ECCM

20

26-30 JUNE

2022

LAUSANNE

SWITZERLAND

Proceedings of the 20th European Conference on Composite Materials

COMPOSITES MEET SUSTAINABILITY

Vol 1 – Materials

Editors : Anastasios P. Vassilopoulos, Véronique Michaud

Organized by :

EPFL

CCLAB Composite Construction Laboratory

Under the patronage of :

LPAC Laboratory for Processing of Advanced Composites

ESCM EUROPEAN SOCIETY FOR COMPOSITE MATERIALS

ECCM 20
26-30 JUNE 2022
LAUSANNE SWITZERLAND

EPFL CCLAB Composite Construction Laboratory LPAC Laboratory for Processing of Advanced Composites

Proceedings of the 20th European Conference on Composite Materials ECCM20 26-30 June 2022, EPFL Lausanne Switzerland

Edited By :

Prof. Anastasios P. Vassilopoulos, CCLab/EPFL
Prof. Véronique Michaud, LPAC/EPFL

Oragnized by:

Composite Construction Laboratory (CCLab)
Laboratory for Processing of Advanced Composites (LPAC)
Ecole Polytechnique Fédérale de Lausanne (EPFL)

ISBN: 978-2-9701614-0-0
DOI: http://dx.doi.org/10.5075/epfl-298799_978-2-9701614-0-0

Published by :

Composite Construction Laboratory (CCLab)
Ecole Polytechnique Fédérale de Lausanne (EPFL)
BP 2225 (Bâtiment BP), Station 16
1015, Lausanne, Switzerland

https://cclab.epfl.ch

Laboratory for Processing of Advanced Composites (LPAC)
Ecole Polytechnique Fédérale de Lausanne (EPFL)
MXG 139 (Bâtiment MXG), Station 12
1015, Lausanne, Switzerland

https://lpac.epfl.ch

Cover:

Swiss Tech Convention Center
© Edouard Venceslau - CompuWeb SA

Cover Design:

Composite Construction Laboratory (CCLab)
Ecole Polytechnique Fédérale de Lausanne (EPFL)
Lausanne, Switzerland

©2022 ECCM20/The publishers

Disclaimer:

The ECCM20 organizing committee and the Editors of these proceedings assume no responsibility or liability for the content, statements and opinions expressed by the authors in their corresponding publication.

ECCM 20
26-30 JUNE 2022
LAUSANNE SWITZERLAND

Editorial

This collection gathers all the articles that were submitted and presented at the 20th European Conference on Composite Materials (ECCM20) which took place in Lausanne, Switzerland, June 26-30, 2022.

ECCM20 is the 20th edition of a conference series having its roots back in time, organized each two years by members of the European Society of Composite Materials (ESCM).

The ECCM20 event was organized by the Composite Construction laboratory (CCLab) and the Laboratory for Processing of Advanced Composites (LPAC) of the Ecole Polytechnique Fédérale de Lausanne (EPFL).

The Conference Theme this year was “Composites meet Sustainability”. As a result, even if all topics related to composite processing, properties and applications have been covered, sustainability aspects were highlighted with specific lectures, roundtables and sessions on a range of topics, from bio-based composites to energy efficiency in materials production and use phases, as well as end-of-life scenarios and recycling.

More than 1000 participants shared their recent research results and participated to fruitful discussions during the five conference days, while they contributed more than 850 papers which form the six volumes of the conference proceedings. Each volume gathers contributions on specific topics:

Vol 1 – Materials

Vol 2 – Manufacturing

Vol 3 – Characterization

Vol 4 – Modeling and Prediction

Vol 5 – Applications and Structures

Vol 6 – Life Cycle Assessment

We enjoyed the event; we had the chance to meet each other in person again, shake hands, hold friendly talks, and maintain our long-lasting collaborations. We appreciated the high level of the research presented at the conference and the quality of the submissions that are now collected in these six volumes. We hope that everyone interested in the status of the European Composites’ research in 2022 will be fascinated by this publication.

The Conference Chairs

Anastasios P. Vassilopoulos, Véronique Michaud

ECCM 20
26-30 JUNE 2022
LAUSANNE SWITZERLAND

Hosting Organizations

Composite Construction Laboratory (CCLab)
Laboratory for Processing of Advanced Composites (LPAC)
Ecole Polytechnique Fédérale de Lausanne (EPFL)

Venue

Swiss Tech Convention Center (https://www.stcc.ch)

Conference Chairs

Chair : Prof. Anastasios P. Vassilopoulos, EPFL, Switzerland
Co-Chair: Prof Véronique Michaud, EPFL, Switzerland

International Scientific Committee

Prof. Malin Åkermo SE
Dr. Emmanuel Baranger FR
Prof. Christophe Binetruy FR
Prof. Pedro Camanho PT
Prof. Konstantinos Dassios GR
Prof. Brian Falzon UK
Prof. Kristofer Gamstedt SE
Prof. Sotiris Grammatikos NO
Prof. Christian Hochard FR
Prof. Marcin Kozlowski PL
Prof. Stepan Lomov BE
Dr. David May DE
Prof. Stephen Ogin UK
Prof. Gerald Pinter AT
Prof. Silvestre Pinho UK
Prof. Yentl Swolfs BE
Dr. Julie Teuwen NL
Dr. Panayota Tsotra CH
Prof. Wim van Paepegem BE
Prof. Dimitrios Zarouchas NL
Dr. Andrey Aniskevich LV
Prof. Christian Berggreen DK
Dr. Nicolas Boyard FR
Prof. Valter Carvelli IT
Prof. Klaus Drechsler DE
Prof. Bodo Fiedler DE
Dr. Nathalie Godin FR
Prof. Roland Hinterholzl AT
Prof. Ian Kinloch UK
Dr. Thomas Kruse DE
Prof. Theodoros Loutas GR
Prof. Veronique Michaud CH
Prof. Alessandro Pegoretti IT
Prof. Joao Ramoa Correia PT
Prof. Jose Sena-Cruz PT
Prof. Antonio T. Marques PT
Prof. Thanasis Triantafillou GR
Prof. Albert Turon ES
Prof. Anastasios P. Vassilopoulos CH
Prof. Martin Fagerström SE
Dr. Alexandros Antoniou DE
Prof. Lars Berglund SE
Prof. Michal Budzik DK
Prof. Lucas Da Silva PT
Dr. Andreas Endruweit UK
Prof. Mariaenrica Frigione IT
Dr. Larissa Gorbatikh BE
Dr. Martin Hirsekorn FR
Prof. Vassilis Kostopoulos GR
Prof. Jacques Lamon FR
Prof. Staffan Lundstrom SE
Prof. Peter Mitschang DE
Dr. Soraia Pimenta UK
Prof. Paul Robinson UK
Dr. Olesja Starkova LT
Prof. Sofia Teixeira de Freitas NL
Dr. Stavros Tsantzalis GR
Prof. Danny van Hemelrijck BE
Prof. Michele Zappalorto IT
Dr. Miroslav Cerny CZ

Local Organizing Committee

Prof. Anastasios P. Vassilopoulos, EPFL
Prof. Véronique Michaud, EPFL
Angélique Crettenand and Mirjam Kiener, Lausanne Tourisme
And all those who helped, colleagues who reviewed abstracts and chaired sessions, and CCLab and LPAC students and collaborators who worked hard to make this conference a success.

ECCM 20
26-30 JUNE 2022
LAUSANNE SWITZERLAND

Sponsors

SHIMADZU
Excellence in Science

Bristol Composites Institute

JEC GROUP

suprem

Surface Measurement Systems
World Leader in Sorption Science

INSTRON

9T LABS

Anton Paar

DIA-STRON
DELIVERING MEASUREMENT SOLUTIONS

AELER

HRC

ICCM 23
BELFAST 2023
30 JULY – 4 AUGUST

TEIJIN

Functional Composite Materials

materials
an Open Access Journal by MDPI

ELSEVIER

Supporting partners

JEC

CertBond
COST Action CA18120

EsSENce

Switzerland Tourism.

SWISS

SBB CFF FFS

sampe
Switzerland

COMPOSITES UNITED | SWITZERLAND

canton de vaud

Lausanne

Contents

Contribution to the Determination of Thermal and Chemical Residual Stresses in Fiber Reinforced Composites Using the Incremental Hole Drilling Method: Numerical and Experimental Approach

A.S Ibrahim Mamane[a], S. Giljean[a], M.-J. Pac[a], and G. L'Hostis[a]

a: Université de Haute-Alsace, Laboratoire de Physique et Mécanique Textiles (UR 4365), F-68093 Mulhouse, France – aboubakar-sedick.ibrahim-mamane@uha.fr

Abstract: *The incremental hole drilling method is widely used to determine the residual stress profile in composite materials. However, the effect of the drilling steps on the local residual stresses and on the raw acquisition data of the relaxation strains is very little studied. In this paper, the thermal and mechanical contributions of the drilling on the acquisition data are explained. The residual stresses of unidirectional carbon/epoxy composite laminates, manufactured by filament winding under different curing conditions, are presented and compared.*

Keywords: Fiber reinforced composites; finite element simulation; incremental hole drilling method; residual stresses.

1. Introduction

Fiber reinforced composite laminates are particularly subject to residual stresses due to their heterogeneity and the complex chemical, mechanical and thermal mechanisms that occur during their processing (1). Residual stresses are known to cause damage accumulation, shape instability and behavior disturbance in composite parts (2). Therefore, residual stresses are important data to consider when sizing composite parts and predicting their behavior.

The Incremental Hole Drilling is one of the most widely used method for measuring residual stresses. This method is semi-destructive and consists of drilling incrementally a hole through the thickness of the material, measuring relaxation strains around the hole for each increment and converting these strains into residual stresses using a matrix of coefficients called calibration coefficients (3). These coefficients are calculated using finite element simulations.

In this paper, the Incremental Hole Drilling Method (IHDM) is used to determine the residual stresses in unidirectional carbon/epoxy composite laminates. The thermal and mechanical effects of drilling on the raw acquisition data of the relaxation strains are also discussed.

2. Material and methods

2.1 Material

The material studied in this work is unidirectional carbon/epoxy composite fabricated by filament winding under industrial conditions. The samples are composite plates composed of 12 layers with a thickness of approximately 0.33 mm each, i.e. a total thickness of 4 mm approximately. T700SC-24000-50C carbon fibers are used with Araldite 1564 epoxy resin. Aradur 3474 hardner is used as curing agent. The fiber content of the composites is 70% by mass and 60% by volume. The material was mechanically characterized by tensile tests in a previous work.

  doi:10.5075/epfl-298799_978-2-9701614-0-0

The longitudinal E_x and transverse E_y Young's moduli are equal to 143 GPa and 7 GPa respectively. In this study, three different composite plates were considered with various curing cycles summarized in Table 1.

Table 1: Curing cycles used to manufacture the composite plates.

Plates	Curing cycle	Cooling
Plate 1	1 hour curing at 80°C then 4 hours at 120°C in an oven (recommended by the manufacturer)	Cooling in the oven
Plate 2	10 hours curing at 70°C in an oven	Cooling in the oven
Plate3	10 hours curing at 70°C in an oven	Ambient air cooling

The dimensions of the manufactured plates are 300x300 mm. To avoid any influence due to the thickness variation, the samples are cut in such a way as to minimize the thickness variation in the same sample. For this purpose, the thicknesses of the plates are determined using a GOM scanner working with the fringe projection principle. The scan head (ATOS core 5M) is equipped with two cameras of 5 million pixels each and a fringe projector (for more details, the reader can refer to reference (4). The measured thickness for plate 3 is shown in Figure 1a. The samples are extracted in areas where the gradient of the thickness is low (Figure 1b and 1c).

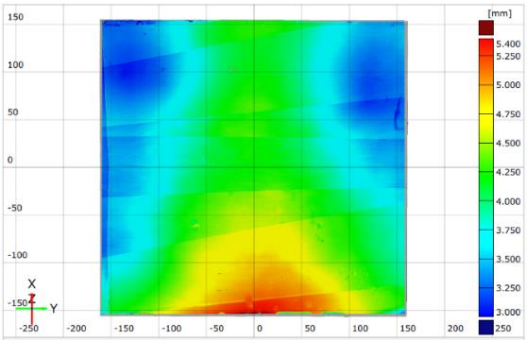

(a)

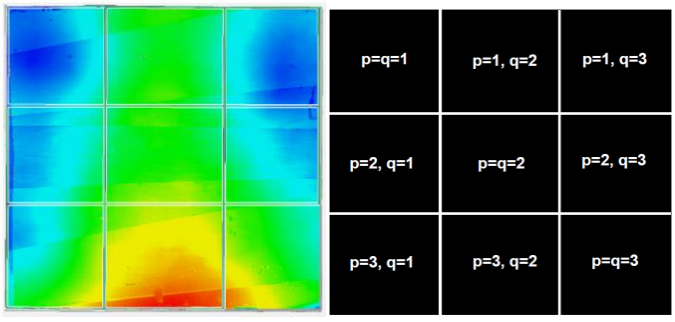

(b) (c)

Figure 1. (a) Thickness of plate 3 determined by 3D scanning (b) Cut of samples from plate 3 in the areas where the thickness gradient is low, (c) Sample identification method as a matrix. For example, sample 1-3 is the sample for which p=1 and q=3

2.2 Methods

The residual stresses are determined by the Incremental Hole Drilling Method (IHDM). The principle of this method is to drill incrementally a hole through the thickness of the material. The removal of material induces a local redistribution of the residual stresses. The corresponding strains (called relaxation strains) are measured using strain gage rosettes (Figure 2). These strains are converted in residual stresses using calibration coefficients, which are calculated by finite element simulations of the IHDM (5) (Figure 3) . The residual stresses of a given increment are equal to the inverse of the calibration coefficients matrix multiplied by the relaxation strains corresponding to this increment, Eq.(1). The relaxation strains of the increment are obtained by subtracting the strains due the previous increments and the total strains recorded by the gages.

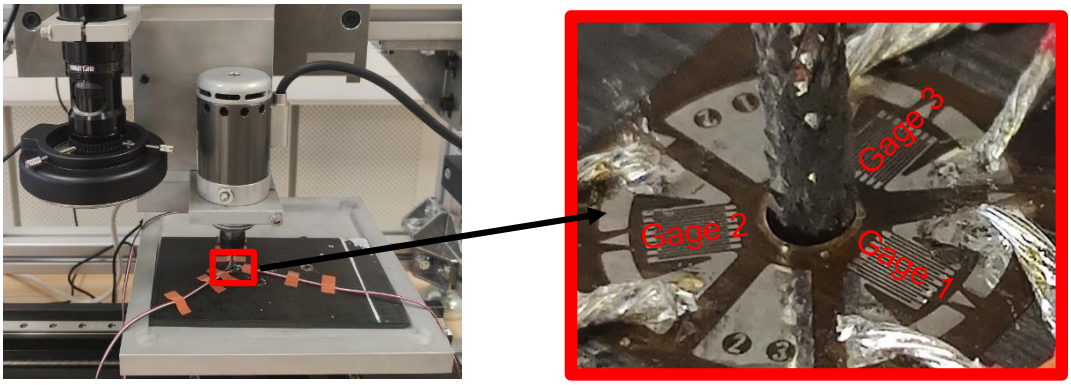

Figure 2. Measurement of the relaxation strains by the Incremental Hole Drilling Method (IHDM) using a strain gage rosette.

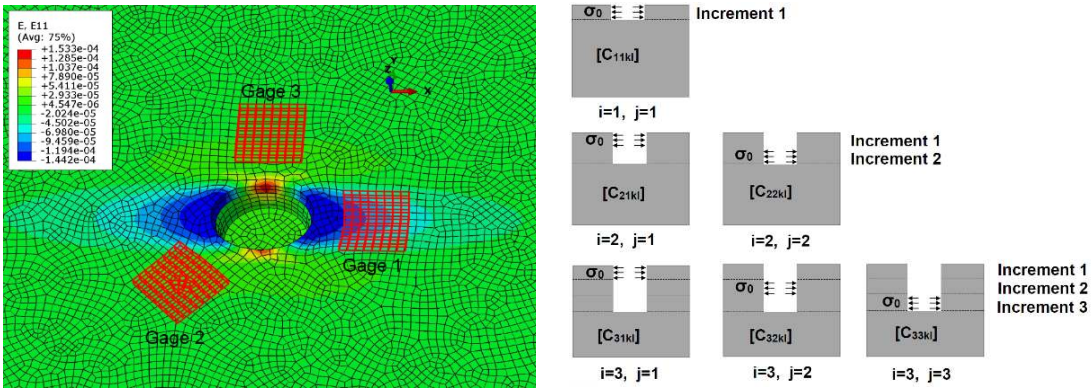

Figure 3. Calculation of the calibration coefficients by finite element simulations: example for 3 increments.

$$\{\sigma_l^i\} = [C_{iikl}]^{-1}\left(\{\varepsilon_k^i\} - \sum_{j=1}^{i-1}[C_{ijkl}]\{\sigma_l^j\}\right),\ 1 \le j \le i,\ 1 \le k,l \le 3 \quad (1)$$

Where:

$\{\sigma_l^i\}$ are the residual stresses of the current increment "i". The subscript "l", $0 < l < 3$, refers to the stress components ($\sigma_1^i = \sigma_x^i, \sigma_2^i = \sigma_{xy}^i, \sigma_3^i = \sigma_y^i$).

$[C_{ijkl}]$ is the matrix of calibration coefficients related to increment "j" when the total number of increments is "i".

$\{\varepsilon_k^i\}$ is the strain given by gage "k", $0 < l < 3$, when the depth of the hole corresponds to "i" increments.

$\sum_{j=1}^{i-1}[C_{ijkl}]\{\sigma_l^j\}$ corresponds to the strains due to the previous increments.

The experimental parameters of the IHDM performed in this study are given in Table 2.

Table 2: Experimental parameters and conditions of the results presented in Figure 4.

Increment depth	Rotation speed	Feed speed	Ambient temperature	Ambient humidity
0.165 mm	5000 rpm	0.01 mm/s	22 ± 2°C	46 ± 2%

3. Results and discussions

3.1 Thermal and mechanical contributions of drilling on raw acquisition data

Figure 4 presents the raw acquisition data obtained for sample 1-3 of plate 3. These data correspond to the strains measured by the gages of the rosette during the incremental hole drilling process. Gage 1 is oriented in the fiber direction (0 degrees), gage 2 at -135 degrees with respect to the fibers and gage 3 in the direction perpendicular to the fibers (90 degrees).

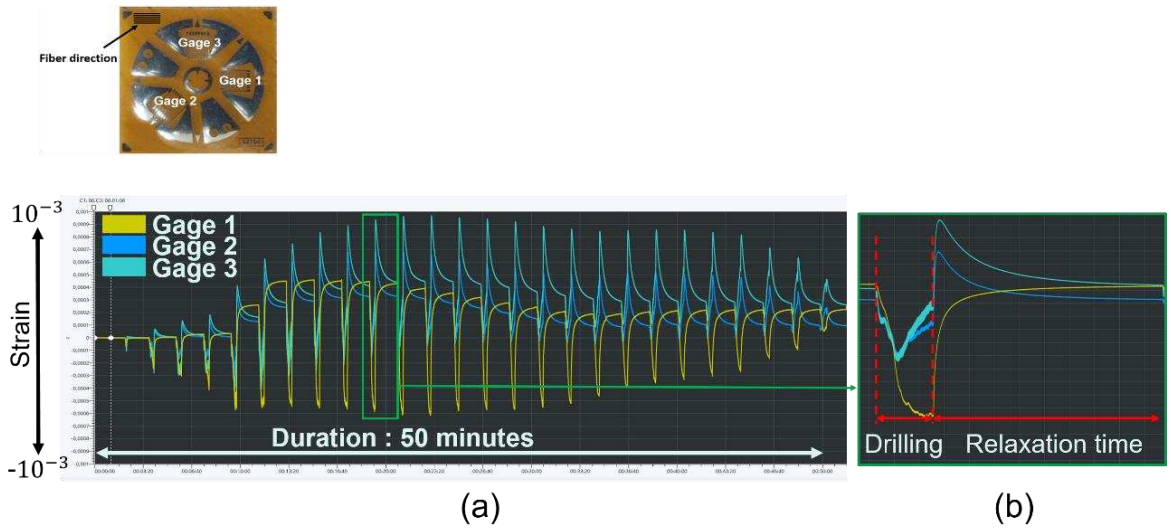

Figure 4. (a) Raw acquisition data obtained for sample 1-3 of plate 3 (See Table 2 for the experimental parameters), (b) Detail of the drilling and relaxation steps for one increment.

Each increment cycle is composed of a drilling step and a relaxation step (Figure 4b). The withdrawal of the milling cutter (end of the drilling step) is followed by an abrupt change of slope of curves. During the drilling, mechanical and thermal strains occur at the same time. Note that the mechanical strains are composed of the strains induced by the milling cutter and the ones induced by the residual stresses. Strains are competing for the gage 2 (oriented at -135 degrees with respect to the fibers) and the gage 3 (oriented in the direction perpendicular to the fibers) and additive for the gage 1 (oriented in the fibers direction). In fact, the heat causes

  doi:10.5075/epfl-298799_978-2-9701614-0-0

negative strains in the fibers direction because of the negative longitudinal thermal expansion coefficients of the fibers. In the resin direction, the induced thermal strains are positive. In the other hand, material removal causes negative strains for all gages. These different strains occurring at the same time explain the particular shapes of the curves during the drilling as well as the jumps recorded for gage 2 and 3 at the onset of the relaxation step.

3.2 Residual stresses in the composite plates

The relaxation strains considered in the calculation of residual stresses are measured at the end of the relaxation time. This allows strains to stabilize after a local redistribution of residual stresses. In this part, one increment per ply is considered for the IHDM. In fact, small increment depths are interesting in areas where residual stress gradient is high. Close to the interfaces of cross-ply laminates for example. Since the material studied here is a unidirectional composite, it is not necessary to refine the depth.

The residual stresses calculated for plate 1, 2 and 3 are presented in Figure 5. Means and dispersions are determined from 3 tests. Here, the calculation of the residual stresses is limited to a hole depth of 0.8 mm because the results become unstable above this depth. This is caused by the fact that the predominant calibration coefficients in the calculation of residual stresses (those of the diagonal) are lower and lower with depth. From a certain depth (0.99 mm here, which corresponds to the third increment), the inverse of these calibration coefficients becomes large enough to generate instability in the calculation. The onset of the instability depends on the material properties and the chosen increment depth. As shown by Zuccarello (6), small increment depths lead to larger instabilities in the residual stress calculation.

In Figure 5, one can observe that the residual stresses σ_x (in the fibers direction, Figure 5a) and σ_y (in the transverse direction, Figure 5b) are lower for plate 1 (manufactured according to the manufacturer's recommended cycle). The residual stresses of plate 3 are slightly higher than those of plate 2. As expected for unidirectional composite laminates, the residual stresses σ_{xy} are very low for the 3 plates.

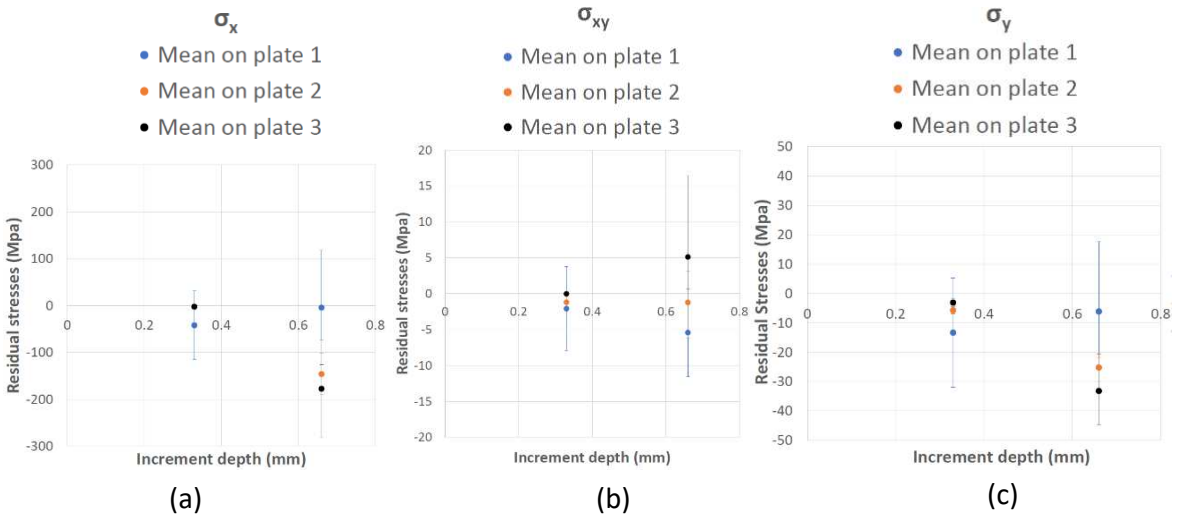

(a) (b) (c)

Figure 5. Residual stresses calculated for plate 1, 2 and 3: (a) σ_x , (b) σ_{xy} and (c) σ_y

The results obtained for plate 1 may seem difficult to analyze since it has undergone the highest temperatures. However, this plate has been annealed (the second cure) at temperature higher than its first glass transition temperature, which can allow the residual stresses to relax while maintaining a high degree of cure. The difference between the results of plate 2 and 3 can be explained by the fact that plate 3 is cooled in ambient air. This rapid cooling generates higher residual stresses.

4. Conclusion

In this work, the residual stresses of unidirectional carbon/epoxy composite laminates fabricated by filament winding were estimated using the Incremental Hole Drilling Method. Investigations were carried out on the thermal and mechanical contributions of the drilling on the raw acquisition data of the relaxation strains. The drilling induces positive thermal strains for gage 2 and 3. However, thermal strains are negative for gage 1 because of the negative thermal expansion coefficient of carbon fibers in the longitudinal direction. In the other hand, the mechanical strains due to material removal is negative for all gages. The combination of these thermal and mechanical strains that occur at the same time allowed to understand the shapes of the raw acquisition data.

The residual stresses were determined for three composite plates manufactured in different curing conditions. The results showed a low level of residual stresses for plate 1 which underwent two dwell temperatures during curing cycle. The residual stresses are believed to relax during the second cure (annealing). Higher residual stresses were obtained for plate 3. This can be explained by the rapid cooling of plate 3, which generates higher residual stresses.

5. References

1. Bogetti TA, Gillespie JW. Process-Induced Stress and Deformation in Thick-Section Thermoset Composite Laminates. J Compos Mater. 1 mars 1992;26(5):626-60.

2. Parlevliet PP, Bersee HEN, Beukers A. Residual stresses in thermoplastic composites – a study of the literature. Part III: Effects of thermal residual stresses. Compos Part Appl Sci Manuf. 1 juin 2007;38(6):1581-96.

3. Akbari S, Taheri-Behrooz F, Shokrieh MM. Characterization of residual stresses in a thin-walled filament wound carbon/epoxy ring using incremental hole drilling method. Compos Sci Technol. 9 avr 2014;94:8-15.

4. ATOS 5: Industrial metrology | high-speed, high-precision [Internet]. [cité 18 avr 2022]. Disponible sur: https://www.gom.com/en/products/high-precision-3d-metrology/atos-5

5. A.S.IBRAHIM MAMANE, S.Giljean, M.-J.PAC, G.L'HOSTIS. Optimization of the measurement of residual stresses by the incremental hole drilling method. Part I: numerical correction of experimental errors by a configurable numerical-experimental coupling. Compos Struct. Publication in progress;

6. Zuccarello B. Optimal calculation steps for the evaluation of residual stress by the incremental hole-drilling method. Exp Mech. 1 juin 1999;39(2):117-24.

  doi:10.5075/epfl-298799_978-2-9701614-0-0

A NOVEL BIO-INSPIRED MICROSTRUCTURE FOR PROGRESSIVE COMPRESSIVE FAILURE IN MULTIDIRECTIONAL COMPOSITE LAMINATES

Torquato, Garulli[a], Emile S., Greenhalgh[a], Silvestre T., Pinho[a]

a: Faculty of Engineering, Imperial College London, UK – t.garulli@imperial.ac.uk

Abstract: *In this study we take inspiration from biological materials to design a modified microstructure for laminated multidirectional (MD) carbon fiber reinforced polymers (CFRP), with the objective of mitigating their compressive failure behavior. We introduce soft inclusions in the form of thin longitudinal strips of foam in 0° load bearing layers, aiming at arresting kinkband propagation. We conceived a bespoke stacking sequence and developed a tailored procedure for manufacturing the microstructure. We then performed in-situ tests on small scale notched specimens from a baseline laminate and a modified one. Results are presented and discussed.*

Keywords: Bioinspiration; Compression; Damage diffusion; Microstructural design

1. Introduction

Longitudinal compressive failure is a major concern for CFRP. In most high-performance unidirectional (UD) composites, failure occurs by fiber kinking. In regions of fiber misalignment, the matrix undergoes shear, leading to further fiber rotation. With increasing load, either this mechanism becomes unstable, or shear fracture of the matrix/interface occurs, leading to unstable collapse and to kinkband formation [1]. In MD laminates, the failure process is more complex and may involve delamination and some progressive damage in the off-axis plies [2]. However, almost inevitably, sudden compressive fracture of load bearing (0°) layers is the final event leading to catastrophic failure, with negligible detectable warning. These complexities lead to a lack of strategies to mitigate the failure process and improve performance.

In this work, we take inspiration from nature to design a novel microstructure for MD CFRP laminates. Several biological materials present alternating stiff and soft zones. The associated periodic stiffness variations are an effective strategy to enhance fracture resistance: a strong decrease in crack driving force occurs when the crack propagates from stiff to soft regions, eventually leading to crack arrest [3]. To replicate such a condition in a MD laminate undergoing compression, we modified its microstructure by replacing continuous 0° composite layers with alternating of stiff (0° composite) and soft (polymethacrylimide -PMI- foam) longitudinal strips, Figure 1, with the objective of creating regions where kinkbands may be arrested, favoring 0° composite strips to fail individually and independently, due to the soft strips isolating them.

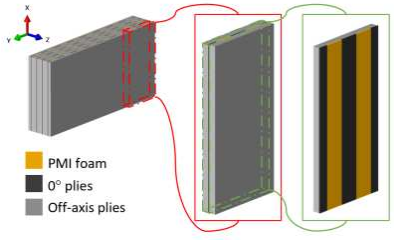

Figure 1. Simplified representation of the devised concept.

  doi:10.5075/epfl-298799_978-2-9701614-0-0

2. Material and methods

2.1 Materials

Since the soft inclusions are not load-bearing, a material with low specific weight is preferable for the soft inclusions. This, along with processing ease and compatibility, led to PMI foams being identified as optimal materials. PMI foam sheets, 0.07 mm thick, were provided by YoneshimaFelt Co. Ltd. Specifically, Rohacell® 200SL foam was used for this study (Table 1). The sheet thickness was chosen by considering commercial availability and compatibility in the design process.

Table 1: Rohacell® 200SL properties from [3].

Density [g/cm^3]	Tensile Modulus [MPa]	Compressive modulus [MPa]	Shear modulus [MPa]
0.205	371	370	123
	Tensile strength [MPa]	Compressive strength [MPa]	Shear strength [MPa]
	10.4	9.6	4.8

A 15gsm MR70/TP402 prepreg, commercially available from North Thin Ply Technologies (NTPT), was selected for this study. MR70 is a high-performance intermediate modulus carbon fiber; TP402 is a 135 °C curing epoxy used for automotive and aerospace applications. Properties for this material are not readily available from open literature, so, for the purpose of this study, they were estimated using micromechanics or assumed, as reported in Table 2 (with the standard notation used in [1]).

Table 2: MR70/TP402 properties.

Density [g/cm^3]	E_1 [GPa] (compressive)	E_2 [GPa]	G_{12} [GPa]	ν_{12}
1.55	153.	9.5	3.16	0.26
X_t [MPa]	X_c [MPa]	Y_t [MPa]	Y_c [MPa]	S_L [MPa]
3880.	1800.	39.	160.	60.

2.2 Configuration design

To test the concept, we developed a bespoke stacking sequence to be used as a baseline, which we called Baseline-No-Foam (BNF), and a modified version for the new microstructure, named Foam Laminate (FL). The two laminate stacking sequences are as follows:

- BNF: $[\pm45/(\pm75/90/\pm75/\pm31_9/0)_{S2}]_S$
- FL: $[\pm45/(\pm75/90/\pm75/\pm31_9/0_{2F})_{S2}]_S$. Here the subscript F indicates the presence of the foam strips in the 0° layers

The BNF laminate was designed to have elastic properties similar to those of a commonly used industrial reference laminate (i.e. $[(\pm45/0/\pm45/90/0)_n]_S$) and to contain a reduced number of 0°

layers. Also, the high number of ±31 layers was tailored to provide a strong support to the laminate at failure of the 0° layers. The FL sequence is obtained from the BNF one by doubling the number of 0° layers. In this case, however, 0° layers are intended as containing foam strips. Specifically, considerations of effectiveness and manufacturability led to the choice of having alternated 1 mm wide 0° composite and foam strips. Therefore, the BNF and FL laminates contain the same volume of composite material (and in the same orientations), the FL one being slightly thicker due to the presence of the foam.

2.3 Manufacturing

Prepreg sheets of the desired orientations were cut with a Blackman and White Genesis 2300 cutting machine. The BNF laminate was laid up manually according to standard practices. To prepare materials for the FL laminate, an Oxford Lasers Diode Pumped Solid State (DPSS) micro-machining system was used as follows:

- 0° prepreg layers, after being laid up in groups of four, $[0_4]$, were cut to have 1 mm wide rectangular slots in the fiber direction
- Foam sheets were cut, in their central region, to be divided into 1 mm wide strips
- PET sheets (125 µm thick) were cut to create templates for positioning of both the 0° prepreg layers and the foam strips

Lay-up of the foam laminate followed standard practices until each of the $[0_4]$ blocks, expected to contain foam strips, was reached; at this point a tailored procedure, exploiting the PET templates and involving multiple steps, was used to create the layer containing the foam strips. More in detail, the strips of 0° prepreg were laid first; afterwards, the foam strips were placed in the slots in between the prepreg. Figure 2 shows three stages of the process.

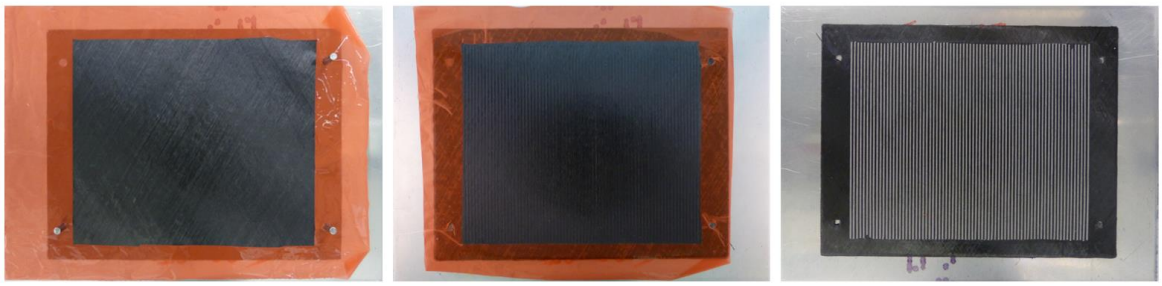

(a) (b) (c)

Figure 2. Three phases of the foam laminate lay-up procedure: (a) right before laying up a $[0]_4$ block containing the foam strips, (b) after laying up 0° prepreg strips, (c) after having laid up both prepreg and foam strips.

For this study, two small scale notched specimens for compression loading, Figure 3, were obtained from each of the two plates. The top and bottom faces of the specimens were ground parallel to ensure optimal loading during compression, while the notch was obtained by means of a disk saw; notch tip radius was found to be, by means of optical microscopy, consistently around 40-50 µm, figure 3 (c).

Due to an incident during manufacturing, the specimens' surface had to be slightly ground, which partially reduced their thickness (about 0.2 mm per specimen) and thus slightly modified their layup (by eliminating outer layers); this may have introduced some variability in the test

performed, but is not expected to have affected the qualitative observations presented here. Table 3 shows the ligament section dimensions and notch tip radii for the four specimens tested.

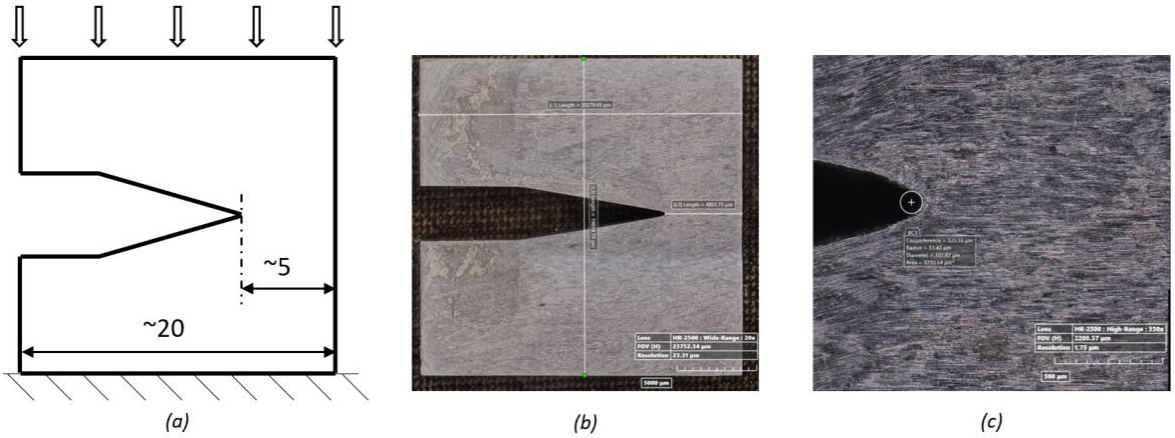

Figure 3. Small scale specimens manufactured: (a) nominal dimensions and loading scheme, (b) actual specimen microscopy with dimensions, (c) detail of the notch tip.

Table 3: Ligament dimensions and notch tip radii of the four specimens tested.

Specimen ID	Ligament length [mm]	Ligament thickness [mm]	Notch tip radius [µm]
BNF1	4.8	2.7	41
BNF2	4.8	2.7	51
FL1	4.9	2.9	43
FL2	4.8	2.9	48

2.4 Test method

The specimens were manually polished and gold coated. They were tested in compression, under displacement control, inside a Hitachi S-3700N SEM by means of a 5 kN in-situ loading stage from Deben UK. The displacement rate was set at 0.1 mm/min and data relative to jaws displacement and load were acquired at 10 Hz. The test was stopped at 400 N intervals to take SEM images of the specimen at different magnifications. The test was run either until complete failure of the specimen or up to a load of about 4.5 kN, in which case it was stopped to prevent damage to the load cell.

3. Results and discussion

The load-displacement curves for the specimens tested are reported in Figure 4. In these curves, small load drops correspond to relaxation occurring during the time the tests are stopped to take images. Both specimens containing foam strips, FL1 and FL2, did not fail by the end of the test. On the other hand, out of the two baseline specimens, BNF1 failed completely at a final load of about 3.83 kN, while specimen BNF2 did not fail by the end of the test.

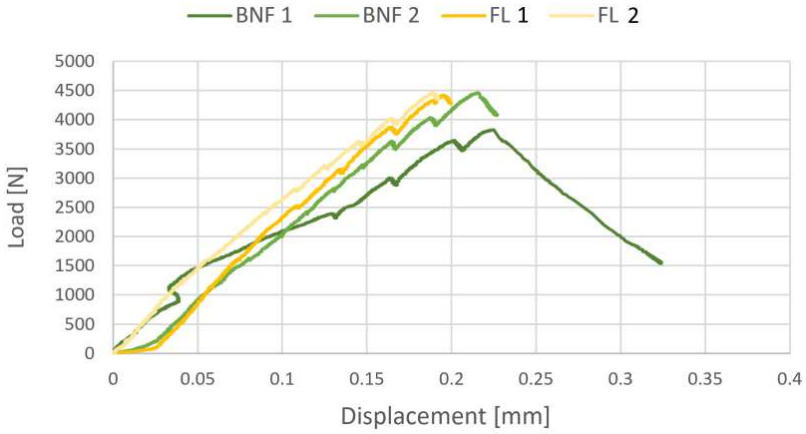

Figure 4. Load displacement curves for the four specimens tested.

Figure 5 shows SEM pictures of all specimens immediately before testing (Figure 5 (a)) and immediately after end of the tests (Figure 5 (b)). For all specimens, surface plies tended to delaminate from the rest of the specimen, and damage in the form of ply splits and fiber fracture is evident on them. By the end of the tests, for specimens BNF1 and BNF2, this damage extends from the notch tip all the way to the opposite specimen's side, and the superficial plies are completely delaminated in this region. In FL1 and FL2 specimens, the damage observed on surface plies is less extended: for FL1, it extends to about 2 mm away from the notch tip; for specimen FL2 a little amount of damage is observed extending from the notch tip toward the bottom side of the specimen.

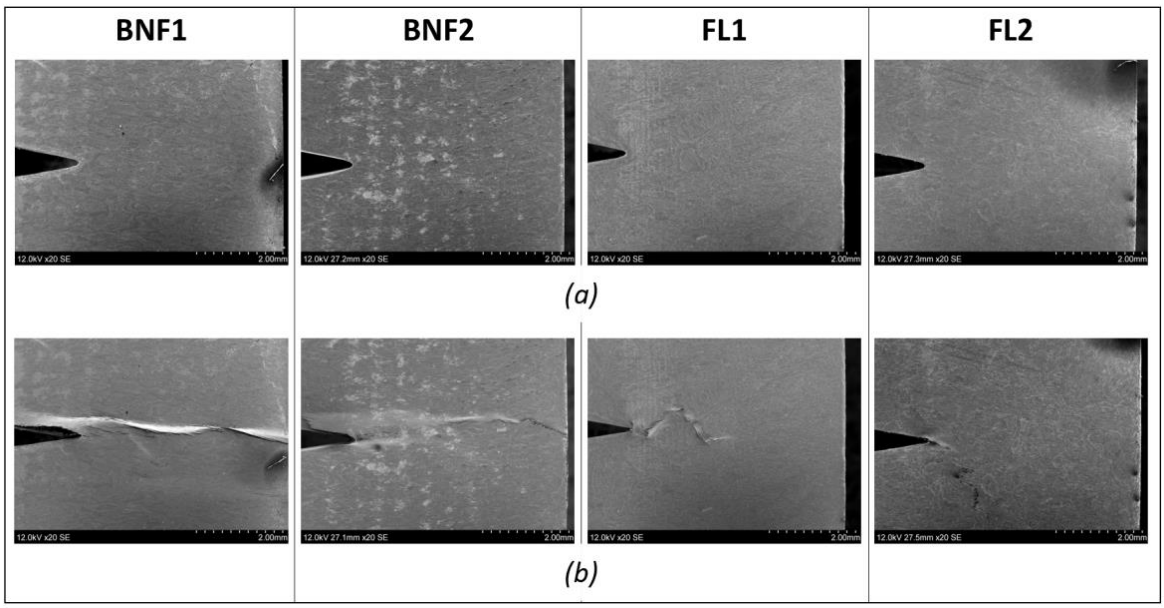

Figure 5. SEM pictures of the specimens' ligament (a) before testing and (b) right after the test.

Figure 6 shows X-ray images of the specimens after testing. One feature common to all the specimens is the presence of clear fracture lines emanating from the notch tip, at an angle of ±31°. The clarity with which these features are observed suggests that they might be somewhat continuous through the specimen thickness, for several layers. Considering the stacking sequence of the laminate (having ±31° ply blocks), it is hypothesized that these may have formed

by initial splitting of the layer with fiber orientation parallel to the direction of the fracture line and subsequent translaminar fracture of the layers with the opposite orientation. It is worth mentioning that X-ray images of FL1 and FL2 specimens show the striped pattern caused by the presence of the foam strips; these latter appearing darker in the images. From this it can be observed that, for both FL specimens, the tip of the notch is located in the middle of a dark region, that is in a region with foam strips.

Specimen BNF1, the only one that failed completely, shows a vast amount of damage going all the way from the notch tip to the opposite specimen's side. Damage probably consists mostly of kinkbands in 0° layers and translaminar fractures in ±31° layers. Additional splits at ±31° are also visible, as well as a wide delamination, as already seen from SEM observations. In specimen BNF2, a narrow damage band extends from the notch across almost the entire ligament length, accompanied by several splits, especially in the lower part of the specimen. Comparing this with BNF1, and considering that by the end of the test specimen BNF2 was still carrying a significant load, may suggest that the damage observed is limited to a few plies through the thickness, while most of the ±31° layers may still be intact and able to carry load. Delamination is also visible in the image, in an area enclosing all other damage observed. Specimen FL1 shows a similarly narrow band of damage extending for about 2.5 mm from the notch tip. An initial wider and brighter band cross a region without foam (lighter colored in the image); possibly this includes kinkbands in 0° layers and additional damage in other layers. As this band reaches the next region with foam strips (darker in the image), it divides into a 31° split, which then deviates into a -75° split, and an almost horizontal narrower band. These two narrow bands then reach the beginning of the next region without foam, where they arrest. Interestingly, specimen FL2 shows no damage at all, except for the already mentioned fracture lines originating from the notch tip. It is likely that these fracture lines and the foam strips present at the notch tip have acted as strong blunting factors, preventing significant stress concentration and damage initiation and propagation from the notch altogether.

Additional fractographic activities will help to fully understand the fracture behavior of the specimens.

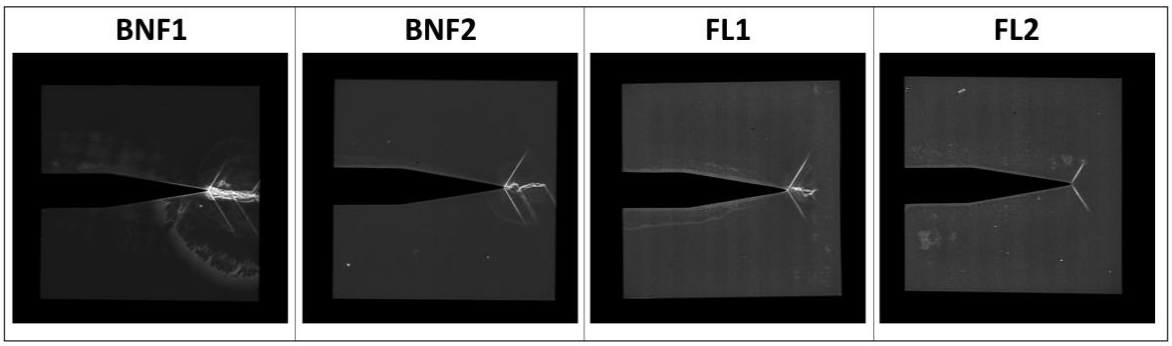

Figure 6. X-ray scans of the four tested specimens.

4. Conclusions

The study presented is concerned with the preliminary design, manufacturing and testing of a bioinspired microstructure for MD CFRP laminates aiming at mitigating compressive failure.

After designing a suitable configuration, a tailored procedure for manufacturing of the desired microstructure was developed. The procedure features adoption of laser cutting for the preparation of the composite prepreg and of the foam sheets used for creating the soft inclusions. Additionally, PET sheets are adopted to create templates for precise positioning of the two former components, with alignment being ensured by means of a system of alignment pins. The developed procedure allows precise manufacturing of the microstructure. In-situ tests were performed on four small scale notched specimens, two baseline ones and two containing soft inclusions. After the tests, X-ray imaging of the specimens was performed to gain a deeper understanding of the specimens' behavior. Out of the four specimens tested, only one baseline specimen failed completely; other tests had to be stopped to avoid damage to the rig's load cell. Our results suggest that splitting and translaminar fracture in off-axis plies from the notch tip occurred and acted as a strong crack blunting mechanism, reducing the stress concentration and the propensity to fracture initiation and propagation from the notch. While the results shown have to be expanded on further experimental activities, it was observed that specimens containing the soft inclusions had a reduced amount of damage when compared to baseline.

Further activities are underway to gain a deeper understating of the results obtained and produce further results to assess the effectiveness of the microstructure designed.

Acknowledgements

The authors kindly acknowledge the funding for this research provided by UK Engineering and Physical Sciences Research Council (EPSRC) programme Grant EP/T011653/1, Next Generation Fibre-Reinforced Composites: a Full Scale Redesign for Compression in collaboration with University of Bristol.

YoneshimaFelt Co. Ltd. and the person of Tomoya Yoneshima are kindly acknowledged for providing PMI foam sheets used for this research.

5. References

1. Pinho ST, Iannucci L, Robinson P. Physically-based failure models and criteria for laminated fibre-reinforced composites with emphasis on fibre kinking: Part I: Development. Composites Part A: Applied Science and Manufacturing 2006; 37:63-73.
2. Tsampas SA, Greenhalgh ES, Ankersen J, Curtis PT, On compressive failure of multidirectional fibre-reinforced composites: A fractographic study. Composites Part A: Applied Science and Manufacturing 2012; 43:454-468.
3. Kolednik O, Predan J, Fischer FD, Fratzl P. Bioinspired Design Criteria for Damage-Resistant Materials with Periodically Varying Microstructure. Advanced Functional Materials 2011; 21:3634-3641.
4. Rohacell® SL datasheet, accessed on 19/04/2022. https://www.rohacell.com/product/peek-industrial/downloads/rohacell%20sl_2020_january.pdf

  doi:10.5075/epfl-298799_978-2-9701614-0-0

FLUORESCENT MARKING OF FIBER REINFORCED POLYMER FOR COMPONENT AND MATERIAL IDENTIFICATION IN THE CONTEXT OF MATERIAL FLOW CANALIZATION

Paul Hoffeins[a], Sebastian Spitzer[a], Vanessa Reich[b], Georg Dost[b], Christian Weidermann[c], Maik Gude[a]

a: Institute of Lightweight Engineering and Polymer Technology, TU Dresden – paul.hoffeins@tu-dresden.de; b: Polysecure GmbH – vanessa.reich@polysecure.eu; c: Siemens AG – christian.weidermann@siemens.com

Abstract: *For a circular economy, the ability of a precise identification of products and materials in all life cycle phases is an enabler. Markers can be used effectively for material identification and they can also be physically integrated into the semi-finished polymer. This paper focuses on the integration of fluorescent particles into fiber-reinforced composites (FRC) via VARI infiltration. Initial experimental studies show possibilities for the application of markers in FRC. Thereby, interaction between marker particles, FRC and manufacturing process variations are analyzed. Additionally, the influence of textile permeability on the particle distribution of markers within the composite is addressed. When processing these polymer mixtures within a VARI process, the reinforcement textiles and processing aids lead to the filtration of marker particles, which is why process execution must be adapted to achieve a more efficient marking process.*

Keywords: Tracer-Based-Sorting; fluorescent particles; continuous fiber reinforced polymers; thermoset polymers; VARI; marker technology

1. Introduction

For a functional and efficient circular economy, the ability to precisely identify products and materials in all life cycle phases is necessary. This is especially relevant for the End-of-Life phase where often no closed chain of information to identify products and materials for efficient reuse or recycling is available. For various product categories surface placed identification technologies are existing such as QR-codes or embossed labels. In addition to these technologies, material integrated solutions are emerging. One of these technologies is the integration of fluorescent particles into the material itself. These particles enable robust material and structure identification possibilities in all product life cycle phases for the realization of circular economies (cf. Figure 1).

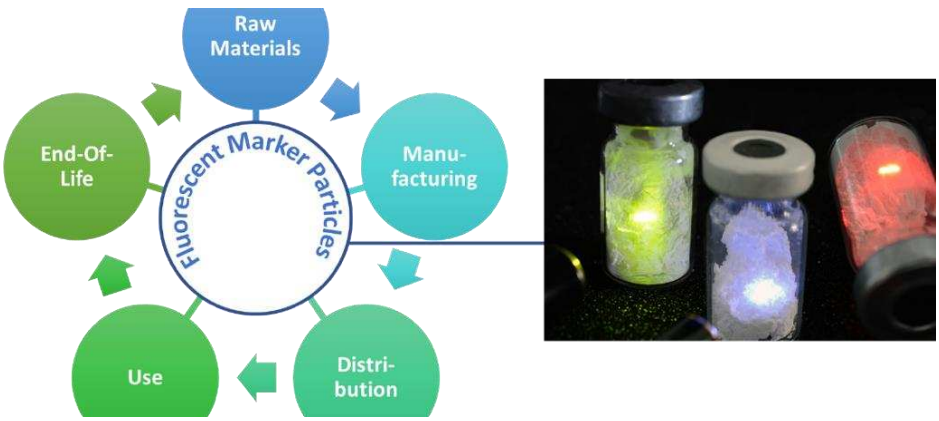

Figure 1: Fluorescent markers for material and structure identification in life-cycle phases

  doi:10.5075/epfl-298799_978-2-9701614-0-0

The market for glass fiber reinforced plastics (GFRP) and carbon fiber reinforced plastics (CFRP) is expected to grow significantly in the next years partly due to the rise in renewable energy activities [1]. While currently there is no widespread established universal recycling method for most of these materials, there is progress in research and development for different recycling technologies in this field [2]. Some of the problems faced are unknown material combinations and other contaminants in the composites. FRCs with continuous fiber reinforcement are expected to bring new challenges to the use of fluorescent particles compared to unfilled plastics, like optical absorption changes, refraction or inhomogeneous particle distribution due to filtration processes. Thus, the interaction between the markers, manufacturing parameters and reinforcement architecture has to be investigated.

As of now there are various research activities for the use of tracer-based-sorting in unfilled and short fiber reinforced thermoplastics for food packaging and window frames, where they show a high potential for enabling circular economy models [3]. Currently there is no research available for the integration of fluorescent particles into fiber reinforced plastics (FRP) with continuous fibers such as CFRP or GFRP.

2. Fluorescent marker technologies for individual product identification

The fluorescent marker particles used in this paper are crystals with a grain size of more than 1 µm. They glow in a characteristic color when excited with near infrared light. Consequently, the fluorescent particles are invisible in ambient light. In addition, the fluorescent particles are thermally and chemically stable and exhibit low solubility behavior. They show good biocompatibility with unobjectionable toxicological test results and are compliant with EU substance law requirements. Due to these properties, fluorescent particles can easily be integrated as an additive in polymeric materials and can be processed in existing production processes. Currently, two distinct technologies that use fluorescent particles are tracer-based-sorting and particle fingerprints.

Tracer Bases Sorting (TBS) opens the possibility of sorting according to arbitrarily definable criteria. It is independent of material properties, robust against deformation and contamination and can be used flexibly. Currently TBS relies on three markers with different spectral properties. To enable identification of more than three different categories, the three markers are mixed in predefined ratios. For example, a 20 % gradation of ratios can generate 21 marker codes. The particles (tracers) can be inserted into the material or applied to the product e.g., by printing or using labels. By mixing the tracers into the material, every part of the material get its own traceable information.

Currently, neat polymers are well detectable by e.g. near infrared sorters and thus subsequently sorted. As this differentiation is usually not sufficient, TBS can be used as an additional decision criterion or as a standalone solution. For example, TBS can be used to separate composites from non-composites. These have the same main polymer on the surface and would thus fall into the same category of NIR sorting. One of the main advantages of material integrated traces for TBS is the robustness against wear and destruction, which enables identification of already crushed material, which is especially beneficial in the recycling industry.

Particle Fingerprints is a technology to apply a unique marking into a product, that is forgery-proof and that can be used to link the product to a database entry e.g., a digital product pass. The technology is based on identification of the geometric distribution of fluorescent particles

  doi:10.5075/epfl-298799_978-2-9701614-0-0

(markers), which have been added to the raw material (e.g. plastic, ceramic, metal or coatings) in advance and thus are arranged in a completely random manner within the production process. Due to the aspect of randomness, the resulting "fingerprint" cannot be copied or reproduced. In contrast, barcodes, RFID tags or digital watermarks are produced by deterministic processes. There is a kind of recipe according to which the codes are produced, which makes it possible to forge and replicate them. The PFP, on the other hand, is unique. Consequently, its use for product identification and authentication is particularly suitable for security and health-related objects and for products that are heavily affected by counterfeiting.

The PFP is particularly suitable for mapping digital product passports because of its high level of protection against forgery and manipulation due to the role of randomization. This also means that an almost infinite number of different fingerprints can be generated.

The main difference between PFP and TBS is that PFP considers the spatial distribution of the markers, while TBS detects the spectral properties of the markers, which is shown in Figure 2. For the best results of these technologies, PFP uses larger particles with a diameter between 30 µm and 50 µm compared to TBS with particle diameters from 5 µm to 10 µm.

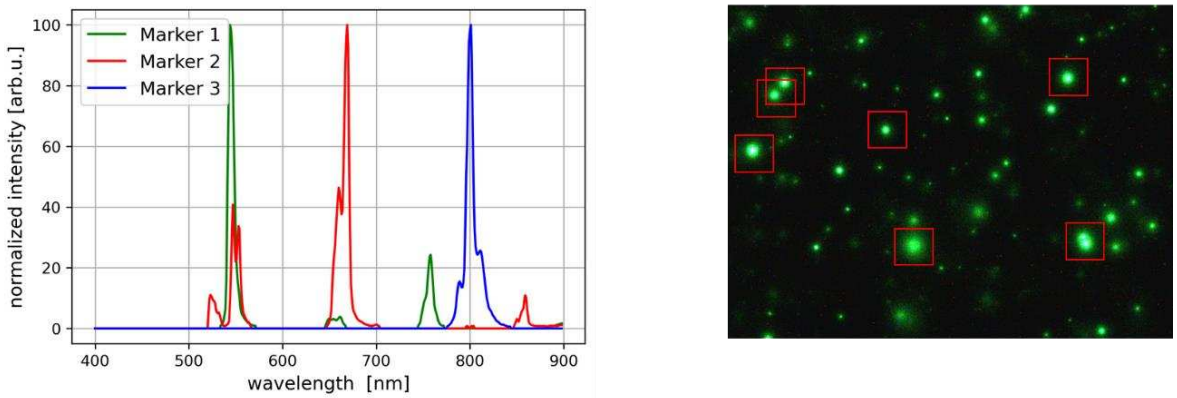

Figure 2: Identification of different TBS markers by spectral analysis (left) and a PFP by spatial distribution analysis (right)

3. Experiments on feasibility of marker integration into continuous fiber reinforced thermosets via vacuum assisted resin infusion

Figure 3 shows the Vacuum Resin Infusion (VARI) process setup to investigate the processability of marker filled resin systems. The main advantages of using the VARI process are, that it enables fast and cost-efficient manufacturing of test specimens due to simple tooling, whilst still providing conclusions on preform related filtration effects for other infusion and injection processes as well as being a relevant manufacturing process for high performance structures.

The preform consists of a layup of 10 layers of unidirectional glass or carbon fiber textiles, which are placed with the same orientation upon a solid glass ground plate.

  doi:10.5075/epfl-298799_978-2-9701614-0-0

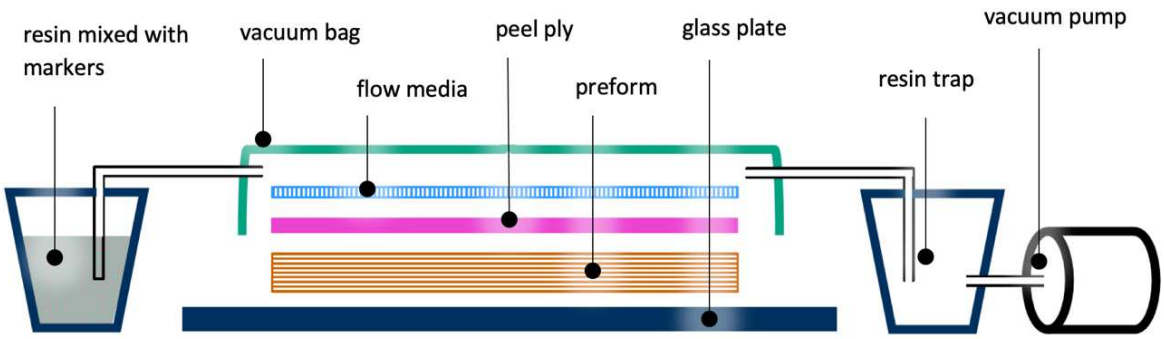

Figure 3: VARI process setup for marker infiltration

A peel ply is placed on top of the preform to ensure a damage free demolding of the FRP after curing. Due to low permeability of the unidirectional textiles, a flow media is used on top of the peel ply, to allow a homogenous resin infusion over the whole textile surface. The layup is covered by a vacuum bag, which is sealed against the glass plate. Vacuum is applied via an outlet tube that connects to a resin trap and vacuum pump. The resin is infiltrated via vacuum through the inlet tube on the other side that connects to a container filled with epoxy resin. The fluorescent particles will be mixed into the resin prior to the infusion.

In the investigations, four combinations of fluorescent particles and preforms are examined, which are shown in Table 1*Table 1*. Thereby, GF-TBS means glass fiber textiles using TBS-technology, CF-TBS means carbon fiber textiles and TBS technology. In case of GF-PFP glass fiber textiles were used in combination with PFP marking technology.

Table 1: Overview of test specimens

ID number	Fiber Type	Textile weight	Textile ply thickness	Marker type
GF-TBS	Glass fiber	250g/m²	0.2 mm	TBS
GF-PFP	Glass fiber	250g/m²	0.2 mm	PFP
CF-TBS	Carbon fiber	200g/m²	0.2 mm	TBS

For all test specimens the same resin (Epoxy L) and curing agent (W300) is used. A total combined weight of 300 g is mixed according to the manufacturer recommended ratio. For all marker types a particle concentration of 300 ppm is chosen, which results in a mass of 0.06 g of marker particles. The particles were mixed homogeneously into the resin before infusion. After infusion, the resin is cured under room temperature.

For evaluating the marker concentration and distribution in the final FRP, the specimens were analyzed using a hyperspectral camera. Therefore, an infrared laser is used for the excitation of the fluorescent particles within the FRP samples. The used setup is shown in Figure 4. Purely optically, the marker particles are not visible in the manufactured test specimen.

  doi:10.5075/epfl-298799_978-2-9701614-0-0

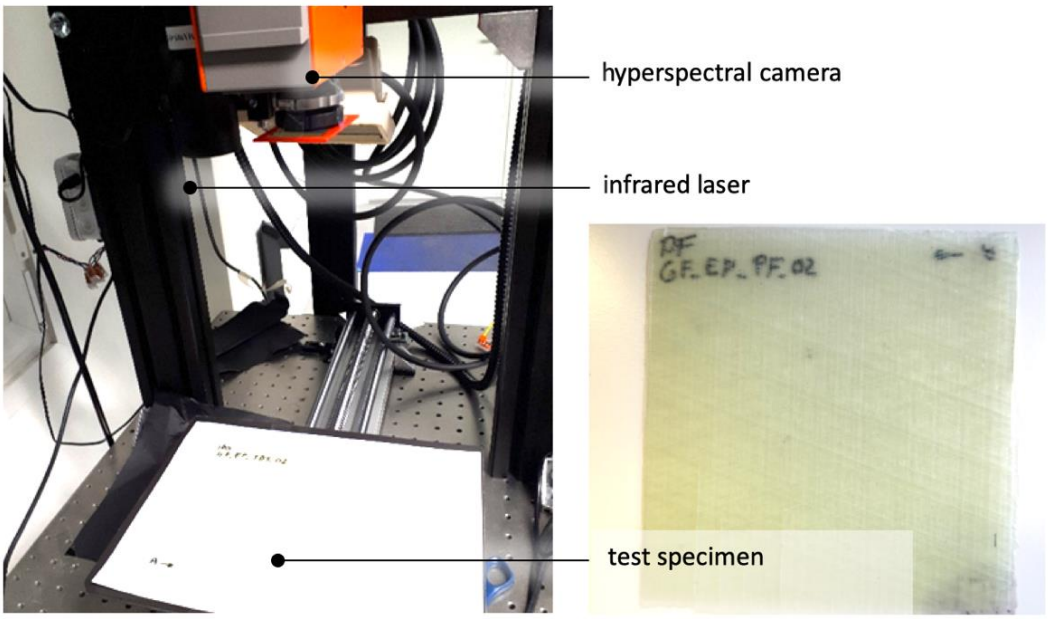

Figure 4: Test setup for the determination of the marker concentration (left) and visual impression of FRP specimen (right)

For all further results, the specimens were excited by laser light showing a wavelength of 980 nm. Additionally, for all specimens the light intensity of the fluorescent particles is measured for the wavelength of 550 nm. To enable the comparison between different specimens all intensities are normalized to the highest measured intensity of the first test specimen.

4. Interpretation of the results

First, the feasibility of mixing the particles into the resin have been analyzed. Therefore, the particles are mixed into the resin using a conventional stirrer. By using an infrared laser pointer with a wavelength of 980 nm, the distribution within the resin can be easily visualized. For both marker types no agglomerations could be identified. Furthermore, since the particle concentration is low, there is no measurable impact to the resin properties, such as viscosity. Thus, the infusion process itself will not be influenced not by the integration of marker particles with these concentrations. This is also shown by the finished FRP specimens, that show no visible quality differences to their counterparts without integrated marker particles.

Afterwards the resulting concentration and distribution of marker particles within the FRPs is analyzed. Figure 5 shows the normalized light intensity at a wavelength of 550 nm for the fluorescent markers with the hyperspectral camera tests for GF-TBS on the tool and non-tool side. Tool side referring to the side oriented towards the glass plate during infiltration.

  doi:10.5075/epfl-298799_978-2-9701614-0-0

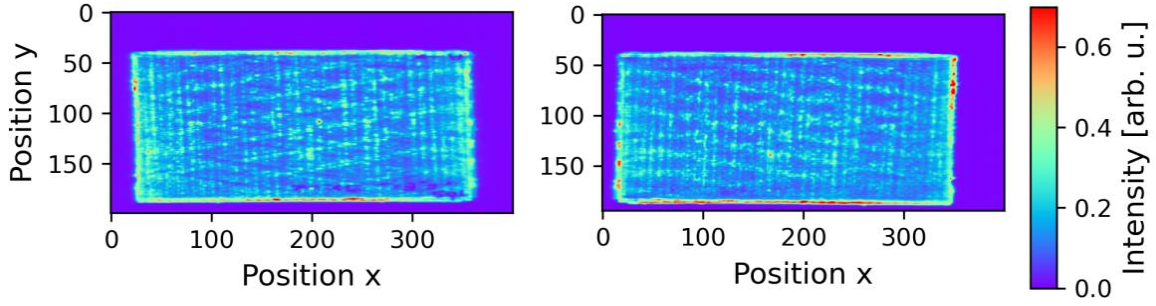

Figure 5: GF-TBS – normalized light intensity at 550 nm wavelength on the tool side (left) and non-tool side (right)

The test setup is not able to measure exact length measurements, which is why the visual results are morphed and not in proper scale. The test specimen orientation can be seen in Figure 6 for comparison. This orientation is true for all further hyperspectral camera results. The TBS marker particles can clearly be identified from both specimen sides. Further analysis shows, that the particles are only situated on the non-tool side of the specimen. This means due to low permeability of the textiles all particles are filtered through it and don't infiltrate through to the tool side. Due to the transparent properties of the glass fibers and thermoset matrix, the particles can still easily be identified on the tool side.

Figure 6 shows normalized intensity results of the fluorescent markers with the hyperspectral camera tests for GF-PFP.

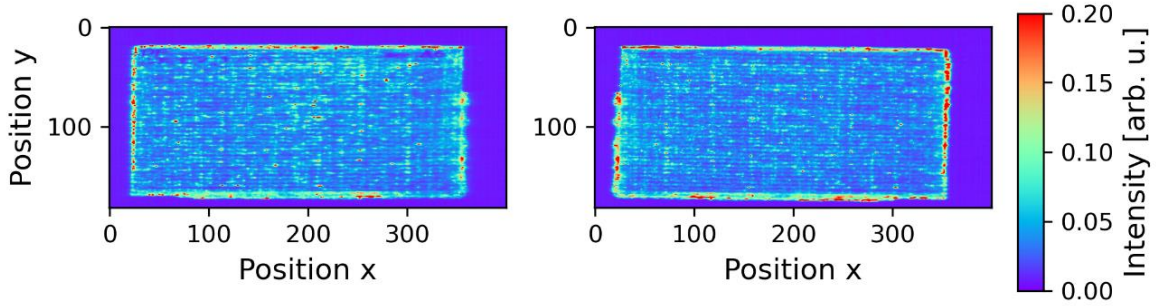

Figure 6: GF-PFP - normalized light intensity at 550 nm wavelength on the tool side (left) and non-tool side (right)

For PFP the particles can also clearly be identified through both sides, however the intensity is lower compared to TBS. This can be a result due to less PFP particle mass in the specimen as well as the larger size of the PFP particles compared to TBS, which can result in a lower luminescence intensity as a certain mass of bigger particles has lower intensity as the same mass of smaller particles due to volume effects.

Looking at the peel ply and flow media through a PFP detection camera setup, it is apparent, that these aids filter the larger PFP particles, which can be seen in Figure 7.

  doi:10.5075/epfl-298799_978-2-9701614-0-0

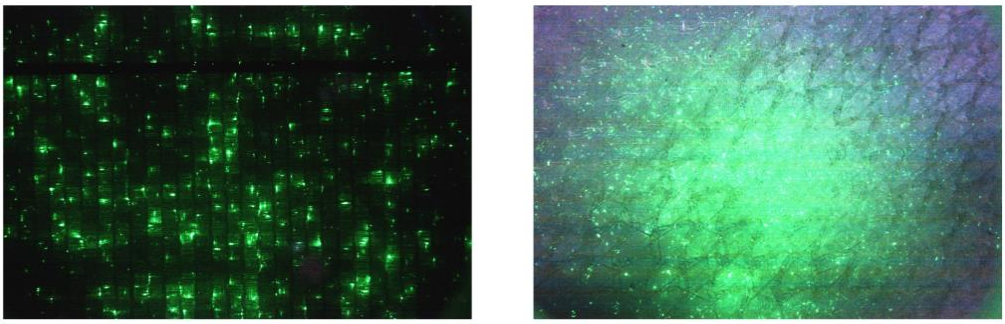

Figure 7: Distribution of the marker particles: PFP particles (green) filtered in the peel ply (left) and the flow media (right)

Thus, the lower intensity for the PFP specimens is caused by the filtration and thus a lower particle concentration in the FRP.

Furthermore, the influence of the substitution of glass fiber with carbon fiber textiles is analyzed. Figure 8 shows the hyperspectral camera results for the CF-TBS specimens.

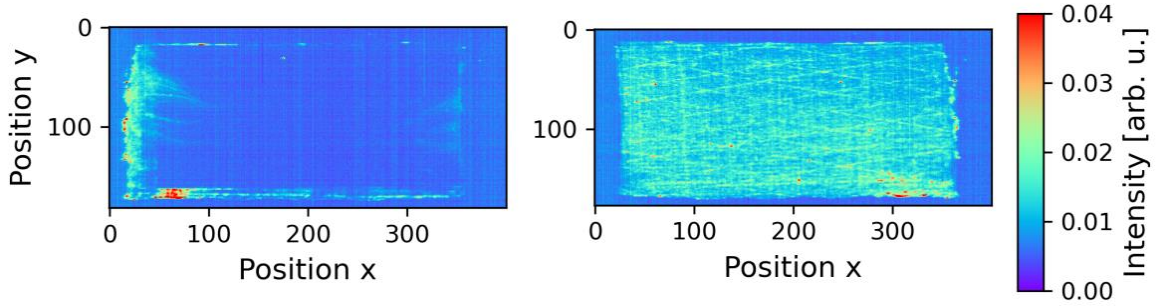

Figure 8: CF-TBS- normalized light intensity at 550 nm wavelength on the tool side (left) and non-tool side (right)

Looking at the tool side, the filtration effect of the textile layup is clearly shown. Particles only overflow on the sides but an infiltration through the textiles is not detectable. Since the carbon fibers are not transparent, identification through the textile layup is not easily possible. The normalized intensity of TBS particles on the top side is significantly lower for CF-TBS compared to GF-TBS. This is due to higher light absorption of carbon fibers which is results in their black color.

5. Conclusions

Within this paper methods and experimental investigations for the traceability of FRP during the whole life cycle considering circular economy are presented. The investigations show that the integration of fluorescent markers into FRPs during manufacturing via VARI process is possible. The markers can be homogenously mixed into the resin and show no significant impact on process parameters for the resin, thus having no direct influence on the infusion process. For both TBS and PFP the textile layups of unidirectional plies show a significant filtration effect resulting in insufficient particle concentrations on the tool side of the FRP specimens. For transparent or translucent fiber/matrix combinations this is a minor problem since the particles can still be identified via both sides of the FRP plates. For non-transparent fiber/ matrix

combinations, such as CFRP, the markers can only be identified from the non-tool side of the specimen.

Due to larger particle size, the use of PFP within the VARI process is prone to filtration effects by process aids, such as peel plies and flow media. Therefore, the standard VARI process setup is not ideal for the use of PFP technology. Possible solutions for the integration of PFP technology could be PFP labels, which then will be integrated on top of the preform during infusion.

The integration of TBS particles into transparent FRPs using the VARI process seems promising, but further research with regard to optimizing process parameters must be conducted. The integration of TBS particles into FRPs with high optical absorption, like carbon fiber reinforced composites results in poor detectability of the particles. A possible solution could be the integration of top layers with low absorption on top of the carbon fiber plies, which could improve the detectability.

6. Acknowledgement

This research was conducted within the project LiKE (Förderkennzeichen: 03LB2008G) which is funded by the German Federal Ministry for Economic Affairs and Climate Action (BMWK) und supported by the funding institution Projektträger Jülich (PTJ).

7. References

1. Composites United e.V. (2020). Composites-Marktbericht 2020. https://composites-united.com/wp-content/uploads/2020/01/GER_CUeV_Marktbericht_2020_CFCap.pdf
2. Karuppannan Gopalraj, S., Kärki, T. A review on the recycling of waste carbon fibre/glass fibre-reinforced composites: fibre recovery, properties and life-cycle analysis. SN Appl. Sci. 2, 433 (2020). https://doi.org/10.1007/s42452-020-2195-4
3. Hopmann C., Dahlmann R., Advances in Polymer Processing 2020: Proceedings of the International Symposium on Plastics Technology, Springer Vieweg, Berlin, Heidelberg (2020). https://doi.org/10.1007/978-3-662-60809-8

  doi:10.5075/epfl-298799_978-2-9701614-0-0

ELECTROFUSION WELDING OF THERMOPLASTIC COMPOSITE PIPES

Maciej Gierulski[a,b], Rachel Tomlinson[a], Matt Smith[a], Mike Troughton[c]

a: University of Sheffield, UK mpgierulski1@sheffield.ac.uk
b: NSIRC, TWI Ltd, Granta Park, Great Abington, Cambridge, CB21 6AL, UK
c: TWI Ltd., Cambridge, UK

Abstract: *Oil and gas operators are attempting to switch from steel to fully non-metallic pipelines, which are less prone to corrosion and potentially more durable. Thanks to recent development in thermoplastic composite pipes (TCPs), products are now available that satisfy the pressure requirements for this application, however TCPs still use steel connectors. The purpose of the project described in this paper is to investigate the possibility of designing a dedicated electrofusion (EF) coupler for glass fibre reinforced polyethylene TCPs. The design process involved first building a finite element model of two TCPs joined with a standard EF coupler, for which the precise properties of the pipe and how it behaves when joined have to be researched. Such joints were then manufactured and two mechanical tests were performed on them in order to verify said model, giving unexpected results. This paper explains why the failures occurred in the way they did and suggests improvements to the testing procedure and setups, allowing for collecting the data required for the design process.*

Keywords: electrofusion welding; thermoplastic composite pipes; reinforced thermoplastic pipes; composite pipelines

1. Introduction

Polyethylene (PE) pipes are a very common solution in gas, water or sewage distribution systems installed nowadays because they are cheap to produce, easy to install, flexible, corrosion resistant and reliable. They are, however, limited in their pressure and temperature capacities compared to steel pipes, although their maximum operating pressure can be increased by reinforcing them with different materials, like glass, carbon or aramid fibre, or even metal. Figure 1 shows the structure of a thermoplastic composite pipe (TCP). The inner layer (liner) contains the fluid, the reinforcement layer provides the strength and the outer cover (jacket)protects the reinforcement layer from the environment. These layers are welded together to produce a solid walled pipe.

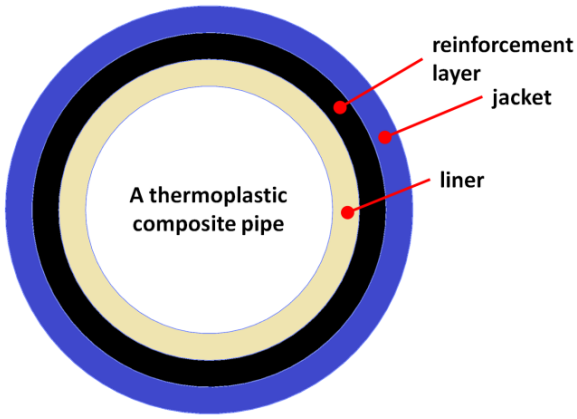

Fig. 1 A cross-section through a thermoplastic composite pipe

  doi:10.5075/epfl-298799_978-2-9701614-0-0

Currently, TCPs are joined together using steel connectors, which are relatively complex, heavy, expensive and prone to corrosion.

This project aims to determine whether it is possible to successfully electrofusion (EF) weld glass fibre reinforced PE TCPs and to develop a dedicated non-metallic electrofusion coupler for this purpose.

Electrofusion welding is a technology widely used for connecting PE pipes. The advantages include maintenance-free service life of 50 years or more, easy installation, corrosion resistance and an axial load resistance better than mechanical joints.

The principle of EF welding is that the ends of two PE pipes are scraped, cleaned and slid into an injection moulded coupler, which has resistance wire coils wound into bore (Fig. 2). Current is applied to the coils, which heat up, melting the surrounding plastic of the coupler and pipe within the fusion zone (FZ). When the plastic cools down and solidifies, a weld is formed. The function of the cold zones visible in the figure is to contain the molten material in the FZ in order to generate the melt pressure required to produce a good quality weld. Apart from melt pressure, the other two important factors influencing the EF welding process are temperature and heating time.

To manipulate these three factors, EF fitting manufacturers can change the heating time, the layout of wiring and cold zones, the clearance between the pipe and coupler, and the material grade for the fitting.

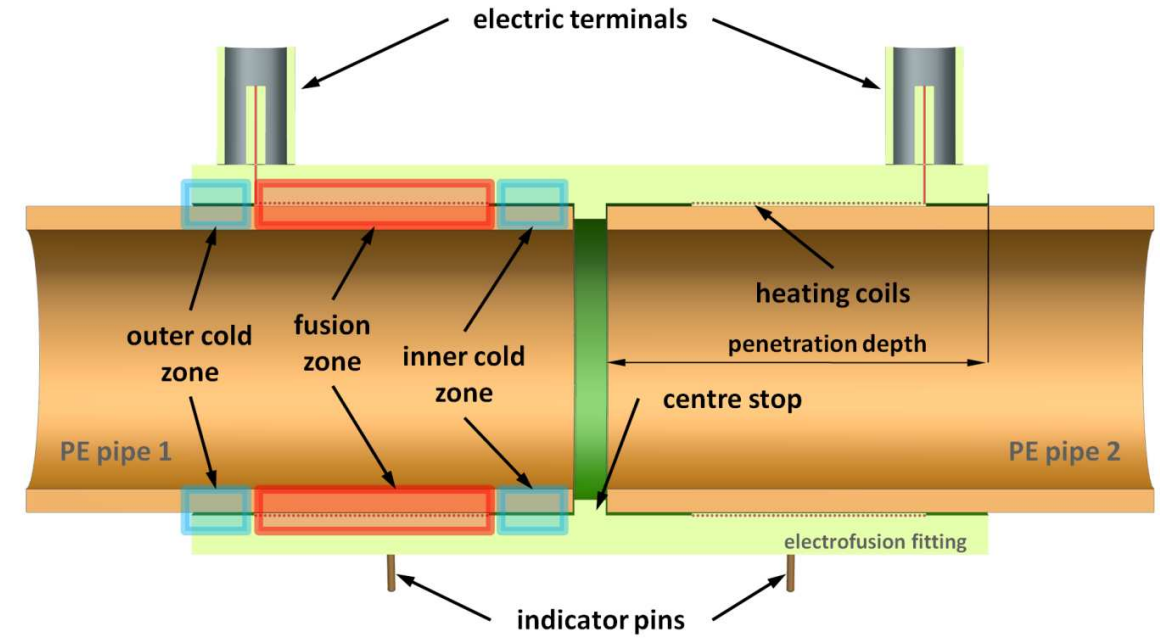

Fig. 2A cross section through an electrofusion joint

Electrofusion joints can function for half a century or more, but they also can fail prematurely if they are not made correctly. In Fig. 3 four typical failure modes are shown. They all correspond to different loading modes. Failure modes 1 and 2 can happen when the weld is not made correctly, for example if the weld interface is contaminated or the weld is underheated or overheated. Modes 3 and 4 happen in correctly made joints which are subjected to excessive stresses or temperatures. Failure mode 3 happens when the internal pressure is too high; a crack forms at the notch formed at the inner cold zone and propagates through the fitting wall, and mode 4 when the axial load on the pipe is too high.

  doi:10.5075/epfl-298799_978-2-9701614-0-0

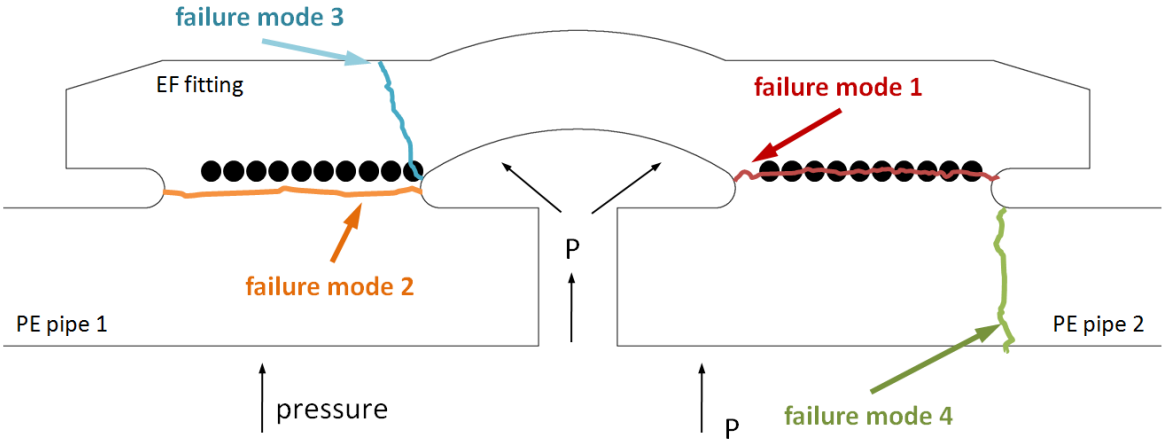

Fig. 3 Typical failure modes of an electrofusion joint. It is most convenient to show features of an EF weld on an axisymmetric cross-section.

2. Simulations and testing

To design a new coupler for joining glass fibre reinforced PE TCPs it is necessary to know how an EF joint using an existing coupler will respond to pressure and axial loads. In order to gain this knowledge, two whole pipe tests were chosen: a hydrostatic pressure test (similar to Annex D of BS EN 12201-3[1]) and whole joint tensile test (similar to Annex B of BS EN 12814-3[2]). Both tests were performed at 65°C, which is the maximum operating temperature of the TCP used. The two tests were finite element (FE) modelled and performed physically with the intention to use the experimental data to verify the model. The samples for the tests were made by welding 60cm lengths of glass fibre reinforced PE TCPs with a standard (unreinforced) EF coupler (Fig. 4). The samples were strain gauged in order to gather data on the material behaviour in the elastic region. 33–35 gauges were used per sample, displaced on both pipes and on the coupler in a way that they could capture both global bending of the sample and local strains due to the applied stress.

Fig. 4 One of three test samples – an electrofusion joint between two lengths of glass fibre reinforced polyethylene TCP

The welding was successful even though the TCPs had noticeable ovality, resulting in an initial maximum gap between the pipe and coupler of 2mm.

The same joints were recreated in Abaqus for FE analysis. Simulations were performed to predict the stresses in the pipe and joint for the two aforementioned tests (see Fig.5). The results suggested that the stress was highest in the cold zone notches in both cases (as suggested in the literature for conventional EF joints in PE pipe [3]). Simulations comparing joints in standard PE pipes with TCPs suggested that the presence of reinforcement in pipes reduces the stresses inside the joint significantly. Considering the yield limit of PE to be

  doi:10.5075/epfl-298799_978-2-9701614-0-0

23 MPa[4], then in the same testing conditions the joints in standard PE pipes would fail, and those in TCPs would not.

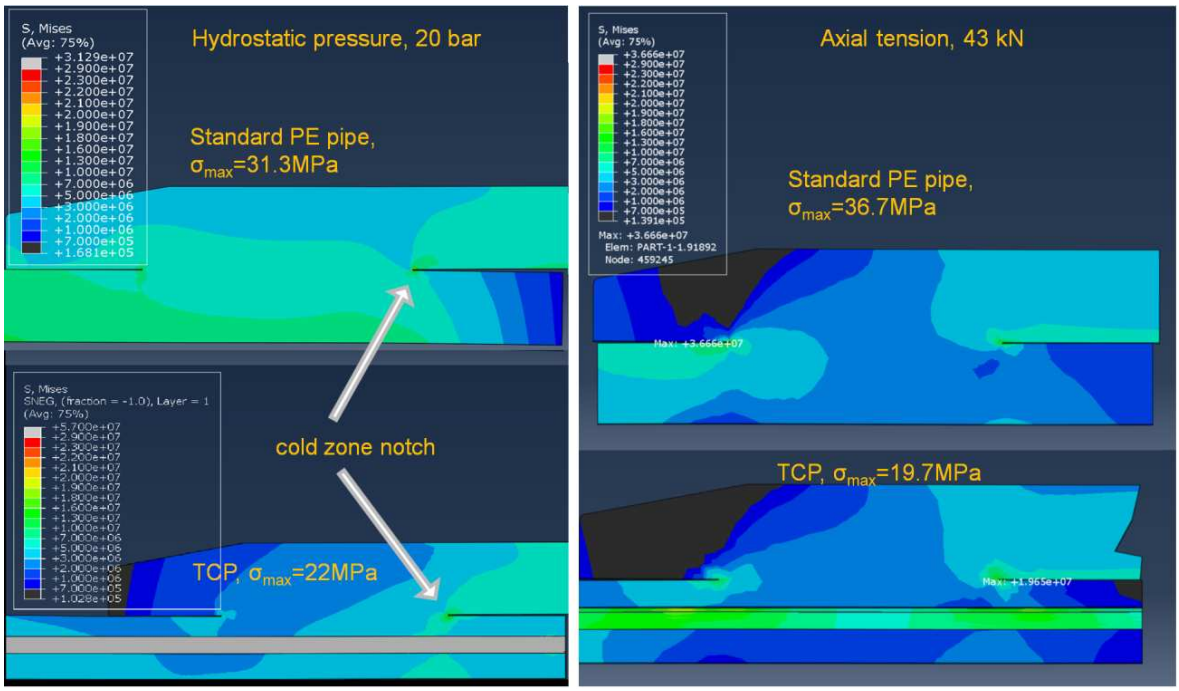

Fig. 5 Results of simulations of the two mechanical tests performed on EF joints in standard PE pipes and TCPs

Abaqus predicted that highest strains and failure should start within the joint at the cold zones notches. However, when the whole joint tensile test was performed, the strains in the coupler were only half those in the pipe in the proximity of the joint and the sample failed at a load of 40-48kN with *mode 4* from Fig. 3, through the outer jacket of the pipe – see Fig. 6. The reason for this was found to be that the EF weld was stronger than the weld between the reinforcement layer and the outer jacket, because, rather than having a fully welded structure, the TCP samples actually had cracks and/or weak interfaces between the three layers. As a result the load was mainly acting on the outside PE layer, so it was sheared off the TCP without substantially affecting the other two layers.

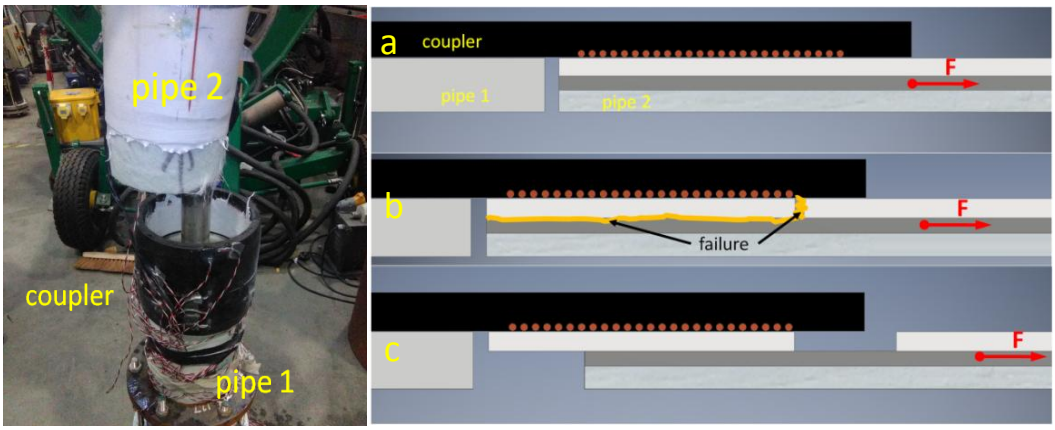

Fig. 6 Photograph of the failed whole joint tensile test sample and a suggestion of the failure mechanism

In the hydrostatic pressure test, initially at low pressure highest strains were recorded on the coupler, as expected from the simulations, but finally the sample failed in the pipe (see Fig. 7) at a pressure of 14 bar.

Fig. 7 Photograph of the failed hydrostatic pressure test sample. A debonded strain gauge is visible on top.

The most probable explanation for the failure is that the pressurized water entered between the reinforcement layer and outer jacket, travelled up the pipe, past the end of the coupler and then burst the outer jacket, as shown in Fig. 8.

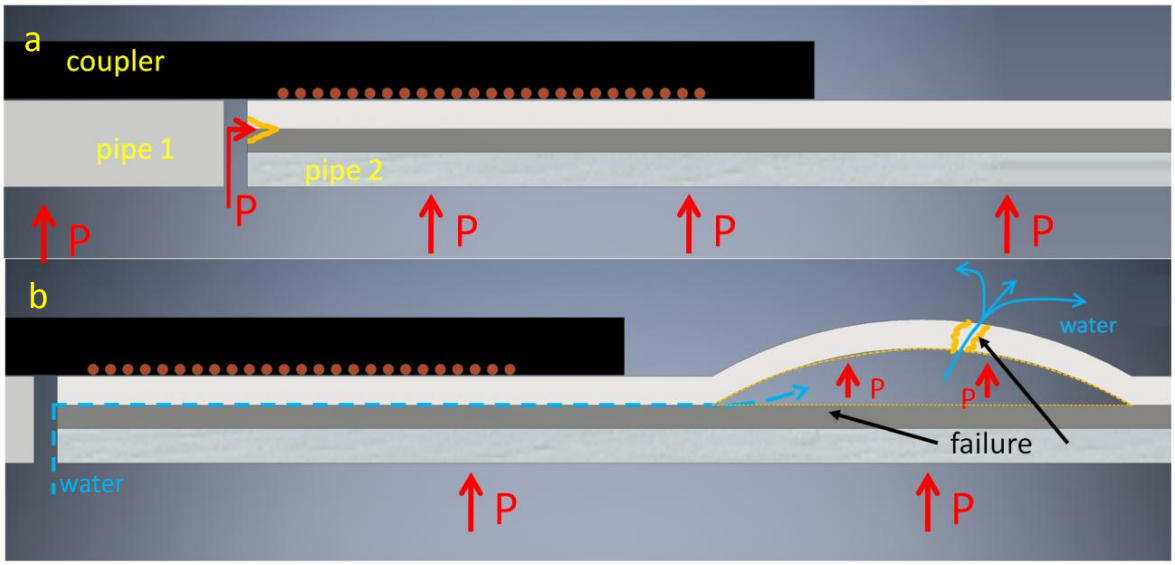

Fig. 8 Proposed failure mechanism for the hydrostatic pressure test: a) hydrostatic pressure separating the outer jacket from the reinforcement; b) water penetrating the crack and creating a bulge, and piercing it.

3. Discussion

The mechanical tests described above were meant to validate the FE model of an EF joint between two TCPs using a conventional unreinforced EF coupler, to allow the model to then

be adapted to design a bespoke EF coupler specifically for joining TCPs. However, the assumption in the FE model that the TCPs provided were fully bonded was incorrect. In fact, the pipes more resembled *semi-bonded reinforced thermoplastic pipes* (RTPs), where the reinforcement layer is not bonded to the outside or inside thermoplastic layers. These findings suggest that it is not possible to electrofusion weld RTPs using a standard EF coupler and give some hints for the design process:

- fluid ingress in between the reinforcement and cover has to be prevented to avoid premature failure of the cover near the EF connector; this could either be done by butt fusion welding the pipes before they are EF welded or by introducing a sleeve inside the coupler that would allow a weld to be created with the liner as well as the outer jacket, as shown in Fig. 9;

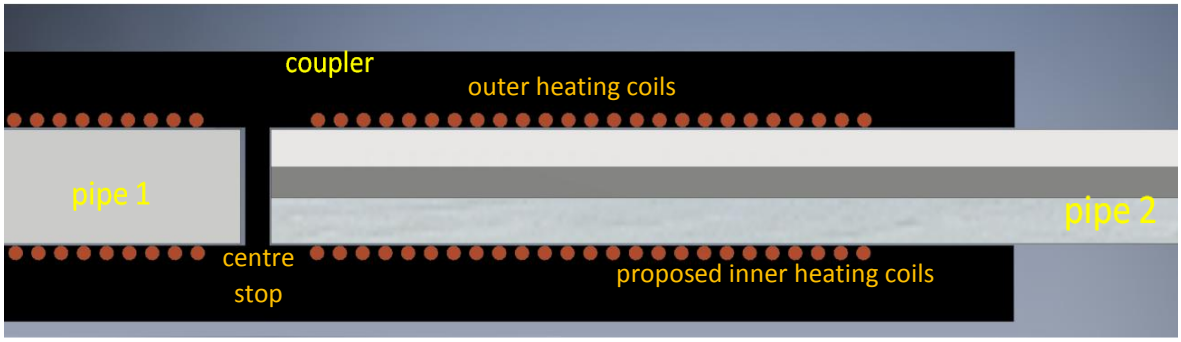

Fig. 9 Proposed concept of an EF coupler to weld both the outer and inner plastic layers.

- the weld interface between the coupler and outer jacket is likely stronger than the one between the outer jacket and reinforcement layer; therefore, the fusion zone must be extended in length to the point that this interface can transfer enough load to the composite layer, and avoid premature failure through shearing of the jacket-reinforcement interface; however, it might be difficult to slide such a long coupler on the TCP if the latter is significantly oval.

4. Conclusions

The purpose of the mechanical tests on EF joints in TCPs was to verify the FE model of these joints under identical conditions. However, due to the unexpected failure modes produced, it was not possible to verify the current model using these tests. However, the two tests can still be modelled, using a low weld strength between the three TCP layers. This will require information about the normal and shear strength of these interlaminar interfaces, which can be obtained from lap shear and tensile tests. This work is planned to be done in the near future. It should then be possible to design an EF coupler that will successfully weld the pipes provided for the project and then give test results that would allow for verifying the relevant FEA model.

5. Acknowledgements

This work was made possible by the sponsorship and support of the **Non-metallic Innovation Centre**. The work was enabled through, and undertaken at, the **National Structural Integrity Research Centre (NSIRC)**, a postgraduate engineering facility for industry-led research into

structural integrity, established and managed by TWI through a network of both national and international universities.

6. References

[1] British Standards, “BS EN 12201-3:2011+A1:2012 Plastics piping systems for water supply, and for drainage and sewerage under pressure — Polyethylene (PE) Part 3: Fittings,” 2003.

[2] British Standards, “BS EN 12814-3:2014 Testing of welded joints in thermoplastics semi-finished products Part 3 : Tensile creep test,” *BS EN 12814-3 2014*, 2014, doi: 10.3403/BSEN12814.

[3] M. Troughton, C. Brown, and M. Piovano, “Comparison of long-term and short-term tests for electrofusion joints in PE pipes,” in *Plastic Pipes XIII Conference Proceedings CDROM*, 2006, vol. 08, no. 1, pp. 1–10.

[4] PE100+ Association, “Polyethylene & HDPE PE100 Pipe: Properties and Types,” 2018. [Online]. Available: https://www.pe100plus.com/PE-Pipes/Technical-guidance/Trenchless/Methods/PE-Pipe-i1341.html. [Accessed: 12-Apr-2022].

  doi:10.5075/epfl-298799_978-2-9701614-0-0

MECHANICAL CHARACTERISATION OF SIMULATED LONG DISCONTINUOUS FIBRE REINFORCED COMPOSITE FOR RECYCLING POTENTIAL ASSESSMENT

Adrien Gonzalez[a], Romain Léger[a], Monica Francesca Pucci[a], Guillaume Ienny[a], Didier Perrin[b], Patrick Ienny[a]

a: LMGC, IMT Mines Ales, University of Montpellier, CNRS, Ales, France – adrien.gonzalez@mines-ales.fr
b: Polymers Composites and Hybrids (PCH), IMT Mines Ales, Ales, France

Abstract:

In order to simulate a recycling process applied to a carbon/epoxy composite, thermal oxydation was performed on discontinuous virgin carbon fibres to remove sizing and binder from their surface. Differences between thermally treated and virgin fibres were evaluated by mechanical and chemical characterization both at the fibre scale and at the composite scale. It appeared that the thermal treatment had no major influence on the mechanical properties and wettability of fibres. Nonetheless, the composite based on thermally treated fibres suffered a significant loss in tensile strength compared to untreated fibres, while the interlaminar shear strength was not significantly impacted.

Keywords: recycling; carbon fibre composite; discontinuous long fibre; mechanical characterization

1. Introduction

Technical composites materials and especially those made of carbon fibres and thermosetting matrix are of great interest today to produce high performance, stiff, lightweight and corrosion very resistant structures in aeronautics, aerospace and general transport sector [1] [2].

For several decades many studies have been carried out on the recycling of these composite materials in view of the large amount of composite structures reaching their end of life. 70% of all composite materials produced every year are made of thermosetting matrix, which means that they cannot be recycled by melting or moulded. According to Jiang [3], it can be expected that 15 000 aircrafts will need to be retired in the next 20 years and this represents at least 200 000 tons of composite materials. For this reason, different valorisation techniques were developed, such as mechanical and chemical recycling and thermal valorisation [4][5][6]. Carbon fibres are very high-quality fibres. The aim of recycling these fibres is to try to keep their physical and mechanical properties intact for re-use in high performance structures. In particular, the conservation of the fibre length is a priority in order to produce new composite materials reinforced with long recycled fibres, offering the best mechanical performance. Among the three valuation techniques mentioned above, only the chemical and thermal recycling can keep the fibre length intact since the mechanical shredding leads to important length reduction [7]. Even though recycling techniques exist to remove thermosetting resin from carbon fibres, it is still extremely difficult to obtain recycled fibres longer than 20 mm.

For this reason, in this work, composite laminates made of long discontinuous carbon fibres of a specific length distribution is investigated. A thermal treatment was chosen to simulate the recycling of fibres. In order to fully characterize the behaviour of the composite, tests at the fibre scale, such as single fibre tensile tests, wettability measurements and atomic force microscopy characterizations

  doi:10.5075/epfl-298799_978-2-9701614-0-0

(AFM), were first carried out. Then, composites made of virgin of thermally treated long discontinuous carbon fibres and epoxy matrix were characterized by tensile tests and interlaminar shear strength tests (ILSS). Tests were performed on a continuous non-woven UD fabric used as reference and on both untreated and treated discontinuous non-woven UD fabrics.

2. Materials and Methods

2.1. Materials under investigation

The material under investigation is an unidirectional carbon fibre reinforced epoxy matrix composite. The Infugreen SR810 epoxy resin and hardener SD 8824 used at a ratio of respectively 100/32 were provided by Sicomin. As reinforcements, two different non-woven fabrics were used. First, a non-woven unidirectional carbon fibre reinforcement T700 Infusion (UD T700 I) provided by Sicomin was used as the reference. The second fabric (UDS) is a non-woven discontinuous STS 40 carbon fibre reinforcement made by Schappe Techniques which fibres length follow a distribution between 20 and 170 mm with an average length of 45mm. The UD T700 I has an areal weight of around 300 g/m² while the areal weight of the UDS is 160 g/m².

In order to simulate the recycling process of carbon fibres, the UDS was thermally treated in an Enitherm DP46 oxygen hoven. The temperature is increased from 30°C to 350 at a rate of 5°C/min, and then hold for 15 min. Finally, the temperature is increased from 350°C to 450°C at 5°C/min. This thermal process was adapted from the ISO 6964 standard. The fibres are hold for 30 min at 450°C in order to remove any organic sizing that can be found on the fibre surface. After thermal treatment, samples are cooled in the hoven at a slow speed. The treated non-woven fibres are reused for composite manufacturing by infusion process instantly after being taken out from the hoven.

Unidirectional laminates of 4 and 10 plies using the UD T700 I with sizes of 150x600 mm² and 150x150mm² respectively were produced by resin infusion at room temperature. The same process was repeated for UDS with 8 and 20 plies of 150x600 mm² and 150x150 mm² respectively. The number of layers was doubled for UDS in order to obtain a similar areal weight for both composites. After a curing time of 24 hours, the infused plates were demoulded and conditioned at 23°C. The composites plates were then cut with a water diamond saw for mechanical testing at the standard sample dimensions according to the ISO 527-4 (250x25mm^2) for the larger plates and the NF EN 2563 (40x10mm^2) for the smaller ones. The porosity of each plate was determined thanks to a density characterization using a Micrometrics gas pycnometer (AccuPyc 1330 Model).

2.2. Characterization methods

2.2.1. Single fibre tensile strength test (STS)

STS tests were performed to provide detailed information on the mechanical properties before and after a treatment of fibres. First, the diameter of each carbon fibre was determined using a Diastron FDAS 770 machine that allows to determine the diameter of the fibre on all its length. Then the fibre was placed into a Diastron LEX 820 apparatus to carry out the tensile test according to the standard ISO 11566:1996. The minimum number of tested samples was set to 20. The Young's Modulus was corrected using a compliance calculated on 12 and 30-mm fibre gauge length. All samples were analysed according to a Weibull model for both gauge lengths of 12 and 30 mm. All fibre ends were glued on plastic tabs with a Dymax Ultra-light weld 3193 UV glue.

During their manufacturing and/or the simulated recycling process performed in this study, defects may appear on the surface or in the core of fibres. Considering a constant diameter for all fibres, the Weibull approach treats these two types of defects indifferently. These flaws may lead to a dispersion of break strength of carbon fibres. For this reason, it was decided to analyse these data using the Weibull's probabilistic model. In a volume *V*, the flaw population is modelled by the parameter λ corresponding to a density of flaw activation under a certain load σ as follows:

$$\lambda = \frac{1}{V_0}(\frac{\sigma}{\sigma_0})^m \quad (1)$$

for which m is the Weibull's modulus.

The failure probability of the fibre can be written as followed:

$$P_f = 1 - \exp(-\frac{V}{V_0}(\frac{\sigma}{\sigma_0})^m) \quad (2)$$

To determine the Weibull's modulus of the fibres, a large number of fibres (superior to 20 according to the literature) must be tested. A non-linear optimisation procedure based on the Generalized Reduced Gradient (GRG) algorithm was used to adjust the material parameters.

2.2.2. Wettability measurements

A single carbon fibre was attached to one plastic tab using the same UV glue used in single fibre tensile test. A high precision force tensiometer, the K100SF from Krüss, was used with different liquids: water, diiodomethane and the Infugreen SR 8100 epoxy resin. During the procedure, the carbon fibre is dipped into the liquid at a speed of 1mm/min, reaching a defined immersion depth. This allows to determine an advancing capillary force. Then the fibre remains at this position for 60 s in order to obtain a static force. Finally, the fibre is withdrawn up to the initial position at a speed of 1mm/min and a receding force is measured. The static force will be used in this work to determine the static contact angles and then the surface energies as made in previous works of Garat et al [8]. The contact angle between the fibre and the liquid is calculated using the Wilhelmy's law as follows:

$$\theta = \arccos(\frac{\gamma_l \times p}{F}) \quad (4)$$

where F is the measured force, , γ_L is the surface tension of the liquid and p is the fibre perimeter. Once the contact angle θ is calculated for each liquid, the Owens-Wendt's [9] formula which is a 2nd degree linear equation can be used to determine the fibre surface energy.

$$\frac{\gamma_L \times (1+\cos(\theta))}{2 \times \sqrt{\gamma_L^d}} = \sqrt{\gamma_s^p} \times \frac{\sqrt{\gamma_L^p}}{\sqrt{\gamma_L^d}} + \sqrt{\gamma_s^d} \quad (5)$$

where γ_L^p is the polar component and γ_L^d is the dispersive component of liquid surface tension and the γ_s^d *and* γ_s^p are the dispersive and the polar component of fibre surface energy respectively.

In order to obtain the surface energy of the fibres, a fit of the equation for four different liquid was done according to previous work by Pucci et al [10].

2.2.3. Topographical Analysis

The nanoroughness of fibres was characterized with an Oxford Asylum Research MFP-3D Infinity AFM using a tapping mode. In order to observe the fibre surface, each end of the fibre was stuck to a glass sheet using a silver glue. Each sample was scanned on 5 x 5 μm^2 area at a scan speed 3.8 µm/s. All

measurements were performed with an AC160TS-R3 silica tip. Thanks to the IGOR Pro 6.37 Software the roughness of the topography can be characterized by the means of two values. The first one is Ra which represents the average roughness of the surface as the second one, Rq, is the quadratic value roughness of the whole surface sample.

2.2.4. Mechanical Tensile Test

Axial tensile test specimen of 250 x 25 x 1.5 mm^3 were produced from the composite plates using a water-cooled diamond saw. Aluminium tabs of 50 x 25 x 2 mm^3 were bonded on each composite end using one-component cyanoacrylate Loctite Super Glue 3. All tests were performed with an MTS Criterion C45.105 tensile machine equipped with a 100 kN load cell at a crosshead speed of 1mm/min according to ISO 527-4 standard requirements. An additional high-resolution camera is placed in front of the sample, and images of its speckled surface are recorded at frequency of 1 Hz. A digital image correlation technique allows measuring the in-plane plane strain tensor and thus the Poisson's coefficient.

2.2.5. Short beam shear test (SBS)

The SBS test is a well-known and used method to study the interlaminar shear strength (ILSS) of laminates. For this test, specimens were cut from the 8 plies plate of UD T700 I and 20 plies plate of UDS in order to have a span of around 20 mm. A Z010/TH Zwick-Roell testing machine equipped with 3 points bending device and a 10 kN load cell was used to apply a load at 1mm/min. The apparent ILSS τ, expressed in MPa is calculated using the following equation:

$$\tau = \frac{3}{4} \times \frac{P_m}{b \times h} \quad (6)$$

Where P_m is the maximum load observed during the test (N), *b* and *h* are the measured width and thickness (mm) respectively.

3. Results and Discussion

3.1. STS tests

Single fibre tensile test results are shown in Table 1 as average value for at least 20 tests. All the tests were carried out in the pure elastic domain of the fibre. Differences between the treated and untreated fibres are not very significant. There was no change on the diameter of the fibres but a loss of 5% of the tensile strength was observed for thermally treated fibres. Considering the Young's modulus, the corrected one is a bit higher than the provider value (around 290 GPa against 250GPa for 12k STS40 EP) but this could be explained by a difference in the fibre holding. In the ISO Standard 11566:1996 the fibre is stuck onto by a paper frame whereas in this work each fibre is glued onto plastic tabs.

Table 1: STS results for UD T700 I, UDS Untreated and TT fibres

Sample Name	d [µm]	σ_{max} [MPa]	E_{corr} [GPa]	m
UD T700 I	6.61 ± 0.33	4150 ± 920	278 ± 20	5.3
UDS Untreated	6.51 ± 0.35	4000 ± 1200	286 ± 18	3.3
UDS TT	6.45± 0.37	3800 ± 870	292 ±17	4.4

The TT seems to have little impact on the mechanical behaviour of fibres except on the standard deviation of the maximum strength which is a bit lower for treated fibres. A Weibull's analysis also

reveals interesting differences with a slight decrease of the fibre strength at Pf = 50% and of the Weibull modulus as it can be seen on the Figure 1.

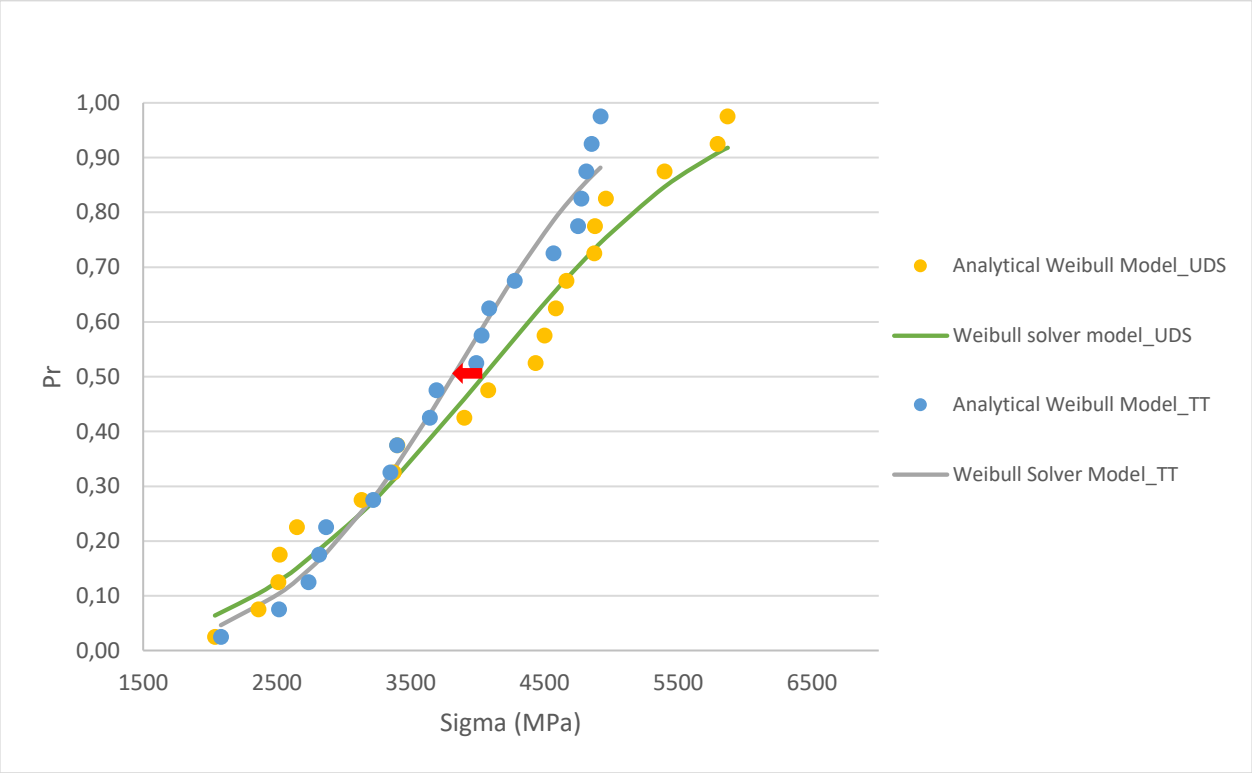

Figure 1. Probability of failure as a function of tensile stress for TT and untreated UDS carbon fibres

The plotted point and solver calculation of the Weibull modulus show that the treated and untreated fibres have a close slope which is observable on the small differences of the Weibull modulus. Nonetheless the deviation of the values is a bit lower for the treated fibres which could be a result of a surface change. It is possible that the heat treatment has made the surface flaws more uniform but these must be proven using surface characterization as with AFM measurements for example.

3.2. Wettability measurements results

3.2.1. Determination of the contact angle

The average results of the tests carried out with the K100SF Tensiometer for 8 single carbon fibres can be found in Table 2. Since the UD T700 I and UDS are not made of the same reference fibres, only untreated and treated UDS fibres were analysed with this method. It appears that treated and untreated have slight differences on contact angles especially with water and diiodomethane, whereas the contact angles values for the Infugreen epoxy shows similar results.

Table 2: Contact angle of treated and untreated fibre for various liquid

Sample Name	Water contact angle [°]	SR 8100 Infugreen Contact angle [°]	Diiodométhan Contact Angle [°]
UDS untreated	51.91 ± 8.5	50.19 ± 5.5	49.94 ± 7.97
UDS TT	61.0 2± 5.2	52.42 ± 5.1	53.94 ± 4.03

3.2.2. Determination of the fibre surface energy

According to the Owens Wendt equation (Eq.6), the static contact angle of the three liquid was used to obtain the fibre surface energies and components. The dispersive component of fibres after treatment remained the same but a small change was observed in the polar component. Nonetheless the values are really close taking the standard deviation in consideration.

Table 3: Surface energy of UDS Untreated and UDS TT

Sample name	Polar component [mJ/m²]	Dispersive component [mJ/m²]	Total component [mJ/m²]
UDS untreated	27.3 ±6.6	22.0 ±1.5	49.3 ±5.8
UDS TT	20.9 ±4	21.6±1	42.5±3.4

3.3. Topographical Analysis

The variation of surface roughness after a desizing treatment have been studied by Yao et al [11] who demonstrated that sizing removal conducts to an increase in roughness. Some topographical analysis were performed by means of AFM on untreated and thermally treated carbon fibres. Measured roughness on both fibres seems to be coherent with results found in the literature. These results will be discussed during the oral presentation.

3.4. Mechanical tensile test

In order to investigate the influence of both the fibre distribution length and the TT on fibre, tensile tests were conducted at composite scale on UD T 700I laminate and both untreated and treated material. To ensure possible differences in the mechanical property tests were carried out on at least 5 samples until failure.

Table 4: Mechanical tensile tests results for Reference, UDS Untreated and UDS TT composites materials

Sample name	Tensile strength R_e [MPa]	Young modulus [GPa]	Poisson coefficient	Porosity [%]
UD T700 I	2145.172	106.8 ± 2.0	0.31 ± 0.02	4
UDS Untreated	1403 ± 85.1	98.6 ± 16.0	0.39 ± 0.1	2.5
UDS TT	1059 ± 112.9	77.9 ± 8.8	0.38 ± 0.1	6.0

On the first hand, the results presented in Table 4 show a good conservation of the Young modulus and Poisson ratio when considering the standard deviation. On the other hand, an important decrease of 25% of the maximum strength was observed for the thermally treated carbon fibres. Since no major differences exist between the two reinforcing non-woven, the adhesion between fibre and matrix after a thermal treatment can be the cause of such loss of properties. The discontinuity of the reinforcements also shows a significant loss of 35% in tensile strength compared to continuous fibres.

3.5. SBS test results

During the SBS test, is the specimen is subjected to longitudinal shear, but also to tension and compression. It is important to confirm the shear failure mode of the specimen by calculating the maximum tensile stress at failure and comparing it to the tensile strength R_e measured previously (Table 4):

  doi:10.5075/epfl-298799_978-2-9701614-0-0

$$\sigma_{max} = \frac{3}{2}\ \frac{FL}{be^2} < R_e \quad (7)$$

With F the load at failure, L the span, b and e the width and thickness of the sample.

It can be seen in the following table that the failure of samples was completely in the shear mode since maximum stress was always lower than the composites tensile strength.

Table 5: SBS test results for UD T 700 I, UDS Untreated and UDS TT composite materials

Sample name	ILSS τ [MPa]	Load at failure [N]	Maximum stress [MPa]	Composite tensile strength [MPa]
UD T700 I	48.1 ± 2.61	1912	386	2145
UDS Untreated	52.4 ± 2.14	2359	420	1403
UDS TT	52.6 ± 1.86	2422	415	1059

Taking the dispersion into account, ILSS displayed in Table 5 does not vary much between the 3 composites. The fact that the discontinuity of fibres has little impact on ILSS is not very surprising since this test is mainly driven by the behaviour of both matrix and interfaces. It can also be observed that the thermal treatment does not influence much the adhesion between fibres and matrix since the ILSS value is 52 MPa for both composite materials.

3.6. Discussion

According to all test carried out, the three type of fibres tested (UD T 700 I, UDS untreated, UDS treated) have similar properties. From a mechanical point of view, only tensile strength and Weibull modulus seem to be impacted by thermal treatment. Tensile strength slightly decreases, while the Weibull modulus increases, reflecting the decrease in the dispersion of the strengths. The major differences between the fibres have been observed for surface topography which is more etched after thermal treatment. This could explain the small difference observed in wettability measurements.

At the composite scale, on one hand, it is understandable that the ILSS showed no evolution when using discontinuous fibres instead of continuous ones as explained previously. On the other hand, it is more surprising not to observe variation with the change in surface of fibres after thermal treatment. This could be explained by a change in the adhesion mode. Before thermal treatment, chemical bond between sizing and matrix were mainly responsible for the adhesion, while after treatment, the rougher surface allows a better mechanical adhesion thanks to interlocking. However, for a better understanding of the shear behaviour of the composites additional characterization needs to be done on the treated fibre such as XPS to observe the sizing removal.

Finally, the 25% drop in strength observed when switching from continuous to discontinuous fibres is directly attributable to the reduction in fibre size. Actually, the mechanical properties of both type of fibres are almost identical. Such a result has been shown several times in the past and was therefore expected. It is all the more important as we are interested in the recycling of these fibres whose size will be reduced after each recycling phase. After heat treatment, an additional drop of 25% is observed and is this time attributed to the change in the adhesion mode. While this change appears to maintain the SBS properties, it is not sufficient for the tensile failure properties.

  doi:10.5075/epfl-298799_978-2-9701614-0-0

4. Conclusion and perspectives

In this study, the recycling process of carbon fibres was simulated by testing the impact on the composite properties of the fibre lenth reduction and the fibre surface state after heat treatment. It was found that the heat treatment did not significantly influence the intrinsic mechanical properties of the fibres, but rather its surface properties in a small but noticeable way. Concerning the composite, modifications are more important, especially on the tensile properties. We note here that the length of the fibres has a predominant impact, as well as the modification of the surface condition of the fibres. These results are all the more important as recycling carbon fibres is an important objective for many companies. It is therefore mandatory to find a solution to compensate for these losses of properties with specific surface treatment such plasma treatments, and to find weaving techniques to produce high quality reinforcements for laminates from long discontinuous fibres.

Acknowledgements

The authors would like to thank Mr. Olivier Thouron and Mr. Jean-Philippe Missonnier from Schappe Techniques for the supply of the non-woven discontinuous carbon reinforcement used in this study.

5. References

[1] C. Soutis, “Fibre reinforced composites in aircraft construction,” *Prog. Aerosp. Sci.*, vol. 41, no. 2, pp. 143–151, 2005.

[2] J. Zhang, V. S. Chevali, H. Wang, and C. H. Wang, “Current status of carbon fibre and carbon fibre composites recycling,” *Compos. Part B Eng.*, vol. 193, no. December 2019, p. 108053, 2020.

[3] H. Jiang, “Trends in Fleet and Aircraft Retirement,” no. June, p. 14, 2015.

[4] J. Howarth, S. S. R. Mareddy, and P. T. Mativenga, “Energy intensity and environmental analysis of mechanical recycling of carbon fibre composite,” *J. Clean. Prod.*, vol. 81, pp. 46–50, 2014.

[5] Y. Liu, J. Liu, Z. Jiang, and T. Tang, “Chemical recycling of carbon fibre reinforced epoxy resin composites in subcritical water: Synergistic effect of phenol and KOH on the decomposition efficiency,” *Polym. Degrad. Stab.*, vol. 97, no. 3, pp. 214–220, 2012.

[6] S. J. Pickering, R. M. Kelly, J. R. Kennerley, C. D. Rudd, and N. J. Fenwick, “A fluidised-bed process for the recovery of glass fibres from scrap thermosetting composites,” *Compos. Sci. Technol.*, vol. 60, no. 4, pp. 509–523, 2000.

[7] A. K. Bledzki and K. Goratsi, “The use of recycled fibre composites as reinforcement for thermosettings,” *Mekhanika Kompoz. Mater.*, vol. 29, no. 4, pp. 473–477, 1993.

[8] W. Garat *et al.*, “Surface energy determination of fibres for Liquid Composite Moulding processes: Method to estimate equilibrium contact angles from static and quasi-static data,” *Colloids Surfaces A Physicochem. Eng. Asp.*, vol. 611, no. xxxx, p. 125787, 2021.

[9] D. K. Owens and R. C. Wendt, “Estimation of Estimation of,” *J. Appl. Polym. Sci.*, vol. 13, pp. 1741–1747, 1969.

[10] M. F. Pucci, M. C. Seghini, P. J. Liotier, F. Sarasini, J. Tirilló, and S. Drapier, “Surface characterisation and wetting properties of single basalt fibres,” *Compos. Part B Eng.*, vol. 109, pp. 72–81, 2017.

[11] L. Yao *et al.*, “Applied Surface Science Comparison of sizing effect of T700 grade carbon fibre on interfacial properties of fibre / BMI and fibre / epoxy,” *Appl. Surf. Sci.*, vol. 263, pp. 326–333, 2012.

  doi:10.5075/epfl-298799_978-2-9701614-0-0

THE MASS PRODUCTION OF MWCNTS/EPOXY SCAFFOLDS USING LATERAL BELT-DRIVEN MULTI-NOZZLE ELECTROSPINNING SETUP TO ENHANCE PHYSICAL AND MECHANICAL PROPERTIES OF CFRP

Asel Ananda Habarakada Liyanage[a,b], Pias Kumar Biswas[a], Mangilal Agarwal[a,], Hamid Dalir[a,*]*

a: Integrated Nanosystems Development Institute, Purdue School of Engineering and Technology, Indiana University−Purdue University Indianapolis, Indianapolis, IN, 46202, USA
b: Multiscale Integrated Technology Solutions LLC, Indianapolis, IN, 46202, USA
Presenting author: ahabarak@iu.edu, *Corresponding author

Abstract: *Electrospinning is the process of ejecting a polymer melt or solution through a nozzle in the presence of a high-voltage electric field, which causes it to coalesce into a continuous filament with various shapes from a submicron to nanometer diameter. This process has gained vast attention because of its versatility, low cost, and ease of processing, leading to a massive demand for translating electrospinning experiments out of the laboratory into commercialized production. This manuscript represents an approach to mass-producing MWCNTs/Epoxy scaffolds using Lateral Belt Driven (LBD) multi-nozzle electrospinning technique to enhance CFRP's physical and mechanical properties. We mitigated the non-uniform electric field distribution challenges with the LBD approach, which helped obtain a single layer and well-uniformed coverage of the electrospun MWCNTs/Epoxy scaffolds onto CFRP sheets. Interlaminar shear strength (ILSS) and fatigue performance under high-stress conditions improved by 29% and 27%, respectively. The energy of barely visible impact damage (BVID) improved by up to 45%.*

Keywords: Nanocomposite; Epoxy-CNT composite; CFRP composite; Electrospinning; Lateral belt-driven multi-nozzle electrospinning

1. Introduction

Since the advent of nanotechnology, researchers worldwide have been advancing the nanocomposite to achieve better properties such as higher mechanical properties, thermal stability, and efficiency through different shapes such as flakes, continuous fibers, and hybrids (1-5). Researchers have studied extruding nanofilaments made from neat thermosetting epoxy and nanocomposites (6). Although progress has been made, fabrication of the nanofilaments through epoxy is quite challenging, and the addition of the nanomaterials to the thermosetting epoxy composite as well. Despite these challenges, our previous group utilized an electrospinning-based approach to overcome these challenges and successfully fabricate the submicron multiwalled carbon nanotube (MWCNTs)/epoxy nanocomposite filaments through the single-nozzle horizontal electrospinning process with an outstanding mechanical improvement (7, 8).

Our next challenge was to develop this technology to an industrial scale. Here the single nozzle electrospinning fiber production and the area of fiber deposition on the CFRP are low due to the required parameters in the electrospinning, such as voltage, distance and the flow rate (between 0.1 ml/hr and 5 ml/hr (9)); therefore, addressing the large volume processing and reproducibility is the primary focus of this study. In order to increase production and efficiency for industry, literature has been published on introducing an auxiliary electrode to increase the jets from a

  doi:10.5075/epfl-298799_978-2-9701614-0-0

single nozzle; the grounded electrode is kept near the spinneret, which creates a strong electrified gradient between the spinner and the electrode (10). However, these improvements still result in slow production rates and add the expense of having a commercial electrospinning line.

Multi-nozzle electrospinning is an approach that seeks to alleviate key limitations in comparison to single nozzle electrospinning (11). Here, the idea is to utilize several jets to achieve higher production rates and more extensive coverage areas. However, a significant challenge is electrostatic interference between multiple nozzles. Studies have been carried out to understand the effects of a multi-nozzle electrospinning setup to enhance the production rates (12, 13). We developed a lateral belt-driven system to overcome these challenges and have uniform layer MWCNTs/epoxy filaments on the CFRP. The current study demonstrates the method of mass-producing MWCNTs/epoxy composites. Studies comparing the interlaminar shear strength, flexural properties, and the fatigue of the resulting materials were undertaken before and after incorporating MWCNTs/epoxy nanoscaffolds. Low-speed energy impact experiments were carried out to inflict barely visible impact damage (BVID) and assess CFRP laminates' impact reaction.

2. Methodology

2.1 Material Preparation

Masterbatch of MWCNTs/epoxy was synthesized using a previously published method by our group (14-16). Bisphenol A (50 - 99 pbw.%) and carbon nanotubes (5 wt.%) were mixed together followed by the addition of Dimethylformamide (DMF) (1:4 volume ratio) and Triton X- 100 (20:1 volume ratio). Then the resulting mixture was sonicated for 10 mins in intervals of 45s and 30s rest between cycles. The same weight of more epoxy was added to the mixtures and 15 mins stirring was done followed by sonication. Finally, to have a uniform viscous mixture, the curing agent was mixed at a ratio of 15:1 and stirred at 50°C for 2 hours to obtain a homogeneous solution. The uniform mixture was then degassed and rested for 16 hrs. prior to electrospinning. For electrospinning, a syringe with a needle gauge of 26 G was filled with MWCNTs/epoxy mixture.

2.2 Experimental setup

Figure 1 shows the schematic of the LBD multi-nozzle linear array platforms investigated in this experiment. 26G Stainless steel nozzles were luer locked with the syringes filled with the MWCNTs/epoxy polymer solutions, loaded to the multi-nozzle platform with the evenly spaced 10 nozzles with a space of 50 mm, and pushed using a modified KD Scientific Legato 180 syringe pump at a constant rate of 0.25 ml/h. The working distance between the nozzle tips and the collector was kept at 12 cm during experiments. Each nozzle was connected to the positive DC terminal, while the collector plate was connected to the negative terminal and grounded. The multi-nozzle syringe holders were then connected to the lateral belt-driven (LBD) platform using a Nema 17 stepper motor with high torque which was programmed using an Adreno and stepper motor drive (DM542T) to have a uniform coverage or overlap of the deposited fiber as shown in figure 1 (b).

The MWCNTs/epoxy solution was extruded from the tip of the nozzle by the strong electric field and deposited on the CFRP prepreg (SE70 Gurit Holding AG, Wattwil, Switzerland) layer fitted on a 60 × 15 cm flat stainless-steel collector, which resulted in the production of an

MWCNTs/epoxy nanofiber scaffold. Each sample collection was conducted for 10 minutes and in ambient conditions.

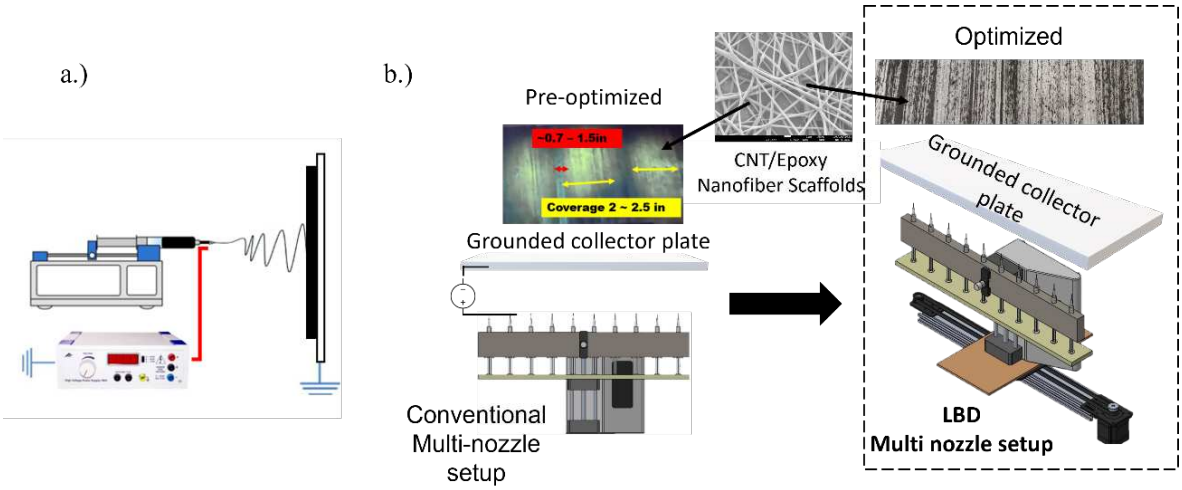

Figure 1. The image of the fiber collection with the multi-nozzle electrospinning syringe setup is arranged vertically in a linear configuration.

2.3 CFRP Laminate Preparation and Mechanical Testing

The control and enhanced MWCNTs/epoxy electrospun CFRP specimens measuring 10 cm × 10 cm were cut from a hot melt epoxy-carbon fiber with a plain weave pattern (SE70 Gurit Holding AG, Wattwil/Switzerland). A hand layup approach was used to reduce the void ratio, followed by vacuum bagging. The CFRP laminates' stacking sequence was $[0/90/\pm45]_{2s}$. Specimens were vacuum bagged for 60 minutes to ensure optimal adhesion between the layers, followed by curing time by placing them in a programable vacuum oven (OV301 Precision Composites Curing Oven, Easy Composite, UK) for 25 minutes at 120° C and 1 bar. The prepared specimens were cooled down to room temperature while maintaining the pressure. A Precision Water Jet Cutting was utilized to fabricate the composite panels for mechanical testing. Short Beam Shearing was carried out for interlaminar bond strength characterization. Within the tight tolerances of the ASTM D2344, the final measurements of the samples were 2mm×4mm×12mm. The test was conducted on an Instron universal testing machine with a crosshead speed of 1.27mm/min and a span-to-depth ratio of 4. For the short beam fatigue test, loads ranged from 60-90% of the ultimate strength with an R-value of 0.1. To define the interlaminar shear strength, ten coupons from baseline (pristine) and electrospun MWCNTs composite panels were cut and tested under static cyclic loading conditions. The mean values from ten tests for each specimen and their standard deviation were measured.

3. RESULTS AND DISCUSSION

3.1 Mechanical Properties and Morphology

Compared to other shear tests, the small dimensions of the Interlaminar Shear Strength (ILSS) test make this method the most suitable. Figure 2 represents load-displacement curves and the corresponding ILSS values for all samples. Here, the load increased with displacement in the linear elastic area until peak load. Assuming the ultimate shear stress produces cracking at the mid-plane point of the composite, the ILSS of the laminate was measured using the maximum

strength achieved throughout the tests. The reinforced matrix (MWCNTs/epoxy) showed a high load of 650.01 N and then decreased sharply as expected. Conversely, the control sample showed a high load of 503.92 N. Therefore, MWCNTs/epoxy reinforced regions hold higher ILSS than the baseline interlayer. Ten independently tested coupons for each laminate structure were run for bending tests and the load bearing capacity increment was always reproducible. The reinforcements in the ILSS properties were increased by 29% just by adding 4% wt. MWCNT in epoxy.

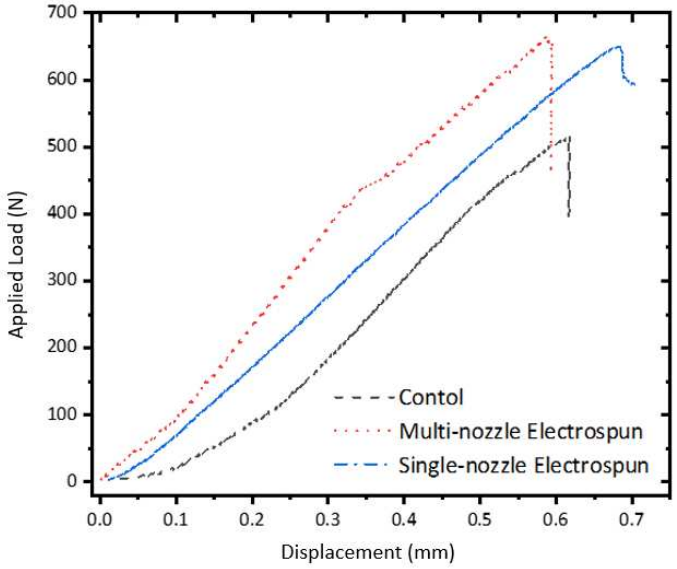

Figure 2. Load vs displacement curves of control and enhanced CFRP laminates.

The fatigue life cycle was measured using an Instron Co. 8801 fatigue tester. The frequency and stress ratio (R) of the fatigue tests were set to be 5 Hz and 0.1 Hz, respectively. Fatigue test samples for baseline sample and MWCNTs/epoxy enhanced samples were measured according to ASTM D3479 standard. All the coupons utilized in the fatigue tests failed at the gauge length center where the impact damage was observed. In all cases, the MWCNT reinforced specimens showed longer fatigue lives. With respect to the control, the fatigue enhancement of specimens was in the range of 25-60% with MWCNTs/epoxy as shown in figure 5. These results indicated that under cyclic loading, adding a small amount of MWCNTs has a significant impact on the mechanical strength of the composite laminate.

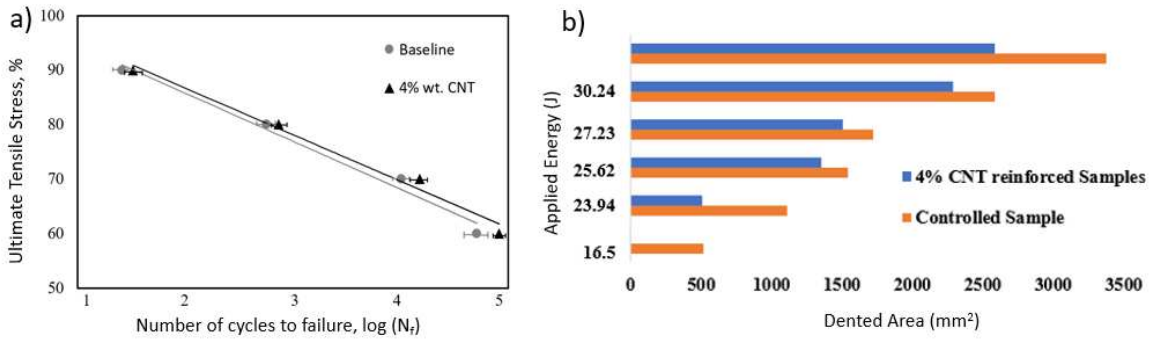

Figure 5. a) Short Beam Fatigue Testing of Baseline and Enhanced Composites Under Cyclic Loading, b) relation between dented area and applied energy on the laminated CFRP sheet surface has been depicted

  doi:10.5075/epfl-298799_978-2-9701614-0-0

Minor damage events are hard to identify on the surface of composites. However, the formation of such damages on the structures over time can have the same significant structural impact as delamination, matrix cracking and fiber fracture. To minimize these effects, minor damages need to be examined using a BVID test to avoid catastrophic failure. In the BVID test, when 16.50J was applied, the first visible dent was found on the controlled sample whereas the surface of 4% CNT reinforced samples looked intact. After increasing the energy level, the first visible dent on of 4% CNT reinforced sample for 23.94J and interestingly the dented area is almost the same as the controlled sample for 16.5J. Similarly, different energy was applied, and in all cases, dented area for the controlled sample was found to be significantly bigger than the 4% MWCNTs/epoxy reinforced sample. For the highest energy applied (35.15J), the impactor almost penetrated the surface of the controlled sample where only a higher dent was visible on the 4% MWCNTs/epoxy reinforced one.

4. CONCLUSION

The mass production of MWCNTs/epoxy scaffolds fabricated successfully using the Lateral Belt Driven (LBD) multi-nozzle electrospinning technique and the mechanical properties, including interlaminar shear strength and BVID of the fabricated composites, were evaluated. Results revealed that by incorporating the electrospun MWCNTs/epoxy nanofiber scaffold, the mechanical properties of the composite were considerably improved. The electrospinning parameters were also optimized for the multi-nozzle system to improve stability and fabricate uniform fiber with smaller diameter fibers. Simulation data and machine learning can be introduced as future work for this study.

Acknowledgements

The authors would like to express their gratitude to the National Science Foundation Major Research Instrumentation Program for supporting this research (#1229514) for FESEM. The authors declare a potential financial conflict of interest. Multiscale Integrated Technology Solutions LLC (MITS), which has been awarded the National Science Foundation (NSF) Small Business Technology Transfer (STTR) (#2036490) grant to conduct research and development (R&D) work on enhancing the strength of carbon fiber reinforced polymer composites, has potential commercial interest in the research presented in this paper.

5. References

1. Vijay Kumar V, Ramakrishna S, Kong Yoong JL, Esmaeely Neisiany R, Surendran S, Balaganesan G. Electrospun nanofiber interleaving in fiber reinforced composites—Recent trends. Material Design & Processing Communications. 2019;1(1):e24.
2. Ling T, Wang J-J, Zhang H, Song S-T, Zhou Y-Z, Zhao J, et al. Freestanding Ultrathin Metallic Nanosheets: Materials, Synthesis, and Applications. Advanced Materials. 2015;27(36):5396-402.
3. Zhao R, Lu X, Wang C. Electrospinning based all-nano composite materials: Recent achievements and perspectives. Composites Communications. 2018;10:140-50.

  doi:10.5075/epfl-298799_978-2-9701614-0-0

4. Gajanan K, Tijare SN. Applications of nanomaterials. Materials Today: Proceedings. 2018;5(1, Part 1):1093-6.
5. Biswas PK, Liyanage AAH, Jadhav M, Agarwal M, Dalir H. Higher strength carbon fiber lithium-ion polymer battery embedded multifunctional composites for structural applications. Polymer Composites.n/a(n/a).
6. Demir MM, Horzum N, Taşdemirci A, Turan K, Güden M. Mechanical Interlocking between Porous Electrospun Polystyrene Fibers and an Epoxy Matrix. ACS Applied Materials & Interfaces. 2014;6(24):21901-5.
7. Wable V, Biswas PK, Moheimani R, Aliahmad N, Omole P, Siegel AP, et al. Engineering the electrospinning of MWCNTs/epoxy nanofiber scaffolds to enhance physical and mechanical properties of CFRPs. Composites Science and Technology. 2021;213:108941.
8. Aliahmad N, Biswas PK, Wable V, Hernandez I, Siegel A, Dalir H, et al. Electrospun Thermosetting Carbon Nanotube–Epoxy Nanofibers. ACS Applied Polymer Materials. 2021;3(2):610-9.
9. Omer S, Forgách L, Zelkó R, Sebe I. Scale-up of Electrospinning: Market Overview of Products and Devices for Pharmaceutical and Biomedical Purposes. Pharmaceutics. 2021;13(2):286.
10. Liu Y, Zhang L, Sun X-F, Liu J, Fan J, Huang D-W. Multi-jet electrospinning via auxiliary electrode. Materials Letters. 2015;141:153-6.
11. SalehHudin HS, Mohamad EN, Mahadi WNL, Muhammad Afifi A. Multiple-jet electrospinning methods for nanofiber processing: A review. Materials and Manufacturing Processes. 2018;33(5):479-98.
12. Yang E, Shi J, Xue Y. Influence of electric field interference on double nozzles electrospinning. Journal of Applied Polymer Science. 2010;116(6):3688-92.
13. Ananda Habarakada Liyanage A, Kumar Biswas P, Siegel A, Agarwal M, Dalir H. Electrospinning optimization of carbon nanotube/epoxy submicron filaments: A numerical study. other. 2021 2021/09/06/.
14. Biswas PK, Aliahmad N, Dalir H, Agarwal M. Nanostructured V2O5-SWCNTs based lithium ion battery for multifunctional energy storage composites: materials synthesis and fabrication. AIAA Scitech 2021 Forum. AIAA SciTech Forum: American Institute of Aeronautics and Astronautics; 2021.
15. Biswas PK, Liyanage AAH, Jadhav M, Agarwal M, Dalir H. Higher strength carbon fiber lithium-ion polymer battery embedded multifunctional composites for structural applications. Polymer Composites. 2022;n/a(n/a).
16. Aliahmad N, Wable V, Biswas PK, Hernandez I, Dalir H, Agarwal M. Carbon nanotube/epoxy submicron filaments for composite reinforcement applications. AIAA Scitech 2021 Forum. AIAA SciTech Forum: American Institute of Aeronautics and Astronautics; 2021.

  doi:10.5075/epfl-298799_978-2-9701614-0-0

THERMO-MECHANICAL MODELLING OF UD COMPOSITES TO INVESTIGATE SELF-HEATING AND THERMAL SOFTENING EFFECT OF POLYMER MATRIX

P. Hao[a,b], R.D.B. Sevenois[a], W. Van Paepegem[a], F.A. Gilabert[a]

a: Mechanics of Materials and Structures (MMS), Department of Materials, Textiles and Chemical Engineering (MaTCh), Faculty of Engineering and Architecture (FEA), Ghent University (UGent), Technologiepark 46, 9052 Zwijnaarde, Belgium
b: SIM M3 Program, Technologiepark Zwijnaarde 48, 9052, Zwijnaarde, Belgium

Abstract: *The mechanical performance of Fibre-Reinforced Polymer Composites (FRPC) relies highly on the nonlinear thermomechanical behaviour of the polymer matrix with rate- and temperature-dependency. In particular, high strain rate loading can increase the temperature due to self-heating. In this work, a fully coupled thermomechanical FEM-based framework is developed. A constitutive material model is developed to accurately capture the polymer matrix response from isothermal to adiabatic conditions. The parameters were identified from the stress-strain curves for a thermoset epoxy and a semi-crystalline polymer PA6, respectively. Thermo-Mechanical Periodic Boundary Conditions (TMPBC) were used in micromechanical models based on Representative Volume Element (RVE). The present model makes it possible to investigate the evolution of local features as a function of the strain rate and temperature. The thermomechanical response of different UD-based FRPCs are compared in order to explore the limits of their mechanical performance and thus proposing improvements.*

Keywords: Fibre-reinforced polymer composite; Thermomechanical modelling; Representative Volume Element; Rate sensitivity; Self-heating

1. Introduction

The mechanical performance of Fibre-Reinforced Polymer Composites (FRPC) relies highly on the interaction and properties of the constituents: fibre, polymer matrix and interface. The nonlinear thermomechanical behaviour of the polymer matrix greatly affects the overall rate- and temperature-response of the composite [1-5]. Different polymers, namely thermoset and thermoplastic, can be used as matrix materials.

Unidirectional (UD) epoxy-based composites have been widely studied [1-4], comparing to thermoplastic-based composites. To study the transverse loading response of the UD epoxy-based composite, Chevalier et al. [2] compared the numerical results of the representative volume element (RVE) analysis with the microscale digital image correlation (μDIC) results of the local strain field. They believed that the discrepancy is due to the excessive strain localization observed through in-situ scanning electron microscope (SEM). Based on RVE, Garoz et al. [3] performed a systematic study using a new proposed periodic boundary conditions (PBC) for conformal and non-conformal meshes in the micromechanical model of a UD carbon fibre epoxy composite. Recently, owing to the strong demands on high-performance thermoplastic composites, different fibre reinforced thermoplastics draw the attention due to their recyclability and suitability of high volume production processes. Hsiao and Daniel [1] show a

  doi:10.5075/epfl-298799_978-2-9701614-0-0

significant rate sensitivity of two different UD composite systems (i.e., carbon/epoxy and carbon/PEEK laminates) under various loading conditions. Under transverse load, both systems showed a similar response in terms of rate-dependent strength and rate-independent failure strain, regardless of the ductility of the PEEK resin. From this evidence, the failure strength is believed to be affected by the viscoelasticity and by the time-dependent damage accumulation of the matrix. The rate- and temperature-dependency of UD composite based on polyamide-6 (PA6) resin was studied by Zhang et al. [5]. Using RVE with thermo-mechanical PBCs (TMPBC), different packing patterns, strain rate, self-heating and thermal softening effects have been investigated for a carbon fibre reinforced PA6 system [6].

In order to have a better understanding of different composite systems, advanced models to characterize different polymer matrices are needed. Polymers suffer from prominent self-heating and thermal softening at elevated strain rates [7-9]. The generated heat from the plastic dissipation in the polymer matrix does not have sufficient time to be diffused when the thermal condition becomes nearly adiabatic, what it causes thermal softening [7]. A fully coupled thermomechanical FEM-based framework is recently developed to capture the response of semi-crystalline polymers (SCP) [9]. Inspired by the yield kinetics in SCPs, a constitutive model was modularly developed to extend its applicability to a broad variety of thermosets or thermoplastics. This model greatly extends the formulation of the hardening evolution of the Boyce-Park-Argon (BPA) model [10], which was validated at different rates and temperatures. The parameter set can be straightforwardly identified from the true stress-strain curves.

This paper investigates the thermomechanical response of an RVE-based UD composite model when its matrix is either a thermoset or a thermoplastic. Section 2 presents the RVE model extended with TMPBCs. Section 3 describes the material model used in the RVE. Literature-obtained data for epoxy [10] and PA6 [11] resins are used as representative thermoset and thermoplastic, respectively. Section 4 shows the polymer model validation along with the numerical investigation on the global and local behaviours when both matrices are use in the UD composite model.

2. FEM-based thermomechanical modelling

This section introduces the RVE model and the corresponding TMPBCs for a transverse loading test. The overall self-heating and thermal softening effects of the composite are assumed to be dominated by the polymer matrix.

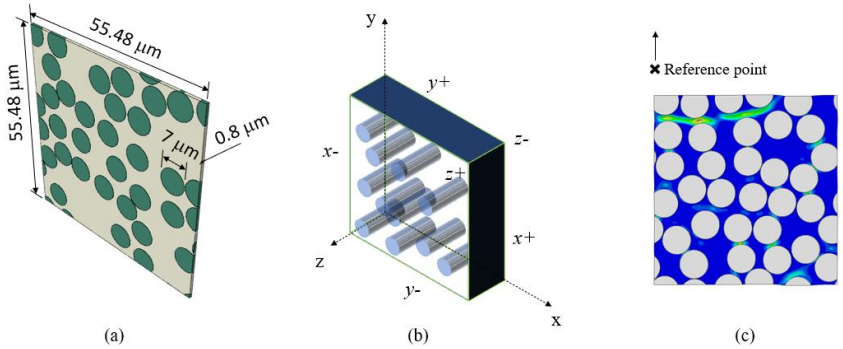

Figure 1. 3D RVE model of UD composites using thermomechanical PBCs: (a) model dimensions, (b) three pairs of opposite surfaces and (c) deformed profile of equivalent plastic strain.

2.1 RVE model of UD composite

Figure 1 shows the 3D RVE model with a fibre diameter 7 μm created with a random generator developed in [12]. The volume fraction was monitored to achieve 40% with 32 fibres embedded in an initially square-shaped RVE of 55.48 μm length and 0.8 μm thickness. Transverse load was applied and the PBC developed in [3] was enriched with temperature. This new TMPBC includes degrees of freedom (DOF) for temperature corresponding with nodes connected via the constraint given by

$$\theta_{\pi+} - \theta_{\pi-} = 0, \tag{1}$$

where $\pi = x, y, z$ represents the three paired surfaces, namely left-right, top-bottom and front-rear.

The fibre-matrix interface was modelled using a traction-separation cohesive zone model. However, to focus the study on the nonlinear response of different polymers and their self-heating-related effects, fibre-matrix perfect bonding was assumed. Thermal conductivity was assigned for the interface allowing the heat exchange from the matrix to the fibres. The interface conductance was assumed the same as the one used for the matrix. The overall response of the UD composite was obtained via homogenization techniques. The stress and strain were obtained using volume-averaged homogenized values, and the temperature was averaged from all the nodes.

2.2 Local strain, self-heating and thermal softening

In order to illustrate the correlation micro-to-macro response, Figure 2(a) shows a typical stress-strain response of a carbon fibre reinforced epoxy composite under transverse compression [2]. All the tested samples gave a rate-insensitive failure strain of 5%, whilst the strength seemed to remarkably depend on the applied rate. It is accepted that the rate-dependency in composites originates from the polymer viscoelasticity [1]. However, this case clearly shows the prominent strain localization taking place at a global strain of 5%. Figure 2(b) depicts a local region of a micro notched specimen using SEM [2]. The maximum local strain reached a value of 20%, which is sufficiently large to trigger self-heating in polymers.

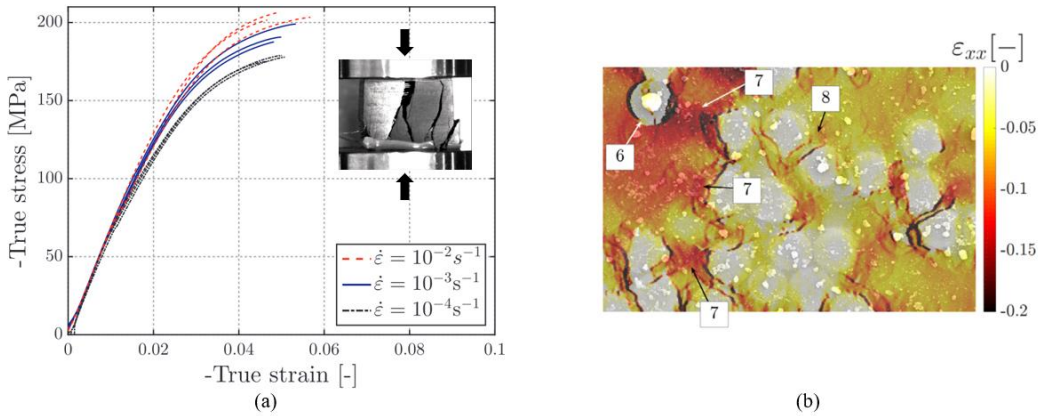

Figure 2. Experimental observation of UD carbon fibre-reinforced epoxy composite by Chevalier et al.[2]: (a) macroscale specimen under transverse compression and (b) μDIC results of a local region of the notched sample using SEM.

To investigate the effect of this localization on the global behaviour, a thermomechanical coupled analysis is needed. A predefined temperature field of 23 °C was applied to the entire RVE model. The heat generated from plastic deformation of the polymer matrix is assumed to be the only heat source. Two user-defined subroutines were used to consistently connect the mechanical and thermal responses. At every increment, the plastic dissipation is calculated and transferred to the thermal model. The new temperature field is updated by solving the heat balance equation. In the subsequent increment, if the thermal softening occurs, a degradation of the mechanical properties follows the predefined temperature-dependent relation [9].

3. Material models

3.1 Carbon fibre

The mechanical properties of carbon fibre are obtained from Ref. [2] assuming a linear elastic and transversely isotropic response. Under transverse loading, fibre failure is unlikely presented, therefore fibre damage and breakage are not incorporated in the present RVE model. Constant thermal properties along and perpendicular to the fibre are assumed [13].

3.2 Matrix: thermoset and thermoplastic

Polymers show a remarkable rate- and temperature-dependency. A classical BPA model has been used to characterize the epoxy by accurately capturing the pre-yield nonlinearity, post-yield strain softening and rubbery effect [10]. The model is developed within the finite strain kinematic framework. The rate of inelastic deformation is given by

$$\boldsymbol{D} = \dot{\bar{\varepsilon}}\boldsymbol{N}, \tag{2}$$

where $\boldsymbol{N}$ is the direction tensor and $\dot{\bar{\varepsilon}}$ is the effecitve plastic strain rate (more details can be consulted in Ref. [10]).

In this approach, two resistances, namely intermolecular and network resistances, are arranged in parallel for the epoxy Epon 862 resin [10]. However, to model the semi-crystalline PA6 tested in Ref. [11], a new extended BPA-based version is developed and used in this work. This model, termed as USCP relies in a unified formulation to describe the intermolecular resistance. This resistance accounts for the yield kinetics of amorphous and crystalline phases simultaneously, in which the saturated states of both phases (s_2 and s_3) are implemented in a new evolution law of the athermal strength denoted by *s* and given by

$$\dot{s} = H_1(\bar{\varepsilon})\left(1-\frac{s}{s_1}\right)\dot{\bar{\varepsilon}} + H_2(\bar{\varepsilon})\left(1-\frac{s}{s_2}\right)\dot{\bar{\varepsilon}} + H_3(\bar{\varepsilon})\left(1-\frac{s}{s_3}\right)\dot{\bar{\varepsilon}} \tag{3}$$

To activate the corresponding yielding occurring in each phase, a series of smooth Heaviside-like functions is formulated as follows

$$H_1(\bar{\varepsilon}) = -h_1\left\{\tanh\left(\frac{\bar{\varepsilon}-\bar{\varepsilon}_p}{f\bar{\varepsilon}_p}\right)-1\right\} \tag{4}$$

$$H_2(\bar{\varepsilon}) = h_2\left\{1-\tanh\left(\frac{\bar{\varepsilon}-\bar{\varepsilon}_p}{f\bar{\varepsilon}_p}\right)\tanh\left(\frac{\bar{\varepsilon}-\bar{\varepsilon}_c}{f\bar{\varepsilon}_c}\right)\right\} \tag{5}$$

$$H_3(\bar{\varepsilon}) = h_3\left\{1 + \tanh\left(\frac{\bar{\varepsilon}-\bar{\varepsilon}_c}{f\bar{\varepsilon}_c}\right)\right\} \quad (6)$$

Table 1 lists the required material parameters. The calibration procedure of epoxy follows the Ref. [9]. However, the PA6 calibration uses a two-step identification procedure. The first step is to identify the amorphous contribution by revisiting Ref. [9]. The second step determines the crystalline-related parameters (s_3, h_3 and $\bar{\varepsilon_c}$) by fitting the true stress-strain curve [14].

Table 1: Material parameters for the investigated epoxy [10] and PA6 [11].

Material parameter	Unit	Epoxy[1]	PA6[2]	Description
Mechanical				
E_{ref}	GPa	2.600	2.616	Modulus at reference temperature
θ_{ref}	K	298	296.15	Reference temperature
ν	-	0.4	0.39	Poisson's ratio
β	-	0.002	0.0036	Temperature dependency
α	-	0.05	0	Pressure sensitivity
$\dot{\varepsilon}_0$	s^{-1}	1.9E+5	3.55E+11	Reference strain rate
m	MPa	0.66	0.80	Exponential factor
A	K/MPa	155	104.0	Active energy
s_0	MPa	104	184.2	
s_1	MPa	135.2	195.6	
s_2	MPa	105	192.6	Heavy-side function
s_3	MPa	-	234.3	
h_1	MPa	7000	32,350.9	
h_2	MPa	350	14,827.2	
h_3	MPa	-	681.2	
$\bar{\varepsilon_p}$	-	0.054	0.00905	
$\bar{\varepsilon_c}$	-	-	0.0295	
f	-	0.3	0.30	
C^R	MPa	5.8	-	Rubbery modulus
N	-	1.44	-	Number of rigid links
Constants				
ρ	kg/m3	1250	1200	Density
k	W/m.K	0.192	0.25	Thermal conductivity
c_p	J/kg.K	1100	1700	Specific heat

[1] Source of material constants: https://www.solvay.com/en/product

[2] Source of material constants: Hao *et al.* [9]

4. Results

This section shows first the model validation for the thermoset and thermoplastic polymers. The parameters listed in Table 1 are used for a cylinder compression (epoxy) and a dog-bone tension (PA6) tests. Later, the rate-dependency of the micromechanical UD model using these two polymers is discussed. Finally, the correlation between the polymer rate-dependency and the thermomechanical global-local response generated by the UD model is analysed.

4.1 Polymers: thermoset and thermoplastic

Thermomechanical coupling analyses were performed to characterize the epoxy and PA6 resins. Because there is no failure criterion implemented, the simulations were terminated according to the minimum failure strain observed in experiments (i.e., 42% for epoxy and 32% for PA6). Figure 3 shows the validation at different strain rates and compares the thermomechanical

  doi:10.5075/epfl-298799_978-2-9701614-0-0

responses of epoxy and PA6. The simulation results conform well with the experimental ones. The self-heating and thermal softening effects are well captured, showing a downwards trend at an elevated strain rate compared to the results (grey) obtained in isothermal condition.

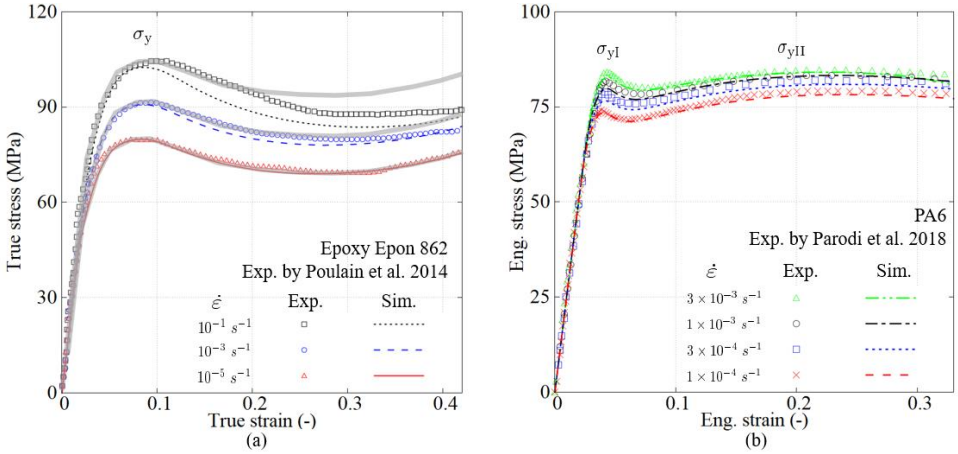

Figure 3. Model validation of (a) pure thermoset epoxy and (b) thermoplastic PA6.

The stress-strain responses of two types of polymers are very distinguishable. The epoxy shows an obvious rubbery effect beyond the low yield point at a strain 30%. For the PA6, two yield stresses can be found in the stress-strain curves, the first yield point is found at the strain of 7% and the second yield σ_{yII} takes place at the strain of 20%. Next, both resins are incorporated in the RVE model to investigate rate-sensitivity of composites.

4.2 UD RVE model: epoxy vs PA6

Figure 4 plots the homogenized stress-strain curves at two different strain rates: 0.0001/s and 0.01 /s. The epoxy- and PA6-based RVE model were used to illustrate the performance of thermoset and thermoplastic composites. Considering that the experimental results generally fail at a low strain level (see Refs. [1,2]), the simulations were terminated at a strain of 3%.

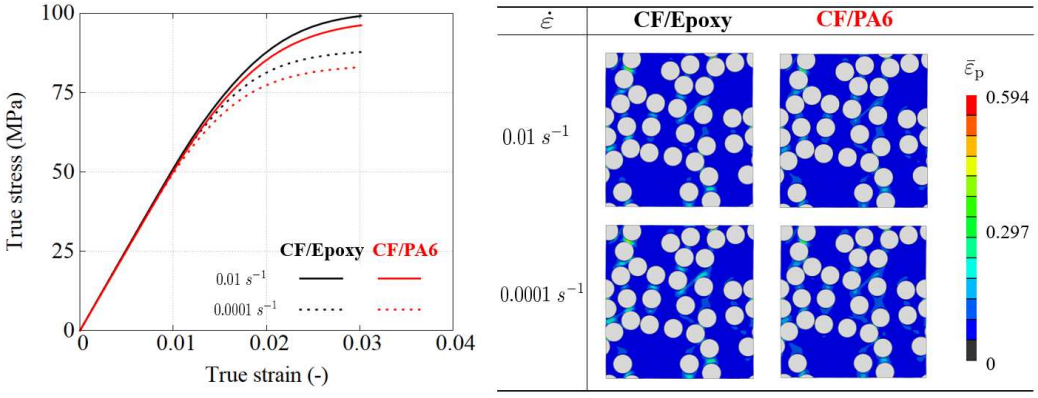

Figure 4. Left: Homogenized true stress-strain response of the UD RVE under transverse tension. Right: Equivalent plastic strain field at the strain of 0.03.

The stress-strain curves show linear elastic response in the strain range below 1%, which is in accordance with the experimental observation [2]. Within this range, both matrices are far from their yield point and the viscoelastic response of polymers is not seen at room temperature [10]. The rate-dependent strength is mainly due to the viscoplastic response of the matrix. Owing to

the homogenized method, local details of different responses of thermoset (rubbery effect) and thermoplastic (double yield) are hidden. Both UD composite systems presented in Figure 3 are substantially affected by loading rate.

4.3 Global versus local response: case of CF/Epoxy

Figure 5 shows a RVE model with a dense fibre packing pattern, leading to a volume fraction up to 60%. Transverse tension was imposed with a high strain rate of 100 /s. It shows that the RVE model experiences a mild increase of temperature from 23 °C to 24 °C. This homogenized temperature increases when the global strain is only 1 %, implying that local plastic deformation occurs, and the self-heating event initiates at this point. This localization can impact the global mechanical response and it is accelerated by the self-heating. Figure. 5 shows that the localization takes place in a rich resin band perpendicular to the loading direction. An excessive strain localization was found when the global strain reaches 2.7%, which corresponds to a local equivalent plastic strain of 67%. Under this situation, the local temperature increases drastically to 31.4 °C causing the main contribution to the increase of the homogenized temperature.

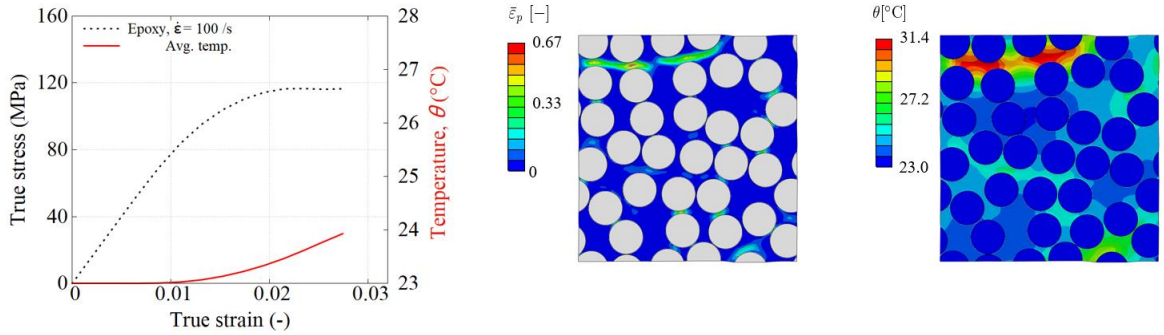

Figure 5. Comparison between the global and the local responses of Carbon/Epoxy with volume fraction 60% under transverse tension.

5. Conclusions

This work focuses on the thermomechanical response of UD composites under transverse loading, providing insight of the self-heating and thermal softening induced by different polymer matrices on the global response. The numerical results show the rate-dependent nonlinear response is attributed to the viscoplastic behaviour of the polymer matrix experiencing important strain localization. The comparison of thermoset- and thermoplastic-based composites shows that the locally observed rubbery effect of epoxy and the double yield phenomenon of PA6 are not detected in the homogenized stress-strain response. The model shows local large deformations taking place even when the composite material still lies within the small strains regime. This feature is caused by rich resin regions resulting from the specific fibre arrangement. The self-heating accelerates the degradation of the overall mechanical properties.

Acknowledgements

The work leading to this paper has been funded by the ICON project ‘‘ProPeL’’ (HBC.2019.0094), which fits in the MacroModelMat (M3) research program, coordinated by Siemens (Siemens Digital Industries Software, Belgium), and funded by SIM (Strategic Initiative Materials in Flanders) and VLAIO (Flemish government agency Flanders Innovation & Entrepreneurship).

R.D.B. Sevenois acknowledges the financial support of the Fonds Wetenschappelijk Onderzoek (FWO) fellowship 12R3221N.

6. References

1. Hsiao, H. M.; Daniel, I. M., Strain rate behavior of composite materials, Composites Part B: Engineering, 1998; 29:521-533.
2. Chevalier, J.; Camanho, P. P. ; Lani, F. ; Pardoen, T., Multi-scale characterization and modelling of the transverse compression response of unidirectional carbon fiber reinforced epoxy, Composite Structures, 2019; 209: 160-176.
3. Garoz, D.; Gilabert, F. A.; Sevenois, R. D. B.; Spronk, S. W. F.; Van Paepegem, W., Consistent application of periodic boundary conditions in implicit and explicit finite element simulations of damage in composites, Composites Part B: Engineering, 2019; 168:254-266.
4. Spronk, S. W. F.; Verboven, E.; Gilabert, F. A.; Sevenois, R. D. B.; Garoz, D.; Kersemans, M.; Van Paepegem, W., Stress-strain synchronization for high strain rate tests on brittle composites, Polymer Testing, 2018; 67:477–486.
5. Zhang, Y.; Sun, L.; Li, L.; Wei, J., Effects of strain rate and high temperature environment on the mechanical performance of carbon fiber reinforced thermoplastic composites fabricated by hot press molding, Composites Part A: Applied Science and Manufacturing, 2020; 134: 105905.
6. Sevenois, R.D.B.; Hao, P.; Van Paepegem W.; Gilabert, F. A., Numerical study on the effect of matrix self-heating on the thermo-visco-plastic response of continuous fiber reinforced polymers under transverse tensile loading (submitted), 2022.
7. Arruda, E. M.; Boyce, M. C.; Jayachandran, R., Effects of strain rate, temperature and thermomechanical coupling on the finite strain deformation of glassy polymers, Mechanics of Materials, 1995; 19:193-212.
8. Garcia-Gonzalez, D.; Zaera, R.; Arias, A., A hyperelastic-thermoviscoplastic constitutive model for semi-crystalline polymers: Application to PEEK under dynamic loading conditions, International Journal of Plasticity, 2017; 88:27-52.
9. Hao, P.; Laheri, V.; Dai, Z.; Gilabert, F. A.; A rate-dependent constitutive model predicting the double yield phenomenon, self-heating and thermal softening in semi-crystalline polymers, International Journal of Plasticity, 2022; 153:103233.
10. Poulain, X.; Benzerga, A. A.; Goldberg, R. K., Finite-strain elasto-viscoplastic behavior of an epoxy resin: Experiments and modeling in the glassy regime, International Journal of Plasticity, 2014; 62:138-161.
11. Parodi, E.; Peters, G.; Govaert, L., Structure–Properties Relations for Polyamide 6, Part 1: Influence of the Thermal History during Compression Moulding on Deformation and Failure Kinetics, Polymers, 2018; 10:710.
12. Gilabert, F.A.; Roux, J-N.; Castellanos, A., Computer simulation of model cohesive powders: Influence of assembling procedure and contact laws on low consolidation states, Physical Review E, 2007; 75.
13. Dong, K.; Liu, K.; Zhang, Q.; Gu, B.; Sun, B., Experimental and numerical analyses on the thermal conductive behaviors of carbon fiber/epoxy plain woven composites, Int. J. Heat Mass Transf., 2016; 102:501–517.
14. Hao, P.; Dai, Z.; Laheri, V.; Gilabert, F. A., A unified semi-crystalline polymer modelling approach capturing double yielding , self-heating and isothermal-to-adiabatic transition, Int. J. Eng. Sci., vol. UNDER REVIEW, 2022.

TOWARDS THE DEVELOPMENT OF LDPE MULTI-LAYERED PACKAGING FILMS WITH ENHANCED BIOACTIVITY

Iro Giotopoulou[a], Arxontoula Giannakopoulou[b], Haralambos Stamatis[b], N.-M. Barkoula[a]

a: Department of Materials Science and Eng., University of Ioannina, Greece – i.giotopoulou@uoi.gr
b: Department of Biological Applications and Technology, University of Ioannina, Greece

Abstract: *With the goal to develop flexible multilayered films with controlled bioactivity the current study incorporated compounds with high antimicrobial and antioxidant activity in low-density polyethylene (LDPE) films in the form of coating. To improve the wettability and enhance the adhesion between the functional coating and the substrate, the surface of LDPE was modified with corona, UV light and chemical etching. The influence of the type of bioactive compound, solvent, plasticizer used to prepare the film coating solution were evaluated. The results showed that the surface modification of LDPE introduced new functional groups which improved the wettability. The mechanical properties were affected by the modification process, while the film forming ability was strongly influenced by the solvent used. This in turn had a great impact on the antimicrobial response of the obtained films.*

Keywords: low density polyethylene; active packaging; bioactive compounds.

1. Introduction

In recent years there is an increasing demand of minimally processed foods that maintain freshness, quality, and safety. Active packaging aims to extend the shelf life and improve the quality and safety over time of food products. Since oxidation and microbial growth are the main factors contributing to the deterioration of the food quality, an attempt is made to use substances of natural origin with antimicrobial and antioxidant properties as alternatives to chemical preservatives [1]. A category of natural preservatives with known antimicrobial and antioxidant properties are secondary metabolites of plants like polyphenols [2]. Their antimicrobial activity is linked with the fact that plants themselves develop these substances as a defense against microorganisms [3]. Thymol and carvacrol are volatile phenolic monoterpenes extracted mainly from plants of the Lamiaceae family and falling into this category [4]. Another natural substance with antimicrobial and antioxidant action is olive leaves extract [5].

Since the direct contact of natural preservatives with food, is linked with their rapid diffusion, reduced effectiveness and side effects, efforts are made to incorporate these substances into food packaging [1]. In that way an active packaging is produced, which either interacts with the food or its environment to maintain food's quality [1]. The most common ways to prepare packaging materials with bioactivity are [6]: a) by using patches with bioactive compounds placed inside the package, b) via blending and/or grafting of the bioactive compound with the polymer before packaging formation, c) through coating of the packaging material with the bioactive compound, d) through encapsulation of the bioactive compound and its subsequent incorporation in the packaging [1]. The addition of the bioactive compound through blending is related with possible loss of the bioactivity during the thermo-mechanical processing of

  doi:10.5075/epfl-298799_978-2-9701614-0-0

packaging, while the use of coatings has been linked with direct release and limited availability of the bioactive compounds during the lifetime of the packaged products[7]. To overcome these issues, one of the recently proposed strategies suggests the development of multi-layered packaging with controlled bioactivity [7]. To this end, as part of an ongoing R&D project, our research team is working towards the development of low-density polyethylene (LDPE) multi-layered films with enhanced bioactivity. The research idea is to create food packaging films with a tri-layered structure, consisting of LDPE as an outer layer, LDPE with dispersed nanocarriers of bioactive compounds as an intermediate layer, and an inner layer that will consist of the bioactive compounds in the form of coating.

As a first step, the current work focuses on the preparation of the inner layer, which entails the effective coating of LDPE with selected bioactive compounds (carvacrol-, thymol-, and olive-based extracts). While LDPE is quite popular as food packaging material due to its good mechanical behavior, low cost, good resistance to wear, barrier properties, etc. [8], it hydrophobic and non-polar nature results in low surface energy with limited ability to adhere with polar molecules. For this reason, several techniques have been developed to modify the surface of different grades of polyethylene, including chemical etching, UV radiation, etc., [9]. In the present study, we have evaluated the effect of corona, UV treatment and chemical etching using sulfuric acid on the wettability and surface activity of LDPE films. Since all three bioactive compounds (i.e., carvacrol-, thymol-, and olive-based extracts) possess both hydroxyl and aromatic groups (polar and non-polar, respectively), different solvents have been employed for the preparation of the bioactive-based solutions/coating. The impact of surface treatment and/or type of solvent on the wettability, antimicrobial efficiency and mechanical performance of the LDPE coated films has been also assessed.

2. Materials and Methods

2.1 Materials

LDPE as well as corona treated LDPE films were kindly provided by Achaika Plastics S.A.. Thymol (T) (purity ≥99%), Carvacrol (C) (purity ≥ 98%) were purchased from Sigma Aldrich, Steinheim Germany. Tween 80 (T) was purchased from Sigma Aldrich, Oakville, ON, Canada. Glycerol (G) (analytical reagent grade of purity ≥99%) was purchased from Fisher Scientific, Loughborough, UK. Methanol (M) (ACS reagent Purity ≥99.8%), Ethanol (E) (Purity ≥99.8%) and Sulfuric acid (purity 95-97%) were purchased from Hooneywell Fluka, Seelze Germany. Olive leaves-based extracts (OE) have been developed by members of the research team following the methodology presented elsewhere [5]. In brief 3 g of OE is obtained after maceration of 30g of dry olive leaves in 250ml ddH_2O, boiling for 1hr and finally filtration and water removal through freeze-drying.

2.2 Methods

Surface treatment of LDPE substrate

Four different types of surface treated LDPE substrates were used in the current study, while unmodified LDPE films were used as reference. More specifically, apart from the unmodified films, LDPE was exposed to Corona, UV, and chemical treatment with sulfuric acid. As aforementioned, corona-treated LDPE films were provided by Achaika Plastics S.A. (undisclosed details). UV treatment was performed using an 18-W UV-A lamp for 1 h at room temperature. The distance between LDPE and UV light source was 1 cm. Chemical etching was obtained using

  doi:10.5075/epfl-298799_978-2-9701614-0-0

sulfuric acid on clean and dry unmodified LDPE films. Chemical etching was performed by immersing the films into a beaker with sulfuric acid for 1 h at two different temperatures (i.e., 25 and 50 °C). After chemical etching the samples were washed with distilled water and dried at 40°C for 20 min. The following designation has been employed for chemically etched LDPE films: SA_25 stands for films treated at 25 °C, while SA_50 for those treated at 50 °C.

Coating solutions – Coated films

Bioactive compounds 5% w/v were dissolved in two different solvents, i.e., methanol and ethanol, mixed with distilled water at 1:1 (v/v) water/solvent ratio. To improve the coating efficiency, glycerol or Tween 80 were added as plasticizers/emulsifiers in selected solutions at 6.7% v/v of the water/solvent content. To keep the ratio of bioactive compound per mass of LDPE substrate constant, certain amounts of the above solutions were placed on LDPE surface to achieve 5% w/w loading of the film. The samples were left to dry at room temperature overnight. Details around the designation of the prepared coating solutions can be found in Table 1.

Contact angle

Contact angle measurements were performed using an automated goniometer by Ossila Ltd (Sheffield, UK). A droplet of 10 µl of wetting liquid was released from a pipette on the surface of untreated LDPE as well as surface-modified LDPE films. To assess the wettability of the LDPE-based substrates two series of measurements were conducted, one using water and the other using the prepared coating solutions as wetting liquid. Three to five measurements were conducted for statistical reasons.

FTIR-ATR

Infrared spectra were collected using a Jasco FT/IR-4700 spectrometer (Pfungstadt, Germany) with external equipment for attenuated reflectance (ATR). One hundred sixty-four scans with resolution 2 cm^{-1} in the wave number range of 600-4000 cm^{-1} were performed. WinSpec software (LISE-Facultés Universitaires Notre-Dame de la Paix, Namur, Belgium) was used to process the obtain data. Measurements on empty cell were performed and subtracted from the FTIR spectra of the films.

Mechanical properties

The mechanical properties LDPE uncoated and coated films were assessed using a universal tensile testing machine, equipped with 2 kN load cell (Jinan Testing Equipment IE Corporation, Jinan, China). Three to five dog-bone specimens were stamped from the LDPE-films, with a cross-section area equal to 0.24 mm^2 and tensioned at a deformation speed of 25 mm/min at 25 °C. Force (N) and deformation (mm) where recorded during the test. Based on these data and the gauge dimensions, Young' s modulus (E), tensile strength (σ_{uts}) and % elongation at break (ε_b) were calculated.

Antimicrobial properties

Initially, 100 µL of bacterial population was inoculated from stock bacterial populations of Escherichia coli BL21DE3 strain, stored in glycerol, in 5 mL of fresh Lysogeny Broth (LB). After incubation at 37 °C, O/N under constant stirring at 180 rpm the pre-culture absorbance was measured at 600 nm and diluted with fresh LB so that the new culture reached an optical density (OD) of about 0.08 absorbance. The new culture was incubated at 37 °C, under stirring at 180 rpm, until the bacterial population present an O.D. of 0.2-0.5. The culture was then centrifuged

  doi:10.5075/epfl-298799_978-2-9701614-0-0

at 4,000 rpm for 5 minutes, the bacterial precipitate was restored and redissolved in saline (0.9% w/v NaCl). After three successive washes the bacterial pellet was redissolved in an equal volume of the culture. Bacterial population samples of 107 CFU/mL were prepared. Approximately 0.5 mg of each sample, was added into an Eppendorf tube containing 100 μL of the bacterial population and it was incubated for 12 hours in a cold chamber. 100μL of bacterial in the absence of sample were used as a control. Then, 25 μL of the bacterial population that interacted with the sample, were inoculated into 225 μL of fresh LB medium in an Elisa microplate well. The microplate was then placed in an incubator chamber at 37 °C and measurements of the O.D. at 600 nm were taken after eight hours.

3. Results

3.1 Characterization of LDPE substrates before – after treatment

As aforementioned, the non-polar nature of LDPE may hinder its coating ability and appropriate modification methods and/or solvents should be selected for the effective adherence of phenolic-based compounds on the proposed films. Figure 1 accesses the wettability of LDPE-based films as a function of surface treatment based on contact angle measurements with water droplets. As observed, untreated LDPE films present contact angles as high as 108°, which confirms their hydrophobic nature and poor wetting properties with water-based solutions/polar liquids [10]. On the other hand, the contact angle of all treated substrates is below 60°. The smallest angle appears in corona-treated LDPE, while chemical etching with sulfuric acid at 50 °C resulted in similar contact angles with those obtained after UV treatment. Furthermore, the increase in the temperature of chemical treatment positively affects LDPE wettability. The obtained results suggest that surface modification through corona, UV and chemical treatment introduce active sites on the LDPE surface that can greatly improve the interaction of LDPE with polar substances.

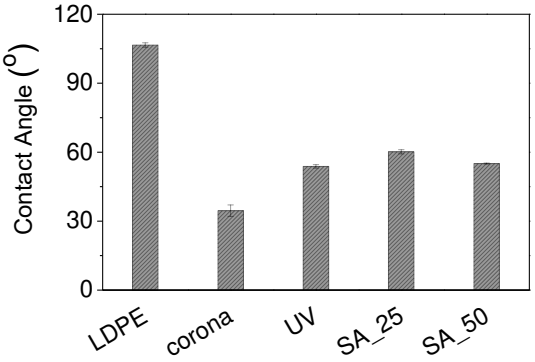

Figure 1. Contact angle of water on as received LDPE films as well as, corona -, UV- and sulfuric acid- treated LDPE at 25°C and 50°C.

To verify the existence of functional groups IR-ATR spectra of as received and treated LDPE films were collected and results are shown in Figure 2. New peaks at 1645 cm^{-1} and 3174 cm^{-1} are observed in Figure 2a for the corona and UV treated samples. These peaks can be attributed to the formation of C=N and N-H bonds respectively due to LDPE photo-oxidation [11]. New functional groups also appear on chemically etched LDPE as seen in Figure 2b. Specifically, new peaks appear at 896 $^{-1}$ and 1045cm^{-1}. This can be attributed on the formation of sulfoxide groups on LDPE surface during chemical modification with sulphuric acid [12]. Based on the above,

  doi:10.5075/epfl-298799_978-2-9701614-0-0 published under CC BY-NC 4.0 license

changes on LDPE wettability can be attributed to the introduction of new polar functional groups on the surface during photo-oxidation or during chemical etching.

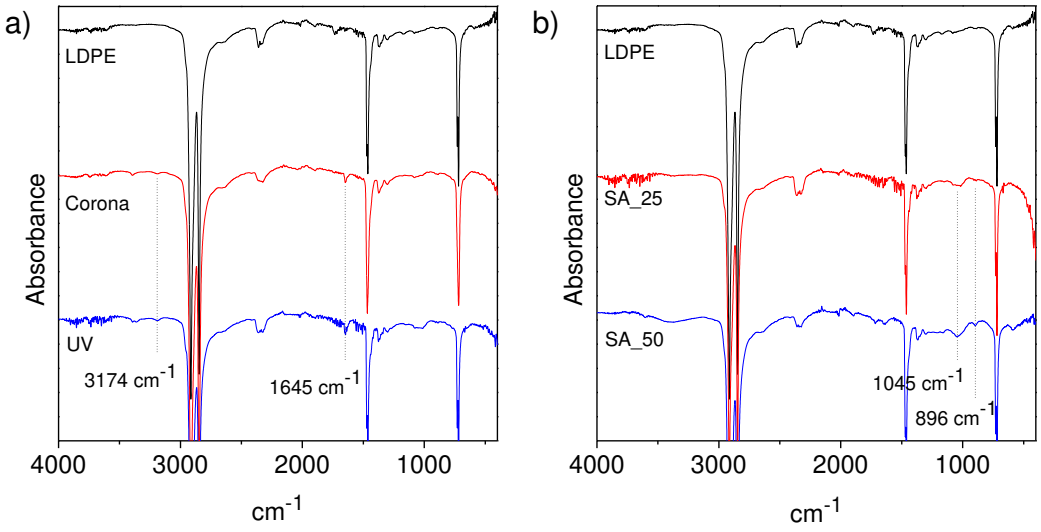

Figure 2. ATR-FTIR of (a) corona and UV treated LDPE and (b), chemically etched with sulfuric acid at 25°C (SA_25) and at 50°C (SA__50), as-received LDPE films are illustrated in both graphs for reference.

Since corona treatment is more effective to reduce the contact angle when water is applied as wetting liquid, further studies with bioactive-based solutions as wetting liquids were performed on as-received and corona-treated LDPE substrates. As illustrated in Figure 3, contact angle of all bioactive-based solutions are below 20 °, on both substrates which indicates that effective coating can be achieved on untreated LDPE. Solutions based on methanol as a solvent present higher contact angles compared to these with ethanol. The observation can be attributed to the higher polarity of methanol with respect to ethanol which limits methanol's interaction with the non-polar substrate.

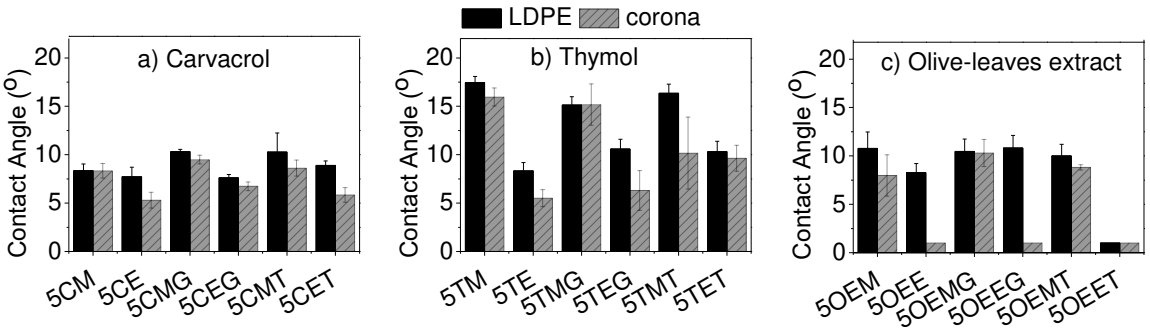

Figure 3. Contact angle of selected bioactive-based solutions on as-received and corona-treated LDPE films: a) carvacrol, b) thymol and c) olive-leaves extract -based solutions

3.2 Characterization of coated LDPE films

It is well accepted that the mechanical performance of packaging films is of paramount importance for their use in different applications. Thus, the effect of coating on the mechanical properties of LDPE films is illustrated in Table 1.

  doi:10.5075/epfl-298799_978-2-9701614-0-0

Table 1: Designation, content of coating solutions, mechanical (E, σ_{uts}, ε_b) and antimicrobial (OD at 600 nm) properties of LDPE films coated with bioactive-based solutions – properties of uncoated LDPE films are added for reference. Please note that coatings have been performed on as-received LDPE films. Control refers to bacterial growth without a sample.

Designation	coating solutions	E (MPa)	σ_{uts} (MPa)	ε_b (%)	OD at 600nm
LDPE	-	178±8	20±1	536±7	-
Control		-	-	-	0.5±0.0
CM	carvacrol/water/methanol	179±1	20±0	477±26	0.6±0.1
CMG	carvacrol/water/methanol/glycerol	255±9	22±1	611±16	0.4±0.0
CMT	carvacrol/water/methanol/tween	184±9	22±0	610±8	0.1±0.0
CE	carvacrol/water/ethanol	180±1	19±1	520±20	0.6±0.1
CEG	carvacrol/water/ethanol/glycerol	257±3	20±1	601±24	0.5±0.1
CET	carvacrol/water/ethanol/tween	178±13	21±1	602±15	0.1±0.0
TM	carvacrol/water/methanol	180±0	20±4	546±2	0.6±0.1
TMG	thymol/water/methanol/glycerol	257±6	22±1	617±14	0.4±0.0
TMT	thymol/water/methanol/tween	178±18	20±2	536±93	0.1±0.0
TE	thymol/water/ethanol	182±7	21±2	587±19	0.6±0.1
TEG	thymol/water/ethanol/glycerol	258±5	21±1	550±31	0.5±0.1
TET	thymol/water/ethanol/tween	182±7	21±1	587±19	0.1±0.0
OEM	OE/water/methanol	181±2	19±1	536±43	0.5±0.0
OEMG	OE/water/methanol/glycerol	264±2	18±4	445±97	0.5±0.0
OEMT	OE/water/methanol/tween	181±2	19±1	536±4	0.6±0.0
OEE	OE/water/ethanol	173±3	19±1	544±30	0.5±0.1
OEEG	OE /water/ethanol/glycerol	263±7	18±4	489±106	0.6±0.0
OEET	OE/water/ethanol/tween	173±3	19±1	544±30	0.6±0.0

As observed the stiffness of the LDPE films is not significantly affected by the application of solutions of bioactive compounds in water/alcohol and/or tween80. Similarly, small variations are observed in the tensile strength of respective films, while their elongation at break shows a small drop, which is more obvious for coatings containing methanol as solvent. Tween-based coatings tend to increase elongation at break while OE-based extracts as bioactive coatings tend to slightly deteriorate the elongation at break of the coated films. These variations can be explained based on optical observation of the coated films before testing, which revealed that

  doi:10.5075/epfl-298799_978-2-9701614-0-0

the surface of OE-coated films was not uniform, showing aggregation of droplets in some spots. Similar observations are made when methanol is used as solvent. On the contrary LDPE films coated with solutions of bioactive compounds with glycerol, present an increase in all mechanical properties, which is more pronounced in the case of the stiffness. These findings can be linked with the presence of glycerol, which acts as a plasticizer and promotes the uniform coating of the substrates. Furthermore, it is speculated that glycerol is beneficial in covering scratches and defects on the LDPE surfaces, and thus minimizing stress concentration points that could otherwise promote crack initiation and propagation. Tween, as emulsifier, contributes to the more uniform distribution of the coating solution on the LDPE surface.

The antimicrobial efficiency of the coated films can be deduced comparing the OD of the control sample with that of the coated LDPE films (see Table 1). As observed, coatings prepared with water/alcohol as solvent do not result in any inhibition capability against E. Coli, since OD values of the films is close or higher than that of the control sample. On the other hand, when glycerol is added in the solution, some inhibition is observed especially in Carvacrol/Thymol-based extracts. Interestingly, when Tween 80 is added as emulsifier, very low OD values (app. 0.1) are obtained indicating almost 100% inhibition for carvacrol, and thymol containing solutions. OE-based extracts do not show any significant effect on the antimicrobial behavior of the films. It is speculated that in case of solutions with water/alcohol as solvent, the bioactive compounds are evaporated during the drying process and very little amounts remain on the surface of the films. Glycerol and more importantly Tween interact with the bioactive compounds, which is maintained in partially “wet” state, contributing to the inhibition of E-Coli growth. In case of OE-based extract it is speculated, that since this extract is a mixture of phenolic and non-phenolic compounds, its inhibition efficiency is reduced and potentially higher wt.% loadings are required to obtain significant improvements in the antimicrobial response of the prepared films.

4. Conclusions

Based on the obtained results it can be concluded that although surface modification greatly improves the wetting properties of LDPE with water, this is not required since, polar solvents such as alcohol/water result in bioactive solutions with very small contact angles and good wetting properties of unmodified LDPE films. Coating of LDPE films does not result in deterioration of mechanical properties, while antimicrobial properties are greatly dependent on the coating solutions. Key to observe significant inhibition of bacteria growth is to obtain a coating that keeps the bioactive compound in a “semi-dry” state. This should be further elaborated since packaging industry requires films in a dry state.

Acknowledgements

This research was co-financed by the European Regional Development Fund of the European Union and Greek national funds through the Operational Program Competitiveness, Entrepreneurship and Innovation, under the call ‘Aquaculture’—‘Industrial Materials’—‘Open Innovation in Culture’ (project: AntiMicrOxiPac, project code: Т6УВП-00232). We would like to thank Achaika Plastics S.A. for providing the LDPE films.

5. References

  doi:10.5075/epfl-298799_978-2-9701614-0-0

1. Nogueira GF, de Oliveira RA, Velasco JI, Fakhouri FM. Methods of incorporating plant-derived bioactive compounds into films made with agro-based polymers for application as food packaging: A brief review. Vol. 12, Polymers. MDPI AG; 2020. p. 1–34.

2. Marchese A, Orhan IE, Daglia M, Barbieri R, di Lorenzo A, Nabavi SF, et al. Antibacterial and antifungal activities of thymol: A brief review of the literature. Vol. 210, Food Chemistry. Elsevier Ltd; 2016. p. 402–14.

3. Othman L, Sleiman A, Abdel-Massih RM. Antimicrobial activity of polyphenols and alkaloids in middle eastern plants. Vol. 10, Frontiers in Microbiology. Frontiers Media S.A.; 2019.

4. Krause ST, Liao P, Crocoll C, It Boachon B, F€ Orster C, Leidecker F, et al. The biosynthesis of thymol, carvacrol, and thymohydroquinone in Lamiaceae proceeds via cytochrome P450s and a short-chain dehydrogenase. Available from: https://doi.org/10.1073/pnas.2110092118

5. Chatzikonstantinou A v., Giannakopoulou A, Spyrou S, Simos Y v., Kontogianni VG, Peschos D, et al. Production of hydroxytyrosol rich extract from Olea europaea leaf with enhanced biological activity using immobilized enzyme reactors. Environmental Science and Pollution Research. 2021;

6. Fu Y, Dudley EG. Antimicrobial-coated films as food packaging: A review. Vol. 20, Comprehensive Reviews in Food Science and Food Safety. Blackwell Publishing Inc.; 2021. p. 3404–37.

7. Krepker M, Zhang C, Nitzan N, Prinz-Setter O, Massad-Ivanir N, Olah A, et al. Antimicrobial LDPE/EVOH layered films containing carvacrol fabricated by multiplication extrusion. Polymers (Basel). 2018 Aug 4;10(8).

8. Wattananawinrat K, Threepopnatkul P, Kulsetthanchalee C. Morphological and thermal properties of LDPE/EVA blended films and development of antimicrobial activity in food packaging film. In: Energy Procedia. Elsevier Ltd; 2014. p. 1–9.

9. Desai SM, Singh RP. Surface modification of polyethylene. Vol. 169, Advances in Polymer Science. 2004. p. 231–93.

10. Habib S, Lehocky M, Vesela D, Humpolíček P, Krupa I, Popelka A. Preparation of progressive antibacterial LDPE surface via active biomolecule deposition approach. Polymers (Basel). 2019 Oct 1;11(10).

11. Diaz E, Olivas-Armendariz I, Rodriguez C, Martel-Estrada S-A, Reyes Blas H. Polyestyrene and Low Density Polyethylene Oregano´s Essential Oil Functionalization for Possible Antimicrobial Active Packaging Applications. The Journal of Applied Packaging Research. 2018 Sep 25;10:70–82.

12. Wang H, Chen SJ, Zhang J. Surface treatment of LLDPE and LDPE blends by nitric acid, sulfuric acid, and chromic acid etching. Colloid and Polymer Science. 2009;287(5):541–8.

  doi:10.5075/epfl-298799_978-2-9701614-0-0

INVESTIGATION OF 3D PRINTED POLYMERS AND MOULDED COMPOSITES IN HOT CONCENTRATED ACID

Damilola Aje[a], Liu Yang[a]

a: Department of Mechanical and Aerospace Engineering, University of Strathclyde, 75 Montrose Street, Glasgow G1 1XJ, UK – damilola.aje@strath.ac.uk

Abstract: *This paper investigates the resistance of polymer composites after being soaked in a hot (85°C) concentrated (85%wt) phosphoric acid solution, it compares the rate of acid intake by different selected polymeric materials, and conduct an analysis on the impact of acid intake and elevated temperature on the baseline mechanical properties of the polymer composites. Four polymers and polymer composites were selected among the common high-performing polymers used in structural applications in this investigation, two of which were 3D printed pure polymers while the other two was an injection moulded polymer composite. Investigation proved that mechanical properties of the selected polymers was not significantly affected by the absorption of the hot acid. The strength and modulus remain unchanged, however, there is a significant drop in strength and modulus for the selected polymers when tested under elevated heat chamber of 95°C.*

Keywords: Polymers; Polymer Composites; Additive Manufacturing; Chemical-aging; Mechanical Properties.

1. Introduction

Polymers and polymer composites are gaining more acceptance in mechanical components industry due to the numerous advantages they possess over the traditional metallic materials. The rising cost of maintenance and repair of existing infrastructural systems is driving the push for a more reliable and cost-effective materials. Polymers are regarded to be a lightweight material and coupled with their high strength, are being regarded as the material needed to drive down the ever-rising cost of production and maintenance [1]. This polymer advantage is very vital, especially in the Aerospace industry where cost saving is desired without jeopardizing the structural integrity of the components [2]. Major companies are now switching into polymer technologies to benefits from its versatile cost saving advantage. Effort is ongoing within most industries in replacing metallic-based components with advanced polymer composites combining with additive manufacturing technology as a productive approach for the next generation of engineering components for mining applications [3].

Light-weighting is seen as the major source of industrial sustainability in the rotating machinery design because of its numerous advantages which includes; Positive effects on natural frequency, reduction in rotating weight and inertia, shaft and bearing down-sizing, and reduction in alloy material usage, coupled with less energy requirement in the casting of 3D printed components as against the traditional casting. Having observed the role of additive manufacturing in other industries such as in aerospace industry, 3D printing has now become a mainstream tool for producing composite parts quickly and efficiently without the usual waste as we have it in traditional manufacturing [3]. Apart from the common reasons of cost-

  doi:10.5075/epfl-298799_978-2-9701614-0-0 published under CC BY-NC 4.0 license

effectiveness, streamlined and efficient production processes and the time-saving nature of the technology as observed in other industries where this technology have been proven, there are other specific advantages these industries has identified to benefit from 3D polymer technologies. Some of these specific advantages includes better supply chain management, quick turn-around of replacement parts, and reduction in manufacturing lead time [3].

Despite the advancement of this non-metallic material, and the fact it is being currently used in engineering applications such as in pipes, pipelines, and tanks, long-term resistance against hot concentrated chemicals remain extremely challenging for most engineering polymers today. Design for this type of applications can be further complicated when the polymers will be used to process chemical fluids at elevated temperature. Understanding the structural behaviour of polymers and polymer composites in different working environments is a vital requirement needed to validate the integrity of polymeric materials in structural applications.

Many researchers have carried out several test on different high performing polymers and have reported polymers to have good corrosion resistance, high strength-to-weight ratio, adequate mechanical properties and have ease of handling. But, little or nothing has been said in the literatures on how hot concentrated acid can affect mechanical performance of the polymers after an extended period of time. M. Amini et all [4] conducted an experimental study of the effect of prolonged corrosive media on the glass fiber/polyester at different temperature levels of 25 oC, 50 oC and 70oC. The polymer specimen was completely submerged into hydrochloric acid solution (10%wt) for various time period. The results indicated that the bending strength, ultimate tensile strength, Young's modulus and hardness of the samples decreased when exposed to longer exposure duration and/or higher temperature.

Temperature is another factor that affect the selection of polymers for structural application as they are more sensitive to elevated temperatures. In general, load-supporting polymers are not suited for long-term use at a temperature higher than their glass transition temperatures (Tg). Glass transition temperature is the temperature at which a polymer turns from a rigid state into a flexible state. Tg of polymers varies and it is determined by the grades, the curing process, and the moisture content. significant performance drop can still occur to polymer composites at above Tg. In addition, creep will become more remarked at above Tg, although fiber reinforcement can mitigate the creep to large extent if the temperature is not too far above Tg [2].

Fluid-structure interaction of polymers and polymer composites was investigated as part of this project through laboratory experiment and testing under coupled thermo-chemical and thermo-mechanical environments. The objective of this work is to investigate the resistance of polymer composites to 85%wt concentrated phosphoric acid solution with elevated temperature at 85oC, compare the rate of acid intake by different polymeric materials, and conduct an analysis on the impact of acid intake and elevated temperature on the baseline mechanical properties of the polymer composites.

2. Experimental

2.1 Material

The detailed review of different polymer materials database was carried out to generate a list of material candidates. These include material software tool known as GRANTA, various material handbooks, and online data sources, as well consultations and discussions with polymer composites suppliers. A list of selected materials was however selected to be tested. Four different high-performing pure polymers and polymer composites were selected and presented in this report. They include.

1. Antero 800 NA – This is a PolyEtherKetoneKetone (PEKK) based thermoplastic with excellent mechanical properties and excellent resistant to most industrial chemicals. They are manufactured by Additive Manufacturing (AM) method known as Fused Deposited Modelling (FDM).

2. Ultem 1010 – This are high performing Polyetherimide (PEI) thermoplastic with high heat resistant and excellent mechanical properties. They are manufactured by Additive Manufacturing method known as FDM.

3. Ketron 30% CF – This is a PolyEtherEtherKetone (PEEK) based thermoplastic polymer. Manufactured by injection moulding methods, Ketron is a 30% carbon fiber reinforced grade with excellent stiffness and strength.

4. Victrex 30% CF – This is a high-performance thermoplastic material which is an Aerospace grade material. It contains 30% carbon fibre reinforced PolyEtherEtherKetone (PEEK) and can be manufactured by injection moulding and extrusion. It is regarded to have a much higher strength and modulus than Ketron.

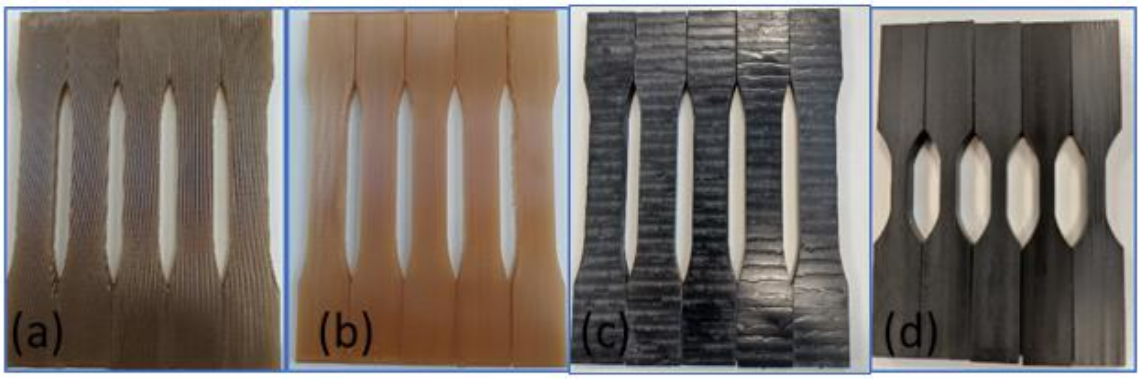

Figure 1 – Polymers under investigation (a) Antero 800NA (b) Ultem 1010 (c) Ketron 30%CF (d) Victrex 30%CF.

2.2 Sample Preparation

A Type 1 dog-bone tensile bar produced in accordance with standard dimensions as per ASTM D638-14 standard. Five different samples were tested for each set of experiment. Each of the test samples were taped at the tab section with PTFE tape to isolate the tab section from the acid solution. This was to ensure that the chemical acid does not affect the tab area for mechanical testing purposes. Sample dimensions (length, breath and thickness) was taken by Spi digital Calliper, and the weight was measured by desktop-based Mettler Toledo weighing machine. The test specimen was conditioned at standard laboratory atmosphere 23 ± 2°C and 50 ± 10 % relative humidity prior to the test in accordance with Procedure A of Practice D618.

  doi:10.5075/epfl-298799_978-2-9701614-0-0

The test was conducted in the standard laboratory atmosphere of 23 ± 2°C and 50 ± 10 % relative humidity.

2.3 Exposure Condition

The specimens were completely submerged into hot concentrated acid (85% wt.) for up to 2000hrs. Some sets of samples were monitored every 24hours to capture the time the fluid intake become saturated. Some others monitored at the end of every 168hours. The sealed container which contained the acid solution and samples was placed in the water bath with constant temperature of 85^{o}C.

2.4 Exposure Condition

Visual inspection of conditioned specimen was observed according to ASTM D638-14. Discolouration of the test medium, the formation of sediments of the samples and surface crack, softening of specimen were physically observed after chemical immersion. An initial discolouration will demonstrate extraction of soluble composites.

2.5 Tensile Testing

The tensile test was carried out on the baseline samples as well as on the chemical conditioned samples. Test was carried out using the 50kN Mechanical Tester (Instron Electromechanical 5969) electromechanical system with a maximum loading capacity of 50kN and equipped with fully integrated video extensometer for contactless measurements. Both Type 1 and Type V tensile testing bars was tested using the appropriate strain rate as per ASTM D638-14. Three samples were tested for each condition, and the average values are presented. See Figure 2b for a typical tensile test machine.

2.6 Microstructural Characterization

The surface topology of the samples was observed in a scanning electron microscope (Leitz Ergolux microscope) from Microscope Systems Limited, UK for detecting physical/surface change due to chemical exposure. The microscope was able to pick the solution absorptions on the surface of the specimens.

2.7 3D Printing Orientation

It is worth noting that, the behaviour of a 3D-printed polymer materials in chemical solutions is affected by the printing orientations adopted during the printing process. There are three printing orientations applicable in every additive manufactured product as shown in Figure 2a.

2.8 Thermo-chemical Testing

The four polymers were conditioned in a hot concentrated acid solution up to 2000 hours. The Weight changes were monitored daily and weekly, the weight percentage versus conditioning time are presented in the results section. Initial weight of the samples was taken prior to conditioning and the weight after were taken immediately the coupons were removed from the container jar and after they were rinsed and dried. Similar behaviour of absorption was observed for after rinsing/drying and before rinsing/drying as presented in Figure 4 and 5. The thickness and width change remain insignificant. No loss of substrate was observed for the four polymers and the colour of the acid solution did not change.

2.9 Thermo-mechanical Testing

Understanding the behaviour of polymer composites in extreme temperature environment was also considered in this work, this is to evaluate how tensile properties, such as strength and modulus have been affected by increased temperature. Tensile testing of the polymers at room temperature was carried out using the 50kN Mechanical Tester (Instron Electromechanical 5969) and the same tester with a heating chamber was used to perform the tensile test at 95°C. The variation in mechanical properties in response to the increased temperature was recorded. Figure 6 presents the graph which shows how strength of polymer materials was affected by elevated temperature.

3 Test Results

3.1 Chemical Solution Absorption Rate

Figure 3 presents the graph which represents rates of chemical intake by the four selected materials with all materials tested to at least 2000hrs of chemical conditioning. Acid intake for polymer composites is seen to be less than that in the pure polymers as observed in the absorption graphs. The increased fluid intake observed in the pure polymers is due to the presence of voids in the crystals of the pure polymers. Also, comparing the two pure polymers, it is seen that Antero (PEKK) behaved better in the acid solution, in terms of acid intake than, its PEI (Ultem 1010) counterparts. Moreover, for both pure polymers, it is observed that the OnEdge (XZ) printing orientation absorbs less fluid than the Upright (ZX) orientation. Hence, the acid intake is affected by the printing orientation.

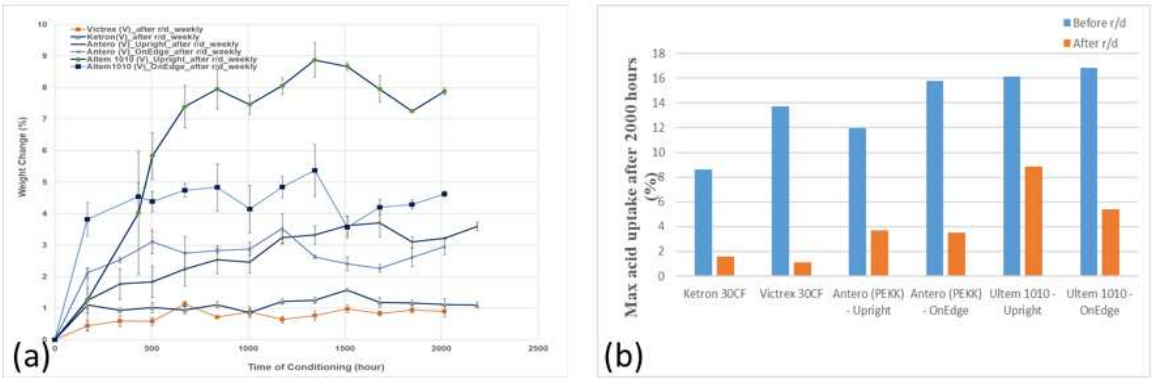

Figure 3 – Chemical Intake Graphs of selected polymers after 2000hrs conditioning (a) weight change versus conditioning time, (b) maximum acid intake before specimen rinsing/after specimen rinsing

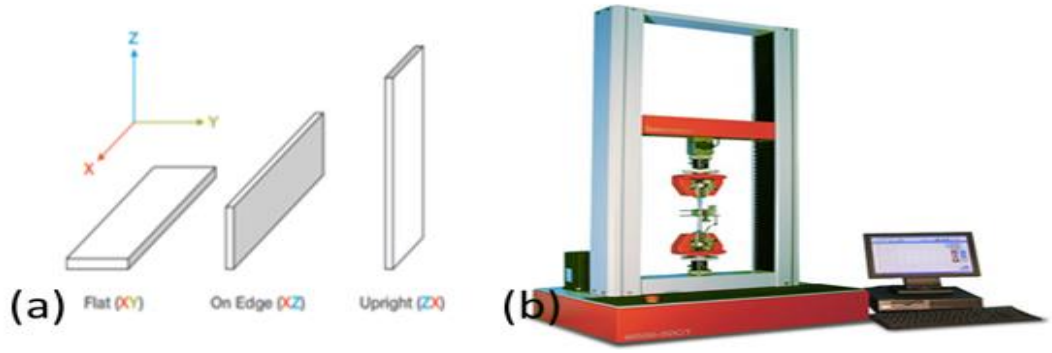

Figure 2 – (a) 3D Printing orientation, (b) Instron Mechanical Test Machine

3.2 Performance Retention Rate

Mechanical testing of the baseline materials and the chemical conditioned materials were done using the 50kN Instron tensile testing machine, (Instron Electromechanical 5969). Baseline data (strength and modulus) for all four selected materials was obtained from the tensile testing and were recorded. Conditioned samples of the four selected materials were also tested after reaching the targeted conditioned period of 2000 hours. The variation in strength and modulus for both the baseline and the conditioned samples were obtained and recorded. The data was used to determine the chemical effects on the selected materials in term of performance retention rate.

From figure 4a & 4b, it is seen that the tensile strength and young modulus of the selected materials does not significantly reduce after 2000 hours of chemical conditioning. Also, Young's modulus unchanged for selected materials after 2000 hours conditioning. There was about 20% increase in modulus for Ketron material after 2000 hours conditioning, further test of Ketron also confirm this increase. Further test was carried out on Ketron material to be sure that the unexpected increase in modulus was not due to measurement error. The ketron material was left in the chemical solution under constant elevated temperature of 85°C for 2000hrs without interruption. The results show similar trend with the previous measurements. Figure 4c presents the graph which includes the data for the interrupted Ketron measurement.

3.2 Tensile Testing with Heating Chamber

In addition to room temperature tensile testing of the polymers using the 50kN Mechanical Tester (Instron Electromechanical 5969), the same tester with a heating chamber was used to perform the tensile test at 95°C. The variation in mechanical properties in response to the increased temperature was recorded. Figure 4d presents the graph which shows how strength of polymer materials was affected by varying temperatures.

  doi:10.5075/epfl-298799_978-2-9701614-0-0

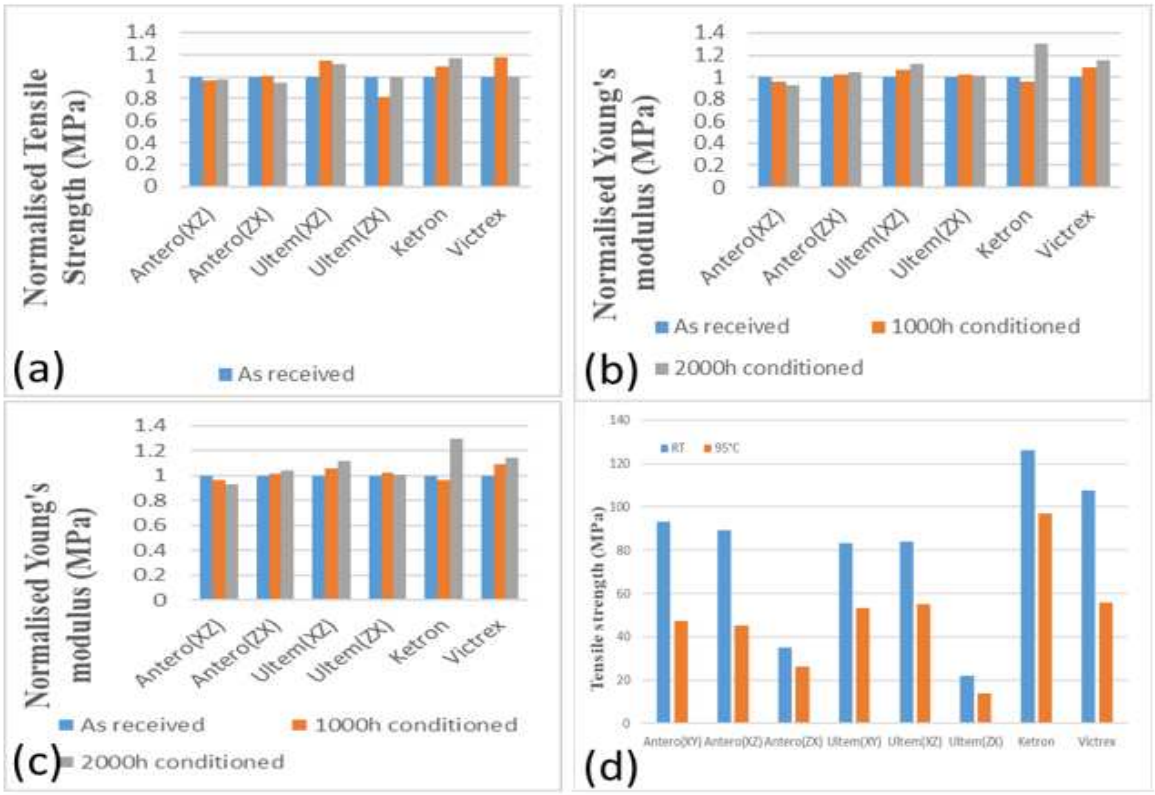

Figure 4 – Test Results after 2000hrs of chemical conditioning (a) Tensile strength, (b) Young Modulus, (c)Young modulus- uninterrupted measurement, (d)Tensile strength at room and elevated temperature.

4 Discussion of Test Results

The results presented in this paper clearly shows that, although, the phosphoric acid solution does not significantly reduce the mechanical properties of the polymers under investigation, they however, degrade significantly with increased temperature. Material stiffness and strength is very critical when deciding on the materials of construction in structural applications. Also, the effect of continual use of such materials in an operating environment must be put in consideration when making this important decision. The summary of the tensile results has proved that the, for the materials under investigation, the reduction in strength and modulus can be as high as 50% reduction when used in a condition with temperature up to 95°C. Hence, in designing a component with the polymers and polymer composites under review, under such elevated temperature, a lower value of strength and modulus should be used rather than the baseline strength and modulus data.

5 Further Work Required

This paper has been able to prove that the selected materials have excellent chemical resistance to 85% phosphoric acid at 85°C in static condition. Static condition is a state where there is no load application on the specimens. But, in the actual operating scenario, the material under investigation will be subjected to series of mechanical loads including dynamic loads. Further work is required to see how these materials will behave in the same concentrated solution but under operating load.

6. References

1. Saleh Alsayed, Yousef Al-Salloum, Tarek Almusallam, Sherif El-Gamal, Mohammed Aqel. Performance of glass fiber reinforced polymer bars under elevated temperatures. Department of Civil Engineering, King Saud University, P.O. Box 800, Riyadh 11421, Saudi Arabia.

2. T. W. Clyne and D. Hull. An Introduction to Composite Materials, Third Edition, Cambridge University Press, ISBN 978-0-521-8609-6.

3. Pakshaal S. Shah. 3D Printing Technology and its Impact on the Mining Industry, Article June 2015, BOROE Advantage Procurement.

4. M. Amini, A. Khavandi. Degradation of Polymer-based Composite in Corrosive Media. Experimental Attempt Towards Underlying Mechansm, faculty of Materials Science and Engineering, K.N. Toosi University of Technology, Tehran, Iran 2 School of Metallurgy and Materials Engineering, Iran University of Science and Technology (IUST), Narmak, 16844 Tehran, Iran. Mech Time-Depend Mater (2019) 23 :153–172 https://doi.org/10.1007/s11043-018-09408-7.

5. Vishwas Mahesh, Sharnappa Joladarashi, Satyabodh M. Kulkarni. A comprehensive review on material selection for polymer matrix composites subjected to impact load. Department of Mechanical Engineering. National Institute of Technology Karnataka Surathkal, Mangalore, 575025, India. Journal homepage: www.keaipublishing.com/en/journals/defence-technology.

6. Gurit, Guide to Composites. Delivering the future of composite solution, www.gurit.com.

7. NV Srinivasulu, V. Tejaswi. Mechanical Properties of Polymer Composite Materials. Department of Mechanical Engineering, Chaitanya Bharathi Institute of Technology, Hyderabad, AP, India, IJRET. International Journal of Research in Engineering and Technology, Volume 01, Issue 01, Sept-2012.

8. GRANTA Edupack 2020, an online engineering material database tool.

9. Kimiyoshi Naito, Hiroyuki Oguma, Chiemi Nagai. Temperature-dependent tensile properties of hybrid carbon/glass thermoplastic composite rods. Polymer Composites. 2020, 41 :3985–3995. wileyonlinelibrary.com/journal/pc. © 2020 Society of Plastics Engineers.

10.Rajan Gupta, Shraddha Shinde, Aswani Yella C, Subramaniam b, Sandip K. Saha c. Thermomechanical characterisations of PTFE, PEEK, PEKK as encapsulation materials for medium temperature solar applications. journal homepage: www.elsevier.com/locate/energy.

11. B. M. Primachenko and K. O. Strokin. Study of The Mechanical Properties of Polymer Composite Material with Different Structures. DOI 10.1007/s10692-019-09991-6 Fibre Chemistry, Vol. 50, No. 4, November, 2018 (Russian Original No. 4, July—August, 2018).

THE EFFECT OF RESORCINOL BIS(DIPHENYL PHOSPHATE) ON THE FLAMMABILITY AND FLEXIBILITY OF FLAME RETARDED EPOXY GELCOATS

Ákos Pomázi[a], Martin Krecz[a], Andrea Toldy[a]*

a: Department of Polymer Engineering, Budapest University of Technology and Economics, Budapest, Hungary – pomazia@pt.bme.hu; pomazi.akos@gpk.bme.hu

Abstract: *During liquid composite moulding technologies, solid flame retardant (FR) particles can be filtered by the reinforcing structure during the injection. This can be avoided by using liquid-only FRs (e.g. resorcinol bis(diphenyl phosphate), RDP) or applying FRs in a coating. Intumescent gelcoats offer excellent fire performance, but they often contain lots of fillers, making the gelcoat brittle and rigid, which leads to cracking and detaching. We prepared epoxy gelcoats containing ammonium polyphosphate (APP) and RDP to control the viscosity, hardness, and thus the flexibility of the gelcoats. We prepared samples with 10% overall P-content with different ratios of APP and RDP. Our goal was to determine which combinations resulted in a viscosity low enough for spraying without a diluent and proper fire performance. The most promising compositions were sprayed onto carbon fibre-reinforced epoxy composites, and their fire performance was investigated using mass loss type cone calorimetry (MLC).*

Keywords: flame retardancy; multifunctional gelcoat; carbon fibre reinforced composites; phosphorus-containing flame retardants

1. Introduction

Carbon fibre reinforced epoxy resin composites are mainly used in aircraft engineering as structural components to replace metal parts. The high flammability of epoxy resins implies the critical need to effectively flame retard them while maintaining their mechanical properties [1]. Previous halogen-containing systems are increasingly being replaced by halogen-free flame retardants such as phosphorus (P). In addition to providing adequate flame retardancy, these materials pose fewer environmental and health risks when used. Some composite manufacturing technologies, such as hand lamination or wet compression moulding, are not productive enough for the aerospace industry; the difficult reproducibility and time-consuming parts production make these methods not profitable. There are more productive manufacturing technologies, such as liquid composite moulding methods (RTM, VARTM). However, if these technologies are used to process resins containing solid FRs, the solid particles may become trapped in the reinforcing structure during injection and may be filtered [2,3]. Particle filtration can be avoided by not adding flame retardants to the matrix material of the composite or by using liquid-only flame retardants (such as resorcinol bis(diphenyl phosphate), RDP) and/or applying a flame retardant coating/gelcoat on the component's surface. Still, there may be other advantages: in an intumescent coating, foaming is not inhibited by the reinforcing structure, and the foaming itself does not cause delamination; the coating protects the component and does not significantly affect the mechanical properties [3]. Although excellent fire performance can be achieved with intumescent gelcoats, they often contain a high amount of fillers, making the gelcoat brittle and rigid. The flexibility of these flame retarded gelcoats is crucial during the application because if the gelcoat is damaged, it cannot fulfil its protective function.

  doi:10.5075/epfl-298799_978-2-9701614-0-0

In our previous research [4], we studied the possibilities of applying the FRs in a separate layer on carbon fibre reinforced composites, and we prepared gelcoats containing both APP (acting in the solid phase) and RDP (acting mainly in the gas phase) since we found that the combination of APP and RDP has synergistic effects on the fire performance. In this study, our goal was to determine the composition with a low-enough viscosity to be applied by spraying without a diluent and providing proper fire performance. We prepared gelcoat samples with 10% overall P-content in different ratios of APP and RDP and investigated the viscosity, the thermal behaviour and the fire performance of the gelcoat materials. The most promising compositions were applied on non-flame retarded (reference) and flame retarded, carbon fibre reinforced epoxy resin composites made by vacuum infusion. The fire performance of the coated composites was carried out by mass loss calorimetry tests (MLC).

2. Materials and methods

2.1 Materials

We used Sicomin SG715 BLANC epoxy gelcoat with Sicomin SD802 hardener as reference and basis for the FR gelcoat formulations. The gelcoat was supplied by Poly-Matrix Ltd, Budapest, Hungary.

As matrix resin system for the composites a tetrafunctional pentaerythritol-based epoxy resin (PER; IPOX MR3016; producer: IPOX Chemicals Ltd, Budapest, Hungary; main component: tetraglycidyl ether of pentaerythritol; viscosity at 25 °C: 0.9-1.2 Pas; density at 25 °C: 1.24 g/cm^3; epoxy equivalent: 156-170 g/eq) with a cycloaliphatic amine hardener (IPOX MH 3122; producer: IPOX Chemicals Ltd, Budapest, Hungary; main component: 3,3'-dimethyl-4,4'-diaminodicyclohexylmethane; viscosity at 25 °C: 80-120 mPas; density at 25 °C: 0.944 g/cm^3; amine hydrogen equivalent: 60 g/eq). The composite samples were prepared with unidirectional carbon fibre reinforcement (PX35FBUD030 consisting of Panex 35 50 k rovings, areal weight: 300 g/m^2; supplier: Zoltek Ltd, Nyergesújfalu, Hungary) in $[0]_5$ layup in each sample.

We used two phosphorus-based flame retardants: solid ammonium polyphosphate (APP; trade name: NORD-MIN JLS APP; producer: Nordmann Rassmann, Hamburg, Germany; P content: 31-32%; average particle size: 15 µm) and liquid resorcinol bis(diphenyl phosphate) (RDP; trade name: Fyrolflex RDP; producer: ICL Industrial Products, Beer Sheva, Israel; P content: 10,7%).

2.2 Methods

To investigate the viscosity, thermal behaviour and fire performance of the gelcoats, we prepared **gelcoat matrix samples**. Components were mixed according to the stoichiometric ratio recommended by the distributor (100:27). In the case of FR gelcoats, the FR additives were mixed into the epoxy component, and then the hardener was added. The prepared mixtures were poured into a silicone mould and cured for 24 h at room temperature. However, the hardener component was not added to the mixture for the viscosity measurement to avoid curing in the device. The prepared samples were the following:

  doi:10.5075/epfl-298799_978-2-9701614-0-0

- SG715_REF
- SG715_5P_APP_5P_RDP
- SG715_6P_APP_4P_RDP
- SG715_7P_APP_3P_RDP
- SG715_8P_APP_2P_RDP
- SG715_9P_APP_1P_RDP
- SG715_10P_APP

Sample names were built according to the following scheme: GELCOAT BASE_P-CONTENT IN MASS %_APP_P-CONTENT IN MASS %_RDP (e.g. SG715_6P_APP_4P_RDP means that the gelcoat base was the SG715/SD802 system, which contained 6% phosphorus from APP and 4% P from RDP).

For the coating process, **composite sheets** were **made by vacuum infusion** using a flexible vacuum bag. The reinforcement layers were stacked in $[0]_5$ layup. To promote and help the mould filling and the proper wetting of the reinforcement layers, we heated the resin mixture for 10-15 minutes at 60 °C to decrease its viscosity. We cured the samples for at least 24 h at room temperature under a vacuum before demoulding.

The coated composite sheets were prepared using a **spraying** gun (nozzle diameter: 2 mm) operating with compressed air (compressed air pressure: 2 bar). We repeated the spraying process until the proper thickness (approx. 500 µm) was achieved. The gelcoat thickness was continuously measured with a wet film thickness gauge.

The temperature dependence of the **viscosity of the gelcoats** was investigated by parallel plate rheometry using a TA Instruments AR2000 device (New Castle, DE, USA). We used a temperature range of 25-80 °C with a temperature ramp of 5 °C/min and a shear rate of 0.1 s^{-1}.

The **thermal behaviour of the gelcoats** was investigated by differential scanning calorimetry (DSC; TA Instruments Q2000 device, New Castle, DE, USA) and thermogravimetric analysis (TGA; TA Instruments Q500 device, New Castle, DE, USA) both in a nitrogen atmosphere. The **DSC** measurements allowed us to determine the effect of the changing APP:RDP ratio on the glass transition temperature (T_g) and the crosslinking characteristics of the gelcoats. We used a heat/cool/heat cycle in each case: first heating from 25 °C to 250 °C with a heating rate of 3 °C/min; cooling from 250 °C to 0 °C with a cooling rate of 10 °C/min; second heating from 0 °C to 250 °C with a heating rate of 10 °C/min. The crosslinking characteristics were determined from the first heating, while T_g was determined from the second heating. The effect of the APP:RDP ratio on the thermal stability of the gelcoats was investigated by **TGA**. The samples were heated in a temperature range of 25-800 °C with a heating rate of 20 °C/min.

We investigated the effect of the APP:RDP ratio on the **fire performance** of the gelcoat by standard limiting oxygen index (LOI) test, UL-94 flammability test and mass loss type cone calorimetry (MLC). The size of the samples used for the LOI test was 120 x 15 x 4 mm. We determined the **LOI** according to ASTM D2863: the oxygen index is the lowest volume fraction of oxygen in an oxygen-nitrogen gas mixture at which the sample burns for more than 3 minutes or burns for a 50 mm section on the specimen during the test. **UL-94 tests** were according to ASTM D3801 and ASTM D635 standards to determine the fire performance of the gelcoats in horizontal and vertical test setups. The dimensions of the samples were 120 mm x 15 mm x 4

  doi:10.5075/epfl-298799_978-2-9701614-0-0

mm. The UL-94 classifications in increasing order are HB, V-2, V-1 and V-0. The **MLC tests** were performed using an instrument from FTT Inc. (East Grinstead, UK), according to ISO 13927. In the case of the gelcoats and the coated composites, a constant heat flux of 25 and 50 kW/m^2 was used, respectively. Gelcoat samples were 100 x 100 x 2 mm, while the coated composites were 100 x 100 x 2.5 mm in size. We used spark ignition during the test. The heat release rate and mass loss were continuously tracked along the burning process.

3. Results and discussion

3.1 Viscosity of the gelcoats

Although we determined the temperature dependence of the dynamic viscosity of the gelcoats, it is essential to mention that these materials are usually used at room temperature. Therefore, only the viscosity values at 25 °C are shown in Figure 1.

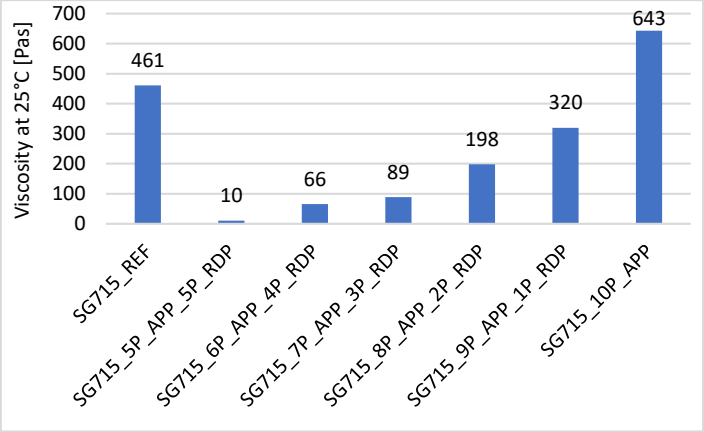

Figure 1. Dynamic viscosity of the gelcoats at 25 °C

The recommended application of SG715 gelcoat is brushing, as its viscosity is relatively high, and the solid APP dispersed in the resin further increases it, making the gelcoat unsuitable for spraying. However, the viscosity of the gelcoat can be adjusted by the addition of a diluting agent that evaporates during crosslinking, which makes spraying application possible. It is clear from the results that the dynamic viscosity of the gelcoats increases with the increasing APP ratio. On the other hand, the increasing ratio of RDP leads to a significant reduction of viscosity; therefore, the gelcoat becomes sprayable without diluent. In addition to viscosity reduction, RDP also eliminates the risk of forming solvent inclusions, as there is no need to dilute further the resin, which also results in a more compact gelcoat microstructure. Based on the results, we concluded that the gelcoats containing 6%P APP + 4%P RDP and 7%P APP + 3%P RDP could be suitable for spraying without diluting.

3.2 Thermal behaviour of the gelcoats

We performed DSC tests to determine the glass transition temperature and crosslinking enthalpy of the gelcoat samples. To better compare the results, we added the specific crosslinking enthalpy (h'_{spec}) to the list of results disregarding the amount of flame retardants since they reduce the crosslinkable material ratio of the resin (Table 1).

Table 1: DSC results of the gelcoats (T_{peak}: temperature of the exothermic peak; h': reaction enthalpy; T_g: glass transition temperature)

Gelcoat	T_{peak} [°C]	h' [J/g]	h'_{spec} [J/g epoxy]	T_g [°C]
SG715_REF	75	188	188	97
SG715_5P_APP_5P_RDP	80	51	135	89
SG715_6P_APP_4P_RDP	77	64	147	97
SG715_7P_APP_3P_RDP	75	83	167	90
SG715_8P_APP_2P_RDP	73	102	183	107
SG715_9P_APP_1P_RDP	72	141	228	119
SG715_10P_APP	74	174	255	120

The addition of flame retardants did not affect the exothermic peak temperature, as it ranged 72–80 °C for all samples. The increasing ratio of APP led to increasing T_g. This can be explained by the well-dispersed spherical APP particles in the gelcoat [5] and the reduction in the RPD ratio. Due to the plasticising effect of RDP, it can decrease the T_g; therefore, lowering the ratio of RDP leads to higher T_g. The addition of flame retardants resulted in lower crosslinking reaction enthalpy compared to the reference since the ratio of epoxy resin capable of crosslinking decreased.

We determined the temperature at 5% and 50% weight loss ($T_{-5\%}$; $T_{-50\%}$), the maximum mass loss rate (dTG_{max}) and its temperature (T_{dTGmax}) (Table 2).

Table 2: TGA results of the gelcoats

Gelcoat	$T_{-5\%}$ [°C]	$T_{-50\%}$ [°C]	dTG_{max} [%/°C]	T_{dTGmax} [°C]	Char yield at 800 °C [%]
SG715_REF	299	375	1.1	346	23.9
SG715_5P_APP_5P_RDP	233	345	0.7	301	31.8
SG715_6P_APP_4P_RDP	224	375	0.7	307	31.8
SG715_7P_APP_3P_RDP	229	388	0.7	310	36.8
SG715_8P_APP_2P_RDP	274	390	0.7	319	39.0
SG715_9P_APP_1P_RDP	243	399	0.6	309	39.1
SG715_10P_APP	300	475	0.9	329	43.2

  doi:10.5075/epfl-298799_978-2-9701614-0-0

The sample with 10%P APP started to decompose at the same temperature as the reference gelcoat; however, the samples containing both APP and RDP had 10-20% lower $T_{-5\%}$, indicating the different decomposition mechanisms of RDP and APP. The presence of RDP lowers the decomposition temperature, which is compensated by increasing APP content. The addition of flame retardants increased the $T_{-50\%}$ of all samples except the one with 5% P APP and 5% P RDP. The results clearly show that the applied FRs reduce decomposition rate, which can be an essential feature in a fire event, as the gelcoat burns more slowly, leaving more time for evacuation.

3.2 Fire performance of the gelcoats

We investigated the flammability properties of the gelcoat samples with limiting oxygen index and UL-94 tests. The results are summarised in Table 3.

Table 3: LOI and UL-94 classifications of the gelcoats

Gelcoat	LOI [V/V%]	UL-94 class.
SG715_REF	21	HB (23 mm/min)
SG715_5P_APP_5P_RDP	35	V-0
SG715_6P_APP_4P_RDP	40	V-0
SG715_7P_APP_3P_RDP	46	V-0
SG715_8P_APP_2P_RDP	50	V-0
SG715_9P_APP_1P_RDP	65	V-0
SG715_10P_APP	62	V-0

All FR samples achieved V-0 (self-extinguishing) classification in the UL-94 tests, which is promising, but not surprising given their 10% P-content. The limiting oxygen index results indicated that the optimal APP:RDP ratio is 9:1. The maximum LOI was reached by this composition, with a 30% increase from the gelcoat with an 8:2 FR ratio. The mixed FR formulations performed better than the gelcoat with 10% P APP, which can be explained by the combined solid and gas-phase effect of the flame retardants [5].

We analysed the fire performance of the gelcoat samples using mass loss calorimetry. Contrary to the composite samples, a heat flux of 25 kW/m^2 was used, as we expected high levels of foaming due to the high FR content. The heat release rates of the gelcoats are shown in Figure 2.

  doi:10.5075/epfl-298799_978-2-9701614-0-0

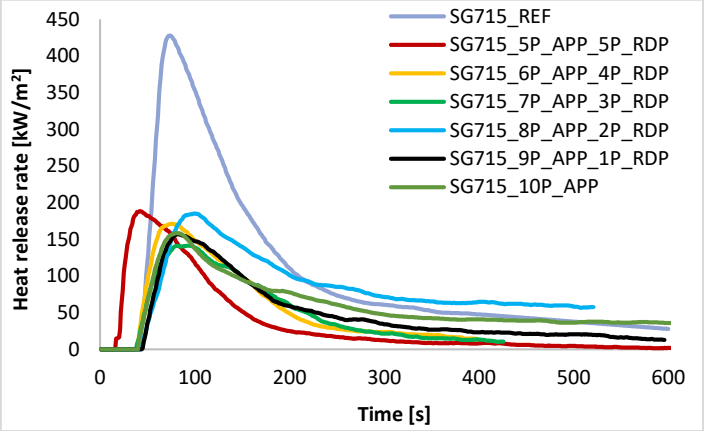

Figure 2. The heat release rate of the gelcoat matrices

During the experiment, the burning of the FR gelcoats was accompanied by intensive foaming and char forming. They also showed a significant reduction in the peak heat release rate and total heat release. While the reference sample had the highest pHRR (428 kW/m^2), the flame-retarded gelcoats only reached the 150–200 kW/m^2 range. Interestingly, the gelcoat with 7% P APP + 3% P RDP reached the lowest pHRR (141 kW/m^2), which is 67% lower compared to the reference. There is no significant difference between the TTI of the samples; the only exception is the sample with 5% P from both FRs, which ignited more than 20 s earlier than all other samples. The reduced TTI can be explained by the gas-phase mechanism of RDP. In addition, the increased amount of RDP significantly reduces the crosslinking density, which can also lead to lower decomposition temperature. Moreover, the FR gelcoats showed an increased time to pHRR and a more elongated, lower heat release. In terms of applicability and fire performance, the proper ratio of APP to RDP in the gelcoat matrix is either 6:4 or 7:3; therefore, in the next phase of our experimental work, we used these two gelcoat formulations to coat the composites.

3.3 Analysis of the coated composites

In the case of the coated composites, a heat flux of 50 kW/m^2 was used during MLC. The chosen composite samples (vacuum infused with 3% P RDP and a non-FR reference) were coated in 0.5 mm thickness with two different gelcoat matrices (6%P APP + 4%P RDP and 7%P APP + 3%P RDP) using a spray gun. The heat release rate of these coated composites is shown in Figure 3.

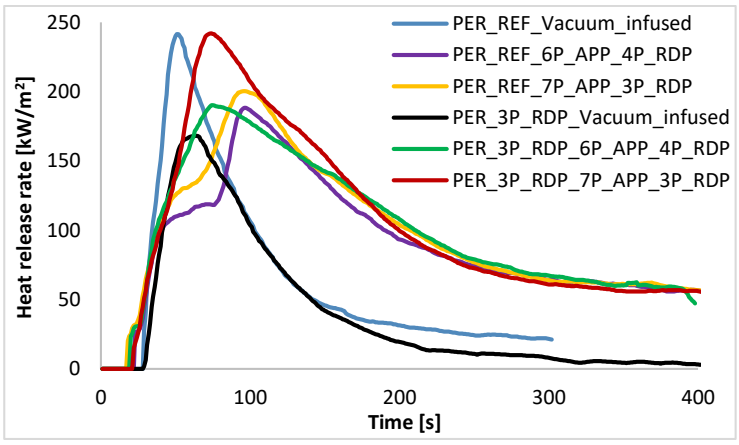

Figure 3. The heat release rate of the coated composites

The pHRR of the flame-retarded samples was in the range of 188–200 kW/m^2, and their THR was between 35 and 39 MJ/m^2. On average, the application of the FR gelcoats lowered the pHRR of the PER reference composite by 20%. As for the PER composite with 3% P RDP, the 6:4 gelcoat could lower the pHRR to the same extent as in the case of the coated reference, but the other gelcoat (7:3) reached as high pHRR as the PER reference composite without coating. In this case, the addition of a further flammable layer could not be compensated by the flame retardant content of the gelcoat. The lowest pHRR (188 kW/m^2) among the FR coated samples was reached by the PER_REF_6P_APP_4P_RDP. It achieved a pHRR reduction of 22% compared to the uncoated PER reference composite and a 6% reduction compared to PER_REF_7P_APP 3P_RDP. The MLC results indicated that the gas-phase effect of 3% P RDP in the gelcoat was insufficient to reduce pHRR effectively; therefore, 6:4 is the preferred flame retardant ratio in the gelcoat formulation. Overall, the fire performance of both reference and FR composites was improved by applying FR gelcoats; however, the effect of the gelcoats was more significant in the case of the reference composite. These results show that it is not necessary to incorporate RDP in the composite matrix of the coated composites. The application of flame-retardants in the coating alone is sufficient to protect the composite.

Acknowledgements

The research reported in this paper and carried out at BME has been supported by the NRDI Fund (TKP2020 NC, Grant No. BME-NCS) based on the charter of bolster issued by the NRDI Office under the auspices of the Ministry for Innovation and Technology. This work was also supported by the National Research, Development and Innovation Office (2018-1.3.1-VKE-2018-00011).

4. References

1. Toldy A, Szolnoki B, Marosi Gy. Flame retardancy of fibre-reinforced epoxy resin composites for aerospace applications. Polymer Degradation and Stability 2011; 96:371-376
2. Louis BM, Maldonado J, Klunker F, Ermanni P. Measurement of Nanoparticle Distribution in Composite Laminates Produced by Resin Transfer Molding. ECCM16 – 16th European Conference on Composite Materials, Seville, Spain 22-26 June 2014
3. Pomázi Á, Toldy A. Particle distribution of solid flame retardants in infusion moulded composites. Polymers 2017; 9:250
4. Pomázi Á, Toldy A. Development of fire retardant epoxy-based gelcoats for carbon fibre reinforced epoxy resin composites. Progress in Organic Coatings 2021; 151:106015
5. Pomázi Á, Toldy A, Szolnoki B. Flame retardancy of low-viscosity epoxy resins and their carbon fibre reinforced composites via a combined solid and gas phase mechanism. Polymers 2018; 10:1081

  doi:10.5075/epfl-298799_978-2-9701614-0-0

CARBON AND GLASS SMC HYBRIDS IN A SANDWICH ARRANGEMENT

Yvonne Aitomäki[a], Daniel Berglund[a]

a: Division Materials and Production , Department Polymer material and composites , Unit Composite Process simulation and Manufacturing, RISE (Research Institutes of Sweden), Sweden, yvonne.aitomaki@ri.se

Abstract: *Hybridisation of different fibres have been shown to increase the functionality of composites [1]. Tested in this study was the combination of carbon and glass SMC material, where a sandwich like material was created, using the stiffer carbon fibres as the skin material and the glass fibres as a core. Two types of glass fibre SMC where tested, one with a fibre volume content of 40wt% and the other with a 35wt%. They were combined with a carbon SMC with 47wt%. The glass fibre material to carbon fibre material was 50%- 50%. The composite was tested in tensile and bending loading conditions and under impact. The tensile and impact results showed, as expected, a hybrid who performance lies between that of carbon and glass, though there was a large variation in all tests. The bending results show that the hybrid composite with 50% glass was on a par with the pure carbon SMC (Modulus 24GPa, Strength 370MPa). The hybrid with glass 35% lay between carbon and glass in both modulus and strength. The bending condition was also simulated, and the result compared well to those found experimentally. The hybrid composite system was then tested in a more complex part with a hat profile and ribs and a bending test used to assess performance. The hybrid carbon-glass modulus and strength were close to or on a par with pure carbon SMC when the differences in weight were taken into account. This hybrid system makes use of the fact that recommendation for using carbon SMC is to have a net coverage between 50 to 70% and that the out of plane flow is small. The advantage is a considerable reduction in the cost of raw material, whilst the impact on performance and weight is marginal.*

Keywords: Sheet moulding compound; hybrid composites; fracture testing;

1. Introduction

The weight of electric vehicles (EVs) is a constant challenge, given that as much carrying capacity as possible needs to be given to batteries. Carbon fibre composites allow a step change in lightweighting however price is a major factor when introducing carbon fibre composites in the car industry. This requires both efficient manufacturing and reducing raw material costs. One way to address this is to use SMC to provide a rapid, press manufacturing method and to mix carbon SMC with glass SMC to reduce costs, whilst maintaining performance and lightweight. To this end, this study investigates the possibility of creating a SMC hybrid in the form of a sandwich. New carbon fibre SMC have a high fibre volume content and it is recommended that the charge cover is 70% of the tooling area. This minimises flow from one layer to another and means it should be possible that a sandwich like structure in the SMC materials is maintained through the manufacturing processing to the final structure. This type of hybrid composites has been studied earlier and have shown in many cases a positive hybridization effect [1] but most literature is on continuous fibres.

  doi:10.5075/epfl-298799_978-2-9701614-0-0

2. Method

2.1 Laminar plates

The materials used were a styrene free carbon SMC from Toray (XMT-000A-20) with a carbon fibre content of 47 wt.% (38 vol%) and two types of glass fibre SMC from Polynt one with a 35 wt.% (20 vol%) glass fibre content (HUP 25/35 RN-1090/43702) the other with a 50 wt.% (32 vol%) glass fibre content (HUP 25/50 RN-1090/43701). The tool had a shear edge allowing pressure to build up in the material and produced flat rectangular parts of 300x 400 x 3 mm. The SMC charge was place in the centre of the tool in different arrangements. Each stack had plies of carbon in the centre and plies of glass SMC as outer layers. The sizes of the stacks were as shown in Table 1 and two of each plate were manufactured.

Table 1: Description of manufactured plates

Description	%v of Carbon	%v of glass	charge size
LowFlow_LC1G50	30%	70%	18 x 30
LowFlow_HC1G50	**50%**	**50%**	**25 x 35**
HighFlow_LC1G50	30%	70%	32 x 8,3
LowFlow_LC1G35	30%	70%	18 x 30
LowFlow_HC1G35	**50%**	**50%**	**25 x 35**
HighFlow_LC1G35	30%	70%	32 x 8,3
LowFlow_G50	0%	100%	25 x 35
LowFlow_G35	0%	100%	25 x 35
LowFlow_C	100%	0%	28 x 40

The tool temperature was 150 °C and the stack was pressed at 2mm/min then held at a pressure of 100 bars for 5 mins to ensure a full cure. The final thicknesses of the parts were between 2.7 and 2.8 mm. The hybrid plates selected for testing were the LowFlow_HC1G50 & LowFlow_HC1G35 as well as the carbon only and glass only plates. These were tested in 3-point bending, tensile and impact. The specimens for 3-point bending were cut from both of the two plates manufactured, 10 specimens from each, 5 in a longitudinal direction and 5 in a transverse direction. For the tensile test, 10 specimens were taken from each material except for the hybrid with glass 35%, where only 2 specimens were taken. The tests were carried out in accordance with ASTM D3039/D3039M-08 on an Instron machine with a load cell of 100 kN and with mounted strain gauges. For the impact tests, the specimens used were as shown in Table 2.

Table 2: Description of specimens used in impact test

SMC composite	Impact E=1.8 J	Impact E=5.8 J	"Quasi-static" impact	Width x Length (mm)	Thickness/(CV) mm/(%)
Pure Glass 35%	1 spec	4 specs	1 spec	50 x 75	2.73 (3%)
Pure Glass 50%	1 spec	3 specs	1 spec	50 x 75	2.74 (2%)
Pure Carbon	1 spec	3 specs	1 spec	50 x 75	2.94 (5%)
Hybrid Carbon/G35 (LowFlow_HC1G50)	1 spec	3 specs	1 spec	50 x 75	2.80 (2%)
Hybrid Carbon/G50 (LowFlow_HC1G35)	1 spec	3 specs	1 spec	50 x 75	2.76 (3%)

For the impact test a Shimadzu 50 kN load cell with an Ø8mm impactor was used on a window size of 62.5x 37.5 mm. A target energy = 5.8 J was set, and a mass of 1.529 kg was dropped from a height of 0.39 m. The deflection was measured with a laser on the back face of the specimen and the impact energy evaluated from the speed and the mass of the impactor.

2.2 Complex form

The complex form used was a hat shape beam with ribs at 45 degrees across the centre of the beam as seen in Figure 1(a).

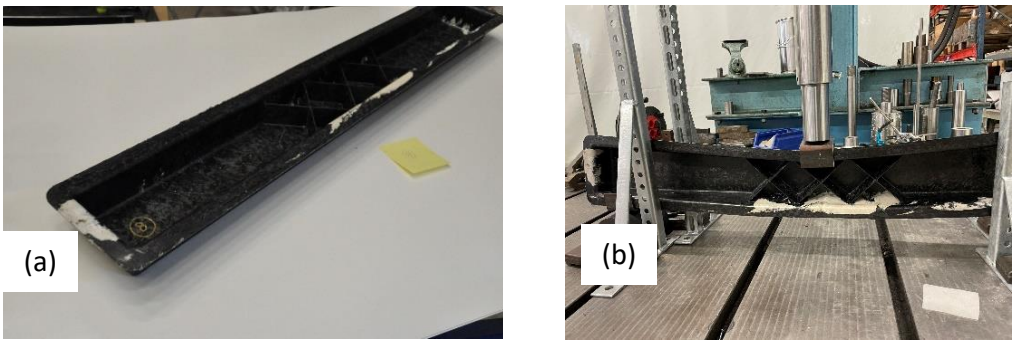

(a) (b)

Figure 1: (a) Hat shaped component with ribs (b) loading case

The design was used to represent a possible arrangement of a side vertical wall on a battery box and hence the load case is as shown in the Figure 1(b). The component was tested in bending (Figure 1(b)). The distance between the supports was 850mm and the test was carried out at a constant loading speed of 100mm/min.

3. Results

3.1 Plates

Where the arrangement had a lower carbon content or with a small charge, resulting in a high flow, the plates where much more uneven and a hybrid structure was not achieved. Testing

therefore focused on the plates where a hybrid structure was achieved. Figure 2 shows a typical hybrid plate and a cross sections of the samples for the low flow, high carbon plates (50% carbon-50% glass).

As can be seen, a sandwich structure was achieved in most but not all parts of all sections.

Figure 2: (a) One of the hybrid plates (b) side view of a stack of samples from the hybrid plate

Figure 3 show the results of the flexural test of the different specimens. They show that the hybrid materials in modulus and strain behave similarly to the carbon SMC material. In flexural strength, the hybrid with 35% glass is slightly lower than the carbon and hybrid with 50% glass but given the high variation the difference is not significant.

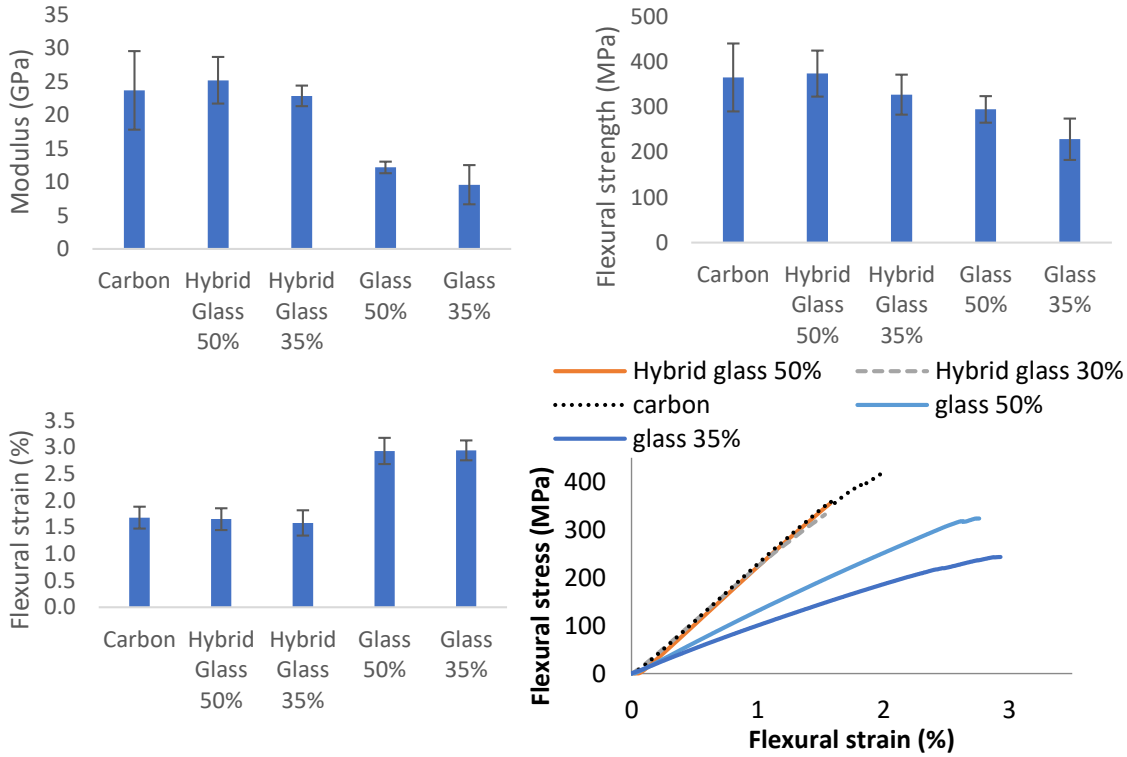

Figure 3: Results of the bending test

Figure 4 shows representative curves from the tensile test. The modulus changes at around 0.2% for all but the carbon SMC material hence the modulus before and after this point are given.

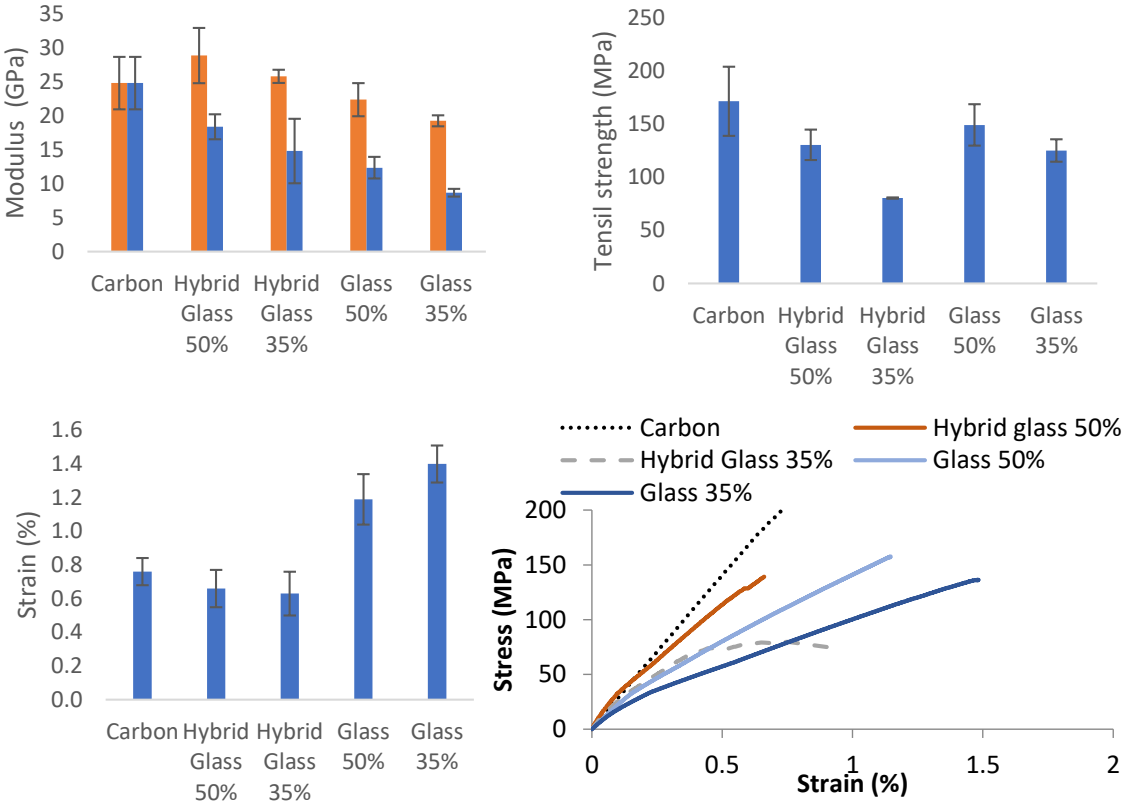

Figure 4: Results of the tensile test

The tensile modulus for the initial part of the curve shows a hybridisation effect where the glass 50% is on a par with the pure carbon. The second part of the modulus show a rule of mixtures like behaviour with the carbon having the highest values going down as the fibre volume and fibre type change to the 30% glass results. The tensile strength is not positive, with the strength of both hybrids being on a par or lower than the glass only composites.

The results of the impact tests followed a similar trend to that of the tensile tests with the carbon plates showing the least damage, followed by the hybrid glass with 50%, hybrid glass with 35% and then the glass 50% and glass 35%. The only material to show a significant difference between static and dynamic loading was the glass with 35% (Figure 5 (a)). It can also be seen that the hybrid glass with 50% absorbed as much energy as the carbon at maximum deflection as shown in Figure 5 (b).

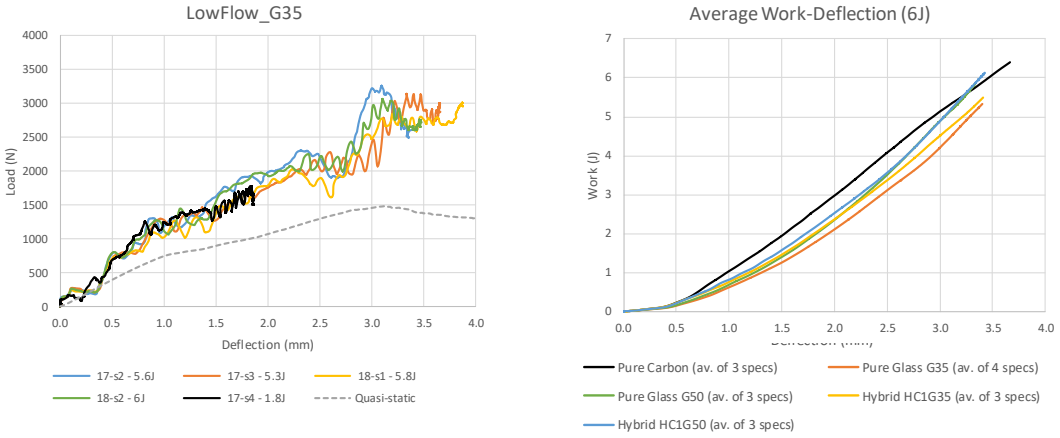

(a) (b)

Figure 5: (a) Comparison of the dynamic and quasi-static impact test for 35%glass plate. (b)average work-deflection in impact of the different materials

3.1 Complex form

For the complex form, the sandwich structure of the material was maintained in most of the structure as can be seen in Figure 1(a) with only small areas on the flanges where glass appears on the surface. The results bending test of the complex form are shown in Figure 6. There was some variation in the amount of material used due to differences in the shape of the preforms used and the weighs are included in the legend in Figure 6(a). However, it can be seen that the hybrid material performed well and on a par with the carbon SMC, when weight is taken into consideration (Figure 6(b).

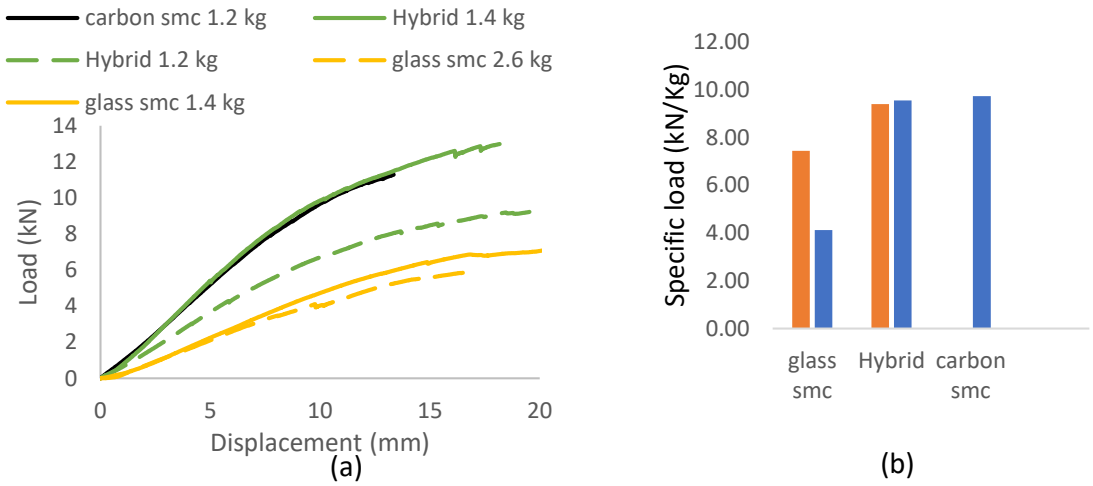

(a) (b)

Figure 6: (a) Load -displacement curve from the bending test of the hat profiles made with the different materials. (b) Specific max load of the different hat profiles in bending

4. Conclusion

The results show that a sandwich structure is maintained through the manufacturing process to the final part if a ratio of 50% glass SMC to 50% carbon SMC is used. This is maintained even in complex forms. However, with higher content of glass, the distribution becomes uneven.

The results in bending give the most positive hybrid effect. The impact and tensile test follow a more rule of mixture type behaviour. There does appear to be a lack of strength in tensile in the hybrid materials however in the complex form, where the structure is designed for bending, the hybrid effects are strong for flexural strength. The performance is maintained in these types of components. Thus, glass can be introduced without affecting the lightweighting advantages of using carbon SMC and cost savings can be achieved. This is a positive result to build on and the next move would be the introduction of recycled carbon in place of the glass to achieve a more sustainable composite with positive hybridisation effects.

Acknowledgements

Special thanks go to Thomas Bru and Alf Bäcklund at RISE for specimen testing. The work was funded in the MAKECAPLIGHTER project through Lighter – a strategic innovation program funded by Vinnova, Swedish Energy Agency and Formas.

5. References

1. Swolfs Y, Gorbatikh L, Verpoest I. Fibre hybridisation in polymer composites: A review. Composites Part A: Applied Science and Manufacturing. 2014 Dec 1;67:181-200.

INVESTIGATING THE EFFECT OF INTERFACE ANGLE AND PLY THICKNESS ON MODE II DELAMINATION BEHAVIOUR OF CARBON/EPOXY LAMINATED COMPOSITES

Sakineh. Fotouhi[a], Ali. Tabatabaeian[a], Saeid Lotfian[b], Amin. Farrokhabadi[c], Mohammad. Fotouhi[a]

a: University of Glasgow, sakineh.fotouhi@glasgow.ac.uk

b: University of Strathclyde

c: Tarbiat Modares University

Abstract: *The effect of angle and thickness of plies are investigated on the fracture energy release rate (ERR) in mode II of carbon/epoxy prepreg laminated composites using finite element modelling. The ply's angle of = 0º, 22.5º, 30º, 45º, 60º, and 90º with 4 different thicknesses are investigated. The finite element modelling is done using the virtual crack closure technique (VCCT) to evaluate the asymmetric effect. The overall stiffness of the laminates is designed to have the least difference from the Mode II standard ASTM test. The results show that by increasing the thickness of the plies, the asymmetric effect and consequently the mode I/Mode II loading contribution is increased. The results show that ERR is decreased by increasing both angle and thickness of the plies. This understanding can help in designing composite materials with better delamination resistant properties under different loadings such as low-velocity impact.*

Keywords: Laminated composites; finite element modelling; ERR; Ply thickness effect; Ply angle effect

1. Introduction

Low-speed impact, manufacturing defects and other factors will cause interlaminar delamination that reduces the load-carrying capacity of laminated composites. Delamination is due to weakness in through-the-thickness direction of these laminates (1). Delamination resistance in terms of ERR or fracture thoughness has been studied in different studies (2,3). Impact-induced delamination tends to be dominated by mode-II fracture (4). ASTM D7905 standard using end notch flexure (ENF) test is mostly used to calculate the mode II ERR (5). This standard is devoted to unidirectional laminated composites, being convenient with uniform crack growth and high contribution of mode II. Meanwhile, multidirectional laminates are mostly used in application and delamination occurs between plies of different angles (6). There are different studies on the mode II behaviour of multidirectional laminated composites. Chen et al. (7) investigated multidirectional carbon epoxy laminated composites with four kinds of ply angles (0°//−0°, 15°//−15°, 30°//−30°, and 45°//−45°) using the ENF test. They showed higher mode II ERR for variable angles of plies. Another ENF test on multidirectional carbon epoxy AS4/3501-6 laminated composites and 0// θ interfaces showed decreasing trend for energy release rate by increasing the off-axis angle (8). Marom et al. Showed a similar trend for mode II ERR for glass, carbon and kevlar laminated composites (9). Ozdil et al. (10) tested glass epoxy specimens with θ //- θ interfaces for delamination starter interfaces and showed three times ERR increasing for the angle variation from 0° to 45°. Pereira et al. (6) performed finite element and experimental analyses on glass epoxy ENF specimens with starter delamination on θ //- θ

  doi:10.5075/epfl-298799_978-2-9701614-0-0 published under CC BY-NC 4.0 license

and 0//θ interfaces. They reported increasing values for ERR mode II for both designed configurations by increasing θ.

Previous works show various issues and contradictory results for the mode II ERR of multidirectional laminated composites. Meanwhile, to the best knowledge of the authors, there is no comprehensive work on ply's angle and thickness effect on mode II ERR of laminated composites. In this study, the main objective is to study the angle and thickness effect simultaneously. Standard D7905/D7905M test is to calculate ERR mode II, GII, using ENF test (11)*. According to this standard, unidirectional zero-degree plies of polymeric composites should be used for manufacturing the specimens to study a pure mode II behavior. When the delamination starter interface consists of different plies' angles, ERR is affected by bending-twisting and membrane–bending couplings* (3,6) *which generates asymmetric behavior. By generating asymmetric behavior, mode I contributes to the total ERR increases. Hence, in this study, thicker specimens are chosen to reduce the asymmetry effect.*

2. Finite Element Modelling

Standard D7905/D7905M test is to calculate ERR mode II, G_{II}, using end-notched flexure (ENF) test (11)*. According to this standard, unidirectional zero-degree plies of polymeric composites should be used for manufacturing the specimens to study a pure mode II behavior. When delamination starter interface consists of different plies' angle, ERR is affected by bending-twisting and membrane–bending couplings* (3,6) *which generates asymmetric behavior. By generating asymmetric behavior, mode I contribution to the total ERR increases. Hence, in this study thicker specimens are chosen to reduce asymmetry effect.* The samples consist of 32 plies with an overall thickness of 4 mm. The stacking sequences of $[0_{16\text{-}n}/\theta_n//0_{16}]$ and ply's angle of θ = 0º, 22.5º, 30º, 45º, 60º, and 90º are chosen (see Figure 1). Where n indicates the non-zero layer' number being 1 to 4 and // indicates the location of the inserted crack.

Figure 1. Schematic of the designed specimens

Modelling was constructed by Abaqus software 3D 8-node brick elements. As it is shown in Figure 2 schematically, ENF specimens have been modelled with the length and width of 125 and 25 mm respectively. 30 mm crack length is considered from the supporting roller to the end of the crack and the span between the supporting rollers is 100 mm. A displacement of 4 mm was applied on the specimen and a general static solver was employed. Material property was defined for IM7/8552 carbon/epoxy pre-pregs according to Table 1.

Table 1. Material properties of IM7/8552

$E_{11} = 161\text{Gpa}$ $\mathrm{E}_{22} = \mathrm{E}_{33} = 11.4\text{Gpa}$
$\vartheta_{12} = 0.3$ $\vartheta_{12} = 0.436$
$G_{12} = G_{13} = 5.17GPa$ $G_{23} = 3.98GPa$

  doi:10.5075/epfl-298799_978-2-9701614-0-0

$$\rho = 1.6g/cm^3$$

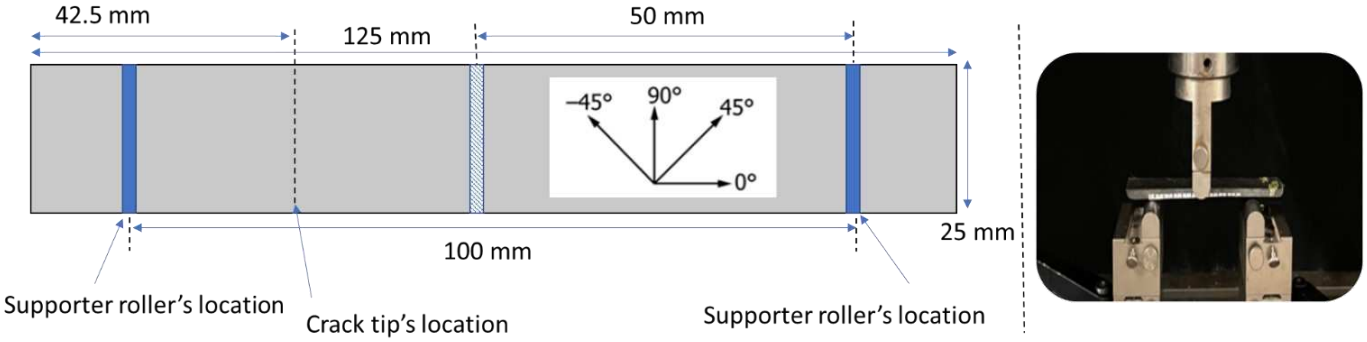

Figure 2. Schematic the ENF test and an experimental view of a ENF test.

Local basic single mesh was applied on the length of the specimens to reduce the element size around the crack tip to get accurate results (see Figure 3). Whole of the specimen was meshed with 8-node linear brick, reduced integration, and hourglass control (C3D8R).

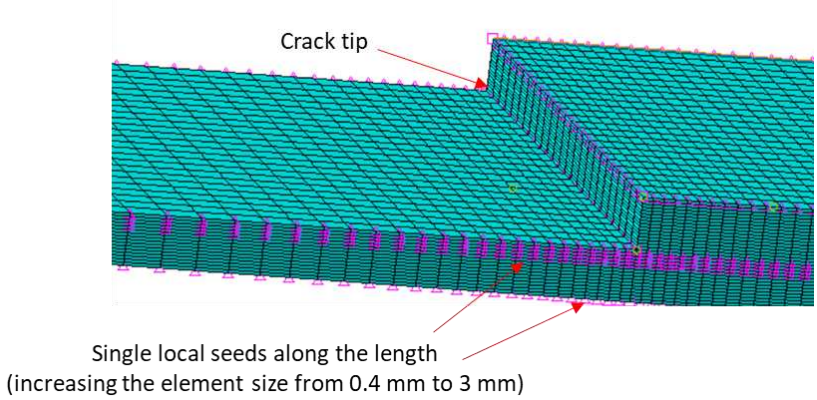

Figure 3. A zoomed area: smaller mesh sizes approaching the crack tip.

To calculate the ERR mode I, mode II, and mode III, i.e., G_I, G_{II}, and G_{III}, Virtual Crack Closure Technique (VCCT) was used. Normal behaviour with hard contact and tangential behaviour with a friction coefficient of 0.3 was defined for the interaction property between the rollers and the specimen. Small sliding and finite sliding were also employed for the cracked surfaces and the rest of the interactions respectively. The energy release rates are calculated using Eq. (1) to Eq. (3), the components of the equations are shown in Figure 4.

$$G_I = \frac{1}{2\Delta A} R_Y \Delta v \quad (1)$$

$$G_{II} = \frac{1}{2\Delta A} R_X \Delta u \quad (2)$$

$$G_I = \frac{1}{2\Delta A} R_Z \Delta w \quad (3)$$

  doi:10.5075/epfl-298799_978-2-9701614-0-0

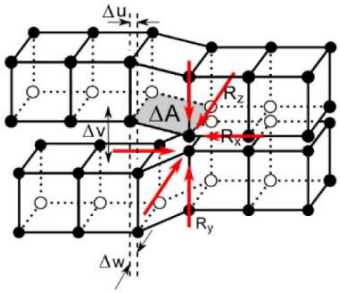

Figure 4. Crack geometry to calculate ERR using VCCT method (12).

3. Results and discussion

Load displacement graphs in Figure 5 show that changing angle and thickness of the plies affect the elastic response. By replacing the central plies' angle, elastic stiffness of the specimens is decreased, and this exceeds by increasing the plies' thickness as well. Table 2 show the maximum load achieved for each of the specimens and

Table 3 indicates how much the elastic response/maximum load varies by changing the angle and thickness of the plies. For the sample with lower angles i.e., 22.5° and 30°, this variation is up to 10% for all the thicknesses, while it is doubled for 90° specimens, reaching 16.20% for the specimen with four 90° plies.

Table 2. Maximum load of each of the specimens (extracted form Figure 5)

n / θ°	1	2	3	4
22.5	22.8744	22.314	22.3444	21.4417
30	22.717	22.0542	21.4312	20.9232
45	22.485	21.6495	20.9185	20.3314
60	22.3444	21.4463	20.6502	20.0332
90	22.2383	21.2739	20.4143	19.5966

*Units are in N and maximum load for the standard (all zero) ENF test is 23.39 N.

Table 3. Stiffness/maximum load difference in % vs the standard (all zero) ENF test's configuration for each of the specimens.

n / θ°	1	2	3	4
22.5	2.20	4.60	4.45	8.30
30	2.87	5.70	8.36	10.50
45	3.85	7.43	10.55	13.06
60	4.46	8.30	11.70	14.34
90	4.90	9.00	12.70	16.20

  doi:10.5075/epfl-298799_978-2-9701614-0-0

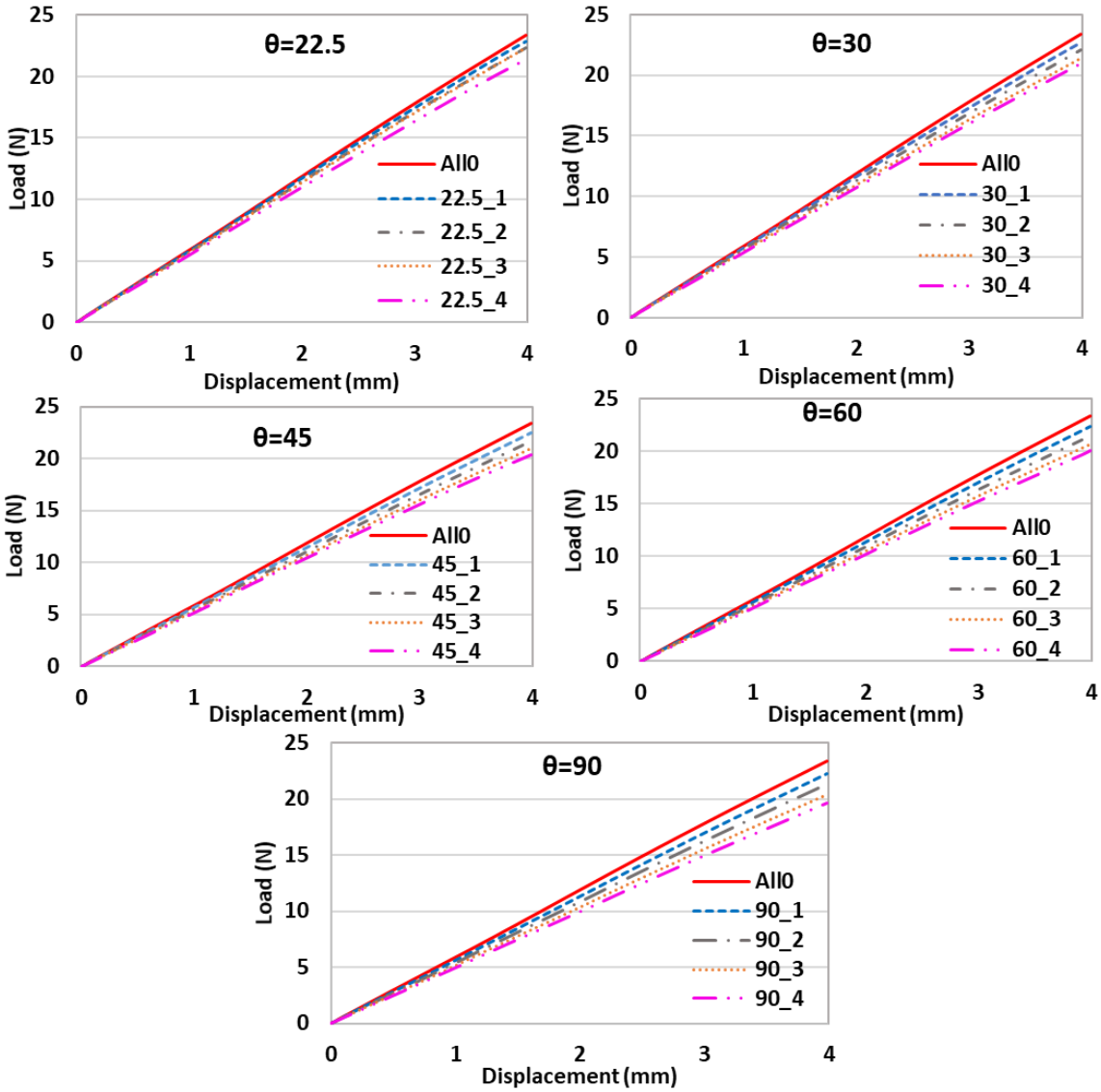

Figure 5. Load displacement graphs of the investigated specimens.

In addition to load and stiffness, energy release rate behavior is investigated. Mode III contribution is negligible for all the specimens. As an example, Figure 6 shows GIII distribution over total ERR (GIII+GII+GI) for the specimen with four 90° plies (90_4) as the extreme case in this study. GIII proportion is around 2.5 percent at the edges of the specimen which reaches rapidly to around zero at the central part of the crack tip. Distribution of GI/GII is shown in Figure 7. The figure shows GI proportion increases with increasing the ply angle and thickness for all the specimens. For the angles of 22.5° to 60°, except for the edges (due to edge effect), the average of this proportion is under 10% for all the ply's thicknesses, but for the 90_4 specimens, this proportion reaches to around 13%. These figures show the current study as a fair one to understand ply and thickness effect on GII behavior.

  doi:10.5075/epfl-298799_978-2-9701614-0-0

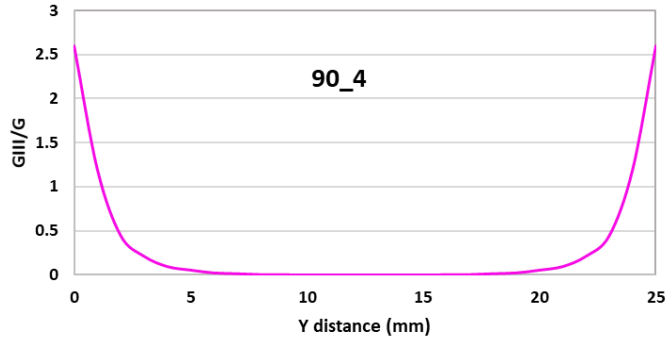

Figure 6. Mode III ratio (G_{III}=G) along the width of the specimen at the crack tip.

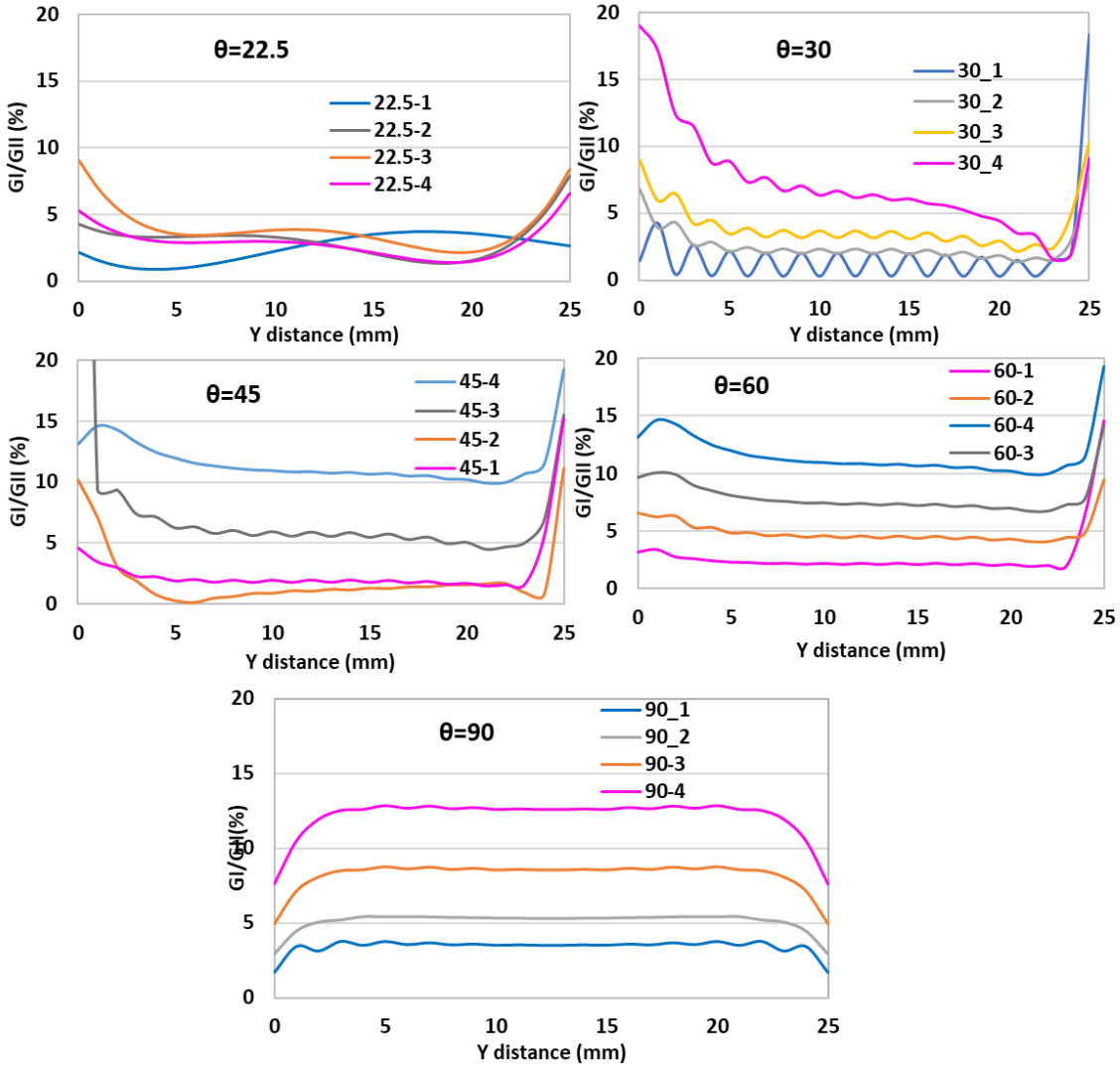

Figure 7. Mode I to mode II ratio (G_I=G_{II}) along the width of the specimens at the crack tip.

Distribution of GII/G at the crack tip is presented in Figure 8. There is usually an oscillatory distribution for the stress component of delamination between plies of different angle. This mostly depends on the crack closure increment (6,13). The GII/G graphs show that oscillatory behavior is more considerable for the lower angles i.e. 22.5° and 30° (see Figure 8). Hence, for the specimen with 22.5° plies, the graphs are smoothed for better demonstration. The average mode II proportion is above 90% of the total ERR except for specimen 90_4, showing a high

contribution of mode II. The higher the plies' degree, the smoother behavior is visible for the specimens.

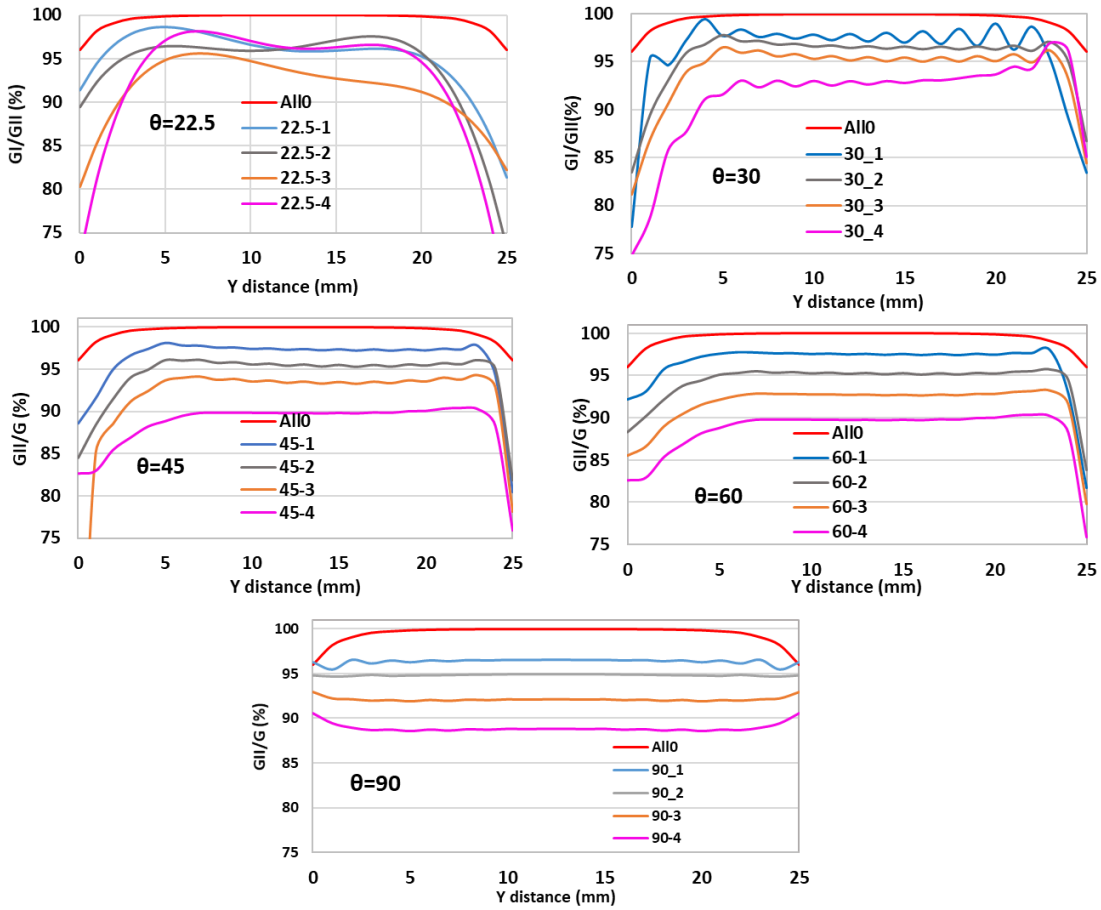

Figure 8. Mode II ratio (G_{II}=G) along the width of the specimens at the crack tip

It is noteworthy that, the specimens with 90-degree plies show different behavior for GII/G distribution. For all the plies' angles, there is a high value at the edges of the crack, but the 90° specimen have a converse behavior. At the crack edges, contribution of mode II is higher than the central part of the crack tip.

4. Conclusions

This study aimed to investigate the effect of interface angle and thickness of the adjacent plies on the delamination behaviour of ENF specimens using finite element method. ENF specimens with configuration of $[0_{16-n}/\theta_n//0_{16}]$ where θ = 0°, 22.5°, 30°, 45°, 60°, and 90°, and n=1, 2, 3, 4 were modelled based on ASTM standard test. Afterwards, VCCT technique was used to calculate ERR for modes I, II, and III. Mode III proportion was negligible and mode I proportion was roughly under 10% for the specimens apart from the specimen with n=4 and θ=90°. It is concluded that the ERR value of 0//0 interface were larger than those of the other interfaces. Furthermore, maximum load and stiffness of the specimens decreased by changing the plies' angle and increasing the thickness.

Acknowledgements

This work was funded under the UK Engineering and Physical Sciences Research Council (EPSRC) Grant EP/V009451/1 on Next generation of high-performance impact resistant composites with visibility of damage. The data necessary to support the conclusions are included in the paper.

5. References

1. Liu C, Gong Y, Gong Y, Li W, Liu Z, Hu N. Mode II fatigue delamination behaviour of composite multidirectional laminates and the stress ratio effect. Eng Fract Mech. 2022;264.

2. Chai H. Bond thickness effect in mixed-mode fracture and its significance to delamination resistance. Int J Solids Struct. 2021;219–220:63–80.

3. Davidson BD, Krüger R, König M. Effect of stacking sequence on energy release rate distributions in multidirectional DCB and ENF specimens. Eng Fract Mech. 1996;55(4):557–69.

4. Davies GAO, Zhang X. Impact damage prediction in carbon composite structures. Int J Impact Eng. 1995;16(1):149–70.

5. Li Z, Wang Z, Lu W, Zhou X, Suo T. Loading rate dependence of mode II fracture toughness in laminated composites reinforced by carbon nanotube films. Compos Sci Technol. 2021;215.

6. Pereira AB, De Morais AB. Mode II interlaminar fracture of glass/epoxy multidirectional laminates. Compos Part A Appl Sci Manuf. 2004;35(2):265–72.

7. Liu C, Bai R, Lei Z, Di J, Wu W, Zou J, et al. Mode II fracture toughness related to ply angle for composite delamination analysis. Mech Adv Mater Struct. 2021;28(23):2417–28.

8. Tao J, Sun CT. Influence of ply orientation on delamination in composite laminates. J Compos Mater. 1998;32(21):1933–47.

9. Marom G, Roman I, Harel H, Rosensft M, Kenig S, Moshonov A. The strain energy release rate of delamination in fabric-reinforced composites. Int J Adhes Adhes. 1988;8(2):73–4.

10. Ozdil F, Carlsson LA, Davies P. Beam analysis of angle-ply laminate end-notched flexure specimens. Compos Sci Technol. 1998;58(12):1929–38.

11. ASTM D7905. Standard test method for determination of the mode II interlaminar fracture toughness of unidirectional fiber-reinforced polymer matrix composites. Astm. 2014;1–18.

12. Gliszczynski A, Wiącek N. Experimental and numerical benchmark study of mode II interlaminar fracture toughness of unidirectional GFRP laminates under shear loading using the end-notched flexure (ENF) test. Compos Struct. 2021;258.

13. Chow WT, Atluri SN. Stress intensity factors as the fracture parameters for delamination crack growth in composite laminates. Comput Mech. 1998;21(1):1–10.

  doi:10.5075/epfl-298799_978-2-9701614-0-0

RANKING THE INFLUENCE OF KEY UNCERTAINTIES IN THE CURING OF THERMOSET LAMINATES

Adam, Fisher[a,b], Arthur, Levy[b], James, Kratz[a]

a: The Bristol Composites Institute, University of Bristol,
Laboratoire de Thermique et Energie de Nantes, université de Nantes
– adamajfisher@bristol.ac.uk
b: Laboratoire de Thermique et Energie de Nantes, Nantes université

Abstract: *The different characteristics of high and low thickness laminates means it is often optimal to process them under different conditions. Processing parts with tapered thicknesses can therefore be an issue as the entirety of the part must be processed in the same environment. To better understand how a processing environment can be optimised to minimise inhomogeneity across a tapered part, sensitivity analyses and Monte-Carlo simulations were performed. The sensitivity analyses showed how changes in key processing parameters affect the sensitivity of cure time to part thickness under different conditions. The results gave strong evidence to suggest that environments with a high heat transfer coefficient and a cure cycle designed for thick laminates were the most conducive to producing tapered parts with the greatest spatial uniformity. Results from the Monte-Carlo simulations showed the cure cycle recommended for thick Hexply M21 laminates was suited to most tapered parts but was highly conservative.*

Keywords: Thermoset; Curing; Modelling

1. Introduction

In many applications it is desirable for a composite part to be tapered, such as with an aircraft wing skin or wind turbine blade, in order to account for the decreasing lift generated towards the tips. Given the entirety of a part must be cured in the same environment, it is of great practical importance to know the characteristics of the curing environment that will result in the most desirable properties throughout the finished part. For example, to minimise the inhomogeneity in the degree of cure across the final part the aim will be to create a processing environment that minimises the cure time disparity between the thickest and thinnest sections of the part.

The curing process of thermoset parts is driven by temperature, as part thickness increases the reduced ability to dissipate exothermic heat causes greater transverse temperature inhomogeneities, leading to greater through thickness cure time variability. To mitigate this, it is common practice to use cure cycles with lower ramp rates and pre-dwells as parts become thicker. However, when a part is tapered the need for a gentler cure cycle will vary across the part, thus introducing a trade-off between part quality and processing efficiency. The question to be answered being, is it optimal to tailor the cure cycle for the thickest section thereby maximising quality throughout or does the optimal cycle lie somewhere between the two extremes? The answer depends on the desired outcome and the material being considered.

This study considers the processing of a tapered composite laminate made with Hexply M21, a high-performance epoxy system that is representative of the class of particle interleaf material systems. The desired outcome considered here was maximising manufacturing efficiency

  doi:10.5075/epfl-298799_978-2-9701614-0-0

through minimising cure time, while keeping the temperature overshoot below 10°C to avoid melting the thermoplastic particles. For superior fidelity, analysis considers uncertainty in material properties and processing conditions, therefore the aim is framed accordingly, achieving a cure time with minimum mean while avoiding temperature overshoots of 8°C (lower to account for thermocouple uncertainty) or more in 95% of cases.

The datasheet for Hexply M21 contains two cure cycle recommendations depending on the thickness of the part, the scenario is explored where the dimensions of a tapered part cover the thickness domains of the two cycles, and when each of the cure cycles should be used to achieve the desired outcome. In addition, a more general analysis is conducted to identify how different combinations of processing conditions affect the sensitivity of cure time to part thickness with the aim of establishing processing environments that are most conducive to minimising degree of cure variability in a tapered part.

Method

Finite Element Model

The curing process in the Hexply M21 carbon fibre laminates were modelled using a finite elements model that coupled transient heat transfer with cure kinetics. The assumption of negligible thickness change during each simulation was used to simplify the heat transfer analysis to a 1D problem [1].

The geometry of the 1D model is represented in Figure 1, it consisted of a homogenised M21/IMA carbon fibre reinforced epoxy laminate in ideal contact with a tool. Simulations were performed with tool thicknesses between 5 and 15mm, with properties representative of invar and a carbon fibre reinforced epoxy composite. Results were reported at the five equally spaced points across the laminate domain shown in Figure 1, this enabled the variations of cure time and temperature overshoot across the thickness to be computed.

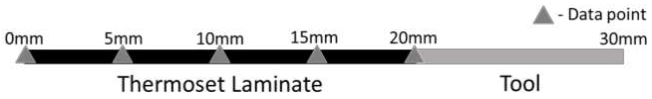

Figure 1. The geometry used in the finite element model (case of 20mm part thickness and 10mm tool thickness)

Cure Kinetics Model

The cure kinetics model for Hexply M21 that was used (Eq. (1)) was based on a variant of the Kamal and Sourour equation [2] and was successfully formulated and validated by Mesogitis et al [3].

$$\frac{d\alpha}{dt} = k_1(1-\alpha)^{n_1} + k_2\alpha^m(1-\alpha)^{n_2} \quad (1)$$

Where α is the degree of cure, n_1, n_2 and m are reaction orders, and k_1 and k_2 are reaction constants which are composed of a diffusion term in addition to a chemical term to capture the effect of diffusion rate limitation phenomena [3], both have Arrhenius temperature dependence. The diffusion term is defined as in Eq. (2).

(2)

  doi:10.5075/epfl-298799_978-2-9701614-0-0

$$k_D = A_D \exp\left(-\frac{E_D}{RT}\right) \exp\left(-\frac{b}{w(T - T_g) + g}\right)$$

Where A_D is the pre-exponential constant, E_D is the activation energy of the diffusion process, R is the universal gas constant, T is temperature, T_g is glass transition temperature and, b, w and g are constants. There is a chemical term for each reaction constant, they are defined in the same manner as Eq. (2) but without the second exponential. An initial degree of cure of 1% was assumed.

Heat Transfer Model

The heat equation used for the composite domain is shown in Eq. (3).

$$\rho C_p \frac{dT}{dt} = k \frac{d^2T}{dx^2} + h(T - T_\infty) + L \frac{d\alpha}{dt} \quad (3)$$

Where ρ is the effective density, C_p is the specific heat capacity, k is the transverse thermal conductivity. The values of these parameters for M21 were obtained in the material characterisation conducted by Mesogetis et al [3]. The second term on the right-hand side represents the convective boundary condition, h is the convective heat transfer coefficient and T_∞ is the cure cycle temperature at time t. The final term, containing volumetric latent heat L and degree of cure α represents the exothermic heat generated during the curing reaction and is responsible for the coupling between the heat transfer model and the cure kinetics model. Volumetric latent heat is defined in Eq. (4).

$$L = \rho_m(1 - v_f)H_T \quad (4)$$

Where ρ_m is the density of the matrix, v_f is the fibre volume fraction and H_T is the total heat reaction obtained through differential scanning colorimetry measurements [3]. Eq. (4) without the last term on the right-hand side was used for the tool domain. The solution of the model involved convective boundary conditions and an initial temperature of 293K through the thickness.

Sensitivity Analysis

Sensitivity analyses were used to identify the set of processing parameters that minimised the influence of part thickness on the cure time. Cure time was defined as the time required to reach a degree of cure of 90% across the thickness. For different sets of processing parameters, cure time was predicted with part thicknesses of 5mm and 25mm, in each case the sensitivity was calculated using these values.

The independent variables considered were convective heat transfer coefficient, tool thickness and tool material, each with two levels. The cure cycle was also varied, the two cure cycles specified in the Hexply M21 datasheet were used, one for laminates with thicknesses less than 15mm, the other for laminates with thicknesses between 15 and 48mm. The cure cycle for thinner laminates consisted of a 2°C per minute ramp to 180°C, followed by a 120-minute dwell at 180°C and finishing with a 5°C per minute cooldown. The cure cycle for thicker laminates consisted of a 1°C per minute ramp to 150°C, an initial 180-minute dwell at 150°C, a 1°C per minute ramp to 180°C, a 120-minute dwell at 180°C and a 5°C per minute cooldown.

  doi:10.5075/epfl-298799_978-2-9701614-0-0

A central difference approximation of the sensitivity of cure time to part thickness was used for the analysis, the metric is defined in Eq. (5).

$$\frac{d\theta}{d\phi} = \frac{\theta(\phi + \Delta\phi) - \theta(\phi - \Delta\phi)}{2\Delta\phi} = \frac{\theta(\phi = 0.025) - \theta(\phi = 0.015)}{0.02} \quad (5)$$

Where $\theta(\phi)$ is cure time when part thickness is ϕ and $\Delta\phi$ is the amount by which the part thickness was shifted. Central difference was used to capture the sensitivity of cure time to part thickness in the thickness domains of both cure cycles using a single metric.

To ensure the parameter space was thoroughly explored, analysis was conducted following the full-factorial experiment design shown in Table 1. The two levels assigned to each parameter are shown in Table 2. The lower heat transfer coefficient value was informed by industrial oven data and the higher by industrial autoclave data to provide values that were relevant to each environment. The two sets of properties given to the tool were obtained from the literature [4] and were intended to represent invar and a cured carbon fibre reinforced epoxy laminate, these properties are presented in Table 3.

To isolate the influence of the independent variables during the sensitivity analyses the remaining parameters were fixed, ensuring the chosen parameter was the only source of variability.

Table 1. A full factorial experiment to determine the processing environment cure time and temperature overshoot are least sensitive to part thickness

Experiment No.	Cure Cycle	HTC	Tool Thickness	Tool Material
1	-	-	-	-
2	-	-	-	+
3	-	-	+	-
4	-	-	+	+
5	-	+	-	-
6	-	+	-	+
7	-	+	+	-
8	-	+	+	+
9	+	-	-	-
10	+	-	-	+
11	+	-	+	-
12	+	-	+	+
13	+	+	-	-
14	+	+	-	+
15	+	+	+	-
16	+	+	+	+

  doi:10.5075/epfl-298799_978-2-9701614-0-0

Table 2. The key defining the two levels of the independent variables in the full factorial experiment (Table 1)

	-	+
Cure Cycle	t < 15 mm	15 < t < 48 mm
HTC	35 $Wm^{-2}K^{-1}$	150 $Wm^{-2}K^{-1}$
Tool Thickness	5 mm	15 mm
Tool Material	Invar	Composite

Table 3. Properties assigned to the tool materials in the heat transfer sub-model

Tool Material	**ρ [kgm^{-3}]**	**C_p [$Jkg^{-1}K^{-1}$]**	**k [$Wm^{-1}K^{-1}$]**
Invar	8100	505	12
Carbon fibre reinforced epoxy composite	1550	800	0.7

Stochastic Simulations

The model described above was incorporated into a stochastic framework, COMSOL Livelink for MATLAB enabled the model to be called repeatedly via a MATLAB script, allowing stochastic data to be generated using the Monte-Carlo method. Monte-Carlo trials were performed with cure kinetics and processing parameters being treated as normal random variables with means and variances derived from experimental data, this is in accordance with a number of previous studies [5, 6]. The means and variances for the cure kinetics parameters were obtained from differential scanning calorimetry data for M21 [3], those for the processing conditions were obtained from measurements within industrial ovens and autoclaves. Simulations were performed with part thicknesses between 5 and 45mm in 10mm increments for both recommended cure cycles. A convergence analysis was used to show 500 Monte-Carlo trials were sufficient to ensure the output distributions produced were repeatable.

The objective was to determine which cure cycle would minimise the cure time while producing temperature overshoots exceeding 8^{o}C less than 5% of the time. Temperature overshoot was defined to be the maximum temperature difference above the 180^{o}C dwell temperature through the thickness. The value of cure time and temperature overshoot were captured for each trial. The results for the two outputs were analysed to ascertain the statistical parameters of interest.

2. Results and Discussion

Sensitivity Analysis

The sensitivity of cure time to part thickness for each experiment in Table 1 is shown in Figure 2. The clearest feature in Figure 2 is that the sensitivity in the first half of experiments is significantly higher than in the second, that is with all other dependent variables the same, the

  doi:10.5075/epfl-298799_978-2-9701614-0-0

sensitivity of cure time to part thickness was consistently lower with the cure cycle recommended for thicker laminates.

With the thicker laminate cure cycle, it is evident that the increase in heat transfer coefficient leads to a reduction in sensitivity. This trend is also observed with the thin laminate cure cycle apart from with the thicker tool, as in experiments 3 and 7 where the tool was invar and, 4 and 8 where the tool was composite.

The influence of tool thickness appears clear with the thick laminate cure cycle, a thicker tool causing an increase in sensitivity. This same trend is observed for the experiments with the thin laminate cure cycle with higher heat transfer coefficient, but the opposite is observed with the lower heat transfer coefficient.

Finally, the effect of going from an invar tool to a composite tool was generally to increase sensitivity. The only exception to this in the data presented was when going from experiment 5 to 6, where the heat transfer coefficient was representative of an autoclave and the thinner tool was used.

Overall, the results from the sensitivity analysis indicated that of the processing environments considered, those in experiment 13 produced the lowest sensitivity of cure time to part thickness. Suggesting that homogeneity in a tapered thermoset composite part is maximised when processing it on a thin, low conductivity tool in an environment with a high heat transfer coefficient using a cure cycle with gentle heating ramps and pre-dwells. However, the closeness of experiments 14, 15 and 16 indicate that heat transfer coefficient and the selection of cure cycle were the most influential parameters. These results point to the suitability of autoclaves for producing tapered parts with uniform quality, due to the ability to augment the heat transfer coefficient with applied pressure. Despite general superiority of the thick laminate cure cycle the conditions during experiments 3 and 6, that is low heat transfer coefficient and a thick invar tool and, high heat transfer coefficient and a thin composite tool respectively, presented a promising compromise between part uniformity and processing efficiency.

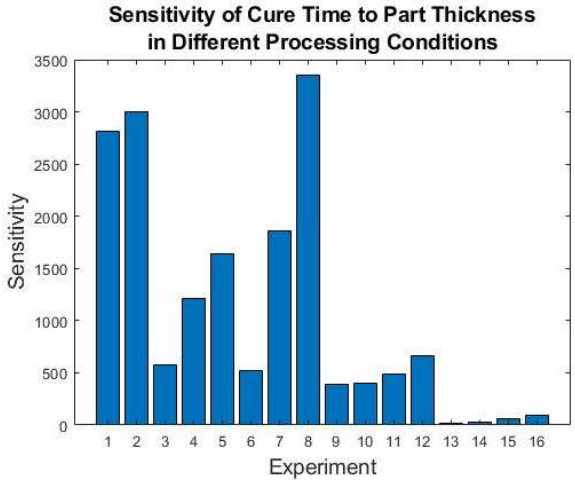

Figure 2. The sensitivity of cure time to part thickness in each processing environment of the full factorial design

Stochastic Analysis

The mean cure times of the 500 Monte-Carlo trials performed using the two cure cycles with part thicknesses from 5 to 45mm are shown in Figure 3. The higher ramp rates and lack of a pre-dwell in the thin laminate cure cycle resulted in mean cure times that were significantly shorter. Cure times were generally similar with the two tool materials, but slightly faster with the composite tool, the lower conductivity made temperature overshoots more likely. Increasing tool part thickness was also shown to have a small influence on the mean cure time, however, a slight positive correlation was evident.

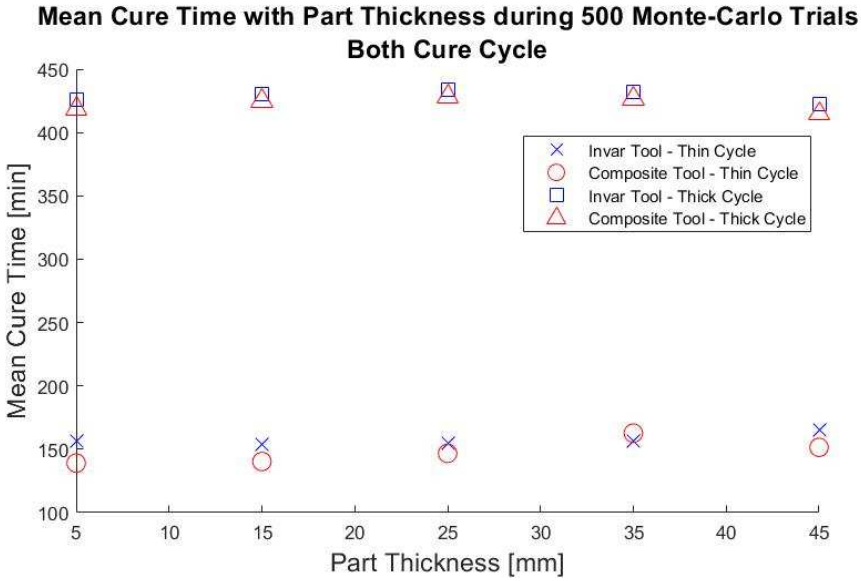

Figure 3. Mean cure time of 500 Monte-Carlo trials with the thin and thick laminate cure cycles

Given the dominance of the thin laminate cure cycle for minimising cure time, it was necessary to use the temperature overshoot criteria to select the appropriate cure cycle in each case. The thin laminate cure cycle was prone to cause larger temperature overshoots, in most cases 8°C was exceeded significantly more than the 5% limit. The only cases that did not violate the limit were part thicknesses of 5 and 15mm with an invar tool. When the tool was composite, the thick laminate cure cycle was required in all cases. This difference was due to the lower conductivity of the composite tool stifling the dissipation of exothermic heat. On the other hand, with the thick laminate cure cycle the temperature overshoot criteria was satisfied in all cases.

Therefore, despite the significantly lower processing efficiency depicted in Figure 3, to produce acceptable tapered composite parts that have thicknesses outside the 5 and 15mm range or when a low conductivity tool is used, the cure cycle designed for thick laminates must be followed. The large difference of the two cure cycles and the universal applicability of the thick laminate cycle, suggests that for the majority of the tapered parts in the specified 15-48mm thickness range this cycle is too conservative and much greater efficiency could be achieved without violating the temperature overshoot criterion.

  doi:10.5075/epfl-298799_978-2-9701614-0-0

3. Conclusion

To determine which combination of the chosen processing parameters resulted in an environment where cure time was least sensitive to part thickness, a campaign of sensitivity analyses was conducted. Clear trends for two of the individual parameters were apparent, these were that the higher heat transfer coefficient and the cure cycle recommended for high thickness laminates consistently resulted in a lower sensitivity and were therefore more conducive to part uniformity. These results gave evidence to suggest that with the parameters considered, processing environments with both a heat transfer coefficient representative of an autoclave with high pressure (i.e., around 7bar) and the Hexply M21 cure cycle recommended for thicker laminates would produce the most uniform tapered parts. Weaker influences were observed for tool material and tool thickness, as such there was no a clear result as to which of the environments with these features would be optimal.

Stochastic simulations showed that the thinner laminate cure cycle resulted in significantly lower cure times. However, the unacceptably large temperature overshoots in the majority of cases meant that the thick laminate cure cycle was almost always required. The thick laminate cure cycle produced acceptable temperature overshoots for all part thicknesses considered with both the invar and composite tools. The universal applicability of this cycle suggested it was overly conservative in most cases. Consequently, future work could investigate a means of tailoring cure cycles to tapered parts with thicknesses in the considered thickness range.**Acknowledgements**

The authors would like to thank the University of Bristol for their support of this research through their scholarship program.
This work was supported by the EPSRC Future Composites Manufacturing Research Hub (EP/P006701/1) Layer by Layer Curing project.

References

1. Guo Z-S, Du S, Zhang B. Temperature field of thick thermoset composite laminates during cure process. Composites science technology. 2005;65(3-4):517-23.
2. Kamal M, Sourour S. Kinetics and thermal characterization of thermoset cure. J Polymer Engineering Science. 1973;13(1):59-64.
3. Mesogitis T, Kratz J, Skordos AA. Heat transfer simulation of the cure of thermoplastic particle interleaf carbon fibre epoxy prepregs. Journal of Composite Materials. 2019;53(15):2053-64.
4. Invar - Nickel Iron Alloy https://www.azom.com/: AZO Materials; [Available from: https://www.azom.com/properties.aspx?ArticleID=515.
5. Mesogitis T, Skordos AA, Long A. Stochastic simulation of the influence of cure kinetics uncertainty on composites cure. Composites Science Technology. 2015;110:145-51.
6. Padmanabhan S, Pitchumani R, Transfer M. Stochastic modeling of nonisothermal flow during resin transfer molding. International Journal of Heat and Mass Transfer. 1999;42(16):3057-70.

  doi:10.5075/epfl-298799_978-2-9701614-0-0

INVESTIGATION OF THE MECHANICAL PROPERTIES OF FUZZY CNT AND CNT/CNC INTEGRATED GLASS FIBER/EPOXY COMPOSITES WITH DIFFERENT REINFORCING STRATEGIES

Melike, Erturk[a-c], Emir, Karci[a-c], Mustafa, Ozdil[a-c], Kaan, Yildiz[a-b-c], Hulya, Cebeci[a-c]

a: Aerospace Research Center, Istanbul Technical University, Istanbul, 34469, Turkey
b: Aviation Institute, Istanbul Technical University, Istanbul, 34469, Turkey
c: Department of Aeronautical and Astronautical Engineering, Istanbul Technical University, Istanbul, 34469, Turkey
erturkm15@itu.edu.tr

Abstract: *Low interfacial properties between fiber and matrix and possible interlaminar failures like delamination cracks have been considered as major problems of fiber-reinforced laminated composites. To promote low fracture toughness and interlaminar properties of fiber-reinforced polymers (FRPs), we aim to investigate the influence of different approaches using both carbon nanotubes (CNTs) and cellulose nanocrystals (CNCs) and their synergistic effect on the interlaminar properties of FRPs. In this study, unidirectional woven glass fiber/epoxy composites manufactured by vacuum infusion process (VIP) are toughened by grafting CNTs on fibers (fuzzy CNT) by chemical vapor deposition (CVD) and by dispersing CNT/CNC mixture in the polymer matrix. The samples investigated in this study include neat glass fiber epoxy composite (GFE), fuzzy glass fiber epoxy composite (FGFE), and neat glass fiber CNT/CNC reinforced epoxy composite (GFCCE) which are compared in terms of short beam shear strength.*

Keywords: Carbon nanotubes (CNTs); cellulose nanocrystals (CNCs); chemical vapor deposition (CVD); vacuum infusion process (VIP); fuzzy CNT; polymer composites

1. Introduction

Fiber-reinforced polymers (FRPs) play a significant role in particular applications where low weight and high strength are essential owing to their substantial stiffness and specific strength. However, they typically suffer from low interlaminar mechanical properties, yielding low fracture toughness and delamination cracks between plies in the out-of-plane direction [1,2]. To promote low fracture toughness and interlaminar properties of FRPs several strategies have been proposed including fiber surface modification and matrix and/or interlayer toughening by means of integration of nanomaterials such as carbon nanotubes (CNTs) [3,4]. Possessing not only excellent mechanical properties like specific strength and stiffness but also superlative thermal and electrical features of CNTs them to be the most preferable toughening materialS in aerospace applications [5]. CNTs can be integrated into composites in two different ways: direct growth on fibers (fuzzy structure) and dispersion in polymer matrices, where the combined effect of these strategies has been investigated by only a few studies [1,2,6,7]. Among these reinforcing strategies, CNT-integration into matrix has been found to be one of the most prominent methods, given that through-the-thickness properties of composites are matrix-dominated. Even though CNT integration has an excellent effect on composite materials, some difficulties occur during may the dispersion process due to the high aspect ratio (>1000) and excessively large surface area of CNT [8].

  doi:10.5075/epfl-298799_978-2-9701614-0-0

In addition to CNTs, cellulose-based alternative nanoparticles such as cellulose nanocrystals (CNCs) are being considered as well to enhance the interfacial interactions between glass fiber and epoxy, thus properties of polymer composites [9,10]. CNCs are abundant in nature, exhibit high mechanical properties, high surface area and aspect ratio, and low density [11]. Furthermore, CNCs can interact with both apolar CNTs and polar solvents because of polar and apolar groups in their own chemical structure [12]. Although CNT dispersion within polymer matrices is challenging, CNCs have proven to help achieve better dispersion and stabilize the CNTs in polymer matrices [13].

In this study, unidirectional woven glass fiber composites manufactured by VIP are toughened by grafting CNTs on fibers by chemical vapor deposition (CVD) and by dispersing CNT/CNC mixture in the polymer matrix. Neat glass fiber epoxy composite (GFE), fuzzy glass fiber epoxy composite (FGFE, and neat glass fiber CNT/CNC reinforced epoxy composite (GFCCE) are produced and their illustrations are shown in Figure 1.

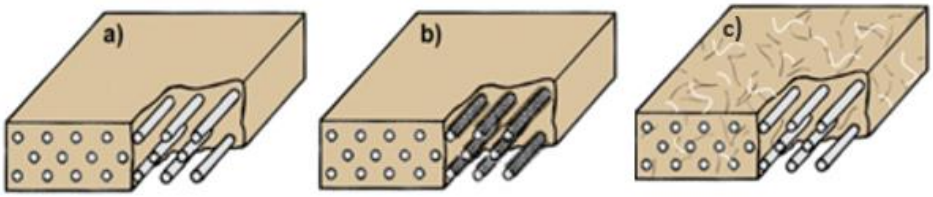

Figure 1 Illustration of different reinforcing strategies a) neat GF epoxy composite (GFE), b) Fuzzy GF and epoxy (FGFE), c) neat GF CNT/CNC reinforced epoxy composites (GFCCE)

The morphological, viscoelastic and mechanical characterizations of the prepared composites were carried out using scanning electron microscopy (SEM), dynamic mechanical analyzer (DMA) and short beam shear test (SBS) under three point bending test.

2. Experimental

2.1 Growth of Fuzzy CNT on Glass Fiber and Production of FGFC Samples

To synthesize CNTs directly on bidirectional glass fiber woven (Dost Kimya, 200 g/m2), the catalysis process was performed on the surface of a fabric with dimensions of 4 cm width and 18 cm length, by immersing into catalysis solution for 20 minutes. Fe catalyst particles in a 50mM solution of iron nitrate ($Fe(NO_3)_3 \cdot 9H_2O$) in isopropyl alcohol (C_3H_8O) were used to grow fuzzy CNTs onto the glass fiber fabrics. After that, the Fe coated fabrics were dried at 30 °C for 8 hours in a furnace.

For the CVD process, the coated fabrics were placed at the predetermined hot zone of the quartz tube. Helium (He), hydrogen (H_2), and ethylene (C_2H_4) gasses were used in the synthesis of CNTs on the glass fibers for purging, nucleation, and growth, respectively. The CNT growth protocol can be summarized as follows:

I. The CVD furnace was heated to 86°C in 2 minutes and purged under constant temperature and 1000 sccm of He for two minutes.
II. The temperature was increased to 650 °C within five minutes while simultaneously introducing 1600 sccm of He and 1000 sccm of H_2. After reaching

  doi:10.5075/epfl-298799_978-2-9701614-0-0 published under CC BY-NC 4.0 license

650 °C, the airflow was continued for an additional 17 minutes to create nucleation sites.

III. After the nucleation is completed, 400 sccm of C_2H_4 fed to the system for 15 minutes to achieve CNT growth, which wwas followed by cooling of the system.

The above mentioned procedure is illustrated in Figure 2 which was used to achieve direct CNT synthesis on glass fiber fabrics.

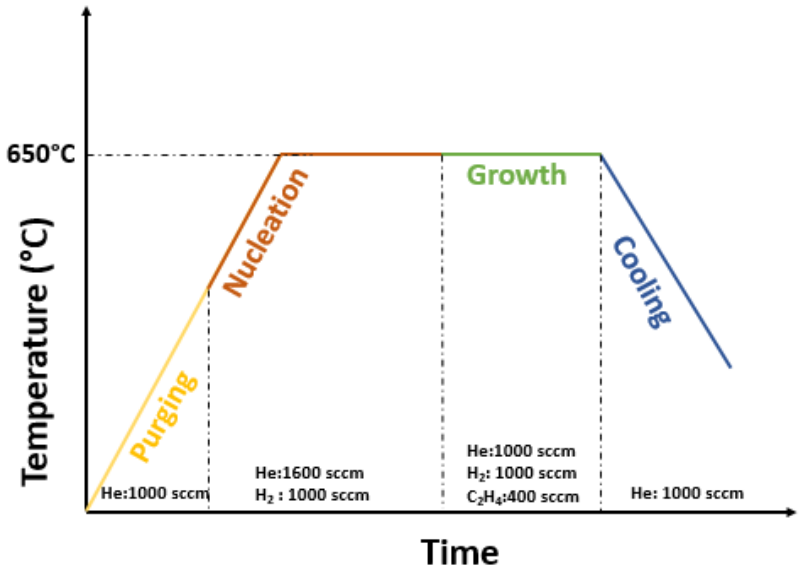

Figure 2. CVD procedure schematic figure

After the CVD process, glass fiber fabrics were cut into the desired size (4x3.5 cm) for the production of composite. In composite fabrication, two types of composites were considered where the first one consists of only fuzzy GF layers while the second one comprises five fuzzy GF layers in the middle and neat GF layers as the exterior. In both cases the number of layers was 15. After the VIP process, the fiber weight fraction of the composites was calculated as ~66%.

2.2 Preparation of CNT/CNC Integrated Epoxy Dispersion and Production of GFCCE Samples

For dispersion, CNTs and CNCs with 1:1 ratio were stirred into distilled water using a mechanical stirrer. Then, the obtained solvent was sonicated by an ultrasound sonication device with 25 seconds on - 35 seconds off pulse under 30% amplitude for 20 minutes. After that, the solvent was evaporated in a fume hood at approximately 80 °C, and CNTs/CNCs in the remaining part of the dispersion were dried at 80 °C for 8 hours to evaporate the remaining distilled water. Finally, coarse particles of CNTs/CNCs were grinded to dust form for dispersion in the epoxy. 1 wt. % CNTs (0.5 wt. %) and CNCs (0.5 wt. %) epoxy dispersion was prepared with different cycles that include an ultrasound sonication device with 10 seconds on - 25 seconds off pulse under two different amplitude values (20% and 40%) for 1 minute and a mechanical mixer operated at 1000 rpm for 3 minutes.

As-prepared dispersion was infused in to glass fiber fabric by VIP. During the VIP process, increased viscosity of the CNTs/CNCs dispersion hindered an adequate flow which resulted in incomplete wetting of the fabrics under vacuum. This problem was referred to as the filtration effect by Fan et al. [17] who also proposed a novel method to overcome the problem. In this work, the proposed method was adopted in which a second vacuum chamber was utilized. The second vacuum chamber helps create gaps between fiber layers because of the pressure

  doi:10.5075/epfl-298799_978-2-9701614-0-0

differences, creating paths for dispersion to travel. Additionally, for the resin flow, the dispersion was fed by an injector rather than the infusion, eliminating the filtration effect. The adopted method is referred to as the syringe feeding method in this study. The details of the classic VARTM and the adopted composite production methods are shown in Figure 3.

Prior to composite fabrication, the 2-component MGS L160/H160 thermoset resin was put into the sonication process and then the sonication process was continued until it was integrated into the system. Since the syringe feeding method was to be used in the composite fabrication, 5x5 cm glass fiber fabrics were placed on the glass mold and taken into a vacuum by placing peel ply and infusion mesh. After the first system was put into the vacuum, the resin inlet was combined with syringes and closed, and the resin outlet was closed by attaching a clamp. Then, since the system was to be taken into a second vacuum, a second vacuum bag was placed around the determined area and a second vacuum area was created carefully to prevent any leakage. After the dispersion was injected into the system, the resin inlet was closed. Due to the low permeability of the fabrics in the vacuum area, second vacuum was applied and the air inlets and outlets were closed. The second vacuum caused the pressure of the first vacuum to decrease and the gaps of the compressed fabric area to increase. After the expansion in the first vacuum area, the injected dispersion was kept at room temperature for 45 minutes. At this stage, the dispersion was able to wet the fabrics sufficiently. Then, the second vacuum was eliminated slowly and it was ensured that the first vacuum area was kept intact. Finally, the first resin outlet was opened, the excess dispersion within was withdrawn and the system was closed. After all these processes, the fabric soaked with the dispersion was left to cure for 24 hours at 25°C.

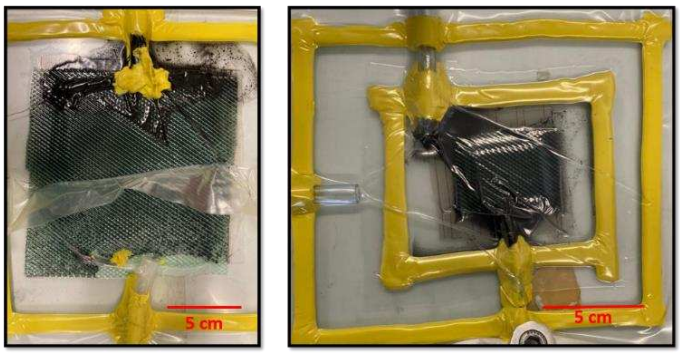

Figure 3. Composite fabrication methods a) classic VIP, b) the adopted method with syringes and second vacuum area

2.3 Testing of Composites

Morphological analysis was performed to ensure that the desired fuzzy CNT was formed on the fabric by using Scanning Electron Microscope (Thermo Fisher Axia SEM) with a secondary electron detector (10.000 kV, 100 and 5000 mag.).

DMA tests were performed using a TA Instruments DMA 850 test machine with a dual-cantilever fixture in the frequency range of 1-100 Hz at 25 °C to observe the effects of nanomaterials on the dynamic mechanical properties of nanocomposites.

The short beam shear test was performed using a Shimadzu universal test machine according to ASTM D2344 standard to report interlaminar shear strength (ILSS) of GFEC (baseline) and FGFE

  doi:10.5075/epfl-298799_978-2-9701614-0-0

and GFCCE samples. The test was applied under three-point bending at a cross-head speed of 1 mm/min until a load drop-off of 30 % was achieved.

3. Results and Discussion

3.1 Morphological Analysis

SEM analysis results showed that the successful growth of fuzzy CNTs on fibers was achieved with the optimized CVD process parameters including the nucleation and growth times, temperature, and the amount of gasses. Fuzzy CNTs on the glass fibers are shown in Figure 4.

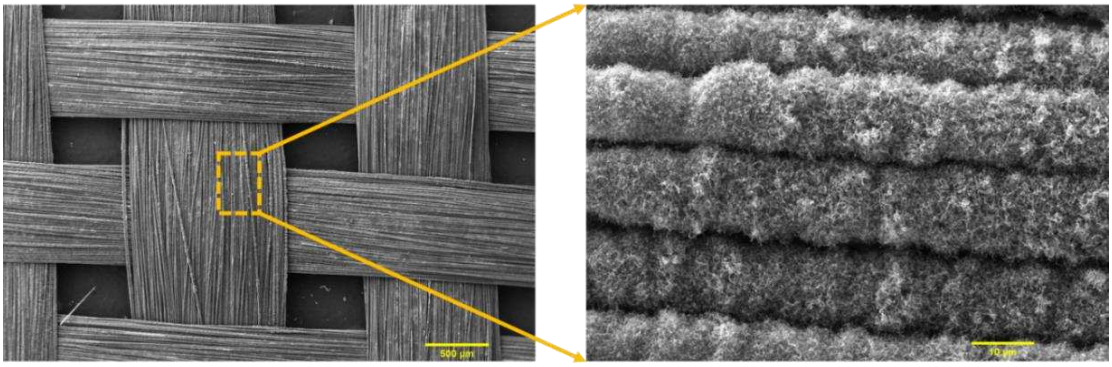

Figure 4. Morphological analysis of fuzzy CNT structure on glass fiber fabric

3.2 Dynamic Mechanical Analysis (DMA) Results

To determine and ensure the dispersion quality of CNT/CNC dispersion and to estimate its effect on the glass fiber composites, dynamic mechanical properties of nanocomposite samples were investigated. The storage modulus of 1 wt. % CNT/CNC epoxy (0.5 wt. % CNT and 0.5 wt. % CNC) with 20% and 40% sonication amplitude samples and the neat epoxy were shown in Figure 5.

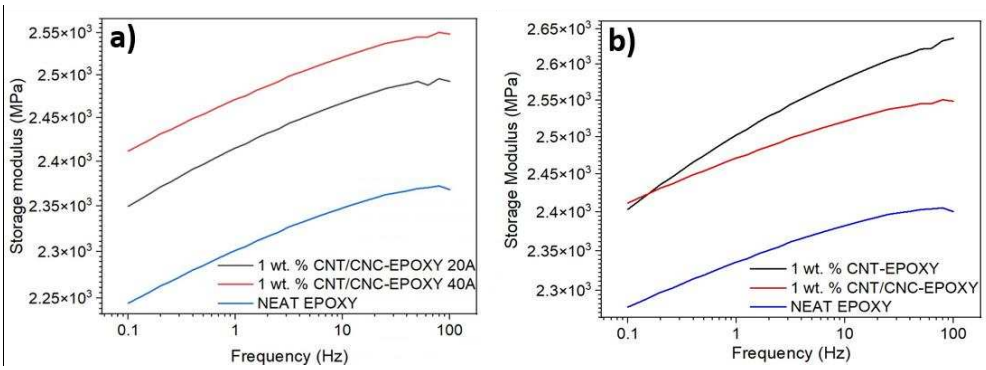

Figure 5. a) The comparison of storage modulus of neat epoxy and 1 wt. % CNT/CNC epoxy with 20% and 40% sonication amplitude, b) The comparison of storage modulus of neat epoxy, 1 wt. % CNT-Epoxy, and 1 wt. % CNT/CNC-Epoxy

The results indicated that CNT/CNC addition to neat epoxy led to increases in the storage modulus compared to neat epoxy, regardless of the sonication amplitude. However, as seen in Figure 5 (a), higher sonication amplitude yielded greater increase which can be explained by the higher amount of energy given to the system to break CNT agglomerations.

  doi:10.5075/epfl-298799_978-2-9701614-0-0

Furthermore, to observe the effect of CNC on the dispersion quality and the storage modulus, 1% wt. CNT epoxy nanocomposites were produced using a sonication amplitude of 40%. Figure 5 (b) shows the storage modulus of neat epoxy, 1% wt. CNT epoxy and 1% wt. CNT/CNC epoxy.

1 wt. % CNT epoxy nanocomposite samples show higher storage modulus than 1 wt. % CNT/CNC epoxy nanocomposites. These results can be attributed to CNT and CNC amount and/or the quality of dispersion processes. Nevertheless, these two nanomaterials have higher storage modulus than neat epoxy samples.

3.3 Short Beam Shear (SBS) Test Results

The test specimens prior to short beam shear tests are shown in Figure 7 and the short beam shear strength results calculated from Eq. (1) are given in Table 1.

$$F^{SBS} = \frac{3}{4} x \frac{P_m}{bxh} \quad (1)$$

P_m is the maximum load in Newton that composites resist during the test. The measured thickness of specimen is h, and the measured specimen width is the b in mm.

Figure 7. The samples of Glass Fiber Epoxy Composite (GFE), Fuzzy Glass Fiber Epoxy Composite (FGFE-1), Fuzzy Glass Fiber Epoxy Composite (FGFE-2), Glass Fiber CNT CNC Epoxy Composite (GFCCE-1), Glass Fiber CNT CNC Epoxy Composite (GFCCE-2)

Table 1. The short beam shear strength results of GFE, FGFE, and GFCCE

Sample Name	Sample Code	Short Beam Shear Strength (F^{SBS}) [MPa]
Glass Fiber Epoxy Composite	GFE (Neat)	41.86
Fuzzy Glass Fiber Epoxy Composite (5 layers Fuzzy in the middle of composite)	FGFE-1	34.54
Fuzzy Glass Fiber Epoxy Composite (All layers are Fuzzy in the middle of the composite)	FGFE-2	22.79
Glass Fiber CNT CNC Epoxy Composite (Glass Fiber 1 wt. % CNT/CNC Epoxy)	GFCCE	28.45
Glass Fiber CNT CNC Epoxy Composite (Glass Fiber 1 wt. % CNT Epoxy)	GFCCE	29.28

  doi:10.5075/epfl-298799_978-2-9701614-0-0

According to test results, FGFE samples, showed lower short beam shear strength values then neat composites. During the CVD process, the temperature reaches approximately 650°C and as a result, the strength of the fibers reduces. In addition, removing the sizing during the catalysis process can be another reason for the decline in the mechanical properties. When FGFE-1 and FGFE-2 samples are compared, the effects of high temperature and catalysis process mentioned above become more apparent. When GFCCE and neat samples are compared, a reduction of the short beam shear strength was observed. Composite production method (VIP), homogeneity of dispersion, and amount of CNT/CNC nanomaterials can be considered as the main reasons for the decrease in SBS strength.

4. Conclusions

Interlaminar shear strength and the dynamic mechanical properties of nanocomposites were investigated in this study. Two different reinforcing strategies, which are matrix toughening and reinforcement toughening, were considered. As first step, the CVD protocol was optimized to obtain fuzzy CNT onto glass fiber surfaces. Then morphological analysis was carried out to investigate the CNT characteristic which was followed by optimization of sonication parameters. Secondly, a modified VIP method which utilizes two vacuum bags was used for composite fabrication to eliminate the filtration effect. According to short beam shear tests, it was observed that short beam shear strength values of FGFE were lower than that of GFE. This can be attributed to the elevated temperatures (650°C) that glass fibers was exposed during CNT growth. To achieve greater short beam shear strength, the number of fuzzy CNT decorated layers was reduced to five and gradual increase was observed. On the other hand, when the CNT/CNC mixture was used to toughen the matrix, SBS values also decreased, indicating dispersion problems. As future work, optimizations on composite production method and the ratio and the amount of CNT/CNC will be carried out to solve problems related to wettability and nanoparticle agglomerations.

Acknowledgments

The authors would like to thank the conference funding for Mrs. Melike Ertürk provided by the TUBITAK 2224-A Support Program for Participation in Abroad Scientific Events.

5. References

1. Yildiz K, Gürkan İ, Turgut F, Cebeci F, Cebeci H. Fracture toughness enhancement of fuzzy CNT-glass fiber-reinforced composites with a combined reinforcing strategy. Compos Commun. 2020;21(December 2019).
2. Karapappas P, Vavouliotis A, Tsotra P, Kostopoulos V, Paipetis A. Enhanced fracture properties of carbon-reinforced composites by the addition of multi-wall carbon nanotubes. J Compos Mater. 2009;43(9):977–85.
3. Gojny FH, Wichmann MHG, Fiedler B, Bauhofer W, Schulte K. Influence of nano-modification on the mechanical and electrical properties of conventional fiber-reinforced composites. Compos Part A Appl Sci Manuf. 2005;36(11):1525–35.
4. Domun N, Hadavinia H, Zhang T, Sainsbury T, Liaghat GH, Vahid S. Improving the fracture toughness and the strength of epoxy using nanomaterials-a review of the current status. Nanoscale. 2015;7(23):10294–329.
5. Coleman JN, Khan U, Blau WJ, Gun'ko YK. Small but strong: A review of the mechanical properties of carbon nanotube-polymer composites. Carbon N Y. 2006;44(9):1624–52.

  doi:10.5075/epfl-298799_978-2-9701614-0-0

6. Wicks SS, Wang W, Williams MR, Wardle BL. Multi-scale interlaminar fracture mechanisms in woven composite laminates reinforced with aligned carbon nanotubes. Compos Sci Technol [Internet]. 2014;100:128–35. Available from: http://dx.doi.org/10.1016/j.compscitech.2014.06.003
7. Godara A, Mezzo L, Luizi F, Warrier A, Lomov S V., van Vuure AW, et al. Influence of carbon nanotube reinforcement on the processing and the mechanical behaviour of carbon fiber/epoxy composites. Carbon N Y [Internet]. 2009;47(12):2914–23. Available from: http://dx.doi.org/10.1016/j.carbon.2009.06.039
8. Ma PC, Siddiqui NA, Marom G, Kim JK. Dispersion and functionalization of carbon nanotubes for polymer-based nanocomposites: A review. Compos Part A Appl Sci Manuf [Internet]. 2010;41(10):1345–67. Available from: http://dx.doi.org/10.1016/j.compositesa.2010.07.003
9. Moon RJ, Martini A, Nairn J, Simonsen J, Youngblood J. Cellulose nanomaterials review: Structure, properties and nanocomposites. Vol. 40, Chemical Society Reviews. 2011. 3941–3994 p.
10. Haque E, Shariatnia S, Jeong TJ, Jarrahbashi D, Asadi A, Harris T, et al. Scalable coating methods for enhancing glass fiber–epoxy interactions with cellulose nanocrystals. Cellulose [Internet]. 2021;28(8):4685–700. Available from: https://doi.org/10.1007/s10570-021-03829-3
11. Asadi A, Miller M, Moon RJ, Kalaitzidou K. Improving the interfacial and mechanical properties of short glass fiber/epoxy composites by coating the glass fibers with cellulose nanocrystals. Express Polym Lett. 2016;10(7):587–97.
12. Ibanez Labiano I, Arslan D, Ozden Yenigun E, Asadi A, Cebeci H, Alomainy A. Screen Printing Carbon Nanotubes Textiles Antennas for Smart Wearables. Sensors (Basel). 2021;21(14).
13. Shariatnia S, Kumar A V., Kaynan O, Asadi A, Asadi A, Asadi A. Hybrid Cellulose Nanocrystal-Bonded Carbon Nanotubes/Carbon Fiber Polymer Composites for Structural Applications. ACS Appl Nano Mater. 2020;3(6):5421–36.
14. Mehdikhani M, Gorbatikh L, Verpoest I, Lomov S V. Voids in fiber-reinforced polymer composites: A review on their formation, characteristics, and effects on mechanical performance. J Compos Mater. 2019;53(12):1579–669.
15. Staal J, Caglar B, Hank T, Wardle BL, Gorbatikh L, Lomov S V., et al. In-series sample methodology for permeability characterization demonstrated on carbon nanotube-grafted alumina textiles. Compos Part A Appl Sci Manuf. 2021;150.
16. Lidston DL, Wicks SS, Wardle BL. Factors controlling infusion processing of laminated composites containing aligned carbon nanotubes. Collect Tech Pap - AIAA/ASME/ASCE/AHS/ASC Struct Struct Dyn Mater Conf. 2011;(April):4–10.
17. Fan Z, Santare M, Advani S. Interlaminar shear strength of glass fiber reinforced epoxy composites enhanced with multi-walled carbon nanotubes. Composites Part A: Applied Science and Manufacturing. 2008;39(3):540-554.

FATIGUE BEHAVIOR OF CARBON FIBER REINFORCED EPOXY POLYMER (CFRP) OF HIGH-PRESSURE HYDROGEN STORAGE TANK

I. Feki[a], M. Shirinbayan[a], R. Tie Bi[b], J. Fitoussi[a]

a: Arts et Metiers Institute of Technology, CNAM, PIMM, HESAM University, Paris, France – imen.feki@ensam.eu
b: Faurecia Clean Mobility, France

Abstract: *The aim of this paper is to study the mechanical properties and damage behavior of Carbon Fiber Reinforced Polymer (CFRP) which is used for manufacturing high-pressure hydrogen storage tanks. The idea of this work is to study the properties of the carbon fiber reinforced epoxy resin in form of tube with the angular orientations of fiber, i-e +/- 15°, +/-30°, +/-45° +/- 86° and multilayer. The analysis such as physical-chemical characterizations, and mechanical tests such as tensile and fatigue tests have been performed. Damage phenomena under monotone and cyclic loadings have been analyzed. The results showed the influence of fiber orientation on the tensile and fatigue behavior of CFRP. In addition, damage mechanisms such as decohesion at the fiber/matrix interface and matrix breakage were observed, followed by delamination just before failure. The obtained results in this study can provide good information for the structural design of hydrogen storage tanks.*

Keywords: *Hydrogen; CFRP; Orientations; Tensile; Fatigue; Damage*.

1. Introduction

Composites can be considered as a superior kind of materials which have a wide range of applications in several industries like aircraft, marine, military, automotive, and medical [1]. One important characteristic of these composites is the possibility to change the stacking sequence of the plies or lamina to obtain structures with the desired mechanical properties. In fact, innovations searched are those that preserve the benefits of cost reduction, lightness, and ease of processing. The primary consideration in the selection of a matrix is its basic mechanical properties [2-4]. For high-performance composites, the most desirable mechanical properties of a matrix are:

- High tensile modulus, which influences the compressive strength of the composite.
- High tensile strength, which controls the interplay cracking in a composite laminate.
- High fracture toughness, which controls ply delamination and crack growth.

In the terms of processing, polymers can be exposed to many treatments that may affect their ability and quality of products. Filament winding is a technique used for the manufacturing of surfaces of revolution such as pipes, tubes, cylinders, and spheres and is often used for the construction of large tanks for chemical production. Properties of the final composite products are reliant on the type of winding pattern [5]. Carbon fiber is attracting great attention in recent years due to its wide range of applications, especially in the field of aeronautics and automobiles, mainly due to its lightweight to strength ratio and good mechanical properties [6].

This research work focused on studying the mechanical properties of carbon fiber reinforced epoxy resin for the manufacturing of hydrogen storage pressure vessels. One can note that Hydrogen is a lightweight gas and has the lowermost volumetric energy density of any fuel at standard temperature and pressure. Concerning its energy characteristics, the gravimetric energy density of hydrogen is about three times higher than gasoline and methane [7]. According to the European Integrated Hydrogen Project EIHP, which is leading the expansion of global regulatory standards for hydrogen

testing and certification of hydrogen refueling infrastructure components and systems, compressed gas hydrogen storage vessels, made using composite materials can be divided into four different types described in Table 1 [8]. A schematic image of the type IV vessels is reported in Fig.1.

Table 1: Types of Hydrogen tanks

Type	Description
Type I	All metallic cylinders (steel/aluminum).
Type II	Metal tank (aluminum) with filament windings like glass fiber/aramid or carbon fiber around the metal cylinder.
Type III	Non-load-bearing metal liner axial and hoop wrapped with resin impregnated continuous filament.
Type VI	Non-load-bearing non-metal liner axial and hoop wrapped with resin impregnated continuous filament.

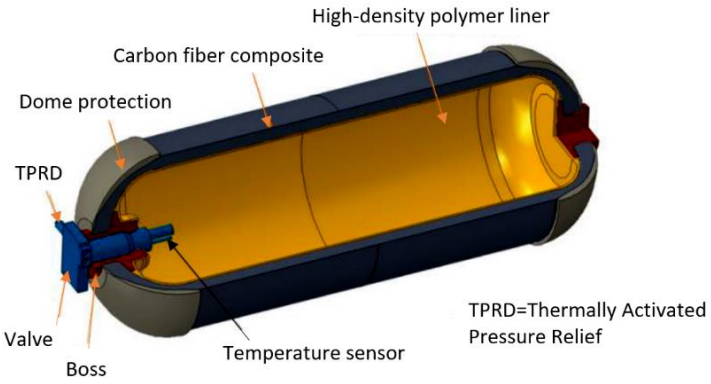

Figure 1. Schematic image of Type-IV compressed hydrogen storage tank [9].

The most innovative lightweight storage system for the case of compressed gas consists of a vessel, which is an advanced composite tank using a non-load-bearing metallic (Type III) or plastic (Type IV) liner axial and hoop wrapped with resin impregnated continuous filaments. These pressure vessels are attracting the high interest of the scientific community [10]. Their structure is based on two essential components: the liner part and the composite part, liner is basically a barrier for hydrogen permeation and the composite structure safeguards the mechanical integrity of the tank. Research is directed towards the expansion of new methodologies for reliable design and safety qualification of these high-pressure storage systems [11-13]. Also, efforts are focused on the extension of these techniques to the next generation of compressed hydrogen storage systems: tanks with complex shapes, optimal use of materials and, of high safety levels.

In this article, the relationship between the fiber orientations, porosity content, and mechanical properties of Carbon Fiber Reinforced Epoxy Polymer (CFRP) produced by the filament winding method is analyzed. The organization of this paper is as follows: after a presentation of the essential physical-chemical characteristics and microstructure of CFRP, a special attention is provided to the porosity calculation and its effect on the mechanical properties of Carbon Fiber Reinforced Epoxy Polymer (CFRP) with the various angular orientations of fiber, i-e +/- 15°, +/-30°, +/-45° +/- 86° and multilayer tube with different angular orientations (±15°/±30°/±45°/±86°). The results of the quasi-static and fatigue loadings up to failure were presented.

2. Material preparation and methods

2.1 Epoxy/carbon fiber composite

Initially, five cylindrical samples of Carbon Fiber Reinforced Epoxy resin with different angular orientations of the fiber, i.e., antisymmetric laminates +/- 15°, +/-30°, +/-45°, +/- 86° and a multilayer (±15°/±30°/±45°/±86°) were prepared as showed in Fig. 2.

In order to realize the thermochemical, physicochemical analysis, and mechanical tests, the samples were sliced from the cylindrical samples, using a cutting machine with rotational blade, into rectangular shaped samples with dimensions 130mm in length, 20mm in width and 3.3mm in thickness.

Figure 2. Schematic illustrations of cylindrical samples of Carbon Fiber Reinforced Epoxy resin with different angular orientation of the fiber.

2.2. Physico-chemical characterization methods

2.2.1. Microscopic observations

The scanning electron microscope HITACHI 4800 SEM makes it possible to qualify the microstructure of the material and particularly the fractured surfaces of the tensile specimens.

2.2.2. Porosity measurement

Porosity or void fraction is the amount of the void spaces in a material and is the ratio between the volume of voids and the total volume of the material. After microstructure analysis, the first step of the experimental work is to analyze the material's porosity. The porosity can be calculated using different methods as shown in Fig. 3:

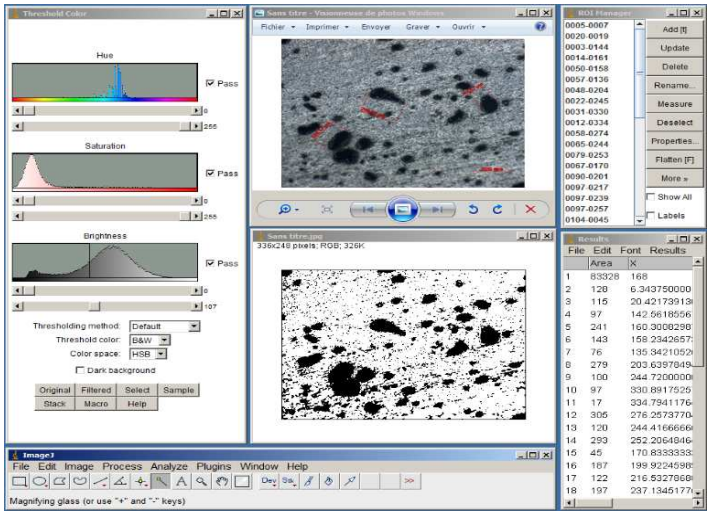

Figure 3. Screen shots of ImageJ software and the process of porosity calculation.

- Calculating percentage mass of fiber (Mf %) or epoxy (Me %): to know the quantity of fiber in the composite material, pyrolysis was performed for all the samples. The samples were heated at 550°C for 5.5 hours, which resulted in degradation of matrix material and the remaining material was carbon fiber. The formula used for the calculation of fiber content is: $M_0 – M_P/M_0 * 100$ (M_0: initial mass and M_P: mass after pyrolysis). Using the density of carbon fiber (1.1 g/cm^3) and the density value of used epoxy (0.8 g/cm^3) the porosity content can be obtained.
- ImageJ software which was used during our research work. SEM analysis is to be done for the sample under the observation and the image taken during SEM is used in the software where the porosity of the material is calculated using a technique through which the pore size and total porosity are calculated. This procedure was taken about 10 times for each sample to obtain the assured value.

2.3. Mechanical characterization

2.3.1. Quasi-static tensile test

Quasi-static tensile tests by the velocity of 20 mm/min are performed with a MTS machine. Tensile tests were performed at temperature of 20 °C. The specimen dimensions are defined in Fig. 4 The value of the thickness is 3.3 mm.

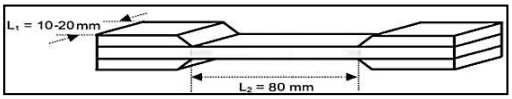

Figure 4. Dimensions of Carbon Fiber Reinforced Epoxy samples

2.3.2. Fatigue test

Tension-tension stress-controlled fatigue tests are performed at different applied maximum stress (s_{max}) on an MTS 830 hydraulic fatigue machine. The minimum applied stress (s_{min}) is always chosen to be equal to 10% of the maximum applied stress. The chosen stress ratio is thus (Rs¼0.1) and the mean stress level is equal to 0.55 s_{max}. The experiments are performed at the frequency of 10 Hz. To precisely measure the stiffness reduction due to the first loading stage, each fatigue test is preceded by a quasi-static tensile loading-unloading-reloading stage.

3. Experimental results and discussion

3.1. Physico-chemical characterization

3.1.1. Microstructure analysis

For microstructure analysis the samples from tubes were obtained and were analyzed in the optical microscope. The observations confirm the structure of a laminated composite that can be seen in Fig. 5. The figure shows the layer-by-layer structure consisting of fiber-matrix bonding and the voids. Considering the key role of porosity on the final mechanical behavior, this parameter was analyzed.

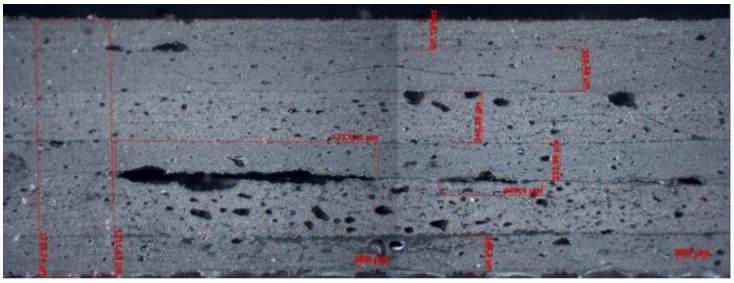

Figure 5. Tube 30° microstructure.

3.1.2. Porosity measurement

The porosity measurement is summarized in Table 2. The volume percentage of porosities for tubes with fiber orientations of 45° and 15° was 12.01% and 7.81%, respectively. The results show the important effect of fiber orientation on the percentage of porosities.

Table 2: Summary for the density of fiber and epoxy and porosity in composite tubes.

Tube		Density [g/cm3]	Fiber-mass [%]	Epoxy-mass [%]	Porosity [%]
Tube 15°	Average	1.45	77.75	22.25	7.81
	SD	±0.023	±1.68	±1.68	±0.84
Tube 30°	Average	1.472	88.54	11.46	11.95
	SD	±0.008	±0.01	±0.01	±0.23
Tube 45°	Average	1.471	87.75	12.25	12.01
	SD	±0.001	±0.59	±0.59	±0.44
Tube 86°	Average	1.46	82.07	16.93	10.11
	SD	±0.012	±3.35	±3.35	±1.02
Tube Mix	Average	1.436	81.37	18.63	10.37
	SD	±0.014	±1.87	±1.87	±0.70

3.4. Tensile behavior

The tensile test for all the samples with the stress to break is reported in Fig. 6. It shows that fiber orientation plays a vital role in load carrying. The samples more oriented to the applied force shows more resistance as in our case tube with fiber orientation of +/-15°. In contrast the samples less oriented to the applied forces showed the least resistance to the applied force as in our case tube with a fiber orientation of +/-86°. The tube with the fiber orientation of 45° showed less resistance to the applied force due to the fact of finer orientation in the composite material to the applied force. However, the deformation with the applied stress is observed as maximum, this is due to the load sharing between the epoxy and carbon fiber. In this tube, the interface between the fiber and matrix plays the key role and epoxy observed the plastic deformation before the rupture.

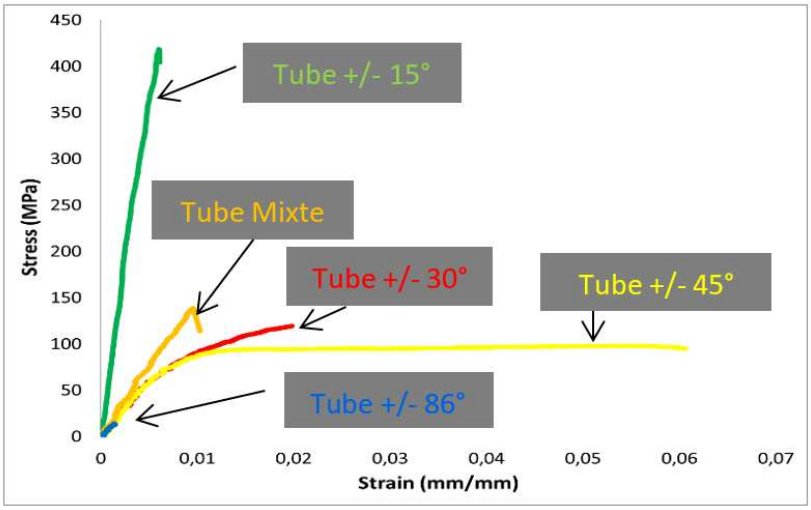

Figure 6. Summary for the tensile curves.

Table 3: Mechanical characteristics at different temperatures

Tube		Tube +/-15°	Tube +/-30°	Tube +/-45°	Tube +/-86°	Tube Mix
E [MPa]	Average	77250	11250	11000	10000	19625
	SD	±7365	±866	±2000	±408	±750
σseuil [MPa]	Average	311.25	60.5	57	8	70.5
	SD	±25.9	±3.1	±2.3	±0	±1.3
εseuil [%]	Average	0.45	0.5675	0.4525	0.1025	0.42
	SD	±0.02	±0.06	±0.07	±0.01	±0.02
σmax [MPa]	Average	407	114.5	99.25	14.75	121.5
	SD	±18.7	±8	±3	±0.9	±14.3
εmax[%]	Average	0.62	2.1175	7.075	0.1675	0.84
	SD	±0.03	±0.50	±1.18	±0.02	±0.12

To illustrate this change in the fracture mode, from ductile to fragile, we also examined the samples on a microscopic scale. The micrographs presented in Table 4 show the microscopic surfaces resulting after a quasi-static tensile test. These micrographs illustrate the decohesion at fiber matrix interfaces followed by fiber breakage.

Table 4. Fractured surfaces of the samples after the quasi-static tensile test.

Macro	Micro
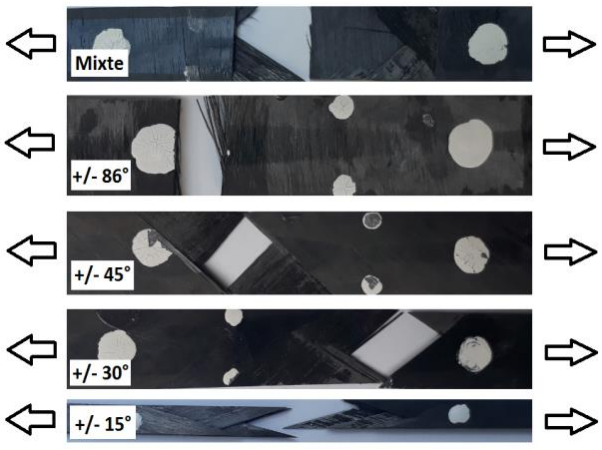	SEM images for tube +/-45° 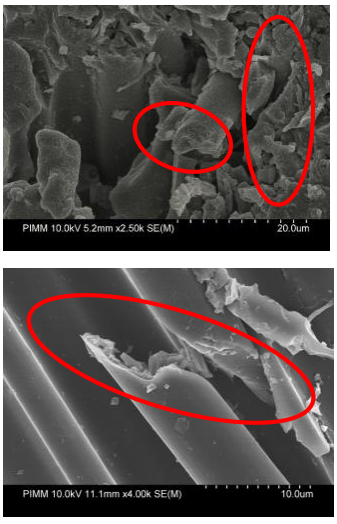

3.4.2. Fatigue behavior

Figure 8 shows the Wohler curves obtained in tension-tension stress-controlled fatigue tests at a frequency of 10 Hz for +/-15°, +/-30°, +/-45°, +/-86°, and a multi-layered samples. It can be noticed that in the case of +/-30° samples for an applied stress equal to 120MPa, the fatigue life is about 1,000 cycles whereas the fatigue life is about 105 cycles for an applied stress of about 80MPa. So, a variation of 33% leads to a fatigue life about 100 times lower. It can be established that the fatigue life is strongly

influenced by the distribution of fiber orientation. It can be established thus that for hydrogen tank, the fatigue design can be efficiently optimized through fiber orientation without critical reduction of material properties in the transverse direction.

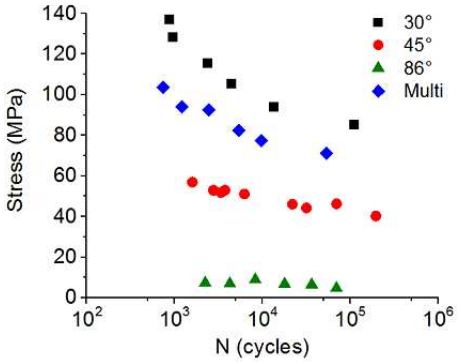

Figure 7. Wohler curves for the tubes.

The damage mechanism of the samples with different angular orientations is reported in Fig. 8. From the curves, the difference in kinetic of damage is clear for different fiber orientations. One can also notice that the macroscopic damage form is similar for all applied stress at one fiber orientation, however the increasing the amplitude the number of cycles at rupture is decreased. For all curves three zones of damage evolution can be observed related to the damage kinetic: 1) no significant damage evolution until near point a, 2) progressive damage until near point b, and 3) a sharp decrease in the rigidity until failure. The obtained results could help us to feed the proposed micromechanical model.

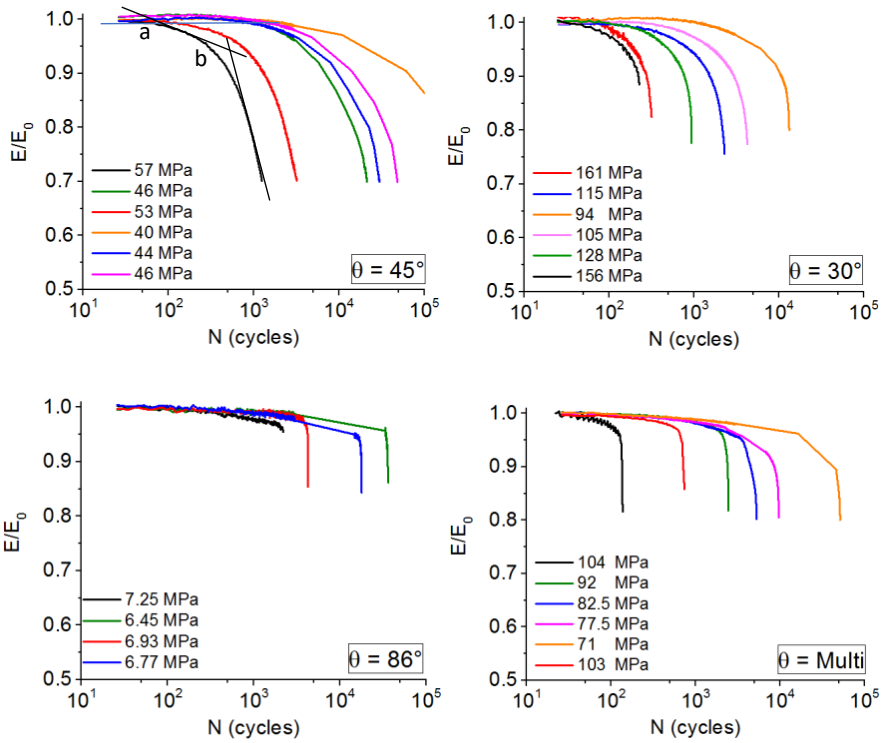

Figure 8. Representative curves of fatigue tests.

4. Conclusion

Storage of pure Hydrogen plays a key role in hydrogen-powered vehicles technology, which is seen as the future of automobile industries. Hydrogen storage technology is still under development.

Regarding the storage of hydrogen, all specified future targets are based on efficient storage of pure hydrogen with economy and the weight of the pressure vessel. The research work conducted in this article was to analyze the mechanical properties of carbon fiber reinforced epoxy resin (CFRP) for hydrogen storage. Firstly, material characterization is performed, which includes porosity and fiber content determination in the composite material. After that, the mechanical characterizations such as tensile and fatigue tests were performed. Microscopic studies and SEM analysis were performed to observe the microstructure of the CFRP. Five samples were analyzed with different angular orientations of fibers i-e +/-15°, +/-30°, +/-45°, +/-86°, and a multi-layered tube. Orientation of the fiber greatly affected the tensile strength as the fiber orientation along the applied tensile force makes it harder to break as we observed for +/-15° (426 MPa) and +/-86° (15.5 MPa) samples. One can note that improving the resin quantity and impregnation during the manufacturing process can improve the quality of the composite tubes.

6. References

1. Yashas Gowda, T.G.; Sanjay, M.R.; Subrahmanya Bhat, K.; Madhu, P.; Senthamaraikannan, P.; Yogesha, B. SSPolymer matrix-natural fiber composites: An overview. Cogent. Eng. 2018, 5, 1446667.
2. Abrate S. Modeling of impacts on composite structures. *Composite Structures*, Vol. 51, p. 129-138, 2001.
3. Gibson, R. F. (2016). Principles of composite material mechanics. CRC press
4. Shirinbayan, M., Fitoussi, J., Bocquet, M., Meraghni, F., Surowiec, B., & Tcharkhtchi, A. (2017). Multi-scale experimental investigation of the viscous nature of damage in Advanced Sheet Molding Compound (A-SMC) submitted to high strain rates. Composites Part B: Engineering, 115, 3-13.
5. Califano, A., Grassia, L., & D'Amore, A. (2019). Fatigue of Composite Materials Subjected to Variable Loadings. Journal of Materials Engineering and Performance, 28(10), 6538-6543.
6. Recker, H. G. (1989). Highly damage tolerant carbon fiber epoxy composites for primary aircraft structural applications. In 34. INTERNATIONAL SAMPE SYMPOSIUM AND EXHIBITION, 1989, (pp. 747-758).
7. Dhaou, H., Mellouli, S., Askri, F., Jemni, A., & Nasrallah, S. B. (2007). Experimental and numerical study of discharge process of metal–hydrogen tank. International Journal of Hydrogen Energy, 32(12), 1922-1927
8. K. H. D. Mori*, «Recent challenges of hydrogen storage technologies for fuel cell vehicles,» international journal of hydrogen energy 34, 2009.
9. FCTO (Fuel Cells Technology Office). 2017. "Hydrogen Storage." Department of Energy. https://www.energy.gov/sites/prod/files/2017/03/f34/fcto-h2-storage-fact-sheet.pdf.
10. N. M. CebollaB.AcostaP.MorettoF.HarskampC.Bonato, «Compressed hydrogen tanks for on-board application: Thermal behaviour during cycling,» International Journal of Hydrogen Energy, p. https://doi.org/10.1016/j.ijhydene.2015.03.035, 2015.
11. H. G. J.BRUNBAUER, «Mechanical properties, fatiguedamage and microstructure of carbon/epoxy laminates depending on fibre volumecontent,» International Journal of Fatigue,, p. 85–92, 2015.
12. A. V. A.VAVOULIOTIS, «On the fatiguelife prediction of CFRP laminates using the Electrical Resistance Change method.,» Composites Science and Technology, p. 630–642, 2011.
13 J. PAYAN, «: Etude du comportement de composites stratifiés sous chargement statique et de fatigue,» France, 2004.

THERMOSET POLYMER SCALING EFFECTS IN THE MICROBOND TEST

David Bryce, James Thomason, and Liu Yang

University of Strathclyde, Glasgow, UK – david.bryce@strath.ac.uk

Abstract: *The curing performance of two epoxy resin systems has been investigated using the microbond test and FTIR spectroscopy. A novel sample preparation technique involving curing epoxy droplets on thin steel filaments allowed for high-throughput determination of microbond droplet cure state using a conventional benchtop spectrometer. Parity between steel filament and glass fibre microbond samples was confirmed by infrared microspectroscopy. It is shown that cure schedules used in the manufacture of composite parts produced microbond droplets with degrees of cure lower than that of bulk matrix specimens subjected to an identical thermal history. For a commercial resin system, testable microbond droplets could only be produced when a room temperature pre-curing time of at least 2 hours was introduced. It is concluded that microbond testing be supported by some method of droplet cure state characterisation to ensure that interfacial effects are not artefacts of droplet sample preparation.*

Keywords: Glass fibres; Epoxy resin; Interfacial shear strength; Microbond test; Infrared spectroscopy

1. Introduction

Optimisation of the stress-transfer capabilities of the fibre/matrix interface region is critical to composite material mechanical performance. The strength of the interface can be defined in terms of interfacial shear strength (IFSS), which can be characterised by a number of micromechanical methods [1]. Such testing methods can be useful tools in the economical and time-efficient development of fibre treatments and assessment of composite processing parameters by enabling screening and optimisation at the single fibre level without the need to scale up to fabric production, laminate processing, and macromechanical testing [2]. Despite apparent IFSS being strongly influenced by the cure state of the matrix, non-ideal droplet curing behaviour is rarely considered.

Microscale curing effects have been identified as an area for improvement in some of the earliest critical reviews of micromechanical [1] and microbond [3] testing methods. Furthermore, these scaling effects may occur across a wide range of thermosetting matrices including epoxy [4], polyester [5], vinyl ester [6], and acrylic resins [7]. Hypotheses on the cause of reduced droplet (and thin film) cure in the current literature include: evaporation of essential polymerisation components (such as volatile curing agents and styrene); adsorption of curing agent onto the fibre surface; absence of a surrounding mould, droplet surface-to-volume ratio; phase separation during sample preparation; imine group formation; fibre surface moisture; anhydride hydrolysis; surface oxidation; interaction with atmospheric moisture; and reduced autoacceleration.

Such variations in droplet cure state may either make microbond testing impossible (depending on matrix and curing agent selection) or result in apparent IFSS being measured in a material with an undefined system chemistry.

  doi:10.5075/epfl-298799_978-2-9701614-0-0

This paper aims to address this fundamental need for a method to directly characterise the cure state of microbond droplet specimens. Previous methods of droplet cure state characterisation have included modified thermomechanical analysis techniques [8] or modelling droplets as thin film specimens [9]. However, a higher throughput solution with less exacting sample preparation requirements is highly desirable. In this paper the microscale curing performance of a commercial epoxy resin designed for wind turbine blade applications and a reference epoxy/tetrafunctional amine system were investigated using novel spectroscopy techniques and the microbond test.

2. Experimental

2.1 Materials

Experiments were carried out using bare (water-sized) E-glass fibres with an average fibre diameter of 17.5 µm from Owens Corning. Two different epoxy resin systems were investigated in this study. One was a multiple-component commercial epoxy/amine system designed for wind turbine blade applications. The other was an experimental system based on a single resin and triethylenetetramine (TETA) curing agent. Resin mixtures were prepared and degassed under vacuum for 10 min to remove entrapped air. Curing cycles consisted of two isothermal stages with intermediate heating rates of 2°C/min and were selected to coincide with curing schedules used in the production of macroscale composite parts. Glass transition temperatures of cured bulk matrix were determined by differential scanning calorimetry (DSC). Details of the epoxy resins used are listed in Table 1.

Table 1: Epoxy resins, curing agents, and temperature schedules used in the investigation

ID	Epoxy Resin	Curing Agent	Cure Schedule	Bulk Tg (°C)
WT1	Epotec YD-535 LV	TH7257	65°C 3.5 h; 75°C 7 h	87
R1	DER332	TETA	60°C 1 h; 120°C 2h	124

2.2 Microbond testing

Microbond testing involves a single fibre being pulled from a restrained droplet of cured matrix while measuring the force required to detach the fibre. IFSS was measured using an in-house designed microbond jig [10]. Successful debonding or instances of droplet plastic deformation were confirmed by in-situ observation of droplet loading using 45x magnification stereo microscopy and a live camera feed.

2.3 Fourier-transform infrared spectroscopy

Fourier-transform infrared spectroscopy (FTIR) was used to characterise degree of cure of microbond droplet and bulk matrix specimens subjected to an identical thermal history. FTIR was performed using a 4100 ExoScan spectrometer and a spherical diamond attenuated total reflectance (ATR) interface. An adjustable probe was used to ensure good specimen contact with the FTIR interface. Analysis was performed in the 4000 to 650 cm^{-1} range with a spectral resolution of 8 cm^{-1} and 64 scans per sample. Glass fibres were replaced by steel wire of diameter 50 µm for spectral measurements using a benchtop spectrometer.

  doi:10.5075/epfl-298799_978-2-9701614-0-0

The benchtop FTIR microbond sample preparation methodology and experimental configuration is illustrated in Figure 1.

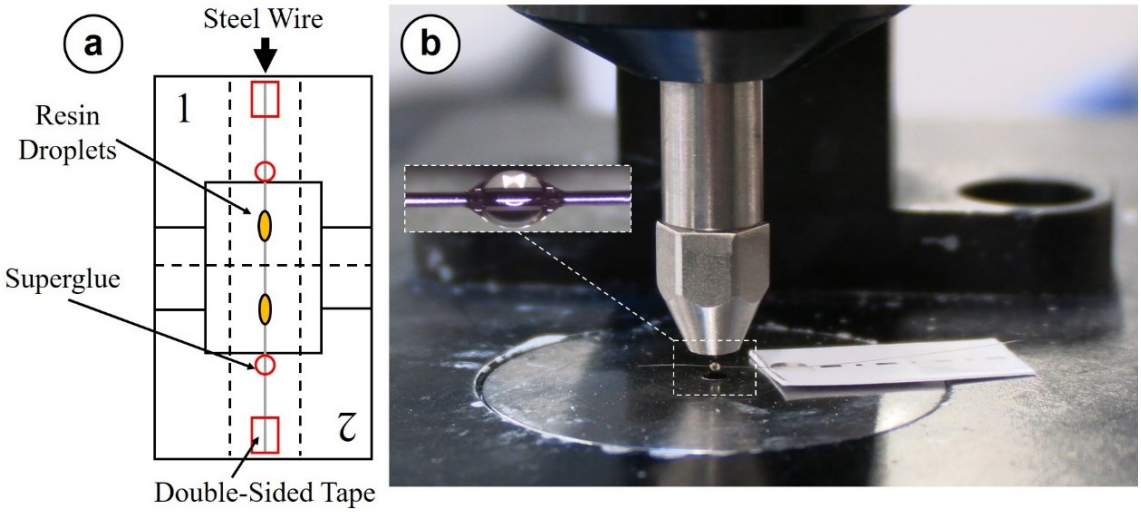

Figure 1: Benchtop FTIR method showing (a) Sample preparation (b) Droplet testing

IR microspectroscopy was performed using a Bruker Hyperion 3000 FTIR microscope equipped with a liquid nitrogen cooled MCT ATR detector in the 4000 to 650 cm^{-1} range with a spectral resolution of 16 cm^{-1} and 32 scans per sample. Glass fibre/epoxy microbond droplet specimens were placed on a glass slide and accurately positioned using a viewing objective and motorised stage.

Degree of monomer conversion was characterised using the reduction of the area of the oxirane group at 915 cm^{-1} against the invariant peak at 1507 cm^{-1} (C=C stretching of the benzene ring) as an internal standard as expressed in Equation 1. Peaks were selected due to stronger relative signal intensities compared to other analytical and reference peaks. Absorbance peak areas were calculated using a baseline integration function between the values of 927–893 cm^{-1} and 1526–1489 cm^{-1}.

$$\alpha = 1 - \frac{(A_{915}/A_{1507})_t}{(A_{915}/A_{1507})_0} \quad (1)$$

3. Results and Discussion

3.1 Microbond testing results

Epoxy resins can be expected to achieve typical apparent IFSS values of 25–35 MPa with unsized glass fibres. Microbond testing of WT1 epoxy resin droplets showed exceedingly low values of apparent IFSS when samples were cured according to the recommended macroscale schedule. As shown in Figure 2(a), in-situ observation during testing showed that the droplets deformed plastically under applied load, indicating incomplete cure. Measurement of IFSS was not possible in such cases and the resulting forces generated during the test can be attributed to frictional effects related to crushing of the droplet and subsequent fibre pull-out from the gel-state matrix. WT1 bulk matrices subjected to identical curing conditions showed T_g of 87°C. Thus, microbond droplets of this epoxy resin should have been capable of producing testable specimens. Conversely, R1 droplets appeared to cure consistently following exposure to immediate elevated temperature heating.

In-situ observation did not show plastic deformation during the test and an apparent IFSS value of around 38 MPa was measured. As shown in Figure 2(b), successful debonding was confirmed by post-test SEM imaging and the presence of a residual meniscus.

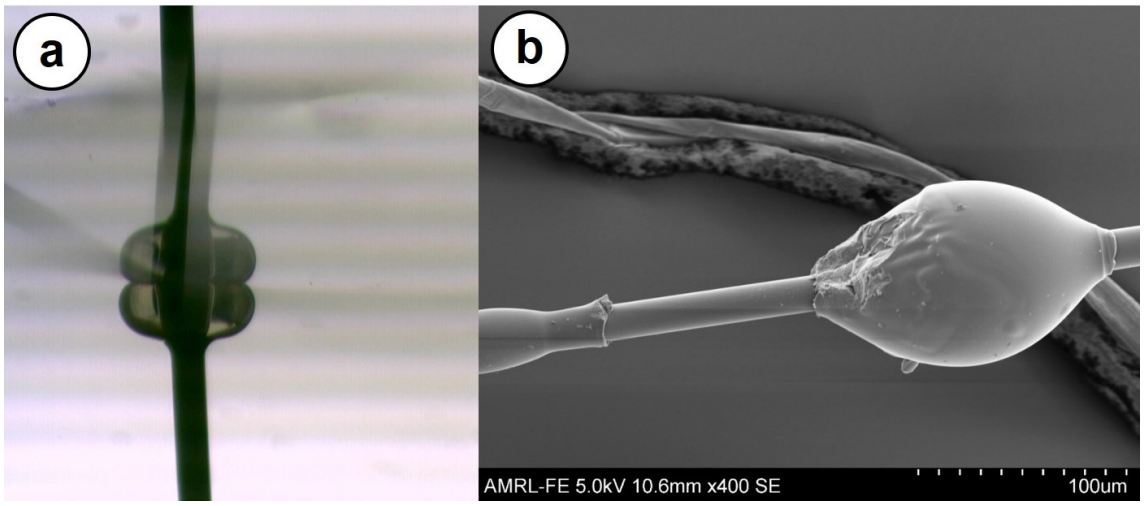

Figure 2: (a) In-situ micrograph of WT1 droplet (b) Post-test SEM of R1 droplet

3.2 Characterisation of microbond droplet cure state

The average mass of individual microbond droplet samples is in the range of 0.5–20 µg. The use of conventional thermal analysis techniques to quantify under-cure was not possible due to insufficient signal to detect T_g or residual exotherm from single droplet specimens. Therefore, droplet spectra collected from microbond specimens cured on thin lengths of 50 µm diameter steel wire were used to study epoxy group conversion. Individual steel filaments were isolated, aligned, and mounted along the vertical axis of a card template using double-sided tape and cyanoacrylate gel superglue before standing for 24 h to fully react. Resins were mixed according to the relevant directions and applied to individual fibres using a thin length of steel wire to produce droplets with embedded lengths of approximately 400 µm. We also performed infrared microspectroscopy on the glass fibre/epoxy microbond droplet specimens used for IFSS measurements to verify that degree of cure values were comparable between glass fibre/epoxy and steel wire/epoxy specimens.

FTIR spectra of WT1 and R1 epoxy microbond droplet specimens cured on glass fibres and steel filaments are shown in Figure 3. A magnified region around the oxirane ring at 915 cm^{-1} is shown in the inset. In all droplet spectra, unreacted epoxy groups were evidenced by increased peak intensities corresponding to vibrations of the oxirane ring at 970, 915, and 760 cm^{-1}. Invariant peaks at 1608 and 1507 cm^{-1} are attributable to C=C and C-C stretching of the benzene ring. The degree of cure of droplets was calculated using Equation 1. Good agreement was shown between spectroscopic methods in that degree of cure values for glass fibre and steel wire epoxy droplets were 0.52 and 0.55, respectively for WT1 specimens. Similarly, degree of cure values for glass fibre and steel wire epoxy droplets were 0.85 and 0.87, respectively for R1 specimens. Accordingly, droplet spectra from resins cured on 50 µm steel filaments were considered comparable models of the cure state of those prepared on unsized glass fibres. This method of sample preparation enables a high-throughput method of droplet cure state assessment by generating sufficient signal strength to allow spectra to be collected from individual droplet specimens.

  doi:10.5075/epfl-298799_978-2-9701614-0-0

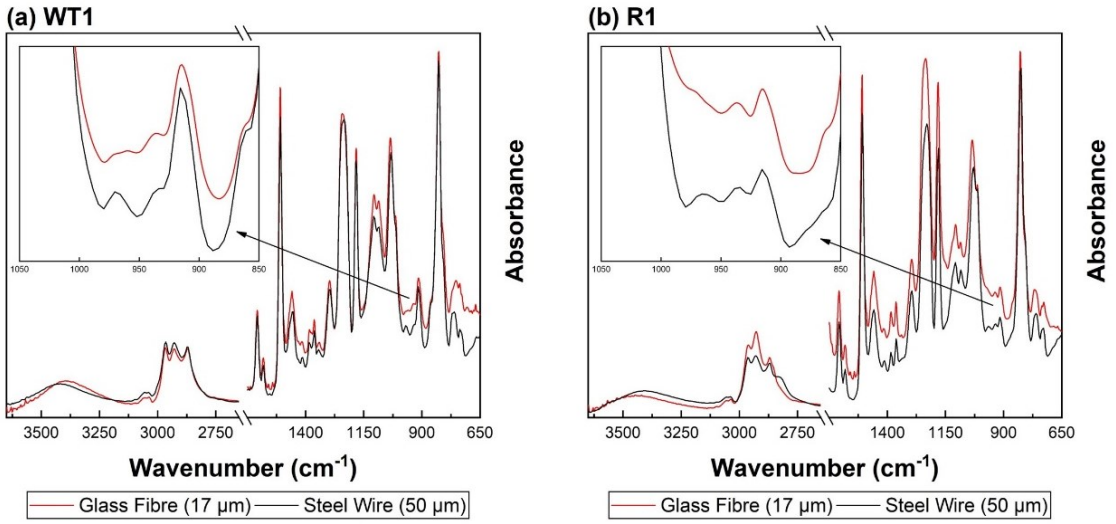

Figure 3: FTIR spectra of epoxy microbond droplets cured on glass fibre and steel wire

3.3 Degree of cure at droplet and bulk matrix scales

FTIR spectra of droplet and bulk matrix specimens subjected to identical thermal histories are shown in Figure 4. Spectra of WT1 microbond samples cured according to the recommended macroscale schedule were commensurate with a non-stoichiometric epoxy/amine network. Unreacted epoxy groups that were not present in comparable bulk matrix spectra were observed. Furthermore, reduced hydroxyl and secondary amine group accumulation (3600–3200 cm^{-1}) and a weaker etherification peak (1100 cm^{-1}) were apparent. The average degree of cure value for these droplet specimens was 0.55. Conversely, cured matrices showed a significantly higher degree of cure values of 0.89. This apparent disparity in curing behaviour may suggest a stoichiometric imbalance due to evaporation of components such as the curing agent. Loss in droplet stoichiometry may have resulted in insufficient amine groups to ensure a strongly cross-linked network structure in the droplet. Poorly cross-linked droplets that show plastic deformation during testing are indicative of a sub-optimal microdroplet T_g. WT1 droplets appeared to have a T_g close to, or below, room temperature and hence do not have a sufficiently high modulus to transmit applied load and enable normal microbond testing to take place.

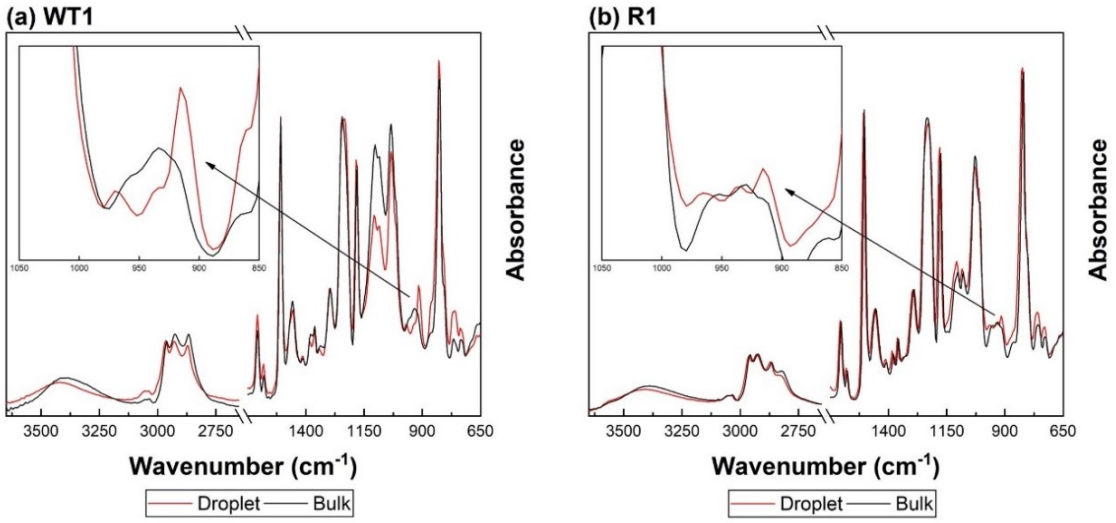

Figure 4: FTIR spectra of microbond droplet and bulk cured matrix specimens

Spectra of R1 microbond droplet specimens were similarly representative of an under-cured matrix formulation, indicated by unreacted epoxy groups at 915 cm^{-1} that were not present in the bulk matrix sample. Degree of epoxy conversion for R1 droplets was 0.87, while comparable bulk specimens reached a conversion of 0.95. These results suggest that the epoxy droplet samples typically associated with the microbond test do not possess material properties comparable to those of bulk matrix specimens, even in cases where good debonding is achieved and reasonable values of apparent IFSS are measured.

It may be suggested that a critical surface-to-volume ratio exists at which some portion of the amine curing agent diffuses to the surface of the droplet and evaporates, despite the fact that vapour pressures for these systems do not indicate particularly high volatility. In any case, spectra of microbond droplet specimens confirmed that the cure state was significantly reduced compared to bulk cured matrices. For a multiple-component commercial resin system, cure state was reduced to the extent that microbond testing was not possible. In a reference epoxy system, droplet degree of cure was lower than that of comparable bulk matrix specimens while remaining sufficiently high to promote good crosslinking and a relatively high droplet T_g.

3.4 Effect of cure cycle modification

Degree of conversion of droplet and bulk matrix specimens subjected to the same range of curing schedules is shown in Figure 5. WT1 droplets cured according to the standard schedule had a degree of cure of 0.55, a value commensurate with a loss of up to 60% of the initial curing agent and a sub-ambient T_g. Droplets that were allowed to pre-cure at room temperature for 2–48 h and partially react prior to curing had degree of cure values between 0.87 and 0.93. Degree of conversion of bulk matrix specimens was not significantly affected by the inclusion of a pre-curing time and in all cases, cured to a higher degree than comparable droplet specimens. For the R1 droplet samples, degree of cure was reduced slightly in the 3–36 h pre-curing range. Degree of conversion was lowest (0.77) following a 36 h pre-cure and was highest when samples were cured immediately (0.87). However, all R1 droplets samples cured to a lower degree than the bulk matrix specimens.

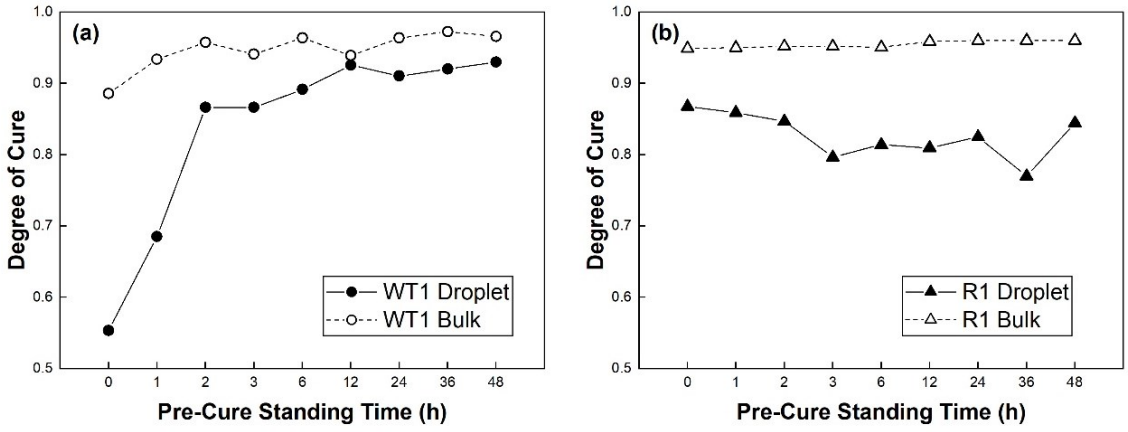

Figure 5: Microbond droplet versus bulk matrix degree of cure

Microbond testing results following the introduction of the same 0–48 h room temperature pre-curing time before the standard curing schedule are shown in Figure 6. The inclusion of a room temperature pre-cure stage had a significant effect on the apparent IFSS of WT1 specimens. Apparent IFSS of R1 samples was entirely independent of pre-cure standing time.

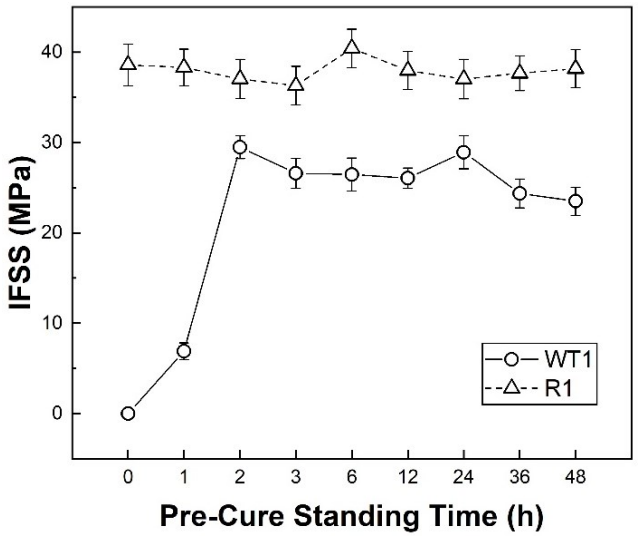

Figure 6: Apparent IFSS versus pre-cure standing time

We report good agreement between micromechanical and spectroscopic methods, in that increased IFSS was measured when droplets had higher degrees of cure. IFSS appeared to show a linear relationship with microdroplet degree of cure up to conversion of approximately 0.8, after which further increases in droplet cure state were not reflected in apparent IFSS. It is possible that an upper threshold IFSS value limited by the adhesion properties and tensile strength of the unsized fibres was reached. Due to the absence of sizing on the fibres, however, it is reasonable to suggest that IFSS was largely dictated by the cure state of the droplet.

The differences in droplet curing behaviour between diamine and tetrafunctional amine cured specimens may be indicative of distinct phenomena that contributes to reduced droplet cure states. For WT1 droplets, diamine curing agent evaporation appeared to result in insufficient amine groups necessary to produce a strongly cross-linked network structure in the droplet. For R1 droplets, cure state may have been lowered by the formation of an imine group or interaction with atmospheric moisture. These phenomena may contribute to depletion of active amine sites available to react with the oxirane ring and reduce droplet degree of cure.

The ability of micromechanical testing methods to inform macroscale materials selection and processing parameters is predicated on an assumption of comparable polymer chemistry and material properties across both scales. The data presented in this study would indicate that this assumption is often invalid for thermoset systems and hence determination of droplet cure state should be considered when employing the microbond test. It should be considered that these data would suggest that even droplets with “ideal” curing behaviour, may in fact have material properties that are inferior to those of the bulk cured matrix and comparable composite part. Interfacial testing methods are often employed to measure the influence of factors such as fibre surface treatments and the application and screening of sizings. Changes in IFSS as the result of such alterations may be masked by the influence of the cure state of the matrix microdroplet. Thus, the route taken in creating microbond samples and the potential effect of microscale curing behaviours contributing to disparity between droplet and bulk matrix material properties must be carefully considered by all practitioners of the microbond test.

  doi:10.5075/epfl-298799_978-2-9701614-0-0

4. Conclusions

In this paper, the curing performance of two epoxy resin systems was investigated using the microbond test and FTIR spectroscopy techniques. The following conclusions were drawn:

- Droplets cured on thin steel filaments are suitable models of typical glass fibre/epoxy microbond droplet specimens and enable high-throughput determination of microbond droplet cure state using a conventional benchtop spectrometer.
- Cure schedules used in the manufacture of composite parts produced microbond droplets with degrees of cure lower than that of bulk matrix specimens subjected to an identical thermal history.
- For a commercial epoxy resin system, testable microbond droplets could only be produced when a room temperature pre-curing time of at least 2 hours was introduced.

The method proposed in this study is suitable for use with extended range of thermoset polymer matrices. Further work in this area may involve characterisation of the cure states of vinyl ester and polyester droplets by monitoring the depletion of C=C peak intensities associated with the polymerisation of these matrices.

5. References

1. Herrera-Franco PJ, Drzal LT. Comparison of methods for the measurement of fibre/matrix adhesion in composites. Composites 1992;23:2–26.
2. Drzal LT, Madhukar M. Fibre-matrix adhesion and its relationship to composite mechanical properties. Journal of Materials Science 1993;28:569–610.
3. Haaksma RA, Cehelnik MJ. A Critical Evaluation of the Use of the Microbond Method for Determination of Composite Interfacial Properties. Materials Research Society Symposium Proceedings 1990;170:71–6.
4. Rao V, Drzal LT. Loss of Curing Agent During Thin Film (Droplet) Curing of Thermoset Material. The Journal of Adhesion 1991;22:245–9.
5. Ash JT, Cross WM, Kellar JJ. Estimation of the true interfacial shear strength for composite materials with the microbond test. Proceedings of the ASME 2013 International Mechanical Engineering Congress and Exposition, 2013.
6. Bénéthuilière T, Duchet-Rumeau J, Dubost E, Peyre C, Gérard JF. Vinylester / glass fiber interface: Still a key component for designing new styrene-free SMC composite materials. Composites Science and Technology 2020;190.
7. Charlier Q, Lortie F, Gérard JF. Interfacial adhesion in glass-fiber thermoplastic composites processed from acrylic reactive systems, a multi-scale experimental analysis. International Journal of Adhesion and Adhesives 2020;98.
8. Rao V, Herrera-Franco P, Ozzello AD, Drzal LT. A Direct Comparison of the Fragmentation Test and the Microbond Pull-out Test for Determining the Interfacial Shear Strength. The Journal of Adhesion 1991;34:65–77.
9. Zinck P, Mäder E, Gerard JF. Role of silane coupling agent and polymeric film former for tailoring glass fiber sizings from tensile strength measurements. Journal of Materials Science 2001;36:5245–52.
10. Yang L, Thomason JL. Development and application of micromechanical techniques for characterising interfacial shear strength in fibre-thermoplastic composites. Polymer Testing 2012;31:895–903.

PLY ORIENTATION EFFECTS IN MULTIDIRECTIONAL CARBON/EPOXY OPEN-HOLE SPECIMENS SUBJECTED TO SHEAR LOADING

Roy C. Bullock[a], Tobias Laux[a], Ole T. Thomsen[a], Janice M. Dulieu-Barton[a]

a: Bristol Composites Institute, University of Bristol, UK – jw21668@bristol.ac.uk

Abstract: *Investigating the shear strength of composite laminates and the factors affecting it remains an important area of study. In addition to altering the number of differently-orientated plys, changing the laminate architecture and stacking sequence (i.e. individual ply thickness and position of the ply in the laminate stack) also has an effect on the laminate's strength. The present work shows the effect of stacking sequence on the open-hole shear strength of CFRP specimens, specifically that not only the ply thickness but also the orientation of the surface ply relative to the shear load direction has a significant effect. This strength difference is caused by a difference in failure mode, which can be observed from out-of-plane displacement plots captured using digital image correlation (DIC).*

Keywords: Laminate Architecture; Modified Arcan Fixture; Digital Image Correlation (DIC)

1. Introduction

The use of CFRP in structural components is well-established across several industries including the aerospace, automotive, and renewable sectors. Despite this history, the factors affecting laminate strength are not fully understood due to complex interactions between the loading configuration, manufacturing method, and laminate architecture.

Previous work has shown that architectural features such as using thinner plies for the same laminate thickness increases strength in unnotched and open-hole compression tests [1] [2]. This is also true for specimens with small holes loaded in tension, although the effect is reversed for larger holes [3]. While the effect of laminate architecture on laminate strength has been investigated using simple uniaxial tension and compression tests, its effects on the shear failure behaviour have rarely been addressed. As a consequence, the understanding of laminate architecture effects on the shear strength is limited.

Therefore, the present work investigates the open-hole shear strength of two different composite laminates using a Modified Arcan Fixture (MAF) [4], which allows CFRP specimens to be tested to failure under a variety of load conditions. In addition to investigating the ply thickness effect as in prior work [4], the effect of the surface ply orientation relative to the shear direction is also investigated.

2. Specimens and testing setup

2.1 Specimen preparation

The specimens were manufactured using an in-autoclave CFRP prepreg, IM7/8552. To investigate stacking effects other than the surface ply orientation, two laminate architectures were tested: a blocked layup of $[+45\ +45\ 90\ 90\ -45\ -45\ 0\ 0]_s$ for a thick-ply case, and a distributed layup of $[+45\ 90\ -45\ 0]_{2s}$ for a thin-ply case. The specimens were waterjet cut according to the slightly waisted design proposed in [4] to promote failure around the hole in a wide variety of

  doi:10.5075/epfl-298799_978-2-9701614-0-0

load cases, including pure shear. Subsequently, the holes were drilled using a tungsten carbide drill bit on a standard pillar drill. Four specimens were tested for the blocked lay-up case, while three specimens were tested for the distributed lay-up cases.

For loading and clamping into the test rig, glass fibre-reinforced polymer (GFRP) tabs were bonded to the specimen ends using an aerospace-grade epoxy adhesive. A black and white speckle pattern, allowing the surface displacements to be tracked with digital image correlation (DIC), was applied with conventional acrylic spray paint.

2.2 Testing setup

To capture the full-field surface displacements, stereo DIC was used to obtain the displacements and strains using MatchID software. Stereo DIC enables out-of-plane displacements to be tracked, as well as correcting for the camera misalignment issues common with single-camera DIC. Two 12 MP cameras and supporting LED lights were used for these tests, with a frame rate of 2 Hz. A specimen loaded by the MAF, mounted in an Instron 1342 servo-hydraulic test machine, is shown in Figure 1.

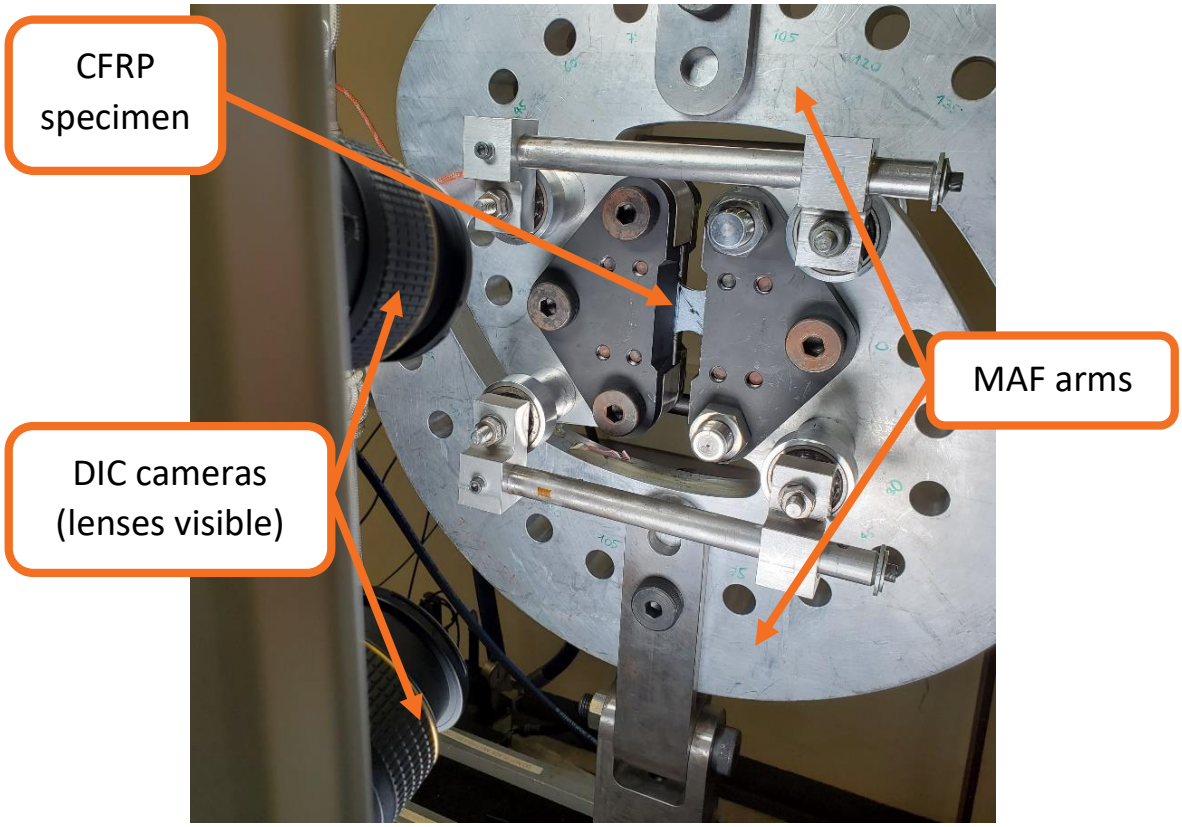

Figure 1. A specimen loaded into the MAF for the 'aligned' load case, with the lenses of the DIC cameras visible in the foreground.

The specimens were loaded into the MAF in an orientation where the +45° plies were either 'aligned' with the shear load or 'against' the shear load, as shown in Figure 2. The MAF was rotated to present the same face of the specimen to the cameras for both specimen orientations. For the quasi-static load condition, the test machine actuator was displaced at a rate of 1 mm/min, with the load and displacement outputs recorded by the DIC system.

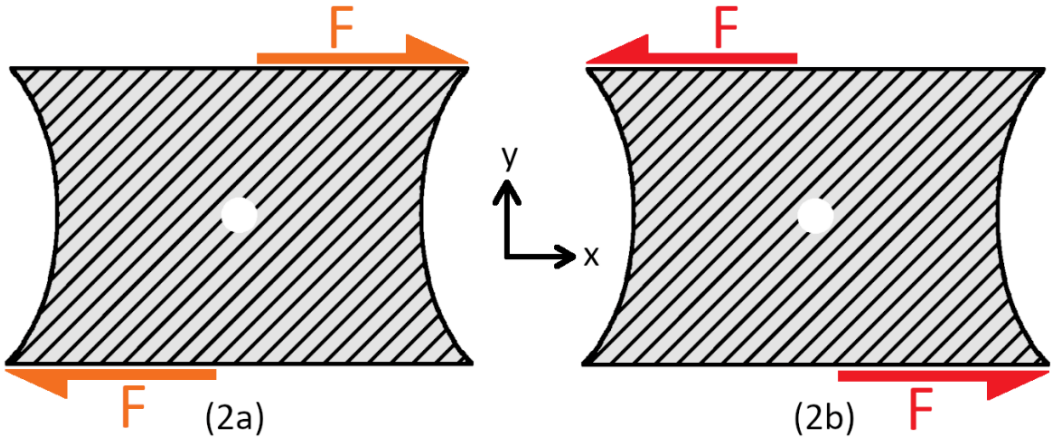

Figure 2. A diagram showing the two shear load directions relative to the surface +45° ply: (a) showing 'aligned' loading and (b) showing 'against' loading.

3. Results

The mean failure loads for each case are shown in Table 1 below, while load-displacement curves up to final failure (using x-direction displacement '*u*' due to the shear case) for representative specimens are shown in Figure 3. The shear displacements used to derive the load displacement curves were extracted from the DIC displacement maps, and the slope of the curve obtained from the 1 to 5 kN load range is also given.

Table 1: Mean failure loads for each test case, as well as the percentage effect (covariance) of surface ply orientation.

Layup	Surface ply orientation	Specimens tested	Failure load [kN]	Orientation effect [%]
Blocked	Aligned	4	12.91	4.96
Blocked	Against	4	13.57	
Distributed	Aligned	3	14.83	2.51
Distributed	Against	3	15.21	

The failure loads in Table 1 clearly show a strength difference based on the specimens tested: the against case is stronger than the aligned case, but the difference is less for the distributed ply lay-up specimens than the blocked ply lay-up specimens. This is currently thought to be due to the relatively thicker unconstrained surface ply in the blocked ply specimens, as discussed further below.

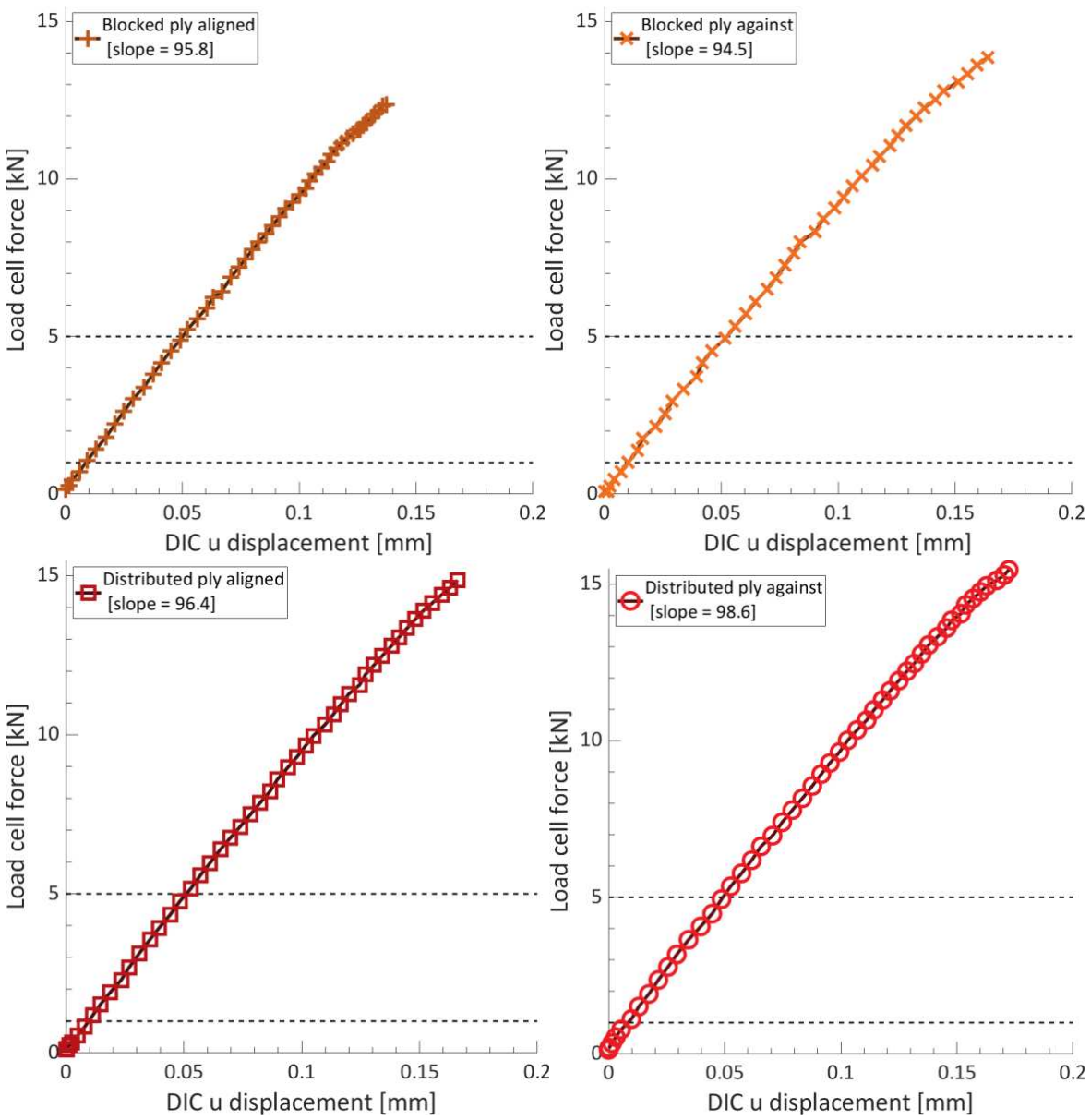

Figure 3: Load-displacement curves for representative specimens (labelled in legend), using the DIC displacements to avoid erroneously capturing the compliance of the test machine and MAF. Slopes are calculated using values from 1 kN to 5 kN (marked with horizontal dotted lines).

The load-displacement curves in Figure 3 show that the laminates largely had the same stiffness (as expected from their layup and classical laminate theory), making it unlikely that the difference in strength was due to manufacturing variation. The distributed ply stiffnesses are slightly greater than those for the blocked ply specimens, attributable to their higher strength with more load required for damage initiation and propagation (and so their effective stiffness remaining greater in the load range used).

Although DIC is a surface technique, plots of out-of-plane displacement '*w*' can be obtained, which allow the onset of subsurface delamination to be identified as the surface ply separates from subsurface plies. The delamination is observable as an abrupt change in the out of plane displacement. The out-of-plane displacement plots showed that the damage progression and failure mode vary significantly between the aligned and against cases, providing a justification

for the difference in strengths shown in Table 1. In the aligned case delamination was clearly visible, with abrupt tensile fibre failure in the surface ply and complete delamination between the surface and inner plies. For the against cases delamination also features, but this was preceded by compressive fibre failure originating from the hole. The resulting failure was more progressive, with gradual delamination around through-thickness cracks leading to matrix cracking and subsequent load drops.

While the failure modes for the aligned and against cases are consistent across the two laminates, the difference is less for the distributed ply specimens than the blocked ply specimens. This is thought to be due to the greater unconstrained ply thickness for the blocked ply laminate – this lay-up shows greater compressive fibre failure pre-delamination which sometimes results in damage in the far-field corners away from the hole (not detected in the distributed ply specimens), although failure still occurred due to the spread of delamination from cracks around the hole. The difference in damage between the two laminates is shown in Figure 4 below via plots of the maximum principal strain ε_1, where high-strain regions (i.e. where the colour scale is at its maximum limit) indicate a displacement discontinuity due to damage rather than a 'real' strain reading.

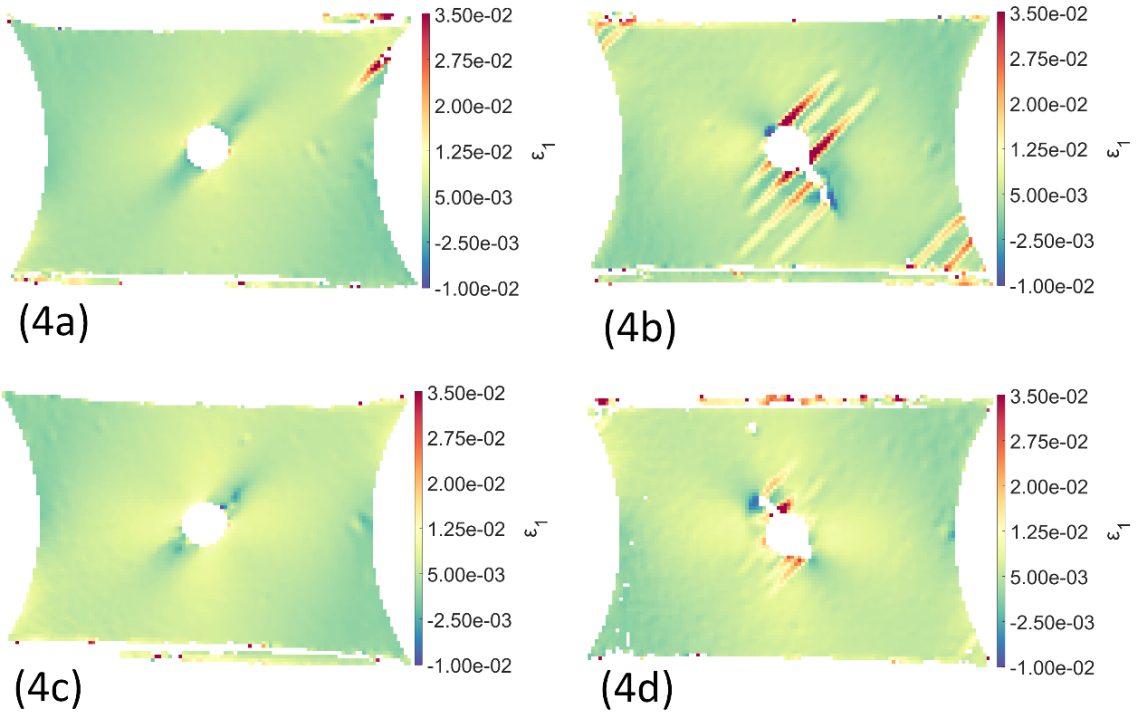

Figure 4. Maximum principal strain ε_1 plots obtained via DIC for a blocked ply aligned-loaded specimen (a), a blocked ply against-loaded specimen (b), a distributed ply aligned-loaded specimen (c), and a distributed ply against-loaded specimen (d) at 99% of the maximum load.

4. Conclusions

It has been demonstrated that the fibre orientation of the surface ply relative to the direction of the applied shear force had a significant effect on the open hole shear strength of CFRP laminates. When the shear force was applied so that its line of action opposed the surface ply fibre direction ('against'), the specimen strength was greater than when the load was applied so

that it aligned with the surface ply fibre direction ('aligned'). This was the case for both specimens with a blocked ply lay-up and a distributed ply lay-up, although the orientation effect was less for the thin-ply laminates. The increased strength of the distributed ply versus blocked ply laminates previously reported for open-hole compression tests [2] is also present here in shear loading, likely due to the same in-situ strength effects preventing damage propagation.

The reason for the difference in strength was identified using plots of out-of-plane displacement obtained using stereo DIC. The aligned failure was observed to be caused mainly by surface ply delamination around the hole before abrupt failure. The against case resulted in compression loading the surface ply, which resulted in a more progressive failure. The distributed ply laminate was less susceptible to the surface ply orientation effect.

Acknowledgements

The research presented was supported by the EPSRC Programme Grant 'Certification for Design – Reshaping the Testing Pyramid' (CerTest, EP/S017038/1) and the Faculty of Engineering, University of Bristol. The support received is gratefully acknowledged.

5. References

1. Yokozeki T, Aoki Y, and Ogasawara T. Experimental characterization of strength and damage resistance properties of thin-ply carbon fiber/toughened epoxy laminates. Composite Structures. 2008; 82(3):382–389.

2. Furtado C, Tavares RP, Arteiro A, Xavier J, Linde P, Wardle BL, et al. Effects of ply thickness and architecture on the strength of composite sub-structures. Composite Structures. 2021; 256.

3. Wisnom MR, Hallett SR. The role of delamination in strength, failure mechanism and hole size effect in open hole tensile tests on quasi-isotropic laminates. Composites Part A: Applied Science and Manufacturing. 2009; 40(4):335–342.

4. Laux T, Gan KW, Dulieu-Barton JM, Thomsen OT. Ply thickness and fibre orientation effects in multidirectional composite laminates subjected to combined tension/compression and shear. Composites Part A: Applied Science and Manufacturing. 2020; 133.

  doi:10.5075/epfl-298799_978-2-9701614-0-0

Composites Meet Sustainability – Proceedings of the 20th European Conference on Composite Materials,
ECCM20. 26-30 June, 2022, Lausanne, Switzerland

CARBON FIBRE FOAMS : INTERNAL STRUCTURE AND MECHANICAL PROPERTIES

Alec De Kuyper[a], Frederik Desplentere[a], Steven K. Latré[b], Kenichi Yoshioka[c],

Masato Honma[c], Hiroaki Matsutani[c], Terumasa Tsuda[c], Ignaas Verpoest[d],

Stepan V. Lomov[d]

a: Research Group ProPoliS, KU Leuven Bruges Campus, Bruges, Belgium –
alec.dekuyper@kuleuven.be
b: Mecha(tro)nic System Dynamics LMSD, KU Leuven Bruges Campus, Bruges, Belgium
c: Composite Materials Research Laboratories CMRL, Toray Industries, Ehime, Japan
d: Composite Materials Group, Department of Materials Engineering, KU Leuven, Belgium

Abstract: *Deconsolidated carbon fibre reinforced thermoplastic polymers combine low density with high resistance to mechanical loads. Toray Industries' "carbon fibre reinforced foam" (CFRF™) is one such new material consisting of carbon fibres in a polymer matrix. The internal structure of these CFRF is investigated via micro-CT-scans. An anisotropic internal structure with almost planar fibre orientations is observed and the polymer is seen as blob-like structures at the fibre junctions or on the fibres. The compression resistance in the out of plane direction for different volume fraction samples was measured. A linear approximation for the compression behaviour is simulated by three types of models: a model of random fibrous assemblies-; a finite element model based on the micro-CT-scans and material properties derived from a Mori-Tanaka homogenization; and a two stage Mori-Tanaka homogenization, the first stage for a solid polymer and fibre mix, the second stage a foam-type homogenization accounting for the voids.*

Keywords: random; fibre; orientation ; foam ; compression

1. Introduction

Toray Industries' "carbon fibre reinforced foam" (CFRF™) is a relatively new type of carbon fibre reinforced thermoplastic [1, 2]. It consists of a directionally expanded "carbon fibre mat in a thermoplastic polymer matrix", the expansion creating voids. These CFRF can be made in complex panel shapes [1] with varying thickness up to several mm and cm and a range of material volume fractions. The panels are lightweight and can handle high compressive loads.

From such CFRF panels, samples with an area of 1cm² or 16cm² and different thicknesses are studied. The thickness of these samples is directly related to the "fibre volume fraction" (VF), which represents the volume fraction of the carbon fibres in the samples, the remaining being occupied by the polymer and the voids in the foamy structure. The amount of carbon fibre and of polymer remains the same for all samples, which only differ in thickness. Inside the solid phase, the relative fraction of carbon fibre volume to polymer and carbon fibre volume is kept constant.

The carbon fibres, produced by Toray Industries, have a diameter of 7 µm and are of the order of several mm in length. The relevant material parameters used in further calculations are shown in Table 1. Further details on the production process of CFRF or the materials used and their relative fractions cannot be disclosed at this time. The notation used in Table 1 is: E = Young's

  doi:10.5075/epfl-298799_978-2-9701614-0-0

modulus; ν = Poisson ratio; G = Shear modulus; L = longitudinal direction of the fibre; T = transverse direction of the fibre.

Table 1: Material parameters of carbon fibre and polymer

Material	E_L	E_T	ν_{LT}	ν_{TT}	G_{LT}	G_{TT}
Carbon fibre (C)	230 GPa	8.0 GPa	0.256	0.3	27.3 GPa	3.08 GPa
Polymer (P)	2.1 GPa		0.43			

2. Internal structure of the CFRF samples

CT-scans of samples with a VF of around 0.08 and 0.04 were carried out at resolutions of 3.5µm and 5µm per pixel. In the resulting scan images, solid material and voids can be distinguished using image processing software Fiji (ImageJ, [3]) to denoise and set intensity thresholds accordingly. After the image processing, the volume of material in the images is close to the expected total material volume for the sample. This indicates that not many thin polymer zones are present, which could have been cut off by the thresholding. Figure 1 shows some selected regions of CT-scans.

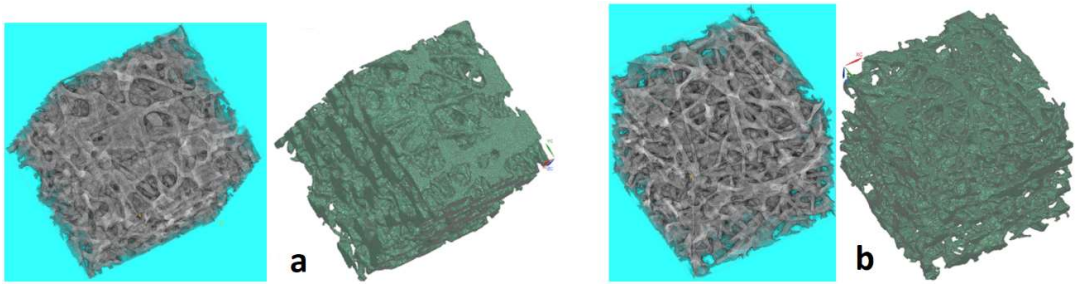

Figure 1. Images and FE meshes of a 0.34mm³ zone of a sample with TVF=0.084 (a) and a 1mm³ zone of a sample with TVF=0.043 (b)

2.1 Fibre orientation distribution

The fibre orientation distribution functions (ODF) are obtained from the CT-scan image stack of 1cm² area samples, using VoxTex [4], a software program using a voxel model and structure tensor to calculate orientation distributions.

Figure 2 shows a resulting ODF. The distribution is almost planar, around a mid-plane of the fibre orientation. We call the direction perpendicular to this mid-plane the “out of plane direction”, which is also the direction of the varying sample thickness and compression direction in the following sections. A random in plane distribution and an out of plane distribution with mean deviation from the mid-plane of approximatively 10°, can be seen in Figure 2. It is noteworthy that the samples with different thickness (different VF) have almost the same out of plane distribution.

  doi:10.5075/epfl-298799_978-2-9701614-0-0

As an approximation to the measured ODF, in the following simulations, the ODF will be set as a uniform distribution for the in-plane angle ϕ and approximated by a normal distribution for the out of plane angle θ, with a standard deviation of 10° .

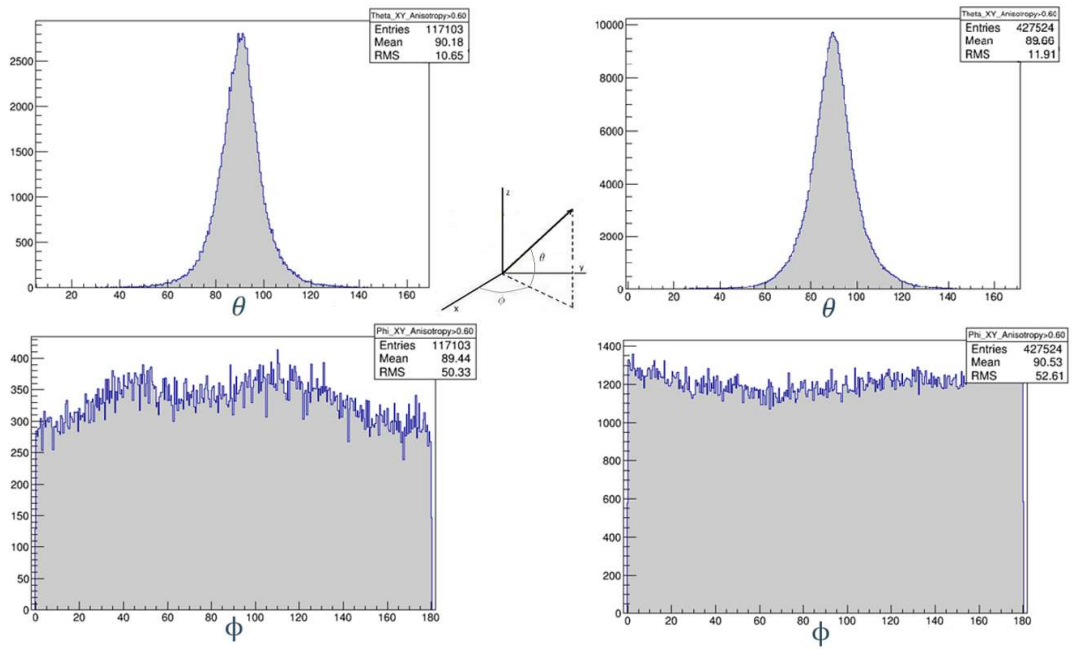

Figure 2. Angle distributions (°) for a sample with VF=0.084 (left) and VF=0.043 (right)

2.2 Polymer distribution

In Figures 1 and 3, we see that the polymer is largely present as blob-like structures at fibre crossings or along the fibre surfaces. The degree to which a blob like distribution is created during the production stage, depends on the materials used. Although some "polymer webs" are also present, see Figure 4, the main structural effect of the polymer will be through the blob like structures connecting the carbon fibres. These effectively function as polymer "spacers" or "bridges" between the fibres, increasing the number of fibre contact points.

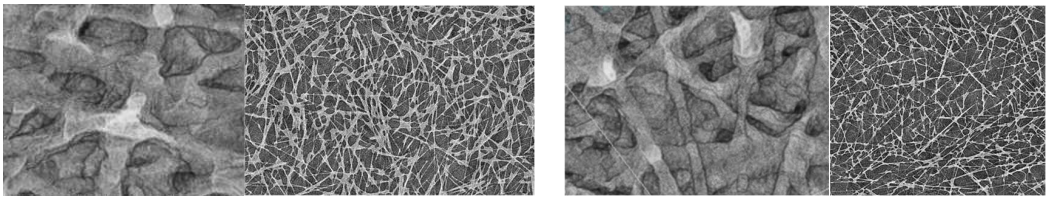

Figure 3. Fibre junction and horizontal slice image for VF=0.084 (left) and VF=0.043 (right)

  doi:10.5075/epfl-298799_978-2-9701614-0-0

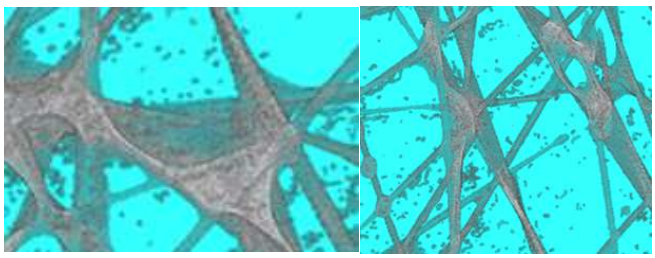

Figure 4. Web-like polymer stretching between fibres for VF=0.04 (higher resolution scan 0.81µm/pixel)

3. Compression modulus: measurements

The compression modulus discussed currently only relates to a linear out of plane-direction compression modulus. For measurements on other moduli, see [2]. CFRF samples were placed between parallel plates on a compression test bench and the force and displacement were measured. The compression rates were set between 0.02 and 0.5 kN/min, depending on sample size. The modulus was measured between the points at 3% and 5% -engineering strain on the compression diagram (see orange points on Figure 5) to calculate this modulus at "4% strain".

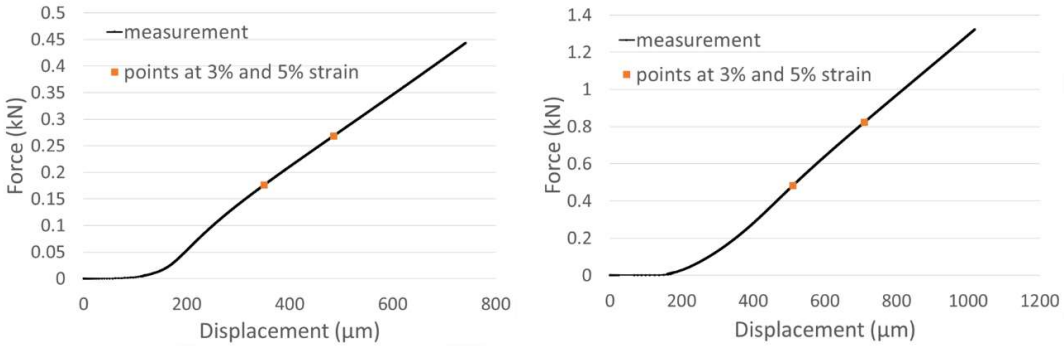

Figure 5. Compression measurements of a sample with $VF = 0.068$ (thickness = 6.7mm, section area 1cm²) (left) and $VF = 0.046$ (thickness = 10.2mm, section area 16cm²) (right)

This range was chosen because it is small enough not to reach any plastic deformation on a macroscopic scale, but large enough past measurement artefacts and non-linear behaviour at initial compression. The compression measurement results are show in Figure 6 (blue points), each point representing a different sample. Some variation in the compression results between the different samples can be seen, indicating statistical variations over a larger scale (> 1cm) in the complete CFRF panels.

  doi:10.5075/epfl-298799_978-2-9701614-0-0

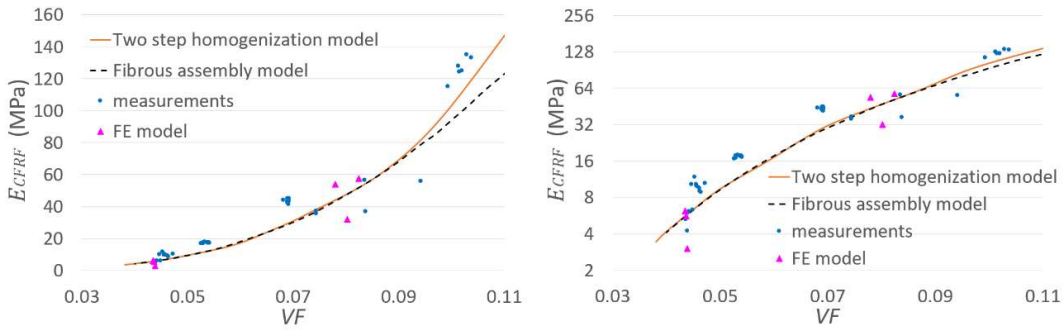

Figure 6. Measured and modelled CFRF compression modulus, lin. scale (left) , log. scale (right)

4. Compression modulus: simulations

The polymer blob-like structures will increase the number of fibre contact points and create a more foam-like structure. Compared to a carbon fibre only assembly, this leads to an increase in the compression resistance. Three models disregarding viscous-, friction- or time dependent effects, are introduced, to calculate the linear compression modulus.

4.1 Fibrous assembly model

This model is based on the works of Komori [5], Lee [6], Carnaby [7] and Pan [8] to which modifications are made to include effects of the "polymer bridges" at the fibre junctions. These fibrous models use a probabilistic fibre distribution and suppose the bending of fibre pieces, as the compliance mechanism for the fibrous assembly. These fibre pieces are supported at the fibre contact points. The vast majority of fibre contact points will be "fixed", by the polymer, so sliding of fibres over each other is not included, compared to the model as explained in [7]. The modifications are (1) a correction for low out of plane fibre orientation distributions; (2) a modification that rests on the idea that the carbon fibres with diameter d_C, are replaced with fibres that have been uniformly coated by polymer. As such they have obtained a diameter $d = d_C + d_P$, with the thickness of the "virtual coating" being $d_P/2$. Thus the distance between two crossing fibres connected by polymer, the "polymer bridge length", is equal to d_P. The bending rigidity of these fibres is still based on the carbon fibre diameter d_C and carbon material properties, but the number of fibre contacts in the assembly increases and the inter-contact-fibre-length decreases due to the addition of the virtual coating. (3) Compressive compliance of the polymer bridges is also included under the assumption is that the polymer bridges have a square cross section with area d_C^2.

The results of using the modified model with an ODF described in section 2.1 and for a bridge length fit parameter $d_P = 3.14\ \mu m$ can be seen in Figure 6 (dotted line). The parameter d_P in this case was obtained by fitting it at $VF = 0.044$ so that the calculated value for the compression modulus approximates the measurement results at this VF. The curve at all other VF is then calculated using the same parameter d_P. Using a constant d_P is another approximation, in general d_P could depend on the VF.

The shape of the fibrous assembly model curve follows the trend of the measurement points quite well, including a steep rise towards higher VF.

  doi:10.5075/epfl-298799_978-2-9701614-0-0

The advantage of this model is that as a fibrous assembly model with only one fit parameter, it has a clear and verifiable physical interpretation via the polymer bridge length. It is also easy to implement and has an extremely low computational cost.

4.2 Finite element model

In this model a linear structural finite element (FE) calculation is performed with a mesh based on the geometry obtained from the CT-scans. A linear tetrahedral mesh for cubic zones in the samples is first constructed using iso2mesh [9] , and then converted to a second order tetrahedral mesh in Siemens Simcenter3D, which is also used to perform the FE calculation. Meshes and the geometries of the corresponding zone are show in Figure 1.

An out of plane displacement for the nodes in the top plane of the cubic zone is imposed, while the nodes in the bottom plane are fixed. No constraints are imposed at nodes in the side planes of the cubic zone. From the resulting force obtained from the FE calculation, a linear compression modulus for the cube zone is derived.

The material properties assigned to the elements in the FE calculation are a homogenized (transverse isotropic-) elasticity tensor for a mix of polymer and carbon fibre. This is an extra approximation, instead of segregating the elements for carbon fibre and polymer.

A Mori-Tanaka (MT) procedure for ellipsoidal inclusions [10] is used to obtain the homogenized elasticity tensor $\boldsymbol{E}_*$. The polymer with elasticity tensor $\boldsymbol{E}_P$ is the host material and the carbon fibres with elasticity tensor $\boldsymbol{E}_C$ are the almost cylindrical inclusions, the orientation of which is defined by the ODF [11]. In this way, the homogenization procedure results in anisotropic properties of the polymer and carbon fibre composite solid phase, which are then introduced in the FE-calculation in order to take into account the intricate foam geometry of the CFRF.

In Figure 6, the averages of FE model results for several cubic zones (10 or 3) at different *VF* are shown (magenta points). Even though the limited amount of cubic zones used for these points, the results are close to measured points.

Using the actual geometry, the FE model has the advantage of a possibility of exploring local effects if a fine enough mesh can be constructed. There is also no necessity to fit any parameters. A disadvantage is that high enough resolution CT scan data is required and a relatively high computational cost for the FE calculation compared to the other models.

4.3 Two stage homogenization model

In this model, in a first stage, the polymer and carbon fibre composite solid phase is homogenized with the same MT procedure as is done in the FE model. In contrast with the FE model, in a second stage, the foam-like geometry of the CFRF is now constructed by introducing voids in the homogenized material of the first stage, while in the FE model, the geometry was obtained from the CT scans. This introducing of voids is done with a Lielens homogenization procedure which is an interpolation of MT and inverse MT homogenization procedures [12]. The reason for using a Lielens procedure is that the volume fraction of voids to be introduced as inclusions is relatively high and there is more uncertainty about the validity of the standard MT procedure at higher inclusion volume fractions.

  doi:10.5075/epfl-298799_978-2-9701614-0-0

A spheroidal shape is assumed for the void inclusions, Figure 8, where the a_3 orientation is aligned with the out of plane direction. All the voids are assumed to be the same shape, hence no averaging for different void inclusions is necessary.

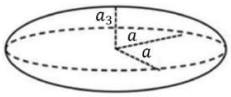

Figure 8. Spheroidal shape of the void inclusions

The two parameters a and a_3 will be dependent on the VF of the samples. We make two assumptions concerning the spheroidal voids of the samples. First, we assume that the number of voids remains the same at different VF. The second assumption is that there is a linear relationship between the in-plane width of a void spheroid a, and the average inter-fibre-contact length of a purely carbon fibre random assembly b_C . Then, the aspect ratio (AR) is fit to approximate measured values at VF = 0.044 , resulting in $AR = \frac{a_3}{a} = 0.0122$.

The very low AR indicates disc like voids, which relates to the almost planar fibre orientation. Results of this two-stage homogenization model are shown in Figure 6 (orange line).

As was the case for the fibrous assembly model, the two-stage model curve follows the trend of the measurement points quite well. The curve for this two-stage model is almost identical to the curve of the fibrous assembly model up to $VF \approx 0.09$.

The advantage of this model is that it is computationally inexpensive and the elasticity tensor for the CFRF is obtained. One has to be aware however that the two assumptions made concerning the spheroidal voids will surely break down for very low void fractions.

5. Conclusions

For the discussed CFRF samples, the polymer is mainly distributed in blob-like structures at fibre crossings or at the surface of the carbon fibres. The carbon fibres have an almost planar orientation distribution that is nearly independent of VF.

The out of plane compression behaviour is non-linear and has some hysteresis, but as a linear approximation, the compression modulus for CFRF samples, ranges between 5 to 140MPa for samples with VF between 0.04 to 0.1 . This is substantially larger than if only the carbon fibres would be present in a similar assembly and is due to the polymer blobs forming a more interconnected structure.

Three models for this linear compression behaviour were proposed. None of the models describe the process of the spreading of the polymer during the production stage and as such still require at least one parameter to be fit or a geometrical description of the CFRF structure to be given. Due to variations between samples, the obtained model curve is very dependent on which points were chosen to approximate via the fit parameter. Nonetheless, the trend of the measured points is captured quite nicely if an appropriate parameter is chosen (fibrous assembly and two stage homogenization models) or enough sample zones are used (FE model).

  doi:10.5075/epfl-298799_978-2-9701614-0-0

Acknowledgements

The FWO large infrastructure I013518N project is acknowledged for their financial support and the KU Leuven XCT Core facility is acknowledged for the 3D image acquisition and quantitative post-processing tools (https://xct.kuleuven.be/)

Support of the work in KU Leuven by Toray Industries through Toray Chair for Carbon Composites, held by IV and SVL, is gratefully acknowledged.

6. References

1. Y. Wan and J. Takahashi, "Deconsolidation behavior of carbon fiber reinforced thermoplastics," J. Reinf. Plast. Compos., vol. 33, no. 17, pp. 1613-1624, 2014.
2. Y. Takebe, N. Hirano, M. Honma, K. Shinohara and T. Fujioka, "A New Foam Material Made from Discontinuous Carbon Fiber Reinforced Plastics", J. of the Society of Materials Science, Japan., vol. 65, no. 8, pp. 555-560, 2016.
3. J. Schindelin, I. Arganda-Carras and E Frise, "Fiji:an open-source platform for biological-image analysis", Nature methods, vol. 9, pp. 676-682, 2012
4. I. Straumit, S. Lomov and M. Wevers, "Quantification of the internal structure and automatic generation of voxel models of textile composites from X-ray computed tomography data", Composites part A, vol. 69, pp. 150-158, 2015
5. T. Komori and K. Makishima, "Numbers of Fiber-to-Fiber Contacts in General Fiber Assemblies" , Textile Research Journal, Vol47, Issue 1, 1977
6. D.H. Lee, "Initial Compressional Behaviour of Fibre Assembly", Doctoral thesis, Seoul National University, 1985
7. G. A. Carnaby and N. Pan, "Theory of the Compression Hysteresis of Fibrous Assemblies", Textile Research Journal, Vol59, Issue 5, 1989
8. N. Pan, "A Modified Analysis of the Microstructural Characteristics of General Fiber Assemblies", Textile Research Journal, Vol63, Issue 6, 1993
9. A. P. Tran, S. Yan and Q. Fang, "Improving model-based fNIRS analysis using mesh-based anatomical and light-transport models", Neurophotonics, Vol.7(1), 0150008, 2020
10. T. Mura, "Micromechanics of defects in solids", ISBN:978-94-009-3489-4, 1987
11. M. Ferrari and G. Johnson, "Effective elasticities of short-fiber composites with arbitrary orientation distribution", Mech. of Materials, Vol.8, pp.67-73, 1989
12. E. Ghossein and M. Lévesque, "Homogenization models for predicting local field statistics in ellipsoidal particles reinforced composites: Comparisons and validations", J. of Solids and Structures, Vol.58, pp.91-105, 2015

  doi:10.5075/epfl-298799_978-2-9701614-0-0

STUDY ON MODE I FRACTURE TOUGHNESS OF COMPOSITE LAMINATES BASED ON THE CORRELATION BETWEEN AE SIGNAL AND CRACK FRONT SHAPE

Hyun-jun Cho[a], Min-Hyeok Jeon[a], Hae-Ri No[a], and In-Gul Kim[a]

a: Department of Aerospace Eng., Chungnam National University, Daejeon, Republic of Korea- jonet123@hanmail.net

Abstract: *The fracture toughness of composite laminates varies with crack length and the crack front shape that has thumbnail shape along with the width. A prediction method of failure behavior considering these complex failure behaviors of composite materials is required. We used 2D FEA and an AE sensor for predicting failure behavior and crack length of composite laminates under Mode I loading. The crack length was measured at the side and widthwise center of the specimen using cameras. An AE sensor was used for measuring elastic waves induced by the fracture of the specimen and predicting crack length. We analyzed acoustic emission signals depending on damage mechanisms and the predicted crack length using these signals. FEA was conducted using a crack front shape and AE signal and the FEA results with the crack length between the side and widthwise center of the specimen was similar to the experimental results.*

Keywords: DCB; Finite element analysis; Crack front shape; AE signal; Equivalent crack length

1. Introduction

The fracture toughness of the composite materials varies with crack length and the crack front shape with a thumbnail shape widthwise. To ensure the integrity of the structures, a prediction method of failure behavior considering the complex fracture behavior of composite materials is required. Mode I fracture toughness has been mainly studied because of its lowest fracture toughness compared to the others, and a double cantilever beam (DCB) test in accordance with ASTM 5528 has been used to analyze the fracture toughness of polymer matrix composites.

An Acoustic Emission (AE) sensor is a powerful tool for analyzing the fracture behavior of composite materials, and many authors [2-6] have studied using it specifically for this purpose. Yousefi et al. [2] reported that the correlation between the AE signal and crack length measured at side of the specimen show a power law and predicted the crack length using an AE signal. Arumugam et al. [5] discriminated frequency ranges (90-120 kHz, 130-200 kHz, 220-245 kHz, 260-295 kHz, and 300-450 kHz) depending on the damage mechanisms, such as matrix cracking, fiber pullout, fiber-matrix de-boding, delamination, and fiber breakage.

The virtual crack close technique (VCCT) and cohesive zone modeling (CZM) are representative methods for predicting fracture behavior using 2D and 3D elements. In particular, finite element analysis (FEA) using 2D element is simple and requires relatively less run-time. However, the crack front shape shows a curvature, and this shape results in less fracture toughness than straight ones [1]. Therefore, we should use the equivalent crack length considering the crack front shape for accurate fracture toughness.

  doi:10.5075/epfl-298799_978-2-9701614-0-0

In this paper, we analyzed the fracture toughness of glass/epoxy composite laminates using an AE signal and 2D FEA. To do this, we discriminated the AE signals depending on damage mechanisms, and analyzed the correlation between the AE signal and crack length. Lastly, the fracture toughness using crack length at side, widthwise center of specimen and a distance to centroid of crack front shape as alternative crack length were adopted in a 2D FEA model, and we compared with experimental results.

2. Experimental procedure

2.1 Specimen Fabrication

DCB specimens were fabricated using glass/epoxy prepreg (UGN 160 B, SK chemicals corporation), and a hand lay-up technique with 32 layers. The polyimide film was inserted in the mid-plane of a specimen as an artificial crack, and the composite laminate was cured using an autoclave machine. Stacking sequence is $[0_{16}//+\theta/-/\theta/0_{14}]$, and '//' indicates a layer inserted an artificial crack. Table 1 and Table 2 show the specifications of the DCB specimen and the material properties of glass/epoxy prepreg, respectively.

Table 1: Specifications of DCB specimen.

Specimen	Stacking sequence	Size (mm)	Thickness (mm)	Artificial crack Length(mm)
Specimen A	$[0_{16}//0_{16}]$	25Wx260L	4	50
Specimen B	$[0_{16}//+30/-30/0_{14}]$			

Table 2: Material properties of glass/epoxy prepreg.

E_1(MPa)	E_2(MPa)	ν_{12}	G_{12}(MPa)
40,710	10,000	0.32	3,570

2.2 AE sensor

An AE sensor (UT1000, Physical Acoustic Corporation) was used for measuring the elastic waves induced by a fracture of the DCB specimen. To record the AE events, a digital oscilloscope (PXI-5102) was used, and the signals were enhanced using a preamplifier. The AE sensor was attached on the upper surface of the specimen using thin double-sided tape. The distance between the AE sensor and loading point was 120 mm. The sampling rate and the sample number was 2MHz with 8 bit of resolution and 200k (0.1 sec), respectively.

2.3 Test procedure

DCB test was conducted in accordance with ASTM 5528 and at a constant crosshead displacement rate of 1 mm/min. Figure 1 represents a schematic diagram of DCB test. The load and displacement data were recorded on a computer at 10 Hz. Two cameras were used for measuring the crack lengths at the side and widthwise center of the specimen, respectively.

The specimen with an artificial crack (a_0=50 mm) was loaded until the crack length based on side of specimen propagated at 5 mm (a_i=55 mm) and then reloaded. After that, the test

continued until crack length reached 100 mm. In the results and discussion section, load, displacement, and crack length data from a crack length of 55 mm to 100 mm were used.

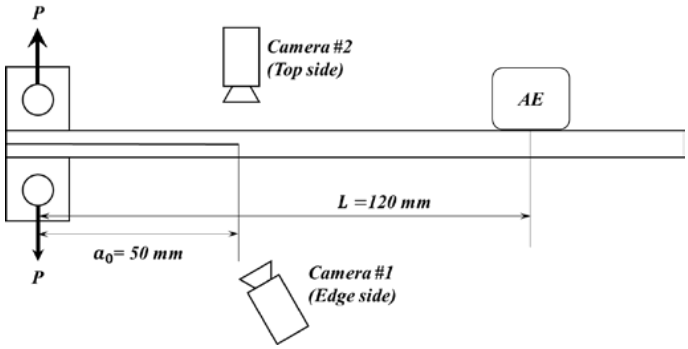

Figure 1. Schematic diagram of the DCB test

3. Finite element analysis

3.1 Cohesive zone modeling

Cohesive zone modeling is a good method to simulate crack propagation. A bi-linear cohesive zone element was used for simulating the crack propagation of the DCB specimen under Mode I loading. Figure 2 represents the constitutive equation of the bi-linear cohesive zone element. The cohesive zone element consists of fracture toughness (G_{IC}), initial interfacial stiffness (K_0), and interfacial strength (σ_{max}), and the failure of the element would occur when the dissipated energy during fracture equals to the fracture toughness.

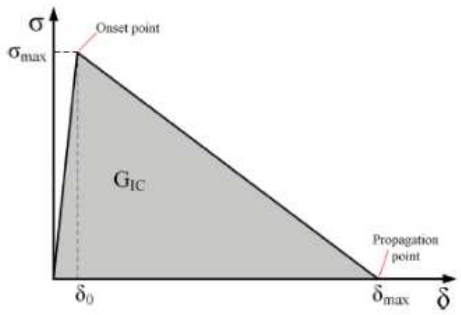

Figure 2. Bi-liner constitutive equation of the cohesive zone element [3]

Figure 3 represents FEA model for the DCB specimen using 2D four-node plane strain element (CPE4) and cohesive zone element (COH2D4). In the case of the composite materials, the fracture toughness varies with the crack length, and these were applied in FEA.

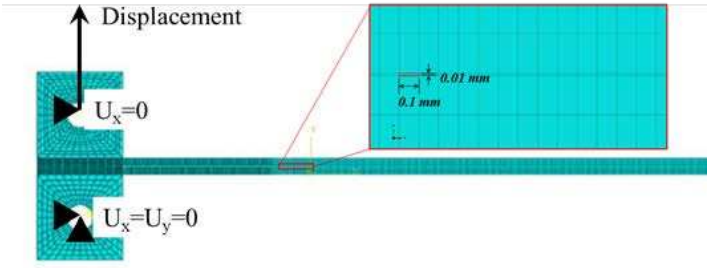

Figure 3. FEA model for the DCB test

4. Results and discussion

4.1 DCB test results

4.1.1 Load and crack length and cumulative AE energy-displacement curve

Figure 4 shows the load, crack length and cumulative AE energy-displacement curve. In case of Specimen A, the load increased linearly and then decreased gradually after the onset of the crack propagation. In contrast, the load increased continuously after the onset of the crack propagation and then decreased gradually in Specimen B. This is due to fiber bridging in the specimen that has an interfacial fiber angle. In case of Specimen B, the cumulative AE energy increased abruptly a few times. This was due to the delamination of the fiber bundle from the crack surface. The signal amplitude was very much higher than the other signal, but this behavior did not lead to an abrupt load decrease, and there was no abrupt crack propagation.

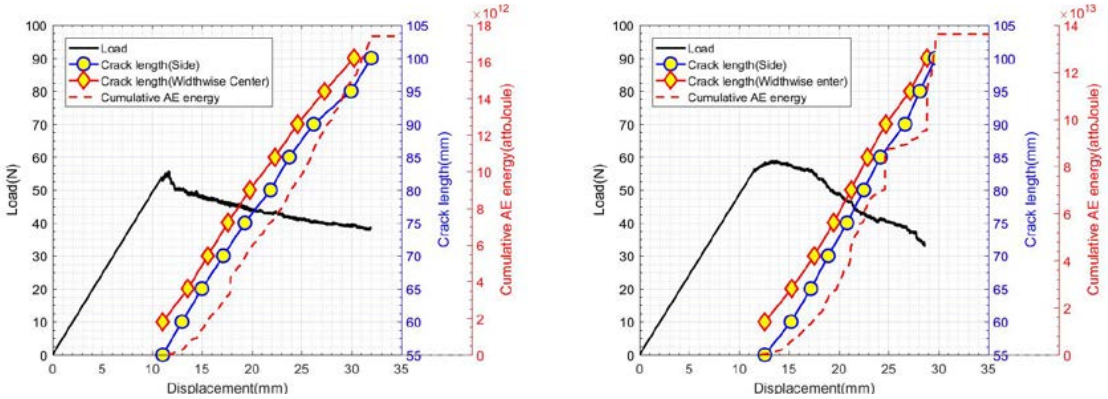

Figure 4. Load and crack length and cumulative AE energy-displacement curve

Figure 5 shows a crack front shape with a crack length of 55 mm, based from the side of the specimen. In the entire specimen, the crack tip at the widthwise center of specimen preceded the crack tip at the side of specimen, and crack front shape showed thumbnail shape.

(a) Specimen A *(b) Specimen B*

Figure 5. Crack front shape

We used two crack lengths in 2D FEA model respectively. In addition, we assumed that the crack front shape is an elliptical shape, and a centroid of the ellipse was applied in FEA model as alternative crack length.

4.1.2 The correlation between accumulative AE energy and crack length

Yousefi et al. [3] assumed that the correlation between the cumulative AE energy and crack length has a power law relation.

  doi:10.5075/epfl-298799_978-2-9701614-0-0

$$a = \alpha \times E_c^{\beta} + \gamma \quad (1)$$

where, E_c is cumulative AE energy, a is crack length, $\alpha, \beta,$ and γ are coefficient related to the power function.

Arumugam et al. [5] discriminated the frequency ranges of the AE signal depending on the damage mechanisms and reported that delamination was found to be in the range of 260-295 kHz. We used these ranges for predicting the crack length using an AE signal.

Figures 6 and 7 show the predicted crack length using Eq. (1) versus the visible crack lengths. Each of them corresponded as expected. However, there were a few errors between 85 mm and 100 mm of displacement in Specimen B. As mentioned in Section 4.1.1, this is due to the signal being higher than the other signal induced by the delamination of the fiber bundle from the crack surface, but it was insufficient to lead to an abrupt crack propagation.

The fracture toughness were calculated using MBT (Modified beam theory) in ASTM 5528, and crack lengths at the side, widthwise center of specimen and a distance to centroid of crack front shape, respectively. Then the fracture toughness were applied in 2D FEA.

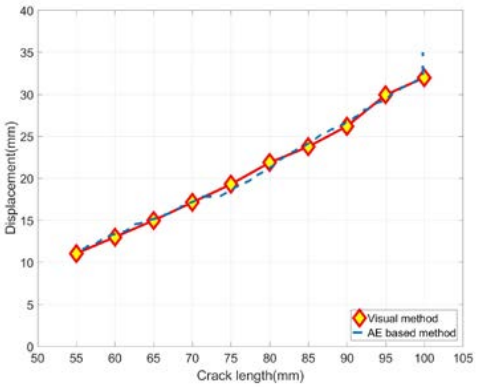

(a) Crack length at the side

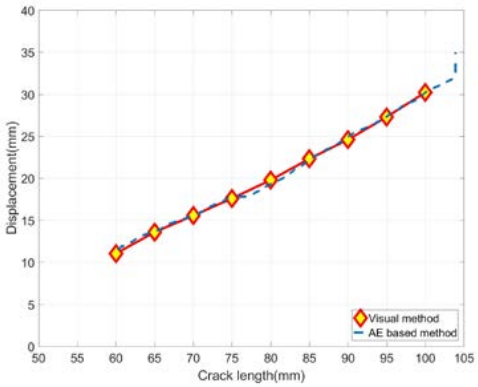

(b) Crack length at the widthwise center

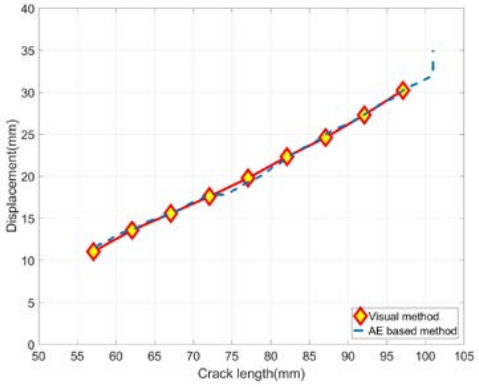

(c) Crack length as distance to centroid

Figure 6. Displacement versus the predicted crack length and the visible crack length for Specimen A

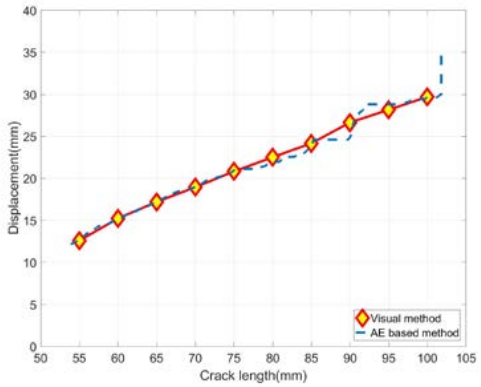

(a) Crack length at the side of specimen

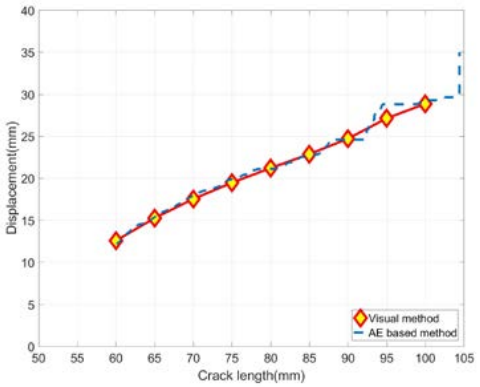

(b) Crack length at the widthwise center

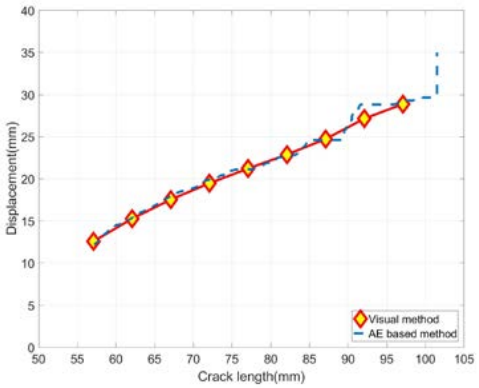

(c) Crack length as distance to centroid

Figure 7. Displacement versus the predicted crack length and the visible crack length for Specimen B

4.2 Finite element analysis results

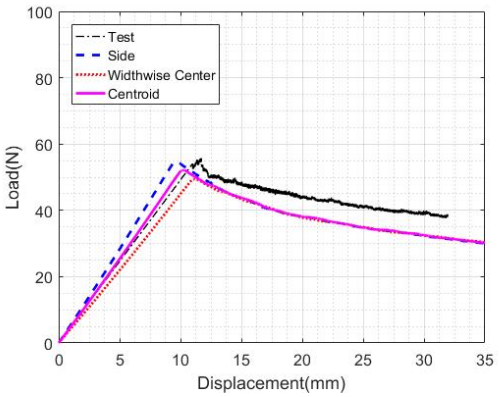

(a) Specimen A

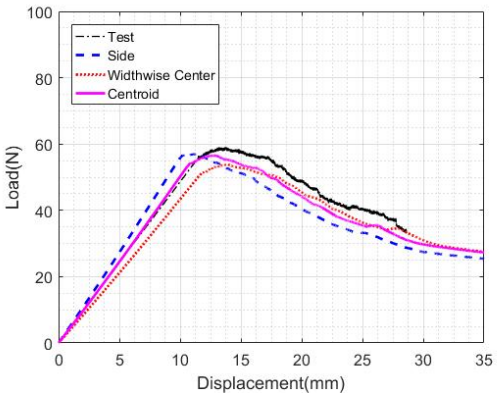

(b) Specimen B

Figure 8. Comparison of the load-displacement curve between the experimental and FEA results

Figure 8 shows comparison of the load-displacement curve between the experimental and FEA results. Based on the range where the load increases linearly the FEA results using the crack length at the side of the specimen were stiffer than the experimental results. In contrast, the results using the crack length at the widthwise center of the specimen were more flexible than

the experimental results. The results using a distance to centroid of crack front shape were similar to the experimental results than other cases. After the onset of the crack propagation, all of cases showed a similar trend.

5. Conclusions

In this paper, we studied the fracture behavior of glass/epoxy composite laminates using the AE signal and 2D FEA. Two cameras were used for measuring the crack length at the widthwise center of the specimen as well as the side. An AE sensor was used for measuring the elastic wave induced by the fracture of the composite DCB specimen.

The crack front shape was recorded by a camera set on the upper surface of the specimen and the crack length at the widthwise center of the specimen preceded the crack length at the side of the specimen. The crack front shape assumed an elliptical shape, and a distance to its centroid was considered as alternative crack length. To divide the crack length measured at intervals of 5 mm in detail, the correlation between an AE signal and the measured crack length was used and was assumed that these have power law relation. The AE sensor receives all of signals induced by many damage mechanisms, so the signal was filtered between 260 and 295 kHz related to delamination. The crack length using AE signal corresponds to the measured crack length. However, there were a few errors in Specimen B because of the relative high amplitude of the signal induced by the delamination of the fiber bundle from the crack surface, although there was no abrupt crack propagation.

To calculate the fracture toughness applied in 2D FEA, the crack length using an AE signal was used. Based on that range where load increases linearly, the FEA results using the crack length at the side of the specimen were stiffer than the experimental results. In contrast, the results using the crack length at the widthwise center of the specimen were flexible than experimental results. Lastly, the results using a distance to the centroid of the crack front shape as crack length were similar to the experimental results than the other cases.

In further work, we should discriminate frequencies depending on the damage mechanisms, combining signal and then analyzing the correlation between the AE signal and the crack length using cumulative the AE counts as well the cumulative AE energy.

Acknowledgements

This research was supported by Basic Science Research Program through the National Research Foundation of Korea (NFR) funded by the Ministry of Education (2020R1I1A3071845).

References

1. Davison DB. An analytical investigation of delamination front curvature in double cantilever beam specimen. Journal of Composite Material 1990; 24:1124-1137.
2. Yousefi J, Mohamadi R, Saeedifar M, Ahmadi M, Hosseini-Toudeshky M. Delamination characterization in composite laminates using acoustic emission features. Journal of Composite Material 2017; 0:1-13.
3. Saeedifar M, Fotouhi M, Najafabadi MA, Hosseini-Toudeshky H. Prediction of delamination growth in laminated composites using acoustic emission and cohesive zone modeling techniques. Composite Structures 2015; 24:120-127.

4. Saeedifar M, Najafabadi MA, Yousefi J, Mohammadi R, Hosseini-Toudeshky M, Minak G. Delamination analysis in composite laminates by means of acoustic emission and bi-liner/tri-linear cohesive zone modeling. Composite Structures 2017; 161:505-512.
5. Arumugam V, Sajith S, Stanly AJ. Acoustic emission characterization of failure modes in GFRP laminates under Mode I delamination. Journal of Nondestructive Evaluation 2011; 30:213-219.
6. Oskouei AR, Ahmadi M. Acoustic emission characterization of Mode I delamination in glass/polyester composites. Journal of Composite Materials 2010; 7:793-807.
7. Shokrieh MM, Daneshjoo Z, Fakoor M. A modified model for simulation of Mode I delamination growth in laminated composite materials. Theoretical and Applied Fracture Mechanics 2016; 82:107-116.
8. Zhao L, Gong Y, Zhang J, Chen Y, Fei B. Simulation of delamination growth in multidirectional laminates under Mode I and mixed Mode I/II loadings using cohesive elements. Composite Structure 2014; 116:509-522.
9. Mohammad HR, Mousa S. Finite element modeling strategies for 2D and 3D delaminates propagation in composite DCB specimens using VCCT, CZM, and XFEM approaches. Theoretical and Applied Fracture Mechanics 2019; 103:102246.
10. ASTM D-5528-13, Standard test method for Mode-I interlaminar fracture toughness of unidirectional fiber-reinforced polymer matrix composite. ASTM international. West Conshohocken, PA, 2013.

THE INFLUENCE OF PRODUCTION WASTES INCORPORATION ON THE PROPERTIES OF THERMOPLASTIC MATRICES

Carolina Borges[a], Pedro Ferreira[a], Andreia Araújo[a,b], Raquel M. Santos[a,b]

a: Institute of Science and Innovation in Mechanical and Industrial Engineering, Rua Dr. Roberto Frias, 4200-465 Porto, Portugal – cnborges@inegi.up.pt
b: Associated Laboratory for Energy, Transports and Aeronautics, Porto, 4200-265, Portugal

Abstract: *The production of polymers has been growing since the 20th century, owing to their application in a wide range of sectors, from packaging and everyday objects to complex structures. Nevertheless, this growth has been brought several societal and environmental challenges, since millions of tons of plastic materials are being discarded every year. Up to now, landfilling and incineration have been the most waste disposal chosen routes. However, both are at the bottom of waste management hierarchy, and can no longer be considered an option due to the waste accumulation and intensive energy consumption. Thus, the implementation of a circular approach focused on the reusing, reintegration and recycling of polymers and their composites is of paramount importance. In the present study, different concentrations of production wastes were incorporated into virgin polymeric matrix by melt compounding. The thermal, electrical, rheological and mechanical properties were assessed for the recycled compounds.*

Keywords: recycling; thermoplastics; composites; sustainability

1. Introduction

The demand for high technological and eco-friendly solutions in highly demanding industries is a contemporary phenomenon. However, todays' generation belongs to a time where it acquired paramount interest, rising extremely stringent technical requirements along with new advanced materials. In such scenario, common materials applied to specific sectors, including light metals and alloys, can no longer assure totally economic and environmental viability. Polymer-based composites now stand out, also responding to the market evolution and the industry growth [1]. Carbon fiber reinforced polymer (CFRP) composites are composed by two or more distinct phases: i) a polymer matrix, which can either be a thermoplastic or a thermoset, and ii) an embedded reinforcement. Several advantages arise when a thermoplastic matrix is applied, such as reusing, repairing, reprocessability, recyclability and sustainability. High-performance and -temperature thermoplastic polymers of the poly(aryl ether ketone) (PAEK) family, in particular the poly(ether ether kethone) (PEEK) have been successfully employed on the development of advanced composites, owing to their unusual thermal, chemical and mechanical properties. PEEK is a linear and semi-crystalline polymer that can be continuously processed up to 350 °C, which is promoted by the presence of diphenylene ketone groups. For niche applications, as satellites, aeronautic and wear resistance components, the performance of PEEK can be further improved by incorporating continuous carbon fibers, giving rise to advanced composite materials [1]–[7].

Driven by new targets to lower carbon dioxide (CO_2) emissions and the need for lightweight structures, composites market size exceeded 10 billion USD in 2020 and it is expected to exhibit

  doi:10.5075/epfl-298799_978-2-9701614-0-0

an annual growth rate of over 7.3 % from 2021 to 2027 [8]. The boost in the CFRP exploitation is now, more than ever, raising awareness about their fate. An important question arises: what to do with the ever-increasing amount of processing scrap (e.g., non-conformities, production surpluses, scraps, cut-offs) and, belatedly, the end-of-life (EoL) of complex material composites? Up to now, landfilling and incineration have been the waste disposal chosen routes for plastics and traditional composites. However, these can no longer be considered viable approaches due to waste accumulation and intensive energy consumption issues, not to mention the increasingly stringent landfilling requirements. Bearing this in mind, and regarding the high energy consumption levels associated to virgin carbon fibers production, it is urgent to enhance composites recycling methods and the quality of the recycled materials [9]–[14]. Therefore, circular economy and sustainability are highlighted, in a world where progressive efforts are being done accordingly.

Notwithstanding, traditional composites recycling is inherently more difficult than thermoplastic matrices due to highly crosslinked nature of the incorporated thermoset resins [1]. Several recycling solutions have been implemented in recent years to improve the recycling yield and the properties of the recovered materials, including mechanical, chemical and thermal. All of them rely on the same principle: fiber size reduction, impurities removal when applicable, re-manufacturing, the production of high-quality recycled materials/products, and costs involved in recovered materials in comparison to virgin raw-materials. Mechanical recycling, the most technologically mature technique, consists of reducing components size by shredding techniques and further grinding or milling to obtain different particle sizes (that can range from fine powder to fibrous constituents). A different approach to attain mechanical recycling is the electrodynamic fragmentation, in which “residues” (secondary raw-materials) are shredded by means of a high voltage impulse. Other less mature recycling solutions can be found, such as electrochemical and biotechnological techniques [1], [10], [13], [15]–[17].

Various researchers have proved the viability associated to composite materials recycling, with special emphasis on CFRP. Roux et *al.* [17] demonstrated the recycling feasibility of high-content carbon fiber reinforced PEEK composites by fragmenting an aerospace part (door hinges) *via* electrodynamical fragmentation and then manufacturing new door hinges by compression molding with 100 % of recycled materials. Door hinges with recycled material exhibited a decrease of only 17 % compared to a novel composite. G. Schinner et *al.* [18] investigated two different possibilities for recycling CFR-PEEK composites, and it was found that PEEK reinforced with carbon fiber composites showed satisfactory processability even at high carbon fiber contents (50 wt.%).

In the present study, the performance of PEEK composites reinforced with recycled CFRP unidirectional tapes will be evaluated. For the purpose, “residues” will be first milled and micronized to obtain a filler used to produce compounds at three loadings, in a co-rotating twin-screw extruder, under different processing conditions. In terms of material characterization, test specimens prepared by injection or compression molding were submitted to mechanical, thermal, rheological and electrical analysis. Scanning electron microscopy analysis was also performed to characterize the fractured surface of the material after mechanical solicitation and rupture.

  doi:10.5075/epfl-298799_978-2-9701614-0-0

2. Experimental Part

2.1 Materials

PEEK 450G™, a suitable grade for injection molding and extrusion, supplied by Victrex™, with a melt viscosity of 350 Pa.s at 400 °C and a density of 1.30 g/cm^3 at 25 °C, was used as polymeric matrix. Unidirectional carbon fiber reinforced PEEK composites, supplied also by Victrex™, were milled into a fine powder and, afterwards, mixed with PEEK pellets at different loadings (2.5, 5 and 10 wt. %). All materials were previously dried overnight at 120 °C. A small portion (< 1 g) of micronized tapes was subjected to a granulometric laser analysis on a Coulter LS 230 Small VolumeModule Plus™, and the results are depicted in Figure 1. The recycled carbon fiber reinforced polymer (rCFRP) presents size distribution from 2 to 310 µm, where d10 = 8 µm, d50 = 48 µm and d90 = 142 µm, and the average particle size is 63 µm **Erro! A origem da referência não foi encontrada.**.

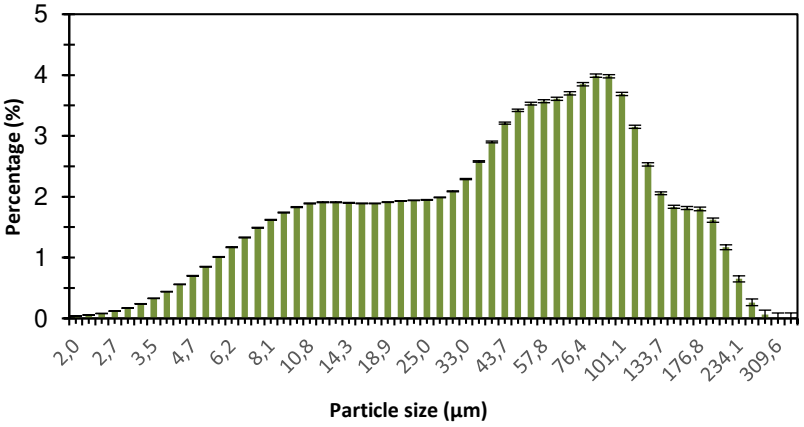

Figure 1 – PEEK tapes granulometric analysis.

2.2 Compounding

The formulations were melt mixed in a co-rotating intermeshing twin-screw extruder, with screws rotating at 180 and 300 rpm, to ensure adequate shear rates and residence times for the dispersion of rPEEK-CF. The temperature profile in the barrel was kept at 365 °C and the die at 375 °C. The screws contain three mixing sections consisting of staggered kneading disks and separated by conveying sections. Extruded filaments were slowly cooled and solidified to ensure an appropriate material recrystallization.

2.3 Injection and compression molding

Virgin PEEK and rPEEK-CF compounds were injected according to the data sheet recommendations supplied by Victrex™. Compression molding was carried out in a hot plate press SATIM TYPE PML 1™, which was used to produce disks for studying the rheological behavior and DC electrical conductivities, at 390 °C for 30 minutes.

2.4 Off-line characterization

2.4.1 Rheology

The rheological properties of PEEK and rPEEK-CF compounds were assessed on a Discovery hybrid rheometer DHR-1™ (from TA instruments™), equipped with a parallel plate geometry

  doi:10.5075/epfl-298799_978-2-9701614-0-0

with a diameter of 25 mm and gap less than 1 mm, at 370 °C. Small amplitude oscillatory shear, SAOS, experiments were performed to the samples at an angular frequency sweep from 0.1 to 10 rad/s. The linear viscoelastic response was previously determined with strain amplitude sweeps from 0.05 to 12.5 % and a strain of 5 % was selected for the frequency sweep tests.

2.4.2 Scanning Electron Microscopy (SEM)

The morphology of rPEEK-CF compounds was analyzed by scanning electron microscopy Zeiss LEO-1530® (Germany). The analysis was performed to verify the interface between the fibers and the matrix. The analysis was conducted on fractured surfaces after specimen's tensile strength determination, which were previously sputtered with a layer of gold/palladium mixture, under argon atmosphere, to avoid electrostatic charging during analysis.

2.4.3 DC electrical behavior

The DC electrical behavior of PEEK and rPEEK-CF compounds was calculated from the slope of I *vs.* V curves, which were measured using an automated Keithley 487™ picoammeter/voltage source, with an applied voltage ranging between -300 and 300 V, at room temperature. Electrodes comprising gold/palladium mixture were deposited onto sample surface by magnetron sputtering using a Polaron SC502™ sputter coater. The geometric parameters were used to calculate the resistivity (ρ) of the samples, which was then converted to electrical conductivity (σ_{DC}) in S/cm.

2.4.4 Crystallization degree evaluation by DSC

The effect of rPEEK-CF contents on the crystallization degree of virgin PEEK was evaluated by Differential Scanning Calorimetry (DSC) (TA Instruments DSC (model Q20™)). All runs were performed at a nitrogen flow of 50 mL/min and samples of 5 to 10 mg were used. Scans were carried out by heating up the sample from 50 to 380 °C at 10 °C/min, cooling down to 50 °C, and reheating to 380 °C at the same heating rate.

2.4.5 Stress-strain behavior

The influence of different loadings of rPEEK-CF on the quasi-static mechanical behavior of PEEK was evaluated using an INSTRON 4208® universal instrument with a load cell of 100 kN and a constant crosshead speed of 1 mm/min until 0.30 % strain followed by 5 mm/min until failure. Analysis was performed by means of ISO-527 standard tensile tests.

3. Results and discussion

3.1 Rheology

Dynamic frequency sweep tests were used to explore the rheological properties of the produced compounds containing different loadings of rPEEK-CF. In addition, the potential conductive network formation by CF-CF contact or interaction (rheological percolation) was also evaluated. The storage modulus (G'), loss modulus (G'') and complex viscosity (|η*|) are displayed in Figure 2.

  doi:10.5075/epfl-298799_978-2-9701614-0-0

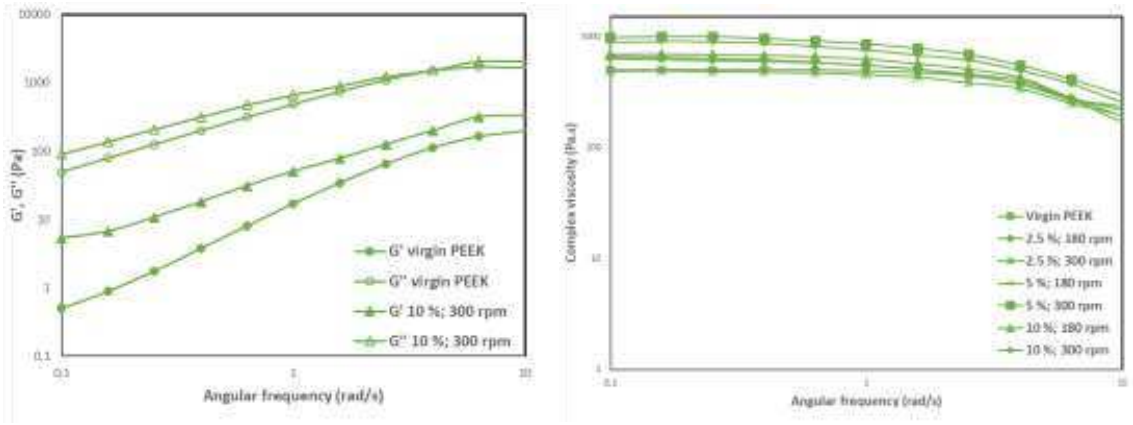

Figure 2 – Storage and loss modulus *versus* angular frequency for virgin PEEK and 10 % loading at 300 rpm ; Complex viscosity *versus* angular frequency for all samples.

The higher values of G' at low frequency region in comparison with neat PEEK is due to the presence of solid phase. Since no rubbery plateau was found with incorporation of 10 wt.% of rPEEK-CF, it can be assumed that the rheological percolation was not achieved, which means that no electrical percolation can be anticipated. For all tested materials, G'' remains virtually unchanged since its behavior is dominated by the flow of the viscous phase, and indicates that the viscous component of the material dominates the elastic counterpart across all frequencies [19], [20]. Moreover, the region where the complex viscosity is independent of the angular frequency, corresponding to the Newtonian plateau, remains very similar for formulation containing different loadings of rPEEK-CF.

3.2 Stress strain behavior

The influence of different loadings of rPEEK-CF in the tensile behavior of PEEK was also evaluated and the results are presented on Figure 3.

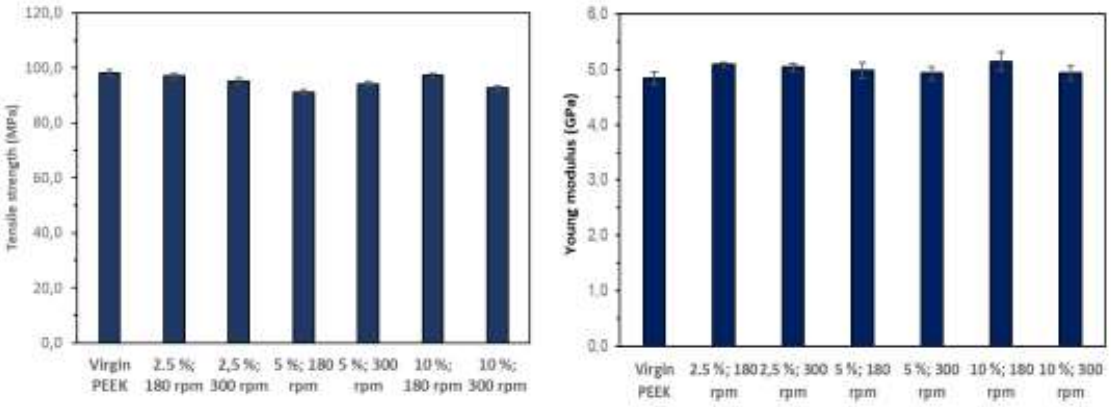

Figure 3 – Tensile strength (MPa) and Young Modulus (GPa) of the produced materials.

According to data summarized in Figure 3, it can be observed that both tensile strength and young modulus are not significantly affected by the incorporation of rPEEK-CF, even at higher loadings. This behavior suggest the following: i) a good dispersion level of rPEEK-CF was found by selecting a specific screw design/geometry and the processing conditions studied (180 and 300 rpm), and ii) the particle size incorporated in neat PEEK is smaller for acting as a mechanical reinforcement.

  doi:10.5075/epfl-298799_978-2-9701614-0-0

3.3 Scanning Electron Microscopy (SEM)

Figure 4 presented SEM images from the fractured surface of the tensile specimens previously tested. Images 1.1 to 1.4 refer to samples with 2.5 wt. % of rPEEK-CF, images 2.1 to 2.4 to 5 wt. % rPEEK-CF, and images 3.1 to 3.4 to 10 wt. % rPEEK-CF.

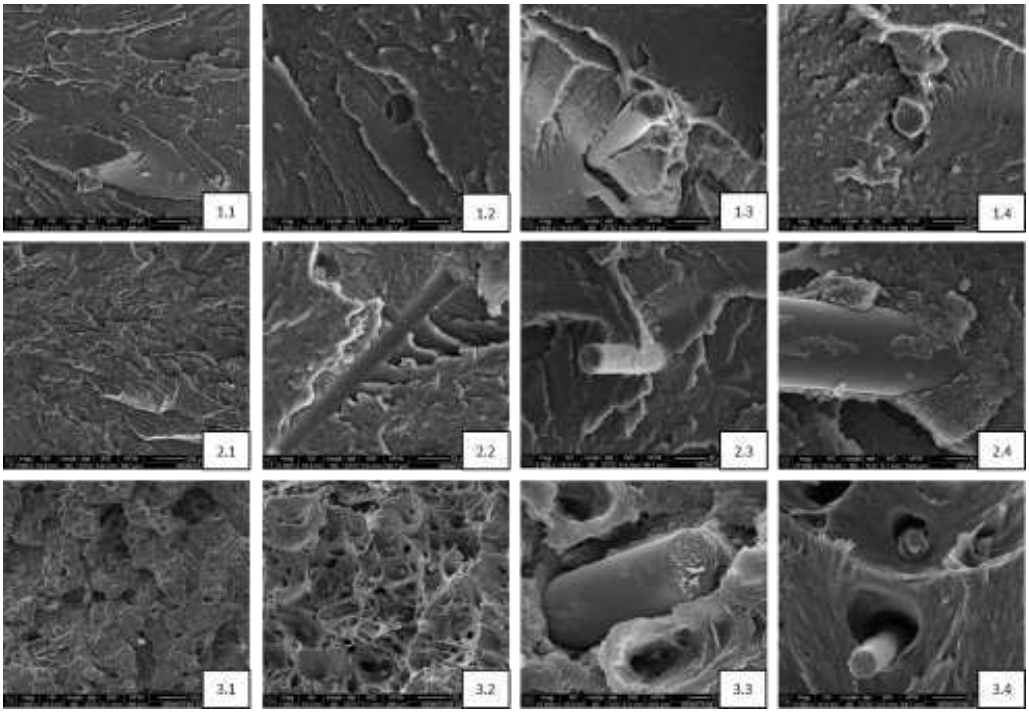

Figure 4 – SEM images (1.1 to 1.4 – 2.5 % rPEEK-CF; 2.1 to 2.4 – 5 % rPEEK-CF; 3.1 to 3.4 – 10 % rPEEK-CF).

The morphology of compounds, for each rPEEK-CF loading, showed the absence of fiber clusters, suggesting that a good dispersion degree was found and confirming that the extrusion conditions were adequate for the development of PEEK composites. No significant differences were found for the developed morphology using 180 or 300 rpm. Moreover, it is observed a good interfacial adhesion between the fibers and the matrix, along with fibers being pull-out probably due to the forces from the tensile test.

3.4 DC electrical conductivity

The influence of different loadings of rPEEK-CF in the DC electrical behavior of neat PEEK is presented on Table 1.

Table 1 - Samples electrical conductivity.

Sample	Electrical conductivity (S/cm)
Virgin PEEK	9.20×10^{-9}
2.5 wt. % ; 180 rpm	8.21×10^{-9}
2.5 wt. % ; 300 rpm	1.71×10^{-8}
5 wt. % ; 180 rpm	7.40×10^{-9}
5 wt. % ; 300 rpm	1.02×10^{-8}
10 wt. % ; 300 rpm	1.18×10^{-8}

  doi:10.5075/epfl-298799_978-2-9701614-0-0

Based on the literature [24], materials with conductivity lower than 10^{-8} S/cm are considered insulators. In this sense, through the analysis of the DC electrical conductivity values presented on Table 1, it is possible to conclude that all developed formulations do not present a significant increase of the DC electrical behavior, as expected from the rheological results, probably due to the low particle size incorporated. J. King et *al.* [25] showed that only PEEK composites containing 30 wt. % carbon fiber presented increased electrical conductivity.

4. Conclusion

In the present work, the performance of PEEK composites reinforced with recycled CFRP residues was assessed. For this purpose, compounds were extruded with different loadings of rCFRP (2.5, 5 and 10 wt. %), while also varying the extrusion speed between 180 and 300 rpm. After the materials characterization, from mechanical, thermal, rheological, electrical analysis and SEM observation, it was possible to conclude that with these low incorporations of residues were not sufficient to attain the desired reinforcement. At the same time, without a network formation between the dispersed CFs, the produced compounds are still insulators. Nevertheless, and promoted by the good dispersion achieved, it should be pointed out that the introduced fillers did not decrease the performance of the PEEK matrix. Further studies will be performed on compounds produced with higher loadings of recycles CFRP, where improvements are expected.

Acknowledgements

This work was supported by the Portuguese PT2020 program Nº17/SI/2019 under the following projects: RREDUCE (47110) and ReCAP (46066).

5. References

[1] J. A. Butenegro, et *al.*, *Materials*, vol. 14, no. 21. MDPI, Nov. 01, 2021.
[2] G. Pedoto, et *al.*, *Mechanics of Materials*, vol. 166, Mar. 2022.
[3] M. Thiruchitrambalam, et *al.*, in *Materials Today: Proceedings*, Jan. 2020, vol. 33, pp. 1085–1092.
[4] V. Mylläri, et *al., Polymer Degradation and Stability*, vol. 120, pp. 419–426, Oct. 2015
[5] A. Patel, V. Venoor, et *al.*, *Polymer Degradation and Stability*, vol. 185, Mar. 2021
[6] H. Li and K. Englund, *Journal of Composite Materials*, vol. 51, no. 9, pp. 1265–1273, Apr. 2017
[7] M. R. Parvaiz and P. A. Mahanwar, *Polymer - Plastics Technology and Engineering*, vol. 49, no. 8, pp. 827–835, May 2010.
[8] Kiran Pulidindi and Akshay Prakash, "Aerospace Composites Market - Global Market Insights," *Aerospace Composites Market Report Coverage*, 2020.
[9] S. Pimenta and S. T. Pinho, *Waste Management*, vol. 31, no. 2, pp. 378–392, Feb. 2011
[10] J. Zhang, V. S. Chevali, et *al.*, *Composites Part B: Engineering*, vol. 193. Elsevier Ltd, Jul. 15, 2020. doi: 10.1016/j.compositesb.2020.108053.
[11] H. Sukanto, et *al.*, "Carbon fibers recovery from CFRP recycling process and their usage: A review," *IOP Conference Series: Materials Science and Engineering*, vol. 1034, no. 1, p. 012087, Feb. 2021

  doi:10.5075/epfl-298799_978-2-9701614-0-0

[12] X. Li, R. Bai, and J. McKechnie, *Journal of Cleaner Production*, vol. 127, pp. 451–460, Jul. 2016

[13] G. Oliveux, L et *al., Progress in Materials Science*, vol. 72. Elsevier Ltd, pp. 61–99, Jul. 01, 2015.

[14] L. Giorgini, et *al.*, *Current Opinion in Green and Sustainable Chemistry*, vol. 26. Elsevier B.V., Dec. 01, 2020.

[15] G. A. Vincent, et *al.*, *Composites Part B: Engineering*, vol. 176, Nov. 2019

[16] P. Anh Vo Dong, et *al.*, "Economic and environmental assessment of recovery and disposal pathways for CFRP waste management Economie and environmental assessment of recovery and disposai pathways for CFRP waste management"

[17] M. Roux, et *al.*, *Journal of Thermoplastic Composite Materials*, vol. 30, no. 3, pp. 381–403, Mar. 2017.

[18] G. Schinner, et *al.*, *Journal of Thermoplastic Composite Materials*, 1996.

[19] P. Wang *et al., Composites Part B: Engineering*, vol. 198, Oct. 2020

[20] C. Ajinjeru *et al.*, "The Influence of Dynamic Rheological Properties on Carbon Fiber Reinforced Polyetherimide For Large Scale Extrusion-Based Additive Manufacturing."

[21] S. S. Yao, et *al.*, *Composites Part B: Engineering*, vol. 142. Elsevier Ltd, pp. 241–250, Jun. 01, 2018.

[22] J. Beauson, et *al.*, *Composites Part A: Applied Science and Manufacturing*, vol. 152, Jan. 2022

[23] D. Yang, et *al.*, *Polymer Testing*, vol. 97, p. 107149, May 2021,

[24] L. A. Fielding, et *al.*, *Chemical Communications*, vol. 51, no. 95, pp. 16886–16899, Sep. 2015

[25] J. A. King *et al.*, *Polymer Composites*, vol. 39, pp. E807–E816, May 2018

  doi:10.5075/epfl-298799_978-2-9701614-0-0

EXTENDED FAILURE MODELS FOR GLOBAL AND LOCAL ANALYSES OF COMPOSITE AEROSTRUCTURES

Giuseppe Corrado[a,b], Albertino Arteiro[a], António Torres Marques[a], Fernass Daoud[b], Florian Glock[b], José Reinoso[c]

a: Department of Mechanical Engineering, Faculty of Engineering, University of Porto (PT) – up201811504@edu.fe.up.pt
b: Airbus Defence and Space GmbH, Manching, Germany (DE) – giuseppe.corrado@airbus.com
c: Group of Elasticity and Strength of Materials, University of Seville (ES).

Abstract: *This work presents the implementation of an advanced phenomenological failure model to perform ``hot-spot" failure analysis and predict the onset of intralaminar damage of fiber-reinforced polymers in large-scale models. The selected failure criteria identify the critical failure mode, accounting for general three-dimensional stress states, which is essential for the design and analysis of composite laminates under higher levels of triaxiality. Then, to represent the quasi-brittle behavior of composite materials up to ultimate strength, these failure criteria are coupled with a smeared crack model for transverse cracking and continuum damage mechanics models for fibre-dominated damage, which together account for the kinematics of matrix cracking and fibre tensile or compressive fracture during damage propagation. Furthermore, cohesive elements are used to predict delamination. A test case involving a stringer runout loaded in tension was selected for the validation of "hot-spot" analysis, while a series of scaled tests on unnotched specimens was used for the validation of the mesoscale model.*

Keywords: Failure criteria; Damage models; Computational methods; Fibre-reinforced polymers

1. Background

Carbon fiber-reinforced plastic (CFRP) materials play an important role in structural applications, namely in aeronautical industry. In fact, thanks to their higher mechanical properties compared with those of traditional lightweight metal alloys, composite materials have been increasingly used in the last decades for manufacturing primary structures. However, the design of aerostructures using composite materials is more complex than using isotropic lightweight alloys, due to the radical increase of design parameters that FRP-composites implies. For this reason, during the early stages of their design, it is important to choose a convenient design strategy to follow, in order to avoid, in a certain measure, the prohibitive cost of their mechanical tests. High performance composites, in fact, are very expensive due to the fact that their beneficial properties usually rely on the use of high-cost raw materials, namely prepregs, and relatively slow and complex manufacturing technologies. These motivations pushed the scientific community towards the development of reliable tools for virtual testing of laminated composites, aiming to reduce the number of mechanical tests required during the design and certification process [1,2].

However, detailed numerical models for large aerospace products result in prohibitive computational costs with the current state of technology. Therefore, to overcome the need of

  doi:10.5075/epfl-298799_978-2-9701614-0-0

high-fidelity models involving millions of degrees of freedom, efficient modelling strategies have been recently proposed, such as global/local approaches. In this framework, ``hot-spot" identification analysis can be used to highlight the most critical structural details where a local model would have a crucial role in capturing more accurately the structural behavior. With the obtained indications, an efficient global/local modelling strategy can be implemented to address the structural response of composite structures.

To model the phenomena of damage propagation, non-linear constitutive models defined in the context of the mechanics of continuum mediums have been developed and implemented in finite elements codes in recent years [3,4]. However, continuum damage mechanics (CDM) approaches alone cannot realistically simulate the response of the laminates that are dominated by delamination, which is discrete in nature and sensitive to the local stress fields and boundary conditions. A more effective computational approach in such cases would have to include a concurrent combination of smeared and discrete models to capture the interaction between the material and structural (or local and global) behavior. For this reason, discrete damage mechanics (DDM) can be a suitable approach to progressive failure modelling when delamination is explicitly introduced into the model via displacement discontinuities, which they create [5].

In this work, the 3D invariant-based failure model was selected and implemented to predict the onset of intralaminar failure in "hot-spot" failure analyses and as damage activation functions in the mesoscale damage model. This set of failure criteria is presented in the section below.

1.1. 3D invariant-based failure criteria

The 3D invariant-based failure theory [6,7] is a set of advanced phenomenological failure theories, selected for the present work due to its unique 3D character. These new criteria are based on the transversely isotropic yield function developed by Vogler et al. [8]. They have an invariant quadratic formulation involving structural tensors that accounts for the preferred directions of the anisotropic material.

The invariant-based failure criterion for transverse matrix failure of unidirectional composites is presented in the equation below, where the failure index FI_M is defined as a function of the stress invariants for matrix failure (I_1, I_2, I_3) and the failure parameters α:

$$FI_M = \begin{cases} \alpha_1 I_1 + \alpha_2 I_2 + \alpha_3^t I_3 + \alpha_{32}^t I_3^2 & for\ I_3 > 0 \\ \alpha_1 I_1 + \alpha_2 I_2 + \alpha_3^c I_3 + \alpha_{32}^c I_3^2 & for\ I_3 \leq 0 \end{cases}, \tag{1}$$

where the stress invariants are given as:

$$I_1 = \frac{1}{4}\sigma_{22}^2 - \frac{1}{2}\sigma_{22}\sigma_{33} + \frac{1}{4}\sigma_{33}^2 + \sigma_{23}^2\,,\ I_2 = \sigma_{12}^2 + \sigma_{13}^2\,,\ I_3 = \sigma_{22} + \sigma_{33} \tag{2}$$

and the failure parameters are:

$$\alpha_1 = \frac{1}{S_T^2}\,,\ \alpha_2 = \frac{1}{S_L^2}\,,\ \alpha_{32}^t = \frac{1 - \frac{Y_T}{2\,Y_{BT}} - \alpha_1 \frac{Y_T^2}{4}}{Y_T^2 - Y_{BT}Y_T}\,,\ \alpha_3^t = \frac{1}{2\,Y_{BT}} - 2\alpha_{32}^t Y_{BT}\,,$$

$$\alpha_{32}^c = \frac{1 - \frac{Y_C}{2\,Y_{BC}} - \alpha_1 \frac{Y_C^2}{4}}{Y_C^2 - Y_{BC}Y_C}\,,\ \alpha_3^c = \frac{1}{2\,Y_{BC}} - 2\alpha_{32}^c Y_{BC}\,. \tag{3}$$

  doi:10.5075/epfl-298799_978-2-9701614-0-0 published under CC BY-NC 4.0 license

The failure parameters in Eq. (3) are function of: S_T and S_L, which are respectively the transverse and in-plane shear strengths; Y_C and Y_{BC}, respectively the transverse uniaxial and biaxial compressive strengths; and Y_T and Y_{BT}, respectively the transverse uniaxial and biaxial tensile strengths. Through the sign of the third invariant I_3, this criterion addresses failure under biaxial stress states.

Fibre failure under tension is predicted using the non-interactive maximum allowable strain criterion, following the LaRC03 criteria [9]:

$$FI_M = \frac{\varepsilon_1}{\varepsilon_{Xt}} \quad for \ \sigma_{11} \geq 0 \tag{4}$$

where ε_{Xt} is the ultimate tensile strain.

Since the failure mechanism under longitudinal compression of fibre-reinforced polymers involves mainly the formation of a kink band, resulting from micro-buckled fibers and local matrix cracking, this theory introduced a 3D kinking model by recalling the invariant-based failure criterion for the transverse case, but in a misalignment frame. In fact, introducing the two angles required for the definition of the frame of the kink band, namely the angle of the kinking plane ψ and the kinking angle φ, it is possible to formulate the invariant-based failure criterion for kinking failure prediction in the misalignment frame.

As it can be observed by the latter frame definition, this set of invariant-based failure criteria is clearly fully 3-dimensional (3D), unlike the Hashin or Puck failure criteria that were initially 2D criteria and then they have been extended to the 3D case.

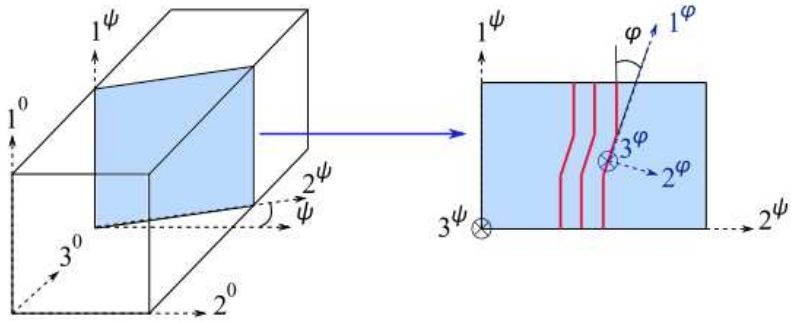

Figure 1. 3D kinking model with the definition of the kinking angle ϕ and the angle of the kinking plane ψ (adapted from [10])

Figure 1 shows the kinking plane and the 3 coordinate systems: the initial coordinate system ($1^0 2^0 3^0$), associated with the material axes of the composite, the coordinate system related with the kinking plane ($1^{\psi} 2^{\psi} 3^{\psi}$) and the coordinate system related with the misaligned fibers ($1^{\varphi} 2^{\varphi} 3^{\varphi}$). In the latter coordinate system, the invariant-based failure criterion for fibre kinking is formulated as a function of the stress invariants and the failure parameters:

$$FI_k = \alpha_1 I_1 + \alpha_2 I_2 + \alpha_3 I_3 + \alpha_{32} I_3^2 \tag{5}$$

with:

$\alpha_3 = \alpha_3^t$, $\alpha_{32} = \alpha_{32}^t$ if $I_3 > 0$, and

  doi:10.5075/epfl-298799_978-2-9701614-0-0

$$\alpha_3 = \alpha_3^c \, , \alpha_{32} = \alpha_{32}^c \text{ if } I_3 < 0. \quad (6)$$

The complete definition of the analytical framework needed to predict failure onset for fiber kinking can be found in [7], where the stress invariants are formulated in the misaligned frame of the kinkband, so as a function of the angle of the kinking plane ψ and the kinking angle φ.

In [6,7,10] several validation studies of these criteria were performed, comparing the predictions with experimental data obtained for different material systems under various scenarios of multiaxial loading, including the case of hydrostatic pressure, which no previous failure criteria have taken into account.

Herein, to show the predictions of this advanced failure theory and compare the with well-known failure criteria, Figure 2 presents the correlation of the predicted envelopes (obtained using Tsai-Wu, Hashin and 3D invariant-based failure criteria) against experimental results from the WWFE-II [11] for T300/PR319. Furthermore, the influence of Y_{BC} on the strength predictions of the invariant-based theory was investigated and the effect of the interaction term F^*_{12} of the Tsai-Wu theory are included in the figure. It can be observed that the 3D invariant-based theory provides a significant flexibility in fitting complex results with Y_{BC}, while the interaction term from Tsai-Wu has a negligible influence for the specific test case and Hashin does not offer flexibility in the predictions with Y_{BC}.

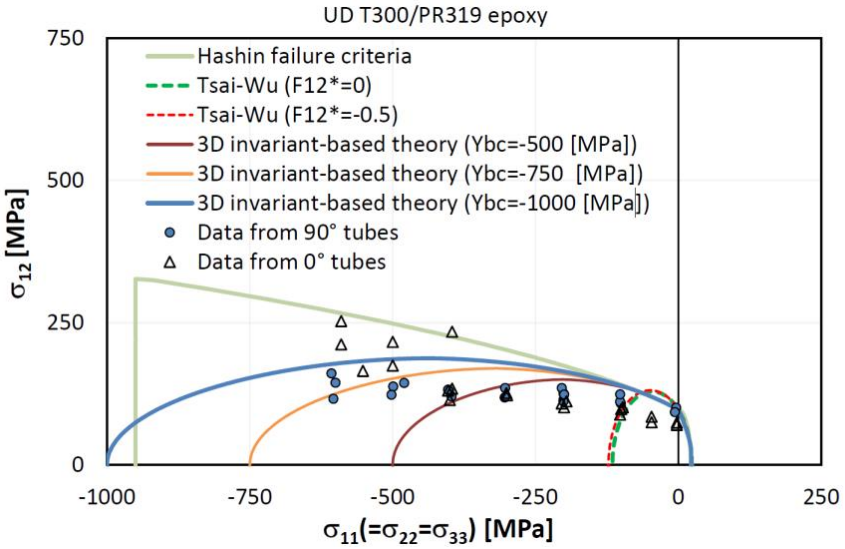

Figure 2. Triaxial failure stress states: shear stress vs. hydrostatic pressure for a UD T300/PR319 epoxy.

2. Hot-spot identification method

The implementation of failure criteria in a FE software for "hot-spot" failure analysis, introduced in [11-13], is a robust method to accurately predict critical locations in large global models. The identification of "hot-spots" in large models, by means of reliable failure criteria, allows to increase the modelling resolution only where required. Advanced phenomenological failure theories have been implemented for this scope, such as the LaRC05 in [11].

As introduced in the previous section, herein the 3D invariant-based failure theory [6] is used for the prediction of first-ply failure (FPF) of laminated composite structures. With this aim, the formulation of this set of criteria was implemented in a post-processing Python script,

  doi:10.5075/epfl-298799_978-2-9701614-0-0

compatible with Abaqus/Standard and Abaqus/Explicit, to generate new element output fields, by using the full stress tensor of each element and computing the failure index for each of the failure modes addressed by the criteria. Because of the fully 3D nature of the implemented failure theory, this approach allows the identification of “hot-spots" and the corresponding failure mechanisms for damage initiation, creating different output variables to predict fibre and matrix failure, under tension and compression.

To verify the correct numerical implementation of this tool and validate it with experimental results, a test case involving an aeronautical reinforced panel under tensile loading was selected, for which experimental results are available. The “hot-spot” failure method was applied to the panel, targeting the identification of the critical locations for damage onset in the runout region. The results of the hot-spot failure analysis are shown schematically in Figure 3. In particular, it can be observed that failure initiates in the skin region close to the runout, where the onset of damage is triggered by fibre kinking. Additionally, in the zoomed view, failure initiation is shown to take place in all the plies of the laminate, in the vicinity of the bolts. Experimental results validated the qualitative predictions obtained with this approach; however they cannot be disclosed in this paper.

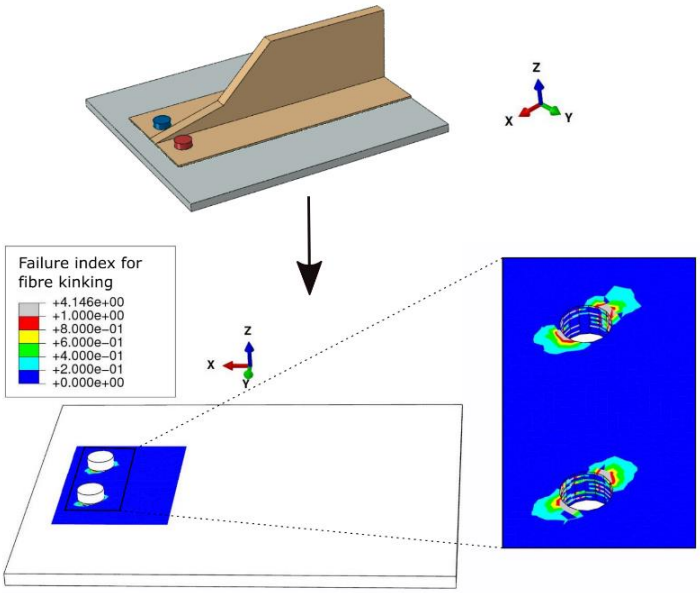

Figure 3. “Hot-spot” failure analysis in the runout region, where the identified critical failure mode is fibre kinking.

3. Detailed damage modelling

Although “hot-spot” FPF analysis can be useful in guiding preliminary design and identifying the most critical areas, it is not sufficient to predict the ultimate load of composite laminates, since failure of these materials is governed by a progressive evolution of damage, which must be addressed for critical areas. Hence, to predict the inelastic deformation up to ultimate failure in local models, these 3D invariant-based criteria are coupled with a smeared crack model that accounts for the kinematics of matrix crack and kink band formation during damage propagation. To predict delamination, cohesive elements are used at the interfaces between layers with different orientation.

  doi:10.5075/epfl-298799_978-2-9701614-0-0

The mesoscale damage model introduced in this paper is an extension of a composite material model proposed in the literature [14], representing the quasi-brittle behaviour of composite structures. It is extended to account for the effect of general 3D stress states in the initiation and broadening of fibre kinking using the 3D invariant-based failure theory [6,7].

A verification study of the mesoscale damage model has been firstly performed at the single element level, to check the correct numerical implementation of the model. Just to give an example of this study, Figure 4 shows the material response of IM7/8552 (material properties from [14]) under an increasing longitudinal compression and constant biaxial transverse pressure. It can be observed that the model is able to capture the increase of strength occurring due to hydrostatic effect.

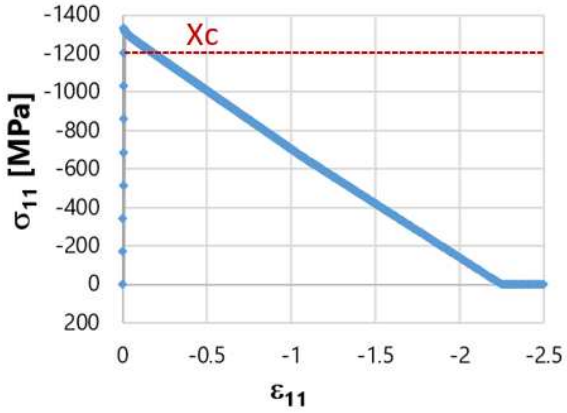

Figure 4. Single element test under longitudinal compressive loading and constant biaxial transverse pressure.

Then, a validation study at the coupon level was performed considering experimental results from [15]. In particular, the idea was to test the damage model in capturing the size effects in the prediction of unnotched tensile strength, i.e. the increase in strength of quasi-isotropic (QI) specimens with size when the thickness was changed by repeating the sublaminate stacking sequence ("*n* scaling", $[45/90/-45/0]_{nS}$) and the decrease in strength when the thickness was increased by changing the ply block thickness ("*m* scaling", $[45_m/90_m/-45_m/0_m]_S$). Additional details can be found in [15].

Figures 16-17 show the numerical results of the finite element analyses (FEA) performed using Abaqus/Explicit and solid elements, and a user subroutine to run the mesoscale damage model. Each case was run with and without cohesive elements to study the effect of delamination in the prediction of the tensile strength. The obtained results show that the numerical predictions fit quite well the experimental results and that delamination plays an important role in the prediction of the tensile strength, especially for ply-level scaled specimens. Furthermore, the developed mesoscale damage model proved to capture the size effect in unnotched tensile strength.

  doi:10.5075/epfl-298799_978-2-9701614-0-0

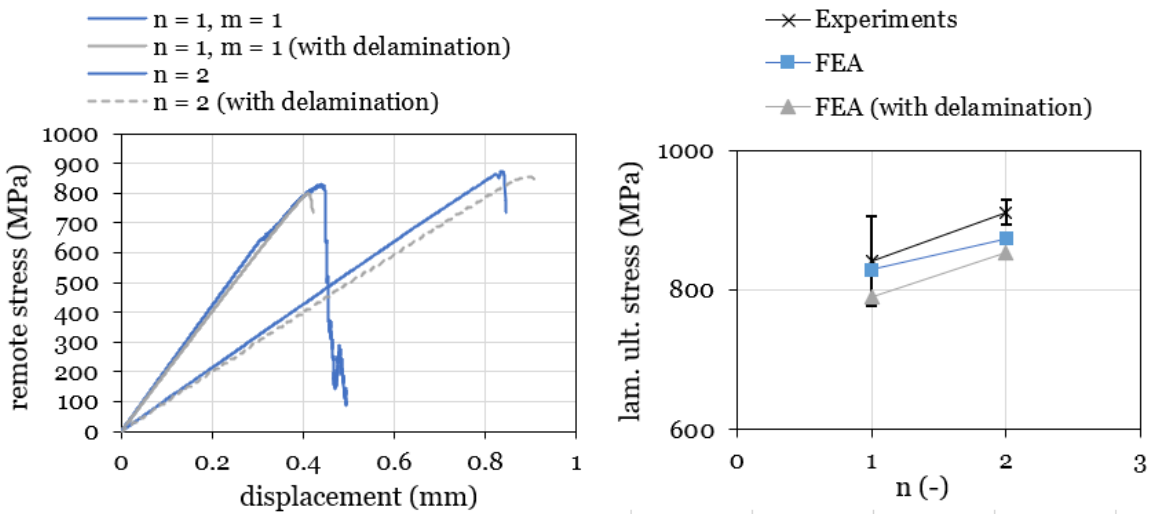

Figure 5. Comparison between the numerical and experimental results for sublaminate-level scaled IM7/8522 ([45/90/-45/0]$_{nS}$) specimens.

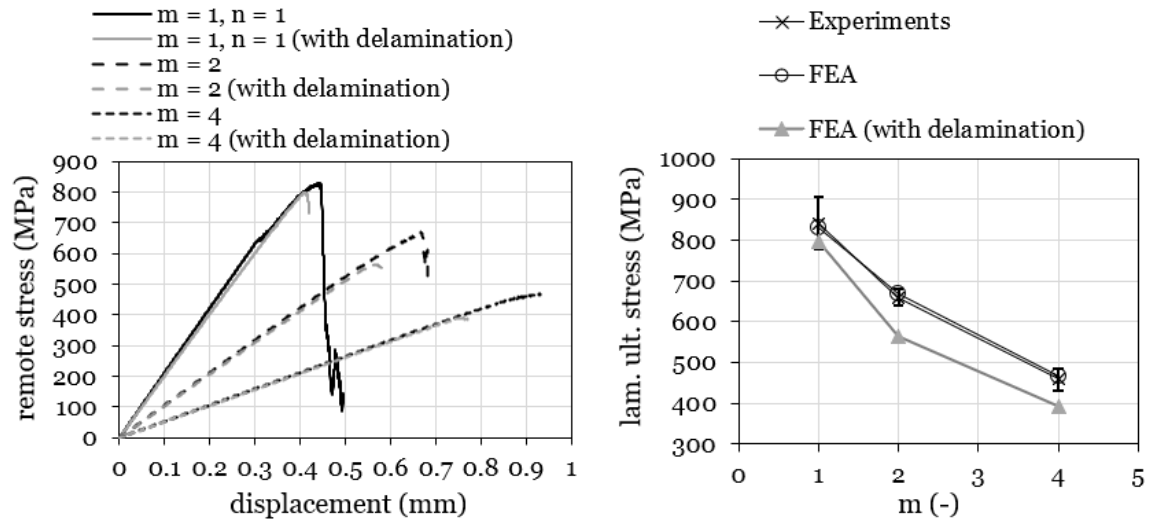

Figure 6. Comparison between the numerical and experimental results for ply-level scaled IM7/8552 [45$_m$/90$_m$/-45$_m$/0$_m$]$_S$ specimens

4. Conclusion

In this work, an advanced phenomenological failure theory was implemented to perform "hot-spot" failure analysis and to extend a mesoscale damage model for general 3D stress states. The fist method allows to identify "hot-spot" for the onset intralaminar failure in large scale models, while the second is suitable for detailed analysis where the mechanical behavior of FRPs up to collapse needs to be investigated.

Validation studies were performed for both methods. The "hot-spot" identification analysis resulted satisfactorily accurate for the prediction of critical locations for intralaminar failure onset in a reinforced panel. Then, the mesoscale damage model was able to capture the effect of hydrostatic pressure in single element tests and the size effect in unnotched tensile strength, with a good correlation with experimental results.

  doi:10.5075/epfl-298799_978-2-9701614-0-0

Acknowledgements

This work was supported by the H2020 Marie Skłodowska-Curie European Industrial Doctorate OptiMACS (Grant 764650). José Reinoso has received funding from the Clean Sky 2 Joint Undertaking under the European Union's Horizon 2020 research and innovation programme under grant agreement No. 785463.

5. References

1. National Institute for Aviation Research. MIL-HDBK-17-3, Composite Materials Handbook, volume 3. Polymer Matrix Composites Materials Usage, Design and Analysis. Department of Defense Handbook 2002.
2. Barile C, Casavola C. Mechanical characterization of carbon fiber-reinforced plastic specimens for aerospace applications. Woodhead Publishing Series in Composites Science and Engineering 2019; 19: 387-407.
3. Maimí P, Camanho PP, Mayugo JA, Dávila CG. A continuum damage model for composite laminates: Part I | Constitutive model. Mechanics of Materials. 2007.
4. Maimí P, Camanho PP, Mayugo JA, Dávila CG. A continuum damage model for composite laminates: Part II | Computational implementation and validation. Mechanics of Materials. 2007.
5. Camanho PP, Hallett SR. Numerical Modelling of Failure in Advanced Composite Materials. Woodhead Publishing Series in Composites Science and Engineering. 2015.
6. Camanho PP, Arteiro A, Melro AR, Catalanotti G, Vogler M. Three-dimensional invariant-based failure criteria for fibre-reinforced composites. International Journal of Solids and Structures. 2015.
7. Camanho PP, Arteiro A, Catalanotti G, Melro AR, Vogler M. Three-dimensional invariant-based failure criteria for transversely isotropic fibre-reinforced composites, Numerical Modelling of Failure in Advanced Composite Materials. Woodhead Publishing, Cambridge 2015, 111–150.
8. Vogler M, Ernst G, Rolfes R. Invariant based transversely-isotropic material and failure model for fiber-reinforced polymers. Computers, Materials and Continua 2010; 16, 1:25–49.
9. Dávila CG, Camanho PP, and Rose CA. Failure Criteria for FRP Laminates. Journal of Composite Materials 2005; 39, 4:323-345.
10. Corrado G, Arteiro A, Marques A, Reinoso J, Daoud F, Glock F. An extended invariant approach to laminate failure of fibre-reinforced polymer structures. The Aeronautical Journal 2021; 1-24.
11. Molker H, Gutkin R, Pinho S, Asp LE. Hot spot analysis in complex composite material structures. Composite Structures 2019, 207:776-786.
12. Zou X, Yan S, Reza M, Brown L, Jones A. An Abaqus plugin for efficient damage initiation hotspot identification in large-scale composite structures with repeated features. Advances in Engineering Software 2021, 153:102964.
13. Molker H, Gutkin R, Asp LE. Implementation of failure criteria for transverse failure of orthotropic Non-Crimp Fabric composite materials. Composites Part A 2017, 92:158-166.
14. Zhuang F, Arteiro F, Furtado C, Chen P, Camanho PP. Mesoscale modelling of damage in single- and double-shear composite bolted joints. Composite Structures 2019. 226, 111210.
15. Wisnom MR, Khan B, Hallett SR. Size effects in unnotched tensile strength of unidirectional and quasi-isotropic carbon/epoxy composites. Compos Struct 2008. 84:21-28.

  doi:10.5075/epfl-298799_978-2-9701614-0-0

HIGH STRAIN RATE CHARACTERIZATION OF TWILL WOVEN CARBON-POLYAMIDE LAMINATE IN LONGITUDINAL COMPRESSION

Arnaud, Clou[a, b], *Jean-Luc, Hanus*[a], *Christophe, Roua*[b], *Patrice, Bailly*[a]

a: INSA Centre Val de Loire, LaMé EA7494, 88 boulevard Lahitolle, 18000 Bourges, France – arnaud.clou@insa-cvl.fr

b: COGIT Composites, 9117 rue des vignerons, 18390 Saint Germain du Puy, France

Abstract: *The proposed contribution concerns the experimental characterization of the strain rate effect on the longitudinal compressive response of a twill woven carbon-polyamide laminate. A specific test fixture was designed to perform quasi-static and dynamic experiments with the same specimen geometry. Quasi-static experiments were conducted using electromechanical machine, and dynamic material characterization, using Split Hopkinson Pressure Bars (SHPB). Particular attention is given to the dynamic stress equilibrium promoted through the use of an appropriate pulse shaper. Thanks to high speed video recording, the failure process is observed and valid failure modes are assessed. Digital Image Correlation (DIC) allows to access to the strain field and to check its homogeneity. In the range from 1.5x10^{-5} s^{-1} to 700 s^{-1}, the experimental results showed a significant increase of +60% in the ultimate compressive strength.*

Keywords: Thermoplastic composite; Longitudinal compression; Dynamic behavior; Split Hopkinson pressure bar; Digital images correlation

1. Introduction

Composite materials with a thermoplastic matrix are increasingly used today in the transport industry. Thanks to their mechanical properties, they make possible to lighten structures compared to metallic materials. Operating costs are therefore reduced thanks to the reduction in fuel consumption while reducing emissions. Compatible with large-scale production thanks to their short cycle times, these materials have a limited environmental impact, compared to composites with a thermoset matrix, due to their recyclability. For example, carbon fiber reinforced with polyamide is used in the automotive industry for structural applications. For that use during service life, the material is subjected to rapid loads such as collisions or impacts. The knowledge of the dynamic behavior and the mechanical properties of these materials is crucial for the sizing of structures and the feeding of representative numerical simulations.

This article focuses on the mechanical characterization in compression of woven carbon fiber reinforced with polyamide. This composite material and its dynamic behavior have been accurately studied in tension but few works have focused on compression. Jendli et al. [1] ascertained the dynamic in-plane tensile and shear properties up to 300 s^{-1} of the 2x2 twill woven carbon fiber reinforced polyamide. Particularly for shear loadings, a positive strain rate effect is noted and is supposed to be due to the viscoplasticity and visco-damage behavior of the thermoplastic matrix. Earlier, Todo et al. [2] characterized a woven carbon fiber composite

  doi:10.5075/epfl-298799_978-2-9701614-0-0

with a polyamide matrix. Linear increases in tensile strength and absorbed energy versus logarithmic strain rate were highlighted.

Split Hopkinson pressure bar system (SHPB) is often used to study the strain rate effects and the mechanical properties of materials. For composite material, to ensure valid experiments, special devices are employed. For flat specimens, Wiegand [3] demonstrated first the suitability of a specific testing fixture to ensure valid compression loading conditions. That's why Koerber and Camanho [4] implemented a specific dynamic fixture to align and stabilize a thin specimen between bars. Carefully developed in order to not disrupt wave propagation, this end-loading test setup provides a state of stress equilibrium in the sample. Ploeckl and al. [5] modified Koerber and Camanho's testing device [4], enhancing end-loaded specimens with bonded glass/epoxy tabs. Ploeckl and al. [6] also improved the previous testing apparatus so as to load flat rectangular specimens, bonded into slotted end caps, by both end- and shear loading. Yokoyama and Nakai [7] investigated rate effects of carbon fiber laminates employing cubic and thick rectangular samples. Brooming and end-crushing are prevented inserting end faces in a square notched steel disk. Nakai and al. [8] applied this last loading method to cylindrical specimens. A positive strain rate effect on the compressive strength is showed from 10^{-3} s^{-1} to 10^{3} s^{-1} in the three principals material axis.

2. Experimental study

2.1 Material, specimen and testing device

The studied material is a polyamide 66 matrix reinforced by 2x2 twill woven carbon fibers. This materials is used in automotive industry to build body panels for example, and for structural sporting goods applications such as helmet shells. Using a hot-press, laminated plates were consolidated in a compression mold during 10 minutes at 285 °C with 0,5 MPa pressure.

20mm long rectangular samples were machined in thick plates with diamond tools, guaranteeing flatness of end-surfaces with close parallel tolerance. An attention is given to the size of the specimen. They must be large enough to contains at least one elementary representative volume of the material to avoid scale effect [1]. Dry lubricant is applied at each end to minimize friction with the loading plates and to ensure an uniaxial state of stress. In order to perform digital images correlation [9], a black and white speckle pattern is applied on the visible face of the specimen.

A specific test fixture (fig. 1) was developed in order to prevent end crushing and premature failure of the specimen while loading. Suitable from low to high strain rate testing, it allows comparison of results at different strain rates. The gripping device consists in two pairs of machined steel clamps mounted at each end of the specimen. The device is assembled in a state of simple contact with the specimen thanks to tightened screws.

  doi:10.5075/epfl-298799_978-2-9701614-0-0

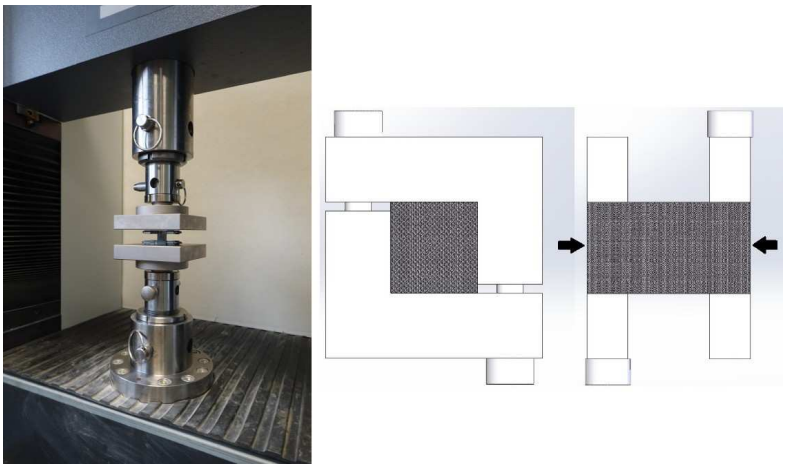

Figure 1. Quasi-static compressive setup (left) and test fixture (right). Front view and side section view. Load application is described by arrows.

2.2 Quasi-static testing apparatus

An electromechanical testing machine with a 100 kN load capacity is used to perform quasi-static experiments. Strain gauges are bonded to the specimen and connected to a data acquisition conditioner via a Wheatstone bridge.

For a basis of comparison, tests according to ISO 14126 standard [10] with IITRI fixture are performed. A-type specimens were employed with bonded glass/epoxy tabs. Characterization tests with the developed device were carried out at several strain rates approximately from 10^{-5} s^{-1} to 10^{-2} s^{-1}. In addition, images of the sample surface sample are recorded with a high definition CCD camera. The system is completed with two 45 W LED lamps to provide a constant lighting of the specimen. Digital image correlation (DIC) is performed with Icasoft software [11], allowing strain calculation on an area corresponding to an elementary representative surface.

2.3 Dynamic test setup

Split Hopkinson pressure bars were employed to determine dynamic compression properties. They are made of 20 mm diameter steel striker, incident and transmission bars respectively 0.5 m, 3.0 m and 1.8 m long. Strain gauges, located at 1.5 m on the incident-bar and 0,38 m on the transmission-bar apart the bar/specimen interface, measure elastic wave propagation. Two sets of strain gauges are bonded on diametrically opposed sides so as to remove bending and torsion effects. Amplified strain signals are recorded at high speed via a digital oscilloscope with a 1 MHz sampling rate. A copper pulse shaper is placed on the incident-bar, on the impacted face, to get a gradual loading of the specimen. This approach has been found well suited for composite materials exhibiting a linear behavior up to failure [4].

So as to verify the absence of dispersion and the accuracy of strain measurement in bars, a bar-together test is performed to validate one-dimensional wave transport. The striker-bar hits the pulse shaper at a speed V_0. The bar wave celerity is obtained by $C_b = (E_b/\rho_b)^{0,5} = 4529$ m/s with $E_b = 160$ GPa the bar Young's modulus and $\rho_b = 7800$ kg/m^3 the bar density. The theoretical amplitude $\varepsilon_b = V_0/2C_b$ is reached. Between incident- and transmission-bar, the 1.4%

  doi:10.5075/epfl-298799_978-2-9701614-0-0

measured strain difference is considered as negligible since no change is revealed in the signal shape. Consequently, dispersion correction is not required.

The test fixture is assembled to the specimen and is the placed between bars. The deforming specimen and its failure modes are observed thanks to high-speed video recording via a Photron camera with a rate of 150 000 frames per second. The homogeneous illumination of the area of interest is provided by two halogen spotlights. According to the previously described protocol, the strain field is also deduced from DIC.

3. Results and discussion

3.1 Quasi-static test results

For each strain rate, three tests are conducted and the longitudinal compression failure stress is measured (tab. 1). The ISO 14126 standard benchmark results are marked with *. The expected brittle elastic mechanical material behavior is confirmed. Digital images correlation attest to the strain field homogeneity in the specimen gauge and so the non-disturbance of test fixture. Noticed failure modes, such as brooming and throught-thickness shear, are away from specimen ends and gripping device. As expected, the results obtained with the proposed device are fully consistent with benchmark results.

*Table 1: Quasi-static test results (*Results according to ISO 14126 standard).*

Strain rate (s^{-1})	Mean failure stress (MPa)	Standard deviation (MPa)	Coefficient of variation (%)
$1.5.10^{-5}$	326	12	3.6
$*6.1.10^{-5}$	*347	*10	*2,8
$1.7.10^{-2}$	396	28	7.0

3.2 Dynamic test results

Forces acting on the specimen at bar ends are calculated from the strain measurement in incident and transmission bars wave propagation. Forces are given by Eq. (1) and Eq. (2), where ε_{inc}, ε_{ref} and ε_{tra} are respectively the incident-, reflected- and transmission-bar strains. S_b is the bar cross section and E_b is the bar Young's modulus.

$$F_{input} = S_b E_b \left(\varepsilon_{inc} + \varepsilon_{ref} \right) \quad (1)$$

$$F_{output} = S_b E_b \varepsilon_{tra} \quad (2)$$

Verifying forces equilibrium and strain homogeneity, the specimen strain rate $\dot{\varepsilon}_s$, strain ε_s and stress σ_s are calculated with Eq. (3), Eq. (4) and Eq. (5), where S_s is the cross section of the specimen.

$$\dot{\varepsilon}_s = \frac{C_b}{l_s} \left(\varepsilon_{tra} - \left(\varepsilon_{inc} - \varepsilon_{ref} \right) \right) \quad (3)$$

$$\varepsilon_s = \int_0^t \dot{\varepsilon}_s \, dt \tag{4}$$

$$\sigma_s = \frac{F_{input} + F_{output}}{2 S_s} \tag{5}$$

A representative example of bar strain signals, recorded during a test, is showed in fig. 2. Post-processed results are given in fig. 3. Due to the early reached stress equilibrium, forces applied at specimen ends jointly evolve over the time (fig. 3). From failure, curves are plotted with dot lines. Both SHPB method and optical measurement provide strain data with a good agreement between the two approaches. Strain homogeneity in the specimen during loading is confirmed by DIC (fig. 4). Longitudinal stress versus strain curve is given in figure 5. Both strain and stress calculated with the SHPB analysis are retained for curve plotting.

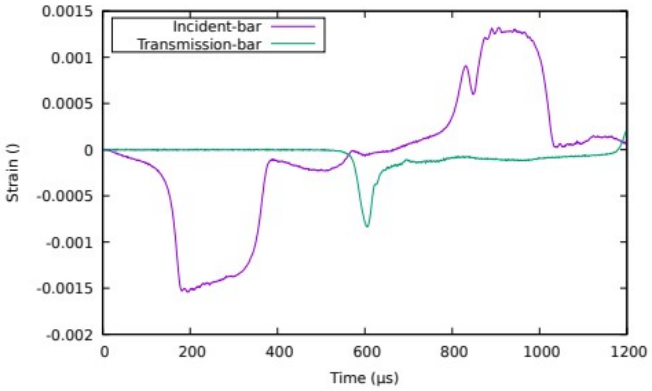

Figure 2. Representative bar strain signal for twill woven carbon-polyamide composite characterization.

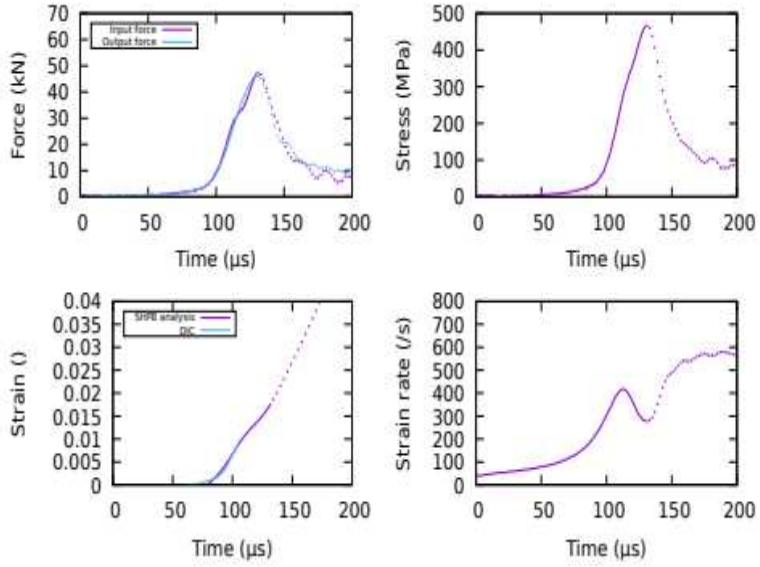

Figure 3. Forces acting at bar ends, specimen stress response, strain obtained via SHPB analysis and DIC, strain rate over the time.

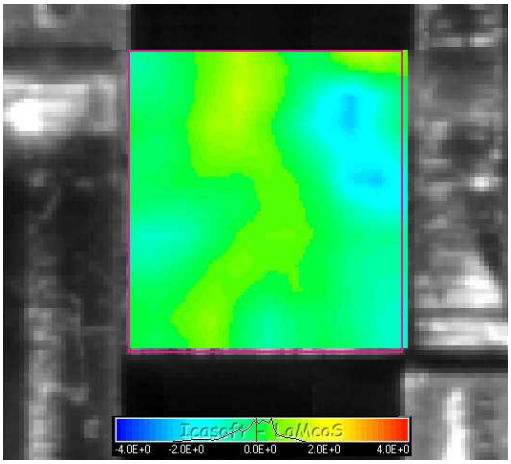

Figure 4. Longitudinal strain field on the horizontally load specimen with SHPB at ε_{11} = 0,29%.

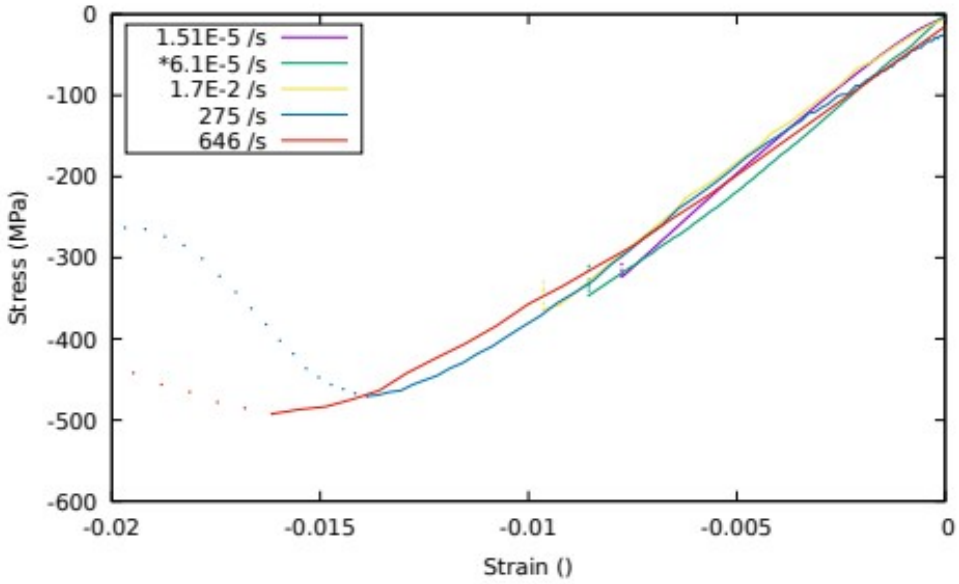

Figure 5. Stress-strain response of twill woven carbon-polyamide laminate in longitudinal compression at different strain rates.

With a coefficient of variation of 5,7% and 5,6%, the mean failure stress is respectively 489 MPa at 265 s^{-1} and 530 MPa at 659 s^{-1}. In comparison to previous observations, failure modes remain valid in the specimen gauge (fig. 6). From quasi-static to dynamic loadings, material behavior exhibits a strain rate sensitivity of its longitudinal compressive failure stress. From 1.5.10^{-5} s^{-1} to 659 s^{-1}, a +60 % increase is noticed.

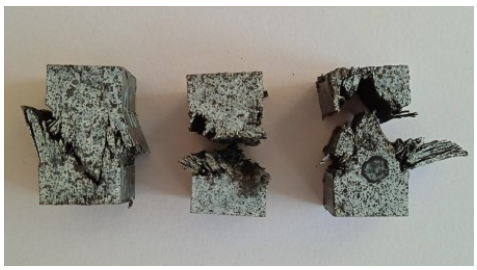

Figure 6. Failure modes in SHPB experiments

  doi:10.5075/epfl-298799_978-2-9701614-0-0

4. Conclusion

This study investigated twill woven carbon fiber reinforced polyamide 66 and its dynamic mechanical behavior. For thick laminated specimens characterization, a specific test fixture device was developed taking care of load introduction and strain homogeneity. Electromechanical machine and split Hopkinson pressure bar were used to perform experiments from quasi-static to dynamic strain rates. High-speed video recording was implemented to calculate strain field via optical measurement and digital images correlation. Brooming and throught-thickness failure modes were observed away from the specimen end faces from low to high strain rates. In the range from $1.5.10^{-5}$ s^{-1} to 10^{3} s^{-1}, a +60% increase of the longitudinal compressive failure stress of twill woven carbon fiber reinforced polyamide 66 is observed.

5. References

1. Jendli Z, Walrick JC, Bocquet M, Fitoussi J. Strain rate effects on the mechanical behavior of carbon-thermoplastic matrix woven composites. Proceedings of ECCM16. 2014.
2. Todo M, Takahashi K, Béguelin P, Henning Kausch H. Strain-rate dependence of the tensile fracture behaviour of woven-cloth reinforced polyamide composites. Composites Science and Technology 2000; 60: 763-771.
3. Wiegand J. Constitutive modelling of composite materials under impact loading. PhD thesis. Oxford University. United Kingdom. 2008.
4. Koerber H, Camanho PP. High strain rate characterisation of unidirectional carbon-epoxy IM7-8552 in longitudinal compression. Composites: Part A 2011; 42: 462-470.
5. Ploeckl M, Kuhn P, Koerber H. Characterization of unidirectional carbon fiber reinforced polyamide-6 thermoplastic composite under longitudinal compression loading at high strain rate. Proceedings of DYMAT conference. 2015.
6. Ploeckl M, Kuhn P, Grosser J, Wolfahrt M, Koerber H. A dynamic test methodology for analyzing the strain-rate effect on the longitudinal compressive behavior of fiber-reinforced composites. Composites Structures 2017; 180: 429-438.
7. Yokoyama T, Nakai K. Impact compressive failure of a unidirectional carbon/epoxy laminated composite in three principal material direction. Proceedings of DYMAT conference. 2009.
8. Nakai K, Fukushima T, Yokoyama T, Arakawa K. High strain-rate compressive properties of carbon/epoxy laminated composites – Effects of loading direction and temperature. Proceedings of DYMAT conference. 2018.
9. Sutton MA, Orteu JJ, Schreier HW. Image correlation for shape, motion and deformation measurements. Springer. 2009.
10. International Organization for Standardization - ISO 14126: 1999. Fibre reinforced plastic composites – Determination of compressive properties in the in-plane direction.
11. Mguil-Touchal S, Morestin F, Brunet M. Various experimental applications of digital image correlation method. Rhodes. CMEM 1997; 97: 45-58.

  doi:10.5075/epfl-298799_978-2-9701614-0-0

DAMAGE CHARACTERISATION IN OPEN-HOLE COMPOSITES USING ACOUSTIC EMISSION AND FINITE ELEMENT, VALIDATED BY X-RAY CT

Neha Chandarana[a,b,], Oliver Helps[a,c], Tobias Laux[b], Paul Fromme[d], Adam Doherty[d], Christopher Thornton[d], Dana Shoukroun[d], and Philip J Withers[a]*

a: Henry Royce Institute, Department of Materials, The University of Manchester, Manchester, UK
b: Bristol Composites Institute and Department of Aerospace Engineering, University of Bristol, Bristol, UK
c: TWI Technology Centre Wales, Port Talbot, UK
d: Department of Medical Physics and Biomedical Engineering, University College London, London, UK
*neha.chandarana@bristol.ac.uk

Abstract: *The development of digital twins for life cycle monitoring of high performance composites is becoming a realistic goal. The use of permanently integrated sensors to obtain structural health information is a promising method by which finite element models could be iteratively updated for remnant life predictions. In the present work, we use acoustic emission (AE) sensors to detect the stress waves generated in open hole composites when damage initiates and grows under quasi-static tensile loading. Damage characterisation is performed on experimental AE data and compared to a finite element (FE)-based damage modelling framework. The results from these techniques are then validated through the use of X-ray computed tomography (CT) scans, conducted on partially loaded specimens. AE monitoring and the FE model show promise in detecting the severity of damage when specimens are subjected to progressive tensile loading, although the FE-based model underpredicts the failure load and further work is required for damage classification using AE signals.*

Keywords: Damage diagnosis; damage detection, ultrasonics; structural health monitoring; non-destructive testing

1. Introduction

Despite advances in the design and manufacture of high performance composite materials, a lack of confidence in their long-term performance remains a challenge. This can result in over-engineered design, laborious inspection procedures, and premature replacement of components. The layered nature of composites can facilitate the permanent integration of acoustic emission (AE) sensors capable of diagnosing the health state of a structure [1]. Provided the signals can be correctly interpreted, the use of such sensors to detect and monitor the presence and growth of defects and damage could lead to a reduction in downtime for inspection and increase the accuracy of lifetime predictions delivered by simulation techniques.

The aim of this work is to demonstrate that damage can be detected using AE sensors, and that the AE data can be combined with a finite element (FE)-based progressive damage model to better interpret the damage process in composites structures. The integrated AE-FE approach will in the short term lead to a better understanding of damage in composites, and in the long term may lead to better structural health monitoring. In the present work, angle-ply carbon

  doi:10.5075/epfl-298799_978-2-9701614-0-0

fibre/epoxy laminates containing 0° and ±45° plies were investigated. Open hole tensile specimens were instrumented with four AE sensors, bonded to the front surface of each specimen. These were used to detect acoustic emissions (AE) produced by changes in the microstructure during loading – such as from the onset and growth of cracks in the matrix, separation of layers (delamination), or fibre fracture. Analysis of the signals and their features can enable identification of different damage mechanisms in composites as well as estimation of the damage locations [2,3]. In parallel, ultrasonic c-scan and X-ray computed tomography (CT) have been employed to characterise the damage in partially loaded specimens. The recorded AE and X-ray CT data were used to better understand failure progression in open-hole specimens, as well as to assess the predictive capability of an FE-based progressive damage model.

2. Materials and methods

2.1 Open-hole tensile loading of composite coupons

Carbon fibre/epoxy laminates constructed from IM7/8552 (134 gm^{-1} fibres, 0.125 mm ply thickness) were provided by Hexcel Composites with a symmetric "angle-ply blocked" lay-up having the stacking sequence $[0_2/-45_2/90_2/+45_2]_S$. Rectangular specimens with a central 4 mm diameter hole (dimensions shown in Figure 1) were subjected to quasi-static tensile loading using an electro-mechanical Instron testing machine equipped with a 50 kN load cell (testing conducted at The University of Manchester). Four Mistras Pico sensors were attached to the top surface for AE monitoring. The delta-T mapping technique [4] was applied to the recorded AE data to locate damage events.

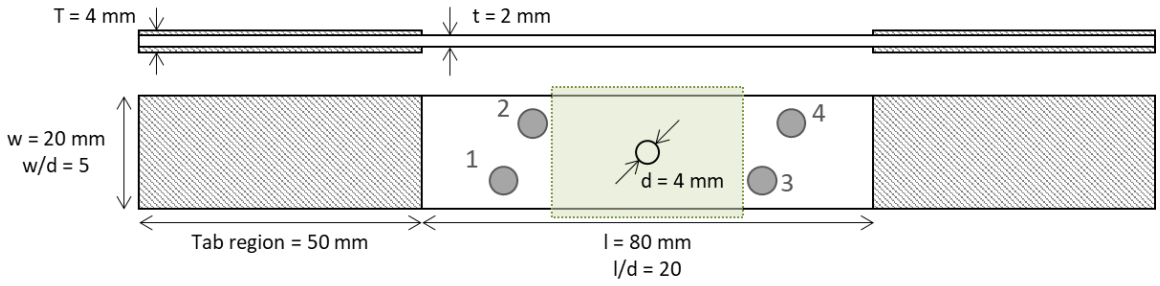

Figure 1. Dimensions of open-hole tensile coupons, with surface mounted AE sensors labelled 1-4. The 23 x 34 mm region of interest imaged by X-ray CT is shown as a green shaded region.

2.2 Finite element simulation

An FE-based damage modelling framework [5,6] was used to simulate the initiation and progression of damage in the angle-ply open-hole composite specimens subjected to quasi-static tensile loading. Intra-ply damage is simulated using a continuum damage model [7,8] with fibre-aligned meshes of single element thickness. Failure initiation is predicted using an approximation of the LaRC 03/04 set of failure criteria [9]. Inter-ply damage (delamination) is accounted for using cohesive elements placed between fibre plies [10]. Material properties for IM7/8552 were taken from [5]. A mesh sensitivity study showed that an in-plane element size of 0.25 x 0.25 mm and loading rate of 1000 mm/min (to accelerate the quasi-static explicit dynamic simulation) provided acceptable results with a reasonable runtime and kinetic enrgy of less than 5% of the internal strain energy. Models were run using a user subroutine (VUMAT) in the commercial FE software, Abaqus.

  doi:10.5075/epfl-298799_978-2-9701614-0-0

2.3 Non-destructive evaluation of partially loaded specimens by X-ray computed tomography

Three angle-ply blocked specimens were selected for non-destructive evaluation by X-ray CT (conducted at TWI Technology Centre Wales). Details of the specimens are given in Table 1. The scans were performed on a North Star Imaging X5000 XCT scanner using an accelerating voltage of 50 kV and tube current of 200 µA. Samples were rotated through 360° capturing 4000 projections with 2 seconds exposure and 3-frame averages, resulting in a total scan time of 8h53min. The scans were reconstructed using the standard North Star filtered back-projection reconstruction software efX-CT 2.2.5.0.

Analysis of the reconstructed datasets was performed in VG studio MAX 3.5.1. Volume registration was conducted using the inbuilt 3-2-1 registration method using two references planes, one fitted to the front face and one to a side face and finally a reference cylinder fitted to the specimens drilled hole. The origin of the co-ordinate axes was defined as the centre of the drilled hole on the front face of the specimen (see Figure 2).

Table 1. Summary of angle-ply blocked composite specimens considered in the study.

Specimen	Applied load (kN)	% of mean failure load
A10	Unloaded	0
A3	29.0	86
A13	33.0	97
A14	35.2	100 (failed)
Mean (6 specimens)	33.9 ± 1.5	100 (all failed)

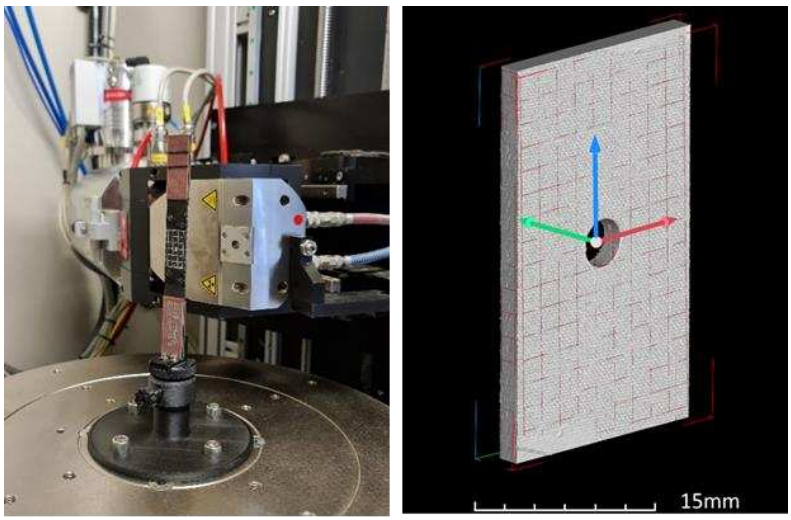

Figure 2. (a) X-ray scanning set-up at TWI Technology Centre Wales, (b) reconstructed specimen volume in VG studio MAX 3.5.1

The total damage in each specimen was visualised using the inbuilt region growing (flooding) algorithm. The algorithm uses a selected seed point in the data and continues to a new voxel within a selected tolerance of the seed points grey level. Due to the low ply deformation

experienced under uniaxial tension, global damage was further segmented in an approximate ply-by-ply manner. Ply-by-ply segmentations were achieved by intersecting the total segmented damage from the region growing with cuboids having a thickness corresponding to the nominal ply thickness of 0.25 mm +0.05 mm tolerance. The interface between plies was visualised through the intersection of cuboids with half nominal ply thickness +0.05 mm tolerance, positioned between two neighbouring ply regions.

3. Results and discussion

3.1 Mechanical properties

The load-displacement curves for the three tested specimens (A14, A13, and A3) are shown in Figure 3. The change in gradient of the three curves is due to the inclusion of the compliance of the test machine in the cross-head displacement value. A comparison of experimental and predicted failure loads from the FE model are given in Table 2. The model underpredicts the failure load by 28% when compared against the mean breaking load obtained from the six failed specimens. Due to the observed discrepancy, comparisons between failure modes observed in partially loaded specimens and model predictions were carried out in terms of the percentage of failure load. Figure 4 shows the extent of fibre and matrix damage in the surface 0° and subsurface -45° plies, as well as the predicted extent delamination between at the 0/-45 interface, near the surface of the specimen. It is evident that matrix damage is first sustained in the -45° (and +45°) plies. Fibre failure in the surface 0° plies is the critical failure mode that leads to ultimate failure.

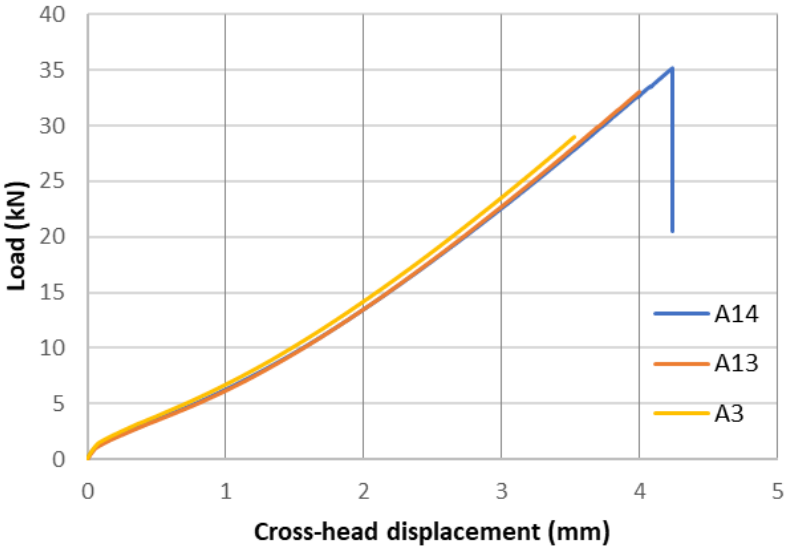

Figure 3. Load-displacement curves for specimens A14, A13, and A3 compared against curved obtained from the FE model (0.25 mm mesh size and 100 mm/min loading rate)

Table 2. Failure load of angle-ply blocked open-hole composites under tensile loading

Method	Failure load (kN)
Experiment (6 specimens)	33.9 ± 1.5
Finite element model	24.2

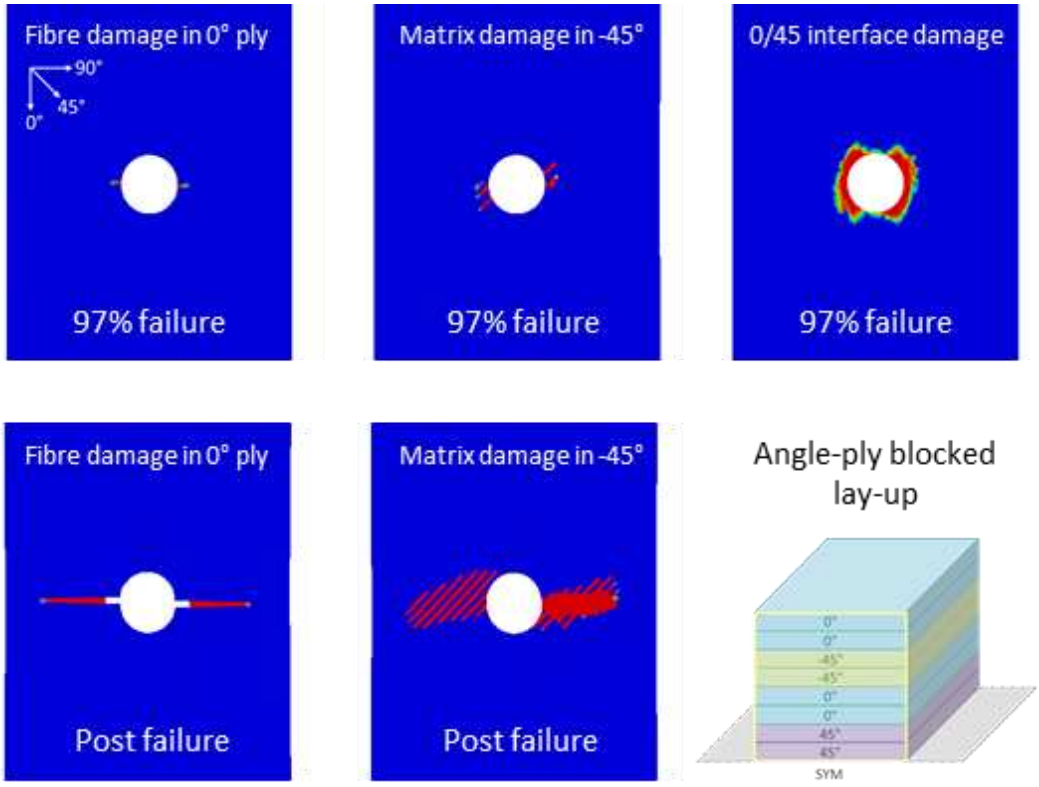

Figure 4. Fibre, matrix, and interface damage in the near-surface plies and interface, as predicted by the FE-model. A schematic of the angle-ply blocked lay-up is shown for reference.

3.2 Acoustic emission monitoring

Figure 5 shows the total number of AE hits recorded by the four mounted AE sensors during loading of specimens A14, A13, and A3. Though the specimens were obtained from a single composite panel, there can be differences in their relative acoustic response due to imperfections and nonuniformity introduced during manufacture. Despite this, we can observe that AE hits are detected from the application of 2 kN load. The number of AE hits recorded increases steadily with loading, with specimen A14 generating the largest number of events – almost 70,000. Figure 5 shows the positioning of all recorded AE hits in the duration versus amplitude feature space. The bulk of signals from all specimens are contained within a point cloud, with a larger number of long duration-high amplitude signals recorded when loading specimens A14 and A13. This suggests the onset and growth of more severe damage in those specimens, particularly delamination and fibre breakage.

3.3 Damage characterisation by X-ray computed tomography

X-ray CT shows low level damage emanating from the backface 0° plies for specimen A10 even prior to loading. This likely indicates that damage was unintentionally introduced by the hole drilling process (see Figure 7). Specimens A3 and A13 show very similar damage morphologies but the progression of damage both laterally and longitudinally from the centre of the hole is evident under the increased loading of specimen A13 (see Figure 7). Fibre splitting was observed in the surface 0° plies and in the -45° plies beneath them. Additionally, the presence of delamination at the 0/-45 interface was prominent, bearing similarities to results found in the literature [11].

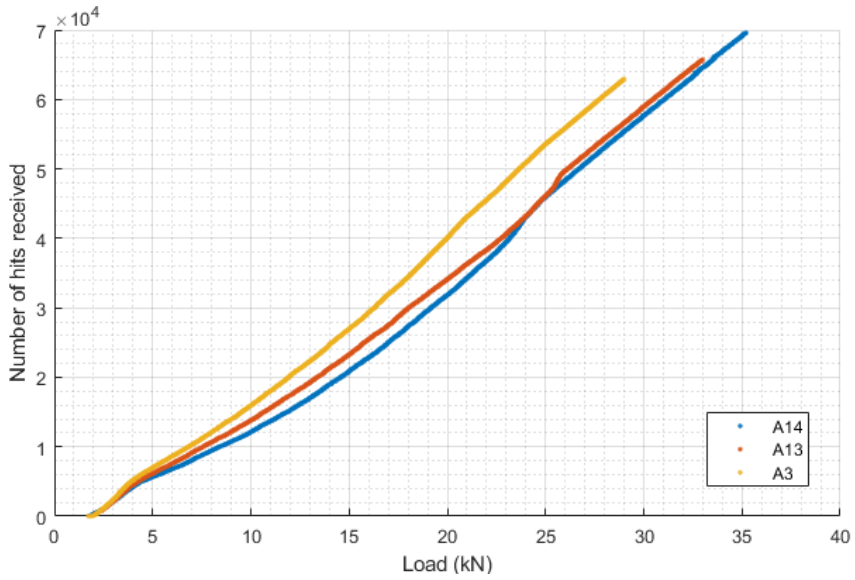

Figure 5. Number of AE hits received by all sensors versus load for specimens A14 (blue), A13 (orange), and A3 (yellow).

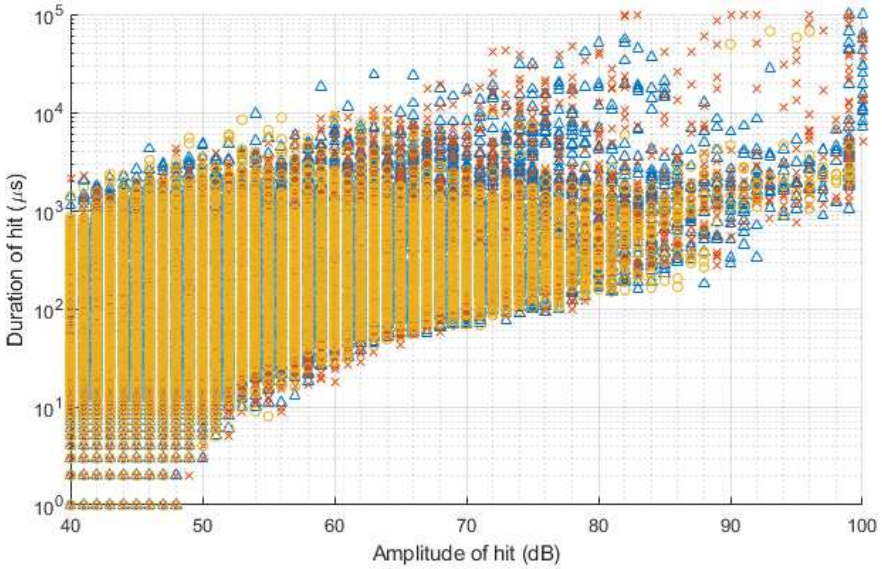

Figure 6. Duration (log scale) versus amplitude of AE hits received by all sensors during loading of specimens A14 (blue), A13 (orange), and A3 (yellow).

1. Summary and outlook

The goal of this on-going work is to make use of an AE-FE combined methodology for the interpretation and characterisation of damage occurrence in open hole composites subjected to tensile loading. The work presented in this paper constitutes a small part of the overall project, in which six composite lay-ups are considered. In the angle-ply blocked lay-up case, the FE model underpredicts the failure load by 28% and fails to predict the severity of the dominant delaminations that are present in the partially loaded specimens at the 0/-45 (Figure 7) and the 0/+45 (not presented) interfaces. The model also fails to predict the longitudinal fibre splitting that are clearly observed in the 0° plies. During loading, these fibre splits are responsible for "notch blunting", which leads to a reduction in stress concentrations around the hole and therefore higher failure loads in the experiment.

The analysis of AE data shows some promise for the detection of damage growth from the hole, but further in-depth analysis is required to determine whether damage classification is possible. The X-ray CT study enabled the visualisation of intra- and inter-ply damage and, importantly, revealed the extent of damage around the hole caused by the drilling process, which has not been accounted for in the FE model. The next steps for this research will involve assessment of the interface failure criteria in the model, source localisation using AE data, with a view to conducting an interrupted tensile test with regular X-ray CT scans to observe early damage initiation.

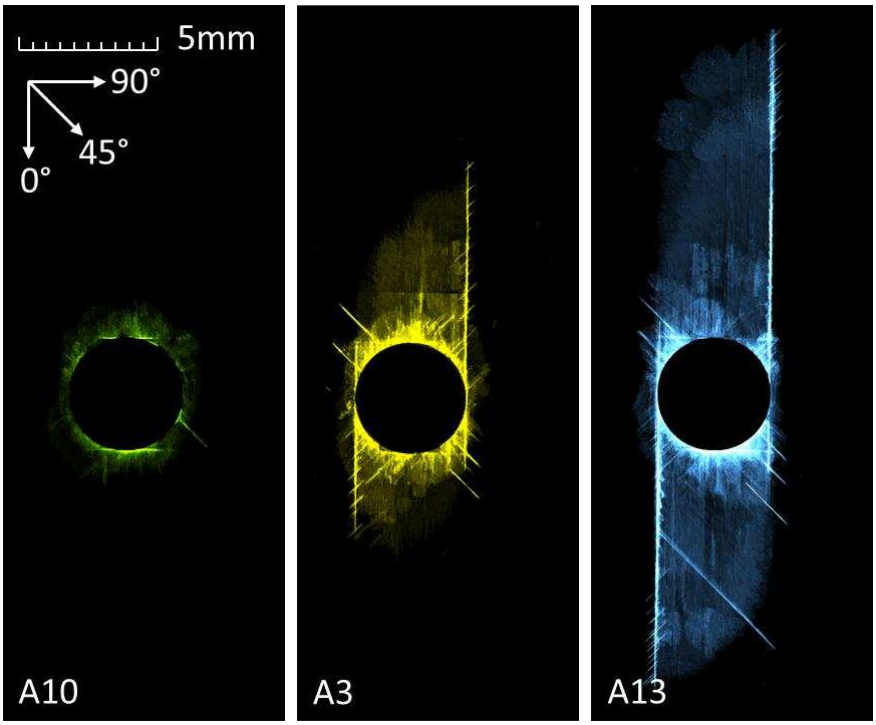

Figure 7. X-ray CT rendering of the through thickness damage for the specimens (A10: unloaded, A3: 85%, and A13: 97% failure load). One ray per display pixel is cast into the segmented damage. The higher the integrated opacity of voxels along a ray, the brighter the corresponding pixel appears in the rendering.

Acknowledgements

The authors would like to acknowledge the following organisations for the provision of financial and technical support throughout this project: (i) EPSRC Doctoral Prize Fellowship awarded to N. Chandarana through the Doctoral Training Partnership (DTP) grant EP/R513131/1; (ii) X-ray facilities at University College London through the National Research Facility for Lab X-ray CT (NXCT) through EPSRC grant EP/T02593X/1; (iii) ESPRC EngD funding for Oliver Helps through the UK Research Centre in Non-Destructive Evaluation (RCNDE) grant EP/L015587/1; (iv) Northwest Composites Centre at The University of Manchester; (v) Prof. P. Camanho's group at the University of Porto for providing the VUMAT used; and (vi) Hexcel Composites for the and provision of prepared OHT composite specimens.

  doi:10.5075/epfl-298799_978-2-9701614-0-0

References

1. Giurgiutiu, V., Structural Health Monitoring with Piezoelectric Wafer Active Sensors, 1st ed., Academic Press, 2008. doi:10.1017/CBO9781107415324.004.

2. Gholizadeh, S.; Leman, Z.; Baharudin, B.T.H.T., "A review of the application of acoustic emission technique in engineering", *Structural Engineering and Mechanics*. **2015**, 54, 1075–1095.

3. Maillet, E.; Baker, C.; Morscher, G.N.; Pujar, V. v.; Lemanski, J.R., "Feasibility and limitations of damage identification in composite materials using acoustic emission", *Composites Part A: Applied Science and Manufacturing*. **2015**, 75, 77–83. doi:10.1016/j.compositesa.2015.05.003.

4. Baxter, M.G.; Pullin, R.; Holford, K.M.; Evans, S.L., "Delta T source location for acoustic emission", *Mechanical Systems and Signal Processing*. **2007**, 21, 1512–1520. doi:10.1016/j.ymssp.2006.05.003.

5. Furtado, C.; Catalanotti, G.; Arteiro, A.; Gray, P.J.; Wardle, B.L.; Camanho, P.P., "Simulation of failure in laminated polymer composites: Building-block validation", *Composite Structures*. **2019**, 226, 111168. doi:10.1016/j.compstruct.2019.111168.

6. Laux, T.; Wui, K.; Tavares, R.P.; Furtado, C.; Arteiro, A.; Camanho, P.P.; Thomsen, O.T.; Dulieu-barton, J.M., "Modelling damage in multidirectional laminates subjected to multi-axial loading : Ply thickness effects and model assessment", *Composite Structures*. **2021**, 266, 113766. doi:10.1016/j.compstruct.2021.113766.

7. Maimí, P.; Camanho, P.P.; Mayugo, J.A.; Dávila, C.G., "A continuum damage model for composite laminates: Part I - Constitutive model", *Mechanics of Materials*. **2007**, 39, 897–908. doi:10.1016/j.mechmat.2007.03.005.

8. Maimí, P.; Camanho, P.P.; Mayugo, J.A.; Dávila, C.G., "A continuum damage model for composite laminates: Part II - Computational implementation and validation", *Mechanics of Materials*. **2007**, 39, 909–919. doi:10.1016/j.mechmat.2007.03.006.

9. Dávila, C.G.; Camanho, P.P.; Rose, C.A., "Failure criteria for FRP laminates", *Journal of Composite Materials*. **2005**, 39, 323–345. doi:10.1177/0021998305046452.

10. Camanho, P.P.; Davila, C.G., Mixed-Mode Decohesion Finite Elements for the Simulation of Delamination in Composite Materials NASA Advanced Air Transport Technology (AATT), 2002. http://www.sti.nasa.gov.

11. Nixon-Pearson, O.J.; Hallett, S.R.; Withers, P.J.; Rouse, J., "Damage development in open-hole composite specimens in fatigue. Part 1: Experimental investigation", *Composite Structures*. **2013**, 106, 882–889. doi:10.1016/j.compstruct.2013.05.033.

AN INVESTIGATION ON THE MECHANICAL PROPERTIES OF SPCS

Daniele Liprandi[a], Seyed Kamal Jalali[a], Maddalena Bertolla[b], Anacleto Dal Moro[b], Tiziano Battistini[b], Nicola Maria Pugno[a,c,]*

a: Laboratory for Bioinspired, Bionic, Nano, Meta, Materials & Mechanics, Department of Civil, Environmental and Mechanical Engineering, University of Trento, Via Mesiano, 77, 38123 Trento, Italy
b: Aquafil S.p.A., Via Linfano, 9, 38062 Arco, Italy
c: School of Engineering and Materials Science, Queen Mary University of London, Mile End Road, London E1 4NS, United Kingdom

Abstract:

Single-polymer composites (SPCs) are an available option as new recyclable material. Fibre-like elements are inserted in a polymeric matrix with the same chemical composition. The unique characteristics of the composite are given by the different crystallinity of the two phases, their geometrical distribution and the interphase between them. One primary advantage of SPCs is the relatively strong stiffness of the interphase between the fibres and the matrix, compared to other fibre-reinforced polymeric composites (FRPs). However, the separation between the fibres and the matrix still plays a role, as it has been reported since the first works on SPCs. In this work, we use a Lattice Spring Model (LSM) to analyse how the mechanical properties of the interface affect the properties of the overall composite. Moreover, we investigate how the behaviours change when different geometries are considered.

Keywords: Fracture; Composites; Lattice Spring Model; Polymers

1. Introduction

In recent decades, one major goal of material science has been the development of recyclable materials with optimized properties. In this context, single-polymer composites (SPCs) emerge as a candidate. Tape and fibre-like elements are inserted in a polymeric matrix with the same chemical composition. The unique characteristics of the composite are given by the different crystallinity of the two phases, their geometrical distribution and the interphase between them.

One primary advantage of SPCs is the relatively strong stiffness of the interphase between the fibres and the matrix, compared to other fibre-reinforced polymeric composites (FRPs). In common FRPs the key actors in the bonding of the fibres are the weak van der Waals forces, therefore coatings or matrix modifications are required to improve the adhesion between phases. in SPCs it is instead possible to observe molecular entanglements, crystalline and amorphous superstructures and other bonding phenomena [1]. However, the separation between the fibres and the matrix still plays a role, as it has been reported since the first works on SPCs [2]. Columnar layers created around the fibres, called transcrystalline layers (TCLs), are reported in the literature for both all-polypropylene (all-PP) and polyamide 6 (all-PA6) SPCs. Recent works have also investigated how the mechanical performances are affected by the amount of polymerization activator and catalyst and by the temperature at which

  doi:10.5075/epfl-298799_978-2-9701614-0-0

polymerization occurs. In all-PA6 composites, a trade-off between ultimate strain and ultimate strength was observed for different dosages of the activator [3].

2. Model definition

2.1 Mechanical behaviour and numerical implementation

A particular condition encountered when working with SPCs is the similarity between the elastic moduli of the matrix and the reinforcing fibre[4,5]. Considering for example Nylon-6 as a reference polymer, literature presents elastic moduli between 0.5 and 4 GPa for both matrix materials, fabrics and single fibres[3,6,7]. The differences in the mechanical behaviour of this polymeric materials are created by their relative humidity, polymerization and crystallization conditions[1,5,8].

Anionic PA6 (APA6) matrices have tensile strength values reported between $60\ \mathrm{MPa}$ and $100\ \mathrm{MPa}$ [3,9–11], while PA6 fibres can usually reach tensile strength values of $600\ \mathrm{MPa}$ [3,12]. A typical stress-strain curve of the APA6 matrix shows an initial linear elastic phase, followed by a softening which is usually reached at a strain value $3\% < \varepsilon_{y_m} < 5\%$ [10]. This softening after the yielding point is affected by the mould temperature and the relative humidity of the caprolactam used in the polymerization, with lower temperatures leading to lower values of the strain at failure, with typical values of the strain at break being $10\% < \varepsilon_{U_m} < 35\%$ [10,11]. PA6 fibres show an elastic behaviour until fracture, with typical values of the strain at break being $15\% < \varepsilon_{U_m} < 25\%$ [3]

In this work, we decided to represent the mechanical properties of the composite phases using bilinear stress-strain laws. Both the matrix and the fibre share the same Young's modulus E_1 until the matrix yielding point ε_{y_m} is reached. After the yielding point, the matrix and the fibre curves proceed with Young's moduli E_{2_m} and E_{2_f}, respectively, until ultimate strain is reached. To simulate the presence of defects and impurities in the different phases, we assign the elongation at break of the computational elements forming the structure according to a statistical distribution. We choosae a two-parameter Weibull distribution

2.2 Lattice Spring Model

Lattice spring models (LSMs) are numerical models based on regular lattices of one-dimensional elements[13–17]. The properties of the single fibres, which can be varied to represent heterogeneous volumes, determine the structural response to the external mechanical load. Lattice models based on Green potentials have already been used to study the behaviour of fibre-based composites [18]. LSMs use a different approach, using ad-hoc elastic bond potentials to correctly simulate the elastic energy in the system. Thus, LSMs are ideal to study the fracture behaviour of heterogeneous elastic structures, since their definition does not require any a-priori knowledge of the fracture path [19] and can be modified to represent non-linear elastic-plastic materials by simply tuning how the elastic energy is represented through the system [17]. To simulate composite failure, fracture occurs when the length of the elongated bonds forming the structure exceeds the critical strain, leading to the release of the stored elastic strain energy. In this work we use two-dimensional x-braced cells, which are able to simulate elastic materials with Poisson's ratio of $\nu \simeq 0.3$ [13].

  doi:10.5075/epfl-298799_978-2-9701614-0-0

2.3 LAMMPS implementation

LAMMPS is a powerful simulator originally developed for molecular dynamics that, today, also accounts for other particle-based algorithms such as DEM, SPH, or Peridynamics [20]. The software is open source and distributed under GNU General Public License (GPL). LAMMPS is gaining notoriety in the computational solid mechanics community thanks to the open definition of the particles and potentials forming the system [21,22]. In this work, we have adapted the LSM formulation to LAMMPS by defining one-dimensional bonds with elastic and elastic-plastic properties connecting two particles of the system. Each lattice spring is defined by two functions, $F_b(r)$ and $\Phi_{\mathrm{b}}(r)$, where F_b is the force applied by the bond to its connecting particles, Φ_b is the bond potential, and r is the distance between two particles.

In this work, we represent each elastic bond forming the structure using the LAMMPS *bond_style table linear* command of the MOLECULE package. This function allows the loading of a generic bond with custom F_b and Φ_b, interpolated by LAMMPS through the usage of a linear function acting on a look-up table provided by the user. We have provided LAMMPS with two tables describing the stress-strain laws for orthogonal and diagonal springs for each phase of the composite, i.e. the matrix, the fibres and the interface.

To apply a tensile load to the structure, we have used the *deform* command, with a fix engineering rate of $R = 10^{-2}\ mm/s$. Each strain increment is followed by a relaxation period: a new strain increment is applied only after the kinetic energy in the sample decreases below a user-defined threshold value. Simulations are performed in a canonical ensemble.

3. Results

3.1 Single fibre verification

It is well known that, in a fibre-reinforced composite, the main mechanism of stress transformation from the matrix to the fibre is the interfacial shear stress, which can be analytically estimated by the shear lag model of Kelly-Tyson [23] by introducing the concept of critical length, l_c. This is defined as the length that the stress transformation between the fibre and the matrix happens which can be estimated as:

$$\frac{l_c}{d} = \frac{\sigma_{U_f}}{2\tau_{y_{m\,0}}} \tag{1}$$

In Eq. (1), d is the diameter of the fibre and τ_{y_m} is the yielding shear stress of the interface which is assumed to be constant in the Kelly-Tyson model. To maximize the strength of the composite, it is important that the length of the fibres, l_f, be higher enough than this critical length to guarantee the proper load carrying by the fibres, $l_f > l_c$.

To study the stress transformation between the fibre and the matrix, first, we consider a single fibre inserted in a uniform matrix media. We identify the fibre, matrix and the interface between them with the symbols f, m, i respectively. We assume $E_f = E_m = 3$ GPa, $\varepsilon_{y_m} = 3\%$, $\sigma_{y_m} = 90$ MPa, $\varepsilon_{U_f} = 20\%$, $\varepsilon_{U_m} = 30\%$, $\sigma_{U_f} = 600$ MPa, $\sigma_{U_m} = 170$ MPa. Regarding the elongation at break, we imposed $\varepsilon_{U_m} = 30\%$, while for the fibre and interface phases we used a two-

  doi:10.5075/epfl-298799_978-2-9701614-0-0

parameter Weibull distribution with a shape factor of $\alpha = 10$ and scale factors of $m_f = \varepsilon_{U_f} = 20\%$. We initially assume a perfect interface, i.e. having the same properties of the matrix.

From Eq.(1) a critical value for the aspect ratio of the fibre is obtained as:

$$\frac{l_c}{d} = \frac{600}{2(45)} = 6.66 \tag{2}$$

In Figure 1, stresses variation along the fibre are shown for a long enough fibre of aspect ratio $\frac{l_c}{d} = 50$. It can be observed that, after an initial transition region near the edges of the fibre, a stress plateau is formed in the middle region, in agreement with our initial assumption of $l_f > l_c$

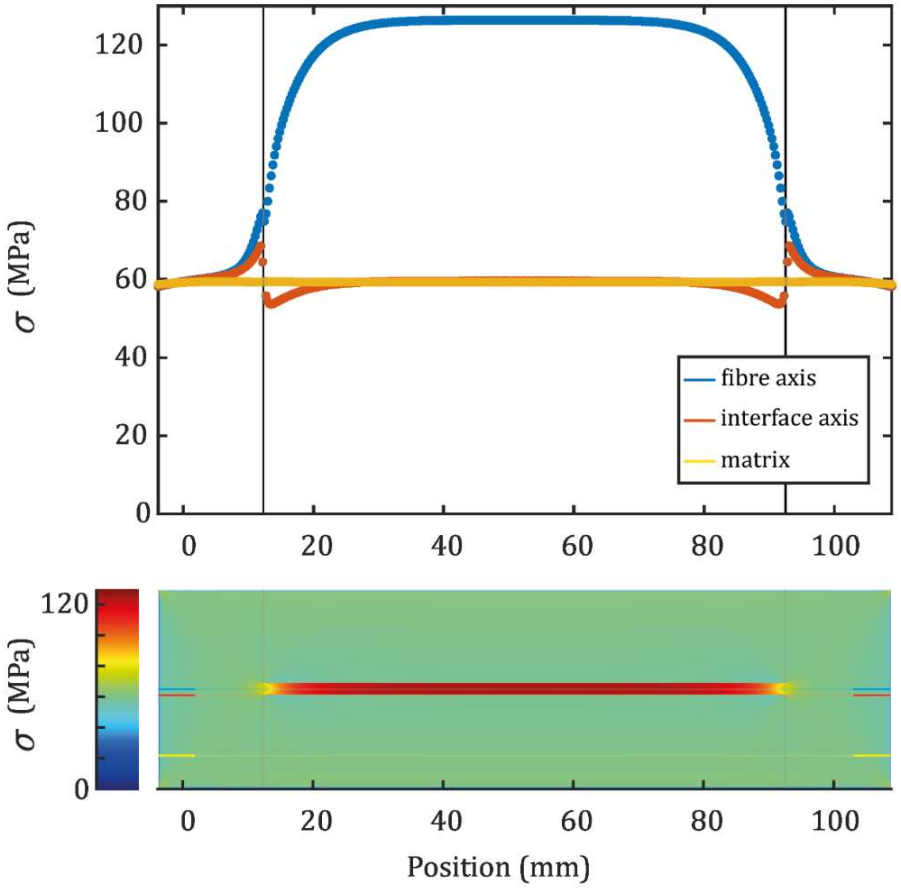

Figure 1. Von Mises stresses in the structure. The stresses are reported along three different lines parallel to the fibre: the fibre mid axis, the bottom interface axis, and at a distance $4d_f$ from the surface of the fibre. Grey vertical lines indicate the edges of the fibre. Coloured horizontal lines in the stress map indicate the three corresponding heights.

3.2 Unidirectional fibres

The main focus of our simulations is to investigate the effect of interface on the strength of composite by considering different values for the stiffness, E_i, and failure elongation, ε_{U_i} of the interphase. To model the effect of interface on the strength, a narrow interphase region of the thickness t_i equals to half the diameter of the fibre d_f is introduced to the model. We start by

  doi:10.5075/epfl-298799_978-2-9701614-0-0

the strongest case assuming a perfect adhesion between the matrix and the fibres, thus, $E_i = E_m$ and $\varepsilon_{U_i} = \varepsilon_{U_m}$. We consider a composite material obtained from 20 parallel long fibres having $l_f = L_c$, where L_c is the length of the composite sample, and a volume fraction of $v_f = 40\%$. We identify this fibre arrangement with the index G1. Results are shown in Table 1. A composite strength $S = 249.1\ \mathrm{MPa}$ is observed. Comparing with the upper limit estimated by direct rule of mixture in Eq. (3) a reasonable agreement is observed which validates the accuracy of the simulation:

$$S_c = v_f \sigma_{U_f} + \left(1 - v_f\right)\sigma_{y_m} = 0.4(600) + 0.6(90) = 294\ MPa \quad (3)$$

We then use two different approaches to reduce the performances of the interface. We consider lower values of E_{i_1}, i.e. a softer interface, and lower values of ε_{U_i}, i.e. a more brittle interface. A 45% decrease of the interface strength S_i leads to a 8% decrease of the composite strength.

Then, the simulation is performed for short, aligned fibres having the length $l_f < L_c$, with L_c being the length of the composite. The results are shown in Table 1. To see the effect of fibre patterning, we have considered two extreme arrangements identified with the indexes G2 and G3. In the G2 arrangement, even and odd rows of fibres are not shifted along their axes, thus leading to a brick-like pattern, see Fig. 2(E and F), while in the G3 arrangement the fibres are also aligned across every row, see Fig. 2(G and H). The Stress-strain curves and the corresponding fracture patterns are reported in Figure 2. The stress concentrations occurring at the edges of the fibres increase the importance of the strength interface. A 45% decrease of the interface properties lead to a 25% to 35% reduction of the composite strength for G2 geometries and 30% to 40% for aligned fibres arrangements.

Table 1: Numerical results for different fibre arrangements and values of the interface Young's modulus E_i and *the interface ultimate strain ε_{U_i}. The theoretical interface strength S_i is reported for each simulation, alongside the numerically obtained composite strength S_c.*

ID	Arrangement	ε_{U_i} [mm/mm]	E_{i_1} [GPa]	S_i [MPa]	S_c [MPa]
ID1	G1	0.3	3	170 MPa	249.1
ID2	G1	0.2	3	140 MPa	242.7
ID3	G1	0.1	3	110 MPa	222.5
ID4	G1	0.3	1	110 MPa	230.1
ID5	G1	0.3	0.5	95 MPa	229.2
ID6	G2	0.3	3	170 MPa	214.0
ID7	G2	0.1	3	110 MPa	142.9
ID8	G2	0.3	0.5	95 MPa	153.8
ID9	G3	0.3	3	170 MPa	172.1
ID10	G3	0.1	3	110 MPa	104.8
ID11	G3	0.3	0.5	95 MPa	117.1

  doi:10.5075/epfl-298799_978-2-9701614-0-0

Focusing on Figures 2D, 2E and 2F, corresponding to the brick-like fibre arrangement G2, the properties of the interface modify the failure mode of the composite. Figure 2D shows shear stress failure modes, since the principal stresses are rotated by 45° with respect to the alignment of the fibres, while Figures 2E and 2F show a failure mechanism associated with the development of normal stresses aligned with the fibres, thus leading to a brittle-like fracture behaviour of the composites. This behaviour is also observed for aligned fibres, G3, as visible in Figures 2G and 2H. Poor interface properties lead to a single point failure at the edges of the fibre, with no visible fracture in the matrix. It must be noticed that, because of the stress concentrations at the edges of the fibres, $S_c < S_m$, i.e. the composite performances are worse than the ones characterizing the pure matrix.

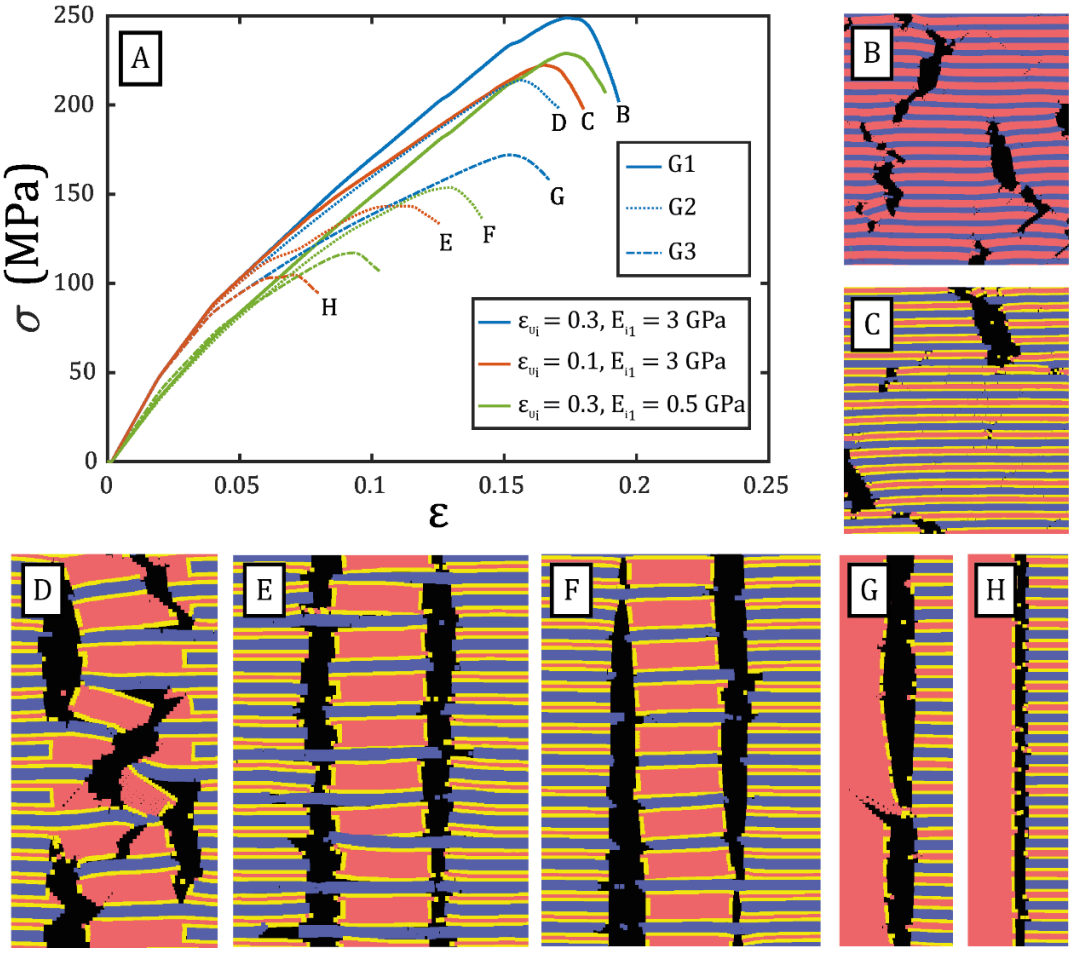

Figure 2. A) Stress – strain curves for different geometries and values of ε_i, E_{i_1}. B-H) Fracture maps. The colours indicate the different phases in the composite: blue – fibre, yellow – interface, red – matrix. The maps correspond to simulations ID1, ID3, ID6, ID7, ID8, ID9, ID10 (in order).

By comparing the two different approaches we used to decrease the interface strength for both G2 and G3 arrangements, it can be observed that softer ductile interfaces (ID8, ID11) lead to higher composite strengths than stiff brittle interfaces (ID7, ID10), regarding having lower interface strengths S_i in our study. Furthermore, in ID7 and ID10 simulations we observed

  doi:10.5075/epfl-298799_978-2-9701614-0-0

debonding phenomena, with multiples crack path being parallel to the fibres. Finally, we observe that for G2 and G3 fibre arrangements, softer interfaces lead to lower values of the strain at maximal stress $\varepsilon|_{\sigma_c=S_c}$, while for G1 we found an increment of 1%. This is compatible with data available in literature [3], showing that for long unidirectional fibres higher activator dosages lead to lower strengths and higher deformations. Further studies are required to investigate this relationship.

4. Conclusions

We have shown how a Lattice Spring Model can be used to study the propagation of fracture in a SPCs, characterized by the similar Young's moduli between matrix and interface. We show how the interface properties become crucial when finite length fibres are considered, and thus the fibre edges play a role in the composite behaviour. This is particularly important in SPCs, where the strength enhancement is limited by the similarity between the composite phases. Our study suggests that for SPCs, long unidirectional fibre arrangement shows a notable potential for enhancement in the mechanical performance, while for short fibres it is observed that the stress concentrations at the edges of the fibres has a destructive effect on the composite behaviour, especially when low strength interfaces are considered

5. References

1. Karger-Kocsis J, Bárány T. 2014 Single-polymer composites (SPCs): Status and future trends. *Composites Science and Technology* **92**, 77–94.
2. Capiati NJ, Porter RS. 1975 The concept of one polymer composites modelled with high density polyethylene. *Journal of Materials Science 1975 10:10* **10**, 1671–1677.
3. Song L, Wang X, Xie P, Ding Y, Dang K, Yang W. 2021 Dissolution window in in situ polymerization preparation of polyamide single-polymer composites. *Polymer Engineering and Science* **61**, 1662–1672.
4. Fakirov S. 2013 Nano- and microfibrillar single-polymer composites: A review. *Macromolecular Materials and Engineering*. **298**, 9–32.
5. Matabola KP, de Vries AR, Moolman FS, Luyt AS. 2009 Single polymer composites: A review. *Journal of Materials Science* **44**, 6213–6222.
6. Dencheva N, Sampaio AS, Oliveira FM, Pouzada AS, Brito AM, Denchev Z. 2014 Preparation and properties of polyamide-6-based thermoplastic laminate composites by a novel in-mold polymerization technique. *Journal of Applied Polymer Science* **131**, 1–11.
7. Tohidi SD, Rocha AM, Dencheva N v., Denchev Z. 2018 Single polymer laminate composites by compression molding of knitted textiles and microparticles of polyamide 6: Preparation and structure-properties relationship. *Composites Part A: Applied Science and Manufacturing* **109**, 171–183.
8. Ageyeva T, Sibikin I, Kovács JG. 2019 Review of thermoplastic resin transfer molding: Process modeling and simulation. *Polymers (Basel)* **11**.
9. Tohidi SD, Denchev Z, Dencheva N v., Rocha AM, Rosa LA, Engesser B. 2020 Development of polyamide 6 based single polymer composites reinforced by novel stitched plain fabrics. *Materials Today Communications* **24**, 101068.
10. van Rijswijk K, Lindstedt S, Vlasveld DPN, Bersee HEN, Beukers A. 2006 Reactive processing of anionic polyamide-6 for application in fiber composites: A comparitive study with melt processed polyamides and nanocomposites. *Polymer Testing* **25**, 873–887.

  doi:10.5075/epfl-298799_978-2-9701614-0-0

11. van Rijswijk K, Bersee HEN, Beukers A, Picken SJ, van Geenen AA. 2006 Optimisation of anionic polyamide-6 for vacuum infusion of thermoplastic composites: Influence of polymerisation temperature on matrix properties. *Polymer Testing* **25**, 392–404.
12. Gong Y, Liu A, Yang G. 2010 Polyamide single polymer composites prepared via in situ anionic polymerization of ε-caprolactam. *Composites Part A: Applied Science and Manufacturing* **41**, 1006–1011.
13. Ostoja-Starzewski M. 2002 Lattice models in micromechanics. *Applied Mechanics Reviews* **55**, 35–59.
14. Zhao SF, Zhao GF. 2012 Implementation of a high order lattice spring model for elasticity. *International Journal of Solids and Structures* **49**, 2568–2581.
15. Chen H, Lin E, Jiao Y, Liu Y. 2014 A generalized 2D non-local lattice spring model for fracture simulation. *Computational Mechanics* **54**, 1541–1558.
16. Zhang T. 2019 Deriving a lattice model for neo-Hookean solids from finite element methods. *Extreme Mech Lett* **26**, 40–45.
17. Buxton GA, Care CM, Cleaver DJ. 2001 A lattice spring model of heterogeneous materials with plasticity. *Modelling and Simulation in Materials Science and Engineering* **9**, 485–497.
18. Zhou SJ, Curtin WA. 1995 Failure of fiber composites: A lattice green function model. *Acta Metallurgica et Materialia* **43**, 3093–3104.
19. Libonati F, Cipriano V, Vergani L, Buehler MJ. 2017 Computational Framework to Predict Failure and Performance of Bone-Inspired Materials. *ACS Biomaterials Science and Engineering* **3**, 3236–3243.
20. Thompson AP *et al.* 2022 LAMMPS - a flexible simulation tool for particle-based materials modeling at the atomic, meso, and continuum scales. *Computer Physics Communications* **271**.
21. Chiang Y, Chiu TW, Chang SW. 2022 ImageMech: From Image to Particle Spring Network for Mechanical Characterization. *Frontiers in Materials* **8**.
22. Albano A *et al.* 2021 How to modify lammps: From the prospective of a particle method researcher. *ChemEngineering* **5**.
23. Gibson RF. 2016 *Principles of Composite Material Mechanics*.

  doi:10.5075/epfl-298799_978-2-9701614-0-0

Hybrid testing for composite substructures

Tobias Laux[a], Jack S. Callaghan[a,b], Sergey G. Kravchenko[c], Janice M. Dulieu-Barton[a,b], Ole T. Thomsen[a]

a: Bristol Composites Institute, University of Bristol, Bristol, UK – tobi.laux@bristol.ac.uk
b: Faculty of Engineering and Physical Sciences, University of Southampton, Southampton, UK
c: Department of Materials Engineering, The University of British Columbia, Vancouver, Canada

Abstract: *A multiaxial substructure test has been devised to investigate the load and failure response of a spar cap to web joint in a wind turbine blade (WTB). The loading configuration has been derived from a finite element model of the full blade subjected to in-service loading conditions. It is now the aim to virtually augment the substructure test, using hybrid testing technology, to account for the evolving interaction between the physically tested substructure and the rest of the structure. The paper provides a brief summary of hybrid testing, the challenges associated with applying this to integrated composite structures, and further gives an overview of the substructure testing being conducted.*

Keywords: Hybrid testing; Subcomponent testing; Composite structures

1. Introduction to hybrid testing

Hybrid testing is a combined experimental and numerical technique that allows physical testing of a subcomponent while the remainder of the structure is modelled numerically. The technique has often been used in earthquake engineering to investigate seismic protection of civil engineering structures as a cost-effective alternative to full-scale shake table tests as shown in Figure 1 [1].

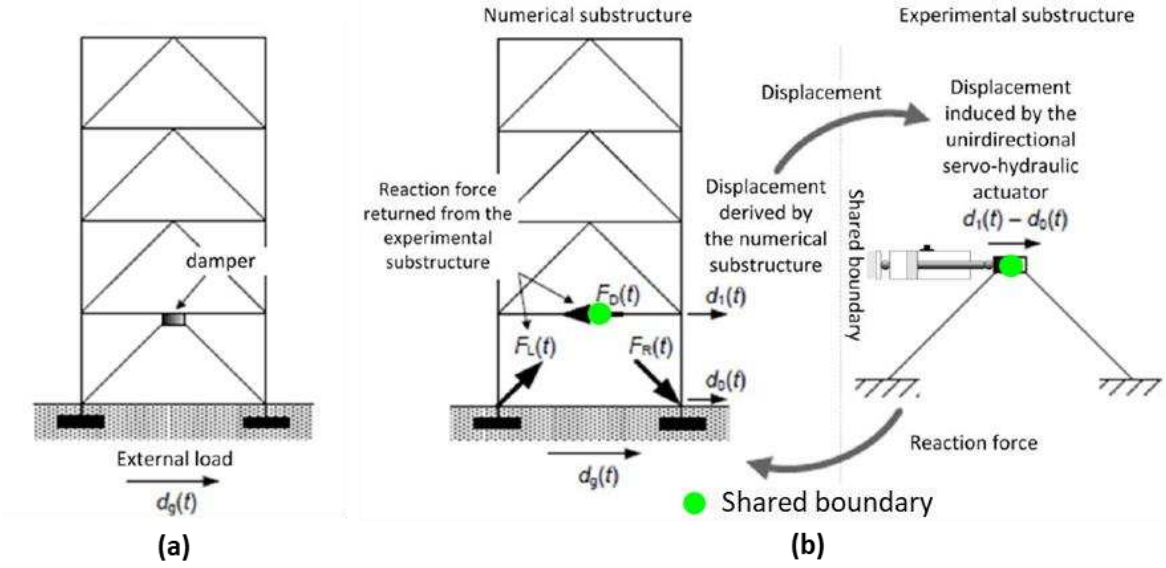

Figure 1. Hybrid test of a building structure to investigate seismic protection: (a) emulated 'full' structure and (b) hybrid test set-up with numerical and experimental substructure [1].

  doi:10.5075/epfl-298799_978-2-9701614-0-0

Typically, parts of the structure with complex physics, i.e. the damper in Figure 1, is experimentally tested, while the substructures with well-understood behaviours, i.e. the steel frames in Figure 1, are modelled numerically. Displacements and force resultants are then exchanged iteratively between the numerical and experimental substructure at the shared boundary (green in Figure 1). The communication loop between the actuator controlling software of the experiment and the numerical model is established through a middleware such as OpenFresco [2] or custom LabVIEW code [3–5].

For the validation of composite structures across the aerospace, wind energy and marine industries, the technique has the potential to spur the development of new substructure test methods at a fraction of the cost of full-scale experiments, while capturing structural effects not present in coupon tests [6]. However, it was found in recent works [3–5] that highly integrated composite structures pose significant challenges for hybrid testing due to their 'continuous' nature, where sub-structuring leads to complex shared boundaries. This is different from most civil engineering structures made from 'discrete' structural members such as columns, beams, and trusses, where sub-structuring leads to relatively simple *discrete* hinge-type or nodal point shared boundaries as shown in Figure 1. The complex *continuous* shared boundaries necessitate the use of multiaxial loading rigs and advanced experimental methods to control and monitor the tests.

The work presented in [3–5] was carried out on simple lab-scale specimens, and application to complex real composite substructures has yet to be demonstrated. The aim of this work is to demonstrate how hybrid testing can be applied to a composite substructure experiment, and further to elaborate the advantages over conventional testing. To this end, a multiaxial WTB substructure is being tested in the Large Structures Testing Laboratory (LSTL) at the University of Southampton, UK, as shown in Figure 2.

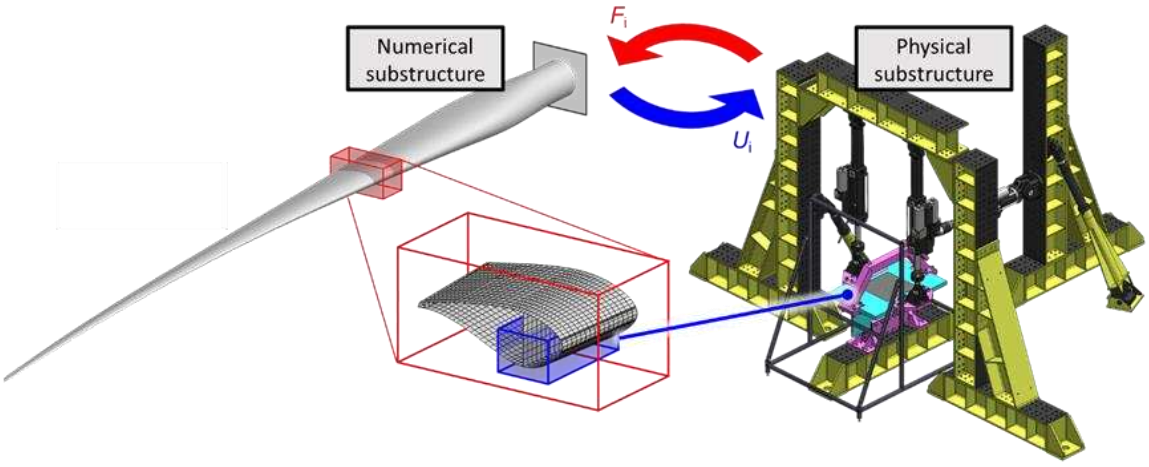

Figure 2. WTB 'T-joint' substructure test currently installed on the LSTL strong floor.

2. Wind turbine blade substructure test

The substructure was down selected from various WTB components in agreement with the manufacturer, due to its complex construction, structural importance, and high strains present in the global (full-scale) WTB analysis. The 'T-joint' shown in Figure 3 is the part of the WTB containing the spar cap, which reacts the large 'flap-wise' bending moments, and the web, which reacts the shear force, and the connection between them.

  doi:10.5075/epfl-298799_978-2-9701614-0-0

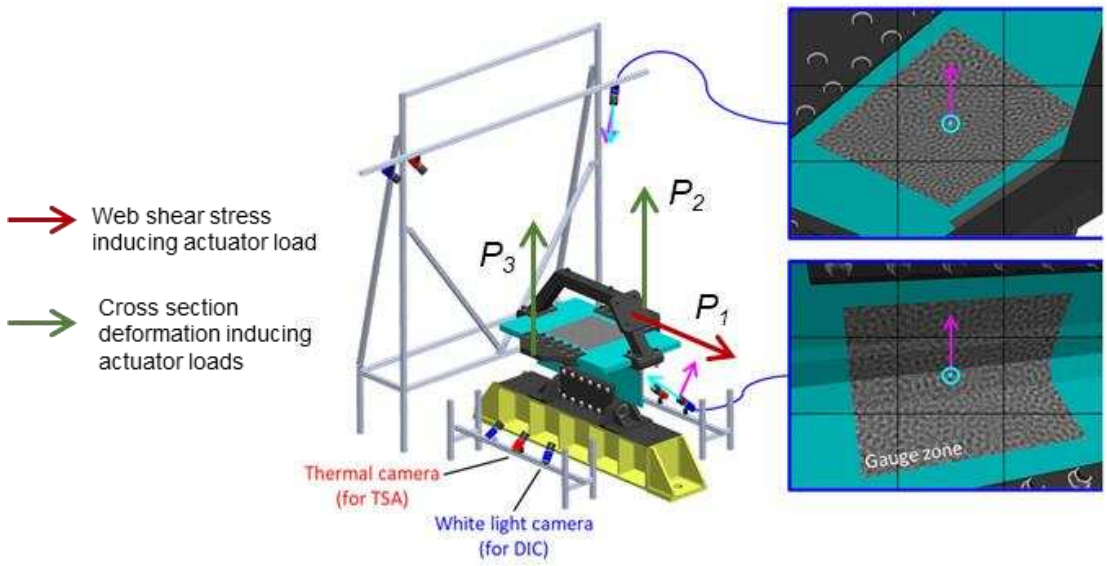

(a) *(b)*

Figure 3. T-joint substructure test: (a) multiaxial load case and imaging device mounting frame (load rig superstructure and actuators hidden), (b) camera views of gauge zone region.

In reality the outer surface of the T-joint is curved as it is part of the WTB aerofoil, however, the specimens used for this research are flat bottomed to simplify manufacturability and reduce production costs. The main constituent material is glass fibre reinforced polymer (GFRP), with wood core materials used for moulding and to form sandwich panels. The layup of the T-joint specimens replicates the actual WTB substructure at the interface between the spar cap and the web, but is continuous across the spar, when in reality it tapers down towards the outside. The specimens are 1.2 m x 0.8 m x 0.4 m.

The test load configuration, as shown in Figure 3, was developed so that it was practically feasible to replicate in an experimental setup while remaining structurally relevant, containing key load components that when tested would provide useful information regarding substructural load response and design allowables. The test load cases were defined by comparing an FEA simulation of the specimen under parameterised loading conditions to the matching substructure within the global WTB FEA model and selecting the parameters that yielded the best match for the general load case components.

The multiaxial test was designed to facilitate full-field imaging of all sides of the central region of the T-joint, referred to as the ‘gauge zone’, resulting in three stereo digital image corelation (DIC) [7] and infrared camera arrangements (Figure 3). DIC is used to monitor the displacement and strain fields, while the infrared cameras capture the thermal information necessary to obtain a stress metric through thermoelastic stress analysis (TSA) [8]. Prior testing was conducted on a ‘two-dimensional’ T-joint cross-section in a uniaxial test machine, from which the imaging analysis methods were developed [9]. The natural progression from uniaxial to multiaxial load state works towards developing the substructural tier of the ‘testing pyramid’. The ability to apply more relevant load cases in substructure tests, along with validated numerical models of such tests, will reduce the dependence on the bottom (coupon-scale) tier

  doi:10.5075/epfl-298799_978-2-9701614-0-0

design allowables with significant knockdown factors, as where relevant, allowables based on substructural response can be used.

3. The opportunity for hybrid testing

Applying the hybrid testing method to the multiaxial test allows to account for the evolving interaction between the physically tested substructure and the rest of the structure, i.e. the numerical substructure. This interaction may change during the test due to occurrence of damage in either substructure. It is this change in the interaction that cannot be accounted for in a traditional substructure test but which may be crucial to accurately represent the load and failure response of the investigated structure as a whole.

Difficulties arise when considering the boundary conditions for the WTB T-joint substructure for hybrid testing, in that the component is enclosed by continuous material on all outside edges, i.e. handling the shared boundaries becomes challenging and will require advanced experimental methods for control. Therefore, the hybrid testing methodology will initially be developed on a dummy T-joint specimen made from steel before its deployment on the composite specimen. Due to the well know material properties of the steel, an accurate reference solution to benchmark the hybrid testing methodology can be obtained based on a FE model of the full structure. The set-up will also be tested virtually where both the physical and numerical substructure are simulated and run as a co-simulation in the commercial FE software Abaqus. Displacements obtained from LVDT as well as strains derived from DIC measurements will be considered in the hybrid testing control loop.

4. Summary and outlook

A multiaxial substructure test has been set-up to investigate the load and failure response of the spar cap to web joint in a composite WTB. The experimental loading conditions were carefully deduced from a full-scale FE blade model, and loading frames and fixtures have been design. Camera equipment and arrangements have also carefully been selecting to enabling DIC and TSA during the substructure test. The next steps are:

- To conduct a conventional quasi-static substructure test where the load cases are known prior to testing as derived from the FE blade model.
- To devise a virtually augmented substructure test, where hybrid testing technology will used to control the experimental boundary conditions, increasing the fidelity of the substructure test by accounting for the interaction between physical substructure and the rest of the blade, i.e. the numerical substructure.
- To compare the hybrid testing approach to the conventional substructure test.

Overall, the developments presented in this paper and the planned future work, will pave the way to a better understanding of hybrid testing in the context of substructure testing of complex integrated composites structures. This in turn will lead to a better understanding of the load and failure response of structures which will aid structural design and model development/validation.

  doi:10.5075/epfl-298799_978-2-9701614-0-0

Acknowledgements

The research presented was supported by the EPSRC Programme Grant 'Certification for Design – Reshaping the Testing Pyramid' (CerTest, EP/S017038/1), and the EPSRC Equipment Grant 'Structures 2025: A High Fidelity, Data Rich, Paradigm Shift For Structural Testing' (EP/R008787/1).

References

[1] Williams MS. Real-time hybrid testing in structural dynamics. 5th Australas. Congr. Appl. Mech. ACAM 2007, 2007.

[2] Schellenberg A, Huang Y, Mahin SA. Structural FE-software coupling through the experimental software framework , openfresco. 14th World Conf Earthq Eng 2008:1–8.

[3] Høgh J, Waldbjørn J, Wittrup-Schmidt J, Stang H, Berggreen C. Quasi-static single-component hybrid simulation of a composite structure with multi-axis control. Strain 2015;51:459–73. https://doi.org/10.1111/str.12157.

[4] Waldbjørn J, Høgh J, Stang H, Bergreen C, Wittrup-Schmidt J, Branner K. Hybrid testing of composite structures with single-axis control. 19th Int. Conf. Compos. Mater., Montreal, Canada: 2013.

[5] Waldbjørn JP. Hybrid Simulation of Wind Turbine Blades. Technical University of Denmark, 2016.

[6] You S, Gao XS, Nelson A. Breaking the Testing Pyramid with Virtual Testing and Hybrid Simulation. Fatigue Aircr Struct 2019;2019:1–10. https://doi.org/10.2478/fas-2019-0001.

[7] Sutton MA, Orteu JJ, Schreier H. Image correlation for shape, motion and deformation measurements. Springer; 2009.

[8] Dulieu-Barton JM, Stanley P. Development and applications of thermoelastic stress analysis. J Strain Anal Eng Des 1998;33:93–104.

[9] Callaghan JS, Thomsen OT, Dulieu-Barton JM, Laustsen S. An integrated methodology for comparing and fusing full-field experimental and numerical data for complex composite substructures. 22nd Int. Conf. Compos. Mater., 2019.

  doi:10.5075/epfl-298799_978-2-9701614-0-0

MECHANICAL CHARACTERIZATION OF 3R-REPAIRABLE COMPOSITES AND 3R BONDING TECHNIQUES PRODUCED BY DIFFERENT PROCESSES AND THEIR REPAIR EFFICIENCY

Maria Kosarli[a], Georgios Foteinidis[a], Kyriaki Tsirka[a], Vincent Gayraud[b], Stefan Weidmann[c], Asier M. Salaberria[d], Nerea Markaide[d], Alain Leroy[e], Alkiviadis S. Paipetis[a]

a: Department of Materials Science & Engineering, University of Ioannina, Ioannina, 45110, Greece, m.kosarli@uoi.gr

b: Composite Unit, EURECAT, Av. Universitat Autònoma, 23, 08290, Barcelona, Spain

c: Leibniz-Institut für Verbundwerkstoffe GmbH, Erwin-Schroedinger-Str. Gebaeude 58, 67663 Kaiserslautern, Germany

d: CIDETEC, Basque Research and Technology Alliance (BRTA), Paseo Miramon 196, 20014 Donostia-San Sebastian, Spain

e: Coexpair S.A., Belgium

Abstract: *In this research, the mechanical properties and the repair ability of vitrimer composites manufactured by different production processes (Resin Transfer Molding- RTM & thermoforming) were studied and compared with conventional composites. The bonding properties of the vitrimer resin were also investigated in terms of adhesive bonding. The mechanical tests were applied to the Interlaminar Shear Strength-ILSS geometry and the Double Cantilever Beam-DCB geometry. For the evaluation of the bonding properties, specimens of a geometry that can simulate a stiffened panel, called lap strap, were manufactured and tested. Results indicated that the specimens recovered their initial properties by 60% to 70% and were able to eliminate any defects that were induced during the manufacturing process, after the repair process.*

Keywords: Composites; vitrimer; repair; repair efficiency;

1. Introduction

Advanced Fiber Reinforced Polymers (FRPs) are among the most important technological materials in the aerospace industry, usually for the replacement of metallic alloys. Their high specific properties as their high stiffness, the excellent modulus of elasticity in combination with the relatively low density are some of the FRPs advantages. They can be used for high end applications where specific material properties are a prerequisite. However, the FRPs' relatively low fracture toughness can result to undesirable fracture phenomena that could compromise the materials structural integrity. One of the most significant disadvantages of the thermoset epoxy polymers and their composites is the difficulty in repair.

  doi:10.5075/epfl-298799_978-2-9701614-0-0

The three-dimensional cross-linking network that thermosets always form make their repair difficult or even impossible [1]. Moreover, their thermoset matrix is non-recyclable and cannot be remolded or reshaped in contrast to the thermoplastics. These properties can now be achieved thanks to a new and innovative epoxy vitrimer resin that is re-processable, repairable and recyclable (3R) [2]. The repair takes place at specific temperature, above the Tg of the resin by applying heat and pressure. In this temperature, the dynamic chemical bonds of the epoxy can be reshuffled and repair resin/fiber delaminations of the damaged part [3].

In this research, the different properties of 3R composites manufactured by different production processes (Resin Transfer Molding- RTM and stacking of 3R prepregs) were evaluated with mechanical tests. The bonding properties of the vitrimer resin were also investigated in terms of adhesive bonding. The mechanical tests applied to the Double Cantilever Beam-DCB geometry and the Interlaminar Shear Strength-ILSS geometry. For the evaluation of the 3R bonding properties, specimens of a new proposed lap strap geometry were manufactured with a 3R resin layer between the two parts and tested [4]. The repair process took place by applying heat and pressure.

2. Experimental

- Manufacturing
    - Materials

The 5HS carbon fabric C-WEAVE™ 280SA5 T800HB 6K 40B- 5HS x125cm with Spunfab 118CHQ 4 g/m^2 1 face and the UD 24K carbon fabric of 280g/m^2 provided by CHOMARAT, were used as primary reinforcement. The AIR-RES-7 3R (vitrimer) epoxy resin developed by CIDITEC used for the repairable composites. The conventional panels were manufactured using the RTM6 aerospace grade epoxy resin by Hexcel S.A.

    - Composites manufacturing
        - 3R panels manufactured by RTM process

For both UD and quasi-isotropic panels, the fabrics were cut at the desired dimensions and the 3R resin was pre-heated at 80^{o}C while degassing took place for 30 min. The manufacturing process was the resin transfer moulding technique (Figure 1). The lamination sequence for the quasi-isotropic panels was [(±45)/(0/90)]4_s and for the UD panel 18 plies of the fabric with a Teflon insert at the midplane, were selected. The mould was heated at 130°C and the injection pressure was 1 bar. Curing took place at 130°C for 1 hour and at 180°C for 0.5 hour according to the curing profile of the 3R resin. The pressure of the mould was set at 4 bars.

        - RTM6 panels manufactured by RTM process

As previously, the conventional panels (both the quasi-isotropic and the UD) were manufactured by RTM process. All fabrics were stacked according to the above lamination and the tooling was closed. The resin (RTM6) was pre-heated and injected to the mold. In this case, the tooling was heated up to 180º C for 1,5 hours. Once the curing process finished the mold was left to cool at room temperature and the panel was extracted.

  doi:10.5075/epfl-298799_978-2-9701614-0-0

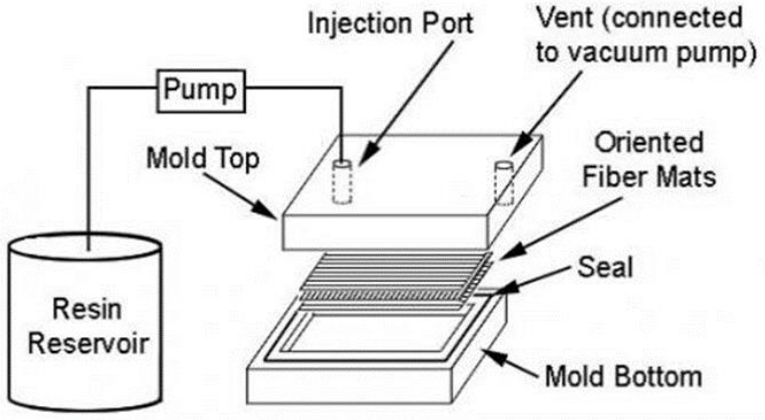

Figure 1. Experimental setup of the manufacturing of the panels by RTM proceess.

- 3R panels manufactured from EPP's

Single layer enduring prepregs (EPP's) were used to produce the quasi-isotropic panels by a hot-pressing process (thermoforming). The manufacturing process of the single layer prepregs is part of another research. The prepregs were stacked on top of each other. In order to improve the toughness properties of the produced laminates, a binder veil (Spunfab 118CHQ, 4 g/m²) was applied on one side of the fabric. To ensure that the individual laminates had the same layer structure, this veil side was defined as the top side. A laboratory press Dr. Collin GmbH P 300 M was used for the thermoforming process. In order to achieve a homogeneous pressure distribution on the laminates in the pressing process, a layer of silicone (HT 60 WHT silicone sheet, thickness 1.5 mm, provided by MVQ-Silicones) was used. Thermoforming took place at 210 °C for two hours under 2 MPa pressure.

- Characterization techniques
  - Interlaminar Shear Strength (ILSS)

The interlaminar shear strength was investigated using the short beam shear geometry. ILSS specimens were cut from quasi-isotropic laminates according to ASTM 2344. Mechanical testing was performed on a Universal Testing Machine WDW-100 by Jinan S.A. equipped with a 100kN loadcell under 3-point bending. The interlaminar shear strength was evaluated by the short beam shear geometry. The maximum strength (MPa) was estimated from equation (1):

$$\text{Strength}_{ILSS} = 0.75 \times \frac{P_{max}}{b \times h} \quad (1)$$

where P is the maximum load (N), b is the width of the specimen (mm) and h the specimen thickness (mm).

  - Mode-I Fracture Toughness (G_{Ic})

The interlaminar fracture toughness of the composites was evaluated using Mode-I test. For this test, Mode-I specimens were extracted from the UD laminates. A two-part epoxy resin Epikote 828 lvel (DGEBA) by Hexion S.A. was used as adhesive to bond two piano hinge tabs (one at each side) at one end of each specimen. Testing took place at an Instron 8001 Universal Testing Machine with a 100kN loadcell according to ASTM D 5528. The displacement rate was set at 2

  doi:10.5075/epfl-298799_978-2-9701614-0-0

mm/min. The strain energy release rate, G_{Ic}, was calculated using the modified beam theory method and equation (2):

$$G_{IC} = \frac{3P\delta}{2b(a+|\Delta|)} \quad (2)$$

where P is the applied load (N), δ is the displacement (mm), b is the width of specimen (mm), a is the delamination length (mm) and Δ is the correction factor.

- Lap Strap (model structure geometry)

Lap Strap specimen geometry can simulate the stiffening of a composite laminate. This geometry is comprised of two parts, the lap and the strap with a resin adhesive layer between them. Both parts were extracted from the quasi-isotropic laminates. Mechanical testing was performed at an Instron 8001 Universal Testing Machine with a 100kN loadcell under tensile mode (Figure 2). The stress was calculated as the ratio of the load over the cross-section area (thickness × width) and the strain as the ratio of the extension over the grip-to-grip distance.

Figure 2. Lap Strap specimen during mechanical testing.

3. Results

- Interlaminar Shear Strength (ILSS)

Table 1 illustrates the initial and repaired strength values that obtained from the ILSS tests. In case of the specimens that manufactured with RTM process, the initial values that achieved was at 37.53 MPa while after the repair the maximum strength reached the 21.74 MPa, with a repair efficiency of ca. 58%. Specimens that produced by stacking of 3R prepregs, exhibited maximum strength values of 7.32 MPa with the repaired values to be increased at 10.98 MPa. In this case, the recovery of the properties exceeded the 100% (150%) since the prepregs that manufactured for this research had a lower resin content than the initial ones.

Table 1: Interlaminar Shear Strength (ILSS) results.

Type of CFRP	Strength (MPa)	Repair efficiency (%)

  doi:10.5075/epfl-298799_978-2-9701614-0-0 published under CC BY-NC 4.0 license

3R CFRP RTM process initial	37.53 ± 6.39	
3R CFRP RTM process repaired	21.74 ± 2.86	57.9
3R CFRP Prepregs initial	7.32 ± 4.27	
3R CFRP Prepregs repaired	10.98 ± 7.69	150.0

- Mode-I Interlaminar fracture toughness

The mode-I interlaminar facture toughness was calculated for specimens that produced with a conventional and aerospace grade resin (RTM6) and specimens with the 3R resin. Table 2 presents the G_{Ic} values for both composites and especially for the repairable composites the values after the repair. As can be seen, the 3R composites exhibited 10% increased properties when compared to the conventional composites. Also, a recovery of the fracture toughness of 34% was achieved.

Table 2: Mode-I results of Interlaminar fracture toughness.

Type of CFRP	G_{Ic} (J/m^2)	Difference of properties (%)
Conventional CFRP	204.67 ± 51.22	
3R CFRP initial	225.38 ± 44.18	+10.12
3R CFRP repaired	76.72 ± 55.25	Repair: 34.0

- Lap Strap geometry

Figure 3 illustrates representative stress vs strain plots from Lap Strap specimens before and after the repair. As can be observed, the debonding of the lap from the strap had a sudden character that mentioned with a small drop of the stress.

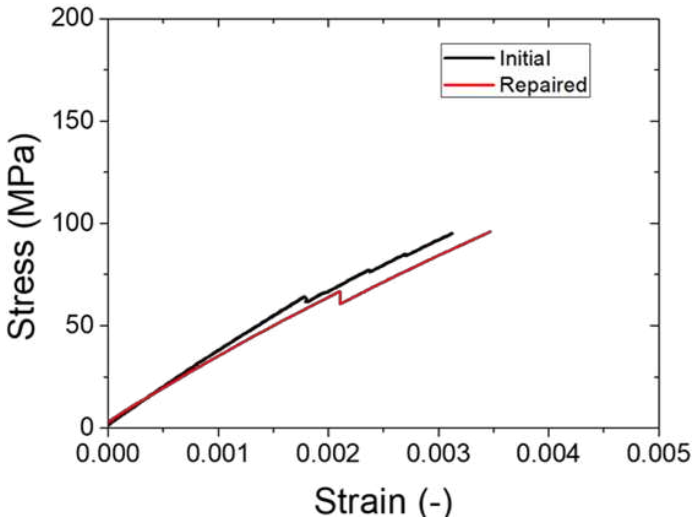

Figure 3. Representative Stress-Strain plots of lap strap specimens before and after repair.

The repaired lap strap specimens presented a recovery of 70% in terms of strength values in comparison to the initial specimens. Specifically, the initial composites showed an average maximum strength of about 76 MPa while the repaired composites exhibited an average maximum strength of about 53 MPa (Table 3).

Table 3: Results of maximum strength of lap strap specimens.

Type of CFRP	Strength (MPa)	Repair efficiency (%)
3R CFRP Lap Strap initial	76.36 ± 11.17	
3R CFRP Lap Strap repaired	53.14 ± 19.59	69.7

4. Conclusions

In this work, innovated composites manufactured with a new vitrimer resin that was re-processable, repairable, and recyclable, called 3R-resin, were demonstrated. Different production processes were used such as the Resin Transfer Molding technique and the stacking of 3R prepregs. Moreover, composites that produced with a typical aerospace grade resin were tested in order to estimate any differences between their values. The repair efficiency of the 3R-repairable composites was also estimated from the values obtained from mechanical tests at the initial composites and those after the repair process.

In terms of ILSS properties, specimens that manufactured with RTM process exhibited a repair efficiency of 58% when specimens that produced using prepregs revealed a recovery of 150% of their initial properties due to the elimination of some defects that induced during the manufacturing. At mode-I interlaminar fracture toughness, the 3R specimens had better mechanical properties by 10% comparing to conventional composites. They also revealed a recovery of 34% of their initial properties after the repair process. The lap strap geometry that is a new proposed testing configuration, presented a repair efficiency of 73% in terms of bonding properties.

Acknowledgements

This work has received funding from the European Union's Horizon 2020 research and innovation program under grant agreement No 769274.

5. References

1. Archer E, McIlhagger A. Repair of damaged aerospace composite structures [Internet]. Polymer Composites in the Aerospace Industry. Elsevier Ltd; 2015. 393–412 p. Available from: http://dx.doi.org/10.1016/B978-0-85709-523-7.00014-1

  doi:10.5075/epfl-298799_978-2-9701614-0-0

2. Ruiz De Luzuriaga A, Martin R, Markaide N, Rekondo A, Cabañero G, Rodríguez J, et al. Epoxy resin with exchangeable disulfide crosslinks to obtain reprocessable, repairable and recyclable fiber-reinforced thermoset composites. Mater Horizons. 2016;3(3):241–7.

3. Yang Y, Xu Y, Ji Y, Wei Y. Functional epoxy vitrimers and composites. Prog Mater Sci [Internet]. 2021;120(June):100710. Available from: https://doi.org/10.1016/j.pmatsci.2020.100710

4. Luterbacher R, Coope TS, Trask RS, Bond IP. Vascular self-healing within carbon fibre reinforced polymer stringer run-out configurations. Compos Sci Technol. 2016;136:67–75.

  doi:10.5075/epfl-298799_978-2-9701614-0-0

DESIGN OF LAMINATED HEATING MODULE FOR ELECTRIC VEHICLES

Ji-Seok Lee[a], Myeong-Hyeon Yu[a], Hak-Sung Kim[a, b]

a: Department of Mechanical Convergence Engineering, Hanyang University, 222, Wangsimni-ro Seondong-gu, Seoul, Republic of Korea - ljs94920@gmail.com
b: Institute of Nano Science and Technology, Hanyang University, 222, Wangsimni-ro, Seongdong-gu, Seoul, Republic of Korea

Abstract: *Recently, to save energy in electric vehicles, there has been a need to develop radiant heating modules to increase the efficiency of vehicle heating systems. In this study, effect of insulation and covering material's properties (thermal conductivity, emissivity, density, and specific heat) on the efficiency of the heating module, was investigated using finite element analysis. The radiant heating module were composed of a covering material, a heating film, an insulation material, and an injection substrate. Leather, cloth, and suede were used as covering material, and honeycomb made of nylon, polyurethane foam, and melamine foam were used as heat insulation materials. ABAQUS joule heating simulation was used to calculate the front temperature, heat flux of the heating module, and heat receiving unit temperature. As a result, the heating module with the melamine foam insulating layer and suede for the covering material has the highest efficiency compared to the other cases.*

Keywords: Laminated Composite Heating Module; Radiation; Electric-Thermal Analysis; View Factor; Optimization

1. Introduction

Since 2014, the European Union has used the Euro 6 standard to regulate emissions in vehicles with internal combustion engines. Therefore, automobile company are attempting to reduce emissions by focusing on electric vehicles that do not emit exhaust gas [1,2]. Internal combustion engine vehicles use engine heat to control the temperature inside the vehicle [3]. However, because electric vehicles do not use a combustion engine as a source of power, it is impossible to heat the vehicle using the engine's residual heat [4]. Therefore, additional energy for heating is necessary, a heating module which use less energy to increase temperature of electric vehicle is required for the passenger's warmth [5]. In this study, the heating efficiency of each material was studied through the joule heating simulation of the heating module varying the insulation and covering material. In case of covering material, woven fabric, leather, and suede were used which are common in vehicle interior materials. PU-foam, melamine-foam, and honeycomb structures were used as insulation. Even when the same thermal energy is given to the heating module, it shows varied energy efficiency depending on the combination of the insulation and covering material, thus it is required to derive an appropriate combination of the insulation and covering material. The front temperature and heat flux of the heating module, as well as the temperature of the heat receiving component, were estimated and compared in the simulation using ABAQUS joule heating simulation. The heating module was laminated with covering, heating film, insulation, and injection substrate. To generate heat in the joule heating simulation, a continuous current was applied to the heating film. Heat was generated and transmitted to other components of the heating module via conduction, raising the temperature

  doi:10.5075/epfl-298799_978-2-9701614-0-0

of the covering material, insulation, and injection substrate. The heating module and the heat receiving unit had a rectangular cross section, and the heat receiving unit was 70 mm apart from the heating module. Radiation from the heating module raised the temperature of the heat receiving unit. A view factor was adopted to define the radiant heat transfer between the heat receiving unit and the radiant heating module. The view factor is a geometric variable that is independent of the radiation surface's attributes, such as emissivity, and can be expressed as the radiation surface's shape, size, and distance. In this study, the simulation was conducted with consideration of the view factor between the heating module and the heat receiving unit.

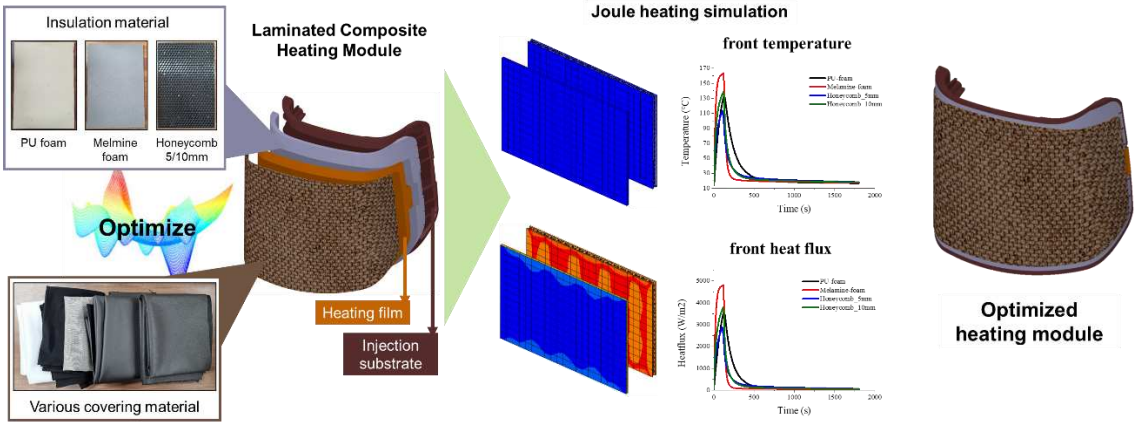

Figure 1. Laminated composite heating module optimization through joule heating simulation

2. Thermal-electrical analysis

2.1 Heat transfer

For the thermal-electrical analysis, three types of heat transfer were considered: conduction, convection, and radiation.

2.1.1 Conduction

Conduction is a phenomenon in which energy is transmitted from a high-energy mass to low-energy mass by interaction between mass. Conduction in solids is caused by vibration by molecules inside the lattice model and energy transfer by free electrons. When the temperatures of both sides of the wall with a thickness Δx and a surface area A are different from T_1 and T_2 , the heat transfer rate transferred from the high temperature to the low temperature can be calculated by Eq. (1) [7].

$$\dot{Q} = kA\frac{T_1 - T_2}{\Delta x} \quad (1)$$

Where k is thermal conductivity which is a quantitative expression of how well it transmits heat. Conduction was reproduced in thermal-electrical simulation by defining that the temperatures of the surfaces in contact were the same, and within same material, conducted through thermal conductivity.

2.1.2 Convection

Convection is heat transfer that occurs at the interface of a solid and a liquid or a solid and a gas, and it is called that natural convection when heat is transmitted by fluid movement produced

  doi:10.5075/epfl-298799_978-2-9701614-0-0

by density changes in the fluid due to temperature changes. Heat transfer by convection can be expressed as the Eq. (2) [7].

$$\dot{Q} = hA(T_s - T_\infty) \tag{2}$$

Where h is the convection heat transfer coefficient, A is the area of convection, T s and T_ are the temperature of the surface where the convection occurred and the temperature of the fluid which has sufficiently distant from the surface. Natural convection is considered to occur at the front of the heating module in all cases in the simulation.

2.1.3 Radiation

Unlike conduction and convection, radiation does not require an intermediate medium to transfer thermal energy. Radiant heat is emitted by any objects having a temperature higher than the absolute temperature, and heat transfer through radiation can be calculated using Eq. (3) [7].

$$\dot{Q} = \varepsilon\sigma A(T_s^4 - T_{surr}^4) \tag{3}$$

Where ε is emissivity, σ is Stefan-Boltzmann constant that has the value of 5.67E-8 W/m^{2}K^4, A is area that emit a radiant energy, T_s is surface temperature, T_{surr} is temperature of surround. In the simulation, the ambient temperature of the heating module was same, but different emissivity was applied for each covering materials.

2.2 View factor

The view factor is a geometric variable used in this study to define radiant heat transfer between the heating module and the heat receiving unit that is unaffected by the surface properties of two objects in radiant heat transfer. Radiant heat transfer between the two surfaces is related not only to the distance but also to the direction of the surface [7,8]. In order to consider the effect of direction and distance in radiant heat transfer between the two surfaces, pure geometric values view factor independent of surface characteristics and temperature are used. The view factor of radiation that is released from surface 1 and directly hits surface 2 is defined as F_{12}, and in this study, the view factor between the heating module and the heat receiving unit is defined by Eq. (4).

$$F_{12} = \frac{2}{\pi\bar{X}\bar{Y}}\left(ln\left[\frac{(1+\bar{X}^2)(1+\bar{Y}^2)}{1+\bar{X}^2+\bar{Y}^2}\right]^{\frac{1}{2}} + \bar{X}(1+\bar{Y}^2)^{\frac{1}{2}}\tan^{-1}\frac{\bar{X}}{(1+\bar{Y}^2)^{\frac{1}{2}}} + \bar{Y}(1+\bar{X}^2)^{\frac{1}{2}}\tan^{-1}\frac{\bar{Y}}{(1+\bar{X}^2)^{\frac{1}{2}}} - \bar{X}\tan^{-1}\bar{X} - \bar{Y}\tan^{-1}\bar{Y}\right) \tag{4}$$

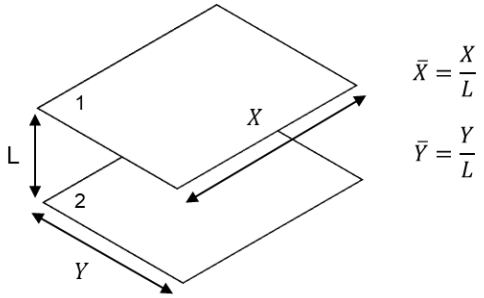

Figure 2. Coaxial rectangular plates

  doi:10.5075/epfl-298799_978-2-9701614-0-0

Where X is length of one side of plate and Y is length of the other side of rectangular plate with same axial. L is distance between two plates. $\bar{X}$ and $\bar{Y}$ are normalized length of each side of plate respect to L (Figure.2).

2.3 Thermal-electrical simulation modeling and material

The cross section of the heating module had a rectangular shape with a 300 mm width and a 200 mm length. Heating modules were laminated with four materials which were described previously. Heat receiving unit was modeled 70 mm away from the front part of heating module with same size (Figure.3). ABAQUS thermal-electrical heating simulation was used in the analysis tool. The electrical current was supplied to the heating film for 120 seconds to generate joule heating in which the heat was generated by the resistivity (2.4E-2 $\Omega \cdot cm$) of the film. The view factor between the heating module and the heat receiving unit was defined only in range of from 0 mm to 70 mm, which is the distance between the heating module and heat receiving unit. In the other range, the view factor was defined as 0 to exclude radiant heat transfer. The front temperature, heat flux, and heat receiving unit temperature were calculated as the average of each side after the simulation.

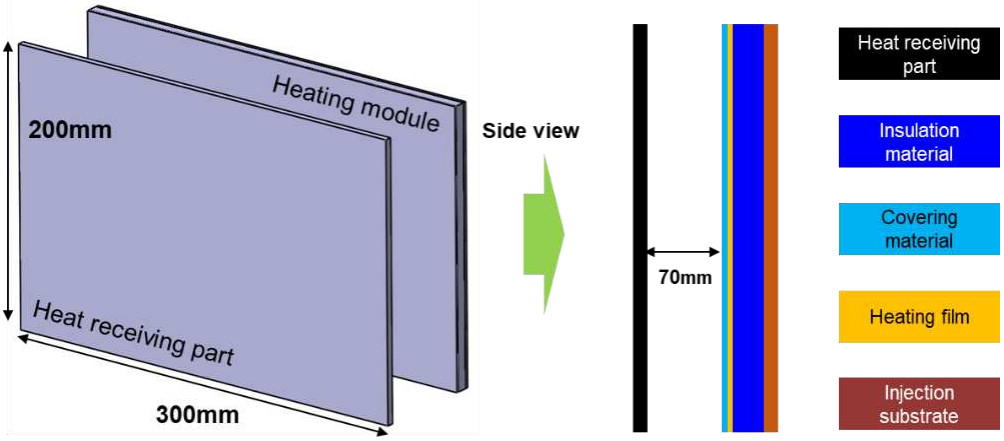

Figure 3. Schematic of simulation model and materials

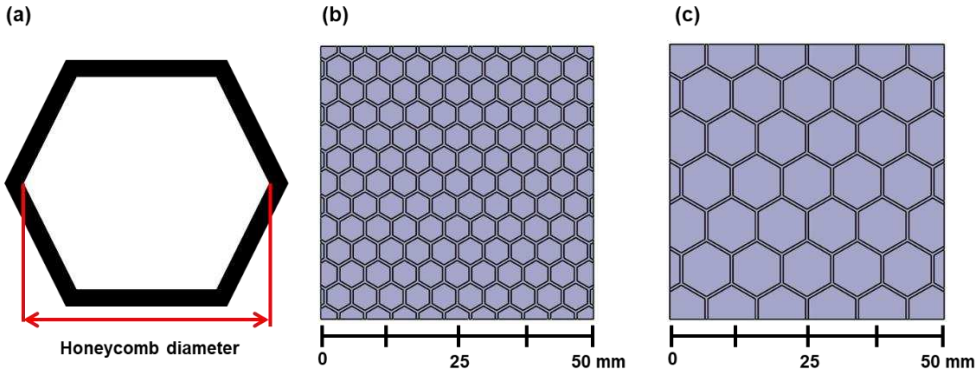

Figure 4. (a) Definition of honeycomb diameter, section view of nylon honeycomb according to diameter: (b) 5 mm, (c) 10 mm

The heating module was laminated with four different parts that were bonded together. First layer was the covering material at the front. The covering material is located closest and visible to the passenger, leather, cloth and suedes were used in the commercial vehicle [6]. Second

  doi:10.5075/epfl-298799_978-2-9701614-0-0

layer was heating film which converts electrical energy into heat to raise the temperature of the heating module. Third layer was insulation layer. In this work, three types of insulation materials were used: polyurethane foam, melamine foam and nylon honeycomb with 5/10 mm diameter (Figure. 4). The last layer was the injection molded polypropylene substrate that can support all of these layers. The thermal properties of these material were shown in the Table 1.

Table 1: Properties of materials that used in joule heating simulation

Material	Property	Value	Material	Property	Value
Leather	Emissivity	0.95	Suede	Emissivity	0.9
	Density [kg/m^3]	563		Density [kg/m^3]	281
	Thermal conductivity [W/m·K]	0.14		Thermal conductivity [W/m·K]	0.2
	Specific heat [J/kg·K]	1500		Specific heat [J/kg·K]	1500
Cloth	Emissivity	0.77	Heating film	Emissivity	0.03
	Density [kg/m^3]	137		Density [kg/m^3]	2700
	Thermal conductivity [W/m·K]	0.045		Thermal conductivity [W/m·K]	205
	Specific heat [J/kg·K]	1300		Specific heat [J/kg·K]	900
PU-foam	Density [kg/m^3]	207	Honeycomb (PA6)	Density [kg/m^3]	1084
	Thermal conductivity [W/m·K]	0.0222		Thermal conductivity [W/m·K]	0.25
	Specific heat [J/kg·K]	2000		Specific heat [J/kg·K]	1310
Melamine foam	Density [kg/m^3]	8	Injection substrate	Density [kg/m^3]	1050
	Thermal conductivity [W/m·K]	0.035		Thermal conductivity [W/m·K]	0.11
	Specific heat [J/kg·K]	1200		Specific heat [J/kg·K]	1920
Heat receiving unit	Emissivity	0.9			
	Density [kg/m^3]	988			
	Thermal conductivity [W/m·K]	0.145			
	Specific heat [J/kg·K]	1670			

  doi:10.5075/epfl-298799_978-2-9701614-0-0

3. Result and Discussion

3.1.1 Front temperature of heating module

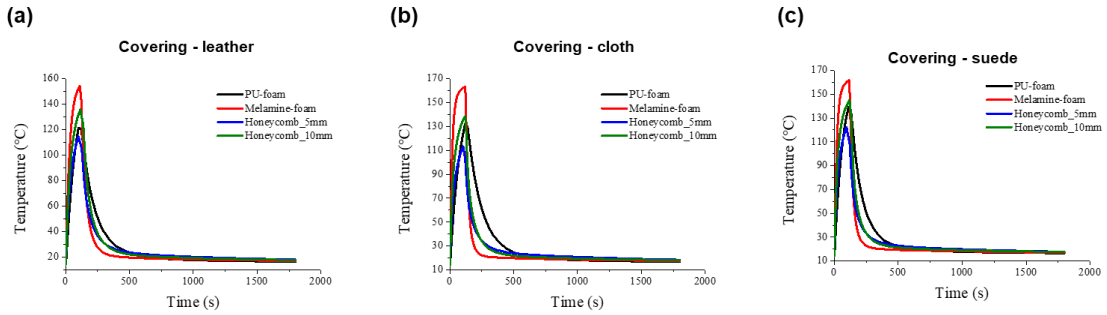

Figure 2. Front temperature of heating module according to covering material

Figure. 5 is the simulation result of the front temperature of the heating module. The heating module with melamine foam insulation reached the highest temperature and the fastest heating rate in all the covering materials. It is because melamine foam has a low thermal mass compared to other insulation materials. Meanwhile, honeycomb with a diameter of 10 mm and polyurethane foam were ranked as the second and third, respectively. The honeycomb with a diameter of 5 mm showed the lowest temperature and slowest heating speed meaning worse efficiency of the heating module.

3.1.2 Front heat flux of heating module

The front heat flux showed a similar tendency to that of the front temperature. Melamine foam shows the highest heat flux emission at the front of heating module. Depending on the covering material, heat flux was high in the order of suede, leather and cloth (Figure.6). Although the emissivity of leather and the suede are similar, heat flux emitted due to radiation as can see in Eq (3) is proportional to the fourth square of temperature. Therefore, suede showed higher heat flux than leather.

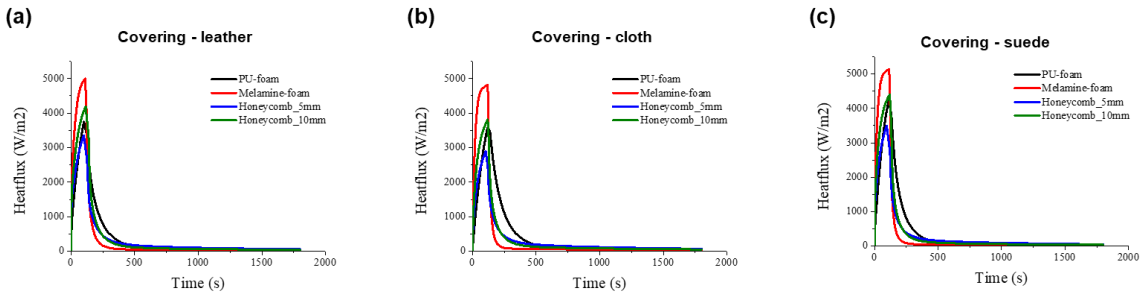

Figure 3. Heat flux of heating module according to covering material

3.1.3 Temperature of heat receiving unit

In the case of the temperature at the heat receiving part, the tendency was slightly different depending on the covering material. When the covering material is leather and suede, the melamine foam showed the highest temperature of heat receiving unit. The temperature were decreased in the order of honeycomb with 10 mm diameter, PU-foam, and honeycomb with 5 mm diameter. When the covering material was cloth, melamine foam and honeycomb with 5

mm diameter were same in order with leather and suede, but honeycomb with 10 mm diameter and PU-foam showed similar temperature of heat receiving part (Figure. 7).

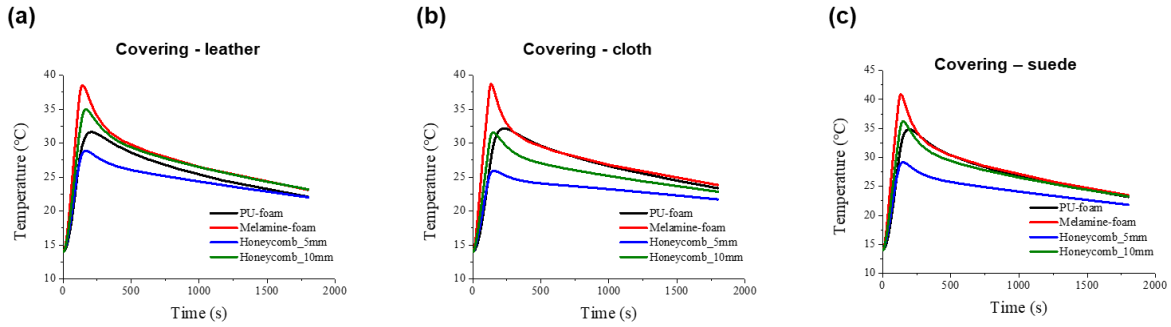

Figure 4. Temperature of heat receiving unit according to covering material

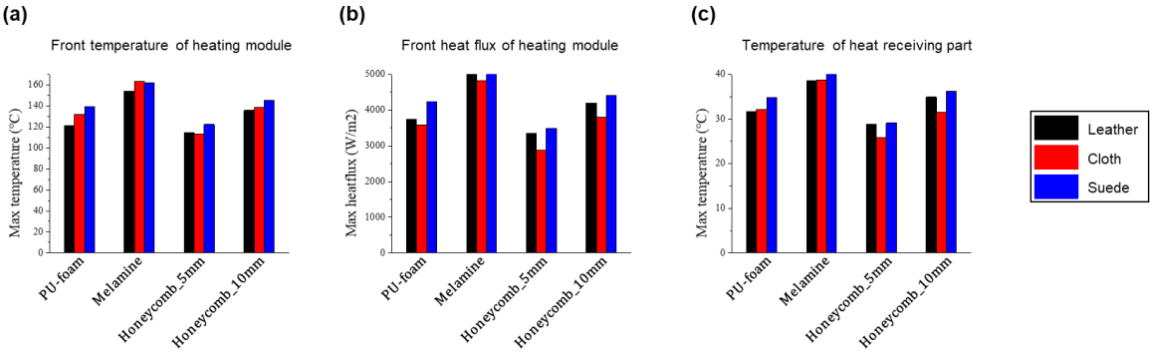

Figure 5. Joule heating simulation according to insulation/covering material: (a) front temperature, (b) heat flux, (c) temperature of heat receiving unit

The efficiency of the radiation heating module could be maximized when the melamine foam was used as the insulation and suede covering was used as the covering material, based on the results of the front temperature, heat flux of the heating module, and heat receiving unit temperature. When honeycomb with 5 mm diameter and cloth were used as the insulation material and covering material, respectively, the radiant heating module's efficiency was the lowest (Figure. 8). The highest efficient module's front temperature, heat receiving unit temperature, and heat flux were 48°C, 15°C, and 78% higher than those of the lowest efficient module. As a result, the most efficient radiant heating module could be designed with the best combination of melamine foam for insulation and suede for covering material.

4. Conclusion

In this study, the heating module was designed and simulated to compare the efficiency of radiant heating module. The module used a laminated composite heating module containing three types of covering materials: leather, cloth, suede and four types of insulation materials: PU-foam, melamine foam, honeycomb with 5/10 mm diameter. In addition, a view factor of two parallel surface was defined to accurately simulate radiant heat transfer between heating module and heat receiving unit. The efficiency of module was evaluated based on the front temperature, heat flux of heating module and temperature of heat receiving part. As a result, the optimum laminated composite heating module combination could be obtained when

  doi:10.5075/epfl-298799_978-2-9701614-0-0

melamine foam and suede were used as insulation and covering material. This result will be used in designing an efficient radiant heater for electric vehicle.

Acknowledgements

This work was partly supported by Korea Evaluation Institute of Industrial Technology (KEIT) grant funded by the Korea government (MOTIE) (Project No. 20014863, Development of 3D formable heating elements and forming technology for energy-efficient radiant heating of electric vehicles)

5. References

1. Zhang Z, Wang J, et al. “The solutions to electric vehicle air conditioning systems: A review” Renewable and Sustainable Energy Reviews 91(2018): 443-463
2. Tie S.F, Tan C.W, “A review of energy sources and energy management system in electric vehicles” Renewable and Sustainable Energy Reviews 20(2013): 82-102
3. Seo JH, Kim HJ, Jung KJ, Kim DW, Yeom JK, Lee MY “Review of conventional air conditioning system for internal combustion engines” Air-Conditioning and Refrigeration 21(2013): 1330001
4. Li W, Liu Y, Lu R, Wang D, Shi J, Yu Z, Cheng L, Chen J “Performance evaluation of secondary loop low-temperature heat pump system for frost prevention in electric vehicles” Applied Thermal Engineering 182(2021): 115615
5. Lee JT, Kwon SJ, Lim YS, Chon MS, Kim DS, “Effect of air-conditioning on driving range of electric vehicle for various driving modes” SAE Technical Paper Series 20(2013)
6. Material developments in car interior and engine compartment, Recticel Flexible Foams 27(2018)
7. Çengel, Y. A., Ghajar, A. H., 2020 Heat and mass transfer: Fundamentals & applications New York, NY: McGraw-Hill Education.
8. Narayana. “View factors for parallel rectangular plates” Heat transfer engineering 19(1998): 59-63.

  doi:10.5075/epfl-298799_978-2-9701614-0-0

FLEXURAL BEHAVIOUR OF POLYURETHANE FOAM FILLED HIGH PERFORMANCE 3-D WOVEN I-BEAM COMPOSITES

Eyuphan, Kucukkalfa[a-b], Melisa, Dincer[a-b], Emir, Karci[a], M. Ali, Vural[a], Kaan, Yildiz[a-b], Elif, Ozden-Yenigun[c], Basak, Ozkendirci[d], Hulya, Cebeci[a-b]

a: Aerospace Research Center, Istanbul Technical University, Istanbul, 34469, Turkey – kucukkalfa16@itu.edu.tr
b: Aviation Institute, Istanbul Technical University, Istanbul, 34469, Turkey
c: School of Design Textiles, Royal College of Art, SW7 2EU, London, UK
d: Faculty of Fine Arts and Design, Dogus University, Istanbul, 34775, Turkey

Abstract: *Sandwich composites have several industrial applications due to their lightweight and high specific strength. Strengthened polymeric foams by nano-reinforcement have high contact surface between core and face-sheets bring advantages including elimination of the face-sheet and core debonding and water accumulation in the structure. Furthermore, filling area between the web and the flanges of I-beams with polymeric foams can enhance strength and load bearing capacity while assisting structural integrity. In this work, polymeric foams and 3-D woven composites are combined to obtain high-performance I-beam composites. Foaming process of neat and 0.1 wt.% carbon nanotube (CNT) reinforced polyurethane foams was achieved in the area between the web and the flanges of 3-D woven glass fibers by a novel free-rise foaming method. Composites were fabricated by the vacuum infusion method, and three-point bending tests were performed to evaluate the increment in load bearing capacity, flexural strength and flexural modulus.*

Keywords: Structural integrity; 3-D woven I-beam composites; polyurethane foam; carbon nanotubes; flexural strength.

1. Introduction

Sandwich composites are commonly used materials especially in aviation, space and marine industry, owing to their great bending strength and lightweight compared to laminated composites or metal alloys with same dimensions. Considering the structural similarity between sandwich composites and I-beams where flanges of I-beams and face sheets of sandwich composites resist higher stresses, while web of the I-beams and cores of sandwich composites transfer stresses and decrease the effect of external loads. Therefore, this structural similarity enhances the usage of sandwich composites where I-beams were traditionally used. Honeycomb cores have been widely used in sandwich composites, however, drawbacks such as moisture absorption and face sheet-core debonding arising from their open cell structure diminish their use in future composites [1]. Novel material concepts such as polymeric foams with higher contact surface area between core and face-sheets due to their closed-celled structure bring advantages including elimination of above-mentioned drawbacks. Furthermore, these innovative foams can be strengthened with the integration of micro and/or nano reinforcements. Carbon nanotubes (CNTs) [2–4] and carbon nanofibers (CNF) [5,6] due to their high strength and cellulose nanocrystals [7,8] because of low-cost and ease of supply are the most preferred nanomaterials used in foam reinforcement studies. Considering the

  doi:10.5075/epfl-298799_978-2-9701614-0-0

enhancement brought by the additives, foam-cored sandwich composites have the potential of replacing honeycomb-core sandwich structures.

Besides being used as a core in sandwich composites, polymeric foams have found applications in strengthening beams. Akrami et al. [9] developed bio-inspired T-joints using polyvinyl chloride (PVC) foams inserted to the intersection of web and flange. The resulting T-joint outperformed its conventional equivalent in terms of peak load in bending by 40% and stiffness by 60%. Their idea can easily be extended to I-beams. On the other hand, instead of placing the polymeric foam at the intersection of web and flanges, filling the area between web and flanges might even lead to greater enhancements in strength and stiffness while assisting structural integrity. Lacki and Derlatka [10] integrated polyurethane (PU) foams into to the area between web and glass fiber reinforced flanges of an I-beam made of aluminum alloy and obtained 200% increase in the buckling resistance.

Recently, 3-D woven composites are under investigation since they have a potential to avert delamination problems, leading to increased structural integrity while enabling manufacturing of near-net complex shapes [11]. 3-D weaving methods can be easily utilized to manufacture ideally delamination-free structural composites such as I-beam structures. The weaving pattern and the amount of resin for impregnation provide a control on the mechanical properties of the resulting composite structures.

This study aims to combine polymeric foams (PU foam) and 3-D woven composites to design and manufacture high-performance I-beam composites. In this work, 3-D woven I-beams were weaved using glass fibers and vacuum infusion method was utilized to fabricate fortified I-beam composites with epoxy resin. Foaming process of neat and 0.1 wt.% CNT reinforced PU foams were directly achieved in the area between web and flanges of the woven glass fibers. This approach brings almost no weight increase compared with conventional material usage while improving the mechanical properties of the structure. Other advantages of this novel free-rise foaming approach include reduced production time and material requirement and enhanced overall structural integrity. To evaluate the influence of the utilized approach on the mechanical properties, three-point bending tests were performed and load bearing capacity, flexural strength and flexural modulus were determined.

2. Experimental

2.1 Materials

600 TEX E-glass fibers with 16µm fiber diameter were purchased from Şişecam, Istanbul. Hexion MGS L160 epoxy resin having a viscosity and density of 700-900 mPas and 1.13-1.17 g/cm^3 at 25°C, and Hexion MGS H160 curing agent were both purchased from Dostkimya, Istanbul. Polyol 9022/100, density of which is 100 kg/m^3, and PMDI for the foaming process were acquired from Active Foam, Istanbul. Multi-walled CNTs with 92% purity and 8-10 nm diameter were purchased from Nanografi, Istanbul.

2.2 Fabrication of I-Beam Composites

3-D woven I-beams were made of 600 TEX E-glass fibers, where TEX implies that the mass of 1000 meter long fiber in terms of grams. The weaving geometry shown in Figure 1 which is called “Load Bearing with X vertical wall” (LB-X) was used to obtain the 3-D geometry using 2D weaving

machine. Since the fabric contains two warp layers with differing lengths, two warp beams were utilized to create the 3-D geometry [12]. Web length and flange width were weaved as 2 cm and 16 cm, respectively. I-beam composites were fabricated using vacuum assisted resin transfer molding method (VARTM) which is one of the main composite fabrication techniques. Epoxy and curing agent were mixed with 4:1 weight ratio during VARTM process. Both peel ply and mesh were placed under and over of the I-beam to make demolding easier and acquire efficient epoxy distribution, respectively. Teflon film coated molds were placed into a gap between web and flanges of I-beam to preserve model shape.

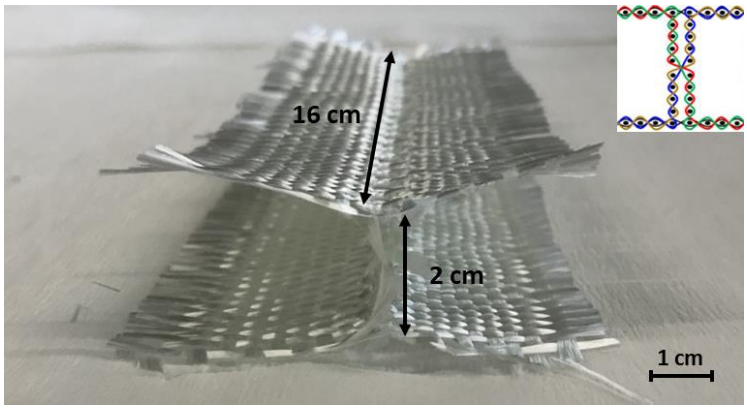

Figure 1: The "LB-X" weaving geometry.

2.3 Foaming Procedure in I-Beam Composites

Instead of pouring PU into a mold and inserting it after sizing with desired dimensions, the foaming process of the PU foam was directly performed in the area between the web and the flanges of I-beam composites without using adhesives. Firstly, for the neat PU foam, polyol and PMDI were mixed at 2000 rpm for 60 seconds with 50:50 weight ratio according to the manufacturer's manual. Then, polyol-PMDI blend was poured into one of the areas between web and flanges and free-rise foaming occurred for 15 minutes at room temperature. As the next step, the specimen was reversed and the other area was filled with foam and the same free-rise foaming procedure was repeated. Finally, I-beam sandwich composite was held in a 40°C oven for 10 hours for curing. All these steps are illustrated in Figure 2.a. For the CNT reinforced PU foams, CNTs were added to PMDI and sonicated for 5 minutes at the %30 amplitude in a beaker wrapped by ice cubes to prevent overheating. The rest of the procedure was the same with neat PU foam. The final appearance of vacant, neat foam-filled and CNT reinforced foam filled I-beam composites are shown in Figure 2.b,2.c and 2.d, respectively.

2.4 Compression Tests of PU Foams

The manufacturing procedure of both neat and CNT reinforced PU foams to obtain compression test specimens is parallel with the process in I-beam composites. The only difference is that the polyol-PMDI blend was poured into an aluminum mold, which was heated in the oven at 40°C for 1 hour before molding, instead of pouring into the gap between the web and the flanges of I-beam structure. The average density of neat and CNT reinforced PU foams were calculated as 111.7 ± 1 and 113.0 ± 1 kg/m^3, respectively. Flatwise compression tests of foams were performed by Shimadzu universal test machine (UTM) according to ASTM C365 standards. Test specimens were cut to 30 x 30 x 15 mm^3 dimensions and 5 specimens were utilized for both neat and CNT reinforced PU foams. Test speed was 0.5 mm/min.

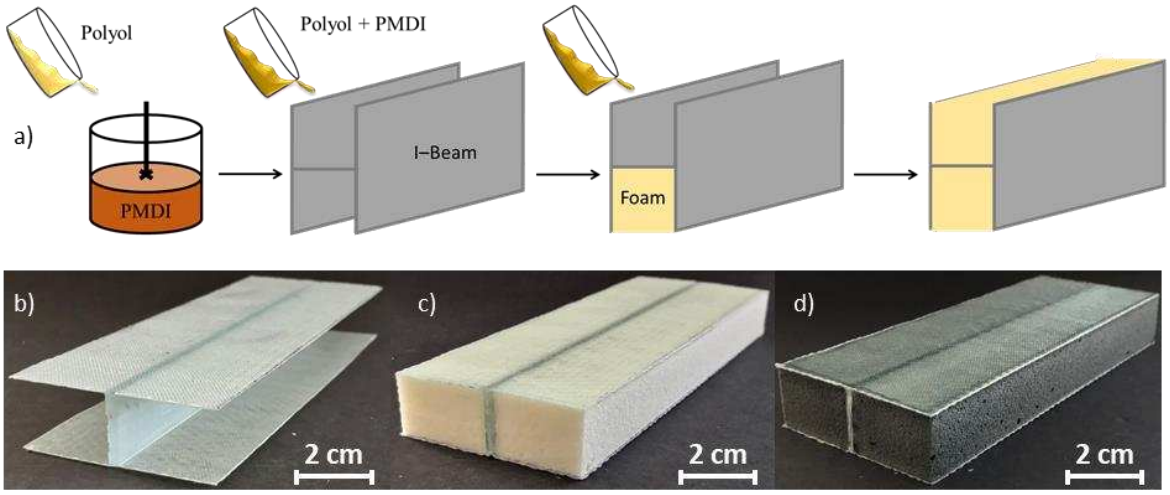

Figure 2: a) Foaming process takes place directly in the area between the web and the flanges of I-beam composites. b) vacant, c) neat foam filled and d) CNT reinforced foam filled I-beam composites.

2.5 Bending Tests of I-Beam Composites

ASTM C393 standard for sandwich composites was used in this work since no corresponding standard was declared for three-point bending tests of 3-D woven I-beam composites. Specimens were sized for both I-beam composites and foam inserted I-beam composites as 140 x 50 x 20 mm^3 and the span length of the test apparatus was set as 90 mm. Test speed was 6 mm/min.

3. Results & Discussion

3.1 Compression Test Results of the PU Foams

The compression test mechanism and the results are given in Figure 3. According to stress/strain curves, compressive strength of neat PU foam (N_PU) and 0.1 wt.% CNT reinforced PU foam (CNT_PU) were 1.07 MPa and 1.09 MPa, respectively. Moreover, compressive modulus of neat foam and CNT reinforced foam were computed as 26.64 MPa and 30.43 MPa, respectively. Therefore, the results indicate that 0.1 wt.% CNT addition let to 1.83% and 14.23% increase in compressive strength and modulus, respectively, as compared to neat PU foams.

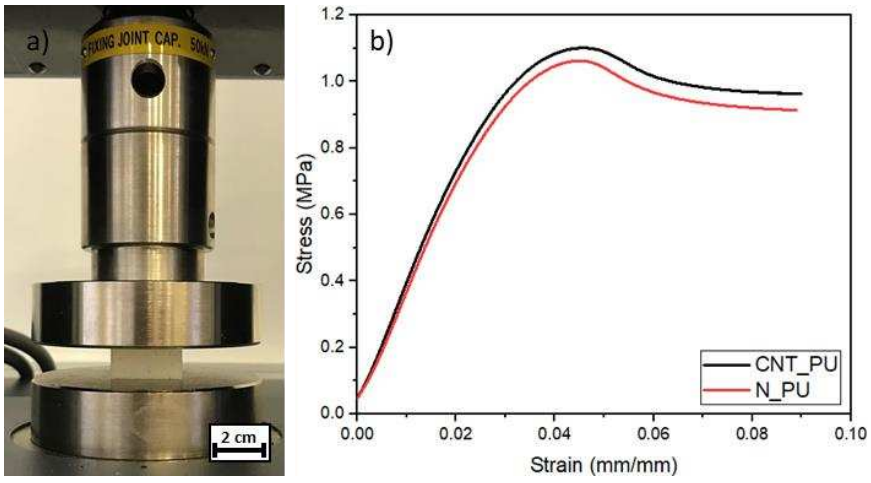

Figure 3: Compression test mechanism and results.

Enhancements in compressive properties of neat foam with CNT addition can be explained by the existence of stiff CNTs within the PU foam and changes of the microstructure. As a result of CNT addition, thicker cell walls and smaller cell sizes occurred and denser foams were obtained.

3.2 Three-Point Bending Tests of I-Beam Composites

Three-point bending test apparatus and stress/strain curves of I-beam composites are shown in Figure 4. The force/displacement data were used to evaluate the load bearing capacities of I-beam composites, and the stress/strain curves were utilized to compute flexural modulus and flexural strength. The corresponding results are summarized in Table 1. According to test results, the load bearing capacity of the I-beam without foam (LBX), neat foam filled (N_PU_LBX) and CNT reinforced foam filled (CNT_PU_LBX) are 2.52 kN, 3.46 kN, and 3.53 kN, respectively. Therefore, the results show that the load bearing capacity was increased by 53.7% with neat and 57% by CNT reinforced foam insertion. Moreover, flexural modulus of LBX, N_PU_LBX and CNT_PU_LBX were calculated as 478.63 MPa, 629.81 MPa, and 670.32 MPa, respectively. Also, 31.59% and 40.05% increase in flexural modulus was obtained by neat and CNT reinforced foam addition. Furthermore, flexural strength values were found as 14.67 MPa, 22.77 MPa and 23.07 MPa for LBX, N_PU_LBX and CNT_PU_LBX, respectively. It was seen that neat and CNT reinforced foam insertion yielded 55.18% and 57.23% increase in flexural strength.

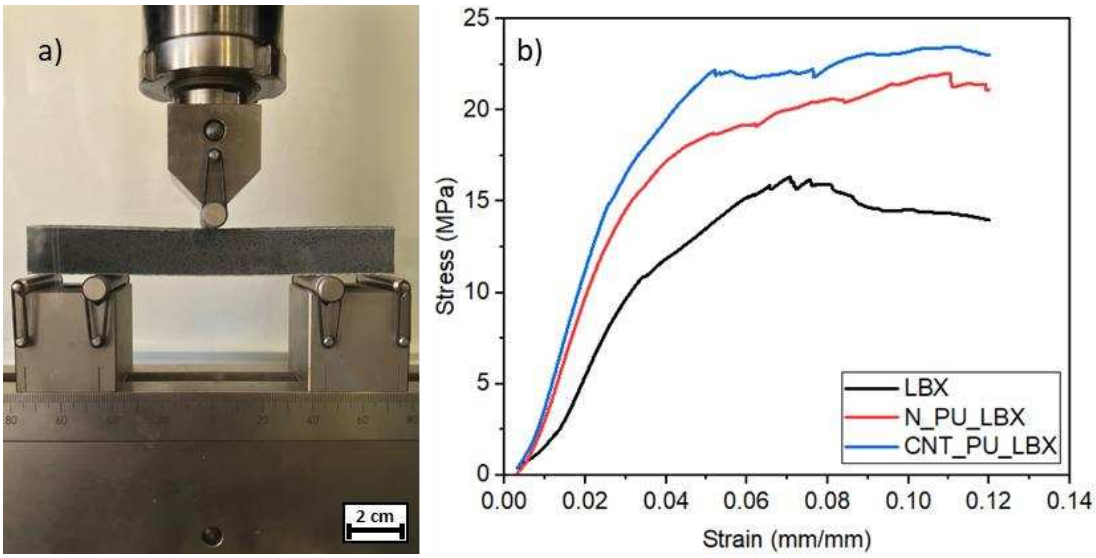

Figure 4: a) Three-point bending test apparatus, b) stress/strain curves.

Table 1: Summary of three-point bending test results.

Specimen	Load Bearing Capacity [kN]	Increase [%]	Flexural Modulus [MPa]	Increase [%]	Flexural Strength [MPa]	Increase [%]
LBX	2.52	-	478.63	-	14.67	-
N_PU_LBX	3.46	53.70	629.81	31.59	22.77	55.18
CNT_PU_LBX	3.53	57.00	670.32	40.05	23.07	57.23

Compared to neat PU insertion, 0.1 wt.% CNT reinforcement of the foam brought additional enhancements of 6.15%, 26.78%, and 3.72% to load bearing capacity, flexural modulus and flexural strength, respectively. Therefore, these results are considered to be substantially promising as greater improvements can be achieved with higher CNT concentrations with negligible weight penalty.

Structural integrity is another aspect that should be considered to design safe and reliable structures, increasing the use of I-beam 3-D woven composites. Similar to an earlier study [12], during three-point bending tests of I-beam (LBX) composites, twisting and/or torsional buckling (Figure 5.a) was observed under high loadings. Strengthening the web and flanges with nanomaterials might increase the material properties but might not be the solution of buckling under bending load. Additionally, adding ribs to the area between web and flanges might avoid the twisting behavior, however, additional challenges such as proper joint design between ribs and I-beam, cracks at joints or new weaving design to maintain single-piece 3-D structure might arise. Due to these issues, foam insertion between web and flanges might be one of the easiest and the most applicable methods. Figure 5.b, illustrates that, with the foam insertion, the delamination between the flanges and the foam occurs shortly before the failure loading. This clearly shows that twisting response of the beam is no longer a concern, and delamination does not exist until failure and the structural integrity of beam was maintained. Furthermore, Figure 5.c shows the foam filled I-beam crushed instead of delamination at similar loading given in Figure 5.b. The reason of this behavior at high loadings was interpreted to be the lack of adhesive between the foam and the beam. Moreover, Figure 5.d indicates that at failure the beam cracks at the center cross-section, the point where the bending moment is maximum. This behavior encourages the idea that the pure bending force was achieved.

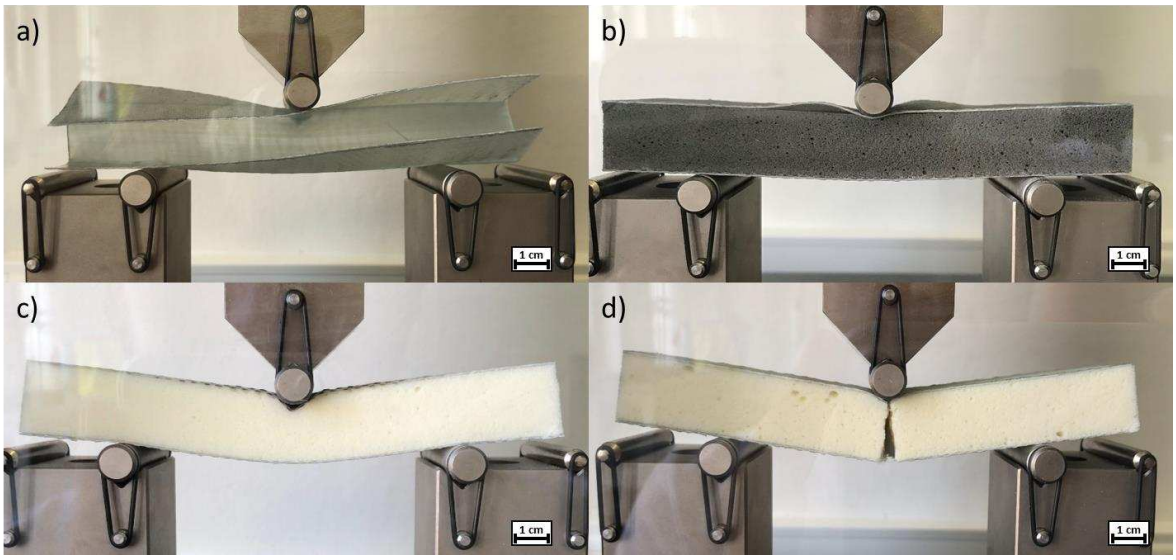

Figure 5: a) Twisting and torsion of LBX, b) delamination between flanges and foam at CNT_PU_LBX, c) structural integrity maintained by foam insertion, and d) crack at the center of N_PU_LBX.

4. Conclusions

In this work, foam insertion by direct manufacturing of free-rising PU foam in the area between the web and the flanges of 3-D woven I-beam structures was investigated. This novel approach

bears the potential of obtaining high-performance composites and acquiring enhanced structural integrity. In accordance with this purpose, neat and CNT reinforced PU foams were utilized and bending properties such as load bearing capacity, flexural modulus, and flexural strength of I-beam composites were determined. The results showed remarkable increases of 57.00 %, 40.05%, and 57.23% in load bearing capacity, flexural modulus and strength with CNT reinforced PU foam insertion, respectively. Furthermore, twisting at higher loadings under the bending test for I-beam composites was suppressed by foam insertion. Therefore, the crucial crack at failure load occurred in the mid-section of the foam-inserted test specimens which implies that the structural integrity was enhanced and pure bending condition was achieved.

For future work, an adhesive layer bonding the foam and the I-beam, can be applied to the inner beam surface before free-rise foaming to avoid or retard delamination. Furthermore, nanomaterial content in PU foam can be optimized to obtain better bending properties with small amounts of weight enhancement. Also, nanomaterials can be combined such as CNT/CNC (Cellulose nanocrystals) or CNT/CNF (Cellulose nanofibrils) to prevent agglomerations and non-uniform distribution in dispersion media at higher nanomaterial concentrations.

Acknowledgments

This study was funded by the Scientific and Technological Research Council of Turkey (TUBITAK) 1003 Primary Subjects R&D Funding Program (Project No. 218M703 and Project No. 218M704) and Career Development Program 3501 (Project No. 121M993). The authors would also like to thank to the conference funding for Mr. Eyuphan Kucukkalfa provided by the TUBITAK 2224-A Support Program for Participation in Abroad Scientific Events. The authors are also thankful to Cagın Emre, Ibrahim Halil Sahin and Burak Yatkin for their support in composite manufacturing.

5. References

1. Pascoe JA, Zarouchas DS, Alderliesten RC, Benedictus R, Xu H, Yin X, et al. Foam core impresses in aircraft study. Composites Science and Technology 2014;59:31–3. https://doi.org/10.1016/s0034-3617(14)70248-6.
2. Dolomanova V, Rauhe JChrM, Jensen LR, Pyrz R, Timmons AB. Mechanical properties and morphology of nano-reinforced rigid PU foam: 2011;47:81–93.
3. Yan D, Xu L, Chen C, Tang J, Ji X, Li Z. Enhanced mechanical and thermal properties of rigid polyurethane foam composites containing graphene nanosheets and carbon nanotubes. Polymer International 2012;61:1107–14. https://doi.org/10.1002/PI.4188.
4. Caglayan C, Gurkan I, Gungor S, Cebeci H. The effect of CNT-reinforced polyurethane foam cores to flexural properties of sandwich composites. Composites Part A: Applied Science and Manufacturing 2018;115:187–95. https://doi.org/10.1016/J.COMPOSITESA.2018.09.019.
5. Kabir ME, Saha MC, Jeelani S. Effect of ultrasound sonication in carbon nanofibers/polyurethane foam composite. Materials Science and Engineering A 2007;459:111–6. https://doi.org/10.1016/j.msea.2007.01.031.
6. Saha MC, Kabir ME, Jeelani S. Enhancement in thermal and mechanical properties of polyurethane foam infused with nanoparticles. Materials Science and Engineering: A 2008;479:213–22. https://doi.org/10.1016/J.MSEA.2007.06.060.
7. Li S, Li C, Li C, Yan M, Wu Y, Cao J, et al. Fabrication of nano-crystalline cellulose with phosphoric acid and its full application in a modified polyurethane foam. Polymer Degradation and Stability 2013;98:1940–4.

8. Septevani AA, Evans DAC, Annamalai PK, Martin DJ. The use of cellulose nanocrystals to enhance the thermal insulation properties and sustainability of rigid polyurethane foam. Industrial Crops and Products 2017;107:114–21.
9. Akrami R, Fotouhi S, Fotouhi M, Bodaghi M, Clamp J, Bolouri A. High-performance bio-inspired composite T-joints. Composites Science and Technology 2019;184:107840.
10. Lacki P, Derlatka A. Influence of PU foam reinforcement of I-beam on buckling resistance. Composite Structures 2018;202:201–9.
11. Neje G, Behera BK. Comparative analysis of mechanical behavior of 3D woven spacer sandwich composites with single and double level structures. Polymer Composites 2020;4885:4898-41.
12. Turgut F, Neje G, Behera B, Ozden-Yenigun E, Cebeci H. Hierarchical carbon nanotubes grown on 3D woven glass fiber preforms for multifunctional structural composites beams. ECCM 2018 - 18th European Conference on Composite Materials 2020:24–8.

  doi:10.5075/epfl-298799_978-2-9701614-0-0

Composites Meet Sustainability – Proceedings of the 20th European Conference on Composite Materials,
ECCM20. 26-30 June, 2022, Lausanne, Switzerland

SECOND LIFE FOR AERONAUTICAL MANUFACTURING MATERIALS

Zulima, Martín-Moreno[a], Maria, Manzanas-Moreno[b], Guillermo, Hernáiz-López[b], Joaquín Andrés Jiménez[b], Asunción Butragueño Martinez[b]

a: AIRBUS (Paseo de John Lennon s/n, Getafe, Spain) – zulima.martin@airbus.com
b: AIRBUS (Paseo de John Lennon s/n, Getafe, Spain)

Abstract: *Polyamide (PA) from the recycling of the vacuum bags – auxiliary material – and short carbon fibre from the recycling of structural prepreg composite materials, both used in the manufacturing process of aircraft composite parts, have been combined to produce PA/short-CF filament for Additive Manufacturing process, and to produce PA/short-CF pellets for Injection molding processes, to manufacture parts with no structural requirements that can be reintroduced again in our product life cycle, following a Circular Economy approach.*

Keywords: sustainability; recycling; reuse; circular economy; composite materials.

1. Introduction

The use of Carbon Fibre Reinforced Polymer (CFRP) composites in the manufacturing processes of aeronautical components is currently the main solution for the design and manufacture of structural elements in the aerospace industry, due to their excellent specific mechanical properties and their outstanding experience during their operation.

This has allowed a significant reduction in greenhouse gas emissions to the level of 63.5 grams per passenger and kilometer traveled in 2020 in the case of Airbus, in addition to a significant reduction in maintenance and operating costs.

However, if we want to maintain, or even increase, the current level of use of high-performance composite materials, some major challenges need to be solved: reduction in the cost of the final structure, reduction in energy consumption during the manufacturing cycle from the base material to the final structure, and develop recycling and reuse technologies to produce materials and structures with high added value.

Sustainability is of paramount importance for Airbus. Therefore, among other initiatives, we are putting a great effort in recycling and reusing the materials employed in our manufacturing processes, not only of the structural carbon fiber (CF) composites, but also, the auxiliary materials used.

This paper will show Airbus work in developing processes to recycle structural carbon fiber composites (uncured pre-impregnated composite material), as well as recycling of auxiliary materials, where the products obtained from these recycling processes will form together a new raw material that will be used in the manufacturing of non-structural aircraft components, thus, reintroducing them again in our product life cycle, following a Circular Economy approach.

Polyamide (PA) from the recycling of used vacuum bags and short carbon fibre from the recycling of structural prepreg composite materials, both used in our manufacturing processes, will be combined to produce PA/short-CF filament for Additive Manufacturing process, and to produce

  doi:10.5075/epfl-298799_978-2-9701614-0-0

PA/short-CF pellets for Injection molding processes. Application scenarios and proof of concept of the components manufactured will be also presented.

2. Experimental

2.1 Materials

A new composite material is proposed. The matrix used is polyamide (PA) coming from vacuum bags used in the manufacturing of aircrafts composite parts (Figure 1).

Figure 1. Vacuum bags used in aircraft composite parts production

It is a multilayer material whose main component is PA6.6, PA6 in less extent, and a polyethylene (PE) sandwiched layer. Prior to a shredding process to reduce the material size and enable a better dosage for compound activities (see Figure 2), the material undergoes an anti-hydrolysis treatment.

Figure 2. Vacuum bags shredding process

The short carbon fibre to be used as reinforcement, is obtained after pyrolysis of Carbon Fibre Reinforced Polymers (CFRP) scrapped from the manufacturing of aircraft parts (either uncured or cured) (Figure 3).

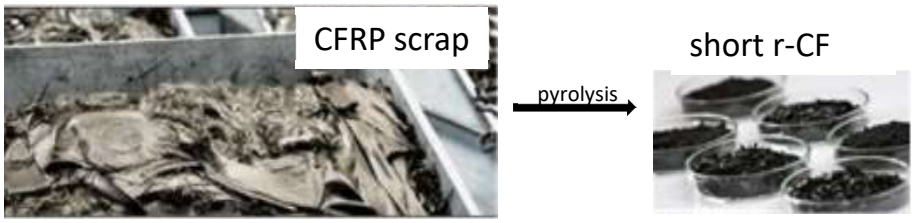

Figure 3. Short recycled carbon fibre (short r-CF)

2.2 Preparation of r-PA/short r-CF composites

A co-rotating twin screw extruder has been employed to:

1) Produce recycled polyamide (r-PA) pellets (Figure 4.a) with controlled rheology properties by the addition of plasticizer, so that the material could be applied to fuse deposition modeling (FDM) and injection molding applications.

  doi:10.5075/epfl-298799_978-2-9701614-0-0

2) Reinforce r-PA pellets with the incorporation of short recycled carbon fibres (short r-CF) (Figure 4.b). The target was incorporating 30% of short r-CF in the r-PA. The parameters of the extrusion process are set in order to ensure proper dispersion and distribution of the fibre while maintaining, as much as possible, the fibre geometry and morphology, so that the final composite meet the required mechanical performance.

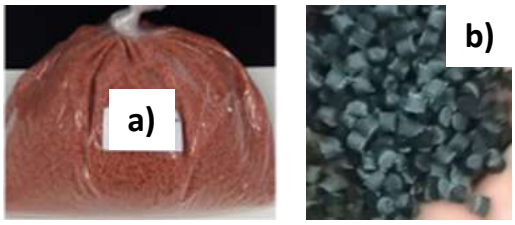

Figure 4. a) r-PA pellets. b) r-PA/short r-CF pellets.

2.3 Differential scanning calorimetry (DSC)

The melting behavior, of the pristine PA (brand new vacuum bag film), of the PA after the recycling process and of the composites obtained from recycled materials, were was investigated by differential scanning calorimetry (DSC) using a *DSC Q2000 – TA Instruments*, according to ISO 11357, operating under a nitrogen flow, using approximately 12 mg of sample sealed in aluminum pans. Melting temperatures measured (Table 1) served as reference of the process temperature in the extruder, and in subsequent steps (filament extrusion, additive manufacturing and injection processes).

Table 1: Melting temperatures values

Specimen	Tm [ºC]
pristine PA	255.8 ± 0.9
r-PA	253.5 ± 2.0
r-PA/short r- CF w.o. plasticizer	255.5 ± 3.5
r-PA/short r-CF + 1% plasticizer	253.9 ± 0.6
r-PA/short r-CF + 2% plasticizer	251.6 ± 0.3

**: samples obtained from brand new vacuum bag film*

2.4 Melt flow index

A *GOTTFERT Mi-5 Flow Index Meter* was used to evaluate the rheological properties of r-PA/short r-CF pellets (Table 2), according to UNE-EN ISO 1133-2. Test conditions were: Weight: 5 kg, temperature 255ºC, nozzle diameter: 2 mm, nozzle length: 8 mm, cutting method: manual, preheating time: 5 min. Pellets were pre-conditioned 4 hours at 90ºC.

  doi:10.5075/epfl-298799_978-2-9701614-0-0

Table 2: Melt flow index values

Specimen	Mass flow rate (MFR) [g/10min]	Volume flow rate (MVR) [cm^3/10min]
r-PA/ short r-CF w.o. plasticizer	4.99 ± 0.12	4.53 ± 3.5
r-PA/ short r-CF + 1% plasticizer	19.2 ± 0.8	18 ± 0.3
r-PA/ short r-CF + 2% plasticizer	65.9 ± 2.2	58.4 ± 2.5

3. Additive Manufacturing with recycled aeronautical manufacturing materials

3.1 Filament extrusion

Filaments to be used in an additive manufacturing process, based on Fused Filament Fabrication (FFF), were obtained from r-PA/short r-CF in a filament extruder (Figure 5).

Figure 5. Filament extrusion and produced spool of filament

3.2 Fused Filament Fabrication (FFF) - Printing trials

A non-structural part was chosen as proof of concept for the printing trials. These were carried out with different part geometries and different designs to set the optimum printing parameters in order to fulfill qualitative aspects, i.e. infill resolution, corner details, surface finish, and to solve process troubles such as warping or extruder nozzle clogging. Figure 6 shows the proof of concept obtained with selected printing parameters.

Figure 6. Flying part trial specimen printed to assess the process

  doi:10.5075/epfl-298799_978-2-9701614-0-0

4. Injection moulding with recycled aeronautical manufacturing materials

4.1 Injection molding of coupons for testing

r-PA/short r-CF pellets were fed into the heated barrel of an injection moulding machine to obtain coupon specimens for characterization testing (Figure 7).

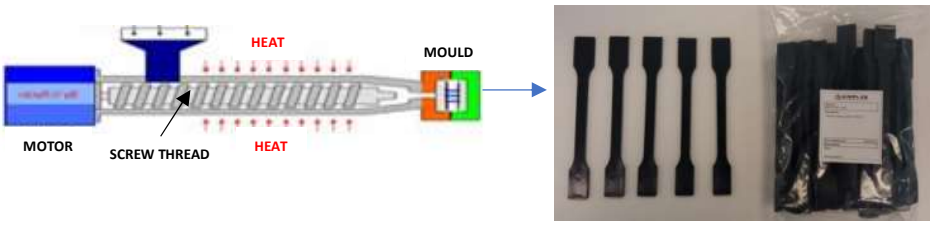

Figure 7. Testing coupons specimens obtained by injection molding

4.2 Tensile properties

A Universal Testing Machine was used to evaluate the tensile properties (Young's modulus and mechanical strength), see Figure 8, of the coupons obtained by injection molding. The tests were carried out according to UNE-EN ISO 527-2 Standard. The environmental conditions during testing were: Temperature (23 ± 2)ºC, RH (50 ± 5) %. For each r-composite composition, five specimens were tested; injected coupons were pre-conditioned 16 hours at the environmental conditions mentioned above.

Testing conditions were: Speed for calculating Modulus E: 1 mm/min, speed for strength test: 50 mm/min, distance between jaws: 115 mm, Reference length: 75 mm, Load cell: 20 kN, mechanical jaws, accuracy of testing machine: Strength (acc. ISO 7500) Class 0.5, and displacement indicator (acc. ISO 9513) Class 0.5. Displacement indicator: clamp extensometer for elastic modulus, makroeXtens for strength characterization.

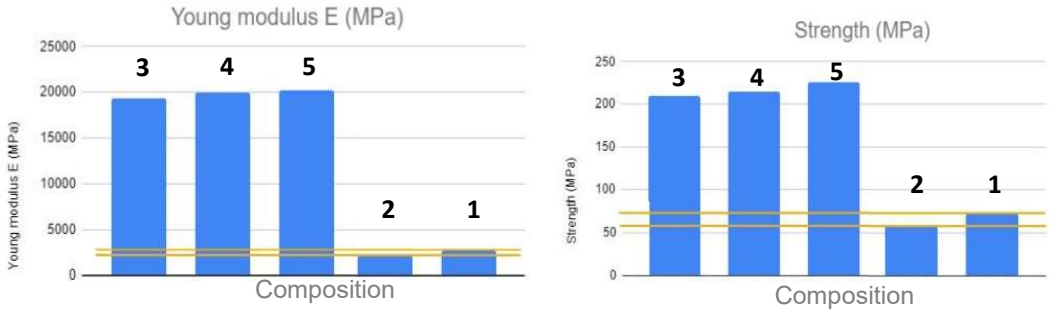

1: pristine PA (from vacuum bag) **2**: r-PA **3**: r-PA/short r-CF
4: r-PA/short r-CF + 1% plasticizer **5**: r-PA/short r-CF + 2% plasticizer

Figure 8. Testing coupons specimens obtained by injection molding

5. Conclusions and way forward

The recycling process on the PA6.6 – vacuum bag film barely affects the thermal properties of the material. There is a slight decrease in the melting temperature. This value recovers when introducing the reinforcement, which could be due to the nucleating effect produced by the fibres, this aspect needs further investigation. The addition of plasticizer, as expected, reduces

the polyamide crystallinity, and thus, the melting temperature. Nevertheless, this reduction is not significant.

However, the effect of the plasticizer is more noticeable in the rheological properties. The addition of 1% of plasticizer increases the mass and volume flow rates four times, and the addition of a 2% of plasticizer, increases these values thirteen times.

A decrease of the 20% in the tensile properties is observed when comparing pristine (vacuum bag film) PA6.6 with r-PA, most likely due to the embrittlement of the PA, thermal aging, during the extrusion process, that could produce a slight decrease in the polymer crystallinity, as indicated by the slight decrease in the melting temperature. When adding the reinforcement, the higher values are observed in the r-PA/short r-CF + 2% plasticizer (Young's modulus 20200 MPa, Tensile strength 226 MPa. These values make the material suitable for applications in non-structural parts of an aircraft.

Several applications have been already identified for both FFF and injection manufacturing technologies, one being more convenient than the other depending on the volume of parts per aircraft, geometric complexity, etcetera; elevator shim, brackets, funnels, drainage tubes, system supports, gaskets, machinery items and accessories. Beyond the aeronautical sector, these materials would also have great potential for use in automobile and sports industries.

As for the way forward, r-PA/short r-CF + 2% plasticizer has been selected for the next trials since appears with the best balance between rheological behavior (easier processing) and mechanical performance. Injection moulding of drainage tube is on-going as proof of concept for this technology. The tube will be later on tested to its specific requirements to confirm if those are met.

This preliminary study proves that a second life for auxiliary and composite materials used in aircraft manufacturing processes is more than possible, enabling an effective circular economy with this greener and zero scrap manufacturing approach.

Acknowledgements

The authors would like to thank the Centre for the Development of Industrial Technology (CDTI) which partially funds this project, with the support of the Spanish Ministry of Science and Innovation and of the "Next Generation EU" funds, specifically by the Recovery and Resilience Facility. Also, we would like to thank AIMPLAS – Technological Institute of Plastic for its contribution in the frame of a subcontracting activity in this project.

  doi:10.5075/epfl-298799_978-2-9701614-0-0

DEVELOPMENT OF FLAME RETARDANT COATINGS FOR ε-CAPROLACTAM-BASED POLYAMIDE 6 COMPOSITES

Zsófia, Kovács[a], Ákos, Pomázi[a], Andrea Toldy[a]*

a: Budapest University of Technology and Economics, Department of Polymer Engineering, H-1111 Budapest, Műegyetem rkp. 3.
* Presenting author: kovacszs@pt.bme.hu

Abstract: *The use of long fibre reinforced thermoplastic composites is increasing due to their short cycle times and ease of recycling. A major representative of thermoplastic matrices is the ε-caprolactam-based polyamide 6 (PA6). Due to the strict safety regulations of the automotive industry, PA6 composites need to be flame retarded. The flame retardant (FR) can be added to the matrix or used as a coating. The use of coatings ensures that flame retardants do not alter the properties of the composites, prevent the solid additives from being filtered out by the reinforcing materials, and prevent delamination caused by intumescent flame retardants. We developed ε-caprolactam-based flame retardant coatings suitable for in-mould coating carbon fibre reinforced PA6 composites during thermoplastic resin transfer moulding (T-RTM).*

Keywords: flame retardancy; in situ polymerisation; ε-caprolactam; polyamide 6

1. Introduction

Due to short cycle times and easy recycling, thermoplastic matrix composites are becoming increasingly important in many technical fields, particularly in the automotive industry [1]. PA6 is one of the most commonly used matrix materials to produce long fibre reinforced thermoplastic composites. PA6 can be produced from ε-caprolactam monomer by anionic ring-opening polymerisation in the presence of an activator and initiator [2]. One of the most promising methods for their production is thermoplastic resin transfer moulding (T-RTM) technology based on in-situ polymerisation, where the polymerisation of the monomer impregnated in the reinforcing materials takes place in the mould. A significant drawback of PA6 is its flammability, as it melts easily in flames, and melt droplets can cause rapid fire spread. The strict fire safety requirements make the flame retardancy of PA6 [3].

There are two basic options for polymer flame retardancy: additive and reactive flame retardancy. In additive flame retardancy, the flame retardant additive can be mixed directly into the unmodified polymer, while in reactive flame retardancy, flame retardant monomers are incorporated into the polymer main chain. Of the methods mentioned above, additive flame retardancy is the most commonly used method for PA6. The disadvantage of this process is that flame retardants that are not soluble in ε-caprolactam may be filtered out by the reinforcing materials. In addition, additives can affect the mechanical properties and viscosity of the matrix, which can cause problems during processing. The use of caprolactam-soluble flame retardants or flame retardant coatings may solve these problems [4].

Höhne et al. [5] used caprolactam soluble hexaphenoxycyclotriphosphazene (HPCTP) for carbon fibre reinforced polyamide 6 composites. The authors found that the PA6 composite flame

  doi:10.5075/epfl-298799_978-2-9701614-0-0

retarded with HPCTP meets the requirements of FAR 25.853 for aerospace applications and achieves a self-extinguishing V-0 rating in UL-94 testing.

HPCTP can also be effectively used in glass fibre reinforced PA6 composites. A V-0 rating and a high oxygen index value can be achieved in UL-94 tests. During the initial stage of thermal decomposition, HPCTP releases mainly non-combustible gases (NH_3, H_2O, and CO_2). In addition to the gas-phase flame retardant effect, a solid-phase effect is also observed in forming a foamed carbon layer [6].

Alfonso et al. [7] achieved a synergistic effect for the combustion inhibition of PA6 by combining red phosphorus with magnesium oxide (MgO) or a polyhalogenated cyclopentadiene derivative (Dechlorane Plus - DP). In the case of MgO, the synergistic effect was explained by the ability of MgO to increase the rate of phosphoric acid formation, which leads to a higher rate of char formation on the surface. In the case of DP, it forms phosphorus-containing radicals from the thermal decomposition of hydrochlorinated hydrocarbons. The authors also found that many flame retardants commonly used for PA6 flame retardancy inhibit the polymerisation reaction of ε-caprolactam and thus cannot be used for its flame retardancy.

Our research investigated the development of flame retardant coatings for carbon fibre reinforced polyamide 6 composites. The flame retardants used were red phosphorus (RP), magnesium oxide (MgO), and expandable graphite. The effect of the flame retardants on crystallinity, glass transition temperature, thermal stability, and fire performance was investigated.

2. Materials and methods

2.1 Materials

To prepare the PA6 matrix, we used AP-NYLON Caprolactam (CL, Brüggemann Chemical) as the monomer. BRUGGOLEN C20P (C20P, Brüggemann Chemical) was used as the activator and Dilactamate (DL, Katchem) as the initiator. Magnesium oxide (MgO, Sigma Aldrich), red phosphorus (RP, Clariant), and two types of expandable graphite (EG ES100 and EG ES350, Graphit Kropfmühl) were used as flame retardants. The difference between the two expandable graphites is their particle size and foaming rate: for the ES100 type, the particle size is in 75% < 150 µm, and the change in volume during foaming is 100 cm^3/g, while for the ES350 type, the particle size is in 80% > 300 µm, while the expansion rate is 350 cm^3/g. We used PX 35 UD 300 carbon fibre from Zoltek to prepare the composites.

2.2 Preparation of coating materials

Reference and flame retardant coatings were tested on their own. The reference PA6 was prepared using 87% CL, 3% activator, and 10% initiator. 10% flame retardant was used to produce flame retarded PA6. The materials were stored in a vacuum oven, and the flame retardants were dried at 80 °C for 4 hours before use. The monomer and activator, and in the case of flame retarded samples, the flame retardant, were mixed and melted at 120 °C using a heated magnetic stirrer. After adding the initiator, specimens were prepared in an aluminium mould at 150 °C.

  doi:10.5075/epfl-298799_978-2-9701614-0-0

2.3 Preparation of composites with coating

An aluminium mould at 150 °C was used to model T-RTM and in-mould coating. In the mould with the dimensions of 100x100x2 mm^3, 5 layers of unidirectional carbon reinforcement were pre-placed in $[0]_5$ layer order. We used 87% CL, 3% C20P and 10% DL for the matrix. The CL and the C20P were mixed and melted at 120 °C. Then, after adding DL, the system got into the closed mould using a syringe, and in-situ polymerisation was carried out between the reinforcing material. The coating was applied to the composite surface in a 2.5 mm deep aluminium mould. The coating was applied using the same method and monomer/activator/initiator ratio with 10% flame retardant.

2.4 Methods

Differential scanning calorimetric measurement (DSC) was performed with a TA Instruments Q2000 device. 2-5 mg samples were analysed in 50 ml/min nitrogen flow. We used heat/cool/heat cycles in a temperature range of 25-250 °C with heating and cooling rates of 10 °C/min.

The thermal stability of the samples was tested using a TA Instruments Q500 TGA device. The test was carried out on 2-5 mg samples under 30 ml/min nitrogen flow. The samples were heated in a temperature range of 30-600 °C with a heating rate of 20 °C/min.

We performed UL-94 flammability test according to ISO 9772 and ISO 9773. The flame spread rate can be determined from the horizontal arrangement (H-type), and the flammability classification can be determined from the vertical arrangement (V-type). The dimensions of the samples were 120x15x4 mm^3.

The oxygen index tests (LOI) were performed according to ISO 4589-1 and ISO 4589-2 standards. LOI is defined as the minimum oxygen content by volume of an oxygen-nitrogen gas mixture flowing at a specified velocity in the test sample that is still burning. The size of the samples was 120x15x4 mm^3.

To determine the complex combustion characteristics of the samples, we used a mass loss type cone calorimeter (MLC, Fire Testing Technologies Inc.). In the test, we exposed samples to a heat flux of 50 kW/m^2 based on the ISO 13927 standard. The dimensions of the coating samples were 100x100x4 mm^3, and the dimensions of the coated composites were 100x100x2.5 mm^3.

3. Results and discussion

Firstly we characterised the coating materials according to thermal and fire behaviour. Then we investigated the coated composites focusing on fire performance.

3.1 The effect of FRs on the glass transition temperature and crystallinity (DSC)

The effect of the flame retardants on the glass transition temperature and the crystallinity was investigated by differential scanning calorimetry. The results are given in Table 1.

The crystalline fraction was calculated from the enthalpy of the first heating curve using the following equation:

$$X_c = \frac{\Delta H_{m1}}{\Delta H_{100\%}(1-\alpha)} \cdot 100 \quad (1)$$

  doi:10.5075/epfl-298799_978-2-9701614-0-0

where $\Delta H_{100\%}$=188 J/g is the theoretical value of the enthalpy of crystallization for 100% crystalline PA6, α [-] is the filler fraction.

Based on the DSC measurements, the added additives had no significant effect on the glass transition temperature of PA6. In general, the T_g and X_c values obtained agreed with those reported in the literature. However, the residual CL in the system may distort the results due to inadequate polymerisation. The CL sublimates at 60 °C, which, in the best case, only occurs in an endothermic peak, but the baseline may be shifted in some cases.

Table 1: DSC results of reference and flame retarded PA6 samples (T_g: glass transition temperature; $\Delta H_{m1,2}$: enthalpy of crystallisation for the first and second heating; ΔH_c: enthalpy of crystallisation; X_c: crystalline fraction.

Sample	T_g [°C]	ΔH_{m1} [J/g]	ΔH_{m2} [J/g]	ΔH_c [J/g]	X_c [%]
PA6	49	78.6	40.5	45.9	42
PA6/10%RP	51	59.4	28.6	32.9	35
PA6/10%MgO	44	73.2	43.7	42.6	43
PA6/10%EGES100	46	66.7	36.2	32.9	39
PA6/10%EGES350	45	104.2	31.1	29.3	62
PA6/5%RP/5%MgO	49	103.6	37.0	37.1	61
PA6/5%RP/5%EGES100	50	80.7	35.2	35.6	48
PA6/5%RP/5%EGES350	47	80.1	50.1	50.2	47
PA6/5%MgO/5%EGES100	46	95.0	47.0	46.3	56
PA6/5%MgO/5%EGES350	49	127.9	28.3	26.9	76

3.2 The effect of FRs on thermal stability (TGA)

The thermal stability of the samples was tested using TGA. The results are presented in Table 2.

The temperature associated with 5 and 50% mass loss was shifted towards higher values than the reference PA6. The improvement in thermal stability was also reflected in an increase in the residual mass, which is favourable from an application point of view. The samples containing expandable graphite performed exceptionally well: although their decomposition usually started below 200 °C, the temperature for 50% mass loss was above 400 °C in all cases, except the samples containing MgO as well, and the maximum decomposition rate occurred at the highest temperatures. For samples containing 5% RP and expandable graphite, the graphite with a larger particle size (EG ES350) led to a higher residual mass due to the larger expansion of the graphite. Similar observations were made for samples containing MgO and expandable graphite.

  doi:10.5075/epfl-298799_978-2-9701614-0-0

Table 2: TGA results of reference and flame retarded PA6 samples ($T_{-5\%}$: the temperature at 5% mass loss; $T_{-50\%}$: the temperature at 50% mass loss; dTG_{max}: maximum moss loss rate; T_{dTGmax}: temperature belonging to the maximum mass loss rate).

Sample	$T_{-5\%}$ [°C]	$T_{-50\%}$ [°C]	dTG_{max} [%/°C]	T_{dTGmax} [°C]	Char yield at 600 °C [%]
PA6	104	324	0.8	139	3.4
PA6/10%RP	332	439	1.5	432	35.0
PA6/10%MgO	155	391	1.2	412	16.3
PA6/10%EGES100	243	446	1.0	437	38.6
PA6/10%EGES350	152	435	1.0	439	27.1
PA6/5%RP/5%MgO	123	383	0.9	435	7.4
PA6/5%RP/5%EGES100	120	407	1.0	436	9.1
PA6/5%RP/5%EGES350	214	425	1.0	442	11.4
PA6/5%MgO/5%EGES100	192	354	1.2	341	6.2
PA6/5%MgO/5%EGES350	111	354	0.7	370	15.4

3.3 Fire performance of PA6 coating materials

The flammability of reference and flame retardant coating materials was analysed by LOI, UL-94, and MLC. The results of the UL-94 and LOI measurements are shown in Table 3.

Table 3: UL-94 and LOI results of reference and flame retardant coating materials.

Sample	UL-94 ranking	LOI [%]
PA6	HB	21
PA6/10%RP	HB	26
PA6/10%MgO	HB	21
PA6/10%EGES100	HB	25
PA6/10%EGES350	V-1	25
PA6/5%RP/5%MgO	V-2	25
PA6/5%RP/5%EGES100	V-0	26
PA6/5%RP/5%EGES350	V-1	25
PA6/5%MgO/5%EGES100	HB	24
PA6/5%MgO/5%EGES350	HB	24

  doi:10.5075/epfl-298799_978-2-9701614-0-0

The oxygen index of the samples containing flame retardant was higher than that of the reference, except for the sample containing pure MgO. Although the oxygen index of the individual compositions is not an outstandingly high value, it can be seen that the UL-94 classification of the samples containing expandable graphite is significantly better than the reference. The PA6/5%RP/5%EGES100 sample has the highest oxygen index (26%) and is the only sample to achieve a V-0 self-extinguishing rating in the UL-94 test.

The complex combustion properties of the samples were investigated using MLC. The results compared to the reference PA6 without flame retardant are shown in Figure 1.

The flame retardants significantly reduced the peak heat release rate (pHRR): the best performing sample (PA6/10%EGES350) had a maximum heat release of only 253 kW/m^2 compared to the reference value of 729 kW/m^2. For samples containing red phosphorus, the ignition time was in all cases shorter than the ignition time of the reference, which can be explained mainly by the gas phase mechanism of the additive. In general, the residual mass of the sample was higher than the reference due to the flame retardant additives. While the reference sample was almost completely burnt, the sample with high graphite additives retained almost one-third of its mass. Neither red phosphorus nor magnesium oxide provided outstanding results when used alone, but their combination with the two types of expandable graphite showed favourable flame retardancy. A significant shift characterised the graphite samples in the times to ignition and peak heat release rate, which in all cases can be explained by the intense foaming of the additives. The intense foaming caused the sample to ignite and reach the peak heat release rate only much later during combustion. The time course of the heat release also illustrates the intensive foaming: These samples foamed into the cone calorimeter, which caused the heat release curve to have an incomplete decay.

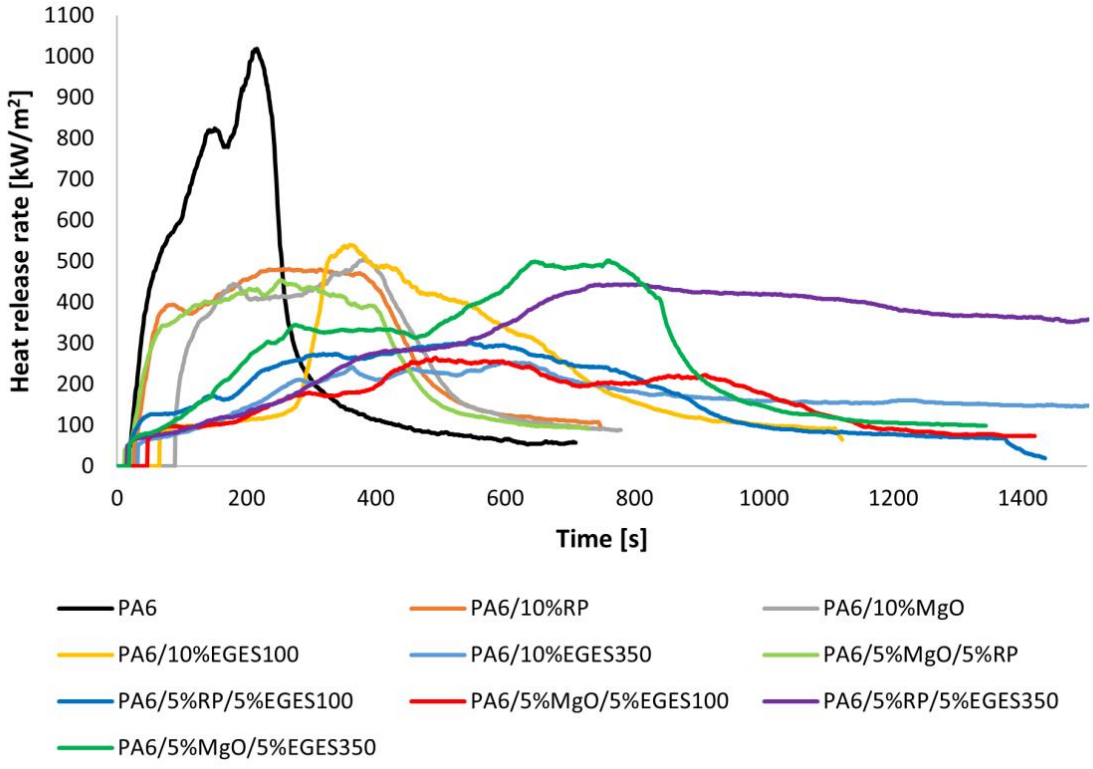

Figure 1. Heat release rate of reference and flame retardant coating materials

Based on preliminary testing of the coatings, the following samples were used as coatings for carbon fibre reinforced PA6 composites: PA6/10%EGES350, PA6/5%RP/5%EGES350, PA6/5%MgO/5%EGES100, PA6/5%RP/5%EGES100.

3.4 Fire performance of coated CF/PA6 composites

The MLC results for the reference and flame retardant coated PA6 composite samples are shown in Figure 2.

Compared to the reference composite without flame retardant (347 kW/m^2), only sample PA6/CF/5%RP/5%EGES100 had a lower heat release (274 kW/m^2). In all cases, the residual mass was increased due to the flame retardants, but the samples ignited sooner than the reference except for PA6/CF/5%RP/5%EGES100. The poorer fire performance of these samples may be explained by the significant sedimentation observed in samples with EG ES350, and a noteworthy amount of the flame retardant remained in the inlet.

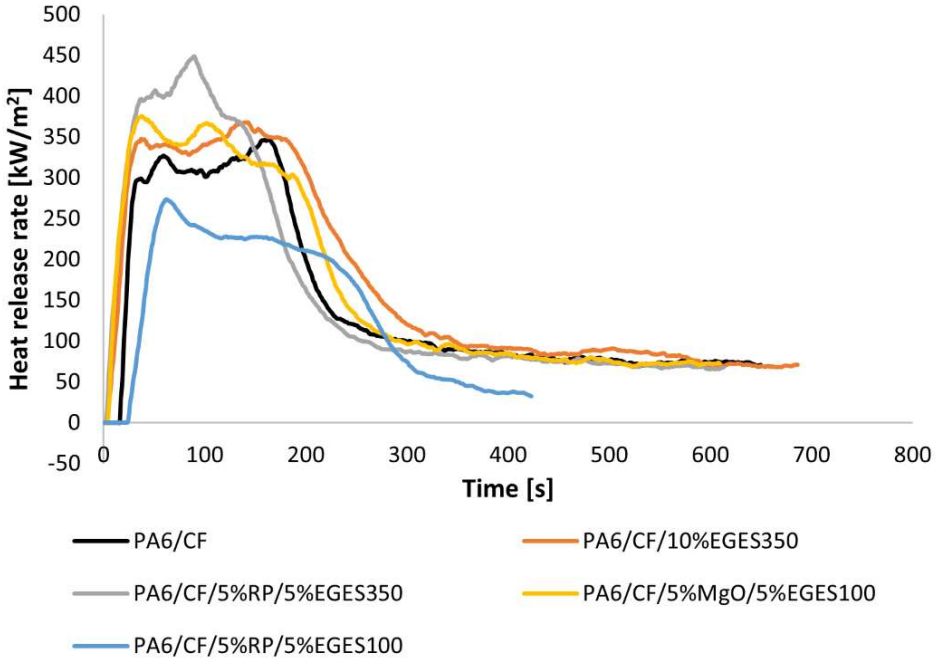

Figure 2. The heat release rate of reference and flame retardant coated carbon fibre reinforced polyamide 6 composites

4. Conclusions

In our work, we first investigated the effect of different flame retardants on the crystallinity, glass transition temperature, thermal stability, and flammability of the PA6 matrix. Red phosphorus, magnesium oxide, and expandable graphite with small and large particle sizes were used as flame retardants. They did not considerably affect the glass transition temperature and crystallinity, but they improved the thermal stability compared to the reference. Neither red phosphorus nor magnesium oxide showed outstanding results when used as sole additives, but their combination with expandable graphite is favourable in terms of flame retardancy. The best formulations were applied to coat carbon fibre reinforced polyamide 6 composites. T-RTM and in-mould coating were modelled by preparing the composites and coatings. The composite

  doi:10.5075/epfl-298799_978-2-9701614-0-0

coated with 5% red phosphorus and 5% small grain expandable graphite showed the best fire performance.

Acknowledgements

The research reported in this paper and carried out at BME has been supported by the NRDI Fund (TKP2020 NC, Grant No. BME-NCS) based on the charter of bolster issued by the NRDI Office under the auspices of the Ministry for Innovation and Technology. This work was also supported by the National Research, Development and Innovation Office (2018-1.3.1-VKE-2018-00011).

5. References

1. Krawczak P. Automotive plastics: What future is there for polymers in tomorrow's electric and autonomous vehicles? EXPRESS Polymer Letters 2021;15:288. https://doi.org/10.3144/expresspolymlett.2021.25.
2. Osváth Z, Szőke A, Pásztor S, Závoczki LB, Szarka G, Iván B. Recent Advances in the Synthesis and Analysis of Polyamide 6 and Products Therefrom: From Polymerization Chemistry of ε-Caprolactam to Thermoplastic Resin Transfer Molding (T-RTM). Acadademic Journal of Polymer Science 2020;4:100118–0012. https://doi.org/https://doi.org/10.19080/AJOP.2020.04.555629.
3. Kovács Z, Pomázi Á, Toldy A. The flame retardancy of polyamide 6—prepared by in situ polymerisation of ε-caprolactam—For T-RTM applications. Polymer Degradation and Stability 2022;195:109797. https://doi.org/10.1016/j.polymdegradstab.2021.109797.
4. Toldy A. Flame retardancy of carbon fibre reinforced composites. EXPRESS Polymer Letters 2018;12:186. https://doi.org/10.3144/expresspolymlett.2018.17.
5. Höhne C-C, Wendel R, Käbisch B, Anders T. Hexaphenoxycyclotriphosphazene as FR for CFR anionic PA6 via T-RTM a study of mechanical and thermal properties. Fire and Material 2016;41:291–306. https://doi.org/10.1002/fam.2375.
6. Yan C, Yan P, Xu H, Liu D, Chen G, Cai G, et al. Preparation of continuous glass fiber/polyamide6 composites containing hexaphenoxycyclotriphosphazene: Mechanical properties, thermal stability, and flameretardancy. Polymer Composites 2021;43:1022–1037. https://doi.org/10.1002/pc.26431.
7. Alfonso GC, Costa G, Pasolini M, Russo S, Ballistreri A, Montaudo G, et al. Flame-resistant polycaproamide by anionic polymerisation of ε-caprolactam in the presence of suitable flame-retardant agents. Journal of Applied Polymer Science 1986;31:1373–1382. https://doi.org/10.1002/app.1986.070310521.

  doi:10.5075/epfl-298799_978-2-9701614-0-0

DEVELOPMENT OF A CARBON FIBER REINFORCED SHEET MOLDING COMPOUND FOR HIGH TEMPERATURE APPLICATIONS

Robert Köhler[a], Florian Gortner[a], Peter Mitschang[a], Hauke Lengsfeld[b], Jan-Pierre Schneider[b]

a: Leibniz-Institut für Verbundwerkstoffe GmbH, 67663 Kaiserslautern, Germany – robert.koehler@ivw.uni-kl.de
b: Schill+Seilacher "Struktol" GmbH, 22113 Hamburg, Germany

Abstract: *Carbon fiber reinforced Sheet Molding Compounds (C-SMC) offer great potential for weight savings by substituting metallic materials in many areas of the mobility sector. However, components in this application area may be subjected to elevated operating temperatures up to 120 °C. In this work, therefore, three SMC materials with epoxy-based resin systems and carbon fiber reinforcement are investigated with respect to their thermomechanical properties. One commercially available material and two newly developed materials are considered. The materials are tested by using dynamic-mechanical thermal analysis in a 3-point bending test. The results to be compared are the dynamic flexural modulus and the glass transition temperature. The materials show a loss of the dynamic flexural moduli between 6 % and 18 % at 120 °C. One of the newly developed materials discloses a small drop of 6 %, which is on a par with the behavior of aluminum. The evaluation of the glass transition temperatures reveals that the materials have a dynamic flexural modulus between 67 % and 72 % at their lowest glass transition temperature. This indicates that the glass transition temperature may not be a suitable value for estimating the maximum operating temperature of the C-SMC.*

Keywords: Sheet Molding Compound; Carbon fiber reinforced Sheet Molding Compound; Dynamic-mechanical Thermoanalysis, Glass Transition temperature; High Temperature Applications

1. Introduction

In order to meet the goals of the Paris Climate Agreement, CO2 emissions in all areas of mobility must be significantly reduced in the upcoming years. In 2018, road transport alone accounted for about 26 % of CO2 emissions within the European Union [1]. This also results in the endeavor to increase the energy efficiency of transport. In addition to switching to alternative propulsion systems, vehicle CO2 emissions can be reduced by weight savings at system and component level, regardless of the propulsion technology [2, 3]. Current developments aim to substitute metallic materials by fiber reinforced polymer composites (FRPC) for weight reduction. However, compared to metallic materials, FRPC often involve higher raw material and manufacturing costs [4]. The higher manufacturing costs usually result from a low proportion of fully automated processes. For this reason, Sheet Molding Compound (SMC) material and process can play an important role to reach these goals. These compounds are compression molded and based on polyester or epoxy resins, which are produced as flat semi-finished products from a resin paste and chopped fibers in a fully automated process. For component manufacture, the semi-finished product is cut to size, stacked to form the component weight and placed in a hot sealing edge mold. Due to the heat effect in the mold, the viscosity of the SMC decreases, it starts to flow and fills the mold completely. The flowing process of the material enables very complex geometries such as ribs and webs. This behavior enables a great design freedom for the components. SMC enabled for the first time to manufacture glass fiber

  doi:10.5075/epfl-298799_978-2-9701614-0-0

reinforced polymer composites (GFRPC) components in large-scale production, which could compete with metallic components in terms of price. Since then, glass fiber reinforced SMC (GF-SMC) have been used primarily as structurally low-stress components, such as outer skin components in the automotive industry or for electrical insulating components. In 2020, 25 % of the mass of FRPC components produced in Europe was based on SMC/BMC, which is the largest production value before open mold processing [5]. In order to economically exploit the potential of FRPC for weight reduction in further areas, current developments aim to use SMC in structurally highly stressed components. To improve the mechanical properties of SMC, the reinforcing glass fibers are replaced by carbon fibers (C-SMC) and the fiber content is increased, typically from 30 wt.-% up to 60 wt.-%. One disadvantage of commercially available C-SMC materials is the drop in the mechanical properties at operating temperatures above 100 °C. Ogi and Yamanouchi investigated the influence of temperature on C-SMC based on a vinylester (VE) resin system. The flexural modulus of elasticity and flexural strength were determined at five temperatures between 20 °C and 110 °C in order to predict the failure behavior of the material. From this, it was found that with increasing temperature, the elastic modulus of C-SMC decreases significantly.[6] C-SMC competes with the widely used aluminum die casting process, which can also reproduce complex component geometries. Aluminum also exhibits a temperature dependence of Young's modulus. Compared to room temperature, this still possesses about 94 % of its flexural modulus at a temperature of 120 °C [7]. This value can be regarded as a benchmark in the context of material development. The lack of mechanical performance of available C-SMC materials at higher temperatures is addressed in this work by the development of a new C-SMC with increased thermomechanical stability at higher temperatures for application in transport and mobility sector.

2. Materials

Three different epoxy-based C-SMC materials were investigated in this work. One commercially available material from the manufacturer ASTAR S.A. called CARBKID PGK5250-R63 (ASTAR 5250), which was available as an already processed test sheet. The semi-finished products of the other two materials were produced in-house at IVW on a SMC line and processed into test panels on a hydraulic press. The resin systems used were "80CF" from the manufacturer Polynt Composites and "XP3424" from the manufacturer Schill+Seilacher "Struktol". In the further course of this work, the semi-finished products and materials based on the resin systems "80CF" and "XP3424" are abbreviated to "Polynt 80CF" and "XP3424". The components recommended by the manufacturers as curing agents and process additives were used. Carbon fibers of the type "PYROFIL TR 50S 15L" from the supplier Mitsubishi Chemical Europe GmbH with a filament count of 15k were used as reinforcing fibers. Due to the selected fibers and restrictions of the cutting unit of the SMC line, a fiber content of 40 % could be achieved in the produced semi-finished products. The manufacturing process of the test panels is illustrated by using the example of the Polynt 80CF material in Figure 1. The semi-finished products were produced in-house on an SMC line (Figure 1 a) and were stacked and placed in a hydraulic parallel-controlled pressing tool (Figure 1 b). The tool occupancy was 50 % and the semi-finished product was inserted in the center of the tool. The direction of production of the semi-finished product is in the x-direction oriented parallel to the shorter side of the pressing tool. The tool temperature was 145 °C and the holding time 540 s. The processing pressure during the production of the test plates with the Polynt 80CF and the XP3424 materials was 15 MPa, which is within the

  doi:10.5075/epfl-298799_978-2-9701614-0-0

recommended range of the respective resin system manufacturers. A finished test panel, which is used for further testing, is shown in Figure 1 c.

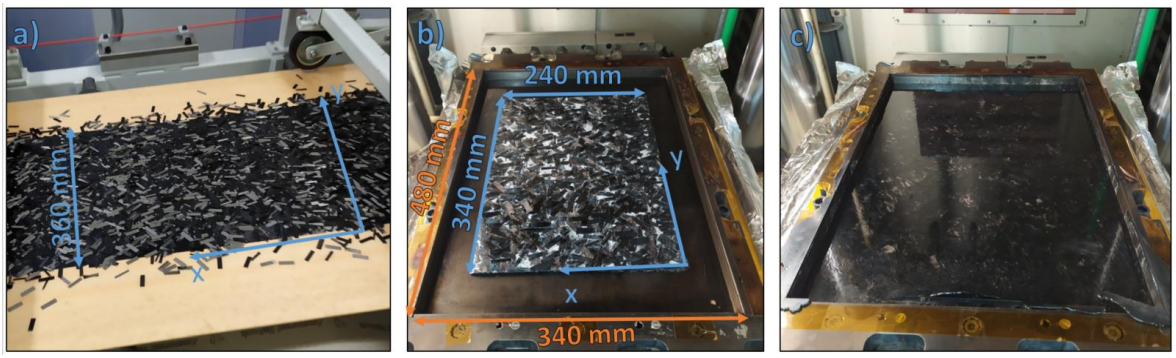

Figure 1: Production of the semi-finished products (a), placement of the stacked semi-finished product in the pressing tool (b), finished test panel in the pressing tool (c)

The known characteristic values of the materials are summarized in Table 1. No manufacturer data on the glass transition temperature is yet available for the XP3424 material. The densities of the Polynt 80CF and XP3424 materials are calculated by using the density and amount of each component being used in the production process.

Table 1: Properties of the used materials

Property	ASTAR 5250	Polynt 80CF	XP3424
Fiber content	52 % *	40 %	40 %
Fiber length	25 mm *	25 mm	25 mm
Density	1.38 g/cm² *	1.38 g/cm²	1.36 g/cm²
Glass-Transition Temperature (Tg)	170 °C *	150 °C *	N/A

* Data from technical Data Sheet

3. Methods

The test specimens were examined by means of dynamic-mechanical thermal analysis (DMTA) in a 3-point bending test in accordance to DIN EN ISO 6721-1 [8]. The Eplexor 100 N system from the manufacturer Gabo was used for this purpose. Four test specimens of size 50 x 10 x 4 mm³ were prepared from each of the test panels according to Figure 2 a. In order to avoid influences of the edge area, which occur during the flow process, the specimens were taken at least 20 mm away from the edge. Furthermore, two of the four specimens were tested in the x-direction shown and another two in the y-direction in order to detect influences of the production direction. The support distance was 40 mm and the specimen was subjected to cyclic loading at a frequency of 10 Hz. During the test, the specimens were in a climatic chamber under a nitrogen atmosphere. The nitrogen was heated from a temperature of 10 °C to 280 °C at a heating rate of 2 K/min. During the test, the force and deformation amplitude as well as the phase shift of these two are permanently recorded. A schematic drawing of the test setup is shown in Figure 2 b.

  doi:10.5075/epfl-298799_978-2-9701614-0-0

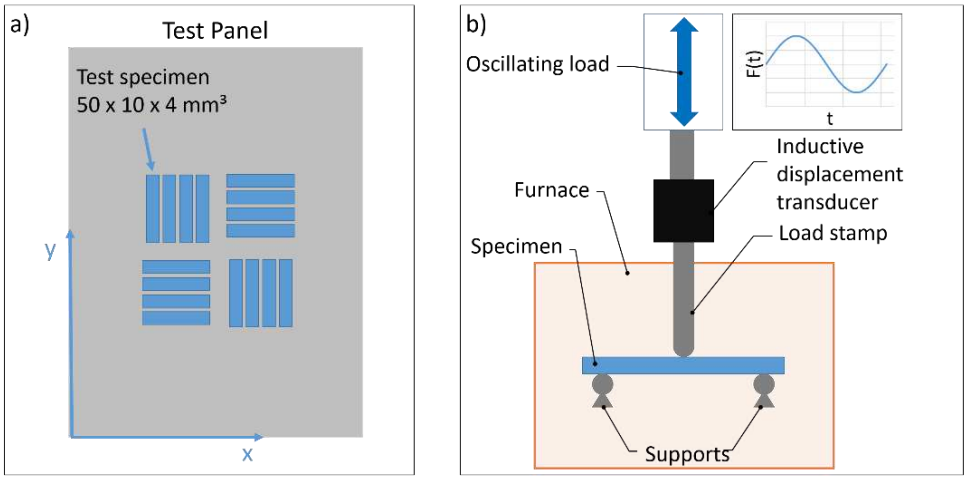

Figure 2: Schematic drawing of the test setup

With this test setup the complex modulus E*, storage modulus E', loss modulus E'' and damping factor tan δ can be determined. The storage modulus E' describes the reversible stored energy during a vibration amplitude, while the loss modulus E'' indicates the dissipated energy. The damping factor tan δ results from the ratio of E' and E''. The absolute value of the complex modulus of elasticity |E*| is called dynamic flexural modulus. It is determined from the initial stress and the resulting deformation and serves as a characteristic value for assessing the stiffness of the materials under investigation. The glass transition temperature Tg can be determined by using DMTA in accordance with ISO 6721-11 [9] with using three different methods. In the onset method, the intersection of two straight lines is used. The first straight line is the result of two points of the storage modulus, which lie before the increasing drop of the modulus. The second straight line is the tangent of the inflection point of the steep drop of the storage modulus. The second method determines the glass transition temperature by the maximum value of the loss modulus E'' and the third method by the maximum value of tan δ. Typically, the largest determined glass transition temperature is via tan δ, followed by loss modulus and onset.

4. Results

The dynamic flexural modulus curves of the three tested materials are shown in Figure 3. For this purpose, the mean value of the four test specimen was calculated at each temperature point. The absolute values of ASTAR 5250 are higher than those of the other two materials being produced at IVW at each temperature. However, this can be explained by the higher fiber content (52 % ASTAR 5250 to 40 % Polynt80CF and XP3424). Apart from the absolute values of the dynamic flexural moduli, the progression for the subsequent component properties is particularly interesting. The material ASTAR 5250 shows a steady decrease of the dynamic flexural modulus over the entire course. Up to a temperature of approx. 130 °C, the modulus drops almost linearly, followed by a steeper drop up to a temperature of approx. 200 °C. The Material Polynt 80CF shows a plateau up to about 50 °C after a short increase of the dynamic flexural modulus between 10 °C and 23 °C. Thereafter, an approximately linear decrease can be monitored up to a temperature of 120 °C. In contrast to the other two materials, the dynamic flexural modulus of the XP3424 material is at a similar level up to a temperature of 120 °C. Above

  doi:10.5075/epfl-298799_978-2-9701614-0-0

this temperature, a steep drop in the modulus is seen within a small temperature range of approx. 40 °C.

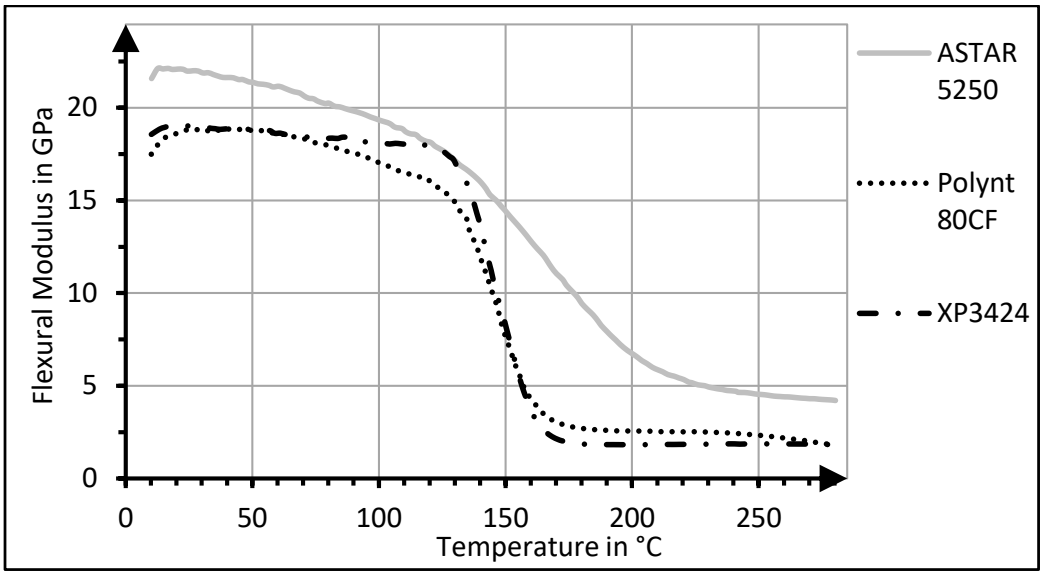

Figure 3: Dynamic flexural modulus of the tested materials

Since the fiber contents of the investigated materials differ, the following Figure 4 shows the decrease of the dynamic flexural modulus as a function of temperature in relation to room temperature. The dynamic flexural modulus at room temperature corresponds to 100 %. This clearly shows, that at a temperature of 60 °C, all materials still have a dynamic flexural modulus of over 95 %. At 100 °C, the dynamic flexural modulus of the materials ASTAR 5250 and Polynt 80CF decreases significantly to 88 % and 91 %, respectively. The material XP 3424 still exhibits a dynamic flexural modulus of 95 % at this temperature. From 100 °C to 120 °C, the dynamic flexural modulus of the XP3424 drops by one percentage point, while the ASTAR 5250 and Polynt 80CF drop by 5 %P. At 140 °C, all materials show the largest drop in dynamic flexural modulus. There, the remaining dynamic flexural moduli range from 64 % to 72 %, with the Polynt 80CF material showing the lowest relative dynamic flexural modulus.

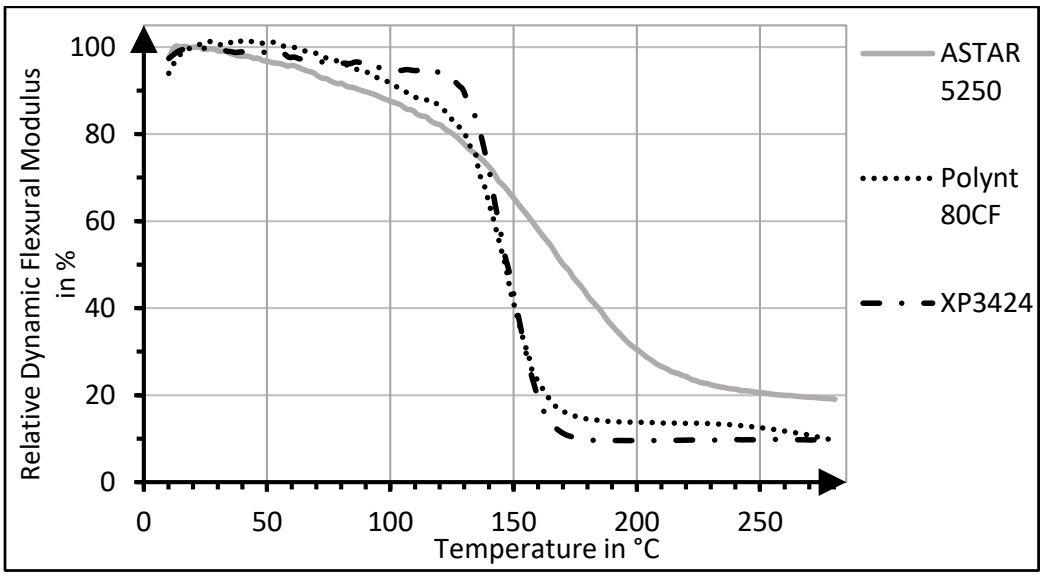

Figure 4: Dynamic flexural modulus of the tested materials in relation to room temperature

  doi:10.5075/epfl-298799_978-2-9701614-0-0

Using the obtained values, the glass transition temperatures of the three materials can be determined. Figure 5 shows an example of the determination of the glass transition temperatures according to the three methods mentioned above, using one test specimen per material. The solid red line indicates the glass transition temperature to be read.

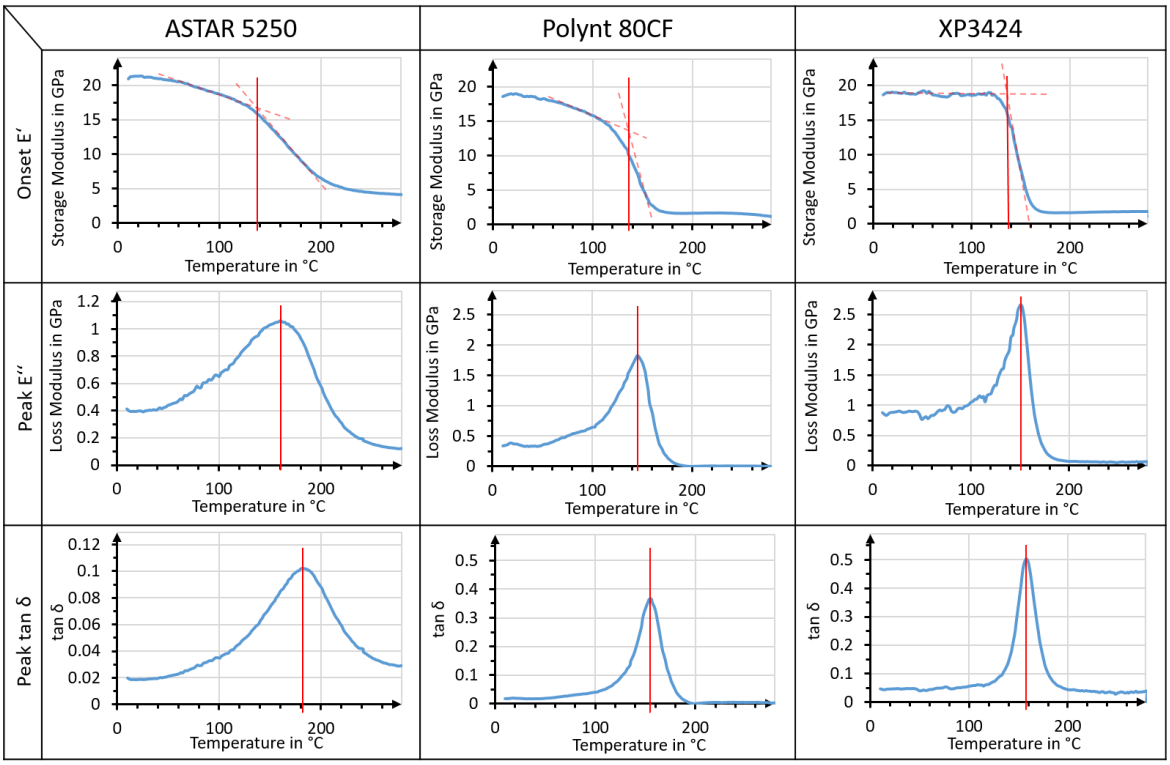

Figure 5: Determination of the glass transition temperature using Onset E', Peak E'' and Peak tan δ method

The glass transition temperature was determined for all four test specimens of the materials. The resulting average value of the glass transition temperatures is listed in Table 2. As expected, the glass transition temperatures are lowest with using the onset E' method, followed by the peak E'' and peak tan δ methods. The glass transition temperatures, which are given in the data sheets of the materials, range between the values by the Peak E'' and Peak tan δ methods for the ASTAR 5250 and the Polynt 80CF.

Table 2: Glass transition temperatures

Method	ASTAR 5250	Polynt 80CF	XP3424
Onset E´	140.58 °C	137.95 °C	140.14 °C
Peak E´´	156.70 °C	146.27 °C	150.33 °C
Peak tan δ	185.10 °C	154.97 °C	158.4 °C
Data sheet	170 °C	150 °C	N/A

In practice, the glass transition temperature is often used as a guide to the maximum operating temperature of the material. Therefore, Table 3 shows the relative values of the dynamic flexural modulus compared to its maximum value. This shows that the dynamic flexural moduli of all

  doi:10.5075/epfl-298799_978-2-9701614-0-0

materials at the glass transition temperature, determined by the onset method, are in a similar range of about 70 %. At the glass transition temperatures, determined by the Peak E'' method, the difference between the materials is more pronounced. Here, ASTAR 5250 still has 60.84 % of its maximum dynamic flexural modulus, while the other two materials have only 48.96 % and 42.59 %, respectively. This trend is also evident in the dynamic flexural moduli at the glass transition temperature determined by the peak tan δ method.

Table 3: Relative value of the dynamic flexural modulus at glass transition temperature compared to peak value

Method	ASTAR 5250	Polynt 80CF	XP3424
Onset E´	72.13 %	67.02 %	70.45 %
Peak E´´	60.84 %	48.96 %	42.59 %
Peak tan δ	39.88 %	27.71 %	22.45 %
Data Sheet	49.92 %	39.56 %	N/A

5. Conclusions

Within the scope of this work, three different C-SMC materials were investigated with respect to their thermomechanical properties by means of a dynamic-mechanical thermal analysis in a three-point bending test. The commercially available material ASTAR S.A. CARBKID PGK5250-R63 (ASTAR 5250) and two newly developed materials based on resin systems from the companies Polynt Composites (Polynt 80CF) and Schill+Seilacher "Struktol" (XP3424) are compared by the dynamic bending moduli as a function of temperature and the glass transition temperatures of the materials. The absolute values of the dynamic flexural modulus of the ASTAR 5250 material are above those of the other two materials at each temperature. This is due to a significantly higher (52 % to 40 %) fiber content of ASTAR 5250. The influence of temperature on the dynamic flexural moduli of the investigated materials is very different in different temperature ranges. The commercially available material ASTAR 5250 shows a steady decrease of the dynamic bending modulus over the whole measured temperature range. The Polynt 80CF material also shows such a drop. Compared to the other two materials, the newly developed material based on the XP3424 resin system shows a small drop in dynamic flexural modulus up to a temperature of 120 °C. There, the XP3424 material still has about 94 % of its flexural modulus compared to room temperature. This value corresponds to that of aluminum, with which C-SMC competes. At this temperature, the material Polynt 80CF shows approx. 86 % and the material ASTAR 5250 still approx. 82 % of its flexural modulus in relation to room temperature. The decrease of the flexural modulus with increasing temperature can have a strong influence on the component properties, since important quantities such as the natural frequency are affected. Furthermore, the glass transition temperatures of the materials were determined by three different methods within the scope of this work. Depending on the method, the materials have between 22 % and 72 % of their flexural modulus at their glass transition temperature in relation to the maximum value. It can be deduced from this, that the glass transition temperature is not a suitable value for deriving the maximum service temperature of the C-SMC, if the stiffness of the component at high operating temperatures is a critical factor. In particular, since the data sheets usually do not mention, which method was

  doi:10.5075/epfl-298799_978-2-9701614-0-0

used to determine the glass transition temperatures. Depending on the application, it might be more useful to give the mechanical properties of the C-SMC materials for different temperatures or to determine the temperature at which the stiffness or strength of the material fell below a certain value (for example, 95%) compared to room temperature. The newly developed material based on the XP3424 resin system shows great potential for use in applications subject to high thermal stress, since the drop in the dynamic flexural modulus at temperatures up to 120 °C is very low compared with commercially available materials. Therefore, further factors influencing the properties of the material are to be identified and optimized in upcoming investigations.

Acknowledgements

This study has been conducted in the frame of the research project “drivEcomp II - Advanced composite solutions for electric drives to increase the power density in ground-based mobility applications” funded by the Federal Ministry of Economic Affairs and Energy (BMWK) on the basis of a decision by the German Bundestag (funding reference 19I20017D).

6. References

1. Statistisches Bundesamt: Straßenverkehr: EU-weite CO2--Emissionen seit 1990 um 24 % gestiegen [Online: 01.03.2022 https://www.destatis.de/Europa/DE/Thema/Umwelt-Energie/CO2_Strassenverkehr.html]
2. Redelbach M, Klötzke M, and Friedrich H. Impact of lightweight design on energy consumption and cost effectiveness of alternative powertrain concepts. [Online: 01.03.2018 https://elib.dlr.de/80771/]
3. Brooker A, Ward J et al. Lightweighting Impacts on Fuel Economy, Cost and Component Losses. in SAE 2013 World Congress & Exhibition: SAE International. 2013. DOI: 10.4271/2013-01-0381.
4. Patel M, Pardhi B, Chopara S, Pal M. Lightweight Composite Materials for Automotive – A Review. in International Research Journal of Engineering and Technology. 2018. e-ISSN: 2395-0056
5. Witten E, Mathes V. Der Markt für Glasfaserverstärkte Kunststoffe (GFK) 2020. 2020. [Online: 01.03.2022 https://www.avk-tv.de/files/20201111_avk_marktbericht_2020.pdf]
6. Ogi, K, Yamanouchi, M. Temperature Dependence of Flexural Strength of a CF-SMC Composite. Appl Compos Mater 18, 397–408 (2011). https://doi.org/10.1007/s10443-010-9171-x
7. Hopkins, D.C. & Baltis, Theodore & Pitarresi, James & Hazelmyer, Donald. (2012). Extreme Thermal Transient Stress Analysis with Pre-Stress in a Metal Matrix Composite Power Package. Additional Conferences (Device Packaging, HiTEC, HiTEN, & CICMT). 2012. 000361-000372. DOI: 10.4071/HITEC-2012-THA25
8. DIN EN ISO 6721-1:2019-09. Kunststoffe - Bestimmung dynamisch-mechanischer Eigenschaften - Teil 1: Allgemeine Grundlagen (ISO 6721-1:2019); Deutsche Fassung EN ISO 6721-1:2019. Beuth-Verlag. Berlin. 2019
9. ISO 6721-11:2019-06. Kunststoffe - Bestimmung dynamisch-mechanischer Eigenschaften - Teil 11: Glasübergangstemperatur. Beuth-Verlag. Berlin, 2019

  doi:10.5075/epfl-298799_978-2-9701614-0-0

DEVELOPMENT OF ELECTRIC VEHICLE UNDERBODY SHIELD USING CARBON FIBER/POLY(ETHYLENE TEREPHTHALATE) AND SELF REINFORCED POLYPROPYLENE COMPOSITES

Hui-Jin Um[a], Hak-Sung Kim*[a,b]

a: Department of Mechanical Convergence Engineering, Hanyang University, 222 Wangsimni-ro, Seongdog-gu, Seoul, Republic of Korea
b: Institute of Nano Science and Technology, Hanyang University, 222, Wangsimni-ro, Seoungdong-gu, Seoul, Republic of Korea
*Email: gog9057@hanyang.ac.kr

Abstract: *The global market of electric vehicles has been extremely growing due to the interest in eco-friendly energy. Therefore, the weight reduction and lithium battery protection are the critical issues in electric vehicles industry. In this study, the underbody shield was designed with carbon fiber reinforced polymer and self-reinforced polypropylene composites to protect the lithium battery pack of electric vehicle from external shock with light weight. The impact simulation was performed, then the optimal shape was designed. The vehicle crash test was conducted with electric vehicle equipped with the manufactured composite underbody shield. As a result, the composite underbody shield could destroy the obstacle, and no electrical or mechanical damage occurred to the battery pack.*

Keywords: CFRP composites; spreading tow; electric vehicle; Finite element analysis.

1. Introduction

The electrical vehicle industries have been rapidly growing in recent years due to the interest in eco-friendly energy [1-2]. Since the lithium battery is the main power source of electric vehicles, the battery packs with several batteries are usually loaded under the vehicle. In the case of lithium batteries, there is a risk of explosion or fire if an external shock is applied. Therefore, the protection of battery pack from external impact must be considered. Excellent mechanical properties are required to protect the battery pack from ground impact, while at the same time reducing the weight of electric vehicles is also an important issue in order to increase the driving range in consideration of energy efficiency. The battery protection pack was mainly designed using metal material such as aluminum and titanium [3]. Therefore, to reduce the weight, the entire battery pack cannot be covered by protection structure, and there are limitations in dimensions such as installing some structures for crushing obstacles in front of the battery pack.

The fiber reinforced polymer (FRP) composites have excellent mechanical properties such as high specific strength and specific modulus. In particular, the carbon fiber reinforced polymer (CFRP) composites shows excellent mechanical strength and modulus compared to the other composites. If a thermoplastic resin is used as a base for a CFRP composite material, a specific shape can be realized through thermoforming, which is an advantage that can reduce the production time in the industrial field. Among the various FRP composites, the hybrid composite has the advantage of being able to implement improved properties by compensating for each other's shortcomings by using a mixture of composite materials with different properties.

  doi:10.5075/epfl-298799_978-2-9701614-0-0

In this study, the underbody shield design was conducted to protect the battery pack of electric vehicle with hybrid composites for weight reduction. The optimal geometry and appropriate hybrid ratio were found through an impact simulation. The CFRP woven composites which was fabricated with spreading carbon fiber (CF) tow and polyethylene terephthalate (PET) tape and self-reinforced polypropylene (SRPP) composites were applied to fabricate the designed underbody shield as hybrid composites. The adhesion properties of hybrid composites were analyzed through weight drop test and the optimal fabrication process condition was investigated. The vehicle crash test was performed with electric vehicle equipped with the designed underbody shield.

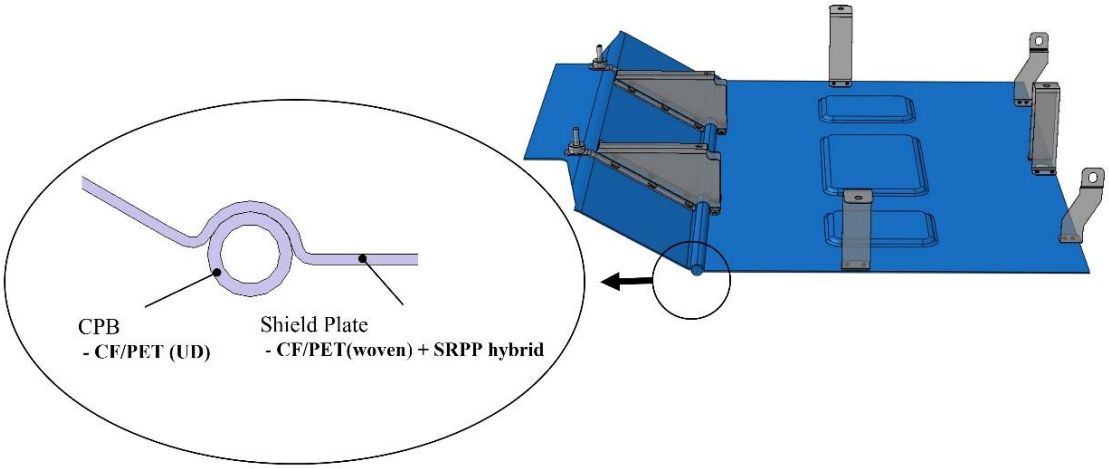

Figure 1. Schematic of underbody shield which was composed with collision profile and shield plate.

2. Underbody shield design

2.1 Geometry of underbody shield

The underbody shield design was conducted based on the battery pack dimension of electric vehicle (Smart EV D2, Semisysco, South Korea). The overall dimension and geometry of underbody shield was shown in Fig. 1 (a). The underbody shield is composed of two parts. The first part is the collision profile, which is primarily responsible for crushing large obstacles. The other one is a shield plate and it covers the entire battery pack to protect from impact loading. As indicated in Fig. 1 (b), the collision profile is hollow cylinder shape with the outer diameter of 20 mm, inner diameter of 14 mm, and the thickness of 3 mm.

The shape design was conducted according to the collision profile position and shield plate angle, and four cases were shown in Fig. 1(c). Cases 1 and 2 show the case where the collision profile is located on the upper surface of the shield plate, and Cases 3 and 4 show the case where the collision profile is located on the underside of the shield plate. And it can be divided into two cases according to the angle that the shield plate wraps around the CPB.

  doi:10.5075/epfl-298799_978-2-9701614-0-0

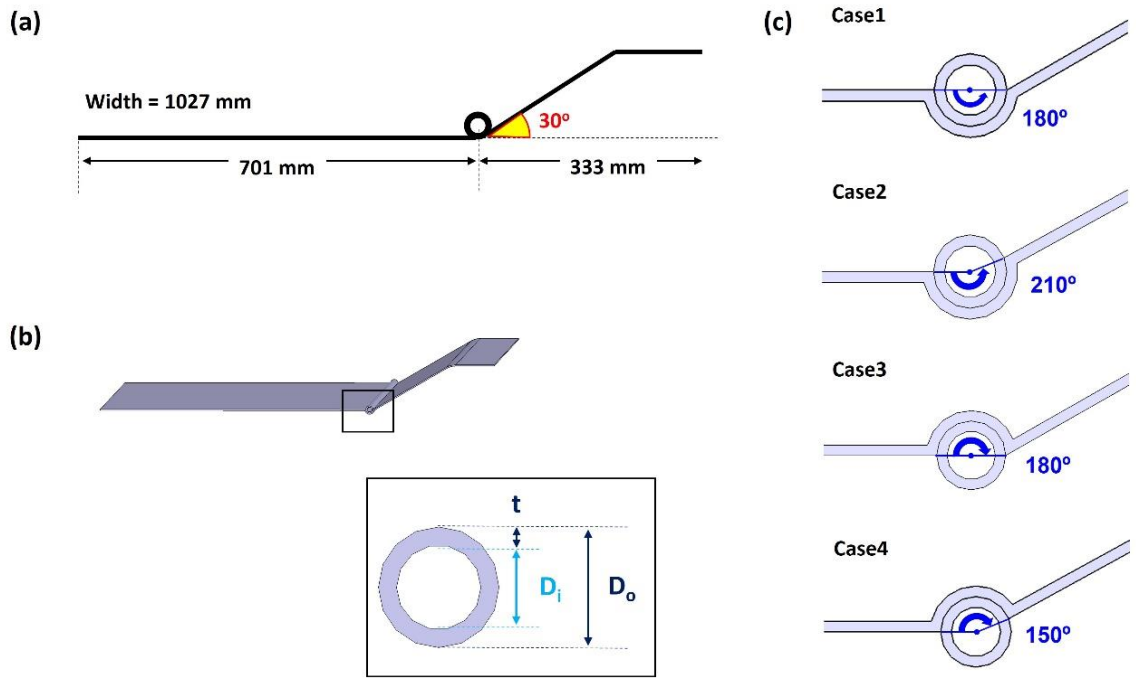

Figure 2. The overall dimension and geometry of (a) underbody shield and (b) collision profile. (c) The four cases of underbody shield according to the geometry

2.2 Hybrid composites design

The hybrid composites were used to the underbody shield plate to maximize the weight reduction. The unidirectional carbon fiber reinforced polymer (CFRP) composite was used for CPB, and the hybrid composite was applied to the shield plate to achieve further lightweight with CFRP and self-reinforced polypropylene (SRPP) composites. The SRPP composites have a lower density than that of CFRP composites, but the mechanical properties were also weaker than that of CFRP composites. Therefore, to achieve both battery pack protection and weight reduction through higher mechanical properties, it is necessary to find the optimal hybrid ratio between the CFRP and SRPP composites. The optimal hybrid ratio was found through finite element analysis using the underbody shield of the appropriate shape determined in the previous section. The hybrid ratio was defined as the number of SRPP plies divided by the number of CF/PET plies.

2.3 Finite element analysis

The impact simulation was performed using commercial finite element software ABAQUS. The CF/PET composites and SRPP composites properties were used in the shield plate part. The collision profile was modeled with unidirectional CF/PET composites properties and the fiber direction was assigned with local coordinate. The fixed boundary condition was assigned to the mounting position. The concrete obstacle was modeled with a cylindrical shape as an impactor, and the brittle-cracking model was applied [4, 5]. The overlap length between the lowest point of underbody shield and top point of concrete impactor was set by 25 mm. For the impact simulation, the speed of 32 km/h was assigned to the concrete obstacle, and this obstacle was

  doi:10.5075/epfl-298799_978-2-9701614-0-0

set to move towards the underbody shield during the simulation. Through this collision simulation, an appropriate shape was selected after performing cases 1-4. After simulation of various thicknesses of shield plate for the determined shape, an appropriate thickness was chosen for the hybrid composite. After that, the optimal hybrid ratio was determined by performing simulations on the hybrid composite. In addition, to analyze the behavior of the underbody shield according to the collision location, three types of collision body positions were analyzed as shown in Fig. 3.

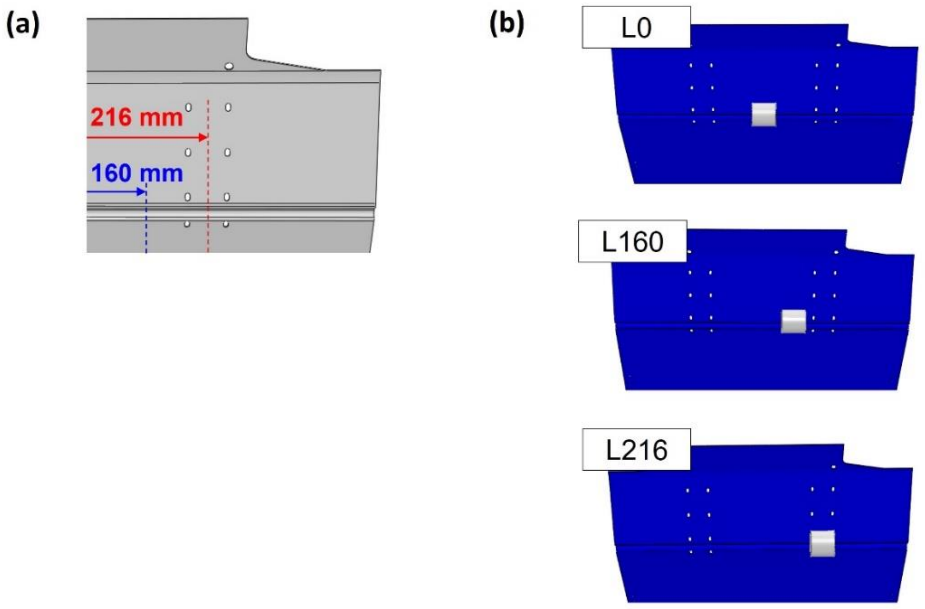

Figure 3. (a) Impact simulation model of underbody shield and (b) various impact location.

3. Mechanical experiments

3.1 Underbody shield fabrication

The CF/PET tape was fabricated with spreading CF tow. The spreading CF tow has advantage in impregnation due to the thin and wide shape as shown in Fig 4. Therefore, when spread CF tow is used, it is possible to produce composites that is uniformly impregnated even in a thermoplastic matrix with high viscosity. Hybrid composite is a CF/PET woven fabric laminated on the outer layer and SRPP composite material on the inner layer. The hot-melt film was inserted between the CF/PET woven composite and SRPP composites to enhance the adhesion. The thermoforming was performed with CF/PET and SRPP composites and the process condition was shown in Table 1.

Table 1: Thermoforming process condition.

	Temperature	Pressure	Time
CF/PET composites	270 ℃	1000 tons	100 seconds
Hybrid composites	170 ℃	500 tons	10 minutes

  doi:10.5075/epfl-298799_978-2-9701614-0-0

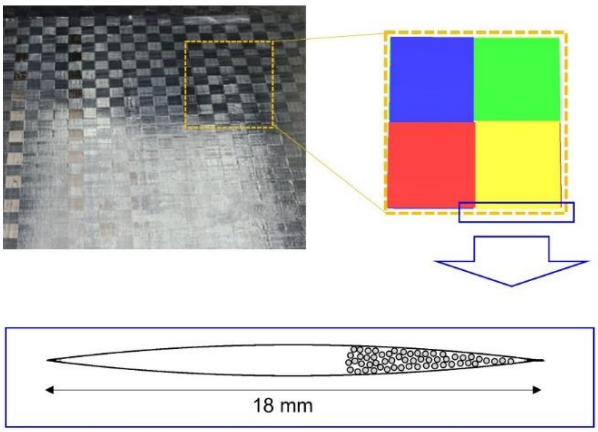

Figure 4. CF/PET woven composites and the schematic of spread CF tow shape

3.2 Weight drop test

The weight drop test was performed to analyze the adhesion properties of hybrid composites based on the ASTM D 7136 [6]. The impact ball mass was 5.0 kg and the impact velocity was 3.13 m/s. Fig. 5(a) shows the weight drop test system, and the rectangular-shaped specimen was fixed to the lower part of the tester using a clamp. The hybrid specimen was fabricated with CF/PET woven and SRPP composites as shown in Fig. 5(b). The final specimen was indicated in Fig. 5 (c) and the dimension of it was 100 mm in width, 150 mm in length.

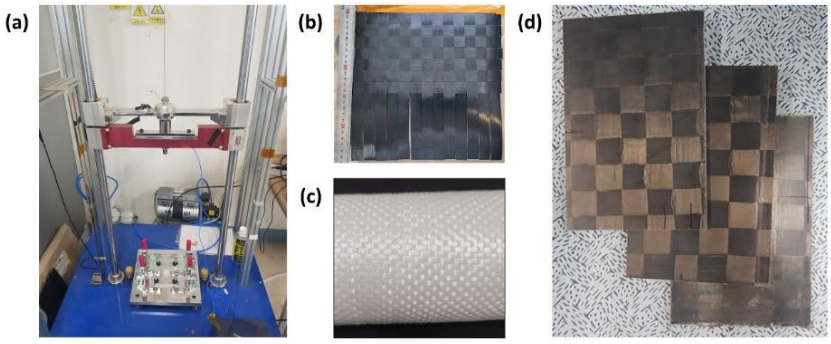

Figure 5. (a) Weight drop test system (b) CF/PET woven composites (c) Polypropylene fiber (d) Hybrid composites specimens of weight drop test.

3.3 Vehicle crash test

The vehicle crash test was conducted with electric vehicle equipped with the designed underbody shield at Automobile technology test center (Ulsan, South Korea). The concrete obstacle was fabricated 7 days before the test as shown in Fig. 6 (a). The concrete obstacle was fixed to the steel plate with bolt joint as shown in Fig. 6 (b-c). The steel plate height was controlled so that the overlap length between the obstacle and underbody shield was 25 mm.

  doi:10.5075/epfl-298799_978-2-9701614-0-0

The deformation amount of underbody shield was measured through laser displacement sensor, and the battery properties were monitored through a sensor attached to the vehicle.

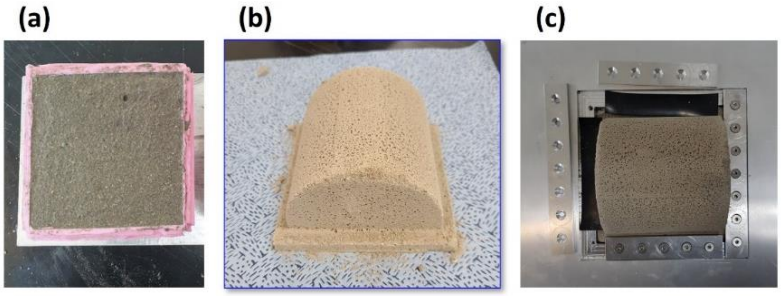

Figure 6. (a) Concrete specimen fabrication process with silicone mold (b) fabricated concrete obstacle (c) Concrete obstacle fastened to the steel plate using bolt joint.

4. Result and Discussion

4.1 Underbody shield design

The deformation behavior of underbody shield was different according to the underbody shield shape. Fig. 7 (b) shows the maximum deformation of each point with respect to the geometry cases. The max deformation amount of point 2 was higher when the collision profile was located on the upper surface of the shield plate such as case 1 and 2. Especially, case 4 shows significantly low deformation amount compared to other cases. It means that if the collision profile receives an impact load first, the underbody shield was deformed less. On the other hand, if the shield plate collided with the concrete obstacle firstly, it was not able to break down the concrete obstacle and large deformation occurred together with it. Therefore, further analysis was performed to find the appropriate thickness of shield plate and optimal ratio of the hybrid composites using case4 shape. As the thickness increased and the CF ratio of hybrid composites increased, the impact deformation was reduced. Since the gap between the underbody shield and the battery pack was 10 mm, it was assumed that deformation of more than 4 mm should not occur in order not to affect the battery pack. Therefore, the thickness of the underbody shield satisfying this condition was 2.4 mm, and the hybrid ratio between CF and SRPP was selected as 2. Fig. 7 (c) shows the deformation with respect to the impact location. The amount of deformation at point 2 was always the largest regardless of the collision location.

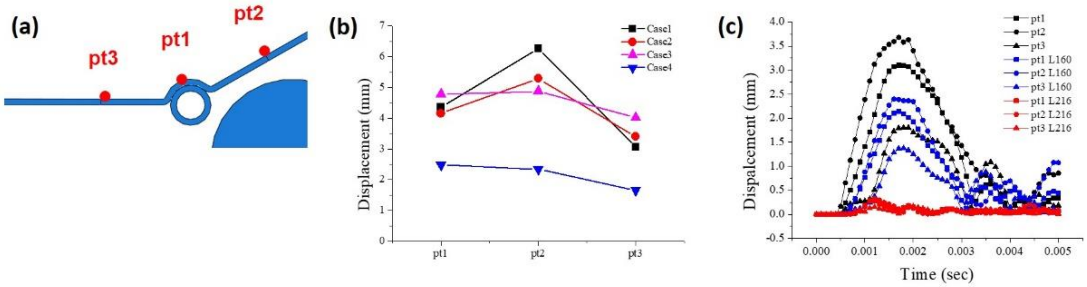

Figure 7. (a) Displacement measurement points of underbody shield model. Impact simulation result according to (b) the geometry cases and (c) impact location.

  doi:10.5075/epfl-298799_978-2-9701614-0-0

4.2 Mechanical characteristics

Fig. 8 shows the result of weight drop test. The separate SRPP plies were observed in the specimen which was fabricated at 150 °C. On the other hand, in the case of specimens manufactured at a higher temperature, SRPP composites did not separate with appropriate consolidation. Therefore, the largest fracture area was found in the specimens manufactured at 150 °C, and relatively large fiber failure occurred in the specimens fabricated at 160 °C. In the case of the specimen fabricated at 180°C, the specimen deformed significantly due to the high temperature, and the optimal process condition was selected at 170 °C.

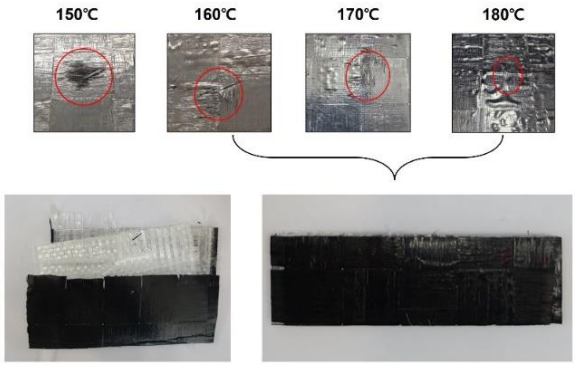

Figure 8. Result of weight drop test for the hybrid composites specimen with respect to the fabrication temperature.

4.3 Vehicle crash test

Fig. 9 (a) shows the vehicle crash test with electric vehicle, and Fig 9(b) is an image captured by a high-speed camera at the moment when the underbody shield collides with the concrete obstacle. As a result of vehicle crash tests, the concrete obstacle was shattered, and the maximum deformation on the underbody shield was around 5 mm, which did not affect the battery pack. In addition, there was no leakage or change in electrical characteristics when the condition of the battery before and after the crash was checked, indicating that the battery pack was successfully protected by the underbody shield.

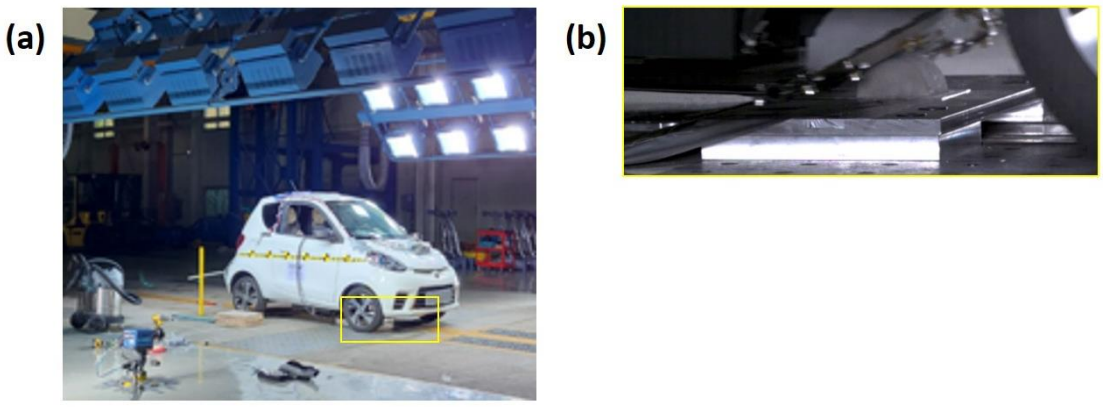

Figure 9. (a) Vehicle crash test with electric vehicle and (b) high-speed camera image at the impact moment

5. Conclusion

In this study, the underbody shield was designed to protect the battery pack of electric vehicle. The optimal geometry and appropriate hybrid ratio were found through an impact simulation. The appropriate fabrication process conditions were determined through the weight drop test to enhance the adhesion between the CF/PET and SRPP composites. The designed underbody shield was fabricated using CFRP and SRPP composites as hybrid composites. The vehicle crash test was performed with electric vehicle equipped with the designed underbody shield. Consequently, the deformation of underbody shield was lower than 5mm and the there was no change in electrical characteristics of battery.

Acknowledgements

This work was supported by Korea Institute of Energy Technology Evaluation and Planning(KETEP) grant funded by the Korea government(MOTIE)(20212020800090, Development and Demonstration of Energy-Efficiency Enhanced Technology for Temperature-Controlled Transportation and Logistics Center). This research was also supported by the BK21 FOUR (Fostering Outstanding Universities for Research) project of the National Research Foundation of Korea Grant.

6. References

1. Chen, Xin, et al. "Electric vehicles body frame structure design method: An approach to design electric vehicle body structure based on battery arrangement." Proceedings of the Institution of Mechanical Engineers, Part D: Journal of Automobile Engineering (2021): 09544070211052957.
2. Shui, Li, et al. "Design optimization of battery pack enclosure for electric vehicle." Structural and Multidisciplinary Optimization 58.1 (2018): 331-347.
3. Schmerler, Rico, et al. "Multi-functional battery housing for electric vehicles." Lightweight Design worldwide 10.5 (2017): 26-31.
4. Jiang, Hua, Xiaowo Wang, and Shuanhai He. "Numerical simulation of impact tests on reinforced concrete beams." Materials & Design 39 (2012): 111-120.
5. Kaewunruen, Sakdirat, Chayut Ngamkhanong, and Chie Hong Lim. "Damage and failure modes of railway prestressed concrete sleepers with holes/web openings subject to impact loading conditions." Engineering Structures 176 (2018): 840-848.
6. ASTM D7136. "Standard Test Method for Measuring the Damage Resistance of a Fiber-Reinforced-Polymer Matrix Composites to a Drop-Weight Impact event." Book of Standards 15 (2005): 03.

  doi:10.5075/epfl-298799_978-2-9701614-0-0

Sustainable epoxy thermosets and carbon fibers based composites with potential applications in the aerospace sector

Roxana Dinu[a], Ugo Lafont[b], Olivier Damiano[c] and Alice Mija[a]

a: Université Côte d'Azur, Institut de Chimie de Nice, France - Alice.Mija@univ-cotedazur.fr
b: ESA, ESTEC, Keplerlaan 1, PO Box 299, NL-2200 AG Noordwijk, The Netherlands
c: Thales Alenia Space, 5 Allée des Gabians, 06156 Cannes la Bocca, France

Abstract: *High glass transitions, high storage moduli, high thermal stability and low water absorption values are crucial criteria of high performant materials. This work proposes the chemical combination of aromatic biobased epoxy monomers with potential biobased anhydrides to produce thermosetting materials with competitive performances. Triglycidyl ether of phloroglucinol (TGPh) and diglycidyl ether of vanillyl alcohol (DGEVA) were copolymerized with hexahydro-4-methylphthalic anhydride (HMPA) or methyl nadic anhydride (MNA). The produced thermosets have high biobased organic carbon content, ~69–77%, high glass transition values (>100 °C for DGEVA-based resins and >200 °C for TGPh resins), high storage moduli (2.7–3.1 GPa at 30 °C), high thermal stability ($T_{5\%}$ = 329–359 °C) and very low water absorption (in average ~1.5% after 15 days). The performances of these biobased thermosets and of their carbon fibers based composites open windows of application in space, aerospace, or naval industries.*

Keywords: aromatic biobased epoxy monomers; vanillin; phloroglucinol; curing; high glass transitions; thermosets for space application

1. Introduction

Epoxy resins are one of the most used thermosetting systems due to their high mechanical properties, good thermal stability, processability and compatibility with other polymers,[1] having a broad range of applications such as composites,, structural materials in civil infrastructures and, in automotive and aerospace industry.[1,2] Over 90% of these epoxy materials are based on bisphenol A (BPA) which has been classified as carcinogen mutagen and reprotoxic (CMR) being submitted to restrictive regulations in numerous countries.[3] Focusing on aerospace and space applications, it is known that thermosets used in these fields have very good mechanical properties but also a good performance at high temperatures. This last characteristic is related to the high temperature values of the glass transition (T_g), which in general, for the aeronautical industry is between -50°C–60 °C, while for the space environment the T_g value is ranged between -150–150 °C.[2] Therefore, the materials used in these fields exceed these upper temperature limits for a higher resistance of components manufactured over time and to special environments. In this context, epoxy monomers derived from biomass such as vanillin and phloroglucinol were used in this work to produce high glass transition biobased thermosets. Vanillin is the main component of the natural vanilla extract and is originally extracted from vanilla orchid pods. The most important industrial process to obtain vanillin is the chemical depolymerization of lignin.[1] Another bio-renewable resource used in this work is the phloroglucinol, compound found in marine brown algae or bark of fruit, but also obtained by synthetic route from benzene.[4]

In this study, the main goal is the development of bio-based epoxy thermosets starting from bio-renewable compounds. DGEVA and TGPh, laboratory made monomers were crosslinked with HMPA or MNA anhydride, the reactions being initiated by 1MIM or 2E4M

Physico-chemical and thermo-mechanical properties of the materials were investigated by thermogravimetric analysis (TGA), dynamic mechanical analysis (DMA), Shore tests, water absorption and gel content. Composites were prepared thereafter using carbon fibers and thermomechanical properties were tested.

2. RESULTS AND DISCUSSIONS

2.1. Curing behaviour of the epoxy/anhydride systems

The non-isothermal curing behaviours of TGPh and DGEVA epoxies were monitored by DSC (Fig.1). Based on reported studies,[2] the curing temperatures for the epoxy resins used in aerospace applications are ranged between 120-135 °C and can increase up to 180 °C. Specific values of crosslinking reaction studied by DSC, such as the reaction peak temperature (T_{peak}), the interval of the thermal curing (T_{onset}-T_{end}) and the reaction enthalpy (ΔH) are given in Table 1. In Fig.1, the TGPh-based formulations display a lower onset temperature of reactions with MNA or HMPA anhydrides (40–60 °C), compared with the homologous formulations with DGEVA. At the same time, TGPh-based formulations have a larger curing interval of temperature ($\Delta T_{reaction}$ ~160 °C) compared to DGEVA ones ($\Delta T_{reaction}$ ~80 °C). An parameter related to the reactivity of the compounds is the T_{peak} value of the DSC exothermic peak: lower is the T_{peak}, higher is the reactivity of the mixtures.[5,6] In Fig.1 can be seen that for both TGPh- and DGEVA-formulations, the curing reactions with HMPA anhydride are slightly more reactive than those with MNA anhydride.

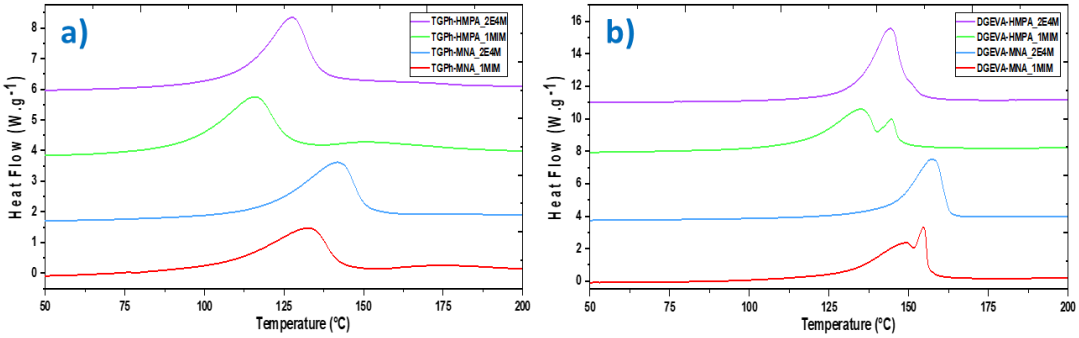

Figure 1. DSC thermograms of heating at 10 °C/min of a) TGPh/anhydride and b) DGEVA/anhydride formulations

Table 1: Dynamic DSC data of the curing process

Formulations	T_{onset} -T_{end} (°C)	T_{peak} (°C)	ΔH (J.g^{-1})
TGPh-MNA_1MIM	45–205	132; 173	257
TGPh-MNA_2E4M	58–212	141	258
TGPh-HMPA_1MIM	36–200	115; 151	315
TGPh-HMPA_2E4M	58–201	127	292
DGEVA-MNA_1MIM	83–174	149; 153	290
DGEVA-MNA_2E4M	99–175	157	284
DGEVA-HMPA_1MIM	68–175	134; 144	319
DGEVA-HMPA_2E4M	90–171	143	343

It can also be seen that the reaction enthalpy of the mixtures was generally few influenced by the nature of the initiator, excepting the DGEVA-HMPA system, where 2E4M is more efficient i.e. higher ΔH, lower T_{peak} value and $\Delta T_{reaction}$.

3.2. Investigation of thermo-mechanical properties of the bio-based epoxy thermosets

The thermomechanical performances of the designed bio-resins were determined by DMA analysis using a three-points bending mode. The temperature-dependent curves of the storage modulus (*E'*) obtained for epoxy thermosets are represented in Fig.2. The *E'* values at 30 °C for all the prepared thermosets are very close, between ~2.7 and 3.1 GPa (Table 2). We used the *E'* values in the rubbery plateau to evaluate the crosslink density (*v*) according with the rubber elasticity theory,[7]:

$$\upsilon = \frac{E'}{3RT} \quad (1)$$

where *E'* is the storage modulus in the rubbery plateau, *R* the gas constant, and *T* the absolute temperature. Table 2 show the crosslink densities values calculated at T_g + 70 °C.

Table 2: Physical and thermo-mechanical properties of the epoxy/anhydride thermosets

Thermosets	Density (g/cm3)	Hardness Shore D tests	E' at 30 °C (MPa)	Glass transition (°C)		υ (mmol·cm-3)	Mc (g/mol)	Gel Content (%)
				Tg (DSC)	tan δ			
TGPh-MNA_1MIM	1.20	89	2822	211 ± 1	210	7.26	165.12	99.88
TGPh-MNA_2E4M	1.22	88	3133	184 ± 1	199	7.98	144.15	99.72
TGPh-HMPA_1MIM	1.17	88	2691	179 ± 1	197	6.68	174.68	99.80
TGPh-HMPA_2E4M	1.16	87	2925	178 ± 1	189	7.62	152.40	99.62
DGEVA-MNA_1MIM	1.12	81	2929	106 ± 1	104	4.598	244.16	99.22
DGEVA-MNA_2E4M	1.13	81	3062	107 ± 1	108	4.193	268.50	96.77
DGEVA-HMPA_1MIM	1.05	80	2729	93 ± 1	96	3.191	326.75	99.70
DGEVA-HMPA_2E4M	1.10	81	2838	94 ± 1	99	3.492	315.38	94.75

The average molecular mass between crosslinks (M_c) was also calculated based on the equation established by Tobolsky:[8]

$$Mc = \frac{3\rho RT}{E'} \quad (2)$$

The trifunctional molecule of TGPh provides the development of a more compacted networks, thus more rigid than those developed with DGEVA. The ν of TGPh-thermosets is ranged between 6.7 and 8 mmol·cm^{-3}, while those with DGEVA are with 40-50% lower, varying between 3.2 and 4.6 mmol·cm^{-3}. Tan δ is associated with the macroscopic T_g transition and is dependent on various physico-chemical and mechanical factors.[9] Its shape is correlated with the network structure, the width of and the breadth of the peak giving information on the degree of homogeneity of the network.[10] TGPh-thermosets have higher tan δ values, with lower amplitude of the peaks and wider curves compared to those developed with DGEVA (Fig.2). We obtained a very good correlation between the tan δ and T_g results, with high values for TGPh-thermosets, around 180–210 °C. Compared to these resins, the materials developed with DGEVA show lower values ranged between 96 and 108 °C. Based on industrial requirements, these resins can be considered suitable for hard material applications.[10,11] The designed TGPh-based resins can successfully be used for structural aerospace components, [2,12] as the obtained T_g values of our resins are comparable with those of commercial products: Park Aerospace Nelco® N5000-30/32 BT: T_g=205 °C; Park Aerospace Nelco® N4000-29: T_g =185 °C; Dow VORAFORCE™ TW 103/TW 158: T_g=175–185 °C; Hexcel® HexPly® 108: T_g=190–210 °C.

A similar behaviour was revealed by the stiffness values (Table 2) of these thermosets, obtained by Shore D hardness tests which are ranging between 80–89 SD. According with the Shore D

scale these materials are enclosed in the extra hard materials category, having similar properties to resins such as Master Bond EP17HTDA-1, Henkel Loctite® Stycast® EO 1058, Epoxy Technology EPO-TEK® OE100-T, which are especially useful for both prototyping and manufacturing in the aerospace, automotive, naval, electronical, applications. Another important parameter for aerospace application is the density of the material which is recommended to be below 1.3 g/cm^3. To demonstrate the importance of the weight of the materials, we can take as an example a large commercial aircraft (150 tons) with 250 passengers for which a reduction of 1 kg leads to a decrease in fuel consumption by about 120 L per year.[13] The developed thermoset epoxy resins show density values ranged between 1.05 and 1.22 g/cm^3, making them suitable candidates for space and aerospace applications.

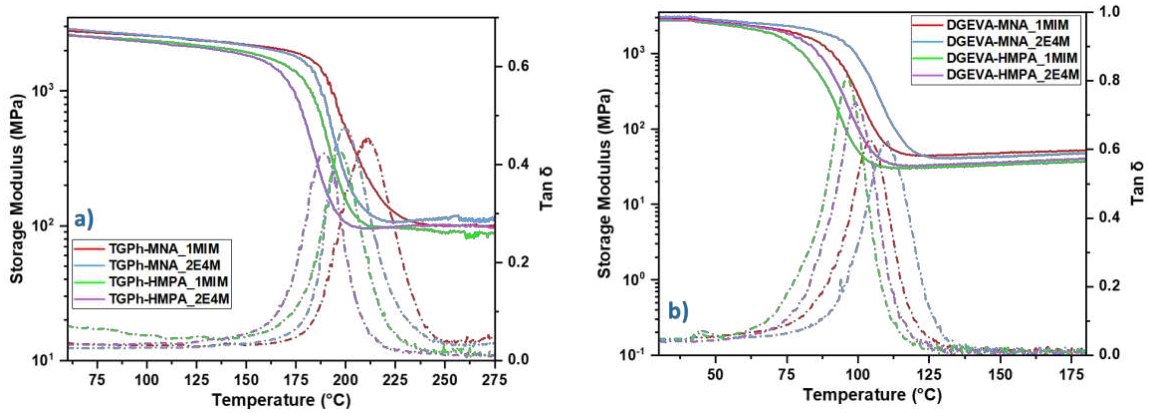

Figure 2 : Storage modulus (E') and tan δ curves of the bio-based epoxy thermosets with a) TGPh and b) DGEVA determined at a heating rate of 3 °C·min^{-1} with a 1.0 Hz oscillating stress and 20 µm amplitude.

3.3. Thermal stability of the TGPH- and DGEVA-based thermosets

The TGA and DTG curves plotted in function of temperature are displayed in Fig.3. The statistic heat-resistance index (T_s) of the bio-based epoxy materials gives an indication of the thermal stability of thermosets and was calculated according with equation (3). [14]

$$T_s = 0.49[T_{5\%} + 0.6(T_{30\%} - T_{5\%})] \quad (3)$$

where $T_{5\%}$ and $T_{30\%}$ represent temperatures for a mass loss of 5% and 30%, respectively.
In Fig.3, both the TGPh and DGEVA thermosets follow a similar thermal degradation pattern under oxidative atmosphere (air), composed from two stages. The main degradation step occurs in the temperature range from 250 to 540 °C. The maximum degradation rate peak for the TGPh resins can be observed at about 369–379 °C, while for the DGEVA systems the T_{dmax} can be seen at 399–409 °C depending on the anhydride nature. This first stage represents the main degradation step, the pyrolysis, the percentage of mass loss for materials with MNA being ranged from 60 to 70% and for HMPA from 72 to 84%. In this step occurs the thermolysis of network structure, with the breaking of aliphatic chains and the loss of small molecules.[15] The second degradation stage with a mass loss of approximately 15–35% takes place above 560 °C, being characteristic to the thermo-oxidative degradation of C–C linkages and other functional groups.[16] The $T_{5\%}$ values for the synthesized materials are ranged from 320 to 360 °C, results comparable to those of commercial materials (Park Aerospace Nelco® N4000-6 FC: $T_{5\%}$=325 °C; Park Aerospace Nelco® N4350-13 RF: $T_{5\%}$=350 °C). The heat resistance index (T_s) represents the temperature of the polymers in the physical heat-tolerance and is ranged in the case of our resins between 178–185 °C, being slightly inferior to the commercial epoxy and polyimide resins [17]

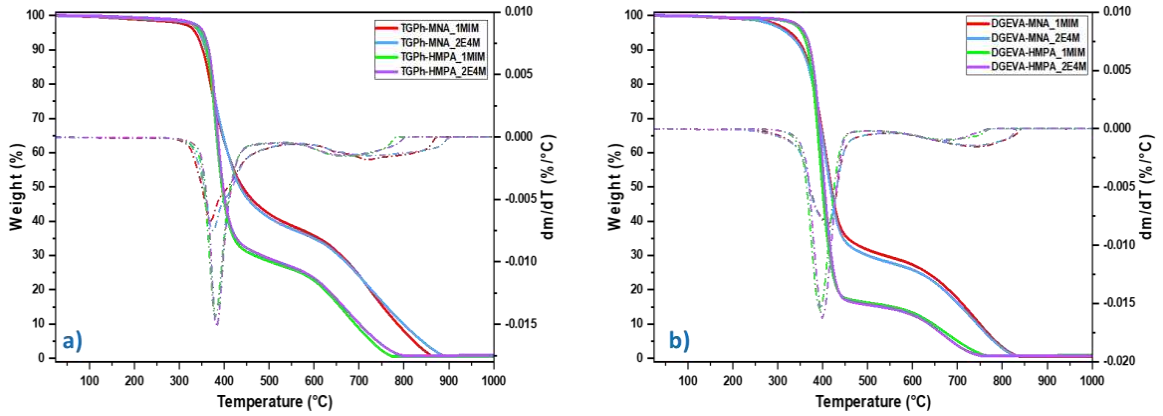

Figure 3 : TGA and derivative thermogravimetric curves (DTG) under oxidative atmosphere of a) TGPh- and b) DGEVA-anhydride thermosets at a heating rate of 10 °C·min^{-1}

3.4. Water absorption

The WA% measurements of prepared thermosets were evaluated based on ASTM D570 standard. The WA% curves of TGPh- and DGEVA-based thermosets present a similar behaviour over time. The materials hydrostability can be impacted by various factors, such as the network density, protocol and the curing parameters, but also the presence of free hydroxyl or other polar groups which can facilitate the polymer-water affinity by hydrogen-bonding.[18,19] The water uptake value is ranged between 1.5 and 1.95%, except for the TGPh-MNA_2E4M matrix which after 15 days of immersion gain the water content equilibrium at the value of about 2.8%. Following the results, we can conclude that these materials present a very low hydrophilicity being comparable with commercial products (Cookson Group STAYCHIP® 3105=1,5%; Cookson Group STAYCHIP® 3100=1,14%; Henkel Loctite® ABLESTIK 2053S Epoxy=1%; Hexcel® F161 Epoxy Resin=2,8%).

The bio-based carbon content (*BCC*) of the materials was determined based on the study of Pan *et al*.[20] were in the first step is calculated the carbon percentage for each compound, and then the bio-based carbon content for all the formulations. Both epoxy monomers and initiators are compounds laboratory synthetised by glycidylation [21–23] of phloroglucinol and vanillin with bio-based epichlorohydrin [24], so they are 100% bio-based, while HMPA and MNA are for the moment petrochemical-based compounds. The *BBC* by weight of the designed thermoset resins was calculated using the equation:

$$\mathrm{BCC} = \frac{\sum(\mathrm{W}_{100\%}\cdot\mathrm{TC}_{100\%})}{\sum(\mathrm{W}_{100\%}\cdot\mathrm{TC}_{100\%})+\sum(\mathrm{W}_{0\%}\cdot\mathrm{TC}_{0\%})}\cdot 100 \quad (4)$$

where $W_{100\%}$ – is the mass of the constituent 100% bio-based, expressed in grams, $TC_{100\%}$ – is the total carbon of the constituent 100% bio-based, expressed as a percentage of the total molar mass of the constituent, $W_{0\%}$ – is the mass of the constituent 0% bio-based, and $TC_{0\%}$ – is the total carbon of the constituent 0% bio-based. The biobased organic carbon (*BOC*) was also calculated using equation (5) and the obtained data are tabulated in Table 3.

$$\mathrm{BOC} = \frac{\sum bio{-}based\ carbon}{\sum \mathrm{bio{-}based\ carbon}+\sum \mathrm{petro{-}based\ carbon}}\cdot 100 \quad (5)$$

From Table 3, it can be seen a close value of *BCC* for all the developed materials, ranged between 55–61%. Knowing that actually the minimum acceptable percentage of biomass plastics is about 25% of the total weight of the materials[25], the designed TGPH and DGEVA-thermosets are satisfying the required criteria

Table 3. Calculated BCC and BOC of the developed thermosets

Thermoset	*BCC (%)*	*BOC (%)*
TGPh-MNA_1MIM	56	74
TGPh-MNA_2E4M	55	74
TGPh-HMPA_1MIM	58	77
TGPh-HMPA_2E4M	58	77
DGEVA-MNA_1MIM	59	69
DGEVA-MNA_2E4M	59	69
DGEVA-HMPA_1MIM	61	73
DGEVA-HMPA_2E4M	60	73

3.5. Carbon fibers composites

Studying the physico-chemical and thermo-mechanical properties of the developed bio-based resins, the TGPh-HMPA-2E4M thermoset was selected as the best option for the development of composites reinforced with carbon fibers (Hexcel). Composites were developed by hand lay-up method using 12 layers of carbon fibers in different angles, the plies being sequentially laid up according to directions of 0 degree, plus 60 degrees, and minus 60 degrees. The obtained samples were then autoclave cured by vacuum bag only (VBO) prepreg process for 3h at 120 °C and 1h at 160°C, and then post-cured at 180°C for 1h. After crosslinking process, the laminated were demolded, cutted at specific dimension (20 mm x 10 mm) and then mechanically tested according with IGC 04 26 235 standard at ambient temperature using a Zwick Z250 traction machine at 250 kN load. Based on the obtained data displayed in Fig.4 and Table 4 it can be seen laminate revealed a rigid character with a maximum force of about 1380 N, a tensile stress of around 73 MPa and an elongation at break approximately 0.26 mm.

Table 4. Mechanical properties of the developed epoxy composites

Sample	Area (mm^2)	Force Max (N)	Tensile stress (MPa)
S1	19.99	1280.48	64.06
S2	19.02	1533.38	80.62
S3	18.56	1496.03	80.61
S4	19.04	1151.13	60.46
S5	18.88	1291.73	68.42
S6	18.68	1522.39	81.50
	Mean	1379	72.6
	Standard deviation	160	17.5

Based the literature studies[26] the general properties of the epoxide composites with carbon fibers are the are the following: tensile strength = 30-80 MPa, elongation at break = 0.5-1 %, and Young modulus = 6-9 GPa. Exploring the www.matweb.com database we were able to conclude that the composite developed in this work can be likened to a number of commercial materials such as Toray T300 Carbon Fiber - Epoxy Composite (σ=76 MPa, ε at break=1.26 %), Toray 2510 Prepreg Laminate with P707AG-15 Fiber (Oven Cure) (σ=44.3 MPa, Young modulus=8.41 GPa), Goodfellow Carbon/Epoxy Composite (σ=50 MPa, ε at break=0.5 %, Young modulus=10 GPa).

  doi:10.5075/epfl-298799_978-2-9701614-0-0

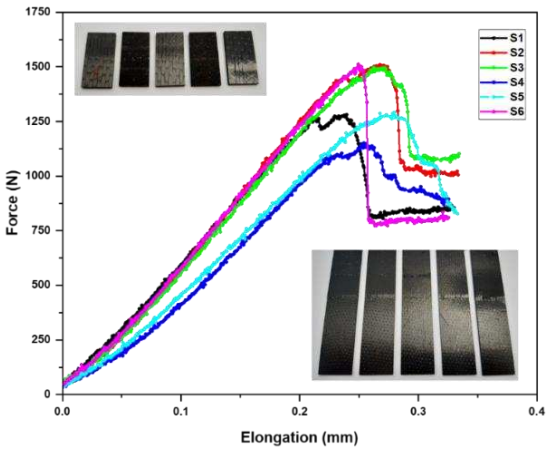

Figure 4 : Force vs. Elongation curves and physical aspects of the TGPh-HMPA-2E4M matrix reinforced with 12 layers of carbon fibers

4. CONCLUSIONS

In this work, starting from two biobased epoxy monomers, laboratory synthesized, TGPh and DGEVA, thermosets with performances for aerospace or space applications were designed. The designed formulations are respecting REACH legislations, in terms of components' toxicity, and those of green chemistry in terms of the processing of curing. The TGPh and DGEVA monomers were copolymerized with two anhydrides having a strong potential to be obtained from renewable resources, the hexahydro-4-methylphthalic anhydride and methyl nadic anhydride. All the tested formulations showed a high reactivity in DSC, with an onset temperature ranged from 35–60 °C for TGPh-formulations and 70–90 °C for DGEVA-formulations, and a maximum temperature of reaction at about 115–150 °C. These curing parameters led to the design of a feasible protocol for up-scaling. DMA analyses showed that the obtained thermosets are stiff materials with values of the storage modulus at 30 °C between 2.7 and 3.1 GPa. The materials' glass transition investigated by DMA and DSC, showed values between 96 and 108 °C for the materials based on DGEVA, and between 189 and 210 °C for those based on TGPh. After 15 days of immersion in water, the developed materials showed a particularly good moisture resistance, the maximum amount of water absorbed being a about 1.5-1.95%. The designed thermosets also showed a high gel content, > 99% for almost all the systems. We can conclude that resins from bio-based and renewable resources, with good physico-chemical and thermo-mechanical performances were successfully designed and developed. Also, the objectives of developing materials with high T_g and feasible industrial manufacturing protocol have been achieved, making these materials sustainable candidates to replace fossil-based materials in important sectors such as naval, aerospace and space industry.

Acknowledgements

This work received financial support from the French government, managed by the National Research Agency under the "Investissements d'Avenir UCA^{JEDI}" project with reference n° ANR-15-IDEX-01 and from the European Space agency under ESA contract 4000134653.

References

1. Wan J, Zhao J, Zhang X, Fan H, Zhang J, Hu D Epoxy thermosets and materials derived from bio-based monomeric phenols: Transformations and performances. Prog Polym Sci. 2020; 108.

2. Paolillo S, Bose RK, Santana MH, Grande AM. Intrinsic self-healing epoxies in polymer matrix composites for aerospace applications. Polymers (Basel). 2021;13:1–32.
3. Moreman J, Lee O, Trznadel M, David A, Kudoh T, Tyler CR. Acute Toxicity, Teratogenic, and Estrogenic Effects of Bisphenol A and Its Alternative Replacements Bisphenol S, Bisphenol F, and Bisphenol AF in Zebrafish Embryo-Larvae. Environ Sci Technol. 2017;51(21):12796–805.
4. Chowdhury MTH, Bangoura I, Kang JY, Park NG, Ahn DH, Hong YK. Distribution of phlorotannins in the brown alga Ecklonia cava and comparison of pretreatments for extraction. Fish Aquat Sci. 2011; 14(3):198–204.
5. Liu X, Xin W, Zhang J. Rosin-based acid anhydrides as alternatives to petrochemical curing agents. Green Chem . 2009;11(7):1018.
6. Ma S, Liu X, Fan L, Jiang Y, Cao L, Tang Z, et al. Synthesis and Properties of a Bio-Based Epoxy Resin with High Epoxy Value and Low Viscosity. ChemSusChem. 2014 ;7(2):555–62.
7. Flory PJ. Principles of Polymer Chemistry. Ithaca, New York: Cornell University Press; 1953.
8. Tobolsky AV. Properties and structure of polymers. New York: Wiley; 1960. 331 p.
9. Kalogeras IM, Hagg Lobland HE. The nature of the glassy state: Structure and glass transitions. J Mater Educ. 2012; 34(3–4):69–94.
10. Terry JS, Taylor AC. The properties and suitability of commercial bio-based epoxies for use in fiber-reinforced composites. J Appl Polym Sci. 2021;138(20):1–12.
11. Mora, Tayouo, Boutevin, David, Caillol. Synthesis of PluriFunctional Amine Hardeners from Bio-Based Aromatic Aldehydes for Epoxy Amine Thermosets. Molecules. 2019 9; 24 (18): 3285.
12. Savonnet E, Grau E, Grelier S, Defoort B, Cramail H. Divanillin-Based Epoxy Precursors as DGEBA Substitutes for Biobased Epoxy Thermosets. ACS Sustain Chem Eng 2018 Aug 6;6(8):11008–17.
13. Gay D. Composite Materials Design and Applications. 3rd editio. New York: CRC Press Taylor & Francis Group; 2014.
14. Ma S, Kovash CS, Webster DC. Effect of solvents on the curing and properties of fully bio-based thermosets for coatings. J Coatings Technol Res. 2017;14(2):367–75.
15. Fang Z, Nikafshar S, Hegg EL, Nejad M. Biobased Divanillin As a Precursor for Formulating Biobased Epoxy Resin. ACS Sustain Chem Eng. 2020;8(24):9095–103.
16. Pan H, Sun G, Zhao T, Wang G. Thermal properties of epoxy resins crosslinked by an aminated lignin. Polym Eng Sci 2015;55(4):924–32.
17. Heat resistance index and classification of plastic profile products . [cited 2021 Jul 26]. Available from: https://www.extrusionplastic.cn/news/plastic-profile-products.html
18. Toscano A, Pitarresi G, Scafidi M, Di Filippo M, Spadaro G, Alessi S. Water diffusion and swelling stresses in highly crosslinked epoxy matrices. Polym Degrad Stab. 2016; 133: 255
19. Capiel G, Uicich J, Fasce D, Montemartini PE. Diffusion and hydrolysis effects during water aging on an epoxy-anhydride system. Polym Degrad Stab . 2018;153:165–71.
20. Pan X, Sengupta P, Webster DC. High biobased content epoxy-anhydride thermosets from epoxidized sucrose esters of fatty acids. Biomacromolecules. 2011;12(6):2416–28.
21. Tess RWH, Calif O. Process for manufacture of glycidyl ethers of polyhydric phenols. US2879259A, 1959.
22. Claire WES. Process for preparing epoxyalkyl aryl ethers. US2892849A, 1959.
23. Reinking NH. Preparation of monomeric glycidyl polyethers of polyhydric phenols. US2943096A, 1960.
24. Bell BM, Briggs JR, Campbell RM, Chambers SM, Gaarenstroom PD, Hippler JG, et al. Glycerin as a renewable feedstock for epichlorohydrin production. The GTE process. Clean - Soil, Air, Water. 2008;36(8):657–61.
25. NCS-16785. Bio-based content certification scheme. 2016.
26. Biron M. Thermosets and Composites Material Selection, Applications, Manufacturing and Cost Analysis. 2nd Edition. Elsevier. 2013.

THE INFLUENCE OF TEMPERATURE AND MATRIX CHEMISTRY ON INTERFACIAL SHEAR STRENGTH IN GLASS FIBRE EPOXY COMPOSITES

Ross F, Minty[a], Liu, Yang[a] and James L, Thomason [a]

a: Department of Mechanical and Aerospace Engineering, University of Strathclyde Glasgow, G1 1XJ, United Kingdom. ross.f.minty@strath.ac.uk

Abstract: *The present work focuses on further investigating the influences of the chemistry of an epoxy system and the testing temperature on the stress-transfer capability of the fibre-matrix interface in a glass fibre-reinforced composite. We discuss how the apparent interfacial shear strength (IFSS) is influenced by the hardener-to-epoxy ratio and testing temperature. The results indicated that the IFSS was strongly dependent on both matrix chemistry and testing temperature. It was observed that the IFSS showed a significant inverse dependence on testing temperature, with IFSS dropping as the temperature was increased for all ratios. Notably it was shown that once the testing temperature was raised above the glass transition temperature (T_g) that ratios possessing excess hardener had larger IFSS values. From the results presented it is hypothesized that residual radial compressive stresses at the interface are influenced by the chemistry of the matrix system and relax away at the higher testing temperatures.*

Keywords: Glass Fibres; Fibre/matrix bond; Interfacial strength; Residual stress.

1. Introduction

With the world's continual growing interest in renewable energy, the designers of wind turbine blades are now under more pressure than ever to produce larger, more powerful wind turbine blades. As such the demand to produce glass fibre-reinforced composites that possess superior mechanical properties has never been higher, with a great level of investment having been placed into research with the goal of broadening our understanding of how to optimize mechanical performance.

If this performance is to be maximised, then it is critical to optimize the stress transfer capability of the interfacial region which exists between the reinforcement fibre and the polymer matrix. If this region is weak, with poor 'adhesion' between the fibre and the matrix, then the composite will fail to reach its true potential in terms of mechanical properties. One accepted mechanically measurable value which can be used to define the strength of the interface is the interfacial shear strength (IFSS) which can be influenced by several factors including the surface chemistry [1], the chemistry of the epoxy system used [2] and the testing temperature [3-4].

Recent work [2-4] has concluded there does seem to be a relationship that exists between stoichiometry, testing temperature and the resulting performance of the interface. However, more work on this subject was warranted in order to fully understand what was occurring at the interface level.

Due to the nature of fibre sizing application, the level of coating applied along the whole length of the fibre is known to vary [5] leading to the potential for localized pockets of epoxy rich or amine rich resin along the entire length of each fibre, threatening overall performance. The influence of these potential small differences in mixture chemistry adhesion with a rubbery

  doi:10.5075/epfl-298799_978-2-9701614-0-0

polymer above T_g has never thoroughly been investigated. This paper thus focuses on studying the relationship between testing temperature, the epoxy resin: curing agent ratio (R) and the fibre-matrix interface strength (IFSS) using a microbond technique designed for use within a thermo-mechanical analyser [3].

2. Experimental

2.1 Materials

The experiments were carried out using boron free E-glass fibres, sized with γ-aminopropyltriethoxysilane (APS), taken from larger roving's manufactured by Owens Corning-Vetrotex. The nominal tex was 1200 g/km and the average diameter was 17.5 µm for both. The epoxy resin used was Araldite 506® (DGEBA) and the curing agent used was Triethylenetetramine (TETA) with a technical grade of 60%. Both were purchased from Sigma-Aldrich and used as received.

2.2 Sample Preparation

Preparation of the microbond samples began with the application of the glass fibres to sections of 20 mm gauge length card through a combination of double-sided tape and Loctite® super glue. Care was taken to ensure that the exposed sections of fibre to be used for the test were protected from contamination, whether through surface or human contact. With the fibres in place, the next task was to apply the droplets of the epoxy resin system.

The mixture of the epoxy system was varied for each batch, with the mass of curing agent applied to the mixture being varied whilst the mass of epoxy resin was maintained at 5 g. This in turn allowed for predefined percentages of TETA to be applied relative to the system. The stoichiometric ratio for the system was calculated as 12.0% TETA, equating to an amine: epoxy group ratio (R) of 1.0. The mass values were monitored to the nearest 0.01 g using a XSE 205 Dual Range analytical balance, manufactured by Mettler Toledo with percentages ranging from as low as 6.8% up to 22.2%, equating to R ratios ranging from 0.55 to 2.08 respectively. The resin mixtures were mixed thoroughly before being degassed for approximately 15 minutes.

The droplet application process involved applying several minute droplets to each fibre, due to the difficulty in producing only a single droplet which would not be too large to test successfully. The application of the minute droplets was completed using a 50 µm piece of steel wire. Once the application process was complete, samples were transferred to a convection oven where they were heated to 60 °C and held isothermally for 1 hour, then further heated to 120 °C and held isothermally for 2 hours. The heating rate was 2 °C/minute for both heating ramps and the samples were left to cool down in the oven overnight.

Prior to testing, all samples were examined under 200x magnification using a Nikon Epiphot inverted microscope to obtain values for the fibre diameter (D_f) and the fibre length (L_E) embedded in the resin droplet. Multiple photos of each fibre were taken to account for all the droplets applied to each sample during the application process. Following testing each sample was re-examined using the Nikon Epiphot inverted microscope to identify the initial primary droplet that had been loaded during the TMA microbond procedure.

2.3 TMA Microbond Procedure

Development of the Thermo-Mechanical Analysis (TMA) microbond technique has been reported previously [3, 6]. The technique uses a TA Q400 thermo-mechanical analyser, in combination with the cooling accessory MCA270 mounted with a film/fibre probe and microbond setup as shown in Figure 1. The droplet applied to the fibre sits on the shearing plate which itself sits on the stationary quartz platform. The movable probe, installed in the centre of the stationary platform, then rests on the paper tab of the sample. It is this probe which applies the load during the test. The entire microbond setup is then enclosed within the TMA temperature controlled, programmable oven. Each sample was initially placed under a very small pre-load of 0.005 N, with the free fibre length between the tab and epoxy droplet maintained at a constant value of 5 mm to match the samples tested in [2].

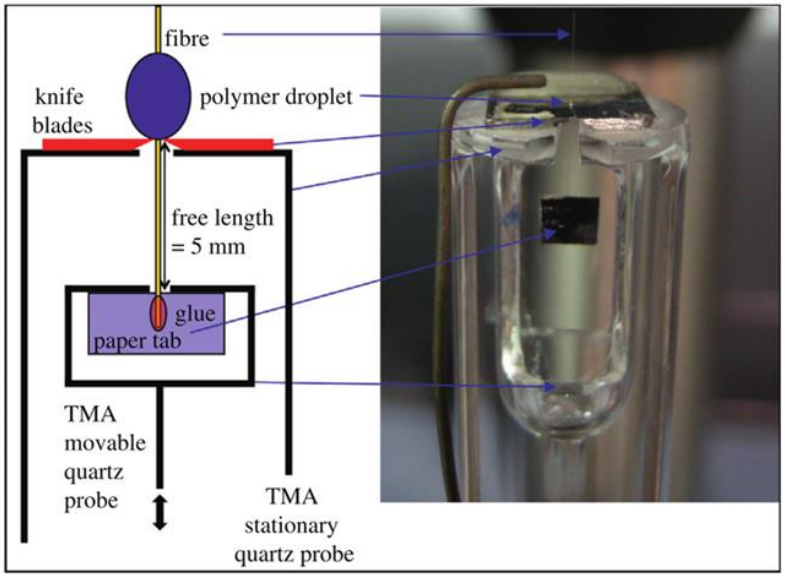

Figure 1. Schematic and close-up photograph of TMA-Microbond test setup.

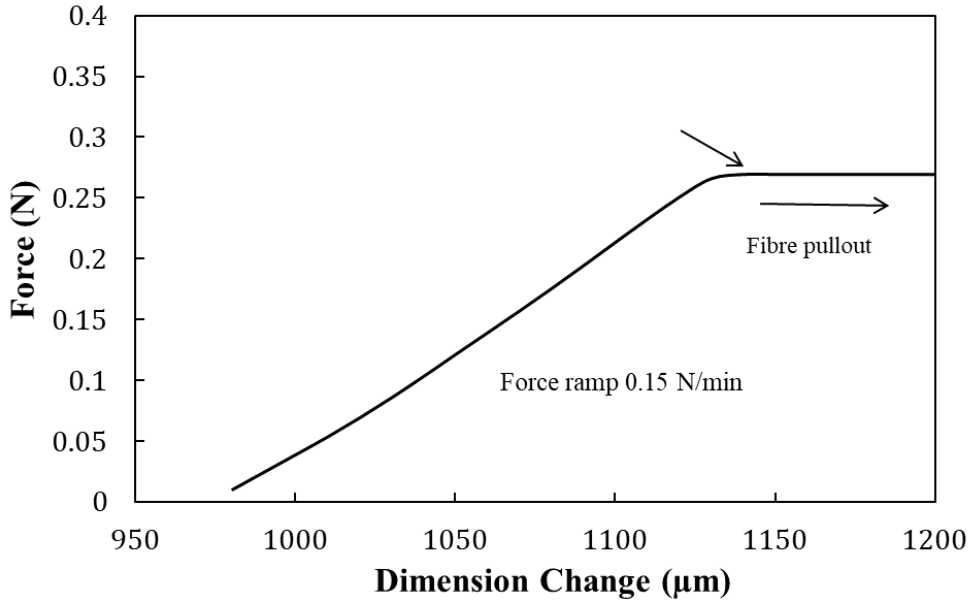

Figure 2. Load/Displacement curve for TMA microbond test.

  doi:10.5075/epfl-298799_978-2-9701614-0-0

The notable difference between the TMA and Instron microbond techniques relates to how each technique loads the sample. The Instron technique [2] is carried out by measuring the load generated during the displacement of a droplet at a constant strain rate however the TMA is unable to operate in this mode. Instead, the TMA had to be configured to measure the sample displacement during a linear force ramp of 0.15 N/min [3, 6]. The testing procedure proceeded as follows: the probe displacement was electronically zeroed and the microbond sample loaded into the shearing plate with the paper tab hanging freely below the movable probe. The movable probe was then carefully lowered onto the paper tab before the furnace was closed. The initial sample length and probe position was then recorded, with the furnace then programmed to equilibrate at the desired test temperature (ranging from 20 °C to 120 °C) with an additional three-minute isothermal segment to ensure a constant equilibrium temperature was achieved. The force ramp was then initiated at 0.15 N/min. As the test proceeded the probe displacement would increase and be recorded until a successful de-bond occurred. All tests were conducted under a nitrogen flow of 50 ml/min with approximately 30 samples per ratio tested. A typical result obtained from a TMA-microbond test is plotted as a force–displacement curve in Figure 2. The max force value recorded at de-bond, along with the measured fibre diameter and embedded length, was used to calculate the apparent IFSS value using Eq. (1).

$$\tau_{app} = \frac{F_{max}}{\pi D_f L_e} \quad (1)$$

3. Results & Discussion

Figures 3 to 6 display peak load versus embedded area plots for the samples studied. Figure 3 shows a comparison between the TMA microbond results at 20 °C and the previous published data collected using the Instron microbond technique [2] for R = 1.22.

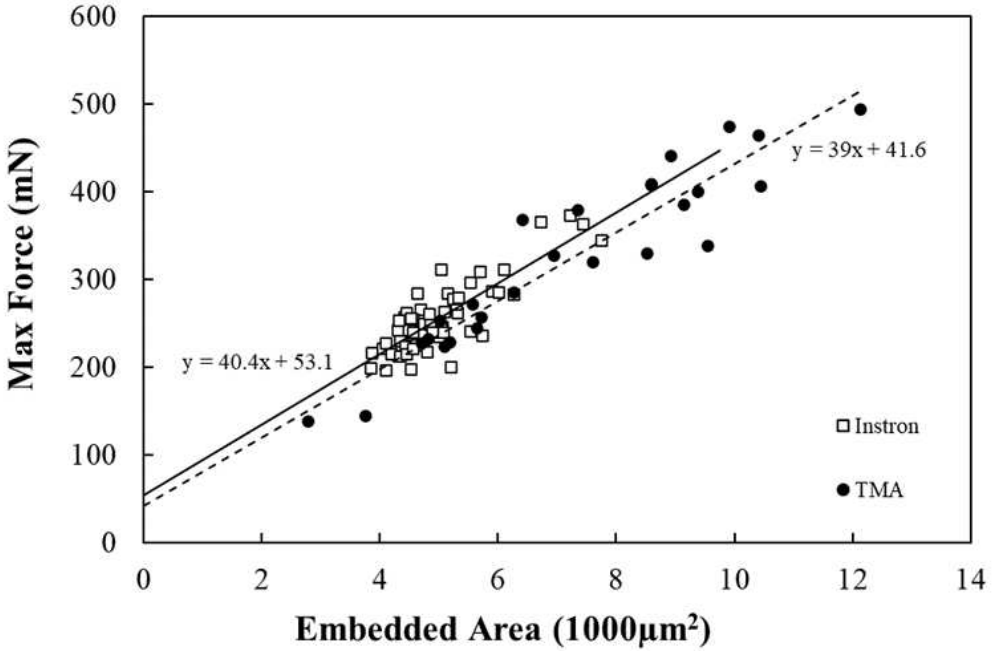

Figure 3. Comparison between force/displacement plots collected using the TMA microbond technique and data collected using the Instron microbond technique, amine: epoxy ratio = 1.22 and testing temperature = 20 °C.

  doi:10.5075/epfl-298799_978-2-9701614-0-0

It can be seen that the results collected using the TMA technique correlate well with the results collected using normal microbond testing. Figure 4 shows a comparison between the different testing temperatures for R = 1.22. We can see that as the testing temperature was increased, the peak load of the microbond samples decreased, with a notable drop once the temperature was raised above the previous published T_g value of 87.3 °C [2].

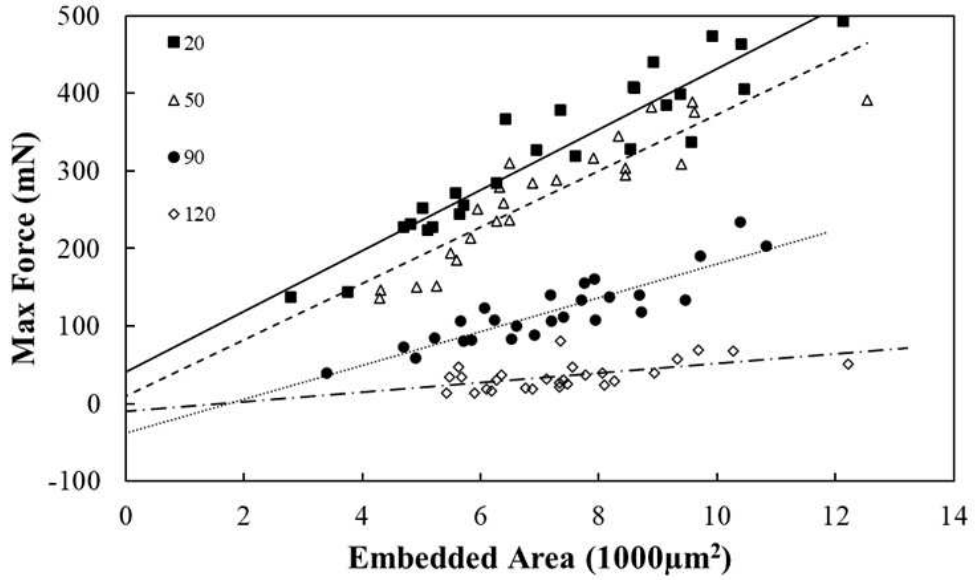

Figure 4. Comparison between force/displacement plots for amine: epoxy ratio = 1.22 at different testing temperatures.

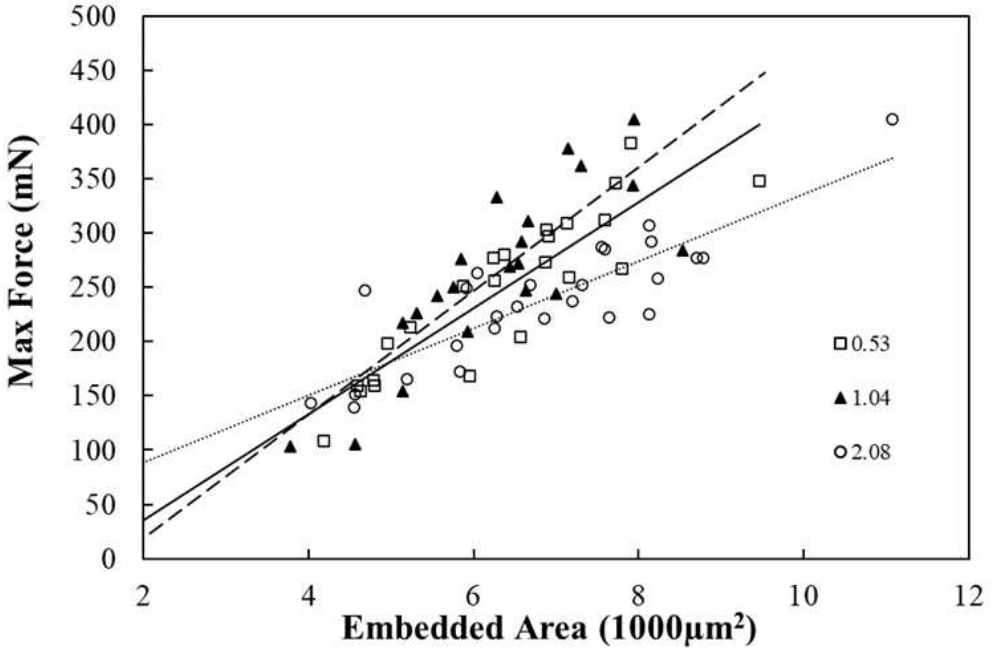

Figure 5. Comparison between force/displacement plots for different amine: epoxy ratios at a testing temperature 50 °C.

Figures 5 and 6 shows plots where the testing temperature was maintained at constant values of 50 °C and 120 °C respectively whilst the R ratio of the matrix system was altered. At 120 °C

  doi:10.5075/epfl-298799_978-2-9701614-0-0

the effect of changing the matrix chemistry appears greater than at 50 °C. This suggests that the importance of the matrix chemistry to the magnitude of the IFSS may be greater above T_g. It can also be seen that the plot shown in Figure 4 does show some correlation with that shown in Figure 6, with both possessing a notable point of transition.

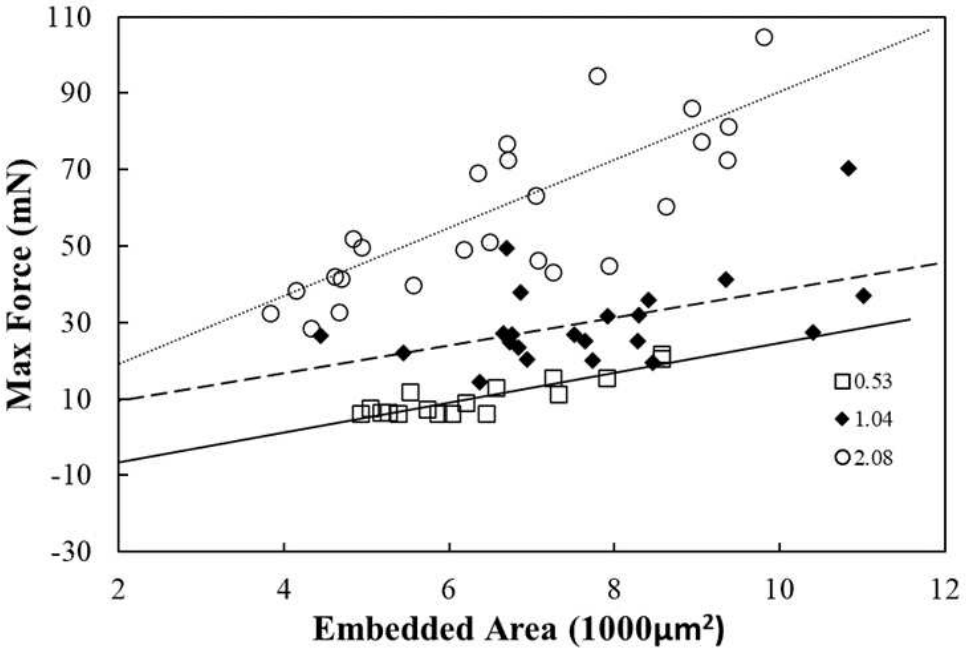

Figure 6. Comparison between force/displacement plots for different amine: epoxy ratios at a testing temperature 120 °C.

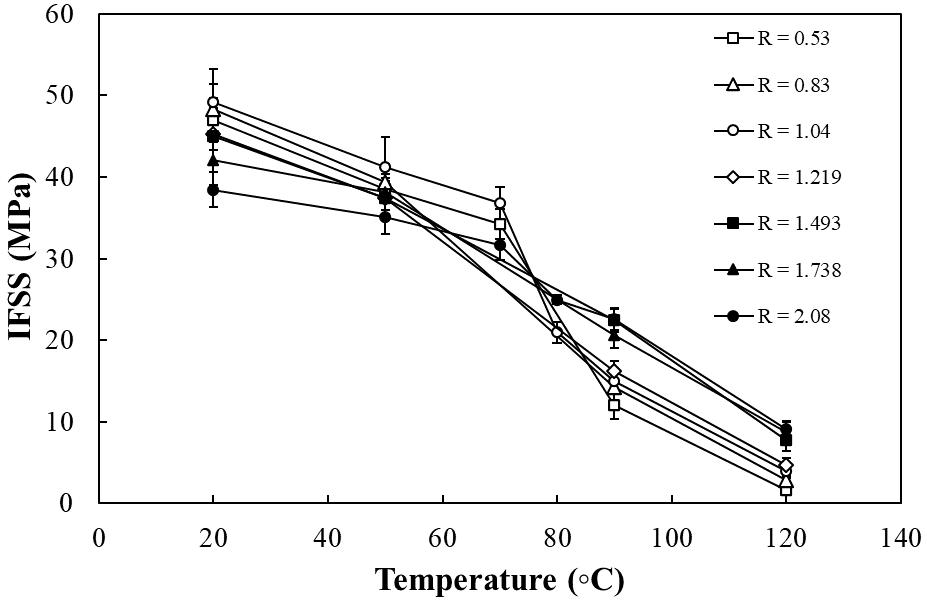

Figure 7. Plot of IFSS versus Testing Temperature.

Figures 7 and 8 present the apparent IFSS values versus the testing temperature and the R ratio of the sample respectively. The data in both figures convey a clear dependence of the IFSS on both the chemistry of the matrix system and the testing temperature. The results in Figure 7 represent the average of individual samples and indicate that the apparent IFSS value decreased

  doi:10.5075/epfl-298799_978-2-9701614-0-0

as the testing temperature was increased for all ratios, with R ratios close to the stoichiometric value initially exhibiting the largest IFSS values for temperatures ≤ 70 °C. Interestingly it can be seen in Figure 8 that at temperatures ≤ 70 °C the polymer mixtures containing excess epoxy (R < 1) appear to possess higher apparent IFSS values than the polymer mixtures containing excess amine. However, once the testing temperature was increased above T_g the apparent IFSS values appear to decrease less for ratios possessing excess amine (R > 1), with this relationship appearing linear at 120 °C. In Figure 7 a notable gap between R >> 1 and R ≈ 1 can be seen at 120 °C. The observed gradient of transition appears to occur differently depending on the specifics of the matrix chemistry, with ratios where R ≤ 1 appearing to lose performance sharply once above 70 °C whilst ratios where R >> 1 appear to be less influenced by crossing this temperature. Figure 8 highlights this further by showing that for temperatures below 70 °C, optimized performance occurs around the stoichiometric value but above 70 °C the apparent IFSS value increases as more amine hardener was added to the system. Interestingly, Figure 8 also suggests that there may exist a critical temperature where the IFSS will remain unchanged with changes to the matrix chemistry. This may be the case since the plots for 70 °C and 80 °C appear to be approaching a mid-point where the transition seemingly occurs.

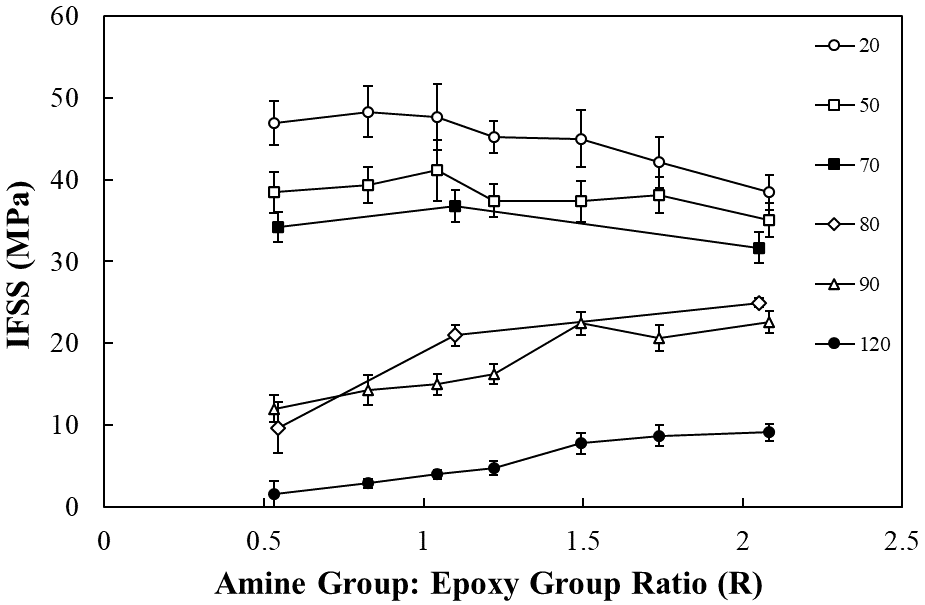

Figure 8. Plot of IFSS versus Amine: Epoxy Ratio (R).

Overall, it appears that the apparent IFSS was clearly influenced by the chemistry of the matrix system as well as the testing temperature, with performance deteriorating consistently as the testing temperature was increased. A potential explanation is that the residual radial compressive stresses (σ_R) formed at the interface during the curing process are being influenced by the properties of the matrix and relaxing away as the test temperature increases [3, 6]. An explanation for the linear apparent IFSS trend shown at 120 °C is that due to the increasing amine content introduced to the system via the extra hardener, there is a combination of an increase in hydrogen bonding as well as an increase in the shear failure behavior of the matrix.

4. Conclusions

The results presented in this paper show that the hardener-to-epoxy ratio and testing temperature both influence the stress transfer capability of the interface in a glass fibre-

reinforced epoxy composite, and in some cases significantly. Each hardener-to-epoxy ratio tested was shown to possess different apparent IFSS values at each testing temperature. Below the epoxy polymer T_g, the highest apparent IFSS value was shown to occur at the stoichiometric value, with apparent IFSS decreasing as the ratio deviated further from this value. However, as the temperature was increased a transition in apparent IFSS was observed when the testing temperature exceeded 70 °C. Whilst interfacial performance continued to decrease overall after this point, the optimum relative apparent IFSS value was shown to improve linearly when more amine was added to the epoxy system. This was the case even at 120 °C.

It was hypothesized that there was some correlation between the deterioration in apparent IFSS observed and the potential relaxation of the "frozen" in residual stresses at the interface as the temperature was increased. It was also observed that at temperatures well above T_g a small value of apparent IFSS still existed, despite the proposed residual stresses having likely relaxed away. It was hypothesized that an increased level of hydrogen bonding, due to the increasing amine content of the matrix system, combined with the variation in shear failure behavior of the matrix due to the differing crosslink densities, was potentially responsible for this.

One practical conclusion from the results presented here is that performance of the interface in thermoset composites is strongly related to the chemistry of the polymer matrix adjacent to that interface as well as the temperature of the surrounding environment. Fibre sizings typically contain chemical reactive groups similar to the polymer matrices in order to promote 'adhesion'. Such coatings are typically not applied consistently, which may well result in unexpected local variations in the R ratio. Hence it is possible that key interface properties of a glass fibre-reinforced epoxy composite may vary along the entire length of the embedded fibre. Small changes in R may result in small variations in the level of adhesion with minimum impact on performance. However, if the variation from the stoichiometric value is large enough then there may be potential for a significant impact on performance of the final composite material, with the effect of this increasing with rising temperatures.

Acknowledgements

The authors gratefully acknowledge the support of the Engineering and Physical Sciences Research Council (EPSRC).

5. References

1. Thomason JL. Glass Fibre Sizings - A Review of the Scientific Literature. 2012.
2. Minty RF, Yang L, Thomason JL. The influence of hardener-to-epoxy ratio on the interfacial strength in glass fibre reinforced epoxy composites. Composites Part A 2018; 112:64-70.
3. Thomason JL, Yang L. Temperature dependence of the interfacial shear strength in glass- fibre polypropylene composites. Composites Science and Technology 2011; 71:1600-1605.
4. Petersen HN, Thomason JL, Minty RF, Brøndsted P, Kusano Y, Almdal K. Testing temperature on interfacial shear strength measurements of epoxy resins at different mixing ratios. Proceedings of the 20th International Conference on Composite Materials (ICCM20), Copenhagen, Denmark, 19-24 July 2015.
5. Thomason JL. Glass fibre sizing: A review, Composites Part A 2019; 127: 105619.
6. Thomason JL, Yang L. Temperature dependence of the interfacial shear strength in glass-fibre epoxy composites, Composites Science and Technology 2014; 96:7–12.

CERAMIC SPATIAL STRUCTURES AS A NEW METHOD OF REINFORCING FERROUS ALLOYS

Łukasz Szymański[a], Michał Pieszczek[a], Agnieszka Bigos[b], Jerzy Józef Sobczak[a], Natalia Sobczak[b], Maciej Asłanowicz[c]

a: AGH University of Science and Technology, Faculty of Foundry Engineering, 23 Reymonta St., 30-059 Cracow, Poland – lukaszszymanski14@gmail.com
b: Polish Academy of Sciences, Institute of Metallurgy and Materials Science, 25 Reymonta St., 30-059 Cracow, Poland
c: FerroTerm sp. z o.o., 176 Przybyszewskiego St., 93-120 Łódź, Poland

Abstract: This work concerns the method for obtaining cast iron castings locally reinforced with ceramic inserts (preforms) having porous spatial structures. The composite castings were fabricated in one step using the pressure less infiltration of ceramic preforms (either alumina or zirconia type) with molten white chromium cast iron during pouring the melt into a mold, in which preforms were properly placed and fixed. The detailed structural characterization by means of scanning electron microscopy coupled with energy dispersive X-ray spectroscopy evidenced uniform and defect-free infiltration of both types of porous ceramic preforms with molten metal matrix and a good bonding between them, despite a lack of wetting of Al_2O_3 and ZrO_2 by selected alloy. This effect is caused from a positive role of Cr that promotes physicochemical interaction between the metal matrix and the reinforcement.

Keywords: composite; ex-situ; casting; wear; ceramic

1. Introduction

Statistical data shows that about 80% of machine and device failures are caused by surface wear due to parts rubbing against each other or hydrogen degradation [1]. Abrasive wear is a costly and serious problem in lots of different branches of industry [2]. Therefore, it is necessary to design materials that offer an attractive combination of price and industrial output.

A couple of good examples are the ex situ and in situ methods of fabricating metal matrix composites by liquid assisted techniques, e.g. casting or sintering [3]. Composites with a ferrous alloy matrix reinforced by different ceramic phases (particles, fibers, whiskers) have become a recent research subject [4]. Due to their high wear resistance, excellent mechanical properties, and high melting temperatures, they are considered to be most promising materials in the view of the potential application in the very fields of the industry: mining, automotive, extractive, or petrochemical [5]. Additionally, alloys based on Fe are commonly used as the base matrix in MMCs (metal matrix composites) on account of their low costs and good mechanical properties [6].

In order to manufacture composite zones, techniques with high-energy density such as thermal spraying, laser plating, laser alloying, or welding methods (TIG – tungsten inert gas) are used [7]. Due to the method of fabricating the phase reinforcement, composite layers can be classified into two groups: ex situ and in situ (the same as with metal matrix composites). Hard ceramic phases such as WC, Al_2O_3, ZrO_2, TiB_2, or TiC are widely used as a reinforcement of metal matrix composites [8].

  doi:10.5075/epfl-298799_978-2-9701614-0-0

The manufacturing of local composite zones with oxide ceramic particles is being extensively discussed in many scientific studies and industrial research; this is evidenced by the availability of a wide range of products that are based on metal matrix composites (MMCs) and offered by well-known global companies.

Over the last decade, many research groups reported the results on synthesis and characterization of ferrous matrix composites containing different oxide reinforcements. The ceramic reinforcements are used in the form of either porous preforms or inserts produced with a use of different types of organic binders [9-11]. Stir casting method is the second common method of obtaining ex-situ composites reinforced by ceramic particles. In stir casting, molten metal is stirred with the help of a mechanical stirrer while the particles are added to the melt. This action disperses the reinforcing phase to create a composite slurry, containing a suspension of reinforcements [12].

The main goal of our research was to manufacture cast iron castings locally reinforced with porous oxide preforms by pressure less infiltration with molten white chromium cast iron directly in a mold.

2. Experimental

The ceramic preforms of porous spatial structures were manufactured by FerroTerm sp. z o.o. using either alumina (Al2O3) and zirconia (ZrO2) powder. For trials, the preforms were placed in a mold cavity as showing Fig. 1. The perforated metal sheets and nails were used as the assembly system to fix ceramic preforms into proper places of sand molds. The molds were poured with molten white chromium cast iron at the temperature of 1633 K; the chemical composition of which is given in Table 1.

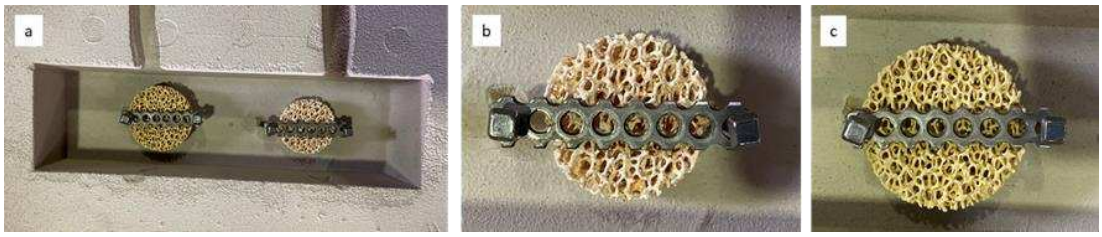

Figure 1 Photos of sand mold (a) along with ceramic preforms (b,c)

Table 1: Chemical composition of base alloy [wt.%]

Chemical composition of base alloy [wt.%]						
C	Si	Mn	Cr	Ni	Mo	Fe
2.81	0.67	0.68	15.5	0.19	1,.43	Bal.

The final castings with the dimensions of 300 × 90 × 50 mm and weighing 14 kg were cut in order to take samples from the locally reinforced areas and matrix alloy. Before structural characterization, the samples were subjected to grinding and polishing.

Microstructural observations of both substrate surface and cross-sectioned substrate were performed by (1) light microscopy (LM) with the help of Keyence VHX-700 microscope allowing 2D and 3D scanning of the ceramic spatial structure as well as the samples, (2) scanning electron microscopy (SEM) using an ESEM FEI XL-30 type microscope and BSE (Backscattered

  doi:10.5075/epfl-298799_978-2-9701614-0-0

Electron) detector. Chemical composition of selected phases were evaluated by Energy Dispersive X-ray Spectroscopy (EDS).

3. Results and discussion

Fig. 2 shows the macrostructure of the casting with the local reinforcement after shaking out process. Designed assembly system was characterized by high thermal stability which can be confirmed by presence of nails (lack of burnout process of metal elements). It is worth noting that the ceramic spatial structures at the first site seem to be infiltrated by liquid alloy, despite lack of the distance between sand mold and ceramic preforms.

The cross section of the composite zones fabricated ex-situ in white chromium cast iron specimens is presented in Fig. 3. The observations carried out did not reveal the occurrence of structural defects within the regions in neither the composite nor the base alloy. Additionally, these observations confirmed that the ceramic spatial structures made from both Al_2O_3 and ZrO_2 were well infiltrated by molten metal matrix (pressure less infiltration).

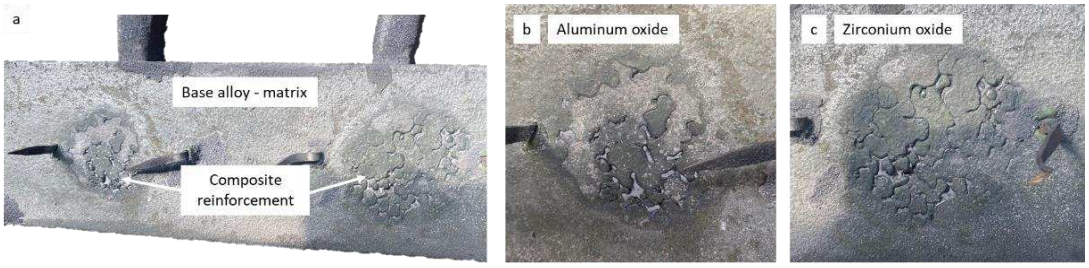

Figure 2 Macrostructure of casting with local composite reinforcement - as cast.

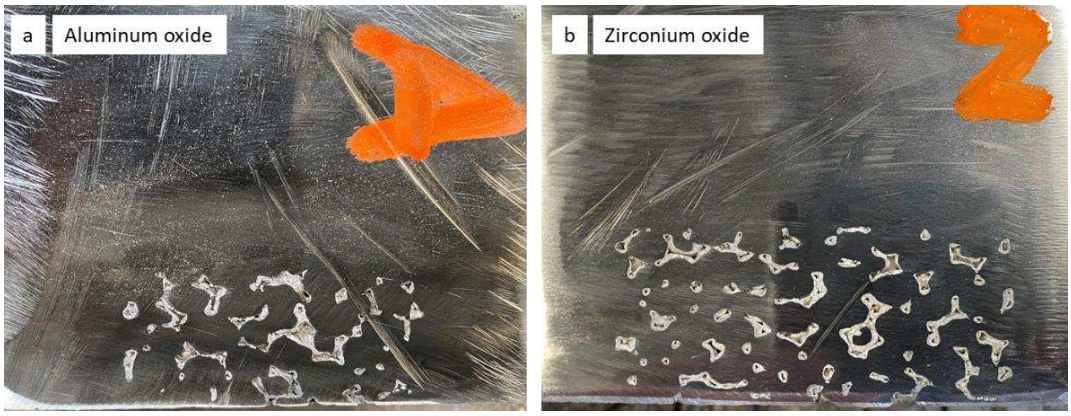

Figure 3 Cross section of casting within area of the local composite reinforcement

The microstructures of the composite zones reinforced by Al_2O_3 and ZrO_2 fabricated ex-situ in white chromium cast iron are presented in Figures 4 and 5, respectively. In both cases, the transition area between ceramics phase and metal matrix alloy are free of discontinuities. Observations conducted by light microscopy (LM) revealed the presence of the porosity within the ceramic preforms only. However, this phenomenon is not caused from infiltration process since it is related directly to technological process of manufacturing ceramic preforms because ceramic preforms reproduce the initial structure of polymer foams used as templets for the production of the ceramic spatial structures. After the soaking process of the foam in the ceramic bulk, they undergo the thermal degradation in the next stages of the process. As a

  doi:10.5075/epfl-298799_978-2-9701614-0-0

consequence, the "closed" porosity can be observed within area of ceramic reinforcement (Fig. 6).

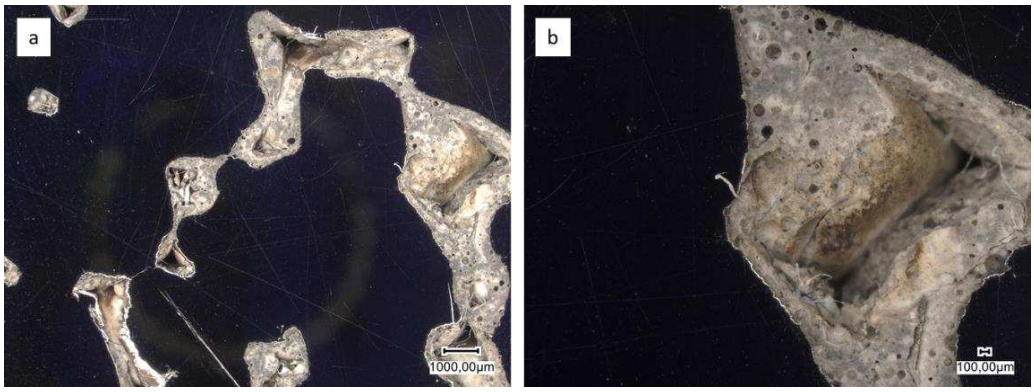

Figure 4 Photos of white chromium cast iron casting locally reinforced with Al_2O_3 preform

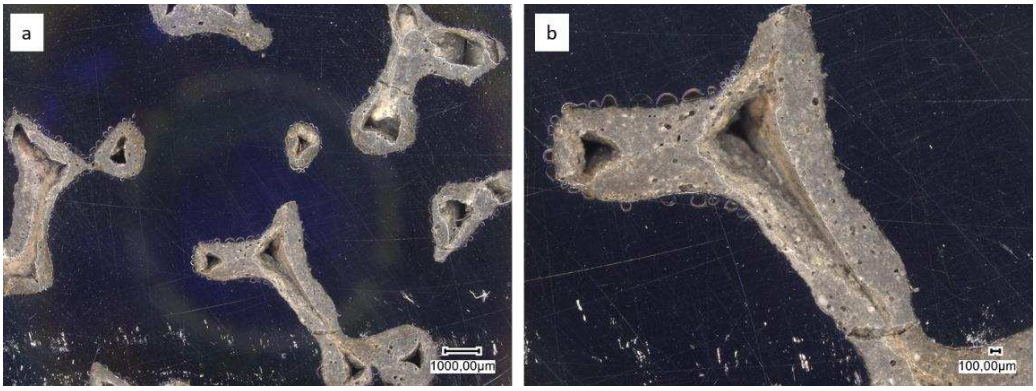

Figure 5 Photos of the white chromium cast iron casting locally reinforced with ZrO_2 preform

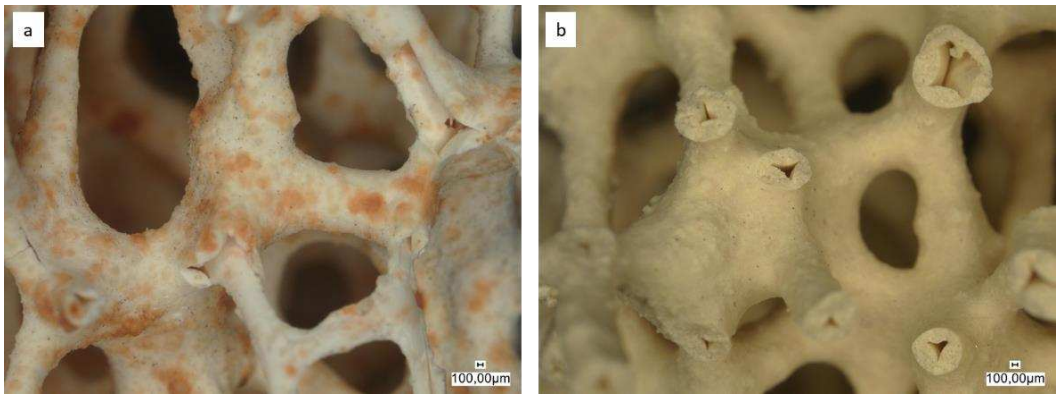

Figure 6 Photos of the ceramic spatial structure with visible porosity: a) preform made from aluminum oxide (Al_2O_3 preform); b) preform made from zirconium oxide (ZrO_2)

The microstructures of the composite materials manufactured ex situ in the cast iron and the selected BSE region of the microstructures of the composite zones with the marked areas of X-ray microanalysis (EDS) are shown in Figs. 7 and 8. Within the areas 1, the occurrence of O and either Al or Zr or Al that corresponds to Al_2O_3 or ZrO_2, respectively. The areas 3 and 5 contain primarily iron, which is the main component of the metal matrix. Areas 2 and 4 contain high amount of Cr, C and Fe which confirmed by the presence of a carbide of the $(Fe,Cr)_7C_3$ type in the microstructures. In composite zone with ZrO_2 preform, a complex phase was identified

  doi:10.5075/epfl-298799_978-2-9701614-0-0

within transition areas noted at the metal matrix/reinforcement interfaces. These areas contain Zr, Al, Mg, Mn, Fe and Cr probably formed by chemical reaction between ZrO_2 and white chromium cast iron.

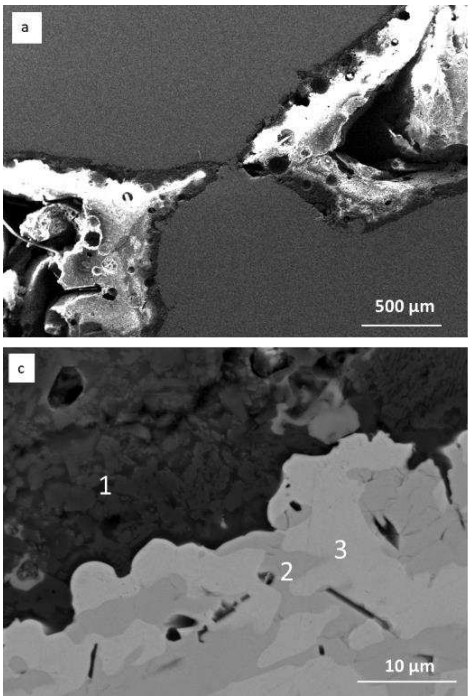

Chemical composition [wt. %]			
	Point 1	Point 2	Point 3
C	-	4.7	3.7
O	42.8	2.6	1.7
Si	12.7	1.3	1.8
Cr	3.5	36.6	17.2
Fe	-	54.8	75.6
Al	41.0	-	-

Figure 7 a, b) SEM BSE microstructures of composite zones type Al_2O_3/white chromium cast iron c) area of X-ray microanalysis (EDS)

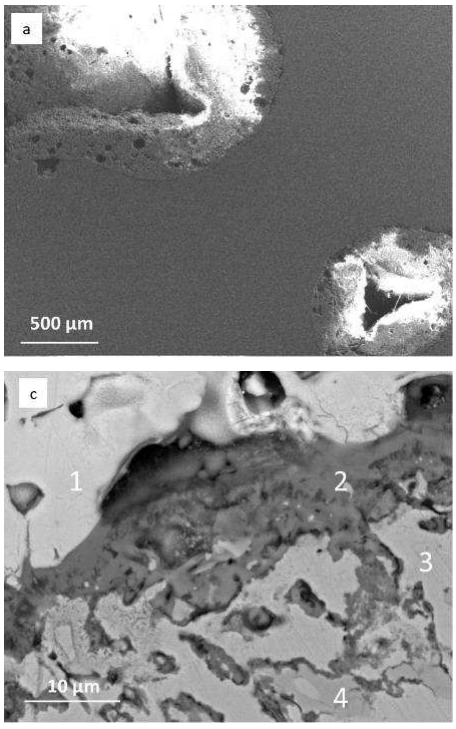

Chemical composition [wt. %]				
	Point 1	Point 2	Point 3	Point 4
C	5.8	3.2	1.8	6.5
O	21.2	25.5	-	-
Mg	2.0	2.5	-	-
Zr	71.0	0.8	-	-
Si	-	-	0.5	1.8
Cr	-	43.1	14.6	17.0
Mn	-	2.9	0.5	0.7
Fe	-	14.3	82.6	74.0
Al	-	7.7	-	-

Figure 8 a, b) SEM BSE microstructures of composite zones type ZrO_2/white chromium cast iron c) area of X-ray microanalysis (EDS)

  doi:10.5075/epfl-298799_978-2-9701614-0-0

4. Conclusions

The local composite reinforcements were manufactured in a cast iron casting as a result of placing ceramic preform in a casting mold cavity. The composite castings were fabricated in one step using the pressure less infiltration of ceramic preforms. Microstructure examinations indicated a positive role of Cr that promotes physicochemical interaction between the metal matrix and the reinforcement.

Acknowledgements

Scientific work financed by The National Centre for Research and Development of Poland, Project No. LIDER/49/0200/L-11/19/NCBR/2020.

5. References

1. Balitskii A, Chmiel J, Kawiak P, Kolesnikov W. Odporność na zużycie ścierne i niszczenie wodorowe austenitycznych stopów Fe-Mn-C. Problemy Eksploatacji 2007; 4:7–16.
2. Rendon J, Olsson M. Abrasive wear resistance of some commercial abrasion resistant steels evaluated by laboratory test methods. Wear 2009; 267:2055–2061.
3. Olejnik E, Szymanski Ł, Kurtyka P, Tokarski T, Grabowska B, Czapla P. Hardness and wear resistance of TiC– Fe–Cr locally reinforcement produced in cast steel. Archives of Foundry Engineering 2016; 2:89–94.
4. Miracle D.B. Metal Matrix Composites – From science to technological significance. Composites Science and Technology 2005; 65 (15-16):2526-2540
5. Niu L, Hojamberdiev M, and Xu Y. Preparation of in situ formed WC/Fe composite on gray cast iron substrate by a centrifugal casting process. Journal of Materials Processing Technology 2010; 210 (14):1986-1990
6. Wang Z, Lin T, He X, Shao H, Tang B, Qu X. Fabrication and properties of TiC reinforced high-strength steel matrix composite. International Journal of Refractory Metals and Hard Materials 2016; 58:14–21.
7. Kumar C, Masanta M. Microstructure and mechanical properties of TiC-Ni coating on AISI304 steel produced by TIG cladding process. Journal of Materials Processing Technology 2017; 240:126-137
8. Chen D, Liu D, Liu Y, Wang H, Zheng Z. Microstructure and fretting resistance of γ/TiC composite coating in situ fabricated by plasma transferred arc cladding. Surface & Coatings Technology 2014; 239:28-33
9. Dulska A, Studnicki A, Cholewa M, Szajnar J. Cast iron reinforced with foaming ceramic insert. Archives of Foundry Engineering, 2018; 2/18:137-140
10. Dulska A, Studnicki A, Szajnar J. Reinforcing cast iron with composite insert. Archives of Metallurgy and Materials 2017; 1/62:255-357
11. Gao Y, Sun S, Qian B, Wang X, Lv S, Zhu Y, Ni H. Preparation and wear resistance of ZrO_2 toughened Al_2O_3 ceramic particles reinforced high chromium cast iron matrix composites by powder sintering and casting. Acta Materiae Compositae Sinica 2021; 8/38:2676-2683
12. P. K. Rohatgi P.K, N. Gupta N, A. Daoud A. Synthesis and processing of cast metal matrix composites and their applications. In casting, ASM Handbook 2008; 15:1149-1164

  doi:10.5075/epfl-298799_978-2-9701614-0-0

LOW VELOCITY IMPACT AND RESIDUAL STRENGTH ANALYSIS OF CARBON FIBER SMC COMPOSITES

Biruk Nega[a], *Robert S. Pierce*[a,b], *Xiaosu Yi*[a], *Xiaoling Liu*[a]

a: Department of Mechanical, Materials and Manufacturing Engineering, University of Nottingham Ningbo China, Ningbo, P.R. China, 315100
Email – Biruk.NEGA@nottingham.edu.cn
b: DTU Wind Energy, Frederiksborgvej 399, 4000 Roskilde, Denmark

Abstract: *In this work, the low velocity impact response, and residual tensile and compressive strengths of carbon fibre Sheet Moulding Compound (SMC) composites have been investigated experimentally. Drop-weight impact tests have been performed at two energies (7.5J and 15J), and the extent of damage has been characterized using ultrasonic inspection. The lower energy impact produced very little observable damage in the SMCs, while large damage areas with visible surface cracking was observed at higher impact energy. The 15J impact samples resulted in 16% and 25% reductions in tensile and compressive strengths respectively, whereas the 7.5J impact caused no observable change in the SMC performance. Digital Image Correlation (DIC) from compression testing showed a relationship between the impact damage area and post-impact fracture initiation sites.*

Keywords: SMC, Low velocity impact; Compression After Impact; Tension After Impact

1 Introduction

Lightweight composite materials are being used increasingly in automotive industry as a key strategy to advance fuel efficient vehicle and cope with rising environmental impact. Sheet Moulding Compounds (SMCs) made from discontinuous fibre reinforcement and thermosetting resins are thus replacing traditional metals due to their high strength-to-weight ratio, low production waste, and suitability for high volume production [1]. With advanced manufacturing techniques for producing discontinuous carbon fibre composites at high fibre volume fractions (>50%), carbon fibre SMC composite have now become an attractive option for structural and semi-structural applications in automotive industry. However, their complex and variable material behaviour presents a significant design challenge, and requires better understanding. For instance, some work has found virtually notch-insensitive damage behaviour in discontinuous composites [2], a unique benefit over continuous fibre composites. While other studies have reported fibre length, bundle size, and notch-diameter dependent notch behaviour [3, 4], emphasizing the challenge in understanding such material performance. Characterisation and optimization work has been done in the past few decades regarding the in-plane quasi-static properties of advanced SMCs. However, their residual strength behaviour has received limited attention. As their application in automotive industry extends to closure body panels, their susceptibility to impact damage (especially at low energy) increases, which can cause a significant strength reduction without being easily detected.

Early studies on the impact response of SMCs, showed an intermediate behaviour between that of a brittle and a ductile material, and failure behaviour that is influenced by the

263/1602 ©2022 Nega et al. doi:10.5075/epfl-298799_978-2-9701614-0-0 published under CC BY-NC 4.0 license

geometry/thickness, microstructure, and constituent material (fibre/matrix) type. For instance, Kau [5] demonstrated that the impact energy absorption of glass fibre-reinforced SMC decreased exponentially with a decrease in sample thickness. Lee et al. [6] also showed specimen thickness to be the most important parameter governing the energy dissipation capability of SMCs subject to low velocity impact (21 – 34J), and that the variation of initial impact velocities had little effect. However, Chaturvedi and Sierakowski [7] investigated the impact response of a glass fibre SMC over a greater range of energies (15 – 52J) and reported significant correlation between impact velocity/energy, damage size, and the residual tensile properties. Impactor size, mass, and shape have also been seen to influence the extent of induced damage and the corresponding failure mechanisms [6, 7]. Moreover, Trauth et al. [8] studied the impact response of SMCs from 1D and 2D flow, and showed that the microstructure, i.e. fibre orientation, significantly influences the damage evolution and failure mechanism.

In addition to the above studies on the impact response of SMCs, several other works have considered the residual post impact properties. Kravchenko et al. [9], for instance, investigated the effect of fibre length on the impact and compression after impact behaviour of carbon fibre SMCs made of prepreg chips, compared with quasi-isotropic continuous fibre laminates. The results showed the short fibre composites to have a larger damage area, greater reduction in the residual compressive strength, but greater energy absorption than SMCs with a longer fibre length or continuous laminates. This was due to the increase in interfacial shear stress between the lower aspect ratio tow chips, which lead to greater energy absorption through delamination[10]. Such works suggest that SMC composites are more prone to impact induced damage [9, 11] than continuous fibre reinforced composites, and exhibit lower post-impact residual properties as a result. However other studies have reported contradictory results, and superior damage tolerance with SMC [12]. Ogi et al. [13] also studied the impact damage and residual tensile strength of 0.3 mm thick carbon fibre SMCs subject to low energy impact (ranging from 1.1 - 3.5J). They observed a clear correlation between the extent of impact damage and residual tensile strength, depending mainly on impact damage depth. Although these studies independently considered the residual tensile and compressive properties of SMCs after low velocity impact, no comprehensive investigation is available to compare the different load cases.

Therefore, this study aims to characterize low velocity impact response of carbon fibre SMC manufactured from Directed Carbon Fibre Preforming (DCFP) process, and their residual strength under both tensile and compressive loads. Digital Image Correlation (DIC) has also been employed to study the correlation between the impact damage and post-impact failure initiation sites.

2 Materials and Manufacturing

In this work, the carbon fibre SMCs were prepared from 25 mm, chopped, T700SC-12k carbon fibre tow in Derakane 782 vinyl ester resin using a DCFP process. Five layers of randomly distributed chopped carbon fibre tows and six layers of resin paste were alternatively deposited over 250x250mm area at a nominal volume fraction of 30%. Each charge was then compacted at room temperature under 10 MPa pressure to improve the through thickness resin infiltration, homogeneity, before it was thermally B-staged at 50°C for an hour. Flat SMC panels of 400x400x4 mm were manufactured by stacking the B-staged charge material at 25% mould

coverage, placed centrally, and compression moulded for 15 minutes at 150°C. A total of six panels were prepared and six test samples were extracted from each panel by abrasive waterjet cutting. Figure 1 shows a representative fibre orientation distribution in the moulded plaques as a result of fibre orientation scanning (based on optical reflectance technique [14]) along with sample cutting plan.

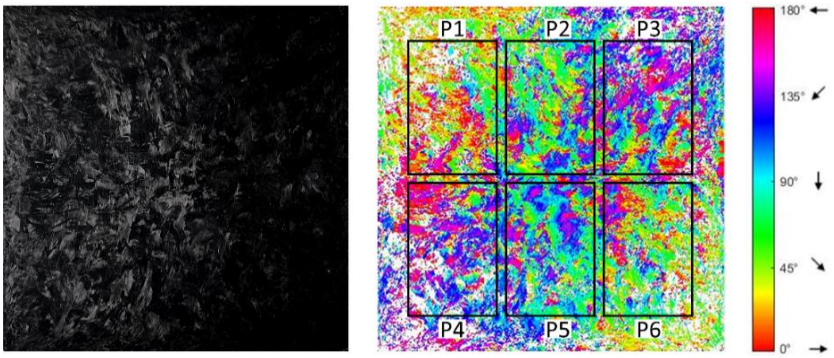

Figure 1: Raw image of the SMC panel (left) and representative fibre orientation distribution in the moulded plaques, along with sample cutting plan (right).

3 Experimental work

Low velocity impact tests were performed on a 150x100 mm standard coupons according to ASTM D7136 [15] standard on Instron CEAST 9340 drop impact tower with automated rebound-catch system. A hemispherical steel impactor of diameter 16 mm and mass 3.265 kg was dropped from a drop height of 234 mm and 468 mm corresponding to impact energies of 7.5J and 15J respectively. Impact force and velocity were digitally acquired from the force sensor and velocity gate connected to the impactor. Five repeat tests were performed for each energy, on samples taken from three different panels, to account intra-plaque variability. Ultrasonic inspection was used to assess the size and extent of the damage. The dent depth on the impacted surface was also measured using a depth micrometre.

Compression After Impact (CAI) testing was performed in accordance with the ASTM D7137 [16] standard for the impact-damaged samples, along with a set of undamaged control samples. Samples were securely fixed within a CAI fixture and tested on a universal testing machine with 100 kN load cell at a loading rate of 1.3 mm/min. Load-displacement curves were then obtained, from which residual compressive strength was determined. After evaluating the impact damage size from ultrasonic C-scan and visual inspection, tension after impact (TAI) test samples were prepared by trimming off 25 mm from each side in the width direction leaving the central 150 x 50 mm, making sure the damage is fully contained in the samples. Then tests were performed with a gauge length of 100 mm at a speed of 2 mm/min. A single camera (2D) Digital Image Correlation (DIC) system was used to assess the full-field surface strain during CAI and TAI tests.

4 Results

4.1 Low velocity impact

The representative force-history and force-displacement responses of the SMC panels under 7.5 and 15J impact energies are shown in Figure 2. The smoother curves of the 7.5J impacted

samples indicate a negligible effect on the composite stiffness. The post-impact ultrasonic inspection (shown in Figure 4) was suggestive of a network of small cracks around the impact site of the 7.5J samples, as well as visible signs of some breakthrough damage at the rear surface. Alternatively, the impact response of the 15J samples shows considerable fluctuations in Figure 2 that are representative of greater damage initiation, internal matrix cracking, and delamination. These samples also showed visible fracture on the back surface of the specimens, and the overall extent of the impact damage can be seen from the low amplitude regions of the C-scan images in Figure 4.

Table 1 also summarizes the low velocity impact response of the two sample groups used for TAI and CAI test. Both 7.5J CAI and TAI groups showed very consistent impact response behaviour, with less than 1% difference in the mean contact force, absorbed energy, and peak displacement. Alternatively, the 15J sample groups generally showed greater variability (8-12%) in these parameters; likely due to the significant difference in mean thickness between the batches (3.57 mm for CAI and 3.98 mm for TAI). Observations of decreasing impact resistance with decreasing sample thickness, as similarly seen here, has been established in related work [6]. From ultrasonic C-scans, this also resulted in a 27% smaller mean damage area for the thicker 15J TAI sample group (365.59 ± 132.15 mm^2) than that of the 15J CAI sample group (503.24 ± 61.86 mm^2). Additionally, the overall mean damage area from all 7.5J impacted samples was 64% smaller than that of the 15J samples. Furthermore, as can be seen from Table 1, the 15J CAI group exhibited greater (63% greater) permanent deformation than the 7.5J sample group, while for the TAI sample groups this difference in dent depth was only 34% (likely due to the thickness effect).

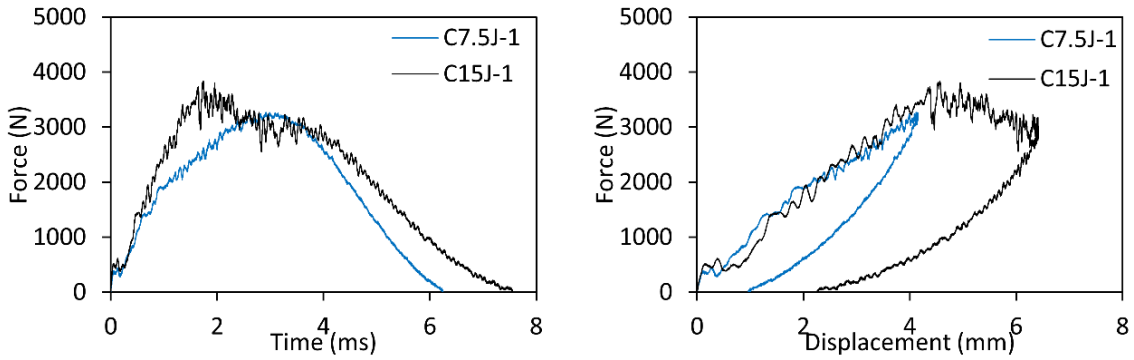

Figure 2: Representative force-time and force-displacement curves of 7.5J and 15J samples (taken from CAI groups).

Table 1: Summary of low velocity impact test results for CAI and TAI sample groups (values in brackets indicate the standard deviation of measured parameters)

Sample group		Thickness, mm	Contact force, N	Absorbed energy, J	Peak disp., mm	Dent depth, mm
CAI	7.5J	3.85 (0.07)	3269.72 (91.94)	3.56 (0.13)	4.31(0.22)	0.20 (0.06)
	15J	3.57 (0.12)	3670.94 (233.07)	10.85 (0.53)	7.05 (0.47)	0.54 (0.32)
TAI	7.5J	3.75 (0.05)	3307.64 (291.89)	3.46 (0.36)	4.27 (0.37)	0.18 (0.04)
	15J	3.98 (0.15)	4576.93(502.94)	9.17 (0.89)	5.73 (0.23)	0.35 (0.10)

4.2 Compression after impact

The residual compressive strengths of the SMC panels are shown in Figure 3 (left) as a function of impact energy. Four pristine samples were also tested as a reference, among which all failed outside the central gauge region. Such "other" failure results serve as a minimum baseline strength under these loading conditions, but may not be representative of the true compressive strength of the panels. Similarly, three of the five 7.5J impacted samples and one of the five 15J impacted samples also failed away from the impact site, and have therefore not failed as a result of the impact damage. The full failure classification and results can be seen in

Table 2 and Figure 3 (left). Quantitatively, there appears to be no significant reduction in the compressive strength of the 7.5J impacted samples, with all valid and invalid tests failing at similar loads to the pristine samples. However, the occurrence of failure initiation through the impacted regions of two samples suggests there may still be a stress concentration and knockdown from the true compressive strength that was simply not measurable with the current testing configuration. For the 15J impacted samples though, a mean 25% reduction of the residual compressive strength was recorded for the four tests with valid failure modes (28% if the invalid test is included). Considering the impact response behaviour of individual samples from Table 1 against the CAI results in Figure 3 (left), there does not appear to so be any correlation between the results. Although plotting the CAI strength against the impact dent depth does reveal 15J samples with greater permanent deformation to have lower residual strength, even when accounting for the sample that failed outside of the central damage region.

The post impact ultrasonic C-scans and full-field strain responses of representative 7.5J and 15J impacted CAI samples can be seen in Figure 4. Surface strains were measured using DIC and are presented at the moments immediately before and after final failure. The image results for

Table 2: Summary of sample failure location and failure modes in CAI test according to ASTM D7137 [16].

Failure type, failure area, failure location	Control	7.5J impacted	15J impacted
Lateral, at/through damage, middle	-	2	4
Lateral, gauge/away from damage, middle	2	2	1
End crushing, at end/edge, top	2	1	-

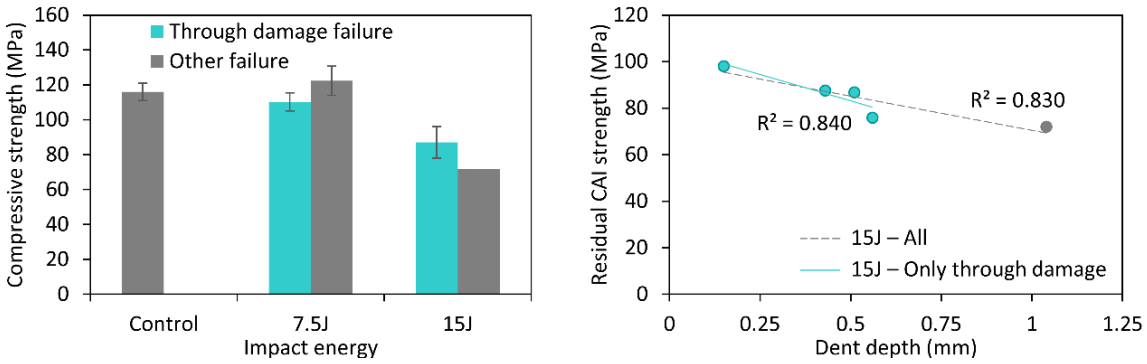

Figure 3: Residual compressive strength as a function of impact energy (left) and residual CAI strength of 15J impacted samples with dent depth (right).

267/1602 ©2022 Nega et al. doi:10.5075/epfl-298799_978-2-9701614-0-0 published under CC BY-NC 4.0 license

samples C7.5J-2 and C15J-3 in Figure 4 are representative of all samples with valid failure modes (through the damage region), while samples C7.5J-3 and C15J-2 are examples of invalid failures. The failure of sample C15J-2 in particular initiated from the conjunction of a manufacturing defect (signified by a surface pock mark and a low attenuation region in the C-scan) and another high strain region propagating from the unconstrained left bottom edge.

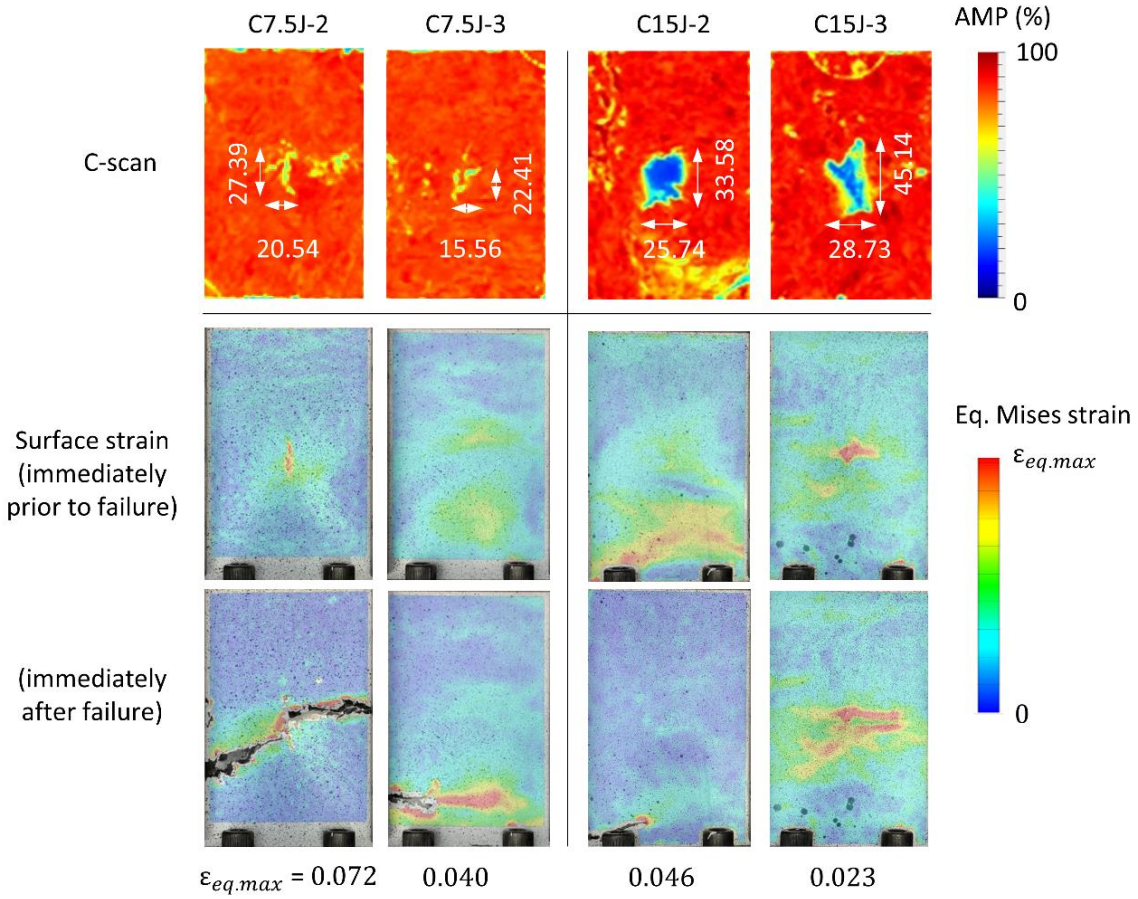

Figure 4: Representative C-scan and the corresponding CAI full-field surface strain immediately prior and post final failure in 7.5J and 15J impacted samples.

4.3 Tension after impact

The residual TAI strength can be seen in Figure 5 for each of the sample batches at different impact energies. Here, the 7.5J impacted specimens also showed no observable strength reduction in tension compared with the control group. However, the 15J impacted samples showed a 16% tensile strength degradation from the baseline. For most samples fracture initiated in the gauge region in the vicinity of the existing impact damage, while samples that failed near the clamps were excluded from the analysis. Although some size effect due to manufacturing variability was identified in the impact response of samples, the SMC plaques showed greater performance (55% to 75%) in tension than in compression consistently for all sample groups. Unlike the CAI results, or other reported literature [13], no clear correlation was observed between the individual dent depth of each specimen and the corresponding residual tensile strength.

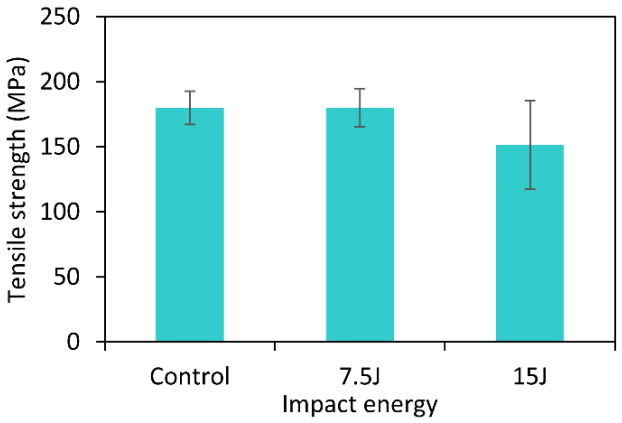

Figure 5: Residual tensile strength as a function of impact energy.

5 Conclusions

In this study, the low velocity impact response and residual compressive and tensile strength of SMC composites was investigated. Ultrasonic C-scan and full-field DIC surface strain measurements were used to assess the extent of low velocity impact damage and its correlation with post-impact compression and tension failure initiation. At lower energy (7.5J) any damage was indiscernible from the inherent material variability, while significant damage areas and visible fibre breakthrough were observed at higher energy (15J). Furthermore, the impact response of the SMCs, i.e., peak force, absorbed energy, damage size and dent depth, showed significant sensitivity to specimen thickness. Lower energy (7.5J) impacted samples showed no strength degradation in both compression and tension, while 25% and 16% reductions were observed respectively at higher energy (15J). This suggests that compression may be the more critical load case for post-impact testing of these composites. Moreover, the correlation between impact damage and post-impact failure initiation sites also appeared to be stronger in compression rather than in tension.

Acknowledgements

The authors would also like to acknowledge the financial support from the Ningbo S&T Bureau under Collaboration Project (Project code: 2017D10033), and the support of the Zhejiang Innovation Team scheme.

6 References

[1] L. T. Harper, T. A. Turner, N. A. Warrior, J. S. Dahl, and C. D. Rudd, Characterisation of random carbon fibre composites from a directed fibre preforming process: Analysis of microstructural parameters, *Compos. Part A Appl. Sci. Manuf.*, vol. 37, no. 11, pp. 2136–2147, (2006).

[2] P. Feraboli, E. Peitso, T. Cleveland, P. B. Stickler, and J. C. Halpin, Notched behavior of prepreg-based discontinuous carbon fiber/epoxy systems, *Compos. Part A Appl. Sci. Manuf.*, vol. 40, no. 3, pp. 289–299, (2009).

[3] L. T. Harper, Discontinuous Carbon Fibre Composites for Automotive Applications, no. August, pp. 1–335, (2006).

[4] J. E. Lindhagen and L. A. Berglund, Application of bridging-law concepts to short-fibre compositesPart 2: Notch sensitivity, *Compos. Sci. Technol.*, vol. 60, no. 6, pp. 885–893, (2000).

[5] H. T. Kou, A Study of the Impact Behavior of Chopped Fiber Reinforced Composite, *Polym. Compos.*, vol. 11, no. 5, pp. 253–264, (1990).

[6] S. Lee, J. Cheon, and Y. Im, Experimental and numerical study of the impact behavior of SMC plates, *Compos. Struct.*, vol. 47, no. 1999, pp. 551–561, (2000).

[7] S. K. Chaturvedi and R. L. Sierakowski, Effects of Impactor Size on Impact Damage-Growth and Residual Properties in an SMC-R50 Composite, *J. Compos. Mater.*, vol. 19, no. 2, pp. 100–113, (1985).

[8] A. Trauth, M. Bondy, K. A. Weidenmann, and W. Altenhof, Mechanical properties and damage evolution of a structural sheet molding compound based on a novel two step curing resin system, *Mater. Des.*, vol. 143, pp. 224–237, (2018).

[9] S. G. Kravchenko, C. Volle, and O. G. Kravchenko, An experimental investigation on low-velocity impact response and compression after impact of a stochastic, discontinuous prepreg tape composite, *Compos. Part A Appl. Sci. Manuf.*, vol. 149, no. June, p. 106524, (2021).

[10] S. G. Kravchenko, D. E. Sommer, B. R. Denos, A. J. Favaloro, C. M. Tow, W. B. Avery, and R. B. Pipes, Tensile properties of a stochastic prepreg platelet molded composite, *Compos. Part A Appl. Sci. Manuf.*, vol. 124, no. July, p. 105507, (2019).

[11] C. Hong, J. Kim, G. Kim, and W. Ji, Effect of stacking sequence on impact resistance performance of hybrid composites laminated with continuous and discontinuous fiber-reinforced layers, *Funct. Compos. Struct.*, vol. 3, no. 2, (2021).

[12] S. Pimenta, A. Ahuja, and A. Y. Lau, Damage tolerant tow-based discontinuous composites, *ICCM Int. Conf. Compos. Mater.*, vol. 2015-July, no. July, pp. 19–24, (2015).

[13] K. Ogi, J. W. Kim, K. Ono, and N. Uda, Impact damage and residual tensile strength of a CF-SMC composite, *Adv. Compos. Mater.*, vol. 22, no. 1, pp. 29–47, (2013).

[14] R. S. Pierce and X. Liu, Exploiting the optical reflectance behaviour of carbon fibre composites for low-cost inspection and orientations analysis, *J. Reinf. Plast. Compos.*, vol. 39, no. 23–24, pp. 869–879, (2020).

[15] ASTM D7136/D7136M-12, Standard Test Method for Measuring the Damage Resistance of a Fiber-Reinforced Polymer Matrix Composite to a Drop-Weight Impact Event, (2012).

[16] ASTM D7137/D7137M − 17, Standard Test Method for Compressive Residual Strength Properties of Damaged Polymer Matrix Composite Plates, (2007).

INFLUENCE OF TEX LINEAR DENSITY ON MECHANICAL PROPERTIES OF 3D WOVEN I-BEAM COMPOSITES

Melisa, Dincer[a-b], Muhammed Ali, Vural[a-b], Emir, Karci[a], Mert, Celikturk[a-c], Ibrahim Halil, Sahin[a-c], Burak, Yatkin[a-c], Cagin, Emre[a-c], Basak, Ozkendirci[d], Elif, Ozden Yenigun[e], Hulya, Cebeci[a-b-c]

a: Aerospace Research Center, Istanbul Technical University, Istanbul, 34469, Turkey– dincer18@itu.edu.tr
b: Aviation Institute, Istanbul Technical University, Istanbul, 34469, Turkey
c: Department of Aeronautical and Astronautical Engineering, Istanbul Technical University, Istanbul, 34469, Turkey
d: Faculty of Arts and Design, Department of Textile and Fashion Design, Dogus University, Istanbul, 34437, Turkey
e: School of Design Textiles, Royal College of Art, SW7 2EU, London, United Kingdom

Abstract: *In heterogeneous structures such as composites, load transfer is one of the most critical issues that need to be improved where poor interphase between the fiber and matrix is observed. Moreover, the weak interface between the composite plies also induces delamination behavior as a dominant failure mechanism. An innovative approach, 3D weaving, is used to eliminate delamination by improving the toughness of out-of-plane yarns in 3D woven fabrics without secondary processing required. In this study, 3D rectangular spacer fabrics were woven from E-glass fibers (GFs) with 600 and 1200 TEX linear densities at the same warp and weft densities Then, 3D composites were fabricated by vacuum infusion process (VIP) coupled with a custom-designed 3D molding. Depending on TEX, void content, fiber volume fraction, mass, and crimp values change and the effect on the specific flexural strength of I-beams has been investigated.*

Keywords: 3D weaving; structural composite; woven preform; flexural strength; composite quality

1. Introduction

Structural elements such as beams are thin-walled structures for which the thickness of the walls is much smaller than the overall cross-section [1–5]. The beam types used as wing spars, control surface spars, floor beams, and wing ribs in these main structures are subjected to major forces. Although beams are used in the empennage and the floor, the most significant beams are the wing spars and must be considered as a critical system because the sufficient load-carrying to remain aloft for the aircraft is much greater in the wing. Shear force and bending moment are created when the wings produce lift, so wings must be designed to withstand critical combinations of direct bending, shear, and torsional loads [6,7].

When other structural members of the wing are subjected to load, most of the stress is transmitted to the spar, which is the most heavily loaded part of an aircraft and is designed as a cantilever beam. While the spar flanges carry most of the direct stresses, the web of the spar is designed to resist shear stresses which is a significant part of the total wing lift. Generally, beams are produced as laminated composites in the aerospace industry so they provide lightness as

  doi:10.5075/epfl-298799_978-2-9701614-0-0

well as sufficient strength, which is undoubtedly the most important key point in the design of aerospace structures. [4,6,8].

The continuing trend towards composites due to their high stiffness and strength properties in aircraft structures is tackling the delamination problem of conventional fiber-reinforced composites. Delamination cracks are easily initiated and then propagated under out-of-plane loading conditions due to the absence of reinforcing through-the-thickness, matrix-rich regions, weak interface, and interphase properties between plies, which makes the structure suffer from low fracture toughness [4,9]. Fabrics produced by the 3D weaving method do not require a secondary process for delamination toughening since they already have yarns out of the plane. It also does not contain resin-rich regions and disorientated fibers. Therefore, properties such as out-of-plane mechanical properties, delamination toughness, impact response, fracture toughness, and damage tolerance can be enhanced by the 3D weaving technique [9,10]. The 3D weaving process is capable of producing preforms in near net shape without the need to join steps and huge trimmings after weaving also made with substantial thickness 3D structures with spacer fabrics [11].

In this study, rectangular spacer fabrics were woven by the 3D weaving method, by transferring the dobby plan created from a weaving design called load-bearing with X-designed vertical wall (LB-X) to a modified 2D weaving machine. The main aim is to study the mechanical properties of 3D I-beam composites (IBCs) based on the effect of 600 and 1200 TEX GFs on 3D woven spacer fabrics. In order to discuss the TEX effect, the warp density and weft density were kept the same in 3D fabrics with the LB-X design. The vacuum infusion process (VIP) was employed to manufacture 3D I-beam composites from 3D woven spacer fabrics. The quality assurance of 3D I-beam composites were studied by the investigation of void content through image processing. The mechanical properties were studied by 3-point bending tests where the flexural strengths of 600 and 1200 TEX IBCs were compared.

2. Experimental

2.1 Weaving I-beam preforms with X vertical wall

By using 600 and 1200 TEX E-glass fiber rovings supplied from Şişecam, 3D rectangular spacer preforms with "Load Bearing X vertical wall" (LB-X) design based on the face-to-face principle [12] were woven on a custom-built weaving machine. The weaving process was performed in 2 steps where initially the top and bottom flanges were woven followed by the vertical wall formation. Simultaneously, four layers of weaving were performed with the required fabric length, flange width, and height of the I-beam. Then, I-beam preforms were extracted from the woven fabric and prepared for composite production. During 3D weaving of the glass fabrics, a weaving plan is employed referring to the vertical wall of the I beam as an “X” appearance with a connection point in the vertical direction. Fig. 1 shows 3D woven I-beams with a flange width of 7 cm and a length of 16 cm and a load-bearing wall of 2 cm. Linear densities (TEX) are an important parameter for the production of woven fabric in appropriate sizes and have affected the warp and weft densities due to yarn widths. 1200 TEX glass fiber has a yarn width greater than 600 TEX, and TEX has created a difference in the beat-up movement to obtain a 4 cm^{-1} weft density at a warp density of 12 cm^{-1}. Therefore, the fabrics produced from the weaving of 1200 TEX glass fiber (LB-X-1200) are tightly woven as it is desired to have the same warp and weft density as 600 TEX (LB-X-600).

  doi:10.5075/epfl-298799_978-2-9701614-0-0

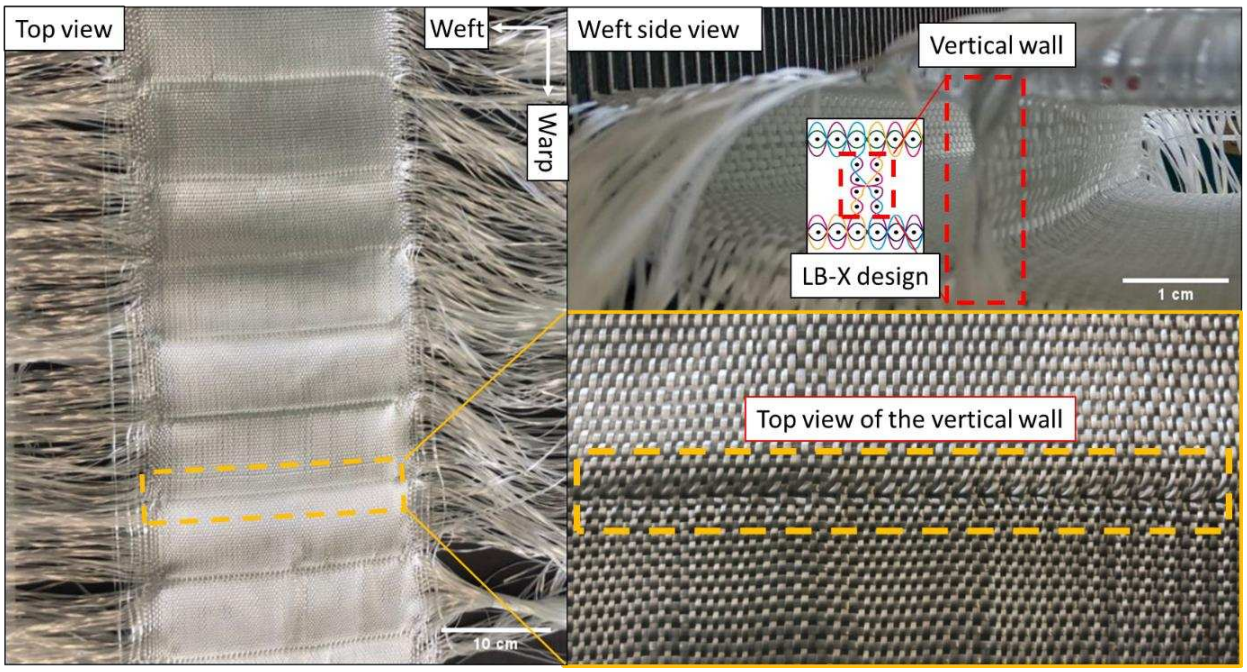

Figure 1. The weft side view of the I-beam preforms obtained by the 3D weaving method, which is based on the weft interlacing perpendicular to the warps

Cover factor, an indicator of the relative looseness or tightness of the fabric, is used to compare the relative closeness of yarns in different fabrics and indicates how much the fabric is filled by the weft in the warp direction and vice versa. Changing the cover factor can affect the strength, thickness, stiffness, stability, and porosity of fabrics [13], [14]. The cover factor is obtained from the formula shown in Eq. (1).

$$K = \frac{n\sqrt{N}}{10} : n = yarn\ count\ per\ centimeter, N = linear\ density\ (TEX) \quad (1)$$

where n, N, and K are yarn count, yarn linear density in TEX, and cover factor, respectively. 3D I-beams are woven separately with 6 warps per cm on the upper and lower flanges, a total of 12 warps. In the cover factor calculation shown in Table 1, only the value of the upper flange has been calculated.

Table 1: Fabric properties of the 3D woven I-beam samples.

Sample Code	Linear Density (TEX)	Warp Density (cm^{-1})	Weft Density (cm^{-1})	Cover Factor
LB-X-600	600	6 (per flange)	4	24.5
LB-X-1200	1200	6 (per flange)	4	34.6

2.2 Fabrication of I-beam composites

Woven I-beam preforms and a mixture of epoxy resin and hardener as a matrix were used for composite production by Vacuum Infusion Process (VIP) which is a manufacturing technique driven by vacuum pressure [15]. Spacer geometries require special molding since they need to

  doi:10.5075/epfl-298799_978-2-9701614-0-0

be supported in vertical and horizontal directions and the void content is aimed to be reduced for a high quality composite manufacturing. Based on this, a custom-designed mold system is used for VIP as presented in Fig. 2 since hollow fabrics were used for composite manufacturing.

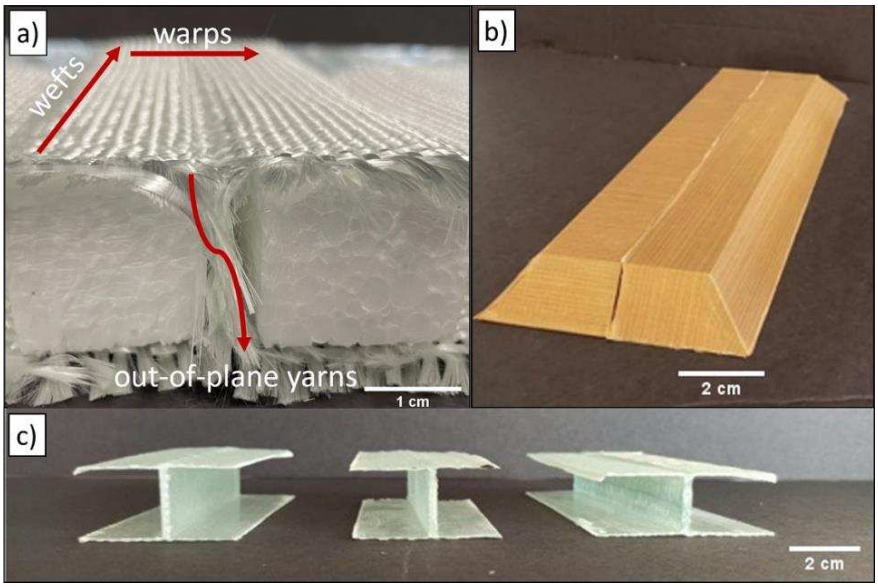

Figure 2. IBCs were produced by VIP method with custom-designed molds that support the flanges of I-beam preforms. a) 3D woven spacer fabrics in I-beam form, b) custom-designed Teflon-coated molds, c) manufactured IBCs

The epoxy resin was purchased as a brand named Hexion MGS L160 having a 700-900 mPas viscosity and 1.13-1.17 g/cm^3 density at 25°C. The hardener for this epoxy was Hexion MGS H160 and the mixing ratio was defined as 4:1. For VIP, infusion mesh and peel ply were placed on a glass mold respectively. While infusion mesh ensures the even flow of resin throughout the mold surface, the peel ply allows the cured structure to be easily stripped from the molds. To retain the preform shape during vacuum, the top and bottom flanges of the woven I-beams were supported by inserts of custom-designed Teflon-coated wooden molds through the left and right gaps of the vertical wall, and then the system was vacuumed by placing a vacuum bag. The wetted fabric was placed aside for 24 hours at room temperature to cure and become a rigid state. In order to compare the void content and flexural strength data, 6 samples of 600 TEX I-beam composites (IBC-600), and 6 samples of 1200 TEX I-beam composites (IBC-1200), a total of 12 samples were produced. Table 2 shows the thicknesses, average weights as well as dimensions of the IBCs.

Table 2: Properties of fabricated I-beam composites (IBCs) and woven I-beams.

Sample Code	Dimensions (L*W*H) (mm)	Vertical Wall Thickness (mm)	Fabric Weight (g)	Matrix Weight (g)	Fiber Weight Fraction (FWF) (%)
IBC-600	160*70*20	20	20	300	46
IBC-1200	160*70*20	20	30	350	55

  doi:10.5075/epfl-298799_978-2-9701614-0-0

3. Results and Discussions

3.1 Characterizations

The structural strength of composites depends on their production quality. It is expected that the strength of composites will be increased by minimizing the negative effects such as stress concentration due to manufacturing defects. Voids, one of the manufacturing defects of fiber-reinforced composites, occur very frequently and have significant detractive effects on the mechanical properties of composite structures. In areas such as aerospace where high-performance structures are required, less than 1–2% void content is generally expected for structural applications so that the loss of strength caused by voids is minimized and risky designs are avoided [16].

In this study, the void content of the flanges and vertical walls was examined with an optical microscope to determine the production quality of IBCs and, accordingly, their strength. For this purpose, optical microscope images of IBCs were taken at positions relative to the resin inlet, and the void content increased from the resin inlet to the outlet as shown in Fig. 3. ImageJ application is used in the calculation of the void content of the composite structure from the images taken by the optical microscope (OM).

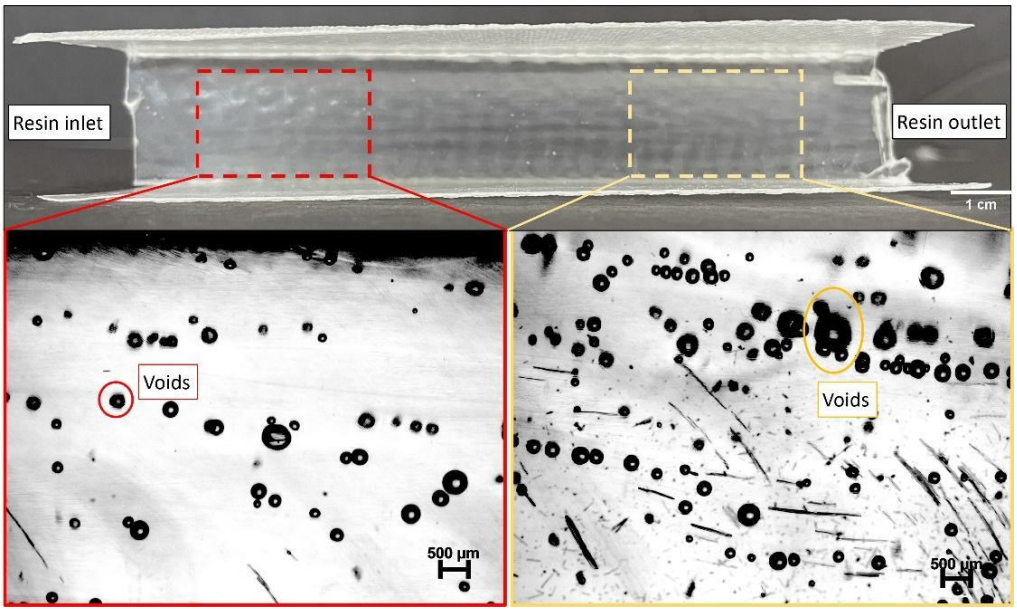

Figure 3. Optical microscope image of the void contents depending on the resin inlet and outlet positions

Because the reduction in resin velocity is related to void formation [15], furthermore, the resin mixture is rich in dissolved gas from the cavities held near the resin inlet zone, then the cavities are driven by the front velocity of the flow, and the motion of the cavities is gradually pushed towards the resin outlet zone [16]. Table 3 shows the cover factor and average void content (for the 12 samples) relations between the IBCs.

  doi:10.5075/epfl-298799_978-2-9701614-0-0

Table 3: Relations between the cover factor and void content of IBCs.

Sample Code	Linear Density, TEX	Cover Factor	Void Content, %
IBC-600	600	24.5	1.9
IBC-1200	1200	34.6	2.6

3.2 3-Point Bending Tests

The produced I-beam composites were also evaluated to determine the mechanical properties according to the ASTM D790 standard on SHIMADZU AGS-X 50 kN universal testing machine. There are two types of roller support diameters 6 mm and 3 mm. The test speed of the 3-point bending test is 1 mm/min. According to the ASTM D790 standard, the span length was evaluated as 80 mm. For the 3-point bending test, 15 N pre-load was applied at 3 mm/min load speed. The load-stroke data of the 3-point bending test applied to the IBCs made according to ASTM D790 were calculated with Eq. 2 and bending stress-strain values were found.

$$\sigma = \frac{3PL}{2bd^2} \tag{2}$$

where: σ, P, L, b, d are stress (MPa), load at a given point on the load-stroke curve (N), support span (mm), width of beam tested (mm), depth of beam tested (mm).

According to the stress-strain shown in Fig. 4a, it was observed that 1200 TEX IBCs with higher fiber content withstand more stress than 600 TEX. This situation shows the relationship between the cover factor and the strength of two IBCs that have the same warp and weft densities but differ in terms of cover factor when it comes to TEX change. During the 3-point bending test of both 600 TEX and 1200 TEX IBCs, an initial local failure, not an overall failure, was observed in the contact of the upper flange and roller of the crosshead [17], as presented in Fig. 4b and Fig. 4c. For 600 TEX IBCs, distortion was observed while the testing, then the maximum flexural stress was observed, but 1200 TEX IBCs had a different behavior where a distortion did not occur. It was understood that distortion of the IBC-600s occurred by warping stresses that dominated the fracture. Kink band formation occurred in both IBCs due to the large shearing of the matrix, and shear failure occurred near the neutral axis at the mid-height of the IBCs. Moreover, since the vertical wall consists of two layers due to the LB-X weaving design, the applied load subjected to the vertical wall separated the layers from each other and caused the first load drop as shown in the stress-strain graph. For a clear discussion of the influence of the TEX on the strength, the length-to-span ratio of IBC-600 and IBC-1200 were kept the same. When examining the strains along the IBCs, it was observed as maximum in the mid-span. All IBCs were manufactured at 2 mm vertical wall thickness and 20 mm height. Therefore, the resin weight ratio of IBC-600 was higher than IBC-1200. As a result, the low fiber content and resin-rich regions of IBC-600 resulted in lower strengths.

  doi:10.5075/epfl-298799_978-2-9701614-0-0

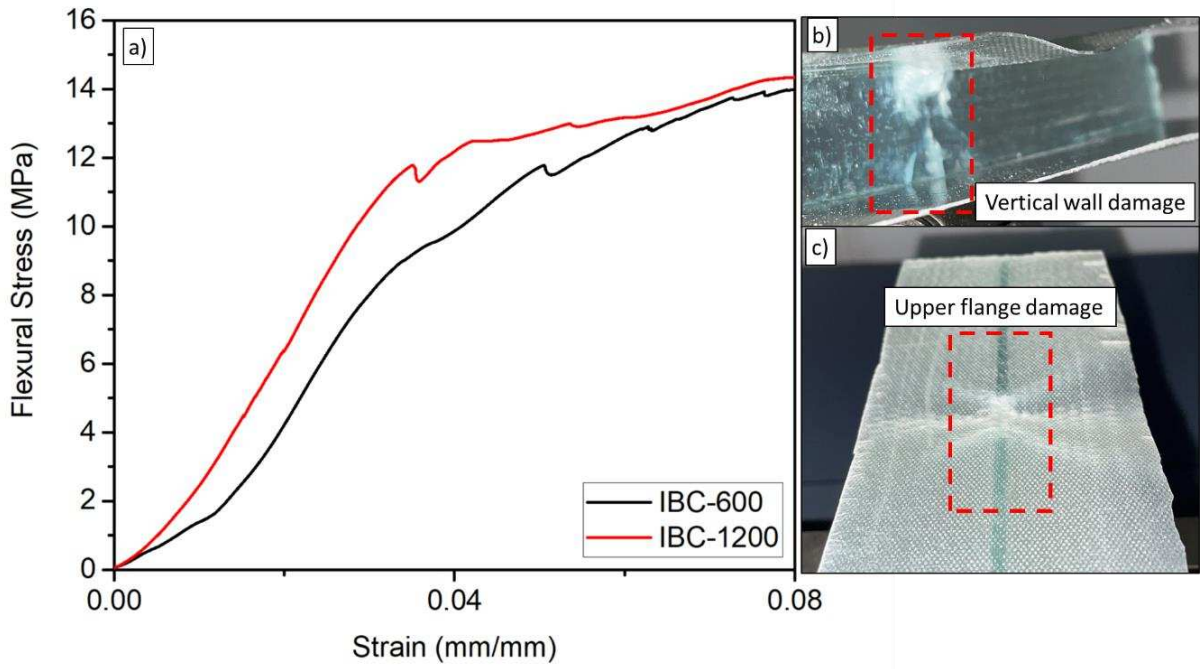

Figure 4. a) The stress-strain curves of the IBCs that manufactured from 600 and 1200 TEX, b) vertical wall damage of the IBCs, c) upper flange damage of IBCs

4. Conclusions

In this study, the flexural strength of IBCs produced from 3D woven spacer fabrics was investigated in terms of void content, TEX, and cover factors. When the 3D woven spacer fabrics with the same yarn densities in the weft and warp directions were compared in terms of TEX, it was calculated that the use of 1200 TEX increased the cover factor by 41% compared to 600 TEX. At the same strain value (0.0352), IBC-1200 showed 26% higher flexural strength than IBC-600. It was observed that the void content in the IBCs increased by 37% with the increase of TEX. Although the destructive effect of the void content reduces the strength of the IBCs, it has not changed the strength increase trend created by the increase in TEX, and it has been observed that sample 1200 TEX IBCs show higher strength as 11.7 MPa. However, the first significant load drop due to the crack formed in the region of the vertical wall near the upper roller of the cross-head was observed at strain less than 1200 TEX. Studies on this subject will be discussed in detail further.

Acknowledgements

This study was funded by the Scientific and Technological Research Council of Turkey (TUBITAK: project number 218M703 (218M704)) 1003 Primary Subjects R&D Funding Program. The authors would also like to thank to the conference funding for Ms. Melisa Dincer provided by the TUBITAK 2224-A Support Program for Participation in Abroad Scientific Events.

We would like to thank Şişecam Elyaf, Turkey's glass fiber producer, for the material support of glass fibers provided for this study.

  doi:10.5075/epfl-298799_978-2-9701614-0-0

5. References

1. Hodges DH, Rimoli JJ, Kardomateas GA, Ruzzene M, White DW. ENHANCEMENTS IN ANALYSIS OF BEAM-LIKE STRUCTURES USING ASYMPTOTIC METHODS [Internet]. Georgia Institute of Technology; 2018 Apr [cited 2021 Feb 27]. Available from: https://smartech.gatech.edu/handle/1853/61073
2. Nguyen XH, Kim N Il, Lee J. Optimum design of thin-walled composite beams for flexural-torsional buckling problem. Compos Struct. 2015;132:1065–74.
3. Sheikh AH, Thomsen OT. An efficient beam element for the analysis of laminated composite beams of thin-walled open and closed cross sections. Compos Sci Technol. 2008;68(10–11):2273–81.
4. Cutler J, Liber J. Understanding Aircraft Structures [Internet]. 4th Editio. Wiley; 2005. 224 p. Available from: https://books.google.com.tr/books?id=wlHBMSmTegUC
5. Deo A, Yu W. Thin-walled composite beam cross-sectional analysis using the mechanics of structure genome. Thin-Walled Struct. 2020 Jul;152.
6. Gudmundsson S. Aircraft Structural Layout. Gen Aviat Aircr Des. 2014 Jan 1;97–131.
7. Donaldson BK. Analysis of Aircraft Structures. Anal Aircr Struct. 2008;1–135.
8. Saha M. Design Survey of Laminated Composite I-Beam. 2018;
9. Kundu AK, Price MA, Riordan D. Conceptual Aircraft Design: An Industrial Approach. 2019. 1053 p.
10. Yildiz K, Gürkan İ, Turgut F, Cebeci F, Cebeci H. Fracture toughness enhancement of fuzzy CNT-glass fiber reinforced composites with a combined reinforcing strategy. Compos Commun. 2020;21(July).
11. Neje G, Behera BK. Investigation of mechanical performance of 3D woven spacer sandwich composites with different cell geometries. Compos Part B Eng [Internet]. 2019;160(September 2018):306–14. Available from: https://doi.org/10.1016/j.compositesb.2018.10.036
12. Chen X. Hollow three-dimensional woven fabrics [Internet]. Advances in 3D Textiles. Elsevier Ltd.; 2015. 53–77 p. Available from: http://dx.doi.org/10.1016/B978-1-78242-214-3.00003-6
13. Gandhi KL, Sondhelm WS. Technical Fabric Structures - 1. Woven Fabrics [Internet]. Second Edi. Vol. 1, Handbook of Technical Textiles: Second Edition. Elsevier Ltd.; 2016. 63–106 p. Available from: http://dx.doi.org/10.1016/B978-1-78242-458-1.00004-2
14. Anand, A. Richard Horrocks SC. Handbook of Technical Textiles Volume 1: Technical Textile Processes [Internet]. Woodhead Publishing; 2016. 396 p. Available from: https://www.sciencedirect.com/book/9781782424581/handbook-of-technical-textiles?via=ihub=#book-description
15. Ince ME. Performance of Composites from 3D Orthogonal Woven Preforms in terms of Architecture and Sample Location during Resin Infusion. North Carolina State University; 2013.
16. Gangloff JJ, Daniel C, Advani SG. A model of two-phase resin and void flow during composites processing. Int J Multiph Flow [Internet]. 2014;65:51–60. Available from: http://dx.doi.org/10.1016/j.ijmultiphaseflow.2014.05.015
17. Turgut F, Koycu A, Cebeci H, Neje G, Behera BK, Ozden-Yenigun E. Hierarchical cnts grown multifunctional 3d woven composite beams for aerospace applications. AIAA Scitech 2020 Forum. 2020;1 PartF(January).

  doi:10.5075/epfl-298799_978-2-9701614-0-0

EFFECT OF FIBER MICROSTRUCTURE ON KINKING IN UNIDIRECTIONAL CARBON FIBER REINFORCED COMPOSITES IMAGED IN REAL TIME UNDER AXIAL COMPRESSION

Katherine Nelms [a], Ying Wang[a], Yunhui Chen [b], Alexander Rack [b], Shelley Rawson[a], Jerome Adrien[c], Eric Maire[c], Philip J. Withers[a]*

a: Henry Royce Institute for Advanced Materials, Department of Materials, The University of Manchester, Manchester, M13 9PL, United Kingdom
b: The European Synchrotron Radiation Facility, Grenoble, 38043 Cédex 9, France
c: MATEIS laboratory, CNRS UMR5510 INSA-Lyon, 69621 Villerbanne Cédex, France
*katherinejnelms@gmail.com

Abstract: *It is well known that the main failure mode of fiber reinforced polymer composites (FRPs) loaded under compression is fiber microbuckling followed by the formation of kink bands. This study uses ultra-fast in-situ synchrotron radiography (50 µs per frame) at the European Synchrotron Radiation Facility's ID19 beam line to study the compressive failure of unidirectional (UD) carbon fibre/epoxy FRPs. High spatial and temporal resolution was used to probe the role of fiber movement on kink band initiation and propagation. Post-mortem micro-CT was used to visualize damage modes in 3D and confirm radiographic results. Radiographs demonstrate the propagation of a region of microbuckled fibers across the width of the sample at a rate of 0.2 µm/µs. This was followed by the initiation and propagation of multiple kink bands in less than 350 microseconds with a transverse band propagation rate of at least 16.3 µm/µs.*

Keywords: X-ray computed tomography (CT); fibre-reinforced composites (FRP); fibre microbuckling; kink band; compressive failure

1. Introduction

Compressive failure of fiber reinforced polymer composites (FRPs) is a critical limitation of their use as structural materials. In particular, the compressive strength of unidirectional FRPs is typically only 60% of their tensile strength [1]. It is well known that the main failure mode under compression is kink band formation, which is often accompanied by fiber microbuckling, fiber fractures, and longitudinal splitting. However, how these failure modes interrelate, and their contribution to kink band initiation and propagation is still debated.

It is agreed that matrix shear yield strength and initial fiber misalignment are key parameters leading to kinking [1-7]. Further, microbuckling is the cooperative bending or rotation of fibers [7-10]; kink bands (fig. 1a) are regions of fibers deflected at a significant angle relative to the loading direction and delineated by planes of fiber fractures. They are accompanied by matrix shear, giving rise to permanent lateral displacement within the damage zone [5, 8, 11-13]. The key geometric features are the kink band width ω, band angle β, and the angle of fiber rotation within the band, $\phi+\phi_0$. Multiple bands tend to form in one of two geometries (fig. 1): complete bands "stacked" on one another [11, 14-15] or smaller (sub-critical) bands which do not propagate across the sample contained within a complete band [5,13,16,17].

Much initial experimental work aiming to investigate kink band formation were limited to 2D studies post mortem [1, 7]. It is only relatively recently that in-situ studies have been published that show a region of microbuckled fibers preceding kink bands. Most of these studies involve

  doi:10.5075/epfl-298799_978-2-9701614-0-0

compressing an FRP to failure, then reload the sample under optical microscope or SEM. [5,11,14,16-17]. Though insightful, especially regarding band propagation, these studies are inherently limited as they cannot capture 3D effects or kink band initiation.

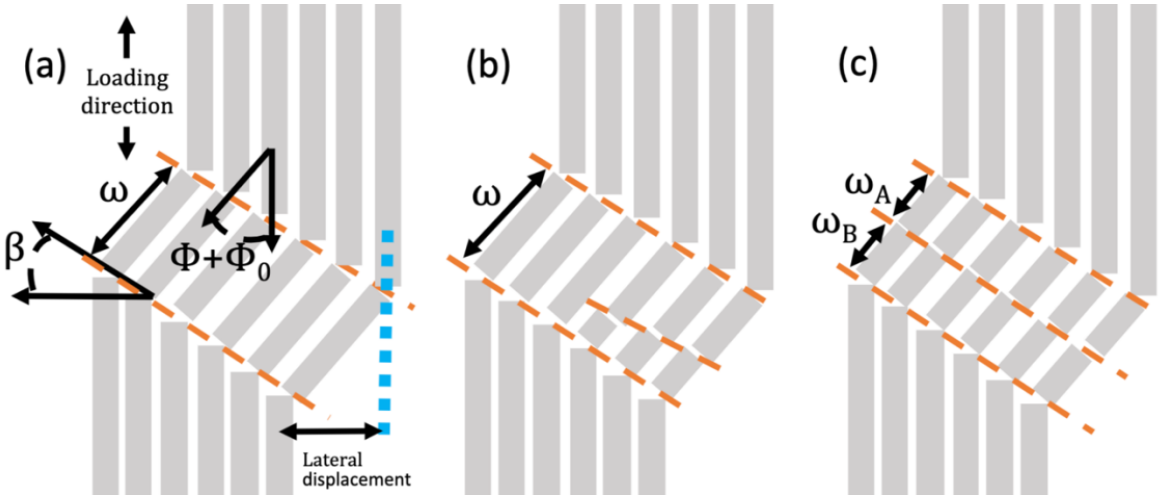

Figure 1. Schematic of (a) single kink band geometry (b) sub-critical bands (c) stacked bands

X-ray computed tomography (CT) presents the opportunity to view 3D images of failed samples [12]. Besides imaging damage in 3D, CT is a non-destructive technique and so avoids introducing damage during sample preparation. A further benefit of CT is the ability to take images in situ or in time-lapse sequences during loading [18]. A tomogram is reconstructed computationally from 100s or 1000s of radiographs collected as the sample is rotated. This methodology limits the temporal resolution and requires that sample movement not occur during the acquisition of the constituent radiographs if one is to prevent motion artifacts.

Previous work by our group has used in-situ synchrotron radiography at 10kHz to view damage propagation in real time [13]. These results confirm that kink bands initiate due to fibre micro buckling and agree with the mechanism proposed in previous in-situ studies: compression causes fibres to buckle, which can additionally lead to longitudinal splits along the fibre direction. These splits open while the matrix fails under shear. After matrix failure, the fibres are then free to bend or rotate due to the lack of lateral constraint from the matrix. Eventually, the fibres cannot bend further, leading to kink band initiation as the fibres fracture. The fractures propagate rapidly across the sample to form the final kink band.

Our previous studies were not able capture the kink event itself due to limited temporal and spatial resolution. The aim of this paper is to use ultra-fast in-situ synchrotron radiography (20kHz frame rate) during compression of a unidirectional (UD) CFRP to capture the kink event and related damage modes.

2. Experimental

2.1 Preparation of Unidirectional FRP

UD FRPs were fabricated from Torayca T700 carbon fibre yarns and Huntsman Araldite LY 564/XB 3486 epoxy resin. A small-scale resin infusion (SSRI) method was developed to achieve cylindrical FRPs with high volume fraction, low porosity, and uniform lateral constraint [9]. Following infusion, CFRPs were cured at 80°C for eight hours. The CFRP cylinders were cut into

  doi:10.5075/epfl-298799_978-2-9701614-0-0 published under CC BY-NC 4.0 license

20 mm samples and a 3mm length by 1.5 mm diameter gauge section was ground in their center (fig. 2). The ends of the sample were inserted into steel end caps to better interface with the compression rig and adhered using Araldite® Strength in Bonding epoxy. Excess epoxy was removed via a small hole drilled in the base of each cap. A notch of 100-200 µm depth was made with a razor blade on one side of the sample in the center of the gauge section. The notch was to encourage the kink band to form within the field of view of the synchrotron detector.

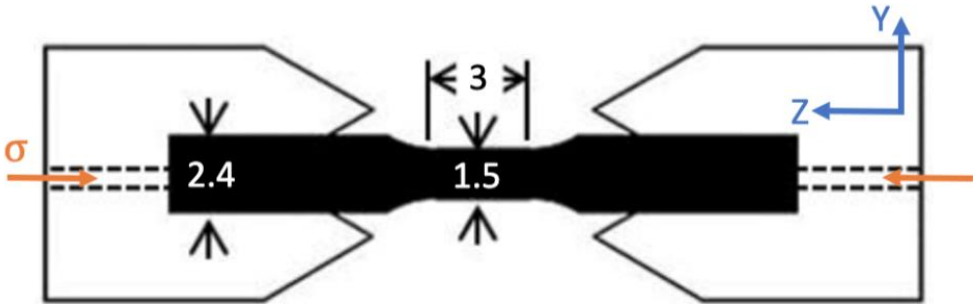

Figure 2. Schematic showing sample dimensions in mm and coordinate system

2.2 In-Situ Synchrotron Radiography

In situ synchrotron x-ray radiography was conducted at the European Synchrotron Research Facility's. Samples were loaded using a tension-compression loading rig developed at INSA-Lyon for in-situ CT studies [19]. The samples were compressed at a displacement rate of 1 µm/s, and radiographs were collected at 20,000 fps using a Photron FASTCAM SAZ. A pink x-ray beam with mean beam energy of 18 keV was used. The resulting voxel size was 1.1 µm and exposure time was 50 µs. The failure was recorded over 25 frames; more than 25 frames total were recorded, however, there the on-board memory of the high-speed camera is limited [19]. The projections were recorded continuously and the oldest image within the buffer is replaced by a new image once the buffer is full. This "rolling" data collection is stopped manually after the failure event. As such, frame 1 does not correspond to a load of 0N but rather just prior to failure.

2.3 Post-mortem Microtomography

Only one of three samples tested failed within the field of view of the imaging detector. This specimen was also scanned on a Zeiss Versa 520 X-ray scanner in the Henry Moseley X-ray Imaging Facility post mortem. A source voltage of 50 kV was used to produce 3201 projections taken over a rotation of 180°. The exposure time was 7 seconds per projection and voxel size was 1.28 µm. The Feldkamp-Davis-Kress (FDK) algorithm [20] was used for reconstruction and the reconstructed volume was analyzed using Avizo 2019 visualization software.

3. Results and Discussion

3.1 Kink Band Geometry Post-Mortem

The central CT slice in Fig. 3 shows the final kink band geometry. The coordinate system shown was chosen post-mortem such that the orientation of the X-Z slice was the predominant shear plane and approximately parallel to the plane of the radiographs. The kink band features, tabulated in table 1, were measured from the final radiograph recorded during loading because the post-mortem tomograph was taken after sample unloading. The values measured from the radiograph generally agree with the CT values; there is 2° difference in mean band angle and 5° difference in mean fiber angle, either due to stress relaxation upon unloading or to possible

  doi:10.5075/epfl-298799_978-2-9701614-0-0 published under CC BY-NC 4.0 license

shifting during transport from the ESRF. However, is it important to note a high inherent uncertainty in the values in table 1 due to the through-thickness nature of the view.

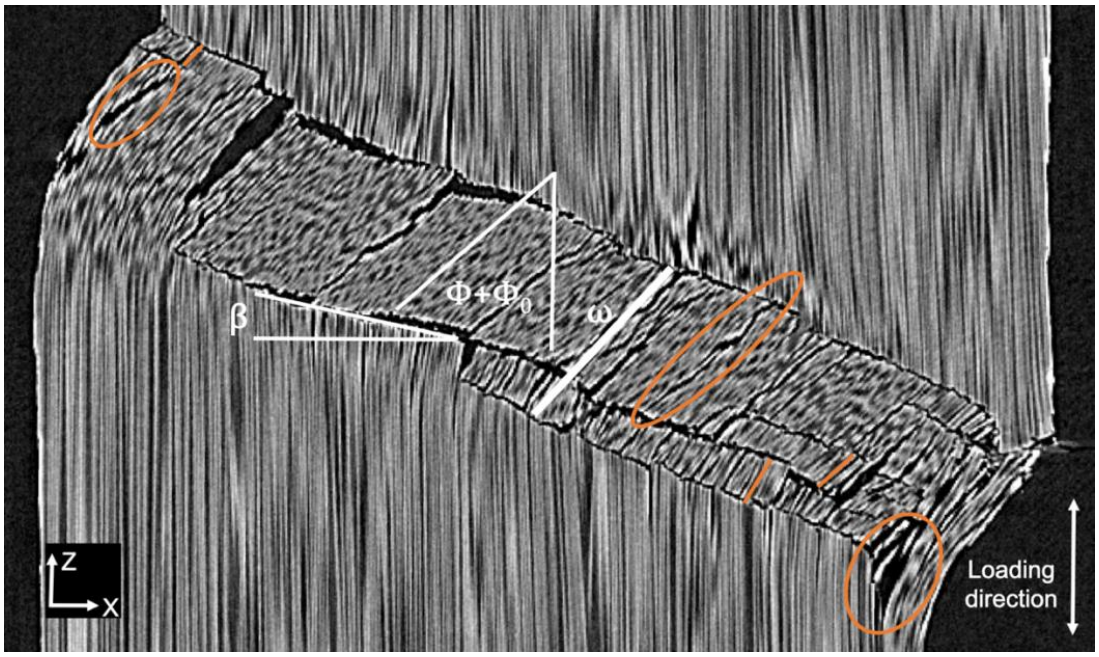

Figure 3. Central CT slice of the UD CFRP sample after failure. Representative fiber fragments within subcritical bands are indicated by orange lines. Orange ellipses indicate longitudinal splits

Characteristically, there are two broadly parallel planes of fiber fractures which delineate the main kink band. The distortion of fibers within the band arises because some of the fibres do not lie precisely within the X-Z plane, indicative of mixed-mode(in- and out-of-plane) kink failure. Several longitudinal splits are evident, and only one plane of fractures propagates across the entire sample width. Instead, the bottom plane of fiber fractures appears truncated by a resin-rich area and is adjacent to severely curved fibers which have not broken due to lack of lateral constraint in this region. This curvature is less severe than in the final radiographs, and each of these observations are consistent with previous findings [13]. There is also a concentration of sub-critical kink bands near the notch. These bands have a similar angle to the main band and fiber fractures but these do not propagate across the full width of the sample.

Table 1: Mean measurements and their uncertainty for characteristic kink band geometric features. Ranges are reported for the sub-critical bands based on measurements of several representative bands in Fig. 3

	β (deg)	$\phi+\phi_0$ (degrees)	ω (μm)
Main band	21 ± 4	52 ± 4	155 ± 4
Subcritical bands	10±2 - 27±2	39±2 - 55±2	13±3 - 66±3

Figure 4 shows orthogonal X-Z slices generated from the reconstructed volume of the post-mortem tomogram selected roughly one-quarter, halfway, and three-quarters through the thickness of the sample along the Y direction. These cross sections show a myriad of longitudinal splits throughout the sample volume in planes parallel to the loading direction, similar to features depicted in [12]. In particular, Fig. 4c shows a two very large splits. These features seem

  doi:10.5075/epfl-298799_978-2-9701614-0-0

to inhibit kink band propagation in the last quarter of the volume along the Y-axis. The region near the largest split is surrounded by highly curved fibers which have not broken due to lack of lateral constraint near the split during compression. This may also explain why the sub-critical kink bands occur mainly in first half of the sample near the notch (fig. 4a, 4b). It is also notable that the kink band is narrower in the central, predominantly, in-plane kink region.

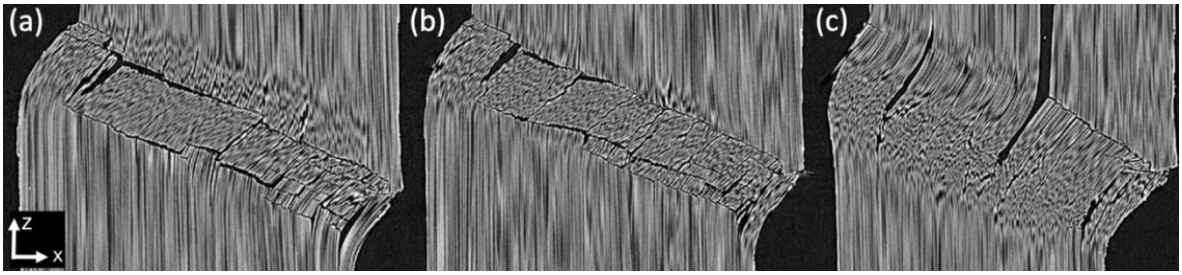

Figure 4. Y-Z slices taken through the thickness of the sample selected roughly (a) one-quarter, (b) halfway, and (c) three-quarters through the thickness of the sample.

3.2 Radiographic Imaging of the Kink Band Formation Sequence

Figure 5 shows the sequence of events leading up to failure captured during loading in-situ by X-ray radiography. It should be borne in mind that some of the features may be misleading because each pixel in a radiograph represents the x-ray attenuation through the thickness of the sample. However, the main features are confirmed by the CT sections in 3.1.

3.2.1 Microbuckle Propagation

Initially, a region of fibers microbuckling elastically in concert can be seen (fig. 5a, 5b). The region appears to become reduced vertically as the fibers rotate with increased loading through frames 1-14. Note, that 11 frames have been omitted between fig. 5a and fig 5b because the per-frame increase in fiber rotation within the microbuckled region is small over this period (600 μs). For each frame, the largest fiber rotation angle is seen near the notch (fig. 5a-c, fig 6). Essentially, this microbuckled region appears to propagate across the sample in 650 μs immediately prior to kink band initiation. Previous in-situ studies have reported a similar propagation of fiber microbuckling followed by kink initiation [5, 11, 13-14,16-17].

To our knowledge, this is the first study with sufficient temporal resolution to report the translation rate at which the microbuckled region moves across the sample, and estimate it to be 0.2 μm/μs based on the initial length of the microbuckled region (Fig. 5a, 529 ± 32 μm) and length just before kinking (Fig. 5b, 637±37 μm). The uncertainty in this value is high due to resolution limits and the radiographic (through-thickness) nature of the data.

3.2.2 Kink Band Initiation and Propagation

The kink initiates at some point between frame 13 and frame 14 (Fig. 5c). In Frame 14, there is evident motion blurring as the fibers move due to lateral motion of the bottom half of the sample. A large longitudinal split can be seen beneath the notch as the matrix fails under shear, and a crack has initiated from the notch following the path of the microbuckled region partway across the sample. In the next frame (Fig. 5d), there is significantly more fiber rotation and nearly all of the lateral displacement has occurred by this frame. Areas of high contrast (dark grey lines) represent longitudinal splits as the matrix yields. The top plane of fiber fractures has extended

  doi:10.5075/epfl-298799_978-2-9701614-0-0

nearly halfway across the sample. It appears that another plane has started to form below it but this is likely radiographic artefact as the plane of fractures is higher (i.e. the kink band wider) near external surfaces than in the center. Sub-critical kink bands appear to have initiated at this point, and the bottom region is blurred as the fibers move. This blurring is indicative of "band broadening", defined as the continuous movement of bending into unkinked fibers [3]. It has been observed in-situ before in [11] and is known to follow fiber lock up, i.e., once it is not energetically favorable for fibers to continue rotating, the band extends reaching until a characteristic band width [2]. Though previously modelled as separate processes [3, 11], our results show band broadening and transverse propagation happening simultaneously.

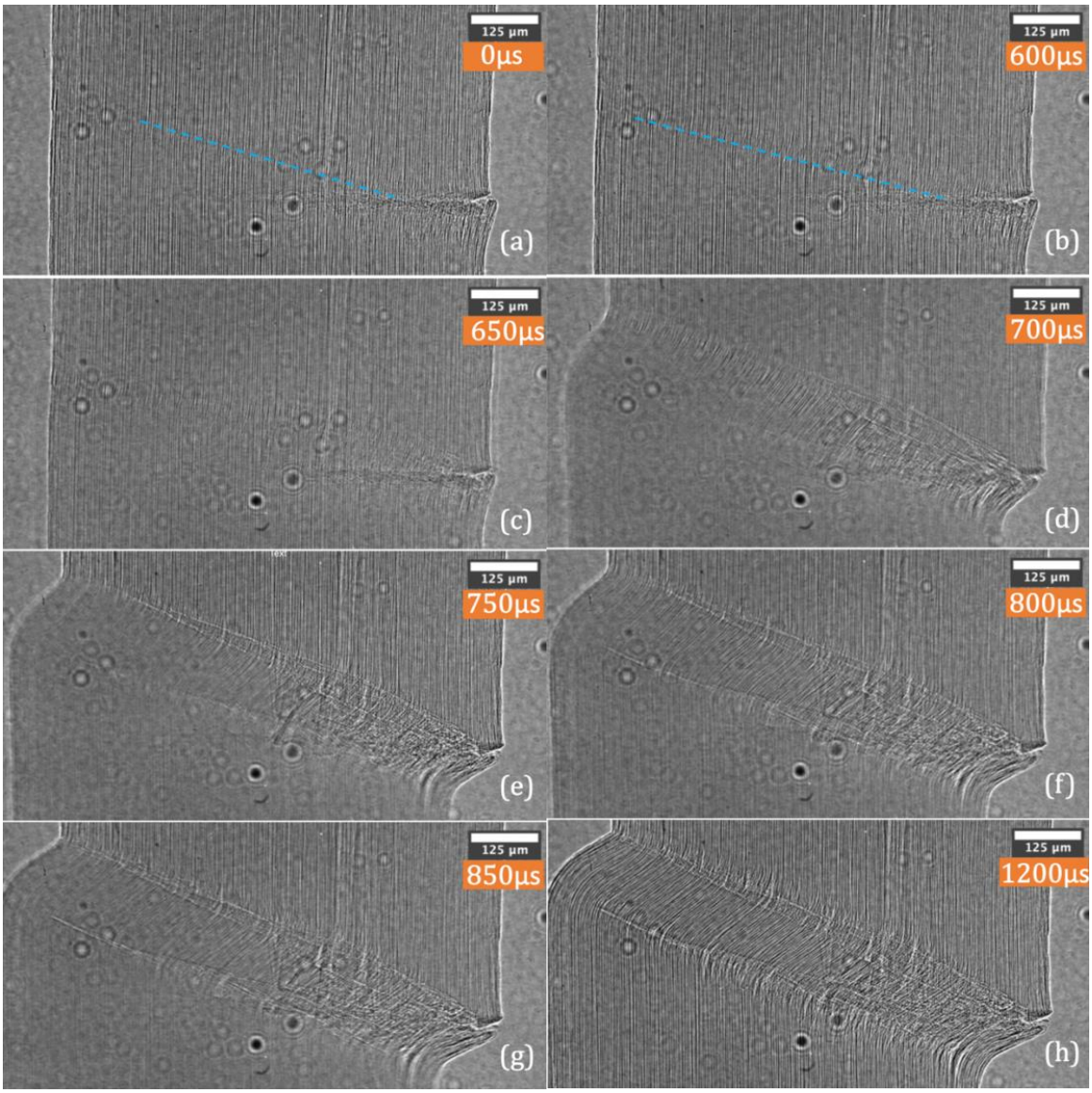

Figure 5. X-ray radiographs leading up to and during failure for frames a) 1, b) 13, c) 14, d)15, e) 16, f) 17, g) 18 and h) 25. The blue lines indicate the length of the microbuckled region.

In Fig. 5e, longitudinal splits have appeared near the base of the notch, indicating severe matrix yielding. Several sub-critical kink bands have also formed. By Fig. 5g, both fracture planes have propagated across the sample, concluding kink band propagation, and no further lateral displacement occurs in the next frame (no further motion blur). Note that kink band initiation

  doi:10.5075/epfl-298799_978-2-9701614-0-0

and propagation had completed within 300 µs, with the frame shown in 5g providing the clearest radiograph because fiber movement had largely completed.

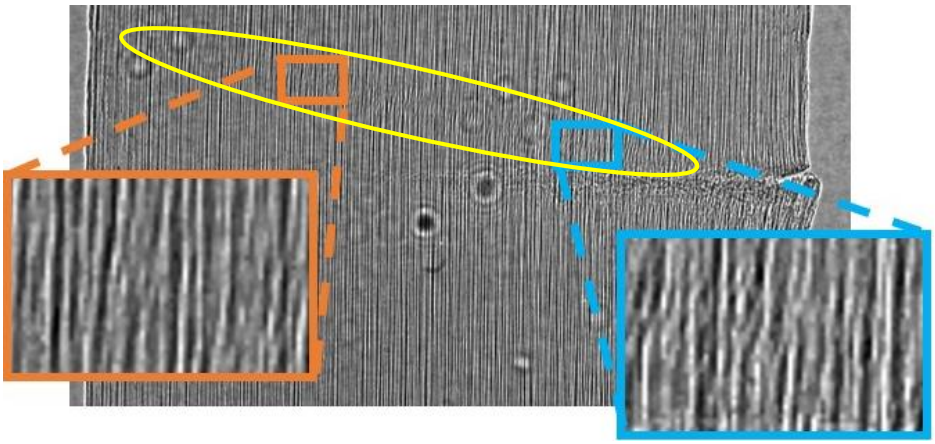

Figure 6: Frame 1 showing region of microbuckled fibers before kink initiation (ellipse). Enlarged regions demonstrate that the severity of the buckle angle increases close to the notch

Building on previous work, our observations suggest that the kink band initiates when severely microbuckled fibers begin to fracture. Then, transverse propagation occurs as the fibers fracture through the sample and rapidly complete their rotation to their final lock up angle. Once locked, band broadening becomes the energetically favorable mode until another plane of fiber fractures is energetically favored. These steps appear to occur locally near the notch forming a series of sub-critical bands before the characteristic bottom plane of fractures occurs.

Finally, the total propagation time was 350 µs between frame 13 and 20. It is clear that the wave of significant fibre rotation and lateral displacement to the lower half of the sample occurs primarily between 5c and d. This suggests that majority of the kink band initiates and propagates within 50 µs and must travel laterally at a speed of at least 16.3 ± 1.3 µm/µsec. The band broadening rate can be roughly estimated as 1 µm/µs based on the band width and frame rate, but further studies with better temporal resolution are required to confirm this value

4. Conclusions

In this study, we present radiographs recorded at 20,000 fps recorded by in-situ synchrotron X-ray radiography during compression testing of unidirectional CFRP. We have captured the sequence of events that occur during microbuckling events and subsequent kink band initiation and propagation. We have observed that a region of microbuckled fibers propagates transverse to the fiber direction immediately prior to kink band formation at a rate of 0.2 µm/µs. A series of sub-critical kink bands form through fiber rotation and fibre fractures, enabling band broadening before the fully developed kink band is formed. This process initiates and propagates within 50µs, giving a translation speed of at least 16.3 µm/µs.

Acknowledgements

We would like to thank the European Synchrotron Research Facility for the beamtime. This work was also supported by the Henry Royce Institute for Advanced Materials, funded through EPSRC grants EP/R00661X/1, EP/S019367/1, EP/P025021/1 and EP/P025498/1, and by the National

  doi:10.5075/epfl-298799_978-2-9701614-0-0

Research Facility for lab CT funded through EP/T02593X/1. We also kindly thank CT-specialists Dr. Tristan Lowe and Dr. Billy Koe for their support.

5. References

1. B. Budiansky and N. A. Fleck, "Compressive Failure of Fiber Composites," Journal of the Mechanics and Physics of Solids, pp. 183-211, 1993.
2. B. Budiansky, "Micromechanics," Computer & Struc, pp. 3-12, 1983.
3. B. Budiansky, N. A. Fleck and J. C. Amazigo, "On Kink Band Propagation In Fiber Composites," Journal of the Mechanics and Physics of Solids, 1998.
4. R. Gutkin, S.T. Pinho, P. Robinson, P.T. Curtis, " Micro-mechanical modelling of sheardriven fibre compressive failure and of fibre kinking for failure envelope generationin CFRP laminates," Composites Science and Technology, 2010.
5. R. Gutkin, S.T. Pinho, P. Robinson, P.T. Curtis, “On the transition from shear-driven fibrecompressive failure to fibre kinking in notched CFRP laminates under longitudinalcompression.," Composites Science and Technology, 2010.
6. P. M. Jelf and N. A. Fleck, "Compression Failure Mechanisms in Unidirectional Composites," Journal of Composite Materials, vol. 26, no. 18, 1992.
7. N. A. Fleck, "Compressive Failure of Fiber Composites," Advances in Applied Mechanics, 1997.
8. P. M. Moran, H. X. Liu and C. F. Shih, "Kink Band Formation And Band Broadening In Fiber Composites Under Compressive Loading," Acta Metallurgica Et Materialia, 1995.
9. Y. Wang, "Damage Mechanisms Associated with Kink-Band Formationin Unidirectional Fibre Composites," The University of Manchester, 2015
10. Y. Wang, M. J. Emerson, K. Conradsen, A. B. Dahl, V. A. Dahl, E. C. Maire and P. C. Withers, "Evolution of fibre deflection leading to kink-band formation in unidirectional glass fibre/epoxy composite under axial compression," Composites Science and Technology, 2021.
11. M. P. Sutcliffe and N. A. Fleck, "Microbuckle Propagation In Carbon Fibre-Epoxy Composites," Acta Metallurgica et Materialia, 1994.
12. Y. Wang, C. Soutis and P. J. Withers, "X-Ray Microtomographic Imaging Of Kink Bands In Carbon Fibre-Epoxy Composites," ECCM16, 2014.
13. Y. Wang, S. C. Garcea, T. Lowe, E. Maire, C. Soutis and P. J. Withers, "Ultra-Fast Time-Lapse Synchrotron Radiographic Imaging Of Compressive Failure In CFRP," ECCM17, 2016.
14. J. Hapke, F. Gehrig, N. Huber, K. Schulte and E. T. Lilleodden, "Compressive Failure of UD-CFRP Containing Void Defects: SEM Microanalysis," Comp. Sci. and Technology, 2011.
15. T. J. Vogler and S. Kyriakides, International Journal of Solids and Structures, 1999.
16. S. Pimenta, "Micromechanics of kink-band formation," Master’s thesis, ICL, 2008.
17. S. Pimenta, R. Gutkin, S. Pinho and P. Robinson, " micromechanical model for kink-band formation: Part 1 Experimental study and numerical modelling," Comp. Sci. and Tech. 2009.
18. S. C. Garcea, Y. Wang and P. Withers, " X-ray computed tomography of polymer composites," Composites Science and Technology, vol. 156, pp. 305-319, 2018.
19. E. Maire, C. Le Bourlot and J. Adrien, "20 Hz X-ray tomography during an in situ tensile test," International Journal of Fracture, 2016.
20. L. A. Feldkamp, D. L. C. and J. W. Kress, "Practical cone-beam algorithm," Journal of the Optical Society of America , 1984.

  doi:10.5075/epfl-298799_978-2-9701614-0-0

EFFECT OF HEAT/FIRE ON STRUCTURAL DAMAGE TO CARBON FIBRES IN CARBON FIBRE-REINFORCED COMPOSITES

Francesca McKenzie [a], Baljinder Kandola [a], Emmajane Erskine [b]

a: IMRI, University of Bolton, Deane Rd, Bolton, BL3 5AB, UK, flm1res@bolton.ac.uk
b: Dstl, Porton Down, Salisbury, SP4 0JQ, UK

Abstract: *At temperatures above 300°C the polymer matrix within carbon fibre-reinforced composites (CFRCs) begins to decompose and starts to burn. At over 550°C the carbon fibres begin to oxidize. This can lead to fibre de-fibrillation which poses harm to the surroundings. For example, carbon fibres are electrically conductive and could interfere with surrounding electronics. This study examines the damage caused by high temperatures/fire to carbon fibres in CFRCs and the effects on their physical properties including fibre diameter reduction, with the aim to provide further insight into potential hazards posed by exposed fibres after high heat situations.*

Keywords: Carbon fibre; composites; heat; fire

1. Introduction

The use of carbon fibre, predominantly used in carbon fibre reinforced composites (CFRCs) is on the rise due to their high strength-to-weight ratio. Combined with their resistance to corrosion, they are rapidly replacing many metals and are particularly attractive to the aerospace and automotive industries. In general, CFRCs have high heat resistance. However, when exposed to temperatures above 300°C the resin, organic matrix breaks down and loses its mechanical properties. At even higher temperatures the resin ignites and at over 550°C, oxidation of the carbon fibres begins to occur [1]. While considerable work has been carried out on assessing the effect of heat/fire on degradation of the composite resin (matrix) [2-4] and CFRCs themselves [5,6] there are limited studies on identifying the damage to carbon fibres within CFRCs, and the hazards posed by the exposed, damaged carbon fibres.

Carbon fibres contain at least 92wt% carbon. The majority of carbon fibres are polyacrylonitrile (PAN)-based, with a small percentage being pitch-based and rayon-based. Fibre diameter is typically 5-10µm and they have good electrical and thermal conductivity along the fibre direction [7]. With the increasing demand for CFRCs, there are growing concerns surrounding the hazards posed by carbon fibres exposed during a high heat situation. Oxidised carbon fibres are still electrically conductive, and due to their lightweight could be transported by winds, potentially interfering with surrounding electronics, as well as provide an adsorbent surface for ambient chemicals and contaminants. They also pose a hazard to human health - broken fibres can be sharp enough to cut through human skin, and under 7µm these particles are considered respirable and upon inhalation they can cause damage to the trachea and lungs [8].

It is generally accepted that when carbon fibres are exposed to heat, above 550˚C in air the fibre diameters decrease and there is a reduction in fibre tensile strength because of the mass loss due to surface oxidation [9]. Mechanical failure at high temperatures reduces the number of application carbon fibres can be used in. Their oxidation behaviour is the main restriction for

  doi:10.5075/epfl-298799_978-2-9701614-0-0

use in high temperature environments. In theory, the oxidation is controlled by these reactions:

$$C(s) + O_2 \rightarrow CO_2$$

$$C(s) + 1/2O_2 \rightarrow CO$$

$$C(s) + CO_2 \leftarrow\rightarrow 2CO$$

The third reaction is referred to as the "Boudouard reaction". It determines the ratio of CO_2 to CO. Below 700°C mainly CO_2 is produced and above 700°C mainly CO [10]. As the temperature increases, so does the rate of carbon oxidisation. At 850°C the oxidisation of the carbon fibres to its gaseous products is complete within a few minutes [11].

By understanding the extent of heat/fire damage to carbon fibre, protective measures can then be put in place to reduce and prevent carbon fibre oxidation. For example, adding flame retardants (FRs) to the resin is a popular method to decrease CFRCs flammability [12]. As the resin (organic polymer matrix), which deteriorates first (above 200˚C) in CFRCs, FRs can increase the resin's cross-linking ability so that when subjected to high heat or fire a highly cross-linked char is formed and the carbon fibres do not become exposed.

2. Experimental

This study examined the oxidative damage caused to carbon fibres within CFRCs under a range of heat and fire conditions. A series of experimental techniques were used to simulate fires which radiate heat at temperatures ranging from 400°C to 1100°C. Mass loss and carbon fibre diameter reduction were used as indicators of the amount of oxidation which occurred.

2.1 Materials

PAN based TR30S 200g 2x2 twill weave 3K carbon fibre from Mitsubishi (Japan). The as-received carbon fibre was characterised with SEM and had a diameter of 7.68 ± 0.23µm. The control CFRC used an epoxy resin (Epilok 60-822 and Curamine 32-790), was 8 plies thick and made via resin infusion. It had a fibre fraction volume of 58.1% and laminate thickness of 2.8mm. 15wt% of the following FRs were also added to the CFRCs resin - Ammonium polyphosphate (CC_APP), Resorcinol bis-(diphenyl phosphate), (CC_RDP), 9,10-Dihydro-9-oxa-10-phosphaphenanthrene 10-oxide (CC_DOPO).

2.2 Thermogravimetric analysis testing

The effect of heat in a controlled environment was studied using thermogravimetric analysis (TGA) (TA Instruments Q600 SDT). Carbon fibre tows were cut to 5mm length pieces and placed in an open platinum pan. These were continuously heated from 23°C to 1050°C, at a rate of 20°C/min, under air at flow rate 100ml/min. In order to confirm the effect of an oxygen-containing atmosphere, TGA was also carried out under the same conditions in a nitrogen atmosphere (flow rate 100ml/min).

  doi:10.5075/epfl-298799_978-2-9701614-0-0

2.3 Cone Calorimeter irradiance testing

To replicate real fire conditions using radiant heat fluxes, the cone calorimeter was used from 50kWm^{-2} to 75kWm^{-2}, where a heat flux of 50kWm^{-2} simulates a standard house fire at the flashover condition. Both the carbon fibre 2x2 twill weave and CFRC strips measuring 25x100mm were exposed to the cone separately for 600s, in order to compare the damage to the fibre and see if the resin provided protection. Samples were placed on an aluminium foil covered holder in the horizontal position. Spark ignition was used to ignite the volatiles from CFRCs. Fibres were removed from the different plies within the CFRC, where fibres from the surface ply (P1) were directly exposed to the cone heater, and P8 is the underneath ply. Schematic is shown in Figure 1.

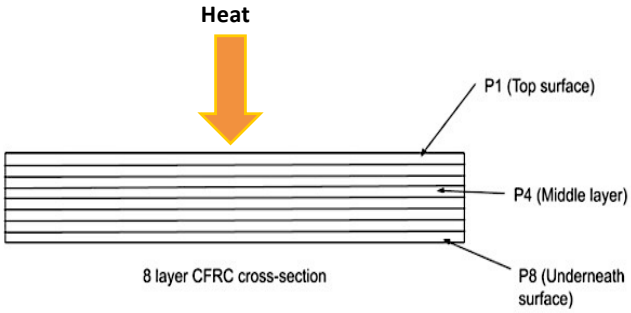

Figure 1: Schematic of CFRC with plies labelled

2.4 Exposure to premixed propane/air flames

Using a propane burner, the effects of extremely high heat flux (116kWm^{-2}), close to thermal conditions in a jet fuel fire, and direct contact with a flame, were studied. The propane burner set-up is given in more detail in [13]. CFRC samples and fibre strips were mounted in a 250x250 mm graphite plate, with a placement holder in the centre of 25x100x3 mm. This was used so edge effects of the composite were negated. Kaowool ceramic fibre was used to insulate the plate (Figure 2a). Each specimen was retained in the sample holder using nickel alloy wire. The sample support system was mounted vertically in a steel holder 1.4metres above the ground. The propane burner set-up employed a 63.5 mm diameter Bullfinch No. 1270 nozzle, a burner-to-plate distance of 350 mm, and a propane burner gas pressure adjusted so the thermocouple 10mm in front of the sample hot face recorded 1,000°C (graph in Figure 2b). It took 19 seconds from when the propane burner was ignited until a stable temperature was measured. There was a time delay associated with thermocouple temperature recording, but for each measurement, the time to stable temperature remained consistent. Exposure to the propane burner lasted for 120s, 300s or 600s.

  doi:10.5075/epfl-298799_978-2-9701614-0-0

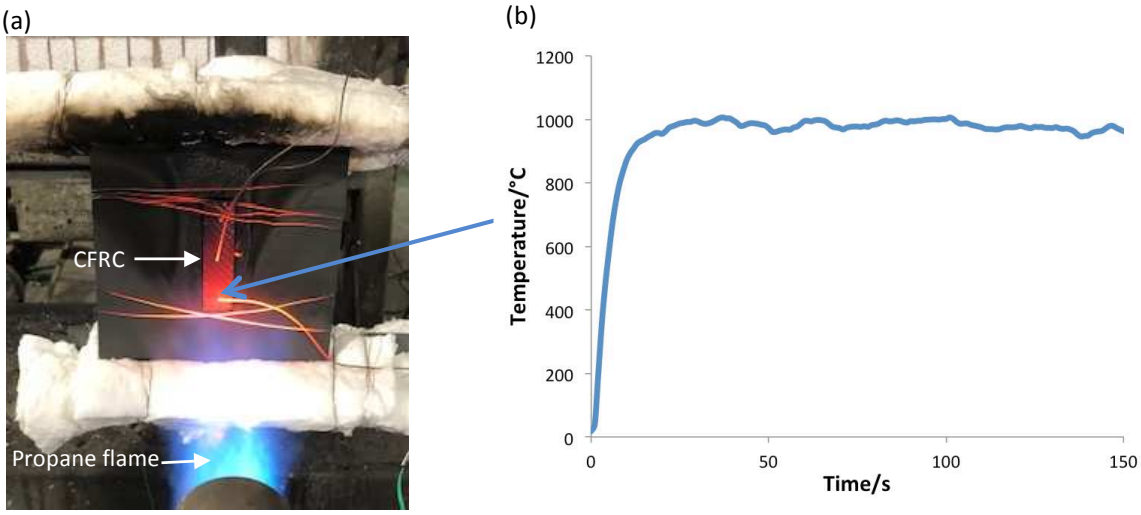

Figure 2: (a) Sample setup (b) Temperatures recorded by the thermocouple in front of flame

Due to the intensity of the flame, some carbon fibres were lost during the experiment so an accurate reduction in fibre mass due to direct exposure to fire could not be recorded.

3. Results and discussion

3.1 TGA

TGA on the as-received carbon fibre was carried out to confirm its oxidation behaviour in air and nitrogen. In a nitrogen atmosphere only a small mass loss of 1.6% was seen at 267°C, this was attributed to the loss of the polymer sizing. This mass loss was also seen in air, with a corresponding small peak on the first derivative (DTG) curve. The major mass loss commenced at around 500°C and continued to 820°C, after which the fibre had been fully oxidised into carbon dioxide and carbon monoxide. TGA is given in Figure 3.

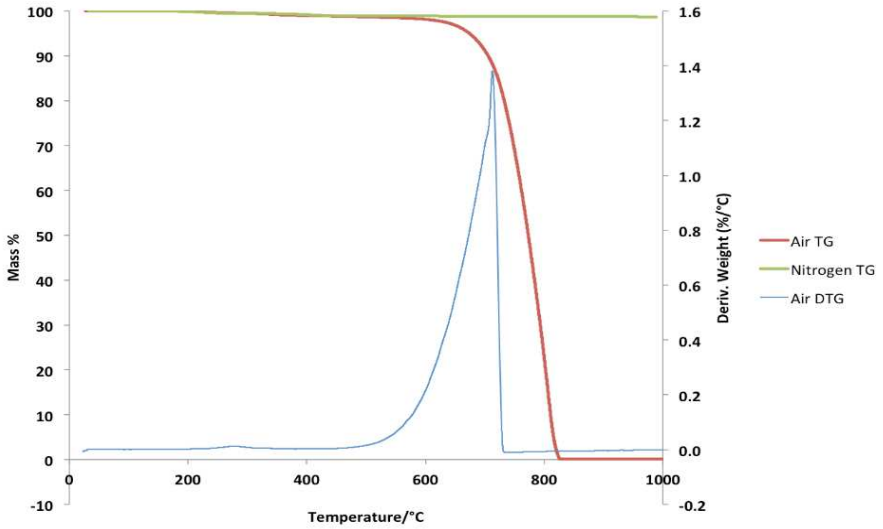

Figure 3: TG curves in air and nitrogen, and first derivative of the mass loss curve in air for TR30S carbon fibre

3.2 Irradiance tests at 50kWm^{-2} and 75kWm^{-2}

Fibres from different plies of the CFRC exposed to 50kWm^{-2} were removed and examined under SEM. Only the underneath ply (P8) had char residue adhering to it. No surface damage to the fibres were observed and no change in fibre diameter.

At 75kWm^{-2} no char or resin was found on the fibres from any ply, and all had undergone oxidation as seen in Figures 4(a-c). Fibre diameter reduction to 5.89 ± 0.11µm and 6.65 ± 0.11µm for P1 and P8, respectively. Fibres from P1 had areas of oxidation along the fibres' striations, while P8 showed uniform surface oxidation. Given the uniformity of the oxidation, it was most likely due to the diffusion of gasses through pores and micro-structural defects.

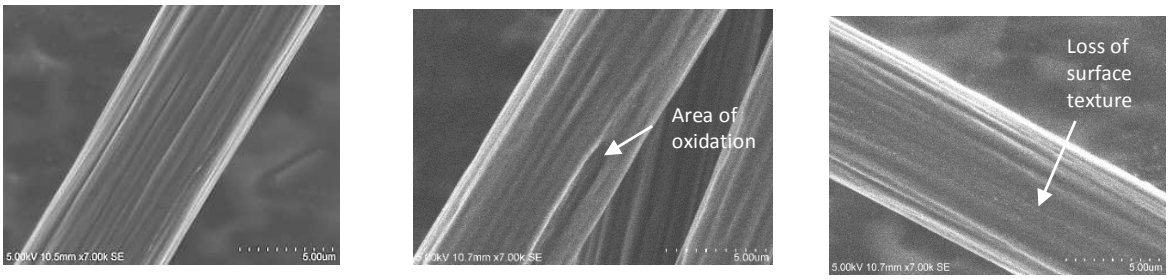

Figure 4: SEMs of (a) as-received fibre, (b) P1 and (c) P8 after heat testing

3.3 Premixed propane/air flames 116kWm^{-2}

CFRCs lost mass within the first minute due to resin decomposition. Between 3 and 5 minutes only a small amount of mass was lost (34.4wt% and 38.7wt% respectively). However, after 10 minutes there was significant loss of mass (53.4wt%) due to oxidation of the carbon fibres. No char residue remained on the fibres, indicating that even at 3 minutes, contact with a propane flame (with a temperature close to 1000°C) is high enough to burn all resin from the CFRC. The mean fibre diameters for 3 and 5 minutes were reduced and within error of each other (7.14 ± 0.17µm and 6.96 ± 0.14µm). However, after 10 minutes there was significant diameter reduction (6.15 ± 0.13µm). While all fibres experienced surface oxidation, over 3 and 5 minutes, the fibres still maintained the raw fibre's inherent striations. At 5 minutes, signs of localised surface damage appeared.

After 10 minutes larger localized areas of oxidation (Figure 5) were observed. Fibres removed from P8 of the CFRC after 10 minutes retained more of their fibre diameter (6.66 ± 0.12µm) and showed more uniform oxidation. As carbon fibre is typically only 92 to 96wt% carbon (over 99wt% carbon they become brittle and are referred to as graphite fibre), there are impurities remaining in the fibre. On contact with the flame these may be vaporised, creating a localised areas of oxidation. Even a few defects in the usual highly ordered structure of carbon fibre can have large effects on strength, leading to fibre breakage.

  doi:10.5075/epfl-298799_978-2-9701614-0-0

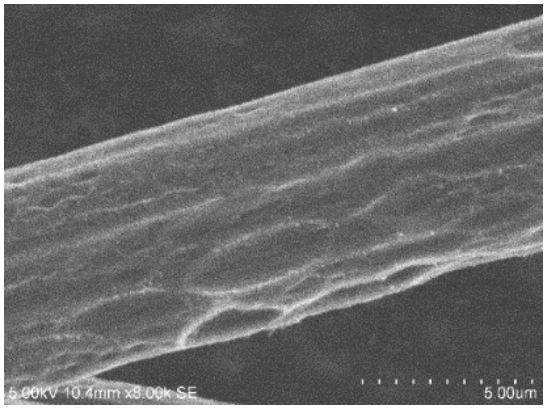

Figure 5: Fibre removed from P1 of CFRCs in direct contact with the flame after 10 minutes

For both exposure to the cone calorimeter and propane burner, fibres from the surface P1, had a larger reduction in diameter, with greater signs of oxidation, compared to those removed from the underneath P8. This implied that upper plies provided a protective barrier in the form of physical shielding and impeded the flow of oxygen to the plies underneath.

3.4 Irradiance tests at 75kWm^{-2} of CFRC with 15wt% flame retardants

Residual fibre removed from CC_DOPO and CC_RDP underwent more surface oxidation than fibres from the control CFRC, with very little char attached to them. However, there was a noticeable reduction in surface oxidation of carbon fibres recovered from CC_APP, with fibre diameter reduction less than the control CFRC. This was attributed to the large amount of char adhering to the removed fibres. Many of these fibres were encapsulated in char and bound together. This increased their mass, making them less likely to be transported by wind to interfere with their surroundings. Based on the char forming ability of APP [14], only this flame retardant resulted in the desired char formation and fibre retention effect. Investigation is ongoing to understand the effect of FRs on residual fibre properties, including tensile strength and electrical conductivity.

4. Conclusions

TR30S carbon fibre was characterised and studied under a range of heat and fire conditions.

- Exposing carbon fibre to high temperatures in a nitrogen atmosphere did not reduce fibre diameter but did remove the polymer sizing (above 450°C).
- TGA results showed fibre oxidation began at 550°C with rapid oxidation between 700 and 850°C. Above 850°C the fibre was fully oxidised.
- Exposing carbon fibre to a heat flux of 50kWm^{-2} for 600s caused no fibre oxidation.
- At 75kWm^{-2} for 600s there was significant carbon fibre oxidation with the dominant mechanism being diffusion of gasses through pores and micro-structural defects.
- After 10 minutes of exposure to the propane burner (116kWm^{-2}), the flame caused vaporisation of contaminant particles creating sites for localised oxidation.
- The addition of 15wt% APP increased char formation which provided protection from oxidation to the fibres within the composite.

  doi:10.5075/epfl-298799_978-2-9701614-0-0

Acknowledgements

We are grateful to Dstl for providing funding for this project.

5. References

1. Mouritz AP, Gibson AG. Fire properties of polymer composite materials. Dordrecht: Springer-Verlag New York. 2006.
2. Kandare E, Kandola BK, Myler P, Gerard E. Thermo-mechanical responses of fibre-reinforced epoxy composites exposed to high temperature environments. Part I: Experimental data acquisition'. J. Composite Materials 2010; 44 (26), pp. 3093-3114.
3. Kandare E, Kandola BK, McCarthy E, Myler P, Edwards G, Jifeng Y, Wang YC, Fibre-reinforced epoxy composites exposed to high temperature environments. Part II: Modelling heat induced mechanical property degradation'. J. Composite Materials 2010; 45 (14), pp. 1511-1521.
4. Mc Carthy ED, Kandola BK, Edwards G, Myler P, Yuan J, Wang YC, Kandare E. Modelling Flaming Combustion in Glass Fibre-Reinforced Composite Laminates. J. Composite Materials 2012; 47 (19), pp. 2371 – 2384.
5. Tranchard P, Samyn F, Duquesne S, Thomas M, Estèbe B, Montès JL, Bourbigot S. Fire behaviour of carbon fibre epoxy composite for aircraft: Novel test bench and experimental study. Journal of Fire Sciences 2015; 33(3), 247–266.
6. Grigoriou K, Mouritz AP. Comparative assessment of the fire structural performance of carbon-epoxy composites and aluminium alloy used in aerospace structures. Materials and Design 2016; 108, pp 699-706.
7. Huang XS. Fabrication and Properties of Carbon Fibers, Materials 2009; 2 pp. 2369-2403
8. Inthavong K, Mouritz AP, Dong J, Tu JY. Inhalation and deposition of carbon and glass composite fibre in the respiratory airway. Journal of Aerosol Science 2013; 65, pp. 58–68
9. Feih S, Mouritz AP. Tensile properties of carbon fibres and carbon fibre– polymer composites in fire. Compos A Appl Sci Manuf 2012; 43 (5) pp. 765-772
10. Yin Y. Binner GP, Cross TE, Marshall SJ. The oxidation behaviour of carbon fibres J Mater Sci 1994; 29, pp. 2250-2254
11. Su F, Huang P, Li T, Yao R. Oxidation of Carbon Fibre and its Effect on Mechanical Properties, 21st International Conference on Composite Materials 2017
12. Braun U, Balabanovich AI, Schartel B, Knoll U, Artner J, Ciesielski M. Influence of the oxidation state of phosphorus on the decomposition and fire behaviour of flame-retarded epoxy resin composites, Polymer 2006; 47 (26) pp. 8495-8508
13. Gibson AG, Wan-Jusoh WNB, Kotsikos G. A propane burner test for passive fire protection (PFP) formulations containing added halloysite, carbon nanotubes and graphene, Polymer Degradation and Stability 2018; 148, p 86-94
14. Kandola BK, Biswas B, Price D, Horrocks AR. Studies on the effect of different levels of toughener and flame retardants on thermal stability of epoxy resin. Polym. Degrdn. Stab. 2010; 95(2), 144-152

  doi:10.5075/epfl-298799_978-2-9701614-0-0

USE OF CARBON PARTICLES IN FIBER/EPOXY UD LAMINATES

Blanka Tomková[a], Miroslava Pechočiaková, Jana Novotná

a: Technical University of Liberec, Dpt. of Material Engineering, Studentská 2,
461 17 Liberec, Czech Republic – blanka.tomkova@tul.cz

Abstract: *This study focuses on changes in mechanical, thermo-mechanical, and electrical properties of epoxy composites reinforced with carbon or glass unidirectional (UD) roving, if the resin is modified with 2.5 wt% of carbon particles (synthesized graphene nanopellets, and milled recycled carbon fibers). Aim of this work is to study the influence of carbon fillers on overall composite properties, and analyse its applicability for improvement of UD epoxy laminates without having to significantly change the production technology.*

Keywords: roving, epoxy composite, recycled carbon fiber, unidirectional (UD) reinforcement

1. Introduction

High demands on fibre reinforced plastic (FRP) for structural application (e.g. the lowest possible weight and high load capacity) led to development of materials made from inorganic multifilaments embedded in polymer matrices. While the technical advantages of these FRP are undisputed, in recent years much attention has been paid to environmental problem they cause when disposed in landfills at the end of their lifetime. This problem is particularly acute with thermoset matrix composites. Although there are numerous attempts to their recycling, suitable technologies are still lagging behind the growing amount of composite waste [1].

Therefore, the development of new "environmentally friendly" composite laminates is one of the fastest growing R&D areas in composite research. The joint idea is to develop a Bio-FRP from renewable and sustainable raw materials, which are as light and resilient as the classic FRP, and if they are bio-degradable and recyclable the better. As for the textile reinforcements, there has been an effort to replace inorganic fibres with natural ones (e.g. hemp or flax), however, for many structural composites high performance (e.g. carbon) fibres are still irreplaceable [2]. In these cases, the research is focused on binder modification. Many recent studies thus present possibilities of improvement for "green" resins or "bio-based" thermo-plastics using different combinations of micro/nanofillers, mainly those made from recycled sources [3-9].

Their selection depends, in the first place, on the property we aim to improve. When, for example, we focus on improvement of thermal/mechanical endurance along with electrical conductivity, we must consider the fact that most polymeric materials belong into category of insulators [10] with electrical conductivity lower than 10^{-14} S/m. To increase both, electrical conductivity, and thermal/mechanical properties, it is necessary to fill polymer matrix with sufficient amount of electro-conductive particles and/or nanoparticles, that concurrently support arrangement of matrix structure. From this viewpoint, electro-conductive carbon/graphite particles of various shapes and sizes seem like very promising material [11]. Their market offer is very wide [12], from chopped or milled carbon fibers, over graphene nanopellets, carbon black, multiwalled or singlewalled carbon nanotubes, to natural fullerens,

  doi:10.5075/epfl-298799_978-2-9701614-0-0

and they can be variously combined. In addition, many of them are made from recycled raw materials and thus meet the requirements for sustainable product development.

And there are many other fillers (various minerals, wood-flour, chopped glass fibers, clays, fly ash, etc.), that are widely used in all polymer types [13]. Filler volume in structural plastics ranges between 15-40wt% depending on the production technology, and requirements on utility properties of final composite product. However, we cannot use such an amount in the resin that serves as the binder in FRP due to striking increase of resin viscosity in higher concentrations. We observed this increase at a concentration around 3wt% [14].

Our study is therefore focused on influence of fillers' morphology on resin properties, and its applicability for improvement of FRP in perspective of appropriate balance between the matrix modification and processing requirements (e.g. resin viscosity) in FRP production. We build on previous research in the development of fibrous assemblies and structural composites from recycled sources [14-20]. For this study we modified green epoxy resin with 2.5wt% of carbon based fillers, which were subsequently applied to carbon, and glass multifilaments, and vacuum cured to obtain fiber/epoxy UD laminates.

2. Experimental

2.1. Materials

Series of composite samples with two types of common inorganic reinforcements (carbon and glass rovings) were prepared in following compositions: one set was embedded in neat epoxy, in the others the matrix was filled with selected type of carbon particles. Their weight ratio (2.5wt%) was set with respect to our previous works [14,17,18].

Fibrous reinforcements

- Carbon roving (Toho Tenax STS40 F13, number of filaments 24 000, linear density of roving 1 600 tex, fiber diameter 7 μm, volume density 1.77 g.cm^{-3})
- Glass roving (Johns Manville's StarRov 086 1200, number of filaments 2350, linear density of roving 1200 tex, fiber diameter 16 μm, volume density 2.54 g.cm^{-3})

Epoxy matrix

Bisphenol A-based low viscosity epoxy resin EnviPOXY 520 (Green epoxy from Spolchemie) certified EPD for significant CO_2 savings in production, low oil content and high content of renewable resources (minimum 28wt% of bio-carbon). It was mixed with cyclo-aliphatic polyamine curing agent Telalit 0492 (mixing ratio 100:30 by weight).

Carbon fillers

Sigma-Aldrich synthesized graphite powder (GNP), and two types of milled particles from recycled carbon – ELG Carbon Fibre's Carbiso (CMF), and carbon web from pyrolysed acrylic fibrous waste (CPAN) [19,20]. Morphology of particles was controlled by scanning electron microscope (SEM) VEGA3 TESCAN. Perimeter of particles was determined from SEM micrographs using Image analysis software NIS Elements, and converted to equivalent diameter, see Table 1.

  doi:10.5075/epfl-298799_978-2-9701614-0-0

Table 1: Geometry of used carbon fillers analysed from SEM

Particles	GNP	CMF	CPAN
Equivalent diameter* d_e[µm]	4,3	3,3	4,8

*The diameter of particle with assumed circular shape, that have the same perimeter p [µm] as the particles observed on the SEM

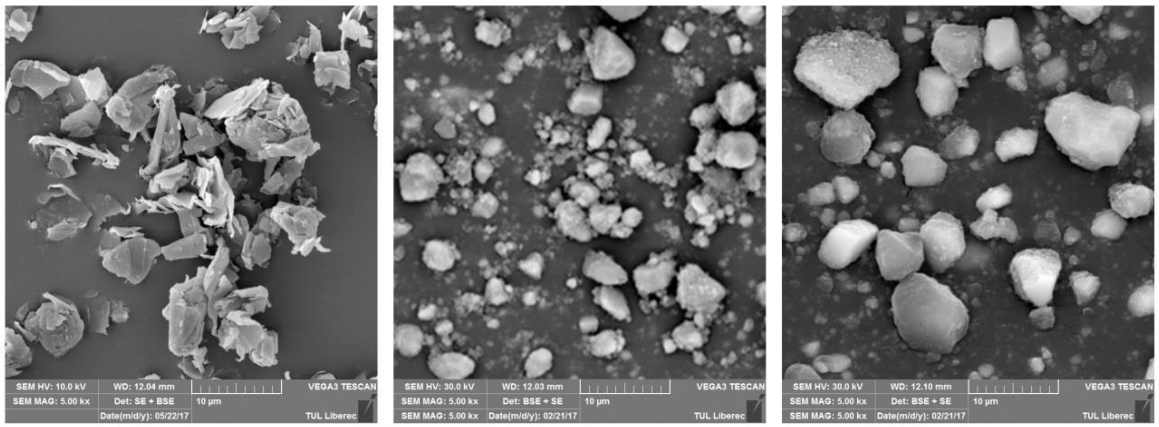

Figure 1. Consecutive from the left: graphite powder (GNP), milled Carbiso fibers (CMF), milled carbon from acrylic waste (CPAN)

Milling of carbon particles

Carbiso fibres and carbon web from acrylic waste were milled by dry pulverization using high energy planetary ball milling, see Fig. 2. Carbon material was placed in 80 ml sintered corundum container and milled by zirconium balls (∅10 mm) for 30 minutes in dry state. Selected balls/material ratio was 10:1, rotation speed was set at 850 rpm.

Figure 2. Milling of carbon particles (https://www.fritsch-international.com/sample-preparation/milling/planetary-mills/details/product/pulverisette-7-premium-line/)

Composite preparation

Composite plates 2 mm thick were made from 8 layers of carbon, and 6 layers of glass roving to achieve 45wt% of UD reinforcement. The layer were impregnated with pre-prepared epoxy resin (neat and modified), then vacuum cured for 24 hour in ambient temperature. This process was followed by post-curing of the resin in 60°C for 15 hours.

  doi:10.5075/epfl-298799_978-2-9701614-0-0

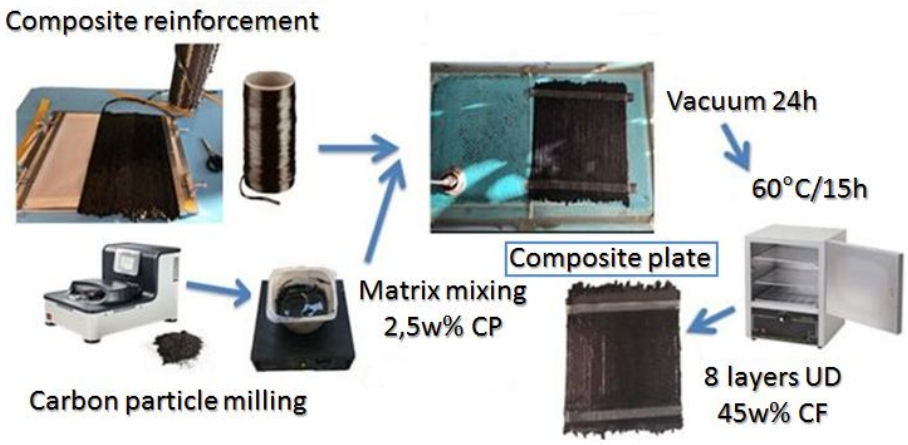

Figure 3. Production scheme for UD fiber/epoxy laminate

2.2 Testing methods

Testing of mechanical properties

Tensile device TIRA TEST 2300 (Labortech) with adjustable measurement modules and corresponding tensile and 3PB jaws was used for analysis of flexural and tensile properties. For testing of flexural properties – 3PB test EN ISO 14125, and for testing of tensile properties - tensile test EN ISO 527-4 were used. Impact test was run according to ISO 179-1:2010, where specimen is laid into horizontal position on Charpy's hammer struts.

Testing of thermo-mechanical properties

Changes of elastic/plastic properties were scanned using DMA1 – 455 (Mettler Toledo) in 3PB mode. The specimen has been loaded as free-fixed beam. The tests have been realized in ambient temperature 25°C under the 1 Hz load frequency. The test time was 30 minutes.

Alternating current (AC) conductivity

AC conductivity σAC [Sm^{-1}] was measured using AGILENT 4294. The measurements were made in the frequency 10 kHz according to ASTM D150-98:2015. A precision analyser was used to measure the sample capacitance C [F] and the loss tangent.

Electromagnetic (EMI) shielding

Electromagnetic shielding was measured according to ASTM D 4935-10 "Standard Test Method for Measuring the Electromagnetic Shielding Effectiveness of Planar Materials", using Rhode and Schwarz FSMR Measuring Receiver. According to this Standard, the shielding effectiveness was analysed in frequency range from 30 MHz to 1,5 GHz, that covers frequencies from long radio waves to the microwave radiation in ultra high frequency spectrum.

3. Results and Discussion

3.1 Mechanical and thermo-mechanical properties

Experimental measurements showed that use of carbon filling improved selected mechanical properties of carbon reinforced specimen (see Fig. 4), if compared to neat epoxy the ones. The same trend we also observed in specimen reinforced with glass rovings.

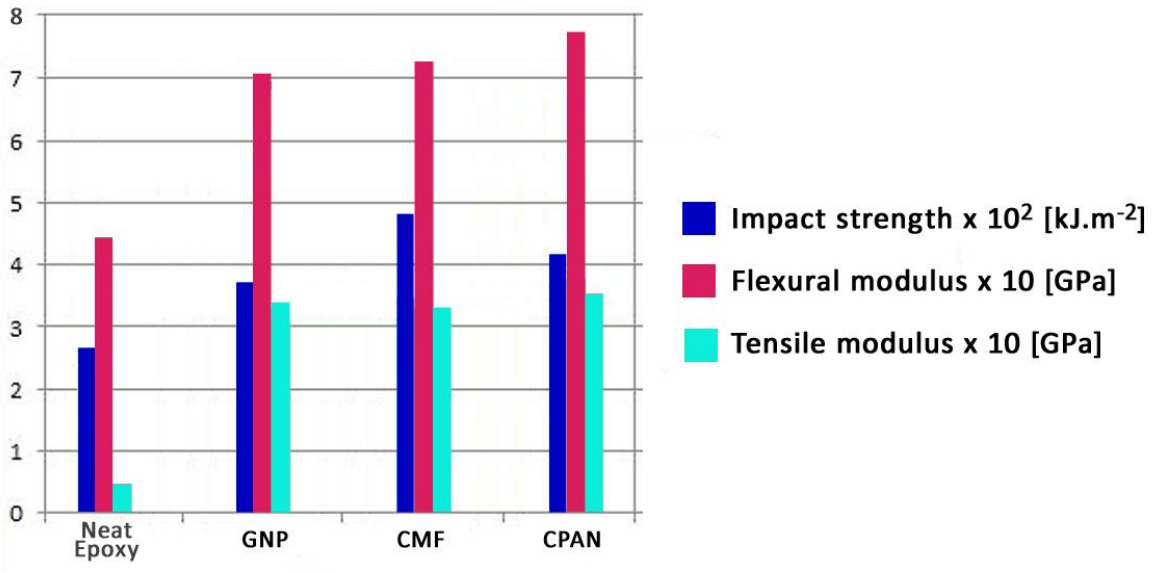

Figure 4. Impact strength, flexural, and tensile moduli of carbon/epoxy laminates

We can observe almost identical results for both, composites with synthetic (GNP), and with recycled (CMF, CPAN) carbon filling. Comparing complex moduli E*[MPa] of neat epoxy, GNP, and CMF specimen via DMA analysis, the same trend showed, see Figure 5. Drop in loss factor tan(delta) is another factor proving the improvement of elastic properties of the studied composite materials, see Figure 6.

As the filling made from synthetic graphene showed results comparable to filling made from recycled carbon fibers, we can state the milled recycled fibers (CMF or CPAN) have great potential as not only cost-effective but also environmentally friendly filling for mechanical improvement of composites.

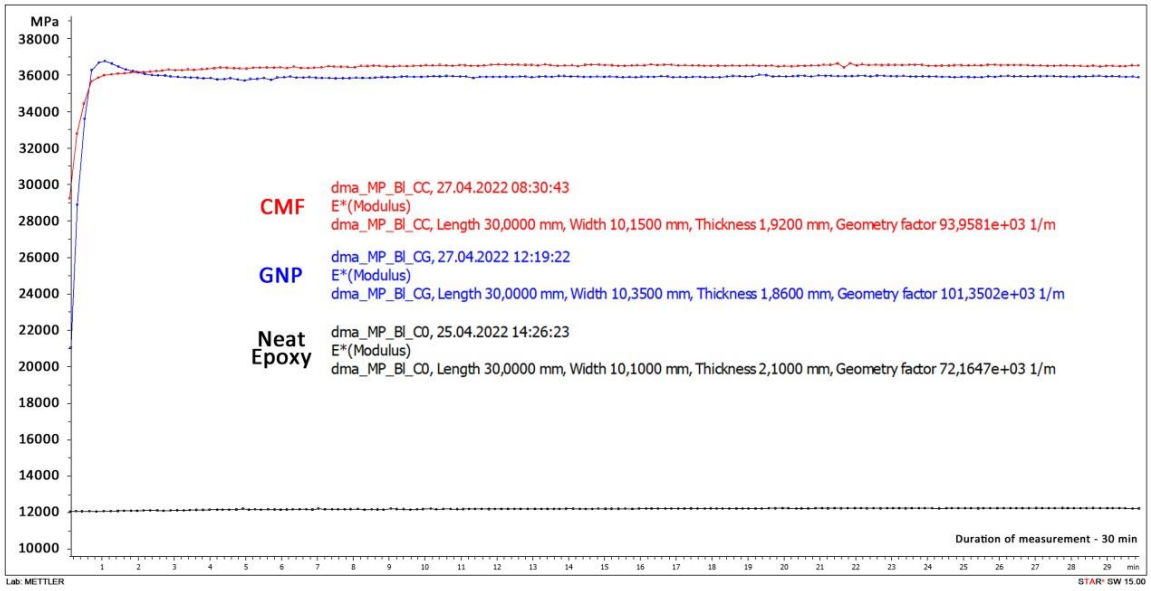

Figure 5. DMA analysis of carbon/epoxy laminates - complex modulus

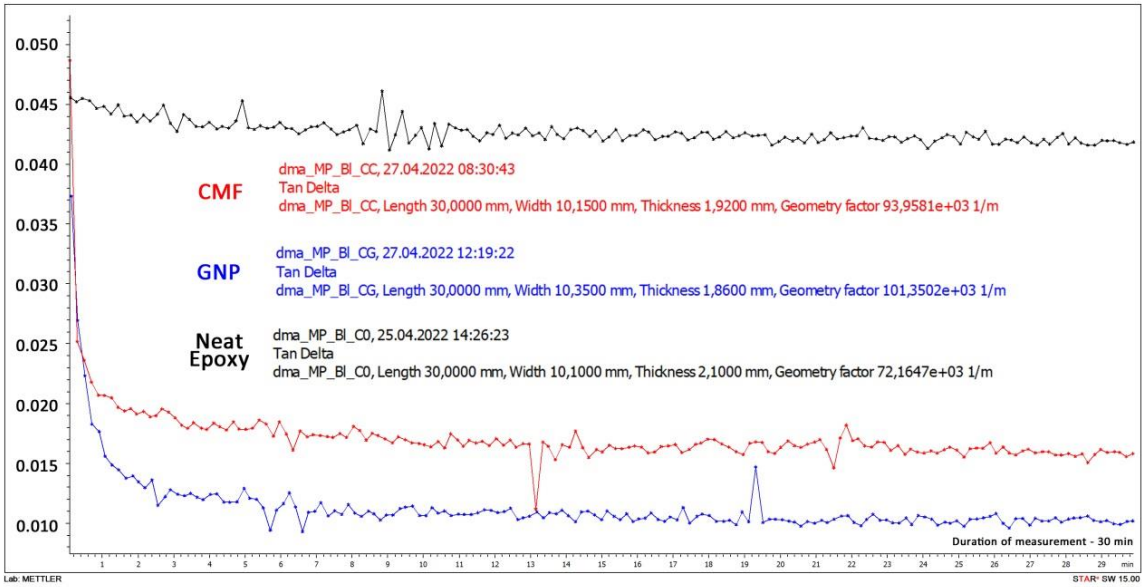

Figure 6. DMA analysis of carbon/epoxy laminates - loss factor

3.2. Electrical properties

Results for surface conductivity and EMI shielding are shown in Figure 7. It is obvious that carbon filling shifted the conductivity of a material, especially when non-conductive fibers (glass roving) are the reinforcement. In this case material shifted from highly insulating to antistatic category, which is very important transformation for many technical applications of such plastics, as it reduces the danger of electrostatic charge. The change of electric conductivity also corresponds to the increase in EMI shielding effectiveness. The increase of efficiency over 10 dB falls within minimum requirements for least shielding effectiveness of protective materials, that expands the potential of glass/epoxy UD laminates in technical applications.

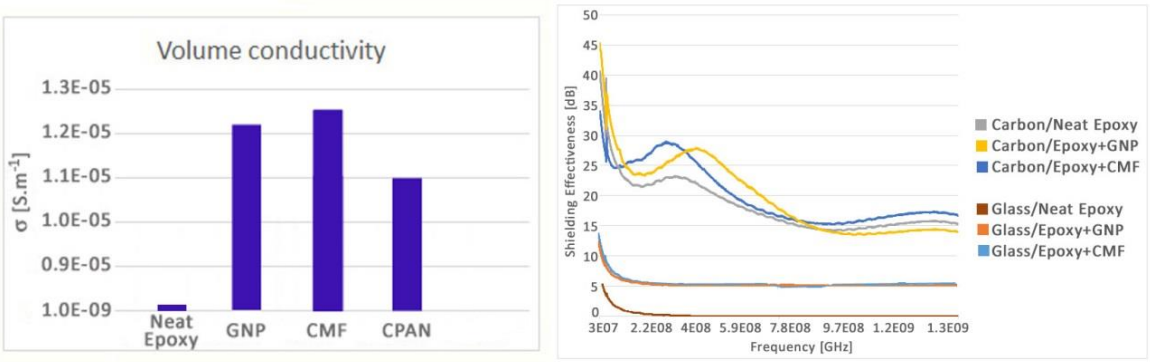

Figure 7. Consecutive from the left: AC Conductivity σ_{AC} [Sm^{-1}] of glass/epoxy laminate and EMI shielding effectiveness of epoxy composites

4. Conclusion

When summarizing the results of experiment, it can be stated that carbon filled FRP composites performed better properties than those with neat epoxy. It shows carbon fillers have great potential for improving the properties of FRP. As an example, we can mention the production of rotor blades, where the researches aim to improve their mechanical properties while maintaining (or reducing) their weight [21].

Theoretically, the simplest way, how to improve its mechanical properties, is to increase the volume fraction of fiber reinforcement, as we can see e.g., when elastic modulus prediction is applied using a simple mixing rule. The problem is, that this modification also leads to an increase in the weight of the structure. If the standard blade from glass/epoxy laminate contains 50% of glass fibers (calculated modulus is approx. 38 GPa), the laminate has a density of about 1650 $kg.m^{-3}$, but at a volume ratio of 60% (calculated modulus is approx. 45 GPa) it already has 1800 $kg.m^{-3}$, which is weight gain 150 kg per cubic meter. For a blade with working area of 5 000 m^2 and thickness of 0.01 m, this means mass increase of 7.5 tonnes. When we use a suitable carbon filler instead, at volume composition glass/epoxy/filler – 50/47.5/2.5 we calculate modulus approx. 44 GPa, while density shifts to 1692 $kg.m^{-3}$, which in abovementioned blades means mass increase of 600 kg only [22].

Another problem are current production technologies (lamination into a negative form or winding of rovings on a positive form), where real composite structure reach maximum fiber volume fraction between 45-55%. These facts point to areas where carbon fillers can make a significant contribution to improvement of structural composites.

It is also remarkable that comparable results as for synthetic graphene were achieved for particles made from recycled carbon fiber sources. Use of such material supports the ecological aspects in design, development, and processing of new fiber/polymer composites.

Although we have not yet explored all the links between filler content and overall performance of studied FRP composites, it is obvious, these materials deserve more detailed studies on microstructure, morphology and material properties, as well as on improvements in composite samples fabrication. This is main challenge for future work.

Acknowledgements

The authors would like to express appreciation for the financial support by the Ministry of Education, Youth and Sports of the Czech Republic and the European Union - European Structural and Investment Funds in the frames of Operational Programme Research, Development and Education (project Hybrid Materials for Hierarchical Structures, Reg. No. CZ.02.1.01/0.0/0.0/16_019/0000843)

5. References

1. Krauklis AE. Composite Material Recycling Technology-State-of-the-Art and Sustainable Development for the 2020s. Journal of Composite Science 2021; 5(28):1-33.
2. Cherif Ch. Textile Materials for Lightweight Constructions. Springer-Verlag, Berlin. 2016.
3. Kotsilkova R, Fragiadakis D, Pissis P. Reinforcement effect of carbon nanofillers in an epoxy resin system: Rheology, molecular dynamics, and mechanical studies. Journal of Polymer Science B 2005; 43(5):522-533.

4. Singh S, Srivastava VK, Prakash R. Influences of carbon nanofillers on mechanical performance of epoxy resin polymer. Applied Nanoscience 2015; 5(3):305-313.
5. Brusentseva TA, et al. Modification of epoxy resin with silica nanoparticles and process engineering of composites based on them. Mechanics of Composite Materials 2015; 51(4):531-538.
6. Baheti V, Militky J, Marsalkova M. Mechanical Properties of Poly-Lactic Acid Composite Films Reinforced with Wet Milled Jute Nanofibers. Polymer Composites 2013; 2133-2141.
7. Almasi A, et al. The Effects of Nanofillers on Composite Materials Mechanical Properties. Revista de Chimie 2017; 68(1):192-199.
8. Gajapriya M, et al. Fillers in Composite Resins – Recent Advances. European Journal of Molecular & Clinical Medicine 2020; 7(1):971-977.
9. Koronis G, Silva A. Green Composites for Automotive Applications. Woodhead Publishing, Elsevier Ltd. 2019.
10. Peliskova M, Saha P. Influence of lightened structure on electrical properties of polymer composites with electroconductive fillers. Chemical Letters 2012 (in Czech); 106:1104-1109.
11. Burchell TD. Carbon Materials for Advanced Technologies. Elsevier Science Ltd. 1999.
12. Delgado JL, et al. The nano-forms of carbon. Journal of Materials Chemistry 2018; 18:1417-1426.
13. Gilbert M. Brydson's Plastics Materials (Eighth Edition). Elsevier Science Ltd., 2017.
14. Tomkova B, et al. Limits of carbon micro/nano particles utilization to improve properties of polymer matrices in fibre reinforced composites. IOP Conf. Series: Materials Science and Engineering 2019; 459:1-6.
15. Rwawiire S, Tomkova B, et al. Acoustic and thermal properties of a cellulose nonwoven natural fabric (barkcloth). Applied Acoustic 2017; 116:177-183.
16. Mishra R, Wiener J, et al. Bio-Composites Reinforced with Natural Fibers: Comparative Analysis of Thermal, Static and Dynamic-Mechanical Properties. Fibers and Polymers 2020; 21(3):619-627.
17. Novotna J, et al. Development of Multilayered Nanocomposites for Applications in Personal Protection. Fibers and Polymers 2018; 19(6):1288-1294.
18. Novotna J, Salacova J, Pechociakova M. C/P carbon composites - reinforcement volume effect on the electrical properties. IOP Conference Series: Materials Science and Engineering 2017; 254:1-8.
19. Baheti V, et al. Optimized preparation of activated carbon nanoparticles from acrylic fibrous wastes. Fibers and Polymers 2015; 16(10):2193-2201.
20. Naeem S, et al. Development of porous and electrically conductive activated carbon web for effective EMI shielding applications. Carbon 2017; 111:439-447.
21. Zangenberg J. et al. Design of a fibrous composite preform for wind turbine rotor blades. Materials and Design 2014; 56: 635-641.
22. Tomkova B. et al. Carbon micro/nano particles utilization in carbon fiber polymer matrix composites. Invited lecture at 26th Advanced Materials Congress, Stockholm, June 10-13, 2019.

Validation of Composite Aerostructures through Integrated Multi-Scale Modelling and High-Fidelity Substructure Testing Facilitated by Design of Experiments and Bayesian learning

Ole Thomsen[a], J.M. Dulieu-Barton[a], S.R.Hallett[a], R. Butler[b]

a: Bristol Composites Institute, University of Bristol, Bristol, UK
b: Materials and Structures Centre, Department of Mechanical Engineering, University of Bath, UK

Abstract: *The aim of CerTest is to develop the building blocks that enable lighter, safer and more cost efficient composite aerostructures. The research will result in a new approach for integrated high-fidelity structural testing and multi-scale statistical modelling through Design of Experiments (DoE) and Bayesian Learning. The underlying assumption is that it is possible to develop a more cost/performance optimised philosophy, by reducing the level of physical testing, especially in the bottom/top levels of the test pyramid. Instead, structural behaviour is accounted for in a new culture of virtual design and validation that promotes a change towards virtual testing, enabling reduction of empiricism, mass savings, expansion of the design and performance envelopes, and reduction of design costs and associated development time.*

Keywords: Performance validation, Composite aero-structures, Sub-component testing, Multi-scale modelling, Bayesian learning, Design of Experiments

1. Introduction

Evidence has emerged, that current test, simulation and certification approaches, as outlined by the generally adopted “building block” approach [1], inhibit the efficient exploitation and optimisation of advanced composite aerostructures. The Programme Grant “Certification for Design: Reshaping the Testing Pyramid” or “CerTest” funded by the UK Engineering and Physical Sciences Research Council [2],[3] seeks to break this impasse. The academic partners are the Universities of Bristol, Bath, Exeter and Southampton. Industrial partners include Rolls Royce, Airbus, GKN Aerospace and BAE Systems. CerTest is also supported by the Alan Turing Institute and The National Composites Institute (NCC), Bristol, UK.

The aim of CerTest is to develop the building blocks that enable lighter, safer and more cost efficient composite aerostructures. The research will result in a new approach for integrated high-fidelity structural testing and multi-scale statistical modelling through Design of Experiments (DoE) and Bayesian Learning. The underlying assumption is that it is possible to develop a more cost/performance optimised philosophy, by reducing the level of physical testing, especially in the bottom/top levels of the test pyramid. Instead, structural behaviour is accounted for in a new culture of *virtual design and validation* that promotes a change towards *virtual testing*, enabling reduction of empiricism, mass savings, expansion of the design and performance envelopes, and reduction of design costs and associated development time.

  doi:10.5075/epfl-298799_978-2-9701614-0-0

2. Research challenges

The CerTest research activities are broken down into 4 key research challenges:

3. **RC1:** Development and validation of a multi-scale statistical modelling framework incorporating Bayesian statistics, iterative solvers, and model order reduction techniques to predict load response, damage initiation and progression in complex composite and structures, including the impact of as-designed subsurface features, manufacturing variability, damage and their statistical distributions.

4. **RC2:** Development and validation of non-destructive evaluation (NDE) toolsets for intrinsic meso-scale features, both as-designed and deviations from design, that can be applied throughout the design and manufacture of composite aerostructures. The toolset will provide an understanding of feature growth and impact on component performance, leading to a knowledge base of structurally important features and in-service damages.

5. **RC3:** Development and validation of novel data-rich experimental techniques to characterise evolving stress and strain due to features, defects and damage and the impact with respect to performance and strength. Furthermore, CerTest develops and validates a novel high-fidelity paradigm for data-rich testing, incorporating full-field imaging and a hybrid testing platform, for composite aerostructures subjected to complex loading.

6. **RC4:** Integration of data-rich experimental procedures for testing of large composite aero-structures and predictive statistical and multi-scale computational models by developing data processing and a closed input/feedback loop based on novel Bayesian Learning and DoE techniques.

A schematic of the CerTest research challenges and their interdependence is shown in Figure 1.

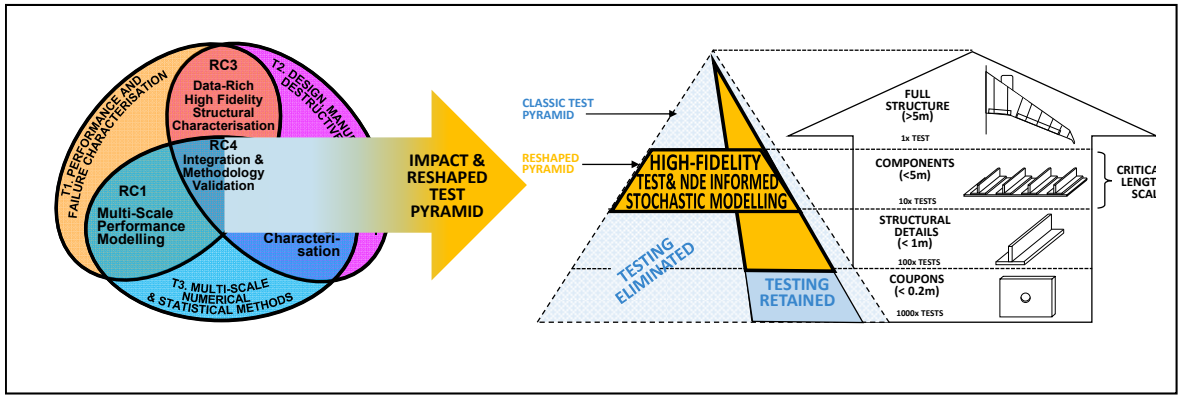

Figure 1. Schematic overview of CerTest research challenges and focus on the sub-structure and component test tier

  doi:10.5075/epfl-298799_978-2-9701614-0-0

2. CerTest research hypotheses

An underlying hypothesis for CerTest is that reliance on physical testing can be reduced by developing the mid-tiers of the testing pyramid. It is at these length scales that are characterised by complexity wrt. material composition, geometric features and load states that, where model benchmarking and validation can be conducted via sufficiently realistic and thus complex complex sub-structure and component tests. The merger of physical test and modelling data, is conducted via a Bayesian inference process or loopomn, which is illustrated in Figure 2.

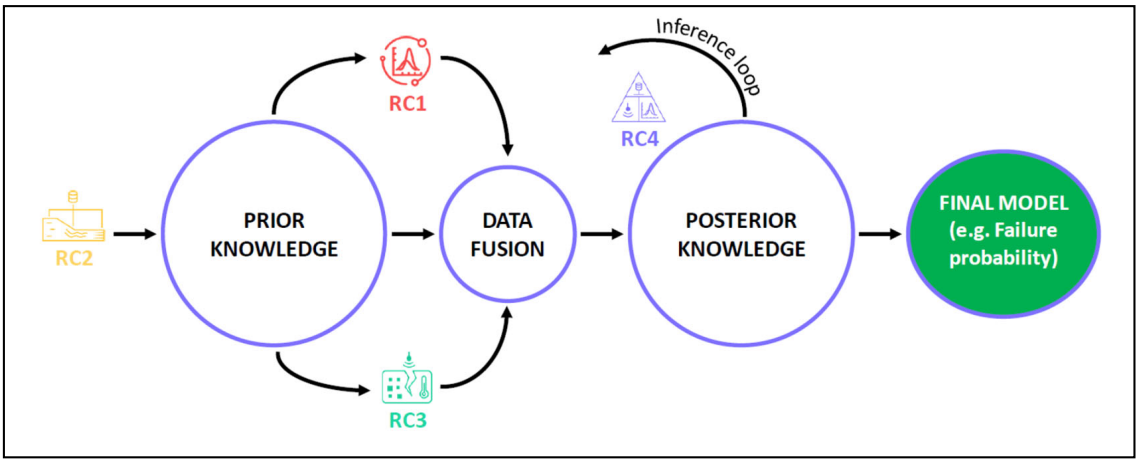

Figure 2. Simplified overview of dataflow in Bayesian processes in CerTest

3. Summary and outlook

CerTest is about halfway through its funding period, and substantial research has been conducted with a focus on multi-scale modelling, characterisation of feature and manufacturing defects in aerospace composite parts, NDE and experimental method development in the 4 research challenges. Presentations covering this research corresponding to RC1, RC2 and RC3 mainly will be presented at the ECCM20.

The current focus, in addition to advancing the research mentioned above, is to develop and validate a Bayesian based Design of Experiments approach to facilitate the validate the multi-scale models, as well as to define and deploy a series of demonstrator cases, where parts or the entirety of the CerTest methodology will be deployed and benchmarked against current validation processes used by aerospace industry.

Acknowledgements

The research is supported by the EPSRC Programme Grant 'Certification for Design – Reshaping the Testing Pyramid' (CerTest, EP/S017038/1 [2]). The support received is gratefully acknowledged.

  doi:10.5075/epfl-298799_978-2-9701614-0-0

4. References

[1] CMH-17-3G, Composite Materials Handbook, Chapter - Polymer Matrix Composites: Materials, Usage, Design, and Analysis, SAE International, June 2012

[2] gow.epsrc.ukri.org/NGBOViewGrant.aspx?GrantRef=EP/S017038/1

[3] www.composites-certest.com

  doi:10.5075/epfl-298799_978-2-9701614-0-0

EASY-REPAIRING OF HIGH PERFORMANCE FIBRE REINFORCED COMPOSITES WITH MULTIPLE HEALING CYCLES AND INTEGRATED DAMAGE SENSING

Thomas D.S. Thorn[a], Yi Liu[b], Emiliano Bilotti[a], Ton Peijs[c], Han Zhang[a]*

a: School of Engineering and Materials Science, Queen Mary University of London, London E1 4NS, UK – t.d.s.thorn@qmul.ac.uk
b: Department of Materials, Loughborough University, Loughborough, LE11 3TU, UK
c: WMG, University of Warwick, Coventry CV4 7AL, UK
Corresponding author: Han Zhang, han.zhang@qmul.ac.uk

Abstract: *An aerospace grade carbon fibre/epoxy laminate with increased fracture toughness and the ability to repeatably repair delamination damage through a scalable phenoxy thermoplastic interleaving method is here-in reported. Compared to a neat carbon fibre/epoxy reference laminate, an increase in the propagation critical strain energy release rate ($G_{IC\text{-}propagation}$) of over 430% is achieved. Recovery of interlaminar fracture toughness of delaminated specimens is realized after a simple compression moulding repairing cycle at elevated temperature. The $G_{IC\text{-}propagation}$ and peak load of interleaved specimens remains greater than the reference composites after five fracture and repair cycles. These results were achieved with laminates containing only 1.0 wt.% phenoxy and a fibre volume fraction >50 %. Moreover, in-situ damage sensing through monitoring electrical resistance has been established alongside a repeatably repairable composite for the first time, with specimens showing an increasing correlation of resistance change to delamination length after the first repair cycle.*

Keywords: Carbon fibre reinforced composite; multifunctional composites; phenoxy; repairing; damage sensing

1. Introduction

Advanced fibre reinforced composite materials are being increasingly adopted in engineering applications to replace metals in multiple engineering sectors, primarily in automotive, aerospace and renewable energy technologies. The reduction in weight with similar or greater in-plane stiffness increases fuel efficiency, thereby reducing costs for large structural parts. However, the orthotropic nature of laminated composites results in poor out-of-plane properties such as impact resistance and interlaminar fracture toughness.

The highly crosslinked chemistry of aerospace grade epoxy matrix composites means damage sustained during service life cannot be repaired without first removing or replacing the damaged area, usually through adhesively bonded patches or scarfs [1]. The addition of thermoplastics such as EMAA [2,3] or PCL [4,5] have been used to achieve both tough and easily repairable fibre-reinforced composites. Unfortunately, most current thermoplastics either produce volatiles during the healing process, and/or possess relatively low melting temperatures (T_m) and below room temperature glass transition temperature (T_g), restricting their use in high temperature environments and reduce flexural properties and in-plane stiffness. In this work, a simple repairing route via thermoplastic interleaves is presented which can significantly toughen the composite laminates and restore the out-of-plane toughness after a repairing process. A

  doi:10.5075/epfl-298799_978-2-9701614-0-0

thermoplastic glass transition temperature above 90°C makes this system compatible for high temperature structural composites, which has not until now been achieved.

Second, continuously measured property changes within composites during service-life can be correlated to the propagation of their internal damages. Changes in electrical resistance within fibre reinforced composites as a result of various damage modes have been previously investigated to assess structural health [6-8]. In this paper a repeatably repairable composite is presented alongside a structural health monitoring system based on electrical method. The benefits to an integrated damage sensing and repairing solution are manyfold, not only in terms of reducing costs for industry through greatly increased service-life and remote damage localization, but also increased safety for end users and greater sustainability in composites through a policy of reusing rather than recycling.

2. Experimental

2.1 Materials

The fibre-reinforced composite system consisted of a high strength cross-ply carbon fabric from Formax (UK), with an areal weight of 303 g/m^2, and MVR444, a 2-part aerospace grade epoxy from Cytec Ltd. (UK). Polyhydroxy ether of bisphenol A (Phenoxy™) in pellet form were procured from InChem®, with a specified average molecular weight (M_w) of 52,000 Da. The particular molecular weight grade, designated PKHH, possesses a glass transition temperature (T_g) of 92°C and a melt flow index (MFI) of 4g/10minutes at 200°C. A polytetrafluoroethylene (PTFE) release film (A6000®) of 12µm thickness was used to act as the specimen pre-crack and was supplied from Aerovac Systems Ltd.

2.2 Composite preparation and manufacture

Interleave fabrication. Thin continuous films of phenoxy were prepared using a melt-compounding method. Pellets of pre-dried phenoxy were first heated to 240°C within a Dr Collin P3100 E Hot Press and then directly compression moulded at a pressure of 240bar. The fabricated interleaves had an average thickness of between 120µm and 130µm.

Fabrication of fibre-reinforced composites. 24-ply laminates were fabricated in a $[0,90,90,0]_{3S}$ lay-up. For interleaved laminates, phenoxy films were placed between the two mid-plies of the lay-up, covering approximately one half of the mid-ply fabric area, with the remaining midply area occupied by a PTFE film to generate the desired pre-crack. Laminates were fabricated using a vacuum-assisted resin infusion (VARI) technique, the details of which can be found in our previous work [9]. The designed curing cycle consisted of a ramp from 30°C to 120°C at 3°C/minute and held for 2 hours, followed by a post-cure at 180°C for a further 3 hours. The calculated estimate of fibre volume fraction for both neat carbon fibre/epoxy and phenoxy interleaved laminates was 0.54.

2.3 Characterization

Specimens were cut from cured panels with approximate dimensions of 130mm in length and 20mm in width and then prepared for double cantilever beam (DCB) testing in accordance with ASTM D5528 [10]. Specimens were tested using an Instron 5566 universal testing frame with a 1kN load cell at a crosshead speed of 1mm/minute. At least 4 reference and 4 interleaved specimens were tested. Crack advancement was visually observed using a traveling optical

  doi:10.5075/epfl-298799_978-2-9701614-0-0

microscope and crack growth was recorded manually and correlated to load-displacement data in order to determine $G_{IC\text{-}propagation}$ values.

Fractured specimens were repaired by hot pressing at 180°C, after a 10 minute pre-heat step. Specimens were pressed at 50bar for 2 minutes, followed by continued pressing while cooling to a temperature below the T_g of the phenoxy (92°C).

The fractured surfaces of specimens from Mode-I testing were examined through scanning electron microscopy (SEM) using an Inspect™ F from FEI Company (Netherlands). Specimens were sputter coated with either an Au or Au/Pd target before inspection with a 10kV accelerating voltage.

Measuring change in electrical resistance during Mode-I testing was achieved by attaching copper wires to the specimen edges using a silver loaded epoxy adhesive, separated by the PTFE pre-crack. Resistance values were recorded with an Agilent 34401A digital multimeter connected to a LabVIEW program.

3. Results

3.1 Load-displacement curves & R-curves

A representative load-displacement curve to indicate crack growth behavior in the phenoxy interleaved specimens during the 1st, 3rd and 5th tests is given in Figure 1a. During the first test, reference specimens of carbon fibre/epoxy exhibit a moderately unstable crack propagation characterized by multiple small load drops and a peak load of approximately 33N and a reference $G_{IC\text{-}propagation}$ of 0.34kJ/m^2.

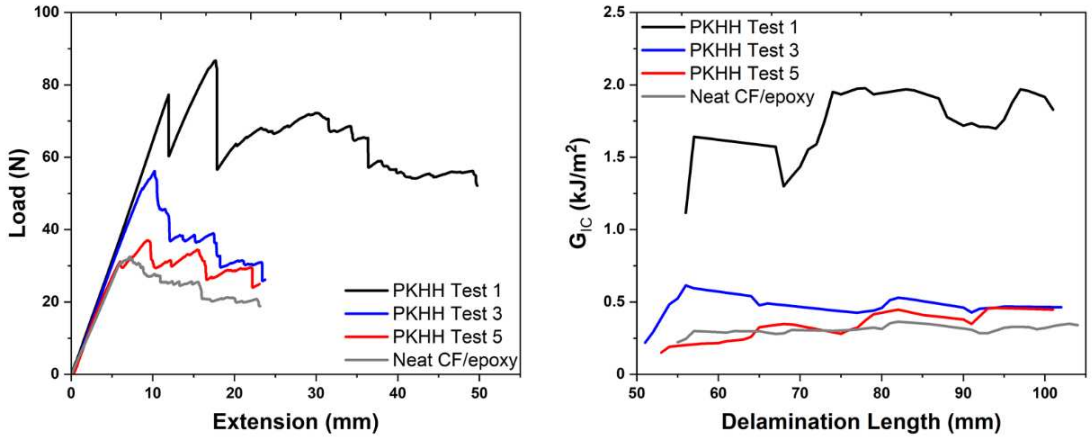

Figure 1. a) The representative load-displacement curves of PKHH interleaved and reference composites, showing the changing fracture behaviour after each repairing cycle, b) associated R-curves, showing the decrease in average G_{IC} after each repair cycle.

The fracture behaviour for reference composites is typical of the brittle fracture associated with highly crosslinked epoxy matrices. Reference specimens are incapable of repair by the hot-press method and therefore only the first test is presented as a comparison to interleaved specimens' fracture behaviour after multiple repairing cycles. Phenoxy interleaved specimens show a dramatic increase in peak load and a stick-slip crack growth behaviour as a result of the

thermoplastic toughening. After each repairing cycle, the peak load decreases and the stick-slip behaviour becomes less pronounced and a more stable propagation emerges.

The corresponding representative R-curves for each load-displacement curve is presented in Figure 1b. The rising nature of the R-curve in interleaved specimens is apparent, while the stick-slip behaviour of specimens in the 1st test results in a large variation in individual G_{IC} values along the delamination length. This behaviour diminishes after each repairing and coincides with the stable crack propagation observed in the load-displacement curves.

3.2 Interlaminar Fracture Toughness & Peak Load

The summarized calculated $G_{IC\text{-}propagation}$ and determined peak load (P_{max}) values for phenoxy interleaved specimens after each repair cycle is given in Figure 2. In the 1st test, interleaving phenoxy dramatically increases the $G_{IC\text{-}propagation}$ value by 432%, from 0.34kJ/m^2 to 1.81kJ/m^2, a similar result found in our previously reported work [9]. The P_{max} is increased by 110%, from 34.7N, to 72.9N. After the first repair cycle (2nd test), the $G_{IC\text{-}propagation}$ decreases from 1.81kJ/m^2 to 0.62kJ/m^2, 34% of the pristine toughness. With each subsequent repair and re-fracture, the $G_{IC\text{-}propagation}$ continues to decrease, but at a low and consistent rate, remaining after 5 complete delaminations greater than the reference toughness. This result demonstrates that phenoxy interleaved composites can be repaired multiple times with a $G_{IC\text{-}propagation}$ in each test greater than that of the reference carbon fibre/epoxy composite.

The P_{max} after the first repair cycle is 72.1N, a 99% retention compared to the first test max load, but then decreases linearly with each subsequent repair cycle. The maximum load is expected to decrease with each repair cycle as some of the polymer chain lengths are severed after each delamination, effectively reducing the average molecular weight of the thermoplastic along the interface between fracture surfaces. There will also be damages to the areas of low thermoplastic concentration such as intralaminar fibre damage and epoxy matrix cracking, which aren't repaired and so reduce the peak load in subsequent tests.

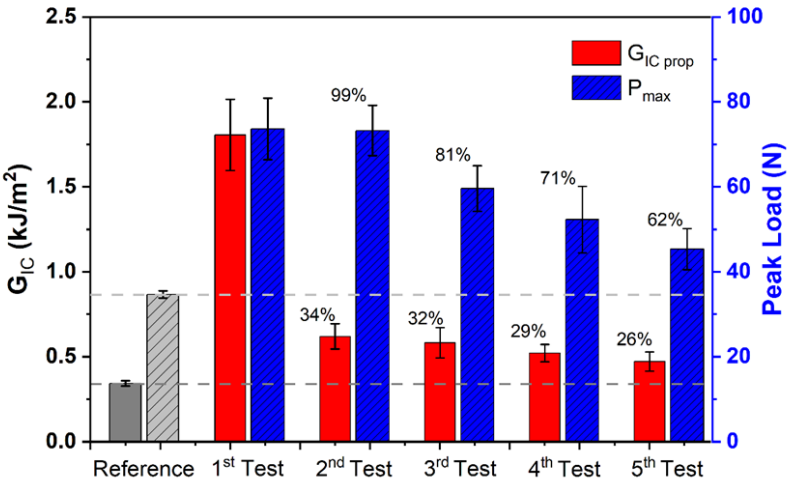

Figure 2. Summarized $G_{IC\text{-}propagation}$ and peak load values for PKHH interleaved composites after each repairing cycle. $G_{IC\text{-}propagation}$ is increased more than four-fold by the introduction of PKHH interleaves. The toughness after repairing is significantly reduced but remains greater than the reference after 5 fracture tests.

  doi:10.5075/epfl-298799_978-2-9701614-0-0

3.3 In situ damage sensing

Changes in electrical resistance during each interlaminar fracture toughness test were recorded and used to correlate the damage state within the composite to its internal electrical properties. The change in resistance compared to the undamaged state is assessed qualitatively as a suitable method for condition-based maintenance within phenoxy interleaved composites.

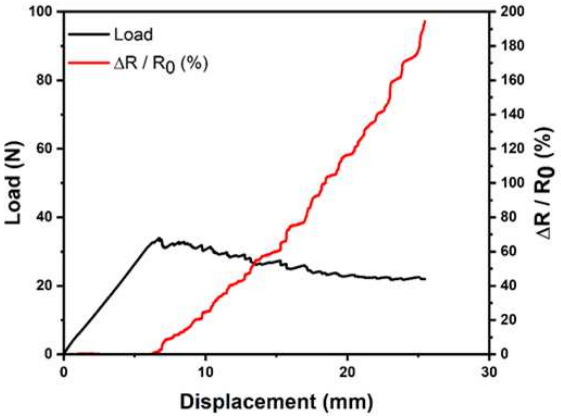

Figure 3. In situ damage sensing curves for a reference carbon fibre/epoxy laminate, showing a steady increase in percent change in resistance with the propagating crack during Mode-I loading.

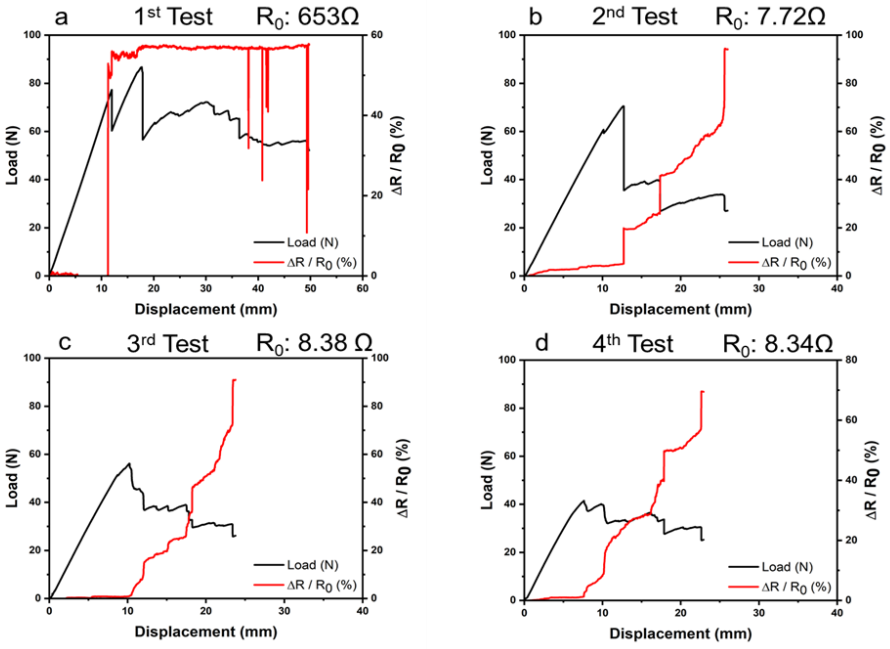

Figure 4. In situ damage sensing results of phenoxy interleaved composites during the first fracture and each subsequent repair and re-fracture, up to the 4th test.

Reference specimens were tested as a baseline for correlation between electrical resistance change and the load-displacement characteristics. As shown in Figure 3, the change in resistance increases steadily with the crack propagation, indicating that there is sufficient carbon fibre bridging and the change in resistance method as a good measure of the damage state within the composite for a condition-based maintenance approach.

  doi:10.5075/epfl-298799_978-2-9701614-0-0

In contrast, Figure 4 shows the representative results for phenoxy interleaved composites from the 1st through 4th tests. During the 1st test, the resistance increases with the first instance of crack growth, but then remains similar or largely unstable for the remainder of the crack propagation, indicating that the through-thickness conductivity is dissimilar along the length of the composite. This finding is in consistent with previous literature where insulating thermoplastic interleaves are placed to block the electron pathways [11]. After the first repairing and retest, the initial resistance decreases from 653Ω to 7.72Ω, while the change in resistance becomes more correlated with the load drops associated with the crack propagation. The through-thickness of the composite becoming more conductive is attributed to the reduced thickness of the insulating thermoplastic midplane due to the pressure applied during the repairing process.

3.4 Fractography

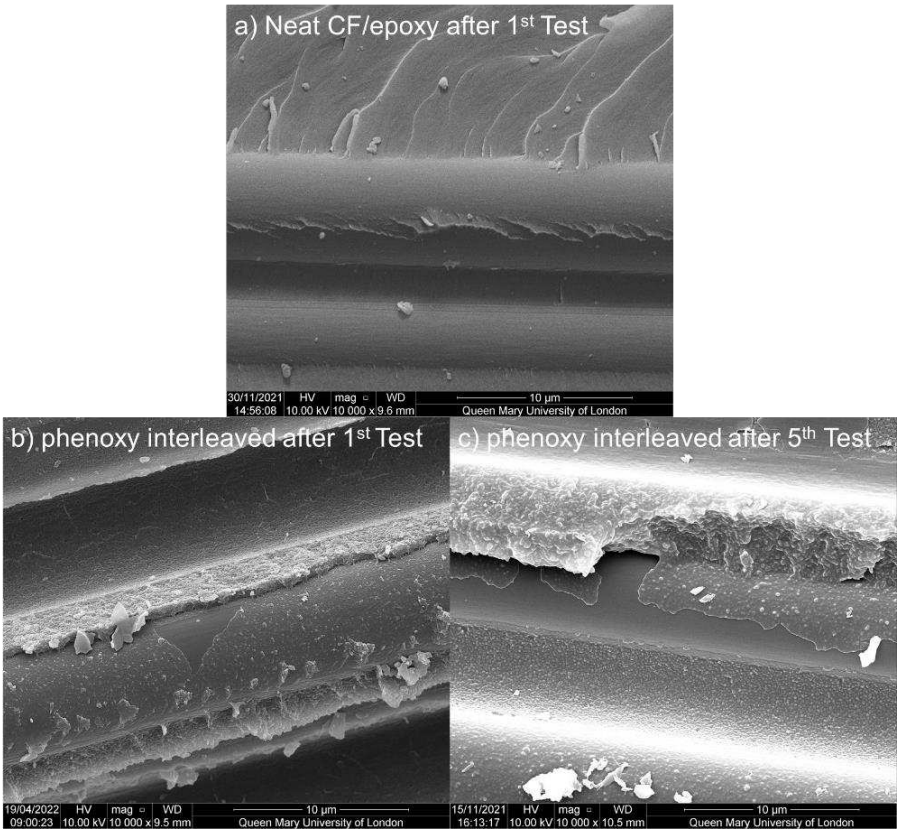

Figure 5. a) reference carbon fibre/epoxy laminate fracture surface, showing a good bonding of epoxy to carbon fibres and relatively smooth matrix fracture, b) phenoxy interleaved composites after the first test, showing attached and pulled of PKHH, c) phenoxy interleaved composites after the 5th fracture, showing similar morphology to after 1st fracture.

SEM of fracture surfaces after DCB testing was undertaken to ascertain and compare the differences in morphology of phenoxy interleaved composites both before and after the repairing process. The reference specimen without phenoxy in Figure 5a highlights the representative fracture surface of a neat carbon fibre/epoxy reference laminate, showing a complete coverage and bonding between epoxy and carbon fibres. The smooth surfaces are typical of the brittle fracture process associated with highly crosslinked thermoset matrix composites.

  doi:10.5075/epfl-298799_978-2-9701614-0-0

In the case of phenoxy interleaved composites, SEM images of the fracture surfaces taken after the 1st fracture, Figure 5b, show carbon fibres covered by a layer of a predominantly thermoplastic phase, identified by the more complex morphology. However, some of the phenoxy which surrounds the carbon fibre is seen to have been peeled off during the fracture process, leaving behind the exposed carbon fibres. After the 5th fracture test, Figure 5c, a similar morphology is seen in comparison to the 1st test, with some carbon fibre areas coated with phenoxy, while in other areas, the phenoxy has been effectively peeled from the fibre surface.

These fracture surfaces provide key evidence to explain the associated toughening and repairing results. Before the first test, the phenoxy is presumed to be well-coated on most fibre surfaces with a very favourable compatibility. The energy required for fracture is greatly increased as a result, with both adhesive failure (between phenoxy and carbon fibres) and cohesive failure (within the phenoxy phase), shown by the partially peeled off phenoxy layer. After the first repairing cycle, the phenoxy is able to bridge fracture surfaces and provide the observed repairing, but may be unable to bond with the carbon fibre to the same degree as before; during the curing and phase separation process. Therefore, the 2nd test $G_{IC\text{-}propagation}$ will be significantly reduced. The morphology of fracture surfaces after each subsequent repair and test is shown by the SEM images to not change significantly, explaining the slower decrease in $G_{IC\text{-}propagation}$ between the 3rd, 4th and 5th tests.

Furthermore, the evidence of peeled off phenoxy from carbon fibres as shown in Figure 5b-c will expose conductive carbon fibres on the fracture surfaces. This in turn will increase the midplane conductivity and may be a further physical mechanism in the more sensitive damage sensing results after the 1st fracture, as seen in the results for in situ damage sensing.

4. Conclusions

Carbon fibre epoxy composites were manufactured with a small loading of phenoxy through a simple and scalable midply interleaving method. Interleaved composites showed an initial 430% increase in fracture toughness compared to a reference carbon fibre/epoxy laminate. An initial repairing efficiency of 34% was reported, determined as the retention in $G_{IC\text{-}propagation}$ compared to the original toughened laminate. Interleaved laminates were capable of repair to a level greater than the original toughness of the reference laminate, even after five DCB fracture tests to the same specimen. Scanning electron micrography of fracture surfaces provides an explanation to the observed toughening and repairing results. Fracture toughness after the 1st repairing is reduced due to the adhesive peeling of between phenoxy and carbon fibres, which occurs during the 1st fracture, and which cannot be completely reestablished by the repairing regime. The similar fracture surface morphology between interleaved specimens after every fracture shows why subsequent repairing will result in a very gradual decrease in $G_{IC\text{-}propagation}$ and multiple cycles of repair are possible. Results from in situ damage sensing show that the initially insulating midply region of interleaved laminates provides a poor correlation between change in resistance and crack propagation. After the 1st repair, there is a significant decrease in initial through-thickness resistance and the change in resistance against crack propagation is well correlated thereafter, providing a means to predict the damage state within repairable composites. This behaviour is attributed to the use of external pressure applied during the repairing regime which will also reduce the size of the mid-ply region. In short, a novel repeatably repairable and toughened composite has been developed for the first time alongside an in situ damage sensing strategy for the purposes of extending the service life of fibre

  doi:10.5075/epfl-298799_978-2-9701614-0-0

reinforced composites. Increased fracture toughness with a favourable repairing efficiency and a quantitative method to assess the damage state after the 1st repairing cycle is a proof of concept that both damage sensing and repairing composites after thermoplastic interleaving is achievable.

Acknowledgements

The authors would like to acknowledge support from the Engineering and Physical Sciences Research Council (ESTEEM, EP/V037234/1), and the Graphene Flagship Core 3 (grant agreement: 881603) which is implemented under the EU-Horizon 2020 Research & Innovation Actions and is financially supported by EC-financed parts of the Graphene Flagship.

5. References

1. Baker A, Dutton S, Kelly D. Composite Materials for Aircraft Structures. 2nd ed. Reston (VA): American Institute of Aeronautics and Astronautics; 2004.
2. Meure S, Furman S, Khor S. Poly [ethylene-co-(methacrylic acid)] healing agents for mendable carbon fiber laminates. Macromolecular Materials and Engineering. 2010 May 18;295(5):420-4.
3. Pingkarawat K, Wang CH, Varley RJ, Mouritz AP. Self-healing of delamination fatigue cracks in carbon fibre–epoxy laminate using mendable thermoplastic. Journal of Materials Science. 2012 May;47(10):4449-56.
4. Cohades A, Daelemans L, Ward C, Meireman T, Van Paepegem W, De Clerck K, Michaud V. Size limitations on achieving tough and healable fibre reinforced composites through the use of thermoplastic nanofibres. Composites Part A: Applied Science and Manufacturing. 2018 Sep 1;112:485-95.
5. Jony B, Thapa M, Mulani SB, Roy S. Repeatable self-healing of thermosetting fiber reinforced polymer composites with thermoplastic healant. Smart Materials and Structures. 2019 Jan 25;28(2):025037.
6. Thostenson ET, Chou TW. Carbon nanotube networks: sensing of distributed strain and damage for life prediction and self healing. Advanced Materials. 2006 Nov 3;18(21):2837-41.
7. Kostopoulos V, Vavouliotis A, Karapappas P, Tsotra P, Paipetis A. Damage monitoring of carbon fiber reinforced laminates using resistance measurements. Improving sensitivity using carbon nanotube doped epoxy matrix system. Journal of Intelligent Material Systems and Structures. 2009 Jun;20(9):1025-34.
8. Zhang H, Liu Y, Huang M, Bilotti E, Peijs T. Dissolvable thermoplastic interleaves for carbon nanotube localization in carbon/epoxy laminates with integrated damage sensing capabilities. Structural Health Monitoring. 2018 Jan;17(1):59-66.
9. Zhang H, Bharti A, Li Z, Du S, Bilotti E, Peijs T. Localized toughening of carbon/epoxy laminates using dissolvable thermoplastic interleaves and electrospun fibres. Composites Part A: Applied Science and Manufacturing. 2015 Dec 1;79:116-26.
10. 5528-01 AD. Standard test method for Mode I interlaminar fracture toughness of unidirectional fiber-reinforced polymer matrix composites. ASTM International; 2001.
11. Zhang H, Liu Y, Huang M, Bilotti E, Peijs T. Dissolvable thermoplastic interleaves for carbon nanotube localization in carbon/epoxy laminates with integrated damage sensing capabilities. Structural Health Monitoring. 2018 Jan;17(1):59-66.

  doi:10.5075/epfl-298799_978-2-9701614-0-0

THE EFFECT OF SHORT CARBON FIBERS ON VISCOELASTIC BEHAVIOR OF UHMWPE

Stephanie, Gonçalves Nunes[ab], Roshan, Swar[a], Nazanin, Emami[a], Janis, Varna[ab]

a: Luleå University of Technology, Department of Eng. Sciences and Mathematics, Sweden - stephanie.nunes@ltu.se

b: Riga Technical University, Institute of Mechanics and Mechanical Engineering, Latvia

Abstract: At service temperatures, ultra–high molecular weight polyethylene (UHMWPE) is a highly viscoelastic (VE) material due to its low glass transition temperature (≈-113 °C). Since the mechanical response changes over time, the ability to predict and improve its performance over lifetime is an engineering concern. Adding short carbon fibers (SCF) as reinforcement (10 wt%) is expected to improve the material instant and long-term properties. VE relaxation functions for UHMWPE and composite at different temperatures (25-100 °C) are obtained from experimental data used to find parameters in a Schapery's type linear VE model. Then, relaxation functions of the SCF (randomly distributed) composite are predicted using the quasi-elastic approach. The results show that fibers affect positively the VE properties of UHMWPE and that the temperature- and time-dependent matrix behavior affects the stress transfer to fibers However, due to uncertainty regarding the input parameters, limiting the applicability of the chosen quasi-elastic approach, the quantitative agreement is not perfect.

Keywords: reinforced thermoplastic; stress relaxation; viscoelasticity; quasi-elastic approach

1. Introduction

Ultra–high molecular weight polyethylene (UHMWPE) is a linear semi crystalline polymer, with mechanical properties dependent on both phases, crystalline and amorphous, giving to the material low glass transition temperature ($T_g \cong$ -113 °C). Therefore, at service temperatures, UHMWPE is highly viscoelastic (VE) with characteristics such as low modulus and hardness, and high creep rate, which significantly limits its applicability, especially when long-term behavior is requested.

Since even under low loading conditions the UHMWPE behaves viscoelastically, with mechanical properties (i.e. creep and stress relaxation) that are rate and temperature-dependent, the ability to predict its performance over lifetime (long-term) is an important engineering concern, [1]. However, to be able to predict the long-term material behavior, long-time tests must to be performed. As an alternative, the time-temperature superposition principle (TTSP) is widely used in polymer science upon linear VE data to estimate long-term properties of polymer-based materials from short-term tests [2].

As UHMWPE usually exhibits unsatisfactory performance for engineering applications, one way to improve its long-term mechanical properties is through reinforcement of such polymer [1,3]. The addition of fiber reinforcements generally improves the overall performance and properties of the composite. According to Vadivel et al. [3], short carbon fibers (SCFs) have the potential to improve the polymer long-term properties and also provide a good interface with the UHMWPE matrix when compression molded.

  doi:10.5075/epfl-298799_978-2-9701614-0-0

Experimental measurements are the most direct method to explore the effect of constituents and microstructural parameters of fiber reinforced polymer behavior, however, they are usually costly and time-consuming. Therefore, accelerated methodology which includes experimental and theoretical tools is needed for faster development of polymer-based materials [4]. If the composite fiber orientation state is known, micromechanics-based models could be used for predicting the effective mechanical properties of such reinforced composites.

In this context, this research aims to estimate the UHMWPE/SCF composite viscoelastic properties through experimental stress relaxation data for pure UHMWPE at different temperatures, identifying relaxation functions in a Schapery's type linear VE model. Then, the so called quasi-elastic approach is used to simulate relaxation functions for composite. In this approach, the composite relaxation function in an arbitrary instant of time is calculated utilizing elastic expressions where the matrix relaxation function's value at that instant is used. Micromechanics-based model is applied to simulate the VE behavior for a short fiber composite with a given fiber orientation distribution and length correction factor. Shear lag model is used to calculate the length factor. The simulated relaxation curves are compared with test data for composites and the applicability of the quasi-elastic approach and used model is assessed.

2. Theoretical considerations

2.1 Viscoelastic material model

A modified Schapery's thermodynamically consistent linear viscoelastic (VE) material model is used, Eq. (1). In the used thermo-rheologically simple (T-R simple) model viscoplastic (VP) effects are not considered and just uniaxial tensile loading (1-D) is described. In this study, data reduction for the matrix and the composite, simulations and analysis will be performed separately for each temperature and, therefore, introduction of time–temperature shift factors and master curves is unnecessary

$$\sigma(t) = E_r\varepsilon + \int_0^t \Delta C(t-\psi)\frac{d(\varepsilon)}{d\psi}d\psi \tag{1}$$

$$\Delta C(t) = \sum_m C^m exp\left(-\frac{t}{\tau_m}\right) \tag{2}$$

where, τ_m are relaxation times and C^m coefficients in Prony series, which are constants, different for tests and simulations at different temperatures (T). The same type of material model is applied for both, the matrix and the composite.

In an idealized relaxation test, where strain ε_0 is applied at $t = 0$ as a Heaviside step function, the stress relaxation, according to Eqs. (1) and (2), is given by

$$\sigma_{rel} = \varepsilon_0\left[E_r + \sum_m C^m exp\left(-\frac{t}{\tau_m}\right)\right] \tag{3}$$

In Eq. (3), the expression in brackets is the stress relaxation function, where its value at $t = 0$ is the epoxy glassy modulus. Eq. (3) together with relaxation test data, is often used to find the coefficients C^m in the Prony series.

In case of loading-holding (L-H) tests performed in this study, the strain is not applied as a Heaviside step-function (Eq. 3) It will increase from zero to ε_0 over a finite time t_1. Therefore, in the L(t_1)-step during the time interval $0 < t \leq t_1$, stress is given by

  doi:10.5075/epfl-298799_978-2-9701614-0-0

$$\sigma(t) = \left[E_r \frac{t}{t_1} + \frac{1}{t_1}\sum_m C^m \tau_m \left(1 - exp\left(-\frac{t}{\tau_m}\right)\right)\right]\varepsilon_0, \quad \varepsilon = \varepsilon_0 \frac{t}{t_1} \tag{4}$$

In the H(t^*)-step, where the strain is held constant in the time interval $t_2 > t \geq t_1$, stress is given by

$$\sigma(t) = \left[E_r + \frac{1}{t_1}\sum_m C^m \tau_m exp\left(-\frac{t}{\tau_m}\right)\left(exp\left(\frac{t_1}{\tau_m}\right) - 1\right)\right]\varepsilon_0, \quad \varepsilon = \varepsilon_0 \tag{5}$$

2.2 The quasi-elastic approach

The quasi-elastic approach is very efficient in calculating relaxation functions of composites based on known relaxation functions of constituents. The value of the composite relaxation function at time instant t is calculated using micromechanics expressions from linear elasticity, using for VE constituents their relaxation function values at the same time instant. Theoretically, this approach is not correct, because the correspondence principle between elastic and VE solutions is valid in Laplace domain, not in the time domain. However, as shown by Schapery, the error by using this approach in time domain is rather small in cases where functions are changing monotonously as it is in an idealized relaxation test described by Eq. (3). More details about the inversion methods between time- and Laplace-domains and their accuracy can be found in Park et al. [5].

2.2.1 Micromechanics-based model

Among the several micromechanics-based models that consider the effects of physical properties and/or geometric parameters of individual phase components for the prediction of effective macroscopic mechanical properties of heterogeneous polymeric composite materials, rule of mixture (ROM) for long fiber composites is the simplest one [4]. Nonetheless, regarding short fibers reinforced composites, ROM has limited applicability. However, due to simplicity and practical issues, ROM has been modified (MROM) based on experimental or numerical data to fit the curves. Therefore, empirical formulas are generally employed to obtain better agreement with experiment.

Approximate models are available to predict the elastic properties of composites reinforced by randomly distributed short fibers by introducing correction factors in ROM. The used MROM adopts the following assumptions: a) fibers are randomly distributed in 3-D ($\eta_\theta = 0.2$); b) perfect bonding between fiber and matrix; and d) introduction of the correction factors of fiber length efficiency (η_l) to reflect the stress distribution in the fiber.

Applying the expressions for the VE case, the matrix related terms become time-dependent. Therefore, in the loading direction, the stress distribution in the composite (σ_c) will be given by,

$$\sigma_c = (\eta_\theta \eta_l(t) V_f E_f + V_m E_m(t))\varepsilon_c(t) \tag{6}$$

for,

$$\eta_l(t) = \left(1 - \frac{2r_f}{l_f \beta(t)} \tanh \beta(t) \frac{l_f}{2r_f}\right) \tag{7}$$

  doi:10.5075/epfl-298799_978-2-9701614-0-0

$$\beta(t) = \sqrt{\frac{2G_m(t)}{E_f \frac{1}{2}\ln(\frac{1}{V_f})}} \tag{8}$$

$$G_m(t) = E_m(t) \cdot \frac{1}{2\big(1+\nu(0)\big)} \tag{9}$$

where E_f and E_m are the elastic moduli of the fiber and matrix, respectively. V_f and V_m are fiber and matrix volume fraction. ε_c is strain applied to the composite. η_θ is the orientation efficiency factor and η_l the length correction factor. r_f is the fiber radius, l_f is the fiber length. β is the shear lag parameter, G_m is the matrix shear modulus and $\nu(0)$ the instant value of Poisson's ratio, which in calculations is assumed T-independent.

3. Material, manufacturing and test routines

3.1 Material and manufacturing

The polymer used as matrix was the MIPELON UHMWPE XM-220 powder (Mitsui Chemicals, Japan) with an average particle size of 30 µm, a molecular weight of 2 x10^6 g/mol, a density of 0.4 g/cm^3, modulus about 1.00 GPa, tensile strength of 20 MPa and ν equal to 0.46.

The short fiber used was a carbon fiber (SCF) provided by Toho Tenax America Inc (Tenax-A HT M100 100 µm), with an average length of 124 ± 62 µm, diameter of 7 µm, modulus of 225 GPa, tensile strength of 4.28 GPa, elongation at break of 1.9%, and bulk density of 1.82 g/cm3.

The manufacturing of the neat polymer and composite samples was in two steps: first, a dry ball milling was used to mix the UHMWPE powder (for neat polymer samples) and UHMWPE with SCF (for composite samples manufacture) powder for 5 min at 100 rpm with 250 Zirconia balls of 5 mm diameter. Then, the powder compositions, neat polymer and UHMWPE/SCF (10 wt%), were formed by compression molding process at 190 °C for 70 minutes, with several short pressing cycles of 105 kN. The final samples size was ≅ 160 x 18 x 4 mm^3.

3.2 Tensile tests

Loading-holding (L-H) tensile tests, described with equations in section 2.1, were performed on neat UHMWPE and UHMWPE/SCF (10 wt%) composites specimens, with gauge length 100 mm, using an Electroplus™ E3000 Instron machine, with a load cell of 5 kN and mechanical grips.

Axial strain was measured using an Instron 2620-601 dynamic extensometer, with 50 mm gauge length. To prevent sample slipping in the clamping area and sliding of the extensometer, pieces of sandpaper were used. The time, strain and load acquisition rate was 1 Hz. All tests were performed in strain-control mode. To test at different temperatures (T=25, 40, 60, 80, 90 and 100 ^{0}C) an Instron environmental chamber 3119-005 was used. To verify the reliability of the chamber regarding the set T, a thermocouple type K was used and a T vs. t curve was provided.

Before the mechanical test, the specimen was held at 0 N while the T of the chamber was increasing to the set mechanical test T. This step was in load controlled mode to prevent buckling due to the weight of the extensometer and to allow for free expansion. The T was held constant for 30 min, to allow the sample to reach thermal equilibrium. Then, the VE response was measured in L-H tests at constant temperature in the range 25 to 100 ^{0}C. The L-H test consisted of two steps:

1. L-step: where strain increased linearly with time, reaching $\varepsilon_0 = 0.3\%$ in $t_1 = 60\ s$.
2. H-step: where ε_0 was held constant for a time t^*=120 min and stress relaxation was recorded.

After all L-H tests, the mechanical response was reversible and strains fully recovered after the H-step in a time interval ≥15t* at the same test T, or during an accelerated recovery for time t^*at 20 °C higher temperature than the test T. Absence of irreversible strains is requested for using Eqs. (4-5). During the whole process only one resin sample and one composite sample was used and they were never removed from the testing machine or grips released, as recommended by Nunes et al. [6].

4. Results and discussion

4.1 Mechanical response of UHMWPE in L-H tests at different temperatures

For the UHMWPE specimen the L-H tests were performed at 6 different temperatures ($T = 25, 40, 60, 80, 90$ and $100\ ^0$C). Using the stress data from this test and Eqs (4) and (5), Prony coefficients for each test temperature were found by fitting. The experimental stress data for 40 and 60 °C test T and fitting curves are shown in Figure 1a. Fitting accuracy is excellent. The fitting coefficients C^m, are shown in Table 1.

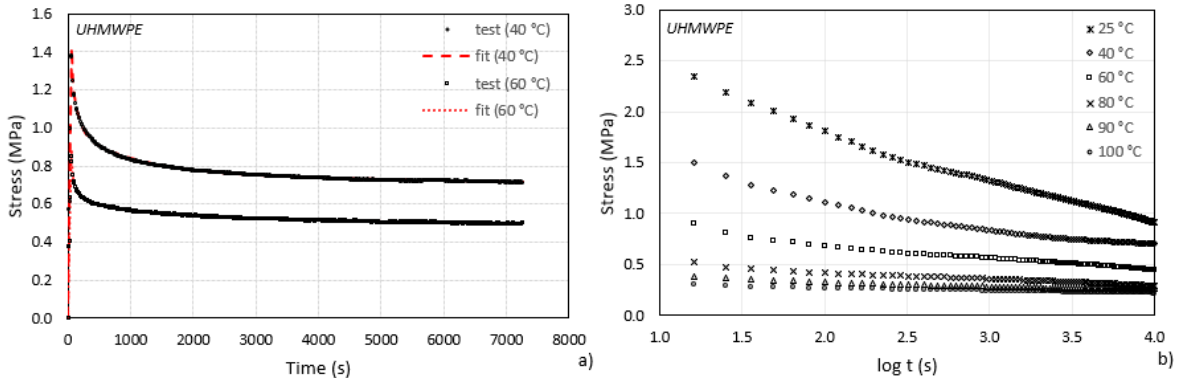

Figure 1. Stress relaxation for UHMWPE sample: a) experimental stress curves and fit in L-H(120 min) test with ε_0= 0.3% at T=40 °C and 60 °C; and b) simulated stress relaxation curves in ideal relaxation test at ε_0= 0.3% for six constant testing T

Then, the Prony coefficients in Table 1 were used to simulate stress relaxation in an ideal relaxation test at the corresponding T with a Heaviside step-function applied. Thus, relaxation functions for different T shown in Fig. 1b were obtained using Eq. (3).

Table 1: Prony coefficients C^m (MPa/%) from fitting L-H(120 min) tests data at six different constant temperatures for UHMWPE sample (E_r = 0).

τ_m (s)	1	10	10^2	10^3	10^4	10^5	10^6	10^7
25 °C	11.60	2.74	2.33	1.15	1.33	2.82	0	0
40 °C	0	2.92	1.31	0.79	0	1.90	0.62	0
60 °C	0	2.10	0.57	0.29	0.31	1.51	0	0
80 °C	0	0.99	0.24	0.16	0.18	0.99	0	0
90 °C	3.34	0.40	0.19	0.15	0	0	0.76	0.13
100 °C	1.17	0.45	0.07	0.09	0.00	0.55	0.23	0

4.2 Mechanical response of composite (UHMWPE/SCF)

  doi:10.5075/epfl-298799_978-2-9701614-0-0

Similarly as for the neat polymer (section 4.1), Prony coefficients for the composite at each temperature were obtained from L-H test data using Eq. (4) and (5). Figure 2a shows the excellent accuracy of the fitting for the composite provided by the found coefficients, indicating its reliability. Then, the coefficients were used in Eq. (3) to obtain idealized relaxation curves indicated with "VE" in Fig.2b.

Then, the quasi-elastic approach and the MROM (Eq. (6) to (9)) were used to simulate relaxation functions for composite. As MROM expressions provide the composite properties based on properties, quantity and arrangement of its constituents, the properties of short carbon fibers (E_f, V_f) and UHMWPE (V_m, $E_m(t)$, ν) and geometrical parameters given in section 3.1) have been used within Eqs (6-9) to find the stress and relaxation modulus of the studied composite.

The simulated stress relaxation curves for composite in ideal relaxation test at ε_0= 0.3% for test T equal to 25, 60 and 100 °C are presented in Figure 2b. They are indicated in legends as "MROM" and shown together with "VE" relaxation curves obtained from experiments as described above.

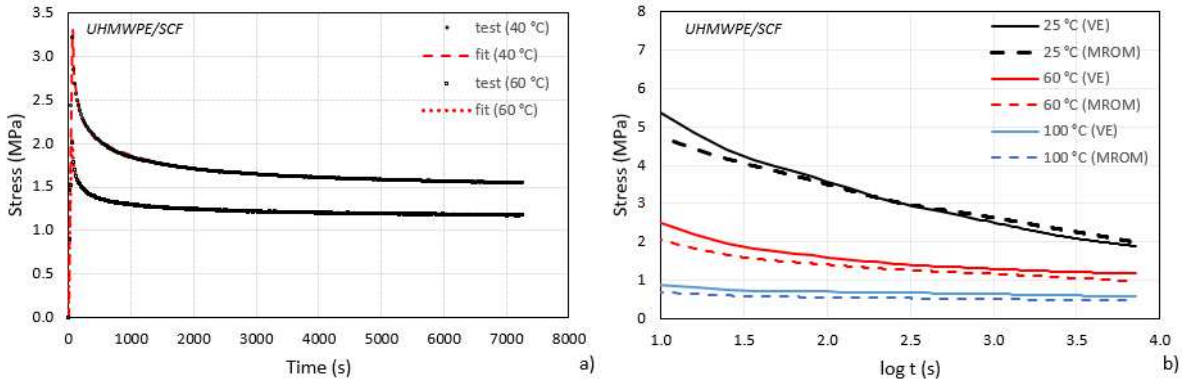

Figure 2. Stress relaxation for UHMWPE/SCF sample: a) experimental stress curves and fit in L-H(120 min) test with ε_0= 0.3% at T=40 °C and 60 °C; and b) stress relaxation curves in ideal relaxation test at ε_0= 0.3% for test T=25, 60 and 100 °C, according to composite test results (VE) and simulated using the quasi-elastic model (MROM).

Comparing the curves, it is possible to observe that the *stress* values for the MROM model are lower. However, the difference between the models decrease as the test T and t increase, providing reasonably accurate relaxation description for such cases. The main reasons for discrepancies could be the assumed 3-D random orientation distribution and uncertainty of the matrix property responsibly for stress into fiber. It should be noted that the obtained η_l for the 25, 60 and 100 °C tests were very low 0.082, 0.041 and 0.020, respectively.

An alternative inspection of the potential of the quasi-elastic approach and the used micromechanics expressions can be performed focusing on the L-step of the performed L-H tests on the polymer and the composite. The loading curves in the rather short (60 s) L-step shown in Fig.1a for matrix and in Fig. 2a for the composite that they are rather linear with a slope decreasing with increasing test temperature. Some researchers would interpret these data as elastic modulus decrease with temperature. Our interpretation is that the slope change is due to much faster stress relaxation at elevated temperature and that the true elastic response is not changing. Thus, the curves in Figures 1a and 2a represent VE response during 60 s.

However, to check the accuracy of the quasi-elastic response and the used micromechanical model (Eq. (6)) we assume now that the response in Figures 1a and 2a have been elastic and

  doi:10.5075/epfl-298799_978-2-9701614-0-0

define an "apparent" modulus dividing the stress reached at the maximum with the corresponding strain 0.3%. The apparent moduli for the matrix are given in Table 2 as columns "E_m" before the length correction factor η_l calculated using Eqs. (7-9). The composite stress value at 0.3% strain from experiment are in column "$\sigma_{0.3\%}$Test"and the apparent composite modulus in "E_c Test".

Table 2: Composite tensile stress ($\sigma_{0.3\%}$) at 0.3% strain and the apparent modulus (E_c) for different test temperatures, obtained using the experimental data for composite and calculated using the quasi-elastic *MROM, having as input the matrix apparent modulus E_m, length correction factor η_l, η_θ=0.2, V_f=0.1 and E_f=225 GPa.*

	MROM parameters		$\sigma_{0.3\%}$ (MPa)		E_c (GPa)	
	E_m (GPa)	η_l	Test	MROM	Test	MROM
25 °C	0.7371	0.164	4.46	4.20	1.49	1.40
40 °C	0.4614	0.111	3.23	2.74	1.08	0.91
60 °C	0.2840	0.072	2.03	1.74	0.68	0.58
80 °C	0.1670	0.044	1.29	1.04	0.43	0.35
90 °C	0.1243	0.033	1.03	0.78	0.34	0.26
100 °C	0.1007	0.027	0.78	0.64	0.26	0.21

The $\sigma_{0.3\%}$ and E_c calculated using the micromechanics model are also presented in Table 2 as "MROM". At room T the quasi-elastic MROM model gives rather good estimate of the composite response to 0.3% strain and the trends with increasing T are described correctly, however, the relative difference increases to 25% at 90 °C.

The increasing inaccuracy in MROM predictions and the systematic under-prediction of the response could be due to a combination of factors. The properties of short fiber composites are highly dependent on the length, orientation, diameter and content of fiber. Due to the method used to manufacture the composites (compression moulding) it was assumed that fibers are randomly 3-D distributed, therefore, the value adopted for the orientation efficiency factor (η_θ) was 0.2 [7]. However, some in-plane distribution preference may have been possible.

Another source of error can be in the length correction factor that is proportional to the average stress in the fiber. The average fiber stress depends on the stress transfer that depends on the matrix properties at the fiber surface. Since the apparent modulus of the matrix at high T is very low, the η_l in Table 2 is very small. In this extreme case the stress transferred to the fiber over fiber ends cannot be neglected. This contribution that is not included in the shear lag model, would increase the η_l values, leading to higher predicted apparent modulus of the composite.

5. Conclusions

The time-temperature-dependent viscoelastic response (VE) of UHMWPE/SCF composite tested at different temperatures (25 to 100 °C) is compared with the simulated response using linear VE description of the neat resin based on modified Schapery's thermodynamically consistent theory. In addition, the quasi-elastic approach together with micromechanics-based modified rule of mixture (MROM) is used to simulate relaxation curves for composite. Using the MROM expressions, the elastic constants of the matrix were replaced by the corresponding instant values of the time-dependent relaxation function (i.e. using Prony coefficients and relaxation

times of the matrix). The agreement with test data is rather good showing the same trends and an increasing accuracy with increasing time.

For further evaluation of the quasi-elastic approach, the data from relatively fast (60 s) loading to 0.3% strain and the reached stress at the end were treated as temperature-dependent elastic response, defining apparent modulus for the matrix and for the composite. Using the apparent matrix modulus in the elastic micromechanics expressions resulted in slightly underestimated predictions for composites. At 90 °C the apparent values provided the highest deviations, reaching almost 25%.

The deviations could be related to the assumptions used in the model, such as fibers being randomly distributed in 3-D ($\eta_\theta = 0.2$) and in the uncertain value of the length correction factor, which is directly related to average stress in the fiber that is transferred to the fiber over side surfaces and fiber ends. At high temperatures, the length correction factor obtained in shear lag analysis is very small and including the stress transfer through fiber ends would increase it.

The short carbon fibers used as reinforcement (10 wt%) for a UHMWPE matrix showed positive effect on viscoelastic material properties, increasing its apparent modulus by about 100%, thus, providing a more resistant to deformation material.

Acknowledgements

The authors would like to thank Kempestiftelserna with funding reference SMK-1738 and ERDF within the Activity 1.1.1.2 and “Post-doctoral Research Aid” of the Specific Aid Objective of the Operational Programme “Growth and Employment” (project No. 1.1.1.2/VIAA/4/20/641) for their financial support.

6. References

1. Macuvele DLPM, Nones J, Matsinhe JV, Lima MM, Soares C, Fiori MA, Riella HG. Advances in ultra-high molecular weight polyethylene/hydroxyapatite composites for biomedical applications: A brief review. Materials Science and Engineering C 2017; 76:1248–1262.
2. Tajvidi M, Falk RH, Hermanson JC. Time–Temperature Superposition Principle Applied to a Kenaf-Fiber/High-Density Polyethylene Composite Journal of Applied Polymer Science 2005; 97: 1995–2004.
3. Vadivel HS, Al-Maqdasi Z, Pupure L, Joffe R, Kalin M, Emami N. Time-dependent properties of newly developed multiscale UHMWPE composites. Polymer Testing 2022; 105: 107400.
4. Zhao S, Zhao Z, Yang Z, Ke L, Kitipornchai S, Yang J. Functionally graded graphene reinforced composite structures: A review. Engineering Structures 2020; 210: 110339.
5. Park SW, Schapery RA. Methods of interconversion between linear viscoelastic material functions. Part I-a numerical method based on Prony series. International Journal of Solids and Structures 1999, 36:1653–1675.
6. Nunes SG, Saseendran S, Joffe R, Amico SC, Fernberg P, Varna J. On temperature-related shift factors and master curves in viscoelastic constitutive models for thermoset polymers. Mechanics of Composite Materials 2020; 56(5); 573–590.
7. Dubey KA, Hassan PA, Bhardway YK. High Performance Polymer Nanocomposites for Structural Applications. Materials under extreme conditions: recent Trends and Future Prospects. Elsevier. 2017, 159-194.

  doi:10.5075/epfl-298799_978-2-9701614-0-0

DEVELOPMENT OF POLYPROPYLENE MELT-BLOWN FINE FIBER INTERLEAVED SINGLE-POLYPROPYLENE COMPOSITES

Yahya Kara[a], Kolos Molnar[a,b]

a: Budapest University of Technology and Economics, Faculty of Mechanical Engineering, Department of Polymer Engineering, Műegyetem rkp. 3., H-1111 Budapest, Hungary – karay@pt.bme.hu

b: MTA–BME Research Group for Composite Science and Technology, Műegyetem rkp. 3., H-1111 Budapest, Hungary

Abstract: *In this study, we aimed to improve the performance of SPCs by interleaving them with melt-blown (MB) fine PP fibers. The PP fine fiber veils, with an average fiber diameter of 2.28 ± 0.23 µm, were generated by melt-blowing. We produced single-Polypropylene composites by film-stacking in which we applied a film as a matrix, woven fabric as primary reinforcement, and MB fiber mats as interleaves. We used compression molding to make the interleaved single-PP composites. Results showed that interleaving increased the tensile modulus in the range of 20-46% and the Interlaminar shear strength (ILSS) over 10% compared to the non-interleaved sample. We found that interleaving enhanced the secant modulus up to 34%, indicating the fine fiber veil improved the load-bearing ability of the laminae. Results implied that melt-blown microfiber interleaving improved the interfacial strength by forming a net-like structure in the interface. Findings implied that the interleaving SPCs with the fine fibers made of the same polymer could be potential candidates to advance environmentally friendly composite structures for various engineering applications.*

Keywords: Polymer fibers; stiffness; delamination; interleaving; self-reinforced composites

1. Introduction

The volume of thermoplastic-based composites used is emerging. The advantage of these composites over their thermoset counterparts is the shorter production cycle times, the fair recyclability, the high toughness, the damage tolerance, and the technically unlimited shelf-life without the need for humidity- or temperature-controlled storage, equating to significant reductions in energy, as well as manufacturing costs (1, 2).

The composite laminates made of reinforcing fibers usually exhibit excellent in-plane material properties; however, out-of-plane properties (e.g., interlaminar shear strength and delamination resistance) are dominated by the matrix material and the fiber-matrix interface bonding; and are relatively poor. Ply to ply interfaces of composite laminates possess the weak points of the structure due to the nature of the laminates. An interlaminar toughening approach can solve this issue by incorporating sub-phases into the reinforcement and matrix interface (3). This issue led to the development of single-polymer composites (SPCs). SPCs are a particular family of thermoplastic composite materials in which both the reinforcing fiber and the polymer matrix are made from the same polymer family. Although the SPCs are not new, difficulties in processing and limited load-bearing ability and thermal performance still hamper SPCs' applicability in industrial utilization (4). In this regard, interlaminar toughening approaches

  doi:10.5075/epfl-298799_978-2-9701614-0-0

involving sub-phases into the interface between the reinforcement and the matrix can overcome this issue (5, 6). Among the other methods, incorporating fine fiber (nano- and submicron) veils can be feasible since only a tiny amount of such fine fibers may be sufficient to achieve improved interfacial adhesion and overall performance. In this regard, melt-blowing is a potential way to generate fine fibers directly from a polymer melt to produce such interleaves. The process possesses several advantages, including but not limited to high-throughput rate, straightforward and solvent-free processing, the utilization of a wide range of polymers, the fair control of fiber morphology, cost-efficiency, etc.

In this study, we investigated the effect of melt-blown fine PP fiber veil interleaving on the performance of SPCs. The SPCs are produced by the film stacking method followed by compression molding. The mechanical behavior of the PP SPCs is investigated, from which we observed that fiber mat interleaves with the same PP material improved the SPCs' properties. Results showed that the MB fiber mat interleaving approach improved the interlaminar mechanical performance without compromising its recyclability.

2. Materials and methods

2.1 Materials

HL912FB type PP homopolymer (Borealis, Austria) was used to prepare fine fiber mats via melt blowing. A plain-woven PPfabric (Tiszatextil Kft., Hungary) with an areal density of 200 g/m^2 (tape count: 5/cm (warp), 4.2/cm (weft)) was used as the composites' primary reinforcement. We compounded a low modulus isostatic PP (iPP, L-MODU S401, Idemitsu, Japan) for the matrix with a random copolymer PP(rPP, RJ470MO Borealis, Austria) in a mass ratio of 1:9.

2.2 Extrusion blending and film production

We produced a PP blend made of 10 wt% L-MODU isotactic PP(iPP) and 90 wt% random PP (rPP) with a counter-rotating twin-screw extruder (Labtech LE 25–30/C, Thailand). The extruder was equipped with two 26 mm diameter, 44 L/D screws; the extrusion temperature was set to 170-180-185-190-200 °C (from hopper to die). The screw and feeder rotation speeds were set to 40 and 10 rpm, respectively. Thin films of the PP blend were prepared with an LF-400 type laboratory extruder followed by a small sheet film line (LabTech LCR300, Thailand). This extruder has one 25 mm diameter, 30 L/D screw. The extruder was equipped with a 200 mm wide coat hanger type sheet die, and the slit distance was set at 0.5 mm. The speeds of the lower and upper take-off rolls (Ø = 72.5 mm) were 2 and 2.8 rpm, respectively. The flat film extrusion temperature was set to 180-185-190-195-200 °C (from hopper to die). The extruder screw and flat film line take-up cylinder pulling speed were set to 40 rpm and 10 rpm, respectively, while the take-up cylinder temperature was set to 70 °C. The thickness of the film produced was 70 ± 5 µm.

2.3 Generating melt-blown fiber mats and related interleaved single-polymer composites

A custom laboratory unit, related details can be seen in (7) was used to generate PP fine fiber mats. The die and extruder temperatures were set to 225 °C. The air temperature and air pressure were set at 275 °C and 2.5 bar, respectively. The extruder screw speed was set at 1 rpm. A drum with a diameter of 160 mm was used as the collector Collector drum rotation speed was set at 28 m/min. The die-to-collector distance (DCD) was set to 400 mm. The collector

drum was covered with the woven PP fabric, and MB fiber mats were collected directly onto those.

The composite stack consisted of 6 layers of film (F) and 5 layers of woven fabric (W), while those composites interleaved with MB fiber mat (MB) had 4 layers of fiber mat distributed in between the film and the woven fabric. The composite sheets were produced by film-stacking with a hydraulic hot press (Polystat 300S, Maschienenfabric Fr. Schwabenthan & Co. Kg., Germany). The compression mold consisted of two matching aluminum halves with a cavity size of 180 mm x 100 (length x width) mm. The layered stack was placed into this mold and then put into the hot press set at the designated molding temperature (*i.e.*, 150, 155, 160 °C). After closing the mold, it was kept 30 s without pressure to equilibrate the temperature. Then the compression molding pressure was set at 5 MPa (actual pressure on the specimen) while the holding time was fixed at 120 s. SPC sheets had a thickness of 1.9 ± 0.1 mm. The PP woven fiber, PP MB fiber and matrix film content of the produced SPCs are given in Table 1.

Table 1. The single-polymer composite samples prepared

Stack description	Woven fabric content [wt%]	Fiber mat veil content [wt%]	Processing temperature [°C]	Sample code
Film + woven fabric	74 ± 1	-	150 °C	150 F/W
			155 °C	155 F/W
			160 °C	160 F/W
Film + woven fabric interleaved with melt-blown fiber mat veil	74 ± 1	4±1	150 °C	150 F/MB/W
			155 °C	155 F/MB/W
			160 °C	160 F/MB/W

2.4 Characterization

The morphology of the fibers and composites was observed by using scanning electron microscopy (SEM; JEOL 6380 LA, Japan). The surface of the fiber mat and composite sample was finely coated using JEOL JFC-1200 (Jeol Ltd., Japan) fine coater with gold (Au) to avoid their charging. With the ImageJ 1.51k software, we measured 150 fibers to determine the fiber diameter distributions of the MB veils.

We studied the thermal properties of the constituent phases and the single-polymer composites by differential scanning calorimetry (DSC) with a Q2000 DSC (TA Instruments, USA) device. The tests were performed in an inert atmosphere (N_2; 50 ml/min purge flow rate) at a temperature range of -50 to 220 °C with a heating and cooling rate of 10 °C/min.

The tensile properties of the MB fiber mat, matrix film and woven fabric were tested at room temperature with a Zwick Z005 (Zwick, Germany) type universal tensile tester equipped with a 5 kN load cell. We prepared rectangular samples for the PP fiber mat sample in 50 x 20 mm, while the blend film and woven were cut in 150 x 20 mm. The gauge length was set at 25 mm.

The sample length and width were measured using a digital caliper (Fowler Promax, USA) with a precision of 0.01 mm. The PP fiber mat samples were weighed using a Sartorius Quintix 125D-1CEU (Sartorius, Germany) semi-micro scale. We calculated the fiber mat cross-section by using Eq. 1.

$$A = \frac{\mathrm{m}_{fm}}{l_{fm}\rho_{bulk}} \quad (1)$$

where, m_{fm} is the fiber mat mass, l_{fm} is the length of the fiber mat and ρ_{bulk} is the bulk density of the hPP (0.891 g/cm^3). The SPC samples were tensile tested at room temperature at 5 mm/min with a Zwick Z020 (Zwick, Germany) machine equipped with a 20 kN load cell. The gauge length was set at 90 mm. We tested 7 specimens for each group. The tensile strength, elastic modulus and secant modulus at 2% strain were evaluated.

The short beam shearing (SBS) tests were conducted at room temperature according to the ISO 14130 standard (8). We cut the composite sheet into 20 x 10 mm specimens. A Zwick Z020 type universal tensile tester with 20 kN load cell at 1 mm/min test speed was used. The test setup was equipped with a 3-point bending fixture, and the span length was set to 10 mm. 7 samples were tested for each group. The interlaminar shear strength (τ_{ILSS}) was determined by using Eq. 2 (8).

$$\tau_{\mathrm{ILSS}} = 0.75 \times \frac{F_{max}}{bt} \quad (2)$$

where, F_{max} is the maximum load observed during the test, b is the specimen width and t is the sample thickness.

3. Results and Discussions

3.1 Analyzing the component's properties

We obtained a PP fiber mat with an average fiber diameter of 2.28 ± 0.23 µm. The areal density of the PP fiber mat was 110.5 ± 35.4 g/m^2. The diameter distribution and an SEM image are shown in Figure 1. Melt-blowing typically generates self-bonded and highly entangled fiber mats that derive their strength from fiber-to-fiber contacts besides the intrinsic material properties (9). And so, the newly formed fiber's ability to penetrate to the fibers already on the collector significantly affects the fiber mat's load-bearing capability upon applied stress. We found that a die-to-collector distance (DCD) of 400 mm results in appropriate fiber mat porosity and fiber entanglement based on our previous experiences (2, 7). High porosity is necessary as the matrix flows through pores at compression molding.

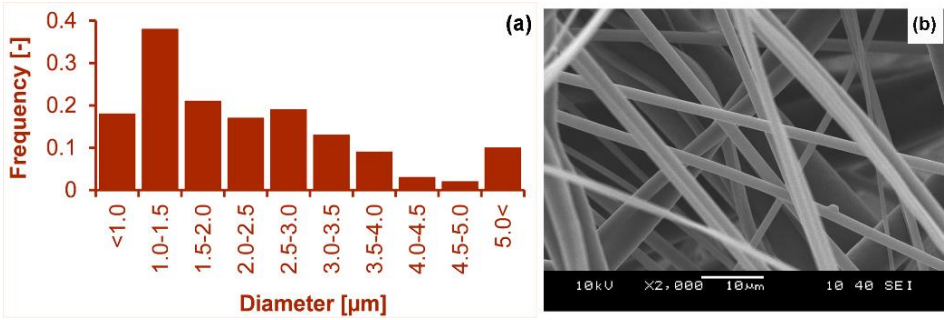

Figure 1. MB PP fiber mat morphology; (a) fiber diameter distribution, (b) SEM image

We conducted DSC tests on the constituent components to examine the processing window. The blend PP film, MB fiber mat and the woven fabric crystalline peak melting temperatures were recorded around 150 °C, 160 °C and 168 °C, respectively, as shown in Figure 2. Results showed that three phases are suitable for producing SPC via compression molding, while the inherent thermal properties possess a narrow processing window.

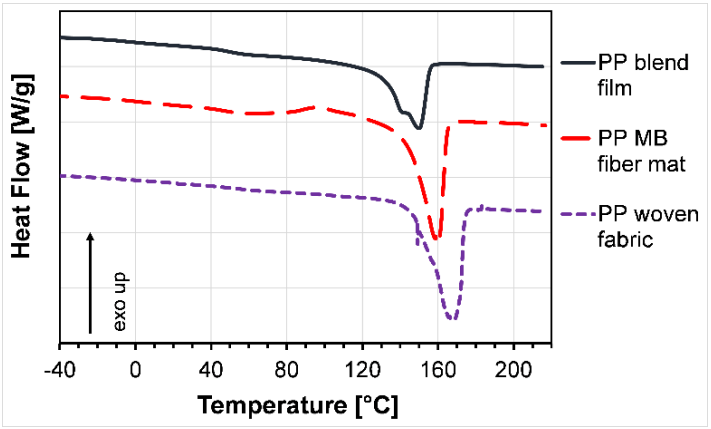

Figure 2. DSC 1st heating thermograms of the blend film, MB fiber mat and woven fabric

We determined the component's tensile behavior. The results obtained are given in Table 2. Results revealed that the MB fiber mat's tensile strength is considerably lower than that of the film and woven fabric. The fiber mat is a randomly aligned and self-bonded structure with high porosity and low solidity. Therefore, comparing fiber mat tensile strength with a bulk material or a woven and densely woven fabric may be misleading. Even though the MB fiber mats' tensile strength was much lower than that of the matrix film and the woven fabric, these continuous fine PP fibers are expected to improve the interfacial adhesion due to their high aspect ratio (length/diameter) (10).

Table 2. Tensile properties of the components

Sample Name	Tensile strength [MPa]
PP blend film	18.1 ± 0.8
PP woven fabric	421 ± 2

PP MB fiber mat	2.5 ± 0.3

3.2 Analyzing the PP MB fiber mat interleaved SPC's performance

Results showed that interleaving via fine fiber mat improves the mechanical properties of the SPCs (Figure 3). Besides, the molding temperature plays a crucial role in the interfacial strength of the laminate. We observed an early tape and interlayer debonding at tensile testing for the 150 F/MB/W SPC due to poor consolidation. The highest tensile strength was recorded for the 150 F/W SPC. This phenomenon is associated with a high fraction of the highly oriented fibers when low compression molding temperature (11, 12) was applied. F/MB/W SPCs tensile strength slightly improved (~7%) with increasing the temperature. The MB fiber mat interleaves increased the tensile modulus in the range of 20-46% (Figure 3 (c)). On the other hand, the MB fiber mat interleaves enhanced the 2% secant modulus between 20-34%, as shown in Figure 3 (d). These findings implied that self-interleaving via a fine fiber veil improves the load-bearing capacity of the SPC.

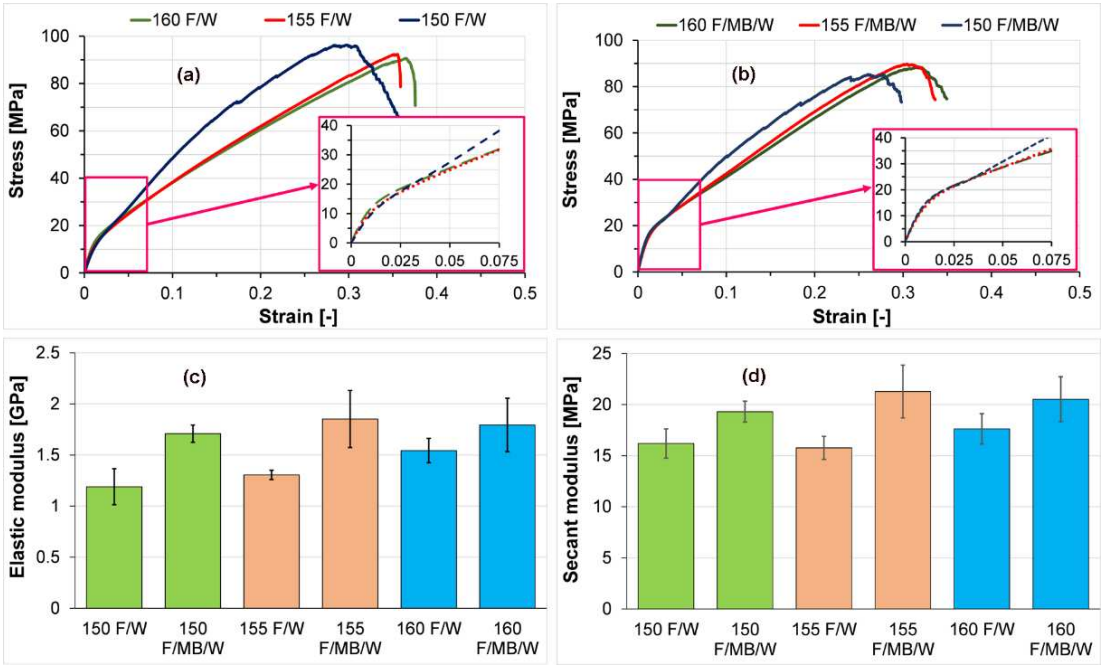

Figure 3. Tensile properties of the SPC's; stress-strain curves of (a) the F/W, (b) F/MB/W SPCs, F/W and F/MB/W SPC's (c) elastic modulus and (d) 2% secant modulus

We conducted short beam shear tests to analyze the effect of interleaving on the interlaminar properties further. The short beam shear (SBS) test of the 150 F/W and 155 F/W samples showed an invalid failure mode (*e.g.,* inelastic deformation and failure under compression load) due to their low stiffness (e.g., high strain to failure); therefore, these results are not given. Low stiffness is related to poor fiber-matrix bonding due to the low temperature. We found that MB interleaving improved the interlaminar shear strength (ILSS) by 17% for the SPC produced at 155 °C. 155 F/MB/W SPC had the highest ILSS, as shown in Table 3. On the other hand, ILSS of 160 F/MB/W SPC was only 6% higher than that of the 160 F/W. Figure 4 illustrates that MB fibers were able to create a well-established net-like structure in the interlaminar region of the

F/MB/W. The formed structure enhanced the interfacial strength, and this, in turn, gives higher ILSS and elastic modulus.

Table 3. Variation of the ILSS and 95% confidence intervals of the SPCs

Sample Code	ILSS [MPa]
150 F/MB/W	2.9 ± 0.17
155 F/MB/W	5.9 ± 0.66
160 F/MB/W	5.3 ± 0.51
160 F/W	5.1 ± 0.21

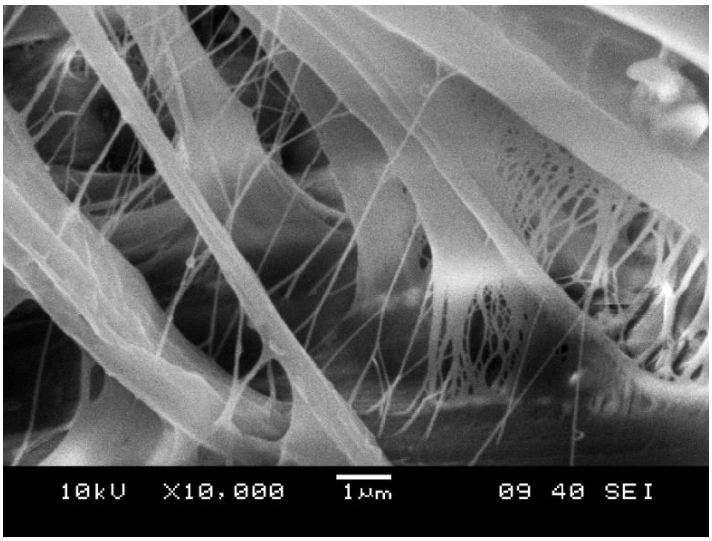

Figure 4. SEM image of the SPC lamina with MB fiber interleaves

4. Conclusion

In this study, we demonstrated a new strategy for enhancing the mechanical behavior of single-PP composites by interleaving those with thin layers of PP fine fiber mats. The MB interleaves increased the SPC's tensile modulus in the range of 20-46% at compression molding temperatures of 155 and 160 °C. The SPC's tensile strength did not change significantly with interleaving. On the other hand, the 2% secant modulus was considerably enhanced. Results implied that the interleaving improved the load-bearing capacity of the SPC, even in the high strain region. Results showed that fine fiber interleaving improved ILSS by 17%. The interleaving considerably reduced the delamination by creating a net-like structure leading to superior interfacial adhesion. These findings prove that the self-interleaving concept with fine fibers of the same polymer enhances SPC's performance.

Acknowledgements

The authors thank Borealis Polymers N.V. and Henk van Paridon for supplying the melt-blowing fiber grade resin used in this work. The authors also thank Idemitsu Kosan Company, Ltd. and Katsuya Kawahara for providing the L-MODU Polypropylene resin used in this work. This paper

created at the Budapest University of Technology and Economics was supported by the "TKP2020, Institutional Excellence Program" of the National Research Development and Innovation Office in the field of Nanotechnology and Materials Science (BME IE-NAT TKP2020). This paper was also supported by the János Bolyai Research Scholarship of the Hungarian Academy of Sciences (MTA), the by the ÚNKP-20-5 New National Excellence Program of the Ministry for Innovation and Technology.

5. References

1. Mallick PK. Thermoplastics and thermoplastic–matrix composites for lightweight automotive structures. In: Mallick PK, editor. Materials, Design and Manufacturing for Lightweight Vehicles. Cornwall, UK: Woodhead Publishing; 2010. p. 174-207.
2. Virág ÁD, Kara Y, Vas LM, Molnár K. Single Polymer Composites Made of Melt-blown PP Mats and the Modelling of the Uniaxial Tensile Behaviour by the Fibre Bundle Cells Method. Fibers and Polymers. 2021.
3. Daelemans L, van der Heijden S, De Baere I, Rahier H, Van Paepegem W, De Clerck K. Using aligned nanofibres for identifying the toughening micromechanisms in nanofibre interleaved laminates. Composites Science and Technology. 2016;124:17-26.
4. Hine P, Olley R, Ward I. The use of interleaved films for optimising the production and properties of hot compacted, self reinforced polymer composites. Composites Science and Technology. 2008;68(6):1413-21.
5. Cheon J, Kim M. Impact resistance and interlaminar shear strength enhancement of carbon fiber reinforced thermoplastic composites by introducing MWCNT-anchored carbon fiber. Composites Part B: Engineering. 2021;217:108872.
6. Acar V, Erden S, Sarıkanat M, Seki Y, Akbulut H, Seydibeyoğlu M. Graphene oxide modified carbon fiber prepregs: A mechanical comparison of the effects of oxidation methods. Express Polymer Letters. 2020;14(12).
7. Kara Y, Molnár K. Revealing of process–structure–property relationships of fine polypropylene fiber mats generated via melt blowing. Polymers for Advanced Technologies. 2021;32(6):2416-32.
8. Fibre-Reinforced Plastic Composites. Determination of Apparent Interlaminar Shear Strength by Short-Beam Method. ISO; 1999.
9. Kara Y, Molnár K. A review of processing strategies to generate melt-blown nano/microfiber mats for high-efficiency filtration applications. Journal of Industrial Textiles. 2021:1-44.
10. He H, Gao M, Illés B, Molnar K. 3D Printed and Electrospun, Transparent, Hierarchical Polylactic Acid Mask Nanoporous Filter. International Journal of Bioprinting 2020;6(4).
11. Swolfs Y, Zhang Q, Baets J, Verpoest I. The influence of process parameters on the properties of hot compacted self-reinforced polypropylene composites. Composites Part A: Applied Science and Manufacturing. 2014;65:38-46.
12. Varga LJ, Bárány T. Development of recyclable, lightweight polypropylene-based single polymer composites with amorphous poly-alpha-olefin matrices. Composites Science and Technology. 2021;201:108535.

TAILORED OUT-OF-OVEN CURING OF HIGH PERFORMANCE FRPS UTILISING A DOUBLE POSITIVE TEMPERATURE COEFFICIENT EFFECT

Xudan Yao[1], Yushen Wang[1], Yi Liu[2], Emiliano Bilotti[1], Han Zhang[1]
[1]School of Engineering and Materials Science, Queen Mary University of London, Mile End Road, London, E1 4NS, UK.
[2]Department of Materials, Loughborough University, Loughborough, LE11 3TU, UK

Email: x.yao@qmul.ac.uk

Abstract: *Making use of the pyroresistive behaviour of conductive polymer composites (CPCs) paves an efficient path for the* out-of-oven (OoO) *curing of fibre reinforced plastics (FRPs). Graphene nanoplatelets (GNPs) filled PVDF as well as HDPE/PVDF binary-polymer were fabricated through melt pressing to achieve both single and double* positive temperature coefficient (*PTC*) *effects. For GNP/PVDF nanocomposites, single PTC as well as self-regulating heating behaviour, were achieved with the switching temperature at around 150 °C, owing to the thermal expansion of PVDF. For the GNP/HDPE/PVDF ternary system, double PTC behaviour accompanied with two self-regulating heating stages were achieved at around 125 °C and 150 °C respectively, with co-continuous phase formed. In particular, the second stage shows higher self-regulating sensitivity owing to its higher PTC intensity. This work provides selections for both single and double PTC systems, which can be tuned and used to safely cure FRP composites OoO through self-regulating Joule heating.*

Keywords: conductive polymer composite (CPC); graphene nanoplatelet (GNP); Positive temperature coefficient effect; Joule heating; out-of-oven (OoO) curing

1. Introduction

With the increasing consideration on environmental impact, low-/zero-carbon technologies are increasingly demanded. Thanks to their high specific strength and stiffness, as well as chemical resistance, fibre reinforced plastics (FRPs) have been widely used as an environmental friendly lightweight solutions in diverse fields, such as aerospace, automotive, civil, energy, sports, etc. Unfortunately, when it comes to the manufacturing of advanced composites, traditional methods including autoclave and oven-based curing procedures lead to high energy consumption as well as size restrictions.

In order to overcome these limitations, our group has performed diverse study in pyroresistive performance of conductive polymer composite (CPC) and achieved reliable self-regulating heating performance, which can be used for sustainable out-of-oven (OoO) curing for high performance composites [1-4]. Compared with the composites cured by traditional methods, OoO curing needs only 1% of energy consumption which significantly contributes to the sustainable manufacturing, especially considering the growing demand of advanced composites need to be manufactured in next decades. Moreover, the integrated CPC layer could also be used for structural health monitoring, anti-/de-icing, etc., to achieve advanced multifunctional lightweight composite structures.

  doi:10.5075/epfl-298799_978-2-9701614-0-0

Single-step positive temperature coefficient (PTC) effect was employed, in which the electrical resistance of the CPC suddenly increased at desired curing temperature, thus, to control the heating procedure and protect the system from over-heating. In the case of high performance FRP composites, the curing cycle commonly consists of two stages of curing and post-curing at different temperatures. In this work, a double or two-step PTC effect is developed to fulfill this requirement in manufacturing high performance composites.

In order to achieve double PTC effect, literatures [5-7] give consistent recommendations on the binary-polymer nanocomposites. The polymer in which conductive fillers tend to disperse should kept as the phase with lower volume fractions, thus the conductive pathways could be broken either within this polymer or at the interface between two polymers when temperature reaching two melting points, which was explained by island-bridge or type I + M (interface + matrix) theories.

Here, CPC layers with both single and double PTC effects were fabricated, in which a selection of different polymers with distinct melting points were combined to fulfill the cure cycle at desired temperatures. In addition, different loadings of conductive fillers were incorporated to provide the conductive and heating paths, among which graphene nanoplatelets were used. Melt-mixing and hot-pressing were utilised to process the CPC composites.

2. Experimental

2.1 Materials

Graphene nanoplatelets (GNPs) from XG sciences (Grade M25) were used as the conductive fillers in this work, which have an average particle diameter of ~ 7.7 µm [8], thickness of 6–8 nm (~ 20 layers of graphene) and density (ρ_g) of 2.2 g cm^{-3}. Solef 1015 PVDF (particle size < 300 µm, density of 1.78 g cm^{-3}) and RIGIDEX HD5218EA HDPE (density of 0.952 g cm^{-3}) were used as the polymer matrix, owing to their PTC switching temperatures of ~120 °C and ~150 °C respectively, which fit well with curing cycle of the epoxy resin system. Polymers were dried at 80 °C in the oven overnight before processing. Strips of 3 mm wide copper tapes combined with 0.056mm copper wires and meshes were used as the electrical buses to connect the samples to a power supply.

2.2 Sample preparation

Thermo Fisher PolyLab OS mixer HAAKE Rheomix600 with the Roller Rotors was used to melt mix GNP with PVDF and HDPE. Sample weight was calculated based on the equation:

$$m = \rho \cdot V_n \cdot 0.7 \quad (1)$$

Where ρ is the melt density, V_n represents net chamber volume (69 cm^3) and 0.7 is the filling percentage. As both PVDF and UHMWPE are semi-crystalline polymers, 80% of their solid densities were used as melt densities.

GNPs were mixed into PVDF with the loading of 22 wt.% under 200 °C, torque of 30 Nm for 10 min. Afterwards, the 22 wt.% GNP/PVDF compound was further mixed with specific amount (HDPE/PVDF volume ratio of 1/4) of HDPE for 5 min, to achieve 20 wt.% GNP/HDPE/PVDF. Then the 22 wt.% GNP/PVDF and 20 wt.% GNP/HDPE/PVDF compounds were hot pressed into films

  doi:10.5075/epfl-298799_978-2-9701614-0-0

(~200 µm thick, for Joule heating) and sheets (~1 mm thick, for pyroresistive behaviour testing) using Dr. Collin P300E at 200 °C under 100 bar and 240 bar respectively.

2.3 Characterization

A FEI Inspect F field emission Scanning electron microscopy (SEM) was used to observe the morphology of GNPs and polymers, as well as brittle fractured cross section surfaces of the nanocomposites.

The pyroresistive behaviour test was achieved by measuring the resistance of the sample under various temperatures. Samples were placed in a temperature-controlled oven and connected to an Agilent 34410A 6½ Digit Multimeter to measure the real time electrical resistance using the two-wire method. A K type thermocouple was attached to the surface of the sample for temperature recording. The resistance and temperature were recorded simultaneously.

A GE EPS 301 power supply was used for Joule heating, with different voltages applied. K type thermocouples accompanied with a TC-08 thermocouple data logger from Pico Technology were used to record the temperature of various positions on the sample surface during the tests.

3. Results and discussion

3.1 Morphology

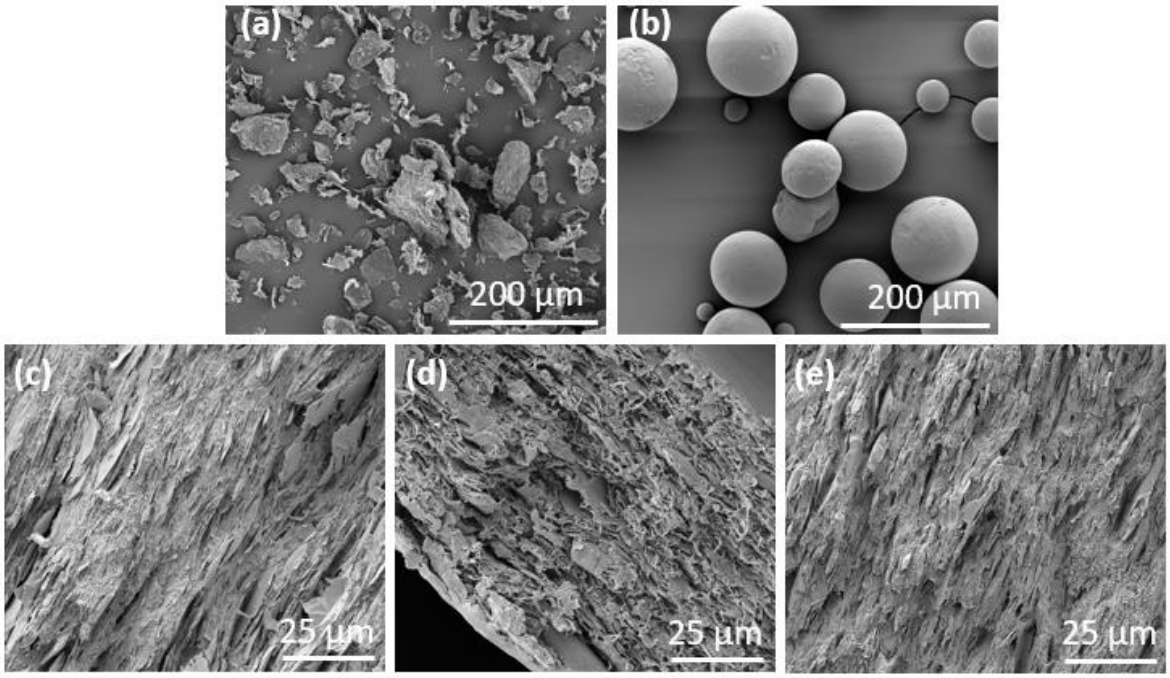

Figure 1. SEM images of as-received (a) M25 GNP, (b) PVDF powder; brittle fractured cross-section of (c) 22 wt.% GNP/PVDF hot pressed under 240 bar, as well as 20 wt.% GNP/HDPE/PVDF hot pressed under (d) 100 bar and (e) 240 bar respectively.

The as-received GNP, PVDF, cross section of 22 wt.% GNP/PVDF and 20 wt.% GNP/HDPE/PVDF were characterized by SEM for their morphology, as shown in Figure 1. It shows that after hot pressing, GNPs distribute highly aligned along the in-plane direction, result in a layered structure (Figure 1c-e). While with the hot-pressing pressure increased, the whole structure was more

  doi:10.5075/epfl-298799_978-2-9701614-0-0

densely packed with GNPs highly aligned, with PVDF and HDPE formed co-continuous phase (Figure 1d, e).

3.2 GNP/PVDF composite

Hot pressed (under 100 bar) rectangular samples (15 mm × 6 mm × 0.97 mm) were used for pyroresistive behaviour tests. As shown in Figure 2 left, 22 wt.% GNP/PVDF sample shows the single-step PTC effect, owing to the thermal expansion of PVDF, with the PTC intensity (peak resistivity/room temperature resistivity) of 2.6 and switching temperature at around 150 °C.

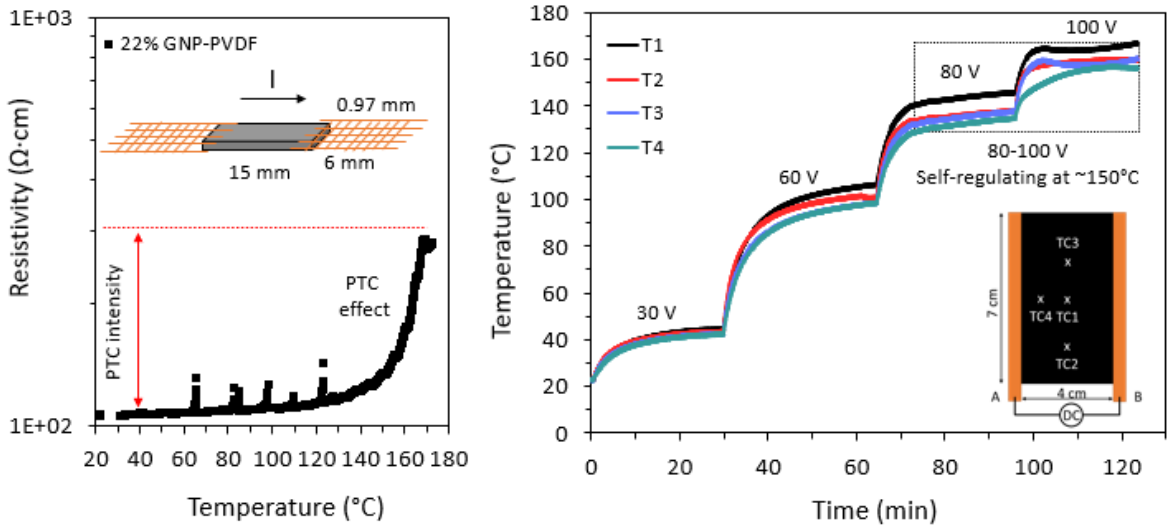

Figure 2. Pyroresistive (left) and Joule heating (right) behaviour of 22 wt.% GNP/PVDF samples, embedded with the sample dimensions and set up, including power supply connection, copper buses and thermocouples (TCs).

In order to check the capability of the compounded nanocomposites for OoO curing FRP composites, Joule heating behaviour of the samples were tested. 22 wt.% GNP/PVDF film was hot pressed into a rectangular shape (7 cm x 4 cm), with the thickness of ~200 µm, resistance of 2.4 kΩ and copper buses applied as the electrodes, as shown in Figure 2 right.

During the Joule heating test, thermal insulating materials (polyester fabric) were used to cover the samples to prevent the major heat loss, convection [9]. In this case, energy generated by resistive heating contributes to heat up the composite accompanied with heat loss via heat conduction and radiation, following the below equation:

$$q_{in} = \frac{U^2}{R} \tag{2}$$

$$q_{out} = c \cdot m \cdot \frac{dT(t)}{dt} + q_{cond} + q_{rad} \tag{3}$$

According to the law of conservation of energy:

$$\frac{U^2}{R} = c \cdot m \cdot \frac{dT(t)}{dt} + kA\frac{T_s - T_\infty}{\Delta x} + \varepsilon\sigma A(T_s^4 - T_\infty^4) \tag{4}$$

Where U is the applied voltage; t is the time; R, T, c and m are the resistance, temperature, specific heat capacity and mass of the samples; A is the heating area; T_s and T_∞ are the sample surface and environmental temperature respectively; Δx is the distance between sample

surface and environment ; k, ε and σ are the thermal conductivity of the insulating material, emissivity and Stefan-Boltzmann constant.

Owing to its PTC effect, resistance of the 22 wt.% GNP/PVDF film increased with increasing temperature, particularly around and after the switching temperature (~150 °C). As a result, further increased voltage (80 V to 100 V) only contributed to limited extra input power ($\frac{U^2}{R}$), as well as a limited temperature increase, thus reaching a self-regulating state.

3.3 GNP/HDPE/PVDF composite

When it comes to the 20 wt.% GNP/HDPE/PVDF, a double or two-step PTC effect was observed, as shown in Figure 3 left, with the PTC intensities of first and second step achieved at 1.6/1.5 and 5.2/5.9 for the samples hot pressed under 100 bar, before/after repeat. When the pressure increased up to 240 bar, the PTC intensities increased to 2.3/2.4 and 7.3/9.4 for the two steps respectively, with the two switching temperatures sit at ~120 °C and ~150 °C contributed by the thermal expansion of HDPE and PVDF respectively.

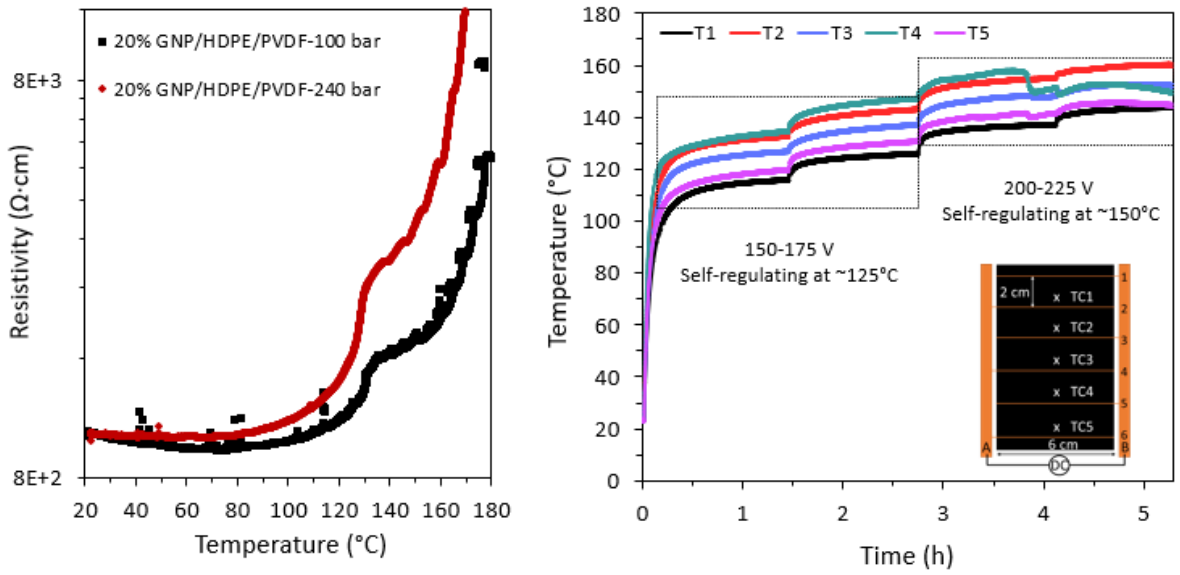

Figure 3. Pyroresistive (left) and Joule heating (right) behaviour of 20 wt.% GNP/HDPE/PVDF samples, embedded with sample dimensions and set up, including power supply connection, copper buses and thermocouples (TCs) at five different positions.

The higher hot-pressing pressure contributed to higher PTC intensities for both the first and second steps, thus 240 bar was used for the 20 wt.% GNP/HDPE/PVDF Joule heating film preparation. Due to the higher resistance, a different circuit was designed for this sample, as shown in the embedded image in Figure 3 right. 2 cm was selected as the interval between copper wires, with six wires in total and three connected to each copper bus at intervals. The whole resistance at room temperature is 7.5 kΩ. After 150 V voltage applied for ~1.5 h, 120 °C, which is the first switching temperature, was reached. In this case, with the voltage further increased up to 175 V, the temperature difference only increased ~10 °C. This is the first self-regulating behaviour contributed by the thermal expansion of HDPE. With the voltage further increasing to 200 V, steady state temperature reached at around 150 °C, which is the second switching temperature, contributed by the thermal expansion of PVDF. Owing to its higher PTC

  doi:10.5075/epfl-298799_978-2-9701614-0-0

intensity (7.3/9.4) at the second step, better self-regulating behaviour was observed as shown in Figure 3 right. After further increased the voltage from 200 V to 225 V, the steady state temperature nearly unchanged, confirming the second stage of the self-regulating heating.

4. Conclusions

GNP filled nanocomposites with both single and double polymer matrix were manufactured through melt mixing and hot pressing. For the single polymer system, single step PTC behaviour was observed owing to the thermal expansion of PVDF. Meanwhile, self-regulating heating behaviour of the system was also observed at around 150 °C, which is the switching temperature of PTC effect. For the double polymer system, double PTC behaviour was achieved via the thermal expansion of both HDPE and PVDF at different temperatures. Consequently, two self-regulating heating stages were achieved at around 125 °C and 150 °C respectively. In particular, the second stage shows higher self-regulating sensitivity owing to its higher PTC intensity. This study provides suitable selections for systems with both single and double PTC behaviour, which can be used to safely cure different FRP composites OoO through self-regulating Joule heating.

Acknowledgements

The authors would like to acknowledge the financial support received from the Engineering and Physical Sciences Research Council (EPSRC) [ESTEEM project, EP/V037234/1]. We also acknowledge Ms Jun Ma for the LabVIEW programming.

5. References

1. Y Liu, T Vliet, Y Tao, JJC Busfield, T Peijs, E Bilotti, H Zhang. Sustainable and self-regulating out-of-oven manufacturing of FRPs with integrated multifunctional capabilities. Composites Science and Technology 2020; 190, 108032.
2. Y Liu, E Asare, H Porwal, E Barbieri, S Goutianos, J Evans, M Newton, JJC Busfield, T Peijs, H Zhang, E Bilotti. The effect of conductive network on positive temperature coefficient behaviour in conductive polymer composites. Composites Part A 2020; 139, 106074.
3. Y Liu, H Zhang, H Porwal, W Tu, K Wan, J Evans, M Newton, JJC Busfield, T Peijs, E Bilotti. Tailored pyroresistive performance and flexibility by introducing a secondary thermoplastic elastomeric phase into graphene nanoplatelet (GNP) filled polymer composites for self-regulating heating devices. Journal of Materials Chemistry C 2018; 6, 2760.
4. Y Liu, H Zhang, H Porwal, W Tu, K Wan, J Evans, M Newton, JJC Busfield, T Peijs, E Bilotti. Universal Control on Pyroresistive Behavior of Flexible Self-Regulating Heating Devices. Advanced Functional Materials 2017; 27, 1702253.
5. X Zhang, S Zheng, H Zou, X Zheng, Z Liu, W Yang, M Yang. Two-step positive temperature coefficient effect with favorable reproducibility achieved by specific “island-bridge” electrical conductive networks in HDPE/PVDF/CNF composite. Composites Part A: Applied Science and Manufacturing 2017; 94:21-31.
6. J Feng, CM Chan. Double positive temperature coefficient effects of carbon black-filled polymer blends containing two semicrystalline polymers. Polymer 2000; 41:4559-4565.
7. W Di, G Zhang, Y Peng, Z Zhao. Two-step PTC effect in immiscible polymer blends filled with carbon black. Journal of Materials Science 2004; 39:695-697.

  doi:10.5075/epfl-298799_978-2-9701614-0-0

8. RJ Young, M Liu, IA Kinloch, S Li, X Zhao, C Valle´s, DG Papageorgiou. The mechanics of reinforcement of polymers by graphene nanoplatelets. Composites Science and Technology 2018; 154:110–116.
9. X Yao, SC Hawkins, BG Falzon. An advanced anti-icing/de-icing system utilizing highly aligned carbon nanotube webs. Carbon 2018; 136:130-138.

  doi:10.5075/epfl-298799_978-2-9701614-0-0

REMOTE ACTIVATION OF FRONTAL POLYMERIZATION FOR SUSTAINABLE MANUFACTURING OF THERMOSETS AND COMPOSITES

Mostafa, Yourdkhani[a,b], Morteza, Ziaee[a], Iman, Naseri[a], Sean, Smith[a]

a: Department of Mechanical Engineering, Colorado State University, Fort Collins, CO, USA
b: School of Advanced Materials Discovery, Colorado State University, Fort Collins, CO, USA
yourd@colostate.edu

Abstract: *In this work, we present a new technique for rapid and energy-efficient manufacturing of thermoset composites using photothermally activated frontal polymerization of a high-performance thermoset resin. Exploiting the high absorptivity of carbon fibers, we use photothermal effect to convert the electromagnetic energy of an incident laser light into thermal energy at a local spot on the surface of carbon fibers. When the generated heat is large enough, it can quickly initiate frontal polymerization of the surrounding matrix resin. We first use a tow of carbon fiber embedded in a bath of resin to understand the role of various parameters, including laser output power and focal area on the activation of frontal polymerization. The insights gained from this study is then used to design a processing technique for multi-point initiation of frontal polymerization and fabrication of a composite panel with a high-volume fraction of carbon fibers.*

Keywords: sustainable manufacturing; frontal polymerization; carbon fiber; photothermal energy conversion; dicyclopentadiene

1. Introduction

Fiber reinforced polymer composites have replaced metals in a wide variety of industrial sectors and applications from space and aerospace to automotive to wind energy because of their excellent strength- and modulus-to-weight ratios, durability, chemical resistance, and fatigue performance [1,2]. One of the major challenges with advanced composites is the underlying slow and energy-intensive manufacturing processes that lead to a high cost of manufacturing and low fabrication rates of composite products. In traditional composites manufacturing, the matrix thermoset resin of composites is heated at high temperatures for several hours using large and expensive equipment (autoclaves, ovens, or heated molds); as a result, such approaches require a large amount of energy, produce a significant amount of carbon dioxide (CO_2), and are cost-inefficient due to the acquisition and maintenance of expensive equipment and high labor cost per unit product [3,4].

In recent years, composite industries and academic researchers have explored alternative approaches to reduce the manufacturing time and/or energy. For example, use of snap-cure resins allows for reducing the cycle times, but such resins have a limited pot life and require heated molds for processing [5]. Various irradiation techniques have been developed to efficiently and uniformly heat up composite materials via radiation, as opposed to inefficient convective heat transfer in autoclaves and ovens, but they require expensive equipment and are limited to the manufacture of small or thin parts [3].

  doi:10.5075/epfl-298799_978-2-9701614-0-0

Frontal polymerization (FP) is a promising alternative to traditional curing strategies that can substantially reduce the manufacturing time, energy, and cost of thermosets and their composites. In FP, a resin solution containing monomers and a latent catalyst can remain stable at room temperature until a local thermal stimulus is applied to the solution. Upon local heating via a thermal stimulus, the latent catalyst becomes active and initiates the polymerization reaction in the heated region, which in turn releases heat as a result of the exothermic chemical reaction. This heat diffuses into the nearby resin, activating more catalyst and polymerizing more resin. The result is a reaction wave which propagates through the resin, transforming all available monomer to a fully cured polymer [6]. This self-sustaining polymerization strategy reduces the manufacturing time by one to two orders of magnitude and manufacturing energy by up to 10 orders of magnitude compared with traditional oven- or autoclave-curing methods [7]. FP has been recently used to produce small aerospace-grade carbon fiber composite panels in less than 5 minutes with minimal energy input, which would otherwise take several hours (more than 6 hours and up to 30 hours) to make using traditional curing strategies [7,8].

Current approaches for activation of FP reactions mostly rely on contact thermal methods such as the use of a hot soldering iron, heater films, or Joule heating of resistive wires [6]. While the contact thermal activation is easy to apply, it suffers from a few drawbacks and limitations. Continued supply of thermal energy to the resin via contact heating makes it difficult to control the amount and spatial distribution of energy delivered to the FP resin, leading to a risk of excessive local heating of the polymer and degradation of the quality and mechanical properties of produced parts. Activation of the FP reaction via conductive heat transfer typically takes several seconds to minutes in a test tube setting but can be quite long and challenging in actual manufacturing setups, especially if the intermediate boundaries have poor thermal conductivity (e.g., thick glass walls) or in hard to access regions.

Alternatively, remote activation methods would allow for better control over energy input and would enable rapid activation of FP reaction in hard-to-access regions and for multi-point initiation of the FP reaction [9]. Remote activation of FP reactions has been previously demonstrated for photo-frontal polymerization reactions, where a focused ultraviolet (UV) light is used to both initiate and sustain the propagation of the underlying chemical reaction [10–12]. Such photopolymerization schemes are limited to a certain class of monomers and cannot be applied to most FP chemistries. In addition, presence of non-transparent fillers and reinforcements prevents the efficient transmission of light to resin, which can inhibit full curing of the photopolymerizable resin. Plasma ignition has also been used for remote activation of FP reaction; however, the short activation distances and the complexity of plasma generation have limited the application of this activation method [13,14]. Another remote activation approach is the conversion of infrared or visible light to heat via photothermal energy conversion effect. Since the incident light energy is converted locally to thermal energy, this approach can be used for thermal activation of most FP chemistries that are thermally driven. However, the main challenges with the photothermal activation approach are the long activation times (ranging from 10 to 60 seconds) as well as the required absorption spectra of the FP resin system.

Here, we present a facile approach for rapid and remote activation of FP reactions via the photothermal effect. In our approach, instead of relying on the low absorptivity of FP resins, we exploit the extremely high absorptivity of carbon fibers to convert the energy of an incident laser light to heat, which consequently can activate the frontal polymerization in the surrounding

  doi:10.5075/epfl-298799_978-2-9701614-0-0

monomer solution. Using this approach, we can activate FP reactions with minimal energy input and in less than one second, reducing the activation time by 1-2 orders of magnitude compared with previously reported FP activation times. This remote activation approach is used to demonstrate multi-point initiation of frontal polymerization to further reduce the manufacturing time and also to successfully initiate the FP reaction in a fiber-reinforced polymer composite layup. The FP chemistry used in this study is based on frontal ring opening metathesis polymerization (FROMP) of dicyclopentadiene (DCPD) in presence of second-generation Grubb's catalyst. The resulting polymer, polydicyclopentadiene (pDCPD) is a high-performance thermoset polymer with good mechanical properties comparable to those of aerospace-grade epoxies, high fracture toughness, and high glass transition temperature (T_g) of ~120 °C, making it an ideal polymer for fabrication of advanced thermosets and composite materials [15–17].

2. Materials and Methods

2.1 Materials

Dicyclopentadiene (DCPD), 5-ethylidene-2-norbornene (ENB), and second-generation Grubbs catalyst (GC2) were purchased from Sigma Aldrich and used as received. DCPD is solid at room temperature, therefore a 95:5 wt% solution of DCPD:ENB was prepared in order to depress its melting point. The DCPD/ENB solution will be referred to as DCPD resin hereafter in this article. Phenylcyclohexane (PCH) and tributyl phosphite (TBP) were obtained from TCI America. PCH is used to facilitate the dissolution of the GC2 catalyst in the resin solution, whereas TPB is used as an inhibitor to control the reactivity and pot life of the resin system. For all experiments, a constant concentration of GC2 in the DCPD solution (100,000 molar equivalent of resin with respect to GC2) was used, but the concentration of inhibitor was varied based on the experimental design. In a typical experiment, 3.21 mg of GC2 was measured and dissolved in 400 μL of PCH. An appropriate amount of TBP (0.3-2 molar equivalents with respect to GC2) was added to the GC2/PCH solution via a volumetric syringe. This solution was then added to 5 mL of DCPD, mixed thoroughly, and used within five minutes to minimize the effect of any potential background polymerization. Carbon fiber yarns (HTS40 E13 200 tex, 3K), generously provided by Teijin Carbon, was used in this study for systematic measurement of the FP activation as a function of resin reactivity and laser light parameters.

2.2 Experimental setup

An experimental setup was designed to systematically measure the activation time of the FP reaction. A disposable glass fixture was designed to suspend small pieces of carbon fiber tow and separate them from bottom surfaces to minimize heat losses through the boundaries. This fixture was designed to fit in a small 35 mm diameter petri dish to minimize material use (Figure 1). A 450 nm blue laser light with a nominal power of 2 W was used to initiate the FP reaction. For precise positioning of the laser with respect to the experimental setup, it was mounted on a high-precision, 3-axis robotic platform that can be automatically moved to adjust the laser beam on the carbon fiber tow.

  doi:10.5075/epfl-298799_978-2-9701614-0-0

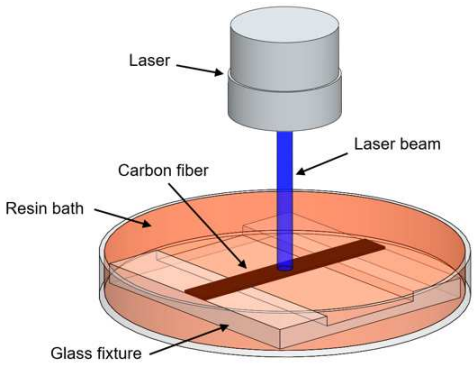

Figure 1. Schematic representation of the experiment setup used for the measurement of the FP activation time

An experimental protocol was developed to measure the activation time of the FP reaction in response to various experimental parameters and conditions. First, the laser beam was aligned on the center of the fiber tow by the guidance of a weak light from the laser source (1% of the maximum power). The laser was then activated for an interval of 50 ms. If the FP reaction was activated and propagated within the resin, then the pulse time was recorded as the activation time. Otherwise, new samples were tested with increasing pulse time until successful activation of the reaction was observed.

3. Results and discussions

The developed experimental setup was used to study the effect of laser parameters (laser intensity and spot size) on the activation time of FP reaction. Activation time was measured at laser powers of 0.4, 0.5, 1, and 2 W at the laser's focal point (Figure 2a). The trend observed is non-linear, with a decrease in power resulting in longer activation times. FROMP is not observed for laser powers below 0.4 W. The activation energies for 0.4 W, 0.5 W, 1 W, and 2 W were 0.4 J, 0.35 J, 0.33 J, and 0.45 J, respectively. The trend in activation time is explained by the activation energy. As laser power decreases, more exposure time is needed to achieve the requisite activation energy, which is around 0.4 J for this experimental condition. We hypothesize that the reason FROMP is not observed for laser powers below 0.4 W is due to heat loss through conduction and convection mechanisms. Due to these thermal transport mechanisms, the temperature at the laser spot does not reach the temperature needed to decompose the GC2-TBP complex and begin FROMP.

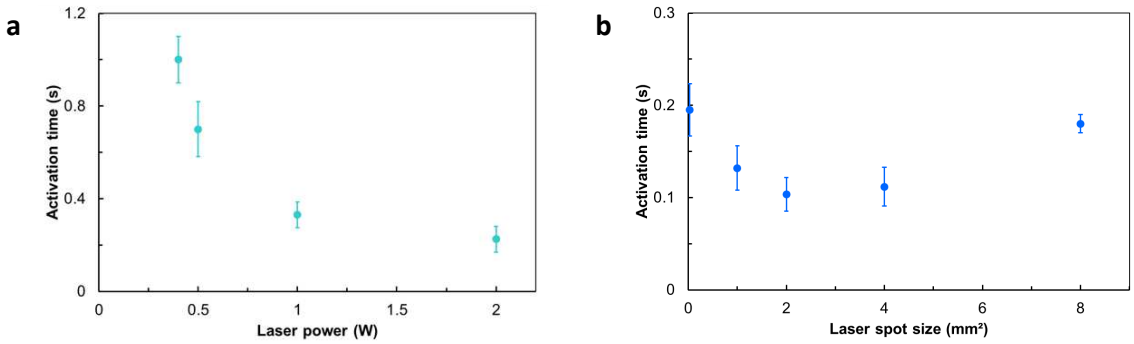

Figure 2. Effect of laser parameters on FP activation time. (a) Effect of laser input power. (b) Effect of laser spot size.

  doi:10.5075/epfl-298799_978-2-9701614-0-0 published under CC BY-NC 4.0 license

To study the effect of laser spot size on activation of FP reaction, activation time was measured for spot sizes of 0.1 mm^2 (area at the focal point) and 1, 2 , 4, and 8 mm^2 with a laser power of 2 W (Figure 2b). As spot size increases from the focal point to 2 mm^2, the activation time decreases from 200 to 100 ms. Increasing the spot size further to 8 mm^2 increases the activation time to ~200 ms. We hypothesize there are two competing factors that are responsible for this result. With a larger spot size, more resin is heated and activated in a shorter timeframe, thus resulting in faster activation times. However, as a temperature of at least 60 °C is needed to decompose the TBP-GC2 catalyst complex and initiate FROMP, large spot sizes result in reduced laser intensity per unit area, requiring longer exposure times to reach the activation temperature, thus increasing the activation time.

Controlling the laser processing parameters allows for designing new applications using this remote FP activation mechanism. For example, adjusting the laser spot size at the focal point enables very fast activation of FP reaction (in less than 100 ms), which can be used for multi-point initiation of FP reaction. To demonstrate multi-point initiation of the FP reaction, a short pulse was first applied to initiate the FP reaction in the first point, then the laser was quickly moved to a second point using the robotic platform to apply a second pulse and initiate the FP in another point (Figure 3). Once both reaction fronts were initiated, they started to propagate radially until they merged at the middle of the petri dish, reducing the cure time by almost one half. The remote activation mechanism was also used to initiate FP curing of a carbon fiber-reinforced composite panel prepared by vacuum-assisted resin transfer molding layup strategy. However, the high concentration of fiber reinforcements required a larger spot size and longer activation times to heat up a larger volume of resin and reaching the activation temperature. Upon local initiation of the FP, the front then propagated within the plane of the layup to successfully cure the composite in a few minutes.

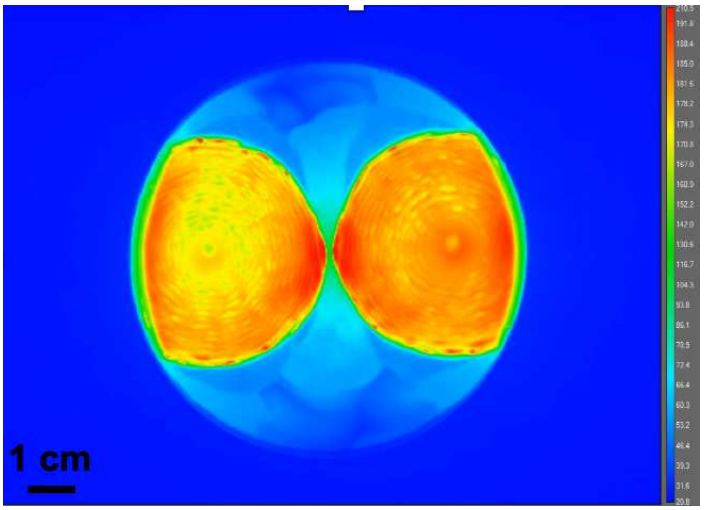

Figure 3. Thermal image of two-point initiation of FP observed from the top of the experimental setup. The reaction was initiated at two points which then propagated radially until they merged and fully cured the available monomer.

4. Conclusions

We used photothermal energy conversion to remotely and rapidly activate thermal frontal polymerization of a thermoset resin for the first time. Exploiting the high absorptivity of carbon fibers allows for quickly converting the energy of an incident laser light to heat and increasing

  doi:10.5075/epfl-298799_978-2-9701614-0-0

the surface temperature of fibers to high temperatures (above 200 °C) in less than a second to initiate frontal polymerization in the surrounding matrix resin. The effect of laser parameters on the activation time of the reaction was systemically studied to determine the fastest activation time that can be achieved using this technique. The results of this study was then used to demonstrate multi-point initiation of frontal polymerization as well as remote curing of a composite panel.

Acknowledgements

This work was supported by startup funds from the Department of Mechanical Engineering at Colorado State University.

5. References

1. Daniel IM, Ishai O. Engineering mechanics of composite materials. Oxford University Press. 2006.
2. Karbhari VM, Seible F. Fiber reinforced composites – advanced materials for the renewal of civil infrastructure. Applied Composite Materials 2000; 7:95–124.
3. Abliz D, Duan Y, Steuernagel L, Xie L, Li D, Ziegmann G. Curing methods for advanced polymer composites - a review. Polymers and Polymer Composites 2013; 21:341–348.
4. Timmis AJ, Hodzic A, Koh L, Bonner M, Soutis C, Schäfer AW, et al. Environmental impact assessment of aviation emission reduction through the implementation of composite materials. The International Journal of Life Cycle Assessment 2015; 20:233–243.
5. Malnati P, Sloan J. Fast and faster: Rapid-cure resins drive down cycle times. 2018. URL: https://www.compositesworld.com/articles/fast-and-faster-rapid-cure-epoxies-drive-down-cycle-times
6. Pojman JA. Frontal polymerization. In: Matyjaszewski K, Möller M, editors. Polymer science: a comprehensive reference. Elsevier. 2012.
7. Robertson ID, Yourdkhani M, Centellas PJ, Aw JE, Ivanoff DG, Goli E, et al. Rapid energy-efficient manufacturing of polymers and composites via frontal polymerization. Nature 2018; 557:223–227.
8. Goli E, Parikh NA, Yourdkhani M, Hibbard NG, Moore JS, Sottos NR, et al. Frontal polymerization of unidirectional carbon-fiber-reinforced composites. Composites Part A: Applied Science and Manufacturing 2020; 130:105689.
9. Zhou ZF, Yu C, Wang XQ, Tang WQ, Wang CF, Chen S. Facile access to poly(NMA-co-VCL) hydrogels via long range laser ignited frontal polymerization. Journal of Materials Chemistry A 2013; 4:7326–7331.
10. Mariani A, Bidali S, Fiori S, Sangermano M, Malucelli G, Bongiovanni R, et al. UV-ignited frontal polymerization of an epoxy resin. Journal of Polymer Science Part A: Polymer Chemistry 2004; 42:2066–2072.
11. Nason C, Roper T, Hoyle C, Pojman JA. UV-induced frontal polymerization of multifunctional (meth)acrylates. Macromolecules 2005; 38:5506–5512.
12. Sangermano M, D'Anna A, Marro C, Klikovits N, Liska R. UV-activated frontal polymerization of glass fibre reinforced epoxy composites. Composites Part B: Engineering 2018; 143:168–171.

  doi:10.5075/epfl-298799_978-2-9701614-0-0

13. Zhou J, Shao H, Tu J, Fang Y, Guo X, Wang CF, et al. Available plasma-ignited frontal polymerization approach toward facile fabrication of functional polymer hydrogels. Chemistry of Materials 2010; 22:5653–5659.
14. Zhou J, Tang WQ, Wang CF, Chen L, Chen Q, Chen S. In situ access to white light-emitting fluorescent polymer nanocomposites via plasma-ignited frontal polymerization. Journal of Polymer Scinece A: Polymer Chemistry 2012; 50:3736–3742.
15. Delaude L, Noels AF. Metathesis. In: Kroschwitz JI, Seidel A, editors. Kirk-Othmer encyclopedia of chemical technology. John Wiley & Sons. 2007.
16. Woodson Jr CS, Grubbs RH. Polymeric composites including dicyclopentadiene and related monomers. US Patent 6,310,121 B1. 2001.
17. Vallons KAM, Drozdzak R, Charret M, Lomov SV, Verpoest I. Assessment of the mechanical behaviour of glass fibre composites with a tough polydicyclopentadiene (PDCPD) matrix. Composites Part A: Applied Science and Manufacturing 2015; 78:191–200.

  doi:10.5075/epfl-298799_978-2-9701614-0-0

SUSTAINABLE MULTIFUNCTIONAL COMPOSITES: FROM ENERGY EFFICIENT MANUFACTURING TO INTEGRATED SENSING AND DE-ICING CAPABILITIES

*Yi Liu [a,b], Emiliano Bilotti [a], Ton Peijs [c], **Han Zhang** [a]*

a: School of Engineering and Materials Science, Queen Mary University of London, Mile End Road, London E1 4NS, UK

b: Department of Materials, Loughborough University, Loughborough, LE11 3TU, UK

email: han.zhang@qmul.ac.uk

Keywords: Sustainable manufacturing; Nanocomposites; Out-of-oven curing; Damage sensing; Positive Temperature Coefficient effect.

With the increasing amount of advanced composite materials employed in various fields like aerospace, automotive and renewable energy, the environmental impact of composite industries has gained more attentions than ever. It is well acknowledged that high performance fibre reinforced plastics (FRPs) can provide lightweight solutions in many structural applications, especially compared to the traditional metal counterparts to achieve higher fuel efficiency and less environmental impact during their usage period. However, in order to stimulate sustainable development of composite materials, both manufacturing stage of FRPs and components' end-of-life options should be borne in mind, where energy efficient manufacturing methods are of great necessity. From energy and capital intensive autoclave few decades ago, to nowadays out-of-autoclave manufacturing methods like vacuum assisted resin infusion and vacuum assisted resin transfer moulding, great efforts have been made in this field to the reduce end-use energy in composite manufacturing.

The advance of carbon nanomaterials like carbon nanotubes (CNTs) and graphene nanoplatelets (GNPs) over last decade has enabled another step towards energy efficient manufacturing of composite materials, with out-of-oven curing performed based on Joule heating effect of percolated conductive network [1-4]. Lee et al. reported an out-of-oven curing technique via resistive heating of an aligned carbon nanotube film, which could be detached after curing. The energy consumption was reported to be over two orders of magnitude lower (14 vs. 0.1 MJ) as compared to the oven cure baseline [2]. Xu et al. fabricated a large scale CNT film as heating

  doi:10.5075/epfl-298799_978-2-9701614-0-0

source to perform the in-situ curing of glass fibre reinforced plastics (GFRPs), leading to outstanding uniformity in thickness, surface resistance and temperature, using only one seventh of the energy consumption of the oven curing process [3]. Although the extremely high heating rate together with high thermal conductivity of these carbon nanomaterials have also brought safety concerns and risks of overheating and subsequent burning and fire hazards.

In this work, a highly energy efficient and intrinsically safe out-of-oven manufacturing method has been developed for advanced composites. Self-regulating heating based on positive temperature coefficient (PTC) effect has been achieved with percolated GNPs in HDPE matrix [5-6]. The fabricated GNP/HDPE nanocomposite film with intrinsic self-regulating heating capability has been embedded and employed to perform curing of thermoset based composites without risk of overheating and without an oven as well (Figure 1).

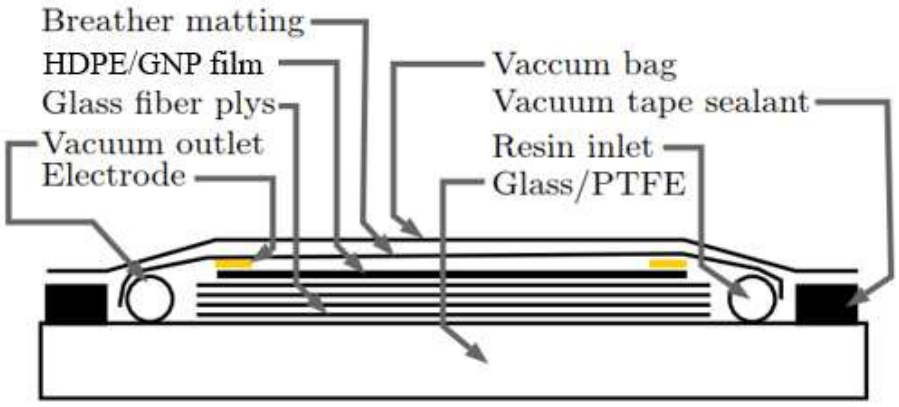

Figure 1 schematic illustration of nanocomposite film placed on top of reinforcing fabrics during the vacuum assisted resin infusion process.

Both temperature and energy consumption during the out-of-oven curing process have been monitored and recorded, with a more than 90% of energy consumption saved compared to traditional convection oven curing (Figure 2). Systematic characterisation such as DSC and DMA have been performed to examine the curing degree as well as thermal mechanical properties like Tg, with no obvious different between two curing methods.

After the composite laminate was cured, the nanocomposite layer is embedded on the surface of the laminate and being utilised as a smart multifunctional layer. Figure 2 (top right) shows the in-situ electrical sensing signals for the current multifunctional composites under flexural

  doi:10.5075/epfl-298799_978-2-9701614-0-0

loading conditions, with clear and consistent sensing signals upon each loading cycle. The de-icing capabilities based on Joule heating has also been examined and presented in Figure 2 (bottom), indicating very good heating capabilities based on embedded nanocomposite film.

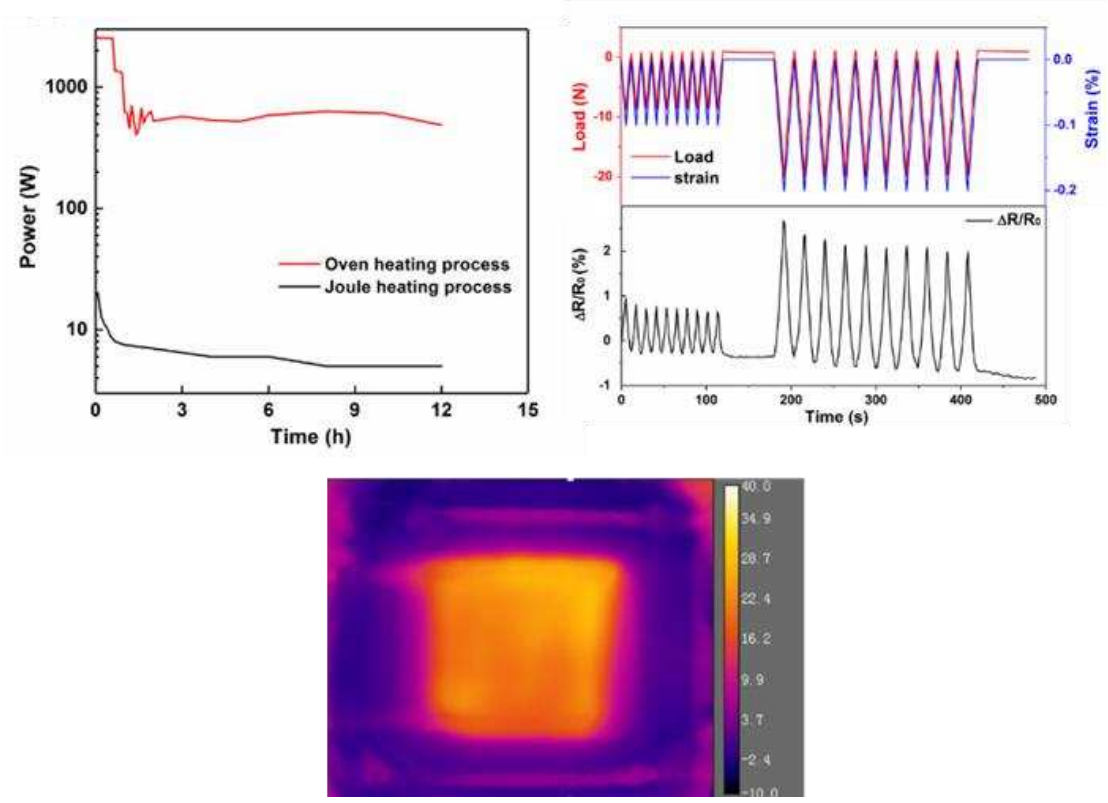

Figure 2. Power consumption comparison between oven curing and current sustainable out-of-oven curing; strain sensing performance under flexural loading; and Joule heating based de-icing performance.

In short, the current sustainable and safe out-of-oven manufacturing based on the PTC effect of nanocomposite layer provides not only a highly energy efficient manufacturing method for composite materials, but also integrated strain/damage sensing capabilities for online structural health monitoring, as well as de-icing for extreme environment. The current multifunctional composites also provide great flexibility for complex shape manufacturing since HDPE/GNP films can be easily made with desired dimensions. Capital costs also can be saved compared to autoclave or oven curing methods. The great preservation of laminate original design with no effects on internal structures has also enables high compatibility with current composite

  doi:10.5075/epfl-298799_978-2-9701614-0-0

manufacturing and applications, providing great potential for sustainable development of composite industries with reduced end-use energy from manufacturing stage.

References

1. B. Mas, J.P. Fernández-Blázquez, J Duval, H Bunyan, J.J. Vilatela. Thermoset curing through Joule heating of nanocarbons for composite manufacture, repair and soldering, Carbon 63 (2013) 523-529.
2. J. Lee, X Ni, F Daso, X Xiao, D King, J.S. Gómez, T.B. Varela, S.S. Kessler, B. L. Wardle. Advanced carbon fiber composite out-of-autoclave laminate manufacture via nanostructured out-of-oven conductive curing, Composites Science and Technology 166 (2018) 150-159.
3. X. Xu, Y Zhang, J Jiang, H Wang, X Zhao, Q Li, W Lu. In-situ curing of glass fiber reinforced polymer composites via resistive heating of carbon nanotube films, Composites Science and Technology 149 (2017) 20-27.
4. T. Xia, D Zeng, Z Li, R.J. Young, C Vallés, I.A. Kinloch. Electrically conductive GNP/epoxy composites for out-of-autoclave thermoset curing through Joule heating, Composites Science and Technology 164 (2018) 304-312.
5. Y. Liu, H. Zhang, H. Porwal, W. Tu, J. Evans, M. Newton, J. Busfield, T. Peijs, E. Bilotti. Universal Control on Pyroresistive Behavior of Flexible Self-Regulating Heating Devices, Advanced Functional Materials 27(39) (2017) 1702253.
6. Y. Liu, et.al., Pyroresistivity in conductive polymer composites: a perspective on recent advances and new applications, Polymer International 68(3) (2019) 299-305.

  doi:10.5075/epfl-298799_978-2-9701614-0-0

IMPROVED ENERGY ABSORPTION OF NOVEL HYBRID CONFIGURATIONS UNDER STATIC INDENTATION

Xun Wu [a], James Finlayson [b], Michael R. Wisnom [a], Stephen R. Hallett [a]*

a: Bristol Composites Institute, Queen's Building, University of Bristol, Bristol, UK, BS8 1TR
b: Rolls-Royce Plc, Derby DE24 8BJ, UK
* Email: Xunxun.Wu@Bristol.ac.uk

Abstract: In the present paper, a series of novel hybrid configurations were designed and tested in order to improve the energy absorption and impact resistance of carbon fibre composites under static indentation. All three hybrid configurations: glass/carbon hybrid with glass on the impact side, carbon/glass hybrid with glass on the rear side and interlayered glass/thin carbon hybrid, showed significant improvements in energy absorption in static indentation compared to the monolithic carbon layup, although the failure mechanisms were different from case to case. The interlayered glass/thin carbon has shown the highest peak load for penetration initiation and energy absorption, attributed to the fibre fragmentation in the thin carbon layers and stable fibre pull-out.

Keywords: Hybridisation; Impact damage; Static indentation; Energy absorption; Delamination

1. Introduction

Carbon fibre composites possess high specific stiffness and strength properties that are attractive for many applications. However, the use of carbon fibre composites has been significantly limited by their low baseline impact resistance and lack of mechanisms for energy absorption under low and high velocity impact loading, which composite structures may experience foreign objects during their service life.

More specifically, compressive strength after impact loading is commonly used to characterise the impact behaviour of carbon fibre composites, as barely visible impact damage (BVID), such as matrix cracking, delamination and even fibre breakage can significantly degrade their compressive strength [1]. In addition, impact behaviour of composite materials can also be characterised by the amount of energy absorbed during penetration and the associated damage area.

A range of damage mechanisms are involved in penetration of composite plates, including crush and contact failure under the projectile which can be related to Hertz contact theory; matrix cracking and delamination; shear plugging in the through-thickness direction; tensile and compressive fibre fractures due to global or localised bending stress. In order to improve impact response and energy absorption of carbon fibre composites, hybridising carbon fibre with high strain materials is a common strategy, since high strain materials have shown flexibility and good energy absorption on their own and open up a larger design space since the behaviour can be modified by using different fibre types, ply thickness and layup [2–5].

  doi:10.5075/epfl-298799_978-2-9701614-0-0

Sayer et al have presented a series of carbon/glass fibre hybrids, with different ratios and relative position of carbon plies to glass plies [4]. They have found that the impact penetration threshold has been improved by up to 30% with high strain fibres on the rear than on the impact surfaces and the ratio of carbon to glass plies has less effect. Whilst Jang et al have observed better energy characteristics in laminates with high strain material on the impact side [5]. The carbon layers on the back surface were severely damaged and the energies dissipated through the damage process at the back surface. An increase in impact energy has also been found in layer-by-layer hybrids due to increased interfaces and delamination [3]. In addition, pseudo-ductile glass/thin carbon hybrids with the damage mechanism of carbon fragmentation, have also shown improved energy absorption in tensile loading [6]. Progressive fragmentation of carbon layers has shown the potential to increase energy absorption under impact loading as the back surface in an impacted panel is in tension. Additional interfaces created in the glass/thin carbon hybrids could be additional mechanisms for energy absorption.

The prediction of behaviour of hybrid laminates is more complex and less understood compared with conventional carbon fibre composites, and some conflicting conclusions have been reported in the literature [4,5]. Therefore, the objectives of this paper are to design hybrid configurations with improved impact energy absorption using different approaches and to make comparisons between them.

2. Design and manufacture

2.1 Configuration design and material selection

Damage mechanisms are found to be associated to bending, shear, membrane and contact indentation loadings which are all involved in static indentation. Design of a hybrid layup would allow to select proper fibre types and layups for each part of a hybrid based on their damage mechanisms in order to improve their energy absorption under impact loading. Two hybrid concepts were used in the present work: block-by-block hybrids and interlayer hybrids.

Table 1. The cured ply properties of all three prepregs.

Prepreg Type	E_1 (GPa)	σ_1 (MPa)	ε_t (%)	ε_c (%)	t (mm)
IM7/8552	161	1780	1.62	1.3	0.125
S2-glass/8552	49.6	2800	4.62	3.0	0.125
T800/TP135	168	3290	1.90	1.0	0.03

On the impact side, the damage is localised and constrained under the indentor, therefore the material on the impact surface was selected to redistribute the contact stress, through either matrix cracking/delamination or early fibre fracture on the impact surface. On the rear side, deformation is at a maximum and large deformation allows more energy absorption, so the rear side has been designed to fail at high strain. An interlayered hybrid configuration - a glass/thin carbon hybrid, has been selected to use on the rear side of the

  doi:10.5075/epfl-298799_978-2-9701614-0-0

panel in order to create extra energy absorption through fragmentation in the thin carbon layers and delamination at the additional interfaces. Based on the considerations above, the following quasi-isotropic hybrid configurations with thicknesses ranging from 4.5mm to 4.75mm, were designed and are presented in this work as shown in Figure 1. Cured material properties for all constituents are given in Table 1.

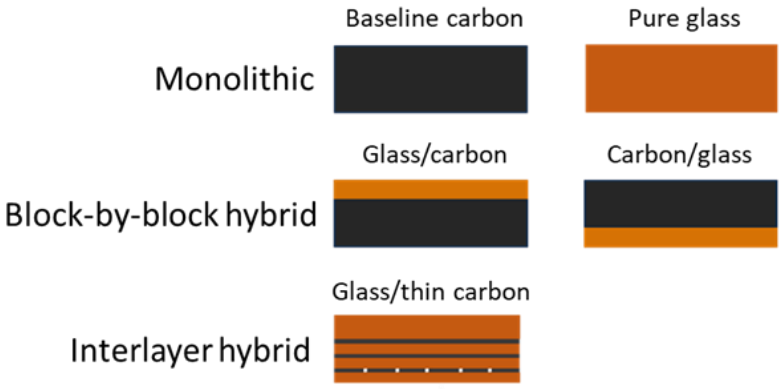

Figure 1. Schematic diagrams for all configurations, where orange and black colour represent S-glass fibre and carbon fibre respectively. The thin black lines in the glass/thin carbon case are continuous and at a later stage fragmented thin carbon layers.

2.2 Manufacture and mechanical testing

The constituent materials for each of these configurations were commercially available prepreg materials as given in Table 1. IM7 and S2-glass prepregs with HexPly 8552 epoxy resin were from Hexcel, and T800 thin plies prepreg with NTPT-TP135 epoxy resin were from North Thin-ply Technology. Both resin systems can be cured with a similar cycle, which includes dwelling at 80 °C for 75 mins, holding at 185 °C for 135 mins and curing at a pressure of 6.5 bar.

Since static indentation gives representative damage sequences and similar overall behaviour, it was selected to be used in this work to replace low-velocity impact [7]. Testing panels were designed according to the ASTM D7136 standard and were machined to the required in-plane dimensions of 150 mm by 100 mm using a waterjet cutting machine. The machined panels were then tested in a static indentation setup using an Instron hydraulically-actuated system with a 25kN load cell, at a loading rates of 0.5mm/min. A hemi-spherical steel indentor with a diameter of 16mm was used and the panels were simply supported over a window of 125mm by 75mm. The details of the test setup and parameters are shown in Figure 2. All the panels were tested until full penetration occurred.

  doi:10.5075/epfl-298799_978-2-9701614-0-0

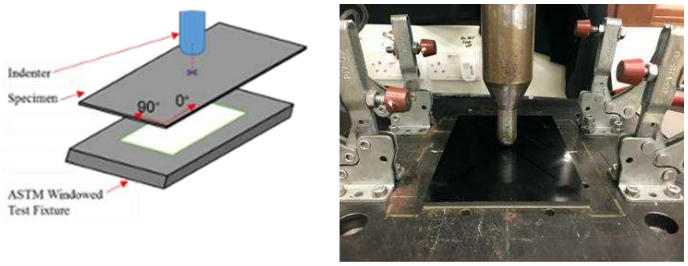

In-plane dimension: 150mm x 100mm
Window size: 125mm by 75mm
Indenter diameter: 16mm
Loading rate: 0.5mm/min

Figure 2. Experimental setup for the static indentation

3. Results and discussions

Full panel penetration has been achieved in all configurations. The typical applied loads versus the displacements for all configurations are plotted in Figure *3*(a) and (b), where Figure *3*(a) is for the monolithic and block-by-block hybrid configurations and Figure *3*(b) is for the interlayered hybrid layups. Due to slight differences in the thickness of each configuration, a thickness scaling factor $k = (t/t_c)^{1.5}$ based on the baseline carbon was applied to all loads to make a fair comparison [8].

Overall, all the panels exhibited similar global behaviour in the initial stage of loading – an early load drop associated with delamination initiation, then a region of load recovering and increasing before the peak load and a major load drop followed by a gradual load reduction. As expected, the baseline carbon panel showed the highest initial stiffness, but also presented the lowest deformation and the largest load drop after the peak load due to the brittle failure of the carbon fibre on both the impact and rear surfaces.

The carbon fibre plates hybridised with a block of high strain S-glass on either the impact or rear side of the panel, both showed improved peak loads and more gradual load-displacement responses especially after the peak load. This indicates that hybridising carbon fibre with high strain S-glass fibre improved the resistance to penetration in impact loading. The low modulus of S-glass fibre and extensive delaminations in the glass plies on the rear side have allowed more deformation. Fibre failure was delayed in this configuration, resulting in a 15% higher peak load and more energy absorbed compared to the S-glass/carbon hybrid, where the energy mainly dissipated via fibre breakage of the carbon layers on the rear surface. The monolithic S-glass panel exhibited the highest peak load due to the lower modulus and higher failure strain of S-glass in both tension and compression.

In Figure *3*(b), the interlayered hybrid configuration showed an even higher peak load and more gradual failure compared to the monolithic glass layup. The load-displacement curve for the S-glass/thin carbon interlayer configuration was almost identical to the pure S-glass panel up to the peak load. However, a higher peak was observed in the glass/thin carbon panel and a region of plateau was observed after peak load which is attributed to the fragmentation and gradual fibre pull-out in the carbon layers on the rear side.

  doi:10.5075/epfl-298799_978-2-9701614-0-0

A ranking based on the normalised total penetration energies for each configuration is presented in Figure *3*(c), where penetration energy was calculated from the total area under the load-displacement curves. All hybrid configurations showed significant improvements in energy absorption by up to 78% compared to the baseline carbon. The interlayered glass/thin carbon hybrid presented the highest energy absorption and penetration thresholds compared with all the other block-by-block hybrids and the monolithic glass panel.

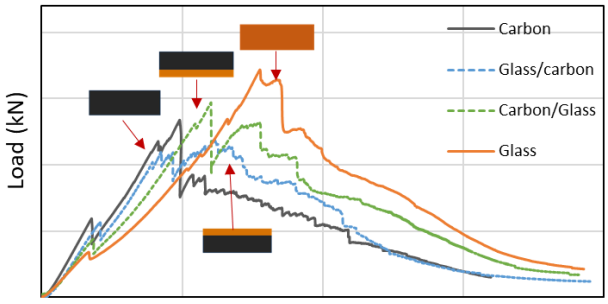

(a)

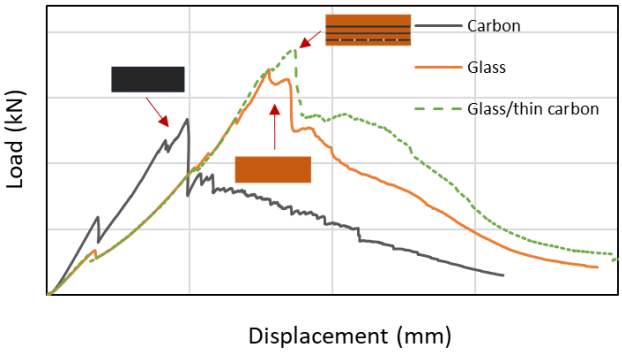

(b)

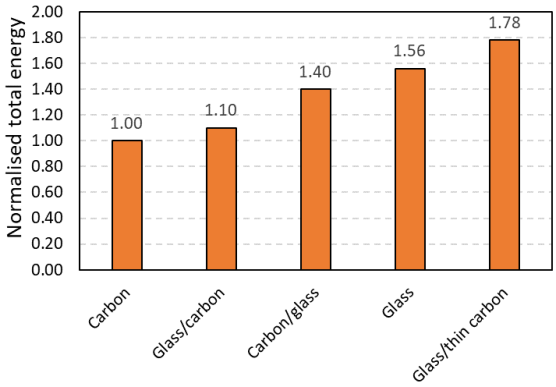

(c)

Figure 3. (a) typical load-displacement curves for the monolithic and block-by-block hybrid configurations, (b) typical load-displacement curves for the monolithic and interlayered hybrid configurations and (c) total energy absorption under static indentation

4. Conclusions

Based on the experimental investigation, the following points can be concluded:

- Energy absorption and resistance to penetration in static indentation have been improved significantly by adding high strain S-glass to the carbon plies.

  doi:10.5075/epfl-298799_978-2-9701614-0-0

- In the two block-by-block hybrid configurations, high strain S-glass on the rear side of the panel showed a 30% higher energy absorption than the configuration with S-glass on the impact side, since the lower modulus of S-glass and delamination on the rear side allowed more deformation, delaying fibre fracture.
- The interlayered glass/thin carbon hybrid exhibited the highest penetration resistance and energy absorption of to all tested configurations. Progressive fibre fragmentation in the thin carbon plies and fibre pull-out are the mechanisms promoting extra energy absorption.

Acknowledgements

This work was funded under the UK Aerospace Research and Technology (ATI) FANDANGO Programme. The authors also would like to acknowledge Rolls-Royce plc. for the support of this research through the Composites University Technology Centre (UTC) at the University of Bristol.

5. References

[1] W.J. Cantwell, J. Morton, The impact resistance of composite materials - a review, Composites. 22 (1991) 347–362. https://doi.org/10.1016/0010-4361(91)90549-V.

[2] Y. Swolfs, L. Gorbatikh, I. Verpoest, Fibre hybridisation in polymer composites: A review, Compos. Part A Appl. Sci. Manuf. 67 (2014) 181–200. https://doi.org/10.1016/j.compositesa.2014.08.027.

[3] A.A.J.M. Peijs, R.W. Venderbosch, Hybrid composites based on polyethylene and carbon fibres Part IV Influence of hybrid design on impact strength, J. Mater. Sci. Lett. 10 (1991) 1122–1124. https://doi.org/10.1007/BF00744101.

[4] M. Sayer, N.B. Bektaş, O. Sayman, An experimental investigation on the impact behavior of hybrid composite plates, Compos. Struct. 92 (2010) 1256–1262. https://doi.org/10.1016/j.compstruct.2009.10.036.

[5] B.Z. Jang, L.C. Chen, C.Z. Wang, H.T. Lin, R.H. Zee, Impact resistance and energy absorption mechanisms in hybrid composites, Compos. Sci. Technol. 34 (1989) 305–335. https://doi.org/10.1016/0266-3538(89)90002-X.

[6] G. Czél, M. Jalalvand, M.R. Wisnom, Design and characterisation of advanced pseudo-ductile unidirectional thin-ply carbon/epoxy-glass/epoxy hybrid composites, Compos. Struct. 143 (2016) 362–370. https://doi.org/10.1016/j.compstruct.2016.02.010.

[7] A.T. Nettles, M.J. Douglas, A comparison of quasi-static indentation to low-velocity impact, NASA Technical Report, TP-2000-210481.

[8] G. Caprino, V. Lopresto, C. Scarponi, G. Briotti, Influence of material thickness on the response of carbon-fabric/epoxy panels to low velocity impact, Compos. Sci. Technol. 59 (1999) 2279–2286. https://doi.org/10.1016/S0266-3538(99)00079-2.

  doi:10.5075/epfl-298799_978-2-9701614-0-0

INFLUENCE OF BRAZIER EFFECT ON THE FAILURE BEHAVIOR OF A GFRP THIN CIRCULAR CYLINDER - AN EXPERIMENTAL AND NUMERICAL STUDY

Yakanna Akkala[a], Subbareddy Daggumati[b], Akash Sharma[c]

a: Discipline of Mechanical Engineering, Indian Institute of Technology Tirupati, Yerpedu, Tirupati-517619, India, Ph.D. Scholar, me20d001@iittp.ac.in
b: Discipline of Mechanical Engineering, Indian Institute of Technology Tirupati, Yerpedu, Tirupati-517619, India, Assistant Professor, subbareddy.daggumati@iittp.ac.in
c: Discipline of Mechanical Engineering, Indian Institute of Technology Indore, Simrol, Indore -453552, India, Ph.D. Scholar, phd1701103003@iiti.ac.in

Abstract: *The observed ovalization phenomenon (flattening of a circular cross-section) under the applied bending loads in the thin-walled long-length cylinder-like structures, such as wind turbine rotor blades has been referred to as the Brazier effect. The Brazier forces tend to reduce the second area moment of the cylinder, and eventually lead to structural collapse. To understand the detailed effect of the Brazier forces on the damage initiation and propagation in composite structures, in the current research work, a GFRP thin cylinder (sub-component level) was manufactured and tested under a compression load to induce the ovalization effect. To predict the stiffness and strength degradation of the cylindrical cross-section caused by transverse loads, along with the ply level strength properties, required mode I and mode II strength and fracture energy values are obtained from experimental coupon level testing. Besides, numerical simulations are accomplished at the coupon level to calibrate the implemented material models. Finally, the obtained load vs. displacement curve from experimental testing of the cylinder was used to validate the results predicted by the detailed FE model.*

Keywords: Brazier effect; ovalization; glass-epoxy composite; delamination; intralaminar damage

1. Introduction

As the world is moving toward renewable energy sources, the generation of electricity from wind energy has rapidly increased over the past two decades. For example, the global wind power capacity in 2001 was 24.33 GW, whereas, in 2019 the power generation reached 650.76 GW with a 20% cumulative annual growth rate [1]. During these years, to increase the efficiency of wind energy production and thereby reduce the Levelized Cost Of Energy (LCOE), the size of wind turbines is increasing exponentially. Consequently, a modern 10 MW size wind turbine rotor blade is more than 90 m long and weighs about 50 tonnes [2]. In general, the aforesaid rotor blades are manufactured using Glass Fiber Reinforced Polymer (GFRP) composites. A typical GFRP wind turbine rotor blade has a hollow circular cross-section at the root that changes into a continuously decreasing airfoil shape while moving towards the blade tip. Currently, the largest wind turbine blade has a length of 107 m making the structure more slender and thin, i.e., in principle, these structures are long and have thin-walled sections with a radius to thickness ratio higher than 10 [3]. Under the applied bending loads, such long-length thin circular structures undergo large deflections and produce compressive and tensile stress above and below the neutral axis, respectively (Fig 1a).

  doi:10.5075/epfl-298799_978-2-9701614-0-0

These stresses, in turn, generate internal forces that have two components, namely longitudinal and transversal (Fig 1a). During the bending load application, the transversal force component reduces the second moment of area of the thin-walled structure leading to a non-linear bending response. At critical load, the structure can no longer sustain externally applied moment, leading to structural collapse [4]. During the load application process, these long-length thin circular sections experience a flattening effect i.e. transforming the circular cross-sections (Fig 1b) into an oval shape (Fig 1c) [5]. Hence it was concluded that the transversal force component is responsible for ovalization. This ovalization phenomenon of thin-walled long-length tubes under non-linear bending has been referred to as the Brazier effect, which was generally characterized by Brazier pressure [6].

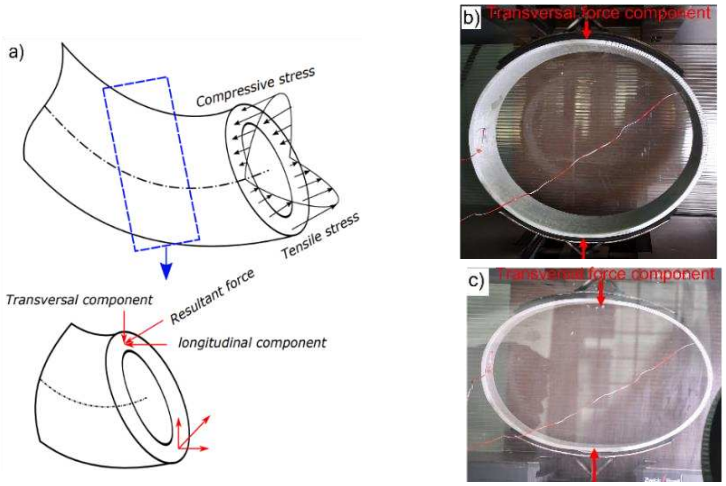

Figure 1. Transversal force component developing brazier effect in the thin-walled structure: a) stress distribution due to global bending load; b) GFRP thin circular composite cylinder before load; c) ovalization due to transverse compression (Brazier crushing pressure).

In order to study the effect of Brazier forces on the damage initiation and propagation of a rotor blade, Jørgensen et al. [7] conducted a full-scale static test on a 25 m long wind turbine blade under flapwise bending load and reported various failure modes for the main spar (load-bearing box girder). Besides, local non-linear deformation caused by Brazier pressure leads to skin wrinkling and debonding from the web. Similarly, Jensen et al. [8] conducted a full-scale static test on a 34 m long wind turbine blade with a load-bearing box girder under flapwise bending load. The aforesaid study concluded that the brazier effect which introduces crushing pressure has a significant influence on web deflection. In addition, it promotes skin debonding from the cap as an initial failure mechanism. The aforesaid mechanism is followed by delamination-driven buckling, which leads to structural collapse. Besides, Jensen et al. [9] developed an FEA model in the blade structural region (0-13 m) by taking non-linear displacement boundary conditions from a full-scale FE model. Deflections of the blade in the flapwise direction agreed well with FEA simulation results. Based on the detailed studies, Jensen et al. [10] strongly recommended that the brazier effect must be taken into consideration during the wind blade design process. Similar to the above discussed studies, Zhang et al. [11] conducted a full-scale static test on a 48.8 m long blade that confirmed the involvement of the brazier effect on structural failure.

  doi:10.5075/epfl-298799_978-2-9701614-0-0

Regarding the effect of fatigue loads on the rotor blade structural failure, H.G. Lee et. al. [12] conducted a full-scale fatigue test on a 3MW turbine blade that is 56 m long. Besides, fatigue load was applied simultaneously in both edge and flap directions. A detailed study was conducted for the root cause analysis of the T-bolt failure at the blade root-end. The aforesaid study leads to an observation that the so-called bumpy deformation of the blade under cyclic loads leads to the delamination at the root end. The aforesaid uneven deformation can be attributed to the Brazier crushing pressure.

As discussed above, in order to study the influence of the Brazier effect on the failure behavior of circular composite cross-sections, several full-scale experiments, and numerical studies have been conducted. The aforesaid studies provide a general outline of the failure behavior of the composite cross-sections influenced by Brazier pressure under the applied bending load. However, a detailed ply-ply modeling approach explaining the damage initiation and final failure in relation to the ovalization phenomenon is missing in the existing literature. Consequently, the current research work presents a detailed ply-ply modeling approach to study the effect of ovalization induced failure behavior of a GFRP cylinder under the applied transverse compression load. To this end, mimicking the typical reinforcement materials that are currently used in commercial rotor blades, a GFRP Uni-Directional (UD) non-crimp fabric (NCF) is used as a primary reinforcement along with the bi-axial fabric for the construction of the cylinder. Using the aforesaid glass fabric combined with epoxy resin, a thin circular cylinder was manufactured and tested (sub-component level) under a transverse compression load. Consequently, a geometrically non-linear deformation profile associated with the Brazier effect was studied. Finally, to conduct a detailed ply-ply failure analysis of the cylinder, several coupon level tests were conducted to estimate the elastic and strength constants of the chosen composite materials system. To simulate the interlaminar failure behavior, coupon level fracture tests and short beam shear tests on NCF glass composite laminates are conducted to obtain mode-I and mode-II fracture energy values and interlaminar tensile and shear strengths. To study the failure process at the substructure level, Hashin's failure theory was implemented to capture crack initiation, and the exponential degradation law was used to analyze the strength and stiffness degradation within the plies. A cohesive zone model (CZM) was implemented to capture interlaminar damage behavior in between the plies. Finally, the presented numerical methodology is thoroughly validated using the experimental damage profiles and the load-displacement curves.

2. Estimating interlaminar shear strength

2.1. Manufacturing process

To obtain elastic and strength constants at the ply level, initially, various test coupons were manufactured using non-crimp fabric (NCF) glass fiber of 1244 GSM as a reinforcement and epoxy matrix supplied by Bhor chemicals (BhorBond®) as a binder material. Vacuum-assisted Resin Transfer Molding (VARTM) technique was used to manufacture composite composites plates. Besides, the plates that were manufactured are cured at room temperature. Moreover, all the in-plane and interlaminar coupons were tested using ASTM standards.

  doi:10.5075/epfl-298799_978-2-9701614-0-0

Considering the length of the manuscript, in the following section, a detailed procedure related to the estimation of mode II interface fracture properties is explained. Followed by the cohesive properties estimation, cylinder FE analysis results are presented that include both intra and interlaminar damage models.

2.2. Inter Laminar Shear Strength (ILSS) - Short beam shear test

In order to estimate the ILSS of the chosen NCF UD composite laminate, the ASTM D2344 test guidelines are followed. As shown in Fig 2a, the specimen has a thickness of 6.44mm and consequently, the chosen support span length is 25.76mm. The specimen was loaded in a displacement-controlled manner with a crosshead speed of 1 mm/min. As soon as the load drop is approximately 20% of the maximum applied load, the test is terminated. A total of five specimens were tested, and respective load-displacement curves were given in Fig 2b. From the obtained load values, using Eqn 1, the ILSS value of 34.25±1.71 MPa was obtained. Moreover, to obtain the surface strain fields and to track the damage initiation and propagation, 2D Digital Image Correlation (DIC) is used. In the following sections, a correlation between experimental and numerical strain profiles is presented.

$$\tau_{ILSS} = \frac{3}{4}\frac{P_{max}}{B*h} \quad (1)$$

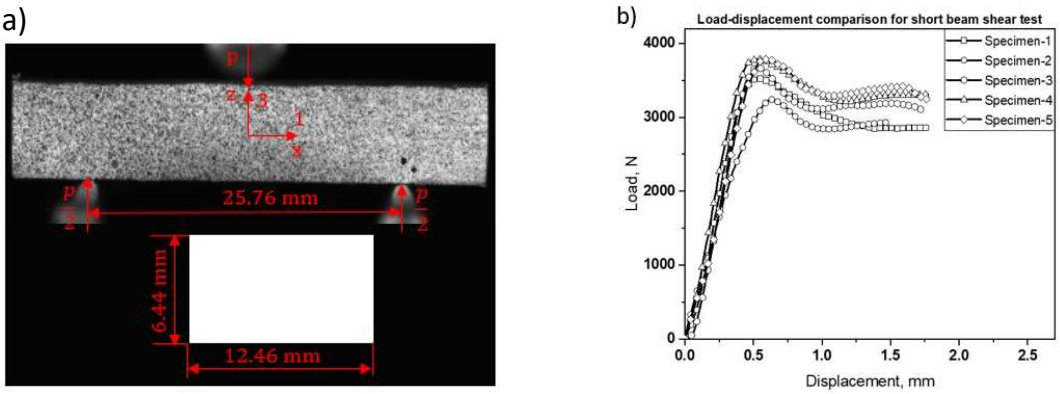

Figure 2. Schematic of short beam shear test: a) experimental setup; b) load vs. displacement curves.

2.3. Estimating mode-II interlaminar fracture toughness

Glass composite plate of thickness 3.41 mm manufactured with four unidirectional NCF plies. An 8 μm thick polytetrafluoroethylene film was inserted in the middle of the layup to create an initial crack. Mode-II fracture test coupons were machined into the required dimensions (Fig 3) as per ASTM D7905 [13]. The experimental setup and loading configuration are shown in Fig 3. Using the experimentally obtained load-displacement curves, the critical fracture energy release of the material is calculated using the below formula:

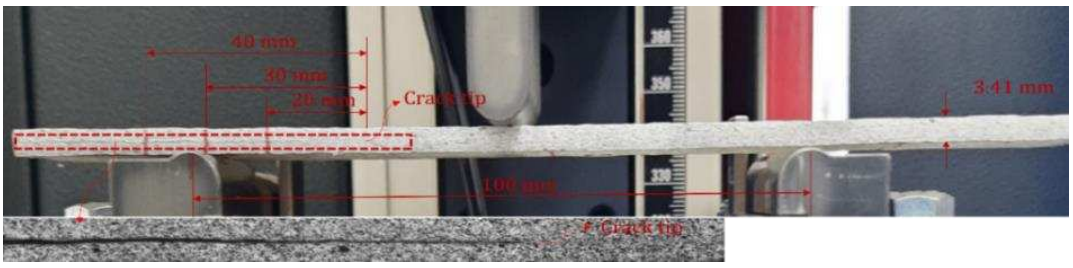

Figure 3. End-Notched Flexure (ENF) test - dimensions and experimental setup.

$$G_{\mathrm{IIc}} = \frac{P^2}{2B}\left(\frac{\mathrm{dC}}{da}\right) \quad (2)$$

In the above equation, P is the maximum load sustained by the beam and B is the width of the beam. Moreover, $\frac{\mathrm{dC}}{da}$ represents the change in beam compliance with respect to the crack growth. Hence, to estimate the (G_{IIc}) value, an expression for compliance (C) in terms of the crack length is required. In the current research work, the compliance calibration (CC) method was used for data reduction. As shown in Fig 3, CC lines were marked at a distance of 30±10 mm and 30 mm from the crack tip towards the initial crack side. All CC tests were performed by placing the specimen at crack length a_i=20,40 mm and the final fracture test is conducted at a_0=30 mm at 0.5mm/min load rate. For each CC test, compliance (C) was calibrated using a Linear least-squares fit between load vs. displacement curve. For the fracture test (a_0=30) compliance was calculated by taking data from 90 N to 50% of peak load. As compliance varies linearly with $(\text{crack length})^3$, an equation C= A+ma^3 was fitted using linear least-squares regression analysis [13]. Upon estimating the 'm' value, interlaminar fracture toughness was estimated to be equal to 1.35±0.37 N/mm using Eqn 3:

$$G_{IIc} = \frac{3mp^2a_0^2}{2B} \quad (3)$$

3. Results and discussion

3.1 Estimating the cohesive properties

As described by Rzeczkowski et al. [14], the peak load obtained from the SBS experiments (Fig 2b) cannot be the accurate interface damage initiation strength. Hence, to estimate the interface damage initiation stress and hence input the cohesive properties, an inverse method is used. It is a trial-and-error method, and cohesive properties can be obtained by matching the numerical load-displacement curve with the experiment. To achieve this, the ENF test specimen was modeled with a 2-D shell element in ABAQUS. The GFRP lamina has a thickness of 0.85 mm. The cohesive layer having a thickness of 0.01 mm was inserted at the center of the ply layup (Fig 4a). The model has a total length of 183 mm with an initial crack length of 63 mm (Fig 4a). GFRP composite layers are meshed with 7320 CPE4R elements, and the interface layer has meshed with 400 COH2D4 elements. For the current FE simulations, cohesive formulations described in [15] are used. Supporting and loading rollers had a radius of 5 mm and were modeled with 2-D discrete rigid elements (R2D2).

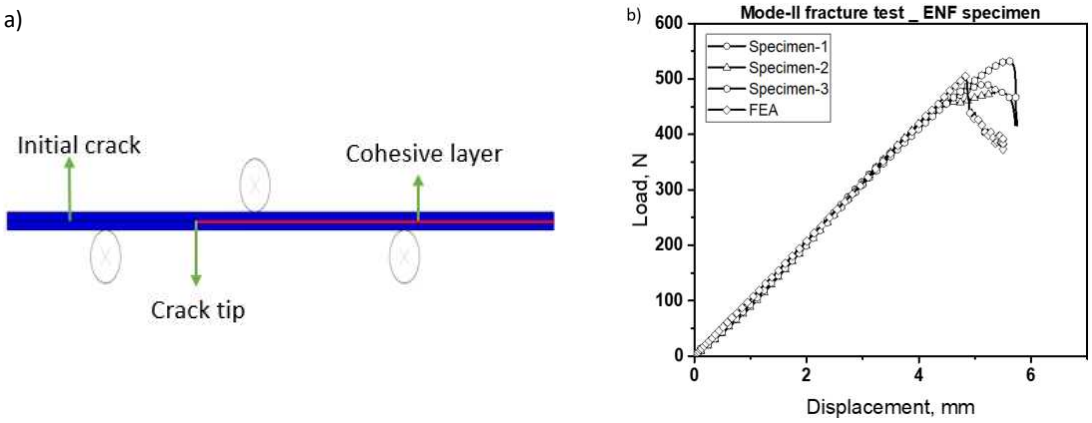

Figure 4. a) Schematic of FEA simulation of ENF test specimen; b) load-displacement comparison between experimental and FEA simulation.

A dynamic explicit solver was used for simulating the load-displacement behavior. In order to obtain the interface damage initiation stress value, the experimentally obtained G_{IIc} (1.35 N/mm) is kept constant and the interface strength value is varied such that the predicted load-displacement curve matches the experimental load-displacement curve (Fig 4b). The predicted mode II interface damage initiation stress value is listed in Table 1. Similarly, mode I experiments are accomplished using Double Cantilever Beam (DCB) experiment (ASTM D5528), and the G_{Ic} value is obtained as 0.645±0.142 N/mm. Finally, mode I interface strength is obtained from the numerical simulations. The experimental critical fracture energy release rates and the calibrated cohesive interface strengths are listed in Table 1

Table 1: Cohesive properties of NCF GFRP UD composite.

Test	***Strength, MPa***	***Interface damage initiation, (estimated) MPa***	***Critical fracture energy release rate, J/m²***
Mode I	*NA*	*12*	*645±142*
Mode II	34.25±1.71	*28*	*1350*±350

3.2. Verification of mode –II cohesive properties

Experimental stress-displacement curves obtained from the short beam shear test were used to verify calibrated cohesive strength (28 MPa). To this end, the short beam shear specimen, which has dimensions and load configuration shown in Fig 2a was modeled in ABAQUS. The FEA model consists of 8 GFRP laminas meshed with 36672 C3D8R elements. Cohesive elements were inserted between each GFRP lamina and meshed with 16044 COH3D8 elements. Loading and support roller meshed with discrete rigid elements (R3D4). Upon running the FE simulations, the predicted stress-displacement curve is compared against the experimental stress-displacement curves (Fig 5a). Using the cohesive properties listed in table 1, the predicted stress-displacement curve closely matches experimental results (Fig 5a). Further strain profiles obtained from DIC were also compared with respective strain profiles from the FEA simulation, and the results were matched well (Fig 5b).

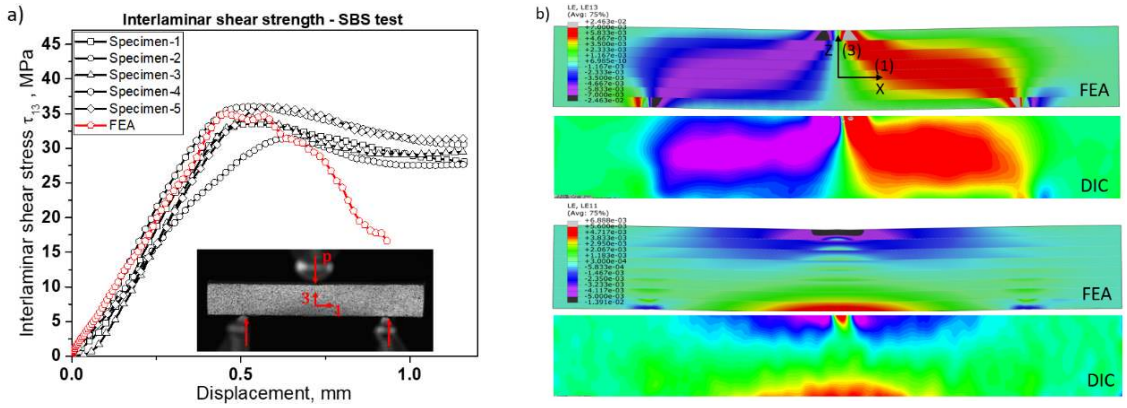

Figure 5. Comparison between experimental and FEA simulation results of short beam shear test: a) Load vs. displacement curve; b) strain profiles at 85% of peak load.

  doi:10.5075/epfl-298799_978-2-9701614-0-0

3.3. GFRP thin composite cylinder under transverse compression – FE modeling

To achieve the objective of this paper, a GFRP thin composite cylinder with an inner radius of 202 mm and an outer radius of 210.99 mm was modeled in ABAQUS. The model consists of 18 plies, consisting of the following $[0/(\pm 45)_2]_{3s}$ stacking sequence. The GFRP laminas meshed with C3D8R elements. Moreover, cohesive elements having a thickness of 0.01mm were inserted between the plies and are discretized with COH3D8 elements. A user-defined material (VUMAT subroutine) was developed to characterize matrix cracking and delamination damage behavior. The aforesaid user materials were developed based on the progressive damage model (PDM). In these models, stiffness degradation starts whenever laminate satisfies the damage initiation criterion. A scalar damage variable was used to degrade stiffness, which varies between 0 at damage initiation and 1 at element deletion. Hashin's failure theory was used for matrix cracking as damage initiation and the exponential progressive degradation law as damage evolution [16]. Similarly, the quadratic nominal stress criterion was used for the interface damage initiation (cohesive elements), and the B-K law was used for interface element deletion. To induce the ovalization effect in the cylinder, a transverse compressive load is applied through a discrete rigid body (R3D4) (Fig 6a). The cylinder underwent a large non-linear deformation before final failure changing the circular cross-section into an oval shape (Fig 6). Due to the Brazier effect matrix cracking in the 45^0 plies is observed as initial damage (Fig 6a). This crack propagated towards the interface, causing delamination damage following the final failure (Fig 6b).

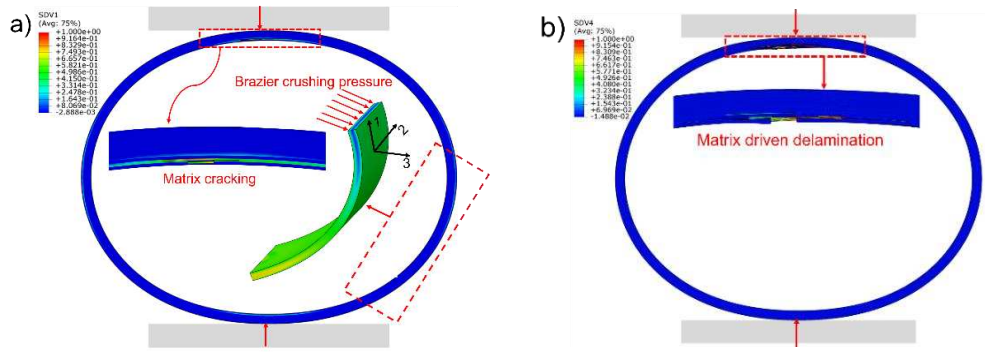

Figure 6. Brazier effect on GFRP thin composite cylinder due to Transverse compression (Brazier crushing pressure): a) matrix cracking; b) delamination.

4. Conclusions

A detailed ply-ply FE model of a GFRP composite cylinder was developed consisting of both intra- and interlayer damage models. Required ply elastic and strength constants, as well as interlaminar strength and fracture energy values, were experimentally determined. Also, cohesive properties were estimated by FEA parametric study by matching experimental load-displacement curves to the predicted curves. Using the GFRP cylinder FE analysis, under the applied transversal force that mimics Brazier crushing force, large deformation (11.68% reduction in diameter of the cylinder in load application direction) is produced while reducing the second area moment by 19.26%. The observed flattening effect led to matrix cracking in 45^0 plies. The aforesaid crack propagated towards the interface causing matrix-driven delamination followed by final failure of the cylinder.

5. References

[1] P. Liu, F. Meng, and C. Y. Barlow, "Wind turbine blade end-of-life options: An economic comparison," *Resour. Conserv. Recycl.*, vol. 180, no. August 2021, p. 106202, 2022, doi: 10.1016/j.resconrec.2022.106202.

[2] D. T. Griffith and T. D. Ashwill, "The Sandia 100-meter All-glass Baseline Wind Turbine Blade : SNL100-00," *Baseline*, no. June, pp. 1–67, 2011.

[3] "A Towering Achievement: This Summer In Holland, GE Will Build The World's Largest Wind Turbine | GE News." .

[4] L. S. Cecchini and P. M. Weaver, "Brazier effect in multibay airfoil sections," *AIAA J.*, vol. 43, no. 10, pp. 2252–2258, 2005, doi: 10.2514/1.11736.

[5] L. G. Brazier and P. R. S. L. A, "On the flexure of thin cylindrical shells and other 'thin' sections," *Proc. R. Soc. London. Ser. A, Contain. Pap. a Math. Phys. Character*, vol. 116, no. 773, pp. 104–114, 1927, doi: 10.1098/rspa.1927.0125.

[6] K. T. Kedward, "Nonlinear Collapse of Thin-Walled Composite Cylinders Under Flexural Loading.," pp. 353–365, 1978.

[7] E. R. Jørgensen *et al.*, *Full scale testing of wind turbine blade to failure - flapwise loading*, vol. 1392, no. June. 2004.

[8] F. M. Jensen, A. S. Puri, J. P. Dear, K. Branner, and A. Morris, "Investigating the impact of non-linear geometrical effects on wind turbine blades-Part 1: Current status of design and test methods and future challenges in design optimization," *Wind Energy*, vol. 14, no. 2, pp. 239–254, Mar. 2011, doi: 10.1002/WE.415.

[9] F. M. Jensen, B. G. Falzon, J. Ankersen, and H. Stang, "Structural testing and numerical simulation of a 34 m composite wind turbine blade," *Compos. Struct.*, vol. 76, no. 1–2, pp. 52–61, 2006, doi: 10.1016/j.compstruct.2006.06.008.

[10] F. M. Jensen, P. M. Weaver, L. S. Cecchini, H. Stang, and R. F. Nielsen, "The Brazier effect in wind turbine blades and its influence on design," *Wind Energy*, vol. 15, no. 2, pp. 319–333, Mar. 2012, doi: 10.1002/we.473.

[11] L. Zhang, Y. Guo, L. Yu, X. Wei, W. Liu, and X. Huang, "Structural collapse characteristics of a 48.8 m wind turbine blade under ultimate bending loading," *Eng. Fail. Anal.*, vol. 106, no. May, p. 104150, 2019, doi: 10.1016/j.engfailanal.2019.104150.

[12] H. G. Lee, M. G. Kang, and J. Park, "Fatigue failure of a composite wind turbine blade at its root end," *Compos. Struct.*, vol. 133, pp. 878–885, 2015, doi: 10.1016/j.compstruct.2015.08.010.

[13] ASTM D7905, "Standard test method for determination of the mode II interlaminar fracture toughness of unidirectional fiber-reinforced polymer matrix composites," *Astm*, pp. 1–18, 2014, doi: 10.1520/D7905.

[14] J. Rzeczkowski, "An experimental analysis of the end-notched flexure composite laminates beams with elastic couplings," *Contin. Mech. Thermodyn.*, vol. 33, no. 6, pp. 2331–2343, 2021, doi: 10.1007/s00161-020-00903-2.

[15] A. Sharma, S. Daggumati, A. Gupta, and W. Van Paepegem, "On the prediction of the bi-axial failure envelope of a UD CFRP composite lamina using computational micromechanics: Effect of microscale parameters on macroscale stress–strain behavior A.," *Compos. Struct.*, vol. 251, no. May, p. 112605, 2020, doi: 10.1016/j.compstruct.2020.112605.

[16] L. B. Andraju and G. Raju, "Continuum and cohesive zone damage models to study intra/inter-laminar failure of curved composite laminates under four-point bending," *Compos. Struct.*, vol. 253, no. June, p. 112768, 2020, doi: 10.1016/j.compstruct.2020.112768.

MULTISCALE INTERFACE BEHAVIOUR AND PERFORMANCE OF GF-PC COMPOSITE

O. Vetterli [a], G. A. Pappas, P. Ermanni

a: Laboratory of Composite Materials and Adaptive Structures, Swiss Federal Institute of Technology Zurich (ETHZ); [a]oliverve@ethz.ch

Abstract: *Fibre-matrix interface performance is essential in fibre reinforced polymer composites, leading to important efforts in quantification and optimization. This is even more relevant for thermoplastics, since interfacial bonding happens only via physical interactions. Standardised mechanical tests provide homogenized composite properties, but fail to isolate the contribution of the interface. Micromechanical ones are designed for this exact purpose, but need complex set-ups and sample preparation. This study adopts a novel multiscale approach to measure mechanical properties of polycarbonate-glass fibre composites, manufactured under different interfacial conditions (sized & desized). This is enabled by use of focused ion beam in precise manufacturing and post-mortem analysis of specimens. The results show an evident difference between tested conditions at the macroscale (mode I), where sized specimens outperform desized ones. At the microscale (mode II), these differences are less pronounced due to the high ductility of the matrix resulting in a cohesive failure of the composite.*

Keywords: Polycarbonate; Glass fibre composites; Microscale; Interface

1. Introduction

The demand for high performing glass fibre (GF) reinforced polymer composites has been growing rapidly, mainly due to their attractive performance to price ratio, making them appealing for lightweight structures [1, 2]. Moreover, due to the sustainability potential, thermoplastic polymers are becoming a valid alternative to thermosets [3]. Also, thermoplastics like polycarbonate (PC), show very high tenacity due to their high ductility, making them appealing for demanding applications such as protective equipment and ballistics [4, 5]. Generally, the performance of composites, not only depends on the constituent material mechanical properties and orientation, but largely, on the interfacial strength [6, 7]. Interactions at this level include physical (like Van der Waals interactions), mechanical (like surface roughening) and chemical (like covalent bonds). In practical terms, bonding is improved via the application of sizing solution, which are complex mixtures that have to fulfil specific requirements [8, 9]. Contrary to thermosets, which are polymerised in-situ, thus, allowing for chemical interaction, thermoplastics only allow for physical interactions with the fibre and sizing.

Being able to precisely quantify interface strength and toughness is of paramount importance to enable the production of better performing composites, and can be done explicitly via micromechanical experiments. Unfortunately, these kind of tests are extremely laborious, lack standards and the high complexity of testing setups prevents direct comparison of results. This limits their implementation at an industrial level, where conventional macro-mechanical tests are used considering a homogenized behaviour [10]. This work will therefore focus on

  doi:10.5075/epfl-298799_978-2-9701614-0-0

investigating the failure behaviour of PC-GF composite at different size scales and processing conditions, via state of the art macromechanical test and innovative micromechanical setup. The micromechanical test set-up resembles designs applied in ceramics [11, 12] and thermosets [6, 13] composites, namely push-out test; where the interface between the matrix and fibre is forced into failure under shear (mode II). However, to precisely control the sample dimension and quality, an innovative manufacturing technique that employs a focus ion beam (FIB) has been developed. Macromechanical testing was also included in this study via transverse tensile test on laminated strip-coupons. In terms of processing conditions, a thermoplastic compatible sized glass fibre mat is compared to a neat one, where the matrix-fibre interface is expected to be lower affecting the overall performance.

2. Materials & Methods

2.1 Materials

Specimens for both macro- & micro-mechanical testing were produced with the same constituent materials. Two types of glass fibre mats were used, 92145 and 92145-FE800, produced by *Porcher Industries Germany Gmbh*. Both materials are unidirectional GF mats with a nominal areal weight of 223±5 g/m^2 (10 g/m^2 weft direction). The only difference is the finishing of the glass fibres. The first one has been fully de-sized via thermal processing (a procedure carried out by the supplier), and the second has a thermoplastic sizing containing silane compounds. The polymeric matrix used is a commercial-grade polycarbonate *Makrofol 1-4 010181,* produced by *Covestro Germany Gmbh* in film form with a thickness of 175 µm.

2.2 Macromechanical specimen manufacturing and testing set-up

Composite plates were prepared via the state-of-the-art film stacking technique, where a 200×200 mm^2 film of polycarbonate is alternated every two layers of a 200×200 mm^2 GF mat, for a total of 6 and 12 layers respectively. This lay-up gives a final nominal fibre volume fraction (FVF) of ~54% after a ~2.5% of matrix bleed.
The laminates were stacked manually and pressed under vacuum. To achieve flat specimens with homogeneous thickness, the material was pressed in a *Fontijne TP 400* hot press, between thick steel plates equipped with 2 mm (nominal) thick spacers to avoid excessive bleeding and restrain over-compaction. The material was heated at a constant rate of 5°C/min up to 320°C under vacuum to avoid degradation. Once the processing temperature was reached, pressure was applied in two steps to facilitate compaction and impregnation: 10 min at 8 bar followed by 20 min at 20 bar. The whole set-up was cooled down to room temperature over a time of 40 min to relax out thermal stresses. Specimens were cut to dimension with a water-cooled circular saw according to ASTM D3039 [14] standards for transverse tensile testing. From each type of plate (2 conditions), 7 samples were produced with nominal values of length L= 200 mm width w= 25 mm and thickness *t*= 2 mm. Prior to testing, quality control was carried out via thermogravimetric analysis *(TGA-2 SF, Mettler Toledo)* and microscopy *(VHX-6000, Keyence)* to evaluate FVF, void content and microstructure.

2.3 Micromechanical specimen preparation and testing set-up

Micromechanical specimens for the push-out geometry were made from the same laminate prepared for transverse tensile test to remove any processing bias. According to the process, initially, strip coupons with the same dimensions as the macromechanical samples are

  doi:10.5075/epfl-298799_978-2-9701614-0-0

manually ground and polished on top and side faces, via a *Tegramin-20, Streuers*, down to a surface roughness of 1 µm. The second step, consists of cutting the polished strips with a fine diamond blade (paying great care not to damage the 2 polished edges), to a final dimension of 8×5×2 mm^3 before fixing it on a scanning electron microscope (SEM) stub with conductive silver glue. Consequently, in order to successfully image the sample with an SEM, a platinum-palladium conductive coating is applied with a thickness of 10 nm via a *CCU-010 Metal Sputter Coater, Safematic* (Figure 1). In the final two steps, the sample is further smoothed and small 'pockets' are milled, by means of a focus ion beam (FIB) *Helios 5 UX Dual Beam, ThermoFisher Scientific*. The previously prepared sample is then mounted on a 45° pre-tilt adaptor and re-inserted into the device.

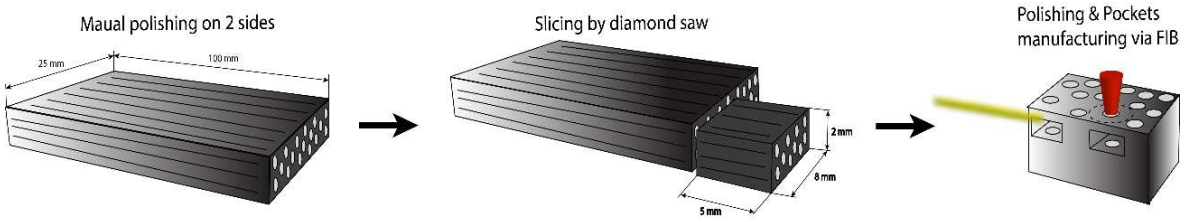

Figure 1: Micromechanical specimen preparation and workflow (not to scale). Left: The top (25×100 mm^2) and side (25×2 mm^2) faces are manually polished. Middle: micromechanical sample is sliced. Right: The sample is mounted on an SEM stub (not shown) and a pocket is milled via FIB.

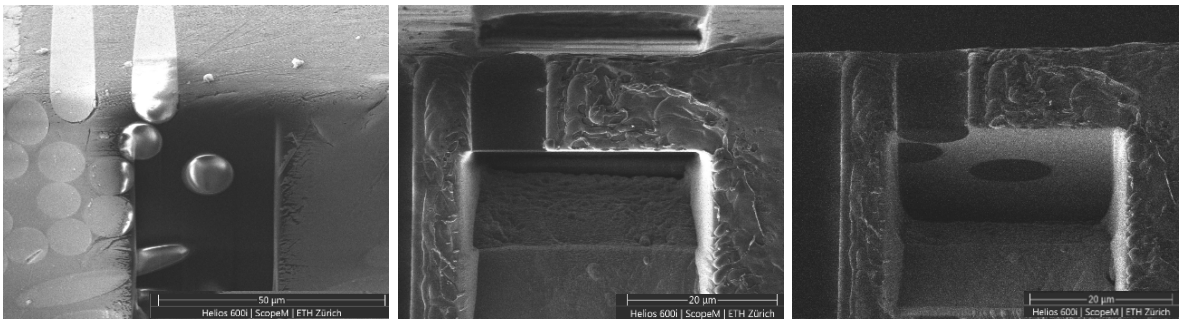

Figure 2: Detail of specimens prepared with the FIB. Left: top view of the polished surface. Middle: front view of the composite layer where the push-out test will be performed. Right: inside view of the pocket, with the single fibre domain prepared for mechanical test.

In detail, once a suitable area has been identified (matrix rich domains with isolated fibre), the top surface is further polished at a stage tilt of 8.5° (1.5° over tilt *w.r.t.* ion source), using cleaning cross sections (CCS). To achieve optimal smoothness, two procedures are run: first, a 30×30 $µm^2$ area is processed with a current of 20 nA. This removes any surface features in the micro-meter range. Secondly, a smaller area of 20×20 $µm^2$ is further processed with a finer current of 9 nA, removing sub-micrometre features.
Then the pocket, where the fibre will be pushed in, is carved out in two steps, both carried out with a gallium ion beam equipped with a water gas nozzle (multichem gun) to enhance the etching rate. First, the bulk material is removed via a regular cross-section (RCS), with a width of 3 times the fibre diameter, 30 µm depth and 20 µm height. Then a further polishing step, with a lower current of 9 nA, is carried out to achieve a smooth finishing of the newly manufactured pocket surface. Depictive SEM images are shown in Figure 2.

The previously prepared push-out samples were tested on *Vega 3 Tescan* SEM equipped with a displacement controlled indenter from *Alemnis*. For the experimental campaign, a 3.5 µm

diamond flat punch indenter, from *Synton MDP*, with a displacement rate of 50 nm/s was used [13].

3. Results & Discussion

The stress-strain plots in Figure 4 together with Table 1 summarize the essential information gathered from the transverse tensile tests. In both cases, sized & desized condition, five specimens provided usable results; for the rest the coupons failed close to the gripping region of the tensile machine clamp, invalidating the results [14].

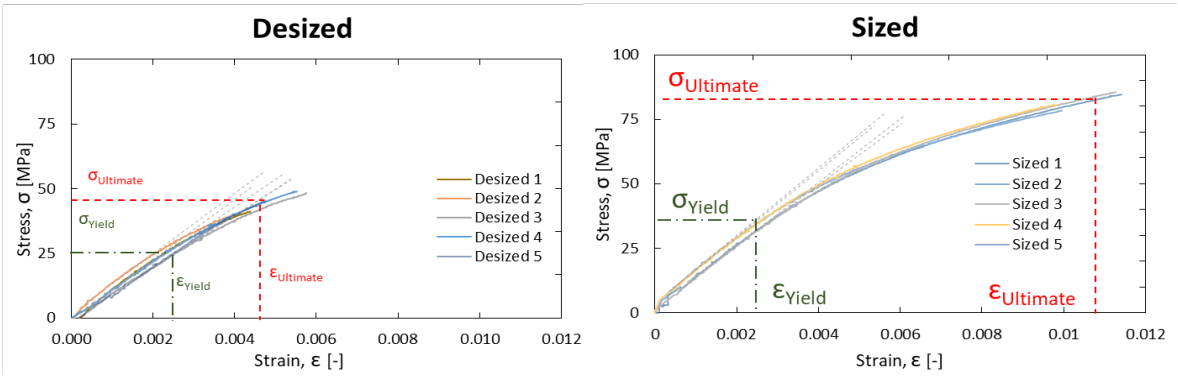

Figure 3: Tensile testing results, plot of Stress vs. Strain values of Left: Desized and Right: Sized GF-PC composite. Dotted red and green line pinpoint the measured ultimate and yield values for strength/strain, respectively.

Table 1: Macromechanical results (averages of n=5, and standard deviation) from transverse tensile test.
**Normalized for FVF= 53.5% and pure UD assumption (without weft effect see text for details)*

Material	Strength* [MPa]		Critical Strain [-]		E_{22}* [GPa]
Sized	σ_{Yield}	31.1±2.2	ε_{Yield}	0.0024±0.0006	12.2±0.5
	$\sigma_{Ultimate}$	78.3±3.0	$\varepsilon_{Ultimate}$	0.0110±0.0005	
Desized	σ_{Yield}	24.1±3.5	ε_{Yield}	0.0027±0.0006	11.0±0.6
	$\sigma_{Ultimate}$	37.8±4.3	$\varepsilon_{Ultimate}$	0.0051±0.0007	

Thanks to the precise manufacturing of the laminate, the void content is <0.5% and the final FVF is 53.7±0.4%; resulting in a fair and reliable comparison between the two tested conditions. To calculate the composite strength and modulus in transverse direction, the contribution of the weft (perpendicular to the bundles in the main fibre direction of the unidirectional fabric) had to be taken into account. In fact, the measured stress-strain response is assumed to be the result of pure 90° (transverse) composite plus the longitudinal glass fibre weft. One can assume the rule of mixtures (ROM, i.e. uniform strain) as a representative approximation of this combination [15]. The theoretical transverse modulus of the pure GF-PC composite in the transverse direction can be approximated by the Halpin-Tsai semi-empirical model (Eq. 1, with $\xi = 2$), which in combination with the weft contribution provides a value for the given ratio of weft and UD. This is then compared with the effective measured modulus, providing a correction factor, in the range of 0.8, for the measured stresses, allowing the evaluation of the true strength in the transverse direction. Moreover, to be consistent with the micromechanical evaluation of the material, yield strength was defined by a 2% deviation from linearity [13].

$$E_{22} = E_{PC}\frac{1+\xi\,\eta\,v_f}{1-\eta\,v_f}, \text{with } \eta = \frac{E_{GF}-E_{PC}}{E_{GF}+\xi\,E_{PC}} \qquad (1a)$$

$$E_{22}^{*} = \frac{\nu_f}{\nu_f + \nu_w} E_{22} + \frac{\nu_w}{\nu_f + \nu_w} E_{GF} \quad (1b)$$

In Eq. 1a & 1b, E_{22} is the modulus in transverse direction; ν_f is the fibre volume fraction in the principal direction; ν_w is the weft-fibre volume fraction; E_{GF}, E_{PC} the moduli of glass fibre and matrix respectively; Note that the total FVF=$\nu_f + \nu_w$.

From the provided data, a substantial influence of sizing can be observed. Compared to desized samples, sized conditions have 52% and 23% higher ultimate and yield strength, respectively. Ultimate strain results follow the same trend, too, with sized conditions having a 54% higher value compared to desized. Though, yield strain values are in the same order of magnitude for both tested conditions. E-moduli have a more contained difference (10%); nonetheless, the overall trend is repeated in this instance too.

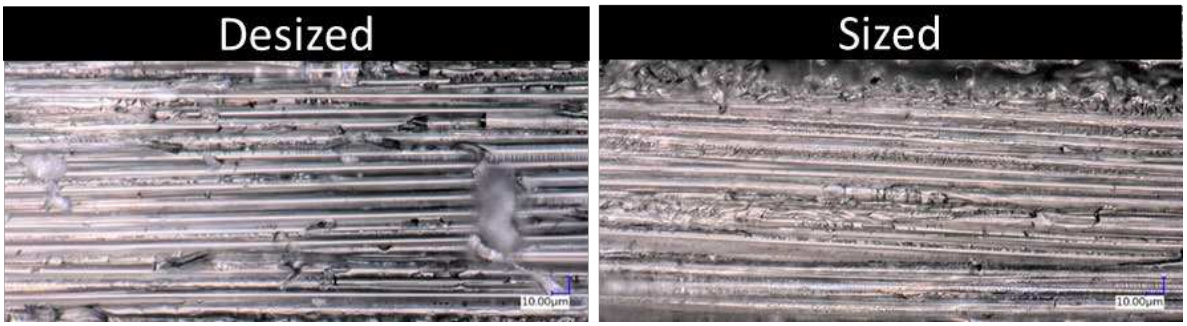

Figure 4: Fractography on surfaces resulting from tensile test. Left: desized surface, with mainly adhesive failure as a result of a weaker matrix-fibre interface. Right: sized surface, with mixed adhesive-cohesive failure.

Interestingly, the presence of sizing allows for a much larger plastic deformation before failure. This can be explained by a stronger interface between the two components and can be seen in the post-mortem microscopy analysis of the cracked specimens, similar to the observations of Montenegro et. al. [16] (Figure 5). Sizing leads to a failure with partially coated fibres after the tensile test, leading to a mixed adhesive-cohesive failure. For desized condition, a considerably larger bare glass fibre surface is exposed, resulting in a predominantly adhesive failure of the specimen. This behaviour observed at the macro scale can be partially seen at the micro-scale too, where the bottom portion of the pushed-out fibre is partially matrix coated for the sized sample and bare for the desized one (Figure 6) as explained hereafter.

In Figure 7 the results from the push-out tests are reported. The nominal effective shear stress is calculated over the contact area between the glass and matrix, where $F_{applied}$ is the force applied by the intender, *r* the fibre radius and *h* the height of the composite layer (Eq. 2). Via this simple calculation, differences in fibre diameter and polymer layer thickness can be accounted for. The first portion of the curve with the initial rise and constant slope, was a result of elastic bending of the thin composite layer and elastic response of the fibre. This was followed by a flattening of the curve and the approaching of critical load where failure happened. Though, in our case, since the interface was stronger than the polymer, contrary to ceramic and often thermoset matrices, this portion of the graph corresponded, mainly, to the plastic deformation of the polymer. Nonetheless, a critical load (marked with a star) has been identified at 2% deviation from linearity, following previously reported procedure on similar geometry [6, 17].

$$\tau_{Nominal} = \frac{F_{applied}}{2\,\pi\,r\,h} \quad (2)$$

  doi:10.5075/epfl-298799_978-2-9701614-0-0

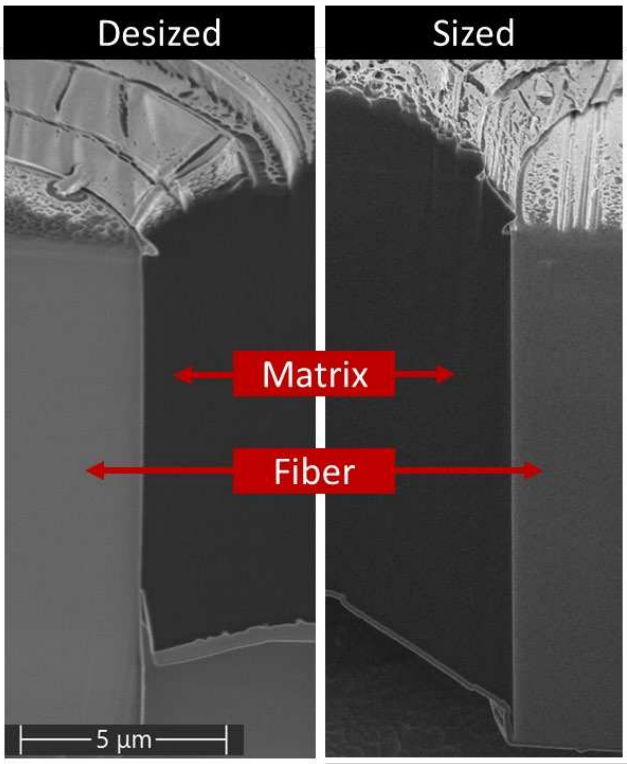

Figure 5: SEM picture of the cross-section of a pushed out fibre.. Left: Desized fibre, where it can be seen that the interface at the bottom of the specimens fails adhesively. Right: Sized fibre, where it can be seen that the matrix has been plastified extensively, and the pushed-out portion of the fibre still has matrix on the surface, leading to a cohesive failure. Note that, the final displacement and force applied is higher for the sized one.

The average value for critical shear stress for sized and desized conditions are 31.0±0.9 MPa and 27.1±2.5 MPa respectively. These values do not correspond to a complete interface failure, because the polymer yields extensively without any pronounced interface failure (Figure 6). This phenomenon is attributed to an interface strength in mode II higher than the matrix shear strength, compared to mode I vs. tensile strength (as in the case of transverse tensile test). Nonetheless, the overall trends can be retrieved and give useful insights into the failure mechanisms.

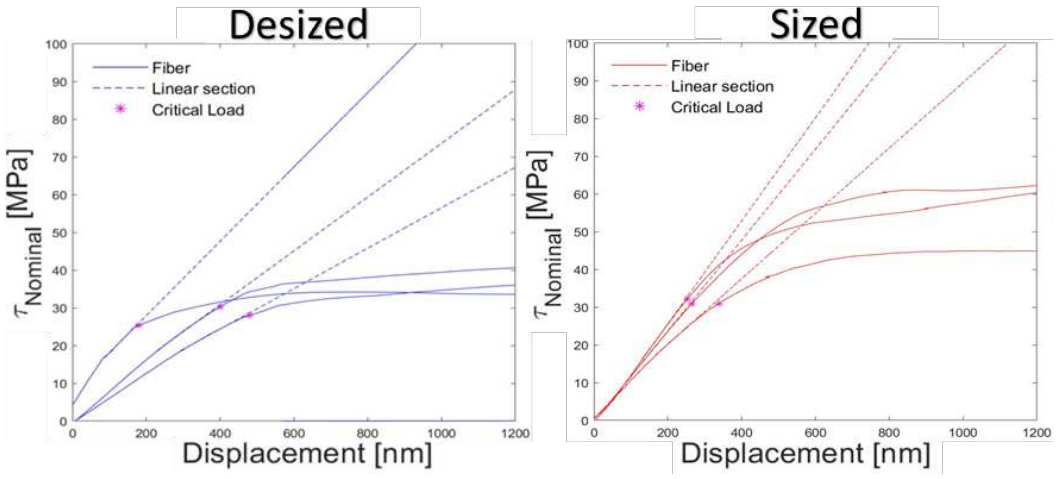

Figure 6: Results of Nominal shear (Eq. 2) vs. displacement from push-out experiments on PC-GF composite (for each condition, n= 3). Left: Desized and Right: Sized.

  doi:10.5075/epfl-298799_978-2-9701614-0-0

Once the mechanical test has been carried out, the specimen is treated, once more, with the FIB to obtain the post-mortem samples (Figure 6). The pushed-out fibre is cut in fibre direction to better visualise the interface between the components and plastic deformation of the matrix. When inspecting this newly manufactured cross-section, a substantial difference can be observed at the bottom end of the layer. This domain is loaded under shear but also tensile stress (due to bending), i.e. partially mixed-mode conditions. Therefore, the interface fails cohesively for the sized sample and partially adhesively for the desized one, following similar trends as in the macromechanical tests. This can be recognised by the fully exposed glass fibre surface for the desized condition (bottom portion of Figure 6, left). On the other hand, in the small portion that has been pushed out in the sized condition, the fibre surface retain a thin layer of polymer (bottom portion of the figure, right), and extensive yielding of the polymer can be observed. Thus, composite action was maintained for a large portion of the experiment in both cases, with essentially cohesive failure, yet, showing a stronger interface than in the desized condition.

4. Conclusion & Outlook

Mechanical analysis of PC-GF composites at different size scales allowed us to identify, quantify and visualise the failure behaviour of this understudied thermoplastic fibre reinforced material. By implementing a FIB procedure in the manufacturing and analysis of the samples, a reliable and precise micromechanical, interface-evaluation scheme has been implemented for thermoplastic composites. In terms of mechanical properties, as expected, the material with the thermoplastic compatible sizing applied to the surface of the glass fibre, performs better at both size scales than the desized one. Moreover, the failure mechanism under transverse tensile loading can be clearly identified by the post mechanical test analysis, where the failure is predominately adhesive and mixed adhesive-cohesive, for desized and sized conditions, respectively.

Thanks to the use of FIB, which allows us to process the specimen after micromechanical testing, the main tendencies observed at the macro scale can be identified at the single fibre level too, contributing to the multi-scale mechanical analysis.

Due to the high degree of ductility of the thermoplastic polymer, as well as the high strength of the PC-GF interface under mode II, the fibre cannot be fully separated (pushed-out) from the matrix. This behaviour diverges from the commonly observed one for thermosets and ceramics. In detail, a brittle interface will lead to a complete separation, but also brittle matrix cracking will have similar effect with a wet fibre though (cohesive failure).

Thus, for PC-GF combination, where we observe high ductility and good interface in mode II, novel micromechanical tests shall be developed and further optimised to achieve a complete interface failure and strength identification. This could be achieved via finite element analysis, where the mechanical contribution of neighbouring fibres, shear and bending forces on the specimen geometry could be simulated to provide insights into mode II interface failure. Of great interest would be to develop a micromechanical test able to induce interface failure in mode I. This would be beneficial since it would allow a more representative comparison to the macromechanical test. Even though, the latter has great complexity, it will allow gaining a better understanding of failure mechanisms at a microscopic level.

Acknowledgments

The authors thank Reuteler Joakim of ScopeM-ETH Zurich and Lauener Carmen from the Laboratory of Nanometallurgy ETH Zurich for their support & assistance in this work.

Reference

[1] C. Schneeberger, N. Aegerter, S. Birk, S. Arreguin, J. Wong und P. Ermanni, «Direct stamp forming of flexible hybrid fibre preforms for thermoplastic composites,» in *SAMPE Europe Conference 2020 Amsterdam: The Future Composite Footprints*, 2021.

[2] C. Schneeberger, J. C. H. Wong und P. Ermanni, «Hybrid bicomponent fibres for thermoplastic composite preforms Part A Applied science and manufacturing,» 2017.

[3] J. L. Thomason, «Glass fibre sizing: A review,» *Composites Part A: Applied Science and Manufacturing,* Bd. 127, p. 105619, 2019.

[4] S. Fu, Y. Wang und Y. Wang, «Tension testing of polycarbonate at high strain rates,» *Polymer Testing,* Bd. 28, p. 724–729, 2009.

[5] N. A. Fleck, W. J. Stronge und J. H. Liu, «High strain-rate shear response of polycarbonate and polymethyl methacrylate,» *Proceedings of the Royal Society of London. A. Mathematical and Physical Sciences,* Bd. 429, p. 459–479, 1990.

[6] C. Medina M, J. M. Molina-Aldareguía, C. González, M. F. Melendrez, P. Flores und J. LLorca, «Comparison of push-in and push-out tests for measuring interfacial shear strength in nano-reinforced composite materials,» *Journal of Composite Materials,* Bd. 50, p. 1651–1659, 2016.

[7] C. González und J. LLorca, «Mechanical behavior of unidirectional fiber-reinforced polymers under transverse compression: microscopic mechanisms and modeling,» *Composites Science and Technology,* Bd. 67, p. 2795–2806, 2007.

[8] J. L. Thomason, «Interfacial strength in fibre reinforced thermoplastics,» in *International Conference on Interfaces & Interphases in Multicomponent Materials (IIMM)*, 2010.

[9] J. Karger-Kocsis, H. Mahmood und A. Pegoretti, «Recent advances in fiber/matrix interphase engineering for polymer composites,» *Progress in Materials Science,* Bd. 73, p. 1–43, 2015.

[10] F. R. Jones, «A review of interphase formation and design in fibre-reinforced composites,» *Journal of Adhesion Science and Technology,* Bd. 24, p. 171–202, 2010.

[11] R. M. G. De Meyere, K. Song, L. Gale, S. Harris, I. M. Edmonds, T. J. Marrow, E. Saiz, F. Giuliani, D. E. J. Armstrong und O. Gavaldà-Diaz, «A novel trench fibre push-out method to evaluate interfacial failure in long fibre composites,» *Journal of Materials Research,* Bd. 36, p. 2305–2314, 2021.

[12] R. S. Hay, E. E. Boakye, P. Mogilevsky, G. E. Fair, T. A. Parthasarathy und J. E. Davis, «Transformation Plasticity in (Gd x Dy 1- x) PO 4 Fiber Coatings During Fiber Push Out,» *Journal of the American Ceramic Society,* Bd. 96, p. 1586–1595, 2013.

[13] F. Naya, J. M. Molina-Aldareguia, C. S. Lopes, C. González, LLorca und J, «Interface characterization in fiber-reinforced polymer–matrix composites,» *Jom,* Bd. 69, p. 13–21, 2017.

[14] A. C. D.-3. on Composite Materials, Standard test method for tensile properties of polymer matrix composite materials, ASTM international, 2008.

[15] I. M. Daniel, O. Ishai, I. M. Daniel und I. Daniel, Engineering mechanics of composite materials, Bd. 1994, Oxford university press New York, 2006.

[16] D. M. Montenegro, G. Pappas, J. Botsis, M. Zogg und K. Wegener, «A comparative study of mode I delamination behavior of unidirectional glass fiber-reinforced polymers with epoxy and polyurethane matrices using two methods,» *Engineering Fracture Mechanics,* Bd. 206, p. 485–500, 2019.

[17] H. Ho und L. T. Drzal, «Evaluation of interfacial mechanical properties of fiber reinforced composites using the microindentation method,» *Composites Part A: Applied Science and Manufacturing,* Bd. 27, p. 961–971, 1996.

  doi:10.5075/epfl-298799_978-2-9701614-0-0

TWO-DIMENSIONAL MODE II DELAMINATION GROWTH IN COMPOSITE LAMINATES WITH IN-PLANE ISOTROPY

Congzhe Wang, Anastasios P. Vassilopoulos, Thomas Keller

Composite Construction Laboratory (CCLab), Ecole Polytechnique Fédérale de Lausanne (EPFL), Station 16, Bâtiment BP, CH-1015 Lausanne, Switzerland. – congzhe.wang@epfl.ch

Abstract: *The two-dimensional delamination growth in fiber composites with in-plane isotropy was experimentally investigated under Mode II fracture condition. Circular-plate specimens were transversally loaded above the centrally embedded pre-crack and clamped along the edge. The cracks propagated symmetrically in all directions, forming a circular pattern, until tensile failure appeared on the bottom of the specimens due to bending. The whole loading process could be divided into three stages based on delamination behavior, i.e. crack initiation, initial propagation and rapid propagation stages. Stiffening mechanisms, such as the stretching in the laminates, which played a particularly important role in 2D delamination, and fiber bridging, and softening mechanism, such as crack propagation, together affected the compliance behavior of the specimens.*

Keywords: 2D delamination; Laminates; Mode II; Crack growth

1. Introduction

Delamination is one of the main failure mechanisms in laminated composites and can be initiated in various scenarios, e.g. originating from a manufacture defect or during structural service [1]. Numerous efforts have been devoted to the investigation of the fracture performance of composites based on beam-like specimens, which have been well-developed in several test standards, i.e. double cantilever beams (DCB) for Mode I [2], end-loaded split (ELS) or end-notched flexure (ENF) for Mode II [3,4] and mixed-Mode bending (MMB) for mixed-Mode [5]. Such standardized specimens benefit from convenient preparation, relatively simple test set-up and post analyses of data. However, rather than exhibiting a constant crack width and a unique crack-propagation direction, real structural components normally behave differently, where crack propagates within the delamination plane in multiple directions, possibly with a continuously changing contour, showing an irregular two-dimensional (2D) pattern.

Many works already stressed the dependency of fracture properties on geometry, in particular on the laminate thickness or adhesive thickness in joints, in composite materials based on beam-like specimens [6–15]. In general, such dependency was attributed to the fiber bridging behavior at the tail of the crack tip for fiber composites [9] and the plastic zone effects ahead of the tip for ductile adhesives [15]. Although large scale fiber bridging can also be present in Mode II fracture condition [16], it was mainly discussed in DCB tests. Thus, for Mode-II delamination in fiber composites, the geometry dependency still remains unclear.

Available literature on 2D fracture performance mostly focused on Mode-I-dominated debonding/delamination induced by buckling [17–20]. Direct investigation of 2D shear mode delamination can be found in [21], where carbon fiber laminates were tested under three-point bending with two circular or elliptical embedded pre-cracks located symmetrically on each span

  doi:10.5075/epfl-298799_978-2-9701614-0-0

(creating a mixed-Mode II/III fracture condition along the crack fronts). Nevertheless, the research mentioned above still assumed the critical strain energy release rate (SERR) to be identical to that of standardized beam-like specimens.

More recent studies on 2D delamination that specifically distinguished the 2D effects were carried out by Cameselle-Molares et al. [22–24] and the authors [25] through a series of experimental and numerical investigations under Mode I fracture condition. The composite plates with an embedded pre-crack were opened via a pair of steel inserts in the center. Numerical simulations based on cohesive zone method were then carried out to estimate the Mode-I SERR, followed by a parametric study on the effects of geometric configuration and fracture resistance. Compared with DCB specimens of the same laminate, the Mode-I SERR obtained from plate specimen was around 40% higher. Specifically, the SERR component at the crack tip was the same, while the component due to fiber bridging increased significantly. To summarize, the previous work revealed the fact that, generally, fracture tests on beam-like specimens cannot represent an actual delamination scenario for structural members, at least in the Mode I domain. In the current work, the investigations were expanded to Mode II to provide a more systematic understanding of the 2D delamination behaviors.

The main objective of this paper was the experimental investigation of 2D Mode-II delamination in composite laminates. For that purpose, a novel experimental set-up was developed, where circular-plate specimens with a centrally embedded pre-crack were clamped along the edge and transversally loaded above the pre-crack, thus propagating the crack in two dimensions under Mode-II fracture condition. In-plane isotropic laminates were chosen to achieve symmetry in all radial directions in order to simplify the understanding of the results. The experimental results are discussed, and the 2D effects on delamination are addressed in the following.

2. Materials and experimental set-up

In consideration of research consistency, laminates reinforced by continuous filament mats (CFM) of 600-g/m^2 weight, which were already employed in the works on Mode I [22–25], were originally chosen for the investigation here. These laminates exhibit the advantages of in-plane isotropy, potential for large scale bridging and translucency for visual observation of the crack. Subsequent trials revealed the necessity of further reinforcements to prevent premature tensile failure on the bottom due to bending. Hence, in addition to fourteen layers of CFM, three multidirectional (quadriaxial 0/45°/90°/-45°) non-stitched fabrics (MD) of 800-g/m^2 weight were introduced on both sides of the laminate to improve the bending performance while maintaining the in-plane isotropy. The fiber layup is presented in Figure 1, and the properties of the glass fibers and epoxy resin are given in Table 1. Three plates were fabricated through a vacuum infusion process with a circular pre-crack in the center of the mid-plane introduced by a 13-µm-thick Teflon film before infusion started. The geometrical dimensions of the plate specimens are presented in Table 2.

The experiments were performed on a Zwick-Roell universal testing machine of 500-kN capacity under displacement-control at a rate of 1 mm/min. Figure 2 presents the experimental set-up, which simulated the condition where a quasi-infinite plate was loaded above its intrinsic defect (most unfavorable loading condition). Specifically, the specimens were placed on a steel ring (with fillet along the inner edge) with a support radius of 150 mm, and then clamped on top by a 15-mm-thick steel frame to constrain the vertical and rotational displacement of the edge.

  doi:10.5075/epfl-298799_978-2-9701614-0-0

Between the specimen and the frame, a ring-shaped Teflon film with grease on both sides was interposed, covering the clamped region, in order to reduce friction and thus release in-plane movement. Hence, the radial constraint at the plate edge was comparable to the sliding boundary condition in ELS tests at the beam end. A cylindrical loading block was placed in the center above the pre-crack to transfer the compressing load from the machine, providing a symmetric Mode II fracture condition. To reduce stress concentration at the loading zone, the bottom of the steel cylinder was machined into a spherical surface (with a radius of 306 mm), and additionally, a small piece of rubber pad of 3-mm thickness was placed under. The load was recorded directly by the machine, while the deflections in the bottom center of the specimens were obtained by a Linear Variable Differential Transducer (LVDT). Three additional measurement systems were used, as shown in Figure 3: a 3D Digital Image Correlation system (DIC), capturing the displacements and deformations of the specimens' top surface on the west side; two fiber optic sensors, measuring the top and bottom radial strains, respectively, in the north and south directions; and a digital camera above the plate, recording the crack propagation in three directions marked with rulers, with illumination from an LED strip below the specimen thanks to the material's translucency.

Table 1 Material properties.

Material	E [GPa]	G [GPa]	ν	ρ [g/cm3]
Epoxy resin	2.96	1.30	0.35	1.14
E-CR* glass (for CFM)	80.00	32.80	0.22	2.62
E glass (for MD)	72.00	29.50	0.22	2.55

*Corrosion-resistant

Table 2 Description of plate specimens.

Specimen number	Thickness [mm]	Radius [mm]	Pre-crack radius [mm]
CP1	14.9	175	40
CP2	15.8	175	40
CP3	16.6	175	40

3. Experimental results and discussion

3.1 Crack propagation pattern and failure mode

An example of the failure mode is shown in Figure 3. For all specimens, the crack propagated stably within the mid-plane without kinking into other layers. Due to the in-plane isotropic nature of the laminate and the symmetry of the experimental set-up, the delamination growth almost showed the same behavior in all directions during loading, presenting a circular pattern. Final average crack radii of around 64 mm, 81 mm and 87 mm were obtained for specimens CP1, CP2 and CP3 respectively. Apart from delamination, no other types of damage were noticed during the loading process until some sounds evincing matrix cracking, quickly followed by a loud noise marking the brittle tensile failure in the center of the lower sub-laminate due to

bending, which resulted in a severe loss in the structural load-bearing capacity and consequently the termination of loading. Thanks to the curved loading block and the rubber pad, no failure appeared in the upper loading zone. In addition, only slight matrix damage was observed along the support line on the bottom surface. Considering the reinforcements applied to the laminate plus the special experimental configuration, it would be extremely difficult to achieve critical Mode-II delamination failure before strength failure for the CFM laminates in actual structures.

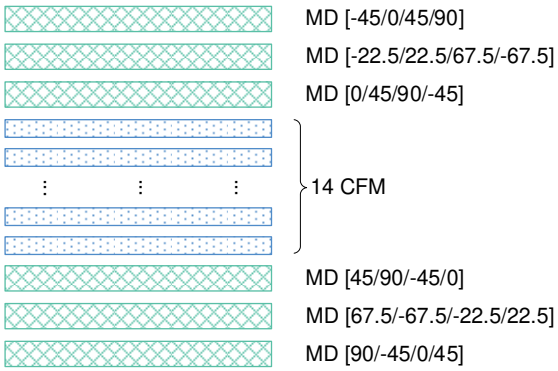

Figure 1. Fiber layup

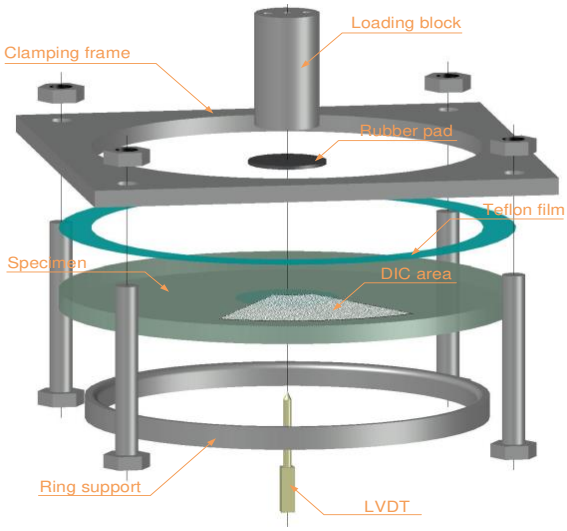

Figure 2. Experimental set-up

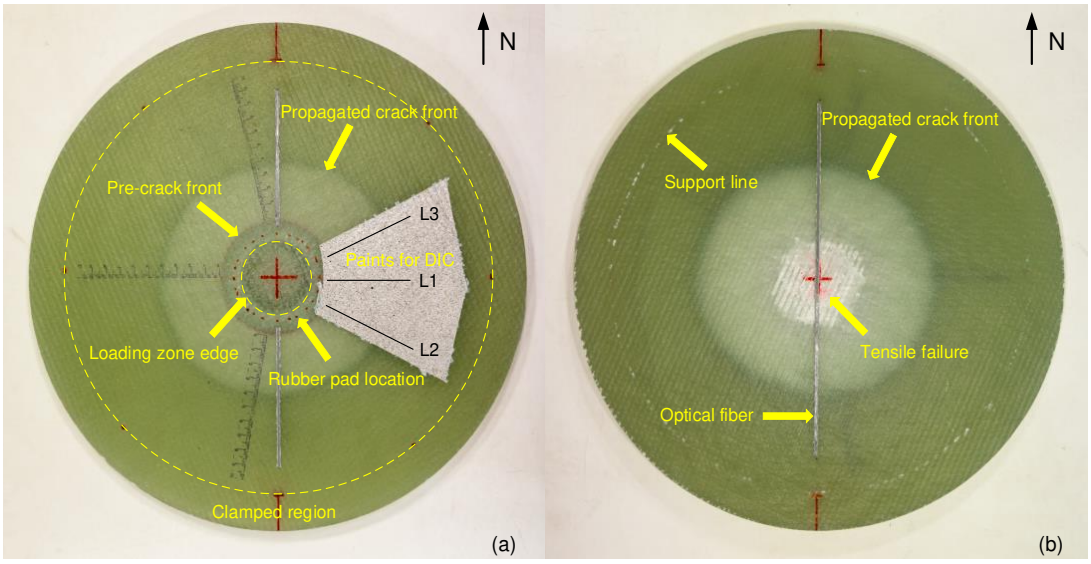

Figure 3. Failure mode (CP2); (a) top view; (b) bottom view

3.2 Load-deflection response and delamination growth behavior

Since displacement data from the machine included the deformation of the rubber pad, the specimens' bottom deflection measured from the LVDT was used for analyses instead. The load-deflection curves for all three specimens are shown in Figure 4. Despite similar ultimate deflection, certain scatter in load levels was observed from the beginning possibility due to different thickness, fabrication qualities and constraint levels (e.g. clamping torque). Continuously increasing loads were obtained up to failure even during crack propagation, in

contrast to ELS tests where the load decreases soon after crack initiation. Such difference was attributed to the different crack growth patterns in the systems: in beam-like specimens, the crack propagates in one direction with an almost constant width; but in plates, an embedded crack is likely to exhibit increasing crack contour during propagation, requiring more load to advance the crack front. Before failure, the slopes of the load-deflection curves reduced except CP1, at around 13.2 mm for CP2 and 13.8 mm for CP3 respectively.

The radial crack lengths, calculated as the distance from the plate center to the crack front, along the three directions marked with rulers (Figure 3) were obtained from the digital camera and plotted in Figure 4. According to the figure, the crack propagation in different directions showed a good agreement for all specimens, denoting a symmetric growth pattern, i.e. a circular crack shape. The cracks initiated (i.e. advanced from the pre-crack front) at deflections of around 4.7 mm, 3.2 mm and 2.7 mm in specimens CP1, CP2 and CP3, respectively, and then propagated stably. Then the propagation rates for CP2 and CP3 increased at deflections of around 13.6 mm and 14.0 mm, which correspond to crack lengths of around 55 mm and 57 mm, respectively, while for CP1 no such increase can be clearly recognized due to similar reasons stated above for its low stiffness. Three stages (A, B and C in Figure 4) can be distinguished based on the crack propagation behavior. In stage A, the crack was under initiation, and the plate bore the load without any growth of the initial pre-crack. In stage B, the crack initiated and propagated stably at a certain rate. This was the main stage that accounted for over 60% of the whole loading process in terms of plate deflection. In stage C (not obvious in CP1), the crack propagation rates were accelerated until structural failure, and the specimen stiffness decreased correspondingly.

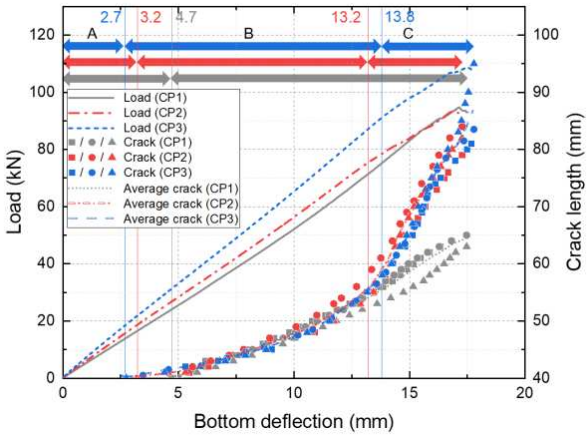

Figure 4. Load and crack length vs bottom deflection curves

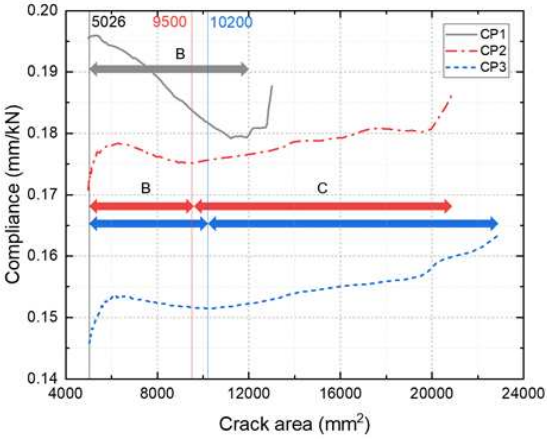

Figure 5. Compliance vs crack area curves

3.3 Compliance behavior

The crack lengths in the three directions described above were averaged to derive a continuous crack length evolution curve for each specimen (Figure 4). The corresponding crack areas were then calculated by taking the average crack lengths as the radii (i.e. pre-crack area was included). Figure 5 presents the changes of compliance, calculated as δ/P, with δ being the specimen's bottom deflection and P the load, over crack area. As already indicated in the load-deflection curves in Figure 4, specimen CP1 exhibited the highest overall compliance and CP3 the lowest. The compliance behavior during crack propagation was a result of competition between the softening mechanisms, i.e. initial readjustment between the specimen and the loading system (including the boundary) and crack propagation, and the stiffening mechanisms, i.e. fiber

  doi:10.5075/epfl-298799_978-2-9701614-0-0

bridging and stretching. In particular, radial stretching arose in the plate since the outer part of the plate acted as a frame that constrained the radial movement during out-of-plane deformation of the central part. In most fracture analyses stretching is disregarded, whereas for the case investigated here, it not only stiffened the plate but also affected the fiber bridging behavior [25]. For all three specimens, the compliance rose sharply at crack initiation and early propagation up to a maximum (mainly due to the special boundary condition, which will be discussed in the following section), after which the stiffening mechanisms prevailed over the softening mechanisms, leading to a descent of compliance as the stretching increased with loading. Specimen CP1 started to exhibit material damage in the bottom center in this state, leading to a significant increase in compliance and subsequently the structural failure; while for CP2 and CP3, as the crack propagated even further with higher rates, the softening mechanism (i.e. crack propagation) again became dominant, and consequently an additional ascending branch was observed before the unstable increase towards failure. Stages B and C defined in Figure 4 can also be recognized from the compliance curves, as the branch from crack initiation to the valley and the second ascending branch, respectively.

3.4 Boundary conditions

During the loading process, bending deformation was found in the steel frame used for clamping due to insufficient thickness and overlong fixing spans (see Figure 6). Thus, the specimens were in fact under a semi-clamped boundary condition, where the vertical and rotational displacements along the edge were only partially constrained. Such constraint exhibited several impacts on the experimental results. First of all, compared with a fully-clamped condition, the specimens showed lower overall stiffness and consequently slower crack propagation. Secondly, the plate deflections were distributed closer to plate edge due to the rotation (i.e. the deformation was less intense in the center), and lower stretching was presented since less radial elongations could be found in the delaminated part at the same central deflections. Finally, it accounted for the softening behavior at crack initiation and early propagation (beginning of stage B in Figure 5).

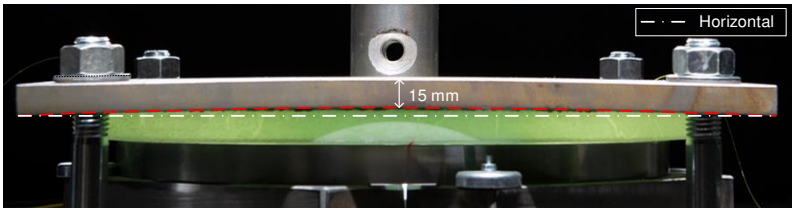

Figure 6. Deformation of steel frame during loading

4. Conclusions

The Mode-II delamination growth in an in-plane isotropic composite laminate was investigated under 2D fracture condition. The delamination growth pattern and failure mode were obtained. Three stages were distinguished from the whole loading process, and the corresponding load-deflection response, crack propagation and compliance behavior were discussed. The following conclusions could be drawn:

1. A novel experimental set-up was developed to promote 2D propagation of a circular embedded pre-crack in composite laminates under Mode-II fracture condition. Symmetric propagation pattern, i.e. a circular crack shape, was observed. The specimens

  doi:10.5075/epfl-298799_978-2-9701614-0-0

failed in tension in the bottom center due to bending before the crack front reached the support line.
2. The load continued to rise during crack propagation due to the increasing crack contour, which distinguished 2D delamination from delamination in traditional beam-like specimens.
3. The specimens experienced three stages before failure: in the crack initiation stage, the plate deformed without growth of the pre-crack; in the initial crack propagation stage, new crack initiated from the pre-crack font and propagated stably; in the rapid crack propagation stage, the propagation rate increased notably with rising compliance.
4. Stretching and fiber bridging, i.e. the stiffening mechanisms, played an important role in 2D fracture process, which accounted for the stiffening behavior of the plate during initial crack propagation.
5. Due to the deformation of the steel frame, the specimens were under a semi-clamped boundary condition, thus exhibiting lower structural stiffness and crack-propagation rates than under fully clamped conditions.

Due to the nature of 2D delamination experiments, fiber bridging behavior, which is expected to differ significantly from that in beam-like specimens, could not be directly observed or measured on site. Furthermore, existing compliance-based data reduction schemes for SERR derivation are no longer applicable here, since the compliance was affected not only by crack propagation but also stretching forces in the plates. Hence, a numerical model is required in future work based on experimental data for a more comprehensive investigation. In addition, new experiments will be carried out using a redesigned clamping system that provides fully-clamped boundary condition.

Acknowledgements

The authors wish to acknowledge the financial support of this research by the Swiss National Science Foundation (Grant No. 200020_185005) and the assistance provided by the technical team of the structural engineering Experimental platform (GIS-ENAC at the Ecole Polytechnique Fédérale de Lausanne (EPFL), Switzerland).

5. References

1. Sridharan S. Delamination Behaviour of Composites. Cambridge, England: Woodhead Publishing Limited; 2008. 1–762 p.
2. ISO 15024:2001. Fibre-Reinforced Plastic Composites - Determination of Mode I interlaminar Fracture Toughness, Gic, for Unidirectionally Reinforced Materials. 2001.
3. ISO 15114:2014. Fibre-reinforced plastic composites - Determination of the mode II fracture resistance for unidirectionally reinforced materials using the calibrated end-loaded split (C-ELS) test and an effective crack length approach. International Standard Organization. Geneva, Switzerland; 2014.
4. ASTM D7905. Standard test method for determination of the mode II interlaminar fracture toughness of unidirectional fiber-reinforced polymer matrix composites. ASTM. 2014.
5. D6671M A. Standard Test Method for Mixed Mode I-Mode II Interlaminar Fracture Toughness of Unidirectional Fiber Reinforced Polymer Matrix Composites. ASTM Int. 2006.
6. Da Silva LFM, De Magalhães FACRG, Chaves FJP, De Moura MFSF. Mode II fracture toughness of a brittle and a ductile adhesive as a function of the adhesive thickness. J Adhes.

  doi:10.5075/epfl-298799_978-2-9701614-0-0

2010;86(9):891–905.
7. Carlberger T, Stigh U. Influence of layer thickness on cohesive properties of an epoxy-based adhesive-an experimental study. J Adhes. 2010;86(8):816–35.
8. Ji G, Ouyang Z, Li G, Ibekwe S, Pang SS. Effects of adhesive thickness on global and local mode-I interfacial fracture of bonded joints. Int J Solids Struct. 2010;47(18–19):2445–58.
9. Manshadi BD, Vassilopoulos AP, Botsis J. A combined experimental/numerical study of the scaling effects on mode I delamination of GFRP. Compos Sci Technol. 2013;83:32–9.
10. Farmand-Ashtiani E, Cugnoni J, Botsis J. Specimen thickness dependence of large scale fiber bridging in mode I interlaminar fracture of carbon epoxy composite. Int J Solids Struct. 2015;55:58–65.
11. Frossard G, Cugnoni J, Gmür T, Botsis J. Mode I interlaminar fracture of carbon epoxy laminates: Effects of ply thickness. Compos Part A Appl Sci Manuf. 2016;91:1–8.
12. Shah OR, Tarfaoui M. Effect of adhesive thickness on the Mode i and II strain energy release rates. Comparative study between different approaches for the calculation of Mode i & II SERR's. Compos Part B Eng. 2016;96:354–63.
13. Kravchenko OG, Kravchenko SG, Sun CT. Thickness dependence of mode I interlaminar fracture toughness in a carbon fiber thermosetting composite. Compos Struct. 2017;160:538–46.
14. Pappas GA, Botsis J. Towards a geometry independent traction-separation and angle relation due to large scale bridging in DCB configuration. Compos Sci Technol. 2020;197(December 2019):108172.
15. Oliveira JJG, Campilho RDSG, Silva FJG, Marques EAS, Machado JJM, da Silva LFM. Adhesive thickness effects on the mixed-mode fracture toughness of bonded joints. J Adhes. 2020;96(1–4):300–20.
16. Shahverdi M, Vassilopoulos AP, Keller T. Mixed-mode quasi-static failure criteria for adhesively-bonded pultruded GFRP joints. Compos Part A Appl Sci Manuf. 2014;59:45–56.
17. Kwon H, Kim H. Buckling and debond growth of partial debonds in adhesively bonded composite splice joints. Compos Struct. 2007;79(4):590–8.
18. Haselbach PU, Branner K. Initiation of trailing edge failure in full-scale wind turbine blade test. Eng Fract Mech. 2016;162:136–54.
19. Riccio A, Raimondo A, Di Caprio F, Scaramuzzino F. Delaminations buckling and growth phenomena in stiffened composite panels under compression. Part II: A numerical study. J Compos Mater. 2014;48(23):2857–70.
20. Rhead AT, Butler R, Hunt GW. Compressive strength of composite laminates with delamination-induced interaction of panel and sublaminate buckling modes. Compos Struct. 2017;171:326–34.
21. Chatterjee SN, Dick WA, Byron Pipes R. Mixed-mode delamination fracture in laminated composites. Compos Sci Technol. 1986;25(1):49–67.
22. Cameselle-Molares A, Vassilopoulos AP, Keller T. Experimental investigation of two-dimensional delamination in GFRP laminates. Eng Fract Mech. 2018;203(April):152–71.
23. Cameselle-Molares A, Vassilopoulos AP, Renart J, Turon A, Keller T. Numerical simulation of two-dimensional in-plane crack propagation in FRP laminates. Compos Struct. 2018;200:396–407.
24. Cameselle-Molares A, Vassilopoulos AP, Renart J, Turon A, Keller T. Numerically-based method for fracture characterization of Mode I-dominated two-dimensional delamination in FRP laminates. Compos Struct. 2019;214(February):143–52.
25. Wang C, Vassilopoulos AP, Keller T. Numerical modeling of two-dimensional delamination growth in composite laminates with in-plane isotropy. Eng Fract Mech. 2021;250(April):107787.

EFFECT OF LIGHTWEIGHT FILLERS ON THE PROPERTIES OF POLYMER CONCRETE

Ruihan, Wang[a], Samuel, Furtado [b], Chamil, Abeykoon[a], Prasad, Potluri[a]

a: Northwest Composites Centre, Department of Materials, The University of Manchester – ruihan.wang@postgrad.manchester.ac.uk

b: Advanced Manufacturing Research Centre (AMRC), The University of Sheffield

Abstract: *Polymer concrete has become increasingly popular material in civil engineering since it was first introduced in the 1950s. Due to its low cost and relatively easy processability, polymer concrete products can be found in high-volume but low-cost applications like shower trays, kitchen worktops, prefabricated panels for construction, etc. Nowadays, special micro-fillers with lightweight, have been applied in the polymer concrete to lower the product weight, which brings a competitive advantage, especially for construction products. In this research, two different lightweight fillers (named lightweight filler and ultra-lightweight filler) were employed and compared with a conventional micro-filler (limestone). The results showed that the product density decreases by 50% with the increase in volume ratio of both lightweight fillers, although both the compressive and flexural strengths were reduced to 34 %-60 %. To improve the sustainability of the polymer concrete, recycled materials (lightweight filler) were employed and evaluated.*

Keywords: Polymer concrete; Lightweight filler; Sustainability; Mechanical properties, Particle mix proportioning

1. Introduction

Nowadays, polymer concrete has become a popular material in engineering and has aroused great interest in more areas due to its obvious advantages, such as good mechanical properties, excellent chemical resistance, fast curing, lightweight and low price. The utilization of polymer concrete can be traced back to the 1950s when it was produced to take the place of cement concrete in some facilities [1]. Initially, polymer concrete was used as a building cladding material and then as construction and structure repair materials. In recent years, precast polymer concrete is widely employed as a component of production, like drains, acid tanks, highway pavements, floor tiles, and so on.

Polymer concrete, also known as resin concrete, is a composite consisting of thermoset resins and aggregates where resins play the role of the matrix, binding the aggregates together. Here the resin replaces the cement in traditional cement concrete. The resins are mainly thermosetting, such as unsaturated polyester, epoxy (EP), furan, vinyl ester (VE), polyurethane (PUR), and phenol (PF), although sometimes thermoplastic (such as ABS) are also used [2]. Apart from resins and aggregates, fibres can also be used as reinforcement in the resin. Additionally, micro-fillers can be added to reduce the voids in the aggregate mixture. As a result, the

  doi:10.5075/epfl-298799_978-2-9701614-0-0

properties of polymer concrete depend on various factors, including the type and resin content, the type and mix proportioning of aggregate, the nature and content of reinforcing fibres, the type and dosage of micro-fillers, etc.[1]

The packing density of a polymer concrete mixture can be defined as the volume fraction of the mixture occupied by the solids [3]. The addition of micro-fillers can result in a higher packing density of the solid mixture by optimising the grain sizes distribution. This leads to the reduction of resin (normally the most expensive element of the mixture) content required for similar viscosity, therefore making it more cost-effective. Theoretically, a solid mixture with maximum packing density has the minimum void content. However, the addition of micro-fillers excessively may result in particle interference and hence could increase the void content of the solid mixture [4]. To achieve optimum particle mixing, particles with different sizes are employed in the solid mixture. Compared with using well-graded particles, the utilization of particles of gap-grade or restricted sizes can decrease the particle interference, even though it may slightly increase the void content [4].

The common micro-fillers used in polymer concrete are calcium carbonate, kaolin, and some recycled products from waste like fly ash and silica fume. To gain the competitive advantage of polymer concrete, lightweight fillers which are lighter than common micro-fillers are introduced to further reduce the production density. In the study, two different lightweight fillers were used to replace the common micro-filler and their effect on the properties of polymer concrete was evaluated. The study can help promote the innovation of the construction material industry and convenient the whole construction process.

2. Experimental

In this research work, the goal was to evaluate the effect of lightweight fillers on the properties of polymer concrete and design a lightweight product with a high packing density (up to 80 V%) while keeping the viscosity as low as possible for better processability. The samples were all made of polyester resin, flow beads and micro-fillers to have a similar viscosity/flowability.

2.1 Materials

The details of the materials used in the study are listed in Table 1, including resin, aggregate mixture, and micro-fillers. The resin used in the study was unsaturated polyester resin. An unsaturated polyester has a wide market share, because of its easy accessibility, excellent mechanical properties, and low cost. According to a recent report [1], the properties of polymer concrete made of polyester with micro-fillers can be similar to those made of epoxy resin. The epoxy resin usually presents better mechanical properties but is more expensive than unsaturated polyester resin. The MEKP catalyst was used to promote the polymerisation process by accompanying the resin. Flow beads is a premixed aggregate mixture, consisting of sand particles of various sizes. The shape of the sphere makes them well “flowable”. Besides, particles with different dimensions result in high packing density, decreasing the dosage of resin.

Limestone is a common micro-filler, a white powder made of Calcium Carbonate with a density of 2.98 g/cm^3, which acts as a micro-filler. Due to fewer processing procedures, it is cheap and commonly used in construction products. The two lightweight fillers are special micro-fillers with

  doi:10.5075/epfl-298799_978-2-9701614-0-0

low density, which are applied to reduce the density of the product and gain more competitive advantages. Between the two fillers, the coarser one, named lightweight filler, is a high-quality sustainable mineral glass microsphere with a density of 1.35 g/cm^3 which is made of recycled glass. It has excellent resistance to fire, moisture, chemicals, and high temperature. Additionally, it is easy to handle and cost-effective. The particle used in the study is uniform and has a dimension of around 0.1~0.3 mm. The other filler used in the study, named ultra-lightweight filler, is a processed glass microsphere with a density of 0.25 g/cm^3, which is inorganic, dormant, harmless and empty with fluctuating shapes. It is applied in a wide range of applications, such as wall patching compounds, cultured marbles, and adhesives.

Table 1: Raw materials used in the project.

Matrix	Reinforcement	
Resin	Aggregate Mixture	Micro-filler (Density)
Polyester	Flow beads	Limestone (2.98g/cm^3) Lightweight filler (1.35g/cm^3) Ultra-lightweight filler (0.25 g/cm^3)

2.2 Methods

2.2.1 Sample design

In this study, a total of 9 samples were produced and analysed. The first sample is the one using traditional micro-filler, limestone, labelled as sample M, where the volume fraction by weight of the components is matrix (resin + catalyst): aggregate: micro-filler = 0.2: 0.4: 0.4.

The following eight samples listed in Table 2 were modified from sample M. The addition of micro-fillers was to reduce the cavities in the flow beads mixture. The type of matrix and the level of dosage of aggregate and the total volume of micro-fillers were not changed. Due to the significant difference in the densities between the limestone and the two lightweight fillers, the design of the samples considered the replacement of equivalent volume contents of the limestone filler. The samples were denoted with labels beginning with L and UL for lightweight filler and ultra-lightweight filler, respectively.

The number in the subscript of each notation represents the percentage volume of lightweight fillers in each micro-filler mixture. The particles of two lightweight fillers were all finer than that of limestone. The increasing content of lightweight fillers resulted in the growth of the total number of aggregate particles. As was observed, when the amount of micro-filler particles reached a critical value, the particle interference occurred and more voids were created, and hence the amount of resin should be increased to maintain the viscosity at a similar level. The amount of resin in the 8 samples started at 20% volume fraction by weight and then increase to 35%. In the case where the solid mixture could not dissolve in the initial resin to an adequate level or the fluidity of concrete mixtures was too low, the additional amount of resin would be added to the concrete mixture gradually until the mixtures were flowable enough. The amount of catalyst was 2wt% of the resin for all the samples.

  doi:10.5075/epfl-298799_978-2-9701614-0-0

Table 2: Micro-filler constituents in the samples

Samples	Micro-filler
M	100% limestone
L_{25}	75% limestone + 25% lightweight filler
L_{50}	50% limestone + 50% lightweight filler
L_{75}	25% limestone + 75% lightweight filler
L_{100}	100% lightweight filler
UL_{25}	75% limestone + 25% ultra-lightweight filler
UL_{50}	50% limestone + 50% ultra-lightweight filler
UL_{75}	25% limestone + 75% ultra-lightweight filler
UL_{100}	100% ultra-lightweight filler

Note: The percentages in front of the micro-fillers represent the volume content of one filler to the total micro-filler mixture.

2.2.2 Density measurement

As lightweight fillers have a quite low density, the evaluation of their influence on the product density was of great interest. For the density measurement of composite, the immersion approach was chosen as the most common and effective method The results were calculated using Eq. (1). [5] The value of water density under room temperature is expressed by Eq. (2). [5]

$$\rho_C = \frac{M_1 \rho_W}{M_1 - (M_2 - M_W)} \quad (1)$$

$$\rho_W = 1.0017 - 0.0002315T \quad (2)$$

Where:

ρ_W is the density of the water (g/cm^3).

M_1 is the dry mass of the composite(g).

M_2 is the immersed mass of the composite(g).

M_W is the mass of the displaced water(g).

T is the temperature of the water (°C).

2.2.3 Volume fraction measurement

Volume fraction measurement was introduced to work out the actual dosage of matrix in the samples. In the process, the specimens were put in the crucibles and burned in the Muffle Furnace at 600°C for an hour. After that the organic materials in the composites, resin and catalyse, were removed and inorganic materials were left in the crucibles, including flow beads and micro-fillers. The whole procedure was carried out according to the standard ASTM D3171-

22. The Equation (3)[6] and Equation (4)[6] illustrate the calculation of matrix volume fraction, in weight and volume content, respectively.

$$W_m = \frac{m_i - m_f}{m_i} \times 100 \quad (3)$$

Where:

W_m is the matrix content (weight percentage).

$\mathrm{m_i}$ is initial mass of the specimen (g), and

$\mathrm{m_f}$ is final mass of the specimen after combustion (g)

Note: The mass of the reinforcement may be gotten by taking the mass of the crucible with reinforcement minus the crucible mass ($m_f = m_{cr.} - m_c$).

$$V_m = \frac{m_i - m_f}{m_i} \times \frac{\rho_c}{\rho_m} \times 100 \quad (4)$$

Where:

V_m is the matrix content (volume percentage).

ρ_c is specimen density (g/cm^3), and

ρ_m is matrix density (g/cm^3).

2.2.4 Mechanical test

To find out the effect of lightweight fillers on the mechanical performance of the polymer concrete, two mechanical tests (compression and bending) were carried out following ASTM D695-15 and ASTM D790-17 standards, respectively. The result of compression strength is expressed in Eq. (5) [7], and the Eq. (6) [8] shows the calculation of flexural strength.

$$\sigma = \frac{F}{A} \quad (5)$$

Where, σ is the compression strength (Pa) and F is the failure load (N).

$$\sigma = \frac{3FL}{2WT^2} \quad (6)$$

Where, σ represents the flexural strength (Pa) and F represents the maximum load (N).

L represents the lower support span length between the two lower supports (m).

W represents the width of the specimen (m).

T represents the thickness of the specimen (m).

3. Results and discussion

3.1 Density and volume fraction measurement

  doi:10.5075/epfl-298799_978-2-9701614-0-0

As for the products used in civil engineering, the property of lightweight will bring convenience to the manufacture, transport and construction process. At least five specimens of each sample were tested to obtain the average value in the study. The measured density values for both lightweight and ultra-lightweight fillers are presented in Fig. 1 and the results for the volume fraction measurement of matrix (resin + catalyst) are shown in Fig. 2. As expected, with the increase of lightweight fillers content, the product density reduced. The density decreased most sharply in the lightweight fillers content within the range of 0~25%. When the limestone was totally replaced by ultra-lightweight filler and lightweight filler, the product density decreased by 34.3% and 27.9%, respectively. It can be seen that, with the introduction of lightweight fillers, the product density dropped sharply at the beginning. However, samples that used ultra-lightweight filler were heavier than those that used lightweight filler, except for the samples when lightweight fillers completely replaced limestone. Particles of ultra-lightweight filler were too fine, which caused more severe particle interference than Lightweight particles, resulting in higher resin content for similar viscosity. Thus, mix proportion and filler grading are key influence factors of polymer concrete density. For this reason, appropriate sizes and ratios of lightweight fillers should be selected in product manufacturing.

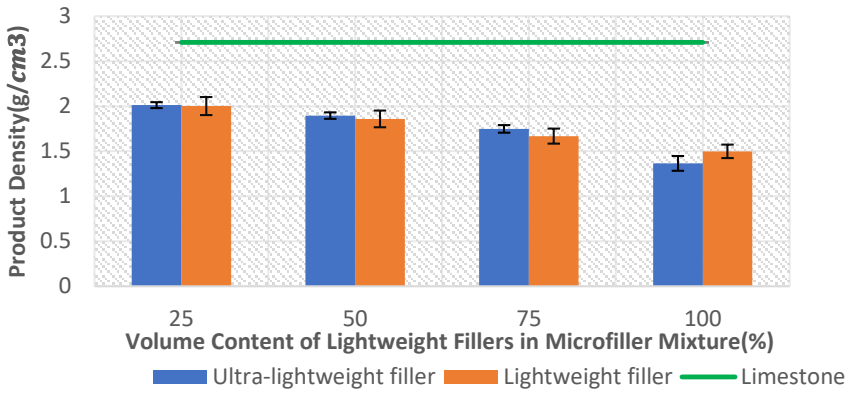

Figure 1: Measured density values for lightweight and ultra-lightweight fillers

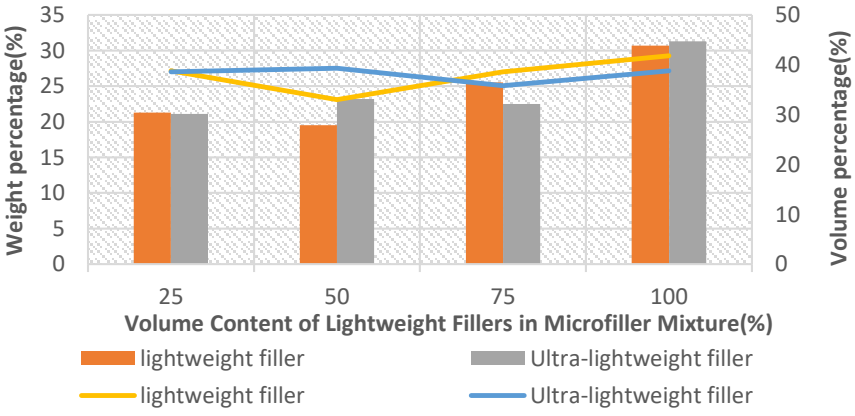

Figure 2: Volume fraction measurement results of the matrix

3.2 Mechanical test

As mentioned previously, to evaluate the mechanical properties of the samples, compression and bending test were carried out and five specimens of each sample were tested. The

measured flexural strength and flexural modulus are plotted in Fig. 3 and the measured compression strength is plotted in Fig.4. The graphs illustrate that the mechanical properties decreased with increased lightweight filler content , especially the compression strength. With the addition of lightweight fillers, the value of compression strength reduced dramatically. The compressive strength of samples UL_{100} and L_{100} were only 22.6% and 42.2% of that of limestone sample, respectively. As it is evident, the lightweight fillers present a higher compressive strength than ultralightweight ones. As for the flexural performance shown in Fig. 3, the ultra-lightweight filler samples had higher strength and modulus than lightweight filler samples in the content ranging from 25% to 75%, whereas the situation reversed from 75% to 100%. According to the sharp decrease in mechanical properties, the load capacity of lightweight fillers was quite lower than limestone. When choosing the proper ratio of lightweight fillers, it is important to consider not only the density of the product but also the other characteristics, such as the minimum requirements of mechanical properties. For instance, the samples made of ultra-lightweight filler had better flexure properties but worse compressive properties than lightweight filler products. Therefore, different lightweight fillers should be selected to satisfy the requirements of different applications. As the lightweight filler is made of recycled glass, it illustrates that fillers made of recycled materials would help to improve the sustainability but achieve a similar and even better physical and mechanical properties.

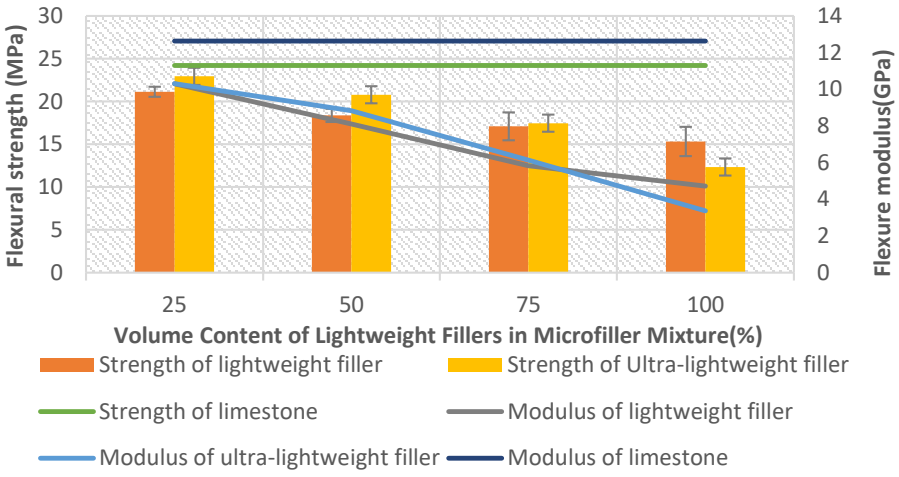

Figure 3: Flexural performance of the polymer concrete

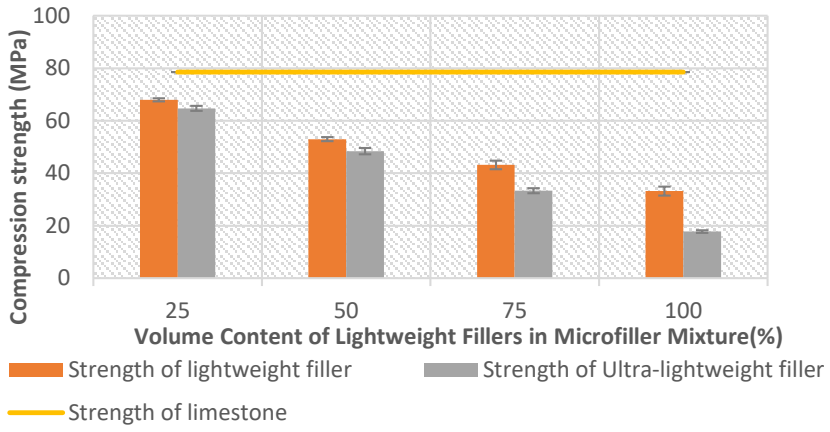

Figure 4: Compression performance results of polymer concrete

  doi:10.5075/epfl-298799_978-2-9701614-0-0

4. Conclusions

Compared with traditional concrete, polymer concrete is a potential material with a low density but with relatively high mechanical properties. This study was conducted to understand and characterise the polymer concrete with a few different lightweight fillers. Lightweight fillers (which are micro-fillers) with low densities can help to develop competitive advantages in product densities and can reduce the cost of unit volume at the same time (up to 17%). Several parameters of lightweight fillers ought to be considered in making an optimum design of the product, including their dimension, density, mechanical performance and so on. First, the size of lightweight fillers would significantly influence the grading of filler mixture as well as the packing density. The employment of too fine particles would result in a restricted size grading, which would initially increase the packing density but it will decrease at last. The higher the packing density, the lower the resin content. Secondly, when considering the benefit of the density of lightweight fillers, their mechanical properties ought to be taken into consideration. The lightweight fillers commonly have low load-bearing capacity than normal micro-fillers, therefore, the mechanical properties of products would decrease sharply with the introduction of lightweight fillers. To acquire an optimal choice of lightweight filler, a balance ought to be made among the requirements of product density and mechanical property. Besides, the ratio of lightweight fillers is a key influential factor as well in the process of manufacturing. The excessive addition of lightweight fillers would cause interference, resulting in a higher content of resin. Moreover, it can be said that to make the best of lightweight fillers in an application, the selection of their types and content ratios should be taken into consideration. Therefore, to meet the requirements of the different products, different types and dosages of lightweight fillers should be chosen. In the future, sizing agents will be introduced to help further improve the mechanical performance of the lightweight fillers used in the polymer concrete.

5. References

1. Bedi, R., R. Chandra, and S. Singh, *Mechanical properties of polymer concrete.* Journal of Composites, 2013. **2013**.
2. Ohama, Y., *Polymers in concrete*. 2003: CRC Press.
3. Stovall, T., F. De Larrard, and M. Buil, *Linear packing density model of grain mixtures.* Powder technology, 1986. **48**(1): p. 1-12.
4. Rao, V.K. and S. Krishnamoothy, *Aggregate mixtures for least-void content for use in polymer concrete.* Cement, Concrete and Aggregates, 1993. **15**(2): p. 97-107.
5. German, R.M., *Particulate Composites*. 2016: Springer.
6. ASTMInternational, *ASTM D3171-22 Standard Test Methods for Constituent Content of Composite Materials*. 2022, ASTM International: USA.
7. ASTMInternational, *ASTM D695-15 Standard Test Method for Compressive Properties of Rigid Plastics*. 2015, ASTM International: USA.
8. ASTMInternational, *ASTM D790-17 Standard Test Methods for Flexural Properties of Unreinforced and Reinforced Plastics and Electrical Insulating Materials*. 2017, ASTM International: USA.

NON-LINEAR ELASTIC BEHAVIOUR OF CARBON FIBRES: MATERIAL OR GEOMETRICAL ORIGIN?

V. Keryvin[a], A. Marchandise[a,b], J.-C. Grandidier[c]

a: Univ. Bretagne Sud, UMR CNRS 6027, IRDL, F-56321 Lorient, France
b: Avel Robotics, F-56100 Lorient, France
c: ISAE-ENSMA, F-86360 Chasseneuil-du-Poitou, France

Abstract: *Carbon fibres and unidirectional continuous carbon fibre composites exhibit a non-linear elastic behaviour. There has long been a debate on the physical origins of such a behaviour for these materials. Indeed, two main mechanisms have been proposed: either the reorientation of graphene sheets in the carbon fibre or that of the fibre itself due to initial fibre waviness arising from composite manufacturing. This paper addresses this issue by performing, on the one hand, specific mechanical tests to extract the non-linear elastic coefficients in a reliable way, and, on the other hand, using specific finite element analyses with a non-local model. The simulations allow us to show that, while both mechanisms come into play for the non-linear elasticity of carbon fibres, the intrinsic behaviour of fibres can be considered as the main contributory mechanism.*

Keywords: Carbon Fibres; Polymer-matrix composites; Elastic Behaviour; Non-linear Behaviour; Non-local modelling

1. Introduction

The non-linear elastic behaviour of carbon fibres was reported as early as the 1960s [1] and then more recently [2]. This mechanism is linked to the reorientation of graphene crystallites in the direction of the tensile loading [3]. Unidirectional carbon fibre reinforced polymer (UD) materials exhibit a non-linear elastic behaviour under tension [4] (stiffening) or compression [5] (softening). The changes in axial moduli close to failure can be dramatic, reaching a one-third reduction in IM fibres for instance [6]. The characterization of this behaviour is usually carried out either in one step accounting for only one type of non-linearity (tension or compression) but not the other one, or in two steps, by tension and compression tests [5]. We have recently proposed an experimental protocol based on four-point bending tests to characterize simultaneously the non-linear elastic behaviour of UD both in tension and compression [6].

The origins of the non-linear elastic behaviour of UD plies in tension and compression have been the subject of debate. It can come from the non-linearity of the carbon fibres or from the initial fibre waviness. In this paper, we would like to quantify the respective contributions to non-linear elasticity due to the type of material (carbon fibre) and geometry (fibre waviness).

  doi:10.5075/epfl-298799_978-2-9701614-0-0

2. Materials and methods

2.1 Materials

Each UD ply is composed of an epoxy resin matrix (M81 from Hexcel) and carbon fibres (intermediate modulus - IM - IM2C form Hexcel and high modulus - HM - HR40 from Mitsubishi) The prepreg batch had a resin weight content of 35 % and fibre weight of 300 g/m². The ply thickness is around 300 µm and the fibre volume fraction is 55 %.

The laminate is composed of 11 blocks of plies with the following stacking sequence: $[+45°|0_6°|+45°/-45°|0_4°|-45°|0_2°]_S$. The plate was manufactured by AVEL Robotics, the layup being performed by a C1-Coriolis Composites Automated Fibre Placement robot. The curing cycle consisted of a one-shot curing. Plates were precisely machined by waterjet cutting into 500x30x10 mm^3 samples. For each sample, the thickness *h* and the breadth *b* were measured with a calliper. The thickness of each block of plies were measured by optical microscopy. The samples were completely symmetric to ensure accuracy of this measurement.

2.2 Mechanical testing

Four-point bending tests (4PB) were carried out with a universal testing machine (Instron 5567, 30 kN load cell). Mono-axial strain gauges (10 mm in length - Kyowa) were glued onto both the compression and the tension sides. Eight to ten monolithic samples were tested. Other details can be found in Ref. [7]. The force on the assembly and the two strain gauge signals were recorded during loading and synchronized. The position of the neutral axis λ vis-a-vis the mid-axis is given by the two strain gauge signals on the compressive side ($\varepsilon^g{}_c$) and the tensile side ($\varepsilon^g{}_t$):

$$\lambda = -\frac{h}{2}\frac{\epsilon_c^g + \epsilon_t^g}{\epsilon_c^g - \epsilon_t^g} \tag{1}$$

The procedure for extracting the elastic properties of the unidirectional plies in the beam direction has been reported in Ref. [6] and will not be reproduced here for sake of clarity. It extracts four parameters: the initial moduli in tension, $E^{T0}{}_{UD}$, and in compression, $E^{C0}{}_{UD}$, as well as the linear decrease of the elastic modulus in tension β with strain $\varepsilon^T{}_{UD}$ and in compression α with strain $\varepsilon^C{}_{UD}$. They are extracted according to Eq. (4) in the range [0.1-0.5] % of strain. In doing so, the coefficients $\alpha' = \alpha / E^{C0}{}_{UD}$ and $\beta' = \beta / E^{T0}{}_{UD}$ are introduced, with respect to Ref. [6].

$$\begin{aligned} \sigma^{\mathrm{T}}_{\mathrm{UD}} &= \mathrm{E}^{T0}_{\mathrm{UD}}\epsilon^{\mathrm{T}}_{\mathrm{UD}}(1+\beta'\epsilon^{\mathrm{T}}_{\mathrm{UD}}) \quad \text{4PB - Tension} \\ \sigma^{\mathrm{C}}_{\mathrm{UD}} &= \mathrm{E}^{C0}_{\mathrm{UD}}\epsilon^{\mathrm{C}}_{\mathrm{UD}}(1+\alpha'\epsilon^{\mathrm{C}}_{\mathrm{UD}}) \quad \text{4PB - Compression} \end{aligned} \tag{2}$$

2.2 Numerical simulations

The idea of the model presented here is to consider the local bending of fibres with beam elements linked to continuum elements as in Ref. [8, 9], but without describing each fibre. The representative volume element (RVE) chosen here is a square of 1.6 mm × 1.6 mm, which is meshed with 6400 beams and 6480 plane stress elements, while the number of nodes is 19763. The initial default is assumed to be constant (fibres undulate in phase) in the structure, being taken as sinusoidal and described by two parameters: amplitude and wavenumber. The wavenumber is chosen as equal to 4 and the amplitude of the defect is equal to either 2.22 or 4.44 µm, which corresponds to a maximum misalignment angle of 1° and 2°, respectively. The anisotropic properties of the 2D continuum medium (stiffness tensor L^{CM}) are defined through the composite cylinder assemblage homogenization scheme [10]. This latter incorporates the determination of the in-plane shear modulus following the generalized self-consistent scheme [11] for a unidirectional composite. The fibre properties are taken from datasheets (tensile modulus) and literature results [12]. The matrix is assumed to be a classical epoxy resin [13] with a Young's modulus of 3.5 GPa and a Poisson's ratio of 0.4. In the fibre direction, the contribution of the fibre stiffness is supported by the beam and should be subtracted from the 2D medium stiffness. All necessary parameters of the model are reported in Tables 1 and 2. The code Abaqus v6.17 (Dassault Systèmes) is used with elements B22 (2D beams) and CPS8 (plane stress continuum elements).

Table 1: Components of the stiffness tensor (in GPa) of the medium (1 is fibre direction)

Carbon Fibre	L_{1111}^{CM}	L_{1122}^{CM}	L_{2222}^{CM}	L_{1133}^{CM}	L_{2233}^{CM}	L_{3333}^{CM}	L_{1212}^{CM}	L_{1313}^{CM}	L_{2323}^{CM}
IM2C	1.67	1.48	11.7	1.48	6.05	11.7	3.70	3.70	2.80
HR40	1.84	1.56	11.0	1.56	5.80	11.0	3.70	3.70	2.60

Table 2: Components of the stiffness tensor (in GPa) of the medium (1 is fibre direction)

Carbon Fibre	Beam Width [µm]	Beam Thickness [µm]	E_f [GPa]	ν_f [-]	E_L [GPa]	E_T [GPa]	G_{LT} [GPa]	ν_{LT} [-]
IM2C	2.11	5.2	296	0.3	164	8.4	3.7	0.31
HR40	1.58	7	360	0.3	200	7.8	3.7	0.31

  doi:10.5075/epfl-298799_978-2-9701614-0-0

3. Results and discussion

Figure 1 shows the evolution of the neutral fibre position. There is a clear shift towards the tensile zone, and this is more pronounced for the HM fibre than for the IM one.

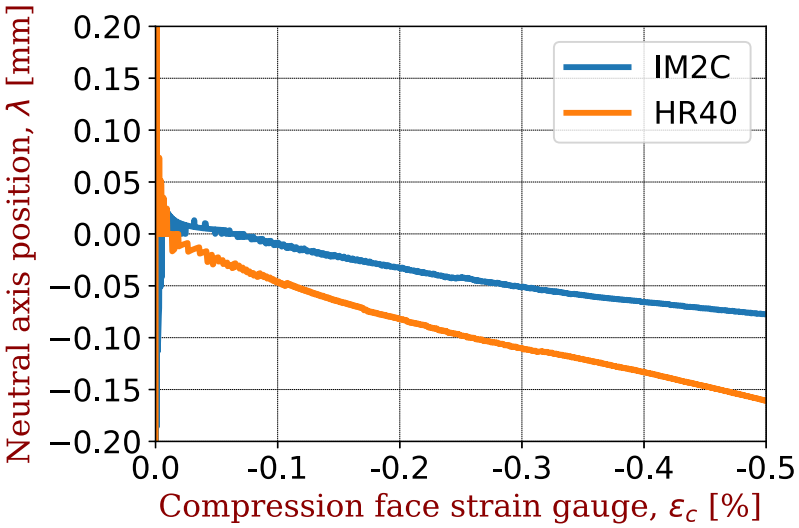

Figure 1. Neutral axis position for the two carbon fibres

All extracted parameters' values are reported on Table 3.

Table 3: Elastic properties of unidirectional plies – Linear and Non-linear

Carbon Fibre	E_{UD}^{T0} [GPa]	E_{UD}^{C0} [GPa]	B' [-]	A' [-]
IM2C	165 ± 4	164	14±4	8±3
HR40	200	200	22±4	22±4

Figure 2 describes the evolution of the axial modulus of a UD ply of epoxy/fibre composite in tension and compression for IM2C and HR40 carbon fibres, as given by the numerical simulations. The moduli for different fibre waviness levels varies as a function of the out-of-plane misalignment angle θ. At 0.5 % strain for the highest angle of 2° considered here (a value beyond reported values, see [13, 14, 15]), we find an increase of ~ 0.5‰ in tension and a decrease of ~ 0.7‰ in compression for the GFRP, which are non-significant differences. On the contrary, at 0.5 % strain, UD with carbon fibres show an increase in their tensile moduli by ~ 0.7 % for IM2C (compared with 1 % for HR40) and a decrease in their compressive moduli by ~ 1.2 % for IM2C (compared with 1.8 % for HR40).

  doi:10.5075/epfl-298799_978-2-9701614-0-0

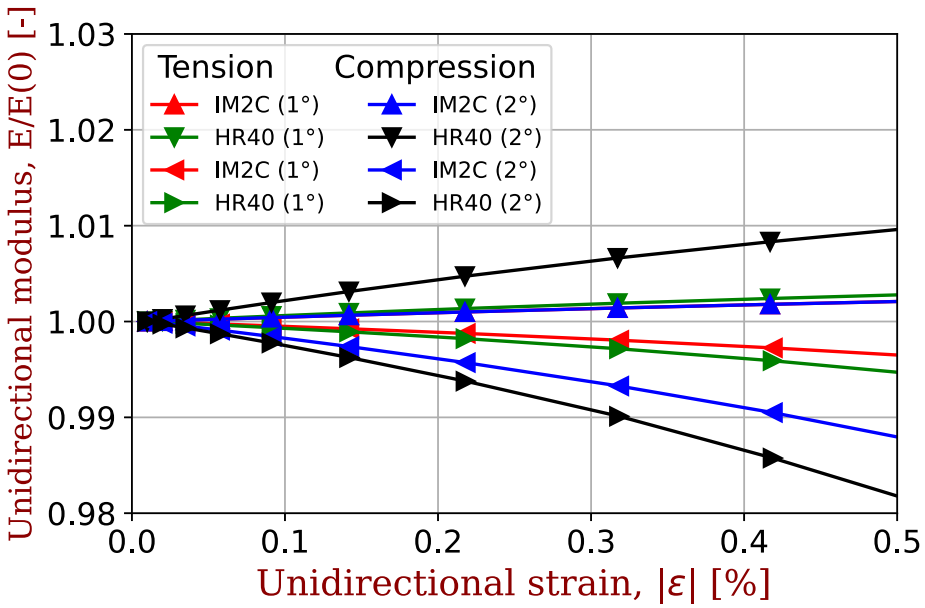

Figure 1. Use the option "Unformatted text" when copying/pasting text from other sources

For IM2C carbon fibre, geometry can explain up to 1/10th of the increase and up to 1/4th of the decrease, by taking an extreme value of the misalignment angle θ=2°. Assuming a more relevant value of 1° for this angle (see [14,15]), the increase and the decrease are limited to ~ 0.2% and 0.35 %, respectively, so we infer that geometry can explain 1/14th and 1/11th of the changes in stiffness in tension and in compression, respectively. For HR40 carbon fibre, geometry can explain up to 1/10th of the increase and up to 1/6th of the decrease by taking an extreme value of the misalignment angle θ =2°. For a more relevant value of 1°for this angle, the increase and the decrease are limited to ~ 0.25 and 0.5 %, respectively, in which case geometry can explain 1/50th and 1/20th of the changes in stiffness in tension and in compression, respectively. Therefore, for a reasonable value of the misalignment angle, and for a maximum strain of 0.5 %, the (extrinsic) contribution of geometry is of a second order, but not negligible, with respect to the (intrinsic) contribution of the carbon fibre.

4. References

1. Curtis, G.J., M., M.J., Reynolds, W.N.. Non-Hookean Behaviour of Strong Carbon Fibres. Nature 1968;220(5171):1024–1025.
2. Hughes, J.. Strength and modulus of current carbon fibres. Carbon N Y 1986;24(5):551–556.
3. Shioya, M., Hayakawa, E., Takaku, A.. Non-hookean stress-strain response and changes in crystallite orientation of carbon fibres. J Mater Sci 1996;31(17):4521–4532.
4. Vandreumel, W.H.M., Kamp, J.L.M.. Non-Hookean Behavior in Fiber Direction of Carbon-Fiber Composites and Influence of Fiber Waviness on Tensile Properties. J Compos Mater 1977;11(Oct):461–469.
5. Wisnom, M.R.. Limitations of Linear Elastic Bending Theory Applied to Four Point Bending of Unidirectional Carbon Fibre-Epoxy. In: 31st Struct. Struct. Dyn. Mater. Conf. Reston, Virginia: American Institute of Aeronautics and Astronautics; 1990,.
6. Keryvin, V., Marchandise, A., Mechin, P.Y., Grandidier, J.C.. Determination of the longitudinal non linear elastic behaviour and compressive strength of a CFRP ply by bending tests on laminates. Compos Part B Eng 2020;187:107863.

  doi:10.5075/epfl-298799_978-2-9701614-0-0

7. Mechin, P.Y., Keryvin, V., Grandidier, J.C.. Limitations on adding nano-fillers to increase the compressive strength of continuous fibre / epoxy matrix composites. Compos Sci Technol 2020;192:108099.
8. Grandidier, J.C., Channakeshava, A.B., Mazziotta, R.. A non-local model to analyse 2D and 3D microbuckling of long carbon fibre epoxy material. Compos Struct 2021;277:114531.
9. Bettadahalli Channakeshava, A., Grandidier, J.C.. A non-local finite element model to assess the compressive strength of composite structures. Eur J Mech - A/Solids 2022;93:104494.
10. Hashin, Z.. Analysis of Composite Materials—A Survey. J Appl Mech 1983;50(3):481.
11. Christensen, R., Lo, K.. Solutions for effective shear properties in three phase sphere and cylinder models. J Mech Phys Solids 1979;27(4):315–330.
12. Guruprasad, T., Keryvin, V., Charleux, L., Guin, J.P., Arnould, O.. On the determination of the elastic constants of carbon fibres by nanoindentation tests. Carbon N Y 2021;173:572–586.
13. Mechin, P.Y., Keryvin, V., Grandidier, J.C., Glehen, D.. An experimental protocol to measure the parameters affecting the compressive strength of CFRP with a fibre micro-buckling failure criterion. Compos Struct 2019;211:154–162.
14. Jumahat, A.. Effect of Nanofillers on Thermo-Mechanical Properties of Polymers and Composite Laminates. Ph.D. thesis; University of Sheffield, UK; 2011.
15. Grabow, M.. Contribution to the investigation of the compressive strength and delamination of continuous fibre laminated composites in the context of competitive sailing. Ph.D. thesis; Univ. Bretagne Sud (France); 2021.

  doi:10.5075/epfl-298799_978-2-9701614-0-0

Composites Meet Sustainability – Proceedings of the 20th European Conference on Composite Materials,
ECCM20. 26-30 June, 2022, Lausanne, Switzerland

EVALUATION OF THE SHEAR BEHAVIOR OF CF-PETG AND CF-PC COUPONS MANUFACTURED USING LARGE-SCALE ADDITIVE MANUFACTURING PROCESSES

Benjamin Steva[a], Kyle Warren[a], Camerin Seigars[a], Britt Helten[a]

a: University of Maine – benjamin.steva@maine.edu

Abstract:

Two ASTM standard shear methods were studied using two different materials to quantify the variation that may occur based on the chosen calculation area of a strain field measured using digital image correlation (DIC). Panels of carbon fiber reinforced polyethylene terephthalate-glycol (CF-PETG) and polycarbonate (CF-PC) were printed using a Cincinnati BAAM work cell. The panels were then faced to 7.5-mm thick and notched coupons were extracted with geometries according to ASTM standards D5379 and D7078. The DIC strain data collected during experiments was post-processed and evaluated using various calculation areas within the coupons. Comparisons were made between the materials, shear test methods, and calculation areas for these large-scale additively manufactured coupons. Recommendations on test method and calculation area are provided.

Keywords: Thermoplastic composites; BAAM; Digital image correlation; Additive manufacturing; Standardized testing

1. Introduction

The advent of large-scale additive manufacturing (AM) has introduced new opportunities to manufacture large, complex parts in one process, while also offering the possibility of cost and waste reduction and increased efficiency. However, the mechanical properties of parts manufactured with this process differ from those of plastics manufactured with more traditional processes, largely due to anisotropy of AM and lack of continuous long-fiber reinforcement.

In this study, the shear properties of carbon fiber reinforced polyethylene terephthalate-glycol (CF-PETG) and polycarbonate (CF-PC) were investigated using digital image correlation (DIC). Both materials were tested according to two standard test methods for determining shear properties in composites: ASTM D5379 [1] and ASTM D7078 [2]. Comparisons between these two test standards have been made in previous studies on chopped fiber composites [3] and on neat and reinforced injection-molded polypropylene [4], [5]. However, previous studies do not provide guidance specific to large-scale additively manufactured coupons and parts. In this study, the two test methods were compared by means of large-scale AM CF-PETG and CF-PC, and recommendations applicable to these materials are made. Additionally, three different calculation areas were used when post-processing to produce shear strains and determine any variation in the resulting shear moduli due to the calculation area.

2. Testing

2.1 Test Standards and Coupon Preparation

Of the available test standards, ASTM D5379 and ASTM D7078 were deemed most suitable for the evaluation of these AM materials, as they apply to fiber reinforced composite materials, which are anisotropic, unlike typical plastics. The standards utilize similar v-notched geometries,

  doi:10.5075/epfl-298799_978-2-9701614-0-0

but load specimens in a different manner. Figure 1 shows a labelled diagram of each specimen geometry. The corresponding dimensions can be found in Table 1. All specimens were cut from one bead thick, AM panels that were faced equally on either side to a panel thickness of 7.5-mm, as opposed to the recommended 3 to 4-mm for ASTM D5379 and 2 to 5-mm for ASTM D7078. A greater thickness was used due to the thickness of the as-printed panels, which had a typical bead width 16.5 to 19-mm. The final test specimens were cut on a water jet from these faced panels according to the dimensions from the standards, using SI units.

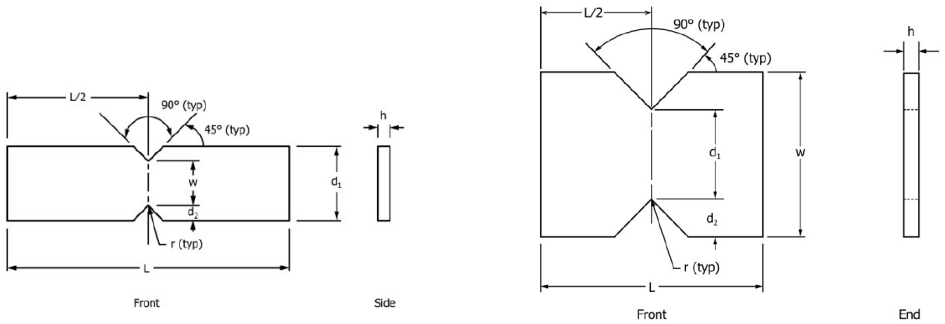

(a) *(b)*

Figure 1. Labelled diagram of (a) ASTM D5379 test specimen [1] and (b) ASTM D7078 test specimen [2].

Table 1: ASTM D5379 [1] and ASTM D7078 [2] test specimen dimensions, in mm (in).

Dimension	ASTM D5379	ASTM D7078
h	7.5 (0.3)	7.5 (0.3)
L	76 (3.0)	76 (3.0)
r	1.3 (0.05)	1.3 (0.05)
d1	19 (0.75)	31.0 (1.20)
d2	3.8 (0.15)	12.7 (0.50)
w	11.4 (0.45)	56.0 (2.20)

The most significant difference between the two ASTM test methods is the method for loading. According to ASTM D5379, specimens are loaded into the fixture and aligned with the loading axis using a pin in the fixture (Figure 2a). The two halves of the fixture are then compressed, loading the specimen on its edges. In contrast, the ASTM D7078 fixture grips the faces of the test specimen (Figure 2b), the fixture halves are pulled apart from one another, and face loading is imparted on the specimen.

(a) *(b)*

Figure 2. Test setup for (a) ASTM D5379 and (b) ASTM D7078.

2.2 Experiments, Data Collection, and Post-Processing

All experiments were performed on a servo-hydraulic Instron machine using a constant displacement rate of 2-mm/min, as specified by both standards. Two orientations were prepared and tested relative to the AM bead orientation. These orientations are shown in Figure 3, where the AM beads are aligned perpendicular to the gauge region in the 13-orientation, and parallel to the gauge region in the 31-orientation. Anisotropic material symmetry supports that the linear-elastic response (shear modulus) should be the same between orientations, though the post-linear response may vary. Both orientations were examined to generate a comparison between the entire stress-strain response of each orientation. DIC was used to collect full-field shear strain measurements for all specimens using a GOM ARAMIS system. The white and black paint pattern used for this data collection can be seen on the specimens in Figure 2.

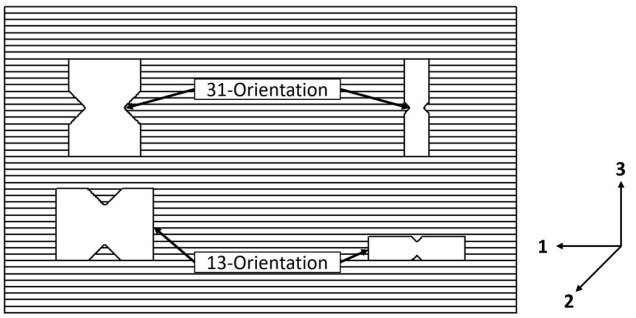

Figure 3. Specimen orientations with reference to AM beads.

Using the GOM Correlate 2021 software, the DIC data collected was post-processed and exported into CSV files, which were used to calculate strengths and moduli for comparisons. GOM's built-in scripting interface was used to create a local coordinate system fitted to each specimen based on a few user-defined points at the notches and corners of the painted surface. The coordinate system set the X-axis along the long axis of the coupon, the y-axis in the loading direction, and the origin at the center of the specimen between the notches. This coordinate system can also be seen in the lower left of Figure 4.

DIC calculates strain fields using the black and white pattern on the specimen surface, and the calculation area selected during DIC data analysis can affect the resulting strains. This study examined three different calculation areas for each test type and average strains within the region were generated and exported via scripting. For each test method, all calculation areas had the same width between the notches (in the local Y-direction) so the only variable in the areas was the length along the long axis of the test specimens (in the local X-direction). The chosen calculation area dimensions are listed below in Table 2, and example calculation areas as seen on a specimen for each standard are shown in Figure 4.

Table 2: Dimensions of calculation areas used in DIC analysis, in mm (in).

Calculation Area ID	Width Across Gauge Section	Length
D5379_CA1	8.89 (0.35)	2.54 (0.1)
D5379_CA2	8.89 (0.35)	5.08 (0.2)
D5379_CA3	8.89 (0.35)	7.62 (0.3)
D7078_CA1	25.4 (1.0)	3.175 (0.125)
D7078_CA2	25.4 (1.0)	6.35 (0.25)
D7078_CA3	25.4 (1.0)	9.525 (0.375)

  doi:10.5075/epfl-298799_978-2-9701614-0-0

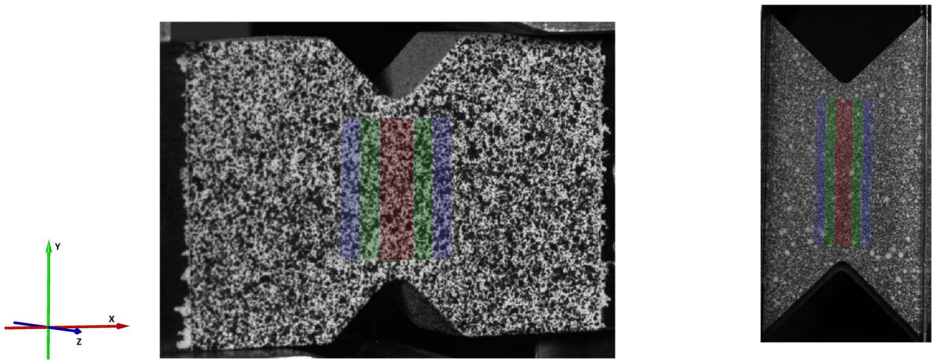

(a) Example of D5379_CA1 (red), D5379_CA2 (green), and D5379_CA3 (blue)

(b) Example of D7078_CA1 (red), D7078_CA2 (green), and D7078_CA3 (blue)

Figure 4. Example calculation areas for (a) ASTM D5379 and (b) ASTM D7078. Calculation areas 2 and 3 are inclusive of the smaller areas shown in the image (i.e., D5379_CA2 includes all red and green areas).

A GOM script was used to calculate the average XY strain from the XY strain field within each calculation area. The average XY strain was then exported to a CSV file along with the corresponding time, load, and position. This CSV and a python post-processing script were then used to determine the average ultimate strength and average chord modulus for each set of data.

3. Results

A representative strain field on an ASTM D5379 and an ASTM D7078 specimen can be seen overlaying the images in Figure 5. Table 3 and Table 4 representative strain fields for all calculation areas at a set displacement for each orientation of an ASTM D5379 specimen and an ASTM D7078 specimen, respectively. The strain fields of the specimens in the 13-orientation appear to be segmented, which can be attributed to the AM beads alignment perpendicular, or nearly perpendicular, to the gauge length. The strain fields of the specimens in the 31-orientation are more homogeneous, especially in the D5379 specimen; the AM beads in this orientation run parallel to the gauge length.

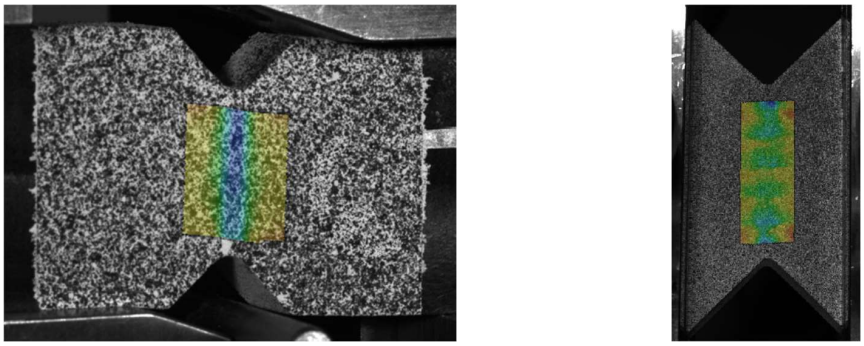

(a) *(b)*

Figure 5 : Representative strain fields as shown on an (a) ASTM D5379 specimen and (b) ASTM D7078 specimen prior to failure.

  doi:10.5075/epfl-298799_978-2-9701614-0-0 published under CC BY-NC 4.0 license

Table 3: Representative strain fields at 2-mm displacement for each calculation area in the 13- and 31-orientations for D5379 specimens.

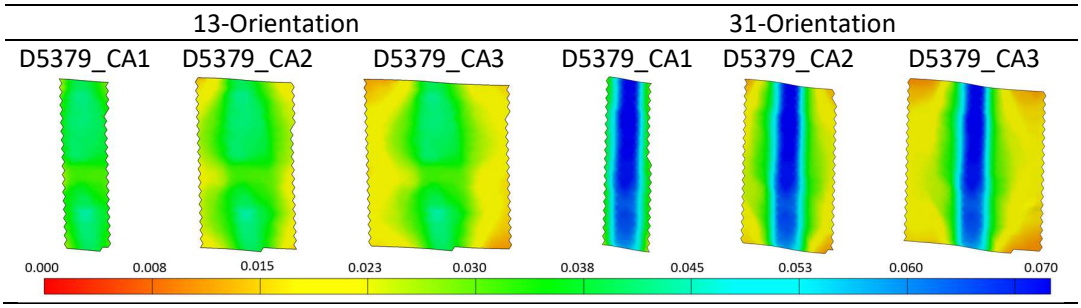

Table 4: Representative strain fields at 1.5-mm displacement for each calculation area in the 13- and 31-orientations for D7078 specimens.

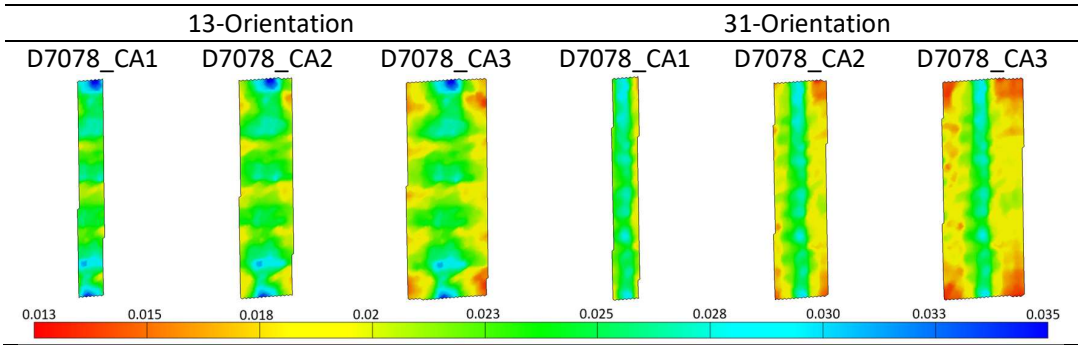

Since the load and cross-sectional area are not affected by the varying calculation area, each specimen has only one ultimate strength. Figure 6 shows the average ultimate strength of each combination of material, orientation, and test standard.

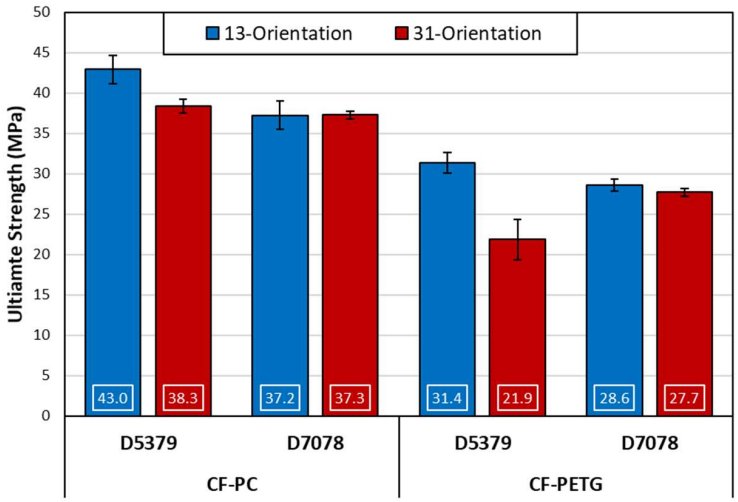

Figure 6. Average ultimate shear strengths for each material, orientation, and test standard combination.

Varying the calculation area affects the resulting strain, which in turn results in a different chord modulus calculation. Visually, the result of the calculation area on the moduli can be viewed within the stress-strain curves created. A representative stress-strain curve for the 13- and 31-orientations can be found below for ASTM D5379 (Figure 7) and ASTM D7078 (Figure 8).

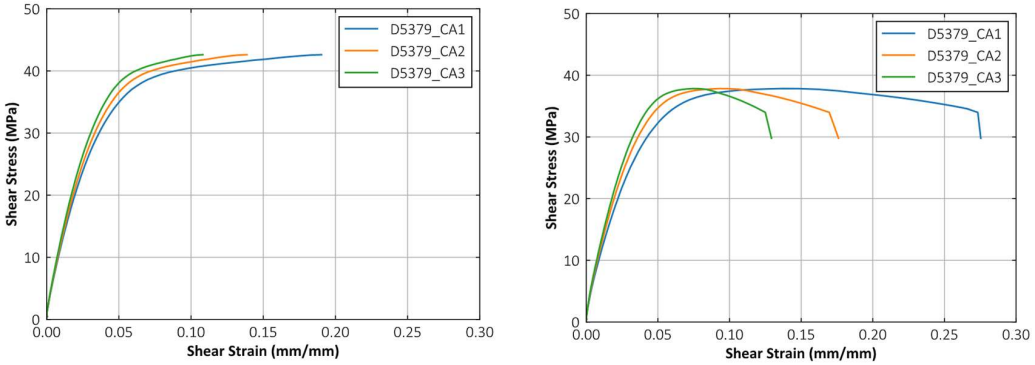

(a) 13-orientation *(b) 31-orientation*

Figure 7. Representative stress-strain curves for each calculation area of a D5379 specimen in the (a) 13-orientation and (b) 31-orientation

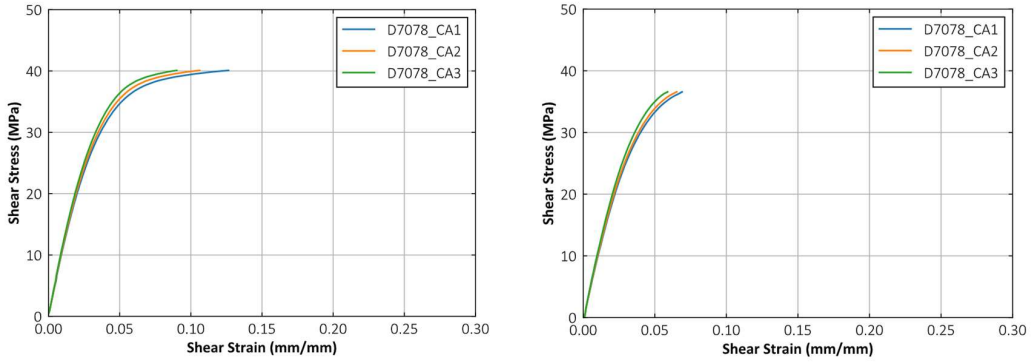

(a) *(b)*

Figure 8. Representative stress-strain curves for each calculation area of a D7078 specimen in the (a) 13-orientation and (b) 31-orientation

For the different calculation areas, the stress-strain curves resemble one another at low strains, but as the strain increases, the curves begin to diverge. To compare the impact of the calculation areas numerically, the average chord moduli were calculated for each calculation area of each test set and can be found below in Table 5. The nominal strain range for calculating the chord moduli was 1,500 to 5,500 με.

Table 5: Average chord moduli by material, test standard, and orientation.

Material	Test Standard	Orientation	Avg. Chord Modulus, CA1 (GPa)	Avg. Chord Modulus, CA2 (GPa)	Avg. Chord Modulus, CA3 (GPa)
CF-PC	D5379	13	1.007	1.081	1.138
		31	0.939	0.985	1.069
	D7078	13	1.097	1.134	1.150
		31	1.027	1.043	1.073
CF-PETG	D5379	13	1.074	1.150	1.228
		31	0.985	1.078	1.173
	D7078	13	1.110	1.125	1.162
		31*	1.134	1.168	1.223

*Three coupons were tested in the 31-orientation for D7078 CF-PETG, as opposed to the recommended five.

To normalize the modulus results, the percentage increase in modulus was determined for calculation areas two and three, relative to calculation area one. Figure 9 shows these percentage increases.

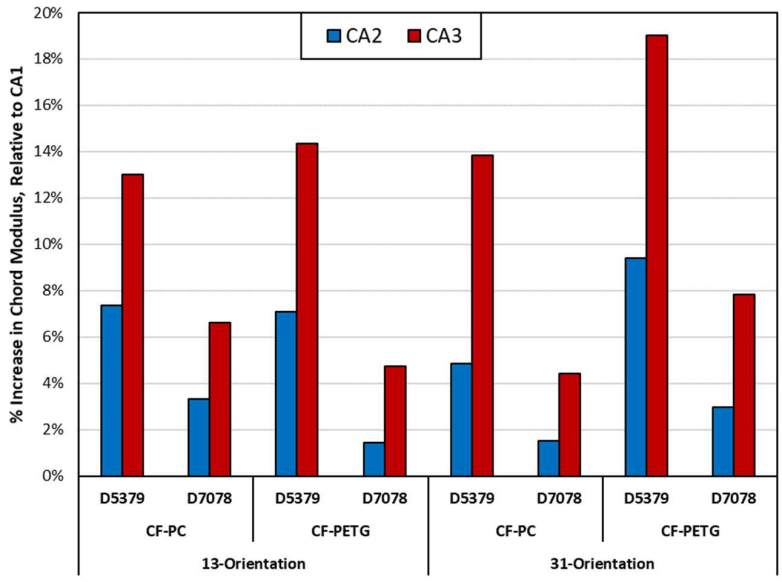

Figure 9. Percent increase in chord modulus for different calculation areas, relative to the smallest calculation area, CA1.

4. Discussion

Two standard test methods for determining shear properties of composites were applied to two carbon fiber reinforced, large-scale AM materials in this study. The effect of varying the calculation area used with DIC was investigated by examining the shear chord modulus. In all cases, the shear chord modulus varied as the calculation area changed; however, no clear pattern was seen when comparing all data across both standards, except that changes in the calculation area affected ASTM D5379 specimens more than they did ASTM D7078 specimens. This suggests that the ASTM D7078 may be better suited as a shear test method when using DIC

  doi:10.5075/epfl-298799_978-2-9701614-0-0

on these materials, due to its lower sensitivity to calculation area. One reason for this lower sensitivity may be the larger gauge region of ASTM D7078 geometry, which could be better suited to the large unit cell size associated with these large-scale AM coupons.

Specimens tested according to ASTM D7078 resulted in similar ultimate strengths between the two orientations. Those tested according to ASTM D7078 saw an average of only 0.15% and 3.14% difference between orientations in CF-PC and CF-PETG, respectively. In contrast, specimens tested according to ASTM D5379 had an 11.34% and 35.80% difference between orientations in CF-PC and CF-PETG, respectively. Additionally, the ultimate strengths of CF-PC were greater those of CF-PETG by an average of 42.95% for those tested according to ASTM D5379 and 27.88% for ASTM D7078.

Based on the data collected in these experiments and discussed in this paper, ASTM D7078 is recommended for testing large-scale AM materials, especially when using DIC to measure strains. This finding is in agreement with the study done by Chen et al. on chopped carbon fiber SMC composites [3]. However, it is in opposition of the findings by Codolini, Li, and Wilkinson, who found more variability in stress-strain curves of homogeneous polypropylene specimens tested according to ASTM D7078 than ASTM D5379 [5]. The results here show that the shear strengths produced using ASTM D7078 were generally more conservative for the two material systems tested in this study, and the choice of test method is less sensitive to the calculation area used with DIC. Finally, the data shows that CF-PC has a higher shear strength than CF-PETG for this manufacturing process.

5. References

1. D30 Committee, “Test Method for Shear Properties of Composite Materials by the V-Notched Beam Method,” ASTM International. doi: 10.1520/D5379_D5379M-19E01.
2. D30 Committee, “Test Method for Shear Properties of Composite Materials by V-Notched Rail Shear Method,” ASTM International. doi: 10.1520/D7078_D7078M-20E01.
3. Z. Chen *et al.*, “A Comparative Study of Two ASTM Shear Test Standards for Chopped Carbon Fiber SMC,” *SAE Int. J. Mater. Manuf.*, vol. 11, no. 4, pp. 277–283, Apr. 2018, doi: 10.4271/2018-01-0098.
4. H. Daiyan, E. Andreassen, F. Grytten, H. Osnes, and R. H. Gaarder, “Shear Testing of Polypropylene Materials Analysed by Digital Image Correlation and Numerical Simulations,” *Exp. Mech.*, vol. 52, no. 9, pp. 1355–1369, Nov. 2012, doi: 10.1007/s11340-012-9591-7.
5. A. Codolini, Q. M. Li, and A. Wilkinson, “Mechanical characterization of thin injection-moulded polypropylene specimens under large in-plane shear deformations,” *Polym. Test.*, vol. 69, pp. 485–489, Aug. 2018, doi: 10.1016/j.polymertesting.2018.06.010.

3D-PRINT PATH GENERATION OF CURVILINEAR FIBER-REINFORCED POLYMERS BASED ON BIOLOGICAL PATTERN FORMING

Naruki Ichihara, Masahito Ueda

Nihon University – csna15018@g.nihon-u.ac.jp

Abstract: *This paper proposed 3D printing of orthotropic material, carbon fiber-reinforced polymers, based on the optimized material orientation and distribution. First, the cross-ply orthotropic material orientation and distribution were optimized using the gradient-based anisotropic topology optimization method to maximize the structural stiffness. Then, the continuous 3D print path was generated from the optimized material orientation and distribution using the biological pattern-forming system. Finally, the optimized structure was 3D printed based on the 3D print path by means of the fused filament fabrication. The proposed structure brought the full potential of orthotropic materials minimizing the structural weight.*

Keywords: 3D printing; Topology optimization; Material orientation; Print path; Fiber-reinforced polymers

1. Introduction

Engineering to utilize materials efficiently is essential to manufacture optimized structures with minimal weight. Notably, the material orientation of anisotropic materials, e.g., fiber-reinforced polymers, within the structure is essential to fully demonstrate the mechanical property. The undesirable material orientation design causes an increase in the structural weight.

In designing material orientation, the optimization method is needed. The gradient-based solver improves the material orientation iteratively to minimize an index for an optimization problem. Many engineering problems accepted this approach to resolve the optimization problems, such as maximizing stiffness [1], strength [2], and natural frequencies [3]. Additive manufacturing for fiber-reinforced polymers, e.g., Automated Tape Placement and 3D printing [4], provides the manufacturing procedure of structures with optimized material orientation. However, a manufacturable 3D print path generation method is needed to integrate these contributions. Generally, the optimization process discretizes the material orientation field to the finite elements or their vertices, and thus the optimization result is a discrete material orientation field that does not provide the manufacturable 3D print path.

Some 3D print path generation methods were proposed, such as the EQS, streamline, and level-set methods [5]. However, the performance of the 3D print path that generates these methods depends on the external shape of the structure. Therefore, engineers should change the strategy for each situation. An alternative approach is based on the stripe pattern aligned with the vector field. Boddeti [6] proposed the path generation method based on Knoppel's stripe pattern [7]. However, this method requires a unique formulation and discretization different from the optimization. The Turing pattern is an advantageous stripe pattern generation method. The Gray-Scott model, the partial differential equation set for the Turing pattern, was adopted for 3D print path generation [8]. This model can be solved by using the same discretization method of optimization. However, the parameters do not have an engineering meaning because the

  doi:10.5075/epfl-298799_978-2-9701614-0-0

model was developed for chemical interactions, which makes the parameter setting difficult. Authors have proposed the 3D print path generation technique based on the Swift-Hohenberg equation [9]. This method generates a continuous and intersection-free 3D print path. However, this method has only been applied to optimized material orientation without topology optimization.

This study proposes the 3D printing of cross-ply carbon fiber-reinforced polymers based on the topology and material orientation optimization. The proposed method was applied to the 2D structure for maximizing stiffness. The proposed optimized design was 3D printed using a Fused Filament Fabrication type 3D printer.

2. Topology and material orientation optimization

2.1 Material fraction and orientation representation

This study considered the minimizing structural compliance problem with material amount limitation. Assume that the two-dimensional design domain D is given. Inside of design domain D, the scalar and vector fields are defined. These fields represent the local material fraction ρ and material orientation $\boldsymbol{\theta}$, respectively.

These fields must satisfy the following constraints:

$$\rho \in [\epsilon, 1], \quad \|\boldsymbol{\theta}\| = 1, \quad 0 < \angle\boldsymbol{\theta} < \frac{\pi}{2} \tag{1}$$

here, $\epsilon = 10^{-3}$ is the small parameter for numerical stability. However, in these constraints, the quarter sector constraint of the vector field requires at all points in the design domain. This large number of non-linear conditions causes difficulties in solving the optimization problem. The isoparametric-projection method was adopted to avoid this problem [10]. The following relaxed constraints are assumed instead of the unit norm constraints:

$$\|\boldsymbol{\theta}\| \leq 1, \quad 0 < \angle\boldsymbol{\theta} < \frac{\pi}{2}. \tag{2}$$

To avoid the point-wise non-linear constraints, a precursor vector field $\boldsymbol{\phi} \in [-1, 1]^2$, which satisfies the box constraints, is introduced. The following isoparametric projection is applied to the precursor field $\boldsymbol{\phi}$ to fulfill the original non-linear conditions:

$$\boldsymbol{\theta} = N(\boldsymbol{\phi}) \tag{3}$$

Here, N is the shape function for 8-noded serendipity elements and defined following:

$$N = \sum_{i=1}^{8} \boldsymbol{N}_i \mathbf{v}_i \tag{4}$$

$\mathbf{v}_i$ is the coordinates of i-th vertex in the physical system. To translate the box constraint to the quarter sector constraint, the $\mathbf{v}_i$ is defined as follows:

$$\mathbf{v}_i = \begin{pmatrix} u_i \\ v_i \end{pmatrix} \tag{5}$$

$$u_i = \begin{cases} 0 & i = 1 \\ \cos(\pi(i-2)/12) & \text{otherwise} \end{cases} \tag{6}$$

$$v_i = \begin{cases} 0 & i = 1 \\ \sin(\pi(i-2)/12) & \text{otherwise} \end{cases} \tag{7}$$

  doi:10.5075/epfl-298799_978-2-9701614-0-0

This transformation is illustrated in Figure 1.

Next, the design fields are regularized by the Helmholtz equation [11].

$$-R_\rho^2\nabla^2\tilde{\rho}+\tilde{\rho}=\rho \tag{8}$$

$$-R_\theta^2\nabla^2\widetilde{\boldsymbol{\theta}}+\widetilde{\boldsymbol{\theta}}=\boldsymbol{\theta} \tag{9}$$

Here R_ρ and R_θ are filter radiuses for the scalar and vector fields, respectively. In this study, the design fields are regularized using finite element analysis by solving equations (8) and (9).

2.2 Optimization problem for cross-ply laminated orthotropic material

The orthotropic material is placed to be symmetric cross-plied laminates at any point. The following stacking sequence is assumed:

$$S_i(\mathbf{x})=\left[\angle\widetilde{\boldsymbol{\theta}}/\angle\widetilde{\boldsymbol{\theta}}+90\right]_{\mathrm{s}} \tag{10}$$

Material orientation angle is a function of the position. The in-plane stiffness tensor A_{ij} is defined as follows using the stacking sequence S_i;

$$\bar{Q}_{ij}^k=\tilde{\rho}^p R^T(S_k)Q_{ij}R(S_k) \tag{11}$$

$$A_{ij}=\sum_{k=1}^4\bar{Q}_{ij}^k\,(h_k-h_{k-1}) \tag{12}$$

where $R(\vartheta)$ is the rotation transform tensor, Q_{ij} is the orthotropic stiffness tensor for the elementary ply, h_k is the ply height of the k-th lamina, and p is the penalty parameter typically set to be 3. Assuming the small deformation, the strain tensor ε is represented as follows;

$$\varepsilon=\frac{1}{2}(\nabla\boldsymbol{u}+(\nabla\boldsymbol{u})^T),\quad [\varepsilon]_i=[\varepsilon_1\ \ \varepsilon_2\ \ 2\varepsilon_{12}] \tag{13}$$

where $\boldsymbol{u}$ is the in-plane displacement vector. The strain energy is calculated by the in-plane resultant forces $N_i=A_{ij}[\varepsilon]_j$ and the Voight represented strain tensor $[\varepsilon]_i$:

$$\Psi=\int_D\frac{1}{2}A_{ij}[\varepsilon]_i[\varepsilon]_j\,\mathrm{d}x. \tag{14}$$

The minimization of the strain energy Ψ maximizes the structural stiffness under the external in-plane loading. Therefore, the optimization problem is defined as follows.

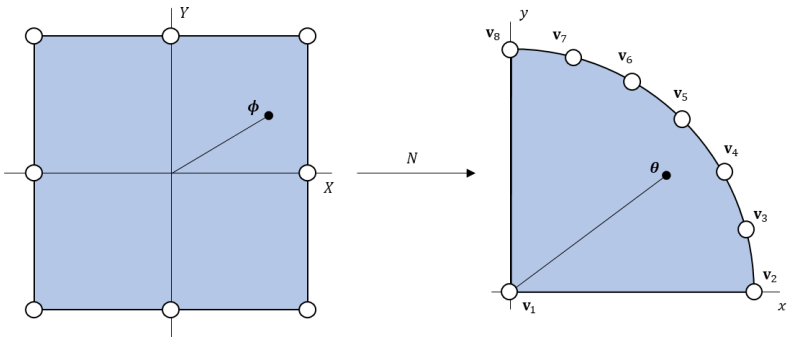

Figure 1. The transformation of the box constraints in the natural coordinate system to the quarter sector constraint in the physical coordinate system.

  doi:10.5075/epfl-298799_978-2-9701614-0-0 published under CC BY-NC 4.0 license

$$\min_{\rho,\boldsymbol{\phi}} \Psi = \int_D \frac{1}{2} A_{ij}[\varepsilon]_i[\varepsilon]_j \, \mathrm{d}x \tag{15-a}$$

subject to

$$\rho \in [\epsilon, 1], \quad \boldsymbol{\phi} \in [-1, 1]^2 \tag{15-b}$$

$$V = \int_D \tilde{\rho} \, \mathrm{d}x, \quad g = V_t - V \geq 0. \tag{15-c}$$

where V and V_t represents the total amount of the material and the target material amount.

2.3 Numerical implementation

The Finite Element Analysis (FEA) was used to calculate the elastic deformation. All design fields were defined at the vertices of the finite element and interpolated by the first-ordered Lagrange element. Hence, the optimization problem has a vast number of design variables. A gradient-based optimization routine is the best choice for this problem. The method of moving asymptotes was used. The FEA package in the Python3, FEniCS, was used. The PETSc's Krylov solver with an algebraic multi-grid preconditioner was used as the FEA solver.

3. 3D-print path generation from the optimized material orientation and distribution

3.1 A stripe pattern generation

The optimized material orientation does not directly provide the 3D print path because of the discretized representation. The discretized optimized material orientation field needs to be converted to the continuous 3D print path. This study used a biological stripe pattern forming method to obtain the 3D print path.

Assume that the design domain D, which is identical to the above optimization problem, is given. The phase-field $\varphi(\boldsymbol{x})$ is introduced in the design domain D to produce the 3D print path. The phase-field $\varphi(\boldsymbol{x})$ emerges a stripe pattern oriented to the optimized material orientation $\boldsymbol{\theta}$. The free energy functional $\mathcal{F}[\varphi]$ of the phase-field $\varphi(\boldsymbol{x})$ is defined to yield the spatial stripe pattern.

$$\mathcal{F}[\varphi] = \int_D \left\{ W(\varphi) + \frac{1}{2}[-2k^2|\nabla\varphi|^2 + (\nabla^2\varphi)^2 + k^4\varphi^2] \right\} \mathrm{d}x \tag{16}$$

where W is the double-well potential that is defined as follows;

$$W(\phi) = -\frac{\phi^2}{2} + \frac{\phi^4}{4}, \tag{17}$$

and k is the field variable parameter that governs the hatch spacing of the stripe pattern. This free energy represents the local activation and global inhibition interaction and develops the spatially periodic pattern. This mechanism explains the pattern of the Benard convection and biological pattern forming. In this study, the anisotropic diffusion term is added to the free energy $\mathcal{F}$ to orient the stripe along with the optimized vector field $\boldsymbol{\theta}$.

$$\mathcal{F}[\varphi] = \int_D \left\{ W(\varphi) + \frac{1}{2}[-2k^2|\nabla\varphi|^2 + (\nabla^2\varphi)^2 + k^4\varphi^2 - 2q^2\nabla\varphi^T(\boldsymbol{\theta}^\perp \otimes \boldsymbol{\theta}^\perp)\nabla\varphi] \right\} \mathrm{d}x \tag{18}$$

where q is the magnitude of the anisotropic diffusion.

The parameter k corresponded with the local material fraction ρ.

  doi:10.5075/epfl-298799_978-2-9701614-0-0

$$k = \sqrt{\pi^2\rho^2 \Big/ w_0^2 - \rho^2 q^2} \tag{19}$$

where w_0 is the default hatch spacing.

This free energy is minimized using the variational method. Consequently, the following time evolution equation is derived:

$$\frac{\partial \varphi}{\partial t} = -(\nabla^2 + k^2)^2\varphi - 2q^2\nabla \cdot \left((\boldsymbol{\theta}^{\perp} \otimes \boldsymbol{\theta}^{\perp})\nabla\varphi\right) - W'(\varphi) \tag{20}$$

This equation is known as the Swift-Hohenberg equation and can be solved by the FEA routine.

3.2 Generation of the 3D print path

Curves are extracted from the stripe pattern obtained by developing the equation (20), which are used as 3D print paths. Here, the 0-level contours were used as 3D print paths $\mathcal{C}$.

$$\mathcal{C} = \{\varphi = 0\}. \tag{21}$$

4. Example of the three-point bending beam problem

This section applied the proposed method to a three-point bending beam problem. The mechanical properties used in the optimization problem are listed in Table 1.

The commercial fused filament fabrication type 3D printer (Composer A4, Anisoprint) was used to fabricate the beam structure. The short-carbon fiber-reinforced polyamide filament (Onyx, Markforged) was used. The nozzle temperature was set to be 270 degrees in Celsius.

The geometry and boundary conditions are illustrated in Figure 2. The target material fraction was 50% of the total amount in this example. The radiuses of the Helmholtz filter in Equations (8) and (9) were 0.8. Figure 3 shows the results of the optimized material distribution $\tilde{\rho}$ with the material orientation $\widetilde{\boldsymbol{\theta}}$. Then, the optimized material distribution and material orientation are used in Equation (20) to obtain the stripe pattern for the 3D print path, as shown in Figure 4.

Figure 5-A shows the print path generated by the stripe pattern in Figure 4, and figure 5-B shows the 3D printed part using the print path in Figure 5-A.

Table 1: Orthotropic material properties of short-carbon fiber-reinforced polyamide

Symbol (Unit)	Value	Description
E_1 (MPa)	2400	Young's modulus in the print direction.
E_2 (MPa)	2400/5	Young's modulus in the transverse direction.
G_{12} (MPa)	2400/10	In-plane shear stiffness.
ν_{12} $(-)$	0.36	In-plane Poisson's ration.

  doi:10.5075/epfl-298799_978-2-9701614-0-0

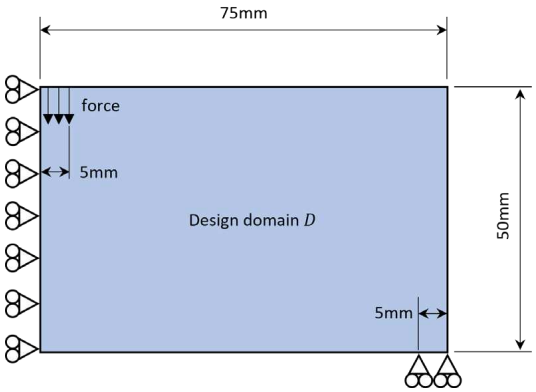

Figure 2. The geometry and boundary conditions of the three-point bending beam problem.

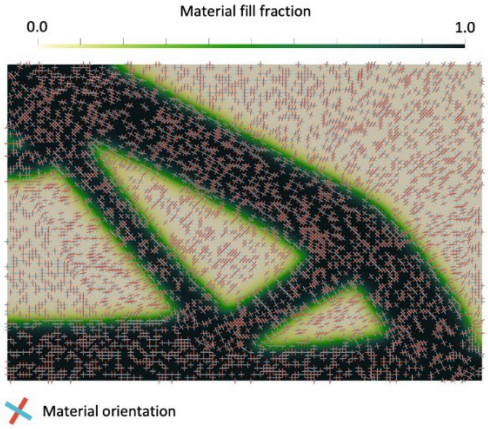

Figure 3. The optimized material distribution and material orientation.

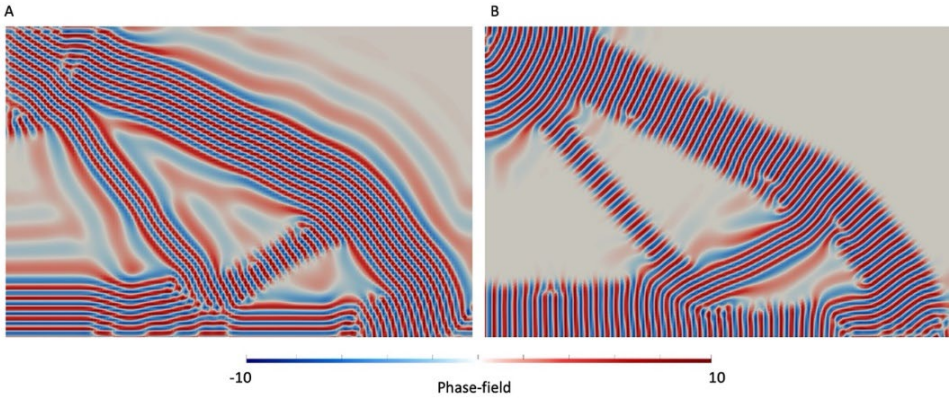

Figure 4. Stripe patterns for the 3D print path.

5. Conclusions

This study proposed the 3D printing of orthotropic material with optimized material orientation and material distribution. Material orientation and distribution was optimized using the gradient-based anisotropic topology optimization method. The 3D print path was generated from the optimized material orientation and distribution using the biological stripe pattern forming method. The optimized structure was successfully 3D printed using short-carbon fiber-reinforced polymers.

  doi:10.5075/epfl-298799_978-2-9701614-0-0

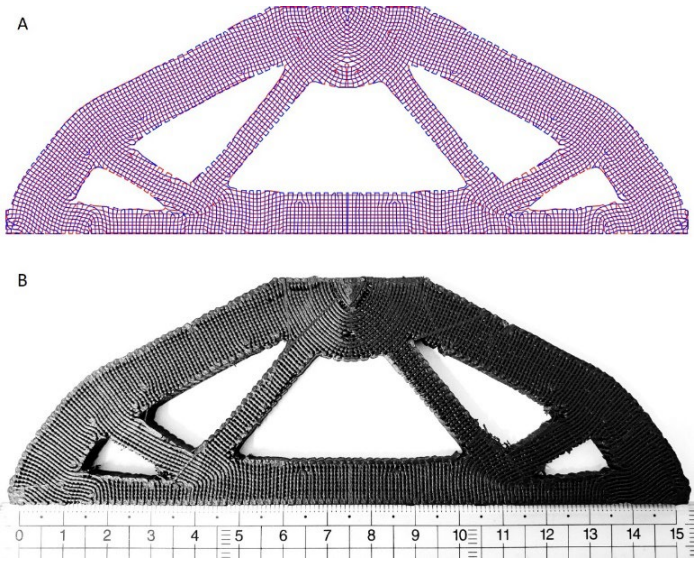

Figure 5. A is the 3D print path, and B is the 3D printed beam structure.

6. References

1. Nomura T, Kawamoto A, Kondoh T, Dede E, Lee J, Song Y, Kikuchi N. Inverse design of structure and fiber orientation by means of topology optimization with tensor field variables. Composites Part B: Engineering 2019; 176:107187.
2. Shimoda M, Muramatsu Y, Tsukihara R. Minimization of maximum failure criterion of laminated composite shell structure by optimizing distributed-material orientation. Structural and Multidisciplinary Optimization 2020; 61(4):1547-1571.
3. Honda S, Igarashi T, Narita Y. Multi-objective optimization of curvilinear fiber shapes for laminated composite plates by using NSGA-II. Composites Part B: Engineering 2013; 45(1):1071-1078.
4. Tian X, Todoroki A, Liu T, Wu L, Hou Z, Ueda M, et. al. 3D Printing of Continuous Fiber Reinforced Polymer Composites: Development, Application, and Prospective. Chinese Journal of Mechanical Engineering: Additive Manufacturing Frontiers 2022; 100016.
5. Papapetrou V, Patel C, Tamijani A. Stiffness-based optimization framework for the topology and fiber paths of continuous fiber composites. Composites Part B: Engineering 2020; 183.
6. Boddeti N, Tang Y, Maute K, Rosen D, Dunn M. Optimal design and manufacture of variable stiffness laminated continuous fiber reinforced composites. Scientific Reports 2020; 10(1):16507.
7. Knoppel F, Crane K, Pinkall U, Schroder P. Stripe Patterns on Surfaces. ACM Transactions on Graphics 2015; 34(4).
8. Nomura T, Dede E. Method of tool path generation for additive manufacturing with vector distribution. U.S. patent 2021.
9. Ichihara N, Ueda M. 3D-print infill generation using the biological phase field of an optimized discrete material orientation vector field. Composites Part B: Engineering 2022; 232:109626.
10. Nomura T, Dede E, Lee J, Yamasaki S, Matsumori T, Kawamoto A, Kikuchi N. General topology optimization method with continuous and discrete orientation design using isoparametric projection. International Journal for Numerical Methods in Engineering 2015; 101(8):571-605.
11. Lazarov BS, Sigmund O. Filters in topology optimization based on Helmholtz-type differential equations. International Journal for Numerical Methods in Engineering 2010; 86(6):765-781.

  doi:10.5075/epfl-298799_978-2-9701614-0-0

SYNCHROTRON RADIATION 3D COMPUTED TOMOGRAPHY STUDY ON IN-SITU MECHANICAL DAMAGE PROGRESSION OF NANOENGINEERED GLASS FIBER REINFORCED COMPOSITE LAMINATES WITH INTEGRATED MULTIFUNCTIONALITY

Palak B. Patel[a], Carolina Furtado[b], Megan Cooper[a], Jeonyoon Lee[a], Keiran Ball[c], Yeajin Lee[c], Albertino Arteiro[b], Marta Majkut[d], Lukas Helfen[e], Luiz Acauan[a], Mark Spearing[b], Iskander Akhatov[f], Stepan V. Lomov[f], Sergey G. Abaimov[f], Brian L. Wardle[a]

a: Massachusetts Institute of Technology, Cambridge, Massachusetts, USA – palak@mit.edu
b: University of Porto, Porto, Portugal
c: University of Southampton, Southampton, UK
d: European Synchrotron Radiation Facility, Grenoble, France
e: Institut Laue-Langevin, Grenoble, France
f: Skolkovo Institute of Science and Technology, Moscow, Russia

Abstract: *Composite materials' lightweight, multi-directional, tailorable, and multifunctional properties are important for weight-critical applications in aerospace vehicles. Aerospace composites nanoengineered with additional multifunctionalities, besides the primary structural function, are further advantaged in weight reduction. In this paper, a glass fiber reinforced polymer (GFRP) laminate is nanoengineered with vertically aligned carbon nanotubes (CNTs) at ply interfaces to have multiple multifunctionalities. A double edge notched tension (DENT) testing campaign was performed to explore the effect of laminate nanoengineering on damage development and progression by performing in-situ tests at the European Synchrotron Radiation Facility. Synchrotron radiation computed tomography (SRCT), to image in 3D the laminate under increasing tensile loads, revealed effective integration of the CNTs from the perspective of progressive damage mechanics.*

Keywords: glass fiber reinforced polymer; multifunctionality; double edge notched tension test; synchrotron radiation computed tomography; damage development

1. Introduction

Lightweight heterogenous materials, such as advanced fiber composites, have enabled the design and development of innovative aerospace structures. The composite materials' lightweight, multi-directional, tailorable, and multifunctional properties are important for weight-critical applications in aerospace vehicles. Aerospace composites with additional multifunctionalities, besides the primary structural function, are further advantaged in weight reduction. This is achieved by adding multifunctionalities in a structural composite while maintaining the structural strength of the composite. Nanoengineering enables the integration of multifunctionalities in composites without needing to modify the design, shape, or load-carrying capability of the composite structure with effectively no increase in weight. While single additional functionalities such as life-cycle enhancement [1-15], structural self-health monitoring, energy savings [9-14], de-icing protection [15], and self-cure monitoring [11-13] have been demonstrated in carbon fiber reinforced polymer (CFRP) composites, the

  doi:10.5075/epfl-298799_978-2-9701614-0-0

combination of multiple multifunctionalities in one composite system has not been demonstrated.

In this paper, a glass fiber reinforced polymer (GFRP) laminate is nanoengineered to have multiple multifunctionalities. Vertically aligned carbon nanotubes (CNTs) and commercial CNT films are integrated into the prepreg laminate to create an integrated multifunctional composite (IMC). The IMC, maintaining its primary structural function, has demonstrated mechanical enhancement with increased interlaminar shear strength due to interlaminar reinforcement provided by CNTs [16, 17]. Here, a double edge notched tension (DENT) testing campaign was performed on the IMC specimens to explore the effect of laminate nanoengineering on damage development and progression of the GFRP IMC. In-situ tests were performed in a micro mechanical tester utilizing synchrotron radiation computed tomography (SRCT) to image in 3D the laminate under tensile loads at the European Synchrotron Radiation Facility in Grenoble, France. This paper will present test results of the IMC laminate in terms of tensile strength and damage development through final failure via 3D SRCT under load for the DENT configuration, sometimes referred to as 4D due to the temporal nature of the in-situ load application, as seen in Figure 1.

2. Integrated Multifunctional Composite Manufacturing

The integrated multifunctional composite is manufactured by nanoengineering multifunctionalities into composites by integrating carbon nanotubes into composite laminates.

2.1 Multifunctional CNT Architectures

Carbon nanotubes are the key to the integration of multifunctional properties in the integrated multifunctional composite. Vertically aligned carbon nanotubes, as seen in Figure 1a, referred to as nanostitch 1.0 [1-6], were synthesized by a thermal catalytic chemical vapor deposition method. In this method, CNTs were synthesized on silicon wafers which have uniform layers of iron and Al_2O_3 catalyst deposited on the surface which were placed in a quartz tube furnace. The carbon nanotubes were synthesized in the furnace under controlled temperature conditions and gas flows of helium, hydrogen, and ethylene. Nanostitch 1.0 with a height of 20 microns was selected to be integrated into the IMC as per a previous study conducted on the influence of

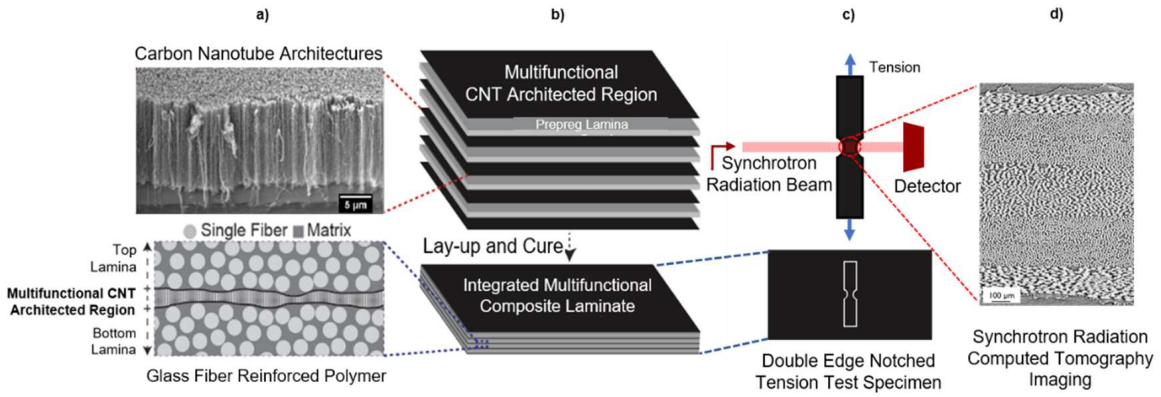

Figure 1. Manufacturing and testing of IMC specimens via in-situ 3D SRCT: a) CNT architecture placed in the IMC, b) lay-up and cure of the IMC, c) DENT test performed in-situ under synchrotron radiation for damage development via 3D imaging (15° tilt not shown), d) SRCT image of the IMC

  doi:10.5075/epfl-298799_978-2-9701614-0-0

carbon nanotube architectures on the interlaminar shear strength of laminates [16]. The second carbon nanotube architecture integrated into the IMC consists of randomly oriented commercial CNT film (Tortech, CNTM4) [17].

2.2 Nanoengineered Glass Fiber Reinforced Polymer Laminate

The glass fiber reinforced polymer (GFRP) chosen for this study, Hexcel NVE 913 E-glass unidirectional autoclave-grade pre-impregnated fibers (prepreg), had a fiber volume fraction of 56%. The laminate was manufactured by performing an 8-ply $[90|0|-45|+45]_s$ quasi-isotropic lay-up. To integrate the multifunctionalities in the IMC laminate via nanoengineering, nanostitch 1.0 was placed in the interlaminar region of the IMC and commercial CNT film was integrated into the top and bottom of the laminate as seen in Figure 1b. The IMC with integrated CNTs, as well as a baseline GFRP laminate without integrated CNTs, were cured in an autoclave following the manufacturer recommended cure cycle [17].

3. Experimental Characterization, Testing, and Results

3.1 In-Situ Double Edge Notched Tensile Test

A scaled down version of the double edge notched tension (DENT) test was performed in-situ during synchrotron radiation computed tomography to map the damage behavior of the nanoengineered laminate IMC under tension, as shown schematically in Figure 1c. DENT test specimens of length 40 mm, width 4 mm, laminate thickness 1.1 mm, and 1.1 mm radius notches were prepared by waterjet machining without further polishing. The micro tensile tester (Deben CT5000) had an X-ray transparent loading rig to enable SRCT imaging. In-situ testing was performed by providing tensile load to the DENT specimen to a particular load step, stopping the test and pausing for stability, performing a SRCT scan to capture laminate damage development, resuming the test, and repeating for different load steps (0%, 70%, 80%, 90%, 95%, and 100% of a previously experimentally determined failure load of baseline DENT specimens) until failure of the specimen.

Due to the limitation on ESRF beam time, two specimens of baseline composite DENT specimens and two specimens of IMC DENT specimens were tested in-situ during SRCT. The in-situ test was performed until failure and the average DENT strength with standard error were calculated. The test resulted in an average tensile strength of 170.82 ± 4.78 MPa of the baseline specimens and 174.14 ± 0.37 MPa of the IMC specimens as seen in Figure 2. A comparison between the DENT strengths of the baseline GFRP composite laminate and the IMC laminate showed that the IMC specimens demonstrated a statistically insignificant increase in DENT strength of 1.94%. These test results showed that the integration of the carbon nanotubes in the IMC, with the purpose of adding multifunctionalities to composites, still allowed the composite to maintain structural integrity under tension.

3.2 Synchrotron Radiation Computed Tomography Damage Development

The synchrotron radiation computed tomography imaging during in-situ testing was performed at the European Synchrotron Radiation Facility (ESRF) ID19 beam line. SRCT was utilized to 3D image the laminates under tensile loads to observe damage progression as tensile loads increased until failure of the laminates. SRCT was performed under the conditions of 19 KeV beam energy, 0.65 µm voxel size, 2500 projections, and 15° tilted test set-up to allow for better

  doi:10.5075/epfl-298799_978-2-9701614-0-0

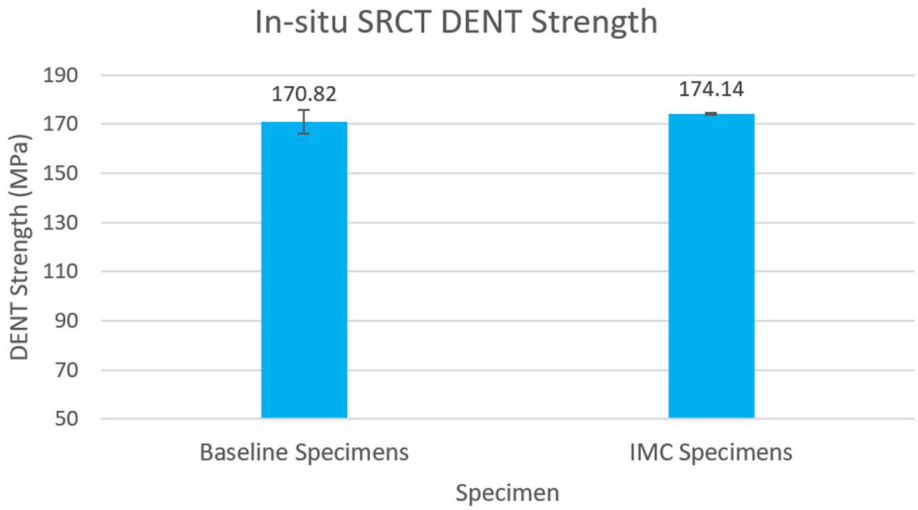

Figure 2. Average in-situ double edge notched tensile strength of baseline and IMC specimens with standard error

imaging of all fiber orientations. This aided in understanding the progression of the damage with increasing loads and the effect of nanoengineering on damage development and progression. A comparison between the damage development and progression in the baseline laminate and the IMC laminate was performed to note the effect of carbon nanotubes and the integration of multifunctionalities in composite laminates.

Figure 3 compares representative SRCT cross-sectional scans of the baseline and IMC laminates under different load percentages. The scans had been taken close to the notch in the DENT specimens. The lighter grey color represents the glass fibers, the darker grey is the matrix, and the darkest grey represents cracks in the laminate. Both baseline and IMC laminates under load showed through ply matrix cracks as well as double ply matrix cracks that progressed as the load on the specimens increased. SRCT images of the baseline specimen after failure depicted more delamination failure than the IMC specimen, but due to the insignificant difference in DENT strength, it could not be determined if the integrated CNTs played a significant role in the difference in delamination failure of the specimens. It is likely that delamination failure is not playing a significant role in the failure of these laminates under this loading, and therefore the CNTs show no positive effect of a stronger and tougher interface. Since the damage development in both baseline and IMC specimens demonstrated similar mechanisms, it was concluded that the CNTs integration in the IMC, with the purpose of adding multifunctionalities to composites, doesn't affect the damage development mechanism of the laminate.

4. Conclusion

It is important to maintain structural integrity of the composite laminate while integrating multifunctionalities through nanoengineering (here, using carbon nanotubes). It has been demonstrated in this paper that the structural integrity of the IMC is comparable to the baseline GFRP composite laminate in terms of tensile strength. The IMC specimens had an average DENT strength 1.94% higher (statistically insignificant) than the baseline laminate specimens. The damage development and progression observed in the baseline and IMC laminates were similar. The integration of the multifunctionality enabling CNTs in prepreg-based GFRP, resulting in the

  doi:10.5075/epfl-298799_978-2-9701614-0-0

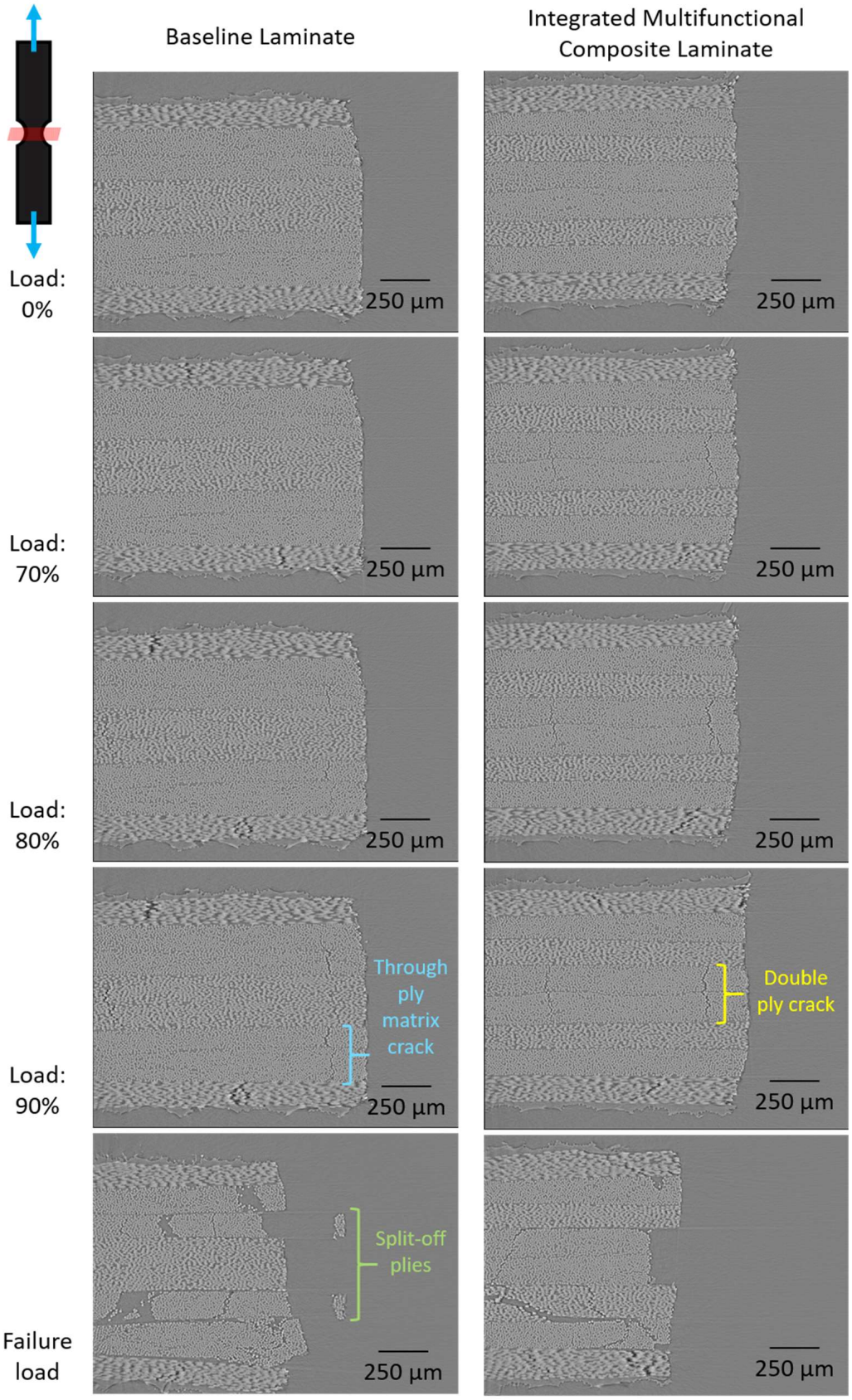

Figure 3. Comparison of damage development in synchrotron radiation computed tomography cross sectional scans of double edge notched tensile baseline and IMC specimens under various loads (0%, 70%, 80%, 90%, and failure) (Testing rig was at 15° tilt during scan)

  doi:10.5075/epfl-298799_978-2-9701614-0-0

formation of an IMC, maintained the structural integrity of the composite in terms of strength of laminate under tension, and damage development and progression. Further work on demonstrating the integrated multifunctionalities, such as piezoresistive strain and damage sensing, and additional mechanical characterizations (particularly where delamination is more a feature of progressive damage), are planned.

Acknowledgements

The SRCT experiments were performed on beamline ID19 at the European Synchrotron Radiation Facility (ESRF), Grenoble, France. This work was supported by the Skoltech NGP Program (Skoltech-MIT joint project "Multifunctional Fusion: Life-cycle enhancements via data-driven nanoengineering of advanced composite structures") and partially supported by Airbus, ANSYS, Boeing, Embraer, Lockheed Martin, Saab AB, and Teijin Carbon America through MIT's Nano-Engineered Composite aerospace Structures (NECST) Consortium. The authors gratefully acknowledge prepreg materials donation from Hexcel.

5. References

1. De Villoria RG, Hallander P, Ydrefors L, Nordin P, Wardle BL. In-plane strength enhancement of laminated composites via aligned carbon nanotube interlaminar reinforcement. Composites Science and Technology. 2016 Sep 14;133:33-9.
2. Kalfon-Cohen E, Kopp R, Furtado C, Ni X, Arteiro A, Borstnar G, Mavrogordato MN, Sinclair I, Spearing SM, Camanho PP, Wardle BL. Synergetic effects of thin plies and aligned carbon nanotube interlaminar reinforcement in composite laminates. Composites Science and Technology. 2018 Sep 29;166:160-8.
3. Ni X, Wardle BL. Experimental investigation of interlaminar fracture micro-mechanisms of aligned carbon nanotube-reinforced aerospace laminated composites. InAIAA Scitech 2019 Forum 2019 (p. 1201).
4. Ni X, Furtado C, Fritz NK, Kopp R, Camanho PP, Wardle BL. Interlaminar to intralaminar mode I and II crack bifurcation due to aligned carbon nanotube reinforcement of aerospace-grade advanced composites. Composites Science and Technology. 2020 Apr 12;190:108014.
5. Ni X, Kalfon-Cohen E, Furtado C, Kopp R, Fritz NK, Arteiro A, Valdes G, Hank T, Borstnar G, Mavrogordato M, Spearing SM. Interlaminar reinforcement of carbon fiber composites using aligned carbon nanotubes. In21st Int. Conf. Compos. Mater 2017 Aug 20 (pp. 40-43).
6. Ni X, Furtado C, Kalfon-Cohen E, Zhou Y, Valdes GA, Hank TJ, Camanho PP, Wardle BL. Static and fatigue interlaminar shear reinforcement in aligned carbon nanotube-reinforced hierarchical advanced composites. Composites Part A: Applied Science and Manufacturing. 2019 May 1;120:106-15.
7. Ni X, Acauan LH, Wardle BL. Coherent nanofiber array buckling-enabled synthesis of hierarchical layered composites with enhanced strength. Extreme Mechanics Letters. 2020 Sep 1;39:100773.
8. Ni X, Wardle BL. Aerospace-grade advanced composites with buckling-densified aligned carbon nanotubes interlaminar reinforcement. InAIAA Scitech 2020 Forum 2020 (p. 0156).
9. Lee J, Stein IY, Kessler SS, Wardle BL. Aligned carbon nanotube film enables thermally induced state transformations in layered polymeric materials. ACS applied materials & interfaces. 2015 Apr 29;7(16):8900-5.

  doi:10.5075/epfl-298799_978-2-9701614-0-0

10. Lee J, Ni X, Daso F, Xiao X, King D, Gómez JS, Varela TB, Kessler SS, Wardle BL. Advanced carbon fiber composite out-of-autoclave laminate manufacture via nanostructured out-of-oven conductive curing. Composites Science and Technology. 2018 Sep 29;166:150-9.
11. Lee J, Daso F, Kessler SS, Wardle BL. Carbon Fiber Prepreg Composite Laminates Cured via Conductive Curing using Nanoengineered Nanocomposite Heaters.
12. Lee J, Wardle BL. Nanoengineered In Situ Cure Status Monitoring Technique Based on Carbon Nanotube Network. InAIAA Scitech 2019 Forum 2019 (p. 1199).
13. Lee J, Stein IY, Antunes EF, Kessler SS, Wardle BL. Out-of-oven curing of polymeric composites via resistive microheaters comprised of aligned carbon nanotube networks.
14. Lee J, Kessler SS, Wardle BL. Void-Free Layered Polymeric Architectures via Capillary-Action of Nanoporous Films. Advanced Materials Interfaces. 2020 Feb;7(4):1901427.
15. Lee J, Brampton CJ, Bowen CR, Wardle BL, Kim HA. Investigation of aligned conductive polymer nanocomposites for actuation of bistable laminates. In23rd AIAA/AHS Adaptive Structures Conference 2015 (p. 1725).
16. Patel P, Furtado CF, Cooper M, Acauan L, Lomov S, Akhatov I, Abaimov S, Lee J, Wardle B. Nanoengineered Glass Fiber Reinforced Composite Laminates with Integrated Multifunctionality. InProceedings of the American Society for Composites—Thirty-Sixth Technical Conference on Composite Materials 2021.
17. Patel PB, Furtado C, Lee J, Cooper M, Acauan L, Lomov SV, Akhatov IS, Abaimov SG, Wardle BL. Building Life-Cycle Enhancement Multifunctionality into Glass Fiber Reinforced Composite Laminates via Hierarchical Assemblies of Aligned Carbon Nanotubes. In AIAA SCITECH 2022 Forum 2022 (p. 0501).
18. Kopp RA. X-ray Micro-Computed Tomography and Deep Learning Segmentation of Progressive Damage in Hierarchical Nanoengineered Carbon Fiber Composites (Doctoral dissertation, Massachusetts Institute of Technology).

  doi:10.5075/epfl-298799_978-2-9701614-0-0

INSIGHT ON INDUCTION WELDING OF REACTIVE PMMA CARBON FIBER COMPOSITES

Barbara Palmieri[a], Angelo Petriccione[b], Giuseppe de Tommaso[b], Angela Pozzi[b], Michele Giordano[a], Alfonso Martone[a]

a: Institute for Polymers Composites and Biomaterials, National Research Council, Ple E Fermi, 1 80055 Portici (NA), Italy
b: Advanced Tools and Moulds srl, Zona Industriale ASI Stabilimento 13, Gricignano d'Aversa (CE).

Abstract: *This study investigates the effectiveness of fusion bonding by induction welding of carbon fibre reinforced composites (CFRC) manufactured by Elium 188-O resin. The welding characteristics of Elium composites were investigated by optimising welding parameters with preliminary Interlaminar shear tests ILSS (Inter-Laminar Shear Strength). The fracture behaviour of CF/Elium composites has been investigated through end notched flexure (ENF) to evaluate the delamination critical energy in mode II. Three joints have been investigated by lap shear tests: adhesive joint (by employing liquid Elium as adhesive), welded joint (by direct welding of adherents) and welding with an additional resin layer laid on the joining area. The results showed a higher lap shear strength for the adhesive joint compared to the induction welded one, but they are nevertheless encouraging for future investigations.*

Keywords: Thermoplastic composites (TPCs); Fracture toughness; Interlaminar fracture; Carbon fiber; Induction Welding

1. Introduction

Fibre-reinforced thermoplastic composites (FRTPCs) are widely used in several industries due to their recyclability, re-processibility and weldability properties, besides their high strength-to-weight ratio [1,2]. Thanks to molecular mobility, thermoplastics (TPs) resins flow like viscoelastic liquids if heated above the glass transition temperature, Tg or at the melting temperature, Tm (in the case of semi-crystalline polymers). Thanks to this property, they can be assembled by the fusion bonding process.

Among the different welding techniques for fusion bonding of thermoplastic composites [3], induction welding is particularly interesting for the high level of automation [4,5]. The induction heating process uses a high-powered coil with an alternating voltage to generate a magnetic field in an electrically conductive and magnetically susceptible material between adherend interfaces. In the case of carbon fibre reinforced polymers, heating can occur only due to a closed electrical path, guaranteed by the use of fabric as reinforcement [6].
While TPs are suitable for joining by fusion bonding techniques, the main disadvantage of these materials is the need for high processing temperature and pressures caused by the high viscosity of melted matrix. Therefore, novel thermoplastic monomers, viscous at room temperature thanks to their short chains, are being developed [7]. An example is the Elium© resin, recently developed by Arkema, which is based on an acrylic thermoplastic and can be also be cured at room temperature [8]. The liquid state at room temperature and the relatively low viscosity of 0.2 Pa·s make it suitable for VARI and RTM processes.

  doi:10.5075/epfl-298799_978-2-9701614-0-0

First, the induction welding characteristics of Elium© composites were investigated by optimising welding parameters with preliminary Interlaminar shear tests (ILSS). Then, the mode II interlaminar fracture of the reference samples was compared to the induction welded one, to investigate the applicability of this fusion bonding technique as a repairing process.
Finally, lap shear tests were performed to evaluate the shear strength of the three joints: adhesive joint (by employing liquid Elium as adhesive), welded joint (by direct welding of adherents) and welding with an additional resin layer laid on the joining area.

2. Materials and Methods

2.1. Materials

The laminated composite was made of carbon fibre fabric (twill 2x2) reinforced Elium® 188 resin (Arkema, Colombes Cedex, France). Elium® 188 resin undergoes radical polymerisation with benzoyl peroxide initiator (BPO, Carlo Erba Reagents, Milano, Italy) at 3% by weight.
The composite laminates were manufactured by Vacuum Assisted Resin Transfer Moulding (VARTM) technique Figure 1.b, and flat panel laminates have dimensions of 500 x 500 x 3 mm, with a stacking sequence of [0, +45, -45,90]s. Moreover, a 13 µm thick PTFE film was also inserted between the adherends before curing to introduce the pre-crack required for ENF testing Figure 1a). Samples for continuous induction welding tests were obtained by the final laminates.

a) b)

Figure 1. Manufacturing process of samples for welding tests

2.2. Induction welding equipment

Fusion bonded samples were induction welded using an experimental set-up available at the A.T.M.srl plant and provided by SINERGO (Italy). The experimental setup is depicted in Figure 2. The coil can be moved manually along the y-axis, while the movement along the x-axis is automatised. The nominal working frequency with the coil used during this study is close to 145 kHz, and the level of power can be set as a fraction of the total 2,2 kVA power. The induction welding head integrates the induction coil, a pyrometer to control surface temperature, one compacting cylinder and one cooling nozzle located on the top of the surface. Typical motion speeds are between 1 and 10mm/s. The cooled inductor is attached to a pneumatic cylinder such that pressure can be applied for consolidation after welding. The CFRP parts are placed

below the inductor. A ceramic plate is placed below the CFRP parts because, contrary to metal, the ceramic material does not heat by induction or does it attract the magnetic field and therefore has a limited effect (conduction only) on the heating of the test parts.

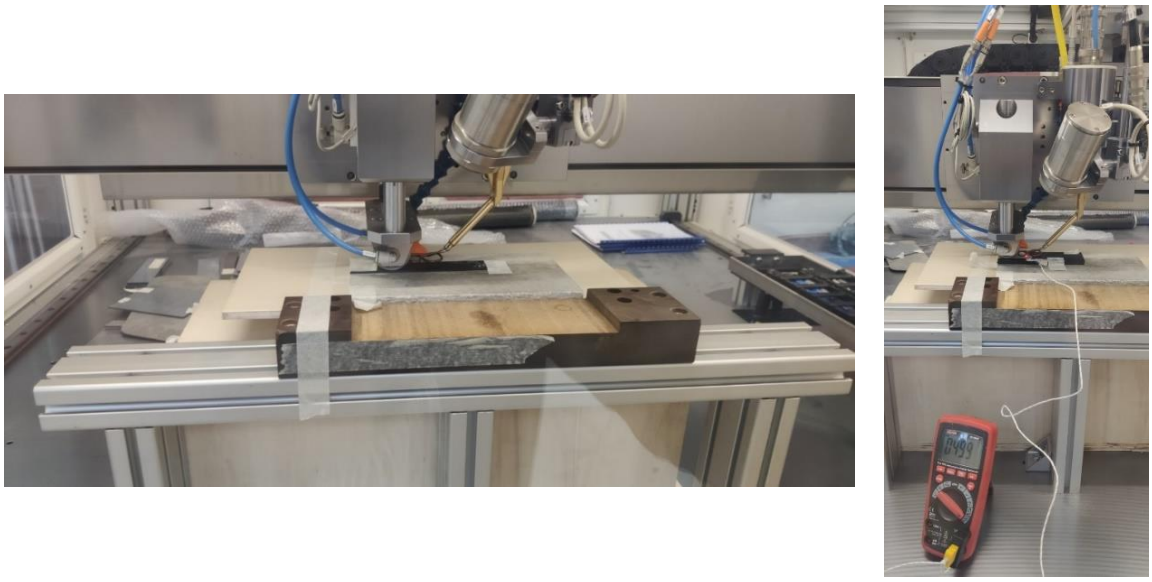

Figure 2. Induction heating system for thermoplastic composite.

The coil geometry was chosen to avoid the edge effect and, consequently, uniform the temperature distribution [9]. The coil was not in contact with the composite laminate, but it was kept at a constant distance of 2 mm from the laminate's surface. The steel roller applied a constant consolidation pressure along the welding area following the coil and simultaneously cools down the molten matrix.

3. Results and Discussion

3.1. ILSS tests

ILSS (Interlaminar Short Beam) mechanical tests were performed to determine the interlaminar shear strength of the welded composites by optimising welding parameters. The tests were carried out with a 50-kN load cell in an Instron 68TM-50 Mechanical tester, according to standard ASTM D2344. For this purpose, three (3) samples were tested for each case investigated. After the test, Nikon SMA-U stereoscopic microscope analysed the fractured SBS specimens to describe failure types. The ILSS was calculated using the classical beam theory (Bernoulli–Euler), and the maximum shear stress acting on the beam section in SBS tests was estimated as [10]:

$$F^{sbs} = \frac{3}{4}\frac{P_{max}}{b\,h} \tag{1}$$

Based on interlaminar shear strength tests, three different welding procedures were chosen to identify the process parameters that guarantee better mechanical performance. Table 1 shows the summary of the induction welding selected parameters for each of the three batches of specimens.

  doi:10.5075/epfl-298799_978-2-9701614-0-0

During the SBS tests, the failure areas, at the welding interface, were observed as shown in Figure 3. The value of ILSS obtained, reported in Table 2, is consistent with the SBS values in the literature [11].

Table 1. Welding parameters

Energy Level	Feed Rate [mm/s]	Peak Temperature [°C]	Roller Pressure [kg]	Power [%]	Air Flow Rate [lit/min]
B1	1	120	6	60	180
B2	1	120	16	90	180
B3	1	170	10	90	180

The lower value obtained by the B3 process depends on, the higher peak temperature, which may cause a matrix's degradation.

Table 2. ILSS Results of the induction welding process

Energy Level	ILSS Mean Value (MPa)	Standard Dev.
B1	38,01	1,027
B2	40.68	0,63
B3	28,22	4,49

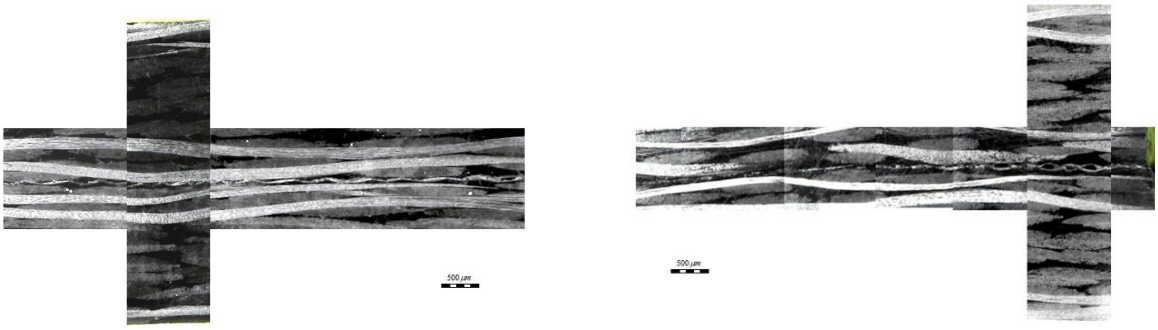

a) b)

Figure 3. Optical microscopy induction heat-sealed specimens: welding parameters B1 (a) and B2 (b)

3.2. ENF tests

Therefore, based on the results of preliminary ILSS tests, best welding parameters were chosen. The mode-II interlaminar fracture (GII_C) was obtained by performing the end notched flexure (ENF) test. The tests were carried out according to ASTM D7905 standard, and a total of five ENF specimens were prepared; the specimens had dimensions equal to 1.9 x 25.2 x 130 mm, while Figure 4 shows the schematic view of the ENF experiment.

a) b)

Figure 4. a) ENF setup; b) ENF tested sample

The Mode II energy release rate (GII_c) was calculated from Eq. (2):

$$GII_c = \frac{9a^2P\delta}{2B(2L^3 + 3a^3)} \quad (2)$$

After the ENF tests, the same samples were repaired by induction welding using the process parameters reported in Table 3.

Table 3. Process parameters for repairing

Feed Rate [mm/s]	Peak Temperature [°C]	Roller Pressure [kg]	Power [%]	Air Flow Rate [lit/min]
1	120	16	95	180

The force-displacement responses of the samples in the ENF tests are depicted in Figure 5. Analysis of the fracture toughness parameters reported in Figure 5, the values of the reference samples are consistent with the literature [12]. Therefore, a gradual decrease in the force and energy release rate (about 20%) was found for the repaired samples, indicating the possible presence of voids at the interface due to the unwelded zone.

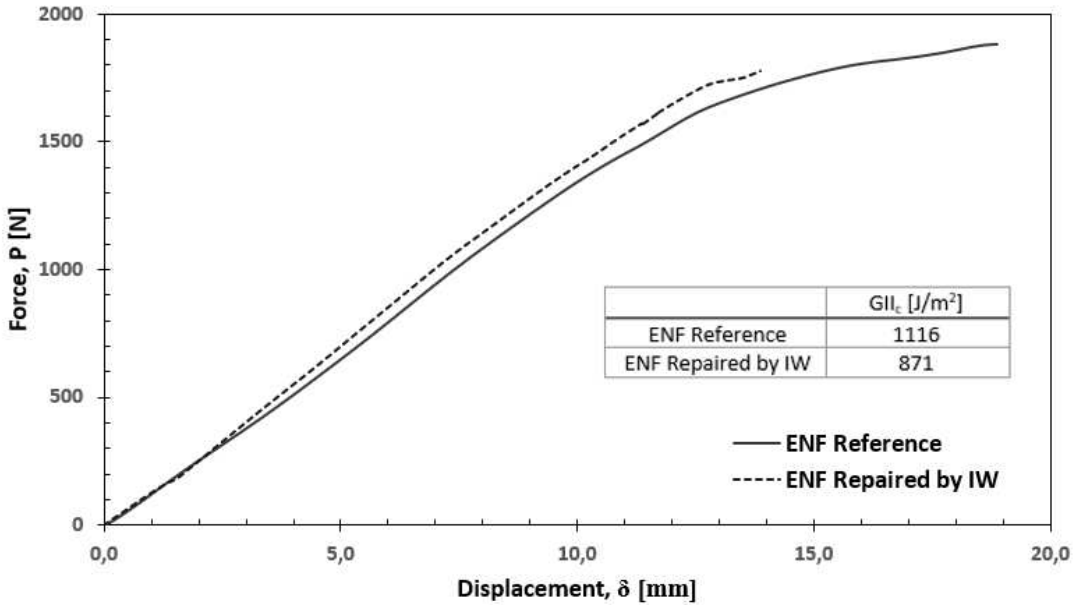

Figure 5. End Notched failure test. Comparison between the pristine sample and repaired by induction welding

  doi:10.5075/epfl-298799_978-2-9701614-0-0

3.3. Lap Shear Strength

To assess the joints' effective strength, lap shear tests were performed according to the ASTM D5868 standard. Three kinds of joints were made in different configurations identified:

- Adhesive joints were realised by employing liquid Elium as adhesive. The adhesive was cured at the room temperature under clamp pressure for a minimum of 48 hours;
- Direct induction welding joints were performed by direct welding of adherents, using the process parameters optimised by ILSS tests (Table 1. Welding parametersTable 1);
- Additional layer aided Induction welding joints. In this case, a film of Elium, about 1 mm of thickness, was cured on an adherend. Later the two adherends were induction welded.

The results of LSS are depicted in Figure 6; the adhesive bonds have higher lap-shear strength than the induction welded joints.
Figure 6 also shows the fracture surface of the adherends for each joint's configuration investigated. In the direct induction welded joints case (Figure 6. A), the trace of the bonding area is evident; this results in a good interfacial bonding and represents a cohesive failure of the sample. Also, the adhesive bonded joints Figure 6. B is characterised by a cohesive failure that indicates that the bond between the adherend and the adhesive is strongest than the adhesive strength.
The lowest value of LSS was obtained by the rich bonded joints, where the interfacial failure occurred, and indicates the poor adhesion of the adhesive to the adherends (Figure 6. C).

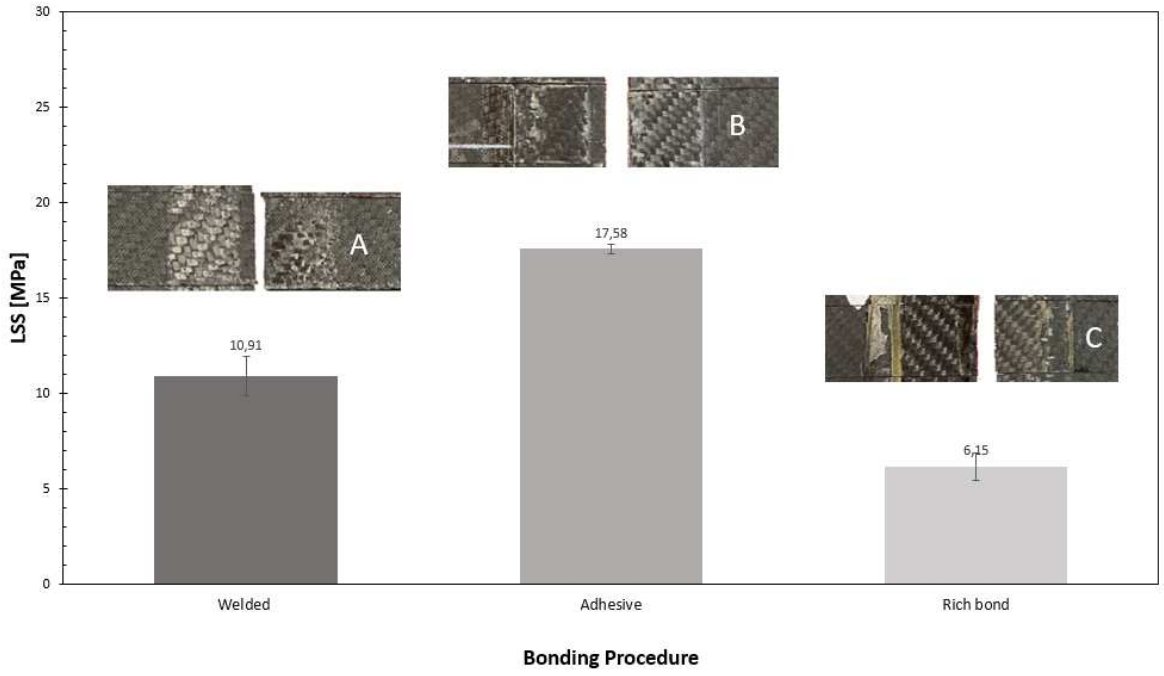

Figure 6. Lap-shear strength of various bond types.

4. Conclusion

In this work, an alternative joining method for infusible thermoplastic resins was investigated. Thermoplastic composites bonds made with standard adhesion technology was compared to induction welded bonds. Various failure modes were observed for welded joining optical

micrograph image was used to identify the failure modes. Repaired joints (by repeating ENF on tested and welded samples) show satisfactory interlaminar fracture toughness (-20%) compared to pristine material. Compared to adhesive joints, induction welding allows achieving a residual strength lower than 30%, while the repairing procedure led to a slight decrease in fracture toughness, lower than 20%. Analysis of the fracture surface highlighted the direct relationship between surface fracture failure and the LSS results. The joints with lower shear strength have shown poor interfacial bonding, probably linked to an uneven melting of the matrix.

5. Acknowledgements

This research was carried out in the framework of the project TIPA, grant number F/050076/01/X32 founded by Italian Government.

6. References

1. Shuaib NA, Mativenga PT. Energy demand in mechanical recycling of glass fibre reinforced thermoset plastic composites. J Clean Prod 2016;120:198–206. https://doi.org/10.1016/j.jclepro.2016.01.070.

2. Bhudolia SK, Gohel G, Joshi SC, Leong KF. Manufacturing Optimization and Experimental Investigation of Ex-situ Core-shell Particles Toughened Carbon/Elium® Thermoplastic Composites. Fibers Polym 2021;22:1693–703. https://doi.org/10.1007/s12221-021-0819-y.

3. da Costa AP, Botelho EC, Costa ML, Narita NE, Tarpani JR. A review of welding technologies for thermoplastic composites in aerospace applications. J Aerosp Technol Manag 2012;4:255–65. https://doi.org/10.5028/jatm.2012.04033912.

4. Palmieri B, Nele L, Galise F. Numerical modeling and experimental validation of thermoplastic composites induction welding. AIP Conf Proc 1960;050013. https://doi.org/10.1063/1.5034886.

5. Lionetto F, Morillas MN, Pappadà S, Buccoliero G, Fernandez Villegas I, Maffezzoli A. Hybrid welding of carbon-fiber reinforced epoxy based composites. Compos Part A Appl Sci Manuf 2018;104:32–40. https://doi.org/10.1016/j.compositesa.2017.10.021.

6. Ahmed TJ, Stavrov D, Bersee HEN, Beukers A. Induction welding of thermoplastic composites—an overview. Compos Part A Appl Sci Manuf 2006;37:1638–51. https://doi.org/10.1016/J.COMPOSITESA.2005.10.009.

7. van Rijswijk K, Bersee HEN. Reactive processing of textile fiber-reinforced thermoplastic composites – An overview. Compos Part A Appl Sci Manuf 2007;38:666–81. https://doi.org/10.1016/j.compositesa.2006.05.007.

8. Palmieri B, Petriccione A, Tommaso G De, Giordano M, Martone A. An Efficient Thermal Cure Profile for Thick Parts Made by Reactive Processing of Acrylic Thermoplastic Composites 2021.

9. Rudolf R, Mitschang P, Neitzel M. Induction heating of continuous carbon-fibre-reinforced thermoplastics. Compos Part A Appl Sci Manuf 2000;31:1191–202. https://doi.org/10.1016/S1359-835X(00)00094-4.

10. Precision WS. Standard Test Method for Short-Beam Strength of Polymer Matrix Composite Materials. Annu B ASTM Stand 2011;00:1–8. https://doi.org/10.1520/D2344.

11. Bhudolia SK, Perrotey P, Joshi SC. Optimizing polymer infusion process for thin ply textile composites with novel matrix system. Materials (Basel) 2017;10. https://doi.org/10.3390/ma10030293.

12. Barbosa LCM, Bortoluzzi DB, Ancelotti AC. Analysis of fracture toughness in mode II and fractographic study of composites based on Elium® 150 thermoplastic matrix. Compos Part B Eng 2019;175:107082. https://doi.org/10.1016/j.compositesb.2019.107082.

LITZ WIRE-BASED MULTIFUNCTIONAL COMPOSITES FOR MANAGING THERMAL AND MECHANICAL LOADS WITHIN ELECTRICAL SYSTEMS

Christof Piefke[a], Simon Bickerton[a], Piaras Kelly[a,b], Tom Allen[a]

a: Centre for Advanced Composite Materials, Department of Mechanical Engineering, The University of Auckland, Auckland, New Zealand
E-mail: cpie420@aucklanduni.ac.nz
b: Department of Engineering Science, The University of Auckland, Auckland, New Zealand

Abstract: *Inductive power transfer (IPT) technology can be used for convenient and straightforward charging of stationary or moving electric vehicles. Primary charging units embedded in pavements incorporate Litz wire to achieve low transmission losses. As it covers most of a charging unit, the multifunctional composite of Litz wire and potting compound defines the structural and thermal response of an IPT charging pad. This research investigates the impact of wire and potting material selection, and manufacturing methods on the infiltration and structural characteristics of Litz wire embedded in an epoxy potting compound. Fluorescent additive Coumarin 1 was added to samples to enable infiltration to be visually analysed from images captured under UV light. Compression tests were conducted on epoxy-Litz wire composites to characterise the compressive modulus and strength. The discussion showed a correlation between Litz wire infiltration and compressive modulus. The structural capabilities of samples with the highly-filled and thermally conductive epoxy were improved through process modification.*

Keywords: Multifunctional composite; Litz wire; Epoxy; Infiltration; Compressive stiffness

1. Introduction

The shift from internal combustion engine to electrically-propelled vehicles can reduce greenhouse gas emissions and slow down man-made climate change. IPT (inductive power transfer) charging technologies are a simple approach to tackle the significant drawbacks of electric vehicles (EV) such as range anxiety and confusing charging systems. If used in roads, dynamic IPT charging systems can reduce the battery size due to constant charging or the use of EVs as temporary energy storage. IPT charging units embedded in electrified roads are subjected to structural (traffic), thermostructural (coefficient of thermal expansion mismatch), and thermal (heat losses and climate) loads. These charging units consist of fragile electric and electromagnetic components that must be protected to ensure a high transmission efficiency over at least a decade. The primary coil is made of Litz wire to reduce losses due to the skin and proximity effect. Better integration of Litz wire into the pad structure with optimised manufacturing methods and potting compounds could improve the structural and thermal behaviour of IPT charging units.

Various manufacturing methods and materials of potted Litz wire have been analysed to improve the infiltration and, subsequently, the thermal capabilities of electrical machines. Richnow et al. [1] studied the thermal behaviour of potted Litz wire in stators using impregnation methods such as variations of dipping and trickling. Nategh et al. [2] manufactured several

  doi:10.5075/epfl-298799_978-2-9701614-0-0

potted motor prototypes using a simple casting approach with highly-filled epoxy, polyurethane, and silicone potting compounds. The potted motors showed a vastly improved thermal behaviour compared to non-potted designs. Shin et al. [3] developed a modified vacuum infusion method for an improved infiltration of Litz wire used in high power density motors in electrified aircraft. Imura et al. [4] studied the structural behaviour of non-potted Litz wire coils in different casing materials embedded in the road for IPT application.

The structural characterisation and optimisation of the multifunctional composite comprised of potted Litz wire have not been presented in existing research. A method to achieve a thermally conductive Litz wire composite showing high compressive stiffness has not been developed.

This paper studies the degree of infiltration and compressive stiffness of a multifunctional composite comprised of Litz wire and epoxy potting compound. Composite samples were potted under ambient and elevated temperatures using both filled and unfilled epoxies. A method was developed to investigate the infiltration of potted Litz wire samples. The fluorescent dye Coumarin 1 was added to the epoxy potting system to increase the visibility of the potting under UV light, especially for opaque highly filled epoxies. Images of the cross-section were taken and processed in ImageJ. A modified compression testing method ASTM D695 was applied to analyse the compressive stiffness of Litz wire and epoxy composites. A correlation was investigated between used materials, manufacturing parameters, infiltration, and compressive behaviour.

2. Materials and Methods

2.1 Materials and manufacturing

The analysed samples comprised a Litz wire embedded unfilled or filled, thermally more conductive, epoxy potting compounds. Two epoxy resins with different filler contents were chosen to emphasise the impact of viscosity (inherent with a high thermal conductivity filled compound) on the Litz wire infiltration. The epoxy West System 105/206 is generally used for liquid composite moulding processes, in scenarios where no increased thermal conductivity and electrical insulation are needed. The viscosity at a temperature of 22°C of the mixed system is 725 mPas [5]. In contrast, the potting compound Electrolube ER2188 is used to encapsulate electronic components due to its increased thermal conductivity, flame retardancy, and electrical insulation capabilities. The filler content of around 50 % leads to mixed system viscosity at a temperature of 23°C of 9000 mPas [6].

The Litz wire consists of six twisted bundles, which comprise of five sub-bundles of twisted individually-insulated strands. Litz wires for this research were purchased from Elektrisola GmbH & Co KG. As shown in Table 1, a type of Litz wire was utilised with 800 strands and a nominal diameter of 4.2 mm. The strands comprised an electrolytic tough pitch copper core with a diameter of 0.1 mm and polyurethane insulation of 0.005 mm thickness. The purchased Litz wire is spirally served with nylon filaments for improved geometrical stability and simple handling. The serving was manually removed for some samples.

Table 1: Specifications of Litz wire

No of strands	Strand diameter (mm)	Thickness insulation (mm)	Average fill factor	Diameter Litz wire (mm)
800	0.1	0.005	0.74	4.2

  doi:10.5075/epfl-298799_978-2-9701614-0-0

The samples were manufactured using a casting process under ambient pressure. The potting compounds were mixed following the datasheet instructions and degassed for five minutes to reduce the occurrence of voids in the samples. The Litz wire segments were hand-tensioned and fixated with spring clamps to the casting mould to reduce undulations that could compromise the structural characteristics. The casting process was undertaken at an ambient temperature of 21°C (+/- 1°C) or an elevated temperature of 40°C (+/- 1°C). At elevated temperature, the mould and resin were preheated, and samples were cured in an oven to ensure a constant temperature. The samples were post-cured at ambient temperature for minimum 14 days to achieve consistent structural characteristics. An overview of all sample parameters is given in Table 2.

Table 2: Overview of sample parameters

Potting compound	Potting temperature	Litz wire serving
WS 105/206	21°C	Yes
ER2188	40°C	No

2.2 Method infiltration analysis

A method was developed to visually quantify the infiltration of embedded Litz wire samples. Preliminary analysis of images taken with a light microscope showed a lack of contrast between the epoxy and uninfiltrated areas. To increase the visibility of areas filled with epoxy, the fluorescent dye Coumarin 1 was added to the potting compound (0.5 % of total weight) prior to casting. Coumarin 1 emits visible light under UV light due to the peak excitation wavelength of 360 nm and the emission wavelength 450 nm [7]. The samples were cut into 20 mm sections perpendicular to the Litz wire on a Buehler Isomet 1000 precission cutter with an Allied High Tech Products Inc. diamond metal bond wafering blade to reduce plastic deformation of soft copper. The cross-sectional surfaces were consecutively polished with 600, 1200, 2000 grit sandpaper under a constant water flow.

As shown in Figure 1, the image acquisition setup consisted of a Canon Eos 800D camera and a Canon EF-S 60 mm macro lens mounted on a tripod. The images were taken with an aperture of f/4, an exposure time of 30 seconds, and ISO set to 100 to maintain contrast and sharpness. The samples were lit with a UV light set to the wavelength of 365 nm.

  doi:10.5075/epfl-298799_978-2-9701614-0-0

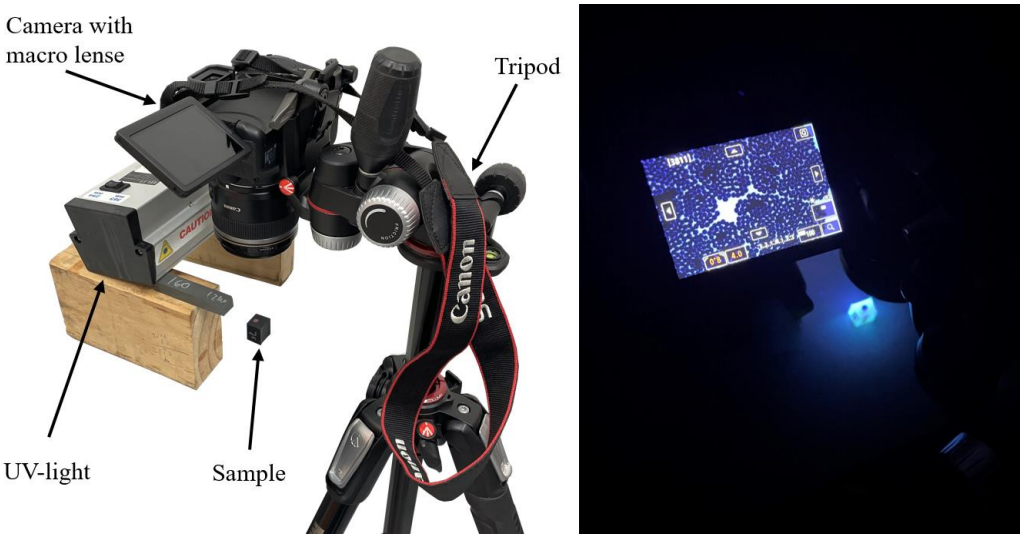

Figure 1: Setup for the acquisition of images of the sample cross-section under UV-light

An algorithm in the image-processing software ImageJ was developed to quantify the potting infiltration. First, the colour images were converted to binary images using the thresholding method. Second, a watershed separation algorithm was applied to distinguish between strands that are in contact. Finally, embedded strands were counted with the particle analysis tool. The infiltration was calculated by forming a fraction from embedded strands and the total number of strands in a Litz wire.

2.3 Method compression testing

The modulus in fibre direction under compression loading of variously embedded Litz wire samples was determined by conducting tests following a modification of the standard ASTM D695 [8]. The samples were manufactured as described in chapter 2.1. Sample dimensions were produced to achieve a fibre volume fraction of 26 %. The sample dimensions were 5.4 mm x 5.4 mm x 60 mm. To achieve flat surfaces, the samples were cut perpendicular to the Litz wire on a Buehler Isomet 1000 precission cutter with an Allied High Tech Products Inc. diamond metal bond wafering blade.

The experiments were conducted on an Instron 5567 universal testing machine with a 30 kN load cell. The load was applied with a compression tool consisting of two flat and parallel surfaces. The testing machine was set to speed-control with 1.3 mm/min crosshead speed. The strain was measured using an Instron axial clip-on extensometer with a gauge length of 25 mm. The maximum stress and the stress-strain diagram were recorded to calculate the compressive strength and the compressive modulus.

3. Results and Discussion

3.1 Infiltration analysis

As shown in Figure 2, images of fluorescent samples give a qualitative understanding of the infiltration with epoxy potting compounds. Areas with a strong contrast between dark strands and bright potting compounds are well infiltrated. Dark spots, more extensive and less defined than strands, indicate a bad infiltration. Samples potted with ER2188 showed a poorer penetration than West Systems 105/206. Samples with non-served Litz wire were better

  doi:10.5075/epfl-298799_978-2-9701614-0-0

infiltrated. However, a loss of geometrical definition of the bundles and strand density could be observed.

The images were processed in an ImageJ algorithm to quantify the infiltration of potting compound. As shown in Table 3, ER2188 and 105/206 samples showed 14 % and 86 % infiltration with served Litz wire. The removal of the Litz wire serving of ER2188 and 105/206 samples led to an increased infiltration of 41% and 97 %. A comparison of the infiltration of samples with Litz wire potted at 21°C and 40°C is given in Table 4. Samples potted at 21°C showed an infiltration of 15 % (ER2188) and 92 % (WS 105/206). An increase in potting temperature to 40°C leads to increased infiltration for ER2188 samples to 40 % and no change for WS 105/206 samples.

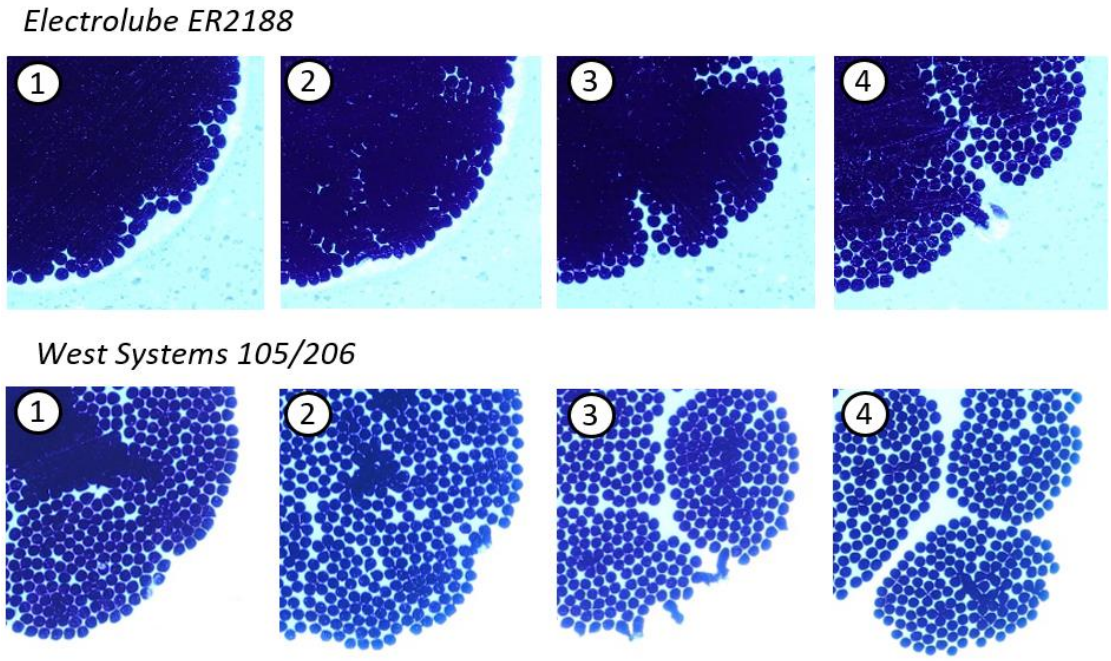

Figure 2 : Cross-sectional images of litz wire type A embedded in Electrolube ER2188 and West Systems 105/206 potting compound. (1) Ambient temperature, served litz wire; (2) elevated temperature, served Litz; (3) ambient temperature, not served Litz wire; (4) elevated temperature, not served Litz

Table 3: Infiltration of samples with served Litz wire vs not served Litz wire

Resin	Litz wire serving	Infiltration (%)	Standard deviation (%)	Number of samples
ER2188	Yes	14	2	6
	No	41	12	6
WS 105/206	Yes	86	12	9
	No	97	2	6

Table 4: Infiltration of samples potted at 21°C vs 40°C

Resin	Potting Temperature	Infiltration (%)	Standard deviation (%)	Number of samples
ER2188	21°C	15	2	6
	40°C	40	12	6
WS 105/206	21°C	92	6	8
	40°C	92	12	7

3.2 Compression testing

The stress-strain curve behaviour and compressive modulus of samples comprising Litz wire embedded in ER2188 and WS 105/206 potting compounds were analysed. As shown in Figure 3, all sample types showed a linear-elastic stress-strain response until 0.3 % strain. The curve flattened in the transition to the plastic area until the failure. The sample failures were initiated by cracking of the epoxy matrix or interfacial failures between epoxy and Litz wire, which led to the final buckling failures.

The elastic response was analysed using the chord modulus between 0.1 % and 0.3 %. Samples potted in ER2188 showed a mean compressive modulus of 6371 MPa (standard deviation of 990 MPa, ambient temperature, serving), 8105 MPa (1516 MPa, 40°C, serving), 8053 MPa (1288 MPa, ambient temperature, no serving), and 10679 MPa (2746 MPa, 40°C, no serving). Samples embedded in WS 105/206 had a mean compressive modulus of 9442 MPa (standard deviation of 876 MPa, ambient temperature, serving), 8814 MPa (615 MPa, 40°C, serving), 9958 MPa (977 MPa, ambient temperature, no serving), and 10854 MPa (1124 MPa, 40°C, no serving).

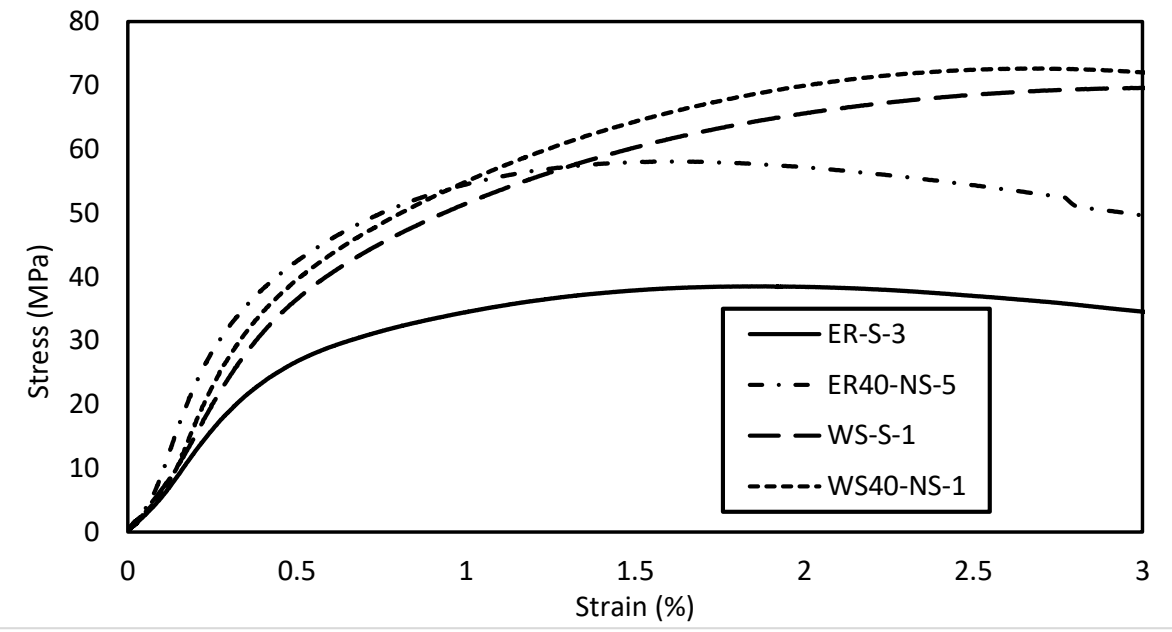

Figure 3 : Stress-strain curves of variously treated samples embedded in ER2188 and WS 105/206

As shown in Figure 4, samples potted in ER2188 showed an increase of compressive modulus with raising infiltration. By potting at elevated temperature and removing the Litz wire serving,

the infiltration was improved to 60 % and the average compressive modulus was increased by 40 % to 10679 MPa compared to samples potted at ambient temperature with served Litz wire. As shown in Figure 5, samples embedded in WS 105/206 were less affected by different manufacturing methods. The best-infiltrated sample group (elevated temperature, no serving) had an improved compressive modulus of 15 % compared to the least infiltrated sample group. However, the difference in infiltration between the weakest and strongest sample groups is 52 % and 12% for ER2188 and WS105/206, respectively.

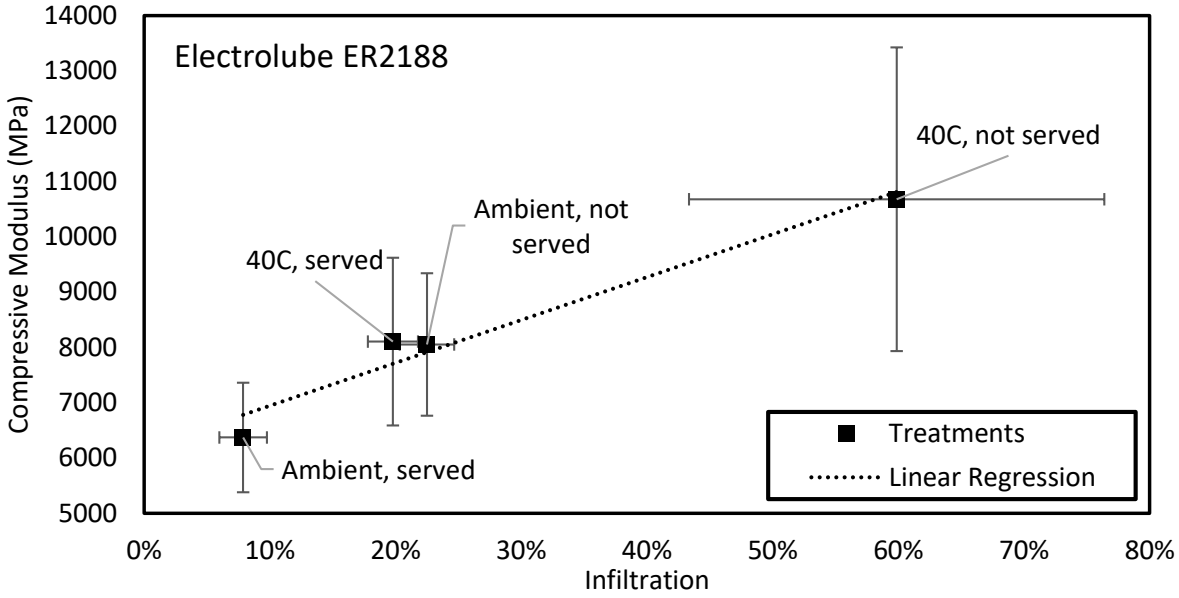

Figure 4: Compressive modulus vs infiltration of ER2188 samples

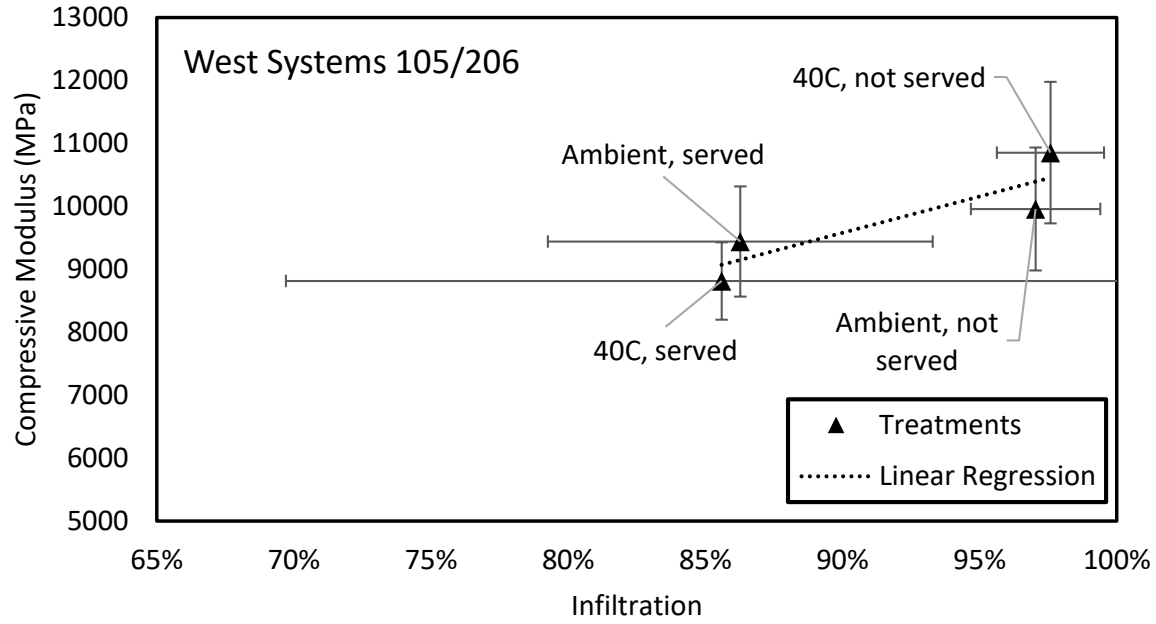

Figure 5: Compressive modulus vs infiltration of WS 105/206 samples

4. Conclusion

This research has focused on the infiltration and structural capabilities of the multifunctional composite comprised of an epoxy potting compound and Litz wire. Several manufacturing parameters, a low viscous potting system, West Systems 105/206, and a high viscous, thermally more conductive epoxy, Electrolube ER2188, have been characterised. The infiltration has been visually analysed using the fluorescent dye Coumarin 1 as a contrast enhancer and an algorithm in ImageJ for quantification. Samples potted in West Systems 105/206 show a higher infiltration than Electrolube ER2188. The infiltration with Electrolube ER2188 can be improved by increasing the potting temperature and removing the nylon Litz wire serving. The compressive modulus has been characterised. A correlation between compressive modulus and infiltration into the Litz wire has been shown. It would be possible to achieve the same structural performance in a roadway embedded inductive power transfer pad with the thermally conductive Electrolube ER2188 as the West System 105/206 by applying the proposed changes of manufacturing parameters.

Acknowledgements

The authors wish to thank the financial support by New Zealand Ministry of Business, Innovation and Employment through MBIE Endeavour Fund UOAX1711.

5. References

[1] J. Richnow, P. Stenzel, A. Renner, D. Gerling, and C. Endisch, “Influence of different impregnation methods and resins on thermal behavior and lifetime of electrical stators,” *2014 4th Int. Electr. Drives Prod. Conf. EDPC 2014 - Proc.*, 2014, doi: 10.1109/EDPC.2014.6984406.

[2] S. Nategh, A. Boglietti, D. Barber, Y. Liu, and R. Brammer, “Thermal and Manufacturing Aspects of Traction Motors Potting: A Deep Experimental Evaluation,” *IEEE Trans. Energy Convers.*, vol. 35, no. 2, pp. 1026–1035, 2020, doi: 10.1109/TEC.2020.2966606.

[3] E. S. E. Shin, “Improved potting of Litz Wires for High Power Density Electric Motor,” no. i, pp. 1–11, 2021, doi: 10.2514/6.2021-3292.

[4] T. Imura, K. Hanawa, K. Sasaki, and N. Abe, “Coil Performance and Evaluation of Pavement Durability of Dynamic Wireless Power Transfer System using Ferrite-less and Capacitor-less Coil for Road Construction Methods,” 2021.

[5] “Data Sheet West Systems 105 Epoxy Resin / 206 Slow Hardener.” p. 1, 2014, [Online]. Available: https://www.westsystem.com/wp-content/uploads/105-206-Epoxy-Resin.pdf.

[6] “Data Sheet Electrolube ER2188.” pp. 1–2, 2019, [Online]. Available: https://electrolube.com/wp-content/uploads/2019/11/ER2188_p4agfz.pdf.

[7] M. Taniguchi and J. S. Lindsey, “Database of Absorption and Fluorescence Spectra of >300 Common Compounds for use in PhotochemCAD,” *Photochem. Photobiol.*, vol. 94, no. 2, pp. 290–327, 2018, doi: 10.1111/php.12860.

[8] ASTM International, “ASTM D695-15 Standard Test Method for Compressive Properties of Rigid Plastics.” pp. 1–8, 2015, doi: 10.1520/D0695-15.2.

SHIFT FACTOR DEPENDENCE ON PHYSICAL AGING AND TEMPERATURE FOR VISCOELASTIC RESPONSE OF POLYMERS

Stephanie, Gonçalves Nunes[abc], Sibin, Saseendran[ad], Patrik, Fernberg[a], Nazanin, Emami[a], Antonella, Esposito[e], Sandro,Campos Amico[c], Janis, Varna[ab]

a: Luleå University of Technology, Department of Eng. Sciences and Mathematics, Sweden
b: Riga Technical University, Institute of Mechanics and Mechanical Engineering, Latvia – stephanie.goncalves-nunes@rtu.lv
c: Federal University of Rio Grande do Sul, Materials Engineering Department, Brazil
d: Research Institutes of Sweden, Department of Polymer Materials and Composites, Sweden
e: Normandie Univ, UNIROUEN, INSA Rouen, CNRS, Groupe de Physique des Matériaux, France

Abstract: *As polymeric resins are used as matrix in reinforced composites, understanding of their viscoelastic-viscoplastic response is critical for long-term performance design. However, during service life, thermosets are not in a thermodynamic equilibrium state, resulting in physical aging, which affects failure and viscoelastic (VE) properties, becoming a concern for industries. In this paper, an alternative methodology for testing and parameter determination for aging polymer, at different temperatures (T_A) and times (t_A), is proposed. The experimental data analysis was performed using a Schapery's type thermo-aging-rheologically simple VE model with constant coefficients in Prony series and the effect of temperature and aging included by two shift factors (a_T, a_A). Results showed that the shift factor can be presented as the product of shifts a_T and a_A. Furthermore, for short t_A the change rate of the a_A with t_A does not depend on T_A, whereas for long t_A at high T_A the rate increases.*

Keywords: Physical aging; viscoelasticity; stress relaxation; shift factors; numerical simulations

1. Introduction

As polymeric resins are broadly used as matrix in reinforced composites for high performance applications, understanding of their viscoelastic-viscoplastic response is critical for long-term performance design. However, during service life, thermoset polymers are mostly used below their glass transition temperature (T_g) and, therefore, they are not in a thermodynamic equilibrium state since the local molecular motions are temperature and time dependent, resulting in a phenomenon known as physical aging [1].

Physical aging, which in out-of-equilibrium amorphous polymers proceeds over years during their service life (simultaneously with long-term creep and stress relaxation), affects failure and viscoelastic (VE) properties, and, consequently, becomes a concern for industries [2]. Therefore, long-term behavior of a VE material cannot be considered without taking physical aging into account.

Physical aging is a reversible process and the amplitude of the change in mechanical properties upon aging into equilibrium depends on the magnitude of the initial departure from equilibrium [3,4]. Therefore, usually the specimen is first annealed at temperature above T_g (to erase the thermal history), and then quenched at temperature below T_g. After, aging is performed for different aging times (t_A) [1,5,6]. Since the aging may accelerate as the service temperature approaches the T_g, for a proper engineering design the physical aging effect needs to be

  doi:10.5075/epfl-298799_978-2-9701614-0-0

considered, especially when high-temperatures are required. Such constantly evolving properties may strongly impair the long-term viscoelastic behavior through a shift in the time scale [5,7].

Researchers have been using the concept of effective time theory (ETT) to analyze VE experiments (i.e. creep or stress relaxation) and using the time-temperature-aging superposition principle to explain the data [5,6,8]. The ETT concept, proposed by [7], assumes that all retardation times are equally affected by aging with a constant aging shift rate. Through this concept, it is possible to predict a data and analyze the material response. However, the mechanical test time needs to be shorter than the aging time before the test, to ensure that no significant aging will occur during each test.

In this research, an alternative methodology for testing and parameter determination for aging polymer is proposed. The experimental aging data analysis for an epoxy material was performed using a Schapery's type thermo-aging-rheologically simple (T-A-R simple) VE model with constant coefficients in Prony series (C^m) and the effect of temperature and aging included by the product of two shift factors, one responsible for aging (a_A) and the other one for testing temperature (a_T).

2. Material Model

2.1 Thermo-aging-rheologically simple viscoelastic model

In this paper, a modified Schapery's thermodynamically consistent linear viscoelastic (VE) material model is used (Eq (1) (1-D tensile loading). In the used thermo-aging-rheologically simple (T-A-R simple) model, where the parameters β and T represent the aging state and the mechanical test temperature, respectively, which may be changing during the loading history. Viscoplastic (VP) effects are not considered.

$$\sigma(t) = E_r\varepsilon + \int_0^t \Delta C(\psi - \psi')\frac{d(\varepsilon)}{d\psi'}d\psi' \tag{1}$$

$$\Delta C(\psi) = \sum_m C^m exp\left(-\frac{\psi}{\tau_m}\right) \tag{2}$$

where, τ_m are relaxation times and C^m coefficients in Prony series, which are constants and are not affected by temperature nor the aging state. ψ is the reduced time. Shift factor a in Eq. (3) is dependent on T and β. It is assumed and validated in this work that a can be written as a product of a T-dependent and an aging(A)-dependent term. Such hypothesis proved to have sufficient accuracy for practical applications [9].

$$\psi(t) = \int_0^t \frac{1}{a(\beta, T)}d\zeta = \frac{t}{a_A(\beta)a_T(T)} \tag{3}$$

In case of an idealized relaxation test (strain ε_0 at $t = 0$), a Heaviside step function is applied and the stress relaxation, according to Eqs. (1), (2) and (3), is given by

$$\sigma_{rel} = \varepsilon_0\left[E_r + \sum_m C^m exp\left(-\frac{\psi}{\tau_m}\right)\right] \quad , \quad \psi = \frac{t}{a_A a_T} \tag{4}$$

In Eq. (4), a_T and a_A depend on the constant values T and β. The expression in brackets is the stress relaxation function, where its value at $t = 0$ is the epoxy glassy modulus.

  doi:10.5075/epfl-298799_978-2-9701614-0-0

For loading-holding (L-H) tests, as the strain increases from zero to ε_0 over finite time t_1, the strain cannot be applied as a Heaviside step-function (Eq. 4). Therefore, the L(t_1)-step, as the strain linearly increases from zero to ε_0 during time interval $0 < t \leq t_1$, is given by

$$\sigma(t) = \left[E_r \frac{t}{t_1} + \frac{a_T a_A}{t_1} \sum_m C^m \tau_m \left(1 - exp\left(-\frac{t}{\tau_m a_T a_A}\right)\right)\right] \varepsilon_0, \ \varepsilon = \varepsilon_0 \frac{t}{t_1}, \ 0 < t \leq t_1 \qquad (5)$$

and for the H(t^*)-step of length t^*, where the strain is held constant, $\varepsilon = \varepsilon_0$, is given by

$$\sigma(t) = \left[E_r + \frac{a_T a_A}{t_1} \sum_m C^m \tau_m exp\left(-\frac{t}{\tau_m a_T a_A}\right)\left(exp\left(\frac{t_1}{\tau_m a_T a_A}\right) - 1\right)\right] \varepsilon_0, \quad t \geq t_1 \qquad (6)$$

3. Material, manufacturing and test routines

3.1 Material and manufacturing

To carry out the proposed study an epoxy system Araldite® LY 5052/Aradur® HY 5052, provided by Hunstsman, was used. This cold-curing resin system presents a low viscosity and long pot-life, what provide an easy impregnation of reinforcement materials.

For the manufacture of the samples, through casting process, epoxy was mixed with the hardener, in a proportion of 100:38 by weight, for 5 min and degassed for ≅ 12 min in a vacuum system to reduce the trapped air content. Then, the mix was poured into a silicon rubber mold and compressed between two metallic plates lined with Teflon fabric to allow easy demolding. The curing started as soon as the resin was poured into a silicone mold, at room temperature (RT) ≅ 23 °C. After 24 h the samples were demolded and post-cured at 105 °C for 4 h, to obtain fully cured (FC) samples (degree of cure α=0.992, determined by Kamal's model [10]). During the curing process, a type K thermocouple, connected with a pico logger data acquisition module TC-08, was inserted in the uncured resin in the mold and the T vs. t was recorded. Temperature fluctuations (±1℃) around the nominal curing temperature were recorded. The manufactured FCRT-24h specimen size, after grinding and polishing, was ≅ 160 x 15 x 4 mm^3.

3.2 Thermal rejuvenation of the epoxy samples

As the samples have different manufacturing dates and storage times, and since physical aging will accumulate as soon as the sample is below T_g, a thermal treatment known as "rejuvenation", achieved by annealing, was used to erase the thermal history of the amorphous epoxy before start any experimental program. Therefore, as physical aging is a thermoreversible phenomenon, any previous aging occurred when the polymer was stored (bellow T_g) could be erased.

To the rejuvenation process, a sample was assembled in an Instron type Universal 3366 machine, with load cell of 10 kN and mechanical grips. The specimen was then loaded at a very low load (2 N, to prevent buckling during thermal expansion), heated above T_g (T = T_g + 20 °C), using an Instron environmental chamber 3119-406, and isothermal holding for 40 min at T=150 °C (as recommended by [3] and [7]). After, the chamber was opened and the sample was cooled down to a room temperature RT≅ 23 °C. The accuracy of the temperature displayed on the control panel of the chamber was checked with a thermocouple, placed close to the sample, providing a T vs. t curve for each thermal rejuvenation process (heating and cooling steps).

  doi:10.5075/epfl-298799_978-2-9701614-0-0

This process was performed for all samples used in this research and every time when the ageing temperature (T_A) was changed for each tested sample. For some specimens the annealing and the whole test program was repeated several times and during the whole process the specimen was never removed from the testing machine or grips released.

3.3 Quasi-static tensile tests

After rejuvenation, aiming to investigate the effect of physical aging on the viscoelastic properties of an epoxy material, specimens, with gauge length 100 mm, were aged at temperature T_A and the VE response after certain aging time t_A was measured in loading-holding (L-H) tests. All tests were performed using an Instron machine, type Universal 3366, with load cell of 10 kN, acquisition rate of 1 Hz and mechanical grips. To prevent sample slipping in the area and, also, sliding of the extensometer, pieces of sandpaper were used. Axial strain was measured using a standard Instron 2620-601 dynamic extensometer, with 50 mm gauge length, which was attached to the sample by means of metallic bands. Using an Instron environmental chamber 3119-406 was possible to test the samples at various L-H testing temperatures (T) and T_A.

To parameters identification (C^m, a_A and a_T) in the viscoelastic model, different test routines were implemented:

a) L-H tests at different T_A and t_A

- the T_A was selected, grips were closed, extensometer attached and the machine was switched to load-control mode. A very low (2 N) constant pre-load was applied (to prevent buckling) and held until the end of the whole temperature-aging-mechanical test program. The stress from the pre-load is about 0.1% of the maximum stress in the L-H test. It took about 20 min to reach and stabilize to the set testing T and to start the first L-H test. Therefore, it was estimated that at this time instant the specimen was aged t_A for ≅20 min.
- Then, a strain-controlled L-H test was superimposed to the pre-load. During data reduction the pre-load was subtracted from the load measured in the L-H ramp. The L-H test was performed at T equal to aging temperature T_A=70 to 110 °C without interrupting the aging process and it consisted of two steps: i) in the L-step the strain increased linearly with time, reaching the final value $\varepsilon_0 = 0.5\%$ in $t_1 = 60\ s$; ii) H-step, where strain ε_0 was held constant for a time t^* and stress relaxation was recorded. The holding time t* was selected based on the reached t_A: during the L-H test the aging state should not change, since a constant value of a_A during the test is assumed in Eqs. (5)-(6). This means that with increasing t_A a larger holding time t* could be used. After, the specimen was unloaded to the pre-load 2 N level, at constant strain rate (0.5%/min).

During the test and during the following strain recovery the aging continued. The time to the next L-H test was long enough to allow for VE recovery and for additional aging.

The final t_A was around 5,000 min, except for one specimen at 100 °C that was aged for more than 10,000 min. At the end of the aging test, the additional effect of aging on the VE response was almost negligible, however, it does not mean that the equilibrium was reached.

After the final aging step, as the L-H showed small changes of the max stress comparing with the previous test, the specimen was considered “fully aged” and no changing in the aging state of

the specimen was considered during the following tests. Nevertheless, one more aging test was performed in the "fully aged" sample for $t_A = 1{,}000$ min to obtain one extra data "point" before the next testing program started. The "fully aged" state will be used as reference ("A-ref").

b) L-H for aged specimens

When the sample was close to equilibrium ("fully aged"), L-H tests at several T was performed for master curve construction, and shift factor a_T and Prony coefficients C^m determination. To avoid additional aging, the T used were below the used T_A and the t^* used in the H(t^*)-step was 60 or 120 min. For example, for a specimen aged at $T_A = 80$ ℃ testing was at 40, 60 and 80℃.

For the used epoxy and test conditions, the mechanical response is reversible and strains fully recover in a time interval ≥10t* [9]. When appropriate, the strain recovery was accelerated performing recovery at 10 ℃ higher than the test T, but only after finding that everything is reversible and repeatable. This condition is requested for using Eqs. (5)-(6). The enhanced T recovery was not used in tests where the t_A was the parameter.

At each T_A one to three specimens were tested and they will be identified in the text as "SpN" (N = 1, 2, 3, …), and when relevant testing T, t_A and T_A also will be included in legends.

4. Results and discussion

4.1 Mechanical response in constant strain rate tensile tests

As, for the chosen methodology, all mechanical tests for the same sample were performed without removing the sample from the machine grips, the results showed to be very stable, with a small scattering in-between repeated test. For example, sample Sp9 tested at 40 ℃ reached during uploading to 0.5% strain (strain rate 0.5%/min) a maximum stress ($\sigma_{0.5\%}$) of 13.75 ±0.01 MPa and at 60 ℃ a $\sigma_{0.5\%}$ = 11.67 ±0.00 MPa.

The efficiency of the rejuvenation process (section 3.2) regarding the repeatability of stress relaxation in L-H tests was also checked. For sp10, aged for $t_A \approx 440\ min$ at T_A =80 ℃, the average between annealing 1 and 2 was $\sigma_{0.5\%}$=8.86 ±0.02 MPa, and for $t_A \approx 1200\ min$, $\sigma_{0.5\%}$=9.08 ±0.01 MPa. The reached stress level is a result of viscoelastic response.

4.2 Physical aging effect on the VE behavior

To determine the aging and temperature effect (at different T_A and t_A) from the L-H tests (described in section 3) in the material VE behavior, the following analysis was performed and results were found:

a) Prony coefficients (C^m): using experimental data provided by testing "fully aged" ("A-ref") epoxy sample in L-H(120 min) tests at T=40, 60 and 80 ℃. C^m (Table 1) were found through fitting the data using Eqs. (5) and (6), assuming $a_T = a_A = 1$, since both shift factors do not change during the test at constant T.

b) relaxation functions: stress relaxation in ideal Heaviside step-loading at a given T and $\varepsilon_0 = 0.5\%$ were simulated using as input the T-dependent C^m obtained in (a) and Eq.(4).

c) master curve and temperature shift factor (a_T): were obtained after manually shifting horizontally the stress relaxation curves (at 40, 60 and 80 ℃) obtained in (b), using $80\ °C$ as the

  doi:10.5075/epfl-298799_978-2-9701614-0-0

reference temperature (T_{ref}). For example, for Sp10 aged for 5466 min ($T_{ref} = 80$ °C) a_T are: 3.5, 2.1 and 0, for temperatures equal to 40, 60 and 80 °C, respectively.

d) master Prony coefficients C^i: were found using data from (c) through the method of least squares. The master C^i (Table 1) together with a_T and a_A are the main parameters in the VE model to simulate arbitrary T- and aging dependent strain or stress-controlled ramps.

e) physical aging shift factor (a_A): the shift factor a_T found in (c) and master C^i found in (d) for a "fully aged" state sample were used to simulate the L-H test for different states of aging during aging at T_A. In simulations $a_T = 1$ ($\log a_T = 0$), since $T_A = T_{ref}$ was used, therefore, $\log a_A$ (Table 2) was the only parameter to be found. The shift factors were used as a parameter to find the best agreement with experimental L-H data.

f) incremental VisCoR code: simulations of L-H tests at arbitrary t_A were performed using experimental time and strain data together with shift factors, obtained in (e). Since the time instants in test and simulations were exactly the same, a simple minimization procedure (to minimize the difference between the simulated and experimental stress curves) was performed using a_A as a variable.

Table 1: Prony coefficients C^m (MPa) for "A-ref" Sp10 (T_A = 80 °C, t_A = 5466 min) at three temperatures (E_r = 0) and Prony coefficients of the master curve, C^i (MPa), for Sp10.

τ_m (s)		0.01	0.1	1	10	10^2	10^3	10^4	10^5	10^6	10^7
C^m	40 °C	0	0	517.0	104.3	96.8	103.0	0	747.5	1297.8	0
	60 °C	0	0	251.2	103.4	86.3	95.2	0	736.7	1177.1	0
	80 °C	0	0	279.1	101.8	95.7	124.1	45.9	1637.8	0	0
C^i		93.1	102.4	99.4	86.6	104.9	111.8	267.8	0	0	1425.4

Table 2: Aging shift factor $\log a_A$ dependence on t_A at $T_A = 80$ °C for Sp10. The aging state "A-ref" is assumed after t_A=5466 min.

Aging time (min)	20	155	444	2502	5466
$\log a_A$	-1.92	-1.22	-0.92	-0.07	0

The procedure of shift factor a_A determination for each individual specimen was based on master curve for the same specimen in fully aged state (*"A-ref")* and its dependence on T_A and t_A is presented in Figure 1a, in which the reference point for a_A is aging state at $t_A = 20$ min (first data point), with assumed value $\log_{10} a_A = 0$.

In Figure 1a a quasi-linear (constant rate) behavior which $\log_{10} a_A$ change can be observed in the range of $20\ \text{min} < t_A < 700\ \text{min}$ for different T_A. Therefore, for all used T_A, $\log_{10} a_A$ dependence on t_A can be obtained by fitting data in Figure 1a and described by the following equation [11]

  doi:10.5075/epfl-298799_978-2-9701614-0-0

$$\log_{10} a_A = 0.8169 \cdot \log_{10} t_A - 1.0735 \ , \ 20 \text{ min} < t_A < 700 \text{ min} \quad (7)$$

This independency on the used T_A of the $\log_{10} a_A$ dependence on t_A was also reported by [3] and [7] through the ETT concept. However, the results observed in Figure 1a show a different effect of the T_A on $\log_{10} a_A$ for $t_A > 700$ min, where a_A at a given t_A is larger if T_A is higher. Predictions extrapolating Eq. (7) to larger region than the used fitting region (Figure 1a dashed red line) were done and showed a good agreement with experimental data for low T_A (70 and 80 °C). However, for higher T_A ($90 - 110$ °C) this dependence is nonlinear and Eq. (7) for $t_A > 700$ min is not applicable.

Assuming T_A –independent behavior could cause an overestimation in the material long-term VE behavior, directly affecting the polymer engineering design, since the aging will not evolve with a constant aging shift rate.

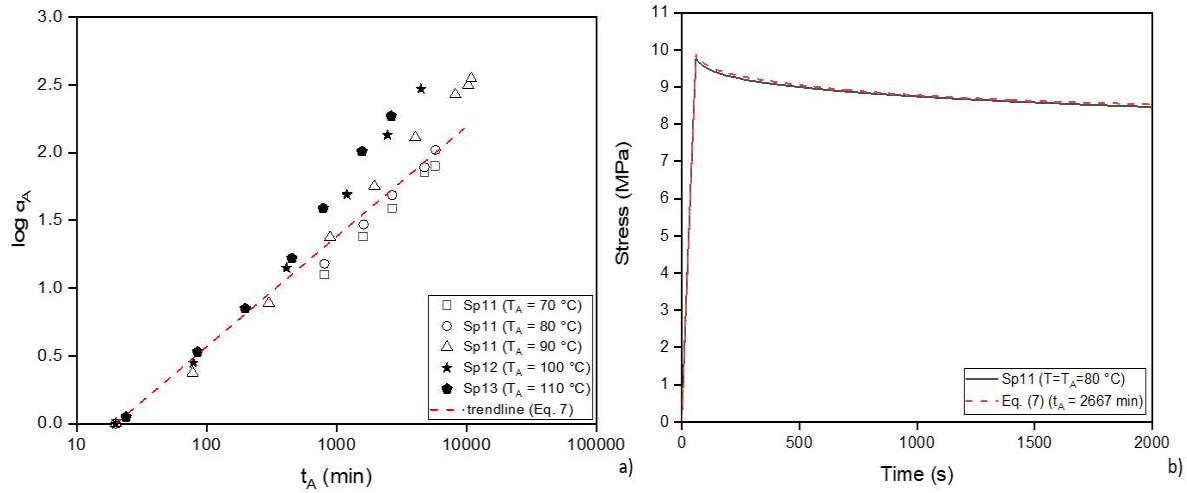

Figure 1. a) Dependence of the aging shift factor a_A on T_A and t_A: all data showing quasi-linear (constant rate) behavior at short t_A and b) stress response in L-H test (ε_0 = 0.5%) at different aging states. C^i for "A-ref" Sp11 (T_A = 80 °C, t_A = 2667 min) were used to simulate tests at different T_A and t_A for T_A = 80 °C.

Using master Prony coefficients (C^i) and shift factors as input for VisCoR code the stress response for Sp11 aged for $t_A = 2667$ min at the same temperature (T=80 °C) was predicted. For the applied methodology, the simulations provided, with a fast convergence, an excellent accuracy over the whole-time interval (Figure 1b). The use of the incremental VisCoR model, has as the main advantage the significant memory saving [12], becoming a very promising tool for the industry.

5. Conclusions

This paper focused on a methodology for testing and parameter determination for aging polymer using a Schapery's viscoelastic (VE) type of model, where the VE response was measured in tensile tests at different temperatures for specimens subjected to different aging temperatures (T_A) and times (t_A).

Results showed that the aging rate (a_A change with t_A in log-log axes) for the first 700 min of aging for all used T_A, is constant. However, with increasing t_A the effect of T_A became significant, with faster a_A change for higher T_A. The on T_A –dependent behavior is contrary to the trend

  doi:10.5075/epfl-298799_978-2-9701614-0-0

reported at literature when a different approach was used. Such dissimilar behavior could provide different VE response, and, therefore, an unreliable long-term material response prediction.

The performed simulations using the incremental VisCoR model provided a good agreement with the test data, attesting the reliability of the proposed methodology and model.

Acknowledgements

The authors would like to thank “Post-doctoral Research Aid” of the Specific Aid Objective of the Operational Programme “Growth and Employment” (project No. 1.1.1.2/VIAA/4/20/641), Higher Education Improvement Coordination (CAPES/Brazil), The Swedish Foundation for International Cooperation in Research and Higher Education (STINT) and Kempestiftelserna with funding reference SMK-1738 and ERDF within the Activity 1.1.1.2 for their financial support.

6. References

1. Cangialosi D, Boucher VM, Alegría A, Colmenero J. Physical aging in polymers and polymer nanocomposites: recent results and open questions, Soft Matter 2013; 9:8619–8630.
2. Odegard GM, Bandyopadhyay A. Physical aging of epoxy polymers and their composites. J Polym Sci B Polym Phys 2011; 49:1695–1716.
3. Lee A, McKenna GB. The physical ageing response of an epoxy glass subjected to large stresses. Polymer, 1990; 31:423-430.
4. Hodge IM. Physical aging in polymer glasses. Science 1995; 267:1945–1947.
5. G'Sell C, McKenna GB. Influence of physical aging on the yield response of model DGEBA/poly(propylene oxide) epoxy glasses. Polymer 1992; 33(10):2103-2113.
6. Barbero EJ, Julius MJ. Time-temperature-age viscoelastic behavior of commercial polymer blends and felt filled polymers. Mechanics of Advanced Materials and Structures, 2004; 11: 287–300.
7. Struik LCE. Physical Aging in Plastics and Other Glassy Materials. Polym Eng Sci 1977; 17(3):165-173.
8. Santore MM, Duran RS, McKenna GB. Volume recovery in epoxy glasses subjected to torsional deformations: the question of rejuvenation. Polymer 1991; 32(13):2377-2381.
9. Nunes SG, Saseendran S, Joffe R, Amico SC, Fernberg P, Varna J. On temperature-related shift factors and master curves in viscoelastic constitutive models for thermoset polymers. Mech Compos Mater 2020; 56(5):573-590.
10. Bolasodun B, Rufai O, Nesbitt A, Day R. Comparison of the isothermal cure kinetics of Araldite LY 5052/4 4’DDS epoxy system using a differential scanning calorimetry and a microwave heated calorimeter. Int J Mater Eng 2014; 4(4):148-165.
11. Nunes SG, Joffe R, Emami N, Fernberg P, Saseedran S, Esposito A, Amico SC and Varna J. Physical Aging Effect on Viscoelastic Behavior of Polymers. Composites JCOMC 2022; 7: 1-11.
12. Saseendran S, Berglund D, Varna J. Viscoelastic model with complex rheological behavior (VisCoR): incremental formulation. Adv Manuf Polym Compos Sci 2020; 6(1):1-16.

  doi:10.5075/epfl-298799_978-2-9701614-0-0

CHARACTERIZATION OF NOVEL SUSTAINABLE COMPOSITE MATERIALS BASED ON ELIUM® 188 O RESIN REINFORCED WITH A COLOMBIAN NATURAL FIBER

Juan Porras[a], Maria A. Morales[a], Alejandro Maranon[b], Camilo Hernandez[c], Véronique Michaud[d], Alicia Porras[a]

a: Grupo de Diseño de Productos y Procesos (GDPP), Department of Chemical and Food Engineering, Universidad de los Andes, CR 1 18a 12, Bogotá 111711, Colombia – js.porras@uniandes.edu.co (J. Porras).
b: Structural Integrity Research Group, Department of Mechanical Engineering, Universidad de los Andes, CR 1 18a 12, Bogotá 111711, Colombia
c: Sustainable Design in Mechanical Engineering Research Group (DSIM), Department of Mechanical Engineering, Escuela Colombiana de Ingenieria Julio Graravito, Autopista Norte AK 45 205 59, Bogotá 111166, Colombia
d: Laboratory for Processing for Advanced Composited (LPAC), Institute of Materials, Ecole Polytechnique Fédérale de Lausanne (EPFL), EPFL-STI-IMX-LPAC, Station 12, CH-1015 Lausanne, Switzerland.

Abstract: *In this work a novel composite material based on Elium® 188 O resin reinforced with Manicaria saccifera fiber was developed and characterized, by vacuum-assisted resin infusion molding (VARIM) manufacturing methodology using two fabric fiber layers configured to 0° and 90°. The influence of the presence of reinforcement was studied on physical, thermal, and mechanical properties. Physical characterization showed that fiber presence increased the density compared to the resin; the moisture content in the composites was not significantly affected, and the water absorption increased due to the presence of Manicaria fiber. The fiber volume fraction was 0.23, and the void content was 3.9%. Thermal analysis showed that the degradation process of the composites started in the same temperature range as the resin. The composite improved the flexural strength and modulus by 36% and 28%, respectively. Manicaria fiber has good potential as a reinforcement for composite materials.*

Keywords: *Manicaria* fiber; natural fiber composite; Elium® 188 O resin; infusion resin; thermoforming.

1. Introduction

Over the last years, the massive production of commodities that are not renewable or sustainable has generated a global because waste derived from these industries remains in landfills for many years. The development of sustainable practices or alternatives to reduce waste has generated significant interest in many governments and industries, which has led to a transition towards new eco-friendly materials [1]. One example is composite materials based on polymeric matrices reinforced with natural fibers, which are emerging as an alternative of great interest from an engineering perspective due to their potential to replace traditional plastic.

In particular, natural fibers are attractive because they display several advantages in contrast to conventional reinforcement materials such as glass or carbon fibers. Their low cost, low density,

  doi:10.5075/epfl-298799_978-2-9701614-0-0

sufficient specific strength, good thermal insulating properties, biodegradability, and renewability constitute the main incentives for their use in composites [2]. In Colombia, the processing and production of coffee, palm oil, corn, rice, cocoa, sugar cane, and bananas generate more than 71 tons of waste per year that end up in landfills or are incinerated [3]. Recently, the need to reduce the environmental impact of the agro-industry led to explore the possibility to exploit the residues produced by this industry as raw materials in other fields. Researchers have focused on developing new technologies and strategies to create value-added products based on agricultural residues or natural fibers, such as composite materials. A Colombian natural fiber of high interest is the fiber extracted from the Manicaria saccifera palm. It can be used with no further treatment as a UD layer, has a high percentage of cellulose, low density, and good thermal and mechanical properties. Its application has been previously explored for use in green composites laminated with PLA as polymeric matrix [4]. The green composites performed good mechanical properties and excellent energy absorption capacity, showing the great potential of Manicaria as PLA reinforcement.

Sustainable composite materials are usually constituted by thermoplastic polymeric matrices, which could be post-formed. The development of Liquid Composite Molding (LCM) manufacturing techniques such as Vacuum-Assisted Resin Infusion Molding (VARIM) by using thermoplastic matrices has contributed to the development of novel liquid resins that are processed as thermoset polymers using in situ polymerization, but that maintain their property of being recyclable and reusable at the end of their useful life. An example of this is the Elium® 188 O resin developed by Arkema Inc., which has low viscosity and can be processed at low temperatures [5]. Although its application has been studied in composite materials reinforced with synthetic and natural fibers, such as Jute or Rayon [6], there is great interest in continuing to investigate its use with other natural fibers to develop novel and low-cost composites with innovative applications.

Therefore, this work aims to present the development and characterization of a novel sustainable composite material based on Elium® 188 resin reinforced with natural fabric obtained from Manicaria saccifera. Vacuum-assisted resin infusion molding (VARIM) manufacturing process of composite laminas was used with two layers of fiber configured to 0° and 90°. The neat resin and composite material's physical, thermal, and mechanical properties were characterized. Density, moisture and void content, water absorption, fiber fraction, thermal analysis (TGA and DSC), flexural test, and thermoforming are analyzed to explore the performance of the materials.

2. Materials and Methods

2.1 Materials

Elium® 188 O resin and Luperox® AFR40 produced by Arkema Inc. were used as polymeric matrix and catalyst. In addition, a chemically treated natural fiber extracted from Manicaria saccifera palm was used as reinforcement in the composite material [4], [7]. Besides, Ipplon® KM1300 vacuum plastic, Greenflow 75 flow mesh, ½" spiral tube, grey vacuum tape, and low-cost anti-adherent fabric (Peel ply) were used as the main inputs for elaborating the vacuum assemblies necessary for the manufacturing processes.

2.2 Resin and composite preparation

  doi:10.5075/epfl-298799_978-2-9701614-0-0

A vacuum-assisted resin casting system was constructed to prepare the resin. 3 wt.% catalyst was used to polymerize the resin specimens and composite lamina. Liquid resin previously mixed with Luperox® AFR40 was deposited in a silicone mold with the geometry of flexure test specimens according to ASTM D790. The mold was placed in a vacuum bag made of Ipplon® KM1300 plastic and sealed with vacuum tape. Acetate sheets and a layer of the breather, a fabric that serves as a resin trap and minimizes contact with air, were placed on top of the mold before the bag was closed. The sealed bag was connected to a GAST DOA-P704-AA vacuum pump that generated a vacuum at a pressure of approximately -430 mmHg. A typical set-up for this process is shown in Figure 1.

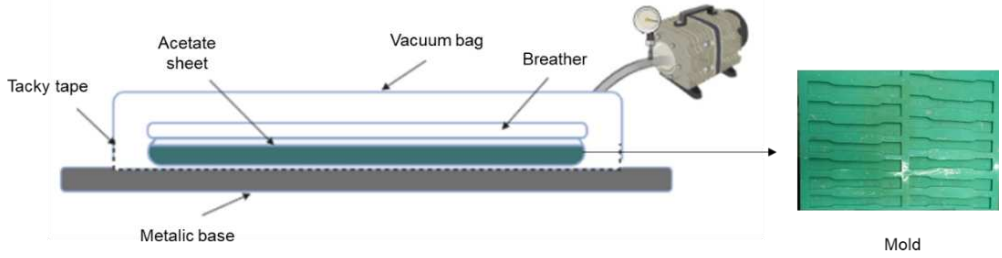

Figure 1. Typical vacuum-assisted resin casting set-up.

Composites based on Elium® 188 O resin and reinforced with Manicaria saccifera fiber were manufactured using vacuum-assisted resin infusion molding [5]. By using this method transfers resin across a surface or mold where the fiber or composite reinforcement rests. Figure 2 shows the assembly used in the elaboration of the composite material.

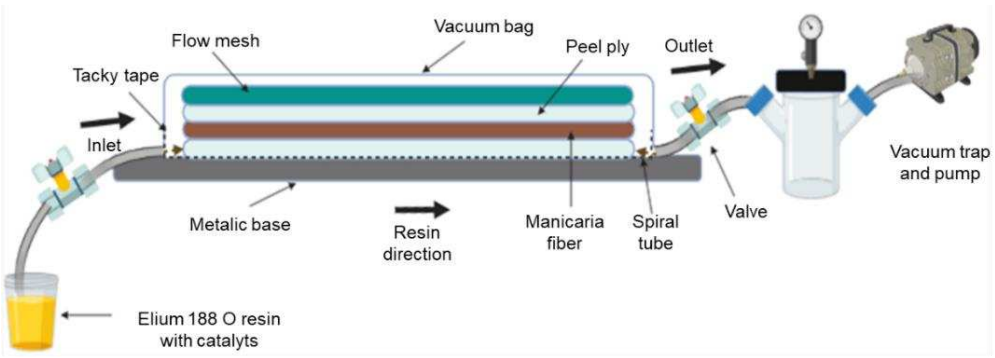

Figure 2. Typical set-up of resin infusion manufacturing of composites based on Elium® 188 O resin reinforced with Manicaria saccifera fiber.

For this study, a GAST DOA-P704-AA vacuum pump was used to generate a vacuum at a pressure of approximately -20 mmHg. This value is indicative of the initial acceleration to which the liquid resin previously mixed with catalyst is subjected. Composite laminate with two layers of reinforcement oriented at 0° and 90° ([0/90]) were manufactured in this work. The composite was cured at room temperature for 24 hours and then post-cured for 24 hours at 60°C.

2.3 Physical characterization

2.3.1 Volumetric density

The density of the materials was determined by the displacement of distilled water at 21.1°C (ρ = 0.998 g/cm3), according to ASTM D792 – method A. Five samples for each material were tested.

  doi:10.5075/epfl-298799_978-2-9701614-0-0

2.3.2 Fiber volume fraction and void content

The fiber volume fraction was determined using Eq. (1) [8],

$$v_i = x_i \frac{\rho_i}{\rho_{ce}} \quad (1)$$

where the mass fraction (x_i) and density of the constituent i (ρ_i) are related to the experimental density of the composites (ρ_{ce}) to calculate the volume fraction of the component (v_i).

Likewise, method B of the ASTM D2734 standard was used to determine the void content in the composites. Eq. (2) was used to calculate the void percentage per unit volume in the structure of the materials.

$$V_{void}\,[\%] = 1 - \rho_{ce}\left(\frac{x_f}{\rho_f} + \frac{(1-x_f)}{\rho_m}\right) \quad (2)$$

where ρ_{ce} represents the experimental density of the compounds, x_f and ρ_f are the mass fraction and density of the fiber, respectively; and ρ_m symbolizes the density of the composite matrix, in this case, Elium® 188 O resin.

2.3.3 Moisture content

The percentage moisture content of the materials was measured according to the ASTM D6980 standard. Each specimen was heated to 105°C until its weight remained constant with an accuracy of 1 mg. The percent moisture content was calculated as the difference between the initial and final weight, divided by the magnitude of the initial weight. Five samples of each material previously stored in a controlled room at 21.9°C and 55.3% relative humidity were tested.

2.3.4 Water absorption

Water absorption was evaluated according to the ASTM D570 standard. Samples of each material were dried at 50°C for 24 hours, then cooled in a desiccator to be immediately weighed. The specimens were immersed in distilled water for 24 hours. Then, samples were removed, and their entire surface was dried with a cloth and finally weighed. Eq. (3) was used to calculate the percentage weight increase during immersion. Three samples of each material were evaluated.

$$\%\ \text{Increased weight} = \frac{W_i - W_0}{W_0} \times 100 \quad (3)$$

where W_i is the weight of the sample after the immersion period and W_0 is the weight after drying.

2.4 Thermal performance

2.4.1 Thermogravimetric analysis (TGA)

Thermo-gravimetric analysis (TGA) test for composite material and Elium® resin were carried out using a TA Instruments SDT Q600 (New Castle, TE, USA) based on the ASTM E1131 standard. The procedure was performed from room temperature up to 500°C with a heating ramp of 10°C/min in an inert nitrogen atmosphere.

2.4.2 Differential scanning calorimetry (DSC)

The thermal behavior of the resin and the composite material was studied using a DSC TA Instruments Q2000 (New Castle, TE, USA) with hermetically sealed aluminum plates according to ASTM D3418 standard. Samples of each material were heated with a ramp of 5°C/min from 25°C to 200°C under an inert nitrogen atmosphere at a 400 mL/min flow rate.

2.5 Flexural test

Flexural tests were performed per ASTM D790 standard. Specimens were loaded at three bending points with a span to depth ratio of 16:1. An Instron Model 3367 equipped with a 500 N load cell was used. Five rectangular specimens (12.7 mm x 63.5 mm) were tested using a crosshead speed of 1.61 mm/min and 0.92 mm/min for neat resin and [0/90] composite.

2.6 Thermoforming

The thermoforming behavior of the composite material was evaluated by transforming a flat panel into a corrugated geometry using an aluminum mold and a Dake model 44-251 molding press. A preheating time of 15 minutes at 160°C was used, and then 18 bar of pressure was applied for 4 minutes.

2.7 Statistical analysis

The influence of the reinforcement in the composite material on the physical and mechanical properties was characterized using an ANOVA one-way test in the Minitab 19 Statistical Software (Minitab Inc., State College, PA, USA). A p-value lower than 0.05 was considered statistically significant.

3. Results and Discussion

3.1 Physical properties

Table 1 presents the physical properties results for Elium® 188 O resin and [0/90] composite. The density in the composites increases due to the presence of Manicaria sheets that present a higher density (between 1.30 and 1.34 g/cm^3) with respect to the resin (1.182 g/cm^3). According to the statistical analysis with a 5% significance, the reinforcement's presence has a significant influence on this property. In terms of the moisture content, it was found that there are no significant differences between the resin and the composite, proving that by using the VARIM manufacturing method, the fiber was impregnated and coupled satisfactorily with the matrix.

Table 1: Physical properties.

Configuration	Volumetric Density [g/cm^3]	Moisture Content [%]	Water Absorption [%]	Void Content [%]
Resin	1.182 ± 0.003	0.084 ± 0.025	0.19 ± 0.03	-
[0/90]	1.213 ± 0.013	0.108 ± 0.031	1.68 ± 0.15	3.91

The hygroscopic behavior of Elium® resin and [0/90] composite was quantified by water absorption. According to Table 1, composite material presents an increase of 784% in the

percentage of water absorption compared to the neat resin due to the hydrophilic behavior of the natural fiber.

On the other hand, the fiber mass fraction was 0.225; therefore, the fiber volume fraction was 0.245 (24.5%), and consequently, the resin fraction was 0.755. Thus, it was obtained that the [0/90] composite presented a void content of 3.91%. Applying higher vacuum pressures or mercerization to the fiber could improve this property and contribute to the manufacture of composites with optimum mechanical and physical properties since the pores generate stress concentrators that may lead to premature failure.

3.2 Thermal analysis

The thermal stability of the materials was studied by thermogravimetric analysis. Figure 3a shows the weight loss and the weight loss derivative curves as a function of temperature. Resin curves present a first loss step between 250 to 300°C, of approximately 15%, attributed to some resin additives. A second step between 310°C to 410°C, with a maximum peak at 375°C, represents mainly the degradation of the PMMA, a polymer that makes up the largest percentage of the resin.

Similar behavior is observed for the composite curves. At temperatures around 250 °C, a weight loss step is observed. This peak is not only attributable to the resin but also to the presence of the lignocellulosic fiber. At 280°C the partial decomposition of the lignin and the decomposition of the hemicellulose takes place. Cellulose, the main component of the fiber, has a degradation peak at 340°C, approximately. Therefore, the decomposition phases of the lignocellulosic material are mixed with the decomposition regions of the resin.

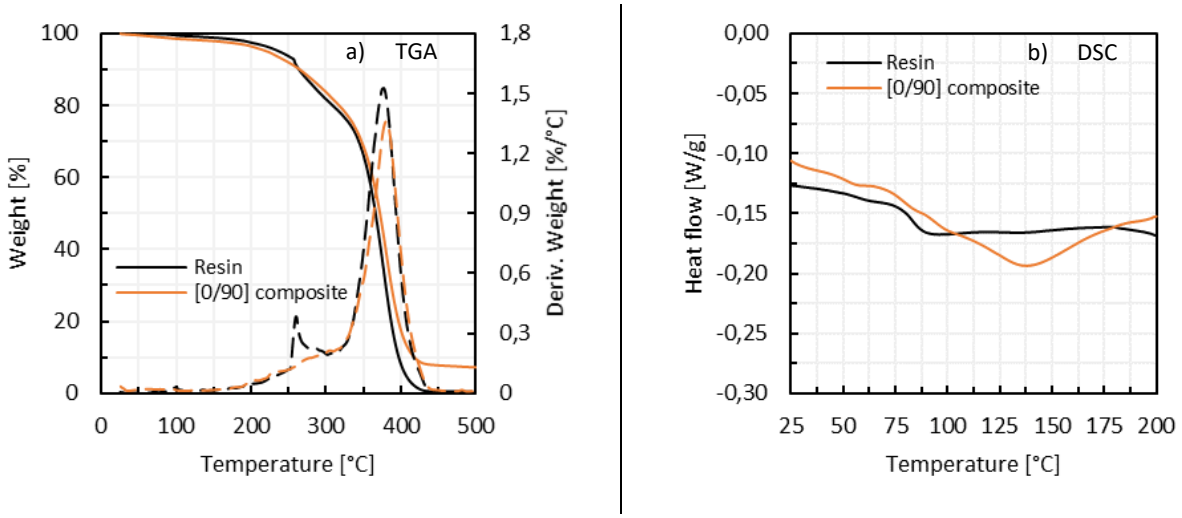

Figure 3. Thermal performance of resin and [0/90] composite. a) TGA. b) DSC.

Figure 3b shows the thermal transitions curves obtained by the DSC testing. It is observed that tested materials (composite and neat resin) do not have a melting point, but they present a glass transition temperature. This behavior is due to the highly amorphous nature of the resin since it is mainly composed of PMMA, a very amorphous polymer [9]. The glass transition temperature of the resin is approximately 83°C, and for the composite, it is around 117°C, producing a deviation with respect to the resin due to the presence of the reinforcement.

3.3 Flexural test analysis

Figure 4 shows the typical behavior of the resin and the [0/90] composite subjected to flexural tests at three loading points. The composite shows a better performance in the typical flexural behavior than Elium® resin due to the presence of the fibers, which make the composite more rigid and stronger because fiber's elastic modulus is higher than Elium® resin [7].

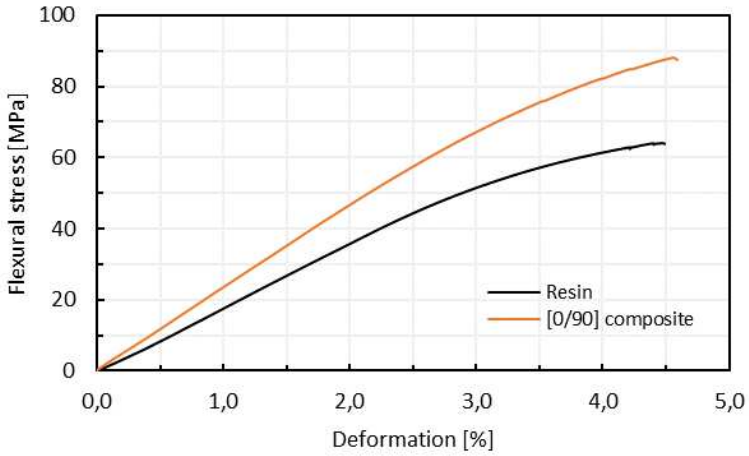

Figure 4. Typical performance of Elium® 188 O resin and [0/90] composite in the flexural test.

Table 2 shows the values of the material properties under flexural tests. In the [0/90] composite, flexural strength and modulus were higher than Elium® resin by 36.2% and 28.4%, respectively. As also was discussed in [10], the good resin-fiber adhesion led to increased strength in natural fiber-reinforced composite, validating that the fiber was linking satisfactorily to the resin using the VARIM manufacturing method.

A study with [0/90] composites based on Elium® resin reinforced with Jute fiber fabric, at 40% fiber volume fraction, reported a value of 87.1 MPa for the flexural strength [6], which is in the range of this study, but with a higher fiber fraction. Therefore, Manicaria fiber adheres better to the resin than Jute fiber, making the flexural properties comparable even though the composite material has a lower fiber volume fraction. Besides, it shows that this type of long fiber fabrics improves mechanical properties because its organized structure, with a high percentage of cellulose, allows a better load distribution in contrast to neat resin.

Table 2: Flexural mechanical properties.

Configuration	Flexural Strength [MPa]	Modulus [GPa]	Deformation at maximum load [%]
Resin	64.09 ± 4.50	1.94 ± 0.15	5.14 ± 0.73
[0/90]	87.28 ± 1.94	2.49 ± 0.18	4.40 ± 0.68

3.4 Thermoforming and potential application

A corrugated structure with a good surface finish was obtained without structural irregularities due to a good fit of the material to the mold, demonstrating that the composite materials could be mechanically recycled, sustainable, and used in thermoformed products design. Figure 5 shows the thermoforming test result.

  doi:10.5075/epfl-298799_978-2-9701614-0-0

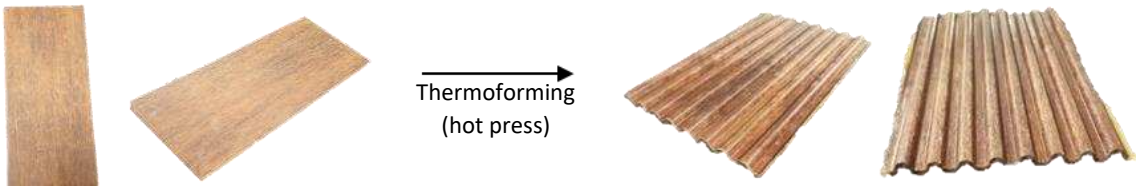

Figure 5. Composite laminate to corrugate structure using thermoforming process.

4. Conclusions

A well-impregnated thermoplastic composite material with Colombian Manicaria saccifera fiber was produced using Elium® resin by vacuum-assisted resin infusion molding. The mechanical and thermal properties of the composite developed showed a great potential of Manicaria fiber as reinforcement for composite materials; an opportunity to generate added value to Colombian biomass through the design of eco-friendly products with potential applications in industries such as automotive, construction, health, among others.

Acknowledgements

This project was supported by Seed Money Grants 2019 call of the University of St. Gallen, Laboratory for Processing of Advanced Composites (LPAC) from EPFL and the Universidad de los Andes. We thank Dr P. Gérard from Arkema for initial resin samples and fruitful discussions.

5. References

1. Mohanty AK, Misra M, Drzal LT. Sustainable Bio-Composites from Renewable Resources: Opportunities and Challenges in the Green Materials World. Vol. 10, Journal of Polymers and the Environment. 2002.
2. Nabi D, Jog JP. Natural Fiber Polymer Composites: A Review. Vol. 18, Advances in Polymer Technology. John Wiley & Sons, Inc; 1999.
3. Peñaranda LV, Montenegro SP, Giraldo PA. Aprovechamiento de residuos agroindustriales en Colombia. Revista de Investigación Agraria y Ambiental. 2018;8(2):141–50.
4. Porras A, Maranon A, Ashcroft IA. Thermo-mechanical characterization of Manicaria Saccifera natural fabric reinforced poly-lactic acid composite lamina. Composites Part A: Applied Science and Manufacturing. 2016 Feb 1;81:105–10.
5. Arkema. Liquid thermoplastic resin for tougher composites. ELIUM® by Arkema. 2019.
6. Khalili P, Skrifvars M, Ertürk AS. Fabrication, Mechanical Testing and Structural Simulation of Regenerated Cellulose Fabric Elium® Thermoplastic Composite System. Polymers (Basel). 2021 Sep 1;13(17).
7. Porras A, Maranon A, Ashcroft IA. Characterization of a novel natural cellulose fabric from Manicaria saccifera palm as possible reinforcement of composite materials. Composites Part B: Engineering. 2015;74:66–73.
8. Torres-Arellano M, Renteria-Rodríguez V, Franco-Urquiza E. Mechanical properties of natural-fiber-reinforced biobased epoxy resins manufactured by resin infusion process. Polymers (Basel). 2020 Dec 1;12(12):1–17.
9. Manjunath L, Sailaja RRN. PMMA-cellulose acetate phthalate nanocomposites reinforced with silane-treated nanoclay. Cellulose. 2014;21(3):1793–802.
10. Fiore V, Scalici T, Vitale G, Valenza A. Static and dynamic mechanical properties of Arundo Donax fillers-epoxy composites. Materials and Design. 2014;57:456–64.

  doi:10.5075/epfl-298799_978-2-9701614-0-0

COMBINED DIC-INFRARED THERMOGRAPHY FOR HIGH STRAIN RATE TESTING OF COMPOSITES

Karthik Ram, Ramakrishnan[a], Gustavo, Quino[a], Janice, Dulieu-Barton[a]

a: Bristol Composites Institute, University of Bristol, Bristol, United Kingdom
* Corresponding author email: Karthik.ramakrishnan@bristol.ac.uk

Abstract: *Infrared Thermography (IRT) is a full-field measurement technique for evaluating defects or damage in a material by localized variation in the surface temperature observed using a thermal camera. The occurrence of damage in composite structure is accompanied by heat dissipation and a subsequent temperature evolution on the specimen surface. The thermal images provide quantitative information about location and magnitude of hot spots and, in turn, of the damage mechanisms. Therefore, surface temperature analysis using an infrared camera can be applied to better understand the damage mechanisms and energy absorption in composites. In this paper, simultaneous high-speed white-light and infrared imaging were conducted to obtain quantitative description of thermomechanical response of the material and to study the formation and propagation of shear localizations from the temperature history.*

Keywords: full-field imaging; high strain-rate; composites; in-plane shear; thermography

1. Introduction

Composites materials are widely used in a diverse range of applications due to the several benefits they provide (lightweight, multifunctionality, corrosion-resistance, etc.). However, composites may encounter dynamic loads during service. For instance, during an impact event such as bird strike, the local strain rates near the impact location are very high and it is known that mechanical properties such as the in-plane shear strength or the fracture toughness are sensitive to the strain rate. Therefore, reliable characterisation of mechanical properties over a wide range of strain rates and temperatures is required to safely design components with these materials. The Split Hopkinson Pressure Bar (SHPB) is an experimental technique used to measure mechanical properties at strain rates in the order of 100 to 1000 s^{-1}[1]. Though there are several works studying the use of SHPB for rate-dependent compressive properties of composite materials, there is limited work investigating tensile or shear properties of composite materials under high rates of loading [2,3]. One of the main failure mechanisms of unidirectional fibre composites is inter-fibre failure under in-plane shear. It is mainly driven by the properties of the polymeric matrix which due to its viscoelastic nature, is highly strain-rate dependent. Some experimental works have investigated the effects of strain rate on the in-plane shear behaviour of composites [4–6]. Cui et al. [4] reported that the shear stiffness and yielding strength increased with strain rate, while the failure strain decreased. The initiation and growth of micro cracks was not only responsible for the shear driven failure, but this failure mechanism also changed considerably with strain rate.

  doi:10.5075/epfl-298799_978-2-9701614-0-0

There is also literature on the application of temperature measurement for the characterisation of the mechanical behaviour of composites. Various authors have used infrared thermography (IRT) to identify damage in FRP materials [7–9]. IRT is a full-field measurement technique based on the principle that electromagnetic radiation in the infrared spectrum (wavelength in the range of 0.75–1000 um) is emitted by all objects above absolute zero temperature. IRT can be used to monitor the surface temperature during loading. In addition to the change in material temperature due to a change in applied stress (thermoelastic effect), heat generation in composites can be due to various mechanisms such as fracture, damping caused by viscoelastic behaviour of the matrix or the frictional sliding between fibre-fibre and fibre-matrix interfaces. Libonati and Vergani [7] studied the damage evolution in GFRP under static loading conditions and showed that IR thermography is a powerful tool for damage analysis and the thermal maps and thermal profiles allowed the detection of defects, damage formation, and evolution. For instance, small amount of energy is dissipated during the formation of microcracks, which can be observed as small temperature increase in the thermal images, while fibre breakage causes large dissipation of energy and a corresponding local increase of temperature. Jiménez-Fortunato et al. [8] explored the possibility of combining Digital Image Correlation (DIC) with thermal imaging conducted using low-cost bolometer IR cameras for assessing defects in composite materials. However, the use of thermography for high strain rate applications is limited by the capabilities of the currently available IR detectors [10]. The temperature variation occurs during a short duration of the order of milliseconds and their visualization is only possible with high-speed imaging. The high acquisition rates (>10kHz) required to capture the phenomena in dynamic tests means reduced integration times which adversely affects the signal to noise ratio. Pan et al. [11] used high-speed thermal imaging to identify localization of temperature rise, adiabatic shear band, resin matrix softening, damages and failures during the dynamic failure of 3-D braided composite material. Johnston et al. [9] used a Telops FAST-IR 2K camera capable of frame rates up to 90,000 frames per second in sub-window mode to capture the temperature fields of a composite panel impacted using a gas gun and found that the generated temperatures in the local region near the point of impact was over 252 °C. This large temperature rise surpassing the glass transition temperature of the matrix causes thermal softening and subsequent deformation localization. Similar localized temperature rise exceeding the Tg of the resin matrix was reported to cause stress concentration and subsequent failure in warp/weft fibre tows in localized positions in non-crimp fabric reinforced polymer composites [12]. Johnsen et al. [13] reported an increase in temperature of almost 50 °C during high strain rate testing of rubber-modified polypropylene, when adiabatic heating conditions are met. It was also noted that the self-heating introduces a softening in the material and increases the locking stretch for higher strain rates. Tarfaoui et al. [3] developed an experimental setup for Hopkinson bar compression tests in which simultaneous full-field deformation and temperature measurements were obtained. It was reported that the observed V-shaped hot zones, localized at the centre of the specimen coincided with the damage area observed from the white light imaging. Similar tests conducted on pultruded glass fibre composites also observed maximum temperatures in the fracture zones exceeding 80 °C and it can be concluded that simultaneous optical and IR imaging can be used to obtain quantitative description of thermo-mechanical response of the material and to study the formation and propagation of shear localizations from the temperature history [14].

  doi:10.5075/epfl-298799_978-2-9701614-0-0

In this paper, we characterise the in-plane shear response of carbon fibre composite laminates at high strain rates using combined white light imaging and infrared thermography. The results will serve as a basis for the development of improved strain rate sensitive, physically-based constitutive models for composites.

2. Experimental setup

2.1 Material

Tensile dogbone specimens were cut by water jet cutting from a 300x300 mm plate made of IM7/8552 prepreg, [+45, -45]8s, with an approximate thickness of 2mm. Specimen geometry is displayed in Fig. 1. 3M DP460 epoxy-based adhesive was employed to glue metallic endcaps to the specimens. The M12 threaded endcaps were impedance matched and used for gripping into the Hopkinson bars. A specially designed rig was used to ensure the alignment and co-axiality of these endcaps during curing of the epoxy. The subset matching based DIC requires surfaces containing a random pattern. Prior to testing, coupons were prepared with a black speckle on white background to obtain full-field measurement of the strains by DIC. The speckle patterns were applied on the samples using the temporary tattoo or water slide paper method developed by Quino et al [15]. In this method, a random speckle pattern created by Speckle Generator software from Correlated Solutions was printed on commercially available special paper for temporary tattoo and wet-transferred to the surface of the specimen.

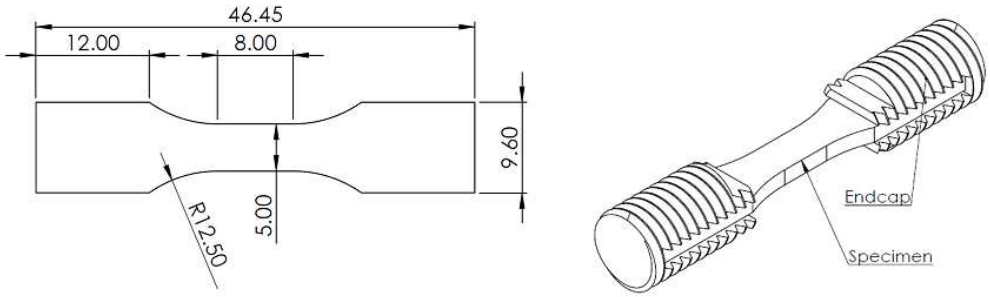

Figure 1 Specimen geometry to characterise the in-plane shear behaviour.

2.2 High rate characterisation

Dynamic characterisation was performed in a Split Hopkinson bar system (see Fig. 2) to achieve strain rates up to 900s^{-1}. The bars were instrumented with three sets of strain gages (see Fig. 2) from which the history of loads across the specimen was calculated following 1D wave propagation theory as described in reference [16]. The calculated axial stress σ_{xx} was then converted into shear stress τ_{12} with $\tau_{12} = -\sigma_{xx}/2$. The history of strains was obtained from DIC analysis of high-speed images taken with a Kirana camera (Specialised Imaging Ltd, UK) at a rate of 250000 fps. The image acquisition of the camera was triggered by the stress pulse arriving at the first strain gage. A delay of 380 μs was set as the Kirana camera can only capture 180 frames. Digital image correlation (DIC) analysis of the high-speed camera images were conducted using Davis software to obtain the displacement across the speckled gage section of the composite specimens and the corresponding strain were evaluated. It was found that the strain distribution within gage area was reasonably uniform and an average strain from the centre of the sample was used to plot the stress vs. strain curves.

  doi:10.5075/epfl-298799_978-2-9701614-0-0

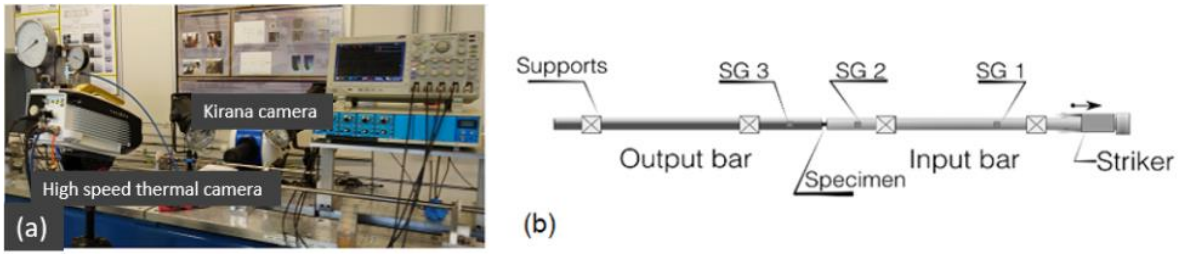

Figure 2 (a) Experimental setup with combined high-speed imaging, (b) Schematic diagram of a Split Hopkinson Tension bar

A Telops FAST M3K photon detector camera was used to capture IR images at a resolution of 64 x 8 pixels and a frame rate of 93000 fps. It was necessary to use a subwindow mode to obtain the high frame rate required for the dynamic test. The sample was heated with a heat-gun to get a clear difference in temperature to the surroundings. The window size was progressively reduced to ensure that the 8 pixels of the width coincided with the width of the composite sample. A typical image of the radiometric temperature plot obtained from the Telops camera is shown in Figure 3. An integration time of 5 µs and calibration range from 0 to 176 °C were used in the experiment. The same trigger signal used for the Kirana was used to trigger image acquisition of the Telops camera.

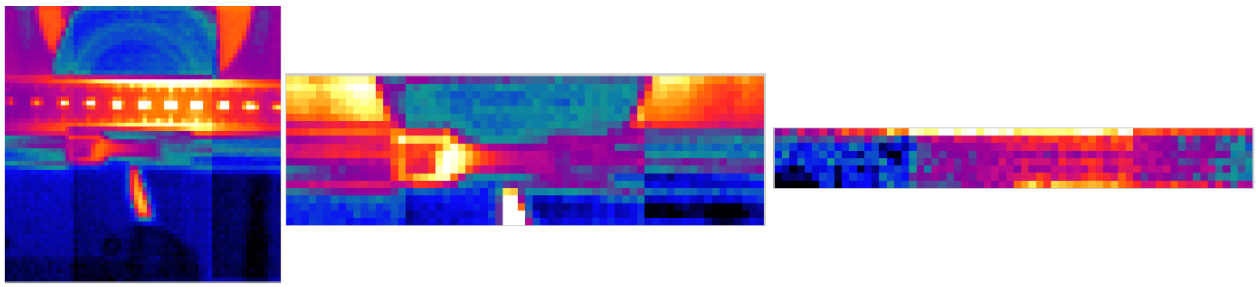

Figure 3 Typical images of surface temperature from IR camera

3. Results and Discussion

The raw signals obtained from the strain gages in the input bar (SG1 and SG2) as well as the output bar (SG3) are shown in Figure 4. The shape of the input pulse obtained from using the rubber pulse shaper is evident. The raw signals from the oscilloscope are post-processed using 1D wave theory equations to obtain the force and stress signals in the composite. The force validity showing equilibrium between the end of input and beginning of output bars is also shown.

  doi:10.5075/epfl-298799_978-2-9701614-0-0

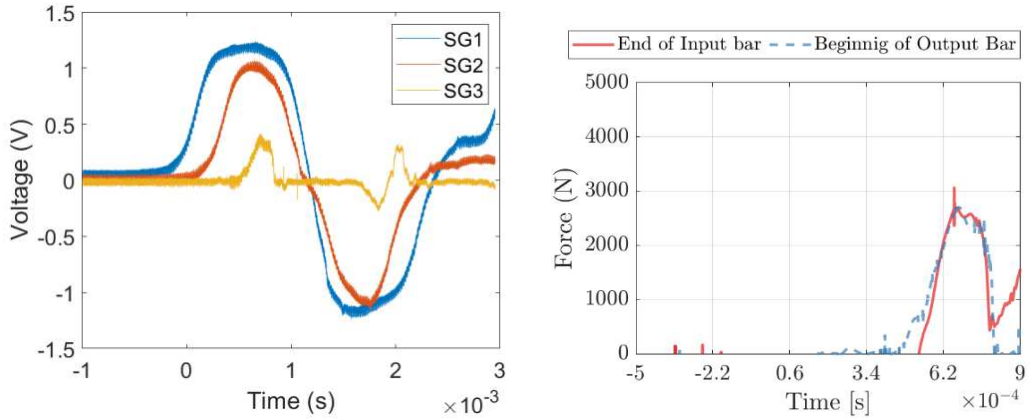

Figure 4 (a) Typical strain gage signals from the SHPB test and (b) Force validity

A time lapse of the images taken with Kirana high speed camera is shown in Figure 5. The threaded endcaps and the speckled pattern in the gage area of the composite are clear. The images are from 80 µs apart and show the shear deformation and failure of the composite.

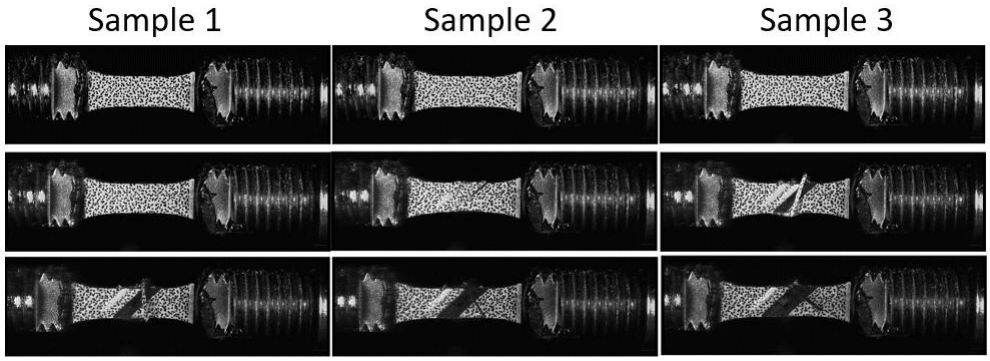

Figure 5 Typical high speed camera images of in-plane shear test of CFRP composite

The displacement measurements in the x-direction (loading direction) obtained from the DIC analysis is shown in Figure 6. A region of interest is chosen in the gage area and a subset size of 17 pixels x 17 pixels was chosen with a step size of 8 pixels. The images correspond to the first image acquired after the trigger (before any stress pulse), (ii) displacement in the composite when the stress wave arrives in the specimen, (iii) localization and beginning of fibre failure and (iv) finally fracture and complete failure of the specimen. It can be noted that the fibre fracture occurs at an angle corresponding to the 45°surface ply.

  doi:10.5075/epfl-298799_978-2-9701614-0-0

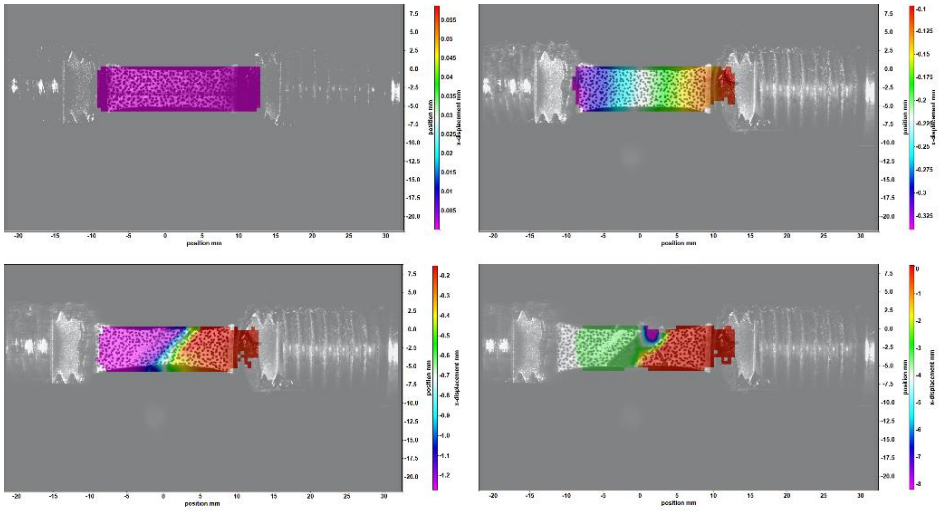

Figure 6 Displacement contours obtained from DIC analysis

The stress obtained from the postprocessing of the strain gage signals and the strain obtained from the DIC analysis were combined to obtain the shear stress vs. strain plot shown in Figure 7. It can be seen that the tests consistently show a nonlinear shear response, and a post-peak strain softening region. The average shear strength measured from the peak stress was 123 MPa, slightly below to the 130MPa reported by Cui et. al for a similar material system [4], possibly because of the higher strain rate in their experiments.

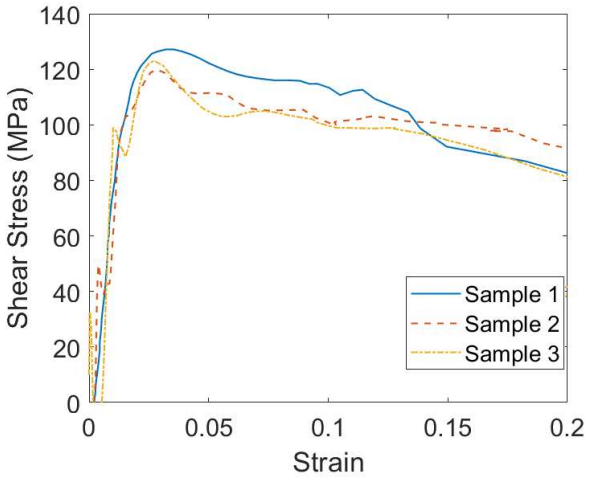

Figure 7 Shear stress vs strain curve at high strain rate for IM7/8552 composite

The radiometric temperature measured from the Telops camera was used to plot the change in temperature (ΔT) in the composite. Figure 8 shows that there is a diffused increase in temperature in the composite during the deformation followed by localized hotspot during fibre fracture. The increase in temperature is almost 100 °C which is consistent with the reported literature. The thermal images clearly show the effect of matrix damage and fibre failure, which will provide additional information about the damage mechanisms in the composite and the effect of the temperature increase on the material performance.

  doi:10.5075/epfl-298799_978-2-9701614-0-0

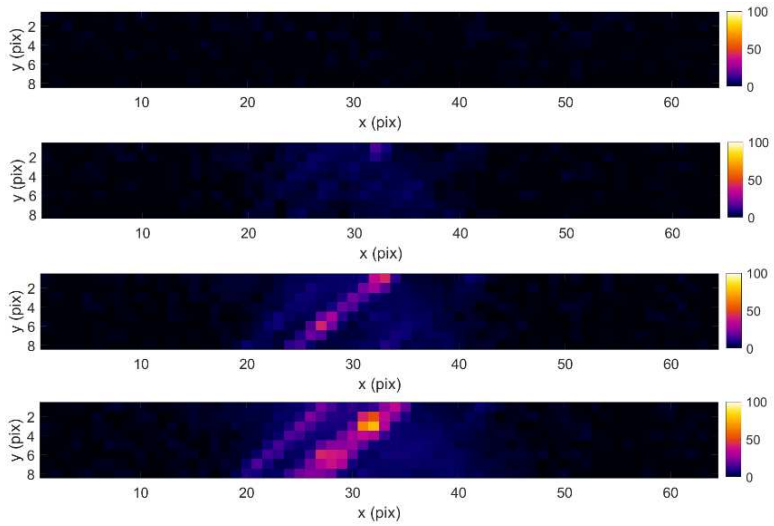

Figure 8 Change in temperature measured from high speed thermal camera

4. Conclusion

A combined high-speed white-light and infrared imaging method was used to study the in-plane shear response of carbon fibre composite at high strain rate. A Split Hopkinson Pressure Bar setup was used to conduct the test on ±45° sample of the composite. DIC analysis of the high speed images were used to obtain the strain history and 1D wave analysis was used to measure the stress history. The thermal images provide quantitative information about location and strength of hot spots and, in turn, of the damage mechanisms. Therefore, surface temperature analysis using an infrared camera can be applied to provide quantitative description of thermo-mechanical response of the material and to study the formation and propagation of shear localizations from the temperature history.

Acknowledgements

The authors acknowledge the Marie Curie Individual Fellowship funded by the European Union's H2020-MSCA-IF-2018 Programme (FIDELITY project, grant agreement n◦ 846458).

5. References

[1] Gerlach R, Kettenbeil C, Petrinic N. A new split Hopkinson tensile bar design. Int J Impact Eng 2012;50:63–7. https://doi.org/10.1016/j.ijimpeng.2012.08.004.

[2] Koerber H, Xavier J, Camanho PP. High strain rate characterisation of unidirectional carbon-epoxy IM7-8552 in transverse compression and in-plane shear using digital image correlation. Mech Mater 2010;42:1004–19. https://doi.org/10.1016/j.mechmat.2010.09.003.

[3] Tarfaoui M, El Moumen A, Ben Yahia H. Damage detection versus heat dissipation in E-glass/Epoxy laminated composites under dynamic compression at high strain rate. Compos Struct 2018;186:50–61. https://doi.org/10.1016/j.compstruct.2017.11.083.

[4] Cui H, Thomson D, Pellegrino A, Wiegand J, Petrinic N. Effect of strain rate and fibre rotation on the in-plane shear response of ±45° laminates in tension and compression tests. Compos Sci Technol 2016;135:106–15.

  doi:10.5075/epfl-298799_978-2-9701614-0-0

https://doi.org/10.1016/j.compscitech.2016.09.016.

[5] Taniguchi N, Nishiwaki T, Kawada H. Tensile strength of unidirectional CFRP laminate under high strain rate. Adv Compos Mater Off J Japan Soc Compos Mater 2007;16:167–80. https://doi.org/10.1163/156855107780918937.

[6] Ledford N, Imbert M, May M. High-rate in-plane shear testing of cfrp using the split hopkinson tension bar. AIAA Scitech 2021 Forum 2021;59:1–8. https://doi.org/10.2514/1.j060269.

[7] Libonati F, Vergani L. Damage assessment of composite materials by means of thermographic analyses. Compos Part B Eng 2013;50:82–90. https://doi.org/10.1016/j.compositesb.2013.01.012.

[8] Jiménez-Fortunato I, Bull DJ, Thomsen OT, Dulieu- JM. On the source of the thermoelastic response from orthotropic fibre reinforced composite laminates. Compos Part A 2021:106515. https://doi.org/10.1016/j.compositesa.2021.106515.

[9] Johnston JP, Pereira JM, Ruggeri CR, Roberts GD. High-speed infrared thermal imaging during ballistic impact of triaxially braided composites. J Compos Mater 2018;52:3549–62. https://doi.org/10.1177/0021998318765290.

[10] Fruehmann RK, Dulieu-Barton JM, Quinn S. Thermoelastic Stress and Damage Analysis Using Transient Loading. Exp Mech 2010;50:1075–86. https://doi.org/10.1007/s11340-009-9295-9.

[11] Pan Z, Wu Z, Xiong J. High-speed infrared imaging and mesostructural analysis of localized temperature rise in damage and failure behavior of 3-D braided carbon/epoxy composite subjected to high strain-rate compression. Polym Test 2019;80:106151. https://doi.org/10.1016/j.polymertesting.2019.106151.

[12] Pan Z, Wu Z, Xiong J. Localized temperature rise as a novel indication in damage and failure behavior of biaxial non-crimp fabric reinforced polymer composite subjected to impulsive compression. Aerosp Sci Technol 2020;103:105885. https://doi.org/10.1016/j.ast.2020.105885.

[13] Johnsen J, Grytten F, Hopperstad OS, Clausen AH. Influence of strain rate and temperature on the mechanical behaviour of rubber-modified polypropylene and cross-linked polyethylene. Mech Mater 2017;114:40–56. https://doi.org/10.1016/j.mechmat.2017.07.003.

[14] Pournoori N, Corrêa Soares G, Orell O, Palola S, Hokka M, Kanerva M. Adiabatic heating and damage onset in a pultruded glass fiber reinforced composite under compressive loading at different strain rates. Int J Impact Eng 2021;147:103728. https://doi.org/10.1016/j.ijimpeng.2020.103728.

[15] Quino G, Chen Y, Ramakrishnan KR, Martínez-Hergueta F, Zumpano G, Pellegrino A, et al. Speckle patterns for DIC in challenging scenarios: Rapid application and impact endurance. Meas Sci Technol 2021;32. https://doi.org/10.1088/1361-6501/abaae8.

[16] Quino G, Tagarielli VL, Petrinic N. Effects of water absorption on the mechanical properties of GFRPs. Compos Sci Technol 2020;199:108316. https://doi.org/10.1016/j.compscitech.2020.108316.

  doi:10.5075/epfl-298799_978-2-9701614-0-0

Effect of gap defects on in-situ AFP-manufactured structures

Lukas, Raps[a], Ines, Schiel[a], Ashley, Chadwick[a]

a: German Aerospace Center (DLR), Institute of Structures and Design, Stuttgart, Germany, lukas.raps@dlr.de

Abstract: *The laser-assisted Automated Fibre Placement (AFP) process has great potential to reduce cycle times for large-scale primary aircraft structures by means of in-situ consolidation. Single- and double-curved structures, such as an aircraft fuselage, require advanced layup strategies and careful evaluation of resulting gap or overlap defects. The work presented in this paper examines the impact of gap defects on tensile and compression strength of AFP-manufactured laminates using in-situ consolidation. Two laminates with gap defects and one reference laminate without defects were manufactured. Computed Tomography scans and microsections were generated to determine resulting defects and porosity in the gap areas. Tensile and compression test samples were prepared and tested. Tensile test results remained at the same level for all configurations. Compression strength decreased for the specimens with gap defects.*

Keywords: Automated Fibre Placement; Thermoplastic Composites; in-situ Consolidation; Gap Defects; Mechanical Properties

1. Introduction

In-situ Automated Fibre Placement (AFP) is a promising manufacturing process, which dispenses with post consolidation process steps as autoclave- or press-consolidation. Instead, the structure is fully consolidated in the course of the additive in-situ process. This process has the potential to reduce production time- and energy, leading towards a more sustainable manufacture of large composite structures. Without a subsequent autoclave- or press-consolidation-process to mitigate resulting defects, detailed analysis and evaluation of the interdependent layup parameters is required to ensure structural integrity of the manufactured components. The manufacture of complex non-developable geometries using AFP inevitably results in defects. The following three interdependent factors determine the type and magnitude of the defects: Fibre angle deviation, fibre steering and gap and overlap defects. The fibre angle deviation is the angular deviation from the required ply angle orientation following layup on a curved surface. This deviation has to be as small as possible. A typical aerospace industry requirement is below $\pm$ 3° [1]. Fibre steering describes the in-plane curvature of the layup path. Steering radii below a critical value result in manufacturing defects. Comprehensive research has been conducted on steering of thermoset AFP layup [2-6]. Zenker et al. [7-8] and Clancy et al. [9] investigated steering effects for thermoplastic AFP. Zenker et al. found increased fibre waviness and resulting local gap defects following steering of CF/PA6 6.35 mm tape. Clancy et al. achieved good results for steering radii as low as 400 mm for 6.35 mm wide CF/PEEK tape. Allowable fibre angle deviation and fibre steering can thus be considered as boundary conditions for the layup strategy. Along with the reference geometry, this results in the third defect category gaps and overlaps. The impact of gap and overlap defects on thermoset composite

  doi:10.5075/epfl-298799_978-2-9701614-0-0

structures has been investigated comprehensively [9-21]. Depending on laminate and defect design, maximum compression strength reductions between 1 % [11] and 55 % [14] were found. Defect-induced out-of-plane waviness was identified as a main factor for the strength decrease [20]. Tensile strength was generally found to be less critical than compression strength with gap- and overlap-induced maximum strength decreases between 3.4 % [11] and 45 % [16]. Nguyen et al. found a strength increase of 20 % for an overlap configuration with 12.7 mm overlaps [16].

Thus far, only two studies focus on AFP gap- or overlap defects for thermoplastic material. Rakhshbahar et al. investigated tensile strength of unidirectional specimens with 3 mm wide pairwise stacked gaps [22]. The specimens were consolidated in a hot press. The decrease in tensile strength was 13 % compared to the reference laminate. Zenker et al. investigated the impact of gap and overlap defects in CF/PPS specimens, which were consolidated in either a variothermal press cycle, autoclave or stamp consolidation process. Defects were included in 0° and 90° plies and 2.5 mm or 7.35 mm in size. Specimens with gap defects in 0° plies showed the largest decrease in ultimate strength of over 70 % and over 60 % for tensile and compressive tests, respectively. Gaps in 90° plies resulted in tensile strength decreases of up to 40 % and compression strength decreases of up to 33 % [23]. To the author's knowledge, no research has been carried out for the effect of gap defects on in-situ AFP manufactured laminates thus far. This work presents a first experimental investigation of gap defects using in-situ AFP.

2. Materials and Methods

2.1 Facility and Specimen Manufacture

The laminates for experimental investigation were manufactured at the thermoplastic AFP facility at the German Aerospace Center (DLR) Institute of Structures and Design in Stuttgart, Germany. The facility uses a 6 kW near-infrared laser combined with a Multi Tape Laying Head end-effector (AFPT GmbH, Dörth) and a cooled compaction roller (Fig. 1).

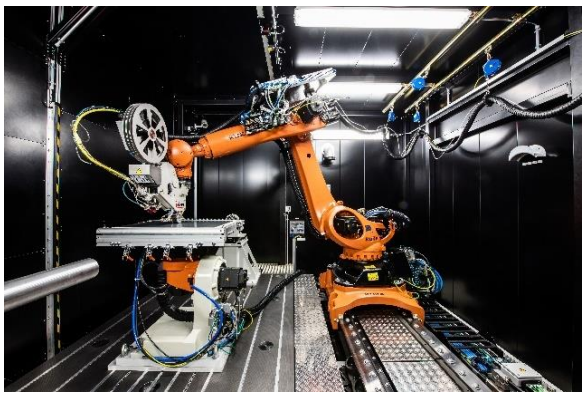

Figure 1. Thermoplastic AFP facility at DLR Institute of Structures and Design, Stuttgart

A closed-loop temperature control system is used, to keep the temperature in the consolidation zone (nip-point) within the optimum process window. This allows for processing of high-temperature thermoplastic composites. In this case, carbon-fibre-reinforced low-melt polyaryl ether ketone (CF/LM-PAEK) prepreg slit tape with a fibre volume fraction of 60 % was used for the experiments. The Material was supplied by Toray Advanced Composites (TC1225) and slit to a tape width of 12.7 mm. Three laminates were manufactured within the scope of this work: one acting as a defect-free reference and the others with different defect (gap) severities. The laminates were manufactured on an unheated tooling. Optimum manufacturing parameters

  doi:10.5075/epfl-298799_978-2-9701614-0-0

were determined in previous work [24,25]. A nip-point temperature of 470 °C, consolidation pressure of 6 bar and a layup speed of 7.5 m/min were used. All three laminates were manufactured using the same balanced and symmetric (quasi-isotropic) ply stacking sequence $[0°/-45°/90/°45°]_{2S}$. Gaps were introduced into the laminates in all four 90° layers, resulting in discrete reductions of ply quantity of 25 % (16 layers to 12). This exaggerated configuration was chosen in order to cause a severe deterioration of the consolidation properties in the gap area and examine possible delamination, out-of plane waviness or other effects occurring due to the in-situ process [11,20,23]. AFP layup of complex geometries results in gap defects of triangular shape, with the shortest side corresponding to the width of the utilised tape material. Common AFP prepreg material widths are 12.7 mm and 6.35 mm (1/2 inch and 1/4 inch). The industry customary gap allowance between adjacent tapes of 0.5 mm [1] was added resulting in expected defect gaps of 13.2 mm and 6.85 mm.

2.2 Computed Tomography

A high resolution microfocus computed tomography (µCT) system (nanotom, GE Sensing & Inspection Technologies GmbH, Wunstorf) was used for the non-destructive inspection of the laminates. The system comprises a microfocus X-ray tube with maximum accelerating voltage of 180 kV and a 12-bit flat panel detector. X-ray parameters 80 kV / 180 µA at an exposure time of 1000 ms enabled a voxel size of 2 µm. The commercial software package VGStudioMax 3.4 (Volume Graphics GmbH, Heidelberg) was used for data analysis and visualisation.

2.3 Microsections

Specimens for microscopic analysis were embedded in epoxy resin and ground using a grinding and polishing system (Struers ApS, Denmark). A VHX-5000 digital microscope (Keyence Deutschland GmbH, Neu-Isenburg) was used for analysis and image visualization.

2.4 Mechanical Testing

From the manufactured laminates, tensile and compression test samples were prepared. The tensile test samples were prepared and tested according to AITM 1-0007 A2 [26] at the DLR Stuttgart facility. Specimen dimensions were 250 mm by 22 mm with 50 mm long end tabs. The specimens were tested to failure using a ZwickRoell 500 kN material testing machine at a rate of 2 mm/min. Ultimate tensile strength was determined using Eq. (1):

$$\sigma_{tu} = \frac{P_u}{t_n \cdot w} \tag{1}$$

P_u is the maximum load, t_n is the specimen thickness and w is the specimen width. The specimen thickness was approximately 2.9 mm.

Compression test samples were prepared according to AITM 1-0008 A2 [27] and tested at COTESA GmbH in Mittweida, Germany. Specimen dimensions were 172 mm by 22 mm with 75 mm end tabs, resulting in a free length of 22 mm. The test rate was 0.5 mm/min and an anti-buckling device was used during the tests. Ultimate compression strength was determined using Eq. (2):

$$\sigma_{cu} = \frac{P_u}{t_n \cdot w} \tag{2}$$

  doi:10.5075/epfl-298799_978-2-9701614-0-0

P_u is the maximum load, t_n is the specimen thickness and w is the specimen width. At least 6 specimens of each configuration were tested for both tensile and compression tests.

3. Results

3.1 Computed Tomography

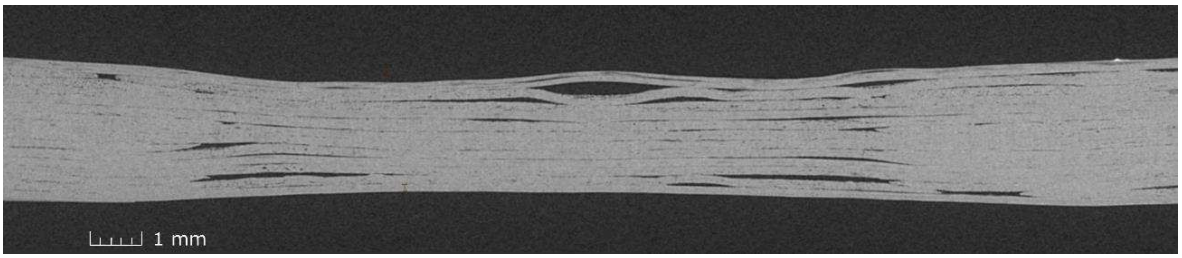

Figure 2. Computed Tomography scan of 13.2 mm gap defect, voxel size: 15 µm

Fig. 2 shows the CT scan of a specimen with 13.2 mm gap configuration. Delamination can be detected in particular in the edge region of the gap close to the ply drops. Poor consolidation is moreover found in the center of the gap between the top layers. Fig. 3 shows a representative section of the reference laminate. Intralaminar porosity is apparent in the first ply at the bottom of the laminate. A large pore of 0.3 mm in width can be detected in ply 4, which is a gap between adjacent courses. Repeated interlaminar porosity can be found throughout the laminate.

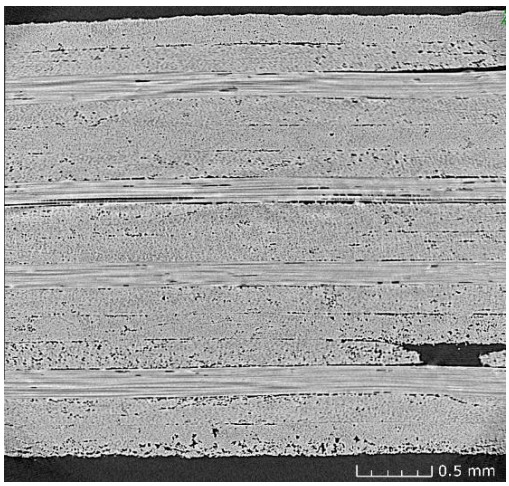

Figure 3. Computed Tomography scan of reference laminate, voxel size: 2 µm

3.2 Microsections

A microsection of the 6.85 mm gap configuration is depicted in Fig. 4 For the purpose of clarity, the dropped 90° plies are highlighted in red. Distinct triangular pores can be recognized adjacent to the ply drops. Within the gap area, the bottom half of the laminate is poorly consolidated with pronounced interlaminar porosity. Fig. 5 shows a microsection of the 13.2 mm gap configuration. Triangular pores are found again in the vicinity of the ply drops. Interlaminar porosity is less pronounced than in the 6.85 mm gap configuration.

  doi:10.5075/epfl-298799_978-2-9701614-0-0

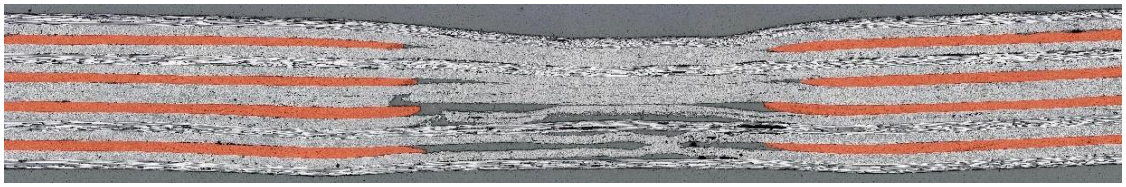

Figure 4. Microsection of 6.85 mm gap configuration

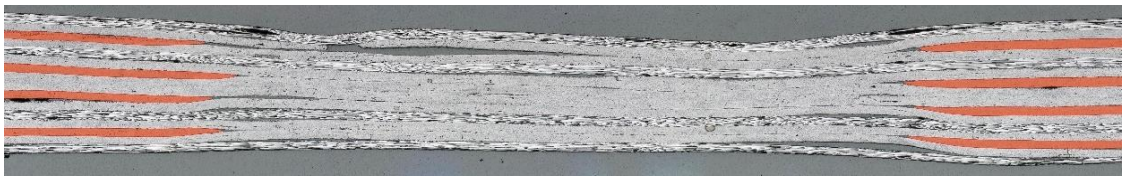

Figure 5. Microsection of 13.2 mm gap configuration

3.3 Mechanical Testing

Fig. 6 shows the tensile strength test results. The reference laminate without gap defects achieved an ultimate median tensile strength of 699 MPa with a standard deviation of 19 MPa. Both gap configurations reached a slightly higher median tensile strength of 721 MPa. The compression strength test results are depicted in Fig. 7. The reference laminate reached a median ultimate compression strength of 224 MPa with a standard deviation of 12 MPa. The 6.35 mm and 13.2 mm gap configuration reached 51 % and 54 % of the reference strength, respectively.

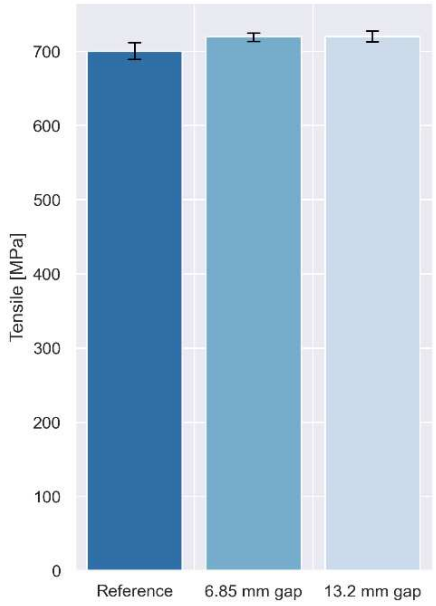

Figure 6. Tensile strength results

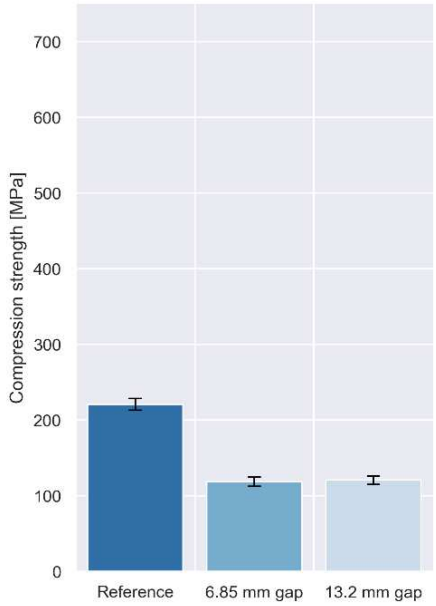

Figure 7. Compression strength results

4. Discussion

Both CT scans and microsections reveal pronounced porosity in the gap region. The triangular pores next to the ply drops are likely due to fibre bridging. The compaction roller has a diameter of 80 mm and a 5 mm-thick silicone cover which is not able to force the stiff tape closer to the step geometry. To ensure a stable process, the tape is held under tension, which adds to the bridging effect. While these triangular pores would be filled with resin during a post-

  doi:10.5075/epfl-298799_978-2-9701614-0-0

consolidation process, the in-situ process results in small pores in these sections. In the case of the 6.35 mm gap configuration, the triangular ply drops, in combination with the tape tension results in a delamination force, which is splitting the newly added tape from the substrate, creating a bridge between the ply drop edges. This effect is less pronounced in the 13.2 mm gap configuration, as a larger area for consolidation is available between the ply drop edges. A second explanation for the suboptimal consolidation in the gap area is a disturbance of the temperature control due to the gap defect. An analysis of the temperature control log revealed a fluctuation in control parameters. Approaching the ply drop off, the temperature control system detected an apparent increase in ply temperature. As a consequence, the laser power was decreased. The nip-point-temperature was thus below the optimum process temperature in the area of the gap defects. Both these effects likely resulted in suboptimal consolidation. The consolidation roller configuration and the temperature control system with respect to ply drop offs will be investigated in future work. The CT results revealed interlaminar porosity not only in the defect areas, but also in the reference laminate. Ongoing investigations address minimisation of porosity through the use of optimised materials and process parameters.

Both gap defect sizes result in similar compression and tensile strength results. This agrees with results by Sawicki et al. showing that further increases in gap size above a threshold of 0.76 mm did not further decrease strength results. Tensile strength was not mitigated by the gap defects. Undulation and porosity in the gap area thus did not affect tensile strength. The chosen gap configuration did not disrupt the main load-bearing 0° plies. Zenker et al. found a slight decrease in tensile strength of around 3 % for a similar stacking sequence and gap configuration (7.35 mm gap width) using isothermal stamping post consolidation and larger tensile strength decreases of up to 40 % for variothermal press consolidation [23]. It is generally viewed as a disadvantage of the in-situ AFP process, that pores and gaps cannot be filled with resin as in a post-consolidation process. In this case however, this might be an advantage as the 0° plies are not weakened by resin passing from the 0° plies to the porous areas. Further analysis of failure mode and detailed comparison with post consolidated samples will be subject to future investigation. Unlike tensile strength, compression strength decreased significantly by almost half of the reference strength value. Significant compression strength decreases were reported also in [10, 14, 20, 21]. Zenker et al. [23] found a compression strength decrease of up to 30 % from 7.35 mm wide defects in 90° plies. While Zenker et al. used a caul plate or press tooling to achieve a uniform laminate thickness, the in-situ AFP process, as well as post consolidation processes with soft tooling, result in decreased laminate thickness in the area of gap defects. The manufactured specimens showed a local thickness reduction of 0.6 to 0.9 mm in the area of the gap defects. While the bottom of the laminate follows the tooling surface, the subsequent plies are increasingly pushed in, resulting in a through thickness asymmetry which leads to a local shift in midplane. This in turn results in a bending moment, similarly reported in work by Nguyen et al. [16]. Furthermore, increased porosity and undulations in the gap area facilitate buckling of the 0° plies. Future work will focus on decreasing porosity in the gap defect area, to mitigate these effects.

5. Conclusion

This paper presents a first investigation into the impact of gap defects on in-situ AFP manufactured laminates. The results were promising with regard to in-situ manufacture of complex structures since the weakening of the laminate was less pronounced than expected.

  doi:10.5075/epfl-298799_978-2-9701614-0-0

The two investigated gap sizes resulted in similar tensile and compression strength results. While tensile strength remained at the same level, compression strength decreased due to suboptimal consolidation in the defect area. Future work will focus on optimising the layup process for disruptions due to ply drops to achieve better consolidation in the gap areas.

Acknowledgements

The results presented here were produced as part of the TRumpf research project (FKZ: 20W1721D) in the Federal Aviation Research Programme V-3. Funding was provided by the Federal Ministry for Economic Affairs and Energy, on the basis of a decision by the German Bundestag.

4 References

1. AIPS03-02-019 Issue 11 June 2016, Airbus Process Specification, Manufacture of Monolithic Parts with Thermoset Prepreg Materials.
2. Wang H, Chen J, Fan Z, Xiao J, Wang X. Experimental Investigation on the Influence of Fiber Path Curvature on the Mechanical Properties of Composites. Materials 2021; 14(10):2602.
3. Rajan S, Sutton MA, Wehbe, R, Tatting B, Gürdal Z, Kidane A, Harik R. Quantifying Wrinkling During Tow Placement on Curvilinear Paths. Advancements in Optical Methods & Digital Image Correlation in Experimental Mechanics 2020; 3:9-12.
4. Rajasekaran A, Shadmehri F. Steering of carbon fiber/PEEK tapes using Hot Gas Torch-assisted automated fiber placement. Journal of Thermoplastic Composite Materials 2022; 0(0):1-29.
5. Wehbe R, Tatting B, Rajan S, Harik R, Sutton M, Gurdal Z. Geometrical modeling of tow wrinkles in automated fiber placement. Composite Structures 2020; 246:112394.
6. Akbarzadeh AH, Nik Arian M, Pasini D. The role of shear deformation in laminated plates with curvilinear fiber paths and embedded defects. Composite Structures 2014; 118:217-227.
7. Zenker T, Gnaedinger M. Consolidation Behavior of Fiber Steered Thermoplastic Automated Fiber Placement Preforms. In Proceedings of the 5th International Conference and Exhibition on Thermoplastic Composites ITHEC 2020; 13-14 .
8. Clancy G, Peeters D, Oliveri V, Jones D, O'Higgins RM, Weaver PM. A study of the influence of processing parameters on steering of carbon Fibre/PEEK tapes using laser-assisted tape placement. Composites Part B: Engineering 2019; 163:243-251.
9. Zhang XZ, Bai RX, Lei ZK, Zhu YG, Geng CH, Feng Y, Zhong Z, Wu W. Study on tensile properties of composite laminates with gap defects. 2nd International Workshop On Materials Science And Mechanical Engineering (IWMSME2018) 2019; 504(1):012079.
10. Sawicki A, Minguett P. The effect of intraply overlaps and gaps upon the compression strength of composite laminates. 39th AIAA/ASME/ASCE/AHS/ASC Structures, Structural Dynamics, and Materials Conference and Exhibit 1998; 1786.
11. Croft K, Lessard L, Pasini D, Hojjati M, Chen Jihua, Yousefpour A. Experimental study of the effect of automated fiber placement induced defects on performance of composite laminates. Composites Part A: Applied Science and Manufacturing 2021; 42(5):484-491.
12. Woigk W, Hallett ST, Jones IM, Kuhtz M, Hornig A, Gude M. Experimental investigation of the effect of defects in Automated Fibre Placement produced composite laminates. Composite Structures 2018; 201:1004-1017.

  doi:10.5075/epfl-298799_978-2-9701614-0-0

13. Lan M, Cartie D, Davies P, Baley C. Microstructure and tensile properties of carbon-epoxy laminates produced by automated fibre placement: Influence of a caul plate on the effects of gap and overlap embedded defects. Composites Part A: Applied Science and Manufacturing 2015; 78:124-134.
14. Lan M, Cartie D, Davies P, Baley C. Influence of embedded gap and overlap fiber placement defects on the microstructure and shear and compression properties of carbon-epoxy laminates. Composites Part A: Applied Science and Manufacturing 2016; 82:198-207.
15. Falcó O, Lopes CS, Naya F, Sket F, Miamí P, Mayugo JA. Modelling and simulation of tow-drop effects arising from the manufacturing of steered-fibre composites. Composites Part A: Applied Science and Manufacturing 2017; 93:59-71.
16. Nguyen MH, Vijayachandran AA, Davidson P, Call D, Lee D, Waas AM. Effect of automated fiber placement (AFP) manufacturing signature on mechanical performance of composite structures. Composite Structures 2019; 228:111335.
17. Del Rossi D, Cadran V, Thakur P, Palardy-Sim M, Lapalme M, Lessard L. Experimental investigation of the effect of half gap/half overlap defects on the strength of composite structures fabricated using automated fibre placement (AFP). Composites Part A: Applied Science and Manufacturing 2021; 150:106610.
18. Guin WE, Jackson JR, Bosley CM. Effects of tow-to-tow gaps in composite laminates fabricated via automated fiber placement. Composites Part A: Applied Science and Manufacturing 2018; 115:66-75.
19. Suemasu H, Aoki Y, Sugimoto S, Nakamura T. Effect of gap on strengths of automated fiber placement manufactured laminates. Composite Structures 2021; 263:113677.
20. Marrouze JP, Housner J, Abdi F. Effect of manufacturing defects and their uncertainties on strength and stability of stiffened panels. ICCM19 Montreal, Canada 2013.
21. Nartey M, Zhang T, Gong B, Wang J, Peng S, Wang H, PengH. Understanding the impact of fibre wrinkle architectures on composite laminates through tailored gaps and overlaps. Composites Part B: Engineering 2020; 196: 108097.
22. Rakhshbahar M, Sinapius M. A novel approach: combination of automated fiber placement (AFP) and additive layer manufacturing (ALM). Journal of Composite Science 2018; 2(3):42.
23. Zenker T, Bruckner F, Drechsler K. Effects of defects on laminate quality and mechanical performance in thermoplastic Automated Fiber Placement-based process chains. Advanced Manufacturing: Polymer & Composites Science 2019; 5(4):184-205.
24. Schiel I, Raps L, Chadwick AR, Schmidt I, Simone M, Nowotny S. An investigation of in-situ AFP process parameters using CF/LM-PAEK. Adv Manuf: Polym Compos Sci 2020; 6:191–197.
25. Raps L, Chadwick AR, Schiel I, Schmidt I. CF/LM-PAEK: Characterisation and sensitivity to critical process parameters for automated fibre placement. Composite Structures 2022; 284:115087.
26. AITM 1-0007 Issue 5 March 2016, Airbus Test Method, Fibre Reinforced Plastics, Determination of Plain, Open Hole and Filled Hole Tensile Strength.
27. AITM 1-0008 Issue 5 March 2016, Airbus Test Method, Fibre Reinforced Plastics, Determination of Plain, Open Hole and Filled Hole Compression Strength.

  doi:10.5075/epfl-298799_978-2-9701614-0-0

POLYPROPYLENE/FLAX FABRIC COMPOSITE LAMINATES: EFFECTS OF PLASMA AND THERMAL PRE-TREATMENTS OF REINFORCING FIBRES

Pietro, Russo[a], Giulia, Leone[b], Gennaro, D'Angelo[b], Pietro, Ferraro[b], Vito, Pagliarulo[b]

a: Institute for Polymers, Composites and Biomaterials (IPCB), National Research Council, via Campi Flegrei 34, 80078 Pozzuoli, Italy – pietro.russo@ipcb.cnr.it
b: Institute of Applied Sciences & Intelligent Systems (ISASI) "E. Caianiello", National Research Council, via Campi Flegrei 34, 80078 Pozzuoli, Italy

Abstract: *In this work, the combined effect of plasma treatment and drying of flax fabrics on the mechanical and physical performance of hot-pressed polypropylene-based laminates is examined. Specifically, flax fabrics exposed for 15 min to a stream of nitrogen plasma were dried at 70 °C in a vacuum oven for different times (0, 3 h and overnight) and incorporated into laminar structures applying pre-optimized process conditions. Wicking tests were performed to analyse their absorption properties, while quasi-static tests in terms of flexural and tensile measurements were made to compare the mechanical performance of all samples prepared. In addition, optical techniques have been used for morphological analyses and damage NDT inspection, i.e. SEM and ESPI, respectively.*

Keywords: Composite laminates; plasma treatment; polypropylene; flax fabric; non-destructive technique.

1. Introduction

In recent years, the "green" market is evolving to face the challenge of climate change. In this respect, the use of natural fibre as reinforcement in composite has grown due to environmental reasons. Thanks to the reduction of the pollution associated with the extraction, production and disposal, natural fibres open the door for new low environmental impact solutions in the aerospace [1], automotive [2] and biomedical [3] industries. From this perspective, green composites were developed for both functional and structural applications replacing traditional materials as demonstrated by Al-Hajaj et al [4] that have carried out non-destructive investigations to state the performance of hybrid composite made by woven Kevlar and flax fibres. Different fibre orientations were taken into account to establish the configuration that best resists low-velocity impact and the results suggest that the measured impact toughness is slightly better compared to those of aluminium alloys and carbon fibre composites. Mocerino et al [5] have focused on the hybridization process of carbon/hemp composite laminate to combine the mechanical performance of the carbon with the ability to adsorb energy of the natural fibres. The results show an improvement of the adsorbed energy capability and a decrease in the delamination extension after an impact event of the hybrid composite compared to the traditional carbon fibre one. A FE model has also been validated to predict the impact response and the crack evolution showing a good agreement with experimental results.

However, natural fibres, due to their inherent hydrophilic nature, are incompatible with most of the polymers that usually have a hydrophobic behaviour that threatens interfacial adhesion. Mechanical performance of the composite is strongly dependent on the quality of the interface

  doi:10.5075/epfl-298799_978-2-9701614-0-0

and an incorrect adhesion can be determinant for the quality of the interfacial phase, limiting the laminate's applications. Surface pre-treatments can be employed to improve the compatibility between the reinforcement and the matrix, such as electric discharge (corona, cold plasma), alkali treatment, silane coupling agent, and so on. In the contribution of Wu et al [6] natural bamboo fibers have been modified with methacrylic anhydride to improve interfacial adhesion in composites processed by 3D printing with photopolymerization of vinyl palm oil-based resins. Kaboglu et al [7] have investigated the effect of the pre-modified maleic anhydride-grafted PP matrix for flax fabric-based composite to enhance the interfacial adhesion. Results confirmed potentials of suitable coupling agents to improve the mechanical behaviour of products by decreasing the out-of-plane displacement under impact loads.

In this regard, superficial plasma treatment is largely employed to modify the natural fibres' surfaces introducing reactive groups without the employment of dangerous chemicals and the formation of toxic reaction products. In addition to surface treatments, it is a common practice to dry fibre to previously remove the water in bulk and more. Fiore et al [8] have investigated the degradation phenomena of natural fibre reinforced composites in order to evidence reversible ones that allow a mechanical recovery after the drying treatment. They demonstrated that flexural strength is strongly dependent on reversible ageing phenomena, while stiffness is related to irreversible ones.

In this work, the combination of plasma and drying treatments was analysed at different parameters, poorly explored in the literature. Based on previous studies, flax fabrics were treated with low-pressure plasma treatment for 15 min and dried in the oven for 0 h, 3 h and overnight. Composite specimens were cut from hot compacted laminates based on plasma treated and eventually dried flax fabric and poly-propylene (PP) matrix. Wettability properties were measured by means of a longitudinal wicking test. The performance of natural fibre composite was examined under tensile and flexural loads. Finally, Electronic Speckle Pattern Interferometry (ESPI) non-destructive testing and Scanning Electron Microscopy (SEM) were performed in order to quantify defects and damage extent in loaded specimens.

2. Experimental

The composite materials studied consist of a commercial woven flax fabrics (density: 200 g/m^2, 2x2 Twill structure) supplied by Composite Evolution (Chesterfield, United Kingdom) and a polypropylene (PP) matrix purchased purchased from Songhan Plastic Technology Co. Ltd under the trade name Topilene J640 (MFI @ 230 °C, 2.16 kg: 10g /10 min).

Preliminarily, the matrix was processed by flat filming to obtain an 80 µm-thick PP film using a Collin Teach-Line E-20 T extruder equipped with a Collin CR 72T calender. The temperature profile along the screw was set equal to 180-190-200-190-185 °C from the hopper to the filming head with a screw speed of 55 rpm.

The reinforcing flax fabric, precut in layers of suitable dimensions, was treated with a low-plasma system (ATTO Type B, Diener Electronic, Germany) created by an inductively coupled RF generator, using nitrogen, N_2, as process gas. The equipment is composed of a cylindrical borosilicate glass chamber with an inner diameter of 211 mm and a depth of 300 mm, connected to a vacuum system that consists of a rotary slide pump with a suction power of 2.5 m^3/h. The fabrics (160 mm x 160 mm) were treated for 15 min at a low frequency of 40 kHz and power of 200 W, and the process pressure was about 0.5 mbar.

In addition, flax fabric layers were also dried at 70 °C in a vacuum oven considering different treatment times corresponding to 0 h, 3 h and overnight.

In the light of already consolidated knowledge on the durability of the plasma treatment efficacy, significantly reduced after only a few days, the treated fabrics were employed to produce composite samples within less than 12 hours of their production. Each laminate was obtained by superimposing 12 reinforcement layers, preliminarily conditioned as above, alternated with PP films, and compacting the stack of layers by means of a Collin Model P400E press at 190 ° C and according a pre-optimized pressure cycle. In this way, 160 mm x 160 mm laminate plates were obtained from which rectangular specimens were cut according to ASTM D3039 and ASTM D790 Standards for tensile and interlaminar shear (ILSS) tests, respectively.

Longitudinal wicking measurements were performed on treated flax fabric in laboratory conditions at 23.9 °C and 55% RH, and results were compared to untreated fabrics values. The vertical testing apparatus is shown in Fig. 1. The fabrics were dipped in a distilled water reservoir to a depth of 5 mm. In order to monitor the water rising speed, the height of the waterfront was recorded for each 10 mm travelled as a function of time and the total duration of each test was 300s.

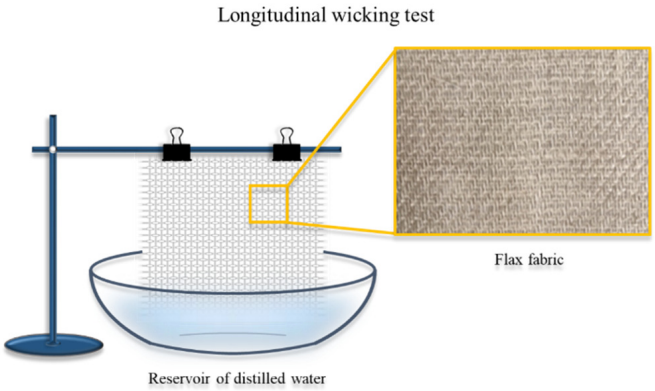

Figure 1. Longitudinal wicking test apparatus: reservoir of distilled water, sample holder and flax fabric sample.

Tensile measurements were carried out setting a crosshead speed of 2 mm/min and Digital Image Correlation (DIC) technique was employed to obtain in-plane surface deformation of the specimens and to measure strains. After collecting the planar specimen surface images during the tensile test, the images were processed by “GOM Correlate” software to evaluate the strains.
ILSS tests were performed with Universal Testing Machine (Instron model 4301), equipped with a 1 kN load cell, setting a ratio between the distance of the supports (span) and the thickness of the specimen equal to 10 and a loading speed concentrated to 2 mm / min. Failure strength and modulus were calculated by processing typical stress-strain curves.

After the mechanical testing, specimens were analysed by optical techniques: Electronic Speckle Pattern Interferometry (ESPI) and Scanning Electron Microscopy (SEM). The typical set-up of the system for recording ESPI measurements can be found in previous works [9]. SEM was adopted to collect images of the fibre-matrix interface using a field emission (FEI Quanta 200) instrument under low vacuum and an acceleration voltage of 30 kV. Before the analysis, specimens were coated with an Au/Pd layer applied with sputter coating equipment.

  doi:10.5075/epfl-298799_978-2-9701614-0-0

3. Results and discussion

The effect of the plasma treatment on flax fabrics was investigated in previous works [10] with the aim to find the optimal exposure time to the N_2 gas that best improves the interfacial adhesion with the PP polymer. For this purpose, the reinforcing fabrics were treated to low-pressure plasma treatment at different times equal to 0 min, 5 min, 10 min and 15 min and opportunely dried. The results in terms of morphological and mechanical properties were compared with respect to the only pre-dried fabrics assumed as a reference sample. Samples with flax fibres treated for the longest time of 15 min were found to exhibit the best performance. Results of the wicking tests suggested that the plasma treatment has a relevant effect on the fibre surface wettability, witnessed by an increase in the speed of the waterfront in accordance with the increase of the treatment time.
Fig. 2 compares the representative tensile stress-strain curves of flax fabric specimens pre-exposed to plasma for different times. Clearly, flax fabric specimens pre-treated for 15 min (Plasma 15') show the best tensile properties while the fabric specimens treated for 5 and 10 min seem to have mechanical parameters even lower than those of the reference pre-dried flax fabric. This behaviour can be ascribed to structural changes induced both by drying and by plasma surface treatment, as partially evidenced by the results of the analyses reported in this contribution.

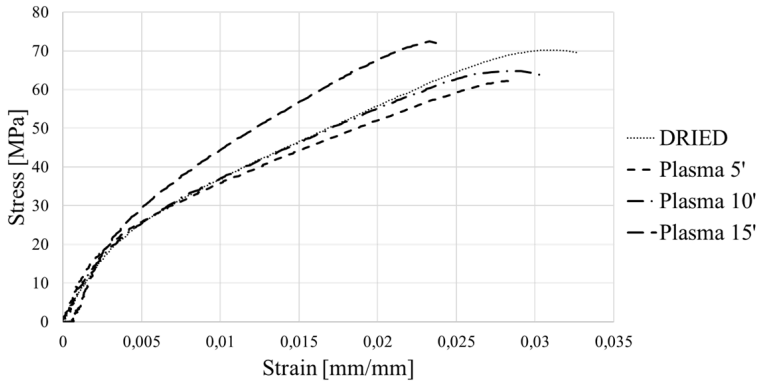

Figure 2. Representative tensile stress-strain curves of FF/PP composites with pre-dried fibres exposed to low-pressure plasma for 0 min, 5 min, 10 min and 15 min.

Considering a fixed low-pressure plasma treatment of 15 min, flax fabrics were dried for 0 h (P15), 3 h (P15 + D3) and overnight (P15 + DOn), then tested for longitudinal wicking and the results were compared to those of the un-treated fabrics (UT).
Wicking tests made it possible to obtain useful information regarding the diffusion of water both from the bundles' fibres surface into the fabric, and between the fibres of the individual bundles by means of capillarity.

Fig. 3 (a) shows the results of the vertical wicking tests in terms of the height of the waterfront as a function of the test time up to 300 s for the untreated fabric and for those exposed to plasma for the three different times considered (5, 10 and 15 min). It is noticed that the representative curves show a linear trend within the first 30 seconds before the change of the slope. This tendency is typically explained by assuming that at the beginning of the test the surface forces are predominant, wetting the fabric, and then the water penetrates among the fibres by capillarity [11]. For each treated fabric the water uptake speed is greater than that

  doi:10.5075/epfl-298799_978-2-9701614-0-0

detected for the un-treated one. The (P15) and (P15 + DOn) samples return the longer travelled final distance.
The capillarity flow regime is generally expressed in literature with the Lucas-Washburn power low equation [12]:

$$h(t) = kt^p \quad (1)$$

where *h* is the height of the water rise, *t* is the time, *k* is the wicking constant and *p* is the wicking rate power low index. The parameters *k* and *p* are determined by transforming the graph of Fig. 3 (a) into a bi-logarithmic scale in Fig. 3 (b). The *k* constant is strongly dependent on capillarity and the highest values are calculated for P15 and P15+D3 samples. While the wicking ratio, *p*, corresponds to the speed of the phenomena relevant for a longer time than those of interest in this work.

Based on the results collected in Table 1, P15 and P15+D3 showed similar wettability and, therefore, it is possible to assume that they are the best candidates to reach a good interfacial adhesion with the hosting matrix.

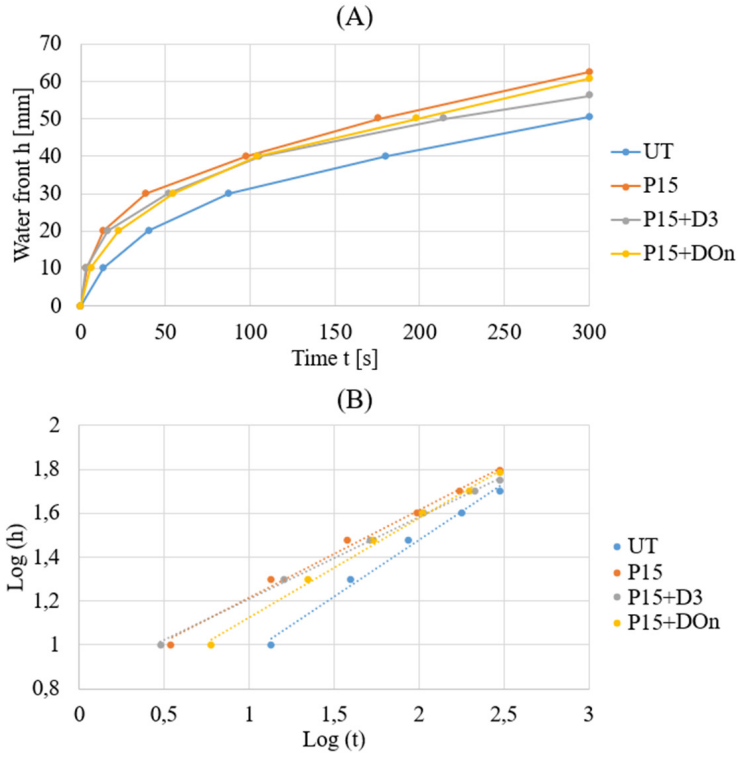

Figure 3. (a) Water uptake evolution of the liquid height, h, along the flax fabrics as a function of time, t, and (b) the bi-logarithmic scale representation.

Table 1: Wicking parameters.

	UT	P15	P15+D3	P15+DOn
p (slope)	0.5169	0.3992	0.3731	0.4563
k (intercept)	0.4444	0.8159	0.8355	0.6668

Figs 4 and 5 show the mean values of the tensile and shear properties, respectively, by histograms. Compared to the only 15 min plasma treatment, for a long time of pre-drying the mechanical performance improves. In detail, with respect to P15, the ultimate tensile strength

and Young's modulus of the P15+DOn sample improve by 14.06% and 5.78%, respectively, while the ILSS strength and modulus improve by 4.02% and 16.15%. For the shorter time equal to 3h of pre-drying the combination of the treatments is not relevant. The higher ILSS modulus of the P15 + DOn specimen has to be attributed to a better impregnation of the reinforcement fabric by the host matrix and, therefore, to a greater ability of the composite to withstand the internal stresses triggered during the loading. This behaviour can be ascribed to the optimal combination between the improvement in interfacial affinity induced by the N2 plasma treatment and the surface drying effect in the vacuum oven.

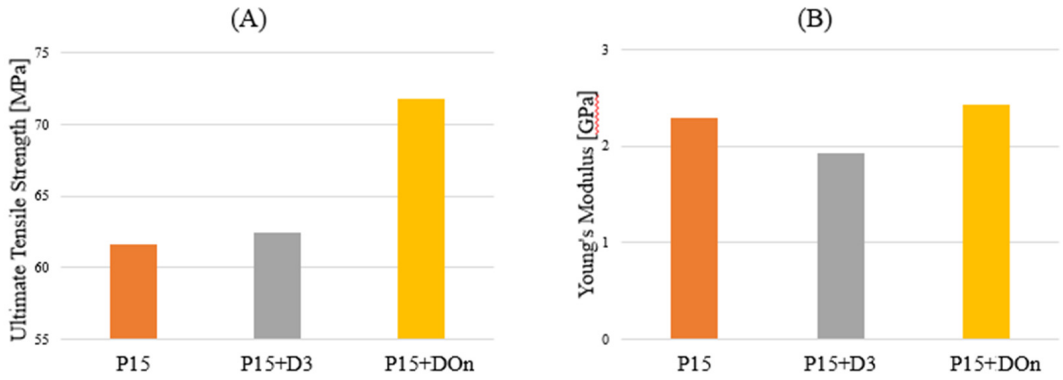

Figure 4. Tensile strength (A) and modulus (B) of flax-PP composites with treated fabrics for 15 min to plasma flow and dried for 0 h (P15), 3 h (P15+D3) and overnight (P15+DOn).

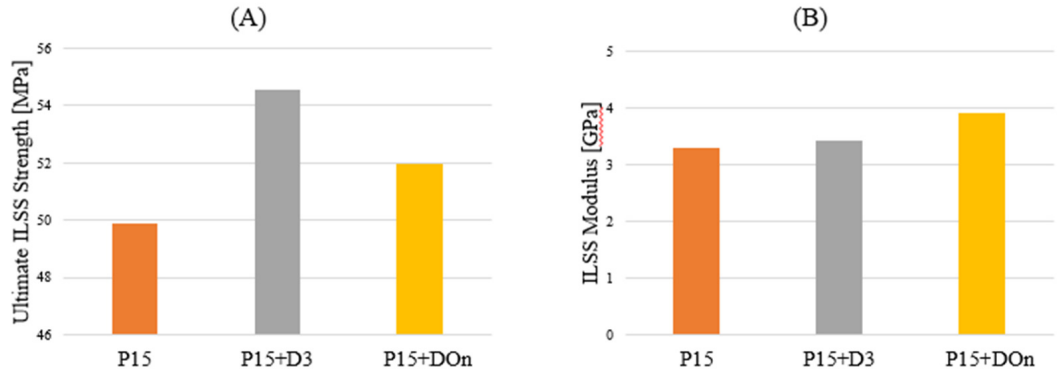

Figure 5. ILSS strength (A) and modulus (B) of flax-PP composites with treated fabrics for 15 min to plasma flow and dried for 0 h (P15), 3 h (P15+D3) and overnight (P15+DOn).

As far as ESPI investigation is concerned, Fig. 6 shows the unwrapped phase-contrast maps obtained by numerical processing using 4-step phase-shifting. Thanks to the grey scale, it is possible to identify in the central part of each specimen the area previously loaded and delaminated after the ILSS test. Using a Matlab code, the damaged areas were calculated and the results are reported in Table 2. With regard to specimens including flax fabric layers exposed to plasma for 15 min (P15) and not dried, it appears that the delaminated area increases if the reinforcing fabric is pre-dried for 3 h and then abruptly decreases for specimens in which the fabric is subject to longer pre-drying times. This evidence is coherent with ILSS modulus results since the highest modulus corresponds to the sample P15+DOn which resists better the out-of-plane deformations, and it is consequently affected by lower delamination. In accordance with

  doi:10.5075/epfl-298799_978-2-9701614-0-0

previous results, ESPI analysis confirms that an overnight drying of the flax fabric in combination with a 15 min plasma treatment is able to ensure the best performance of polypropylene-based composites.

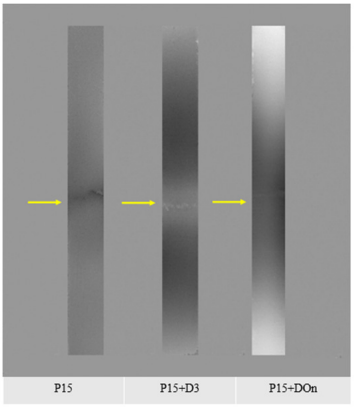

Figure 6. ESPI unwrapped phase image of the composite with flax fabrics exposed to plasma for 15 min and additionally dried for 0 h (P15), 3 h (P15+D3) and overnight (P15+DOn), left to right.

Table 2: Damaged area measured by ESPI technique.

	P15	P15+D3	P15+DOn
Area [mm^2]	42.22	51.56	35.02

In Fig. 7 SEM micrographs, collected at different magnifications, highlight interface details between the treated flax fabrics and the PP matrix. Drying appears to induce a fraying effect of the fibres and laminates seem to be less compacted with the increase of the treatment time. This effect can increase the surface/volume ratio promoting the matrix penetration and consequently enhancing the interfacial fibre/matrix interlocking. Thus, for sufficiently long treatment times, the resin can better penetrate the fibre bundles, increasing the interface bonds. Only some pull out phenomena is noted (see arrows), essentially due to a localized loss of adhesion between the fibre bundle and the matrix.

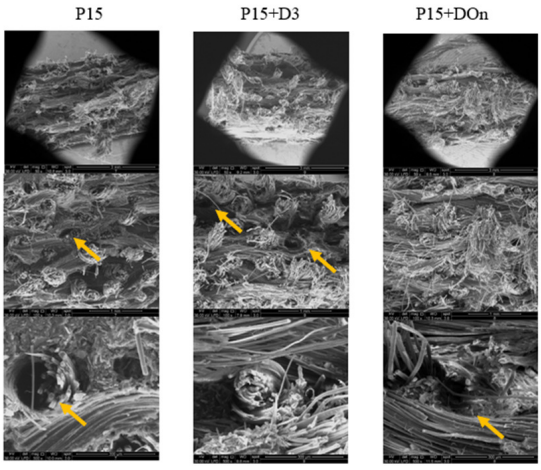

Figure 7. SEM images of the composite with flax fabrics exposed to plasma for 15 min and additionally dried for 0 (P15), 3 h (P15+D3), and overnight (P15+DOn) at different magnifications. Arrows indicate pull-out phenomenon.

4. Conclusions

The results achieved so far show that an appropriate combination of plasma treatment and drying of the reinforcing fabrics can generate interesting performances of the produced composites. Specifically, considering that the benefits induced by the plasma pre-treatment of the reinforcing fabric, on the mechanical properties of the relative composites, appear to increase over time for exposures lasting up to 15 min, mechanical tests, supported by morphological observations, have clearly shown that such improvements, slightly compromised by short pre-drying steps, can be further magnified by prolonged ones.

5. References

1. Mohit H, Mavinkere Rangappa S, Siengchin S, Gorbatyuk S, Manimaran P. Alka Kumari C, Khan A and Doddamani M. A comprehensive review on performance and machinability of plant fiber polymer composites. Polym. Compos. 2022; 43(1): 608-623.
2. Pantaloni D, Ollier L, Shah DU, Baley C, Rondet E and Bourmaud A. Can we predict the microstructure of a non-woven flax/PLA composite through assessment of anisotropy in tensile properties?. Compos. Sci. Technol. (2022); 218: 109173.
3. Sathish T, Palani K, Natrayan L, Merneedi A, de Poures MV and Singaravelu DK. Synthesis and characterization of polypropylene/ramie fiber with hemp fiber and coir fiber natural biopolymer composite for biomedical application. Int. J. Polym. Sci. 2021; 2462873 (8 pages).
4. Al-Hajaj Z, Sy BL, Bougherara H and Zdero R. Impact properties of a new hybrid composite material made from woven carbon fibres plus flax fibres in an epoxy matrix. Compos. Struct. 2019; 208: 346-356.
5. Mocerino D, Boccarusso L, De Fazio D, Durante M, Langella A, Meo M, Pinto F and Rizzo F. Prediction of the Impact Behavior of Bio-hybrid Composites Using Finite Element Method. ESAFORM 2021 (2021).
6. Wu Y, Li C, Chen T, Qiu R and Liu W. Photo-curing 3D printing of micro-scale bamboo fibers reinforced palm oil-based thermosets composites. Compos. Part A Appl. Sci. Manuf. 2022; 152:106676.
7. Kaboglu C, Liu J, Liu H, Russo P, Simeoli G, Lopresto V, Dear JP and Maharaj C. The effect of a coupling agent on the impact behavior of flax fiber composites. J. Eng. Mater. Technol. Trans. ASME 2021; 143(3):031008 (10 pages).
8. Fiore V, Calabrese L, Miranda R, Badagliacco D, Sanfilippo C, Palamara D, Valenza A and Proverbio E. On the response of flax fiber reinforced composites under salt-fog/dry conditions: Reversible and irreversible performances degradation. Compos. Part B Eng. 2021; 230:109535.
9. Papa I, Ricciardi MR, Antonucci V, Langella A, Tirillò J, Sarasini F, Pagliarulo V, Ferraro P, Lopresto V. Comparison between different non-destructive techniques methods to detect and characterize impact damage on composite laminates. J. Compos. Mater. 2020; 54(5):617-631.
10. Leone G, D'Angelo GA, Russo P, Ferraro P, Pagliarulo V. Plasma treatment application to improve interfacial adhesion in polypropylene-flax fabric composite laminates. Polym. Compos. 2022; 43(3): 1787-1798.
11. Raja D, Ramakrishnan G, Babu VR, Senthilkumar M and Sampath MB. Comparison of different methods to measure the transverse wicking behaviour of fabrics. J. Ind. Text. 2012; 43(3):366–382.
12. Hamdaoui M and Nasrallah S Ben. Capillary Rise Kinetics on Woven Fabrics: Experimental and Theoretical studies. Indian J. Fibre Texile Res. 2015; 40(2):150-156.

  doi:10.5075/epfl-298799_978-2-9701614-0-0

IMPROVING THE MODE II DELAMINATION BRIDGING PERFORMANCE OF FIBROUS COMPOSITE Z-PINS

Eduardo, Santana de Vega[a], Giuliano, Allegri[a], Bing, Zhang[a], Ian Hamerton[a], Stephen R, Hallett[a]

a: Bristol Composites Institute, University of Bristol

Abstract: *Composite Z-pins have been traditionally manufactured employing carbon fibres combined with a bismaleimide (BMI) resin. These materials allow a substantial enhancement of the mode I interlaminar fracture toughness of Z-pinned laminates to be achieved. Nonetheless, the improvements in mode II toughness are much more modest, due to the inherent brittleness of the combination of carbon/BMI. In order to increase the mode II dominated toughness of Z-pins, fibrous Z-pin rod-stocks were manufactured employing matrix and fibre materials with mechanical properties dissimilar to those of carbon/BMI. The novel through-thickness reinforcement candidates were inserted in quasi-isotropic glass fibre/epoxy laminates and their single-pin delamination-bridging performance was characterised under a mode II dominated loading configuration. Polybenzoxazole (PBO) fibre pins showed an increase in average energy dissipation per pin by as much as 113 mJ (2000% increase) compared to the 5mJ dissipated by traditional carbon fibre/BMI pins. The effect of twisting the fibre yarns was characterized by including Z-pins manufactured out of twisted PBO fibres. These showed 10-fold increase in performance compared to carbon fibre, albeit a reduction of 50% compared to unidirectional PBO.*

Keywords: fibre-reinforced polymer; through-thickness reinforcement; delamination; z-pins

1. Introduction

Interlaminar toughness of laminates is a critical mechanical performance indicator of most composite structures. Delamination is the predominant failure mechanism of these materials and must be accounted for in any sort of structural design. The incorporation of through-thickness reinforcement (TTR) has been the preferred way to tackle this problem. TTR consists of different methods of embedding fibrous reinforcement that bridge the load-bearing layers of the laminate and the interface between these, increasing the energy required for interlaminar cracks to appear and propagate [1]. Methods of TTR are numerous and can vary from the quasi-orthogonal insertion of fibre tows, such as those used in tufting [2] and stitching [3], to the production of dry-fibre preforms with a woven or braided 3D reinforcement architecture [4]. Most of these methods have been designed with dry fibre and resin infusion manufacturing in mind. Z-pinning is a TTR method which relies on thin metallic or composite rods, which are typically inserted orthogonally to the surface of the laminate. The stiffness of these cured rods allows them to be introduced into laminates which have been preimpregnated with resin and are the only suitable method for prepeg lamination manufacturing [5].

Most research has been aimed at studying the behaviour of commercially available steel and carbon fibre-reinforced bismaleimide (CF/BMI) composite z-pins. There is an extensive body of research dedicated to the delamination bridging behaviour of metal and CF-based composites [1,6,7]. This has exposed the advantages and drawbacks of using either type of z-pin. In both

  doi:10.5075/epfl-298799_978-2-9701614-0-0

cases, the bridging behaviour is largely dependent on the delamination mode and the resultant load mode-mixity. Metallic pins typically excel under mode II delamination bridging [8]. In contrast, CF/BMI pins show significant delamination toughening when the load applied results in primarily mode I displacements. In each case, as the level of mode mixity shifts towards its complementary delamination mode, the toughening effect observed is considerably reduced. Current CF/BMI z-pins will pull-out of the host laminate at load mode-mixities below 0.2-0.5. Above this, they will typically rupture transversely and exhibit extensive fibre failure [9,10]. To address this, this study explores the use of alternative fibre/matrix combinations that can successfully bridge mode II delamination cracks and provide extensive toughening under these loading conditions. Rodstock was successfully manufactured using unidirectional and twisted high-strength, high-toughness fibrous reinforcement in combination with a tough thermosetting resin. The bridging behaviour of these novel z-pins under mode II loads is evaluated and directly compared to that of the most commonly available z-pin type. SEM micrography is used to assist in characterizing the failure mode and effectiveness of this novel structures.

2. Materials and Methods

2.1 Materials

E-glass/913 epoxy prepreg used as the reinforced laminate was supplied by Hexcel UK. CF/ BMI matrix z-pins were supplied by DPP B.V. The novel Z-pins were manufactured by pultrusion of a continuous fibre tow of either 1k carbon fibre or poly(*p*-phenylene-2,6-benzobisoxazole) fibre or PBO. The latter is commercially traded as Zylon and was obtained from Toyobo, Japan. High toughness epoxy resin used was obtained from Huntsman Corporation, UK.

2.2 Manufacturing

Novel Z-pin rodstock was manufactured through pultrusion of continuous fibre tows. Reinforcement fibres are pulled through a resin bath containing an epoxy resin blend (Araldite©LY3508 resin and Aradur©22962 hardener). The impregnated fibres are then forced into a heated die which gels and shapes the system into a composite rod. The z-pin rodstock subsequently undergoes a full post-cure cycle to allow the mechanical properties of the resin to develop. Three types of z-pins were manufactured using this method. The afore-mentioned epoxy resin was used as the main matrix (EPX) together with a combination of different fibre materials and architectures, namely unidirectional CF, unidirectional PBO fibre (uPBO) and twisted PBO fibre (tPBO). A fourth z-pin type was also included to represent the traditional z-pin material combination of carbon fibre and bismaleimide resin (CF/BMI).

Figure 1 shows a schematic representation of the z-pinned coupons used in this study. Each coupon comprises 56 plies of unidirectional E-Glass within a Hexcel 913 epoxy resin. They are stacked into a quasi-isotropic layup with individually symmetric top and bottom halves separated by a PTFE film. The overall layup of the laminate is antisymmetric with top and bottom stacking sequences of $[(0/45/90/\text{-}45)_3/0]_S$ and $[(90/\text{-}45/0/45)_3/90]_S$ respectively. The 0/90 mid-plane reduces nesting [11,12] of the fibres, which would otherwise contribute to the mode II traction loads. The cure cycle used follows that recommended by the manufacturer, with prolonged times at the lower temperatures during heating to reduce the risk of exotherm.

  doi:10.5075/epfl-298799_978-2-9701614-0-0

2.3 Testing

Mechanical testing was carried out using the arcan rig shown in Figure 1, mounted to an electro-mechanical tensile test machine loaded with a 1kN load cell. The rig allows single-pin delamination bridging tests of coupons through the full mode-mixity range by rotating the samples by 15° at a time from 0° to 90°. It is worth noting that pin misalignment is unavoidable during insertion, which will affect the load mode mixity acting on the pin. The effect of misalignment can be accounted for by calculation introduced by researchers at the University of Bristol [9,10,13]. The effect on load mod mixity is most significant at delamination modes close to Mode I. In this study, the specimens were tested using the 90°configuration, which corresponds to a nominal load mode-mixity of 1, or mode II delamination. Accounting for pin-misalignments of up to 15°, the load mode mixity will above 97% mode II dominated. Thus, specimens have been assumed to have similar load mode-mixities for statistical simplicity. Regardless, it is important to note this occurrence and the implication that pure mode II is not possible unless no misalignment is present.

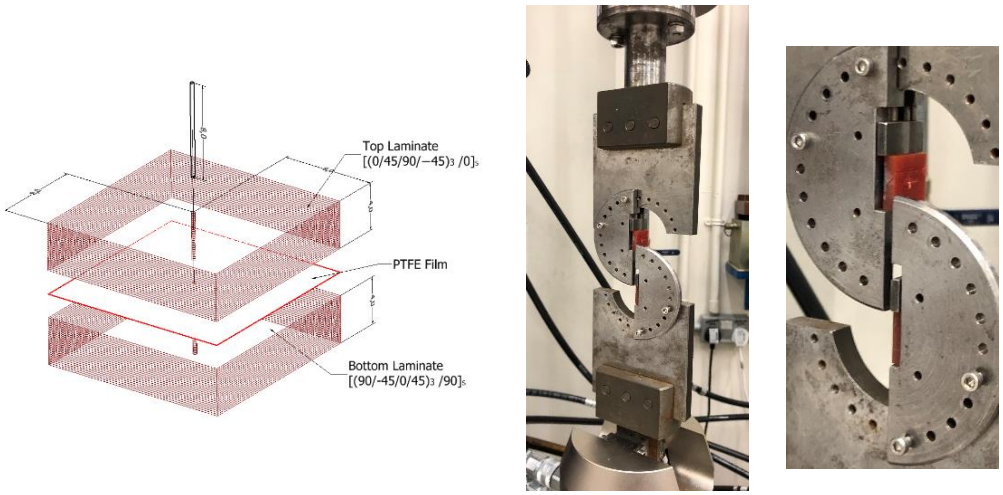

Figure 1 - Schematic representation of a single-pin bridging test coupon (left). Arcan test rig with Mode II-dominated set up (right).

3. Results and discussion

3.1 Energy dissipated and max force

The single pin bridging test results for all four pin types are summarised in Table 1 and Figure 2. Two key variables were obtained from the load displacement graphs for each specimen set, energy dissipated and maximum force. The energy dissipation corresponds to the area under the load displacement graph. It is a measure of the energy absorbed by the pin whilst bridging the delamination. The maximum force is the peak of the load displacement graph, which can correspond to the failure load of the pin or its peak traction load.

The total energy dissipated by the PBO-based z-pins was superior to that of the CF based pins. uPBO-EPX specimens dissipated 113 mJ of energy more on average than the commercially available CF-BMI pins. This corresponds to a 2307% improvement in delamination bridging toughness. Similarly, tPBO-EPX pins showed an improvement of 1006% in comparison to their CF counterparts. It also implies that unidirectional PBO is twice as effective bridging a delamination as twisted PBO.

Table 1 - Summary of key results from the load-displacement curves of the pin bridging tests.

Fibre	Matrix	Abbreviation	Average Energy Dissipated [mJ]	Maximum Force [N]	Notes
Unidirectional Carbon	BMI	CF-BMI	4.3	54.4	Commercial pins
Unidirectional Carbon	Epoxy	CF-EPX	5.4	56.0	Control resin
Unidirectional PBO	Epoxy	uPBO-EPX	117.9	60.2	-
Twisted PBP	Epoxy	tPBO-EPX	54.2	51.7	2mm lay-length

did not result in statistically significant differences between CF-BMI and CF-EPX. Both pin types exhibited an average energy dissipation value between 4 and 5 mJ. In terms of peak load, all four Z-pin categories displayed similar peak loads in their load-displacement curves, with standard deviation bars overlapping between them. On average, the maximum load sustained during the test varied from 50 to 60N. The following sections will analyse and compare the failure characteristics of each z-pin type to understand the energy dissipation values observed.

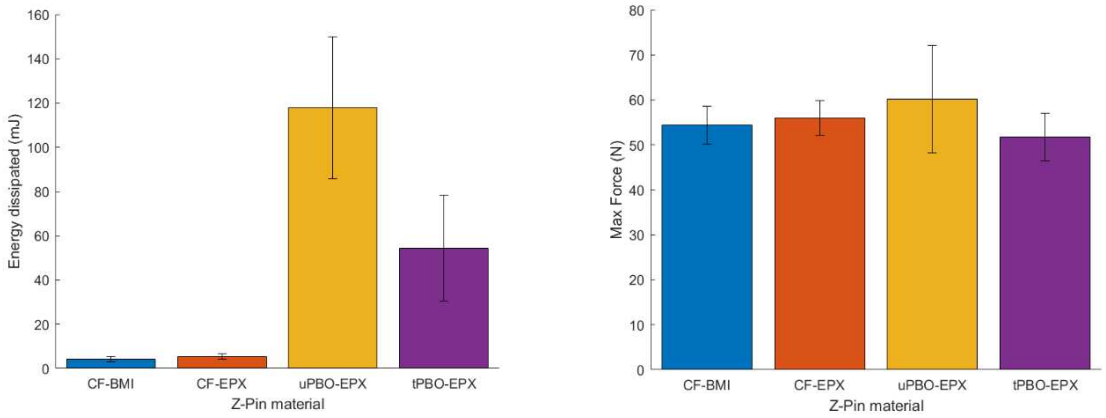

Figure 2 - Mean energy dissipated per z-pin type during bridging tests (left). Mean maximum force carried by each (right).

3.1 Matrix Comparison

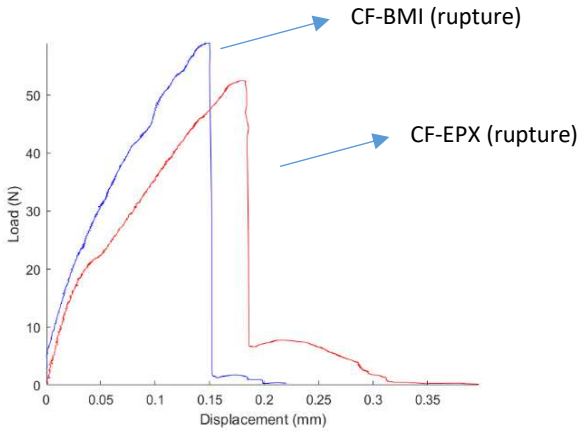

Figure 3 – Typical load-displacement curves for single pin bridging tests of CF-BMI and CF-EPX.

Before directly comparing the effect of altering the fibrous reinforcement on the z-pin bridging performance, it was necessary to compare the behaviour of a typical CF-BMI z-pin with CF z-pins manufactured using the same procedure and resin system as that of the novel z-pins presented. As it is clear from the energy dissipation charts in Figure 2 and from the load displacement chart (Figure 3), the difference in Mode II performance is statistically negligible. The load-displacement curves reveal a similar behaviour for both types of pin. Those manufactured out of the high elongation resin showing a larger displacement and higher compliance as expected, albeit not enough to increase energy dissipation significantly. This correlates with previous modelling of mode II bridging [10,13] which suggest that mode II delamination bridging is solely fibre-property dominated.

3.2 Effect of fibre material

Figure 4 shows the typical load displacement curves for both novel z-pin comprising PBO fibres, compared to that of commercial CF-BMI pins. Energy dissipation corresponds to the area under the load displacement curves. This implies that the best performing z-pin will be able to sustain a large traction load [14] through a large displacement. Under mode II-dominated conditions such as these, CF-based z-pins failed by transverse rupture, as has been previously reported [5,15,16], with complete tensile failure of the CFs [10]. However, PBO-based pins are able to de-bond from the laminate and pull-out from the insertion hole without rupturing. This partial or full pull-out mechanism results in a displacement along which work is carried out against an opposing traction force. The load is a combination of the friction between the pin and the surrounding laminate as it slides out and a snubbing [17] effect as the pin is pushed into the laminate. This energy absorption mechanism through pin pull-out of composite Z-pins has been documented [1,5,15] albeit only at load mode mixities close to Mode I or in metallic Z-pins. This is the first account of a composite-based z-pin able to pull-out of the host laminate without rupturing during mode II delamination.

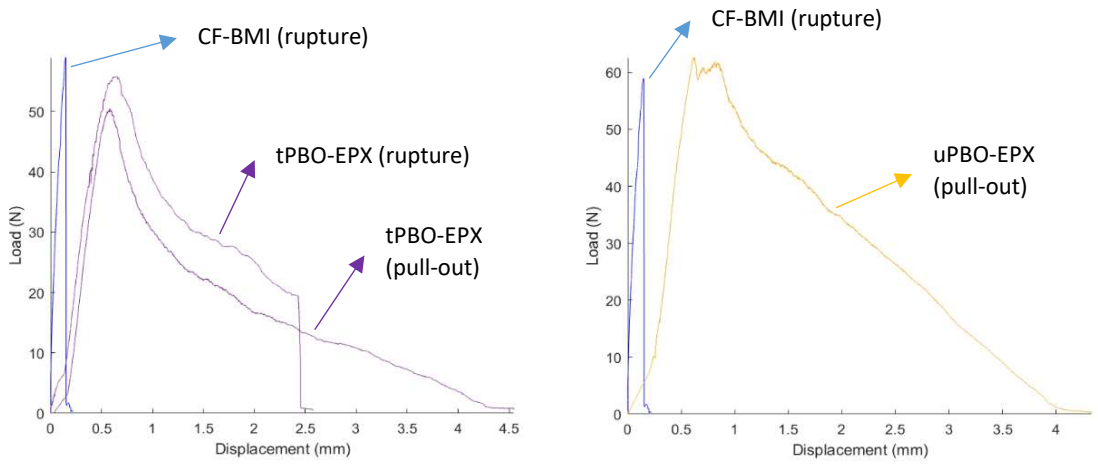

Figure 4 - Comparison of the typical load-displacement curves of CF-BMI with tPBO-EPX (left) and uPBO-EPX(right)

SEM micrographs of failed uPBO in Figure 5 can help understand the failure mechanisms behind the pull-out of PBO-based pins during mode II delamination. The pin is permanently deformed, pushed against the delamination plane. There is extensive matrix longitudinal cracking and separation of the fibre tow into smaller fibrils. This behaviour results from the combination of high strength and high toughness of the PBO fibres. The high toughness and noticeably higher

elongation at break (2.5% compared to 1.5% of carbon fibre) allows them to bend under mode II-dominated conditions. As the pin bends, the load acting on the pin is transferred and carried axially, along the fibre orientation. This is combined with a tensile strength as high as 5.5 GPa (as quoted by Toyobo, Japan), which reduces the risk of tensile fibre failure. Both factors synergistically improve the bridging performance of the pin, allowing it to be pulled out and dissipate energy during delamination.

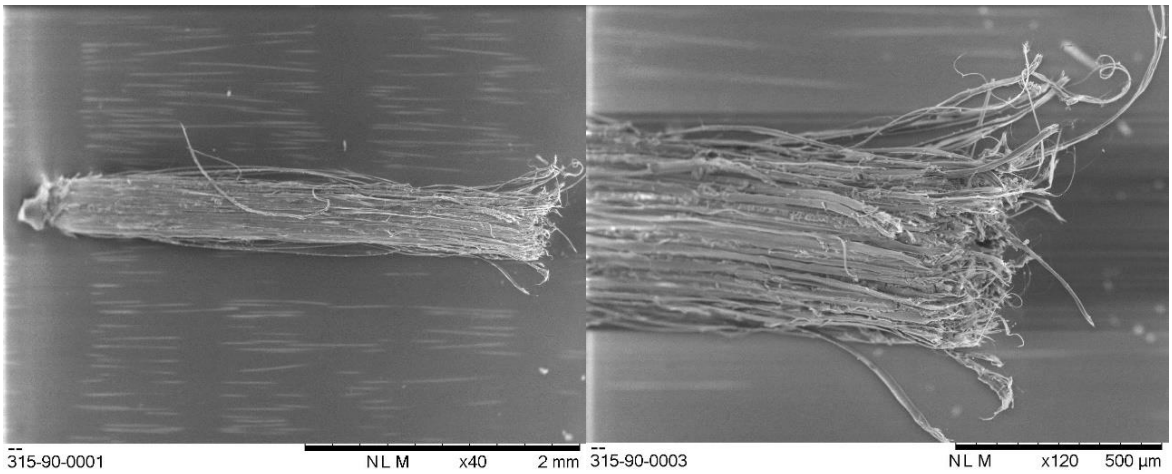

Figure 5 - SEM failure micrographs of uPBO-EPX z-pins under mode II-dominated loading.

3.3 Effect of fibre architecture

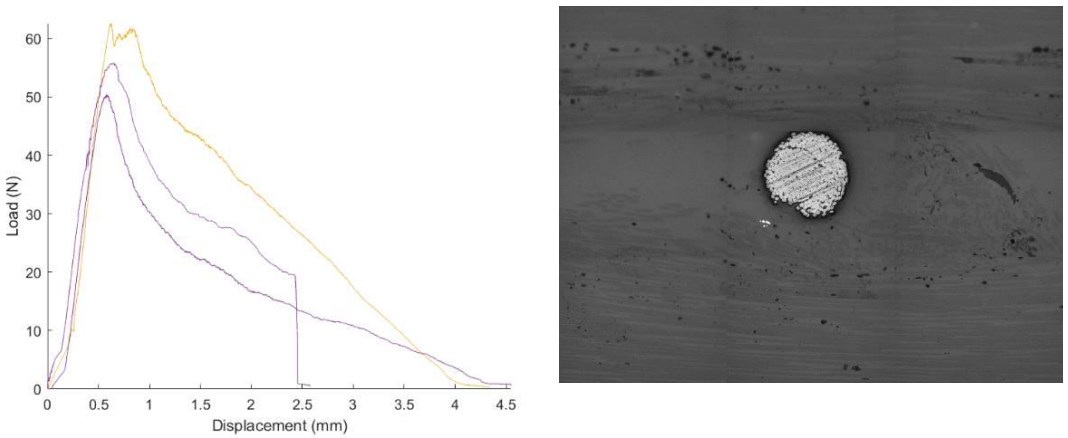

Figure 6 - Comparison of the typical load-displacement curves of uPBO-EPX with tPBO-EPX (left) and microstructure of a tPBO pin within a laminate (right).

The effect of using two twisted tows of PBO fibre to alter the z-pin architecture is apparent from the load-displacement curve in Figure 6 and the overall energy dissipation chart in Figure 2. There appear to be two factors that reduce the performance of the twisted pins compared to unidirectional tows. The average traction force against displacement is significantly lower and some pins are only partially pulled out. Both of these factors contribute to a lower energy dissipation through bridging. The lower overall traction load may be caused by the tendency of the twisted yarn to form a more geometrically consistent and smoother pin. Figure 6 shows how one of the twisted yarns completely envelops the other, forming an almost perfectly cylindrical structure. Secondly, the tendency of this pins to rupture during pull-out may be a

result of the increased stress concentrations at the points of fibre overlap. As the pin is pulled under tension, both individual yarns tend to de-bond from each other as can be observed in Figure 7. They are then able to slide past each other and form points of contact with increased stress concentration. At these points, the individual bundles may not be able to slide past each other anymore and in some cases fibre failure may occur, as seen in Figure 7. It is worth noting how dissimilar this failure is compared to typical CF failure. The thinning of the filaments and filament bundles observed suggests a more progressive and plastic mechanism.

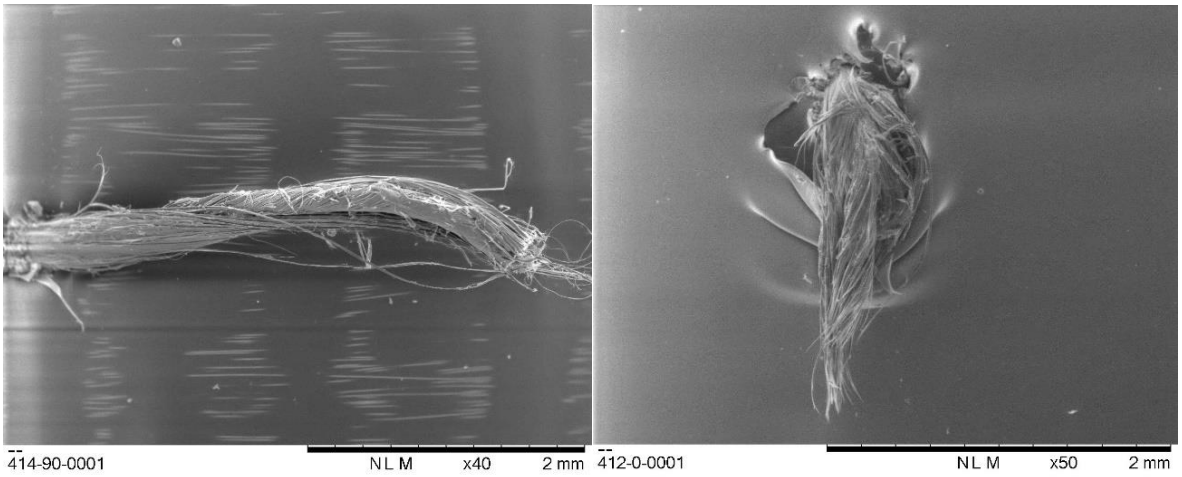

Figure 7 - SEM micrographs of tPBO-EPX pins failed by pull-out (left) or rupture (right).

4 Conclusion

Novel z-pins have been manufactured by pultrusion and employing alternative materials and architectures to those commonly used. Single pin delamination bridging tests have revealed that pins comprising PBO fibre are able to pull out from the laminate under 97-99% mode II dominated delamination loads. Unidirectional PBO z-pins have shown an energy dissipation improvement of over 2000% compared to conventional CF pins. The superior performance of PBO based pins has been attributed to the high strength, high toughness characteristics of PBO fibre, which allows large deformations without rupture and support of high axial loads. Twisted PBO yarn has shown a better manufacturability albeit a significant reduction in bridging performance compared to its unidirectional counterpart. This study marks the discovery of composite z-pins with metallic z-pin-like mode II bridging behaviour.

Acknowledgments

The authors wish to acknowledge the support of Rolls-Royce plc through the Composites University Technology Centre (UTC) at the University of Bristol and the EPSRC through the ACCIS Centre for Doctoral Training grant, no. EP/G036772/1.

5 References

1. Mouritz AP. Review of z-pinned composite laminates. Compos Part A Appl Sci Manuf [Internet]. 2007 Dec 1 [cited 2019 Jun 5];38(12):2383–97. Available from: https://www.sciencedirect.com/science/article/pii/S1359835X07001479

  doi:10.5075/epfl-298799_978-2-9701614-0-0

2. Dell'Anno G, Treiber JWG, Partridge IK. Manufacturing of composite parts reinforced through-thickness by tufting. Robot Comput Integr Manuf. 2016 Feb 1;37:262–72.
3. Velmurugan R, Solaimurugan S. Improvements in Mode I interlaminar fracture toughness and in-plane mechanical properties of stitched glass/polyester composites. Compos Sci Technol. 2007 Jan 1;67(1):61–9.
4. Mouritz AP, Bannister MK, Falzon PJ, Leong KH. Review of applications for advanced three-dimensional fibre textile composites. Compos Part A Appl Sci Manuf [Internet]. 1999 Dec 1 [cited 2019 Jun 26];30(12):1445–61. Available from: https://www.sciencedirect.com/science/article/pii/S1359835X99000342
5. Cartié DDR, Partridge IK. Effect of Z-Fibres on the delamination behaviour of carbon fibre / epoxy laminates. Sch Ind Manuf Sci. 2000;PhD(December).
6. Kostopoulos V, Sarantinos N, Tsantzalis S. Review of Through-the-Thickness Reinforced z-Pinned Composites. J Compos Sci. 2020;4(1):31.
7. Mouritz AP. Review of z-pinned laminates and sandwich composites. Vol. 139, Composites Part A: Applied Science and Manufacturing. Elsevier Ltd; 2020. p. 106128.
8. Warzok F, Allegri G, Gude M, Hallett SR. Experimental study of Z-pin fatigue; understanding of mode I and II coupon behaviour. Compos Part A Appl Sci Manuf. 2019 Dec 1;127:105615.
9. Yasaee M, Lander JK, Allegri G, Hallett SR. Experimental characterisation of mixed mode traction-displacement relationships for a single carbon composite Z-pin. Compos Sci Technol. 2014 Apr 9;94:123–31.
10. Allegri G, Yasaee M, Partridge IK, Hallett SR. A novel model of delamination bridging via Z-pins in composite laminates. Int J Solids Struct. 2014 Oct 1;51(19–20):3314–32.
11. Cui H, Yasaee M, Kalwak G, Pellegrino A, Partridge IK, Hallett SR, et al. Bridging mechanisms of through-thickness reinforcement in dynamic mode I&II delamination. Compos Part A Appl Sci Manuf. 2017 Aug 1;99:198–207.
12. M'membe B, Yasaee M, Hallett SR, Partridge IK. Effective use of metallic Z-pins for composites' through-thickness reinforcement. Compos Sci Technol. 2019 May 3;175:77–84.
13. Zhang B, Allegri G, Yasaee M, Hallett SR. Micro-mechanical finite element analysis of Z-pins under mixed-mode loading. Compos Part A Appl Sci Manuf [Internet]. 2015 Nov 1 [cited 2019 Jun 14];78:424–35. Available from: https://www.sciencedirect.com/science/article/pii/S1359835X15002389
14. Mouritz AP, Koh TM. Re-evaluation of mode i bridging traction modelling for z-pinned laminates based on experimental analysis. Compos Part B Eng [Internet]. 2014 Jan 1 [cited 2019 Jul 16];56:797–807. Available from: https://www.sciencedirect.com/science/article/pii/S1359836813005295
15. Cartié DDR, Cox BN, Fleck NA. Mechanisms of crack bridging by composite and metallic rods. Compos Part A Appl Sci Manuf [Internet]. 2004 Nov 1 [cited 2019 Jun 17];35(11):1325–36. Available from: https://www.sciencedirect.com/science/article/pii/S1359835X04000715
16. Pegorin F, Pingkarawat K, Daynes S, Mouritz AP. Influence of z-pin length on the delamination fracture toughness and fatigue resistance of pinned composites. Compos Part B Eng [Internet]. 2015 Sep 1 [cited 2019 Jun 27];78:298–307. Available from: https://www.sciencedirect.com/science/article/pii/S1359836815002255
17. Cox BN. Snubbing effects in the pullout of a fibrous rod from a laminate. Mech Adv Mater Struct. 2005 Mar;12(2):85–98.

STUDY ON THE EFFECT OF STRAIN RATE AND TEMPERATURE ON THE MECHANICAL BEHAVIOR OF POLYPROPYLENE AND THERMOPLASTIC OLEFIN

Se-Min, Lee[a], Gyu-Won, Kim[a], In-Soo, Han[b], Hak-Sung, Kim[c]…

a: Department of Mechanical Convergence Engineering, Hanyang University, 222, Wangsimni-ro, Seongdong-gu, Seoul, Republic of Korea – minhappy96@hanyang.ac.kr
b :Hyundai Motor Group R & D Division, Gyeonggi-do, 18280, Republic of Korea
c: Institute of Nano Science and Technology, Hanyang University, 222, Wangsimni-ro, Seongdong-gu, Seoul, Republic of Korea

Abstract: *In this study, the strain rate dependent tensile properties of Polypropylene (PP) and Thermoplastic olefin (TPO) were investigated under the high strain rate by using the Split Hopkinson Pressure Bar (SHPB). The SHPB is the most widely used apparatus to characterize dynamic mechanical behavior of materials at high strain rates between 100/s and 10,000/s. Also, the dynamic properties of TPO and PP were measured under temperature from -35 ℃ to 85 ℃. The SHPB test is based on the wave propagation theory which was developed to give the stress, strain and strain rate in the specimen using the strains measured in the incident and transmission bars. In addition, to verify the strain data obtained from SHPB, the strain distribution of the specimen was photographed with a high-speed camera and the strain data obtained through the Digital Image Correlation (DIC) and compared with the strain value from the SHPB test.*

Keywords: Split Hopkinson Pressure Bar (SHPB); High strain rate ; Thermoplastic Olefin(TPO), Polypropylene (PP)

1. Introduction

High fuel efficiency and high efficiency are emerging as important issues in the automobile industry. If the weight is reduced by using various lightweight materials and plastics, fuel efficiency can be maximized. For this purpose, thermoplastic olefin (TPO) such as polypropylene (PP) are used as automotive interior materials. Thermoplastic composites are increasingly being applied to automotive materials, especially due to their simple manufacturing process, low material cost, and excellent impact force.[1]

The advantage of these materials is that fuel can be saved due to the weight reduction of the vehicle due to the low specific gravity. In order to develop reliable automotive lightweight products for such TPO and PP, it is very important to predict the material properties under impact load. Materials deform rapidly during a vehicle crash, and in general, materials tend to increase in strength and stiffness as the strain rate increases. In particular, it is essential to secure accurate dynamic properties as the vehicle interior material proceeds at a high strain rate of over 1000/s during a automotive collision [2]. Therefore, in the event of an automotive collision, an accurate automotive design should be conducted based on the collision analysis considering the dynamic properties.

  doi:10.5075/epfl-298799_978-2-9701614-0-0

In this paper, the dynamic properties proceeding at a dynamic strain rate (100/s ~ 10000/s) were measured using a Hopkinson Bar (SHPB) experiment. Also, the dynamic properties of PP and TPO were measured under temperature from -35 ℃ to 85 ℃. The temperature range is considered by the cryogenic and high temperature regions on Earth. The SHPB method was proposed in 1949 through Kolsky's Stress Wave Theory. Using the strains measured at the incident bar and transmission bar in the device, the stress, strain, and strain rate of the specimen can be obtained [3]. In this work, the tensile behavior according to the strain rate of the PP and TPO materials was obtained using the SHPB.

2. Experimental design

2.1 Experimental materials

In this study, PP (polypropylene) and TPO (Thermoplastic olefin), which are widely used in the automobile industry as lightweight parts, were selected as experimental materials. Both of materials composition on ingredients were represented as shown in Table 1 and Table 2. Also, mechanical and physical properties of materials were represented as shown in Table3.

Table 1: Polypropylene composition on ingredients

Chemical name	CAS No.	Contain Ratio (%)
1-Propene polymer with ethene	9010-79-1	59 ~ 69
Ethylene-1-octene copolymer	26221-73-8	19 ~29
Talc (Containing no asbestos fibers)	14807-96-6	3 ~ 13

Table 2: Thermoplastic olefin composition on ingredients

Chemical name	CAS No.	Contain Ratio (%)
1-Butene polymer with ethene	25087-34-7	37 ~ 47
1-Propene polymer with ethene, block	106565-43-9	24 ~ 34
1-Propene polymer with ethene	9010-79-1	15 ~ 25
Talc (Containing no asbestos fibers)	14807-96-6	1 ~ 5

Table 3 : Mechanical and physical properties of materials

Properties	Test Conditions	Units	PP	TPO
Density	-	g/cm3	0.95	0.89
Tensile Strength at Yield	50mm/min	MPa	19	10
Elongation at Break	50mm/min	%	222	353
Flexural Strength	2mm/min	MPa	28	12

  doi:10.5075/epfl-298799_978-2-9701614-0-0

Flexural Modulus	2mm/min	MPa	1,860	480

2.2 Specimen design

In this work, the specimens for the tensile test were prepared based on the ASTM D3039. For the designing of the shape of specimen, the gage length must be short enough to allow stress equilibrium to be reached in the dynamic tests and also to achieve sufficiently high strain rates. For this reason, a dog-bone specimen was designed with the shape and dimensions as shown in Figure 1. The specimen width was designed to minimize stress concentration at its ends by selecting a smooth radius of curvature in the transition region.

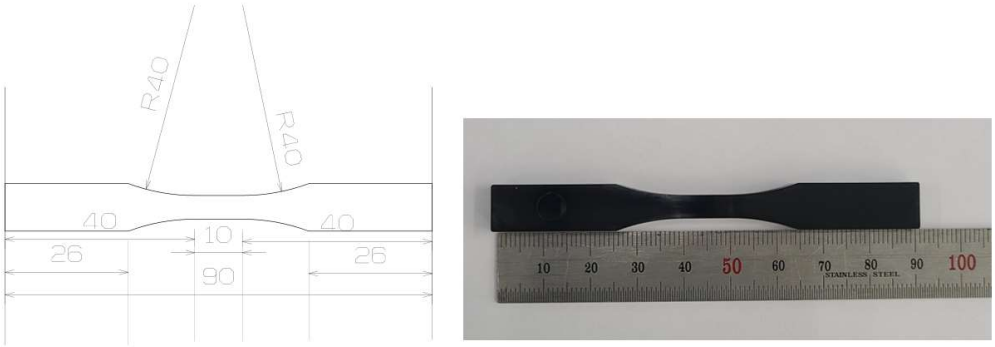

Figure 1. The specimen dimensions in mm (Thickness = 3mm)

2.3 Experimental Set-up

Dynamic tensile test were performed using a modified tensile SHPB as sketched in Figure 2. The SHPB is largely composed of a striker, incident bar and transmission bar. When the striker fired through the gas gun strongly collides with the incident bar, the specimen located between the incident bar and the transmission bar is stretched in tensile mode generating a tensile wave. This elastic wave is transmitted through the incident bar and then reaches the boundary between the incident bar and the specimen. On reaching the specimen, a part of this incident pulse is reflected, and the rest is transmitted to the transmission bar. [4]. In this experiment, the stress, strain, and strain-rate versus time can be obtained from the records of strain gages on the incident and transmission bars by using the well- established elementary linear elastic wave propagation theory. Based on this theory, the strain in the specimen is directly proportional to the time integral of the reflected pulse and stress is directly proportional to the amplitude of the transmitted pulse.

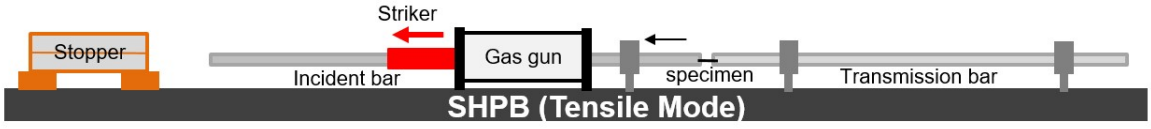

Figure 2. Schematic of Split Hopkinson Pressure Bar

As shown in Figure 3, when the initial length of the specimen located between incident bar and transmission bar is L_s and the displacement of both ends of the specimen is u_1, u_2. The average strain of the specimen can be expressed as follows.

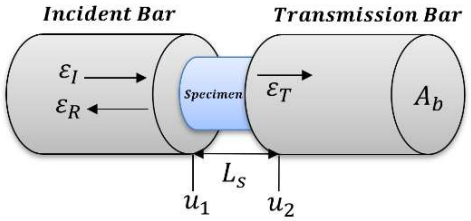

Figure 3. Testing section of Split Hopkinson Pressure Bar

$$\varepsilon_s = \frac{u_2 - u_1}{l_0} \tag{1}$$

$$u_1 = C_b \int_0^t \varepsilon_I \, dt + (-C_b) \int_0^t \varepsilon_R \, dt = C_b \int_0^t (\varepsilon_1 - \varepsilon_R) \, dt \tag{2}$$

$$u_2 = C_b \int_0^t \varepsilon_T \, dt \tag{3}$$

C_b is elastic wave speed of bars. The applied load at the each ends of the specimen can be expressed as follows.

$$P_1 = E_b A_b (\varepsilon_I + \varepsilon_R) \tag{4}$$

$$P_2 = E_b A_b \varepsilon_T \tag{5}$$

Where E_b is Young's modulus of the bars, A_b is cross-sectional area of the bars. The stress through the specimen is constant because of assumption that the short specimen is in equilibrium statement during the deformation. So, it can be expressed

$$P_1 \approx P_2 \text{or } \varepsilon_I + \varepsilon_R \approx \varepsilon_T. \tag{6}$$

Finally, the average stress, strain, and strain rate in the specimen are obtained based on hypothesis of equilibrium using the following expressions

$$\sigma_s = \frac{P_1 + P_2}{2A_s} = \frac{A_B}{A_s} E_B \varepsilon_T \tag{7}$$

$$\varepsilon_s = \frac{u_1 - u_2}{l_0} = \frac{C_b}{l_0} \int_0^t \varepsilon_R \, dt \tag{8}$$

$$\dot{\varepsilon}_u = \frac{C_b}{l_0} \varepsilon_R \tag{9}$$

Table 4: Physical properties of incident and transmission bars

Properties	Units	6061 aluminum alloy
Density	g/cm3	2.70
Young's modulus	GPa	68
Tensile strength	MPa	310
Length	M	2
Bar diameter	mm	20

  doi:10.5075/epfl-298799_978-2-9701614-0-0

2.3 Temperature control

In the SHPB experiment, there was a constraint that the incident bar and transmission bars had to pass through the environmental chamber and that chamber should have a small dimension, so the environmental chamber was directly fabricated and configured to control temperature. The PID control system can be used to control the target temperature. A ceramic heater was used to raise the temperature, and liquid nitrogen was purged for cryogenic temperatures to control the target cryogenic temperature.

2.4. Digital Image Correlation (DIC)

In this study, to secure the reliability of the strain data obtained through SHPB, comparison with the strain data obtained through Digital Image Correlation (DIC) was conducted. The DIC technique is a non-contact measurement method that can obtain the strain rate of the specimen during the deformation process by analyzing the digital image of the speckle pattern. The DIC technique was performed with GOM's Aramis Professional software. In order to obtain a uniform strain field in the plane from the speckle-patterned surface, the image resolution of the high-speed camera was set to 800 × 164 and the frame rate to 65,000 fps. In addition, to ensure the in-plane strain field due to the deformation of the specimen, high-speed camera video recording for the DIC technique was performed simultaneously during the high-speed compression test through the Hopkinson bar.

3. Results and discussions

3.1 Effect of strain rate on mechanical properties

The voltage amplitude measured by strain gauge attached at the incident bar and the transmission bars recorded by oscilloscope. The voltage data can be converted to strain experienced by each strain gauge, thus stress, strain and strain rate in the specimen can be calculated using equations (7) and (8).

Figure 4. represents the results of dynamic tensile test of PP and TPO. Dynamic tests were carried out by using the $1000s^{-1}$, $1500s^{-1}$, $2000s^{-1}$ of strain rates. It can be seen that the tensile modulus and failure strain strengths of both materials increased with the strain rates. This is because the materials can withstand the higher load under the high strain rate since the amount of accumulated damage at the particular strain level decreases as strain increases. This is because the loading rate is increased, the time for the damage to develop is less.[7~8]

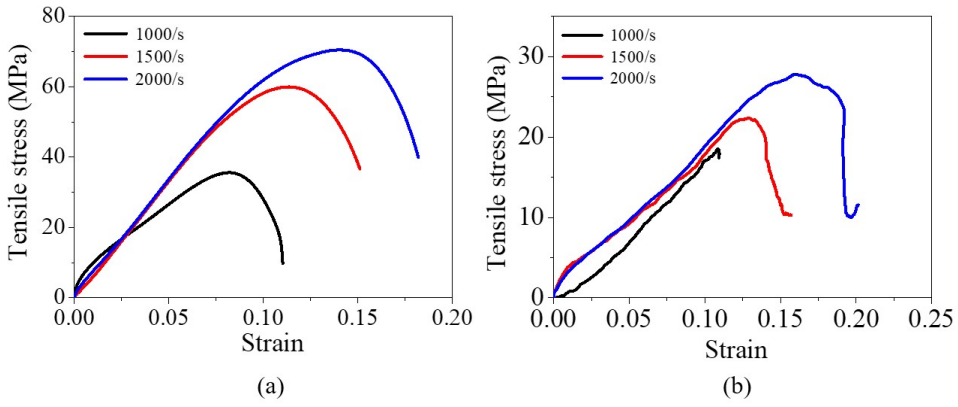

Figure 4. Stress-strain response for different high strain rates: (a) PP ; (b) TPO

3.2 Mechanical properties at temperature effect

Figure 5. represents the results of dynamic tensile test of PP and TPO in temperature -35 ℃, 23℃, 85 ℃. The results show that the tensile modulus and tensile strength of both materials increased at the low temperature. In general, the material tends to a stiffer mechanical behavior at the low temperature.

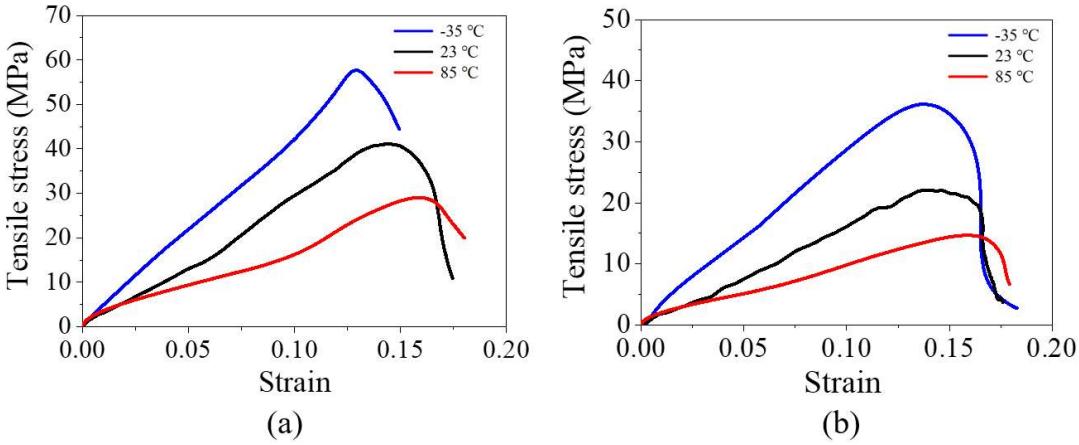

Figure 5. Strain-Stress curves at the strain rate of 1500 s^{-1} : (a) PP ; (b) TPO

3.3 Verification of consistency of SHPB data through DIC

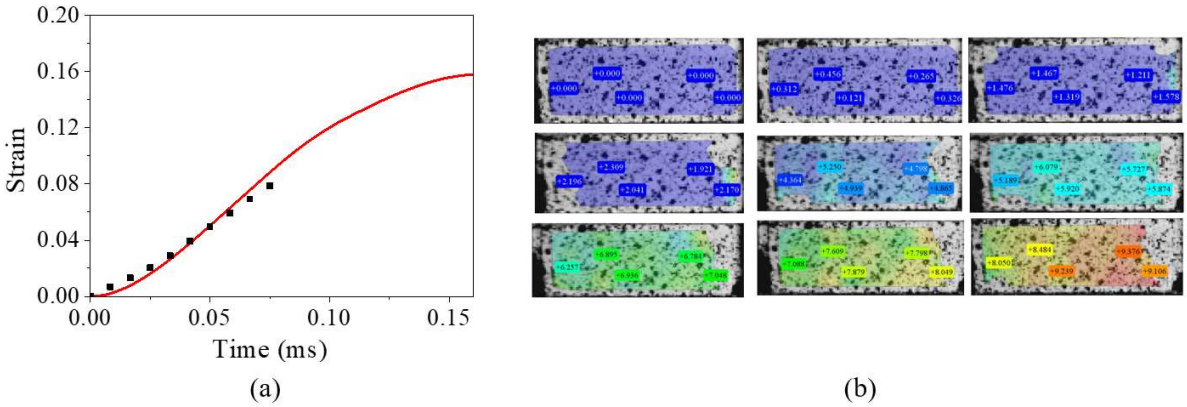

Figure 6. (a) Comparison of strain data from SHPB experiment and DIC , (b) The image of TPO by the high speed camera and DIC

Figure 6 shows the results of SHPB experiments and DIC results. In all the strain data before failure, it can be seen that the two data are almost similar, whereas from 0.08ms, the strain field on the surface of the specimen is distorted as the strain begins to occur in the specimen.

Through this, it was confirmed that the strain measurement of SHPB was reliable through similarity to the DIC data until the DIC analysis area was broken.

4. Conclusions

  doi:10.5075/epfl-298799_978-2-9701614-0-0

In this study, the strain rate dependent mechanical behavior of PP and TPO was investigated under the high strain rate and various temperatures by using the split Hopkinson bar equipment. Dynamic mechanical properties such as the stress, strain and strain rate of the specimen was obtained by elastic wave theory. Firstly, the dynamic tensile tests were performed with respect to the strain rate. Then the behavior according to temperature was also confirmed with strain rate.

Acknowledgements

This work was supported by Korea Institute of Energy Technology Evaluation and Planning (KETEP) grant funded by the Korea government (MOTIE)(20202020800360, Innovative Energy Remodelling Total Technologies for the Aging Public Buildings). This work was supported by a grant from the Human Resources Development program (no. 20204010600090)of the Korea Institute of Energy Technology Evaluation and Planning (KETEP), funded by the Ministry of Trade, Industry, and Energy of the Korean Government.

References

1. Fri ich, K., and Almajid, A.A., “Manufacturing Aspect of Advanced Polymer Composites for Automotive Applications,” Applied Composite Materials, Vol. 20, 2013, pp. 107-128.
2. Kim D-H, Kang S-Y, Kim H-J, et al. Strain rate dependent mechanical behavior of glass fiber reinforced polypropylene composites and its effect on the performance of automotive bumper beam structure. Compos Part B Eng 2019; 166: 483–496.
3. Chen, W.W., and Song, B., Split Hopkinson (Kolsky) Bar : Design, Testing and Applications, Springer Science & Business Media, 2010.
4. Al-Mousawi M, Reid S, Deans W. The use of the split Hopkinson pressure bar techniques in high strain rate materials testing. Proc Inst Mech Eng, Part C: J Mech Eng Sci 1997;211(4):273–92.
5. Abrate S. Behavior of composite materials under impact: strain rate effects, damage, and plasticity. ASME Appl Mech Div-Publ-AMD 2001; 250: 41–50.
6. Kapoor, Rajat, Laxman Pangeni, Aswani Kumar Bandaru, Suhail Ahmad, and Naresh Bhatnagar. "High strain rate compression response of woven Kevlar reinforced polypropylene composites." Composites Part B: Engineering 89 (2016): 374-382.
7. Abrate S. Impact on laminated composite materials. Appl Mech Rev 1991;44(4):155–90.
8. Abrate S. Behavior of composite materials under impact: strain rate effects, damage, and plasticity. ASME Appl Mech Div-Publ-AMD 2001;250:41–50.

  doi:10.5075/epfl-298799_978-2-9701614-0-0

SIMULTANEOUS SPINNING OF RECYCLED THERMOPLASTICS AND GLASS FIBERS FOR HYBRID YARNS USED IN SUSTAINABLE COMPOSITES

Christina Scheffler[a], Ricardo Bernhardt[a], Ines Kühnert[a], Axel Spickenheuer[a], Markus Stommel[a,b]

a: Leibniz-Institut für Polymerforschung Dresden e. V. (IPF), Hohe Str. 6, D-01069 Dresden, Germany, scheffler@ipfdd.de
b: Institute of Material Science, Faculty Mechanical Engineering, Technical University Dresden, D-01062 Dresden, Germany

Abstract: *Plastic packaging, predominantly made from polypropylene (PP) and polyethylene terephthalate (PET), has a low service life and is currently the main purpose of synthetic polymers. A lot of effort has been made to keep this valuable resource within a material cycle, however, a significant decrease in many material properties is usually observed, which is also referred to as downcycling. In contrast, the subject of this work is to explore the potential of recycled thermoplastics for upcycling processes using them as thermoplastic matrix in fiber-reinforced composites. Therefore, different types of recycled PP (rPP) and PET (rPET) were characterized in terms of viscosity and molecular weight to be used in a polymer melt spinning process that is combined with a glass fiber spinning line to enable the manufacturing of hybrid yarns. The comparison of unidirectional rPP and virginPP-based composites by using the hybrid yarns reveals a slight decrease in composite performance, serving as a first benchmark for such an approach.*

Keywords: polymer melt spinning; hybrid yarn; recycled polymers; fiber-reinforced thermoplastic composites

1. Introduction

It is known that multiple processing of thermoplastic polymers leads to degradation of the molecular chains due to high process temperatures and shear forces. This is accompanied by losses in terms of further processing and usage properties. The extent to which these take effect in turn determines for which areas of application and under which processing conditions the use of recycled polymers makes sense. Plastic packaging, which is predominantly made from polyolefins and PET, has a short service life and is currently the main use for synthetic polymers. The object of this work is to explore the potential of recycled thermoplastics for upcycling processes in which they are used as a thermoplastic matrix in fiber-reinforced composites.

Hybrid yarns are an ideal material in order to produce thermoplastic composites. The matrix material is placed in form of endless thermoplastic filaments between the endless reinforcing fibers (Figure 1), so that the high viscous melt must pass very short flow paths during composite manufacturing resulting in outstanding consolidation quality. Especially, complex thermoplastic light weight parts produced by Tailored Fiber Placement (TFP) technology benefit from the usage of hybrid yarns since it allows the arrangement of fibers even along small radii [1]. Further, the amount of required reinforcing fibers for composite manufacturing is reduced to a minimum by TFP, so that this approach inherently fulfils the demand of resource efficiency.

  doi:10.5075/epfl-298799_978-2-9701614-0-0

Based on the wide experience on polymer melt spinning as well as the simultaneous spinning of glass and thermoplastics for hybrid yarn manufacturing recycled polypropylene (rPP) and polyethylene terephthalate (rPET) are used to serve as raw material in this work [2].

Since recycled thermoplastics are subjected to degradation when passing through several processing cycles their molecular weight is reduced. Moreover, the introduction of fillers, pigments, and processing additives as well as residuals from packaging are accumulated in the recycled thermoplastic and lead to new challenges for subsequent processing; in particular, the fiber spinning process requires defined processing windows of viscosity and purity of the polymer melt. The aim of this work is: (i) a feasibility study to define the conditions that allow a stable hybrid yarn spinning with recycled thermoplastics for TFP made preforms and (ii) providing benchmarking data for the comparison of the mechanical performance of composites produced by virgin against recycled materials.

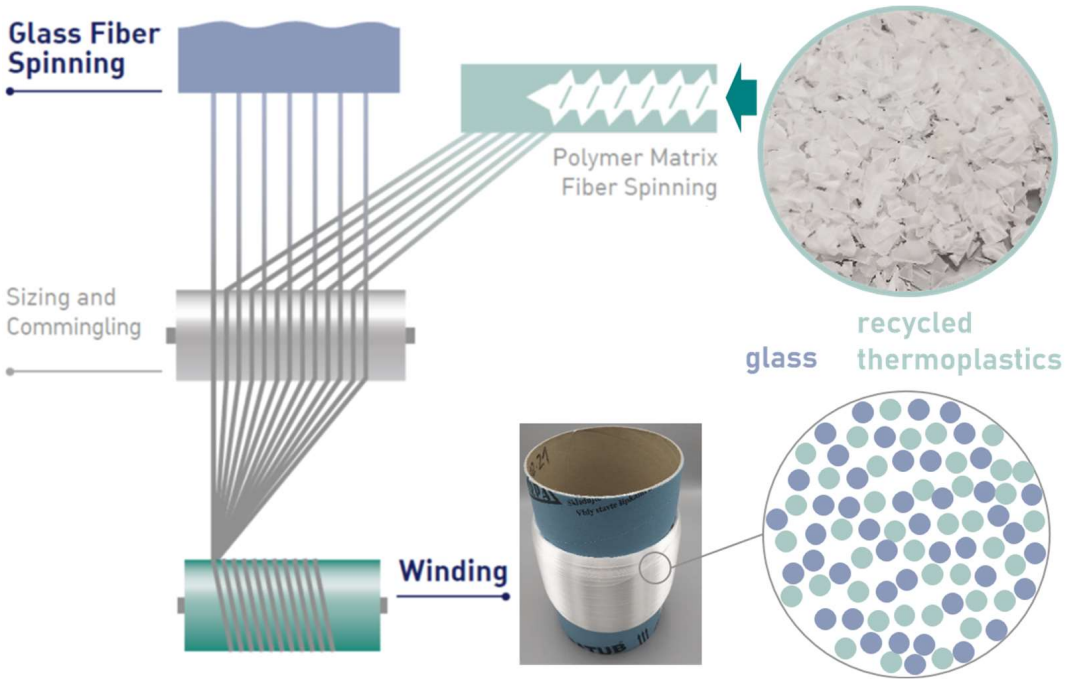

Figure 1 : Scheme of the simultaneous spinning process of glass and thermoplastic filaments for hybrid yarns

2. Experimental

2.1 Materials

As a virgin and reference material a homopolymer PP was used (granulated, HG475FB, Borealis) that is known to provide good spinnability. The melt flow rate (MFI) at 230 °C/2.16 kg is MFI = 27 g/10 min, and the melting temperature is given with 161 °C determined by differential scanning calorimetry. The recycled PP (rPP) was provided in form of flakes (Thees Natur PP, Thees Kunststoffverarbeitung GmbH, Germany) with MFI = 40 g/10 min.

  doi:10.5075/epfl-298799_978-2-9701614-0-0

As a PET virgin material PET RT20 (INVISTA Resins & Fibers GmbH, Germany) was used. The recycled PET types C/TR-04, O-08 und O-12 (Veolia MultiPet GmbH, Germany) were provided with increasing degrees of impurity in form of bottle flakes.

The glass fiber spinning was carried out using a standard E-glass composition. During hybrid yarn spinning the same standard PP-compatible sizing was applied on all produced yarns. The sizing, consisting mainly of a PP-film forming agent (Aquacer 598, BYK, Germany) and aminosilane (AMEO, Evonik, Germany), is applied on both types of filaments during the commingling process by the sizing applicator roll.

2.1 Methods

Polymer processing. Many of the recycled PP and PET materials are provided in form of flakes that are made by shredding different packaging materials. The melt spinning process requires a homogenous polymer to avoid differences in the polymer viscosity that would lead to unstable spinning conditions or even fiber rupture. This homogenization is received by an additional compounding and extrusion step so that granules are produced out of the flakes. In this work this was done by a twin-screw compounder (ZE 25 R/A Ultra Glide, Berstorff). Further, residuals in forms of particles and fibers (Figure 2) resulting from previous usage are still present in the polymer. In order to increase the polymer purity to avoid clogging of the spinning nozzles, the residuals are filtered out by sieves of different mesh sizes. Selected PP samples have therefore been extruded two or three times; filtering was realized by sieves of 15 µm up to 120 µm mesh size; the extrusion was carried out at 220 °C or 250 °C, respectively.

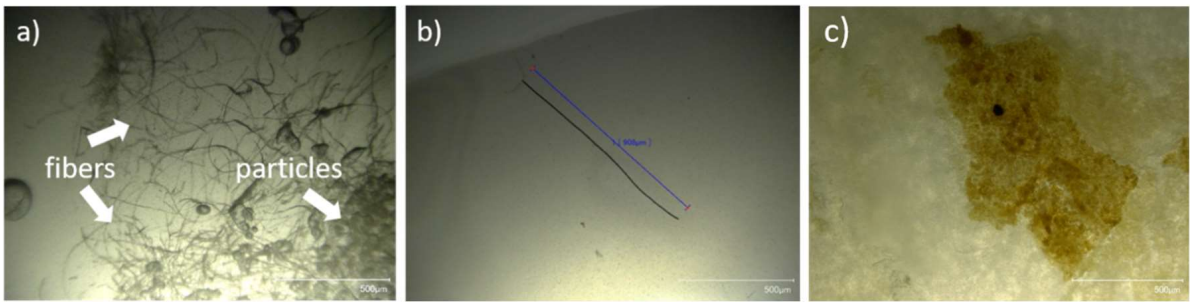

Figure 2 : Examples of typical residuals found in rPP and recycled PET C-TR 07; light microscope images of thin polymer layers received by pressing a melt droplet between glass sheets, a) fiber bundles and particles (PP); b) a single fiber with a length of 908 µm (PP), c) label residue (PET)

Polymer and hybrid yarn spinning. Principle tests of spinnability were carried out at a piston spinning device that was constructed and built up at IPF with different spinning parameters. The hybrid yarns we spun utilizing a pilot spinning line by combining a glass melt spinning and polymer melt spinning process using a drawing velocity of 486 m/min. This velocity is sufficient to draw the polymer into filaments that will serve as matrix provider during composite manufacturing.

Molecular weight. For the molecular weight analysis (number and weight average M_n and M_w) the high temperature gel permeation chromatography (HT-GPC) was utilized (GPC220, Polymer Laboratories) with a streaming velocity of 1.0 ml/min at 150 °C.

  doi:10.5075/epfl-298799_978-2-9701614-0-0

Viscosity. The complex viscosity was determined by the rotational rheometer ARES-G2 (Waters TA Instruments, USA). All experiments were performed in parallel plate geometry, 25 mm diameter, at temperatures of 180 °C-250 °C for PP and 260 °C-300 °C for PET.

Unidirectional composites. Filament winding of the hybrid yarns followed by compression molding was used to manufacture unidirectional composites with a glass fiber volume fraction of 50 %. The processing regime was as follows: heating up to 250 °C with a heating rate of 15 K/min at 10 bar; increasing the pressure to 45 bar for 2 min; reduction of the temperature and pressure down to 165 °C and 10 bar; cooling down to 40 °C with 15 K/min. Specimens for mechanical testing were cut out of the unidirectional plates using a rotating diamond saw. Tensile tests (ISO 527-5) and transverse tensile tests (ISO 527-4) were performed.

Micro-computed tomography (µCT). The particle size and distribution of impurities inside the recycled polymers were caried out with µCT investigations (CT-ALHA, Procon X-Ray GmbH, Sarstedt). The samples were scanned with 960 projections using X-Ray of 90 keV/120 µA. With a resulting image resolution of 4 µm the particle quantification was done with 3D image analysis software VG Studio MAX 3.5 (Volume Graphics GmbH, Heidelberg).

3. Results

3.1 Viscosity

The complex viscosity has been determined for PP and PET in the temperature range that will be achieved during polymer spinning for the hybrid yarns. As a rule of thumb, the complex viscosity of the thermoplastic polymers should range between 100 Pa·s and 1000 Pa·s to fulfil the requirements of spinning. Both, the virgin-PP and rPP type meet this demand even at high temperatures of 250 °C. In the case of PET, a significant reduction of the viscosity is observed already at very low angular frequencies. Besides the virgin PET, the recycled PET type C/TR-04 reveals an appropriate viscosity. In contrast, the viscosity of the recycled PET types O-08 and O-12 strongly ranges underneath the limit of 100 Pa·s, so that they have not been considered for spinning trials.

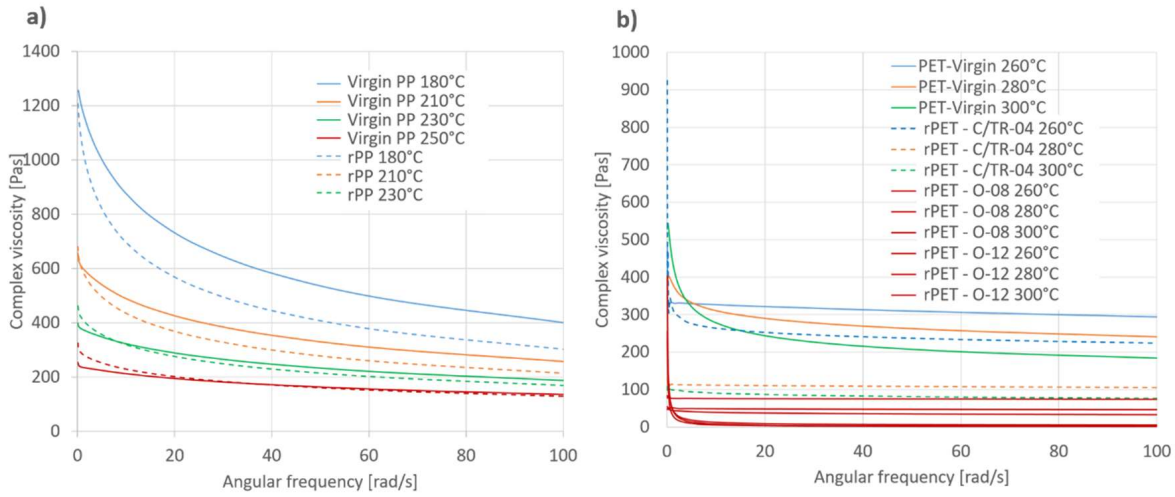

Figure 3 : Complex viscosity depending on the angular frequency determined for a) PP types and b) PET types at different temperatures

  doi:10.5075/epfl-298799_978-2-9701614-0-0

3.2 Molecular weight analysis

The number (M_n) and weight average molecular weight (M_w) was determined for virgin PP (vPP) and rPP after passing through various process steps. Since the virgin PP and rPP are not of the same polymer type, the values of both materials cannot be compared directly, however, it becomes obvious, that the molecular weight of rPP is on a much lower level that corresponds to roughly one third of the virgin PP. However, the treatment by the different extrusion cycles and temperatures did not lead to any further decrease. Also, the additional heat and shearing stresses during spinning using the piston spinning device did not result in further reduction of M_w and M_n.

The PET samples have been analyzed in the as-received state and the values of M_n were found to range between M_n = 51,000 g/mol for the virgin-PET, as well as 42,000 g/mol for C/TR-04, 33,000 g/mol for O-08 and 32,000 g/mol for O-12. Referring to the low values of complex viscosity the reduction of M_n by more than 10,000 g/mol does strongly limit the spinnability.

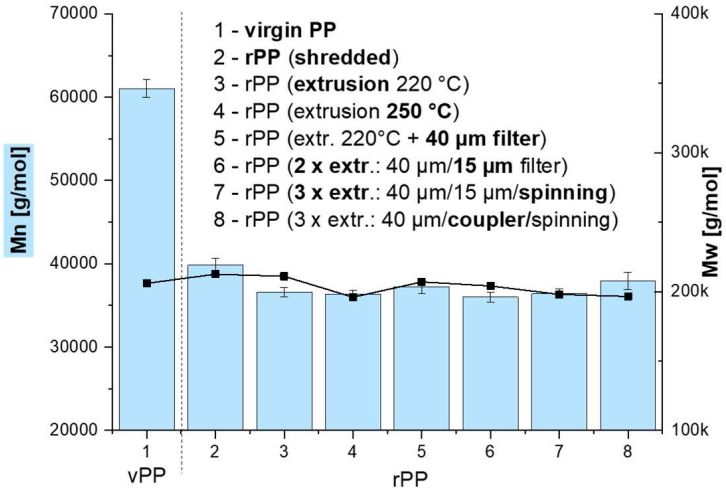

Figure 4 : Number and weight average molecular weight of recycled PP before and after different compounding and extrusion events

3.3 Purification

The size of the particles and fibers that were found as residuals in the recycled polymers does not only need to be considered with regards to nozzle blocking. The filtration of polymers during processing is done as a standard procedure to prevent any damage of the devices by big particles of any origin. The always available residual particles in recycled polymers carry the risk of high-pressure build-up in the processing equipment due to clogging of those filters. As a standard sieve a mesh size of 40 µm is used in the spinning devices. The rPP was selected to determine the particle diameter distribution after processing the material at 220 °C by using mesh sizes underneath and above this value to learn about the achievable purification. The particle diameter distribution in Figure 5 shows that a clear purification effect is observed by the sieve with a mesh size of 15 µm. In the other cases, the maximum values are reduced or a wider distribution can be observed. Further investigation was done by µCT-analysis (Figure 6) after

filtration by a 40 µm and a combined filtration of 40 µm and 15 µm mesh size. Again, it shows the effectiveness of the small mesh. However, the filtration by larger mesh sizes is necessary as a first step since otherwise the pressure in the compounding unit increases drastically.

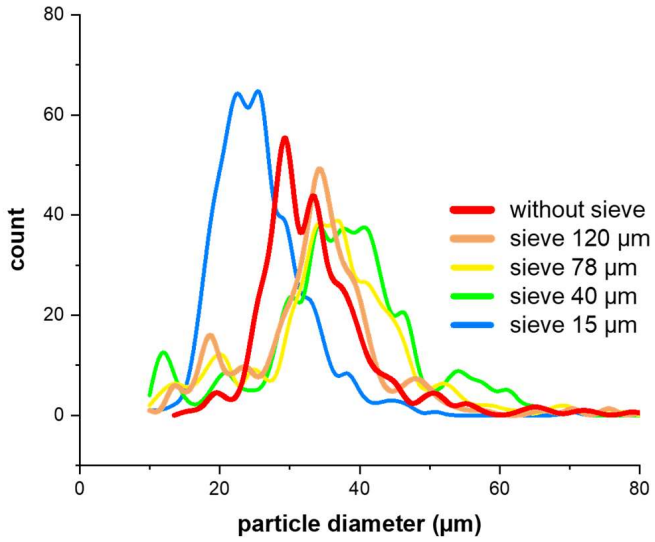

Figure 5 : Particle diameter distribution after filtration of rPP at 220 °C using different sieves

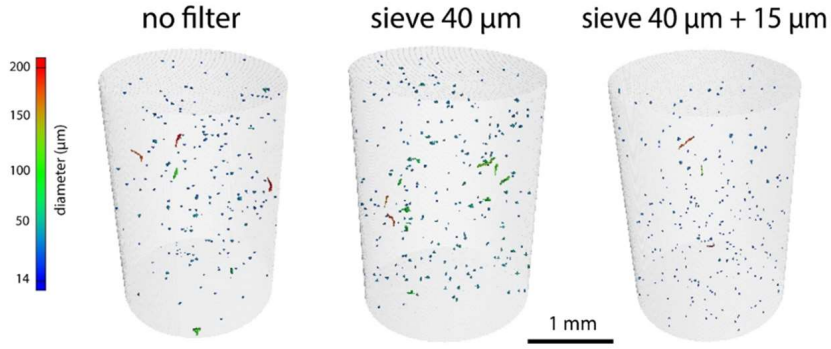

Figure 6 : µCT-analysis of particle distribution in rPP after filtration using sieves with a mesh size of 40 µm or a combination of 40 µm and 15 µm

3.4 Hybrid yarn manufacturing and composite testing

rPP was selected for the upscaling in hybrid yarn spinning trials. The material was filtered accordingly and rovings with a total fineness of 160 tex (118 tex glass, 42 tex polymer) have been manufactured at a temperature of 220 °C for rPP and 235 °C for virgin PP adding 2% coupling agent (SCONA TPPP 9212 GA, BYK, Germany).

The unidirectional composites made of the produced hybrid yarns have been tested transverse and along the fiber direction (Figure 7). Since the same sizing was applied on both hybrid yarns the reduction of the properties is mainly attributed to the degradation of the matrix. However, it should be kept in mind that the interphase properties are also determined by the interaction of the sizing with the matrix polymer [3] that might be different if the molecule chain length of

the matrix polymer is shortened. The matrix degradation during processing leads to a reduction of the tensile strength that is more pronounced in transverse direction, as expected, by about 32%.

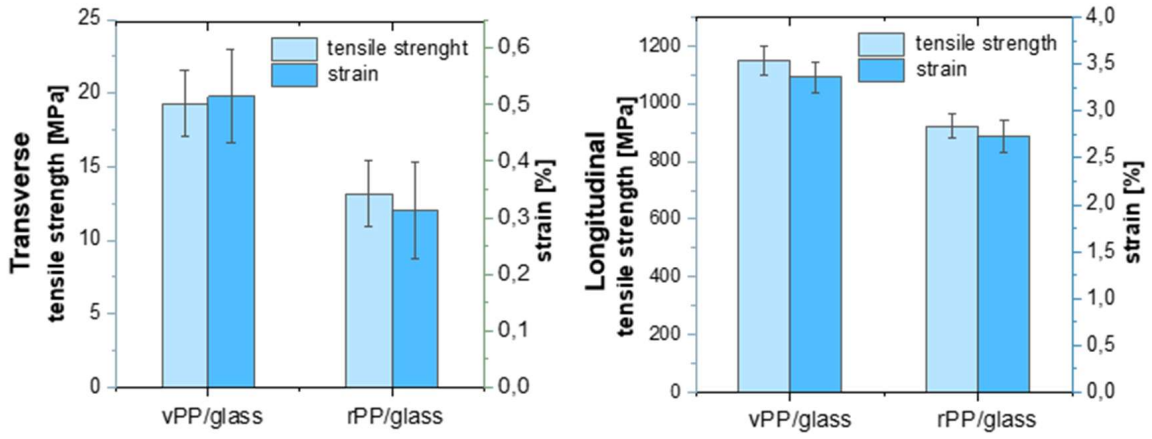

Figure 7 : Comparison of the mechanical properties of unidirectional composites produced by winding of hybrid yarns made of vPP and rPP

4. Summary

This work showed the feasibility in principle of using recycled PP in hybrid yarns to serve as matrix polymer for composites; the usage of recycled PET was limited by the low melt viscosity of recycled PET types. It can be assumed that the usage of additives and also the adaption of the sizing in subsequent works might lead to an increase of the achieved mechanical composite performance. However, the filtration efforts that are required to enable fiber spinning are a clear downside and need to be evaluated with regards to economic efficiency.

References

1. Spickenheuer A, Scheffler C, Bittrich L, Haase R, Weise D, Garray D, Heinrich G. Tailored fiber placement in thermoplastic composites. Technologies for Lightweight Structures 2017 (TLS), 1(2).
2. Wiegand N, Mäder E. Commingled yarn spinning for thermoplastic/glass fiber composites. Fibers 2017; 5(3), 26.
3. Kamps J. H., Scheffler C, Simon F, van der Heijden R, Verghese N. Functional polycarbonates for improved adhesion to carbon fibre. Composites Science and Technology 2018, 167, 448-455.

  doi:10.5075/epfl-298799_978-2-9701614-0-0

REPROCESSABLE VITRIMER COMPOSITES

Vincent SCHENK [a,b,c,], Karine LABASTIE [a], Mathias DESTARAC [a,b], Marc GUERRE [b,*], Philippe OLIVIER [c,*]*

a: IRT Saint Exupéry, bâtiment B612 3 rue Tarfaya, 31405 Toulouse cedex 4, France. E-mail: vincent.schenk@irt-saintexupery.com
b: Laboratoire des IMRCP, Université de Toulouse, CNRS UMR5623, Université Paul Sabatier, 118 route de Narbonne, 31062 Toulouse Cedex 9, France. E-mail: marc.guerre@cnrs.fr
c: Institut Clément Ader, Université de Toulouse, CNRS UMR5312, Université Paul Sabatier, 3 rue Caroline Aigle, 31400 Toulouse Cedex 4, France. E-mail: philippe.olivier@iut-tlse3.fr

Abstract: *The industry uses more and more thermoset composites owing to their outstanding properties and high versatility. Nevertheless, this class of materials which cannot be repaired nor recycled raise a major problem regarding the transition from a linear towards a circular economy. One solution to this problem involves a new class of materials coined vitrimers. Herein, we develop a promising high-performance epoxy vitrimer with a high glass transition temperature for aeronautics applications and compatible with conventional composite manufacturing processes. The ability of these vitrimers to fulfil all processing specifications such as viscosity, reactivity and gel time was verified. For the first time a complete rheological study was performed on high performance epoxy vitrimer systems possessing the same thermomechanical properties as the reference thermoset analogue. The first results were promising for making reprocessable epoxy vitrimer composites.*

Keywords: vitrimer; composite; epoxy; rheology; reprocessable

1. Introduction

Aeronautics uses more and more thermosets for high performance applications (e.g. structural parts such as fuselage or wings) thanks to their outstanding mechanical properties, resistance to solvents and versatility in application. They are also used in many other areas such as transportation in general or energy (e.g. wind turbines). Nevertheless, these important materials raise a major problem regarding their recyclability as they are intrinsically insoluble and infusible. Even if these properties are considered as major assets during their lifetime, they become important drawbacks at the end of their life as they are very difficult to recycle. (1)

To improve their mechanical properties, thermosets are generally associated with reinforcements such as carbon fibres, glass fibres, carbon nanotubes, graphene and many others. One of the challenges regarding the recycling process consists in separating the reinforcement from the matrix. Current processes use thermolysis (the matrix is degraded at high temperature) (2,3), solvolysis (4) or other methods (5) enabling reinforcements recovery but mostly with altered mechanical properties. Therefore, these fibres cannot be recycled several times and used for the same applications as they were initially designed for. (6,7)

An interesting way to recycle thermoset composites would be to work on the chemical structure of the thermosets before they are produced in order to introduce reprocessable and recyclable properties. Vitrimers open up great opportunities towards sustainable materials by producing

  doi:10.5075/epfl-298799_978-2-9701614-0-0

reprocessable thermosets based on dynamic exchanges endowing the vitrimers with a behaviour similar to that of glass above the glass transition temperature (Tg). (8)

Many efforts have been made in the past two decades to produce reprocessable, healable and recyclable thermosets by introducing reversible bonds into the polymeric networks, including reversible non-covalent interactions (e.g. hydrogen bonds) and reversible covalent exchanges. Thermosets with non-covalent interactions are often weak and could not withstand large stress making them not suitable for structural applications. Alternatively, polymer networks with reversible covalent bonds, known as covalent adaptable networks (CANs), offer an attractive way to make thermosets with good mechanical integrity combined with thermoplastics-like behaviour at high temperature. CANs are generally divided into two groups depending on their exchange mechanism: dissociative CANs and associative CANs. The first group, dissociative CANs, are constituted of reversible chemical reactions based on dissociative exchange mechanisms, meaning the cross-link bonds break upon heating and reform at lower temperature resulting in a decrease of network connectivity and modification of the cross-linking degree during network rearrangement. Hence, such exchange reactions lead to a sudden drop of viscosity with the increasing temperature; as a result, the network cannot maintain its dimensional integrity at high temperature. For instance, the Diels-Alder (DA) reaction is typically representative of dissociative CANs. The second group, associative CANs, keep their cross-link density constant during thermal activation with an unchanged number of chemical bonds during reprocessing. In fact, bond breaking only occurs when a new bond is formed. (9–11)

In 2011, Leibler and co-workers coined this new polymeric material based on associative CANs, “vitrimer”. This first vitrimer was obtained by adding transesterification catalysts into epoxy/acid or epoxy/anhydride polyester networks. This catalyst promoted transesterification reactions with control over the exchange kinetics by varying the quantity of catalyst initially introduced. (12) Vitrimers are now considered as the third class of polymeric material alongside thermoplastics and thermosets. At service temperature, vitrimers behave like traditional thermosets, which have good thermal and mechanical properties. However, when heated above a specific temperature, the exchangeable reaction (such as transesterification) occurs. In the past decade, various chemistries have been implemented for vitrimers purposes including carboxylate transesterification (13–15), transamination of vinylogous urethanes (16–18), transalkylation (19–21), disulfide exchange (22–25) or imine exchange (26–28), to name a few.

From the composite standpoint, vitrimer matrices based on chemistries cited above have started to be used to produce composite materials with different reinforcements such as carbon fibres (29–31), carbon nanotubes (32–34), graphene (35–37), glass fibres (38) and few others (39–41).

Despite the significant scientific interest of those chemistries, their use in practical industrial applications is not straightforward. Indeed, many issues are inherent to the chemical nature of each system such as scalability, use of a catalyst, thermal stability or low mechanical properties. Here we report a catalyst-free new epoxy vitrimer system based on the commercial epoxy resin RTM6-2, readily upscalable with composite manufacturing processes and which could be reprocessable, repairable and recyclable.

2. Experimental

2.1 Materials

  doi:10.5075/epfl-298799_978-2-9701614-0-0

HexFlow® RTM6-2 Part A (4,4'-Methylenebis[N,N-bis(2,3-epoxypropyl)aniline]) and Part B (4,4'-Methylenebis(2,6-diethylaniline) 60-100%, 4,4'-Methylenebis(2-isopropyl-6-methylaniline) 30-60%) were purchased from Hexcel. 4-aminophenyl disulfide (4-AFD) was purchased from Molekula group.

2.2. Characterizations

Differential scanning calorimetry (DSC) analyses were performed with a DSC 25 TA instruments under nitrogen atmosphere at a heating rate of 10°C/min from -50°C to 350°C.

Thermogravimetric analyses (TGA) were performed with a TG 209 F3 Tarsus Netzsch under nitrogen atmosphere at a heating rate of 10°C/min from 30°C to 950°C.

Rheological analyses were performed with a rheometer MCR 302 Anton Paar. Oscillatory measurements using parallel plates of 25 mm diameter with a gap of 0.5 mm, an angular velocity of 10 rad/sec and a strain of 4% were typically used.

2.3. Synthesis of RTM6-2 vitrimer

The reference epoxy network was prepared following the recommendation of Hexcel by adding 6.81 g of RTM6-2 part B preheated at 90°C to 10 g of RTM6-2 Part A preheated at 80°C both for 12 hours. Then, the mix was stirred slowly at 80°C for 30 minutes.

For the vitrimer network, 5.45 g of 4-AFD preheated at 80°C was added to 10 g of RTM6-2 Part A preheated at 80°C both for 12 hours and then stirred slowly at 80°C for 30 minutes. This was followed by a curing process at 180°C for 90 minutes for the RTM6 and 130°C for 60 minutes then 180°C for 15 minutes for the RTM6 vitrimer to obtain the plates.

3. Results and discussion

To prepare the above-mentioned vitrimer, the harderner usually used in the Hexcel formulation was fully replaced by a dynamic hardener (4-AFD). This harderner is constituted of disulfide linkages which undergo exchanges at high temperature introducing the desired vitrimer properties. This change in hardener is expected to have an influence on the curing behaviour of the RTM6 resin. To better evaluate this influence, different experiments were conducted to study the reactivity of 4-AFD with the RTM6 resin. Through this study, a careful comparison was conducted between the non-dynamic RTM6 reference and the vitrimer counterpart.

The thermal stability analysed by TGA (Table 1) of the network which is an important criterion for processing and reprocessing showed that dynamic network possesses a lower degradation temperature compared to the non-dynamic reference. An onset degradation of 5% is observed at 286.5 °C for the vitrimer while the reference is stable up to 345 °C. Luzuriaga and coworkers observed the same decrease of degradation temperature with their DGEBA counterpart (31). This difference is very likely due to the presence of the disulfide bridges, known to be less thermally stable than the carbon-carbon bonds.

From DSC thermograms (Figure 1), similar glass transition temperatures were obtained for the reference and vitrimer network. However, the enthalpy of crosslinking of the vitrimer was largely increased by 27% compared to that of the reference network, indicating its internal energy is higher. Furthermore, the exothermic peak has been lowered by more than 40°C for

  doi:10.5075/epfl-298799_978-2-9701614-0-0

the vitrimer compared to RTM6, showing that crosslinking reactions occurred at lower temperatures (Table 1).

Table 1: Thermal properties of RTM6 and RTM6 vitrimer obtained by DSC and TGA analyses.

	Tg_0 [°C]	Enthalpy [J/g]	Exothermic peak [°C]	Tg_∞ [°C]	T_d [°C]
RTM6	-16.50	459.9	242.0	222.51	345.0
RTM6 vitrimer	-10.51	585.1	200.5	233.06	286.5

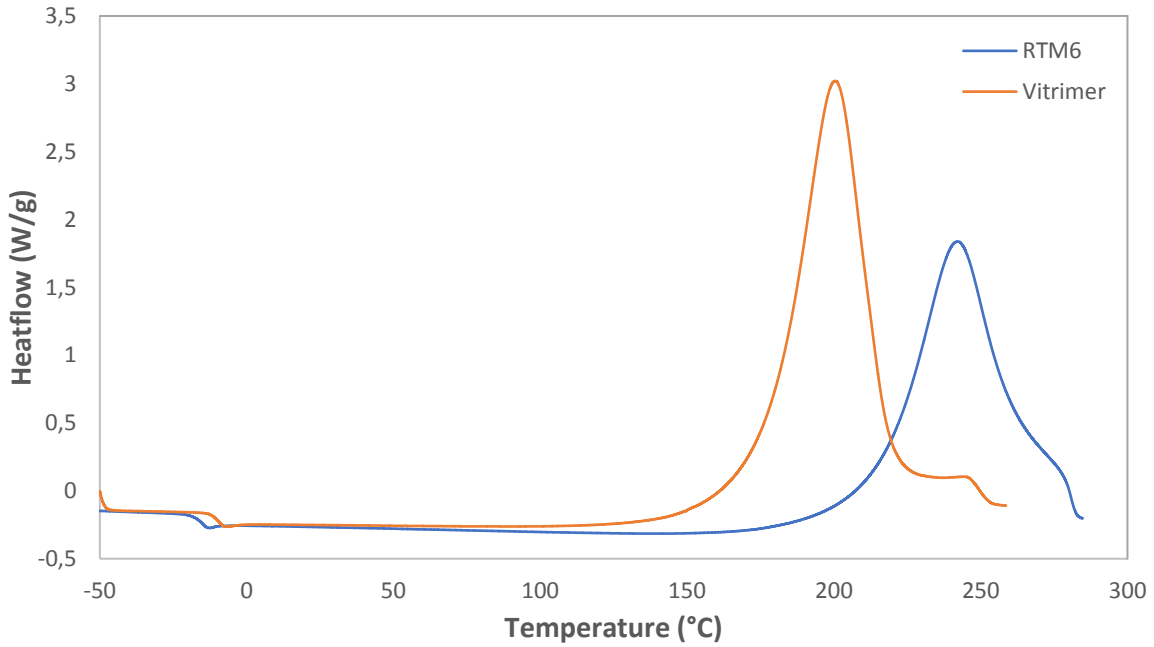

Figure 1: DSC thermograms of the uncured RTM6 and RTM6 vitrimer.

Before evaluating the crosslinking kinetics, the linearity zones at different isothermal temperatures in oscillation mode were determined. A strain of 4% and an angular frequency of 10 rad/s were selected and used in all curing profiles.

The initial complex viscosities for RTM6 and RTM6 vitrimer all lie between 50 and 100 mPa.s for isotherms ranging from 110°C up to 150°C (Figure 2). This indicates that the introduction of 4-AFD as hardener does not considerably change the viscosity of the resin at the initial curing stage which is an important parameter for processing techniques such as RTM. Nevertheless, even if the initial complex viscosities are comparable for both networks, the time to reach 10^6 mPa.s is much faster for the RTM6 vitrimer. Indeed, the reactivity seems faster for the vitrimer system in accordance with the DSC thermograms obtained previously.

In addition to the complex viscosity, the storage and loss modulus were also followed during crosslinking kinetics. Gel times corresponding to the time at which the evolving dynamic storage (G') and loss (G'') moduli cross over during an isothermal cure were determined at different temperatures (Table 2).

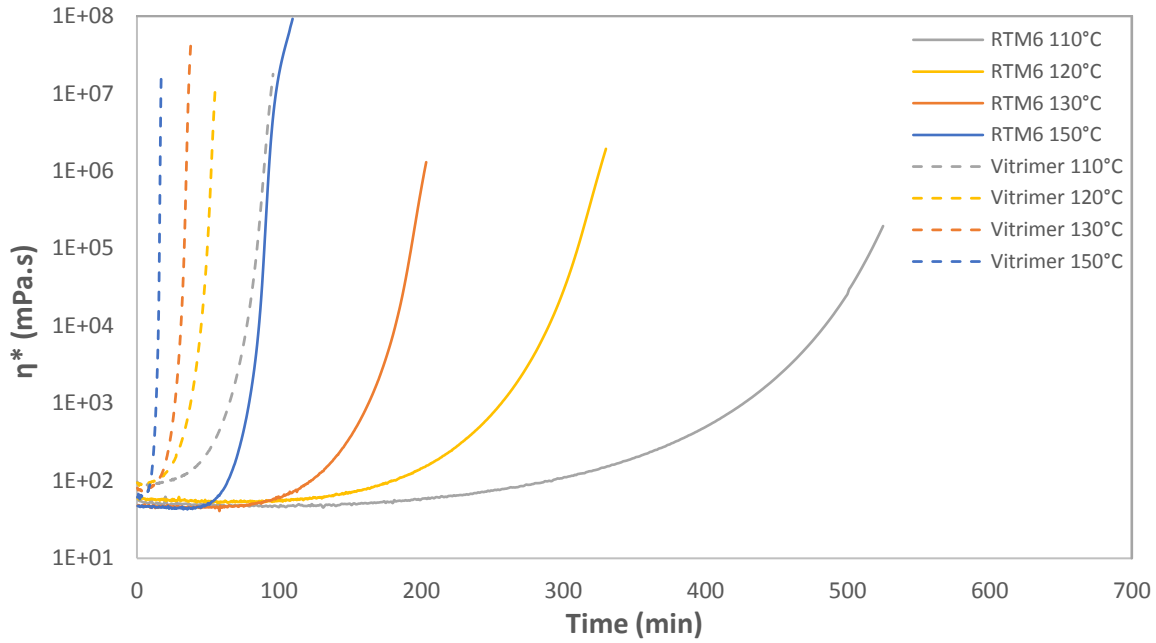

Figure 2: Complex viscosity as a function of time during curing at different isotherms for RTM6 and RTM6 vitrimer to assess the crosslinking kinetics.

Table 2: Gel times for curing at different isotherms for RTM6 and RTM6 vitrimer.

Gel time [min]	120°C	130°C	140°C	150°C
RTM6	340	202	140	91
RTM6 vitrimer	53.5	34.5	21.5	16

The gel times are much shorter for the RTM6 vitrimer compared to standard RTM6, confirming the increase of reactivity and crosslinking kinetics with the 4-AFD hardener. This information is important to further adapt the processing conditions for composite manufacturing.

Subsequently, to prove the capacity of the RTM6 vitrimer to be reprocessable, the material was ground and reprocessed above its glass transition temperature by compression moulding at 220 °C for 30 min. The new plate obtained had a satisfying aspect (Figure 3).

Figure 3: RTM6 vitrimer (Tg >210°C) reprocessed using a hot-press after grinding.

4. Conclusions

In our work, we produced an epoxy vitrimer from the high performance RTM6-2 epoxy thermoset and 4-AFD hardener containing dynamic disulfide bonds. We have shown that both networks have comparable properties although the RTM6 vitrimer crosslinks at lower temperatures and has a higher reactivity, while showing new features such as reprocessability as presented previously. Therefore, the RTM6 vitrimer could be used as a matrix to manufacture polymer composites using industrial manufacturing processes such as resin transfer moulding or infusion. Furthermore, raw materials are already available in large volumes, which offers great opportunities for manufacturing high performance vitrimer composites at an industrial scale.

Acknowledgements

The authors would like to thank the technological research institute Saint Exupéry for financial support.

5. References

1. Utekar S, V k S, More N, Rao A. Comprehensive study of recycling of thermosetting polymer composites – Driving force, challenges and methods. Composites Part B: Engineering. 2021 Feb 15;207:108596.
2. Boulanghien M, R'Mili M, Bernhart G, Berthet F, Soudais Y. Fibre characterisation of steam thermal process recycled carbon fibre/epoxy composites. In: ICCM 19 -19th International Conference on Composite Materials [Internet]. Montreal, Canada; 2013 [cited 2022 Apr 19]. p. p.9087-9094. Available from: https://hal.archives-ouvertes.fr/hal-01741814
3. Boulanghien M, R'Mili M, Bernhart G, Berthet F, Soudais Y. Mechanical Characterization of Carbon Fibres Recycled by Steam Thermolysis: A Statistical Approach. Advances in Materials Science and Engineering. 2018 May 20;2018:e8630232.
4. Oliveux G, Bailleul JL, Gillet A, Mantaux O, Leeke GA. Recovery and reuse of discontinuous carbon fibres by solvolysis: Realignment and properties of remanufactured materials. Composites Science and Technology. 2017 Feb 8;139:99–108.
5. Jlassi S, Berthet F, Bernhart G. Investigation of mechanical properties of nonwoven second generation composite material elaborated through a mixture of carbon fibers and filament lengths. In 2018 [cited 2022 Apr 19]. Available from: https://hal-mines-albi.archives-ouvertes.fr/hal-01862432
6. Zhang J, Chevali VS, Wang H, Wang CH. Current status of carbon fibre and carbon fibre composites recycling. Composites Part B: Engineering. 2020 Jul 15;193:108053.
7. Verma S, Balasubramaniam B, Gupta RK. Recycling, reclamation and re-manufacturing of carbon fibres. Current Opinion in Green and Sustainable Chemistry. 2018 Oct 1;13:86–90.
8. Yang Y, Xu Y, Ji Y, Wei Y. Functional epoxy vitrimers and composites. Progress in Materials Science. 2020 Jun 25;100710.
9. Kloxin CJ, Scott TF, Adzima BJ, Bowman CN. Covalent Adaptable Networks (CANs): A Unique Paradigm in Cross-Linked Polymers. Macromolecules. 2010 Mar 23;43(6):2643–53.
10. Bowman CN, Kloxin CJ. Covalent Adaptable Networks: Reversible Bond Structures Incorporated in Polymer Networks. Angewandte Chemie International Edition. 2012;51(18):4272–4.
11. Kloxin CJ, Bowman CN. Covalent adaptable networks: smart, reconfigurable and responsive network systems. Chemical Society Reviews. 2013;42(17):7161–73.

  doi:10.5075/epfl-298799_978-2-9701614-0-0

12. Montarnal D, Capelot M, Tournilhac F, Leibler L. Silica-Like Malleable Materials from Permanent Organic Networks. Science. 2011;334(6058):965–8.
13. Capelot M, Montarnal D, Tournilhac F, Leibler L. Metal-Catalyzed Transesterification for Healing and Assembling of Thermosets. Journal of the American Chemical Society. 2012 May 9;134(18):7664–7.
14. Yu K, Taynton P, Zhang W, Dunn ML, Qi HJ. Reprocessing and recycling of thermosetting polymers based on bond exchange reactions. RSC Advances. 2014;4(20):10108–17.
15. Brutman JP, Delgado PA, Hillmyer MA. Polylactide Vitrimers. ACS Macro Letters. 2014 Jul 15;3(7):607–10.
16. Denissen W, Rivero G, Nicolaÿ R, Leibler L, Winne JM, Du Prez FE. Vinylogous Urethane Vitrimers. Advanced Functional Materials. 2015;25(16):2451–7.
17. Liu Z, Zhang C, Shi Z, Yin J, Tian M. Tailoring vinylogous urethane chemistry for the cross-linked polybutadiene: Wide freedom design, multiple recycling methods, good shape memory behavior. Polymer. 2018 Jul 18;148:202–10.
18. Taplan C, Guerre M, Bowman CN, Prez FED. Surface Modification of (Non)-Fluorinated Vitrimers through Dynamic Transamination. Macromolecular Rapid Communications. 2021 Jan 11;n/a(n/a):2000644.
19. Obadia MM, Mudraboyina BP, Serghei A, Montarnal D, Drockenmuller E. Reprocessing and Recycling of Highly Cross-Linked Ion-Conducting Networks through Transalkylation Exchanges of C–N Bonds. Journal of the American Chemical Society. 2015 May 13;137(18):6078–83.
20. Hendriks B, Waelkens J, Winne JM, Du Prez FE. Poly(thioether) Vitrimers via Transalkylation of Trialkylsulfonium Salts. ACS Macro Letters. 2017 Sep 19;6(9):930–4.
21. Huang J, Zhang L, Tang Z, Wu S, Guo B. Reprocessable and robust crosslinked elastomers via interfacial CN transalkylation of pyridinium. Composites Science and Technology. 2018 Nov 10;168:320–6.
22. Rekondo A, Martin R, Ruiz de Luzuriaga A, Cabanero G, Grande HJ, Odriozola I. Catalyst-free room-temperature self-healing elastomers based on aromatic disulfide metathesis. Materials Horizons. 2014;1(2):237–40.
23. Martin R, Rekondo A, Ruiz de Luzuriaga A, Cabanero G, Grande HJ, Odriozola I. The processability of a poly(urea-urethane) elastomer reversibly crosslinked with aromatic disulfide bridges. Journal of Materials Chemistry A. 2014;2(16):5710–5.
24. Azcune I, Odriozola I. Aromatic disulfide crosslinks in polymer systems: Self-healing, reprocessability, recyclability and more. European Polymer Journal. 2016 Nov 1;84:147–60.
25. Li B, Zhu G, Hao Y, Ren T. An investigation on the performance of epoxy vitrimers based on disulfide bond. Journal of Applied Polymer Science. n/a(n/a):51589.
26. Zhang H, Wang D, Liu W, Li P, Liu J, Liu C, et al. Recyclable polybutadiene elastomer based on dynamic imine bond. Journal of Polymer Science Part A: Polymer Chemistry. 2017;55(12):2011–8.
27. Feng Z, Yu B, Hu J, Zuo H, Li J, Sun H, et al. Multifunctional Vitrimer-Like Polydimethylsiloxane (PDMS): Recyclable, Self-Healable, and Water-Driven Malleable Covalent Networks Based on Dynamic Imine Bond. Industrial & Engineering Chemistry Research. 2019 Jan 23;58(3):1212–21.
28. Chao A, Negulescu I, Zhang D. Dynamic Covalent Polymer Networks Based on Degenerative Imine Bond Exchange: Tuning the Malleability and Self-Healing Properties by Solvent. Macromolecules. 2016 Sep 13;49(17):6277–84.
29. Yu L, Zhu C, Sun X, Salter J, Wu H, Jin Y, et al. Rapid Fabrication of Malleable Fiber Reinforced Composites with Vitrimer Powder. ACS Applied Polymer Materials. 2019 Sep 13;1(9):2535–42.

  doi:10.5075/epfl-298799_978-2-9701614-0-0

30. Liu YY, He J, Li YD, Zhao XL, Zeng JB. Biobased epoxy vitrimer from epoxidized soybean oil for reprocessable and recyclable carbon fiber reinforced composite. Composites Communications. 2020 Dec 1;22:100445.
31. Luzuriaga AR de, Martin R, Markaide N, Rekondo A, Cabañero G, Rodríguez J, et al. Epoxy resin with exchangeable disulfide crosslinks to obtain reprocessable, repairable and recyclable fiber-reinforced thermoset composites. Mater Horiz. 2016 May 3;3(3):241–7.
32. Yang Y, Pei Z, Zhang X, Tao L, Wei Y, Ji Y. Carbon nanotube-vitrimer composite for facile and efficient photo-welding of epoxy. Chemical Science. 2014;5(9):3486–92.
33. Zhang J, Lei Z, Luo S, Jin Y, Qiu L, Zhang W. Malleable and Recyclable Conductive MWCNT-Vitrimer Composite for Flexible Electronics. ACS Appl Nano Mater. 2020 May 22;3(5):4845–50.
34. Zhou F, Guo Z, Wang W, Lei X, Zhang B, Zhang H, et al. Preparation of self-healing, recyclable epoxy resins and low-electrical resistance composites based on double-disulfide bond exchange. Composites Science and Technology. 2018 Oct 20;167:79–85.
35. Chen J, Huang H, Fan J, Wang Y, Yu J, Zhu J, et al. Vitrimer Chemistry Assisted Fabrication of Aligned, Healable, and Recyclable Graphene/Epoxy Composites. Frontiers in Chemistry. 2019 Sep;7:632.
36. Liu Y, Tang Z, Chen Y, Wu S, Guo B. Programming dynamic imine bond into elastomer/graphene composite toward mechanically strong, malleable, and multi-stimuli responsive vitrimer. Composites Science and Technology. 2018 Nov 10;168:214–23.
37. Krishnakumar B, Prasanna Sanka RVS, Binder WH, Park C, Jung J, Parthasarthy V, et al. Catalyst free self-healable vitrimer/graphene oxide nanocomposites. Composites Part B: Engineering. 2020 Mar 1;184:107647.
38. Post W, Cohades A, Michaud V, van der Zwaag S, Garcia SJ. Healing of a glass fibre reinforced composite with a disulphide containing organic-inorganic epoxy matrix. Composites Science and Technology. 2017 Nov 10;152:85–93.
39. Yue L, Amirkhosravi M, Ke K, Gray TG, Manas-Zloczower I. Cellulose Nanocrystals: Accelerator and Reinforcing Filler for Epoxy Vitrimerization. ACS Appl Mater Interfaces. 2021 Jan 20;13(2):3419–25.
40. Niu Z, Wu R, Yang Y, Huang L, Fan W, Dai Q, et al. Recyclable, robust and shape memory vitrified polyisoprene composite prepared through a green methodology. Polymer. 2021 Jul 16;228:123864.
41. Ji F, Liu X, Sheng D, Yang Y. Epoxy-vitrimer composites based on exchangeable aromatic disulfide bonds: Reprocessibility, adhesive, multi-shape memory effect. Polymer. 2020 May 27;197:122514.

  doi:10.5075/epfl-298799_978-2-9701614-0-0

CHARACTERIZING THE TENSILE AND COMPRESSIVE BEHAVIOR OF PETG/CF AND PC/CF MANUFACTURED USING LARGE SCALE ADDITIVE PROCESSES

Camerin Seigars, Kyle Warren, Benjamin Steva, Christopher Murphy, Britt Helten

Advanced Structures and Composites Center
University of Maine
camerin.seigars@maine.edu

Abstract: *The large-scale additive manufacturing (AM) process provides unique potential with the ability to fabricate large thermoplastic composite structures with complex features by leveraging extrusion processes. To design load bearing structures manufactured with this technology it is essential that engineers have a deep understanding of the material systems that can be processed with this equipment. Material characteristics such as elastic modulus, ultimate strength, and strain to failure are essential for engineers to design safe and predictable structures and parts. The quasi-static tensile and compressive response was evaluated in the two primary directions within the 13-plane (along and through the thickness of the printed bead) for parts manufactured from short carbon fiber reinforced polyethylene terephthalate-glycol (PETG) and polycarbonate (PC) on a Cincinnati Big Area Additive Manufacturing (BAAM) work cell.*

Carbon reinforced PETG and PC were chosen as they provide a balance between feedstock cost and mechanical performance appropriate for structural applications. Tensile properties were measured using a thickness-modified ASTM D638-14 with as-printed coupons. Compressive properties were measured using ASTM D6641-16 with printed samples that were machined into a flat plate to characterize the continuous area at the center of the deposited extrudate. Digital image correlation was used on all specimens during experiments to capture full-field strain behavior. Tensile and compressive performance of carbon reinforced PETG and PC was compared in various orientations to establish engineering properties that can be used for structural design inputs.

Keywords: Large-scale additive manufacturing; thermoplastic composites; big area additive manufacturing (BAAM); standardized testing.

1. Introduction

This paper summarizes and then compares the tensile and compressive quasi-static response of two carbon fiber reinforced thermoplastic materials manufactured into panels using large-scale polymer extrusion additive manufacturing on a Cincinnati BAAM machine. Tensile and compressive properties including strength and elastic modulus are important in the design of structural elements. This study used methods based on ASTM D638-14 standard test method for tensile properties of plastics [1] to measure the tensile properties of as-printed type III dumbbell-shaped specimens and ASTM D6641-16 standard test method for compressive properties of polymer matrix materials using a combined loading compression test fixture [2] to measure the compressive properties of machined flat material. These two standards were chosen in order to evaluate their potential for characterizing large-scale additively

  doi:10.5075/epfl-298799_978-2-9701614-0-0

manufactured composites and to explore what adaptations may be necessary in order to use these existing test standards for a wider array of material systems.

The material used in this study was printed in a box configuration modeled as solid rectangular boxes on a BAAM machine as shown in Figure 1. There was no infill, top, or bottom layers, and only one perimeter. The bead width achieved was nominally 15.9-mm thick in the walls. The boxes were cut into panels in a secondary process and as-printed tension samples were extracted. Some areas of panel were faced equal amounts on both sides using a Laguna Computer Numerical Controlled (CNC) router to expose a 7.5-mm thick flat continuous center of the extruded panel for prismatic compression samples. Two materials were printed for this study: PETG/CF using TechmerPM Electrafil 1711 3DP [3] feedstock and PC/CF using Sabic feedstock.

Figure 1: Image of BAAM print

A coordinate system was adopted to describe the directionality of the material, shown in Figure 2 with a representative graphic of a panel of as-printed AM material in the 13-plane.

Figure 2: Additively manufactured material cartesian coordinate system

2. Quasi-static Testing Methods

2.1 Tensile Testing

Tensile testing was conducted using ASTM D638-14, a widely accepted standardized test method for characterizing the tensile response of plastics. A modified type III specimen [1] was used with the thickness that was determined by the as-printed thickness of the panel the samples were extracted from. The rate of testing chosen was 1.2-mm/min based on previous work done at the University of Maine combined with guidance for tensile polymer-matrix composite testing given in ASTM D3039-17 [4], which calls for a standard rate of crosshead displacement of 0.05-in/min (roughly 1.2-mm/min). All specimens were conditioned at standard laboratory conditions for at least 88-hours prior to testing in accordance with ASTM D618-21 procedure A [5].

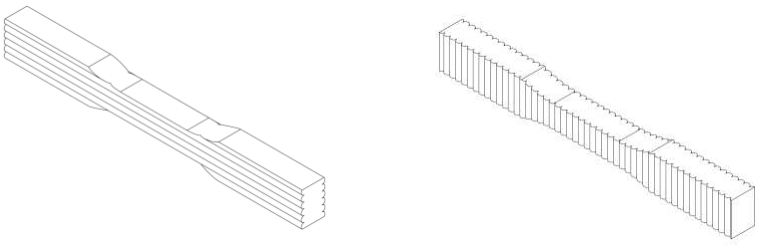

Figure 3 : ASTM D638-14 type III specimen geometry
(a) longitudinal 11-specimen & (b) through-thickness 33-specimen

Tests were conducted with an Instron WaveMatrix program designed to drive the position-controlled test using a constant crosshead displacement linear rate of 1.2-mm/min as the speed of testing. This was found to produce failures in an acceptable amount of time as outlined in section 8.2 of ASTM D638-14. Figure 4 shows the tensile testing setup that was used during this study. A spray painted stochastic patten was generated using a flat white background speckled with flat black dots for use with a digital image correlation (DIC) system. Post-processing of DIC data was conducted in GOM Suite 2021 [6] and a screenshot of a tensile coupon's full-field strain from GOM Correlate Pro is shown in Figure 5 below.

Figure 4 : ASTM D638-14 test setup

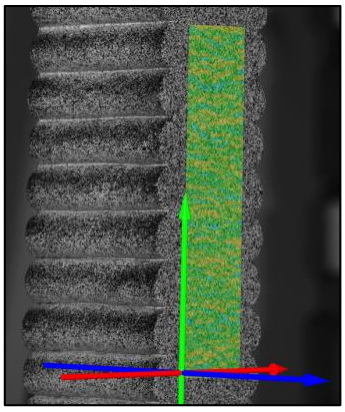

Figure 5 : Screenshot from GOM Correlate to show calculation area

  doi:10.5075/epfl-298799_978-2-9701614-0-0

2.2 Compression Testing

Compression testing was conducted using a method developed based on ASTM D6641-16 standard test method for compressive properties using a combined loading test fixture [2]. Figure 6 below shows the specimen geometry that was cut from the 7.5-mm thick flat panels using a waterjet.

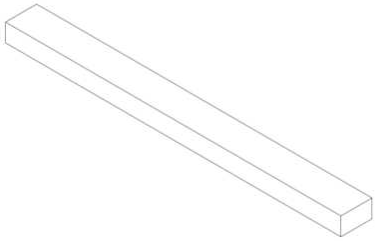

Figure 6 : ASTM D6641-16 combined loading compression (CLC) specimen geometry

Figure 7 shows the test setup used to conduct position controlled constant head speed quasi-static compression tests at a crosshead displacement rate of 1.3-mm/min. This test fixture is used to characterize the compressive properties by loading the specimen in both direct end-loading and shear-loading. Full-field strain measurements were collected using the same methods described for tensile testing in the previous section and a screenshot of the strain field shown in the analysis software is given in Figure 8.

Figure 7 : ASTM D6641-14 CLC test setup

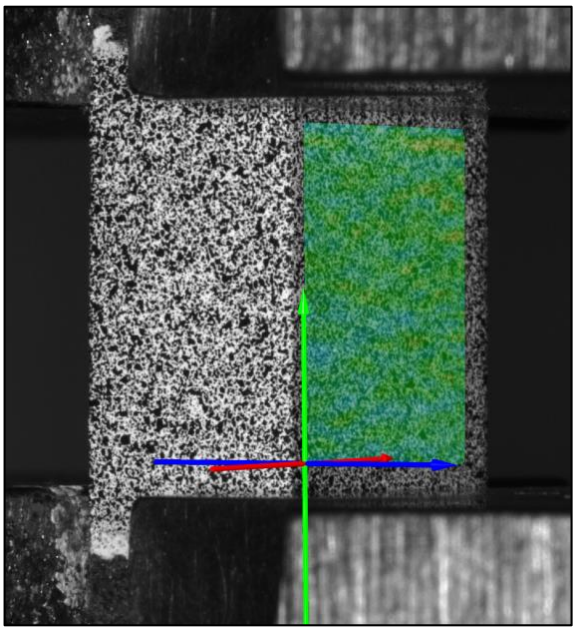

Figure 8 : Screenshot from GOM Correlate to show calculation area

The setup and use of the CLC test fixture has more steps than simply gripping the tensile samples in the Instron grips for ASTM D638-14. The procedure used with the CLC fixture was as follows; insert specimen into the fixture using an alignment jig in order to assure a consistent and centered location within the fixture, torque all eight bolts on the fixture to 25-in-lb as indicated in ASTM D6641-16, and then load the fixture into the Instron test frame on top of a fixed platen and then bring the top of the fixture into contact with a self-leveling platen.

  doi:10.5075/epfl-298799_978-2-9701614-0-0

3. Quasi-static Testing Results

3.1 Tensile Testing

Tension tests were conducted on specimens oriented in two directions within the 13-plane: the longitudinal or axial 11-direction, and the through-thickness 33-direction. Multiple specimens were tested in each orientation and the results were averaged to provide a single value for characterization. Figure 9 shows on the left typical failed PETG/CF and on the right typical failed PC/CF specimens tested for this study with 11 samples on top and 33 on bottom. All specimens used in this study had failures in the straight narrow region of the specimen or right at the termination of the radius leading into this section of the coupon.

Figure 9: Tension testing – failed specimen images (left) PETG/CF & (right) PC/CF

Table 1 gives a summary of the average tensile properties for both material systems in both the print direction (1) and build direction (3) as well as the associated coefficients of variation (COV) and number of specimens tested (N). Figure 10 gives two representative stress-strain curves for the tensile data collected. On the left shows the representative curves for PETG/CF and on the right shows the representative curves for PC/CF.

Table 1 : Tabulated tension data for PETG/CF and PC/CF

Material Property	Units	PETG/CF		PC/CF	
		11 (N = 7)	33 (N = 9)	11 (N = 5)	33 (N = 7)
Ultimate Strength	MPa (% COV)	86.9 (2.47)	10.9 (9.53)	88.2 (4.35)	28.2 (1.91)
Elastic Modulus	GPa (% COV)	12.1 (3.65)	2.72 (1.61)	8.08 (3.75)	2.61 (1.63)
Poisson's Ratio	- (% COV)	0.378 (7.19)	0.387 (9.30)	0.392 (11.5)	0.388 (2.28)
Strain at Failure	% (% COV)	1.29 (6.81)	0.435 (14.4)	1.57 (5.04)	1.22 (2.12)

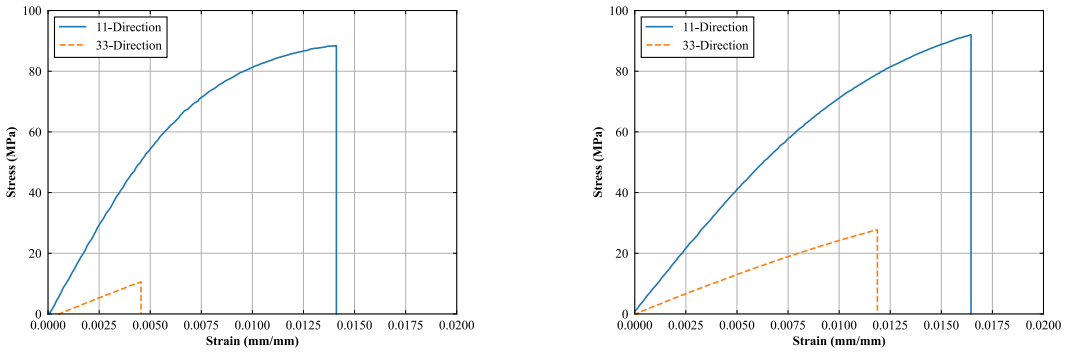

Figure 10: Representative tensile stress-strain curves (left) PETG/CF & (right) PC/CF

3.2 Compression Testing

Compression tests were conducted in the same orientations as tensile testing; the longitudinal 1-direction aligned with the print direction and the build (through-thickness) 3-direction. Multiple specimens were tested in each orientation and the results were averaged to provide a single value for characterization. Figure 11 shows on the left typical failures observed in PETG/CF specimens and on the right PC/CF specimens tested for this study. All compression specimens failed in the gauge region.

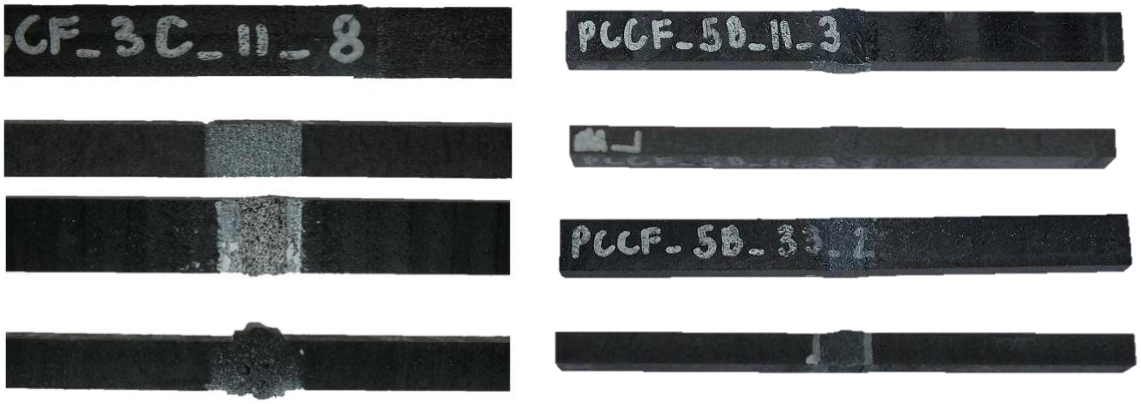

Figure 11 : Compression testing – failed specimen images (left) PETG/CF & (right) PC/CF

Table 2 gives a summary of the average tensile properties for both material systems evaluated as well as the associated coefficients of variation (COV) and number of samples tested (n). Figure 12 gives two representative stress-strain curves for the tensile data collected. On the left shows the representative curve for PETG/CF and on the right shows the representative curve for PC/CF.

Table 2 : Tabulated compression data for PETG/CF and PC/CF

Material Property	Units	PETG/CF		PC/CF	
		11 (N = 5)	33 (N = 4)	11 (N = 5)	33 (N = 5)
Ultimate Strength	MPa (COV)	109 (2.78)	93.6 (1.76)	117 (1.42)	138 (7.43)
0.2% Offset Strength	MPa (COV)	80.9 (5.72)	53.2 (4.27)	65.1 (5.76)	43.1 (25.6)
Elastic Modulus	GPa (COV)	11.5 (5.89)	3.94 (3.08)	8.34 (4.45)	3.47 (11.4)
Poisson's Ratio	- (COV)	0.422 (12.3)	0.175 (24.6)	0.438 (2.61)	0.143 (28.6)
Strain at Failure	% (COV)	5.21 (18.2)	13.2 (7.29)	4.12 (5.64)	15.3 (9.81)

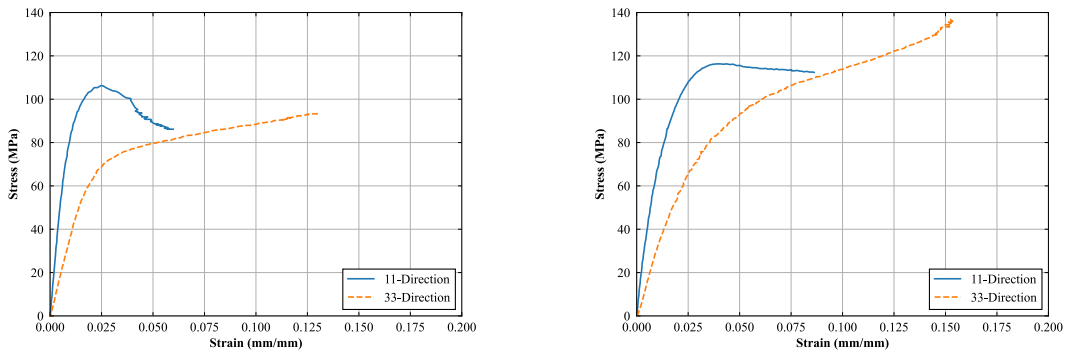

Figure 12 : Representative compressive stress-strain curves (left) PETG/CF & (right) PC/CF

3.3 Results Comparison

This section presents a side-by-side comparison of the PETG/CF and PC/CF results for tension and compression testing done in Table 3 followed by some discussion in the conclusions section of this paper.

Table 3 : Summary of results – tension and compression for PETG/CF and PC/CF

Result Type			Material Property			
Material	Test	Orientation	Ultimate Strength MPa (% COV)	Elastic Modulus GPa (% COV)	Poisson's Ratio - (% COV)	Strain at Failure % (% COV)
PETG/CF	Tension	11 (N = 7)	86.9 (2.47)	12.1 (3.65)	0.378 (7.19)	1.29 (6.81)
		33 (N = 9)	10.9 (9.53)	2.72 (1.61)	0.387 (9.30)	0.435 (14.4)
	Compression	11 (N = 5)	109 (2.78)	11.5 (5.89)	0.422 (12.3)	5.21 (18.2)
		33 (N = 4)	93.6 (1.76)	3.94 (3.08)	0.175 (24.6)	13.2 (7.29)
PC/CF	Tension	11 (N = 5)	88.2 (4.35)	8.08 (3.75)	0.392 (11.5)	1.57 (5.04)
		33 (N = 7)	28.2 (1.91)	2.61 (1.63)	0.388 (2.28)	1.22 (2.12)
	Compression	11 (N = 5)	117 (5.64)	8.34 (4.45)	0.438 (2.61)	4.12 (5.64)
		33 (N = 5)	138 (7.43)	3.47 (11.4)	0.143 (28.6)	15.3 (9.81)

4. Conclusions

The experimental mechanical characterization in tension and compression in this study used two standard test methods ASTM D638-14 and ASTM D6641-16 respectively on AM PETG/CF and PC/CF materials showing that they exhibit similar mechanical performance with regards to strength, stiffness, and strain response.

In tension the PC/CF had a slightly higher ultimate strength in the 1-direction, only 1.5% higher than the PETG/CF, however, a higher retention of strength through the thickness was exhibited with 61% higher strength in the 3-direction compared to the PETG/CF. In the loading direction the PETG/CF was 33% and 4% stiffer than the PC/CF in the 1 and 3-directions, respectively. All ultimate strength and elastic modulus values calculated in the 1-direction had coefficients of variation (COV) less than 5% and less than 10% for the 3-direction that showed more variation for the PETG/CF 3-direction ultimate strength. The compressive properties also showed a mix of which material exhibited higher properties with the PC/CF again having strengths at 6.8% and 32% higher for the 1 and 3 directions respectively. Like the tensile response the PETG/CF was also exhibited higher stiffness in compression by 27% and 12% for the 1 and 3-directions respectively. COVs for ultimate strength and elastic modulus in compression were all less than 10% except for PC/CF 3-direction elastic modulus, which has a COV just above 10% of 11.4%. From this study it was seen that the PC/CF had higher ultimate strengths in both tension and compression and the PETG/CF exhibited higher stiffness in tension and compression regardless of orientation. In addition, both materials showed higher compressive strengths and similar stiffnesses in both tension and compression.

  doi:10.5075/epfl-298799_978-2-9701614-0-0

Tensile and compressive mechanical properties presented in this paper had relatively low COVs for testing conducted on reinforced composite materials, therefore, allowing for confidence in their use in supporting engineering analyses and design applications. In addition, the relative consistency of the results indicate that ASTM D638-14 and ASTM D6641-16 may be applicable for use in characterizing large-scale additively manufactured materials, however, with regards to the ASTM D638-14 dumbbell-shaped specimens more than half of the failures observed in this study occurred outside of the gauge region defined in the test standard, but within the narrow region or termination of the radius leading into that region. This phenomenon of failures outside the center-region of the specimen and near this radius warrants further investigation. The relatively low COVs on elastic moduli, which used strain values captured using DIC show that this versatile non-contact measurement method shows promise for use with large-scale AM materials. Additional work is required to better understand failure modes and mechanisms as well as investigation of the full-field strains captured using DIC.

5. References

1. D20 AI. ASTM D638-14 standard test method for tensile properties of plastics. In: Book of standards volume 0801 [Internet]. 100 Barr Harbor Drive, PO Box C700, West Conshohocken, PA 19428-2959, United States: ASTM International; 2014. (ASTM Standards). Available from: https://compass.astm.org/document/?contentCode=ASTM%7CD0638-14%7Cen-US

2. D30 AI. ASTM D6641/D6641M-16 standard test method for compressive properties of polymer matrix composite materials using a combined loading compression (CLC) test fixture. In: Book of standards volume 1503 [Internet]. 100 Barr Harbor Drive, PO Box C700, West Conshohocken, PA 19428-2959, United States: ASTM International; 2016. Available from: https://compass.astm.org/document/?contentCode=ASTM%7CD6641_D6641M-16E02%7Cen-US

3. Techmer Polymer Modifiers. Electrafil PETG 1711 3DP. Techmer Polymer Modifiers (TechmerPM); 2020.

4. D30 AI. ASTM D3039/D3039M-17 standard test method for tensile properties of polymer matrix composite materials. In: Book of standards volume 1503 [Internet]. 100 Barr Harbor Drive, PO Box C700, West Conshohocken, PA 19428-2959, United States: ASTM International; 2017. Available from: https://compass.astm.org/document/?contentCode=ASTM%7CD3039_D3039M-17%7Cen-US

5. D20 AI. ASTM D618-21 standard practice for conditioning plastics for testing. In: Book of standards volume 0801 [Internet]. 100 Barr Harbor Drive, PO Box C700, West Conshohocken, PA 19428-2959, United States: ASTM International; 2021. Available from: https://compass.astm.org/document/?contentCode=ASTM%7CD0618-21%7Cen-US

6. GOM Correlate Pro: Strains and displacements from motion pictures [Internet]. [cited 2022 Apr 15]. Available from: https://www.gom.com/en/products/gom-suite/gom-correlate-pro

  doi:10.5075/epfl-298799_978-2-9701614-0-0

INFLUENCE OF MECHANICAL PROPERTIES OF MATRIX ON BENDING STRENGTH OF UNI-DIRECTIONAL VINYL ESTER COMPOSITE

Takumi Shimano[a], Kiyotaka Obunai[b], Kazuya Okubo[b] Yukiko Fujita[c]

a: Department of Mechanical Engineering, Doshisha University, Japan – ctwg0569@mail4.doshisha.ac.jp
b: Faculty of Science and Engineering, Doshisha University, Japan – kiobunai@mail.doshisha.ac.jp
c: DIC Corporation – yukiko-fujita@ma.dic.co.jp

Abstract:

The purpose of this study is to investigate the influence of mechanical properties of matrix on bending strength of uni-directionally reinforced vinyl ester composite. Four types of vinyl ester were prepared as the matrix of the composite, where the mechanical properties were varied. Bending strengths and Mode-1 fracture toughness of monolithic resin plates were measured by three-point bending tests and single-edge-notch bending tests, respectively. Interfacial shear strengths were also investigated by micro-droplet tests. Changes of bending strengths of the composites were investigated by three-point bending tests. 2. The bending strength of the composites was the highest, when the bending strength of the matrix resin and the interfacial shear strength was high. For the materials studied in this research, achieving the consistency of high bending strength of the resin and high interfacial shear strength was effective for improving the bending strength of the composite.

Keywords: Uni-directionally reinforced composite; Vinyl ester; Bending strength

1. Introduction

Because composite material has high ratio strength and ratio rigidity, is superior in fatigue-resistant properties, it is essential materials in industry [1]. Composite which functionalized a particularly lightweight and high-strength carbon fiber as a reinforcement is used widely in the field of not only the field of aerospace but also public industry, and it is predicted that by its lightness and the superior dynamics characteristic the market size of the composite will be enlarged in future [2],[3]. In late years, in matrix resin used for composite, vinyl ester resin which had workability of the unsaturated polyester resin and mechanical properties and adhesive properties of epoxy resin attracts attention. In particular, vinyl ester resin was superior in corrosion resistance and use of composite which used vinyl ester as matrix resin spread in the fields such as chemical equipment or ship [4],[5]. The strength of the composite is not solely dependent on the strength of the fibers, but the properties of the matrix determine the damage that occurs first, so the properties of the matrix resin must also be considered. Vinyl ester resin with various performance including high strength and high tenacity was developed. On the other hand, influence of resin properties on mechanical properties of composites which use vinyl ester resin as matrix has not been well known yet. In this study, the purpose of this study is to investigate the influence of mechanical properties of matrix on bending strength of uni-directionally reinforced vinyl ester composite. Four types of vinyl ester were prepared as the

  doi:10.5075/epfl-298799_978-2-9701614-0-0

matrix of the composite, where the mechanical properties were varied. Bending strengths and Mode-1 fracture toughness of monolithic resin plates were measured by three-point bending tests and single-edge-notch bending tests, respectively. Interfacial Shear Strengths (IFSS) was also investigated by micro-droplet tests. The uni-directional composite plates were then fabricated by conventional pressing method at elevated temperature condition. Changes of bending strengths of the composites were investigated by three-point bending tests. The relationships between the bending strength of the composite and the bending strength, Mode-1 fracture toughness of the resin plate specimen and interfacial shear strength were investigated.

2. Material and Testing Description

2.1 Material

Four types of vinyl ester resins (hereinafter referred to (A), (B), (C), and (D) resins) (DIC Corporation) with styrene as the monomer were prepared as the materials of matrix resins. Stitched unidirectional carbon fiber cloth with 3.4GPa of nominal tensile strength and 230GPa of Young's modulus (TORAYCA cloth UT70-40G, Toray Industries) was prepared as the reinforcement.

2.2 Fabrication process of monolithic resin plate and composite plate

Figure 1 and 2 shows the fabrication process of monolithic resin plates and composite plates, respectively. Each resin was cured at 25 °C for 12 hour and then at 180 °C for 12 hours in the mold having thin rectangular space to make the monolithic resin plate. The monolithic resin plates with 2 mm and 6mm were obtained after the curing. The number of cloths aligned in the unidirectional orientation and the volume fraction of the fibers in the composite plate was 4 and 50, respectively. The composite plates were obtained by heat pressing under 4 MPa at 25 °C for 12 hours and then at 180 °C for 12 hours.

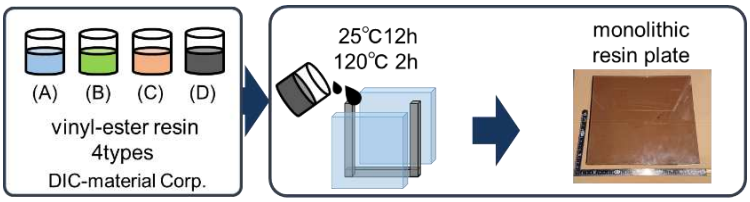

Figure 1. Fabrication process of monolithic resin plates.

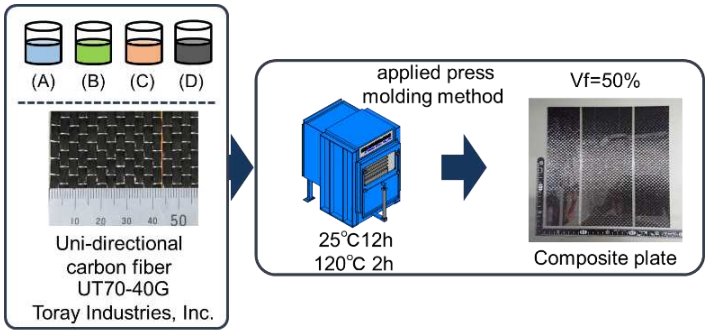

Figure 2. Fabrication process of composite plates.

2.3 Bending test

Bending test was employed using a universal testing machine (Autograph AG-I, Shimadzu Corporation). Figures 3 and 4 show schematic illustrations of test specimen. Coupon specimens with the dimensions of 80 mm long × 10 mm wide × 4 mm thick and 100 mm long × 15 mm wide × 2 mm thick were cut from the monolithic resin plate and composite plate, respectively. The sides of the specimens were finished with a sandpaper before the tests. The test speed and the distance between the fulcrums were 2.0 mm/min and 64 mm in accordance with ASTM D5023 for the test of monolithic resin specimens, and 5.0 mm/min and 80 mm in accordance with ASTM D7914 for composite specimen, respectively.

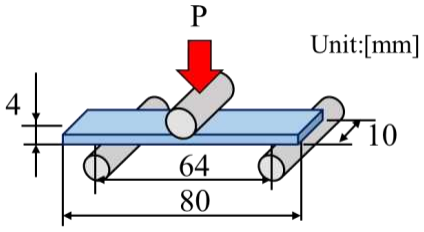

Figure 3. Specimen of resin plates for bending tests.

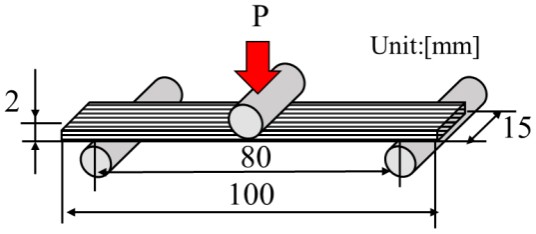

Figure 4. Specimen of composite plates for bending tests.

2.4 SENB test

Single-edge-notch bending (SENB) test was employed using a universal testing machine (Autograph AGS-X, Shimadzu Corporation). Figures 4 shows schematic diagram of test specimen. Thick coupon type specimens with the dimensions of 80 mm long × 6 mm wide × 12 mm thick were cut from the monolithic resin plates. Notches were introduced as the initial cracks. A pre-crack was then introduced by sliding a razor blade across the tip of the notch. The test speed was 10 mm/min in accordance with ASTM D5045. Critical stress intensity factor K_{IC} was determined from the failure load Pm by Equation (1) [6], and the fracture toughness in mode1 of the test specimens were evaluated.

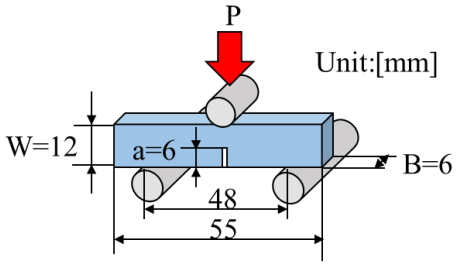

Figure 4. Specimen of resin plate for SENB tests.

$$K_{IC} = \left(\frac{P_m}{BW^{\frac{1}{2}}}\right) f(x) \quad (1)$$

$$f(x) = 6x^{\frac{1}{2}} \frac{\left[1.99 - x(1-x)\left(2.15 - 3.93 + 2.7x^2\right)\right]}{(1+2x)(1-x)^{\frac{3}{2}}}$$

$$x = \frac{a}{W}$$

2.5 Micro-droplet test

Micro-droplet test was employed using test device (HM410, Toei Sangyo Co., Ltd.) shown in figure 5. Figures 6 shows schematic diagram of test specimen. The test speed was 0.12 mm/min.

Interfacial shear strength τ was determined from pull-out load P, fiber diameter d and micro-droplet length L by Equation (2).

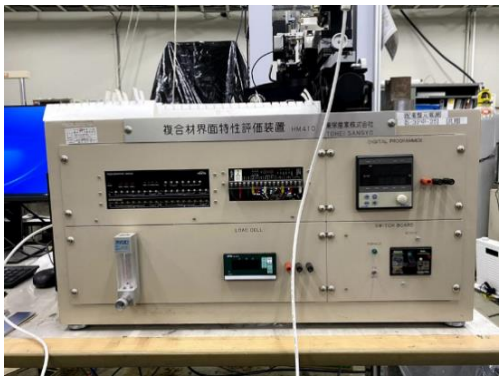

Figure 5. Test machine for micro-droplet tests.

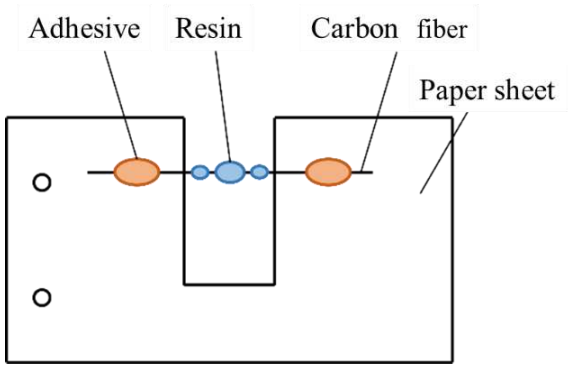

Figure 6. Specimen for micro-droplet tests.

$$\tau = \frac{F}{\pi d L} \quad (2)$$

3. Results

3.1 Mechanical properties of resin and interfacial property

The mechanical properties of the resin plate specimen obtained from the test results are shown in the table 1. It was observed that test results of fracture toughness in mode1 showed trade-off relations to those of bending strength and interfacial shear strength.

Table 1: Mechanical properties of resin and interfacial property.

	(A)	(B)	(C)	(D)
Bending strength [MPa]	135.2	137.5	131.1	86.7
Fracture toughness in Mode 1 [MPa$\sqrt{m}$]	1.32	1.41	1.42	1.75
Interfacial shear strength [MPa]	22.8	29.2	15.7	12.6

3.2 Bending strength of composite specimen

Figures 7 and 8 show stress-strain diagrams and the comparison of bending strengths of the composite specimen, respectively. The bending strength of the composites was the highest, when the resin (B) was applied as the matrix resin where the bending strength of the resin and the interfacial shear strength was high. On the other hand, the bending strength of the composites was lowest, when the resin (D) was applied as the matrix resin where bending strength of the resin and interfacial shear strength was low. The fracture strain of the composites was also the highest when the resin (B) was applied as the matrix resin, while the lowest fracture strain was observed, when the resin (D) was applied. Difference of fracture states after bending tests are shown in Figure 9. Brittle fracture behavior was observed, when the resin (D) was applied as the matrix resin. On the other hand, ductile fracture behavior was observed, when the resin (B) was applied as the matrix resin.

  doi:10.5075/epfl-298799_978-2-9701614-0-0

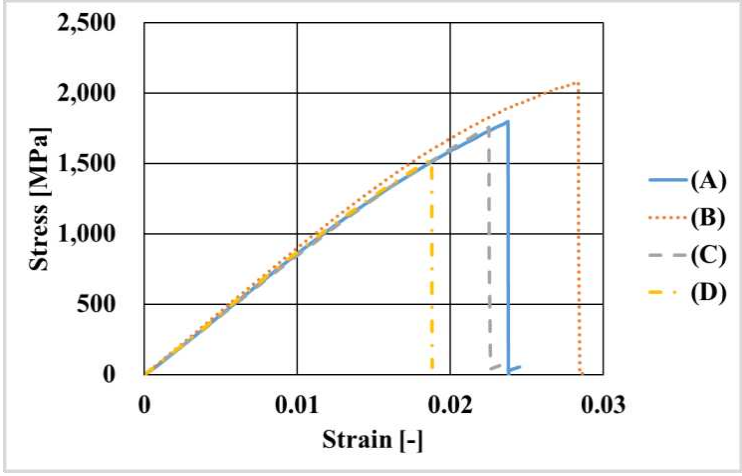

Figure 7. Stress-Strain diagrams.

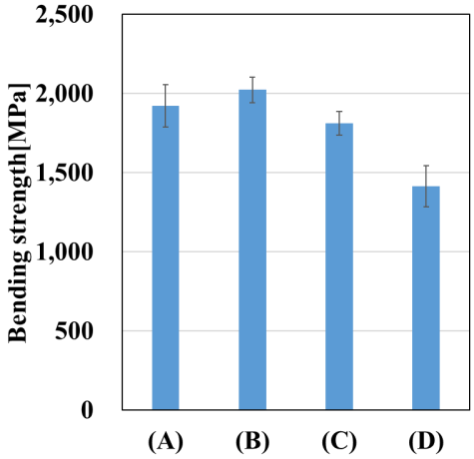

Figure 8. Change of bending strength of composites.

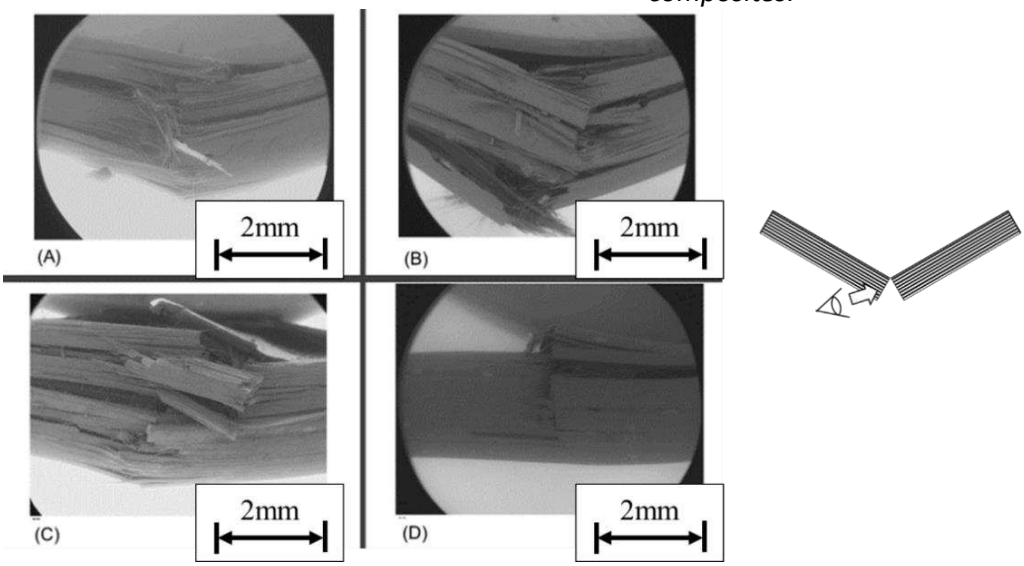

Figure 9. Difference of fracture states after bending tests.

The relationships between the bending strength of the composite and the bending strength, mode I fracture toughness of the resin plate specimen and interfacial shear strength are shown in Figures 10-12, respectively. In order to compare the relationship between the bending strength of composite and the matrix resin properties, each resin properties were normalized by the lowest value investigated in this study. The bending strength of the composite was increased as the bending strength and interfacial shear strength of the resin were increased, even if the fracture toughness in mode1 of the resin was decreased. On the other hand, the bending strength of composite was decreased when the bending strength of the resin and interfacial shear strength was decreased. These results indicated that, for the materials studied in this research, achieving the consistency of high bending strength of the resin and high interfacial shear strength was effective for improving the bending strength of the composite.

  doi:10.5075/epfl-298799_978-2-9701614-0-0

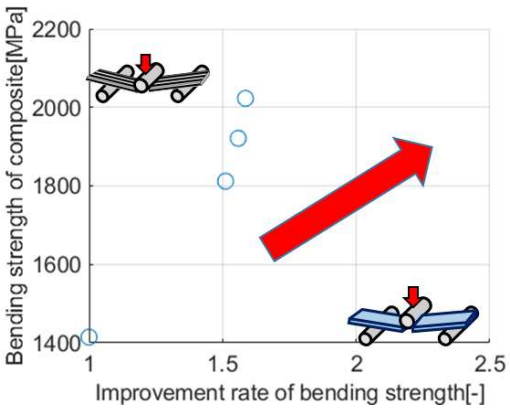

Figure 10. Change of bending strength of composite with respect to bending strength of resin.

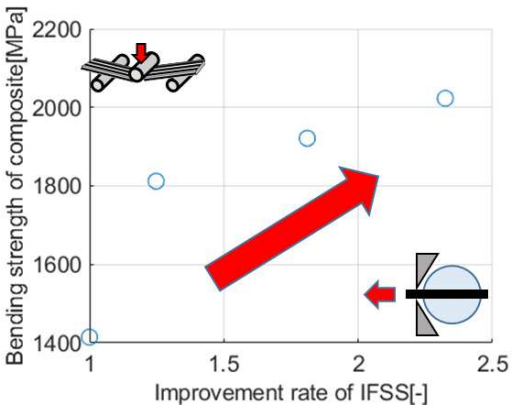

Figure 11. Change of bending strength of composite with respect to IFSS.

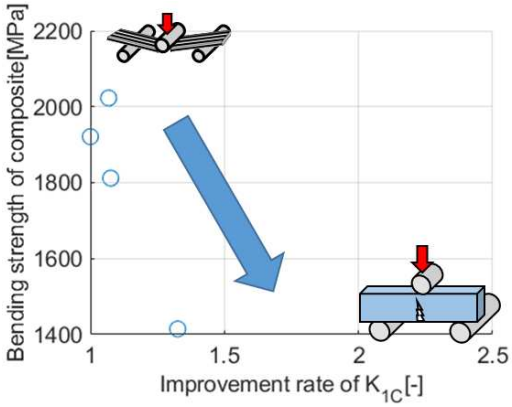

Fig.12 Change of bending strength of composite with respect to mode-1 fracture toughness of resin.

4. Discussion

Difference of crack propagations was explained by a schematic model shown in Figures 13. When only the strength of the resin was comparatively high, the interfacial cracks were significantly initiated and propagated, even if cohesive failure was prevented and additional cracking due to cohesive crack propagation was also prevented. On the other hand, when only the interfacial shear strength was comparatively high, cohesive failure was significantly initiated and propagated, then cohesive failure dominated the strength of composite, even if the initiation of the interfacial crack that would be initial cracks was delayed. When these both effects were introduced at once, combination of delay of the initial crack initiation and delay of the additional cracking was achived and ductile fracture occurred. As a result, either of elemental improvement was not effective to prevent total damage of the composite. This study found that achieving the consistency of high bending strength of the resin and high interfacial shear strength was effective to improve the bending strength of the composite.

  doi:10.5075/epfl-298799_978-2-9701614-0-0

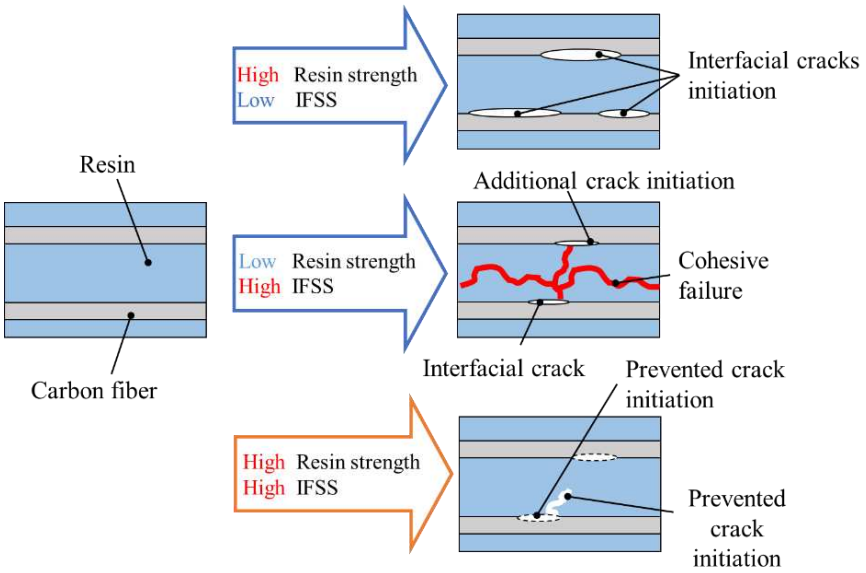

Figure 13. Difference of crack propagations.

5. Conclusion

1. It was observed that test results of fracture toughness in mode1 showed trade-off relations to those of bending strength and interfacial shear strength.
2. The bending strength of the composites was the highest, when the bending strength of the matrix resin and the interfacial shear strength was high. On the other hand, the bending strength of the composites was the lowest, when the bending strength of the matrix resin and interfacial shear strength was low.
3. For the materials studied in this research, achieving the consistency of high bending strength of the resin and high interfacial shear strength was effective for improving the bending strength of the composite.

References

1. Ronald F.Gibson, A review of recent research on mechanics of multifunctional composite materials and structures. Composite Structures 2010; 92: 12: 2793-2810.
2. Mark Holmes, Carbon fiber reinforced plastics market continues growth path. Reinforced Plastics 2013; 57: 6: 24-29.
3. Weihao Liu, Haihong Huang, Huanbo Cheng, Zhifeng Liu. CFRP Reclamation and Remanufacturing Based on a Closed-loop Recycling Process for Carbon Fibers Using Supercritical N-butanol. Fibers and Polymers; 21: 604-618.
4. Christopher Wonderly, Joachim Grenestedt, Göran Fernlund, Elvis Cĕpus. Comparison of mechanical properties of glass fiber/vinyl ester and carbon fiber/vinyl ester composites, Composites Part B: Engineering 2005; 36: 5: 417-426.
5. Kunigal N. Shivakumar, Gowthaman Swaminathan, Mathew Sharpe. Carbon/Vinyl Ester Composites for Enhanced Performance in Marine Applications, Journal of Reinforced Plastics and Composites 2006; 25: 10: 1101-1116.
6. ASTM Designation D5045-99, Standard Test Methods for Plane-Strain Fracture Toughness and Strain Energy Release Rate of Plastic Materials, 1999; 1-9.

  doi:10.5075/epfl-298799_978-2-9701614-0-0

STRAIN SENSING OF COMPLEX SHAPED 3D WOVEN COMPOSITES USING MXENE NANOPARTICLES

Prasad, Shimpi [a], Vladimir, Spacek [b], Daiva, Zeleniakiene [a]

a: Department of Mechanical Engineering, Kaunas University of Technology, Studentų street. 56, Kaunas-51424, Lithuania- prasad.shimpi@ktu.edu (P.S)
b: SYNPO, akciová společnost, S. K. Neumanna 1316, Pardubice-53207, Czech-Republic

Abstract: *This study aims to develop smart 3D woven nano composite by vacuum infusion process, which can sense deformation and damage at the joints of complex shapes like T-profile. The MXene were delaminated by chemical etching and dispersed in deionised water. In next stage, they were sprayed directly on the joint of 3D woven T-profile composite to form a conductive coating. The resultant nano composites were subjected to tensile loading to study the sensitivity of MXene to applied elongation. Results show that the MXene network is sensitive to tensile deformation. It can be concluded from the study that MXene smart strain gauge manufactured during this research work can be used for in-situ deformation monitoring of complex shaped composites while being cost effective and easy to manufacture.*

Keywords: 3D woven composite; MXene; mechanical testing; T-profile

1. Introduction

The quality evaluation of fibre reinforced composites in aerospace, civil and mechanical engineering structures is usually accomplished by locating damage via different techniques. These damage detection techniques can be broadly classified into two major categories namely destructive and non-destructive testing (NDT). Bulk manufactured cost-efficient components are often evaluated by destructive testing whereas large complex components, which are not feasible to be damaged are evaluated via NDT. Researchers combine various scientific techniques to develop systems for sensing damage in the composite structures. Some of the NDT methods are ultrasonic testing, radiography, thermographic, acoustic [1], and shearography testing [2] etc. However, these methods fail to evaluate the component during its actual usage. The concept of structural health monitoring (SHM) becomes important in such scenarios where quality of the component needs to be evaluated during its actual usage.

The most feasible method of SHM is by integrating sensor elements during various stages of composite manufacturing. A brief overview of such methods is integrating metallic wires, optical fibres [3], yarn coated with conductive dyes [4] etc., in the composite layup or in the fabric preform during weaving process. However, placing sensor elements during fabric layup introduces defect in the composite structure while integrating the sensor at weaving stage of fabric manufacturing imparts damage to the sensor element and often results in improper functioning of the sensor. To resolve this problem and enhance the sensing efficiency, conductive nanoparticles like MXene [5], carbon nanotube (CNT) [6], graphene [7] etc., are either dispersed in matrix or applied as coating on the composite. The mechanical deformation of composite structure affects the electrical properties of these nanoparticles, which forms the basis of monitoring the structural health of the material.

  doi:10.5075/epfl-298799_978-2-9701614-0-0

The MXene nanoparticles are two dimensional (2D) structures of titanium carbide $Ti_3C_2T_z$ synthesized from its MAX phase via various etching and delamination methods. The manufacturing process of MXene allows bonding of functional groups such as -O, -OH and/or-F, denoted as T_z in the formula, to impart wide range of properties. The reported tensile strength of MXene nanoparticles is 570 MPa (940 nm thick film) [8]. Recent studies have successfully modified MXene to achieve high adhesion with epoxy resin [9].

The most common research methodology of effective SHM by MXene nanoparticles is focused only on planar surfaces [10]. However, the practical applications of composites consist of complex shapes. Such shapes are usually in the form of 'T' or 'I'. One of the most extensively used shape is T-profile, which transfers load between mutually perpendicular directions. The conventional method of manufacturing T-joint composites is by laying up fabric plies on 2 opposing 'L' shaped rigid mould [11]. The laminated T-joint composite manufactured in this manner is reported to have less load bearing capacity and prone to delamination [12]. To overcome the structural limitations of laminated composite, the layers of fabric plies are either z pinned/tufted [13] or the T-profile preform is 3D woven directly on weaving machine. Numerous studies have shown that the 3D woven T-profile composites exhibit higher mechanical properties without delamination of constituent layers [14].

Majority of the research on NDT techniques for SHM of laminated and 3D woven composite T-profile has been done via process such as ultrasonic vibration [15], integrating piezoresistive layers [16] and electromechanical response of CNT [17], etc. However, there is a research gap in deformation and damage sensing of complex shapes by MXene nanoparticles. The aim of this research work was to develop smart 3D woven composite T-profile capable of monitoring its deformation and damage in real time using MXene nanoparticles. T-profile preform was woven on shuttle loom and infused with epoxy resin to manufacture composite. In the next step, the MXene nanoparticles were sprayed at the composite junction region and copper wires were soldered to measure the resistance via multimeter. The electromechanical response of MXene coating was studied while subjecting the sample to tensile loading.

2. Materials and Methods

2.1 Preparation of MXenes

The MXenes were sourced in their Ti_3AlC_2 MAX phase. The etching process was done by adding the MAX phase to hydrochloric acid and lithium fluoride solution. After stirring for 24 h, the multilayer MXene sediment was delaminated using 99 wt.% LiCl. The $Ti_3C_2T_z$ MXene nanoparticles were further centrifuged at 3500 rpm for 10–15 times and rinsed with deionised water until the pH of the supernatant reached 6.5. After measuring the concentration of MXenes in the supernatant to 0.335 mg/mL, it was finally concentrated to 3.3 mg/mL by centrifuge to obtain conductivity in the order of 10^5 Ω.

2.2 Weaving of T-profile preform and composite manufacturing

Fibre reinforcement in the shape of T-profile was woven in folded form on an 8 head shaft dobby loom with shuttle insertion. The draft and denting plan as shown in Figure 1a was designed to thread glass rovings of 300 tex. The thread density (warp and weft) measured in final fabric was 8 threads/cm.

  doi:10.5075/epfl-298799_978-2-9701614-0-0

Bisphenol F resin hardener system CR-122 was used as matrix and the woven T-profile was used as reinforcement to manufacture composite via resin transfer moulding process in double 'L' shaped metal mould. The wet preform was then subjected to 101.3 kPa vacuum for 3 h. The preform was cured at room temperature for 24 h and post cured in oven at 80 °C for 5 h.

To increase the hydrophilicity of epoxy surface, T-profile composite was subjected to argon-oxygen plasma and sprayed with 10 layers of MXene using airbrush with a 0.4 mm diameter nozzle. The composite T-profile was cut into dimensions as shown in Figure 1b.

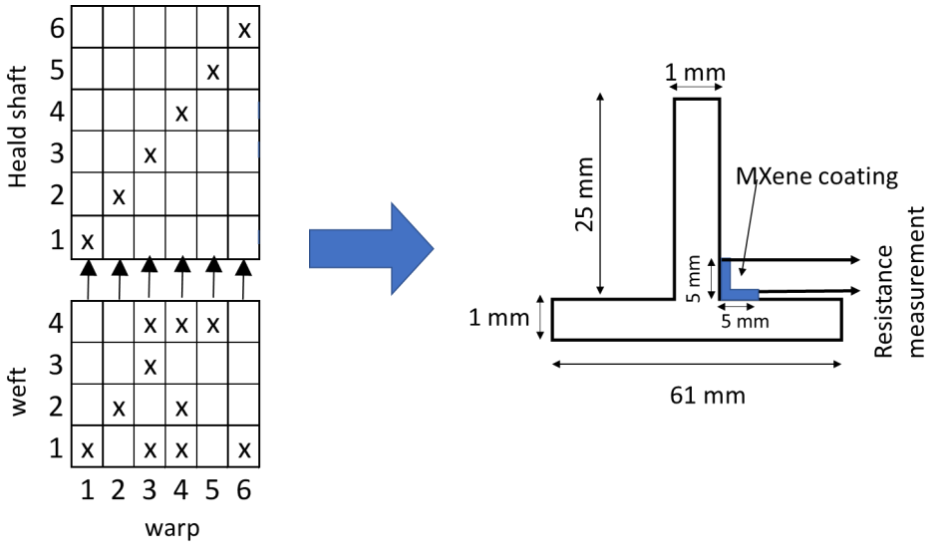

Figure 1. 3D woven composite T-profile: (a) Weave design and draft; (b) Sample dimensions and resistance measurement scheme

2.3 Tensile testing

The tensile testing of five composite specimens was carried out on Instron ElectroPuls E10000T machine with optical strain sensor and testing speed of 2 mm/min. The specimen dimensions and mounting scheme are as shown in Figures 1b and Figure 2, respectively. The copper wires were soldered on the MXene coating and silver paste was applied to reduce the contact resistance. The resistance measurement was performed with Fluke 287 RMS multimeter by using two-probe method.

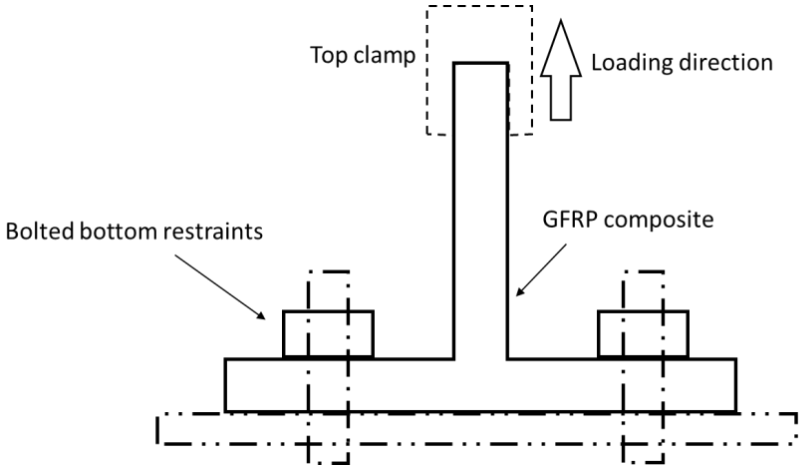

Figure 2. Tensile testing of T-profile composite

  doi:10.5075/epfl-298799_978-2-9701614-0-0 published under CC BY-NC 4.0 license

3. Results and Discussion

3.1 Tensile testing results and discussion

Due to premature failure at the bottom restraints, four out of five samples were successful in demonstrating monotonic relation between deformation and resistance values of the MXene coating. The graphs of $\Delta R/R_0$ against force-displacement for one representative sample is shown in Figure 3. ΔR is change in resistance and R_0 is initial resistance of the MXene coating. A typical graph on T-joint composites can be divided in two distinct zones i.e., initial failure and final failure. Initial failure is usually detected as drop in the tensile load values for the 1st time.

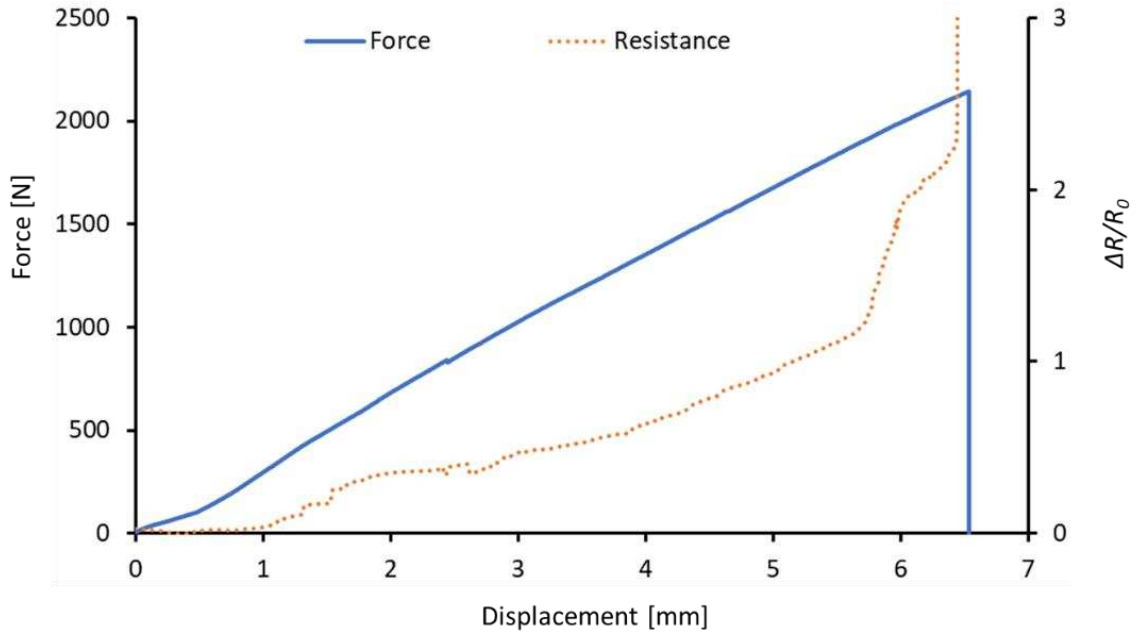

Figure 3. Real time deformation monitoring of composite T-profile during tensile loading

With increase in the tensile load, the stress started to accumulate at the junction region of T-profile. At 2.47 mm the initial failure occurred. Further loading beyond this point lead to crack propagation and ultimate failure of the composite at 6.54 mm in the junction region. The major failure mode observed was yarn/matrix damage.

The resistance values of MXene coating increased linearly in proportion to the applied stress which matches well with the previous studies related to MXene based SHM of composites [5], [10]. The initial failure of composite was detected as disturbance in the resistance value while the deformation due to stress accumulation till failure was detected as steady increase in the resistance of the MXene coating. The main source of change in MXene coating resistance is quantum tunnelling and contact resistance. Quantum tunnelling is the phenomenon where the electrons can transfer between nano flake structures, which has a gap in the order of magnitude 1 nm. Contact resistance is due to the overlapping of MXene over each other, thus providing a continuous path for electrical conductivity. The applied deformation of the composite tends to increase the contact and tunnelling resistance of the MXene coating, thereby leading to sensing of the damage and deformation.

  doi:10.5075/epfl-298799_978-2-9701614-0-0

4. Conclusions

The 3D woven composites T-profile were manufactured by resin transfer moulding process and MXene coating was sprayed at the junction region to monitor deformation and damage. The results show that the composites were able to sense the initial failure and deformation at the junction in real time under tensile loading. The graphs of change in resistance versus force-displacement were plotted to study the electromechanical response of the MXene layer. The following conclusions can be derived from the study:

- The concept of spraying MXene nanoparticles at the junction of complex shaped composite is feasible for real time deformation monitoring.
- During tensile testing of the samples, the MXene layer was able to sense the total deformation till failure in response to the applied displacement.

Acknowledgements

This project has received funding from the European Union's Horizon 2020 research and innovation programme under the Marie Skłodowska-Curie grant agreement No 777810.

5. References

1. Jolly M, Prabhakar A, Sturzu B, Hollstein K, Singh R, Thomas S, et al. Review of Non-destructive Testing (NDT) Techniques and their Applicability to Thick-Walled Composites. Procedia CIRP. 2015; 38:129–136.
2. Gholizadeh S. A review of non-destructive testing methods of composite materials. In: Procedia Structural Integrity. 2016. p. 50–57.
3. N.Rajic; M. Veidt; A. Mita; N. Takeda; W.K. Chiu, editor. In-Situ Strain Monitoring in Deltoid of Composite T-joints using Optical Fiber. In: Structural Health Monitoring: 8th Asia Pacific workshop on structural health monitoring. Queensland, Australia; 2021. p. 161–169.
4. Nauman S, Cristian I, Koncar V. Intelligent carbon fibre composite based on 3D-interlock woven reinforcement. Textile Research Journal. 2012;82:931–944.
5. Shimpi P, Omastova M, Aniskevich A, Zeleniakiene D. In Situ Deformation Monitoring of 3D Woven Composite T-Profile Using MXene Nanoparticles. Materials 2022, 15:2730.
6. Shimpi P, Aniskevich A, Zeleniakiene D. Improved method of manufacturing carbon nanotube infused multifunctional 3D woven composites. Journal of Composite Materials. 2021 Nov 14. 2022; 56:479-489.
7. Tang LC, Wan YJ, Yan D, Pei YB, Zhao L, Li YB, et al. The effect of graphene dispersion on the mechanical properties of graphene/epoxy composites. Carbon N Y. 2013. 60:16-27
8. Zhang J, Kong N, Uzun S, Levitt A, Seyedin S, Lynch PA, et al. Scalable Manufacturing of Free-Standing, Strong $Ti_3C_2T_x$ MXene Films with Outstanding Conductivity. Advanced Materials. 2020; 32:2001093.
9. Zukiene K, Monastyreckis G, Kilikevicius S, Procházka M, Micusik M, Omastová M, et al. Wettability of MXene and its interfacial adhesion with epoxy resin. Materials Chemistry and Physics. 2021; 257:123820.
10. Wang X, Lu J, Lu S, Li B, Zhang L, Ma C, et al. Health monitoring of repaired composite structure using MXene sensor. Composite Communications. 2021;27.

  doi:10.5075/epfl-298799_978-2-9701614-0-0

11. Stickler PB, Ramulu M. Experimental study of composite T-joints under tensile and shear loading. Advanced Composite Materials. 2006; 15:193–210.
12. Bai JB, Dong CH, Xiong JJ, Luo CY, Chen D. Progressive damage behaviour of RTM-made composite T-joint under tensile loading. Composite Part B Engineering. 2019;160:488–497.
13. Bigaud J, Aboura Z, Martins AT, Verger S. Analysis of the mechanical behavior of composite T-joints reinforced by one side stitching. Composite Structures. 2018; 184:249–255.
14. Yan S, Zeng X, Brown L, Long A. Geometric modeling of 3D woven preforms in composite T-joints. Text. Res. J. 2018;88:1862–1875.
15. Ooijevaar TH, Loendersloot R, Warnet LL, de Boer A, Akkerman R. Vibration based Structural Health Monitoring of a composite T-beam. Composite Structures. 2010; 92:2007–2015.
16. Panda SK, Mishra PK, Panda SK. Damage Propagation Prediction of Adhesion Failure in Composite T-joint Structure and Improvement using PZT Patch. Scientia Iranica, 2021; 28: 3232-3245
17. Wan Y, Hu W, Yang B, Zhao X, Xian G, Yuan Y, et al. On-line tensile damage monitoring of WGF/epoxy T-joint by the embedded MWCNT@WGF sensor. Composite Communications. 2021;23:100541.

  doi:10.5075/epfl-298799_978-2-9701614-0-0

COMPARISON OF THE FIRE REACTION OF A CARBON-EPOXY COMPOSITE LAMINATES AT SMALL AND LARGE SCALE

Clément VICTOR[a,b], Alexis COPPALLE[b], Benoit VIEILLE[c], Jennifer DUPUIS[a] , Mathieu PREAU[a] , Thierry LE DOCTE[a]

a: Safran Nacelles, 76700 Gonfreville l'Orcher
b: Normandie Univ, UNIROUEN, INSA Rouen, CNRS, CORIA, 76000, Rouen, France
c: Normandie Univ, UNIROUEN, INSA Rouen, CNRS, Groupe de Physique des Matériaux, 76000, Rouen, France

Abstract: *To study the fire-proofness of materials panels, assemblies or components, certification standards require significant 448x448mm² samples to withstand a kerosene flame for fifteen minutes tests. To better analyse thermo-physicals phenomena involved in a flame exposition of composite-based samples, a laboratory test bench composed of a small-scaled air-kerosene burner has been developed. The current work presents the development of a representative Jet A-1 burner by finding the right settings for the flame parameters and by comparing the degradation process of several four-plies epoxy-composite samples. Two laboratory-scale articles are tested and compared to one large sample tested on a standardized fire test bench.*

Keywords: Fire reaction; Kerosene burner; Aeronautical composite materials; CFRP Epoxy panels; Fireproof

1. Introduction

To reduce airplane fuel consumption and improve efficiency, thinning and lightering of aeronautical structures were achieved using alternatives to conventional metallic materials. Nowadays, composite materials are widely used in the aircraft industry and represent more than 50 per cent of the total materials in an aircraft (A350, B787). As safety requirements increase each year, the use of carbon-epoxy composite materials represents a major concern for companies in charge of structural design, especially in areas close to engines referenced as “fire zone”. For the development of a new aircraft, fire tests on materials, assemblies or components within a determined fire zone must be carried out as part of a certification process to comply with authority’s regulations. At the heart of concerns for aeronautical industrials, these standardized fire requirements have ensured the safety of aircraft’s operational life for many years by preventing major incidents to become major accidents.

2. Specimen tested and experimental set-ups

2.1 Specimen description

As part of a certification campaign within a business jet program, a large painted composite (LPC) material of 448mmx448mm dimensions was tested on a certification test bench (cf. Figure 8a). The laminate consists of a 4-plies epoxy matrix reinforced with a 5-harness satin weave of carbon fibres. There is on the unexposed side an additional ply improving its lightning protection composed of a bronze mesh with a secondary epoxy-based resin. Finally, the sample is fully

  doi:10.5075/epfl-298799_978-2-9701614-0-0

painted with a blue primary layer to close pores and an additional cosmetic white paint layer on the front side.

To compare the thermal aggression of the two different scale benches, two similar test specimens with smaller 230mmx230mm dimensions were produced. The first one (SPC) was exactly equal to the certification specimen as it was covered with the same layers of paint (cf. Figure 8b) while the second one (SC) was not painted at all (cf. Figure 8c).

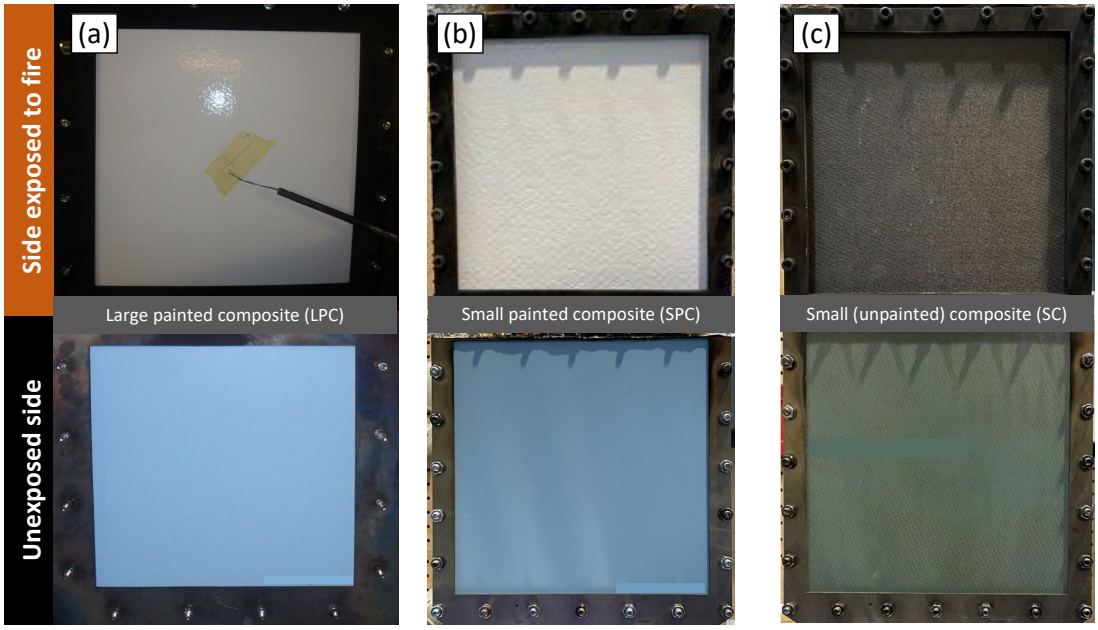

Figure 1 – Raw state of (a) the large painted composite, (b) the small painted composite and (c) the small unpainted composite

2.2 Standardised fire tests

Demonstrating the fireproof capability of material panels is only one part of an aircraft's overall fire certification process. For this assignment, significant 448x448mm² samples are exposed to an air-kerosene flame of a standard Jet A-1 burner for a 15 minutes test [1-2]. Taking place within a dedicated facility, the purpose of these tests is to prove that structural parts are able to contain and isolate a fire that would come from an engine dysfunction, therefore acting as a fire barrier for a given duration. For ground testing conditions, the standardised test setup consists of a fuel burner to generate an air-kerosene flame, a frame with a mounting area to fasten the test sample, a few measurement tools to calibrate the flame parameters, a vibrating pot to recreate engine-like conditions and finally CCD cameras to record the test (cf. Figure2).

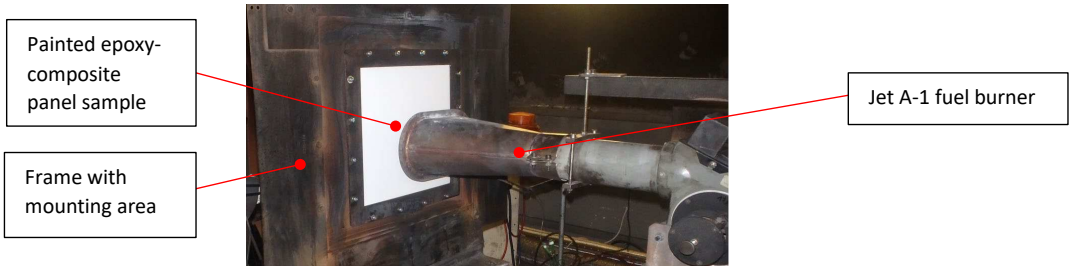

Figure 2 – Painted epoxy-composite sample in front of an air-kerosene burner before the start of a fire test in a dedicated facility (LEFAE, Lyon, France)

  doi:10.5075/epfl-298799_978-2-9701614-0-0

As burner manufacturers may vary from one facility to another, standardisation of flame parameters is realised from a calibration phase before starting to fire the sample. Calibration of the air-kerosene flame is based on the compliance of two thermal characteristics. Firstly, a flame heat flux density of 116 +/- 10 kW/m² is measured with a water calorimeter (cf. Figure 3). The water calorimeter allows the calculation of heat flux across a heat transfer device section by considering Eq. (1).

$$q = \frac{q_v.\rho.c_p(T_2-T_1)}{A} \quad (1)$$

Where q is the heat flux density, q_v is the water flow, ρ is water density, Cp is the water heat capacity, T_1 and T_2 are water temperatures at the entry of and at the exit from the heat transfer tube respectively and A is the surface of exchange between the flame and the heat transfer device. Surface A is the product of the heat transfer device length impinged by the flame (380mm) and its external perimeter.

Secondly, a flame temperature of 1100 +/- 80 °C is measured with a rake of seven K-type thermocouples of 1.6mm diameter spread across the horizontal axis of the burner, hence acquiring temperature data across the flame length (cf. Figure 4). Tests on the sample and calibration devices are all made at a fixed distance of 100mm from the burner edge to provide similar heat transfer conditions [3]. If the following conditions are met, the exposure of the test sample to the calibrated flame is performed.

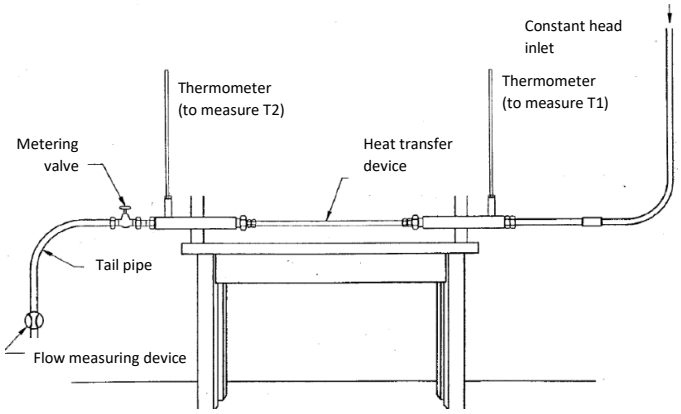

Figure 3 - Apparatus for measuring heat-flux density

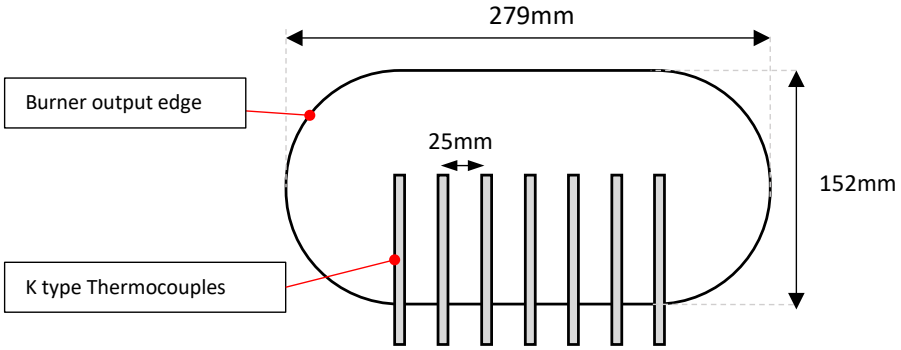

Figure 4 – Normalized burner output dimensions and thermocouple rake position for measuring the flame temperature

Failures occurring on the test sample before reaching the required 15 minutes test duration usually come out of two main reasons. Firstly, flame penetration occurs when the flame burns through the sample. It can either occur from a complete thermal breakdown of the material or, in the case of assemblies, if the flame can slip across lap joint gaps. Secondly, a backside ignition takes place when another flame appears on the unexposed side of the specimen. This is usually the case when samples outgas during flame exposure, producing highly flammable gaseous emissions that may generate a flame on the "cold side" [4]. If one of these events occurs during the test, the sample is therefore not fireproof and the test status is failed.

2.3 Laboratory scale fire tests

Within CORIA Laboratory, a small-scale version of the standardized air-kerosene burner used in fire certification tests has been developed with the purpose of testing and analysing small-scale samples compare to the standard one (cf. Figure 5). The small-scale burner has been designed to provide the same thermal aggression like the one used in dedicated standard facilities. For this purpose, the small-scale burner parameters have been adjusted and a comparison of the degradation process of four-plies graphite-epoxy-composite laminates tested on the two different benches was performed.

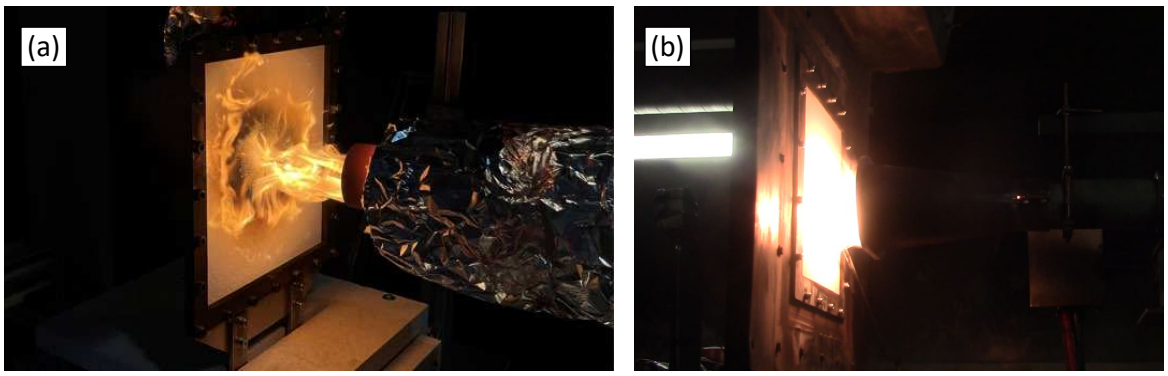

Figure 5 – Painted epoxy composite performing a fire test against (a) a laboratory scale burner (CORIA), (b) a fire-certification burner (LEFAE)

Some adaptations had to be made as part of the reduction in burner size to recreate a thermal stress equivalent to that of a large standardized burner. Therefore, the differences between the two benches must be considered before comparing the responses of samples to a thermal aggression.

Firstly, the laboratory burner does not have a cone-shaped outlet but a converging cylindrical tube with a radius of 50 mm, which means that the burner shape and flame size are different. Secondly, a ventilation hood placed above the laboratory test bench allows gaseous emissions from the flame and the degradation of the sample to be extracted with a low flow rate to avoid any disturbances. Only thermal stresses were applied to samples and no vibrating pot has been installed on the laboratory bench.

Then, on calibration measurement devices (cf. Figure 6); The flame temperature was measured by means of five K-type thermocouples of 1mm diameter, equally spaced along the 50mm horizontal axis of the burner output, meaning that three of them are positioned inside of the flame and the two others are at the burner edges. Regarding the two thermocouples in the edges, the flame exchanges heat with the surrounding air, which means that the measured

temperature is lower at this location. However, both sensors can be used to check if the flame is correctly oriented and does not have a side angle.

The flame heat flux measurement is carried out using a Gardon sensor (Capthec, Captherm) due to the difficulties to obtain relevant measurements using a suitably sized water calorimeter. A Gardon sensor is a gradient flux meter with a differential thermocouple that measures the temperature difference between the centre and the circumference of a thin circular foil disk [5]. The 25mm disk, made of constantan (Ni-Cu alloy) is bonded to a circular opening in a cylindrical water-cooled heat sink made of stainless steel. These materials produce an electrical potential output, which is directly proportional to the heat flux absorbed by the sensitive surface. The exposed side of the sensor is coated with a high absorbance black coating to obtain a significant signal [6].

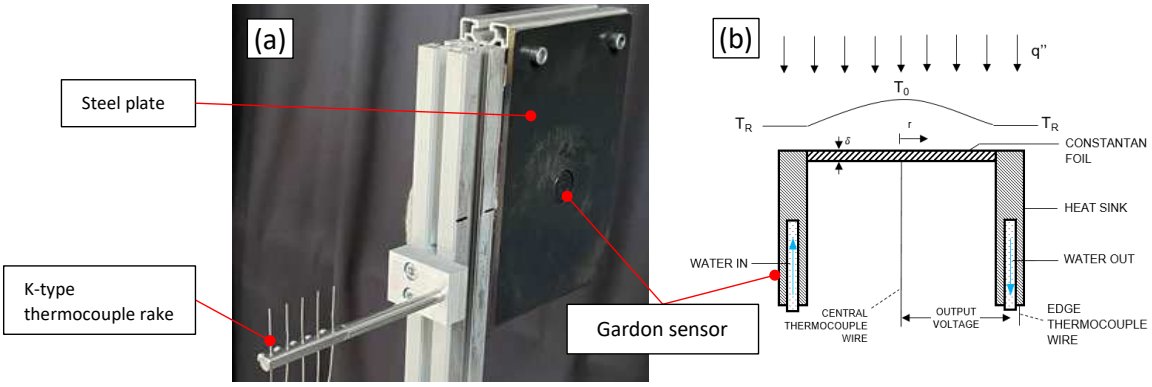

Figure 6 - Calibration devices of the laboratory scale bench (a) and a Gardon sensor scheme (b)

The major difference between the water calorimeter used in standard tests and the Gardon sensor is the measurement surface used to calculate the heat flux density. On one side, the water calorimeter provides a mean heat flux density over the length of the heat transfer device (380mm) which is much larger than the burner outlet plan (279mm) and thus the flame size, and is almost insensible to the radiation. On the other side, the Gardon sensor provides a more punctual total heat flux density measurement with a sensitive surface of 25mm, which can be completely covered within the 50mm laboratory scale burner outlet plane. Therefore, it makes sense that 116kW/m² measured with the water calorimeter on the large-scale bench is not similar to the 116kW/m² measured on the laboratory-scale bench with the Gardon sensor.

To overcome this problem, measurements of the heat flux density with the Gardon sensor were performed over the central horizontal axis of a certification burner within a dedicated facility. By mounting the Gardon sensor on a translation system, it was possible to acquire the highest thermal stress data and its position within the flame. This setup made it possible to define the necessary heat flux density to be achieved with the laboratory burner to remain representative and conservative concerning the thermal stress encountered on a certification bench (cf. Figure 7). A small offset due to a disturbance was applied to the recorded data and the heat flux density chosen for the laboratory tests was set to 143kW/m² with the use of the Gardon sensor as a calibration device.

  doi:10.5075/epfl-298799_978-2-9701614-0-0

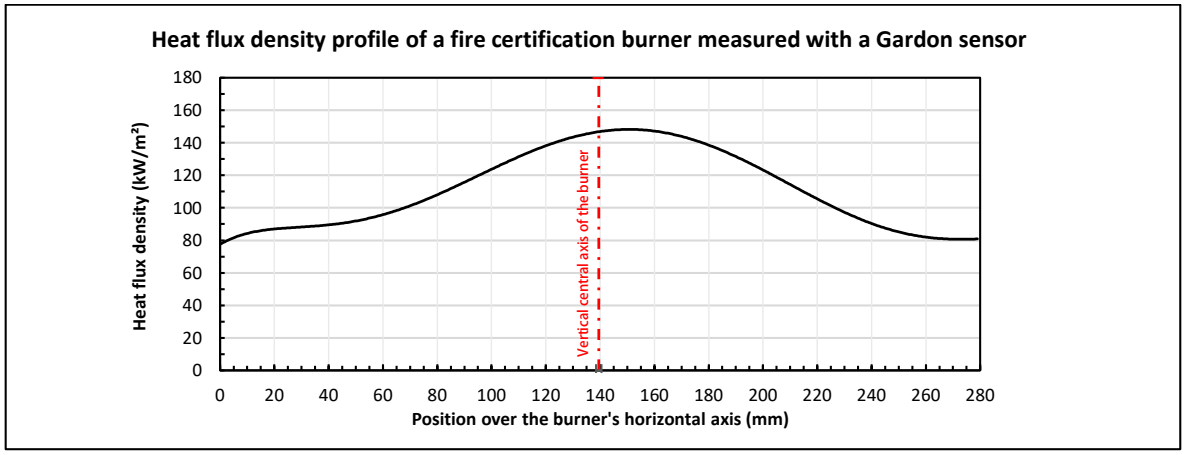

Figure 7 - Heat flux density measurements of the Gardon sensor over a fire certification burner's horizontal axis

Finally, additional non-destructive measurement tools have been added to acquire more information from laboratory samples. A balance (Mettler Toledo: XSR4002S) has been added to acquire the mass loss of samples during tests and two thermal imaging cameras were used. The first thermal camera (FLIR PM595 and then, later on, FLIR T540) views the backside of the test specimen to acquire its temperature field and to possibly measure its backside temperatures. The second thermal camera (FLIR A6750), views the front surface of specimens. At a constant wavelength of 3.9 µm, it allows the front surface condition of the test specimen to be monitored without being blinded by the flame luminous intensity within the visible spectrum (cf. Figure 7).

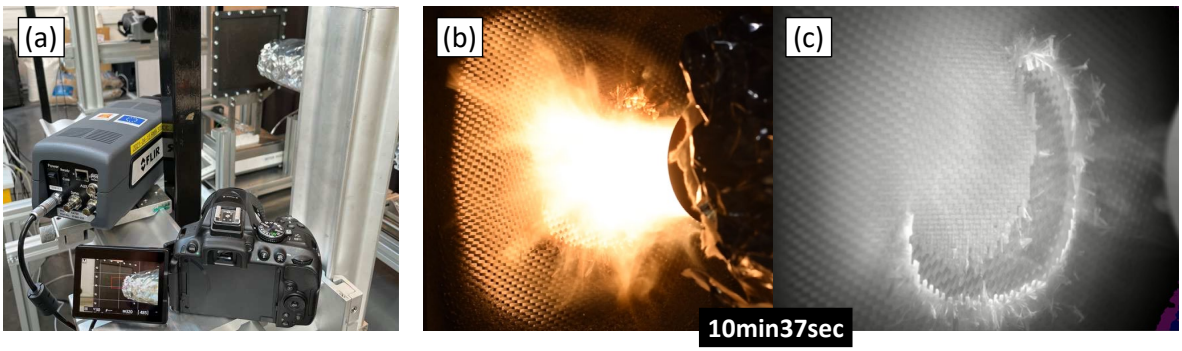

Figure 8 – Front side camera set-up (a) and a snapshot 10 minutes and 37 seconds after the start of a laboratory fire test on a carbon-epoxy composite with (b) a NIKON D5300 video camera and (c) a FLIR A6750 infrared camera

  doi:10.5075/epfl-298799_978-2-9701614-0-0

3. Experimental results and discussion

The reference in terms of thermal degradation is the Large Painted Composite (LPC). The main sources of information available for this test are:

- The initial flame settings to ensure it was compliant with the standards.
- The video recordings during the test to timestamp the appearance of multiple visible thermal degradation events.
- Photographs of the sample after the 15-minute test to analyse the final degradation residue

For the laboratory specimens, the same sources are available as well as additional measurements as mentioned in section 2.3.

The flame parameters of the three tests are presented in Table 1.

Table 1: Tests flame parameters

Specimen	Mean temperature [°C]	Heat flux density [kW/m²]
LPC	1103°C	118kW/m²
SPC	1147°C	146kW/m²
SC	1158°C	142kW/m²

All the mean temperatures are in the [1020-1180] °C range of the standard requirements. However, temperature data shows a small increase of about 40-50°C between laboratory tests (SPC & SC) and certification tests (LPC). This is the result of the different sizes of thermocouples used.

All heat flux density data meet their respective requirements of [106/126] kW/m² measured with the water calorimeter for the LPC and the proximity of the 143kW/m² required for the SPC and the SC.

Timestamps of major thermal degradation events that occurred during fire tests of the three samples are presented in Table 2.

Table 2: Major thermal degradation events of composites samples during tests

Sample Face	Degradation event	Timestamps (min'sec)		
		LPC	SPC	SC
Front	Flare-Up	00'10 - 01'23	00'10 - 00'53	00'08 - 00'45
Back	Outgassing	00'10 - 05'40	00'09 - 03'40	00'08 - 02'48
Front	Paint peeling	00'14	00'49	None
Back	Paint peeling	10'03 - 15'00	None	None
Front	1st composite ply opening	10'48	None	10'48
Front	2nd composite ply opening	14'46	None	14'48

  doi:10.5075/epfl-298799_978-2-9701614-0-0

Back	4th composite ply oxidation	13’20 – 15’00	None	05’01 – 07’38
Both	Breakthrough	None	None	14’58

This non-exhaustive list is essential to compare samples’ degradation and therefore the influence of thermal stress from one case to another. The event called Flare-Up is the ignition of the front panel outgassing of matrix resin [7]. Outgassing on the front and backside of composite specimens happens virtually at the same time, early in the fire test. When front side gases make their way out of the sample, they will directly face the flame and its flow (cf. Figure 9, “zone 1”). Being pushed out towards the periphery by following the impingement flow [8], these gas will at some point mix with the oxygen present in the ambient air and ignite instantly due to the heat and propagation provided by the burner flame. This creates a second flame area located on the periphery of the sample (cf. Figure 9, zone 2). A small difference in the start of outgassing about two seconds can be noticed between painted and unpainted samples. The paint might be responsible for small additional protection that delayed the outgas starting time. Overall, the outgas lasts a little longer on the LPC than on the SPC and the SC, this might be due to a sample size effect and differences between flame shapes (circular for SPC or SC and oval for LPC).

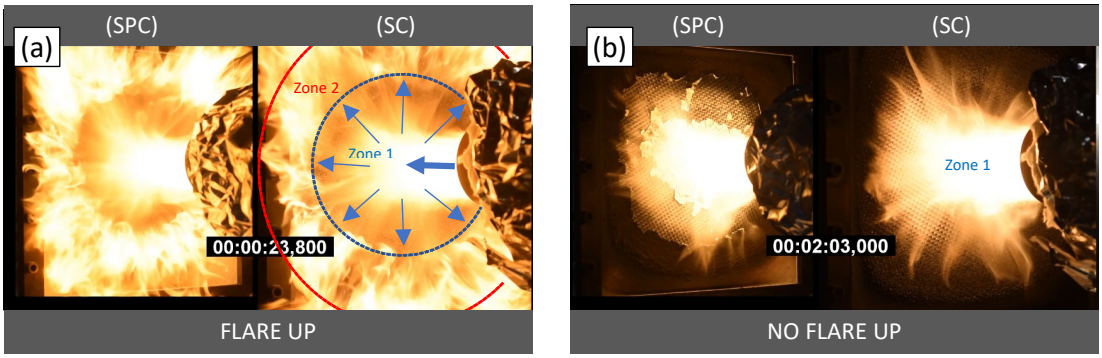

Figure 9 – (a) Flare-up and (b) no flare-up snapshot comparison during fire tests of SPC and SC

Paint peeling appears on the front side of both painted composite samples (LPC and SPC) and only on the backside of the large painted composite after 10’03. The paint will firstly melt and its colour will change to black. It will then become white and very brittle with the appearance of cracks. The presence of a vibrating pot on the LPC test bench allows cracks to peel fast. All of the paint layers on the exposed side drop early in the fire test. After 20 seconds, there is no more paint on the front face of the LPC specimen at the flame location, leaving the first composite ply facing the flame for the rest of the test. Due to peeling using a vibrating pot on the LPC, the front side paint does not have a key role in fire protection.

However, on the SPC, minor paint peeling appears later than on the LPC but, due to the lack of vibration pot on the laboratory test bench, some paint parts will stick to the front face and keep their adherence to the 1st ply using the flame flow pressure (can be seen on Figure 9 (b), SPC). This adhesive paint layer protects the first ply by acting as a barrier and prevents the next degradation events from happening such as delamination. Because of that, the SPC is not representative of the LPC degradation.

  doi:10.5075/epfl-298799_978-2-9701614-0-0

1st ply delamination occurs on both LPC and SC at 10’48. Figure 10 shows the state of the front surface before and after the first ply delamination.

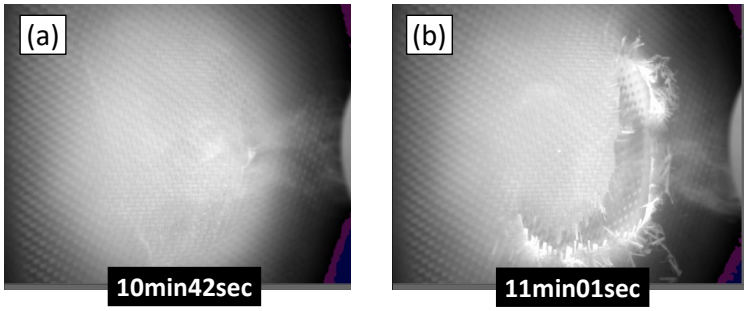

Figure 10 - Snapshot of thermal imaging (a) before and (b) after the first ply delamination

The same event appears on the second composite ply at 14’46 and 14’48 for the LPC and SC respectively. These close timings of front side degradation events indicate a similarity in terms of degradation reaction between the two samples tested on two different benches. This exposes the fact that the thermal stress applied to these samples is similar.

Finally, a noticeable difference occurs on the backside of the LPC and the SC specimens, with the fourth ply fibres being oxidised earlier on the SC. The unpainted backside of the SC specimen, results in more contact of the last ply fibres with ambient air, therefore increasing the oxidation process of carbon fibres. This oxidation phenomenon decreases the strength of carbon fibre plies by turning them into a thin brittle layer. For the SC specimen, the same thing is probably happening on the third ply after that the fourth has become very brittle. This should explain why the SC specimen experienced a breakthrough right after the second ply opening at 14’58.

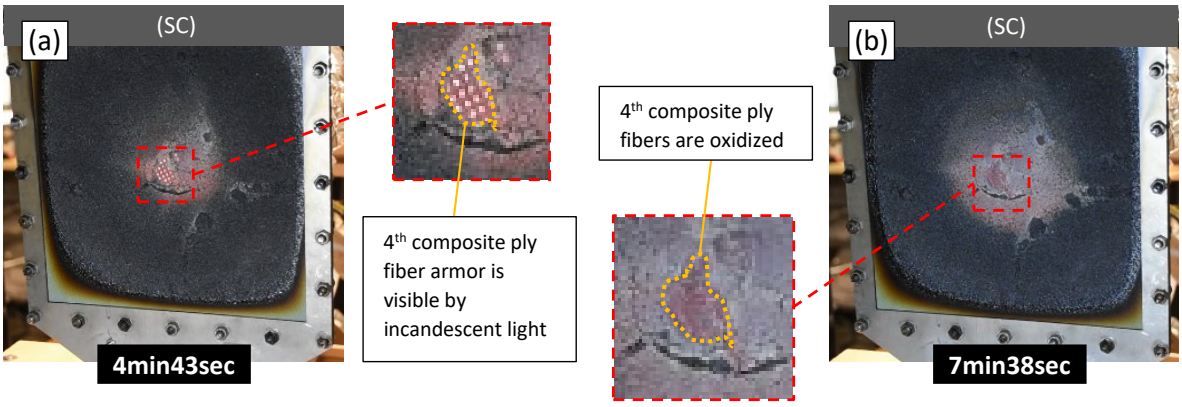

Figure 11 - Backside snapshot (a) before fourth ply oxidation, (b) after fourth ply oxidation

4. Conclusion

It has been demonstrated that the large painted composite quickly becomes unpainted on the exposed flame side due to the brittleness of the paint and peeling from vibrations. This allowed comparing the degradation timings of a large painted composite tested on a certification test bench to a small unpainted composite tested on a small scale laboratory test bench. The similarities in phenomena occurring on the front side of the samples confirm the similarity of the thermal stresses applied. However, the lack of paint on the backside of the small composite specimen result that the fourth and third ply of carbon fibre being oxidised earlier in the test compared to the large painted composite. This led to a breakthrough of the small unpainted composite shortly after the delamination of its second ply and two seconds before the end of the required 15 minutes. Although the test results differ due to paint effects, these composite specimens have highlighted that for a 116kW/m² heat flux density measured on the certification test bench with a water calorimeter, comparable results are achieved for tests done at 143kW/m² measured with a Gardon sensor.

5. References

1. ISO 2685, Aircraft. Environmental conditions and test procedures for airborne equipment. Resistance to fire in designated fire zones. International standard 1992.
2. AC 20-135, US Department of Transportation, Federal Aviation Administration, Powerplant installation and propulsion system component fire protection test methods, standards, and criteria. Change 1, 2018
3. O'Donovan T, Jet impingement heat transfer, International journal of heat and mass transfer, 2007
4. Grange N, Etude du comportement au feu de matériaux composites destines à des applications aéronautiques: experiences et Modélisation. INSA Centre Val de Loire, 2018
5. Ballestrin J, Estrada C.A, Rodriguez-Alonso M, Perez-Rabago C, Langley L.W, Barnes A, Heat flux sensors: Calorimeters or radiometers? Solar energy 80, 2006
6. Guillot E, Alxneit I, Ballestrin J, Sans J.L, Willsh C, Comparison of 3 heat flux gauges and a water calorimeter for concentrated solar irradiance measurement, SolarPACES 2013
7. Li H, Wang N, Han X, Yuan H, Xie J, Mechanism identification and kinetics analysis of thermal degradation for Carbon Fiber/Epoxy Resin
8. Viskanta R, Heat transfer to impinging isothermal gas and flame jets, Experimental and thermal fluid science, 1993

  doi:10.5075/epfl-298799_978-2-9701614-0-0

LEFFICIENT AND VERSATILE 3D WOVEN COMPOSITE MANUFACTURING: NOVEL APPROACHES ON THE QUALITY OF COMPOSITE FABRICATION

Muhammed Ali Vural[a,b], Emir Karci[a,c], Melisa Dincer[a,b,c], Mert Celikturk[a,c], Ibrahim Halil Sahin [a,c], Burak Yatkin[a,c], Cagin Emre[a,c], Basak Ozkendirci[d,e], Elif Ozden Yenigun[f], Hulya Cebeci[a,b,c]
a: Aerospace Research Center, Istanbul Technical University, Istanbul, 34469, Turkey
vural20@itu.edu.tr
b: Aviation Institute, Istanbul Technical University, Istanbul, 34469, Turkey
c: Department of Aeronautical and Astronautical Engineering, Istanbul Technical University, Istanbul, 34469, Turkey
d: Faculty of Fine Arts and Design, Dogus University, Istanbul, 34437, Turkey
e: Department of Textile and Fashion Design, Dogus University, Istanbul, 34775, Turkey
f: School of Design Textiles, Royal College of Art, SW7 2EU, London, United Kingdom

Abstract: *The complex and hollow nature of 3D spacer fabrics require novel approaches to achieve efficient transfer of resin to the structure with a uniform fashion. In this work, a custom-built spray system is designed and built to achive an effective wetting of 3D I-beam fabrics for a high-quality composite manufacturing of a spacer structure. The spray-wetted 3D I-beam composites were manufactured with a custom-designed 3D molding for 600 TEX glass fiber and epoxy resin. Since achieving high-quality composites is essential to accomplish the required mechanical characteristics, the 3D I-beam composites fabricated with vacuum infused process were also compared with spray-wetted and molded specimens. The quality of both specimens was evaluated by optical microscopy images for void content and the results clearly demonstrated a higher void content of 5,65 times more for spray wetted specimens compared to produced ones with vacuum infusion. The results of the three-point bending tests were in line with the calculated void content. 3-point bending results of vacuum infused 3D composites were measured as 13,3 MPa where the spray-wetted 3D composites presented as 11,6 MPa.*

Keywords: 3D weaving; structural composite; woven preform; flexural strength; composite quality

1. Introduction

Laminated composite structures were studied expensively due to their high load-bearing ability and low weight. However, in 2D laminated structures the fiber breakage, matrix cracking and delamination are still important challenges where innovative approaches to conventional solutions are demanded (1). For solving the delamination problem, various novel studies have been carried out as z-pinning (2), braiding (3), and stitching (4) to increase the resistance of laminated composite structures against out-of-plane stresses.

As an innovative approach, 3D weaving is an alternative route to develop delamination-free composite structures in various architectures. Unlike 2D woven fabrics, 3D woven structures have fibers on the z-axis, which enhance the composite materials resistance to out-of-plane stress and hence provide delamination resistance (5). Chen et al. divided 3D composite materials into four groups according to their structures: Solid, Hollow (Spacer), Shell, and Nodal. Spacer fabrics such with hollow geometries brings many advantages to 2D laminated systems however

  doi:10.5075/epfl-298799_978-2-9701614-0-0

the composite manufacturing of systems are still under development (6). Conventional composite manufacturing systems such as the vacuum assisted resin transfer method (VARTM) or vacuum infusion processes can be employed to produce composites from 3D woven fabrics; however, non-homogenous wetting and operator-related problems were encountered (7). K. Großmann et al. developed a 3D woven composite fabrication method referred to as Hot Compression-Moulding Technique (HCMT) with a limited geometrical capability of manufacturing only 3D spacer composites with rectangular weaving (8). Hence, developing methods and tools for complex geometries and patterns of 3D woven fabrics is essential to investigate the potential of novel 3D woven composites when high-quality manufacturing can be performed.

The aim of the research is to create an automated spraying system and a manufacturing procedure that will assure uniform resin impregnation of 3D I-beam fabrics while reducing operator-related issues. A modified loom machine was used to weave rectangular cross-section 3D spacer fabrics with LB-II vertical wall design. Since the vertical wall is presented for load-bearing capabilities, the design of it is very critical for an efficient load transfer. The details were explained in the experimental section in briefly. 3D I-beam fabrics were cut from the weaved fabrics, and 3D I-beam composites were produced from I-beam fabrics with two different resin wetting methods as i) spray-wetted resin and ii) resin infusion by vacuum. Both wetting processes were followed by composite manufacturing with custom-designed tool systems followed by vacuum processes. The mechanical characterizations of 3-point bending test and void content analysis were correlated to discuss the quality dependence of 3D composites manufactured with two distinct processes. The results confirmed that the spray-wetted samples test results were comparable to the vacuum infusion samples.

2. Experimental

2.1 Weaving of 3D I-beams with LB-II vertical wall design

The 3D I-beam fabrics were weaved with a 600 TEX glass fiber. A woven pattern with a vertical wall design called LB-II was utilized to produce 3D I-beam fabrics. Since this vertical wall presents the load-bearing, the custom weaving pattern is established uniquely for 3D I-beam structures. A dobby-loom machine is used for the 3D fabric weaving and the new wall design is referred as LB-II vertical wall. The 3D I-beam fabrics produced have a warp density of 20cm^{-1} and a weft density of 4 cm^{-1}. The modified dobby loom and theLB-II vertical wall design are shown in Figure.1.

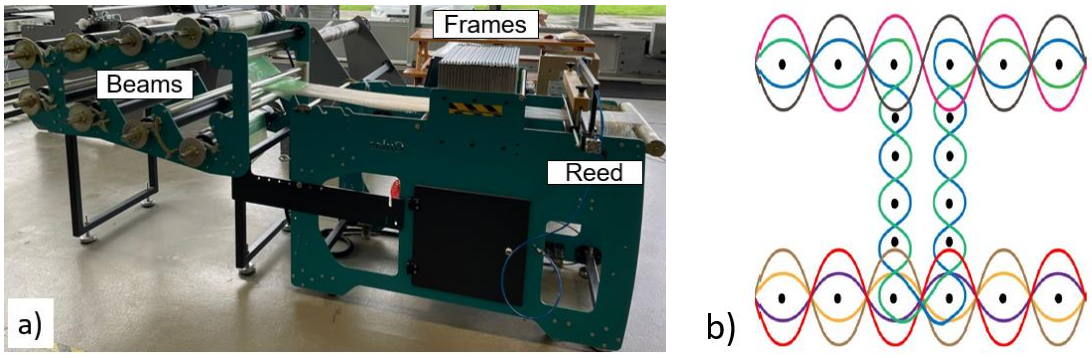

Figure 1. 3D I-beam fabric: a) modified dobby loom, b) vertical wall design.

  doi:10.5075/epfl-298799_978-2-9701614-0-0

2.2 Production of 3D I-beam composites

For resin infusion as mentioned earlier, two different wetting processes are performed. The first one is referred as spray-wetted by a custom-built spraying system uniquely designed for these 3D spacer fabrics. The second method is infusion of resin by vacuum as conventional methods, extensively studied in the literature (9, 10). The wetted specimens with both of the methods are molded with custom-tools under vacuum and manufactured as 3D I-beam composites. The effectiveness of spray wetting and vacuum resin infusion are compared within these studies.

2.2.1 Vacuum infusion process (VIP)

VIP was used to create 3D I-beam composites from 3D I-beam fabrics. Teflon-wrapped wooden molds were used to produce a near net shape from the produced I-beam fabrics. Diglycidyl Ether Bisphenol A epoxy resin (Resin: CE-A 1546 and Hardener: CE-B 10560) was employed at a mixing ratio of 4:1 in VIP. The 3D I-beam composites were vacuumed during 4 hours at 80 ℃ for curing. Production of 3D I-beam composite with VIP is shown in Figure.2.

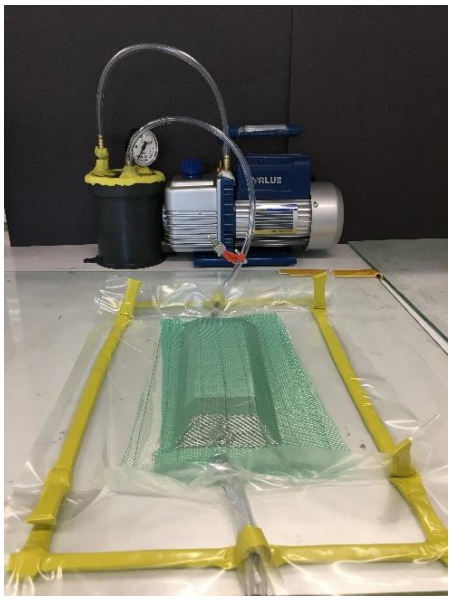

Figure 2. *3D I-beam composite fabrication with VIP.*

2.2.2 Custom-built spraying system

A custom-built spray system was designed and built to wet the 3D I-beam fabrics or any kind of spacer fabrics. This system includes a spraying mechanism for wetting the 3D I-beam fabrics, as well as a dosing device for controlling the epoxy amount on the fabric coupled with a designed control system. In Figure.3, the picture of custom-built system is presented with the dosing section. A 4:1 mixing ratio of Diglycidyl Ether Bisphenol A epoxy resin (Resin: CE-A 1546 and Hardener: CE-B 10560) was used. After the 3D I-beam fabrics are wetted with the spray system, Teflon coated wooden molds inserted to the hollow structures and the 3D I-beam fabric were vacuum bagged with the teflon molds. The curing was applied upon the given technical data sheet by the manufacturer as at 80 ℃ for a period of 4 hours.

  doi:10.5075/epfl-298799_978-2-9701614-0-0

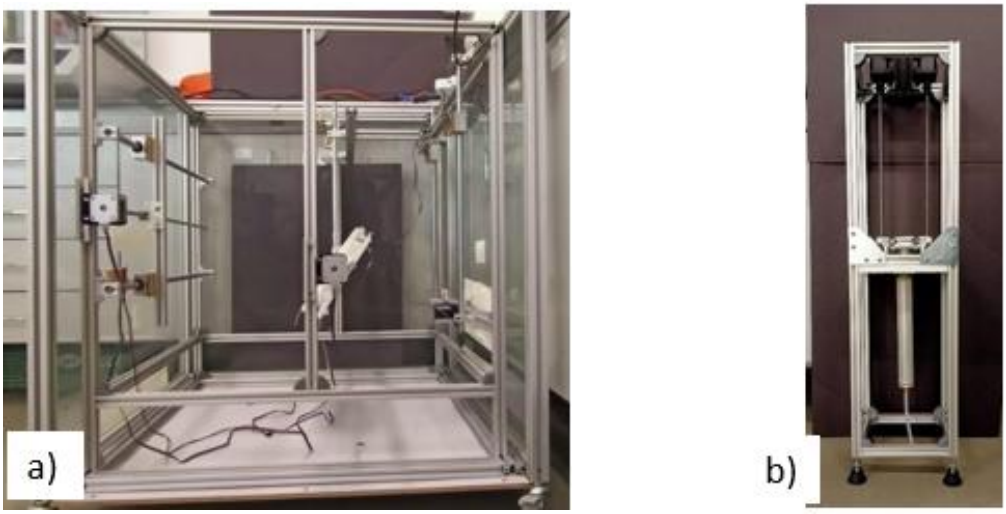

Figure 3. Custom-built spray system: a) spraying mechanism, b) dosing device.

2.3 Characterization of 3D I-beam composites

The air bubbles that remain afterwards the composite manufacturing are one critical aspects effecting the mechanical properties of composites. Similarly for 3D beam composites the manufacturing quality of the composites were evaluated through comparing the void content by the two different wetting processes studied in here. Since the custom-built spray system is the innovative approach for such spacer fabrics with hollow geometries, the optimization of this process will be one important step that needs to be further studied. Recently, preliminary work for comparing the wetting of 3D I-beam fabrics will be presented however more studies are still ongoing to finalize the coresponding results. To establish the relation in between the quality of composite manufacturing to mechanical properties.

The optical microscope (OM) images are taken to investigate the amount of air bubbles through an image processing by Image J-tool software. The 3-point bending tests produced with VIP and custom-built spray system were perromed with SHIMADZU Universal Test Machine using a 50 kN load cell. The ASTM D790 standard was employed throughout the testing, and the span to height ratio was set at 4:1 and the test speed was set to 1 mm/min. Five different samples with a length of 14 cm, a span of 8 cm and a height of 2 cm were tested for each composite manufacturing process and results were discussed in details.

3. Results and Discussion

The 3D I-beam composite samples produced by the wetting through spray method and vacuum infusion were subjected to void content analysis and 3-point bending tests. 3D I-beam composite samples produced VIP as conventional composite manufacuturing process and spray wetting as an innovative approach for hollow 3D fabrics are shown in Figure.4.

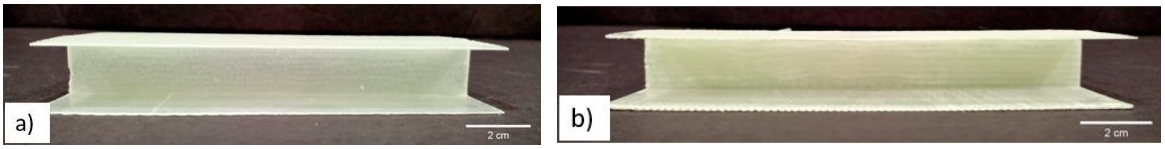

Figure 4. 3D I-beam composites with different wetting mechanism as a) vacuum infusion of resin and b) spraying of resin followed by vacuum bagging method for composite manufacturing

The void content analysis was performed on the load-bearing vertical walls of the 3D I-beam composites produced within these two distinct resin wetting processes, and the content of voids

  doi:10.5075/epfl-298799_978-2-9701614-0-0

formed on the vertical walls of the samples were compared. The voids formed in the load-bearing vertical walls were determined for five samples, and the average of the obtained void content values were compared with the voids formed in the vertical walls of the two manufacturing processes.

According to the void content analysis through Image J tool, the voids at vertical wall of the 3D I-beam composites produced by VIP was 0.748%, while the vertical wall of the 3D I-beam composites produced with the spraying method was 4.23%. Although, the void content in spraying method for resin wetting is higher than the VIP, they are both below 5%. Since the optimization of the sprayin process will be performed for various viscosity of epoxies and sprayin speeds, the initial results with such a custom-built system was resulted as promising for further studies. Optical microscope images of the vertical wall of the 3D I-beam composites produced by VIP and Spraying Method are shown in Figure 5.

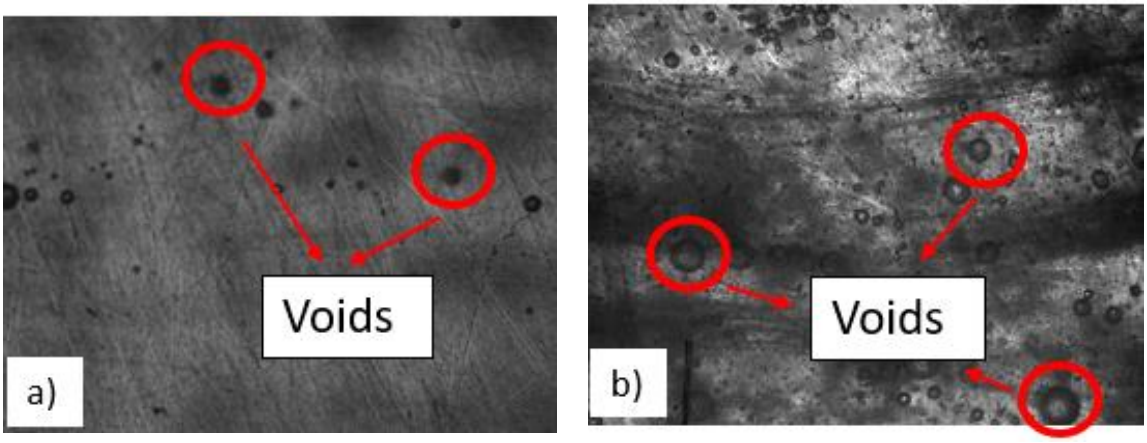

Figure 5. Optical microscope images of vertical wall: a) VARTM, b) spraying method.

The 3-point bending tests were performed to investigate the mechanical properties of 3D I-beam composites. The flexural stresses of spray-wetted and resin infused 3D beam composites were as 11.6 MPa and 13.3 MPa, respectively. Figure 6 depicts the average results of 3-point bending tests of all 5 samples from each manufacturing processes. The lower void content of the VIP samples also presented a higher flexural strain for the first ply failure as also presented through the kinks seen in Figure.6. Additionally, the increase in strength after the first ply failure has been continued with an increasing trend for VIP manufactured 3D I-beam composites. However, the spray-wetted composites did not present a similar trend which may be attributed to the higher void contents.

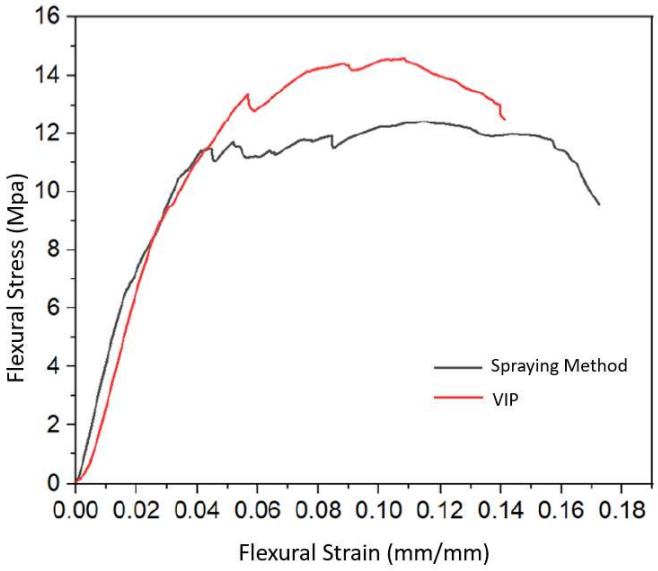

Figure 6. 3-point bending test results for spraying method and VIP for wetting of resin followed by vacuum bagged composite manufacturing.

4. Conclusions

A novel automated custom-built spray system and a 3D composite production method with a molded tools were developed in this study. It is intended that by using such a custom-built spray method, the challenges such as operator related manufacturing problems and ability to manufacture complex architecures can be overcome. To achieve high-quality of such 3D composites is essential to have mechanical properties required for load bearing applications. In here, 3D I-beam composites, as an important engineering geometry is investigated. The 3D weaving allows to achieve delamination-free structures. However, the challenges arisen from composite manufacturing quality lowers the potential of these 3D composites. So far, to the best of our knowledge none of the literature studies have explored the quality of 3D spacer composites where hollow geometries are considered that requires much attention. This study aimed to perform a comparative study for manufacturing of 3D I-beam composites when two different wetting processes of resins were considered. Spray-wetted 3D I-beam composites and resin infused 3D I-beam composites were investigated through comparing the void content of the overall composites. All void content analysis were performed at the vertical wall of I-beams. The initial results without further parametric studies revealed that the void content is 5.7 times more compared to conventional process as resin infusion. Although the spray-wetted system presented a higher void content, with such a novel method, the overall void content was lower than the 5%. 3-point bending tests were studied to investigate the mechanical properties of 3D I-beam composites and the flexural strength was found as 13% less in spray-wetted to resin infused composites structures. Further studies will be performed to improve the quality of spray-wetted 3D spacer fabric composites with the novel method as introduced in this study as custom-designed spray system.

Acknowledgements

This study was funded by the Scientific and Technological Research Council of Turkey (TUBITAK: project number 218M703 (218M704)) 1003 Primary Subjects R&D Funding Program. The

authors would also like to thank to the conference funding for M.Ali Vural provided by TUBITAK 2244-A Support Program for Participation in Abroad Scientific Events.

We would like to thank Şişecam Elyaf, Turkey's glass fiber producer, for the material support of glass fibers provided for this study.

5. References

1. Jinlian Hu. 3-D Fibrous Assemblies Properties, Applications and Modelling of Three-Dimensional Textile Structures. 3-D fibrous assemblies. 2008.

2. Mouritz AP. Review of z-pinned composite laminates. Compos Part A Appl Sci Manuf. 2007;38(12):2383–97.

3. Bilisik K. Three-dimensional braiding for composites: A review. Vol. 83, Textile Research Journal. 2013. p. 1414–36.

4. Mouritz AP, Leong KH, Herszberg I. A review of the effect of stitching on the in-plane mechanical properties of fibre-reinforced polymer composites. Vol. 28, Composites Part A: Applied Science and Manufacturing. 1997. p. 979–91.

5. Ding YQ, Yan Y, McIlhagger R, Brown D. Comparison of the fatigue behaviour of 2-D and 3-D woven fabric reinforced composites. J Mater Process Tech. 1995;55(3–4):171–7.

6. Chen X, Taylor LW, Tsai L ju. An overview on fabrication of three-dimensional woven textile preforms for composites. Text Res J. 2011;81(9):932–44.

7. Neje G, Behera BK. Investigation of mechanical performance of 3D woven spacer sandwich composites with different cell geometries. Compos Part B Eng [Internet]. 2019;160(September 2018):306–14. Available from: https://doi.org/10.1016/j.compositesb.2018.10.036

8. K. Großmann, A. Mühl, C. Cherif, K.-H. Modler FA, Krahl M. FutureTrendsInProductionEngine. Proc. 1st Conf. German Academic Society for Production Engineering (WGP). 2013. 143 p.

9. Hsiao KT, Mathur R, Advani SG, Gillespie JW, Fink BK. A closed form solution for flow during the vacuum assisted resin transfer molding process. J Manuf Sci Eng Trans ASME. 2000;122(3):463–75.

10. Hsiao KT, Heider D. Vacuum assisted resin transfer molding (VARTM) in polymer matrix composites. Manufacturing Techniques for Polymer Matrix Composites (PMCs): A Volume in Woodhead Publishing Series in Composites Science and Engineering. 2012. p. 310–47.

  doi:10.5075/epfl-298799_978-2-9701614-0-0

ELECTRICAL CONDUCTIVITY AS AN INSTRUMENT FOR DAMAGE DIAGNOSTIC OF NANOMODIFIED GLASS FIBER REINFORCED PLASTIC

Stanislav, Stankevich[a], Olga, Bulderberga[a], Sergejs, Tarasovs[a], Daiva, Zeleniakiene[b], Veronika, Zahorodna[c], Vitalii, Balitskyi[c], Ivan, Baginskiy[c], Oleksiy, Gogotsi[c], Andrey, Aniskevich[a]

a: Institute for Mechanics of Materials, University of Latvia, Jelgavas St. 3, Riga, LV-1004, Latvia – Stanislavs.stankevics@lu.lv
b: Department of Mechanical Engineering, Kaunas University of Technology, Studentų St. 56, 51424 Kaunas, Lithuania
c: Materials Research Center, Krzhizhanovskogo St. 3, Kyiv 03680, Ukraine

Abstract: *Two types of modified glass fiber reinforced plastic (GFRP) were studied: with epoxy matrix modified by multiwall carbon nanotubes (MWCNT); with built-in interleave based on conductive nanofillers such as MXene and MWCNT. Structural approach was approbated for electrical conductivity prediction of MWCNT modified GFRP plate. The numerical analysis on electrical conductivity for modified composite plates with various fiber orientation angles showed a good agreement with experimental results. The investigation of the damaged composite plate was carried out by measuring the distribution of electrical potential in the bulk of the material for both GFRP with MWCNT modified matrix and impregnated interleave with MXene coating. The voltage distribution measured throughout the laminate allowed detecting the damage in its volume. Implementation of the conductive interleave in GFRP showed good potential to determinate the location, quantification, and geometry of the damage in the lamina.*

Keywords: Glass fiber reinforced plastic; Carbon nanotubes; MXenes; Electrical conductivity; Damage diagnostic.

1. Introduction

Electrically conductive fillers, such as MWCNT, 2D carbides MXene, graphene nanoplatelets, etc., can be incorporated into polymer matrixes of fiber reinforced plastics to produce structural composites with enhanced mechanical performance and electrical conductivity [1, 2]. For successful application of such advanced composite with specific electrical conductivity, it needs to be evaluated prior manufacturing process. The infill amount of MWCNT in the modified matrix, reinforcement angle, and stacking sequence of the laminated plate are the most crucial factors influencing the electrical conductivity of the composite. Previously approbated [3] structural mechanic approach will be used for electrical conductivity prediction of MWCNT modified GFRP plate. Due to gained electrical conductivity, such composites possess the ability for strain and damage monitoring [1, 4, 5]. By applying the electrode network among the conductive volume of modified composite, it is possible to measure the voltage distribution throughout the laminate with followed damage detection in its volume [3].

Damage diagnostic can be achieved as well with an implementation of conductive elements in the structure of GFRP. These methods give an opportunity for health diagnostic of complex composite structures during its service time. Considering very high interest in the implementation of damage sensing technology inside the composite structures, the reliability of such a technique still remains inconsistent.

  doi:10.5075/epfl-298799_978-2-9701614-0-0

The aim of this study was to analyze the possibilities of damage detection via electrical conductivity monitoring of the nanomodified composite with volumetric and local in-plane nanoparticles introduction and provide insight for future design of damage diagnostic of nanomodified GFRP. Firstly, the possibility of the electrical conductivity prediction of modified GFRP was checked. Secondly, electrical conductivity response of the modified composite plate to a generated damage was evaluated.

2. Materials

The GFRP composite under investigation was based on unidirectional (UD) glass fabric (GF) with a density of 500 g/m^2 supplied by Havel Composites CZ Company Ltd. (Czech Republic), and two-component epoxy resin system Biresin ® CR122 supplied by SIKA (Germany).

MWCNT NC7000™ supplied by Nanocyl SA (Belgium) was utilized for epoxy modification. MXene for spray coating was produced and supplied by research group from Materials Research Center (MRC) in Kiev (Ukraine). Delaminated MXene was supplied as highly concentrated aqueous solution. All necessary electrical contacts were created using conductive silver paint ELECTRON 40 AC.

High shear mixer DISPERMAT® LC30 was used to disperse directly added MWCNT in the volume of epoxy resin. A disk blade of 40 mm width at the speed of 10000 rpm was used to initiate the de-agglomeration process. Solution was degassed at a pressure of -0.98 bar and low speed mixed with hardener at 400-500 rpm. The final 10 min degassing cycle was applied prior to specimen manufacturing.

During MWCNT modified GFRP manufacturing GF layers were impregnated one by one with nanomodified epoxy resin and sealed in a vacuum bag. The vacuum of -0.98 bar was applied at the room temperature of 20 °C. In such conditions, the vacuum bag was left for 18 h straight. The post-curing procedure was done according to epoxy system manufacturer recommendations: heating at rate 0.2 °C/min until 110 °C; keeping steady at 110 °C for 10 h; cooling down at rate -0.5 °C/min to avoid unexpected structural distortions due to the thermal shock. The volume fraction of glass fiber in the composite specimens prepared during this work was kept at 68%.

3. Electrical conductivity of nanomodified GRFP

3.1 Structural approach

To characterize the electrical conductivity of multi-layered composites, the conductivity of matrix, reinforcement angle, and stacking sequence of the laminated plate should be taken into account. Electrical conductivity of GFRP as a second rank tensor were calculated similarly as in micromechanics using the conductivity of the nanomodified matrix. For that reason, the structural approach that is widely used for the prediction of mechanical and thermal properties [6, 7] was adopted. According to such an approach, conductivity characterization of the multi-layered composite plate could be considered on several structural levels:

1. Micro-scale level of the composite. A fiber reinforced UD composite could be considered a set of long parallel glass fibers embedded in a polymer matrix at the micro-scale level. In that case tensor of electrical conductivity σ_{ij} could be defined as follows:

  doi:10.5075/epfl-298799_978-2-9701614-0-0

$$\sigma_{ij} = \begin{pmatrix} \sigma_{11} & 0 & 0 \\ 0 & \sigma_{22} & 0 \\ 0 & 0 & \sigma_{33} \end{pmatrix} \quad (1)$$

As long as UD GF are lined to axis 1, $\sigma_{22} = \sigma_{33}$. This means that σ_{11} and σ_{22} fully define the material and may be found using the rule of the mixture and already known equations from thermal conductivity, diffusivity, etc. [7]:

$$\sigma_{11} = \eta\sigma_{11}^{f} + (1-\eta)\sigma^{m} \quad (2)$$

and

$$\sigma_{22} = \sigma^{\mathrm{m}}\left[1 + \frac{\eta}{\sigma^{\mathrm{m}} / (\sigma_{22}^{f} - \sigma^{m}) + (1-\eta)/2}\right] \quad (3)$$

where η is the volume fraction of glass fibers, σ^{m} and $\sigma^{f}=0$ are conductivity for matrix and fibers, respectively.

2. Monolayer with various angle of GF reinforcement. The specific case needs to be evaluated to calculate conductivity with GFRP orientation at a reinforcement angle ϑ rather than 0°. Calculation of each ply should be transformed in accordance to the angle ϑ at which fibers are rotated [1]:

$$\sigma'_{11} = \sigma_{11}\cos^{2}\theta + \sigma_{22}\sin^{2}\theta \quad (4)$$

$$\sigma'_{22} = \sigma_{11}\sin^{2}\theta + \sigma_{22}\cos^{2}\theta \quad (5)$$

$$\sigma'_{12} = \sigma'_{21} = (\sigma_{22} - \sigma_{11})\sin\theta\cos\theta \quad (6)$$

3. Laminate. Stack of conductive layers oriented in different angles provides conductivity of a multi-layered GFRP laminate as presented schematically in Figure 1.

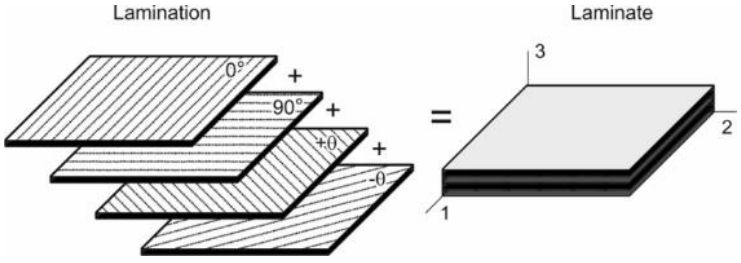

Figure 1. Scheme of laminate with angles 0, 90, and ±ϑ°

For the specific layup $[\pm\vartheta°]_4$ conductivity tensor components were defined by the Eq. (7) and (8) [1]:

$$\bar{\sigma}'_{11} = \frac{1}{H}\sum_{i=1}^{N} h_i(\sigma_{11}\cos^{2}\theta_i + \sigma_{22}\sin^{2}\theta_i) \quad (7)$$

$$\bar{\sigma}'_{22} = \frac{1}{H}\sum_{i=1}^{N} h_i(\sigma_{11}\sin^{2}\theta_i + \sigma_{22}\cos^{2}\theta_i) \quad (8)$$

  doi:10.5075/epfl-298799_978-2-9701614-0-0

3.2 Verification

To validate the prediction of electrical conductivity by the structural approach, calculated data were compared to the experimental ones on different structural levels. Nanomodified GFRP laminates were cut into smaller samples and separated to groups with reinforcing angles of 0, 90, and 45°. Electrical conductivity evaluation of those specimens was done using 4-point probe method. Electrical conductivity data calculated by Eq. (7) and (8) were compared with experimentally acquired in Figure 2.

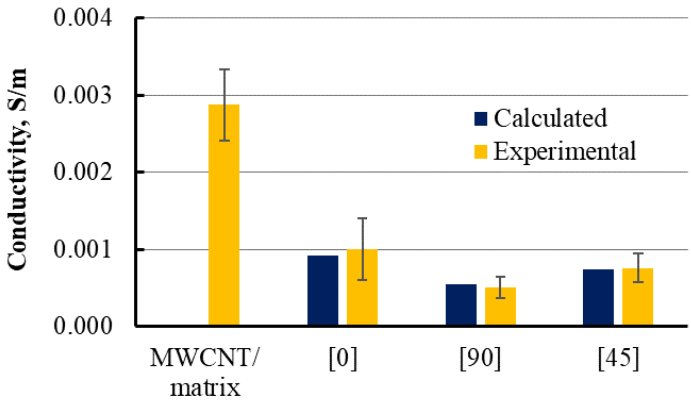

Figure 2. Calculated and experimental conductivity of UD GFRP with 0.3 wt.% MWCNT modified epoxy matrix and its based composite bars with reinforcing angles 0, 90, and 45°

Noticeable electrical anisotropy was observed for MWCNT modified UD GFRP specimens due to the orientation of non-conductive fibers. Electrical conductivity values for composite along the fibers were three times higher than those for transverse direction. Such behavior could be described with a higher number of obstacles for current to flow around created by transverse orientated fibers. Calculated and experimental electrical conductivity data for various fiber orientation angles were in good agreement.

4. Voltage distribution in damaged nanomodified GFRP

To evaluate electrical conductivity usage for composite plate's damage diagnostic two types of modified glass fiber reinforced plastic (GFRP) were studied: with epoxy matrix modified by multiwall carbon nanotubes (MWCNT); with built-in conductive interleave based on MXene.

4.1 GFRP with nanomodified epoxy resin

According to the composite manufacturing process described in Sec. 2, MWCNT modified composite plate was prepared with reinforcement orientation of $[0°, 90°]_4$ for an equal conductivity in the *x* and *y* directions. Considering the conductive matrix, characterization of voltage distribution throughout the laminate was performed by creating an electrode network of 8×8 contacts by applying conductive paint directly on the polished top surface of the composite plate.

4.2 GFRP plate with conductive interleave

With volumetric matrix nanomodification, only integral damage diagnostic can be provided in all specimen's volume. Thus, the whole structural element is a single sensor, and in that case, damage localization is impossible. The situation changes with the embedding of thin conductive

sensor to the structural element. This was realized via the implementation of spray coated conductive layer inside the GFRP structure. Such conductive interleave was created using MXene conductive nanoparticles. MXene aqueous concentrate was diluted with deionized water and mixed using probe ultrasonicator at 140 W for 30 min with two 5 min pauses in-between.

Woven GF with a density of 390 g/m^2 was utilized to create 8-layered composite. Woven type was chosen to maintain the integrity of sprayed film during composite manufacturing process. In order to apply and receive electric signal from conductive inner layer, 64 metallic nails were implemented in the composite plate prior spraying. Nails were polished, sharpened, and their caps were dramatically thinned, so they can fit between 4th and 5th layers of the composite without affecting the whole structure (see Figure 3).

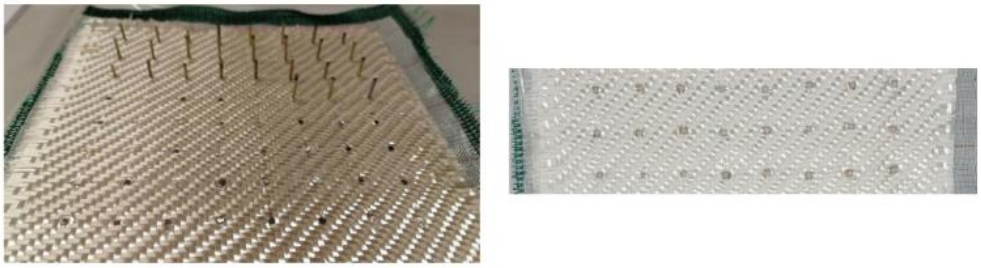

Figure 3. Polyethylene vacuum film, breathable net, nylon ply and 4 layers of GF plies are pressed into polyurethane foam using 64 metal nails (left). Glued nails` heads to the 4th GF layer of the composite (right)

To maintain the integrity of the conductive layer during composite production, nails` heads were glued to the 4th GF layer prior spraying using conductive paint (see Figure 3). MXene aqueous solution was used to create single layered spray coated conductive film on top of the 4th GF ply together with glued contact heads. Spray coating procedure was carried out by spray-gun SAP-CR 0.2 supplied by STAR®, with a nozzle size of 0.2 mm at the pressure of 0.1 MPa. The amount of MXene in mass per area was held at $3.0 \cdot 10^6$ g/mm^2 during spray coating procedure. The rest of the composite was stacked on top of the sprayed layer. Stacked layers were impregnated with epoxy resin by vacuum infusion. The vacuum and post curing procedure were kept as described in Sec. 2.

Health diagnostic of complex composite systems may require a large number of signal pins (output electrodes), which can adversely affect the mechanical properties of the monitored structure. In this case, it is necessary to reduce the number of signal outputs to a minimum with minimal loss in structural damage diagnostic accuracy. For that reason, one more type of GFRP laminate was prepared with decreased amount of electrodes (from 64 to 28) implemented into the composite as shown in Figure 4.

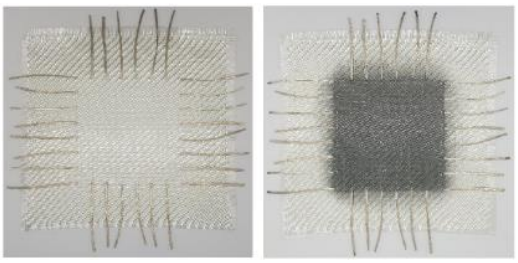

Figure 4. Neat (left) and MXene spray coated (right) GF plies

Spray coating procedure was carried out using same spray-gun properties and MXene aqueous solution as for previous GFRP modified plate. Modernized GF ply was used in a place of a regular GF ply during composite manufacturing. This means that any layer in the composite structure can be upgraded in that way. Thus, allowing more local selection of the preferable damage detection zone within composite structure.

4.3 Verification

To evaluate electrical conductivity usage for composite plate's damage diagnostic, MWCNT modified composite plate was utilized. The voltage of 20 V was applied between the diagonally opposite corners of the plate (upper left and lower right corners). The voltage distribution of initial composite plate was obtained by the voltage drop measuring on each contact.

Three different cases of damage were consecutively created and examined: (1) a circular hole of diameter 9.8 mm in the middle; (2) a notch of 31 mm length and 1.8 mm width; (3) a notch of 70 × 1.8 mm. Using the network of 64 contacts, the distribution of voltage in the GFRP plate was measured experimentally at each sequential damage state (U_0 – initial state (case 0), U_1 - first damaged state (case 1), U_2 – second damaged state (case 2), U_3 – third damaged state (case 3)). Voltage data was compared between adjacent states and presented in Figure 5.

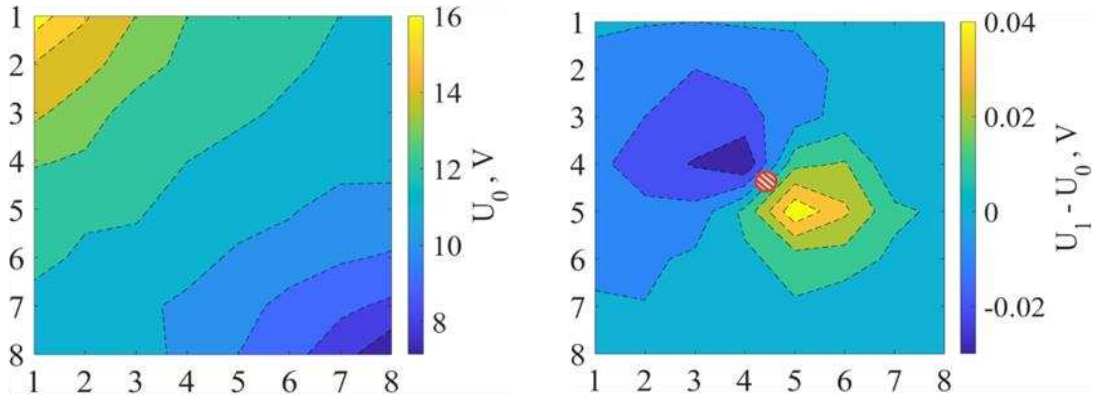

Figure 5. Experimentally obtained voltage distribution of initial plate (left). Voltage distribution difference between the cases (1) and (0) (right). Damaged areas are red line highlighted. Vertical and horizontal numbers from 1 to 8 define the coordinates of electrodes on the composite plate

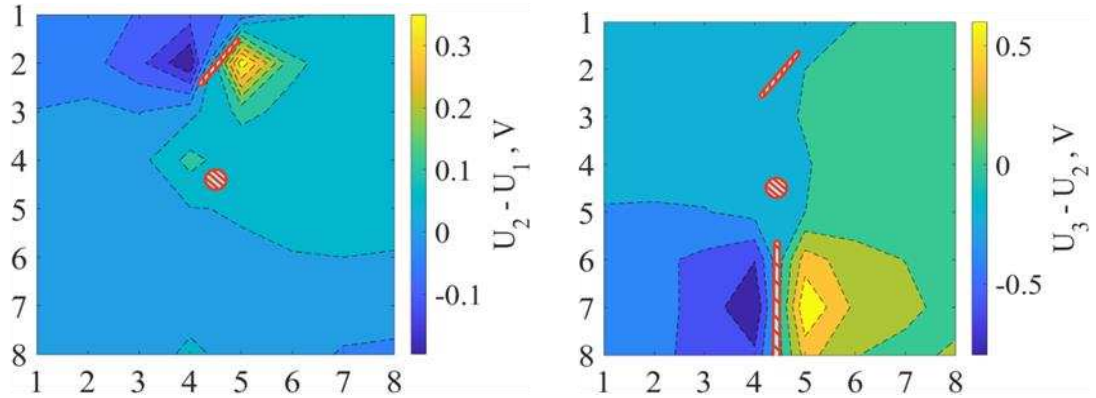

Figure 6. Experimentally obtained voltage distribution difference between the cases (2) and (1) (left), cases (3) and (2) (right)

As seen from Figure 5 and Figure 6, equipotential lines' front in the nearest area of the damage mimicked the geometry of the aperture. Thus, voltage distribution maps for all damage cases showed the aperture's proper position and geometry.

The distribution of the electric field potential in a plate for all damage states was simulated using two-dimensional static electric analysis by finite element method (FEM) in Ansys. For evaluation of damage characterization capability by voltage distribution monitoring, experimental data were compared with the simulation model. Relative error δ between experimental and calculated data for different damage cases were found using Eq. (9)

$$\delta = \frac{1}{64}\sum_{i=1}^{64}\frac{\left|U_{\text{FEM}}^{i} - U_{\text{exp}}^{i}\right|}{U_{\text{exp}}^{i}} \cdot 100\% \tag{9}$$

where i is a consecutive number of composite plate's electrode. The average relative error of $\delta = 6.2 \pm 0.2\%$ for all states of the composite plate showed an excellent resemblance between calculated and experimental voltage data.

5. Delamination crack monitoring in double-cantilever beams

In composite structures, in addition to bulk damage, the process of delamination is no less important. That is why damage diagnostic for interlaminar defects is interesting topic and was approbated earlier for composite structures [1, 8, 9]. That was done by finding the relationship between resistance and interlaminar crack propagation for double-cantilever beam (DCB) specimens during Mode I (opening mode) interlaminar fracture toughness test. Electrical resistance response was used to characterize interlaminar fracture of DCB specimens: (1) with nanomodified conductive matrix. Electrical conductivity through all volume of a specimen was provided in this case, which means that whole specimen is a single sensor and only integral damage diagnostic can be achieved; (2) with MWCNT modified interleave that provided conductivity of the thin layer only in the middle of a specimen and allowed for more local damage detection.

Results demonstrated that electrical resistance could be successfully used for the diagnostic of the crack propagation during interlaminar fracture of the MWCNT modified GFRP [1].

Conclusions

The electrical conductivity of the GFRP composite was experimentally and theoretically considered on different structural levels. Calculated and experimental electrical conductivity of multi-layered GFRP with MWCNT modified epoxy matrix were in good agreement.

It was proved that electrical conductivity monitoring could be successfully used for damage diagnostic of the GFRP lamina with the MWCNT-doped polymer matrix. Determining the location, quantification, and geometry of the damage in the MWCNT modified GFRP lamina can be performed by monitoring the voltage distribution throughout the composite plate. The shape of equipotential voltage lines near the defect in the plate was precisely mimicking the geometry of the defect. Furthermore, voltage distribution in damaged GFRP plate calculated by FEM showed an excellent resemblance with experimental data for all damage states.

  doi:10.5075/epfl-298799_978-2-9701614-0-0

Implementation technology of conductive interleave with output electrodes into GFRP structure was developed. Results demonstrated that introduction of thin conductive spray coated interleave in the GFRP can lead towards more local damage diagnostic of the structure.

Acknowledgements

This work has received funding from the European Union's H2020-MSCA-RISE-2017 project Nano2Day, "Multifunctional polymer composites doped with novel 2D nanoparticles for advanced applications", grant agreement No 777810.

6. References

1. Stankevich, S., et al., *Electrical conductivity of glass fiber-reinforced plastic with nanomodified matrix for damage diagnostic.* Materials, 2021. **14**(16).
2. Kilikevičius, S., et al., *Novel Hybrid Polymer Composites with Graphene and MXene Nano-Reinforcements: Computational Analysis.* Polymers, 2021. **13(7)**: p. 1-12.
3. Aniskevich, A., S. Stankevich, and J. Sevcenko, *Prediction method of electrical conductivity of nano-modified glass fibre reinforced plastics.* IOP Conference Series: Materials Science and Engineering, 2019. **500**: p. 012010.
4. Viets, C., S. Kaysser, and K. Schulte, *Damage mapping of GFRP via electrical resistance measurements using nanocomposite epoxy matrix systems.* Composites Part B: Engineering, 2014. **65**: p. 80-88.
5. Monastyreckis, G., et al., *Strain Sensing Coatings for Large Composite Structures Based on 2D MXene Nanoparticles.* Sensors, 2021. **21**: p. 2378.
6. Aniskevich, K., et al., *Long-term deformability and aging of polymer matrix composites.* Long-Term Deformability and Aging of Polymer Matrix Composites, 2012: p. 1-190.
7. Christensen, R. and J. McCoy, *Mechanics of Composite Mateials.* Journal of Applied Mechanics, 1980. **47**: p. 460.
8. Zhang, H., et al., *Improved fracture toughness and integrated damage sensing capability by spray coated CNTs on carbon fibre prepreg.* Composites Part A: Applied Science and Manufacturing, 2015. **70**: p. 102-110.
9. Wan, Y., et al., *Mode I interlaminar crack length prediction by the resistance signal of the integrated MWCNT sensor in WGF/epoxy composites during DCB test.* Journal of Materials Research and Technology, 2020. **9**(3): p. 5922-5933.

  doi:10.5075/epfl-298799_978-2-9701614-0-0

ENERGY EFFICIENT OUT-OF-OVEN MANUFACTURING FOR NATURAL FIBRE COMPOSITES WITH INTEGRATED DEFORMATION SENSING

Yushen Wang[a], Xudan Yao[a], Yi Liu[b], Emiliano Bilotti[a], Han Zhang[a]

[a] School of Engineering and Materials Science, Queen Mary University of London, London E1 4NS, UK – yushen.wang@qmul.ac.uk
[b] Department of Materials, Loughborough University, Loughborough, LE11 3TU, UK

Abstract: *This study developed an extremely energy efficient out-of-oven (OoO) manufacturing method based on a graphene biopolymer nanocomposite film to fabricate natural fibre reinforced composites (NFRCs) with integrated multi-functionalities throughout their life cycles. The smart nanocomposite layer works as a self-regulating heating source to cure the NFRCs at the desired temperature. Extremely high energy efficiency has been achieved with a significantly reduced energy consumption (> 95 % compared with traditional oven curing), thanks to the conduction heating from the surface layer directly to the laminates. After the composite manufacturing, the nanocomposite film embedded on the surface of the laminate subsequently becomes an integrated multifunctional layer to the NFRCs, providing real-time deformation and damage sensing capabilities with enhanced water barrier properties to prolong the usage stage of the natural fibre composites.*

Keywords: Sustainable manufacturing; Out-of-oven curing; Natural fibre reinforced composites; Damage sensing; Barrier properties

1. Introduction

With the increasing concern for the environment and the necessity of sustainable development in composite sector, significant efforts have been made to develop eco-friendly and biodegradable materials. Natural fibre reinforcements and bio-based resins provide an opportunity to reduce the carbon footprint of structural composites while improving environmental sustainability [1]. However, traditional composite manufacturing methods such as autoclave or resin transfer moulding are capital and energy-intensive, also generate a large amount of greenhouse gases during conventional manufacturing stage [2]. Recently, some energy-efficient manufacturing methods have been developed to cure fibre-reinforced composites, such as microwave methods for conductive carbon fibre composites [3]. Nevertheless, a highly energy-efficient curing method for insulating NFRCs is still yet to be developed.

Very recently, Liu *et al.* showed that an extremely high energy efficiency can be achieved during composite manufacturing with a significantly reduced energy consumption by using a conductive polymer composite films with a positive temperature coefficient (PTC) behaviour as a heating layer for laminate curing [4]. Due to the mismatch in thermal expansion between matrix and fillers, the electrical resistivity will increase drastically when the conductive polymer composites approach to their melting temperature, leading to a PTC effect with a sudden increase in electrical resistance [5, 6]. Based on the PTC effect of fabricated conductive polymer

  doi:10.5075/epfl-298799_978-2-9701614-0-0

composites, self-regulating heating can be achieved by applying the Joule heating effect onto the film and cure the fibre reinforced thermoset composites without an oven.

In this study, a bio-degradable thermoplastic polycaprolactone (PCL) was chosen as the matrix of the functional surface film. PCL is an aliphatic polyester considered as an eco-friendly polymer, which is usually applied in biodegradable plastic products, including controlled drug releases, bone scaffolds, tissue engineering, packaging, etc [7]. The relative high coefficient of thermal expansion (CTE) of semicrystalline PCL (~ 130 10-6/°C) provides an opportunity to manufacture the conductive film with a PTC effect for self-regulating heating and out-of-oven composite manufacturing. Furthermore, it could also act as a water barrier layer to prolong NFRCs' usage life [8].

2. Materials and methods

2.1 Materials

Polycaprolactone pellets from Ingevity (PCL, Capa™ 6800, M_n = 6900 ± 3500, M_w = 112000 ± 5500) and graphene nanoplatelets from XG Science (GNP, Grade M, thickness of 6-8 nm and lateral dimension of 25 µm according to the manufacturer) were used to fabricate the multifunctional surface nanocomposite film. The NFRCs consisted of flax fabrics (EcoTechnilin, FLAXTAPE 110) with an areal weight of 110 g/m^2 and a bio-based epoxy (PRO-SET, M1049 & M2049) with a pre-curing stage at room temperature for 24 hrs and a post-curing stage of 50 °C for 16 hrs.

2.2 Manufacturing methods

The multifunctional PTC film was fabricated by a solution casting method. The PCL pellets were dissolved in chloroform with a concentration of 20 wt.%. Graphene nanoparticles were dispersed in another bottle of chloroform by an ultrasonic probe. A 10 mg/ml concentration was chosen to disperse graphene in chloroform solution. After mixing two chloroform solutions, the mixed solution was magnetically stirred and degassed in an ultrasonic bath. Finally, the degassed solution was poured onto a release film for solvent evaporation to obtain a 5.5 wt.% PCL/GNP film.

The 5.5 wt.% PCL/GNP film was then compress moulded at elevated temperature to achieve a homogeneous thickness of 150 µm. Six parallel copper wires with an interval of 1.5 cm were also hot-pressed into the film to act as electrodes for Joule heating function.

The NFRCs have dimensions of 10 × 10 cm^2, consisting of eight layers of unidirectional flax fibre with a layer of multifunctional surface film on top. The panels were fabricated by vacuum-assisted resin infusion (VARI) and cured by two different methods (conventional convection oven curing, and out-of-oven curing by Joule heating of surface nanocomposite film).

2.3 Characterization

Scanning electron microscopy (SEM, Inspect F) was applied to observe the morphology of the GNP embedded PCL films. Specimens were immersed in liquid nitrogen to create the cryo-fractured surfaces on PCL films, while the film-cured NFRCs laminates were polished to reveal the cross-sectional views. Both specimens were gold-sputtered before imaging.

The PTC effect of PCL/GNP composites was measured in a small oven connected to a thermocouple recorder (Pico Technology, TC-08) attached to the specimen surface for temperature recording and two-probe electrodes embedded on both sides of specimens for resistance measuring. The voltage supply given to the PCL/GNP film was provided from an DC power supply (GE EPS 301). The power consumption of the convection oven and Joule heating film curing were recorded by a plug-in power monitor (2000MU-UK).

Dynamic mechanical analysis (DMA, TA Instruments Q800) was used to observe the thermomechanical performance of the NFRP laminates fabricated by different curing methods. The PCL/GNP surface layer was removed before the tests. Three-point bending was performed with a temperature scan from 30 °C to 90 °C with a frequency of 1 Hz and a strain of 1 %.

The real-time deformation and damage sensing performance of fabricated multifunctional composites were monitored based on an electrical signal measurement system consisting of a universal test machine (Instron 5566) and a multimeter (Agilent 34401A) connected with the LabView program. Cyclic loadings in the three-point bending test were applied to specimens with a maximum strain of 0.1 % and 0.2 % at a 1 %/min strain rate. Three-point bending (TPB) test was used to obtain the flexural properties of the laminates, with tests and calculation performed in accordance with ASTM D790-10.

Water vapour transmission test was performed according to ASTM E96. Neat PCL film and 5.5 wt.% PCL/GNP film with the same thickness of 150 μm were prepared by aforementioned compression moulding process. Two test dishes were filled with water and sealed with testing films, placed in a desiccator with a sustained relative humidity of 5 %. The dishes were taken from the desiccator to measure daily weight loss. Water absorption test was performed by recording the sample weight after removing the top water layer on the sample surface, with all surfaces except the top surface sealed by the hydrophobic polyisobutylene tape.

3. Results and discussion

3.1 PTC effect and self-regulating property

The positive temperature coefficient effect describes the increase of electrical resistance when the specimen is subject to a rising temperature, which usually exists in the conductive polymer composites. During the thermal expansion of the polymer matrix, the conductive filler network will be rearranged and separated, providing an autonomous cut off during Joule heating and set a safety limit for heating. The thermal expansion coefficient reaches the highest value near the melting point in the semi-crystalline polymer. Therefore, the resistance of the conductive polymer composites will jump when the temperature approaches to the melting temperature of the matrix.

*Figure 1*a shows the resistance changes of 5.5 wt.% PCL/GNP with an increasing temperature. The resistance increased slightly from room temperature upon heating, with a clear jump and a change in slope when temperature approached to the melting point of the PCL, followed by a negative temperature coefficient (NTC) effect when further heating was applied with temperature above the melting point. The NTC effect can be attributed to the GNP re-agglomeration after the melting of the matrix with a significantly reduced viscosity. *Figure 1*b shows the surface temperature of the PCL/GNP film with a given voltage from 10 V to 150 V. With an increased voltage from 10 V to 120 V, an obvious temperature increase can be observed

due to the increasing amount of power input into the system. Once the temperature reached the self-regulating temperature (around 58 °C), a relatively stable temperature profile can be observed even at much higher voltage applied (up to 150 V). This can be attributed to the self-regulating heating capability of the film due to the thermal expansion with the disconnecting motion of the conductive network.

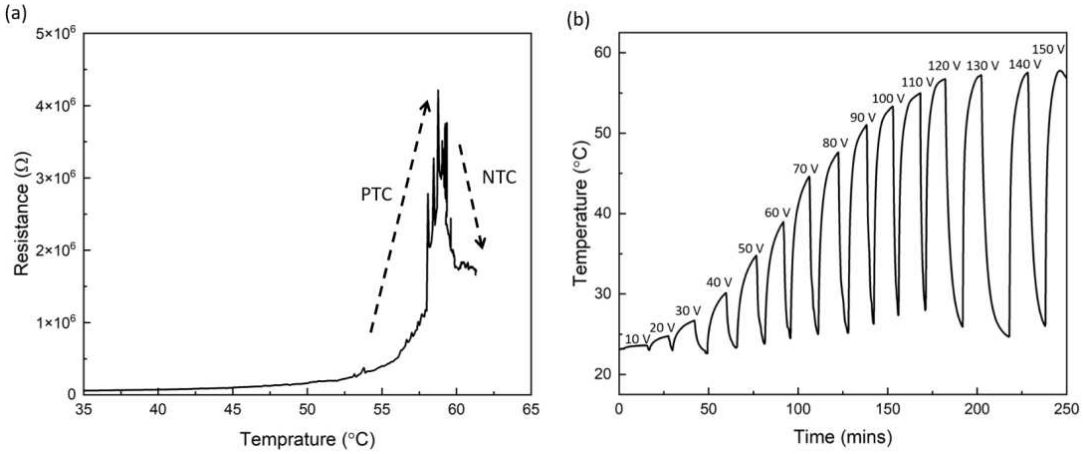

Figure 1 (a) The PTC and NTC effect of 5.5 wt.% PCL/GNP specimen. The resistance of PCL/GNP composite has a relatively sharp increase before the melting point of PCL, where the conductive network was separated by the matrix thermal expansion; (b) the temperature of PCL/GNP film during the self-regulating heating at various applied voltages. The temperature stabilised at self-regulating temperature, with an obviously reduced heating rate when increasing the voltage from 120 V to 150 V.

3.2 Thermomechanical, flexural properties and morphologies of natural fibre laminates

NFRC panels with UD flax fibre were cured by traditional oven method as well as developed surface nanocomposite film out-of-oven. *Figure 2*a-b display thermomechanical performance of the laminates measured by DMA tests. The glass transition temperature and the storage modulus of the film-cured specimens were slightly higher than the oven-cured laminate, resulting in from the slightly higher curing temperature of film-cured panel than the oven-cured one. From the three-point bending results in *Figure 2*c, the flexural modulus of the film-cured panel processed a similar value but slightly lower than the oven-cured panel. This difference in flexural modulus was resulted from the existence of PCL surface film on NFRC specimens, leading to a higher thickness (around 0.15 mm of PCL film without reinforcing fibres as shown in *Figure 3*a-b) used for the modulus calculation. The PCL/GNP film was designed to stay attached to the NFRCs panel for the TPB sensing test, while the film was removed in the DMA test to obtain a more accurate value on NFRCs' mechanical property. Nevertheless, the mechanical property of the two curing methods did not exhibit any significant difference, indicating the functional film possesses a proper heating ability to cure NFRCs.

  doi:10.5075/epfl-298799_978-2-9701614-0-0

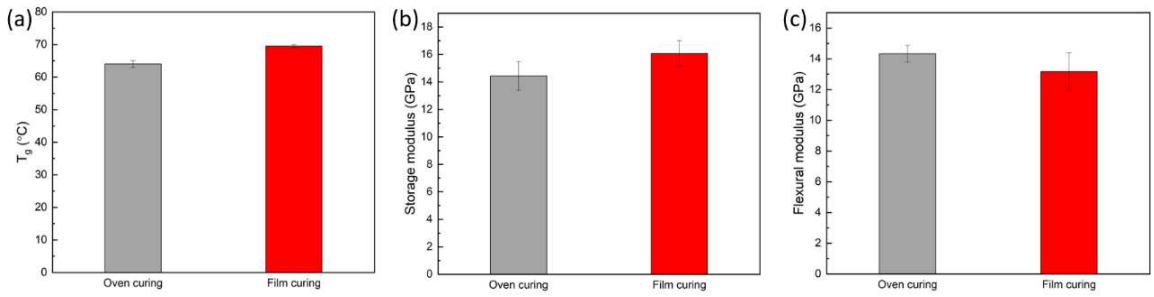

Figure 2 Thermomechanical and flexural properties of natural fibre composites cured by traditional oven and out-of-oven film method: (a) The glass transition temperature and (b) the storage modulus value from DMA measurement, (c) The flexural modulus from the three-point bending test. Similar values were obtained from two curing methods, indicating the feasibility and effectiveness of using out-of-oven manufacturing for natural fibre composites.

The good attachment between film and laminates surfaces can be observed in *Figure 3*a-b, which guaranteed the energy transferring from heating film to epoxy. It is also clear that the laminates cured by PCL/GNP functional film did not exhibit any obvious voids from both front-view and side-view cross-section of specimens. *Figure 3*c displayed the unidirectional orientation of graphene nano sheets in PCL matrix, attributing to the hot-press process after solution casting.

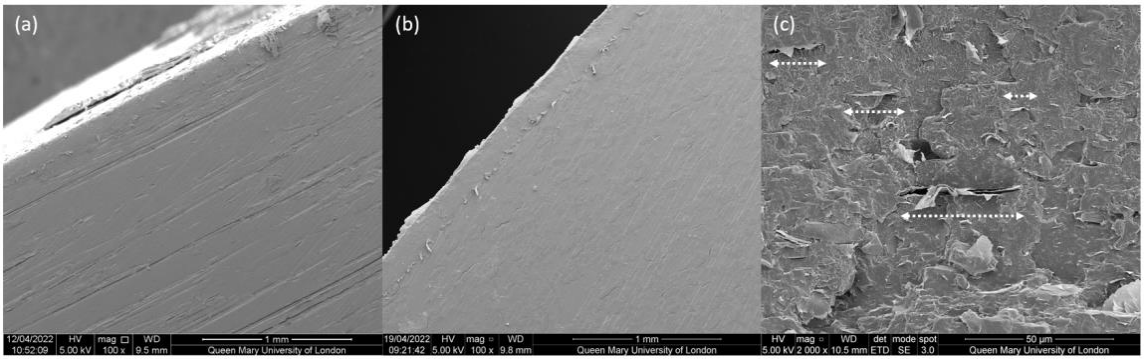

Figure 3 The SEM images: (a) the side-view and (b) the front-view of cross-section in polished NFRC laminate with PCL/GNP film after curing with PCL film well attached to the bio-epoxy. (c) PCL/GNP film's cryo-fractured surface after hot-pressing exhibited a laminated orientation of GNP nanoparticles in PCL polymer (see arrows).

3.3 Energy consumption

The real-time power-consumption and the final energy consumption of both curing methods are shown in *Figure 4*. The oven curing method consumed ~6.83 kWh, nearly twenty times the curing process's energy based on self-regulating heating film (~0.35 kWh). The main reason for such a vast difference is that the Joule heating film was directly attached to the NFRCs laminates as the heating source for curing, while in convection oven, the air was heated first then transferred the energy to the laminates. Due to the low thermal conductivity and the large heat capacity of the air, a large portion of energy was used to heat up the air. From an energy consumption and heat transfer viewpoints, it is clearly advantageous to have a heating film in direct contact with the laminates to promote conduction heating rather than traditional convection oven. Furthermore,

  doi:10.5075/epfl-298799_978-2-9701614-0-0

the self-regulating heating function of the PTC film could also prevent the overheating by the high voltage supply, making it safer than other Joule heating materials.

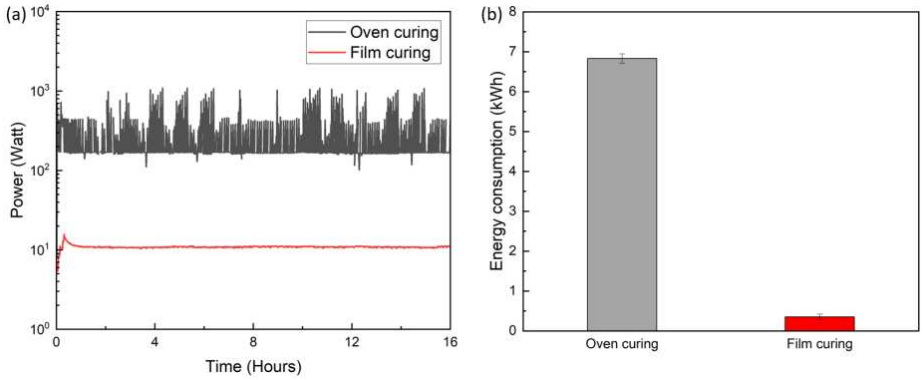

Figure 4. (a) The real-time power consumption and (b) total energy consumption value of traditional oven curing and Joule heating film curing methods, showing a significantly enhanced energy efficiency from the Joule heating film curing method over traditional oven.

3.4 Real-time deformation and damage sensing

Although the natural fibre composites are electrically insulating, the introduction of PCL/GNP nanocomposite surface layer allows the electrical sensing methods to be used to detect deformation and damage. The in-situ deformation sensing of developed multifunctional composites was examined by a cyclic loading profile (*Figure 5*a). The relative resistance of the PCL/GNP film ($\Delta R/R_0$) was used as the sensing signals to detect the strains. It was observable that a GNP loading of 5.5 wt.% in the PCL matrix displayed a relatively distinguished signal under 0.2 % strain deformation, while the sensing layer was less sensitive to 0.1 % strain.

Damage sensing has also been demonstrated via the PCL/GNP sensing layer as shown in *Figure 5*b. The conductive PCL/GNP nanocomposites was at the bottom surface (under tension) during the three-point bending tests, showing a clear increasing trend of the sensing signals with applied load from the beginning of the test. With the fracture of the specimen alongside clear load drops, the sensing signals shown a sudden jump with a very clear correlation with the damage of the laminates.

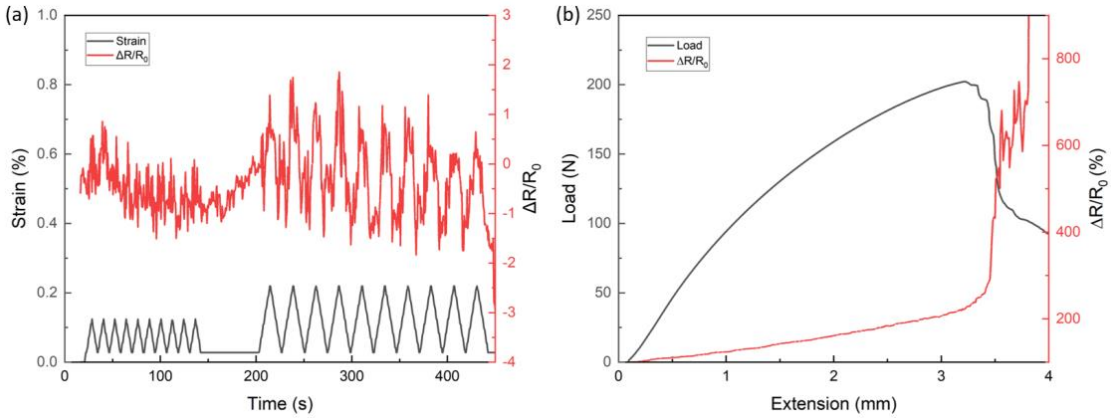

Figure 5 (a) The real-time deformation sensing signal from PTC film attached NFRCs specimen under cyclic three-point bending mode. (b) The damage sensing of developed multifunctional

NFRC under three-point bending tests, showing a correlation between the electric signal from multifunctional film and the load response on NFRC laminates at different strain level.

3.5 Water barrier properties

*Figure 6*a-b presents the values of water mass loss from the sealed cavity of dishes to the outside environment, with illustrations of two dishes covered by the pure PCL film and the PCL film containing 5.5 wt.% GNP, respectively. It is noticeable that the water loss speed of PCL with 5.5 wt.% GNP was slower than the pure PCL film. According to the calculation method in ASTM E96, the water permeability test results of pure PCL film and 5.5 wt.% PCL/GNP were 0.503 e^{-13} (kg m/s m^2 Pa) and 0.216 e^{-13} (kg m/s m^2 Pa), respectively, which confirmed that PCL with 5.5 wt.% GNP filler possessed a higher water molecular shielding property than the pure PCL film. The hot-press process produced a uniform orientation of graphene nanoparticles in the polymer (*Figure 3*c), turning the GNP network into tortuous paths thus prolonging the water molecular cross distance [9]. The water permeability of polymer films with graphene filler could possesses a maximum reduction level up to 93 % at a filler loading up to 0.1 wt.% [10]. In this study, the water permeability has a reduction of 57.1 %, which is a relatively good improvement for nanocomposites in water barrier properties.

Water absorbing experiments were designed to identify the water protection ability between the NFRC laminates with or without the PCL/GNP smart surface film. The water-absorbing mass of the same volume and shape samples has shown in *Figure 6*c-d. It can be observed that the NFRC laminates covered by the PCL/GNP film have a reduced water update compared to the specimen without surface film, indicating the PCL/GNP film could be used as a shielding on the NFRCs, especially in humid environments.

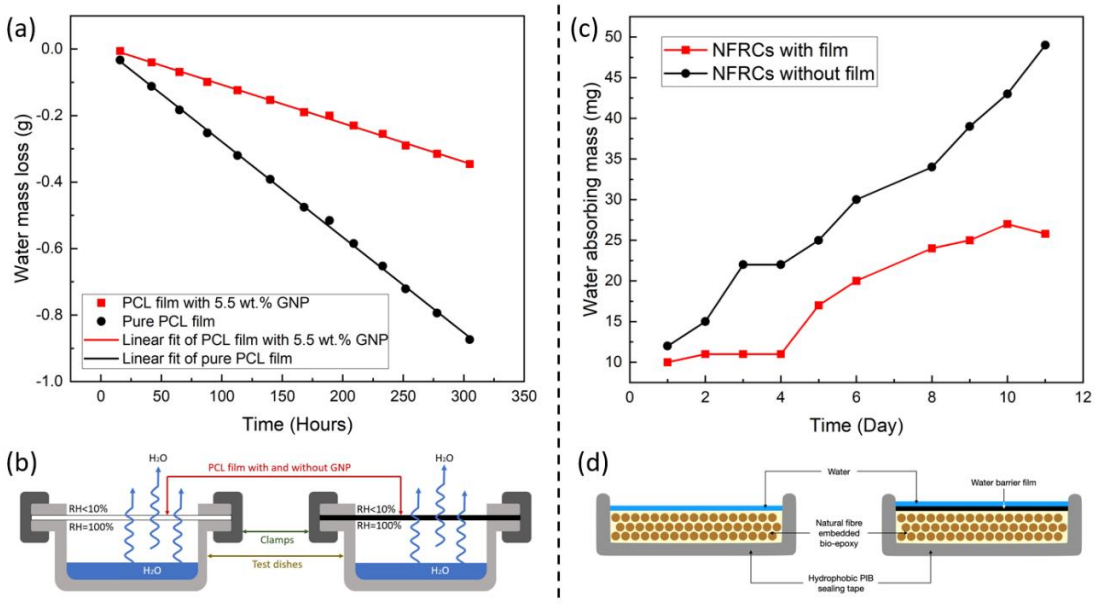

Figure 6 (a)-(b) The water vapour transmission curve of pure PCL film and 5.5 wt.% PCL/GNP film by water method testing. The water mass loss of pure PCL film was significantly higher and faster than the graphene embedded PCL film. (c)-(d) The water-absorbing mass of oven-cured and film-cured NFRCs. The weight of film cured NFRCs has a slight weight change compared to the NFRCs without the film layer.

  doi:10.5075/epfl-298799_978-2-9701614-0-0

4. Conclusions

This study developed an energy-efficient curing method for NFRCs based on a PCL/GNP nanocomposite film with integrated multifunctionalities. The smart biopolymer layer has a self-regulating heating function for desired curing temperature during Joule heating without the risk of overheating. The energy efficient out-of-oven cured NFRC laminates exhibited almost the same thermomechanical and mechanical properties in comparison with the conventional oven cured laminates. Besides, the PCL/GNP layer attached to NFRCs could also provide real-time deformation and damage sensing capabilities with water barrier property to prolong the usage stage of the natural fibre composites.

Acknowledgements

This work was supported by the Engineering and Physical Sciences Research Council (EPSRC) [ESTEEM, grant number EP/V037234/1]. YW is grateful to the China Scholarship Council for the financial support.

5. References

1. Gholampour A, Ozbakkaloglu T. A review of natural fiber composites: Properties, modification and processing techniques, characterization, applications. Journal of Materials Science. 2020;55(3):829-92.
2. Abliz D, Duan Y, Steuernagel L, Xie L, Li D, Ziegmann G. Curing methods for advanced polymer composites-a review. Polymers and Polymer Composites. 2013;21(6):341-8.
3. Mgbemena CO, Li D, Lin M-F, Liddel PD, Katnam KB, Thakur VK, et al. Accelerated microwave curing of fibre-reinforced thermoset polymer composites for structural applications: A review of scientific challenges. Composites Part A: Applied Science and Manufacturing. 2018;115:88-103.
4. Liu Y, van Vliet T, Tao Y, Busfield JJ, Peijs T, Bilotti E, et al. Sustainable and self-regulating out-of-oven manufacturing of FRPs with integrated multifunctional capabilities. Composites Science and Technology. 2020;190:108032.
5. Park S-J, Kim H-C, Kim H-Y. Roles of work of adhesion between carbon blacks and thermoplastic polymers on electrical properties of composites. Journal of colloid and interface science. 2002;255(1):145-9.
6. Liu Y, Zhang H, Porwal H, Busfield JJ, Peijs T, Bilotti E. Pyroresistivity in conductive polymer composites: a perspective on recent advances and new applications. Polymer International. 2019;68(3):299-305.
7. Mohamed RM, Yusoh K. A review on the recent research of polycaprolactone (PCL). Advanced materials research. 2016;1134:249-55.
8. Sanchez-Garcia M, Gimenez E, Lagaron J. Morphology and barrier properties of solvent cast composites of thermoplastic biopolymers and purified cellulose fibers. Carbohydrate Polymers. 2008;71(2):235-44.
9. Tan B, Thomas NL. A review of the water barrier properties of polymer/clay and polymer/graphene nanocomposites. Journal of Membrane Science. 2016;514:595-612.
10. Tsai M-H, Chang C-J, Lu H-H, Liao Y-F, Tseng I-H. Properties of magnetron-sputtered moisture barrier layer on transparent polyimide/graphene nanocomposite film. Thin Solid Films. 2013;544:324-30.

  doi:10.5075/epfl-298799_978-2-9701614-0-0

CONTROLLING ELECTRICAL PERCOLATION IN THERMOPLASTIC COMPOSITES THROUGH INFORMED SELECTION OF FILLERS

Kailing Lin[a,b], Yubao Deng[a,b], William Sampson[a], Mark Bissett[a], Ian Kinloch[a]

a: National Graphene Institute, Henry Royce Institute and Department of Materials, School of Natural Sciences, The University of Manchester, Manchester M13 9PL, U.K
Email address: Kailing.lin@postgrad.manchester.ac.uk
b: Dutch Polymer Institute, P.O. Box 902, 5600 AX Eindhoven, The Netherlands

Abstract: *Carbonaceous nanofillers, such as graphene, carbon nanotube (CNT) and carbon black (CB), have been proved to be excellent candidates for conductive polymer composites recently due to their low density, high electrical conductivity, and good mechanical. These three types of carbon nanofiller were used to fabrication polycarbonate composites to study the effect of filler morphology and orientation in the composites. Conductive AFM was applied to study the conductive network formed in the composites. It is found that the better dispersion of CNT and CB lead to more effective conductive network thus resulting in higher conductivity while agglomeration of GNP due to flake-flake interaction results in poor electrical connection among fillers. Moreover, orientation of CNT in injection moulding was found and result in reduction of filler connection thus decreasing the conductivity.*

Keywords: Polymer composites; nano carbon fillers; electrical performance; conductive atom force microscopy

1. Introduction

Compared with conventional conductive material like metal and intrinsic conductive polymer, conductive polymer composites (CPC) possess the advantages of tuneable conductivity by varying loading of conductive filler, anti-corrosion, ease of fabrication, low cost and flexibility. (1) Consequently, CPCs have been attracted enormous academic and industry interest and have a wide range of applications, such as antistatic material used in fuel tank, electromagnetic interference shielding, conductors and sensors. Carbonaceous nanofillers, such as graphene, carbon nanotube (CNT) and carbon black (CB), have been proved to be excellent candidates for CPC recently due to their low density, high electrical conductivity, and good mechanical properties combining with ease of recycling. Lots of reports in literature have shown that incorporation of graphene, CNT and CB improved electrical properties of polymer greatly. (2-5) However, the relationship between filler structure and electrical properties of composites has not been studied sufficiently yet. Conductive atom force microscopy, which can simultaneously measure the topography of sample and the electric current flow through the tip of conductive cantilever and sample surface, can visualize the conductive network formed in the composites thus can help to build the relationship among filler morphology – filler network – properties of composites.(6-9)

In this work, CB, CNT and graphene reinforced polycarbonate composites were fabricated by melt mixing and were hot press for further study. The effect of filler morphology, status of filler dispersion on the formation of conductive network in composites have been studied with the hot press samples. On the other hand, CNT composites were also injection moulded to study the

  doi:10.5075/epfl-298799_978-2-9701614-0-0

effect of filler orientation on conductive network and electrical conductivity. Overall, this work aimed to build up the relationship of filler morphology / processing method – filler network – electrical properties of composites.

2. Materials and methods

2.1 Materials

Polycarbonate were achieved from Sabic, grade 172, with melt volume flow rate of 26 cm^3/10min (300℃ / 1.2kg). The graphene nanoplatelets (GNP) were purchased from XG Sciences Inc. Lansing, Michigan, USA, and used as received. Carbon black were received from Nouryon, which was grade EC 600JD. Carbon nanotube were purchased from Nanocyl, which was grade 7000. Detail comparison of these three types of fillers were showed in Table 1.

Table 1. Comparison of dimensions of carbon nanofillers.

	CB 600JD	C750 GNP		MWCNT Nanocyl 7000	
Size	Average diameter(nm)	Flake length(μm)	Thickness (nm)	Average diameter (nm)	Average length (μm)
	47 ± 6[a]	2[b]	<2[b]	9.5[b]	1.5[b]
BET surface area (m^2/g)	1266[a]	120-150[b]		250-300[b]	
Density g/cm^3	2.25[b]	2.2[b]		1.7~1.9[b]	

[a] value obtained from experiment; [b] value from supplier.

2.2 Composites Fabrication

Melt mixing

Masterbatch of C750 GNP / CB 600JD / CNT 7000 composites with polycarbonate were fabricated by melt mixing with co-twin extruder (HAKKE Rheomex PTW 16/25 OS). Loadings of filler were 15, 10, 8wt% respectively for GNP, CB and CNT which were limited by the extruder. The extrusion temperature was 280℃. Carbon nanofillers and polycarbonate matrix were fed into extruder by gravimetric and volumetric feeder respectively. The extruded strand went through water bath to solidify and was chopped into pellets by pelletizer. Actual filler contents in the masterbatch were confirmed by thermogravimetric analysis, which were 9.79±0.15wt%, 14.96±0.57wt% and 7.58±0.64wt% for CB, GNP and CNT respectively.

Composites with GNP, CB and CNT at different loadings were fabricated by diluting the masterbatch with pure polycarbonate. The same temperature and extruder used in fabrication of masterbatch were also used in the dilution procedure. Speed of screws were set to be 20 rpm. Loadings were set to be 0.5, 1, 2, 4, 5, 6, 8, 10, 12wt%.

Compression moulding

The composites pellets were moulded into slabs of sizes of 10cm ×10cm×1mm by hot press at 280℃. The slabs were then cut into pieces of sizes of 10mm × 10mm × 1mm for electrical properties characterization.

2.3 Characterization

The impedance of composites were tested on 10mm ×10mm x 1mm solid specimens. All impedances were tested using a PSM 1735 Frequency Response Analyzer from Newtons4th Ltd connected with Impedance Analysis Interface (IAI) at the range of frequencies from 1 to 10^6Hz. The specific conductivities (σ) of the materials were calculated from the measured impedances using:

$$\sigma(\omega) = |Y^*(\omega)|\frac{t}{A} = \frac{1}{Z^*} \times \frac{t}{A} \quad (1)$$

where Y*(ω) is the complex admittance, Z* is the complex impedance, t and A are the thickness and cross section area of the sample, respectively.

The specific surface area was determined by N2 adsorption at 77 K with BET (Brunauer, Emmett and Teller) method using Quadrasorb EVO surface area and pore size analyser.

The morphology of composites were analysed using a transmission electron microscope (TEM) FEI Tecnai G2 20 (LaB6) operated at an acceleration voltage of 200 kV. For this, thin sections with a thickness of 80 nm were prepared using a diamond knife mounted on an ultramicrotome. The cuts were performed at room temperature in direction perpendicular to press direction in the middle of the samples.

Atomic force microscopy (AFM) and conductive AFM were performed using a JPK NanoWizard 4 XP NanoScience atomic microscope equipped with a conductive AFM module. The images were recorded using a Pt−Ir coated silicon probe (PPP-EFM, Nanosensor).

3. Result and Discussion

3.1 Effect of filler morphology on conductive network

Three types of carbon nanofillers of different dimensionality were chosen to study the effects of filler morphology on electrical conductivity of composites. Carbon blacks were considered as 0 dimension fillers; carbon nanotubes were considered as 1D fillers; graphene nanoplatelets (GNP) were considered as 2D fillers. The morphology of the as chosen fillers and their dispersion in composites were investigated by TEM as shown in Figure 1. GNP flakes are tend to form agglomerates in the composite which might result from the $\pi - \pi$ interaction between flakes. Also the GNP agglomerates seem to isolate from each other which might reduce the connection among fillers. On the other hand, CBs and CNTs distribute more evenly in the composites than GNP with less large agglomerates can be found. CBs form chain-like network in the composites while CNT form web-like network.

  doi:10.5075/epfl-298799_978-2-9701614-0-0

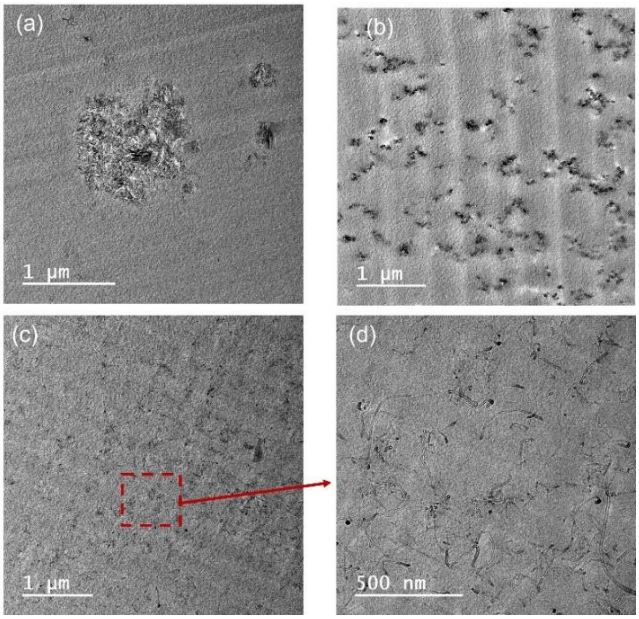

Figure 1. TEM images of C750 GNP composites (a); CB composites (b); CNT composites with different magnifications (c) and (d); all the composites at loading of 4wt%.

Conductive AFM image can collect the topography and current image from sample surface simultaneously and thus the morphology of filler network and conductive network can be compared as shown in Figure 2. The topography images (Figure 2.(a, b, c)) of CB, CNT and GNP composites are consistent with the result from TEM image that CB and CNT disperse evenly in the composites while GNPs form agglomerates. As for the current mapping in Figure 2.(d, e, f), the conductive area (brighter area in the image) in CB and CNT composites is similar to the network observed in topography image and TEM which indicated n effective network formed in the composites. However, no conductive area can be found in the current mapping of GNP composite and the current flow through the sample surface are two orders of magnitude lower than that of CB and CNT which reveals that no effective conductive network forms in the composites due to the agglomeration of GNP fillers.

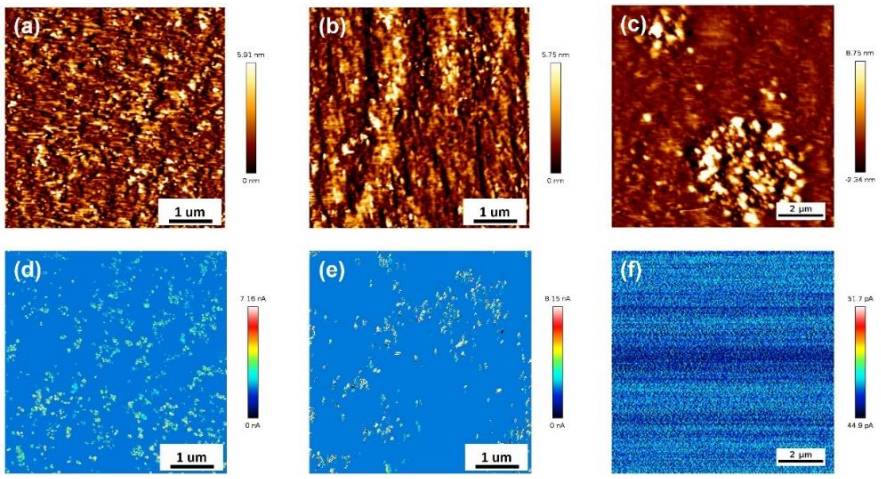

Figure 2. Topography (top) and current (bottom) image of 4wt% CB composite (a, d); 4wt% CNT composite (b, e); 4wt% GNP composite (c, f) obtained from conductive AFM.

The bulk electrical conductivity of these three types of composites were measured and compared with various fillers loading. At filler loading of 4wt%, CNT composite shows the highest conductivity while the conductivity of CB composite is slightly lower that CNT composite. Moreover, the conductivity of GNP composites at 4wt% is much lower than the other two composite, which can be considered insulating. This result corresponds to the current mapping that better dispersion of CB and CNT results in effective filler network for electron conduction thus leading to higher conductivity while the agglomeration of GNPs results in poor connection among fillers and no conductive network can be formed.

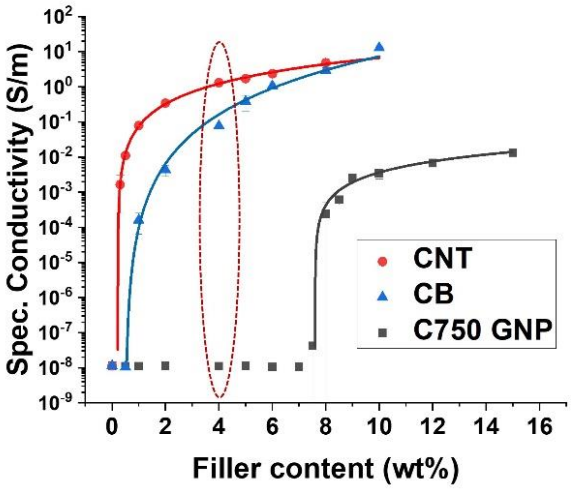

Figure 3. Semi-log plot of conductivity as a function of weight fraction for CB, CNT and GNP composites at frequency of 1Hz. The solid line were fitting from percolation theory equation.(10)

3.2 Effect of injection moulding on the micro and macro conductivity of composites

Previous work in the Advance Nanomaterials Group in the University of Manchester has found that the shear force induced in injection moulding can lead to orientation of filler in the side region in injected samples while the fillers in the core region remain random orientation due to the low shear force in the core region (11). The extruded CNT composites were further injection moulded to study the effects of filler orientation on filler network formation and electrical conductivity. The TEM images (Figure 5. (b, e)) shows that in the side region where the high shear force was generated, CNTs tend to orientated to a certain direction while fillers in the core region show a more random orientation. The orientation distribution of filler can be obtained by analysis of TEM images.

  doi:10.5075/epfl-298799_978-2-9701614-0-0

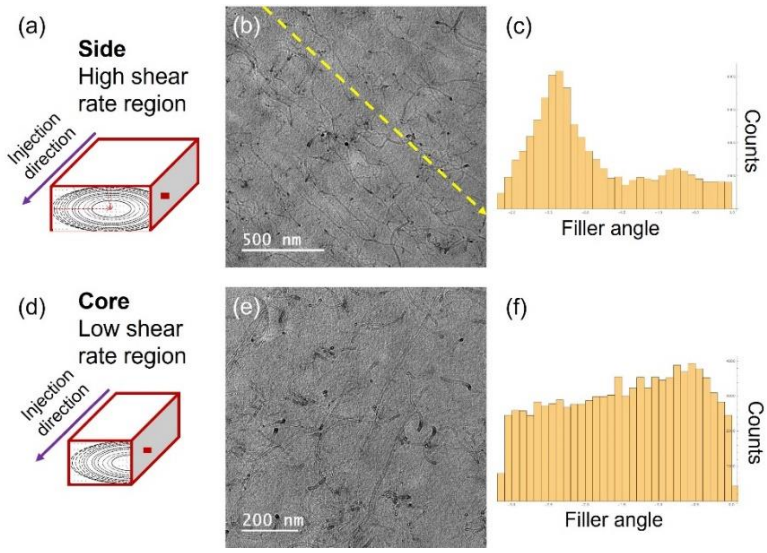

Figure 5. Schematic of TEM sample cutting from the side (a) and core (d) region parallel to injection direction; TEM image of 4wt% CNT composites from the side (b) and core (e) region; orientation distribution of filler from TEM image analysis.

Conductive AFM was applied to analysis the distribution of filler in the injection moulded 4wt% CNT composites. The conductive area in the side region is shaped like bundles of "noodles" which represent the orientated CNTs form the conductive network in a particular direction. Moreover, in the core region, the conductive area is distributed randomly in the composite which consistent with the random orientation of filler in the core region. The calculation of ratio of conductive area as well as the resistance also reveal the effect of orientation with lower resistance and higher conductive area ratio in the core region. This indicates that the orientation of filler reduce the connection thus increasing resistance.

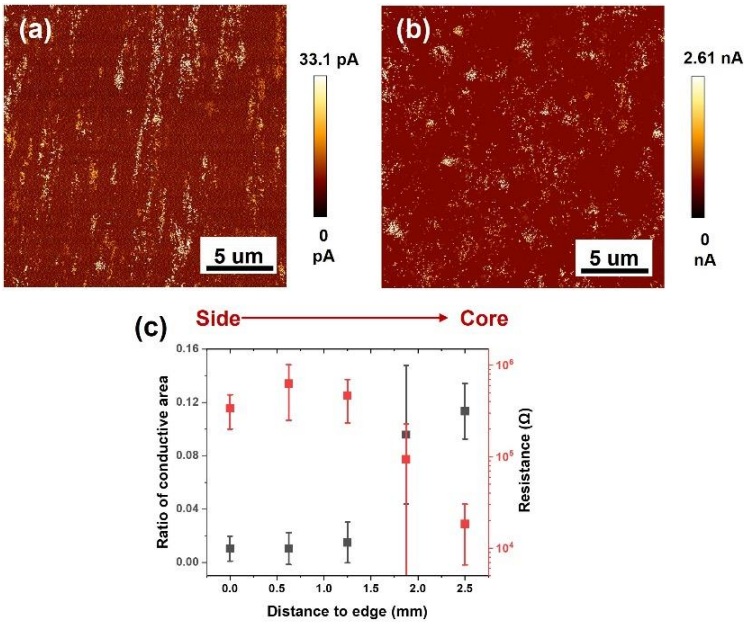

Figure 6. Current image of 4wt% CNT composites from side region (a) and core (b) region; ratio of conductive area and resistance calculated from CAFM images verse various distance to the sample edge (c).

  doi:10.5075/epfl-298799_978-2-9701614-0-0

The electrical conductivity of bulk composites was measured in two directions which were perpendicular and parallel to the injection direction as shown in Figure 7.(a). Conductivity in perpendicular direction is lower than that in the parallel direction at all loadings. Electron conduction in perpendicular direction is dominated by the side region in the composites while the conduction in parallel direction is dominated by the core region, which causes the difference of conductivity in the two directions.

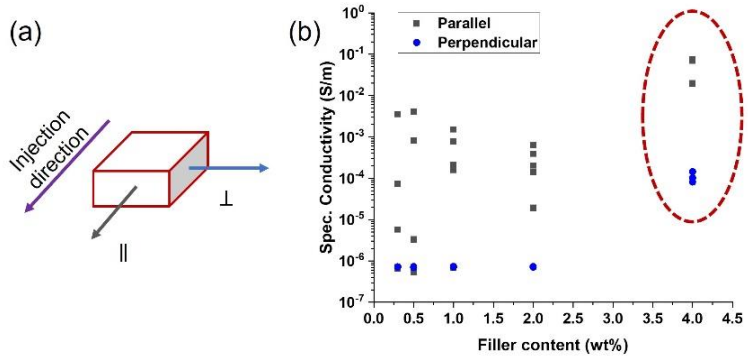

Figure 7. (a) Schematic of direction of conductivity measurement; (b) Semi-log plot of conductivity as a function of weight fraction for injection moulded CNT composites at frequency of 1Hz.

4. Conclusion

Three types of fillers, CB, CNT and GNP were melt mixing with polycarbonate to fabricate conductive polymer composites in order to study effect of filler morphology on conductivity. For the hot press composites, good dispersion of CB and CNT were confirmed with TEM and topography image while large agglomerates of GNP can be found, which leads to more efficient conductive network in CB and CNT and can be confirmed by the CAFM current mapping. Consequently, conductivity of CB and CNT composites are higher than GNP composites.

For the injection moulded CNT composite, orientation of filler can be found which also leads to orientation of conductive area. The orientation of filler reduces the connection of fillers thus resulting in lower conductivity in the composites.

Acknowledgements

This research forms part of the research program of Dutch Polymer Institute (DPI), PP 2.0 project #819.

5. References

1. Choi H-J, Kim MS, Ahn D, Yeo SY, Lee S. Electrical percolation threshold of carbon black in a polymer matrix and its application to antistatic fibre. Scientific Reports. 2019;9(1).
2. Zhang Q, Wang J, Zhang B-Y, Guo B-H, Yu J, Guo Z-X. Improved electrical conductivity of polymer/carbon black composites by simultaneous dispersion and interaction-induced network assembly. Composites Science and Technology. 2019;179:106-14.

3. Bauhofer W, Kovacs JZ. A review and analysis of electrical percolation in carbon nanotube polymer composites. Composites Science and Technology. 2009;69(10):1486-98.
4. Socher R, Krause B, Hermasch S, Wursche R, Pötschke P. Electrical and thermal properties of polyamide 12 composites with hybrid fillers systems of multiwalled carbon nanotubes and carbon black. Composites Science and Technology. 2011;71(8):1053-9.
5. Qu M, Nilsson F, Schubert DW. Novel definition of the synergistic effect between carbon nanotubes and carbon black for electrical conductivity. Nanotechnology. 2019;30(24):245703.
6. Trionfi A, Wang DH, Jacobs JD, Tan LS, Vaia RA, Hsu JW. Direct measurement of the percolation probability in carbon nanofiber-polyimide nanocomposites. Phys Rev Lett. 2009;102(11):116601.
7. Alexeev A, Loos J, Koetse MM. Nanoscale electrical characterization of semiconducting polymer blends by conductive atomic force microscopy (C-AFM). Ultramicroscopy. 2006;106(3):191-9.
8. Viswanathan R, Heaney MB. Direct imaging of the percolation network in a three-dimensional disordered conductor-insulator composite. Phys Rev Lett. 1995;75(24):4433-6.
9. Ozhukil Kollath V, Arjmand M, Egberts P, Sundararaj U, Karan K. Quantitative analysis of nanoscale electrical properties of CNT/PVDF nanocomposites by current sensing AFM. RSC Advances. 2017;7(52):32564-73.
10. Essam JW. Percolation theory. Reports on progress in physics. 1980;43(7):833.
11. Liu M, Papageorgiou DG, Li S, Lin K, Kinloch IA, Young RJ. Micromechanics of reinforcement of a graphene-based thermoplastic elastomer nanocomposite. Composites Part A: Applied Science and Manufacturing. 2018;110:84-92.

  doi:10.5075/epfl-298799_978-2-9701614-0-0

MACROSCALE MAGNETIC ALIGNMENT OF MULTIPLE DISCONTINUOUS FERROMAGNETIC FIBRES IN A POLYMER MATRIX

Cédric, De Schryver[a], Dries, Vanoost[b], Bart, Buffel[a], Davy, Pissoort[b],

Frederik, Desplentere[a]

a: Department of Materials Engineering, ProPoliS Research Group, KU Leuven Bruges Campus, Spoorwegstraat 12, 8200 Bruges, Belgium
Email: cedric.deschryver@kuleuven.be
b: Department of Electrical Engineering, M-Group (Mechatronics Group), KU Leuven Bruges Campus, Spoorwegstraat 12, 8200 Bruges, Belgium

Abstract: *The mechanical properties of a discontinuous fiber composite depend on the properties of the individual components and the orientation of the fibers with respect to the loading direction. The smaller the misalignment angle between fiber and load orientation, the higher the strength and stiffness of the composite. In this paper, discontinuous steel fibers are dispersed in non-reactive polydimethylsiloxane (PDMS). The fiber alignment is performed by magnetic manipulation using static magnetic fields. Video and image analyses are carried out to calculate the fiber realignment. The influence of parameters like the matrix viscosity, the fiber volume fraction and the magnetic field strength are discussed. The average fiber orientation angle is calculated as a function of time, for different parameter sets.*

Keywords: Magnetics; Polydimethylsiloxane; Ferromagnetic Fibers; Optical Microscopy; Fiber Orientation

1. Introduction

In the last decades, discontinuous fiber-filled composites have been widely used to replace comparable products in steel or aluminum. Between 1960 and 2004, the United States' market for composites increased by a factor of 16, while steel consumption doubled during the same period [1]. Especially in high-demanding industries (e.g. the automotive and aerospace industry), composite components are more frequently used. The mechanical properties of a discontinuous fiber composite depend on several factors. Besides the properties of the individual components (matrix and dispersed phase), the fiber volume fraction, the fiber length distribution, the fiber-matrix adhesive properties and the fiber orientation distribution play an important role [2]. Fu and Lauke [3,4] showed that the composite's elastic modulus strongly depends on the mean fiber orientation angle relative to the load direction. Any deviation in fiber orientation from this direction leads to a decrease in composite stiffness. For higher fiber volume fractions, it is also seen that the decline of the elastic modulus becomes more pronounced.

When discontinuous fiber composites are processed with commonly known processing techniques (e.g. injection molding or extrusion), the formation of the fiber structure is primarily controlled by the processing parameters, rheological characteristics of the matrix-fiber blend and geometry of the part. It is often impossible to change the dispersed phase's morphology without affecting other predetermined part specifications. Many techniques have been tried to change the structures in a non-invasive way. The technique of fiber manipulation employing

  doi:10.5075/epfl-298799_978-2-9701614-0-0

magnetic field interaction has been a popular choice in many fields of study over the last decades. The advantages of magnetic manipulations have introduced this method to many domains. For instance, in injection molding, the integration of permanent magnets [5,6] and electromagnets [7,8] inside the mold improved structural and magnetic properties for the injected composite. This technique applies the magnetic field during the injection phase, when the polymer viscosity is low at high temperatures and high shear forces. This low viscosity allows the dispersed phase to realign before the solidification of the matrix occurs. Further studies [9,10] on the magnetic alignment of filler materials in shear flow and in the presence of a perpendicular applied external field discuss the dynamics of the realignment process. During the process, a magnetic fiber torque, which is a function of the applied magnetic field intensity and fiber properties, is countered by a viscous torque caused by the fluid viscosity. The alignment rate is influenced by the applied magnetic field, material parameters of the fibrous phase, and the fluid viscosity.

This paper discusses the results from experiments with steel fibers dispersed in a polydimethylsiloxane (PDMS). In Section 2, the different materials and setup are explained. Section 3 reports the test methodology and results with varying parameters of process. The conclusions end the paper in Section 4.

2. Experiments

2.1 Materials

Ferromagnetic fibers (FeCrAl alloy) were obtained in continuous bundles from Bekaert NV in Belgium. These bundles were manually cut into discontinuous fibers with a length of 1 mm. Non-curable polydimethylsiloxanes (also referred to as silicone oils) from Wacker were used as the matrix material. These materials are transparent and retain their liquid properties in ambient conditions, making them excellent for optical microscopy. Two different viscosities were chosen for the tests: 10 Pa·s and 100 Pa·s. The fibers were manually dispersed in the fluid and stirred to obtain a random orientation at the start of the experiment. The samples were degassed in a low vacuum (± 200 – 300 mbar) to avoid air bubbles from interfering with the fibers during the alignment process.

2.2 Setup

The experiments were conducted on a lab-scale setup. This setup consists of an aluminum block with a small cavity. The cavity holds additively manufactured plastic cups for the fluid mixtures. Two handmade electromagnets are used to create a unidirectional static magnetic field. The coils consist of an iron core and are mounted on a soft iron block. The magnetic field strength varies with the applied current, which is provided by a Keysight E36313A power supply. The magnetic field strength was also verified with a Phywe digital Teslameter. Videos of the process were made with a Motic Moticam 3.0 USB camera mounted on an optical microscope. Videos and images were analyzed using open-source Kinovea software (version 0.8.15) and the Image Processing Toolbox in MathWorks MATLAB (version R2019b). Figure 1 (left) shows an image of the setup, with the electromagnets installed and a 3D-printed cup for the mixtures. Figure 1 (right) shows a schematic representation of a fiber in a static magnetic field $\vec{H}_0$. A fiber that is oriented perpendicular to the magnetic field direction, is indicated by an orientation angle of 0°.

  doi:10.5075/epfl-298799_978-2-9701614-0-0

After switching on the magnetic field, the fiber aligns parallel with the magnetic field, which is indicated by a 90° orientation angle.

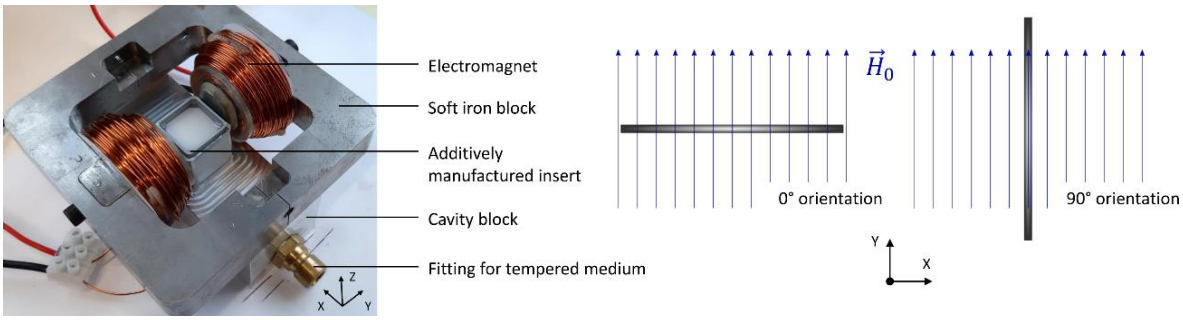

Figure 1. Lab scale setup with two electromagnets installed and a 3D-printed cup in the center (left). The chosen convention of orientation by magnetic realignment (right): a fiber perpendicular to the magnetic field direction (parallel to the x-axis) equals a 0° orientation. Fibers aligned with the magnetic field direction (parallel to the y-axis) equal a 90° orientation.

3. Results

An automated MATLAB script was developed to process the images from the experimental tests. At every time step, an average of 140 different fibers were evaluated. Figure 2 shows an example of a test using a silicone oil of 100 Pa·s. The magnetic field strength was 47.7 x 10^3 A/m. The fiber length was 1 mm and the fiber thickness 35 µm. The fiber volume fraction was 0.14 % (or 1 % of fibers by mass). This is low compared to conventional discontinuous fiber filled composite structures, which can have a maximum fiber volume fraction in the range of 40 – 45 % (to guarantee the practical processing with general equipment [2]). Keeping the fiber volume fraction low during the tests, facilitates the fiber response and clustering of fibers. The mean in-plane fiber orientation angle at the start was 38.1° (standard deviation: ± 25.6°), which equals a random orientation (see Figure 2 – A). After five seconds, the mean orientation angle was 86.8° (standard deviation: ± 3.1°) (see Figure 2 – B), with most fibers oriented parallel to the magnetic field direction. From Figure 2 – A, it is observed that some of the fibers in the mixture tend to cluster (indicated with yellow arrows).

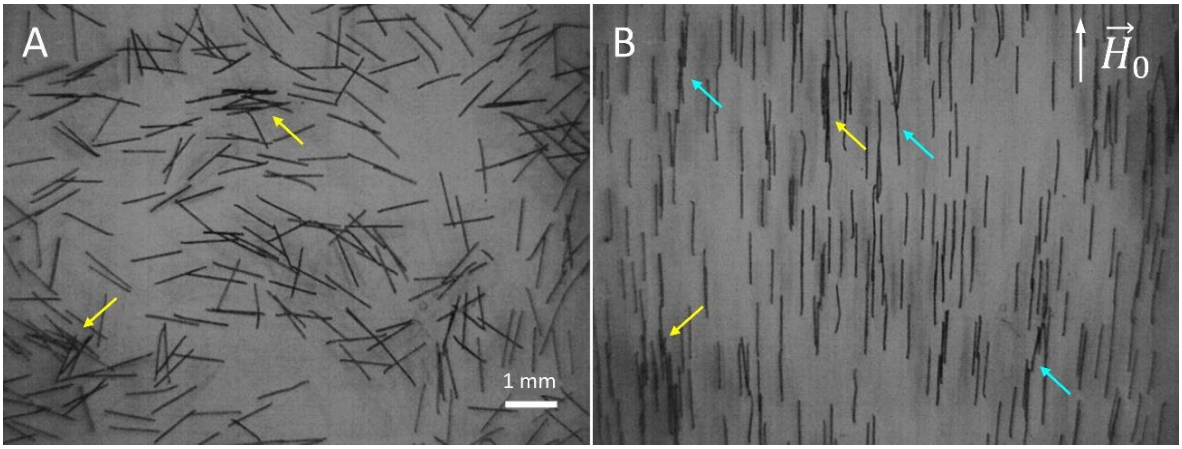

Figure 2. Example of the magnetic alignment of ferromagnetic fibers in a silicone fluid of 100 Pa·s. The magnetic field strength was 47.7 x 10^3 A/m. The fiber length was 1 mm and the fiber thickness 35 µm. The fiber volume fraction was 0.14 %. Fiber clusters are indicated with yellow arrows. Blue arrows indicate misalignment caused by fiber network formation and clustering.

  doi:10.5075/epfl-298799_978-2-9701614-0-0

This is caused by remanent magnetism inside the ferromagnetic material. Additional friction due to the rough fiber surfaces may increase the amount of initial fiber contact. After initiation of the magnetic field, the clusters of closely positioned fibers are aligned parallel to the magnetic field direction. The close contact remains after the magnetization, despite the rapid motion and the new in-plane orientation of every fiber.

The mean fiber orientation angle was calculated in MATLAB. Overlapping fibers were detected and every image was checked for double-counted fibers. The experimental results from the tests are displayed in Figure 3. The mean fiber orientation angle as a function of time is plotted, together with the error bars indicating the standard deviation.

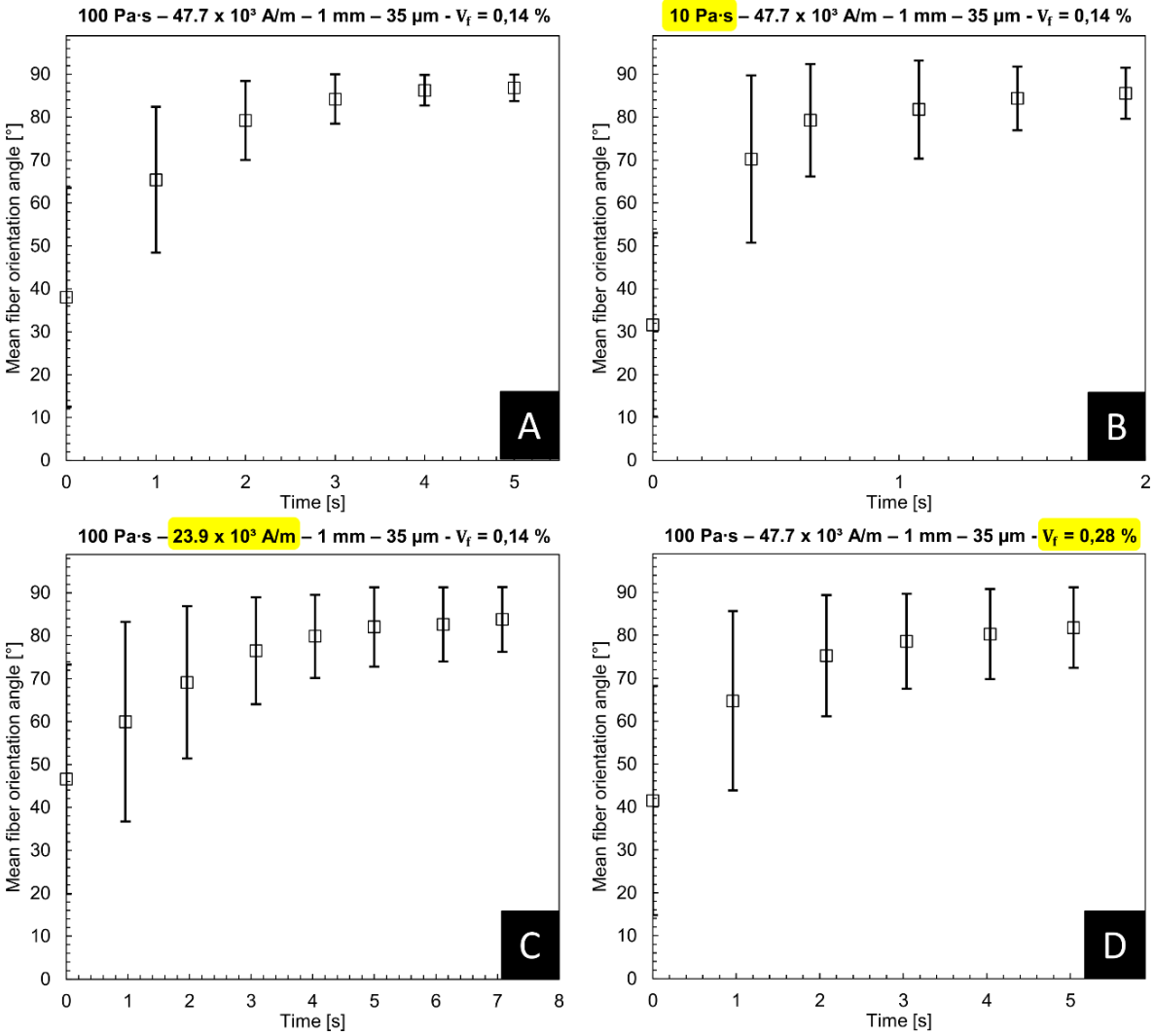

Figure 3. Experimental results showing the mean fiber orientation angle (with standard deviation error bars) as a function of time. The test conditions are shown above each graph. Figure 3(A) shows the results with the same parameters as explained in Figure 2. Parameters highlighted in yellow have been changed from the test conditions in Figure 3(A). In Figure 3(B), the matrix viscosity was changed to 10 Pa·s. In Figure 3(C), the magnetic field strength was decreased to 23.9 x 10³ A/m. In Figure 3(D), the fiber volume fraction was doubled to 0.28 %.

Figure 3 – A shows the results from the test as explained in Figure 2. From the video analysis, it is shown that the angular reorientation is the predominant motion at the start of the

  doi:10.5075/epfl-298799_978-2-9701614-0-0

experiment. This realignment is initiated by the misalignment angle between the primary axis of the fiber and the magnetic field direction. In this phase, mutual fiber interaction occurs as well as network formation between adjacent magnetized fibers. When the fibers are aligned parallel to the magnetic field direction, a translational fiber motion is observed. This is due to the position of each fiber relative to the solenoids and the magnetic attraction towards them. The translational movement initiates more network formation as a function of time.

In Figure 3 – A, the mean orientation angle after 5 seconds is 86.8°. A lot of fibers were able to move freely, resulting in a high mean orientation angle for the sample, with a low standard deviation. Additional realignment was hindered due to fiber clustering. This is indicated in Figure 2 – B with blue arrows. In Figure 3 – B, the matrix viscosity was lowered to 10 Pa·s. This implies that the viscous torque on the fiber is lower, resulting in a faster alignment response. A mean orientation angle of 84.4° (± 8°) was achieved in 1.92 seconds. The standard deviation is higher compared to the test results in Figure 3 – A. This is due to the higher amount of clustering caused by the lower viscous torque which also causes increased translational fiber movement. The result of the test is displayed in Figure 4 – B.

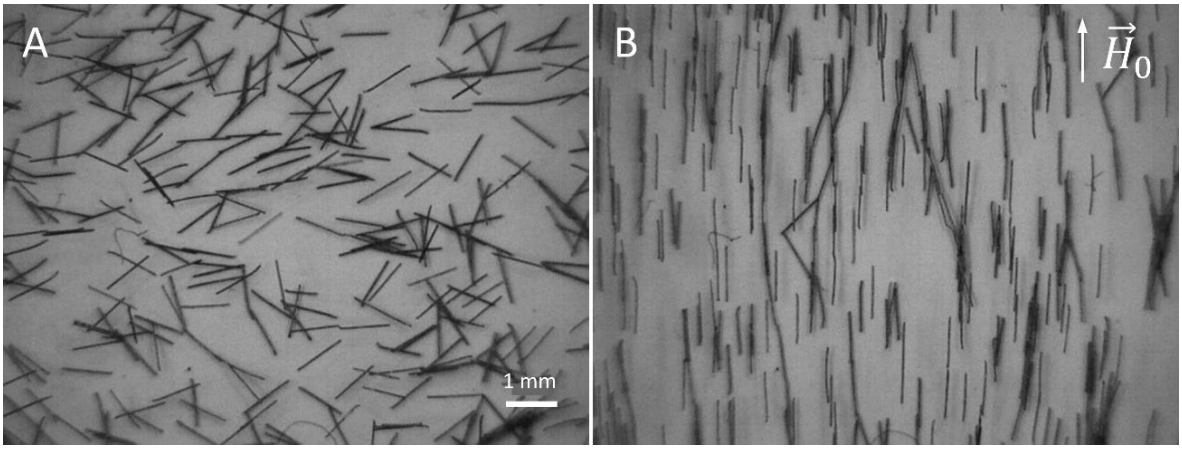

Figure 4. Magnetic alignment of fibers in a silicone fluid with a viscosity of 10 Pa·s (A). The magnetic field strength was 47.7 x 10³ A/m. The fiber length was 1 mm and the fiber thickness 35 µm. The fiber volume fraction was 0.14 %. Clustering of fibers due to the low viscosity after 1.92 s (B).

In Figure 3 – C, the magnetic field strength was decreased by a factor of 2. Although the matrix viscosity was constant compared to the test in Figure 3 – A, the lower magnetic torque causes the fibers to rotate slower. A mean orientation angle of 83.8° (± 7.5°) was noted in 7.08 seconds. The slower rate of fiber alignment also gives the fibers the opportunity to attract adjacent magnetized fibers, resulting in a higher amount of fiber interaction and overall higher standard deviation. Finally in Figure 3 – D, the amount of fibers was doubled, leading to a faster response compared to the results in Figure 3 – C. Due to the higher fiber volume fraction, the number of evaluated fibers was also higher. On average 280 fibers were taken into account during the orientation angle assessment. An overall mean orientation angle of 81.8° (± 9.4°) was found in 5.04 seconds.

  doi:10.5075/epfl-298799_978-2-9701614-0-0

4. Conclusion

The magnetic fiber reorientation process for discontinuous ferromagnetic fibers dispersed in silicone oils was studied. Different parameters in the process were varied to asses the fiber alignment response. Every test started with a random fiber orientation. The results showed that for every test, an overall mean orientation angle of > 80° was achieved. This corresponds to a structure in which the majority of the fibers are aligned according to the magnetic field direction. By decreasing the matrix viscosity, the viscous torque on the fiber's solid body also decreases, resulting in a higher rate of fiber alignment. Besides the viscous forces, the magnetic torque, induced by the magnetic field strength, influences the process. The limiting factor in achieving a perfect alignment relative to the magnetic field direction, was the amount of fiber-fiber interaction. The attraction between adjacent magnetized fibers leads to fiber clustering which hinders the structure from further alignment.

Acknowledgements

The authors would like to thank IMCD Benelux for providing the PDMS silicone oils. The authors would also like to thank Bekaert Fiber Technologies for providing the continuous steel fiber bundles and sharing their knowledge on this topic.

5. References

1. Agarwal BD, Broutman LJ, Chandrashekhara K. Analysis and Performance of Fiber Composites. Wiley; 2006. 576 p.
2. Fu S-Y, Lauke B. Science and engineering of short fibre reinforced polymer composites. 2009. 364 p.
3. Fu S-Y, Lauke B. The elastic modulus of misaligned short-fiber-reinforced polymers. Compos Sci Technol. 1998;58(3–4):389–400.
4. Fu S-Y, Lauke B. An analytical characterization of the anisotropy of the elastic modulus of misaligned short-fiber-reinforced polymers. Compos Sci Technol. 1998;58(12):1961–72.
5. Chung C, Chen S, Lin K. Effect of Magnetic Field on the Fiber Orientation during the Filling Process in Injection Molding , Part 1 : Simulation and Mold Design. 2018;(October).
6. Chen S, Chung C, Tseng Y. Effect of Magnetic Field on the Fiber Orientation during the Filling Process in Injection Molding , Part 2 : Experiments and Electrical Conductivity Measurements. Mater Sci Forum. 2018;936(October):136–41.
7. Volpe V, Auria MD, Sorrentino L, Davino D, Pantani R. Injection molding of magneto-sensitive polymer composites. Mater Today Commun [Internet]. 2018;15(March):280–7. Available from: https://doi.org/10.1016/j.mtcomm.2018.03.016
8. Gardocki A, Drummer D. Improvement of the filler orientability during injection molding of multi-polar SmCo-magnets by premagnetization. 2012 2nd Int Electr Drives Prod Conf EDPC 2012 - Proc. 2012;1–5.
9. Gómez-Ramírez A, Kuzhir P, López-López MT, Bossis G, Meunier A, Durán JDG. Steady shear flow of magnetic fiber suspensions: Theory and comparison with experiments. J Rheol (N Y N Y). 2011;55(1):43–67.
10. Martin JJ, Riederer MS, Krebs D, Erb RM. Understanding and overcoming shear alignment of fibers during extrusion. Soft Matter. 2015;11:400–5.

  doi:10.5075/epfl-298799_978-2-9701614-0-0

LASER-INDUCED GRAPHENE CARBON FIBER REINFORCED COMPOSITES FOR MULTIFUNCTIONALITY

Despoina I. Batsouli[a], Aspasia Antonelou[b], Grigorios Koutsoukis[a], Athanasios Baltopoulos[a], Stavros Tsantzalis[c], Vassilis Kostopoulos[c], Spyros N. Yannopoulos[b] & Antonios Vavouliotis[a]

a: Adamant Composites Ltd., Aghias Lavras and Stadiou St., GR-26504, Rio Patras, Greece - batsouli@adamant-composites.com
b: Foundation for Research and Technology – Hellas, Institute of Chemical Engineering Sciences (FORTH/ICE–HT), P.O. Box 1414, GR-26504, Rio-Patras, Greece
c: Department of Mechanical Engineering and Aeronautics, University of Patras, 26500 Rio, Patras, Greece

Abstract: *A novel method for graphene deposition on carbon-fiber-reinforced composites (CFRPs) via an industrially relevant process was established. The process consists of forming a graphene oxide (GO) layer onto the CF prepreg surface by spraying GO aqueous-dispersion, followed by laser-assisted GO reduction directly on prepreg to form conductive graphene at ambient conditions. Two composite plates, namely neat-reference and graphene-enabled, are manufactured to investigate their multifunctionality. The graphene film morphology and the quality of produced graphene are assessed with SEM and Raman spectroscopy. The electrical, thermal, and mechanical properties of the composites were also studied. The GO was successfully reduced with an energy flow 4J/m^2. The graphene film results in optimization of the CFRP properties yielding a 63%, 8% and 42% increase in flexural stress, thermal conductivity, and electrical conductivity, respectively. However, the mechanical interaction along the interlaminar region is influenced by the graphene presence and consequently the interlaminar properties are decreased.*

Keywords: Laser induced graphene; Smart materials; Carbon fiber reinforced composites; Multifunctional composites

1. Introduction

Graphene-enabled carbon fiber reinforced composites (CFRPs) have attracted significant interest from both industries and researchers due to their attractive attributes, such as enhanced engineering properties (mechanical, electronic, optical, thermal, and magnetic properties) [1-3]. A variety of methods have been employed for the synthesis and large volume production of graphene with relatively high crystalline quality. These methods include mechanical exfoliation, chemical exfoliation, epitaxial growth, pyrolysis, and chemical vapor deposition [4]. A frequently used approach adopts graphene oxide (GO) as the precursor to be reduced to graphene-like sheets by removing the oxygen-containing groups with the recovery of a conjugated structure by thermal, chemical, or electrical treatments. Laser irradiation is considered a very promising technique for the in-situ conversion of GO to reduced graphene oxide (rGO). This method eliminates the use of highly corrosive and toxic chemicals and avoids the requirement for high temperatures [5, 6].

In this work, water-based graphene oxide (GO) dispersion is sprayed on the surface of carbon fiber pre-impregnated fabric (prepreg). Laser-assisted reduction of GO takes place towards the

  doi:10.5075/epfl-298799_978-2-9701614-0-0

formation of conductive graphene directly on the surface of prepreg at ambient conditions [6]. The rGO film morphology and the quality of the produced graphene are assessed with scanning electron microscopy (SEM) and Raman spectroscopy. The purpose of this study is to simultaneously improve the properties of the composite and introduce multifunctionality. Therefore, two composite plates, namely neat-reference and treated, are manufactured to investigate comparatively their electrical, thermal, and mechanical properties. The results show that the graphene film results in optimization of the thermomechanical properties and provides thermal and electrical conductivity to carbon reinforced composites.

2. Experimental

2.1 Manufacturing of laser-assisted graphene carbon fiber reinforced composites

Commercial graphene oxide aqueous dispersion (Graphenea S.A., Spain) with a concentration of 4 mg/mL is used. GO is sprayed onto woven carbon fiber pre-impregnated fabric-prepreg (SHD Composites, UK) utilizing a roll-to-roll (R2R) spraying pilot line equipped with air atomizing nozzles (Spraying Systems Co.). The spraying process was performed with a spraying air pressure of 2.1 bar and a spraying liquid pressure of 1.5 bar, and the GO coating was dried at 60 ^{o}C for 10 min in the pilot line heating zone. The thickness of the GO layers was estimated to be within 500 and 700 nm, measured with a stylus profilometer (Ambios XP-1). For the reduction of GO, the R2R laser pilot line equipped with a laser StarPulse 150 System (COHERENT, laser power 40 W, wavelength 1064 nm) is employed. The laser beam is directed and focused onto the substrate with the aid of a galvo mirror system. The laser-assisted GO reduction was performed with single pulse irradiation, using a wide focusing spot (~8 mm), fluence in the range 4-6 J/cm^2 and pulse length duration 1-2 ms. The whole process took place at ambient conditions. Due to the Gaussian beam profile, overlapping steps comparable to the radius of the focused spot were used to ensure homogeneous irradiation.

To produce CFRP laminates (neat-reference and graphene-enabled), sheets were cut from the neat prepreg and graphene-enabled prepreg, respectively. A total of 6 laminates (200 x 200 mm^2) consisting of 6 plies prepreg sheets were manufactured for mechanical, thermal, and electrical tests. Additionally, 2 laminates (260 x 150 mm^2) consisting of 10 plies prepreg sheets and a polytetrafluoroethylene (PTFE) film were manufactured for Mode-I tests. The PTFE was placed in the middle plane of each laminate to generate the initial delaminated region according to the test standard. Following the lamination process, the plates were closed in a vacuum bag and then cured in an autoclave at 120 °C for 45 min under 6 bar of gauge pressure.

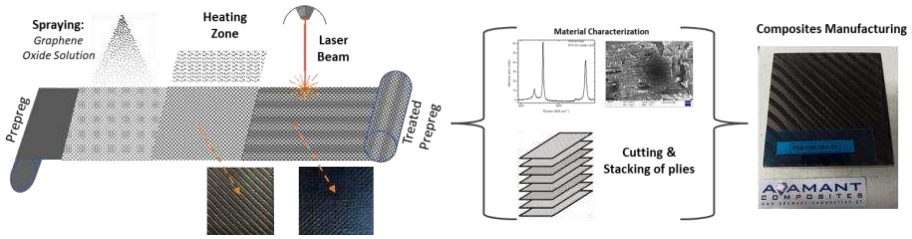

Figure 1. Manufacturing process for neat-reference and graphene-enabled CFRP laminates.

2.2 Characterization methods

A high-resolution field-emission scanning electron microscope (FE-SEM) instrument (Zeiss, SUPRA 35VP) operating at 15 kV was employed to record micrographs of the graphene-coated

  doi:10.5075/epfl-298799_978-2-9701614-0-0

substrates. Electron microscopy images were recorded from graphene-enabled prepreg, neat CFRP and graphene-enabled CFRP. Raman spectra was obtained with a Kimon He-Cd Laser apparatus at a laser excitation wavelength of 441.6 nm to investigate the graphene oxide reduction and CFRPs. The scattered light is analyzed by a LabRam HR800 (Jobin Yvon) micro-Raman spectrometer at a spectral resolution of about 2.0 cm^{-1}. A microscope objective with 50× magnification is used to focus the light onto a spot of about 3 μm in diameter.

Five specimens were cut according to the test standards from the manufactured plates for each testing. The glass transition temperature T_g and the storage modulus of the two CFRPs (neat and graphene-enabled) were specified by Dynamic Mechanical Analysis (DMA) measurements (DMA 50 Metravib). The measurements were conducted at 1 Hz from ambient room temperature to 250°C at a heating rate of 2°C/min. Three-point bending (3 PB) and Interlaminar Shear Strength (ILSS) tests were performed using an Instron 8872 servo-hydraulic testing machine in accordance with EN ISO 14125:1998 and ASTM D2344, respectively. The test speed of 3PB and ILSS tests was 1 mm/min. Double cantilever beam (DCB) tests were carried out to measure the opening Mode-I interlaminar fracture toughness energy (G_{IC}) according to the AITM 1.0005 standard. The DCB tests were performed in a servo-hydraulic test machine (Instron 8872) and the crosshead speed was set at 10 mm/min. The applied loading and the opening displacement of each specimen were recorded to measure the G_{IC}, while the location of the crack tip was tracked down in regular intervals and was recorded along with the load and the displacement at each measured crack extension. G_{IC} was calculated according to the following equation:

$$G_{IC} = \frac{A}{a+w} * 10^6 \quad (1)$$

where A = energy to achieve the total propagated crack length, α = propagated crack length, and w = specimen width.

Electrical measurements were performed using digital multimeter (Keysight) through four-wire resistance at room temperature. The electrical conductivity was calculated according to the following equation:

$$\sigma = \frac{l}{R*A} \quad (2)$$

where l = length of the specimen, R = electrical resistance of a uniform specimen of the material, and A = cross-sectional area of the specimen.

Measurements of thermal conductivity of the developed materials were performed by using a thermal conductivity analyzer (TCi Mathis). TCi Mathis Analyzer measures directly and rapidly the through thickness thermal conductivity of sample at room temperature, providing a detailed overview of its thermal characteristics. All measurements reported are the average of at least five specimens.

3. Results and discussions

3.1 Graphene oxide reduction

Based on the electron microscopy images (Figure 2), it is observed that the reduction of graphene was carried out evenly over the entire surface of the prepreg.

  doi:10.5075/epfl-298799_978-2-9701614-0-0

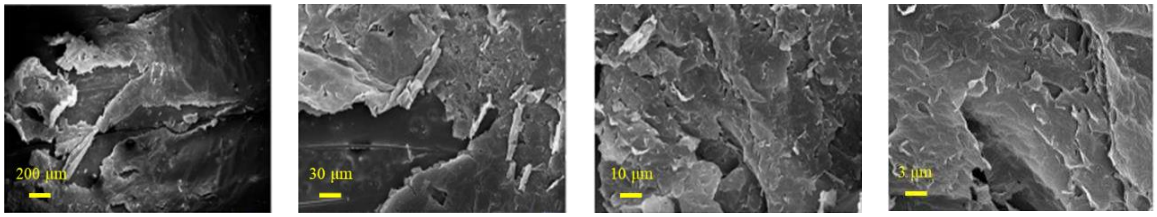

Figure 2. Scanning electron microscopy images, at different magnifications, of laser-assisted reduced GO on pre-impregnated carbon fiber fabric for energy flow 4 J/cm^2.

Raman spectroscopy was used to characterize the developed graphene layer produced and the extent of reduction of the GO. Various band parameters such as the relative intensity ratio of D, G and 2D bands (i.e. I^D / I^G, I^{2D} / I^G), the amplitude of the G band, the spectral shape of the 2D band and so on, are frequently employed as reliable indicators of the graphene quality, structure and sp^3 to sp^2 relative fraction. Figure 3 shows the Raman spectra of laser-assisted reduced GO on pre-impregnated carbon fiber fabric for energy flow of 4 J/cm^2 and 6 J/cm^2. For the irradiation conditions used the spectrum displays significant reduction of the GO. It is evident that laser irradiation results in several spectral changes. These include, appreciable decrease of the I^D/I^G ratio, narrowing of the D and G bands, and increase of the I^{2D}/I^G ratio.

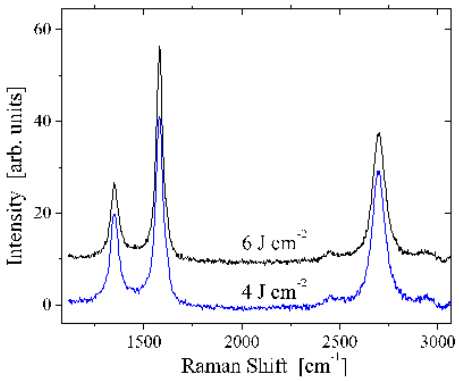

Figure 3. Typical Raman spectra of laser-assisted reduced GO on CF prepreg at ambient conditions for two different fluences.

3.2 Laser-assisted graphene carbon fiber reinforced composites

SEM observation was conducted to determine the surface morphology changes of CFRP produced with laser-assisted reduced GO prepregs. Figure 4 shows the SEM images for both neat and graphene-enabled composites. These images reveal the morphology of the cross section of the specimens. Specifically, Figures 4 (a) and (b) depict images of the neat CFPR, where the layering of the fibers with a different (vertical) orientation between them is observed at low magnification. At higher magnification the morphological characteristics of the fibers and parts of the resin which surrounds the fibers are observed. Figures 4 (c) and (d) present the graphene-enabled CFRP, where the interface between the prepreg layers contains rGO produced by laser irradiation. These images reveal that the presence of the laser-reduced GO, and possible laser transformation of the resin, modify the material volume at the interface, thus making the observation of the discrete carbon fibers less obvious than in the previous case (neat), as shown by the larger magnification image in Figure 4 (c). At higher magnifications the formation of a phase is observed whose morphological characteristics differ from the corresponding interface, without the presence of reduced graphene oxide. This morphology may be due to the mixing of

  doi:10.5075/epfl-298799_978-2-9701614-0-0

reduced graphene particles with the resin, which has also decomposed to some extent due to irradiation.

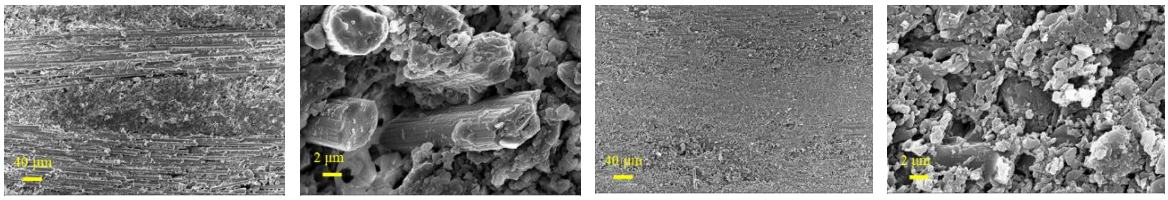

(a) *(b)* *(c)* *(d)*

Figure 4. Representative SEM images taken from interface of multi-functional composite material specimens (a), (b) neat-reference, (c) and (d) graphene-enabled.

Raman spectra were obtained from the specimen interface. For the neat specimen, the spectrum that corresponds to the resin region (away from carbon fibers area) is shown in Figure 5 (a). In the range 1800-2700 cm^{-1}, a wide and strong peak is observed, which is attributed to fluorescence signal emerging from the resin. In this spectrum, the carbon D and G bands are observed at ~1355 cm^{-1} and ~1585 cm^{-1}, respectively. The remaining bands (~ 1307 cm^{-1}, ~ 1461 cm^{-1}, ~ 1554 cm^{-1}, ~ 1610 cm^{-1}) are assigned to the polymer of the composite material. A representative Raman spectrum obtained from the region where the carbon fibers are located in the neat specimen is illustrated in Figure 5 (b). The spectrum is characteristic of nanocrystalline carbon or carbon material with a high sp^3/sp^2 hybridization content. The main vibration bands, D and G are located at ~ 1366 cm^{-1} and ~ 1599 cm^{-1}, respectively, being quite wide. A deconvolution of these broad bands to individual components, typically reveal additional peaks at ~ 1503 cm^{-1} and ~ 1568 cm^{-1}. A broad background is also evident in the spectral area 2100-2700 cm^{-1}, which is attributed to fluorescence. Representative Raman spectra recorded from the graphene-enabled specimen are shown in Figure 5 (c). Raman spectra were obtained in the intermediate region between the locations where the carbon fibers are located. This spectrum exhibits several peaks assigned to the polymer, as well as, weak D and G bands of the reduced graphene oxide, which are narrower compared to the corresponding peaks of the carbon fibers, while their degree of overlap is much smaller.

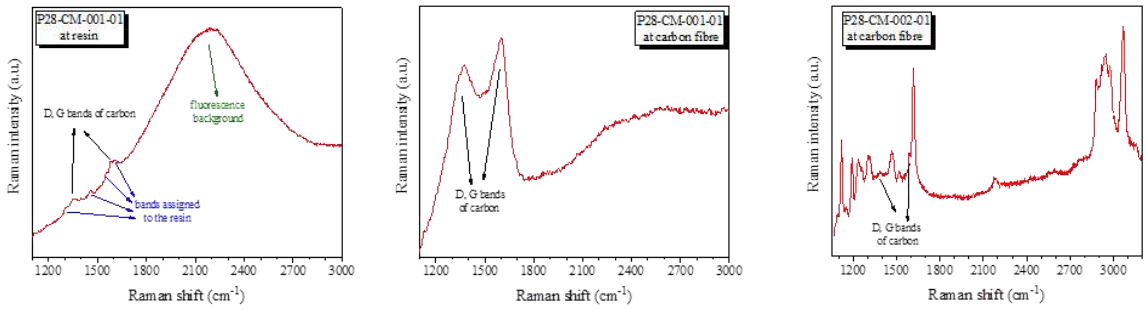

(a) *(b)* *(c)*

Figure 5. Raman spectra of multi-functional CFRP in (a) resin region of neat specimen, *(b)* carbon fibers region of neat specimen *and (c)* carbon fibers region of treated specimen.

The influence of reduced graphene produced by laser irradiation on storage modulus and glass transition temperature was studied by conducting dynamic mechanical thermal analysis (DMA). The presence of graphene had active properties as there was an increase in E' from 37 GPa (±2.7 GPa) to 42.8 GPa (±1.2 GPa), which corresponds to a 16% increase (Figure 6 (a)). Respectively,

  doi:10.5075/epfl-298799_978-2-9701614-0-0

for the glass transition temperature (T_g) an increase of about 3 °C was observed from 125.3 °C (±3.2°C) to 128.6 °C (±6.4°C), as shown in Figure 6 (b).

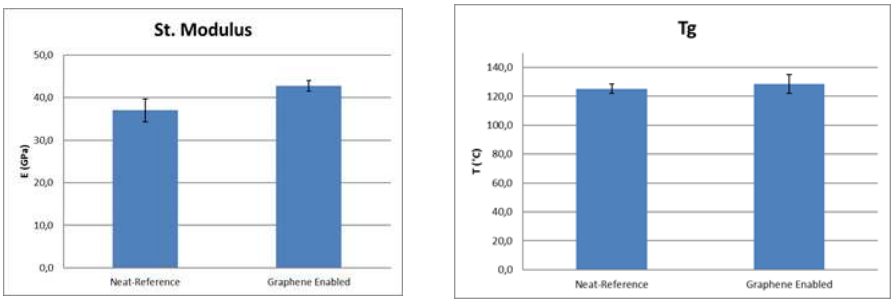

(a) *(b)*

Figure 6. Dynamic Mechanical Analysis *of multi-functional CFRP in* neat and modified specimens *(a) Storage Modulus (E') and (b) Glass Transition Temperature (T_g).*

Comparative three-point bending (3PB) test was carried out between the reference CFRP and the graphene-enabled CFRP. Figure 7 depicts the force and flexural stress of 3PB test. The increase of the maximum bending load from 331.9N (± 80.5N) to 501.2N (±52.6N) is obvious, which based on the dimensional characteristics of each test corresponds to an increase of the maximum stress from the 580.9 MPa (± 120.1MPa) to 942.7MPa (± 40.1MPa). The above results correspond to a relative increase of about 63%.

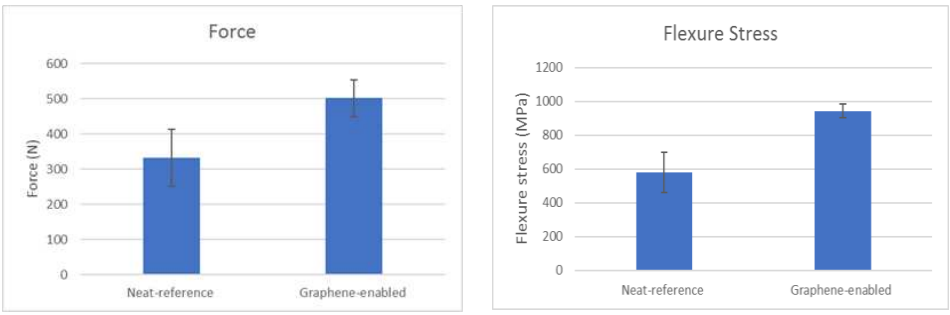

(a) *(b)*

Figure 7. Three-point bending of multi-functional CFRP in neat and modified specimens (a) Force and (b) Flexural stress.

The effect of the presence of reduced graphene was also studied by the interlaminar shear strength test (ILSS). A reduction of the maximum load was observed from 68.51 MPa (±1.58 MPa) to 22 MPa (±1.46 MPa) corresponding to a relative reduction of about 68%, as shown in Figure 8. ILSS is dominated by the properties of the fiber-matrix interface, thus, the degradation of interface with the presence of graphene produced by laser irradiation is responsible for its decrease.

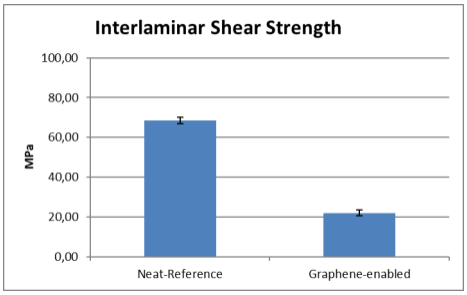

Figure 8. Interlaminar shear strength of multi-functional CFRP in neat and modified specimens.

  doi:10.5075/epfl-298799_978-2-9701614-0-0

To measure the opening Mode-I interlaminar fracture toughness energy (G_{IC}), DCB tests were carried out. Figure 9 depicts the influence of reduced graphene produced by laser irradiation on the force and G_{IC}. A decrease in the maximum load was observed from 107.89N (± 8.95 N) to 53.87N (± 10.79N) due to the presence of graphene on the outside side of prepreg (graphene-enabled CFRP) causing an overall degradation of the corresponding properties. Thus, for example, the corresponding interlaminar fracture toughness energy shows a significant reduction of 70% from 641.69 ± 10.71 J/m^2 to 190.27 ± 52.05 J/m^2.

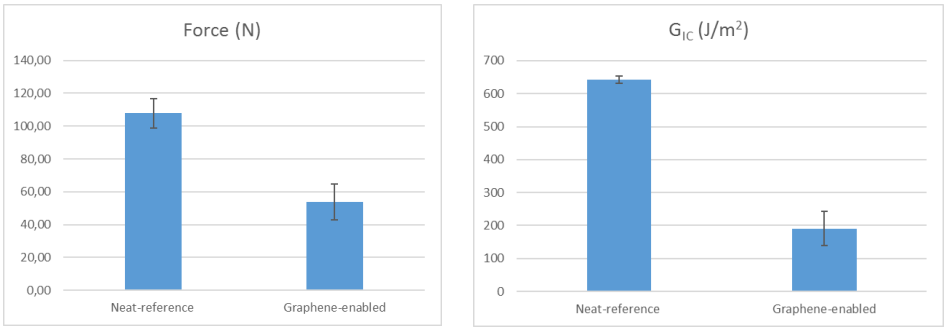

(a) *(b)*

Figure 9. Double cantilever beam (DCB) tests of multi-functional CFRP in neat and modified specimens (a) Force and (b) G_{IC}.

Thermal conductivity measurements were performed through the thickness on both sides of the specimens. The total of tests performed on both the top and bottom side of the specimens to eliminate any external variation in surface quality that significantly affects its respective measurements, is presented in Figure 10 (a). An increase in thermal conductivity was observed from 0.55 W/mK (± 0.05 W/mK) to 0.59 W / mK (± 0.05 W/mK), which corresponds to an increase of about 8% and is enhanced by the presence of the graphene. The electrical conductivity study showed an increase in the modified specimens from 6.54 S/m (±3.18 S/m) to 9.30 S/m (±3.9 S/m) due to the presence of graphene, which corresponds to an increase of about 42%, as shown in Figure 10 (b).

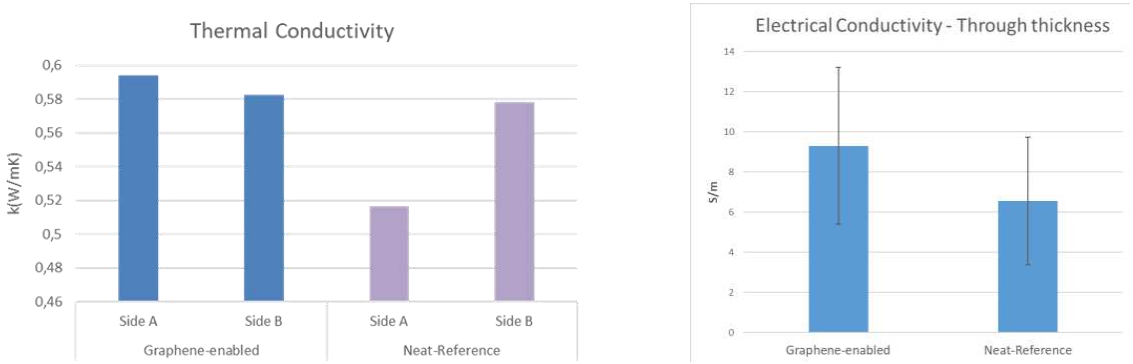

(a) *(b)*

Figure 10. Performed measurements through the thickness of (a) thermal conductivity and (b) electrical conductivity.

4. Conclusions

Laser-assisted reduction of graphene oxide (GO) was successfully carried out onto woven carbon fiber pre-impregnated fabric (prepreg). The whole process was conducted utilizing an R2R spraying pilot line, where GO is deposited onto the prepreg surface and an industrial type laser

  doi:10.5075/epfl-298799_978-2-9701614-0-0

coupled to the R2R pilot was used to irradiate and reduce the GO layer. Two CFRP plates (neat-reference and graphene-enabled) were manufactured to examine the influence of graphene presence in composite material. Specifically, electron microscopy images were recorded from graphene-enabled prepreg, neat CFRP and graphene-enabled CFRP and Raman spectra was obtained to investigate the graphene oxide reduction and CFRPs. Dynamic Mechanical Analysis, Three-point bending, Interlaminar Shear Strength (ILSS) and Double cantilever beam tests were performed to study the mechanical properties of CFRPs. In addition, thermal conductivity and electrical conductivity measurements were carried out to investigate the thermal and electrical properties, respectively. Electron microscopy analysis revealed that the laser-assisted reduced graphene oxide was successfully formed onto prepreg substrate. The Raman spectra showed that the laser-induced reduction of GO produces high quality graphene-like structures. Additionally, the graphene film enhances the properties of CFRP yielding a 63%, 8% and 42% increase in flexural stress, thermal conductivity, and electrical conductivity, respectively. Finally, the interlaminar properties are decreased since the mechanical interaction along the interlaminar region is influenced by the graphene presence.

Overall, the direct graphene deposition on the surface of carbon fiber reinforced composites has been successfully demonstrated using a R2R laser-assisted method. The graphene formed in this way, can act as nanoscale structural element in these composites to provide fast and cost-effective mechanical performance improvements and multifunctionality for structural applications.

Acknowledgements

This work is funded by the Greek national funds through the Operational Program Competitiveness, Entrepreneurship, and Innovation, under the call RESEARCH – CREATE – INNOVATE (project code: T1EDK-03167).

5. References

1. Papageorgiou DG, Kinloch IA, Young RJ. Mechanical properties of Graphene and Graphene based nanocomposites. Progress in Materials Science 2017; 90:75–127.
2. Kostopoulos V, Masouras A, Baltopoulos A, Vavouliotis A, Sotiriadis G, Pambaguian LA. Critical review of nanotechnologies for composite aerospace structures. CEAS Space Journal 2017; 9, 2017:35–57.
3. Kavouras P, Dragatogiannis DA, Batsouli DI, Charitidis CA. Effect of local microstructure on the indentation induced damage of a fiber reinforced composite. Polymer Testing 2017; 61:197-204.
4. Lee HC, Liu W, Chai S, Mohamed AR, Aziz A, Khe C, Hidayaha NMS, Hashima U. Review of the synthesis, transfer, characterization and growth mechanisms of single and multilayer graphene. RSC Advances 2017; 7, 15644–15693
5. Wan Z, Streed EW, Lobino M, Wang S, Sang RT, Cole IS, Thiel DV, Li Q. Laser-Reduced Graphene: Synthesis, Properties, and Applications. Advanced Material Technology 2018; 170-315
6. Antonelou A, Sygelou L, Vrettos K, Georgakilas V, Yannopoulos SN. Efficient defect healing and ultralow sheet resistance of laser-assisted reduced graphene oxide at ambient conditions. Carbon 139 2018; 492–499

  doi:10.5075/epfl-298799_978-2-9701614-0-0

INFLUENCE OF FIBER/MATRIX INTERFACE ON GAS PERMEABILITY PROPERTIES OF CF/TP COMPOSITES

Gautier Allusse[a], Olivier De Almeida[a], Quentin Govignon[a], Fabrice Schmidt[a]

a: Institut Clément Ader (ICA), Université de Toulouse, CNRS, IMT Mines Albi, INSA Toulouse, ISAE SUPAERO, UT3, Toulouse, France – gautier.allusse@mines-albi.fr

Abstract: *One of the main properties to be satisfied in hydrogen applications is low gas permeability. In composite materials, this property depends on the processing parameters and in particular on the residual porosity, but also on the quality of the fiber/matrix interface. This is particularly the case in composites involving a thermoplastic matrix with carbon fibers as the lack of reactive group on the fiber surface can limit the level of interfacial interaction between the reinforcement and the matrix. In this study, the role of the interface is therefore analyzed through the investigation of the hydrogen permeability of CF/PVDF and CF/PPS composites manufactured with different grades of polymers and reinforcements. The hydrogen permeability of the composites was determined, and a correlation with the crystallization behavior of the matrix on the fiber surface could be identified. Hydrogen permeation decreases when the fiber favors matrix nucleation.*

Keywords: Composite ; Thermoplastic ; Permeability ; Fiber/matrix interface ; Hydrogen.

1. Introduction

The energy transition is seeing the development of numerous applications based on hydrogen, which has been identified as a necessity for reducing greenhouse gas emissions. Many technologies have been developed or are still being developed in this way, whether for the production, storage or use of hydrogen. In particular, new designs of hydrogen storage tanks are explored with the aim at obtaining durable lightweight solutions for transport applications.

Composite materials are suitable candidates for tank application as they combine lightness, corrosion and mechanical resistance adapted to high pressure hydrogen storage. However, the permeability of composite materials to gases [1] and in particular to hydrogen which is a light gas with a small molecular size [2] still needs to be better understood. Indeed, although the literature reports that gas permeability properties are retained for thermoset matrix composites [3], indicating good control of the fiber/matrix interface, very little data on thermoplastic matrix composites is available.

Thermoplastics (TP) have intrinsically good gas impermeability properties, of the order of 10^{-10} $mol.m^{-1}.s^{-1}.MPa^{-1}$, close to thermosets [3,4]. On the other hand, carbon and glass reinforcements also exhibit low permeability [5]. Studying hydrogen permeation in thermoplastic composites therefore consists in investigating the role of the interface on this property.

Interface issues are well known in composites. Reinforcements are generally sized before forming to improve mechanical strength but also to ensure good adhesion with the resin. Regarding hydrogen permeability, adhesion is however not necessarily the key criteria and this study therefore proposes an in-depth analysis of the interfacial interactions in thermoplastic composites and its influence on hydrogen permeability.

  doi:10.5075/epfl-298799_978-2-9701614-0-0

To do so, the behavior of carbon fiber reinforced composites manufactured with matrices of different nature was investigated. Poly(Vinylidene Fluoride) (PVDF) was first chosen for its good intrinsic gas permeability [5]. PVDF is a fluorinated semi-crystalline polymer known for its excellent chemical resistance, dielectric properties, excellent UV and moisture resistance, low coefficient of friction and very good thermal stability between -40°C and 150°C [6]. PVDF is therefore particularly suitable for use in fluid storage and transport applications (piping), in membranes for the medical field or in piezoelectric applications [7]. However, because of the high electronegativity of the fluorine element, this polymer exhibits poor chemical interaction with its environment which limits bond formation with carbon fibers in composite applications.

For comparison purpose, Poly(Phenylene Sulfide) (PPS) was selected as this thermostable thermoplastic has a hydrogen permeability of the same order of magnitude as PVDF [4]. This semi-crystalline thermoplastic polymer is widely used in composites for its high mechanical performance, high temperature stability, fire resistance and high chemical resistance [8] and has a better compatibility with carbon fibers.

PVDF and PPS polymers and their respective CF composites are studied and compared. After checking the impregnation quality, the hydrogen permeability properties are measured to highlight the influence of the fiber/matrix interface, through different fiber/matrix pairs. Morphological and crystallization analysis at the interface were then used so as to identify the main factors that control the hydrogen permeability.

2. Experimental

2.1 Materials

In order to compare the influence of the fiber/matrix interface on the gas permeability properties, two grades of PVDF were characterized and used for the manufacture of composite. The polymers used were in the form of 100 µm thick films. The first grade is a homopolymer PVDF (PVDF-H) while the second grade is a grafted PVDF (PVDF-G) which grafted function improves the chemical affinity of PVDF. Studies on similar grafted-PVDF show a decrease in the contact angle of PVDF on carbon fibers, leading to an improvement in wettability as well as an improvement in interlaminar shear strength, indicating an improvement in the quality of the CF/PVDF interface [9,10]. The gas permeability behavior of PVDF was compared to that of PPS, used as a 50 µm film.

Composite plates were manufactured with the different thermoplastic polymers, in combination with two different carbon reinforcements in the form of a mat with a weight of 465 g/m². The reinforcement (CF-A) is an unsized reinforcement while the reinforcement (CF-B) has been treated to modify the surface of the carbon fiber. The surface activation treatment modified the chemistry of the surface and therefore induced a different interfacial interaction with the semi-crystalline polymers.

2.2 Composite manufacturing

The panels were manufactured by thermocompression molding using the film stacking method. The film stacking method consists of heating and compressing a stack of alternating layers of polymer film and dry reinforcement. The conventional thermo-compression processing cycle first consisted in a low-load heat-up phase. The reinforcement/matrix system was then loaded

  doi:10.5075/epfl-298799_978-2-9701614-0-0

when the matrix temperature was beyond its melting point in order to promote polymer flow within the fiber reinforcement. The composite was finally cooled under pressure to set the structure of the impregnated composite and demolded when the temperature decreased below 50°C.

2.3 Characterization

Void content

The impregnation quality of composite panels was characterized by the presence or absence of porosity within the manufactured material. Samples taken from the plates in identical locations were polished with silicon carbide abrasive paper and then observed under an optical microscope. The image analysis technique was then used to determine the size and distribution of the porosities in the volume of the samples and the residual void content.

Hydrogen permeability

The hydrogen permeability properties of the plates were measured by the pressure differential method using a homemade equipment. A hydrogen overpressure p_{H_2} of 1 bar was applied on one side of the composite panel. The amount of hydrogen Q in ppm that had passed through the panel of area A and thickness e during time t was measured on the other side. The permeability Pe coefficient [mol.m^{-1}.s^{-1}.MPa^{-1}] was then calculated under standard temperature and pressure conditions, from equation 1:

$$P_e = \frac{Q\ e}{t\ A\ p_{H_2}} \tag{1}$$

Cryo-fractured samples

Cryo-fractures were performed on the composite samples for analyzing the fiber-matrix adhesion. The samples were immersed in liquid nitrogen for 3 min and broken with tweezers. The low temperature of the sample allowed preventing plastic deformation during fracture. The fibre/matrix interface of the samples was then platinum coated and observed under a scanning electron microscope (SEM) in secondary electrons mode.

Differential Scanning Calorimetry

DSC measurements were carried out with a Perkin Elmer 8500 DSC equipment to determine the melting temperatures and enthalpies of fusion of the polymers and composite matrices. Sealed aluminum sample pans were prepared with 15 to 20 mg of polymer and composite. The samples were then heated from 50°C to 220°C in the case of PVDF and from 50°C to 330°C in the case of PPS, at 10°C/min. The melting temperature was recorded at the maximum of the heat flow peak, and the degrees of crystallinity of the polymers and composites were calculated from equation 2:

$$X_c = \left(\frac{\Delta H_m}{\chi_m \times \Delta H_m^0}\right) \times 100 \tag{2}$$

In equation 2, χ_m and ΔH_m are the mass fractions (equal to 100% in the case of pure polymer) and the enthalpy of fusion of the polymer, respectively. ΔH_m^0 is the enthalpy of fusion of a pure polymer crystal, which is 104.6 J/g for PVDF [11] and 76.5 J/g for PPS [12].

  doi:10.5075/epfl-298799_978-2-9701614-0-0

Polarized Optical Microscopy (POM)

Isothermal crystallization from the molten state was finally studied using Polarized Optical Microscopy (POM) by means of a Linkam THMS-600P hot stage. Thin samples containing single carbon filaments were first prepared by thermocompression molding with two polymer films (PVDF and PPS) and carbon fibers taken from the reinforcements. The material systems were heated to 200°C and 295°C for PVDF and PPS respectively over short times to avoid degradation, and pressed to obtain samples with a thickness of between 40 and 50 µm.

The crystallization study under hot stage was achieved from the molten state by first heating the polymers to temperatures of 220°C and 320°C for PVDF and PPS respectively. The samples were held at this temperature for 3 min to remove the thermal history. The samples were then cooled at a rate of 50°C/min to the set crystallization temperature (160°C for PVDF and 260°C for PPS). The direct observation of spherulitic growth during polymer crystallization under polarized optical microscope allowed identifying the bulk nucleation density and fiber-induced nucleation density.

3. Results and discussion

3.1 Impregnation quality

The plates manufactured by thermocompression using the film stacking method exhibited a low residual porosity rate (figure 1.a), and of the same order for all materials. Microscopic observations (figure 1.b) confirmed the good impregnation quality of the composite panels with no visible porosity. The differences in the hydrogen permeability behavior of the composite panels can not therefore be explained by the impregnation step as such and the presence of a different porosity level.

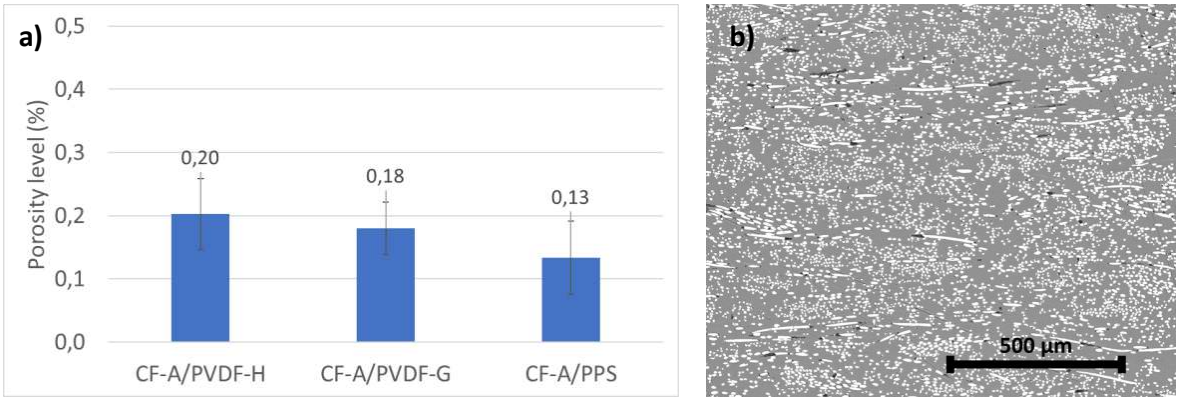

Figure 1. a) Residual porosity level in the composites and b) Microscopic observation of the CF-A/PPS composite.

3.2 Gas permeability

Figure 2 presents the hydrogen permeability measurements of the pure polymers (PVDF-H, PVDF-G and PPS) and their respective composites with the two carbon fiber references CF-A and CF-B. The pure polymers have a low hydrogen permeability in accordance with data from literature. The results also show that PVDF has a slightly lower permeability than PPS which confirms the renewed interest in PVDF for hydrogen applications.

  doi:10.5075/epfl-298799_978-2-9701614-0-0

After coupling the polymers with the carbon reinforcement, the composites show a strong increase in hydrogen permeability of several orders of magnitude. As shown previously, this result can not be attributed to an effect of the void content since all composite panels were showing a high impregnation quality. The differences in gas permeability behavior are therefore related to the quality of the fiber/matrix interface.

It should be noted that the CF-A/PVDF-G composite has a slightly lower hydrogen permeability than the CF-A/PVDF-H composite. The addition of the grafted functions improved the quality of the fiber/matrix interface [10].

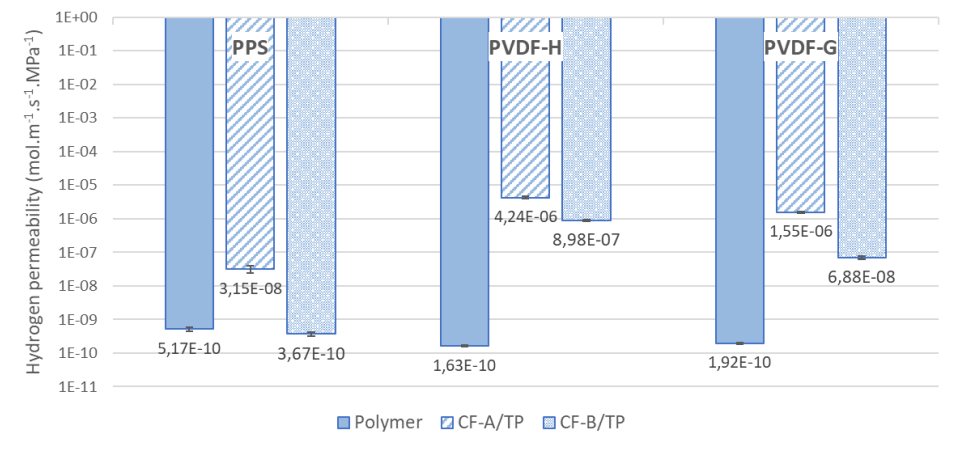

Figure 2. Hydrogen permeability of polymers (PVDF-H, PVDF-MAH and PPS) and their composites with CF-A and CF-B reinforcements, respectively.

These observations are confirmed by the hydrogen permeability measurements performed on the CF-B/PVDF-H, CF-B/PVDF-MAH and CF-B/PPS composites (figure 2). These composites, involving the activated reinforcement, show a lower hydrogen permeability than in the case of CF-A reinforcement. The functions created on the surface of the fibers during the treatment improved the quality of the fiber/matrix interface [10], leading to improved gas permeability properties of the composites. However, figure 2 shows a different behavior according to the fiber/matrix pairs. The coupled effect of the grafted functions in PVDF with the activated reinforcement improves the gas permeability properties of the CF/PVDF composites. However, the hydrogen permeability measurements remain lower than those of the CF-B/PPS composite, highlighting the influence of the fiber/matrix interface on the hydrogen permeability.

3.3 Fiber/matrix adhesion

As shown in figure 3, the SEM observations of the fractured surfaces all show poor quality interfaces. First, the presence of numerous cavities indicates that many fibers were pulled out of the matrix during the fracture. Then, little or no polymer residue can be observed on the fiber surface, indicating poor adhesion of the polymer to the carbon fibers.

The surface observation of the fiber/matrix interfaces does not allow clearly differentiating the samples. Therefore, differences in hydrogen permeability can not be correlated to different fiber-matrix adhesion levels in the composites. Nevertheless, the very high cooling rate associated with the liquid nitrogen treatment can have damaged the fiber/matrix interface. Indeed, because of the different thermal expansion coefficients of the matrix and reinforcement, the stress induced to the fiber-matrix interface upon cooling may have damaged

  doi:10.5075/epfl-298799_978-2-9701614-0-0

the interface before cryo-fracture leading to cryo-fractures that are not representative of the actual interface. Observations of fractured surfaces generated at very high speed (Charpy test) could better reveal the actual adhesion at the interface.

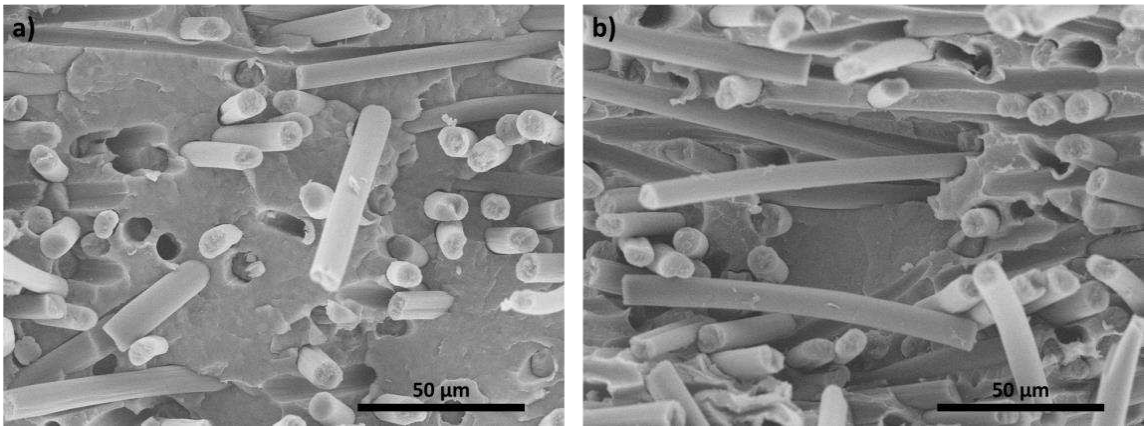

Figure 3. SEM observation of cryo-fractures of composites a) CF-A/PVDF-H and b) CF-B/PPS.

3.4 *Influence of fibers on crystallization*

The good adhesion of the matrix with the fiber is a source of improvement of the gas permeability as it may limit the gas paths in the interphase between the fiber and the matrix. However, this condition is necessary but not sufficient. Indeed, Monson *et al.* [13] showed in their study that a higher proportion of crystalline phase led to an improvement in gas permeability properties. As in the case of fillers, crystalline phases increase the effective path length of gases through the composites.

During the manufacturing process, the composite panels were cooled at a cooling rate of about 10°C/min. Such cooling rates have little effect on the crystallization of PVDF-H, PVDF-G, PPS and their respective composites. As shown in figure 4, the degrees of crystallinity of the polymers and the corresponding composites are of the same order of magnitude. The differences in crystallinity in the volume do not explain the differences in permeability behavior.

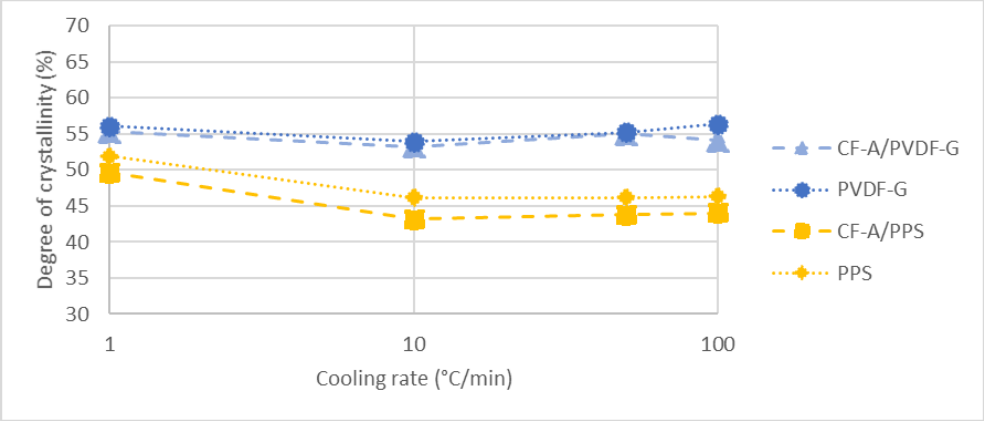

Figure 4. Degree of crystallinity of polymers and composites from DSC measurements.

  doi:10.5075/epfl-298799_978-2-9701614-0-0

In order to highlight the effect of fibers on crystallization, numerous images were taken during the spherulite growth process and the surface of the image covered with spherulites was monitored by using image analysis method. The influence of fibers was assessed by measuring the percentage of the image covered by spherulites in an area close to the fiber. In the present case, a distance of 25 µm around the fiber was considered (figure 5.a) for defining this area. The same percentage was calculated in the rest of the image, *i.e.* in an area far from the fiber, therefore representing the bulk crystallization process. The ratio between the two percentages was then used as an indicator of the influence of the fiber, a value close to unity demonstrating an absence of fiber influence on the crystallization process.

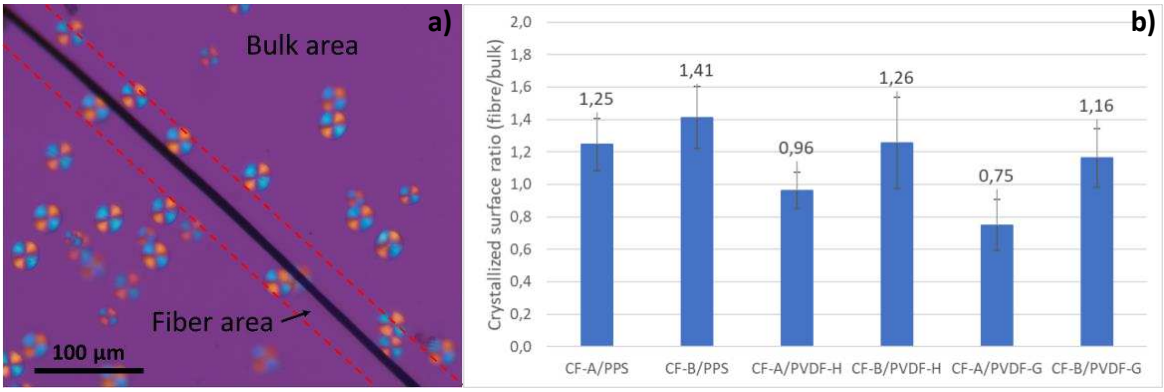

Figure 5. Influence of the fiber zone on the crystallized surface for different combinations of reinforcements and matrices. (a) Observation of growing spherulites by optical microscopy; (b) Ratio between the surface of the micrographs covered by spherulites in the fiber area and in the bulk area.

According to figure 5.b, the CF-A reinforcement has a low influence on the crystallization of PVDF and even a negative effect of the fiber, as shown by ratios lower than unity. On the other hand, the presence of the fibers impacts the crystallization of PPS, possibly through a greater nucleation effect on the fiber surface. This results in a stronger loss of permeability properties in the case of PVDF composite than for PPS composite.

By adding CF-B, the activated surface of the carbon fiber increases the ratio, indicating a higher influence of the carbon surface on crystallinity that can be correlated with the improvement of the hydrogen impermeability of the composites. The higher ratio can be due to a higher nucleating effect of the activated carbon fiber that may induce a densification of the interface [13] therefore locally reducing the hydrogen permeability.

The benefit of using a grafted PVDF appears to be very low on crystallization, although it significantly improves the permeability property of the composite when combined with CF-B (one order of magnitude difference). This suggests that other phenomena also influence the permeability property at the fiber/matrix interface, adhesion being one of the parameters to be considered.

  doi:10.5075/epfl-298799_978-2-9701614-0-0

4. Conclusion

This study demonstrates the influence of fiber/matrix interface in carbon fiber reinforced thermoplastic composites on the hydrogen permeability properties. In particular, the nucleating effect of the fiber surface appears as a key factor for improving the permeability property, most likely because of an interphase densification at the fiber-matrix interface. The combination of a grafted polymer with an activated reinforcement allows to significantly decrease the hydrogen permeability. This improvement is attributed to the better affinity of the polymer with the reinforcement. The same observation was made with PPS, which exhibit a higher affinity with the activated carbon fiber leading to a permeability property similar to that of the neat polymer.

5. References

1. Flanagan M, Grogan DM, Goggins J, Appel S, Doyle K, Leen SB, et al. Permeability of carbon fibre PEEK composites for cryogenic storage tanks of future space launchers. Compos Part Appl Sci Manuf. 2017;101:173-84.
2. Klopffer MH, Flaconneche B. Transport Properdines of Gases in Polymers: Bibliographic Review. Oil Gas Sci Technol. mai 2001;56(3):223-44.
3. Humpenöder J. Gas permeation of fibre reinforced plastics. Cryogenics. janv 1998;38(1):143-7.
4. Massey LK. Permeability properties of plastics and elastomers: a guide to packaging and barrier materials. Cambridge University Press; 2003.
5. Schultheiß D. Permeation barrier for lightweight liquid hydrogen tanks. 2007.
6. Drobny JG. Blends and composites based on fluoropolymers. In: Macromolecular Symposia. Wiley Online Library; 2001. p. 149-56.
7. Humphrey JS, Amin-Sanayei R. Vinylidene Fluoride Polymers. In: Encyclopedia of Polymer Science and Technology. John Wiley & Sons, Ltd; 2001.
8. Rahate AS, Nemade KR, Waghuley SA. Polyphenylene sulfide (PPS): state of the art and applications. Rev Chem Eng. 2013;29(6):471-89.
9. Liu P, Zhang S, Lu C, Yuan H. Increased interfacial adhesion between carbon fiber and poly(vinylidene fluoride) by an aqueous sizing agent: MPVDF sizing agent for CF/PVDF composites. Surf Interface Anal. déc 2016;48(13):1410-7.
10. Tran MQ, Ho KKC, Kalinka G, Shaffer MSP, Bismarck A. Carbon fibre reinforced poly(vinylidene fluoride): Impact of matrix modification on fibre/polymer adhesion. Compos Sci Technol. juin 2008;68(7-8):1766-76.
11. Nakagawa K, Ishida Y. Annealing effects in poly(vinylidene fluoride) as revealed by specific volume measurements, differential scanning calorimetry, and electron microscopy. J Polym Sci Part -2 Polym Phys. nov 1973;11(11):2153-71.
12. Brady DG. The crystallinity of poly(phenylene sulfide) and its effect on polymer properties. J Appl Polym Sci. sept 1976;20(9):2541-51.
13. Monson L, Moon SI, Extrand CW. Permeation resistance of poly(ether ether ketone) to hydrogen, nitrogen, and oxygen gases. J Appl Polym Sci. 5 févr 2013;127(3):1637-42.

  doi:10.5075/epfl-298799_978-2-9701614-0-0

TRIBOLOGICAL STUDY ON WOOD AND GRAPHENE REINFORCED HIGH DENSITY POLYETHYLENE

Zainab, Al-Maqdasi[a], Ugo, Jantel[a], Roberts, Joffe[a], Nazanin, Emami[b]

a: Division of Materials Science, Department of Engineering Science and Mathematics, Luleå University of Technology – zainab.almaqdasi@ltu.se
b: Division of Machine Elements, Department of Engineering Science and Mathematics, Luleå University of Technology

Abstract: *Wear rate and coefficient of friction for neat high-density polyethylene (HDPE) and reinforced with wood flour (WF) and/or graphene nanoplatelets (GNPs) are studied. The pin-on-disc tribotest configuration on samples with different moisture contents are performed. The effect of the different scales of reinforcement (micro- and nano-) on these properties is discussed. The morphological/microstructural changes at the materials´ surface induced by the motion in contact and/or moisture content in the bulk are investigated by differential scanning calorimetry and scanning electron microscopy. Results show that reinforcing the polymer with WF or GNPs reduces the wear rate significantly, compared to neat HDPE. The hybrid multi-scale reinforcement contributes to maximum improvement in wear resistance (>98%) and in the reduction of coefficient of friction (>11%). The improvement in the tribological behavior of bio-based polymer composites has a significant impact on sustainable development through the improved design, durability, and environmental impact.*

Keywords: Tribology; Wood Polymer Composite; graphene; multi-functional composites; multiscale reinforcement

1. Introduction

One of the ways to reduce carbon footprint is to use more eco-friendly materials and industrial processes. Wood polymer composite (WPC) is used in applications as alternative to natural wood that can still preserve the wooden appearance but with cheaper prices, less required maintenance and better chances to utilize recycled materials [1]. Moreover, WPC offers a good lightweight, low cost, chemical resistant alternative to metals that is also easily processed and recycled. On the other hand, due to the hydrophilic nature of wood fibers, WPC have its limitations in durability against moisture that needs to be addressed.

For load-bearing applications where materials are in contact, coefficient of friction (COF) and wear rate (WR) are used to assess the material's serviceability and service life. Those parameters are not intrinsic for the specific material but are very much affected by the surrounding environment, the mating material and surface properties and the tribological system conditions. However, it is very important for the design and selection of any material to understand the influence of different factors on its behavior. Research has been carried out to study the physico-mechanical properties of WPC in quasi-static conditions [2], but little research has been devoted to study their tribological properties [3]. It has been shown that solid self-lubricants such as graphitic derivatives can improve the tribological performance of polymers by improving the transfer film formation on the surface [4]. The improvement in the tribological behavior of

  doi:10.5075/epfl-298799_978-2-9701614-0-0

systems is tightly connected to energy conservation and conversion. Moreover, the use of bio-based materials has a significant impact on sustainable development through the improved design, durability, and environmental impact [3].

A previous study by the authors [5] showed that mechanical performance of HDPE reinforced with WF and/or GNPs was improved significantly, and a new thermal conducting functionality was introduced. Synergistic effect of combining hybrid, multi-scale reinforcement has shown to surpass the positive impact of the individual reinforcement. In the current work, the tribological performance (e.g., WR and COF) of neat HDPE and HDPE-based wood composite with different moisture contents is evaluated by means of a pin-on-disc (PoD) tribotest configuration. Changes of materials' structure and response to various parameters are also investigated.

2. Experimental

2.1 Materials

High-density polyethylene (HDPE, MG9647S, Borealis AG) in pellet form with a density of 0.964 g/cm^3 is used as the base polymer. A master batch of graphene in HDPE (heXo HDPE1-V20/35, NanoXPLOre) with 35 wt% GNPs is used to incorporate the nanoparticles into the composites. According to the manufacturer's technical data sheet, the platelets in the masterbatch have an average of 40 layers graphene sheets with a thickness of 20 nm and a lateral dimension of 50 µm. The platelets are functionalized at the edges by the supplier to enhance compatibility with the polymer. Wood flour (WF, Scandinavian Wood Fiber AB) is a sawdust of spruce and pine wood with 75% of its particles in the size range of 200–400 µm. Maleic anhydride-grafted polyethylene (MAPE, E265, DuPont), is used as a compatibilizer for the wood composites. Table 1 shows the composition of the studied materials with their designation names.

Table 1. Sample designation and composition of constituents

Sample code	HDPE (wt%)	GNP (wt%)	WF (wt%)	MAPE (wt%)
HDPE	100	-	-	-
HDPE15	85	15	-	-
40WPC	58.5	-	40	1.5
40WPC15	43.5	15	40	1.5

2.2 Methods

Composites were manufactured by melt compounding the dry constituents in a co-rotating twin screw extruder followed by compression molding under 100 bars. Samples for tribological test were machined from composite sheets to nominal dimensions of 4mm × 4mm × 4mm cubes. Edges were carefully cleaned with razor blades to remove the excess polymer lint that might disturb the test. Tests were performed on the faces in contact with the compression mold plates which were preserved without polishing. Sample conditioning environments were prepared by using saturation salts in sealed glass containers (MgCl2 for 33% RH and NaCl for 78% RH ± 5%) at room temperature. Samples were dried in the oven at 50 °C for several days and initial weight was registered. The moisture saturation in the samples was monitored by weighing the mass increase on predefined time intervals, until the difference between three successive

  doi:10.5075/epfl-298799_978-2-9701614-0-0

measurements is less than 0.1% (the duration varies depending on the type of sample and ranges from 3 weeks for neat polymer and 6-7 weeks for the highly loaded wood samples).

Friction and wear measurements were obtained using a TE67 pin-on-disc tribometer measurements. The linear volumetric wear was calculated using a linear variable differential transformer. Stainless steel disc (EN 1.4307 alloy - 18% chromium and 8% nickel) having a finished surface roughness of 0.3 µm was used as a counter surface (CS) rotating with a rotational velocity equivalent to a linear speed of 0.13 m/s. The two surfaces were brought into contact and a dead-weight of 80 kg (resulting in a contact pressure of ≈5 MPa) was applied. Test was running for a sliding distance of 4000 m.

Morphological changes of materials due to friction have been investigated by differential scanning calorimetry (DSC) utilizing Mettler Toledo DSC281 equipment. The thermal history of the samples was not removed by an initial heating run as it also contain the thermal information from the test. Therefore, the change induced by the test conditions was evaluated by comparing the two ends of each sample, assuming that they have gone through the same thermal history, except for the additional effect at the friction end in contact with the CS. A single heating run was implemented with a heating rate of 10 K/min in an inert atmosphere (Argon, 80 ml/min) in the temperature range 25 °C – 250 °C. Crystallinity was evaluated using heats of fusions obtained from the DSC data. For reinforced materials, the fraction of reinforcement is taken into account according to Eq. (1) and only melting enthalpy of the polymer crystals is considered. In this equation, $\%\chi_c$ is the crystallinity of the polymeric phase, ΔH_f is the measured melting enthalpy of the sample, ΔH_f^0 is the theoretical melting enthalpy of 100% crystalline PE (293 J/g) and W_f is the weight fraction of the reinforcement.

$$\%\chi_c = \frac{\Delta H_f}{\Delta H_f^0} \times \frac{1}{1-W_f} \times 100 \quad (1)$$

Microscopic observations were performed using scanning electron microscope (SEM, Jeol JCM-6000) and stereo microscope (Nikon SMZ1270) on the CS as well as the pin samples after the test to analyze the wear mechanisms.

3. Results and Discussions

3.1 Moisture Uptake

As different materials reach different saturation levels based on the affinity to moisture and the available free volume for water molecules, Table 2 shows the final moisture content at saturation for the conditioned samples at the different relative humidity levels.

Table 2. Moisture content of the samples after saturation in controlled environment

	Moisture content (%)			
	HDPE	HDPE15	40WPC	40WPC15
RH 33%	<0.01-0.05	<0.01	0.18-0.42	0.04-0.14
RH 79%	<0.01-0.08	0.01-0.1	1.33-1.42	1.27-1.39

The hydrophobic polymer and its nanocomposites do not show significant changes in mass as they do not absorb moisture. On the contrary, the addition of the hydrophilic wood immediately impacts the moisture uptake of the composites and cause it to increase. Further addition of the

  doi:10.5075/epfl-298799_978-2-9701614-0-0 published under CC BY-NC 4.0 license

GNPs causes the moisture uptake of WPC to reduce, especially at 33% RH. The difference in mass evolution during conditioning between the WPCs and the WPC with GNP are not as obvious as expected for the environment containing relative humidity of 79%. As graphene is a hydrophobic material, the addition of graphene should have decreased the moisture absorption compared to the WPC. These results can be the consequences of inhomogeneity of the samples with the presence of wood-clusters and voids among them that increases the available free volume for moisture uptake [6]. This is possible at high content of reinforcement in the composite. In a complementary study, the impact of graphene in composites reinforced with 25% wood fiber appears to be visible both in the 33% RH or 79% RH environment (unpublished results). A decrease in water absorption was clearly visible between samples containing 25% wood and samples containing 25% WF and 10% GNPs. Correlation between the homogeneity of samples and their moisture uptake has been reported previously [6][7].

3.2 Tribology

The results obtained for the COF of the samples with different moisture contents, shown in Figure 1, reveal an increase in this coefficient for the WPC compared to neat polymer and the other formulations at all conditions. It is highest at 33% RH for the 40WPC and no clear trend for the effect of moisture content on the COF can be observed. Conflicted results are available in literature on the effect of addition of WF on the COF of thermoplastic matrix as both decrease [8] and increase [9] in COF have been reported. It is possible that the very little moisture content is being evaporated at the point of contact due to the heat development at interface, before being able to lubricate the surface, this, however, needs to be validated. The impact of adding GNPs on the WPC is noticeable as the coefficient of friction of 40WPC15 is significantly lower than that of 40WPC but also slightly lower than those of the neat polymer and the nanocomposite. These improvements for the 40WPC15 are probably due to the improved distribution of the GNPs over the scaffold-like structure provided by wood fibers that can elevate the lubricating nature of GNPs.

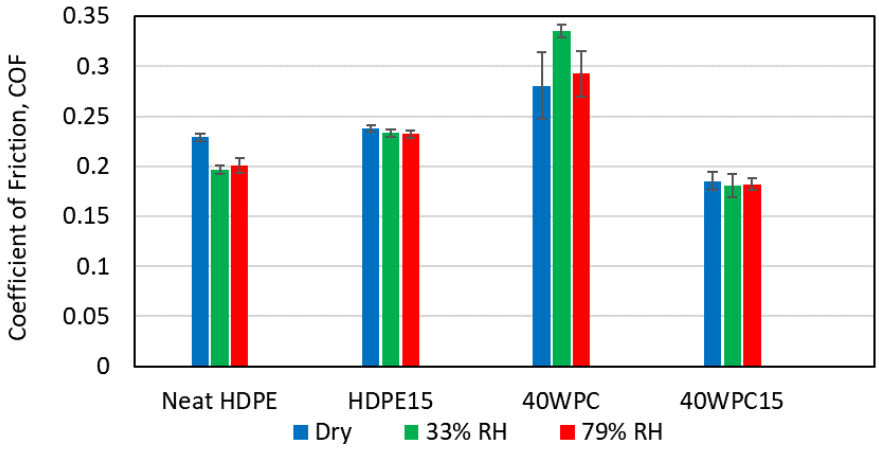

Figure 1. COF for the neat polymer and the composites at different moisture saturation level

On the other hand, the linear volumetric wear rate decreases significantly for all composites, regardless of the type of reinforcement, compared to the neat polymer, see Figure 2. Both types of reinforcement reduced the wear rate by about 80% compared to the neat HDPE at the dry conditions. However, with these testing conditions, almost no wear was noticeable for the 40WPC15 as the wear rate for this formulation was less than 1% of that in HDPE. Statistical

  doi:10.5075/epfl-298799_978-2-9701614-0-0

analysis of variance (ANOVA) revealed no statistical significance effect of moisture on the samples containing nanoparticles (i.e., HDPE15 and 40WPC15). The wear rate has though been affected by moisture for the neat polymer and the wood containing samples compared to the wear rate of their dry counterparts. It is expected that the moisture present in the sample results in plasticization of the polymer that it becomes softer, easier to deform but less prone to wear and detach from the surface (i.e., more ductile). On the other hand, once the surface layer of polymer has been transferred to the counter surface and fibers are exposed, the fibers act as protection for the polymer surface against wear reducing the wear rate significantly and resulting in the increase of the friction coefficient as was noticed earlier. It is worth noting that the wear rate presented in Figure 2 is calculated from the linear part of the volume loss curve over distance and the complete curve varies in the nonlinearity between the different materials under study. Other authors [10] have reported significant increase in the specific wear rate of natural fiber reinforced composites after water immersion due to fiber degradation despite the use of reinforcement in a woven form that is highly resistant to wear. Even though randomly oriented fibers are more prone to debond and detach from the polymer due to friction forces, the deterioration by the effect of moisture sorption could be less significant compared to water immersion. Extended exposure to water promotes the formation of type II bond water where water molecules are bonded chemically by multiple hydrogen bonds to the polymer chains rather than single bond or freely filling the nano-pores [11]. This highlights the difference in durability and serviceability of the material based on the intended application.

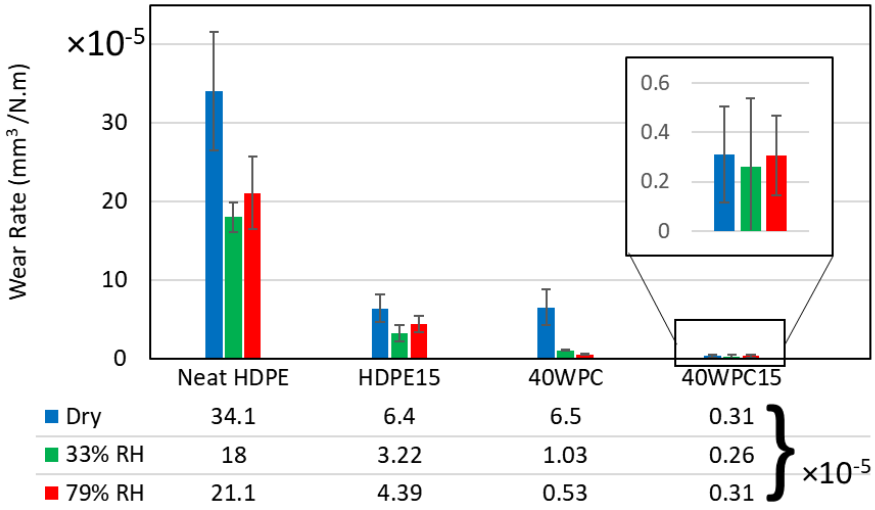

Figure 2. Wear rate of materials at different moisture saturation levels.

The effect of addition of the GNP on the wear mechanism is shown in Figure 3. It can be seen that the presence of GNPs resulted in the formation of discontinuous transfer film on the CS, which was helping smearing the polymer debris on the surface, rather than removing them away. This is also visible on the surface of the pins (micrographs to the right) as it appears smoother (with well embedded patches of debris) than that of the neat polymer pin (with polymer particles barely attached to the surface). However, the presence of discontinuous transfer film means that there would be repeatable polymer-polymer adhesion at the contact points with the film that does not reduce the global COF after the tested sliding distance.

The effect of the moisture content on the wear mechanism is examined in Figure 4 for the 40WPC at different moisture saturation levels. This sample was selected for comparison as it

  doi:10.5075/epfl-298799_978-2-9701614-0-0

showed a significant dependence of wear rate on the moisture content. With the increase in moisture content, the polymer gets softer and more ductile that it is easier to spread over the counter surface creating more continuous transfer film.

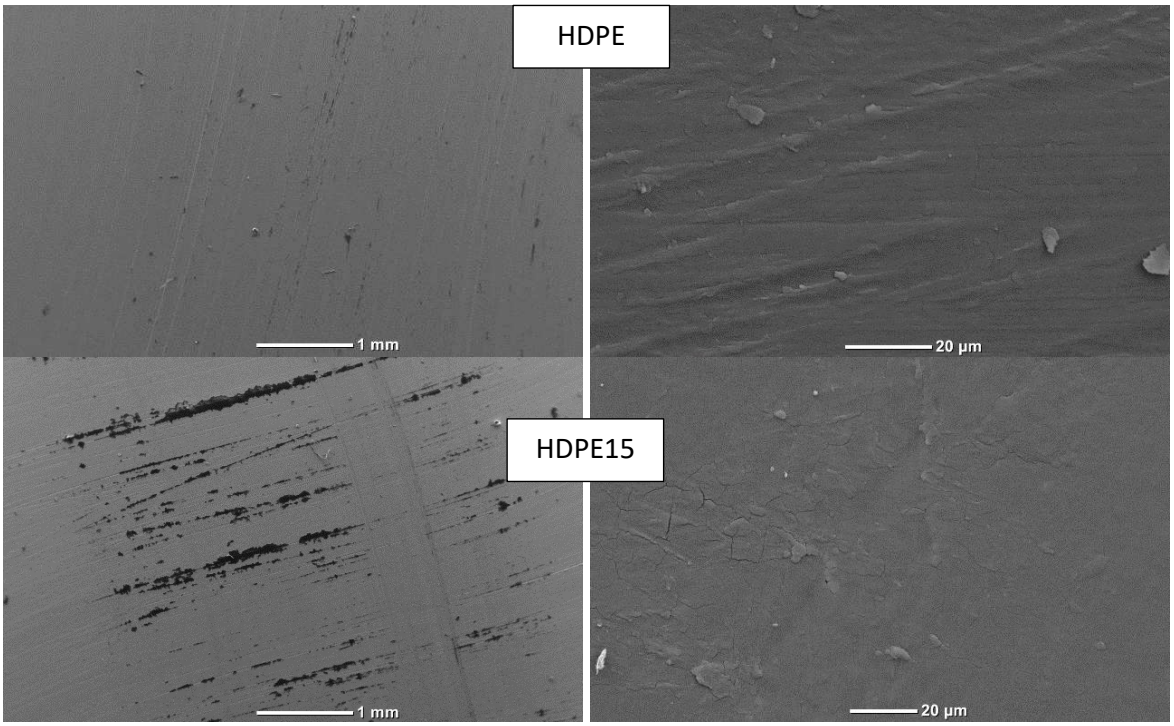

Figure 3. SEM images of CS (left) and pins (right) for the HDPE (top) and HDPE15 (bottom) at a moisture saturation level of 33% RH

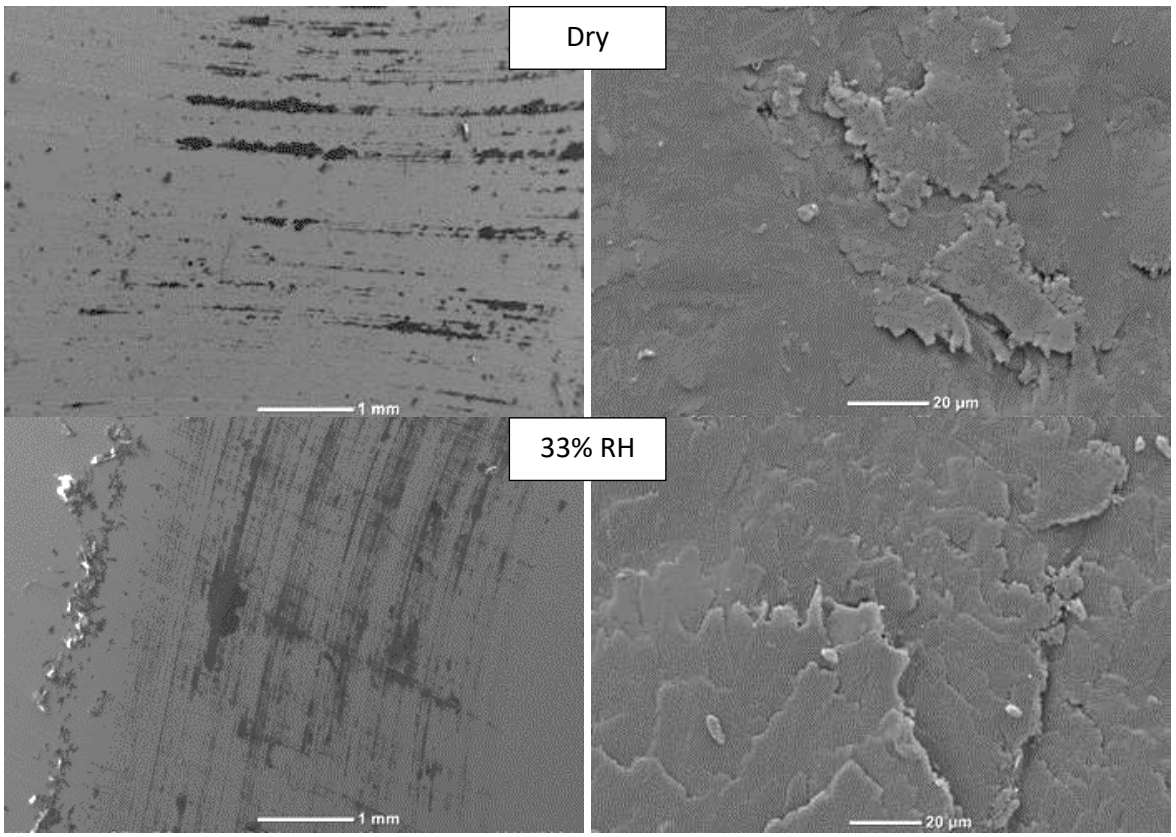

  doi:10.5075/epfl-298799_978-2-9701614-0-0 published under CC BY-NC 4.0 license

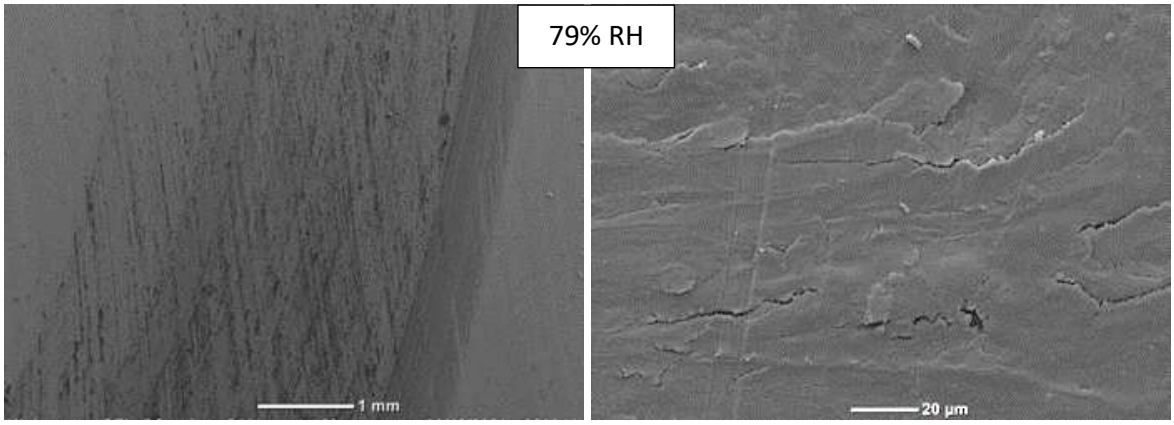

Figure 4. SEM images for CS (left) and WPC pins (right) with different moisture content examined after the wear test on a PoD configuration

3.3 Morphology

Crystallinity of the materials calculated by Eq. (1) is presented in Figure 5. For most of the materials the crystallinity does not change significantly between the Friction-side and the Opposite-side, so the correlation between these two parameters is not relevant under the tested conditions. It could also be possible that the sliding time is insignificant to cause the expected variation. Contact layer for the material of large wear rate is being removed continuously before the friction and contact pressure could induce changes to the microstructure. On the other hand, it could be speculated that during the sliding deformation, the surface layer of the polymer (especially the reinforced samples which does not wear much) undergoes time-dependent deformation where compaction of the amorphous part rather than crystallization occur which is then being relaxed until the time of DSC test. Repeating the tests for longer sliding distances could confirm the results. Earlier studies on UHMWPE samples revealed noticeable changes in the crystallinity of the polymer at similar sliding distances by the effect of reorientation of the polymer chains at the surface of contact [12]. Nonetheless, crystallinity has been changed by the effect of the moisture content, for the materials that showed significant moisture uptake (WPC and WPC with GNP). The crystallinity has increased almost linearly with the increase in moisture content. That could be explained by the possible swelling of the fibers that could cause increased local mechanical stresses on the polymer chains leading to the change in crystallinity.

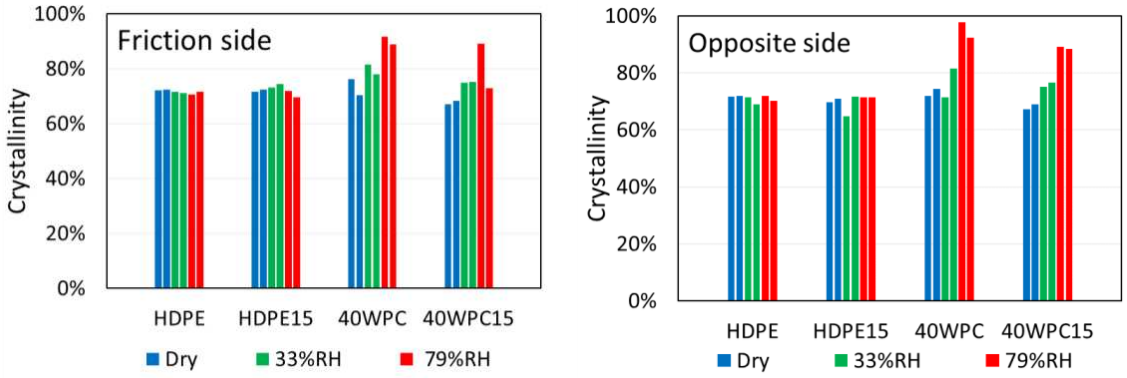

Figure 5. DSC results on the crystallinity change due to test parameters

4. Conclusions

The current study has shown that significant improvement in the tribological performance of WPC based on HDPE could be achieved by reinforcing the polymer with wood fibers (micro-sized) and graphene nanoplatelets (nano-sized). Up to 99% reduction in the wear rate and 11% in the COF was registered for samples reinforced with 40 wt% wood fibers and 15 wt% GNPs. Moisture content in the samples did not have a significant impact on the COF when GNPs are present. However, it contributed to the change in the wear mechanisms of the WPC and the degree of crystallinity of the materials undergone noticeable mass change due to moisture uptake. Challenges in obtaining homogeneous samples have been reflected in the large scatter of the results, especially because of the small size of the samples used for the characterization. Better distribution and more homogeneous samples could be achieved if lower concentrations of the reinforcements are considered.

Acknowledgment

Support of Nano2Day project (Marie Skłodowska-Curie, grant No 777810) is acknowledged.

5. References

1. Mavinkere Rangappa S, Parameswaranpillai J, Hemanth Kuma M, Siengchin S, editors. Wood Polymer Composites: Recent Advancements and Applications. Springer Nature; 2021. 268 p.
2. Gogoi R, Manik G. Mechanical Properties of Wood Polymer Composites. 2021;113–36.
3. Tzanakis I, Hadfield M, Thomas B, Noya SM, Henshaw I, Austen S. Future perspectives on sustainable tribology. Renew Sustain Energy Rev. 2012;16(6).
4. Bahadur S, Schwartz C. The effect of nanoparticle fillers on transfer film formation and the tribological behavior of polymers. In: Tribology of Polymeric Nanocomposites: Friction and Wear of Bulk Materials and Coatings: Second Edition. 2013.
5. Al-Maqdasi Z, Gong G, Nyström B, Emami N, Joffe R. Characterization of Wood and Graphene Nanoplatelets (GNPs) Reinforced Polymer Composites. Materials (Basel). 2020;13(9):2089.
6. Peltola H, Pääkkönen E, Jetsu P, Heinemann S. Wood based PLA and PP composites: Effect of fibre type and matrix polymer on fibre morphology, dispersion and composite properties. Compos Part A Appl Sci Manuf. 2014;61:13–22.
7. Mysiukiewicz O, Sterzyński T. Influence of Water on Tribological Properties of Wood-Polymer Composites. Arch Mech Technol Mater. 2017;37(1).
8. Aurrekoetxea J, Sarrionandia M, Gómez X. Effects of microstructure on wear behaviour of wood reinforced polypropylene composite. Wear. 2008;265(5–6).
9. Chen Q, Zhang R, Qin D, Feng Z, Wang Y. Modification of the physical-mechanical properties of bamboo-plastic composites with bamboo charcoal after hydrothermal aging. BioResources. 2018;13(1).
10. Chaudhary V, Ahmad F. Effect of moisture absorption on the wear and dynamic mechanical behavior of polymer composites. J Reinf Plast Compos. 2020;39(15–16).
11. Fan XJ, Lee SWR, Han Q. Experimental investigations and model study of moisture behaviors in polymeric materials. Microelectron Reliab. 2009;49(8).
12. Golovkova EA, Teplov AA, Tsetlin MB, Tikhomirov SA, Belousov SI. Effect of Friction on the Degree of Crystallinity of Composite Materials Based on Ultra-high-molecular-weight Polyethylene and Polytetrafluoroethylene with Quasicrystalline Filler Al–Cu–Fe. Crystallogr Reports. 2020;65(4).

  doi:10.5075/epfl-298799_978-2-9701614-0-0

STRUCTURAL HEALTH MONITORING (SHM) ON FIBRE REINFORCED COMPOSITE T-JOINT GEOMETRY MANUFACTURED BY A NOVEL 3R RESIN

Georgios Foteinidis[a], Maria Kosarli[a], Kyriaki Tsirka[a], Alaitz Ruiz De Luzuriaga[b], Stefan Weidmann[c], Alain Leroy[d], Thibault De Lumley Woodyear[e], Alkiviadis S. Paipetis[a]

a: Department of Materials Science & Engineering, University of Ioannina, Ioannina, 45110, Greece
b: CIDETEC, Basque Research and Technology Alliance (BRTA), Paseo Miramon 196, 20014 Donostia-San Sebastian, Spain
c: Leibniz-Institut für Verbundwerkstoffe GmbH, Erwin-Schroedinger-Str. Gebaeude 58, 67663 Kaiserslautern, Germany
d: COEXPAIR SA
e: SONACA S.A., Gosselies, Belgium

Abstract: *Due to the increased demand for fibre-reinforced composites in various fields, i.e., transportation and energy fields, the necessity of repairing damaged structures efficiently and with low cost was increased. For this reason, self-healing strategies were developed, including a novel vitrimer resin, 3R resin. In this research, the adhesion properties of the 3R resin were investigated on a T-joint geometry. Specimens with conventional resin were also manufactured in order to compare their properties. Additionally, Electrical Resistance Change Method (ERCM) was selected as an NDE technique and applied to T-joint geometries to monitor their behaviour during mechanical testing until the failure of the specimens.*

Keywords: NDE; SHM; CFRP; t-joint; vitrimer

1. Introduction

Fibre-reinforced composites nowadays possess a leading position in the aeronautics industry for primary aircraft components (e.g., Boeing 787, Airbus A350). Composite materials are mainly manufactured by thermoset resins. Although the thermosets have the advantage of the high strength to weight ratio, their repair is complicated and expensive. Due to these reasons, several self-healing approaches have been developed, including the micro-capsules containing the healing agent, vascular networks, or intrinsic polymers approaches [1–3]. This work presents a novel Re-processable, Repairable and Recyclable (3R) thermoset resin. The 3R properties are due to the reversible crosslinking in the cured thermoset resin. This resin can reduce costs and the time of repair [4].

Structural Health Monitoring (SHM) can provide vital information about the integrity of the component in real-time. Several Non-Destructive Techniques (NDT) are utilised for the SHM. Furthermore, some techniques exploit the inherent properties of the materials to identify their changes, such as electric-based methods. In this case, the materials used as reinforcing phases in composite, i.e., the electrical conductivity of the carbon nanotubes or the carbon fibres, also act as sensors. Impedance spectroscopy was utilised successfully on laminate to identify and locate delaminations after impact damage [5,6]. The laminate was manufactured by nano-

  doi:10.5075/epfl-298799_978-2-9701614-0-0

reinforced epoxy matrix and glass fibres, while a tailor-made layout of carbon fibres, which acted as electrodes, was introduced between specific layers [7].

In this research, Electrical Resistance Change Method (ERCM) was applied to T-joint geometries to monitor their behaviour during mechanical testing. The T-joints were manufactured using the novel 3R resin. Additionally, conventional T-joint specimens were subjected to the same tests to compare their differences.

2. Experimental

2.1 3R-T-joint manufacturing

For pull-off tests, T-joints were manufactured. Firstly, T-profiles were manufactured by prepreg hand lay-up and curing in the autoclave. A three-part mould was used in order to achieve the T-profile shape. The used material, lay-up, manufacturing setup and geometries are shown in Figure 1.

Material ID	Resin	Fabric	Resin content (%wt.)
3R-CF-PP	AIR-RES-7	C-WEAVE™ 280SA5 T800HB 6K 40B- 5HS with Spunfab 118CHQ 4 g/m2	35%
3R-GF-PP	AIR-RES-7	Glass fabric Hexforce 220, 109 g/m2	35%
NF	AIR-RES-7-C	TEXTREME Carbon tape 38 g/m2 (Torayca M30SC 18 k, unidirectional)	65%

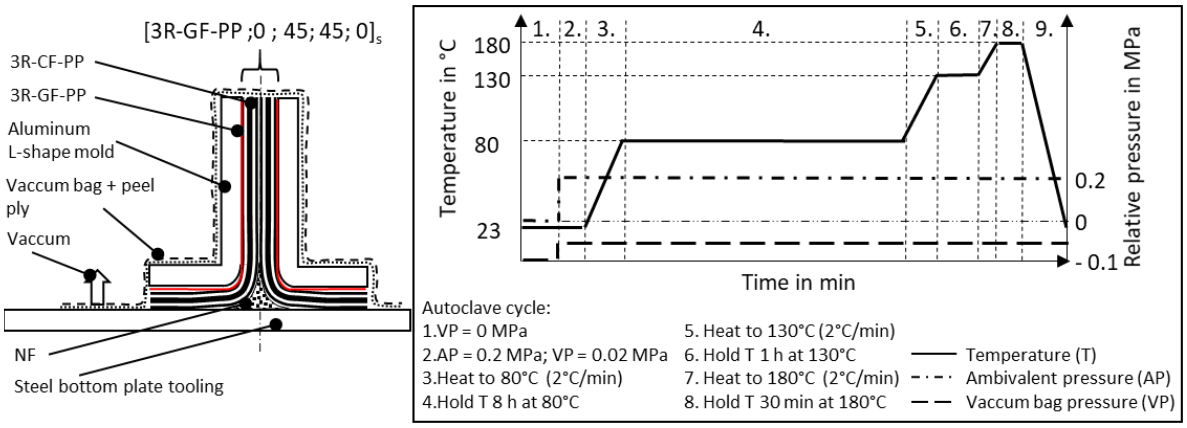

Figure 1: Manufacturing of T-profile in autoclave.

After manufacturing, the T-profile has to be joined to a flat laminate with a functional AIR-RES-7 coating, manufactured in an SQRTM process. For bonding preparation, the joining zone of the T-profile and the corresponding joining zone of the SQRTM flat laminate were sanded (grit 400) and degreased by using isopropanol. A 3R adhesive film (AIR-ADH-16F2-3) was placed between the sanded surfaces in order to achieve better bonding. The experimental setup and temperature profile used for joining the T-profile to the SQRTM laminate are shown in Figure 2.

  doi:10.5075/epfl-298799_978-2-9701614-0-0 published under CC BY-NC 4.0 license

Material ID	Resin	Description
T-profile	AIR-RES-7	See figure XX
AIR-ADH-16F2-3	AIR-RES-7	Optiveil 20103A Glass Veil (17 g/m²) as carrier material, impregnated with AIR-RES-7; thickness 0.26 mm; Glass transition temperature (T_g) = 55 °C
SQRTM laminate	Epoxy + AIR-RES-7 functional coating	Prepreg: CFRP 8552/AS4; Lay-up: 3R;(0/90/45/135/0/0/135/45/90/0);3R; Thickness: 2.22 mm

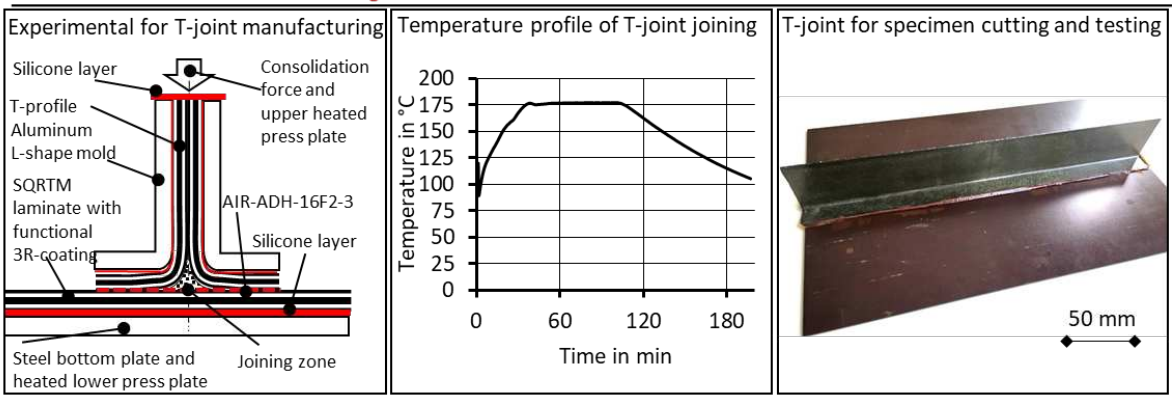

Figure 2: Joining of T-profile to SQRTM laminate by using a hot press.

A preheated hot-press was used to apply the necessary pressure to join the T-profile to the SQRTM-laminate by using the L-shaped-molds from the T-profile manufacturing as force introduction elements. In order to achieve a homogeneous pressure distribution of 2 MPa in the joining zone, silicone layers were placed below the SQRTM-laminate and on top of the T-profile flanges.

The same process was repeated for the manufacturing of reference T-joint specimens. A conventional 8552 layer of resin was used on the joining zone of the T-profile and the SQRTM flat laminate instead of the 3R film.

2.2 Mechanical characterisation

Mechanical testing was performed on a Universal Testing Machine WDW-100 by Jinan S.A. equipped with a 100kN loadcell. A special experimental setup for t-joint debonding (Figure 3) was used, and the displacement rate was set to 1 mm/min.

Figure 3. Special experimental setup for t-joint debonding.

  doi:10.5075/epfl-298799_978-2-9701614-0-0

2.3 Electrical resistance change method

A two-probe multimeter (Agilent 34401A) was utilised for the electrical resistance measurements. Copper electrodes were attached to the red marked areas of T-joint specimens with conductive silver resin, as depicted in Figure 4. The ERCM measurements were applied to the T-joint specimens simultaneously with the mechanical testing (online monitoring).

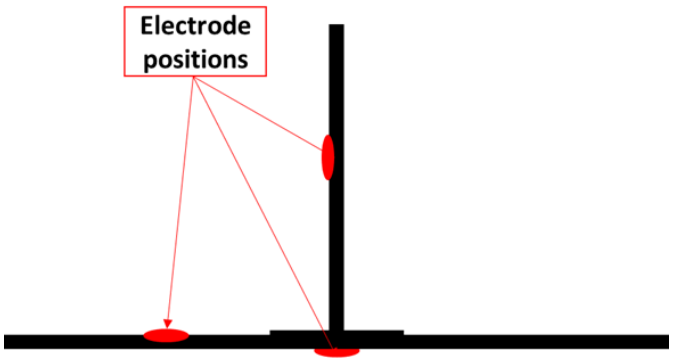

Figure 4: Schematic representation of T-joint geometry and the marked red areas where the electrodes were attached.

3. Results and discussion

3.1 Mechanical results

The results of the mechanical testing are presented in Figure 5. It can be observed that the specimens with the 3R resin film had a two-step failure, while the conventional one-step failure. This was attributed to the different failure modes of the 3R and conventional T-joint specimens. In the case of 3R specimens, the failure was cohesive, and the first step indicated the initiation of the adhesive layer failure in the centre (Figure 6-right) [8]. When the failure of the layer extended from the centre to the edges, a sudden second failure occurred. However, the conventional specimens revealed a single step that stated an adhesive failure (Figure 6-left). The mean max load of the conventional and the 3R specimens was 1.55 ± 0.14 kN and 1.12 ± 0.09 kN, respectively (Table 1).

  doi:10.5075/epfl-298799_978-2-9701614-0-0

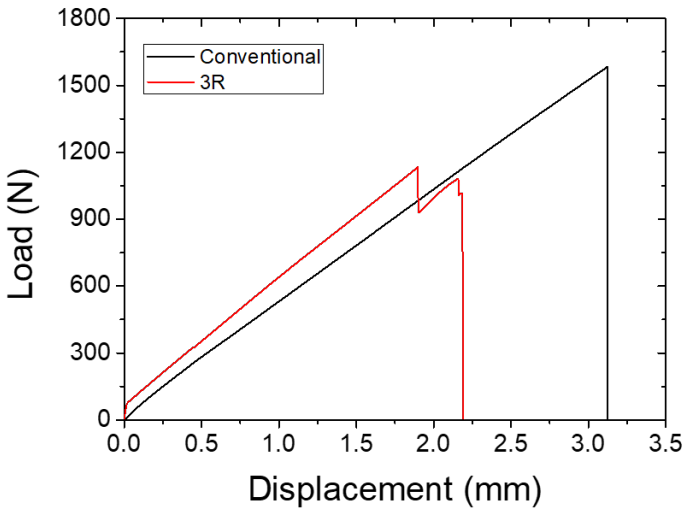

Figure 5: Representative mechanical results of T-joint specimens.

Table 1: Mechanical results of T-joint specimens.

Type of specimen	Max Load (kN)
Conventional	1.55 ± 0.14
3R	1.12 ± 0.09

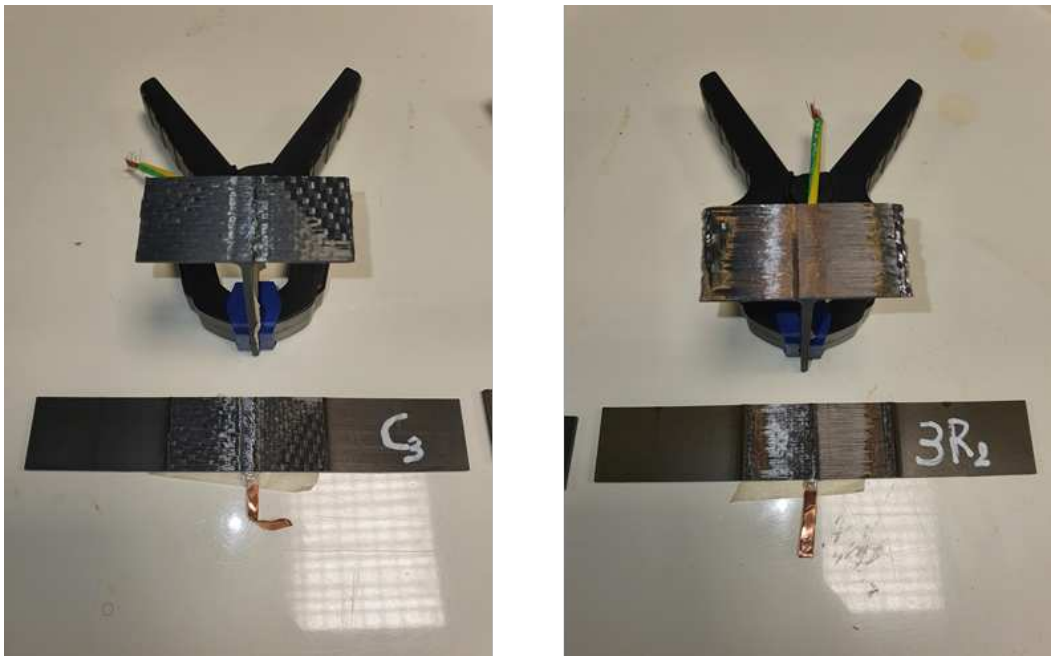

Figure 6: Pictures of the debonding area between the T-profile and the flat laminate of conventional (left) and 3R (right) T-joint specimens.

3.2 ERCM results

  doi:10.5075/epfl-298799_978-2-9701614-0-0 published under CC BY-NC 4.0 license

ERCM was applied to monitor the electrical resistance changes during mechanical testing. Figure 6 illustrates the Load (black curve) and the electrical resistance change (blue curve) versus Time results. The conventional specimen presented a strain sensitive area before the specimen failure, where the resistance was decreased. This decrease occurred due to bending flexural stress at the flat laminate before the failure of the specimen [9]. During the bending, the adjacent carbon fabrics were compressed in the through-thickness direction.

Additionally, the alignment of the fabrics was improved due to tensile forces on the opposite side of the flat panel. These two effects were responsible for the decrease of the resistance before failure. The debonding was designated by a sharp resistance increase, as the conductive path was corrupted.

On the other hand, the 3R laminate exhibited a less sensitive strain area. This occurred due to their increased stiffness and lower strength compared to the conventional specimens. The two-step failure was successfully observed, as the first debonding caused a slight increase in the resistance, while the second step led to the destruction of the conductive path.

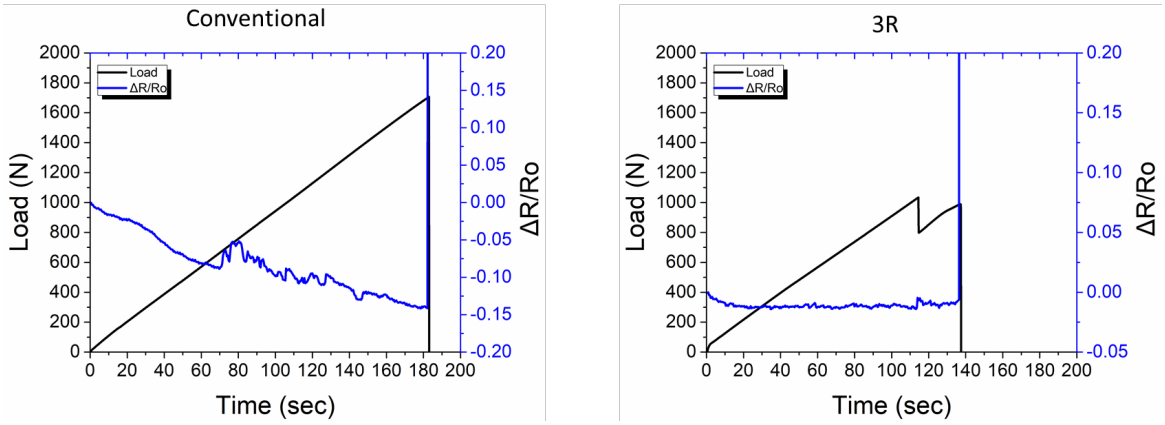

Figure 7: Representative ERCM results of conventional (left) and 3R (right) T-joint specimens.

4. Conclusions

In this research, a novel 3R resin was tested as an adhesion film between the T-profile and the flat laminate of T-joint geometry. Conventional specimens were also manifested in order to compare the mechanical properties. The Max Load of 3R specimens was decreased by 27.7% compared to conventional specimens. Furthermore, the failure mode was different, an adhesive failure was observed for the conventional specimens and a cohesive for the 3R. Regarding the ERCM, the 3R exhibited less sensitivity to the strain area than the conventional specimen. All debonings were recorded successfully in both types of specimens

5. References

1. Bekas DG, Baltzis D, Paipetis AS. Nano-reinforced polymeric healing agents for vascular self-repairing composites. Mater Des [Internet]. Elsevier Ltd; 2017;116:538–44. Available from: http://dx.doi.org/10.1016/j.matdes.2016.12.049
2. Kosarli M, Foteinidis G, Tsirka K, Bekas DG, Paipetis AS. Concurrent recovery of mechanical and electrical properties in nanomodified capsule-based self-healing epoxies. Polymer (Guildf) [Internet]. Elsevier Ltd; 2021;227:123843. Available from: https://doi.org/10.1016/j.polymer.2021.123843

  doi:10.5075/epfl-298799_978-2-9701614-0-0

3. Kosarli M, Polymerou A, Foteinidis G, Vazouras C, Paipetis AS. Healing efficiency of CNTs-modified-UF microcapsules that provide higher electrical conductivity and EMI shielding properties. Polymers (Basel). 2021;13.
4. Ruiz De Luzuriaga A, Martin R, Markaide N, Rekondo A, Cabañero G, Rodríguez J, et al. Epoxy resin with exchangeable disulfide crosslinks to obtain reprocessable, repairable and recyclable fiber-reinforced thermoset composites. Mater Horizons. 2016;3:241–7.
5. Grammatikos SA, Gkikas G, Paipetis A. Monitoring strain and damage in multi phase composite materials using electrical resistance methods. 2011;7982:1–6.
6. Grammatikos SA, Kouli M, Gkikas G, Paipetis AS. Structural health monitoring of aerospace materials used in industry using electrical potential mapping methods. 2012;8346:1–7.
7. Foteinidis G, Paipetis AS. A novel composite with structural health monitoring functionality via 2d and 3d impedance mapping topography. Appl Sci. 2021;11:1–19.
8. Zhang Y, Zhou Z, Tan Z. Compression shear properties of bonded-bolted hybrid single-lap joints of C/C composites at high temperature. Appl Sci. 2020;10.
9. Roh HD, Lee SY, Jo E, Kim H, Ji W, Park Y Bin. Deformation and interlaminar crack propagation sensing in carbon fiber composites using electrical resistance measurement. Compos Struct [Internet]. Elsevier; 2019;216:142–50. Available from: https://doi.org/10.1016/j.compstruct.2019.02.100

ACKNOWLEDGEMENTS:
"This project has received funding from the European Union's Horizon 2020 research and innovation program under grant agreement No 769274".

  doi:10.5075/epfl-298799_978-2-9701614-0-0

THE USE OF RECYCLED MATERIALS TOWARDS SUSTAINABILITY: BIOCOMPOSITES MANUFACTURED IN MELT COMPOUNDING

Luísa, Rosenstock Völtz [a, b] and Kristiina, Oksman [a, b,c]

a: Division of Materials Science, Department of Engineering Sciences and Mathematics, Luleå University of Technology, SE-97187 Luleå, Sweden – luisa.voltz@ltu.se
b: Wallenberg Wood Science Center (WWSC), Luleå University of Technology, SE-97187 Luleå, Sweden
c: Department of Mechanical & Industrial Engineering (MIE), University of Toronto, ON M5S 3G8 Toronto, Canada

Abstract. *Currently, there is a need in developing sustainable materials with an emphasis on reusing and recycling, to meet the sustainable development goals outlined by the United Nations for 2030. This work aimed to use recycled materials, such as recycled jeans and recycled rubber to replace the additive used in commercial wood polymer composites (WPCs) (reference material) to make it more sustainable without affecting its technical performance. The feeding of the post-used jeans fabric directly into the extruder was accomplished successfully with an increase in strength, modulus, and impact properties when compared with the reference material. The fracture surfaces showed that the fiber pullout contributed to the enhancement in fracture toughness with the addition of recycled jeans, further the addition of recycled rubber led to the matrix modification keeping the toughness at the same level as the reference material.*

Keywords: recycled materials; biocomposites; sustainability; mechanical properties

1. Introduction

Wood-polymer composites (WPCs) have been used as an excellent alternative to replace petroleum-based materials with the motivation to reduce environmental impact and make better use of natural resources, in addition to their specific properties such as low density, and high stiffness [1]. Due to environmental and sustainability requirements, the global WPC market is expected to reach $ 9 billion by 2027 compared with $ 4.7 billion in 2019 [2]. Several studies have focused on WPCs as a green material for applications such as construction, automotive, and furniture; however, the low impact strength is one of the major disadvantages of the WPCs [3].

The toughness of WPCs can be enhanced by modifying the matrix polymer and/or by the addition of long and tough fibers [4,5]. Elastomers such as EPDM (ethylene propylene diene monomer), and SEBS (styrene-ethylene butylene styrene) with and without maleic anhydride (MA) have been used as impact modifiers in WPCs [5–7]. For example, an addition of 10 wt.% of EPDM-rubber in PP-wood flour increased the notched Izod impact strength from 26 J/m to 38 J/m and 10 wt.% EPDM-MA increased it furthermore to 48 J/m [5]. Long and tough fibers such as sisal and man-made viscose fibers can also be used to increase the impact strength. In a previous study, long viscose fibers (10 wt.%) were used as an impact modifier in PP-jute composites resulting in excellent improved impact strength and toughness [4,8].

  doi:10.5075/epfl-298799_978-2-9701614-0-0

In 2015, the 17 Sustainable Development Goals (SDGs) were adopted by the members of the United Nations to move toward health and well-being worldwide, generating pressure in developing materials with reuse-recycling solutions [9]. For example, more than 27 million tons of cotton are produced every year globally. The cotton industry is one of the dirtiest industries in the world, responsible for considerable carbon dioxide emissions, and is very water-demanding, taking more than 10 tons of water to produce a single pair of jeans [10]. Because of the impacts, it is necessary to rethink alternatives reuses of post-consumer clothes. Few studies have been reported about the use of waste cotton in composites. In terms of raw materials, most of them use waste cotton fabrics or fibers from the leftover in the production line [11–15], and a few used post-consumer textile fabrics [16,17]. However, chemical pre-treatments [12,15,17] as well as energy-demanding processes to separate the cotton fibers from the textile [12,13,17] prior to their use in composites. In terms of composite manufacturing, the majority of the studies are about resin impregnation and compression molding [11,14,18–20] to create laminated composites, and only a few use melt processing [13,15,17]. According to our knowledge, our processing technique, to feed the textile into the extruder and separate it into cotton fibers in the compounding step is novel.

This study aims to investigate the effect on mechanical properties, focusing on the toughness of using post-consumer textile fabric with no pre-treatment, and recycled rubber in substitution of the existing commercial elastomer in WPC and contribute to the SDGs.

2. Materials and Method

2.1 Materials

- Commercial wood polymer composites consisting of 60 wt.% polypropylene copolymer (PP), 30 wt.% thermomechanical pulp (TMP), 10 wt.% elastomeric additive, and a minor amount of maleic anhydride polypropylene (MAPP) coupling agent – referee here as WPC30/10A, was kindly supplied by Stora Enso (Hylte Mill, Hylte, Sweden).
- Commercial wood polymer composite consisting of 60 wt.% PP, 40 wt.% TMP, and a minor amount of MAPP coupling agent, were kindly supplied by Stora Enso (Hylte Mill, Hylte, Sweden), referred to here as WPC40.
- Polypropylene copolymer was kindly supplied by Stora Enso (Hylte Mill, Hylte, Sweden).
- MAPP was kindly supplied by Stora Enso (Hylte Mill, Hylte, Sweden).
- Recycled rubber (TPRR 450) containing a 60 wt.% mixture of recycled polypropylene and high-density polyethylene (HDPE) and 40 wt.% recycled elastomer additives with an MFI of 7 g/min (230 °C/2.16 kg) was kindly supplied by Ecorub AB (Lövånger, Sweden).
- Lubricant (LUB) Struktol TPW113 was purchased from Struktol Company of America (Stow, OH, USA).
- Post-used textile fabric from a pair of jeans (called here recycled jeans). The recycled jeans fabric was cut into a 10 mm wide strip, no pre-treatment was performed before the compounding. All the materials were oven-dried overnight at 60 °C.

2.2 Method

2.2.1 Biocomposite processing

A masterbatch of the PP and textile fabric was first produced, having a targeted fiber content of 40 wt.%, PP content of 57.5 wt.%, 2 wt.% MAPP and 0.5 wt.% LUB. The compounding was made

using a co-rotating twin-screw extruder (Coperion W&P ZSK-18 MEGALab, Stuttgart, Germany). PP, MAPP, and LUB were premixed and fed using K-Tron gravimetric feeder (Niederlenz, Switzerland) to the main inlet in the extruder. The recycled jeans were fed using LFT (long-fiber-thermoplastic) process, in which the textile strip was fed into the side extruder, as shown in Figure 1a. The fiber content was controlled with screw speed and it was calculated using targeted fiber content, the weight of the textile strip per meter, length of screw revolution, and time [21]. The total throughput was 4 kg/h, the feeding rate of the polymer mixture was 2.4 kg/h, and the feeding rate textile strip was 1.6 kg/h. The side screw speed was 122 rpm. The extruder speed was 200 rpm and the profile temperature for the 7 zones was: 180, 185, 190, 190, 190 195, and 195 °C, respectively. The material was cooled using a water bath and pelletized. The pellets were dried in an oven.

The material formulations are shown in Table 1. The masterbatch was mixed with WPC40 before extrusion to produce WPC30/10J. The recycled rubber (TPRR 450) was also premixed before the extruder to produce WPC30/10R. For both compounding processes, the extruder screw speed was 300 rpm with a 3 kg/h throughput rate. The temperature setup was: 180, 185, 190, 195, 195, 200, and 200 °C. The material was cooled using a water bath and pelletized. The pellets were dried in an oven.

Table 1: Materials formulation.

Materials	PP (wt.%)	Fibers (wt.%)	IM (wt.%)[1]	MAPP (wt.%)	LUB (wt.%)
Masterbatch	57.5	40	-	2	0.5
WPC30/10J	58	30	10	2	-
WPC30/10R	58	30	10	2	-

[1] IM stands for impact modifier.

The WPC30/10A, WPC30/10J, and WPC30/10R (Figure 1b) were injection molded using Haake II MiniJet Pro Piston Injection Molding System (Thermo Fisher Scientific International, Karlsruhe, Germany). The pellets were manually fed into the cylinder (200 °C), the injection pressure was 400 bar for 40 s, and the mold temperature was set to 75 °C, the cooling pos-pressure was set to 150 bar for 30 s. The dog-bone shape specimens are following ASTM D638 (specimen type IV) [22]. Those specimens were used for tensile testing.

For the fracture toughness and impact test, the produced biocomposites were compressed molded using LabEcon 300 Fontijine Grotness press (Vlaardigen, The Netherlands). The pellets were placed into a mold between Millard-covered steel plates, pre-heated for 360 s at 200 °C, and pressed at a pressure of 5.9 MPa for 60 s, followed by cooling to room temperature (for 240 s). The desired specimen size was cut using a laser cutter machine (CMA0604-B-A, GD Han's Yueming Laser Group Co. Ltd., Guangdong, China).

2.2.2 Characterizations

The mechanical properties were tested according to ASTM D638 [22], using a Shimadzu Autograph AGX universal testing machine (Kyoto, Japan) with a 5 kN load cell, a gauge length of 25 mm, and a strain rate of 2.5 mm/min, connected to a non-contact video extensometer (DVE-201, Shimadzu, Kyoto, Japan). At least five samples were tested, and the average was presented.

  doi:10.5075/epfl-298799_978-2-9701614-0-0

The fracture surfaces were analyzed using a scanning electron microscope JEOL (JSM-IT300, Tokyo, Japan) with 10 kV acceleration voltage. The fracture surfaces were sputter-coated with platinum (10 nm).

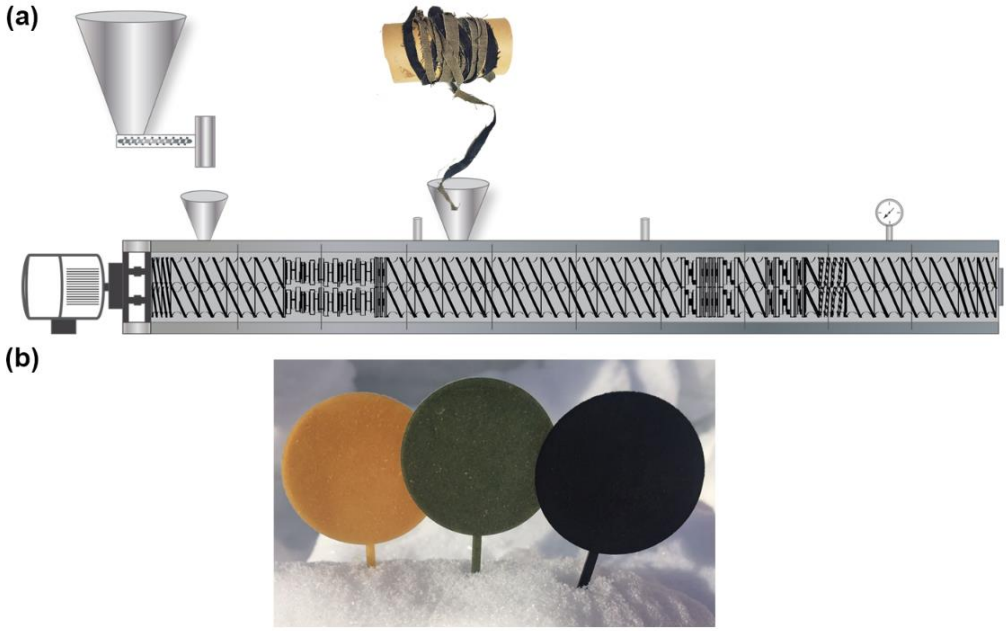

Figure 1. (a) Melt extrusion processing showing how the recycled jeans were fed into the extruder, and (b) the biocomposites from left to right (WPC30/10A, WPC30/10J, and WPC30/10R).

Fracture toughness tests were carried out in a universal test system Instron 4411 (Instron, Norwood, MA, USA) using a three-point bending test, following ASTM D5045 [23], with a load cell of 500 N and a test speed of 10 mm/min. The specimen's size was 28x6x3 mm³. The notch was produced by a saw cutting (0.5 mm width) with an average depth of 2 mm. The pre-cracking was produced by slowly pressing a fresh blade in the notch, attaching the blade to the upper grip of the universal testing machine, and compressing to the specimen at a constant speed of 0.1 mm/min until reaches a maximum extension of -1.2 mm. At least three samples were tested, and the average was presented. After breakage, measurements of crack propagation were done using a Nikon Stereomicroscope (SMZ1270, Tokyo, Japan).

The load-displacement impact curves of the samples were investigated using an Instron Dynatup mini-tower drop weight tester (Instron, Norwood, MA, USA). The compression-molded samples size was 100x100x1.4 mm³ and was fully clamped on the sample holder. The clamped samples were impacted with a velocity of 1.6 m/s, and 3.6 kg drop mass, resulting in 4.9 J of impact energy.

The one-way analysis of variance (ANOVA) and Tukey's HSD (Honestly Significantly Different) tests, with a 5% significance level, were applied for tensile results, with the calculations performed by Past 4.0 software. The specimens were conditioned for 40 hours at 25 °C and 50% relative humidity before the test for all characterizations mentioned above.

3. Results and Discussions

  doi:10.5075/epfl-298799_978-2-9701614-0-0

Figure 2 shows the tensile testing results, it shows that the addition of recycled jeans increases the modulus and strength when compared with other materials. The modulus increased from 2.4 (±0.1) GPa to 3.7 (±0.4) GPa with the addition of 10 wt.% recycled jeans. The modulus for WPC30/10R was around 2.3 (±0.1) GPa. The recycled jeans had an increment of 17% in strength to around 46 (±1) MPa, while the strength of WPC30/10R was around 30 (±1) MPa. The addition of recycled rubber contributes to a slightly better elongation at break, around 4.1 (±0.6) %. The toughness (absorbed energy) calculated from the area under the curve is shown in Table 2, where it can be noted that all materials presented similar values for the toughness.

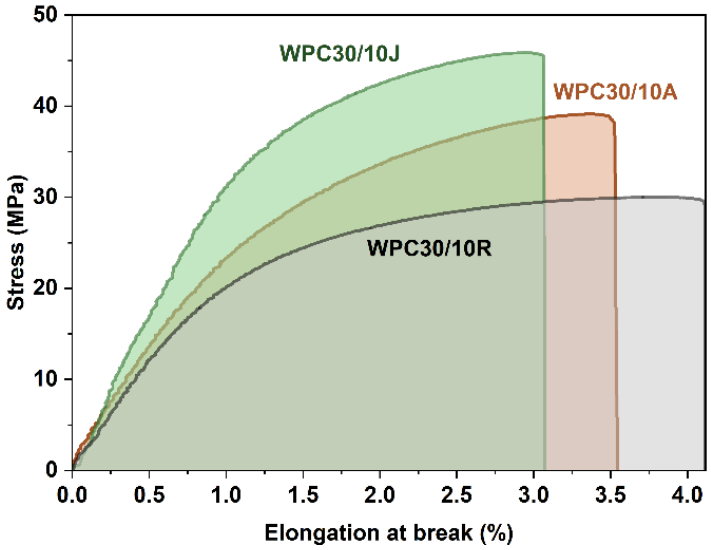

Figure 2. Representative tensile testing curves.

Table 2: Toughness calculated by the area under tensile curves.

Biocomposites	Toughness (MJ/m³)
WPC30/10A	1.0 (±0.1) [A]
WPC30/10J	1.1 (±0.1) [A]
WPC30/10R	1.1 (±0.2) [A]

[A/B] Marked with the same letter within the same column is not significantly different at a 5% significant level based on ANOVA and Tukey's tests.

The SEM images from the fracture surface of tensile samples are shown in Figure 3. The presence of fiber pullouts is visible, indicated with white arrows, which are expected to correspond to the cotton fibers separated from the jeans (Figure 3a). In addition, the wood fibers (indicated by black arrows) are characterized more by fiber breakage or fiber tearing. Regarding the addition of the recycled rubber (Figure 3b), small round rubber particles, indicated by the red arrow, are visible in the PP matrix, it is more difficult to see the fibers in these composites which indicate a good interface and adhesion between the matrix and the fibers.

The load-displacement curves of the fracture toughness are shown in Figure 4a and the load-time curves from the impact test are shown in Figure 4b. It can be noted that the failure load for the fracture toughness specimens presents the highest value with the addition of the recycled jeans, around 26 N, failure load is around 21 N for the WPC30/10A and 19 N for WPC30/10R.

  doi:10.5075/epfl-298799_978-2-9701614-0-0

The load-time curves for the falling weight impact test show similar behavior compared with the fracture toughness, the impact load for WPC30/10J around 115N and the values around 104 N for WPC30/10A and WPC30/10R. The fracture toughness and impact test results together with the SEM images indicate that the recycled jeans can contribute to a higher energy absorbance because of the long fiber pull-out mechanism.

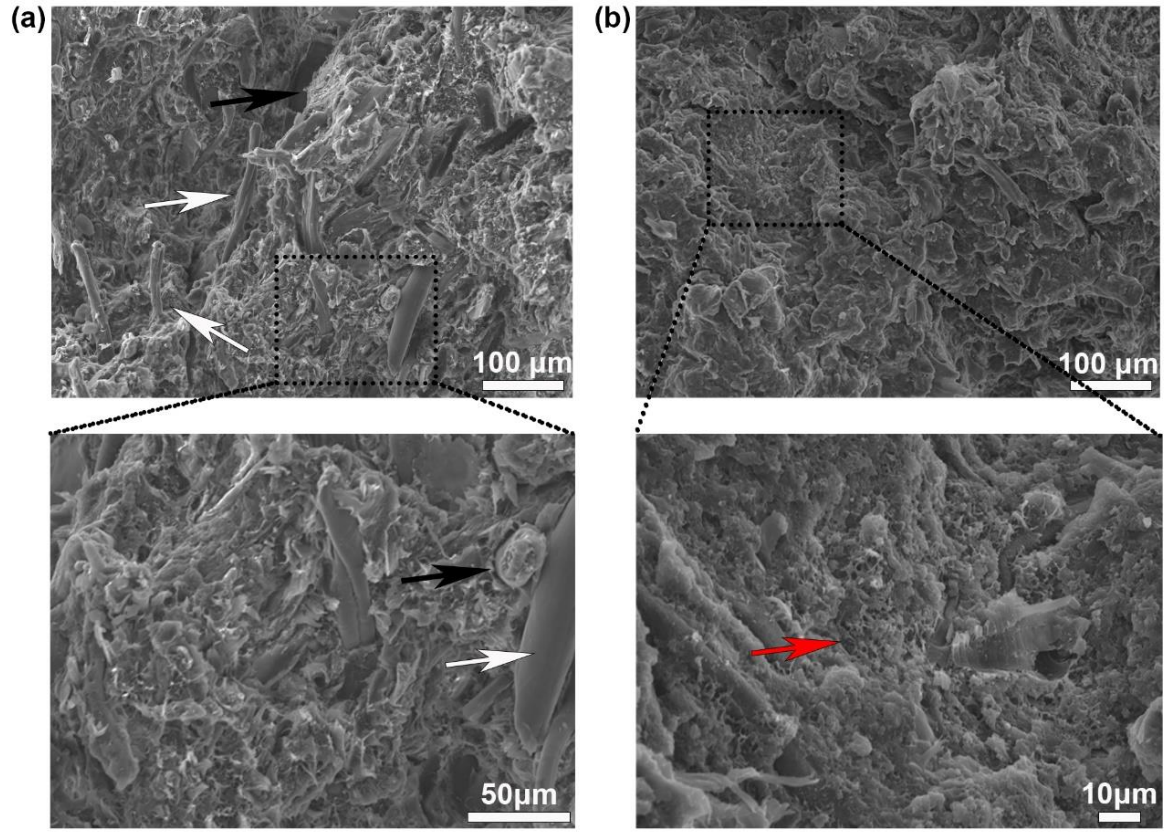

Figure 3. SEM micrographs of (a) WPC30/10J and (b) WPC30/10R.

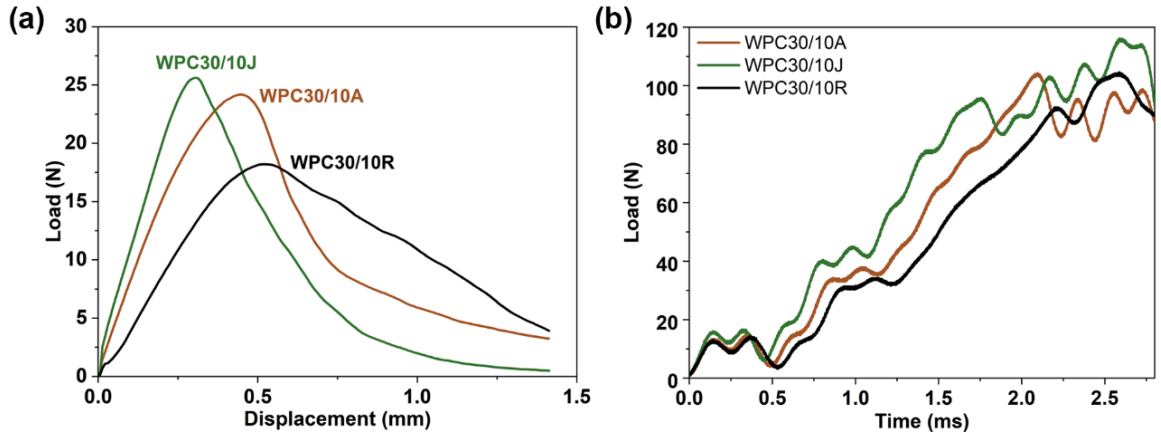

Figure 4. (a) Load-displacement curve from fracture toughness and (b) Load-time curve from impact test.

This study has demonstrated that giving a second chance of a pair of jeans and used as an additive without any pre-treatments and direct feeding using an extrusion process show improved mechanical properties of the WPC in substitution of 10 wt.% elastomeric additive. The

  doi:10.5075/epfl-298799_978-2-9701614-0-0 published under CC BY-NC 4.0 license

addition of recycled rubber showed that besides a slight decrement in tensile properties still recycled EPDM can be used in substitution of the elastomeric additive since the impact properties were similar compared with the reference WPC. The substitution of the elastomeric additive for recycled materials can contribute to a more sustainable future without compromising the properties of the material. To improve our knowledge in this study digital image correlation and x-ray diffraction microtomography are being performed.

Acknowledgments

The authors would like to thank Stora Enso AB and Knut och Alice Wallenbergs Stiftelse for their financial support. In addition, the authors would like to thank Mr. Matthew Smith from Stora Enso AB, and Mr. Mattias Karlsson from Ecorub AB for providing the materials. Also, thank the Wallenberg Wood Science Center.

4. References

1. Faruk O, Bledzki AK, Fink H-P, Sain M. Biocomposites reinforced with natural fibers: 2000–2010. Prog Polym Sci. 2012 Nov 1;37(11):1552–96.

2. Wood Plastic Composite Market Size, Share | Report, 2020-2027 [Internet]. [cited 2022 Mar 28]. Available from: https://www.fortunebusinessinsights.com/wood-plastic-composite-market-102821

3. Huang L, Wu Q, Li S, Ou R, Wang Q. Toughness and crystallization enhancement in wood fiber-reinforced polypropylene composite through controlling matrix nucleation. J Mater Sci. 2018 May;53(9):6542–51.

4. Ranganathan N, Oksman K, Nayak SK, Sain M. Effect of long fiber thermoplastic extrusion process on fiber dispersion and mechanical properties of viscose fiber/polypropylene composites. Polym Adv Technol. 2016;27(5):685–92.

5. Oksman K, Clemons C. Mechanical properties and morphology of impact-modified polypropylene–wood flour composites. J Appl Polym Sci. 1998;67(9):1503–13.

6. Hasanpour M, Mazidi MM, Aghjeh MKR. The effect of rubber functionality on the phase morphology, mechanical performance and toughening mechanisms of highly toughened PP/PA6/EPDM ternary blends. Polym Test. 2019 Oct 1;79:106018.

7. da Silva ALN, Coutinho FMB. Some properties of polymer blends based on EPDM/PP. Polym Test. 1996 Jan 1;15(1):45–52.

8. Oksman K, Mathew AP, Långström R, Nyström B, Joseph K. The influence of fibre microstructure on fibre breakage and mechanical properties of natural fibre reinforced polypropylene. Compos Sci Technol. 2009 Sep;69(11–12):1847–53.

9. THE 17 GOALS | Sustainable Development [Internet]. [cited 2022 Mar 28]. Available from: https://sdgs.un.org/goals?msclkid=885717cbae7911ec87732a2526bc70e5

10. TheWorldCounts. World Cotton Production Statistics [Internet]. [cited 2022 Mar 23]. Available from:

https://www.theworldcounts.com/challenges/consumption/clothing/world-cotton-production-statistics/story?msclkid=ed4ac57aaab011ec984e981e5229856b

11. Mishra R, Behera B, Militky J. Recycling of textile waste into green composites: Performance characterization. Polym Compos. 2014;35(10):1960–7.

12. Serra A, Tarrés Q, Claramunt J, Mutjé P, Ardanuy M, Espinach FX. Behavior of the interphase of dyed cotton residue flocks reinforced polypropylene composites. Compos Part B Eng. 2017 Nov 1;128:200–7.

13. Montava-Jordà S, Torres-Giner S, Ferrandiz-Bou S, Quiles-Carrillo L, Montanes N. Development of Sustainable and Cost-Competitive Injection-Molded Pieces of Partially Bio-Based Polyethylene Terephthalate through the Valorization of Cotton Textile Waste. Int J Mol Sci. 2019 Jan;20(6):1378.

14. Wei B, Xu F, Azhar SW, Li W, Lou L, Liu W, et al. Fabrication and property of discarded denim fabric/polypropylene composites. J Ind Text. 2015 Mar 1;44(5):798–812.

15. Araújo RS, Rezende CC, Marques MFV, Ferreira LC, Russo P, Emanuela Errico M, et al. Polypropylene-based composites reinforced with textile wastes. J Appl Polym Sci. 2017;134(28):45060.

16. Haque Anma, Naebe M. Sustainable biodegradable denim waste composites for potential single-use packaging. Sci Total Environ. 2022 Feb 25;809:152239.

17. Petrucci R, Nisini E, Puglia D, Sarasini F, Rallini M, Santulli C, et al. Tensile and fatigue characterisation of textile cotton waste/polypropylene laminates. Compos Part B Eng. 2015 Nov 1;81:84–90.

18. Lee JT, Kim MW, Song YS, Kang TJ, Youn JR. Mechanical properties of denim fabric reinforced poly(lactic acid). Fibers Polym. 2010 Feb 1;11(1):60–6.

19. Todor M-P, Kiss I, Cioata VG. Development of fabric-reinforced polymer matrix composites using bio-based components from post-consumer textile waste. Mater Today Proc. 2021 Jan 1;45:4150–6.

20. Sezgin H, Kucukali-Ozturk M, Berkalp OB, Yalcin-Enis I. Design of composite insulation panels containing 100% recycled cotton fibers and polyethylene/polypropylene packaging wastes. J Clean Prod. 2021 Jul 1;304:127132.

21. Ranganathan N, Oksman K, Nayak SK, Sain M. Structure property relation of hybrid biocomposites based on jute, viscose and polypropylene: The effect of the fibre content and the length on the fracture toughness and the fatigue properties. Compos Part Appl Sci Manuf. 2016 Apr 1;83:169–75.

22. Standard Test Method for Tensile Properties of Plastics [Internet]. [cited 2022 Mar 3]. Available from: https://www.astm.org/d0638-14.html

23. Standard Test Methods for Plane-Strain Fracture Toughness and Strain Energy Release Rate of Plastic Materials [Internet]. [cited 2022 Mar 3]. Available from: https://www.astm.org/d5045-14.html

FULLY BIO-BASED EPOXY-AMINE RESINS FROM CIRCULAR ECONOMY: CONCEPTION, MULTISCALE STRUCTURAL AND MECHANICAL BEHAVIOUR CHARACTERIZATION TOWARD LOW CARBON-FOOTPRINT COMPOSITES

Nour MATTAR, Valérie LANGLOIS, Estelle RENARD, Agustin RIOS DE ANDA

Institut de Chimie et des Matériaux Paris-Est (CNRS) – agustin.rios-de-anda@u-pec.fr

Abstract: In this study, fully bio-based epoxy-amine thermoset resins were synthetized and formulated. Formulations based on resorcinol diglycidyl ether (RE) were cured with an aliphatic (hexaméthylènediamine – HMDA), a cycloaliphatic (diamine-limonene – DA-LIM), or an aromatic (diamine-allyl eugenol – DA-AE) structure. Diglycidyl ether of bisphenol A (DGEBA) cured with HMDA served as a petrosourced benchmark. By considering a multiscale experimental approach combining thermal analyses (DSC and DMA), mechanical testing (bending, fracture toughness, creep and fatigue crack propagation), and Time-Domain NMR, it was found that the resins depend on the network structure characterized by the chemical and physical crosslink density. It was demonstrated that the three considered fully bio-based matrices showed better mechanical behavior compared to DGEBA/HMDA. These formulations were then reinforced with recycled carbon fibers. The obtained fully-biobased composites exhibited better mechanical properties than the petrosourced benchmark, which was explained by a better fiber-matrix interface wetting and interactions. This work shows that the studied fully bio-based can be considered as potential candidates for functional applications. Finally, the proposed multiscale approach combining macroscopic mechanical studies with molecular time-domain NMR allowed us to soundly deepen the understanding of the structure−property relationship for such functional materials.

Keywords: biosourced thermosets; renewable composites; multiscale analysis; mechanical behavior

1. Introduction

For the past several years, increasing interest on bio-based thermoset materials as functional matrices for technical applications has been experienced [1−4]. Indeed, the aim and challenge of such studies are to obtain similar thermal and mechanical properties compared to existing materials obtained from fossil resources, while contributing to a greener chemistry and materials science approach. Moreover, a means to reinforce such matrices through a carbon footprint reduction is to consider recycled carbon fibers versus natural or synthetic fibers [5,6]. In that regard, in our group, neat epoxy-amine-based thermosets and recycled carbon reinforced composites with these same matrices have been successfully synthesized, formulated, and studied [7-9]. The epoxy monomer was resorcinol diglycidyl ether (RE), which is commonly obtained from glucose or from waste from the paper industry [10] Two amines synthesized from (R)-(+)-limonene (citrics) and eugenol (wood industry), potentially obtainable through circular economy, were used as in-house hardeners in such studies. A third amine, hexamethylenediamane (HMDA), was also used. HMDA is usually obtained from petrochemistry processes but can be produced nowadays from bio-based sources [11]. Thus, HMDA can also be considered as a biosourced hardener in the forthcoming future. The aim of this abstract is to briefly summarize the synthesis of the aforementioned two novel amine hardeners (*i.e.* derived

  doi:10.5075/epfl-298799_978-2-9701614-0-0

from limonene and eugenol), their formulation with RE to obtain thermoset epoxy-amine resins, their mechanical characterization both for instantaneous (DMA, bending, fracture toughness) [7,8] and aging tests (creep, fatigue crack propagation) [7,12], and their potential as matrices for recycled carbon fiber composites [7,9]. Such an investigation is carried out through a multiscale approach relating the thermosets' inner chemical and network structure characterized by ^{1}H Time Domain Double Quantum (TD-DQ) NMR to their macroscopic mechanical behaviors [12,13]. This approach allowed us to fully understand the applicative potential of these novel resins compared to standard petrosourced materials.

2. Results and discussion

The synthesis of limonene- and eugenol-based biosourced amines (DA-LIM and DA-AE respectively) as well as the formulation of the fully biosourced and benchmark petrosourced resins with either RE or DGEBA has been detailed in [7,8]. Figure 1 shows the chemical structures of each monomer and the obtained resins after optimized curing.

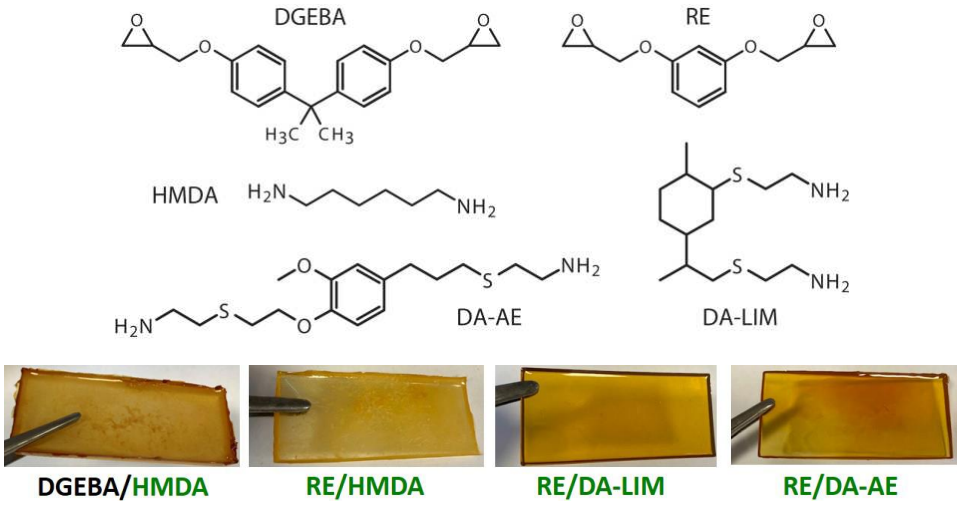

Figure 1. Chemical structures of DGEBA, RE, HMDA, DA-AE, and DA-LIM, and optimized cured resins obtained in this work.

Details on experimental measurements are detailed in [7-9,12,13]. Once the resins where obtained, their mechanical properties were studied. The flexural modulus E_F, strength σ_F, and strain ε_F were determined by three-point bending tests. The obtained values are listed in Table 1, where it can be seen that the flexural properties of all the resins are reasonably comparable.

Table 1: Bending and fracture toughness data for the studied resins.

Resin	Bending			Fracture toughness	
	E_F (GPa)	σ_F (MPa)	εF (%)	K_{IC} (MPa·m$^{1/2}$)	G_{IC} (J/m^2)
DGEBA/HMDA	2.5 ± 0.4	89 ± 15	6 ± 2	0.63 ± 0.05	±
RE/HMDA	3.0 ± 0.8	93 ± 16	7 ± 2	0.63 ± 0.03	±
RE/DA-AE	2.2 ± 0.5	85 ± 11	15 ± 2	0.81 ± 0.10	±
RE/DA-LIM	2.7 ± 0.7	99 ± 16	8 ± 3	0.93 ± 0.05	±

  doi:10.5075/epfl-298799_978-2-9701614-0-0

Indeed, all resins have flexural strengths σ_F close or greater than 80 MPa while the flexural moduli E_F vary between 2 and 3 GPa. Such values are similar to those reported for petroleum-based thermosets. To deepen the understanding regarding the influence of the chemical structure on the mechanical properties of the studied resins, the flexural moduli E_F were plotted as a function of the number of atoms per theoretical repeating unit. Figure 2a shows an example of a theoretical unit for RE/HMDA while Figure 2b shows this plot.

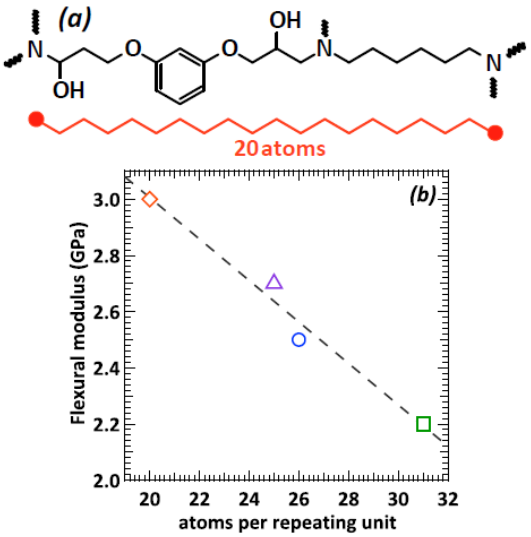

Figure 2. (a) Schematic representation of the number of atoms per repeating unit for RE/HMDA and (b) evolution of the flexural modulus EF with the number of atoms per repeating unit for the studied resins. The dashed line is a linear fit and serves as a guide for the eyes.

Figure 2b shows that when the number of atoms per theoretical repeating unit increases, EF decreases and interestingly, that it follows a linear relationship, leading to conclude that for the studied resins, when the number of atoms per repeating unit increases, E_F decreases.

Concerning the fracture toughness properties, it is clearly noticed in Table 1 that RE/DA-LIM and RE/DA-AE matrices have greater K_{IC} and G_{IC} values than those obtained for DGEBA/HMDA and RE/HMDA. This means that RE/DA-LIM and RE/DA-AE are tougher and resist better to the propagation of cracks. The difference of fracture toughness behavior can be also linked to the choice of the hardener, since both DGEBA and RE epoxy monomers possess aromatic rings in their structure. Indeed DA-AE and DA-LIM seem to yield networks with more mobile chains between two crosslink points, leading to tougher resins [7,8]. From a benchmark approach, the fully bio-based resins cured with the amine hardeners synthesized in this work possess higher fracture toughness values not only to our petrosourced internal reference (*i.e.* DGEBA/HMDA). This means that to reach the same toughening behavior, these biosourced resins can avoid the use of external common toughening agents such as nano-particles (*i.e.* montmorillonite, nano-CNT's, nano-silica, and nano-rubbers) to improve their fracture toughness.

Afterwards, the creep behavior of these resins was evaluated. Figure 3 shows that all of the studied samples exhibit a similar creep lifetime span within the temporal limits of the SSM accelerated method. Furthermore, when comparing a given flexural load, Figures 3a (*i.e.* 20% of max. load), 3b (*i.e.* 40% of max. load), and 3c (*i.e.* 60% of max. load) show that the fully biobased RE/HMDA, RE/DA-LIM, and RE/DA-AE resins can sustain, in this order, a higher strain deformation for a similar lifetime span resistance when compared to the petro-sourced

  doi:10.5075/epfl-298799_978-2-9701614-0-0

DGEBA/HMDA formulation. This is somehow surprising as from a visco-elastic perspective a ductile material (*i.e.* for which its plastic behavior is larger than that of a stiffer material) under creep loads will tend to deform easily, leading to an early failure under prolonged loads [14,15]. The fact that the three fully bio-based formulations are able to stand larger strain or deformations without failing within the same lifetime span when compared to a stiffer petro-sourced formulation lead to deduce that such materials possess a good compromise between toughness and creep resistance.

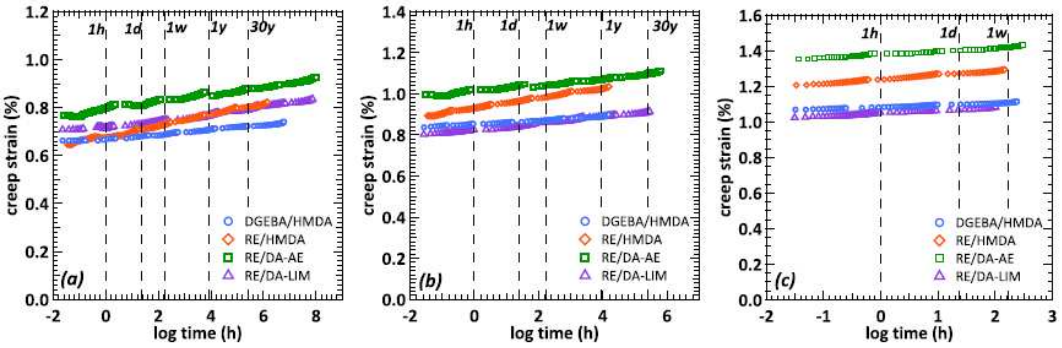

Figure 3. Estimated long term creep properties measured at 23°C for all samples at (a) 20%, (b) 40%, and (c) 60% of their maximum flexural load.

To deepen this study, lifetime aging prediction tests under dynamic loading were considered. Fatigue Crack Propagation (FCP) measurements were carried out on all formulations at 23°C. Figure 4 shows the obtained crack propagation rate *da/dN* as a function of the stress intensity factor *ΔK* for all samples.

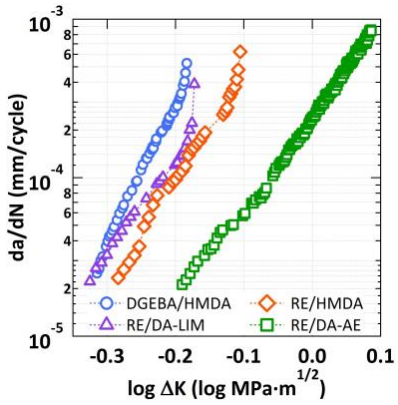

Figure 4. Fatigue crack propagation behavior at 23 °C for all studied samples.

Figure 4 shows that the fully bio-based resins, *i.e.* RE/HMDA, RE/DA-LIM, and RE/DA-AE possess better FCP properties when compared to DGEBA/HMDA, indeed the propagation of cracks in these materials happens for larger stress intensity factor *ΔK* values. This can be translated as the need to apply a higher amount of energy to propagate the crack, leading to tougher, more resistant materials. Moreover, the trends observed by creep and FCP measurements do not follow the same trend observed for the flexural and fracture toughness instantaneous static properties presented before. The only sample for which its static and aging behaviors seem to be directly correlated is for the DGEBA/HMDA which possesses a high flexural modulus E_F and a low fracture toughness resistance K_{IC}, while exhibiting the lesser creep and FCP resistance. For the rest of the formulations, such a direct correlation is not observed. For instance RE/HMDA

had a higher flexural modulus E_F and a lower fracture toughness resistance K_{IC} when compared to RE/DA-LIM. This would mean that as regards static measurements RE/HMDA has a more brittle behavior than RE/DA-LIM, which is not observed concerning creep and FCP measurements. To clarify this, the inner network structure was obtained by ^{1}H TD-DQ NMR. Specifically, the dipolar residual constant D_{res}, which is analogous to the crosslink density was calculated from such measurements. Figure 5 shows the obtained D_{res} values as a function of the crosslink density v_C calculated by DMA for the studied resins.

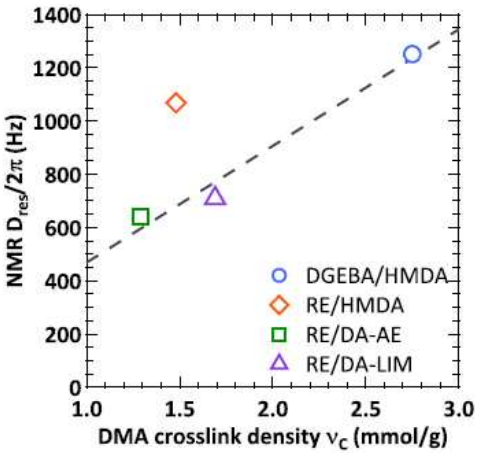

Figure 5. Fatigue crack propagation behavior at 23 °C for all studied samples.

Figure 5 shows that DGEBA/HMDA, RE/DA-LIM, and RE/DA-AE follow the same linear trend linking D_{res} and v_C. However RE/HMDA does not follow this trend. This could be due to the fact that RE/HMDA has a faster curing kinetics compared to the other three resins [7,12]. It can be thus expected that RE/HMDA is a readily reactive resin and the network gelates quickly at the beginning of curing. As the system is tightly crosslinked in this phase, reactive ends still available would not be able to find each other through simple diffusion as part of the matrix is already thermoset. This would eventually lead to these reactive ends to not wholly react and form a partially crosslinked matrix and would be observed experimentally as a material with lower a chemical crosslink density than expected. Nevertheless, RE/HMDA exhibits a D_{res} value significantly higher than that for RE/DA-LIM and RE/DA-AE and somehow comparable to that of DGEBA/HMDA. Indeed, this is due to the capacity of ^{1}H TD-DQ NMR to be able to probe and quantify physical entanglements and chemical crosslinks, whereas DMA can only quantify chemical crosslinks [12,13]. This means that RE/HMDA possesses more physical entanglements, thus, the difference between instantaneous and aging mechanical behaviors for this resin can be then attributed to a synergetic compensatory effect between a low chemical crosslink density with a large concentration of physical entanglements. These physical entanglements would act as semi-hard mechanical reinforcements, increasing the instantaneous mechanical behavior of the matrix. Yet, since these entanglements are not solidly bonded to the network, their influence would be less important than that of chemical nodes over long periods of time (*i.e.* aging) as the former tend to relax faster than the latter. This would lead RE/HMDA to have an improved ductile behavior, exhibiting a better resistance to creep and FCP when compared to more brittle matrices such as DGEBA/HMDA.

Finally, these matrices were reinforced with PAN-based recycled carbon fibers via Vacuum Assisted Resin Infusion (VARI) process. We investigated the mechanical properties of these

  doi:10.5075/epfl-298799_978-2-9701614-0-0

composites while proposing an alternate low carbon-footprint approach to obtain low carbon-footprint functional polymers for structural applications. Figure 6 shows the tensile, compression and flexural properties of the obtained composites.

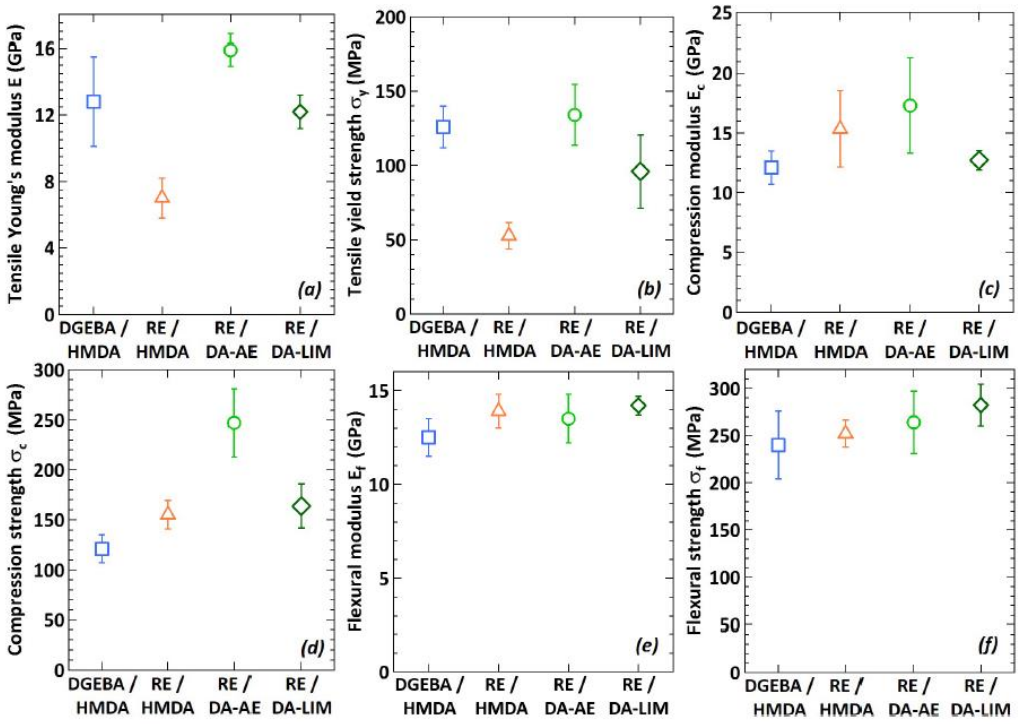

Figure 6. Tensile, compression and flexural mechanical properties of all composites.

Figure 6 shows that fully bio-based composites exhibit overall comparable to better mechanical properties when compared to DGEBA/HMDA. This amelioration was attributed to better matrix-fiber interactions for RE/DA-AE and RE/DA-LIM evidenced by SEM images shown in Figure 7.

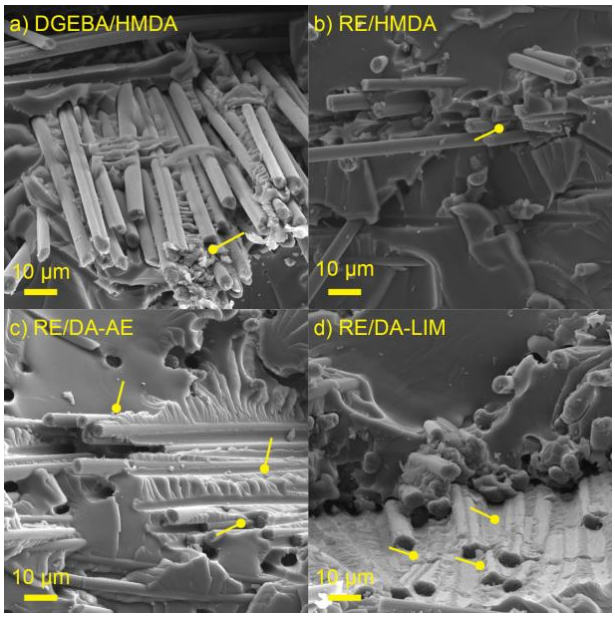

Figure 7. SEM images of the fracture surfaces of bending samples for all composites.

  doi:10.5075/epfl-298799_978-2-9701614-0-0

For DGEBA/HMDA and RE/HMDA, debonding of the fiber-matrix interface was observed whereas for RE/DA-AE and RE/DA-LIM, the mechanical failure occurred in the matrix, leading to conclude that the interface effectively complied with its role to transfer mechanical loads from the matrix to the fibers.

3. Conclusion

This work summarizes the synthesis of two novel amine hardeners from biobased molecules. These hardeners were then used to cure a biobased epoxy to obtain fully-biobased thermoset resins. The instantaneous and aging mechanical properties of these resins were investigated. These measurements demonstrated that the three fully bio-based matrices (*i.e.* RE/HMDA, RE/DA-LIM, and RE/DA-AE) possessed a better compromise between flexural, fracture toughness, creep and fatigue crack propagation (FCP) behaviors when compared to to the petrosourced benchmark material (*i.e.* DGEBA/HMDA). Furthermore, a multiscale experimental approach combining the aforementioned experiments with ^{1}H Time-Domain DQ NMR allowed us to discern the evolution of the resins mechanical behavior with its network structure. It was observed for DGEBA/HMDA, RE/DA-LIM, and RE/DA-AE that the mechanical properties depend directly on the resin's network morphology, characterized by their chemical and physical crosslink densities. In the case of RE/HMDA, the physical entanglements probed by ^{1}H TD-DQ NMR seem to behave as semi-hard mechanical reinforcements acting as stress relaxation points against creep and FCP. These entanglements would allow the material to possess instantaneous thermomechanical properties (*i.e.* flexural and fracture toughness) closer to those of brittle materials while conferring a ductile behavior over long periods of time. This synergetic phenomenon would lead to an improvement of its FCP properties, as observed in this work. Moreover, although not mentioned in this abstract, previous investigations showed that these same materials possessed interesting glass-transition temperature Tg, mechanical properties and good composite processability and mechanical behavior compared to other biosourced and similar petrosourced resins [7-9,12,13]. A signature of this is that the fully bio-based resins reinforced with recycled carbon fibers exhibited the best mechanical properties in tensile, compression and flexural modes when compared to a petrosourced benchmark material. The improvement of such a behavior was attributed to a better fiber-matrix interface interaction for these bio-based resins. By combining these results, it can be established that these bio-based epoxy-amine resins possess outstanding functional mechanical properties and could be candidates for potential resin and fiber-reinforced composite structural applications. Finally, the original proposed multiscale approach presented in this work, *i.e.*, combining macroscopic mechanical characterizations with molecular ^{1}H Time-Domain DQ NMR measurements, had not yet been considered so far for such thermoset resins. This approach presents itself as a sound and robust tool to deepen the understanding on the structure−property relationship for functional materials.

Acknowledgements

This project was funded by the I-SITE Future (Ph.D. thesis funding for Nour Mattar) and the International Mobility Grant from the Université Paris Est (Uiversité Paris Est Créteil-ICMPE & University of Bayreuth collaboration).

  doi:10.5075/epfl-298799_978-2-9701614-0-0

4. References

1. Aouf C, Nouailhas H, Fache M, Caillol S, Boutevin B, Fulcrand H. Multi-functionalization of Gallic Acid. Synthesis of a Novel Bio-based Epoxy Resin. Eur. Polym. J. 2013; 49: 1185−1195.
2. Maiorana A, Spinella S, Gross RA. Bio-based Alternative to the Diglycidyl Ether of Bisphenol A With Controlled Materials Properties. Biomacromolecules 2015; 16: 1021−1031.
3. Ma S, Li T, Liu X, Zhu J. Research Progress on Bio-based Thermosetting Resins. Polym. Int. 2016; 65: 164-173.
4. Mashouf Roudsari G, Mohanty AK, Misra M. Green Approaches to Engineer Tough Biobased Epoxies: A Review. ACS Sustainable Chem. Eng. 2017; 5: 9528-9541.
5. Meyer LO, Schulte K, Grove-Nielsen E. CFRP-recycling following a pyrolysis route: process optimization and potentials. J. Compos. Mater. 2009; 43: 1121-1132.
6. Pimenta S, Pinho ST. Recycling carbon fibre reinforced polymers for structural applications: Technology review and market outlook. Waste Manage. 2011; 31: 378-392.
7. Mattar N. Matériaux Composites Biosourcés pour la Construction Durable. Ph.D. Thesis, Université Paris Est Créteil, France, 2021.
8. Mattar N, Rios de Anda A, Vahabi H, Renard E, Langlois V. Resorcinol-Based Epoxy Resins Hardened with Limonene and Eugenol Derivatives: From the Synthesis of Renewable Diamines to the Mechanical Properties of Biobased Thermosets. ACS Sustainable Chem. Eng. 2020; 8: 13064-13075.
9. Mattar N, Langlois V, Renard E, Rademacker T, Hübner F, Demleitner M, Altstädt V, Ruckdäschel H, Rios de Anda A. Fully Bio-Based Epoxy-Amine Thermosets Reinforced with Recycled Carbon Fibers as a Low Carbon-Footprint Composite Alternative. ACS Appl. Polym. Mater. 2021; 3: 426-435.
10. Gioia C, Banella MB, Vannini M, Celli A, Colonna M, Caretti D. Resorcinol: A Potentially Bio-based building block for the Preparation of Sustainable Polyesters. Eur. Polym. J. 2015; 73: 38-49.
11. Jiang Y, Loos K. Enzymatic Synthesis of Biobased Polyesters and Polyamides. Polymers 2016; 8: 243.
12. Mattar N, Hübner F, Demleitner M, Brückner A, Langlois V, Renard E, Ruckdäschel H, Rios de Anda A. Multiscale Characterization of Creep and Fatigue Crack Propagation Resistance of Fully Bio-Based Epoxy-Amine Resins. ACS Appl. Polym. Mater. 2021; 3: 5134-5144.
13. Mattar N, Renard E, Langlois V, Rios de Anda A. Multiscale Network Structure Analysis by Time Domain 1H DQ NMR and DMA of Resorcinol Diglycidyl Ether-Jeffamine Matrices. ChemistrySelect 2020 ; 5 : 11291-11298.
14. Grellmann W, Seidler S. Polymer Testing. Carl Hanser Verlag. 2013.
15. Hallary JL, Lauprêtre F, Monnerie L. Polymer Materials, Macroscopic Properties and Molecular Interpetrations. John Wiley & Sons. 2010.

  doi:10.5075/epfl-298799_978-2-9701614-0-0

MECHANISM-BASED ASSESSMENT OF CELLULOSE-BASED BIOCOMPOSITE COTTONID FOR SUSTAINABLE CONSTRUCTION

Ronja Scholz, Frank Walther

TU Dortmund University, Chair of Materials Test Engineering (WPT)
Baroper Str. 303, D-44227 Dortmund, Germany – ronja.scholz@tu-dortmund.de

Abstract: *Exploitation of finite resources and climate change are critical consequences of industrialization and lead to the urgent demand for new approaches concerning sustainable materials, especially in the building industry, which is defined by huge resource consumption. Cellulose-based biocomposites are a promising material class, since they are sustainable and have physical and mechanical similarities to wood as construction material. In this study, Cottonid as a traditional cellulose-based technical biopolymer is characterized concerning its structural performance. Quasi-static tests are performed on two different material variants in varying hygrothermal test conditions using mechanical testing systems in combination with integrable climate chambers. Accompanying microstructural in situ experiments in analytical devices enable an understanding of effective material-specific damage mechanisms. The results are used as an experimental basis for optimization of the manufacturing process as well as mathematical description of the humidity- and temperature-dependent deformation behavior, which can directly be used for dimensioning of Cottonid elements for reliable structural applications.*

Keywords: Sustainable construction; technical biopolymers; Cottonid; thermoelasticity; temperature and humidity dependency

1. Introduction

Todays' constitution of earth's climate system and its reserves of resources is alarming, so the need for direct action is urgent if we want to preserve our natural habitat. Since industrial processes and products, especially in the building industry, are heavily resource and energy consuming, sustainable approaches in this field can make a considerable contribution to increase sustainability in engineering. Further, the possibility of ecological recirculation of the used resources during production as well as at the end of the product lifetime is an important topic to reduce pollution due to non-degradable and environmentally harmful materials. [1]

Cellulose-based biocomposites are an attractive alternative to building materials based on finite resources, like crude oil and minerals, since cellulose is the main molecular component of plant material and therefore very accessible. Wood as traditional construction material is a so-called naturally grown biocomposite and constitutes of cellulose, hemicelluloses and lignin as main molecular components, which give wood its outstanding mechanical property spectrum. Since sustainable construction gets more and more popular due to the environmental awareness of the society, the demand on wood and wood products has increased considerably in the last decades, which is a good development in terms of sustainable and environmentally friendly materials, but, on the other hand, leads to an increasing destruction of existing forests, since wood is a slowly growing resource, and hence to poorer air quality. Therefore, the technical

  doi:10.5075/epfl-298799_978-2-9701614-0-0

qualification of cellulose-based biocomposites with comparable properties to wood has to be focused to introduce new approaches in the field of sustainable construction. [2, 3]

Cottonid is a fully cellulose-based biocomposite, which was already patented before industrialization as the first modified natural material, with a mechanical strength comparable to some technical plastics and wood and a pronounced deformation capacity. These attributes underline the technological potential of Cottonid and qualify the material for the aforementioned challenge to act as a new option to contribute to resource efficiency and preserve existing forests. [4]

Within this study, the humidity- and temperature-dependent strength-deformation behavior of industrially available as well as structurally optimized Cottonid variants are determined and correlated with their process-related microstructure. Quasi-static investigations in application-oriented surrounding atmospheres and instrumented with thermometry to detect material's reactions during loading are performed. For the implementation as building material, especially the transition between elastic and plastic deformation is of interest, since yielding of the material within the application, which would lead to damage and therefore failure of the construction, has to be avoided. The mechanical values at the end of the elastic region can therefore be defined as maximum load capacities and be used for the dimensioning of Cottonid elements for construction-related applications. To identify material-specific damage and failure mechanisms, mechanical in situ experiments within a computed tomography system are performed to visualize the inner structures of the material during loading and derive essential findings.

2. Experimental procedure

2.1 Biocomposite Cottonid

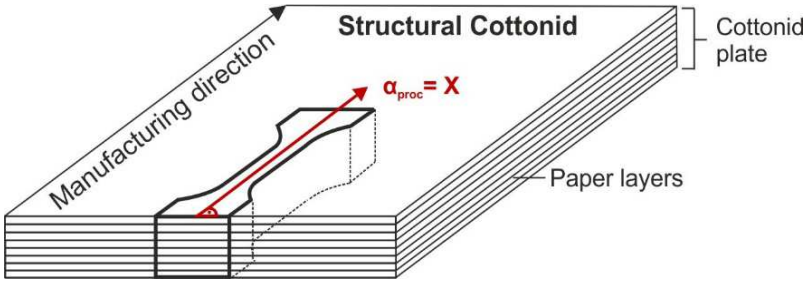

Figure 1. Scheme of specimen location parallel to manufacturing direction $\alpha_{proc} = X$ in a plate of structural Cottonid (h_{mat} > 1 mm) for mechanical tests; according to [5].

The manufacturing principle of Cottonid is called parchmentizing. Unsized paper layers with a high content of α-cellulose are treated with a chemical catalyst to produce new hydrogen bonds between the cellulose short fibers. This results in a homogenization of the microstructure within one paper layer and enhances its material properties, i.e. mechanical strength and ductility. This procedure can also be used to combine several paper layers with each other to produce a homogeneous structural material with varying thickness based on the amount of paper layers used in this process step. [4] Due to the directed paper making process, the cellulose short fibers contained in the layers have a preferred orientation in manufacturing direction, which is still visible after the parchmentizing procedure. For Cottonid, this results in direction-dependent properties, e.g. increased strength parallel to manufacturing direction and an increased

  doi:10.5075/epfl-298799_978-2-9701614-0-0

deformability perpendicular to it. Therefore, within a mechanical assessment, the location and orientation of the specimen is highly relevant. Figure 1 shows a schematic sketch of a Cottonid plate, in which a dogbone shaped specimen geometry is indicated. The orientation of the specimen according to manufacturing direction is termed α_{proc}. [5]

For the investigations, industrially available Cottonid material (*Hornex*, Ernst Krueger) and the structurally optimized variant M60Z50 is used, which was developed in cooperation with the Technical University of Munich. For structural optimization, decisive manufacturing parameters, like cellulose source CS, reaction time t_{react} in catalyst bath, chemical catalyst Cat and process temperature T_{Cat} have been adjusted in a laboratory-scale test setup and Cottonid variants with varying process-related microstructures have been produced. Pretests revealed increased mechanical properties for the parameter combination M60Z50, see Table 1, so a mechanical benchmark study for this variant is presented in comparison to the industrial standard. [6] Specimens were prepared out of Cottonid plates parallel (α_{proc} = X) to manufacturing direction with a thickness of h_{mat} = 2.5 mm.

Table 1. Manufacturing parameters of structurally optimized Cottonid variant M60Z50.

Cellulose source CS	Reaction time t_{react} [sec]	Chemical catalyst Cat	Process temperature T_{Cat} [°C]
Cotton linters M	60	Zinc dichloride solution Z	50

2.2 Test setup and procedure

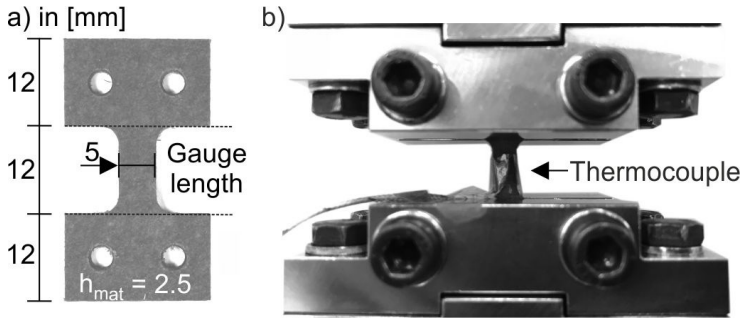

Figure 2. Mechanical testing: a) Specimen geometry, according to [7], [b) mounted specimen instrumented with thermocouple.

For the determination of tensile properties of Cottonid, a customized specimen geometry was chosen, see Figure 2 a), to be able to correlate the results with accompanying in situ investigations in a micro computed tomograph (µCT). Tests were carried out using a servohydraulic testing system (F_{max} = 30 kN, Shimadzu) with a strain rate of $\dot{\varepsilon}$ = 2x10^{-3} s^{-1} according to the corresponding standard [8] for the determination of tensile properties of plastics. To monitor material's reactions during loading, specimens were instrumented with a thermocouple, see Figure 2 b), to interpret damage initiation and evolution before final failure.

For the superimposition of application-oriented test conditions, an integrable climate chamber (THC, Shimadzu) was used. The respective combinations of ambient temperature T_{amb} and

  doi:10.5075/epfl-298799_978-2-9701614-0-0

relative humidity φ_{amb} were chosen by orienting on earth's climate zones [9] and are summarized in Table 2.

Table 2. Hygrothermal test conditions.

Test condition		Ambient temperature T_{amb} [°C]	
		MT	HT
Relative humidity [%]	LH	23°C, 10%	60°C, 10%
	MH	23°C, 50%	60°C, 50%
	HH	23°C, 95%	60°C, 95%

2.3 In situ experiments

For the in situ identification of material-specific defects and damage mechanisms and the investigation of damage initiation and evolution in Cottonid due to a quasi-static mechanical load, a micro tensile/compression testing module (F_{max} = 5 kN, 5000CTGCT-RT, Deben UK) was integrated into a µCT (max. beam voltage $U_{B,max}$ = 160 kV, X TH 160, Nikon Metrology). Tensile tests with a crosshead speed of v = 0.5 mm/min were interrupted at respective stress steps until final failure of the specimen, and three-dimensional volumes of the gauge length were reconstructed out of 1583 projections per scan ($U_{B,scan}$ = 125 kV) with an effective pixel size of 7 µm with industrial CT software (VGStudio Max V.2.2, Volume Graphics) via threshold defect analysis. [7]

3. Results and discussion

3.1 Tensile tests

In Figure 3, tensile stress σ_T is plotted over nominal total strain ε_t for industrial (Ind.) and structurally optimized (M60Z50) Cottonid material for α_{proc} = X and MT-MH test conditions (see Figure 1 and Table 2). Also shown is the thermal response ΔT of the material variants onto the mechanical loading.

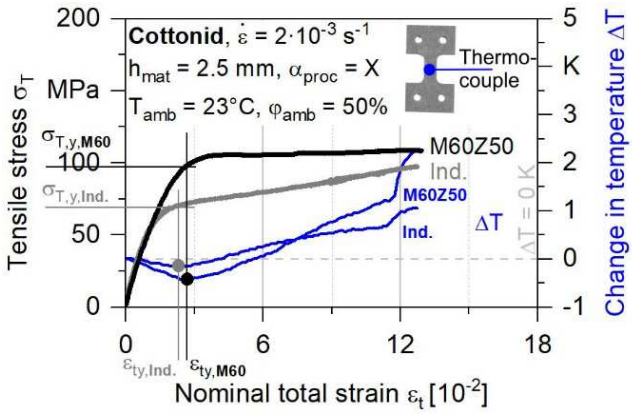

Figure 3. Stress-strain curves of Cottonid (industrial, M60Z50) at MT-MH test conditions with monitoring of temperature profile during loading, according to [10].

Cottonid is characterized by an elastic-plastic deformation behavior with a continuous transition between the two regions. In the plastic region, the industrial material shows a strengthening effect until final failure, whereas for M60Z50 this effect is not visible and it rather behaves nearly linear elastic-plastic. In general, the adjustment of the manufacturing parameters results in enhanced structural behavior, since with a tensile stress at yield of $\sigma_{T,y,\mathbf{M60}}$ = 95.59 MPa (nominal yield strain $\varepsilon_{ty,\mathbf{M60}} = 2.48 \cdot 10^{-2}$) the yield strength of M60Z50 is ~50% higher compared to the industrial material with $\sigma_{T,y,\mathbf{Ind.}}$ = 65.26 MPa ($\varepsilon_{ty,\mathbf{Ind.}} = 1.53 \cdot 10^{-2}$). This finding will be correlated with the respective microstructure and discussed further in chapter 3.2. [10]

With regard to the thermal response of the two material variants, Cottonid is characterized by thermoelastic material behavior typical for polymeric materials [11], which is defined by a decrease of ΔT until reaching the yield strength. When passing $\sigma_{T,y}$ and ε_{ty}, respectively, a nearly linear increase of ΔT can be detected, which is interrupted by a sudden leap in ΔT occuring right before final failure of the specimens at σ_m. Elastic deformation of Cottonid therefore obviously results in a temperature decrease, which can be attributed to decreasing entropy of the system. Since Cottonid is based on cellulose short fibers, a rearrangement of the fibers in loading direction, i.e. a higher structural order due to elastic deformation of the system, is expected, resulting in the described entropy-based thermoelastic effect. [12] Because of this behavior, the thermal response of Cottonid during loading enables a precise determination of the onset of yielding, which is difficult for materials with a continuous transition between the elastic and the plastic region, like Cottonid. Mechanical values at failure are comparable for both material variants with $\sigma_{m,\mathbf{M60}}$ = 108.82 MPa ($\varepsilon_{tb,\mathbf{M60}} = 12.92 \cdot 10^{-2}$) and $\sigma_{m,\mathbf{Ind.}}$ = 97.43 MPa ($\varepsilon_{tb,\mathbf{Ind.}} = 12.79 \cdot 10^{-2}$). Since in technical applications plastic deformation of components is critical, $\sigma_{T,y}$ and the relation between $\sigma_{T,y}$ and σ_m are important values for component design and can obviously be improved during manufacturing. [10]

Following this procedure, quasi-static tests were performed on industrial Cottonid material for all hygrothermal test conditions summarized in Table 2. The results for tensile properties at yield, i.e. $\sigma_{T,y}$ and ε_{ty}, are depicted in Figure 4.

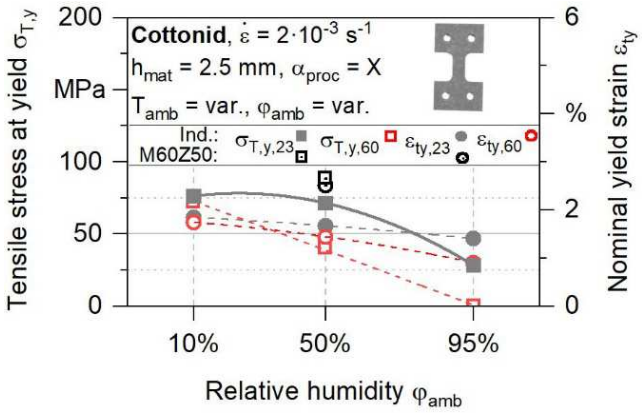

Figure 4. Humidity- and temperature-dependent tensile properties ($\sigma_{T,y}$, ε_{ty}) of industrial (Ind.) and structurally optimized (M60Z60) Cottonid material, according to [10].

Compared to MT–MH test conditions, low values of φ_{amb} result into a slightly increased yield strength of $\sigma_{T,y,\mathbf{MT-LH}}$ = 72.50 MPa (+9%), whereas it decreases to $\sigma_{T,y,\mathbf{MT-HH}}$ = 23.75 MPa (-64%) corresponding to high values of φ_{amb}. Since Cottonid is a hygroscopic material, it takes up water molecules from the atmosphere at high values of φ_{amb} and releases them again, when φ_{amb} is

  doi:10.5075/epfl-298799_978-2-9701614-0-0

low, which influences its strength and deformability. It is noticeable, that for MT in LH and MH test conditions, tensile properties at yield stay relatively constant, whereby for HH test conditions (φ_{amb} = 95%), a significant drop in yield strength is visible. With regard to research on wood, this can be correlated with hydrogen bonds contained in the material, which form crystalline regions at low values of φ_{amb}, which means, that the material has a higher resistance against yielding. [13] Also depicted are the results for M60Z50 in MT–MH test conditions to demonstrate the possibility of performance enhancement through microstructural tuning. [6, 10] To describe the interdependencies between the onset of yielding of industrial Cottonid material and environmental parameters for modeling of the material behavior and lifetime prediction, polynomial functions were used, which fit the obtained data points with $R^2 \geq 0.9$. The resulting mathematical description for $\sigma_{T,y}$ as a function of φ_{amb} at MT test conditions is given in Eq. (1). [10]

$$\sigma_{T,y,\boldsymbol{Ind.,23}} = 72.6 + \frac{\varphi_{amb}}{2} - \frac{(\varphi_{amb})^2}{100} \text{ [MPa]} \quad (1)$$

Table 3. Humidity- and temperature-dependent tensile properties of Cottonid (industrial, M60Z50; h_{mat} = 2.5 mm, α_{proc} = X), according to [10].

Test condition		Tensile properties			
T_{amb}	φ_{amb}	$\sigma_{T,y}$ [MPa]	ε_{ty} [%]	σ_m [MPa]	ε_{tb} [%]
MT	LH	71.26 ± 1.08	1.84 ± 0.10	88.44 ± 0.43	9.30 ± 0.50
HT		69.72 ± 8.09	1.74 ± 0.09	81.84 ± 2.45	4.40 ± 0.21
MT	MH	66.23 ± 0.73	1.67 ± 0.19	93.81 ± 3.41	12.31 ± 0.42
		88.62 ± 5.77 (M60Z50)	2.5 ± 0.18 (M60Z50)	108.71 ± 3.57 (M60Z50)	13.28 ± 1.66 (M60Z50)
HT		39.18 ± 2.03	1.44 ± 0.10	70.46 ± 2.45	12.08 ± 0.71
MT	HH	24.18 ± 0.31	1.40 ± 0.08	78.17 ± 0.59	23.01 ± 0.46
HT		0.44 ± 0.07	0.90 ± 0.18	26.76 ± 1.04	25.28 ± 2.06

Tests were repeated at elevated temperature T_{amb} = 60°C (HT) to investigate temperature influences. For HT–MH and HT–HH test conditions a pronounced decrease of strength-related values, i.e. σ_T and $\sigma_{T,y}$, can be detected. It is assumed, that higher values for T_{amb} result in a drying effect, which reduces the deformability of Cottonid and affects its strength. In HT–HH test conditions, Cottonid shows an enormous deformability, like in MT–HH test conditions, but nearly no mechanical strength is left, so these surrounding conditions are unsuitable for structural applications of Cottonid elements. [10]

In sum, variations in φ_{amb} have an influence on the deformability of Cottonid but its mechanical strength seems not to affected heavily at medium values of T_{amb}. With standard deviations between 5 – 6%, see Table 3, Cottonid's strength properties are very reliable for MT test conditions, therefore, Eq. (1) for mathematical description of the humidity-dependent yield

  doi:10.5075/epfl-298799_978-2-9701614-0-0

strength of industrially available Cottonid material are an appropriate approach for the humidity-dependent design of Cottonid elements for structural applications. Also, the results of the test series with M60Z50 show a high reproducibility, which verificates the enhancement of the structural behavior of Cottonid due to adjustment of manufacturing parameters.

3.2 In situ investigations

Detected void volume percentages for industrial and M60Z50 Cottonid material in relation to the initial condition are plotted over applied σ_T in Figure 5. It is remarkable, that the structurally optimized variant inherits a much smaller amount of initial defects, i.e. pores and microcracks, in comparison to the industrial standard, which can be correlated with the enhanced tensile properties at yield (see Figure 3 and Figure 4). Further, for the industrial standard, the overall void volume increases significantly until final failure of the specimen, whereas for M60Z50 it nearly stays the same. [7] The adjustment of manufacturing parameters to produce M60Z50 therefore obviously leads to less defects in initial condition, i.e. a higher structural integrity, and enables the production Cottonid elements with customized properties.

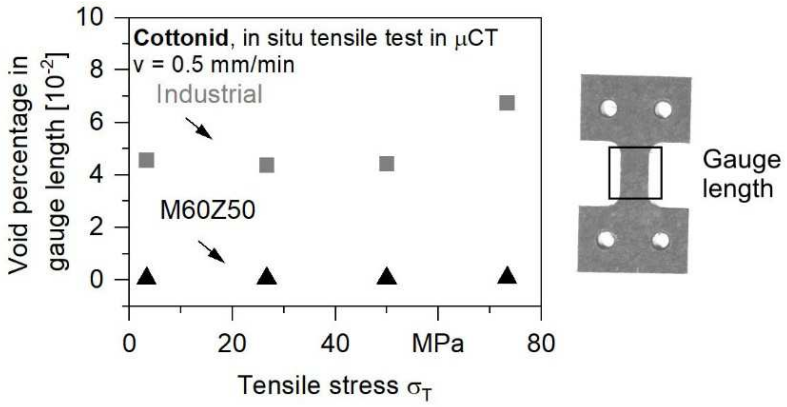

Figure 5. Percentage development of void volume for Cottonid (industrial, M60Z50; h_{mat} = 2.5 mm, α_{proc} = X), according to [7].

4. Summary and outlook

To implement sustainability into construction-related applications, especially within the building industry, Cottonid can serve as an alternative to conventional building materials based on mineral resources and can reduce the critical demand on wood and wood products. This work provides basic design guidelines for Cottonid elements with respect to microstructural and environmental factors. Based on this research it is now possible to estimate the structural performance of Cottonid in different service conditions and to optimize manufacturing parameters to reach a higher structural integrity resulting in enhanced mechanical properties. The implementation of structurally optimized Cottonid variants with customized strength-deformation behavior for construction-related applications can help to counteract to critical earth trends described above.

In future investigations, physical sensors will be implemented in Cottonid material, e.g. optical fibers, to realize a structural health monitoring, like it is state of the art for long-term monitoring of engineering structures in service.

  doi:10.5075/epfl-298799_978-2-9701614-0-0

Acknowledgements

The authors thank the German Research Foundation (Deutsche Forschungsgemeinschaft, DFG) for funding the research projects "Biomechanical qualification of the structurally optimized functional material Cottonid as an adaptive element" (WA 1672/23-1, ZO 113/22-1) and "Mechanism-based development and validation of a structural health monitoring for climate adaptive architectural Cottonid elements" (WA 1672/23-2, ZO 113/22-2), project no. 325009350. Further thanks to the colleagues from TUM, Cordt Zollfrank and Matthias Langhansl, for providing M60Z50 material within an excellent scientific collaboration, and the Ernst Krueger GmbH & Co. KG for providing industrial reference material.

5. References

1. World Wide Fund For Nature. Living planet report 2018. WWF 2018, Gland. ISBN 978-2-940529-90-2.
2. AL-Oqla F M, Omari M A. Sustainable biocomposites: Challenges, potential and barriers for development. Green Biocomposites, Green Energy and Technology 2017; 13-29. http:\\doi.org\10.1007/978-3-319-46610-1_2.
3. Forest Products Laboratory. Wood handbook - Wood as engineering material. Forest Products Laboratory. Centennial edition. United States Department of Agriculture (USDA), Washington 2010. ISBN 978-0891-161240.
4. Taylor T. U.S. patent 114,880. 16 March 1871.
5. Scholz R, Mittendorf R-M, Engels JK, Hartmaier A, Kuenne B, Walther F. Direction-dependent mechanical characterization of cellulose-based composite vulcanized fiber. Materials Testing 2016; 58(10):813-817. http:\\doi.org\10.3139/120.110929.
6. Scholz R, Langhansl M, Zollfrank C, Walther F: Humidity-sensing material Cottonid – Microstructural tuning for improved actuation and fatigue performance. Frontiers in Materials 2020; 7:1-10. http:\\doi.org\10.3389/fmats.2020.00156.
7. Scholz R, Delp A, Walther F. In situ characterization of the damage initiation and evolution in sustainable cellulose-based Cottonid. TMS 2021 Annual Meeting & Exhi-bition Supplemental Proceedings, The Minerals, Metals & Materials Series 2021; 867-878. http:\\doi.org\10.1007/978-3-030-65261-6_77
8. DIN EN ISO 527-1. Plastics – Determination of tensile properties - Part 1: General principles. Beuth, Berlin 2012.
9. Hegger M, Fuchs M, Stark T, Zeumer M. Energie Atlas. Birkhäuser, Basel 2007. http:\\doi.org\10.11129/detail.9783034614498.
10. Scholz R. V. Mechanism-based assessment of structural and functional behavior of sustainable Cottonid. Dissertation, TU Dortmund University, Springer Vieweg, Wiesbaden 2022, ISBN 978-3-658-37539-3.
11. Godovsky Y K. Thermophysical properties of polymers. Springer, Berlin 1992. ISBN 978-3-642-51670-2. http:\\doi.org\10.1007/978-3-642-51670-2.
12. Pitarresi G. Found M S. Patterson E A. An investigation of the influence of macroscopic heterogeneity on the thermoelastic response of fibre reinforced plastics. Composites Science and Technology 2005; 65(2):269-280. http:\\doi.org\10.1016/j.compscitech.2004.07.008.
13. Ramage M H, Burridge H, Busse-Wicher M, Fereday G, Reynolds T, Shah D U et al. The wood from the trees: The use of timber in construction. Renewable and Sustainable Energy Reviews 2017; 68:333-359. http:\\doi.org\10.1016/j.rser.2016.09.107.

  doi:10.5075/epfl-298799_978-2-9701614-0-0

NOVEL CELLULOSE BASED COMPOSITE MATERIAL FOR THERMOPLASTIC PROCESSING

Amélie, Tribot[a], Asta, Nurmela[a], Tuomas, Turpeinen[a], Jussi, Virkajärvi[a], Pia, Willberg-Keyriläinen[a], Kirsi, Immonen[a]

a: VTT Technical Research Centre of Finland Ltd., FI-02044 Espoo, Finland
– amelie.tribot@vtt.fi

Abstract: *Novel solutions using renewable materials are needed to tackle sustainability issues in industry. Totally cellulose-based composites, suitable for thermoplastic processing are introduced in this paper. The polymer matrix was a thermoplastic cellulose ester, Thermocell. Composites reinforcing fibres consisted of microcellulose, bleached softwood kraft pulp fibres, or long regenerated viscose fibres. The latest allowed to improve composites mechanical performance, especially at 20 wt-% loading. In the extrusion process, fibres oriented along processing direction, giving hopes for a future use in extrusion type additive manufacturing (AM). However, further developments of the AM system are required to print this material. With 20 wt-% microcellulose, the composite could be 3D printed using a fused granular fabrication process. Improved microcellulose dispersion was achieved with 2 wt-% tall-oil fatty acid lignin ester or cellulose ester ether additives. Wood-based additives also helped to decrease the internal porosity, leading to better mechanical performance of 3D printed materials.*

Keywords: Cellulose; Composites; Injection-molding; 3D printing; Microtomography

1. Introduction

The industry using thermoplastic materials is in transition towards novel sustainable solutions, either using recycled or renewable materials. Cellulosic raw materials are abundant and from renewable origin, therefore they are key to answer today's needs for safer and more eco-friendly materials. However, high cellulosic content materials applied for thermoplastic processing are poorly available. This paper presents developments of all-cellulose composites suitable for injection-molding, extrusion and extrusion additive manufacturing (AM), based on a novel thermoplastic cellulose material, Thermocell (1). Its synthesis was performed in a homogeneous system, using molar mass-controlled cellulose from softwood further esterified with bio-based fatty acid with side chain length of C16. In many composite materials, issues often arise to achieve proper polymer-fibre adhesion, causing a reduction of their mechanical performance. To exceed the properties over polymer matrix, coupling agents should therefore be employed (2). In this paper where both Thermocell matrix and fillers were from same cellulosic origin, such challenge was minimised.

As the market for thermoplastic 3D printing materials is growing (21%CAGR for 2021-2026) (3), bio-based solutions should also be available in this area. Lamm et al. (2020) reviewed the wood-based fillers used in materials extrusion AM processing (4). The composite materials for extrusion AM that contain cellulose fibres typically have a PLA or ABS main polymer matrix and compatibility challenges may occur (4,5). Also, we see the cellulose content limited by the amount of fibrous/filling material. Thus, cellulose esters have been found promising for AM (6,7).

  doi:10.5075/epfl-298799_978-2-9701614-0-0

Fused deposition modeling (FDM) of rigid cellulose acetate (CA) and flexible cellulose acetate propionate (CAP) has been reported on different fabrics (8). Then, solvent evaporation methods are mostly reported for AM of CA by dissolving first the polymer in acetone (5,9). Fused filament fabrication (FFF) of commercial CA polymer was presented by Böhler et. al, where CA contained 29 wt-% of plasticizer (10). Unlike literature examples, the Thermocell matrix was processed without plasticizer or solvent evaporation method. The concept of using Thermocell in AM was previously introduced by some of the authors (6,7). In the following results presented in this paper, Thermocell was combined with microcellulose (MC) and wood-based additives for AM purposes or regenerated cellulose fibres for improved mechanical performance. A fused granular fabrication (FGF) process allowed to skip the step related to filament making. Mechanical properties (Charpy impact strength, tensile strength, and Young modulus) of injection-molded and 3D printed samples are presented. By X-ray microtomography, we evaluated fibres size and orientation after processing, the quality of fibre-matrix interface, microcellulose dispersion in matrix, and porosities of the printed samples.

2. Materials and Methods

2.1 Materials

Thermoplastic cellulose matrix (Thermocell) was produced from commercial softwood dissolving grade pulp (Domsjö Fabriker AB, Sweden), esterified with vegetable bio-based fatty acids with side chain C16 (11,12). Composites reinforcing fibres consisted of microcellulose (MC) Arbocel UFC-100 (JRS Pharma GmbH, Weissenborn, Germany), bleached softwood kraft pulp fibres (SWP) (Metsä, Äänekoski, Finland), or regenerated viscose fibres (RF) Danufill 1,7 dTex with 3 mm or 5 mm length (Kelheim Fibres GmbH, Kelheim, Germany). The first additive, TOFA (tall-oil fatty acid) lignin ester, was obtained using Lignoboost lignin (UPM) and TOFA (Forchem, Rauma, Finland) containing 3.5% saturated and 86.3% unsaturated fatty acids respectively (13). The second additive, cellulose ester ether (hexanoate of hydroxypropyl cellulose, HPC-C6) was synthetized from commercial softwood dissolving grade pulp (Domsjö Fabriker AB, Sweden) as starting material. The third additive, rosin ester Sylvalite® 9100 from pine crude tall-oil feedstock, with 93% biobased content, was provided by Kraton, Sweden. Analytical grade reagents chloroform, and triethyl dichlomethane were purchased from Rathburn Chemicals. Other commercial reagents were purchased from Sigma-Aldrich in the highest purity grade.

2.2 Methods

In material chemical synthesis, Thermocell with DS of 1 was prepared using the homogeneous method presented by Willberg-Keyriläinen et al. (1,14) with ozone pretreated pulp. Synthesis and characterization of TOFA lignin ester have been performed as described by Hult et al (13). HPC-C6 was prepared using two-step synthesis. First, hydroxypropylation of cellulose was carried out in aqueous alkaline conditions. The cellulose was mixed with water, t-butanol and aqueous NaOH. Then, propylene oxide was added. The reaction was allowed to proceed at 30°C for 24 hours. After the reaction, the product was ultrafiltrated and dried using spray dryer. In a second phase, esterification of hydroxypropylated cellulose (HPC) was conducted. The dry HPC was dissolved in DMAc and pyridine was added to the homogeneous mixture. After that hexanoic anhydride was added, the mixture was stirred 24 hours at 35°C. The product was then precipitated and washed using water.

  doi:10.5075/epfl-298799_978-2-9701614-0-0

Processing of composite materials was performed by first drying materials at 50°C overnight prior to compounding. Compounding of Thermocell and fibres (20 wt-% MC, 20 wt-% SWP, 10 wt-% RF-3mm, 20 wt-% RF-3mm, or 20 wt-% RF-5mm) was performed with corotating twin-screw extruder (Berstorff ZE 25x33 D, Berstorff GmbH, Hanover, Germany) with temperatures ranging from 160°C to 175°C, screw speed of 100 rpm and output of 3 kg/h. The pure Thermocell was identically extruded to give the same thermal history as for the other compounds. In the case of MC composites with additives (2 wt-% lignin ester, HPC-C6, or rosin ester) a pre-mixing was performed with blade blender (Kenwood Chef XL Elite). Granules from compounding were further processed by injection-molding (Engel ES 200/50 HL, Engel Maschinenbau Geschellschaft m.b.H, Schwefberg, Austria) to test specimens according to the ISO 527. The processing temperatures were from 160 to 170 °C in the screw, 175 °C at nozzle, and a 60 °C mold temperature. Other test specimens for tensile and impact strength testing were prepared using fused granular fabrication (FGF) AM system delivered by Brinter®, Finland (6,7). Based on preliminary 3D printing trials, a printing speed of 15 mm/s and brass nozzles, type E3D-V6, with a diameter of 0.8 mm were selected and used in manufacturing of all samples. Extrusion AM was performed horizontally using a concentric infill pattern and 100% infill percentage. The number of layers were respectively 4 and 8 for tensile and impact strength samples, with 0.5 mm layer hight for both.

X-ray microtomography (XμCT) employed RX Solutions Desktom 130 (RX Solutions SAS, Chavanod, France) XμCT device. Injection-molded samples containing MC were imaged with 4 μm resolution (50 keV, 80 μA, and 0.75/s frame rate). Other samples were imaged with 7 μm resolution (50 keV, 300 μA and 4/s frame rate). In each XμCT scan, 1440 projection images and average of 2 frames for each projection were taken. RX Solutions Xact-software was used for the filtered backprojection reconstruction. Image analysis was done with VTT in-house analysis software, partially based on Miettinen opensource software Pi2 (15). In injection-molded samples containing MC, the volume distributions of MC aggregates were solved. Objects smaller than 960 μm^3 were removed from the volume distribution analysis as being mixed with noise. In 3D printed samples, volume fractions of extrusion and internal voids were calculated. Separation between the pore types was realized by looking at the form factor of the pores, the extrusion pores being longer and stretching over the sample length along the printing direction.

Tensile tests were performed according to the ISO-527 standard using an Instron 4505 Universal Tensile Tester (Instron Corp., Canton, MA, USA) and an Instron 2665 Series High Resolution Digital Automatic Extensometer (Instron Corp., Canton, MA, USA). For injection-molded samples, a 10 kN load cell and a 5 mm/min crosshead speed was used. For printed samples, a 1 kN load cell and a 2 mm/min crosshead speed was used. Five parallel specimens were tested for each sample material to obtain average values of the tensile properties. Impact strengths were determined according to the ISO-179 standard using a Charpy Ceast Resil 5.5 Impact Strength Machine (CEAST S.p.a., Torino, Italy). Charpy impact strength tests in edgewise orientation were carried out on unnotched specimens on five to ten replicates to obtain an average value and variance. Test specimens were kept in standard conditions (23°C, 50% relative humidity) for at least five days before mechanical tests.
Melt flow index (MFI) was measured from the material granules straight after compounding. MFIs of the material compounds were analyzed using a RAY-RAN Melt Flow Index-er, Model 3A (Industrial Physics, Theme, UK). Tests were performed at 210°C under a weight of 2.16 kg with four parallel samples.

  doi:10.5075/epfl-298799_978-2-9701614-0-0

3. Results and discussion

3.1 Injection-molded and extruded cellulose-based composites

Addition of microcellulose (MC), lignocellulosic softwood pine fibres (SWP), or regenerated viscose fibres (RF) in Thermocell matrix provided a reinforcing effect with systematic increase of tensile strength and Young modulus (Figure 1). XµCT reconstructed 3D images of the injection-molded and extruded samples evidenced a very good fibre-Thermocell matrix adhesion (Figure 2) with no void formation around fibres at observed resolutions. In injection-molded samples containing RF, fibre length decreased because of shear forces in place during the process, knowing that the cutting of lignocellulosic fibres in plastic processing is typical (16). Nevertheless, aspect ratio of the 5 mm RF was still high enough to provide consequent reinforcement in 20RF-5mm sample, with 2.4 fold increase of Young modulus, 1.8 fold increase in impact strength, and +44% increase in tensile strength compared to neat Thermocell. The reinforcing effect was more important for 20 wt-% fibre loading (20RF-3mm) than for 10 wt-% (10RF-3mm), as impact strength, for instance, increased by 1.5. The impact of fibres aspect ratio and fibre content on the composite mechanical properties were in alignment with literature findings (17). Lignocellulosic SWP were strongly agglomerated, and a dispersion agent would be required to solve this issue (2). In injection-molded samples, the RF were cut to smaller size, and also highly bended and twined, but in extruded samples they retained their size and aligned within the processing direction. Thus, RF have potential to provide the cellulose-composite with improved performance and could be suitable for extrusion additive manufacturing (4). This article further investigates 3D-printability of the cellulose-based composites.

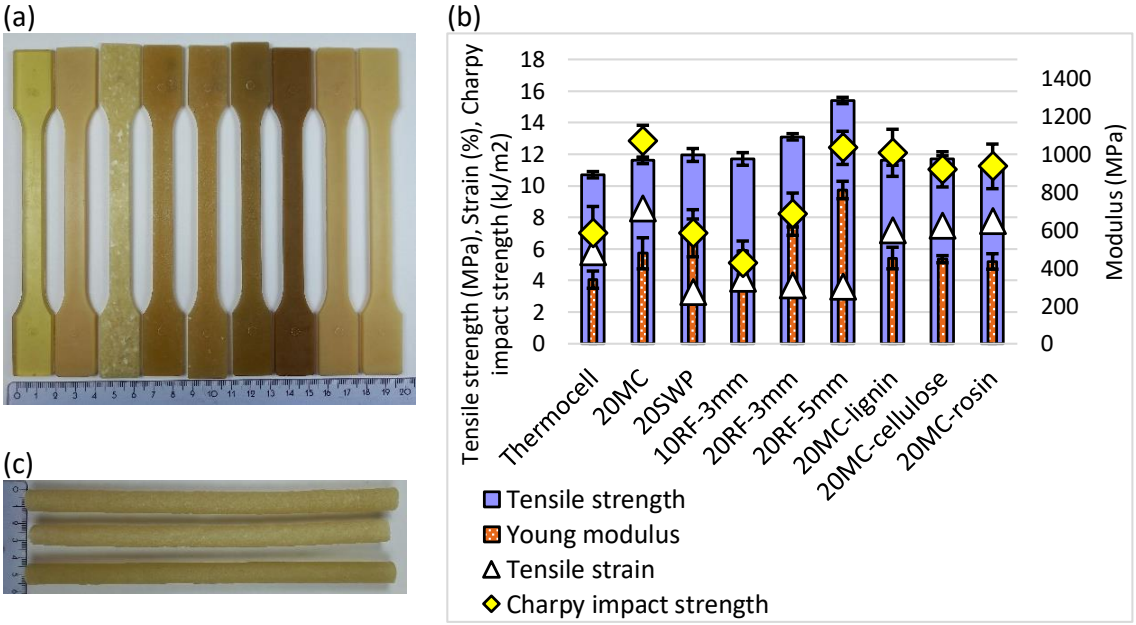

Figure 1. Injection-molded samples with Thermocell matrix (a) and their mechanical properties (b), containing from left to right: 0 wt-% fibres, 20 wt-% microcellulose (MC), 20 wt-% softwood pine fibres (20SWP), 10 wt-% 3mm regenerated fibres (10RF-3mm), 20 wt-% 3mm regenerated fibres (20RF-3mm), 20 wt-% 5mm regenerated fibres (20RF-5mm), 20 wt-% MC and 2 wt-% lignin ester (20MC-lignin), 20 wt-% MC and 2 wt-% cellulose ester ether (20MC-cellulose), 20 wt-% MC and 2 wt-% rosin ester (20MC-rosin). (c) Extruded samples, from top to bottom 10RF-3mm, 20RF-3mm, 20RF-5mm.

  doi:10.5075/epfl-298799_978-2-9701614-0-0

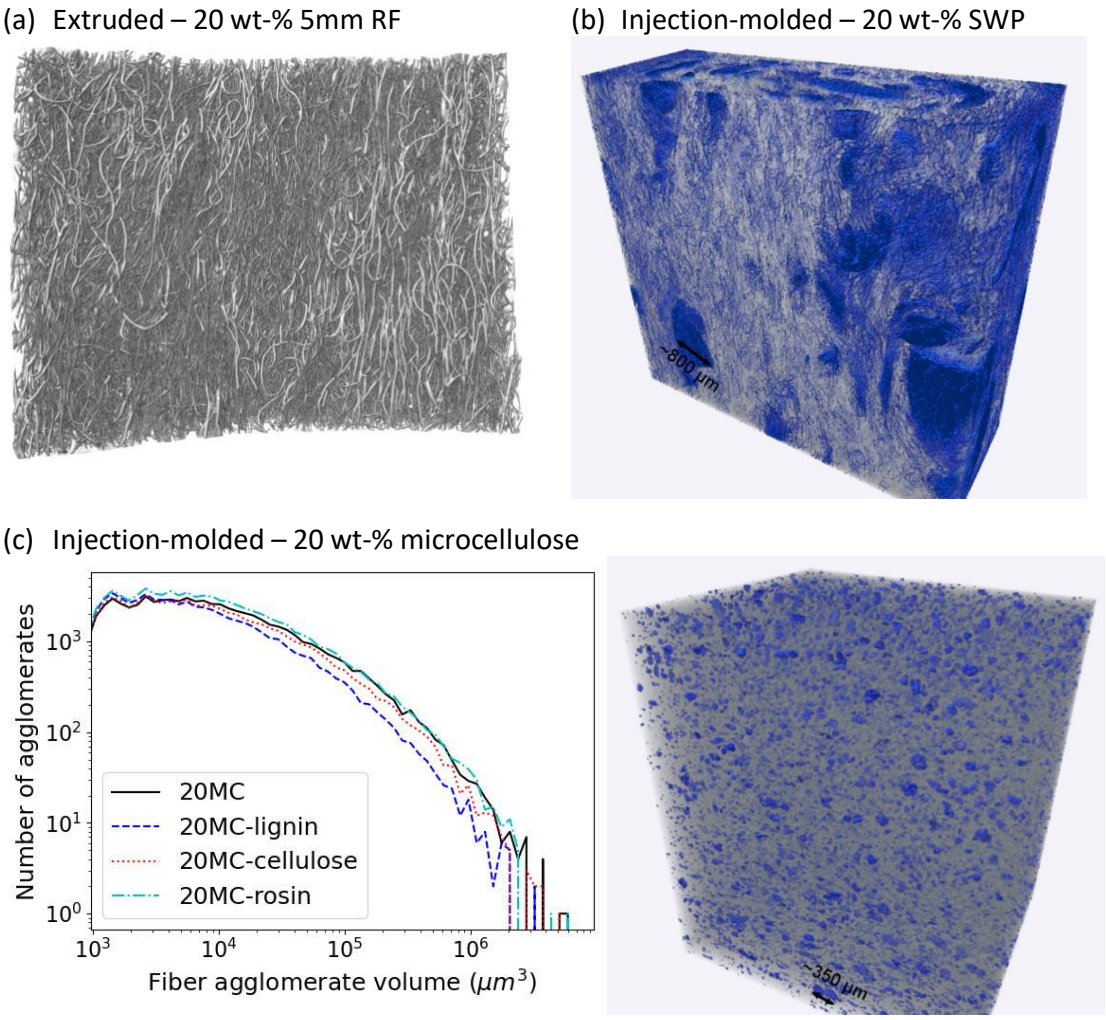

Figure 2. X-ray microtomography (XµCT) visualizations of composites containing Thermocell matrix and regenerated viscose fibres (a), softwood pine fibres in blue (b), or microcellulose (MC) in blue (c) with calculation of MC agglomerates (size – amount) from XµCT scans in 21.9 mm³ volume including in total 67871 (20MC), 60906 (20MC-lignin), 63986 (20MC-cellulose), and 78914 (20MC-rosin) number of agglomerates (c). Note: scale bars, showing the size of certain agglomerates are only indicative, as there is a perspective in the 3D visualizations.

Further developments of the printing system are required in the case for RF-filled composites whereas printing of the 20MC material could be investigated. Two out of the three wood-based additives needed for 3D printed recipes enabled dispersion of MC into injection-molded samples (Figure 2c). Lignin ester was the most effective additive to reduce the size of MC agglomerates and also their total number in the studied volume. As a consequence (2), slight improvement of mechanical properties compared to 20MC reference were measured (Figure 1b).

3.2 Fused granular fabrication (FGF) of cellulose-based composites

During FGF, the thermoplastic cellulose matrix exhibited a sticky behaviour, which often led to nozzle blocking. In addition, the melt flow was inconstant, as shown by high standard deviation in MFI measurements (Table 1).

  doi:10.5075/epfl-298799_978-2-9701614-0-0

Table 1: Melt flow index (MFI), tensile strength (TS), Young modulus, and impact strength (IS) of materials with Thermocell matrix, containing 20 wt-% microcellulose (MC), and 2 wt-% of respectively lignin ester (20MC-lignin), cellulose ester ether (20MC-cellulose), or rosin ester (20MC-rosin).

Sample	MFI (g/10 min)	TS (MPa)	Modulus (MPa)	IS (kJ/m2)
Thermocell	40.25 ± 28.57	-	-	-
20MC	29.08 ± 22.43	-	-	5.10 ± 0.88
20MC-lignin	3.41 ± 1.13	7.26 ± 0.72	510.25 ± 174.40	7.30 ± 1.65
20MC-cellulose	2.70 ± 0.83	6.69 ± 0.64	477.96 ± 80.50	7.10 ± 0.92
20MC-rosin	5.73 ± 2.95	6.90 ± 0.99	339.63 ± 42.37	6.40 ± 0.56

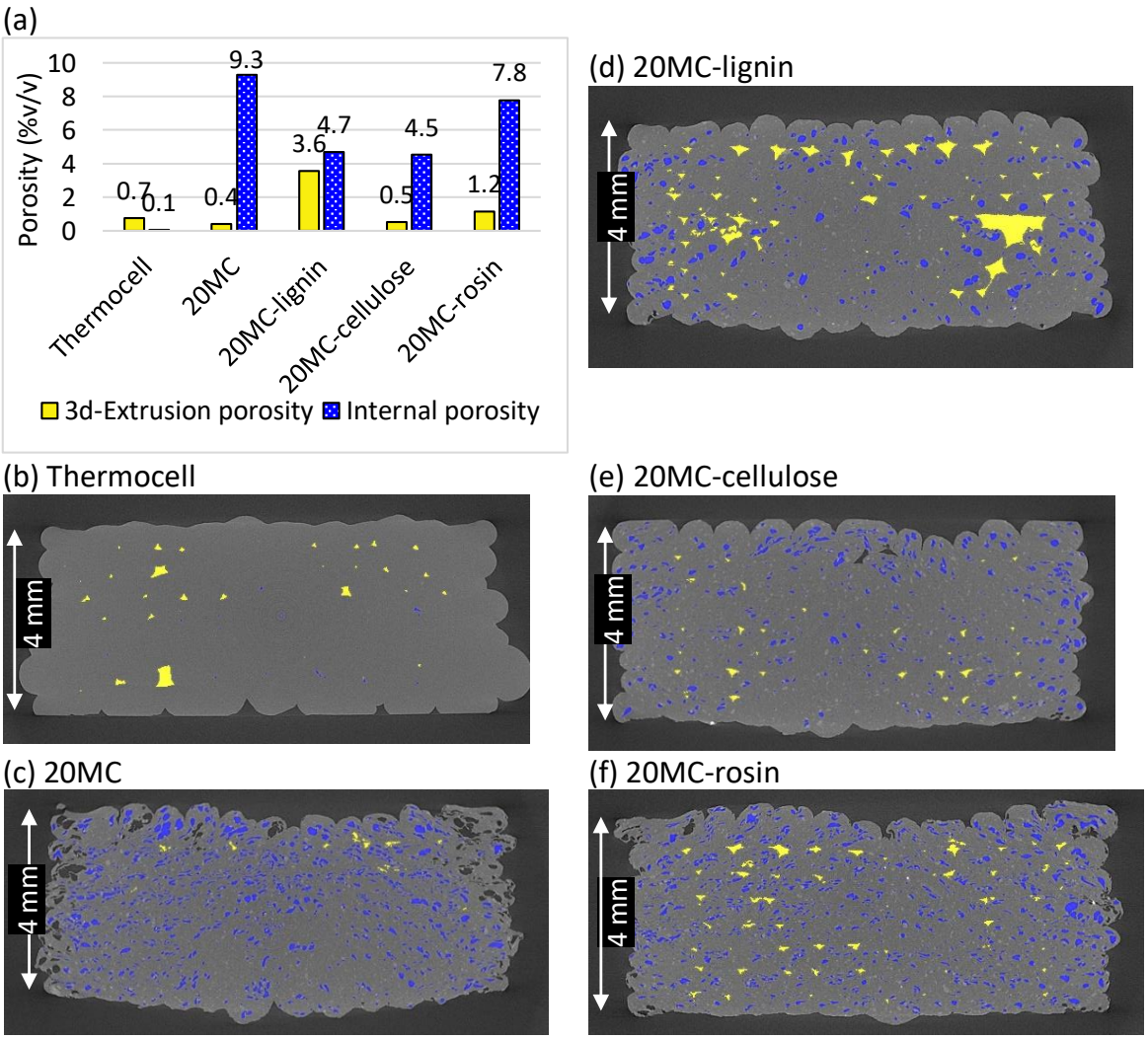

Figure 3. (a) Evidence of 3D-Extrusion porosity (in yellow, formed during the printing process at the interface of two deposited layers) and internal porosity (in blue, related to the material composition) by X-ray microtomography in thermoplastic cellulose (b) with 20 wt-% microcellulose (c) and 2 wt-% lignin ester (d), cellulose ester ether (e), or rosin ester (f).

Upon addition of 20 wt-% MC, printability was enhanced, but dimensions of the mini-printed dog-bone shapes were not reproducible enough for testing purpose and more internal porosity appeared as evidenced in XμCT scans (6) (Figure 3a). Porosity in composites can be defined as air-filled cavities inside a continuous matrix material and is often caused by the mixing and consolidation of two discrete components (18), presently Thermocell and MC. Upon addition of solely 2 wt-% of lignin-, cellulose-, or rosin-based additive, the material was then suitable for 3D printing, with MFI bellow 10g/10min (19) and both impact and tensile mini-test specimens were printed. The wood-based additives provided increased impact strength of the printed material, probably because they also enabled to lower the internal porosity (Figure 3a). As discussed in previous section (Figure 2c), the lignin- and cellulose-based additives were also efficient for improving the dispersion of MC in polymer matrix (reduced number and smaller size of the MC agglomerates). Those observations seem to correlate with the differences in internal porosity inside 3D printed samples. Inter-fusion of printed strands could be enhanced further by changing the printing parameters for instance. Finally, it can be noted that the cellulose ester ether additive (Figure 3e) led to less voids in between deposited strands than the lignin ester additive (Figure 3d).

3.3 Conclusion

Developments related to all-cellulose based composites applied for thermoplastic processing (e.g. injection-molding, extrusion, fused granular fabrication) were presented. A novel thermoplastic cellulose material, Thermocell, was synthetized from commercial softwood dissolving grade pulp and utilized as a polymer matrix. Regenerated cellulose fibres (RF) provided the material with improved mechanical performance, especially with 20 wt-% RF. This material could be extruded and fibres got orientated along processing direction, giving hopes for its future use for extrusion type additive manufacturing (AM) as highly reinforcing material. However, further developments of the AM system are required to print this material. In the case of bleached softwood kraft pulp fibre compounds, the fibres were agglomerating too much for 3D printing purposes, showing the need for better dispersion. With 20 wt-% microcellulose content, the composite could be 3D printed successfully with wood-based additives. Improved microcellulose dispersion was achieved with 2 wt-% tall-oil fatty acid lignin ester and cellulose ester ether additives. The wood-based additives also helped to decrease the internal porosity, leading to better mechanical performance of 3D printed materials.

Acknowledgements

The authors thank Sini-Tuuli Rauta, Petri Kuusipalo, and Olli Linjamaa for material processing and contribution in sample analytics.

4. References

1. Willberg-Keyriläinen P, Talja R, Asikainen S, Harlin A, Ropponen J. The effect of cellulose molar mass on the properties of palmitate esters. Carbohydrate Polymers 2016; 151:988–95.
2. Pickering KL, Efendy MGA, Le TM. A review of recent developments in natural fibre composites and their mechanical performance. Composites Part A: Applied Science and Manufacturing. 2016; 83:98–112.

  doi:10.5075/epfl-298799_978-2-9701614-0-0

3. LLC BCC Research. Global Markets for 3D Printing 2021; MFG074B. 2021.
4. Lamm ME, Wang L, Kishore V, Tekinalp H, Kunc V, Wang J, et al. Material Extrusion Additive Manufacturing of Wood and Lignocellulosic Filled Composites. Polymers 2020; 17;12(9):2115.
5. Mohan D, Teong ZK, Bakir AN, Sajab MS, Kaco H. Extending Cellulose-Based Polymers Application in Additive Manufacturing Technology: A Review of Recent Approaches. Polymers 2020; 12(9):1876.
6. Immonen K, Willberg-Keyriläinen P, Ropponen J, Nurmela A, Metsä-Kortelainen S, Kaukoniemi O-V, et al. Thermoplastic Cellulose-Based Compound for Additive Manufacturing. Molecules 2021; 26(6):1701.
7. Immonen K, Metsä-Kortelainen S, Nurmio J, Tribot A, Turpeinen T, Mikkelson A, et al. Recycling of 3D Printable Thermoplastic Cellulose-Composite. Sustainability 2022; 14(5):2734.
8. Tenhunen TM, Moslemian O, Kammiovirta K, Harlin A, Kääriäinen P, Österberg M, et al. Surface tailoring and design-driven prototyping of fabrics with 3D-printing: An all-cellulose approach. Materials & Design 2018; 140:409–19.
9. Pattinson SW, Hart AJ, Pattinson SW, Hart AJ. Additive Manufacturing of Cellulosic Materials with Robust Mechanics and Antimicrobial Functionality. Advanced Materials Technologies 2017; 2(4):1600084.
10. Böhler S, Bartel M, Bohn A, Jacob R, Ganster J, Büsse T, et al. Highly dense cellulose acetate specimens with superior mechanical properties produced by fused filament fabrication. Polymer 2020; 194:122388.
11. Willberg-Keyriläinen P, Vartiainen J, Harlin A, Ropponen J. The effect of side-chain length of cellulose fatty acid esters on their thermal, barrier and mechanical properties. Cellulose 2017; 24(2):505–17.
12. Willberg-Keyriläinen P, Orelma H, Ropponen J. Injection Molding of Thermoplastic Cellulose Esters and Their Compatibility with Poly(Lactic Acid) and Polyethylene. Materials 2018; 11(12):2358.
13. Hult EL, Ropponen J, Poppius-Levlin K, Ohra-Aho T, Tamminen T. Enhancing the barrier properties of paper board by a novel lignin coating. Industrial Crops and Products 2013; 50:694–700.
14. Willberg-Keyriläinen P, Vartiainen J, Harlin A, Ropponen J. The effect of side-chain length of cellulose fatty acid esters on their thermal, barrier and mechanical properties. Cellulose 2017; 24(2):505–17.
15. Miettinen A. Process Image 2 (Pi2) software [Internet]. Available from: https://github.com/arttumiettinen/pi2
16. le Baillif M, Oksman K. The Effect of Processing on Fiber Dispersion, Fiber Length, and Thermal Degradation of Bleached Sulfite Cellulose Fiber Polypropylene Composites. 2009; 22(2):115–33.
17. Thomason JL, Rudeiros-Fernández JL. A review of the impact performance of natural fiber thermoplastic composites. Frontiers in Materials 2018; 5:60.
18. Madsen B, Lilholt H. Physical and mechanical properties of unidirectional plant fibre composites—an evaluation of the influence of porosity. Composites Science and Technology 2003; 63(9):1265–72.
19. Wang S, Capoen L, D'hooge DR, Cardon L. Can the melt flow index be used to predict the success of fused deposition modelling of commercial poly(lactic acid) filaments into 3D printed materials? Plastics, Rubber and Composites 2018; 47(1):9–16.

  doi:10.5075/epfl-298799_978-2-9701614-0-0

TOWARDS MORE EFFICIENT AND ENVIRONMENTAL FRIENDLY FLAX-BASED ECO-COMPOSITE THROUGH DIRECT F_2 FLUORINATION AS A COMPATIBILIZATION TREATMENT

Olivier Téraube[a,b], Jean-Charles Agopian[a,b], Monica Francesca. Pucci[c], Pierre-Jacques Liotier[d], Nicolas Batisse[a], Samar Hajjar-Garreau[e], Karine Charlet[b] Marc. Dubois[a]

a: UCA, Clermont Auvergne INP, ICCF, BP 10448, 63000 Clermont-Ferrand, France
b: UCA, Clermont Auvergne INP, Institut Pascal, BP 10448, 63000 Clermont-Ferrand, France –
c: LMGC, IMT Mines Ales, Univ Montpellier, CNRS, Alès, France
d: Polymers Composites and Hybrids (PCH), IMT Mines Ales, Alès, France
e: IS2M, CNRS-UMR 7361, Université de Haute-Alsace, 68057 Mulhouse, France

olivier.teraube@uca.fr

Abstract: *Because of their specific properties, vegetal fibers are increasingly used as sustainable polymer reinforcements for eco-composites. Nevertheless, their polar character hinders them from being used more frequently at industrial scale due to their incompatibility with mostly dispersive polymers (the cheapest and most common ones). In this study, direct fluorination treatment was carried out to covalently graft fluorine atoms at the outmost surface of flax fibers, allowing the polarity of flax fibers to be significantly decreased. Thanks to this polarity reduction, the gap between the surface energies of the fibers and polymer matrix (epoxy) was reduced improving the wettability of the fibers during the infusion process. Thereby, porosity of the composite thus formed is significantly reduced, increasing its Young's modulus by 25%, its maximal flexural stress by 10% whereas the percentage of maximal elongation is decreased by 15%. These improvements are achieved without any chemical coupling agent or solvent harmful to the environment.*

Keywords: Vegetal fibers composite; Fluorination; Wettability; Interface; Porosity

1. Introduction

Vegetal fibers are increasingly used to substitute glass fibers for polymer strengthening to make eco-composites. Indeed, in addition to the fact that vegetal fibers and glass fibers present equivalent specific properties, the use of the former allows to valorize bio-based and local resources while lightening the overall weight and reducing the cost of composites. Therefore, all these advantages provide to vegetal fibers to be more and more used in the transport industry (aeronautics, automotive, etc.); this trend is expected to increase in light of current environmental issues and the emerging context of the bio-economy aimed at continuing economic growth while preserving the environment and earth resources.

However, one of the main difficulties arising when using these vegetal compounds as polymer matrix reinforcement is their incompatibility with a large part of the latter. Indeed, the hydrophilic nature of vegetal fibers makes them sensitive to moisture absorption and difficult to wet by hydrophobic resins (which represent the majority of polymer matrices used). This incompatibility results in a poor effective adhesion, partly due to micro-porosities, between fibers and matrix that would greatly weaken the mechanical performance of these eco-composites [1].

  doi:10.5075/epfl-298799_978-2-9701614-0-0

In order to obtain the optimal mechanical performance of these composites, it is often considered necessary to compatibilize these vegetal fibers with the polymer matrix. Over the years, several chemical and/or physical methods have been developed for this purpose (thermal treatment, electric discharge, acetylation, MAPP treatment, mercerization, etc. [2]). If these treatments allow to decrease the polarity of the fibers and thus to reduce the presence of cavities at the fiber/matrix interface, they are generally harmful for the environment because of the use of chemical reagent, solvent and/or a high energy cost, inducing in all cases an increase of the carbon footprint of the composites, which is incompatible with the very principle of "eco-composite" aiming at reducing as much as possible the environmental impact of these materials.

The fluorination treatment takes place in this context. Indeed, thanks to the reaction of molecular fluorine F_2 onto flax fibers surface (or any other lignocellulosic fibers [2,3]), it is possible to covalently graft fluorine by this chemical element. This treatment of natural fibers, carried out only at a laboratory scale up to now, allows the polarity of the substrate to be significantly decreased without modifying its bulk properties. Moreover, as a gas/solid reaction, fluorination is performed without using toxic solvent in a closed reactor, *i.e.* without release of any toxic substance in the atmosphere, and the reaction occurs spontaneously at room temperature; so this treatment exhibits a very low environmental footprint.
In addition, direct fluorination treatment is already an industrial process employed to treat commercial polymers in order to add the superficial properties of a fluoropolymer at the substrate surface [4,5]. Moreover, this method is fast, without any human contact with the reactant, reproducible, and thus presents all the advantages required for an eco-responsible industrial way to reduce the vegetal fibers' polarity in order to compatibilize this filler with hydrophobic polymer.

Thereby, the present work aims at carrying out fluorination of flax fibers at a semi-pilot scale in order to increase the quantity and size of fluorinated fibers per batch allowing the manufacture of eco-composites with long fiber reinforcement. Therefore, fluorinated flax fibers and epoxy resin (with a polar component typically measured below 5mN/m [6]) will be employed together *via* Composite Vacuum Resin Infusion, to form eco-composite. Those composites will be then tested by flexural test to evidence the enhancement of the mechanical performance of the fluorinated fillers based material as expected because of the fiber polarity reduction, according to the literature [1].

2. Materials and methods

2.1 Materials

Flax fibers were pieces of FlaxTape™ 110, purchased from Eco-Technilin. These fibers which are 40cm width tape of unidirectional flax fibers with a weight of 110g/m^2 have undergone a fluorination treatment described below (noted "fluorinated"). For comparison, other fibers were used "as received" (noted "Raw" in the following) to make composite materials.

Composite were manufactured using an epoxy resin: resoltech 1050, coupled with 1056S hardener, both purchased from SF Composite. Resin and harderner were mixed together with a 100/35 weigh ratio.

  doi:10.5075/epfl-298799_978-2-9701614-0-0

2.2 Fluorination

Fluorination of flax fibers was performed inside a 50L passivated nickel reactor (covered with NiF_2) in static conditions. The flax fibers were distributed into the fluorination reactor over 4 trays, each being 65cm long and 21cm wide Figure 1a.
The reactive gas consists of a mixture of pure elemental fluorine, purchased from Solvay Fluor (less than 0.1 vol.% of admixtures, mainly oxygen) and pure Nitrogen (99,999 % purity). Before each reaction, fibers were first outgassed during 2h under primary vacuum (10^{-3} mbar) at 120 °C (setpoint) within the reactor. Then, the heating is turned off, and the reactor is left to cool down overnight.
After that, the chamber (still under primary vacuum, *i.e.* 10^{-3} bar) was filled with the gases. In a first step, N_2 is injected into the reactor during 5min at 400 mL/min flow rate. Then, the reactive F_2/N_2 mixture was introduced during 20 min in the reactor with N_2 and F_2 flow rates which are set at 400 and 100 mL/min, respectively. At the end of this step, the pressure inside the reactor is of 200mbar. Thereafter, N_2 is added (600mL/min) in the reactor until a pressure of 1 bar was reached. The reactor is then immediately flushed with pure nitrogen gas overnight to both stop the reaction and remove the traces of unreacted F_2, HF¸ CF_4, and C_2F_6 (those gases were removed by a soda lime trap). Finally, the fibers are once again outgassed for 1 h under nitrogen at 120 °C for the completion of removal of all fluorine-based gases from the sample surface.

2.3 Composite manufacturing

Composite plates are prepared by Composite Vacuum Resin Infusion (that we will call infusion afterwards). To manufacture these plates, a PMMA mold of 400mm long, 40mm wide and 3mm thick was used. For each infusion, 6 fibers (raw or fluorinated) plies are cut (length in the fiber direction) to the mold dimensions and placed within it (Figure 1b). Then, 2 cylindrical gaskets (in black on Figure 1b) are placed in the location provided, to ensure the vacuum tightness of the mold. After that, the counter mold is placed, and the 2 parts of the mold firmly closed and held in position thanks to C-clamps (Figure 1c). Thereafter, resin was mixed with its corresponding hardener and mixture was stirred for 5min. Once mixed, the resin pot is connected to the mold by a plastic pipe, and the whole infusion device was put under vacuum (10^{-3} bar). After 5 minutes, circuit upstream of the resin is returned to atmospheric pressure, while the mold is still under vacuum, driving the resin inside the mold. Once the infusion done, the set is left 24 hours to obtain a composite plate dried enough to be demolded. Then the plate is demolded and dried for, at least, 2 weeks at room temperature.

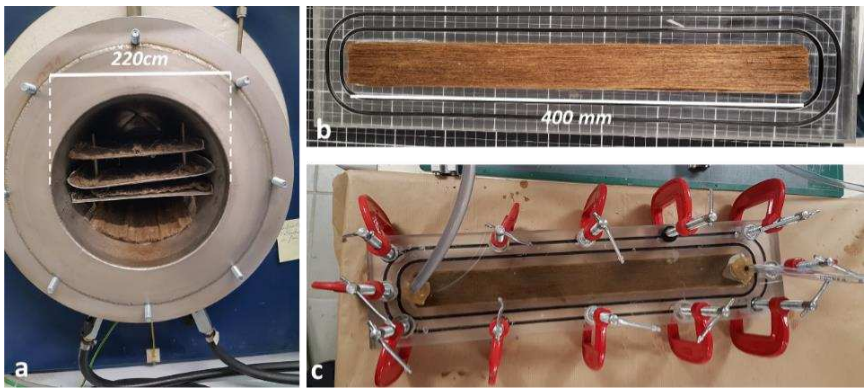

Figure 1: (a) 50L fluorination reactor with 4 trays inside ; (b) and (c) composite manufacturing

  doi:10.5075/epfl-298799_978-2-9701614-0-0

2.3 Characterization

FTIR experiments were carried out with a Nicolet 6700 FT-IR (Thermo Scientific) spectrometer in ATR mode. For each spectrum, 32 scans with 4 cm^{-1} resolution were collected between 4000 and 524 cm^{-1}.

^{19}F solid state NMR spectra were recorded using a 300 MHz Bruker Avance spectrometer. A magic-angle spinning (MAS) probe operating with 2.5 mm rotors was used allowing a 30 kHz spinning rate. A simple sequence was used with a single π/2 pulse with a duration of 4.0 µs. ^{19}F chemical shifts were externally referenced to CF_3COOH and then referenced to $CFCl_3$ (δ_{CF_3COOH} = -78.5 ppm vs δ_{CFCl_3})

In order to estimate the change in the surface energy due to treatments, the determination of the contact angle between fibers and different liquids is necessary. To measure this contact angle, the most common method is the "sessile drop" technique [7]. However, this technique cannot be employed with fibers and fabrics, because of their shape and texture that induce a fakir effect distorting the measurements. Thereby, several methods have been developed along time in order to perform this measurement on single fibers [8–11]. Among them, the tensiometric one seems the most convenient. As described by Qiu *et al.*[9], it is based on the use of a Wilhelmy balance and the Wilhelmy relationship (1)

$$F = \gamma_l \, p \, \cos\theta \tag{1}$$

where F is the capillary force (mN), p (m) the wetted length, ϑ (°) the contact angle and γ_l (mN/m) the surface tension of the liquid.

Using the method described in Pucci *et al.* [12], measurements were performed using a Krüss K100SF tensiometer. To measure the contact angle with a given liquid, a single fiber was first extracted from the strips of fibers. This one was placed in a clamp within the tensiometer and placed as close as possible to a crystallizer filled with the liquid without touching it. This crystallizer moved at a speed of 1mm/min and came in contact with the fiber. Then it went up to a depth immersion of 5 mm, the tensiometer allowing to measure the capillary force exerted by the liquid on the fiber.

To determine the polar and the dispersive components of the surface energy of fibers, the Owens-Wendt method was considered [13]. This theory is based on the equation (2) that allows to determine the dispersive and polar components of the fiber surface energy (γ_s^d and γ_s^p).

$$\frac{\gamma_l(1+cos(\theta))}{2\sqrt{\gamma_l^d}} = \sqrt{\gamma_s^p}\left(\frac{\sqrt{\gamma_l^p}}{\sqrt{\gamma_l^d}}\right) + \sqrt{\gamma_s^d} \tag{2}$$

For each sample, at least 5 measurements were carried out with different test liquids, and the mean value of θ was used to plot data. The uncertainties on surface energy components were measured using the maximum and minimum slopes techniques.

To evaluate the impact of the fluorination treatment on flexural properties, three points bending tests have been conducted following ASTM D790-03 [14]. However, only 4 samples

were tested instead of 5 because of the limited amount of space available on composites. Dimensions of the samples were 120×18x3mm^3, and because the standard requires a span-to-death ratio larger than 16:1 at minimum and recommends it higher than 32:1, we have set our support span to 100mm (span-to-death ratio = 33:1). Experimentations were carried out on a Zwick UTS20K machine equipped with a 20 kN capacity load cell, at a crosshead displacement rate of 1 mm/min.

3. Result and discussion

3.1 Homogeneous fluorine grafting

Fluorination of flax fibers, as well as other lignocellulosics materials, is known to graft fluorine atoms at the outmost surface of these compounds in replacement of -OH groups [2,3]. Therefore, the fact that fluorination of lignocellulosic materials is possible were previously discussed in a previous paper [3,15].

According to the high reactivity of F_2 gas, the tubular geometry of the reactor with a gas injection on one side may result in inhomogeneous fluorination rate along the fibers during the scale-up with a reactor of 50L volume: chemical analysis of fibers must be carried out to check the homogeneity of the treatment. Figure 2 displays the IR and ^{19}F NMR spectra of fluorinated flax fibers, as a function of the location of the fibers tape in the reactor. These spectra were recorded with samples collected at 0cm and 65cm from the edge, in the center of the fibers width (the 0cm side corresponding to the width closest to the fluorine insertion) on the 4 trays that were placed one above another into the reactor. The presence of bands on ^{19}F NMR spectra demonstrates the covalent grafting of fluorine atoms at the flax fibers surface as already observed on previous work; formation of -CHF, -CF_2 and with less extend -CF_3 groups is then evidenced [16]. In addition, because of both the *quasi* overlapping of both ^{19}F NMR and FT-IR lines whatever the location of the sample in the trays and the perfect similarity of these lines for the case in between 0 and 65cm, we clearly notice that treatment is chemically and quantitatively almost identical whatever the observed area. These results demonstrated that the chosen treatment conditions allow a high homogeneity over the whole length of the samples. This characteristic is a prerequisite for the use of the mechanical properties.

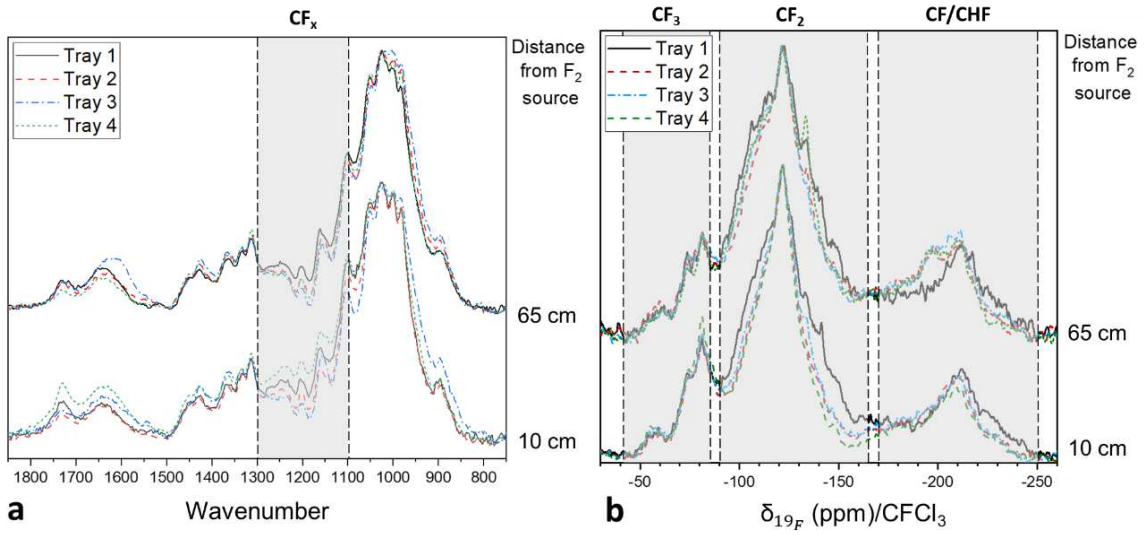

Figure 2: (a) IR and (b) ^{19}F NMR spectra of fluorinated flax fibers

  doi:10.5075/epfl-298799_978-2-9701614-0-0

3.2 Modification of surface energy

When controlled, fluorination of flax fiber allows to modify the surface energy of the latter, by reducing its polar component (γ_s^p). In order to identify and quantify the modifications resulting from the treatment, wetting tests by tensiometric method were carried out.
Table 1 summarizes the evolution of polar (γ_s^p), dispersive (γ_s^d) and total (γ_s) surface energy of both pristine and fluorinated flax fibers. This treatment significantly lowered the polarity of fibers, from 19.1 ± 9 $mN.m^{-1}$ to 5.8 ± 2.4 $mN.m^{-1}$.
In addition, when considering the experimental uncertainties, it is evident that the fluorinated fibers are more homogeneous than the raw ones; vegetal fibers being natural materials, they present a disparity between them [17]. When it is well controlled, fluorination treatment allows this variability to be limited and a surface energy with a reduced data dispersion is obtained for treated fibers compared to the raw ones. From an industrial point of view, this appears as extremely promising.
On the contrary, we noticed that the dispersive component remains nearly constant after the fluorination treatment. Therefore, and knowing the fact that the dispersive constant is strongly related to the surface texture [18], the absence of changes may suggest the maintaining of the surface roughness during the fluorination treatment.

Table 1: Polar, dispersive and total surface energy of raw and fluorinated flax fibers

Sample	γ_s^p (mN/m)	γ_s^d (mN/m)	$\gamma_s^{tot.}$ (mN/m)
Raw	19.1 ± 9.0	22.5 ± 2.0	41.6 ± 11
Fluorinated	5.8 ± 2.4	21.1 ± 3.6	26.9 ± 6.0

3.2 Effect of fluorination treatment on mechanical properties of composite

Liotier *et al.* [1] have already demonstrated that, if the polar component of vegetal fibers fiber is reduced by a given treatment (thermal treatment in their case), the wettability of fibers by the polymer matrix will be improved and therefore, the overall mechanical behavior of composites manufactured is improved with treated fibers (even if fiber properties at rupture are reduced). This phenomenon was related to the improvement of the wettability of the fibers by the matrix, allowing to reduce the micro-porosity at the filler/matrix interface as already observed in the literature [3,12].
Thereby, in order to evaluate the impact of the flax fiber fluorination on the mechanical performance of eco-composite formed with this natural reinforcement, laminates plates of composites were manufactured with raw flax fibers reinforcement on one side and fluorinated flax fiber reinforcement on the other. The materials thus formed were then analyzed by flexural tests in the exactly same conditions in order to be compared. Results (Figure 3) evidenced a 25% increase of the Young's modulus (E) and a 10% increase of the maximal flexural stress (σ_m) whereas a 15% decrease of percentage of maximal elongation (A%) is observed. It is to note that the changes of these 3 values are achieved without overlapping the experimental uncertainty bars, demonstrating that the enhancements are significant. In addition, the improvements of E and σ_m while A% is decreased highlight a stiffening of the material thanks to the fluorination of its reinforcements (vegetal fibers).

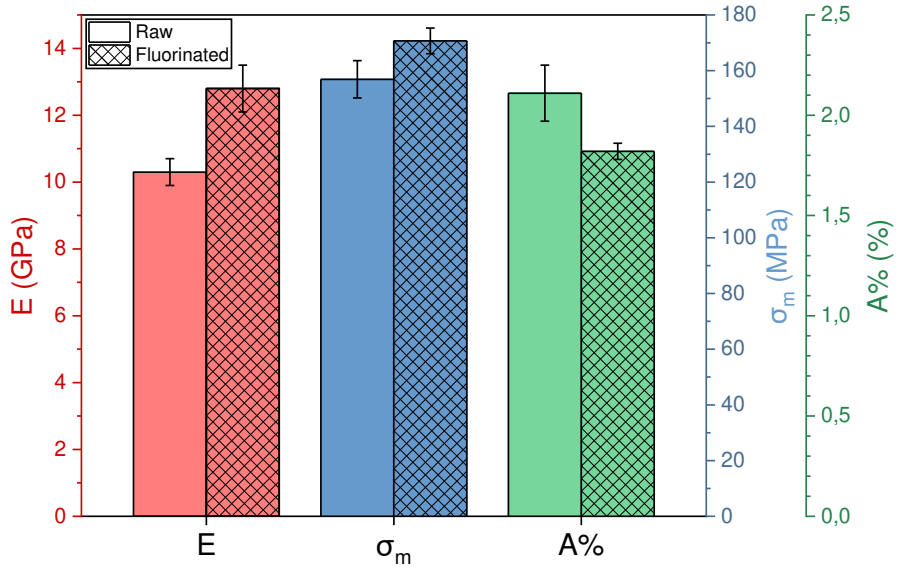

Figure 3: Flexural properties of composites made from raw and fluorinated flax fibers (E = Young's modulus; σ_m = Ultimate tensile strength; A% = percentage of maximal elongation)

4. Conclusion

The present work was focused on the effect of the fluorination treatment of flax fibers on the mechanical behavior of composites reinforced by fluorinated fibers. Fluorination has been realized at a large scale in a 50L reactor and have allowed to covalently graft fluorine atoms at the outmost surface of flax fibers. In addition, this treatment was carried out homogeneously over the 65cm length and the 4 trays of fibers introduced into the reactor and has allowed to reduce the fibers' polar component of surface energy. Thanks to this polarity decrease, the gap between the surface energies of the fibers and polymer matrix (Epoxy) was reduced; in other words, the wetting of the fiber by the polymer is improved during the infusion process (probably due to the fact that the porosity of the composite thus formed is significantly decreased). Therefore, mechanical performance of these composite is improved (a 25% increase of the Young's modulus (E) and a 10% increase of the maximal flexural stress (σ_m)), without any chemical coupling agent harmful to the environment or solvent for the chemical reaction.

Acknowledgements

This work was financially supported by the Région Auvergne-Rhône-Alpes through the FLUONAT Project and encouraged by Solvay Group.

5. References

[1] Liotier P-J, Pucci MF, Le Duigou A, Kervoelen A, Tirilló J, Sarasini F, et al. Role of interface formation versus fibres properties in the mechanical behaviour of bio-based composites manufactured by Liquid Composite Molding processes. Composites Part B: Engineering 2019;163:86–95. https://doi.org/10.1016/j.compositesb.2018.10.103.

[2] Pouzet M, Dubois M, Charlet K, Béakou A, Leban J-M, Bada M. Fluorination renders the wood surface hydrophobic without any loss of physical and mechanical properties 2019;133:133–41. https://doi.org/10.1016/j.indcrop.2019.02.044.

  doi:10.5075/epfl-298799_978-2-9701614-0-0 published under CC BY-NC 4.0 license

[3] Saulnier F, Dubois M, Charlet K, Frezet L, Beakou A. Direct fluorination applied to wood flour used as a reinforcement for polymers. Carbohydr Polym 2013;94:642–6. https://doi.org/10.1016/j.carbpol.2013.01.060.
[4] Kharitonov AP, Taege R, Ferrier G, Teplyakov VV, Syrtsova DA, Koops G-H. Direct fluorination—Useful tool to enhance commercial properties of polymer articles. J Fluor Chem 2005;126:251–63. https://doi.org/10.1016/j.jfluchem.2005.01.016.
[5] Kharitonov AP, Moskvin YuL, Syrtsova DA, Starov VM, Teplyakov VV. Direct fluorination of the polyimide matrimid® 5218: The formation kinetics and physicochemical properties of the fluorinated layers: Direct Fluorination of Matrimid® 5218. J Appl Polym Sci 2004;92:6–17. https://doi.org/10.1002/app.13565.
[6] Pucci MF, Liotier P-J, Drapier S. Tensiometric method to reliably assess wetting properties of single fibers with resins: Validation on cellulosic reinforcements for composites. Colloids and Surfaces A: Physicochemical and Engineering Aspects 2017;512:26–33. https://doi.org/10.1016/j.colsurfa.2016.09.047.
[7] Young T. An Essay on the Cohesion of Fluids. Philosophical Transactions of the Royal Society of London 1805;95:65–87.
[8] Schellbach SL, Monteiro SN, Drelich JW. A novel method for contact angle measurements on natural fibers. Mater Lett 2016;164:599–604. http://dx.doi.org/10.1016/j.matlet.2015.11.039.
[9] Qiu S, Fuentes CA, Zhang D, Van Vuure AW, Seveno D. Wettability of a Single Carbon Fiber. Langmuir 2016;32:9697–705.
[10] Hodzic A, Stachurski ZH. Droplet on a fibre: Surface tension and geometry. Composite Interfaces 2001;8:415–25. https://doi.org/10.1163/156855401753424451.
[11] Van Hazendonk JM, Van der Putten JC, Keurentjes JTF, Prins A. A simple experimental method for the measurement of the surface tension of cellulosic fibres and its relation with chemical composition. Colloids and Surfaces A: Physicochemical and Engineering Aspects 1993;81:251–61.
[12] Pucci MF, Liotier P-J, Seveno D, Fuentes C, Van Vuure A, Drapier S. Wetting and swelling property modifications of elementary flax fibres and their effects on the Liquid Composite Molding process. Compos Part A: Appl Sci Manuf 2017;97:31–40. https://doi.org/10.1016/j.compositesa.2017.02.028.
[13] Owens DK, Wendt RC. Estimation of the surface free energy of polymers. J Appl Polym Sci 1969;13:1741–7. https://doi.org/10.1002/app.1969.070130815.
[14] ASTM D790-03, Standard Test Methods for Flexural Properties of Unreinforced and Reinforced Plastics and Electrical Insulating Material. ASTM International; 2017.
[15] Pouzet M, Dubois M, Charlet K, Béakou A, Leban J-M, Bada M. Fluorination renders the wood surface hydrophobic without any loss of physical and mechanical properties 2019;133:133–41. https://doi.org/10.1016/j.indcrop.2019.02.044.
[16] Pouzet M, Dubois M, Charlet K, Béakou A. The effect of lignin on the reactivity of natural fibres towards molecular fluorine. Mater Des 2017;120:66–74. http://dx.doi.org/10.1016/j.matdes.2017.01.086.
[17] Charlet K, Baley C, Morvan C, Jernot JP, Gomina M, Bréard J. Characteristics of Hermès flax fibres as a function of their location in the stem and properties of the derived unidirectional composites. Compos Part A: Appl Sci Manuf 2007;38:1912–21. https://doi.org/10.1016/j.compositesa.2007.03.006.
[18] Kharitonov AP, Simbirtseva GV, Tressaud A, Durand E, Labrugère C, Dubois M. Comparison of the surface modifications of polymers induced by direct fluorination and rf-plasma using fluorinated gases. J Fluor Chem 2014;165:49–60. https://doi.org/10.1016/j.jfluchem.2014.05.002.

FLAX FIBRE SIZINGS FOR FIBRE-REINFORCED THERMOSETS - INVESTIGATING THE INFLUENCES OF DIFFERENT SIZING AGENTS ON THE COMPOSITE PROPERTIES

Jan-Marten Sprenger[a,b], Milan Kelch[b], Claas Hoffmann[b], Jörg Müssig[c], Farzin Javanshour[d] and Régis Voillat[e]

a: Faculty of Production Engineering, University of Bremen, D-28359 Bremen, Germany – janmarte@uni-bremen.de
b: Training Centre for Fibre Composite Technology, Fraunhofer IFAM, D-28359 Bremen, Germany
c: The Biological Materials Group, Department of Biomimetics, HSB – City University of Applied Sciences, D-28199 Bremen, Germany
d: Faculty of Engineering and Natural Sciences, Tampere University, FI-33014 Tampere, Finland
e: Bcomp Ltd., CH-1700 Fribourg, Switzerland

Abstract: *The functionalisation of the fibre surface offers high potential to improve the fabric properties and fibre-matrix adhesion. For this purpose, the application of sizings is promising. Sizings are conventionally used to maintain fibre quality during the weaving process and are not specifically designed as a coupling agent between fibre and matrix for structural composites. The present work provides a comparative study of flax fibre reinforced composites (FRCs) containing 2, 6 and 12 % sizing volume fraction relative to the fibre volume using oxidised starch, polyvinyl acetate (PVAc) and cellulose acetate (CA) as sizing agents. The composite porosity was one of the main aspects influenced by the sizing. PVAc and low amounts of CA sizing improved the Young's modulus of the composite up to 13 % without lowering the tensile strength. The performance of the composites containing PVAc sizings was almost independent of the sizing volume fraction.*

Keywords: Sizing; Fibre-matrix adhesion; Complex Interphase; Epoxy resin; Porosity

1. Introduction

In our fast-paced modern world, lightweight design is one of the main aspects to match sustainability demands. Therefore, natural fibre-reinforced composites (NFRCs) are becoming increasingly relevant [1]. In addition to their environmental friendliness, other advantages include good stiffness, low densities, and better end of life options compared to synthetic fibres. Thanks to advancing developments, natural fibres are progressively able to replace synthetic fibres for composite materials. Manufactured fibres such as various plastics, carbon fibres and glass fibres are often fossil-fuel based, their production is energy-intensive, and they are poorly recyclable. In contrast, natural cellulosic plant fibres such as flax and hemp originate from natural renewable resources. In addition to their environmental friendliness, other advantages include good stiffness and low densities compared to glass fibres [2]. For the production of textiles, fibre coatings, so-called sizings, are extensively used to maintain the fibre quality by reducing yarn hairiness and abrasion, thus preventing fibre slippage and yarn tearing during machining processes such as pultrusion, knitting or weaving and the further fabric handling steps. Therefore a sizing solution should provide enough flexibility for fibres to be processed

  doi:10.5075/epfl-298799_978-2-9701614-0-0

without breaking, regulate the moisture content of the yarns, and provide a uniform coating for fibres within a yarn. The most prominent and commonly used sizing agent up until today is starch and its derivatives [3]. The sizing is usually removed after weaving for clothing textiles and other traditional fibre applications to prevent interference with subsequent processing steps such as dyeing. Hence, traditional sizings are not designed for use in composite applications and are far from optimal for facilitating a strong fibre matrix adhesion [4]. The sizings functionality can be extended and define the properties of the fibre-matrix interphase, which is the interpenetrating and heterogeneous region between fibre and matrix, which, in the case of NFRCs, especially with the use of sizings, can also be called the "complex interphase" [5,6]. The sizing can have major impacts on the manufacturing and the composite quality, potentially leading to improved composite properties. Sizing, which is also often referred to as the "heart of weaving", and according to Thomason [4], is possibly the most critical component in fibre manufacturing and their composites remain a "black-box" technology. While the complex interaction of often ten or more sizing components with each other is quite inadequately researched, even less is known about their highly complex interplay with natural fibres, the matrix resin and their composites [3,4]. Consequently, this work aimed to provide fundamental knowledge on the effect of different sizing agents and sizing amounts on the composite's mechanical properties. The employed test procedures were selected to examine the interaction of sizing and flax fabric, the effects on the composite manufacturing and the influence on the mechanical properties of the composites. The latter was evaluated using a quasi-static longitudinal tensile test to measure the tensile strength and Young's modulus and a transverse tensile test to measure the transverse tensile strength. Fabric surfaces and fracture surfaces were analysed using Scanning Electron Microscopy (SEM).

2. Materials and Methods

2.1 Materials

Composites were produced with a flax fibre fabric provided by Terre de Lin (TdL) (Saint-Pierre-le-Viger, France) (growing region: Normandy, France). The fabric was made from an untreated roving (210 g / m^2, stitching thread: nylon) where the fibres were bound together by a helically wound nylon wrapping yarn. The polymers used as sizing agents were oxidised starch, cellulose acetate (CA) and polyvinyl acetate (PVAc) (Carl Roth GmbH, Karlsruhe, Germany).

2.2 Fabric Sizing Process

Two different solvents were used for the polymers to produce immersion baths for the flax fabrics – namely deionised water to dissolve starch and acetone (purity grade 99.5 %: analytical) as a solvent for PVAc and CA. Due to the different polarity and chemical nature of both solvents, they affect the fibre impurities (e.g., pectins, waxes and lipids) and the surface structure. As a result, prior to the fibre coating, the mass loss of the fibres in both solvents were evaluated to determine the exact amount of the sizing agents on the flax fabrics. The targeted sizing volume fractions were 2, 6 and 12 %. Due to the different densities of each polymer, an additional concentration in the solvent has to be used to produce fibre coatings with the same volume fraction of the sizing agents. The respective polymer concentrations in the solvents were identified in preliminary tests. The polymers were dissolved using a magnetic stirrer for 60 minutes. Starch was dissolved at 80 °C, PVAc and CA at 40 °C. For the sizing process, single layers of untreated UD flax fabric were cut, and their edges were maintained with masking tape. To

  doi:10.5075/epfl-298799_978-2-9701614-0-0

ensure sufficient fabric wetting, every layer was impregnated in the bath for two seconds from each side. Afterwards, the layers were spread out on steel grids to dry.

2.3 Composite Manufacturing

For each sizing type and sizing volume fraction, one composite plate (250 x 200 x 2 mm^3) was manufactured using a vacuum bag set-up. As a matrix system, an epoxy IMP503Z-HT prepreg film (120 g / m^2, ρ = 1.2 g / cm^3) supplied by Impregnatex Compositi S.R.L. (Castano Primo, Italy) was used. For easier handling during manufacturing, two layers were pasted on top of each other to get a double matrix film with backing film on both sides. Then, five UD flax layers and six double matrix layers (12 single layers), with 250 mm x 200 mm dimensions, were stacked alternatingly onto the mould. After pasting every double matrix layer onto a UD flax layer, a vacuum was applied to compress the layers and make the matrix film adhere to the fibres properly before removing the backing film and continuing with the next UD layer. Additionally to the conventional set-up, a semi-permeable membrane, only allowing air to pass through, was used to ensure a consistent fibre volume fraction of the composite plates of 37 %. The curing cycle for the plates was at 140 °C for two hours (heating rate: 1 °C / min, cooling rate: 2 °C / min). The finished plates were then cut dry with a chop saw to the required specimen geometries.

2.4 Quasi-static Longitudinal Tensile Test

The longitudinal tensile properties of the composites were measured according to the DIN EN ISO 527- 4 testing standard on a Zwick/Roell Z150 universal testing machine (Zwick/Roell GmbH, Ulm, Germany) with a maximum force of 150 kN and a 150 kN load cell. The force was applied by a constant crosshead speed of 1 mm/min, and the pre-pressure of the pneumatic clamps was at 50 bar. The data were recorded at a frequency of 25 Hz. Of each variety, six specimens were tested. The specimens had a length of 250 mm, a width of 13.27 mm $\pm$ 0.18 mm and a thickness of 2.30 mm $\pm$ 0.25 mm (n = 66). The gauge length was 115 mm. The tensile properties were calculated from measured tensile forces, and the specimen deformations were measured via a videoXtens extensometer (Zwick Roell GmbH, Ulm, Germany). The optical measurement marks on the specimens were set with a lacquer containing reflective particles for better recognition and applied 1 cm over and under the clamps. The specimen cross-section was determined by the mean value of three measurements from thickness and width using a digital sliding calliper (d = 0.01 mm) (Vogel GmbH, Germany).

2.5 Quasi-static Transverse Tensile Test

The transverse tensile test was chosen to characterise the fibre-matrix adhesion in composites. The test was performed on the Zwick/Roell Z150 universal testing machine with a 30 kN load cell (Xforce K, Zwick/Roell GmbH, Ulm, Germany). The force was applied through wedge clamps at a constant crosshead speed of 1 mm / min. The data were recorded at a frequency of 25 Hz. Of each variety, seven specimens were tested. The specimens had a length of 31.85 mm $\pm$ 3.49 mm, a width of 24.36 mm $\pm$ 0.57 mm and a thickness of 2.24 mm $\pm$ 0.24 mm (n = 77). The gauge length was 10 mm. The tensile properties were calculated from measured tensile forces and specimen deformation measured via videoXtens extensometer (Zwick Roell GmbH, Ulm, Germany). The specimen cross-section was determined by the mean value of three measurements from thickness and width using a digital sliding calliper (d = 0.01 mm) (Vogel GmbH, Germany).

2.6 Optical Examination of Fabrics Sizings and Fracture Surfaces

The fabric sizings and fracture surfaces of composites were examined using SEM. Therefore a JSM-6510 Series Scanning Electron Microscope (Jeol Ltd., Akishima, Japan) was used for the fabrics and a Helios Nanolab 600 (FEI - Thermo Fisher Scientific Inc., Massachusetts, USA) for the fracture surfaces. The images were recorded with the secondary electron mode and an acceleration voltage of 10 kV. The specimens were placed on a conductive adhesive carbon carrier and coated with a 15 nm thick gold layer in an argon atmosphere. Further parameters of the recordings are listed in the respective images.

3. Results and Discussions

3.1 Interaction of Sizings with Flax Fabric

As shown in Figure 1, exemplarily for 6 % sizing volume fractions, the different sizing agents lead to varying sizing surface qualities. While the sizings with starch and PVAc show smooth surfaces, the CA sizing forms more extensive membranes between the elementary fibres, and the surface looks rougher, containing small CA shreds. The more brittle the sizing agent behaves, like in the case of CA sizings, the more likely it is that the sizing agent's surface will break during fabric handling, causing the development of shreds and a rough fabric surface. Djordjevic et al. [8] described inconsistent sizing and a rigid and brittle character for starch sizings. The SEM observation cannot confirm this because no quantitative studies on this exist, and no statement can be made for CA and PVAc sizings.

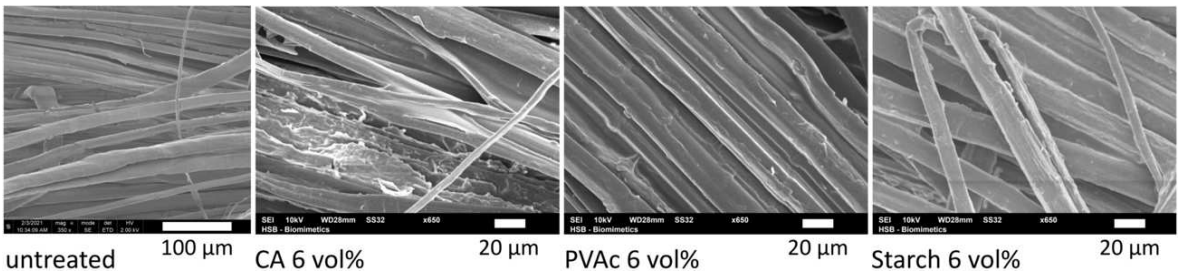

Figure 1. SEM images of coated and uncoated UD fabrics.

3.2 Composite Manufacturing

The fabric sizings can, directly and indirectly influence the composite properties. Certain parameters of the manufacturing process can potentially control these influences. High amounts of sizing with the formation of membranes between single fibres and high surface roughness of the fabric might act as a barrier and negatively affect the infiltration of the fabric with the matrix. An insufficient wetting and infusion of the fabric with matrix will introduce porosity (voids), weakening the fibre matrix adhesion and the properties of the complex interphase. The surface quality and composite porosities are qualitatively shown in Figure 2. The untreated composite shows almost no porosity. The starch sized flax epoxy composites exhibit the highest surface porosities already at a low sizing amount, which seemingly increases with increasing sizing volume fraction. In contrast, the PVAc sizings exhibit all together almost no porosity. Composites processed with CA sized fabrics at 2 vol% show minor surface porosity, which increases at higher sizing volume fractions.

  doi:10.5075/epfl-298799_978-2-9701614-0-0

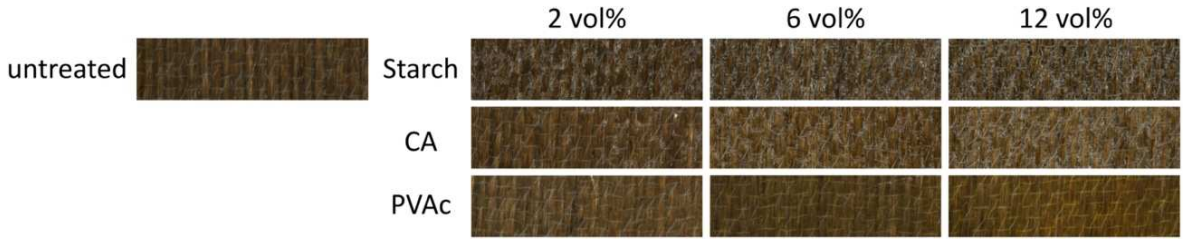

Figure 2. Composite plate surfaces, qualitatively show different levels of porosity.

A low glass transition temperature (Tg) of the sizing agent might be advantageous, as the sizing agent could reach lower viscosities early during the curing process. This could additionally be improved by applying pressure on the composite during the curing process, e.g., using an autoclave or an increased curing temperature. The plate´s porosity may also have resulted from the evaporation of moisture from the fibre during the curing process within the matrix system. This relates to the different abilities of the sizings to act as a barrier for water absorption and desorption. A well-known problem with the wettability of flax fibres with epoxy resin is the fibres' heterogeneous surface character [5]. However, fibre sizing can potentially produce a homogenous surface for the fabric, which might lead to uniform properties of the fibre-matrix interface and eventually even a complex interphase. With the selection of the sizing agent, the chemical interaction of the fabric surface with the matrix can be modified.

The chemical character of oxidised starch offers a high polarity and good compatibility with the OH groups of cellulose, but also with the OH groups of the epoxy and the oxygen atoms of its ether groups. Further, the more hydrophobic character of oxidised starch in comparison to the hydrophilic flax fibre surface might improve the wetting of the fabric with epoxy. Although starch coated flax fibres and fabrics have smooth surface structure, their composites have notable surface porosities. This might be a consequence of the large-sized starch molecules and high viscosity of the sizing bath, providing a good surface structure of the fabric but eventually causing weak infiltration of fibre bundles and penetration of the fibre surfaces. Encapsulated air and moisture inside the fabric due to starch membrane might introduce pores during the composite curing process [9]. In PVAc, the oxygen atoms within acetate groups (ester linkages) offer the opportunity to form hydrogen bonds with the OH groups of the flax fibre surface. The same interaction can be assumed with the OH groups of the epoxy, potentially leading to strong interfaces. Furthermore, PVAc is known to disperse within the epoxy matrix during the curing process, explaining the low porosity levels in the composites [10,11]. According to Sanchez-Cabezudo et al. [11], higher curing temperatures above 150 °C can further improve this homogenisation of the complex interphase. In the chemical structure of CA, there are OH groups next to the ester linkages of the acetate groups. Thus, it offers the possibility to interact with both the flax fibre surface and the epoxy matrix with the formation of hydrogen bonds. However, CA sizings exhibit a poor surface quality on the fabric (see Figure 1). This behaviour is possibly due to the larger molecule size compared to PVAc and the strong membrane forming character. In addition, with its higher Tg, this might introduce the formation of pores within the composites.

3.3 Longitudinal Tensile Properties

The longitudinal tensile testing results of composites are shown in Figure 3. Comparing the tensile performance of composites with and without fibre sizing shows a decrease in the tensile

strength and Young's elastic modulus with increasing sizing volume fraction for the starch and CA coatings. This observation can mainly be attributed to the weakening of the fibre matrix adhesion by pores. In contrast, increasing PVAc sizings content on fibres does not negatively affect the tensile strength and elastic modulus of composites. This behaviour underlines the hypothesis for the dispersion of PVAc within the epoxy matrix during the curing process, improving resin infiltration Composites with 2 vol% PVAc exhibit the highest mean tensile strength, next to the ones with 2 vol% CA and the untreated composite. The Young's modulus can be significantly improved with all PVAc sizings compared to the untreated composite.

The results for the tensile strength and Young's elastic modulus agree with the qualitative observations for the composite porosity, depending on the used sizing agent and sizing volume fractions. All of the used sizings decrease the maximum strain. Generally, pores within the complex interphase and the matrix will reduce the ability of the matrix to transfer the stresses between the fibres uniformly (with starch sizings). This will increase local stress peaks within single fibres, causing early fibre and composite failure. On the other hand, a strong fibre matrix adhesion will reduce the deformation of the fibre (with PVAc and CA sizings). With starch sizings, the strain again decreases with the increasing sizing amount. The results are mainly determined by the weaker interphase, exhibiting the overall highest levels of porosity. PVAc sizing strain results are again comparatively constant over varying sizing amounts. CA, however, shows an optimum at 6 vol% with the highest strain of all sized fabrics. Additionally to the correlation of the tensile test results with the composite porosity, the results indicate different chemical interactions of the sizing agents with the epoxy resin. The 2 vol% CA sizing exhibits equally high tensile strengths and moduli as the PVAc sizings, while the apparent porosity seems to be higher, indicating stronger chemical interaction with the flax fibre surface and the epoxy matrix. The porosity increases visibly with increasing CA volume fractions, significantly reducing the strength and modulus. Furthermore, the Young's moduli results also indicate an improvement of the fibre-matrix interface with all PVAc sizings and the 2 vol% CA sizing compared to the untreated composite.

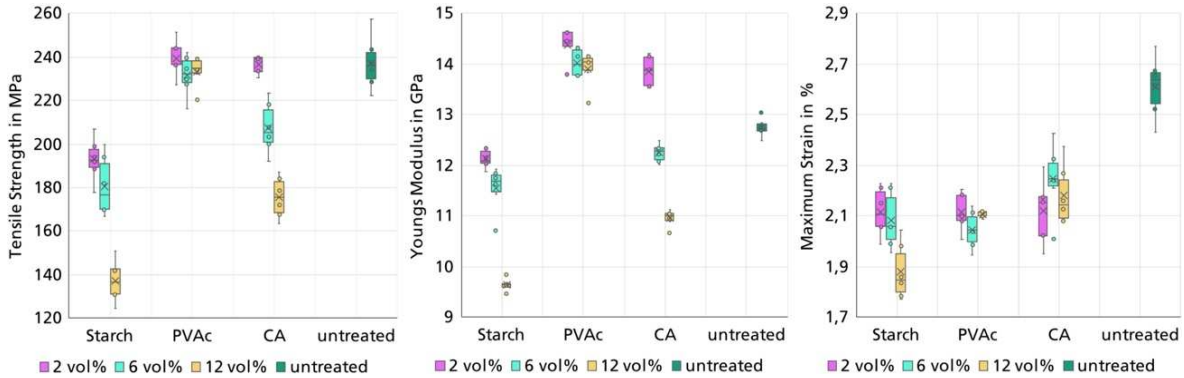

Figure 3. Box-and-whisker plots from tensile test results (n = 6)

3.4 Transverse Tensile Properties

Although the standard deviations of the transverse tensile test results, shown in Figure 4, are comparatively large, the results exhibit the same trend as observed for the longitudinal tensile test results. The larger deviations can be explained by the orientation of the fabric layers during the lay-up composite manufacturing process and misaligned fibres in the fabric (e.g., hairiness). Also, the fabrics contain a nylon wrapping yarn whose orientation is longitudinal to the

transverse load direction, contributing to the transverse tensile properties, even though its volume fraction within the composite is comparatively low.

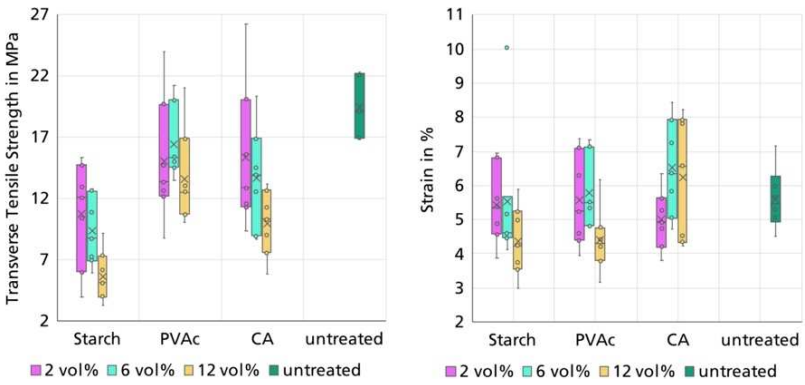

Figure 4. Results from the transverse tensile test (n = 7).

In contrast to the untreated composite, the fracture surfaces with sized fabrics show peeling of the fibre surface layers (fibrillation), indicating a failure within the interphase between sizing and fibre (see Figure 5). Thereby the level of the fibrillation varies qualitatively with the number, length and width of the shreds. The untreated composite exhibits the lowest fibrillation level. As for the composites containing sizings, an increase of the fibrillation with increasing sizing volume fraction is qualitatively noticeable for all sizing agents. Generally, the fibrillation of the flax fibre surface indicates a strong fibre-matrix or fibre-sizing adhesion. Hence, a strong chemical and physical interaction as the bond of the sizing agent with the flax fibre surface is strong enough to separate cellulose microfibrils from each other.

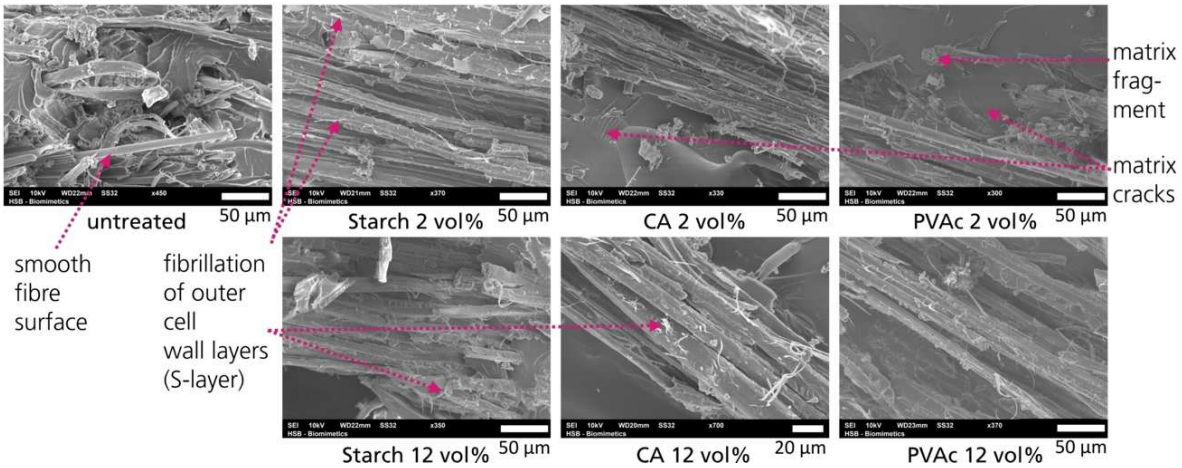

Figure 5. SEM images of fracture surfaces from transverse tensile test specimens.

4. Conclusion

The development of NFRCs in general but especially using sized fabrics requires a holistic and interdisciplinary understanding. Amongst others, this includes the chemical and physical properties of the sizing agents and important factors for the sizing process (solvents, concentrations, immersion times), as well as the properties of the epoxy matrix system and the composite manufacturing process. The sizing can homogenise the fibre surface whereby the coating, wetting and encapsulation of the fibres with matrix might be improved. Therefore, lower sizing volume fractions seem to be advantageous as higher amounts might act as wetting

barriers and increase porosity. This effect might be mitigated by choosing sizing agents with low Tg. This is underlined by the results of the composites containing PVAc sizings which exhibit the lowest levels of porosities and lead to increased elastic modulus compared to the untreated composite without lowering the tensile strength (1 % improvement at 2 vol% sizing amount). The Young's modulus can be improved by about 13, 10, and 9 % with all tested PVAc sizings, respectively, at 2, 6 and 12 vol% compared to the untreated reference. Differences in the sizing quality and the composite properties regarding the sizing agent type and the sizing volume fraction could be observed. Generally, the use of a sizing can improve the composite properties. However, this highly depends on the sizing agent especially seen for starch and PVAc, but also the sizing volume fraction as seen for CA. The composite porosity, being substantially affected by different sizings, is one of the main aspects. The results show that the sizing in general, but pure starch sizings in particular, do not necessarily lead to improved composite properties, underlining the need for further research and the importance of new developments in the field of natural fibre sizings for composite applications.

5. References

1. Müssig J. Preface. Industrial Applications of Natural Fibres. Müssig J. (Ed.). John Wiley & Sons Ltd., UK. 2010, xiii-xiv.
2. Müssig J, Haag K. The use of flax fibres as reinforcements in composites. Biofiber Reinforcement in Composite Materials. Ed. by Faruk O and Sain M. Elsevier Science 2015, 35-85.
3. Goswami BC, Ananjiwala RD, Hall DM. The Sizing Process. Textile Sizing. Ed. by Kozlowski RM and Mackiewicz-Talarczyk M. 1. Marcel Dekker Inc. 2004, 1-17.
4. Thomason JL. Glass fibre sizing: A review. Composites Part A: Applied Science and Manufacturing 127 2019. 1-24.
5. Duigou A, Kervoelen A, Le Grand A, Nardin M, Baley C. Interfacial properties of flax fibre-epoxy resin systems: Existence of a complex interphase. Composites Science and Technology 100 2014, 152-157.
6. Müssig J, Graupner N. Test Methods for Fibre/Matrix Adhesion in Cellulose Fibre-Reinforced Thermoplastic Composite Materials: A Critical Review. Reviews of Adhesion and Adhesives 8 2020, 68-129.
7. DIN EN ISO 527-4:1997-07. Plastics - Determination of tensile properties - Part 4: Test conditions for isotropic and anisotropic fibre-reinforced plastic composites (ISO 527- 4:1997). Beuth Publishing 1997.
8. Djordjevic S, Kovacevic S, Djordjevic D, Konstantinovic S. Sizing process of cotton yarn by size from a copolymer of methacrylic acid and hydrolysed potato starch. Textile Research Journal 89 2019, 3457-3465.
9. Li Y, Li Q, Ma H. The voids formation mechanisms and their effects on the mechanical properties of flax fiber reinforced epoxy composites. Composites Part A: Applied Science and Manufacturing 72 2015, 40-48.
10. Mallarino S, Chailan JF, Vernet JL. Glass fibre sizing effect on dynamic mechanical properties of cyanate ester composites I. Single frequency investigations. European Polymer Journal 41 2005, 1804-1811.
11. Sanchez-Cabezudo M, Prolongo MG, Salom C, Masegosa RM. Sisal Cellulose Whiskers Reinforced Polyvinyl Acetate Nanocomposites. Journal of Thermal Analysis and Calorimetry 86 2006, 699-705.

ELABORATION OF HYBRID BIO-COMPOSITES WITH THERMOPLASTIC MATRIX: OPTIMAL FORMULATION AND MODELLING OF THE QUASI-STATIC BEHAVIOUR FOR AN AUTOMOTIVE STRUCTURAL APPLICATION PARTS

Wassim GUERFALA[a,b], *Patrick ROZYCKI*[a], *Christophe BINETRUY*[a]

a: Nantes Université, Ecole Centrale Nantes, CNRS, GeM, UM618,[F-44000 Nantes],France

wassim.guerfala@ec-nantes.fr

b: Department Body in White Research and innovation Unit Bertrandt

Keywords

Composite materials; natural fibres; hybrid composite; homogenisation; thermo-compression

Abstract

The environmental impact is becoming increasingly important in the automotive industry, pushing OEMs to reduce CO2 emissions through clean engines and structural weight reduction. Composite materials offer an excellent alternative to standard steels with considerable weight reduction. The main objective of this study is the application of bio-composite materials in automotive structure. This study is divided into two phases: the first step aims to develop a new hybrid composite material that can meet the mechanical, thermal and economic specifications [1]. In the second phase of this project a multiscale homogenisation approach [2] was used to predict and understand its elastic mechanical behaviour. This paper presents the experimental results that show the interest of hybridisation to improve the stiffness of this composite.

1. Introduction

The application of composite materials remains limited in the automotive industry due to various technical, economic, and environmental constraints. Knowledge of the technical aspects of manufacturing (processes and production rate), of the mechanical behaviour of these heterogeneous materials (behaviour law and simulation tools) and of their lifespan is still insufficient for mass production. On the economic aspect, the high price of fibres such as carbon fibres and the high manufacturing cost related to cycle time are the main obstacles to the development of these materials. Furthermore, the environmental impact became increasingly critical with new European regulations for reducing the CO2 emission and the Carbone footprint of the life cycle automotive structures. The main objective of this research work is to define a new concept for semi-structural automotive parts (hood, door, dashboard…) that can meet the various industrial requirements while respecting the environmental regulations. Therefore, the initial work has focused on the selection of

  doi:10.5075/epfl-298799_978-2-9701614-0-0

materials among a broad spectrum of natural fibres and bio-sourced polymers with suitable characteristics. Then we focused on the characterisation of hybrid composite materials through different quasi-static mechanical tests.

This article presents the results of a comparative study of natural fibres and a choice of the hybrid combination for the composite material. The second part concerns the experimental study of the developed materials, basalt/PA11, flax/PA11 and Hyb/PA11 for different orientations (0°/45°/90°).

The objective of this study is to understand the impact of the hybridisation on the evolution of the mechanical behavior of this composite.

2. Materials choice

Different bio-composite materials based on natural fibres and bio-sourced matrices are used in industry for several reasons [1], [8]: mass reduction [8], [3], environmental impact limitation [8], [9], [10], good recycling capacity [11], [12].

The choice of these materials is essential and is linked to the final characteristics required for the semi structural part. Different matrices and fibres were compared according to manufacturing constraints, processing conditions, environmental impact, and economic requirements.

The hybridisation concept uses two or more fibres within the same matrix. This concept provides adequate flexibility to design the optimal material. The main idea is to eliminate the weakness of one of the fibres with maintaining the advantages of the other(s). This composite material offers many qualities but needs an in-depth study to define the best combination of compatible fibres [32]. The mechanical properties of the hybrid composite (fibre A and fibre B) are often the weighted average of the respective mechanical properties of both fibres. A better combination can create a synergetic effect which enhances the hybrid composite properties compared to the constituent composites (composite with fibre A and composite with fibre B) [32].

There are two leading families of fibres: synthetic fibres and natural fibres (mineral fibres, plant fibres and animal fibres) [2]. We are interested in natural fibres whose mechanical properties are similar to those of glass fibres. Mineral fibres have good mechanical and thermal characteristics due to their chemical compositions based on silicon (e.g., asbestos, basalt). Plant fibres have a wide range of varieties depending on the nature of the plant and its origin (leaves, stems, seeds or fruits) [8] Table 1

  doi:10.5075/epfl-298799_978-2-9701614-0-0

Fibres	Young's Modulus (GPa)	Ultimate elongation (%)	Tensile strength (MPa)	Density	References
Glass E	72	1.7-2.1	1200-2000	2.54	[8]
Carbone T300	230	1.5	3530	1.7-1.9	[8]
Bamboo	32-44	3.8-5.8	1200-1610	1.41	[14] [15]
Hemp	23.5-90	1-3.5	270-900	1.45	[16][17][18]
Jute	20-40	1.5-1.8	280-773	1.44	[19][20][21]
Sisal	9-21	3-7	350-700	1.45	[23][24]
Basalt	93-110	3.1	4150-4800	2.6	[8]
Flax	38-75	1.7-3	600-1400	1.5	[22]

Table 1 Mechanical properties of synthetic and natural fibres

We selected natural fibres through bio-composite studies applications [3], [8], industrial aspect of fibre production (followed by product quantity and quality) and the industrial requirements (structural lightness, mechanical performance, cost, environmental impact and durability).

It was decided to select flax and basalt as fibre reinforcement and a PA11 matrix [3]. These different constituents are compatible and have complementary mechanical properties. Flax fibre has good mechanical properties [8], [22] and low density (1.4 g/cm³) [8], while basalt fibre provides high stiffness (Young's modulus of 93 GPa) [8], high humidity resistance (water absorption rate of 0.03%) [8] and excellent temperature resistance (maximum application temperature: 850°C) [8]. The choice of a thermoplastic matrix and natural fibres improves the recyclability of this hybrid bio-composite.

3. Experimental tests

The main objectives of the experimental phase were to indentify the mechanical characteristics (Young's modulus, Poisson's ratio, strength and strain at failure) of the PA11 matrix and the composites flax/PA11 (twill, 4 plies, 2 mm thick, Vf 40%), basalt/PA11 (UD, 8 plies, 4 mm thick, Vf 30%) and hybrid 50/50 (twill, 4 plies and 2 mm thick, Vf 35 %). The quasi-static tests were carried out on a tensile-compression machine type INSTRON 5584 , which allows a tensile force or a displacement applied as a function of time.

In order to determine the various mechanical properties of the studied materials, we carried out several quasi-static in the dry state (RH0 : relative humidity 0), at ambient temperature (T 23°C) and for different orientations (0°/45°/90°) The 0° orientation provides the longitudinal mechanical characteristics, 45° for the shear characteristics and 90° for the transverse characteristics of the composite. The choice of the hygrometry level and the temperature was made to eliminate their impact on the composite mechanical behaviour, as flax fibres are sensitive to humidity and high temperature |8], in this paper we want to foucs only on the hybridisation impact

For each test, five samples were used to ensure the reproducibility of the results Table 2.

	RH0/T +23°C
Flax twill/PA11	0°/45°/90°
UD Basalte/PA11	0°/45°/90°
Twill Hybrid/PA11	0°/45°/90°
PA11	X

Table 2 Characterisation test matrix for flax, basalt, hybrid and PA11

The digital image correlation (DIC) method has been adopted to determine the strain field of the specimens. A high-definition camera (STEMMER GT6600) is used to acquire images during the tensile test and they are subsequently processed using the VIC -2D software, which allows the calculation of the global longitudinal and transverse deformations.

The analysis of the monotonic tensile tests provides the mechanical characteristics of these materials (elasticity relationship and stress/strain at failure). Unidirectional composite laminates are considered as transversely isotropic materials due to their geometrical symmetries [6]. This hypothesis makes it possible to simplify the relationships between stresses and strain for the different orientations. Table 3 shows the quantities calculated as a function of the different laminates.

	Tensile test$[0]_4$	Tensile test $[90]_4$	Tensile test $[45]_4$
Flax twill/PA11	E11, υ12, ε11R	E22, ε22R	G12
UD Basalt/PA11			

Table 3 Mechanical parameters of flax/PA11, basalt/PA11 and hybrid/PA11 composites

$$E_{11} = \frac{\sigma_{11}}{\varepsilon_{11}} \quad (1)$$

$$E_{22} = \frac{\sigma_{22}}{\varepsilon_{22}} \quad (2)$$

$$G_{12} = 2\,\frac{\sigma_{12}}{\varepsilon_{12}} \quad (3)$$

$$\vartheta_{12} = -\frac{\varepsilon_{11}}{\varepsilon_{22}} \quad (4)$$

4. Experimental results and discussion

Figure 1 compares the different mechanical behaviours of the flax/PA11, basalt/PA11 and hyb5050/PA11 composites.

  doi:10.5075/epfl-298799_978-2-9701614-0-0

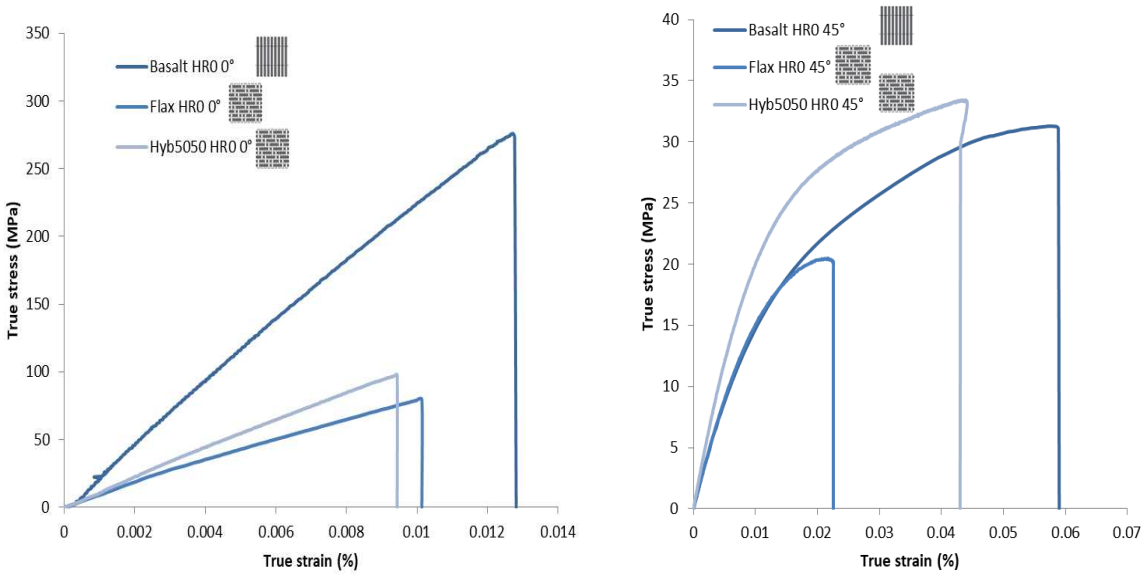

Figure 1 Tensile test Flax/PA11, Hyb5050/PA11 & basalt/PA11 for RH0 and 0° and 45° at T 23°C

With the aim of improving the mechanical characteristics of the hybrid composite 5050 /PA11 compared to the flax/PA11 composite; one can see that the hybrid composite is 20% stiffer than the flax composite Figure 1. The different mechanical properties for the studied composites are reported in the Table 4.

	Flax		Basalt		Hyb 50 50	
0°	E11(MPa)	υ 12	E11(MPa)	υ 12	E11(MPa)	υ 12
	9193	0.02	22658	0.26	11056	0.05
	σ 11 failure	ε 11 failure	σ 11 failure	ε 11 failure	σ 11 failure	ε 11 failure
	80	0.01	276	0.01	98	0.01
90°	E22(MPa)		E22(MPa)		E22(MpPa)	
	12926		4460		12555	
	σ 22 failure	ε 22 failure	σ 22 failure	ε 22 failure	σ 22 failure	ε 22 failure
	90	0.01	77	0.02	102	0.01
45°	G12(MPa)		G12(MPa)		G12(MPa)	
	977		862		1317	
	σ 12 failure	ε 12 failure	σ 12 failure	ε 12 failure	σ 12 failure	ε 12 failure
	41	0.02	63	0.07	67	0.05

Table 4 Mechanical characteristics of Hyb5050/PA11, basalt/PA11 and flax/PA11 composites for RH0 and for orientations (0°/45°/90°) at 23°C

Figure 2 shows the typical dispersion of the mechanical behaviour, especially for the flax/PA11 composite. Although, this dispersion is essentially due to the plant nature of the flax fibres, the mechanical characteristics of flax fibres depend on the nature of the fibres, the growth conditions (temperature and humidity), and the treatment carried out to process these fibres [8], [9].

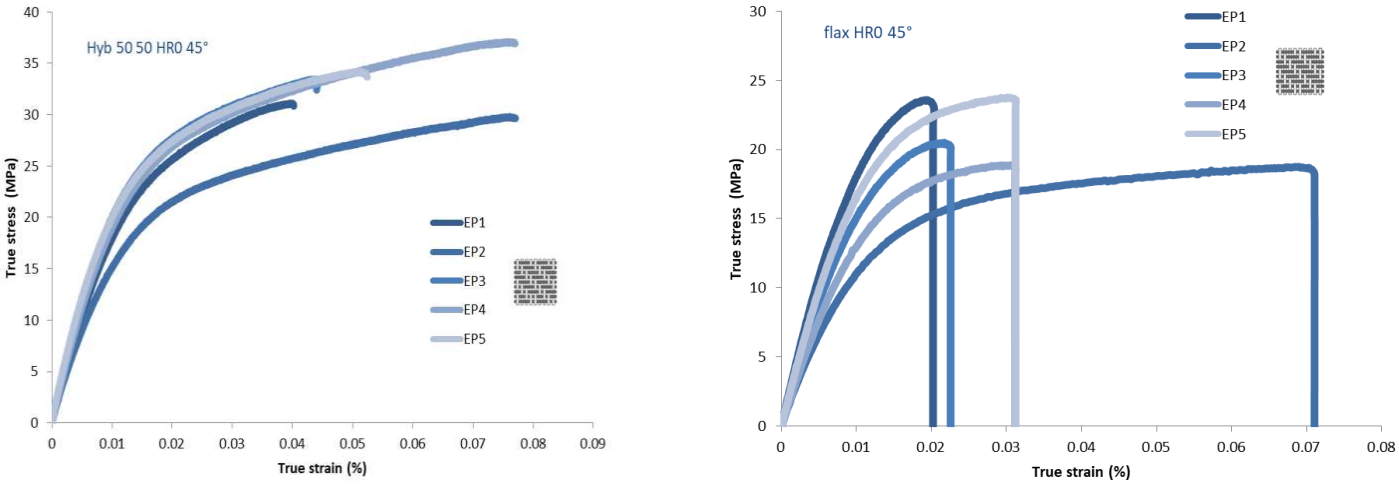

Figure 2 Tensile tests for Flax/PA11 & Hyb5050/PA11 45° for RH0 at 23°C

Hybridisation of flax fibres with basalt fibres reduced the scattering of the mechanical characteristics of the flax/PA11 composite. The hybrid composite 5050/ PA 11 shows a much lower scattering compared to the flax/ PA11. Like glass fibre, basalt has good mechanical stability due to its chemical composition and manufacturing process [34], [35].

5. Conclusions

The main objective of this study is to highlight the interest of applying bio-composite materials in structural parts by understanding their mechanical behaviour.

In the first phase, we start by studying natural fibres and thermoplastic matrices to determine the best fibre/matrix combination. Then we validated the thermo-compression parameters (temperature, holding time and pressure), which meet the industrial requirements. The second phase was devoted to the experimental characterisation for the different composites materials (flax, basalt and hybrid) and the matrix (PA11); the purpose of this part is to identify the mechanical properties of the studied materials in the dry state and at room temperature.

The results of the characterisation tests highlight the interest of hybridisation. Indeed, the use of basalt fibres with flax fibres improves the mechanical performances of the hybrid composite compared to the flax/PA11 composite and reduce its density by increasing the potential mass gain compared to the basalt/PA11 composite. Furthermore, we have also found that the basalt fibres allowed the homogenisation of the hybrid composite mechanical behaviour by reducing the scattering of flax fibre composites.

In the second step of this project, we correlated the numerical and the experimental result through a multiscale homogenisation approach to study the impact of the interface fibre/matrix on the mechanical behaviour of the composite material and to understand the impact of the moisture on the mechanical behaviour of plant fibres. Also, the numerical tool offers the possibility to compare the three scales of hybridisation; the laminate scale, the layer scale (by co-weaving) and the fibre

scale (by commingling of two different fibres), and help us to make the suitable choice of hybridisation for the targeted application.

Acknowledgements

We would like to acknowledge the support of the company Bertrandt for the funding of this research work

6. References

[1] Gay, Composite Materials Design and Applications. 2016.
[2] Swolfs,Y., Gorbatikh, L., Verpoest, I. (2014) , Fibre hybridisation in polymer composites : A review , Composite Part A: Applied Science and Manufacturing, p. 181-200.
[3] Fragassa, C., Santulli, C., Pavlović, A., & Šljivić, M.(2015), Improving performance and applicability of green composite materials by hybridisation, Contemporary Materials, p. 35-43.
[4] A. Thuault, S. Eve, J. Bazin, K. Charlet, F. Destaing, M. Gomina ,J. Bréard, (2011), Morphologie, biocomposition et comportement mécanique des fibres de lin, Matériaux et techniques,p 275-280.
[5] Barbulée, A ,Jernot J.P, Bréard J,(2014),Damage to flax fibre slivers under monotonic uniaxial tensile loading, Composite Part A Applied Science and Manufacturing,64:107-114.
[6] Baley C., Morvan C., Grohens Y. «Influence of the Absorbed Water on the Tensile Strength of Flax Fibers». Macromolecular Symposia, Vol. 222, pp. 195–202, 2005.
[7] Baley. C, Bourmaud A, (2014), Average tensile properties of French elementary flax fibres, Materials letters, p159-161.
[8] Baley C, (2020), Fibres naturelles de renfort pour matériaux composites, matériaux plastiques et composites, technique de l'ingénieur, AM5130 V3
[9] Le duigou A,Davies P., Baley C, (2011), Environmental impact analysis of the production of flax fibres to be used as composite material reinforcement. J Biobased Mater Bioenergy; 5:p.153-65
[10] Joshi S ,Drzal L,Mohanty A, Arora S, (2004), Are natural fiber composites environmentally superior to glass fiber reinforced composites? Compos Part A ApplSci Manuf; 35:p.371-6
[11] Pervaiz M, Sain M.M, (2003), Carbon storage potential in natural fiber composites. Resour ConservRecycl; 39:p.325-40
[12] Bourmaud A, Baley C, (2007), Investigations on the recycling of hemp and sisal fibre reinforced polypropylene composites. Polym Degrad Stab; 92:p.1034-45
[13] Bourmaud A, Baley C, (2009), Rigidity analysis ofpolypropylene/vegetalfibrecom- posites afterrecycling. PolymDegradStab; 94 :p.297-305
[14] Ren D, Yu Z, Li W, Wang H, Yu Y, (2014), The effect of ages on the tensile mechanical properties of elementary fibers extracted from two sympodial bamboo species. Ind Crops Prod ; 62 : p. 94-9
[15] Yu Y, Jiang Z, Fei B, Wang G, Wang H, (2011), An improved micro tensile technique for mechanical characterisation of short plant fibers : a case study on bamboo fibers. J Mater Sci ; 46 : p. 739-46
[16] Bourmaud A, Baley C, (2009), Rigidity analysis of polypropylene/vegetal fibre composites after recycling. Polym Degrad Stab ; 94 : p. 297-305
[17] Duval A, Bourmaud A, Augier L, Baley C, (2011), Influence of the sampling area of the stem on the mechanical properties of hemp fibers. Mater Lett ; 65 : p. 797-800

  doi:10.5075/epfl-298799_978-2-9701614-0-0

[18] Marrot L, Lefeuvre A, Pontoire B, Bourmaud A, Baley C,(2013), Analysis of the hemp fiber mechanical properties and their scattering (Fedora 17). Ind Crops Prod ; 51 : p. 317-27
[19] Roe P.J, Ansell M.P, (1985), Jute-reinforced polyester composites. J Mater Sci ; 20 : p. 4015-20
[20] Tanguy M, Bourmaud A, Baley C, (2016), Plant cell walls to reinforce composite materials : Relationship between nano indentation and tensile modulus. Mater Lett ; 167 : p. 161-4
[21] Lee B.-H, Kim H.-J, Yu W.-R, (2009),Fabrication of long and discontinuous natural fiber reinforced polypropylene biocomposites and their mechanical properties. Fibers Polym; 10 : p. 83-90
[22] Baley C, Bourmaud A, (2014), Average tensile properties of French elementary flax fibers. Mater Lett; 122: p. 159-61
[23] Li Y, MAI Y.-W, YE L, (2000), Sisal fibre and its composites: a review of recent developments. Compos Sci Technol; 60: p. 2037-55
[24] Silva F. de A, CHAWLA N, FILHO R.D. de T, (2008), Tensile behavior of high performance natural (sisal) fibers. Compos Sci Technol; 68: p. 3438-43
[25]Abida M, Gehring F, Mars J, Vivet A,(2020), Hygro-mechanical coupling and multiscale swelling coefficients assessment of flax yarns and flax / epoxy composites, Composites Part A Applied Science and Manufacturing,p136-143
[26] V. Fabre, G. Quandalle, N. Billon, and S. Cantournet,(2017), Time-Temperature-Water Content equivalence on dynamic mechanical response of polyamide 6,6, Polymer, p2-3.
[27] Coussa et al., (2017), influence of rate effects on the mechanical behavior of thermoplastic matrix woven composites', in JNC 20–Ecole des Ponts ParisTech – 28 - 30 juin 2017.
[28] El Hadi S, Scida D, Assarar M, Sabhi H, Ayad R (2017), Composite hybride lin-verre : effet de l'hybridation sur la cinétique de diffusion et les propriétés mécaniques en traction. Journée Nationales des Composites
[29] Rozycki P, Mbacke M, Dau A, (2018), Multiscale Homogenisation of a glass-PA66 Fabric Composite Behavior for crash studies, ECCM18-18th European Conference on Composite Materials,p24-28
[30] Gu,H. « Multigrid methods for 3D composite material simulation and crack propagation modeling based on a phase field method»,Ph.D. Thesis, Lyon University, 2016
[31] Swolfs.Y, Verpoest.I,Gorbatikh.L, (2019), Recent advances in fibre hybrid composites : materials selection, opportunities and applications, International materials reviews, p181–215.
[32] Hearle J.W.S.,(1986), The fine structure of fibres and crystalline polymers - Interpretation of the mechanical properties of fibres, Journal of applied polymer science , p1207-1223.
[33] Mukherjee P.S., Satyanarayana K.G., (1986), An empirical evaluation of structure-property relationships in natural fibres and their fracture behaviour", Journal of Materials Science, p4162-4168.
[34] Shubhalakshmi.B.S, Dr. H.N.Jagannatha Reddy, K.Arjun (2016), International journal of engineering sciences & research technology, ISSN: 2277-9655.
[35] Singha.K, (2012), A short review on basalt fiber, International journal of textile science, p.19-28.
[36] ALLAIRE G, « Introduction to homogenisation theory », in : CEA-EDF-INRIA school on homogenisation, Ph.D.thesis, Ecole Polytechnique, 2010.

  doi:10.5075/epfl-298799_978-2-9701614-0-0

CONVERTING RECYCLED GLASS FIBRE AND POLYPROPYLENE TO FEEDSTOCK (FILAMENT) FOR MATERIAL EXTRUSION ADDITIVE MANUFACTURING

Pouyan Ghabezi [a], Noel M. Harrison [a, b], Tomas Flanagan [c]
a: School of Engineering, National University of Ireland Galway, Ireland,
E-mail: Pouyan.ghabezi@nuigalway.ie
b: I-Form Advanced Manufacturing Research Centre, Dublin, Ireland
c: Eirecomposites Teo, Údarás Industrial Estate An Choill Rua, Inverin, Co. Galway, Ireland

Abstract: *3D Printing, specifically material extrusion, is a potential candidate manufacturing method for the use of recycled plastics and composite off-cut fibres gathered from industrial and domestic waste. In this work, off-cut glass fibres and recycled mushroom containers made of Polypropylene (PP) have been combined in an extruder to make short fibre reinforced filaments as an engineering grade feedstock for material extrusion manufacturing. A Noztek Touch Dual PID filament maker was utilized to make reinforced PP with 0%, 2%, 5%, and 8% glass fibre weight fractions. The extruding parameters including motor speed, heating temperatures, cooling fan status, and pulling load were optimized to produce a filament with average diameter of 1.45mm and desired surface quality, void content, and profile. Tensile testing, microscopy and differential scanning calorimetry were conducted to assess the effect of adding short on the properties of recycled filaments.*

Keywords: Recycling; *Polypropylene*; extruding; Filament; Composites;

1. Introduction

On the 16th January 2018, the European Commission (EC) published a European Strategy for Plastics in a Circular Economy requiring all Member States to reuse and recycle 50% of all plastic packaging waste by 2025 and 55% by 2030 [1]. Polypropylene (PP) is a cheap thermoplastic polymer with exclusive properties such as Good thermal resistance, Good impact and fatigue resistance, Good heat resistance, Smooth surface finish. PP is a widely used plastic to make end products for customers, such as plastic packaging, and accounts for 16 % of the worldwide plastics market [2]. According to the Gulf Petrochemicals and Chemicals Association, the rate of post-consumer recycling of PP worldwide is just about 1 %, therefore, huge amounts of PP go to landfills, subsequently compounding the plastic pollution quandary [3]. The PP reinforced by short fibres may be formed into filaments for industrial market segmentation. Automotive industry has been a candidate for applying this composite [4]. 3D printing has shown advantages over traditional molding methods, due to this researchers are seeking to find optimum printing parameters for well-known thermoplastics and overcome the limited variety of the materials that can be formed into filament and fed into printers [5, 6, 7].

Sodeifian et al. [4] have investigated the mechanical, morphological, rheological, and crystallinity properties of pure polypropylene, polypropylene reinforced with glass fiber (GF), and PP/GF composites containing maleic anhydride polyolefin (POE-g-MA) at 10, 20 and 30 fibre weight fractions. The pure PP was observed to be shrunk, detached from the platform surface,

  doi:10.5075/epfl-298799_978-2-9701614-0-0

and finally distorted, due to weak adhesion, while adding GF provided convenient adhesion for the melt layers on the platform surface. Li et al. [8] developed recycling process to create a value-added composite from a PEEK/CFC waste stream that maximizes the carbon fibre-reinforced composites attributes. Zander et al. [7] evaluated processing of PET, polypropylene (PP), and polystyrene (PS) into fibres, equal part blends of each combination of polymers (50/50 wt % of PS, PET, PP), as well as a tri-component blend of PS, PET, and PP (33/33/33 wt %) through centrifugal spinning technique. In Mutiva et al. research [9], the recycled waste PET materials were converted into high value and useful products such as dog bones test samples, 3D printing filaments, mobile robot chassis, drone blades etc. There are many ways to modify and improve the mechanical properties of recycled thermoplastics such as adding a certain percentage of virgin material to the recycled material. This method enhance the average linear chain length, therefore improving the properties of the material as a whole. Also, blending in other additives such as fibre to form composite materials is another method of improving the mechanical. Blending in reinforcing fibres provides a range of advantages including increased mechanical properties and reductions in shrinkage [10, 11].

While polypropylene is widely used in the plastic injection industry, it is not used as much in additive manufacturing because it is not the easiest thermoplastic to print. Before overcoming the printing difficulties of PP, it is critical to produce a good quality filament from recycled waste thermoplastics and upcycle them by adding short fibres in order to improve their mechanical properties. In this work, 100% recycled mushroom containers made of PP were incorporated by different weight fractions of off-cut short glass fibres to fabricate reinforced filaments suitable for fused deposition modeling 3D printing method.

1. Materials and Extruding

Domestic mushroom trays made of polypropylene were collected, sorted, washed and shredded into small flakes with maximum length of 5mm. As a reinforcement, off-cuts E-Glass 200 TEX fibres with the average length of 4.5mm were utilized. Three different fibre weight fractions, 2%, 5%, and 8%, were selected to make the reinforced filaments

A Noztek Touch Dual PID filament maker with a stainless barrel and screw was utilized to make polypropylene and reinforced PP with 0%, 2%, 5%, and 8% weight fractions short glass fibre. The extruding parameters including motor speed, heating temperatures, cooling fan status, and pulling load have been optimized to produce a filament made from these waste materials with the desired surface quality, void content, and profile. The mushroom containers were washed, dried and shredded to be able to pour them into the extruder hopper with different percentages of short fibres. Different extruding temperatures were examined along with different motor speeds to have a good molten flow at the nozzle. The next challenging parameter to control is the diameter of filament and and prevent waviness in the produced filaments. To do this a filament winder with a speed controller was used and the extruder motor speed and dragging speed of the filament winder were modified to produce a filament with constant diameter (Figure 1).

The used Noztek extruder has two controllable heating regions which according to the trials and errors, the optimum temperatures were set as 220°C and 225°C for nozzle temperature and barrel temperature respectively, ambient temperature = 22°C and the motor speed was 7 RPM while fan status was off. The consistency of the filament diameter was elevated by adding sort

fibres and the die swell reduced.

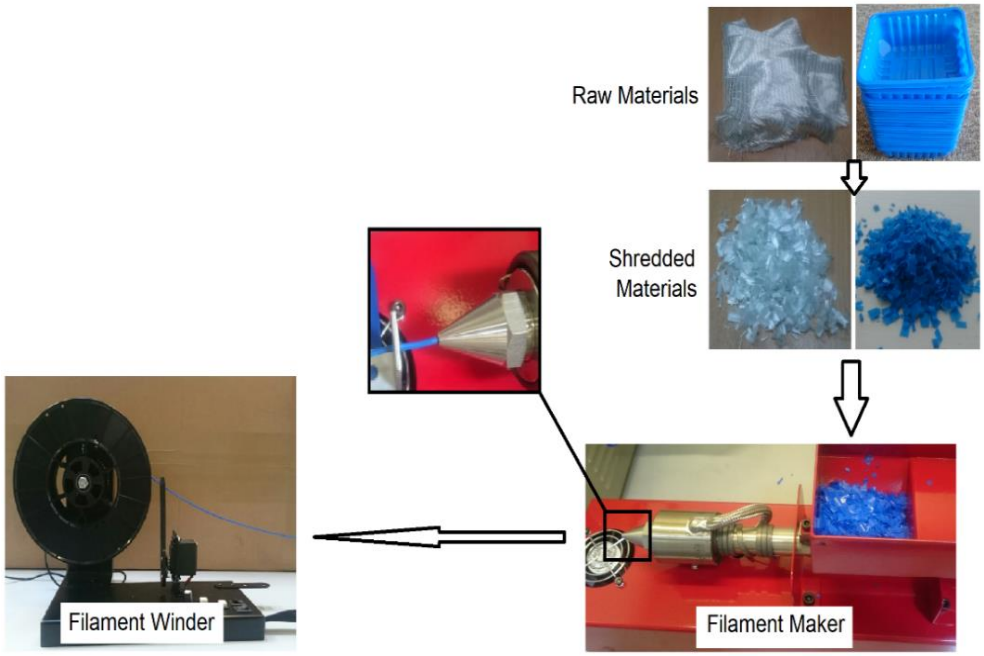

Figure 1: Filament making process.

2. Microscopic Assessment

During the making of a filament, it is crucial to assess the profile of the filament including diameter, void content, etc. along the filament length and monitor the basalt fibre dispersion with different weight fractions into the PP matrix. Microscopy images were obtained using a light microscopy instrument, Olympus BX51M equipped with a UC30 camera to assess abovementioned factors and any unwanted inclusions through image processing techniques. The microscopic images from cross-section area of the PP filaments and the reinforced ones (Figure 2) revealed that the short glass fibres with 2%, 5%, and 8% weight fractions were distributed uniformly into the thermoplastic.

The images captured from the longitudinal cross section of the recycled filaments confirmed the fibres were embedded in the direction of extruding as was predictable. The microscopic images confirmed that there was no voids in the filaments, and the average filament diameter was calculated as 1.37mm while the nozzle diameter was 1.6mm. According to the experimental trials and figure 2, adding short fibres change the viscosity and dynamic of the flow helping the consistency of the filament diameter and cross section area profile. The microscopy did not show any de-bonding between the fibres and the matrix which confirm the utilized setting for the filament making process including temperatures and speeds. It should be taken into account that 3D printing of filaments with high weight (volume) fraction would be difficult because of higher possibility of blocking nozzle by short fibres. Fiji is an image processing package [12], a "batteries-included" distribution of ImageJ, bundling a lot of plug-ins which facilitate scientific image analysis. The percentage of pixels in the images have been highlighted in red using Image>Adjust>Threshold. Then the area fraction in different polished layers of different reinforced filaments was calculated via ImageJ software to illustrate the average volume fraction of fibres. According to the fibre volume fraction analysis the maximum fibre content was 3%.

  doi:10.5075/epfl-298799_978-2-9701614-0-0

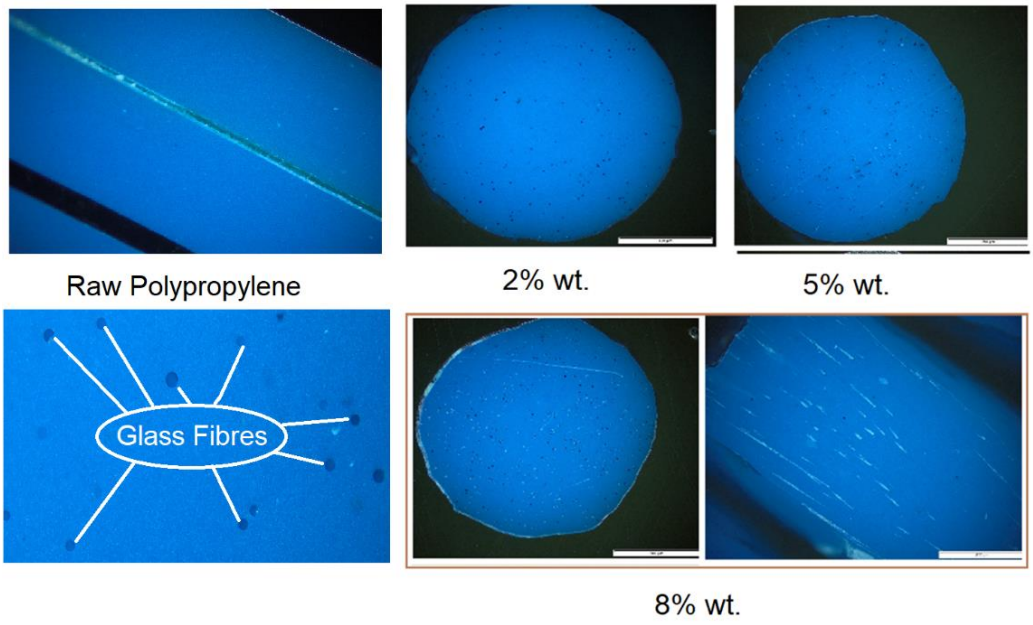

Figure 2: Short glass fibre distribution in PP matrix.

3. Melting and Crystallization Temperatures

Differential scanning calorimetry (DSC) determines the difference in the amount of heat required to increase the temperature of a sample and reference material, as a function of temperature. The output from a DSC experiment is a plot of heat flux versus temperature or versus time. These data are then used to calculate enthalpies of transitions, such as melting and crystallization temperatures. The DSC measurements were performed using a DSC 214 Polyma system with software Proteus® 7.0 manufactured by NETZSCH with an airflow of 50 mL/min. A temperature scan was performed on less than 10mg PP samples from 40 °C to 250 °C at a heating rate of 20 °C /min. For the second scan, the samples were cooled from 250°C to 40°C; in the last scan, the samples were again heated to 250°C and then cooled to 40°C. For all scans, the samples were held for 5 min at 40°C and at 250°C. According to the differential scanning calorimetry (DSC) testing the melting temperature and crystallization temperature of raw polypropylene thermoplastic were 175.63±1.17°C and 118.97±0.68°C, respectively, while these temperatures were measured for the recycled filaments as 169.43±1.68°C and 116.60±1.91°C, respectively. It is apparent from the DSC results that melting temperature has reduced (3.53%) during filament making process, like the crystallization temperature which reduced in 2% showing that degradation has happened during melting and extruding process.

4. Mechanical Testing

A ZwickRoell Uniaxial tensile machine with a 100N load cell was employed to measure the tensile strength of reinforced Polypropylene with different percentages of short glass fibre along the filament length. The length of the tested filaments was 70mm and the testing speed was 2mm/min. The tensile strength of the polypropylene filaments was measured as 31.79MPa. The experimental result showed that incorporating 2% wt. of glass fibre increased the tensile strength equal to 17.7% compared to the recycled PP filaments. The samples with higher fibre weight fractions, 5% and 8%, showed a rise as 22.7% (39.02MPa), and 38.6% (44.06MPa) in tensile strength, respectively. Generally, the higher fibre weight fraction the higher tensile

  doi:10.5075/epfl-298799_978-2-9701614-0-0

strength (Figure 3). Figure 4 shows the elastic modulus values for the recycled polypropylene and the reinforced PP with different short glass fibre. The elastic modulus of the recycled PP filaments was calculated as 615.82±29.99MPa, and adding 2% wt. short glass fibre caused a 33.76% in the elastic modulus (823.72±40.83MPa). The elastic modulus of the samples with higher fibre weight fractions, 5% wt. and 8% wt., were calculated as 976.43±15.05MPa (58.58%) and 1110.97±67.09MPa (80.4) respectively.

According to the experimental tensile testing, the fibre reinforced filaments showed a more brittle behaviour than the pure PP filaments, which was apparent from the fracture pattern in the tested specimens (necking phenomena was clearly seen during the filament tensile testing of PP samples).

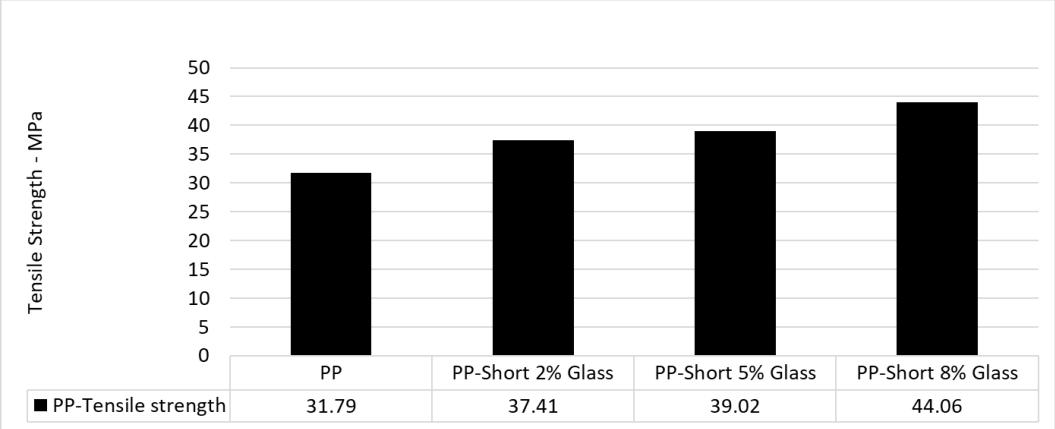

Figure 3. Tensile strength of recycled reinforced filaments.

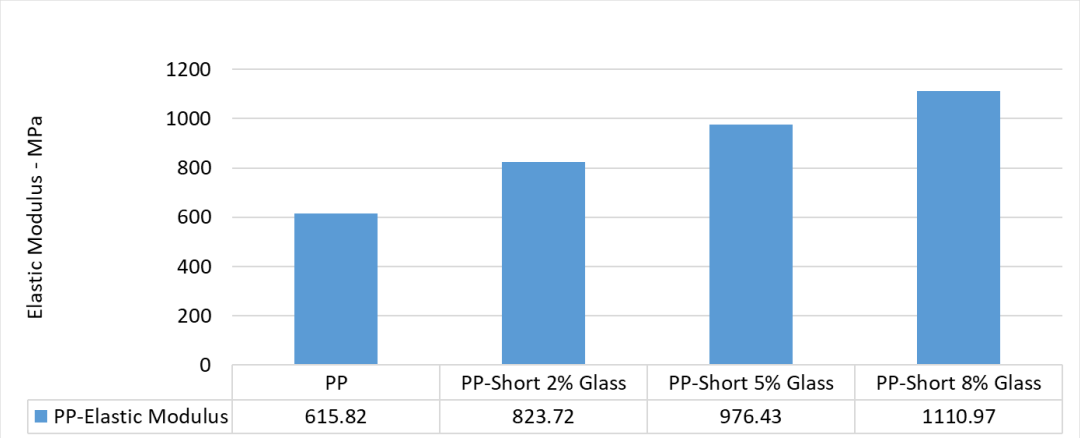

Figure 4. Elastic modulus of recycled reinforced filaments.

5. Conclusion

The increased mechanical properties of recycled waste materials investigated in this work along with the uniform distribution of fibre into the matrix make them a good candidate for feedstock in material extrusion to produce products with high strength lightweight applications. The future work would be developing a 3D printer to be able to print the manufactured filaments with short fibres.

Establishing the appropriate fibre weight fraction have an important impact on the quality of the filaments (cross-section profile, void content, fibre dispersion). The recycled reinforced PP

filaments with 8% wt. of off-cut glass fibre had the highest tensile strength and elastic modulus compared to the filaments with 2% and 5% wt. short glass fibre.

The degradation during the melting and filament making process at 225°C was confirmed by the differential scanning calorimetry test results.

Acknowledgements

This project has received funding from the European Union's Horizon 2020 research and innovation programme under the Marie Skłodowska-Curie grant agreement No. 847402.

6. References

1. Plastic Packaging Recycling Strategy 2018-2030, September 2018, https://repak.ie/images/uploads/downloads/Plastic_Packaging_Recycling_Strategy_2018-2030.pdf
2. Bora R.R., Wang R., You F., Waste Polypropylene Plastic Recycling toward Climate Change Mitigation and Circular Economy: Energy, Environmental, and Techno economic Perspectives, ACS Sustainable Chemistry & Engineering, 8 (43) (2020), pp. 16350-16363.
3. Gulf Petrochemicals and Chemicals Association. GCC Petrochemicals & Chemicals Industry 2012.
4. Sodeifian G., Ghaseminejad S., Yousefi AA., Preparation of polypropylene/short glass fiber composite as Fused Deposition Modeling (FDM) filament, Results in Physics Volume 12, March 2019, Pages 205-222.
5. Ranjan R., Kumar D., Kundu M., Chandra Moi S., A critical review on Classification of materials used in 3D printing process, Materials Today: Proceedings, 2022,
6. Li H., McDonald AG., Fractionation and characterization of industrial lignins. Indus Crop Product 2014; 62: 67–76.
7. Zander NE., Gillan M., Sweetser D., Composite Fibres from Recycled Plastics Using Melt Centrifugal Spinning, Materials (Basel). 2017 Sep; 10(9): 1044. Published online 2017 Sep 6. doi: 10.3390/ma10091044.
8. Li H., Englund K., Recycling of carbon fibre-reinforced thermoplastic composite wastes from the aerospace industry, Journal of Composite Materials, 2017, Vol. 51(9) 1265–1273.
9. Mutiva BL., Byiringiro JB., Muchiri PN., A Study on Suitability of Recycled Polyethylene Terephthalate for 3D Printing Filament, IOSR Journal of Mechanical and Civil Engineering (IOSR-JMCE) e-ISSN: 2278-1684,p-ISSN: 2320-334X, Volume 15, Issue 2 Ver. III (Mar. - Apr. 2018), PP 04-09
10. Tan H.S., Yu Y.Z., Xing L.X., Zhao L.Y. , Sun H.Q., Polymer-Plastics Technology and Engineering, 52, 257-260 (2013).
11. Dai M.F. D., Wood fibres as reinforcments in natural fibre composites, In Natural Fibre Composites: Materials, Processes and Properties R.S. A.Hodzic, Ed.; Woodhead Publishing Limited: Cambridge, UK, pp 3-43 (2014).
12. https://imagej.net/Fiji

  doi:10.5075/epfl-298799_978-2-9701614-0-0

TURNING OIL PALM WASTE INTO ALL-CELLULOSE FIBREBOARDS UTILISING REFINED PULP FIBRES

Dharu Smaradhana[ab], Koon-Yang Lee[ac]

a: Department of Aeronautics, Imperial College London, SW7 2AZ London, United Kingdom
b: Department of Mechanical Engineering, Universitas Sebelas Maret, 57126 Surakarta, Indonesia
c: Institute for Molecular Science and Engineering, Imperial College London, SW7 2AZ London, United Kingdom
dharu.smaradhana16@imperial.ac.uk

Abstract: *Empty fruit bunch (EFB) of oil palm is one of the primary wastes resulted from the production of palm oil. This work shows the potential of EFB to be produced into green fibreboard without any synthetic binder. Pulp fibres were used as binder to hold the otherwise loose efb fibres. Mechanical refining using a re-circulating colloid mill was performed to improve the binding performance of pulp fibres. This method is usually applied for improving the mechanical properties of paper. Characterisations including porosity and tension were carried out to investigate the performance of EFB fibreboards. The manufactured EFB fibreboards have the potential to be a substitute for commercial fibreboards and particleboards.*

Keywords: Empty fruit bunch; pulp fibres; oil palm; cellulose; fibreboard

1. Introduction

Oil palms (*Elaeis Guineensis*) are essential oil-producing plants nowadays due to their versatility in various products, including foods (chocolates, margarine and cooking oils), cosmetics and biodiesel (1,2). It is cultivated in more than 40 countries worldwide with Indonesia and Malaysia as the largest palm oil producers (3). According to the United States Department of Agriculture's report (4), Indonesia generated 44.5 million metric tons of palm oil in 2020. However, the production of crude palm oil (CPO) is followed by solid matter in the form of lignocellulosic waste (5,6). This lignocellulosic waste includes empty fruit bunch (EFB) of oil palm, trunks, fronds, and mesocarp (3). Among that fibrous biomass, one-third of them is EFB, which can yield up to 73% fibres (7). According to Karina et al. (8), every ton of CPO production generates 1.1 tons of EFB. The massive number of these lignocellulosic residues evokes a significant problem in the environment (9). Realising the potential of fibres from EFB with decent cellulose content (42.7%-65%), many efforts have been made to use EFB fibres to produce bio-based composite products, one of which is fibreboard panels (10–12).

To produce truly green fibreboards, there is a problem encountered in the industry: the use of synthetic binders. The role of binders is to distribute the load between the fibres, increasing the modulus and strength to produce robust fibreboard panels. The most common synthetic binders used in the industry are formaldehyde-based resin such as phenol-formaldehyde and urea-formaldehyde (13). These adhesives are chosen due to their low cost, high performance, and low cure temperature (12).

The use of nano-sized cellulose as binder has been introduced before, whereby sisal fibres were soaked into a suspension containing bacterial cellulose (BC) followed by vacuum filtration,

  doi:10.5075/epfl-298799_978-2-9701614-0-0

consolidation, and drying (14). A robust sisal fibre preform was produced utilising hydrogen bonding from nanocellulose networks to hold the otherwise loose sisal fibres together. However, this method is not suitable for industrial application because the price of nanocellulose is expensive.

Therefore, in this work, micrometre-sized cellulose from pulp fibres that have lower price than nanocellulose are used as binder. Mechanical refining was conducted to improve the binding performance of pulp fibres. Paper-making process were carried to produce EFB fibreboard containing 10 wt% of pulp fibres. Porosity and tensile properties of EFB fibreboard were investigated.

2. Experimental Sections

2.1 Materials

EFB fibres were purchased from PT. Polytech (Karawang, Indonesia). EFB was obtained from oil palm plants grown in West Kalimantan, Indonesia. The fibre strands were extracted from the bunch through several stages including rolling crushing, shredding, hammer milling, and drying. Acacia wood pulp was kindly supplied by Asia Pasific Resources International Limited (APRIL, Riau, Indonesia) in the form of pressed pulp sheets (grammage = 500g/m^2).

2.2 Manufacturing method

Pressed pulp sheet was cut into small pieces and soaked into de-ionised water overnight before blended using kitchen blender. The suspension containing pulp fibres were then fed into re-circulating colloid mill (JM-60, Shanghai Tiangang Machine Manufacture Co. Ltd., Shanghai, China) for refining stage for 10 mins. After refining stage, de-ionised water was added into suspension to make the concentration to be 0.25% before soaking EFB fibres into the suspension. The suspension was left overnight. Afterwards, the filtration and hot pressing step were performed to completely EFB fibreboards. Finally, EFB fibreboards with grammage of 2000 g/m^2 containing 10 wt.% of (un)refined pulp fibres were manufactured. EFB fibreboard without any binder was also produced for comparison. The schematic procedure of EFB fibreboards manufacturing steps is shown in figure 1.

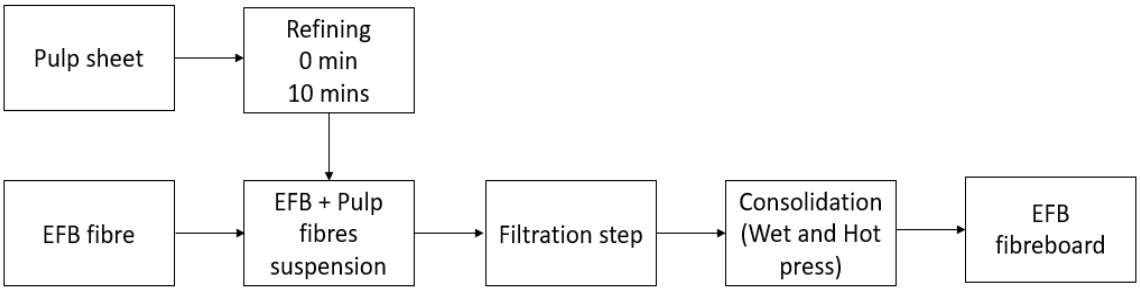

Figure 1. Schematic procedure of manufacturing steps of EFB fibreboards

2.3. Characterisation

Porosity was measured using Helium pycnometry (AccuPyc II 1340, Micrometrics Ltd., Dunstable, UK). Before applying the test, the weight of EFB fibreboard was measured. The porosity can be determined using equation (1) after the true density was obtained. The tensile properties were investigated using universal testing machine (Instron 5969, Instron GmbH, and Buckinghamshire, UK). Before the test, the sample was prepared by cutting the fibreboards into 100 x 15 mm.

$$P = \left(1 - \frac{\rho e}{\rho}\right) x\ 100 \qquad (1)$$

3. Results and discussion

EFB fibreboards with (un)refined pulp fibres used as binder was manufactured (figure 2a). it can be seen that EFB fibreboards containing pulp fibres could hold the otherwise loose EFB fibres together. Without the use of pulp fibre as binder, the loose EFB fibres were only held by fibre entanglements and friction between the fibres. The fibreboard produced without binder could not support a very low load (figure 2b).

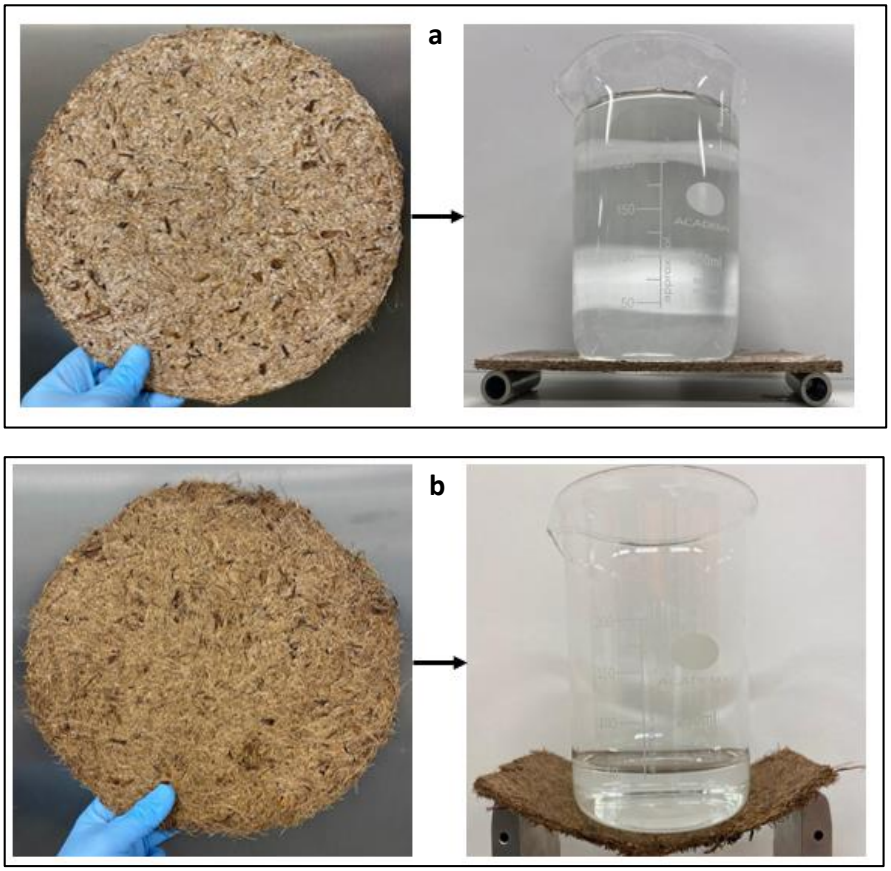

Figure 2. The produced EFB fibreboards: (a) EFB fibreboards containing 10wt% of unrefined pulp; (b) EFB fibreboards without binder

3.1. Porosity

Table 1 shows the densities and porosities of EFB fibreboard using 10wt % of (un)refined pulp fibres as binder. There are two factors influencing the density and porosity of fibreboard: the amount of binder and the refining times of pulp fibres as binder. The higher amount of binder increased the density and reduced the porosity of the fibreboards. This is because the higher binder content increased the potential for pulp fibres to bind and hold the otherwise loose EFB fibres which reduced the gaps between the EFB fibres resulting in a denser fibreboard. On the one hand, increasing refining times also contributes to the enhancement of density and the decrease in the porosity of fibreboards.

Table 1: Density and porosity of EFB fibreboard

Refining times(mins)	Density	Porosity
0	0.63	59 ± 1.64
10	0.66	57 ± 2.66

3.2. Tensile properties

Table 2 summarises tensile properties of EFB fibreboards using (un)refined pulp fibres as binder. Neat EFB fibreboard without binder cannot be measured as only friction and fibre entanglement holding the loose EFB fibres. It can be seen that the tensile strength of EFB fibreboards containing pulp fibres refined for 10 mins is higher than EFB fibreboards with unrefined pulp fibres. It is hypnotised due to the fibrillation of pulp fibres as a result of refining process that can increase the contact area between pulp fibres and EFB fibres. Fibrillation is also likely to increase the fibre-fibre bonding between pulp fibres. This hypothesis will be proven in further work by investigating the morphology of unrefined and refined pulp fibres.

Table 2: Tensile properties of EFB fibreboard

Refining times(mins)	Tensile strength (kN/m)	Tensile index (N m/g)
0	6.84 ± 2.49	3.42 ± 1.25
10	13.98 ± 1.14	6.99 ± 0.57

4. Conclusions

In this work, we show that EFB fibres can be produced into sustainable materials with higher added value, green fibreboards. Pulp fibres were used as binder to hold the otherwise EFB fibres. Refining pulp fibres for only 10 mins not only reduced the porosity but also improved the tensile strength of EFB fibreboards. It is recommended for further works to increase the refining times and the amount of binder content to investigate the optimised performance of EFB fibreboards with refined pulp fibres as binder.

5. References

1. Chaiwong W, Samoh N, Eksomtramage T, Kaewtatip K. Surface-treated oil palm empty

  doi:10.5075/epfl-298799_978-2-9701614-0-0

fruit bunch fiber improved tensile strength and water resistance of wheat gluten-based bioplastic. *Composites Part B: Engineering*. [Online] Elsevier Ltd; 2019;176(August): 107331. Available from: doi:10.1016/j.compositesb.2019.107331

2. Basiron Y, Weng CK. The Oil Palm and its Sustainability. *Journal of Oil Palm Research*. 2004;16(1): 1–10.

3. Shinoj S, Visvanathan R, Panigrahi S, Kochubabu M. Oil palm fiber (OPF) and its composites: A review. *Industrial Crops and Products*. [Online] Elsevier B.V.; 2011;33(1): 7–22. Available from: doi:10.1016/j.indcrop.2010.09.009

4. USDA. Oilseeds : World Markets and Trade Evaporate on Lower Demand Soybean Oil Price Differential. 2021;(October): 40 pages. Available from: https://apps.fas.usda.gov/newgainapi/api/Report/DownloadReportByFileName?fileName=Oilseeds and Products Annual_Manila_Philippines_04-01-2021.pdf

5. Maitah M, Prochazka P, Pachmann A, Šrédl K, Řezbová H. Economics of palm oil empty fruit bunches bio briquettes in Indonesia. *International Journal of Energy Economics and Policy*. 2016;6(1): 35–38.

6. Lewis K, Rumpang E, Kho LK, McCalmont J, Teh YA, Gallego-Sala A, et al. An assessment of oil palm plantation aboveground biomass stocks on tropical peat using destructive and non-destructive methods. *Scientific Reports*. [Online] Springer US; 2020;10(1): 1–12. Available from: doi:10.1038/s41598-020-58982-9

7. Wirjosentono B, Guritno P, Ismail H. Oil palm empty fruit bunch filled polypropylene composites. *International Journal of Polymeric Materials and Polymeric Biomaterials*. [Online] 2004;53(4): 295–306. Available from: doi:10.1080/00914030490429942

8. Karina M, Onggo H, Dawam Abdullah AH, Syampurwadi A. Effect of oil palm empty fruit bunch fiber on the physical and mechanical properties of fiber glass reinforced polyester resin. *Journal of Biological Sciences*. [Online] 2008;8(1): 101–106. Available from: doi:10.3923/jbs.2008.101.106

9. Fithri L, Puspaningsih NNT, Asmarani O, Ni'matuzahroh, Fitrah Dewi GD, Arizandy RY. Characterization of Fungal Laccase Isolated from oil palm empty fruit bunches (OPEFB) and Its Degradation from The Agriculture Waste. *Biocatalysis and Agricultural Biotechnology*. [Online] Elsevier Ltd; 2020;27(March): 101676. Available from: doi:10.1016/j.bcab.2020.101676

10. Mahmood H, Moniruzzaman M, Yusup S, Akil HM. Pretreatment of oil palm biomass with ionic liquids: A new approach for fabrication of green composite board. *Journal of Cleaner Production*. [Online] Elsevier Ltd; 2016;126: 677–685. Available from: doi:10.1016/j.jclepro.2016.02.138

11. Abdul Khalil HPS, Nur Firdaus MY, Anis M, Ridzuan R. The effect of storage time and humidity on mechanical and physical properties of medium density fiberboard (MDF) from oil palm empty fruit bunch and rubberwood. *Polymer - Plastics Technology and Engineering*. [Online] 2008;47(10): 1046–1053. Available from: doi:10.1080/03602550802355644

12. Ibrahim Z, Ahmad M, Aziz AA, Ramli R, Wahab NA, Alias AH, et al. Oil Palm Empty Fruit Bunches (EFB): Influence of Alkali and Acid Treatment on the Mechanical Properties of Medium Density Fibreboard (MDF). *Journal of Advanced Research in Fluid Mechanics*

and Thermal Sciences. [Online] 2020;79(1): 44–53. Available from: doi:10.37934/ARFMTS.79.1.4453

13. Shmulsky R, Jones PD. *Forest Products and Wood Science An Introduction: Sixth Edition*. [Online] Forest Products and Wood Science An Introduction: Sixth Edition. 2011. Available from: doi:10.1002/9780470960035

14. Lee K, Ho KKC, Schlufter K, Bismarck A. Hierarchical composites reinforced with robust short sisal fibre preforms utilising bacterial cellulose as binder.

SOFT COMPOSITES FROM BIO-BASED RESOURCES

Markus, Schwaiger[a]; Marcel, Bender[b]; Johannes, Taesler[c]; Heiko, Schirmer[c]; Katharina, Resch-Fauster[a]

a: Materials Science and Testing of Polymers, Montanuniversitaet Leoben, Leoben, Austria
E-Mail: markus.schwaiger@unileoben.ac.at
b: Processing of Composites, Montanuniversitaet Leoben, Leoben, Austria
c: Kobleder GmbH, Sankt Martin im Innkreis, Austria

Abstract: *This study focusses on the development and investigation of soft composites from bio-based materials. The matrix material was based on epoxidized linseed oil and the knitted reinforcements with 3 or 6 threads were made of Lyocell fibers. The composites were manufactured by a modified vacuum bagging process. Mechanical properties were measured in tensile and 3-point bending tests in wale and course direction, whereas specific focus was on the analysis of the anisotropic behavior. In wale direction, the tensile strength was higher but the bendability was lower (higher flexural stiffness). The 3-threaded composite showed a stronger anisotropic behavior compared to the 6-threaded composite.*

Keywords: soft composites; bio-based composites; epoxidized linseed oil

1. Introduction

Soft composites in terms of fiber reinforced mechanical flexible composites, can combine high tensile strength with good bendability. Compared to conventional composites, which usually exhibit high specific stiffness, they open up completely new possibilities. They have the potential to be used in a wide range of applications such as apparel, furniture and sporting goods as well as technical leather, technical canvas and damping elements. For applications that require specific anisotropic mechanical properties, like sporting goods or medical applications (orthopedics), the composites' characteristics can be adapted by tailoring the reinforcement structure.

By using bio-based components instead of petrochemical ones, composites become more environmentally friendly and sustainable [1]. A bio-based alternative to petrochemical resins are functionalized plant oils, which can be used for a broad spectrum of mechanical and thermal properties in dependence on the respective hardener [2]. The usage of such functionalized plant oils as matrix material in soft composites has already been demonstrated for an ecological leather-like material used in footwear [3]. An alternative to conventional reinforcement fibers are plant fibers or synthetic fibers based on renewable resources, such as rayon, which exhibit a uniform fiber quality in comparison to plant fibers.

The present research work addresses the development of soft composites fully based on renewable resources. As reinforcement knitted fabrics were used, which have unique draping characteristics [4]. The mechanical properties of the manufactured soft composites were investigated by tensile and bending tests in wale and course direction. Specific focus was on the analysis of the composites' mechanical anisotropy.

  doi:10.5075/epfl-298799_978-2-9701614-0-0

2. Experimental

2.1 Materials and processing

For the knitted fabrics, Lyocell fibers (167 dtex, Lenzing, Austria) were used. The fabrics were produced with 3 and 6 threads on a flat bed knitting machine (type Stoll CMS 330 TC, Gauge E12). The applied knitting type was interlock (DIN EN ISO 23606 [5]) and the structures were 300 mm wide (course direction) and 650 mm long (wale direction). Knitting parameters like take-down, yarn tension and loop-length were kept constant.

For the bio-based matrix material, epoxidized linseed oil was used as resin and crystalline sebacic acid was used as hardener. Both were provided by bto-epoxy GmbH (Austria). The used molar mixing rate of epoxy/carboxyl groups was 0.69. This matrix system exhibited a glass transition temperature of 5 °C (curing at 140 °C for 16 h). Thus, it is soft enough to provide mechanical flexibility. Unlike most 2-component resin systems used in fiber reinforced composite manufacturing, the bio-based resin system consists of a fluidic resin and a solid hardener. For this reason, the resin and hardener mixture had to undergo a wet milling process (ceramic balls in a metal cannister) at ambient temperature for 24 h. By reducing the particle size of the solid hardener, this procedure improved the processability, hardener distribution and homogeneity of the degree of cross-linking.

However, this process did not reduce the particle size to a degree, which makes the resin formulation suitable for vacuum infusion or resin-transfer-molding process, since the fabrics filter the hardener. This would lead to a gradient of the degree of cross-linking across the composite, which would further result in inhomogeneous physical properties of the matrix system (excess of resin or hardener). To prevent this filter effect, a coating-like process was developed, utilizing a film applicator to cover both fabrics surfaces with a constant resin layer of 0.7 mm. The complete fabric saturation through thickness was ensured by a modified vacuum bagging process, utilizing a semi-permeable membrane with an inner vacuum bag. This reduced the effective flow length to the thickness of each fabric. Additionally, vacuum was applied after reaching the curing temperature of 140 °C, so that the hardener is liquid during saturation (melting temperature of 133.5 °C). The resin was cured at 140 °C under -0.96 bar vacuum pressure in a convection oven for 16 h.

2.2 Characterization

The fiber volume content V_F of manufactured composites was calculated following Eq. (1). Herein m_T is the weight of the fabric and m_C the weight of the composite. The densities of the matrix (ρ_M) and composites (ρ_C) were determined gravimetrically by buoyancy method in deionized water (T=24 °C) according to DIN EN ISO 1183-1 [6] .

$$V_f = 1 - \frac{\frac{m_C - m_f}{\rho_M}}{\frac{m_C}{\rho_C}} \quad (1)$$

Tensile tests were performed on a universal testing machine (Z250, Zwick/Roell GmbH & Co. KG, Germany) at ambient temperature with a 10 kN load cell. The clamping length was 150 mm and the strain was measured with an extensometer with a gauge length of 50 mm. Specimens were measured with a crosshead speed of 50 mm/min until failure. The Youngs's modulus was

measured with a crosshead speed of 2 mm/min between a strain of 0.05 and 0.25 %. The Young's modulus was calculated by linear regression. Measurements were performed in wale and course direction. A minimum of 5 specimens (250 mm x 50 mm) were tested for both composite types (3 and 6 threads) in both directions.

As visualized in Figure 1, the composites showed good bendability. Due to the knitted structure, the bending stiffness was highly anisotropic. This anisotropic behavior was quantified by performing 3-point bending tests.

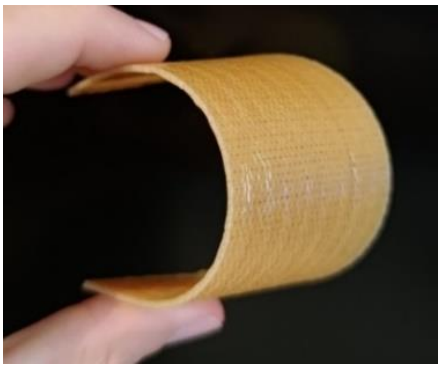

Figure 1: Demonstration of the bendability of a soft composite in course direction.

These 3-point bending tests were performed on a universal testing machine (Z250, Zwick/Roell GmbH & Co. KG, Germany) at ambient temperature with a 500 N load cell. The support span L was 30 mm and the flexural strain was measured with an extensometer. Samples (50 mm x 50 mm) were pre-loaded with 0.4 N and measured with a crosshead speed of 1 mm/min. The flexural modulus E_{flex} was calculated by linear regression between a flexural strain of 0.05 and 0.25 %. To prevent damage, the measurement was stopped after reaching a flexural strain of 0.5 %. Each specimen was measured three times in course and wale direction. In advance a "conditioning" measurement in the respective direction was performed to prevent unwanted curvature of the soft samples, which might affect the measurement. This procedure is summarized in Figure 2. For both composites 5 specimens were measured.

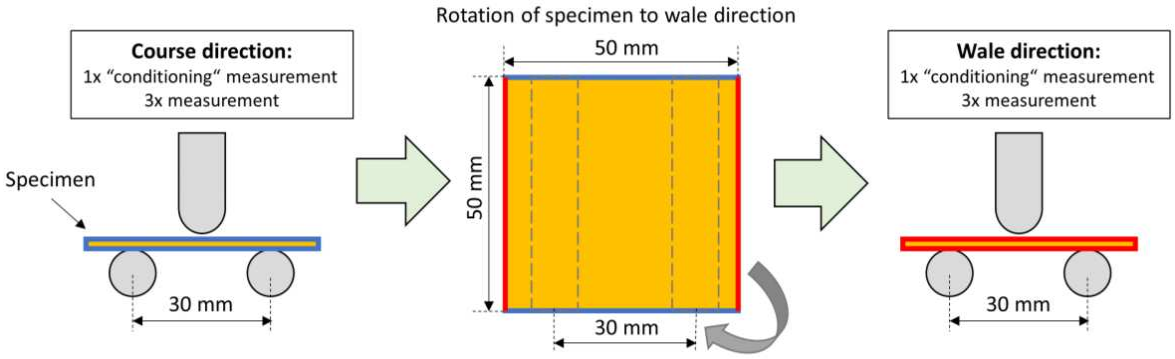

Figure 2: Procedure for the measurement of the flexural modulus of the soft composites.

The flexural stress and strain were calculated using Eq. (2) and (3), whereas F is the applied force, b is the width, L is the support span, h is the thickness and s is the deflection.

$$\sigma_{flex} = \frac{3 * F * L}{2 * b * h^2} \tag{2}$$

  doi:10.5075/epfl-298799_978-2-9701614-0-0

$$\varepsilon_{flex} = \frac{6 * s * h}{L^2} \quad (3)$$

3. Results

3.1 Tensile properties

The determined fiber volume content V_f was 22.6 % for the 3-threaded and 33.6 % for the 6-threaded composite. The lower V_f of the 3-threaded composite is related to the manufacturing process and the less dense fabric. Therefore, the tensile properties were normalized in respect of the determined V_f for a better comparability of the results.

In Figure 3 the normalized stress-strain curves of tensile measurements in wale and course direction are shown. In course direction the stress decreases after reaching a strain of 6 and 10 % for the 6-threaded and the 3-threaded composites, respectively. This is caused by crack formation in the matrix system. The subsequent increase of the stress is mainly related to the fabric. This behavior is not observed in wale direction, as the fabrics exhibit lower stretchability in wale direction compared to course direction. In wale direction, the 6-threaded composite shows only a slight flattening in the stress-strain curve in this strain range, while the 3-threaded composite already fractures at a strain of 10 %.
Figure 4 displays the resulting values of normalized tensile modulus, strain at break and normalized tensile strength for 3- and 6-threaded composites. The normalized tensile modulus ranges between 201 and 688 MPa. Especially for the 3-threaded composite, a higher normalized tensile modulus was observed in wale direction (factor 3.4) compared to course direction. Both composites show a higher strain at break in course direction (93 – 117 %) compared to wale direction (10-20 %) due to the higher stretchability of the fabrics in course direction. Nevertheless, the strain at tensile strength was similar (3-threaded) or even higher (6-threaded) in wale direction. The normalized tensile strength (first maximum of stress) ranges between 9 and 67 MPa. In wale direction the normalized tensile strength is higher by a factor of 4.6 – 4.8. Further, the 3-threaded composite show a higher normalized tensile strength for both directions (factor of 1.6).

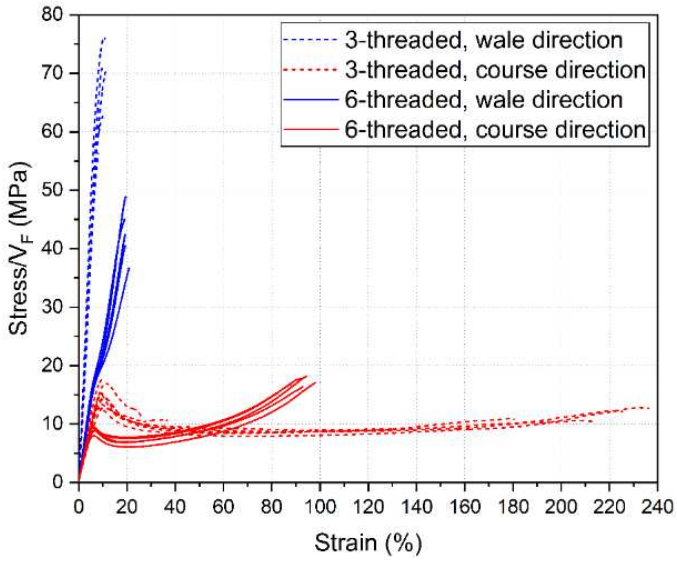

Figure 3: Normalized stress-strain curves of the soft composites with 3- and 6-threaded knitted fabrics in wale and course direction.

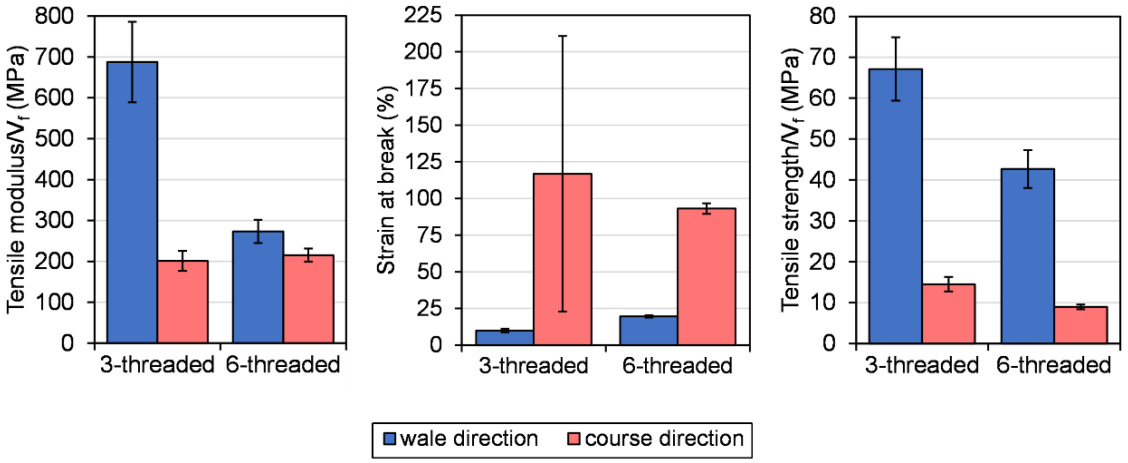

Figure 4: Comparison of normalized tensile modulus, strain at break and normalized tensile strength (in order left to right) of the soft composites with 3- and 6-threaded knitted fabrics in wale and course direction.

3.2 Flexural modulus

Figure 5 shows E_{flex} of repeated measurements normalized to the respective first measurement by using Eq. (4) in order to demonstrate the applicability of the procedure given in Figure 2. Resulting damage from a previous measurement would cause a decreasing E_{flex}, which cannot be observed here. The 6-threaded composite shows no significant change of E_{flex} and the measurements are reproducible (standard deviation ≤ 5 %). The 3-threaded composite shows a continuously increase of E_{flex}, which can be especially observed in course direction. This is related to the curvature of some specimens (very low E_{flex} (28 MPa)), which decrease with each measurement. The difference of the curvature of the specimens also leads to the much higher standard deviation here.

$$AvChange_x = 100\% * \frac{1}{5}\sum_{i=1}^{5}\frac{E_{flex\_a\_i}}{E_{flex\_1^{st}\_i}} \qquad \text{for a = } 1^{st};\ 2^{nd};3^{rd} \text{ measurement}, \quad \text{i … specimen number} \tag{4}$$

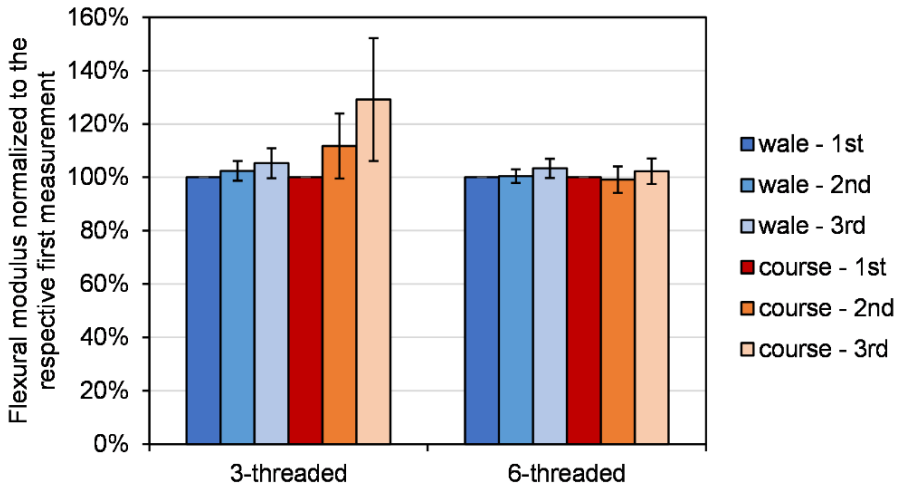

Figure 5: Flexural modulus of repeated measurements normalized to the respective first measurement.

Resulting stress-strain curves of the respective 3rd measurement of each specimen are presented in Figure 6. In the evaluated area (0.5 – 0.25 % flexural strain) the curves show good linearity (average $R^2 > 99.5$ %). Absolut values of the averaged E_{flex} are given in Table 1 and range between 28 and 207 MPa. The 6-threaded composite exhibits a higher E_{flex} compared to the 3-threaded composite, which might be explained by the higher V_F. In wale direction both the 3- and 6-threaded composites exhibit a higher E_{flex}, which is related to the structure of the knitted fabrics. The ratio of E_{flex} between wale and course direction was found to be higher for the 3-threaded composite (factor of 3.9). However, for the 6-threaded composite the E_{flex} still differs by a factor of 2.6.

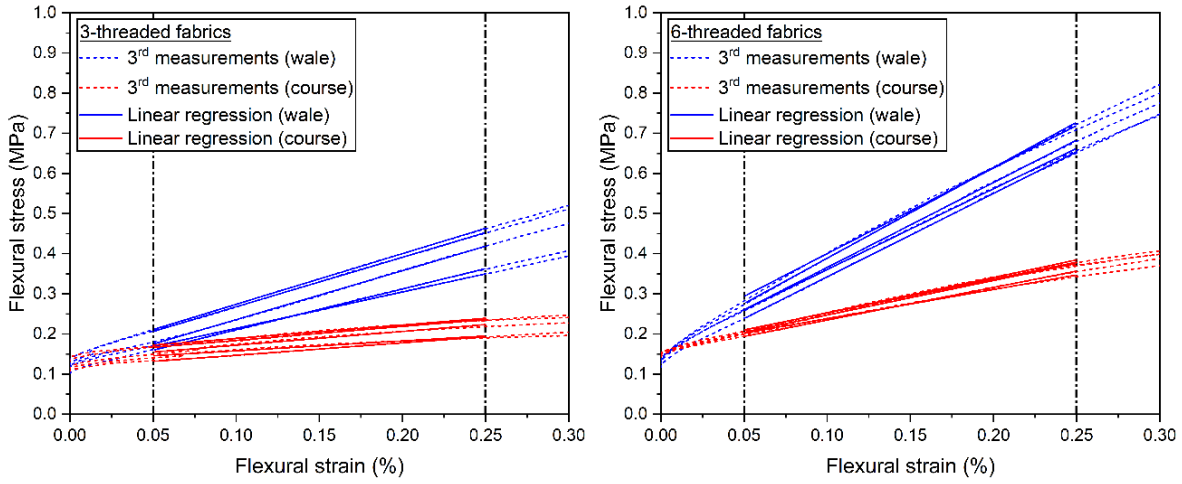

Figure 6: Stress-strain curves of the 3rd flexural modulus measurement with linear regression between 0.05 and 0.25 % strain; left: 3-threaded fabric; right: 6-threaded fabric.

Table 1: E_{flex} of measured soft composites in wale and course direction.

Fabric	E_{flex_wale} [MPa]	E_{flex_course} [MPa]	E_{flex_wale}/ E_{flex_course} [-]
3-threaded	110 ± 15	28 ± 4	3.9 ± 0.3
6-threaded	207 ± 11	81 ± 7	2.6 ± 0.3

4. Conclusion

Soft composites from bio-based resources could be successfully manufactured by a modified vacuum bagging process. Strong anisotropic mechanical properties were shown in tensile and bending tests, which is related to the structure of the knitted fabrics.
In wale direction the composites exhibit a higher tensile strength, but also a higher flexural stiffness (lower bendability). By using 3-threaded fabrics, the anisotropy of tensile and flexural moduli is increased and a higher normalized tensile strength is achieved compared to 6-threaded fabrics.
Next step is to correlate the results with the mechanical properties of the unimpregnated fabrics and to adapt the mechanical properties by tailoring the fabric's structure.

  doi:10.5075/epfl-298799_978-2-9701614-0-0

Acknowledgements

The research project is funded by the Austrian Ministry for Climate Action, Environment, Energy, Mobility, Innovation and Technology in frame of the program “Produktion der Zukunft” under contract no. 871403, within the context of the project “Semiflexible and flexible composites based on renewable resources”.

5. References

1. La Mantia FP, Morreale M. Green composites: A brief review. Composites Part A: Applied Science and Manufacturing. 2011;42:579–88. doi:10.1016/j.compositesa.2011.01.017.
2. Baroncini EA, Kumar Yadav S, Palmese GR, Stanzione JF. Recent advances in bio-based epoxy resins and bio-based epoxy curing agents. J of Applied Polymer Sci 2016. doi:10.1002/app.44103.
3. Cao H, Wool RP, Bonanno P, Dan Q, Kramer J, Lipschitz S. Development and evaluation of apparel and footwear made from renewable bio-based materials. International Journal of Fashion Design, Technology and Education. 2014;7:21–30. doi:10.1080/17543266.2013.859744.
4. Leong KH, Ramakrishna S, Huang ZM, Bibo GA. The potential of knitting for engineering composites—a review. Composites Part A: Applied Science and Manufacturing. 2000;31:197–220. doi:10.1016/S1359-835X(99)00067-6.
5. DIN EN ISO 23606:2009-08, Textilien - Maschenstoffe - Darstellungsformen und Patronierung (ISO 23606:2009); Deutsche Fassung EN ISO 23606:2009. Berlin: Beuth Verlag GmbH. doi:10.31030/1476504.
6. DIN EN ISO 1183-1:2019-09, Kunststoffe - Verfahren zur Bestimmung der Dichte von nicht verschäumten Kunststoffen – Teil 1: Eintauchverfahren, Verfahren mit Flüssigkeitspyknometer und Titrationsverfahren (ISO 1183-1:2019, korrigierte Fassung 2019-05); Deutsche Fassung EN ISO 1183-1:2019. Berlin: Beuth Verlag GmbH. doi:10.31030/3023324.

ALL LIGNOCELLULOSE BIOCOMPOSITES FOR WOODY LIKE MATERIALS

Sergejs Gaidukovs, Sergejs Beluns, Oskars Platnieks, Gerda Gaidukova

a: Institute of Polymer Materials, Faculty of Materials Science and Applied Chemistry, Riga Technical University, P.Valdena 3/7, LV-1048, Riga, Latvia

Abstract: *Wood-like or woody mimic biocomposite materials can be formulated from lignocellulose and hemicellulose matrices loaded with lignocellulose components. For example, xylan and plant-based oil matrix-based biocomposites can be prepared with diverse cellulose micro-and nano fillers and fibers. Those are prospective mutual biobased and biodegradable materials derived from renewable resources, while lignocellulose could be delivered from forest and plant biomass waste. We propose lignocellulose nanoparticles assembly strategy from solution and processed by hot press fabrication and resin infusion that can be used to process woody mimic biocomposites. Performance properties have been dependent on the chosen material composition, formulation process, lignocellulose modification route, and biocomposite fabrication. Rigid, soft, and ductile biocomposites' mechanical behavior can be achieved. Thermal, tensile, viscoelastic, thermo-mechanical, dynamic-mechanical, rheological, and biodegradation properties of the wood-mimic composites are reported. The obtained biomaterials can be a sustainable alternative to replace fissile source polymers and conventional composites, e.g. wood polymer composite.*

Keywords: lignocellulose; nanocellulose; nanopaper; foams; aeorgels

1. Introduction

Global production must strive to use renewable feedstock and raw materials, design safe chemicals and products, and reduce our dependence on fossil resources. Agriculture and forestry have the potential to be a significant sources of biobased chemicals and materials. While most products are used in the long term, the primary source of waste and pollution are various packaging materials and single-use products (1). An emerging material, cellulose nanopaper, is known for its dense structure and good mechanical and barrier properties (2). However, cellulose is sensitive to moisture because of its hydrophilicity, limiting its application (3). As a result, much of the research has been focused on making cellulosic materials more hydrophobic and improving their properties in humid environments (4).

Lignin and hemicellulose are green and abundant materials found naturally in plants; they are also produced as by-products in various industries; for example, lignin is a significant by-product of the paper industry (5). They offer protection for cellulose in wood and plant structures by reducing the environmental impact of UV irradiation and microbial attacks. Some studies have characterized changes in the mechanical properties of NPs obtained with partial or full purification of NFC from lignin and hemicellulose (6). However, these processes are often hard to control and repeat and depend on the source of cellulose (7). Thus, there is a basis for exploring the controlled addition of these natural components rather than their removal from the NFC structure.

  doi:10.5075/epfl-298799_978-2-9701614-0-0

Nanopaper production can be done in a relatively clean route involving mechanical cellulose, wastepaper, and biowaste processing into nanofibrillated cellulose (NFC). Efficient mechanical processing of cellulose into nanocellulose has been demonstrated and is currently being tested in various industrial pilot plants (8). This form of cellulose processing is only limited by electricity consumption and avoids different toxic and corrosive processes (9). NFC is a versatile material and can be used to prepare various membranes. Applications such as tight aqueous ultrafiltration membranes and membranes for oil/water separation have been proposed (10). Nevertheless, in nanopaper form, it can also be applied to food packaging, sensors, and even electronics (11).

We research possibilities to obtain all lignocellulose composite materials in the present work. The main concept is shown in Figure 1 (12). The properties of the obtained materials were extensively tested before and after exposure to simulated environmental impacts, and UV-VIS, and FTIR spectroscopies were used to supplement the analysis. We selected lignin and xylan as green, cheap, and nontoxic natural cellulose surface modifiers for NPs and examined their interface and interphase formation mechanisms to enhance properties. The analysis was supplemented with extensive SEM characterization that explored structural changes and showed aging damage to NPs. The characterization of properties also includes the produced hemp-based nanocellulose, nanopapers, and foams, assessed by XRD, FTIR, thermal conductivity, TGA, BET, and structural and mechanical analysis.

2. Results

Kraft lignin was suspended in DI water and stirred magnetically at 85 °C for 1 h. A strong alkaline solution of NaOH was slowly added to stabilize pH at 10. The final concentration of suspension was adjusted to 10 wt % lignin. Similarly, xylan was dissolved in DI and stirred magnetically at 85 °C for 1 h. After preparation, suspension and solution were cooled to room temperature (20 °C). The 1 wt % NFC suspension was combined with previously prepared lignin suspension or xylan solution using a blender (800W, 5 min). Further homogenization was achieved with magnetic stirring for two h at room temperature (20 °C). Polystyrene (PS) Petri dishes were used for film casting and drying at room temperature (20 °C). Dry films were further dried in a thermostat at 50 °C for 24 h. Modified CNPs were prepared with the following concentrations of lignin or xylan: 1, 2.5, 5, 10, 20, 30 wt %. Nanopaper from pure NFC with no modifiers, i.e., cellulose nanopaper (CNP), was also produced for comparison. Prepared NPs were abbreviated, combining letters from lignin (L) or xylan (X) with their loading in wt % (e.g., X1 sample corresponds to NP with 1 wt % xylan and 99 wt % NFC loadings, L1 sample—lignin 1 wt % and NFC 99 wt %). Densities of prepared NPs are listed in Table 3. Samples with thicknesses around 0.1 mm in the shape of strips, 10 mm in width and 40 mm in length, were cut from films. Before testing, samples were stored at 50 °C and RH < 10% in a thermostat. These samples are considered dry reference samples.

Films were irradiated with 1.6 W/cm2 intensity and at a fixed distance of 25 cm from the source. A deep UV exposure lamp (Hg, 1000 W) with a broad emission spectral range from 200 to 600 nm was used as an irradiation source in an air environment. The temperature of 80 °C was maintained in the experimental chamber with the UV lamp. Exposure time was set to 6, 12, and 24 h. After irradiation, samples were collected in sealable plastic bags and kept for 24 h before performing a tensile test.

  doi:10.5075/epfl-298799_978-2-9701614-0-0

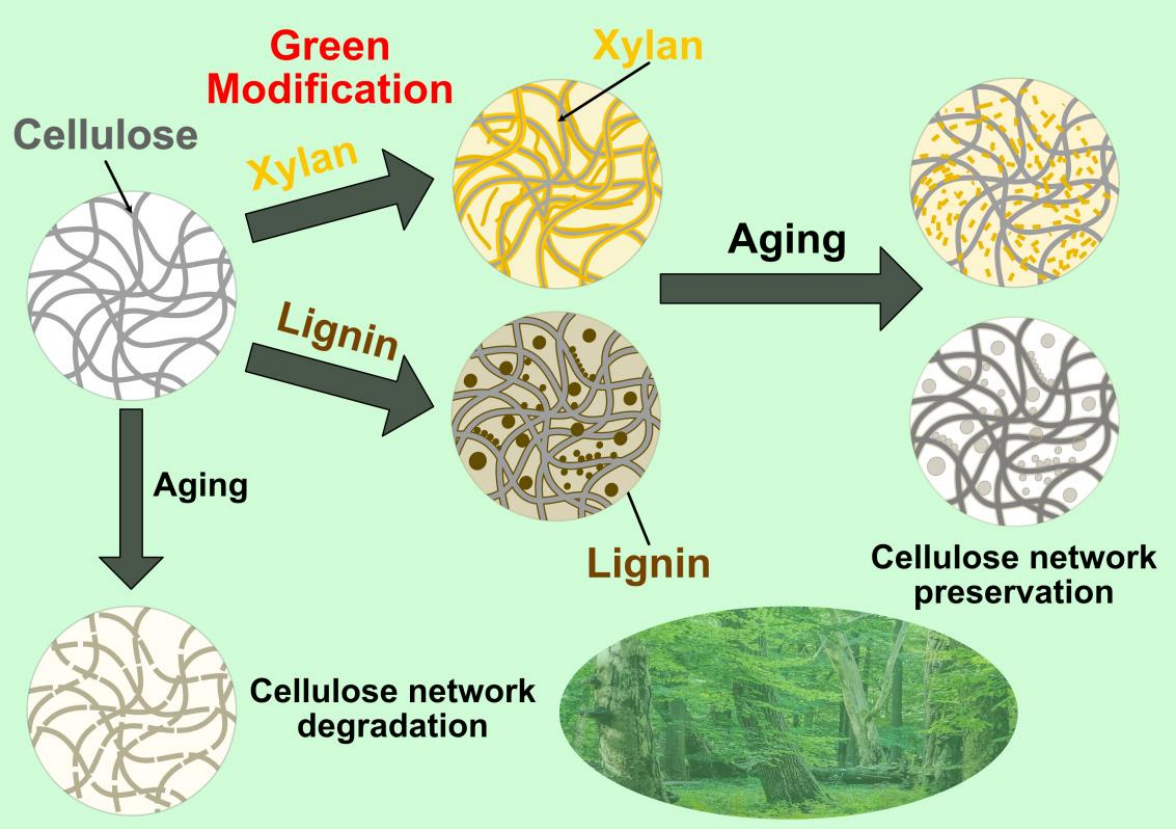

Figure 1. Schematic preparation of lignocellulose composite concept

Samples were conditioned in desiccators under different relative humidity environments (RH%) at room temperature 22 °C. The humid environments were created by using different saturated salt solutions: KC2H3O2 (RH24%), NaCl (RH75%), and K2SO4 (RH97%). Gravimetric measurements were made with an accuracy of 0.01 mg, and the relative weight changes of samples w [%] were determined as weight gain per weight unit. Moisture saturation was achieved within 3–7 days. Retention of the mechanical properties after moisture desorption was studied on samples initially saturated at RH75% and RH97% and then conditioned at RH24% until weight stabilization, which was abbreviated as RH75 (> 24%) and RH97 (> 24%), respectively.

  doi:10.5075/epfl-298799_978-2-9701614-0-0

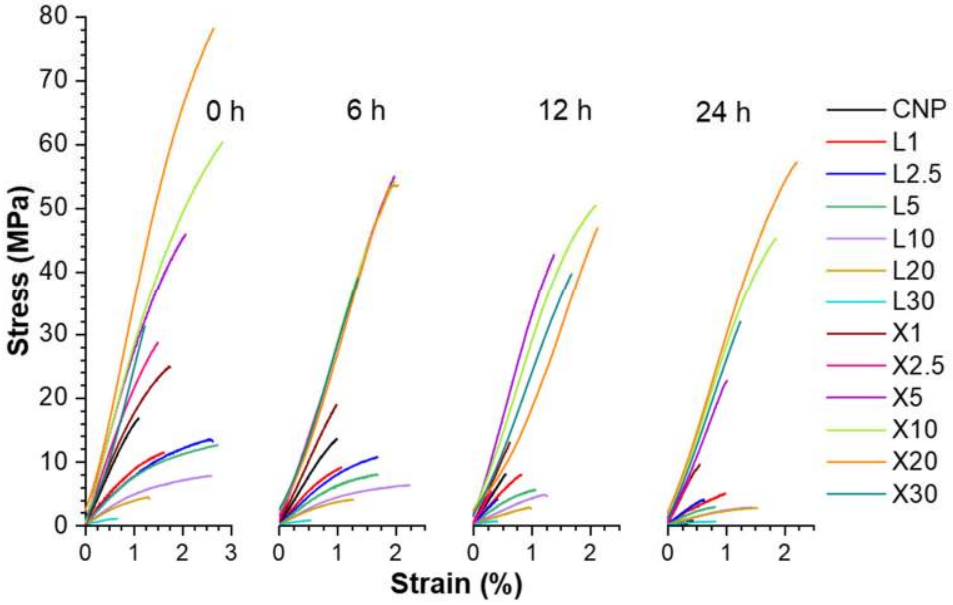

Figure 2. Representative stress-strain curves of nanopapers for pristine and aged samples at different times of UV irradiation

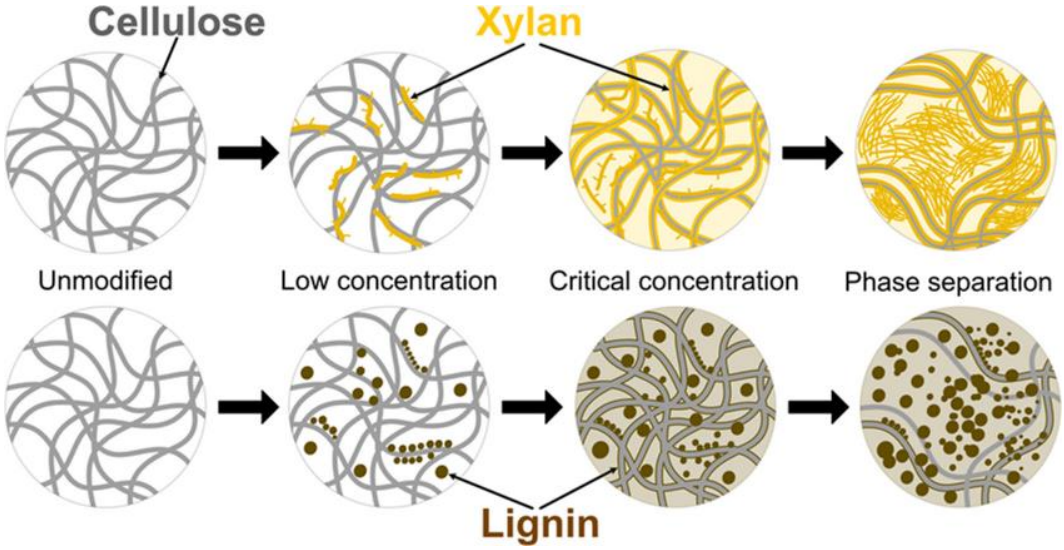

Figure 3. Schematic representation of the developed composite structure

3. Summary

The proposed cellulose nanopapers modification, using lignin and xylan additives, provides simple and sustainable route to engineer the interface in the developed mesh material and control the materials durability to the UV irradiation, moisture, and temperature. The tensile properties as shown in Figure 2 are significantly enhanced with the addition of xylan and lignin interface modifiers. The UV irradiation showed a milder impact on the cellulose modifications with 5 and 10 wt % xylan concentrations. In comparison, the moisture absorption test showed the

  doi:10.5075/epfl-298799_978-2-9701614-0-0

overall best performance for xylan's 2.5 wt % composition. Xylan interface development as revealed in Figure 3 in all sample concentrations showed remarkable improvements in the UV and heat resistance of NP. Lignin also strongly improved the UV resistance of NP. Cellulose NP without interface modifiers exhibited a catastrophic decrease in tensile properties after UV exposure. The UV irradiation damage is revealed in SEM analysis.

The oxidation and depolymerization of lignin and xylan at the protective interface for the cellulose (Figure 3) was indicated by UV-Vis spectroscopy as a shift in absorption peak intensities and regions. Similar observations were made from FTIR spectra analysis. The moisture sorption capacity of the NP increases with moisture level and with lignin and xylan loadings. Absorbed moisture significantly affects the elastic modulus (Figure 2). The lignin modifier resulted in higher moisture absorption capacity and, as a result, higher properties' sensitivity to humidity changes due to the strong agglomeration and phase segregation effect. However, remarkably, lignin NP showed better property retention even at high moisture content compared to CNP. The retention of the elastic modulus and strength after moisture desorption is in the range of 60–95%; lignin-modified compositions show the highest property retention.

The NP films of X10 and L2.5 have presented the highest durability performance characteristics against UV-irradiation and humidity aging (Figure 2). The improvements were achieved by improving the interface (xylan), while the developed interphase layer covered the cellulose mesh. These completely sustainable NP film compositions are being considered for the food packaging application, which is now underway as validation for berries, fruits, and vegetables.

4. Acknowledgments

This research is funded by the Latvian Council of Science, project RealHLC No. lzp-2019/1- 0390.

5. References

1. Roman L, Schuyler Q, Wilcox C, Hardesty BD. Plastic pollution is killing marine megafauna, but how do we prioritize policies to reduce mortality? Conservation Letters. 2021 Mar 3;14(2).

2. Barhoum A, Samyn P, Öhlund T, Dufresne A. Review of recent research on flexible multifunctional nanopapers. Nanoscale. 2017;9(40):15181–205.

3. Ferreira ES, Rezende CA, Cranston ED. Fundamentals of cellulose lightweight materials: bio-based assemblies with tailored properties. Green Chemistry. 2021;23(10):3542–68.

4. Cunha AG, Gandini A. Turning polysaccharides into hydrophobic materials: a critical review. Part 1. Cellulose. Cellulose. 2010 Oct 11;17(5):875–89.

  doi:10.5075/epfl-298799_978-2-9701614-0-0

5. Mimini V, Kabrelian V, Fackler K, Hettegger H, Potthast A, Rosenau T. Lignin-based foams as insulation materials: a review. Holzforschung. 2018 Dec 19;73(1):117–30.

6. Xiao S, Gao R, Lu Y, Li J, Sun Q. Fabrication and characterization of nanofibrillated cellulose and its aerogels from natural pine needles. Carbohydrate Polymers. 2015 Mar;119:202–9.

7. Batishcheva E v., Sokolova DN, Fedotova VS, Sokolova MP, Nikolaeva AL, Vakulyuk AY, et al. Strengthening Cellulose Nanopaper via Deep Eutectic Solvent and Ultrasound-Induced Surface Disordering of Nanofibers. Polymers (Basel). 2021 Dec 26;14(1):78.

8. Reid MS, Villalobos M, Cranston ED. Benchmarking Cellulose Nanocrystals: From the Laboratory to Industrial Production. Langmuir. 2017 Feb 21;33(7):1583–98.

9. Bharimalla AK, Deshmukh SP, Patil PG, Vigneshwaran N. Energy Efficient Manufacturing of Nanocellulose by Chemo- and Bio-Mechanical Processes: A Review. World Journal of Nano Science and Engineering. 2015;05(04):204–12.

10. Mautner A, Lee KY, Tammelin T, Mathew AP, Nedoma AJ, Li K, et al. Cellulose nanopapers as tight aqueous ultra-filtration membranes. Reactive and Functional Polymers. 2015 Jan;86:209–14.

11. Trache D, Tarchoun AF, Derradji M, Hamidon TS, Masruchin N, Brosse N, et al. Nanocellulose: From Fundamentals to Advanced Applications. Frontiers in Chemistry. 2020 May 6;8.

12. Beluns S, Platnieks O, Gaidukovs S, Starkova O, Sabalina A, Grase L, et al. Lignin and Xylan as Interface Engineering Additives for Improved Environmental Durability of Sustainable Cellulose Nanopapers. International Journal of Molecular Sciences. 2021 Nov 29;22(23):12939.

DILATOMETRIC AND FRACTURE MECHANISM INVESTIGATIONS ON POLY(LACTIC ACID) PLA- CALCIUM CARBONATE BIOCOMPOSITES

Laura, Aliotta[a,b], Vito, Gigante[a,b], Maria-Beatrice Coltelli[a,b] Andrea, Lazzeri[a,b]

a: Pisa University, Department of Civil and Industrial Engineering, 56122 Pisa, Italy – laura.aliotta@unipi.it
b: National Interuniversity Consortium of Materials Science and Technology (INSTM), 50121 Florence, Italy

Abstract: *The rigid filler toughening mechanism was investigated introducing calcium carbonate particles, treated with stearic acid on their surface, into a poly (lactic acid) (PLA) matrix. To favour the plastic deformation and the stretching of interparticle ligaments, a biobased and biodegradable plasticizer Acetyl Tributyl Citrate (ATBC) was added into the PLA matrix. It was proved that the best impact, fracture toughness and ductility performance were achieved with a calcium carbonate content of 10 vol.%. With this content, a more controlled growth of voids formation, was registered during the tensile dilatometric tests made thanks to the help of a videoextensometer able to record in real time the axial and transversal elongation during the tensile test. The fracture toughness, determined with the multispecimen procedure in critical conditions (medium/high crosshead speed), has been also carried out*

Keywords: Poly (lactic acid); Biocomposites; Fracture mechanics; Micromechanics; Dilatometry;

1. Introduction

Poly(lactic acid) (PLA) is one of the most studied biodegradable and renewable polymer that can substitute conventional fossil based polymers in different industrial sectors especially in the packaging field [1]. Generally, PLA possesses a high tensile stress and elastic modulus but has poor impact resistance and toughness. At this purpose a valid alternative to toughen a polymer matrix without losing the initial materials stiffness, is the use of rigid inorganic fillers [2,3]. The typology of adopted filler is fundamental to effectively toughen the polymeric matrix. In fact, according to the Argon and Cohen theory [4,5], a low adhesion among the filler and the matrix, is necessary to favor debonding that generates voids around the filler. Thanks to the voids formation the interparticle ligament can deform plastically absorbing a great quantity of energy, thus increasing the materials toughness. However, the amount of filler to be added should be optimized because excessive voids decrease the macroscopic elastic resistance. Furthermore, the higher is the filler content, the higher will be the possibility of filler agglomerations that act as stress intensification factor leading to the premature failure of the material [6,7].
Good results in improving the PLA toughness were achieved in a previous work [7] with Calcium Carbonate particles treated with Stearic Acid (SA) on their surface. It has been demonstrated that the particle surface coating favors the particles dispersions, reduces the filler/matrix adhesion, and favors debonding. In fact, SA was found to be effective in reducing the adhesion with the polymeric matrix; it reacts at the calcium carbonate particle surfaces and forms calcium stearate bicarbonate [8]. This treatment with SA, coats the filler surface making it hydrophobic without forming strong bonds [9]. SA molecules lying perpendicular to the filler surface, forms

  doi:10.5075/epfl-298799_978-2-9701614-0-0

a closely packed layer with a thickness of about 2.5 nm that reduces the filler/matrix adhesion favoring the debonding [10,11].
Nevertheless, PLA alone is intrinsically fragile, and its plasticization is necessary to ensure the plastic deformation and the stretching of interparticles ligaments. Starting from the results previously obtained [7], different amount of surface treated micrometric calcium carbonate particles were added into a plasticized PLA. ATBC (Acetyl Trybutyl Citrate) was used to plasticize the matrix, but its content was drastically reduced from 20 wt.% to 5 wt.%. The reason of this decrement was twofold. On one hand, the ATBC content was too high and, as it was observed in literature [12,13], it creates long-term plasticizer diffusion problems. On the other hand, the influence of ATBC content reduction combined with the optimization of filler content deserves to be investigated, in view of achieving a PLA toughness increment. The study was supported by dilatometric study useful to separate the micromechanical deformation processes: debonding and stretching of the interparticles ligaments; the latter, indeed, is the main absorbing energy mechanism. The application of multiple specimen resistance curve approach for measuring the J-fracture toughness of the composites, at high-medium speeds (10 mm/min) was also evaluated.

2. Materials and Methods

2.1 Materials

The materials used for this work were:

- Poly (lactic acid), trade name PLA 2003D, purchased from NatureWorks. It is an extrusion grade PLA with melt flow index (MFI) of 6 g/10 min (210 °C, 2.16 kg), nominal average molar mass of 200,000 g/mol and density of 1.24 g/cm^3. According to the producer data sheets it contains about 4% of D-lactic units.
- Acetyl Tributyl Citrate (ATBC) plasticizer was purchased from Tecnosintesi S.p.A., it is a colorless liquid having a molecular weight of 402.5 g/mol and density of 1.05 g/cm^3.
- Micro sized $CaCO_3$ particles, trade name OMYACARB 2T-AV, were kindly provided by OMYA®. It is a dry grinded Calcium Carbonate grade having a mean particle size ($d_{50\%}$) of 2.6 µm, top cut diameter ($d_{98\%}$) of 15 µm, it has a cubic shape and density of 2.7 g/cm^3. These $CaCO_3$ particles have a surface coating of stearic acid (SA) that, according to technical data sheet, is below 2 wt.%.

2.2 Methods

2.2.1 Blends and samples preparation

Composites containing increasing amount of $CaCO_3$ (from 5 vol.% to 20 vol.%), were produced in granules using a semi-industrial COMAC EBC 25HT twin screw extruder. Blends name and compositions are reported in *Table 1*. Before the extrusion all solid materials were dried in an oven for at least 24 h.

Table 1: Formulation composition

Name	PLA:ATBC ratio	$CaCO_3$ wt.%	Corresponding $CaCO_3$ volumetric content vol.%

PLA_ATBC	95:5	-	-
PLA_ATBC_5C	95:5	10	5
PLA_ATBC_10C	95:5	20	10
PLA_ATBC_15C	95:5	28	15
PLA_ATBC_20C	95:5	35	20

The extrusion temperatures in the zones from 1 to 11 were: 150/175/180/180/180/185/185/185/185/190/190 °C, with the die zone at 190 °C; the screw speed was 250 rpm and the flow rate was 10 kg/h. The screw rate was 250 rpm. After the extrusion all pellets were finally dried in a Piovan DP 604-615 dryer at 60 °C. Subsequently, the extruded materials were reprocessed in a Thermo Scientific MiniLab Haake twin-screw extruder (at 110 rpm/min, extrusion temperature equal to 190°C and a cycle time of 60 s) at the exit of the Haake extruder the molten materials were transferred, through a preheated cylinder, to a Thermo Scientific Haake MiniJet II mini-injection moulder for preparation of specimens for tensile and impact tests. The cylinder temperature was set at 190°C while the injection molding conditions were: mold temperature 60°C, injection pressure 670 bar for dogbone specimens and 720 bar for Charpy specimens and residence time of 10 s. After their injection molding, the specimens, before the mechanical characterization, were stored in a desiccator at room temperature and 50% of HR.

2.2.2 Mechanical characterization

All the mechanical characterization were carried out not before 24h from specimen extrusion and injection molding. For tensile and dilatometry tests Haake Type 3 dog-bone tensile bar (gauge dimensions: 25 × 5 × 1.5 mm) were used. Tensile tests were carried out, at room temperature, at a crosshead speed of 10 mm/min on an MTS Criterion model 43 universal testing machine equipped with a 10 kN load cell; the machine is interfaced with a computer through the MTS elite software (MTS Testsuite version 4.1). At least five specimens were tested for each composition and the average values were reported. Tensile dilatometry tests were carried out with the same MTS testing machine model at a crosshead speed of 10 mm/min. Dilatometry tests were performed only for those composites that were visibly toughened and at least five specimens for each materials were tested. Transversal and axial specimen elongations were measured, during tensile test, using a video extensometer (Genie HM1024 Teledyne DALSA camera) interfaced with a computer running ProVysis software (Fundamental Video Extensometer) and able to transfer the data in real time to the MTS Testsuite software. The volume strain was calculated, assuming the two lateral strain components to be equal, according to the following equation [14]:

$$\frac{\Delta V}{V_0} = (1 + \varepsilon_1)(1 + \varepsilon_2)^2 - 1 \quad (1)$$

where ΔV is the change in volume, V_0 is the original volume, ε_1 is the longitudinal (or axial) strain, and ε_2 is the lateral strain.

  doi:10.5075/epfl-298799_978-2-9701614-0-0

The Charpy impact tests were performed on parallelepiped specimens (10 mm width, 80 mm length, 4mm thickness) V-notched with a V-notch of 2mm. The standard ISO 179:1993 was adopted and the machine used was an Instron CEAST 9050 pendulum. For each blend, at least ten specimens have been tested at room temperature.
The same parallelepiped specimens adopted for Charpy were used for the measuring of nonlinear elastic J-fracture toughness of the material adopting a critical medium/high speed rate (not 1 mm/min but 10 mm/min). The specimens were single-edge-notched and tested with a three-point bending configuration adopting the before mentioned MTS machine. A sharp notch at the half of the total length was made by a manual cutter refrigerating the cutting zone with cool air. The ESIS TC4 multispecimen procedure [15] was adopted that requires several identical test specimens to be loaded to varying displacements to elicit different corresponding amounts of crack growth. The specimens are then unloaded and broken to expose the fracture surface for crack growth measurement (that was performed by an optical microscope). The J-R curve is obtained experimentally and fitted with a power law equation reported below:

$$J = C_1 \Delta a^{C_2} \quad (2)$$

where C_1 and C_2 are the fitting parameters and Δa is the crack growth. The J_{Ic} is taken equal to the J value at which 0.2 mm of crack growth occurred. To stay within the J-controlled region crack growth, crack growths were limited to 6% of the ligament [16].

3. Results and discussion

The addition of rigid filler $CaCO_3$ reduces the plasticizer amount and it is still effective in increasing the PLA toughness. In fact, it can be observed from the mechanical results reported in *Table 2,* that a marked decrement of the yield stress occurred when the filler amount is increased, moreover a considerable increment of the elongation at break (that it is reflected in a tensile toughness increment) was also registered.

Table 2: Main mechanical properties

Name	Elastic modulus (GPa)	Stress at break (MPa)	Elongation at break (%)	Yield stress (MPa)	Elongation at yielding (%)	Charpy impact resistance C.I.S. (kJ/m^2)
PLA_ATBC	3.25 ± 0.1	35.1 ± 0.7	15.1 ± 0.3	53.3 ± 0.6	3.8 ± 0.1	2.98 ± 0.35
PLA_ATBC_C5	3.72 ± 0.1	29.2 ± 2.3	164.7 ± 3.9	49.6 ± 0.8	3.2 ± 0.1	3.47 ± 0.42
PLA_ATBC_C10	4.20 ± 0.1	25.5 ± 2.2	195.6 ± 3.3	41.5 ± 0.7	2.6 ± 0.1	4.43 ± 0.31
PLA_ATBC_C15	4.8 ± 0.1	24.3 ± 1.2	143.9 ± 8.2	36.8 ± 0.5	2.3 ± 0.1	4.13 ± 0.18
PLA_ATBC_C20	5.1 ± 0.1	18.7 ± 2.1	32 ± 3.2	31.9 ± 1.2	2.1 ± 0.2	3.18 ± 0.14

The elongation at break is considerably improved and increases with the filer content up to 10 vol.% then a decrement was registered at 15 vol.% while at 20 vol.% an abruptly decay due to the excessive filler quantity was registered. Interesting is also to observe the stiffening effect caused by the introduction of the rigid filler that, as it could be expected, increments the Young's modulus of the material as a function of the filler content added. The tensile results are coherent

  doi:10.5075/epfl-298799_978-2-9701614-0-0

with the C.I.S results and the J_{IC} values (reported in *Figure 1* together with the correspond J-R curves); in addition, a maximum value in correspondence of 10 vol.% of $CaCO_3$ was registered.

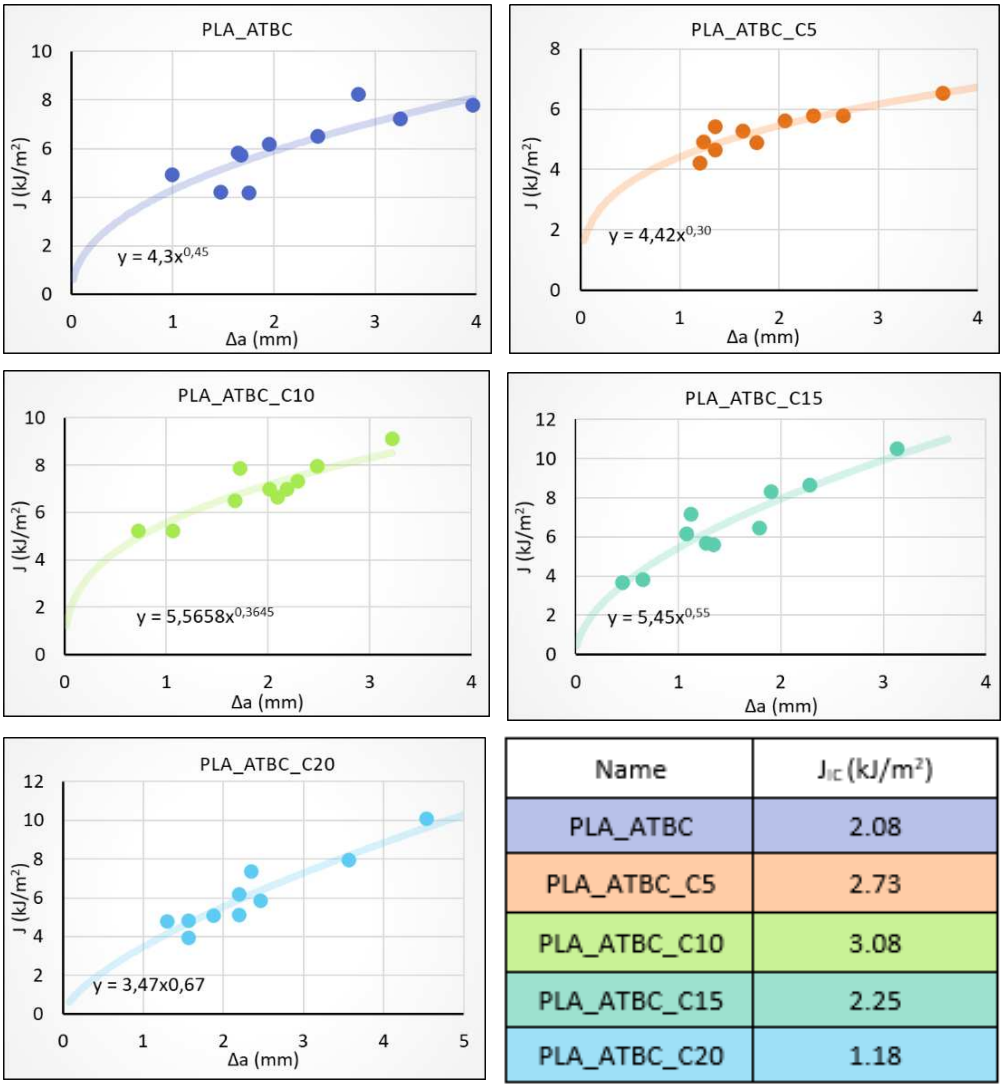

Name	J_{IC} (kJ/m²)
PLA_ATBC	2.08
PLA_ATBC_C5	2.73
PLA_ATBC_C10	3.08
PLA_ATBC_C15	2.25
PLA_ATBC_C20	1.18

Figure 1. J-R curves and their corresponding J_{IC} values.

To better understand the toughening mechanism, particular attention was dedicated to the tensile dilatometry results; the separation of the volume evolution of the polymeric matrix in the composite was carried out in the hypothesis that the volume matrix contribution is not affected by the filler presence. Thus, the overall composite strain can be described by the following equation:

$$\left(\frac{\Delta V}{V_0}\right)_C = \left(\frac{\Delta V}{V_0}\right)_M (1-\varphi) + \left(\frac{\Delta V}{V_0}\right)_V \quad (3)$$

where $(\Delta V/V_0)_C$ is the volume strain of the composite, $(\Delta V/V_0)_M$ is the volume strain of unfilled matrix, φ is the filler volume fraction and $(\Delta V/V_0)_V$ is the volume strain due to debonding and void growth. Thanks to Eq.1 it is possible to calculate, experimentally both the volume strain of the unfilled matrix ($(\Delta V/V_0)_M$) and of the composites ($(\Delta V/V_0)$); consequently, applying Eq.3, the $(\Delta V/V_0)_V$ contribution can be obtained for the analyzed composites. The obtained results, reported in Figure 2, show a linear increment of the volume variation as a function of the axial

  doi:10.5075/epfl-298799_978-2-9701614-0-0 published under CC BY-NC 4.0 license

strain. In particular, the liner increment can be divided in two stages at which corresponds two different slopes correlated to two different filler-related micromechanical deformation processes [7,14,17]. The most significant volume increment is registered in correspondence of the second stage while for the first a little volume variation is observed, and it is almost equal for all composites.

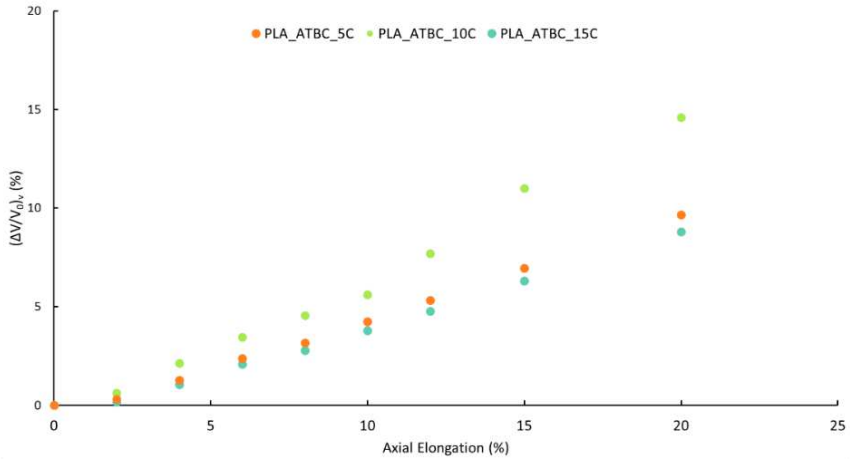

Figure 2. Volume strain due to void growth and debonding, $(\Delta V/V_0)_V$ calculated from Eq. (3), plotted versus longitudinal strain.

The first micromechanical deformation mechanism that occurs is debonding, associated to the first stage; it was observed in literature [7,14,18] that debonding occurs before yielding and, at this stage, little volume variations are observed. The deformation at which debonding approximately starts can be easily calculated by a simple geometric construction (reported in *Figure 3*) thus determining the intersection point where the slope change occurs.

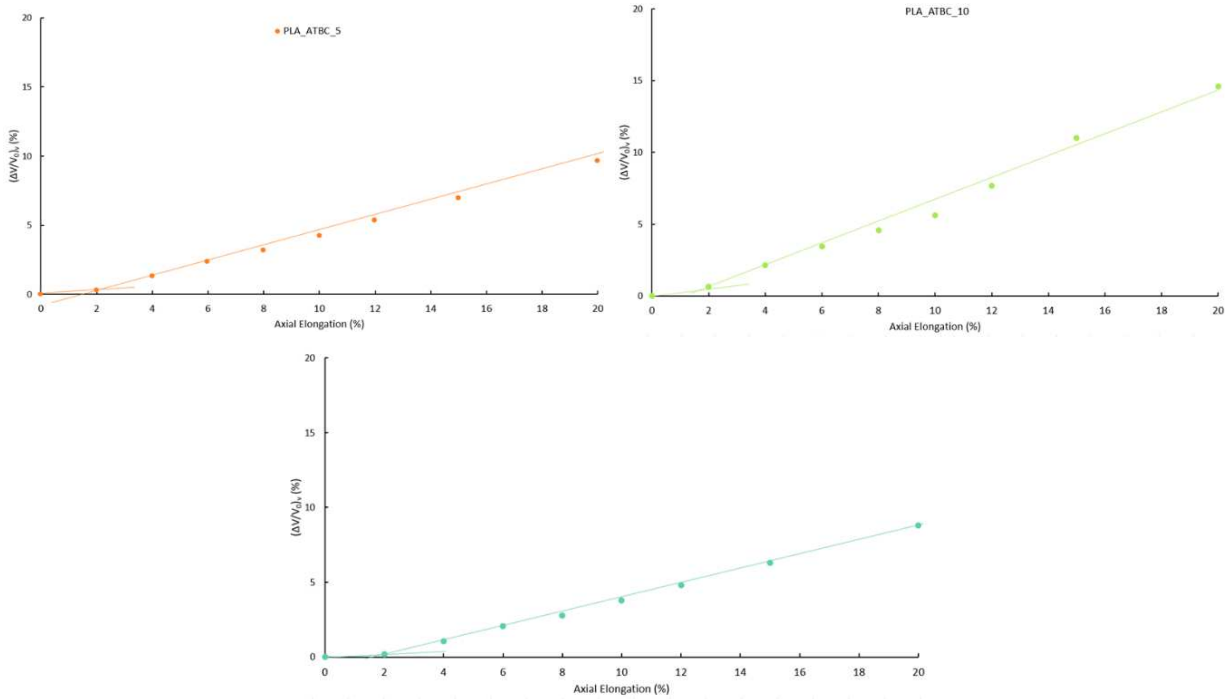

Figure 3. Graphical determination of axial elongation at debonding.

It can be observed that, for all the composites, debonding occurs around at 2% of axial elongation and, by comparing the elongation at yielding values (*Table 2*), it is confirmed that the

debonding process starts before yielding. However, the major differences to the volume variation that are responsible of the main composite differences in the mechanical response, are correlated to the second stage associated to the voids volumetric growth along the stretching direction. This second mechanism is the main absorbing energy mechanism and it is responsible of the tensile toughness improvement. The better composition that guarantees a good balance between the filler content and an efficient voids growth is the 10 vol.% for which the highest volume increment was observed. The SEM micrographs of the surface of the tensile specimen cryo-fractured along the draw direction, reported in *Figure 4*, confirms the presence of many different voids that have been generated around the CaCO3 particles indicating that debonding occurred; also elongated voids along the tensile direction are clearly visible.

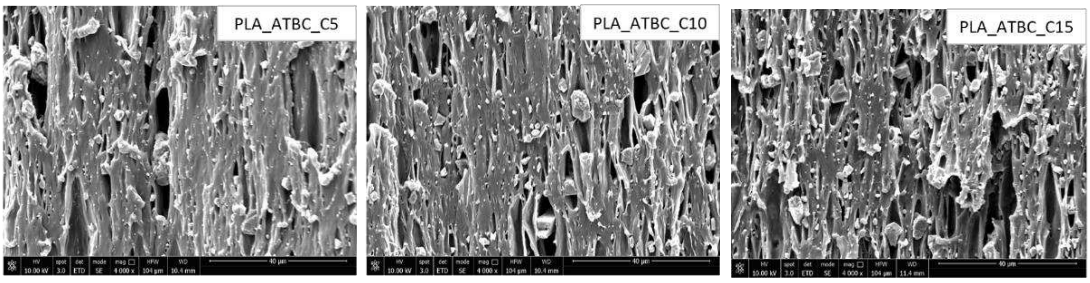

Figure 4. SEM micrographs of the surface tensile specimen cryo-fractured along the tensile direction

When the filler content is excessive the voids around the particles cannot efficiently grow due to the presence of the other adjacent fillers leading to a reduction of the tensile toughness and of the volume variation. 10 vol.% is thus the best composition able to maximize voids growth thus leading to a significant increment not only of the tensile toughness but also of the fracture toughness.

4. References

[1] Balla E, Daniilidis V, Karlioti G, Kalamas T, Stefanidou M, Bikiaris ND, Vlachopoulos A, Koumentakou I, Bikiaris DN. Poly(lactic Acid): A Versatile Biobased Polymer for the Future with Multifunctional Properties—From Monomer Synthesis, Polymerization Techniques and Molecular Weight Increase to PLA Applications. Polym 2021, Vol 13, Page 1822 2021; 13:1822.

[2] Bigg DM. Mechanical properties of particulate filled polymers. Polym Compos 1987; 8:115–122.

[3] Fu SY, Feng XQ, Lauke B, Mai YW. Effects of particle size, particle/matrix interface adhesion and particle loading on mechanical properties of particulate-polymer composites. Compos Part B Eng 2008; 39:933–961.

[4] Argon AS, Cohen RE. Toughenability of polymers. Polymer (Guildf) 2003; 44:6013–6032.

[5] Argon AS, Bartczak Z, Cohen RE, Muratoglu OK. Novel mechanisms of toughening semi-crystalline polymers. ACS Publications; 2000.

[6] Williams JG. Particle toughening of polymers by plastic void growth. Compos Sci Technol 2010; 70:885–891.

[7] Aliotta L, Cinelli P, Coltelli M-B, Lazzeri A. Rigid filler toughening in PLA-Calcium

  doi:10.5075/epfl-298799_978-2-9701614-0-0

Carbonate composites: effect of particle surface treatment and matrix plasticization. Eur Polym J 2018.

[8] Osman MA, Suter UW. Surface treatment of calcite with fatty acids: Structure and properties of the organic monolayer. Chem Mater 2002; 14:4408–4415.

[9] Lazzeri A, Zebarjad SM, Pracella M, Cavalier K, Rosa R. Filler toughening of plastics. Part 1—the effect of surface interactions on physico-mechanical properties and rheological behaviour of ultrafine CaCO3/HDPE nanocomposites. Polymer (Guildf) 2005; 46:827–844.

[10] Rothon 1944- (viaf)29689163 RN. Particulate-filled polymer composites. Harlow : Longman scientific and technical; 1995.

[11] Zuiderduin WCJ, Westzaan C, Huétink J, Gaymans RJ. Toughening of polypropylene with calcium carbonate particles. Polymer (Guildf) 2002; 44:261–275.

[12] Aliotta L, Vannozzi A, Panariello L, Gigante V, Coltelli M-B, Lazzeri A. Sustainable micro and nano additives for controlling the migration of a biobased plasticizer from PLA-based flexible films. Polymers (Basel) 2020; 12.

[13] Castle L, Jickells SM, Sharman M, Gramshaw JW, Gilbert J. Migration of the plasticizer acetyltributyl citrate from plastic film into foods during microwave cooking and other domestic use. J Food Prot 1988; 51:916–919.

[14] Lazzeri A, Thio YS, Cohen RE. Volume strain measurements on CACO3/polypropylene particulate composites: The effect of particle size. J Appl Polym Sci 2004; 91:925–935.

[15] Williams JG. Fracture Mechanics Testing Methods for Polymers Adhesives and Composites. ESIS Publication - Elsevier; n.d.

[16] Joyce J. Elastic-Plastic Frcature Test Methods: the User's Experience 2nd Volume. 1991.

[17] Pukánszky B, Van Es M, Maurer FHJ, Vörös G. Micromechanical deformations in particulate filled thermoplastics: volume strain measurements. J Mater Sci 1994; 29:2350–2358.

[18] Thio YS, Argon AS, Cohen RE, Weinberg M. Toughening of isotactic polypropylene with CaCO 3 particles. Science (80-) 2002; 43:3661–3674.

  doi:10.5075/epfl-298799_978-2-9701614-0-0

EFFECT OF FIBRILLATION OF FLAX MAT BINDER ON THE IMPACT RESPONSE OF UNIDIRECTIONAL FLAX/EPOXY COMPOSITES AND COMPARISON WITH A GLASS/EPOXY COMPOSITE

Samer, El Khoury Rouphael[a,b,c], Gilbert, Lebrun[a], Fabienne, Touchard[b], Thuy-Quynh, Truong-Hoang[c]

a: Institut d'Innovations en Écomatériaux, Écoproduits et Écoénergies à base de biomasse (I2E3), Université du Québec à Trois-Rivières (UQTR), C.P. 500, Trois-Rivières, Québec, Canada – samer.el.khoury.rouphael@uqtr.ca
b: Institut PPRIME, CNRS-ENSMA-Université de Poitiers, Département Physique et Mécanique des Matériaux, ENSMA, 1, Av. Clément Ader, B.P. 40109, 86961 Futuroscope Cedex, France
c: ESTACA'LAB, Pôle Mécanique des Matériaux Composites et Environnement, ESTACA – Campus Ouest, Rue Georges Charpak, BP, Laval Cedex, France

Abstract: *In this study, the behavior of flax fiber (FFC) and glass fiber composite (GFC) laminates under a series of low velocity impact loads from a drop weight impact tower is analyzed and compared. All laminates are made by stacking unidirectional (UD) layers of reinforcement, where the UD flax fibers are combined to short flax fibers used as a mat binder to form the base architecture of this reinforcement denoted by UD-mat. Two types of short flax fibers are taken into consideration for the mat binder: one is unmodified fibers while the second one undergoes a refining modification. When comparing the two types of flax/epoxy laminates, the FFC with refined short flax fibers shows the highest permanent and maximal displacements. Results show that, for all impact energies the maximum load for FFC with unmodified short fibers is higher than that with refined fibers. The flax/epoxy composites absorb more energy than the glass/epoxy ones.*

Keywords: Natural composites, flax, impact behavior, fibrillation, damage.

1. Introduction

Composite materials are widely used in structures and as substitutes for metals in various sectors like aerospace and automotive. However, their response to localized impact is one of their limitations [1]. The impact properties of a given composite material depend on several factors. Namely, the type of matrix and its ductility, the type of fibers and their architecture as well as their orientation, the quality of the interface between the fibers and the matrix and the thickness of the laminate [2]. The most used method to characterize the response of a composite to a low-velocity impact is that of the drop tower [3]. This method simulates tools drops and other scenarios during materials manufacture and maintenance [4]. The use of natural fibers in high performance applications has been limited due to a lack of information on their durability facing fatigue loads and impact scenarios. Because of the natural origin of bast fibers, the mechanical behavior of their composites varies remarkably, unlike glass fiber reinforced composites. This is the result of variations in the fiber properties due to many factors such as the seasonal variations, fiber location along the plant stem and fiber defects, to name a few [5]. Ramakrishnan et al. [6] found a similarity in the performance of flax fiber reinforced composites made from a PP matrix and an epoxy matrix. For the epoxy composite, a fiber dominant damage

  doi:10.5075/epfl-298799_978-2-9701614-0-0

is detected. Fiber breakage in the back face appeared with limited delamination. Panciroli and Gianni [5] compared the impact response of epoxy composites (using quasi-isotropic configurations) reinforced with non-crimp and twill flax fabrics and UD glass fabrics. They showed that the damage region expands with the increase of the impact energy while fiber breakage, for the flax/epoxy composites, took place at each impact energy. Habibi et al. [7] studied flax/epoxy laminate with UD-mat reinforcements (the same reinforcements used in this work). They found that for low energy levels the cracks on the back face of the specimen are parallel to the UD fibers. As the impact energy increases, cracks in the direction transverse to the UDs (resulting in fiber breakage) begin to appear. Finally, the damage area widens with the increase in the impact energy. Liang et al. [8] also investigate the effect of low-velocity impacts on quasi-isotropic flax/epoxy composites. A microcrack initiation energy is found at 4 J for their materials. The increase in the impact time is linked to an increase in the damage accentuation. This phenomenon is explained by the development of the damage in the material, which is perceptible by the growth of the macrocracks length.

Surface fibrillation consists in the refinement of short fibers with a partial pealing of the microfibrils located at the surface of fibers. Fiber refining is well known in the paper industry, and Afra et al. [9] have found an enhancement of the bonding between fibers resulting in increased tensile strength of the produced papers. For this purpose, the present work is conducted on reinforced epoxy composites using flax UD-mat reinforcements made of non-fibrillated and fibrillated short fibers for the mat phase. The results are then compared to laminates made of UD E-glass reinforcements. The impact behavior is analyzed using force-time and force-displacement curves and photos of the impacted faces of the specimens are shown in support to the analysis.

2. Materials and methods

2.1 Reinforcements preparation and laminates fabrication

The same fabrication procedure for the UD-mat flax reinforcement, described in previous works [10, 11], is applied for this study. The UD phase consists in Tex 400 flax strands supplied by Safilin Inc. (France). Tex 5000 flax strands, also supplied by Safilin, are chopped into short fibers of 6 ± 1 mm, which are used for the mat phase of the reinforcement. It is important to note that this length is chosen to stay over the minimum length/diameter fiber aspect ratio below which fiber debonding and loosening could occur during testing. There is also a length limit of about 10 mm, after which the projection of short fibers/water mixture is difficult considering the risk to obstruct the projection nozzle in the fabrication process. For the preparation of the reinforcements with refined short flax fibers, the fibrillation process is performed according to the following procedure. First, the desired quantity of short fibers is placed in a disintegrator (Figure 1a), water is added, and the mixture homogenized. Next, a quasi-homogeneous thick sheet is obtained using a static former (Figure 1b). The sheet is then tear into small pieces and placed inside a PFI mill (Figure 1c) consisting in a rotor and stator assembly which, by rotation of the rotor, allow the refinement of fibers (surface fibrillation). The refinement level is controlled by the number of rotor revolutions and for this study, this number is set to 400 based on ongoing works. Finally, after fibrillation, the fibers are mixed with water in a proportion 0.06% by weight. The mixture is used next to fabricate the reinforcement, procedure described in previous works [10, 11]. After fabrication, the short fiber mat acts as a binder layer ensuring a natural adhesion between the UD yarns while keeping them well aligned. The average surface

  doi:10.5075/epfl-298799_978-2-9701614-0-0

density of the reinforcements is 299 ± 11 g/m^2, including the 50 g/m^2 mat binder. Before molding, the reinforcements are dried at 105°C for 15 minutes to remove humidity. The glass UD reinforcements, supplied by Texonic Inc. (Québec, Canada), have been chosen to have a surface density of 295 ± 2 g/m^2, close to that of UD-mat flax reinforcement. The same laminate sequence of $[0]_8$ was chosen in both types of composites to allow comparisons in the analysis.

The laminates are produced using the resin transfer molding (RTM) process. The resin SikaBiresin CR72 and the hardener SikaBiresin CH72-3, both supplied by Sika Industry (USA) are mixed at a resin to curing agent weight ratio of 100:18 according to the technical data sheet. Degassing vacuum was applied for 10 minutes before the start of injection. After injection, part was cured at a temperature of 80°C for 12h. The measured thickness of the flax/epoxy specimens with unmodified (standard) and refined short flax fibers was respectively of 4.28 ± 0.09 mm and 4.07 ± 0.06 mm corresponding to fiber volume fractions of 38.84 ± 2.10 % and 40.84 ± 1.47 % respectively. The measured thickness of the glass/epoxy specimens is 2.34 ± 0.04 mm with a fiber volume fraction equal to 37.98 ± 2.17 % measured by calcination. Note that the flax/epoxy with standard and fibrillated short fibers are termed FUM0S, FUM0F, respectively. While the glass/epoxy composites are called GUD0.

Figure 1. The different eauipements used for the short flax fibers refining: a) Desintegrator, b) Static former, c) Refiner (PFI mill).

2.2 Impact tests

The sample dimensions follow the recommendations of ASTM D7136/D7136M standard. An Instron CEAST 9350 drop tower (Figure 2a) is used to perform the impact tests with a load cell of 22 kN. Three impact curves are recorded: load-time, load-displacement, and energy-time. Using the information of these curves, the maximum load and displacement at impact are determined along with the permanent displacement and absorbed energy. The samples had the following dimensions: 150 mm x 90 mm x measured thickness for the FFCs and 150 mm x 100 mm x measured thickness for the GFCs. For reasons related to the reinforcement fabrication, the width of the flax samples was 90 mm instead of the 100 mm recommended by the standard. Considering the relatively smaller size of damage after impact, this had no influence on the results. The length of the sample corresponds to the longitudinal (UD fiber) direction of the composite. The impact energies applied in this study are 3 J, 5 J, 8 J and 11 J. For each impact energy, three specimens are tested for the FFCs and two specimens for the GFCs, which are more repeatable. The impacts are performed with a hemispherical impactor (Figure 2b) of a diameter of 20 mm. The samples are fixed between a lower fixed support and an upper movable support, at a clamping pressure of 7 bar, and the internal and external diameter of supports are 40 mm and 60 mm respectively.

  doi:10.5075/epfl-298799_978-2-9701614-0-0

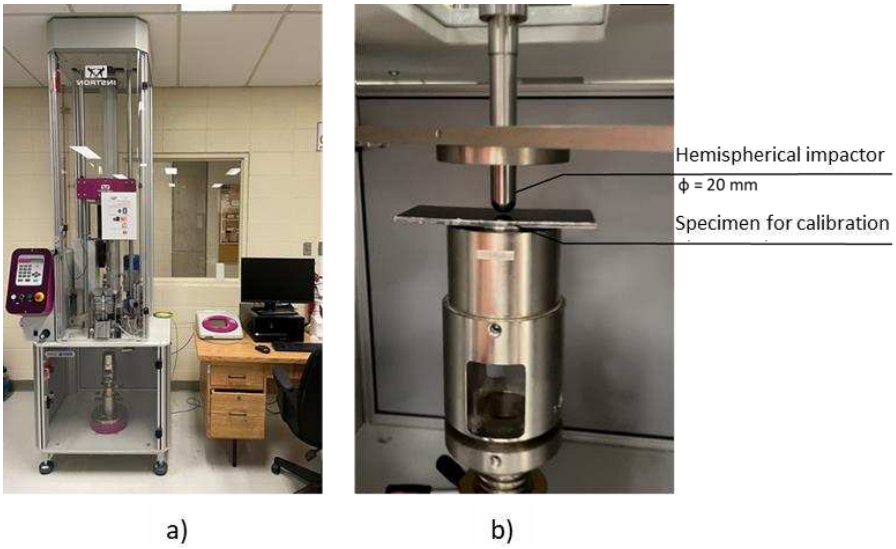

Figure 2. The impact machine used in this study: a) Instron drop-tower and the data acquisition system, b) the impactor with a specimen between the supports

3. Results and discussion

3.1 Force-time curves

The force-time curves of the materials impacted at 8J are shown in Figure 3 for the three types of composites. The peak load of the FUM0S is around 2900 N, with an impact time equal to 8 ms, while the FUM0F have a slightly lower peak load around 2700 N with the same impact time. The GUD0 have the highest peak load at approximately 4000 N (40% higher than the flax/epoxy composites) with a slightly lower impact time of 7.3 ms.

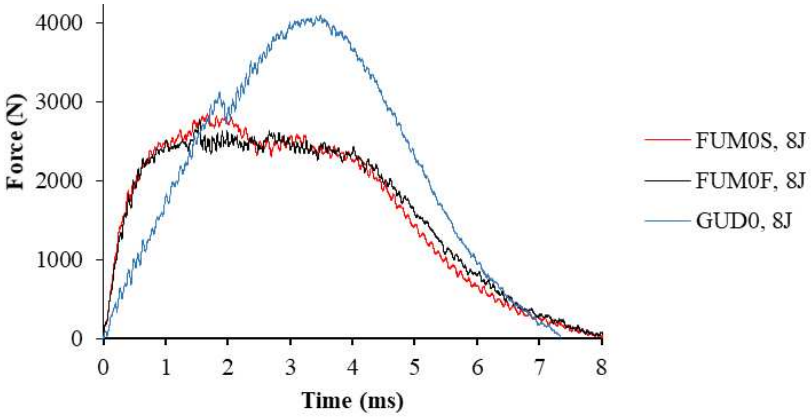

Figure 3. Force-time curves of the FUM0S, FUM0F, and GUD0 laminates.

When comparing the force-time curves, those of FUM0S and FUM0F reach a plateau with a quasi-constant force maintained for the same duration, followed by a decrease. This plateau corresponds to progressive damages taking place in the material. On the other hand, the glass/epoxy curve has a sinusoidal shape, which means a more brittle damage occurs leading to a lower energy dissipation [5]. The small, abrupt load drop occurring at 3000 N can signify that a sudden damage occurred such as delamination which can be observed by visual inspections. In this case, the damage threshold is exceeded without the occurrence of a plateau in the force-time curve. Figure 4 shows the peak loads reached for each type of laminate at each impact

  doi:10.5075/epfl-298799_978-2-9701614-0-0

energy. Comparing the response of the FFCs (FUM) and the GFC (GUD), the peak load of the glass/epoxy composite is always higher, the difference being larger at higher impact energies (see Figure 4). Finally, and compared to the standard flax UD-mat reinforcement, it appears that surface fibrillation of short mat fibers did not have an evident influence on the peak load between 3 J and 8 J. Otherwise, fibrillation seems to reduce the peak load at the higher 11 J impact energy.

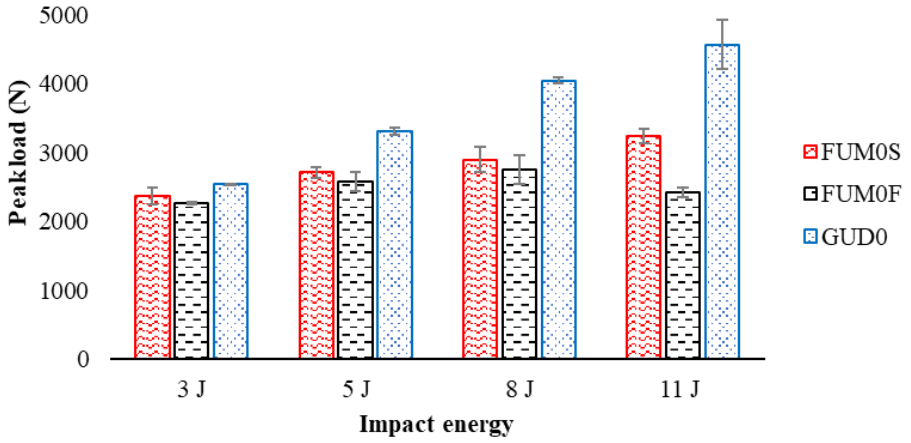

Figure 4. Peak loads registered at the four impact energies (3 J, 5 J, 8 J and 11 J) for the FUM0S, FUM0F and GUD0

3.2 Force-displacement curves

Typical force-displacement curves at 8 J are shown in Figure 5. It is observed that the fibrillated flax/epoxy specimens show a slightly larger permanent and maximum displacement than the specimens with standard mat. The average permanent displacement of FUM0S is 2.045 ± 0.290 mm, 15% lower than that of the FUM0F which is 2.417 ± 0.197 mm. However, this result must be considered with care considering the overlap of standard deviations. The force-displacement history of FUM0S and FUM0F are very similar showing a plateau with a larger surface area under these curves compared to GFC. Instead, the curve shows lower dissipated energy, and the damage threshold is exceeded with a continuous load increase. Finally, the GUD0 showed a maximum displacement comparable to that of the FUM0F, but the permanent displacement of the GUD0 is much less pronounced than that of the FUM0S and FUM0F, so more energy was restituted in the glass-epoxy laminate compared to the flax-epoxy ones.

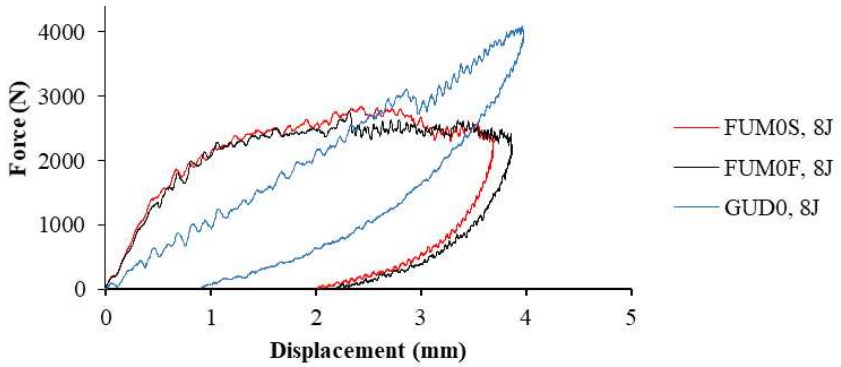

Figure 5. Force-displacement curves of the FUM0S, FUM0F, and GUD0 laminates.

  doi:10.5075/epfl-298799_978-2-9701614-0-0

Figure 6 shows the mean permanent displacements for all tests. In line with Figure 5, the permanent displacement is always lower for the glass-epoxy laminate. The permanent displacements of the FFCs are similar at low energies, but that of fibrillated composites (FUM0F) becomes larger at 8 and 11 J. The standard flax UD-mat reinforcement seems to perform better than the fibrillated one as concern the impact behavior of UD flax laminates.

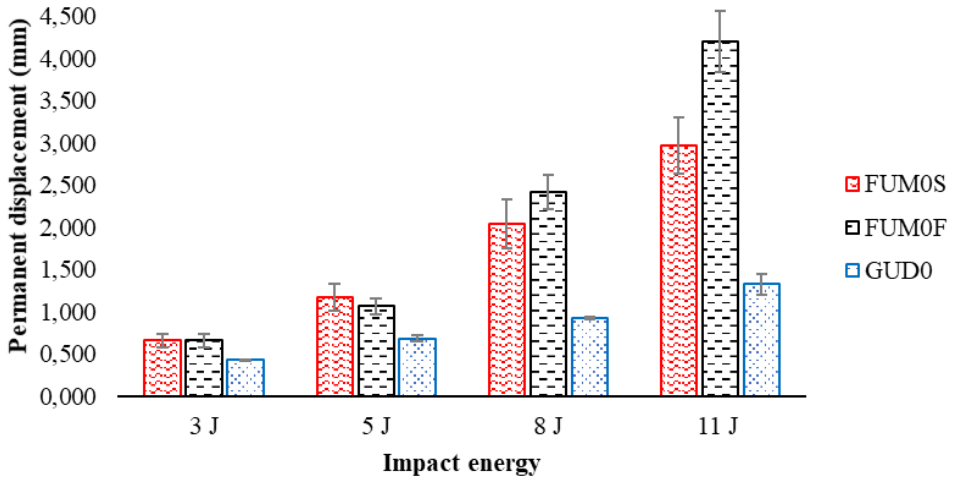

Figure 6. Permanent displacements registered at the four impact energies (3 J, 5 J, 8 J and 11 J) for the FUM0S, FUM0F and GUD0

Globally, the energy absorbed by the biocomposites is higher than that absorbed by the GFC, as shown in Figure 7. The absorbed energy and the energy absorption ratio increase progressively with the applied impact energy for the three types of laminates. It should be noted that no full penetration occurred.

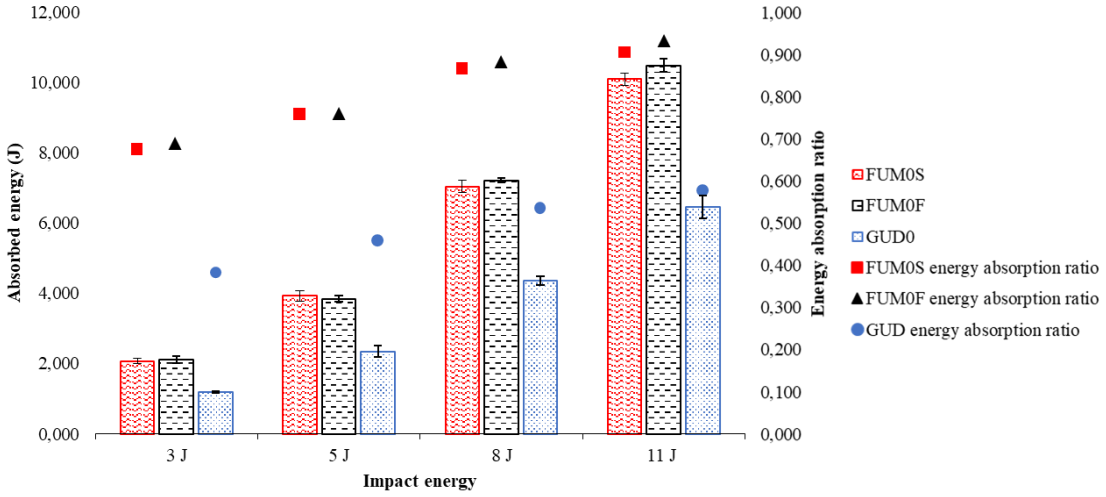

Figure 7. Absorbed energy and the energy absorption ratios for the four impact energies (3 J, 5 J, 8 J, 11 J) for the FUM0S, FUM0F and GUD0

3.3 Damage analysis

Figure 8 shows example images of the front and rear faces of the different specimens impacted at 8 J. It can be seen that the impacted flax/epoxy specimens present on the front face two large longitudinal cracks that spread on a length of about 36 mm. On the rear face, the damage is

highlighted by a central longitudinal crack of about 41 mm with other smaller longitudinal cracks, and a large transverse fracture. Moreover, delamination has been visually detected on the rear face of the FUM0S and FUM0F specimens impacted at 11 J. The damaged surface takes an elliptical shape with the longitudinal and transverse cracks being its primary and secondary axes, respectively. In a study conducted by Habibi et al. [7] on the same type of flax UD-mat/epoxy composites oriented at 0° with the same V_f of 40%, the form of damage that were identified are matrix tension cracks, fibers breakage, delamination, and shear matrix cracks. The difference in the size of damages in their material compared to the ones of this study can be explained by the use of a conical impactor in their work. They also used thinner 2.95 mm plates, compared to the 4.07 and 4.28 mm thick fibrillated and standard flax laminates in the actual work. The main damages occurring in the glass/epoxy impacted specimens are matrix cracks and delamination (see GUD0 in Figure 8). Delamination was detected due to the transparency of this composite. In line with previous observations in Figure 6, it is important to note that fiber breakage occurred only in the FFCs, which may explain the difference in permanent displacement between FFCs and GFC. Visual inspections of the damages at the front and rear faces of impacted flax/epoxy specimens (at 8 J) show the presence of fiber breakage, which can explain the appearance of the plateau in Figures 3 and 5.

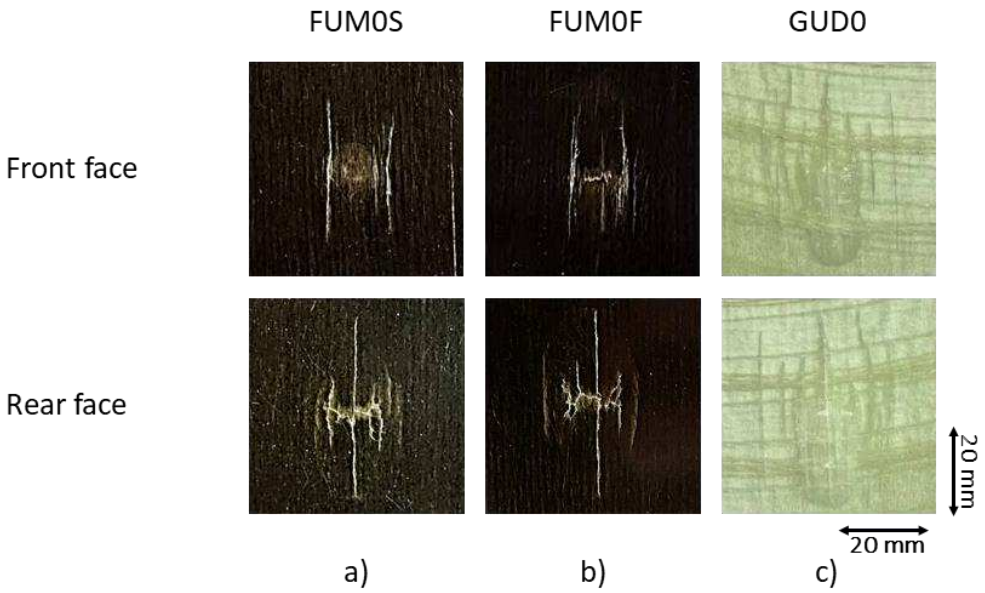

Figure 8. Front and rear faces of the impacted specimens at 8 J : a) FUM0S, b) FUM0F, and c) GUD0

4. Conclusion

In conclusion the flax/epoxy laminates with refined short flax fibers exhibit the highest permanent displacement for the impact energies of 8 J and 11 J when comparing to standard FFCs. In addition, the maximum load for FFC with unmodified short fibers is slightly higher than that with refined fibers, and the difference becomes remarkable for the impact energy of 11 J. For this reason and for the energy levels tested, it can be concluded that the fiber refining does not provide a higher performance of the FFC under impact loading. On the other hand, the GFC exhibits the highest maximal load and absorbs less energy than the FFCs. In terms of damage mechanisms, delamination and matrix cracks are observed in GFC while matrix cracks, fiber breakage and delamination occurred in FFCs. It may be concluded, at least for the studied

  doi:10.5075/epfl-298799_978-2-9701614-0-0

parameters and UD laminate types, that the fibrillation did not offer an improvement for the flax/epoxy UD composites and the glass fiber is more resistant than flax fiber facing a low velocity impact. For the upcoming studies, the effect of fibrillation will be explored while considering cross-ply flax/epoxy composites.

5. References

1. T. Yuanjian et D. H. Isaac, « Combined impact and fatigue of glass fiber reinforced composites », Compos. Part B Eng., vol. 39, no 3, p. 505-512, avr. 2008, doi: 10.1016/j.compositesb.2007.03.005.
2. F. Bensadoun, D. Depuydt, J. Baets, I. Verpoest, et A. W. van Vuure, « Low velocity impact properties of flax composites », Compos. Struct., vol. 176, p. 933-944, sept. 2017, doi: 10.1016/j.compstruct.2017.05.005.
3. D. S. D. Vasconcellos, « Comportement en fatigue avant et après impact de composites tissés chanvre/époxy », PhD ENSMA (France) 2014.
4. S. I. Thorsson, A. M. Waas, et M. Rassaian, « Low-velocity impact predictions of composite laminates using a continuum shell based modeling approach Part b: BVID impact and compression after impact », Int. J. Solids Struct., vol. 155, p. 201-212, déc. 2018, doi: 10.1016/j.ijsolstr.2018.07.018.
5. R. Panciroli et O. Giannini, « Comparing the impact resistance of flax/epoxy and glass/epoxy composites through experiments and numerical simulations », Compos. Struct., vol. 264, p. 113750, mai 2021, doi: 10.1016/j.compstruct.2021.113750.
6. K. R. Ramakrishnan, S. Corn, N. Le Moigne, P. Ienny, et P. Slangen, « Experimental assessment of low velocity impact damage in flax fabrics reinforced biocomposites by coupled high-speed imaging and DIC analysis », Compos. Part Appl. Sci. Manuf., vol. 140, p. 106137, janv. 2021, doi: 10.1016/j.compositesa.2020.106137.
7. M. Habibi, S. Selmi, L. Laperrière, H. Mahi, et S. Kelouwani, « Experimental investigation on the response of unidirectional flax fiber composites to low-velocity impact with after-impact tensile and compressive strength measurement », Compos. Part B Eng., vol. 171, p. 246-253, août 2019, doi: 10.1016/j.compositesb.2019.05.011.
8. S. Liang, L. Guillaumat, et P.-B. Gning, « Impact behaviour of flax/epoxy composite plates », Int. J. Impact Eng., vol. 80, p. 56-64, juin 2015, doi: 10.1016/j.ijimpeng.2015.01.006.
9. E. Afra, H. Yousefi, M. M. Hadilam, et T. Nishino, « Comparative effect of mechanical beating and nanofibrillation of cellulose on paper properties made from bagasse and softwood pulps », Carbohydr. Polym., vol. 97, no 2, p. 725-730, sept. 2013, doi: 10.1016/j.carbpol.2013.05.032.
10. H. Mohamed, L. Laperrière, G. Lebrun, et L. Toubal, « Combining short flax fiber mats and unidirectional flax yarns for composite applications: Effect of short flax fibers on biaxial mechanical properties and damage behaviour », Compos. Part B Eng., vol. 123, mai 2017, doi: 10.1016/j.compositesb.2017.05.023.
11. M. Habibi, G. Lebrun, et L. Laperrière, « Experimental characterization of short flax fiber mat composites: tensile and flexural properties and damage analysis using acoustic emission », J. Mater. Sci., vol. 52, no 11, p. 6567-6580, juin 2017, doi: 10.1007/s10853-017-0892-1.

MORPHOLOGICAL IMAGE ANALYSIS: A CANDID TECHNIQUE TO DETERMINE DENSITY OF A FIBER AND PERMANENT DAMAGE DUE TO INTERACTION WITH WATER MOLECULES

Mengstu Asherbe, Arefe[a,b], Mulualem Gebregiorgis, Gebremariam[b], Aart Willem Van Vuure[a]

a: Department of Materials Engineering KU Leuven, Kasteelpark Arenberg 44, box 2450, 3001 Leuven, Belgium– mashebre@yahoo.com
b: School of Mechanical and Industrial Engineering, Ethiopian Institute of Technology-Mekelle (EiT-M), Mekelle University, Mekelle, Ethiopia

Abstract: *This paper presents a morphological analysis to study the density of natural fiber and the effect of surface treatment. It further studies the dimensional change of the fiber when exposed to water molecules. An interactive MATLAB and GIMP (image manipulation software) were employed for microstructural image analysis for fiber dimensions and fiber damage due to hygroscopic swelling. A noble method has been well established to determine the density from the fiber constituents and lumen contribution. To measure the density and dimensional change caused by fiber treatment, alkali, acetylation, and alkali-acetylation treated fibers were compared to untreated fibers. The fibers have shown a large dimensional change due to alkali and alkali-acetylation treatments and swelling: while the treatments reduce the equivalent diameter of the fibers due to collapsing of the elementary fibers, the interaction with water molecules has put a permanent size change on the technical fibers.*

Keywords: Morphologic analysis; fiber density; treatment; fiber swelling

1. Introduction

Bio-based fibers are gaining superiority in low-loading applications and are becoming viable options for load-bearing engineering structures, thanks to the extensive research and development works. These fibers have a low density, allowing them to demonstrate remarkable qualities in their specific strength and modulus capabilities, and are replacing synthetic fibers like glass (1). Understanding the density and microstructural properties of bio-based fibers, on the other hand, remains a challenge. In the study of the mechanical performance of fiber-reinforced composites, density is an important factor to consider in defining the fiber volume fraction. The common measuring instruments used to investigate the density of natural fibers are largely inconclusive(2) (3). Researchers almost always assume that the density of the fiber is the same as the density of the solid component of the fiber. This indicates that the effect of the core hollow component of the elementary fiber, the lumen, is ignored. Furthermore, chemical treatments of fibers, such as alkali treatment, may strongly affect the microstructure, which might result in collapsing the lumen completely due to the aggressive penetration of the solution into the fiber constituents (4). However, the effect of fiber treatment on density is often overlooked, and the density of treated and untreated fibers has been often considered the same. As a result, erroneous density values could lead to a miscalculation of the material's performance properties.

Moreover, natural fibers are sensitive to moisture and their mechanical properties degrade due to changes in the microstructure(5). Moisture enters the composite structures due to diffusion and capillary action. The moisture can create a differential swelling inside the cell wall due to

  doi:10.5075/epfl-298799_978-2-9701614-0-0

the difference in hydrophilicity of the constituents (cellulose, hemicellulose, lignin, and pectin) which may lead to internal stress and structural damage within the fiber (6). Moreover, moisture molecules plasticize the interface of the fiber and the matrix due to asymmetric fiber and matrix swelling capacity. These phenomena establish damage to the structure and lead to degrading the performance properties of the composite when in use (7).

The goal of this study was to use morphologic image analysis to assess the density of bio-based fibers and to investigate the influence of fiber treatment. Moreover, the study aimed to investigate the average equivalent diameter of the fiber in untreated and treated conditions and the irreversible dimensional change of fiber due to swelling when a fiber-reinforced polymer composite is subjected to water molecules.

2. Materials and Methods

2.1. Materials

We investigated an exotic fiber called Enset fiber from the Enset plant in Ethiopia's Wolliso district in the south. Enset plants belong to the Ventricosum plant family, which includes plants that create their stems by stacking up their leaves over time and are known for their high water content. The plant's false stem is harvested when it is deemed to be ripe enough to give an excellent yield of starch-rich food. Fibers were collected during food extraction and stretched along their length axis by putting stiff cylindrical wooden materials within to straighten them out during drying and preservation.

2.2 Fiber treatment

To investigate the effect of various treatments on the untreated fiber and the relative advantage of them, treated and untreated fibers were created. Three treatment methods were conducted: 1) **Alkali treatment:** fibers were immersed in a 5 (w/w) % NaOH-distilled water solution for three hours, which is the most used NaOH concentration in natural fiber modification (8). The treated fibers were then rinsed in distilled water several times to remove alkali ions and cuticles, then air-dried for 12 hours. 2) **Acetylation treatment:** fibers were first immersed in a glacial acetic acid solution for an hour followed by being rinsed in an acetic anhydride solution with a droplet of sulfuric acid as an initiator for an hour(9). Fibers were soaked repeatedly with distilled water to remove the cuticles and stabilize the fiber neutrality and then dried in air. 3) **Alkali-Acetylation treatment:** the alkali-acetylation treatment process combines the alkali and acetylation treatment procedures.

2.3 Sample preparation

Enset reinforced polyester composite samples of a rectangular size of 100*15*15 mm^3 were produced from the treated and untreated fibers in a manually operated press machine. These rectangular samples were cut and polished into cubes of 15 mm in length (figure 1). The cubic

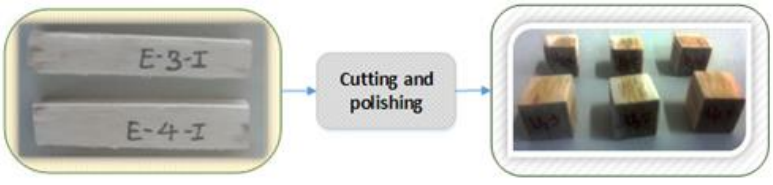

Figure1. Cubic samples of fiber-reinforced composite for microstructural imaging, dimensional change due to fiber treatment, and fiber swelling

  doi:10.5075/epfl-298799_978-2-9701614-0-0

samples were further embedded with epoxy resin, degassed and cured in the air for 24 hours. Grinding was done with successive grinding tissues of 320-4000 grit size to obtain an expected surface finish of 6µm followed by polishing in the automated machine with 3µm and 1µm suspensions. Final polishing was carried out using OPS (active Oxide polishing suspensions) projected to produce a 0.25 µm resolution surface of the microstructure.

2.4 Density of the fiber

The density of the fiber was studied using a noble approach that combines both image analysis and the rule of mixtures. An optical microscope was used to capture images of the microstructure of technical fibers and their corresponding elementary fibers from the composite samples. The areal profile of the central lamella, as well as the cell walls of elementary fibers and their lumen, were created using modeling software. An assumption was formulated that the central lamella is made up of pectin, and the elementary cell wall is formed from cellulose, hemicellulose, and lignin, while the lumen is a hollow structure filled with air. Because the primary cell wall is destroyed during extraction(10), it is not included in the study. Therefore, the contribution of the cellulose, hemicellulose and lignin that make up the cell wall structure of the elementary fiber was gathered from research reports, and the density of the secondary cell wall, ρ_w, was calculated using the rule of mixtures Eq. (1):

$$\rho_w = \rho_c * \%_c + \rho_h * \%_h + \rho_l * \%_l \quad (1)$$

Where $\%_c$, $\%_h$, and $\%_l$ represent the percentage share of cellulose, hemicellulose, and lignin in the cell wall of the elemental fiber, respectively. This procedure provides the density of the solid component of the fiber.

The density of the fibers was further measured using a helium pycnometer to validate the results from the new measurement approach. The helium pycnometer can only measure the solid component of objects because helium gas can enter nano-dimensional holes of an object under study (3). Therefore, this method of density measurement does not consider the effect of the lumen. As a result, the density of the solid component of the fibers created by the rule of mixtures and the helium pycnometer was compared. To avoid the thermogravimetric effect during density measurement with the pycnometer, samples were chopped into an approximate length of 2mm and dried in an oven at 60°C for 24 hours before being sealed in a vacuum bag. Once the density of the cell wall structure is defined, areal contribution-based density measurement can be applied to determine the effective density of the technical fiber, ρ_f, using the rule of mixtures Eq. (2).

$$\rho_f = \frac{A_w}{A_f} . \rho_w + \frac{A_p}{A_f} . \rho_p \quad (2)$$

Where A_w, A_p, and A_f are the areas of the cell wall, central lamella/pectin, and technical fiber, respectively; and ρ_p, is the density of the central lamella.

2.5 Diameter of the fiber and effect of fiber treatment

The diameter of the fiber was determined from microstructural image analysis. Microscopic images of the fiber cross-section have been taken and postprocessing of the images has been executed using MATLAB. Due to the complex structure of the fibers and the small difference in density between the matrix and the fiber which largely affects the contrast of the image, we

  doi:10.5075/epfl-298799_978-2-9701614-0-0

introduce GIMP (Image manipulation program) to manually assist MATLAB for image segmentation and contact region separation. Statistical data were extracted in 'region analyzer', an application tool in MATLAB. To investigate the influence of fiber treatment on fiber size, representative samples of NaOH-treated and untreated fibers were taken and the dimensional change of the fibers was evaluated based on the equivalent diameter. The untreated samples represent any fiber condition including treatments that do not result in any microstructural change, while the NaOH samples represent treatments that bring microstructural change.

2.6 Swelling induced fiber damage

To study the dimensional change due to fiber swelling on the natural fiber composites, the cubic composite samples were first dried in an oven at 60°C until a stable weight was obtained. The samples were then sealed on all four sides with silicone rubber to allow water molecules to only pass through in the fiber direction, then immersed in polypropylene beakers filled with distilled water and kept at room temperature. To establish effective equilibrium moisture conditions and keep the level consistent, the immersed samples were held for 40 days.

Samples were then dried at 60°C until they reached a stable dry weight, then stored in air at 20°C and 50 % RH for another forty days to stabilize the moisture and heat impact. After polishing, microstructural images were taken with a confocal microscope from immersed and non-immersed samples of both treated and untreated images. Through the same procedure of image analysis, the equivalent diameter of the fibers generated and dimensional change was measured by comparing the diameter between the immersed and non-immersed samples.

3. Result and discussion

3.1 Fiber density

The study of fiber density was divided into two steps: step one involved determining the density of the solid component of the fiber and step two involved determining the density of the technical fiber. The density and percentage contribution of the fiber components are obtained from the literature to determine the density of the solid part of the fiber. According to (10,11), the percentage share of cellulose, hemicellulose, lignin, and pectin in Enset fiber is 67 %, 21 %, 6 %, and 6 %, respectively. These fiber components' densities (g/cc) are 1.55, 1.52, 1.33, and 1.52 in that sequence (3). The solid component here symbolizes the secondary cell wall, which comprises cellulose, hemicellulose, and lignin. It is tactically decided to exclude the central lamella from the calculation of density of the solid component simply because its area is defined and hence can help to implement the rule of mixtures to calculate the overall density of the fiber from the components' volume fractions. When the density and percentage contribution of the cell well components are substituted into Eq (1), the density of the secondary cell wall is found to be 1.52 g/cc. Helium Gas Pycnometer, which yields a density of the solid components, was used to validate the result obtained using the rule of mixtures. This method yields a density of 1.46 ± 0.01 g/cc for the fiber. This demonstrates that the 'rule of mixtures' can be considered a candid technique to assess the density of the fiber in the solid component of the fiber.

The density of the technical fiber comprises the central lamella, the lumen, and the secondary cell wall. Figure 2 shows the modeling of the technical fiber and its corresponding elementary fibers. A representative single technical fiber has been first created to find a representative density for the solid component and the complete technical fiber (the fiber that considers the

  doi:10.5075/epfl-298799_978-2-9701614-0-0

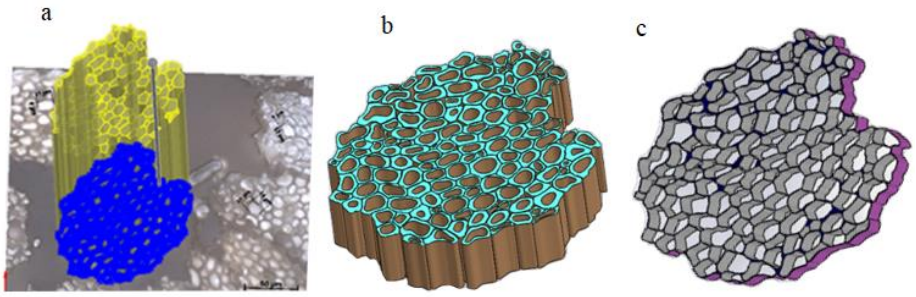

Figure 2. Modeled Fiber microstructure replicated and from the microscopic image of a technical fiber. 3D models of a) technical fiber, b) elemental fibers that show the lumen and the solid components and c) central lamella

lumen structure). Modeling technical fiber involves obtaining the cross-sectional area of the secondary cell wall, lumen, and central lamella. Table 1 demonstrates the cross-sectional area of these constituents. The lumen has a large contribution to the fiber structure which is projected to provide a low density to the technical fiber.

Table 1: The areal contribution of components of the technical fiber

Component	Area (mm^2)	Areal Cont. (%)
Cell wall	5.23E-03	51.9
Central Lamella	9.28E-04	9.2
Lumen	3.92E-03	38.9
Technical Fiber	1.01E-02	100

The density of the technical fiber is then determined by substituting the density of the components and the areal/volume contribution using Eq. (2). Substituting the density and the areal contribution provides a density of 0.93 g/cc for the technical fiber. Three additional technical fibers have been considered and a similar procedure has been carried out which produces a representative average density of 0.94g/cc.

3.2 Effect of fiber treatment on the fiber density

A microstructural image of the treated and untreated fibers is shown in Figure 3. The alkali and alkali-acetylation treatments modified the internal structure of Enset fibers significantly. This implies that alkali-related treatments may have a significant influence on density because they

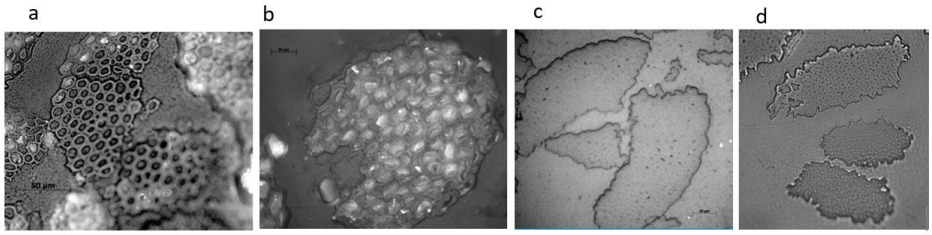

Figure 3: The microstructure of a) untreated fibers, b)acetylated, c)Alkali, and d)Alkali-acetylation treated fiber

collapsed the elementary fibers and increased the volumetric contribution of the solid component significantly. Furthermore, NaOH is said to dissolve hemicellulose which increases the percentage share of cellulose and lignin contents in the fiber. As a result, there will be a small contribution of density difference in the solid component in the untreated and alkali-treated fibers. The interior structures of the fibers, on the other hand, are unaffected by the acetylation treatment. As a result, it is possible to conclude that the treatment of fibers with acetylation does not affect the density of these fibers.

Ray and Sarkar (12) reported the weight loss of fiber components with 5% alkali solution at 2 and 4 hours. By interpolating the weight loss at 3 hours, 0.4%, 9.25% and 0.26% weight reduction were recorded for cellulose, hemicellulose, and lignin, respectively. Considering the same reduction in enset fiber for 3 hrs with alkali and alkali-acetylation treatment and recalculating the percentage share for cellulose, hemicellulose, lignin and pectin can be approximated into 73.93%, 13.04%, 6.37% and 6.57%, respectively. Modifying Eq. (1) into Eq. (3) to include density, ρ_p, and percentage contribution, $\%_p$, of pectin provides the density of alkali and alkali-acetylation treated fibers.

$$\rho_w = \rho_c * \%_c + \rho_h * \%_h + \rho_l * \%_l + \rho_p * \%_p \quad (3)$$

Table 3: Helium gas pycnometer analysis of treated fibers and the density of the fibers calculated from the microstructural analysis of the fiber.

Fibers	Density (g/cc)	
	Pycnometer	Calculated
NaOH treated	1.48 ± 0.01	1.53
NaOH-Acetylation treated	1.49 ± 0.02	1.53
Acetylation treated	1.49 ± 0.02	1.52

On the other hand, the microstructural arrangement of the fibers in the acetylation treatment is identical to that of the untreated ones. As a result, the acetylated fibers' calculated density is the same as the density of the untreated fibers. The density of these treated fibers was also measured using a helium gas pycnometer. Table 3 shows the density of the treated Enset fibers as measured by the pycnometer and the calculated density with the rule of mixtures.

3.3 Fiber dimension, the effect of fiber treatment, and fiber damage due to fiber swelling

The diameter of treated and untreated fibers was measured from the post-processed microscopic image of the fiber structure with the help of MATLAB and an Image analyzer. The accuracy of the post-processing was validated by first extracting the edge of the segmented image and laying it up on the original image. This is needed because morphologic processing of images can show up an increase or decrease in the size of the technical fibers to some amount as the manipulation codes have the power to do so. Figure 4 shows the layup of the extracted edge of the technical fibers from the post-processed microstructural image over the fibers from the same but unprocessed image.

  doi:10.5075/epfl-298799_978-2-9701614-0-0

It is observed that the extracted edges are in good alignment with the microscopic image, and the dimensional data retrieved from the post-processed image is very indicative of true fiber dimensions. The equivalent diameter, which is calculated from the fiber cross-sectional area by assuming a circular shape, is used to characterize the measured size of these fibers because they do not have a circular shape. The equivalent diameter is also used to evaluate the treatment's impact and swelling-induced dimensional changes.

It is reached via this method that the Enset fiber has an average diameter of 97.5 µm (figure 5). The alkali treatment reduced the fiber's equivalent diameter by 42%, which is largely due to collapsing the lumen. On the other hand, because acetylation does not affect the microstructure, the diameter is assumed to be the same as for the untreated fiber.

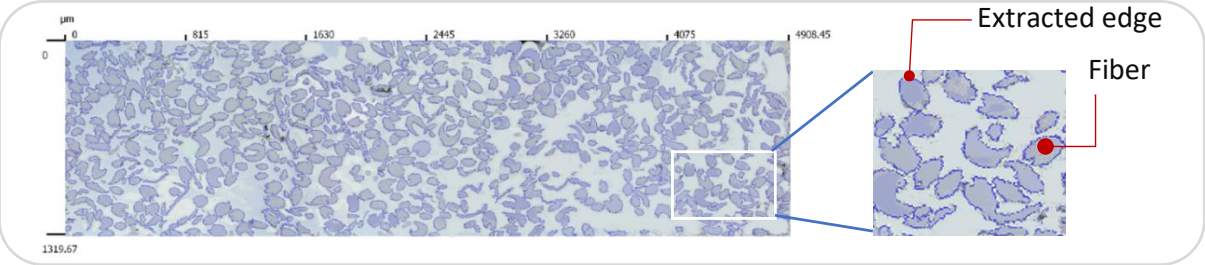

Figure 4: Microstructural image from the confocal microscope with a layup of the extracted edges of the segmented and post-processed image

Figure 5 also demonstrates the fiber's dimensional change as a result of fiber swelling. The fiber diameter of the untreated and alkali-treated fibers increased by 10 % and 9 %, respectively, after swelling. Because the experiment was conducted a considerable time after the sorption and desorption processes, we may classify this impact as hygroscopic-induced persistent fiber damage (5).

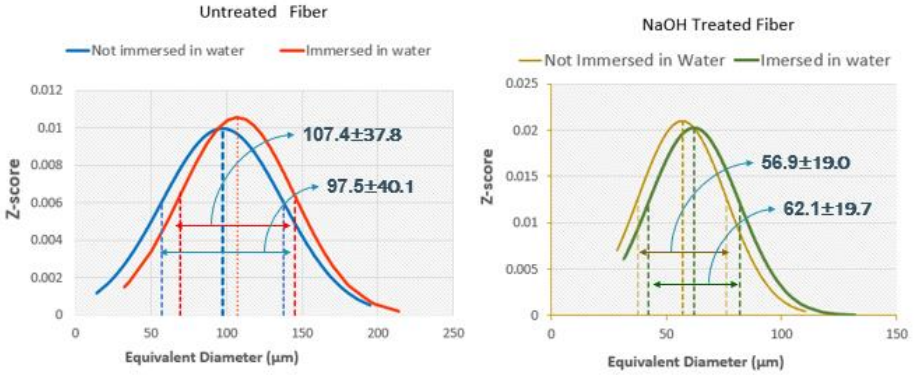

Figure 5: fiber diameter and dimensional change due to fiber treatment and ingression of water molecules

4. Conclusion

In this study, a noble approach was established to study the density of Enset fiber. The density in solid and porous state of the fiber, which is related to considering the contribution of the lumen, was measured using the rule of mixtures. The density of the solid component was measured from the density and percentage contribution of fiber constituents (cellulose, hemicellulose, lignin, and pectin) whereas the density of the technical fiber was determined from the volumetric contribution of the lumen, central lamella, and the secondary cell wall. In

  doi:10.5075/epfl-298799_978-2-9701614-0-0

addition, morphologic image analysis was used to identify the fiber's density and dimensional change due to treatment and swelling. The alkali and alkali-acetylation treatments resulted in significant dimensional reduction due to lumen collapsing and presumed hemicellulose dissolution, whereas the acetylation treatment did not. Furthermore, fiber swelling resulted in a significant permanent alteration in the dimensions of the fiber.

5. References

1. Jaiswal D, Devnani GL, Rajeshkumar G, Sanjay MR, Siengchin S. Review on extraction, characterization, surface treatment and thermal degradation analysis of new cellulosic fibers as sustainable reinforcement in polymer composites. Current Research in Green and Sustainable Chemistry. 2022 Jan 1;5.
2. Truong M, Zhong W, Boyko S, Alcock M. A comparative study on natural fibre density measurement. Journal of the Textile Institute. 2009 Aug;100(6):525–9.
3. Boyer B, Rudie A. Single Fiber Lignin Distributions Based on the Density Gradient Column Method. 2007.
4. Sukmawan R, Kusmono, Rahmanta AP, Saputri LH. The effect of repeated alkali pretreatments on the morphological characteristics of cellulose from oil palm empty fruit bunch fiber-reinforced epoxy adhesive composite. International Journal of Adhesion and Adhesives. 2022 Apr 1;114.
5. Rocha IBCM, Raijmaekers S, Nijssen RPL, van der Meer FP, Sluys LJ. Hygrothermal ageing behaviour of a glass/epoxy composite used in wind turbine blades. Composite Structures. 2017 Aug 15;174:110–22.
6. Cadu T, van Schoors L, Sicot O, Moscardelli S, Divet L, Fontaine S. Cyclic hygrothermal ageing of flax fibers' bundles and unidirectional flax/epoxy composite. Are bio-based reinforced composites so sensitive? Industrial Crops and Products. 2019 Dec 1;141.
7. Péron M, Célino A, Castro M, Jacquemin F, le Duigou A. Study of hygroscopic stresses in asymmetric biocomposite laminates. Composites Science and Technology. 2019 Jan 5;169:7–15.
8. Raju JSN, Depoures MV, Kumaran P. Comprehensive characterization of raw and alkali (NaOH) treated natural fibers from Symphirema involucratum stem. International Journal of Biological Macromolecules. 2021 Sep 1;186:886–96.
9. Kabir MM, Wang H, Lau KT, Cardona F. Chemical treatments on plant-based natural fibre reinforced polymer composites: An overview. Composites Part B: Engineering. 2012 Oct;43(7):2883–92.
10. Berhanu Lemma H, Kiflie Z, Yimam Ali A. Chemical and Morphological Analysis of Enset (Ensete Ventricosum) Fiber, Leaf, and Pseudo stem Deinking of Black Toner Ink from Laser Printed Paper by Using Anionic Surfactant View project Titanium dioxide (TiO2) based photocatalysis for drinking water disinfection under vis-LED and sunlight View project [Internet]. Available from: https://www.researchgate.net/publication/318702231
11. Teli MD, Terega JM. Chemical, Physical and Thermal Characterization of Ensete ventricosum Plant Fibre. International Research Journal of Engineering and Technology [Internet]. 2017; Available from: www.irjet.net
12. Ray D, Sarkar BK. Characterization of Alkali-Treated Jute Fibers for Physical and Mechanical Properties. Vol. 80, J Appl Polym Sci. 2001.

COST-EFFECTIVE HEMP STAPLE FIBRE YARNS FOR HIGH-PERFORMANCE COMPOSITE APPLICATIONS

Nina Graupner[a], David E. Weber[a], Erik G. Bell[b], Karl-Heinz Lehmann[b], Hans-Willi Hilgers[c], Herbert Randerath[b], Thomas Gries[b], Isabel Walenta[d], Marc Joulian[d], Jörg Müssig[a]

a: HSB – City University of Applied Sciences, The Biological Materials Group, Dept. of Biomimetics, Neustadtswall 30, D-28199 Bremen, Germany; nina.graupner@hs-bremen.de
b: Institut für Textiltechnik of RWTH Aachen University, Otto-Blumenthal Straße 1, D-52074 Aachen, Germany
c: Wenzel & Hoos GmbH, Berliner Straße 35, D-36304 Alsfeld-Leusel, Germany
d: INVENT GmbH, Christian-Pommer-Straße 47, D-38112 Braunschweig, Germany

Abstract: *The present study deals with the development of yarns from cost-effective hemp from a disordered separation process (total fibre line) for the use in composite materials. Yarns from the rotor spinning process and yarns with almost unidirectional fibre orientation in the core (staple fibre yarn) were produced from hemp fibre bundles. Composites in the form of round and rectangular rods were made from the yarns using a miniature pultrusion process to analyse the reinforcing effect compared to a flax staple fibre yarn produced in a previous study. The results show that around 90% of the flexural strength and flexural modulus of identically produced flax composites could be achieved. The yarns were additionally used to create quasi-unidirectional fabrics to produce composite laminates by using vacuum infusion, resin transfer moulding and a resin injection process in an autoclave. Hybrid materials were also produced from glass and hemp fabrics. The characteristic values of hemp and hemp/glass laminates are sufficient to use these materials in applications with higher mechanical requirements.*

Keywords: staple fibre yarn, rotor yarn, quasi-unidirectional fabric, hemp, mechanical properties, hybrid hemp/glass composites

1. Introduction

Increasing environmental awareness and finite fossil resources lead to a growing use of renewable raw materials in the composites sector [1]. Their biological origin mainly drives the use of hemp fibres in various applications. In general, natural fibres show benefits for the environment like biodegradability, renewability of base material, and reduction in emission of greenhouse gasses [2]. Bast fibres like hemp display comparatively high strength and stiffness compared to many other vegetable fibres [3]. In recent years increasing attention on using bast fibres for higher loaded applications occurred. In particular, flax fibres and flax fibre-reinforced plastics were examined in detail [4,5]. Compared to flax, hemp fibres are often more difficult to handle. An overview of steps to be taken for using hemp in high-performance composites is given in [5].

A major disadvantage of bast fibre-reinforced plastics, and hemp fibre-reinforced composites (HFCs) in particular, is a relatively low toughness which is significantly lower compared with glass fibre-reinforced composites (GFC) [6], often limiting their use to applications that do not have to withstand high impact loads. Damping properties of bast fibre-reinforced composites are usually better than GFC [7]. Hybrid materials are now being used with increasing frequency for

  doi:10.5075/epfl-298799_978-2-9701614-0-0

highly stressed composite materials to minimise the disadvantages of HFC and GFC. Above all, the toughness of HFC and the damping behaviour of GFC can be significantly improved by hybridisation.

Another big problem with the industrial use of bast fibres for high-value applications is the high price of semi-finished products. Currently, long flax is used for highly stressed natural fibre-reinforced components, which is very cost-intensive due to the complex and intense harvesting and processing technology. The semi-finished product costs can almost reach the level of carbon fibre semi-finished products [8]. In a previous study, we have already shown that comparable composite characteristics can be achieved with less expensive flax from tow by producing an alternative staple fibre yarn compared to composites produced by a unidirectional flax roving available at the market [9,10]. It is well known that the twist of ring-spun yarns prevents the full utilisation of the fibre reinforcement potential in a composite [11]. Therefore, the developed staple fibre yarn possesses an almost unidirectional fibre orientation. The yarn costs are significantly lower compared to low-twist yarns or rovings available on the market. Hemp may provide approximately comparable mechanical properties to flax. Compared with the previously used flax tow, it is even cheaper (~1.0 €/kg compared to ~1.4 €/kg for flax) [10]. The aim of the present study was to reach 80% of the properties of the flax-reinforced composites. A detailed description of the results can be found in [10].

2. Materials and methods

Raw hemp fibre bundles (USO 31; Planéte Chanvre, Aulnoy, FR) were processed into slivers, yarns, fabrics, and composites. Fibres and fibre bundles were prepared from the yarns and characterised regarding their width, length, and tensile characteristics to analyse the influence of the different processing steps. The reinforcing effect of the developed yarns is verified by testing unidirectional composites produced by pultrusion and compared with the results of the previously developed flax staple fibre yarn [9]. Laminates of hemp fabrics and hybrids of hemp and glass fabrics were produced with project partners from the industry by vacuum infusion, resin-transfer-moulding (RTM) and a resin injection process in an autoclave. Thermosetting epoxy matrices were used for composite production. Composites were analysed with bending, unnotched Charpy impact, tensile and short beam shear tests. A detailed description of applied materials and methods can be found in [10]. Composites were produced from different semi-finished products and by different processes:

- Pultruded yarns and rovings (fibre mass fraction of round rods: ~40% and of rectangular rods: ~30%):
    - Rotor yarn version 1 (V1), 588 tex
    - Rotor yarn version 2 (V2), 550 tex
    - Rotor yarn version 3 (V3), 604 tex
    - Rotor yarn version 4 (V4), 581 tex
    - Staple fibre yarn version 1 (V1), 294 tex
    - Staple fibre yarn version 2 (V2), 285 tex
    - Flax staple fibre yarn version 9 (V9), 200 tex

  doi:10.5075/epfl-298799_978-2-9701614-0-0

- Processed fabrics (vacuum infusion, resin transfer moulding, resin injection in an autoclave; fibre volume fraction: ~30-40%):
    - Fabric from staple fibre yarn V2, processed by vacuum infusion (4 layers), autoclave injection (4 layers) and RTM (4 layers)
    - Flax fabric from flax yarn V9, processed by vacuum infusion (4 layers) and autoclave injection (5 layers)
    - Glass fabric, processed by vacuum infusion (6 layers), autoclave injection (9 layers) and RTM (9 layers)
    - Hybrid - glass and hemp fabric, processed by vacuum infusion (1 layer glass, 3 layers hemp, 1 layer glass), autoclave injection (1 layer glass, 3 layers hemp, 1 layer glass) and RTM (1 layer glass, 3 layers hemp, 1 layer glass)

3. Results and discussion

3.1 Influence of processing on the fibre properties

The influence of the different processing steps during yarn and fabric production on fibre bundle length, width and tensile properties was analysed. Results have shown that raw hemp consists of coarse fibre bundles with lengths partly higher than 25 cm. The following production of the slivers resulted in significant refinement of the fibre bundles and a related shortening. The spinning process led to a further slight shortening, whereas further processing into fabric did not result in any further change of length. The fibre lengths in the rotor yarns are significantly shorter compared with the staple fibre yarns. Nevertheless, the length values (~5cm) are clearly higher than the critical fibre length required to reinforce a thermosetting composite. At the same time, the width appeared to be lower compared to the fibre bundles from the staple fibre yarn. The fibre bundle lengths from the hemp staple fibre yarn are slightly higher than the fibre bundle lengths from the flax staple fibre yarn. It follows that hemp could be processed with similar care as flax. Compared to the fibre bundles from the flax staple fibre yarn with a median value of 24.0 µm, the fibre bundles in the hemp staple fibre yarn are significantly coarser with a median width of 36.3 µm. The analysis of the tensile properties showed that the processing did not significantly change mechanical properties. I.e. the manufacturing process of the yarns is protective enough not to damage the fibres.

3.2 Reinforcing potential of the yarns

In order to analyse the reinforcing effect of the different yarns, unidirectional fibre composites were produced using the pultrusion process with an epoxy matrix [9]. Round samples with a fibre volume fraction of approx. 40% and rectangular samples with a fibre volume fraction of approx. 30% were produced. The pultruded samples were analysed by impact and bending tests.

The results of the unnotched Charpy impact strength are shown in Figure 1. The data of the samples from the rotor yarns and the unidirectional staple fibre yarns from hemp are compared with the results of the composites produced from flax staple fibre yarns. The results of the round and rectangular rods show the same trend. Due to the lower fibre content, the values of the rectangular rods are slightly lower than those of the round rods. No hemp yarn could achieve the impact strength of the flax-reinforced sample. The rotor yarn reached 43% and 46% of the impact strength of flax with the round and rectangular samples, respectively. The hemp staple

  doi:10.5075/epfl-298799_978-2-9701614-0-0

fibre yarn V2 shows the highest values achieving 56% and 63% of the impact strength of the round and rectangular flax samples.

The fibre orientation plays an essential role in the mechanical characteristics of fibre-reinforced composites [11]. While staple fibre yarns show nearly no twist, the rotor yarns have a twist which is assumed to be the main reason for the different impact strength values.

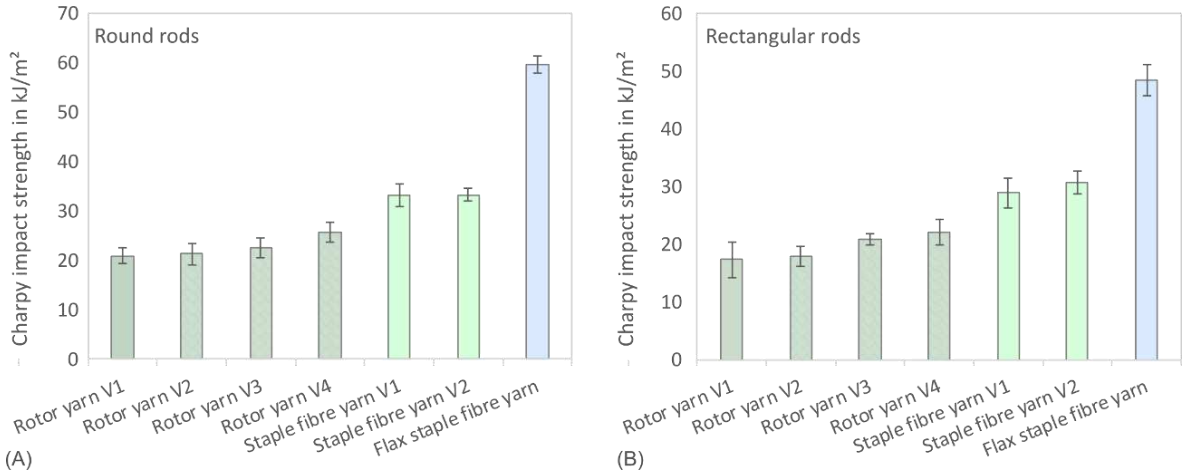

Figure 1. Unnotched Charpy impact strength (mean value ± standard deviation) of pultruded round rods with a fibre volume fraction of 40% (A) and rectangular rods with a fibre volume fraction of 30% (B) [Results from previously published study [10]]

The bending properties are summarised in Figure 2. As described for the impact strength, similar trends are obtained for the different test specimen geometries. Due to the lower fibre volume fraction of rectangular specimens of 30% compared to 40% of the round rods, the characteristic values of rectangular rods are lower (Figure 2A & C). Compared to the impact strength, the reinforcement effect of the hemp yarns is considerably better. The flax-reinforced composite provides the highest characteristic values with 290 MPa for the round rods and 210 MPa for the rectangular rods. However, the hemp staple fibre yarn V2 also provides good characteristic values, with 282 MPa for the round rods and 186 MPa for the rectangular rods, which corresponds to 97% and 89% of the bending strength of the flax samples, respectively. The rotor yarns V1 and V2 showed the lowest bending strength overall. As described for the impact strength, this effect may be attributed to the high yarn twist angle of approx. 40 °. It can be seen that a lower twist angle of the rotor yarns V3 and V4 (~35 °) leads to slightly higher characteristic values.

The trend described for the flexural strength was also found for the flexural modulus (Figure 2B & D). Likewise, the flax fibre-reinforced composite shows the highest values with 23.5 GPa for the round rods and 14.4 GPa for the rectangular rods. Composites reinforced with the hemp staple fibre yarns come very close, reaching values of 23.4 GPa for the staple fibre yarn V2 and 12.9 GPa for the rectangular rods, corresponding to 99.6% and 89.4% of the properties of the flax composite. The bending moduli of the composites reinforced with the rotor yarns were significantly lower, with a trend towards slightly higher characteristic values when using the yarns with the lower twist angle (rotor yarns V3 and V4).

In summary, the best reinforcement effect for the staple fibre yarn V2 with bending strengths of 282 and 186 MPa and bending moduli of 23.4 and 12.9 GPa was achieved for the round rods

  doi:10.5075/epfl-298799_978-2-9701614-0-0

with 40% fibre volume content and the rectangular rods with 30% fibre volume content, respectively. The hemp staple fibre yarns exceeded the goal of achieving a reinforcement effect of at least 80% of the flax yarns in terms of bending properties.

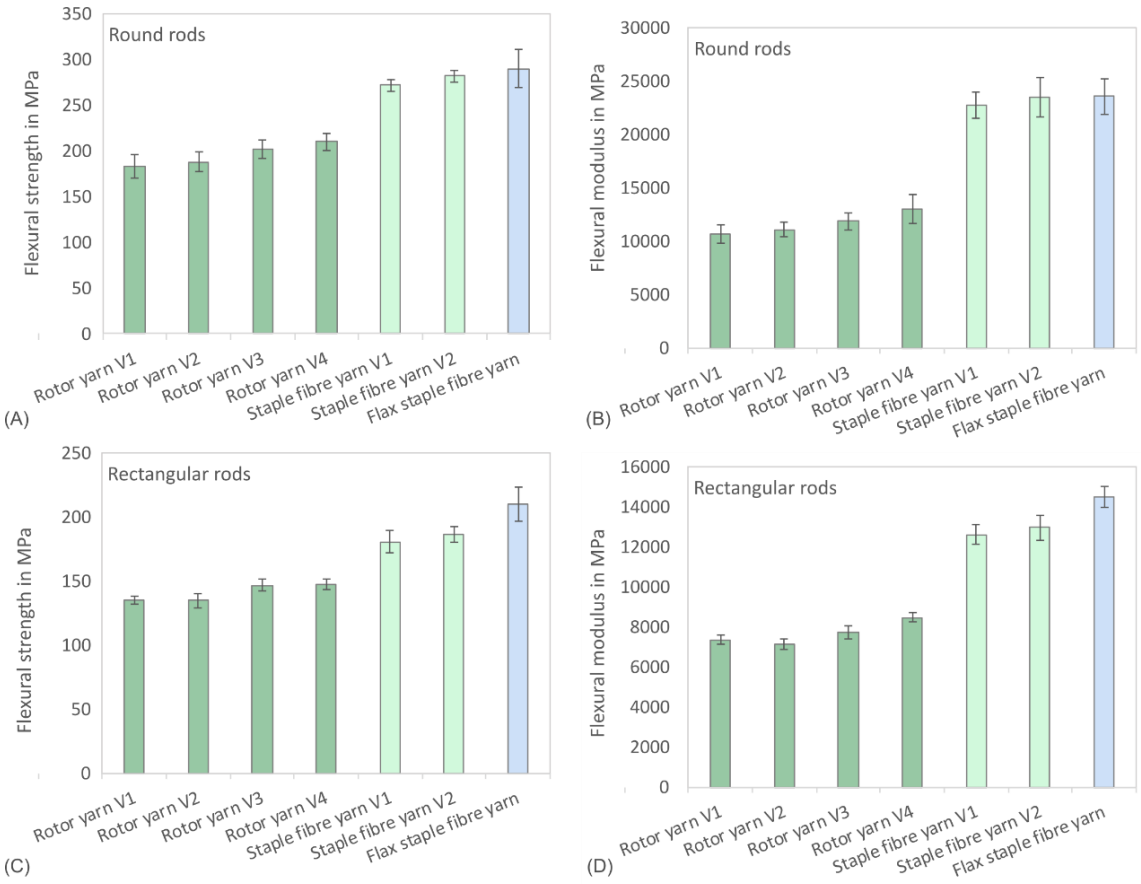

Figure 2. Flexural strength and flexural modulus (mean value ± standard deviation) of pultruded round rods with a fibre volume fraction of 40% (A & B) and rectangular rods with a fibre volume fraction of 30% (C & D) made from yarns obtained from different stages of development [Results from previously published study [10]]

3.3 Composite laminates

Fabrics were processed by vacuum infusion with an epoxy resin and by autoclave injection and RTM with a bio-based epoxy (PTP-L). For the combination of the properties of hemp and glass fibres, hybrid materials were also produced, and a glass fibre-reinforced laminate was used as a reference sample. The autoclave injection process leads to significantly higher fibre volume fractions (39-43%) than the vacuum infusion (29-31%) and the RTM process (30-38%).

The tensile properties of the different laminates produced are shown in Figure 3. As expected, the glass laminates offer the highest tensile strength and Young's modulus values. The hemp laminates, which were produced using the vacuum infusion and the RTM process, show comparable characteristics with tensile strengths around 150 MPa and Young´s moduli between 16.1 and 16.7 GPa (Figure 3A, B, E, F). The strength and Young's modulus values of the hemp laminates from the autoclave injection process are slightly higher (154 MPa and 19.4 GPa), presumably due to the higher fibre volume content (Figure 3C & D). The hemp laminate produced in the autoclave injection process achieved 72% of the strength and 90% of Young's

  doi:10.5075/epfl-298799_978-2-9701614-0-0

modulus of the flax laminate. The vacuum infusion process yields 78% and 99% of the strength and Young's modulus of the flax laminate. Hybrid laminates clearly show higher characteristic values but significantly lower values than the GFC.

The reinforcement effect is additionally affected by the crimp of the fabrics. It was shown in a previous study that the flax yarns, processed in the same way as the hemp yarns, were not completely aligned, and some crimp was present in the fabric [9]. Due to the lower fineness of the hemp yarns (300 tex) compared to the flax yarns (200 tex), it is assumed that the crimp may be more pronounced, and the reinforcing effect of the hemp yarns in the fabric is slightly reduced.

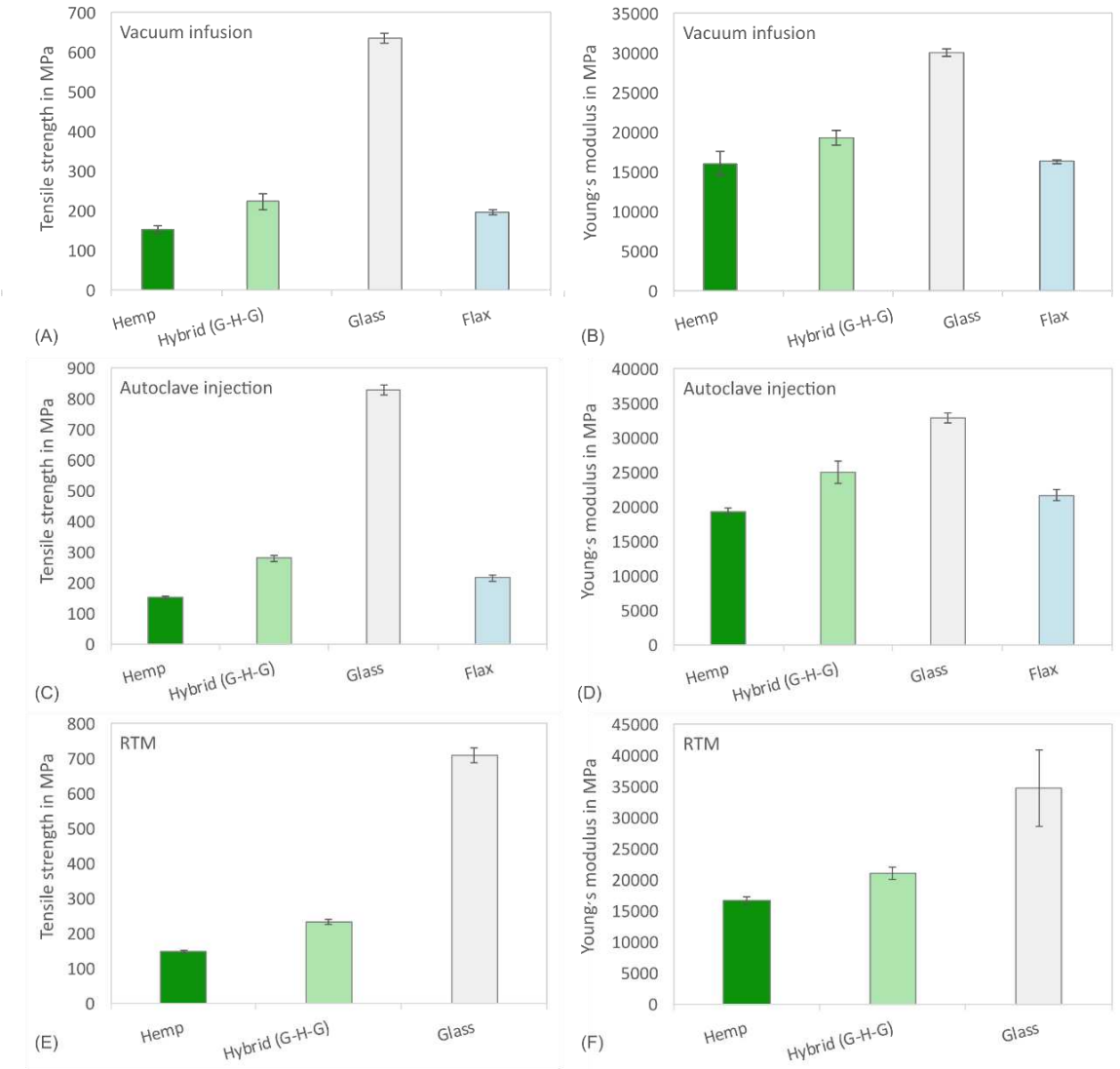

Figure 3. Tensile strength and Young´s modulus (mean value ± standard deviation) of composite laminates produced by vacuum infusion (A & B), autoclave injection (C & D) and RTM (E & F) [Results from previously published study [10]]

The results of the unnotched Charpy impact strength of composite laminates are shown in Figure 4. The glass fibre-reinforced laminates offer the highest characteristic values. It is known that GFC have a higher toughness compared with bast fibre-reinforced composites, especially hemp fibre-reinforced plastics [6], and the fracture behaviour is different [12]. The impact strength of

  doi:10.5075/epfl-298799_978-2-9701614-0-0

the hemp laminates ranges between 10 kJ/m² for the laminate produced with the RTM process and 24 kJ/m² for the laminate manufactured with the autoclave injection process.

Compared to the tensile properties, it is noticeable that the use of hybrid materials leads to a more significant improvement in impact strength than the hemp laminate. As described for the round and rectangular rods, the hemp fibre bundles in the laminates also lead to low impact strength than the flax fibre-reinforced laminates. For the laminates produced in the autoclave injection process and vacuum infusion process, the impact strength corresponds only to 57% and 52% to the values of the flax fibre laminate.

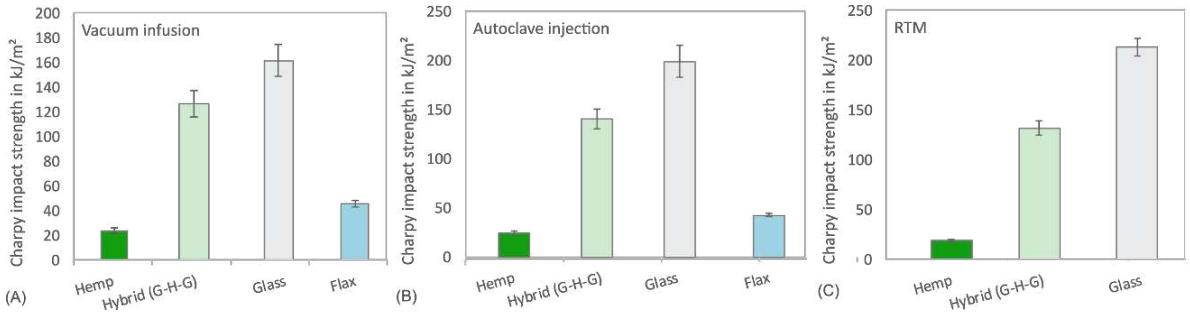

Figure 4. Unnotched Charpy impact strength (mean value ± standard deviation) of composite laminates produced by vacuum infusion (A), autoclave injection (B) and RTM (C) [Results from previously published study [10]]

4. Summary and conclusions

The aim was to achieve at least 80% of the reinforcing potential of comparable flax composites. It has been shown that the fibre bundles in the staple fibre yarns with almost unidirectional fibre orientation were considerably less shortened by the spinning process than the fibre bundles in the rotor yarns. Nevertheless, the rotor yarns contained fibre bundles with considerably higher lengths than the critical fibre length necessary to reinforce composites. However, in contrast to the staple fibre yarns, the rotor yarns exhibited a rather large twist. Therefore, the reinforcing effect of the staple fibre yarns was significantly higher. With the staple fibre yarns, the aim was achieved for the tensile and bending properties and was in some cases even considerably exceeded for the unidirectional pultruded composites. The impact properties represented a deficit. The unnotched Charpy impact strength only ranged between 50 and 60% of the flax composites.

Quasi-unidirectional fabrics were manufactured from the staple fibre yarns and processed into composite laminates. The achieved tensile and bending properties were relatively high. It is expected that these can be further increased with an improved fabric structure. The present crimp leads to a reorientation of the fibres and thus reduces the reinforcement effect.

The development of hybrid materials from hemp and glass is a solution to improve the low toughness of hemp laminates. At the same time, tensile and bending properties increased, whereas the damping properties of glass laminates will probably be improved.

In the overall consideration, it could be shown that good semi-finished textile products can be produced with cost-efficient hemp from the disordered fibre line, which leads to good tensile and bending properties for use in components subject to higher loads.

  doi:10.5075/epfl-298799_978-2-9701614-0-0

Acknowledgements

Our special thanks go to our project partners, without whom we would not have been able to realise the project: Novacom Verstärkte Kunststoffe GmbH (Lisa Bruns, Luisa Berger & Albert Bruns), SachsenLeinen GmbH (Torsten Brückner & Kay Kölzig) & BAFA Neu GmbH (Bernd Frank). Moreover, we would like to thank our student co-workers Alexander Behrens, Steffen Deutsch, Charlotte Spelsberg, Julia Kubitz and Timo Acktun, who supported us with practical experiments during the project.

5. References

1. Tanasă, F., Zănoagă, M., Teacă, C.-A., Nechifor, M., Shahzad, A. Modified hemp fibers intended for fiber-reinforced polymer composites used in structural applications - a review. i. methods of modification 2020, *Polymer Composites*, 41(1):5–31
2. Thyavihalli Girijappa, Y.G., Rangappa, S.M., Parameswaranpillai, J., Siengchin, S. Natural fibers as sustainable and renewable resource for development of eco-friendly composites: A comprehensive review 2019 *Frontiers in Materials*, 6:226
3. Müssig, J. *Industrial applications of natural fibres: structure, properties and technical applications 2010,* John Wiley & Sons, Ltd., Chichster, UK, 1. Edition
4. Baley, C., Gomina, M., Breard, J., Bourmaud, A., Davies, P. Variability of mechanical properties of flax fibres for composite reinforcement. a review 2020, *Industrial Crops and Products*, 145:111984
5. Müssig, J., Amaducci, S., Bourmaud, A., Beaugrand, J., Shah, D.U. Transdisciplinary top-down review of hemp fibre composites: From an advanced product design to crop variety selection 2020, *Composites Part C: Open Access*, 2:100010
6. Patel, H., Ren, G., Hogg, P. J., Peijs, T. Hemp fibre as alternative to glass fibre in sheet moulding compound. Part 2 – impact properties. Plastics 2015, *Rubber and Composites*, 44(7):291–298
7. Buksnowitz, C., Adusumalli, R., Pahler, A., Sixta, H., Gindl, W. Acoustical properties of lyocell, hemp, and flax composites 2010, *Journal of Reinforced Plastics and Composites*, 29 (20):3149–3154
8. Deimann, F. Personal communication with Mr. Friedrich Deimann about prices for biaxial flax fabrics from 13.11.2020, 2020.
9. Graupner, N., Lehmann, K.-H., Weber, D. E., Hilgers, H.-W., Bell, E. G., Walenta, I., Berger, L., Brückner, T., Kölzig, K., Randerath, H., Bruns, A., Frank, B., Wonneberger, M., Joulian, M., Bruns, L., von Dungern, F., Janßen, A., Gries, T., Kunst, S., Müssig, J. Novel Low-Twist Bast Fibre Yarns from Flax Tow for High-Performance Composite Applications 2021, 14(1): 105
10. Graupner, N., Weber, D.E., Bell, E.G., Lehmann, K.-H., Hilgers, H.-W., Randerath, H., Gries, T., Walenta, I., Joulian, M., Müssig, J. Hemp From Disordered Lines for New Staple Fibre Yarns and High-Performance Composite Applications 2022; 8: 807004
11. Zhang, L., Miao, M. Commingled natural fibre/polypropylene wrap spun yarns for structured thermoplastic composites 2010, *Composites Science and Technology*, 70(1):130 – 135
12. Cordin, M., Bechtold, T., Pham, T. Effect of fibre orientation on the mechanical properties of polypropylene-lyocell composites 2018 *Cellulose*, 25(12):7197–7210
13. Bonnafous, C., Touchard, F., Chocinski-Arnault, L. Damage mechanisms in hemp-fibre woven fabric composite, and comparison with glass-fibre composite 2011, *Polymers and Polymer Composites*, 19(7):543–552

  doi:10.5075/epfl-298799_978-2-9701614-0-0

INFLUENCE OF WET/DRY CYCLING ON MECHANICAL PROPERTIES OF HEMP-REINFORCED BIOCOMPOSITES

Quentin, Drouhet[a], Fabienne, Touchard[a], Laurence, Chocinski-Arnault[a]

a: Département Physique et Mécanique des Matériaux
Institut Pprime, CNRS – ISAE-ENSMA – Université de Poitiers
1, Avenue Clément Ader, 86961 Futuroscope Chasseneuil, France
quentin.drouhet@ensma.fr

Abstract: *The interest of manufacturers in natural fibers as reinforcements in composite materials is growing due to global warming and environmental policies. The hydrophilic behavior of natural fiber-reinforced composites must be taken into account for structural applications using these types of materials. This study aims to assess the effect of water absorption fatigue on the mechanical properties of hemp-reinforced biocomposites. In order to simulate the service conditions to which the materials could be subjected, a series of wet/dry cycles is applied. Three different polymers are used as matrices in hemp-reinforced biocomposites: Epolam, Greenpoxy and Elium. The absorption behavior of these composites during wet/dry cycles is studied. Mechanical tests and X-Ray microtomography analyses are performed for different numbers of wet/dry cycles to better understand the damage evolution. Results show that the water absorption fatigue leads to interfacial damage, which degrades the mechanical properties of such hemp composites, whatever the resin used.*

Keywords: Wet/dry cycling; water absorption; mechanical properties; micro-CT; damage

1. Introduction

The study of biocomposites is more and more developed for structural applications, especially for the energy and transport industry. Indeed, global warming and environmental policies imply a growth in the use of natural fibers as reinforcements [1,2]. Hemp fibers are ones of the less environmentally damaging to manufacture biocomposites and compete with synthetic fibers as for glass/epoxy composites [3,4]. The thermoset resins usually used to manufacture glass/epoxy composites come from non-recyclable fossil resources. So, alternative resins have to be taken into account. In this study, the three matrices used are Epolam 2020, Greenpoxy 56 and Elium 188. The first one is an epoxide resin, traditionally used in glass-reinforced composites. Greenpoxy 56 is also a thermosetting resin, but it is partially bio-based; 56% of its carbon atoms are biosourced [5,6]. Elium 188 is a liquid methylmethacrylate thermoplastic. The high interest in this last polymer is its recyclability and its thermoformability [7,8]. According to the manufacturer, this thermoplastic polymer is equivalent to an epoxide thermoset in terms of mechanical properties. One of the major issues in the use of plant fiber-reinforced biocomposites is the lifetime of these materials in outdoor applications. In fact, the hydrophilic behavior of natural fibers compared with the hydrophobic behavior of the polymer matrix has to be taken into account. The absorption of the environmental humidity by fibers implies damage at the interface, such as debonding between fiber and matrix [9]. This has a direct consequence on the mechanical properties [10,11]. Some studies also analyze the effect of the temperature of water immersion [12,13]. In this paper, the aim is to analyze the consequences of several wet/dry cycles on mechanical properties and on damage mechanisms in hemp-

  doi:10.5075/epfl-298799_978-2-9701614-0-0

reinforced biocomposites. The aging conditions consist in immersing samples in 60°C water until reaching the maximum water uptake (during twelve days) and drying these specimens for two days at 40°C. In this paper, the results obtained for two aging states are presented: after one wet/dry cycle and after ten wet/dry cycles. All results are compared to the reference state called "Ambient storage" which consists in storing samples at room temperature and humidity.

2. Materials and methods

2.1 Tested materials

The three studied materials are made of seven plain-woven plies of the same hemp fabric with an areal density of 290 ± 10g/m². Different matrices are used. One matrix is an epoxide thermoset polymer called Epolam 2020 produced by the company *Axson Technologies*. The second matrix is also an epoxide thermoset polymer. This one is provided by the company *Sicomin* and it is a partially bio-based resin, named Greenpoxy 56. The third matrix of the study is a thermoplastic polymer, Elium 188, developed by the company *Arkema*. Some properties of raw materials are provided in Table 1. The vacuum infusion process has been used for the manufacturing of the composite plates and appropriate heat treatments have been carried out for each biocomposite. Hemp/Epolam plates were cured for 3 hours at 40°C, 2 hours at 60°C, 2 hours at 80°C and 4 hours at 100°C. Hemp/Greenpoxy plates were cured for 24 hours at 40°C, 16 hours at 60°C, 8h hours at 80°C and 30 minutes at 95°C. Hemp/Elium plates were heated for 4 hours at 80°C. Rectangular samples were cut from each plate to get 140mm long, 20mm wide and 4mm thick samples with two different reinforcement orientations (±45° and 0°/90°). The fiber volume fractions V_f have been measured for each sample and they are equal to 40.3 ± 2.4% for Hemp/Epolam, 41.8 ± 1.7% for Hemp/Greenpoxy and 39.7 ± 1.6% for Hemp/Elium.

Table 1. Properties of used materials

	Density ($g.cm^{-3}$)	Young's modulus (GPa)	Strength (MPa)	References
Hemp yarn	1.48	23	601	[14,15]
Epolam 2020	1.16	3.1	69	[9,15]
Greenpoxy 56	1.18	2.8	67	
Elium 188	1.19	3.3	76	Manufacturer's data sheet

2.2 Aging conditions and water uptake modeling

Three different conditionings are considered for this study to analyze the influence of wet/dry cycling on mechanical behavior and damage mechanisms of previously described hemp-reinforced composites:

- "Ambient storage" (AS): samples were stored at room conditions,
- "1 wet/dry cycle" (1 wd): samples were immersed in water at 60 ± 1.5°C for 12 days and dried during 2 days at 40 ± 1.5°C,
- "10 wet/dry cycles" (10 wd): samples were subjected to ten identical wet/dry cycles.

The immersion temperature has been chosen in order to accelerate absorption and to reach water saturation faster than at room temperature. The water uptake of the samples has been

measured with a precision balance during the immersion phases. Weight gain, noted M_t, follows the Eq. (1):

$$M_t = 100 * \frac{m(t) - m_0^i}{m_0^i} \quad (1)$$

where m_0^i is the initial weight of the sample for the wet/dry cycle number i and $m(t)$ is the sample weight at time t. An approximation of the one-dimensional Fick's model has been used [16] (Eq. (2)) and the diffusion coefficient for each wet/dry cycle is expressed by Eq. (3):

$$\frac{M_t}{M_\infty} = 1 - \exp\left(-7.3\left(\frac{Dt}{h^2}\right)^{3/4}\right) \quad (2)$$

$$D = \pi\left(\frac{hk}{4M_\infty}\right)^2 \quad (3)$$

where M_∞ is the maximum of weight gain, D is the Fick diffusion coefficient (mm²/s), h is the thickness of the sample (mm) and k is the initial slope of the M_t-$\sqrt{t}$ curve.

2.3 Mechanical tests

All the mechanical tests have been carried out in ambient conditions by using an *Instron 5982* tensile machine with a crosshead speed of 0.5mm/min. A 12.5mm gauge length extensometer has been used to measure the axial strain. In order to take into account the variation of the composites geometry due to the aging conditions, the sample section was measured just before each mechanical test.

2.4 Micro-CT

An *UltraTom CT* scanner manufactured by the company *RX Solutions* has been used to perform image acquisitions. In this study, the voxel size was 15µm and a voltage of 50kV was used. To obtain this resolution, four hours of image acquisition are required for each sample. An algorithm based on the filtered back-projection procedure for Feldcamp cone-beam geometry has been applied for the reconstruction.

3. Results and discussion

3.1 Water uptake and Fick's law

The water absorption curves measured during ten wet/dry cycles are shown in Figure 1 for the three different materials. It has been observed that the reinforcement orientation (±45° or 0°/90°) does not influence these curves. Therefore, only one example for each material is plotted in Figure 1. Weight variations are normalized by the fiber volume fraction to consider differences in fiber content between the samples and the X-axis is the square root of time (in seconds) normalized by the thickness (in millimeters) of the specimens. To plot Figure 1, weight gain M_t is calculated from Eq. (1) using m_0^1, the initial weight before the first wet/dry cycle. Figure 1 shows that the wet/dry cycle parameters chosen allow to reach the water saturation in less than twelve days and samples are almost dry after two days in an oven at 40°C. It also appears that the duration to reach the maximum water absorption stiffly decreases. Indeed, time to reach 95% of the saturation in water decreases by almost 30% for Hemp/Epolam and Hemp/Greenpoxy specimens and it decreases by 60% for Hemp/Elium samples. Despite this, whatever the number of wet/dry cycles, the diffusion properties of the composites studied follow a Fickian behavior.

  doi:10.5075/epfl-298799_978-2-9701614-0-0

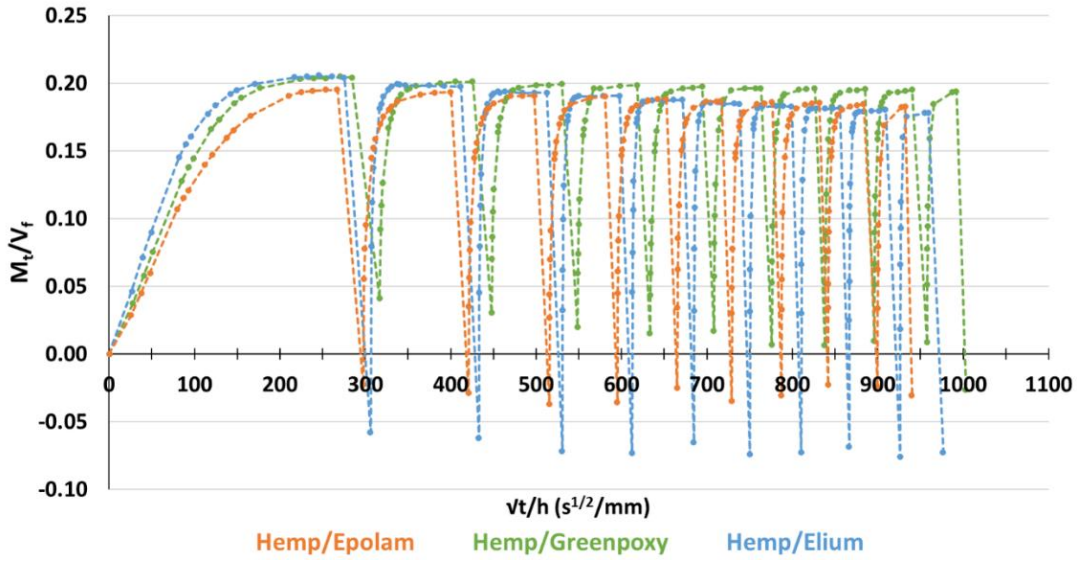

Figure 1. Weight variations normalized by fiber volume fraction during ten wet/dry cycles for the three biocomposites studied.

The values of the maximum weight gain normalized by fiber volume fraction (M_∞/V_f) and of the Fick's diffusion coefficient have been determined. The comparison of the values obtained after one wet/dry or ten wet/dry cycles shows that there is an increase in M_t/V_f of about 25% for Hemp/Epolam samples ($\left(M_\infty/V_f\right)_1 = 0.218$; $\left(M_\infty/V_f\right)_{10} = 0.262$) and for Hemp/Elium ones ($\left(M_\infty/V_f\right)_1 = 0.219$; $\left(M_\infty/V_f\right)_{10} = 0.283$). For Hemp/Greenpoxy specimens, results are different: there is no significant variation in the maximum weight gain ($\left(M_\infty/V_f\right)_1 = 0.202$; $\left(M_\infty/V_f\right)_{10} = 0.204$)). It also appears that the diffusion coefficient drastically increases between the first and the tenth immersion for all biocomposites. For Hemp/Epolam specimens, the diffusion coefficient is multiplied by eight, it is multiplied by eleven for Hemp/Elium samples and 'only' by five for Hemp/Greenpoxy ones. Therefore, the water absorption behavior of the Hemp/Greenpoxy samples seems to be less sensitive to the wet/dry cycles than the one of the two other materials.

3.2 Tensile behavior

Tensile tests have been proceeded to characterize the mechanical properties of $[\pm45°]_7$ and $[0°/90°]_7$ biocomposites for the three different conditionings: "Ambient storage" (AS), "1 wet/dry cycle" (1wd) and "10 wet/dry cycles" (10wd). The obtained stress-strain curves for 0°/90° orientation are shown in Figure 2. Young's moduli of each biocomposite for all the conditionings and orientations are summarized in the bar chart in Figure 3. The values of strength and axial strain at failure are given in Table 2 for $[0°/90°]_7$ biocomposites and in Table 3 for $[\pm45°]_7$ ones.

First, mechanical properties of the three biocomposites at ambient storage are discussed. For $[0°/90°]_7$ samples, all strains at failure are similar and equal to about 3%. Hemp/Epolam and Hemp/Greenpoxy samples have almost the same Young's modulus and maximum stress. Young's modulus of Hemp/Elium is slightly lower for ambient storage than the thermoset biocomposites of the study. The strength of Hemp/Elium $[0°/90°]_7$ is 35% lower than for Hemp/Epolam or Hemp/Greenpoxy samples. For $[\pm45°]_7$ specimens, mechanical properties are very close for the three materials.

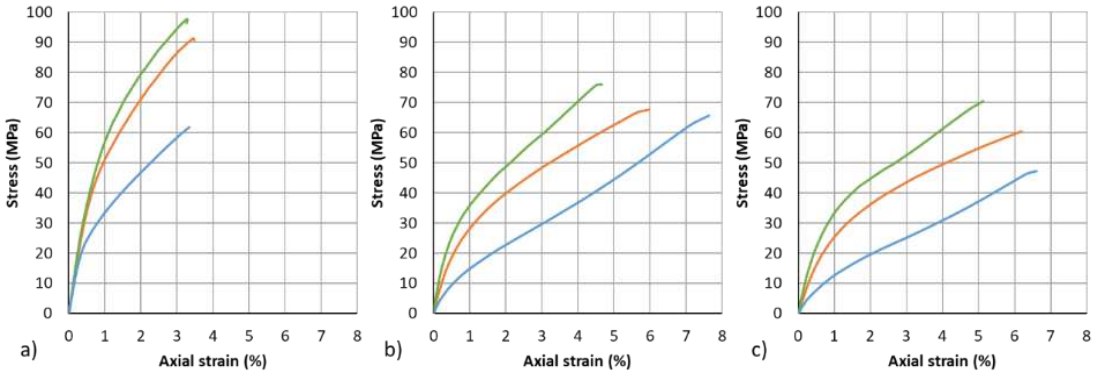

Figure 2. Tensile stress-strain curves of $[0°/90°]_7$ composites after ambient storage a), one wet/dry cycle b) and ten wet/dry cycles c): orange for Hemp/Epolam, green for Hemp/Greenpoxy and blue for Hemp/Elium.

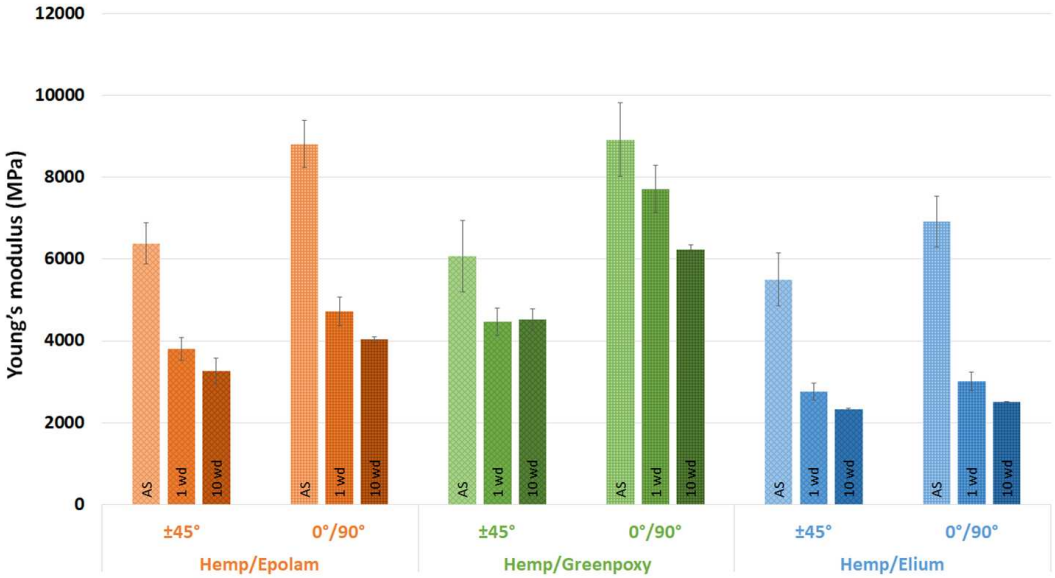

Figure 3. Young's modulus values measured after the three conditionings for the different hemp composites with the two orientations (±45° and 0°/90°).

Then, the influence of one and ten wet/dry cycles on both reinforcement orientations and on the three biocomposites is analyzed. Mechanical properties are differently affected depending on the material. Concerning Young's moduli of $[0°/90°]_7$ composites, Hemp/Epolam loses 45% of its initial value after one cycle and 55% after ten wet/dry cycles. Young's modulus of Hemp/Greenpoxy samples decreases by 13% after one wet/dry and 30% after ten cycles. A high reduction in modulus is observed for Hemp/Elium specimens: -58% and -64% after one and ten wet/dry cycles respectively. The $[±45°]_7$ composites are also affected. There is a drop in Young's moduli of around 45% for Hemp/Epolam, 25% for Hemp/Greenpoxy and 55% for Hemp/Elium (average decrease between one and ten wet/dry cycles).

Regarding the maximum stresses, whatever the reinforcement orientation, Hemp/Epolam and Hemp/Greenpoxy biocomposites lose about 25% after one wet/dry cycle and 30% after ten cycles. The strength of $[0°/90°]_7$ Hemp/Elium is not affected by one wet/dry aging but after ten wet/dry cycles the decrease is about 20%. The drops in strength for [±45°] Hemp/Elium after one and ten wet/dry cycles are quite similar to those of the other biocomposites: -22% and -30% respectively.

  doi:10.5075/epfl-298799_978-2-9701614-0-0

Finally, the strains at failure increase rapidly during the water absorption fatigue. Indeed, whatever the reinforcement orientation, after one and ten wet/dry cycles, the ultimate strain is multiplied by 2 for Hemp/Epolam samples, by 1.6 for Hemp/Greenpoxy specimens and by 2.5 for Hemp/Elium ones.

Table 2: Tensile strength and strain at failure values of the three biocomposites for 0°/90° orientation for ambient storage, one wet/dry cycle and ten wet/dry cycles.

	Strength (MPa)			**Strain at failure (%)**		
	Hemp Epolam	Hemp Greenpoxy	Hemp Elium	Hemp Epolam	Hemp Greenpoxy	Hemp Elium
Ambient storage	93 ± 2	98 ± 5	62 ± 1	3.0 ± 0.3	3.5 ± 0.3	2.7 ± 1.0
1 wet/dry cycle	68 ± 3	76 ± 4	63 ± 3	6.0 ± 0.3	4.7 ± 0.2	7.4 ± 0.4
10 wet/dry cycles	60 ± 1	71 ± 1	48 ± 1	6.2 ± 0.3	5.2 ± 0.1	6.6 ± 0.1

Table 3: Tensile strength and strain at failure values of the three biocomposites for ±45° orientation for ambient storage, one wet/dry cycle and ten wet/dry cycles.

	Strength (MPa)			**Strain at failure (%)**		
	Hemp Epolam	Hemp Greenpoxy	Hemp Elium	Hemp Epolam	Hemp Greenpoxy	Hemp Elium
Ambient storage	59 ± 2	56 ± 3	54 ± 1	3.9 ± 0.1	4.0 ± 1.1	5.3 ± 0.6
1 wet/dry cycle	44 ± 2	46 ± 2	42 ± 2	6.8 ± 0.3	6.7 ± 0.4	12.6 ± 0.6
10 wet/dry cycles	40 ± 1	41 ± 1	38 ± 1	9.1 ± 0.9	7.8 ± 1.0	13.2 ± 0.3

3.3 Damage observations

X-ray microtomography analyzes have been carried out to better understand the damage evolution during the water absorption fatigue. Figure 4 presents examples of pictures obtained for the three $[0°/90°]_7$ biocomposites of the study for ambient storage and ten wet/dry cycles after tensile tests. The images shown are from the core of each sample. The horizontal x-axis represents the direction of the tensile loading and the z-axis corresponds to the sample thickness.

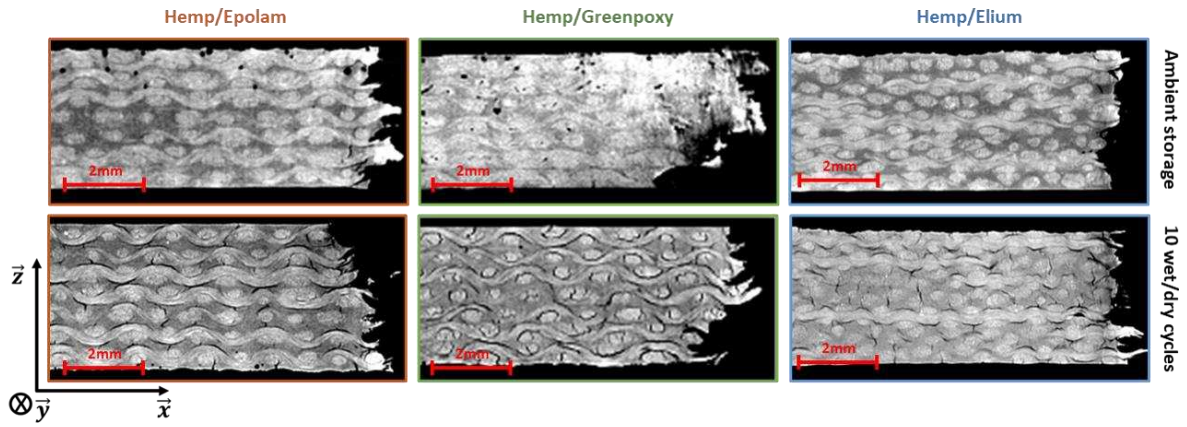

Figure 4. Micro-CT images of the three different biocomposites (orientation 0°/90°) after tensile testing for two conditionings: ambient storage and ten wet/dry cycles.

Micro-CT observations show that some specimens contain pores due to the manufacturing process. For example, it is the case for the Hemp/Epolam and Hemp/Greenpoxy samples with AS condition presented in Figure 4. However, there is no specific damage due to the presence of these pores. Figure 4 shows that, for all biocomposites, the damage is localized in the failure zone for AS conditioning. On the opposite, after 10 wet/dry cycles, the damage is present all along the observed zone of the samples. Debonding at fiber/matrix interfaces and matrix cracks are observed. Damage is far more developed than for ambient storage condition, demonstrating the role of wet/dry cycles on damage mechanisms. The water absorption fatigue leads to the degradation of the fiber/matrix interfaces, facilitating the development of damage during the tensile tests. This explains the decrease in the mechanical properties of the materials.

4. Conclusion

In this study, the influence of wet/dry cycles on three different biocomposites - Hemp/Epolam, Hemp/Greenpoxy and Hemp/Elium - with two orientations (0/90 and ±45) was analyzed. The applied wet/dry cycle consisted in two phases: immersion of the samples in water at a temperature of 60°C during twelve days and drying of the samples in an oven at 40°C for two days. A Fickian behavior was observed whatever the biocomposite and the number of wet/dry cycles. The duration to reach 95% of the saturation in water decreases between one and ten wet/dry cycles for all the biocomposites. The maximum water uptake of Hemp/Epolam and Hemp/Elium for the tenth wet/dry cycle is higher than for the first wet/dry cycle, whereas it remains similar for Hemp/Greenpoxy. At the same time, the diffusion coefficients are all increased with the number of cycles. Tensile tests with an axial extensometer were also carried out. Results showed important differences in the behavior of the biocomposites after one and ten wet/dry cycles or after ambient storage. Mechanical properties drop with one wet/dry cycle. After ten wet/dry cycles, the mechanical properties continue to decrease, but the reduction is less significant. The damage mechanisms were analyzed after tensile testing by microtomography. For “ambient storage” specimens, no clear damage is visible in the materials outside the failure zone. On the contrary, after ten wet/dry cycles, numerous debondings at fiber/matrix interface and cracks are observed, whatever the biocomposite. This explains the evolution of the mechanical properties of these materials.

Acknowledgements

This work was partially funded by the French Government program “Investissements d'Avenir” (EQUIPEX GAP, reference ANR-11-EQPX-0018) and by the CPER FEDER project of Région Nouvelle Aquitaine. It pertains to the French Government program “Investissements d’Avenir” (EURINTREE, reference ANR-18-EURE-0010). The authors also thank *Arkema* for the manufacture of the Elium-based composites.

  doi:10.5075/epfl-298799_978-2-9701614-0-0

5. References

1. Zwawi M. A Review on Natural Fiber Bio-Composites, Surface Modifications and Applications. Molecules. 2021 Jan 14;26(2):404.
2. Faruk O, Bledzki AK, Fink H-P, Sain M. Biocomposites reinforced with natural fibers: 2000–2010. Progress in Polymer Science. 2012 Nov;37(11):1552–96.
3. Marrot L, Alao PF, Mikli V, Kers J. Properties of Frost-Retted Hemp Fibers for the Reinforcement of Composites. Journal of Natural Fibers. 2021 Apr 17;1–12.
4. Madsen B, Hoffmeyer P, Thomsen AB, Lilholt H. Hemp yarn reinforced composites – I. Yarn characteristics. Composites Part A: Applied Science and Manufacturing. 2007 Oct;38(10):2194–203.
5. Essid S, Hegde VJ, Mahieu A, Bizet L, Leblanc N, Saouab A. Comparison of the properties of flax shives based particleboards prepared using binders of bio-based lignin and partially bio-based epoxy resin. International Journal of Adhesion and Adhesives. 2021 Sep;109:102915.
6. Gbadeyan O, Adali S, Bright G, Sithole B, Lekha P. Mechanical, microstructure, and dynamic mechanical analysis of nano-shell and plant fiber hybrid biocomposite. Journal of Composite Materials. 2021 Oct;55(24):3345–58.
7. Allagui S, El Mahi A, Rebiere J-L, Beyaoui M, Bouguecha A, Haddar M. Effect of Recycling Cycles on the Mechanical and Damping Properties of Flax Fibre Reinforced Elium Composite: Experimental and Numerical Studies. Journal of Renewable Materials. 2021;9(4):695–721.
8. Khalili P, Blinzler B, Kádár R, Blomqvist P, Sandinge A, Bisschop R, et al. Ramie fabric Elium® composites with flame retardant coating: Flammability, smoke, viscoelastic and mechanical properties. Composites Part A: Applied Science and Manufacturing. 2020 Oct;137:105986.
9. Perrier A, Touchard F, Chocinski-Arnault L, Mellier D. Quantitative analysis by micro-CT of damage during tensile test in a woven hemp/epoxy composite after water ageing. Composites Part A: Applied Science and Manufacturing. 2017 Nov;102:18–27.
10. Malloum A, Mahi AE, Idriss M. The effects of water ageing on the tensile static and fatigue behaviors of greenpoxy–flax fiber composites. Journal of Composite Materials. 2019 Sep;53(21):2927–39.
11. Muñoz E, García-Manrique JA. Water Absorption Behaviour and Its Effect on the Mechanical Properties of Flax Fibre Reinforced Bioepoxy Composites. International Journal of Polymer Science. 2015;2015:1–10.
12. Sala B, Gabrion X, Trivaudey F, Guicheret-Retel V, Placet V. Influence of the stress level and hygrothermal conditions on the creep/recovery behaviour of high-grade flax and hemp fibre reinforced GreenPoxy matrix composites. Composites Part A: Applied Science and Manufacturing. 2021 Feb;141:106204.
13. Scida D, Assarar M, Poilâne C, Ayad R. Influence of hygrothermal ageing on the damage mechanisms of flax-fibre reinforced epoxy composite. Composites Part B: Engineering. 2013 May;48:51–8.
14. Wambua P, Ivens J, Verpoest I. Natural fibres: can they replace glass in fibre reinforced plastics? Composites Science and Technology. 2003 Jul;63(9):1259–64.
15. Perrier A, Ecault R, Touchard F, Vidal Urriza M, Baillargeat J, Chocinski-Arnault L, et al. Towards the development of laser shock test for mechanical characterisation of fibre/matrix interface in eco-composites. Polymer Testing. 2015 Jul;44:125–34.
16. Shen C-H, Springer GS. Moisture Absorption and Desorption of Composite Materials. Journal of Composite Materials. 1976 Jan;10(1):2–20.

  doi:10.5075/epfl-298799_978-2-9701614-0-0

BIODEGRADABLE POLYMER FILMS TO PREVENT BIOFILM FORMATION FOR FOOD PACKAGING APPLICATION

Ekaterina, Kukushkina[a,b], Mari Chiara, Sportelli[a], Nicoletta, Ditaranto[a,b], Nazan, Altun[c], Pelayo, Gonzalez[c], Rosaria Anna, Picca[a,b], Nicola, Cioffi[a,b]

a: Department of Chemistry, University of Bari "Aldo Moro", Bari, Italy – ekaterina.kukushkina@uniba.it
b: CSGI (Center for Colloid and Surface Science) Bari Unit, Bari, Italy
c: ASINCAR (Research Association of Meat Industries of Principado de Asturias), Noreña, Spain

Abstract: *Safe and effective materials for food packaging application are in high demand due to misuse and overuse of non-degradable plastics with a negative impact on nature. In food industry, especially in food processing, another alarming problem exists, which is the uncontrolled growth of resistant pathogens and biofilms. In this work, we report potentially compostable and/or biodegradable chitosan-based polymer film, which has inorganic antimicrobial nanophases tightly and homogeneously spread within the matrix. The homogeneity and some physico-chemical properties were studied and preliminary antipathogen tests were carried out. The antibiofilm effect was detected, when material was used in a form of a thin coating on stainless steel samples.*

Keywords: antibiofilm; nanocomposite; silver nanoparticles; polymer.

1. Introduction

In the recent years scientists pay close attention to the uncontrolled usage of plastic packaging materials, which lead to leakage of tons of the waste into the environment. Better, optimized design of the "green" packaging materials could result in neutral impact on the nature, instead of the harmful one. When searching for a better and greener alternatives, it is necessary to take into account not only biodegradability or compostability of the final materials, but also the potential impact of the production and utilization of the starting material-related processes.

Chitosan (CS) is an abundant and cheap biopolymer and is known for its attractive properties, like biodegradability, intrinsic antimicrobial activity and non-toxicity. In particular, CS films might find application as an advantageous alternative to petroleum-based packaging materials: potentially, these eco-friendly biopolymer materials are able to prevent food spoilage caused by foodborne pathogens and inhibit the formation of biofilms. Many works have been reported on the potential industrial application of CS-based films. The biggest advantage, which was specifically highlighted in all the works, is their ability to not cause harmful impact on nature and environment.

Another emerging problem humanity is facing nowadays is antimicrobial resistance (AMR). The uncontrolled growth of biofilms and rise of AMR cause significant damage in many industrial and public sectors, especially in food industry and healthcare sector. The need of novel efficient antimicrobial composites calls for fast response from a research community, but at the same time they should be designed in a way to protect and harm the environment. CS can be

  doi:10.5075/epfl-298799_978-2-9701614-0-0

potentially combined with other antimicrobial components (e.g. antibiotics), organic (small antimicrobial molecules) and inorganic species (metal ions), which can both increase polymer's mechanical performance and enhance antimicrobial properties [1–3]. The list of potential safe and effective candidates is big, but there are several requirements that the additive(s) must meet. First, upon combination with CS, it should improve the mechanical robustness of the CS-based composite in humid environment, for example by crosslinking mechanism; second, it should bring the enhanced and synergistic effect to the overall antimicrobial performance, by generation of ions or reactive oxygen species (ROS); and the last, but not the least, maximum safety and minimum toxicity, when combined together, of the components are required. One of the candidates is tannic acid (TA), natural abundant polyphenolic compound with pronounced antioxidant properties. It has been proved to be an efficient crosslinking agent, when combined with CS and other polymers, with intrinsic antimicrobial action. Several works reported antibacterial efficiency of CS and TA in combination [4].

To provide even more pronounced antimicrobial effect and additional action against resistant pathogens, inorganic nanophases, in particular metal nanoparticles, could be incorporated or in situ synthesized and immobilized in the polymer matrix [5]. This way, the inorganic component can promote the generation of reactive oxygen species (ROS) and ion release directly from the polymer matrix, making the composite work in several directions against pathogens. In order to provide controlled and continuous release of active components from the matrix, it is necessary to ensure good colloidal stability of the nanophases. Silver, in a form of nanoparticles, was successfully combined with CS alone and with TA-crosslinked CS, showing enhanced antimicrobial effect against pathogens like *E. Coli.*

In this work, we report modified method of in situ synthesis of spherical AgNPs, stabilized by highly crosslinked polymer network, consisting of CS, TA and one of the classical crosslinking agent, glutaraldehyde (GA). Preliminary results have demonstrated the killing of the bacteria, *Salmonella Enterica*, when this material is used in a form of a coating on stainless steel. This way, it might work as promising solution to reduce negative effect of the biofilm formation on various surfaces in industrial environments, like meat processing units.

2. Materials and Methods

2.1 Synthesis of polymer supported AgNPs

In order to synthesize nanocomposite with AgNPs incorporated in polymer matrix, CS solution was prepared by dissolving medium molecular weight CS in acetic acid solution (2% v/v) until the final solution was transparent, with a final concentration of 1.5% w/v. Silver nitrate (0.1 M aqueous solution), glutaraldehyde (2.5% v/v aqueous solution) and tannic acid, were introduced. In the typical synthesis, for every 10 ml of CS solution amounts of other components were the following: 2 ml of 0.1 M $AgNO_3$, 0.3 ml of GA, 0.016 g of TA. The reaction mixture was left for 4 h, at a constant stirring and heating (65-75°C). Then, 2 ml of absolute EtOH was introduced to a system for a soft enhancement of solidification and polymerisation. Resulting colloidal solution CS/GA/TA/AgNPs was subjected to further analysis and application. The presence and rough estimation of AgNPs morphology and size were investigated by UV-vis spectroscopy (Shimadzu UV-1601) and transmission electron microscopy (TEM, Techai F 12 TEM, Tokyo, Japan), crosslinking event and immobilization of inorganic nanophases on polymer matrix

  doi:10.5075/epfl-298799_978-2-9701614-0-0

were studied with Fourier-Transform Infrared Spectroscopy (FTIR, Perkin Elmer Spectrum Two) and homogeneity of AgNPs within polymer matrix was assessed by means of scanning electron microscopy (SEM, JEOL JSM- 5600).

All the reagents were of analytical grade. Milli-Q water was used throughout the synthesis and for sample preparation for analysis.

2.2 Preliminary antibiofilm tests and Confocal Laser Scanning Microscopy (CLSM)

In order to get the preliminary data on antipathogen properties of the synthesized polymer composites, the colloidal solution was deposited on Stainless Steel (SS) industrial samples (5x10 cm^2) by immersion method, dried in the oven for 3 h at 55°C and subjected to biofilm growth protocols developed by ASINCAR, Noreña, Spain, using *Salmonella Enterica* as a biofilm-forming bacteria. As a control, uncoated SS sample was incubated in bacterial suspension, coated SS sample was incubated for the same time and conditions. At the end of the incubation, SS samples were washed carefully in 100 ml of phosphate buffer saline (PBS), and directly subjected to the observation by CLSM (Confocal Microscope Leica TCS-SP8X). To do so, 3-6 µL of SYTO® 9 fluorescent dye was deposited on the area of interest, liquid-air interface, to stain all microbial cells attached to the surface of SS sample.

3. Results and discussion

3.1 Characterization of the nanocomposite in the colloidal liquid and solid state

Freshly synthesized nanocolloids were subject to basic analysis in order to detect: presence of AgNPs, crosslinking events due to the addition of GA and TA, homogeneity of distribution of the inorganic nanophases within the polymer and their morphology.

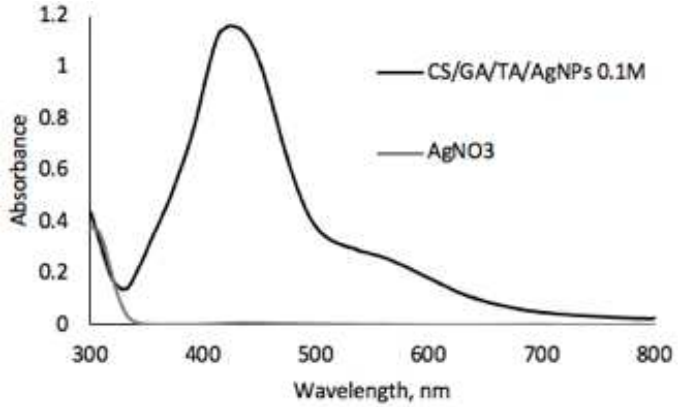

Figure 1. UV-vis spectra (black) of freshly synthesized nanocomposite (CS/GA/TA/AgNPs), with a typical SPR band of AgNPs at 422 nm; (grey) of silver nitrate solution as a control.

In order to prove the presence of AgNPs and get a rough size estimation, UV-vis spectra of the diluted aqueous colloidal solutions were recorded (Figure 1). Peak associated with SPR of AgNPs is located at 422 nm, which is in agreement with the references [5]. Depending on the stabilizer, at this wavelength AgNPs could be of the size from ~15 to 35 nm .

  doi:10.5075/epfl-298799_978-2-9701614-0-0

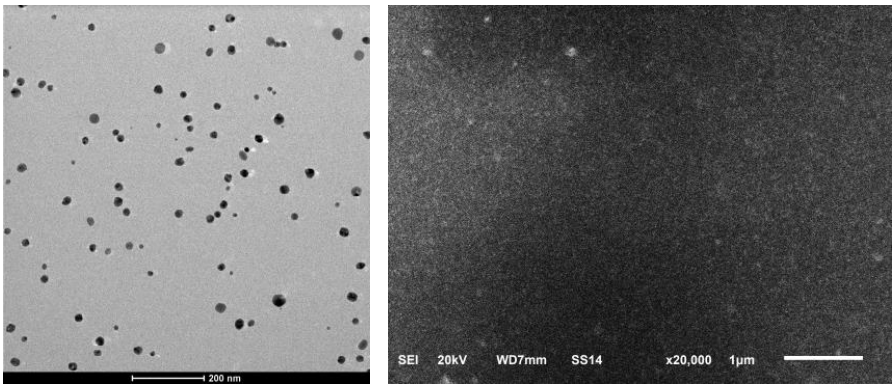

Figure 2. On the left: TEM micrograph of the colloidal AgNPs, stabilized by polymer matrix. On the right: SEM micrograph of the deposited on Si wafer colloidal solution of CS/GA/TA/AgNPs, bright spots are corresponding to a presence of AgNPs.

In order to directly observe morphology and measure the size of the inorganic nanocolloids, TEM analysis was carried out. On the Figure 2, left, TEM micrograph is shown. Individual nanophases appear spherical, evenly distributed and have the size of ~20 nm, which is in agreement with UV-vis data. On the right side of Figure 2, we can see the appearance of bright spots within polymer on SEM image. These correspond to evenly distributed metal NPs, which are immobilized in polymer.

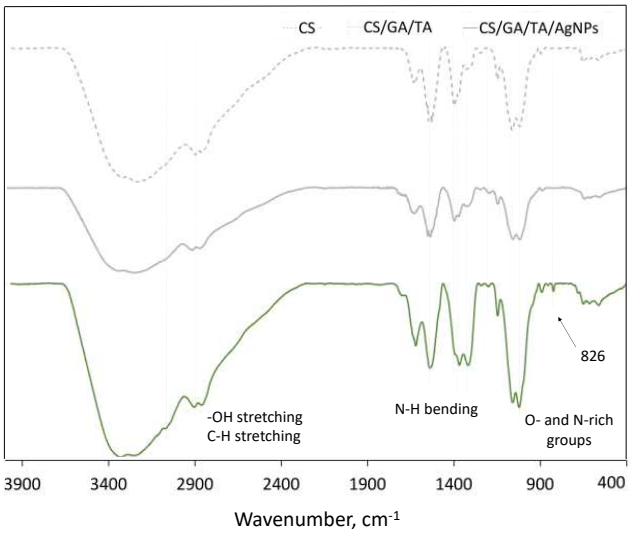

Figure 3. FTIR spectra of CS (control), CS/GA/TA, CS/GA/TA/AgNPs composite materials.

To potentially improve mechanical stability and bring additional antimicrobial effect, GA and TA were introduced to CS. It was expected to detect crosslinking by FTIR and spectral changes. Indeed, when pure CS and CS/GA/TA is compared, we can observe changes in the band intensities in the N-H bending region (1100-1600 cm^{-1}) and in the wavenumber range from 900 to 1100 cm^{-1}, which is attributed to the O- and N-rich functionalities. Upon addition of AgNPs to the system, appearance of the peak at 826 cm^{-1} is proving direct immobilization of the nanophases within the polymer matrix [6].

  doi:10.5075/epfl-298799_978-2-9701614-0-0

3.2 Antibiofilm tests

Since this material was designed for a potential application in food industry sector, it was important to run preliminary antimicrobial activity tests. *Salmonella Enterica*, one of the most widespread foodborne pathogens, can form biofilms on various surfaces.

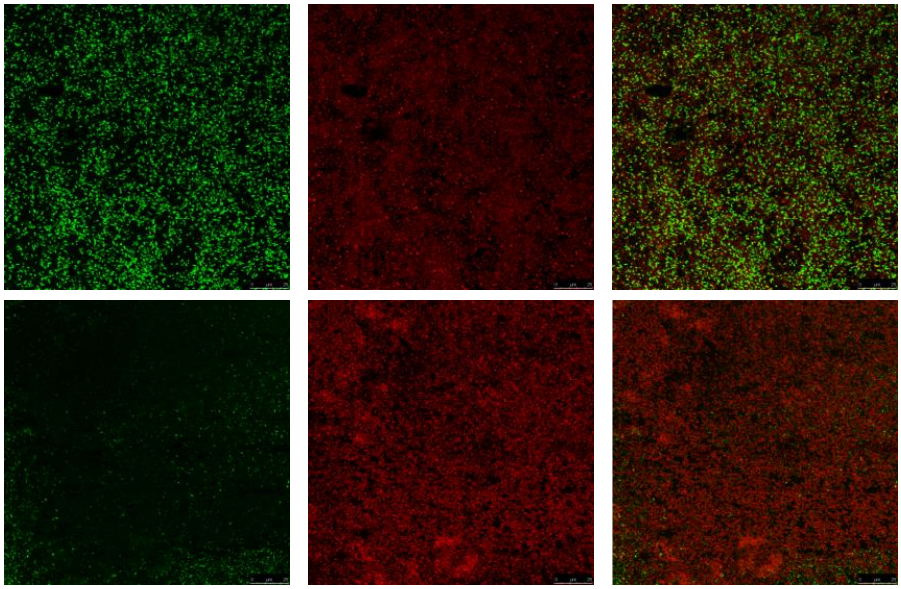

Figure 4. CLSM analysis of (upper) Salmonella Enterica biofilm of uncoated Stainless Steel sample and (bottom) CS/GA/TA/AgNPs coated SS sample. Both of the samples were observed and images recorded directly after incubation. Alive bacteria appear in green and dead bacteria appear in red.

Surface of a SS sample was exposed to the bacterial suspension for 5 days, uncoated and coated with nanocomposite. After incubation, it was necessary to observe the bacterial behavior and see if the inhibition/bacterial killing took place. With CLSM and fluorescent labeling 2 types of bacteria were observed: alive, which appear in green, and dead, which have a red color on microscopy images. The uncoated control SS sample has predominantly alive bacteria, tightly arranged in a biofilm. On contrary, in case of the coating, the death of bacteria was observed. This is an indication of the antibacterial action of the composite material, when used in a form of thin coating.

3.3 Conclusions and perspectives

We successfully optimized in situ synthesis of Chitosan-stabilized AgNPs. They appear spherical in shape, homogeneously distributed and not aggregated. Tannic acid was used to obtain synergistic active coatings. Preliminary antibiofilm tests revealed activity against biofilm-forming *Salmonella Enterica*, when the material is deposited on a solid substrate in a form of a thin coating. The following steps include stability tests, study of the influence of different parameters on the antibiofilm and antimicrobial performance and further optimization steps.

Acknowledgements

Financial support is acknowledged from European Union’s 2020 research and innovation program under the Marie Sklodowska-Curie Grant Agreement No. 813439. CLSM and SEM

  doi:10.5075/epfl-298799_978-2-9701614-0-0

experiments have been performed in the Scientific and technical Services Centre, University of Oviedo, Spain.

4. References

1. Yilmaz Atay, H. Antibacterial Activity of Chitosan-Based Systems. Funct. Chitosan 2020; 457–489.
2. Badawy, M.E.I.; Lotfy, T.M.R.; Shawir, S.M.S. Preparation and Antibacterial Activity of Chitosan-Silver Nanoparticles for Application in Preservation of Minced Meat. Bull. Natl. Res. Cent. 2019; 43, 83.
3. Ahmed, S.B.; Mohamed, H.I.; Al-Subaie, A.M.; Al-Ohali, A.I.; Mahmoud, N.M.R. Investigation of the Antimicrobial Activity and Hematological Pattern of Nano-Chitosan and Its Nano-Copper Composite. Sci. Rep. 2021; 11, 9540.
4. Cano, A.; Contreras, C.; Chiralt, A.; González-Martínez, C. Using Tannins as Active Compounds to Develop Antioxidant and Antimicrobial Chitosan and Cellulose Based Films. Carbohydr. Polym. Technol. Appl. 2021; 2, 100156.
5. Kukushkina, E.A.; Hossain, S.I.; Sportelli, M.C.; Ditaranto, N.; Picca, R.A.; Cioffi, N. Ag-Based Synergistic Antimicrobial Composites. A Critical Review. Nanomaterials 2021; 11, 1687.
6. Roy, S.; Zhai, L.; Kim, H.C.; Pham, D.H.; Alrobei, H.; Kim, J. Tannic-Acid-Cross-Linked and TiO2-Nanoparticle-Reinforced Chitosan-Based Nanocomposite Film. Polymers 2021; 13, 228.

  doi:10.5075/epfl-298799_978-2-9701614-0-0

Composites Meet Sustainability – Proceedings of the 20th European Conference on Composite Materials, ECCM20.
26-30 June, 2022, Lausanne, Switzerland

LIFE CYCLE ASSESSMENT OF NATURAL FIBRE REINFORCED POLYMER COMPOSITES. A COMPARATIVE STUDY

Vassilis Kostopoulos[a], Nikolitsa Gkoloni

a: Department of Mechanical Engineering & Aeronautics, University of Patras, Greece.
kostopoulos@upatras.gr

Abstract: *The increased environmental awareness worldwide towards achieving the reduction of our carbon emissions to net zero and product sustainability, has spurred great efforts in using more environmentally friendly materials in product design. One direction that has been intensively investigated during the last 10 years is the application of Natural Fiber Composites (NFCs) as an alternative for replacing synthetic composites. To this direction, the use of natural fibers to reduce the dependence on synthetic fibers as reinforcement materials for polymer composites is a significant step towards greening of composite industry. Three different polymer composites containing flax fibers were manufactured by infusion and cured using different out of autoclave curing processes, that conclude to products having similar fiber volume fraction and mechanical performance. These NFCs were evaluated from an environmental perspective by means of Life Cycle Assessment (LCA) applying the cradle-to-gate approach and compared against their typical glass fiber epoxy counterpart. It is evident that the use of flax fibers reinforcement together with bio-resin matrix material and microwave curing concludes to minimum environmental impact.*

Keywords: flax fibers, composites, micro-wave curing, bio-resin, LCA

1. Introduction

The growing demand for new eco-friendly composites is driving the natural fiber reinforced composites (NFCs) market. They can be used in diverse applications such as automotive, building materials, aircraft interiors and household appliances. The natural fiber reinforced composites market is estimated to reach 3,740 metric tons in 2022 and is expected to register a Compound Annual Growth Rate (CAGR) of more than 9% during the period 2022-2027[1]. Among the various natural fibers that have been used as reinforcement, flax represented 50% of the market share for composites in 2012 [2] and comes fourth in production out of the different commercially major fiber sources available [3]. The increasing trend on the application of NFCs is contributed to its lightweight, environmental, and cost superiority, and can easily replace glass fiber composites due to the similar mechanical properties that some of the natural fibers have compared against glass [4].

Natural fiber reinforcements have many advantages over their inorganic competitor (E-glass). They have low density, high specific properties, are biodegradable, are derived from renewable resources, have a small carbon footprint, and provide good thermal and acoustical insulation. Those relative advantages explains why the automotive industry is at the forefront of NFC adoption [4].

The market share of natural fibers composites has significantly increased. In 2012 they encompassed close the 2% of the total fiber reinforced composite (FRP) market, while in 2024 it is expected to represent the 28% of the FRP market. Currently, NFCs have been well accepted by the automotive industry and they are used to produce secondary-tertiary structures such as interior components, door panels, head liners etc. Natural Fibre Polymer Composites have proven to have a higher environmental performance in the automotive sector and are emerging as an option for weight reduction in aircrafts interior, as an additional effort to contribute to ACARE goal for recyclable aircraft, in the direction to reduce and finally avoid the

  doi:10.5075/epfl-298799_978-2-9701614-0-0

consumption of non- renewable materials. Thus, many meaningful solutions have to be developed and combined in an intelligent way to achieve these ambitious goals that cannot be fulfilled with a simple, single solution. In recent decades, the use of plant fibers is not only a material substitution. They are specifically chosen because: they are from a renewable source, they are both durable and biodegradable, the specific mechanical performance of certain fibers is very good, they require considerably less energy than glass fibers to produce, and their End of Life (EoL) management is easier [5]. On the other hand, petroleum- based polymeric resins used as matrix materials in fiber reinforced polymers (FRPs) (epoxies, polyester, vinylester, PU resins etc) are primarily composed of chemicals which are fundamentally unsustainable. By replacing the matrix of the FRP with a bio-sourced resin, the environmental impact associated with production of the FRPs could be further reduced.

Finally, with increasing deployment of the fiber-reinforced composites, curing processes have been developed to improve the composite quality and production time cycle. Autoclave processing cures composite prepreg by heating and pressurizing the air inside the autoclave chamber. However, autoclave processing requires a long time, because of the time required to heat the air that then heats the composite prepreg by convection [6,7]. An alternative technique, prepreg compression forming (PCF), directly heats a metallic mold to reduce production costs [8,9]. Nonetheless, this technique can still require a long processing time depending on the thermal conductivity of the mold. In recent development, pressure assisted resin transfer molding (RTM) has effectively reduced the processing time by injecting the resin at relatively high pressure and temperature [10,11], but this process still incurs substantial energy costs in addition to the initial setup costs for the resin injection system [12]. A microwave-based curing process (MCP) is one solution for reducing the energy consumption by shortening the process cycle and the necessary energy consumption. This advantage has stimulated interest in the MCP as a replacement for conventional autoclave and out of autoclave curing processes [13].

2. Goal and scope of the study

The aim of this study is to assess and quantify the environmental impact and the resulted environmental differences between four different composite plates manufactured for serving needs of aircraft interiors. The reference composite material is a glass fiber reinforced epoxy, manufactured by using infusion technique with epoxy matrix, cured by using a conventional oven and finally post cured for concluding its final properties (Scenario 1). The first alternative is to replace the glass fibers by flax fiber, keeping the same type of matrix material, manufacturing, curing and post-curing processes (Scenario 2). The second alternative is the use of flax fibers as reinforcing material for the epoxy matrix and then after applying infusion process for the manufacturing of the plate, to use microwave oven for the curing and the same conventional oven for the final step of post curing (Scenario 3). The final alternative is the use of flax fibers as reinforcing material, to replace the epoxy resin with a bio-resin matrix material and then after applying infusion process for the manufacturing of the plate, to use microwave oven for the curing and the same conventional oven for the final step of post curing (Scenario 4). In all four cases the mechanical properties of the final composite plate are the same both for the modulus of elasticity and the tensile strength.

The functional unit used for this LCA analysis in all the scenarios is defined as the manufacturing of a 250x200x2 mm3 composite laminate. In conclusion, the following combination of materials and manufacturing scenarios are considered:

- Scenario 1: Glass fiber reinforcement with epoxy matrix and curing in conventional oven
- Scenario 2: Flax fiber reinforcement with epoxy matrix and curing in conventional oven
- Scenario 3: Flax fiber reinforcement with epoxy matrix and microwave curing
- Scenario 4: Flax fiber reinforcement with bio-resin matrix and microwave curing.

3. Methodology

  doi:10.5075/epfl-298799_978-2-9701614-0-0

3.1 Materials and manufacturing method

In all cases, a 150 g/m^2 flax fiber plain weave, supplied by Lineo (France) was used as textile reinforcement or the manufacturing of the flax fiber composites. The produced panels consist of eight fabric layers and were manufactured using Infusion process. The fiber volume fraction in all the cases were close to 40%. The epoxy resin used is the LY1564 with Aradur2954 hardener, while the bio-resin is a partly bio-based system that contains 40% soya-bean oil [14]. In details, after cutting of the woven fabrics to the predefined dimensions the 8 cut woven fabrics are laid up as a dry stack of materials in a symmetric way into the appropriate open mold. The fiber stack is then covered with peel ply and a knitted flow distribution mesh. The whole dry stack is then vacuum bagged, and once bag leaks have been eliminated, epoxy or bio-resin is allowed to flow into the laminate under vacuum conditions. Rather than starting with excess and drawing epoxy or bio-resin out, Vacuum Infusion Process starts and pushes resin in. Ideally, any excess epoxy or bio-resin that is introduced will eventually be sucked out into the vacuum line. As a result, only the minimum amount of resin is introduced to the mold. After filling the mold with the necessary quantity of epoxy or bio- resin the system is placed into the oven for curing, followed by a post curing stage.

In the case of flax fiber reinforcement, the flax fabrics must be firstly thermally treated and conditioned in a conventional oven for drying before use. Furthermore, for the needs of the present study in the case of flax fiber/epoxy or bio-resin laminates the curing process is executed either into a conventional oven or in a microwave oven, after optimizing the curing conditions to conclude to a high-quality flax composite laminate. In all four cases the mechanical properties of the final composite plate are the same both for the modulus of elasticity and the tensile strength.

3.2 Life cycle assessment

Engineers, designers, manufacturers and researchers are increasingly turning to Life Cycle Assessment (LCA) as an environmental impact analysis method to clearly communicate the advantages of bio-composites material. As a tool, LCA is very broad and can be applied to various industries, areas, and types of products. Thus, a guideline cannot specify how to carry out each individual step because the exact procedure can vary drastically between products. ISO has established guidelines for LCA to harmonize the basic procedure of studies. ISO 14040 outlines the principles and framework of LCA, and ISO 14044 outlines the requirements and guidelines of LCA [15, 16]. Based on the standards, the steps are (1) identify the goal and scope of the analysis, (2) compile a life cycle inventory (LCI), (3) complete a life cycle impact assessment (LCIA), and (4) interpret the results. In the present study OpenCLA is used to perform the Environmental Assessment [17] and Ecoinvent database is used for the processes in the Inventory stage [18].

3.3 System boundaries.

As the steps after laminate production (use and end of life) are identical and only small weight variations between scenarios are assumed, for the scope of the study, a ‘cradle to gate’ LCA is carried out. The geographical boundary for this study was set to be within Europe and the European average power mix is applied for all operations. All raw materials production for flax and glass fiber as well as for epoxy resin are considered with their transportation and their intermediate production steps. The manufacture of consumable materials required for each manufacturing processes is also considered as well as their disposal after use, assumed to be through incineration with energy recovery.

3.3.1 Building of LCI model

  doi:10.5075/epfl-298799_978-2-9701614-0-0

As the most time-consuming and extensive phase, LCI requires identifying and quantifying the resource flows for the system [19]. The purpose of LCI is to create an inventory of all inputs and outputs of materials, wastes, and natural resources for all processes, in relation to the functional unit. The system diagram of the manufacturing process for all scenarios are given in Figures 1 (Scenario 1), 2 (Scenarios 2 and 3) and 3 (Scenario 4).

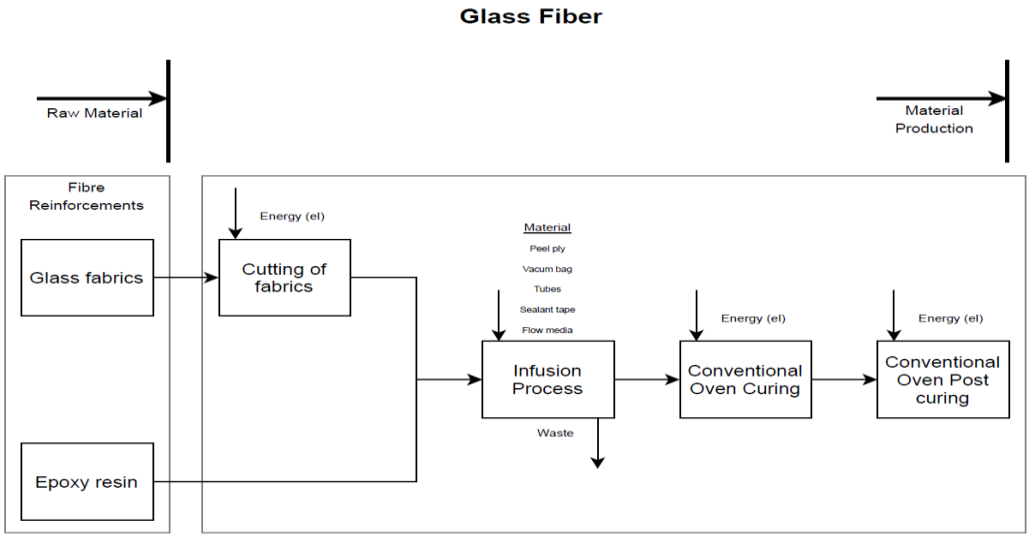

Figure 1. System diagram for Glass Fiber Epoxy Composite Production

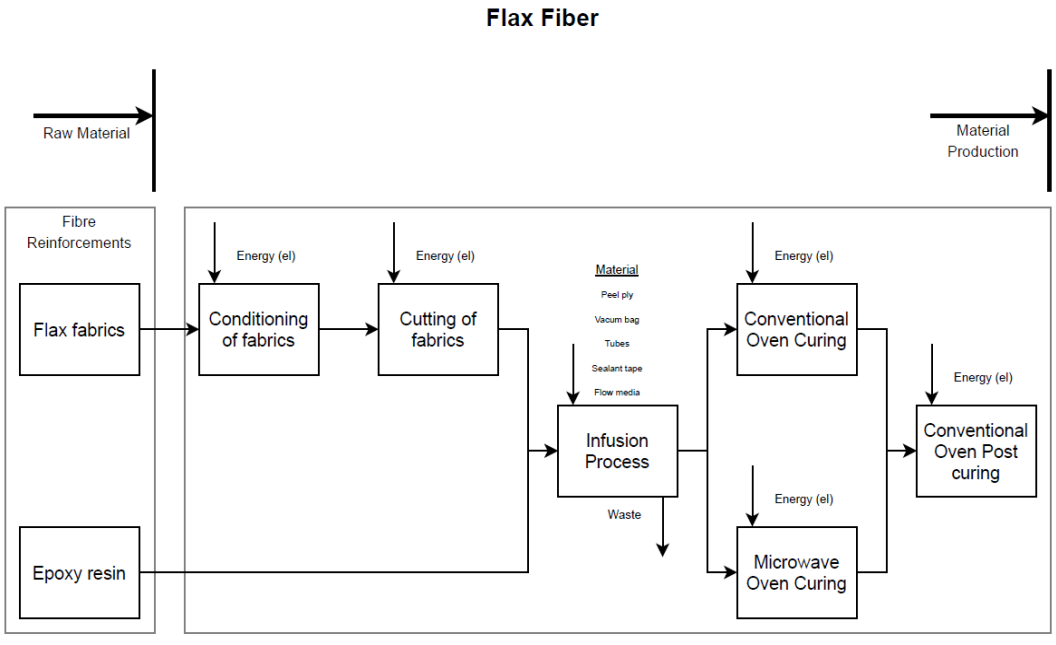

Figure 2. System diagram for Flax Fiber Epoxy Composite Production

  doi:10.5075/epfl-298799_978-2-9701614-0-0

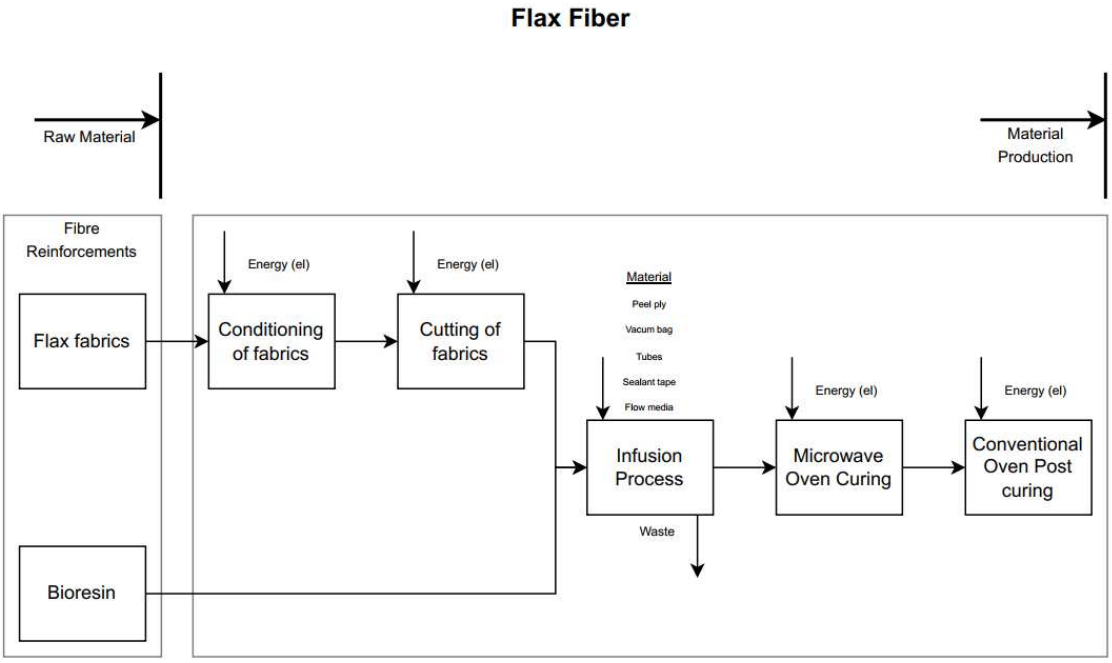

Figure 3. System diagram for Flax with bio-resin matrix composite production

3.3.2 Inventory data and sources

The summary of materials quantities and energy use for each production scenario is shown in Table 1, where «waste» refers to off-cuts from consumables. In the cases of flax fiber production, glass fiber production and consumable materials, which direct inventory data of flows were not available, the flows were obtained for Ecoinvent Centre. Table 2 lists the consumable and fiber type with the associated materials and processes chosen.

Table 1. Summary of materials quantities and energy use for each production

Flow	Scenario 1 Amount	Scenario 2 Amount	Scenario 3 Amount	Scenario4 Amount	Unit
electricity, low voltage	4,15	4,1	2,9	2.9	kWh
epoxy resin, liquid/bioresin	0,27	0,27	0,27	0,27	kg
fibre, flax		0,05	0,05	0,05	kg
fible, glass	0,1				kg
flow media	0,003	0,003	0,003	0,003	kg
peel_ply	0,003	0,003	0,003	0,003	kg
sealant_tape	0,504	0,504	0,504	0,504	kg
tube insulation, elastomere	0,00374	0,00374	0,00374	0,00374	kg
vacuum	0,005	0,005	0,005	0,005	kg
waste	0,63374	0,63374	0,63374	0,63374	kg

  doi:10.5075/epfl-298799_978-2-9701614-0-0

Table 2. Materials and process selected from Ecoinvent to represent Inventory data

Product	**Materials**
flax fiber	fiber production, flax, retting | fiber, flax | Cutoff, ROW
glass fiber	glass fiber production | glass fiber | Cutoff, RER U
Epoxy resin	LY1564/Aradur2954 | Cutoff, RER U
Bio resin	Epoxy resin | Cutoff, RER U Soybean oil | Cutoff, REE U
Peel ply	nylon66, at plant/RER U
	weaving, cotton/GLO U
Flow media	polypropylene, granulate, at plant/RER U
	Melt spinning, cotton/GLO U
Tube	Silicone product, at plant/RER U
	Extrusion, plastic pipes/RER U
Sealant tape	tetrafluoroethylene, at plant/RER U
	Melt spinning, cotton/GLO U
vacuum bag	synthetic rubber, at plant/RER U
	Melt spinning, cotton/GLO U
electricity	market low voltage electricity /GR

3.4 Results of LCIA and Discussion

A comparative life cycle impact assessment (LCIA) was carried out. In general, ISO defines three broad impact categories to be included: damage to human health, ecosystem health, and resources. If the LCA uses these general categories, the study can be classified as an “end-point damage” model. However, a “mid-point damage” model can instead be used, when impact categories are made more specific. Thus, for the aim of this study we use ILCD Midpoint and Recipe 2011 Endpoint to compare the results and to have a variety of impact categories that can help policy decision makers. The results of the two assessment methods for all production scenarios are presented and compared in the bar chart of Figure 4 and Figure 5 respectively. For each indicator the maximum result is scaled to 100% and the results of the variants are displayed in relation to this result. In ILCD midpoint assessment, Flax fiber reinforcement with bioresin matrix and microwave over curing has a lower value for all the environmental impact indicators, except land use, which is expected since the soya been oil comes from natural resources. In case this substance comes from recycled products this index diminishes. However, in the Recipe Endpoint and especially in indicator “Land use”, scenario 4 is the friendliest solution.

In conclusion, results showed that materials, in particular flax fiber reinforcement fabrics shows to have a beneficial effect to the environmental impact of the final composite in compare with glass fiber. In the case of using flax fiber reinforcement in combination with Microwave oven curing and bioresin matrix, the final composite product has a considerably lower environmental impact. In offing, the proposed framework can be extended by modelling “cradle-to-grave” assessment because in green composites, the end-of-life disposal can vary significantly from those of synthetic composites.

  doi:10.5075/epfl-298799_978-2-9701614-0-0

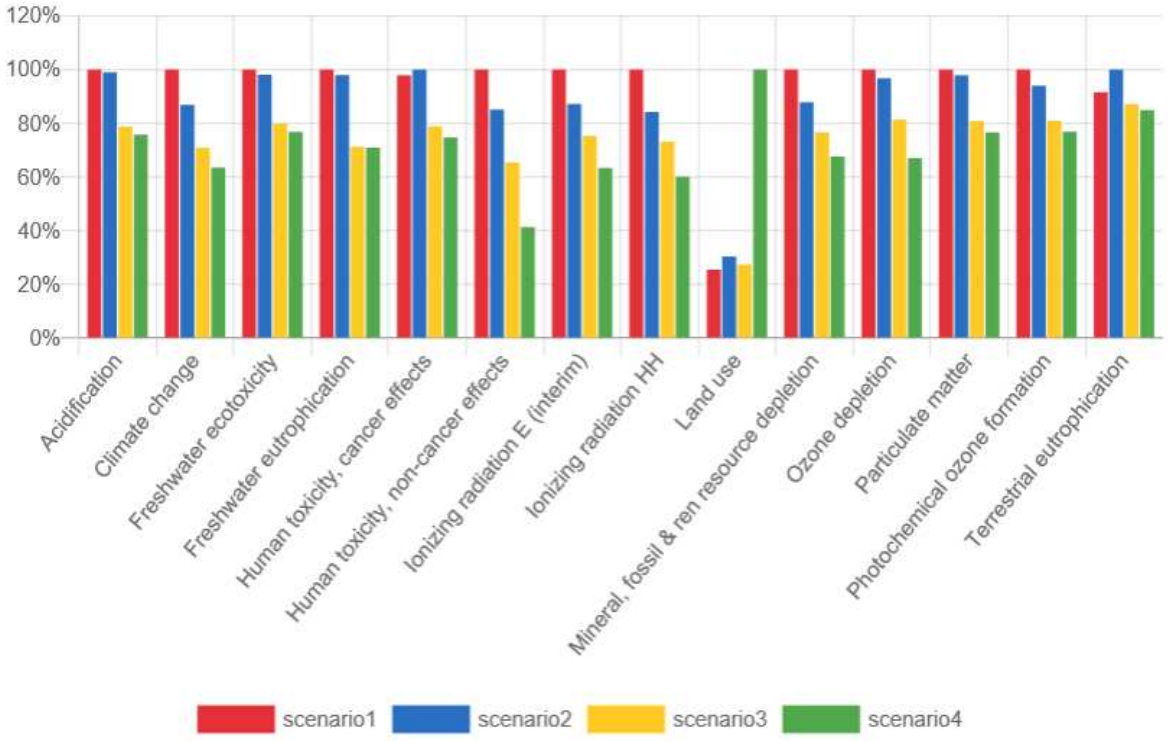

Figure 4. Indicators and results of ILCD midpoint LCIA

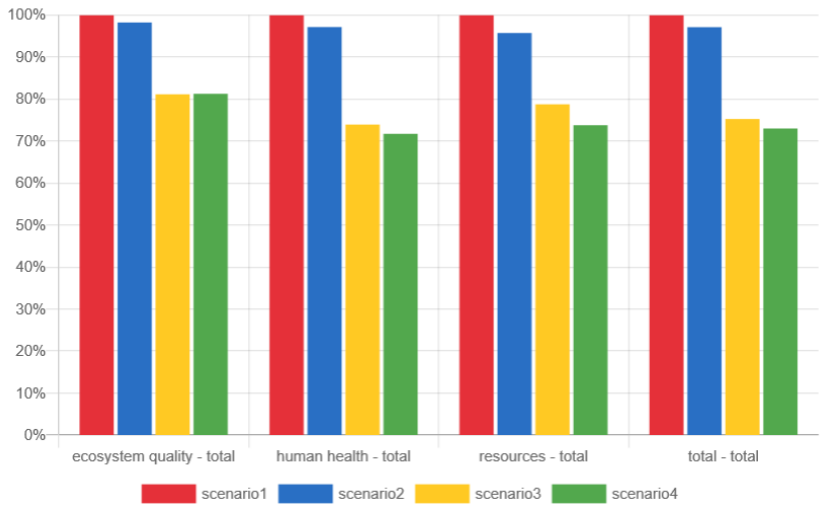

Figure 5. Indicators and results of Recipe Endpoint LCIA

  doi:10.5075/epfl-298799_978-2-9701614-0-0

4. References

1. Market Report. Natural Fiber Reinforced Composites Market - Growth, Trends, COVID-19 Impact, and Forecasts (2022 - 2027). Available: https://www.reportlinker.com/p06241287/Natural-Fiber-Reinforced-Composites-Market-Growth-Trends-COVID-19-Impact-and-Forecasts.html?utm_source=GNW. Accessed on 3/4/2022
2. Barth M, Carus M. Carbon Footprint and Sustainability of Different Natural Fibres for Biocomposites and Insulation Material. nova-Institut GmbH. 2019
3. Faruk O, Bledzki K, Fink H, Sain M, 2012. Bio- composites reinforced with natural Fibers: 2000e2010. Prog. Polym. Sci. Top. Issue Polym. Biomater. 2012; 11:1552-96.
4. Sanjay M.R, Madhu P, Jawaid M, Senthamaraikannan P, Senthil S, Pradeep S. Characterization and properties of natural fiber polymer composites: a comprehensive review. Journal Clean Prod. 2018; 172:566-81.
5. Christophe B, Alain B, Peter D. Eighty years of composites reinforced by flax fibres: A historical review, Composites Part A: Appl.Sci. Manuf .2021;144: 1-8.
6. Centea T, Grunenfelder L.K, Nutt S.R. A review of out-of-autoclave prepregs—Material properties, process phenomena, and manufacturing considerations. Compos. Part A Appl. Sic. Manuf. 2015; 70: 132–154.
7. Vita A, Castorani V, Germani M, Marconi M. Comparative life cycle assessment and cost analysis of autoclave and pressure bag molding for producing CFRP components. Int. J. Adv. Manuf. Technol. 2019; 7:1–16
8. Wulfsberg J, Hermann A, Ziegmann G, Lonsdorfer G, Stöß N, Fette, M. Combination of carbon fibre sheet moulding compound and prepreg compression moulding in aerospace industry. Procedia Eng. 2014; 81: 1601–07.
9. Lee J.M, Kim B.M, Ko D.C. Development of vacuum-assisted prepreg compression modling for production of automotive roof panels. Compos. Struct. 2019; 213: 144–52.
10.Rondina, F.; Taddia, S.; Mazzocchetti, L.; Donati, L.; Minak, G.; Rosenberg, P.; Bedeschi, A.; Dolcini, E. Development of full carbon wheels for sport cars with high-volume technology. Compos. Struct. 2018, 192, 368–378.
11. Han B.J, Jeong Y.C, Kim C M, Kim R.W, Kang M. Forming characteristics during the high-pressure resin transfer molding process for CFRP. Adv. Compos. Mater. 2019; 28: 365–82.
12. Baskaran M, de Mendibil I.O, Sarrionandia M, Aurrekoetxea J, Acosta J, Argarate U, Chico D. Manufacturing cost comparison of RTM, HP-RTM and CRTM for an automotive roof. Proceed. 16th Eur. Conf. Comp.M., Seville, Spain, 22–26 June. 2014; pp. 1–7.
13. Mishra R.R, Sharma A.K. Microwave-material interaction phenomena: Heating mechanisms, challenges and opportunities in material processing. Compos. Part A Appl. Sic. Manuf. 2016; 81: 78–97.
14. Qiuyu T, Yahua C, Huizhi G, Qian L,et al. Bio-Based Epoxy Resin from Epoxidized Soybean Oil. Available on: https://www.intechopen.com/chapters/64421. Accessed on 2/2/2022
15. ISO. Environmental management-Life cycle assessment-Principles and framework. Geneva,2006; https://www.iso.org/ standard/37456.html. Accessed on7/1/2022.
16. ISO. Environmental management-Life cycle assessment-Requirements and guidelines. Geneva, 2006; https://www.iso. org/standard/38498.html.Accessed on 7/1/2022.
17. Green Delta GmbH. OpenLCA. Available online: http//www.openlca.org. Accessed online on 6/1/2022.
18. Ecoinvent Centre. Available online: https://ecoinvent.org/. Accessed on 28/12/2021
19. Mansor MR, Salit MS, Zainudin ES, et al. Life cycle assessment of natural fiber polymer composites. Springer Intern. Publ. 2015; 121–41.

.

DEVELOPMENT OF QUASI-UNIDIRECTIONAL WOVEN FABRICS WITH 100% HEMP ROVINGS FOR COMPOSITE MATERIALS APPLICATIONS

Chaimae, Laqraa[a], Manuela, Ferreira[a], Ahmad-Rashed, Labanieh[a], Damien, Soulat[a]

a: University of Lille, ENSAIT – GEMTEX, 59000 Lille, France – Chaimae.laqraa@ensait.fr

Abstract: *The present study deals with developing 100% hemp quasi-unidirectional woven fabric from cost-effective hemp for composite application. Untreated hemp rovings were used for the first time to produce a quasi-unidirectional fabric by weaving process. Weaving process was challenging since the raw materials have higher hairiness and low cohesion between fibers. In this context, low crimping, fiber alignment and high roving density in the weft direction were targeted. This innovative hemp fabric is then used to produce composites by using the thermocompression molding process with thermosetting matrices. Multi-scale characterization was then performed at the different scale of production (yarns, fabric and composite). Results at composite scale, clearly show competitive properties compared to literature. Thus, the tensile strength achieved 300 MPa and the Young's modulus 25 GPa for a fiber volume fraction of 45%. This new quasi-unidirectional reinforcement is promising since it provides competitive characteristics that are sufficient for some composites application.*

Keywords: Hemp rovings; quasi-unidirectional fabric; multi-scale characterization; composites

1. Introduction

Due to increasing environmental awareness and finite fossil resources, more and more materials based on renewable raw materials are being used in the composites sector [1,2]. Natural fibers display benefits for the environment like biodegradability, renewability of raw material, and reduction in emission of greenhouse gasses [3], and especially bast fibers like hemp display comparatively high strength and stiffness compared to many other vegetable fibers [4,5]. Besides the fiber characteristics and processing methods, the properties of the composites can be significantly influenced by the reinforcement structure, as shown by several studies on flax fiber-reinforced composites or hemp fiber reinforced composites [6–15]. Thus, to obtain the best properties in the loading direction, the ideal reinforcement should maximize the number of fibers aligned in this direction [16,17]. But due to the finite length of plant fibers and the high number of selectable process parameters, the production of yarns, rovings and fabrics is complex [1] and the consequence of the use of these semi-products appears, sometimes, only on the final scale properties of the composites. Madsen et al. [18] in a study on hemps yarns produced in two different years, which have not significant differences in linear density and fiber size distribution from a textile point of view, resulted in different properties at the composite scale. Another biggest problem with the industrial use of bast fibers for high-value applications is the high price of semi-finished products. Increasing production volumes to reduce these costs results in the use of high-twist yarns to increase tenacity, minimize hairiness and reduce thread breakage during weaving process. But it is well known that a high level of twist prevents a good impregnation in a composite [19,20]. The higher the yarn twist, the lower the mechanical composite properties [6,7,9]. Consequently, the use of low-twist roving from bast fibers is preferred. Graupner et al. [1] have recently developed a new staple hemp yarns for high

  doi:10.5075/epfl-298799_978-2-9701614-0-0

performance composite applications. At industrial scales, pure unidirectional (UD) fabrics in the form of tapes have also been developed and commercialized with flax fibers, such as FlaxtapeTM by the company Lineo-Ecotechnilin [21,22]. In a previous study, quasi-unidirectional (QUD) fabrics from hemp roving were produced by weaving process [15]. This type of fabric has several advantages, as to align most of the fibers in a main direction, to minimize the crimp effects, compared to pure woven fabrics, but also to reinforce transverse direction with low density of yarns. Indeed, in pure unidirectional tapes, fibers are poorly bonded transversely, which can be problematic to the handling of the fabric or during the forming stage of the liquid composite molding (LCM) process [23,24]. These hemp fibers quasi-unidirectional fabrics were then used as reinforcement in composite samples and their tensile properties were compared with those given in the literature with unidirectional flax tapes, noncrimp fabrics and quasi-unidirectional woven fabrics made of flax fibers. The results highlighted the competitiveness of this hemp-based quasi-UD composite in terms of stiffness in both material directions compared to these products. These QUD fabrics contained, in low density, twisted yarns (222 turns/m) in warp direction, which can compress the low-twisted rovings, used in weft direction, in the interlaced area and generate some stress concentration. In this study we propose to optimize this QUD pattern with the use of only low-twisted rovings in warp and weft direction. Properties identified at the fabric and composite scales are compared with those of this previous paper.

2. Materials and methods

2.1 Materials

Two types of hemp rovings, in the form of low-twisted rovings provided by an Italian Company, Linificio e Canapificio Nazionale, were used to manufacture quasi-unidirectional woven fabric for biobased composites. Their textiles and mechanical properties are listed in Table 1. The first roving named R1 was subjected to chemical treatment, while the second roving R2 was not treated. The chemical treatment used is a conventional treatment, called mercerization, used in the textile industry to improve the mechanical properties of the rovings and thus facilitate their weaveability. The linear density of these rovings was measured according to the standard NF G07-316 [25], the twist level according to the standard NF G07-079 [26], and the tenacity at break according to the standard NF EN ISO 2062 [27].

The treated roving has lower linear density than the untreated roving, which is induced by the applied chemical treatment that decreases the mass of fibers by removing the impurities. This treatment leads as a result to higher tenacity and low hairiness. Previous study of Corbin et al. [15] has shown that this kind of treatment improves weaveability of rovings without damaging fibers and final composites properties. Furthermore, since untreated rovings R2 do not have the required strength for preparing the weaving process, treated rovings R1 were used to maintain the cohesion of the fabric.

Table 1: Hemp rovings properties.

	Linear density (Tex)	Twist level (turns/m)	Hairiness H ± sh	Tenacity (cN/Tex)	Strain at break (%)
Hemp roving with chemical treatment (R1)	282.4 ± 4.7	38.5 ± 2.5	9 ± 4	25 ± 4	5,3 ± 0,5

  doi:10.5075/epfl-298799_978-2-9701614-0-0

Hemp roving without chemical treatment (R2)	316 ± 4	39 ± 2	18 ± 7	11 ± 5	2.4 ± 0.3

2.2 Methods

- **Woven fabric manufacturing:**

Quasi-unidirectional woven fabric, later named QUD1, was produced with the two hemp rovings R1 and R2 on a manual dobby loom, a Leclerc WeaveBird weaving machine, as shown in Figure 1. The treated hemp rovings R1 were used in the warp direction, with a very low yarn density (0.6 yarns/cm) to maintain and provide cohesion to fabric and to limit the crimping level in this direction. In the weft direction, the untreated rovings R2 were inserted using a shuttle by packing highly to maximize the fiber content and density in this direction to 10 yarns/cm. Thus, the fiber mass fraction in this direction reached 94% and 6% in the warp direction. The QUD1 fabric was produced with a plain weave pattern.

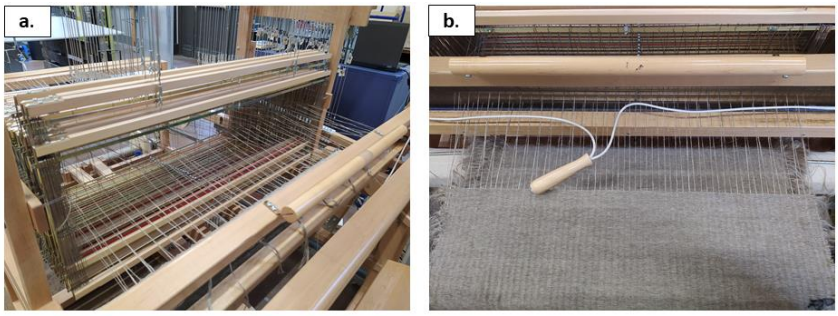

Figure 1. Weaving machine: a. view of the warp yarn insertion b. weft yarn insertion.

- **Characterization of QUD fabric:**

The areal density, thickness and air permeability of the produced fabric were measured on 10 samples according to the standard NF EN 12127 [28], NF EN ISO 5084 [29] and NF EN ISO 9237 [30] respectively. Air permeability test is used to measure the air flow rate that pass perpendicularly through the fabric with defined area (20 cm^2), time (1 minute) and pressure drop (200 Pa). The mechanical properties in terms of bending rigidity and tensile strength were characterized. Tensile tests were conducted according to the standard NF EN ISO 13934-1 [31] on a MTS Criterion 45 tensile machine with a load cell of 10 kN, a gauge length of 200 mm, a crosshead displacement rate of 20 mm/min and a preload of 5 N. Fives samples were prepared with a length of 300 mm and a width of 50 mm. Only the weft direction of the fabric was characterized. The same samples, were firstly used to measure their bending rigidity by a cantilever test according to the standard ISO 4604 [32]. Bending modulus was then calculated by using the procedure described in the study of Corbin et al. [15].

- **Composite manufacturing:**

Composite plates based on the developed QUD fabric were produced using the thermocompression molding process. A partially biosourced epoxy pre-polymer (GreenPoxy 56®) and its hardener (SD7561) provided by Sicomin® were used as matrix. The produced plates

  doi:10.5075/epfl-298799_978-2-9701614-0-0

are composed of two plies both oriented in the same direction of the fabric and which were conditioned at least 24h before the manufacturing process at a temperature of 23°C and a relative humidity of 50%. The two plies were hand layed-up and impregnated manually in an open mold with the epoxy resin following the protocol proposed in the study of Corbin et al. [15]. The mold was placed in a hot-press Agila® 100 kN Press following the curing cycle: procuring at 40°C for 15 minutes and curing at 60°C for 1 hour, then when the temperature reached 40°C, a pressure of 3 bars was applied on the plate. A post-curing step at 130°C was then applied for 1 hour. After this manufacturing process, the plates were conditioned at 23°C and 50% RH during at least four weeks. The fiber and void volume fraction in these composite are equal to 48.8% and 1.5% respectively.

- **Composite characterization:**

The mechanical properties of the produced plates were determined from tensile tests. Tensile tests were carried out according to the ASTM D3039 [33] standard on a MTS Criterion 45 machine with a crosshead speed of 1 mm/min. The strain was measured by using an Instron 2620-601 contact extensometer with a gauge length of 50 mm and a full range of ±10%. The tensile modulus of these plates were calculated in the strain range of 0.01 to 0.15%.

3. Results and discussions

3.1 Fabric properties

- **Textiles properties**

Table 2 presents the textile properties of the produced QUD1 fabric as well as the textile properties of the quasi-unidirectional, named later QUD2 as reference for comparison, produced during the study of Corbin et al. [15]. This QUD2 fabric was manufactured by using twisted hemp yarns (characterized by a linear density of 153 Tex, a twist level of 222 turns/m) and a tenacity of 37 cN/tex) in the warp direction and low-twisted hemp roving (R1) in the weft direction. Both fabrics were woven with the same weave pattern and warp density, but the weft density of QUD2 is two times higher than that of QUD1. This difference is generated during the manual weaving process by packing highly the fabric during the insertion step of the weft yarns. Therefore, the linear density and the thickness of the QUD2 fabric are higher than that of QUD1. The higher number of rovings in the weft direction leads to a heavier and thicker fabric.

Table 2: Textiles properties of the woven fabrics.

Fabric properties	QUD1	QUD2 [15]
Warp yarns	Low-twisted rovings (R1)	Twisted yarns
Weft yarns	Untreated rovings (R2)	Low-twisted rovings (R1)
Warp density (yarns/cm)	0.6	0.6
Weft density (yarns/cm)	10	20
Areal density (g/m²)	424 ± 21	649 ± 3
Thickness (mm)	2.13 ± 0.06	2.97 ± 0.14

  doi:10.5075/epfl-298799_978-2-9701614-0-0

Air permeability (L/m²/s)	603 ± 89	424 ± 19

- **Mechanical properties**

The tensile properties of the produced reinforcements in terms of maximal load and strain at maximal load are shown in Figure 2. The high weft density of these structures leads to a higher fibers content in this direction compared to warp direction. Thus, the tensile properties are highly unbalanced between the two directions and are maximal in the weft direction. The weft density of QUD2 fabric is two times higher than that of QUD1 fabric, which leads to a higher maximal load at break for this structure. Furthermore, in order to evaluate the effect of the architecture, the maximal load is reported to the number of yarns in the weft direction and the linear density of the used roving in this direction. This comparison shows that the maximal load of QUD1 is higher than that of QUD2 even if QUD2 has a weft density two times higher than QUD1. This can be explained by the presence of twisted yarn in the structure of QUD2 compared to the low-twisted roving in QUD1. The presence of twisted yarn leads to a lower interlacement area between the two directions of this fabric. In addition, using treated rovings in the weft direction of QUD2 resulted on higher strain at maximal load compared to QUD1.

The bending properties, in terms of bending modulus, of the two structures are presented in Figure 2.d. Bending modulus is correlated to fiber content of the fabric, where, higher bending modulus is obtained in weft density direction since the fiber content in this direction is much higher than in the warp direction. Thus, QUD2 with higher weft density exhibited higher bending modulus than QUD1.

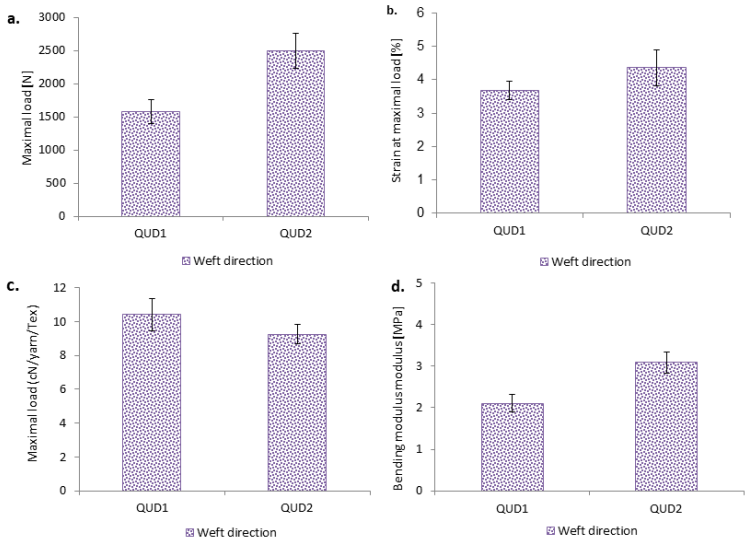

Figure 2. Tensile and bending properties of QUD1 and QUD2 fabrics in weft direction.

3.2 Composites properties

Table 3 presents the characteristics in terms of mechanical properties and intrinsic composition of the two produced composites in the fiber direction. Composite plates developed from the above-mentioned QUD fabric QUD1 and QUD2 are designed by QUDH1 and QUDH2 respectively. Stress and modulus are reported to an equivalent fiber volume ratio of 45% by using the rule of mixture to fairly compare their properties. For both composites, quasi-

unidirectional structure permits to reach higher fiber content in the composite. That result in higher global strength and stiffness for these structures in comparison for example to composites made of woven reinforcements. However, the transverse direction of these composites structure has lower tensile properties (not presented in the present study). Furthermore, the stiffness of the QUDH1 composites developed in this study is similar, considering the standard deviation, to that obtained for QUDH2 composites. Thus, even if the QUD1 fabric is produced by using untreated hemp rovings that have tenacity two times lower than that of treated rovings used for the production of QUD2 fabric, properties at composite scale are similar. Indeed, the presence of twisted yarns in the structure of QUDH2 composites induces disorientation of the hemp rovings within the structure. For the strength at failure of these composites, the obtained strength for QUDH1 is higher than the strength obtained for QUDH2. A difference of 37% is observed between the two types of composites and this difference can be attributed to the presence of the twisted yarns in the warp direction of QUD2 structure. Indeed, in the study of Corbin et al. [15], the microscopic view highlighted some cracks within the warp yarns and fracture profile of the tested samples confirmed that the initiation of the failure occurs in the region where the twisted yarns are located. These zones, constitute weak points for the composite where most of the strength are concentrated. It can be concluded, that even if the rovings present lower properties at the yarn scale, their associated composites exhibited good properties compared to composites made from strong rovings. Thus, the transverse direction plays an important role in the failure mechanisms of the composite materials.

Table 3: Composites properties.

Composites plates	Stress [MPa]	Strain [%]	Tensile Modulus [GPa]
QUDH1	297 ± 25	1.79 ± 0.02	25.2 ± 1.1
QUDH2 [15]	216 ± 31	1.36 ± 0.17	24.1 ± 0.5

4. Conclusion

The aim of this work was to produce a quasi-unidirectional hemp fabric by using untreated and low-twisted rovings by the manual weaving process. The main challenges, were to combine easy handling, fiber alignment, better impregnation by resin and lightness of the fabric. In this context, the quasi-unidirectional fabric was produced by using the untreated rovings in the weft direction with a high density and only few treated hemp rovings in the warp direction. This reinforcement was less heavy and less thick than other quasi-unidirectional reinforcement developed within the same project. However, this property still higher compared to conventional flax unidirectional fabrics already commercialized on the market. Otherwise, the fabrication process of this structure permitted to obtain higher fiber content in the main direction of the fabric and low crimping compared to woven structure. Thus, during weaving process of quasi-unidirectional fabric, the properties of rovings are less affected. Composites plates were then produced by the thermocompression process and characterized by tensile tests to compare their properties with previous study. Indeed, using this type of structure, result

on composite with high fiber content in the main direction and that leads to higher stiffness and strength properties in this direction and poor properties in the transverse direction.
The experimental results highlighted competitive properties both at fabric and composite scale, when compared them to previous development.

Acknowledgements

The authors would like to thank the Italian Company Linificio e Canapificio Nazionale for providing the hemp rovings used in this study. This study was carried out within the European SSUCHY program.

5. References

1. Graupner N, Weber DE, Bell EG, Lehmann K-H, Hilgers H-W, Randerath H, et al. Hemp from Disordered Lines for New Staple Fibre Yarns and High-Performance Composite Applications. Frontiers in Materials. 2022;8.
2. Tanasa F, Zănoagă M, Teacă C, Nechifor M, Shahzad A. Modified hemp fibers intended for fiber-reinforced polymer composites used in structural applications—A review. I. Methods of modification. Polymer Composites. 2019;41.
3. Thyavihalli Girijappa YG, Mavinkere Rangappa S, Parameswaranpillai J, Siengchin S. Natural Fibers as Sustainable and Renewable Resource for Development of Eco-Friendly Composites: A Comprehensive Review. Frontiers in Materials. 2019 ;6.
4. Bourmaud A, Beaugrand J, Shah DU, Placet V, Baley C. Towards the design of high-performance plant fibre composites. Progress in Materials Science. 2018; 97:347-408.
5. Müssig J, Fischer H, Graupner N, Drieling A. Testing Methods for Measuring Physical and Mechanical Fibre Properties (Plant and Animal Fibres). Industrial Applications of Natural Fibres. John Wiley & Sons, Ltd; 2010. p. 267-309.
6. Goutianos S, Peijs T, Nystrom B, Skrifvars M. Development of Flax Fibre based Textile Reinforcements for Composite Applications. Appl Compos Mater. 2006; 13:199-215.
7. Baets J, Plastria D, Ivens J, Verpoest I. Determination of the optimal flax fibre preparation for use in unidirectional flax–epoxy composites. Journal of Reinforced Plastics and Composites. SAGE Publications Ltd STM; 2014; 33:493-502.
8. Poilâne C, Zine Eddine C, Richard F, Vivet A, Ben Doudou B, Chen J. Polymer reinforced by flax fibres as a viscoelastoplastic material. Composite Structures. 2014;
9. Scida D, Bourmaud A, Baley C. Influence of the scattering of flax fibres properties on flax/epoxy woven ply stiffness. Materials & Design. 2017;122.
10. Shah D, Schubel P, Clifford M, Licence P. Mechanical Property Characterization of Aligned Plant Yarn Reinforced Thermoset Matrix Composites Manufactured via Vacuum Infusion. Polymer-Plastics Technology and Engineering. 2013;53.
11. Müssig J, Amaducci S, Bourmaud A, Beaugrand J, Shah DU. Transdisciplinary top-down review of hemp fibre composites: From an advanced product design to crop variety selection. Composites Part C: Open Access. 2020; 2:100010.
12. Corbin A-C, Soulat D, Ferreira M, Labanieh A-R, Gabrion X, Malécot P, et al. Towards hemp fabrics for high-performance composites: Influence of weave pattern and features. Composites Part B: Engineering. 2020; 181:107582.
13. Abbas Z, Shahid S, Nawab Y, Shaker K, Umair M. Effect of glass microspheres and fabric weave structure on mechanical performance of hemp/green epoxy composites. Polymer Composites. 2020; 41:4771-87.
14. Sala B, Gabrion X, Trivaudey F, Guicheret-Retel V, Placet V. Influence of the stress level and hygrothermal conditions on the creep/recovery behaviour of high-grade flax and hemp fibre

reinforced GreenPoxy matrix composites. Composites Part A: Applied Science and Manufacturing. 2021; 141:106204.
15. Corbin A-C, Sala B, Soulat D, Ferreira M, Labanieh A-R, Placet V. Development of quasi-unidirectional fabrics with hemp fiber: A competitive reinforcement for composite materials. Journal of Composite Materials. SAGE Publications Ltd STM; 2021; 55:551-64.
16. Swolfs Y, Verpoest I, Gorbatikh L. Recent advances in fibre-hybrid composites: materials selection, opportunities and applications. International Materials Reviews. Taylor & Francis; 2019; 64:181-215.
17. Baley C, Gomina M, Breard J, Bourmaud A, Drapier S, Ferreira M, et al. Specific features of flax fibres used to manufacture composite materials. Int J Mater Form. 2019; 12:1023-52.
18. Madsen B, Hoffmeyer P, Thomsen AB, Lilholt H. Hemp yarn reinforced composites – I. Yarn characteristics. Composites Part A: Applied Science and Manufacturing. 2007; 38:2194-203.
19. Shah DU, Schubel PJ, Clifford MJ. Modelling the effect of yarn twist on the tensile strength of unidirectional plant fibre yarn composites. Journal of Composite Materials. SAGE Publications Ltd STM; 2013; 47:425-36.
20. Madsen B, Thygesen A, Lilholt H. Plant fibre composites-porosity and stiffness. Composites Science and Technology. 2009; 69:1057-69.
21. Decorme J, Duval A, VANFLETEREN E, VANFLETEREN F. Method for producing a continuous web of fibres comprising long natural fibres, and associated apparatus and web. 2014.
22. Khalfallah M, Abbès B, Abbès F, Guo YQ, Marcel V, Duval A, et al. Innovative flax tapes reinforced Acrodur biocomposites: A new alternative for automotive applications. Materials and Design. 2014; Complete:116-26.
23. Corbin A-C, Soulat D, Ferreira M, Labanieh A-R. Influence of Process Parameters on Properties of Hemp Woven Reinforcements for Composite Applications: Mechanical Properties, Bias-extension Tests and Fabric Forming. Journal of Natural Fibers. Taylor & Francis; 2020; 0:1-13.
24. Labanieh AR, Garnier C, Ouagne P, Dalverny O, Soulat D. Intra-ply yarn sliding defect in hemisphere preforming of a woven preform. Composites Part A: Applied Science and Manufacturing. 2018; 107:432-46.
25. AFNOR NF G07-316. Textiles - Tests of yarns - Determination of linear density. 1988.
26. AFNOR NF G07-079. Textiles - Testing threads - Determining the twisting of threads by untwisting/retwisting with a double re-test. 2011.
27. AFNOR NF EN ISO 2062. Textiles - Yarns from packages - Determination of single-end breaking force and elongation at break using constant rate of extension (CRE) tester. 2010.
28. AFNOR NF EN 12127. Textiles - Fabrics - Determination of mass per unit area using small samples. 1998.
29. AFNOR NF EN ISO 5084. Textiles - Determination of thickness of textiles and textile products. 1996.
30. AFNOR. NF EN ISO 9237. Textiles - Determination of permeability of fabrics to air. 1995.
31. AFNOR. NF EN ISO 13934-1. Tensile properties of fabrics - Part 1: determination of maximum force and elongation at maximum force using the strip method. 2013.
32. AFNOR ISO 4604. Reinforcement fabrics - Determination of conventional flexural stiffness - Fixed-angle flexometer method. 2011s.
33. ASTM International ASTM D3039 / D3039M-17. Standard Test Method for Tensile Properties of Polymer Matrix Composite Materials. West Conshohocken; 2017.

  doi:10.5075/epfl-298799_978-2-9701614-0-0

EFFECT OF DIFFERENT NATURAL FIBRES ON MECHANICAL AND DISINTEGRATION PROPERTIES OF COMPOSTABLE BIOBASED PLASTICS

Vincent Röhl[a], Corinne van Nordenne[b], Hansjörg Wieland[c], Jörg Müssig[a]*

a: HSB – City University of Applied Sciences, Dept. of Biomimetics, The Biological Materials Group, Neustadtswall 30, D-28199 Bremen, Germany; jmuessig@bionik.hs-bremen.de

b: NHL Stenden, Rengerslaan 8-10, 8917 DD Leeuwarden, The Netherlands

c: 3N Kompetenzzentrum Niedersachsen Netzwerk Nachwachsende Rohstoffe und Bioökonomie e.V., Kompaniestraße 1, 49757 Werlte, Germany

Abstract: *Compounds containing the compostable biobased plastic PHBH and 30 mass% of cotton, merino-wool, wood fibres, and hemp fibres, respectively, were created, and foils were manufactured using a laboratory hot press. Samples for mechanical characterisation were also produced by injection moulding. Samples were submerged in bioactive soil for 16 weeks to determine the influence of fibre type on the biodegradation speed in soil. The degradation was measured by subsequent excavation and determination of dry mass loss and visual inspection. All kinds of natural fibres generally improve degradation speed. The most significant improvement was reached by samples containing cotton and wool, which experienced similar mass loss, followed by the ones containing hemp fibres. The smallest increase in degradation speed was achieved by samples containing wood fibres. Mechanical properties and cost saving potential were increased in the samples containing cotton and hemp.*

Keywords: Biodegradation; PHBH; 3-Hydroxyhexanoate and 3-Hydroxybutyrate; Home Compostable; Natural Fibres

1. Introduction

Compostable thermoplastics may solve severe littering and microplastic generation problems in a large range of products (Bauchmüller et al., 2021). While the production capacities and demand are rising for these types of polymers, the price is still relatively high. Natural fibres are often mentioned as a way of reducing material costs, which is only valid if the mechanical properties of the composite are not critically reduced. To assess the suitability of a material to substitute an existing one without sacrificing performance and at the same time reducing cost can be evaluated using material indices, depending on the mechanical load case (Ashby, 2005). The cost-saving potential can be quantified by using these indices.

Depending on the application, an increased rate of material disintegration may be beneficial. Due to the entirely different chemical composition of different types of natural fibres, the degradability in soil differs greatly. Wool seems to be particularly interesting in this context (Röhl & Müssig, 2022). In animal hair, the disulphide bond between cysteine molecules can be broken by ceratinolytic microorganisms under the appropriate environmental conditions, and the hair can be degraded (Solazzo, 2013). During the biodegradation of wool in the soil, sulphur and

  doi:10.5075/epfl-298799_978-2-9701614-0-0

nitrogen are made available to the plants and act as fertilisers. Gorecki & Gorecki (2010) have shown that 1 g of washed wool per cubic decimetre of soil can increase the fruit yield of tomato and pepper plants by up to 30 % (Gorecki & Gorecki, 2010).

In the context of the presented investigations, the question arose of how the degradation rates of the compostable biobased plastic PHBH change through the addition of different natural fibres. For this purpose, composite materials with 30 mass% of cotton, merino wool, wood fibres and hemp fibres were produced. The degradation rates were investigated after burying the samples in bioactive soil.

2. Materials & Method

Compounds were created according to the recipes in Table 1, using different natural fibres, including bast fibres, wood fibres, animal hair and seed fibres. PHBH type Kaneka X331N was supplied as a polymer matrix by H&P Moulding Emmen B.V. (Emmen, The Netherlands). The current market price for this polymer was given at roughly 10 €/kg. The prices and sources for the fibres are listed in Table 1. Prices for Merino wool at the given fineness are taken from the Micron Price Guide (AWI MPG, 2022) for Week 35 in 2021. The cotton price is assumed, given the current market reports and currency rates (USDA, 2022).

Table 1: Compositions of the created compounds as well as fibre sources and prices

Nr.	Matrix	Fibre Type	Fibre content in % mass	Fibre source	Fibre Price in € / kg
1	Kaneka X331N	Cotton fibres	30	Buckmann Handel (Bremen, DE)	2.4
2	Kaneka X331N	Arbocel UFC100 (wood fibres)	30	Rettenmeier Holding AG (Willburgstetten, DE)	3.3
3	Kaneka X331N	Merino wool (20 mic)	30	Wollknoll GmbH (Oberrot, DE)	9.4
4	Kaneka X331N	Hemp fibres (55 mm)	30	HempFlax Group B.V. (Oude Pekela, NL)	1.0
5	80 % Kaneka X331N + 20 % Nuvolve (TPS)	Merino wool (20 mic)	30	Wollknoll GmbH (Oberrot, DE)	9.4
6	Kaneka X331N	-	0	-	

For tensile and impact testing, samples were injection moulded into cold moulds of temperature 25 °C. The cooling time inside the mould was 30 seconds. For the degradation testing, foils of thickness 0.4 mm were produced using a laboratory hot press (LaboPress P200S der Firma Vogt, Berlin, DE). The pressing temperature was set to 170 °C at a pressing time of 5 minutes. Before pressing, the granulate was placed in the press and was given 5 minutes to warm up. Final thickness was achieved using Teflon foil as spacers. Eighteen strips of size 2 x 8 cm² were cut from each sample so that 3 samples could be dug up at each sampling point (after 1, 2, 4, 8, 12 and 16 weeks). The sample's dry mass was measured, and afterwards, the samples were

  doi:10.5075/epfl-298799_978-2-9701614-0-0

submerged into bioactive soil in an indoor testing facility at room temperature. The soil's moisture was checked weekly, and water was added if necessary.

Mechanical properties were tested on the injection-moulded samples. Tensile testing was performed on a Zwick/Roell Z020 universal testing machine (Zwick GmbH and Co., Ulm, DE), equipped with a 20 kN load cell, using a testing speed of 2 mm/min. The strain was measured using a video extensometer (VideoXtens, Zwick/Roell GmbH, Ulm, DE). The Charpy impact strength was measured on unnotched samples cut from the tensile bars using an impact hammer with a maximum energy of 2 J (type 5101 (Zwick GmbH, Ulm, DE).

In order to assess the cost-saving potential of the different compounds in applications limited by tensile strength performance, a model was used to determine the cost for a plate under uniform load following Ashby (2005). Material indices for the cost-saving potential were derived, taking into account raw material and manufacturing costs as well as mechanical properties. For this, a compounding cost of 70 ct/kg was assumed. A higher index value resembles a greater cost-saving potential. The material index for a plate under uniform load is derived as:

$$M = \frac{\sqrt{R_m}}{C_v} \quad (1)$$

R_m: Tensile strength

C_v : Cost per unit Volume

The costs per unit volume takes into account the material density, prices of fibre and matrix, as well as compounding costs:

$$C_v = \left(\varphi * C_f + (1 - \varphi) * C_m + C_c\right) * \rho \quad (2)$$

φ : Fibre mass fraction

C_f : Cost per kg of the fibres

C_m: Cost per kg of the matrix

C_c : Cost per kg for compounding

ρ : Composite density

3. Results & Discussion

3.1 Mechanical characterisation

The results of the mechanical tests are summarised in Table 2. Youngs-modulus was improved in all samples compared to the neat matrix. The highest stiffness was reached by hemp fibres, with cotton being close below at roughly 6 GPa. This is quite surprising, as common literature usually gives a Young's modulus of 10 – 12 GPa for cotton fibres. When modelling the expected composite Young's modulus using the Halpin-Tsai model for 2D-randomly oriented short fibres (Tsai & Kardos, 1976), the results, even assuming very optimistic fibre lengths of 2 mm, are nowhere near the measured values. In ongoing research, this phenomenon will be further investigated.

  doi:10.5075/epfl-298799_978-2-9701614-0-0

Concerning tensile strength, the highest values are reached by the samples containing cotton, with an increase of over 50 % compared to the neat matrix. While hemp fibres also led to increased tensile strength, even though not as severe as in the cotton samples, all other fibre types led to a decrease compared to the neat matrix.

Promising results were obtained in testing impact strength, where cotton samples gained the highest strength. The second highest values were reached by samples containing merino wool, even though tensile strength was reduced in these samples, which could be due to the high strain potential of these fibres. This effect was not visible in the samples with merino wool and the 20 % thermoplastic starch in the matrix, which could be due to reduced deformability of the matrix due to TPS presence. In all other samples, impact strength was reduced compared to the neat matrix.

When calculating the material indices for the cost-saving potential, it is clear that cost savings can be realised for the samples containing cotton and hemp. This is due to the improved tensile strength in combination with the relatively low price for the raw fibres. No cost savings can be directly achieved for the samples containing wood fibres. But due to the small difference in the material index, this material may still be used to replace the neat matrix if an increased tensile stiffness is desirable. Due to the high price of merino wool, combined with a low tensile strength, product costs cannot be reduced when using this material. This is to be expected as fine merino wool is sought after for use in garments and textiles. A possibility would be to use coarser wool types, often discarded and therefore low priced. But as previous investigations have shown (Roehl & Müssig, 2022), a drop in tensile strength is to be expected due to low fibre-matrix interaction.

Table 2: Results of the mechanical testing as well as the calculated material index. For materials with indices higher than the value of the neat matrix (0.439), cost can be saved by substitution.

Nr.	Young's Modulus in GPa	Tensile strength in MPa	Impact strength in kJ/m²	Density in g / cm³	M
1 – Cotton	6 ± 0.2	42.6 ± 0.5	18.9 ± 3.8	1.26	0.615
2 – Wood	4.4 ± 0.1	23.7 ± 0.4	6.4 ± 0.5	1.28	0.438
3 – Wool	3.1 ± 0.1	23.0 ± 0.3	17.9 ± 2.7	1.21	0.377
4 – Hemp	6.6 ± 0.2	32.8 ± 0.4	10.9 ± 1.4	1.27	0.564
5 – Wool (mod. Matrix)	3.8 ± 0.2	17.2 ± 0.4	7.6 ± 1.1	1.25	0.315
6 – Neat	2 ± 0.1	27.3 ± 0.6	12.6 ± 2.3	1.19	0.439

3.2 Degradation tests

The visual disintegration of the submerged pieces is shown in Figure 1. Visually, it seems that the highest disintegration was present in the samples containing wool, with only small fragments being left after 16 weeks. The second highest disintegration was achieved by cotton samples,

followed by hemp. Visually, the neat matrix and the samples containing wood fibres are only slightly damaged with an intense colour change and loss of transparency.

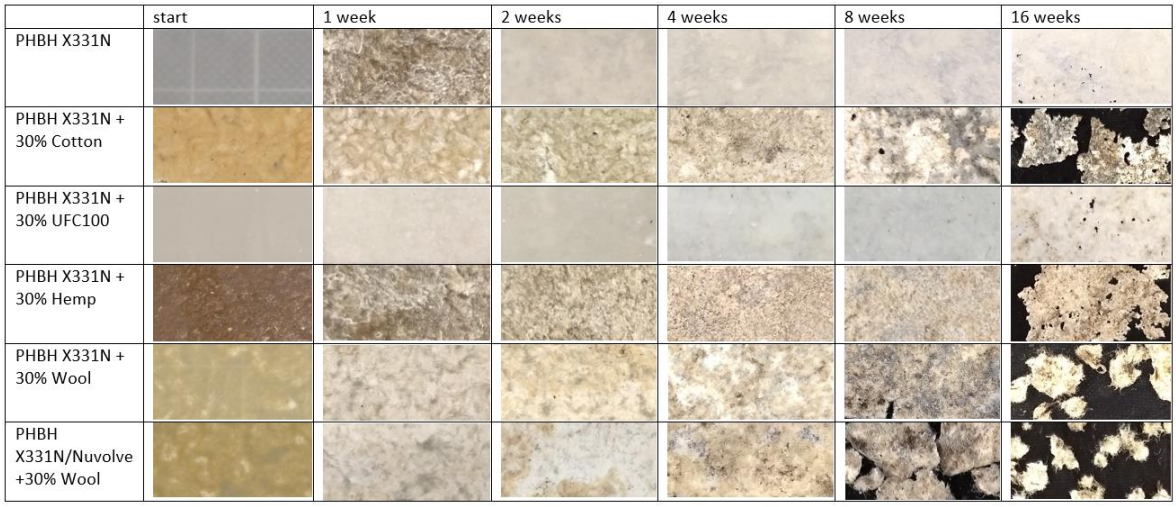

Figure 1: Visual inspection of the excavated pieces after the given time period. The first picture is brighter due to a different environment. Picture after 1 week of submerging should be used as a reference.

Figure 2 shows the relative mass loss of the samples over the course of 16 weeks. The coloured areas show the standard deviation range inside each sample (n=3). It is visible that the largest mass loss is achieved for the specimens containing wool, followed by the ones containing cotton. These are followed by the samples containing hemp fibres. The standard deviation of the mass loss after 16 weeks is very high in the specimens containing cotton and hemp so that no significant difference can be stated unless the experiment were to be repeated with more specimens, even though the visual inspection seems to undermine the observation that disintegration is stronger in the wool specimens. The lowest mass loss was measured in the neat matrix, with the introduction of short wood fibres leading only to a slight increase in disintegration severity.

  doi:10.5075/epfl-298799_978-2-9701614-0-0

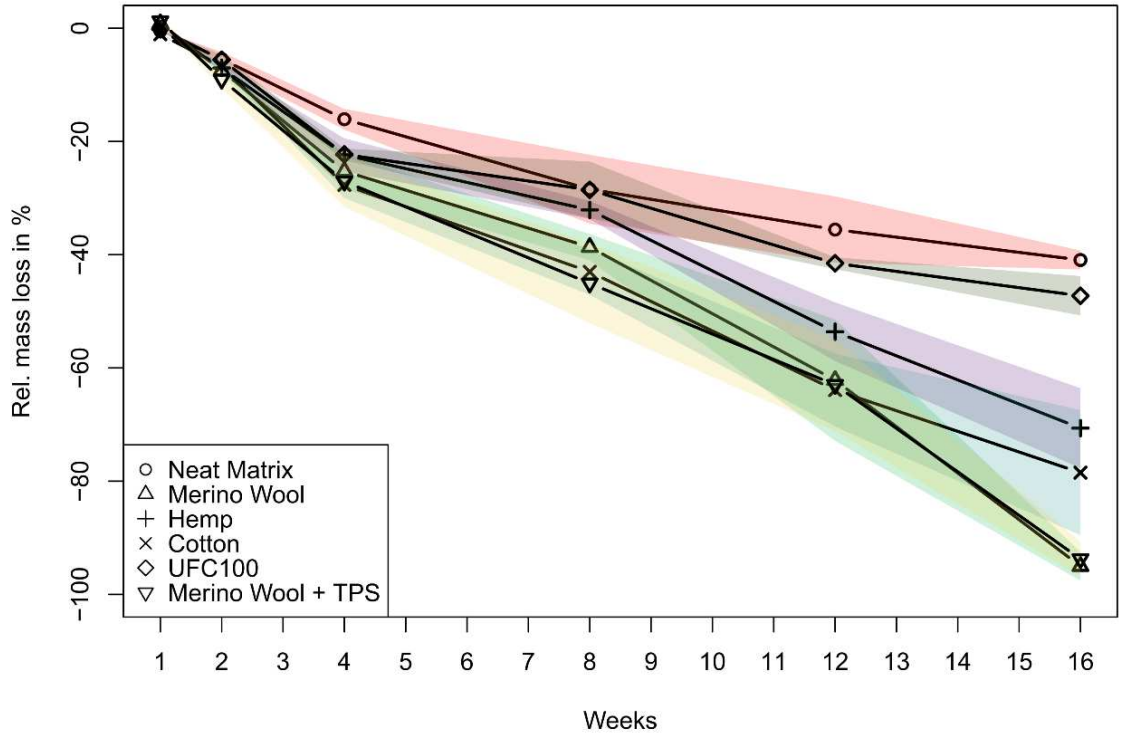

Figure 2: Relative mass loss of the samples submerged in soil. Coloured areas specify the range of the respective standard deviation; 3 specimens were excavated for each date and material.

3.3 Discussion

The introduction of natural fibres is auspicious for improving the degradation rates of compostable thermoplastics. Cotton shows large cost-saving potential due to the high mechanical properties achieved in combination with the low cost. A strong influence of fibre type on the disintegration rate of the composites was observed. The effect was especially strong in the samples containing wool fibres, which is probably due to the nurturing substrate that wool gives to ceratinolytic bacteria as well as a large number of cracks and increased surface area due to exposed fibres on the surface and a rather weak fibre-matrix interaction. It is also interesting to note that the impact toughness was improved relative to the neat matrix. If a cheaper wool type could be utilised in composite applications without sacrificing the mechanical properties, a cost-saving effect could be implemented while improving toughness and allowing faster biodegradation.

4. Conclusion

It has been shown that the degradability of compostable polymer materials such as polyhydroxybutyrate (PHB) can be controlled by the use of natural fibres. Cotton is an attractive candidate from different points of view. In addition to good degradability properties, it also

  doi:10.5075/epfl-298799_978-2-9701614-0-0

showed excellent mechanical properties, especially impact strength. Wool, too, showed exciting potential in the studies by improving the degradation rate, and a possible fertilising effect could result in unique advantages in an agricultural environment. Due to the high wool prices for the textile industry, the use of previously unused wool from waste and residual streams is favoured, but the influence of these wool types on the mechanical properties, as well as the possibilities for improving fibre-matrix interaction, should be investigated.

Acknowledgements

This research took place within the framework of Project Bioeconomy. We acknowledge the funding agencies within the cross-border project "Bioeconomy – Green Chemistry "(https://edr.eu/project/bio-oekonomie-gruene-chemie), funded within the programme 'INTERREG V A-Germany – Netherlands' by the European Fund for Regional Development (EFRE) co-financed by the state of Lower-Saxony, the Dutch ministry of economics and the Dutch provinces Drenthe, Flevoland, Fryslân, Gelderland, Groningen, Noord-Brabant and Overijssel.

5. References

1. Ashby, M.F., 2005. Materials Selection in Mechanical Design, 3rd ed. Elsevier Butterworth Heinemann, Linacre House, Jordan Hill, Oxford OX2 8DP, ISBN 0750661682.
2. AWI MPG, 2022. Micron price guide, weekly report by the Australian Wool Innovation Ltd., <https://www.wool.com/market-intelligence/weekly-price-reports/> (2022-03-01).
3. Bauchmüller, V., Carus, M., Chinthapalli, R., Dammer, L., Hark, N., Partanen, A., ... & Lajewski, S. 2021. BioSinn-Products for Which Biodegradation Makes Sense. nova-Institut für politische und ökologische Innovation GmbH, Hürth, Germany.
4. Górecki, R., Górecki, M., & others, . 2010. Utilisation of waste wool as substrate amendment in pot cultivation of tomato, sweet pepper, and eggplant. Polish Journal of Environmental Studies, 19(5), 1083 – 1087.
5. Tsai, H., & Kardos, J. L. (1976). The Halpin-Tsai Equations. Polym. Eng. Sci, 16, 344-352.
6. Röhl, V. & Müssig, M. 2022: Wool fibre-reinforced thermoplastic polymers for injection moulding and 3D-printing. In: Thomas. S. & Seiko, J. (Eds.): Wool-Polymer composites, ELSEVIER, Amsterdam, NL (in press)
7. Solazzo, C., Dyer, J., Clerens, S., Plowman, J., Peacock, E., & Collins, M. 2013. Proteomic evaluation of the biodegradation of wool fabrics in experimental burials. International Biodeterioration & Biodegradation, 80, 48 – 59. Elsevier.
8. USDA, 2022. Monthly price statistics. Cotton market news division, Memphis, USA. <www.ams.usda.gov/mnreports/cnmcps.pdf> (2022-03-01)

  doi:10.5075/epfl-298799_978-2-9701614-0-0

HIGH-STRENGTH RIGID BOARDS MADE FROM INDUSTRIALLY PRODUCED BACTERIAL CELLULOSE

Katrin G. Hoffmann[a], Gustav Nyström[a], Thomas Geiger[a]

a: Laboratory for Cellulose & Wood Materials, Empa – Swiss Federal Laboratories for Materials Science and Technology, Überlandstrasse 129, 8600 Dübendorf, Switzerland

Abstract: *The desire for independence of petroleum promotes the development of novel biopolymers as future substitute for conventional polymer materials. Here, industrially produced bacterial cellulose was dewatered using an optimized thermo-compression process with a subsequent drying step, resulting in mechanically very stable boards with several millimeter thickness. The removal of impurities from the bacterial cellulose fermentation by moderate bleaching with NaClO and NaOH led to an exceptional flexural stiffness of 22 GPa and a flexural strength of 225 MPa. The uptake of moisture induced a reversible plasticization of the material with a decrease of flexural and tensile properties, still outperforming most conventional plastics. Moreover, the original mechanical properties were regained even after repetitive wetting and drying of the material. The mouldability into 3D shapes during dewatering and drying was demonstrated.*

Keywords: cellulose nanofibrils; *nata de coco*; thermo-compression; mouldability

1. Introduction

The desire for independence of petroleum promotes the development of novel biopolymers as future substitutes for conventional polymer materials. However, inefficient processing, insufficient material properties as well as a poor price/performance ratio are still reasons for limited industrial use of these biomaterials. Yet the advantages of biopolymers are evident. Cellulose, for example, has a renewable origin, is biodegradable as well as environmentally friendly, recyclable, and CO_2-neutral when incinerated. In addition, the chemical structure of cellulose macromolecules allows for self-assembly into fibrils and fibers through hydrogen bonding, resulting in mechanically high-strength bulk materials. Especially when exceptional mechanical stability is required for technical applications, this self-bonding property of cellulose is an advantage that standard plastics do not possess. Instead, additional reinforcement must be introduced by compounding the plastics with artificial or natural fibers. The self-binding property of highly disintegrated cellulose fibers from plants was already discovered at the beginning of the 20th century and a process for the production of solid horn-like bodies was patented [1]. One century later, advanced fibrillation technology enabled the production of boards made from nanofibrillated cellulose from wood pulp with strongly increased mechanical properties of 16 GPa for flexural modulus and 250 MPa for flexural strength [2].

We are now the first to report the production and characterization of rigid boards from industrially produced bacterial cellulose (BC). One advantage of BC over wood-based cellulose materials is its inexpensive production by glucose fermentation in large scale with low energy requirement as an alternative to the more costly and energy demanding wood pulping process with subsequent mechanical disintegration to cellulose nanofibrils (CNF). Without the use of

  doi:10.5075/epfl-298799_978-2-9701614-0-0

solvents, binders or other chemical additives, rigid boards of several millimeter thickness were produced by thermal compression of BC. Different types of industrial BCs and varying processing parameters were studied.

2. Experimental section

2.1 Materials and board fabrication

Bacterial cellulose was obtained as *Nata de coco* from 99 Gold Data Trading Co., Ltd. (Thành phố Hồ Chí Minh, Vietnam). It consists of flakes (edge length approx. 10 mm) with a solid content of 6–7 wt. % and a pH of 1–2 (*BC-01*). It was rinsed with deionized water for seven days to remove residual sugars and proteins from bacteria cultivation (*BC-02*). Further purification was achieved through treatment with 2 wt. % NaOH (aq.) at ambient temperature for 16 h and rinsing with deionized water until pH was below 10. This was followed by a treatment with 0.5 wt. % NaClO (aq.) for 6 h and extensive rinsing with deionized water (*BC-03*). Before the preparation of boards, both *BC-02* and *BC-03* were partly dewatered in a sieve basket under a mass of 200 kg to a solid content of 5.6–6.3 wt. %. Purified BC pellicles (*BC-04*) for cosmetic use were purchased from fzmb GmbH (Bad Langensalza, Germany).

For production of rigid squared boards in the size of 100 x 100 x 2 mm³, a corresponding amount of BC material was filled into a porous mold (Figure 1a). Sealings and four layers of stainless-steel fabric covering the holes in the lower and upper part of the mold prevented BC material from escaping the mold's cavity during compression with a laboratory press (4122 12-12H, Carver, Inc., Wabash, IN, USA). Initial dewatering was done at ambient temperature under 10.8 MPa for 30 min, followed by hot pressing at 120 °C under 10.8 MPa for 120 min and subsequent drying at 105 °C for 24 h in a convection oven under a 5 kg mass. For *BC-02*, the duration of either the hot pressing or the duration of the oven drying step was varied from 0 to 120 min and from 0 to 39 h, respectively, while maintaining the other at 120 min or 24 h to study the influence of processing parameters on mechanical properties. Plate thickness was monitored during hot pressing by measuring the height of the mold cavity and plate mass was measured during drying in regular intervals. The dried boards were stored in a desiccator filled with silica gel.

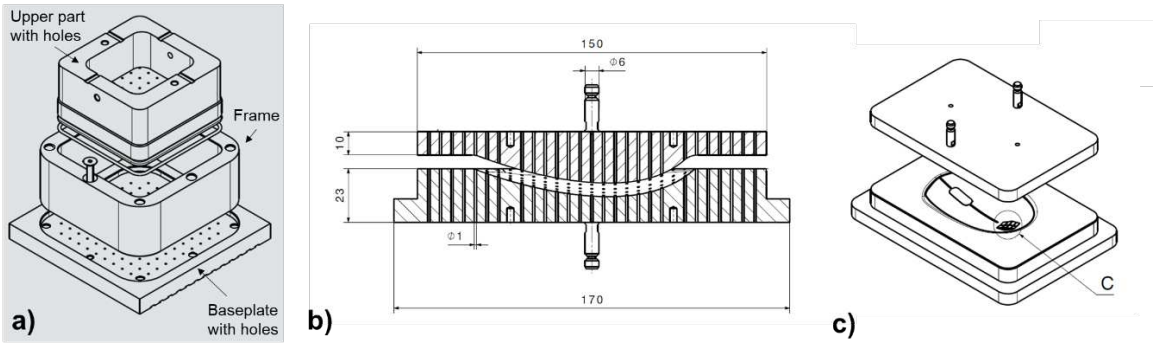

Figure 1. Mold used for the thermo-compression of BC boards (a), porous inserts (b) and solid body inserts (c) for 3D-moulding of mouse cover.

2D-molding experiments with *BC-02* and *BC-04* were conducted after short preliminary dewatering at 90 °C and 5 MPa for 2–3 min using the equipment above (targeted board thickness of 0.25 mm). Hot pressing at 120 °C and 10.8 MPa was then performed between two

  doi:10.5075/epfl-298799_978-2-9701614-0-0

stainless-steel plates with a matching repetitive 2D-trapezoid geometry. For 3D-moulding of a mouse cover, a specially designed mold with changeable inserts was used in a 150 t laboratory press (Gottfried Joos Maschinenfabrik GmbH & Co. KG, Pfalzgrafenweiler, Germany). *BC-04* sheets for a targeted board thickness of 1.2 mm were placed between porous mold inserts, where the holes in both insert parts were covered with two layers of stainless-steel wool and peel ply fabric (Figure 1b). Dewatering at ambient temperature to a thickness of approx. 10 mm took 15 min. Drying was then performed in the mold with solid body inserts (Figure 1c), without sealings and one layer of peel ply around the BC molding for escape of water vapor. The height of the cavity was slowly decreased from 10 mm to 4 mm over 80 min at 90–100 °C. After removing the peel ply, the BC mouse cover was finished by compressing at 120 °C and 100 MPa for 15 min with a preceding pressure increase over 15 min.

2.2. Flexural and tensile properties

Specimen preparation for mechanical tests (n = 5) was done with a laser cutter (Nova 24, 60 W, Thunder Laser USA LLC., Quitman TX, US) with 80 % cutting power and a cutting speed of 17 mm/s. Three-point flexural testing was conducted following DIN ISO 178 using a universal testing machine (Z100, ZwickRoell GmbH & Co. KG, Ulm, Germany) equipped with 1 kN load cell. Specimen geometry was 10 x 80 mm² and the span width equaled 16 times board thickness. The pre-force was 5 N and testing speed 1 mm/min. Tensile testing followed DIN EN ISO 527-2 using a load cell of 100 kN. The dog-bone shaped specimens 1BA were clamped with a pre-load of 5 N. The testing speed was 0.25 mm/min for the determination of the tensile modulus and then increased to 1 mm/min. If not stated differently, specimens were conditioned for three days before testing in a desiccator with silica gel at ambient temperature. Humid conditioning was performed either at 50 % relative humidity and 23 °C or at 85 % relative humidity and 20 °C. The specimen's mass change was monitored for calculation of water content. After testing, the specimens were dried at 105 °C for 24 h to determine the dry mass.

To investigate the influence of water uptake and release, tensile specimens were stored in weekly alternating climate conditions switching between 85 % in a climate chamber and < 5 % relative humidity in a desiccator with silica gel. After each week at dry conditions, five specimens were withdrawn, and their tensile properties determined as described above. Deviating, the testing speed was 0.5 mm/min after modulus determination. At each change of climate conditions, specimen mass and thickness were recorded. After the experiment, all specimens were dried at 105 °C for 24 h to determine the dry mass and thickness.

3. Results and Discussion

BC has several advantages over plant cellulose nanofibrils. It consists of an exceptionally homogeneous, three-dimensional interwoven network of hierarchically organized cellulose fibrils that exhibit both high crystallinity and a high degree of polymerization. In addition, the BC network has good water holding capacity, excellent mechanical properties and good formability. Also known as *nata*, BC can be produced by fermentation of *Acetobacter xylinum* using fruit juices as nutrient medium. *Nata de coco* is the term used for BC produced in coconut water as nutrient medium. It is a common food in Asian countries such as the Philippines, Indonesia, Vietnam, Thailand, or Indonesia [3]. After fermentation, raw *nata de coco* contains over 90 % of water, cellulose fibrils, and impurities including bacteria, proteins, nucleic acids, and residual carbohydrates [4].

  doi:10.5075/epfl-298799_978-2-9701614-0-0

Partial dewatering or complete drying of *nata de coco* is an important aspect for its industrial processing in order to reduce transport volume and thus costs. Numerous publications therefore report on methods to efficiently reduce or remove water from the BC hydrogel [5-11]. Furthermore, it has been recognized that in the production of paper-like films for various applications, such as packaging or membranes for loudspeakers, the level of impurities in the BC has a significant influence on the mechanical properties of the dried material. In general, it was found that higher stiffness and strength can be achieved with a higher degree of purity. Subsequently, cleaning processes using aqueous solutions of sodium hypochlorite and sodium hydroxide were described [12], which were also applied here. However, the use of a bleach can also have a negative effect on the mechanical properties due to its influence on the crystallinity and molecular weight of the cellulose. Therefore, the solution's concentration, time and temperature for cleaning must be optimized for obtaining maximum properties.

For our study, four different BC materials were used: commercially available raw *nata de coco BC-01*, rinsed *nata de coco BC-02*, purified *nata de coco* (bleached with NaOH and NaClO) *BC-03* and commercial available BC sheets (purified by the company with an alkaline solution and sterilized in water) *BC-04*.

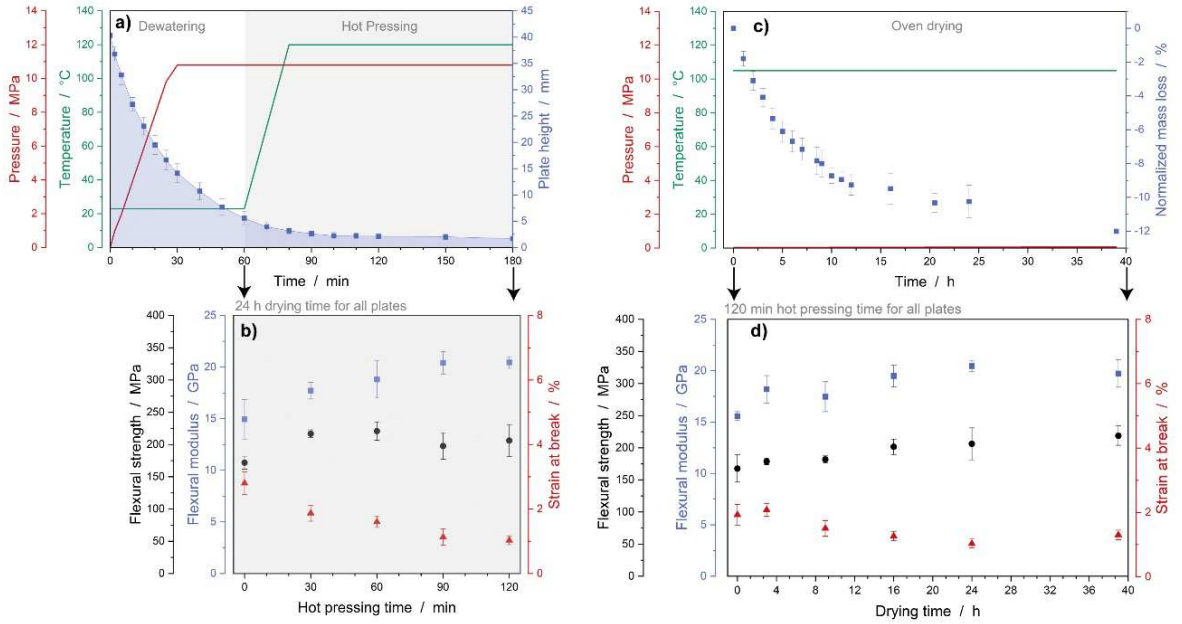

Figure 2. Plate height during thermo-compression (a) and mass loss during oven drying (c) of BC boards. Flexural properties after fabrication with varying hot pressing (b) and oven drying times (d). The error bars represent the standard deviation.

With the aim of reducing the time and energy consumption required to produce anhydrous BC boards while maintaining the mechanical properties, hot pressing and drying time were varied accordingly (Figure 2). When dewatering *BC-02* in the porous mold with increasing pressing pressure from 0 to 10.8 MPa at ambient temperature, no further dewatering and thus change in thickness of the board was observed after 60 min. Only if temperature was increased to 120 °C while maintaining the constant pressure of 10.8 MPa, further dewatering and change in plate thickness was observed. With increasing dwell time under these conditions, an increase in flexural modulus and flexural strength as well as a decrease in strain at break was determined.

  doi:10.5075/epfl-298799_978-2-9701614-0-0

After 90 to 120 minutes of hot pressing, the sheet thickness of *BC-02* did not vary further and the mechanical properties changed only insignificantly. This trend is also observed for specimens where the duration of hot pressing was kept constant with 120 min while the duration of the oven drying step at 105 °C was varied. Specimens continued to lose up to up to 11 % of their mass during 24 h of drying and showed maximum flexural modulus (20.5 GPa) and flexural strength (206 MPa) after 24 h. Interestingly, a longer drying time of 39 h at 105 °C led to a further loss of mass (12 %) but no increase of stiffness or strength. Thus, a hot pressing time of 120 min at 10.8 MPa and a drying time of 24 h at 105 °C were chosen for further investigations.

In order to investigate the influence of impurities, such as proteins or residues of carbohydrates, on the mechanical properties of BC, rigid boards were prepared from *BC-01*, *BC-02*, *BC-03* and *BC-04* (Figure 3a-d) and their flexural modulus and strength were determined (Figure 3e). In general, with decrease of impurities (*BC-01* to *BC-04*) the flexural moduli increased from 18.0 to 24 GPa, i.e., the material became increasingly stiffer. This can be explained by a maximum formation of intra- and intermolecular hydrogen bonding at *BC-04*, since impurities hindering the bond formation are not present here. Moreover, during the fabrication of *BC-01* plates, the impurities led to cavern formation, which are also a reason for the early failure during flexural loading. Flexural strength increased from 141 MPa to 225 MPa from *BC-01* to *BC-03* due to increasing degree of purity. But, for *BC-04*, the flexural strength (158 MPa) decreased again. In these plates, which were pressed from hydrogel sheets and not flakes, early delamination between the sheet layers was observed, leading to premature failure.

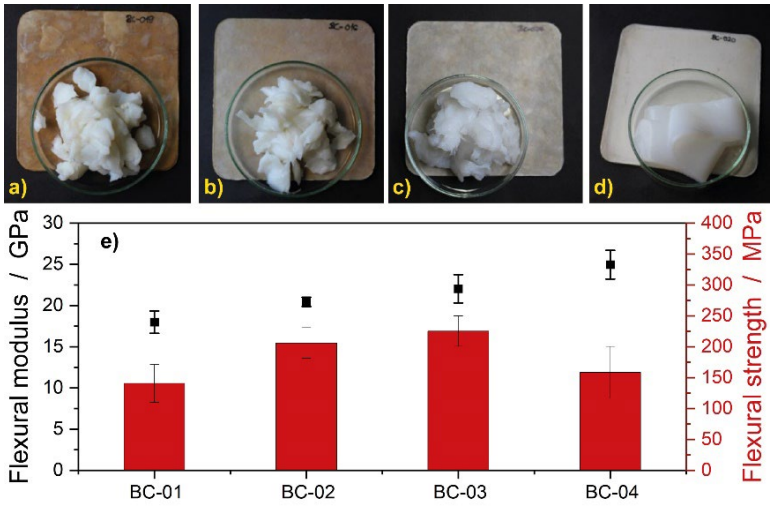

Figure 3. Different BC materials and resulting boards, as well as their flexural properties: BC-01 (a), BC-02 (B), BC-03 (C) and BC-04 (d). The error bars represent the standard deviation (e).

Compared to the above-mentioned impurities, water has by far the greatest influence on the mechanical properties of the dried BC boards. By nature, cellulose is hydrophilic and water accumulates in several layers on the surface of cellulose [13]. It has been demonstrated that even after drying cellulose, a layer of water molecules cannot be removed due to the strong hydrogen bonding to the cellulose. Thus, 100 % water-free BC materials are technically not feasible. If *BC-02* is processed into rigid boards by thermo-compression and the flexural and tensile specimens are conditioned at different humidity levels (23 °C/< 5 % RH, 23 °C/50 % RH, and 20 °C/85 % RH), a strong influence of water content on the stiffness and strength can be observed (Figure 4). Apparently, dried BC material still has a residual water content of 1.3 to

  doi:10.5075/epfl-298799_978-2-9701614-0-0 published under CC BY-NC 4.0 license

1.6 wt. %. At this water content, a flexural modulus of 20.5 GPa and a flexural strength of 208 MPa, as well as a tensile modulus of 25.0 GPa and a tensile strength of 112 MPa were determined. Surprisingly, the conditioning at 50 % RH, only led to a doubling of the water content to 2.7 to 2.9 wt. %. The mechanical properties do not significantly deteriorate and a flexural modulus of 19.1 GPa and a flexural strength of 199 MPa, as well as a tensile modulus of 21.5 GPa and a tensile strength of 115 MPa were measured. Apparently, this level of moisture is not sufficient to intercalate formed intra- and intermolecular hydrogen bonds considerably and thus to plasticize the cellulose. If the moisture (85 % RH) increases further during conditioning, the water content in the material rises to 6.0 to 6.9 wt. % and stiffness as well as strength decrease to approximately half of their original values. A flexural modulus of 12 GPa and a flexural strength of 103 MPa, as well as a tensile modulus of 11.5 GPa and a tensile strength of 76 MPa were determined here. In general, even at high water content the BC material is outperforming most conventional polymers.

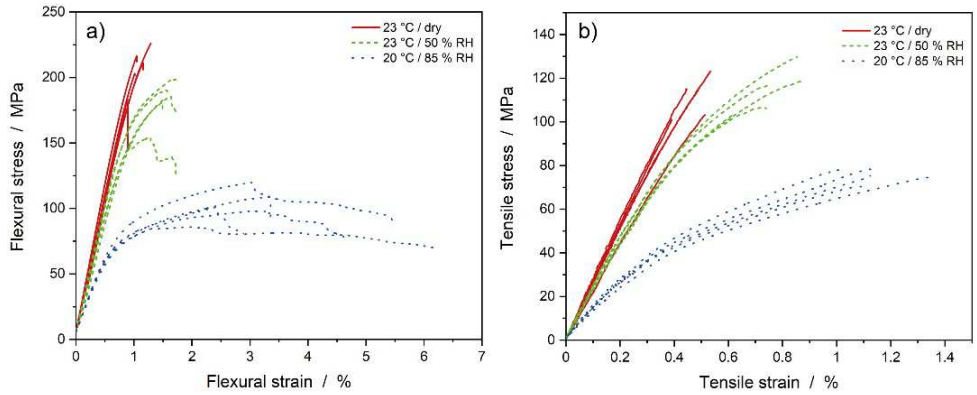

Figure 4. Stress-strain diagrams from flexural (a) and tensile (b) testing of BC-02 boards after conditioning at different humidity levels.

In addition to a single exposure to moisture, the influence of repetitive drying and wetting on the BC material is of interest (Figure 5). The experiment clearly showed that the plasticizing effect of moisture uptake is reversible. Even over three cycles of wetting and subsequent drying, the initial mechanical stability of the rigid boards was maintained. Although both water content and thickness of the tensile specimens increased by 5 to 6 % in relation to the dry state during the seven-day storage at 85 % RH due to swelling, the absorbed water was completely released upon drying and the specimen regenerated to the original thickness and water content.

With regard to later applications of rigid BC boards, preliminary investigations were carried out to study the formability of BC material during the thermo-compression process. For this purpose, *BC-02* and *BC-04* were formed into different two and three-dimensional shapes (Figure 6). It was observed that pellicle flakes (*BC-02*) are only conditionally suitable for forming over edges. Pellicle sheets (*BC*-04) are more suitable here and form edges without cracks or flaws. The pellicle sheets can also be used to produce more complex 3D shapes, such as a cover for a commercially available computer mouse. For obtaining a smooth surface, the pre-dried mouse cover was subjected to a finishing hot-pressing step between polished pressing surfaces under increased temperature and pressure. In addition, the introduction of a well-defined embossing (Empa logo) was achieved in this step.

  doi:10.5075/epfl-298799_978-2-9701614-0-0

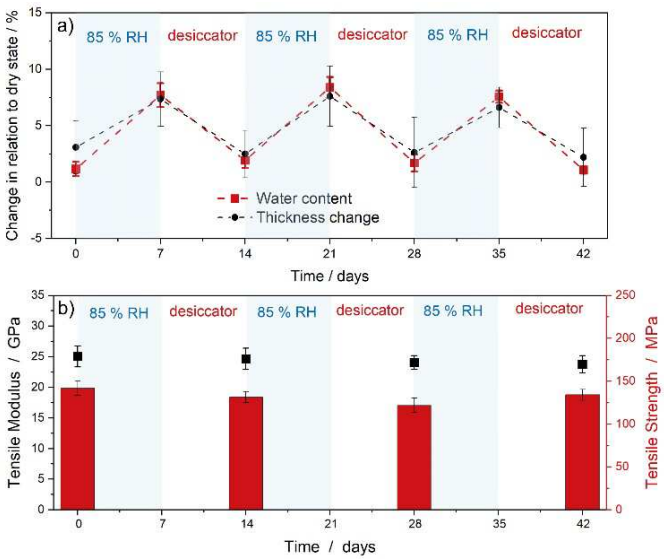

Figure 5. Change of water content and thickness (a) as well as tensile properties of dried specimens (b) after repetitive wetting and drying. The error bars show the standard deviation.

In terms of mechanical stability and formability, the rigid BC material can be seen as a sustainable biobased and biodegradable alternative to conventional plastics made from petroleum and a justified use in consumer goods can be considered. Further studies will be dedicated to the use of coatings or additives for e.g., water repellency, flame retardancy and coloring to broaden the range of possible applications of rigid BC boards.

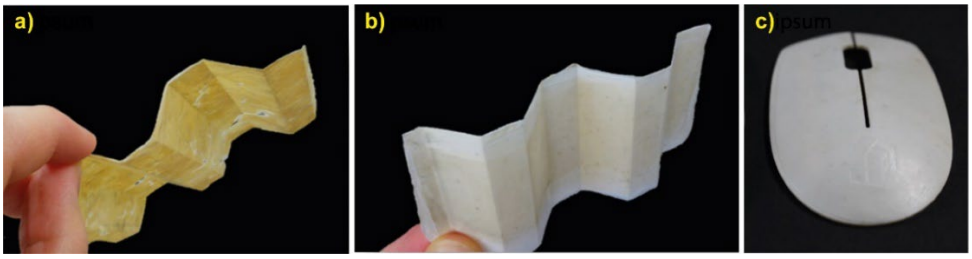

Figure 6. 2D-shaped boards made from BC-02 (a) and BC-04 (b) and 3D-shaped mouse cover made from BC-04 (c).

4. Conclusion

Bacterial cellulose or *nata de coco* (in the case of coconut milk as nutrient medium) contains an exceptionally homogeneous network of nanofibrils of high-purity cellulose in a hydrogel. The material is produced on an industrial scale by fermentation and is available in various processing forms as cut flakes or sheets. By optimized thermo-compression and subsequent drying, the BC can be dewatered, resulting in mechanically very stable boards with several millimeter thickness. It has been shown that the removal of impurities from the fermentation by moderate bleaching with NaClO and NaOH leads to an improvement of the mechanical properties (flexural modulus of 22 GPa). The influence of moisture disturbs the inter- and intramolecular hydrogen bond network of cellulose fibrils by intercalation of water and leads to plasticization. Flexural and tensile modulus as well as strength decrease. However, the incorporation of water is reversible. The original mechanical properties are regained even after repetitive wetting and

  doi:10.5075/epfl-298799_978-2-9701614-0-0

drying. BC hydrogels can be molded into 3D shapes during dewatering and drying. The production of a mouse cover was used as an example to demonstrate the potential for later technical application. More detailed studies on hydrophobization and the use of additives without affecting the internal structure and thus the mechanical stability are in progress.

Acknowledgements

We thank the following collaborators for their support and many valuable discussions: Anja Huch (SEM), Walter Risi, Roman Elsener (mechanical testing), Urs Hintermüller, Erwin Pieper (mold design and construction) and Gion Barandun and his team (exchange about processing).

5. References

1. Schönbeck, DE334494, 1921.
2. Yano H, Nakahara S. Bio-composites produced from plant microfiber bundles with a nanometer unit web-like network. Journal of Materials Science. 2004;39(5):1635-8.
3. Phisalaphong M, Tran TK, Taokaew S, Budiraharjo R, Febriana GG, Nguyen DN, et al. Nata de coco Industry in Vietnam, Thailand, and Indonesia. Gama M, Dourado F, Bielecki S, editors. Amsterdam: Elsevier Science Bv; 2016. 231-6 p.
4. Iguchi M, Yamanaka S, Budhiono A. Bacterial cellulose—a masterpiece of nature's arts. J Mater Sci. 2000;35(2):261-70.
5. Chung YC, Shyu Y. The effects of pH, salt, heating and freezing on the physical properties of bacterial cellulose - nata. Int J Food Sci Technol. 1999;34(1):23-6.
6. Pa'e N, Abd Hamid NI, Khairuddin N, Zahan KA, Seng KF, Siddique BM, et al. Effect of Different Drying Methods on the Morphology, Crystallinity, Swelling Ability and Tensile Properties of Nata De Coco. Sains Malays. 2014;43(5):767-73.
7. Zhao Y, Koizumi S, Yamaguchi D, Kondo T. Hierarchical structure in microbial cellulose: what happens during the drying process. Eur Phys J E Soft Matter. 2014;37(12):129.
8. Vasconcellosa VM, Farinas CS. The Effect of the Drying Process on the Properties of Bacterial Cellulose Films from Gluconacetobacter hansenii. Chemical Engineering Transactions. 2018;64:145-50.
9. Illa MP, Sharma CS, Khandelwal M. Tuning the physiochemical properties of bacterial cellulose: effect of drying conditions. J Mater Sci. 2019;54(18):12024-35.
10. Indriyati, Irmawati Y, Puspitasari T. Comparative Study of Bacterial Cellulose Film Dried Using Microwave and Air Convection Heating. J Eng Technol Sci. 2019;51(1):121-32.
11. Sederaviciute F, Domskiene J, Baltina I. Influence of Drying Temperature on Tensile and Bursting Strength of Bacterial Cellulose Biofilm. Mater Sci-Medzg. 2019;25(3):316-21.
12. Nishi Y, Uryu M, Yamanaka S, Watanabe K, Kitamura N, Iguchi M, et al. The Structure and Mechanical-Properties of Sheets Prepared from Bacterial Cellulose .2. Improvement of the Mechanical-Properties of Sheets and Their Applicability to Diaphragms of Electroacoustic Transducers. J Mater Sci. 1990;25(6):2997-3001.
13. Sinquefield S, Ciesielski PN, Li K, Gardner DJ, Ozcan S. Nanocellulose Dewatering and Drying: Current State and Future Perspectives. ACS Sustainable Chemistry & Engineering. 2020;8(26):9601-15.

  doi:10.5075/epfl-298799_978-2-9701614-0-0

MANUFACTURING AND MECHANICAL CHARACTERISATION OF UNIDIRECTIONAL FIQUE FIBRES REINFORCED POLYPROPYLENE COMPOSITES

Guillermo Idarraga[a], Johnattan Vargas[b], Meisam Jalalvand[c], Juan Meza[b], Liu Yang[a]

a: Department of Mechanical and Aerospace Engineering, The University of Strathclyde, 75 Montrose Street, Glasgow G1 1XJ, UK
b: National University of ColombiaDesign of Advanced Composite Structures DADCOMP, 75th Street 79A-56, Building M17, Medellín, Colombia
c: Engineering Materials Research Group, School of Engineering, University of Southampton, Southampton, SO17 1BJ, UK

Abstract: *New sustainable composites have gained considerable attention in recent years and implementing natural fibres as reinforcement in composites is growing faster in engineering applications. This work presents the development, processing, and characterisation of a new composite material by combining textile polypropylene (PP) and long Fique fibres (a South American Andes native fibre). The samples are made out using coated Fique fibres and compared with samples of only PP. The consolidation is carried out using hot pressing at 185°C and a pressure of 10MPa. Tensile, bending, Charpy and DSC tests are conducted to evaluate the thermo-mechanical properties of the new material. The PP-Fique composite with coated fique fibres shows a remarkable increment in the mechanical properties in comparison with PP. Implementing Fique fibres as reinforcement in PP will reduce the amount of plastic required keeping mechanical performance.*

Keywords: Fique Fibres; Hot Pressing; textile polypropylene; Composites; thermo-mechanical properties

1. Introduction

Agro-based structural materials are growing in different industrial applications and natural fibres are gaining attention due to their low cost, low density, minimal health hazards, biodegradability and specific mechanical properties [1-3]. Natural fibres are widely used in geotextiles, sorbents, filters, structural and non-structural parts and among others. Being implemented in industries such as packaging, building, furniture, sport and automotive [4,5]. The use of natural fibres in composites materials is growing by 6% annually, being wood fibres the most used followed by more sustainable fibres such as jute, sisal, kenaf and hemp [6,7]. Natural fibres can even replace some synthetic fibres, having distinct advantages over glass fibre in application with low loading requirements. Natural fibres have comparable strength to glass fibre and a similar specific modulus [8,9]. As an example, Flax fibres have a tensile strength of 600 to 2000 MPa and Young's modulus ranging between 12 to 100 GPa, being comparative with E-glass and having 40% lower density [10].

Fique Fibres are relatively unknown natural fibres native to the South American Andes and obtained from the leaves of the fique plant. Fique fibres are mainly made of cellulose, hemicellulose and lignin with average contents of 52.3, 23.8 and 23.9% respectively [11]. Colombia produces approximately 30.000 tons of fique fibres per year and despite Fique fibres showing good mechanical properties for engineering application, the use of Fique fibres as a

  doi:10.5075/epfl-298799_978-2-9701614-0-0

reinforcement of composite materials has not been widely investigated [12-14]. Fique fibres are mainly found in the Colombian market as ropes, cordages, textiles and sackcloth for agricultural products such as coffee sacks and the cost of processed fique fibres vary between US$0.36 to US$0.45 per kg [15].

On the other hand, plastic is widely applied across all areas, and it represents one of the most important elements of modern life. More than 300 million tons of plastic materials are produced every year with most discarded-on land fills, in the ocean or incinerated [16,17]. Polypropylene is the second plastic more used after polyethene and represents 20% of the market and continues to grow [18]. Polypropylene is a thermoplastic, with good stiffness, low density, chemical resistance and low cost and it is used in different applications such as automobile bumpers, boat hulls, household goods, containers and among others [19-21].

Plastic waste causes global environmental and health problems such as pollution and loss of biodiversity. This project proposes a new composite material using polypropylene fabric and natural Fique fibres as reinforcement. The use of Fique fibres allows an increment in the flexural, tensile and impact properties of the polypropylene, reducing the cross-section area and therefore the amount of material needed in certain applications.

2. Materials

Fique fibres and polypropylene fabric are provided by the Colombian company Compañia de Empaques. The fibres are obtained from the leave of the Fique plants through mechanical decortication, cleaned in water at room temperature for 12 to 15 hours and dried naturally by the sun. During the production process, a vegetal oil is sprinkled to reduce friction and the fibres are aligned to obtain a continuo yarn. On the other hand, PP corresponds to a plain homopolymer PP fabric. The PP yarns are flat tape of PP with a width of 2.5mm and a thickness of 41µm manufactured in a drawing process. Table 1 shows some properties of the Fique fibres and PP tapes in tension.

Table 1: Summary of the mechanical properties.

Property	Fique Fibres	PP Tapes
Young modulus [GPa]	9.3 GPa (SD: 3.2GPa)[a]	6.7 GPa (SD: 0.3 GPa)[b]
Tensile strength [MPa]	340 MPa (SD: 106) [a]	382 MPa (SD: 6MPa) [b]
Elongation at break [%]	3.8% (SD: 1.5) [a]	24.9 (SD: 2.0) [b]

[a] Average value taken from [22]

[b] Measured during this work

3. Composite manufacturing

3.1 Fique laminates and coating process

To produce the unidirectional laminates of Fique, the continuo yarn is manually combed to remove impurities and reduce waviness. Groups of yarns are placed next to each other and tied using a fique fibre as a warp, unidirectional fique laminates are obtained as Figure 1a shown. For the coating, virgin pellets of the homopolymer PP are used, the pellets are diluted in Xilol in a proportion of 20ml of Xilol per 1g of PP. The pellets of PP and the Xilol are mixed at 120°C for 25 minutes, time enough to make the PP diluted completely. Then, the unidirectional Fique laminates are introduced in the bath for 10 minutes as Figure 1b shows. Microscopy images of

  doi:10.5075/epfl-298799_978-2-9701614-0-0

the Fique fibre after coating indicate that the fibres are completely coated by the PP showing that the coating process is implemented properly, see Figure 1c.

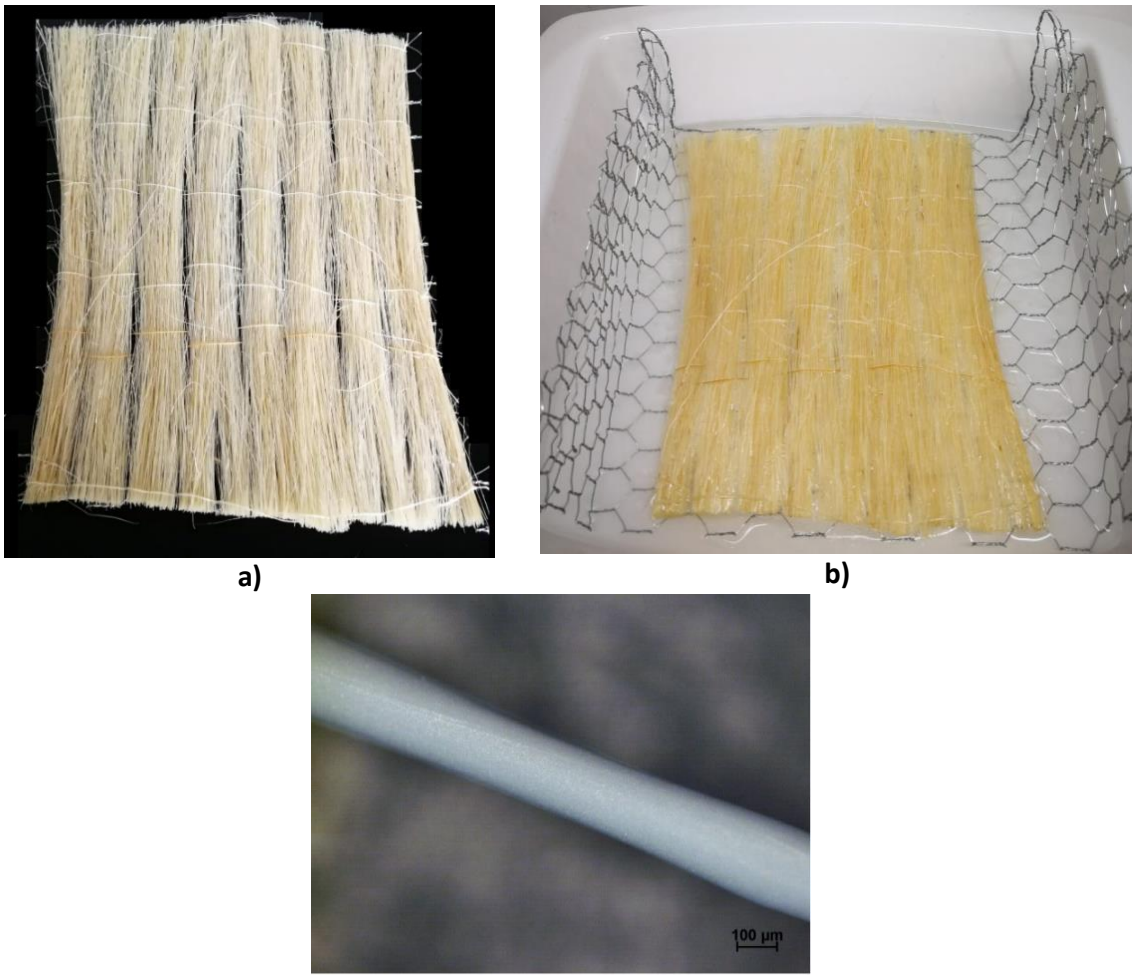

Figure 1. a) Unidirectional laminates, b) coating process, c) microscopy image of a fibre coated with PP.

3.2 Processing temperature

To determine the temperature of the consolidation process using hot pressing, a differential scanning calorimetry (DSC) test is carried out on the Fique fibres and the PP. According to the DSC, two exothermic reactions are identified. The first reaction is produced by the degradation of hemicellulose, starting at 260°C with a peak at 295°C and the second reaction is produced by the degradation of the cellulose, starting at 360°C with a peak at 390°C. Because lignin is a complex polymer it has a wide range of thermal degradation temperatures (115°C - 500°C) [22,23]. The DSC results of PP show an endothermic reaction at 165°C which corresponds to melting point. Considering that the processing temperature should be enough to melt the PP but not too high to degrade the Fique fibres, 185°C is set as the processing temperature.

3.3 Hot pressing

The consolidation of composites is conducted in a Wickert hot pressing machine. For the process, rectangular steel moulds are used, the layers are introduced in the mould at room temperature (~25°C) and compressed to reach 10MPa. The layers are heated up to 185°C at a

  doi:10.5075/epfl-298799_978-2-9701614-0-0

rate of 10°C per minute and kept at that temperature for 15 minutes. Then the layers are cooled down using a water-cooling system until a temperature of 90°C. At this temperature, the pressure is released and finally, the material is removed from the mould at 60°C.

Preliminary consolidations show that uncoating fibres generate clusters with poor penetration of the PP inside of the fibres while coated laminates show a better distribution of fibres in the composite. Figure 2 shows micrographs of uncoating and coating Fique fibres used as reinforcement in the PP laminate.

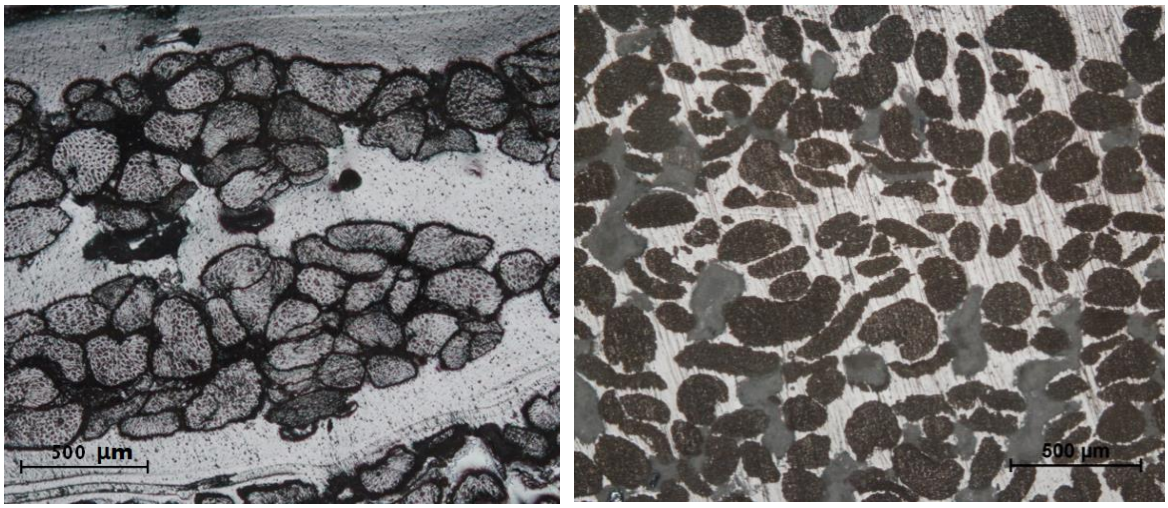

a) b)

Figure 2. microscopy image of a laminate with a) uncoated fibres b) coated fibres.

4. Tests and results

4.1 Fique Fibres Tensile tests

For the tensile tests, the samples are manufactured according to the method described in section 3.3. A rectangular mould is used with dimensions of 160x140x3mm, height, width and thickness respectively. The stacking sequence for PP-Fique laminates is [PP_2/Fique/PP/Fique/PP/Fique /PP_2], while for the laminates of only PP, 35 layers are used to keep similar thickness, [PP_{35}]. After hot-pressing, the samples are cut using a laser cutting machine, obtaining dog-bone samples with a test length of 45 mm (SD:1.0mm), test width of 12.7mm (SD:0.1mm) and a thickness of 3.0 mm (SD: 0.1mm), see Figure 3.

Figure 3. Samples for tensile tests PP reinforced with coated Fique fibres

The tensile tests are conducted in a computer-controlled Instron 3382 universal servo-electric test machine with a displacement control crosshead speed of 2 mm/min. Figure 4a shows the results of only PP samples. The first part of the stress-strain curves (red rectangle in Figure 4a) has high stiffness with a Young modulus of 2.8 GPa (DS: 0.1GPa). After 3.2% (DS: 0.3%) of strain, the modulus decreases considerable reaching 78.9MPa (SD:15.1MPa). In the final section of the curves, the samples have high deformation with a brittle final failure. The maximum average

stress and strain are 70.0MPa (SD:10.0MPa) and 51.5% (SD: 7.6%). On the other hand, Figure 4b show the results of the tensile tests of PP reinforced with coated fibres. The samples have an average Young modulus of 6.0GPa (SD: 0.5GPa), a strength of 90.4MPa (SD: 7.7 MPa) and the strain at the maximum stress corresponds to 3.3% (SD: 0.3%).

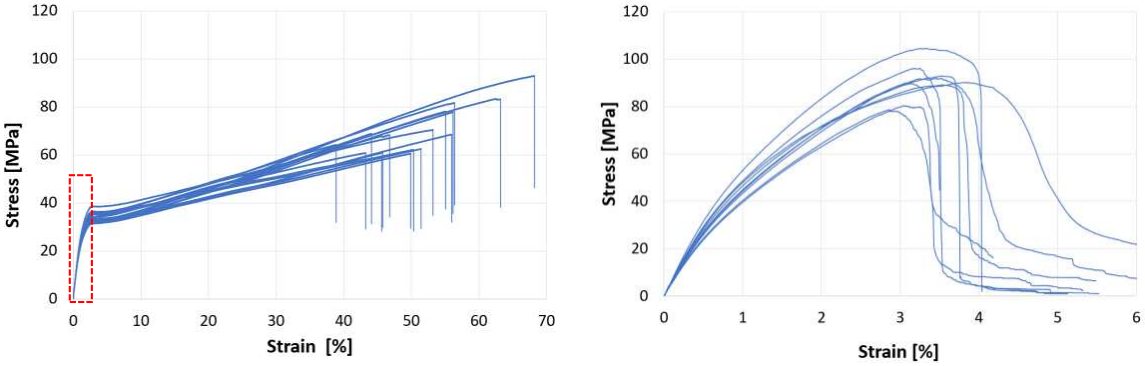

a) **b)**

Figure 4. Strain-strain curve obtained from tensile tests a) samples made of only PP, b) PP reinforced with coated Fique fibres.

4.2 Bending tests

For the bending tests, the samples are manufactured according to the method of section 3.3, using a rectangular mould of 190x120x3mm in height, width and thickness respectively. For the bending tests, 48 layers of PP are used, [PP_{48}], and the stacking sequence for PP-Fique laminates corresponds to [PP_2/Fique/PP/Fique/PP/Fique/PP/Fique/PP_2]. After hot-pressing, the samples are cut using a laser cutting machine, obtaining rectangular samples, see Figure 5a. The samples have a width of 14.8mm (SD: 0.4mm), a length of 170mm (SD: 1.2mm) and a thickness of 3.6mm (SD: 0.1mm). The tests are carried out using a three-point bending fixture as Figure 5b shown. The loading and support noses have a diameter of 10mm and the distance between the support noses is 60mm. For the tests, a displacement control crosshead speed of 2 mm/min is used.

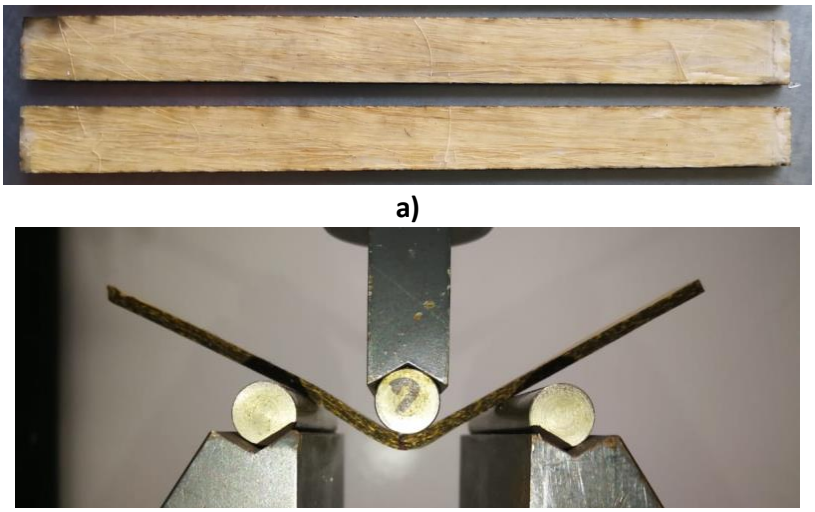

a) **b)**

Figure 5. a) Samples for bending tests PP reinforced with coated Fique fibres b) three-point bending test.

Figure 6 shows the results of the bending tests. Despite the high dispersion obtained in the results using coated Fique fibres, the flexural strength and the Young modulus increase in comparison to the composites of only PP. The average flexural strength and the Young modulus of only PP are 51.4 MPa (SD: 3.0 MPa) and 2.0 GPa (SD: 0.2) respectively. On the other hand, for the PP composites reinforced with the coated Fique fibres, the strength is 81.5 MPa (SD: 17.8) and the Young modulus is 5.8 GPa (SD: 0.5).

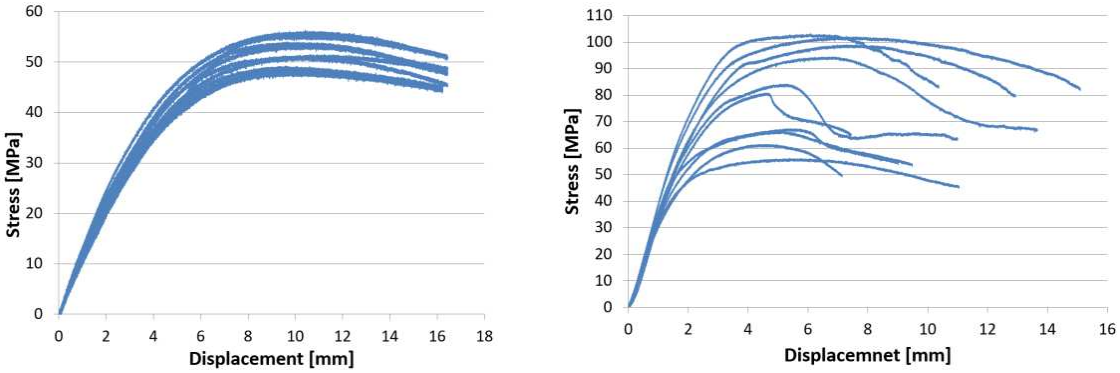

b) **c)**

Figure 6 Bending tests results, a) only PP, b) PP reinforced with coated Fique fibres c) PP reinforced with uncoated Fique fibres.

4.3 Charpy impact tests

The samples correspond to an unnotched prismatic rectangular shape of 15mm in width, 50mm in length and 3mm in thickness with the same stacking sequence used for tensile tests. For the tests, a pendulum with a mass of 0.48kg with a drop high of 330mm and angle of 107.46 is used. The velocity of the pendulum just before the impact corresponds to 2.9m/s. The amount of energy dissipated for the Only PP samples is 275.1 J/m (SD: 21.6 J/m), while energy dissipated by the samples of PP reinforced with coated Fique fibres corresponds to 454 J/m (SD: 87.6 J/m).

5. Discussion and conclusions

Table 2 summarises the mechanical properties measured in tension, bending and impact tests. At the end of Table 2, the improvement in properties between results using only PP and the composites of PP reinforced with coated Fique fibres is shown. It is possible to see that despite the high dispersion found during the tests, the coated Fique fibres used as a reinforcement of PP laminate can contribute to obtain a better performance of the material reducing the amount of plastic needed in low loading applications.

Table 2: Summary of results.

	Tensile Test		**Bending Test**		**Charpy Test**
	Strength [MPa]	Y. Modulus [GPa]	Strength [MPa]	Y. Modulus [GPa]	Energy [J/m]
Only PP	70.0 (DS: 10.0)	2.8 (DS: 0.1)	51.4 (SD: 3.0)	2.0 (SD: 0.1)	275.1 (SD: 21.6)
PP & Coated Fique	90.4 (SD: 7.7)	6.0 (SD: 0.5)	81.5 (SD: 17.8)	5.8 (SD: 0.5)	454 (SD: 87.6)

  doi:10.5075/epfl-298799_978-2-9701614-0-0

Improvement [%]	29.0	111.5	58.5	187.6	65.0

The high variation in the results using fique fibres is produced because the manufacturing method is not completely standardised, especially the production of the laminates, being not available in the market a laminate of Fique fibre with high quality. The coating proposed in this work contributes to obtaining a better dispersion of the fibres in the composites, avoiding dry zones related to fibres agglomeration.

Acknowledgements

The authors acknowledge the financial support provided by the Royal Academy of Engineering and the Newton Fund: Industry-Academia Partnership Programme, IAPP18-19/29 and to the company Compañia de Empaques for providing the material using in this work. Author G. Idarraga would like to thank Colciencias of the Colombian government for the Doctoral grant, Colciencias, call 647 and The National University of Colombia.

6. References

1. Kumaran S, Shamprasad MS, Varadarajan YS, Sangamesha MA. Coconut coir fiber reinforced polypropylene composites: Investigation on fracture toughness and mechanical properties. Materials Today: Proceedings Volume 46, Part 7, 2021, Pages 2471-2476.
2. Ifuku S, Yano H. Effect of a silane coupling agent on the mechanical properties of a micro fibrillated cellulose composite. International Journal of Biological Macromolecules Volume 74, March 2015, Pages 428-432.
3. Khondker O, Ishiaku U, Nakai A, Hamada H. Fabrication and mechanical properties of unidirectional Jute/PP composites using Jute yarns by film stacking method. Journal of Polymers and the Environment, April 2005, Vol. 13, No. 2.
4. Mathijsen D. The renaissance of flax fibers. Reinforced Plastics, May/June 2018, Volume 62, No. 3.
5. Mathijsen D. Fully bio-based fiber reinforced thermoplastics can now challenge polypropylene composites. Reinforced Plastics, March/April 2021, Volume 65, No. 2.
6. Worldwide Textile Industry to 2026 - Increasing Demand for Natural Fibers is Driving Growth September 23, 2021 05:33 ET | Source: Research and Markets.
7. Global Natural Fiber Composites Market 2020-2024. $ 1.49 Billion Growth in Natural Fiber Composites Market During 2020-2024 | 38% Growth to Come from North America | Technavio. January 27, 2021. Source: www.businesswire.com
8. Wambua P, Ivens J, Verpoest I. Natural fibers: Can they replace glass in fiber reinforced plastics? Compos. Sci. Technol. 2003, 63, 1259-1264.
9. Santulli C. Mechanical and impact properties of untreated jute fabric reinforced polyester laminates compared with different E-glass fibre reinforced laminates. Science and Engineering of Composite Materials, 2000, Vol. 9, No 4.
10. Charlet K, Jernot JP, Gomina M. Mechanical properties of flax fibers and of the derived unidirectional composites. Journal of Composite Materials, 2000, Vol. 44, No. 24.
11. Ovalle S, Blanco C, Combariza M. Exploring the composition of raw and delignified Colombian fique fibers, tow and Pulp. Cellulose, 2018, 25:151–165.

  doi:10.5075/epfl-298799_978-2-9701614-0-0

12. Gómez C, Alvarez V, Gañán P, Vázquez A. Fique Fibers: Enhancement of the Tensile Strength of Alkali Treated Fibers During Tensile Load Application. Fibers and Polymers 2012, Vol.13, No.5, 632-640.
13. Castellanos LJ, Blanco-Tirado C, Hinestroza JP, Combariza MY. In situ synthesis of gold nanoparticles using fique natural fibers as template. Cellulose, 2012, 19:1933–1943.
14. Chacón M, Blanco C, Hinestroza JP, Combariza M. Biocomposite of nanostructured MnO2 and fique fibers for efficient dye degradation. Green Chemistry, 2013, 15, 2920.
15. Echeverri R, Franco L, González M. Fique en Colombia. Fondo Editorial ITM, diciembre de 2015.
16. Sezgin H, Kucukali-Ozturk M, Berkalp O, Yalcin-Enis I. Design of composite insulation panels containing 100% recycled cotton fibers and polyethylene/polypropylene packaging wastes. Journal of Cleaner Production, 2021, 304, 127132.
17. Ritchie H, Roser M. Plastic Pollution. Published online at OurWorldInData.org.
18. Belokon TD, Kurganova YA, Bragin DA, Kovalev MN. Increasing the efficiency of the recycling of propylene - polyethylene raw materials. Russian Metallurgy (Metally), Volume 2017, Issue 13, pp.1099-1102
19. Kim M, Park T, Hong S. Experimental determination of the plastic deformation and fracture behavior of polypropylene composites under various strain rates. Polymer Testing 93, 2021, 107010.
20. Ghasemi FA, Ghasemi I, Menbari S, Ayaz M, Ashori A. Optimization of mechanical properties of polypropylene/talc/graphene composites using response surface methodology. Polymer Testing 53, 2016, 283–292.
21. Bahlouli N, Pessey D, Raveyre C, Guillet J, Ahzi S, Dahoun A, Hiver JM. Recycling effects on the rheological and thermomechanical properties of polypropylene-based composites. Materials and Design, 33, 2012, 451–458.
22. Vargas J. Análisis interfacial de un material compuesto fabricado en matriz polimérica reforzado con fibras de fique para potenciar sus propiedades mecánicas. Master thesis, National University of Colombia, 2020.
23. McLean S. Fique fibre characterisation for use in composites and potential applications. Thesis BEng Mechanical Engineering, University of Strathclyde, 2019.

  doi:10.5075/epfl-298799_978-2-9701614-0-0

BEHAVIOUR AND REPAIR OF FLAX/ELIUM BIOCOMPOSITES LOADED IN LOW VELOCITY IMPACT

Racha Manaii[a,b], Laurent Guillaumat[a], Svetlana Terekhina[a], Davy Duriatti[b]*

a: LAMPA, ENSAM, esplanade des Arts et Metiers, 49100 Angers, France
laurent.guillaumat@ensam.eu
b: Depestele, 5 rue de l'église, Bourguébus 14540, France

Abstract: Several studies have been carried out over recent years to investigate the mechanical behaviour of vegetal fibre-based composites. Composite structures are submitted to static, cyclic and dynamic loads during their life cycle. Low Velocity Impact (LVI) is one of the most important loadings applied on composites. This study focuses on damage, repair and environmental aspect of thermoplastic biocomposite plates. The composite used is a combination of woven flax fibres and Elium®188 thermoplastic resin developed by Arkema. Two stacking sequences [0/90] and [±45] have been considered. Quasi-static tests reproducing the impact conditions allowed a comparison between the dynamic and quasi-static response of the plates. Furthermore, bending tests were carried out to assess the residual performance. Different impact – repair cycles have been applied on a sample at two kinetic energies. The sample without fibre breakage has a similar behaviour whatever the number of cycles but on contrary with broken fibres the stiffness coupon decrease.

Keywords: biocomposites; flax fibres; thermoplastic matrix; recyclability; dynamic behaviour

1. Introduction

A large number of composites using synthetic and non-synthetic fibres with different thermoset and thermoplastic matrices have been already investigated. But, thanks to their eco-friendly property and low cost production with interesting physical and mechanical properties natural fibres are gathering a growing scientific and economic interest [1].

Thus, some studies have been conducted over recent years to investigate the mechanical behaviour of plant fibre-based composites. Moreover, composite structures are loaded under static, cyclic and dynamic loads during their life cycle. However, low Velocity Impact (LVI) is one of the most important loadings and it is difficult to set up these parameters because of its random nature. Understanding the behaviour of composite when subjected to LVI loading is necessary for designing structures as it is a common issue and damages are usually not apparent to the naked eye.

Finally, this study focuses on the LVI damage and the reparability of thermoplastic biocomposite plates. For this purpose, impact tests were carried out and post-impact bending tests as well. Moreover, to demonstrate repairability, two batches of impact tests were conducted with and without fibre breaks.

2. Material, manufacturing and samples

2.1 Material

  doi:10.5075/epfl-298799_978-2-9701614-0-0

The material used in this study is a biocomposite made of thermoplastic matrix with flax fibres. Fibres are available as woven twill flax fabrics. The matrix is an innovative liquid thermoplastic matrix named Elium®188, recently formulated by Arkema company.

Plates, of dimensions 1000×750 mm^2 and a thickness which ranges from 4.5 - 4.8 mm, were manufactured by CMP Company using Vacuum Resin Infusion (VRI) (figure 1). This latter is usable although it used thermoplastic matrix because of the very low resin viscosity.

The flax twill fabric has an area density of 360 g/cm^2 and is produced and provided by Depestele Company.

Two stacking sequences were considered for this study: $[0/90]_6$ and $[\pm45]_6$.

Figure 1. biocomposite plate

2.2 Impact samples

Samples with dimensions of 100 x 150 mm^2 were cut from the previous plates according to Airbus standard AITM 1-0010 [2]. However, a main difference in our study is in the boundary conditions as discussed below.

Two batches have been prepared according to both stacking sequences.

2.3 repair method

An in-house thermocompression device (Figure 2) was designed in our laboratory to manufactured thermoplastic-based composites. But, in our case, it had been used to repair the impacted plates using a temperature of 200 °C and a very low pressure to avoid changing the dimensions and more especially the thickness of the plates.

Samples were put in between the two aluminium trays and we just added an weight of 5 kg on the upper plate. 5 minutes was enough to make flat again the impacted samples.

  doi:10.5075/epfl-298799_978-2-9701614-0-0

Figure 2. Conventional hot press.

3. Devices

3.1 drop tower

Low velocity impact (LVI) means that the velocity ranges from 1 m/s to 10 m/s [3]. The falling weight impact setup, (so called drop tower), is the most efficient device to reproduce low energy impacts.

Our drop tower (Figure 3) consists of two parts. The first one is the dropping mass and the second one is the boundary conditions. As mentioned previously, the boundary conditions we used are not like in the standard. We clamped the sample on two metallic supports closed to 3 points bending configuration.

Displacements (centre of the impacted plate and position of the striker) were measured using laser sensors and the force by a piezoelectric sensor.

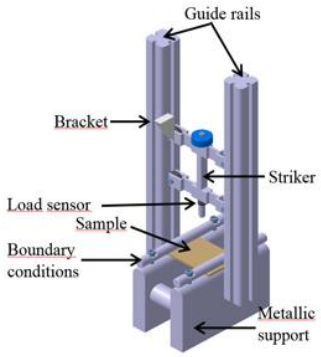

Figure 3. Scheme of the Drop Tower.

The mass of the striker was around 1 kg and we used 3 heights: 1, 2 and 3 m. Moreover, one batch of samples with the stacking sequence $[0/90]_6$ was aged at 75%HR at room temperature.

3.2 Quasi-static tests

  doi:10.5075/epfl-298799_978-2-9701614-0-0

Quasi-static tests have been done to compare results to dynamical tests. To ensure the same experimental conditions in both cases, the plates were clamped with a similar support and the same hemispherical tip used for impact applied the quasi-static loading (Figure 4).

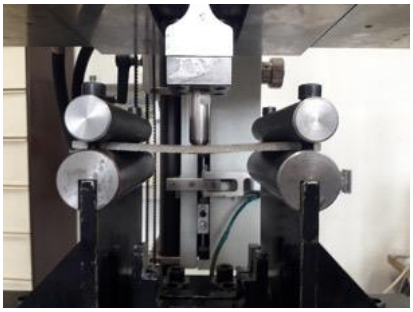

Figure 4. Quasi-static device.

Finally, conventional 3 points bending tests were conducted to estimate the residual resistance. This test was chosen over the compression after impact (CAI) because in the thermoplastic-based composites delamination is not the main damage mode during an impact due to the ductility of the matrix.

4 Results and discussion

Post-impact visual inspections revealed an indentation on the impacted face which increase with the energy of impact for all impacted specimens even at 1 meter height.

The back face, as expected, exhibits a damage shape according to the stacking sequence (figure 5).

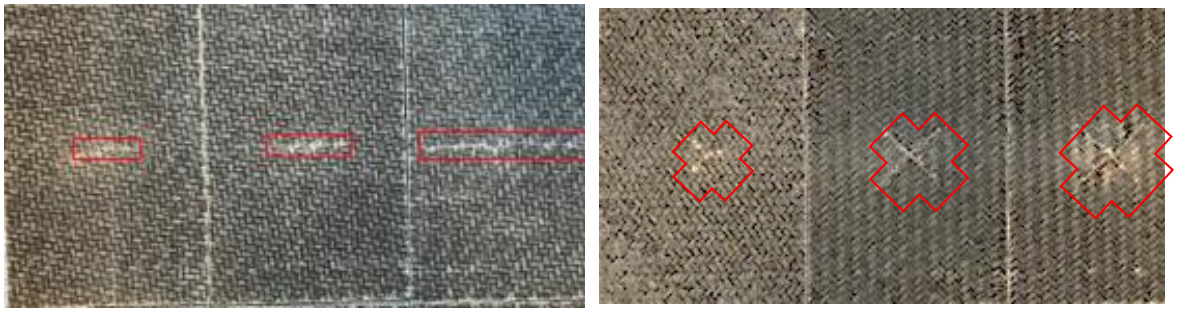

Figure 5. Damage evolution from 1 to 3 m (a) $[0/90]_6$, (b) $[\pm45]_6$.

Optical microscopy observations confirm that no large delamination occurred during the impact loading. It is why CAI is probably not the best test to estimate the residual properties. But we observed cracks inside the yarns or often at the border with the surrounding matrix (figure 6).

  doi:10.5075/epfl-298799_978-2-9701614-0-0

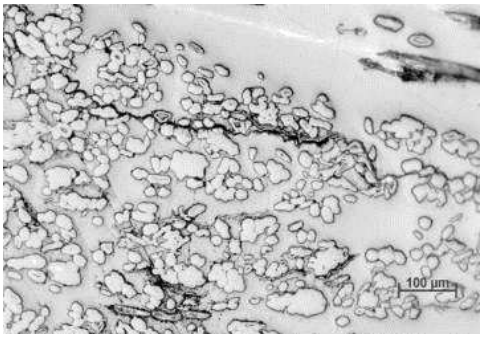

Figure 6. Crack in a yarn.

The force versus time curves for the 3 different energy levels for the 3 batches ($[0/90]_6$, $[\pm45]_6$ and ([0/90]6 aged) are shown at Figure 7. Curves exhibit significant oscillations which can be mainly due to the vibration of the specimen according to its eigen modes [4].

it can be observed that, for both stacking sequences, the contact duration between the sample and the striker during impact increases slowly with respect to time. This phenomenon is due to the decrease of the stiffness because of the growth of the macro-crack located at the back face as illustrated in the figure 5. Thus, it is well known that the contact duration depends strongly on the striker mass and on the stiffness of the impacted structure. It can be noted that the maximum force increases slightly with the incoming energy too. The maximum force increases slightly too with the incoming energy as expected.

Post-impact bending tests were preferred to compression as discussed above to evaluate the residual properties. The results (figure 8)**Erreur ! Source du renvoi introuvable.** for both orientations. Indicate that the performance of the stacking $[0/90]_6$ is much more sensitive to specimens $[\pm45]_6$ compared to the refence one. It is well known that he fibres angle has a strong influence on the mechanical responses and of course a angle of 0° increases strongly the young modulus but then these fibres break this latter decreases strongly too. This explanation is confirmed by the damage induced by the impact (figure 5). Effectively, we can observe that the crack for the $[0/90]_6$ is transverse to the span creating a strong effect on the sample stiffness contrary to the $[\pm45]_6$ for which the damage is more located at the centre of the specimen.

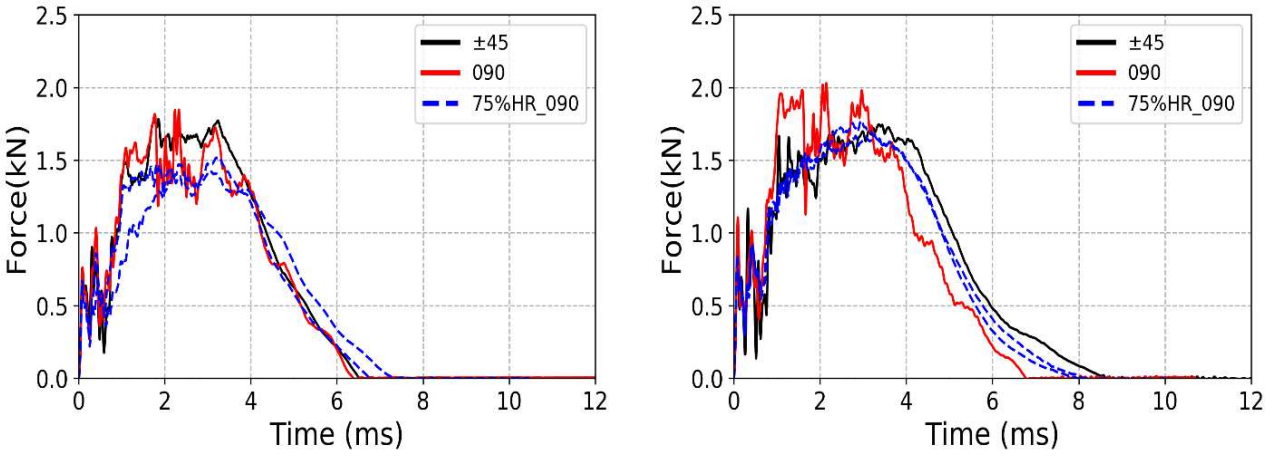

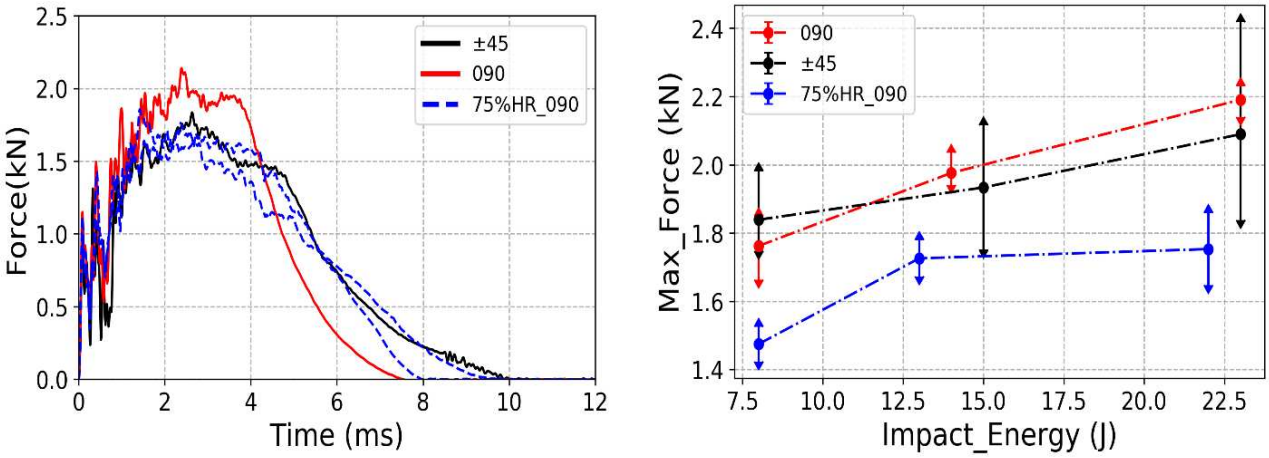

(c) (d)

Figure 7. Load versus time during impact for around (a) 8 J, (b) 15 J, (c) 22J, (d) max force evolution versus impact energy.

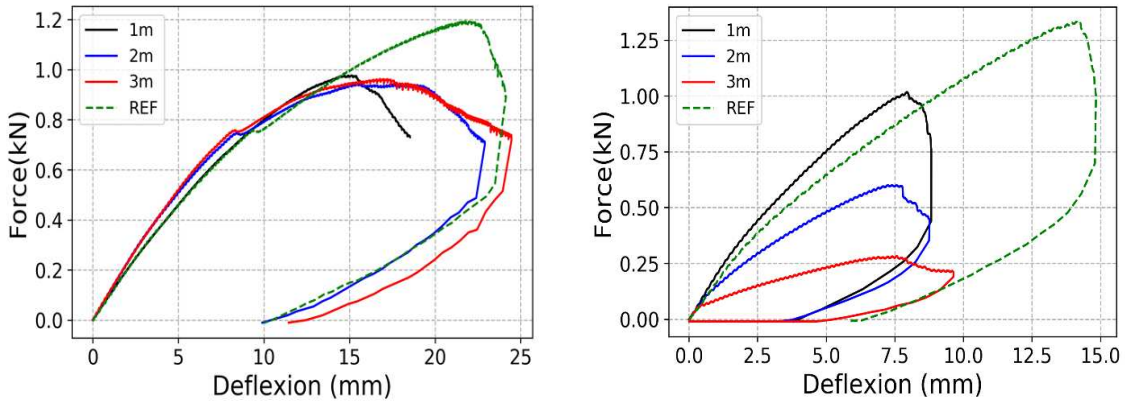

(a) $[\pm 45]_6$ (b) $[0/90]_6$

Figure 8. Residual performance after impact compared with the quasi-static test (called REF).

Finally, several cycles impact – repair have been done on the $[0/90]_6$ composite with two levels of the incoming energy (0,5 and 1 m). The main objective was to prepare samples with and without broken fibres on the back face but matrix cracks can exist.

The curves figure 9 show the evolution of the force versus time according to the number of cycles. In the case of the sample with broken fibres (a) the stiffness of the sample decreases with the number of cycles: the maximum force decreases and the contact duration increase. On the contrary, if the sample doesn't contain broken fibres (b) it can maintain the same stiffness even after several cycles impact-repairs (figure 9 – b). Moreover, we observed that the macro-cracks increase slightly with the number of cycles in both cases but the repair was sufficient to ensure constant mechanical properties in the case (b).

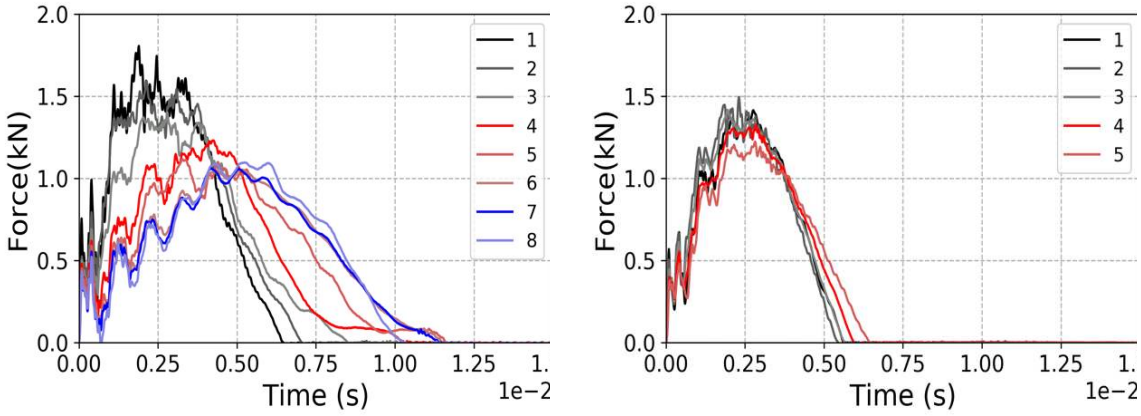

(a) 1m (b) 0.5m

Figure 9. *Force vs Time curves for the multiple impact - repair cycle on* $[0/90]_6$ *plate loaded at 1m (a) and 0.5m (b).*

5 Conclusion

This paper dealed with behaviour of flax/Elium composites LVI loading. The experiments have to main objective to determine the behaviour of plates, to identify damages and the reparability of thermoplastic bio-composite plates. Visual observations allowed to determine the damage mechanisms which was mainly microcracks and plastic deformation.

Quasi-static tests have been conducted and had showed that specimens exhibit, barely the same response excepted of oscillations representing the vibratory response in case of the impacted specimens. Bending tests have been performed to evaluate the residual strength after impact in place of compression because specimens did not develop large delamination.

The repair of the plates was successful for the impacted plates without broken fibres. Repetitive impact and repair cycles have shown that the force and time of impact are a function of the stiffness.

6 References

1. O. Faruk, A. Bledzki, H.-P. Fink, and M. Sain, “Biocomposites reinforced with natural fibres: 2000-2010,” *Prog. Polym. Sci.*, vol. 37, pp. 1552–1596, 2012, doi: 10.1016/j.progpolymsci.2012.04.003.
2. AITM1-0010, “Airbus Test Method: Determination of Compression Strength after Impact,” Blagnac, 2005.
3. G. A. Schoeppner and S. Abrate, “Delamination threshold loads for low velocity impact on composite laminates,” Compos. Part A Appl. Sci. Manuf., vol. 31, no. 9, pp. 903–915, 2000, doi: 10.1016/S1359-835X(00)00061-0.
4. S. Liang, L. Guillaumat, and P. B. Gning, “Impact behaviour of flax/epoxy composite plates,” Int. J. Impact Eng., vol. 80, pp. 56–64, 2015, doi: 10.1016/j.ijimpeng.2015.01.006.

ON THE FLEXURAL STRENGTH AND ACTUATION OF WOOD BRANCHES – MECHANISMS USEFUL IN COMPOSITE DESIGN?

Marie Hartwig[a], E. Kristofer Gamstedt[a], Malin Wohlert[a], Corentin Briot[b]

a: Division of Applied Mechanics, Department of Materials Science and Engineering, Upspala University, Uppsala, Sweden – kristofer.gamstedt@angstrom.uu.se
b: École Nationale Supérieure de Mécanique et des Microtechniques, Rue de l'Épitaphe, Besançon, France

Abstract: *In trees, reaction wood, different from the main wood tissue, is formed in branches in order to carry high bending moments and actuate the branch towards upward growth. In conifer species, such as pine and spruce, compressive wood is formed on the lower side of the branch, whereas the upper side is similar to normal wood, prevalent in most parts of the tree. This study explores the function of the compression wood, and shows how it contributes significantly to the flexural strength of the branch, and also serves as a moisture-driven actuator for branch bending. From a composite material perspective, the wood branches show an elegant way to design a beam with high flexural strength and an active bending function in a natural material with a limited number of building blocks (cellulose fibrils in a lignin/hemicellulose matrix). The cellular material is light, strong and stiff in bending, even in the presence of moisture.*

Keywords: Wood; Bending; Actuation; Design; Composite beam

1. Introduction

Wood material in tree branches have evolved to carry load, transport nutrition and to grow in a given direction. In conifers, typically recognized by their needles and cones, such as spruce and pine, the branches are composed of two different types of tissues, namely compression wood and opposite wood, where the latter is very similar to the normal wood found in the bulk of the tree. It can be assumed that the special features of compression wood are designed in such a way to improve the functions particular to branches, i.e. to carry bending moments [1] and grow in a suitable direction with respect to gravity [2]. This work explores, both by simple models and some experiments, the mechanisms behind a significant increase in flexural strength and the ability to hydraulically actuate branch growth by bending. It has been found that the compression wood has a suitable combination of stiffness, strength and hygroexpansion coefficient for the branch to carry bending moment and to deflect by swelling in the fibre direction. Finally, parallels to these findings are drawn in structural design in bending of composite components and in reinforced concrete beams. Potentials of moisture-induced actuation are also presented, which could have applications in e.g. climate-controlled devices.

Beam theory can be used to predict bending stresses, curvature, maximum moments etc. The relatively well-defined geometry of slender conifer branches makes beam theory an attractive option for such predictions, considering the alternative with finite element modelling which would have to be repeated for each new geometry and material composition. The input would then only be the stiffness, strength and hygroexpansion coefficients of the two phases

  doi:10.5075/epfl-298799_978-2-9701614-0-0

(compression wood and early wood) and the cross-sectional geometry. The axial stiffness, i.e. Young's modulus and axial strength (different in tension and compression) are available in literature for Norway Spruce, but the hygroexpanion coefficients need to be determined experimentally, which constitute the experimental part of this study, described in the following section.

Figure 1. X-ray CT cross section of a Norway spruce branch, where the slightly darker, i.e. denser, region below with pith constitutes mainly of compression wood. The diameter of the branch is about 2 cm.

2. Experimental methods

Norway spruce samples were taken from branches with an approximate diameter of 2 cm. The samples were cut into cubes with a length of 5 mm from each side. The samples were taken from opposite sides of the branch, i.e. containing mostly compression wood on the lower side, and opposite wood on the upper side. The samples were stored and equilibrated in chamber with relative humidity of 45%. This serves as the reference state, from which the hygroexpansion behavior was characterized for higher levels of relative humidity, corresponding also to higher moisture contents. These were 75% and 98% relative humidity, respectively. Equilibration was assured by measuring the mass on a sensitive balance on several occasions. The dimensional

  doi:10.5075/epfl-298799_978-2-9701614-0-0

changes were not measurable with micrometer gauges. The precision of X-ray micro-CT was needed to measure these small strains.

Figure 2. A stack of wooden cubes in the X-ray micro-CT, encapsulated in plastic foil with salt equilibration at given levels of relative humidity.

Several samples were stacked on top of each other in the measurement chamber in an X-ray micro-CT Skyscan 1172, as shown in Figure 2. In this way, the data from multiple samples could be generated in one scan. The samples were not constrained to any significant degree by the adjacent samples. The stack was sealed in plastic foil, inside which constant humidity conditions prevailed. The irradiation was kept low enough so that the samples did not heat up during the data acquisition.

In Figure 3, a cross section of a cubic sample is shown. Out of this plane, the samples are well oriented along the grain of the sample, but the radial and tangential directions of the annual rings are not consistently in line with the axes of the cube, despite the small dimensions of the sample. The hygroexpansion values obtained for the radial and tangential directions along the cube faces must therefore be regarded as radially and tangentially dominated values only. A numerical model must be used to back-calculate the corresponding values for the polar orthotropic wood samples.

  doi:10.5075/epfl-298799_978-2-9701614-0-0

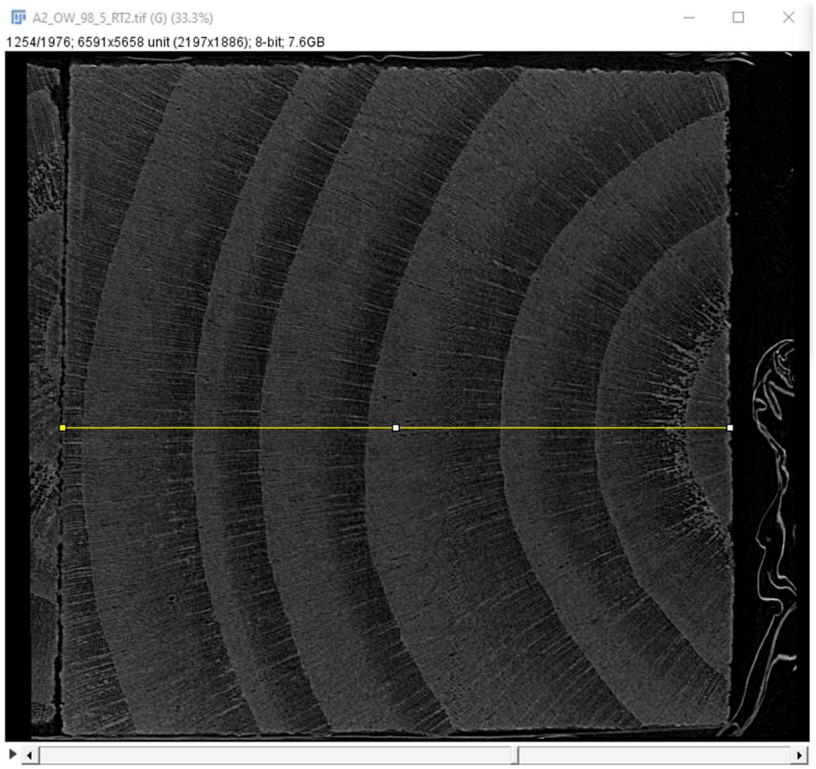

Figure 3. The hygroexpansion of wood cubes was measured with image analysis of cross-sections from rotated 3D images. This example shows a 5 mm cube where the radial expansion was measured. The same procedure was used for the longitudinal and tangential expansions.

3. Results and discussion

3.1 Flexural strength

Based on input values of the longitudinal Young's moduli of compression and opposite wood and values of the longitudinal strength in compression and tension of the same tissues, the maximum pure moment can be calculated for a given percentage of compression wood. The values and beam model is presented in Ref. 1. This maximum bending moment can be normalized with the maximum bending moment obtained for the case of neat opposite wood cross section. It turns out that the results are independent of the aspect ratio of any elliptical cross section. The curve in Figure 4 presents the failure envelope if the relative amount of compression wood is varied from the lower side of the branch. Low maximum moments are found if the branch wood consist of only opposite wood or only of compression wood. Somewhere between these to extremes, a maximum value is found. The discontinuities in the curve present transitions from one failure mode to another. The green zone indicates percentages of compression wood found in the literature for real branches. Indeed, the maximum value falls in this domain. It can thus be assumed that the wood branch in designed in such a way through the compression wood, to optimize its bending strength, which is the most prevalent type of loading from its own weight, snow loads etc. In addition to increased bending strength, the compression wood can also have the function to push growth in the upward direction through moisture-induced actuation, which is addressed in the following.

  doi:10.5075/epfl-298799_978-2-9701614-0-0

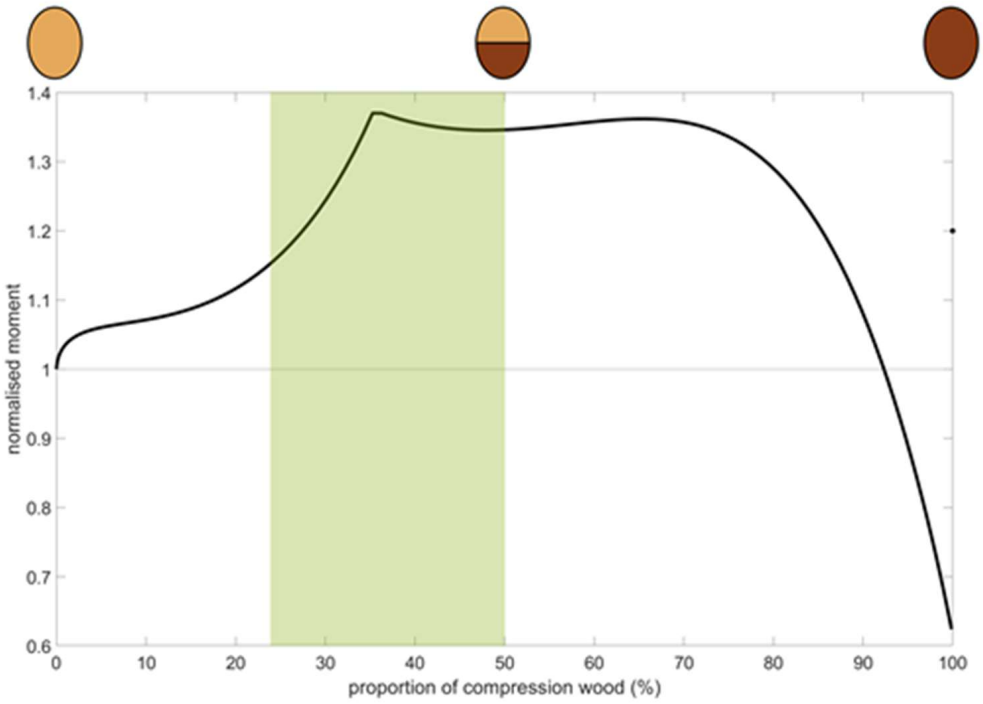

Figure 4. The maximum moment normalized with pure opposite wood moment with respect to percentage compression wood, where the green band corresponds to compression wood fractions found experimentally in cross-sections.

3.2 Moisture expansion

At this state in the ongoing studies, we will limit ourselves to present the hygroexpansion coefficients of the compression wood and opposite wood materials. Such values have not been presented before, to our knowledge. The actuating bending mechanism of a two-phase beam will be presented in further detail at the conference, and is the intended topic of a forthcoming publication. In Figure 5 below, the results from two branches are shown. For the bending mechanism, the longitudinal values (in the branch direction, blue colour) are of most interest. The hygroexpansive strain is calculated with respect to the initial state with a relative humidity of 45%. It can be noticed that the hygroexpansion is consistently significantly higher for compression wood than for opposite wood, for both levels of relative humidity. This proves that the swelling compression wood on the lower side of a branch can actuate the branch in a concave and upwards deflecting growth, as seen in growing trees where the branches strive upwards towards the canopy.

The structure of the compression wood with high microfibril angles and circular cross section with not middle walls attached to adjacent fibres also promote swelling in the longitudinal direction compared with the structure of opposite wood.

  doi:10.5075/epfl-298799_978-2-9701614-0-0

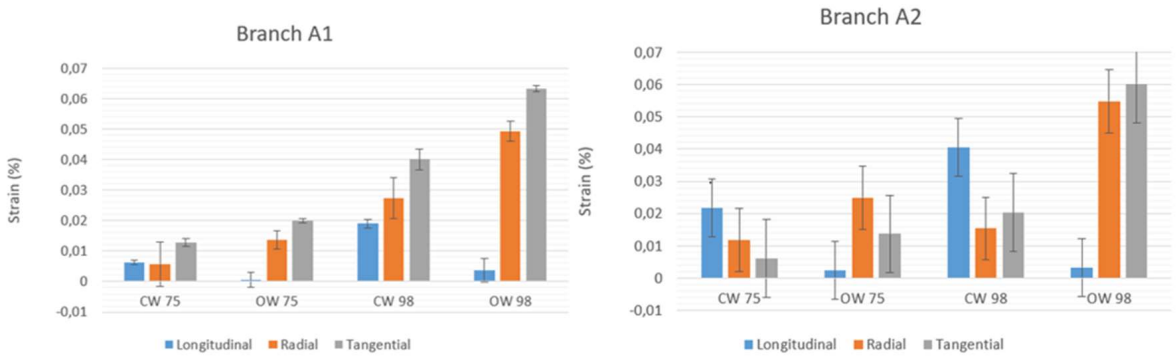

Figure 5. An example of hygroexpansion of two specimens of opposite wood (OW) and compression wood (CW) at 75% and 98% relative humidity, compared with the initial state at relative humidity of 45%.

Acknowledgements

MH acknowledges financial support from the Research Council of Sweden.

4. References

1. Hartwig M, Gamstedt EK. On the composite design of wood branches leading to improved bending strength. Institute of Physics Conference Series: Materials Science and Engineering, 2020; 942:012008.
2. Joffre T, Neagu RC, Bardage SL, Gamstedt, EK. Modelling of the hygroelastic behaviour of normal and compression wood tracheids. Journal of Structural Biology, 2014; 185:89-98.

  doi:10.5075/epfl-298799_978-2-9701614-0-0

MECHANICAL MODELLING OF VISCOELASTIC HIERARCHICAL SUTURE JOINTS AND THEIR OPTIMIZATION AND AUXETICITY

Federica Ongaro[a], Nicola M. Pugno[a,b]

a: Laboratory for Bio-inspired, Bionic, Nano, Meta Materials & Mechanics, Department of Civil, Environmental and Mechanical Engineering, University of Trento, 38123 Trento, Italy
b: School of Engineering and Materials Science, Queen Mary University of London, Mile End Road, London E1 4NS, United Kingdom

Email addresses: federica.ongaro@unitn.it (F. Ongaro), nicola.pugno@unitn.it (N. M. Pugno)

Abstract: *Suture joints are the key factor for the exceptional balance of stiffness, strength, toughness and energy dissipation typical of many biological systems as the cranium, ammonite fossil shells and carapace of the turtle. In the literature, many works discuss this aspect, with a particular attention on the role of the suture's geometry on the overall behavior. However, in very few investigations the viscoelasticity of the suture's components has been taken into account. To provide a contribution in this limitedly explored research area, this paper presents explicit expressions for the effective properties of viscoelastic hierarchical suture joints with a general trapezoidal waveform. The example of a self-similar hierarchical structure with eleven levels of hierarchy is considered, from which optimal levels of hierarchy have been identified. A parametric analysis also reveals that particular suture's morphologies lead to an auxetic behavior. These results, suggesting a possible idea for bioinspired devices, are reported here for the first time.*

Keywords: viscoelasticity; hierarchy; suture joints; effective properties; auxeticity

1. Introduction

Suture joints with different geometries are commonly found in biology as in the carapace of the turtle, the woodpecker beak, the cranium, the seedcoat of the *Portulaca oleracea* and *Panicum miliaceum* and ammonite fossil shells, among others. From a mechanical point of view, suture joints are composite structures typically including two interdigitating stiff components, the teeth, joined by a thin compliant interface layer. This configuration allows the biological system not only a high level of flexibility to accommodate the vital functions, but also an excellent balance of stiffness, strength, toughness and energy dissipation [1-3]. These fascinating performances, however, are strongly affected by the suture's geometry that, in nature, varies among and within species as a result of an evolutionary process. Starting from the pioneering contributions in [4-6], where the geometric characterization of different types of biological suture joints is reported, several existing studies confirm this aspect. [7], for example, explains how the high sinuosity and complexity of the suture lines in ammonites lead to a decrease in stresses and deformations. [1,8], in addition, discuss the role of geometry on the suture's effective properties including stiffness, strength and fracture toughness. By focusing on the wavy-patterned suture joints of the common millet (*Panicum miliaceum*) seedcoat, [3,9] illustrate the important role played by suture interfaces in resisting indentation loads. An extension of the theory in [1,8] to the case of hierarchical suture joints is presented in [10],

  doi:10.5075/epfl-298799_978-2-9701614-0-0

where analytical relations between the effective properties and the geometric and mechanical features are derived. Finally, the fracture resistance and damage tolerance of composite materials with a wavy configuration is investigated in [11], while the damping performances of suture structures with a viscoelastic interface layer are considered in [2]. From the suggested examples, it can be said that, in the literature, many works deal with the mechanical characterization of suture joints. Surprisingly, very few investigations concern suture joints where one or both phases display a viscoelastic behavior, as it happens in biology. Also, in spite of the proven benefits distinguishing the biological hierarchical sutures, a limited number of studies are currently available on this topic. To make a contribution to this incomplete research area and to provide some useful tools for practical applications, this paper focuses on the effects of adding hierarchy into a two-dimensional viscoelastic suture joint having a general trapezoidal configuration. The work is organized in 4 sections, including this introduction. Initially, based on the elastic-viscoelastic correspondence principle, in Section 2 the modelling technique leading to closed-form relations for the effective moduli and damping properties is illustrated. Some considerations about the influence of the suture's geometric and mechanical characteristics on the effective properties are presented in Section 3, where it emerges that particular suture's configurations lead to an auxetic behavior. Optimal levels of hierarchy are also identified. As a conclusion, Section 4 summarizes the main findings.

2. Effective properties of viscoelastic hierarchical suture joints: basic concepts and assumptions

2.1 Problem statement

Let us focus on Figure 1, where a schematic representation of a suture joint with a general trapezoidal profile is reported. This system can be represented as a composite material including two trapezoidal interdigitating stiff phases, the teeth, joined by a thin compliant element, the interface layer, along the seam line. Both the teeth and the interface layer are assumed to be homogeneous and perfectly bonded at the slant interfaces. Their mechanical response is linear elastic, in the case of the teeth, and viscoelastic, in the case of the interface layer. Regarding the latter, the Kelvin-Voigt model [2] has been used.

2.2 Effective properties

Closed-form relations for the effective in-plane Young's moduli, shear modulus and Poisson's ratios accounting the viscoelastic effect can be obtained in the frequency domain by applying the elastic-viscoelastic correspondence principle, according to which the effective properties can be derived as in the elastic case just by replacing the elastic material parameters with their frequency-dependent complex counterparts. For the examined viscoelastic interface layer, they are given by

$$\tilde{G}_L \equiv G_L + i\omega\eta, \qquad \tilde{E}_L \equiv E_L + i\omega\xi \tag{1}$$

being G_L and E_L the layer's shear modulus and Young's modulus, η and ξ the layer's viscosity coefficients for the shear and normal deformations modes, ω the circular frequency.

With reference to Figure 1, it emerges that the effective Young's moduli in the e_1 and e_2 directions and shear modulus are expressed, respectively, by

$$E_1 = \left(\frac{\lambda_S - 2h_L}{\lambda_S E_T} + \frac{2h_L}{\lambda_S} \left(\frac{\cos^2\alpha_S \sin^2\alpha_S}{\tilde{G}_L} + \frac{\cos^4\alpha_S}{\tilde{E}_L} \right) \right)^{-1} \equiv E_1' + iE_1'', \tag{2}$$

$$E_2 = \frac{\lambda_S - 2h_L}{\lambda_S} \left(\frac{\Psi}{E_T} + \frac{h_L(\lambda_S - 2h_L)}{2A_S^2} \left(\frac{\cos^4\alpha_S}{\tilde{G}_L} + \frac{\cos^2\alpha_S \sin^2\alpha_S}{\tilde{E}_L} \right) \right)^{-1} \equiv E_2' + iE_2'' \tag{3}$$

and

$$G_{12} = \frac{(\lambda_S - 2h_L)\,\Phi_1/\lambda_S}{\frac{\Phi_1}{4\Phi_2}\left(3 + \frac{5\Phi_2}{4E_T \tan^2\beta_S}\right) + \frac{\lambda_S \tan\alpha_S}{2A_S}\left(\frac{2h_L}{\lambda_S \psi_{\alpha\beta}} + \frac{3\tilde{G}_L}{2\Phi_2}\left(1 + \frac{3\Phi_2}{4E_T \tan^2\beta_S}\right)\right)} \equiv G_{12}' + iG_{12}'', \tag{4}$$

where the parameters A_S and λ_S are, on order, the amplitude and wavelength of the suture profile, h_L the thickness of the interface layer, α_S and β_S the angles that define the suture's geometry, i.e., trapezoidal, rectangular, triangular and anti-trapezoidal, E_T and G_T the Young's modulus and shear modulus of the teeth. The quantities Ψ, Φ_1, Φ_2 introduced in Equations (3), (4) are reported in Appendix A.

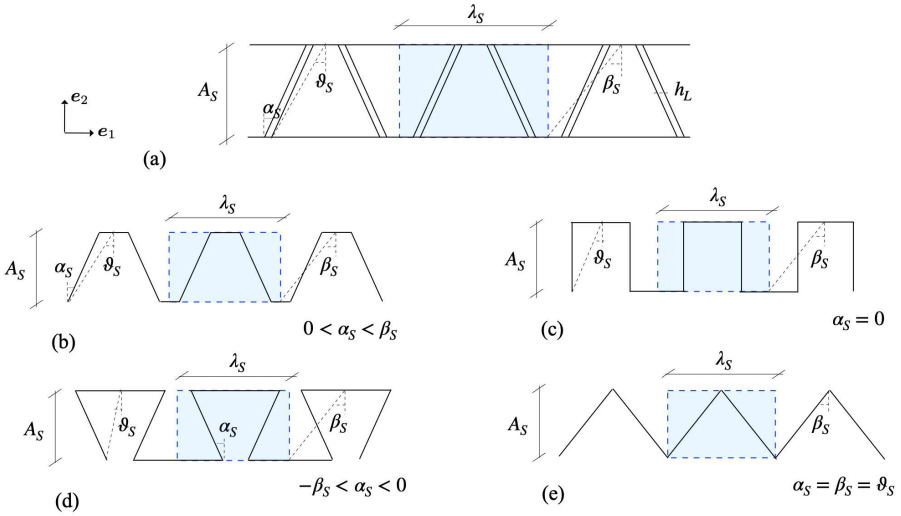

Figure 1. Schematic representation of a trapezoidal suture joint indicating (a) the most relevant geometric parameters and the geometric profiles corresponding to different values of the angles $\alpha_S, \beta_S, \vartheta_S$: (b) trapezoidal, (c) rectangular, (d) anti-trapezoidal, (e) triangular.

As it can be seen, the effective moduli listed in Equations (2)-(4) are complex quantities, with $(\cdot)'$and $(\cdot)''$denoting, on order, the storage and loss moduli of the suture joint, whose ratio defines the loss tangent

$$\tan\delta_1 \equiv \frac{E_1''}{E_1'}, \qquad \tan\delta_2 \equiv \frac{E_2''}{E_2'}, \qquad \tan\delta_{12} \equiv \frac{G_{12}''}{G_{12}'}, \tag{5}$$

a useful parameter giving a measure of the ratio of the energy lost to the energy stored in a cyclic deformation [12]. Finally, regarding the effective Poisson's ratios, it emerges

$$\nu_{12} = \frac{\lambda_S}{2A_S}\left(\nu_T A_S + \frac{E_T\tilde{\nu}_L}{\tilde{E}_L}\frac{h_L}{\tan\beta_S} - h_L\Phi_4\right)\left(\frac{\lambda_S}{2} + h_L\Phi_3\right)^{-1}, \quad (6)$$

$$\nu_{21} = \left(\nu_T A_S + \frac{\tilde{\nu}_L E_T}{\tilde{E}_L}\frac{h_L}{\tan\beta_S} - h_L\Phi_4\right)\left(1 + \frac{2h_L}{\lambda_S}(\Phi_3 - 1)\right)\left(\left(\frac{h_L\Phi_3}{2A_S} + \frac{A_S\Psi}{(\lambda_S - 2h_L)}\right)(\lambda_S + 2h_L\Phi_3)\right)^{-1}, \quad (7)$$

with ν_T and $\tilde{\nu}_L$ in turn, the Poisson's ratio of the teeth and the interface layer, Φ_3 and Φ_4 in Appendix A.

2.3 Hierarchical extension

Let us consider the viscoelastic suture joint in Figure 1 and let us imagine to modify its architecture by replacing the interface layer with a structural element having the same composite configuration of the starting system, i.e., two stiff components articulated via a thin suture layer. If we iterate this modification at successively smaller length scales, we obtain the novel class of viscoelastic hierarchical suture joints in Figure 2, where the general case of a hierarchical suture element having *n* levels of scale is illustrated.

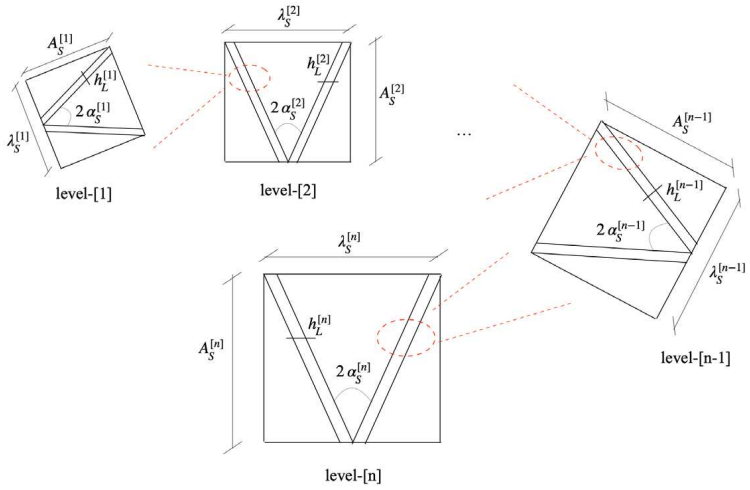

Figure 2. Viscoelastic hierarchical suture joint: schematic representation and principal geometric parameters in the case of a self-similar triangular configuration

By assuming [13] that the size of the layer's microstructure is fine enough to be negligible with respect to the underlying large architecture, it is possible, at each hierarchical level, to treat the interface layer as a continuum with effective properties given by Equations (2)-(4), (6), (7). This assumption, in conjunction with the elastic-viscoelastic correspondence principle, allow us to obtain closed-form relations for the effective properties of a viscoelastic hierarchical suture having a general number of hierarchical levels *n.* Such relations, in particular, have the same form of Equations (2)-(4) and (6), (7) with the two set of parameters $A_S, \lambda_S, \alpha_S, \beta_S, h_L$ and $G_T, E_T, \nu_T, \tilde{G}_L, \tilde{E}_L, \tilde{\nu}_L$ substituted by $A_S^{[n]}, \lambda_S^{[n]}, \alpha_S^{[n]}, \beta_S^{[n]}, h_L^{[n]}$ and $G_T^{[n]}, E_T^{[n]}, \nu_T^{[n]}$,

$G_L^{[n-1]} \equiv G_{12}^{[n-1]}$, $E_L^{[n-1]} \equiv E_1^{[n-1]}$, $\nu_L^{[n-1]} \equiv \nu_{12}^{[n-1]}$ that specify the geometric, the first, and mechanical, the second, characteristics of the level-[n] suture. Note that in approximating the layer with an equivalent continuum, the effective properties in the longitudinal direction e_1 have been considered.

3. Discussion

3.1 How the effective properties are affected by the suture's characteristics

This section aims at understanding how the suture's geometric and mechanical parameters affect the effective properties in the not-hierarchical case. The analysis involves a suture joint having wavelength $\lambda_S = 15$ mm, amplitude $A_S = 15$ mm and where the teeth and the interface layer have, respectively, the following mechanical properties: $E_T = 10$GPa, $\nu_T = 0.3, G_T = 2$ GPa and $E_L = 10^{-2}E_T, G_L = 10^{-2}G_T, \nu_L = 0.3, \eta = \xi = 5Pa \cdot s$. Finally, a teeth volume fraction of $\phi_T = 0.75$ has been selected. As illustrated in Figures 3 and 4, four different configurations have been investigated, corresponding to different values of the ratio α_S / β_S = -0.6, 0.3, 0, 1, providing, in turn, a suture joint with an anti-trapezoidal, trapezoidal, rectangular and triangular profile (Fig. 1).

In general, Figures 3(a,b,c) suggest that increasing the tooth tip angle β_S leads to an increase in the normalised Young's modulus E'_1/E_T , which is more significant for $\alpha_S/\beta_S = 1$, and to a rapid decrease in the normalised Young's modulus E'_2/E_T . A slightly different trend emerges in the case of the normalised shear modulus G'_{12}/E_T : an initial rapid increase for small values of β_S, followed by a peak region and a final decrease. Analogous considerations can be derived by focusing on the loss tangent tan δ_1, tan δ_2, tan δ_{12} illustrated in Figures 3(d,e,f), from which it emerges a large increase provided by even a small increase of β_S. Regarding the effective Poisson's ratios ν_{12} and ν_{21}, Figure 4 shows a 'Poisson's switch' from positive to negative values obtained by varying the angle β_S. However, the value of β_S at which the 'Poisson's switch' occurs is affected by the parameter α_S / β_S , being located, for example, at $\beta_S = 20°$ for $\alpha_S/\beta_S = -0.6$ and at $\beta_S \approx 47°$ when $\alpha_S/\beta_S = 0.3$ (Fig. 4a). These findings, in accordance with [14], reveal the possibility to obtain a large control in the effective properties of suture joints and, in particular, an auxetic behavior can be obtained just by tailoring the geometric characteristics of the two constituents.

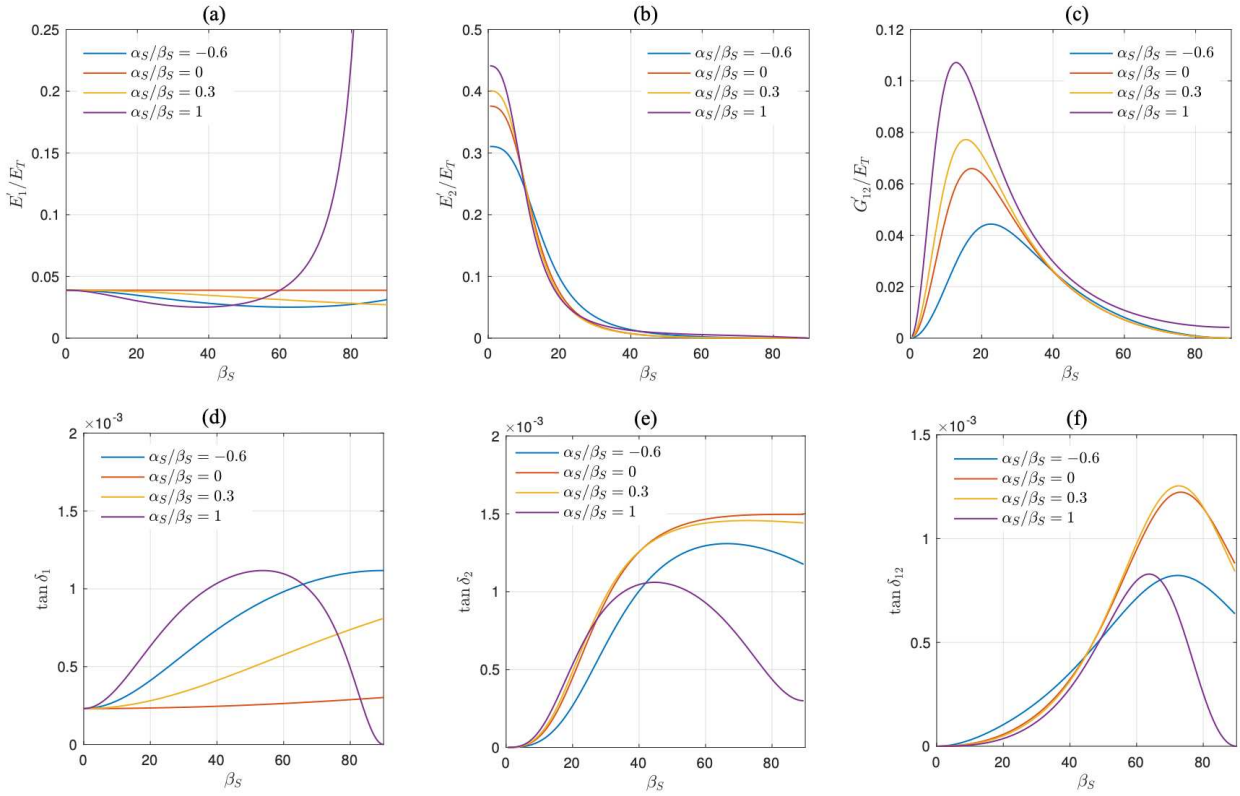

Figure 3. Viscoelastic suture joints: the influence of the tooth tip angle β_S into the (a), (b), (c) effective moduli and (d), (e), (f) loss factors.

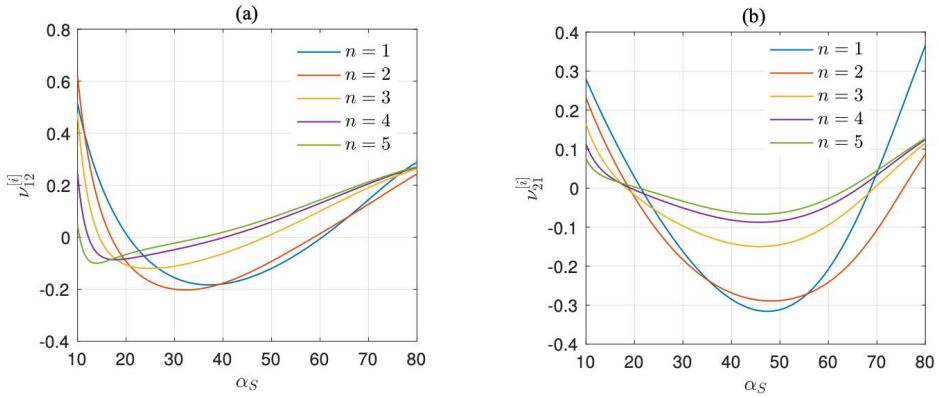

Figure 4. The influence of the tooth tip angle β_S into the effective Poisson's ratio of viscoelastic suture joints.

3.2 Hierarchical suture joints: parametric analysis and optimal values

Motivated by the findings of Section 3.1 where, interestingly, even an auxetic behavior can be achieved for particular values of the tooth tip angle, in this section the analysis is extended to the case of structural hierarchy. Our investigation deals with a self-similar viscoelastic hierarchical suture joint having up to 11 levels of hierarchy and, considering its abundant

presence in biology, a triangular configuration with a constant value of teeth volume fraction, $\phi_T^{[i]} \equiv \phi_T = 0.75$, at all levels. The starting element of the examined system, the level-[1] in Figure 2, has the same amplitude, wavelength and mechanical characteristics of the not-hierarchical suture considered in Section 3.1. The outcome of the analysis is summarised in Figure 5, where the effective stiffness $(E_1^{[i]})'/E_T$, $(E_2^{[i]})'/E_T$, $(G_{12}^{[i]})'/E_T$ and loss tangent tan $\delta_1^{[i]}$, tan $\delta_2^{[i]}$, tan $\delta_{12}^{[i]}$ are plotted versus the number of levels, and in Figure 6, where the effective Poisson's ratios $\nu_{12}^{[i]}, \nu_{21}^{[i]}$ are plotted versus the tooth tip angle $\alpha_S = \beta_S$. Note that, according to the assumption of self-similarity, α_S is constant at all levels. Regarding the effective moduli, Figures 5(a,b,c) suggest that, generally, the benefit obtained by adding orders of hierarchy is limited to a number of levels *n*<5. A different trend can be observed in Figures 5(d,e,f) where, in the case of the loss tangent, introducing hierarchical levels leads to a significant improvement only for particular values of α_S. For example, if we focus on the loss tangent tan $\delta_2^{[i]}$ in Figure 5(e), we can see that hierarchy is detrimental for $\alpha_S = 30°, 40°$ while, for $\alpha_S = 60°$, adding hierarchy leads to an improvement up to the second level that coincide with the optimum level of this particular configuration.

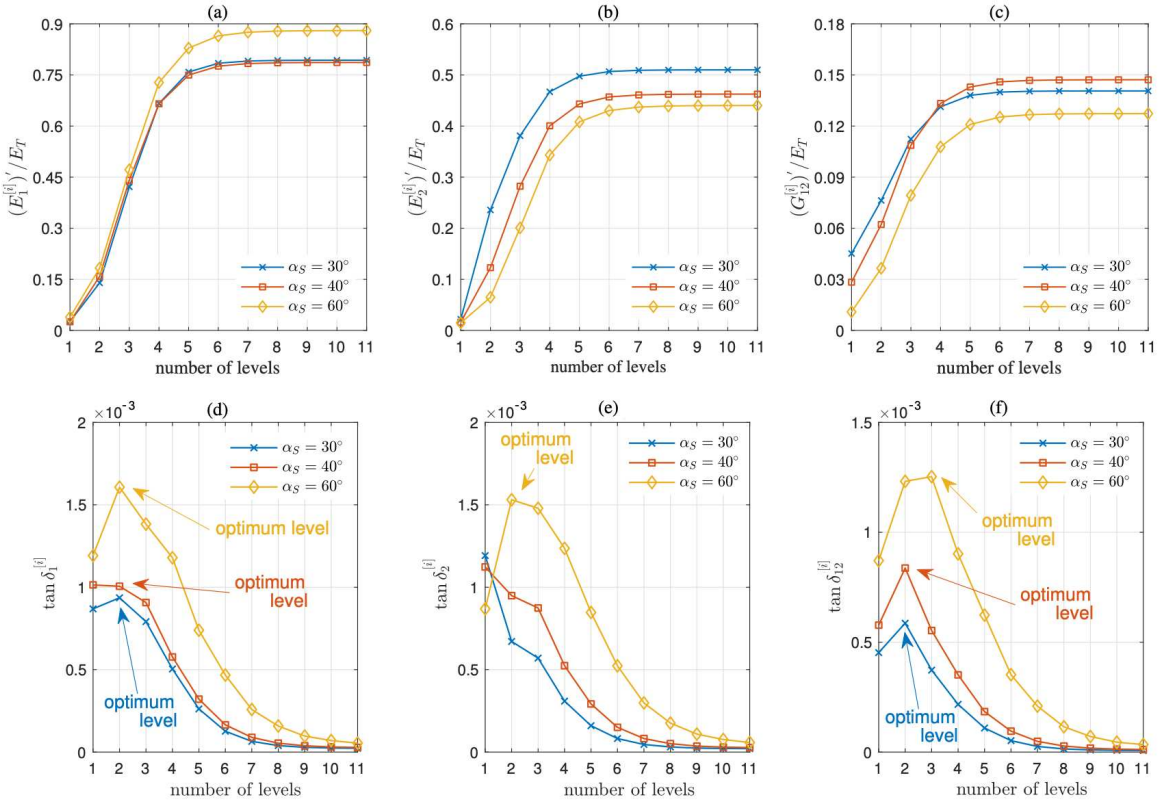

Figure 5. Viscoelastic hierarchical suture joints: (a), (b), (c) effective moduli and (d), (e), (f) loss factors vs number of levels.

Finally, in terms of $\nu_{12}^{[i]}, \nu_{21}^{[i]}$ in Figure 6, it emerges an auxetic behavior for particular values of α_S. A large variability in the values of $\nu_{12}^{[i]}$ and $\nu_{21}^{[i]}$ can also be obtained just by modifying the number of hierarchical levels.

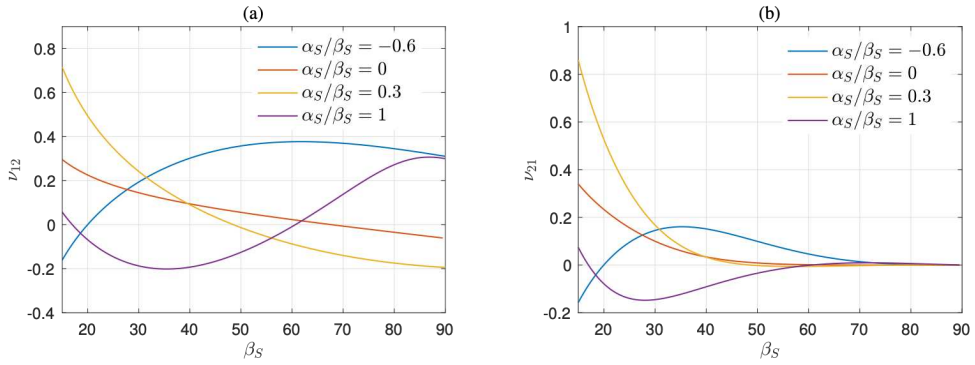

Figure 6. The influence of the tooth tip angle β_S into the effective Poisson's ratio of viscoelastic hierarchical suture joints.

3. Conclusions

This paper deals with the analysis of viscoelastic hierarchical suture joints having a general trapezoidal waveform. Initially, based on the elastic-viscoelastic correspondence principle, closed-form expressions for the effective properties and loss factors are presented for both the not-hierarchical and hierarchical arrangement. A strong influence of the suture's geometric and mechanical characteristics on the effective behavior can be observed and a parametric analysis has been established to thoroughly investigate this aspect. We found that for particular suture's configurations it is possible to obtain not only an improvement in the effective stiffness and loss moduli but also a negative value of the Poisson's ratios, revealing the system's auxetic response. The example of a self-similar hierarchical suture with eleven orders of hierarchy is also presented. It emerges that introducing hierarchy leads to an enhancement of the effective moduli and loss factors, together with the existence of optimal levels of hierarchy. As far as we know, in the context of suture joints, the two fundamental ingredients of hierarchy and viscoelasticity are simultaneously considered here for the first time.

Acknowledgements

F. Ongaro and N. M. Pugno are supported by the EU H2020 FET-Open project Boheme, Grant agreement No. 863179.

4. References

1. Li YN, Ortiz C, Boyce M. A generalized mechanical model for suture interfaces of arbitrary geometry. J. Mech. Phys. Solids 2013;1144-1167.
2. Yu Z, Liu J, Wei X. Achieving outstanding damping performance through bioinspired sutural tessellations. J. Mech. Phys. Solids 2020.

  doi:10.5075/epfl-298799_978-2-9701614-0-0

3. Gao C, Li Y. Mechanical model of bio-inspired composites with sutural tessellation. J. Mech. Phys. Solids 2019; 122:190-204.
4. Jaslow CR. Mechanical properties of cranial sutures. J. Biomech. 1990; 23.
5. Saunders WB. Evolution of complexity in Paleozoic ammonoid sutures. Science 1999; 286:760-763.
6. Hubbard RP, Melvin JW. Flexure of cranial sutures. J. Biomech. 1971; 4:491-496.
7. De Blasio FV. The role of suture complexity in diminishing strain and stress in ammonoid phragmocones. Lethaia 2008; 41:15-24.
8. Li YN, Ortiz C, Boyce M. Stiffness and strength of suture joints in nature. Physical Review E 2011; 84.
9. Hasseldine BPJ, Gao C, Collins JM, Jung HD, Jang TS, Song J. Mechanical response of common millet (Panicum miliaceum) seeds under quasi-static compression: Experiments and modeling. Journal of the Mechanical Behavior of Biomedical Materials 2017; 73:102-113.
10. Li YN, Ortiz C, Boyce M. A bio-inspired mechanical, deterministic fractal model for hierarchical suture joints. Phys. Rev. E 2012;85.
11. Liu J, Wei X. A universal fracture analysis framework for staggerd composites composed of tablets with different wavy topologies. J. Mech. Phys. Solids 2021; 151.
12. Ferry J. Viscoelastic properties of polymers. John Wiley and Sons 1980.
13. Lakes R. Materials with structural hierarchy. Nature 1993; 361:511-515.
14. Gao C, Hasseldine BPJ, Li L, Weaver JC, Li Y. Amplifying strength, toughness, and auxeticity via wavy sutural tessellation in plant seedcoats. Adv. Mater. 2018.

Appendix A

$$\Psi := \begin{cases} 1 & \text{triangular} \\ 2/3 & \text{rectangular} \\ 2 - \dfrac{1}{\psi_{\alpha\beta}} + \dfrac{\left(1-\psi_{\alpha\beta}\right)^2}{2\psi_{\alpha\beta}^2} \ln\left(\dfrac{1+\psi_{\alpha\beta}}{1-\psi_{\alpha\beta}}\right), & \text{trapezoidal, anti-trapezoidal} \\ \psi_{\alpha\beta} := \dfrac{\tan\alpha_S}{\tan\beta_S}, \end{cases} \tag{A1}$$

and

$$\Phi_1 := \tilde{G}_L \tan^2\alpha_S + \tilde{E}_L, \qquad \Phi_2 := \frac{G_T\left(\lambda_S - 2h_L\right) + 2\tilde{G}_L h_L}{\lambda_S}, \tag{A2}$$

$$\Phi_3 := E_T\left(\frac{\cos^2\alpha_S \sin^2\alpha_S}{\tilde{G}_L} + \frac{\cos^4\alpha_S}{\tilde{E}_L}\right), \qquad \Phi_4 := \cos^3\alpha_S \sin\alpha_S\left(\frac{1}{\tilde{G}_L} + \frac{1}{\tilde{E}_L}\right) \tag{A3}$$

BIOBASED GLASS FIBER SIZINGS FOR COMPOSITES IN MEDICAL AND TECHNICAL APPLICATIONS

Rudi, Reichenbächer[a], Cindy, Elschner[a], Julia, Eichhorn[b], Martin, Groß[b], Markus, Stommel[a,c], Christina, Scheffler[a]*

a: Leibniz-Institut für Polymerforschung Dresden e. V., Hohe Str. 6, D-01069 Dresden, Germany
reichenbaecher@ipfdd.de
b: Technische Universität Bergakademie Freiberg, Institut für Glas und Glastechnologie, Leipziger Str. 28, D-09599 Freiberg, Germany
c: Technische Universität Dresden, Institut für Werkstoffwissenschaft, D-01062 Dresden, Germany

Abstract: *Glass fibers are the most widely applied reinforcing fibers in polymeric composites and provide stiffness, strength as well as thermal and chemical resistance. Such glass fibers are available with suitable sizings to be chemically compatible to the selected polymer matrix. In light of the increasing use of biobased polymers, the challenging point of composite recycling is addressed in this work. A new approach for the development of biodegradable glass fiber reinforced composites is presented, based on both a degradable matrix and hydrolytically active glass fibers that also includes the use of biobased and degradable sizings. In our work, we successfully treated degradable glass fibers with silanes and biocompatible film formers with the aim to enhance the fibers' tensile strength, but also to show the effect of the sizing process on the fibers' degradation. The biobased sizings increased the single fiber tensile strength, however, the film formation on the surface needs to be further improved.*

Keywords: hydrolytically active glass fibers; biobased polymers; biodegredation; biocomposites; sizing.

1. Introduction

Today, glass fiber reinforced composites find use in many fields ranging from application in lightweight structures in automotive and transport to wind turbines or construction. However, with the development of biodegradable, biocompatible or bioactive glass compositions by *Larry Hench* in 1969 the application of glasses in medical fields and the creation of sustainable polymeric composite materials with the possibility of composite recycling came into view [1]. Bioactive glasses interact with water by dissolving the glass structure and releasing ions. The Bioglass® created by *Hench* is a SiO_2-Na_2O-CaO-P_2O_5-system that is bioresorbable and shows bioactive properties through the degradation products promoting bone growth [2]. Applications of this glass and similar glass compositions developed in the wake of *Henchs'* discovery are used primarily in orthopaedics, dentistry, and oral and maxillofacial surgery [3]. Because of the potential angiogenetic properties of the glasses, they can also be used for wound healing in a textile form [4]. A main focus when using bioactive glasses is the development of novel bone scaffold materials using the osteogenic properties of this new group of materials. However, for this specific approach bioactive glasses have only been used in the form of granules, pastes or short fibers which cannot be loaded during the healing process. Significant advantages could arise from a load bearing bioactive glass containing bone scaffold material. To make such a

  doi:10.5075/epfl-298799_978-2-9701614-0-0

mechanically strong composite possible, the glasses would have be processed in the form of continuous fibers. Currently, no continuous fibers made from bioactive glass compositions on the market, but they have been successfully fabricated as described previously [6].

By using these glasses as a reinforcing phase in plastic matrices, it should be possible to selectively rebond the composite and cleanly separate the matrix from the fibers when they are released from the matrix into an aqueous phase. With the development of biodegradable glass fibers, a fully degradable system could be achieved and thus application in medicine as well as lightweight construction can become feasible. Especially for the use in construction, this could pave the way for fully sustainable "green" composite alternatives. However, for the development of such a system it is indispensable to develop a suitable biodegradable and biobased sizing in order to improve the mechanical properties of the composite while keeping the system fully biocompatible. A scheme presenting the development process of a sizing for a fully degradable composite material is shown in Fig. 1.

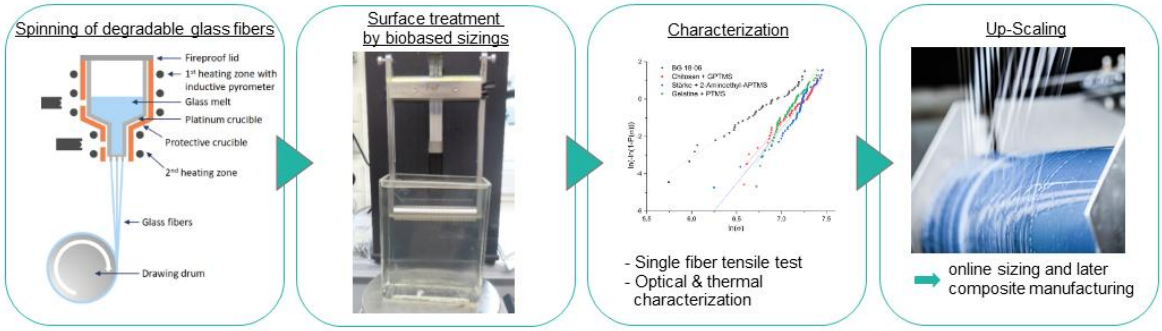

Figure 1. Scheme for the development of a biobased sizing for degradable glass fibers

The fiber-matrix-adhesion is very important for mechanical performance of each composite. The properties of this interface are mainly determined by the sizing applied to the fibers prior to composite manufacturing. The sizing has three main functions: improving the tensile strength of the fiber by bridging defects on the surface of the glass fiber network, protecting it from degradation as well as during processing and optimizing the fiber-matrix-adhesion [5]. The latter is especially important in order to be able to provide strength and stiffness to the overall composite. If a fully degradable composite is targeted, the sizing must furthermore be biobased and biodegradable and has to be water-based.

Accordingly, the aim of this work was to develop a suitable biodegradable and biobased sizing for degradable glass fibers drawn from biocompatible glass compositions to improve the fibers' tensile strength and to show the influence of the sizings on the fibers' degradation process. This will provide the basis for manufacturing of an adjustable biodegradable glass fiber reinforced composite.

2. Materials and methods

2.1 Fiber manufacturing

The fibers were produced at TU Freiberg by melt spinning, i. e. by downdrawing them from bushing tips as described previously [6]. Composition 18-06 (65 SiO_2:1,5 B_2O_3:18,4 Na_2O:15

CaO:0,1 MgO, in wt%) had been chosen because of its good mechanical properties and slow degradation rate in aqueous media.

2.2 Sizing compositions

The sizing consisted of three ingredients. A silane acting as networking agent, a biobased film former and water as a solvent.

Four different silanes supplied by Evonik Industries AG were chosen as networking agents: Dynasylan® GLYMO ((3-Glycidyloxypropyl)trimethoxysilane - GPTMS), Dynasylan® DAMO (N-(2-Aminoethyl)-3-aminopropyltrimethoxysilane), Dynasylan® AMEO (3-Aminopropyltriethoxy-silane; APTES) and Dynasylan® PTMO (Propyltrimethoxysilane). As filmformers three biopolymers were used: chitosan, starch (from potatoes) and gelatin (from bovine skin). Starch and gelatin were supplied by Sigma-Aldrich while chitosan was provided by BioLog Heppe GmbH in the form of a 2 % solution.

Chitosan was chosen for its very good cohesion and adhesion as well as antibacterial properties. As a by-product of the fishing industry, its production proves to be environmentally friendly. Gelatin exhibits excellent film forming abilities and is one of the best materials to imitate natural collagen. Finally, starch is the most readily available and least expensive material with the smallest environmental footprint, also showing good film forming properties. As film formers chitosan, gelatin and starch were examined.

2.3 Single fiber dip-coating

For the single fiber dip coating, sizings were prepared in low volumes. For the preparation of the sizing water was placed in a beaker and the silane was slowly added under stirring. The silanes were added with an amount of 2 wt% and their hydrolyzation was carried out for 0,5 to 1 hour in water. After the hydrolyzation of the silane, the film former was added at 1 wt%. This low amount of film former is ascribed to the high viscosity of the chitosan solution and for the sake of comparability the other film formers were used in the same amounts. For chitosan, acetic acid was added to the watery solution of the silane and the chitosan was slowly added to the solution under stirring. For starch and gelatin, the silane solution was heated and the film formers in the form of powders were weighed in and added to the solution under stirring.

Simultaneously, a metal frame was prepared and mounted with single glass fibers. This frame could then be dipped into the sizing solution at a fixed speed of 80 mm/min and was kept in the solution at the lowest point for 1 minute. During dipping the sizing solution was constantly stirred. The starch and gelatin sizings were kept at an elevated temperature during the immersion process. After dipping, the fibers were dried at room temperature for 24 h.

2.4 Fiber characterization using single-fibre-tensile tests and SEM/EDX analysis

The fiber samples were mechanically tested by single fiber tensile tests with a FAVIMAT from *TexTechno Herbert Stein GmbH & Co. KG*. The determination of the mechanical parameters provides information about the distribution of the coatings and their efficiency in healing defects in the fiber surface. The device also allows for the measurement of fiber diameters through the vibroscopic method by exciting vibrations of the fibers and measuring their resonant frequency.

  doi:10.5075/epfl-298799_978-2-9701614-0-0

The fractures strength of the samples are analysed through a Weibull distribution. This statistical method is reasonable since the defects on the glass fiber surface are also spread randomly. The homogenous healing of defects by the sizing can therefore be analysed. As a result, the Weibull modulus and the characteristic strength of the fibers are acquired. The Weibull modulus is a measure of the distribution of surface defects on the fiber. The higher the modulus, the more homogenous the distribution of surface defects.

Finally, the surface of the sized fibers was analyzed by Scanning electron microscopy (SEM) with enery-dispensive X-ray (EDX) detection to evaluate the film homogeneity and to identify individual elements. The fibers were embedded in an epoxy resin (Epofix) to fix them, then embedded in Epofix for a second time and grinded. The surface was then sputtered with carbon. SEM-EDX investigations were done in an UltraPlus device (*Zeiss*, Germany) with an EDX detector XFlash 5060F (*Bruker*, Germany) with an excitation voltage of 6 keV at different positions with different magnifications.

3. Results and discussion

3.1 Single fiber tensile tests

The samples included fibers sized with both networking agent only and with the combinations of networking agents and biobased film formers.

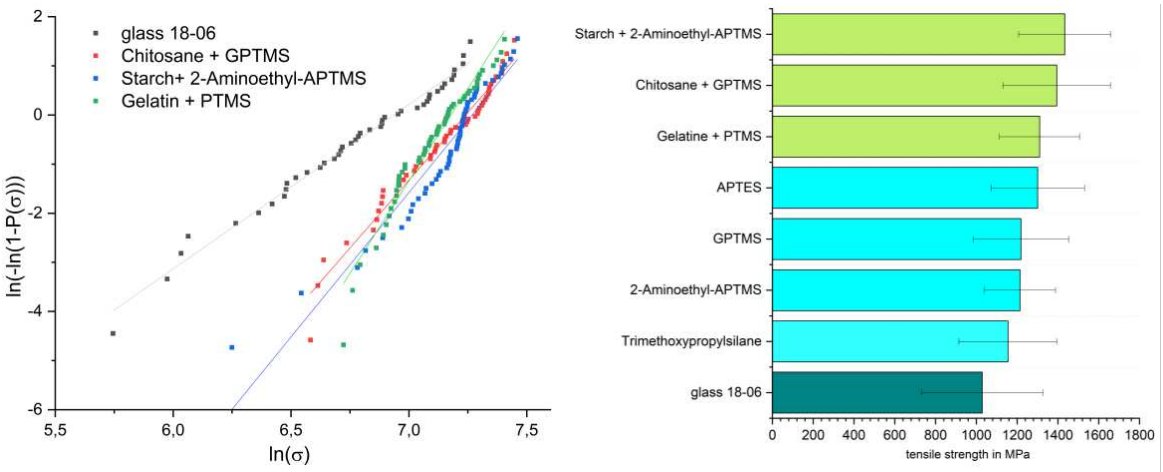

Figure 2. Weibull diagrams of the sizings showing the highest tensile strengths (left) and comparison between the fracture strength of the unsized glass 18-06, the fibers sized with various silanes and with full sizing compositions (right)

In comparison to the unsized fibers, enhanced mechanical properties could be achieved both through the sizing with networking agent (silane) only but also in combination with a film former. For the silanes the highest value for the fracture strength could be achieved with 3-aminopropyltriethoxysilane (APTES) at 1300±228 MPa. The overall improvement of the tensile strength of the fibers can be explained by the formation of a siloxane network by the silane molecules. This network closes the defects that occur in the silica network on the fiber surface. The defects can therefore no longer act as a weak point in the fiber structure. A relative improvement of up to 30 % could be observed. Consequently, the homogenous healing of the defects in the glass structure led to significantly higher Weibull moduli in all samples, increasing from 3.35 (glass 18-06 unsized) to up to 7.53 (sizing Gelatin+PTMS). The silanes therefore exhibited the same functionality on degradable glass as on AR- or E-glass, where they are

commonly applied in sizing formulations. The fiber surface is – on a molecular level – rather rough due to the occurrence of defects mentioned. Hence, it is likely that the silanes are present as covalently bond monolayers on the fiber surface [7].

By combining the networking agents with the biobased film formers, fracture strenghts of consistently above 1300 MPa were achieved. However, through the application of the film formers the Weibull modulus didn't change significantly in comparison to the silane only sized fibers. The biopolymers do not contribute to the healing of defects on the fiber surface but reinforce them mechanically by forming of a thin film that strengthens the fiber longitudinally. A relative mechanical improvement of 40 % could be observed. This is comparable to the effects silanes can have on other glasses such as AR-glass fibers [8]. These improvements, however, are not correlating with the results of the trials with the silanes alone, as can be seen especially with PTMS. The decisive factor for the effects of the film formers is how they interact with the silane layer present on the fiber surface. The biopolymers can be either chemically or physically bonded to the layer beneath. For some combinations, mechanisms for copolymerization of the silane and the polymer are known. The epoxy ring of GPTMS reacts with the primary amine of chitosan in low pH conditions and the hydroxyl group of starch can copolymerize with the primary amine of APTMS [9]. The covalent bonding between the two sizing components explains the good mechanical improvement of the fiber in these both cases. Nevertheless, the film former must not be chemisorbed in all cases. For other combinations, the interface between silane and the polymer can be described as an interpenetrating network, presenting a physisorbed gradient interface which can also lead to good mechanical improvements [5, 7].

The fiber diameters do not change significantly in either the silane-only application or the full sizing formulas. The slight decrease (from 18.6±2.1 µm to 17.4-18.1 µm) could also be ascribed to the storage time of the degradable glass fibers. The non-decreased diameters suggest that the water-based sizing treatment of degradable fibers has not significantly weakened the fiber due to degradation. However, it is of importance to note that the trials were conducted with glass 18-06, which degrades slowly. Tests with other, more hydrolytically active glasses will further reveal the effects of a water-based sizing on the glass fibers.

3.4 SEM-EDX imaging

SEM/EDX experiments were done to assess the quality of the sizing film and to identify individual elements. Two examples are shown below.

In general, the sized fibers feature a very homogenous and smooth surface area with minimal or no inhomogeneities. A polymeric film on the fiber surface cannot be unequivocally determined with this method. However, a smooth fiber surface is a good indicator considering the degradation tendencies of the fiber. Apparently, the sizing process, involving a contact with water, did not visibly degrade the fiber. As the silane is certainly bound to the fiber surface in form of a nanoscale layer, it is not detectable using SEM. The biopolymeric film former, however, becomes visible when its weight share is increased from 1 wt% to 5 wt%, as shown in Fig. 3 – right.

  doi:10.5075/epfl-298799_978-2-9701614-0-0

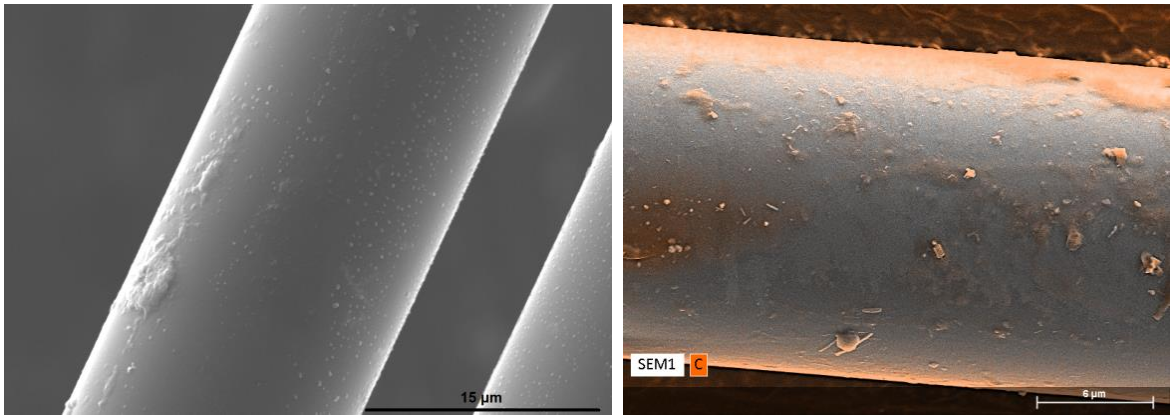

Figure 3. SEM image of APTMS (2 wt%) sized fibers (left) and SEM/EDX result of fibers sized with starch + APTMS (5 wt% + 2 wt%; right)

The carbon originating from the starch molecules could be identified and is distributed unevenly across the fiber surface in the form of small agglomerates. Because of the polar character of the glass fiber surface and the nonpolar character of starch, a direct coupling of the starch polymers to the silica surface seems unlikely. Rather, the silane is covalently bonded to the silica network of the glass and offers its organic functional group to the biopolymer molecules, forming a copolymer [9]. These results also show that optimizing the sizing composition using characterization methods such as SEM/EDX is necessary to obtain the desired properties.

4. Conclusions

The fiber/ matrix interface has a significant influence on the mechanical properties of composites. Particularly in biodegradable composites, major attention must be paid to the sizing that mediates adhesion between fiber and matrix, as it is also released during degradation. In this study, aqueous sizing compositions based on common industrial silanes and bio-based film formers were investigated on 18-06 type biodegradable glass fibers. It was observed that the silanes were responsible for an increase in the fracture strength of the glass fibers. A relative increase of tensile strengths of up to 40 % could be achieved in comparison to unsized fibers. Especially the combinations of Chitosan + GPTMS, Gelatin + PTMS and Starch + N-(2-Aminoethyl)-3-APTMS proved to be effective. It was also important to show that with this glass composition, the surface finish is not affected by the dip coating process. However, it is conceivable that with more hydrolytically reactive glass compositions, dissolution of the fiber surfaces already occurs during sizing. Future studies are still needed to detect the sizing components on the glass surfaces satisfactorily and to analyze the effects of the sizing process on the stability of the degradable glass fibers.

Acknowledgements

The authors thank Janett Hiller and Matthias Krüger for their great assistance in the lab. Many thanks also to Regine Boldt for the SEM-EDX studies performed on the glass fibers

  doi:10.5075/epfl-298799_978-2-9701614-0-0

5. References

1. Hench LL, Jones JR Bioactive Glasses: Frontiers and Challenges. Front. Bioeng. Biotechnol. 2015; 3:2296-4185.
2. Chajri S, Bouhazma S, Adouar I, et al Synthesis, characterization and evaluation of bioactivity of glasses in the CaO-SiO_2-P_2O_5-MgO system with different CaO/MgO ratios. J. Phys.: Conf. Ser. 2019, 1292.
3. Valliant EM, Romer F, Wang D, et al. Bioactivity in silica/poly(gamma-glutamic acid) sol-gel hybrids through calcium chelation. Acta Biomaterialia 2013, 9, 7662-7671.
4. Baino F, Hamzehlou S, Kargozar S, et al. Bioactive Glasses : Where Are We and Where Are We Going? J. Funct. Biomater. 2018, 9, 25.
5. Thomason JL Glass fibre sizing: A review. Composites Part A: Applied Science and Manufacturing 2019, 127.
6. Eichhorn J, Elschner C, Groß M Spinning of Endless Bioactive Silicate Glass Fibres for Fibre Reinforcement Applications. Appl. Sci. 2021, 11, 7927.
7. Ishida H A review of recent progress in the studies of molecular and microstructure of coupling agents and their functions in composites, coatings and adhesive joints. Polym. Compos. 1984, 5, 101-123.
8. Scheffler C Zur Beurteilung von AR-Glasfasern in alkalischer Umgebung. Diss., Technische Universität Dresden, 2009.
9. Connell LS, Romer F, Suarez M, et al Chemical characterisation and fabrication of chitosan-silica hybrid scaffolds with 3-glycidoxypropyl trimethoxysilane. J. Mater. Chem. B 2014, 2, 668-680.
10. Fraga AN, Williams RJJ Thermal properties of gelatin films. POLYMER 1985, 26.

  doi:10.5075/epfl-298799_978-2-9701614-0-0

THE EFFECT OF HUMIDITY ON THE MECHANICAL PROPERTIES OF FLAX-POLYESTER BIOCOMPOSITES WITH DIFFERENT FIBRE ARCHITECTURES

Ali Moghimiardekani(*) , Jan Ivens, Aart Willem van Vuure

KU Leuven, Department of Materials Engineering, , Kasteelpark Arenberg 44, 3001 Leuven, Belgium

(*)Email: Ali.moghimiardekani@kuleuven.be

Abstract: *An experimental investigation was performed to study the effect of humidity on the mechanical properties of non-dry flax/polyester biocomposites. A better understanding of the relationship between environmental factors, particularly humidity, and mechanical properties allows to assess the long-term durability of these materials. This work aims to provide a better insight into the effect of humidity, 55%, 65%, and 85%(RH), on the evolution of the flexural properties of flax/polyester biocomposites. Composites with three different unidirectional fibres, ±45 fabrics from two different suppliers, and 0/90non-crimp fabric are prepared by Vacuum Assisted Resin Infusion (VARI) process. Flexural test results show that a 14% - 25% reduction in modulus of unidirectional NFCs is observed due to the increasing humidity from 55%RH to 85%RH. Furthermore, at 85%RH, the modulus of composites made of non-dry ±45 fabrics and 0/90 fabrics is decreased 27-34% and 21% respectively in comparison with 55%RH.*

Keywords: Bio-Composites; Humidity Effect; Flexural Properties; Fibre Architectures

1. Introduction

In recent years, the use of natural fibres especially flax fibres as a suitable alternative to glass fiber in fiber-reinforced polymer (FRP) is more attractive. Lightness and a lower environmental impact are two crucial factors that can distinguish Natural Fibre Composites (NFCs) from synthetic fibre reinforced polymers[1]. Among various types of natural fibres, bast fibres especially flax ones are so attractive and used in industry due to their high specific stiffness. But their applications have been limited due to the nature of these materials[2]. They interact with humid environments because of the hydrophilic properties of the natural fibre reinforcements mainly explained by their complex multi-scale structure and biochemical composition. Although the effect of humidity and water absorption on the mechanical properties of NFCs have been investigated by many researchers[3], few researchers have embedded non-dried fibre in their composites. Lu et al[1]. found that the durability of these materials increases by making composites with non-dried fibres, because the pre-swollen fibres swell and shrink less in in-use humidity conditions. Hence, in order to have a better understanding of the effect of humidity on the NFCs with non-dried fibre, some biocomposites with different fibre architectures (UD, ±45, 0/90 non-crimp fabric) and partially bio-based polyester resin are prepared. Using a partially bio-based resin combined with a cobalt-free accelerator enhances the environmentally friendly character of NFCs[1]. The results of this work not only depict the effect of humidity on NFCs with different architectures but also reduce the concern over the biocompatibility of NFCs.

2. Materials and Methods:

  doi:10.5075/epfl-298799_978-2-9701614-0-0

2.1. Materials

As described in Table 1 different fibres with various fibre architectures were used as the reinforcement to make flax fibre reinforced composites. Furthermore, the partially bio-based polyester resin(1580 IB, Polynt) with peroxide curing agent (Butanox LPT-IN, Nouryon), cobalt free accelerator (Nouryact CF-12N, Nouryon), and an inhibitor (NLC-10, Nouryon) were used for the matrix preparation. The proportions of resin/accelerator/peroxide/ inhibitor were 100/1/2/0.4 wt% respectively.

Table 1. Flax fibre characteristics

Fibre architechtures	Areal weight (g/m^2)	Suppliers
Non-crimp UD fabric	420	Terre de lin
Quasi-UD	280	Bcomp
UD tape	200	Lineo
0/90 Non-crimp fabric	800	Terre de lin
±45 Non-crimp fabric A	750	Terre de lin
±45 Non-crimp fabric B	350	Bcomp

2.2. Natural fibre composites manufacturing method

All fabric layers were conditioned at 65% RH to have a non-dried fibre prior to the manufacturing of the NFCs. Biocomposite plates were prepared using the vacuum-assisted resin infusion (VARI) technique with a theoretical volume fraction of 35%-40%.

2.3. Flexural test

Flexural tests in the longitudinal direction of the fibres were conducted in accordance with ASTM D790 standard, with a test span of 64 mm. Three-point bending tests were performed on a universal testing machine (Instron 5567) with a 1 kN capacity load cell. All flexural tests were done after sample conditioning for at least 14 days in the standard salt solution boxes with different humidity conditions of 55%, 65%, and 85% RH.

3. Results and discussions

3.1. Flexural test and moisture effect

Table 2. summarizes the flexural properties of the various NFCs at 55% RH. Since fibre volume fraction (FVF%) is a potential variable in the composite manufacturing methods such as VARI, the longitudinal flexural properties were linearly normalised to the FVF%. Hence, Fig 1. depicts the normalized flexural properties of Unidirectional NFCs. As shown in Fig 1. flexural strength and modulus of UD Tape are higher than for the rest of unidirectional NFCs. The lower flexural properties of NFCs with quasi-UD and Non-crimp UD fabric could be due to the twisted fibre and stitched fibre in both NFCs respectively. These effects on the mechanical properties of NFCs have been evaluated by various researchers[4][5] and also it could be confirmed by Micro-CT evaluation. The stitches could make a resin-rich area and cracks could propagate in this area. So

  doi:10.5075/epfl-298799_978-2-9701614-0-0

the mechanical properties of these composites might be reduced. This effect will be addressed by Micro-CT test results in future work.

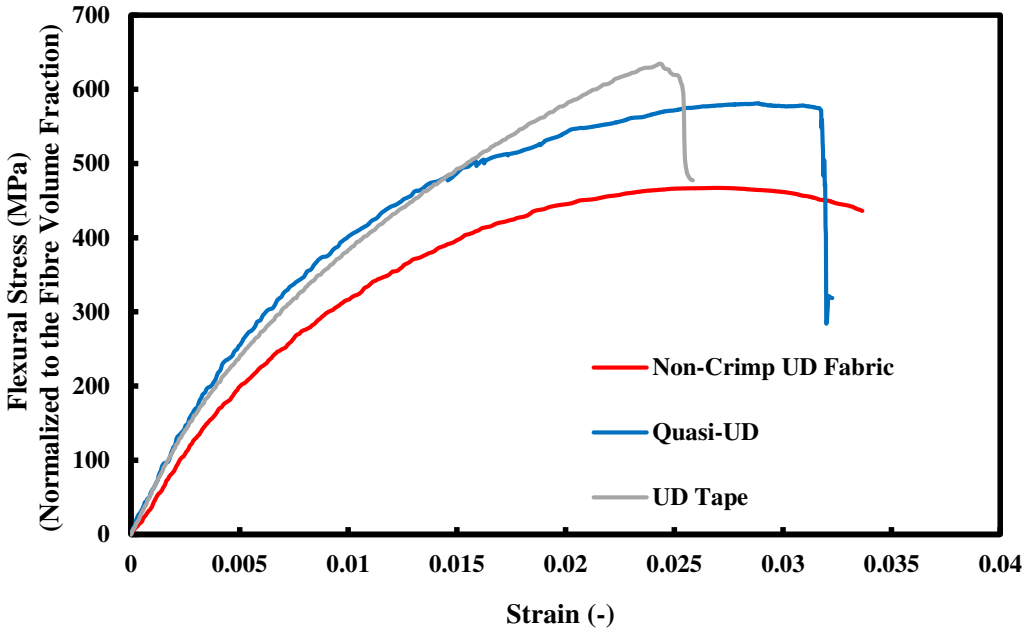

Figure 1. Normalized flexural properties of Unidirectional NFCs, according to the rule of mixtures

Furthermore, Fig. 2 represents the flexural properties of NFCs after conditioning at different relative humidity conditions. As shown in Fig 2.a, the flexural modulus of NFCs with Quasi-UD at 55% RH is 24.23 GPa, while this property at 85%RH is 18.14 GPa. Hence a 25% reduction in flexural modulus due to the increasing humidity from 55%RH to 85%RH is observed. Moreover, the drop in modulus in the rest of unidirectional NFCs is about 14%. Thus, the maximum reduction in flexural modulus in NFCs is seen with the Quasi-UD. It might be due to the twist effect or micro impregnation issues with certain yarns. As shown in Fig 2.b, the flexural modulus of NFCs with ±45 Non-Crimp fabric B (somewhat twisted fibre) is 25% greater than the flexural modulus of NFCS with ±45 Non-Crimp fabric A, the type of stitches in both fabrics might be the reason for this behaviour. Furthermore, the drop in modulus after conditioning at 85% in the first composite with twisted fibre is about 7% higher than in the second type of composite. Hence, the effect of twisted fibre or micro impregnation issues could be some hypotheses for this downward trend.

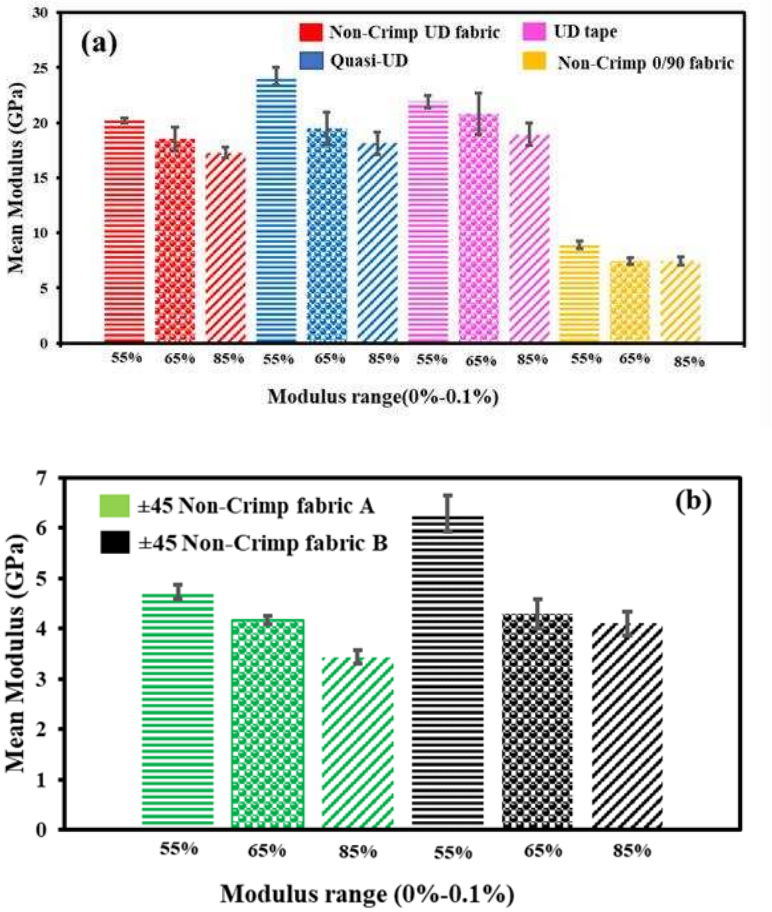

Figure 2. (a) Humidity effect on the flexural modulus of NFCs (a)UD and 0/90 fabrics, (b) ±45 fabrics

Table 2. Flexural properties of NFCs with different architectures (at 55 %RH and RT)

Fibres	Mean Strength (MPa)	Mean Modulus (GPa)	Strain to Failure (-)	FVF (%)
Non-Crimp UD Fabric	182.38 ± 7.96	20.18 ± 0.24	0.023 ±0.002	41.3
Quasi-UD	242.41 ± 2.79	24.23 ± 0.79	0.029 ± 0.001	40.8
UD Tape	234.3 ± 5.62	21.92 ± 0.58	0.024 ± 0.001	37.6
±45 Non-Crimp fabric A	81.45 ± 4.51	4.73 ± 0.15	0.033 ± 0.004	43.1
±45 Non-Crimp fabric B	80.56 ± 6.20	6.29 ± 0.36	0.036 ± 0.004	43.8
0/90 Non-Crimp fabric	162.12 ± 5.94	8.92 ± 0.76	0.035 ± 0.003	36.7

Fig 3. shows the theoretical and experimental flexural properties of NFCs with ± 45 fabrics which were obtained from ESAComp software. ESAComp results, which were obtained based on Classical Laminate Theory(CLT), represent that the flexural modulus ratio(Exp/Theo (%)) of NFCs with ±45 fabric A is 54% whilst this value for NFCs with Non-Crimp UD fabric is 73%, and these values are the lowest ratios in comparison with the rest of ±45 fabric and UD biocomposites.

  doi:10.5075/epfl-298799_978-2-9701614-0-0

Since these two types of fabrics are stitched fabrics, it might be indicative of the effect of the stitches. Moreover, the fibre alignment should be another important factor so further research is required to evaluate the effect of fibre misalignment on the mechanical properties of NFCs.

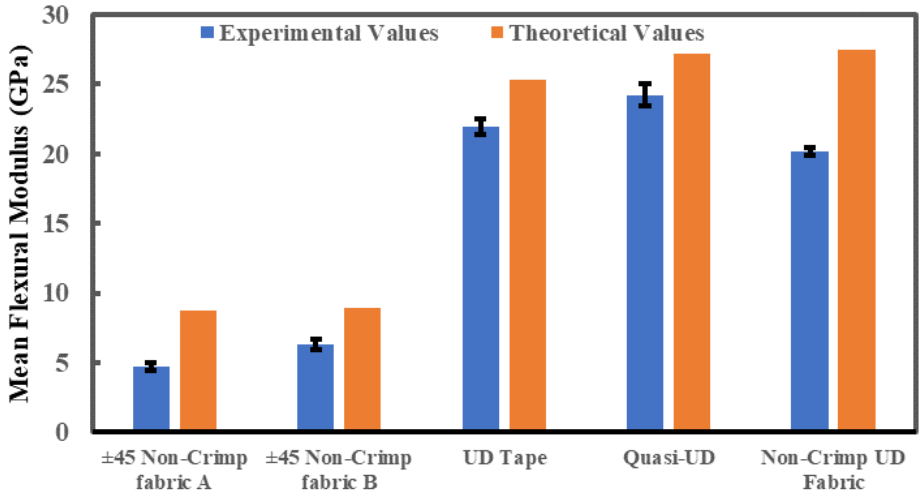

Figure 3. Experimental and theoretical flexural modulus of NFCs

4. Conclusions

The reduction in E-modulus at high humidity is remarkably lower than usually reported in the literature[6], where reductions up to 50% are seen. Quasi-UD flax fibre reinforced epoxy composites showed a higher decline in flexural modulus when subjected to the higher relative humidity in comparison with the rest of unidirectional NFCs. The significant drop in flexural modulus of "Non-Crimp UD Fabric " and "±45 Non-Crimp fabric A" depict the effect of stitches. Moreover, fibre misalignment could be a crucial factor to demonstrate other reduction parameters of flexural properties.

Acknowledgments

The authors would like to acknowledge the financial support from Interreg North-West Europe, under grant agreement No NWE 993 – Smart Circular Bridge project.

5. References

1. Lu MM, Van Vuure AW. Improving moisture durability of flax fibre composites by using non-dry fibres. Composites Part A: Applied Science and Manufacturing 2019;123:301–9.
2. Azwa ZN, Yousif BF, Manalo AC, Karunasena W. A review on the degradability of polymeric composites based on natural fibres. Materials and Design 2013;47:424–42.
3. Koolen G, Soete J, van Vuure AW. Interface modification and the influence on damage development of flax fibre - Epoxy composites when subjected to hygroscopic cycling. Materials Today: Proceedings 2019;31:S273–9.
4. Mouritz AP, Leong KH, Herszberg I. A review of the effect of stitching on the in-plane mechanical properties of fibre-reinforced polymer composites. Composites Part A: Applied Science and Manufacturing. 1997;28:979–91.
5. Mouritz AP, Gallagher J, Goodwin AA. Flexural strength and interlaminar shear strength of

stitched GRP laminates following repeated impacts. Composites Science and Technology. 1997;57:509–22.
6. Scida D, Assarar M, Poilâne C, Ayad R. Influence of hygrothermal ageing on the damage mechanisms of flax-fibre reinforced epoxy composite. Composites Part B: Engineering 2013;48:51–8.

  doi:10.5075/epfl-298799_978-2-9701614-0-0

FUNCTIONALIZED WOOD COMPOSITES FOR MECHANICAL ENERGY HARVESTING AND VIBRATION SENSING

Farsa Ram,[a] and Lars Berglund[a]*
[a]Wallenberg Wood Science Center and Division of Biocomposites, Department of Fibre and Polymer Technology; KTH Royal Institute of Technology, Stockholm SE-10044, Sweden- farsa@kth.se

Abstract: *Sustainable energy technologies require the development of sustainable composites using novel methods and materials with a minimal environmental impact. Piezoelectric effect-based mechanical energy harvesting (MEH) and sensing offer great potential as a sustainable technology for low-grade mechanical energy harvesters and self-powered sensors. Herein, we utilize ZnO to functionalize the delignified wood surface for MEH and vibration sensing applications, where wood act as robust support to well adhered piezoelectric ZnO nanoparticles. This surface functionalization strategy is a reasonable substitute for the bulk ZnO films, which offer optimal utilization of active material at relatively low content. The wood/ZnO composite device is utilized for vibration sensing and MEH. The device (25 cm^2) resulted in a peak to peak output voltage of ~15 mV and a peak to peak current of ~2.2 nA under the influence of mechanical vibrations from the periodic motion of a linear motor operating at the acceleration of 50 ms^{-2}. The scalable fabrication approach signifies the practical use of wood-based composites for piezoelectric mechanical energy harvesting.*

Keywords: Sustainable bio-based composites; mechanical energy harvesting; ZnO; wood composites,

1. Introduction

This work reports the utilization of ZnO surface-functionalized wood veneers as a mechanical energy harvester and vibration sensor. Mechanical energy harvesting is realized via the piezoelectric effect, where employed devices are known as piezoelectric nanogenerators (PENG). PENGs play a significant role in the development of sustainable technology as they can utilize waste mechanical energy from wind, sound, waves, human physiological motions, or machines and infrastructures vibrations converting into electricity for running small portable electronics or the array of sensors for the Internet of Things (individually identifiable smart devices connected over the internet). Additionally, PENGs can also act as self-powered mechanical sensors, flexible electronic skin, wearable sensors for technological applications, or human health monitoring.[1]

Wood is a ubiquitous material that is majorly comprised of cellulose, hemicellulose, and lignin.[2] The presence of these chemical motifs and their rich functionalities in wood provide a platform for various modifications for numerous technological applications.[3] Recently, delignified balsa wood was explored for mechanical energy harvesting and sensing applications, where piezoelectric properties in the wood were attributed to crystalline cellulose.[4] Delignification using hydrogen peroxide or selective fungal decay of wood not only enhances the

  doi:10.5075/epfl-298799_978-2-9701614-0-0

cellulose content but also the compressibility of the wood leading to enhanced energy generation, which resulted in the output voltage of 0.84 V under 22.2 kPa stress, and 0.87 V at 10 N force (45 kPa) stress.[5,6] However, these reports were limited to the balsa wood only, and fungal treatment takes about ten weeks, making it an unfavorable process from the scalability point of view. Previously, cellulose piezoelectricity was improved by the ZnO coating.[7] However, cellulose films are prepared via a bottom-up approach in which cellulose fibers of the wood are broken down using chemical or physical methods and then reassembled to form a cellulose macroscopic structure. On the other hand, in a top-down approach, wood structure and/or its compositions are engineered to obtain functional properties without compromising its original hierarchical anisotropic structure. Usually, the top-down approach requires less energy consumption, making it a more eco-friendly process.[3]

In this row, we functionalized wood surfaces with ZnO nanoparticles coating to demonstrate their potential application in mechanical energy harvesting and vibration sensing. The functionalization of wood with ZnO has been vastly explored, due to several advantages such as enhanced moisture resistivity, photostability, fire retardancy, and antibacterial properties of the wood substrate.[8,9] ZnO adheres well to wood or cellulose due to the higher binding affinity of Zn^{2+} toward the oxygen atom in hydroxyl or carboxyl functionalities.[8,9] The surface functionalization strategy is unique to previous approaches to composite preparation, wherein active piezoelectric particles embedded in a polymer matrix can hinder their effective utilization.[10] However, surface functionalization of wood with ZnO nanoparticles coating ensures the effective utilization of active material, and a similar output can be achieved at lower ZnO content. Additionally, this method is independent of the wood substrate, as ZnO functionalization of wood has been utilized for numerous wood species.[8] Moreover, wood functionalization by ZnO can be achieved at a larger scale, which signifies its potential for large-area applications such as wooden floors.

2. Results and discussion

The birch wood veneers were treated in a bleaching solution (6 wt % hydrogen peroxide, 1 wt % trisodium citrate dihydrate, and 1 wt % sodium hydroxide in deionized water) at 65 °C for 2 h and washed 2 to 3 times using deionized water. The bleaching treatment partly removes the lignin and modifies its chromophores while retaining the structural integrity of the wood veneers. Figure 1a shows the Fourier Transformed Infrared (FTIR) spectroscopic analysis of native wood (NW) and delignified wood (DW), where peaks intensities at 1460, 1505, and 1595 cm^{-1} corresponding to lignin were reduced slightly owing to only partial removal/modification of lignin. This treatment does not destroy the aromatic backbone of lignin such that the structural integrity of the wood is not compromised. The intensity of the peak at 1734 cm^{-1} disappeared due to the deacetylation of hemicellulose. Additionally, the intensity of the peak near 1233 cm^{-1} reduced due to the modification of C-O bonds in hemicellulose and lignin. Further, wood veneers were solvent exchanged from water to ethanol, and ZnO nanosol was prepared by dropwise addition of ethanolic sodium hydroxide in a zinc acetate dihydrate solution at 65 °C. The delignified wood was further functionalized with ZnO by ZnO nanosol infiltration under vacuum followed by drying at 110 °C for 3 min. These steps were subsequently repeated four times to ensure the homogenous coverage of ZnO on the wood surface. The ZnO content was found to be ~7 wt% as determined by thermal gravimetric analysis in oxygen. Figure

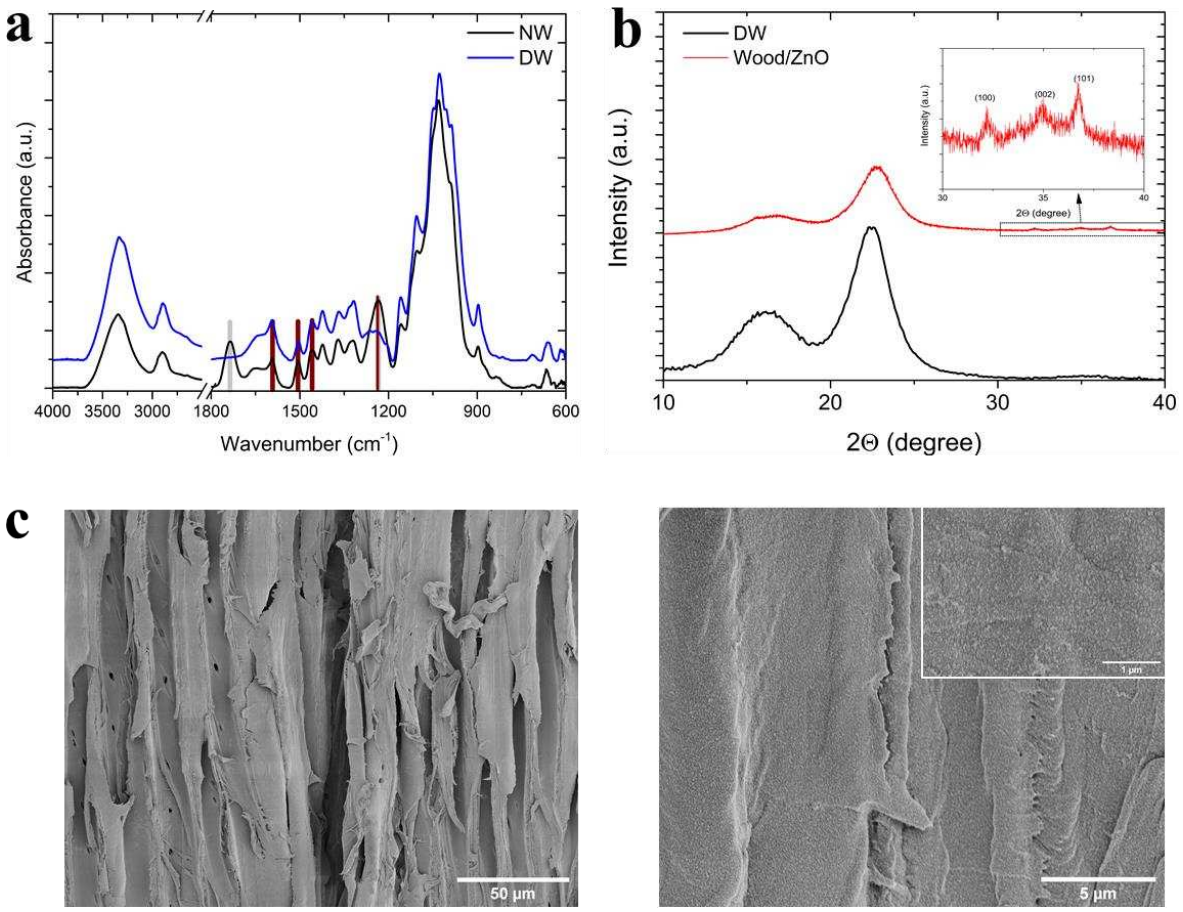

Figure 1: (a) FTIR spectra of native and delignified wood. The peaks changed due to lignin and hemicellulose modification are shown in dark brown and grey, respectively. The data was obtained using PerkinElmer spectrum 100 FT-IR equipped with an MKII Golden Gate, a single-reflection accessory unit with a diamond ATR crystal (Graseby Specac Ltd., UK). SEM images of ZW. (b) X-ray diffraction pattern of DW and wood/ZnO (c) Overview of wood structure along with the fiber direction, (d) Fiber surface shows ZnO nanoparticle coating and zoom-in image in inset shows the ZnO nanoparticle morphology. The data were obtained using a Field Emission Scanning Electron Microscope (Hitachi S-4800, Japan).

1b shows the X-ray scattering diffraction pattern of DW and wood/ZnO. The inset image shows the ZnO crystalline planes (100), (002), and (101).[11] Figures 1c and 1d show the Scanning Electron Microscopy (SEM) images of ZnO functionalized wood veneers. Since the wood veneers were cut along the fiber direction, ZnO deposition was majorly limited to only the fiber surface or in the exposed lumens. The wood surface shows the exposed fiber lumen and fiber surfaces (Figure 1c). After ZnO functionalization, small granular ZnO nanoparticles can be observed on the fiber surface as shown in Figure 1d. The ZnO particle size ranges from 20 - 40 nm as shown in the inset image of Figure 1d.

A device or PENG was fabricated by attaching two electrodes at the top and bottom of the wood/ZnO veneer (5 x 5 cm^2) followed by soldering two copper wires. Finally, the whole device was encapsulated in an insulating matrix (Figure 2a) to eliminate other contributions during the testing. In the practical environment, mechanical energy is abundant in the form of vibrations. Every running machine, equipment, and infrastructure like wooden floor, flyover, etc. produces vibrations. These vibrations have a unique frequency associated with them, which can

  doi:10.5075/epfl-298799_978-2-9701614-0-0 published under CC BY-NC 4.0 license

change under external stimuli or malfunction, and they can be used as a mechanical source for mechanical energy harvesting or sensing. For a demonstration, we utilize the device for vibration sensing. The vibrations were produced by the periodic movements of the linear motor (Linmot, USA) operating at an acceleration of 50 ms^{-2}. Figure 2b shows the device mounted on the linear motor. The output voltage and current were recorded using Keithley's DMM 7510. When the linear motor was at the rest, no signal was observed and marked as “Off” in Figure 2c. When the periodic motions of the linear motor started, the signals appeared, which is marked as “On” in Figure 2c. The vibrations act as a mechanical input, which mechanically deforms the wood/ZnO

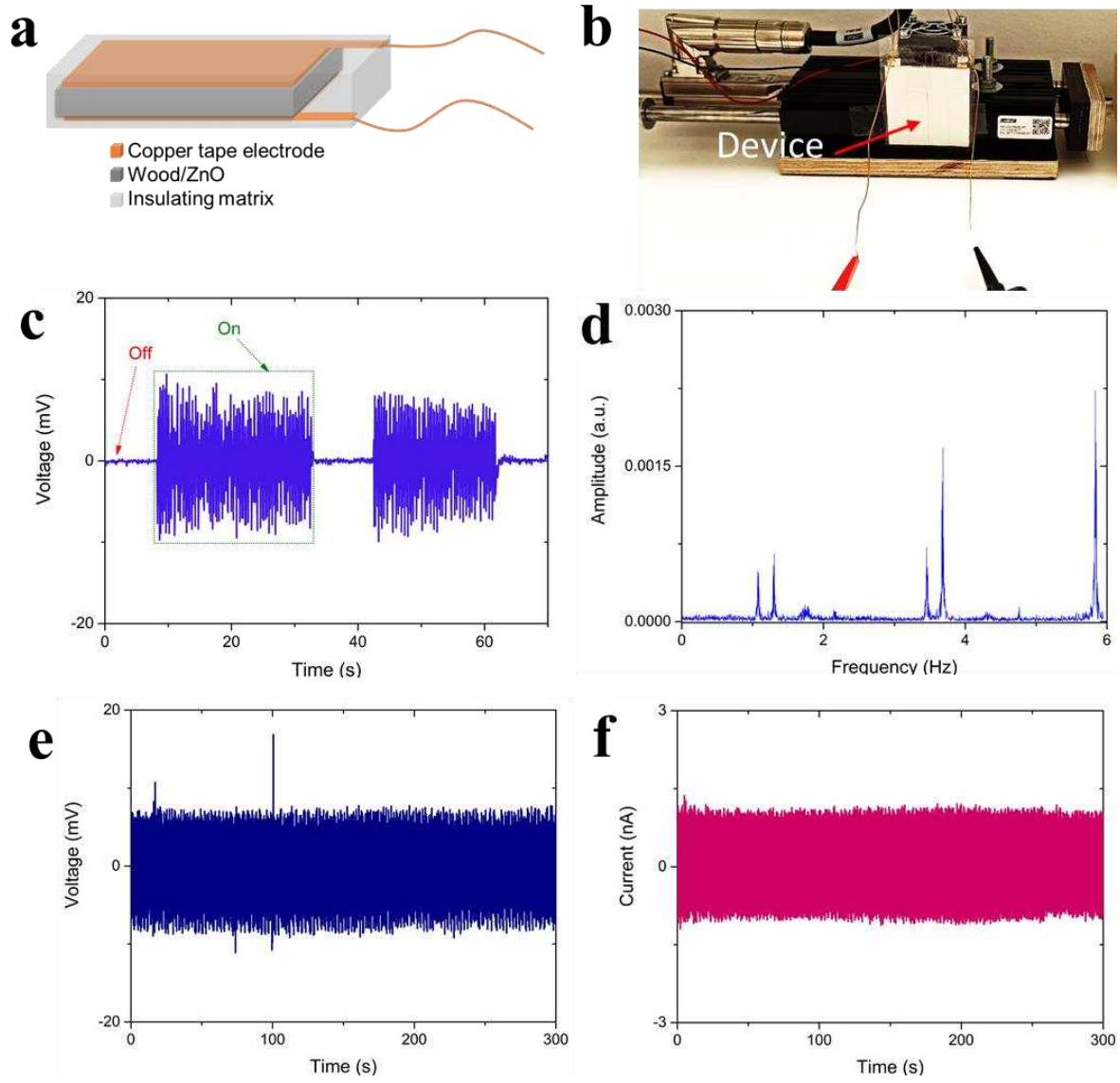

Figure 3: Vibration sensing and mechanical energy harvesting from ZnO functionalized wood. (a) Schematic illustration of the piezoelectric nanogenerator fabricated from wood/ZnO. (b) A linear motor setup for producing the vibrations, and images show the device mounted on the linear motor setup. (c) The vibration sensing ability of wood/ZnO device, where the vibrations are produced by a linear motor operating at the acceleration of 50 ms^{-2}. (d) Fast Fourier Transformed analysis of voltage signal showing frequency range of vibrations. Mechanical energy harvesting from vibrations produced by the periodic motion of the linear motor, (e) the output voltage, and (f) output current.

  doi:10.5075/epfl-298799_978-2-9701614-0-0

substrate. In a response to the mechanical deformations, the wood/ZnO produces electrical signals owing to its piezoelectric properties. Hence, the wood/ZnO device act as a self-powered vibration sensor. The Fast Fourier Transformed (FFT) analysis of output signals (Figure 2d) revealed that at the acceleration of 50 ms^{-2}, the prominent frequency of the linear motor setup vibration was ~5.8 Hz. Additionally, these low-grade vibrations were also used for mechanical energy harvesting. The device resulted in an output voltage of ~15 mV (Figure 3e) and a current of ~2.25 nA (Figure 3f) from these vibrations. Hence, low-cost, scalable wood/ZnO composites-based piezoelectric nanogenerators demonstrated their potential in mechanical energy harvesting and vibration sensing toward the development of sustainable technologies.

3. Conclusions

We report the wood/ZnO sustainable composite-based vibration sensing and mechanical energy harvesting devices. The wood/ZnO composite can be prepared by surface functionalization of delignified wood veneers. This method offer advantages of effective utilization of active material along with scalability potential. A device fabricated from the wood/ZnO composite (25 cm^2) demonstrated its potential as a self-powered vibration sensor. It could sense low-frequency vibrations produced by the periodic motions of the linear motor. These vibrations were also utilized as a mechanical input for MEH, which resulted in an output voltage of ~15 mV and a current of ~2.2 nA. Thus, low cost, easy to prepare wood/ZnO offer potential for their application in mechanical energy harvesting and sensing application, where they can be employed under wooden floors.

Acknowledgements

FR and LB thank Knut and Alice Wallenberg foundation, and Wallenberg Wood Science Center for the postdoctoral fellowship and funding. FR thanks Xioying Xu for helping with XRD measurements.

4. References

1. Cao X, Xiong Y, Sun J, Zhu X, Sun Q, Wang ZL. Piezoelectric Nanogenerators Derived Self-Powered Sensors for Multifunctional Applications and Artificial Intelligence. Advanced Functional Materials. 2021 Aug;31(33):2102983.

2. Saka S. Structure and chemical composition of wood as a natural composite material. InRecent Research on Wood and Wood-Based Materials 1993 Jan 1 (pp. 1-20). Elsevier.

3. Chen C, Berglund L, Burgert I, Hu L. Wood nanomaterials and nanotechnologies. Advanced Materials. 2021 Jul;33(28):2006207.

4. Fukada E. Piezoelectricity as a fundamental property of wood. Wood Science and Technology. 1968 Dec;2(4):299-307.

5. Sun J, Guo H, Ribera J, Wu C, Tu K, Binelli M, Panzarasa G, Schwarze FW, Wang ZL, Burgert I. Sustainable and Biodegradable Wood Sponge Piezoelectric Nanogenerator for Sensing and Energy Harvesting Applications. ACS nano. 2020 Sep 16;14(11):14665-74.

6. Sun J, Guo H, Schädli GN, Tu K, Schär S, Schwarze FW, Panzarasa G, Ribera J, Burgert I. Enhanced mechanical energy conversion with selectively decayed wood. Science Advances. 2021 Mar 1;7(11):eabd9138.

7. Mun S, Ko HU, Zhai L, Min SK, Kim HC, Kim J. Enhanced electromechanical behavior of cellulose film by zinc oxide nanocoating and its vibration energy harvesting. Acta Materialia. 2016 Aug 1;114:1-6.

8. Kong L, Tu K, Guan H, Wang X. Growth of high-density ZnO nanorods on wood with enhanced photostability, flame retardancy and water repellency. Applied Surface Science. 2017 Jun 15;407:479-84.

9. Dong Y, Yan Y, Ma H, Zhang S, Li J, Xia C, Shi SQ, Cai L. In-situ chemosynthesis of ZnO nanoparticles to endow wood with antibacterial and UV-resistance properties. Journal of Materials Science & Technology. 2017 Mar 1;33(3):266-70.

10. Shin DM, Tsege EL, Kang SH, Seung W, Kim SW, Kim HK, Hong SW, Hwang YH. Freestanding ZnO nanorod/graphene/ZnO nanorod epitaxial double heterostructure for improved piezoelectric nanogenerators. Nano Energy. 2015 Mar 1;12:268-77.

11. Makarona E, Koutzagioti C, Salmas C, Ntalos G, Skoulikidou MC, Tsamis C. Enhancing wood resistance to humidity with nanostructured ZnO coatings. Nano-Struct. Nano-Objects 2017;10:57-68.

DEVELOPMENT OF BIO-BASED CFRP LAMINATES FOR STRENGTHENING CIVIL ENGINEERING STRUCTURES. PRELIMINARY RESULTS OF THE BIOLAM PROJECT

Marina Santos[a], Mateus Hofmann[a], Mário Garrido[a], João R. Correia[a], João Carlos Bordado[b], Filipe Dourado[c]

a: CERIS, Instituto Superior Técnico, University of Lisbon
b: CERENA, Instituto Superior Técnico, University of Lisbon
c: S&P Clever Reinforcement Ibérica, Rua José Fontana nº 76, Amora

Abstract: *The BioLam project, currently being developed by Instituto Superior Técnico and pultrusion company Clever Reinforcement Ibérica, envisages the development of more sustainable carbon-FRP (CFRP) laminates. The main goal of the project is to develop a bio-based resin system and replace its current petrochemical-based thermosetting counterpart in the production of pultruded CFRP laminates for the strengthening of reinforced concrete structures. This paper presents an overview of the BioLam research project, namely of the various tasks. The paper presents, in more detail, (i) results of mechanical characterisation tests of pultruded CFRP laminates, produced with a bio-based resin already developed and a conventional counterpart, and (ii) preliminary results of durability tests on those two types of laminates after 1 and 3 months of accelerated hygrothermal ageing.*

Keywords: Construction; Sustainability; Bio-polymers; Composites; CFRP laminates; Strengthening.

1. Introduction

Approximately one third of global CO_2 emissions are attributed to the construction industry; thus, increasing its efficiency and introducing innovative and more sustainable materials are key strategies to reduce the environmental impacts of this sector [1,2]. Fibre reinforced polymer (FRP) composites have gradually gained acceptance in construction due to their several advantages over conventional materials [3]. However, their polymeric matrix is usually derived from petrochemical sources, generating significant environmental impacts and undesirable dependency from crude-oil. Over the past century, the price of both petrochemical monomers and petro-based products gradually raised due to increasing consumption and decreasing raw material availability. One way to reduce the dependence from petroleum is to favour the use of renewable raw materials [4,5].

Pultruded carbon fibre reinforced polymer (CFRP) laminates are now often used in the structural strengthening of civil engineering infrastructure, such as bridges and buildings (

Figure *1*). They have a typical fibre volume of 70% and their resin matrix is usually made of petrochemical-based vinyl ester or epoxy resins. In this context, there is an opportunity to improve the sustainability of CFRP laminates by using resins obtained from bio-based materials, the so-called bio-resins, provided that they present similar performance to conventional polymeric resins [2,5].

The most promising path for the development of bio-composites for structural applications is the synthesis of polymers from renewable raw materials, such as vegetable oils or biomass [6].

  doi:10.5075/epfl-298799_978-2-9701614-0-0

Lignocellulosic biomass is an abundant renewable resource, composed mainly of cellulose, hemicellulose, and lignin. Phenolic compounds from biomass can be incorporated in the polymeric chain at a competitive cost, increasing the bio-content, improving fire performance and, consequently, the sustainability and performance of resins and composites in which they are incorporated [7,8].

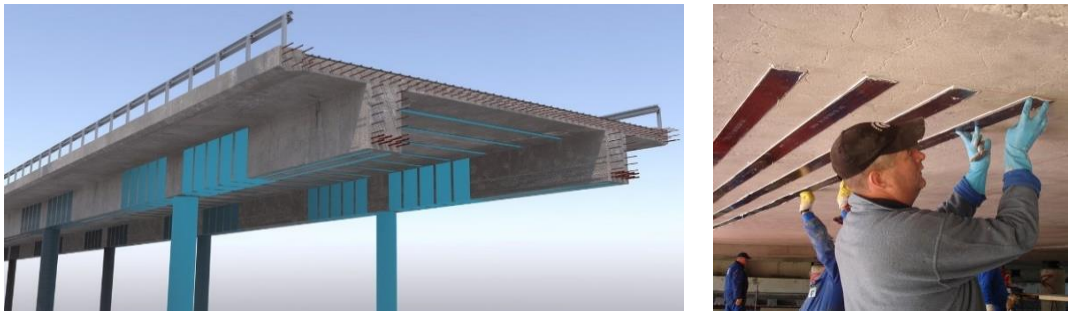

Figure 1. CFRP laminates and sheets strengthening of bridge and building structures [9].

The ongoing BioLam project aims to address the above-mentioned challenge – the aim of this project is to develop a bio-based polymeric resin system able to replace current petroleum-derived resins, and use it in the development of CFRP laminates for structural strengthening in civil engineering applications. In particular, the bio-based CFRP laminates to be developed should provide comparable mechanical and structural performance to existing conventional CFRP laminates produced with vinyl ester or epoxy resins, a more competitive price, better fire properties and superior environmental sustainability.

The BioLam project is led by the company S&P - Clever Reinforcement Ibérica, specialized in the manufacturing of pultruded CFRP laminates used in structural strengthening, in consortium with Instituto Superior Técnico, through its research units CERIS and CERENA, specialized respectively in the development and implementation of FRP materials and structures, and the synthesis and processing of polymers. The project includes the following articulated tasks:

- Preliminary study of strategies for synthesizing bio-resins and preliminary assessment of their viability;
  Experimental assessment of high potential bio-resins;
- Production of specimens and prototypes;
- Experimental characterization of the selected bio-resin(s) and the corresponding CFRP bio-laminates;
  Application of CFRP bio-laminates in the strengthening of reinforced concrete structural members and their experimental characterization;
- Life cycle analysis (LCA) of bio-laminates compared to current solutions.

The following sections of the paper provide a brief overview of the activities involved in the abovementioned tasks. Further details are given about (i) the results of mechanical characterisation tests of pultruded CFRP laminates produced with a bio-based resin already developed and with a conventional epoxy-based resin (CVE), used as reference, and (ii) preliminary results of durability tests on those two types of laminates after 1 and 3 months of hygrothermal ageing.

  doi:10.5075/epfl-298799_978-2-9701614-0-0

2. Preliminary study of strategies for synthesizing bio-resins and their viability

This task has been carried out via two routes: (i) development of a bio-phenolic resin obtained directly from raw biomass; and (ii) adjustment of a bio-polyester resin, previously developed at IST in the scope of the EcoComposite project [10,11], in light of the requirements for manufacturing (pultrusion) and outdoor exposure of CFRP laminates.

Regarding the first route, although more disruptive and innovative (TRL 2), after an initial research period, this was suspended due to logistical and technical difficulties in obtaining liquefied biomass at a large enough scale. Moreover, the laboratorial effort to produce the organosolv lignin (liquefied biomass after separation treatments) did not show to be promising as the amount of material produced was quite low, not enough to produce resin plates for laboratory testing.

The second route is currently being pursued via modification (TRL 7) of the polymeric chain of a bio-based polyester (BUPE) resin recently developed at IST and already tested in the pultrusion process [10]. This resin was produced by synthesising monomers (diacids and diols) derived from renewable raw materials - 1,3-propanodiol, isosorbide, fumaric acid, and phthalic anhydride - and using a mixture of styrene and HEMA as a reactive diluent. Currently, efforts are being made to improve the initial viscosity and pot life of the bio-based resin, as well as to increase its resistance to hydrolysis and/or plasticization.

3. Experimental assessment of high potential bio-resins

3.1. Requirements for the processing, physical and mechanical properties of bio-resins

In the development (adjustment) of the modified bio-based polyester (BUPEM) resin, requirements concerning the target values for the resin gel time at 180°C (DIN 16945) and apparent viscosity (ASTM D4287) were set. The gel time target value is 80 s, similar to that of the conventional epoxy-based resin that is currently in use. The viscosity target value is 500 cP, considered as acceptable for resin processing in pultrusion; in fact, higher viscosities can increase the production time and cause risk of voids and formation of defects in the composite part [12].

Pure resin specimens of the BUPEM resin are being produced and their physical and mechanical properties assessed to verify the resin requirements for the pultrusion process. Standard experimental procedures are used to determine the hardness (ASTM D2583), density (ASTM D792) and water absorption (ASTM D570) of the bio-resins, and also the mechanical behaviour in tension (ASTM D638) and shear (ASTM D5379/D5379M). The following target values were set for the main control properties: (i) Barcol hardness of 15-30, (ii) maximum water absorption of 1%, (iii) tensile strength above 50 MPa, (iv) tensile modulus above 2.5 GPa, and (v) tensile strain at failure above 2.5%.

3.2. Pilot application in the pultrusion of bio-laminates

A first pilot production of bio-laminates by pultrusion was carried out using the original BUPE resin described previously (Figure 2). A new production will be carried out at a later stage, after the successful development and characterisation of the BUPEM resin. Regarding the bio-

  doi:10.5075/epfl-298799_978-2-9701614-0-0

laminates produced in the first pilot production, the following tests were performed to determine and compare their mechanical properties with those of their conventional counterparts: tensile (ASTM D638, ASTM D7565/D7565M) and interlaminar shear (ILS) (ASTM D5379/D5379M) tests. In both cases, the laminates have cross section of 1.4 x 20 mm^2, comprising a (unidirectional) fibre volume content of 66%. The results of these tests for the first pultrusion iteration with BUPE resin have suggested a good adhesion between the bio-resin and the carbon fibre rovings, as the mean value of ILS strength (ILSS) of the bio-based CFRP laminate was only 10% lower compared to the conventional laminate (Table 1 and Table 2, respectively).

Figure 2. Pilot production of pultruded CFRP bio-laminates using the BUPE resin.

Table 1. Interlaminar shear tests of BUPE-laminates

	Interlaminar shear strength (MPa)
$\bar{x}$	40,4
σ	1,1
ν	2,7%

Table 2. Interlaminar shear tests of CVE-laminates

	Interlaminar shear strength (MPa)
$\bar{x}$	44,9
σ	1,8
ν	4,0%

The results of the tensile tests of BUPE and CVE laminates are shown Table *1* Tables 3 and 4 respectively. The short-term mechanical properties in tension (strength, σ_{MAX}, modulus of elasticity, E, and strain at failure, ε_U) of both types of laminates were very similar. For instance, the mean value of the tensile strength of the bio-laminates was slightly (4%) higher, the modulus of elasticity was slightly (4,5%) lower, and the deformation capacity was higher (10%) when compared to the conventional counterpart, demonstrating the potential of the bio-based resin to be used in a high-structural-performance composite product.

Table 3. BUPE-laminates tensile tests

	σ_{Max} (MPa)	E (GPa)	ε_U(%)
$\bar{x}$	2030,8	165,8	1,4
σ	171,0	4,0	0,1
ν	8,4%	2,4%	9,9

Table 4. CVE-laminates tensile tests

	σ_{Max} (MPa)	E (GPa)	ε_U (%)
$\bar{x}$	1946,8	173,6	1,3
σ	44,5	3,7	0,1
ν	2,3%	2,2%	10,2

  doi:10.5075/epfl-298799_978-2-9701614-0-0

4. Strengthening of structural members using bio-laminates

In the final part of the project, a proof-of-concept will be carried out aiming at assessing and demonstrating the structural efficiency of the CFRP bio-laminates through: (i) CFRP-concrete bond tests (double lap and pull-out); and (iii) flexural tests of CFRP-strengthened reinforced concrete beams. The results will be compared to those using conventional CFRP laminates.

4.1. Double-lap tensile tests

The interface between FRP composites and a concrete substrate is expected to transfer the loads from the concrete to the FRP composite, so the system performance is highly influenced by the properties of the adhesive layer [13]. The objective of these tests is to evaluate the structural effectiveness of the CFRP bio-laminates, namely by assessing the adhesion between concrete specimens and CFRP bio-laminates bonded with epoxy adhesive by means of double-lap tensile tests. Tests will be performed also using conventional CFRP laminates to compare their mechanical behaviour and failure modes. The following parameters will be measured: (i) the load and cross-head displacement of the test machine; (ii) the slip along the bonded length of the CFRP laminates, measured at the beginning and end of the bonded length; and (iii) the axial strains at the centre and along the bonded length of the CFRP laminates.

4.2. Pull-off tests

Pull-off tests between concrete blocks and CFRP laminates bonded with epoxy adhesive will be carried out according to ASTM D7522/D7522M. The direct tension will be applied by means of a standard pull-off test fixture to measure the bond strength between the CFRP and the concrete substrate to determine the maximum tensile load (stress) that the CFRP–epoxy-concrete interfaces can resist. These tests will be performed both with BUPE and CVE CFRP laminates to compare their relative performance.

4.3. Flexural tests on CFRP-strengthened reinforced concrete beams

This task comprises flexural tests on reinforced concrete beams (lightly to moderately reinforced), before and after strengthening in bending with CFRP laminates, both conventional and bio-based. These tests will serve mostly as a proof of concept of the bio-based CFRP laminates to be developed. Full scale four-point bending tests will allow determining the load *vs*. midspan deflection responses of the beams and assessing the contribution of the CFRP strengthening system in terms of cracking load, ultimate load, maximum deformation, and failure modes.

5. Durability

The durability of the BUPE and CVE CFRP laminates is being assessed through hygrothermal ageing followed by mechanical tests at predetermined periods (up to 12 months). The specimens are being immersed in tap water at three different temperatures of 20, 35 and 50°C. Moreover, to evaluate the photo-degradation of the CFRP laminates, they will be placed in a QUV chamber and mechanically tested after 750 h, 1500 h and 3000 h of exposure. The mechanical characterization tests consist of tensile (ASTM D638, ASTM D7565/D7565M) and in-plane shear (ASTM D5379/D5379M) tests. Mechanical tests were already performed after 1 and

  doi:10.5075/epfl-298799_978-2-9701614-0-0

3 months of hygrothermal ageing (with the CFRP laminates in wet condition); additional tests will be performed after 6 and 12 months, to determine and predict (extrapolate) the long-term behaviour of the CFRP laminates [14]. The same hygrothermal aging and mechanical characterisation tests will be performed for bio-based resin BUPEM, presently under development (adjustment). In addition, tests will also be performed to assess the durability of the CFRP-epoxy-concrete bond; for this purpose, double lap tensile test specimens will be subjected to the same hygrothermal exposure.

Figure 2 shows the results of the tensile tests for the BUPE and CVE CFRP laminates before and after 1 and 3 months of hygrothermal ageing at 20, 35 and 50 °C. The results after 1 month of immersion indicate that the bio-based resin matrix suffered severe hygrothermal degradation, particularly at 35 °C - for this exposure condition, the tensile strength decreased 39% compared to its initial capacity. However, the BUPE resin may have experienced significant (competing) post-curing at 50 °C - for this highest immersion temperature, the decrease of tensile strength after 1 month of immersion was only 5%. On the other hand, the conventional VE resin was able to maintain the tensile strength of the CFRP laminate after immersion at 20°C, at 35°C the tensile strength of the CFRP laminate experienced a small (5%) increase (due to post-curing), and at 50 °C the tensile strength decreased 14%. After 3 months of immersion at 20, 35 and 50 °C, the reductions in tensile strength were 15%, 17% and 19% for the bio-laminate and 7%, 18% and 1% for the conventional laminate, respectively. These results seem to indicate that the hygrothermal degradation of the BUPE resin is more severe than that experienced by the conventional epoxy-based resin. Results of future tests will allow confirming these initial trends.

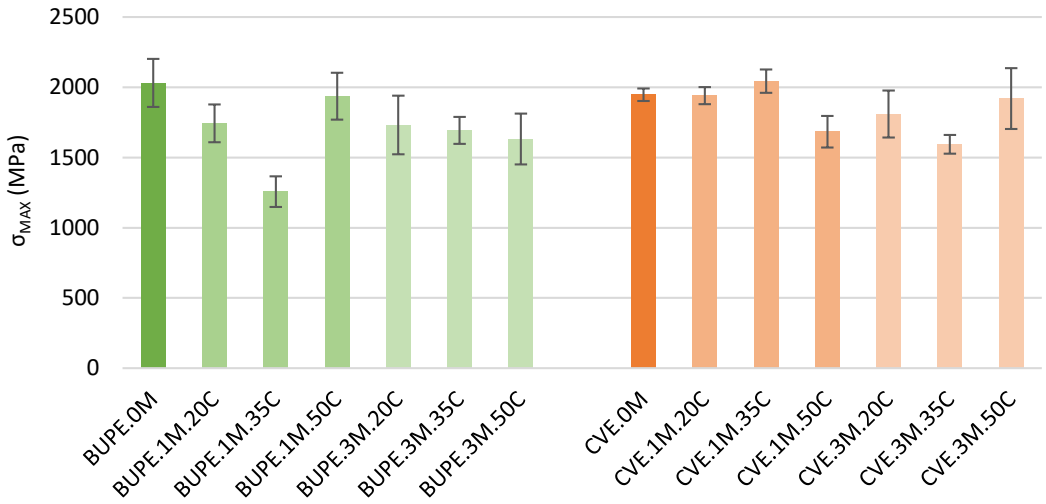

Figure 2. Tensile test results after 1 and 3 months of hygrothermal aging at 20, 35 and 50 °C for BUPE and CVE CFRP laminates

Figure 3 shows the results of ILS tests for the BUPE and CVE CFRP laminates before and after 1 and 3 months of hygrothermal ageing at 20, 35 and 50 °C. The CVE CFRP laminates did not present significant degradation of the ILSS; compared to the initial condition, after immersion at 20 and 35 °C, the ILSS even increased (between 14% and 24%, after 3 months), possibly due to the effects of post-curing, while after immersion at 50 °C it remained roughly unchanged. On the other hand, hygrothermal ageing had a clear detrimental effect at the fibre-matrix interface of the BUPE CFRP laminate, and such degradation is increasing with the immersion duration -

after 3 months, compared to the initial condition, the ILSS decreased 33%, 28% and 47% respectively for 20, 35 and 50 °C. The magnitude of these reductions is indicative of a severe effect of hydrolysis and/or plasticization on the fibre-matrix interface of the BUPE CFRP laminates. The above-mentioned adjustments (ongoing) on the BUPE resin aim at improving its resistance to moisture.

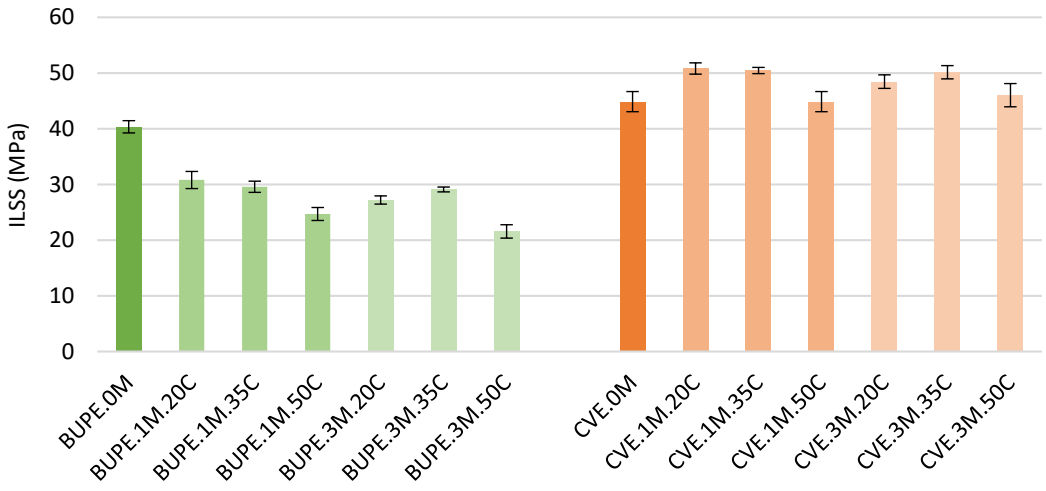

Figure 3. ILS test results after 1 and 3 months of hygrothermal aging at 20, 35 and 50 °C for BUPE and CVE CFRP laminates

6. LCA of bio-laminates compared to current solutions

The environmental impacts of bio-resins and bio-laminates will be compared with those of materials currently used by S&P. A “cradle-to-gate” approach will be considered, evaluating all impacts from the acquisition of raw materials to the final product at the gate of the factory. The assessment of impacts will be based on (i) the “carbon footprint”, which considers carbon dioxide emissions during all stages of production, and (ii) embodied energy, which considers all energy consumption incurred to produce the laminates. Based on this analysis, it will be possible to identify the raw materials and production stages with the greatest environmental impacts, allowing a critical assessment in terms of their environmental sustainability.

7. Final remarks

This paper presented an overview of the ongoing BioLam research project, whose main goal is to develop bio-based CFRP laminates to strengthen civil engineering structures. The paper presented a brief description of the main tasks and challenges of the BioLam project.

Initial results of mechanical characterisation tests of pultruded CFRP laminates, produced with a bio-based polyester resin already developed and a conventional epoxy-based counterpart, showed the short-term potential of the bio-based CFRP laminates developed so far. On the other hand, the preliminary results of durability tests of those two types of laminates revealed the occurrence of more severe hydrolysis and/or plasticization on the bio-based CFRP laminates compared to their conventional counterparts. These preliminary results point out the need to introduce changes in the structure of the polymeric bio-based resin recently developed at IST.

  doi:10.5075/epfl-298799_978-2-9701614-0-0

Acknowledgements

The first author acknowledges the financial support of Fundação para a Ciência e a Tecnologia (FCT) for the doctoral grant SFRH/BD/04675/2020. The support of FCT through project PTDC/ECI-EGC/29597/2017 (EcoComposite) is also gratefully acknowledged. The support of ANI through COMPETE POCI-01-0247-FEDER-039769 LISBOA (BioLam) and of CERIS (UIDB/04625/2020) and CERENA research units of IST is also gratefully acknowledged.

References

[1] B.I. Observatory, Advanced Building Materials, Adv. Mater. Res. 250–253 (2011).

[2] United Nation Environment Programme, Buildings and Climate Change, Unep. (2009) 1–62.

[3] F.O. Sonmez, Optimum Design of Composite Structures: A Literature Survey (1969–2009), J. Reinf. Plast. Compos. 36 (2016) 3–39. https://doi.org/10.1177/0731684416668262.

[4] B. Lochab, S. Shukla, I.K. Varma, Naturally occurring phenolic sources: Monomers and polymers, RSC Adv. 4 (2014) 21712–21752. https://doi.org/10.1039/c4ra00181h.

[5] E. Frollini, C.G. Silva, E.C. Ramires, F. Oliveira, Bio-based composites derived from thermoset phenolic-type matrices and lignocellulosic fibers, in: 2011: pp. 1–2.

[6] Y. Zhu, C. Romain, C.K. Williams, Sustainable polymers from renewable resources, Nature. 540 (2016) 354–362. https://doi.org/10.1038/nature21001.

[7] C. Li, X. Zhao, A. Wang, G.W. Huber, T. Zhang, Catalytic Transformation of Lignin for the Production of Chemicals and Fuels, Chem. Rev. 115 (2015) 11559–11624. https://doi.org/10.1021/acs.chemrev.5b00155.

[8] M. Asim, N. Saba, M. Jawaid, M. Nasir, M. Pervaiz, O. Y. Alothman, A review on Phenolic resin and its Composites, Curr. Anal. Chem. 13 (2017) 185–197. https://doi.org/10.2174/1573411013666171003154410.

[9] S&P Clever Reinforcement, C-Laminates, A Simpson Strong-Tie® Company., 2021. https://doi.org/https://www.sp-reinforcement.eu/en-EU.

[10] M.A. Hofmann, A.T. Shahid, M. Garrido, M.J. Ferreira, J.R. Correia, J.C. Bordado, Biobased Thermosetting Polyester Resin for High-Performance Applications, ACS Sustain. Chem. Eng. (2022). https://doi.org/10.1021/acssuschemeng.1c06969.

[11] M. Hofmann, Sustainable bio-based resins and fibre-polymer composites for civil engineering structural applications, PhD Thesis in Civil Engineering, Universidade de Lisboa, Instituto Superior Técnico, 2022.

[12] S.K. Yadav, K.M. Schmalbach, E. Kinaci, J.F. Stanzione, G.R. Palmese, Recent advances in plant-based vinyl ester resins and reactive diluents, Eur. Polym. J. 98 (2018) 199–215. https://doi.org/10.1016/j.eurpolymj.2017.11.002.

[13] L.C. Bank, Composites for Construction, John Wiley & Sons, Inc., Hoboken, NJ, USA, 2006. https://doi.org/10.1002/9780470121429.

[14] M. Garrido, J.M. Sousa, J.R. Correia, S. Cabral-Fonseca, Prediction of long-term performance and definition of a moisture conversion factor for the durability design of pultruded GFRP profiles under hygrothermal exposure, Constr. Build. Mater. 326 (2022) 126856. https://doi.org/10.1016/j.conbuildmat.2022.126856.

  doi:10.5075/epfl-298799_978-2-9701614-0-0

BIO-BASED VACUUM INFUSED GLASS FIBRE REINFORCED UNSATURATED POLYESTER COMPOSITES FOR HIGH-PERFORMANCE STRUCTURAL APPLICATIONS

Mateus Hofmann[a], Abu T. Shahid[a], Mário Garrido[a], João C. Bordado[b], João R. Correia[a]

a: CERIS, Instituto Superior Técnico (IST), University of Lisbon
mateus.hofmann@tecnico.ulisboa.pt
b: CERENA, Instituto Superior Técnico (IST), University of Lisbon

Abstract: *There is potential to increase the sustainability of fiber-polymer composite products since they are typically manufactured from raw materials derived from non-renewable resources. This paper presents a study about the development, mechanical and thermo-mechanical characterization of a glass fiber-reinforced polymer (GFRP) composite produced by vacuum infusion using a bio-based unsaturated polyester (UP) resin developed in-house; this resin contains over 50 wt.% of bio-content and has a reactive diluent using 50 wt.% less styrene compared to typical oil-derived counterparts. The main development stages of the bio-based resin and the resulting GFRP composite are presented, as well as the evaluation of their tensile-compressive behavior and glass transition temperature* (T_g)*. The bio-based UP resin and GFRP composite showed similar (and in some cases even better) tensile-compressive and T_g properties compared to those produced with a conventional UP resin. Thus, our approach of combining glass fibers with a bio-based UP resin (containing high bio-based content) to manufacture more sustainable GFRP composites for high-performance applications was validated at a high technological readiness level.*

Keywords: bio-based resin; bio-based composite; bio-based GFRP; vacuum infusion

1. Introduction

The use of high-performance thermoset matrices derived from renewable raw materials for the manufacturing of fiber-polymer composites can be considered as a significant advancement towards a more sustainable composites industry [1–3]. However, despite the efforts to develop new bio-based resins, currently, most bio-based thermosets commercially available for manufacturing composites – suitable for applications in various industries, such as naval, automotive, energy, and consumer products – still have reduced incorporation (about 30-35%) of sustainable raw materials [4–6]. In addition, although new commercial bio-based resins have recently been made available [7], the composites market for structural applications still lacks bio-based thermosets with processing characteristics suitable for current manufacturing techniques, such as vacuum infusion and pultrusion, and that present the required mechanical and thermomechanical properties (after curing) for load-bearing composite structures.

In this context, there are challenges to be overcome for the development of more sustainable UP resins with potential to achieve, at the same time: (i) mechanical and thermomechanical behavior suitable for structural applications, (ii) processing characteristics compatible with typical techniques used to manufacture large-scale fiber-polymer composite parts, such as vacuum infusion and pultrusion, and (iii) having high bio-content from raw materials derived

  doi:10.5075/epfl-298799_978-2-9701614-0-0

from renewable sources. In addition, the characterization of relevant mechanical and thermomechanical properties of bio-based composites developed to date is still scarce, namely in what concerns the compressive, interlaminar shear and in-plane shear properties, and the glass transition temperature (T_g) from DMA tests; this last information is essential for the structural design of bio-based GFRP composites, since the determination of T_g by DMA is more relevant (compared to DSC) to determine the stiffness reduction of fibre-polymer composites caused by the temperature increase – in fact, DMA is the method specified in the future European Technical Specification for the "*Design of Fibre-Polymer Composite Structures*" [8].

This paper presents the manufacturing, mechanical and thermo-mechanical characterization of a bio-based GFRP composite, produced by vacuum infusion, combining glass fibers and a bio-based UP resin recently developed in-house [9], which was synthesized using monomers derived from renewable sources. The cured bio-based resin has a bio-based mass content of more than 50%, while containing less volatile organic compounds in the liquid resin compared to typical conventional petroleum-based alternatives. Thus, the main innovation of this study is the development of a bio-based GFRP composite with (i) high bio-based content that meets or exceeds the one of previously referenced works, and (ii) tensile-compressive properties and T_g capable of competing with those of its conventional counterparts, manufactured with petroleum-derived UP resins. For this purpose, an experimental campaign was conducted towards the manufacturing and subsequent mechanical and thermomechanical characterization of bio-based and conventional GFRP composites, which were produced and tested under the same conditions.

2. Experiments

2.1 Materials

Bio-based UP resin (Resin-B) was used as a matrix for glass fiber impregnation during the production of a bio-based GFRP composite (GFRP-B). Resin-B was produced by synthesizing monomers derived from renewable raw materials. The bio-based polyester prepolymer obtained from the polycondensation reaction was subsequently incorporated using a mixture of styrene and 2-hydroethyl methacrylate (HEMA) as a reactive diluent (RD) [9] – see Figure 1.

The main features of Resin-B are the following: (i) the replacement of maleic anhydride and ethylene glycol (both petroleum-derived) by fumaric acid, isosorbide and 1,3-propanediol (renewable source-derived); (ii) suitable viscosity (750 cP at 23 °C) for the vacuum infusion technique; and (iii) mechanical and thermomechanical properties that match or exceed those of its petroleum-derived counterparts. For a comparison, a conventional petroleum-derived UP resin (Resin-C) with viscosity of 300 cP at 23 °C, obtained from Scott Bader, under the commercial designation of Crystic U 904 LVK™, was also used to produce a conventional GFRP composite (GFRP-C).

Finally, both Resin-B and Resin-C were post-cured at 100 °C for four hours, and their mechanical and thermomechanical characterization was performed under identical conditions. Table 1 shows the tensile-compressive and T_g results obtained for the cured resins, namely the mean values of: (i) strength ($\sigma_{t,max}$ and $\sigma_{c,max}$), modulus of elasticity (E_t and E_c) and strain at failure ($\varepsilon_{t,max}$ and $\varepsilon_{c,max}$) in tension (t) and compression (c); and (ii) the T_g based on the onset value of the storage modulus decay.

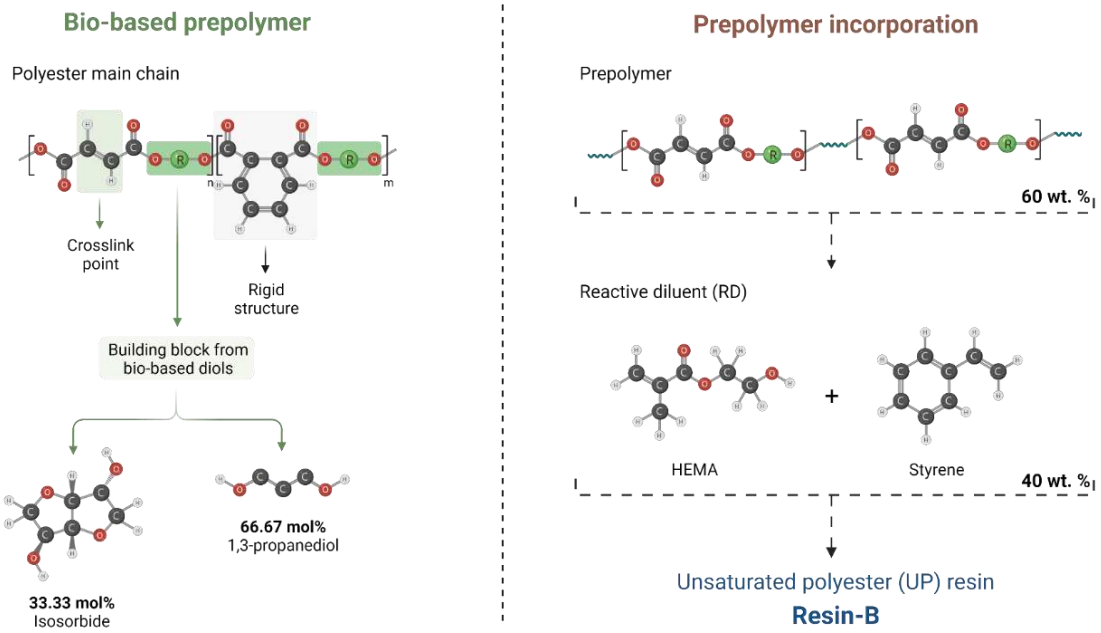

Figure 1. Main steps to obtain the Resin-B used in this study (more details can be found in [9]).

Table 1: Mean values of tensile-compressive and T_g properties of Resin specimens.

Specimen	$\sigma_{t,max}$ [MPa]	E_t [GPa]	$\varepsilon_{t,max}$ [%]	$\sigma_{c,max}$ [MPa]	E_c [GPa]	$\varepsilon_{c,max}$ [%]	T_g [°C]
Resin-B	60.7	3.0	1.9	131.5	4.5	5.2	75
Resin-C	62.1	3.4	2.4	119.4	3.8	5.3	65

The glass reinforcement comprised: (i) unidirectional fiberglass mats (WR-500) with 500 g/m^2, obtained from Castro Composites (Spain); and (ii) bidirectional (0°/90°) fiberglass mats (G-Sheet E 90/10, Type A) with 440 g/m^2, obtained from S&P Clever Reinforcement Ibérica.

2.2 Composites manufacturing

The fiber architecture of the GFRP-B and GFRP-C composites consisted of six layers of unidirectional (UD) fiber mat and four layers of bi-directional (BD) fiber mat, arranged in the following symmetrical and balanced layup: $[U/B/U/B/U]_S$. The composites were produced by vacuum infusion (see Figure 2).

A steel mold (base plate) was coated with a release agent, followed by a breather layer, peel ply, the fiber mats and infusion mesh (resin distribution medium), topped with an additional layer of peel-ply, a breather fabric, and the vacuum bag. The UD glass fibre mats and the infusion mesh mats were positioned according to the percolation direction of the resin to allow a better impregnation between fibrous layers. After impregnation, the composites were pre-cured at room temperature for 24 hours. The GFRP-B and GFRP-C composites were then cut using a CNC milling machine (Figure 2) to obtain the specimens required for the tensile-compressive and T_g

characterization tests – with dimensions according to each test standard (*cf.* section 2.3). Before testing, the GFRP specimens were also post-cured at 100 °C for four hours.

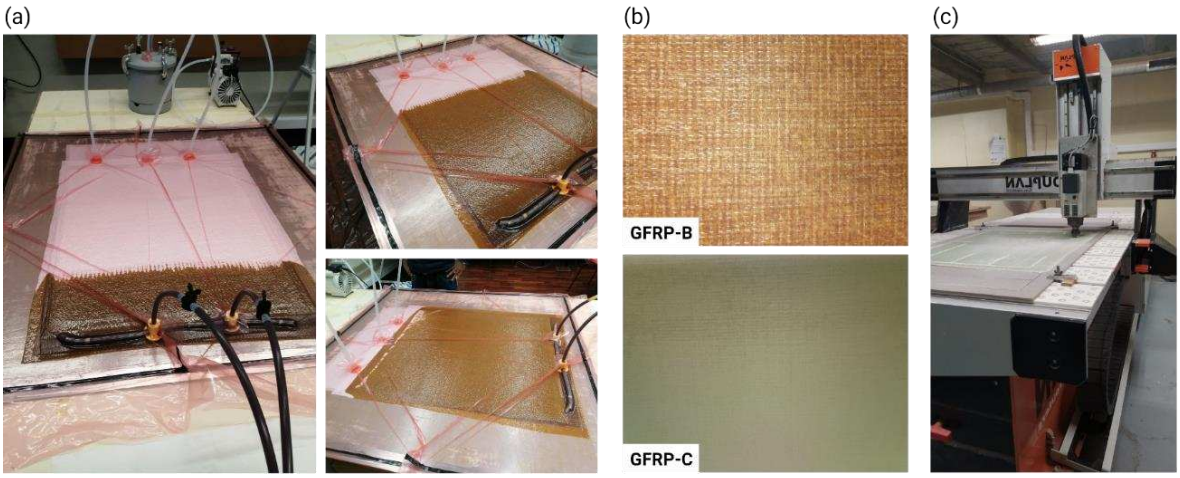

Figure 2. Composites manufacturing: a) infusion process (representation for GFRP-B plate); b) produced plates; and c) cutting plates to obtain specimens for characterization tests.

2.3 Characterization

Tensile tests: according to parts 1 and 4 of ISO 527 in specimens with 25 mm by 300 mm (without end tabs), using an Instron 8800D universal test machine (UTM) under displacement control at a loading rate of 2 mm/min, and a video-extensometer (high-definition Sony™ video camera, model XCG 5005E, Fujinon – Fujifilm HF50SA-1 lens) to measure deformations.

Compressive tests: according to ASTM 6641/D6641M standard in specimens with geometry of 25 mm by 147 mm, using a combined loading compression (CLC) test fixture in a UTM under displacement control at a rate of 1.3 mm/min, with strain monitoring by video-extensometer.

Dynamic mechanical analysis (DMA): according to parts 1 and 5 of ISO 6721 using a dynamic mechanical analyzer from TA Instruments, model DMA Q800. The specimens with geometry of 10 mm by 60 mm were tested with a strain amplitude of 15 µm, and constant frequency of 1 Hz. The temperature range was -30 °C to 150 °C with an increment rate of 2 °C/min. The T_g was defined from the onset value of the storage modulus decay.

Calcination tests: according to ISO 1172, where the samples (3 for each type of resin) were heated in a muffle furnace up to 700 °C, and the weight of the residual fibers (no inorganic filler was added to the resin matrix) was used to calculate the fiber mass fraction.

The experimental programme included also in-plane shear tests and interlaminar shear tests. Full details about these tests, not described herein, are available in [10,11].

3. Results and discussion

3.1 Tensile and compressive behavior

Figure 3 presents representative stress-strain curves that allow comparing the axial behavior of GFRP-B and GFRP-C composites under tensile and compressive stresses; this figure also includes, as a reference, representative stress-strain curves of the corresponding resins Resin-C and Resin-B, obtained in [9]. For both GFRP-B and GFRP-C tensile specimens, the curves present the typical

  doi:10.5075/epfl-298799_978-2-9701614-0-0

tensile behavior of fiber-polymer composites, with an initial linear branch, followed by a gradual loss of stiffness for higher strains, until the occurrence of brittle tensile failure.

Regarding GFRP-B and GFRP-C compressive specimens, the behavior was approximately linear up to failure, which also occurred in a brittle way. However, compared to the tensile response, higher scatter was found within each series and the compression stress-strain curves are not as "linear". This was considered to stem from the smaller gauge length used in the compression tests, which affects the precision of the strain calculations made from the video-extensometer measurements.

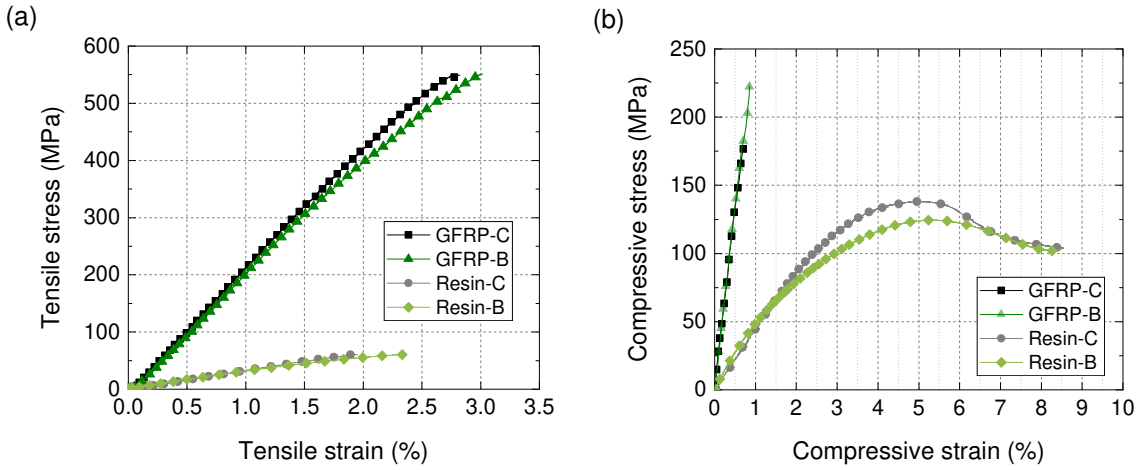

Figure 3. Representative nominal axial stress-strain curves of GFRP and resin specimens: (a) tensile and (b) compressive.

Table 2 summarizes the resulting mechanical properties in tension and compression of both GFRP-C and GFRP-B specimens. Very similar tensile properties were obtained for both types of GFRP composites: (i) the modulus of elasticity of GFRP-B (20.6 ± 0.7 GPa) was about 6% lower compared to GFRP-C (21.9 ± 0.9 GPa); (ii) the tensile strengths were nearly identical at 538.1 ± 23.6 MPa and 533.0 ± 16.5 MPa for GFRP-B and GFRP-C, respectively; and (iii) the tensile strain at break of GFRP-B (3.0 ± 0.1%) was approximately 10% higher compared to GFRP-C (2.7 ± 0.2%). Although a direct comparison is not possible (due to differences in fiber content and architecture), these results generally match or exceed those found in the literature (for example, the ones reported by Hosseini *et al.* [12]).

Table 2: Tensile and compressive properties of GFRP specimens (mean ± standard deviation).

Specimen	$\sigma_{t,max}$ [MPa]	E_t [GPa]	$\varepsilon_{t,max}$ [%]	$\sigma_{c,max}$ [MPa]	E_c [GPa]	$\varepsilon_{c,max}$ [%]
GFRP-C	533.0 ± 16.5	21.9 ± 0.9	2.7 ± 0.2	169.6 ± 10.8	25.1 ± 0.3	0.7 ± 0.1
GFRP-B	538.1 ± 23.6	20.6 ± 0.7	3.0 ± 0.1	210.4 ± 27.8	24.9 ± 2.2	0.8 ± 0.1

The above-mentioned results, as well as the curves depicted in Figure 2 attest the mechanical potential of GFRP-B composite compared to its petroleum-derived counterpart regarding the mechanical behavior in tension, as well as the effectiveness of the bio-based Resin-B in distributing stresses among glass fibers, one of the main roles of the polymer matrix of composites subject to tension. Regarding the compression results, which are also summarized

in Table 2, prompt the following comments: (i) the modulus of elasticity in compression of GFRP-B (24.9 ± 2.2 GPa) matched that of GFRP-C (25.1 ± 0.3 GPa); (ii) the compressive strength of GFRP-B (210.4 ± 27.8 MPa) was 24% higher compared to GFRP-C (169.6 ± 10.8 MPa); and, accordingly, (iii) the strain at break in compression of GFRP-B (0.8 ± 0.1 %) was also 14% higher than that of GFRP-C (0.7 ± 0.1 %).

Comparing the tension *vs.* compression behavior, it is worth referring also that while the values of the tensile strain at break of the resins and the corresponding composites are relatively similar, that is not the case for the values of the compressive strain at break, which are much lower in GFRP composites than in their corresponding resins. This is mainly due to the resins' capability to deform plastically in compression, which is a behavior not exhibited by the composites.

It is worth noting the magnitude of the relative differences between the average values of compressive strength of both types of composites, despite the relatively high scatter of this property, e.g., coefficient of variation (CoV) of 13% for GFRP-B. The higher performance of GFRP-B in terms of compressive strength may be due to the higher strain at break and shear strength (not reported here, but available in [10,11]) of the bio-based resin, which in both cases were 11% higher compared to the conventional resin. The failure of composites in compression involves delamination and fiber kinking (as observed here). Delamination typically occurs due to transverse tensile stresses (from the Poisson effect) and, therefore, induce tensile strains in the matrix – such strains at break were higher in Resin-B. On the other hand, fiber kinking depends strongly on the shear strength of the polymer matrix, which was also higher in Resin-B. This may (at least partly) explain the higher compressive strength of GFRP-B.

3.2 Thermomechanical behavior

DMA was used to determine the thermomechanical properties of the composites, which are particularly relevant for high-performance civil engineering applications, especially those located outdoors in temperate to warm climates, where the temperature-dependence of mechanical properties is quite relevant. The T_g is a common indicator of such performance.

Figure 4 presents the results of DMA tests, namely the storage modulus (E') as a function of temperature, for the GFRP-C and GFRP-B composites and their corresponding resins. It is worth referring that the GFRP-C composite included a slightly higher fibre mass fraction (64 wt.%) than GFRP-B (60 wt.%).

The E' curves of both types of resins and their composites present a well-defined and sharp drop with temperature increase across the glass transition region. In this respect, the E' of both groups of curves (composite-resin) are quite consistent, and the small relative differences between the resins and the corresponding composites may be attributed to (i) variability in estimation of the onset value of the E' decay, and (ii) the effects of the fibre reinforcement in the response measured from DMA tests. The results obtained prompt the following comments: (i) the E' reduction of the Resin-B is very similar to that of the Resin-C; however, for the former resin, the reduction is steeper and occurs for slightly lower temperatures, resulting in T_g estimates of 66 °C and 75 °C for Resin-B and Resin-C, respectively; (ii) the same is observed for the corresponding composites, with GFRP-C presenting slightly (10%) higher T_g (71 °C) than GFRP-B (64 °C).

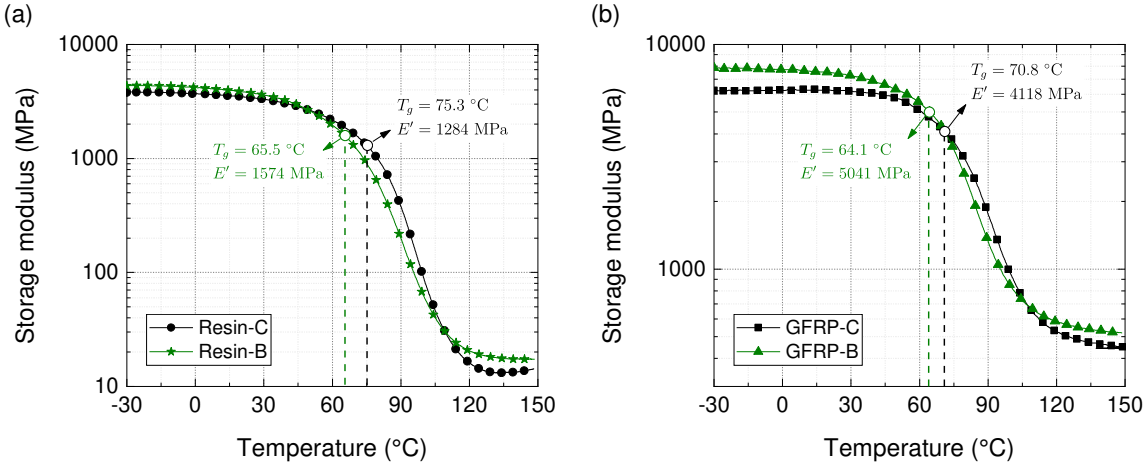

Figure 4. Storage modulus curves of GFRP and resin specimens.

Overall, the DMA results show that the T_g presented by GFRP-B is slightly lower compared to GFRP-C, however it is still considered suitable for civil structural applications, particularly considering the recent European Technical Specification for the "*Design of Fibre-Polymer Composite Structures*" [8], which recommends a minimum T_g of 60 °C.

4. Conclusions

This study assessed the prospects of using an innovative bio-based unsaturated polyester resin in the manufacturing of high-performance GFRP composites for civil engineering structural applications, providing an alternative to traditional petroleum-derived composites.

The production of the GFRP composites was successful, and the bio-based resin proved to have the potential to be used in the vacuum infusion technique. The mechanical characterization results showed that the tensile and compressive properties of the bio-based GFRP composite are equivalent to those of its petroleum-derived counterpart, demonstrating bio-based resin's capability to impregnate the glass fibre reinforcement and provide adequate fibre-matrix adhesion in the cured product. In addition, although the T_g of the bio-based GFRP composite was slightly lower than its conventional counterpart (about 10%), it was still above the 60 °C threshold enabling its use in civil engineering structural applications.

The overall results presented here validate the use of the bio-based GFRP composite for high-performance structural applications, providing an alternative to conventional oil-based thermoset composites which is partially based on renewable resources. Further studies are ongoing, addressing different aspects of the bio-based GFRP composite, namely the quantification of its environmental performance, as well as its long-term durability.

Acknowledgements

The support of Fundação para a Ciência e a Tecnologia (FCT) through project PTDC/ECI-EGC/29597/2017 (EcoComposite) and through funding of the research units CERIS (UIDB/04625/2020) and CERENA of IST are gratefully acknowledged. The first author also acknowledges FCT for the doctoral grant SFRH/BD/139863/2018.

5. References

1. Correa JP, Montalvo-Navarrete JM, Hidalgo-Salazar MA. Carbon footprint considerations for biocomposite materials for sustainable products. J. Clean. Prod. 2019;208:785–794.

2. La Rosa AD, Recca G, Summerscales J, Latteri A, Cozzo G, Cicala G. Bio-based versus traditional polymer composites. A life cycle assessment perspective. J. Clean. Prod. 2014;74:135–144.

3. Fitzgerald A, Proud W, Kandemir A, Murphy RJ, Jesson DA, Trask RS, et al. A Life Cycle Engineering Perspective on Biocomposites as a Solution for a Sustainable Recovery. Sustainability. 2021;13(3).

4. Easy Composites. LB2 Epoxy Laminating Bio Resin. Infusion bio-resin. 2022; Available from: https://www.easycomposites.eu/LB2-epoxy-laminating-resin

5. INEOS Composites. Envirez™. Unsaturated Polyest. resin. 2021; Available from: https://www.ineos.com/businesses/ineos-enterprises/businesses/ineos-composites/products/unsaturated-polyester-resins/envirez/

6. Sicomin Epoxy Resin. Bio-based epoxy. SR GreenPoxy56/SD7561. 2018; Available from: https://sicomin.com/products/epoxy-systems/bio-based-epoxy

7. TFC Biomass biobased chemicals. Biorez™ series. 2022; Available from: https://www.transfurans.be/products

8. Correia, João Râmoa; Keller, Thomas; Knippers, Jan; Pérez, Marta Gil; Mottram, Toby; Paulotto C. prEN 19101:2021. Design of Fibre-Polymer Composite Structures. European Comission; 2020.

9. Hofmann MA, Shahid AT, Garrido M, Ferreira MJ, Correia JR, Bordado JC. Biobased Thermosetting Polyester Resin for High-Performance Applications. ACS Sustain. Chem. Eng. 2022;10(11):3442–3454.

10. Hofmann M., Sustainable bio-based resins and fibre-polymer composites for civil engineering structural applications, PhD Thesis in Civil Engineering, Universidade de Lisboa, Instituto Superior Técnico, 2022.

11. Hofmann M, Shahid AT, Machado M, Garrido M, Bordado J, Correia JR. GFRP composite produced by vacuum infusion with a novel high-performance bio-based unsaturated polyester resin: manufacturing and mechanical characterisation. Composites Part A: Applied Science and Manufacturing. [Submitted on March 2022]

12. Hosseini N, Webster DC, Ulven C. Advanced biocomposite from highly functional methacrylated epoxidized sucrose soyate (MAESS) resin derived from vegetable oil and fiberglass fabric for composite applications. Eur. Polym. J. 2016;79:63–71.

  doi:10.5075/epfl-298799_978-2-9701614-0-0

HYGROTHERMAL AGEING OF A GFRP COMPOSITE PRODUCED BY VACUUM INFUSION WITH A NOVEL BIO-BASED UNSATURATED POLYESTER RESIN

Abu T. Shahid[a], M. Hofmann[a], M. Garrido[a], J.R. Correia[a]

a: CERIS, Instituto Superior Técnico (IST), University of Lisbon
toyobshahid@tecnico.ulisboa.pt

Abstract: *One of the major challenges towards the development of bio-based resins derived from renewable resources is the need to ensure suitable long-term performance and durability, as many applications of fibre reinforced polymer (FRP) composites require relatively long service lives under often harsh environmental conditions. This study presents the results of an ongoing assessment of the durability in hygrothermal ageing of a glass-FRP (GFRP) composite produced by vacuum infusion using a novel partially bio-based unsaturated polyester (UP) resin. Accelerated ageing was carried out in water immersion in isothermal conditions at temperatures of 20 °C, 35 °C, and 50 °C for periods of up to 180 days. Its effects were assessed through (i) mechanical characterisation in tension, compression, and interlaminar shear, as well as (ii) thermo-mechanical characterization using dynamic mechanical analysis (DMA). The results obtained so far highlight the occurrence of significant hydrolysis of the bio-based UP resin, as well as the need for the further development and improvement of this bio-based UP resin.*

Keywords: Bio-based resin; unsaturated polyester resin; bio-based GFRP; vacuum infusion; hygrothermal ageing.

1. Introduction

The demand for fibre reinforced polymer (FRP) composites has been steadily increasing across several different industries due to their various advantages over conventional alternatives, such as lightness, high specific strength and stiffness, the possibility of achieving application-tailored material properties, among others [1]. FRP composites are generally produced with petro-based polymer resins (epoxy, unsaturated polyester (UP), vinyl ester), reinforced with synthetic fibres, such as carbon or glass, which are produced through relatively energy-intensive processes. However, the increasing volatility in the availability and cost of petroleum as feedstock poses a threat to the steady supply of petro-based raw materials. Moreover, the sustainability and the reduction of the environmental impacts of the composites industry are motivating a search for more environmentally friendly materials.

In this context, the development of bio-based polymer resins, fully or partially derived from renewable resources, is one of the most promising routes [2-6]. Recently, a novel bio-based UP resin with over 50% of renewable content (wt.%) has been developed at IST by replacing petro-based chemical monomers with bio-based alternatives [7]. The potential for using this resin in the development of glass fibre reinforced polymer (GFRP) composites has been shown [8], and the short-term performance of these composites was found to be competitive with respect to conventional (oil-based) GFRP. However, the durability and the need to assess the life cycle performance of these bio-based products are two major concerns limiting their widespread applicability. In fact, the existing data regarding long term durability of bio-based resins and their FRP composites is still very scarce. Considering the detrimental effects of already well-known

  doi:10.5075/epfl-298799_978-2-9701614-0-0

degradation mechanisms caused by exposure to moisture of GFRP composites (e.g., leaching, etching, plasticisation, swelling, hydrolysis, micro-cracking, fibre-matrix debonding, among others [9]), it is imperative to assess the durability of novel bio-based GFRP composites when exposed to hygrothermal ageing.

This paper presents the preliminary results of an ongoing durability assessment of a bio-based GFRP composite produced by vacuum infusion with the bio-based UP resin previously developed at IST. Accelerated ageing of the composites involved hygrothermal exposure, and the induced degradation was assessed through mechanical and thermomechanical characterization after predefined periods of ageing. To provide a basis for comparison regarding the durability performance of the bio-based GFRP, the same procedures were adopted for a conventional GFRP composite comprising a petro-based UP resin and similar glass fibre architecture, and produced with the same manufacturing method.

2. Experimental program

2.1 Materials

Bio-based UP resin: A bio-based UP resin developed in-house at IST was used to produce the bio-based GFRP composite. This orthophthalic polyester resin was produced by synthesizing a UP prepolymer from bio-based renewable monomers (di-acids and diols) in a polycondensation reaction, which was subsequently incorporated with a mixture of reactive diluents (RD) (60 parts of bio-UPE pre-polymer: 40 parts of RD). The main building blocks used in the prepolymer were obtained from phthalic anhydride (PA), fumaric acid (FA), 1,3-propanediol (PDO), and isosorbide (ISO), whereas the reactive diluent contained equal parts of 2-hydroxy ethyl methacrylate (HEMA) and styrene (a carcinogenic compound), where the content of styrene was reduced compared to typical petro-based UP resin counterparts [7]. For curing, peroxide (PMEK, 2%) was used together with octoate cobalt (1%) as initiator. A petro-based orthophthalic UP resin was adopted for comparison with the bio-based UP resin, with the selected product being obtained from Scott Bader under the commercial designation of Crystic U 904LVKTM. The cure initiation for this resin was also achieved using PMEK (1%).

Glass fibre mats: Two types of glass fibre (E-type) mats, (a) unidirectional (0°) and (b) bi-directional (0°/90°), were used in the fibre layup. The unidirectional and bi-directional glass fibre mats were obtained from S&P Clever Portugal and Castro Composites (Spain), respectively. The areal weight of the unidirectional glass fibre mat was 440 g/m^2, containing 90% in 0° direction and 10% in 90° direction for stitching. The density and tensile strength in the main direction were 2.6 gm/cm^3 and 3740 N/cm respectively. The bi-directional mat had areal weight of 500 g/m^2 with 54.5% fibre in warp and 45.5% in weft. The density and tensile strength of the warp and weft were 2.4 gm/cm^3 and 2.0 gm/cm^3, and 1440 N/cm and 1200 N/cm, respectively. Both fibre mats comprised yarns of 1200 tex.

2.2 Production of GFRP composites

The fibre architecture of the GFRP composites consisted of six layers of unidirectional (UD) fibre mat and four layers of bi-directional (BD) fibre mat, arranged in the following symmetrical and balanced layup: $[U/B/U/B/U]_S$. The vacuum assisted resin infusion method (VARIM) was used for the production of composite laminates. A steel mould (base plate) was coated with a release agent, followed by a breather layer, peel ply, the fibre mats and infusion mesh (resin distribution

  doi:10.5075/epfl-298799_978-2-9701614-0-0

medium), topped with an additional layer of peel-ply, a breather fabric and the vacuum bag. The resin infusion was carried out at a continuous pressure (vacuum) of 0.95 bar at room temperature. After impregnation, the composites were pre-cured at room temperature for 48 hours followed by post-curing at 100°C for four hours. The resulting GFRP composite laminates had nominal thickness of 4.6 mm.

2.3 Ageing environments

GFRP composites are typically exposed to diverse environments in different applications, including indoor, outdoor, aquatic, and saline conditions, with varying temperature, humidity, and UV radiation. Exposure to moisture with elevated temperature is one of the most critical conditions for environmental ageing of GFRP materials. In this study, hygrothermal ageing environments were selected to investigate the susceptibility to degradation of the bio-based GFRP composite laminate. For both bio-based and petro-based GFRP, the laminates were immersed in tap water and placed in a thermal chamber at 20 °C. For accelerated hygrothermal ageing, composite laminates were additionally immersed in water at elevated temperatures of 35 °C, and 50 °C. Before ageing, the GFRP laminates were cut in a CNC router to dimensions of 35 cm by 25 cm; the test specimens were later extracted from such laminates, thus minimizing the length of exposed cut sections during ageing (which are preferable points for water ingress). The effects of hygrothermal ageing were assessed through mechanical and thermomechanical analyses, as described in the following section.

2.4 Experimental procedures

Dynamic mechanical analysis (DMA): The thermomechanical behaviour of the composites was assessed according to parts 1 & 5 of ISO 6721 standard using a specimen geometry of 10 mm by 60 mm, a strain amplitude of 15 µm, and constant frequency of 1 Hz. The temperature range was -30 °C to 150 °C with an increment rate of 2 °C/min. The glass transition temperature (T_g) was determined from the onset of the storage modulus decay.

Tension: According to parts 1&4 of the ISO 527 standard, the tensile properties of the material were determined in specimens with geometry of 25 mm by 300 mm (without end tabs), using a universal test machine (UTM) with load capacity of 100 kN at a displacement rate of 2 mm/min.

Compression: To determine the compression properties, a combined loading compression (CLC) test setup was used and the geometry of the specimens was 25 mm by 147 mm according to the ASTM 6641/D6641 M standard. Tests were carried out mounting the CLC fixture in a UTM under displacement control at a rate of 1.3 mm/min.

Interlaminar shear: The ISO 14130 standard was used to determine the apparent interlaminar shear strength of the GFRP composites by the short beam method, in specimens with geometry of 46 mm by 23 mm; tests were performed under displacement control at a rate of 1 mm/min.

At least five specimens were considered for each series of mechanical tests and two specimens for each series of DMA tests. The specimens were tested in a saturated condition, being kept in water until immediately before testing. In this paper, and regarding the mechanical properties of the aged materials, only the strength values and their retention over ageing time are presented and discussed.

  doi:10.5075/epfl-298799_978-2-9701614-0-0

3. Results and discussion

3.1 Initial properties

The mechanical and thermomechanical properties of both bio-based and petro-based GFRP composites are provided in Table 1. In the table and following discussion, **GFRP_G** represents the bio-based GFRP, while **GFRP_C** indicates the petro-based GFRP.

Table 1: Initial properties of bio-based and petro-based GFRP (average ± SD values when applicable).

Properties	**GFRP_G**	**GFRP_C**
T_g (onset modulus) (°C)	55	72
Tension		
σ_t (MPa)	538.1 ± 23.5	533.0 ± 16.5
E_t (GPa)	21.6 ± 0.8	22.3 ± 0.8
Compression		
σ_c (MPa)	205.7 ± 19.5	173.3 ± 18.2
E_c (GPa)	25.5 ± 1.0	24.7 ± 1.9
Interlaminar Shear		
σ_{sbs} (MPa)	21.0 ± 2.5	21.0 ± 0.7

The DMA tests indicated a lower T_g value for the bio-based GFRP. Both composites exhibited relatively similar properties, particularly in tension and interlaminar shear. The compressive strength of GFRP_G was around 20% higher than for GFRP_C.

3.2 DMA

Figure 1 shows the retention (%) of T_g after 1, 3, and 6 months of immersion in water at 20°C, 35°C, and 50°C with respect to the unaged material, for both GFRP_G and GFRP_C composites. It is noticeable that for GFRP_G there was a significant initial reduction of T_g after 1 month irrespective of the immersion temperature, while GFRP_C was less affected. For GFRP_G, after 1 month the retentions were 50%, 50%, and 54% for water immersion at 20°C, 35°C, and 50°C, respectively; for GFRP_C, these figures were 88%, 90%, and 86%. However, after this initial degradation in both types of materials, the properties recovered slightly after 3 months and did not experience further significant changes. After 6 months, the retentions of T_g for the GFRP_G composite were 62%, 60%, and 62% for water immersion at 20°C, 35°C, and 50°C, respectively; for GFRP_C, these figures were 90%, 89%, and 94%. The initial steep reduction in T_g was mostly attributed to the initially dominant hydrolysis reaction in the ester chains in combination with water absorption and leaching of plasticizers. The inversion of property reduction after 3 months can be attributed to additional post-curing phenomena, which competed with the hydrolysis of the polymer chain. Moreover, the much more severe degradation of GFRP_G is attributed to the inherent hydrophilicity of some of the constituent materials of the bio-based resin, such as HEMA, ISO, and PDO.

  doi:10.5075/epfl-298799_978-2-9701614-0-0

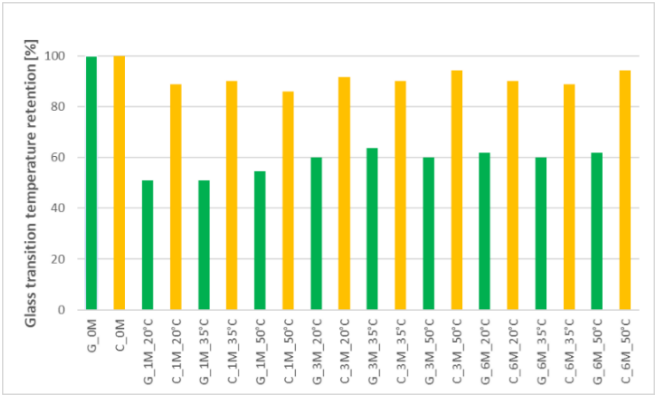

Figure 1: Retention of glass transition temperature for bio-based (GFRP_G) and petro-based (GFRP_C) GFRP composites during hygrothermal ageing

3.3 Tensile strength

The retention (%) of tensile strength is shown in Figure 2 for GFRP_G and GFRP_C composites under hygrothermal ageing at 20 °C, 35 °C, and 50 °C temperatures. For both types of composites, the tensile properties reduced sharply (20-30%) after 1 month, with continued reductions up to 3 months for GFRP_G irrespective of temperature. After 6 months of immersion, the tensile strength of GFRP_G did not present significant additional variations, with the exception of water immersion at 50 °C, for which it decreased an additional 6% after 6 months of immersion. The tensile strength of GFRP_C was less affected comparing to GFRP_G and, after the steeper initial degradation after 1 month of immersion, this property was found to have some recovery and fluctuation within a relatively small range, presumably due to the aforementioned post-curing phenomena. After 6 months, the retentions in tensile strength of GFRP_G were 64%, 65%, and 56% for hygrothermal immersion at 20°C, 35°C, and 50°C temperatures, respectively; for GFRP_C, these figures were 88%, 84%, and 91%. In both composites, but particularly for GFRP_G, comparing to the retention of glass transition temperature, which is a matrix-dominated property, lower reductions were observed in tensile strength, which agrees with the fibre-dominated nature of this property. However, due to the proneness to hydrolysis of the bio-based resin, the reductions in tensile strength were higher for GFRP_G composites compared to their conventional counterparts.

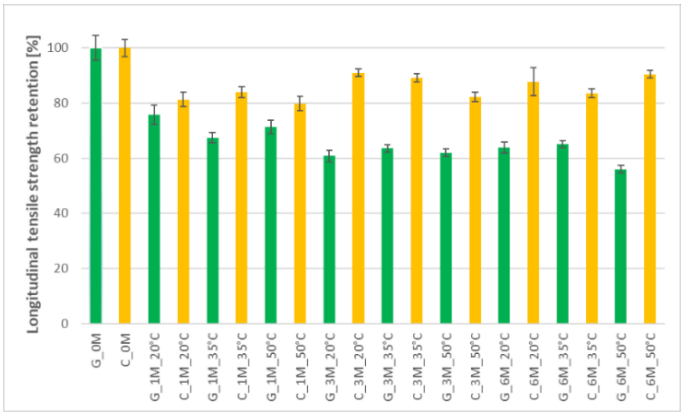

Figure 2: Retention of longitudinal tensile strength for bio-based (GFRP_G) and petro-based (GFRP_C) GFRP composites during hygrothermal ageing

  doi:10.5075/epfl-298799_978-2-9701614-0-0

3.4 Compressive strength

Figure 3 presents the evolution in retention (%) of compressive strength for GFRP_G and GFRP_C under hygrothermal immersion in water at 20 °C, 35 °C, and 50 °C. There was a global reduction trend noticed for both types of composite laminates. However, the reductions were significantly more severe for GFRP_G, showing a clear agreement with the retentions of T_g shown previously, with both properties being markedly matrix-dominated. In GFRP_G, the initial reduction was steep and it increased with temperature. Further reductions were observed after 3 months of ageing, however at a slower rate. After 6 months of ageing, the strength values seem to have recovered slightly or stabilized. The initial abrupt degradation was attributed to hydrolysis of the polymer matrix, possibly in combination with micro-cracking and some fibre-matrix debonding. This degradation pattern was attenuated or recovered slightly over time due to post-curing. The retentions in compressive strength for GFRP-G in water immersion at 20°C, 35°C, and 50°C were 35%, 32%, and 28%, respectively, after 6 months of exposure.

For GFRP_C, initially the reductions in compressive strength were lower comparing to GFRP_G. However, the trend of strength reduction significantly increased with temperature and exposure time up to 3 months, with the exception of the material exposed at 35°C. After 6 months of ageing, the compressive strength of GFRP-C somewhat stabilized, showing small variations, and the retentions in compressive strength in water immersion at 20°C, 35°C, and 50°C were 85%, 85%, and 81%, respectively. However, it is worth referring that the scatter in results increased significantly for this ageing period, possibly indicating some variability in the degree of degradation as well as post-curing experienced by these laminates.

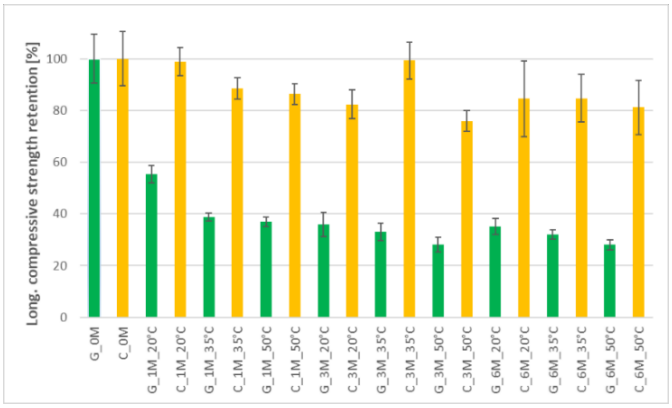

Figure 3: Retention of longitudinal compressive strength for bio-based (GFRP_G) and petro-based (GFRP_C) GFRP composites during hygrothermal ageing

3.5 Interlaminar shear strength

The retention (%) of interlaminar shear strength as a function of time and temperature in hygrothermal ageing is provided in Figure 5. The results obtained are in agreement with those shown previously for the compressive strength for both types of composites. There was a general trend of initial reduction, more pronounced for the bio-based composite. For GFRP_G, the reductions observed were more severe with increasing temperature, and continued until 3 months of ageing. The reasons for these reductions should be identical to those highlighted previously (plasticization, hydrolysis, matrix micro-cracking and debonding along the fibre-matrix interface). For GFRP_C, these degradation mechanisms were less severe and, after an

initial reduction, some property recovery was observed after 3 months of ageing and continued after 6 months with only small variations being observed. It is worth noting that, as for the compressive strength, the GFRP_C_3M_35°C series showed significant property increase. This suggests that for this combination of ageing time and temperature, the post-curing of the oil-based resin outweighs the hygrothermal degradation that is experienced. However, for longer time periods or higher exposure temperatures, this balance reverts and resin degradation becomes more relevant, hence the reduction in the strength retention.

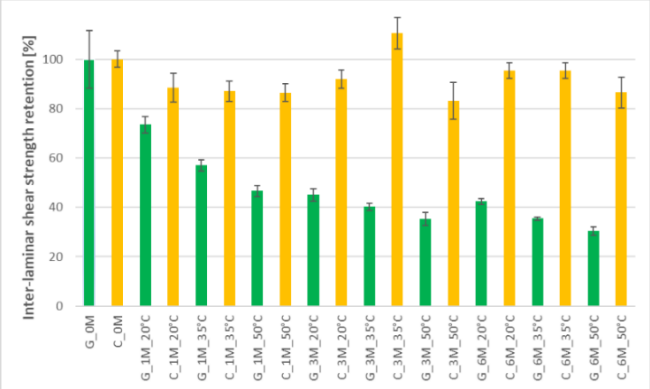

Figure 5: Retention of interlaminar shear strength for bio-based (GFRP_G) and petro-based (GFRP_C) GFRP composites during hygrothermal ageing

For GFRP_G, the retentions of interlaminar shear strength due to hygrothermal ageing at 20°C, 35°C, and 50°C were 42%, 35%, and 30%, respectively, after 6 months; for GFRP_C, these figures were 95%, 95%, and 87%.

4. Conclusions

This paper presented the results of an ongoing study about the durability of a bio-based GFRP composite under hygrothermal ageing, involving water immersion at 20 °C, 35 °C, and 50 °C. The bio-based GFRP composite was produced using a bio-based resin developed in-house with over 50% of renewable content (wt.%). A conventional oil-based GFRP composite was also produced using a similar production technique (VARIM) and fibre architecture, and it was aged following the same procedures to provide a direct basis of comparison. So far, both materials were aged for 6 months with periodic assessment of their thermomechanical and mechanical properties after 1, 3 and 6 months. The variations in their glass transition temperature, tensile strength, compressive strength and interlaminar shear strength were presented and discussed.

Hygrothermal ageing induced much more severe degradation in the bio-based GFRP composite than in the conventional GFRP composite, for all properties assessed. As expected, this degradation was accentuated for higher exposure temperatures. Although both composites presented initial degradation of all properties assessed, the rate of reduction of their properties was generally reduced after 3 months. Slight property recovery or stabilization was noticed after 6 months of ageing in the bio-based composite, with this also being noticed for the conventional GFRP after 3 months of ageing. These experimental observations can be attributed to early-stage irreversible hydrolysis reactions, as well as leaching and plasticization of the polymer matrices. These degradation phenomena may have also caused micro-cracking and fibre-matrix debonding. These degradation mechanisms were particularly severe for the bio-based resin, evidencing its proneness to hydrolysis. The property recovery observed for later ageing periods

  doi:10.5075/epfl-298799_978-2-9701614-0-0 published under CC BY-NC 4.0 license

can be attributed to post-curing phenomena, stemming from residual bonding over time of unreacted bonds within the polymer chain. Among the strength properties of the bio-based GFRP, those which are fibre-dominated, such as tensile strength, were significantly less affected comparing to matrix-dominated properties, such as glass transition temperature, and compressive and interlaminar shear strengths. Therefore, the more severe degradation of the bio-based composite was most likely caused by hydrolysis reactions affecting the bio-based UP resin, mainly due to its hydrophilic constituents, such as HEMA, ISO, and PDO. These results are particularly useful, being instrumental in the further development and improvement of this bio-based UP resin; they also provide valuable information on the durability properties of bio-based resins and monomers.

5. Acknowledgement

The support of Fundação para a Ciência e a Tecnologia (FCT) through project PTDC/ECI-EGC/29597/2017 (EcoComposite) and of CERIS (UIDB/04625/2020) and CERENA research units of IST are gratefully acknowledged.

6. References

[1] Proença M, Garrido M, Correia JR, Gomes MG. Fire resistance behaviour of GFRP-polyurethane composite sandwich panels for building floors. Composites Part B: Engineering, 2021, 224.

[2] Zhu Y, Romain C, Williams CK. Sustainable polymers from renewable resources. Nature, 2016, 540:354–62.

[3] SSUCHY. Sustainable structural and multifunctional biocomposites from hybrid natural fibres and bio-based polymers. CORDIS EU research results, 2022.

[4] Harmsen PFH, Hackmann MM, Bos HL. Green building blocks for bio-based plastics. Biofuels, Bioproduction and Biorefining, 2014, 8:306–24.

[5] Gandini A, Lacerda TM. From monomers to polymers from renewable resources: Recent advances. Progress in Polymer Science, 2015, 48:1–39.

[6] Rosenboom J-G, Langer R, Traverso G. Bioplastics for a circular economy. Nature Reviews Materials, 2022, 7:117–137.

[7] Hofmann M, Shahid AT, Garrido M, Ferreira MJ, Correia JR, Bordado J. Bio-based Thermosetting Polyester Resin for High-performance Applications. ACS Sustainable Chemistry & Engineering, 2022, 10(11), 3442-3454.

[8] Hofmann M, Shahid AT, Machado M, Garrido M, Bordado J, Correia JR. GFRP composite produced by vacuum infusion with a novel high-performance bio-based unsaturated polyester resin: manufacturing and mechanical characterisation. Composites Part A: Applied Science and Manufacturing. [Submitted on March 2022]

[9] Sousa JM, Garrido M, Correia JR, Cabral-Fonseca S. Hygrothermal ageing of pultruded GFRP profiles: Comparative study of unsaturated polyester and vinyl ester resin matrices. Composites Part A: Applied Science and Manufacturing, 2021, 140, 106193.

  doi:10.5075/epfl-298799_978-2-9701614-0-0

Toward adhesives-free Bio-Based Composites via UV assisted interfacial cross-linking

*V. Rajasekhara Bade[1], Beate Gebert[2], Christina Schippers[2], Larisa Tsarkova[2], Thomas Bahners[2] & Jörg Mussig[1]**

[1] The Biological Materials Group, Dept. of Biomimetics, HSB – City University of Applied Sciences Bremen, Neustadtswall 30, D-28199 Bremen, Germany
[2] German Textile Research Center North-West gGmbH, Germany

Abstract: *Man-made fibres from bio-based polymers such as regenerated cellulose or polylactide offer a sustainable approach to producing composites by reducing the CO_2 footprint. Regenerated cellulose fibres have several advantages for their usage in high-performance composites due to their defined surface properties and diverse availability. However, it must be considered that the incompatibility issues between the hydrophilic reinforcing fibres and hydrophobic polyolefin matrix affect the fibre/matrix adhesion and decrease the composite performance. In the present research, industrially developed continuous regenerated cellulose fibres and polyethene (potentially of bio-based origin) are used to manufacture fibre-reinforced composites by introducing an intermediate step of UV irradiation of a semi-finished sample. This approach assumes that a cross-linked transition layer can be formed at the interface between UV transparent matrix and UV adsorbing fibres, thus avoiding petrochemical adhesion promotors. The performed mechanical tests confirm the potential of the proposed fabrication toward high-performance adhesives-free bio-based composites.*

Keywords: Bio-based composites; UV irradiation; Adhesive-free composites

1. Introduction:

Over the decades, composites material application has been increased in a wide range of applications, including aerospace, automobile, sports, and marine applications. The majority of the composite industry is dominated by petrochemical materials, i.e., carbon fibres and fossil-fuel-based polymer materials. Despite their excellent mechanical properties, commercial composites cause major environmental issues in mechanical recycling and utilisation through thermal recycling (1). Due to the increased concern over environmental issues, great efforts have been made over the decades to use natural fibres (for example, flax, hemp, and kenaf) in composites manufacturing (3).

In practice, natural fibre-reinforced plastics are sometimes difficult to process, partly due to the fluctuating properties of the fibres. In contrast to natural fibres, such as flax, hemp or kenaf, bio-based regenerated cellulose fibres have several advantages for their usage in high-performance composites due to their defined surface properties and diverse availability as textile pre-product (continuous fibre, staple fibre, fleece, fabric). Despite their advantages over natural fibres, bio-based cellulose fibres as reinforcement in polyolefin matrix result in poor fibre/matrix adhesion, which is a significant drawback that inhibits the extended use of these fibres (2). This poor fibre/matrix interaction is due to the hydrophilic character of the cellulose fibres and the hydrophobic nature of the polyolefin matrix (3–6). In the past, extensive studies have been carried out to improve the fibre/matrix adhesion by modifying the fibre surfaces (7, 8), adding

  doi:10.5075/epfl-298799_978-2-9701614-0-0

additives (9–11) or treating the entire composite structures (12, 13). Overall, a maximum improvement of fibre/matrix adhesion through these additives and surface modifications by a factor of 1.5 - 2 is reported by Müssig et al. (4). Despite optimising the fibre/matrix adhesion in composites, there is often a sharp transition in stiffness at the thin fibre/matrix interface. Therefore, achieving gradient transition of mechanical properties, i. e., tensile, shear and elastic properties, is also important, along with optimising the compatibility between the fibre surface and the matrix. In nature, plant structures often have a gradient transition between strengthening elements and the surrounding matrix. These gradients result in good damping behaviour and high toughness of the plant structure (14). In technical composites, this is usually achieved by an adhesive, an intermediate layer between fibre and matrix (15), consisting of a sizing agent to protect fibres and adhesion promotors.

In an earlier study by Bahners et al. (3), a decrease in the wettability of the hydrophilic viscose fibres and an increase in their affinity towards matrix polymer were achieved by deposition of a hydrophobic organic thin layer on reinforcement fibres through photo-polymerisation. Thin coatings have been deposited on the fibre surfaces by UV induced polymerisation of allylene or acrylates such as diallyl phthalate (DAP) and pentaerythritol triacylate (PETA). The improved composite performance has been attributed to the activation of functional end groups that interact with cellulose's OH groups and the non-polar chain of polyolefin. The single fibre pull-out test, the measurements of the interfacial shear strength (IFSS), as well as fatigue analysis showed that a significant improvement in fibre-matrix adhesion achieved was achieved by the deposition of a thin layer on the fibre surface through UV irradiation. According to the state of the art, the use of additives or modifiers, which are typically petrochemical, is still required to improve the mechanical performance of the regenerated cellulose/polyolefin composites (3). To respond to the trend toward reduction of CO_2 footprint and reduction of petrochemicals in industrial fabrication, a concept of adhesives-free composites has been proposed.

The aim of this research is to develop an intermediate transition layer through UV activation of the interface between UV transparent matrix and UV absorbing fibres and subsequent cross-linking of the matrix polymer. Accordingly, the effect of UV radiation on the fibre/matrix adhesion of regenerated cellulose fibres embedded in polyolefins without further adhesion-optimising additives was investigated. The fibre/matrix adhesion was characterised by the single fibre fragmentation tests.

2. Experimental

2.1 Materials

In this research, single fibres made of viscose regenerated cellulose fibres (Danufil®- Kelheim Fibres GmbH, Kelheim, DE) of fineness 28 dtex, and 3,3 dtex were used. As a matrix polyethene (NR 000491 Lupolen, LyondellBasell Industries, Rotterdam, NL) was used.

2.2 PE Sheet Production

To produce thin PE sheets of thickness 100 – 200 µm, 4,5 g of PE granulate were placed between Teflon sheets and then compressed in a hydraulic press (Typ LaboPress P200S der Firma Vogt, Berlin, DE) at a temperature of 180 °C and a pressure of 40 bar for 5 minutes. The press was then automatically cooled down to 40 °C in 5 minutes by maintaining 5 bar pressure.

  doi:10.5075/epfl-298799_978-2-9701614-0-0

2.3 Specimen preparation

The fabrication process of the single fibre fragmentation specimens for bio-based/thermoplastic model composites is described below in a stepwise approach.

(1) The produced PE sheets were cut into a rectangular shape with dimensions of 145 mm x 105 mm, and then a total of ten single fibres were fixed onto the PE sheet at a distance of 15 mm with a Tesa tape (Tesa SE, Norderstedt, DE) as shown in Figure 1a. Both ends of the single fibres are fixed on the PE sheets to ensure fibre alignment during the press processing.

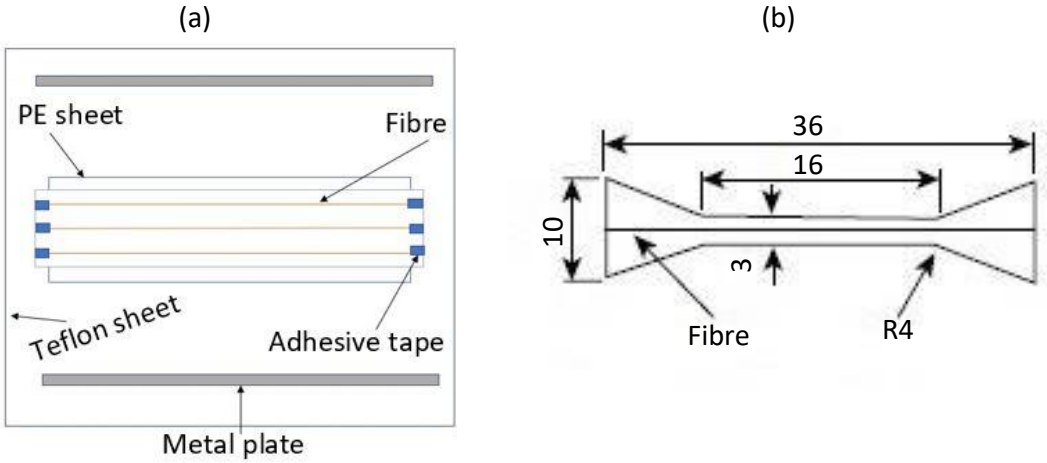

Fig 1: Single fibre composite fabrication and fragmentation sample geometry according to Graupner (16).

(2) The PE sheets with fixed fibres were placed in an oven for 24 h at 60 °C to reduce the moisture content from the fibres.
(3) Once the drying process was completed, it was made sure all the fibres were parallel to each other along the length axis of the PE sheet, and a second PE sheet was placed on the top of the fibres.
(4) The two PE sheets were placed between two Teflon foils (oil type 0903 AS; Böhme Kunststofftechnik GmbH + Co. KG, Schwarzenbek, DE) pressed in a hydraulic press at a temperature of 180 °C for 5 min under a pressure of 10 bar. Later the press was cooled down to 40 °C, and the samples were released from the Teflon sheets.
(5) Only straight fibres were considered to cut the tets specimens from the model composite sheets. These test specimens are prepared with dimensions, as shown in Figure 1b. The final specimen thickness was measured by a slide gauge.

2.4 UV Irradiation

The irradiation of the model composites was performed using a broadband UV lamp with a main emission band from 250 to 300 nm (UVACUBE 2000, Dr Hönle, Munich, DE). With the lamp emitting at a constant specific power of 50 W/cm (total emitted optical power per length of tube) and a constant lamp-to-sample distance of 10 cm, the irradiation dose was varied only by variation of exposure time. Inert conditions were realised by flooding the irradiation zone with argon at a pressure slightly above normal to prohibit competitive reactions with oxygen and ozone radicals.

  doi:10.5075/epfl-298799_978-2-9701614-0-0

2.5 Single fibre fragmentation test (SFFT)

Single fibre fragmentation testings were carried out using the Zwick/Roell universal testing machine Zwick/Roell, Ulm, DE) type Z 020 operating with a load cell of 500 N and a testing speed of 2 mm/min. The gauge length was set to 16 mm. The test was finished before the specimen was destroyed, i.e., the specimens were strained up three times the strain of the single fibres. Before testing, all the test specimens were climatised for at least 24 h at 23 °C and 50 % relative humidity (17). The fragment lengths of the individual specimens were measured under a polarisation microscope ADL-601-P (Bresser GmbH, DE). The measured fragment lengths allow the calculation of both the critical fragment length L_{fc} in mm according to Feih et al. (18) (Eq. 1). The critical fragmentation lengths were compared directly as an indicator for fibre/matrix adhesion. Therefore, the diameter and tensile strength are assumed to be equal for every tested fibre. A good fibre/matrix adhesion should lead to lower critical fragmentation lengths and vice versa.

$$\boldsymbol{L_{fc} = \frac{4}{3} * \bar{l} = \frac{4}{3} \sum_{i=0}^{n} \frac{l_i}{n}} \quad (1)$$

With L_{fc} = critical fragment length in mm, $\bar{l}$ = average fragment length in mm, n = number of measurements and l_i = single fragment length in mm.

3. Results and discussion

3.1 Influence of UV irradiation on fibre/matrix adhesion

3.1.1 Critical fragmentation length

To investigate the influence of the UV irradiation on the fibre-matrix adhesion between PE-Danufil 3,3 dtex, single fragmentation tests were conducted on the untreated specimens and on the specimens that were UV irradiated for 3 min and 8 min. These specimens were subjected to tensile stress until 69 % strain, i.e., three times the strain of the viscose fibres of fineness 3,3 dtex, which is 32 %.

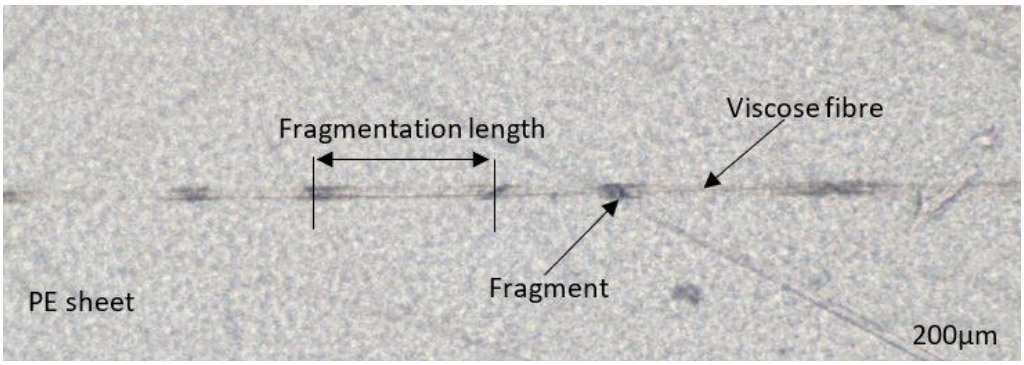

Fig 2: A fragmented viscose fibre in a polyethene matrix after the fragmentation test

Critical fragmentation lengths of the UV treated and untreated samples were determined at 16 mm gauge length based on the equation (1). The determined mean values and standard deviations are shown in Figure 7. From the investigation, the shortest critical fragmentation length of 0.24 mm was measured for 8 min UV irradiated specimens, followed by 3 min UV irradiated specimens with 0.30 mm, and then the highest critical fragmentation length of 0.52

  doi:10.5075/epfl-298799_978-2-9701614-0-0

mm has seen in the untreated samples. The fragmentation results show that UV irradiation decreases the critical fragmentation length indicating an increased fibre/matrix adhesion. The effect depends on irradiation dose, as could be demonstrated by increasing the irradiation time from 3 min to 8 min. Compared to untreated specimens, 3 min and 8 min treated specimens showed a 43 % and 53 % decrease in critical fragmentation length. The critical fragmentation length results show that the UV irradiation significantly influences the fibre/matrix adhesion in the PE-viscose composites. Graupner et al. (19) investigated the fibre/matrix adhesion of cellulose fibres in different matrices, i.e., PLA, PP, and MAPP. A critical fragmentation length of 2.5 mm has been observed in cellulose and PP samples, which was improved to 1.46 mm by modifying the matrix with the coupling agent maleic anhydride. The PP matrix modification with maleic anhydride resulted in a 41.6 % decrease in the critical fragmentation length. However, in this research, 8 min UV irradiation on the cellulose fibres embedded in the PE matrix without any additional coupling agents resulted in a 53 % decrease in critical fragmentation length. This states that UV irradiation has a higher influence on the fibre/matrix adhesion than modifying the matrices with coupling agent maleic anhydride. This proves that UV irradiation could become an alternative to coupling agents in achieving better performances in bio-based composites.

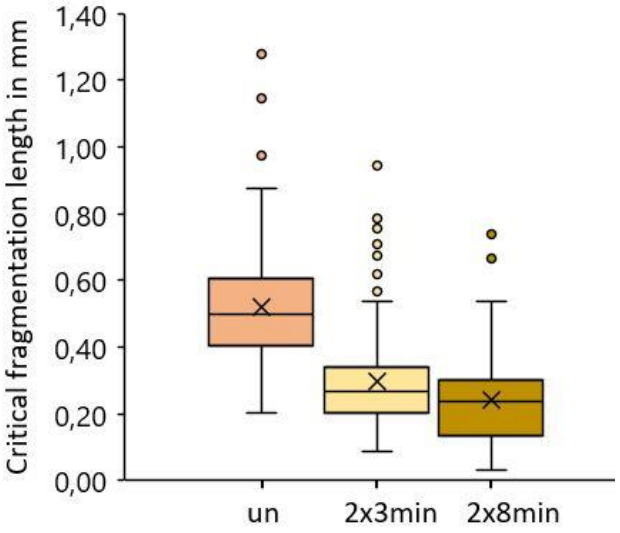

Fig 3: Fragmentation lengths of viscose fibres embedded in a polyethene matrix. The untreated (un) sample is compared with the samples UV irradiated on both sides for 3 and 8 min. The box plots show the median in a box between the first and last quartile. Whiskers show the lowest and highest values, which are 1.5 times the interquartile range.

The results show that UV exposure and exposure time positively affect fibre/matrix adhesion, comparable to conventional adhesion promoters. An explanation of the observed phenomenon is seen in a mechanism proposed in a paper by Bahners et al. (20), where model composites made of PET fabric and PE matrix were UV irradiated with a mercury broadband lamp. As the PE matrix was entirely transparent for UV irradiation between 200 nm and 300 nm, the UV photons penetrate the matrix and are strongly absorbed at the PE/PET interface. Using a peel test, the authors observed a significant difference between the irradiated sample and non-irradiated sample after peeling the PE matrix from the PET fabric; a residual of PE film bonded to the PET fibres was observed, which was the result of cross or interlink formation formed at the interface

  doi:10.5075/epfl-298799_978-2-9701614-0-0

between PE and PET. This cross-linking at the PE/PET interface was created by the radicals generated on the PET through the penetration of photons by UV irradiation (19). Müssig et al. (3) described that direct UV irradiation on viscose fibres results in increased affinity of the non-polar groups. At the same time, a decrease in the moisture content in the viscose fibres proves that viscose fibres are highly absorbable to UV irradiation (3). Given this background and, according to the hypothesis, the performed experiments confirmed the effect of UV radiation on the fibre/matrix adhesion of viscose fibres in polyethene matrix without adhesives.

4. Conclusions

The effect of UV irradiation on the fibre/matrix adhesion between viscose fibres embedded in a PE matrix without any additional coupling agent was investigated using the fragmentation test. Overall, UV exposure and exposure time improved fibre/matrix adhesion. Enhancements comparable to the use of conventional petrochemical adhesion promoters have been achieved. The improved fibre/matrix adhesions are assumed to be based on one primary effect: A cross-linked interface formation between viscose fibres and the PE through UV irradiation.

To elucidate the mechanisms behind the enhanced adhesion and resolve the interfacial region structure induced by UV irradiation, spectroscopic, physio-chemical, mechanical and thermomechanical analysis will be performed in ongoing research. This information, together with the characterisation of the mechanical properties of fibre- or textile-reinforced composites, is used to optimise the performance of bio-based composites.

Acknowledgments The research project IGF-Nr. 21818 N of Forschungskuratorium Textil e. V. was funded by the Bundesministerium für Wirtschaft und Energie in the framework of the program Industrielle Gemeinschaftsforschung (IGF) on the basis of a decision by Deutscher Bundestag. The kind help from Kelheim Fibres GmbH (Kelheim, Deutschland) and LyondellBasell Industries (Rotterdam, NL) by providing material for the experiments is greatly acknowledged. Additionally, we thank Felicitas Hannah Kuhn for her support in experimental work during the research project at HSB.

5. References

1. K. P. Matabola, A. R. De Vries, F. S. Moolman, A. S. Luyt.
Matabola2009_Article_SinglePolymerCompositesAReview.

2. Albano C, González J, Ichazo M, Kaiser D. Thermal stability of blends of polyolefins and sisal fiber. Polymer Degradation and Stability 1999; 66(2):179–90.

3. Bahners T, Kelch M, Gebert B, Osorio Barajas XL, Schmidt TC, Müssig J et al. Improvement of fibre–matrix adhesion in cellulose/polyolefin composite materials by means of photo-chemical fibre surface modification. Cellulose 2018; 25(4):2451–71.

4. Müssig J, Kelch M, Gebert B, Hohe J, Luke M, Bahners T. Improvement of the fatigue behaviour of cellulose/polyolefin composites using photo-chemical fibre surface modification bio-inspired by natural role models. Cellulose 2020; 27(10):5815–27.

5. Shah DU. Developing plant fibre composites for structural applications by optimising composite parameters: a critical review. J Mater Sci 2013; 48(18):6083–107.

  doi:10.5075/epfl-298799_978-2-9701614-0-0

6. Müssig J. Industrial Applications of Natural Fibres: Structure, Properties and Technical Applications. 1st ed. New York, NY: John Wiley & Sons; 2010.

7. S. J. Eichhorn, C. A. Baillie, N. Zafeiropoulos, L. Y. Mwaikambo, M. P. Ansell, A. Dufresne, K. M. Entwistle, P. J. Herrera-Franco, G. C. Escamilla, L. Groom, M. Hughes, C. Hill, T. G. Rials & P. M. Wild. Review: Current international research into cellulosic fibres and composites.

8. Belgacem MN, Gandini A. The surface modification of cellulose fibres for use as reinforcing elements in composite materials. Composite Interfaces 2005; 12(1-2):41–75.

9. Mechraoui A, Riedl B, Rodrigue D. The effect of fibre and coupling agent content on the mechanical properties of hemp/polypropylene composites. Composite Interfaces 2007; 14(7-9):837–48.

10. Duhovic M, Horbach, S. & Bhattacharyya, D., J.Biobased Mater. and Bioenergy, 2009, 3, 188-198.

11. Khan JA, Khan MA, Islam, R. & Gafur, A. Mater. Sci. Appl., 2010, 1, 350-357.

12. Kowalczyk M, Piorkowska E, Kulpinski P, Pracella M. Mechanical and thermal properties of PLA composites with cellulose nanofibers and standard size fibers. Composites Part A: Applied Science and Manufacturing 2011; 42(10):1509–14.

13. Quan H, Li Z-M, Yang M-B, Huang R. On transcrystallinity in semi-crystalline polymer composites. Composites Science and Technology 2005; 65(7-8):999–1021.

14. Speck T, Speck O. Quo vadis plant biomechanics: Old wine in new bottles or an up-and-coming field of modern plant science? Am J Bot 2019; 106(11):1399–403.

15. Jones FR. A Review of Interphase Formation and Design in Fibre-Reinforced Composites. Journal of Adhesion Science and Technology 2010; 24(1):171–202.

16. Graupner N. Analyse und Optimierung der Struktur- und Eigenschaftsbeziehungen von cellulosefaserverstärkten Polylactid-Verbundwerkstoffen [Zugl.: Clausthal, Techn. Univ., Diss., 2013]. 1. Aufl. Clausthal-Zellerfeld: Papierflieger-Verl.; 2014. (Materialwissenschaft und Werkstofftechnik : 2, Polymerwerkstoffe und KunststofftechnikBd. 11).

17. DIN EN ISO 291:2005. Kunststoffe Normalklimate für Konditionierung und.

18. A.Kelly W. Testing procedure for the single fiber fragmentation test; 1483(Risø-R-1483(EN)).

19. Graupner N, Rößler J, Ziegmann G, Müssig J. Fibre/matrix adhesion of cellulose fibres in PLA, PP and MAPP: A critical review of pull-out test, microbond test and single fibre fragmentation test results. Composites Part A: Applied Science and Manufacturing 2014; 63:133–48.

20. Bahners T, Gutmann JS. Photo-Initiated Lamination of Polyethylene (PE) and Poly(ethylene terephthalate) (PET). Journal of Adhesion Science and Technology 2012; 26(1-3):121–30.

  doi:10.5075/epfl-298799_978-2-9701614-0-0

TOWARDS INTEGRATED HEALTH MONITORING OF BIO-BASED COMPOSITE STRUCTURES: INFLUENCE OF ACOUSTIC EMISSION SENSOR EMBEDMENT ON MATERIAL INTEGRITY

Guillem SEYCHAL[a], Xavier GABRION[a], Emmanuel RAMASSO[a], Gilles BOURBON[a], Patrice LE MOAL[a], Vincent PLACET[a]
a: Université Franche-Comté - FEMTO-ST Institute - Dept Applied Mechanics (Besançon, FR)

Abstract: *Structural Health Monitoring (SHM) and Natural Fibres Composites (NFC) have lived since early 2000's important progress due to the needs of reducing material consumption and weight in operating structures while limiting the environmental footprint and increasing the safety of such structures. Acoustic Emission (AE) is one of the numerous solutions that appears to be suitable to predict service life and assess damage in composite structures. NFCs have shown promising properties for structural applications but their complex behaviour and the limited knowledge on their long-term durability still hinder their full development. In that sense, AE-based SHM could allow a more important breakthrough of bio-based composites by monitoring damage evolution and assessing their remaining life in service conditions. The new generation of AE-sensors offers also opportunities of embedment thanks to their smaller size, leading to better protection of the sensors and increased sensitivity. We propose in this work to study the effect of the embedment of millimetric-size dummy sensors in flax/epoxy laminates on the monotonic tensile behaviour and damage kinetic up to failure through AE methods. Results highlight a limited effect of the presence of dummy sensors on the mechanical behaviour and properties. AE results coupled with X-ray tomography pictures however highlight a change in location of damages that are more likely to append in the insert vicinity, and in the onset of the most severe damages, which appears at lower global deformation levels.*

Keywords: Natural fibres; Mechanical properties; Acoustic emission; Smart materials; Biobased Composites

1. Introduction

Natural fibre composites have known an important development over the last two decades. These fibres have shown promising properties [1], competitiveness and process have been enhanced so far that structural biobased composites are now a reality and start to be commercially available [2]. However, design of composite structures and durability prediction still suffers a lack of confidence over damage evolutions and structural integrity. This is due to their complex behaviour and failure mechanisms which may lead to the use of conservative safety factor values and then significant over design, mass increase and material consumption. In that sense, structural health monitoring (SHM) techniques could fill this gap by assessing damages in these structures in real time, by evaluating the remaining lifetime and integrity [3] and thus allowing design optimisation and mass saving. Acoustic-emission (AE) based SHM is particularly adapted to polymer matrix composites to assess, locate and identify real-time damages and propagation in qualitative and quantitative ways with a limited number of equipment [4]. Embedment of small sensors (millimetre-sized) within the laminate could be an opportunity to get smart materials with enhanced sensitivity while easing the instrumentation and improving the durability of the sensors. Several studies [5–7] have already shown major

  doi:10.5075/epfl-298799_978-2-9701614-0-0

advantages in embedding directly sensors within the materials allowing a better coupling between the sensor and the material and providing a packaging around the sensors, thus, limiting the effects of the environment. Moreover, if acoustic emission tends to generate an important amount of data, major breakthrough has been made in the last decades. Nowadays, efficient and reliable signal processing and data mining, through denoising, hits detection and data clustering lead to a fine understanding of the transient acoustic waves induced by damages when composite structures are subjected to loads [8–11]. Sensor technologies and materials have also evolved to improve the signal quality. Among the numerous options, capacitive micromachined ultrasonic transducer (CMUT) technologies are of particular interest. They rely on the use of arrays of small micromachined silicon unit membranes of different resonance frequencies potentially increasing the bandwidth and signal-to-noise ratio of the sensor. Such sensors could be embedded in composite laminates as shown in Figure 1.

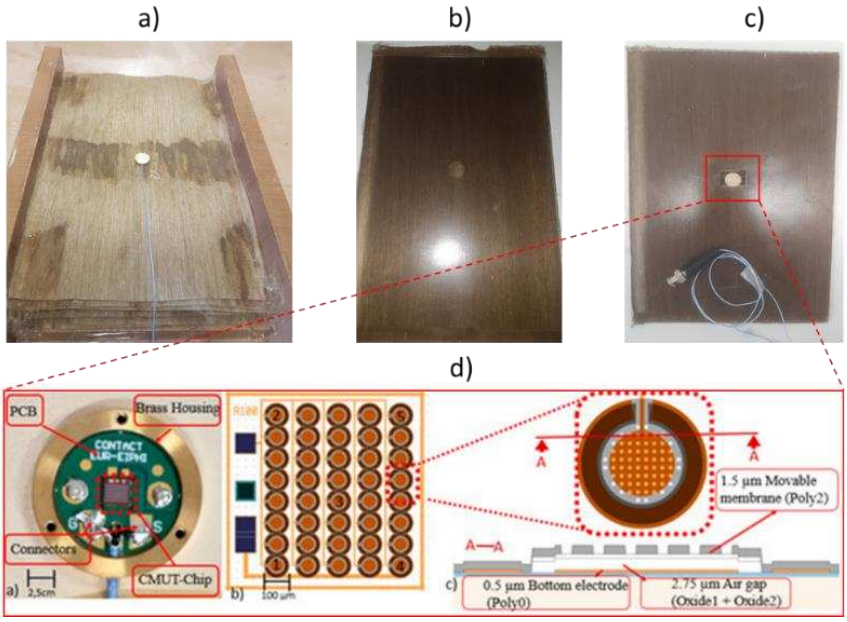

Figure 1 : Embedded CMUTs in a unidirectional flaxtape/GreenPoxy laminate. a) during lay-up; b) after curing, c) after laser cutting to observe the sensor and d) overview of CMUT sensor from [12].

In this work, we propose to study the effect of the embedment of brass parts mimicking CMUT-type AE-sensors on the properties and behaviour of flax-epoxy laminates under monotonic loads conditions as well as on the damage modes and kinetics.

2. Material and methods

Flax/epoxy composites were manufactured by thermocompression. Twenty plies of an unidirectional flax reinforcement (FlaxTape UD110 from Ecotechnilin®) were stacked into a Teflon coated steel mould. Epoxy resin (GreenPoxy 56 from Sicomin®) was poured between the different layers in the middle of the ply's length all along its width. The mould was then closed except on the length extremities to allow air and matrix excess to flow out. Laminates were then cured in a hot press in two step process: a first impregnation step at 40°C and 3bars for 15min and a curing step at 60°C and 3bars for an hour. Additionally, laminates were post-cured at 130°C.

For embedded insert samples, 10x5x1mm³ brass mimicking sensor parts were dipped into the resin and then placed at the middle ply of the laminate (*Figure 2*a), on the symmetric axis. Samples were laser cut (*Figure 2*b). Few samples were also polished to observe the effect on the microstructure (*Figure 2*c). More details about the process can be found in [13]. Samples were tested under monotonic tensile loads on a MTS Criterion tensile machine at 1mm/min.

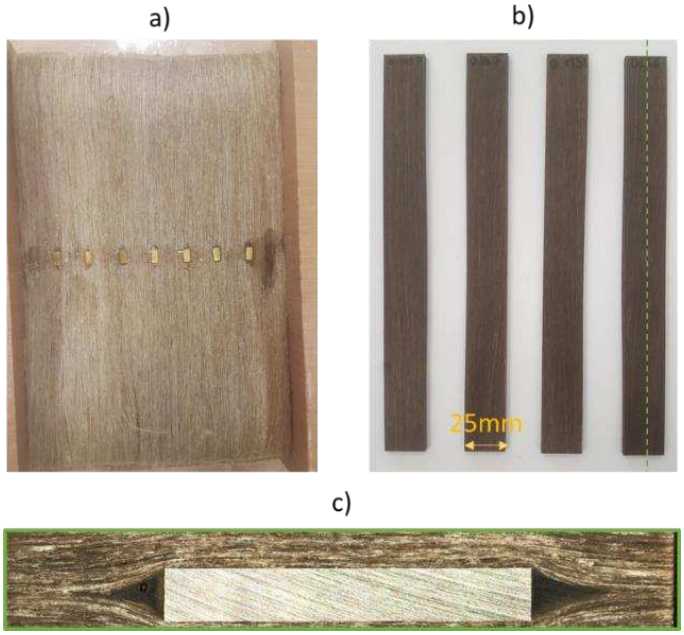

Figure 2 : Dummy sensor embedding a) during manufacturing, b) after laser cut, c) longitudinal microstructural effect of the sensor with matrix rich region in the alignment of the sensor

AE hits were recorded during monotonic tensile tests to evaluate damage modes and kinetics. Each tested specimen was monitored by acoustic emission using two external piezoelectric transducers coupled to the sample. Raw AE data were recorded during the test through a digital picometer and then processed using an algorithm developed in the lab. The raw data were denoised, hits were then identified and matrix of 42 descriptors were extracted. Complete details about AE equipment and processing can be found in [8,13]. Five clusters were then identified using an unsupervised Gustavsson-Kessel algorithm. All combination of 5 parameters were tested and the best set of parameters was retained to plot the representative AE behaviour. The clustering descriptors retained by the algorithm will not be discussed in this paper. This unsupervised clustering method have already been discussed in previous studies [10,11]. X-ray microtomographic images of the broken samples were acquired to enhance AE interpretation, the method details are described in [13].

3. Results and discussions

3.1 Effect of the embedding of dummy sensors on the monotonic properties

Pristine and embedded samples were subjected to monotonic tensile load. The values of the tensile properties are summarised in Table 1. The strain-stress curves are presented in Figure 3. The behaviour of unidirectional laminates is assumed to be bilinear with a first high stiffness (E_1 =31 ± 1 GPa) step between 0% and 0.15% and a second phase after 0.3-0.4% longitudinal strain where the second apparent modulus is significantly lower (E_2 = 25.5 ± 0.5 GPa). Samples have

brittle failure between 1.2 and 1.5% of longitudinal strain with a stress at break of 340.9 ± 12.9 MPa.

Table 1 : Monotonic tensile properties of pristine and embedded laminates

	Pristine	Embedded	Effect
V_f[1] (%)	49.9 ± 2.8	47 ± 0.5	-
V_p [2](%)	3.1 ± 0.8	4.5 ± 0.4	-
E_1[3] (GPa)	31.0 ± 1.0	27.7 ± 1.9	-10 %
E_2[4] (GPa)	25.5 ± 0.5	22.7 ± 1.1	-11%
ν_{LT}	0.44 ± 0.02	0.44 ± 0.01	0%
σ_{max} (MPa)	340.9 ± 12.9	276.9 ± 17.0	-19%
ε_L (%)	1.32 ± 0.02	1.21 ± 0.01	-8%
ε_T (%)	0.51 ± 0.02	0.51 ± 0.02	0%

[1]Fibre volume fraction calculated as $V_f = (m_f/\rho_f)/((m_f/\rho_f) + (m_m/\rho_m))$;[2] Porosity content $V_p = 1-\rho_c(w_f/\rho_f + w_m/\rho_m)$; [3]First apparent modulus calculated between 0.05% and 0.15%;[4]Second apparent modulus calculated between 0.4% and break

Interestingly, the presence of a brass part mimicking sensor does not affect the behaviour of the laminates subjected to tensile loads as the bilinear behaviour remains present with a yield point at the same strain level. The two apparent moduli are only slightly decreased (by about 10%) when a dummy sensor is embedded, emphasizing that the presence of sensors would not lead to oversizing materials to obtain comparable structural stiffness. Moreover, ultimate strain is only decreased by 8% when a dummy sensor is embedded. The stress at break appears to be the most affected properties. Indeed, the UTS drop of 19% from 340.9MPa to 276.9MPa when a dummy sensor is inserted. This could be attributed to stress concentration in the matrix rich region located in the insert vicinity. This stress concentration could thus lead to early matrix cracks coalescence, delamination and debonding triggering earlier fibre breaking.

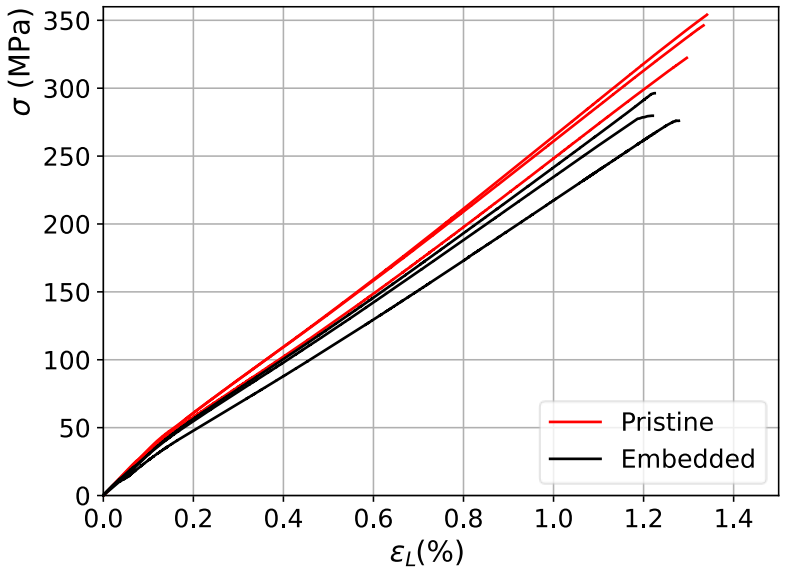

Figure 3 : Monotonic tensile test of pristine and embedded samples

3.2 Effect of sensor embedment on damage modes and kinetics during monotonic tensile testing

Acoustic emission clustering is an useful tool to discriminate damage modes and record damage kinetics during mechanical testing. Traditionally, amplitude, hits number and energy are the preferred AE signal features for clustering, in particular in supervised mono- or multi--parametric methods [14,15] as well as in unsupervised approaches. High energy and amplitude hits are generally correlated to severe damage (such as fibre breaking) that compromise the structural integrity and lead to failure while low energy and amplitude hits are more likely to be related to minor damages (such as matrix cracks) [14–17]. However, even if the utility of AE to discriminate changes in damage modes and kinetics is interesting and clustering methods bring even better insight, one must keep in mind that it is based on a complex unsupervised technique with some unknown about environmental effect and complex behaviour of the waves propagating within the material. Indeed, it has been shown that damages affect the AE signals themselves [9] and this could be even more pronounced when a metallic part is inserted. In that sense, it is preferred in this study to keep an overview of the results to analyse major tendencies without attributing a specific damage mode to a cluster. In addition, X-ray microtomography images of the failed samples, as presented in Figure 4, were analysed to identify the existing damage modes and their location and to ease the understanding and interpretation of changes in AE activity. The evolution of each cluster cumulative hits and energy as function of strain during monotonic tensile testing for both pristine and embedded samples are presented in Figure 5(a) and (b) respectively. Figure 5(c) and (d) represent the amplitude of the hits during the test and Figure 5(e) and (f) represent the energy of the hits during the tests.

For pristine sample, the first three clusters start in the early beginning of the test. For clusters 1 and 2, it is attributed to external sources (such as friction in the clamps) and minor damages (such as microcracking) that occur all along the applied strain. Some early damages and geometrical changes (such as fibres reorientation) of higher amplitude (Cluster 1) also appear in the beginning but slow down after 0.2% strain. At this point, a new cluster (Cluster 4) starts and evolves continuously during the test. This slowing of one cluster while another takes place highlights a change in the damaging behaviour. It is interesting to note that this change occurs simultaneously with the characteristic ill-point of flax composite tensile curves, where the apparent modulus decreases. So, the AE activity in this cluster could be related to nano- and micro-structural changes in the fibre wall. Finally, the fifth cluster starts at much higher strain (0.9%) that can be attributed to much severe damages leading to the final failure. For this cluster, the energy is more important and represents a wide part of the total energy dissipated by the laminate as compared to the other one while the number of hits of this cluster is significantly lower than the other clusters. The clustering result highlights the complexity of the damages occurring in the material, and the chronology of appearing of these damages.

  doi:10.5075/epfl-298799_978-2-9701614-0-0

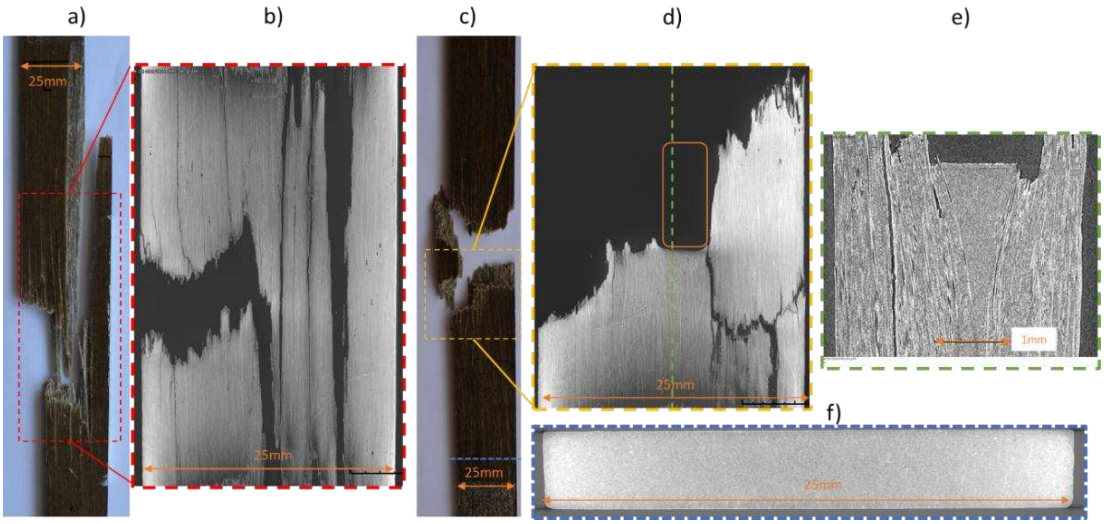

Figure 4 : Failure facies and tomographic observations of the broken a-b) pristine and c-f) embedded samples

Failure facies of pristine sample and tomography reveal long splitting of the laminates and damages in the whole volume. Such observations are coherent with a high number of hits of low energy induced by matrix cracks initiation and propagation in the whole samples. Once the coalescence is important enough, it initiates more energetic breakage of fibres in stress concentrated areas, leading to an energetic brittle fracture.

For embedded samples, it is interesting to note that the overall clusters chronology and trends are comparable to the pristine one with the three early starting clusters. The last two clusters however start at lower strain levels with faster increase in the number of recorded hits than for pristine samples. The number of total hits recorded for embedded samples is slightly lower than for pristine ones while energies are comparable. From these observations, it is important to note that the presence of a brass dummy sensor does not affect damage modes and identified cluster evolution but tends to provoke earlier severe damages leading to a premature failure as highlighted by the lower strain level required to see the last two clusters to start. Interestingly, the cracks in the embedded samples appears to be concentrated in the insert vicinity with failure cracks starting from the matrix rich region. When looking at points far away from the break area, the material seems to be not damaged. Thus, AE and tomography results highlight that the insert concentrate damages in its vicinity conducting to early severe damages thus provoking the failure prematurely. Such observations are in accordance with the observed effect highlighted in Section 3.1 and emphasize the conclusion that the effect of the embedment of dummy sensors affects only moderately the laminates in terms of overall monotonic tensile properties but changes in a more complex way damage initiation and propagation in material. Thus, this subtle effect must be taken with care when sizing structures subjected to more complex loads.

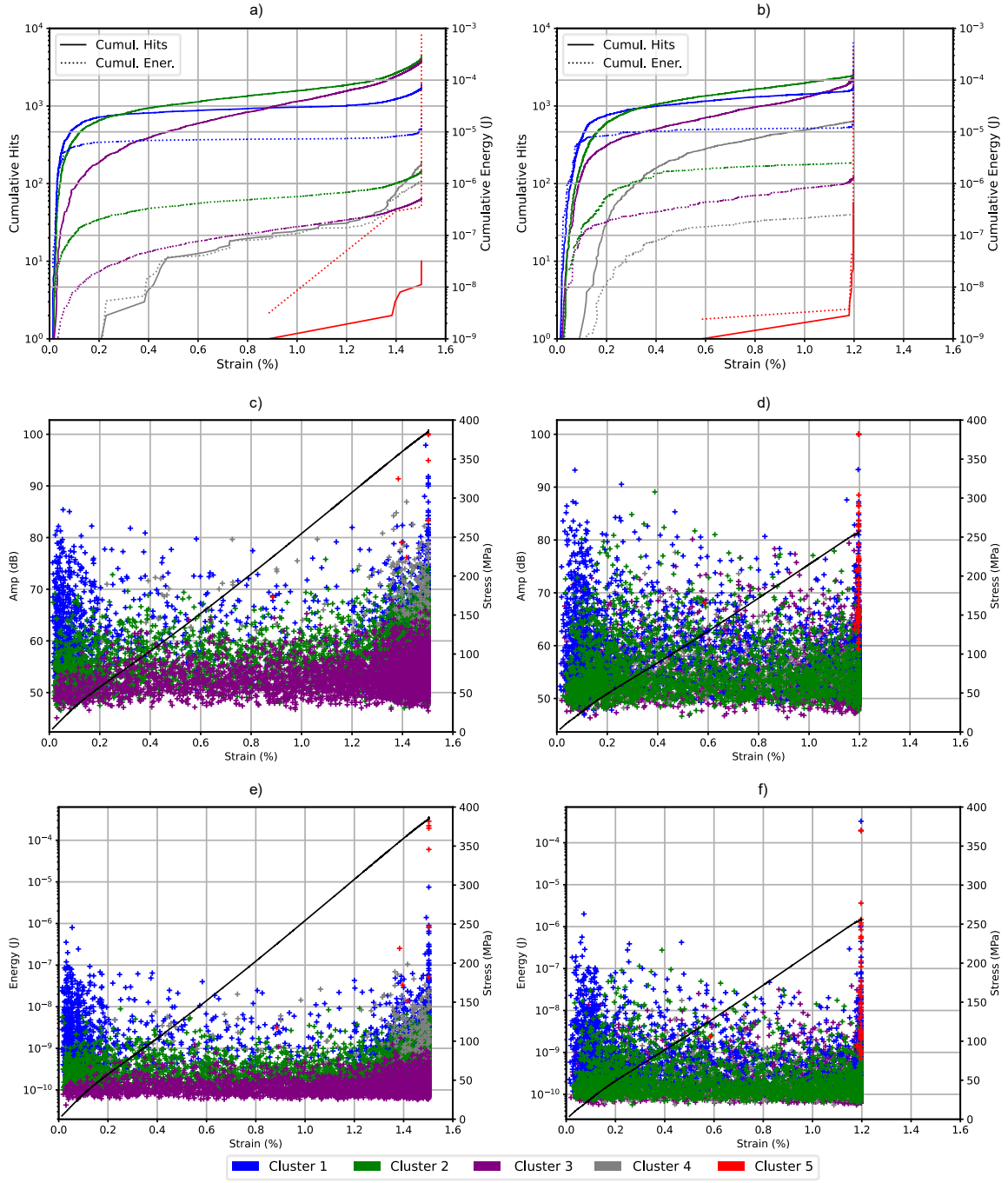

Figure 5 : a) Representative cumulative AE hits and cumulative energy detected per cluster as function of strain for pristine samples and b) embedded samples; c) amplitude of the hits as function of strain for pristine and d) embedded samples; e) energy of the hits as function of strain for pristine and f) embedded samples.

4. Conclusion

Natural Fibres Composites are a promising route to replace glass fibres composite as they showed high mechanical properties. However, their complex behaviour and their properties scattering inherent to their natural origin still limit industrial applications. The use of structural health monitoring such as acoustic emission could thus reduce the unknowns and increase the

reliability of bio-based structures. In this work, we assessed the effect of the embedment of dummy sensors on the integrity of flax/epoxy laminates. Results highlights a limited impact of the integration with no major effect on the overall monotonic tensile behaviour and properties. Regarding damages, the embedment of dummy sensors does not induce the appearance of new damage modes. Only a change in their spatial localisation and their onset times was observed. The presence of a sensor leads to a concentration of damage in its vicinity, leaving the rest of the volume free of damage. It also induces a premature onset of the major damages. However, the global stress at break is only slightly decreased and the effects could be even more reduced by optimising sensor geometry and manufacturing process. So, it can be concluded that in-situ acoustic emission is feasible for bio-based composited and opens opportunities to more sustainable structures.

Acknowledgements

Acknowledgements can be added at the end of the paper, before the references if applicable. This work has been supported by EIPHI Graduate School (contract “ANR-17-EURE-0002”) and the French RENATECH network through its FEMTO-ST technological facility and staff (MIMENTO Clean room). The authors are also grateful to MIFHySTO technological platform (FEMTO-ST, France) for the support in X-ray nanotomography characterisation.

5. References

[1] Jeannin T, Berges M, Gabrion X, Léger R, Person V, Corn S, et al. Influence of hydrothermal ageing on the fatigue behaviour of a unidirectional flax-epoxy laminate. Compos Part B Eng 2019;174:107056. https://doi.org/10.1016/j.compositesb.2019.107056.

[2] Mutel F. Flax and Hemp Fiber Composites, a Market Reality: The Biobased Solutions for the Industry. JEC Group; 2018.

[3] Mitsheal D. A Review of Structural Health Monitoring Techniques as Applied to Composite Structures 2017:57.

[4] De Rosa IM, Santulli C, Sarasini F. Acoustic emission for monitoring the mechanical behaviour of natural fibre composites: A literature review. Compos Part Appl Sci Manuf 2009;40:1456–69. https://doi.org/10.1016/j.compositesa.2009.04.030.

[5] Masmoudi S, El Mahi A, Turki S. Use of piezoelectric as acoustic emission sensor for in situ monitoring of composite structures. Compos Part B Eng 2015;80:307–20. https://doi.org/10.1016/j.compositesb.2015.06.003.

[6] De Rosa IM, Sarasini F. Use of PVDF as acoustic emission sensor for in situ monitoring of mechanical behaviour of glass/epoxy laminates. Polym Test 2010;29:749–58. https://doi.org/10.1016/j.polymertesting.2010.04.006.

[7] Tuloup C, Harizi W, Aboura Z, Meyer Y, Khellil K, Lachat R. On the use of in-situ piezoelectric sensors for the manufacturing and structural health monitoring of polymer-matrix composites: A literature review. Compos Struct 2019;215:127–49. https://doi.org/10.1016/j.compstruct.2019.02.046.

[8] Kharrat M, Ramasso E, Placet V, Boubakar ML. A signal processing approach for enhanced Acoustic Emission data analysis in high activity systems: Application to organic matrix composites. Mech Syst Signal Process 2016;70–71:1038–55. https://doi.org/10.1016/j.ymssp.2015.08.028.

[9] Kharrat M, Placet V, Ramasso E, Boubakar ML. Influence of damage accumulation under fatigue loading on the AE-based health assessment of composite materials: Wave

  doi:10.5075/epfl-298799_978-2-9701614-0-0

distortion and AE-features evolution as a function of damage level. Compos Part Appl Sci Manuf 2018;109:615–27. https://doi.org/10.1016/j.compositesa.2016.03.020.
[10] Ramasso E, Butaud P, Jeannin T, Sarasini F, Placet V, Godin N, et al. Learning the representation of raw acoustic emission signals by direct generative modelling and its use in chronology-based clusters identification. Eng Appl Artif Intell 2020;90:103478. https://doi.org/10.1016/j.engappai.2020.103478.
[11] Ramasso E, Placet V, Boubakar ML. Unsupervised Consensus Clustering of Acoustic Emission Time-Series for Robust Damage Sequence Estimation in Composites. IEEE Trans Instrum Meas 2015;64:3297–307. https://doi.org/10.1109/TIM.2015.2450354.
[12] Boubenia R, Le Moal P, Bourbon G, Ramasso E, Joseph E. CMUT-Based Sensor for Acoustic Emission Application: Experimental and Theoretical Contributions to Sensitivity Optimization. Sensors 2021;21:2042. https://doi.org/10.3390/s21062042.
[13] Seychal G, Ramasso E, Le Moal P, Bourbon G, Gabrion X, Placet V. Towards in-situ acoustic emission-based health monitoring in bio-based composites structures: Does embedment of sensors affect the mechanical behaviour of flax/epoxy laminates? Compos Part B Eng 2022:109787. https://doi.org/10.1016/j.compositesb.2022.109787.
[14] Godin N, Reynaud P, Fantozzi G. Émission acoustique et durabilité des composites. 2018.
[15] Marec A. Damage characterization of polymer-based composite materials: Multivariable analysis and wavelet transform for clustering acoustic emission data. Mech Syst Signal Process 2008:24.
[16] Monti A, El Mahi A, Jendli Z, Guillaumat L. Mechanical behaviour and damage mechanisms analysis of a flax-fibre reinforced composite by acoustic emission. Compos Part Appl Sci Manuf 2016;90:100–10. https://doi.org/10.1016/j.compositesa.2016.07.002.
[17] Munoz V, Valès B, Perrin M, Pastor ML, Welemane H, Cantarel A, et al. Damage detection in CFRP by coupling acoustic emission and infrared thermography. Compos Part B Eng 2016;85:68–75. https://doi.org/10.1016/j.compositesb.2015.09.011.

THE EMERGING ERA OF VISIONARY COMPOSITES BY PLANT-GROWN MATRIX AND REINFORCING FIBRES: THE CELLULAR ADHESION

Mikko, Kanerva[a], Olli, Orell[a], Jarmo, Laakso[a], Alexandros, Prapavesis[b], Aart-Willem, van Vuure[b], Vladimir, Yudin[c], Ari-Pekka, Mähönen[d], Yrjö, Helariutta[d]

a: Tampere University, Engineering and Natural Sciences, Finland – mikko.kanerva@tuni.fi
b: KU Leuven, Department of Materials Engineering (MTM), Belgium
c: Institute of Macromolecular Compounds (IMC), Russian Federation
d: Helsinki University, Viikki Plant Science Centre (ViPS), Finland

Abstract: *The truly sustainable future with engineering materials will require completely new ways of creating materials. A significant part of emissions and energy consumption originates due to the processing of materials for various products, especially in the case of advanced composites. The more circular economy and recycling is to be applied, the more emphasis must be put on the processing of materials. In nature, the 'processes' of synthesis and material circulation are completely sustainable. This work includes actual field trials that were started during the year 2018 – aiming to the studies about the generation of fibre-reinforced visionary composites with the help of natural adhesion and cellular growth in pine trees.*

Keywords: bio-inspired; tree surgery; adhesion; cell proliferation, implantation

1. Introduction

It is not difficult to give reasons for why we should change the way our products, the materials in them, are produced nowadays. The global concentration of CO2 and the growth of its increase has only accelerated during the recent decades [1] – noting that CO2 emissions are regarded as one of the main parameters used to compute any (human) process-induced impact on the climate change. The reported values are already beyond the limits that could have been fought down – proper 'safeguarding' would have allowed to save the global economy [2, 3]. Similar large increases in the CO2 concentration of atmosphere, in the Earth's history, have only been related to total ecological phase changes along with the climate in the planet's history during tens of millions of years [4]. Most of the human's energy consumption is related to processing of Earth resources into different products as well as transporting the raw materials and products from a place to another all over the globe [5]. The activity related to various processes by humanity has long led to significant appropriation on the scale of the Earth ecosystem [6]. Only completely different processes of making materials and products for human needs can be sustained in the future. For future materials, humans must learn to adapt with the synthesis, or conversion, of matter in nature.

Purely from the point of view of engineering, wood – after harvesting and dehydration – has good static strength (e.g., 173 MPa for mararie, *Karrabina benthamiana*) and Young's modulus (e.g., 19 GPa for yellowwood, *Cladrastis kentukea*). These values are significantly higher than those of any polymeric matrix used in the advanced fibre reinforced composites today. Recently, Kyoto University and a company launched a development project about the use of wood materials in satellite enclosures to prevent waste accumulation in Earth orbit [7]. Plywood has

  doi:10.5075/epfl-298799_978-2-9701614-0-0

been used in primary and secondary load-carrying structures in aircraft for decades. Wood and plant stems in general are anisotropic, in terms of the structure and (mechanical) properties, and this suggests that the functional properties as well as mechanics can theoretically be tailored in the final material system [8]. It is important to note that anisotropy is basically the reason why modern fibre reinforced polymer composites (FRPCs) can be much further optimized per application than any isotropic alloy or amorphous material. Interestingly, over the recent few tens of years, scientists have pursued to improve the fibre-matrix interphases in fibrous composites [9]. In this study, the efforts aim to hierarchical, controlled anisotropy in future visionary FRPCs with nature. It is well known that tailored interphases in fibrous composites with multi-scale structuring can give engineering materials not only targeted static mechanical performance but improved fatigue and dynamic response, to be exploited in the design of high-tech products [10]. Wood structure is inherently hierarchical, anisotropic, and specifically controlled for each stress condition by trees themselves [11].

2. Experimental

2.1 Materials

This study was carried out with pine (*Pinus sylvestris*) and synthetic fibres for selected functionalities and as implant parts. In general, of all plants, pine trees naturally exist on all the continents of the Northern Hemisphere. They are available in massive amounts without any industrial cultivation and exist nearby local engineering industries. Therefore, pine tree-based materials have the potential to be used sustainably without long-distance transportation between different continents. Additionally, conifer forests are the largest terrestrial carbon sink. Pine trees have been studied for decades and there are large amounts of scientific literature available about the tissue structure, growth, evolution, and extractives (resins) of various pine trees, making this tree genus a scientifically rather well-defined organism.

The four different fibres representing the implant materials were: 1) carbon (carbon) fibres with the minimum surface finish (Elur®-p-0.08, by Argon LLC, provided by the Institute of Macromolecular Compounds (IMC)), 2) ECR (electrical/ chemical resistance) glass (glass) fibres (provided by Kevra Oy, Finland), 3) high-density polyethylene (PE) fibres (PE melt-spun as described in the previous work [12]) using CG9620 granulate (Borealis Polymers, Austria), and 4) diamond-like carbon (DLC) coated aramid fibres (coating [10] by DIARC® Bindo, by Oerlikon Balzers Coating, Finland) of grade Twaron® 2200 (by Teijin, Japan). Carbon fibre has the greatest potential to improve the stiffness and strength for any alive or post-cut wood-carbon fibre composite as well as it conducts heat and electricity.

For adjusting the compatibility between the cell proliferation and fibre surfaces, pine gum rosin (Forchem, Finland) was used as treatment. The treatment (i.e., dilute solution of dissolved rosin and acetone) was applied by dipping. Whenever tree surface (bark) gets broken, a path is formed via wounds for insects and fungi to attack the internal tree tissue. Therefore, the surface treatments with rosin targeted to ensure healthy, well-grown wounds. The rosin treatment was studied for carbon (carbon-R) and glass fibres (glass-R) series.

  doi:10.5075/epfl-298799_978-2-9701614-0-0

2.2 Outdoor field trial with tree surgery

The growth-integrated composites were grown in Finnish forest using pine (*P. Sylvestris*). The alive meristem cells within the vascular cambium were reached from U-cuts from the bark layer (see Fig. 2 a). Each implant material was studied for two different implantation techniques: I) upward U-cut with half of fibre bundle left outside tree surface, for later characterization with a pull-out method, and II) upward U-cut with full embedment. Each tree, and each cut (manually done by using a sterilized surgeon scalpel Cutfix®, B. Braun Melsungen), was in details identified by the cut length, cut location (direction, height, number of branch fork), and tree dimeter at the surgery location prior implantation. The length of the implant (fibre) samples was 20 mm for full embedment (U-cut length 22-40 mm) giving a length to diameter ratio of ≈1000 (fibre diameter for the different fibres 10-80 µm). All the implanted tree individuals were grown inside a 100 sqm plantation with as similar lighting, weather, and nutrients (soil type) as possible for the outdoor forest-based field trial. The wounds (at implantations) were treated with wound wax (080E1, Neko) and wrapped by tar-treated fabric tape (batch 10.04.002, Finland) as is a typical wound treatment. The tape was removed after two months of tree growth to allow normal bark formation. The healing (proliferation) period (during the years 2018-2019) was in total 17.5 months (i.e., two radial growth terms for pine). Sections were extracted from the pine stems and cut pieces were dehydrated slowly in standard room conditions (21±1 °C, 65% RH) over 12 months. The final pieces included control pieces of un-intervened wood and the growth-integrated pieces.

2.3 Mechanical testing

The dehydrated wood pieces were fine-cut and polished into specimens for three-point bending testing to study increases in flexural strength (28 mm × 8 mm × 8 mm, length × width × height). A three-point bending test fixture was used for flexural testing with a span length of 22 mm, loading pin diameter of 10 mm, and support pin(s) diameter of 5 mm. A universal test machine was used to generate the compressive load (5967, Instron, operated at a 1.0 mm/min test rate). Each specimen was loaded up to the failure load. Peak force and failure mode were recorded. The flexural (longitudinal) strength was defined for the failure with Eq. (1):

$$\sigma_u = \frac{3 \cdot F_u \cdot s}{2 \cdot w \cdot h^2} \quad (1)$$

where F_u is the peak force during a test, s is the support pin span, w is the test specimen's width, and h is the test specimen's height. Flexural strength was calculated for each specimen with specimen's individual exact dimensions. Three pure wooden (no fibres) specimens (see Fig. 2 b) were tested to determine the average reference strength (σ_{ref}). The effect of the grown-integration of fibres was studied via the difference between the flexural strength of fibre-integrated specimen and reference strength ($\Delta\sigma_u$). The conditions during the tests were recorded (20.5 °C, 23% RH).

A new method was generated to pull out and test for adhesion the specimens with growth-integrated glass fibres. In the pull-out testing, fibres or a set of fibres (bundle) were pulled out of the matrix amid (here wood or combination of wood and rosin). The higher is the force (stress) needed to pull, the higher is the interfacial adhesion reflected by the test. The designed test setup is illustrated in Fig. 2 c. A universal test machine was used to generate the load (5967, Instron, operated at a 1.0 mm/min test rate, 5.0 N miniature load cell). To grip a fibre or bundle,

  doi:10.5075/epfl-298799_978-2-9701614-0-0

thin veneer tabs were used; fibre (bundle) was adhesively (using polyvinyl acetate glue) connected between two tabbing pieces.

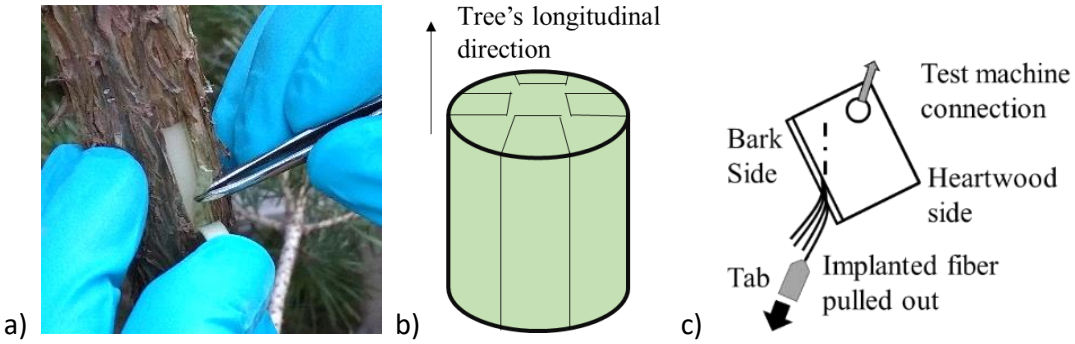

Figure 2. a) U-cut for fibre integration (DLC series in the image); b) pieces extracted from pine tree stem for flexural testing; c) the pull-out test method concept.

2.4 Microscopy and characterization

Field emission (FESEM) scanning electron microscopy (ULTRAplus, Zeiss) was used to study the integration of fibres amid the grown cellular wood structure. Cross-sectional ion polishing (CSP) was used to reveal the ultracellular structure of the adhered cells amidst the fibres and these samples were imaged by FESEM. Compositional analysis (x-ray energy dispersive spectroscopy, EDS) was used to observe fibres.

The fibre integration and fracture formations in the flexural specimens were studied with the help of 3D imaging with X-ray Computed Tomography (XCT) using TESCAN UniTOM HR scanner, equipped with a 160 kV/25 W microfocus & nanofocus X-ray tube, with a tungsten reflection target and a detector of 2916 x 2280 pixels, with a 50 µm pixel pitch. The source voltage and power were set to 55 kV and 0.8 W. Based on the source-to-object distance two voxels size (VS) magnifications were acquired; a) a 10 µm VS scan for the overall inspection of the specimen and b) high resolution scans of 1 µm VS in selected volumes of interest. In total 2600 radiographic projections were acquired over a 360° sample rotation, each with an exposure time of 1200 ms and frame averaging set to 5 to reduce the random noise, resulting in acquisition times of 260 min per scan. Thereafter, cross-sectional reconstruction to tomographic slices performed on the acquired radiographic projections by applying a filter back-projection algorithm in the TESCAN reconstruction software Panthera. Image analysis and 3D visualization of the scans was performed in Avizo 3D v 2021.1 (ThermoFisher)

2.5 Finite element analysis

The pull-out test method was analyzed using simulation on the finite element (FE) basis. The modelling and computations were carried out in ABAQUS (Standard) (2021). The part geometries included 3D models of a wooden part (2 mm × 1 mm × 0.4 mm) and fibre (ø 18 µm, length 4.5 mm). Rigid contacts (tie) were used between the wood and fibre parts. Wood was modelled to be an anisotropic elastic body (moduli $9.7{\cdot}10^{-3}$ N/µm^2, $5.8{\cdot}10^{-4}$ N/µm^2, $5.8{\cdot}10^{-4}$ N/µm^2, shear moduli $3.6{\cdot}10^{-3}$ N/µm^2, $3.6{\cdot}10^{-3}$ N/µm^2, $2.8{\cdot}10^{-4}$ N/µm^2, Poisson's ratios 0.33, 0.33, 0.02, in a Cartesian coordinate system XYZ, respectively, with X-axis matching with the longitudinal (upwards) tree growth [13]). The fibre part was modelled to be an isotropic body (glass, 0.07 N/µm^2, Poisson's ratio 0.3). The fibre was divided into three parts: the free end (50 µm) of the fibre was rigid for a clamped boundary condition, and the portion inside wood

  doi:10.5075/epfl-298799_978-2-9701614-0-0 published under CC BY-NC 4.0 license

was divided into two portions (fibre and a 0.5 mm-internal portion). The internal portion was modelled either 1) glass fibre, or 2) softer, rosin-imitating material ($1 \cdot 10^{-6}$ N/µm^2, Poisson's ratio 0.3). The fibre part was integrated into the wood part at a pull-out angle of 15°. Linear hybrid tetras (C3D10) were used for meshing (nominal size at the interfaces 8 µm). The total mesh included 133 178 elements. The simulation of the pull-out test was run for a constant pull-out force of 0.1 N (point load at the bottom of the wood part). It was estimated that, in a typical real test, there are in average 10 fibres pulled out simultaneously for an experimental peak of ≈1 N.

3. Results and analysis

3.1 Wound healing and cellular structure

The total tree mass was measured at the time of cutting (after the field trial): 8.3 kg, 7.2 kg, 9.1 kg, 6.3 kg, for the trees used in grow-integration of PE, DLC, glass, carbon series, respectively. The increase of diameter at the implantation location was: 38 % (15.8 mm), 49 % (20.6 mm), 58 % (25 mm), 37 % (14.7 mm) for PE, DLC, glass, carbon series, respectively.

The wounds healed so that the U-cut was grown back over all its edges (Fig. 3 a) for all the glass and carbon series. For PE and DLC series, the wounds did not heal well and, especially for the partly embedded fibres, the U-cut did not grow back but was left partly open. For all glass and carbon series, the fibres were adhered, i.e., grown several millimeters inside the wood. The intervention led to secretion of rosin by the tree, as was revealed by the FESEM imaging (Fig. 3 b). For the carbon series where no rosin-treatment was applied, the rosin secretion was significant and visually observable after breakage of the specimen within flexural testing. For the rosin-treated carbon fibres, the secreted rosin was less but clearly visible in XCT analysis on micro-scale (Fig. 4 a-b).

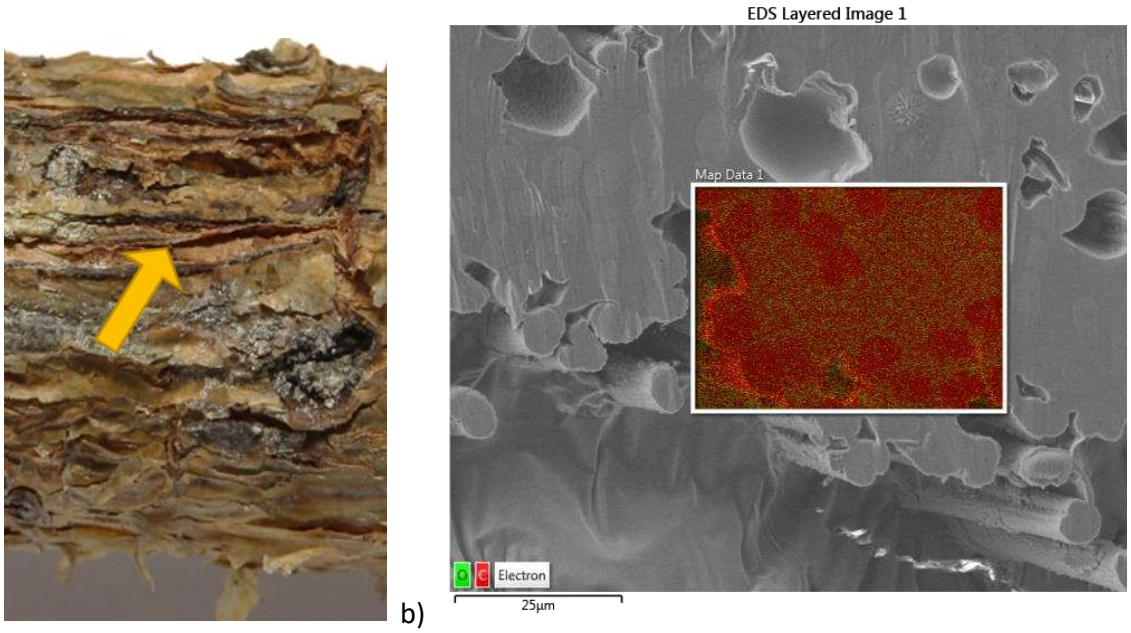

Figure 3. a) Wound healing on pine stem for carbon fibres (without rosin treatment) fully implanted. b) FESEM and related EDS analysis of carbon-series specimen.

  doi:10.5075/epfl-298799_978-2-9701614-0-0 published under CC BY-NC 4.0 license

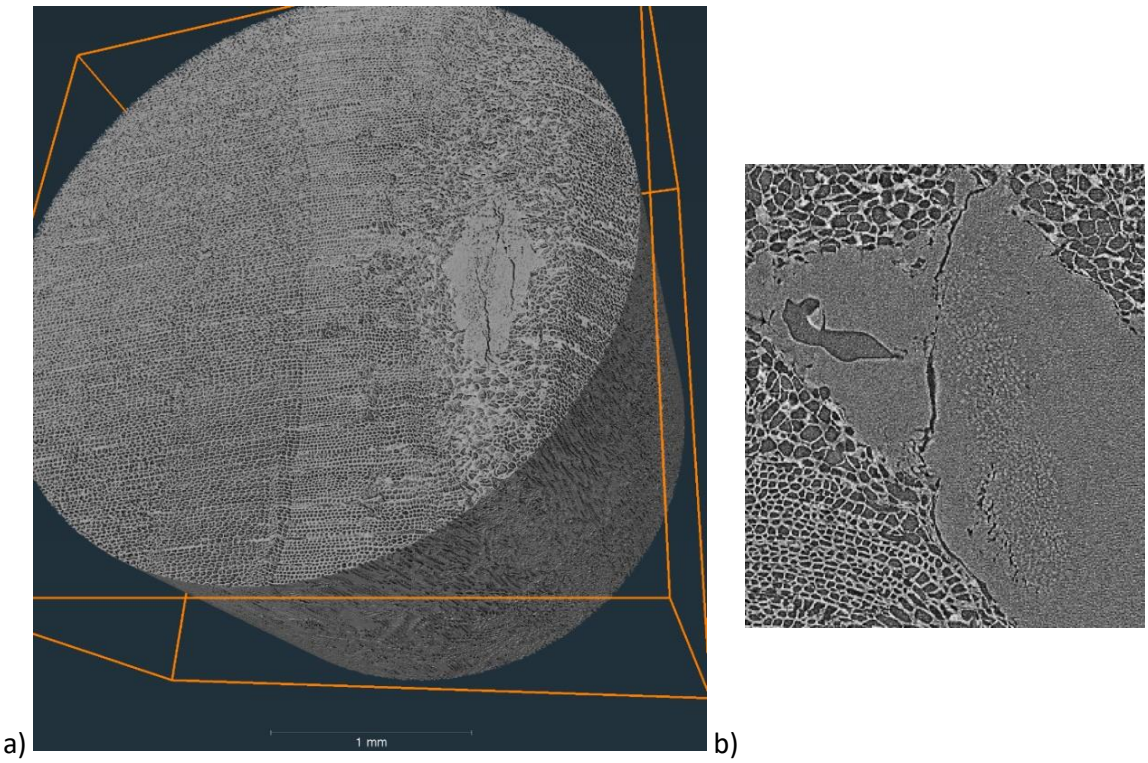

Figure 4. a) 3D analysis of the carbon fibres inside the wood piece based on the XCT analysis; b) 2D cross-section by the XCT analysis of carbon fibres, surrounded by secreted rosin.

3.2 Improvements of mechanical performance

The results of the flexural testing are shown in Fig. 5. a, and the results of pull-out tests in Fig. 5 b. The flexural strength was improved by fibre-integration for all the series except for carbon fibres without the rosin surface treatment. The rosin treatment improved the flexural strength for the carbon fibre integration by 32 % and for the glass fibre integration by 3 %. The fibre integration with rosin treatment, compared to pure wood, increased the strength by 8 % for the carbon series (carbon-R) and 15 % for the glass series (glass-R). Fibre volume fraction was estimated based on cross-sectional areas of specimen ($64 \cdot 10^{-6}$ m^2) and fibres ($\pi r^2 = 80 \cdot 10^{-12}$ m^2; for 100 fibres in a bundle yields $80 \cdot 10^{-10}$ m^2) the longitudinal dimension being essentially equal (specimen's length). This estimation gives a fibre volume fraction of 0.1-0.2 ‰ in the fibre-integrated samples. It should be noted that the flexural strength was significantly increased for the PE and DLC series although the implanted fibres were not well integrated (unsuccessful healing). This indicates that the surgery for implantation is a type of intervention that leads to wound tissue of a higher strength. In other words, the improvements of flexural strength in Fig. 5 a are not only due to the implanted fibres but also due to the changes in the cell structure of wood (see variation in Fig. 4 a) compared to the non-intervened wood of reference specimens.

Significant improvements in (flexural) strength would require good adhesion between the implanted fibres and the proliferated cell tissue amid. However, there are no test methods for measuring the mechanical adhesion forces for wood-fibre materials with grown adhesion. Therefore, a pull-out method was developed and studied. The results of pull-out testing for the glass series are shown in Fig. 5 b. It was found that the peak force can be related to various failure modes, such as partial pull-out and fibre (bundle) breakage. Further research is needed to improve and analyze the pull-out method in detail.

  doi:10.5075/epfl-298799_978-2-9701614-0-0

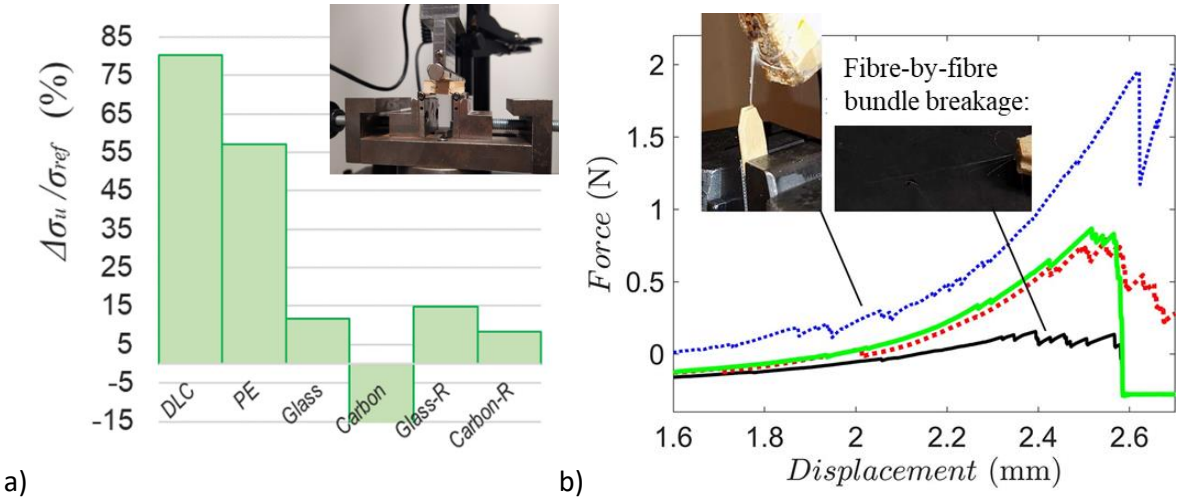

Figure 5. a) Change in flexural strength due to grown-integrated fibres; b) the force-displacement performance of glass fibres pulled out from wood.

3.3 Numerical analysis of the pull-out test method

The von Mises maps are shown in Fig. 6. The stresses at the fibre-wood interface were carried approximately by a portion up to 1 mm of length (inside the wood part). It should be noted that (unhomogenized) real cell structure of wood would allow local yield and the stress-carrying length could be longer, yet the effect is anticipated up to a factor of two. Therefore, in the real test, fibre pull-out clearly requires breakage of fibre near the specimen surface or crack growth along the fibre-wood interface because the fibres were grown to adhesion along a length of approximately 20 mm of fibre inside the wood.

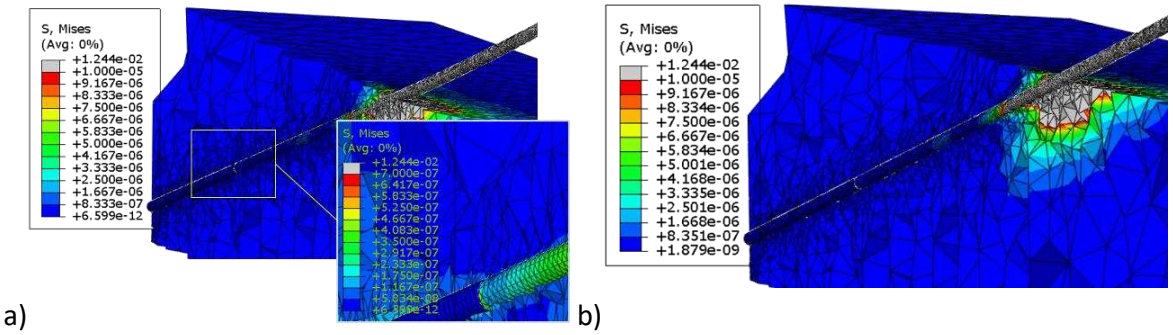

Figure 6. FE analysis results for simulated fibre pull-out tests at a peak force of 0.1 N: a) fibre integrated at a depth of 0.7 mm followed by a rosin-filled cavity; b) fibre integrated throughout (1.2 mm). A half of the wood part have been removed from the visualization for clarity. In the stress legends, the unit of stress is N/μm², e.g., 1·10⁻⁵ N/μm² = 10 MPa.

4. Conclusions

This work confirmed that making advanced composites can be done in close collaboration with alive plants. Different fibres were implanted into alive pine tree stem and the performance was studied after extraction of composite pieces formed by the fibres and grown cellular tissue. The

  doi:10.5075/epfl-298799_978-2-9701614-0-0

healed tissue is irregular and affects the composite properties in addition to the fibres and when compared to the intact wood around the integration volume.

Nowadays, human civilization establishes its 'intelligence' in terms of war and disregard of nature. A change in the mindset is necessary to focus altogether on collaborative living, produce and use physical matter in a harmony with nature – right now and in future.

Acknowledgements

This study made use of the Microscopy Center of Tampere University. The authors want to thank J. Alonso-Serra (RDP-INRAE-ENS de Lyon, France) for collaboration.

5. References

1. Dlugokencky E, Tans P. Global Annual Mean Dioxide Growth Rate. NOAA Research/GML. cited: March 2022. https://www.esrl.noaa.gov/gmd/ccgg/trends/gl_gr.html
2. Steffen W, Broadgate W, Deutsch L, Gaffney O, Ludwig C. The trajectory of the Anthropocene: The Great Acceleration. The Anthropocene Review 2015; 2: 81-98.
3. Figueres C, Schellnhuber HJ, Whiteman G, Rockström J, Hobley A, Rahmstorf S. Three years to safeguard our climate. Nature 2017; 546: 593-595.
4. Anagnostou E, John EH, Edgar KM, Foster GL, Ridgwell A, et al. Changing atmospheric CO2 concentration was the primary driver of early Cenozoic climate. Nature 2016; 533: 380-384.
5. Haberl H, Erb KH, Krausmann F, Gaube V, Bondeau A, et al. Quantifying and mapping the human appropriation of net primary production in earth's terrestrial ecosystems. PNAS 2017; 104: 31
6. World Energy Outlook 2019. Flagship report — November 2019. IEA. 2019. Cited: March 2020. https://www.iea.org/reports/world-energy-outlook-2019
7. Harper J. Japan developing wooden satellites to cut space junk. BBC News. 2020. Cited: March 2022. https://www.bbc.com/news/business-55463366
8. Zhongsen Zhang, Shenming Cai, Yan Li, Zhen Wang, Yu Long, et al. High performances of plant fiber reinforced composites—A new insight from hierarchical microstructures. Composites Science and Technology 2020; 194: 108151.
9. Qian H, Greenhalgh ES, Shaffer MSP, Bismarck A. Carbon nanotube-based hierarchical composites: a review. Journal of Materials Chemistry 2010; 20: 4751-4762.
10. Kanerva M, Korkiakoski S, Lahtonen K, Jokinen J, Sarlin E, et al. DLC-treated aramid-fibre composites: Tailoring nanoscale-coating for macroscale performance. Composites Science and Technology 2019; 171: 62-69.
11. Alonso-Serra J, Shi X, Peaucelle A, Rastas P, Bourdon M, et al. The ELIMÄKI Locus is Required for Vertical Proprioception in Birch Trees. 2019. Available at SSRN: https://ssrn.com/abstract=3444593 or http://dx.doi.org/10.2139/ssrn.3444593
12. Kanerva M, Puolakka A, Takala TM, Elert AM, Mylläri V, et al. Antibacterial polymer fibres by rosin compounding and melt-spinning. Materials Today Communications 2019; 20: 100527
13. Green DW, Winandy JE, Kretschma DE. Mechanical Properties of Wood. Forest Products Laboratory. 1999. In: Wood handbook—Wood as an engineering material. Gen. Tech. Rep. FPL–GTR–113. Madison, WI: U.S. Department of Agriculture, Forest Service, Forest Products Laboratory.

  doi:10.5075/epfl-298799_978-2-9701614-0-0

LEMONGRASS PLANT LEAF AND CULM AS POTENTIAL SOURCES OF REINFORCEMENT FOR BIO-COMPOSITES

Vincenzo, Fiore[a], Luigi, Botta[a], Roberto, Pirrone[a], Suchart, Siengchin[b], Sanjay Mavinkere, Rangappa[b]

a: Department of Engineering, University of Palermo, Viale delle Scienze, Building 6, 90128 Palermo (Italy) – vincenzo.fiore@unipa.it
b: King Mongkut's University of Technology, 1518 Pracharat 1, Wongsawang Road, 10800 Bangkok (Thailand)

Abstract: *A possible source of natural reinforcement for bio-composites can be represented by lemongrass plant (Cymbopogon flexuosus), a clumped and perennial grass which belongs to the Poaceae family. This plant is extensively used for several applications such as pharmacology, food preservation and cosmetics but, to the best of our knowledge, few papers were published on its use as source for reinforcement of composites and no one article was focused on the comparison between lemongrass leaves and culms as potential source of natural reinforcement. To this aim, a preliminary investigation on leaf and culm fibers was carried out to compare their physical and chemical features as well as their tensile properties. Furthermore, bio-composites based on a biodegradable starch-derived matrix (MaterBi®) and lemongrass leaf and culm particles were manufactured via extrusion and compression molding. For both fillers, two compositions (i.e., 10% and 20 wt.%) were investigated in terms of morphological and mechanical properties.*

Keywords: natural fibers; biodegradable polymers; lemongrass; bio-composites

1. Introduction

The use of natural fibers as reinforcement for bio-composites has received a great interest both from the academic world and several industrial fields since the 1970s. This attention is motivated by serious environmental issues correlated both to the unsustainable manufacturing processes of synthetic fibers and plastics, and to the limited recyclability of "traditional" composites and their end of life disposal options.

In addition to the most widely investigated and used natural fibers such as flax, jute, sisal and hemp, several researchers focused their attention in the last decade on the use of less common fibers, extracted from local plants, due to several beneficial aspects such as low cost, wide availability and quite good properties [1].

Indeed, the high demand for natural fibers requires discovering new lignocellulosic reinforcements with adequate properties for composite reinforcement.

Driven by this impulse, more than 40 papers were published on this topic just in the past two years. For instance, new natural fibers extracted from Chrysanthemum morifolium stem [2], Calotropis gigantea fruit bunch [3], Aristida adscensionis [4], Eleusine indica grass [5], Stipa obtusa and Jarava ichu leaves [6] and Strelitzia reginae plant [7] were recently investigated.

  doi:10.5075/epfl-298799_978-2-9701614-0-0

In such a context, we focused our attention on lemongrass plant (Cymbopogon genus) with the aim of comparing the leaf and the culm (i.e., stem) of this perennial grass as possible source of reinforcement for bio-composites.

Cymbopogon genus grows worldwide comprising more than 55 species. Among them, Cymbopogon flexuosus and Cymbopogon citratus are the most important ones with the latter widely cultivated to extract their essential oils used in perfumery as well as in food industry [8-9]. Other important applications of lemongrass plant are due to its antiseptic, antibacterial, antimicrobial, antifungal, and anti-inflammatory properties in pharmacology [10-11].

To the best of our knowledge, just a limited research was focused on the use of lemongrass as reinforcement of composites [12-13]. Furthermore, no investigation was addressed to compare lemongrass leaf and culm as potential source of natural reinforcement to date.

To fill this gap, a preliminary investigation was performed out allowing to evaluate which part of this plant (i.e., leaf or culm) is the best one to obtain natural reinforcement having promising features. In particular, the chemical composition of leaf and the culm lemongrass fibers was investigated through standard methods. The main properties of these fibers were assessed by means of thermogravimetric analysis (TGA), scanning electron microscope (SEM), Fourier transform-infrared spectroscopy (FT-IR) and helium pycnometer analysis. Fifty tensile tests were performed on both fibers and the two-parameter Weibull statistical model was applied to interpret statistically the experimental data.

Furthermore, a biodegradable starch-derived matrix (MaterBi®) was reinforced with lemongrass leaf and culm particles (i.e. < 500 μm). For both fillers, two bio-composites were manufactured at varying the particles weight content (i.e., 10% and 20 wt.%) through extrusion and compression molding and their rheological, morphological and mechanical properties were investigated.

2. Materials and Methods

2.1 Fibers

Lemongrass plants were collected in the area of Bangkok, Thailand. After collecting the raw plant, the culm was separated from the leaves. Both parts were first washed several times with tap water to remove dirt and other impurities and then dried at room temperature for 24 hours. Afterward, fibers were extracted from culms and leaves by mechanical separation.

Fifty tensile tests were carried out on both fibers by using a Universal Testing Machine (U.T.M.) model Z005 by Zwick-Roell, equipped with a load cell of 200 N, bonding each single fibers onto a paper frame before clamping to the screw grips of the U.T.M. According to ASTM D3822 standard, the strain rate and gauge length were set equal to 2.5 mm/min and 30 mm, respectively. Before tensile test, the diameter of each fiber was measured at three different random locations along its length thorough a Leica optical microscope model MS5 and the apparent cross-section area was measured by considering it as perfectly circular [14]. Furthermore, due to the large variability in the mechanical properties of natural fibers, a statistical approach (i.e., two-parameter Weibull distribution) was used to interpret the experimental data.

  doi:10.5075/epfl-298799_978-2-9701614-0-0

The cellulose and the hemicellulose contents of lemongrass fibers were evaluated through Kushner and Hoffer method [15] and NFT 12-008 standard, respectively. The lignin amount was measured using APPITA P11s-78. Ash content was determined according to ASTM E 1755-61.

The fibers chemical structure was also analyzed via Fourier-transform infrared spectroscopy (FTIR) using an infrared spectrometer model Spectrum II by PerkinElmer. The analysis was performed in transmission mode in a wavenumber range from 400 cm^{-1} to 4000 cm^{-1} with a scan rate equal to 4 cm^{-1}.

The thermogravimetric analysis (TGA) was performed by using a thermobalance TG/DTA model SDT Q600 by TA instruments. Fiber samples were placed in an alumina crucible heated from 30 °C to 1000 °C at a heating rate of 10 °C/min in an inert atmosphere.

The experimental density was evaluated by using a helium pycnometer by Thermo Electron Corporation model Pycnomatic ATC and an analytical balance model AX 224 by Sartorius. The morphological analysis of leaf and culm lemongrass fibers was performed through Scanning Electron Microscopy (SEM) investigation by using a FEI microscope model Quanta 200, operating at 10 kV. Before the observations, all samples were coated with a thin layer of gold and rubbed upon a 25 mm diameter aluminum disc.

2.2 Composites

The biodegradable polymer used as matrix for bio-composites is a sample of Mater-Bi® (Mater-Bi HF51L2 by Novamont SpA) with melt flow index (190 °C/2.16 kg), melting temperature and density equal to 4.5 g/10 min, 150°C and 1.21 g/cm^3, respectively. After drying at room temperature for 24 hours the fresh culms and leaves, they were ground by means of a grinding machine. After that, lemongrass particles were sieved to obtain a fraction with maximum size equal to 500 µm.

Before the composites preparation, both the Mater-Bi and lemongrass particles were dried under vacuum at 60 °C for 12 hours with the aim of protecting the polymeric matrix by hydrolytic scission phenomena during processing. For both lemongrass particles, two bio-composites (i.e., containing 10 and 20 wt.% of lemongrass) were manufactured via extrusion and compression molding. In particular, bio-composites particles were first prepared by using a modular co-rotating twin screw extruder (OMC Italy, D = 19, L/D = 35). For the sake of comparison, neat Mater-Bi matrix was processed under the same conditions. The thermal profile adopted was 120–130–140–150–160–170–170 °C while the rotational speed was set to 180 rpm. The molten material obtained from the extruder die was cooled on line in a water bath, pelletized and used for the further manufacturing step.

Afterwards, the so obtained pellets were dried under vacuum at 60°C for 12 hours before the preparation of the samples for the mechanical, rheological and morphological characterizations were prepared via compression moulding by using a Carver Laboratory press (T = 160 °C, P = 27 bar, time = 3 min).

The bio-composites will be identified in the next with the codes L10, L20, C10 and C20, were the letter (i.e., L or C) indicates the lemongrass part (i.e., leaves or culms) and the number (i.e., 10 or 20) the particle weight content.

Tensile tests were performed on composites according to ASTM D638 standard, with the same U.T.M. used for fiber characterization, equipped with a load cell of 5 kN. Five Dumbbell samples for each composite were tested by setting the crosshead speed equal to 5 mm/min for elongation percentage values up to 8% and then equal to 50 mm/min.

The morphological observation of the fractured surfaces of Dumbbell samples was carried out by using the same scanning electron microscope used for the fiber characterization.

3. Experimental results

3.1 Fibers

The typical stress-strain tensile curves of leaf and culm fibers, shown in Figure 1, evidence the brittle behavior of both fibers. By comparing these curves, it can be noticed that the mechanical properties of lemongrass fibers are function of the part of the plant from which they have been extracted. In particular, leaf fibers show higher strength and stiffness than culm fibers, even though the latter reach break at greater elongation percentages.

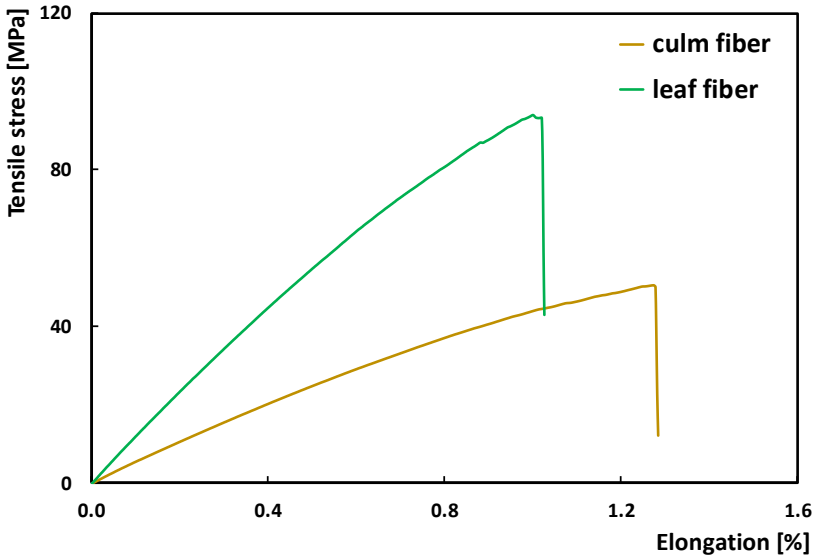

Figure 1. Tensile stress-strain curves of culm and leaf fibers

The statistical analysis of the mechanical results through Weibull model provided a reasonable approximation of the experimental data, furnishing the Weibull shape and scale parameters (i.e., the characteristic values of the distribution) for both properties (i.e., tensile strength and modulus). In particular, it was shown that the tensile strength and modulus of leaf fibers are about 55% and 76% higher in comparison to culm fibers, respectively. Vice versa, the elongation at break of culm fibers is just slightly higher than that of leaf fibers.

The chemical analysis of leaf and culm fibers showed that both fibers contain similar amounts of α-cellulose (i.e., 45.5% and 44.2% for leaf and culm fibers, respectively), hemicellulose (i.e., 29.1% and 28.1%) and lignin (i.e., 17.0% and 17.3%, respectively). These compositions cannot justify the noticeable mismatch between the mechanical properties of leaf and culm fibers. The only remarkable difference is the ash content, about 2% lower in leaf fibers, which explains at least partially the better mechanical properties of leaf fibers than culm ones.

  doi:10.5075/epfl-298799_978-2-9701614-0-0

The FTIR results shown in Figure 2 confirm that the compared fibers can be considered similar in terms of chemical composition.

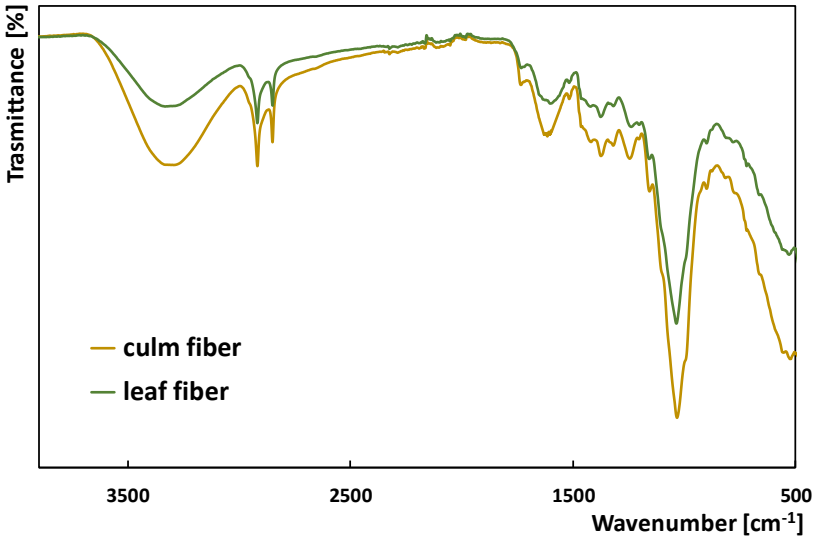

Figure 2. FTIR spectra of culm and leaf fibers

In particular, by comparing these spectra, it is possible to notice that only two peaks are noticeably different. The first one, at about 3325 cm^{-1}, is due to the O-H stretching vibration and hydrogen bond of the hydroxyl groups [16]. The second one, located at about 1600 cm^{-1}, is strictly correlated with the presence of water in the fibers [17]. Both peaks are greater for culm fibers, thus indicating that the latter contain a larger amount of water in comparison to leaf fibers.

Basically, the thermogravimetric analysis confirm this finding. Overall, both leaf and culm fibers experienced three different decomposition stages at around 100, 250 and 310°C, related to the water vaporization, hemicellulose degradation and α-cellulose decomposition, respectively. However, and more interestingly, it was shown that the weight loss found for culm and leaf fibers at 150 °C are respectively equal to about 12% and 8%, thus indicating that a greater amount of water is absorbed in culm fibers in comparison to leaf ones.

The experimental densities measured though helium pycnometer are equal to 1.02 g/cm^3 and 1.14 g/cm^3 for culm and leaf fibers, respectively. The higher density evidenced by leaf fibers meaning that the latter are characterized by a more compact structure in comparison to culm fibers, as clearly shown by observing the SEM micrographs in Figure 3.

  doi:10.5075/epfl-298799_978-2-9701614-0-0

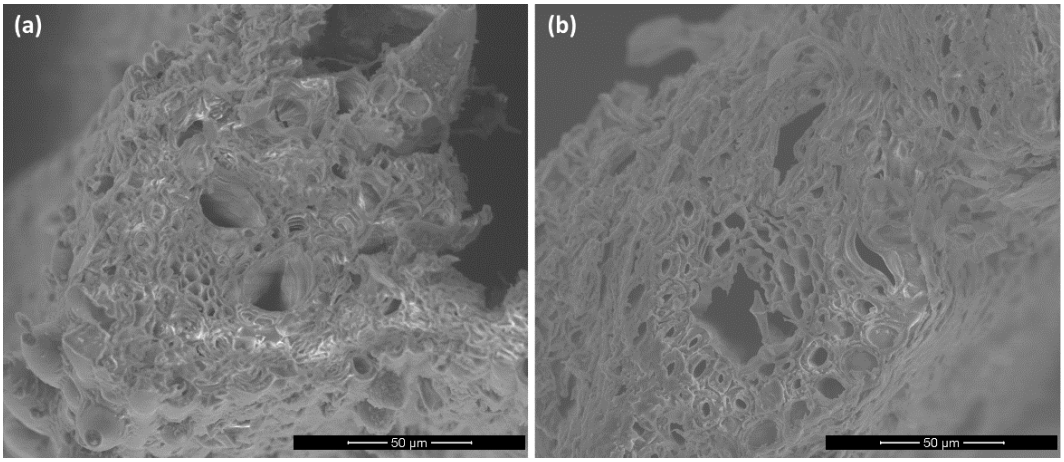

Figure 3. Cross section morphology of (a) leaf and (b) culm fibers

3.2 Composites

The tensile properties of neat matrix and bio-composites are reported in Table 1. All the composites show higher tensile moduli than Mater-Bi. In particular, the tensile modulus strongly increases on increasing the filler content. Furthermore, for both the compositions, the composites incorporating leaf particles exhibit higher stiffness than those containing culm particles. In particular, the L10 and L20 show tensile moduli about 81% and 186% higher than neat matrix, whereas the C10 and C20 show tensile moduli about 53% and 124% higher than Mater-Bi. It is worth noting that, the addition of relatively low content of lignocellulosic particles used in this study, led to remarkable increments of the tensile stiffness of the composites. Despite the positive effect on tensile modulus, the addiction of lemongrass particles led to a reduction in the tensile strength and elongation at break of all the composites compared to neat matrix. However, the reduction is less pronounced for composites incorporating the leaf particles. The decrease in the tensile strength of the bio-composites can be ascribed to the premature failure of the samples, which is expected when rigid particles are loaded in polymer matrices.

Table 1: Tensile properties of bio-composites.

	Strength [MPa]	Modulus [MPa]	Elongation at break [%]
Neat matrix	13.4 ± 0.5	62.5 ± 3.8	665.8 ± 79.8
L10	8.3 ± 0.4	113.3 ± 3.2	196.9 ± 45.4
L20	7.2 ± 0.1	178.9 ± 5.9	51.4 ± 14.9
C10	6.9 ± 0.3	95.7 ± 4.7	146.3 ± 44.8
C20	5.9 ± 0.1	140.0 ± 5.3	51.0 ± 15.5

The higher mechanical performances exhibited by bio-composites incorporating leaf particles can be probably attributed to the better morphology shown by these materials in comparison with the bio-composites incorporating the culm particles, as suggested by analysis of SEM

micrographs. In particular, the latter exhibited a worse adhesion between the matrix and the filler, as clearly visible in the micrographs reported in Figure 4.

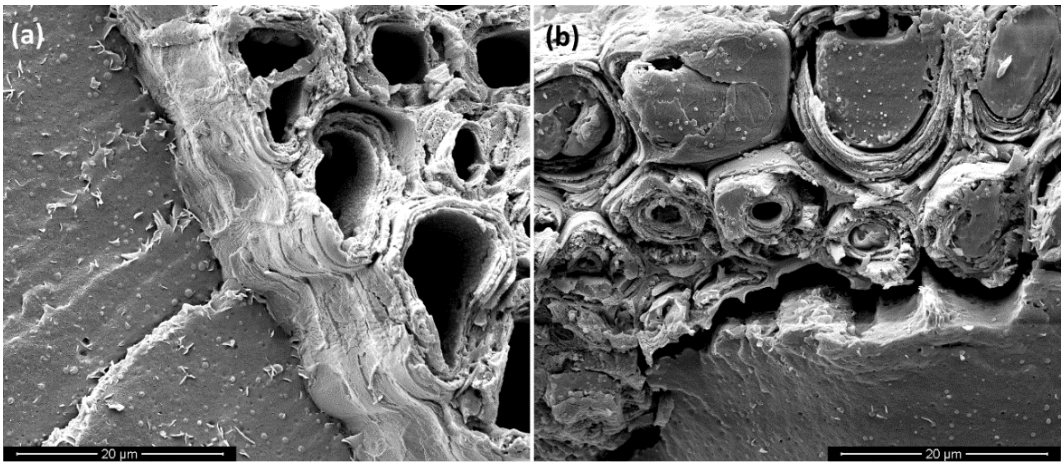

Figure 4. SEM micrographs of nitrogen-fractured surfaces of biocomposites (a) L10 and (b) C10.

Acknowledgements

This research was supported by the project "Progetti di ricerca sviluppati da gruppi di ricerca - Anno 2020", Department of Engineering, University of Palermo.

4. References

1. Sarasini F, Fiore V. A systematic literature review on less common natural fibres and their biocomposites. Journal of Cleaner Production 2018; 195:240-67.
2. Dalmis R, Kilic GB, Seki Y, Koktas S, Yasin Keskin O. Characterization of a novel natural cellulosic fiber extracted from the stem of Chrysanthemum Morifolium. Cellulose 2020; 27:8621-34.
3. Narayanasamy P, Balasundar P, Senthil S, Sanjay MR, Siengchin S, Khan A, Asiri MA. Characterization of a novel natural cellulosic fiber from Calotropis Gigantea fruit bunch for ecofriendly polymer composites. International Journal of Biological Macromolecules 2020; 150:793-801.
4. Manimaran P, Saravanan SP, Sanjay M, Jawaid S, Siengchin S, Fiore V. New Lignocellulosic Aristida Adscensionis Fibers as Novel Reinforcement for Composite Materials: Extraction, Characterization and Weibull Distribution Analysis. Journal of Polymers and the Environment 2020;28: 803-11.
5. Khan A, Vijay R, Lenin Singaravelu Lenin D, Sanjay MR, Siengchin S, Verpoort F, Alamry KA, Asiri MA. Extraction and characterization of natural fiber from Eleusine indica grass as reinforcement of sustainable fiber reinforced polymer composites. Journal of Natural Fibers 2021;18:1742-50.
6. Mori S, Charca S, Flores E, Savastano H. Physical and thermal properties of novel native Andean natural fibers. Journal of Natural Fibers 2021;18:475-91.
7. Lemita N, Deghboudj S, Rokbi M, Rekbi FML, Halimi R. Characterization and analysis of novel natural cellulosic fiber extracted from Strelitzia Reginae plant. Journal of Composite Materials 2022;56:99-114.

  doi:10.5075/epfl-298799_978-2-9701614-0-0

8. Haque ANMA, Remadevi R, Naebe M. Lemongrass (Cymbopogon): A review on its structure, properties, applications and recent developments. Cellulose 2018;25:5455-77.
9. Tran TH, Tran TKN, Ngo TCQ, Pham TN, Bach LG, Phan NQAP, Le THN. Color and composition of beauty products formulated with lemongrass essential oil: Cosmetics formulation with lemongrass essential oil. Open Chemistry 2021;19: 820-9.
10. Kamaruddin ZH, Jumauin R Selamat MZ, Ilyas RA. Characteristics and Properties of Lemongrass (Cymbopogan Citratus): A Comprehensive Review. Journal of Natural Fibers 2021 ; in press.
11. Mukarram M, Choudhary S, Khan MA, Poltronieri P, Masroor M, Khan A, Ali J, Kurjak D, Shahid M. Lemongrass Essential Oil Components with Antimicrobial and Anticancer Activities. Antioxidants 2022;11:20.
12. Jing H, He H, Liu H, Huang B, Zhang C. Study on properties of polylactic acid/lemongrass fiber biocomposites prepared by fused deposition modeling. Polymer Composites 2021;42: 973–86.
13. Soma Sundaram Pillai, Raja, Rajamoni R, Suyambulingam I, Goldy IRS, Divakaran D. Synthesis and characterization of cost-effective industrial discarded natural ceramic particulates from Cymbopogon Flexuosus plant shoot for potential polymer/metal matrix reinforcement. Polymer Bulletin 2021; in press.
14. De Rosa IM, Kenny JM, Puglia D, Santulli C, Sarasini F. Morphological, Thermal and Mechanical Characterization of Okra (Abelmoschus Esculentus) Fibres as Potential Reinforcement in Polymer Composites. Composites Science and Technology 2010;70:116-22.
15. Kushner R., Hoffer A. Cellulose and Cellulose Derivate. Fresenius' Journal of Analytical Chemistry 1993;92:145-54.
16. Seki Y, Sarikanat M, Sever K, Durmuşkahya C. Extraction and properties of Ferula Communis (Chakshir) fibers as novel reinforcement for composites materials. Composites Part B 2013;44:517-2.
17. Olsson AM, Salmén L. The association of water to cellulose and hemicellulose in paper examined by FTIR spectroscopy. Carbohydrate Research 2004;339:813-18.

A NOVEL METHOD TO QUANTIFY SELF-HEALING CAPABILITIES OF FIBRE REINFORCED POLYMERS

Cecilia, Scazzoli[a], Robin, Trigueira[a], Amaël, Cohades[a], Véronique, Michaud[b]

a: CompPair Technologies Ltd., cecilia@comppair.ch
b: École Polytechnique Fédérale de Lausanne, Laboratory for processing of advanced composites

Abstract: *Since the early 2000, self-healing fibre reinforced polymers (FRPs) have increasingly been addressed by researchers with the goal to develop more sustainable materials. However, a practical challenge remains for material / process screening: to propose relevant characterization methods allowing to quantitatively assess the healing efficiency of the matrix within composite parts and to provide comparative results. In the present study, a novel and practical characterization method is proposed: assessing the capacity to recover low-velocity impact damage via three-point bending flexural tests in samples with different fibre orientations. Laminates with fibre oriented at ± 45° showed no signs of fibre rupture after impact damage and hence proved to be the most relevant to prove efficient matrix self-healing capabilities. Such method demonstrated to be: i) representative of early-stage damage of composite FRPs, ii) a fast and reliable characterization technique requiring the use of a limited amount of material.*

Keywords: self-healing; circular economy; composites

1. Introduction

In recent years FRPs have been more and more frequently used for structural applications in aerospace, automotive, wind, marine and sport industries, thanks to their outstanding strength to weight ratio. High service temperatures that might be reached in such applications and exposure to important mechanical loads and solvents make epoxy resins one of the preferential choices as a matrix for their high glass transition temperature (Tg), stiffness and solvent resistance. However, unless toughened like for example in the aerospace field, they have a major drawback: brittleness. Furthermore, fibre reinforced composites naturally have a heterogeneous structure and hence are subjected to complex damage mechanisms: cracks occurring in the matrix, at the fibre/matrix interface, between plies, in the reinforcing fibres, or sometimes originating from processing defects such as porosities or dry zones. Most of the times, these cracks are not visible when looking with bare eyes at the part. Consequently, industry is forced to periodically inspect FRPs with expensive non-destructive techniques, like for example x-rays or ultrasound. When the detected damage event is too extensive, parts are very often trashed, generating large amounts of unrecycled waste. Alternatively, when damage is rather localised, but threatens the structural performances, costly, invasive and time-consuming techniques have been developed for on-site repair (1). According to Suschem (2), this modus operandi (classical repair techniques and simply discarding compromised parts) produces 40’000 tons of composite waste annually, either in the form of scraps or defective parts, just in Europe. By the end of 2015, 304’000 tonnes of composite waste were estimated to have been produced worldwide and most of them lay in land fields (2). Projections estimate that by 2025 683 thousands of tonnes of composite wastes will be generated (3).

  doi:10.5075/epfl-298799_978-2-9701614-0-0

An approach which would enable to save a lot of resources consists in addressing damage at an early stage, i.e. most likely in the form of microcracks and delamination, which, extending progressively, can induce catastrophic failure. Exactly with this purpose, taking inspiration from natural phenomena, like bones regeneration and blood clotting, more and more efforts have been devoted by researchers towards the development of self-healing composites (4). Extrinsic and intrinsic approaches exist. The first is based on isolated reservoirs of unreticulated polymers, stocked inside hollow fibres or capsules, which will break during damage events, fill the cracks and polymerize, while the second one exploits functionalities of the polymeric matrix itself. Many examples are reported in the scientific literature (5,6), but only few are found which reached a high technology readiness level (TRL). One of these are vitrimers, but the drawback is represented by the challenge of maintaining structural performances at the healing temperature (7–11). Another approach, currently commercially provided by CompPair Technologies Ltd., is HealTech™ , a prepreg enabling to build FRP parts in which repair can be triggered simply with the application of moderate heat, while retaining enough stiffness and strength to remain structural during healing (12).

No matter what the self-healing approach is, apart from the main challenge of maintaining a high volume fraction of the reinforcing fibres and adequate mechanical properties for the healable composite, another critical point is represented by the difficulty in finding a common healing efficiency testing method, shared among all the scientific community. The most frequently adopted test methods are either non-destructive analysis, like C-scans, or are based on mechanical tests like Mode I double cantilever beam (DCB), tapered double cantilever beam (TDCB), Mode II end-notched flexure (ENF) testing, compression after impact (CAI), bending after indentation, fatigue, tensile and bending testing (5,6,11,13–29,). The fundamental difference between these characterization methods makes the comparison of the various self-healing matrix systems difficult. Furthermore, such methods are often either not fully representative of real damage occurring throughout the lifetime of a composite part in an industrial environment, or cumbersome or require the use of large amounts of material.

The present work aims at presenting a rapid and efficient solution to overcome the described limitations, using HealTech™ composites to demonstrate the principle. The goal is to assess matrix healing only and thus to avoid breaking fibres which will not heal, so as to concentrate on the matrix healing efficiency within the composite. Composite samples were first damaged via low velocity impact, a relevant mechanism for the aerospace industry, but also for the sports and marine industries. The capacity to mend impact damage has then been evaluated via 3-point bending flexural tests, comparing the flexural modulus and ultimate flexural strength of pristine, impact damaged and healed samples. Healing efficiency was thus computed as the recovery in flexural modulus and ultimate flexural strength. This approach is similar to what has been reported by Kling et al. in (30), but in addition, the present work analyses the influence of fibre orientation on the healing efficiency. Overall, a simple and industrially relevant test that can be further used as a benchmark for many commercial applications is described in the following sections.

2. Materials and methods

2.1 Materials and samples preparation

  doi:10.5075/epfl-298799_978-2-9701614-0-0

FRP laminates were produced with HealTech™ T300-TW200-42RW-1250, a commercial self-healing resin pre-impregnated Torayca T300 3K twill 2x2 fabric, with aerial weight of 200g/m^2, provided by CompPair Technologies Ltd.. Two different types of layups were chosen: $[(0/90)]_{18}$ and $[(+45/-45)]_{18}$. Laminates were cured under vacuum in an oven at 140 °C for 3 hours and post-cured at 180 °C for 2 hours. The obtained fibre volume fractions for the cured laminates were 52.93 ± 0.33 % and 50.71 ± 0.36 % respectively for the $[(0/90)]_{18}$ and $[(+45/-45)]_{18}$ layups.

Table 1: Description of the different types of analyzed and tested samples.

Sample type	Layup	Description
V	$[(0/90)]_{18}$ and $[(+45/-45)]_{18}$	As produced, undamaged
D1	$[(0/90)]_{18}$	Once the laminates were cured, samples were cut and subjected to 30 impacts of 6,86 J, always in the centre of the sample
D2	$[(0/90)]_{18}$ and $[(+45/-45)]_{18}$	Once the laminates were cured, samples were cut and subjected to 30 impacts of 13,72 J, always in the centre of the sample
H1	$[(0/90)]_{18}$	Once the laminates were cured, samples were cut and subjected to 30 impacts of 6,86 J, always in the centre of the sample; samples were then healed in an oven for 30 min at 150 °C.
H2	$[(0/90)]_{18}$ and $[(+45/-45)]_{18}$	Once the laminates were cured, samples were cut and subjected to 30 impacts of 13,72 J, always in the centre of the sample; samples were then healed in an oven for 30 min at 150 °C.

The plates, 150 mm by 130 mm in size, were then cut into rectangular samples 13 x 100 mm^2, 4 mm thick. On one hand, for $[(0/90)]_{18}$ FRPs five types of samples with different treatments were prepared: (i) virgin (V), undamaged, (ii) damaged 1m (D1), (iii) damaged 2m (D2), (iv) healed 1m (H1) and (v) healed 2m (H2). On the other hand, for $[(+45/-45)]_{18}$ FRPs, three types of samples were prepared: (i) virgin (V), undamaged, (ii) damaged 2m (D2) and (iii) healed 2m (H2). Damaged samples are defined as samples which have been subjected to repetitive low velocity impacts with the aid of an impact machine built and customized for the presented test campaign. A wood panel was used as a support for the specimens, which were impacted 30 times, always in the same location, the center of the sample, via a free fall from 1 m (D1) or 2 m height (D2) of a steel impactor of 73 mm in diameter. An electromagnet enabled to release the impactor in a controlled way. The equivalent corresponding energy of each impact was respectively 6,86 J and 13,72 J. The impact set-up is illustrated in Figure 1. H1 and H2 samples were impacted as just described and subsequently placed in an oven at 150 °C for 30 minutes to repair the created delamination, before testing.

  doi:10.5075/epfl-298799_978-2-9701614-0-0

All tests variants are summarized in Table 1.

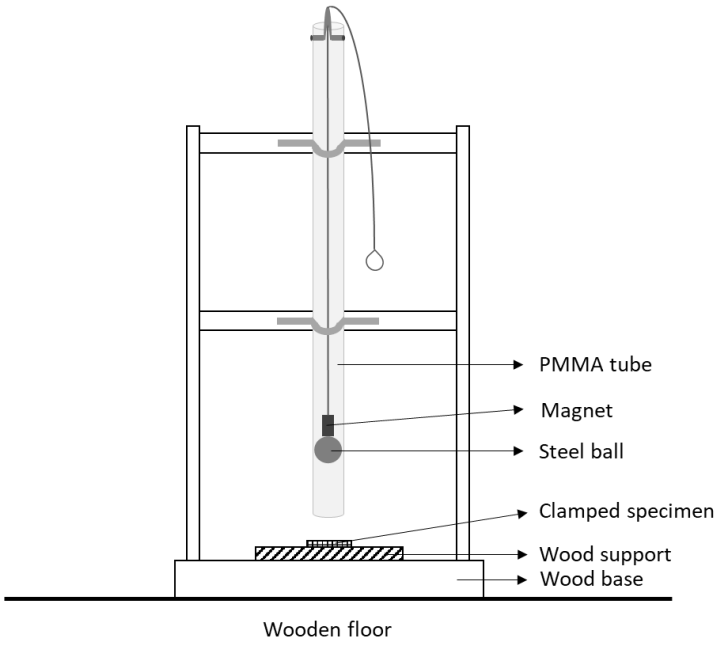

Figure 1: The impact setup used to damage the specimens.

2.1 Morphological characterization

The cross section of damaged samples prior to flexural tests was observed with a *Keyence VHX-5000* in reflexion digital microscopy so to assess (i) the type and extent of damage induced by the impact procedure in $[(0/90)]_{18}$ and $[(+45/-45)]_{18}$ samples.

2.1 Three-point bending flexural characterization

Three-point bending flexural tests were conducted on 100x13 mm^2 samples, following the standard ASTM D7264. At least three samples per each condition (virgin, damaged and healed) were tested. A 125 kN load cell for the $[(0/90)]_{18}$ samples and a 10 kN load cell for the $[(+45/-45)]_{18}$ samples were respectively installed on a universal tensile machine (UTM) Series LFM-125kN (*Walter & Bai*) with a span-to-thickness ratio of 16:1. The testing speed was set at 1 mm/min for the $[(0/90)]_{18}$ samples and 3 mm/min for the $[(+45/-45)]_{18}$ samples.

A healing efficiency, η, was computed based on the assessment of both the flexural modulus, E, in the different states

$$\eta = \frac{E_{healed} - E_{damaged}}{E_{virgin} - E_{damaged}} \quad (1)$$

and the maximum flexural strength, σ, in the different states

$$\eta = \frac{\sigma_{healed} - \sigma_{damaged}}{\sigma_{virgin} - \sigma_{damaged}} \quad (2)$$

3. Results & discussion

3.1 Flexural tests

Figure 2 (a) shows the results of flexural tests performed on V, D1 and H1 $[(0/90)]_{18}$ samples. It is evident that the damage imparted to samples by a 6.86 J impact is limited and especially in

terms of flexural modulus, which decreased by 12.9% after the impact. The recovery of flexural modulus and flexural strength attained over the healing process for this damage condition was relatively poor and the average healing efficiency computed according to Eq. (1) and (2) was respectively 37.9% and 33.8%, as some carbon fibres were already broken during the damage event, and the initial loss of property is limited.

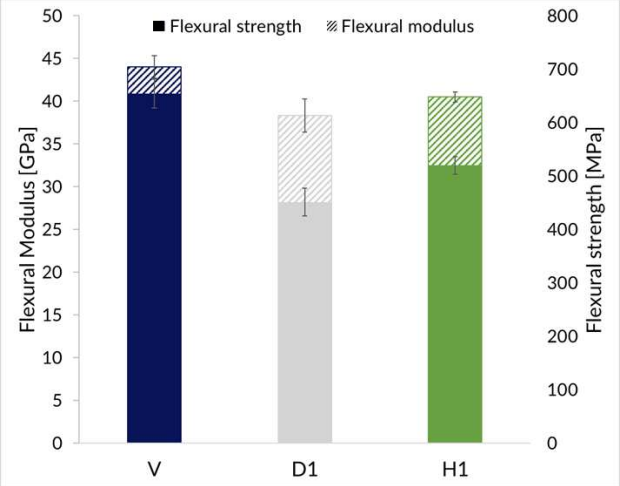

Figure 2: (a) the flexural modulus and the flexural strength for V, D1 and H1 $[(0/90)]_{18}$ specimens.

On the other hand, a 13.72 J impact entailed a 41.68% and a 49.98% decrease respectively in flexural modulus and flexural strength for $[(0/90)]_{18}$ samples and a 30.02% and a 24.66% decrease for the same properties in $[(+45/-45)]_{18}$ samples. Figure 3 presents a summary of the flexural modulus and flexural strength for V, D2 and H2 $[(0/90)]_{18}$ and $[(+45/-45)]_{18}$ specimens. The average healing efficiency computed according to Eq. (1) and (2) resulted to be respectively 72.1% with respect to the flexural modulus and 32.1% with respect to the flexural strength when fibres were oriented at 0/90° and 92.8% with respect to the flexural modulus and 90.1% with respect to the flexural strength when fibres were oriented at ± 45°.

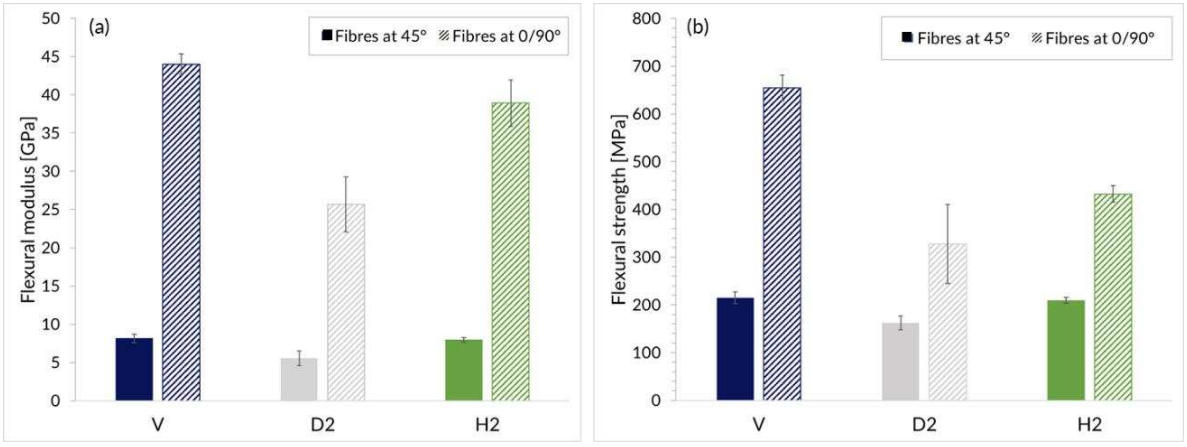

Figure 3: a summary of (a) the flexural modulus and (b) the flexural strength for V, D2 and H2 samples with fibres oriented at 45° or at 0/90°.

Figure 4 and Figure 5 show pictures of the side surface of the specimens undergoing 3-point bending flexural tests. In the case of $[(0/90)]_{18}$ FRPs it is clear that the failure mode for D2 and

H2 samples is similar and implies interlaminar fracture, while this is not the case for virgin samples, in which failure starts with fibre breakage at the plies which are solicited in compression and is followed by the rupture of fibres solicited in traction. Contrarily, in the case of $[(+45/-45)]_{18}$ FRPs, interlaminar fracture characterizing failure in D2 specimens cannot be observed in H2 and V specimens.

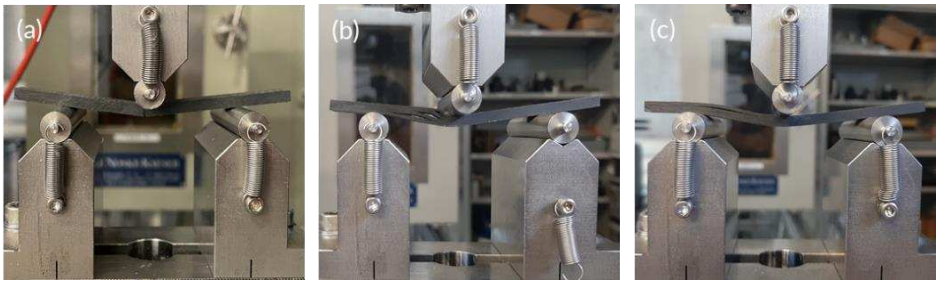

Figure 4: Pictures of the side surface of $[(0/90)]_{18}$ samples during the flexural tests depicting the typical failure of (a) V, (b) D2 and (c) H2 samples.

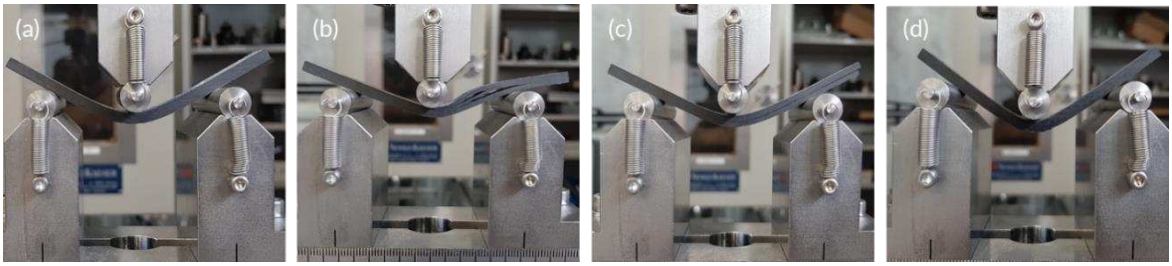

Figure 5: Pictures of the $[(+45/-45)]_{18}$ samples during the flexural tests depicting the typical failure mode of (a) V, (b) and (c) D2 and (d) H2 samples.

A summary of the healing efficiencies attained in the different test conditions is depicted in Figure 6.

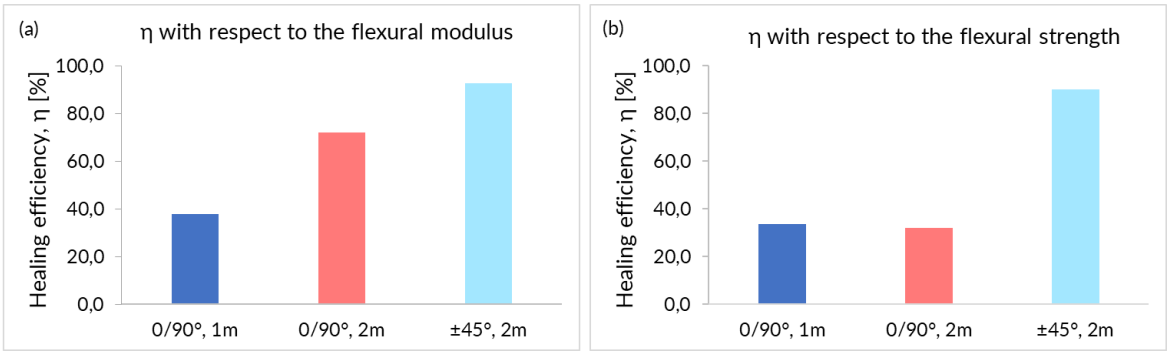

Figure 6: A summary of the healing efficiency obtained for the different impact energies (6.86 J and 13.72J) and fibres orientation (0/90° or ±45°) with respect to (a) the flexural modulus and (b) the flexural strength.

3.2 Morphological characterization

Optical microscopy observations reported in Figure 7 highlight that fibre breakage occurred in D2 samples with fibres oriented at 0/90°, while only delamination was observed when fibres were oriented at ±45°. This justifies why better healing performances could be reached in this latter condition, as HealTech™ enables matrix damage healing, but not fibre rupture recovery.

  doi:10.5075/epfl-298799_978-2-9701614-0-0

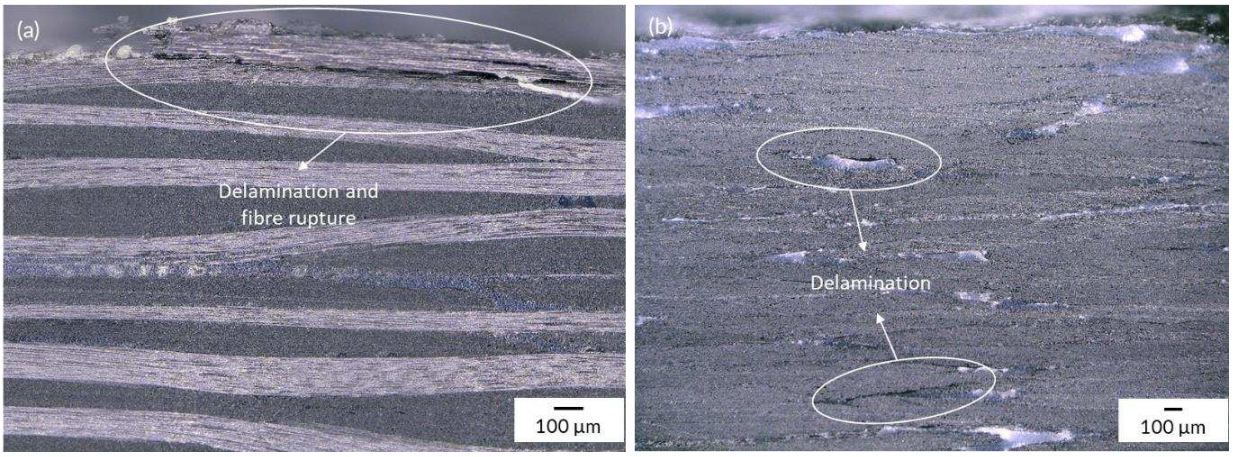

Figure 7: optical microscopy image of the cross section of (a) a D2 $[(0/90)]_{18}$ samples, clearly displaying some broken fibres and (b) D2 $[(+45/-45)]_{18}$ sample showing signs of delamination and cracks.

4. Conclusions

The performed tests proved that, probably also due to the samples' dimensions, FRPs with fibre oriented at ±45° guarantee a higher deformation capability to the fibres subjected to low velocity impact, hence generating matrix delamination, but not fibre rupture. Consequently, evaluating the capacity of $[(+45/-45)]_{18}$ FRPs to recover low velocity impact damage via three-point bending tests demonstrated to be a fast and efficient methodology to assess the matrix self-healing capabilities of a composite material. On the contrary, when fibres are oriented only at 0/90° they are more prone to break hence preventing a relevant evaluation of the matrix self-healing potential.

5. References

1. Katnam KB, Da Silva LFM, Young TM. Bonded repair of composite aircraft structures: A review of scientific challenges and opportunities. Prog Aerosp Sci. 2013;61:26–42.
2. Suschem. Polymer Composites Circularity. 2018;21.
3. Assocompositi, Anev, Futura E. Verso una gestione sostenibile e circolare per il fine vita delle pale eoliche. 2021.
4. Urdl K, Kandelbauer A, Kern W, Müller U, Thebault M, Zikulnig-Rusch E. Self-healing of densely crosslinked thermoset polymers—a critical review. Prog Org Coatings. 2017;104:232–49.
5. Cohades A, Branfoot C, Rae S, Bond I, Michaud V. Progress in Self-Healing Fiber-Reinforced Polymer Composites. Adv Mater Interfaces. 2018 Sep 1;5(17):1800177.
6. Kanu NJ, Gupta E, Vates UK, Singh GK. Self-healing composites: A state-of-the-art review. Compos Part A Appl Sci Manuf. 2019;121(April):474–86.
7. Denissen W, De Baere I, Van Paepegem W, Leibler L, Winne J, Du Prez FE. Vinylogous Urea Vitrimers and Their Application in Fiber Reinforced Composites. Macromolecules. 2018;51(5):2054–64.
8. Han J, Liu T, Hao C, Zhang S, Guo B, Zhang J. A Catalyst-Free Epoxy Vitrimer System Based on Multifunctional Hyperbranched Polymer. Macromolecules. 2018;51(17):6789–99.
9. Zheng P, McCarthy TJ. A surprise from 1954: Siloxane equilibration is a simple, robust, and obvious polymer self-healing mechanism. J Am Chem Soc. 2012;134(4):2024–7.

  doi:10.5075/epfl-298799_978-2-9701614-0-0

10. Ruiz De Luzuriaga A, Martin R, Markaide N, Rekondo A, Cabañero G, Rodríguez J, et al. Epoxy resin with exchangeable disulfide crosslinks to obtain reprocessable, repairable and recyclable fiber-reinforced thermoset composites. Mater Horizons. 2016;3(3):241–7.
11. Kamble M, Picu C, Koratkar N. Vitrimer composites for rotorcraft components. 77th Annu Vert Flight Soc Forum Technol Display, FORUM 2021 Futur Vert Flight. 2021;1–5.
12. Cohades A, Trigueira R. Healable composites to improve circularity. JEC Compos Mag. 2020;(N°136 September-October):41–3.
13. Michaud Véronique, Cohades Amael HN. Healable composites and their performance through mechanical and durability testing. 2019;
14. Cohades A, Michaud V. Thermal mending in E-glass reinforced poly(ε-caprolactone)/epoxy blends. Compos Part A Appl Sci Manuf. 2017;99:129–38.
15. Manfredi E, Cohades A, Richard I, Michaud V. Assessment of solvent capsule-based healing for woven E-glass fibre-reinforced polymers. Smart Mater Struct. 2015 Jan 1;24(1):015019.
16. Cohades A, Michaud V. Damage recovery after impact in E-glass reinforced poly(ε-caprolactone)/epoxy blends. Compos Struct. 2017;180:439–47.
17. Kamble M, Vashisth A, Yang H, Pranompont S, Picu CR, Wang D, et al. Reversing fatigue in carbon-fiber reinforced vitrimer composites. Carbon N Y. 2022;187:108–14.
18. Sordo F, Michaud V. Processing and damage recovery of intrinsic self-healing glass fiber reinforced composites. Smart Mater Struct. 2016 Aug 1;25(8):084012.
19. Williams GJ, Bond IP, Trask RS. Compression after impact assessment of self-healing CFRP. Compos Part A Appl Sci Manuf. 2009 Sep 1;40(9):1399–406.
20. Patrick JF, Hart KR, Krull BP, Diesendruck CE, Moore JS, White SR, et al. Continuous Self-Healing Life Cycle in Vascularized Structural Composites. Adv Mater. 2014 Jul 1;26(25):4302–8.
21. Jony B, Mulani SB, Roy S. Interlaminar shear fracture healing of thermoset CFRP composite using multiphase thermoplastic healing agents. Compos Struct. 2022;279(August 2021):114807.
22. Beylergil B. Interlaminar fracture and crack-healing capability of carbon fiber/epoxy composites toughened with 3D-printed poly-ε-caprolactone grid structures. J Appl Polym Sci. 2021;
23. Luterbacher R, Trask RS, Bond IP. Static and fatigue tensile properties of cross-ply laminates containing vascules for self-healing applications. Smart Mater Struct. 2015;25(1):15003.
24. Tesoro GC, Sastri V. Reversible crosslinking in epoxy resins. I. Feasibility studies. J Appl Polym Sci. 1990 Apr 5;39(7):1425–37.
25. Park JS, Kim HS, Thomas Hahn H. Healing behavior of a matrix crack on a carbon fiber/mendomer composite. Compos Sci Technol. 2009 Jun 1; 69(7–8):1082–7.
26. Meure S, Wu DY, Furman S. Polyethylene-co-methacrylic acid healing agents for mendable epoxy resins. Acta Mater. 2009 Aug 1;57(14):4312–20.
27. Zhang P, Li G. Advances in healing-on-demand polymers and polymer composites. Prog Polym Sci. 2016;57:32–63.
28. Hia IL, Vahedi V, Pasbakhsh P. Self-Healing Polymer Composites: Prospects, Challenges, and Applications. Polym Rev. 2016;56(2):225–61.
29. Lucas SS, Von Tapavicza M, Schmidt AM, Bertling J, Nellesen A. Study of quantification methods in self-healing ceramics, polymers and concrete: A route towards standardization. J Intell Mater Syst Struct. 2016;27(19):2577–98.
30. Kling S, Czigány T. Damage detection and self-repair in hollow glass fiber fabric-reinforced epoxy composites via fiber filling. Compos Sci Technol. 2014;99:82–8.

  doi:10.5075/epfl-298799_978-2-9701614-0-0

ENABLING REPAIRABILITY AND REUSE OF EPOXY COMPOSITES: EPOXY VITRIMERS

Barbara Palmieri, Eugenio Amendola, Alfonso Martone, Michele Giordano*

Institute for Polymers, Composites and Biomaterials, P.le Enrico Fermi, 1, 80055 Portici (NA)
*presenting author email: eugenio.amendola@cnr.it

Abstract: *Epoxy Vitrimers are gathering attention as a development in the field of more easily re-processable and self-healing thermosets. The incorporation of a catalyst should activate the transesterification reaction within the polymeric macromolecule inducing topological modification of the network. By reacting epoxy precursors with suitable anhydrides and acids will promote exchange reactions between esters and beta-hydroxyls adding the vitrimeric behaviour. In the present work, a commercial epoxy system suitable for CFRP manufacturing has been modified to induce vitrimeric behaviour by exploiting the catalytic activity towards the transesterification reaction of Zn^{2+}. Creep experiments confirm that the resin starts to flow above a critical "Vitrimeric" temperature (T_v).*

Keywords: Vitrimers; Epoxy resin; Thermoset recycling; Self-healing; Covalent Adaptable Networks

1. Introduction

Unlike thermoplastic polymers, thermosetting resins and their composite materials are very difficult to recycle. The presence of a stable cross-linked structure prevents any long-range molecular mobility necessary to activate the flow of material at temperatures high enough to carry out reforming and recycling. As a result, thermosetting composites are hardly recycled, and most of the components are sent to landfills at the end of their service life.

Increasing environmental awareness and industrial competitiveness encourage introducing and developing repairable and recyclable structural materials to reduce polymer waste and extend their service life. Recently, the development of thermoreversible crosslinked networks has been introduced as a viable alternative to produce composite components that can be recycled and reformed as thermoplastic materials [1]. Introducing a thermoreversible covalent bond in the crosslinked backbone allows the topological reshuffling of polymeric networks and makes it possible to rework and reform the crosslinked material.

A well-established approach for designing and synthesising covalent adaptable networks (CAN) is the dissociative Diels–Alder reaction between furans and maleimides [2]. As a further development in more easily re-processable and self-healing thermosets, vitrimers are gathering attention for outdoing current drawbacks of CANs. One of the possible mechanisms enabling the vitrimeric behaviour in epoxy resins is based on transesterification exchange reactions between esters and beta-hydroxyls formed by reacting epoxy precursors with suitable acids/anhydrides [3,4]. Incorporating a catalyst activates the transesterification reaction and induces topological variations, stress relaxation and flow in the crosslinked networks, even though the total number of crosslinks does not change [5,6].

However, there have been difficulties in realising such behaviour in rigid thermosets until 2011, when Leibler et al. [7] introduced a new group of materials named vitrimers. They applied the

  doi:10.5075/epfl-298799_978-2-9701614-0-0

well-established transesterification reaction to the hydroxyl and ester groups present in an anhydride-cured epoxy matrix to create a reworkable thermosetting network [7]. During transesterification, the network's connectivity is altered via exchange reactions, inducing stress relaxation and plastic flow at elevated temperatures without depolymerisation. In the presence of a transesterification catalyst, it was shown that both elastomeric epoxy/acid and rigid epoxy/anhydride networks possess gradually decreasing viscosity with increasing temperature, as is characteristic of other vitreous materials such as inorganic glass. Shi et al. investigated the capability of such systems to weld and to be reprocessed [8]. Demongeot et al. investigated the mechanism of action of the catalytic zinc species active in these materials[9]. Capelot et al. [3] investigated the use of organic catalyst, as alternative to zinc salts, for elastomeric epoxy/acid systems.

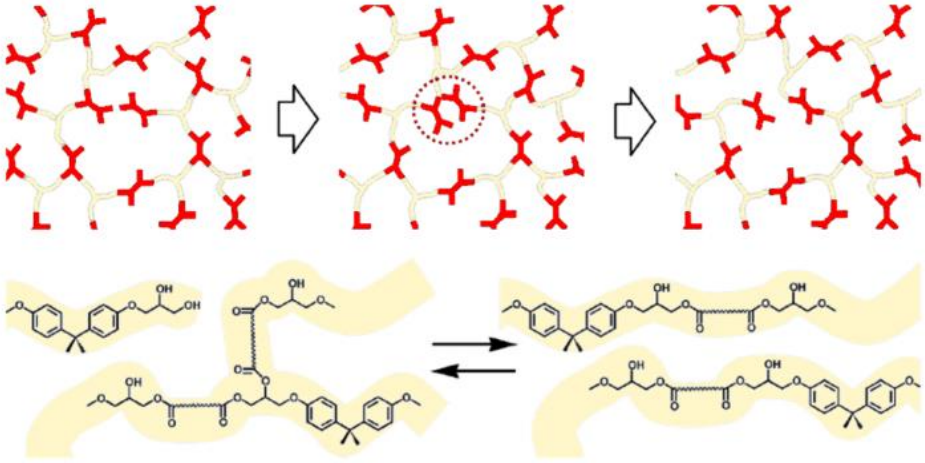

Figure 1. Exchange reaction scheme and related topological changes. Adapted from [9,10]

In the present work, a commercial epoxy system (ARALDITE® LY 3508 and ARADUR® 917-1 by Huntsman Corporation) suitable for CFRP manufacturing was selected for its modification as vitrimer. The zinc acetate was selected as a transesterification catalyst. Two formulations at different stoichiometric ratio between epoxy precursor and curing agent have been prepared and modified by adding Zinc acetate into anhydride. Creep experiments showed a flow above a critical temperature (about 170°C) that confirms the achievement of a vitrimeric behaviour.

2. Materials and Methods

2.1 Chemicals and Reagents

Bisphenol A diglycidyl ether (DGEBA) epoxy resin with an Epoxy Equivalent Weight (EEW) of 196.5 g/eq, tetrahydro-methyl phthalic anhydride (THMPA) curing agent and 2,4,6-tris(dimethyl aminomethyl)phenol as catalyst were kindly provided by Huntsman corporation with product names ARALDITE® LY 3508, ARADUR® 917-1 and Accelerator 960-1 respectively. Anhydrous zinc acetate ($ZnAc_2$) (99.99%) was purchased by Merck Sigma-Aldrich. All reagents were used without further purification.

  doi:10.5075/epfl-298799_978-2-9701614-0-0

2.2 Sample preparation

Epoxy resin formulation. Epoxy resin ARALDITE® LY 3508 and crosslinking anhydride ARADUR® 917-1 were mixed at room temperature with a mechanical mixer in a glass beaker until a homogeneous mixture was achieved. Subsequently, the Accelerator 960-1 was added and further mechanically mixed. The total weight of the prepared mixture was in the range of 75g.
Two different formulations were realised, varying the epoxy to acyl ratio between 0.6 (M2) to 1.0 (M2A).
Vitrimeric epoxy resin formulation. Zinc acetate is added to the epoxy resin formulations to promote the ester interchange reaction and to induce the vitrimeric behaviour of crosslinked resin. First, an adduct is synthesised between tetrahydro-methyl phthalic anhydride (THMPA) and zinc acetate. The required amount of Aradur 917-1 (20.00 g, 0.120 mol) and zinc acetate (3.22 g, 0.018 mol) are reacted in a round bottom flask at 120°C for 2 hours under nitrogen flow. The THMPA/zinc acetate adduct is cooled to room temperature and used without further purification. The epoxy vitrimeric mixture is prepared according to the above mentioned procedure while substituting ARADUR® 917-1 with the THMPA/zinc acetate adduct.
After mixing, samples were degassed under vacuum and cured for 1h @ 120°C and 2h at 140°C. The completion of the crosslinking reaction was monitored by calorimetric analysis.
Table 1 summarises the crosslinked sample condition realised.

Table 1. Crosslinked sample composition

Sample Codex	LY 3508 [phr]	Aradur 917-1 [phr]	960-1 acc. [phr]	r epoxy/acyl ratio	$ZnAc_2$ * [%]
*M2 **	*100*	*70*	*3*	0.6	-
M2A	100	40	3	1.0	-
M2-V	100	70	3	0.6	7.3
M2A-V	100	40	3	1.0	7.3

* $ZnAc_2$ percentage is calculated with respect to the total acyl groups.
** Commercial Huntsman formulation

2.3 Experimental methods

Differential Scanning Calorimetry (DSC). DSC was performed with a Discovery DSC of TA Instruments under a nitrogen atmosphere with a heating and cooling rate of 10 °C min^{-1}, from room temperature to 250°C. About 10 mg samples were encapsulated in aluminium pans before measurements.

Dynamic Mechanical Analysis (DMA). DMA experiments were conducted with a Dynamic Mechanical Analyzer Q800 from TA Instruments in the single cantilever mode. Samples were measured from 30 to 160 °C at 3 °C/min, a strain amplitude of 15 µm, and a frequency of 1 Hz. The samples were cut into a rectangular shape of 25 mm × 5.5 mm and thickness of ca. 2.5 mm.

Creep behaviour measurement. Creep tests were performed using a Dynamic Mechanical Analyzer Q800 from TA Instruments. The Tension Film clamp with preload of 0.1 N was applied. The specimen dimensions were c.a. 10x5.5x2 mm^3. Five minutes of isothermal hold was used before each creep segment, starting from 70°C up to 220°C with 50°C incremental steps to

evaluate sample strain variation from the glassy to the rubbery state. The stress of 0.1 MPa was applied for 45 minutes.

3. Results and Discussion

The preparation of crosslinked systems with semi-flexible molecular structure facilitates topological interchange reactions, however it reduces the glass transition temperature and elastic modulus. Therefore, a balance must be sought between the reactivity of interchange linkages and thermomechanical properties. It is well known that bifunctional epoxy precursors can be crosslinked with monocarboxylic anhydrides using either an excess or a defect of the curing agent. In both cases, a crosslinked network results. Usually, the reaction is promoted by the presence of substituted amines as the catalyst. If a stoichiometric ratio between epoxy and acyl groups is used, the crosslinked density is lower, but the presence of hydroxyl and ester groups highly facilitates the ester interchange reaction [11]. The transesterification reaction can be activated by the presence of Zn^{2+} ions at an elevated temperature beyond T_v, leading to a topological rearrangement.

In this study, the influence of the THMPA/$ZnAc_2$ molecular ratio on the mechanical properties of the epoxy formulations will be discussed. In addition, the occurrence of molecular long-range rearrangements has been verified by temperature-dependent creep experiments.

Starting from the producer directions, epoxy mixture M2 described in Table 1 has been formulated as reference material. The epoxy is used with a stoichiometric defect, with a mole ratio epoxy/acyl equal to 0.6. The acyl groups in stoichiometric excess can further react with –OH groups formed due to oxirane ring addition to carboxylic acid.

The curing behaviour and glass transition temperature of the M2 system are illustrated in Figure 2a. The absence of an exothermic peak in the second heating ramp of DSC is a clear indication of a complete conversion. The observed Tg is about 120°C. The epoxy mixture M2A has subsequently been prepared with a stoichiometric ratio between epoxy and acyls equal to unity. The cure of M2A system is illustrated in Figure 2b (DSC Thermogram). As expected, the Tg drops to 99°C due to a lower crosslinking density.

Both the system have been modified by introducing zinc acetate as a suitable catalyst for ester interchange reactions. The amount of zinc acetate has been fixed at 7.3% of the acyl groups, according to Demongeot et al. [9], the obtained systems have been named M2_V and M2A_V, respectively.

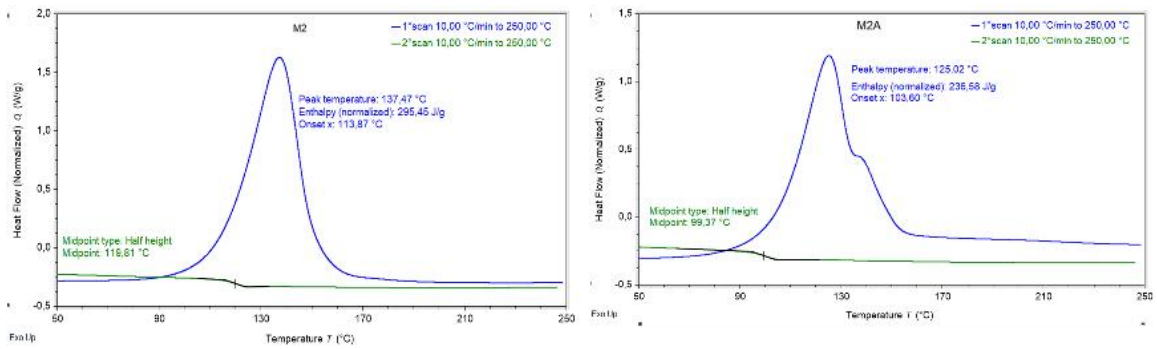

a) b)

Figure 2. DSC curves of the samples at different epoxy/acyl ratio. Reference resin a); stoichiometric ratio (epoxy/acyl 1.0, M2A) b).

  doi:10.5075/epfl-298799_978-2-9701614-0-0

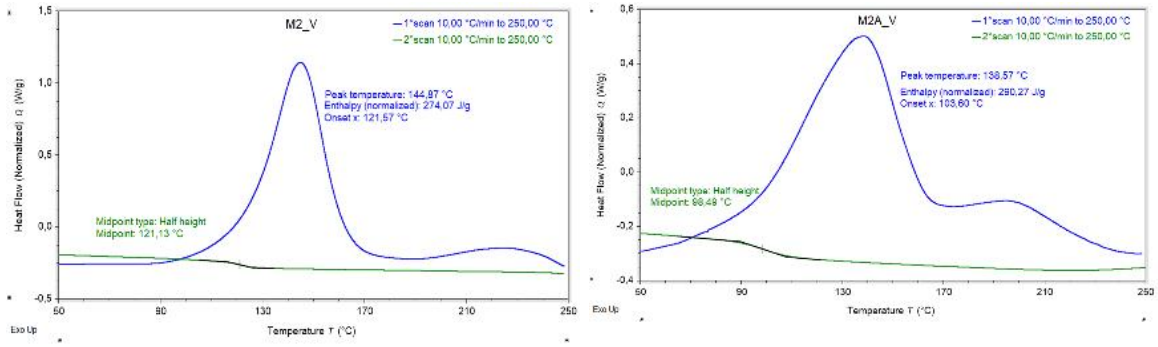

a) b)

Figure 3. DSC curves of the samples at different epoxy/acyl ratio. Modified formulation, "Vitrimers" M2_V a) and M2A_V b).

The zinc acetate influences the primary crosslinking reaction and activates a secondary reaction in the temperature range between 180 and 230°C, while the Tg of the crosslinked sample appears to be dominated by the ratio between epoxy and acyl groups (Figure 3 a/b).
DMA experiments have been performed in the linear viscoelastic deformation range to confirm the glass transition temperatures and elastic modulus of crosslinked samples.
The effects of catalyst addition and the different stoichiometric ratio between epoxy and acyls are shown in Figure 4 and highlight three main phenomena:

a) The glass transition temperatures obtained by DMA confirm the corresponding values measured by DSC;
b) The addition of Zn2+ catalyst produces an increase in the glassy elastic modulus;
c) The tanδ (ratio between loss and storage moduli) of vitrimeric systems (M2-V and M2A-V) @ 160°C is higher than corresponding conventional formulations (M2 and M2A, respectively). Indeed, this experimental observation could be related to a residual viscous flow, confirmed by following creep experiments.

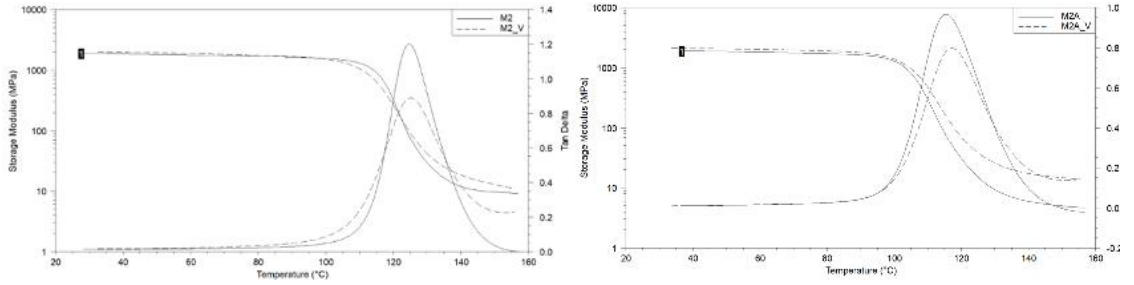

a) b)

Figure 4. DMA curves at different epoxy/acyl ratio M2 and its vitrimer a); M2A and its vitrimer b).

In addition to the DMA experiment, the clear and robust confirmation of vitrimeric behaviour due to thermoreversible cross-linking rearrangements has been obtained by creep experiments. Samples in the form of thin slabs have been subjected to creep experiments under tension deformation. The creep experiments have been performed in the temperature range between 70 and 220°C.

  doi:10.5075/epfl-298799_978-2-9701614-0-0

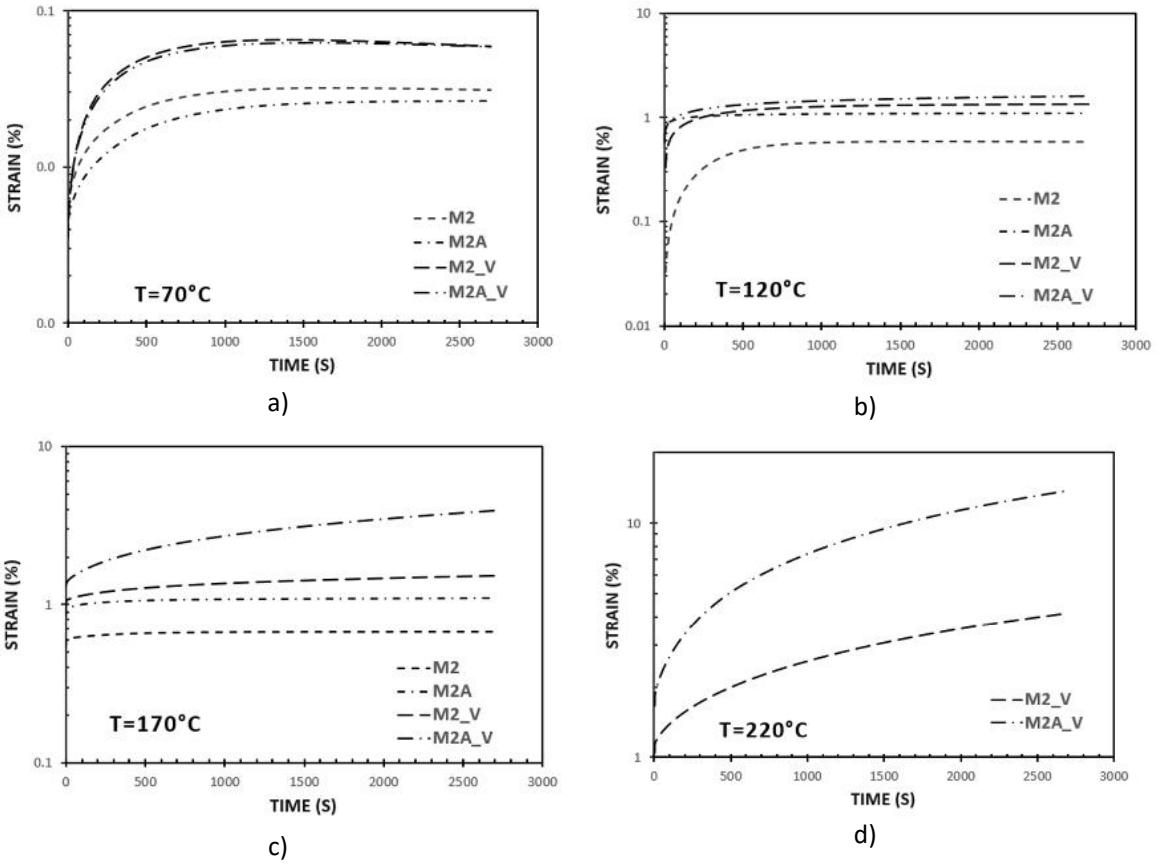

Figure 5. Creep curves at different temperatures.

Specimen M2 and M2A showed a stable behaviour, in fact, creep is negligible at each temperature. Even at temperatures higher than Tg no molecular flow has been observed.
Things change when the zinc acetate is added to the formulation. The presence of metallic ions strongly catalyses the ester interchange reaction, resulting in evident creep of samples subjected to tensile load at different temperatures, as reported in Figure 5. The effects are higher in the case of the M2A-V sample with an equivalent amount of epoxy and acyls (r=1.0).

4. Conclusions

The epoxy groups can efficiently react with carboxylic acids or anhydrides. Therefore, bi/multifunctional epoxy precursors can be efficiently crosslinked with carboxylic anhydrides, resulting in very stable materials with a glass transition temperature in the range of 100-140°C and an elastic modulus in the range of 1.5-2.0 GPa.

In this work, two different formulations with the adjustable stoichiometric ratio between epoxy precursor and curing agent have been prepared. In order to promote the polymer modification into vitrimer the catalyst Zn^{2+} has been introduced into the formulation by synthesising an adduct between $ZnAc_2$ and the THMPA curing agent, with a catalyst concentration of 7.3 % than to acyl groups.

  doi:10.5075/epfl-298799_978-2-9701614-0-0

The starting resin formulation and the modified vitrimers have been characterised by DSC, DMA and CREEP experiments. The Table 2 summarise the thermomechanical properties of the analysed systems.

Table 2. Thermo-mechanical properties

Description	Tg (DSC) [°C]	Reaction Enthalpy [J/g]	Elastic Modulus [GPa]
M2	119.8	295.5	1.88
M2A	99.4	236.6	1.89
M2-V	121.1	274.1	2.25
M2A-V	98.5	290.3	2.11

The presence of metallic ions strongly catalyses the ester interchange reaction, resulting in evident creep of samples subjected to tensile load at different temperatures. Arising from specific features of vitrimers, fascinating properties such as self-healing, recyclability, and weldability may extend the application fields for thermosets to improve their lifespan and sustainability.

Acknowledgements

This work has been supported by the Research Project LAMPO (code CDS00750), founded by Ministry of Economic Development. The authors would like to thank M. De Angioletti, F. Docimo, M. R. Marcedula and C. Leone for their support to experiments

5. References

1. Obadia MM, Mudraboyina BP, Serghei A, Montarnal D, Drockenmuller E. Reprocessing and Recycling of Highly Cross-Linked Ion-Conducting Networks through Transalkylation Exchanges of C-N Bonds. J Am Chem Soc 2015;137:6078–83. https://doi.org/10.1021/JACS.5B02653.

2. Dello Iacono S, Martone A, Pastore A, Filippone G, Acierno D, Zarrelli M, et al. Thermally activated multiple self-healing diels-alder epoxy system. Polym Eng Sci 2017;57:674–9. https://doi.org/10.1002/pen.24570.

3. Capelot M, Unterlass MM, Tournilhac F, Leibler L. Catalytic control of the vitrimer glass transition. ACS Macro Lett 2012;1:789–92. https://doi.org/10.1021/mz300239f.

4. Wang S, Ma S, Li Q, Xu X, Wang B, Yuan W, et al. Facile: In situ preparation of high-performance epoxy vitrimer from renewable resources and its application in nondestructive recyclable carbon fiber composite. vol. 21. 2019. https://doi.org/10.1039/c8gc03477j.

5. Denissen W, Winne JM, Du Prez FE. Vitrimers: Permanent organic networks with glass-like fluidity. Chem Sci 2016;7:30–8. https://doi.org/10.1039/C5SC02223A.

6. Capelot M, Montarnal D, Tournilhac F, Leibler L. Metal-catalyzed transesterification for

healing and assembling of thermosets. J Am Chem Soc 2012;134:7664–7. https://doi.org/10.1021/ja302894k.

7. Montarnal D, Capelot M, Tournilhac F, Leibler L. Silica-like malleable materials from permanent organic networks. Science (80-) 2011;334:965–8. https://doi.org/10.1126/science.1212648.

8. Shi Q, Yu K, Dunn ML, Wang T, Qi HJ. Solvent Assisted Pressure-Free Surface Welding and Reprocessing of Malleable Epoxy Polymers. Macromolecules 2016;49:5527–37. https://doi.org/10.1021/ACS.MACROMOL.6B00858.

9. Demongeot A, Mougnier SJ, Okada S, Soulié-Ziakovic C, Tournilhac F. Coordination and catalysis of Zn2+ in epoxy-based vitrimers. Polym Chem 2016;7:4486–93. https://doi.org/10.1039/C6PY00752J.

10. Capelot M, Montarnal D, Tournilhac F, Leibler L. Metal-catalyzed transesterification for healing and assembling of thermosets. J Am Chem Soc 2012;134:7664–7. https://doi.org/10.1021/JA302894K/SUPPL_FILE/JA302894K_SI_001.PDF.

11. Yang Y, Peng G, Wu S, Hao W. A repairable anhydride-epoxy system with high mechanical properties inspired by vitrimers. Polymer (Guildf) 2018;159:162–8. https://doi.org/10.1016/j.polymer.2018.11.031.

LOW VELOCITY IMPACT RESPONSE AND POST IMPACT ASSESSMENT OF HEALABLE CFRPS MODIFIED WITH DIELS-ALDER RESIN APPLIED BY MELT ELECTRO-WRITING PROCESS

*Anna Geitona[a], Athanasios Kotrotsos[a], Gregory Tzavaras[a], Gregory Petropoulos[a], Filippos Tourlomousis[b], and Vassilis Kostopoulos[a,c,]**

a: Department of Mechanical Engineering and Aeronautics, University of Patras, Patras University Campus, GR-26504 Patras, Greece.
b: Biological Lattice Industries, National Center for Scientific Research 'Demokritos', GR- 15341 Athens, Greece.
c: Foundation of Research and Technology, Institute of Chemical Engineering Sciences (FORTH/ICE-HT), Stadiou Str., GR-26504 Patras, Greece.
*: Corresponding author: kostopoulos@mech.upatras.gr; Tel.: +30-2610-969441

Abstract: *The present work reports a novel approach in terms of the incorporation of the self-healing agent (SHA) into quasi-isotropic carbon fiber reinforced plastics (CFRPs). More precisely, Bismaleimide-Diels-alder (BMI-DA) type resin, containing or not graphene nanoplatelets (GNPs), was integrated locally in high performance CFRPs by melt electro-writing process (MEP) technique. After manufacturing, both reference and modified CFRP plates were subjected to low velocity impact (LVI) and compression after impact tests (CAI). Compression tests were also performed prior LVI, to identify potential degradation effects and after the activation of the healing process to determine potential improvement of the residual compressive properties. C-scan inspections prior and after LVI revealed macroscopically 100% restoration of the damage area after healing process for the modified CFRPs while the residual compressive properties where slightly improved.*

Keywords: Self-healing, Bis-maleimides, impact, compression test

1. Introduction

Composite materials and especially laminated CFRPs present multiple advantages over traditional materials but during the service life are prone to impact events. Potential impact phenomena, even of low energy, usually results in micro-crack and delamination formation, thus leading to a premature failure of composite parts or of the entire composite structures. Repairing of composite materials through conventional methods is a rather time consuming, costly and cannot be easily applied everywhere. Based on literature, various strategies have been adopted with an aim to improve composites' mechanical properties to extend the service life. The use of nano-fillers has proven to be beneficial [1,2]. Among them, high surface area carbon nano-fillers have shown to improve the resistance of CFRPs when exposed to impact events [1].

Lately, on the focus of various researchers, has been the development of new materials able to repair cracks and delamination within the composite matrix. These newly materials are called self-healing (SH) materials and were first reported by White and Sottos in 2001 [3]. SH systems can be either autonomous (extrinsic type) or non-autonomous (intrinsic type). Intrinsic SH approach seems to be the most promising as it allows multiple healing events to be performed

  doi:10.5075/epfl-298799_978-2-9701614-0-0

due to the unlimited thermal reversibility of the incorporated SH agents at specific areas within a composite structure. Intrinsic SH approach can be achieved through thermoplastic polymer blending, supramolecular chemistry based polymers and special covalent bonding interaction-based polymers (i.e., BMI-DA polymers). Polymers having complex molecular architecture can be easily selected as SH agents, due to their functional groups design at molecular level. A new class of SH polymers takes advantage of the DA reaction mechanism, which provides a thermally reversible polymer network. These polymers, exhibit a resin-type nature at ambient conditions, but when heated, de-crosslink through the retro DA reaction mechanism (reverse DA) then flows and fills potential damaged sites within composites' matrix. When cool down, the properties of the polymer network are automatically restored.

The way which a SH agent is incorporated into a composite structure is of high importance. Usually, when a SH system is incorporated into the composite an increase of the thickness may occur resulting in degradation of the mechanical properties. Electrospinning process (EP) is a rapidly evolving technique that has gained much research interest due to its ability to produce continuous fibers with a typical diameter of a few tens nanometers to a few hundred micrometers, using a high voltage electric field. Among several electrospinning variants, melt electro-writing process (MEP) is a processing technique for producing fibers from a polymer melt. The conductivity of the polymeric melt is much lower comparing to the polymer's solution which results in a better control of the fibers' deposition. MEP attracts interest in both academic and industrial level due to the absence of toxic solvents, the direct deposition of fiber mats on a chosen substrate and the ability to design a process according to desired final application [4, 5].

The current investigation is extending and complementing work of previous study [6] conducted by the authors. More precisely, the same DA-BMI polymer network was selected as SH agent to modify high performance CFRP laminates, through the solution electrospinning process (SEP). Here, the DA-BMI polymer network containing or not 1 wt% GNPs, was integrated into CFRPs by using the MEP technique. After composites' manufacturing, potential degradation effects were investigated due to SHA incorporation while all CFRP types were exposed to LVI tests. After LVI, CAI tests were performed prior and after the activation of the healing process to identify potential improvement of the residual compressive properties if the CFRPs. Finally, prior and after the healing process c-scan inspections were performed to macroscopically identify the damage area and to calculate the healing efficiency (H.E.).

2. Experimental Part: Materials and Methods

2.1 Materials

A commercial unidirectional (UD) carbon fiber-epoxy pre-preg tape (identification code: CE-1007150-38), was supplied by SGL Group, Germany and was further used for the manufacturing of the high performance CFRPs. BMI-1700 (M_w=1700 Da), was kindly supplied by Designer Molecules (San Diego, CA, USA). The four layered graphene nanoplatelets (GNPs), having lateral dimensions of 1–2μm, average thickness ≤4 nm, surface area ≥750 m^2/gr and purity ≥99% were supplied by Cheap Tubes Inc., Cambridgeport, Cambridge, MA, USA. In this work a cross-linked BMI-1700 network as well as a doped one containing GNPs at the amount of 1% by weight, played the SHA role and the preparation procedure of them are fully described elsewhere [6, 7, 8].

2.2 Incorporation of the SHA and composites' manufacturing

  doi:10.5075/epfl-298799_978-2-9701614-0-0

The incorporation of the SHA (containing or not GNPs) into CFRPs was performed by using the MEP technique, following the procedure described in Ref. [7]. In Figure 1a, the MEP set-up is sketched in detail while Figure 1b illustrates fibers' deposition onto pre-preg's surface just after the MEP. The MEP set-up consists of a heated metallic hopper (melt container), a high voltage power supply, a capillary (needle) and a grounded collector. After pre-pregs' surface modification the manufacturing and the curing of the laminates was performed by using autoclave technologies. After curing, quality control of the fabricated laminates was performed and the testing of them. Briefly, quasi-isotropic CFRP laminates containing 16 plies having [+45/0/−45/90]2S stacking sequence were manufactured; the reference laminates, modified ones containing the SHA in pure or in nano-modified form. Based on these, each CFRP plate contains 15 surface-modified pre-pregs. The final dimensions of the plates prior testing were 100 mm × 150 mm × 2.1 mm and the fiber volume fraction (Vf) of the composites was calculated to be close to 60± 2%. After CFRPS' modification by SHA, a negligible increase in the thickness of the laminates was observed, as the SHA itself was positioned only in center of each pre-preg ply (60 mm x 60 mm) and replaced part of the host epoxy resin as anticipated (see Figure 1b). Non-destructive quality control for all CFRPs was performed prior testing by using ultrasonics (C-scan technique) to secure absence of potential defects due to manufacturing process. C-scan inspections was performed also just after LVI as well as just after the healing process in order the induced damage at each stage to be determined and the H.E. to be calculated..

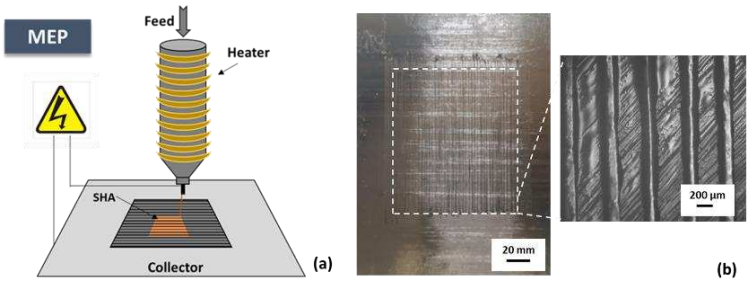

Figure 1 : a) Deposition of the SHA onto pre-preg's surface by using the MEP technique and b) optical microscopy image providing the fibrous mesh morphology of the deposited SHA.

2.3 Low velocity impact (LVI) and compression tests

After manufacturing, all CFRP samples (reference and both modified)were exposed to compression tests in order potential knock-down effects (due to the presence of SHA) to be identified. Then, LVI and CAI tests were conducted in order the residual compressive properties to be identified prior and after the healing process. Based on that, several specimens passed through the healing process to investigate potential restoration of the compressive properties through CAI tests. All tests were performed according to AITM1-0010: 2015 standard of Airbus [9], at ambient conditions. A drop tower equipped with a 16-mm diameter hemispherical aluminum impactor with a mass of 1.720 kg was employed for the LVI tests. A moderate amount of impact energy (13 J) was achieved by adjusting the initial height of the impactor. The impactor was left to drop on the CFRP plate and was restrained of striking for a second time. The provided amount of energy is considered sufficient to cause extended delamination and matrix cracking but not enough to cause fiber breakage. The compressive properties were determined by using an INSTRON 8802 hydraulic machine having a capacity of 250 kN and the samples were loaded under displacement control at a cross head velocity of 0.5 mm/min up to failure.

  doi:10.5075/epfl-298799_978-2-9701614-0-0

2.4 Healing process:

After LVI testing, damaged CFRPs were positioned into a hot-press machine in order the healing process to be activated. The healing cycle consists of uniform heating at 130 °C under 1 kN loading (0.67 bar pressure) for 30 minutes and then left to cool-down up to room temperature (RT). After healing, C-scan inspections were repeated to identify the H.E. (i.e., the proportion of the damage restoration).

3. Results and discussion

3.1 Low velocity impact response of CFRPs

Reference, BMI-modified and BMI & GNP-modified CFRPs were subjected to LVI according to specifications of section 2.3. Diagrams of Figure 2 provide the impact force versus time (Figure 2a) and the impact energy versus time (Figure 2b), for all material sets.

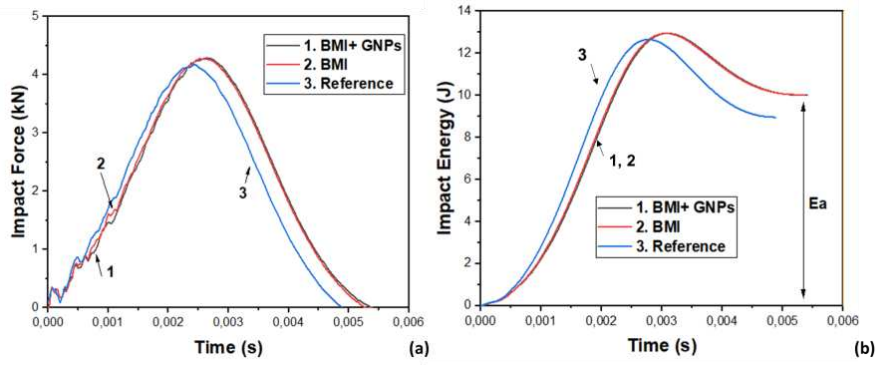

Figure 2: Low velocity impact (LVI) tests for all types of CFRPs; a) force vs time curve, b) impact energy vs time curve.

Figure 2a, provides the force vs.time diagrams for all material sets during impact testing. Thus, the maximum load that each plate receives during LVI as well as the contact duration between the impactor and the specimen, are provided. The geometry of the impactor significantly affects the contact duration of it (the spherical heads result in a longer contact duration) as well as by the impact energy. Higher impact energy provides longer contact duration. The initial load reduction corresponds to the creation of the first delamination and afterwards several oscillations of the curve are observed, until the load reaches its maximum point [10, 11]. These oscillations are a result of delaminations' growth within the composite structure during the impact. Although the maximum load value do not significantly differ for the three CFRP categories, a slight increase was observed for BMI & GNP-modified CFRPs (~4.3 kN). On the other hand, the absorbed impact energy by the CFRP plated during LVI was calculated taking into consideration the force vs time curves of Figure 2a and taking into account specifications of Ref. [9]. For all CFRP materials an increase of the energy value up to 13 J was reached while part of the energy is being restituted to the impactor in the form of kinetic energy. The absorbed energy can be considered as the amount of the dissipated energy within the impacted CFRP plate, without taking into consideration any other energy consumption mechanisms (e.g. friction, energy transfer to the impactor etc.). Modified specimens seem to absorb more energy compared to the reference ones. More precisely, BMI-modified CFRPs absorbed 11% more energy, while BMI & GNP-modified CFRPs absorbed 11.4% more energy when compared to the reference ones. According to C-plots of Figure 3 it was shown that BMI & GNP-modified CFRPs

presented larger damaged area by 19% than the corresponding BMI-modified ones (see Figure 3b & 3e). The above-mentioned behavior probably is attributed to the GNP presence within the SHA structure that led to less resistance to delamination. The presence of the GNPs, may serve as potential starting points of failure. Based on previous publication by the authors reference CFRPs presented comparable damage area as in the case of BMI modified CFRPs [6].

3.2 Effect of the healing process on CFRPs

After LVI testing damaged healable CFRPs underwent the healing process. C-scan inspections were repeated in order to be compared with the images taken just after LVI in order to be compared. The damage area of the c-scan plots was quantified by using the ImageJ software. During the healing process, the retro DA reaction takes place and the cross-linked SHA "breaks" into the primary components, namely BMI-1700 and trifuran (cross-linker) compound. While each specimen is under pressure in the heat-press, the primary components (characterized by low molecular weight compared to the original cross-linked network), flow in between and fill the matrix cracks and the delaminated areas. Upon cooling, the DA reaction takes place and provides a new polymeric network that finally have “filled-in” the induced damage. In Figure 3, c-scan images of the initial CFRP plates (unimpacted form) (a,d), in impacted form (b,e) and in healed situation (c,f) are provided for both modified CFRPs.

In the case of the BMI-modified CFRPs the induced damage due to LVI appears to have been fully healed, as expected, while in the case of the BMI & GNP--modified CFRPs, the damaged area was not entirely healed. This behaviour may is attributed to the fact that the damaged area for these specimens is higher and probably the SHA amount is insufficient. In addition, the presence of the GNPs tend to increase the viscosity of the polymer material when melted having as a result to reduce the capability of it to flow within the damaged sites of the composite structure. Potential increase of the SHA amount and/or the duration of the healing cycle, may result in better H.E. values.

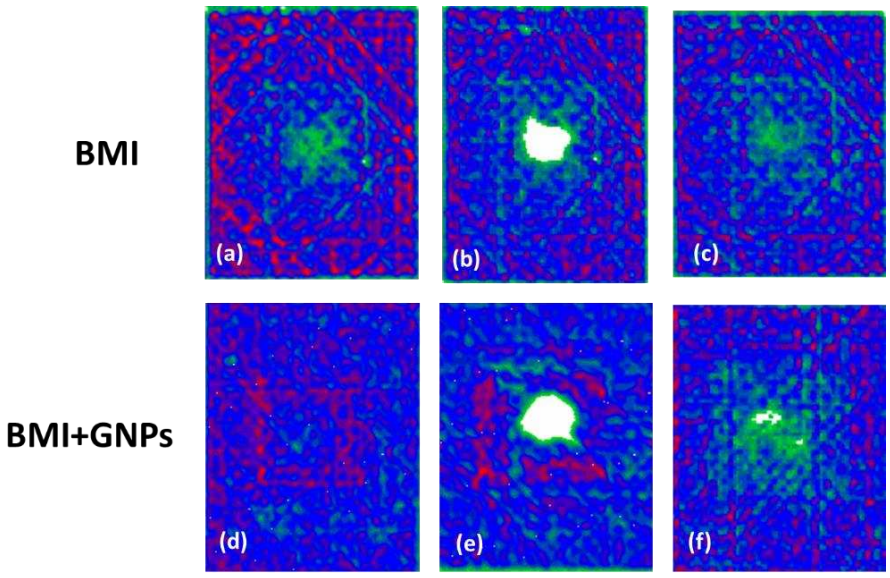

Figure 3 : C-scan plots for BMI- and BMI & GNP-modified CFRPs ; (a,d) before LVI, (b,e) after LVI and (c,f) after the healing process.

3.3 Investigation of potential “knock-down” effect due to SHA presence

In this section the compression tests on the BMI-modified the BMI & GNP-modified and the reference CFRPs were conducted in order potential degradation effects to be identified due to SHA incorporation. The samples at this stage are tested before exposing to LVI testing. Thus, compression before impact tests (CBI) are conducted. As it is clearly shown, in the stress-strain(%) diagrams of Figure 4a, all material sets presented brittle failure. Reference and modified CFRPs exhibit the same trend as the applied stress increases linearly up to failure. In the corresponding bar chart of Figure 4b) the compressive properties (strength, modulus) are summarized. The results indicate a partial loss of the mechanical strength (σ_{max}) due to the SHA presence by 21% and 27% for the BMI- and the BMI & GNP- modified CFRPs respectively. The compressive modulus also presented a decrease by 3% and 12% for the BMI- and the BMI & GNP- modified CFRPs respectively. The reduction of the compressive properties is mainly attributed to the SHA presence (having lower mechanical properties compared to epoxy matrix) that in its turn replace part of the host epoxy matrix. Another factor is the sight thickening effect in local scale due to the incorporation of the healing zone.

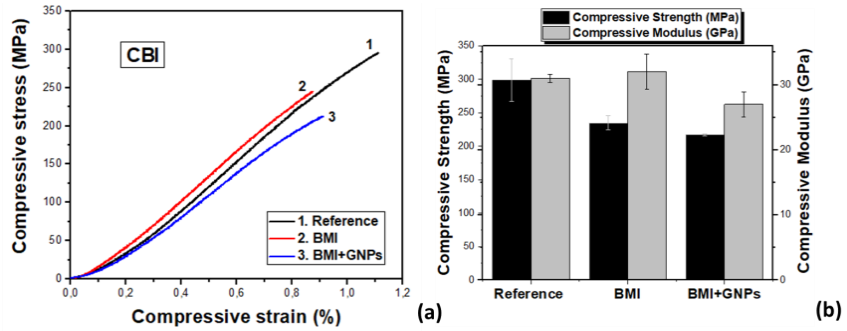

Figure 4 : (a) Compressive stress versus compressive strain (%) curves for the reference and both modified CFRP types and (b) bar chart diagram providing the compressive properties (strength and modulus) prior impact testing.

3.4 Residual compressive properties (CAI) and investigation of the healing effect

Compression strength is the property that mostly suffers after an impact event of a composite structure. Based on that, it is necessary to determine the residual compressive properties of it. In Figure 5, compressive stress versus compressive strain curves for all materials are illustrated. As expected, the damage creation due to LVI test negatively affected the compressive properties of all CFRPs. The presence of cracks and delaminations into the composites interfere the transfer of the applied load from the matrix to the reinforcement (in our case the carbon fibers), resulting in premature failure of the structures. In the case of the BMI-modified specimens, a decrease of 11% in compressive strength and 6.5% in compressive modulus was observed, while in modified specimens by BMI & GNPs the reduction was calculated to be 21.5% and 2% respectively for the same properties. In the case BMI & GNPs CFRPs, the presence of higher damage area led to a significant drop of the residual mechanical properties.

  doi:10.5075/epfl-298799_978-2-9701614-0-0

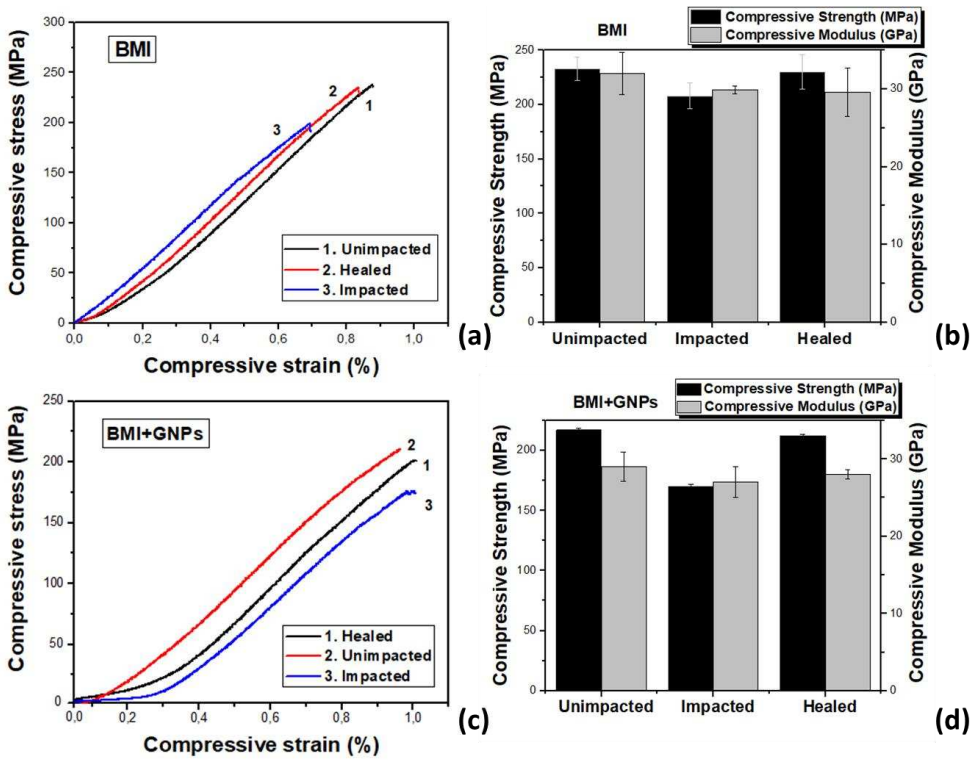

Figure 5 : (a,d) Compressive stress versus compressive strain (%) curves for both modified CFRP types, (b,d) bar chart diagram providing the compressive properties (strength and modulus) after impact testing (for damaged and healed CFRPs respectively).

All modified CFRPs that passed through the healing cycle, presented an increase in the σ_{max} value if compared to the impacted ones (unhealed ones) while no difference was observed for the compressive modulus values. Repairing of cracks and delaminations resulted in partly restoration of load transfer from the matrix to the fibers and thus CFRPs were able to carry higher loads. BMI-modified CFRPs exhibited a restoration of 10.6% in compressive strength, while the modified specimens with BMI & GNPs, which underwent the healing process, regained their compressive strength by 24.5% after LVI.

4. Conclusions

BMI-DA resin, containing or not GNPs at the amount of 1 wt%, was successfully and locally integrated into high performance CFRPs by MEP technique. CBI tests revealed a degradation effect on compressive properties of the composites as modified CFRPs exhibited decreased mechanical properties if compared to the reference ones. According to LVI tests, the BMI & GNP CFRPs presented slightly larger damage area based on c-scan plots while after the healing process the damage area was restores up to 100%. Finally, CAI tests showed the expected degradation due to the presence of the damage for all CFRPs while after the application of the healing process part of the compressive properties were restored.

Acknowledgements

This research is co-funded by Greece & European Union (European Social Fund – ESF), through the Operational Program "Human Resources Development, Education and Lifelong Learning" in the context of the project "Reinforcement of Postdoctoral Researchers- 2nd Cycle" (MIS-5033021), implemented by the State Scholarships Foundation (IKY).

5. References

1. Dimoka P, Psarras S, Kostagiannakopoulou C, Kostopoulos V. Assessing the damage tolerance of Out of Autoclave manufactured carbon fibre reinforced polymers modified with multi-walled carbon nanotubes. Materials 2019; 12(7):1080.
2. Zafeiropoulou K, Kostagiannakopoulou C, Sotiriadis G, Kostopoulos V. A Preliminary Study of the Influence of Graphene Nanoplatelet Specific Surface Area on the Interlaminar Fracture Properties of Carbon Fiber/Epoxy Composites. Polymers 2020; 12(12):3060.
3. White SR, Sottos NR, Geubelle PH, Moore JS, Kessler MR, Sriram SR, Brown EN, Viswanathan S. Autonomic healing of polymer composites. Nature 2001; 409:794–797.
4. Tourlomousis F, Ding H, Kalyon DM, Chang RC. Melt Electrospinning Writing Process Guided by a "Printability Number". Journal of Manufacturing Science & Engineering 2017; 139: 081004.
5. Zhang LH, Duan XP, Yan X, Yu M, Ning X, Zhao Y, Long YZ. Recent advances in melt electrospinning. RSC Advances 2016; 6:53400–53414.
6. Kostopoulos V, Kotrotsos A, Geitona A, Tsantzalis S. Low velocity impact response and post impact assessment of carbon fibre/epoxy composites modified with Diels-Alder based healing agent. A novel approach. Composites Part A Applied Science & Manufacturing 2021; 140: 106151.
7. Kotrotsos A, Michailidis G, Geitona A, Tourlomousis F, Kostopoulos V. Toughening and Healing of CFRPs by Diels–Alder-Based Nano-Modified Resin through Melt Electro-Writing Process Technique. International Journal of Molecular Sciences 2022; 23(7):3663.
8. Liu YL, Hsieh CY. Cross-linked Epoxy Materials Exhibiting Thermal Remendablility and Removability from Multifunctional Maleimide and Furan Compounds, Journal of Polymer Science Part A: Polymer Chemistry 2006; 44:905–913.
9. AITM 1. 0010. Airbus industry test method, Carbon fiber reinforced plastics, Determination of compression strength after Impact, 2005, Issue 3.
10. Shyr TW, Pan YH. Impact resistance and damage characteristics of composites laminates. Composite Structures 2003; 62:193–203.
11. Uyaner M, Kara M. Dynamic response of laminated composites subjected to low-velocity impact. Journal of Composite Materials 2007; 41:2877–2896.

  doi:10.5075/epfl-298799_978-2-9701614-0-0

EVALUATION OF THE SELF-HEALING CAPABILITY OF A POLYCAPROLACTONE FUNCTIONALIZED INTERPHASE FOR POLYMER COMPOSITE APPLICATIONS

Laura Simonini[a], Haroon Mahmood[a], Andrea Dorigato[a], Alessandro Pegoretti[a]

a: Department of Industrial Engineering, University of Trento, Trento, Italy – laura.simonini@unitn.it

Abstract: *In this work, a self-healable interphase was studied for polymer composite applications. Polycaprolactone (PCL) nanoparticles were synthetized and deposited by electrophoretic deposition on the surface of glass fibers to form a coating that acted as an interphase with an epoxy matrix. The glass fibers were provided both with and without the superficial sizing to investigate its effect with the coating. The morphology of the nanoparticles and the coated fibers were observed by field emission scanning electron microscopy that revealed an efficient particles preparation and their homogeneous deposition on the fibers. Micro-composites were prepared by depositing a single micro-drop of epoxy resin on each fiber filament. Micro-debonding tests were performed to evaluate the healing efficiency upon thermal healing. A 50% recovery of the interfacial adhesion properties was obtained for both types of fibers.*

Keywords: self-healing; interphase; polycaprolactone; micro-debonding; polymer composites

1. Introduction

The performances of composite materials do not depend only on the mechanical properties of its constituents (i.e., matrix or fibers), but it also relies on the nature of the interphase, the region that separates the two phases [1]. The failure of the interphase prevents the matrix from transferring the load to the fibers, ultimately causing the composite to fail. To ensure the long-term reliability of the component, it is therefore essential to enhance the stability of the interphase. In this region, several adhesion interactions are established, like surface adsorption and wettability, molecular interdiffusion, electrostatic attraction, chemical bonds, and mechanical adhesion [2], which dictate the mechanical properties of the final composite. Chemical and physical treatments of the fibers surface can improve those interactions [3-5]. Recent works demonstrated the validity of surface coating as a powerful method for the mechanical optimization of the interphase while imparting specific functionalities to the final composite, like energy storage, healing, sensing, and strain monitoring capabilities [6-7]. The idea behind this work is thus to create a multifunctional interphase by coating the glass fibers with a low-weighted small-sized nanomaterial to address good mechanical properties and self-healing capabilities. Polycaprolactone nanoparticles were selected as the healing media in this application. After a damage event, the self-healable interphase can restore the interaction between the two phases, if subjected to external stimuli, for example to heat. The healing process extends the service life of the composites, reducing the waste and the repairing costs, therefore improving the sustainability.

  doi:10.5075/epfl-298799_978-2-9701614-0-0

2. Experimental part

2.1 Materials

WINDSTRAND® glass fibers were provided by Owens Corning (Frankfurt, Germany) as a roving of fiber bundles, both silane sized (GF_1) and unsized (GF_2). They were used as the reinforcing phase for polymer micro-composites.

A bicomponent epoxy system made by an epoxy base (EC157.1) and an aminic hardener (W342) was provided by Elantas Italia S.r.l. (Collecchio, Italy) and it was used as the matrix for the polymer micro-composites. Both components were mixed at a ratio of 100:30 and cured for 8 h at room temperature, then 40 h at 50 °C.

FacilanTM Polycaprolactone (PCL) was provided by 3D4makersB.V. as a continuous filament and used as the nanosized healing agent at the interphase.

Poly(vinyl alcohol) and Polysorbate 80 (Tween®80) were provided by Sigma Aldrich (Missouri, USA) as a powder and a viscous liquid respectively and used as stabilizers for the preparation of PCL nanoparticles.

2.2 Experimental methods

The solvent displacement technique was used to reduce the PCL filament to nanoparticles dispersed in water solution (0.03 wt.% PCL). This was used as source to coat the glass fibers by electrophoretic deposition (EPD). During EPD, the time of deposition and the applied voltage were selected after a careful deposition analysis.

The morphological observation of PCL nanoparticles, uncoated glass fibers and PCL coated glass fibers was performed by field emission scanning electron microscopy (FESEM) by using a Zeiss Supra 40 microscope (Berlin, Germany). For the PCL nanoparticles observation, a single drop of the staring solution was diluted in Milli-Q water at a ratio 1:10 and manually deposited on a sample holder, then left at room temperature till dried. For the fibers, a piece of uncoated and dried coated fiber bundle (about 10 mm length) was cut and glued on a sample holder by using a bi-adhesive carbon tape. Prior to analysis, all the samples were sputtered by a platinum/palladium alloy (80:20) for 20 seconds to make them conductive.

The interface healing was performed by heating micro-composites, prepared by depositing a single micro-drop of an epoxy resin on the uncoated and the PCL coated fibers, at 80°C for 1h. From the micro debonding tests, the interfacial shear strength (IFSS) of both the uncoated and PCL coated fibers was evaluated after ($IFSS_{PCL\_2}$) and before ($IFSS_{PCL\_1}$) the healing process. It was calculated as the ratio between the maximum load from the mechanical micro-debonding load-displacement curves (F_{max}) and the geometrical dimension of the fibers (d, fibers diameter) and the epoxy micro-drops (L, micro-drops length), as reported by Eq. (1).

$$IFSS = \left(\frac{F_{max}}{\pi d L}\right) \quad (1)$$

From the values of IFSS, the healing efficiency was calculated as reported by Eq. (2).

$$HE_{\%} = \left(\frac{IFSS_{PCL\_2}}{IFSS_{PCL\_1}}\right) \cdot 100 \quad (2)$$

3. Results

3.1 Morphological characterization of PCL nanoparticles

The morphological observation of PCL nanoparticles is reported in Figure 1, with the statistical distribution of the particles size.

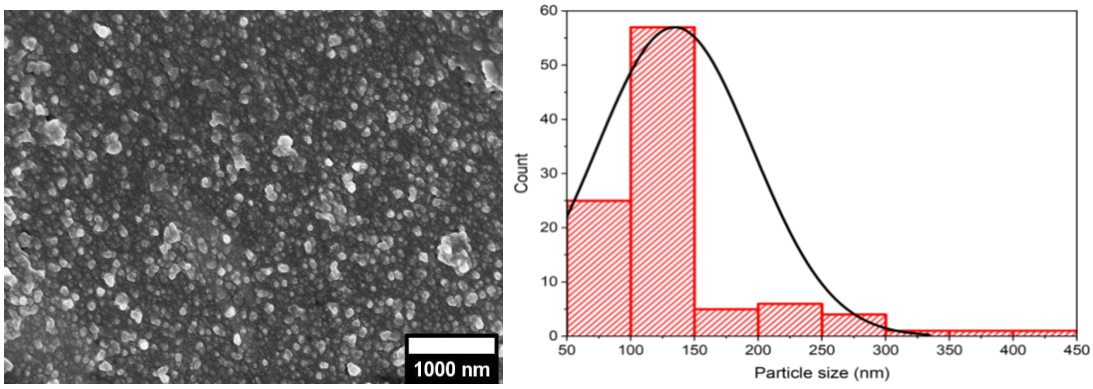

(a) (b)

Figure 1. (a) SEM image of PCL nanoparticles and (b) their statistical size distribution.

The particles appeared to be of quite regular shape and they presented a low level of agglomeration, indication of an efficient preparation method. The average particle size was estimated equal to 134 ± 61 nm.

3.2 Morphological characterization of PCL coated glass fibers

In Figure 2, SEM images of GF_1 and GF_2 surfaces are reported.

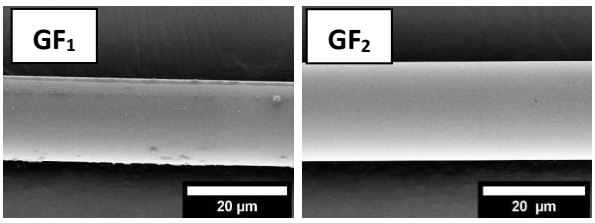

(a) (b)

Figure 2. SEM images of uncoated (a) GF1 and (b) GF2 surfaces.

The surfaces appear to be smooth and free of defects. It is possible to distinguish the presence of the silane sizing on GF1.

In Figure 3, SEM images of the PCL coated fibers are reported and compared. The effect of the variation of the supplied voltage on the deposition's quality was observed, assuming the time constant and equal to 60 seconds for each bundles side.

  doi:10.5075/epfl-298799_978-2-9701614-0-0

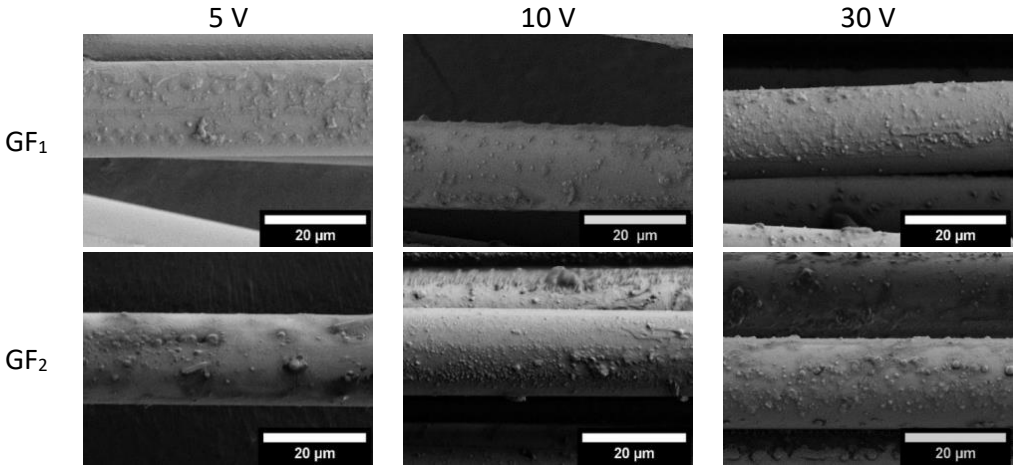

Figure 3. SEM images of PCL coated GF_1 and GF_2 surfaces, varying the applied voltage (5-30V) and keeping the deposition time constant (60 second for each side of the bundles).

Increasing the applied voltage, the deposition of PCL nanoparticles on GF increased. A consistent and homogeneous deposition was observed by selecting ΔV = 30V.

In Figure 4, SEM images of the PCL coated fibers are reported and compared. The effect of the variation of the deposition time on the deposition quality was observed, assuming the supplied voltage constant and equal to 30 V.

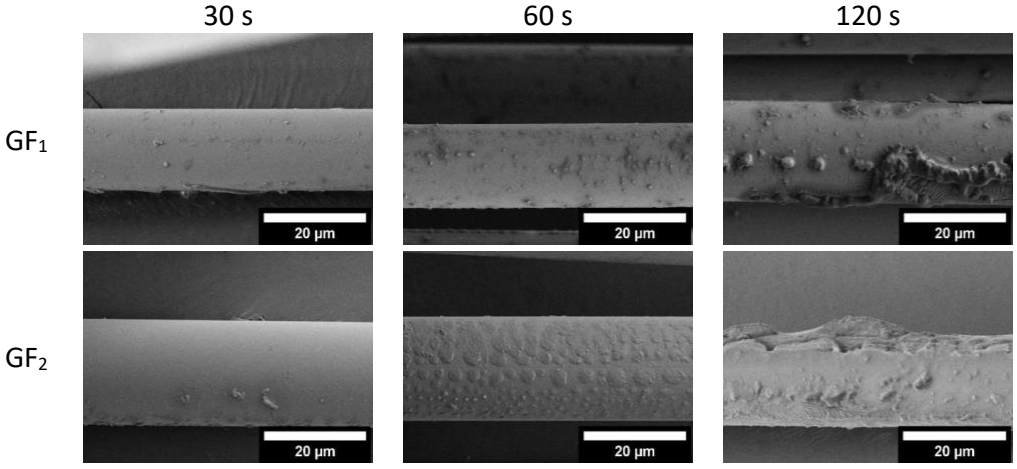

Figure 4. SEM images of PCL coated GF_1 and GF_2 surfaces, varying the deposition time (30-120s) and keeping the applied voltage constant (30 V).

It can be seen that the longer is the deposition time, the worse is the homogeneity of the coating. A compact and homogeneous coating was observed by selecting the time equal to 60 seconds for each bundles side (total deposition time = 120 seconds). It was also observed that this value of deposition time prevented the oxidation of the copper electrodes which began after about 150 seconds of deposition (at ΔV = 30V) by showing a change of the solution color that passed from matt white to green, index of the release of copper ions. This phenomenon was more and more noticeable by waiting longer.

  doi:10.5075/epfl-298799_978-2-9701614-0-0

3.3 Mechanical properties of PCL coated glass fibers/epoxy micro-composites

In Figure 5, the representative load–displacement curves obtained from micro-debonding tests on the PCL coated glass fibers are reported, together with those of the uncoated GF sample. For each specimen, the values of the critical load (F_{max}) were used for the calculation of the interfacial shear strength (IFSS), as described in Eq. (1).

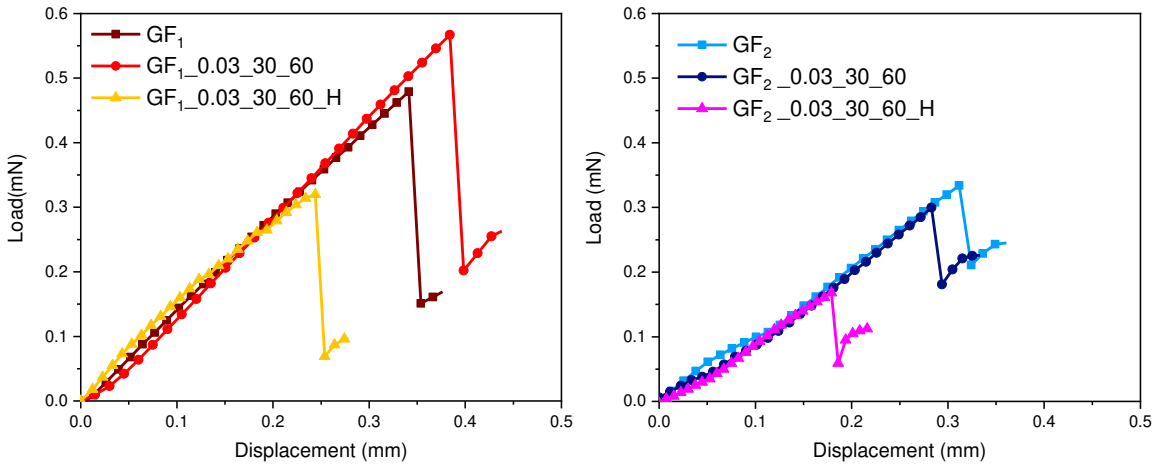

(a) (b)

Figure 5. Comparison of micro-debonding tests of the uncoated and PCL coated (a) GF_1 and (b) GF_2.

A comparison of the calculated IFSS values is reported in Figure 6.

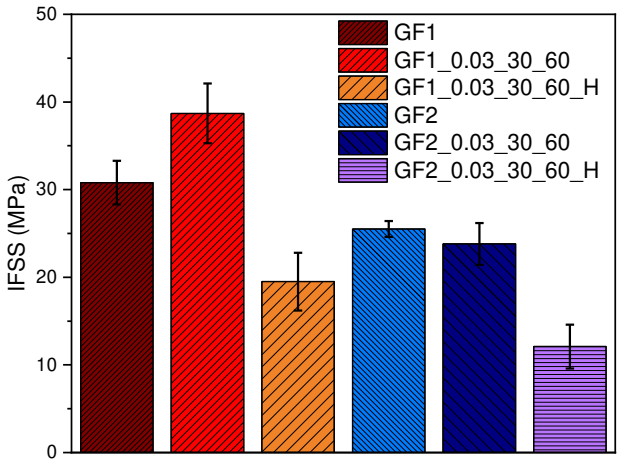

Figure 6. Interfacial shear strength (IFSS) values for GF_1 and GF_2.

From Figure 6, it is possible to notice that the interfacial adhesion value of GF_1 is higher than GF_2 due to the presence of the superficial sizing, as expected by the literature review. The corresponding coated samples (GF_1_0.1_30_60 and GF_2_30_60, respectively) demonstrate that the presence of the PCL interphase provides a positive effect in terms of interfacial shear strength in the case of GF_1 (+26%), while no significant modifications are obtained for GF_2. This indicates that the presence of the PCL interphase provides an optimum interaction with the

  doi:10.5075/epfl-298799_978-2-9701614-0-0 published under CC BY-NC 4.0 license

superficial sizing, whose contact results in enhanced interfacial properties between the fiber and the matrix.

From the values of the interfacial shear strength (IFSS), the healing efficiency was calculated as described in Eq. (2) (Figure 7).

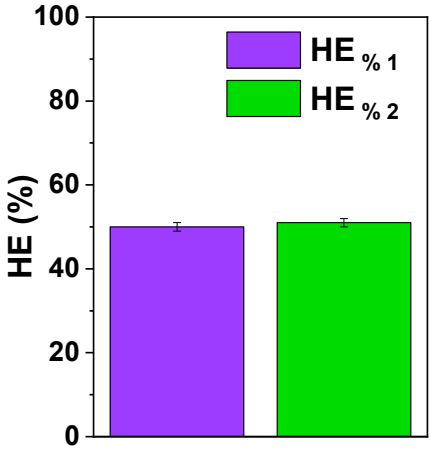

Figure 7. Values of self-healing efficiency for GF_1 ($HE_{\%1}$) and GF_2 ($HE_{\%2}$).

The calculation of the gross healing efficiency (Figure 6) demonstrates that the functionalized interphase provides a recovery of the 50% of the mechanical properties upon thermal healing for GF_1 and 51% for GF_2.

4. Conclusions

For the first time, polycaprolactone (PCL) was used to create a self-healing interphase between an epoxy matrix and glass fibers. PCL nanoparticles were prepared by solvent displacement technique and they were dispersed in a water solution. PCL nanoparticles deposition on the glass fibers surface was performed by electrophoretic deposition (EPD). The morphological analysis showed that the deposition is a function of time and voltage. A homogeneous PCL deposition on the glass fibers was obtained applying 30V of voltage for 60 seconds on each side of the fibers. Epoxy micro-droplets were deposited on the coated fibers and micro-debonding tests were performed on the micro-composites to evaluate the interfacial shear strength (IFSS). A 26% improvement in the IFSS values was found for the micro-composites containing PCL as an interphase compared to neat composites. The thermal healing allowed to recover about 50% of the adhesion mechanical properties, for both the sized and the unsized fibers.

5. References

1. Kaw AK. Mechanics of composite materials. CRC press 2005; 490.
2. Da Silva L, Marques E, Campilho R. Design Rules and Methods to Improve Joint Strength. Handbook of Adhesion Technology 2018; 773-810.
3. Chen J, Zhu Y, Ni Q, Fu Y, Fu X. Surface modification and characterization of aramid fibers with hybrid coating. Applied Surface Science 2014; 321:103-8.
4. Vedrtnam A, Sharma SP. Study on the performance of different nano-species used for surface modification of carbon fiber for interface strengthening. Composites Part A: Applied Science and Manufacturing 2019; 125.

  doi:10.5075/epfl-298799_978-2-9701614-0-0

5. Raphael N, Namratha K, Chandrashekar BN, Sadasivuni KK, Ponnamma D, Smitha AS, et al. Surface modification and grafting of carbon fibers: A route to better interface. Progress in Crystal Growth and Characterization of Materials 2018; 64(3):75-101.
6. Jones AR, Cintora A, White SR, Sottos NR. Autonomic healing of carbon fiber/epoxy interfaces. ACS Appl Mater Interfaces 2014; 6(9):6033-9.
7. Mahmood H, Simonini L, Dorigato A, Pegoretti A. Graphene Deposition on Glass Fibers by Triboelectrification. Applied Sciences 2021; 11(7).

HIGHLY CONDUCTIVE POLYPROPYLENE BASED COMPOSITES FOR BIPOLAR PLATES FOR POLYMER ELECTROLYTE MEMBRANE FUEL CELLS

Mariona Diaz-Rodenas[a], Moritz Thommen[a], Christian Rytka[a], Jean-Marc Le Canut[b], Grégoire Gschwend[b], Sawsane Queloz[c], Panagiota Tsotra[d], Julien Roussel[b], Jean-Francois Weber[b]
a: Institute of Polymer Engineering, School of Engineering, University of Applied Sciences and Arts Northwestern Switzerland FHNW, Windisch, Switzerland - mariona.diaz@fhnw.ch
b: GreenGT, Zone Industrielle Les Rosses 15, Collombey-Muraz, Switzerland
c: TOSA Swisstech, Switzerland innovation park, Allée des sciences 2, Courroux, Switzerland
d: KATZ Kunststoff Ausbildungs- und Technologie-Zentrum, Aarau, Switzerland

Abstract: *In the present work, highly conductive polymer compounds are developed for the production of fuel cell bipolar plates. The composite plates need to fulfil certain requirements concerning electrical and thermal conductivity, mechanical properties, and additionally ensure an easy implementation in industry. A multi-filler approach, based on commercially available compounds and masterbatches is followed in order to achieve these ambitious goals. As the amount of fillers needed to achieve the high electrical conductivity values is over 70 weight percent, the processing of the compounds becomes challenging. The ordinary polymer processing has to be pushed to the limits. We demonstrate that the developed compounds can be processed successfully via compression moulding.*

Keywords: Fuel cells; Conducting materials; Carbon; Graphene; Nanotubes

1. Introduction

In the near future most engines will be powered electrically by batteries or by fuel cells. One of the major factors limiting fuel cell commercialization is the development of bipolar plates (BPP). Their characteristic requirements are a challenge for any class of material, and none meets yet these requirements entirely. Bipolar plates significantly influence the gravimetric and volumetric power density of a fuel cell, typically accounting for more than 80% of the weight of a stack and nearly two third of the volume [1].

In a previous work, we have successfully developed innovative polymer-based composites suitable for fuel cell bipolar plates [2]. Various potentially suitable electrically conductive fillers, such as graphite, carbon black, carbon fibers, carbon nanotubes, and expanded graphite were added to a polypropylene (PP) matrix. The samples were tested with regard to their through-plane electrical conductivity, in-plane thermal conductivity, flexural properties and corrosion resistance. The effect of plate thickness and filler composition was systematically investigated. It was also found that the surface preparation of the samples and the applied pressure during the electrical resistance measurements had a significant effect on the electrical conductivity. The materials showed very good processability with compression moulding which results in a maximum electrical conductivity of 46 S cm^{-1}, using a multi-filler approach with carbon based fillers of different form and size. The conductivity was measured in a 4-pole device obtaining a value that showed a combination of in-plane and through-plane electrical conductivity.

The main objective of this study is to develop PP-based composite compounds which can meet the requirements of bipolar plates and is based on commercially available compounds and

  doi:10.5075/epfl-298799_978-2-9701614-0-0

masterbatches. A multi-filler approach was followed and different combinations of fillers and matrix were tested, aiming to find a good compromise between electrical and mechanical properties, easy processability and efficient production. The effect of the plate thickness on the measurements of the through-plane electrical conductivity was investigated. Also, a new approach for measuring purely the through-plane electrical conductivity was proposed.

2. Experimental

2.1 Materials

Three different commercial PP-based compounds were used in this study: TECACOMP PP HTE PW black 1014974 from Ensinger GmbH, with graphite (Gr) as filler, Plasticyl PP2001 from Nanocyl, filled with carbon nanotubes (CNT) and Pre-Elec PP 17147 from Premix, with carbon black (CB) and carbon fibers (CF). Moreover, a dispersion agents BYK 9076 from BYK-Chemie GmbH and a titanate coupling agent, TYTAN™ from Lawrence Industries, were tested.

2.2 Compounding

The above mentioned materials were used as received for further compounding. This took place at a kneader (HAAKE™ Rheomix OS Lab Mixer from Thermo Fischer). The appropriate amounts of each material were mixed in order to achieve the targeted fillers contents at the final compounds. An overview is given in Table 1.

Table 1: Manufactured compounds.

Compound	PP [wt%]	Gr [wt%]	CB + CF [wt%]	CNT [wt%]	Additive [wt%] / Type
A	13	81	3	1	0.5/ Titanate 2.5/ BYK 9076
B	15	76	5	1	0.5/ Titanate 2.5/ BYK 9076
C	17	72	8	-	0.5/ Titanate 2.5/ BYK 9076
D	19	72	5	2	0.5/ Titanate 2.5/ BYK 9076
E	22	65	11	-	0.5/ Titanate 2.5/ BYK 9076
F	23	65	7	2	0.5/ Titanate 2.5/ BYK 9076
G	25	60	11	1	0.5/ Titanate 2.5/ BYK 9076

2.3 Plate manufacturing

The compounds were pressed into plates via compression moulding. The cavity of the mould was rectangle with a length of 170 mm and width of 85 mm. A special insert showed in Figure 1 was designed for the mould and used in the process to create four areas of different thicknesses into the final plate. In this way, the effect of thickness on the measured through-thickness conductivity could be investigated, as explained in the following paragraphs.

The amount of compound for filling the targeted thicknesses of 1, 2, 3 and 4 mm was calculated and filled in the mould. The mould was placed in a press heated at 240°C for 10 minutes and

  doi:10.5075/epfl-298799_978-2-9701614-0-0

afterwards pressed with 150 bar for 5 min. Then, the mould was cooled until a temperature of 25°C was reached and the plate was demoulded.

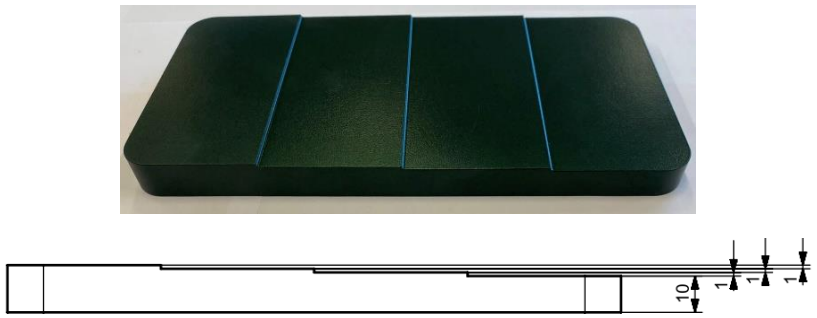

Figure 1: Insert used for compression moulding (above) Drawing of the insert with dimensions in millimetres (below).

2.4 Testing

The flexural strength was determined with a three-point flexural test in compliance with the standard DIN EN ISO 178. For the characterization of the through-plane conductivity, a digital micrometer (MI 3250 MicroOhm 10A from METREL) was used to measure the resistance. The cross-section area of the gold- coated copper electrodes was 6.25 cm^2 (25 mm × 25 mm), while plates of various thickness were tested. A pressure of 1.6 MPa was applied. The measured resistance was R_{tot} given by Eq. (1)

$$R_{tot} = R_{app} + R_{plate} \quad (1)$$

where R_{plate} is the resistance of the plate and R_{app} is the contribution of all resistances that are not the bulk resistance of the plate. This includes the contact resistances between the electrodes and the surface of the plate as well as the resistance of the apparatus itself. $R_{plate,}$ the bulk resistance of the plate, depends on the resistivity of the material ρ_{mat}, the thickness of the plate t, and the area of the electrode A (Eq. (2)).

$$R_{plate} = \rho_{mat} \cdot t / A \quad (2)$$

Inserting Eq. (2) in Eq. (1) one gets:

$$R_{tot} = R_{app} + \rho_{mat} \cdot t / A \quad (3)$$

Thus, according to Eq. (3), plotting the total resistance of plates of various plate thickness as a function of t yields a straight line of slope ρ_{mat}/A and an ordinate at the origin of R_{app}. The material conductivity can then be obtained from the slope according to Eq. (4):

$$\sigma_{mat} = 1/ \rho_{mat} \quad (4)$$

The method presented above is adapted from Cunningham *et al.* [3] and allows to separate the contributions of the resistance as material property from other phenomena. Although this method is experimentally simple and only needs basic apparatus, it nevertheless requires the preparation of several plates of various thicknesses which is time and material consuming. However, the special insert for the compression moulding, explained in the previous paragraph, significantly simplified the process.

  doi:10.5075/epfl-298799_978-2-9701614-0-0

In the case of composite bipolar plates in proton-exchange membrane fuel cells (PEMFC), it can be interesting to measure the resistance of the bipolar plate and gas diffusing layer (GDL) assembly rather than the resistivity of the materials [4]. In this case, the method proposed here is not adapted (since the thickness of the plates must be varied) and other procedures should be followed [5].

The electrical conductivity of the previous method was compared with the values obtained using Eq. (5) for the different thicknesses:

$$\sigma = t / (A\ R_{tot}) \quad (5)$$

where t and A are the thickness of the plate and cross-section area within the electrodes, respectively, and R_{tot} is the measured resistance.

3. Results and Discussion

To achieve high conductivity values, a very large amount of conductive fillers is required. However, this filler content is limited by processability if the material needs to have a reasonably low viscosity for the filling of plates by injection moulding as a highly efficient process, alternatively to compression moulding. Additionally, plates get too brittle if matrix content is too low. Compounds with different amounts of fillers were proposed and the amounts were gradually increased with different additive and filler combinations. All compounds were successfully pressed to plates. A plate with Ensinger TECACOMP PP HTE PW black 1014974 was pressed as reference, composed of 90% graphite as single filler.

For determining the through-plane electrical conductivity, the resistance of the plate was measured at four different thicknesses. Figure 2 shows the values measured with the ohmmeter as well as the regression curves. The corresponding equations are also shown, where the slope is ρ_{mat}/A and the intercept is $R_{app.}$ Thus, the resistivity and conductivity were obtained.

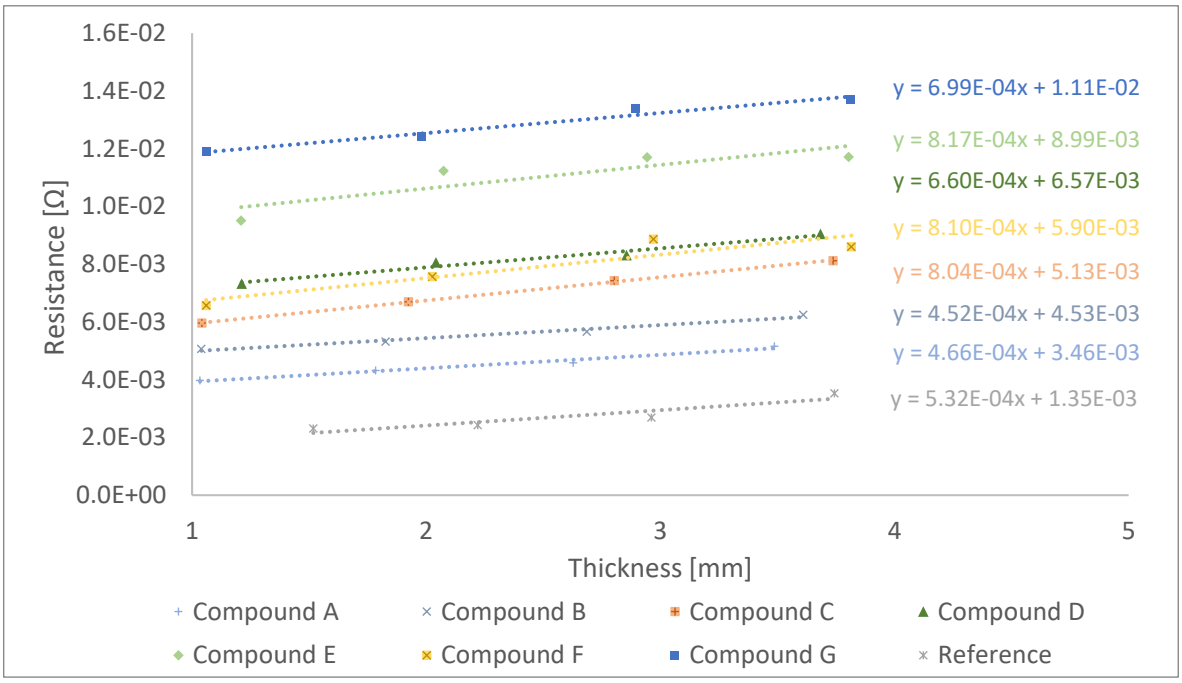

Figure 2: Measured resistance in plates of different thicknesses for compounds A to G and the reference material.

  doi:10.5075/epfl-298799_978-2-9701614-0-0

In Figure 2, it can be seen that some measurements deviate from the regression curves. Indeed, a deviation on the plate thickness has been observed during the measurement what may have an influence on the R_{app}. In some compounds the resistance measured in the 4 mm thick part was lower than the ones measured for the other thicknesses, although a higher value was expected. This is related to a probable uneven distribution of pressure at different thicknesses transferred from the insert into the plate during compression moulding process. This corresponds to studies showing that the compression moulding pressure has a high influence on the electrical conductivity [6].

Figure 3 shows a comparison between the proposed method and the one obtained through Eq. (5) for evaluating conductivity is given. As stated before, the measured resistance is an addition of the bulk resistance and the resistance associated to the surface and the apparatus. For this reason, a correlation between the thickness and the electrical conductivity can be observed in the second method, despite the electrical conductivity is an intrinsic property of the material. While the proposed method shows electrical conductivity through-plane independent of the thickness. Hence, this method was considered the most accurate one for obtaining the electrical conductivity.

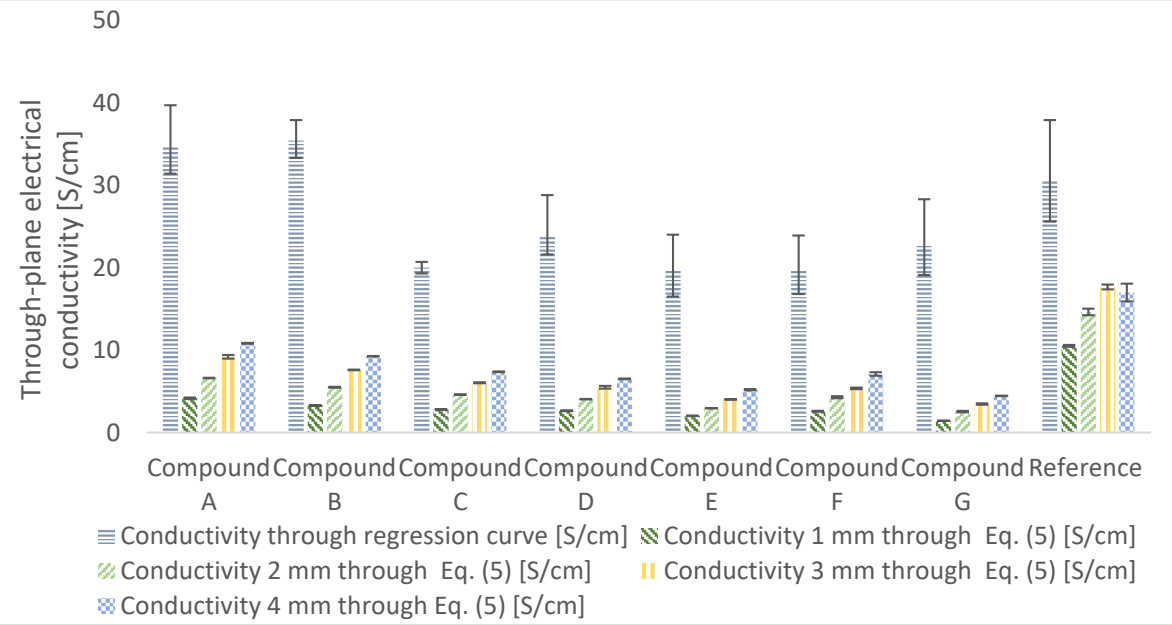

Figure 3: Comparison of through-plane electrical conductivity values with an 80% confidence interval obtained through regression curve and Eq. (5) for different thicknesses

Additionally to the electrical conductivity, flexural properties of the compounds were also evaluated. The flexural strength together with the through-plane electrical conductivity are given in Figure 4. The challenge of finding the compromise between electrical conductivity and good mechanical properties is evident: A compound with high conductivity such as compound A or B shows low mechanical performance. The relation between these two properties can be confirmed in Figure 5, where a correlation value of 0.61 is given for the analysed data.

Compound A and compound B show better through-plane electrical conductivity than the reference material, despite their higher matrix content. This is attributed to the synergistic effect by adding carbon black, carbon fibers and carbon nanotubes as a partial replacement of the

graphite. In the same line, compound D shows better electrical conductivity than compound C. This verifies the positive influence of the carbon nanotubes showed already in literature [7]. Positive influence of carbon black is also found when comparing the compounds A and B, showing a better performance of compound B despite lower amount of PP. This difference lies in the addition of carbon black and carbon fibers.

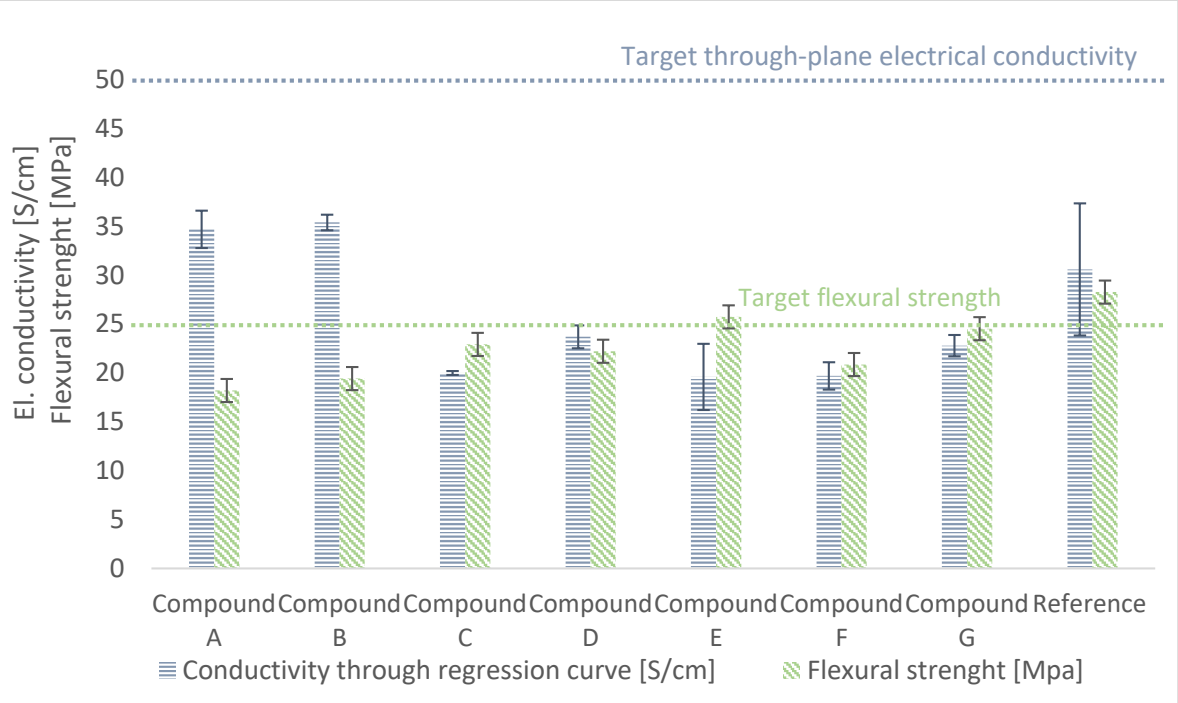

Figure 4. Comparison of the electrical and mechanical properties with an 80% confidence interval of compounds A to G and the reference material produced by compression moulding

Also, the influence in the flexural strength of the carbon fibers that are present in the Pre-Elec compound as proven in previous studies [8]. Compounds E, G and C with higher amount of CB and CF mixtures (11%, 11% and 8% respectively) show the best mechanical performance.

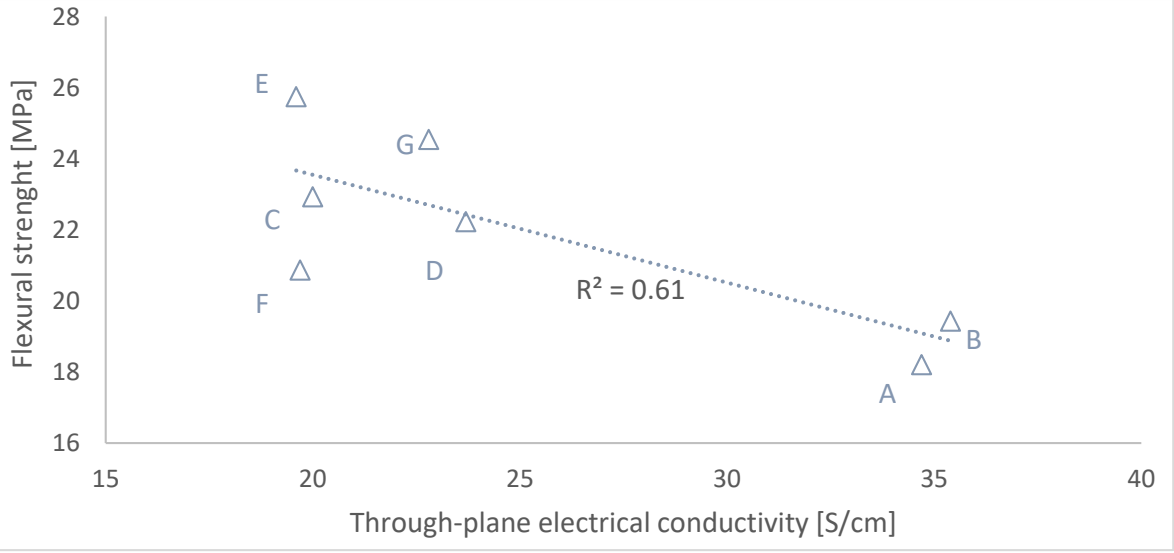

Figure 5. Correlation of the electrical and mechanical properties of compounds A to G produced by compression moulding.

  doi:10.5075/epfl-298799_978-2-9701614-0-0

The encouraging observation of these results is that a small increase in fillers (e.g. 2% between compound B and C) can lead to huge enhancement of the electrical conductivity (respectively by 44%, reaching 35.4 S/cm). Therefore, the target of 50 S/cm can be most probably achieved in next formulations. Future work will focus on further improvement of Compound B towards reaching both through-plane electrical conductivity and flexural strength targets.

Additionally, the compounds will be processed by injection moulding with optimized thermal management to be able to fill the bipolar plates moulds despite the high melt viscosities of the compounds.

Acknowledgements

The authors would like to acknowledge the Swiss Innovation Agency (Innosuisse) for the financial support of this research work. Project number: 43005.1 IP-ENG.

4. References

1. Antunes RA, de Oliveira MCL, Ett G, Ett V. Journal of Power Sources 2011; 196: 2945.
2. Bühler R, Thommen M, Le Canut J-M, Weber J-F, Rytka C, Tsotra P. Fuel Cells. 2021; 21:155.
3. Cunningham N, Lefèvre M., Lebrun G., Dodelet J.P., Journal of Power Sources 2005;143:93-102
4. Yeetsorn R, Fowler M, International Journal of Applied Science and Technology 2014; 7:13-21
5. Sadeghifar H., Energy Conversion and Management 2017; 154:191-202
6. Suherman H, Sahari J, Sulong AB, Ceramics International 2013; 39:7159-7166
7. Ma Y, Wu D, Liu Y, Li X, Qiao H, Yu Z, Composites Part B 2014; 56:384:391
8. Zakaria MY, Sulong AB, Sahari J, Suherman H, Composites Part B 2015; 83:75-80

  doi:10.5075/epfl-298799_978-2-9701614-0-0

CONDUCTIVE SMART NANOCOMPOSITE MATERIALS FOR STRUCTURAL HEALTH MONITORING AND MOTION DETECTION

Olalla. Sanchez-Sobrado, Daniel del Rosario, Ricardo Losada and Elena. Rodriguez*
Advanced Materials, AIMEN, O Porriño, Spain.
**olalla.sanchez@aimen.es*

Abstract: *Presented work collects results from evaluation of different polymeric based composite materials for Structural Health Monitoring and Strain Detection. With the aim of show the variety of key materials in sectors like civil aviation, wind energy, automotive or railway that present this ability, specimens of very different nature have analyzed: a) thermoplastic commercial 3D printing filaments loaded with carbonic nanofillers; b) epoxy resin loaded with graphene and c) Long carbon fiber reinforced resin composite. Measurements of electrical properties of resulting materials were taken to evaluate capability to detect the presence and the size of a structural defect as well as its spatial location. On the other hand, simultaneous measurements of electrical resistivity and mechanical strain during tensile tests were performed to analyze the behavior of materials as strain detectors. All composites studied have shown a positive response (modification of electrical performance) to external mechanical stimulus: induced damage and deformations.*

Keywords: conductive nanocomposites; structural health monitoring; motion detection; carbonic nanomaterials; graphene, carbon nanotubes.

1. Introduction

Structural maintenance in several industrial sectors like civil aviation, wind energy, automotive or railway is being currently based on scheduled maintenance on-ground inspections, in which Non-Destructive Inspections (NDI) are used to detect damage within the structural materials. In this scenario, in-service Structural Health Monitoring (SHM) of nanocomposite material parts plays a key role in the assessment of their performance and structural health [1]. Conductive carbon-based materials networks like those based in carbon nanotubes (CNTs) and others have been recently utilized as in situ sensors to detect microcracking and deformations in polymer and fiber reinforced polymer composite materials by using resistivity change method [2], [3]. The low electrical percolation threshold of these conductive materials allows forming an electrically conductive network withing the composite structure. This network allows identification of the formation of microcracks due to the changes in the electrical resistance as well as the detection of mechanical deformations of the structure [4].

The resistivity change method to perform SHM is since the generation of a microcrack in the polymer matrix of a composite material breaks conducting chains in the percolating conductive material or nanofiller network producing a modification on the electrical resistivity that can be related with the formation and size of the produced crack [5]. However, the spatial localization remains difficult. To overcome this drawback, resistance maps have been proposed to locate damage position [6] together with multi-scale modelling approach for simulating crack sensing [7]. On the other hand, the use of the coupled electro-mechanical response of these materials to self-sense their strain and damage during mechanical loading has been also widely studied

  doi:10.5075/epfl-298799_978-2-9701614-0-0

[8]. Carbonic materials like CNTs (but not only) have been deeply analyzed as candidate for strain and motion sensors at the macroscale, due to the dependence of the electrical properties on mechanical deformation at the nanoscale due to piezoresistive behavior. Many publications report the use of this carbonic based polymer nanocomposite for in textile-based, wearable sensing system for real-time motion detection [9], muscle, breathing and pulse motion [10] or electronic skins [11].

In the presented work, electrical properties, and both damage and strain dependent electrical resistance characteristics of several different carbon-based/polymer composite and nanocomposite materials were investigated: (a) CNTs reinforced RTM6 Epoxy resin, (b) different carbon-based nano additives thermoplastic composite for 3D printing technologies prepreg composite: PLA/CB; ABS/CNTs; PETG/CNTs and PEKK/CNTs and (c) long carbon fiber composite laminates. To analyze the ability of the different developed materials to detect different structural defects, the evolution of the electrical resistance when the size of the produced hole is increased has been analyzed for each composite. Systematically, large, and linear enhancement is obtained, even for the smallest defects. This behavior places polymeric composites integrating carbonic materials and nanomaterials as one of the most promising solutions for SHM applications. Some preliminary tests to evaluate capacities for failure detection have been as well performed. On the other hand, in this work we show a study of the capabilities presented by reinforced polymeric composites for motion detection. Simultaneous measurements of strain and electrical resistance were taken for representative composite coupons during tensile tests. The signal-matching presented by the different materials has been discussed as a direct estimation of the capability for strain sensing and potential use for motion detection applications.

2. Experimental

- FFF 3D printing manufacturing process.

Four dog-bone-type specimens and four rectangular specimens were printed for each of the four purchased filaments, with the commercial materials described below. The printing machine used was a 3D printing: A2V4 printing machine (3nt r) and Ultimaker 2+.

- Resin coupons preparation

Epocyl is the trade name of an epoxy resin with a indetermined load of CNTs that was purchased from Nanocyl. To cure mixtures a mixture of accelerator and hardener were used: Aradur 1571 (50%)/ Accelerator 1573 (50%). The 24 parts of the mixture by 76 of the mixture of resins and we cure at 120º C for 2h. The catalyst mixture is heated slightly before hand-mix it well and is mixed with the resins just before curing.

- Prepreg layup manufacturing process

The layers of Carbon Fiber prepreg, purchased from Toray, were cut manually with (0º,90º, +45º,-45º). First, a release agent was applied on the tool surface. The stack of plies was piled up manually. After the first ply was laid, debulking was made to ensure a good adhesion of the pre-preg to the tool surface. The rest of the plies were positioned following the stacking sequence. Debulking was performed for each four plies or when wrinkles appeared during stacking. This

step was accomplished by placing a non-perforated bleeder film and breather layer under a flexible vacuum bag, and by applying 0,9 bar of vacuum. After placing all the prepreg layers, the coupon was covered by a peel ply, a layer of perforated bleeder film and a non-woven breather cloth. Before introducing the tool on the oven, a vacuum test was performed to check the bag's integrity. Afterwards, the coupon was left under vacuum following the programmed curing cycle. After curing a demoulding phase was carried out.

- Measurements of electrical properties.

Once manufactured, two silver contacts 1 cm thick and 5 cm apart are painted and the ohmic resistance is measured with crocodiles in the acquirer. Data acquisitor system Keysight DAQ970A with an integrated DAQ901A-20 channels armature multiplexer module. This system acquires simultaneously measurements of electrical resistance and mechanical strain to analyse the SHM behaviour.

- Estimation of Conductivity and resistivity

Shape Factor (F)=S/L = 2x0,5/5 (mm) F=0,002 m

Conductivity $\sigma=1/\rho=1/R*0,02$ (S/m)

- Tensile tests.

They were carried out following the ASTM D3039/D3039M standard, the speed was 1mm/min, 10 cycles of ascent and descent were carried out in displacement control, until reaching the target tensions of 50, 100, 150, 200, 250, 300, 350, 400, 450 and 500 MPa. The speed of the section from 0 to 50 MPa is carried out at 0.5 mm/min. The speed of the rest of the sections is 1 mm/min. Due to the placement of the sensors on the specimen, the transverse extensometer cannot be installed.

3. Results and discussion

3.1 3D printing comercial thermoplastic filaments with nano-carbonic additives

Six dense dumbbell-type specimens were printed for each of the four purchased filaments, commercial filaments are described in Table 1. These consisted basically in thermoplastic-based polymers of different type and characteristics: PLA, ABS, PETG and PEKK. All these thermoplastics are nowadays highly considered for applications in numerous industrial sectors like aeronautics, wind energy, automotive, health, construction, or railway. All studied materials presented electrical conductivity due to small loads of different carbonic-based nanofillers: carbon nanotubes (CNTs) and Carbon Black (CB). To evaluate their conductivity, measurements of electrical resistance were taken. Once manufactured, two silver contacts of 1 cm thick and separated by 5 cm were painted directly on the polymeric surface and the ohmic resistance is measured using crocodiles with the acquirer system. The estimated values for conductivity calculated using procedure explained in experimental section, are presented in column 4 of Table 1.

Table 1: Thermoplastic based conductive polymeric filament used to evaluate conductive, SHM and Strain detection capacities.

  doi:10.5075/epfl-298799_978-2-9701614-0-0

Coupon	Description	Supplier	Resistance (ohm)
PLA	Carbon Black (load 20%)	Protopasta	0,588E3
ESD safe ABS	Unknown load of MWCNTs	3DXSTAT	0,464E6
CNT PETG	Unknown load of CNTs	3DXSTAT	0,346E9
PEKK-ESD	Unknown load of CNTs	3DXSTAT ESD	48.5E6

With the aim of analyze the potential of 3D printing conductive filaments made structures for self-monitoring the produced damage, holes of gradually increased size were performed in the center of each sample (hole enlarged using different drill bits). All materials show gradual change (resistivity increase, conductivity decrease) with increasing defect size. Results corresponding to PLA, PTGE and ABS are shown in graphs displayed in Figure 1. All materials respond positively to the formation of a defect so they could be proposed for SHM purposes, nevertheless and despite being the least conductive, CNT-PTGE is considered the best candidate since it presents the greatest change in conductivity. The type of filler integrating the nanocomposite plays a key role in this performance. Depending on the type of filler, two behaviors are observed. A) *Linear behavior* like when carbon black is the conductive filler. In this case, the change in conductivity with the size of the defect is remains linear for the whole range of defect-sizes evaluated. B) *Percolation behavior* like in the case of the CNTs used as fillers. In the second case, two regions can be set. Up to 5mm slow fall. From 5 mm abrupt drop (optimum zone). In this region a small variation in the size of a produced defect leads to high conductivity change, the higher change the easiest to detect so hence, these types of materials (filled with CNTs) are optimum for SHM purpose for a large range of defect sizes but specially above 5mm.

Figure 1 : Evolution of conductivity change with defect size for PLA, PTEG and ABS.

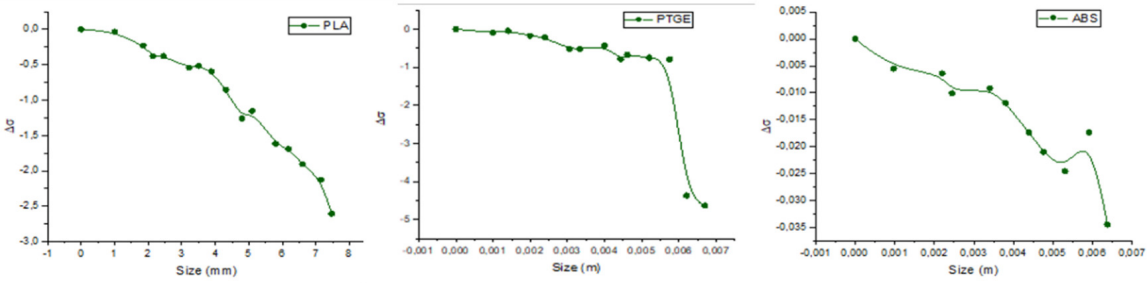

For the four polymeric filaments analyzed, simultaneous measures were taken for the variation of the strain and the variation of resistivity during a tensile test to evaluate the ability of these materials to detect mechanical deformation and evaluate their capacity for applications in body motion and strain detection. The results, shown in graphs of Figure 2 are very satisfactory: for all materials, resistivity increases during deformation, and as soon as deformation ceases and the material returns to its original state, resistivity also decreases. As expected, when polymers reach their respective break point, bot curves resistivity change and strain collapses. All polymers analyzed present have a similar value of elongation being PETG is the most "elastic", ABS is half elastic than PETG while PEKK is the one that endures more cycles as expected since

it belongs to the polymer family known as “high performance polymers” characterized by their extraordinary mechanical properties.

Figure 2. Simultaneus measurements of resistivity change (red lines) and strain (blue lines) for conductive ABS, PLA, PETG and PEKK respectively.

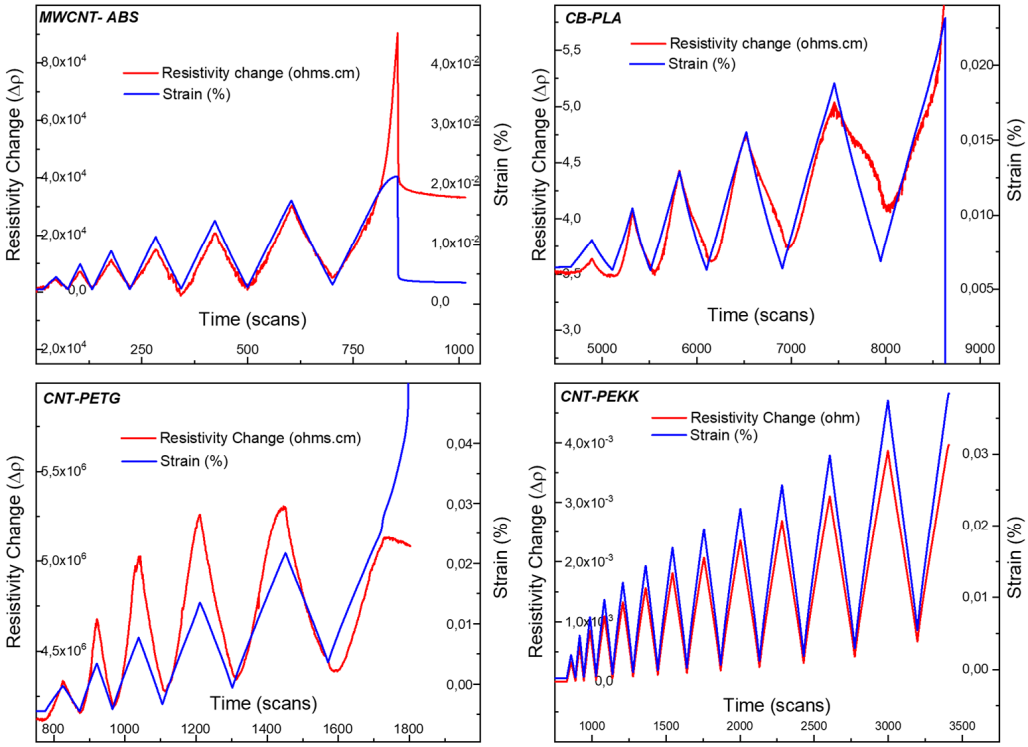

3.2 Epoxy resin with CNTs

With the aim of study the percolation curve of epoxy resin loaded with an undetermined amount of CNTs, we prepare different blends of epoxy resin RTM6 and Epocyl resin containing the CNTs load. Results corresponding to the electrical conductivity of each blend for each different blend is represented in Fig 3a. The expected plateau after reaching maximum of percolation curve is not achieved even for the blend containing a 100% of Epocyl resin. For the following experiments this was the blend selected. We prepare a batch of dog-bone test tubes for mechanical tests and a batch of rectangular (4 x 10 cm) tests to measure evolution of resistivity when the hole size increases gradually since the geometry is simpler. Results are presented in Fig 3b, the resistivity change before and after the production of the defect increases linearly with the gradual increase of size defect. For the window of hole size analyzed, a big range of resistivity is acquired which indicates that CNTs based epoxy resin is an excellent candidate for SHM, since even the smallest variation of defect size produces a clearly measured conductivity change. The reason of the good response is the effect of the breaking of the percolation chains of the CNTs dispersed in the resin. On the other hand, capability for strain detection was also evaluated by simultaneously measuring of the variation of the strain and the variation of resistivity during a tensile test. The results, shown in Fig 3c are very satisfactory: resistivity increases during deformation, and as

  doi:10.5075/epfl-298799_978-2-9701614-0-0

soon as deformation ceases and the material returns to its original state, resistivity also decreases. Results shows good capability of this material for strain and motion detection applications.

Figure 3. a) Percolation curve of Epoxy resin filled with CNT- based Epoxy resin. b) Evolution of change of the resistivity with defect size. c) Simultaneus measurements of resistivity change (red lines) and strain (blue lines) for conductive epoxy resin.

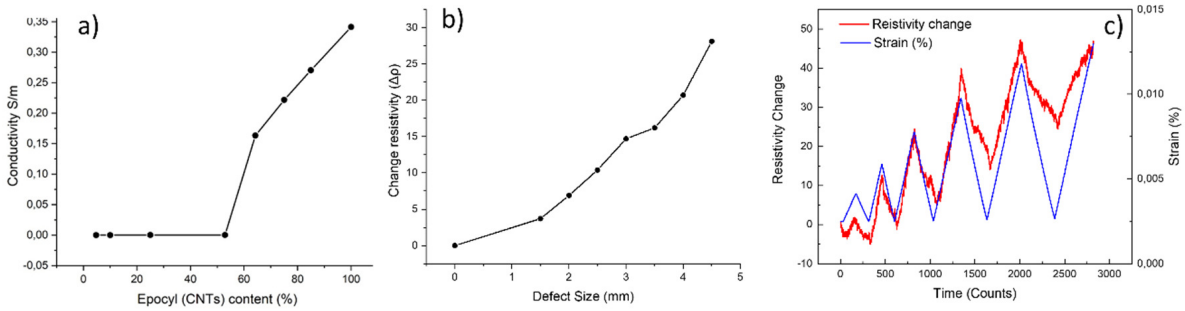

3.3 Carbon fiber reinforced polymer composite

The study of evolution of conductivity properties with the increasing size of drilled hole reveals that this material does not respond well when defect-sizes are low (below 7 mm, see Fig 4a). The reason lies in the fact that long fibers do not create percolation nets allowing conductivity changes. By expanding the range of the defect size, its influence on the conductivity measurements begins to be noticed. This means that, for defects larger than 8 mm, this material is valid for SHM by the electrical resistivity method.

We simultaneously measured the variation in resistance between two electrodes separated by a distance of 5 cm, as well as the deformation generated in the specimen during a tensile test (fig 4b). Changes in resistivity were measured using electrodes and strain using strain gauges. The electrodes consist of silver paint directly on the previously sanded surface in the center of the specimen, then the crocodiles are placed and fastened with copper tape (note, the copper tape ends up coming loose). The gauges are placed symmetrically on both sides of the specimen between the electrodes with glue.

We have started to do cycles of loading and unloading that are clearly shown in graphs displayed in fig 4b. Three different phases might be distinguished: Phase 1: The resistance measurements at the beginning follow well those of traction in phase and intensity. During this phase, at the end of the discharge cycle, the value of $\Delta R/l$ is zero. Phase 2: In phase 2, the first cracks appear and the permanent damage, therefore, at the end of the discharge cycles, $\Delta R/l$ always has a value other than zero due to the permanently open cracks (black dashed line). In this phase, the two signals (mechanical and resistive) also begin to shift. Phase 3: After the eighth cycle, the gauges stop measuring, it is assumed that there is a big damage produced in the resin until finally reach the breakage.

With the aim of evaluate failure location capacities of this material, measurements using an electrode configuration consisting of silver electrodes painted on the edges of the 20 x 20 cm

specimen (picture of Fig 4.c): 5 pairs of electrodes on the X axis and 4 pairs of electrodes on the Y axis separated by 5 cm. Two holes located at the positions indicated in the drawing of Fig4e were made using a drill, two 1.5 cm in diameter and the other 2 x 1 cm. Resistance values were measured between faced pair of electrodes, results are displayed in bars graphics of Fig 4e for pairs in X axis and Y axis. For positions where the resistivity change is reach higher values, a defect is assumed, and from values represented these graphics we can conclude that the material might self-detect the production and position of a defect of 2 x 1 cm located at X4Y4.

Figure 4. a) Evolution of resistivity change with defect-size. b) Simultaneus measurements of resistivity change (red lines) and strain (blue lines). C) Picture of the conductivity measurements set up. d) Carbon fiber based epoxy resin composite coupon prepared to evaluate failure detection capacities. e) measurements of resistivity change for different faced pairs of électrodes when holes are drilled.

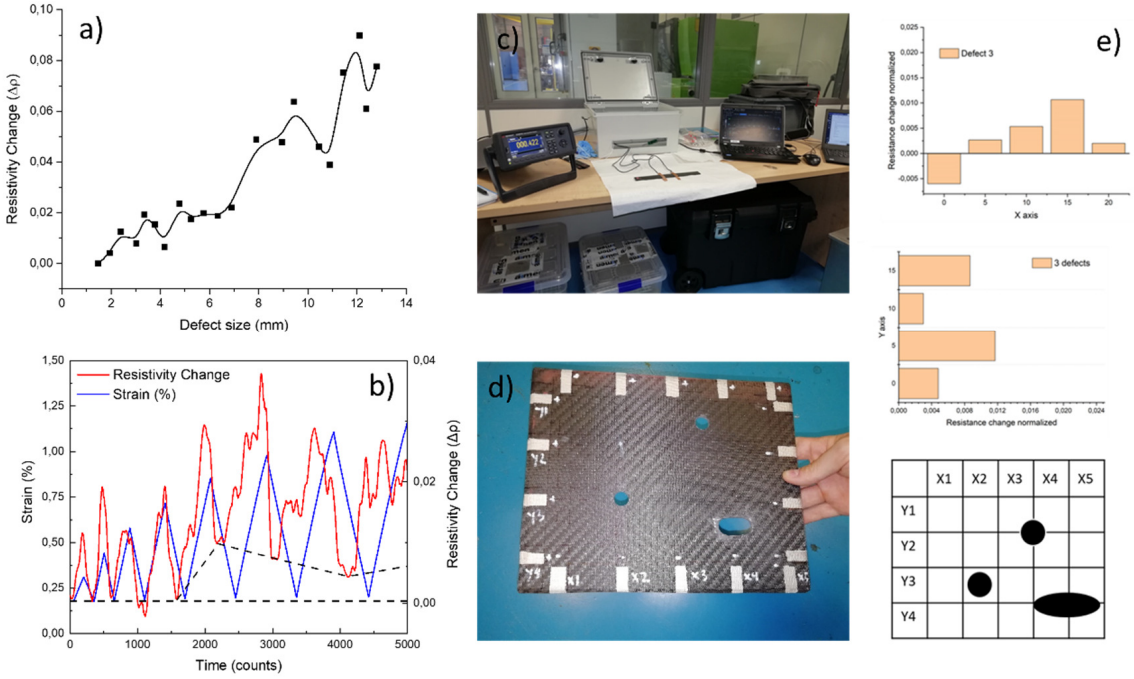

4. Conclusions

In the presented work, electrical properties, and both damage and strain dependent electrical resistance characteristics of several different carbon-based/polymer composite and nanocomposite materials were investigated: (a) CNTs reinforced RTM6 Epoxy resin, (b) different carbon-based nano additives thermoplastic composite for 3D printing technologies prepreg composite: PLA/CB; ABS/CNTs; PETG/CNTs and PEKK/CNTs and (c) long carbon fiber composite laminates.

All polymeric conductive composite and nanocomposite materials evaluated in this work present response to the formation of structural damage, being nanocomposite based in small amount of nanomaterials like CNTs the most sensitive and promised for applications in SHM.

All polymeric conductive composite and nanocomposite materials evaluated of different nature (thermoset and thermoplastic) have been proved suitable for applications in strain and motion

detection. Long carbon fiber-based composites, allow to detect the production of microcracks during tensile tests.

Long carbon fiber-based composites, allow to detect the production and the location of defects of 2 x 1 cm.

5. Acknowledgements

Works presented in this paper have been funded by the Spanish National Science and Technology Minister through the project READI (Ayudas Cervera para Centros Tecnológicos EXP - 00122598 / CER-20191020) of the Red Cervera programm.

6. References

1. K. Diamanti, et al. Structural health monitoring techniques for aircraft composites tructures. Progress in Aerospace Sciences 46 (2010) 342–352.
2. Myounggu Park, et al. Strain-dependent electrical resistance of multi-walled carbon nanotube/polymer composite films. Nanotechnology 19 (2008) 055705 (7pp). doi:10.1088/0957-4484/19/05/055705.
3. Erik T Thostenson et al. Real-time in situ sensing of damage evolution in advanced fiber composites using carbon nanotube networks. Nanotechnology 19 (2008) 215713 (6pp). doi:10.1088/0957-4484/19/21/215713.
4. Limin Gao, et al. Sensing of Damage Mechanisms in Fiber-Reinforced Composites under Cyclic Loading using Carbon Nanotubes. Adv. Funct. Mater. 2009, 19, 123–130. DOI: 10.1002/adfm.200800865.
5. Joung-Man Park et al. Inherent sensing and interfacial evaluation of carbon nanofiber and nanotube/epoxy composites using electrical resistance measurement and micromechanical technique. Composites: Part B 38 (2007) 847–861.
6. Christian Viets, et al. Damage mapping of GFRP via electrical resistance measurements using nanocomposite epoxy matrix systems. Composite part B. 2013. dx.doi.org/10.1016/j.compositesb.2013.09.049.
7. http://www.eco-compass.eu/context-2
8. Rui Zhang et al. Strain sensing behaviour of elastomeric composite films containing carbon nanotubes under cyclic loading. Composites Science and Technology 74 (2013) 1–5.
9. Katsunori Suzuki. Rapid-response, Widely Stretchable Sensor of Aligned MWCNT/Elastomer Composites for Human Motion Detection.2016. DOI: 10.1021/acssensors.6b00145.
10. Conor S Boland et al. Sensitive, High-Strain, High-Rate Bodily Motion Sensors Based on GrapheneRubber Composites. 2017. (DOI: 10.1002/adfm.201606604).
11. Hongfei Zhu. Versatile Electronic Skins for Motion Detection of Joints Enabled by Aligned Few-Walled Carbon Nanotubes in Flexible Polymer Composites.2017. DOI: 10.1002/adfm.201606604.

THE EFFECT OF CONDUCTIVE NETWORK ON POSITIVE TEMPERATURE COEFFICIENT BEHAVIOUR FOR MULTIFUNCTIONAL COMPOSITES: FROM FLEXIBLE SENSING TO SUSTAINABLE MANUFACTURING

Yi, Liu[a], Han, Zhang[b], Ton, Peijs[c], Emiliano, Bilotti[b]

a: Department of Materials, Loughborough University, Epinal Way, Loughborough Leicestershire, LE11 3TU, UK - y.liu2@lboro.ac.uk
b: School of Engineering and Materials Science, Queen Mary University of London, Mile End Road, London E1 4NS, UK
c: Materials Engineering Centre, WMG, University of Warwick, Coventry, CV4 7AL, UK

Abstract: *Conductive polymer nanocomposites with capability to detect the change in temperature or provide autonomous self-regulated heating are of great potentials for use in applications such as healthcare devices, soft robotics, artificial skins, and wearable electronics. In this work, we propose a systematic study to explore the PTC phenomenon and the underlying mechanism, from a conductive network viewpoint, taking account of both conductive fillers and polymer matrices. Three representative conductive fillers with distinct dimensions and shapes were selected to elucidate the effect of the "robustness" of different conductive networks on PTC behaviour in conductive polymer composites (CPCs). The desired conductive network can be obtained by selecting preferentially larger filler size, lower filler aspect ratio and/or selective distribution of filler. The highest PTC intensity was observed around the "critical" percolation threshold, in correspondence of networks with the lowest number of inter-particle contacts. With the properly selected matrix and filler, the composites can serve not only as a self-regulating heater, but also as a sensor to detect different stimuli, such as strain and damage sensing.*

Keywords: Positive temperature coefficient (PTC); conductive polymer composites (CPCs); self-regulating heating; strain and damage sensing.

1. Introduction

With the rapid development of functional and intelligent devices, there is an increasing demand for technological progress on new materials and devices, which can respond to external stimuli spontaneously. Benefiting from a large variety of polymer matrices and conductive fillers available, conductive polymer composites (CPCs) can be easily fabricated with desired properties, fulfilling a broad spectrum of requirements in various applications [1,2].

Certain CPCs, in particular, can show a pyroresistive behaviour ("pyro" is a Greek word meaning "fire/heat"), with their electrical resistivity changing with temperature. Pyroresistivity can manifest in two ways: (i) an increase in electrical resistivity with increasing temperature – known as positive temperature coefficient (PTC) effect – and (ii) a decrease in electrical resistivity with increasing temperature – known as negative temperature coefficient (NTC) effect [1,3]. Different hypotheses on the factors dominating the PTC effect have been proposed, based on experimental observations from different systems, some showing evident inconsistencies. For instance, some researchers in early studies found that the polymer crystalline phase change with temperature has a strong influence on the electrical conductivity of CPCs [4,5]. Luo *et al.* investigated composites based on carbon black (CB) and polymers with different degree of

  doi:10.5075/epfl-298799_978-2-9701614-0-0

crystallinity; from high to low, high density polyethylene (HDPE), low density polyethylene (LDPE), LDPE/ethylene–vinyl acetate (EVA) blends and amorphous polymethylmethacrylate (PMMA). The results have showed a correlation between polymer crystallinity and PTC intensity, namely the higher the crystallinity the higher the PTC intensity. Amorphous PMMA/CB composites showed the smallest PTC intensity, usually below one order of magnitude [4]. This finding is in agreement with the work on CB-based polymer composites by Meyer in early 1970 s [6]. Thermal volume expansion is phenomenologically one of the leading factors for the polymeric PTC transition, as reported by Yi et al. for HDPE/CB systems [7]. In semicrystalline polymers, the change of crystallites to an amorphous melt around the melting temperature leads a step change in volume expansion and an increase in the coefficient of thermal expansion (CTE). No such step change occurs instead in an amorphous polymer. However, although polymer crystallinity has been widely believed to be a dominant factor for the PTC effect, contrasting results have also been reported from literature, in which no correlation between PTC intensity and crystallinity was found [8,9]. For example, a surprisingly large PTC intensity (five orders of magnitude) has been reported for an amorphous CPC system based on PMMA containing 40 wt% Ag coated glass beads by Kar et al. [10]. The same group reported three orders of magnitude change in resistance in a nickel coated graphite (40 wt%) filled polycarbonate (PC). Overall, it is understandable and reasonable to believe that although the polymer matrix crystallinity has a significant influence on the PTC effect, other factors such as filler size and topology might also play a role, and in some cases a more dominant one.

Many researchers have revealed that CPCs with larger average filler size exhibit a higher PTC intensity and higher resistivity at room temperature than those systems with smaller filler size at similar filler content, possibly linked to the increase of average interparticle distance with increasing particle size [11,12]. The effect of different filler content and the use of a combination of different conductive fillers were shown to have an even more complex influence on the PTC effect [13]. It is believed that the PTC behaviour of conductive composites relies on the "robustness" of the conductive network formed within the polymer matrix [14,15]. Therefore, the conductive network in the CPCs can be considered the real dominating factor that influences the PTC effect, containing effects from both filler and matrix. Unfortunately, to date, a comprehensive study of the effect of the matrix, the filler and its formed conductive network on the PTC effect is still lacking.

Herein, an investigation into the understanding of how the conductive network affects the PTC behaviour has been performed. The contributions and influences of different types of filler and polymer matrix on the PTC performance are considered, exploring effects arising from the use of conductive fillers with different shapes and dimensions as well as different polymer matrices. Three classes of conductive fillers with distinct dimensional features have been employed in this work, ranging from spherical zero-dimensional (0D) silver coated glass spheres (AgS), 1-dimensional (1D) carbon nanotubes (CNT), and 2-dimensional (2D) graphite nanoplates (GNP) [16]. The motivation behind this selection is to explore the influence of dimensionality of the fillers on the electrical properties of the composites, the different conductive networks formed and their subsequent pyroresistive behaviour. In addition, three representative polymer matrices with distinct structure and properties have been selected: high density polyethylene (HDPE), thermoplastic polyurethane (TPU) and polycarbonate (PC). HDPE is a typical semicrystalline polymer widely used for PTC materials, while TPU is a thermoplastic elastomer for flexible applications, with the presence of hard blocks, acting as physical crosslinks upon

  doi:10.5075/epfl-298799_978-2-9701614-0-0

crystallisation. PC is a typical amorphous engineering polymer with outstanding strength, and impact resistance. With this systematic and comprehensive study, the factors that affect the pyroresistive (both PTC and NTC) behaviours as well as their underlying mechanisms are explored, providing a material selection guideline for self-regulating heating applications in the fields like healthcare, robotics, and smart heater.

Conventional PTC composites are often limited by the rigid nature of the polymer matrices, particularly at high conductive filler concentrations. The use of appropriate fillers and polymers are the key points in terms of increasing the performance of composites [2].

2. Experimental

2.1 Materials

The materials used in this study are listed in Table 1. All the polymers are in the form of pellets and dried overnight at 80 °C before compounding.

Table 1: Information on polymers and conductive fillers used in this study. [17]

	Materials	Trade name	Information
Polymer	Thermoplastic polyurethane (TPU)	Lubrizol Estane® 58,437	Density 1.19 g/cm3
	High density polyethylene (HDPE)	Rigidex® HD5218EA	Density 0.95 g/cm3
	Polycarbonate (PC)	Bayer Material Science Makrolon 2805	Density 1.20 g/cm3
Conductive filler	Multi-wall carbon nanotubes (MWCNTs)	Nanocyl® NC7000TM	Average diameter of 9.5 nm, carbon purity 90%
	Silver coated glass spheres (AgS)	Potters Industries Ltd.	Average diameter of 2.5 µm, 50 µm, 100 µm with the density of around 3.6, 2.6 and 2.5 g/cm3, respectively
	Graphite nanoplates (GNPs)	xGnP® Grade M	Average particle diameters of 15 µm, density 2.2 g/cm3, carbon content > 99.5%

2.2 Fabrication of composites

A Collin Lab twin-screw compounder P (ZK25, 25 mm, L/D = 40) was used to produce masterbatches of TPU with 5 wt% CNT and of HDPE with 24 wt% GNP. Extruder throughput was 2 kg/h using a screw speed of 50 rpm and 220 rpm for CNT and GNP, respectively, with a temperature profile ranging from 190 °C to 240 °C, over 8 heating zones [18]. Apart from the masterbatches, the remaining compounds and diluted composites from the masterbatches were prepared by melt mixing using a DSM X'plore MC 15 micro-compounder (Netherland). Both HDPE and TPU based composites were melt compounded at 200 °C using a screw speed of 50 rpm for 5 min in nitrogen atmospheres, while PC based composites were processed at a

  doi:10.5075/epfl-298799_978-2-9701614-0-0

temperature of 280 °C. The composites prepared in this study are listed in Table 2. The extruded strands were chopped into pellets and subsequently compression moulded into rectangular shaped samples with dimensions of 30 × 10 × 2 mm, using a Collin hot press P300E, at 220 °C for 5 min under 60 bar pressure. Two pieces of copper mesh (0.16 mm aperture wire diameter) were embedded at mid-depth and on both sides of each specimen during compression moulding and used as the electrodes for all electrical characterisations.

2.3 Characterisation

Scanning electron microscopy (FEI Inspector-F, Netherlands) was used to observe the morphology of as-received materials, as well as the fabricated conductive composite specimens. All the surfaces analysed were gold sputtered before imaging. The images were taken at different magnifications with an accelerating voltage of 20 kV. Electrical resistance was measured by the two-point probe technique and used to calculate the electrical resistivity, obtained using a picoammeter (Keithley 6485, USA) and a DC voltage source (Agilent HP 6614C, USA). As the electrodes are embedded into the compression moulded CPC, the contact resistance between the materials and electrodes are consistent and relatively low. The pyroresistive behaviour of all samples was tested with an apparatus consisting of a temperature-controlled oven (heating rate of 2 °C/min) and an in-situ two-point resistance measurement unit, obtained by combining a picoammeter (Keithley 6485, USA) with a DC voltage source (Agilent HP 6614C, USA). A thermocouple was placed close to, but not touching, the specimen to ensure reliable temperature reading. A constant voltage (1 V) was applied during heating and cooling cycles on the rectangular samples (30 × 10 × 2 mm), while the current and temperature were monitored and recorded simultaneously. Since the size difference induced by thermal expansion of the matrix during heating is very small compared to the sample dimension, it has been neglected from the electrical resistivity calculation. Voltage was applied with 1 s on/off intervals, to avoid electric field-induced filler alignment and network alteration. A minimum of three samples was tested for all characterisations.

3. Results and discussion

3.1 Morphology

It is essential to investigate the microstructure of the composites in order to obtain a better understanding of the conductive networks formed within the polymer matrices and their influence on the electrical and pyroresistive properties of CPCs. To understand the effect of filler size on the microstructure of the composite and any preferential distribution of conductive fillers within the matrix, AgS fillers with distinctly different diameters (2.5 µm, 50 µm, and 100 µm in Figure 1) were selected [17]. It is worth noting that, for the same filler concentration in a given volume of composite, smaller sized fillers (i.e. 50 µm) are present in larger numbers compared to larger fillers (i.e. 100 µm). This also implies that smaller (spherical) fillers present a higher specific surface area, with more potential contact points (or points close enough for tunnelling) between fillers to form conductive pathways, as compared to larger spherical fillers. This difference in the number of contact points is believed to have a significant impact on the electrical properties of the CPCs.

  doi:10.5075/epfl-298799_978-2-9701614-0-0

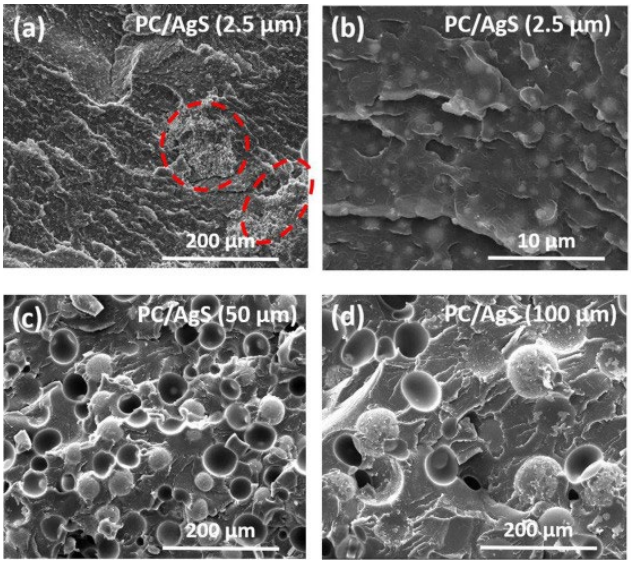

Figure 1. SEM images of cryo-fractured cross-sectional areas of PC based composites containing 30 wt% (above percolation) of 2.5 µm AgS, at a magnification of (a) 500x and (b) 10000x; (c) 40 wt% (above percolation) of 50 µm AgS, showing several contact points between fillers; and (d) 40 wt% (below percolation) of 100 µm AgS, without obvious contact points between fillers.

3.2 Pyroresistive properties

To examine the pyroresistive behaviour of AgS (2.5 µm, 50 µm and 100 µm) filled HDPE, TPU and PC composites, the electrical resistivity of the composites was monitored as a function of temperature (Figure 2). The effect of both polymer matrix and filler size on the observed pyroresistive behaviour have been studied, in order to establish a systematic understanding of their influence on PTC behaviour.

As shown in Figure 2a, AgS (2.5 µm) based composites exhibit a relatively small PTC intensity, regardless of the polymer matrix. Among the three composites, HDPE/2.5 µm AgS (25 wt%) shows the highest PTC intensity (about two orders of magnitude), more than one order of magnitude higher than for TPU and PC based AgS (2.5 µm) composites [17]. This difference is attributed to polymer crystallinity and the greater thermal expansion associated with the melting of the crystal phase. However, as known from the morphological study, small-sized AgS (2.5 µm) with a larger number of contact points build more robust conductive networks, which are more difficult to disrupt under the effect of the matrix thermal expansion. This explains, phenomenologically, why the PTC intensity of HDPE/AgS (2.5 µm) composite is much lower than the PTC intensity of HDPE composites containing larger AgS spheres (50, 100 µm). The same is true for the other polymer matrices. All the 50 µm and 100 µm AgS based composites, independently on the polymer matrix (HDPE, TPU, and PC), show a very high PTC intensity, of about eight orders of magnitude (Figure 2b and c) [17]. It is suggested that spherical conductive fillers of large size can induce a high PTC intensity as the number of conductive filler contact points is limited, which makes the conductive network more sensitive to perturbations, regardless of the polymer matrix. This is consistent with previous studies by our group and the concept of “robustness” of the conductive filler network [14]. The smaller the filler size, the more “robust” the conductive network is, as the number of specific conductive pathways increases, and the more difficult it is for the conductive network to be disrupted. However, the

PTC intensity is not a monotonic function of filler size. In fact, the PTC behaviour of composites based on the 50 µm and 100 µm AgS is very similar.

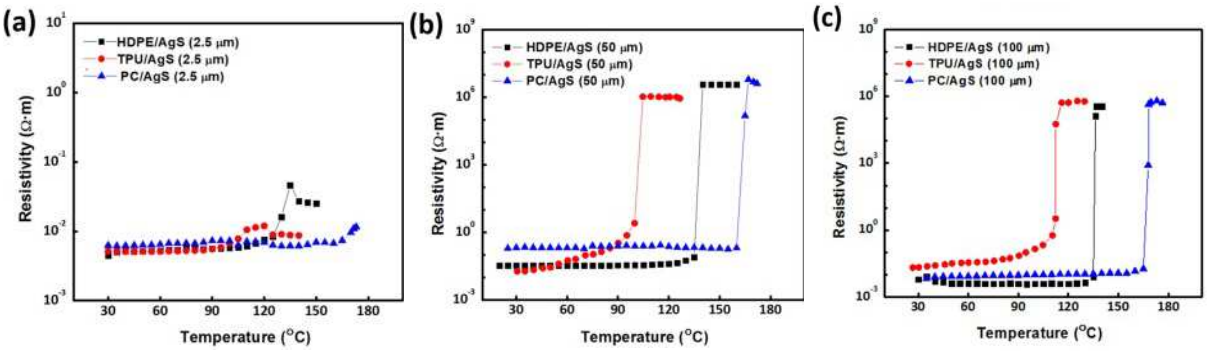

Figure 2. The pyroresistive behaviour of HDPE, TPU and PC filled with (a) 2.5 µm AgS (25 wt%, 30 wt% and 35 wt%); (b) 50 µm AgS (50 wt%); and (c) 100 µm AgS (50 wt%).

A considerable variation of PTC intensity has been observed for different filler shapes, ranging from eight orders of magnitudes, two orders of magnitude, to less than one order of magnitude, for AgS (50 µm), GNP and CNT in HDPE composites, respectively (Figure 3) [17]. This finding can be explained from the viewpoint of how the conductive network (or contact points between fillers) behave upon heating. Comparing the conductive network for 0D, 1D, and 2D fillers, it can be concluded that 0D AgS has the least number of contact points due to their lowest specific surface area. On the other hand, 1D nanotubes, exhibiting the highest aspect ratio and largest surface areas, can form robust, entangled and interconnected networks, leading to a large number of contact points which are the least likely to be separated by thermal expansion of the polymer matrix. 2D GNPs present an intermediate case in terms of both aspect ratio and number of contact points but without the possibility of entanglements, forming a network that is partially affected by the temperature approaching the PTC switch point with a trace of associated NTC behaviour. A similar trend was found in amorphous TPU, with a reduced PTC intensity or even a predominant NTC effect alongside an increasing number of contact points between conductive fillers, i.e. a more robust and interconnected network when moving from 0D to 1D fillers.

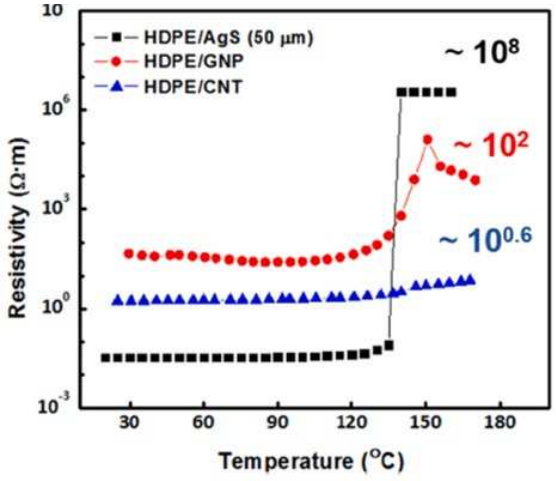

Figure 3. A comparison between the effect of 0D, 1D, and 2D filler conductive networks on the pyroresistive behaviour of HDPE/AgS (50 µm), HDPE/GNP and HDPE/CNT composites.

  doi:10.5075/epfl-298799_978-2-9701614-0-0

4. Applications

The composites can also serve as a sensor to detect different stimuli, such as strain and damage sensing [19]. For example, when the PTC composite layer (HDPE/GNP) is placed on top of fibre-reinforced composites, Figure 4 shows the relative resistance change (ΔR/R0) during cyclic loading to a strain of 0.1% and 0.2%, both at a strain rate of 1%/min. Overall, a good correlation between strain and resistance change of the composite was observed, enabling the current electrical sensing method to be used to monitor structure deformation by correlating sensing signals to mechanical deformation of composite structures. Moreover, it can be a useful tool for out-of-oven fibre reinforced composite curing, with only 1% of energy consumption [20].

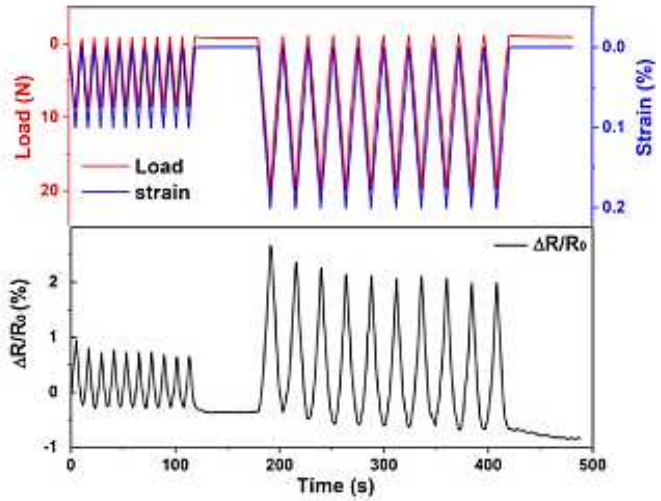

Figure 4. Electrical sensing data under cyclic loading at the strain of 0.1 and 0.2%, showing excellent correlation between sensing signals and mechanical deformation.

Acknowledgements

The authors gratefully acknowledge the financial support from LMK Thermosafe Ltd and Innovate UK (KTP number: KTP009619).

5. References

1. Liu Y, Zhang H, Porwal H, Busfield JJ, Peijs T, Bilotti E. Pyroresistivity in conductive polymer composites: a perspective on recent advances and new applications. Polymer International. 2019;68(3):299-305.
2. Liu Y, Zhang H, Porwal H, Tu W, Evans J, Newton M, Busfield JJ, Peijs T, Bilotti E. Universal Control on Pyroresistive Behavior of Flexible Self‐Regulating Heating Devices. Advanced Functional Materials. 2017;27(39):1702253.
3. Xiang ZD, Chen T, Li ZM, Bian XC. Negative temperature coefficient of resistivity in lightweight conductive carbon nanotube/polymer composites. Macromolecular Materials and Engineering. 2009;294(2):91-5.
4. Luo Y, Wang G, Zhang B, Zhang Z. The influence of crystalline and aggregate structure on PTC characteristic of conductive polyethylene/carbon black composite. European polymer journal. 1998;34(8):1221-7.
5. Deng H, Skipa T, Zhang R, Lellinger D, Bilotti E, Alig I, Peijs T. Effect of melting and crystallization on the conductive network in conductive polymer composites. Polymer. 2009;50(15):3747-54.

  doi:10.5075/epfl-298799_978-2-9701614-0-0

6. Meyer J. Glass transition temperature as a guide to selection of polymers suitable for PTC materials. Polymer Engineering & Science. 1973;13(6):462-8.
7. Yi XS, Shen L, Pan Y. Thermal volume expansion in polymeric PTC composites: a theoretical approach. Composites science and technology. 2001;61(7):949-56.
8. Xiong C, Zhou Z, Xu W, Hu H, Zhang Y, Dong L. Polyurethane/carbon black composites with high positive temperature coefficient and low critical transformation temperature. Carbon. 2005;8(43):1788-92.
9. Fournier J, Boiteux G, Seytre G, Marichy G. Positive temperature coefficient effect in carbon black/epoxy polymer composites. Journal of materials science letters. 1997;16(20):1677-9.
10. Kar P, Khatua BB. Highly reversible and repeatable PTCR characteristics of PMMA/Ag‐coated glass bead composites based on CTE mismatch phenomena. Polymer Engineering & Science. 2011;51(9):1780-90.
11. Ota T, Fukushima M, Ishigure Y, Unuma H, Takahashi M, Hikichi Y, Suzuki H. Control of percolation curve by filler particle shape in Cu-SBR composites. Journal of materials science letters. 1997;16(13):1182-3.
12. Jing X, Zhao W, Lan L. The effect of particle size on electric conducting percolation threshold in polymer/conducting particle composites. Journal of materials science letters. 2000;19(5):377-9.
13. Xu HP, Wu YH, Yang DD, Wang JR, Xie HQ. Study on theories and influence factors of PTC property in polymer based conductive composites. Rev. Adv. Mater. Sci. 2011;27(2):173-83.
14. Asare E, Evans J, Newton M, Peijs T, Bilotti E. Effect of particle size and shape on positive temperature coefficient (PTC) of conductive polymer composites (CPC)—a model study. Materials & Design. 2016;97:459-63.
15. Zhang X, Zheng S, Zou H, Zheng X, Liu Z, Yang W, Yang M. Two-step positive temperature coefficient effect with favorable reproducibility achieved by specific “island-bridge” electrical conductive networks in HDPE/PVDF/CNF composite. Composites Part A: Applied Science and Manufacturing. 2017;94:21-31.
16. Bianco A, Cheng HM, Enoki T, Gogotsi Y, Hurt RH, Koratkar N, Kyotani T, Monthioux M, Park CR, Tascon JM, Zhang J. All in the graphene family–A recommended nomenclature for two-dimensional carbon materials. Carbon. 2013;65:1-6.
17. Liu Y, Asare E, Porwal H, Barbieri E, Goutianos S, Evans J, Newton M, Busfield JJ, Peijs T, Zhang H, Bilotti E. The effect of conductive network on positive temperature coefficient behaviour in conductive polymer composites. Composites Part A: Applied Science and Manufacturing. 2020;139:106074.
18. Liu Y, Zhang H, Porwal H, Tu W, Wan K, Evans J, Newton M, Busfield JJ, Peijs T, Bilotti E. Tailored pyroresistive performance and flexibility by introducing a secondary thermoplastic elastomeric phase into graphene nanoplatelet (GNP) filled polymer composites for self-regulating heating devices. Journal of Materials Chemistry C. 2018;6(11):2760-8.
19. Tao Y, Liu Y, Zhang H, Stevens CA, Bilotti E, Peijs T, Busfield JJ. Smart cord-rubber composites with integrated sensing capabilities by localised carbon nanotubes using a simple swelling and infusion method. Composites Science and Technology. 2018;167:24-31.
20. Liu Y, van Vliet T, Tao Y, Busfield JJ, Peijs T, Bilotti E, Zhang H. Sustainable and self-regulating out-of-oven manufacturing of FRPs with integrated multifunctional capabilities. Composites Science and Technology. 2020;190:108032.

  doi:10.5075/epfl-298799_978-2-9701614-0-0

GRAPHITE FILLED THERMOPLASTICS FOR THERMALLY CONDUCTIVE PIPES

André Kayser[a], Marco Grundler[a], Kevin Buchalik[b], Reinhard Schiffers[b]
a: Zentrum für BrennstoffzellenTechnik GmbH (Duisburg, DE) – a.kayser@zbt.de
b: University of Duisburg-Essen, Institute of Product Engineering (IPE), Duisburg, Germany

Abstract: *Aim of an ongoing research project at ZBT is the development of an extrusion process and a thermoplastic-graphite-compound for the production of a plastic pipe with an increased thermal conductivity (TC) in the range of 2 - 5 W/mK (in radial direction) and the standardized strength requirements for pipes made of PE and PP. The product dimensions of the pipe to be developed should meet nominal diameters from DN25 to DN32 with an internal pressure resistance of PN6 (6 bar). The particle orientation of flaky graphite in an extruded pipe is to be influenced by an innovative extrusion tool in order to achieve a high thermal conductivity with the lowest possible filler content and thus to achieve the required strength and bending stiffness. On the one hand, applications such as heat exchangers can thus be opened up that were previously reserved for metallic materials, and on the other hand, the efficiency of pure polymer heat exchangers already in use can be significantly improved.*

Keywords conductive compound; heat exchanger; thermal conductivity

1. Introduction

Plastics are a widespread material that is used in almost all applications. From everyday life to highly specialized and highly stressed components in mechanical engineering, plastics are taking on more and more functions. On the one hand, this is due to their low density with relatively good mechanical strength, which leads to weight savings compared to metals. On the other hand, due to their low melting point and good flowability, plastics can be molded into complex shapes by processes such as extrusion or injection molding. This allows greater design freedom for components compared with metals.

Domains previously dominated by metals are those of electrical and thermal conductors. Plastics typically exhibit insulating properties due to their chemical structure. Thus, areas where high thermal or electrical conductivity was required often relied on metallic materials in the past. By incorporating conductive fillers such as graphite or carbon black into plastics, electrical and thermal conductivity (TC) can be induced. In further steps, these compounds can then be formed into the desired shape. In the project on which this paper is based, highly filled compounds are converted into pipes by continuous extrusion using a pipe extrusion die.

Until now, corrosion resistant metals such as titanium have been used for highly corrosive applications such as seawater desalination. These have high corrosion resistance combined with good TC. However, titanium is a very expensive material. Available alternatives such as plastic heat exchangers, however, do not have comparable heat exchange performance. Compounds that have high TC and are made of inexpensive materials can be an alternative here. In order to be used in heat exchangers, however, compounds must have sufficiently good mechanical properties in addition to their conductivity and a surface that is not susceptible to fouling.

  doi:10.5075/epfl-298799_978-2-9701614-0-0

Within the project, a process for continuous pipe extrusion was to be developed in which sufficiently stable pipes with a TC of 2-5 W/mK can be produced. To achieve high TC at a low filler content a novel extrusion die was designed which induces an orientation into the melt for graphite particle to orient perpendicular to extrusion direction.

2. Background

A material mixture of a plastic and one or more fillers is called a compound. The plastic is the so-called matrix material and is mixed with the filler. The thermal, mechanical or rheological properties of compounds are thus composed of the respective properties of the plastic and the filler, whereby these are mainly determined by the filler due to the high filler content. The compounds investigated here primarily consider the introduction of large amounts of graphite into various thermoplastics and the resulting change in material properties.

Graphite has a hexagonal crystal structure, with the individual carbon atoms forming covalent bonds with three other carbon atoms within the planar basal planes, the graphene layers. However, only weak Van der Waals forces prevail between the basal planes [1]. These different bond strengths lead to the pronounced anisotropy of the characteristic properties of graphite, such as electrical and TC, but also mechanics which also translate into the compound characteristics. In literature it could be demonstrated that TC correlates with particle size and shape of filler [2]. Since heat is transported by phonons and each individual phase transfer between particles and/or polymer leads to a scattering of phonons, fewer transfers between particles to cross a certain length leads to better heat transport [3]. Bigger particles and particles with larger aspect ratios therefore have an advantage and show better TC [4].

With processes that lead to an orientation parallel to the surface in the final product, such as pipe extrusion, the through-plane TC is decreased, as particles are oriented in in-plane direction. To circumvent this problem an extrusion die which leads to an orientation of filler particles perpendicular to extrusion direction could lead to significant improvements [5].

3. Materials and Methods

3.1 Materials and compound preparation

A commercially available high-density polyethylene (PE-HD) from LyondellBasell (Hostalen ACP 9255 PLUS) was used as matrix material. Two different commercially available graphite types from LUH corporation were used. The first has a plate like morphology and a D90 of 150 µm (G150). The second has a plate like structure as well and a D90 of 300 µm (G300). Based on previous experience filler contents of 30 wt. %, 40 wt. % and 50 wt. % were chosen.

Binary compounds consisting of graphite and polyethylene were produced using a Ringextruder RE3 made by CPM extrusion group. The mass flow was 30 kg/h and the number of revolutions was 200 rpm. Polymer and graphite input were achieved by gravimetrically controlled dosers. Polymer was added in the main feed section whereas graphite was added in a split-feed process further downstream using a sidefeeder. Added air and other volatile components were removed by two degassing units. An extrusion temperature of 200 °C was used.

  doi:10.5075/epfl-298799_978-2-9701614-0-0

3.3 Production of pipes

For the production of pipes, the compound was extruded using a single screw extruder by Brabender (Compact Extruder KE 30/25D) and downstream processing equipment by GRAEWE consisting of vacuum cooling calibration (VT 63/2/3), haul-off (BA 32/600), cutter (SC 40) and pipe-coiler (EW 1000).

For extrusion four different die concepts were used. They were designed by the Institute of Product Engineering (IPE) in Duisburg according to industry standards and based on fluid simulations. A modular design was developed which allowed to change concepts with only replacing the core, sleeve and relaxation ring and therefore keeping most parts constant. This should lead to better comparability between concepts.

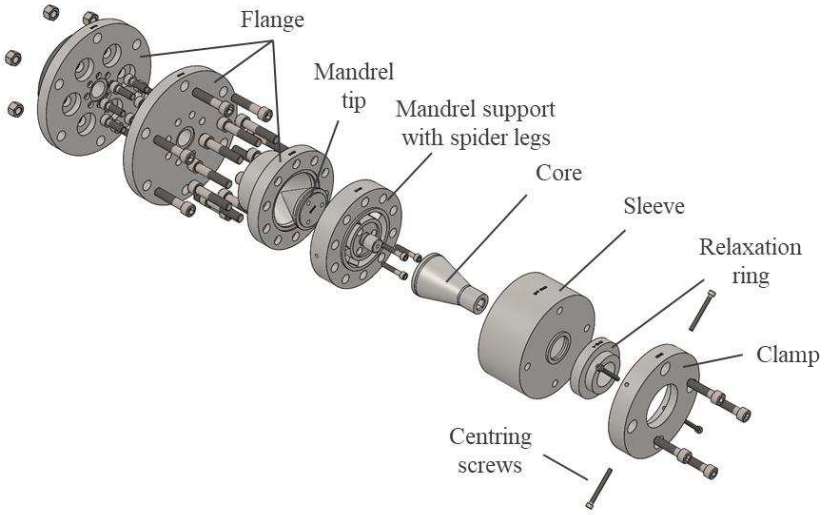

Figure 1: Pipe extrusion die IPE – Reference DN32

The four different concepts with the simulated shear rates are presented below. Concept A was a classical pipe extrusion concept where the shear rate at the outlet in the center of the melt approaches zero and increases towards the wall leading to an alignment of the melt in extrusion direction. Concept B uses a sudden narrowing of the flow path close to exit of the die with a consecutive widening. This leads to a compression of the melt followed by an expansive flow. This expansive flow is supposed to create an alignment of the melt in radial direction. The following relaxation zone is shortened to prevent realignment.

  doi:10.5075/epfl-298799_978-2-9701614-0-0

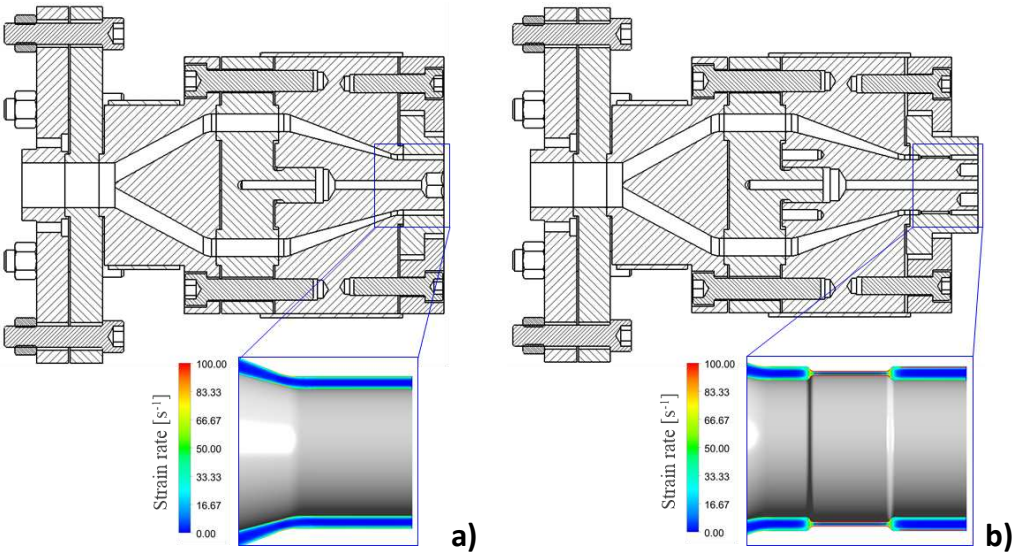

Figure 2: Left: Concept A, Right: Concept B

Concept C uses three separate zones where the melt is sheared in zone 1 and zone 2, so that it can be assumed that the melt has aligned in direction of the flow while the melt is led through a curved shape. In zone 3 the flow is led through a sharp turn followed by an expanded flow channel. This turn is designed to induce wall slip behavior, which is supposed to keep the orientation in the melt in direction of zone 2. The following expansion helps maintain this orientation in the melt. Concept D uses a different approach. Here additional flow walls are installed into the melt flow creating a three-dimensional flow profile. If the wall spacing is lower than the channel width this should result in an additional creation of shear induced orientation leading to further orientation. However, it is unclear if this shear leads to beneficial alignment and whether the following relaxation zone will be short enough to not cancel out this effect.

All die concepts were made in DN32 geometry and DN25 geometry.

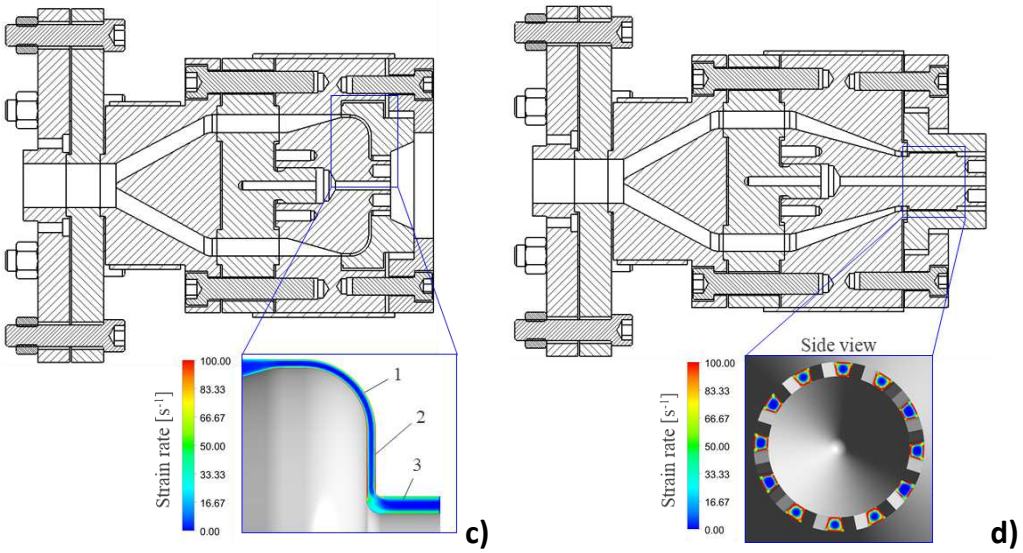

Figure 3: *Left: Concept C, Right: Concept D*

3.4 Measurement of thermal conductivity (ex-situ)

The TC of the compound materials was determined on a NETZSCH LFA 457 MicroFlash instrument according to DIN EN ISO 22007-4. The laser flash method is an unsteady (transient)

one-dimensional measuring method with which the thermal diffusivity of a specimen material is determined. The specimen is heated uniformly on the underside by a short laser pulse. The temperature increase on the upper side of the specimen is measured with an infrared detector and the temperature signal is plotted against time, from which the thermal diffusivity can be calculated. The through-plane thermal conductivities are determined on one specimen per compound. For this purpose, each test specimen is measured 3 times and the measured values averaged. Due to the fact that the specific heat capacity of compound materials is unknown, it is determined during the measurements by comparison with a known reference sample. The TC λ is then the product of the material density ρ, the thermal diffusivity a and the specific heat capacity cp. Since LFA measurements require a flat sample, a sample from the pipe is taken, flattened under pressure and temperature to achieve the necessary sample geometry.

3.5 Measurement of thermal conductivity (in-situ)

Since true TC in case of a pipe heat exchanger is not only influenced by through-plane conductivity but also in-plane conductivity, the extruded pipes were tested in a heat exchanger environment. A special test rig was developed where the produced pipe could be installed into a double wall heat exchanger. To measure TC the volume flow of water and temperature at the entrance and exit of the heat exchanger were measured. Using this and the geometry of the extruded pipe the TC necessary to achieve this difference in temperature can be calculated according to [6]. To achieve proper thermal stability each measurement was performed for 1.5 hours

4. Results and discussion

4.1 Measurement of thermal conductivity (ex-situ)

The following figure (fig. 4) shows the measured through-plane TC measured with LFA for all concepts and three filler contents and a pipe dimension of DN25. First of all, it is evident, that all three concepts that induce orientation (namely concept B-D) result in a higher TC compare to the classic die design in concept A. The only outlier in this case is the sample of 30 wt.% graphite G150G150. On average concept C and D achieve the highest thermal conductivities.

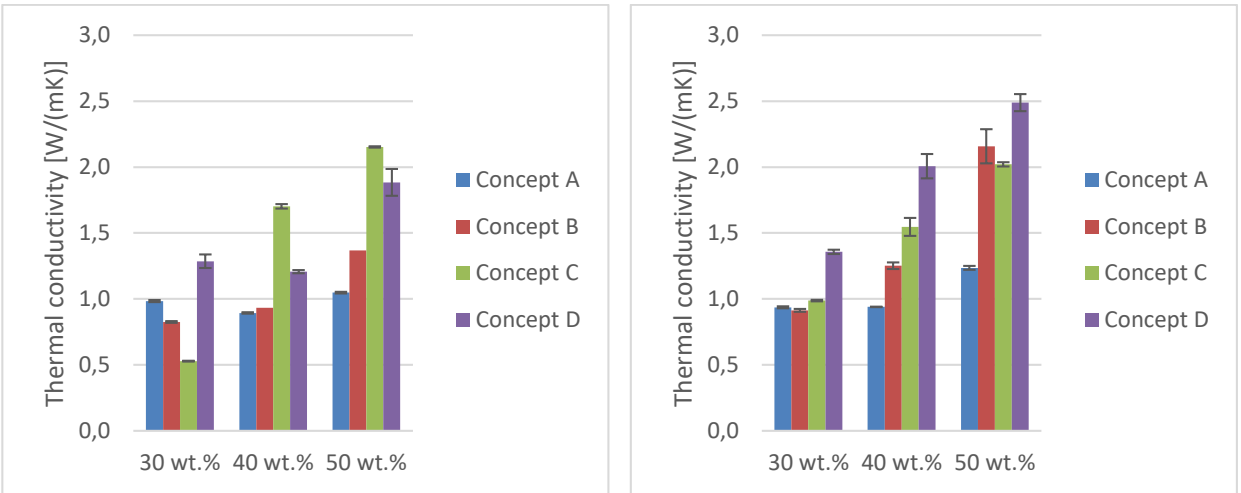

Figure 4:TC of regular extrusion vs. new extrusion concept measured by LFA, DN25, left: Graphite G150, right: Graphite G300

  doi:10.5075/epfl-298799_978-2-9701614-0-0

Comparing the results for diameter DN25 between the two graphite, the smaller graphite G150G150 achieves higher conductivities with concept C, while the larger graphite achieves highest conductivities with concept D. Overall the graphite with larger particles G300 reaches higher conductivities ranging up to around 2.5 W/mK in the DN25 diameter samples.

Comparing the results for diameter DN32 (fig. 5) between the two graphite, the results are quite similar to the findings in the smaller diameter when comparing concepts. Again, all concepts designed to improve TC achieve this goal. Concept C shows the highest overall TC with the small graphite, while concept D shows highest TC with the larger graphite. Overall, the values of TC are substantially higher in the smaller graphite, while being similar to the reference concept in the larger graphite.

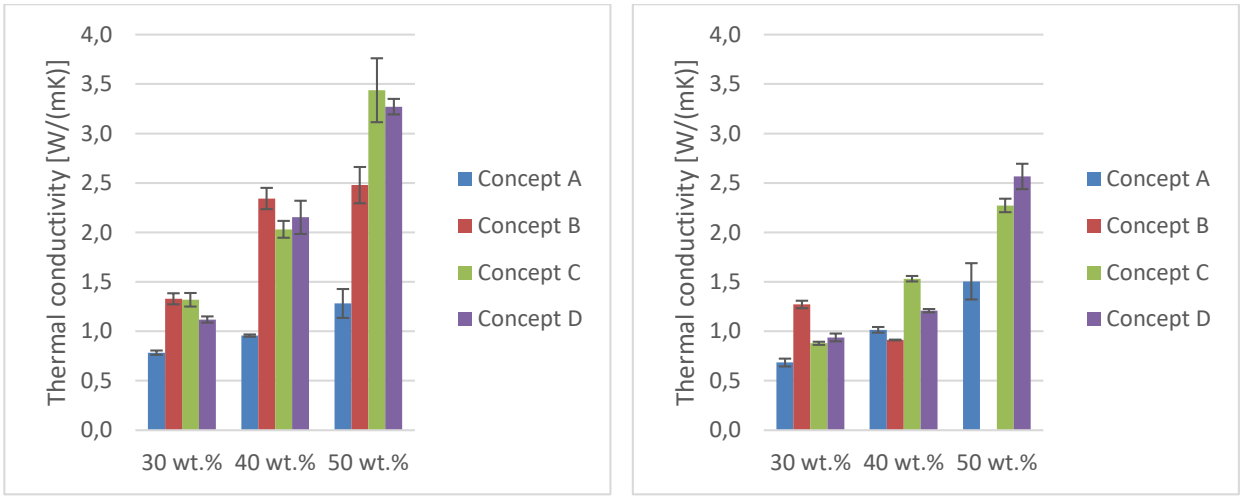

Figure 5: TC of regular extrusion vs. new extrusion concept measured by LFA, DN32, left: Graphite G150, right: Graphite G300

4.2 Measurement of thermal conductivity (in-situ)

The following figure (fig. 6) shows the in-situ measurement results for pipes with the smaller diameter of DN25.

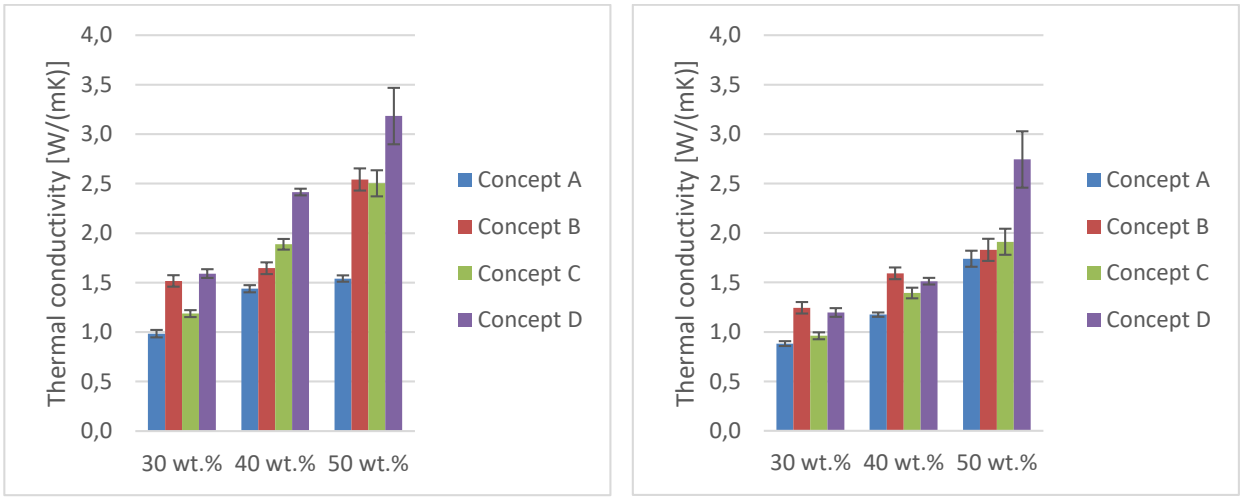

Figure 6: TC of regular extrusion vs. new extrusion concept measured by in-situ test, DN25, left: Graphite G150, right: Graphite G300

  doi:10.5075/epfl-298799_978-2-9701614-0-0

Comparing the results for DN25, all concepts lead to an improvement compared to the reference concept A. Overall concept D achieves the highest improvements on average. With the smaller graphite the overall improvements are larger and the resulting TC is higher. With the larger graphite the TC of the reference sample is higher compared to the reference sample with the small graphite. The improvements with the large graphite (G300) and filler contents of 30 wt.% and 40 wt.% are comparatively small. Only 50 wt.% shows a significant improvement using concept D. Using the smaller diameter, highest TC was achieved using graphite G150 and concept D.

The following figure (fig. 7) shows the results for in-situ measurement of TC of pipes with the larger diameter DN32. Using the larger graphite (G300) pipes of higher filler contents could not be extruded using concept B.

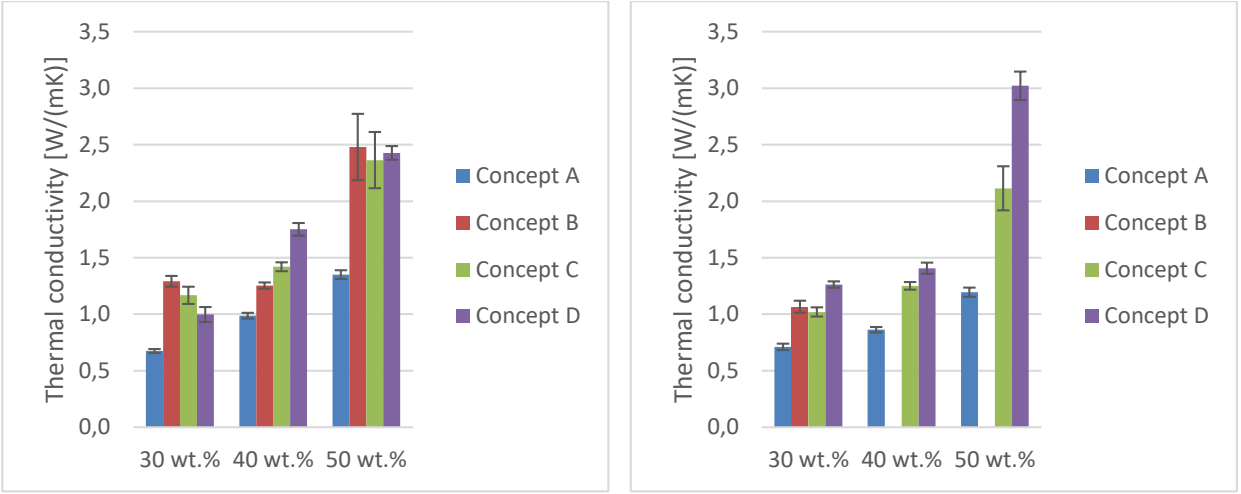

Figure 7 *TC of regular extrusion vs. new extrusion concept measured by in-situ test, DN32, left: Graphite G150, right: Graphite G300*

Comparing the results for the larger diameter DN32, concepts B-D achieve an improvement in TC compared to reference concept A. For graphite G150 there is no best concept overall and the degree of improvement for each concept varies with the filler content. For high filler contents concept B-D achieve similar thermal conductivities. For graphite G300 concept D is the overall best concept regardless of filler contents. Highest overall TC was achieved with graphite G300 and concept D. Therefore, the results of the larger diameter and graphite G300 are comparable to the results with smaller diameter, while results for graphite G150 are different for each diameter. This suggests that the flow profile difference for the different diameters has a greater impact on the smaller graphite.

5. Conclusion

Within this paper three different concepts for inducing orientation into a melt of polymer-graphite-compound were designed and compared with a more conventional pipe extrusion die. To test the dies, compounds of two graphite types and three filler contents were produced and used for pipe extrusion. Pipes with diameter of DN25 and DN32 were produced. The TC of resulting pipes was measured using LFA and a specifically designed test-rig for in-situ testing.

Out of the three die concepts for improving TC, all three lead to a significant improvement while maintaining pressure stability. Different concepts appear to be favorable depending on graphite

  doi:10.5075/epfl-298799_978-2-9701614-0-0

size. Pipe diameter which is directly correlated to thickness of the pipe also affects the resulting TC. These results were verified with a through-plane measurement using an LFA and an in-situ heat exchanger test bench. The results of both methods were similar though not identical. It stands to reason that the in-plane TC has an effect in the in-situ test, as heat is also transported along the pipe, leading to further homogeneity. Over all the in-situ test shows lower TC compared to LFA. Between the concepts, concept D shows highest improvement of TC. TC of the materials could be more than doubled, so that pipes with only 50 wt.% of graphite reach thermal conductivities of up to 3 W/mK.

Acknowledgements

This research is funded by the state Nordrhein-Westfalen (Germany) using funds from the Europäischen Fonds für regionale Entwicklung (EFRE) 2014-2020. This publication was created in the context of this research project (EFRE-0801478).

6. References

1. P. W. Atkins and J. de Paula, Physikalische Chemie, 5., [komplett überarb.] Aufl. (Wiley-VCH Verl., Weinheim, 2013).
2. J. Lee, T. S. Yun, and S.-U. Choi, Materials (Basel, Switzerland) 8, 3975 (2015).
3. C. Huang, X. Qian, and R. Yang, Materials Science and Engineering: R: Reports **132**, 1 (2018).
4. P. E. P. R. S. A. Devpura, Microscale Thermophysical Engineering **5**, 177 (2001).
5. M. Qu, F. Nilsson, and D. Schubert, Fibers **6**, 3 (2018).
6. *VDI-Wärmeatlas*, Mit 320 Tabellen, 11., bearb. und erw. Aufl. (Springer Vieweg, Berlin, Heidelberg, 2013).

  doi:10.5075/epfl-298799_978-2-9701614-0-0

RECYCLING OF GRAPHITIC BIPOLAR PLATES FOR VANADIUM REDOX BATTERIES

Marco Grundler, André Kayser, Paul Stannek
Zentrum für BrennstoffzellenTechnik GmbH (Duisburg, DE) – m.grundler@zbt.de

Abstract: *While energy storage solutions such as redox flow batteries are considered a key component for the turnaround in energy policy, recyclability of individual components has not yet been intensively studied. In an ongoing research project "Re3dOx" (funded by Federal Ministry of Economic Affairs and Climate Action) ZBT GmbH investigates the recycling of graphite-polymer-compounds that were used as bipolar plate material in redox flow batteries. Production of bipolar plates in a resource-saving manner is the main goal of the project. Currently, incorrectly produced bipolar plates are being disposed of, which leads to a high reject rate during production and post-processing. In order to conserve resources, recycled raw materials and rejects are to be reused. This recyclate is tested for its compatibility in the redox flow battery and subsequently processed to bipolar plates again. The plates are characterized in order to evaluate the influence of the recycled raw materials on the board quality.*

Keywords filled compound; bipolar plate; redox flow battery; recycling

1. Introduction

Vanadium Redox Flow Batteries (VRFB) are promising devices for energy storage especially with respect to short time stationary demand [1]. The intensified use of renewable energy requires efficient, save, and low-cost battery technologies. Great advantages of VRFBs are their independent adjustability of power and capacity, long cycle stability as well as their safety. VRFB, which are available in the kWh to MWh range, have already been intensively studied [2,3,4]. VRFBs use the same element as active material in both half cells. The VO^{2+}/VO_2^{+} couple in sulfuric acid as positive electrolyte and the V^{2+}/V^{3+} couple being applied as negative electrolyte [5]. Both electrolytes are stored in external tanks and pumped through the battery cells during charging and discharging. Reduction and oxidation take place at porous carbon fiber electrodes, which are placed between the graphitic bipolar plate and the membrane.

Therefore, the bipolar plate is one of the key components of the VRFB. The bipolar plates electrically conduct and physically separate adjacent battery cells in series. A high electrical conductivity, sufficient impermeability, mechanical stability as well as long-term chemical and electrochemical resistivity of bipolar plate is required, because of harsh conditions in VRFB like acidic vanadium electrolyte and high potential differences [6].

However, until now, VRFBs have not been able to widely capture this new market, which is mainly due to their high investment costs [7]. The total costs are composed of the production, electrolyte and component costs. For those, the recycling of graphite-polymer-bipolar-plates is determined to reduce VRFB costs and to produce bipolar plates in a resource-saving manner.

For VRFB contents of more than 85 wt% of graphite in thermoplastic polymer are needed to function as bipolar plate material. Since highly filled compound characteristics differ widely from that of neat polymers, recycling of highly functionalized graphite-compound requires an entirely

  doi:10.5075/epfl-298799_978-2-9701614-0-0

new process. The effect of recycling on properties such as electrical conductivity or mechanical stability and degradation of polymer and filler features have been studied.

2. Materials and Methods

2.1 Materials and sample preparation

As a high conductivity of the resulting bipolar plates is essential, high filler content in only a small quantity of polymeric matrix material is required. The thermoplastic compounds thus show a very high melt viscosity leading to demanding injection molding process parameters and restriction of the maximum bipolar plate size that can be produced. In order to be able to injection mold bipolar plates a commercially available polypropylene from LyondellBasell was used as matrix material. Graphite platelets (KS 500) with spherical like morphology obtained from company Imerys of 580 µm average size (D90) were mixed with polymer powder with a filler content of 85 wt%.

Firstly, 10 kg of the compound mixture was prepared in a twin-screw extruder PTW25 from Haake/ThermoScientific and then injection molded to plates with dimensions of 60x60x2 mm³ with a 35t injection molding machine Boy 35EHV. Mass flow of compounding was 4 kg/h at 200 rpm and melt temperature of 216 °C. Polymer and graphite input were achieved by gravimetrically controlled dosers. Polymer was added in the main feed section whereas graphite was added in a split-feed process further downstream using a sidefeeder. Added air and other volatile components were removed by two degassing units.

The injection molding process parameters were consistent during the five recycling steps. Cylinder temperature was 295 °C and mold temperature was 80 °C. The necessary injection pressure for complete filling of mold was measured. In total 50 plates were injection molded. 5 plates were removed, the remaining plates were ground by means of a mill and the recycled granules were again injection molded into plates. This process was repeated five times and 5 plates were removed at each recycling step.

2.2 Characterization methods

Measurement of electrical conductivity occurs with a four-pole-measuring procedure at a test rig at ZBT. Measurements of samples take place between two gas diffusion layers (GDL) that are based on polished and galvanized measuring poles made of copper. For measurement the sample is placed between the two poles, the poles are then pressed on the sample's surface and a preset current is applied. Two voltages are observed during this process: a voltage at the measuring poles (Uges) and a voltage at the measuring tip (Utip). The voltages are saved by software and are needed for calculation of resistance. Measurements are carried out at four different pressures (5, 10, 20, 30 bar) and four different currents (0,5 A; 1,0 A; 1,5 A; 2,0 A). The data is averaged for each measurement after the process.

In order to quantify the mechanical properties (flexural strength, flexural modulus and maximum deflection) three-point flexural tests were performed using an Instron 5565 measuring setup. Testing parameters and procedure were used as specified in DIN EN ISO 178:2010+A1:2013. Using the injection molded plates firstly five samples were cut to 60x25 mm² size having 2 mm thickness. The specimens were tested by keeping each one on the testing area of Instron 5565. In the center of the specimens a force was applied by an adaptor moving with

a speed of 1 mm per second until the breaking point was reached. During the procedure the applied force and the deflection of the specimens was measured.

Differential Scanning Calorimetry (DSC) measurements were carried out to determine the melting behavior of virgin compound and after each step of recycling. For this purpose, a DSC from TA Instruments was used. Experiments were carried out under nitrogen atmosphere. The samples were heated up to 240 °C with a ramp of 10 °C and then cooled down to 80 °C again. Subsequently, they were heated up again to 240 °C. The crystallinity was determined using the equilibrium enthalpy for PP of 207 J/g.

A Thermogravimetric Analysis (TGA) was performed to determine changes in filler content and filler particle size due to recycling. For this purpose, a TGA from TA Instruments was used. The samples were heated to 500 °C under nitrogen atmosphere with a ramp of 40 °C/min to pyrolyze the polypropylene. At 500 °C the atmosphere was switched to air and the samples were heated up to 1000 °C with a ramp of 10 °C/min.

Using Size Exclusion Chromatography (SEC) dissolved molecules are separated by size by pumping them through special columns containing microporous filling material. Molecules small enough penetrate the pores of the gel swollen with solvent. Within the pores, the particles can only move by diffusion and elution is therefore delayed. Large molecules cannot penetrate the pores and therefore migrate quickly through the channels between the gel particles. Thus, they are the fastest to be eluted. The determination of the molecular weights of the individual fractions is carried out by comparison with calibration substances.

3. Results and discussion

3.1 Electrical conductivity

The electrical conductivity of bipolar plates is an essential property for a good performance of the VRFB. The through-plane electrical resistance values of the injection molded plates are influenced by the recycling steps (Fig.1). It is found that 100% recycling of injection molded bipolar plates results in a reduction in volume resistance through each step of recycling. This can be caused by the crushing of the filler particles and/or by the damage of the polymer content in the compound caused by the recycling steps.

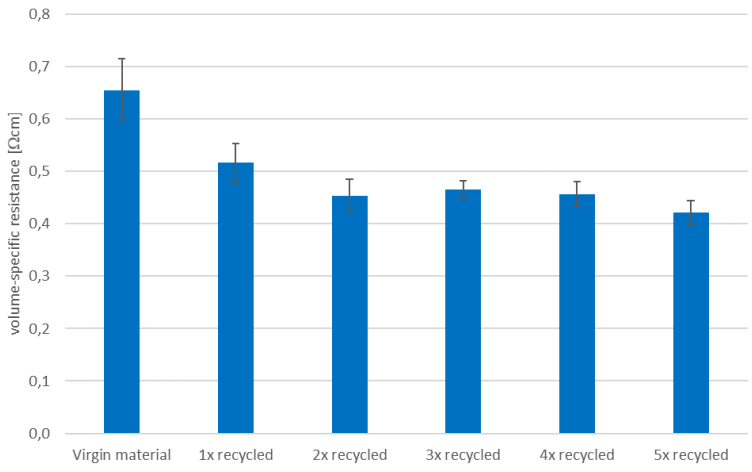

Figure 1: V*olume-specific resistance of injection molded plates over 5 steps of recycling*

3.2 Mechanical properties

Within the VRFB stack bipolar plates are exposed to compressive forces in order to provide an impervious system and to decrease the contact resistance between bipolar plates and carbon felts. The mechanical characterization shows a significant increase in bending strength through each step of recycling (Fif.2 left) but at the same time a significant reduction in elongation at break (Fig.2 right). Changes in the filler particles or the polymer due to recycling thus have a significant effect on the mechanical properties.

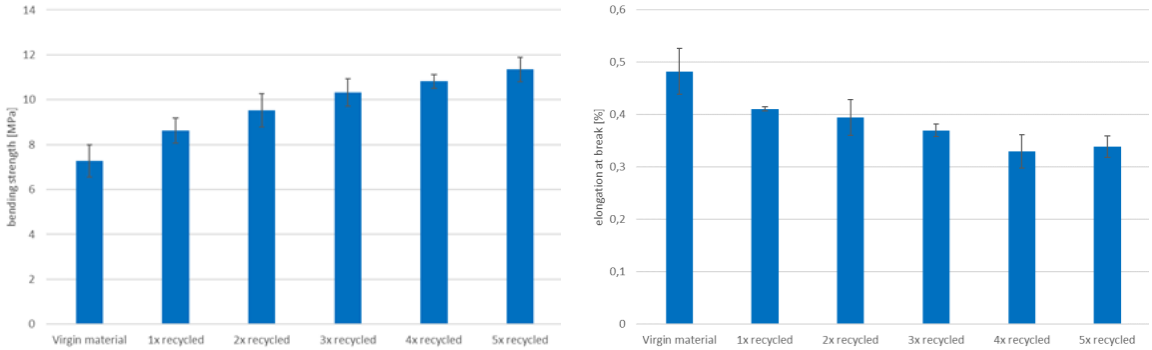

Figure 2: *Bendin*g strength and elongation at break over 5 steps of recycling

3.3 Thermogravimetric analysis

Thermogravimetric analysis was investigated to determine changes of the filler due to the recycling process. First of all, it could be shown that there are no significant changes in filler content due to grinding and further injection molding. As Fig.3 shows there is a plateau of all curves at approx. 500 °C with a filler content of 85 wt%. This means that there is no loss of filler material, e.g. due to dust formation during the grinding process. In the temperature range >650 °C, the neat sample shows the slowest combustion rate, while the recycled materials have a higher rate of mass loss. Since combustion is linked to particle size by the available surface for oxidation, it becomes apparent that the recycling process leads to a comminution of the filler particles and hence shifting of the curves towards lower temperatures with each step of recycling. It also becomes clear that this comminution already takes place during the first recycling step and continues with increasing number of recycling steps.

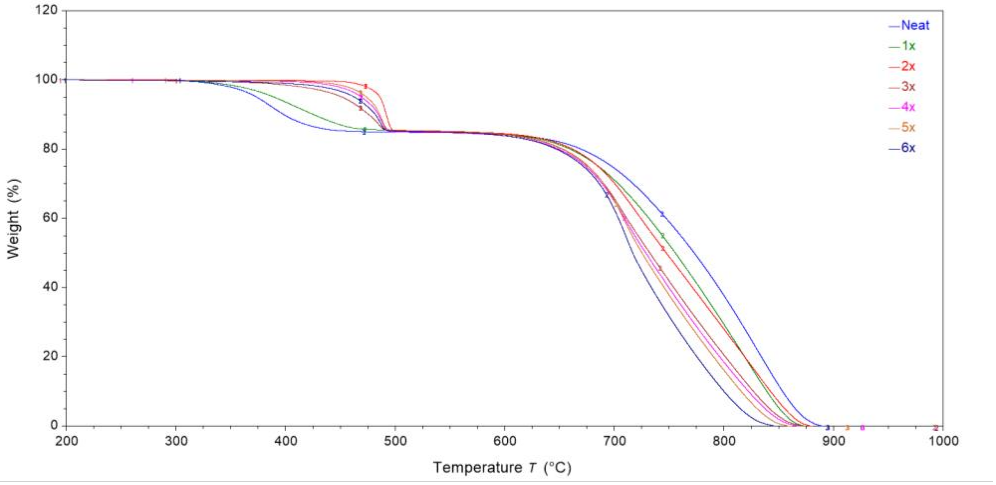

Figure 3: Results of thermogravimetric analysis of neat compound and after each step of recycling

  doi:10.5075/epfl-298799_978-2-9701614-0-0

To further quantify this process the temperature at which 10 wt% (T10), 50 wt% (T50) and 90 wt% (T90) of graphite is combusted is shown in the table 1. These values are characteristic for the combustion process and therefore give insight into the particle comminution. A continuous lowering of the combustions temperatures by each recycling step can be seen. While the T50 and T90 values decrease almost linearly with recycling, T10 temperature shows an initial drop from neat to the third recycling step and then stays almost constant. This suggests that there is a lower particle size where particles are so small that they are not altered by the recycling process anymore.

Table 1 : T10, T50 and T90 for neat and recycled material

	T10 [°C]	**T50 [°C]**	**T90 [°C]**
Neat	691	791	857
1x	678	772	843
2x	679	766	847
3x	670	749	831
4x	669	745	827
5x	670	741	821
6x	666	729	804

3.4 Differential scanning calorimetry

On the basis of DSC measurements carried out, a shift of the melting point of the recycling materials in the first DSC heating curve towards lower melting temperatures with an increase in the number of recycling steps was detected (Fig. 4 top). These indicates a change in the polymer due to the recycling steps. However, the second heating curve from the DSC measurement did show higher melting temperatures with each step of recycling (Fig. 4 below). So, analyzed only by DSC, it is not quite clear if polymer degradation takes places. That's why further tests with Size Exclusion Chromatography (SEC) were carried out for suitable analyzing of changes in the polymer through the recycling steps.

  doi:10.5075/epfl-298799_978-2-9701614-0-0

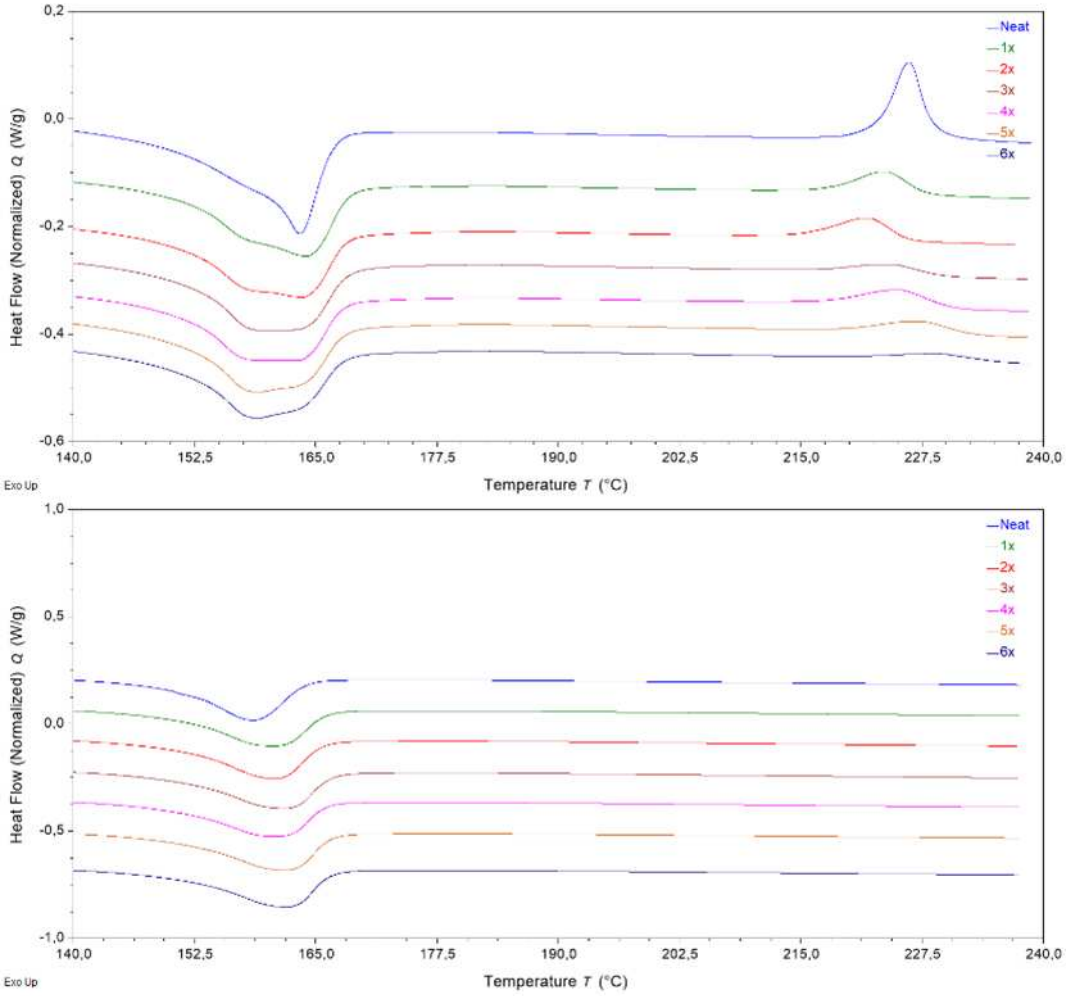

Figure 4: Heat flow (first and second heating) by differential scanning calorimetry measurements of neat compound and after each step of recycling

3.5 Size Exclusion Chromatography

Since the DSC investigations did not provide clear results regarding the damage to the polymer by the recycling steps, the materials were studied by size exclusion chromatography. The pure polymer was also considered, followed by the compound material, followed by the recycling materials at each injection molding step. Starting from the pure polymer, the processing in the extruder to produce the compound already leads to a shift in the molar mass distribution to smaller molecules (Fig.5). This means that the polymer is already damaged in this first processing step. The subsequent injection molding process, including the recycling of the material after each step, reinforces this trend. With each further processing step, the material is further damaged what is shown by a shift in the molar mass distribution towards smaller molecular weights with each step of recycling. Noticeable again is a convergence during the recycling process where the difference is largest between the neat material and the compound and then decreases between each recycling step. This suggest that there is a lower bound of polymer degradation, where further recycling will only lead to marginal difference in product quality.

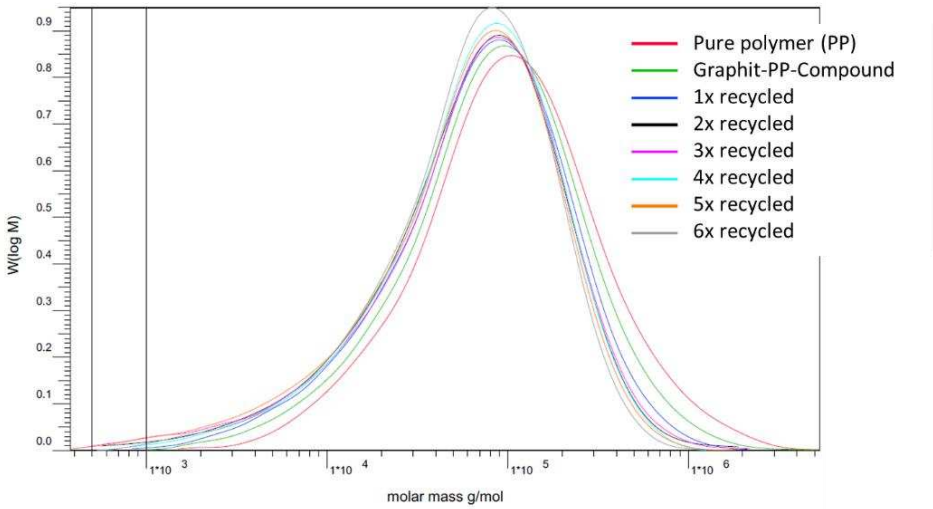

Figure 5: Molecular weight distribution curves of pure polymer, virgin compound and after each step of recycling

4. Conclusion

The 100% recycling of injection molded bipolar plates considered in this study poses a particularly high challenge to the material, but serves to accelerate the investigation. It will thus be possible to notice clear changes in the material properties already after the first recycling step and to identify clear trends after only a few recycling steps. By means of TGA and SEC, it was shown that each processing step (compounding + injection molding steps) of this highly filled compound leads to a comminution of the filler particles and to a degradation of the polymer. The investigations by means of DSC, on the other hand, did not provide any clear conclusions. Since both effects (filler comminution & polymer degradation) run in parallel, they also have a combined effect on the material properties. The current results, however, do not yet allow a statement on which effect dominates. In summary, the multiple recycling of the materials causes a significant increase in the electrical conductivity, but also a significant reduction in the max. elongation capacity of the material, whereas the strength is significantly increased. The results also indicated that the changes in properties during recycling decreased with more recycling steps, which indicates that properties may change asymptotically. To verify this a larger number of recycling steps would have to be studied.

In principle, the study showed that even these extremely highly filled polymer compounds can be recycled. However, depending on the application (design, structure, requirement profile of the VRFB), an assessment must be made as to which effect is acceptable for the application or should be prevented. Accordingly, the proportion of recyclate should be tested and adjusted for the respective product, as is usual in the plastics industry.

Acknowledgements

This work is part of the joint project “Re3dOx” (03ET6156). The authors thank the Federal Ministry of Economic Affairs and Climate Action (BMWK) for funding.

5. References

1. Sánchez-Díez E, Ventosa E, Guarnieri M et al (2021) Redox flow batteries: status and perspective towards sustainable stationary energy storage. J Power Sources 481:228804. https://doi.org/10.1016/j.jpowsour.2020.228804
2. Soloveichik GL (2015) Flow batteries: current status and trends. Chem Rev 115:11533–11558. https://doi.org/10.1021/cr500720
3. Cunha Á, Martins J, Rodrigues N et al (2015) Vanadium redox flow batteries: a technology review. Int J Energy Res 39:889–918. https://doi.org/10.1002/er.3260
4. Arenas LF, Ponce de León C, Walsh FC (2019) Redox flow batteries for energy storage: their promise, achievements and challenges. Curr Opin Electrochem 16:117–126. https://doi.org/10.1016/j.coelec.2019.05.007
5. Kroner I, Becker M, Turek T (2020) Determination of Rate Constants and Reaction Orders of Vanadium-Ion Kinetics on Carbon Fiber Electrodes. ChemElectroChem Vol.7, Issue 21
6. Satola B (2021) Review—Bipolar Plates for the Vanadium Redox Flow Battery. Journal of The Electrochemical Society, 2021 168 060503
7. Minke C, Turek T (2018) Materials, system designs and modelling approaches in techno-economic assessment of all-vanadium redox flow batteries – A review. J. Power Sources, 376, 66 – 81. DOI: https://doi.org/10.1016/j.jpowsour.2017.11.058

DAMAGE SENSING BASED ON ELECTRICALLY CONDUCTIVE NANOPARTICLES IN SANDWICH-STRUCTURED COMPOSITES

Gediminas Monastyreckis[a], Andrey Aniskevich[b], Daiva Zeleniakiene[a]

a: Department of Mechanical Engineering, Kaunas University of Technology, Kaunas, Lithuania
gediminas.monastyreckis@ktu.edu
b: Institute for Mechanics of Materials, University of Latvia, Riga, Latvia

Abstract: *Interlaminar delamination and buckling of the core are crucial defects in sandwich-structured composites. Not identifying these damages in time can lead to further interlaminar cracking, fibre fracturing and a total composite failure. This work aims to develop a self-sensing sandwich-structured composite modified with carbon nanotubes (CNT) and through-the-thickness conductive dip-coated aramid honeycomb using MXene nanoparticles. The morphology of partly-delaminated $Ti_3C_2T_z$ MXenes and CNT modified glass fibre composite is investigated using scanning electron microscopy. The structural health monitoring method proposed in this research is based on a simple piezoresistive effect in different composite layers. The damage location in the composite is evaluated according to electrical resistance change and intensity.*

Keywords: MXenes; carbon nanotubes; sandwich-structured composites; damage sensing

1. Introduction

The most commonly used sensors for structural health monitoring (SHM) are piezoelectric transducers, optical fibres, accelerometers and strain gauges. These sensors are usually attached to the surface or embedded into the composites during the moulding process. However, sensor detachment and internal cracking of the composite can occur over the exploitation period, leading to health monitoring interruption and decreased mechanical properties [1]. Methods that determine structural damage without external sensors are based on electrically conductive materials such as carbon fibres (CF) [2], nanoparticle coated glass fibres (GF), and polymer matrices modified with various conductive nanofillers [3]. The conductivity can be controlled by the amount of coating layers or filler weight percentage. In the event of damage, the condition of the composite structure can be evaluated according to the electrical resistance change. In sandwich-structured composites, the most critical defects that are hardly visible are the delamination of laminates and core indentation. These defects can lead to unexpected composite failure. Therefore, SHM methods that can identify them in real-time are in high demand.

The composite's interlaminar delamination monitoring according to electrical resistance change using carbon nanotubes (CNT) was studied by Kravchenko et al. [4]. A similar approach was investigated by Stankevich et al. [5], who evaluated the crack propagation length of double cantilever beam specimens according to the resistance increase in a CNT interlayer. Aly et al. [6] studied the impact damage detection based on CNT stripes. Grigoriou et al. [7] used vertically knitted carbon rods and estimated the delaminated area by total resistance change. Shimpi et al. [8] proposed a new CNT impregnation method and showed that even complex 3D woven

  doi:10.5075/epfl-298799_978-2-9701614-0-0

composites could be modified and turned into strain-sensing composites. Despite matrix modification, composites can also be coated with novel conductive 2D nanoparticles such as MXenes [9]. One such research showed the capabilities of MXene nanocoatings for the strain-sensing of GF composites [10].

This work aimed to develop a damage sensing sandwich-structured composite based on CNT modified GF laminates and through-the-thickness conductive MXene coated aramid honeycomb core.

2. Materials and methods

2.1 Materials

Partly-delaminated $Ti_3C_2T_z$ MXenes were prepared from Ti_3AlC_2 MAX phase (MRC, Ukraine), using 37 wt% hydrochloric acid and 99 wt% lithium fluoride (Sigma Aldrich, Germany). After 24 h of stirring, the solution was centrifuged and washed 10 times at 3500 rpm, until a neutral pH value was reached. The MXene sediment was reconcentrated to 15 mg/mL aqueous solution.

Epoxy masterbatch with 2 wt% of CNT was prepared following these steps. Firstly, 0.26 g of multi-walled CNT (NC7000™, Nanocyl SA, Belgium) were uniformly dispersed in 200 mL hexane (Sigma Aldrich, Germany) using 10 min 100 W power probe sonication (UP400S, Hielscher Ultrasonics GmbH, Germany). Then, epoxy resin Bisphenol F-epichlorohydrin (Biresin® CR-122, Sika, Germany) was slowly poured into the solution and mechanically stirred for 10 minutes until most CNT were embedded in the epoxy, and a transparent hexane solution was obtained again. Finally, the CNT/epoxy masterbatch was removed from the solution and degassed under vacuum and 50°C for 1 h to completely remove hexane residues.

CNT/epoxy masterbatch was further diluted with epoxy and hardener (Biresin® CH-122-5, Sika, Germany), thus making the final concentration of 0.25 wt% CNT. 3 mm thick aramid honeycomb (R&G Faserverbundwerkstoffe GmbH, Germany) was two times dip-coated in aqueous MXene solution (Figure 1) and dried with a fan for 5 min at 60 °C. The sandwich-structured composite samples (7 × 3 cm) were prepared by hand layup and vacuum bagging, using two bottom plies of CF (twill-weave 163 g/m², Porcher Industries, Germany), two top plies of modified GF with 0.25 wt% CNT/epoxy, and MXene coated honeycomb in between. After the post-curing in a convection oven for 5 h at 90 °C, copper wires (Analog 1 and ground) were soldered directly onto the top and bottom plies using conductive polylactic acid (PLA) (Protoplant Inc., Canada).

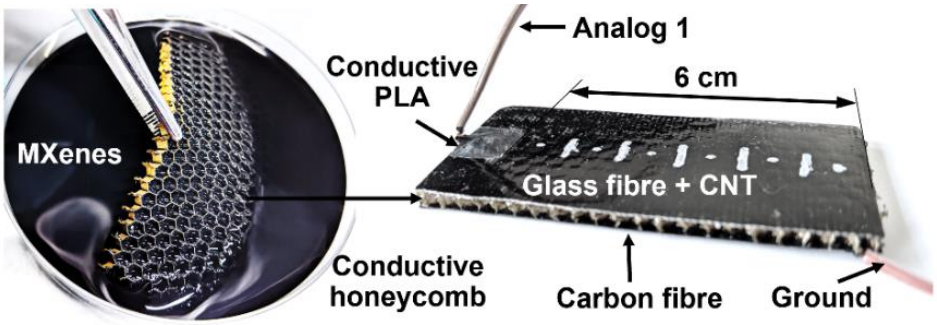

Figure 1. Damage sensing sandwich-structured composite scheme: left – MXene dip-coated aramid honeycomb; right – a sample configuration with wiring and dimensions

2.2 Characterisation and testing

MXene nanoparticles were characterised on dip-coated silicon wafers (1 × 1 cm) using scanning electron microscopy (SEM) (S-3400N, Hitachi, Japan) with an accelerating voltage of 5 kV, while 0.25 wt% CNT-GF composite sample pieces were imaged under 20 kV (Quanta 200 FEG, FEI, US).

Through-the-thickness electrical resistance of the dip-coated aramid core (dry form) was measured between two slightly pressed glass plates covered with aluminium. The resistance was measured using a two-probe Fluke 287 True-RMS multimeter (Fluke Corporation, US), and the mass growth (%) after the dip-coating was measured using analytical scales of 0.01 mg readability (KERN & SOHN GmbH, Germany).

The indentation of the sample was performed using GUNT WP 300 testing machine and a linear indenter (G.U.N.T. Gerätebau GmbH, Germany). The specimens were compressed through the width at every 5 mm distance from the conductive PLA. The electrical resistance was monitored between Analog 1 and ground (Figure 1) during each indentation. In addition, the piezoresistive effect of CNT-GF laminate and MXene coating was monitored during three-point bending tests using Tinius Olsen H25 KT (Tinius Olsen, UK) and ISO-178 standards. Electrical resistance changes of tensiled and compressed surfaces during the bending were measured between two silver paint stripes at the edges of the specimen.

3. Results

3.1 Characterisation

The morphology of MXene nanoparticles and CNT distribution in the composite were studied using SEM (Figure 2). Partly-delaminated $Ti_3C_2T_z$ MXene is presented in Figure 2a. Here, a multilayered MXene structure of roughly 10 µm can be seen. However, such particles cannot form a uniform and highly conductive nanocoating, but they tend to be more electrically sensitive to the deformation by losing flake to flake connections when the honeycomb core is compressed. In Figure 2b, a broken GF specimen with 0.25 wt% CNT in the epoxy matrix is presented. These nanotubes make a conductive network between individual GF filaments and behave as a piezoresistive sensor. In a magnified region, an agglomeration of CNT can be observed (1 µm scale bar).

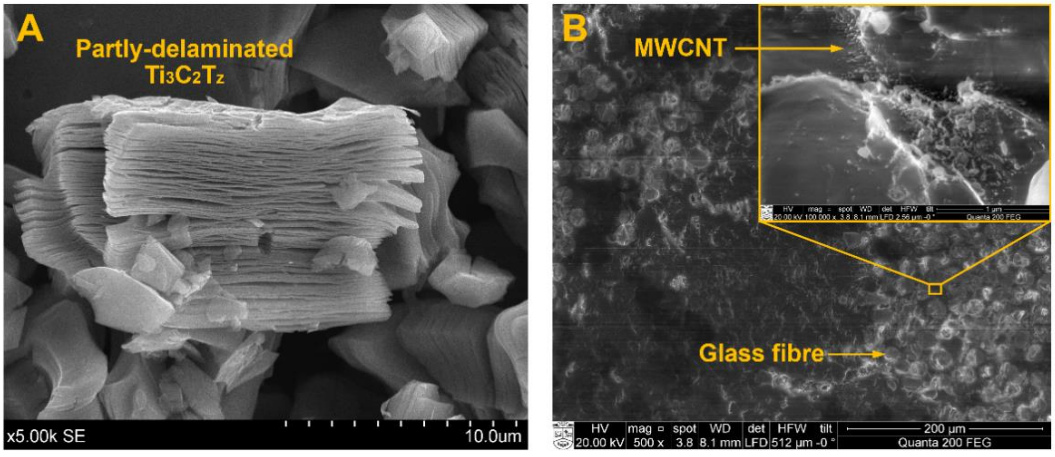

Figure 2. Scanning electron microscopy images: (a) partly-delaminated multilayered $Ti_3C_2T_z$ MXene; (b) GF composite modified with 0.25 wt% multi-walled CNT

  doi:10.5075/epfl-298799_978-2-9701614-0-0 published under CC BY-NC 4.0 license

Average electrical resistance values of aramid honeycomb (12 samples) under 2 times dip-coating (R_1, R_2) are presented in Table 1. Besides resistance, another important parameter is the absorbance of MXenes and the honeycomb's mass growth (Δm_1, Δm_2). An average mass growth after the first dipping was 1.57%, and the second dipping – 2.77%, compared to the initial honeycomb core mass (m_0). From the average values of weight ratio increase during the second dipping ($\Delta m_2/\Delta m_1$) and the resistance decrease ratio (R_1/R_2), we can notice that the mass of absorbed MXenes increased by 76%, and the electrical resistance decreased 4 times. This experiment shows that using simple and scalable dip-coating methods, it is possible to achieve tunable through-the-thickness conductivity with a marginal mass increase.

Table 1: MXene-coated aramid honeycomb core: electrical resistance and mass change.

R_1 [Ω]	R_2 [Ω]	m_0 [g]	Δm_1 [%]	Δm_2 [%]	$\Delta m_2/\Delta m_1$	R_1/R_2
2572	654	0.22093	1.57	2.77	1.76	4.06

3.2 Piezoresistive effect

The piezoresistive effect was monitored under three-point bending separately for lower and upper surfaces, deforming under tension and compression, respectively (Figure 3). The samples were deflected for 2 mm, which gave a flexural surface strain of 1%. Tensiled MXene coating showed a slight increase in electrical resistance by 2.15%, while the values under compression decreased by 1.53%. In comparison, 0.25 wt% CNT-GF composite resulted in more than twice higher values – 4.68% for tension, while compressions results were -0.91%.

Both samples showed a similar tendency of piezoresistance – an electrical resistance increase under tension and a decrease under compression. If the sample or a coating was damaged due to laminate cracking, the resistance increased to infinite. In such a way, when the honeycomb core was compressed, through-the-thickness conductivity in the damaged area was lost. These results indicate that besides composite damage, a small variation in resistance during the deformation occurs, and under cyclic loading, the sensing capability of the composite is expected to degrade slightly.

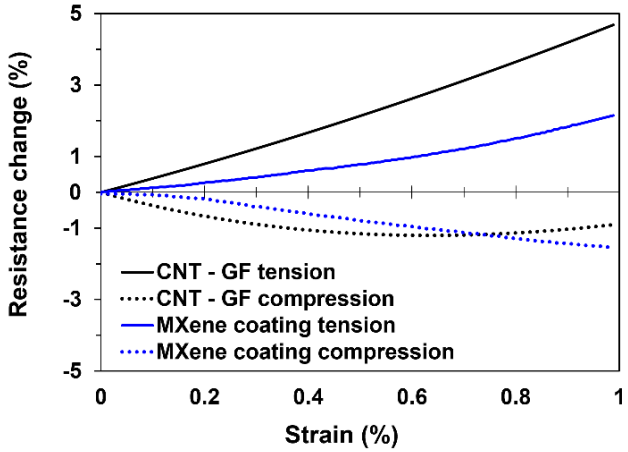

Figure 3. Piezoresistive effect monitored under three-point bending of 0.25 wt% CNT-GF composite and MXene coating

3.3 Damage sensing

The electrical resistance increase of the composite under the indentation test is presented in Figure 4. The first test was performed with 7 indentations with a 0.5 cm step, starting from 4 cm distance from the Analog 1, and ending at 1 cm (Figure 4a). The first indentation at 4 cm resulted in a relative resistance ($\Delta R/R_0$) increase of 4.9%. The second indentation at 3.5 cm distance was roughly followed after 5 s, and the resistance increased to 20.3%. When the compression was performed closer with every step, the resistance increased to 47, 147 and 419% for 3, 2 and 1 cm, respectively.

The same procedure was repeated in the opposite direction (Figure 4b). The first damage was performed at 1 cm distance, and the resistance increased by 17.5%. When the sample was compressed further from Analog 1, the relative resistance intensity decreased with the distance. At 2, 3 and 4 cm, the resistance increased to 37.4, 44.1 and 46.2%, respectively. The results show that the intensity of resistance change differs between the damage direction. Also, it shows different values according to the distance from Analog 1, by which a damaged location can be identified. These results show that the noticeable resistance changes according to indentation damage are limited to 4 cm from Analog 1. Therefore several analogs that would sense a larger area should be spaced by 8 cm. This method could also monitor a damaged area or crack propagation in real-time by using a wire grid. Additionally, the sensing radius can be improved by increasing the conductivity of the top CNT-GF layers and by decreasing through-the-thickness conductivity of the MXene coated honeycomb core.

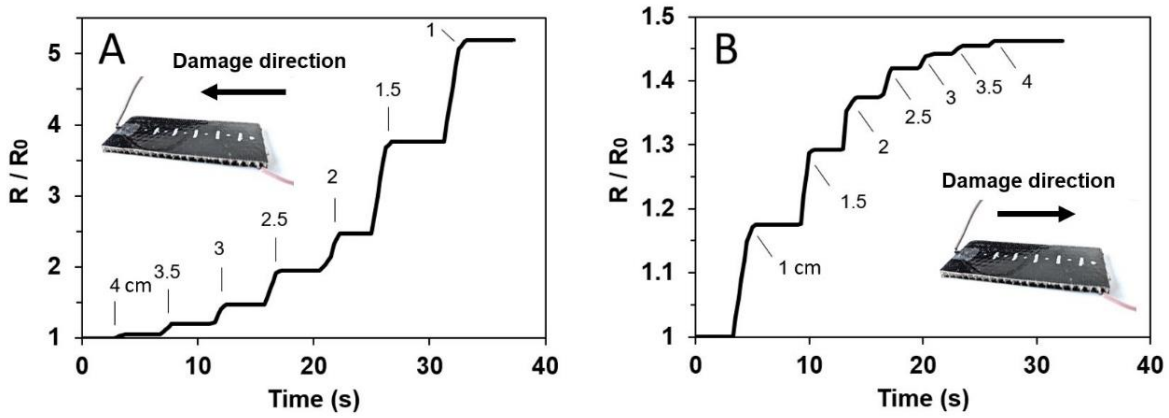

Figure 4. Damage sensing of sandwich-structured composites based on electrical resistance change: (a) linear indentation damage direction to Analog 1; (b) from Analog 1

Conclusions

In this study, a self-sensing sandwich-structured composite was developed using CNT modified GF laminates and MXene coated aramid honeycomb. The morphology of MXenes and CNT-GF composite was investigated using SEM. The piezoresistive effect was studied under three-point bending, and electrical resistance increase for both MXenes and CNT-GF was obtained under tension, and decrease under compression. The SHM method proposed in this research was based on electrical resistance change in different composite layers. The electrical resistance intensity depended on the distance from Analog 1, which led to identifying damage location and propagation in real-time.

Acknowledgements

This project has received funding from the European Union's Horizon 2020 research and innovation program under the Marie Skłodowska-Curie grant agreement No. 777810.

4. References

1. McGugan M, et al. Damage Mechanism Based Approach to the Structural Health Monitoring of Wind Turbine Blades. Coatings 2020, 10, 1223. https://doi.org/10.3390/coatings10121223
2. Vavouliotis A, et al. On the fatigue life prediction of CFRP laminates using the Electrical Resistance Change method. Comp. Sci. Tech. 2011, 71, 5, 630-642. https://doi.org/10.1016/j.compscitech.2011.01.003
3. Valorosi F, et al. Graphene and related materials in hierarchical fiber composites: Production techniques and key industrial benefits. Comp. Sci. Tech. 2020, 185, 107848. https://doi.org/10.1016/j.compscitech.2019.107848
4. Kravchenko OG, et al. Incorporation of plasma-functionalized carbon nanostructures in composite laminates for interlaminar reinforcement and delamination crack monitoring. Journal of Physics and Chemistry of Solids 2018, 112, 163-170. https://doi.org/10.1016/j.jpcs.2017.09.018
5. Stankevich S, et al. Electrical Conductivity of Glass Fiber-Reinforced Plastic with Nanomodified Matrix for Damage Diagnostic. Materials (Basel). 2021, 14, 1–18. https://doi.org/10.3390/ma14164485
6. Aly K, et al. Real-time impact damage sensing and localization in composites through embedded aligned carbon nanotube sheets. Comp. Part B 2019, 162, 522-531. https://doi.org/10.1016/j.compositesb.2018.12.104
7. Grigoriou K. et al. Electrical properties of multifunctional Z-pinned sandwich composites. Comp. Sci. Tech. 2019, 170,60-69. https://doi.org/10.1016/j.compscitech.2018.11.030
8. Shimpi P, et al. Improved method of manufacturing carbon nanotube infused multifunctional 3D woven composites. Journal of Composite Materials. 2022;56(3):479-489. https://doi.org/10.1177/00219983211055823
9. Venkateshalu S, et al. MXenes—A New Class of 2D Layered Materials: Synthesis, Properties, Applications as Supercapacitor Electrode and Beyond. Appl. Mater. Today 2020, 18, 100509. https://doi.org/10.1016/j.apmt.2019.100509
10. Monastyreckis G, et al. D. Strain Sensing Coatings for Large Composite Structures Based on 2D MXene Nanoparticles. Sensors (Switzerland) 2021, 21, 1–14. https://doi.org/10.3390/s21072378

A NOVEL LIGHTNING STRIKE PROTECTION SYSTEM COMPRISING AN ALL-POLYMERIC CONDUCTIVE RESIN

Yu Zhou, Tomohiro Yokozeki

Department of Aeronautics and Astronautics, The University of Tokyo
yu-zhou1103@aastr.t.u-tokyo.ac.jp

Abstract: *Modern aircraft now consists of more than 50 wt% parts made of composite materials for their high specific strength. However, components made of carbon fiber reinforced plastics(CFRP) are vulnerable to lightning strikes, which statistically happens to an aircraft nearly once a year. This work presents a promising alternative to the currently used copper-based lightning strike protection(LSP) system. An all-polymeric conductive resin made of polyaniline(PANI) was utilized as the CF laminate matrix and showed a high electrical conductivity. Such a conductive laminate was evaluated by a simulated lightning strike test, and the damage behavior was investigated. Results indicate that the conductive CF laminate shows a self-protection ability against lightning strikes.*

Keywords: conductive composite; lightning strike protection; polyaniline; residual properties;

1. Introduction

Carbon fiber reinforced plastics (CFRPs) are now commonly seen in structural applications due to their remarkable specific strength (strength to weight ratio). Especially in the aircraft industry, CFRP structures offer decreased fuel consumption and increased payloads while maintaining outstanding structural strength. Modern aircraft now consist of up to 50 weight present or more parts made of CFRP laminate or honeycomb hybrid structures. This proportion is still growing due to the development of new materials and new structure designs.

Statistically, an aircraft is expected to encounter extreme environmental conditions such as lightning strikes roughly once a year[1]. However, CRRP structures are vulnerable to lightning strikes due to their structural nature. Carbon fiber is highly electrically conductive in the longitudinal direction but not in the transverse direction. On the other hand, the epoxy matrix in the CFRP is insulated. Hence, the electrical breakdown happens when lightning strikes on the CFRPs and causes severe damage such as matrix pyrolysis due to the Joule heating effect[2]. Damage caused by a lightning strike can range from no damage to severe ones and requires extensive repairs, which can take the airplane out of service for an extended period. The current lightning strike protection (LSP) technique utilized expanded metal foil (copper) on top of the CFRPs structures, which is adequate but inefficient. Although the expanded copper foil (ECF) is included in the basic design of an aircraft, such an additional layer of metal foil increases the total weight of an aircraft and introduces other kinds of issues, such as galvanic corrosion.

Various new designs and materials have been proposed as alternative LSP strategies. Our research presents a novel all-polymeric resin series comprising intrinsically conductive polymer—polyaniline (PANI). Previous PANI research mainly focused on its electrical properties rather than structural applications because PANI is difficult to process. Nevertheless, our research proposed a new PANI-based all-polymeric conductive resin, and its application as the resin matrix of CFRP laminate[3]. Moreover, we present the mechanical properties of the CF/PANI laminate and its performance against simulated lightning strike investigation.

  doi:10.5075/epfl-298799_978-2-9701614-0-0

2. All-polymeric electrically conductive resin

Polyaniline is the most studied intrinsically conductive polymer(ICP) because of its ease of synthesis, tunable conductivity, eco-friendly and better stability compared to other ICPs. Unlike most linear thermoplastics, polyaniline is principally insoluble and infusible, which has been proved by numerous experimental studies[4]. However, doping with dodecylbenzene sulfonic acid(DBSA) has been verified to improve PANI's processability significantly[2]. Several approaches have tried to blend DBSA doped PANI with traditional epoxy resin to achieve a PANI/Epoxy conductive resin. Yet, the typical amine hardener inevitably leads to the de-doping of PANI because of the strong nucleophilicity of amine[5].

2.1 PANI-DBSA conductive resin system

Previous research in our group has demonstrated a PANI-DBSA/divinylbenzene(DVB) thermosetting resin system by physically dispersing a semi-doped PANI-DBSA complex into DVB. When the resin has been heated, the un-doped DBSA, or free DBSA would either continuously dope onto PANI or initiate the cationic polymerization of DVB to form a crosslinking network[6]. Although the PANI-DBSA/DVB resin system shows high electrical conductivity and can be cured upon heating, the mechanical properties of PANI-DBSA/DVB are inferior to the conventional epoxy resin.

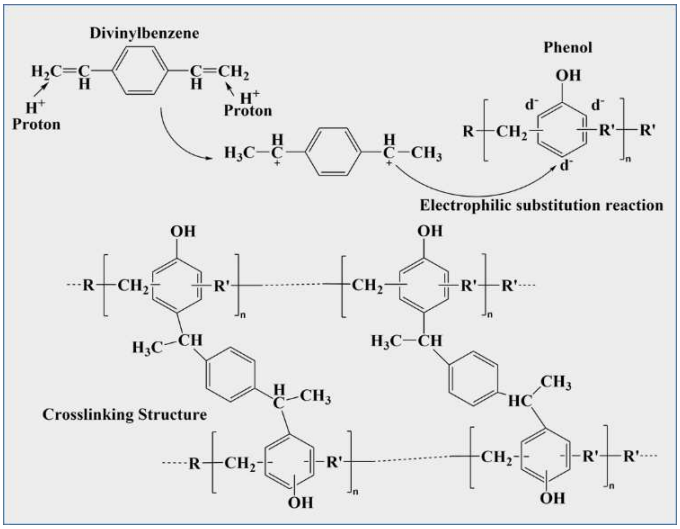

Figure 2.1. The reaction mechanism of phenolic oligomer and DVB

K. Mori et al. has demonstrated a crosslinking reaction between the phenolic oligomer and DVB with the presence of proton[7]. We adopted this reaction to our system to enhance the mechanical properties of our conductive resin. The curing mechanism of the newly developed PANI-DBSA/Phenol-DVB resin, or PDPD resin, is shown in Figure 2.1. The mechanical properties and electrical conductivity of the cast PDPD resin are shown in Table 2.1. The properties of a conventional XNR/H6815 epoxy resin (Nagase ChemteX Corp.) and a standard diglycidyl ether of bisphenol-A (DGEBA)[8] are shown in Table 2.1 as well for comparison. Although the PDPD resin still shows inferior mechanical properties to epoxy resin, the electrical conductivity of the PDPD resin is more than ten orders of magnitude higher than the conventional epoxy resin. The combination of mechanical properties and electrical conductivity was rarely reported before in the all-polymeric domain.

  doi:10.5075/epfl-298799_978-2-9701614-0-0

Table 2.1 Mechanical properties and conductivity of PDPD and conventional epoxy

Resin	Flexural Modulus (GPa)	Flexural strength (MPa)	Electrical conductivity (S/cm)
PDPD	2.43 ± 0.11	51.92 ± 7.63	0.26 ± 0.06
XNR/H6815	3.20 ± 0.10	65.72 ± 2.19	1.61 * 10^-13
DGEBA[8]	2.95 ± 0.13	76.41 ± 4.12	2.33 * 10^-11

3. CF/PDPD conductive composite laminate

The properties of the CFRP made with the newly developed PDPD resin are of vital importance for possible future applications. CF/PDPD laminates were made with a hand lay-up process. The resin was prepared in advance and then applied on woven fabrics (TR3110M, TR30-3K, 200 GSM, Mitsubishi Rayon Co. Ltd.) The prepregs were then stacked in 0°/90° direction and used hot-press to cure. CF/Epoxy laminates were fabricated with identical woven fabric and processes to compare with the CF/PDPD laminates directly. Figure 3.1 shows the comparison between the properties of the CF/Epoxy and CF/PDPD laminates. The conductivity in z means the conductivity in the out-of-plane or through-thickness direction. The measurement process has been introduced in previous publications[9].

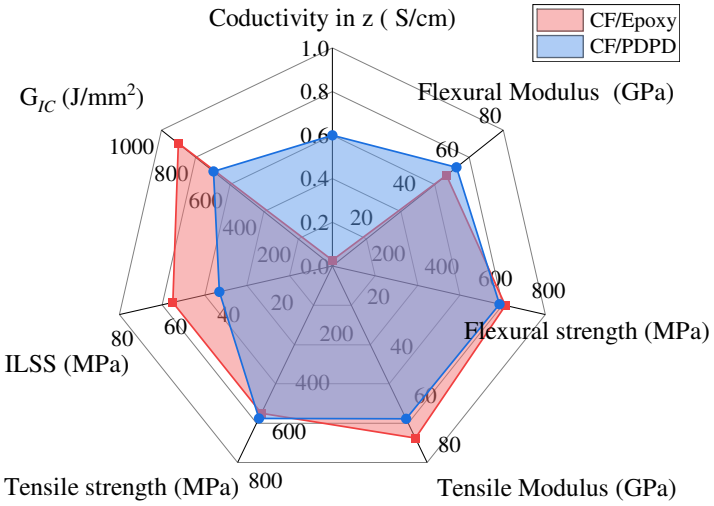

Figure 3.1. The properties comparison of CF/Epoxy and CF/PDPD laminate

As shown from Figure 3.1, the mechanical properties of CF/PDPD laminate are approaching the CF/Epoxy laminate made with identical fabric and process. However, CF/PDPD shows inferior toughness than CF/Epoxy, which might cripple the actual application in the aircraft industry. Further improvement is needed to provide better toughness to this resin matrix. Apart from the mechanical properties, the electrical conductivity of the CF/PDPD shows a 20 times enhancement compared to CF/Epoxy. Our previous research has demonstrated that the through-thickness conductivity dramatically reduces the lightning strike damage to the composite laminate[10].

4. Simulated lightning strike investigation of CF/epoxy and CF/PDPD laminates

  doi:10.5075/epfl-298799_978-2-9701614-0-0

The most important part of this study is a simulated lightning strike test. Laminates made with PDPD conductive resin matrix were evaluated with artificial lightning. Original laminates were made with the same profile as Section 3 with a size of 220mm*200mm. Then a 150mm*150mm panel was cut from each panel for the lightning strike test. The rest of the panel evaluated the pristine mechanical properties and the original through-thickness conductivity. The simulated lightning current amplitude and an ARP standard recommended waveform is shown in Figure 4.1 a; the test setup is shown in Figure 4.1b. The panel was fixed on a copper-made jig which is properly grounded. A maximum of -93.6kA electrical current was applied on the CF/PDPD panel through a jet-diverting electrode, which memes the actual lightning strike event. High-speed and thermal cameras recorded the phenomenon during the strike event.

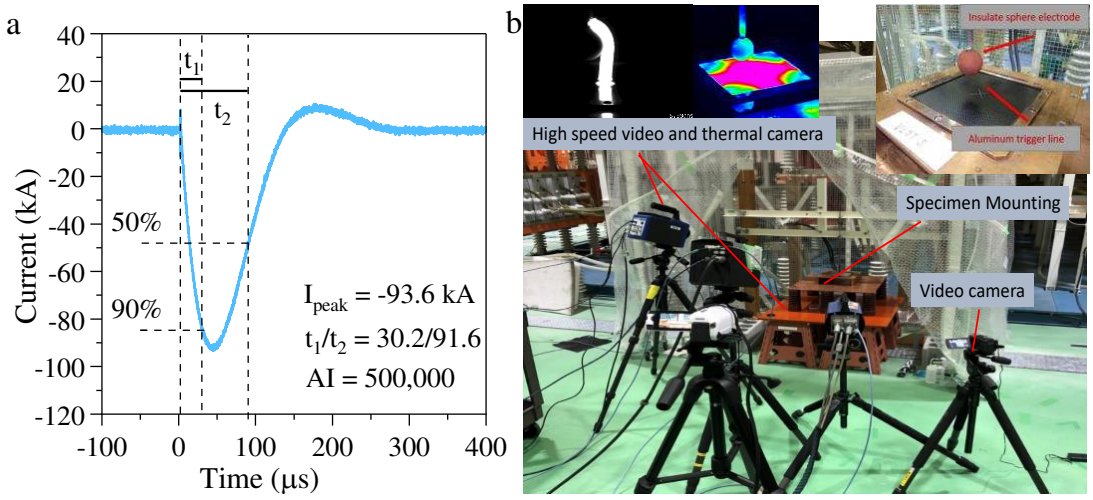

Figure 4.1 The current waveform and test setup of the simulated lightning strike test

The results of the CF/PDPD against the simulated lightning strike are summarized in Figure 4.2. Figure 4.2a shows the photos of the specimens on the copper mount before and after the lightning strike, and the corresponding ultrasonic NDI results. Only minor damage can be identified from the panel surface after the strike. Moreover, no delamination was detected from the NDI results. The NDI results only show some tiny spots corresponding to the barely visible damage on the surface. Figure 4.2b shows the images from the high-speed camera at specific time points. This result shows that the lightning arc travels uniformly on the panel marked by the round-shaped light emission. As we know that this panel is fabricated with plain-woven fabric in the cross-ply direction. The electrical conductivity is much higher in the fiber direction. The result of the high-speed camera indicates that the conductive resin helps dissipate the electrical current fast and uniformly.

Figure 4.2c shows the result of the thermal camera, which is now present as temperature histories of four different points on the panel. We chose four different points on the panel and exported their time history to plot as a figure. Then we focus on the first 30 milliseconds to see how the temperature changes at these four points. We can see that the maximum temperature of the panel center dropped to 150°C after five milliseconds from the stroke. Although the sudden high temperature of the arc might evaporate a small amount of the surface resin, this high temperature lasts less than five milliseconds and has minor effects on the PDPD matrix.

  doi:10.5075/epfl-298799_978-2-9701614-0-0

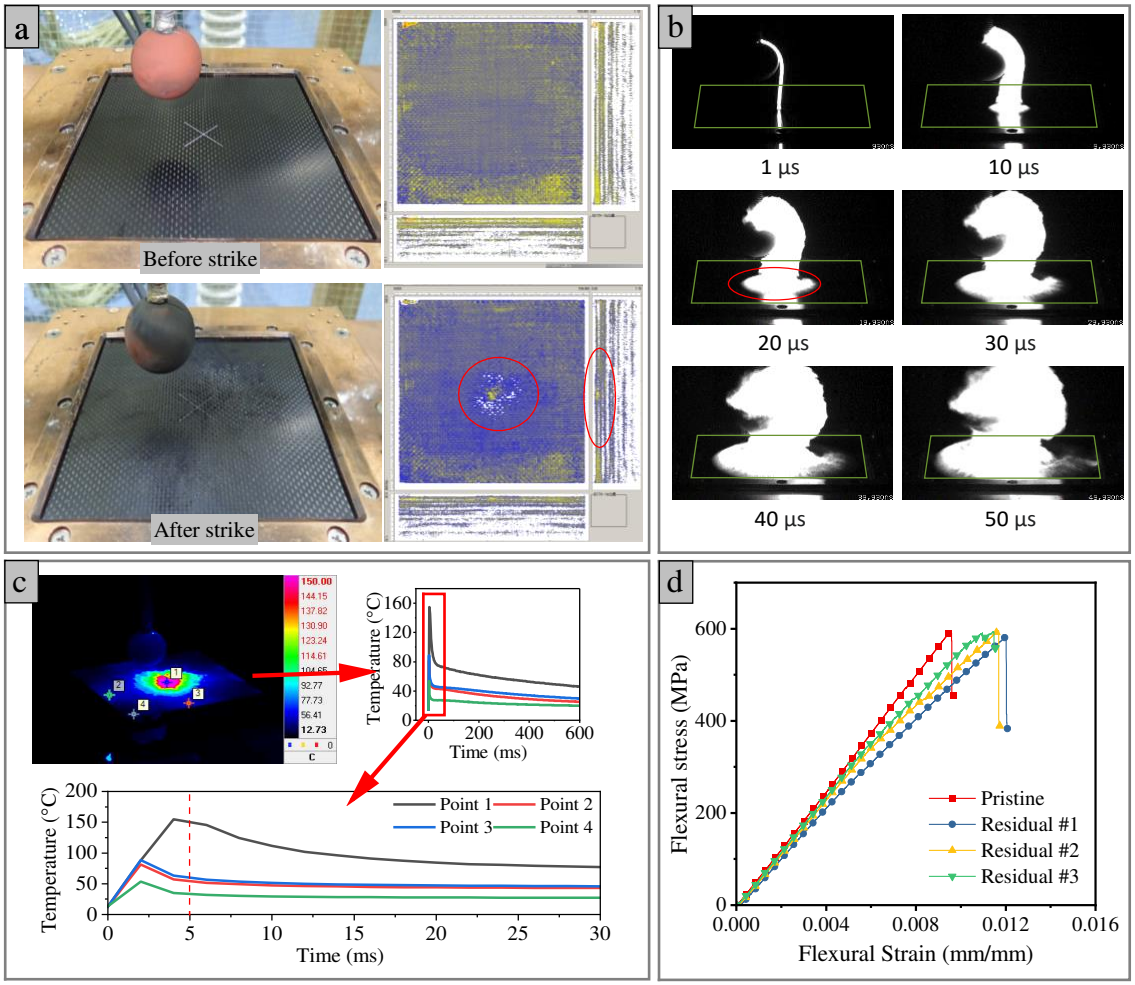

Figure 4.2 a) The photos and NDI results before and after simulated lightning strike test[11]*; b) The image of high-speed camera videos; c) The temperature history result from thermal camera; d) The result of residual strength evaluation.*

The residual strength is of vital importance to evaluate the performance of this newly developed lightning strike protection. Three specimens were cut from the panel center after the strike and the mechanical properties were evaluated through the bending test, same as the pristine properties. The flexural strain to stress curves is shown in Figure 4.2d. As shown in the figure, the modulus and fracture strength of the panel after simulated lighting strike is not affected much compared with the pristine strength. The minor damage to the panel surface does not affect the panel's overall mechanical properties. This result further reflects the advantage of this newly developed LSP system.

5. Summary

This work presents a promising alternative to the currently used copper-based lightning strike protection(LSP) system. An all-polymeric conductive resin made of polyaniline(PANI) was developed, and the electrical conductivity and mechanical properties were compared with the customarily utilized Epoxy resin matrix. This newly developed PDPD resin was then evaluated as the CF laminate matrix and showed a high electrical conductivity and comparable mechanical properties. Such a conductive laminate was evaluated by a simulated lightning strike test, and the damage behavior was investigated. Results indicate that the conductive CF laminate shows

  doi:10.5075/epfl-298799_978-2-9701614-0-0 published under CC BY-NC 4.0 license

a self-protection ability against lightning strikes. Such a conductive CF laminate can be used as an alternative lightning strike protection system.

Acknowledgments

This work was supported by the Japan Society for the Promotion of Science for Grant-in-Aid for Scientific Research (No. 21H01525). This work is a supplemental study of a work published in *Composite science and technology*[11]. The authors also would like to credit Mr. Takeo Sonehara from Shoden corporation, Mr. Katsunori Takida from IHI Jet Service, and staff from Japan Aerospace Exploration Agency (JAXA) for technical support for the simulated lightning strike test.

References

[1] M. Gagné and D. Therriault, "Lightning strike protection of composites," *Prog. Aerosp. Sci.*, vol. 64, pp. 1–16, 2014.

[2] S. Kamiyama, Y. Hirano, T. Okada, and T. Ogasawara, "Lightning strike damage behavior of carbon fiber reinforced epoxy, bismaleimide, and polyetheretherketone composites," *Compos. Sci. Technol.*, vol. 161, no. February, pp. 107–114, 2018.

[3] T. Yokozeki *et al.*, "Development and characterization of CFRP using a polyaniline-based conductive thermoset matrix," *Compos. Sci. Technol.*, vol. 117, pp. 277–281, 2015.

[4] B. Wessling, "New insight into organic metal polyaniline morphology and structure," *Polymers (Basel).*, vol. 2, no. 4, pp. 786–798, 2010.

[5] S. Desvergne, A. Gasse, and A. Pron, "Electrical characterization of polyaniline-based adhesive blends," *J. Appl. Polym. Sci.*, vol. 120, no. 4, pp. 1965–1973, May 2011.

[6] V. Kumar, T. Yokozeki, T. Goto, and T. Takahashi, "Mechanical and electrical properties of PANI-based conductive thermosetting composites," *J. Reinf. Plast. Compos.*, vol. 34, no. 16, pp. 1298–1305, 2015.

[7] K. Mori, T. Inoue, and T. Ikeda, "New Phenolic Resins by the Reaction between Phenols and Divinylbenzene," pp. 1–10, 2005.

[8] L. C. Tang *et al.*, "Fracture toughness and electrical conductivity of epoxy composites filled with carbon nanotubes and spherical particles," *Compos. Part A Appl. Sci. Manuf.*, vol. 45, pp. 95–101, 2013.

[9] V. Kumar, T. Yokozeki, T. Goto, T. Takahashi, S. R. Dhakate, and B. P. Singh, "Irreversible tunability of through-thickness electrical conductivity of polyaniline-based CFRP by de-doping," *Compos. Sci. Technol.*, vol. 152, pp. 20–26, 2017.

[10] V. Kumar *et al.*, "Effect of through-thickness electrical conductivity of CFRPs on lightning strike damages," *Compos. Part A Appl. Sci. Manuf.*, vol. 114, no. September, pp. 429–438, 2018.

[11] Y. Zhou, S. N. V Raghu, V. Kumar, T. Okada, and T. Yokozeki, "Simulated lightning strike investigation of CFRP comprising a novel polyaniline / phenol based electrically conductive resin matrix," *Compos. Sci. Technol.*, vol. 214, no. March, p. 108971, 2021.

  doi:10.5075/epfl-298799_978-2-9701614-0-0

LOW TEMPERATURE GROWTH OF CARBON NANOTUBES ON FIBERS USING COPPER AS CATALYST

Luiz, Acauan[a], Matteo, Lilli[b], Christina, Scheffler[c], Jacopo, Tirillò[b], Fabrizio, Sarasini[b], Brian, Wardle[a,d]

a: Department of Aeronautics and Astronautics, Massachusetts Institute of Technology, 77 Massachusetts Ave., Cambridge, MA, 02139, USA - lacauan@mit.edu
b: Department of Chemical Engineering Materials Environment, Sapienza-Università di Roma & UdR INSTM , Via Eudossiana 18, 00184 Roma, Italy
c: Leibniz-Institut für Polymerforschung Dresden e.V., Group Fibre-Engineering, Hohe Straße 6, 01069 Dresden, Germany
d: Department of Mechanical Engineering, Massachusetts Institute of Technology, 77 Massachusetts Ave., Cambridge, MA, 02139, USA

Abstract: *The aim of this work is to compare the growth of carbon nanotubes (CNTs) at low temperature (480°C) using copper as a catalyst over fibers from two opposite extremes: well-known state-of-the-art structural carbon fibers (CF) and natural, eco-friendly, cost-effective and relatively new basalt fibers (BF). The synthesis has shown to be independent of the type of microfiber substrate, resulting in "bamboo-like" CNTs, homogeneously distributed over both fibers. The CFs displayed no loss in mechanical properties after the CVD growth, while increasing by 23% and 35.5% the total pull out work and interfacial shear strength, respectively. However, CNT-grafted BF showed only a small increase in the interfacial shear strength and a considerable decrease in single fiber tensile strength and total pull out work.*

Keywords: Fiber/matrix interface; CVD; Carbon Fibers; Basalt fibers; Carbon Nanotubes

1. Introduction

Fiber-reinforced polymers are deeply inserted into the aerospace, automotive, marine, and construction industries. The superior performance combined with high strength, high fatigue resistance, high corrosion resistance and weight reduction makes carbon fibers (CFs) the most widely used as reinforcing material for advanced composites[1,2]. Natural fibers such as basalt fibers (BFs) also stand out by their recyclability, fire resistance, good resistance to chemically active environments with a lower price, while having great mechanical proprieties, especially compared to other natural fibers like the vegetable ones[3–5].

The interface between the reinforcement and resin matrix plays a critical role in controlling the overall properties of the composites, however, smooth and chemically inert fiber surfaces usually result in poor matrix compatibility and weak adhesion between fiber and matrix reinforced composites[6,7]. The ability to grow carbon nanotubes (CNTs) directly over these fibers can provide through-thickness reinforcement and better load transfer at the fibers/matrix interface, and also enable other multifunctionalities due to the higher surface area, electric and thermal properties of these nanomaterials[8,9]. Nevertheless, the high temperatures involved in CVD process (usually above 600°C) can significantly reduce the strength of the fibers, so the synthesis process must be tailored to maintain the fibers original mechanical properties[10–13].

  doi:10.5075/epfl-298799_978-2-9701614-0-0

To address these issues, herein we describe synthesis of CNTs by chemical vapor deposition using a copper-based catalyst at 480°C directly at the surface of carbon and basalt fibers[14]. Hence, we compared the mechanical and interfacial properties of both of these CNT-grafted fibers (*a.k.a* "fuzzy" fibers) by single fiber tensile and pull out tests.

2. Materials and methods

2.1 Raw materials

Unsized BF, supplied by Mafic as a continuous roving, with a nominal diameter of 13 µm and a linear density of 450 tex, and unsized CF, supplied by Toho Tenax as a weave, with a nominal diameter of 7 µm and a linear density of 200 tex were used as substrates for the CVD and also named "bare fiber" in the tests. The micro composites for single fiber pull-out tests were prepared using an epoxy resin EPIKOTE Resin MGS® RIM 135 with EPIKURE Curing Agent MGS® RIM H 137 (Hexion). For the catalyst solution it was used: 0.005 M copper acetate (copper (II) acetate monohydrate from Acros, 98%) in acetonitrile (≥ 99.5%, Sigma Aldrich).

2.2 Catalyst deposition

The carbon and basalt fibers where set in a Teflon support at the center of a flask containing 100 ml of the copper acetate solution. The flasks were placed under vacuum to evaporate the solvent until the solution meniscus passed below the support level. After removing the fibers from their respective solutions, they were placed on a rack under room temperature and room pressure to dry overnight. The BFs had an extra step of annealing at 300°C for 1 hour in air before CVD.

2.3 CVD growth

The catalyst-coated fibers were placed on top of a quartz support and inserted at the center of a quartz tube furnace. Before heating the furnace and after growth during cooling, the chamber was purged with inert gas to remove any other gas residue. The samples were heated under an argon and hydrogen flow (100 and 400 sccm, respectively), and when the temperature of 480°C was reached, the argon gas was replaced by acetylene (17 sccm) for 30min[14].

2.4 Single fiber tensile testing

The mechanical properties of the single fibers were evaluated following the ASTM C1557 standard. The tensile tests were performed at room temperature on a Zwick/Roell Z010 equipped with a 100 N load cell with a sensitivity of 0.2 N. Tests were performed in displacement control at a cross-head speed of 2 mm/min. For each series of fibers, a minimum number of 30 fibers were glued on paper supports with 25 mm gauge length. The diameters of the fibers were measured using an optical microscope Nikon Eclipse 150L with the image analysis software Lucia Measurement.

2.5 Single fiber pull-out test

The interfacial shear strength (IFSS) was evaluated with single fiber pull-out tests in an in-house constructed device from the Leibniz-Institut für Polymerforschung (Dresden, Germany) [15,16]. To prepare the micro composites with epoxy resin, the single fibers were embedded at 45°C for a length (l_e) of 100 µm. The cure of the samples consisted of 1 hour at 85°C in the embedding chamber followed by drying for 6 hours at 80°C in an oven before being cooled to room temperature. The pull-out machine worked with a force accuracy of 1 mN, a displacement

  doi:10.5075/epfl-298799_978-2-9701614-0-0

accuracy of 0.07 µm and a loading rate of 0.01 µm/s under ambient conditions. Around 15-20 samples were tested for each fiber type. The apparent interfacial shear strength (τ_{app}) was calculated by the Eq. (1):

$$\tau_{app} = \frac{F_{max}}{\pi d_f l_e} \quad (1)$$

where F_{max} is the maximum force required to extract the fiber out of the matrix, and d_f is the fiber diameter. The total pull-out work (W) is the area under the curve force/displacement from the pull-out test [17].

2.6 Morphological and structural characterizations

The morphology of the fuzzy fibers was analyzed through scanning electron microscopy (Zeiss Sigma 300 VP Field Emission SEM) operating at 1 kV and the samples were coated with 10 nm gold to reduce charging. Transmission electron microscopy (TEM) imaging of the CNTs was performed by a FEI Tecnai (G2 Spirit TWIN) operated at an accelerating voltage of 120 kV using lacey carbon copper grids (01894 - PELCO NetMesh)

3. Results and Discussion

3.1 CNTs grafting and morphology

Both carbon and basalt fibers were coated with the catalyst by the same copper-based solution, only differing by an extra annealing step at 300°C in air. This step converts the copper acetate into copper oxide[18], which is expected to have stronger interaction with the surface of the BF (composed mainly by Si-O and Al-O bonds) reducing the dewetting of the catalyst during the CVD process. Tests performed without the pre-annealing resulted in poor or no CNT growth.

Despite the differences in surface chemistry from carbon and basalt fiber substrates, the growth morphology was very similar. Figure 1 shows the BF and CF covered by CNTs (named BF/CNT and CF/CNT, respectively). The fuzzy fibers are uniformly surrounded by a relatively dense array of misaligned CNTs.

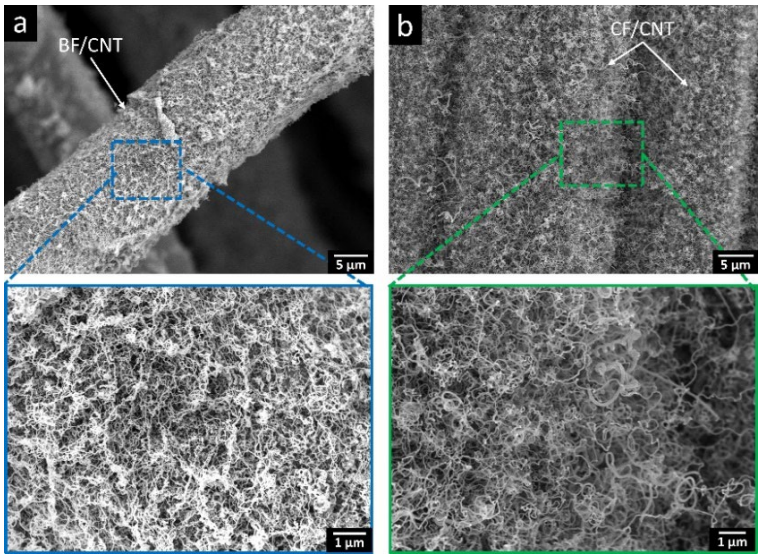

*Figure 1. SEM images from **a)** BF/CNT and **b)** CF/CNT.*

As illustrated in figure 2, the crystalline nanostructure of these nanocarbons synthesized on BF and CF is also very similar. The CNTs are made up of separated hollow compartments and "bamboo" knots which grow straight along the axis, which are known as "bamboo-like CNTs"[19]. They are composed of a broad range of walls in a highly tortuous shape, leading to the fuzzy morphology seen in figure 1. The CNTs from both fibers have very similar diameters, with the CNTs from CFs containing a higher number of walls which reduce the size of the hollow compartments.

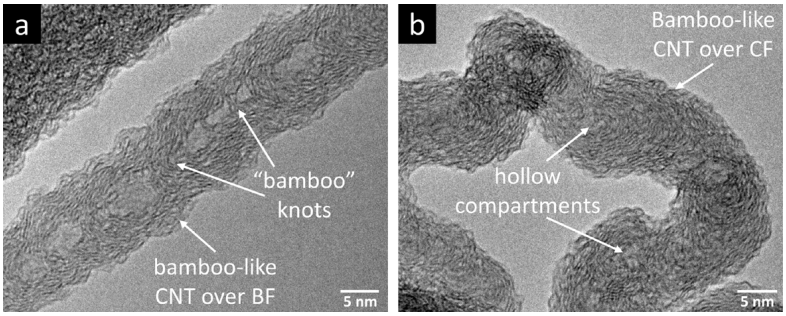

*Figure 2. TEM images from CNTs grown over **a)** BF and **b)** CF.*

3.2 Effects of CVD on the mechanical properties of BF/CNT and CF/CNT

Whereas the results from the CVD growth were very similar for both fibers, the mechanical tests exhibited a very different trend. To evaluate the consequences of the exposure to the CVD process on the tensile behavior of the fibers, the tensile strength of bare and fuzzy fibers was determined at room temperature by single fiber tensile tests. The results, summarized in figure 3, revealed a strength loss of 19.5% for the BF/CNT compared to the bare BF. Although the reduction in tensile strength of the BF at this temperature was relatively large, the loss was much lower than described in other works (>50% [12,20]), indicating that CVD conditions applied in this work are potentially less harmful to the basalt fibers than heat treatments in air. For the CF/CNT, there was no statistical change in tensile strength compared with the bare CF, in accordance with a recent work on fuzzy CF[21,22], confirming that CF are more suitable for CNT growth by CVD.

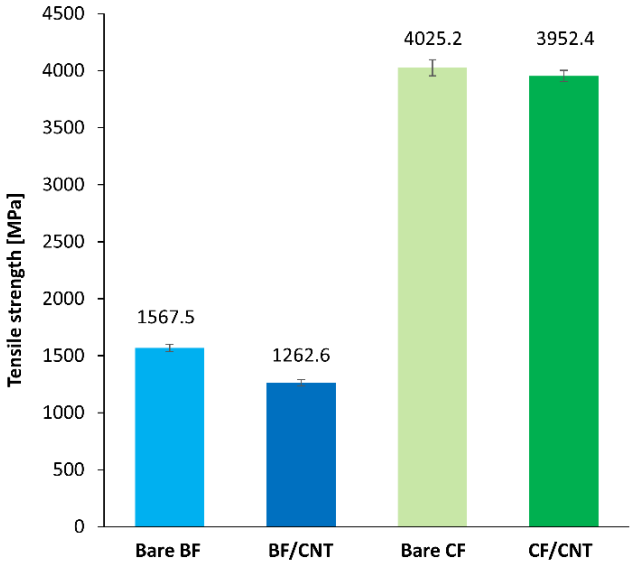

Figure 3. Single fiber tensile tests for BF and CF, bare and after CVD growth

3.3 Characterization of epoxy/fiber interface

The interfacial properties of grafted basalt and carbon fibers with carbon nanostructures was investigated through the single fiber pull-out technique, one of the most accurate techniques for measuring interfacial adhesion. For this analysis, two main parameters were considered: the apparent interfacial shear strength (τ_{app}) and the total pull-out work (W). Figure 4 display these parameters for both fibers, with and without CNTs.

The BF/CNT exhibited only a small, but statistically insignificant, increase in interfacial shear strength combined with a 23.8% decrease in pull-out work compared to the bare BF. This indicates that although a small bonding between the CNTs and the BF might have been established, the overall deterioration of the BF at the CVD conditions contributes negatively for the overall epoxy/BF adhesion.

For the CF/CNT, a large increase in interfacial shear strength and pull-out work is achieved (35.5 and 23.1%, respectively) by the grafting of the CNTs on the CF. These results suggest a strong adhesion between CNTs and CF, effectively bridging CF and epoxy matrix, leading to a stronger interface. Previous work has showed that the synthesis of these CNTs follow a tip-growth mechanism[14], which facilitates a pure carbon-carbon bonding between CNT and CF (no copper in between). This type of covalent bond not only adds strength, but also conceivably allow a good electrical conductivity between CF and CNT, which could be hindered by the presence of a metal oxide nanoparticle at its interface (considering that the copper catalyst will likely oxidize when exposed to atmosphere).

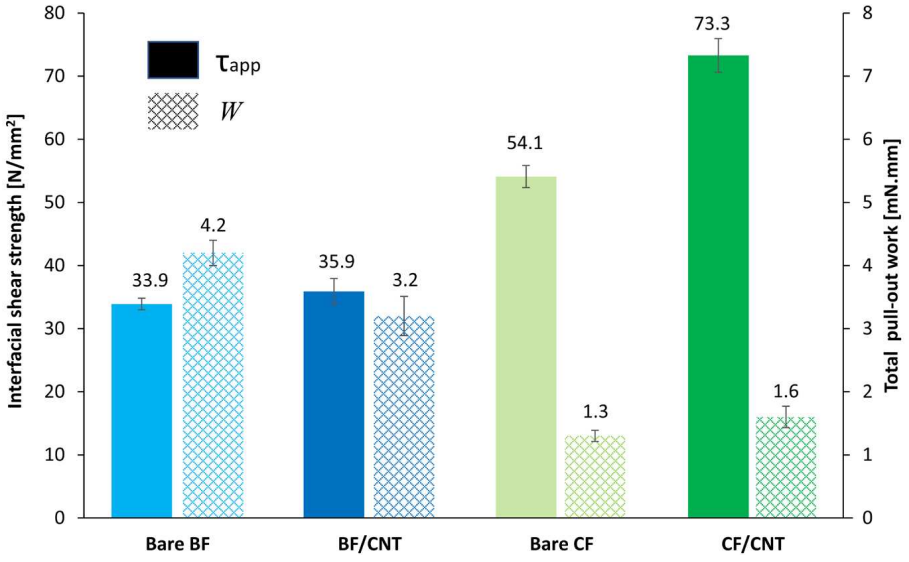

Figure 4 - Interfacial shear strength (left axis) and total pull-out work (right axis) from single fiber pull-out tests of BF and CF, bare and after CVD growth.

4. Conclusions and future work

In the present work we investigated the synthesis of carbon nanostructures over BFs and CFs by CVD at 480°C using copper as catalyst and compared their mechanical and interfacial properties.

Despite their highly different chemical structures, both fibers were uniformly coated with bamboo-like CNTs, demonstrating no major influence in the CVD process.

Our results indicated that the BFs do not profit from the grafting on CNTs under the conditions applied here. The tensile strength was dramatically reduced with little to no increase in the interfacial shear strength and a decrease in debonding work in an epoxy matrix. Future work will attempt to grow carbon nanostructures over BFs at even lower CVD temperatures to reduce the deterioration of the fibers and allowing a gain in the interfacial properties.

CF/CNTs on the other hand showed a substantial improvement both in interfacial shear strength and total pull-out work with no loss in tensile strength, indicating that the CNTs are effectively grafted to the CFs without damaging the fiber. Moreover, the bamboo-like CNTs synthesized here can enable other functionalities for these CF/CNTs. These structures have a well distributed number of defects and a higher ratio of edge-to-plane sites along their surface, which grant them better electrochemical properties than the straight, hollow CNTs[23,24], as well as excellent hydrogen and lithium storage capacity[25,26]. Further research will focus on exploring these multifunctionality aspects, such as investigating the CF/CNT application as structural electrodes.

5. Acknowledgements

The authors would like to acknowledge Airbus, ANSYS, Boeing, Embraer, Lockheed Martin, Saab AB, and Teijin Carbon America through MIT's Nano-Engineered Composite aerospace STructures (NECST) Consortium.

6. References:

1. Paiva MC, Bernardo CA, Nardin M. Mechanical, surface and interfacial characterisation of pitch and PAN-based carbon fibres. Carbon. 2000 Jan 1;38(9):1323–37.

2. Chae HG, Kumar S. Making Strong Fibers. Science. 2008 Feb 15;319(5865):908–9.

3. Morozov NN, Bakunov VS, Morozov EN, Aslanova LG, Granovskii PA, Prokshin V V, et al. Materials Based on Basalts From the European North of Russia. Sci Ceram Prod. 2001;58(3):24–7.

4. Sim J, Park C MDY. Characteristics of basalt fibre as a strengthening material for concrete structures. Compos Part B. 2005;36:504–12.

5. Maxineasa SG, Taranu N. 24 - Life cycle analysis of strengthening concrete beams with FRP. In: Pacheco-Torgal F, Melchers RE, Shi X, Belie ND, Tittelboom KV, Sáez A, editors. Eco-Efficient Repair and Rehabilitation of Concrete Infrastructures [Internet]. Woodhead Publishing; 2018 [cited 2022 Apr 13]. p. 673–721. (Woodhead Publishing Series in Civil and Structural Engineering). Available from: https://www.sciencedirect.com/science/article/pii/B9780081021811000241

6. S. Khandelwal and K. Y. Rhee. Recent advances in basalt-fiber-reinforced composites: Tailoring the fiber-matrix interface. Compos Part B Eng. 2020;192(November 2019).

7. Montes-Morán MA, Young RJ. Raman spectroscopy study of HM carbon fibres: effect of plasma treatment on the interfacial properties of single fibre/epoxy composites. Carbon. 2002 May 1;40(6):845–55.

8. Li R, Lachman N, Florin P, Wagner HD, Wardle BL. Hierarchical carbon nanotube carbon fiber unidirectional composites with preserved tensile and interfacial properties. Compos Sci Technol. 2015 Sep 29;117:139–45.

9. Yamamoto N, Guzman de Villoria R, Wardle BL. Electrical and thermal property enhancement of fiber-reinforced polymer laminate composites through controlled implementation of multi-walled carbon nanotubes. Compos Sci Technol. 2012 Nov 16;72(16):2009–15.

10. Qian H, Bismarck A, Greenhalgh ES, Kalinka G, Shaffer MSP. Hierarchical Composites Reinforced with Carbon Nanotube Grafted Fibers: The Potential Assessed at the Single Fiber Level. Chem Mater. 2008 Mar 11;20(5):1862–9.

11. Thostenson ET, Li WZ, Wang DZ, Ren ZF, Chou TW. Carbon nanotube/carbon fiber hybrid multiscale composites. J Appl Phys. 2002 May;91(9):6034–7.

12. Sarasini F, Tirillò J, Seghini MC. Influence of thermal conditioning on tensile behaviour of single basalt fibres. Compos Part B Eng. 2018 Jan;132:77–86.

13. Mittal G, Rhee KY. Chemical vapor deposition-based grafting of CNTs onto basalt fabric and their reinforcement in epoxy-based composites. Compos Sci Technol. 2018 Sep;165:84–94.

14. Acauan LH, Ashley KL, Wardle BL. Direct Synthesis of Carbon Nanomaterials via Surface Activation of Bulk Copper. Carbon. 2021 Feb;in press.

15. Mäder E, Grundke K, Jacobasch HJ, Wachinger G. Surface, interphase and composite property relations in fibre-reinforced polymers. Composites. 1994;25(7):739–44.

16. Zhandarov S, Mäder E, Scheffler C, Kalinka G, Poitzsch C, Fliescher S. Investigation of interfacial strength parameters in polymer matrix composites: Compatibility and reproducibility. Adv Ind Eng Polym Res. 2018 Oct 1;1(1):82–92.

17. Kruppke I, Scheffler C, Simon F, Hund RD, Cherif C. Surface Treatment of Carbon Fibers by Oxy-Fluorination. Materials. 2019 Feb 14;12(4):565.

18. Youssef I, Sall S, Dintzer T, Labidi S, Petit C. Forward Looking Analysis Approach to Assess Copper Acetate Thermal Decomposition Reaction Mechanism. Am J Anal Chem. 2019;10(05):153–70.

19. Lobo LS, Carabineiro SAC. Explaining Bamboo-Like Carbon Fiber Growth Mechanism: Catalyst Shape Adjustments above Tammann Temperature. C — J Carbon Res. 2020 Mar 30;6(2):18.

20. Bhat T, Fortomaris D, Kandare E, Mouritz AP. Properties of thermally recycled basalt fibres and basalt fibre composites. J Mater Sci. 2018 Feb;53(3):1933–44.

21. Yao Z, Wang C, Wang Y, Lu R, Su S, Qin J, et al. Tensile properties of CNTs-grown carbon fiber fabrics prepared using Fe–Co bimetallic catalysts at low temperature. J Mater Sci. 2019 Sep;54(18):11841–7.

22. Tanaka K, Hinoue Y, Okumura Y, Katayama T. EFFECT OF THE CNT GROWTH TEMPERATURE ON THE TENSILE STRENGTH OF CARBON FIBER. In Tallinn, Estonia; 2017 [cited

2022 Apr 15]. p. 273–9. Available from:
http://library.witpress.com/viewpaper.asp?pcode=MC17-028-1

23. Yook heng L, Chou A, Yu J, Chen Y, Gooding J. Demonstration of the advantages of using bamboo-like nanotubes for electrochemical biosensor applications compared with single walled carbon nanotubes. Electrochem Commun. 2005 Dec 1;7:1457–62.

24. Banks CE, Davies TJ, Wildgoose GG, Compton RG. Electrocatalysis at graphite and carbon nanotube modified electrodes: edge-plane sites and tube ends are the reactive sites. Chem Commun. 2005 Feb 7;(7):829–41.

25. Xu X, Tan H, Xi K, Ding S, Yu D, Cheng S, et al. Bamboo-like amorphous carbon nanotubes clad in ultrathin nickel oxide nanosheets for lithium-ion battery electrodes with long cycle life. Carbon. 2015 Apr 1;84:491–9.

26. Chen L, Xia K, Huang L, Li L, Pei L, Fei S. Facile synthesis and hydrogen storage application of nitrogen-doped carbon nanotubes with bamboo-like structure. Int J Hydrog Energy. 2013 Mar 19;38(8):3297–303.

EFFECT OF NANOARCHITECTURE ON EMI SHIELDING PROPERTIES OF NANOCOMPOSITES AT HIGH CONTENT OF GRAPHITE NANOPLATELETS

Fabrizia Cilento[a], Claudio Curcio[b], Alfonso Martone[a], Angelo Liseno[b], Amedeo Capozzoli[b], Michele Giordano[a]

a: IPCB, Institute of Polymers, Composite and Biomaterials, CNR, Portici, Italy– fabrizia.cilento@ipcb.cnr.it

b: Dipartimento di Ingegneria Elettrica e delle Tecnologie dell'Informazione, Università di Napoli "Federico II", Via Claudio 21, 80125 Napoli, Italy

Abstract: *Nacre-like materials respond to the rising demand for EMI shielding materials, followed by the advancements in wireless technology and increased signal sensitivity in electrical/electronic devices, especially for the safety of aircraft and other structures. In this work, the EMI shielding properties of high content of graphene nanoplatelet (GNP) based nanocomposites are investigated. The shielding effectiveness (SE) of different nanocomposites has been determined in order to investigate the capacity of the material to attenuate the electromagnetic waves in the X band (8-12 GHz). Two different configurations have been considered, compact and porous, varying the filler content (from 10 wt% to 90 wt%) and the thickness of the samples. Specifically, four different systems have been tested: thin (i) and thick (ii) compact laminates and thin (iii) and thick (iv) porous coatings.*

Keywords: Graphene; EMI shielding; nacre-like materials

1 Introduction

With the development of electronic technologies and increasing uses of electronic devices, the exposure to electromagnetic field radiations has widely increased [1,2]. This results in an increased need for electromagnetic shielding and shielding materials, capable of blocking the EM waves [3]. These materials are characterized by excellent electrical conductivity and electromagnetic properties. To date, this function is performed by metals, but their use could be limited due to their weight and their susceptibility to corrosion. To overcome these drawbacks, researchers investigated the possibility of using nanocomposites reinforced with carbonaceous nanofillers [4,5]. Specifically, bidimensional lamellar nanoparticles, such as graphene, are optimal candidates thanks to their high thermal and electrical conductivities and intrinsic barrier properties [6,7]. Graphene also possesses wave absorption capabilities and could have good reflecting properties with unique electrical and mechanical features. Nevertheless, the main challenge is to reproduce on the macroscale the mechanical and functional properties of the nanometric reinforcement. To do this, special architectures can be considered, mimicking existing materials, such as nacre [8]. Thanks to its particular brick and mortar (B&M) architecture, constituted by a high quantity of stiff but brittle nanoparticles, bonded together by a small amount of soft but tough phase (<5 vol%), this material exhibits excellent performance. The oriented nanoplatelets form a conductive path along the in-plane direction, resulting in a higher in-plane conductivity rather than the out-of-plane conductivity [9,10].

In this work, the EMI shielding capacity of high content GNP based nanocomposites is investigated. The shielding effectiveness of different systems has been determined in order to assess the capacity of the material to attenuate the electromagnetic waves in the X band. Two

  doi:10.5075/epfl-298799_978-2-9701614-0-0

different configurations have been considered, compact and porous, varying the filler content and the thickness of the sample. In particular, four different systems have been tested with the waveguide measurement technique in the microwave band of the electromagnetic spectrum within 8-12 GHz: compact thin films (i) thick nanolaminates(ii) and thin (iii) and thick (iv) porous coatings. The morphology of the material has been assessed in order to determine the influence of nanostructure on the absorption capacity of the material.

2 Materials and methods

Graphite nanoplatelets (GNP) with a lateral size of 30 µm and thickness of 14 nm and epoxy resin HexFlow® RTM6 are employed to fabricate nanocomposites.

Porous and compact samples with different filler content and thickness have been fabricated following a top-down approach. The phases of the fabrication process are sketched in Figure 1. GNPs are dispersed in acetone (m/V=1.4%) and mixed with a solution of epoxy diluted in acetone previously prepared by ultra-sonication (Step 1). The obtained paste is first deposited on a silicon non-sticky support using a semiautomatic tri-axes pantograph (Step 2). Then, the material is dried at room temperature all night to let the solvent evaporate. The result, at this stage, is a porous deposition. Porous coating of different thicknesses and filler content of 50 wt%, 70 wt% and 90 wt% have been fabricated.

Compact samples are produced by adding a calendering step in the fabrication process (Step 3). The porous deposition of Step 2 is compacted, promoting particle orientation, and reducing the thickness by about four times. The final pre-impregnated layer is obtained by pressing and curing the layer at increasing compaction pressure up to 10 bars [11,12]. This process allows the production of flexible thin films with different filler content (from 10 to 90 wt%) [9,11,13]. Since these films are impregnated with polymer, they can be assembled to fabricate thick laminates, through a compression moulding process, applying a pressure of 40-50 bar. Samples with filler contents of 50, 70, and 90 wt% are manufactured at a nominal thickness of 1 mm (~20 stacked films).

The list of fabricated samples is reported in Table 1.

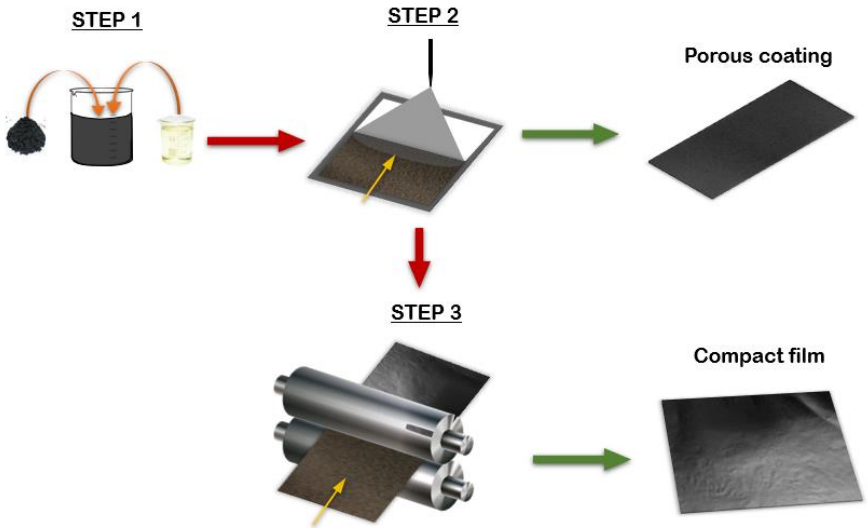

Figure 1. Manufacturing process: Step 1) Dispersion and mixing of GNP particles in acetone with epoxy; Step 2) spray deposition; Step 3) Calendering

  doi:10.5075/epfl-298799_978-2-9701614-0-0

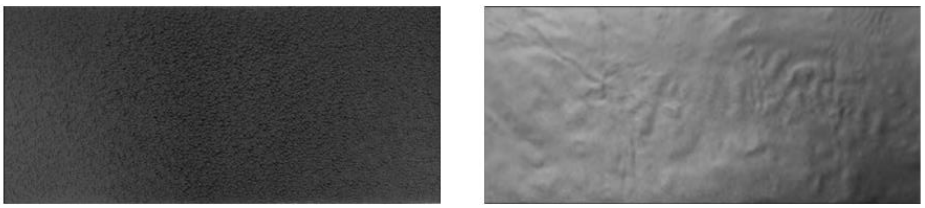

(a) (b)

Figure 2. Surface of porous (a) and compact (b) sample

Table 1. List of tested material: C=compact; P=Porous

System	Fabrication process	Level of compaction	Thickness [mm]	Filler content [wt%]
(i)	Spray + calendaring	C	~ 0.10	10, 20, 40, 50, 70, 80, 90
(ii)	Spray + calendaring+ Compression moulding	C	~ 1.00	50, 70, 90
(iii)	Spray	P	~ 0.07	50, 70, 90
(iv)	Spray	P	~ 0.20	50, 70, 90

The morphology of the two architectures, porous and compact, has been investigated employing scanning electron microscopy (SEM) (FEI Quanta 200 FEG). Samples are fractured in nitrogen to have a picture of the internal cross-section.

The shielding ability of the sample listed in Table 1 is investigated, in the X-band, using a waveguide measurement setup. Rectangular samples of dimensions 22.86 mm x 10.16 mm are placed, filling the section of a WR-90 rectangular guide, and five measurements are collected for each sample (see Figure 3).

The reflection, absorption, and transmission contributions are computed according to Eq.(1) [14].

$$R = |S_{11}|^2$$
$$T = |S_{21}|^2 \quad (1)$$
$$A = 1 - (R + T)$$

S_{11} and S_{21} are the reflection and transmission coefficient at the sample, respectively (see Figure 3).

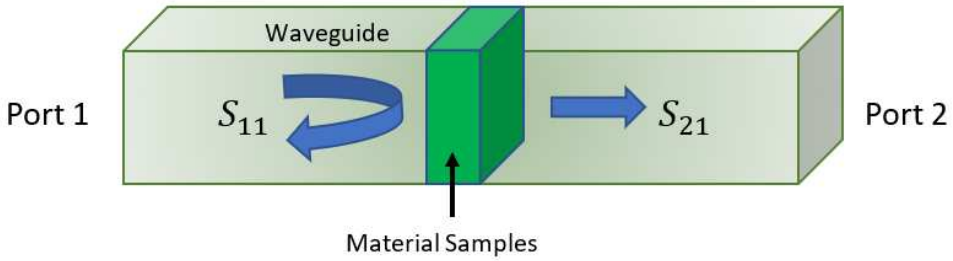

Figure 3. Measurement Setup

3 Results and discussion

Figure 4 and Figure 5 report SEM images of the cross-section (fractured surface) of porous and compact samples. By comparing the pictures, it is evident that the morphology significantly modifies when the calendaring process is added, passing from a chaotic to a well-aligned nanoarchitecture.

Also, by observing SEM images of compact samples (Figure 5), it appears that the nanostructure significantly modifies with increasing filler content. For samples with 10 and 20 wt% GNPs contents, the nanostructure is chaotic, while for filler content greater than 50 wt% the particles are highly oriented, with a laminated inner architecture and uniform texture. The nanoparticles geometry (i.e. high aspect ratio) combined with the processing technology ensure a good alignment in the plane at high filler content, resembling nacre architecture. However, samples with GNP content of 70 wt% show a more organised inner structure with nanoplatelets leaned on the film plane. Above this critical content the inner structure is threatened by dry spots and empty areas.

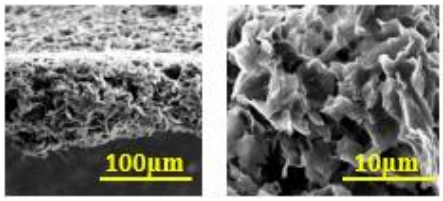

Figure 4. SEM images at two different magnifications of "porous" sample with 50/50 wt/wt

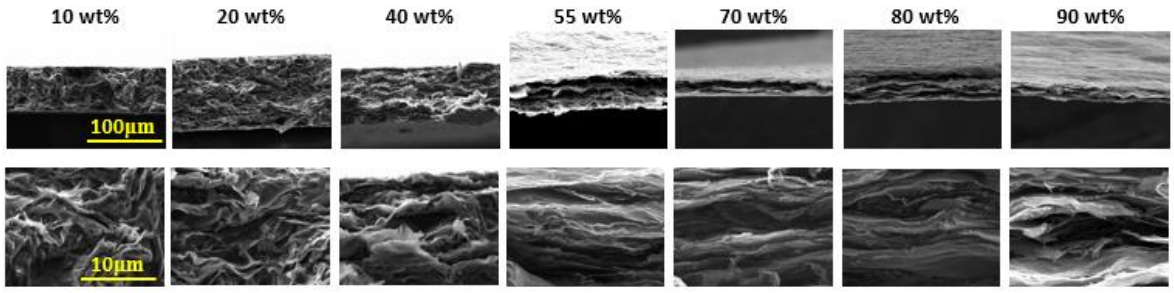

Figure 5. SEM images at two different magnifications of "compact" sample with different nominal filler content

The results of the X-band waveguide measurement are reported in Figure 6. Reflection and absorption contributions are computed according to Eq. (1).

A comparison between thin compact and porous samples for different filler content is reported. It appears that by making the nanostructure porous, the reflection coefficient decreases, and absorption increases. Also, in the compact sample, two different trends can be identified according to filler content:

- For w_f<40% reflection and absorption have an increasing and a decreasing trend respectively, with increasing filler content;
- For w_f>40% the influence of filler content is negligible.

In general, the power transmitted through the sample diminishes when reflection and absorption increase. Both reflection and absorption depend on the material characteristics and thickness of the sample.

  doi:10.5075/epfl-298799_978-2-9701614-0-0

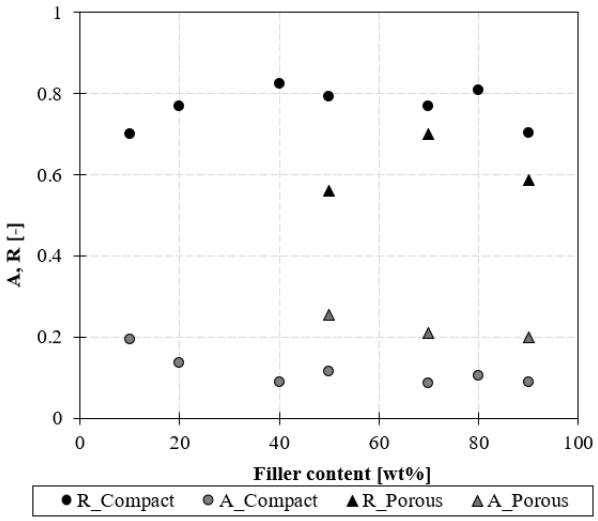

Figure 6. Reflection and absorption contribution of thin compacted vs porous samples at a different filler content

According to the SEM images in Figure 4 and Figure 5, it appears that for high filler content, the material has a well-ordered nanostructure with nanoplatelets oriented in the plane direction. In this configuration, when the EM waves cross the material, reflection increases. On the contrary, for low filler content, the nanostructure is less organized, with nanoparticles randomly oriented in the volume. In this case, a small absorption contribution appears.
The absorption capacity of the material can be expressed in terms of the effective absorption coefficient, as:

$$A_{eff} = \frac{A}{1-R} \tag{2}$$

Thus, a comparison between reflection, effective absorption, and transmission coefficients for the four systems (i-iv), for filler content of 50, 70 and 90 wt%, is reported in Figure 7. It appears that:

- Reflection (*R*) increases with thickness, and slightly decreases from compact to porous structures.
- Effective absorption (A_{eff}) increases with thickness, both for compact and porous structures.
- Transmission (*T*) decreases with increasing thickness both for compact and porous structures.

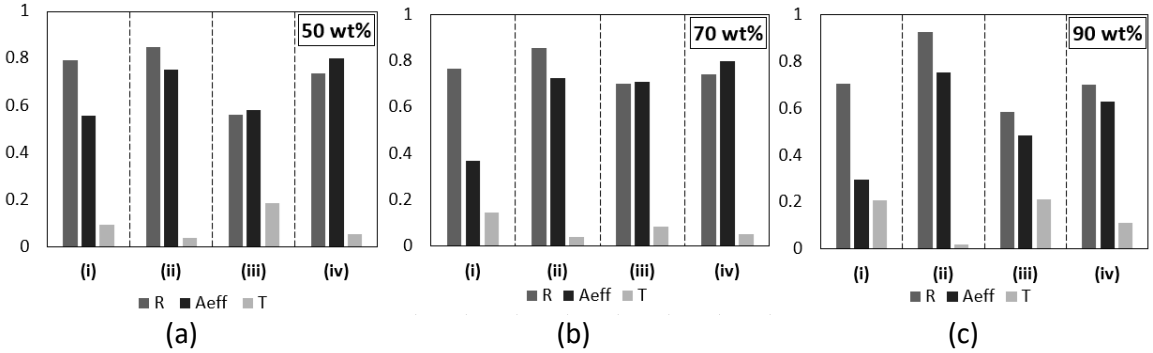

Figure 7. Contributions of reflection, absorption, and transmission for the four systems for samples with 50 wt% (a); 70 wt% (b) and 90 wt% (c)

By making the nanostructure porous, reflection decreases, and absorption increases [15]. Both for compact films at low filler content and porous samples, the chaotic structure allows better absorption. At the same time, the randomly oriented nanostructure reduces the reflection capacity of the material due to a worse alignment of the nanoplatelet of the surface.
By increasing the thickness of the sample, both reflection and absorption increase. In the case of compact samples, a higher compaction pressure applied during the fabrication process leads to a higher level of alignment of the nanoplatelet, which results in a higher reflection capacity of the material [16]. For both porous and compact samples, absorption increases with increasing thickness due to the higher amount of material.
On the contrary, the reflection mechanism, which appears linked to the level of alignment, could be related to the electrical conductivity, which is here measured referring to the static case, and reported in **Errore. L'autoriferimento non è valido per un segnalibro.**.

Table 2. Electrical conductivity of compact GNP/Epoxy films

F/M [wt/wt]	Electrical conductivity [S/m]
50/50	1.6×10^4
70/30	4.5×10^4
90/10	4.7×10^4

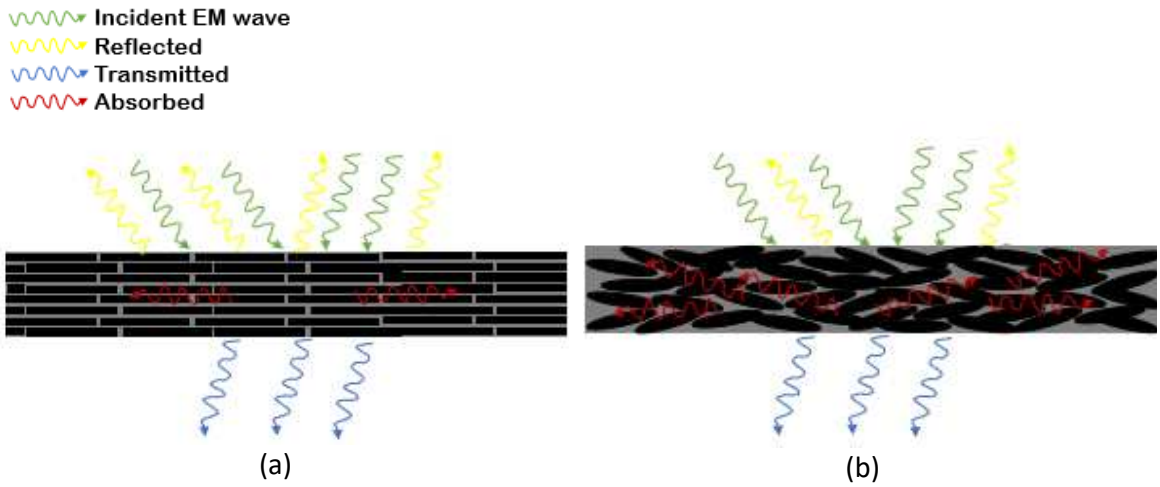

Figure 8. Schematic representation of (a) aligned/compact (i, ii) and (b) chaotic/porous (iii, iv) nanoarchitecture

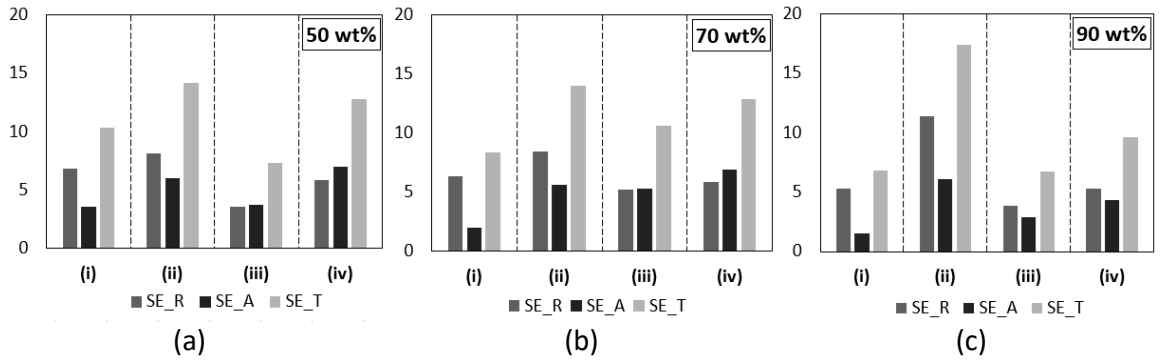

Figure 9. Shielding effectiveness in reflection, absorption and transmission for the four systems for samples with 50 wt% (a); 70 wt% (b) and 90 wt% (c)

A quantitative measure of the EM shielding is the shielding effectiveness (SE), which is measured in decibels (dB) [14]. The shielding effectiveness of the material has been computed according to Eq.(3), and it is reported in Figure 9. The shielding effectiveness in transmission increases with increasing thickness both for compact and porous systems and it is maximum in the case of nanolaminates (ii).

$$SE_R = 10\log_{10}\left[\frac{P_i}{P_i - P_r}\right] = -10\log_{10}(1-R)$$
$$SE_A = 10\log_{10}\left[\frac{P_i - P_r}{P_i - P_r - P_a}\right] = -10\log_{10}(1-A_{eff}) \quad (3)$$
$$SE_T = 10\log_{10}\left[\frac{P_i}{P_t}\right] = SE_R + SE_A$$

P_i, P_r, P_t and P_a are the incident, reflected, transmitted and absorbed power referred to the sample, respectively.

4 Conclusions

The shielding effectiveness in the X band of graphene-based nanocomposites has been experimentally investigated. The effect of the material architecture on the capacity to attenuate the electromagnetic waves has been assessed through experimental analysis.
It is found that at low filler content, given the random orientation of nanoplatelets within the volume, the EM waves are partly absorbed. On the contrary at high GNP content, given the high level of organization and alignment in the plane of the nanoparticles, the EM waves are mostly reflected. In a laminated compact structure, the SE is mainly governed by reflection, since the densely stacked platelets are more favourable for reflecting the EM waves. On the other hand, in the porous structure, waves pass through the surface of the material, moving in a cell-like configuration. According to these observations, it is found that porous-thick samples (iii) promote absorption, while compact-thick samples (iv) promote reflection. Maximum effective absorption of 80% was shown for system (iii) with 50 wt%, while a maximum reflection of 93% was shown for system (iv) with 90 wt%.
Therefore, the materials are able to block the incident radiation, thanks to a combined effect of absorption and reflection, with a maximum shielding effectiveness of 18 dB.

Acknowledgements

This work has been supported by the Research Project LAMPO (code CDS00750), founded by the Ministry of Economic Development

  doi:10.5075/epfl-298799_978-2-9701614-0-0

References

1. Li Y, Zhang H, Liu Y, Wang H, Huang Z, Peijs T, et al. Synergistic effects of spray-coated hybrid carbon nanoparticles for enhanced electrical and thermal surface conductivity of CFRP laminates. Compos Part A Appl Sci Manuf. 2018;105:9–18.
2. Das S, Sharma S, Yokozeki T, Dhakate S. Conductive layer-based multifunctional structural composites for electromagnetic interference shielding. Compos Struct. 2021;261(November 2020).
3. Kondawar SB, Modak PR. Chapter 2 - Theory of EMI shielding. In: Joseph K, Wilson R, George GBT-M for PEMISA, editors. Elsevier; 2020. p. 9–25.
4. Abbasi H, Antunes M, Velasco JI. Recent advances in carbon-based polymer nanocomposites for electromagnetic interference shielding. Prog Mater Sci. 2019;103:319–73.
5. Devi N, Ray SS. Electromagnetic interference cognizance and potential of advanced polymer composites toward electromagnetic interference shielding: A review. Polym Eng Sci. 2022;(December 2021):591–621.
6. Kumar P, Shahzad F, Yu S, Hong SM, Kim YH, Koo CM. Large-area reduced graphene oxide thin film with excellent thermal conductivity and electromagnetic interference shielding effectiveness. Carbon N Y. 2015;94:494–500.
7. Neto AHC, Guinea F, Peres NMR, Novoselov KS, Geim AK. The electronic properties of graphene. Rev Mod Phys. 2009;81(January-March).
8. Sun J, Bhushan B. Hierarchical structure and mechanical properties of nacre: a review. RSC Adv. 2012;2(20):7617.
9. Cilento F, Martone A, Cristiano F, Fina A, Giordano M. Effect of Matrix Content on Mechanical and Thermal Properties of High Graphene Content Composites. MATEC Web Conf. 2019;303(201 9):01002.
10. Han J, Du G, Gao W, Bai H. An Anisotropically High Thermal Conductive Boron Nitride/Epoxy Composite Based on Nacre-Mimetic 3D Network. Adv Funct Mater. 2019 Mar 1;29(13):1900412.
11. Cilento F, Martone A, Pastore Carbone MG, Galiotis C, Giordano M. Nacre-like GNP/Epoxy composites: Reinforcement efficiency vis-à-vis graphene content. Compos Sci Technol. 2021 Jul;211:108873.
12. Formicola C. Insight of thermo-mechanical and fire properties of an aerospace epoxy matrix loaded with micro and nano fillers . Insight of thermo-mechanical and fire properties of an aerospace epoxy matrix loaded with micro and nano fillers . 2008.
13. Cilento F, Martone A, Carbone MGP, Giordano M, Galiotis C. Load transfer in high content graphite nanoplateles composites. AIP Conf Proc. 2019;2196(December).
14. Barani Z, Kargar F, Mohammadzadeh A, Naghibi S, Lo C, Rivera B, et al. Multifunctional Graphene Composites for Electromagnetic Shielding and Thermal Management at Elevated Temperatures. Adv Electron Mater. 2020;6(11):1–12.
15. Lai D, Chen X, Wang Y. Controllable fabrication of elastomeric and porous graphene films with superior foldable behavior and excellent electromagnetic interference shielding performance. Carbon N Y. 2020;158:728–37.
16. Li J, Huang L, Yuan Y, Li Y, He X. Mechanically strong, thermally conductive and flexible graphene composite paper for exceptional electromagnetic interference shielding. Mater Sci Eng B Solid-State Mater Adv Technol. 2021;263(November 2020):114893.

  doi:10.5075/epfl-298799_978-2-9701614-0-0

RAPID AND FACILE PREPARATION OF MULTIFUNCTIONAL BUCKYPAPER NANOCOMPOSITE FILMS

Behnam, Ashrafi[a], Iman, Naseri[b], Michael, Jakubinek[c], Yadienka, Martinez-Rubi[c], Mostafa, Yourdkhani[b]

a: Aerospace Research Centre, National Research Council Canada, Montreal, QC, Canada
b: Department of Mechanical Engineering, Colorado State University, Fort Collins, CO, USA
c: Security and Disruptive Technologies Research Centre, Emerging Technologies Division, National Research Council Canada, Ottawa, ON, Canada
Behnam.Ashrafi@cnrc-nrc.gc.ca

Abstract: *Buckypaper is gaining increasing importance in various applications due to its high thermal and electrical conductivity, flexibility, biocompatibility along with its nanoscale, porous structure. Impregnation of buckypaper with polymer resins allows for creating polymer nanocomposite films with superior functional and mechanical properties; however, existing approaches for fabrication of buckypaper-based nanocomposites often require arduous, long processing conditions and are not suitable for scalable fabrication of nanocomposites. Here, we present our recent progress on rapid and facile development of buckypaper-thermoset nanocomposite films at ambient conditions and without any expensive equipment using a low-viscosity resin system that easily impregnates into the carbon nanotube network and that can be cured rapidly in a few minutes with minimal energy input.*

Keywords: buckypaper, frontal polymerization, rapid curing, nanocomposites

1. Introduction

Addition of nanoparticles (e.g., carbon nanotubes, graphene, boron nitride nanotubes) to polymers and creation of polymer nanocomposites is a widely used approach for imparting various functional properties to the host polymer (e.g., electrical and/or thermal conductivity) and/or for enhancing the mechanical properties of polymers. Early approaches for creation of nanocomposites mainly relied on mixing/dispersing nanoparticles into polymers via solvent-based approaches or direct mechanical mixing techniques [1,2]. While these approaches are useful for bulk preparation of polymer nanocomposites, they suffer from challenging processing steps, safety hazards, and limited amount of nanoparticles that can be added to polymers [1]. For example, in preparation of carbon nanotube-modified polymers, often less than 1 wt.% of nanotubes can be added to polymers, as increasing the nanotube content substantially increases the resin viscosity, making the processing conditions quite challenging. Additionally, it is extremely difficult to evenly disperse all nanotubes, resulting in agglomeration of nanoparticles in the polymer matrix and degradation of mechanical properties of produced nanocomposites compared to the pristine polymer.

An alternative approach for preparation of polymer nanocomposites with a high content of nanoparticles is creation of papers or films of nanoparticles followed by impregnation of the produced nanostructured papers by polymer resins. Buckypaper, which is a macroscopic assembly of carbon nanotubes, is one of such papers that has been produced at large scales and

  doi:10.5075/epfl-298799_978-2-9701614-0-0

is commercially available in rolls of hundreds of square meters [3,4]. Other examples of nanostructured papers include sheets of graphene and boron nitrite nanotube (BNNT) papers [5,6]. Use of such papers allows for creating polymer nanocomposites with high concentrations of nanoparticles (up to 30 vol.%) while enabling easier and safer handling of nanoparticles compared to bulk counterparts. We have previously used buckypapers and BNNT papers to produce epoxy-based nanocomposite films with desired electrical and thermal properties [6–9]. Nanocomposite films were previously prepared by infiltration of nanoparticle networks with a thermosetting resin under vacuum and often at elevated temperatures to reduce the resin viscosity and facilitate the impregnation of the highly dense, porous network of nanotubes. Following the infiltration step, the material was cured in an oven according to the cure cycle of the thermosetting resin, which can typically take several hours for achieving a fully crosslinked polymer network. These processing steps make the manufacturing process slow and energy intensive.

Here, we present a facile approach for rapid and energy-efficient fabrication of thermoset-based nanocomposite films at room temperature without using any vacuum conditions or ovens and in a few minutes as opposed to several hours of processing required in traditional approaches. In this new approach, we use a low-viscosity resin (η ~1.5 cP) based on dicyclopentadiene (DCPD) that can readily impregnate buckypaper networks at room temperature and ambient pressure. Following the rapid impregnation, the DCPD-based resin is cured via frontal polymerization [10]. Frontal polymerization (FP) is a promising alternative to traditional curing strategies that can substantially reduce the cure time and manufacturing energy of thermosets and their composites. In FP, a monomer solution containing a latent catalyst is heated locally to activate the latent catalyst and initiate an exothermic polymerization reaction [11]. The released heat is used to activate more catalyst and polymerize more resin. As a result, a self-propagating reaction wave is formed that propagates through the monomer solution until all available monomer is converted to polymer. Use of the frontally polymerizable DCPD resin system in processing of the nanocomposite films allows for rapid and net-zero energy curing of the thermoset matrix. The resulting frontally cured polymer is polydicyclopentadiene (pDCPD), which is a high-performance thermoset polymer with mechanical properties comparable to those of aerospace-grade epoxies, high fracture toughness (K_{IC} ~3 MPa.m$^{0.5}$), and high glass transition temperature (T_g ~120 °C), making it an ideal polymer for fabrication of durable and tough nanocomposites [12–14].

2. Experimental

Dicyclopentadiene (DCPD), 5-ethylidene-2-norbornene (ENB), and second-generation Grubbs catalyst (GC2) were purchased from Sigma Aldrich and used as received. DCPD is solid at room temperature, therefore a 95:5 wt% solution of DCPD:ENB was prepared in order to depress its melting point. The DCPD/ENB solution will be referred to as DCPD resin hereafter in this article. Phenylcyclohexane (PCH) and tributyl phosphite (TBP) were obtained from TCI America. PCH is used to facilitate the dissolution of the GC2 catalyst in the resin solution, whereas TPB is used as an inhibitor to control the reactivity and pot life of the resin system. In a typical experiment, 3.21 mg of GC2 was measured and dissolved in 400 μL of PCH. An appropriate amount of TBP (1 molar equivalent with respect to GC2) was added to the GC2/PCH solution via a volumetric syringe. This solution was then added to 5 mL of DCPD and thoroughly mixed. Buckypapers were prepared in-house using the vacuum filtration technique.

  doi:10.5075/epfl-298799_978-2-9701614-0-0

Nanocomposite films were prepared by droplet casting of resin onto the surface of buckypaper. Upon dropping a few droplets of resin, the resin was let to saturate the nanotube network, after which the excess resin was removed using a Kimwipe. Frontal polymerization was initiated by heating the DCPD-impregnated buckypaper using a laboratory-scale hot plate at ~140 °C. Since the thickness of the film is low (~100-200 μm), the propagation of the FP reaction through the thickness was not noticeable, and the overall cure process, from initiation to full cure, was done within a few minutes. In other words, the resin was used here as a cure-on-demand resin system rather than as an FP-curable resin.

2. Results and discussions

An ideal resin system for fabrication of buckypaper-based nanocomposites with a high density of nanotubes and low void content should have a low initial viscosity, long pot life at room temperature while being rapidly curable at elevated temperatures, and chemical compatibility with buckypaper for easy impregnation. Additionally, the resulting polymer should exhibit excellent thermomechanical properties. DCPD offers most of these attributes; therefore, we studied the processing of buckypapers impregnated with this cure-on-demand resin to explore the feasibility of fabrication of pDCPD-buckypaper nanocomposite films under mild processing conditions compared to traditional approaches used for epoxy resins.

The results of room-temperature rheological measurements on the DCPD resin are shown in Figure 1a,b. The initial viscosity of resin remained unchanged for approximately two hours, after which it slowly increased and reached a value of 750 Pa.s after five hours (Figure 1a); however,

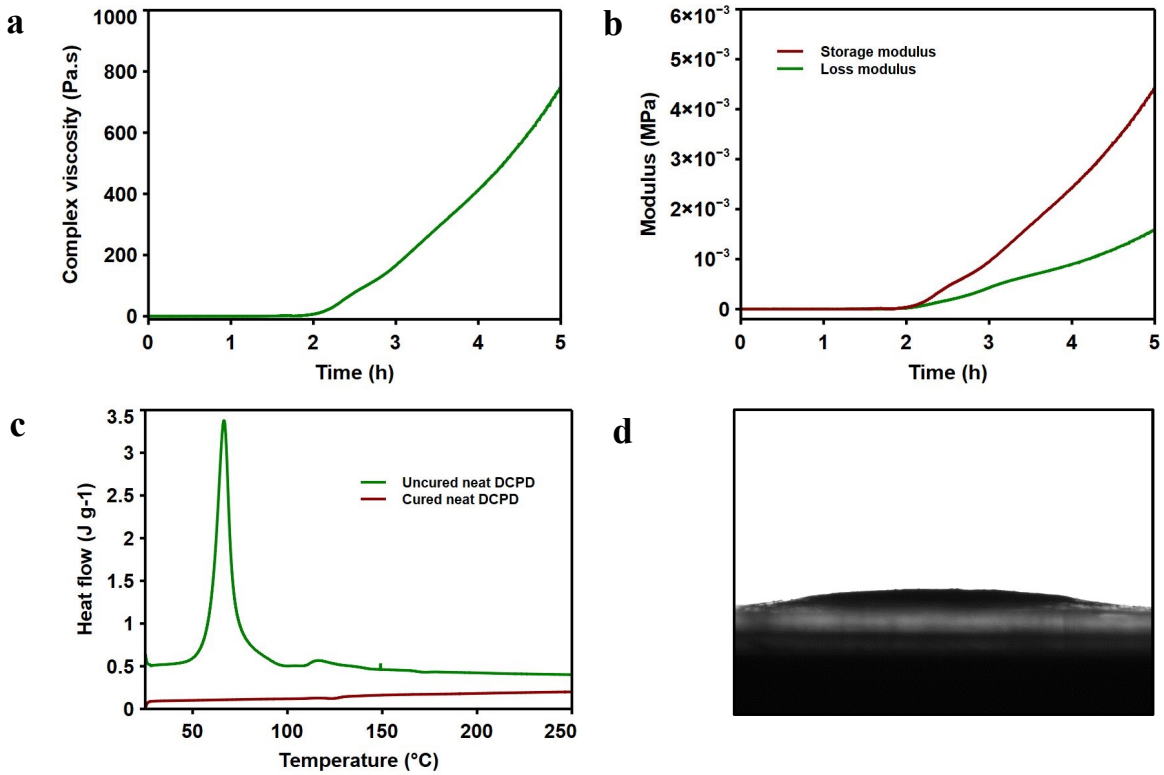

Figure 1. (a, b) Rheological profile of the DCPD resin system. (c) Thermal profile of an uncured resin sample and a cured polymer sample measured by DSC. (d) Contact angle measurement for a droplet of DCPD resin on the buckypaper substrate.

  doi:10.5075/epfl-298799_978-2-9701614-0-0

no gelation was observed within the five hours of the measurement (Figure 1b). As opposed to conventional epoxy resins, which have a high initial viscosity and short pot life, the low initial viscosity along with the long pot life of DCPD resin enable facile impregnation of buckypaper at room temperature and ambient pressure without the need for adding any solvents, which is highly desirable from the processing point of view. In addition, while the catalyzed dicyclopentadiene resin is stable for a few hours at room temperature, it rapidly cures at elevated temperatures and yields a fully cured solid polymer within a few minutes. Figure 1c shows the results of differential scanning calorimetry (DSC) measurements on an uncured DCPD resin sample as well as a sample cured at 140 °C for 5 min. The tall and sharp exothermic peak observed in the thermal profile of the uncured resin sample, which indicates the cure temperature range, clearly disappeared in the thermal profile of the cured sample. As a result, a high degree-of-cure (~99%) could be achieved by curing the resin for only five minutes.

Contact angle measurements were also carried out to evaluate the wettability of buckypaper by the DCPD resin (Figure 1d). While an instant contact angle of 17° was formed between DCPD resin and buckypaper, the resin completely infused into the porous structure of buckypaper within a few seconds due to its low viscosity, demonstrating excellent compatibility between the resin and buckypaper.

Several nanocomposite samples were prepared using droplet casting method. Compared to the pristine buckypaper, which is weak and fragile, the nanocomposite films are mechanically robust and can withstand various forms of deformation including twisting and bending. Scanning electron microscopy imaging (SEM) was used to observe the microstructure of the cured

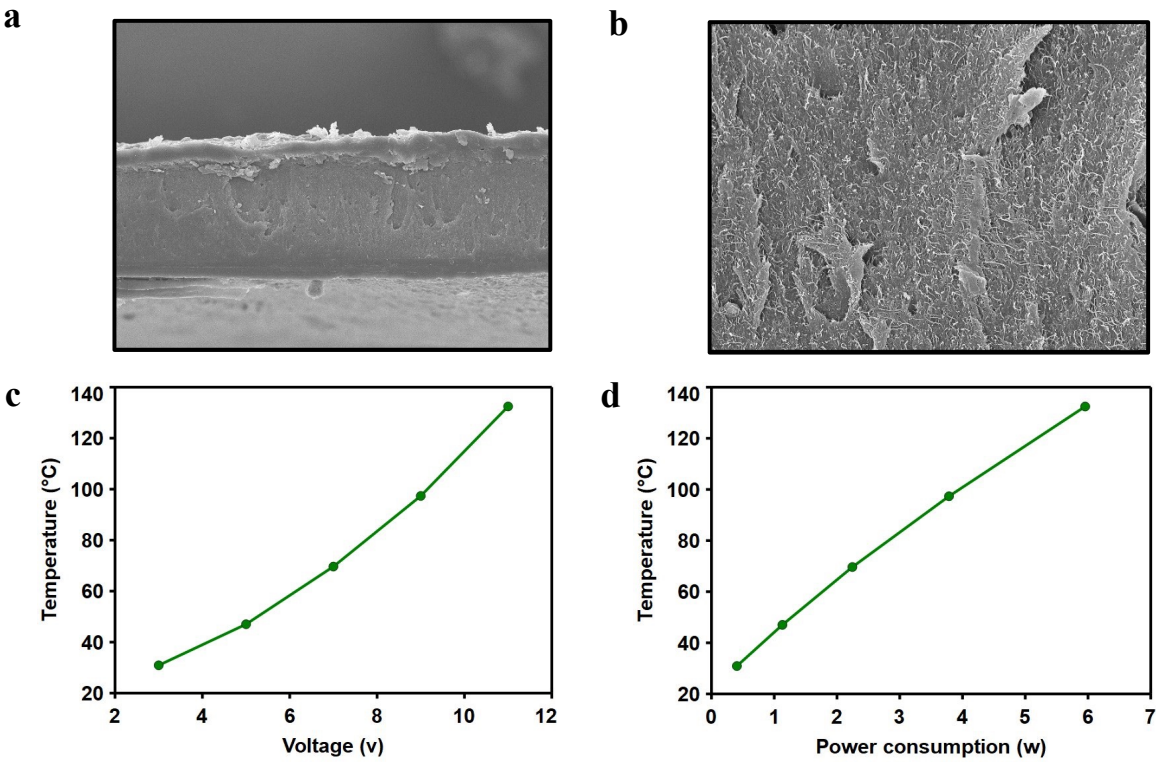

Figure 2. (a, b) Scanning electron microscopy (SEM) images from the cross-section of a nanocomposite film at two magnifications: (a) 500x and (b) 5000x. (c, d) Results of electrothermal measurements on nanocomposite films: (c) Correlation between input voltage and the saturated temperature, and (d) Steady-state temperature as a function of input power.

nanocomposite samples and gain an understanding of the quality of the impregnation process. Figures 2a,b present the SEM images taken from the cross-section of a nanocomposite sample at two different magnifications. The image captured at the higher magnification (Figure 2b) reveals a high quality of impregnation and low volume fraction of pores in the produced nanocomposite film, which are necessary for producing films with a good mechanical performance. The low-magnification image shows a thin layer of neat resin is formed at the surface (Figure 2b), which might affect electrical and mechanical properties of the produced nanocomposite.

We evaluated the electrothermal (Joule heating) performance of the nanocomposites by applying various input voltages across the specimens and measuring their time-dependent temperature profiles. The nanocomposites demonstrate excellent electrothermal performance, where a steady-state temperature of ~135 °C was realized at a low input voltage of 11 V (Figure 2c). The linear relationship between input power and steady-state temperature also demonstrates that the nanocomposite heater follows Joule's law (Figure 2d).

3. Conclusions

We used a frontally curable thermoset resin with a low initial resin viscosity to fabricate buckypaper-based polymer nanocomposites. The low resin viscosity allowed for quick impregnation of the carbon nanotube network at room temperature and ambient pressure. Following the impregnation step, complete curing of the matrix resin was achieved in a few minutes via through-thickness heating of the material. The quality of produced nanocomposite films was determined by performing thermal characterization and electron microscopy imaging. Additionally, excellent electrothermal performance was obtained for the produced nanocomposites. Future efforts will focus on characterizing the tensile properties of nanocomposite films and comparing them with buckypapers and neat resin films.

Acknowledgements

This work was supported by startup funds from the Department of Mechanical Engineering at Colorado State University and in part by the Ideation Fund from National Research Council Canada (Grant Agreement # 967242).

4. References

1. Ma PC, Siddiqui NA, Marom G, Kim JK. Dispersion and functionalization of carbon nanotubes for polymer-based nanocomposites: a review. Composites Part A: Applied Science and Manufacturing 2010; 41:1345–1367.
2. Chakraborty AK, Plyhm T, Barbezat M, Necola A, Terrasi GP. Carbon nanotube (CNT)–epoxy nanocomposites: a systematic investigation of CNT dispersion. Journal of Nanoparticle Research 2011; 13:6493–6506.
3. Miralon® carbon nanotube-based advanced materials. 2019. URL: http://miralon.com/nanocomp-technologies-products
4. Xu X, Zhang Y, Jiang J, Wang H, Zhao X, Li Q, et al. In-situ curing of glass fiber reinforced polymer composites via resistive heating of carbon nanotube films. Composites Science and Technology 2017; 149:20–27.

  doi:10.5075/epfl-298799_978-2-9701614-0-0

5. Dong L, Hu C, Song L, Huang X, Chen N, Qu L. A large-area, flexible, and flame-retardant graphene paper. Advanced Functional Materials 2016; 26:1470–1476.
6. Kim KS, Jakubinek MB, Martinez-Rubi Y, Ashrafi B, Guan J, O'Neill K, et al. Polymer nanocomposites from free-standing, macroscopic boron nitride nanotube assemblies. RSC Advances 2015; 5:41186–41192.
7. Ashrafi B, Jakubinek MB, Martinez-Rubi Y, Rahmat M, Djokic D, Laqua K, et al. Multifunctional fiber reinforced polymer composites using carbon and boron nitride nanotubes. Acta Astronautica 2017; 141:57–63.
8. Ashrafi B, Guan J, Mirjalili V, Hubert P, Simard B, Johnston A. Correlation between Young's modulus and impregnation quality of epoxy-impregnated SWCNT buckypaper. Composites Part A: Applied Science and Manufacturing 2010; 41:1184–1191.
9. Jakubinek MB, Ashrafi B, Guan J, Johnson MB, White MA, Simard B. 3D chemically cross-linked single-walled carbon nanotube buckypapers. RSC Advanced 2014; 4:57564–57573.
10. Robertson ID, Yourdkhani M, Centellas PJ, Aw JE, Ivanoff DG, Goli E, et al. Rapid energy-efficient manufacturing of polymers and composites via frontal polymerization. Nature 2018; 557:223–227.
11. Pojman JA. Frontal polymerization. In: Matyjaszewski K, Möller M, editors. Polymer science: a comprehensive reference. Elsevier. 2012.
12. Delaude L, Noels AF. Metathesis. In: Kroschwitz JI, Seidel A, editors. Kirk-Othmer encyclopedia of chemical technology. John Wiley & Sons. 2007.
13. Woodson Jr CS, Grubbs RH. Polymeric composites including dicyclopentadiene and related monomers. US Patent 6,310,121 B1. 2001.
14. Vallons KAM, Drozdzak R, Charret M, Lomov SV, Verpoest I. Assessment of the mechanical behaviour of glass fibre composites with a tough polydicyclopentadiene (PDCPD) matrix. Composites Part A: Applied Science and Manufacturing 2015; 78:191–200.

  doi:10.5075/epfl-298799_978-2-9701614-0-0

INVESTIGATION OF THE THERMAL AND MECHANICAL PROPERTIES OF COMPOSITE MATERIALS WITH AMINE-FUNCTIONALIZED REDUCED GRAPHENE OXIDE INCLUSIONS

Annika C. Ackermann[a,b,c], Michael Fischer[a,c], Alexander Wick[a,c], Stefan Carosella[a,c], Bronwyn L. Fox[b,c], Peter Middendorf[a,c]

a: University of Stuttgart, Institute of Aircraft Design, Pfaffenwaldring 31, 70569 Stuttgart, Germany. E-mail: ackermann@ifb.uni-stuttgart.de
b: Swinburne University of Technology, Manufacturing Futures Research Institute, Hawthorn, Victoria 3122, Australia
c: ARENA2036 Research Campus, Pfaffenwaldring 19, 70569 Stuttgart, Germany

Abstract: *The incorporation of graphene materials can further improve the thermal and mechanical properties of composites. Yet, the use of graphene derivatives that were functionalized using plasma treatment is relatively unexplored. This study evaluates the change of the thermal and dynamic mechanical properties of nanocomposites and graphene-enhanced carbon fiber reinforced polymers (g-CFRP) by incorporating a non-functionalized form of reduced graphene oxide (rGO) and its amine-functionalized derivative (frGO) which was subjected to plasma treatment. The nanocomposites exhibited a strong increase of the thermal diffusivity and conductivity by up to 27% especially with high weight fractions of frGO. This was in contrast to the g-CFRP specimens that demonstrated a drastic reduction of these two thermal characteristics, but also exhibited a high void content. An increased storage modulus was established for nanocomposites with (f)rGO inclusions, but the g-CFRP demonstrated no significant change.*

Keywords: Nanoparticles; Resins; Thermosets; Thermal analysis; Surface treatment

1. Introduction

The ever-increasing demands required from composite materials have resulted in the incorporation of new materials such as graphene and its derivatives. Given the outstanding mechanical [1], thermal [2] and electrical [3] properties as well as the very large specific surface area, very low contents of graphene materials can lead to drastic changes in the composite's performance [4,5].

In order to improve the dispersibility and bonding strength between graphene materials and the polymeric matrix, a tailored non-covalent or covalent functionalization can be applied to the particles [6,7]. Given that a covalent functionalization usually allows a stronger bonding of the functional groups to the particle's surface, it also enables a more pronounced enhancement of the composite's material properties [8-11]. In addition, it permits a much larger range of different properties than a non-covalent functionalization [6]. For composite materials that use epoxies as their polymeric matrix, a functionalization of the used graphene materials with amine groups is particularly important as these functional groups can take part in the polymerization process [12,13].

  doi:10.5075/epfl-298799_978-2-9701614-0-0

A covalent functionalization of graphene materials is usually carried out using tedious chemical processes in which large volumes of hazardous solvents and reagents are applied in a number of various non-robust and time-consuming processing steps that cannot be scaled to large quantities [14,15]. An alternative covalent functionalization process is the application of plasma treatment. Here, the ionized forms of gases such as NH_3 or O_2 are employed to create the respective functional groups on the particle's surface with very short process times of a few seconds to minutes [6,16]. Furthermore, plasma treatment is comparatively easy to scale by extending the size or number of reactors. Yet, the characteristics of nanocomposites as well as graphene-enhanced carbon fiber reinforced polymers (g-CFRP) that incorporate graphene materials that underwent a plasma functionalization process is currently not well understood.

This work evaluates the influence of two varieties of reduced graphene oxide on the thermal and mechanical properties on nanocomposites and g-CFRPs. Both types of composite materials were comprised of an epoxy matrix and incorporated either a non-functionalized or an amine-functionalized grade of reduced graphene oxide for which the amine functional groups were created by plasma treatment. The thermal properties of the neat polymer, nanocomposite, neat carbon fiber reinforced polymer (CFRP) and g-CFRP were evaluated by quantifying the specific heat capacity, thermal diffusivity and thermal conductivity. Similarly, the mechanical performance of the materials was evaluated by means of dynamic mechanical analysis. This information will facilitate the choice of materials for various applications.

2. Materials and methods

2.1 Materials

Graphit Kropfmühl GmbH (Hauzenberg, Germany) supplied two varieties of graphene derivatives in the form of a non-functionalized reduced graphene oxide EXG 98300 R (rGO) and an amine-functionalized reduced graphene oxide EXG 98300 R FNH (frGO) for which the functionalization was realized by the manufacturer by applying NH_3 in a low-pressure gas plasma. These two particulate materials were used as received. The epoxy resin Biresin® CR83 and the amine-based hardener Biresin® CH83-10 were obtained from Sika Deutschland GmbH (Stuttgart, Germany) and used as the matrix material. This system has a low mixed viscosity (155 mPa s at 25 °C) and matches the functional groups of the frGO particles. ZOLTEK™ (Bridgeton, USA) PX35 tow 50k with 200 g m^{-2} unidirectional carbon fibers were incorporated in the case of the CFRP samples.

2.2 Sample preparation

The dispersion of the (f)rGO particles in the epoxy resin using the three roll mill 80S PLUS from EXAKT Advanced Technologies GmbH (Norderstedt, Germany) to create (f)rGO/resin masterbatches are explained in detail elsewhere [17]. For the manufacturing of the neat polymer and nanocomposite specimens, the (f)rGO/resin masterbatches were manually mixed with the required amount of hardener and, if applicable, more resin to dilute the suspension to lower (f)rGO weight fractions. The resin/hardener mixing ratio of 100:30 parts by weight was used for all specimens. Next, the uncured suspensions were degassed in a vacuum chamber and subsequently casted into molds. The unidirectional g-CFRP laminates with 1.50 wt% (f)rGO with respect to the matrix were produced at room temperature using the automated laboratory-scale prepreg plant at the University of Bayreuth, Germany. After prepreg creation, the rolls were stored at -20 °C until they were further processed by hand lay-up. Depending on the required

  doi:10.5075/epfl-298799_978-2-9701614-0-0

specimen thickness, four or eight plies were stacked on top of each other at 0° fiber direction and enclosed by a vacuum bagging set-up. The neat CFRP laminate was produced using a vacuum resin infusion set-up. Both the nanocomposite and (g-)CFRP samples were left to cure for 48 h at room temperature and experienced a thermal post-curing in which they were heated from room temperature to 70 °C with 0.2 °C min^{-1}, maintained at 70 °C for 12 h and cooled to room temperature at 0.5 °C min^{-1}.

2.3 Characterization

Differential scanning calorimetry (DSC) was used to determine the specific heat capacity c_p of the various materials. Using a TA Instruments (New Castle, USA) DSC 2920 and in accordance to DIN EN ISO 11357-4:2021 [18], the specimen was first maintained at -20 °C for 2 min and subsequently heated to 70 °C at a heating rate of 5 °C min^{-1}. Three samples per material configuration were evaluated in a nitrogen atmosphere and using a modulated DSC.

Laser flash analysis (LFA) was applied to measure the thermal diffusivity a of the materials in accordance to DIN EN ISO 22007-4:2017 [19]. A total of three specimens per material configuration was analyzed using a Netzsch (Selb, Germany) Nanoflash LFA 447 for the neat polymer as well as nanocomposites and a Netzsch 467 Hyperflash for the (g-)CFRP laminates. Each specimen was analyzed four times in succession at the isothermal testing temperatures of room temperature, 40 °C and 60 °C. This data in conjunction with the determined specific heat capacity and density was used to calculate the thermal conductivity λ using

$$\lambda = c_p a \rho. \quad (1)$$

The density ρ of the neat polymer, nanocomposites and (g-)CFRP materials was measured using the procedure as detailed in DIN EN ISO 1183-1:2004 [20]. The fiber volume fraction V_f and void content V_o of the various (g-)CFRP laminates was evaluated by acid digestion based on DIN EN ISO 2564:2018 [21].

Dynamic mechanical analysis (DMA) was conducted to examine the thermomechanical and viscoelastic performance of the different composites. In accordance to DIN 65583:1999 [22] and using a TA Instruments DMA 2980, three specimens per material configuration were heated from room temperature to 130 °C at a heating rate of 3 °C min^{-1} and a frequency of 1 Hz.

3. Results and discussion

3.1 Thermal properties

The mean specific heat capacity of the various material configurations with respect to temperature is illustrated in Figure 1. A slight increase of the specific heat capacity with increasing temperatures can be observed for all samples. Small variations can be established between the neat polymer and nanocomposite samples, but the error of the measurements is too large to establish a significant effect of the (f)rGO particles. Similarly, no significant effect can be confirmed between the neat CFRP and the g-CFRP specimens.

In contrast to the specific heat capacity, the thermal diffusivity of the neat polymer and nanocomposites is approximately constant with increasing temperatures (cf. Figure 2(i)). Yet, a significant effect of the presence of (f)rGO can be established. Increasing contents of (f)rGO result in a higher thermal diffusivity and the impact is more pronounced for frGO than for rGO.

  doi:10.5075/epfl-298799_978-2-9701614-0-0

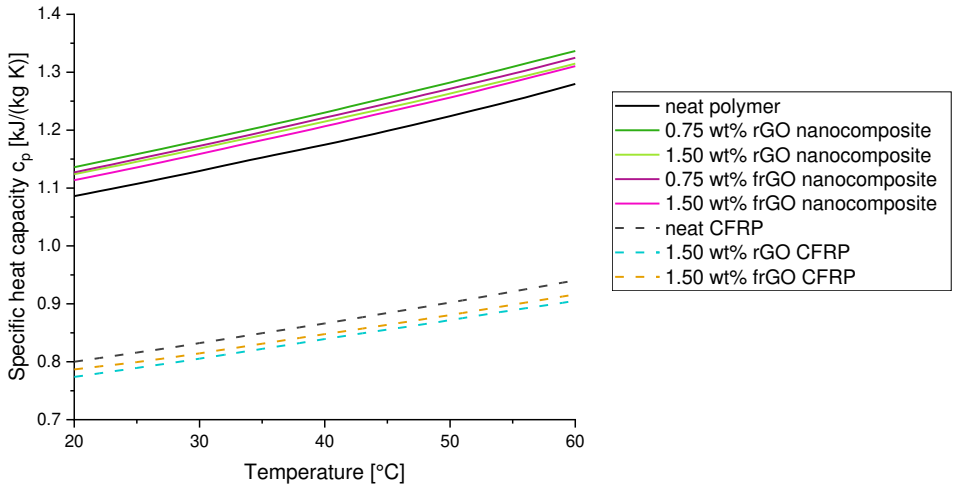

Figure 1. Mean specific heat capacity of the evaluated composites as obtained by DSC.

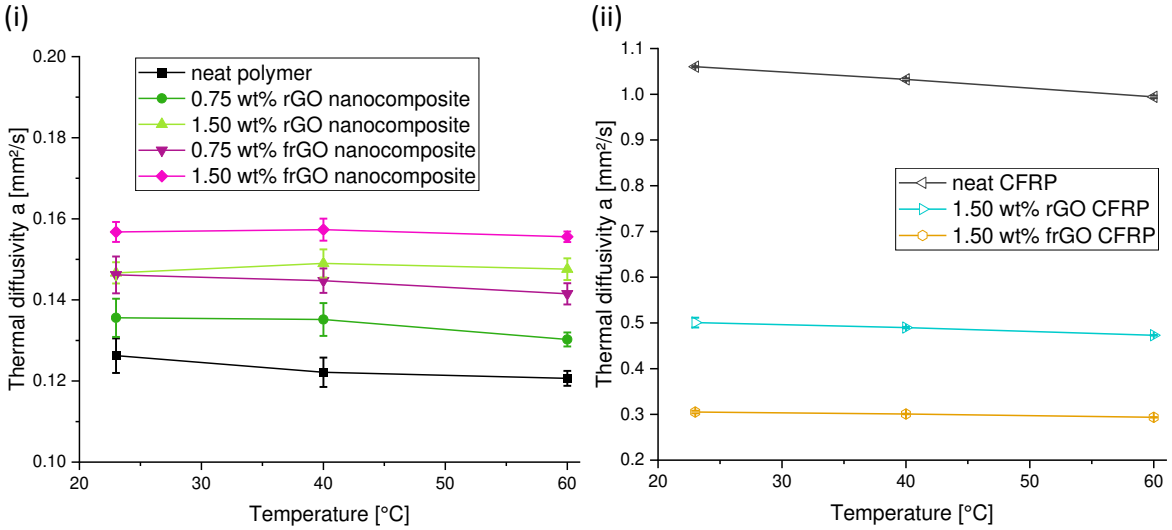

Figure 2. Mean thermal diffusivity and respective expanded uncertainty for a coverage probability of 95% of the evaluated composites as obtained by LFA. (i) Neat polymer and nanocomposites. (ii) Neat CFRP and g-CFRPs.

For example, the thermal diffusivity of the 1.50 wt% frGO nanocomposite is 7% and 24% higher than the thermal diffusivities of the 1.50 wt% rGO nanocomposite and neat polymer at room temperature respectively. Unlike the behavior of the nanocomposite samples, the (g-)CFRP specimens exhibit a small decrease of the thermal diffusivity with rising temperatures (Figure 2(ii)) which is expected for composite materials with high weight fractions of carbonaceous materials [23]. Nonetheless, a drastic reduction by 54% (72%) in comparison to the neat CFRP can be established for the 1.50 wt% rGO CFRP (1.50 wt% frGO CFRP) specimens. This is contrary to expectations as the available literature establishes an increase of the thermal diffusivity with the addition of graphene materials to CFRPs [24]. This inferior performance of our g-CFRP materials is most likely linked to the high porosity of those specimens. As can be deduced from Table 1, the specimens demonstrate similar fiber volume fractions. However, the void content of the g-CFRP laminates is drastically higher and the densities are slightly lower than those observed in the neat CFRP. Our previous work [17] has shown that the nanocomposites exhibit a homogeneous distribution of the graphene materials with no visible voids or agglomerates.

  doi:10.5075/epfl-298799_978-2-9701614-0-0

Furthermore, the viscosity of the suspensions with 1.50 wt% (f)rGO was several times higher than the viscosity range of 1.5 – 2.4 Pa s that is recommended for the production of high quality laminates to enable a suitable processing behavior and a sufficient wetting of the fibers [25]. Consequently, the high void content of our g-CFRP samples can be ascribed to the high viscosities of the used suspensions that limit the processability for the used vacuum bagging setup. These voids are also associated with a reduction of the thermal diffusivity [26,27]. Moreover, the decrease of the thermal diffusivity is also linked to the shape of the laminate's voids. For example, unidirectional fiber reinforced polymers like the ones analyzed in this work typically exhibit pores with the shape of elongated ellipsoids which are also associated with a more drastic reduction of the thermal diffusivity than spherical pores [27,28].

Table 1: Mean fiber volume fraction, void content and density of the neat CFRP and g-CFRP specimens. The error (expanded uncertainty) is stated for a coverage probability of 95%.

Matrix of CFRP	Fiber volume fraction V_f [%]	Void content V_o [%]	Density ρ [g/cm³]
neat polymer	53.1 ± 1.9	1 ± 1	1.5 ± 0.0
1.50 wt% rGO	51.6 ± 1.0	6 ± 1	1.4 ± 0.0
1.50 wt% frGO	52.8 ± 3.3	5 ± 1	1.4 ± 0.0

The thermal conductivity is influenced by the specific heat capacity as well as the thermal diffusivity and the established results for the various material configurations are visualized in Figure 3. Similar to the specific heat capacity, the thermal conductivity of all samples increases with rising temperatures. Moreover, the influence of (f)rGO is similar to the thermal diffusivity as a significant increase of the nanocomposites' thermal conductivity can be observed with higher (f)rGO loadings. Comparably, a drastic reduction of the thermal conductivity of the g-CFRP materials must be noticed.

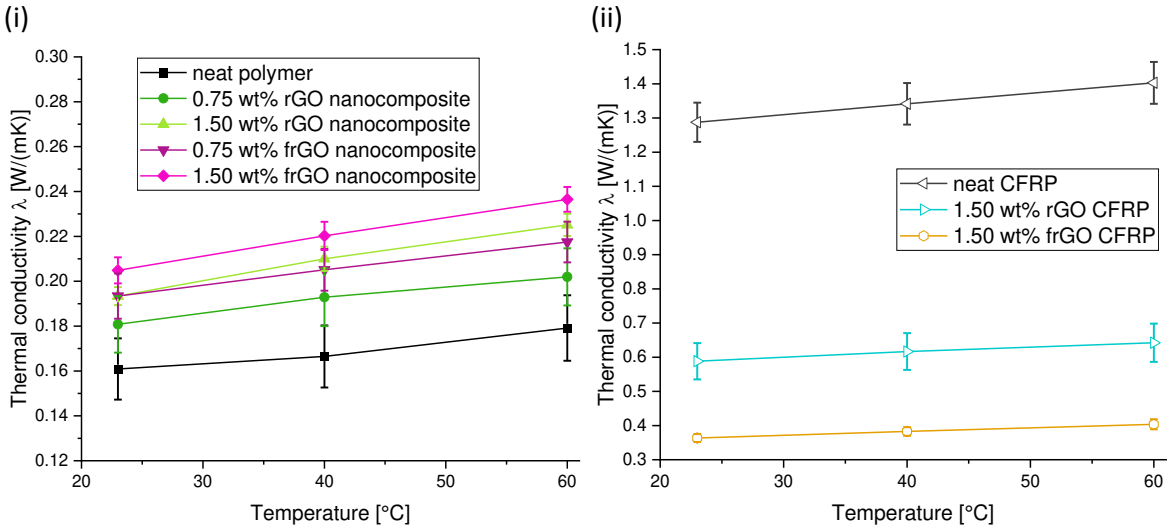

Figure 3. Calculated mean thermal conductivity and respective expanded uncertainty for a coverage probability of 95% of the evaluated composites. (i) Neat polymer and nanocomposites. (ii) Neat CFRP and g-CFRPs.

  doi:10.5075/epfl-298799_978-2-9701614-0-0

3.2 Mechanical properties

The mechanical characteristics were analyzed by the use of DMA and the results are visualized in Figure 4. When comparing the nanocomposite samples to the neat polymer, a significant increase of the storage modulus in the glassy region E'_g can be observed. A maximum increase of 38% (35%) with respect to the neat polymer can be established for the 1.50 wt% rGO (1.50 wt% frGO) nanocomposite. The stiffness of the neat CFRP and g-CFRP specimens as established by the storage modulus below the glass transition temperature exhibits no significant differences as this material characteristic is primarily governed by the carbon fibers and not the matrix material. Yet, a decrease of tan δ and a wider peak broadness can be established for the nanocomposite and g-CFRP materials. This indicates an improved interfacial bonding especially in the case of the frGO particles [29].

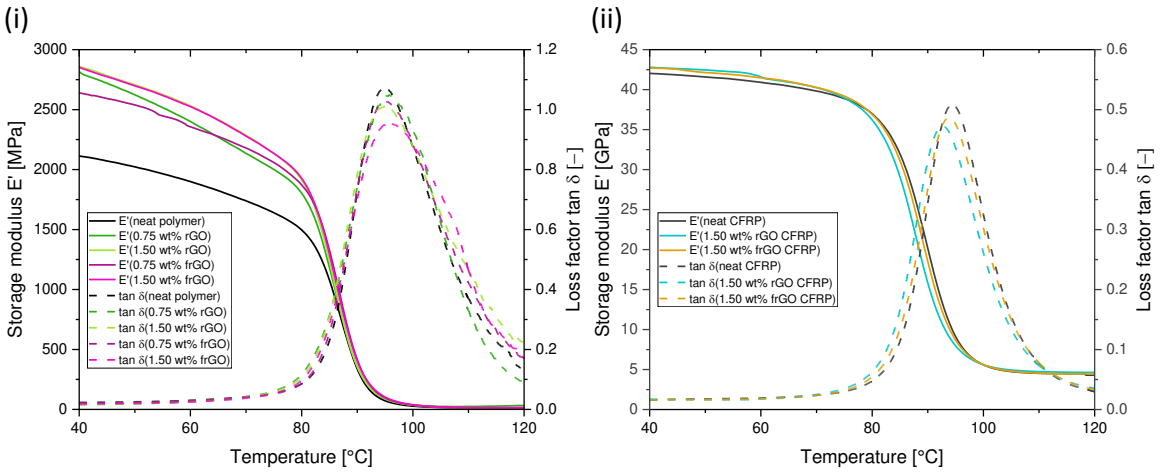

Figure 4. Mean dynamic mechanical properties of the evaluated composites as obtained by DMA. (i) Neat polymer and nanocomposites. Note that the curves for 1.50 wt% rGO and 1.50 wt% frGO are nearly identical. (ii) Neat CFRP and g-CFRP.

4. Conclusion

This work examined the impact of the addition of rGO and plasma-treated frGO to epoxy-based nanocomposites and g-CFRPs on the thermal and mechanical properties. The presence of (f)rGO particles in the nanocomposites as well as the g-CFRPs did not affect the specific heat capacity. Yet, the nanocomposites demonstrated an enhanced thermal diffusivity and thermal conductivity of up to 24% and 27% respectively in the case of 1.50 wt% frGO. A drastic reduction of the thermal diffusivity as well as conductivity was, however, observed in the g-CFRP specimens which was likely to be caused by the high void content in these specimens. The characterization of the mechanical properties by DMA established an increasing stiffness of up to 38% in the case of nanocomposites with higher weight fractions of (f)rGO. No significant effect on the storage modulus was established between the neat CFRP and g-CFRPs as this parameter is primarily affected by the fibrous reinforcement. Yet, an enhanced interfacial bonding in the nanocomposites and g-CFRPs was observed especially in the case of frGO. These results suggest the opportunities for the use of rGO and particularly frGO in composite materials. Nonetheless, efforts are required to realize g-CFRPs with a high laminate quality that enable the use of the full potential of rGO as well as frGO.

  doi:10.5075/epfl-298799_978-2-9701614-0-0

Acknowledgements

This research and development project is funded by the German Federal Ministry of Education and Research (BMBF) within the framework concept “Forschungscampus” ARENA2036 (funding number: 02P18Q643) and managed by the Project Management Agency Karlsruhe (PTKA). The author is responsible for the contents of this publication. The authors thank Graphit Kropfmühl GmbH and Sika Deutschland GmbH for the supply of materials and University of Bayreuth, Department of Polymer Engineering for the preparation of the g-CFRP laminates and LFA measurements.

5. References

1. Lee C, Wei X, Kysar JW, Hone J. Measurement of the elastic properties and intrinsic strength of monolayer graphene. Science 2008; 321(5887):385–8.
2. Balandin AA, Ghosh S, Bao W, Calizo I, Teweldebrhan D, Miao F et al. Superior thermal conductivity of single-layer graphene. Nano Letters 2008; 8(3):902–7.
3. Bolotin KI, Sikes KJ, Hone J, Stormer HL, Kim P. Temperature-Dependent Transport in Suspended Graphene. Physical Review Letters 2008; 101(096802):1–4.
4. Zhu Y, Murali S, Cai W, Li X, Suk JW, Potts JR et al. Graphene and graphene oxide: Synthesis, properties, and applications. Advanced Materials 2010; 22(35):3906–24.
5. Saritha A, Malhotra SK, Thomas S, Joseph K, Goda K, Sreekala MS. State of the Art - Nanomechanics. In: Thomas S, Joseph K, Malhotra SK, Goda K, Sreekala MS, editors. Polymer composites: Volume 2: Nanocomposites. Wiley-VCH. 2013, pp. 1–12.
6. Alam A, Wan C, McNally T. Surface amination of carbon nanoparticles for modification of epoxy resins: Plasma-treatment vs. wet-chemistry approach. European Polymer Journal 2017; 87:422–48.
7. Li Z, Chu J, Yang C, Hao S, Bissett MA, Kinloch IA et al. Effect of functional groups on the agglomeration of graphene in nanocomposites. Composites Science and Technology 2018; 163:116–22.
8. Burger N, Laachachi A, Ferriol M, Lutz M, Toniazzo V, Ruch D. Review of thermal conductivity in composites: Mechanisms, parameters and theory. Progress in Polymer Science 2016; 61:1–28.
9. Ma J, Meng Q, Zaman I, Zhu S, Michelmore A, Kawashima N et al. Development of polymer composites using modified, high-structural integrity graphene platelets. Composites Science and Technology 2014; 91:82–90.
10. Ahmadi-Moghadam B, Sharafimasooleh M, Shadlou S, Taheri F. Effect of functionalization of graphene nanoplatelets on the mechanical response of graphene/epoxy composites. Materials and Design 2015; 66:142–9.
11. Fang H, Bai S-L, Wong CP. Microstructure engineering of graphene towards highly thermal conductive composites. Composites Part A 2018; 112:216–38.
12. Schürmann H. Konstruieren mit Faser-Kunststoff-Verbunden. Springer-Verlag Berlin Heidelberg. 2007.
13. Pascault J-P, Williams RJJ. General Concepts about Epoxy Polymers. In: Pascault J-P, Williams RJJ, editors. Epoxy polymers: New materials and innovations. Wiley-VCH. 2010, pp. 1–12.
14. Hirsch A, Englert JM, Hauke F. Wet chemical functionalization of graphene. Accounts of Chemical Research 2013; 46(1):87–96.

  doi:10.5075/epfl-298799_978-2-9701614-0-0

15. Park J, Yan M. Covalent functionalization of graphene with reactive intermediates. Accounts of Chemical Research 2013; 46(1):181–9.
16. Paredes J, Martínez-Alonso A, Tascón JMD. Atomic-scale scanning tunneling microscopy study of plasma-oxidized ultrahigh-modulus carbon fiber surfaces. Journal of Colloid and Interface Science 2003; 258(2):276–82.
17. Ackermann AC, Carosella S, Rettenmayr M, Fox BL, Middendorf P. Rheology, dispersion, and cure kinetics of epoxy filled with amine- and non-functionalized reduced graphene oxide for composite manufacturing. Journal of Applied Polymer Science. 2022; 139(8):e51664.
18. DIN Deutsches Institut für Normung e.V. Plastics - Differential scanning calorimetry (DSC) - Part 4: Determination of specific heat capacity; DIN EN ISO 11357-4. Beuth Verlag. 2021.
19. DIN Deutsches Institut für Normung e.V. Plastics - Determination of thermal conductivity and thermal diffusivity - Part 4: Laser flash method; DIN EN ISO 22007-4. Beuth Verlag. 2017.
20. DIN Deutsches Institut für Normung e.V. Plastics - Methods for determining the density of non-cellular plastics - Part 1: Immersion methods, liquid pyknometer method and titration method; DIN EN ISO 1183-1. Beuth Verlag GmbH. 2004.
21. DIN Deutsches Institut für Normung e.V. Aerospace series - Carbon fibre laminates - Determination of the fibre, resin and void contents; DIN EN 2564. Beuth Verlag. 2019.
22. DIN Deutsches Institut für Normung e.V. Aerospace - Fibre reinforced materials - Determination of glass transition of fibre composites under dynamic load; DIN 65583. Beuth Verlag. 1999.
23. Kuribara M, Nagano H. Anisotropic Thermal Diffusivity Measurements in High-Thermal-Conductive Carbon-Fiber-Reinforced Plastic Composites. Journal of Electronics Cooling and Thermal Control, 2015; 05(01):15–25.
24. Seyyed Monfared Zanjani J, Saner Okan B, Pappas P-N, Galiotis C, Menceloglu YZ, Yildiz M. Tailoring viscoelastic response, self-heating and deicing properties of carbon-fiber reinforced epoxy composites by graphene modification. Composites Part A 2018; 106:1–10.
25. Siddiqui NA, Khan SU, Ma PC, Li CY, Kim J-K. Manufacturing and characterization of carbon fibre/epoxy composite prepregs containing carbon nanotubes. Composites Part A 2011; 42(10):1412–20.
26. Ciecierska E, Boczkowska A, Kubis M, Chabera P, Wisniewski T. Enhancement of thermal and electrical conductivity of CFRP by application of carbon nanotubes. ECCM16 - 16th European Conference on Composite Materials, Seville, Spain, 22-26 June 2014.
27. Mayr G, Plank B, Sekelja J, Hendorfer G. Active thermography as a quantitative method for non-destructive evaluation of porous carbon fiber reinforced polymers. NDT & E International 2011; 44(7):537–43.
28. Mayr G, Hendorfer G, Plank B, Sekelja J, Thompson DO, Chimenti DE. Porosity determination in CFRP specimens by means of pulsed thermography combined with effective thermal diffusivity models. AIP Conference Proceedings 2010(1211): 1103–10.
29. Panwar V, Pal K. Dynamic Mechanical Analysis of Clay–Polymer Nanocomposites. In: Jlassi K, Chehimi MM, Thomas S, editors. Clay-polymer nanocomposites. Elsevier; 2017, p. 413–441.

  doi:10.5075/epfl-298799_978-2-9701614-0-0

THE APPLICATION OF CARBON NANOTUBES IN LIGHTWEIGHT METAL MATRIX COMPOSITES

Nur Syazana Natasha, Hisham[a], Milo, Shaffer[b], Qianqian, Li[a]

a: Department of Aeronautics, Imperial College London – ssh516@ic.ac.uk
b: Department of Chemistry, Imperial College London

Abstract: *The main challenges in the development of CNTs reinforced metal matrix composites are the inhomogeneous distribution of CNTs in the metal matrix and the poor interfacial bonding between CNTs and metal. Thus, surface modification of CNTs with a suitable coating material prior to composite processing is a promising solution to overcome these issues. In this work, coated CNTs are used to improve the dispersion and the wettability of CNTs by the Mg matrix. This investigation found that a more homogeneous dispersion and better wettability could be achieved by using Ni-coated CNTs in comparison to pristine CNTs in AZ91 matrix.*

Keywords: carbon nanotubes; coating; lightweight metal; metal matrix composites

1. Background

The use of advanced lightweight materials specifically in the automotive and aerospace industries is highly potential to produce vehicles with excellent performance and to reduce the energy consumption and greenhouse gas emission which would fulfill future emission regulations [1,2]. Consequently, the increasing demands for energy efficient materials leads to a growing interest in magnesium (Mg) which is widely abundant and known as the lightest structural metal offering up to 30 and 70% weight saving in comparison to the more commonly used aluminium (Al) and steel, respectively. Mg possesses many desirable properties such as excellent specific strength, good castability and machinability, high damping capacity, good electromagnetic shielding and nontoxicity [3,4]. However, the use of Mg and its alloys is limited due to their poor creep resistance, low strength and modulus at high temperatures, and low wear resistance [5].

The limitations of Mg and its alloys can be overcome through the fabrication of Mg composites by adding metallic or ceramic reinforcements. Among the various types of reinforcements, nanoscale reinforcements are more preferred than the micron-sized reinforcements since the later tend to severely decrease the ductility and strength of the composite due to their susceptibility to cracking and forming large voids at the particle-matrix interface [4]. Particularly, multiwalled carbon nanotubes (MWCNTs) are considered as ideal reinforcements in Mg matrix composites due to their high aspect ratio and superior mechanical and thermal properties [6,7]. In the recent years, many works based on the fabrication of CNTs reinforced Mg matrix composites which showed significant improvement in the mechanical properties of the composites have been reported in the literature. Some of these results are highlighted in Table 1.

  doi:10.5075/epfl-298799_978-2-9701614-0-0

Table 1: Summary of highlighted works based on the fabrication of CNTs reinforced Mg matrix composites

Type of composite	MWCNTs loading (wt%)	% increase relative to the pure matrix			Ref
		Yield strength	Ultimate strength	Ductility	
Mg-MWCNTs	1.3	Tensile: 11	Tensile: 9	Tensile: 69	[8]
AZ31-MWCNTs	0.5	Compression: 58	Compression: 3	Compression: 5	[9]
		Tensile: 10	Tensile: 17	Tensile: 68	
AZ31-MWCNTs	1.0	Tensile: 17	Tensile: 3	Tensile: 24	[10]
AZ31-MWCNTs	1.0	Tensile: 31	-	Tensile: 124	[11]
AZ91- MWCNTs	0.1	Compression: 10	Compression: 20	Compression: 36	[12]
AZ91-MWCNTs	1.0	Tensile: 47	Tensile: 64	Tensile: 112	[13]

However, comparison between the experimental and theoretical yield strength shows a large discrepancy in the results due the idealistic assumptions used in the theoretical calculations where the MWCNTs are perfectly aligned and individually dispersed with an ideal interface with the matrix [12]. CNTs tend to agglomerate due to their large surface area that promote inter-tube bonding via the van der Waals forces therefore leading to an inhomogeneous dispersion of the nanotubes in the matrix. Additionally, CNTs cannot be wetted by Mg which prevents an ideal stress transfer from the matrix to the CNTs to occur. Therefore, the main challenges in the fabrication of CNTs reinforced Mg matrix composites are (1) to obtain a homogeneous distribution of the CNTs in the matrix and (2) to achieve a good wettability between the CNTs and the matrix. In this work, coated CNTs are used in the fabrication of AZ91 composite in order to improve the wettability between the CNTs and the matrix and subsequently to achieve a uniform dispersion of the CNTs in the matrix.

2. Results and discussion

2.1 Characterisation of coated CNTs

Figure 1 shows the characteristics of pristine and Ni-coated CNTs as investigated by using TEM. In comparison with the pristine CNTs, the Ni-coated CNTs shows the formation of spherical aggregates with an average size of 7.0 ± 1.9 nm that are also connected with a thin layer of coating with a rough thickness of 2.2 ± 1.9 nm therefore giving a quasi-continuous layer of Ni coating along the individual tubes. Based on the coating morphology and the good wettability between Ni and Mg AZ91 which had been reported in the literature [16], it can be presumed that the individual tubes can be sufficiently wetted by the matrix during the composite fabrication.

  doi:10.5075/epfl-298799_978-2-9701614-0-0

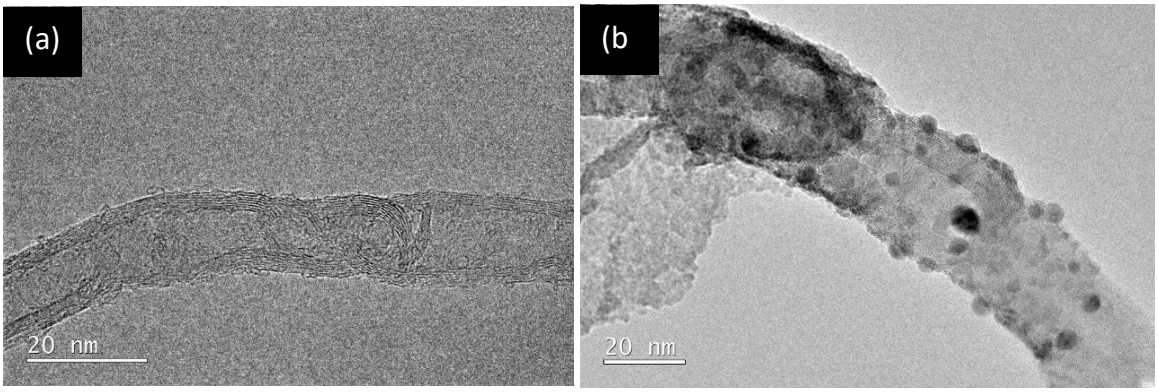

Figure 1. TEM images of (a) pristine and (b) Ni-coated CNTs.

2.2 Effect of coating on the dispersion of CNTs

In order to investigate the state of dispersion of CNTs, the pristine and Ni-coated CNTs were first ultrasonicated in ethanol for 30 min. Figure 2 shows the optical micrographs of pristine and Ni-coated CNTs dispersions in ethanol after the ultrasonication treatment. The pristine CNTs dispersion in Figure 1(a) shows large agglomerates of CNTs that are entangled together meanwhile much smaller agglomerates and a more homogeneous distribution of particles are observed in the Ni-coated CNTs dispersion in Figure 1(b). The improvement in the dispersion of Ni-coated CNTs can be attributed to the presence of Ni-coating layer which prevents the surface of the CNTs from being attracted together to form agglomerates. This investigation shows that a homogeneous dispersion of CNTs can be achieved by using ultrasonication either before or during the composite processing.

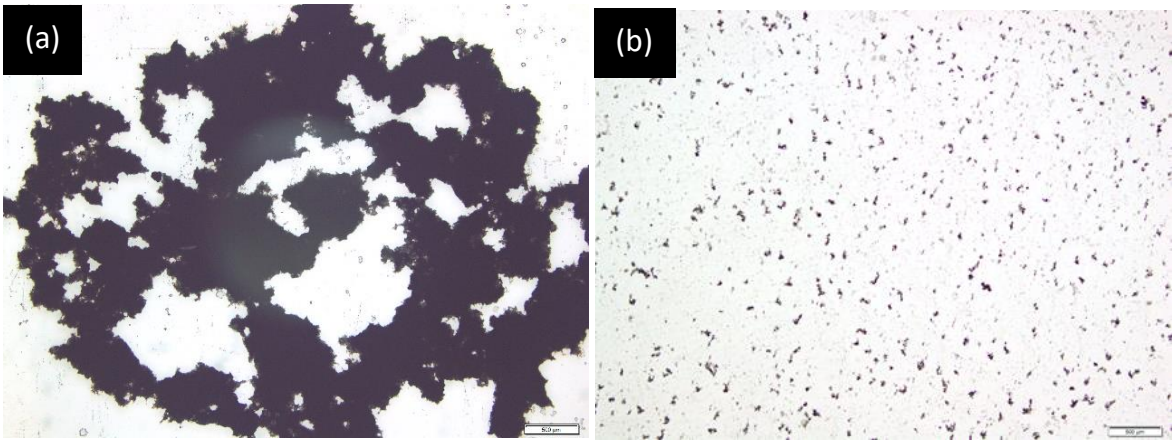

Figure 2. Optical micrographs of (a) pristine and (b) Ni-coated CNTs dispersions in ethanol.

2.2 Effect of coating on the strengthening of AZ91 matrix

Pristine CNTs and Ni-coated CNTs reinforced AZ91 composites were fabricated by using a melt stirring technique as described in [12]. To investigate the strengthening effect of AZ91 matrix by the CNTs via grain refinement, the grain size of pure AZ91 alloy, and pristine CNTs and Ni-coated CNTs reinforced AZ91 composites was calculated as shown in Figure 3. The results showed that

  doi:10.5075/epfl-298799_978-2-9701614-0-0

a grain size reduction by about 20% could be achieved by the addition of both pristine and Ni-coated CNTs therefore contributing to the strengthening of the matrix by grain refinement. It is likely that the similarity in the grain size of pristine CNTs and Ni-coated CNTs reinforced AZ91 composites is due to the low loading of CNTs used i.e. at 0.1 wt% pristine CNTs equivalent.

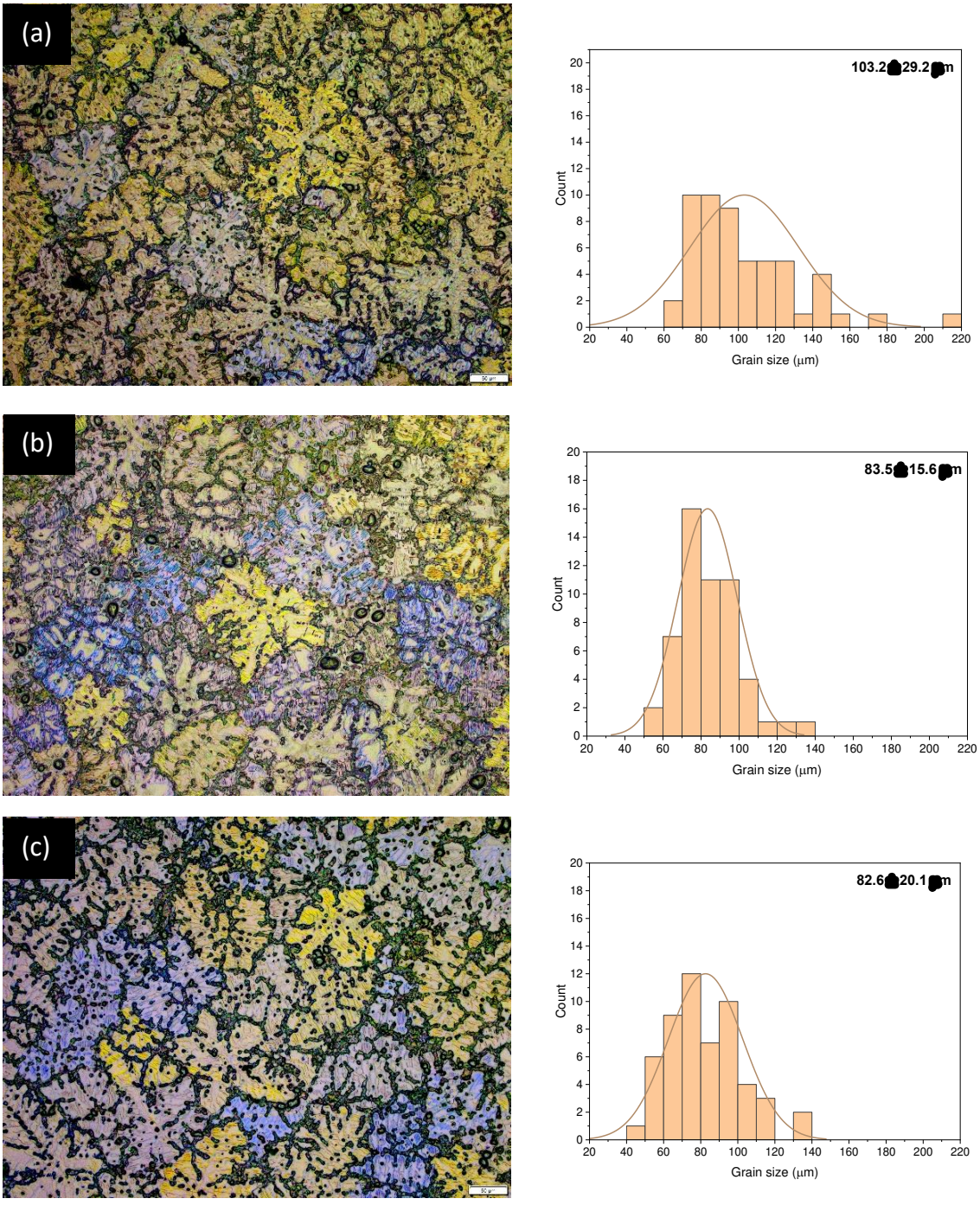

Figure 3. Representative grain structures and grain size distribution of (a) pure AZ91, (b) pristine CNTs and (c) Ni-coated reinforced AZ91 composites

Furthermore, the wettability of the pristine and Ni-coated CNTs by the matrix were also investigated by SEM and the results are shown in Figure 4. Pristine CNTs were found in the matrix

978/1602 ©2022 Hisham et al. doi:10.5075/epfl-298799_978-2-9701614-0-0 published under CC BY-NC 4.0 license

as a huge agglomerate which was poorly wetted by the matrix therefore leading to the formation of a pore (Figure 4(a)). On the other hand, Ni-coated CNTs were observed to be almost completely infiltrated by the matrix (Figure 4(b)). This evidence shows that the presence of Ni coating can improve the wettability of CNTs by the Mg matrix which increases the potential of matrix strengthening via load transfer.

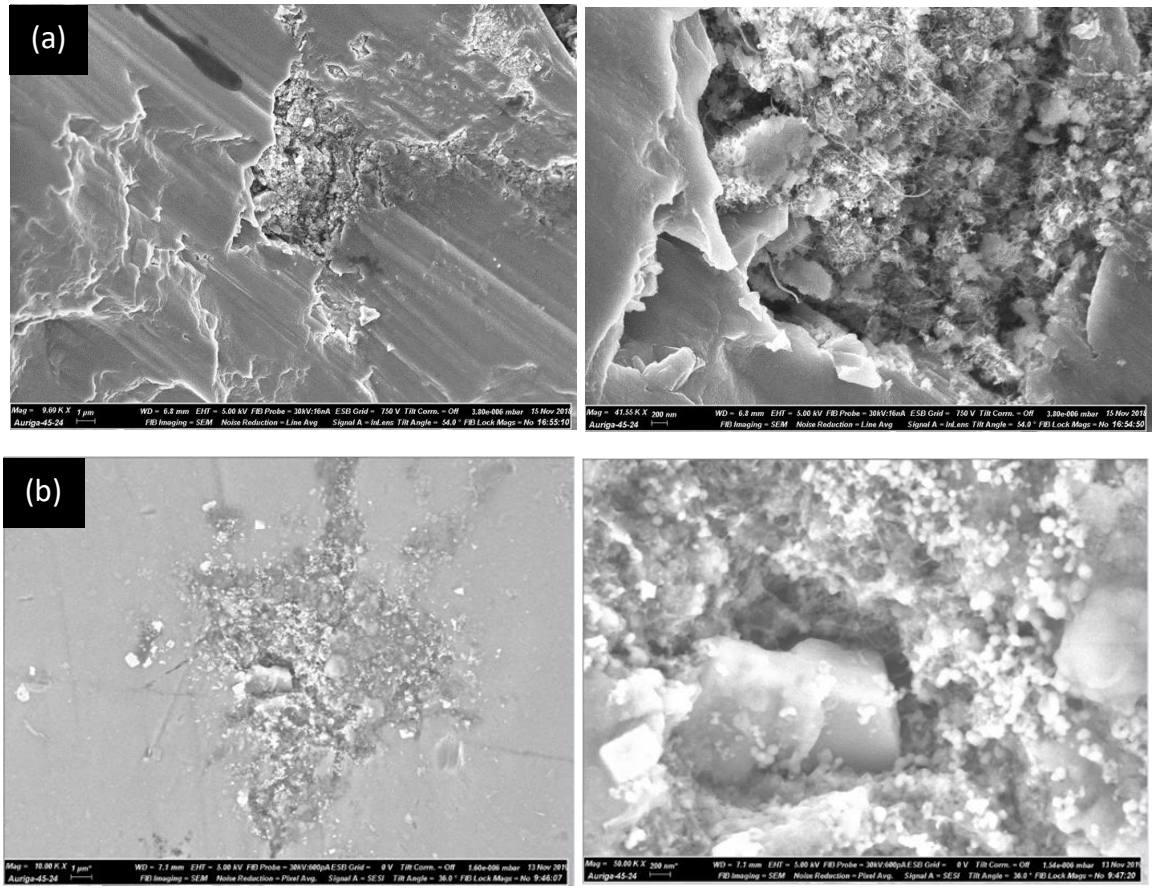

Figure 3. SEM images of (a) pristine CNTs and (b) Ni-coated CNTs found in the AZ91 matrix.

3. References

1. Helms H, Kräck J. Energy savings by light-weighting-2016 Update. Institute for Energy and Environmental Research, Heidelberg, Germany. 2016.
2. Edenhofer O, editor. Climate change 2014: mitigation of climate change. Cambridge University Press; 2015.
3. Kulekci MK. Magnesium and its alloys applications in automotive industry. The International Journal of Advanced Manufacturing Technology. 2008; 39(9):851-65.
4. Gupta M, Wong WL. Magnesium-based nanocomposites: Lightweight materials of the future. Materials Characterization. 2015; 105:30-46.
5. Blawert C, Hort N, Kainer KU. Automotive applications of magnesium and its alloys. Trans. Indian Inst. Met. 2004; 57(4):397-408.
6. Tjong SC. Recent progress in the development and properties of novel metal matrix nanocomposites reinforced with carbon nanotubes and graphene nanosheets. Materials Science and Engineering: R: Reports. 2013; 74(10):281-350.

  doi:10.5075/epfl-298799_978-2-9701614-0-0

7. Demczyk BG, Wang YM, Cumings J, Hetman M, Han W, Zettl A, Ritchie RO. Direct mechanical measurement of the tensile strength and elastic modulus of multiwalled carbon nanotubes. Materials Science and Engineering: A. 2002; 334(1-2):173-8.
8. 9Goh CS, Wei J, Lee LC, Gupta M. Simultaneous enhancement in strength and ductility by reinforcing magnesium with carbon nanotubes. Materials Science and Engineering: A. 2006; 423(1-2):153-6.
9. Paramsothy M, Hassan SF, Srikanth N, Gupta M. Simultaneous enhancement of tensile/compressive strength and ductility of magnesium alloy AZ31 using carbon nanotubes. Journal of Nanoscience and Nanotechnology. 2010 Feb 1;10(2):956-64.
10. Srivatsan TS, Godbole C, Paramsothy M, Gupta M. Influence of nano-sized carbon nanotube reinforcements on tensile deformation, cyclic fatigue, and final fracture behavior of a magnesium alloy. Journal of Materials Science. 2012; 47(8):3621-38.
11. Hashim J, Looney L, Hashmi MS. Metal matrix composites: production by the stir casting method. Journal of materials processing technology. 1999; 92:1-7.
12. Li Q, Viereckl A, Rottmair CA, Singer RF. Improved processing of carbon nanotube/magnesium alloy composites. Composites Science and Technology. 2009; 69(7-8):1193-9.
13. Yuan QH, Fu DM, Zeng XS, Yong LI. Fabrication of carbon nanotube reinforced AZ91D composite with superior mechanical properties. Transactions of Nonferrous Metals Society of China. 2017 Aug 1;27(8):1716-24.
14. Bakshi SR, Agarwal A. An analysis of the factors affecting strengthening in carbon nanotube reinforced aluminum composites. carbon. 2011; 49(2):533-44.
15. Shinozaki N, Morita J, Wasai K. Wetting of graphite by molten magnesium. JOURNAL-JAPAN INSTITUTE OF LIGHT METALS. 2005; 55(7):310.
16. Liang J, Li H, Qi L, Tian W, Li X, Zhou J, Wang D, Wei J. Influence of Ni-CNTs additions on the microstructure and mechanical properties of extruded Mg-9Al alloy. Materials Science and Engineering: A. 2016; 678:101-9.

  doi:10.5075/epfl-298799_978-2-9701614-0-0

NANOPARTICLE REINFORCED LIGHTWEIGHT METAL COMPOSITES

Qianqian Li[a], Daniel Markcoons[a], Zhuocheng Xu[a], Syazana Hisham[a], Samaneh Nasiri[b], Milo S.P. Shaffer[c,d], Michael Zaiser[b]

a: Department of Aeronautics, Imperial College London, London, United Kingdom.
Qianqian.li@imperial.ac.uk
b: Institute of Material Simulation (WW8), University of Erlangen-Nuremberg, Fuerth, Germany
c: Department of Chemistry, Imperial College London, London, United Kingdom
d: Department of Materials Science, Imperial College London, London, United Kingdom

Abstract: *The interest to use carbon nanotubes (CNTs) to reinforce light metals has increased in recent years due to their potential application as lightweight high performance materials. One challenge in producing CNT composites is to achieve a homogenous dispersion of CNTs in the metal matrix. In order to effectively disperse CNTs in the Mg melt, we for the first time introduced the idea of using metal coated CNTs to promote the integration into Mg matrix. In this paper, Pt was selected to coat the CNT surface. TEM and EDX confirm that atomic Pt has been successfully deposited onto CNTs. The dispersion and stability of metal coated CNTs in solution have been investigated and compared to CNTs without metal coating. The Pt coated CNT reinforced Mg composites were also produced via a melt stirring process. The mechanical properties of such composites also showed a clear upward tendency, which we attribute to the Pt coating to help the dispersion of CNTs.*

Keywords: Lightweight metal composites; carbon nanotubes, dispersion, wettability.

1. Introduction

The automotive and aerospace industries have a perpetual need for advanced lightweight materials to enhance vehicle performance and to satisfy future legislation regarding greenhouse gas emissions. The aviation industry is one of the fastest growing sources of greenhouse gas emissions [1] and it is recognised that the uptake of emerging advanced materials is imperative for meeting future emission targets [2]. It has also been calculated that a 100kg weight reduction of an automobile can reduce the CO2 emissions by around 1600kg over a 10 year lifetime [3]. The UN Intergovernmental Panel on Climate Change estimated that “material substitution and advanced design could reduce the weight of vehicles by 20-30%” with the explicit mention of Al and Mg metals [4]. This highlights the importance of lightweight material development.

Metal matrix composites reinforced with microscale particles have been shown to be a competitive alternative to unreinforced metals due to their improved strength, stiffness and hardness. However, these superior properties usually come at the expense of the ductility and machinability of the metal, and so this has limited their widespread use. Recently, research has transitioned from micro to nanoscale reinforcements. The manufacture of metal matrix nanocomposites (MMNCs) has shown the potential of improving metal strength whilst maintaining or even improving the metal’s ductility [5, 6]. Whilst the exact mechanisms underpinning the effects that nanoparticle reinforcements have on the metal matrix remain

  doi:10.5075/epfl-298799_978-2-9701614-0-0

unclear, it is well understood that a homogenous dispersion is critical for the exploitation of the potential improvements in mechanical properties; however, homogenous dispersion is extremely difficult to achieve. Therefore, a host of manufacturing methods have been explored for their sound fabrication, of varying cost effectiveness and scalability.

Recently chemists have managed to coat metal atoms directly on the CNTs surface [7]. One promising way is to create an electrical charge on the surface of the CNTs by using different polyelectrolytes and then deposit the metal on the CNT surface. Coatings of CNTs with different metals give us the idea that it could help the dispersion of the CNTs in the metal matrix because the high specific surface energy can be reduced by the coated metals. Also an improved wettability of the metal coated CNTs in a metal matrix could be obtained through the metal coating, which may lead to a better interfacial bonding. Another advantage is that the metal coating can survive through the high process temperature of producing metal composites. The variety of metal coatings is big, for example copper, iron and nickel [8], platinum, palladium and tin [9], different metal complexes contained Pt, Mo and Pd [10] have all been tried. Simulations have been done to check the binding affinities and the interfacial structures of metal particles onto CNTs in a gold matrix [11]. One experimental example for such a MMC is a Sn-Ag-Cu solder with nickel-coated CNTs as reinforcements from Han [12].

In our previous research, we have successfully produced CNT reinforced AZ91 composites by a two step process including a pre-dispersion and melt stirring [13-15]. In this work, we will coat CNTs with metal and produce their AZ91 composites. The metal coating and the composites will be characterized by various methods.

2. Experimental

CNTs were added to a beaker with aqueous solution of sodium chloride and then sonicated for one hour. Afterwards 400 mg of a PDDA solution was weighted in and stirred with 100 rpm for half an hour to make sure that the separated CNTs were covered with the positive electrolyte PDDA. The excess PDDA was removed by centrifugation cycles. The centrifuge was operated with a speed of 11000 rpm and a duration time of 8 min. The collected CNTs were redispersed in distilled water and 80 mg of the polyelectrolyte PSS. The solution was stirred at 100 rpm for another 30 min. The excess PSS was extracted by centrifugation with the same parameters like the PDDA before. Then the centrifuged CNTs were redispersed and another 400 mg PDDA was added, stirred again and washed by centrifugation afterwards using exactly the same parameters which were mentioned above. Now the CNTs have been coated by three polyelectrolyte layers on the surface and the outer polyelectrolyte has a positive charge on the CNTs outside wall. For the metal coating, the CNTs were diluted in 120 ml water. 85.9 mg H_2PtCl_6 and 240 mg of trisodium citrate dehydrate were added and sonicated for 30 min. Afterwards sodium sulfite aqueous solution with a concentration of 0.05 Mol/l was added drop by drop under mild sonification. As the last step the solution was centrifuged by 6 cycles to get rid of the residual such as the non-reacted metal-salt. After the last washing step the solution was dried by a heater at 80°C to get the resulted metal coated CNTs.

The Pt-coated MWCNT/AZ91 composite was produced by the same two-step process [13]. Using the same process other samples such as non-coated MWCNT/AZ91 composite and pure AZ91 alloy were produced for comparison. A FEI Titan3 80-300 transmission electron microscope

(TEM) equipped with an image aberration corrector was employed for analyzing the coating status of Pt on the surface of MWCNTs. Mechanical properties of the composites were measured by compression test.

3. Results and discussion

Initially to verify the metal or metal compound on the surface of CNTs, high resolution images were recorded by HRTEM and the corresponding metal element was checked by EDX. Figure 1a shows the metal coating on the surface of a CNT. The black dots indicate the presence of platinum clusters which can be confirmed by EDX (Figure 1b).

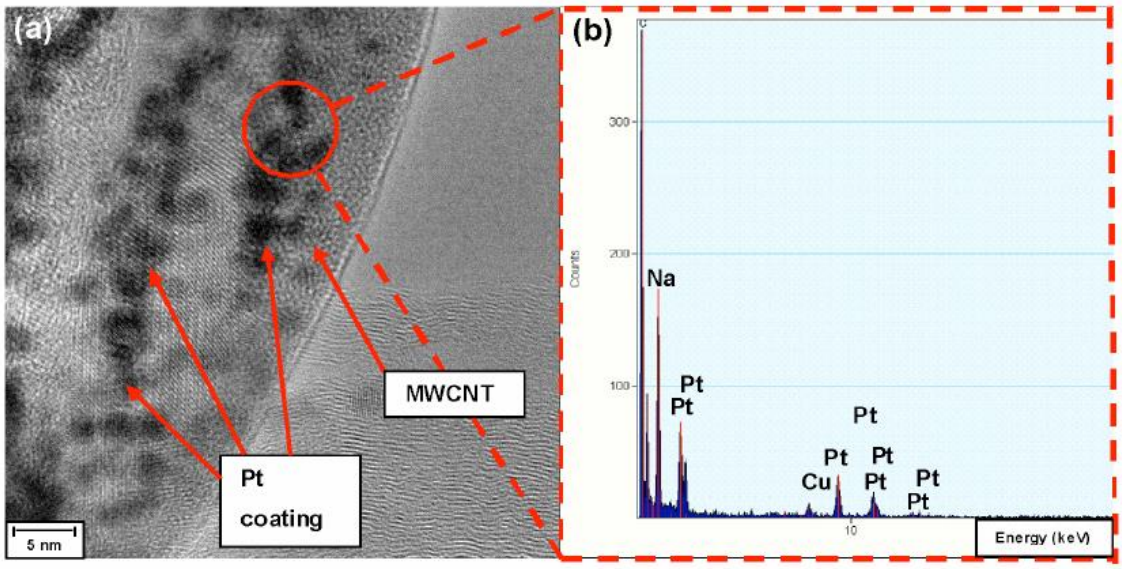

Figure 1 (a) TEM image of Pt coating on the surface of individual MWCNTs; (b) EDX acquire at selected area on surface on Pt-coated MWCNTs.

Different from coating continuous metal layers on CNTs as described in [16], surface decoration of CNT with metals as achieved as in Figure 1a may provide further benefits. If, instead of a continuous coating layer, isolated metal nanoparticles as in Figure 1a are deposited on the CNT surface then these nanoparticles may serve a dual purpose that goes well beyond what can be achieved by a continuous coating. Firstly, discrete metal nanoclusters on the CNT surface can help to prevent agglomeration by the simple means of acting as geometrical 'spacers'. This effect is well known in the context of graphene where decoration of exfoliated graphene sheets with Pt nanoclusters was shown to prevent face-to-face aggregation of the sheets [17]. Secondly, attaching metal nanoclusters rather than continuous metal coatings to CNT may have additional benefits. If a metal such as Pt or Ni bonds well to sp2 carbon and the interfaces between the nanoclusters and the CNT are strong, then such nanoclusters may act as 'nano-rivets' enhancing interfacial shear stress transfer if the decorated CNT is embedded in a metal matrix.

The mechanical properties of Pt coated CNT reinforced Mg composites were measured and showed improved properties compared to pure AZ91 and to AZ91/CNT composites based on uncoated CNTs as shown in Figure 2.

  doi:10.5075/epfl-298799_978-2-9701614-0-0

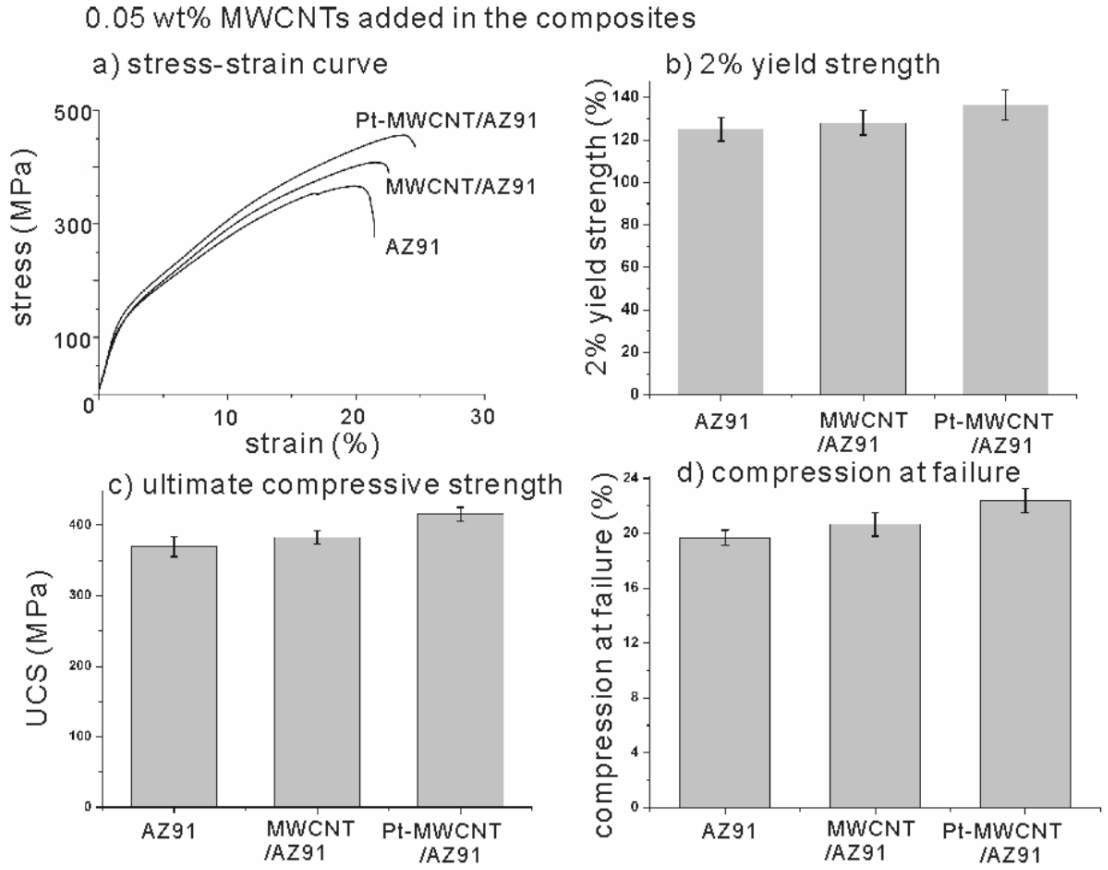

Figure 2 (a) Typical stress-strain curves of pure AZ91, 0.05 wt% raw MWCNT/AZ91 composite and 0.05 wt% Pt-MWCNT/AZ91 composite. Comparison of (b) 2 % yield strength, (c) ultimate compressive strength (UCS) and (d) compression at failure of 36 samples.

However the change is relatively small compared to the usual scatter of experimental results. The reason for affinity of the average values is that the real amount of metal coated CNTs in the AZ91 composites is less than real 0.05 wt% due to the big amount of waste during the metal coating process. At the calculation of the amounts of metal coated CNTs for the composites, we assumed that there is no loss of metal coated CNTs. The weight of the CNTs after the metal coating also differs a lot because of the non-uniform coating with platinum. Nevertheless, an upwards tendency of the mechanical properties can still be found by using metal coated CNTs to produce CNT/ AZ91 composites. This can be attributed to an improved dispersing of CNTs, as well as a possible wettability. More experiments are required.

4. Conclusions

Pt has been deposited on the surface of multiwall carbon nanotubes. By adding small amounts of Pt coated MWCNTs, an upward trend in the mechanical properties of Mg AZ91 composites could be observed when compared to adding raw MWCNTs. Our explanation for this tendency is that a better dispersion of metal coated CNTs in AZ91 melt can be achieved as metal coating weaken the Van de Waal force between CNTs. On the other hand it is apparent that the improvement in mechanical properties is relatively small, hardly beyond the usual scatter band of results. This leads us to the conclusion that further improvements to the deposition process are required.

  doi:10.5075/epfl-298799_978-2-9701614-0-0

Acknowledgements

Financial support by the German Research Foundation (DFG) under grant LI 1847/2-1 is gratefully acknowledged. The authors also gratefully acknowledge the support of the Cluster of Excellence 'Engineering of Advanced Materials' at the University of Erlangen-Nuremberg, which is funded by the German Research Foundation (DFG) within the framework of its 'Excellence Initiative' under grant EXC 315-1. We thank Dr. Jan Schwerdtfeger for fruitful discussions.

5. References

1. Reducing emissions from aviation. 2015 [cited 2019 09/04/2019]; Available from: https://ec.europa.eu/clima/policies/transport/aviation_en.
2. Challenges and Opportunities for Composite Materials Transitions in Aerospace. in ECCM18. 2018. Aerospace Technology Institute.
3. Hinrich Helms, U.L., The Potential Contribution of Light-Weighting to Reduce Transport Energy Consumption. International Journal of Life Cycle Assessment, 2007.
4. Transport and Infrastructure; 4th assessment report of the IPCC. 2007, UN Intergovernmental Panel on Climate Change.
5. Liu, G., et al., Nanostructured high-strength molybdenum alloys with unprecedented tensile ductility. Nature Materials, 2013. 12(4): p. 344-350.
6. Chen, L.Y., et al., Processing and properties of Mg containing a dense uniform dispersion of nanoparticles. Nature, 2015. 528(7583): p. 539.
7. Vossoughi, M., et al., Engineering Letters, Removal of Phenols from Wastewater with Encapsulated Horseradish Peroxidase in Calcium Alginate. 2009. 17(4).
8. Bakshi, S.R., et al., Journal of Alloys and Compounds, Interface in carbon nanotube reinforced aluminum silicon composites: Thermodynamic analysis and experimental verification. 2009. 481(1-2): p. 207-213.
9. Zhong Z. et al., Chemical Physics Letters, Dispersing and coating of transition metals Co, Fe and Ni on carbon materials. 2002. 362: p. 135.
10. Han, L., et al., A direct route toward assembly of nanoparticle-carbon nanotube composite materials. Langmuir, 2004. 20(14): p. 6019-6025.
11. H. Uozumi et al. Fabrication process of carbon nanotube/light metal matrix composites by squeeze casting. Mater. Sci. Eng. A 495, 282 (2008).
12. Han Y.D., et al., Conference: Electronic Components and Technology Conference, 2010. 979.
13. Q. Li, A. Viereckl, C.A. Rottmair and R.F. Singer, Improved processing of carbon nanotube/magnesium alloy composites. Comp. Sci. Tech. 69, 1933 (2009).
14. Q. Li, C.A. Rottmair and R.F. Singer, CNT reinforced light metal composites produced by melt stirring and by high pressure die casting. Comp. Sci. Tech. 70, 2242 (2010).
15. Q. Li and R.F. Singer, U. Kainer (Ed.), 8^th Inter. Conf. on Mg and their App. (Wiley-VCH , Weimar, 2009), p. 661.
16. Yang, D.Q., J.F. Rochette, and E. Sacher, Functionalization of Multiwalled Carbon Nanotubes by Mild Aqueous Sonication. Journal of Physical Chemistry B, 2005. 109(16): p. 7788-7794.
17. Goh, C.S., et al., Nanotechnology, 2006. 17(1): p. 7-12.

  doi:10.5075/epfl-298799_978-2-9701614-0-0

SELF-ASSEMBLY OF NBR AND NOMEX VIA ELECTROSPINNING: RUBBERY NANOFIBERS FOR IMPROVING CFRP DELAMINATION RESISTANCE

Emanuele Maccaferri[a], Laura Mazzocchetti[a,b], Tiziana Benelli[a,b], Tommaso Maria Brugo[b,c], Andrea Zucchelli[b,c], Loris Giorgini[a,b]

a: Department of Industrial Chemistry "Toso Montanari", University of Bologna, Viale Risorgimento 4, 40136 Bologna, Italy – emanuele.maccaferri3@unibo.it
b: Interdepartmental Center for Industrial Research on Advanced Applications in Mechanical Engineering and Materials Technology, CIRI-MAM, University of Bologna, Viale Risorgimento 2, 40136 Bologna, Italy.
c: Department of Industrial Engineering, University of Bologna, Viale Risorgimento 2, 40136 Bologna, Italy.

Abstract: *Metal replacement by Carbon Fiber Reinforced Polymers (CFRPs) is common to benefit lightness structures and components. However, composite laminates suffer from delamination, limiting their usage. Recently, rubbery nanofibers have been proposed for hindering delamination, thanks to their high toughening ability. In this work, the use of Nitrile Butadiene Rubber (NBR)/Nomex mixed nanofibers is presented as an effective reinforcement for epoxy-based CFRP laminates. NBR/Nomex nanofibers with a high rubber content (60 %wt) were produced via single-needle electrospinning, without the need for NBR crosslinking to maintain the nanofibrous structure. The two polymers arrange in a self-assembled fashion, whose disposition depends on the applied electrospinning process conditions. Delamination tests demonstrate that the interlaminar fracture toughness increases up to near 200 % in Mode I. The significant improvement of delamination resistance, together with the retention of original thermal and mechanical laminate properties, make rubbery NBR/Nomex nanofibrous mats a valid solution for contrasting delamination.*

Keywords: Nitrile butadiene rubber; Polyaramid; Electrospinning; Self-assembled nanofiber; Toughening

1. Introduction

Since years, epoxy-based Carbon Fiber Reinforced Polymers (CFRPs) have been proposed as a valid alternative to metals for reducing components weight, tough maintaining a high mechanical performance. Often, CFRP laminates represent the preferred choice to produce structural components. However, the laminar structure implies relatively low mechanical properties along the perpendicular direction with respect to the lamina plane. Indeed, the component failure by delamination, i.e. the debonding of the constituent laminae due to the formation and propagation of microcracks, is the most common failure mode of composite laminates [1]. For this reason, searching for systems able to prevent or limit delamination is of paramount importance. The integration of sensors capable of promptly detect out-of-plane loads (impacts) can be a valid (but expensive) solution to monitor the component health. Several solutions have been proposed, as the embedding of Bragg fibers and piezoelectric materials, even nanostructured, to avoid delamination induced by the integration of such sensors [2,3]. On

  doi:10.5075/epfl-298799_978-2-9701614-0-0

the other hand, it is possible to reduce the component failure making delamination more difficult to occur. In this case, the laminate modification aims at increasing the interlaminar fracture toughness, i.e. the energy required for promoting delamination. CFRPs intended for high performance applications requires a matrix with high thermal and mechanical properties, such as epoxy resins. Because of the valuable stiffness and glass transition temperature (T_g), the matrix has a brittle behaviour, making the CFRP laminate susceptible of delamination. Consequently, matrix toughening is a viable solution to improve delamination resistance. Rubbers are ideal candidates for this aim. The toughening material can be directly added to the bulk resin as uncrosslinked or crosslinked rubber, as well as core-shell particles [4–8]. However, the bulk modification of resin may lead to a relevant lowering of laminate stiffness and T_g [6], thus reducing its application field. A smarter approach involve the localized toughening of the laminate only in the interlaminar regions most subjected to stress, such as free edges, holes, ply-drops and adhesive bondings [9]. This approach allows to sensibly limit the weaknesses that often affect modified laminates (reduced stiffness and T_g, increased weight). The integration of electrospun nanofibrous mats is effective at improving the interlaminar fracture toughness [10]. In the literature, almost all the nanofibrous mats used for reducing delamination are made of non-elastomeric thermoplastic polymers [10–13].

Recently, the Authors demonstrated that rubbery nanofibers based on Nitrile Butadiene Rubber (NBR) strongly hinder delamination, especially under Mode I loading: the enhancement in G_I reaches a +480 % [14,15]. Moreover, such nanofibers are able to improve composite damping up to +77 % [16]. However, due to the low melting temperature of the polycaprolactone (PCL) blended with the NBR for producing dimensionally stable uncrosslinked nanofibers, the composite T_g may be strongly reduced, depending on the modification extent.

To overcome the abovementioned drawback, in the present work the thermoplastic PCL is replaced by Nomex, an aromatic polyamide characterized by a T_g higher than the laminate curing cycle temperature. NBR/Nomex nanofibers with a prevalent rubber content (60 %wt of NBR, 40 %wt of Nomex) are produced via single-needle electrospinning and integrated into epoxy CFRP laminates. Investigations via Scanning Electron Microscopy (SEM) reveal that NBR and Nomex self-assemble in a particular fashion. The delamination behaviour of the nanomodified composite under Mode I loading is investigated by Double Cantilever Beam (DCB) test.

2. Materials and methods

2.1 Materials

Carboxylated Nitrile Butadiene Rubber (NBR), Nipol 1072CGX, was purchased from Zeon Chemicals [68 %mol butadiene (Bu), 28 %mol acrylonitrile (ACN), 4 %mol methacrylic acid (MAA)]. Poly(*m*-phenylene isophtalamide) (Nomex) and lithium chloride were dried before use in an oven at 110 °C for 3 and 24 h, respectively. *N,N*-dimethylacetamide and chloroform were used without any preliminary treatment. Plain weave carbon fabric, 200 g/m^2, in epoxy matrix prepreg (GG204P IMP503Z-HT) for composite production was supplied by G. Angeloni s.r.l., Venezia, Italy.

2.2 Nanofibrous mat production

NBR solution (10 %wt) was prepared in chloroform, while the Nomex one (10 %wt) in *N,N*-dimethylacetamide with lithium chloride (3.5 %wt with respect to the total solution weight). The NBR/Nomex 60/40 blend for producing mixed rubbery nanofibers with 60 %wt of NBR was prepared simply mixing the two starting solutions in a 60:40 wt proportion. For a detailed procedure, refer to [17].

The NBR/Nomex nanofibrous mats were produced via single-needle electrospinning technique, using a 4-needles machine (Spinbow®) equipped with 5 mL syringes. Needles, having an internal diameter of 0.51 mm, were joined to syringes via Teflon tubing. Nanofibers were collected on a rotating drum covered with poly(ethylene)-coated paper at a tangential speed of 0.39 m/s. The rubbery mat (15 × 20 cm) has a grammage of 10 ± 1 g/m^2. The electrospinning process parameters are reported in Table 1. The process was conducted in the air atmosphere at 25 °C and 30 % relative humidity.

Table 1: Electrospinning process parameters.

Nanofiber	Flow rate [mL/h]	Potential [kV]	Distance [cm]
n-60/40_*f*	0.20	25	18
n-60/40_c	1.10	25	11

The nanofibrous mat morphology was assessed via Scanning Electron Microscopy (SEM). The disposition of NBR and Nomex in the nanofiber was investigated via selective removal of the NBR fraction, carried out via two consecutive washes in chloroform (1 h each).

2.3 Rubbery-modified CFRP production and characterization

The NBR/Nomex nanofibrous mats were washed in distilled water to remove lithium chloride before composite lamination.

Double Cantilever Beam (DCB) specimens were prepared via hand lay-up. Single and double nanofibrous mats were integrated in the central interface (7 CFRP plies / 1 or 2 rubbery mat(s) / 7 CFRP plies), using a Teflon film as a crack trigger. For the sake of comparison, unmodified specimens (7 + 7 CFRP plies) were produced too. Laminate panels were cured according to the following procedure: i) pre-treatment of 2 h at 45 °C under vacuum to favour nanofibers impregnation; ii) curing cycle in autoclave for 2 h at 135 °C, under vacuum, 6 bar external pressure, heating/cooling ramp 2 °C/min).

DCB tests were carried out using a universal testing machine (Remet TC-10) equipped with a 1 kN load cell. DCB specimens were tested at 3 mm/min cross-head separation rate. At least 3 specimens for each CFRP sample were tested.

  doi:10.5075/epfl-298799_978-2-9701614-0-0

The energy release rate in Mode I loading (G_I) was calculated according to the following equation [18]:

$$G_{\mathrm{I}} = \frac{3P\delta}{2ba} \qquad (1)$$

where P is the load, δ the cross-head displacement, a the crack length, b the specimen width.

3. Results and discussion

The production of uncrosslinked NBR nanofibers is prevented by the rubber cold flow arising from its low T_g. Trying to electrospin plain NBR leads to film formation over time instead of nanofibers (Figure 1), as already demonstrated [19].

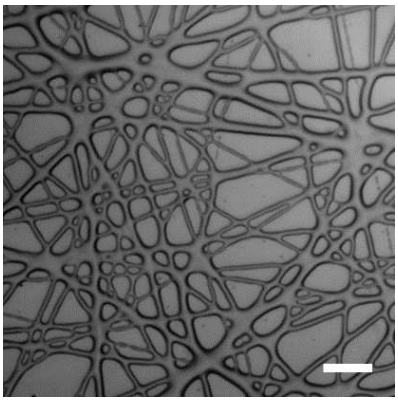

Figure 1. Electrospinning of plain NBR, scale bar 10 μm.

Shaping rubbers into nanofibers is hard, and usually, crosslinking is necessary to maintain the fibrous structure [20]. A different approach involve the rubber blending with a semi-crystalline polymer: the crystal phase (melting temperature ≈60 °C [19]) enables the overall structure retention, as happens for NBR/PCL blend nanofibers [19]. Here, a similar approach is exploited: the polyester PCL is replaced by Nomex, a polyaramid with a high T_g (274 °C [17]). Its excellent thermal properties can be exploited for reducing the impact of the nanofibrous mat on the final CFRP properties.

NBR/Nomex 60/40 blend electrospinning produces defect-free nanofibers (Figure 2A,B), characterized by a mean fiber diameter of 450 nm (standard deviation of ≈100 nm). The resulting membrane exhibits a ductile behavior with respect to Nomex-only [17] and common Nylon 66 ones [21].

While the morphology of both as-spun *n*-60/40_*f* and *n*-60/40_*c* mats is similar, the selective removal of NBR reveals a completely different arrangement of NBR and Nomex into the nanofiber (Figure 2C,D).

  doi:10.5075/epfl-298799_978-2-9701614-0-0

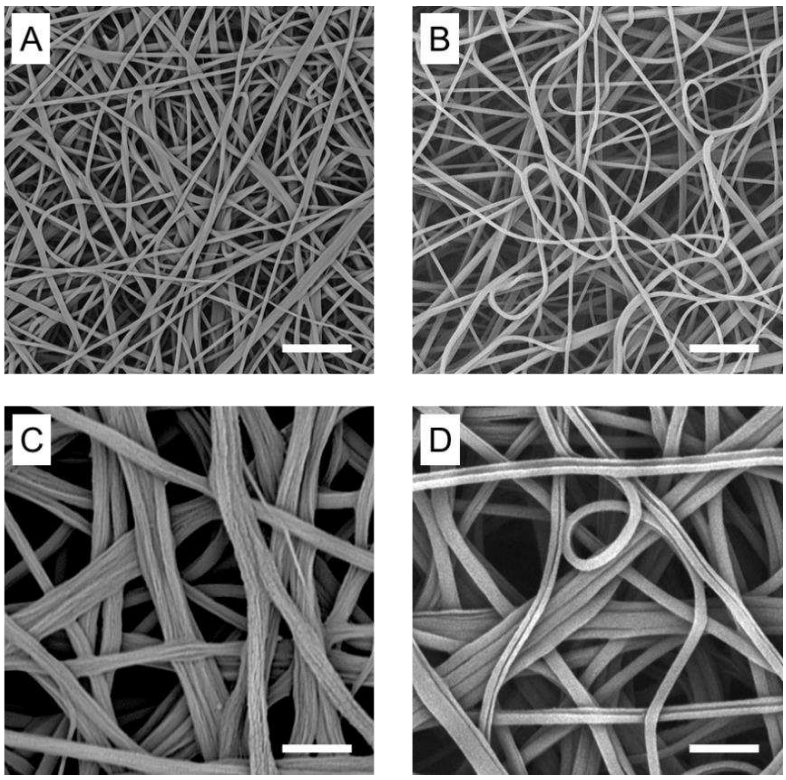

*Figure 2. NBR/Nomex 60/40 mat as-spun: A) n-*60/40*_f and B) n-*60/40*_c*, scale bar 10 μm*. Mats after NBR removal via $CHCl_3$ washing: B) n-*60/40*_f and C) n-*60/40*_c*, scale bar 2 μm.

The only difference between the production of *n*-60/40*_f and n*-60/40*_c* membranes is the applied electrospinning processing conditions, as reported in Table 1. During the process, NBR and Nomex self-assemble, forming peculiar morphologies. A low flow rate generates a "fibril-like" structure made of Nomex, while a higher one nanofibers resembling a quasi-core–shell morphology, with the rubber in the inner channel.

3.1 Mode I delamination (DCB test)

The CFRP delamination behaviour was evaluated by Double Cantilever Beam (DCB) test, in which the specimen beams are subjected to a perpendicular load with respect to the crack propagation plane.

The rubbery-modified laminates behave significantly better than the reference CFRP (Figure 3). The quasi-core–shell mat (*n*-60/40*_c*) is more effective at contrasting delamination than the fibril-like one (*n*-60/40*_f*).

  doi:10.5075/epfl-298799_978-2-9701614-0-0

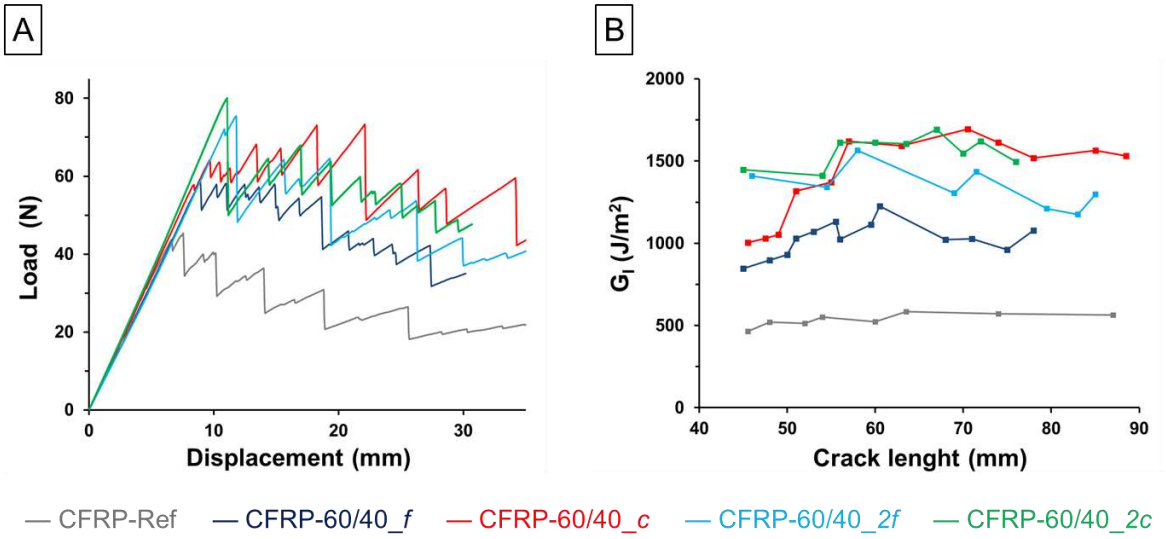

Figure 3. Mode I delamination test: A) load-displacement curves, B) G_I vs. crack length trends.

By analyzing G_I data (Table 2), the CFRP modified with the *n*-60/40_*c* mat shows a +113 % in $G_{I,C}$ and a +179 % in $G_{I,R}$, while the one with *n*-60/40_*f* enhancements of 76 % and 108 %, respectively. Moreover, it is possible to boost the interlaminar fracture toughness by integrating two nanofibrous mats, reaching a maximum enhancement near 200 % (CFRP-60/40_2*c*).

Table 2: DCB test results.

CFRP	Interleaved mats	Maximum load [N]	$G_{I,C}$ [J/m^2]	$G_{I,R}$ [J/m^2]
CFRP-Ref	0	46 ± 5	517 ± 106	558 ± 65
CFRP-60/40_*f*	1	64 ± 5 (+39 %)	910 ± 55 (+ 76 %)	1161 ± 155 (+108 %)
CFRP-60/40_*c*	1	75 ± 3 (+63 %)	1102 ± 107 (+ 113 %)	1559 ± 238 (+179 %)
CFRP-60/40_2*f*	2	76 ± 4 (+65 %)	1346 ± 144 (+ 160 %)	1403 ± 208 (+151 %)
CFRP-60/40_2*c*	2	73 ± 3 (+59 %)	1458 ± 184 (+ 182 %)	1663 ± 188 (+198 %)

Since Nomex-only nanofibers promote delamination [17] due to potential slowing/hindering of epoxy curing [22] and/or bad adhesion to the matrix, the enhancement of the interlaminar properties should be ascribable to the high NBR toughening ability. Indeed, as evidenced by SEM micrographs of delamination surfaces, the matrix fracture is more ductile when NBR/Nomex mixed nanofibers are integrated (Figure 4). Moreover, when adding two veils of nanofibers, the lack of continuity between the two independent layers do not negatively affect the final performance.

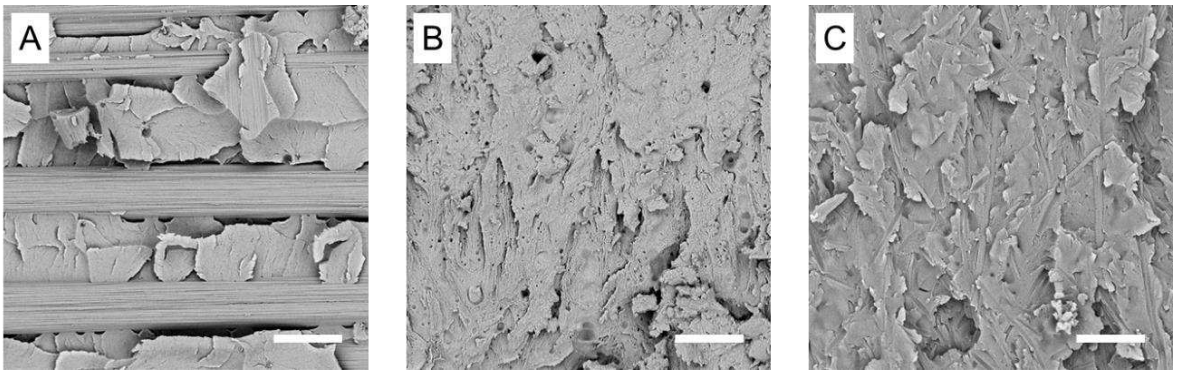

Figure 4. Delamination surfaces of DCB specimens after tests: A) unmodified CFRP, B) CFRP-60/40_2*f, and C)* CFRP-60/40_2*c, scale bar 10 μm.*

4. Conclusions

NBR and Nomex processed via single-needle electrospinning self-assemble, forming peculiar morphologies in which the arrangement of the two polymers depends on the processing parameters. Two completely different nanofibrous morphologies can be obtained: one showing a fibril-like structure of Nomex, the other resembling a quasi-core–shell fiber with the rubber in the inner. Both NBR/Nomex nanofiber types significantly enhance the CFRP interlaminar fracture toughness. The quasi-core–shell morphology gives a better reinforcing action than the fibril-like one (up to +179 % in G_I vs +108 %, respectively). The hindering action can be further improved by integrating two independent nanofibrous mats at the same interface, achieving a maximum G_I boost near 200 %. The work demonstrates the high toughening ability of NBR/Nomex 60/40 nanofibers for contrasting delamination in epoxy-based CFRP laminates, showing also an easy tailoring of the effect playing on the number of integrated veils.

5. References

1. Wu X-F, Yarin AL. Recent progress in interfacial toughening and damage self-healing of polymer composites based on electrospun and solution-blown nanofibers: An overview. *Journal of Applied Polymer Science* 2013; 130: 2225–37.
2. Tuloup C, Harizi W, Aboura Z, Meyer Y, Khellil K, Lachat R. On the use of in-situ piezoelectric sensors for the manufacturing and structural health monitoring of polymer-matrix composites: A literature review. *Composite Structures* 2019; 215: 127–49.
3. Brugo TM, Maccaferri E, Cocchi D et al. Self-sensing hybrid composite laminate by piezoelectric nanofibers interleaving. *Composites Part B: Engineering* 2021: 108673.
4. Wise CW, Cook WD, Goodwin AA. CTBN rubber phase precipitation in model epoxy resins. *Polymer* 2000; 41: 4625–33.
5. Riew CK, Siebert AR, Smith RW, Fernando M, Kinloch AJ. Toughened Epoxy Resins: Preformed Particles as Tougheners for Adhesives and Matrices. *Toughened Plastics II*. Vol252. American Chemical Society, 1996: 33–44.
6. Bagheri R, Marouf BT, Pearson RA. Rubber-toughened epoxies: A critical review. *Polymer Reviews* 2009; 49: 201–25.

  doi:10.5075/epfl-298799_978-2-9701614-0-0

7. Caldona EB, De Leon ACC, Pajarito BB, Advincula RC. A Review on Rubber-Enhanced Polymeric Materials. *Polymer Reviews* 2017; 57: 311–38.
8. Williams RJJ, Rozenberg BA, Pascault J. *Reaction-Induced Phase Separation in Modified Thermosetting Polymers*., 1997.
9. O'Brien TK. Delamination of Composite Materials. *Composite Materials Series* 1991; 4: 181–98.
10. Palazzetti R, Zucchelli A. Electrospun nanofibers as reinforcement for composite laminates materials – A review. *Composite Structures* 2017; 182: 711–27.
11. Zheng N, Liu H-Y, Gao J, Mai Y-W. Synergetic improvement of interlaminar fracture energy in carbon fiber/epoxy composites with nylon nanofiber/polycaprolactone blend interleaves. *Composites Part B: Engineering* 2019; 171: 320–8.
12. Daelemans L, van der Heijden S, De Baere I, Rahier H, Van Paepegem W, De Clerck K. Damage-Resistant Composites Using Electrospun Nanofibers: A Multiscale Analysis of the Toughening Mechanisms. *ACS Applied Materials & Interfaces* 2016; 8: 11806–18.
13. Daelemans L, Kizildag N, Van Paepegem W, D'hooge DR, De Clerck K. Interdiffusing core-shell nanofiber interleaved composites for excellent Mode I and Mode II delamination resistance. *Composites Science and Technology* 2019; 175: 143–50.
14. Maccaferri E, Mazzocchetti L, Benelli T, Brugo TM, Zucchelli A, Giorgini L. Rubbery nanofibrous interleaves enhance fracture toughness and damping of CFRP laminates. *Materials & Design* 2020.
15. Maccaferri E, Mazzocchetti L, Benelli T, Brugo TM, Zucchelli A, Giorgini L. Rubbery-Modified CFRPs with Improved Mode I Fracture Toughness: Effect of Nanofibrous Mat Grammage and Positioning on Tanδ Behaviour. *Polymers* 2021; 13: 1918.
16. Povolo M, Maccaferri E, Cocchi D et al. Damping and mechanical behaviour of composite laminates interleaved with rubbery nanofibers. *Composite Structures* 2021: 114228.
17. Maccaferri E, Mazzocchetti L, Benelli T, Brugo TM, Zucchelli A, Giorgini L. Self-Assembled NBR/Nomex Nanofibers as Lightweight Rubbery Nonwovens for Hindering Delamination in Epoxy CFRPs. *ACS Applied Materials & Interfaces* 2022; 14: 1885–99.
18. ASTM D5528-13 - Standard Test Method for Mode I Interlaminar Fracture Toughness of Unidirectional Fiber-Reinforced Polymer Matrix Composites. *American Society for Testing and Materials*2013.
19. Maccaferri E, Mazzocchetti L, Benelli T, Brugo TM, Zucchelli A, Giorgini L. Rubbery nanofibers by co-electrospinning of almost immiscible NBR and PCL blends. *Materials and Design* 2020; 186: 108210.
20. Thielke MW, Bruckner EP, Wong DL, Theato P. Thiol-ene modification of electrospun polybutadiene fibers crosslinked by UV irradiation. *Polymer* 2014; 55: 5596–9.
21. Maccaferri E, Cocchi D, Mazzocchetti L et al. How Nanofibers Carry the Load: Toward a Universal and Reliable Approach for Tensile Testing of Polymeric Nanofibrous Membranes. *Macromolecular Materials and Engineering* 2021; 306: 2100183.
22. Merighi S, Maccaferri E, Belcari J et al. Interaction between polyaramidic electrospun nanofibers and epoxy resin for composite materials reinforcement. *Key Engineering Materials* 2017; 748 KEM: 39–44.

  doi:10.5075/epfl-298799_978-2-9701614-0-0

CHEMICAL COMPATIBILIZER AS AN APPROACH TO IMPROVE THE MECHANICAL PROPERTIES OF POLY(PROPYLENE) REINFORCED WITH GRAPHENE NANOPLATELETS

Luiza R. Melo de Lima[a,b,c], Tito Trindade[b,c] and José M. Oliveira[a,c]

a: EMaRT Group – Emerging: Materials, Research, Technology, School of Design, Management and Production Technologies Northern Aveiro, University of Aveiro, 3720-509 Oliveira de Azeméis, Portugal – luizalima@ua.pt
b: Department of Chemistry, University of Aveiro, Campus Universitário de Santiago, 3810-193 Aveiro, Portugal
c: CICECO – Aveiro Institute of Materials, University of Aveiro, Campus Universitário de Santiago, 3810-193 Aveiro, Portugal

Abstract: *Poly(propylene) (PP)-based graphene nanoplatelets (GnPs) nanocomposites were prepared by melt blending technique. To improve the adhesion between PP and GnPs, compatibilizers with different chemical active sites were employed during the nanocomposites' processing. The influence of GnPs and 3 different compatibilizers presence on structural characteristics of the PP-based GnPs nanocomposites, as well as in their mechanical properties was analysed and discussed. The compatibilizers addition promoted chemical modifications on nanocomposites' polymeric chains, affecting their mechanical properties in different ways. For instance, the addition of maleic anhydride (MA) compatibilizer improved the mechanical properties of nanocomposite when compared to analogous non-compatibilized nanocomposite. The morphological characterization confirmed that the presence of compatibilizers plays an important role in enhancing the adhesion between PP and GnPs, resulting in an improvement of the nanocomposites' mechanical performance.*

Keywords: PP-based GnPs nanocomposites; Graphene nanoplatelets; Chemical compatibilizers; Injection moulding; Automotive applications

1. Introduction

Thermoplastics are a class of polymers that represent more than 80% of overall plastic consumption. This tendency is attributed to their certain characteristics namely high productivity, low density, and recyclability [1,2]. In the automotive industry, for example, the most common thermoplastic used is poly(propylene) (PP), which represents more than half of the polymeric raw material employed in auto parts [3]. Nevertheless, its structural applications can be limited by its low stiffness and poor impact toughness [4]. The addition of structural fillers begins as an approach to improve these properties. The PP-based composites developed with conventional fillers, such as short glass and carbon fibres [5], and talc [6] are used in auto parts to enhance their mechanical properties, but they must be used in a high load to be more effective [7]. On the other hand, the use of nanofillers such as graphene-based materials (GBM) can be effective at a relatively lower amount

Recently, graphene nanoplatelets (GnPs) have emerged as promising GBM for reinforcing the PP matrix. GnPs are constituted by several graphene monolayers stacked together, able to be produced more easily and economically than totally exfoliated graphene sheets [8]. However,

  doi:10.5075/epfl-298799_978-2-9701614-0-0

the properties and performance of the PP-based GnPs nanocomposites depend mainly on the type of interactions between the PP and GnPs [9]. Thus, physicochemical modifications of the PP and/or GnPs have been reported as an important approach to improving these interactions [2]. The methods of modifying PP and GnPs can be mainly divided into chemical and non-chemical modifications. The chemical modifications are characterized by covalent bonding between functional groups. On the other hand, the non-chemical modifications are mainly based on non-covalent attachment between molecules and the surface of nanoplatelets; *i.e.*, this process involves mainly physical interactions such as van der Walls forces and π-π stacking interactions [10,11]. Both modification methods can induce the improvement of nanocomposites' properties; however, chemical modification is often more effective. To date, various routes for chemical bonding have been proposed such as amidation, silanization, esterification, and substitution [12,13]. For instance, Park & Kim [14] prepared PP/dodecylated GnPs nanocomposites by melt blending process, however, the GnPs surface modifications were previously performed via solution mixing. During the solution mixing, to achieve the GnPs alkylation using dodecylamine (DDA), the authors performed an amidation and epoxide ring-opening reaction between amine groups of DDA and carboxyl or epoxy groups of the GnPs' surfaces. Lee et al. [15] also employed the solution mixing process to modify the GnPs surface with pyrene-functionalized PP grafted maleic anhydride (PPgMA) through π-π interactions. The authors confirmed through morphological analyse that the GnPs modification improved their dispersion within the matrix, as well as their adhesion with the matrix.

So far, investigations focusing on the employing of solvent-free chemical and non-chemical modifications are limited. Trusiano et al. [2] reported the preparation of PP/GnPs nanocomposites by melt blending process and described that the addition of PPgMA enhanced the GnPs dispersion and their adhesion with the matrix. In addition to the use of PPgMA, Al-Saleh et al. [16] also related the incorporation of ethylene-octene elastomer grafted MA (POEgMA) as compatibilizer in PP/GnPs nanocomposites. Based on the tensile properties of nanocomposites, the authors observed that PPgMA had better performance than POEgMA due to its stronger reactivity with PP; however, higher impact strength was achieved when POEgMA was used.

In the present study, part of a project whose objective is to develop PP-based nanocomposites for automotive applications, we prepared PP-based GnPs nanocomposites by melt blending technique. Compatibilizers with different chemical active sites were studied to improve the adhesion between matrix and nanofillers. The effect of the compatibilizers on the structural characteristics of the nanocomposites as well as in their mechanical properties was evaluated and prioritized.

2. Experimental

2.1 Materials

PP homopolymer (PP 595A) from SABIC, Germany, with a melt flow index of 47 g/10 min (230 °C, 2.16 kg) and density of 0.905 g cm^{-3}, was used as a thermoplastic matrix. GnPs from XG Sciences Inc. (xGnP, Grade C), USA, were applied as reinforcement phase of the nanocomposites. As compatibilizers, MA 99% and DDA 98% were used and dicumyl peroxide (DCP) 98% was employed as the initiator of MA grafting in the PP matrix. MA, DDA, and DCP were purchased from Sigma Aldrich, USA.

  doi:10.5075/epfl-298799_978-2-9701614-0-0

2.2 Preparation of PP–based GnPs nanocomposites

The nanocomposites were compounded by melt blending technique, using a Brabender type internal mixer. Before compounding, PP pellets were dried at 60 °C for 24 h. Firstly, the PP pellets were loaded into the Brabender and melted for 2 min at 180 °C and 40 rotations per minute. Then, a certain amount of GnPs and compatibilizer were added and the system was mixed for an additional 10 min. To initiate the graft reaction of MA onto the PP matrix, the DCP (mass ratio of 0.1 DCP/MA) was added simultaneously with MA into the Brabender (MAd compatibilizer). Finally, to assess the individual effect of GnPs on the PP matrix, a formulation without compatibilizers was prepared by the same experimental approach. The nanocomposites formulations are described in Table 1. The compatibilizers' amount was based on previous studies [14,17].

Table 1: Sample code and formulations.

Sample code	PP (wt.%)	GnPs (wt.%)	DDA (wt.%)	MA (wt.%)	MAd (wt.%)
PP	100.0	-	-	-	-
PP/GnPs	99.0	1.0	-	-	-
PP_{DDA}/GnPs	94.0	1.0	5.0	-	-
PP_{MA}/GnPs	89.0	1.0	-	10.0	-
PP_{MAd}/GnPs	89.0	1.0	-	-	10.0

2.3 Characterization of PP–based GnPs nanocomposites

The attenuated total reflection–Fourier transforms infrared (ATR–FTIR) spectra of nanocomposites were performed on FTIR spectrometer (FTIR Bruker Tensor 27), using an ATR Golden Gate (diamond) system. The spectra were collected in the 4000 – 600 cm^{-1} range, with 256 scans recorded at 4 cm^{-1} resolution. The tensile tests were performed using a universal machine for mechanical testing (Shimadzu AG–IS), with a speed of 50 mm min^{-1} at room temperature. The tensile strength (σ_{max}) and elongation at break (ε_{max}) were obtained from the curve of stress *versus* strain. Young's modulus (E) was calculated from the initial curve slope by linear regression. The Charpy impact tests were carried out using a universal pendulum impact system (Ray Ran RR/IMT). The tensile and Charpy impact tests were executed on five and ten specimens, respectively, and the results reported are average values. To obtain the specimens for both mechanical tests, a micro-injection moulding machine (BABYPLAST® 6/10P) from CRONOPLAST S.L. was used. The morphology characterization of samples after tensile tests was performed by scanning electron microscopy (SEM, Hitachi S4100). The samples were coated with Au/Pd for 3 min under Ar atmosphere and observed at an acceleration voltage of 25 kV. The GnPs distribution into the PP matrix was observed using a stereo microscope with LED and HD Camera (Leica EZ4HD). The experimental procedure for the preparation of samples for stereo microscope analysis was previously described [17].

3. Results and discussion

3.1 Structural characterization

  doi:10.5075/epfl-298799_978-2-9701614-0-0

Figure 1 shows the FTIR spectra of samples and compatibilizers agents. The typical peaks of neat PP can be identified, such as the vibration peak at around 2917 cm^{-1}, which is ascribed to CH_2 asymmetrical stretching, and the vibration peaks at 1456 cm^{-1} and 1375 cm^{-1}, both corresponding to the CH_3 symmetrical bending [18,19].

Concerning the PP/GnPs nanocomposite, the addition of GnPs resulted in a spectrum almost identical to that of neat PP, suggesting that adding GnPs into PP had a negligible effect on the chemical structure of PP. In the case of compatibilized nanocomposites, some chemical structural modifications were identified. Regarding the addition of DDA (PP_{DDA}/GnPs), beyond the already identified PP characteristic peaks, another two weak peaks were identified which suggested the DDA modification of PP: the NH stretch related to an emergence of secondary amine (at 3307 cm^{-1}), which may have resulted from the interaction between NH_2 primary observed on DDA spectrum (box delimited area in Figure 1a) and functional groups of the PP, and the NH bend vibration of primary amine (at 1610 cm^{-1}) also verified at around 1645 cm^{-1} of DDA spectrum.

The spectra of PP_{MA}/GnPs and PP_{MAd}/GnPs exhibited similar vibration peaks of the neat PP spectrum, with exception of a vibration peak at 1456 cm^{-1} that shows a tendency to shift to a lower wavenumber. The formation of hydrogen bonds can cause some absorption peaks to shift in position and shape. Furthermore, the anhydride group of MA may have esterified with the hydroxyl group present on the GnPs surface under melt blending circumstances. This intermolecular reaction can improve the interfacial compatibility between PP and GnPs [20,21]. Additionally, it was observed the emergence of a weak band at around 1780 cm^{-1} in the PP_{MAd}/GnPs spectrum, thus indicating that MA was grafted onto the PP chain due to the DCP presence as the initiator [22]. For the MA spectrum, it is visible its characteristic vibration peaks at 1753 and 1774 cm^{-1} related to the asymmetric stretching of the carbonyl group (C=O) of the cyclic anhydride [23].

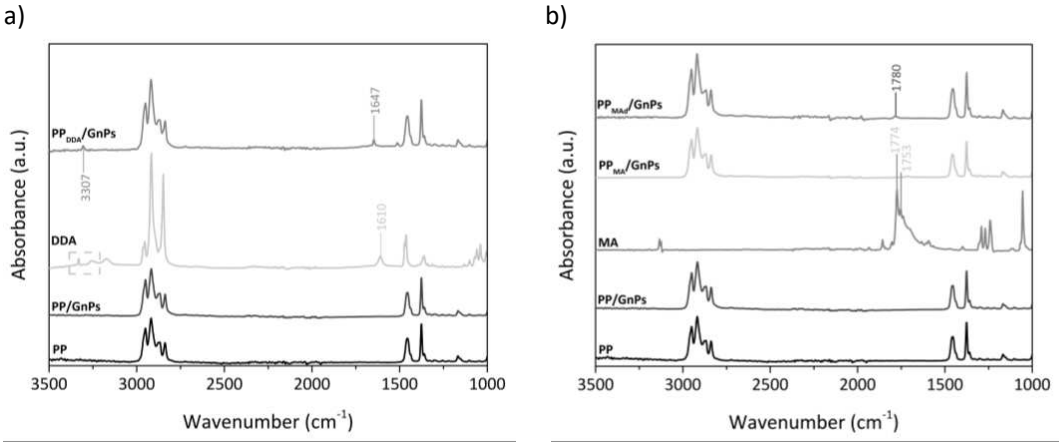

Figure 1. FTIR spectra of samples and compatibilizers agents: a) PP, PP/GnPs, DDA, and PP_{DDA}/GnPs; b) PP, PP/GnPs, MA, PP_{MA}/GnPs, and PP_{MAd}/GnPs.

3.2 Mechanical characterization

The mechanical properties of samples namely σ_{max}, ε_{max}, E, and impact strength are presented in Figure 2. Compared to neat PP, the presence of GnPs increased by ≈ 12% on the σ_{max} and ≈ 13% on E of PP/GnPs, inferring an enhancement of the tensile properties with a stiffening effect of the nanocomposite due to the GnPs' presence. Studies have reported similar outcomes on

thermoplastic-based GnPs nanocomposites [24,25]. The increase of stiffness is also reflected in a marked decrease of ≈ 98% on ε_{max} due to the high restriction of PP chain movement. Additionally, the GnPs incorporation led to a decrease of ≈ 33% in the impact strength. The deterioration of impact strength could be related to weak compatibility between polymer matrix and nanofillers, which leads to failure in effective load transfer [16,26]. The use of nanocomposites in structural auto parts requires a compromise between σ_{max}, E, and impact strength. Typically, attempts to improve one of these properties show an adverse effect on the others. Therefore, the improvement of one or more of these mechanical properties is frequently taken into account depending on the end application [11]. It is recognized that other aspects can affect the mechanical behaviour of PP/GBM nanocomposites, such as (1) the compatibility degree between GBM and matrix; (2) the GBM load; and (3) the dispersion into the polymeric matrix [7,11,27]. To improve the mechanical performance of PP/GnPs, the use of compatibilizers agents as an approach to promote the adhesion between PP and GnPs was evaluated.

Compared to PP/GnPs nanocomposite, as a result of the addition of DDA, a decrease of ≈ 19% on σ_{max} and of ≈ 46% on E of PP_{DDA}/GnPs was attained. This mechanical behaviour suggested that DDA created a poor mechanism of stress transfer between PP and GnPs. On the other hand, it was noticed a significant increase of ≈ 4000% on ε_{max} and ≈ 29% on the impact strength. This deterioration of σ_{max} and E, together with the improvement of nanocomposite' ductility and toughness suggested a plasticizer effect of DDA molecules in the PP_{DDA}/GnPs [14]. The addition of both MA and MAd resulted in a decrease of ≈ 10% on σ_{max} and a marginal effect on E of PP_{MA}/GnPs and PP_{MAd}/GnPs, respectively. In contrast, the MA and MAd presence increased by ≈ 36% and 32% on ε_{max}, respectively, also indicating an increase in plastic regime due to a plasticizer effect of MA-based compatibilizers, which retarded the breaking point of these nanocomposites [20]. Regarding the impact toughness, the addition of MA increased by ≈ 45% the impact strength. This improvement in the energy absorption capacity of PP_{MA}/GnPs can be attributed to the enhancement of interaction between PP and GnPs [2,28]. The MA created a strong interfacial adhesion between nanoplatelets and PP chains, favouring the GnPs distribution into the matrix (as will be confirmed by the morphological analysis) and leading to an enhancement of PP_{MA}/GnPs mechanical compromise. In contrast, the MAd introduction caused a decrease of ≈ 23% in the impact strength, suggesting that the graft of MA onto PP, as well as the chain scission initiated by the DCP presence, may have deteriorated the PP_{MAd}/GnPs' impact toughness.

Sutar et al. [28] reported an increase of up to 43% in impact strength of PP-based nanocomposites after the GnPs incorporation. The authors suggested that GnPs increased the energy dissipation during crack propagation. Similar behaviour was identified by Juan [29] in PP/graphene nanocomposites with an increase of up to 26.7%. On the other hand, Al-Saleh et al. [16] observed that GnPs loading decreases the impact strength of PP/GnPs nanocomposites due to the incompatibility between PP and GnPs. However, with the addition of compatibilizer agents, namely PPgMA and POEgMA, the authors verified an improvement of the impact strength, indicating the increase of nanocomposite fracture toughness due to the enhanced adhesion between PP and GnPs.

  doi:10.5075/epfl-298799_978-2-9701614-0-0

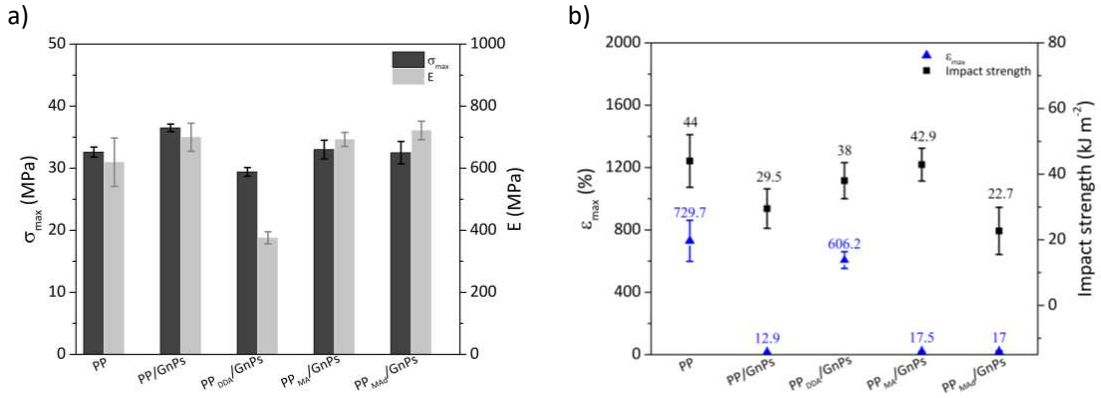

Figure 2. Mechanical properties of samples: a) tensile strength (σ_{max}) and Young's modulus (E); b) elongation at break (ε_{max}) and impact strength.

3.3 Morphological characterization

The morphological analysis of specimens after tensile tests were performed through SEM (Figure 3). SEM micrographs of the neat PP surface showed a smooth and regular surface. All nanocomposites revealed a full encapsulation of GnPs into the PP matrix The PP/GnPs nanocomposite exhibited a rough surface with some voids. The compatibilizers' incorporation changed the fracture surface of nanocomposites. Regarding the PP_{DDA}/GnPs surface, it is evident the plastic deformation of the polymer is due to many coarse fibrillation structures. These fibrillations are signs of crazing in the nanocomposite, which increase the plastic deformation, as also verified by its significant increase on ε_{max}. In contrast, the PP_{MA}/GnPs nanocomposite exhibited a more regular surface when compared with non-compatibilized and compatibilized nanocomposites, indicating a better interface adhesion between PP and GnPs. The PP_{MAd}/GnPs surface also showed a plastic deformation, with a small number of fibres on the fracture surface [2].

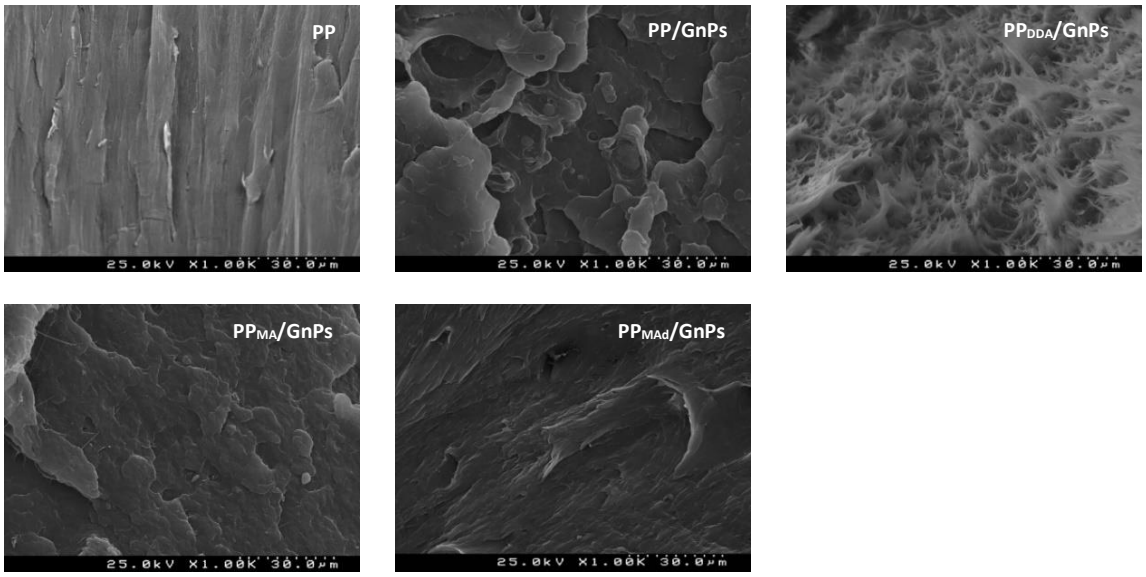

Figure 3. SEM micrographs of samples.

In the stereo microscope micrographs (Figure 4) was observed a homogeneous GnPs distribution in all nanocomposites. The use of compatibilizers has been employed as a strategy to improve the interaction between polymer matrix and fillers, which contribute to a reduction of GnPs aggregation into the matrix [2]. The PP_{MA}/GnPs micrographs showed the lowest agglomeration

tendency of GnPs, implying once again the efficiency of MA as a compatibilizer able to improve the final performance of PP_{MA}/GnPs nanocomposite.

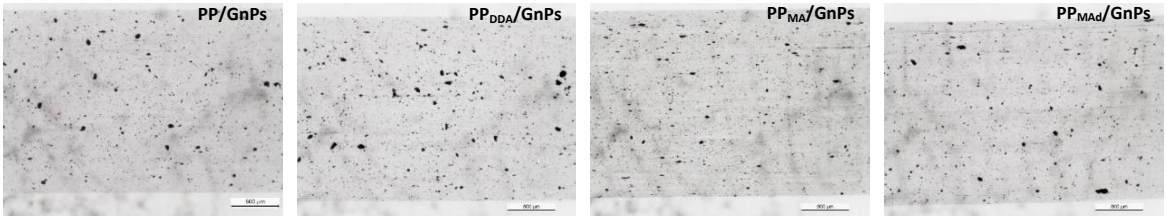

Figure 4. Stereo microscope micrographs of the samples (scale = 500 µm).

4. Conclusions

The influence of GnPs and compatibilizers presence on structural characteristics and mechanical properties of the PP-based GnPs nanocomposites were evaluated. The results confirmed the ability of chemical compatibilizers to promote surface modifications, able to improve the interactions between PP and GnPs. The mechanical properties suggested that GnPs caused a stiffness effect on the PP matrix, however, the results showed the importance of compatibilizer incorporation to achieve a compromise between σ_{max}, E, and impact strength. The MA was the compatibilizer that better achieved this compromise, suggesting that the PP_{MA}/GnPs formulation can be employed in auto parts for structural proposal.

5. Acknowledgements

This work was supported by COMPETE 2020 – Programa Operacional Competividade e Internacionalização within NANO–SIM 3D project (POCI–01–0247–FEDER–039842). This work was also developed within the scope of the project CICECO–Aveiro Institute of Materials, UIDB/50011/2020, UIDP/50011/2020 & LA/P/0006/2020, financed by national funds through the FCT/MEC (PIDDAC).

6. References

1. Voltes-Dorta A, Perdiguero J, Jiménez JL. Are car manufacturers on the way to reduce CO2 emissions?: A DEA approach. Energy Econ [Internet]. 2013;38:77–86. Available from: http://dx.doi.org/10.1016/j.eneco.2013.03.005
2. Trusiano G, Matta S, Bianchi M, Rizzi LG, Frache A, Applicata S, et al. Evaluation of Nanocomposites Containing Graphene Nanoplatelets: Mechanical Properties and Combustion Behavior. Polym Eng Sci. 2019;2062–71.
3. Quiles-Díaz S, Enrique-Jimenez P, Papageorgiou DG, Ania F, Flores A, Kinloch IA, et al. Influence of the chemical functionalization of graphene on the properties of polypropylene-based nanocomposites. Compos Part A Appl Sci Manuf. 2017;100:31–9.
4. Liang J zhao. Effects of graphene nano-platelets size and content on tensile properties of polypropylene composites at higher tension rate. J Compos Mater. 2017;1–8.
5. Fu SY, Lauke B, Mäder E, Yue CY, Hu X. Tensile properties of short-glass-fiber- and short-carbon-fiber-reinforced polypropylene composites. Compos Part A Appl Sci Manuf. 2000;31:1117–25.
6. Świetlicki M, Chocyk D, Klepka T, Prószyński A, Kwaśniewska A, Borc J, et al. The structure and mechanical properties of the surface layer of polypropylene polymers with talc additions. Materials (Basel). 2020;13:1–13.
7. Müller K, Bugnicourt E, Latorre M, Jorda M, Echegoyen Sanz Y, Lagaron J, et al. Review on the Processing and Properties of Polymer Nanocomposites and Nanocoatings and Their Applications in the Packaging, Automotive and Solar Energy Fields. Nanomaterials. 2017;7(4):74.

8. Botta L, La Mantia FP, Ceraulo M, Mistretta MC. Effect of processing temperature and mixing time on the properties of PP/GnP nanocomposites. Polym Degrad Stab. 2020;181:109321.
9. Mylvaganam K, Zhang L. Some Mechanical Properties of Graphene and Their Role in Forming Polymer Nanocomposites. In: Aliofkhazraei M, Ali N, Milne WI, Ozkan CS, Mitura S, Gervasoni JL, editors. Graphene science handbook Mechanical and chemical properties. First. Boca Raton, FL: Taylor & Francis Group; 2016.
10. Bello RH, Coelho LAF, Becker D. Role of chemical funcionalization of carbon nanoparticles in epoxy matrices. J Compos Mater. 2017;1–16.
11. Hu K, Kulkarni DD, Choi I, Tsukruk V V. Graphene-polymer nanocomposites for structural and functional applications. Prog Polym Sci. 2014;39(11):1934–72.
12. Woo JH, Park SY. Polypropylene nanocomposite with polypropylene-grafted graphene. Macromol Res. 2016;24:508–14.
13. Nguyen TT, Bandyopadhyay P, Li X, Nam Hoon K, Lee JH. Effects of grafting methods for functionalization of graphene oxide by dodecylamine on the physical properties of its polyurethane nanocomposites. J Memb Sci. 2017;540:108–19.
14. Park SM, Kim DS. Preparation and physical properties of polypropylene nanocomposites with dodecylated graphene nanoplatelets. Compos Interfaces. 2017;24:335–45.
15. Lee MG, Lee S, Cho J, Jho JY. Improving Dispersion and Mechanical Properties of Polypropylene/Graphene Nanoplatelet Composites by Mixed Solvent-Assisted Melt Blending. Macromol Res. 2020;28(12):1166–73.
16. Al-Saleh MA, Yussuf AA, Al.Enezi S, Kazemi R, Wahit MU, Al-Shammari T, et al. Polypropylene/Graphene Nanocomposites: Effects of GNP Loading and Compatibilizers on the Mechanical and Thermal Properties. Materials (Basel). 2019;12:1–11.
17. Melo de Lima LR, Magalhães da Silva SP, Trindade T, Oliveira JM. Rheological behavior of poly(propylene) reinforced with graphene nanoplatelets for injection molding. J Appl Polym Sci. 2022;Accept.
18. Andreassen E. Infrared and Raman spectroscopy of polypropylene. In: Karger-Kocsis J, editor. Polypropylene: An A-Z Reference. Kluwer Publishers; 1999. p. 320–8.
19. Fang J, Zhang L, Sutton D, Wang X, Lin T. Needleless Melt-Electrospinning of Polypropylene Nanofibres. J Nanomater. 2012;2012:1–9.
20. Magalhães da Silva SP, Antunes T, Costa ME V, Oliveira JM. Cork-like filaments for Additive Manufacturing. Addit Manuf. 2020;101229:1–9.
21. Miao M, Wei C, Wang Y, Qian Y. Effect of Compatibilizer on the Interface Bonding of Graphene Oxide/Polypropylene Composite Fibers. Polymers (Basel). 2018;10:1283.
22. Krause-Sammartino LE, Lucas JC, Reboredo MM, Aranguren MI. Maleic anhydride grafting of polypropylene: Peroxide and solvent effects. Plast Rubber Compos. 2006;35:117–23.
23. Kučera F, Petruš J, Bálková R, Jančář J. Solid-state grafting of maleic anhydride onto polypropylene: The influence of morphology of polypropylene on heterogeneous reaction. Polym Eng Sci. 2020;60(5):1076–82.
24. Evgin T, Turgut A, Hamaoui G, Spitalsky Z, Horny N, Micusik M, et al. Size effects of graphene nanoplatelets on the properties of high-density polyethylene nanocomposites: morphological, thermal, electrical, and mechanical characterization. J Nanotechnol. 2020;11:167–79.
25. Liang JZ, Du Q, Tsui GCP, Tang CY. Tensile properties of graphene nano-platelets reinforced polypropylene composites. Compos Part B Eng. 2016;95:166–71.
26. Jun YS, Um JG, Jiang G, Lui G, Yu A. Ultra-large sized graphene nano-platelets (GnPs) incorporated polypropylene (PP)/GnPs composites engineered by melt compounding and its thermal, mechanical, and electrical properties. Compos Part B Eng. 2018;133:218–25.
27. Melo de Lima LR, Martins FP, Lagarinhos JN, Santos L, Lima P, Torcato R, et al. Characterization of commercial graphene-based materials for application in thermoplastic nanocomposites. Mater Today Proc. 2020;20:383–90.
28. Sutar H, Mishra B, Senapati P, Murmu R. Mechanical, Thermal, and Morphological Properties of Graphene Nanoplatelet-Reinforced Polypropylene Nanocomposites: Effects of Nanofiller Thickness. J Compos Sci. 2021;5:1–18.
29. Juan L. Simultaneous Improvement in the Tensile and Impact Strength of Polypropylene Reinforced by Graphene. J Nanomater. 2020;2020:1–5.

  doi:10.5075/epfl-298799_978-2-9701614-0-0

PIEZORESISTIVITY OF NANOCOMPOSITES: ACCOUNTING FOR CNT CONTACT CONFIGURATION CHANGES

Stepan V. Lomov[a] , Jeonyoon Lee[b], Brian L. Wardle[b], Iskander S. Akhatov[a] and Sergey G. Abaimov[a]*

[a] Center for Design, Manufacturing, and Materials, Skolkovo Institute of Science and Technology Moscow, 121205 Russia, s.lomov@skoltech.ru

[b] Department of Aeronautics and Astronautics, Massachusetts Institute of Technology, Cambridge, Mass., MA 02139 USA

Abstract: *In simulations of piezoresistivity of carbon nanotubes (CNT)-based nanocomposites, finite element (FE) analysis is commonly used to predict the local details of the deformation and change of the tunneling contact distances between the CNTs. This is computationally intensive, making Monte Carlo calculations and optimizations involving variability of the RVE difficult. The present paper proposes a simplified, non-FE model for local changes of the tunneling distances. The CNTs are represented as trusses in an RVE, randomly generated according to the CNT volume fraction and their random orientation description. The analytical model of deformation in contacts combines the uniformity of micro-scale deformation over the CNT network (which defines translation of the contacting CNTs) with amplification of the deformation in the CNT contacts (which is the result of rotation of CNT sections near the contact). The model is benchmarked against full FE modelling and the predictions for random and aligned CNT nanocomposites are compared with literature data.*

Keywords: carbon nanotubes; electrical conductivity; intrinsic conductivity; tunneling conductivity; gauge factor

1. Introduction

The resistor networks model [1] was applied to CNT nanocomposites in early 2000. Such a model uses random generation of a CNT assembly which is transformed into a resistor network and then the conductivity is homogenized. At a given volume fraction of the filler, the input to the model includes geometrical characteristics of the CNTs (single- or multiwall as well as the wall count, outer diameter, length distribution), their waviness, geometrical characteristics of the CNT assembly (orientation distribution, level of agglomeration) and, finally, the electrical characteristics of the CNTs and their contacts. These electrical characteristics are intrinsic conductivity of CNTs themselves and tunneling conductivity of their contacts; the latter depends on the inter-CNT contact distances, which change with the material deformation.

The resistor network approach is a basis for models of piezoresistive behavior of CNT nano-composites [2-9]. These models use finite elements (FE) analysis of the CNT network deformation, extracting from the deformation fields change of the CNT tunneling distance, feeding this change to the calculation of the tunneling resistance of the contacts and then re-homogenizing the conductivity (or resistance) of the whole network. The relative difference between the homogenized resistance after and before the deformation, divided by the applied deformation, defines the *gauge factor* of the material.

  doi:10.5075/epfl-298799_978-2-9701614-0-0

Because of randomness of the CNT networks, such calculations are performed as a part of Monte Carlo simulations, with tens – hundreds of CNT network realizations. Therefore, it is highly desirable to reduce the computational time for each realization. With large number of CNTs in a representative volume (several thousands), there are two bottlenecks: (1) FE analysis of deformation, which should use hundreds of thousands degrees of freedom, even if superimposed meshes (also called embedded regions in Abaqus) are used for CNTs and the matrix; (2) analysis of electric circuit, which is performed either also with FE [4], or via nodal analysis with hundreds of thousands of CNT contacts.

The present paper proposes an analytical model for approximate calculations of the inter-CNT distances change, caused by applied average deformation. The proposed approach drastically reduces the time needed to step (1) above. Hence processing of hundreds of Monte Carlo realizations becomes feasible, and statistics of the gauge factor of CNT nanomaterials can be evaluated with confidence. The model is benchmarked against full FE calculations, taken from [4], and used to calculate statistical distribution of gauge factor of a nanocomposite with aligned CNTs.

2. Geometric modelling of an RVE

The CNT generation algorithm uses random choice of the direction of the generated CNT path segment, as it is widely done in literature, for example, in [10, 11], but with constraints, introduced in [12]. A centerline of a CNT is created as segments. For generation of an aligned assembly, the spherical angles of the segment orientation are defined in relation to a global Cartesian coordinate system with z-axis corresponding to the direction of the forest growth; for generation of a random isotropic assembly, the angles are defined on a local coordinate system with z-axis corresponding to the direction of the previous segment. The algorithm uses random choice of the direction of the generated segment, with the amplitude of the deviations from z-axis depending on the waviness of the CNTs. The randomly generated angles are restricted by given maximum curvature and maximum torsion of the CNT centerline; these restrictions make the statistical characteristics of the CNT centerline independent of the chosen length of the segment. The reader is referred to [12] for details.

Geometric periodicity of the RVE is assumed: if a CNT crosses an RVE face, then it is continued from the opposite face till the full length of the CNT is reached. The number of CNTs in the model is defined based on the prescribed fiber volume fraction (VF).

3. Homogenization of the RVE electrical conductivity

Once an RVE is created, the geometric network of the CNT assembly is analysed for contacts between the CNTs and then transformed into the set of nodes, connected with electrical resistances / conductances, which are assigned to the tunneling contacts and to the CNT sections between the contacts. The electrical boundary conditions are periodical. The homogenized conductivity tensor is then calculated. The details of the homogenization procedure can be found in [12].

Conductance G_{CNT} of the CNT segment of length l_{seg} is calculated as:

$$G_{CNT} = g_{intr}\frac{A}{l_{seg}}, \quad (1)$$

  doi:10.5075/epfl-298799_978-2-9701614-0-0

where *A* is the CNT cross-section area, g_{intr} is the effective volumetric conductivity of the CNT. The area is taken as the full area of the cross-section, $A = \pi d^2/4$, where *d* is the outer CNT diameter.

The tunneling conductance is calculated using Simmons' formula [13, 14], which for low voltage on the contact is [15]:

$$G_{tunn} = G_0 \frac{\tau}{s} \frac{d^2}{32} \exp(-\tau s), \quad (2)$$

where *s* is the distance between the CNT surfaces, $s \geq s_{min}$, s_{min} is usually taken as 0.34 nm (van der Waals distance), *d* is the CNT outer diameter, $G_0 = 2e^2/h$ = 7.722·10^{-5} S (*e* = 1.602·10^{-19} C is the electron's charge, *h* = 6.626·10^{-34} J·s is Plank's constant), and

$$\tau = \frac{4\pi\sqrt{2m\Delta E}}{h}, \quad (3)$$

where *m* = 9.109·10^{-31} kg is electron mass, and ΔE is the potential barrier. The potential barrier ΔE is shown by [15] to have different values (ΔE_1 and ΔE_2) for the contact distances below and above the "polymer cutoff distance", assumed to be equal to 0.6 nm.

Under deformation of the CNT network, the length of the CNT segments changes negligibly because of much higher axial stiffness of the CNTs (~ 1 TPa) in comparison with the stiffness of the matrix (~ 1 – 3 GPa) and homogenized stiffness of the nanocomposite (~ 12 GPa, CNT content ~ 1 wt%). The deformation affects inter-CNT distance *s*, which enters the expression of the tunneling conductance, Eq (2).

4. Piezoresistivity model

4.1 Inter-CNT distances and the tunneling conductance

At deformation, distances *s* of the tunneling contacts, Eq (2), are changing, causing the change in the tunneling part of the conductivity. When modelled, care should be taken to apply correct values of potential barriers. As it was discussed in section 3, in the undeformed state potential barrier ΔE_1 is applied at distances shorter than the polymer cutoff distance 0.6 nm, while at larger distances the value of the potential barrier is switched to ΔE_2. The reason behind this is that at distances between two CNTs larger than 0.6 nm, polymeric chains begin to penetrate into ,this gap while at shorter distances it is prevented by the van der Waals' forces.

When the deformation is applied, distances between CNTs are changing. We assume that no polymer interpenetrates the opening gaps in this process. Then in the case when *s* becomes larger than 0.6 nm, the value of the potential barrier must be evaluated with the reference to the undeformed configuration, the potential barrier still remains ΔE_1 without changing to ΔE_2.

On the contrary, when the gap is not opening, but closing, we expect the van der Waals' forces to push the polymer out of this gap, changing thereby the potential barrier. Then in the case when *s* becomes smaller than 0.6 nm, the potential barrier switches from ΔE_2 to ΔE_1.

Finally, we assume that pairs of contact points, at which tunneling is happening, stay unchanged at deformation, and in the deformed configuration no search for new contact points is performed.

  doi:10.5075/epfl-298799_978-2-9701614-0-0

The piezoresistive gauge factor (*GF*) for uniaxial tension deformation ε in *i* direction is defined as

$$GF = \frac{1}{\varepsilon}\frac{g_{ii}-g'_{ii}(\varepsilon)}{g_{ii}}, \quad (4)$$

where g_{ii} and $g'_{ii}(\varepsilon)$ are *ii* diagonal components (no summation) of the homogenized conductivity tensors before and after the deformation.

4.2 Change of the inter-CNT distances under deformation

Consider uniaxial tension of a nanocomposite, with applied deformation ε. Assumed a value for Poisson's ratio of the nanocomposite, for example $\nu = 0.3$ [16]. Calculations of the distances of the tunneling CNT contacts proceed in the following steps, as illustrated in Figure 1.

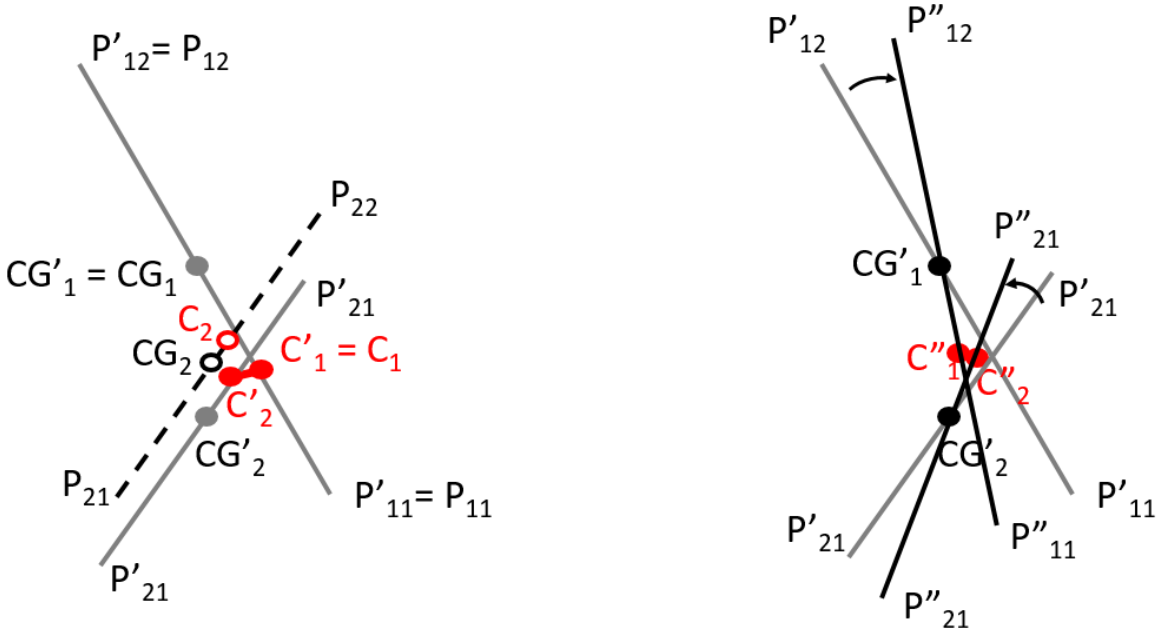

Figure 1. Calculation of the change of the tunneling contact distance under tension in vertical direction: Decomposition of CNT contact geometry into (a) relative displacement of the centers of gravity; (b) rotation of straight sections of the both CNTs.

1. The change of a tunneling distance in a contact **C** between two CNTs (two contact points C_1 and C_2 on the centerlines) is defined by deformation of a "deformation element" (Figure 1a), which comprises sections *(P_{11}, P_{12})* and *(P_{21}, P_{22})* of the CNTs with the length ½ of the inter-contact CNT lengths between subsequent contacts on the both sides from the contact **C** on each of the CNTs.
2. The deformation element is approximated by two straight lines, with contact points belonging to these lines, length of the lines equal to the length of the CNT sections $||P_{11}, P_{12}||$ and $||P_{21}, P_{22}||$, orientation of the lines is the same as of vectors $\overrightarrow{P_{11}, P_{12}}$ and $\overrightarrow{P_{21}, P_{22}}$, positions of the contact points on the lines is the same as on the CNT sections in terms of distance from the contact points to the ends of the sections.
3. Average deformation state of all deformation elements is the same and is defined by the applied deformation:

  doi:10.5075/epfl-298799_978-2-9701614-0-0

$$\varepsilon_{11} = -\nu\varepsilon, \varepsilon_{22} = -\nu\varepsilon, \varepsilon_{33} = \varepsilon\ . \quad (5)$$

4. Conformal deformation of the CNTs in the deformation element has two components:
a. displacements of the centers of gravity (CG) of the CNT sections in the element according to the deformation eq (5), the section length is not changed:

$$\overrightarrow{CG'_1CG'_2} = \begin{bmatrix} -\nu\varepsilon & 0 & 0 \\ 0 & -\nu\varepsilon & 0 \\ 0 & 0 & \varepsilon \end{bmatrix} \overrightarrow{CG_1CG_2}\ ;\ \|P'_{12} - P'_{11}\| = \|P_{12} - P_{11}\|$$

b. rotation of the CNT sections around the displaced centers of gravity (CG'); the rotation increases the Z-distance between the ends of each CNT section by a factor (1+ε) and preserves the section length:

$$|P''_{12z} - P''_{11z}| = |P'_{12z} - P'_{11z}|(1+\varepsilon)\ ;\ \|P''_{12} - P''_{11}\| = \|P'_{12} - P'_{11}\|$$

The new tunneling distance is the distance defined by the new positions of the contact points, C''_1 and C''_2, which result from the described deformation of the CNTs, which transforms their initial positions C_1 and C_2 first, after translation, in $C'_1 = C_1$ and C'_2, and then, after rotation, in C''_1 and C''_2.

4.3 Comparison with FE modelling

To validate the approximate algorithm, described above, a comparison is done with FE calculations of the change of the inter-CNT contact distances and the nanocomposite resistivity, performed in [4]. Table 1 shows parameters of the model, and illustrates the random RVE realizations (centerlines of CNTs are shown). Table 2 compares results of calculations of homogenized conductivity in [4], performed using FE modelling, and the present calculations, done with nodal analysis of the electric circuit. Good correspondence between the results allow further comparison of the change of the RVE resistivity with deformation.

Table 1: Parameters of the test model, multiwall CNTs [4]

Parameter	*Value*	*RVE image*
CNT diameter	50 nm	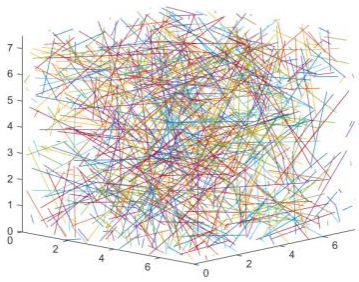
CNT wall thickness	5 nm	
CNT length	5 μm	
CNT max curvature and torsion	1 μm^{-1}	
CNT volume fraction	1%	
RVE size	7.5*7.5*7.5 μm	
Number of CNTs inside the RVE	430	

Table 2 compares relative change of resistance $\Delta R/R$, resulting from uniaxial tension deformation, applied to the RVE, under different levels of the applied strain calculated using FE modelling in [4] and with the present algorithm. The correspondence of the values is pretty good, given a very approximate character and strong assumptions of the proposed algorithm. Time-wise the present calculations of the change of the CNT contacts and the nodal analysis take few seconds per RVE random realization of a PC Intel(R) Core(TM) i9-9880H CPU @ 2.30 GHz, 32 GB RAM.

Table 2: Comparison of the calculated conductivity and relative resistance change according to [4] *and the present modelling*

Homogenized conductivity, S/m			Relative resistivity change, VF = 1%		
VF	[4]*	present calculations**	strain	[4]**	present calculations***
0.75%	0.15	0.15 ± 0.20	0.2%	0.01	0.013
1%	1.2	1.15 ± 0.33	0.3%	0.02	0.030
2%	15	14.5 ± 0.80	0.4%	0.04	0.044
			0.5%	0.08	0.054

* based on [4], Figure 9 *** based on [4], Figure 10

** mean and standard deviation **** logarithmic mean

5. Piezoresistivity of aligned CNT assembly

The model is illustrated on random and aligned CNT nanocomposites [17, 18]. The model parameters are shown in Table 3. Figure 2 shows the calculated distribution of the gauge factor of the nanocomposites under uniaxial tension deformation, for 100 random realizations of the CNT configurations. The calculated range of the gauge factor corresponds to the experimentally observed values for the similar materials [19, 20], which are in the range 1 – 4 along CNTs and 4 – 6 for the VF in the range 1% - 10%.

Table 3: Parameters of the modelled CNT nanocomposites

Parameter	*Random CNTs*	*Aligned CNTs*
Data source	[17]	[18]
CNT outer diameter, nm	1.6	8.0
CNT length		
distribution type	Weibull	constant
mean length, µm	2.0	20
Weibull modulus	3.0	n/a
Weibull scale, µm	2.24	n/a
CNT orientation		
distribution type	uniform	aligned
CNT shape		
maximal curvature, 1/µm	5	5
maximal torsion, 1/µm	5	5
Volume fraction variants	0.5%; 1%	2.5%; 7%

  doi:10.5075/epfl-298799_978-2-9701614-0-0

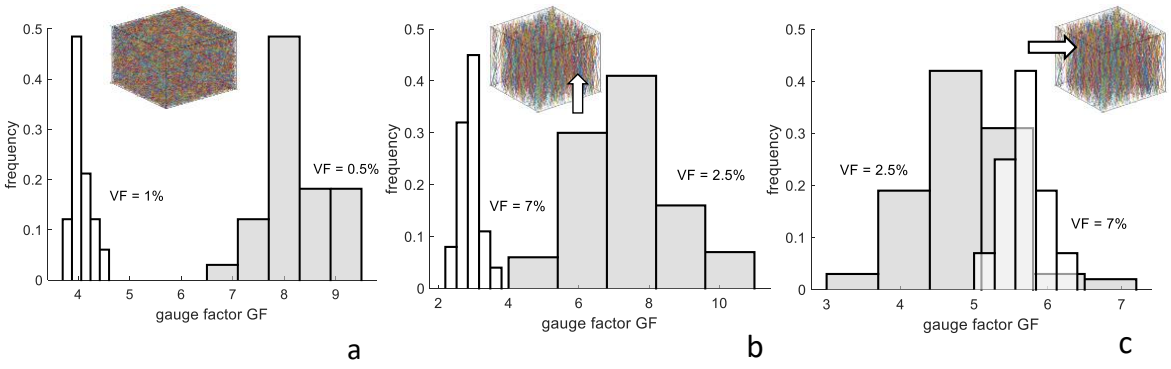

Figure 2. Gauge factor, histograms of the distributions: (a) random CNTs, VF = 0.5% and 1%, (b,c) aligned CNTs, along (b) and across (c) CNTs, VF = 2.5% and 7%. Intrinsic CNT conductivity 10^4 S/m, tunneling potential barrier 3 eV. Sampling size 100. White arrows show the deformation direction.

6. Conclusions

The proposed analytical model for calculating change of the inter-CNT distances and the related change of the tunneling inter-CNT resistances has been validated against the full-FE simulations and provide predictions of the CNT-based nano-composite gauge factors corresponding to the experimentally measured values.

Acknowledgements

This work was supported by Skoltech NGP Program (Skoltech-MIT joint project “Multifunctional Fusion: Life-cycle enhancements via data-driven nanoengineering of advanced composite structures”).

References

1. Kirkpatrick, S., Percolation and Conduction. Reviews of Modern Physics, 1973. 45(4): p. 574-588.
2. Hwang, M.-Y. and L.-H. Kang, CNT network modeling and simulation of the electrical properties of CNT/PNN-PZT/epoxy paint sensor. Journal of Mechanical Science and Technology, 2017. 31(8): p. 3787-3791.
3. Naghashpour, A. and S. Van Hoa, Requirements of amount of carbon nanotubes for damage detection in large polymer composite structures. Polymer Testing, 2017. 63: p. 407-416.
4. Matos, M.A.S., V.L. Tagarielli, P.M. Baiz-Villafranca, and S.T. Pinho, Predictions of the electro-mechanical response of conductive CNT-polymer composites. Journal of the Mechanics and Physics of Solids, 2018. 114: p. 84-96.
5. Alian, A.R. and S.A. Meguid, Multiscale modeling of the coupled electromechanical behavior of multifunctional nanocomposites. Composite Structures, 2019. 208: p. 826-835.
6. Lebedev, O.V., A. Trofimov, S.G. Abaimov, and A.N. Ozerin, Modeling of an effect of uniaxial deformation on electrical conductance of polypropylene-based composites filled with agglomerated nanoparticles. International Journal of Engineering Science, 2019. 144: p. 103132.

  doi:10.5075/epfl-298799_978-2-9701614-0-0 published under CC BY-NC 4.0 license

7. Tanabi, H. and M. Erdal, Effect of CNTs dispersion on electrical, mechanical and strain sensing properties of CNT/epoxy nanocomposites. Results in Physics, 2019. 12: p. 486-503.
8. Lebedev, O.V., S.G. Abaimov, and A.N. Ozerin, Modeling the effect of uniaxial deformation on electrical conductivity for composite materials with extreme filler segregation. Journal of Composite Materials, 2020. 54(3): p. 299-309.
9. Lebedev, O.V., A.N. Ozerin, and S.G. Abaimov, Multiscale numerical modeling for prediction of piezoresistive effect for polymer composites with a highly segregated structure. Nanomaterials, 2021. 11(1): p. 162.
10. Romanov, V., S.V. Lomov, I. Verpoest, and L. Gorbatikh, Modelling evidence of stress concentration mitigation at the micro-scale in polymer composites by the addition of carbon nanotubes. Carbon, 2015. 82: p. 184-194.
11. Stein, I.Y. and B.L. Wardle, Mechanics of aligned carbon nanotube polymer matrix nanocomposites simulated via stochastic three-dimensional morphology. Nanotechnology, 2016. 27(3): p. 035701.
12. Gudkov, N.A., S.V. Lomov, I.S. Akhatov, and S.G. Abaimov, Conductive CNT-polymer nanocomposites digital twins for self-diagnostic structures: Sensitivity to CNT parameters Composite Structures, 2022 in print.
13. Simmons, J.G., Generalized formula for the electric tunnel effect between similar electrodes separated by a thin insulating film. Journal of Applied Physics, 1963. 34(6): p. 1793-1803.
14. Matthews, N., M.J. Hagmann, and A. Mayer, Comment: "Generalized formula for the electric tunnel effect between similar electrodes separated by a thin insulating film" J. Appl. Phys. 34, 1793 (1963). Journal of Applied Physics, 2018. 123(13).
15. Penazzi, G., J.M. Carlsson, C. Diedrich, G. Olf, A. Pecchia, and T. Frauenheim, Atomistic modeling of charge transport across a carbon nanotube-polyethylene junction. Journal of Physical Chemistry C, 2013. 117(16): p. 8020-8027.
16. Dastgerdi, J.N., G. Marquis, and M. Salimi, Micromechanical modeling of nanocomposites considering debonding and waviness of reinforcements. Composite Structures, 2014. 110: p. 1-6.
17. Butt, H.A., S.V. Lomov, I. Akhatov, and S. Abaimov, Self-diagnostic carbon nanocomposites manufactured from industrial epoxy masterbatches. Composite Structures, 2021. 259: p. 113244.
18. Cebeci, H., R. Guzman de Villoria, A.J. Hart, and B.L. Wardle, Multifunctional properties of high volume fraction aligned carbon nanotube polymer composites with controlled morphology. Composites Science and Technology, 2009. 69: p. 2649–2656.
19. Aviles, F., A.I. Oliva-Aviles, and M. Cen-Puc, Piezoresistivity, strain, and damage self-sensing of polymer composites filled with carbon nanostructures. Advanced Engineering Materials, 2018. 20(7): p. 1701159.
20. Sánchez-Romate, X.F., J. Artigas, A. Jiménez-Suárez, M. Sánchez, A. Güemes, and A. Ureña, Critical parameters of carbon nanotube reinforced composites for structural health monitoring applications: Empirical results versus theoretical predictions. Composites Science and Technology, 2019. 171: p. 44-53.

IONIC POLYDIMETHYLSILOXANE-SILICA NANOCOMPOSITES: FROM SYNTHESIS AND CHARACTERIZATION TO SELF-HEALING PROPERTY

Clément Mugemana [a], Ahmad Moghimikheirabad[b], Didier Arl[a], Frédéric Addiego[a], Daniel F. Schmidt[a], Martin Kröger[b] and Argyrios V. Karatrantos[a]*

a: Materials Research and Technology, Luxembourg Institute of Science and Technology, 5, Avenue des Hauts-Fourneaux, L-4362 Esch-sur-Alzette, Luxembourg
b: Polymer Physics, Department of Materials, ETH Zurich, Leopold-Ruzicka-Weg 4, CH-8093 Zurich, Switzerland
Clement.mugemana@list.lu

Abstract: *Polydimethylsiloxane (PDMS)-based nanocomposites have attracted increasing attention due to their inherent outstanding properties. Nevertheless, the realization of high levels of dispersion of nanosilicas in PDMS represents a challenge arising from the poor compatibility between the two components. Herein, we explore the use of ionic interactions located at the interface between silica and PDMS matrix by combining anionic sulfonate-functionalized silica and cationic ammonium-functionalized PDMS. A library of ionic PDMS nanocomposites was synthesized and characterized to highlight the impact of charge location, density, and molecular weight of ionic PDMS polymers on the dispersion of nanosilicas and the resulting mechanical reinforcement. The use of reversible ionic interactions at the interface of nanoparticles-polymer matrix enables the healing of scratches applied to the surface of the nanocomposites. Molecular dynamics simulations were used to estimate the survival probability of ionic crosslinks between nanoparticles and the polymer matrix, revealing a dependence on polymer charge density.*

Keywords: Nanocomposites; PDMS, Self-Healing; Ionic interactions; Simulation**.**

1. Introduction

Polydimethylsiloxane (PDMS) is the most widely explored and utilized polysiloxane, possessing an extremely low glass transition (T_g), excellent thermal stability, high permeability and good biocompatibility. [1] As a liquid at room temperature, most applications require PDMS to be chemically crosslinked and/or combined with nanofillers to realize the requisite mechanical properties. Cross-linking PDMS via reversible dynamic bonds based on hydrogen bonds, ionic interactions, metal complexes and dynamic transesterification has led to smart materials exhibiting self-healing, high stretchability and recyclability.[2] A plethora of nanofillers has been used for reinforcement of the PDMS matrix, and fumed silica has been one of the most favored reinforcing nanofillers for silicones due to strong hydrogen-bond mediated interactions between hydroxyl groups from the fumed silica surface and PDMS siloxane bonds.[3] However, amorphous fumed silica nanoparticles consist of nanoparticles and clusters resulting in inhomogeneous size distribution of nanoparticles. While mechanical reinforcement of PDMS by nanofillers is well-known, the realization of consistently high levels of dispersion in a PDMS matrix remains a challenge. One of the existing strategies to improve nanoparticle dispersion consists of grafting oppositely charged ionic functional groups to the nanoparticle surface and the polymer matrix, respectively, creating nanoparticle ionic materials (NIMS).[4] This approach has been used to design ionic nanocomposites with high levels of nanosilica dispersion in

  doi:10.5075/epfl-298799_978-2-9701614-0-0

poly(ethylene oxide),[5] polylactide, poly[ε-caprolactone-co-D,L-lactide] [6] and polyurethane matrices.[7] Herein, we explore the use of ionic interactions to enhance the distribution and dispersion of nanosilica in a PDMS matrix by combining cationic ammonium-functionalized PDMS and anionic sulfonate-functionalized nanosilicas. The effects of PDMS molecular weight (MW), charge density and charge location on nanosilica dispersion and mechanical reinforcement are investigated. In addition, the use of reversible ionic interactions located at the interface between nanosilica and ionic PDMS matrix was exploited to trigger the scratch healing of the ionic PDMS nanocomposites films. The experimental studies have been complemented by coarse grained molecular dynamics simulations of ionic nanocomposites to estimate the expected lifetimes of ionic crosslinks between ionic nanoparticles and polymers.

2. Results

A library of ionic PDMS polymers with molar masses in the range of 6 500 – 50 000 g mol^{-1} and trimethylammonium concentrations varying from 0.07 to 1.73 mmol g^{-1} were prepared either by a direct quaternization of (aminopropylmethylsiloxane-*r*-dimethylsiloxane) copolymers or hydrosilylation of (methylhydrosiloxane-*r*-dimethylsiloxane) copolymers in a two-step reaction. The hydrosilylation of poly(methylhydrosiloxane-*r*-dimethylsiloxane) copolymers having molar masses of 6 500 and 25 000 g mol^{-1} with respective concentrations of 0.87 and 0.69 mmol g^{-1} of methylhydrosiloxane was performed in the presence of *N,N*-dimethyl allylamine and PtO_2 catalyst. The quaternization reaction in the presence of methyl bromide was performed in a second step to give the trimethylammonium-functionalized PDMS corresponding to P1 and P2, respectively. The direct quaternization of poly(aminopropylmethylsiloxane-*r*-dimethylsiloxane) copolymers having molar masses of 20 000 (P3) and 50 000 (P4) g mol^{-1} with respective cationic charge densities of 1.73 and 0.83 mmol g^{-1} was achieved in the presence of a large excess of methyl bromide and sodium bicarbonate in THF over 4 days. The impact of charge location on nanosilica dispersion was investigated by functionalizing the chain-ends of PDMS with trimethylammonium from aminopropyl-terminated PDMS having molar masses of 5 000, 25 000 and 50 000 g mol^{-1} to yield P5, P6 and P7, respectively.

- Thermal and rheological properties of ionic PDMS

The synthesized ionic polymers were characterized by DSC to determine the impact of cationic pendant group location and concentration on the glass transition temperature (T_g) and crystalline melting point (T_m). (Table 1) It is well-known that linear PDMS is a semi-crystalline polymer that melts around -40°C, crystallizes at approximately -90°C and vitrifies upon cooling around -125°C. The DSC analysis of ionic PDMS polymers revealed the expected PDMS T_g at ≈ -120°C and a second T_g attributed to the ionic component of the copolymer, in the range of 70 to 85°C. The latter assignment is supported by analysis of the highly functionalized P3 copolymer, which showed a single T_g at 75°C. In contrast, with the aforementioned systems, where no obvious MW effects were observed, the introduction of ionic groups at the chain ends alone impacted the thermal property of the PDMS as a function of MW. The P5 exhibited a T_g of -124°C with no melting peak, while the P6 and P7 of higher MW additionally revealed single melting peaks at -46°C and -43°C, respectively. This is consistent with observations that, as with other polymers, very low molecular PDMS crystallizes poorly compared to its high molecular weight counterparts. Crystallization was also observed in the aminopropyl-terminated P6 precursor, which displayed a melting point of -43°C and a T_g of -124°C. Double melting peaks

  doi:10.5075/epfl-298799_978-2-9701614-0-0

were observed at -45 and -38°C for the P7, consistent with other reports on the complexities of PDMS crystallization behavior. [8]

Table 1. Thermal and rheological properties of ionic PDMS.

Ionic Polymer	Mw (Kg/Mol)	Cation Content Mmol/g	Charge Location	Thermal transitions (DSC, °C)			Rheological properties (1 Hz, RT)		
				T_{g1}	T_{g2}	T_m	G'	G''	η
P1	6.5	0.87	Grafted	-119			1.2	2.8	0.5
P2	25	0.69	Grafted	-119			8.4	17.5	3.1
P3	20	1.73	Grafted		76				
P4	50	0.83	Grafted	-117	85		4.8	11.4	1.9
P5	5	0.58	Chain-ends	-124			13.1	10.6	2.7
P6	25	0.14	Chain-ends			-46	77.4	24.3	12.9
P7	50	0.07	Chain-ends			-43	101	8.6	16.1

The viscoelastic properties of the ionic PDMS copolymers were assessed through frequency sweep analysis by measuring the storage and loss moduli G'(ω) and G"(ω) as a function of angular frequency at room temperature. The trimethylammonium-grafted PDMS copolymers (P1, P2 andP4) were dominated by a viscous response, with G"(ω) higher than G'(ω) over almost the entire range of studied frequencies and with crossover observed only at the highest frequencies. In contrast to the ionic-grafted PDMS copolymers, the ammonium-terminated P6 and P7 displayed a much greater propensity for solid-like behavior over the range of studied frequencies, with higher plateau moduli vs. grafted systems of similar MW and with crossover observed at much lower frequencies, i.e. 0.079 Hz and 0.016 Hz, respectively. Below the entanglement molecular weight, Me (12 000 g/mol), the measured moduli of the P5 dropped and no plateau modulus was observed in contrast with PDMS of higher MW, but the material remained solid-like at most frequencies, with a cross-over point at 0.039 Hz. One possible explanation for these observations is that repulsion between high concentrations of cationic groups in the grafted systems makes the formation of physical crosslinks (in the form of entanglements) exceptionally difficult, thus ensuring that liquid-like behavior dominates in such materials. In contrast, in end-functional systems, the tendency of small concentrations of polar end-groups to phase-separate and form clusters with reduced mobility may actually cause the formation of additional physical crosslinks vs. non-functionalized PDMS. This would explain why such a low crossover frequency is observed even in the lowest MW end functionalized PDMS, which would otherwise be expected to behave as a liquid at all frequencies.

- Dispersion of nanosilica in ionic PDMS

PDMS-silica nanocomposites films were prepared by mixing sulfonate-functionalized nanosilicas with trimethylammonium-functionalized PDMS. PDMS nanocomposites were prepared by dissolving the synthesized trimethylammonium-grafted PDMS in DMSO. In tandem, an aqueous nanosilica dispersion was diluted with an equal volume of DMSO, then concentrated under low pressure using a rotovap to remove the water. Nanosilicas dispersed in DMSO were then added to the ionic PDMS solution in a Teflon dish and the mixture was heated at 150°C for two hours, then dried under vacuum overnight to yield transparent PDMS-silica nanocomposite films. A second set of PDMS-silica nanocomposites was prepared from trimethylammonium-terminated

P5, P6 and P7 polymers in the presence of sulfonate-functionalized nanosilicas. Due to lower solubility of the trimethylammonium-terminated PDMS in DMSO, other polar organic solvents had to be tested. P5 polymer was found to be soluble in DMF, and thus the corresponding nanocomposites were prepared following the same procedure as for the ionic grafted-PDMS copolymers in DMSO. Using the aforementioned approach, a series of PDMS-silica nanocomposites films was prepared by mixing the ionic PDMS with 10 wt% of sulfonate-functionalized nanosilica into different ammonium-functionalized PDMS polymers. The weight fraction of nanosilica in different nanocomposite films was estimated by TGA analysis and the concentration was found to be between 11 and 14 wt% except for the P3 (20.3 wt%), P5 (16.8 wt%) P7 (16.9 wt%). This discrepancy may be reflective of an inhomogeneous distribution of nanoparticles in these materials, resulting in higher nanoparticle concentrations in the materials sampled for TGA. To assess nanosilica dispersion levels, Scanning Transmission Electron Microscopy (STEM) was performed. The dispersion and distribution of the nanosilica was found to depend on the charge density of the PDMS as well as the corresponding MW.

Considering first those systems based on PDMS with ionic group grafted along the chain, well-dispersed nanosilica was observed in all cases as shown as an example for the P4 loaded with 10 wt.% of silica. (Figure 1. a) The observation of high levels of dispersion is consistent with the effects of a combination of repulsive ionic interactions between nanosilica particles and attractive (electrostatic) interactions between nanosilica and the PDMS matrix.

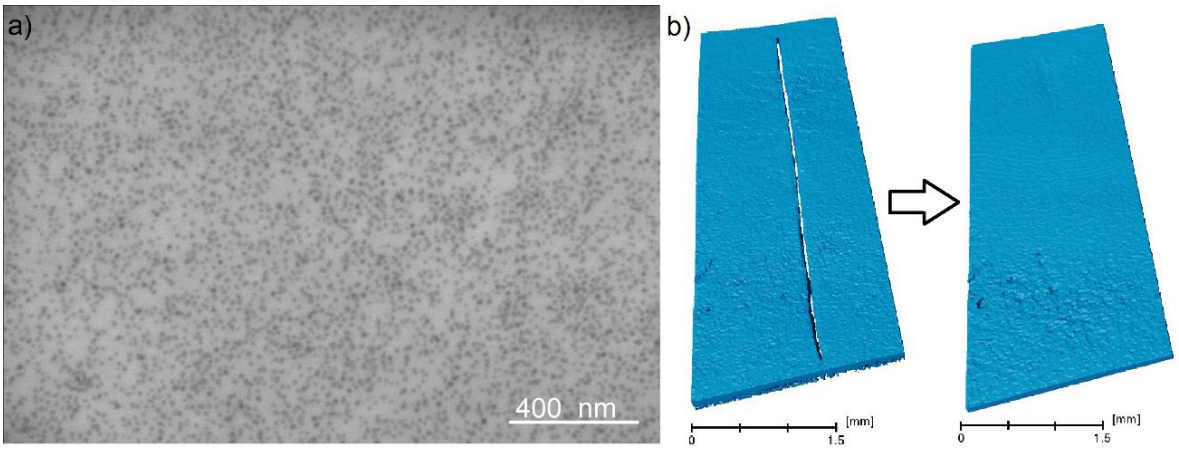

Figure 1. STEM images of the bulk from the PDMS-Silica nanocomposites films prepared from P4 (a) and the self-healing behavior of a P1 nanocomposite film as evidenced by Micro-CT images (b).

PDMS-silica nanocomposites prepared from PDMS bearing ionic groups at the chain ends were also tested to investigate the impact of charge location on the dispersion of nanosilica. While the use of PDMS with MW above 25 000 g/mol resulted in nanoparticle aggregation, the P5-based nanocomposites of higher charge density displayed improved nanosilica dispersion. This observation of high levels of dispersion in a non-entangled (ionic) PDMS matrix agrees with a prior report that layered silicates may be dispersed in non-entangled PDMS with polar end groups, and that, more broadly, layered silicate dispersion in PDMS is driven by polar group content.[9]

  doi:10.5075/epfl-298799_978-2-9701614-0-0

- Mechanical properties of ionic PDMS-silica nanocomposite

While the unfilled polymers here were too weak / liquid-like in character to enable such work, quasi-static tensile testing was performed on trimethylammonium-grafted PDMS-based nanocomposite films. Tensile test analysis was performed on a PDMS-silica nanocomposite film prepared from P1 and 10wt% of silica. While rheometry revealed viscous behavior influenced by interactions between cationic groups within the PDMS chains, the addition of nanosilica resulted in mechanical reinforcement with a tensile strength of 0.16 MPa ± 0.03 and a break strain of 118 ± 1%. Increasing the MW of ionic PDMS to 25 000 g/mol (P2) (above the entanglement MW) resulted in significantly greater mechanical performance at 10 wt% nanosilica loading, with a tensile strength of 0.91 ± 0.20 MPa but a reduced break strain of 68 ± 12%. This decrease in break strain was interpreted as indicative of higher nanosilica mobility in a low MW matrix. [10] The mechanical reinforcement by nanosilica in a higher MW PDMS copolymer of 50 000 g/mol was also tested. P4 containing 10 wt% nanosilica exhibited lower mechanical strength (0.18 MPa ± 0.05) and break strain (25 ± 1%) than the corresponding lower MW P2-based nanocomposites.

Given the levels of mechanical performance observed with 10 wt% nanosilica, the P2 matrix was chosen to study the effects of variations in nanosilica loading. Decreasing the nanosilica loading to 7.5 wt% gave results in line with the expected reductions in crosslink density, with a lower break stress (0.41 ± 0.01 MPa) and a higher break strain (90 ± 6%) observed. While better reinforcement might be expected at higher nanoparticle loadings (20 wt%) given an anion to cation ratio closer to 1, the onset of nanosilica aggregation resulted in nanoparticles clustering and poor mechanical reinforcement when the nanosilica loading was doubled. A tensile strength of only 0.21 ± 0.07 MPa and a strain at break of 20 ± 1% were measured, confirming the optimum nanosilica loading as 10 wt%. The same effect was observed when the charge density of the polymer was doubled (to 1.7 mmol g-1 in the case of P3) while maintaining a nanoparticle loading of 10 wt%, resulting in the lowest observed break stress and break strain values (0.16 ± 0.01 MPa and 16 ± 5%, respectively).

For end-functionalized P5, mechanical reinforcement was assessed by rheology since no free-standing polymer film could be prepared. In this case nanosilica addition was observed to reduce the RT storage modulus at both 5 and 10 wt% nanosilica. While a substantial reduction in loss tangent vs. that of the unfilled polymer was observed in both cases, as would be expected given an increase in crosslink density, the apparent reduction in absolute stiffness was a surprise. One possible explanation for this is that the clustering of the chain ends in the unfilled polymer, previously posited to give rise to its significant increase in solid-like character, might be disrupted through nanosilica addition, with the subsequent interactions with the nanosilica being unable to make up for this change.

- Self-healing of ionic PDMS nanocomposites

Cross-linking PDMS through reversible interactions promises the possibility of self-healing behavior as previously demonstrated on linear polymer chains, [11] polymer conetworks [12] and coatings [13]. The self-healing in ionic PDMS nanocomposites was tested by creating a scratch on the surface of various ionic PDMS nanocomposite films and monitoring the scratch over time, both by optical microscopy and micro-computed x-ray tomography (micro-CT). Two polymer matrix materials were chosen, namely P2 (which gave a nanocomposite with the

highest break stress of any tested) and P1 (which gave a nanocomposite with the highest break strain of any tested). The film samples (180 ± 20 µm thick) were placed on a glass substrate and a scratch was created a using a scalpel, giving a scratch width of 25 ± 5 µm. A healing temperature of 80°C was chosen based on the observation of a glass transition between 70 and 85°C (Table 1) previously assigned to the ionic groups in the system. It was posited that the heating of the ionic nanocomposite films to temperatures close to the glass transition would induce scratch healing as previously demonstrated in polyurethane-based ionic nanocomposites. [7] The first healing tests were performed for 24 hours at 80°C on three samples: P2-10%, P2-7.5% and P1-10%. However, no healing was observed in any case. -It was hypothesized that the high strength of the ionic interactions between the nanoparticles and the PDMS matrix might be impeding healing under these conditions. To test this, the healing experiment was repeated with the sample placed in a humid environment (a sealed glass desiccator with water placed below the sample shelf in place of desiccant; RH = 100 %), then heated to 80°C for 24 hours. In this case, optical microscopy revealed that, among the three samples, the P1-10% possessed the ability to heal rapidly, presumably due to the higher mobility of nanosilica in a non-entangled PDMS matrix. A decrease in scratch width in this system was observed after 30 minutes and after one hour, complete healing of the scratch was observed. This was confirmed with micro-CT analysis, which revealed a scratch 5 mm and 25 ± 5 µm wide prior to healing vs. the near-complete disappearance of the scratch following healing in a warm and humid environment (Figure 1-b). These results confirm the sensitivity of the ionic interactions in these systems to the presence of moisture, and its very strong impact on nanoparticle mobility and relaxation of the polymer chains.

- Modeling of crosslinks in ionic nanocomposites

Complementing the experimental work described here, we have used coarse grained molecular dynamics simulations of both ionic and traditional (attractive, nonionic) nanocomposites to shed light on the formation of ionic crosslinks between ionically functionalized nanosilicas and PDMS chains. The model is composed of spherical nanoparticles with surface beads, to mimic nanosilicas, and multibead-spring linear polymer chains (Kremer–Grest model) with N=200 monomers (this corresponds to a ratio of N/Ne > 2, where Ne is the number of monomers between entanglements 42) at two nanoparticle volume fractions (ϕ=0.062, 0.12). Polymeric and surface beads may or may not carry a permanent charge, while the nanocomposite systems are overall neutral in each case. Details about the simulations and the model used in this study can be found elsewhere in the literature. [14] We model polymers of different charge densities, charged either on their chain ends or along the backbone (one charge every three monomers = p3 type; one charge every 10 monomers = p10 type; one charge every 25 monomers = p25 type), or entirely without charges but incorporating a short-range attraction between polymers and the nanoparticle surface.[15] It is observed by coarse grained simulations [16] that nanoparticle dispersion depends on the ratio of electrostatic strength to distance between charges, rather than on the matrix MW. For all ionic nanocomposites modeled in this work, nanoparticle dispersion in the entangled polymer matrix has been observed.

  doi:10.5075/epfl-298799_978-2-9701614-0-0

3. Conclusion

A library of PDMS-based polymers containing cationic groups was successfully synthesized and characterized to study the impact of charge density and charge location on the structure and properties of nanocomposites formed with oppositely charged nanosilica. Thermal analysis of ionic polymers revealed higher thermal stability in the case of end-functionalized PDMS vs. cation-grafted PDMS. The viscoelastic properties of these materials as assessed by frequency sweep experiments in a parallel plate rheometer showed evidence of a significant viscous response in the case of cation-grafted PDMS, while end-functionalized PDMS exhibited solid-like behavior. The dispersion and distribution of nanosilica in these ionic PDMS matrix materials was driven at least as much by charge location and charge density as by charge balance, with good dispersion possible in all cation-grafted PDMS (albeit with more and more inhomogeneous nanosilica distribution observed as charge density increased), whereas in the end-functionalized PDMS case, only the system with the highest charge density produced high levels of nanosilica dispersion. The highest break stress was observed in the entangled P2 (MW > Me) with a nanosilica loading of 10 wt%. Here, the relatively low overall charge density helps to avoid the formation of a kinetically trapped nanostructure exhibiting inhomogeneous nanosilica distribution. High levels of nanoscale dispersion coupled with uniform distribution and an entangled polymer phase all contribute to increased break stress. The highest break strain was observed in P1 with a nanosilica loading of 10 wt%. This is ascribed to the higher mobility of nanosilica dictated thanks to the presence of non-entangled PDMS chains. The aforementioned nanocomposite also displays rapid (within 30-60 minutes) self-healing at 80°C in a humid environment, consistent with the proposition of high mobility coupled with the reversible nature of ionic interactions.

Acknowledgements

This work was supported by the Swiss National Science Foundation through grant 200021L_185052 and by the Fonds National de la Recherche Luxembourg through grant INTER/SNF/18/13289828. The authors declare no conflict of interest.

4. References

1. Wolf MP, Salieb-Beugelaar GB, Hunziker P, PDMS with Designer Functionalities—Properties, Modifications Strategies, and Applications. Progr. Polym. Sci. 2018, 83, 97-134.
2. Li CH, Wang C, Keplinger C, Zuo JL., Jin L, Sun Y, Zheng P, Cao Y, Lissel F, Linder C, You XZ, Bao Z, A Highly Stretchable Autonomous Self-Healing Elastomer. Nat. Chem. 2016, 8 (6), 618-624
3. Inagi S, Ogoshi T, Miyake J, Bertolucci M, Fujiwara, T, Galli G, Chiellini E, Chujo Y, Wynne KJ, Appearing, Disappearing, and Reappearing Fumed Silica Nanoparticles: Tapping-Mode AFM Evidence in a Condensation Cured Polydimethylsiloxane Hybrid Elastomer. Chem. Mater. 2007, 19 (9), 2141-2143.
4. Rodriguez R, Herrera R, Archer LA, Giannelis EP, Nanoscale Ionic Materials. Adv. Mater. 2008, 20 (22), 4353-4358.
5. Fernandes NJ, Akbarzadeh J, Peterlik H, Giannelis EP, Synthesis and Properties of Highly Dispersed Ionic Silica–Poly(ethylene oxide) Nanohybrids. ACS Nano 2013, 7 (2), 1265-1271.

  doi:10.5075/epfl-298799_978-2-9701614-0-0

6. Odent J, Raquez JM, Samuel C, Barrau S, Enotiadis A, Dubois P, Giannelis EP, Shape-Memory Behavior of Polylactide/Silica Ionic Hybrids. Macromolecules 2017, 50 (7), 2896-2905.
7. Odent J, Raquez JM, Dubois P, Giannelis EP, Ultra-Stretchable Ionic Nanocomposites: from Dynamic Bonding to Multi-Responsive Behavior. J. Mater. Chem. A. 2017, 5 (26), 13357-13363.
8. Klonos PA, Crystallization, Glass Transition, and Molecular Dynamics in PDMS of Low Molecular Weights: A Calorimetric and Dielectric Study. Polymer 2018, 159, 169-180.
9. Schmidt DF, Clément F, Giannelis EP, On The Origins of Silicate Dispersion in Polysiloxane/Layered-Silicate Nanocomposites. Adv. Funct. Mater. 2006, 16 (3), 417-425.
10. Shah D, Maiti P, Jiang DD, Batt CA, Giannelis EP, Effect of Nanoparticle Mobility on Toughness of Polymer Nanocomposites. Adv. Mater. 2005, 17 (5), 525-528.
11. Li CH, Wang C, Keplinger C, Zuo JL, Jin L, Sun Y, Zheng P, Cao Y, Lissel F, Linder C, You XZ, Bao Z, A Highly Stretchable Autonomous Self-Healing Elastomer. Nat. Chem. 2016, 8 (6), 618-624.
12. Mugemana C, Grysan P, Dieden R, Ruch D, Bruns N, Dubois P, Macromol. Chem. Phys. 2020, 221, 1900432.
13. Mugemana C, Anouk M, Dieden R, Ruch D, Dubois P, Macromol. Chem. Phys. 2021, 222, 2000331.
14. Moghimikheirabadi A, Mugemana C, Kröger M, Karatrantos AV, Polymer Conformations, Entanglements and Dynamics in Ionic Nanocomposites: A Molecular Dynamics Study. Polymers 2020, 12 (11), 2591
15. Moghimikheirabadi A, Kröger M, Karatrantos AV, Insights from Modeling into Structure, Entanglements, and Dynamics in Attractive Polymer Nanocomposites. Soft Matter 2021, 17 (26), 6362-6373.
16. Karatrantos A, Koutsawa Y, Dubois P, Clarke N, Kröger M, Miscibility and Nanoparticle Diffusion in Ionic Nanocomposites. Polymers 2018, 10 (9), 1010

  doi:10.5075/epfl-298799_978-2-9701614-0-0

Mechanical behaviour of ultrathin carbon nanomembranes for water purification

Marinos Dimitropoulos[1, 2], George Trakakis[2], C. Pavlou[1, 2], C. Kostaras[1, 2], N. Meyerbröker[3], R. Dalpke[3], P. Angelova[3], A. Schnieders[3], Costas Galiotis[1, 2] and Konstantinos Dassios[1, 2*]

[1]Department of Chemical Engineering, University of Patras, Patras, Greece

[2]Institute of Chemical Engineering Sciences, Foundation for Research and Technology Hellas, Patras, Greece

[3]CNM Technologies GmbH, Morgenbreede 1, Bielefeld, Germany

*kdassios@upatras.gr

ABSTRACT

In order to successfully address the target application, a material or composite structure created for a certain function must meet certain specifications. Mechanical properties of membranes are important in pressure-driven membrane processes, as these materials carry the mechanical loads generated by the flow of liquids. The membranes may be subjected to substantial physical compression at high working pressures, which can diminish or even destroy their performance. When a membrane's functional portion has poor intrinsic mechanical qualities or its dimensions prevent it from operating at high pressures, one approach is to support it with a porous substrate with appropriate mechanical stability. As a result, the mechanical behavior of both the active membrane and the substrate of a composite membrane is noteworthy and must be thoroughly investigated. Carbon nanomembranes (CNMs) are a type of two-dimensional material created by using low-energy electron irradiation to cross-link self-assembled monolayers (SAMs) of aromatic precursor molecules. The thickness and porosity of CNMs can be adjusted according on the precursor molecules and the preparation circumstances, from which they also inherit their terminal functionality. In contrast with macro-materials, measurement of the mechanical properties of nanometer-thick membranes is a very challenging task. For this reason, the membranes were suspended over patterned substrates and evaluated quantitatively in their intrinsic mechanical properties via Atomic Force Microscopy (AFM). The mechanical properties of substrates and composite membranes were studied by tensile experiments using a DebenTM micro-test tensile stage. The effect of the thickness and porosity of the substrates were also examined.

KEYWORDS: Carbon nanomembranes, mechanical properties

1. INTRODUCTION

A material or composite structure produced for a specific function must meet certain standards in order to successfully handle the target application. Membrane mechanical characteristics are critical in pressure-driven membrane processes because these materials carry the mechanical loads generated by liquid flow. At high operating pressures, the membranes may be subjected to significant physical compression, which might reduce or even destroy their performance. When the functional section of a membrane has weak inherent mechanical properties or its dimensions preclude it from operating at high pressures, one solution is to support it with a porous substrate with adequate mechanical stability. As a result, the mechanical behavior of both the active membrane and the substrate of a composite membrane is significant and warrants more investigation.

Carbon nanomembranes (CNMs) are two-dimensional materials synthesized by cross-linking self-assembled monolayers (SAMs) of aromatic precursor molecules using low-energy electron irradiation [1]. CNMs can have different thicknesses and porosities depending on the precursor molecules and preparation parameters, from which they also get their final functionality. CNM Technologies (a spin out of the University of Bielefeld) has modified these membranes to CNM-composite membranes. By combining CNMs with a polymer support with micron-sized pores the CNM-composite membrane can be produced without the delicate process of transferring the active layer (CNM) from the original growth substrate to a porous support.

Measuring the mechanical properties of nanometer-thick membranes, in contrast to macro-materials, is a difficult undertaking. To perform such demanding analysis, the membranes were suspended over patterned substrates and their intrinsic mechanical properties were quantified using Atomic Force Microscopy (AFM). The mechanical properties of the polymer substrates and composite membrane were studied using a Deben^{TM} micro-test tensile. Performing such mechanical tests, the influence of substrate thickness and porosity was determined. Finally, Thermogravimetric Analysis was used to investigate the behavior of composite membranes at high temperatures (TGA).

2. METHODOLOGY

CNMs and CNM-composite membranes were produced by CNM Technologies in Bielefeld, Germany. Three types of samples were used: **a) CNM (NBPS)** [2]: a self-assembled monolayer of [3-([4'-Nitro-1,1'-biphenyl]-4-yloxy)-propyl]-phosphonic acid (NBPS) was prepared on an aluminised polyethylene terephtalathe (PET) film by immersion of the substrate into a solution of the precursor molecule in technical ethanol. The molecular layer was crosslinked by irradiation with low energy (100 eV) electrons with an electron dose density of 50 mC/cm². The CNM/Al/PET was then protected by a spin-coated layer of polymethylmethacrylate (PMMA). After the production of sandwiched structure of PMMA/CNM/Al/PET, a transfer process was performed to lay CNMs on flat or perforated substrates. A lab scissor is used to cut the samples into 1 cm^2

squares. Then, an etching procedure is carried out at a temperature of 80 °C in an aqueous solution of 20 wt % NaOH. The etchant intercalates after a few minutes, and the Al substrate begins to dissolve. The PET support is separated when the Al layer has completely disintegrated, and the PMMA/CNM composite is left floating on the solution's surface. The NaOH solution is then replaced with three times deionized water, and the item is washed numerous times. Finally, the composite is "fished out" by the substrate of choice and dried overnight in a nitrogen atmosphere. Afterwards, the sample is soaked twice in an acetone bath for 10 minutes each time to remove the PMMA coating, then dried overnight. SiO_2/Si, quartz glass slide, and Si_3N_4 perforated with 0.8 µm holes were used as substrates in our research. **b) CNM-composite membranes:** they were made by casting and crosslinking a molecular thin layer of NBPS precursor molecules on an ion-beamed PET-film with subsequent one-sided etching of the ion-tracks into open pores. Since the CNM on top acts as an etch-stop, the track-etched pores in the PET-support are covered with a free-standing CNM [3]. **c) NBPS/PET-CNM:** By complete etching other PET-support, it is possible to release the active CNM layer and handle it as a freestanding layer (after a transfer equivalent to that described above).

All AFM measurements were carried out in a noise isolation chamber under ambient settings using a Bruker Dimension Icon. Silicon TESPA-V2 probes (R=8nm, k=37N/m, f=320kHz) were employed for topographic imaging using PeakForce-Quantitative nano-Mechanical (PF-QnM). To gain a clearer representation of the finer sample features, the forces were kept as low as possible. In addition to the topography, nanomechanical data was collected and correlated. The tip was calibrated for deflection sensitivity on a sapphire standard for quantitative nanomechanical characteristics, and the Sader method was employed for spring constant [4]. For non-contact imaging of the suspended membranes, the same probes were employed.

Tensile mechanical studies were carried out in a Deben™ micro-test tensile stage to investigate the mechanical behavior of substrates and composite membranes. The stage was built specifically for determining the mechanical properties of thin films. It has a 250 N load cell, allowing great sensitivity on samples with minimal force demands. Samples were cut into 30 mm × 2 mm strips and evaluated at a displacement rate of 1.5 mm/min for each sample. Force-displacement pair data were continually recorded throughout the test, and stress-strain curves were generated from their analysis.

3. RESULTS AND DISCUSSION

A transfer from the sandwiched structure to a SiO_2/Si substrate was required to analyze the various produced CNMs for topographic characteristics and inherent mechanical properties. An atomically flat surface is critical for the best potential results on the intrinsic properties of ultrathin films like CNMs. Both contact and tapping modes were used to collect topography, and the findings were in good agreement.

For mechanical measurements, it's critical to choose a tip that can generate enough sample deformation while maintaining high force sensitivity. Furthermore, the tip has to be calibrated for deflection sensitivity on a sapphire reference sample and spring constant using the Sader method [4] in order to obtain quantitative data. The maximal force was chosen to ensure that any deformations that occurred throughout the scan were completely elastic. **Figure 1** shows topographical data as well as mappings of mechanical characteristics of CNM (NBPS) transferred to a SiO_2/Si surface for a random region. With an approximate roughness of 0.5 nm, the topography and mechanical properties of transferred CNMs show excellent homogeneity. The energy dissipation for the CNM is low because the experiments were done in the elastic regime. PMMA residues from the transfer process were visible in all obtained channels and could be differentiated from the CNM by their nano-mechanical properties. The adhesion force between the tip and the sample was estimated to be around 10 nN, while the Young's modulus was ~8 GPa.

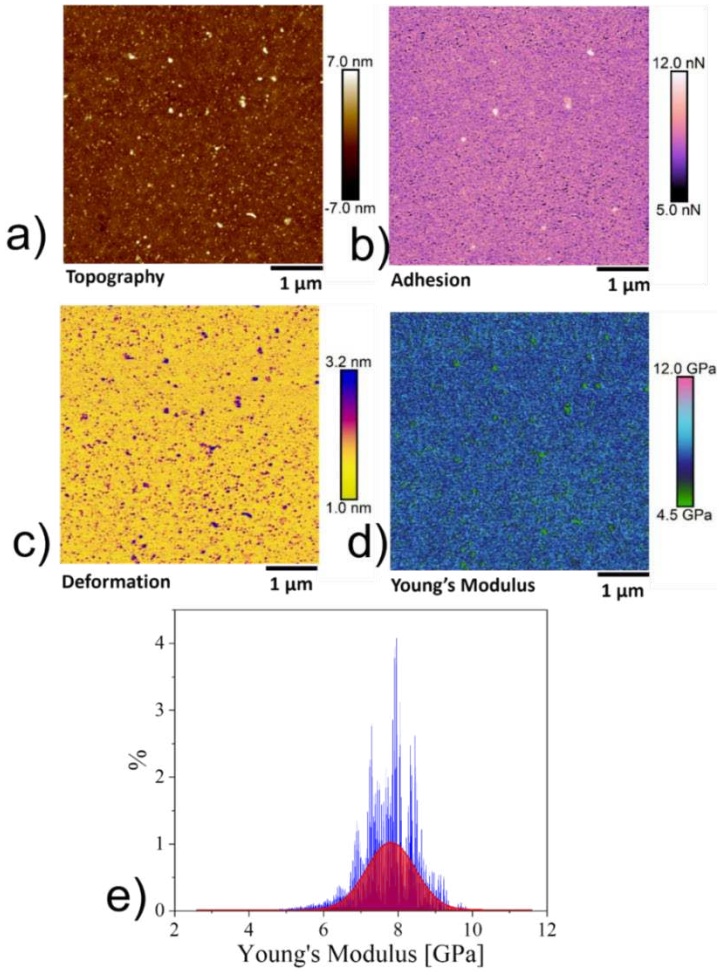

Figure 1: Representative area of CNM (NBPS) with its respective nano-mechanical properties. The images display mappings of (a) Topography, (b) adhesion, (c) deformation and (d) Young's modulus. The white dots on the topography denote PMMA residues from the transfer of the membrane on the SiO2/Si substrate. (e) Histogram of the point-by-point analysis for the Young's modulus mapping.

In order to measure the mechanical characteristics of the ultrathin active CNM-layer of a CNM-composite membranes, which is critical for pressure-driven membrane applications, they were transferred to normal patterned Si_3N_4 substrates with 0.8 µm diameter holes (NBPS/PET-CNM). This allowed for membranes to be suspended, which could then be used to acquire the suspended material's intrinsic mechanical properties without the need for a substrate. Surface forces, such as van der Waals interactions between the substrate surface and the supported membrane, induce thin films to adhere to the inner walls of the supporting substrate after thin membranes are suspended on a substrate (**Figure 2a**).

The outer ring of the suspended material exhibits a change in mechanical properties, as shown by the mappings (**Figure 2**). This change tends to impart unequal tension on the suspended membrane, resulting in a fluctuation in mechanical characteristics within the "drum." More particular, in the top-right region, the tip-sample adhesion is lower, indicating that the material is not well attached to the substrate walls. As can be seen from the profile distribution inside the hole, this difference in adhesion results in a difference in the suspended membrane's Young's modulus. This is also supported by the deformation channel, which shows greater values along the hole's edge, indicating that it is simpler to distort for the same force. This unequal load distribution and the reduction of mechanical characteristics is problematic for membrane applications because they can act as failure spots. As a result, it's clear that transfer processes have an impact on the system's mechanical properties. Outside of the hole, the CNM's mechanical performance is quite homogeneous, as one would expect given the excellent contact and adhesion between the flat Si_3N_4 and the membrane. Young's modulus values extracted for CNM/PET-CNM were 2.5-3 GPa.

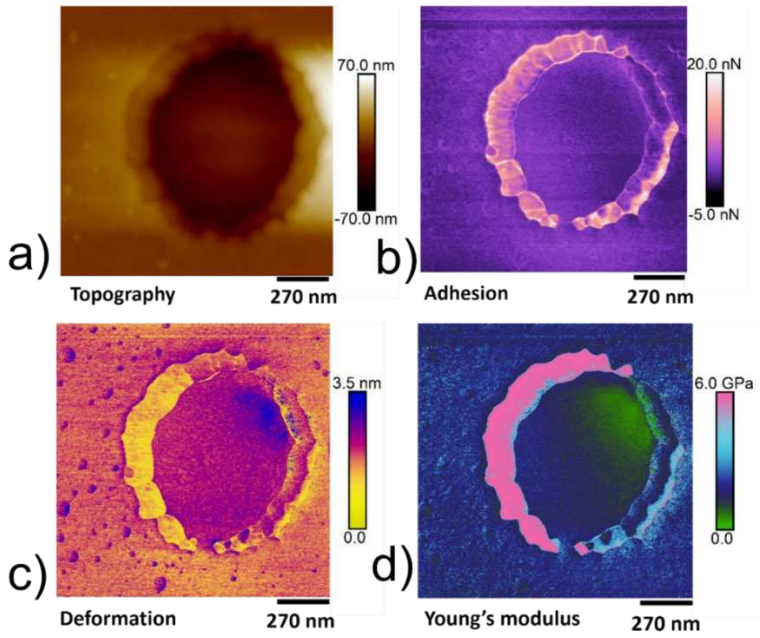

Figure 2: Representative mechanical properties of suspended CNM (NBPS/PET-CNM). Mappings of (a) Topography, (b) adhesion, (c) deformation and (d) Young's modulus.

Finally, the mechanical characteristics of CNM-composite membranes were examined, taking in account the etching time, the pores sizes and density. For the various parameters investigated, the composites are labeled 01, 02, and 03 (A to C). **Table 1** shows the composites' detailed features. **Figure 3** present the stress-strain curves for each sample family, as well as the effect of etching duration on mechanical performance. The engineering values taken from the curves are given in **Table 2**.

Table 1: Characteristics of the prepared CNM-composite membranes. Etching time was 10 minutes for A samples, 8 minutes for B samples and 0 minutes for C samples.

Sample	Etching time (min)	Thickness (µm)	Pore density (cm^{-2})
01A	10	36	20E+6
01B	8	36	20E+6
01C	0	36	20E+6
02A	10	23	20E+6
02B	8	23	20E+6
02C	0	23	20E+6
03A	10	23	1.5E+6
03B	8	23	1.5E+6
03C	0	23	1.5E+6

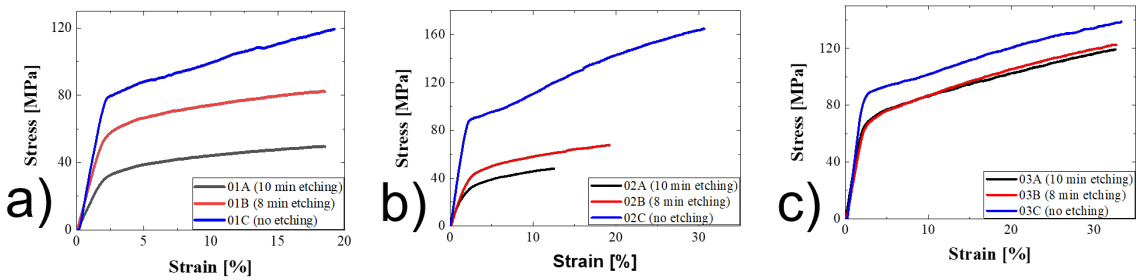

Figure 3: Characteristic stress-strain behavior of (a) 01, (b) 02 and (c) 03 sample series.

Table 2: Extracted engineering values from the stress-strain curves.

Sample	Young's modulus (GPa)	Ultimate strength (MPa)	Strain (%)
01A	2.1 ± 0.3	55 ± 8	16.3 ± 2.0
01B	3.2 ± 0.6	83 ± 9	17.6 ± 2.5
01C	4.5 ± 0.4	119 ± 11	19.2 ± 2.7
02A	1.7 ± 0.3	46 ± 4	12.0 ± 2.0
02B	2.1 ± 0.3	62 ± 12	19.3 ± 0.5
02C	5.2 ± 0.7	159 ± 14	30.1 ± 1.5
03A	3.5 ± 0.3	121 ± 8	32.6 ± 2.5
03B	3.6 ± 0.7	123 ± 3	33.0 ± 1.7
03C	4.8 ± 0.2	141 ± 12	35.1 ± 2.8

All three-sample series, as shown in **Figure 3**, shows the characteristic tensile behavior of polymers, i.e., elastic behavior for small strains with lengthy plastic deformations for larger strains. The range of engineering values observed is comparable to those of a normal PET sample (100 MPa strength, 3.5 GPa Young's modulus, and 20% maximum strain). Unetched specimens (C type samples) have values that are extremely comparable to virgin PET, while pores have no negative impact on mechanical properties. On the other hand, substrate etching has a negative impact on mechanical performance since it reduces the tensile characteristics of the etched samples. In fact, longer etching times result in a more pronounced loss of characteristics. The above findings prove the mechanical potential of using composite CNM/PET membranes in demanding water separation applications.

ACKNOWLEDGEMENTS

This project has received funding from the European Union's Horizon 2020 research and innovation programme under grant agreement No 899528.

REFERENCES

1. Turchanin, A. & Golzhauser, A. (2016). *Advanced Materials*. 28 (29): 6075-6103.
2. *METHOD FOR MANUFACTURING OF A CARBON NANOMEMBRANE, EP 3 368 197 B1, European Patent Office*
3. *CARBON NANOMEMBRANES ON POROUS MATERIALS, WO2019228956A9, World intellectual property organization*
4. Sader, J.E., Chon, J.W.M. & Mulvaney, P. (1999). *Review of Scientific Instruments*. 70 (10): 3967-3969.

INTENSE PULSED LIGHT WELDING PROCESS WITH SIMULTANEOUS MECHANICAL ROLL-PRESSING FOR HIGHLY CONDUCTIVE SILVER NANOWIRE/POLYETHYLENE TEREPHTHALATE COMPOSITE ELECTRODE

Young-Min Ju[a], Jong-Whi Park[a], Simon S. Park[b] and Hak-Sung Kim[a, c]

a: Department of Mechanical Convergence Engineering, Hanyang University, 222, Wangsimni-ro, Seongdong-gu, Seoul, Republic of Korea – zenicmin1111@gmail.com
b: Department of Mechanical and Manufacturing Engineering, University of Calgary, Calgary, AB T2N 1N4, Canada
c: Institute of Nano Science and Technology, Hanyang University, 222, Wangsimni-ro, Seongdong-gu, Seoul, Republic of Korea

Abstract: *In this study, an intense pulsed light (IPL) welding process and mechanical roll-pressing method were employed to enhancing performance for the silver nanowire/polyethylene terephthalate (AgNW/PET) composite electrode. The conditions of two processes were optimized to maximize welding and embedding of AgNWs. Scanning electron microscope (SEM) analysis was conducted to investigate the welded and embedded AgNW network. The surface roughness of AgNW/PET composites were observed and evaluated using atomic force microscope (AFM). The optical properties (transmittance and haze) of AgNW/PET composites were measured by UV-vis spectrometer. The AgNW composite electrode with IPL irradiation and roll-pressing showed a high electrical conductivity, high transmittance, and a reduced surface roughness. Finally, heating film based on AgNW/PET composite electrode was successfully operated showing stable performance.*

Keywords: transparent conductive composite; surface roughness; flexible; silver nanowire;

1. Introduction

Due to excellent optical performance (Transmittance > 90%) and electrical performance (sheet resistance (< 20 $\Omega \cdot sq^{-1}$), Indium tin oxide (ITO) has been used widely for transparent conducting electrodes (TCEs) material[1]. Although ITO have such performance for optoelectronic application, ITO has limiations such as high temeperature conditions, high cost, and brittleness. In those limitation, the brittle charateristic of ITO was critical issue for flexible transparent conducting electrode (FTECs)[2]. To overcome such problems, various materials such as graphene[3], carbon nanotube[4], metal grid[5, 6] and nanowires[7] for FTCEs have been applied. Among these materials, the silver nanowire (AgNW) was attracted attention as apporpiate candidate for FTCEs because it has excellent optical, electrical, and mechanical properties than other matal materials[8]. However, the conductivity of AgNW-based composite electrodes were degraded by contact resistance between nanowire junctions. In addition, the high surface roughness due to nanowire junction cause the electrical short in nano-scale electronic devices. Thus, the junction of AgNWs needs to be reduced by the effective welding process.

To weld the junction of AgNWs, various welding process such as thermal annealing[9], a mechanical pressing[10], and plasmonic welding[11] have been studied. Normally, thermal

  doi:10.5075/epfl-298799_978-2-9701614-0-0

annealing process for polymer-based composite electrode was inappropriate because of their low glass transition temperature (terephthalate, Tg: 80 – 110 ℃)[12]. In case of mechanical pressing method, it requires high pressure conditions to weld and embed AgNWs effectively. Such harsh processes, the AgNW/polymer-based composite electrode can be damaged by excessive heat and pressure. Thus, welding process should be applied at low temperature and pressure to minimize the damage. As an alternative to the conventional welding processes, the intense pulsed light (IPL) welding process was suggested as an effective welding process for the junction of AgNWs[13]. The IPL welding process can weld and embed the junction of AgNWs without any damage in substrate because of the short process time. Many researchers have been reported that the conductivity of AgNW composite electrode could be enhanced by IPL irradiation[14]. However, the surface roughness of AgNWs was not prominently reduced. Therefore, the advanced process to minimize the surface roughness of the AgNW FTCEs has been required.

In this study, we propose a novel approach to weld and embed AgNWs by combining the IPL welding process and mechanical roll-pressing. Such two processes conditions were optimized to weld the junction of AgNWs effectively and embed the AgNWs into the PET substrate. The sheet resistance of AgNW composite electrode was measured by a four-probe method and their surface morphologies were characterized by scanning electron microscopy (SEM) and atomic forced microscopy (AFM).

2. Experiment section

2.1 The IPL welding process for AgNW composite electrode

The AgNW (Diameter: 20 $\pm$ 5 nm, Length: 30 $\pm$ 5 nm) dispersed in D.I water (0.1 wt%) was coated on the polyethylene terephthalate (PET) film (Thickness: 40 um) by bar-coating method. After coating process, the AgNWs were dried by NIR (Near-Infrared Radiation) lamp at a power of 40 W for 300 s. The AgNWs were welded by IPL welding process at room temperature under ambient conditions. The xenon lamp from IPL system emits the intense pulsed light which had a visible wavelengths range (350 nm – 950 nm). In this process, the IPL irradiation energy was used at 5 to 9 J/cm^2. The pulse duration (10 ms) and pulse number (1 pulse) were fixed in such IPL welding process.

2.2 The IPL irradiation with simultaneous mechanical roll-pressing

The schematic diagram of the IPL irradiation with the mechanical roll-pressing were shown in Figure 1. The AgNW composite electrode on the quartz plate was irradiated by intense pulsed light from xenon ramp and was roll-pressed by steel-roller simultaneously. During one pulse irradiation, the entire PET side of AgNW composite electrode was pressed by steel-roller moving at a constant speed (60 mm/s). The conditions of IPL irradiation with the mechanical roll-pressing were divided according to number of irradiation and roll-pressing. The specific conditions of two method were shown in Table 1.

  doi:10.5075/epfl-298799_978-2-9701614-0-0

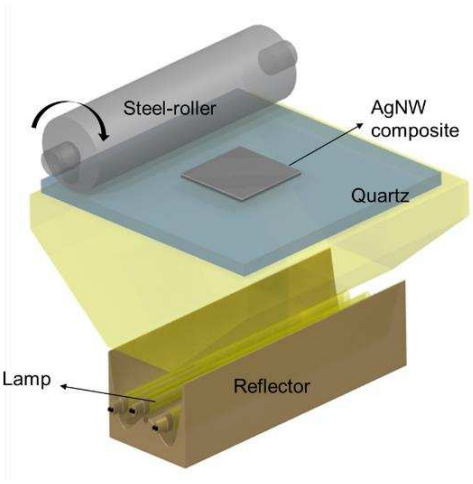

Figure 1. The schematic diagram of IPL irradiation with simultaneous mechanical roll-pressing

Table 1: The conditions of the IPL irradiation with mechanical roll-pressing

Case	IPL pulses [counts]	Irradiation energy per pulse [J/cm^2]	Number of roll-pressing [counts]
1	1	7	1
2	2	3.5	2
3	3	2.33	3
4	4	1.75	4

2.3 Characterization

The four-point probes method was used to measure the sheet-resistance of AgNW composite electrode. The surface morphology of AgNW composite electrode was observed using a scanning electron microscope (SEM, S4800; HITACHI). The surface roughness of AgNW composite electrode was measure by atomic force microscope (AFM, XE-100; Park systems).

3. Result and discussion

3.1 The IPL welding of AgNW composite electrode

The sheet resistance of the AgNW composite electrode respect to various IPL irradiation energies (5 J/cm^2 - 9 J/cm^2) were shown in Figure 2. As shown in Figure 2, the sheet resistance of the AgNW composite electrode before IPL irradiation was 50 Ω/sq. The sheet resistance of AgNW composite electrode decreased as the IPL irradiation energy increased from 5 J /cm^2 to 7 J/cm^2 because AgNWs were welded and the polymer binder was evaporated by generated heat.[14] The lowest sheet resistance was measured at an IPL irradiation energy of 7 J/cm^2. As shown in Figure 3(b), it is obvious that the AgNW network were more welded and embeded than before the IPL irradiation (Figure 3(a)). However, the AgNW network were not fully welded and embedded despite IPL irradiation. The sheet resistance of the AgNW composite electrode was increased at high IPL irradiation energies (8 – 9 J/cm^2). Such results indicated that excessive IPL irradiation energy cause to damage in AgNW and PET. Figure 3(c) shows cracking of AgNWs and

  doi:10.5075/epfl-298799_978-2-9701614-0-0

melting of PET substate by high IPL irradiation energy (9 J/cm^2). From these results, only IPL welding process for AgNW composite electrode was not enough to weld and embed the AgNW network to the PET substrate completely. Therefore, the advanced process must be applied to welding and embedding of AgNWs to improve its electrical and mechanical performance effectively.

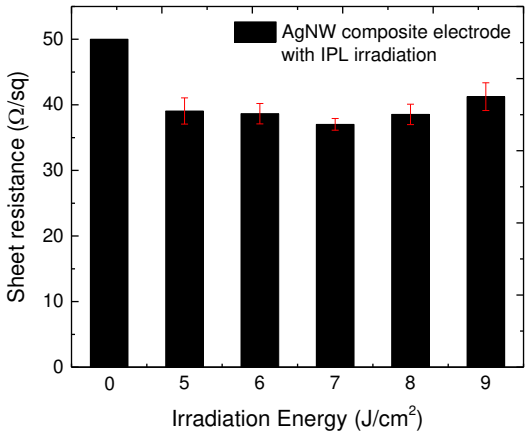

Figure 2. The sheet resistance of the AgNW composite electrode with IPL irradiation according to IPL irradiation energies.

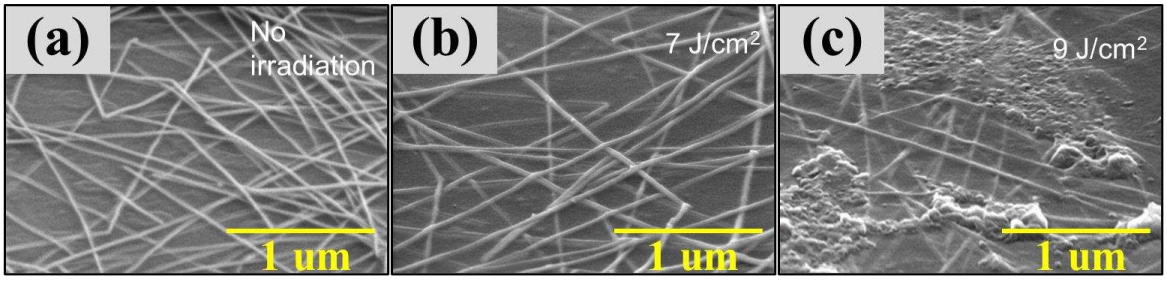

Figure 3. The SEM image of the AgNW composite electrode with various IPL irradiation energies: (a) No irradiation, (b) 7 J/cm^2, and (c) 9 J/cm^2

3.2 The IPL irradiation with simultaneous roll-pressing for AgNW composite electrode

In this study, the IPL irradiation and the roll-pressing method were conducted to improve electrical and mechanical performance of AgNW composite electrode. Photo-induced heat is generated at AgNWs junction due to surface plasmon resonance when IPL is irradiated on AgNW composite electrode[15]. The generated heat melted the AgNWs junction and immediately softened the PET substrate for a few milliseconds. In these states, the AgNWs might be easily welded and embedded into PET substrate assisted by mechanical pressure. To maximize the synergistic effect of IPL irradiation and roll pressing, two processes were simultaneously applied as shown in Figure 1.

As shown in Figure 4(a), the sheet resistance of AgNW composite electrode treated by IPL irradiation with simultaneous roll-pressing was observed. It is noteworthy that the sheet resistance of AgNW composite electrode was meaningfully decreased compared to the IPL welded AgNW composite electrode. Specifically, the sheet resistances of AgNW composite

electrode after IPL irradiation with simultaneous roll-press were 33.0 Ω/sq (Case 1), 28.3 Ω/sq (Case 2), 23.9 Ω/sq (Case 3), and 30.2 Ω/sq (Case 4), respectively. From these results, the IPL irradiation with mechanical roll-pressing could enhance the electrical properties effectively. The surface morphology of AgNW composite electrode after IPL irradiation with mechanical roll-pressing was shown in Figure 4(b). The junctions of AgNWs were fully welded and embedded into PET substrate, formed a continuous pathway for electric carriers. Thus, the sheet resistance of AgNW composite could be reduced dramatically compared IPL welding process.

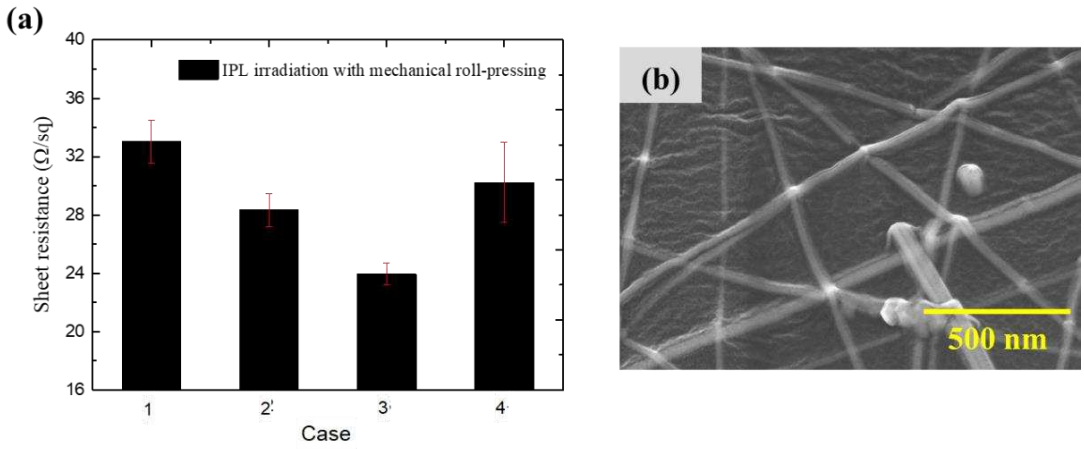

Figure 4. (a) The sheet resistance of the AgNW composite electrode with IPL irradiation with mechanical roll-pressing, (b) The SEM image of AgNW with simultaneous IPL irradiation and roll-pressing (Case 3)

3.3 The analysis of surface roughness of AgNW composite electrode

To investigate embedding of AgNWs, the surface roughness of AgNW composite was measured and analyzed using AFM analysis. Figure 5 showed the AFM images of AgNW composite electrode after IPL irradiation and IPL irradiation with simultaneous roll-pressing, respectively. As shown Figure 5(a), the maximum surface roughness of AgNW composite with IPL irradiation was similar to twice the diameter of the AgNW. It was found that the embedding of AgNWs is insignificant even though the AgNW were irradiated by IPL. On the other hand, the surface roughness of AgNW composite electrode with IPL irradiation and mechanical roll-pressing simultaneously was almost identical to the dimeter of the AgNW (See Figure 5(b)). Again, it was because the junction of AgNWs could be fully welded and embedded into PET synergetic effect of the plasmonic local heating with simultaneous mechanical pressing.

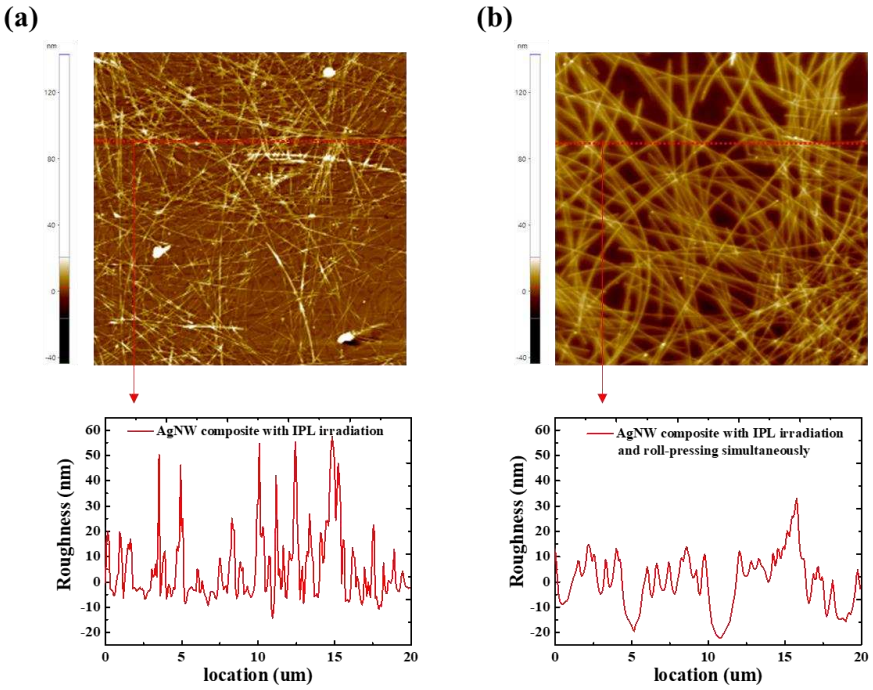

Figure 5. The AFM image and line profile of AgNW composite electrode according to (a) IPL welding process and (b) IPL irradiation with mechanical roll-pressing

4. Conclusion

In this work, a highly conductive, and smooth surface AgNW composite electrode were fabricated by IPL irradiation with simultaneous mechanical roll-pressing. Due to synergetic welding and embedding of AgNWs with plasmonic local heating and mechanical roll pressure, the sheet resistance of AgNW composite electrode could be decreased dramatically compared to AgNW composite electrode with no irradiation. In addition, the surface roughness was also reduced effectively due to fully welding and embedding of AgNW network.

Acknowledgements

This research was supported by the MOTIE (Ministry of Trade, Industry, and Energy) in Korea, under the Fostering Global Talents for Innovative Growth Program (P0008748, Global Human Resource Development for Innovative Design in Robot and Engineering) supervised by the Korea Institute for Advancement of Technology (KIAT). This work was supported by Korea Institute of Energy Technology Evaluation and Planning(KETEP) grant funded by the Korea government(MOTIE)(20212020800090, Development and Demonstration of Energy-Efficiency Enhanced Technology for Temperature-Controlled Transportation and Logistics Center). This work was supported by Korea Institute of Energy Technology Evaluation and Planning(KETEP) grant funded by the Korea government(MOTIE)(20202020800360, Innovative Energy Remodeling Total Technologies(M&V, Design, Package Solutions, and Testing & Verifications Technologies) for the Aging Public Buildings)

References

1. Gulen M, Yildirim G, Bal S, Varilci A, Belenli I, Oz M. Role of annealing temperature on microstructural and electro-optical properties of ITO films produced by sputtering. Journal of Materials Science: Materials in Electronics. 2013;24(2):467-74.
2. Sierros KA, Morris NJ, Ramji K, Cairns DR. Stress–corrosion cracking of indium tin oxide coated polyethylene terephthalate for flexible optoelectronic devices. Thin Solid Films. 2009;517(8):2590-5.
3. Han T-H, Kim H, Kwon S-J, Lee T-W. Graphene-based flexible electronic devices. Materials Science and Engineering: R: Reports. 2017;118:1-43.
4. Bradley K, Gabriel J-CP, Grüner G. Flexible nanotube electronics. Nano Letters. 2003;3(10):1353-5.
5. Yi F-S, Bi Y-G, Zhang X-L, Yin D, Liu Y-F, Feng J, et al. Highly flexible and mechanically robust ultrathin Au grid as electrodes for flexible organic light-emitting devices. IEEE Transactions on Nanotechnology. 2019;18:776-80.
6. Xu J-L, Liu Y-H, Gao X, Sun Y, Shen S, Cai X, et al. Embedded Ag grid electrodes as current collector for ultraflexible transparent solid-state supercapacitor. ACS Applied Materials & Interfaces. 2017;9(33):27649-56.
7. Im H-G, Jin J, Ko J-H, Lee J, Lee J-Y, Bae B-S. Flexible transparent conducting composite films using a monolithically embedded AgNW electrode with robust performance stability. Nanoscale. 2014;6(2):711-5.
8. Kwon J, Suh YD, Lee J, Lee P, Han S, Hong S, et al. Recent progress in silver nanowire based flexible/wearable optoelectronics. Journal of Materials Chemistry C. 2018;6(28):7445-61.
9. Lagrange M, Langley D, Giusti G, Jiménez C, Bréchet Y, Bellet D. Optimization of silver nanowire-based transparent electrodes: effects of density, size and thermal annealing. Nanoscale. 2015;7(41):17410-23.
10. Tokuno T, Nogi M, Karakawa M, Jiu J, Nge TT, Aso Y, et al. Fabrication of silver nanowire transparent electrodes at room temperature. Nano research. 2011;4(12):1215-22.
11. Wan H, Gui C, Chen D, Miao J, Zhao Q, Luan S, et al. Scattering force and heating effect in laser-induced plasmonic welding of silver nanowire junctions. Applied Optics. 2020;59(7):2186-91.
12. Alves N, Mano JF, Balaguer E, Dueñas JM, Ribelles JG. Glass transition and structural relaxation in semi-crystalline poly (ethylene terephthalate): a DSC study. Polymer. 2002;43(15):4111-22.
13. Jang Y-R, Chung W-H, Hwang Y-T, Hwang H-J, Kim S-H, Kim H-S. Selective wavelength plasmonic flash light welding of silver nanowires for transparent electrodes with high conductivity. ACS applied materials & interfaces. 2018;10(28):24099-107.
14. Jang Y-R, Joo S-J, Chu J-H, Uhm H-J, Park J-W, Ryu C-H, et al. A review on intense pulsed light sintering technologies for conductive electrodes in printed electronics. International Journal of Precision Engineering and Manufacturing-Green Technology. 2021;8(1):327-63.
15. Chung W-H, Jang Y-R, Hwang Y-T, Kim S-H, Kim H-S. The surface plasmonic welding of silver nanowires via intense pulsed light irradiation combined with NIR for flexible transparent conductive films. Nanoscale. 2020;12(34):17725-37.

  doi:10.5075/epfl-298799_978-2-9701614-0-0

SURFACE FUNCTIONALIZATION OF QUARTZ FIBRES BY DIRECT GROWTH OF CARBON NANOSTRUCTURES

Ginevra, Lalle[a], Matteo, Lilli[a], Luiz H., Acauan[b], Brian L., Wardle[b,c], Ilaria, Rago[d-e], Gianluca, Cavoto[d-e], Francesco, Pandolfi[e], Fabrizio, Sarasini[a], Jacopo, Tirillò[a]

a: Department of Chemical Engineering Materials Environment, Sapienza-Università di Roma, Via Eudossiana 18, 00184, Roma, Italy– ginevra.lalle@uniroma1.it
b: Department of Aeronautics and Astronautics, Massachusetts Institute of Technology, 77 Massachusetts Ave., Cambridge, MA, 02139, USA
c: Department of Mechanical Engineering, Massachusetts Institute of Technology, 77 Massachusetts Ave., Cambridge, MA, 02139, USA
d: Dipartimento di Fisica 'Sapienza' Università di Roma and INFN Sezione di Roma, Piazzale Aldo Moro 2, 00185, Rome, Italy
e: INFN Sezione di Roma, Piazzale Aldo Moro 2, 00185, Rome, Italy

Abstract: *The aim of the present work is to investigate the direct growth of carbon nanostructures (CNSs) onto quartz fibres to improve interfacial properties in polymer composites. Mechanical properties of quartz fibres are known to be reduced due to exposure to typical conditions (primarily temperature) for CNS growth, e.g., herein quartz fibres at 600 °C for 1h in air give a strength loss of 58%. Cu as a novel low-temperature (<500 °C) catalyst is explored as an alternative to the more typical Fe which requires temperatures higher than 600 °C. As part of a larger study, Cu- and Fe-catalysed CNS growth on quartz fibres are shown at high temperature (740 °C). Weibull analysis of the tensile data, FE-SEM investigation and X-ray diffraction analysis were carried out to identify possible damage mechanisms in the exemplary heat-treated fibres, setting up additional work to compare results at lower-temperature CNS growth known to be achievable with copper.*

Keywords: Quartz fibres; Chemical vapour deposition (CVD); Carbon nanostructures; Interface/Interphase

1. Introduction

Grafting carbon nanostructures (CNSs) onto the surface of microscale reinforcing fibres improves the structural performance of fibre-reinforced polymers (FRPs) by enhancing fibre/matrix interfacial adhesion and matrix-dominated properties [1]. Moreover, due to the unique properties of CNSs, their incorporation into composite materials offers the opportunity to implement additional electrical, chemical, or thermal functions.

Among the techniques reported to graft CNSs onto the fibre surface, direct growth through chemical vapour deposition (CVD) is often preferred as it ensures excellent control over the density and orientation of CNSs [2]. Direct CNS growth has been explored on various fibre materials, including carbon, glass, and alumina fibres. However, depending on the substrate, the high temperatures involved in the CVD process (≥600 °C) may have detrimental effects on the mechanical properties of the fibres. The most severe thermal degradation is observed in the case of E-glass fibres, which exhibit appreciable strength losses at temperatures as low as 250 °C [3]. Quartz fibres, also known as ultrapure silica glass fibres, are designed to withstand service temperatures much higher than E- or S-glass fibres. Therefore, they are emerging as a promising

  doi:10.5075/epfl-298799_978-2-9701614-0-0

candidate for the direct growth of CNSs. Recently, De Luca et al. [4] achieved uniform coverage of carbon nanotubes (CNTs) on quartz fibres resulting in both a 12% improvement of IFSS and a piezo-resistive response suitable for strain-sensing applications. Nevertheless, they detected a 50% decrease of the tensile strength of the fibres exposed to 760 °C for 30 minutes in N_2. A significant drop of quartz fibre tensile strength was also reported by Zheng et al. [5] after 10-hour exposure in the temperature range 600-900 °C in air atmosphere. However, whilst the thermal strength loss of general-purpose glass fibres has been widely investigated, mechanisms behind quartz fibre strength loss still need to be clarified.

To preserve the mechanical properties of the pristine fibres, a new catalyst, namely copper, can be employed to reduce CNS growth temperature, as it requires lower temperatures to be activated (<500 °C) [6] than the more common catalysts based on Fe, Ni and Co. This work is part of a larger study aiming at (i) assessing the effects of thermal exposure to medium-high temperatures (400-800 °C) on the mechanical properties of quartz fibres and discussing the resulting damage modes, and (ii) achieving low-temperature CVD growth of CNSs on quartz fibres using Cu as an innovative catalyst. In particular, this paper discusses at first the behaviour of quartz fibres exposed for 1h at 600 °C in air as a benchmark for highlighting the decrease in mechanical properties and then reports on Cu- and Fe-catalysed CNS growth at high temperature (740 °C), as a preliminary research aimed at achieving lower-temperature CNS growth by means of future optimization of the process parameters. It is worth noting that thermal exposure in air usually represents the worst scenario for fibre degradation compared to inert atmospheres [3].

2. Materials and methods

2.1 Raw materials

Quartz fibres (Quartzel® C14 1600 QS1318) with a commercial epoxy resin compatible sizing were kindly provided by Saint-Gobain as a continuous roving with a nominal fibre diameter of 14 µm. Catalyst precursors for the CVD process were iron (III) nitrate nonahydrate ($Fe(NO_3)_3 \cdot 9H_2O$, ≥98%) and copper(II) acetate monohydrate ($Cu(CH_3COO)_2 \cdot H_2O$, ≥98%). Such precursors were dissolved in 2-propanol ($(CH_3)_2CHOH$, ≥99.5%) and acetonitrile (C_2H_3N, ≥99%), respectively.

2.2 Mechanical characterization of single fibres

A tube furnace (Lenton Thermal Designs Ltd., Hope, UK) was used to heat treat bundles of as-received quartz fibres at 600 °C for 1 hour in air atmosphere. Cooling of the fibres was carried out outside the furnace at room temperature. After the heat treatment, tensile tests were conducted at room temperature on both as-received and heat-treated fibres. Tests were carried out in accordance with ASTM C1557, using a Zwick/Roell Z010 tensile machine equipped with a 100 N range load cell. Displacement control and a cross-head speed of 2 mm/min were selected. At least 60 specimens with a gauge length of 20 mm were tested for each group of fibres. The actual specimen elongation was calculated by subtracting the displacement related to the system compliance from the total cross-head displacement. To evaluate the system compliance, specimens of as-received fibres were tested at three different gauge lengths, i.e., 20 mm, 30 mm, and 40 mm.

The data of the tensile strength and Young's modulus were analysed using the two parameter Weibull distribution in equation (1)

  doi:10.5075/epfl-298799_978-2-9701614-0-0

$$F(\sigma) = 1 - \exp\left[-\left(\frac{\sigma}{\sigma_0}\right)^m\right] \quad (1)$$

where *F(σ)* is the probability of failure at a stress *σ*, *m* is the Weibull modulus and σ_0 is a scale parameter. The probability of failure was estimated according to equation (2):

$$F_j = \frac{j-0.5}{N} \quad (2)$$

where *N* is the number of tested specimens and *j* is the rank of the *j*th data point.

2.3 Growth procedure of carbon nanostructures

Prior to the CVD growth, catalyst precursors were deposited onto the surface of quartz fibres by dip-coating. To achieve the deposition of a Fe-based catalyst precursor, bundles of as-received fibres were dipped into a 50 mM solution of iron(III) nitrate nonahydrate in 2-propanol for 5 minutes. The Cu-based precursor was deposited by dipping into a solution of copper(II) acetate monohydrate in acetonitrile. The molarities (1, 2.5 and 5 mM) and the immersion times (3, 4.5 and 6 h) were varied to find the optimal conditions for uniform CNS growth onto the fibre surface. Both processes were carried out at room temperature. After the deposition process, fibres were allowed to dry at room temperature overnight.

Subsequently, catalyst-solution coated quartz fibres were located on the heating element of a high vacuum reaction chamber to achieve the growth of CNSs through Fe- and Cu-catalysed CVD. To reduce the catalyst precursor and achieve a homogeneous distribution of active nanoparticles on the fibre surface, an annealing treatment was first performed. H_2 was introduced into the chamber up to a partial pressure of $8 \cdot 10^{-1}$ mbar and temperature was raised at 720 °C for 4 minutes. Afterwards, the actual growth process was carried out at 740 °C for 10 minutes by introducing acetylene as a carbon source up to a partial pressure of 60–70 mbar. Finally, the fibres were allowed to cool down to room temperature.

2.4 Morphological and structural characterizations

Morphological investigations of lateral and fracture surfaces of the fibres were carried out by means of a Mira3 field emission scanning electron microscope (FE-SEM) by Tescan. To investigate the effects of high temperature exposure on quartz fibre structure, X-ray diffraction analysis (XRD) was carried out at room temperature on as-received and heat-treated fibres by means of a Philips X'Pert PRO powder diffractometer (Cu_{K1} α radiation = 1.54060 Å, Cu_{K2} α radiation = 1.54443 Å). XRD patterns were collected in the range of 2θ = 10°–70° with a scan rate of 1°/min and a scan step 2θ = 0.02°.

3. Results and Discussion

3.1 Effects of heat treatment on the mechanical properties of quartz fibres

To evaluate the consequences of exposure to typical CVD temperatures on the tensile behaviour of quartz fibres, a heat-treatment at 600 °C for 1 hour in air atmosphere was performed. Afterwards, the tensile strength and Young's modulus of untreated and heat-treated fibres were determined at room temperature by single fibre tensile tests. The results, summarized in Table 1, revealed a strength loss of ∼58% for heat-treated fibres, while Young's modulus did not undergo significant changes, in accordance with a recent work on quartz fibres [4].

  doi:10.5075/epfl-298799_978-2-9701614-0-0

Table 1: Results of tensile tests for as-received (R.T.) and heat-treated single quartz fibres in terms of average value (standard deviation).

Heat-treatment temperature [°C]	Tensile strength [MPa]	Young's modulus [GPa]
R.T.	2379.1 (355.4)	89.0 (3.3)
600	1002.1 (194.9)	84.1 (5.2)

A FE-SEM investigation of the fibre fracture surfaces (Fig. 1) revealed a failure mechanism typical of brittle materials, with a characteristic morphology composed of three different regions, namely mirror, mist, and hackle, originated by changes in the crack propagation rate during breakage. The fracture mechanism did not change for heat-treated fibres, but the size of the mirror zone was found to increase, in accordance with previous works on other ceramic fibres [3,7]. For both untreated and heat-treated fibres, the location of the mirror zone indicated that the flaws responsible for failure were located on the fibre surface.

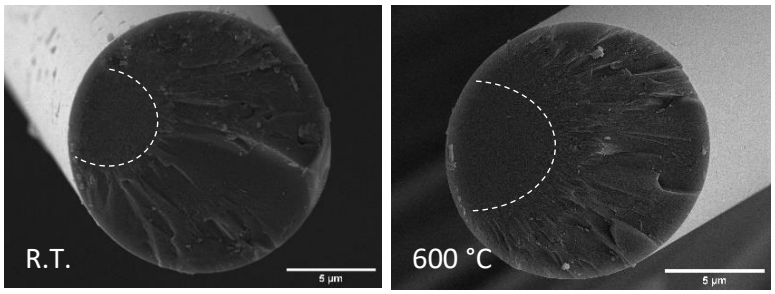

Figure 1. SEM micrographs of the fracture surfaces of as-received (R.T.) and heat treated (600 °C) quartz fibres. The mirror zone is highlighted with a white dashed line.

The outcomes from the tensile tests were analysed through a two-parameter Weibull distribution, obtaining the results reported in Table 2. The linear trend in the Weibull graph in Fig. 2 suggests the existence of a single population of defects and seems to indicate that thermal exposure does not affect the nature of defects, but rather their concentration and severity.

Table 2: Weibull distribution parameters for as-received (R.T.) and heat-treated quartz fibres.

Temperature [°C]	Tensile strength		Young's modulus	
	m_σ	σ_0 [MPa]	m_E	E_0 [GPa]
R.T.	8.0	2526.4	31.1	90.5
600	5.9	1082.7	19.5	86.4

As a confirmation, a morphological characterization of the fibre lateral surfaces (Fig. 3) revealed that, after heat treatment, the smooth morphology observed for as-received quartz fibres is replaced by a more irregular one. This can be ascribed to the total, or at least partial, loss of the protective sizing, which caused the exposure of the inherent fibre flaws, as previously reported

for glass fibres [8]. It is also worth noting that sizing removal directly implies a loss in the fibre/matrix interfacial adhesion of the composite material [9].

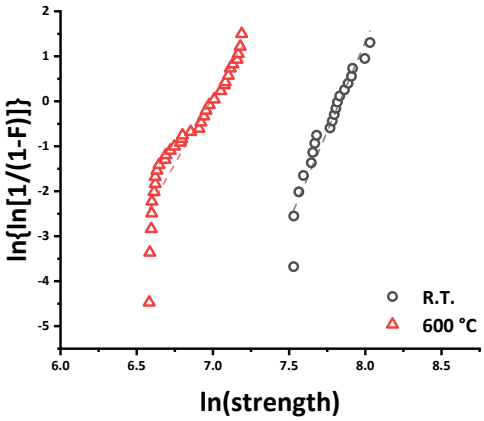

Figure 2. Weibull plot of fibre strength for as-received (R.T.) and heat treated (600 °C) quartz fibres.

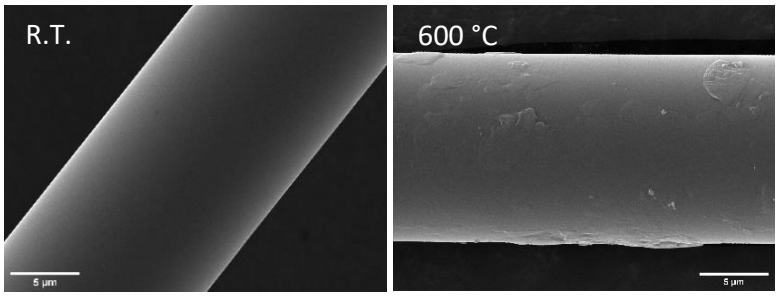

Figure 3. SEM micrographs detailing the lateral surface of as-received (R.T.) and heat treated (600 °C) quartz fibres.

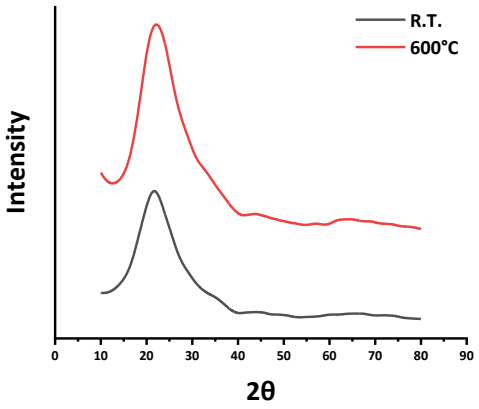

Figure 4. X-ray diffraction patterns for as-received (R.T.) and heat treated (800 °C) quartz fibres.

According to the XRD spectra reported in Fig. 4, the thermal exposure of quartz fibres did not involve crystallization phenomena, as a fully amorphous structure was identified for both as-received and heat-treated quartz fibres.

In the current study, a strength reduction mechanism that occurs predominantly at the surface of quartz fibres was identified. This is consistent with the obtained XRD spectra, which revealed no bulk structural rearrangement. The measured Young's modulus, which was hardly affected

by the heat treatment, confirms the irrelevance of any bulk modification phenomena. On the contrary, Young's modulus has been found to increase for other ceramic fibres, especially general-purpose glass fibres and basalt fibres, due to structural relaxation mechanisms occurring in the bulk of the fibres.

However, it is worth noting that structural relaxation is a phenomenon that occurs faster at the surface than in the bulk of the fibre, as previously reported by Feih et al. [3] for E-glass fibres and demonstrated by Lilli et al. [7] for basalt fibres. Therefore, due to the high drawing stress during quartz fibre fabrication, the occurrence of surface relaxation phenomena cannot be excluded, but detailed investigations are needed.

3.2 CVD growth of carbon nanostructures on quartz fibres

As a baseline for the CVD growth of CNSs onto quartz fibres, a Fe-catalysed CVD process was performed. Highly dense arrays of vertically aligned CNSs were obtained (Fig. 5). CNS diameter was around 40 nm while the length of longer CNS arrays fluctuated from 15 to 80 µm. The organization of CNSs onto the fibre surface followed a 'Mohawk' morphology, previously observed for CNSs grown on other fibres [10]. In fact, when CNS length is larger than the fibre diameter, the radial symmetry is broken and CNSs continue to grow in a common direction due to van der Waals interactions among nearby CNSs.

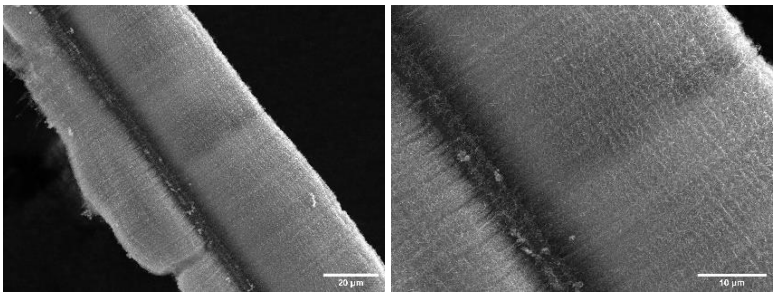

Figure 5. SEM micrographs of CNS-grafted quartz fibres following the Fe-catalysed CVD process.

Temperatures above 700 °C were necessary to achieve the Fe-catalysed growth of carbon nanostructures, in accordance with temperatures usually reported for Fe-catalysed thermal CVD [11,12]. Therefore, to meet the need for a low temperature process, Cu-catalysed thermal CVD growth of CNSs was investigated. Although copper was initially thought to be inactive towards CNS growth, in the last decade many works have demonstrated Cu-catalysed CVD growth of different CNSs, including multi-wall and single-wall CNTs [13,14]. Copper's activity towards the growth of carbon nanofibres has been proved at temperature as low as 250 °C [6], making it a promising option for low temperature CVD.

To assess the possibility to grow CNSs onto quartz fibres using Cu as a catalyst, CVD conditions were left unchanged from those previously found to be effective for Fe-catalysed growth. On the other hand, catalyst deposition conditions were varied in terms of immersion time and concentration of copper(II) acetate monohydrate in acetonitrile. A uniform growth of CNSs was achieved for fibres dipped in a 5 mM solution for 4.5 hours (Fig. 6), confirming the activity of Cu towards CNS growth. Cu-catalysed CVD led to a tangled CNS morphology with a CNS carpet thickness ranging from 2 to 8 µm. Moreover, the obtained CNSs have bigger diameters (~80 nm or more) than those catalysed by Fe.

  doi:10.5075/epfl-298799_978-2-9701614-0-0

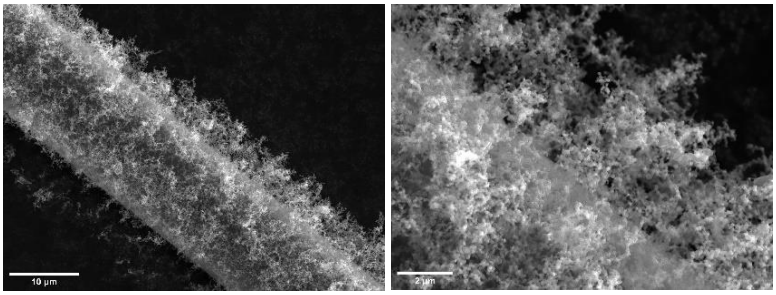

Figure 6. SEM micrographs of CNS-grafted quartz fibres following the Cu-catalysed CVD process.

4. Conclusions

The present work investigates quartz fibres as a candidate substrate for the direct growth of CNSs. The exposure to a typical CVD temperature (600 °C) for 1 hour in air atmosphere caused the strength of quartz fibres to decrease by ∼58%, while no significant changes were detected for Young's modulus. These findings confirmed the higher thermal resistance of quartz fibres compared to E-glass fibres, for which strength losses of more than ∼70% have been reported [8]. On the other hand, they highlighted a significant strength decay, which has been ascribed to damage mechanisms occurring at the fibre surface. To preserve the fibre mechanical properties, a first step towards the development of a low temperature growth has been taken by using an innovative catalyst, namely copper. By varying dip-coating parameters (i.e., immersion time and concentration), optimal catalyst deposition conditions were identified. A Cu-catalysed CNS growth was successfully achieved for fibres dip-coated for 4.5 hours in a 5 mM solution, using the same CVD conditions previously proved to be effective for a Fe-catalysed growth. While the Fe-catalysed CVD led to the growth of dense arrays of aligned CNSs, a tangled morphology of CNSs with bigger diameters was obtained following the Cu-catalysed process. Future work will optimize the CVD parameters of the Cu-catalysed process to control the diameter, density, and orientation of CNSs and achieve a low temperature growth.

Acknowledgements

Luiz H. Acauan and Brian L. Wardle would like to acknowledge Airbus, ANSYS, Boeing, Embraer, Lockheed Martin, Saab AB, and Teijin Carbon America through MIT's Nano-Engineered Composite aerospace STructures (NECST) Consortium.

5. References

1. Qian H, Greenhalgh ES, Shaffer MSP, Bismarck A. Carbon nanotube-based hierarchical composites: A review. Journal of Materials Chemistry 2010; 20(23):4751–62.

2. Sharma P, Pavelyev V, Kumar S, Mishra P, Islam SS, Tripathi N. Analysis on the synthesis of vertically aligned carbon nanotubes: growth mechanism and techniques. Journal of Materials Science: Materials in Electronics 2020; 31:4399–4443.

3. Feih S, Boiocchi E, Mathys G, Mathys Z, Gibson AG, Mouritz AP. Mechanical

properties of thermally-treated and recycled glass fibres. Composites Part B Engineering 2011; 42(3):350–8.

4. De Luca HG, Anthony DB, Greenhalgh ES, Bismarck A, Shaffer MSP. Piezoresistive structural composites reinforced by carbon nanotube-grafted quartz fibres. Composites Science and Technology 2020; 198: 108275.

5. Zheng Y, Wang S. Effect of moderately high temperature heat treatment on surface morphology and structure of quartz fibers. Applied Surface Science 2012; 258(10): 4698–701.

6. Acauan LH, Kaiser AL, Wardle BL. Direct synthesis of carbon nanomaterials via surface activation of bulk copper. Carbon 2021; 177:1–10.

7. Lilli M, Rossi E, Tirillò J, Sarasini F, Di Fausto L, Valente T, et al. Quantitative multi-scale characterization of single basalt fibres: Insights into strength loss mechanisms after thermal conditioning. Material Science & Engineering A 2020; 797:139963.

8. Thomason JL, Yang L, Meier R. The properties of glass fibres after conditioning at composite recycling temperatures. Composites Part A: Applied Science and Manufacturing 2014; 61:201–8.

9. Thomason JL, Nagel U, Yang L, Bryce D. A study of the thermal degradation of glass fibre sizings at composite processing temperatures. Composites Part A: Applied Science and Manufacturing 2019; 121:56–63.

10. Yamamoto N, John Hart A, Garcia EJ, Wicks SS, Duong HM, Slocum AH, et al. High-yield growth and morphology control of aligned carbon nanotubes on ceramic fibers for multifunctional enhancement of structural composites. Carbon 2009; 47(3):551–60.

11. Rago I, Rauti R, Bevilacqua M, Calaresu I, Pozzato A, Cibinel M, et al. Carbon Nanotubes, Directly Grown on Supporting Surfaces, Improve Neuronal Activity in Hippocampal Neuronal Networks. Advanced Biosystems 2019; 3(5):1800286.

12. Ulloa Severino L, Perissinotto F, Rago I, Goldoni A, Santoro R, Pesce M, Casalis L, Scaini D, Carbon nanotubes substrates alleviate pro-calcific evolution in porcine valve interstitial cells. Nanomaterials (Basel) 2021; 11(10): 2724-44.

13. Hsiao CH, Lin JH. Growth of a superhydrophobic multi-walled carbon nanotube forest on quartz using flow-vapor-deposited copper catalysts. Carbon 2017; 124:637–41.

14. Takagi D, Homma Y, Hibino H, Suzuki S, Kobayashi Y. Single-walled carbon nanotube growth from highly activated metal nanoparticles. Nano Lett 2006;6(12):2642–5.

CHARACTERISATION OF GRAPHENE-ENHANCED CARBON-FIBRE/PEEK MANUFACTURED USING SPRAY-DEPOSITION AND LASER-ASSISTED AUTOMATED TAPE PLACEMENT (ATP)

Peter Kreider, Chris Stokes-Griffin, Christopher Leow, Silvano Sommacal, Paul Compston*

ARC Training Centre for Automated Manufacture of Advanced Composites, Australian National University, Canberra, ACT 2600, Australia.

*Corresponding author: peter.kreider@anu.edu.au

Abstract: *The inclusion of nanomaterials within fibre-reinforced polymer composites can enable novel high-performance structures, and graphene is one of the most promising candidate nanomaterials with a unique combination of exceptional mechanical, electrical, and thermal properties. Near-term graphene nanocomposites need to adopt both a scalable nanomaterial synthesis technique and a scalable method to integrate nanomaterials into composites during the manufacturing process. This work explores the spray-deposition of liquid phase exfoliated graphene for the interlaminar enhancement carbon-fibre reinforced polyether ether ketone (PEEK) composites. This approach enables spray-deposited nanomaterial thin films that can be incorporated directly into composites during advanced manufacturing processes such as laser-assisted automated tape placement, which we demonstrate here. Our preliminary investigations suggest that the presence of graphene can enhance the thermal history of the composite during manufacturing in addition to enhancing the properties of the manufactured composite material.*

Keywords: graphene; nanocomposite; laser-assisted automated tape placement

1. Introduction

Nanocomposites, composite materials including one or more components with dimensions on the nanoscale (1–100 nm), have demonstrated great potential to improve upon the already outstanding properties of engineered composites [1]. The combination of fibre reinforcement and high-performance nanomaterials could provide important advantages through increased thermal stability, electrical conductivity, toughness, and strength/stiffness. However, the interaction between the nanomaterials, the polymer matrix, and the reinforcing fibres could also have detrimental effects on the manufacturing process and on composite material properties, especially after traversing the many processing steps during manufacture. The fabrication technology and processing conditions used to manufacture composites can strongly affect material properties and structure on the nanoscale and, as a consequence, manufacturing composites and composite structures with retained nanostructure remains a challenge [1–3]. Traditional thermo-mechanical composite processing such as hot pressing and autoclaving creates an environment conducive to mechanisms like grain growth and aggregation, which have a tendency to eliminate or degrade the beneficial properties associated with nanostructure [2, 4]. Thus, modifications must be made to these manufacturing processes before they are capable of effectively enabling nanomaterial-enabled improvements at the macroscale [2, 4]. Alternatively, non-equilibrium processing techniques such as laser-assisted automated tape

  doi:10.5075/epfl-298799_978-2-9701614-0-0

placement (LATP) are excellent candidates for successful nanocomposite consolidation because they are rapid and avoid prolonged periods of time at high temperature and pressure [2].

Graphene-like materials have emerged as particularly promising nanomaterials for enhancing composites because they possess impressive intrinsic material properties such as strength, stiffness, and conductivity [5]. Their 2D nanoplatelet geometry allows for increased surface area to volume ratios and also enable self-assembly into laminated structures which is significant for imparting anisotropic properties (e.g. fracture toughness, permeability) [6], and they are galvanically compatible with carbon fibres unlike metallic nanomaterials [7]. From a cost, scalability, and nanomaterial quality perspective the ideal technique for graphene generation is liquid-phase exfoliation (LPE) [8]. However, LPE-produced nanosuspensions must be further processed to generate graphene solids and so significant work is required to effectively integrate graphene from suspension into consolidated composite materials. Given the excellent scalability of LPE for graphene synthesis, it is likely that graphene and similar high-performance 2D nanomaterials will be commonly supplied in liquid-phase suspension; therefore, developing manufacturing and processing techniques that leverage those suspensions will be worthwhile.

Interlayer modifications (e.g. interlayers/interleaves or localised nanoadditions like spray deposition) have demonstrated capability for nano-enhanced composite materials [9–12]. However, it is still unclear to what extent the nano-addition to interfacial regions translates to an enhancement in full-scale consolidated parts. Limitations of these interlayer modification techniques can include the possibility of delamination between plies that have thick interlayer additions [12] and migration of nanomaterials away from ply surfaces after infusion/consolidation [13]. Spray deposition is a particular attractive option because it is a simple and effective way to add high-performance nanomaterials to precise locations within the composite, which is a scalable pathway for realistic, industrial-scale nanocomposites manufacturing [9, 10]. Our recent work has successfully demonstrated the enhancement of composite materials via the spray-deposition of nanosuspensions [14, 15]. Successful nanosuspension formulations would enable rapid generation of spray-templated, functionalised nanocoatings that can be incorporated directly into composites during manufacturing processes.

In this work, we investigate the integration of a nanomaterial spray-deposition system with LATP manufacturing, as visualised in Figure 1. Aqueous graphene nanosuspension synthesised using LPE methods was aerosolised and sprayed to generate graphene thin films on CF/PEEK. The resultant graphene thin films were characterised using both microscopy and surface profiling, while the chemical structure of graphene was chemically analysed using Raman spectroscopy. Finally, the interactions between graphene and the IR laser in LATP was studied in a simulated consolidation process.

  doi:10.5075/epfl-298799_978-2-9701614-0-0

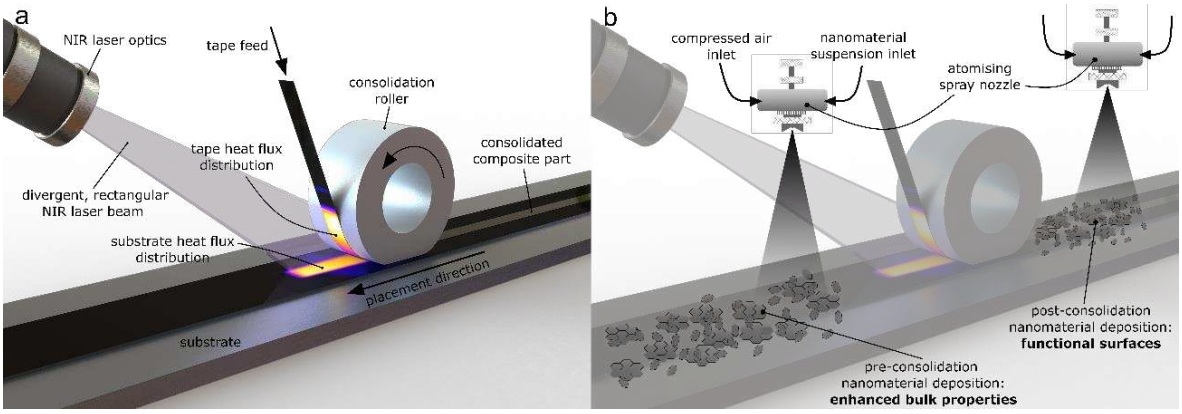

Figure 1. (a) The laser-assisted automated tape placement (LATP) concept based on commercial systems for thermoplastic-based carbon composites (adapted from [16]*) and (b) the LATP process with integrated nanomaterial spray-deposition either pre- or post-consolidation.*

2. Materials and Methods

Concentrated aqueous graphene suspension (1.5 wt% graphene, FlexeGRAPH Pty Ltd) was synthesised using surfactant-assisted liquid phase exfoliation in a continuous flow cell with a Q700 sonicator and 1" diameter probe tip attachment (Qsonica, USA) following the methodology developed by Notley [17]. Graphite was used as the feedstock material and non-ionic pluronic F68 surfactant (Sigma Aldrich) was continuously added for the first half of 240 hrs exfoliation time for a final graphite:F68 feed ratio of 1:1. 90x40 mm plies of carbon fibre (AS4)/polyether ether ketone (CF/PEEK) unidirectional tapes supplied by Toray Cetex (fibre volume fraction 59%) were used as the composite substrate material.

The graphene nanosuspensions were sprayed using a 30 mm diameter syringe filled with graphene suspension and placed in a NE-300 syringe pump (New Era Pump Systems Inc.). The suspension was fed into a flat fan air atomising nozzle (SUE15, Xinhou Industrial Co. Ltd) at a flow rate of 5 mL/min and aerosolised at 1 bar, as shown in Figure 2a. The substrate was placed at a distance of 300 mm and sprayed for 30 s before being placed on a hot plate at 50°C to dry. This process was repeated five times to generate the graphene thin film.

The CF/PEEK plies and spray-deposited graphene thin films on CF/PEEK (hereafter referred to as G-CF/PEEK) were characterised using optical microscopy and white light interferometry (WLI). Nikon Eclipse E200 microscope captured on a DS-Vi1 microscope camera (Nikon). Surface topography and roughness measurements were conducted on VEECO Wyko NT9100 Optical Profiling System using Vertical Scanning Interferometry (VSI) techniques. Five scans were taken at different locations on the sample for average root-mean-square roughness measurements.

Renishaw inVia confocal Raman microscope was used at a magnification of × 50 to chemically characterise graphene quality. Samples were exposed to a 532 nm wavelength laser at about 0.3 mW power with use of a 1200 mm−1 grating to isolate the signal and measurements were integrated over a period of 1 s with 10 accumulations to reduce signal to noise ratios.

For the LATP work, the optics on the laser tape placement head (AFPT GmbH) are supplied with a NIR laser beam (λ = 940–1100 nm) via fibre optic cables connected to a 4 kW laser (Laserline GmBH). A representative schematic of the LATP process is shown in Figure 1a. A 6-axis robot

  doi:10.5075/epfl-298799_978-2-9701614-0-0 published under CC BY-NC 4.0 license

arm (KUKA KR series) is used to control the position of the laser tape placement head and associated laser optics. To simulate graphene thin films being present during LATP consolidation, both CF/PEEK and G-CF/PEEK were irradiated with the AFPT tape placement head consolidation laser with a fixed laser power of 470 W and a tape placement head movement speed of 100 mm/s. The approximate dimensions of the laser spot projected on the sample are 55 mm and 23 mm in the process and transverse directions respectively, at a 60° angle of incidence.

3. Results and Discussion

Optical microscopy and WLI were used to characterise the quality and uniformity of the spray-deposited graphene thin film. The optical microscope images clearly show the carbon fibres and the presence of a light-scattering graphene thin film after spray deposition (Figure 2b, d). F68 surfactant is also present in the thin film but is not visually distinguishable from graphene. The natural gaps and channels in the CF/PEEK prepreg result in a surface roughness (R_{RMS} = 3.3 µm) as shown in Figure 2c. The aerosolisation and deposition of graphene nanosuspension covers the surface and fill in the gaps between fibres, resulting in a relatively smooth, conformal graphene thin film (R_{RMS} = 1.86 µm) on the surface of CF/PEEK (Fig 2e).

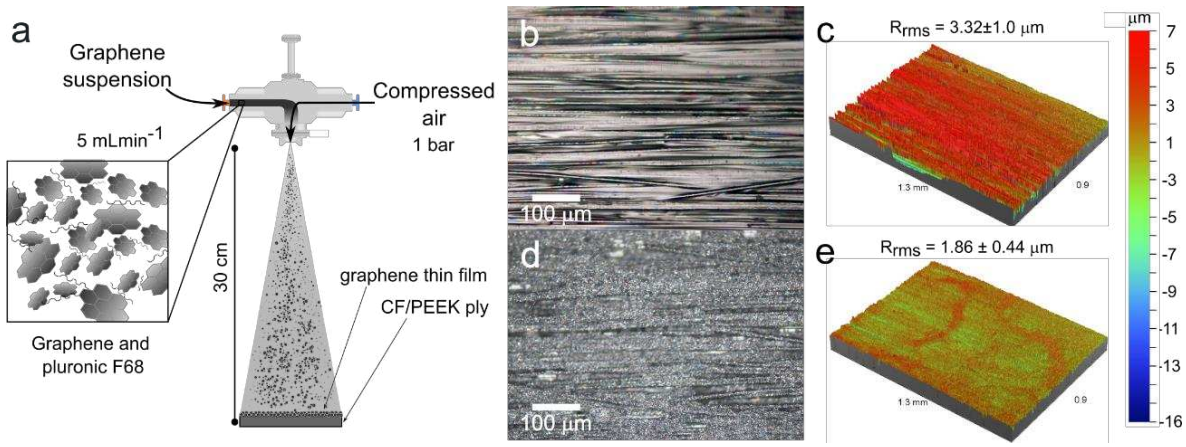

Figure 2. (a) Spray deposition process and parameters to aerosolise and deposit graphene suspension onto CF/PEEK composite plies. Graphical representation of graphene and pluronic F68 surfactant suspension inset. Optical microscope images (b ,d) and white light interferometry surface profiles (c,e) at 5x magnification of the CF/PEEK substrate and graphene thin film on CF/PEEK, respectively.

CF/PEEK and G-CF/PEEK materials were then subjected to IR laser heating in a simulated LATP manufacturing process. This simple process involved measuring the process parameter data both with and without graphene present pre-consolidation. The data from process monitoring for both CF/PEEK and G-CF/PEEK is shown in Figure 3. The in-situ process monitoring thermal camera is used to control the LATP consolidation parameters and is not directly equivalent to surface temperature due to process control algorithms and data processing. However, that surface temperature data is shown here as an indicator of how the graphene thin film affects heating rates and surface temperatures of both CF/PEEK and G-CF/PEEK materials.

  doi:10.5075/epfl-298799_978-2-9701614-0-0

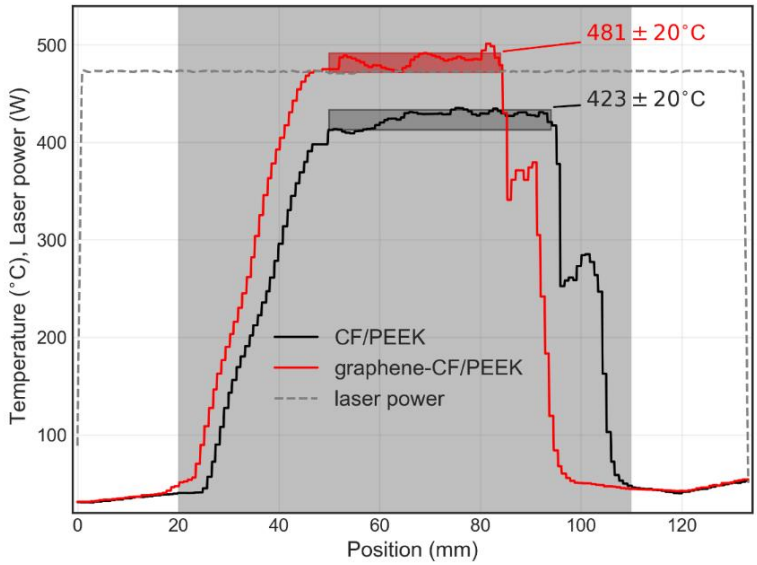

Figure 3. Process control thermal camera temperature and output laser power from the LATP placement head. The grey region represents the area covered by the 90 mm long prepreg plies as the head passes over the sample. The rectangular boxes indicate the 95% confidence interval for average steady-state surface temperature from the process thermal camera.

The G-CF/PEEK material heats up at a faster rate and to a greater temperature (481 ± 20 °C, 95% confidence) than neat CF/PEEK (423 ± 20 °C, 95% confidence). This is likely due to direct heating of graphene within the thin film, as exfoliated graphene can show a strong and broad absorption in the infrared region [18]. This suggests that the presence of graphene on the surface enhances absorption of the IR radiation, which could be beneficial to LATP manufacturing. Rapidly heating nanocarbon materials in air could negatively impact their properties. Therefore, the quality of graphene in the spray-deposited thin films before and after laser irradiation was assessed using Raman spectroscopy, shown in Figure 4.

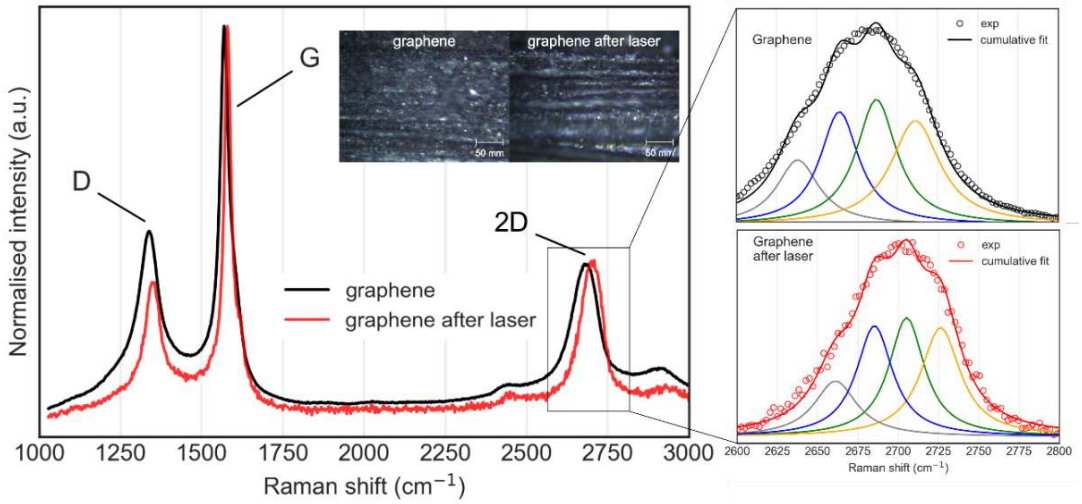

Figure 4. Raman spectra (microscope images from the Raman microscope inset) of the as-deposited graphene thin film on CF/PEEK and the same thin film after exposure to the LATP consolidation laser at 470 W power moving at 100 mm/s.

The G peaks on both the as-deposited graphene thin film and the graphene thin film post-laser exposure can be fit with one Lorentzian curve at 1572 cm^{-1} before and 1581 cm^{-1} after laser exposure. The G peak is associated with the frequency of aromatic carbon rings stretching at ≈1580 cm^{-1} [19]. The D peak fit was centred at 1338 cm^{-1} before and 1351 cm^{-1} after laser exposure; the D peak is activated when defects are present in the graphene due to elastic scattering of charge carriers which only occurs when armchair edges are present [20, 21]. There is virtually no D' band present at 1620 cm^{-1} which suggests a low number of edge defects [20]. The D and D' peaks only occur when there is some level of disorder present in the graphene structure [20] and can be related to corrugations (e.g. ripples, wrinkles), topological defects (e.g. dislocations and grain boundaries), and atomic vacancies or adatoms (i.e. missing carbons, extra carbons, or carbon substitutions in the structure) [22]. The I_D/I_G peak intensity ratio increases with disorder and correlates with reduced charge carrier mobility [23]; the I_D/I_G ratio of the thin films in this work was equal to ≈0.5 before and ≈0.375 after laser exposure, typical for ultrasonic exfoliation synthesis [20, 24]. For context, the I_D/I_G ratio is ≈0 for pristine monolayer graphene and as high 1.31 for graphite [25]. The analysis of the D and G peaks in the spray-deposited graphene thin film are indicative of nanocrystalline carbon with few edge defects [20, 26]. The 2D peaks represent valance (π) and conduction (π*) bands where single layer graphene (SLG) can fitted using a single Lorentzian peak [27]. In bilayer and few-layer graphene (< 5 layers), electronic interactions between the layers cause the π and π* bands to split into four phonons which requires four Lorentzian bands to fit the 2D peak [28]. Four bands appeared at 2638, 2664, 2687, 2711 cm^{-1} before and 2661, 2685, 2705, 2726 cm^{-1} after. The 2D peak centres at 2682 cm^{-1} before and 2700 cm^{-1} after laser exposure. The intensity ratio of G to 2D (I_G/I_{2D}) both before and after laser exposure are both ~2.35, which falls in the appropriate range for exfoliated few layer graphene about 5 layers thick [29]. The full width half maximum of the 2D peak is 112 cm^{-1} before and 79 cm^{-1} after laser treatment which correlates to five or more graphene layers, but the 2D peak centres of ≈2700 cm^{-1} is indicative of 2–4 layer graphene [27]. The general blue shift of all peaks could be due to a laser-driven reduction in the number of layers in graphene, while a reduction in D band intensity could be due to a reduction of graphene edge defects. Blue shift could also arise because of the removal of surfactant after laser heating, which could change graphene surface strain. Collectively, the Raman spectroscopy analysis above suggests that the spray-deposited graphene thin films are high-quality exfoliated graphene roughly 4 to 7 layers thick [30]. After IR laser heating, the graphene Raman spectra presents a lower intensity D band, a slightly more pronounced 2D peak, and a general blue shift by about 13 cm^{-1}, which indicates laser-driven reduction in graphene edge defects and possible reduction in average graphene layer number. Overall, Raman analysis indicates that the graphene thin films are well suited to functionalising carbon fibre composites both before and after laser exposure.

4. Conclusion

The aerosolisation of aqueous graphene suspensions was able to generate smooth thin films on CF/PEEK prepreg tapes (RMS roughness 1.86 μm). The presence of this graphene thin film improved absorption of IR radiation from the LATP consolidation laser at fixed laser power (470 W), allowing surface temps to rise faster and to reach higher temperatures than CF/PEEK alone (481°C with vs 423°C without graphene). This suggests that a graphene thin film enables more efficient surface heating than neat CF/PEEK in LATP. Raman spectroscopy of the graphene thin films shows that high-quality multilayer graphene is present both before and after IR laser irradiation. The next step in this workflow is to consolidate a graphene-enhanced CF/PEEK

  doi:10.5075/epfl-298799_978-2-9701614-0-0

laminate using spray-deposition and LATP and to subsequently measure the mechanical, electrical, and thermal properties of that material. X-ray microCT scans will be also be used to explore the microstructure of graphene-modified CF/PEEK composites.

Acknowledgements

The authors acknowledge FlexeGRAPH for supplying the graphene suspension and J. Bradby for providing the facilities for Raman spectroscopy measurements. This project was conducted within the ARC Training Centre for Automated Manufacture of Advanced Composites (IC160100040), supported by the Commonwealth of Australia under the Australian Research Council's Industrial Transformation Research Program.

5. References

1. Njuguna J, Pielichowski K, Desai S (2008) Nanofiller-reinforced polymer nanocomposites. Polym Adv Technol 19:947–959
2. Viswanathan V, Laha T, Balani K, Agarwal A, Seal S (2006) Challenges and advances in nanocomposite processing techniques. Mater Sci Eng R Reports 54:121–285
3. Hussain F, Hojjati M, Okamoto M, Gorga RE (2006) Review article: Polymer-matrix nanocomposites, processing, manufacturing, and application: An overview. J Compos Mater 40:1511–1575
4. Zhang H, Peijs T (2020) Multifunctional composites based on hierarchical micro–nanostructures: design, manufacturing, properties, and applications. Fiber-Reinforced Nanocomposites Fundam Appl. https://doi.org/10.1016/b978-0-12-819904-6.00009-8
5. Mirabedini A, Ang A, Nikzad M, Fox B, Lau KT, Hameed N (2020) Evolving Strategies for Producing Multiscale Graphene-Enhanced Fiber-Reinforced Polymer Composites for Smart Structural Applications. Adv Sci. https://doi.org/10.1002/advs.201903501
6. Hu K, Kulkarni DD, Choi I, Tsukruk V V. (2014) Graphene-polymer nanocomposites for structural and functional applications. Prog Polym Sci 39:1934–1972
7. Kandare E, Khatibi AA, Yoo S, Wang R, Ma J, Olivier P, Gleizes N, Wang CH (2015) Improving the through-thickness thermal and electrical conductivity of carbon fibre/epoxy laminates by exploiting synergy between graphene and silver nano-inclusions. Compos Part A Appl Sci Manuf 69:72–82
8. Raccichini R, Varzi A, Passerini S, Scrosati B (2015) The role of graphene for electrochemical energy storage. Nat Mater 14:271–279
9. Zhang H, Liu Y, Kuwata M, Bilotti E, Peijs T (2015) Improved fracture toughness and integrated damage sensing capability by spray coated CNTs on carbon fibre prepreg. Compos Part A Appl Sci Manuf 70:102–110
10. Li Y, Zhang H, Liu Y, Wang H, Huang Z, Peijs T, Bilotti E (2018) Synergistic effects of spray-coated hybrid carbon nanoparticles for enhanced electrical and thermal surface conductivity of CFRP laminates. Compos Part A Appl Sci Manuf 105:9–18
11. Kumar V, Sharma S, Pathak A, Singh BP, Dhakate SR, Yokozeki T, Okada T, Ogasawara T (2019) Interleaved MWCNT buckypaper between CFRP laminates to improve through-thickness electrical conductivity and reducing lightning strike damage. Compos Struct 210:581–589
12. Kumar V, Yokozeki T, Okada T, Hirano Y, Goto T, Takahashi T, Ogasawara T (2018) Effect of through-thickness electrical conductivity of CFRPs on lightning strike damages. Compos Part A Appl Sci Manuf 114:429–438

13. Qin W, Vautard F, Drzal LT, Yu J (2015) Mechanical and electrical properties of carbon fiber composites with incorporation of graphene nanoplatelets at the fiber-matrix interphase. Compos Part B Eng 69:335–341
14. Leow C, Kreider PB, Notthoff C, Kluth P, Tricoli A, Compston P (2021) A graphene film interlayer for enhanced electrical conductivity in a carbon-fibre/PEEK composite. Funct Compos Mater. https://doi.org/10.1186/s42252-020-00015-9
15. Kreider PB, Cardew-Hall A, Sommacal S, Chadwick A, Hümbert S, Nowotny S, Nisbet D, Tricoli A, Compston P (2021) The effect of a superhydrophobic coating on moisture absorption and tensile strength of 3D-printed carbon-fibre/polyamide. Compos Part A Appl Sci Manuf 145:106380
16. Stokes-Griffin CM, Compston P (2015) A combined optical-thermal model for near-infrared laser heating of thermoplastic composites in an automated tape placement process. Compos Part A Appl Sci Manuf 75:104–115
17. Notley SM (2012) Highly concentrated aqueous suspensions of graphene through ultrasonic exfoliation with continuous surfactant addition. Langmuir 28:14110–14113
18. Quinn MDJ, Wang T, Al Kobaisi M, Craig VSJ, Notley SM (2018) PEO-PPO-PEO surfactant exfoliated graphene cyclodextrin drug carriers for photoresponsive release. Mater Chem Phys 205:154–163
19. Vázquez-Santos MB, Geissler E, László K, Rouzaud JN, Martínez-Alonso A, Tascón JMD (2012) Comparative XRD, Raman, and TEM study on graphitization of PBO-derived carbon fibers. J Phys Chem C 116:257–268
20. Childres I, Jauregui LA, Park W, Caoa H, Chena YP (2013) Raman spectroscopy of graphene and related materials. New Dev Phot Mater Res 403–418
21. Acik M, Chabal YJ (2011) Nature of graphene edges: A review. Jpn J Appl Phys. https://doi.org/10.1143/JJAP.50.070101
22. Yang G, Li L, Lee WB, Ng MC (2018) Structure of graphene and its disorders: a review. Sci Technol Adv Mater 19:613–648
23. Ma B, Rodriguez RD, Ruban A, Pavlov S, Sheremet E (2019) The correlation between electrical conductivity and second-order Raman modes of laser-reduced graphene oxide. Phys Chem Chem Phys 21:10125–10134
24. Saidin NU, Ying KK, Foo CT, Hazan R, Mahmoud ME (2019) Direct exfoliation of graphite and its Raman spectroscopic study. Mater Today Proc 7:798–802
25. Dubale AA, Su WN, Tamirat AG, Pan CJ, Aragaw BA, Chen HM, Chen CH, Hwang BJ (2014) The synergetic effect of graphene on Cu2O nanowire arrays as a highly efficient hydrogen evolution photocathode in water splitting. J Mater Chem A 2:18383–18397
26. Lucchese MM, Stavale F, Ferreira EHM, Vilani C, Moutinho MVO, Capaz RB, Achete CA, Jorio A (2010) Quantifying ion-induced defects and Raman relaxation length in graphene. Carbon N Y 48:1592–1597
27. Hao Y, et al., (2010) Probing layer number and stacking order of few-layer graphene by Raman Spectroscopy. Small 6:195–200
28. Ferrari AC, Meyer JC, Scardaci V, et al (2006) Raman spectrum of graphene and graphene layers. Phys Rev Lett 97:1–4
29. Gayathri S, Jayabal P, Kottaisamy M, Ramakrishnan V (2014) Synthesis of few layer graphene by direct exfoliation of graphite and a Raman spectroscopic study. AIP Adv. https://doi.org/10.1063/1.4866595
30. Kumar V, Kumar A, Lee DJ, Park SS (2021) Estimation of number of graphene layers using different methods. Materials (Basel). https://doi.org/10.3390/ma14164590

HIGH SPEED IMAGING OF THE ULTRASONIC DEAGGLOMERATION OF NANOPARTICLES IN WATER

Zhuocheng Xu[a], Catherine Tonry[b], Christopher Beckwith[b], Andrew Kao[b], Milo S. P. Shaffer[c,d], Koulis Pericleous[b], Qianqian Li[a]

a. *Department of Aeronautics, Faculty of Engineering, Imperial College London, London, UK*
b. *School of Computing and Mathematical Sciences, Faculty of Engineering and Science, University of Greenwich, London, UK*
c. *Department of Chemistry, Faculty of Natural Sciences, Imperial College London, London, UK*
d. *Department of Materials Science, Faculty of Engineering, Imperial College London, London, UK*

Abstract: *Ultrasonic treatment is effective in deagglomerating and dispersing nanoparticles during composite manufacturing via liquid state processing route. However, the exact deagglomeration mechanisms were difficult to observe owning to opaque metal melt and containers. Here, an analogue experiment was carried out in de-ionize water to study the deagglomeration mechanisms and the influence of sonotrode amplitude during ultrasonication of multiwall carbon nanotubes in light-weight metal melt. Particle image velocimetry was applied to the captured images with a higher Field of View to calculate the average streaming speeds distribution. These data allowed direct comparison with modelling results. For images captured at higher frame rates and magnification, different patterns of deagglomeration were identified, and categorized based on different stages of cavitation zone development and for regions inside or outside the cavitation zone. The results obtained and discussed in this paper can be also relevant to a wide range of carbonaceous and other high aspect ratio nanomaterials.*

Keywords: High-speed imaging; ultrasonication; analogue experiment; CNTs

1. Introduction

Light-weight metal matrix nanocomposites (LMMNC) have attracted the attention of researchers in the last two decades due to their ability to attain good mechanical properties while maintaining low density (1). However, the high tendency for nanoparticles to agglomerate in the as-received state and during the composite fabrication process (especially in the melt route) (2) bottlenecked the real-life application for these materials by forming pre-mature cracks under loading.

High-frequency vibration, e.g., ultrasonication (US) was proven to be an effective method for deagglomerating nanoparticles in the melt route fabrication (3). During US, many tiny cavitation bubbles will be generated and imploded within the solutions or melt within one acoustic cycle (4) which created a shockwave that dramatically increased the pressure and temperature in the neighbouring region (5). This generated pressure was sufficient to overcome the Van der Waal's attraction between the individual nanoparticles that result in cluster breaking (6). In addition to the localised acoustic cavitation effect describe above, US could also lead to a macroscopic streaming effect which further disperses the deagglomerated particle throughout the melt (7). A further complexity in the case of CNTs is that scission may occur, attributed to axial acceleration or buckling of these high aspect ratio particles (6, 8). According to Huang *et al.* (6, 8), the implosion of cavitating bubbles near CNTs not only leads to individual nanotube separation but also shortening above a critical shear-lag length. They attributed this scission

  doi:10.5075/epfl-298799_978-2-9701614-0-0

mechanism to the stress built-up along CNTs by the radial acceleration during the implosion of nearby bubbles. In contrast, Guido *et al.* (9) simulated the dynamic behaviour of a single CNT near a collapsing bubble, as a function of length. This model assumes that the CNTs aligns tangentially to the growing bubble during the initial stages; the results suggest a length-dependent bending or rotation which may break the CNTs by buckling or stretching above a critical threshold. However, due to the opacity of the alloy melt and crucible and relative high processing temperature (typically 600 – 700 °C), the exact mechanisms for US induced deagglomeration in the nanocomposite (especially CNT nanocomposite) melt were still under investigation (3, 10-12) due to the lack of appropriate techniques.

Due to the advancement of 3rd generation X-ray synchrotron, in-situ observation of ultrasonic cavitation process within the alloy melt become possible(4, 13-16). For example, Mirihanage et al (17) compared the radiographs of pure Al-10%Cu alloy melt and the melt with Al_2O_3 nanoparticles addition during US. Their result showed a higher cavitation bubble propensity and flow speed in the melt with nanoparticle addition which may result from more cavitation nucleus due to nanoparticles addition. However, both the individual nanoparticles and their clusters cannot be resolved in the radiograph, hence, no direct observation of the de-agglomeration process was captured.

An alternative method for in-situ observation of the US deagglomeration process in of 'melt like' organic transparent solutions through high-speed imaging (10, 18, 19). The in-situ observation of these special transparent liquids has been used to analogue the metal behaviour since 1965 (20) which for example included the study of the interaction between particles and solidification front (21) and dendrite fragmentation (22). Tzanakis et al. (23) compared a few parameters related to flow and materials properties between three common transparent analogue liquids and Al melt at 700 °C. They found that water should share very close flow properties as Al melt during US due to their closed Reynold numbers and Ohensorge number. After the theoretical studies, they compared the acoustic spectrum between these two liquids and confirmed their closing flow behaviour during US by showing a similar pattern across the whole spectrum broadband. This work provides a theoretical basis for future analogue experiments in transparent liquids. Later, cavitation induced de-agglomeration of MgO cluster in water was observed in-situ by Mi's group (10). The result suggested this process happen from the surface of agglomerates rather than from the inside. This process more resembles chipping off individual particles from the surface rather than rupture of agglomerate from within its bulk This explains why the de-agglomeration takes such a long time. In recent work, Morton et al. (18) (first ever) used high-speed imaging to study the sono-exfoliation of graphite in DI water. By taking advantage of the high frame rate, four specific cavitation bubbles related phenomena during graphite exfoliation were captured and identified. Similar to in-situ X-ray CT, this alternative method still cannot resolve individual nanoparticles, however, the micron-sized agglomerates can be easily observed in each frame. Table 1 below compared the advantages and drawbacks between these two methods.

Table 1: The advantages and drawbacks of X-ray CT and optical analogue experiment.

Techniques	Advantages	Drawbacks

  doi:10.5075/epfl-298799_978-2-9701614-0-0

X-ray CT	1. Direct in-situ observation in the alloy melt.	1. Very expansive equipment and setups (22). 2. Relative low FOV (22) → Cannot give overall dispersion. 3. Thin container, the free growth of the sample and development of acoustic flow field was constrained (13). Hence, the results were not representative to the bulk sample. 4. Large data size, thus quickly saturating the storage capacity of the camera imaging system (13). 5. Alloys compositions need to be adjusted to give a better contrast (13, 24). 6. Cannot fully characterize the flow pattern in the melt. 7. No qualitative info about dispersity in the melt (No sign of change in X-ray absorption). 8. Limited to a small sample volume (23).
Optical analogue experiment	1. Cheaper experiment setups. 2. Relative larger FOV. 3. De-agglomeration of micron size clusters can be captured.	1. Nearly all of the in-situ study using transparent organic materials has the Hele-Shaw confinement effect that can potentially impact the quality and relevance of the results (25). 2. It has been known that the behaviour of transparent alloys is not completely identical to that of metallic systems, because of their low thermal conductivity, in particular, in alloys, dendritic growth is mainly controlled by solute diffusion, because the thermal diffusivity is much higher than the solute diffusivity, typically about three orders of magnitude (26, 27). 3. Organic transparent alloys and solutions are very different from liquid metal alloys in terms of density, viscosity, surface tension, mass transfer coefficient and sound velocity (14).

In this paper, the dispersion of MWCNTs in DI water during UST was captured for the first time by using high-speed imaging. The amplitude of the UST generator was varied to study the influence of input UST intensity. Furthermore, the distributions of average streaming flow speed at 20% amplitude was calculated and compared with simulations for model validation and theoretical studies. Different MWCNT deagglomeration mechanisms were also identified and categorised based on different stages of cavitation zone development and for regions inside or outside the cavitation zone.

2. Experimental

The detailed experimental setup and numerical modelling for this work was describe in somewhere else (28). To be short, 27 mg of NC-7000 MWCNTs (average diameter of 9.5 nm and length of 1.5 µm) and 54 ml of DI water were mixed in a transparent rectangular vessel (3B scientific) with an inner dimension of 77 x 74 x 23 mm^3 (length x height x thickness). The UST system was Sonic VCX 750 processor equipped with a standard 12.7 mm diameter and 139.0 mm length Ti64 probe. For the imaging system, a high intensity LED was used as a light source. A Phantom VEO 640 high-speed camera and Tokina 100 mm F2.8 Macro lens were used for high-speed filming. two resolutions (2560 × 1600 and 640 × 480) were used to capture the distribution of MWCNTs in the bulk solution (in high resolution for wider Field of View (FoV)) and the dynamic interaction between cavitation bubbles and agglomerates (in lower resolution for higher frame rate) in three different amplitudes (24, 36 to 48 µm). LaVision Davis 10 with Flowmaster package was used for image processing and PIV analysis. A three-dimensional coupled numerical model has been developed using COMSOL Multiphysics to predict the acoustic streaming within the vessel. The vessel dimensions and process conditions in the numerical model were assumed to be the same as the experimental work. The Navier-Stokes equations coupled with a nonlinear Helmholtz-type model (29) were used to simulate the acoustic pressure field and acoustic streaming.

3. Results and discussion

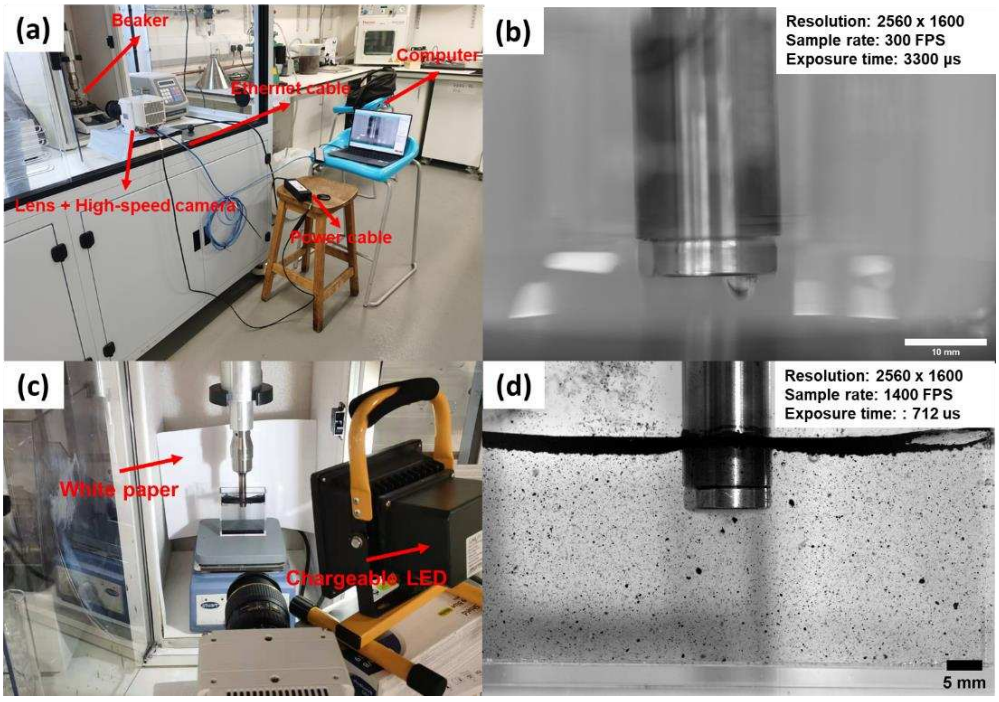

Figure 1. (a) The original experimental setup with a cylindrical glass breaker. (b) Cines captured by the original experimental setup and image information. (c) Final experimental setup. (d) Cine captured by final experimental setup and image information.

The experimental setup for high-speed imaging was adjusted to obtain high quality image ready for PIV analysis. At the beginning, a transparent cylindrical beaker (Fig. 1 (a)) was used as the apparatus for high-speed observation. However, artefacts were shown in the captured film due to the reflection caused by the curved glass wall. Also, the sample rate of the film cannot reach

the full potential of the camera (1400 FPS) and showed flickers due to the AC nature of the weak indoor light source. Therefore, the equipment setup was adjusted and finalized by using a rectangular vessel and strong chargeable LED light source (Fig. 1 (c) & (d)). By using this setup, all the reflection artefacts were removed, and the full potential of the camera can be achieved.

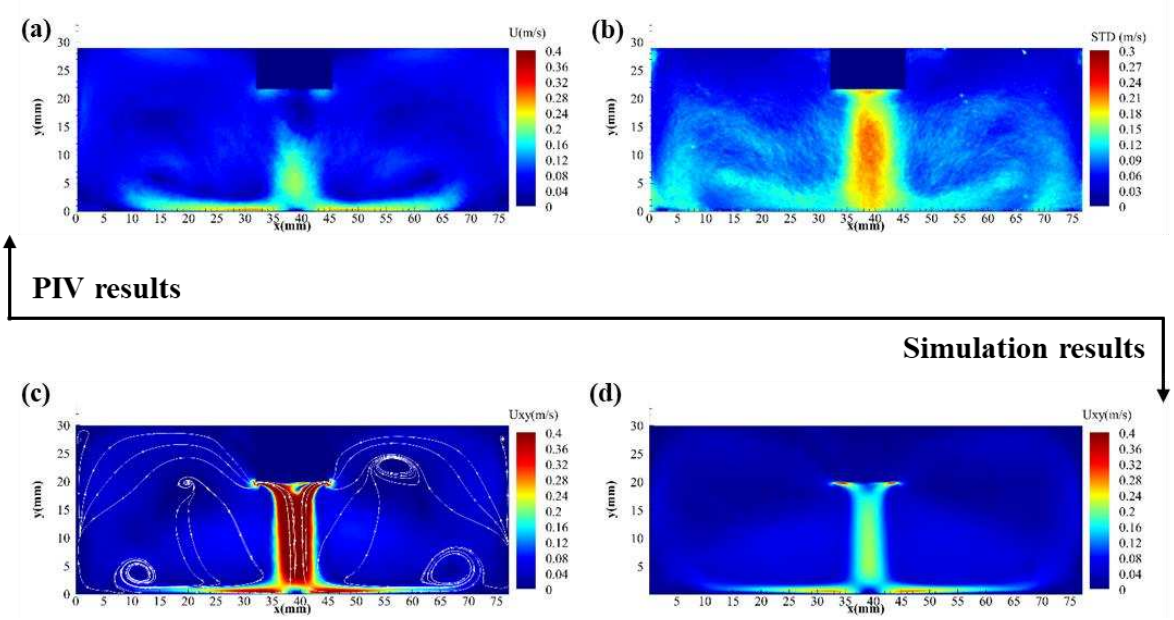

Figure 2. Plots of velocity magnitude for the average over 0.5 s for experimental PIV data for 24 µm amplitude (a), and standard deviation of the PIV data (b), a center xy slice in the numerical model (c), the average velocity in z for the numerical model (d), Note, numerical and experimental scale bars have been matched to highlight the bulk flow.

The deagglomeration and dispersion of MWCNTs were successfully captured by the high-speed camera. Using PIV, the experimental images were converted to give the averaged fluid velocity as Fig. 2. (a) along with the corresponding standard deviation (Fig. 2 (b)) for 24 µm amplitude. The PIV procedure was not able to capture the main downward flow jet, directly below the sonotrode, due to the excessive velocities. This region appears blank in Fig. 2. (a) and coincides with the highest standard deviations from the PIV measurements. The numerical modelling results predict that there should be a high velocity jet below the sonotrode. These results can be plotted as a slice of the numerical solution in the mid-plane of the vessel, containing the centre of the sonotrode (Fig. 2. (c)), or as averaged velocities along the z direction representing a 'projection' of the velocity field (Fig. 2. (d)). A direct comparison of the numerical and experimental data is difficult as PIV is a 2-dimensional representation of what is inherently a 3-dimensional particle velocity field, due to the relatively large length scale in z and uncertain focal depth (The focusing plane for this study was chose as the middle cross-section of the sonotrode).

By considering the hydrophilic and porous nature of the CNTs agglomerate (30), bubbles or air pockets were expected on the surface and inside the MWCNTs agglomerates after adding them to water. These pre-existing bubbles tend to continuous oscillation and coalescence with each other or other bubbles to form a micro-bubble clusters (31). These micro-bubbles showed a chaotic motion with continuous splitting and coalescence during oscillation, which perpetually eroded the surface of the MWCNTs clusters by impelling liquid entrainment through micro water jets (31, 32) (known as the sono-capillary effect). This corresponded to the 'comet' feature

observed in Fig. 3. After a period of oscillation, these microbubbles would either separate from the parent agglomerates through implosion. Other deagglomeration mechanisms have also been observed and identified, however, due to page limit, these results has been summarized somewhere else.

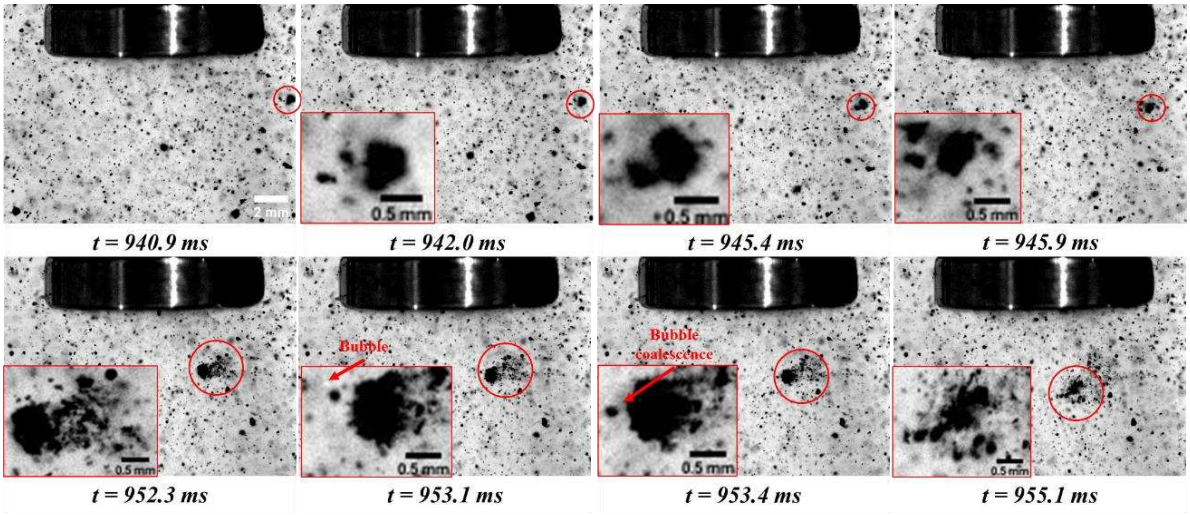

Figure 3. A deagglomeration process captured near the ROI near sonotrode.

4. Conclusion

In this paper, UST assisted deagglomeration and dispersion of MWCNTs in DI water by UST were captured and analysed for the first time by using high-speed imaging and numerical modelling. The experimental setup was adjusted to capture films with no reflection artefacts or flickers. PIV analysis was applied to calculate average flow speeds and compared with numerical modelling which suggested the PIV failed to capture the acoustic streaming jet flow directly underneath the sonotrode due to its 2D nature and limited spatial resolution. However, the remainder of the flow field matched well with the simulation results providing model validation. Films capture at higher frame rate enabled obviously deagglomeration phenomena to be captured, and the reasons for that were inferred as sonocapillary effect and micro-bubble explosion.

1053/1602 ©2022 Zhuocheng et al. doi:10.5075/epfl-298799_978-2-9701614-0-0 published under CC BY-NC 4.0 license

Reference

1. Baig Z, Mamat O, Mustapha M. Recent Progress on the Dispersion and the Strengthening Effect of Carbon Nanotubes and Graphene-Reinforced Metal Nanocomposites: A Review. Critical Reviews in Solid State and Materials Sciences. 2018;43(1):1-46.
2. Li Q, Rottmair CA, Singer RF. CNT reinforced light metal composites produced by melt stirring and by high pressure die casting. Composites Science and Technology. 2010;70(16):2242-7.
3. Dieringa H. Processing of Magnesium-Based Metal Matrix Nanocomposites by Ultrasound-Assisted Particle Dispersion: A Review. Metals. 2018;8(6):431.
4. Wang B, Tan D, Lee TL, Khong JC, Wang F, Eskin D, et al. Ultrafast synchrotron X-ray imaging studies of microstructure fragmentation in solidification under ultrasound. Acta Materialia. 2018;144:505-15.
5. Nguyen TQ, Liang QZ, Kausch H-H. Kinetics of ultrasonic and transient elongational flow degradation: a comparative study. Polymer. 1997;38(15):3783-93.
6. Huang YY, Terentjev EM. Dispersion of carbon nanotubes: Mixing, sonication, stabilization, and composite properties. Polymers. 2012;4(1):275-95.
7. Nowak T, Cairós C, Batyrshin E, Mettin R, editors. Acoustic streaming and bubble translation at a cavitating ultrasonic horn2015 2015-01-01: AIP Publishing LLC.
8. Huang YY, Knowles TPJ, Terentjev EM. Strength of Nanotubes, Filaments, and Nanowires From Sonication-Induced Scission. Advanced Materials. 2009;21(38â39):3945-8.
9. Pagani G, Green MJ, Poulin P, Pasquali M. Competing mechanisms and scaling laws for carbon nanotube scission by ultrasonication. Proceedings of the National Academy of Sciences. 2012;109(29):11599-604.
10. Eskin DG, Tzanakis I, Wang F, Lebon GSB, Subroto T, Pericleous K, et al. Fundamental studies of ultrasonic melt processing. Ultrasonics Sonochemistry. 2019;52:455-67.
11. Barbosa J, Puga H. Ultrasonic Melt Treatment of Light Alloys. International Journal of Metalcasting. 2019;13(1):180-9.
12. Sardar S, Karmakar SK, Das D. Ultrasonic Assisted Fabrication of Magnesium Matrix Composites: A Review. Materials Today: Proceedings. 2017;4(2):3280-9.
13. Zhang Z, Wang C, Koe B, Schlepütz CM, Irvine S, Mi J. Synchrotron X-ray imaging and ultrafast tomography in situ study of the fragmentation and growth dynamics of dendritic microstructures in solidification under ultrasound. Acta Materialia. 2021;209:116796.
14. Mi J, Eskin D, Connolley T, Fezzaa K. Understanding the Highly Dynamic Phenomena in Ultrasonic Melt Processing by Ultrafast Synchrotron X-ray Imaging. Light Metals 2019: Springer International Publishing; 2019. p. 1539-44.
15. Huang H, Shu D, Fu Y, Zhu G, Wang D, Dong A, et al. Prediction of Cavitation Depth in an Al-Cu Alloy Melt with Bubble Characteristics Based on Synchrotron X-ray Radiography. Metallurgical and Materials Transactions A. 2018;49(6):2193-201.
16. Tan D, Lee TL, Khong JC, Connolley T, Fezzaa K, Mi J. High-Speed Synchrotron X-ray Imaging Studies of the Ultrasound Shockwave and Enhanced Flow during Metal Solidification Processes. Metallurgical and Materials Transactions A. 2015;46(7):2851-61.
17. Mirihanage W, Xu W, Tamayo-Ariztondo J, Eskin D, Garcia-Fernandez M, Srirangam P, et al. Synchrotron radiographic studies of ultrasonic melt processing of metal matrix nano composites. Materials Letters. 2016;164:484-7.
18. Morton JA, Khavari M, Qin L, Maciejewska BM, Tyurnina AV, Grobert N, et al. New insights into sono-exfoliation mechanisms of graphite: In situ high-speed imaging studies and acoustic measurements. Materials Today. 2021.

  doi:10.5075/epfl-298799_978-2-9701614-0-0

19. Shu D, Sun B, Mi J, Grant PS. A High-Speed Imaging and Modeling Study of Dendrite Fragmentation Caused by Ultrasonic Cavitation. Metallurgical and Materials Transactions A. 2012;43(10):3755-66.
20. Jackson KA, Hunt JD. Transparent compounds that freeze like metals. Acta Metallurgica. 1965;13(11):1212-5.
21. Sekhar JA, Trivedi R. Solidification microstructure evolution in the presence of inert particles. Materials Science and Engineering: A. 1991;147(1):9-21.
22. Wang S, Kang J, Guo Z, Lee TL, Zhang X, Wang Q, et al. In situ high speed imaging study and modelling of the fatigue fragmentation of dendritic structures in ultrasonic fields. Acta Materialia. 2019;165:388-97.
23. Tzanakis I, Lebon GSB, Eskin DG, Pericleous KA. Characterizing the cavitation development and acoustic spectrum in various liquids. Ultrasonics Sonochemistry. 2017;34:651-62.
24. Guo E, Shuai S, Kazantsev D, Karagadde S, Phillion AB, Jing T, et al. The influence of nanoparticles on dendritic grain growth in Mg alloys. Acta Materialia. 2018;152:127-37.
25. Daudin R, Terzi S, Lhuissier P, Salvo L, Boller E. Remelting and solidification of a 6082 Al alloy containing submicron yttria particles: 4D experimental study by in situ X-ray microtomography. Materials & Design. 2015;87:313-7.
26. Daudin R, Terzi S, Lhuissier P, Tamayo J, Scheel M, Babu NH, et al. Particle-induced morphological modification of Al alloy equiaxed dendrites revealed by sub-second in situ microtomography. Acta Materialia. 2017;125:303-10.
27. Bogno A, Nguyen-Thi H, Reinhart G, Billia B, Baruchel J. Growth and interaction of dendritic equiaxed grains: In situ characterization by synchrotron X-ray radiography. Acta Materialia. 2013;61(4):1303-15.
28. Zhuocheng Xu CT, Christopher Beckwith, Andrew Kao, Hayley Wong, Milo S. P. Shaffer, Koulis Pericleous, Qianqian Li. High-Speed Imaging of the Ultrasonic Deagglomeration of Carbon Nanotubes in Water. 2022.
29. Zhang L, Li X, Li R, Jiang R, Zhang L. Effects of high-intensity ultrasound on the microstructures and mechanical properties of ultra-large 2219 Al alloy ingot. Materials Science and Engineering: A. 2019;763:138154.
30. Liu H, Zhai J, Jiang L. Wetting and anti-wetting on aligned carbon nanotube films. Soft Matter. 2006;2(10):811-21.
31. Priyadarshi A, Khavari M, Subroto T, Prentice P, Pericleous K, Eskin D, et al. Mechanisms of ultrasonic de-agglomeration of oxides through in-situ high-speed observations and acoustic measurements. Ultrasonics Sonochemistry. 2021;79:105792.
32. Ohl CD, Ikink R. Shock-Wave-Induced Jetting of Micron-Size Bubbles. Physical Review Letters. 2003;90(21).

  doi:10.5075/epfl-298799_978-2-9701614-0-0

EFFECTS OF MICROWAVE-ASSISTED CROSS-LINKING ON THE CREEP RESISTANCE AND MEASUREMENT ACCURACY OF THE COAXIAL-STRUCTURED FIBER STRAIN SENSOR

Seung Yoon, On[a], Seong Su, Kim

a: Department of Mechanical Engineering, KAIST (Korea Advanced Institute of Science and Technology), 291 Dahak-ro, Yuseong-gu, Daejeon, Republic of Korea – osy1471@kaist.ac.kr

Abstract: *Conductive particle reinforced nanocomposite-based strain sensors have been widely investigated owing to their unique material properties. Numerous studies on nanocomposite strain sensors have focused on the enhancement of stretchability, flexibility, and gauge factor (GF) for wearable and health care applications. However, flexible polymer-based strain sensor has a limitation for use in high temperature such as cure monitoring of composite structures due to the semi-crystalline structure of the polymer. The semi-crystalline polymers have a substantial creep when the slippage of the molecular chain at the amorphous region is occurred. Moreover, the slip phenomena are maximized at the high temperature because the mobility of the polymer chain is increased, which results in overestimated strain. The cross-linking process of thermoplastic is one of the possible solutions to reduce creep at high temperature. Conventionally, melt-mixing method has been used for the fabrication of cross-linked thermoplastics. However, the melt-mixing method is not suitable for fabricating fiber shape owing to extremely high viscosity because polymer melting and cross-linking reaction are occurred simultaneously. In this work, microwave-assisted cross-linking method was introduced to overcome the limitation of conventional cross-linking process. The ultra-high molecular weight polyethylene (UHMWPE) core fiber was fabricated by using a dry-jet wet spinning system. Microwave post-treatment was performed under the peroxide bath to enhance the creep resistance through the cross-linking reaction. By using the creep resistance enhanced core fiber, coaxial-structured fiber strain sensor which has multi-layer structured shell parts was fabricated by using a facile dip-coating method. The load carrying capacity and creep resistance of the core fiber were estimated by measuring the tensile strength and minimum creep rate at the high temperature. Sensitivity and linearity of the fiber sensor were checked by means of an electronic test equipment during static tensile test. In addition, accuracy of the fiber sensor at high temperature was evaluated and compared with that of a conventional strain gauge.*

Keywords: Microwave post treatment; Fiber structured strain sensor; Core-shell structured fiber; Creep resistance; Multi-layer structure.

1. Introduction

Over the years, post-processing such as stretching[1], drawing[2], and heat setting[3] methods have been investigated to enhance the creep resistance of polymer by increasing crystalline contents. But, these conventional methods are limited to enhance the creep resistance because the amorphous region is still remaining after the post-treatment. To overcome these problems, the crosslinking method of thermoplastic has been deemed as a highly promising technology because the intermolecular movement in the amorphous region can be strongly constrained by a covalent bond. Conventionally, melt blending method[4] with crosslinking agent and Gamma-

  doi:10.5075/epfl-298799_978-2-9701614-0-0

ray or Electron beam irradiation process[5] have been used for fabricating cross-linked thermoplastic materials. The melt blending method is one of the easy ways to fabricate the cross-linked polymer, however, bi-products after crosslinking reaction are remaining in the final products. Also, the blending process is proceeding at a higher temperature than the melting point of the polymer so that it can affect the mechanical properties of the cross-linked polymer due to thermal degradation. Additionally, the microscale products with a large aspect ratio such as fiber are hard to manufacture using the melt blending method, because the polymer melting and crosslinking reaction simultaneously occur during the mixing process so that the viscosity of the mixture is extremely increased. On the other hand, the irradiation crosslinking method has an advantage that can be applied to manufactured products. But, it has limitations that required extremely high energy sources and polymer chain scissoring has simultaneously occurred during crosslinking process.

Herein, we report the novel microwave-assisted crosslinking method of a ultrahigh molecular weight polyethylene (UHMWPE) fibers for enhancing the sensing accuracy of UHMWPE core fiber based coaxial structured fiber strain sensors through the enhancing the creep resistance of core fibers (Figure 1). Cross-linked UHMWPE core fibers were fabricated by using a microwave treatment under the hydrogen peroxide bath to enhance the creep resistance and the load carrying capacity of fiber sensor at the high temperature. The coaxial structured soft strain sensing layer was introduced to consist of polyurethane (PU) layers and MWCNT layers formed by dip coating method. The chemical composition change and crystallinity after microwave treatment was investigated using a Fourier-transform infrared spectroscopy (FT-IR) and X-ray diffractometer (XRD), respectively. Furthermore, the crosslinking densities were calculated using solvent extraction method. The creep resistance and the load carrying capacities of cross-linked core fibers at the high temperature were estimated by measuring the minimum creep rate and tensile strength at various microwave treatment conditions. The strain sensitivity (i.e. gauge factor) and temperature sensitivity were checked by means of electronic test equipment. Finally, the measurement accuracy at the high temperature was evaluated to compared with the conventional strain gauges.

2. Experimental

2.1 Dry-jet spinning process

A UHMWPE fiber was fabricated by the dry-jet wet spinning method with the 4 wt.% spinning solution and a lab-scale spinning instrument (Wet spinning system, DISSOL, Republic of Korea) as shown in Figure 1. The spinning solution was fed to the 0.65 mm diameter of spinneret under 170 °C. The UHMWPE fibers were formed by solidification of the polymer solution extruded from the spinneret in a coagulation bath containing distilled water at 25 °C. The residual solvent after solidification process was removed by rinsing process using hexane (Sigma-Aldrich Inc., USA) for 24 h at 25 °C. The hot-stretching process was introduced to enhance the initial crystallinity of as-spun UHMWPE fibers. The stretching ratio and treatment temperature was adjusted by 14 and 120 °C, respectively.

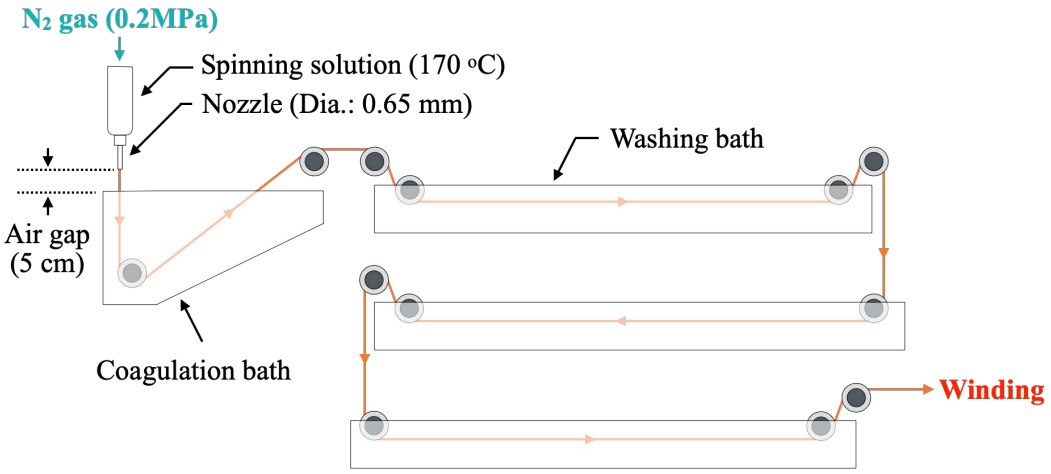

Figure 1. Dry-jet spinning process of UHMWPE core fiber

2.2 Microwave post-treatment

The microwave-assisted crosslinking post-treatment process was introduced for the enhancement of mechanical properties and creep resistance at the high temperature of UHMWPE fibers. The microwave treatment consisted of two parts as shown in Figure 2. In the step 1, the stretched UHMWPE fiber was fixed on the ceramic mold. The fiber was irradiated for 2 min., 3 min., 4 min., and 5 min. with microwaves with an effective intensity per unit mass of 12 kW/kg at 2.4 GHz under the 3% concentrations of hydrogen peroxide (386790-M, Sigma-Aldrich, USA) solution bath. In step 2, the mold was taken from the bath, and then, the UHMWPE fiber was dried by microwaves for 4 min. to remove the excessive water and hydrogen peroxide.

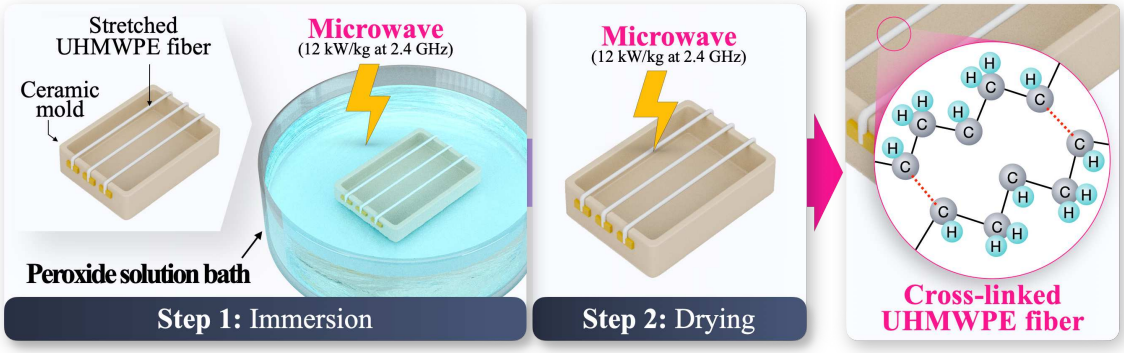

Figure 2. Microwave crosslinking post-treatment process

2.3 Dip coating process

Figure 3 shows the schematic configuration of creep resistance enhanced fiber sensors, consisting of the following sequency from the core outward: the microwave treated UHMWEP core fiber, 1st PU layer, multi-conductive MWCNT layer, and 2nd PU layer, sequentially. The shell parts of fiber sensor was coated using simple dip-coating method using PU solution (Akuarane 26302, T&L Co., Ltd., Republic of Korea) and MWCNT solution (K-Nanos 100P, Kumho petrochemical Co., Ltd., Republic of Korea).

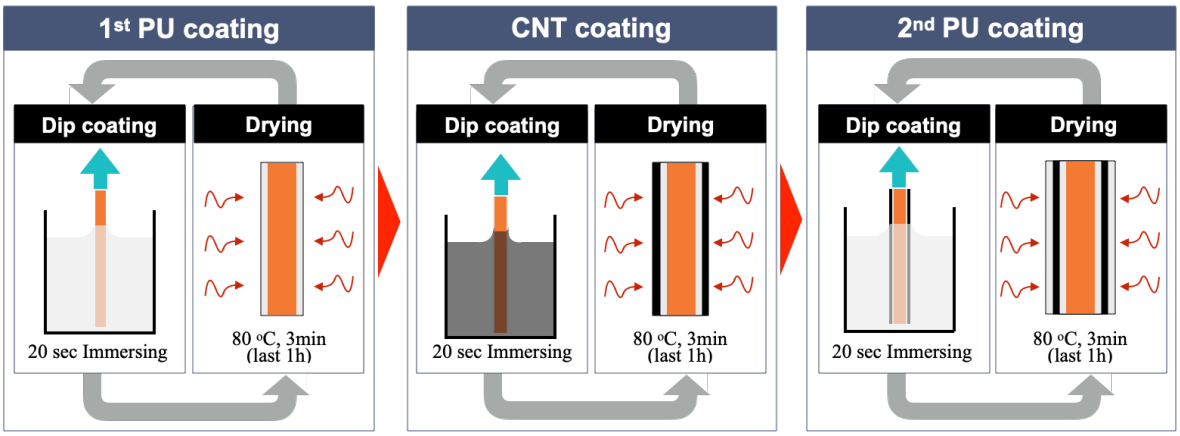

Figure 3. Dip coating process

2.4 Characterization of fiber sensors

The strain sensitivity and temperature sensitivity was measured for calibration process of fiber sensors. The fabricated fiber sensor was attached on the center of tensile test specimen of UD laminated composite and the conventional strain gauge (KFRPB-5-120-C1-11, Kyowa Electronic Instruments Co., Ltd., Japan) was attached on the beside of specimen. Then the relative resistance change from fiber sensor by LCR meter (E4980A, Keysight Technologies, USA) and strain value from strain gauge by DAQ (NI-9235, National Instruments Corp., USA) was measured under the tensile load, simultaneously. Fiber sensor and K-type thermocouple was attached on the ceramic plate. Then the relative resistance changes and temperature data was measured under room temperature to 125 °C using LCR meter and DAQ, respectively.

The measurement signal comparison between conventional strain gauge and fiber sensor under 80 °C, and 125 °C was performed to evaluate the sensing performance of the fabricated fiber sensor. The schematics of specimens was same as strain sensitivity measurement. The conversion of relative resistance change to strain value was performed using flowing equations with measured gauge factor and temperature sensitivity coefficient.

$$\Delta R/R_0 = K_T \Delta T + K_\varepsilon \Delta\varepsilon \quad (1)$$

where $\Delta R/R_0$ is the measurement results of relative resistance change, K_T is the temperature sensitivity coefficient, ΔT is the measured temperature, K_ε is the gauge factor of fiber sensor.

3. Result and discussion

3.1 Effects of microwave-assisted crosslinking methods

Figure 4 shows the measurement result of the tensile properties of UHMWPE core fiber with respect to the post-treatment methods. It was confirmed that the tensile strength and modulus enhanced by 26% and 94%, respectively, compared to the neat fiber. These results show that the mechanical properties increase rate is higher than that of the heat setting method, which is

a conventional post-treatment method used to improve the mechanical properties of the fiber material. Therefore, it is considered that the mechanical properties of the core fibers are significantly improved as crosslinks are formed between the main chains of UHMWPE by the microwave-assisted crosslinking reaction.

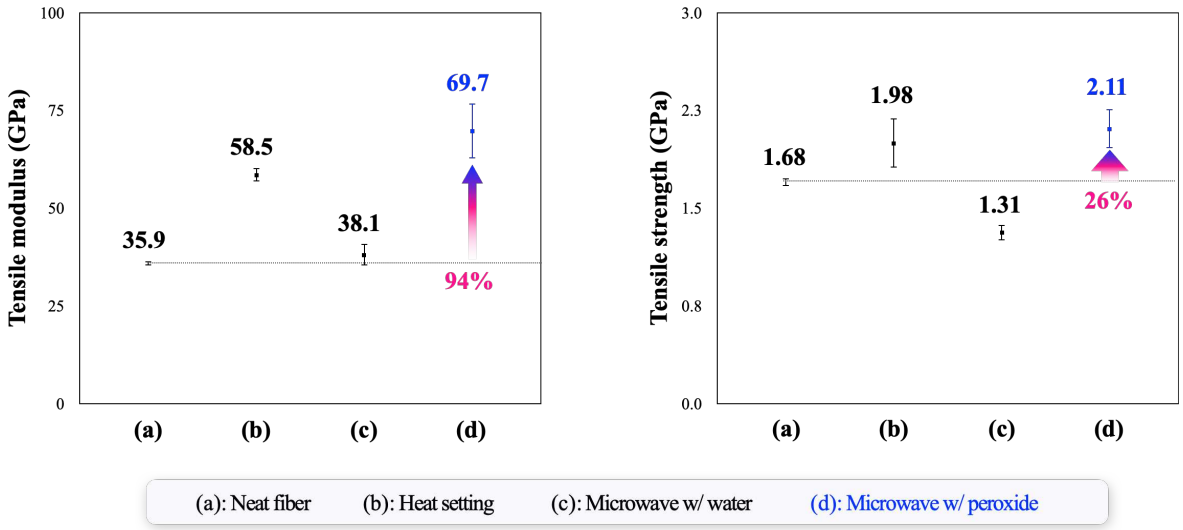

Figure 4. Mechanical properties of microwave treated UHMWPE core fiber

3.2 Evaluation results of sensing performance

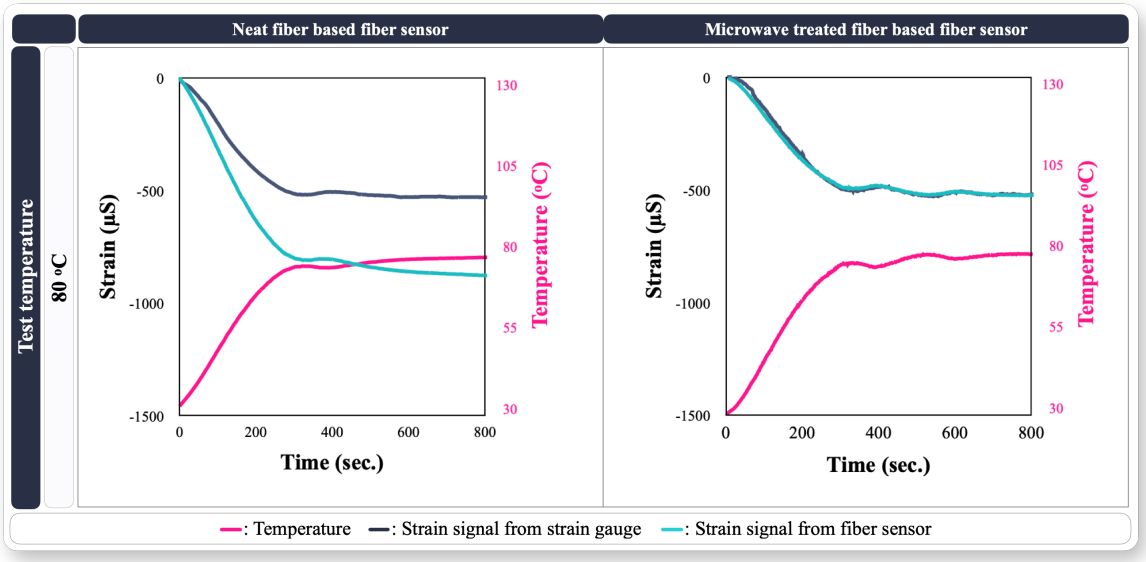

Figure 5. Sensing performance of fiber sensors

Strain signal comparison results between general strain gauge and fiber sensors to evaluate the sensing accuracy of fabricated fiber sensors were shown in Figure 5. In the case of the sensor using the neat fiber, the measurement error between the strain gauge and the fiber sensor measurement result was extensive in high temperature environments where the measurement

error was up to 96% at 80 °C. In addition, measurement error increased after the converging of temperature because the neat fiber, which has the lowest creep resistance, was used as core fiber. By contrast, the measurement error of the fiber sensor with microwave treated core fiber shows the 3% at 80 °C compared with the strain gauge. After temperature converging, the measured signal was stable compared with the neat and heat set core fibers. Consequently, the measurement accuracy of the fiber sensor with microwave treated core fiber was significantly improved through the increased creep resistance by the cross-link formation after the microwave treatment.

4. Conclusions

In this study, microwave-assisted cross linking method was introduced to enhance the mechanical properties and creep resistance of core fibers. The effects of microwave treatment were investigated by measurement of high temperature tensile strength and modulus, and sensing response. Based on the results the following conclusions were obtained.

(1) The tensile test results of microwave treated UHMWPE core fiber showed enhanced mechanical properties. The tensile strength and modulus of microwave treated fiber sensors increased by 29% and 92%, respectively.

(2) Comparison results of measurement accuracy between strain gauge and fiber sensor showed a effects of microwave treated core fiber. The measurement error decreased by 3% at the 80 °C when microwave treated core fiber was applied as core fiber of fiber sensor.

Acknowledgements

This work was supported by the National Research Foundation of Korea(NRF) grant funded by the Korea government(MSIT) (No. 2020R1A2C201096512). This research was financially supported by the Institute of Civil Military Technology Cooperation funded by the Defense Acquisition Program Administration and Ministry of Trade, Industry and Energy of Korean government under grant No. UD10044TU.

5. References

1. Hong, K, Rastogi, A, Strobl, G. A model treating tensile deformation of semicrystalline polymers: Quasi-static stress− strain relationship and viscous stress determined for a sample of polyethylene. Macromolecules 2004; 37:10165-10173.
2. O'Connell, Paul A, Hutcheson, Stephen, McKenna, Gregory. Creep behavior of ultra-thin polymer films. Journal of Polymer Science Part B: Polymer Physics 2008; 46: 1952-1965.
3. Chen, Ying, Ding, Xin, Li, Yuling, Zhao, Xueqian. The Infuence of Heat Setting Conditions on Mechanical Properties of PTT Filaments. Journal of Fiber Bioengineering and Informatics 2011; 4:51-58.
4. Khonakdar, HA, Morshedian, J, Wagenknecht, U, Jafari, SH. An investigation of chemical crosslinking effect on properties of high-density polyethylene. Polymer 2003; 44:4301-4309.
5. Oral, Ebru, Muratoglu, Orhun K. Radiation cross-linking in ultra-high molecular weight polyethylene for orthopaedic applications. Nuclear Instruments and Methods in Physics Research Section B: Beam Interactions with Materials and Atoms 2007; 265:18-22.

MECHANICS OF REINFORCEMENT OF POLYMER-BASED NANOCOMPOSITES BY 2D MATERIALS

Robert J Young [a], Zheling Li[a], Ian A Kinloch[a], Fang Wang[a], Weimiao Wang[a]

a: National Graphene Institute, Henry Royce Institute and Department of Materials, University of Manchester, Manchester, M13 9PL, UK – robert.young@manchester.ac.uk

Abstract: *Graphene is known to have high levels of stiffness and strength and so is an obvious candidate for the reinforcement of polymers. The mechanics of reinforcement by graphene are now understood through a theory we developed to predict the stiffness of the bulk nanocomposites from the mechanics of stress transfer from the matrix to the graphene reinforcement based upon the rule of mixtures and shear-lag deformation. Here we demonstrate how this theory can be extended to other types of ultrathin 2-dimensional (2D) materials, hexagon boron nitride, hBN and tungsten disulfide, WS_2.*

Keywords: 2D materials; nanocomposites; micromechanics; Raman spectroscopy; photoluminescence

1. Introduction

Following the successful exfoliation of graphene [1], ultrathin 2-dimensional (2D) materials with excellent and diverse mechanical, optical, thermal and electronic properties [2, 3] have attracted attention worldwide. In particular, nanometer-thick 2D hexagonal boron nitride (hBN) nanosheets (BNNSs), successfully exfoliated in Manchester [4] a few months after the first reports of graphene, have been the subject of particular interest. BNNSs are different from graphene, having a ~6 eV indirect band gap [5], and exhibit superior oxidation resistance [6], chemical and thermal stability [7, 8] compared with their carbon analogues. The reduced electron-delocalization in the B-N π bonds leads to the BNNSs having a large band gap [9], making them both electrically insulating and optically transparent.

Graphene is an electrical conductor that limits its wider applications where a bandgap is needed. Hence, transition metal dichalcogenides (TMD have started to attract attention since their tunable bandgap offers more controllability. As a typical example of TMDs, tungsten disulfide (WS_2) has received significant interest for applications in transistors [10], photo-detectors [11], photovoltaic devices [12] and composites [13]. Of particular interest is that WS_2 exhibits a transition from a direct- to indirect-bandgap semiconductor both as the number of layers increases [14] and when the WS_2 flakes are subjected to strain [15]. Beyond the electronic applications, WS_2 flakes have also been found to have a reasonable interfacial interaction with polymers as reflected by their good reinforcement of polymers, determined by their lateral size and its distribution, even at a low loading [16]. This sets the foundation for making use of WS_2 for the next generation multifunctional nanocomposites for a number of different applications, such as transistors, sensors, photo-detectors, photovoltaics and absorbers etc. [10-12].

In present study, we have used Raman spectroscopy to follow the deformation of BNNNs and combined Raman and photoluminescence spectroscopy to monitor the strain distributions in mechanically-cleaved monolayer WS_2 flakes, both deformed on flexible substrates.

  doi:10.5075/epfl-298799_978-2-9701614-0-0

2. Deformation of hBN nanosheets

Large single crystals commercial hexagonal boron nitride (hBN) were exfoliated mechanically and the flakes transferred using the standard tape cleavage technique The BNNSs were exfoliated using adhesive tape and deposited directly on the centre of a rectangular PMMA beam with no top coat applied. The BNNSs on the PMMA beams were identified and characterised using the Zeiss optical microscope on a Horiba LabRAM Evolution HR spectrometer with a 488 nm sapphire laser and a 50× lens. The in-situ Raman deformation analysis was conducted by inserting the BNNS-loaded PMMA beams into a four-point-bending rig fixed on the Raman microscope stage. A resistance strain gauge was used on the PMMA beam surface to monitor the strain applied on the PMMA substrate. The beams were deformed up to 0.4% strain in ~0.04% intervals and Raman spectra were collected and peak fitted at each strain level. The exposure time for each Raman scan was 20 s with a power output ~1.3 mW and a laser spot size of ~2 μm using a 50x objective lens. The most prominent Raman band of hBN is the E_{2g} mode which originates from in-plane atomic displacement and is equivalent to the G band of graphene. Raman line mapping was undertaken using a 100x objective lens.

Our previous work on 1L graphene [17] has demonstrated that it is possible to monitor stress transfer from a substrate to the flake of a 2D material by mapping the strain along the flake. Figures 1(a&b) shows a hBN nanosheet of 11 μm length and 17 nm (Figure 1(c)) in thickness deformed in tension parallel to its axis. An intense G band for the BN nanosheet can be seen in Figure 1(d). Figure 1(e) shows the Raman spectra obtained from the middle of the nanosheet (marked by a black square in Figure 1(b)) before and after 0.2% strain was applied. It can be seen that the G band clearly shifts to lower frequency and broadens after deformation. As shown in Figure 1(f), there is a linear red shift of the G band with stepwise straining up to 0.15%. The shift stops at 0.2% strain and eventually became irregular when a higher tensile strain was applied.

The Raman G band position was monitored along the solid line in Figure 1(b) in 1 μm steps. Figure 1(g) shows the variation of axial strain across the BNNSs flake when a low strain (~0.1%) was applied to PMMA substrate. It can be seen that the strain builds up from the two edges and becomes constant along the middle of the nanosheet where the strain in the flake equals to the applied matrix strain. This is analogous to what we observed for the strain distribution of a polymer-sandwiched graphene monolayer under relatively low strain (<0.4%) [17] for which there was good bonding between 2D material and polymer matrix. This behaviour can be analyzed by the well-established shear-lag theory [18] where it is assumed that the elastic stress is transferred from the matrix to the reinforcement through a shear stress at 2D material/polymer interface. The variation of strain in the BNNS, εBNNS, is given as

$$\varepsilon_{\mathrm{f}} = \varepsilon_{\mathrm{m}}\left[1 - \frac{\cosh\left(ns\frac{x}{l}\right)}{\cosh(ns/2)}\right] \qquad \text{where } n = \sqrt{\frac{2G_m}{E_{\mathrm{f}}}\left(\frac{t}{T}\right)} \qquad (1)$$

and ε_{m} is the applied matrix strain, s is the aspect ratio of the BNNS, x represents the position in the flake, l is the length of the flake, G_{m} is the matrix shear modulus, E_{f} is the Young's modulus of the 2D material, t is the thickness of the BNNS and T is the thickness of polymer matrix. The parameter n has been widely accepted as a parameter for evaluating the interfacial stress

1063/1602 ©2022 Robert et al. doi:10.5075/epfl-298799_978-2-9701614-0-0 published under CC BY-NC 4.0 license

transfer efficiency. The dashed line in Figure 1(g) is a reasonable fit of Equation (1) to the Raman mapping results using ns ~ 10. The aspect ratio for the hBN nanosheet in Figure 1 is s = 10 µm/17 nm ~ 590. Since for this BNNS, ns = 10 and so n = 0.017. This value of n is some 30x larger that the value of n = $6x10^{-4}$ determined for a sandwiched graphene monolayer on a polymer substrate [17]. The higher value of n implies that better stress transfer can be expected between BNNSs and a polymer matrix than for graphene, presumably a result of the more polar nature of the bonding in hBN.

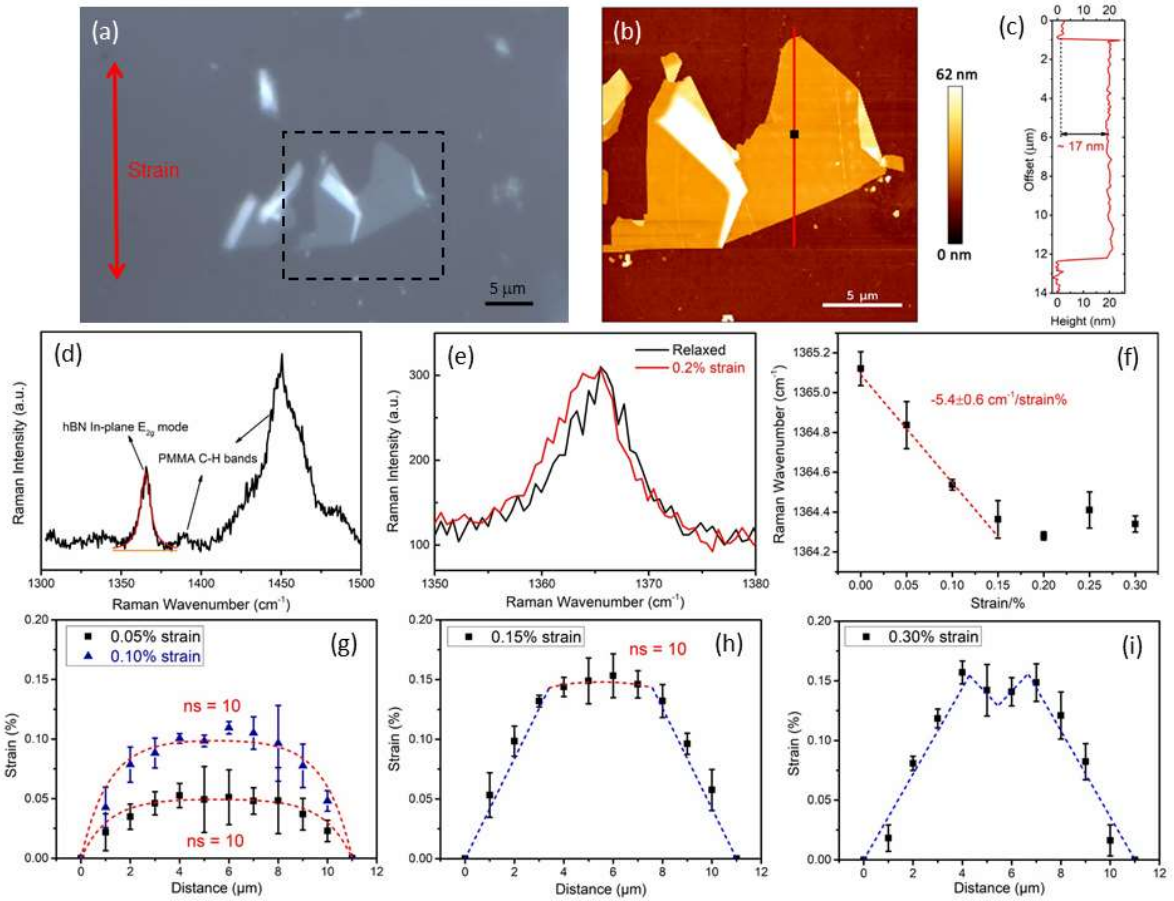

Figure 1. (a) Optical micrograph and (b) AFM image of the hBN nanosheet (outlined in (a)) used for linear Raman strain mapping (the black square in (b) marks the spectra collection position for (d-f)). (c) The AFM height profile corresponding to the solid red line in (b). (d) Raman spectrum of the hBN nanosheet. (e) Raman spectra of the BNNS obtained before and after a 0.2% tensile strain was applied. (f) The position of G band position as a function of tensile strain. (The error bars are the standard deviations of 5 measurements taken at the same position). Distribution of strain in the hBN nanosheet in the direction of the tensile axis along the solid line in (b) at: (g) 0.05%, 0.1% strain, (h) 0.15% strain and (i) 0.30% strain.

3. Deformation of WS_2 flakes

Monolayer WS_2 flakes were obtained by the exfoliation through the micromechanical cleavage of bulk WS_2 crystals with an average grain size of 200. The bulk WS_2 crystals were peeled repeatedly with an adhesive tape until very thin flakes were obtained. The flakes obtained were then transferred to the PMMA substrate by pressing the back of the adhesive film. After the

transfer, monolayer flakes were located and identified using optical microscopy and a combination of Raman and photoluminescence (PL) spectroscopy.

For deformation of the monolayer WS_2 flakes, the PMMA substrate was mounted on a 4-point bending rig and placed under the microscope stage of the Raman spectrometer. A resistance strain gauge was fixed to the PMMA beam close to the WS_2 flakes to monitor the strain. The specimen was then deformed stepwise with the Raman or PL spectra collected for each strain step. Mapping was undertaken using a grid sizes of 0.5 µm x 0.5 µm or 1 µm x 1 µm depending upon sizes of the flakes and the degree of precision needed. The laser was polarised parallel to the direction of tensile strain.

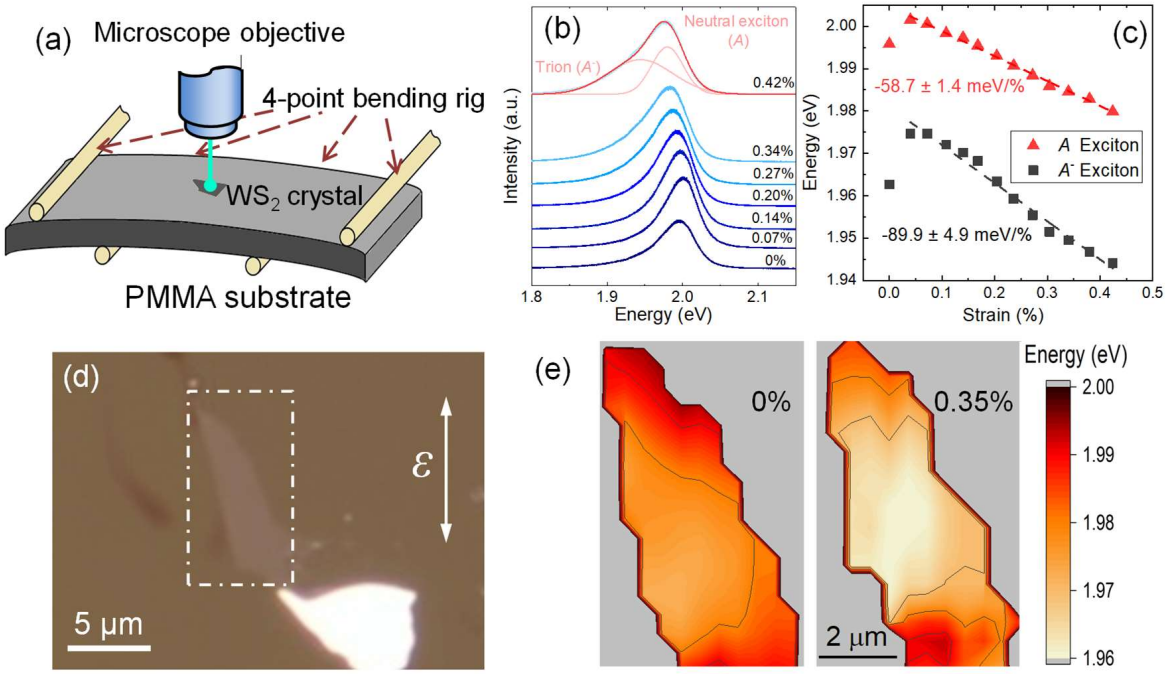

Figure 2. (a) Schematic drawing of the 'in-situ' deformation set up in PL and Raman spectroscopy. (b) Evolution of the PL spectrum of a monolayer WS_2 flake as strain increases. (c) The energies of A exciton and A^- exciton peaks as a function of strain, with the solid lines being the linear fitting. (d) Optical image of one monolayer WS_2 flake. (e) Map of the A exciton peak energy over the flake at (a) 0% and (b) 0.35% strain.

Figure 2a is the schematic diagram of the PMMA substrate in the 4-point bending rig placed on the stage of the Raman spectrometer. It should be noted that the size of WS_2 flake (~10 µm) is three orders of magnitude smaller than the length of substrate (~70 mm) so that the flake can be assumed to be strained uniaxially. A clear red-shift of the PL peak can be seen as the strain level increases, with the peak fitted with two Gaussian peaks (Figure 2b). In more detail, as the strain increases, the red-shift of both the A exciton peak and A- exciton peak is in the order of tens of meV as shown in Figure 2c, which agrees with other studies on TMDs. The shift rate is found to be -58.7 ± 1.4 meV/% strain for the A exciton peak, and 89.9 ± 4.9 meV/% strain for the A- exciton peak, respectively. The apparent tension at 0% strain is likely to be due to the residual strain induced during specimen preparation. The high values can be attributed to the better stress transfer efficiency as a result of the improved interaction of the WS_2 flake with the substrate in this present study.

1065/1602 ©2022 Robert et al. doi:10.5075/epfl-298799_978-2-9701614-0-0 published under CC BY-NC 4.0 license

The PL spectra *x-y* mapped on a 0.5 µm x 0.5 µm grid across a monolayer WS_2 flake without any visible contamination (Figure 2d) were collected at both 0% and 0.35% strain, A reduction of the energy (bandgap) can be clearly seen towards the centre of the flake for 0.35% strain (Figure 2e). This implies that the simple uniaxial tension applied to the monolayer flake on the substrate generates a non-uniform bandgap distribution across an individual WS_2 flake. This is of particular relevance for local fine tuning of the bandgap in a TMD flake through strain engineering [18]. The PL energy varies by some 40 meV over a regions of a few microns in the WS_2 monolayer crystals at 0.35% strain. Moreover this variation of PL energy can be controlled by the application of external strain to the substrate as long as the WS_2 monolayer crystals remain intact and do not debond from the substrate.

In order to investigate the micromechanics of monolayer WS_2 flake using Raman spectroscopy, the PMMA beam was deformed initially to a strain ~0.55%. The specimen was then released and top-coated with a thin layer of SU-8 photoresist polymer. In the second cycle the specimen was then loaded to the same strain of ~0.55%. Using the calibration between the Raman E^{1}_{2g} band and strain established earlier [5], the strain distributions of the uncoated monolayer WS_2 at 0% and 0.55% applied strain were mapped using a 1 µm x 1 µm grid as shown in Figure 3a&b, respectively. It can be seen that the strain distribution is quite uniform at 0% strain, apart from the compression at the edge of flake perhaps due to sample preparation. The similarity between the strain distributions shown in Figure 1 for a BNNS obtained using Raman spectroscopy and those obtained for a similar WS_2 monolayer specimen using PL in Figure 2 is striking.

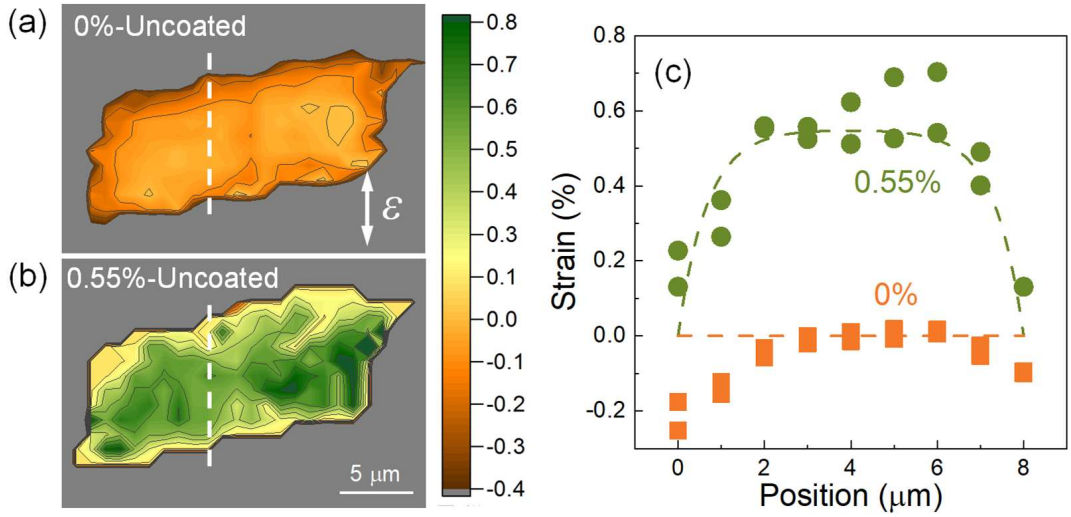

Figure 3. Strain distribution of uncoated monolayer WS_2 flake at (a) 0% and (b) 0.55% applied strain. (c) Extracted strain distribution in the region along the white dashed lines in (a) and (b) determined from the frequency of E^{1}_{2g} mode. The dashed lines are indicative of strain distribution at 0% and 0.55% strain drawn using the shear-lag analysis Eq. 1 with ns=12.

When the specimen was subjected to a strain of 0.55%, the strain in most of the WS_2 flake increased to about 0.55%, demonstrating effective stress transfer from the substrate to the flake. However, a slight strain concentration, higher than the applied strain ~0.55%, can be found in the bottom part perhaps due to defects. The data points extracted along the vertical dashed white lines in tensile strain direction (Figure 3c) clearly show a strain plateau in the middle of the flake at the strain of 0.55%, suggesting that monolayer WS_2 flake also follows the

  doi:10.5075/epfl-298799_978-2-9701614-0-0

shear lag behaviour [18]. Similarly, by using *ns* = 12 in Equation 1, the 'shear-lag' curve is drawn for an applied strain ~0.55% (Figure 3c) confirming the validity of shear-lag theory.

4. Conclusions

Stress transfer both between the individual layers within exfoliated hBN nanosheets and between a hBN nanosheet and a polymer substrate has been followed through the use of Raman spectroscopy. Overall, it has been demonstrated that the efficiency of stress transfer both between the individual hBN layers in the nanosheets and between the nanosheets and the substrate is better for BNNSs than for mono- or multi-layer graphene. The efficiency of interlayer stress transfer is 99% for hBN nanosheets [19] compared with around 70% for multilayer graphene. The critical aspect ratio for stress transfer to the substrate is only ~350 for BNNSs compared with >104 for monolayer graphene implying that better stress transfer to the substrate can be achieved with hBN nanosheets. The implication of this study is that BNNSs should also give rise to better reinforcement in nanocomposites than exfoliated graphene nanosheets as long as the BNNS/polymer interface remains intact. Also, it is less important to achieve a high degree of exfoliation to very thin nanosheets, when using hBN in nanocomposites, than in the case of graphite and graphene. Further details can be found in our recent publication [19].

Photoluminescence and Raman spectroscopy have been combined to successfully monitor the strain distribution and stress transfer of monolayer WS_2 on a flexible polymer substrate. It is demonstrated that monolayer WS_2 still follows continuum mechanics. Particularly, a non-uniform bandgap distribution has been achieved by strain engineering even within a single WS_2 flake due to the non-uniform strain distribution through stress transfer from the substrate. It has been demonstrated that this could have useful applications in optoelectronics in producing tuneable micron-sized PL emitters on a substrate. Their effective Young's modulus is around 30% of their theoretical modulus [20] which means that their reinforcement efficiency is comparable to that of few-layer graphene-reinforced nanocomposites. Further details and the extension of the study to high volume fraction nanocomposites an can be found in our recent publication [20].

Acknowledgements

This research has been supported by funding from the European Union Seventh Framework Programme under grant agreement n°604391 Graphene Flagship and the EPSRC (award no. EP/I023879/1). One of the authors (W. Wang) is grateful to the China Scholarship Council for financial support. We also wish to acknowledge support from the Royce Institute (EP/S019367/1, EP/P025021/1, & EP/R00661X/1).

5. References

1. Novoselov K S, Geim A K, Morozov S V, Jiang D, Zhang Y, Dubonos S V, Grigorieva I V and Firsov A A, 2004, Electric field effect in atomically thin carbon films, Science 306 666-9
2. Gupta A, Sakthivel T and Seal S, 2015, Recent development in 2D materials beyond graphene, Progress in Materials Science 73 44-126
3. Weng Q, Li G, Feng X, Nielsch K, Golberg D and Schmidt O G, 2018, Electronic and optical properties of 2D Materials constructed from light atoms, Advanced Materials 30 e1801600

4. Novoselov K S, Geim A K, Morozov S, Jiang D, Katsnelson M I, Grigorieva I, Dubonos S, Firsov and AA, 2005, Two-dimensional gas of massless Dirac fermions in graphene, Nature 438 197-200
5. Cassabois G, Valvin P and Gil B, 2016, Hexagonal boron nitride is an indirect bandgap semiconductor, Nature Photonics 10 262-6
6. Li L H, Cervenka J, Watanabe K, Taniguchi T and Chen Y, 2014, Strong oxidation resistance of atomically thin boron nitride nanosheets, ACS Nano 8 1457-62
7. Paine R T and Narula C K, 1990, Synthetic routes to boron nitride, Chemical Reviews 90 73-91
8. Weng Q, Wang X, Wang X, Bando Y and Golberg D, 2016, Functionalized hexagonal boron nitride nanomaterials: emerging properties and applications, Chemical Society Reviews 45 3989-4012
9. Jiang X-F, Weng Q, Wang X-B, Li X, Zhang J, Golberg D and Bando Y, 2015, Recent progress on fabrications and applications of boron nitride nanomaterials: A Review, Journal of Materials Science & Technology 31 589-98
10. Cui Y, Xin R, Yu Z, Pan Y, Ong Z Y, Wei X, Wang J, Nan H, Ni Z, Wu Y, Chen T, Shi Y, Wang B, Zhang G, Zhang Y W and Wang X 2015 High-performance monolayer WS_2 field-effect transistors on high-kappa dielectrics, Advanced Materials 27 5230-4
11. Tan H, Fan Y, Zhou Y, Chen Q, Xu W and Warner J H 2016 Ultrathin 2D photodetectors utilizing chemical vapor deposition grown WS_2 with graphene electrodes, ACS Nano 10 7866-73
12. Bernardi M, Palummo M and Grossman J C 2013 Extraordinary sunlight absorption and one nanometer thick photovoltaics using two-dimensional monolayer materials, Nano Letters 13 3664-70
13. Wang F, Kinloch I A, Wolverson D, Tenne R, Zak A, O'Connell E, Bangert U and Young R J, 2017, Strain-induced phonon shifts in tungsten disulfide nanoplatelets and nanotubes, 2D Materials 4 015007
14. Gutierrez H R, Perea-Lopez N, Elias A L, Berkdemir A, Wang B, Lv R, Lopez-Urias F, Crespi V H, Terrones H and Terrones M, 2013, Extraordinary room-temperature photoluminescence in triangular WS_2 monolayers, Nano Letters 13 3447-54
15. Blundo E, Felici M, Yildirim T, Pettinari G, Tedeschi D, Miriametro A, Liu B, Ma W, Lu Y and Polimeni A, 2020, Evidence of the direct-to-indirect band gap transition in strained two-dimensional WS_2, MoS_2 and WSe_2, Physical Review Research 2 012024
16. Eksik O, Gao J, Shojaee S A, Thomas A, Chow P, Bartolucci S F, Lucca D A and Koratkar N, 2014, Epoxy nanocomposites with two-dimensional transition metal dichalcogenide additives, ACS Nano 8 5282-9
17. Gong L, Kinloch I A, Young R J, Riaz I, Jalil R and Novoselov K S, 2010, Interfacial stress transfer in a graphene monolayer nanocomposite, Advanced Materials 22 2694-7
18. Young R J, Liu M, Kinloch I A, Li S, Zhao X, Vallés C and Papageorgiou D G, 2018, The mechanics of reinforcement of polymers by graphene nanoplatelets, Composites Science and Technology 154 110-6
19. Wang W, Li Z, Marsden A J, Bissett M A, Young R J, 2021, Interlayer and interfacial stress transfer in hBN nanosheets, 2D Materials, 8 035058
20. Wang F, Li S H, Bissett M A, Kinloch I A, Li Z, Young R J, 2020, Strain engineering in monolayer WS_2 and WS_2 nanocomposites, 2D Materials, 7 045022

ENHANCED MECHANICAL PROPERTIES OF HIERARCHICAL MXENE/CF COMPOSITES VIA LOW CONTENT ELECTROPHORETIC DEPOSITION

Yi Hu[a,b], Shaojie Pang[b], Jialiang Li[b], Jianjun Jiang[b], Dimitrios G. Papageorgiou[a]*

a: School of Engineering and Materials Science, Queen Mary University of London, London, E1 4NS, UK. *email: d.papageorgiou@qmul.ac.uk
b: School of Mechanical Engineering, Northwestern Polytechnical University, Xi'an 710072, P. R. China

Abstract: *The weak fiber-matrix interface is a bottleneck hindering the development of carbon fiber composites. In this work, an optimized electrophoretic deposition (EPD) approach was explored to improve the interface by depositing uniformly two-dimensional MXene ($Ti_3C_2T_x$) nanoparticles onto the surface of carbon fibers (CF). The MXene-CF hybrids were then used to fabricate continuous carbon fiber reinforced polymer (CFRP) composites. The results manifested that the presence of MXene nanoparticles on the CF surfaces could significantly increase the fiber surface energy and wettability, as well as their surface roughness. As a result, a remarkable increase of the interfacial strength and flexural properties of CFRP has been observed. The functionalized MXene-CF-epoxy composites witnessed a prominent enhancement of interlaminar shear strength (ILSS), flexural strength and monofilament tensile strength compared to their unfunctionalized counterparts (i.e., 75%, 50.4%, and 32.7%). The versatile EPD strategy proposed herein, constitutes a promising approach for CFRP modification that can lead to significantly improved performance.*

Keywords: MXene ($Ti_3C_2T_x$); nanocomposite; Carbon fiber reinforced resin matrix composites (CFRP); Electrophoretic deposition; Interfacial properties;

1. Introduction

Carbon fiber reinforced polymer composites (CFRP) have developed rapidly over the last decades due to their outstanding multifunctional properties, their light weight and possibilities for high volume manufacturing. However, despite their suitability for a number of applications such as in aviation, automotive, civil engineering, and sports, a number of obstacles remain to be solved. The low wettability of CFs and their poor interaction with the polymer matrices, induced by their hydrophobic characteristics and chemical inertness usually result in inferior off-axis properties of CFRPs [1]. Indeed, the weak out-of-plane performance of CFRPs is closely associated with resin-dominated attributes in the radial direction. The resin-rich regions are located between the fiber laminates, where stress is commonly concentrated and cracks firstly initiate and then propagate. On that basis, engineering a strong fiber-matrix interface by selectively reinforcing matrix-rich regions can be beneficial in enhancing the load-transfer capability in order to fully exploit the superior mechanical properties of CFRPs [2].

A number of treatments have been proposed in the literature to improve the interface between the fibres and the matrix. One of the most commonly used strategies is the surface modification of CFs by introducing nanoparticles onto fiber surface via chemical vapor deposition (CVD) [3],

  doi:10.5075/epfl-298799_978-2-9701614-0-0

electrolytic deposition (ELD). [4], spray coating [5], surface desizing, and chemical grafting [6], as well as electrophoretic deposition (EPD) [7]. Unfortunately, some of these strategies do not induce significant improvements due to intrinsic restraints. For example, ELD is restricted to the deposition of metal particles, while fiber sizing decreases the surface roughness which leads to a deterioration of the stress transfer ability and energy-absorbing capacity. Additionally, the CVD treatment can lead to detrimental effects on the fibre structure due to high temperatures, while it inevitably degrades their intrinsic strength. The high growth temperatures in combination with pre-deposited catalysts make it also impractical for large-scale production. Spray coating is quite effective but involves a large amount of chemicals needed to disperse the nanomaterials that are necessary to be fully evaporated from the CF surface before the introduction of the resin. Finally, chemical grafting requires complicated chemical reactions on the CF surface, accompanied with an excessive use of solvents, while processing times tend to be quite long. Compared to these strategies, EPD can enhance the deposition quality and production efficiency at the same time. With the application of EPD it is possible to achieve controllable coating thickness and uniform material deposition on flexible substrates with different shapes and sizes, making it easier to realise an automated manufacturing process. Finally, EPD can lead to a homogeneous nanoparticle deposition at low solution concentrations which is very important for large-scale, continuous industrial production [8].

High-performing nanomaterials such as graphene and carbon nanotubes (CNTs) have been introduced by EPD onto the surface of carbon fibres. MXenes are 2D nanomaterials originating from MAX phases with the general formula $M_{n+1}AX_n$ (where n=1-3 and M denotes an early transition metal, A represents III A group and IV A group elements and X stands for carbon and/or nitrogen) that have shown great potential as reinforcements in composites due to their inherent properties [9]. A $Ti_3C_2T_x$ monolayer has been reported to display a Young's modulus of 0.33±0.03 TPa as measured by nanoindentation, comparable with that of graphene oxide (~0.2 TPa) [10]. The covalent/ionic/metallic character of the M-X bond and the metallic character of the M-A bond endow MXenes with ultra-strong interlayer bonding that cannot be broken by shear or any mechanical means. This makes them highly suitable for improving the strength of the fibre/matrix interface. A number of functional, MXene-reinforced hierarchical composites present a huge application potential in the electromagnetic absorption/interference field as a result of the exceptional conductivity of MXene nanoplatelets. Up to now, the incorporation of MXene nanoparticles into CFRP composites by EPD remains largely unexplored, and the potential impact of MXenes on the field is still unknown. For instance a major problem lies in the fact that MXenes can be easily oxidised; that can lead to a significant deterioration of their mechanical and electrical properties, which is in contrast with the behaviour of GO and CNT.

During EPD, the amount of the deposited particles is related to the electric field strength. The nonuniformity of the electric field tends to produce an inhomogeneous deposition [11]; thus, a highly homogeneous electric field is indispensable to ensure a successful EPD process with high deposition density. Unfortunately, CF fabrics possess anisotropic electrical conductivity, so once they’re immersed into the solution bath, the distinct differences of voltage will appear vertically along with the immersed depth and cause non-uniform deposition thickness [12]. As a result, many works utilized conductive metal frames to clamp the edges of a CF fabric in an attempt to reduce variations in the intensity of the electric field [13]. This method can provide some improvements when the area of CF fabric is small and the processing time is not an issue. However, the deposition density of nanoparticles in these works tended to present an

  doi:10.5075/epfl-298799_978-2-9701614-0-0

undesirable gradient; The deposition efficiency adjacent to the conductive frame was higher, while the center of the CF fabric displayed the lowest deposition content [14]. As can be understood, such phenomena will be more evident for large-area deposition by EPD, which can also lead to longer deposition times of charged particles for low electric field areas. Quite interestingly, the utilization of a copper mesh can be a viable choice to overcome such a dilemma. Compared with the gradient electric field commonly induced by metal frames, a more homogeneous electric field can be achieved with the help of the copper mesh thanks to its spatial structure and superior conductive properties, leading to a uniform nanoparticle deposition thickness.

Given the above considerations, this work utilized MXene nanoparticles homogeneously deposited onto CF surfaces through a modified EPD process to improve the fiber-matrix interface in a CFRP. The EPD method was carefully optimized to impose a uniform electric field and to prevent oxidation and agglomeration of MXenes onto the CFs. The $Ti_3C_2T_x$ nanoplateletes were initially synthesized through consecutive etching, intercalation and freeze-drying. Desizing and oxidation pre-treatments were performed on the carbon fibres to enhance the wettability and reactivity of CF fabrics. The ultra-low concentration MXene suspension was employed to perform the EPD process. Once the MXenes were deposited onto the CF preform, the hybrid structure was infused with the epoxy resin through vacuum-assisted resin infusion (VARI). The effects of MXene-CF on the interfacial CFRP properties were evaluated through a series of characterizations and mechanical tests.

2. Methods

2.1 Electrophoretic deposition of $Ti_3C_2T_x$ onto CFs

The anodic electrodeposition technique was adopted due to the high electronegativity of MXene nanoparticles. However, since MXenes can be oxidized quite easily [15], two optimized processes have been introduced. The first process is illustrated in Fig. 1a, where the pre-treated CF tow was the rectangular positive electrode; fixed copper sheets were positioned alongside the four edges to achieve a uniform electrical field and prevent the fabrics from deformation. Two planar graphite plates were used as the cathode to electrophoretically deposit MXenes onto CF. The process reduced the deposition time to half (10 min) than the original method (20 min) introduced in [16], which used only one graphite sheet, while the CF fabric must be manually reversed to realize a nanomaterial deposition in both sample sides during EPD. To overcome the current dilemma where researches are commonly focusing on a simple planar shape electrode, we utilized a cylindrically shaped graphite plate as the cathode (Fig. 1b). The anode presented a core-shell appearance, with CF fabric as the mandrel, and a copper mesh (which displays excellent electrical conductivity and ductility) was used to tightly surround the CF surface to produce a spatially uniform electric field. The obtained product is denoted as m-MXene-CF, where m stands for modified. The optimized process enhanced both the MXene deposition efficiency and homogeneity. The circumferentially wrapped copper mesh onto the surface of the pretreated CF bundle prevented the fiber tow from deformation and bending, making it easier to deposit nanoparticles uniformly. Additionally, the superior electrical conductivity of the copper net could effectively reduce any variations in the intensity of the electric field, which led to a more homogeneous deposition of nanoparticles for the CF bundle.

  doi:10.5075/epfl-298799_978-2-9701614-0-0

During the EPD process the distance between anode and cathode was 2 cm and a 0.1 M NaOH solution was used to adjust the pH to 10 to form a stable and homogeneous MXene slurry. Notably, an ultra-low MXene suspension concentration of 0.125 mg/mL was adopted to relieve the agglomeration of nanoparticles and decrease the producing cost. A low voltage of 20 V for 10 min was employed through DC power supply. Ultrasonication was used to reduce the formation of agglomerates of large nanoparticles and reduce the bubbles that water-electrolysis produced, contributing to a homogeneous deposition layer. Finally, an ice bath was utilized during the EPD process to maintain a low suspension temperature as excessive voltage and ultrasonication in the presence of the electrolyte would produce much Joule heat that can lead to the development of a hydrothermal environment, which can potentially and undesirably oxidise the MXene nanofillers.

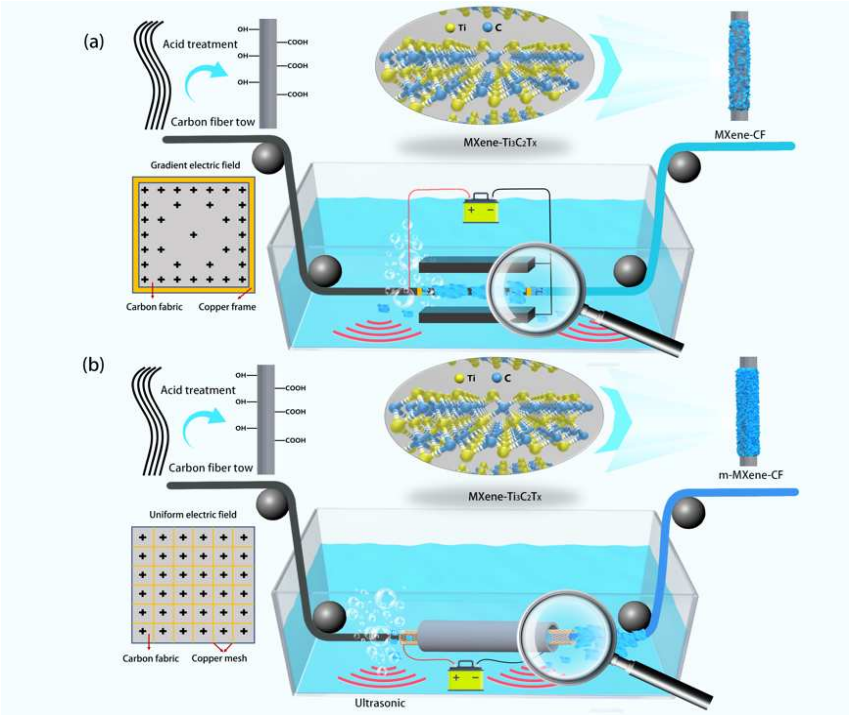

Fig. 1. The EPD process for the fabrication of (a) MXene-CF and (b) m-MXene-CF.

2.2 Preparation of CF/epoxy resin composites by liquid composite molding

The CFRP composites were prepared by vacuum assisted resin infusion (VARI). Firstly, CF fabrics pretreated by desizing, oxidation and MXene deposition processes were laid up unidirectionally on the surface of the aluminium mold. The vacuum compaction was carried out under -0.1 MPa for one hour. Afterwards, the 5015 epoxy resin monomer and curing agent were uniformly blended with a mass ratio of 100:30. The vacuum pumping of the contained gas in the resin took place for 30 mins, followed by resin infusion. Finally, the curing process took place in a vacuum oven at 90℃ for 8h. The final fiber mass loadings of desized CFRP, oxidized CFRP, Mxene-CFRP and m-MXene-CFRP were 57.4%, 58.2%, 58.4% and 58.5%.

  doi:10.5075/epfl-298799_978-2-9701614-0-0

3. Results and Discussion

3.1 Primary characterization of MXene nanoplatelets

The SEM images (Fig. 2a and Fig. 2b) show the evolution from a dense multilayer MAX phase to a loosely stacked MXene structure as a result of etching and exfoliation treatments. The surface morphology of the nanoplatelets from AFM (Fig. 2c) indicated that the MXene nanosheets displayed a thickness of 2.76 nm, demonstrating that 2-3 nanosheet layers were stacked together [17]. Fig. 2d shows the synthesized MXene nanopowders in a glass vial. Fig. 2e shows the typical Tyndall effect of a MXene suspension in a water medium.

XRD was employed to characterize the MXene structure (Fig. 2f). The characteristic peak located at 39° assigned to reflection from the (104) plane was apparent in Ti_3AlC_2 diffraction patterns, while after etching, that peak vanished for $Ti_3C_2T_x$. This is an indication that the Al element has been etched successfully. Additionally, the (002) peak shifted towards a lower angle, from 9.52° (d = 0.92 nm) for the original Ti_3AlC_2 to 6.22° (d =1.42 nm) for $Ti_3C_2T_x$, verifying once again the successful intercalation process. The increased layer spacing should be ascribed to the intercalation effect of Li+ and ethanol [18].

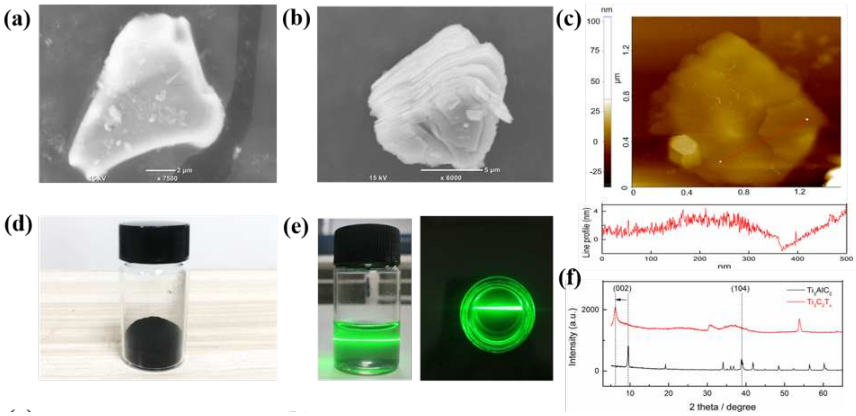

Fig. 2. (a) SEM image of Ti3AlC2; (b) SEM image of Ti3C2Tx; (c) AFM image and line profile of Ti3C2Tx; (d) Image of synthetic Ti3C2Tx powder; (e) Tyndall effect of Ti3C2Tx water solution; (f) XRD patterns of Ti_3AlC_2 and $Ti_3C_2T_x$

3.2 Surface morphology of CF

AFM and SEM were used to ascertain the effect of desizing, oxidizing, and EPD processes. It can be clearly seen in Fig. 3 that the surface of the desized CF was smooth (the surface roughness, R_a was 61 nm) with a few narrow crenulations observed in the longitudinal direction (Fig. 3a). After the nitric acid treatment, as expected, the oxidized CF surface became rougher (R_a=87 nm), and deeper grooves appeared on the CF surface due to etching (Fig. 3b). A significantly rougher surface increases the friction between disparate surfaces to inhibit interlaminar sliding and provide more contact sites for mechanical interlocking between the epoxy matrix and carbon fiber. Meanwhile, it could significantly improve the interfacial adhesion by enhancing the fiber surface wettability, which is crucial for enhancing the interfacial properties through improved fiber-matrix adhesion [19].

During the EPD process, the negatively charged Ti_3C_2-OH nanoparticles moved to the vicinity of CF hydroxy/carboxyl units under the applied electric field, and then hydrogen bonds were

1073/1602 ©2022 Papageorgiou et al. doi:10.5075/epfl-298799_978-2-9701614-0-0 published under CC BY-NC 4.0 license

formed when the MXene nanosheets were homogeneously deposited onto the surface of CFs. Consequently, the CF surfaces became coarser (Fig. 3c,d) (R_a=123 nm for MXene-CF, R_a=142 nm for m-MXene-CF) and the formation of these bonds led to an improvement of the MXene/CF interfacial adhesion while it also helped to prevent any agglomeration during EPD. In conclusion, MXene particles were uniformly distributed on the CF surface via EPD, and the m-MXene-CF samples demonstrated a more homogeneous dispersion and a higher deposition rate than the MXene-CF as a result of the application of a more homogeneous electric field thanks to the assistance of the strategically positioned copper mesh.

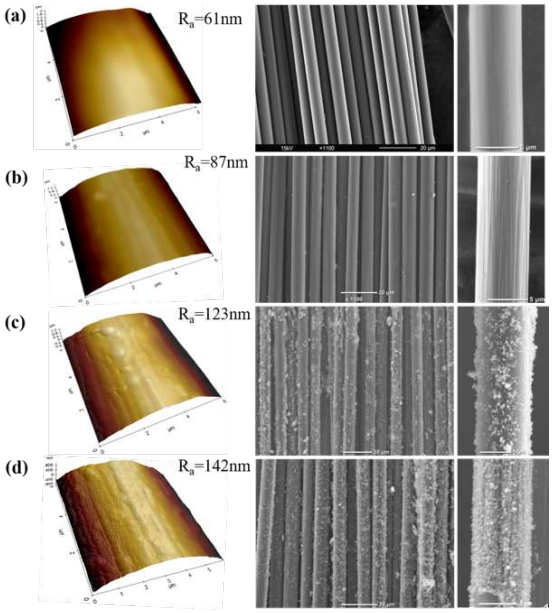

Fig. 3. AFM (left) and SEM (right) morphologies of treated CF. (a) Desized CF; (b) Oxidized CF; (c) MXene-CF; (d) m-MXene-CF.

3.3 Three-point bending of CFRP composites

Three-point bending tests were utilized to assess the flexural performance of CFRP composites. Based on the stress-strain curves presented in Fig. 4 (a), the corresponding flexural strength and modulus could be calculated and the results are presented in Fig. 4(b). The four curves display linear elastic behaviour at low strains. Subsequently, it is very possible that some cracks were formed in the resin and the load values presented a catastrophic decline with continuous increase of strain. It is interesting that the CFRP laminate displayed typical progressive damage behaviour as a result of enhanced bearing stress bearing capacity. The oxidized CF CFRPs showed a superior load-bending resistance (8.4% enhancement in bending strength compared with the desized CF/EP composite) but fracture took place much faster. For the EPD-deposited MXene-CF samples (MXene-CF/EP and m-MXene-CF/EP), the flexural properties were further improved; the MXene-CF/EP composite displayed a flexural strength of 531.3 MPa (an improvement of 22.2% compared to desized CF (435.04 MPa)). After the optimization of the EPD process, the flexular strength further increased to 654.38 MPa, while the flexural modulus presented a similar changing tendency, with the m-MXene-CF/EP composite displaying an increase of 16% compared to the desized CF composites.

1074/1602 ©2022 Papageorgiou et al. doi:10.5075/epfl-298799_978-2-9701614-0-0 published under CC BY-NC 4.0 license

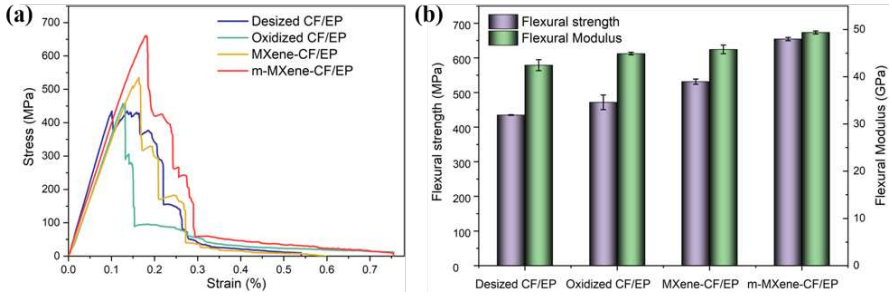

Fig. 4. (a) The stress-strain curves and (b) flexural properties of the produced CFRP composites.

3.4 Interlaminar Shear Stress of CFRP composites

Finally, short beam shear experiments were performed to evaluate the strength of the interphase between the carbon fibre and the matrix. The fractography of the ILSS specimens was also studied from SEM images. From the stress-strain curves in Fig. 5(a), the maximum stress and the slope of the curves gradually increased from the minimum values displayed by the desized CF/EP composite up to the maximum values from the m-MXene-CF/EP composite. The results indicate the improved interlaminar performance with each modification step. Additionally, as illustrated in Fig. 5(b), the m-MXene-CF/EP composites presented the optimum interfacial adhesion with the highest ILSS value (56.4 MPa), an improvement of 75% compared with that of desized CFRP (32.31 MPa). This fact clearly reveals the effectiveness of the modification of the EPD process that is proposed herein and the beneficial characteristics of MXene nanoparticles as CF coating.

The fracture topographies presented Fig. 5(d)-(g) showed that the fractured surfaces were smooth for the desized CFRP composites (Fig. 9d). The evident interfacial debonding revealed that the interfacial adhesion between fiber and matrix was weak. For the oxidized CFRP composites (Fig. 5e), the areas where the matrix fractured became slightly rougher, and the fracture morphology presented feather-like features. These can be regarded as evidence that the fracture mode was not brittle as in previous samples. As soon as the CFs were processed with EPD (Fig. 5f-g), the MXene nanoparticles were compactly attached to the fiber surface. The fracture process took place simultaneously for the resin and the carbon fiber under the synergistic work of enhanced CF surface roughness and local stiffening effect that oxidation and EPD of MXenes induced. Notably, the m-MXene-CF/EP composites displayed a highly homogeneous MXene nanoparticle distribution which led to an optimal ILSS performance. It is impressive that in the present work such a small amount (0.125 mg/mL) of the MXene suspension led to such a pronounced improvement (75% increase) in the ILSS of the CFRP composite. The effectiveness of our method remains outstanding even if compared to other deposition methods (chemical grafting, dip coating, etc.) of nanoparticles (MXene, CNT, GO, GNPs) onto similar types of CF (such as commercial CF, unsized CF, oxidized CF, NH_2-CF and others).

1075/1602 ©2022 Papageorgiou et al. doi:10.5075/epfl-298799_978-2-9701614-0-0 published under CC BY-NC 4.0 license

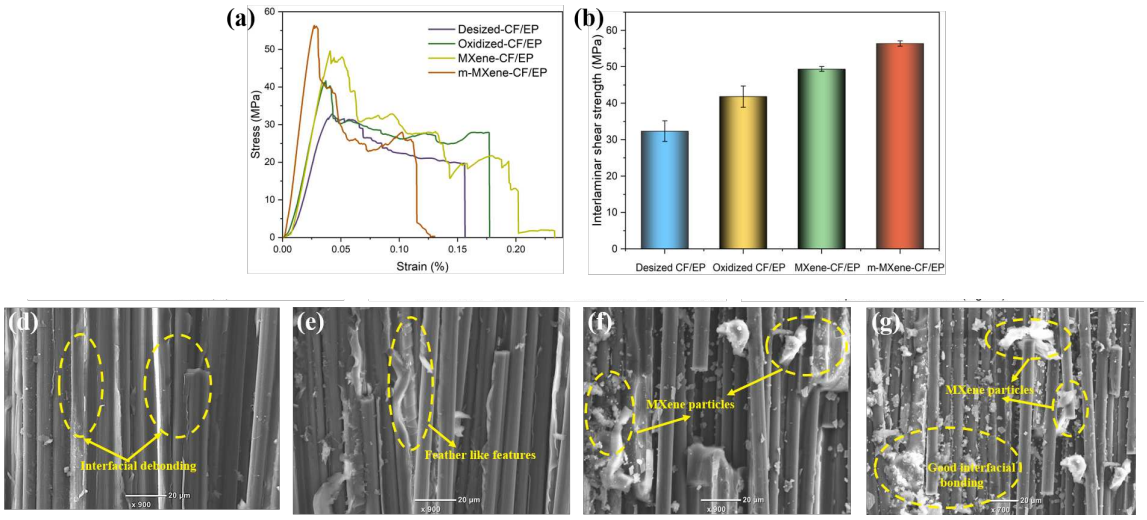

Fig. 5. (a) Stress-strain curves from short beam bending of the CFRP composites; (b) ILSS of the CFRP composites. SEM images of the fracture morphology of (d) Desized CF/EP; (e) Oxidized CF/EP; (f) MXene-CF/EP and (g) m-MXene-CF/EP.

4. Conclusions

A MXene-based EPD process was explored and optimized in this present work. The presence of the copper mesh attached to the CF surfaces enabled an improved homogeneity of the MXene nanoparticles deposition in virtue of a significantly more homogeneous electric field. Through a series of characterization processes, it was realized that MXenes could significantly strengthen the attachment between CF and resin matrix at the composite interface by mechanical interlocking, local stiffening, and hydrogen bonding. Consequently, the constructed hierarchical composite structure (m-MXene-CF-EP) displayed exceptional mechanical properties. The ILSS was improved by 75% (highest values amongst similar samples in the literature), the flexural strength was enhanced by 50%, and the monofilament tensile strength was augmented by 32%. This work has proven successfully that the use of MXene nanomaterials in combination with the EPD method can lead to a significant improvement of the interfacial properties of CFRP. The proposed practice is beneficial for further exploring and building a continuous EPD production line to manufacture superior mechanical CF/MXene/EP hierarchical composites on an industrial scale while it also provides valuable guidance for the successful production of nanoparticle-modified smart fabrics via EPD on nonconducting substrates such as glass, cotton, and cellulose.

Acknowledgements

This research is supported by the “National Natural Science Foundation of China” (No. 11902256, 51573148) and the Natural Science Basic Research Program of Shaanxi (No.2019JQ-479). D.G.P. acknowledges the support from “Graphene Core 3” GA: 881603 which is implemented under the EU-Horizon 2020 Research & Innovation Actions (RIA) and is financially supported by EC-financed parts of the Graphene Flagship. Y.H. would like to thank the Chinese Science Council for funding his stay at QMUL.

  doi:10.5075/epfl-298799_978-2-9701614-0-0 published under CC BY-NC 4.0 license

References

[1] Ding R, Sun Y, Lee J, Nam J-D, Suhr J. Enhancing interfacial properties of carbon fiber reinforced epoxy composites by grafting MXene sheets (Ti2C). Composites Part B: Engineering. 2021;207:108580.
[2] Kim S-H, Park S-J. Effect of graphene oxide/graphitic nanofiber nanohybrids on interfacial properties and fracture toughness of carbon fibers-reinforced epoxy matrix composites. Composites Part B: Engineering. 2021;227:109387.
[3] Anthony DB, Qian H, Clancy AJ, Greenhalgh ES, Bismarck A, Shaffer MS. Applying a potential difference to minimise damage to carbon fibres during carbon nanotube grafting by chemical vapour deposition. Nanotechnology. 2017;28:305602.
[4] Hou D, Zhou W, Liu X, Zhou K, Xie J, Li G, et al. Pt nanoparticles/MoS2 nanosheets/carbon fibers as efficient catalyst for the hydrogen evolution reaction. Electrochimica Acta. 2015;166:26-31.
[5] Li Y, Zhang H, Liu Y, Wang H, Huang Z, Peijs T, et al. Synergistic effects of spray-coated hybrid carbon nanoparticles for enhanced electrical and thermal surface conductivity of CFRP laminates. Composites Part A: Applied Science and Manufacturing. 2018;105:9-18.
[6] Wu G, Ma L, Jiang H, Liu L, Huang Y. Improving the interfacial strength of silicone resin composites by chemically grafting silica nanoparticles on carbon fiber. Composites Science and Technology. 2017;153:160-7.
[7] Lee JU, Park B, Kim B-S, Bae D-R, Lee W. Electrophoretic deposition of aramid nanofibers on carbon fibers for highly enhanced interfacial adhesion at low content. Composites Part A: Applied Science and Manufacturing. 2016;84:482-9.
[8] Wu Y, Dhamodharan D, Wang Z, Wang R, Wu L. Effect of electrophoretic deposition followed by solution pre-impregnated surface modified carbon fiber-carbon nanotubes on the mechanical properties of carbon fiber reinforced polycarbonate composites. Composites Part B: Engineering. 2020;195:108093.
[9] Gogotsi Y, Anasori B. The rise of MXenes. ACS Publications; 2019. p. 8491-4.
[10] Lipatov A, Lu H, Alhabeb M, Anasori B, Gruverman A, Gogotsi Y, et al. Elastic properties of 2D Ti3C2T x MXene monolayers and bilayers. Science advances. 2018;4:eaat0491.
[11] An Q, Rider AN, Thostenson ET. Electrophoretic deposition of carbon nanotubes onto carbon-fiber fabric for production of carbon/epoxy composites with improved mechanical properties. Carbon. 2012;50:4130-43.
[12] Kwon YJ, Kim Y, Jeon H, Cho S, Lee W, Lee JU. Graphene/carbon nanotube hybrid as a multi-functional interfacial reinforcement for carbon fiber-reinforced composites. Composites Part B: Engineering. 2017;122:23-30.
[13] Yuan X, Zhu B, Cai X, Qiao K, Zhao S, Zhang M, et al. Micro-configuration controlled interfacial adhesion by grafting graphene oxide onto carbon fibers. Composites Part A: Applied Science and Manufacturing. 2018;111:83-93.
[14] Joung YS, Buie CR. Antiwetting fabric produced by a combination of layer-by-layer assembly and electrophoretic deposition of hydrophobic nanoparticles. ACS applied materials & interfaces. 2015;7:20100-10.
[15] Zheng Z, Guo C, Wang E, He Z, Liang T, Yang T, et al. The oxidation and thermal stability of two-dimensional transition metal carbides and/or carbonitrides (MXenes) and the improvement based on their surface state. Inorganic Chemistry Frontiers. 2021;8:2164-82.
[16] Jiang J, Yao X, Xu C, Su Y, Deng C, Liu F, et al. Preparation of graphene oxide coatings onto carbon fibers by electrophoretic deposition for enhancing interfacial strength in carbon fiber composites. Journal of The Electrochemical Society. 2016;163:D133.
[17] Monastyreckis G, Mishnaevsky Jr L, Hatter C, Aniskevich A, Gogotsi Y, Zeleniakiene D. Micromechanical modeling of MXene-polymer composites. Carbon. 2020;162:402-9.

  doi:10.5075/epfl-298799_978-2-9701614-0-0

[18] Wang L, Chen L, Song P, Liang C, Lu Y, Qiu H, et al. Fabrication on the annealed Ti3C2Tx MXene/Epoxy nanocomposites for electromagnetic interference shielding application. Composites Part B: Engineering. 2019;171:111-8.
[19] Li Q, Church JS, Naebe M, Fox BL. Interfacial characterization and reinforcing mechanism of novel carbon nanotube–Carbon fibre hybrid composites. Carbon. 2016;109:74-86.

  doi:10.5075/epfl-298799_978-2-9701614-0-0

REMOTE FIELD INDUCED RESPONSE OF POLYMER NANOCOMPOSITES EMBEDDED WITH SURFACE-FUNCTIONALISED DIELECTRIC NANOPARTICLES

Danning Li[1,], James Barrington[2], Stephen James[2], David Ayre[1], Marcin Słoma[3], Meng-Fang Lin[4], Hamed Yazdani Nezhad[1,5,*]*

[1]Enhanced Composites and Structures Centre, School of Aerospace, Transport and Manufacturing, Cranfield University, Cranfield, UK
[2]Centre for Engineering Photonics, School of Aerospace, Transport and Manufacturing, Cranfield University, Cranfield, UK
[3]Faculty of Mechatronics, Warsaw University of Technology, Warsaw, Poland
[4]Department of Materials Engineering, Ming Chi University of Science and Technology, New Taipei, Taiwan
[5]Aeronautics and Aerospace Research Centre, Department of Mechanical Engineering and Aeronautics, City, University of London, London, UK
*Corresponding authors: danning.li@cranfield.ac.uk and hamed.yazdani@city.ac.uk

Abstract: M*atrix toughening is one of the most popular approaches to improve the overall fracture toughness of polymer composite materials. The most widely known approach for matrix toughening is the addition of a second phase such as rigid or/and rubber particles to dissipate the fracture energy, and vessels that containing healing agents that prevent further crack propagation when ruptured. Only a few studies have shown an alternative 'active toughening' by introducing an internal compressive stress field in the matrix via the mismatch in filler/matrix thermal expansion under heating. In this study, epoxy composite materials with embedded ferroelectric barium titanate nanoparticles are fabricated with the aid of silane surface functionalisation. Surface-bonded fibre grating sensors are employed to investigate the strain and temperature change of the epoxy nanocomposite materials under microwave exposure, as an attempt to introduce such field aided strain tailoring of the epoxy matrix as an active toughening mechanism.*

Keywords: Multifunctional nanocomposites; Matrix toughening; Ferroelectrics; Barium titanate; Domain wall movement

1. Introduction

High-performance composites have two major damage initiation modes when exposed to dynamic events; intra-laminar damage (e.g., matrix cracking, fibre fracture and fibre-matrix debonding) and inter-laminar damage (e.g., delamination). The intra-laminar damage is mainly dominated by matrix, fibre, and fibre-matrix interphase properties. However, it is challenging to tailor the properties of the fibre during composite's fabrication process. Therefore, the most widely adopted approach is matrix toughening owing to the diverse feasibility of its manufacturing [1]. A composite is mainly made of thermoset resins such as epoxy with a highly cross-linked structure to achieve optimal mechanical properties and thermal stability. Despite its advantageous properties, epoxy has its drawbacks of having inherent brittleness that tends to fail at relatively low fracture energy, especially under transversal direction or when subjected

  doi:10.5075/epfl-298799_978-2-9701614-0-0

to high strain rate or impact loading [2-4]. Alternatively, thermoplastic-based FRPs could hinder microcracks coalesce and growth owing to their relatively higher toughness and semi-crystalline structures in variants such as poly-ether-ether-ketone (PEEK) [5], widely used for engineering applications in the aeronautical and automotive sectors [6]. To overcome these property-driven drawbacks, numerous researches have been carried out for property enhancement via modifying epoxy with the inclusion of various micro- and nano-fillers as a second phase, such as rubber toughenens [7], silica particles [8], carbon nanoparticles [9, 10], clay [11] and others [12-16]. Although the modified epoxy with particles exhibits a promising future with excellent toughening performance, microcracks still formed in FRPs when subjected to varying or extreme operating conditions or during the manufacturing [17], indicating an inherent level of uncertainty in the material's response that will require active toughness enhancement across the material.

In this study, dielectric nanomaterials exhibiting electric field induced strain are utilized as a vision for an active toughening mechanism. Such induced strain is attributed to intrinsic mechanisms from lattice deformation and extrinsic mechanisms due to domain wall (DW) movement [18], extensively used as actuators and transducers. The inclusion of such material within a rigid epoxy materials can impose a compressive stress field in its surrounding epoxy matrix when activated its DW movements by external electric field stimulation. As result of the DW movements, a microwave stimulation at GHz frequencies induces effective dipolar displacement (leading to intrinsic strains) to the nanomaterial's molecules that, at the interface with their surrounding rigid polymer, is converted to compressive mechanical strain (Figure 1). The hypothesis of this research was based upon suggesting that microcrack propagation during dynamic and impact events would be suppressed under such microwave induced compressive field, i.e. higher strain energy would be required to create new fracture surfaces, however the current article presents attempts on the quantification of the field induced strains.

In a mono-domain ferroelectric crystal, the electric field-induced strain is generated by the intrinsic electrostriction and piezoelectric effect. In both poly-domain single crystal and polycrystalline ferroelectric materials, the domains that contain spontaneous polarisation in various directions can be aligned to the same direction by applying an external electric field. In a poly-domain ferroelectric crystal, the macroscopic strain is significantly dominated by the contribution of extrinsic strain [19]. Extrinsic effects occur at longer length-scales and the main contributor is domain wall motion, a major motivation for the hypothesis behind the development of the current research. The non-180° domain wall motion is the primary but not the only contribution of the extrinsic strain effect. Furthermore, the 90° domain wall movement also contributes to enhanced electromechanical performance in tetragonal BaTiO3 single crystals with nanodomain configurations [20, 21]. The 90° domain switching in BaTiO3 introduces a large electro-strain due to the exchange of two different crystallographic axes, and the field induced strain is one or two orders of magnitude larger than the linear electro-strain of piezoelectric materials. BaTiO3 crystals exhibit more complex domain structures due to different crystallographic axes in the tetragonal phase. Apart from the normal parallel 180° domains, there also exist adjacent domains that are polarised at 90° to each other. It is observed by Hsiang et al. [18] that the 40-80 nm BaTiO3 powders exhibit a single-domain structure while powders with sizes larger than 80 nm are polydomain tetragonal structures (the case examined by this research). Moreover, Dudhe et al. observed the 90° and 180° nano-domains of 80 nm BaTiO3 nanoparticles. Other studies focused on the polydomain structure of BaTiO3 nanoparticles with

  doi:10.5075/epfl-298799_978-2-9701614-0-0

the grain size of 50-70 nm found that the domain size is 10-12 nm [22]. In this research, polydomain BaTiO3 nanoparticles is employed to achieve the field-induced strain effect.

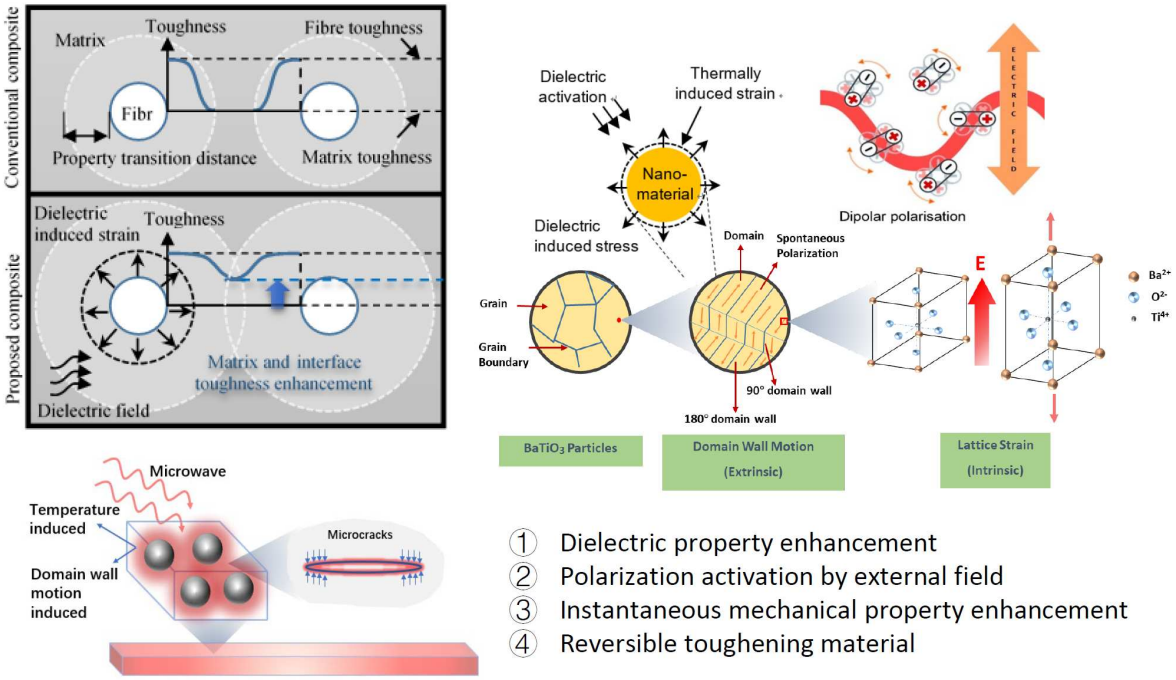

Figure 1. Schematic diagram of the extrinsic strain and intrinsic strain that contributes to macroscopic strain in a BaTiO3 particles embedded epoxy

2. Materials and Fabrication

The epoxy used in this study was Araldite LY1564, a diglycidyl ether of bisphenol A (DGEBA) and the curing agent was Aradur 3487, an amine hardener, supplied by Huntsman, UK. This epoxy resin system has relatively low viscosity and high flexibility mainly for aerospace and industrial structural composites parts. The coupling agent for surface functionalisation selected in this study was 3-glycidoxypropyl trimethoxysilane (3-GPS) supplied by Sigma-Aldrich, US. Hydrogen peroxide (H2O2, 30%) and acetic acid (C2H4O2, 99.9%) used as functionalisation aids were supplied by Sigma-Aldrich, US, and the ethanol (C2H6O, 99.9%) used for BaTiO3 dispersion by Fisher Scientific International, Inc., UK. BaTiO3 powders were supplied from Nanostructure & Amorphous Materials Inc., US. All the chemicals except BaTiO3 powders were used as received without further treatment.

The BaTiO3 powders were prepared using combustion method, therefore, firstly they were pre-treated in H2O2 for hydroxylation process to add hydroxyl group (-OH) to the surface [23]: 10g BaTiO3 nanoparticles were added into a 230mL solution of H2O2 in a round bottom flask. The mixture was then sonicated in an ultrasonic bath for 30 min and then refluxed at the boiling temperature of 30% H2O2 solution at 108°C at 100 rpm using a mechanical stirrer for six hours to facilitate the process by heating without losing H2O2. The nanoparticles were retrieved by centrifuging the resulting solution at 4500 rpm for 15 min, and washed three times with deionized water. The achieved BaTiO3 nanoparticles were dried in an oven at 80°C for 24 hours. The reflux and particle retrieving processes were similar as in the surface functionalisation with 3-GPS. 3-GPS was then applied to BaTiO3 nanoparticles to improve the

1081/1602 ©2022 Yazdani et al. doi:10.5075/epfl-298799_978-2-9701614-0-0 published under CC BY-NC 4.0 license

processability and filler dispersion in nanocomposites; the solution of 1 wt.% of 3-GPS with respect to BaTiO3 was prepared. 150mL aqueous solution of ethanol and deionized water (9:1) was firstly mixed in a beaker. Adding the acetic acid drops using a pipette and stir vigorously after each drop until the pH value of 3.5-4 measured by a METTLER TOLEDO pH meter was reached, stirred vigorously again for 3mins to form a clear solution. The low pH values of the solution facilitate the silane functionalisation process [24]. After the addition of the 0.1g 3-GPS solution to the acidified solution using a pipette, the mixture was left in an ultrasonic bath for 30mins to form a homogenous solution. 10g hydroxylated BaTiO3 powders was then added to the silane solution, and mixed under ultrasonic bath for 10mins for better filler wetting. Finally, the mixture was refluxed at the boiling temperature of ethanol, 78°C [25], at 100 rpm using a mechanical stirrer for six hours using a silicone oil bath over a hotplate. After refluxing, the BaTiO3 was washed three times with deionized water and retrieved using centrifugation at 4500 rpm. The silane treated BaTiO3 (Si-BaTiO3) powders were dried at 110°C for 24 hours to avoid any condensation of silanol groups at the surface. In the end, the powders were crushed in a mortar and pestle for the nanocomposites preparation. The size distribution of Si-BaTiO3 particles was analysed in its epoxy nanocomposite form.

The epoxy nanocomposite fabrication process including Si-BaTiO3 functionalisation is schematically illustrated in Figure 2. The epoxy resin nanosuspension with 1, 5, 10, 15 wt.% Si-BaTiO3 nanoparticles and 5, 10, 15 wt.% untreated BaTiO3 nanoparticles are were prepared as follows: Firstly, the weighed amount of BaTiO3 powders was added to ethanol and sonicated with an ice water bath for 2 min with a 10s pulse to form a homogenous solution. Then a weighed amount of epoxy and the previous mixed solution were blended in a beaker using a mechanical stirrer at 300 rpm and 80°C overnight under the fume hood to gradually remove the ethanol without precipitation of the particles. The mixture was weighed before and after the previous step to ensure the complete removal of ethanol. The curing agent was then added to the mixture with a weight ratio recommended by the company and stirred for a further 3mins. Finally, the mixture was placed in the vacuum oven at 30°C for 1 hour to remove bubbles at 29 inHg and achieve complete removal of ethanol. The whole mixture was poured into a mould made of two pieces of glass clamped with a 3 mm silicone gasket in-between. A uniform thickness of each sample was achieved with the assistance of this type of glass mould. They were then cured in the oven for 8 hours at 80°C as prescribed by the manufacturer, then cooled down to room temperature. The final samples were of size 160×140×3 mm3, and cut to different sizes using a precision cut-off machine BRILLANT 220.

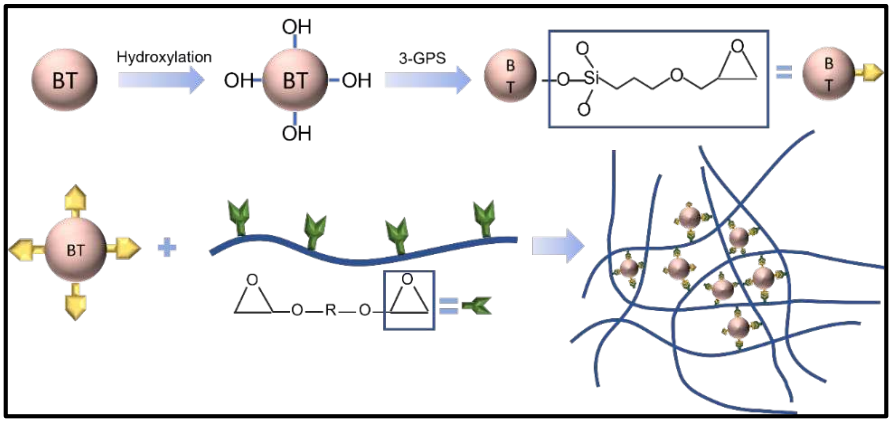

Figure 2. Schematic illustration of the hydroxylation and silane functionalisation process for the BaTiO3 nanoparticles.

3. In-situ Field-induced Strain Measurements

The microwave field was selected to be the external stimulator as BaTiO3 exhibit a peak in a dielectric loss at the microwave frequency range. Most importantly, the design of the experiment becomes more feasible with remote stimulation from the microwave field owing to the spacious cavity. The mechanical strain evolution in the nanocomposite was investigated under a microwave field within a temperature-controlled microwave cavity Panasonic NN-SF464MBPQ running at 2.45 GHz and cavity size of 354×338×230 mm3. In contrast with the conventional one, this oven, equipped with inverter technology, has a circuit board that replaces the transformer, hence the output power can be adjusted linearly by varying the pulse width to ensure a more precise and continuous microwave exposure [99]. The unique flat-bed design of this model is equipped with a stationary ceramic plate that allowed more space to place the sample and its holder.

The strain field introduced by the BaTiO3 nanoparticles to the surrounding epoxy, activated by microwave field, was studied by real-time strain measurements on the surface of the nanocomposite samples with the incorporation of Fibre optic sensors utilising fibre Bragg gratings (FBG) technique. The sensors were placed apart in equal distance from one another within a 90mm straight line. This is theoretically aligned with the microwave's half wavelength (~60mm) as also was experimentally observed during real-time temperature measurements. The sensors were located to ensure overlapping with at least three nodes and antinodes of the microwave cycle. The FBG sensors were fabricated by a periodic intense laser light applied onto the core of an optic fibre. The laser light exposure introduced a permanent increase in the refractive index of the fibre's core and a fixed modulation was created subsequently. Each FBG was approx. five mm long with a grating period of one micron. Two arrays with three FBGs for each sample were fabricated. FBG arrays were then adhesively bonded to the surface of two geometrically identical 135×10×3 mm3 samples made of Si-BaTiO3 epoxy nanocomposites. The strain array was bonded to the surface by adhesives at the FBG regions while the temperature array is firstly packaged into a capillary glass tube, and then bonded parallel to the strain array. The arrays were placed at the same location with the same distance in-between. The strain experienced by the samples was transferred to the FBG sensors, and the measurements were also affected by the temperature. Therefore, the temperature array only measured the temperature change, and compensated the strain measurements accordingly.

A preliminary test via a FLIR One Pro LT Thermal Camera was carried out to inspect the temperature change in different samples under different microwave power levels. Samples were placed at a designed location as shown in Figure 3. The exposure time was then carefully selected based on the heating profiles of each sample to control the temperature of samples well below Tg during the exposure to avoid any interference in strain measurements from the post-cure shrinkage. The sample was clamped on one end by a designed sample holder made of polytetrafluoroethylene (PTFE) to ensure minimum interaction with the microwave field owing to its extremely low dielectric loss. The size and location of the load inside the cavity were two primary factors that affect the microwave field distribution [26]. To control the microwave field distribution, the sample and the holder were placed at the designed location

  doi:10.5075/epfl-298799_978-2-9701614-0-0

shown in the figure, for all tests. The power level of 100W and 440W were initially selected to avoid temperature surges in samples within a short period of time. Exposure time was set to be 650s for 100W and 148s for 440W to limit the temperature below Tg (80°C) based on the preliminary results obtained by the thermal camera.

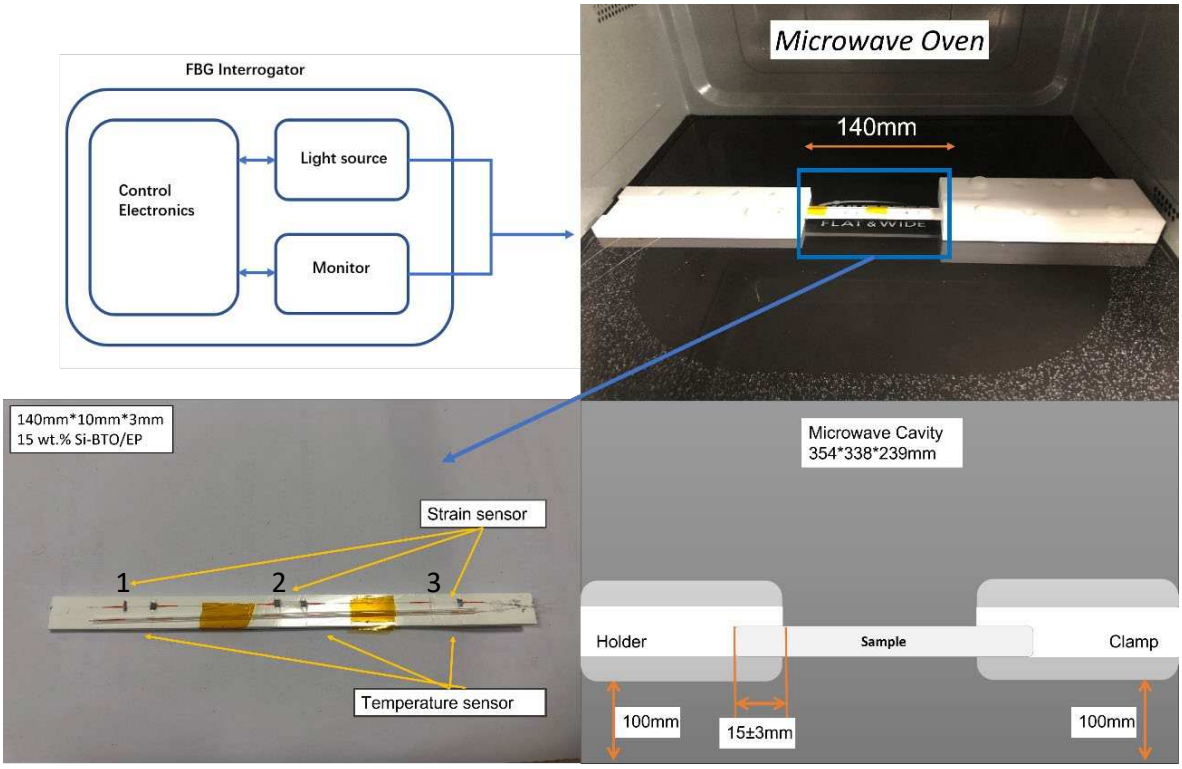

Figure 3. Illustration of the sample of epoxy nanocomposite with BaTiO3 on the PTFE holder in the microwave oven with surface bonded FBG arrays connected to an interrogator.

Neat epoxy, BaTiO3 nanoparticles, and adhesive used for bonding FBGs possess different thermal expansion coefficients (CTE) and microwave heating patterns. Microwave field interaction with the neat epoxy and adhesive have been investigated, thereafter. Two arrays with five FBGs of five mm long and one micron grating period were fabricated for each test. First, the adhesive response under microwave radiation was studied by two arrays of FBGs adhesively bonded to the surface of a PTFE block. It is assumed that measured strain and temperature change are solely due to the microwave heating of adhesive as PTFE has neglectable thermal response (temperature rise) under the microwave. The PTFE block is placed in the microwave oven at the designed location to locate the first FBG sensor on the left end at the same location as the one in the previous exposure on the nanocomposites. The tests have been performed under 100W for 650s and 440W for 110s. Data was recorded on the interrogator 10s prior to the microwave exposure for each run to ensure no data is missing after the microwave starts. The effect of neat epoxy with the FBG sensors bonded to its surface was investigated as a controlled group to the test of 15 wt.% nanocomposites at 10 W for 600s and 440W for 60s. Neat epoxy sample geometrically identical with 15 wt.% nanocomposites in the nanocomposite's exposure test was placed in the designed location with surface-bonded arrays of FBGs. The whole measurements from adhesive and the neat epoxy were compared with the results from the previously performed test on the

  doi:10.5075/epfl-298799_978-2-9701614-0-0

nanocomposites for better distinguishing the BaTiO3-epoxy nanocomposite's response to the microwave exposure.

4. Results and Discussion

Labelling for strain and temperature FBG arrays is illustrated in Figure 3. Field-induced strains in the nanocomposites with 15 wt.% BaTiO3 (the highest wt.% examined) has been investigated within a microwave exposure at 100W and 440W (Figure 5 and Figure 6, respectively). The evolution of strain and temperature have been measured in situ by the two arrays; one array measures the strain while the other one measures the temperature. Sudden drastic fluctuations and absent data presented in the figures are due to Bragg wavelengths moving into adjacent spectral windows that were set up on the sensor interrogator.

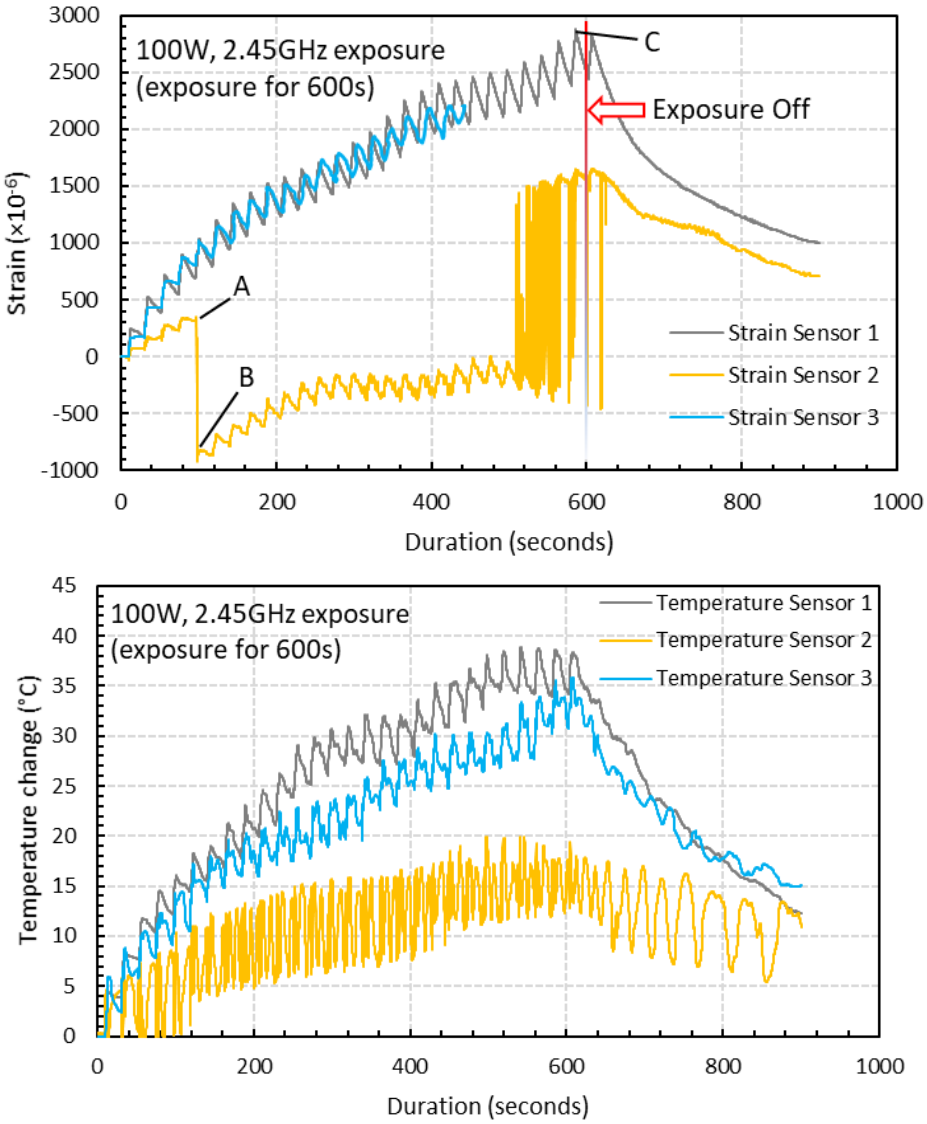

Figure 5. Strain and temperature change measurements of 15 wt.% silane-treated BaTiO3/Epoxy samples under 100W for 600s.

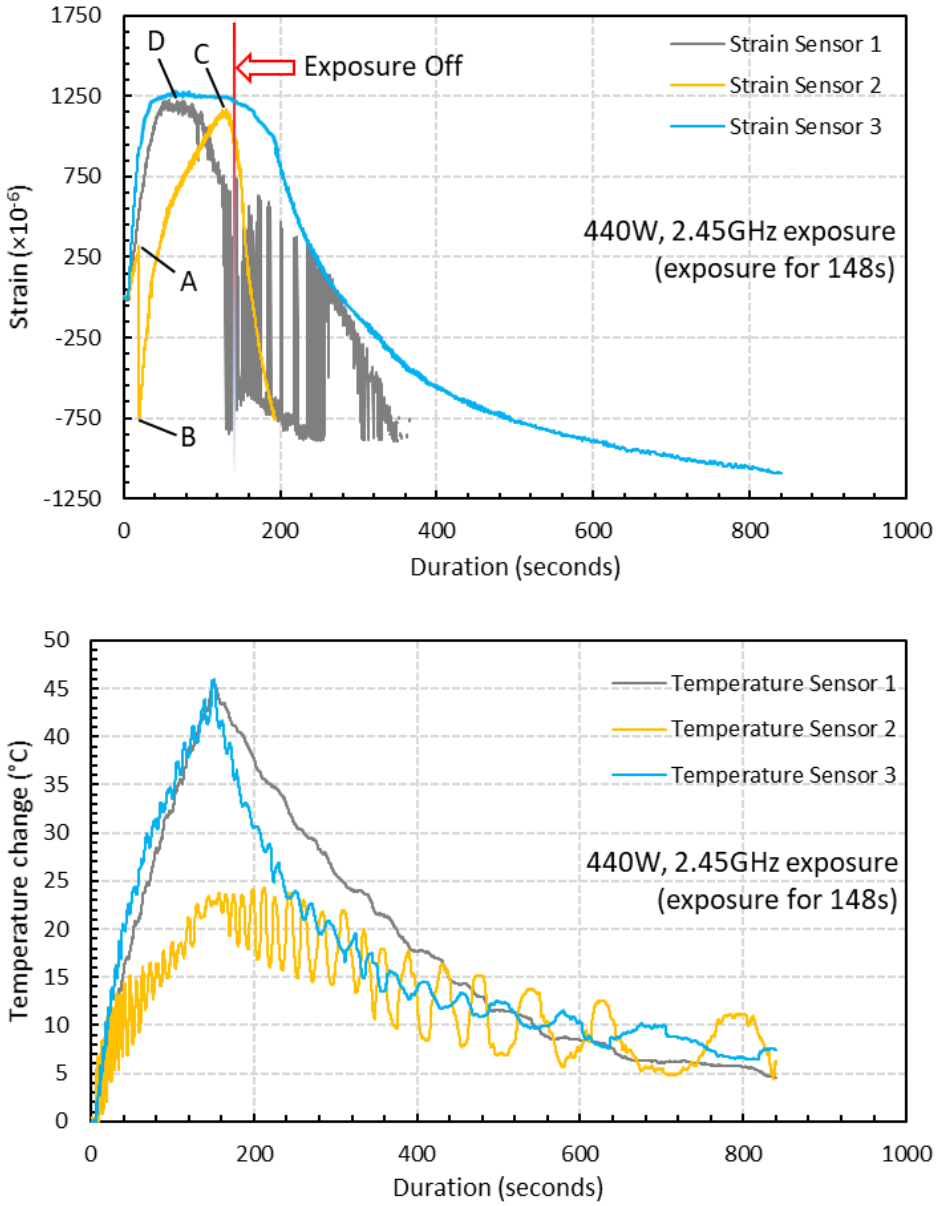

Figure 6. Strain and temperature change measurements of 15 wt.% silane-treated BaTiO3/Epoxy samples under 440W for 148s.

The strain and temperature data exhibit a general increasing trend with the exposure. They drop gradually, immediately, after the microwave stopped. The temperature appeared to be higher at both ends of the specimen (sensor 1 and 3, located left and right respectively) compared to the middle (sensor 2), which is in accordance with the 'hot spot' theory due to microwave nonuniformity. Sensors 1 and 3 data also follows more similar temperature increasing trend (magnitude and rate).

Under the 100W and 440W, the strain measured at the beginning of the microwave radiation in strain sensors 1 and 3 have similar trends of increasing as predicted when the temperature sensors 1 and 3 measurements have close gradients, having higher temperatures than that measured by sensor 2. A sudden drop in the strain measurements of the middle sensors (strain 2) can be observed in both cases soon after the initial surge, labelled as A-B. It instantaneously alters the strains by nearly identical 1162 and 1008 micro-strains (difference between A and B)

under 100W and 440W, respectively. Such decline in the strain measurements is the evidence of attributed to an immediate development of a compressive strain in response to the microwave exposure, as hypothesised. Note that sensor 2 temperature is the lowest amongst the three sensors, in which the thermally induced strain is negligible. Such phenomenon could not be associated with the temperature rise since the temperature change is approximately 12°C and 5.7°C from room temperature 19°C when the sudden drop occurs at point A, which is remarkably lower than 170°C when post-curing shrinkage is introduced as indicated by the exothermic peak in our DSC measurements, and lower than the Tg to have any detrimental effect. Moreover, it is observed that unloading the specimen from the 440W exposure results in a residual compressive strain in all sensors' locations. This occurs after the high non-linear variation of strains in the case of 440W, unlike the linear strain behaviour under 100W. This is analogous to mechanical field introduction in which unloading an elastic-plastic specimen beyond its elastic regime under tensile loading may introduce a compressive residual strain distribution depending on the hardening behaviour (i.e. kinematic or isotropic). The strain and temperature measurements as a function of energy absorbed in Joules are presented below, under 100W and 440W.

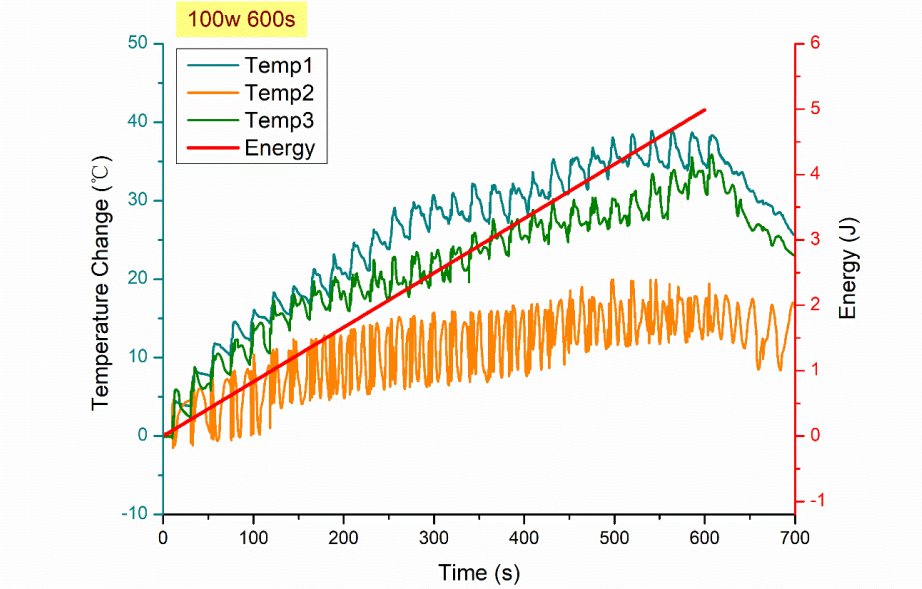

Figure 7. Temperature change measurements (micro-strain) by FBG sensors (left), and energy absorbed (right) versus time (s) under 100W.

  doi:10.5075/epfl-298799_978-2-9701614-0-0

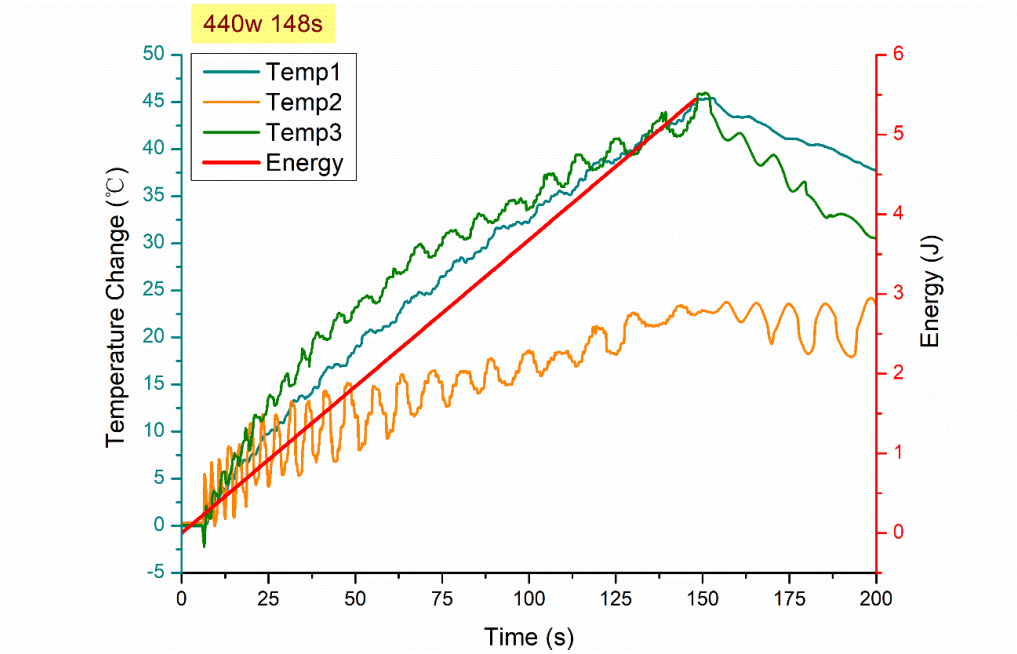

Figure 8. Temperature change measurements (micro-strain) by FBG sensors (left), and energy absorbed (right) versus time (s) under 440W.

It could be observed that, the energy absorption rate is close to the rate of temperature rise in the FBG sensors. At the beginning of the microwave exposure, the temperature rise exhibits a similar rate compared with the energy absorption rate. As the exposure time increases, the temperature rise becomes significantly slower. The 'hot spot' theory due to the non-uniformity of microwave fields is proposed to be the possible explanation of this phenomenon as described formerly.

5. Conclusion

The quantitative research on microwave field-nanocomposite interaction was conducted to study the ferroelectric materials' response in high-performance (rigid) epoxy composite that offers reversible microwave activated electro-strains introduced by a second dielectric phase (BaTiO3). The data presented a pioneering investigation as no investigations have been reported, thus far, on the micromechanical (extrinsic) strain response of rigidly constrained ferroelectric materials in polymer under external electromagnetic fields. FBG sensors-based technique was employed, in-situ with the microwave exposure, for real-time monitoring of the strain and temperature response of the nanocomposite subjected to a 2.45GHz microwave field at controlled exposure power and energy, followed by newly developed theoretical constitutive equations underpinning field-material interactions.

A time-dependent strain field is introduced, proportional to the exposure time/energy, in the multi-domain BaTiO3 nanoparticles under the stimulation of a microwave field, linearly under 100W and non-linearly under 440W. A sudden drop in micro-strain data by the value of approx. 1000 compressive micro-strains was observed in the BaTiO3-epoxy composites at the beginning phase of the exposure under the different exposure powers examined, a potential for active toughening. Such phenomenon has not been reported thus far in the existing literature, and is under investigation of our research group.

  doi:10.5075/epfl-298799_978-2-9701614-0-0

6. Acknowledgment

The authors would like to acknowledge the grants received for this research from the UK Engineering & Physical Sciences Research Council (EPSRC), Ref. EP/R016828/1 (Self-tuning Fibre-Reinforced Polymer Adaptive Nanocomposite, STRAINcomp) and EP/R513027/1 (Study of Microstructure of Dielectric Polymer Nanocomposites subjected to Electromagnetic Field for Development of Self-toughening Lightweight Composites), and Foundation for Polish Science (FNP) under Grant Number First TEAM/2016-1/7, co-funded by the European Regional Development Fund.

References

[1] Ozdemir, N.G., et al., Toughening of carbon fibre reinforced polymer composites with rubber nanoparticles for advanced industrial applications. Express Polymer Letters, 2016. 10(5): p. 394-407.
[2] Cantwell, W.J. and J. Morton, The impact resistance of composite materials — a review. Composites, 1991. 22(5): p. 347-362.
[3] Yazdani Nezhad, H., et al., Numerical analysis of low-velocity rigid-body impact response of composite panels. International Journal of Crashworthiness, 2015. 20(1): p. 27-43.
[4] Camanho, P.P., et al., Prediction of in situ strengths and matrix cracking in composites under transverse tension and in-plane shear. Composites Part A: Applied Science and Manufacturing, 2006. 37(2): p. 165-176.
[5] Hernandez, T.P.A., A.R. Mills, and H. Yazdani Nezhad, Shear driven deformation and damage mechanisms in High-performance carbon Fibre-reinforced thermoplastic and toughened thermoset composites subjected to high strain loading. Composite Structures, 2021. 261: p. 113289.
[6] Alshammari, B.A., et al., Comprehensive Review of the Properties and Modifications of Carbon Fiber-Reinforced Thermoplastic Composites. Polymers, 2021. 13(15): p. 2474.
[7] Ratna, D. and A.K. Banthia, Rubber toughened epoxy. Macromolecular Research, 2004. 12(1): p. 11-21.
[8] Ma, J., et al., Effect of inorganic nanoparticles on mechanical property, fracture toughness and toughening mechanism of two epoxy systems. Polymer, 2008. 49(16): p. 3510-3523.
[9] Thostenson, E.T. and T.-W. Chou, Processing-structure-multi-functional property relationship in carbon nanotube/epoxy composites. Carbon, 2006. 44(14): p. 3022-3029.
[10] Eqra, R., K. Janghorban, and H. Daneshmanesh, Mechanical properties and toughening mechanisms of epoxy/graphene nanocomposites. Journal of Polymer Engineering, 2015. 35(3): p. 257-266.
[11] Liu, T., et al., Morphology and fracture behavior of intercalated epoxy/clay nanocomposites. Journal of Applied Polymer Science, 2004. 94(3): p. 1236-1244.
[12] An, Q., A.N. Rider, and E.T. Thostenson, Hierarchical Composite Structures Prepared by Electrophoretic Deposition of Carbon Nanotubes onto Glass Fibers. ACS Applied Materials & Interfaces, 2013. 5(6): p. 2022-2032.
[13] Yazdani Nezhad, H., and Thaku, V.K., Effect of morphological changes due to increasing carbon nanoparticles content on the quasi-static mechanical response of epoxy resin. Polymers, 2018. 10(10): 1106.
[14] An, D., et al. Ultra-thin electrospun nanofibers for development of damage-tolerant composite laminates. Materials Today Chemistry, 2019. 14: 100202.

  doi:10.5075/epfl-298799_978-2-9701614-0-0

[15]Bregar, T., et al. Carbon nanotube embedded adhesives for real-time monitoring of adhesion failure in high performance adhesively bonded joints. Scientific Reports, 2020. 10(1): p.1-20
[16]Khaleque, T., et al. Tailoring of thermo-mechanical properties of hybrid composite-metal bonded joints. Polymers, 2021. 13(2): 170.
[17]Awaja, F., et al., Cracks, microcracks and fracture in polymer structures: Formation, detection, autonomic repair. Progress in Materials Science, 2016. 83: p. 536-573.
[18]Damjanovic, D., Contributions to the piezoelectric effect in ferroelectric single crystals and ceramics. Journal of the American Ceramic Society, 2005. 88(10): p. 2663-2676.
[19]Jones J.L., N.J.C., Pramanick A., Daniels J.E, Time-Resolved, Electric-Field-Induced Domain Switching and Strain in Ferroelectric Ceramics and Crystals. In: Eckold G., Schober H., Nagler S. (eds) Studying Kinetics with Neutrons. Springer Series in Solid-State Sciences, vol 161. Springer, Berlin, Heidelberg. https://doi.org/10.1007/978-3-642-03309-4_6. 2009.
[20]Gao, J.H., et al., Recent Progress on BaTiO3-Based Piezoelectric Ceramics for Actuator Applications. Actuators, 2017. 6(3): p. 20.
[21]Shen, Z.-Y. and J.-F. Li, Enhancement of piezoelectric constant d33 in BaTiO3 ceramics due to nano-domain structure. Journal of the Ceramic Society of Japan, 2010. 118(1382): p. 940-943.
[22]Hsiang, H.I. and F.S. Yen, Effect of crystallite size on the ferroelectric domain growth of ultrafine BaTiO3 powders. Journal of the American Ceramic Society, 1996. 79(4): p. 1053-1060.
[23]Polotai, A.V., A.V. Ragulya, and C.A. Randall, Preparation and Size Effect in Pure Nanocrystalline Barium Titanate Ceramics. Ferroelectrics, 2003. 288(1): p. 93-102.
[24]Zhou, T., et al., Improving Dielectric Properties of BaTiO3/Ferroelectric Polymer Composites by Employing Surface Hydroxylated BaTiO3 Nanoparticles. Acs Applied Materials & Interfaces, 2011. 3(7): p. 2184-2188.
[25]Ambrożewicz, D., et al., Fluoroalkylsilane versus Alkylsilane as Hydrophobic Agents for Silica and Silicates. Journal of Nanomaterials, 2013. 2013: p. 631938.
[26]UK, F.S. https://www.fishersci.co.uk/shop/products/ethanol-absolute-200-proof-molecular-biology-grade-fisher-bioreagents-5/16606002. 2021.
[27]Bansal, P., E. Vineyard, and O. Abdelaziz, Advances in household appliances- A review. Applied Thermal Engineering, 2011. 31(17): p. 3748-3760.

  doi:10.5075/epfl-298799_978-2-9701614-0-0

EFFECTS OF HYBRIDIZATION AND PLY THICKNESS ON CARBON/CARBON COMPOSITE LAMINATES STRENGTH AND TOUGHNESS

Federico, Danzi,[a,b(*)], Rodrigo, Tavares[b,c], José, Xavier[d], Daniele, Fanteria[e], Pedro Ponces, Camanho[a,b]

a: INEGI, Portugal – fdanzi@inegi.up.pt
b: DEMec, Faculdade de Engenharia, Universidade do Porto, Portugal
c: AMADE, Polytechnic School, University of Girona, Spain
d: UNIDEMI, Department of Mechanical and Industrial Engineering, NOVA School of Science and Technology, NOVA University Lisbon, Caparica, Portugal
e: DICI, Dipartimento di Ingegneria Civile e Industriale, Università di Pisa, Italy
(*) Email: fdanzi@inegi.up.pt

Abstract: *This work presents the results of an experimental study performed on carbon/epoxy composite materials manufactured using a ply-level hybridization technique to promote a pseudo-ductile failure and enhance their longitudinal fracture toughness. Three hybrid layup configurations with different total ply thicknesses and expected mechanical responses were selected for the investigation. The experimental campaign included longitudinal and transverse tensile tests together with in-plane shear and double edge notched tensile (DENT) specimens for the characterization of intralaminar longitudinal toughness. Although fracture toughness does not increase appreciably with hybridization, an effect on the failure modes is observed characterized by more widespread damage with distinctive fragmentation and pull-out. The combination of the thicker ply blocks with hybridization resulted in a diffused damaged scenario with clear advantages in terms of energy dissipation.*

Keywords: Polymer matrix composites ; carbon fibre ; hybrid; thin-ply ; mechanical properties

1. Introduction

High-performance carbon/epoxy composites are nowadays well-established materials for aerospace structures. Notwithstanding their superior specific properties, their intrinsic brittleness is a non-trivial drawback that leads to the application of high safety factors during the design process of any composite components. To overcome this limitation, improvements in their fracture properties are required. In particular, the enhancement of the longitudinal tensile fracture toughness. New possibilities to achieve this goal result from the recent availability of thin-ply composites and the chance to design hybrid composites with tailored failure mechanisms [1-2].

Promising results with significant modifications in the failure properties and modes under longitudinal tensile loads were obtained from the preliminary experimental studies performed on thin-ply glass-carbon hybrid composites [3-4]. For these hybrid composites a remarkable mismatch in both stiffness and failure strain allowed to achieve a stable damage mechanism named pseudo-ductility.

Carbon-carbon hybrid composites were also recently designed and their mechanical bahoviour investigated. Thin and conventional prepregs with intermediate and ultra high

  doi:10.5075/epfl-298799_978-2-9701614-0-0

modulus fibers were investigated and the pseudo-ductile failure was achieved both for unidirectional and multidirectional laminates [5-6]. Moreover, a reduced notch sensitivity was demonstrated in hybrid in open-hole and sharp-notched laminates thanks to a damage localization and the induced load re-distribution around the notches [7].

Although relevant information about the failure properties of all-carbon hybrid composites has already been identified, a systematic and quantitative analysis of their failure properties is still missing. The objective of this work is to provide additional insight into the effects of ply-by-ply hybridization on the relevant properties of carbon/carbon composite materials. The novelty of this work lies in the quantitative characterization of the longitudinal fracture toughness for full-carbon hybrid composite systems including a critical analysis of two concurrent factors, the ply thickness and the ply-by-ply hybridization. Moreover, this work demonstrates the feasibility of carbon-carbon hybrid materials with carbon fibers currently used in the aerospace industry only.

2. Materials and methods

2.1 Baseline materials and hybrid ply-block design

Two carbon epoxy fibres with different modulus and failure strain were considered as baseline materials for the hybridization. The intermediate modulus Toray T800 with a high failure strain, and the high modulus Pyrofil HR40 with a low failure strain. Unidirectional prepreg rolls were supplied by NTPT with different material grades 50 g/m^2 for the T800 based prepreg and 20 g/m^2 for the HR40. Table 1 shows the main mechanical properties of the carbon fibers used in this study.

Table 1: Carbon fiber properties.

Fiber \ Property	E_L [GPa]	σ_L [GPa]	ε_L [%]
T800	294	5.88	2.0
HR40	395	4.11	1.1

Three stable hybrid ply blocks were selected via the ''damage mode map'' [7]: a 3 layers block [T800/HR40/T800] with an expected ply-block thickness of 125 µm named H1, a 5 layers [2T800/HR40/2T800] with a thickness of 230 µm named H2 and the H3 with 8 layers [3T800/2HR40/3T800] and an expected thickness of 364 µm.

2.2 Test matrix

The tensile stiffness and failure in-plane properties of the selected laminates were determined in compliance with ASTM standards [8-9] while the longitudinal fracture toughness was measured using the size-effect law of tensile tests on double edge notched cross-ply specimens. The data regression method as well as the details on the estimation of the R-curve of the 0◦ plies lamina can be found in Bažant et al. [10] and Catalanotti et al. [11]. The tests were carried out on prismatic specimens (length 2l and width 2w) that have an initial double side notch of size a0. Five different specimen widths were investigated from 10 mm to 25 mm with a 5 mm step. The notch to width ratio was kept constant at 0.6 for all the samples. The

  doi:10.5075/epfl-298799_978-2-9701614-0-0

DIC and CT analyses were used to complement the study by providing further information on the failure modes.

The full experimental campaign carried out within this study is summarised in Table 2, where the T350 layup represents a material with a ply-block composed of 7 layers of 50 g/m^2 T800 plies for a total expected ply-block thickness of 360 µm.

Table 2: Test campaign.

Test \ Layup	T800	H1	H2	H3	HR40	T350
ASTM-D3039 [6]	$[0]_{20}$	$[0]_{8}$	$[0]_{4}$	$[0]_{3}$	$[0]_{50}$	-
ASTM-D3039 [6]	$[90]_{30}$	$[90]_{12}$	-	-	$[90]_{75}$	-
ASTM-D3518 [7]	$[\pm45]_{25}$	$[\pm45]_{10}$	-	-	$[\pm45]_{64}$	-
DENT [9]	$[90/0]_{10\$}$	$[90/0]_{5\$}$	$[90/0]_{3\$}$	$[90/0]_{2\$}$	$[90/0]_{25\$}$	$[90/0]_{2\$}$

3. Results

3.1 Lamina properties

Typical longitudinal tensile stress vs. strain curves for the investigated materials are shown in Figure 1a. The ply-by-ply hybridization showed a mild effect on the H1 while the H2 and H3 materials highlighted a prolonged pseudo-ductile stable phase followed by a final hardening before the final failure occurred. From the analysis of the H2 and H3 samples, a stable fragmentation of the low failure strain layers was observed and a fragment length of about 2 mm was measured (see Figure 1b).

Transverse tensile coupons, instead highlighted a mild change in stiffness while a brittle matrix failure was observed on all the investigated material systems. In-plane shear loading results showed a pronounced plastic deformation with evident fiber rotation and delaminations. An increase in the inelastic phenomena before the final softening was observed in the material with the highest percentage of low stiffness plies.

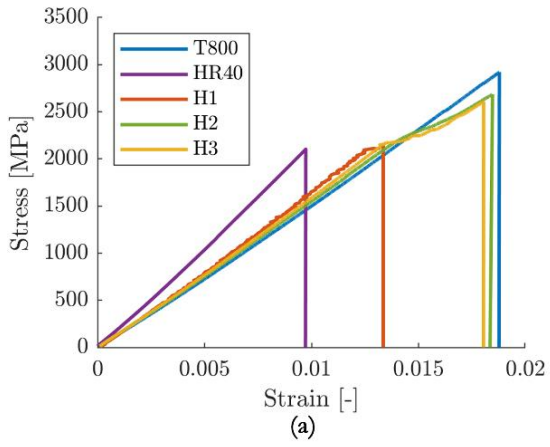

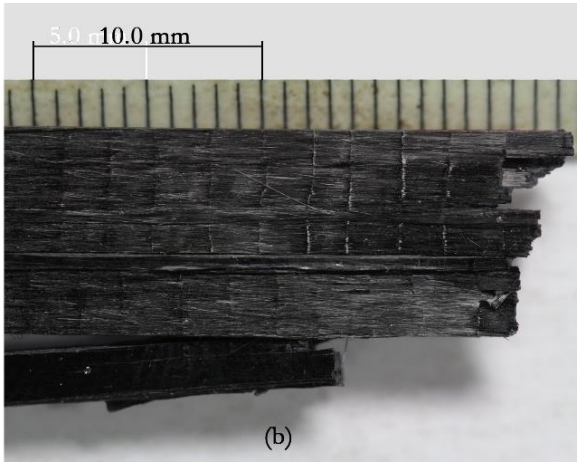

Figure 1: (a) Typical longitudinal tensile stress vs. strain behaviour, (b) Fragmentation on H3 specimen

3.2 Intralaminar fracture toughness

The DENT tests were characterized by a fibre-dominated failure mode, with fibre fracture and pull-out along the ligament section. Figure 2 shows both the remote failure stress and the calculated R-curves for the different materials. Figure 2a highlights how a reduction in the remote failure stress with the specimen thickness is present for all the investigated material systems. This shows how a remarkable improvement in fracture toughness can be reached through both the ply-by-ply hybridization and the increase of the ply-block thickness. From a comparison of the R-curves (Figure 2b) it is evident how the materials system with the highest thickness (the T350 and the H3 with a ply-block thickness of 360 µm) have also the highest values of fracture toughness. Moreover, it is worth noting that the H1 material with a ply-block thickness of 125 µm has results comparable with the T800/M21 with the same ply thickness [12].

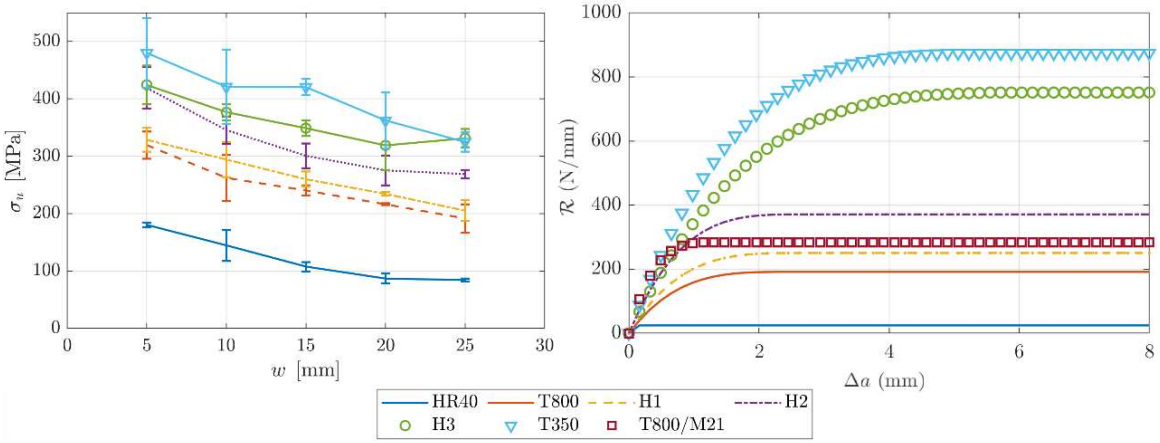

Figure 2: (a) Remote failure stress reduction with specimen size, (b) R-curves comparison.

A comparison of the fracture surfaces of the DENT specimens provides insight into the reasons for the observed change in toughness. While the low failure strain material (HR40) presented flat fracture surfaces that indicate a brittle behaviour, both the T800 based and the hybrid composites showed fibre pull-out mechanisms. Moreover, from the DIC and the post-mortem CT images of the H2 and the H3 system a concurrent failure mechanism was observed, the matrix fragmentation of the 90 layers. Figure 3 shows the longitudinal strain field for the H2 and H3 specimens captured during the test at 95% of the specimen failure load.

  doi:10.5075/epfl-298799_978-2-9701614-0-0 published under CC BY-NC 4.0 license

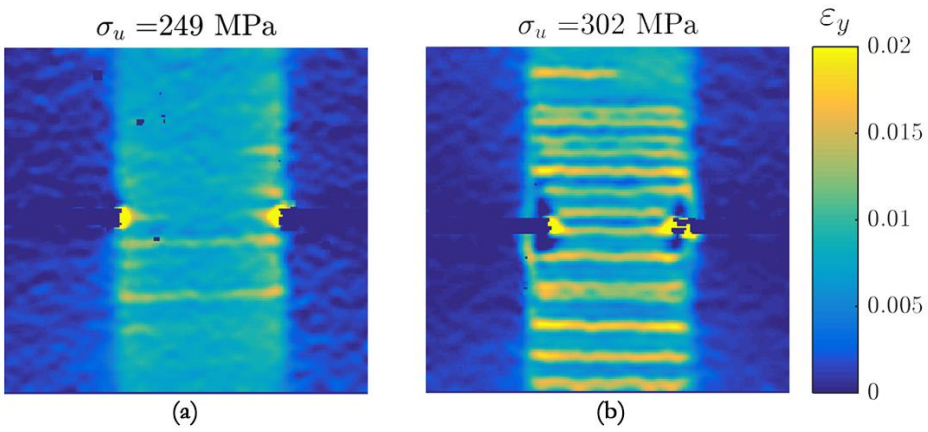

Figure 4: DIC strain field along the loading direction: (a) H2, (b) H3.

The statistical analysis of the fragment distance showed on all the samples an average value of approximatively 0.6 mm. None of the other investigated materials presented any fragmentation mechanisms before the final failure.

Figure 4 confirms how in the hybrid specimens a widespread fiber pull-out is achieved along the specimen width and the matrix fragmentation of the 90 layers on multiple fracture planes is present through the whole thickness of the coupon. These results confirm how in hybrid composites when a stable fragmentation is achieved, multiple failure mechanisms are constantly involved, the fiber fracture, the matrix fragmentation and the delamination. No clear evidence of fiber fragmentation was instead recorded in the notched specimens.

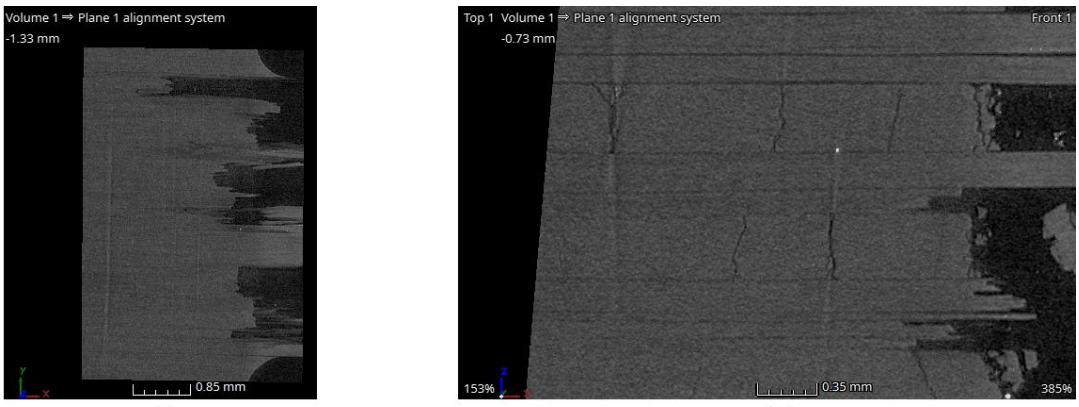

Figure 4: H3 10 mm wide specimen: (a) Top view at the specimen mid-plane, (b) Through-the-thickness view in the center of the speciment.

.

4. Conclusions

The presented results pointed out the possibility to induce the stable fragmentation mechanism in carbon-carbon hybrid composites. This effect, confirmed for the unnotched

tension, leads to a pseudo-ductile effect. In the case of notched cross-ply coupons instead, the combination of the hybridization with thicker ply blocks resulted in a diffused damaged scenario. This results in promoting multiple energy dissipation mechanisms before the unstable fracture occurs.

5. References

1. Sihn, S, Kim, RY, Kawabe, K, et al. Experimental studies of thin-ply laminated composites. Compos Sci Technol 2007.
2. Arteiro A, Furtado C, Catalanotti G, Linde P, Camanho PP Thin-ply polymer composite materials: A review. Compos A Appl Sci Manuf 2020.
3. Czél G, Wisnom M. Demonstration of pseudo-ductility in high performance glass/epoxy composites by hybridisation with thin-ply carbon prepreg. Compos Part A: Appl Sci Manuf 2013.
4. Czél G, Jalalvand M, Wisnom, MR. Design and characterisation of advanced pseudo-ductile unidirectional thin-ply carbon/epoxy-glass/epoxy hybrid composites. Compos Struct 2016.
5. Czél G, Jalalvand M, Wisnom MR, Czigány T. Design and characterisation of high performance, pseudo-ductile all-carbon/epoxy unidirectional hybrid composites. Compos B Eng, 2017.
6. Sapozhnikov, S, Swolfs, Y, Lomov, S. Pseudo-ductile unidirectional high modulus/high strength carbon fibre hybrids using conventional ply thickness prepregs. Compos B Eng 2020.
7. Czél G, Rev T, Jalalvand M, Fotouhi M, Longana ML, Nixon-Pearson OJ, Wisnom MR. Pseudo-ductility and reduced notch sensitivity in multi-directional all-carbon/epoxy thin-ply hybrid composites. Compos Appl Sci Manuf, 2017.
8. Jalalvand M, Czél G, Wisnom MR. Damage analysis of pseudo-ductile thin-ply ud hybrid composites - A new analytical method. Compos Part A: Appl Sci Manuf 2015
9. ASTM International. ASTM D3039 - Standard Test Method for Tensile Properties of Polymer Matrix Composite Materials , 2008.
10. ASTM International. ASTM D3518 - Standard Test Method for In-Plane Shear Response of Polymer Matrix Composite Materials by Tensile Test of a ±45◦ Laminate, 2013.
11. Bazant Z, Planas J. *Fracture and size effect in concrete and other quasibrittle materials*. New directions in civil engineering. Taylor & Francis, 1997
12. Catalanotti G, Arteiro A, Hayati M, et al. Determination of the mode I crack resistance curve of polymer composites using the size-effect law. Eng Fracture Mech 2014.

  doi:10.5075/epfl-298799_978-2-9701614-0-0

EFFECT OF WEATHERING ON THE LONG-TERM PERFORMANCE OF NATURAL FIBER REINFORCED RECYCLABLE POLYMER COMPOSITES FOR STRUCTURAL APPLICATIONS

Subrata Chandra Das, Angela D. La Rosa, Stergios Goutianos, Sotirios A. Grammatikos

Laboratory of Advanced and Sustainable Engineering Materials (ASEMlab), Group of Sustainable Composites, Department of Manufacturing and Civil Engineering, Norwegian University of Science and Technology (NTNU), Gjøvik 2815, Norway
Email: subrata.c.das@ntnu.no

Abstract: *Due to the growing global environmental concern and focus on circular economy, sustainable composite materials fabricated from natural fibers and recyclable polymer matrices have attracted special attention recently. The current work studies the long-term performance of flax fiber reinforced composite laminates based on a recyclable bio-polymer matrix. The performance of the developed recyclable composites was assessed by means of flexural and viscoelastic properties, after accelerated weathering. The weathering was conducted in a simulated environment at lab-scale, using a weathering chamber (QUV/Spray, Q-Lab) for 7, 14, 28 and 56 days. After weathering, the performance of composite coupons was characterized and compared with that of a conventional composite laminate, fabricated with glass fibers and standard cold-curing epoxy resin. The results of this work provide an understanding on the potential of fully recyclable composites to replace conventional polymer composites in structural applications.*

Keywords: Natural fiber composites; flax fiber composites; sustainable composites; accelerated weathering; structural degradation.

1. Introduction

The poor durability of natural fiber reinforced polymer composites makes their application challenging and troublesome in the advanced structural components in civil, maritime, sports and recreations, automotive, and aerospace industries [1]. Usually, natural fiber composites possess lower strength and stiffness than those of conventional counterparts such as GFRPs (Glass Fiber Reinforced Plastics) and CFRPs (Carbon Fiber Reinforced Plastics) [2, 3]. However, due to the lower environmental impact, higher specific stiffness, and biodegradability of natural fibers than glass fibers, natural fiber composites now become a popular topic of research interest. Moreover, due to the shift of the fossil-based industry towards bio-based and/or circularity in industrial products, especially in the post-pandemic era, the growth of natural fiber reinforced (bio-polymer) composites, or recyclable composites is expected to rise significantly in the coming years to keep the environment sustainable and to limit CO_2 emissions [4-7].

Studies on durability and accelerated weathering (UV/water spray) of natural fiber reinforced polymer composites have been conducted by several authors, however, research on accelerated weathering of flax fiber composites is still limited. Salim et al. [8] studied the accelerated weathering of kenaf fiber reinforced acrylic-based polyester composites in Q-SUN Xe-3 xenon arc chamber up to 1500 h, including dark and light cycle alternatively. The UV radiation dose was

  doi:10.5075/epfl-298799_978-2-9701614-0-0

around 0.55 W/m^2 at 340 nm wavelength. After 1500 h of UV exposure, very low degradation of bending properties was observed due to photochemical oxidation. Further, approximately 80% of bending properties recovered after drying the aged composite samples. Accelerated weathering also reported for hemp fiber reinforced bio-composites [9-11]. Tensile, flexural and mode I fracture toughness decreased for all the hemp/PLA composites, however, the impact strength increased. On the other hand, alkali treated hemp/PLA composites experienced lower degradation than untreated composites [9]. Similar degradation of mechanical properties was reported by Dayo et al. [11]. Badji et al. [10] developed a correlation between natural and artificial weathering of hemp/polypropylene composites and found a similar degradation pattern. Yan et al. [12] reported accelerated weathering of flax/epoxy composites for 500 h, 1000 h and 1500 h in an artificial weathering chamber. After 1500 h of exposure, the tensile strength and tensile modulus was dropped around 30% and 35%, respectively. On the other hand, approximately 10% decline of bending strength or stiffness occurred. After comparing with synthetic and hybrid natural/synthetic fiber composites in accelerated weathering conditions, it was observed that the degradation of flax fiber composite was more severe than the degradation of synthetic fiber- and hybrid- composites. The effect of weathering of chemically treated flax fiber bio-composites was reported by Taylor et al. [13] and Massoud et al. [14] reported the accelerated UV ageing of flax/glass/polypropylene hybrid composites.

The present work deals with the fabrication and characterization of unidirectional flax fiber reinforced bio-based- and recyclable- polymer matrix composites. For weathering, the fabricated composite samples were exposed in an accelerated chamber under UV exposure and water spray up to 56 days. After weathering for 56 days, the performance of the exposed composite samples was assessed to validate their durability to use in the external environmental conditions for advanced structural components such as automobiles, sporting equipment (skis), and small wind turbine blades.

2. Materials and Methods

2.1 Materials

The unidirectional flax fabric (FlaxDry UD 180, areal density 180 g/m^2, fiber density 1.45 g/cm^3) was procured from EcoTechnilin, France, and unidirectional glass fabric (areal density 220 g/m^2, fiber density 2.5 g/cm^3) was purchased from Haufler Composites, Germany. Figure 1 shows photos of the unidirectional flax fabric (a) and the unidirectional glass fabric (b). Petroleum based epoxy resin system (SP 106 resin and SP 106 slow hardener, mix ratio 100:18) was procured from Gurit, UK; biobased epoxy resin system (Polar Bear, with Recyclamine hardener, mix ratio 100:22) was procured from R*Concept, Spain.

2.2 Methods

All the composite laminates were prepared by cold compression molding technique and the fabricated laminates were post-cured according to the resin system. Finally, the obtained fabricated composite laminates are (i) flax fiber reinforced recyclable bio-based epoxy resin composite (flax/bio-epoxy), (ii) flax fiber reinforced petroleum-based epoxy resin composites (flax/petro-epoxy), (iii) glass fiber reinforced recyclable bio-based epoxy resin composites

  doi:10.5075/epfl-298799_978-2-9701614-0-0

(glass/bio-epoxy), and (iv) glass fiber reinforced petroleum-based epoxy resin composites (glass/petro-epoxy).

Table 1: Properties of flax fibers and E-glass fibers [4, 15].

Properties	Flax fibers	E-glass fibers
Density (g/cm^3)	1.4 - 1.5	2.5 - 2.59
Tensile strength (MPa)	343 - 2000	2000 - 3500
Tensile Modulus (GPa)	27.6 - 103	70 - 76
Specific Modulus (approx.) (GPa/g/cm^3)	45	29
Elongation (%)	1 - 1.8	1.8 - 4.8
Moisture content (wt.%)	8 - 12	-
Production energy consumption (Fiber mat) (MJ/kg)	9.55	54.7

(a) (b)

Figure 1. Unidirectional flax fabric (a) and unidirectional glass fabric (b).

- **Accelerated Weathering**

The accelerated weathering was conducted in a simulated environment at a lab-scale, using a weathering chamber (QUV/Spray, Q-Lab, USA). The selected weathering cycle (12 h) consisted of irradiation (0.8 W/m^2 UVA radiation, 60°C, 6 h), water condensation (40°C, 4 h), and water spray (room temperature, 2 h). After 7, 14, 28, and 56 days of weathering, the performance of composite laminates was characterized and compared.

- **Characterization**

The composite samples were characterized by flexural and DMA (Dynamic Mechanical Analysis) testing. The flexural tests were conducted according to ISO 14125 standards in an Universal Testing Machine (Instron 5966, 10 kN load cell). The bending flexural strength and flexural modulus were calculated using the following formulas:

Bending strength, $\sigma_f = \frac{3PL}{2bd^2}$ (1)

1099/1602 doi:10.5075/epfl-298799_978-2-9701614-0-0

Bending modulus, $E = \frac{L^3 m}{4bd^3}$ (2)

Where, P = the maximum applied load, L = the length of support span, m = the slope of the tangent, b = the width of the specimen, and d = the thickness of the specimen.

The DMA test was done according to ASTM D 5023 using a dynamic mechanical analyzer (DMA 850, Discovery, USA).

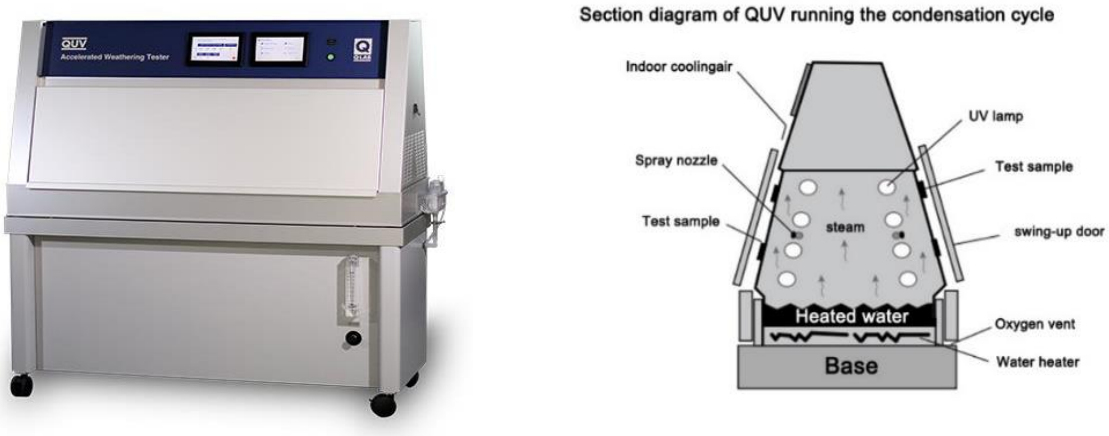

Figure 2. Accelerated weathering tester (Model QUV/Spray) [16].

3. Results and Discussions

Figures 3 and 4 depict the flexural strength and flexural modulus of the composite samples before and after accelerated weathering, respectively. The flexural strength of unaged or reference flax/bio-epoxy, flax/petro-epoxy, glass/bio-epoxy and glass/petro-epoxy samples is 0.28, 0.26, 0.99 and 0.79 GPa, respectively. On the other hand, the flexural modulus of unaged or reference flax/bio-epoxy, flax/petro-epoxy, glass/bio-epoxy and glass/petro-epoxy samples is 26.5, 26.7, 46.0 and 47.0 GPa, respectively. After 56 days of weathering, the flexural strength and modulus drop for all the exposed composite samples. However, flexural strength of glass/petro-epoxy composite increased after 56 days of accelerated weathering. It is found that the decrease of flexural properties is higher in flax fiber composites than that of glass fiber composites, as shown in Figures 3 and 4. Yan et al. [12] reported the similar pattern of degradation of flexural properties of woven flax fabric reinforced petroleum-based epoxy composites under accelerated weathering for 1500 h.

The storage modulus of the composites before and after accelerated weathering is shown in Figure 5. The storage modulus of the unaged or reference flax/bio-epoxy, flax/petro-epoxy, glass/bio-epoxy and glass/petro-epoxy samples is 20.9, 22.8, 34.8 and 37.8 GPa, respectively. After 56 days of accelerated weathering, the storage modulus decreased by 35%, 21%, 10%, and 23% for flax/bio-epoxy, flax/petro-epoxy, glass/bio-epoxy and glass/petro-epoxy composites, respectively, as can be seen in Figure 5. Yorseng et al. [17] also reported the decrease of storage modulus of weathered natural fiber composites and hybrid composites.

  doi:10.5075/epfl-298799_978-2-9701614-0-0

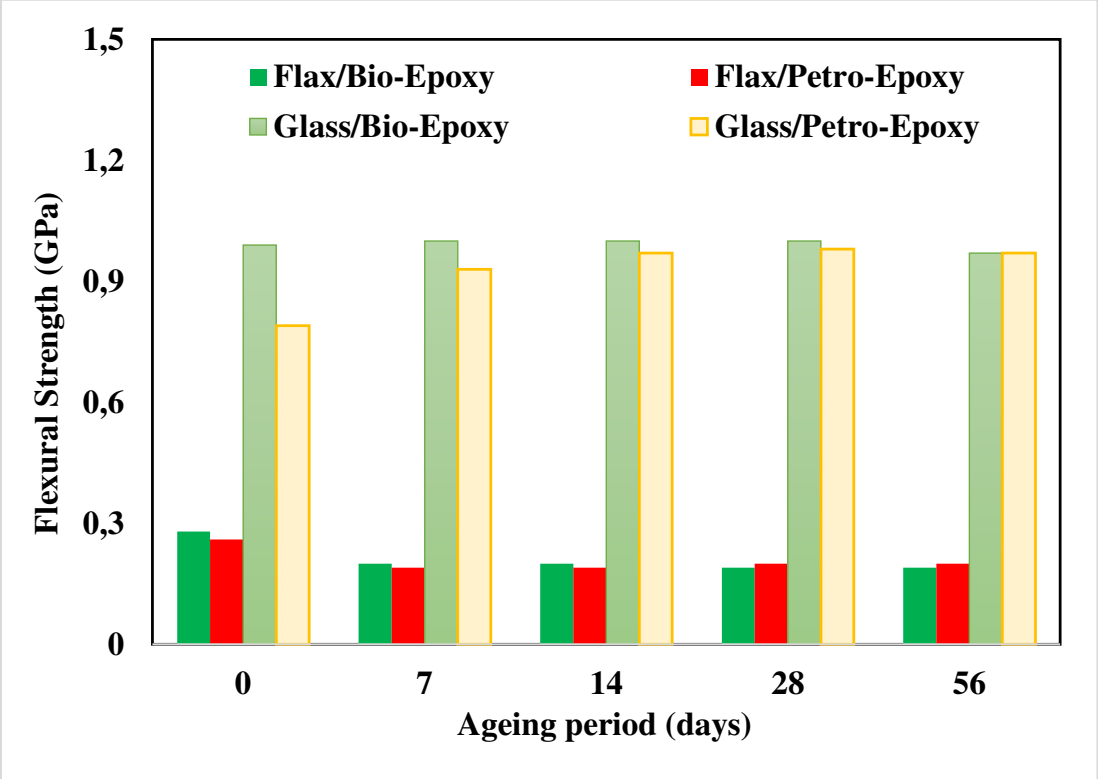

Figure 3. Flexural strength of composite samples before and after accelerated wearing.

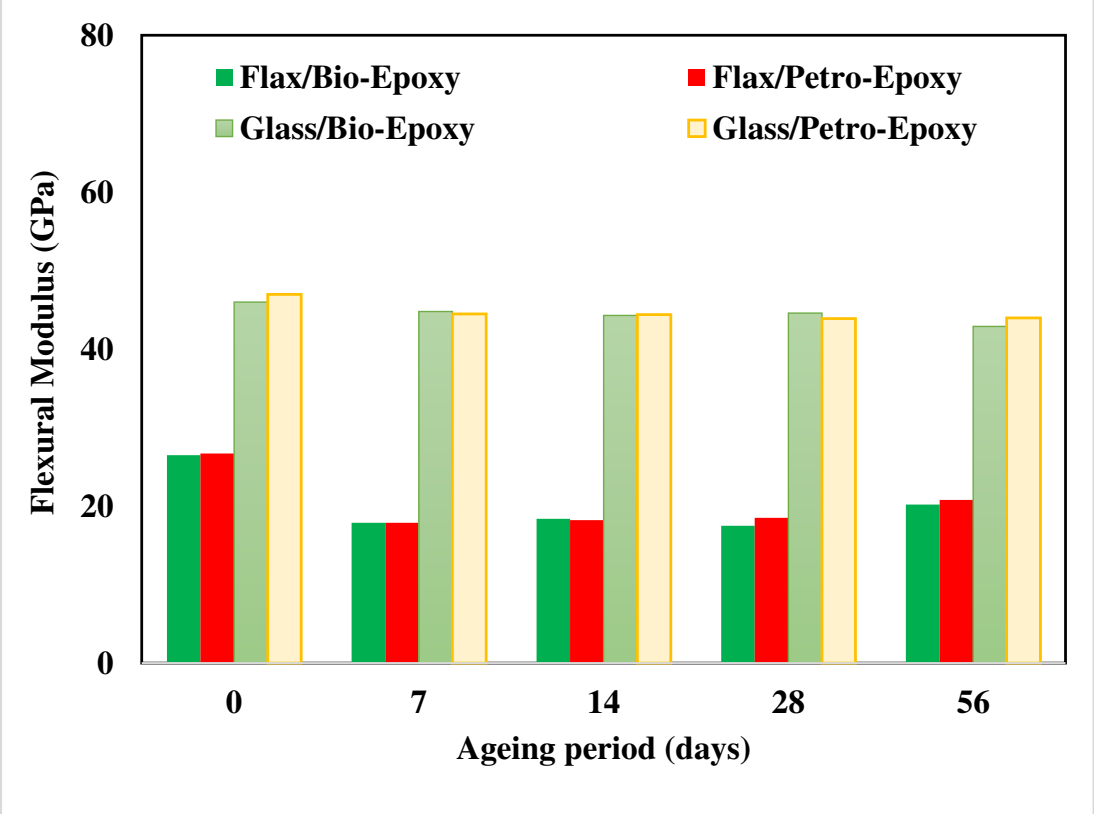

Figure 4. Flexural modulus of the composite laminates before and after accelerated weathering.

1101/1602 ©2022 Das et al. doi:10.5075/epfl-298799_978-2-9701614-0-0 published under CC BY-NC 4.0 license

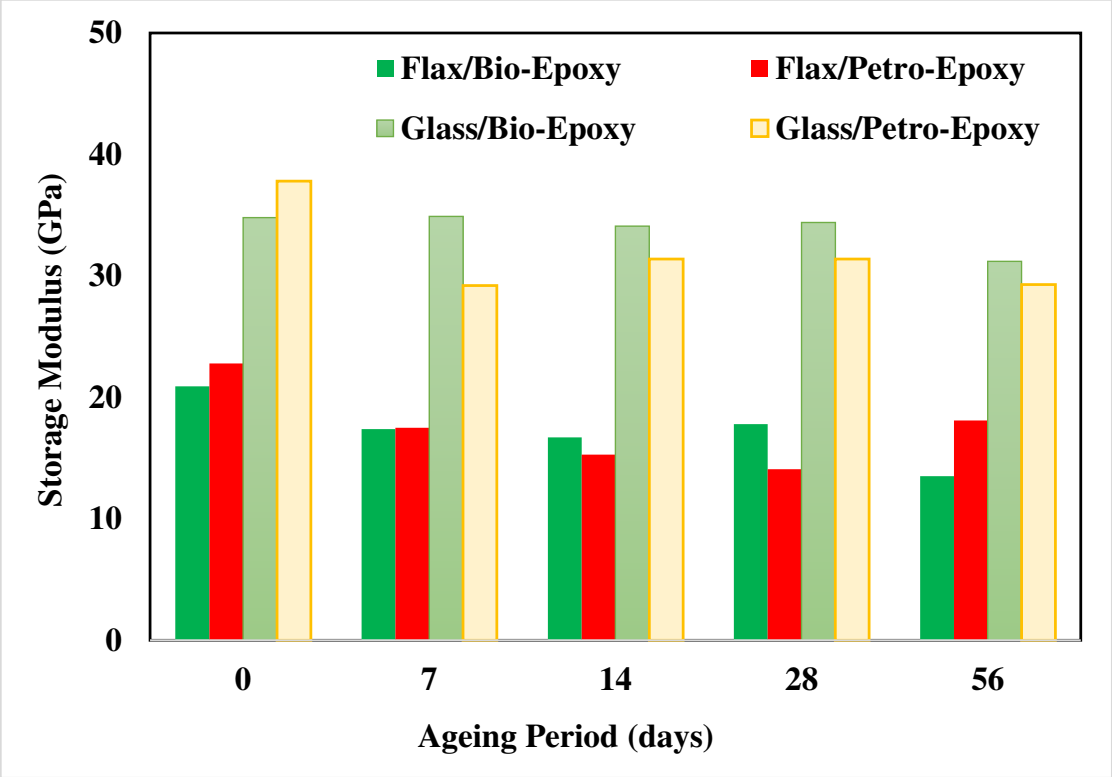

Figure 5. Storage modulus of the composites before and after accelerated weathering.

4. Conclusions

The present study concerns the durability of flax fiber composites with recyclable bio-based polymer matrix under the exposure of accelerated weathering up to 56 days. From the study, it is found that flax fiber composites with bio-epoxy and petro-epoxy resin exhibit almost similar behavior in performance after weathering, implying that the effect of polymer matrix is not affecting significantly the durability of the composites. On the other hand, glass fiber reinforced epoxy (both petro- and bio-based) composites showed higher degree of resistance of their mechanical and dynamic mechanical properties than their flax-based counterparts, which was expected. However, the performance of flax fiber composites was affected more than that of glass fiber composites, after ageing, revealing the low resistance of flax fiber reinforcement to weathering. Further research is required to understand the underlying mechanisms that lead to degradation due to weathering, and also to improve the weathering performance of flax fiber-based bio/recyclable polymer matrix composites. This way, these sustainable natural fiber recyclable matrix composites will become suitable for structural engineering applications such as automotive, civil engineering, wind energy, etc. taking full advantage of their low environmental impact.

Acknowledgements

The authors gratefully acknowledge the funding by NTNU for the PhD work of Subrata Chandra Das (Project no. 649420) and project ECOGLIDE, funded by the Research Council of Norway, RFF INNL (Ref: 328481).

  doi:10.5075/epfl-298799_978-2-9701614-0-0

5. References

1. Chang, B.P., A.K. Mohanty, and M. Misra, *Studies on durability of sustainable biobased composites: A review.* RSC Advances, 2020. **10**(31): p. 17955-17999.
2. Das, S.C., et al., *Effect of stacking sequence on the performance of hybrid natural/synthetic fiber reinforced polymer composite laminates.* Composite Structures, 2021. **276**: p. 114525.
3. Das, S.C., et al. *A comparative study between jute and glass fiber reinforced composites*. in *Key Engineering Materials*. 2021. Trans Tech Publ.
4. Joshi, S.V., et al., *Are natural fiber composites environmentally superior to glass fiber reinforced composites?* Composites Part A: Applied science and manufacturing, 2004. **35**(3): p. 371-376.
5. Mohanty, A.K., et al., *Composites from renewable and sustainable resources: Challenges and innovations.* Science, 2018. **362**(6414): p. 536-542.
6. Dahiya, S., et al., *Biobased products and life cycle assessment in the context of circular economy and sustainability.* Materials Circular Economy, 2020. **2**(1): p. 1-28.
7. Shogren, R., et al., *Plant-based materials and transitioning to a circular economy.* Sustainable Production and Consumption, 2019. **19**: p. 194-215.
8. Salim, M.S., et al., *Accelerated weathering and water absorption behavior of kenaf fiber reinforced acrylic based polyester composites.* Frontiers in Materials, 2020: p. 26.
9. Islam, M.S., K.L. Pickering, and N.J. Foreman, *Influence of accelerated ageing on the physico-mechanical properties of alkali-treated industrial hemp fibre reinforced poly (lactic acid)(PLA) composites.* Polymer Degradation and Stability, 2010. **95**(1): p. 59-65.
10. Badji, C., et al., *Correlation between artificial and natural weathering of hemp fibers reinforced polypropylene biocomposites.* Polymer Degradation and Stability, 2018. **148**: p. 117-131.
11. Dayo, A.Q., et al., *Effects of accelerated weathering on the mechanical properties of hemp fibre/polybenzoxazine based green composites.* Composites Part A: Applied Science and Manufacturing, 2020. **128**: p. 105653.
12. Yan, L., N. Chouw, and K. Jayaraman, *Effect of UV and water spraying on the mechanical properties of flax fabric reinforced polymer composites used for civil engineering applications.* Materials & Design, 2015. **71**: p. 17-25.
13. Taylor, C., et al., *Development and weatherability of bio-based composites of structural quality using flax fiber and epoxidized sucrose soyate.* Materials & Design, 2017. **113**: p. 17-26.
14. Ghasemzadeh-Barvarz, M., C. Duchesne, and D. Rodrigue, *Mechanical, water absorption, and aging properties of polypropylene/flax/glass fiber hybrid composites.* Journal of Composite Materials, 2015. **49**(30): p. 3781-3798.
15. Dittenber, D.B. and H.V. GangaRao, *Critical review of recent publications on use of natural composites in infrastructure.* Composites Part A: applied science and manufacturing, 2012. **43**(8): p. 1419-1429.
16. 06.04.2022]; QUV ACCELERATED WEATHERING TESTER]. Available from: https://www.q-lab.com/products/quv-weathering-tester/quv.
17. Yorseng, K., et al., *Influence of accelerated weathering on the mechanical, fracture morphology, thermal stability, contact angle, and water absorption properties of natural fiber fabric-based epoxy hybrid composites.* Polymers, 2020. **12**(10): p. 2254.

  doi:10.5075/epfl-298799_978-2-9701614-0-0

FIBRES HYBRIDIZATION FOR THERMOPLASTIC MATRIX COMPOSITES

L. Amorim[a,b], D. Gomes[a], M. Martins[a], R. Santos[a,b]*

a: INEGI – Institute of Science and Innovation in Mechanical and Industrial Engineering, Porto, Portugal – lamorim@inegi.up.pt
b: LAETA – Associated Laboratory of Energy, Transports and Aeronautics, Porto, Portugal

Abstract: *In this work, the experimental process optimization of continuous polyphenylene sulphide (PPS) and carbon fibres (CF) hybrid yarns with a feeding CF volume fraction of 55 % was carried out for the development of thermoplastic components, which will be used in energy applications. Processing optimization was conducted using a commingling equipment where three main process variables were evaluated, including fibres overfeed, air pressures and air-jet design. Optimized PPS/CF commingled yarns were then characterized according to their final CF volume fraction and linear density. Visual inspection, and optical and scanning electron microscopy (SEM) analyses were also performed to assess fibres integrity and distribution inside hybrid yarns. Additionally, a new prototype setup was built to produce PPS/CF hybrid yarns in a parallel hybridization way. Those new hybrid yarns produced were compared to the optimized in commingling process. Finally, adhesion between PPS and CF was evaluated based on composite laminate manufactured by hot-press.*

Keywords: Commingling; Hybrid yarns; Optimization; Thermoplastic composites; Processing.

1. Introduction

The usage of fibres reinforced polymers (FRP) has shown a significative growing in the last half-century especially regarding their remarkable in-plane mechanical properties and low density, comparatively to traditional structural materials, as metals and alloys. Moreover, the possibility to customize those materials, depending on the requirements of the final application, put them on the top list for highly demanding sectors, as aeronautic, defence and renewable energies [1], [2].

Recently, thermoplastic based-composites have been getting a lot of scientific and technological attention due to their higher sustainability and mechanical performance under impact and shear loading conditions, when compared to thermoset composites [2], [3] However, fibres impregnation processes on thermoplastic composites still is a major challenge due to the high shear viscosity of these polymers [4]. One way to overcome this issue is by minimizing thermoplastic melt mass transfer distance during composites processing through mixing thermoplastics and reinforcement fibres in a hybrid yarn [5]. Among the several yarn hybridization processes developed along the last decades [3], [6], [7], commingling fibres by air pressure appears as a versatile and effective technique where hybrid yarns with a uniform distribution of fibres can be produced using a wide range of commercially available fibres, in a customized way [1]. Nevertheless, this process can be very aggressive for the reinforcement fibres, due to their brittle behaviour, promoting some damages owing to the pressure and turbulence inside air-jet nozzle [5]. Therefore, to obtain commingled yarns with finest quality it

  doi:10.5075/epfl-298799_978-2-9701614-0-0

is required a careful processing optimization that is highly dependent on the selected process, raw-material and equipment parameters [4].

In this context, this work aims to optimize the production of continuous PPS/CF commingled yarns, with 55 % CF volume fraction, in a commercial commingling equipment for the development of thermoplastic components that will be used in renewable energy applications. In an attempt to minimized damages during hybridization process, a parallel hybridization prototype based on Diao et *al.* [7] and Irfan et *al.* [8] published works has been developed. Optimized commingled and parallel hybridized PPS/CF yarns were then characterized and compared according to their integrity and homogeneity. Additionally, the adhesion between PPS and carbon fibres was evaluated on commingled yarns based composites.

2. Experimental

2.1 Materials

Regarding the leakage on the market of thermoplastic sized carbon fibres, in this work continuous commercial 6k epoxy sized CFs (Tenax®-E HTA40 E13 6K 400tex) from Toray®, Japan, were used. As thermoplastic fibres, commercial polyphenylene sulphide (PPS) having 100 filaments per tow (Torcon® 440dtex), also from Toray, Japan, were selected. According to the suppliers' data sheet, a single PPS and CF have a nominal diameter of 20 and 7 μm, respectively. Based on this information, it was calculated the number of PPS tows needed to be fed to achieve a CF volume fraction of 55 % on the final yarn, and it was found that a combination of 6 PPS and 1 tow of 6k carbon fibres is required. The 6 PPS tows were previously joined together using winding unit of commingling equipment.

2.2 Commingling and hybridization processes

In this work, PPS/CF hybrid yarns were produced using two different processes: i) commercial commingling equipment from Retech®, Switzerland, and ii) a homemade parallel hybridization prototype, which are depicted in Figure 1. In both cases, commingling and parallel hybridization the production speed was set at 20 m/min.

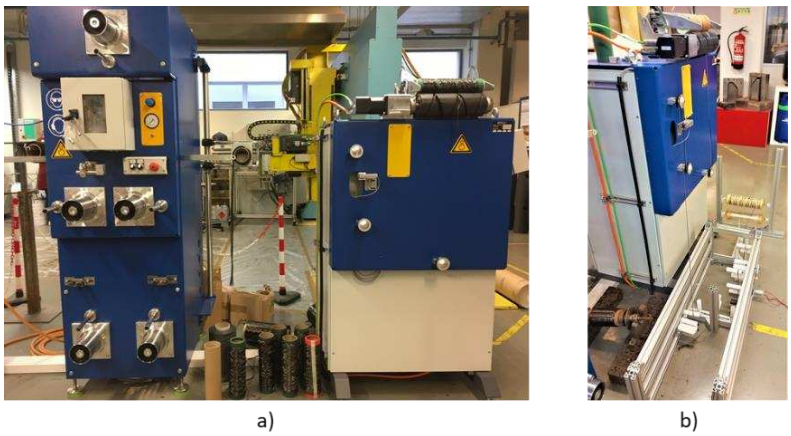

Figure 1. Photography of the a) conventional commingling process and b) parallel hybridization prototype.

Commingling process: The commingling equipment is composed by two main part, the feeding/commingling and the winding unit. In this process, both fibre tows are pulled out from

the creel independently by feeding rolls, and then they are forced to converge to an air-jet device where the air turbulence mingle both fibres. Afterwards, the commingled yarns are pulled out and winded in the winding unit. Even when well-controlled processing conditions are used, commingling technique is typically very aggressive to the fibres leading to their damages. Therefore, it is of paramount importance to carefully optimize all processing parameters, aiming to minimize damage and obtain finest quality yarns. The optimization of commingling process in this study was carried out regarding three main variables: i) air pressure inside the air-jet, ii) overfeed percentage of PPS and carbon fibres, individually, and iii) air-jet design.

The overfeed percentage is defined as the ratio between the feeding speed of each fibre tow into the air-jet and the pulling speed of commingled yarn from the air-jet. The equation 1 expresses the overfeed calculation:

$$Overfeed = \frac{V_{Pf,CF} - V_{CY}}{V_{CY}} \times 100\% \quad (1)$$

where, V_{CY} and V_{Pf} or V_{CF} (represented by $V_{Pf,CF}$) are the pulling speed commingled yarns out of the air-jet, and the feeding speed of polymer and carbon fibre into the air-jet, respectively.

Parallel hybridization process: A homemade parallel mingling prototype was built to produce PPS/CF hybrid yarns. Both fibre tows are pulled out together through a set of rolls in a constant speed, and the constant friction between them and the rolls lead to a mechanical mingling of fibres. The idea behind this strategy is to reduce fibres breaking caused in the traditional commingling process. It is wreath to mention that additional studies will be carried out to improve the parallel hybridization process.

2.3 Characterization tests

A testing campaign was defined to characterize raw-materials and optimized PPS/CF commingled/hybrid yarns. A brief description of the procedures used is given below.

Density (immersion test) – The density of PPS and CF was determined using the immersion method following ISO 1183 standard procedures. A digital weighting scale with an accuracy of 1 X 10^{-4} g was used, and five samples were first weight in air and then immersed in a well-defined density solvent (2-propanol).

Differential scanning calorimetry (DSC) - The melting point of PPS fibres was determined in a TA20 DSC equipment, from TA instruments. Two PPS samples were tested in a range of temperatures between -20 and 300 °C at a heating rate of 10 °C/min.

Linear density – The linear density of as-received fibres and hybrid yarns was determined experimentally over by weighting ten samples, having all of them 1 meter, using a digital weighting scale with an accuracy of 1 X 10^{-4} g. In this work, the linear density is presented in *tex* units, which is equal to the weight of 1 km tow or yarn.

Calcination and carbon fibre volume fraction - Three samples of as-received PPS and carbon fibres, with 1 m length, were cut and putted in individual crucibles. Then, each crucible with the sample inside was weight individually and calcinated inside a muffle at 500 °C for 6 hours. After calcination, crucibles were weight and the remaining residue determined. The same procedure was applied to PPS/CF hybrid yarns. After some calculation corrections using fibres density and

calcination remaining residue of as-received fibres, carbon fibre volume fraction of hybrid yarns was determined.

Optical microscopy - Carbon and PPS fibres diameter was assessed under optical microscopy. At least 20 fibres were measured for each type of fibre. This technic was also used to evaluate fibres distribution into produced hybrid yarns.

Scanning electron microscopy (SEM) - Morphology of carbon and PPS fibres surface was observed under SEM, before and after hybridization process. By this method, it was possible to evaluate how hybridization processes affect fibres integrity, and the adhesion between PPS and carbon fibres. The adhesion of composites based on PPS/CF was also evaluated by SEM.

3. Results and discussion

3.1 Raw-materials characterization

Prior to hybridization, PPS and carbon fibres were characterized according to their nominal diameter, density and linear density and, in the case of PPS, its melting temperature (*Tm*). A summary of these properties is presented in Table 1.

Table 1. Carbon and PPS characteristics/properties experimentally determined.

Property	units	PPS fibres	Carbon
Nominal fibre diameter	μm	21.7 ± 0.4	7.2 ± 0.5
Density	g/cm^3	1.318 ± 0.009	1.725 ± 0.010
Linear density	*tex*	44 ± 0	398 ± 2
Melting temperature (*tm*)	*ºC*	284.30 ± 0.08	-

According to Table 1, the nominal diameter of PPS fibres is slightly higher (±22 μm) than that indicated by the provider (20 μm). From the calculations, the CF volume fraction obtained for hybrid yarns is of approximately 50 %, lower than the value theoretically estimated of 55 %.

3.2 Commingling yarns process optimization

The air pressure optimization tests were conducted at three different air pressures, namely 1, 1.5 and 2 bar. Adapted from a previous project, the overfeed percentages used here were between 1 and 3.3 %.

After 5 min. production using each condition, it was observed an increase of broken fibres inside the sound box where air-jet is installed as the air pressures increased, as it can be seen in Figure 2. At 2 bar of air pressure, the fuzzy aspect of PPS/CF commingled yarns suggests large fibre damages, on the other hand, at 1 bar the process became unstable with the yarn getting out of the guiders after air-jet. Therefore, and considering these observations, 1.5 bar of air pressure was considered the better condition.

  doi:10.5075/epfl-298799_978-2-9701614-0-0

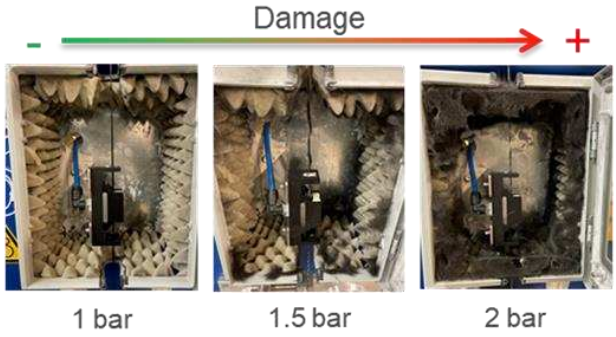

Figure 2. Amount of broken fibres inside the sound box for different air pressures.

The overfeed study was developed by varying, independently, the overfeed of PPS (Of_{PPS}) and carbon (Of_{CF}) fibres using four different percentages, namely 1.5, 3, 6, and 8 %. All tests were conducted using the commercial air-jet and the air pressure was set at 1.5 bar, and results are depicted in Figure 3.

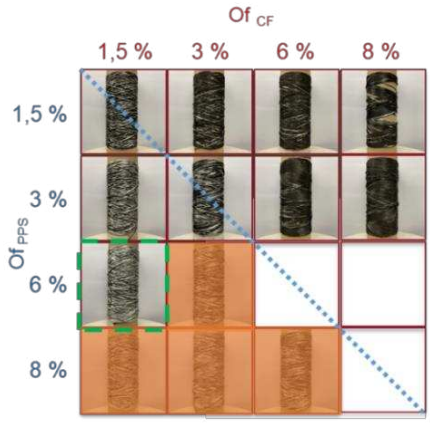

Figure 3. Photography of PPS/CF commingled yarns produced using different overfeed conditions.

In Figure 3, the visual aspect of PPS/CF commingled yarns bobbins, produced at different overfeed conditions, is presented. The blue dotted diagonal line identifies the processing condition where PPS and CF have the same overfeed percentage. Above this diagonal, the percentage of CF fed to air-jet is higher than PPS, while bellow the opposite is imposed. Up to an overfeed of 6 % of PPS and 1.5 of CF, the process is stable, although after this point (orange shaded images) some instabilities were observed, such as fibres tension loss before air-jet or commingled yarn jumping off guiders immediately after air-jet. Therefore, these conditions were not considered for further studies, since it is impossible to produced commingled yarns.

At conditions above the diagonal line, bobbins presented a fuzzy dark aspect, which is indicative of an excess of carbon fibres. On the other hand, conditions below the diagonal line presented a whiter and woolly appearance. Both commingled yarns, produced with conditions along and above the diagonal, have shown visible damages of carbon fibres, therefore, all of them were discarded. Based on the visual inspection of commingled yarns produced using the two remaining conditions, PPS/CF commingled yarns with a CF overfeed of 1.5 % and PPS overfeed 6 % was considered acceptable (green dotted square in Figure 3). Under these overfeed conditions, PPS fibres are clearly tangled around carbon fibres for long lengths, forming a single

  doi:10.5075/epfl-298799_978-2-9701614-0-0

yarn, while in commingled yarns produced by the other conditions (Of_{PPS} = 1.5 % and Of_{CF} = 3 %), PPS and CF remain apart from each other for long extensions. Despite the apparent good aspect of PPS/CF commingled yarns produced under this condition, the attained CF volume fraction was lower than the expected (41 %), and therefore slight adjustments were carried out, leading to a carbon fibre volume fraction close to the expected, 51 %. The optimal overfeed percentages for PPS and carbon fibres were found to be 5 % and 3 %, respectively.

Air-jet study was carried out using the optimal overfeed and air pressure conditions. The visual inspection of PPS/CF commingled yarns produced by the circular cross-section air-jet has revealed a completely segregation between PPS and carbon fibres. To overcome this issue, the air pressure was readjusted but no improvements were achieved, meaning that the design of the commercial air-jet is most suitable for the PPS/CF commingled yarns production.

To summarize, commingling optimization demonstrated that the best processing condition to achieve high quality PPS/CF commingled yarns is by using 1.5 bar of air pressure with overfeeds of 5 % for PPS and 3 % for CFs, and the commercial air-jet geometry.

3.3 PPS/CF hybrid yarns characterization

Table 2 presents the experimental results of PPS/CF hybrid yarns, in terms of linear density and CF volume fraction, while values in parentheses correspond to the theoretically expected.

Table 2. Linear density and carbon fibre volume fraction of PPS/CF hybrid yarns.

	units	Commingling	Parallel hybridization
Linear density	*tex*	663 (662)	664 (662)
Carbon fibre volume fraction	%	52 (50)	42 (50)

It is possible to observe that, independently on the production process, both hybrid yarns presented similar linear densities that are very close to those expected theoretically. Regarding CF volume fraction, optimized commingled yarn revealed a similar value to expected, while parallel hybrid yarns have shown to be 8 % lower. This may result from an instability of PPS fibres trajectory during the process, leading to an excess of the thermoplastic counterpart.

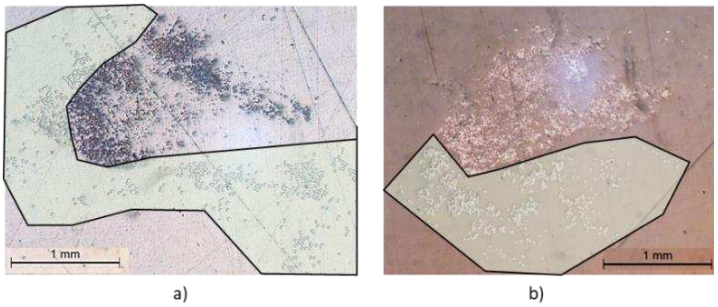

Figure 4. Optical microscopy images of PPS/CF a) commingled and b) hybridized yarns.

Optical microscopic images of commingled and parallel hybridized yarns are shown in Figure 4 a) and b), respectively. Through the cross-section inspection of commingled yarns, it is possible to observe PPS surrounding carbon fibres. Mingling between PPS and carbon fibres was also

observed at the interface (green shade area), which was further confirmed by SEM images [Figure 5 a)]. On the other hand, hybrid yarns produced on new hybridization setup revealed that PPS and carbon fibre are concentrated in tow clusters side-by-side. Nevertheless, signs of mingling also observed at the interface were also verified by SEM, according to the Figure 5 b). Commingled yarn SEM image, in Figure 5 a, also revealed broken and misalignment carbon fibres regarding to PPS counterparts, resulting from a turbulent environment inside the air-jet. For parallel hybridized yarn, in Figure 5 b), fibres seem to mostly kept their integrity without significant misalignments.

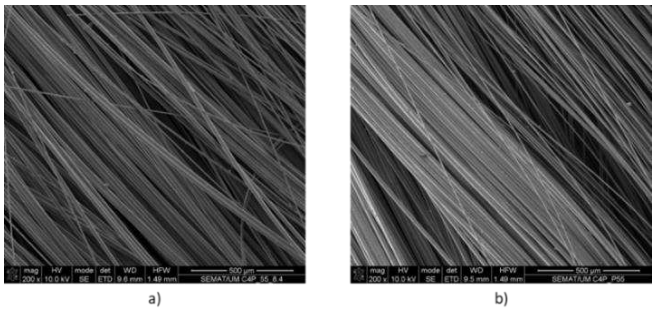

Figure 5. Optical microscopy images of PPS/CF a) commingled and b) hybridized yarns.

3.3 PPS/CF adhesion

To evaluate the adhesion between PPS and carbon fibres, 200 g of commingled yarns were weight and cut in equal parts with 100 mm length. Then, they were carefully aligned in the same direction inside a 100x100 mm metallic frame and the whole set was finally placed between two hot plates. No pressure was applied during the consolidation that occurred at 320 °C for 50 min, and the composite laminate was then cooled to room temperature.

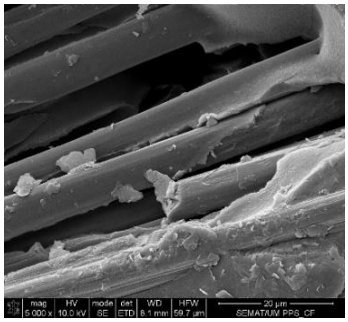

Figure 6. SEM image of a cryogenic fracture on PPS/CF composite.

In Figure 6, it is presented the SEM image of an artificial cryogenic fracture on PPS/CF composite, where it is possible to observe an apparent good wettability between PPS and fibres. A closed look over the image revealed some interfacial debonding and carbon fibres negative prints on PPS, suggesting a mechanical bonding between both. Sizing debonding during commingling process can result in a rough carbon fibres surface, allowing a better mechanical bonding between them and PPS.

4. Conclusions

In this work, the experimental process used for hybridization of PPS and carbon fibres was optimized, allowing the development of composite laminates with 55 % of CF volume fraction,

  doi:10.5075/epfl-298799_978-2-9701614-0-0

for wind and tidal energy applications. Processing optimization was conduct in a commercial commingling equipment and the results were compared to those obtain from PPS/CF yarns produced by a new parallel hybridization prototype. Furthermore, the adhesion between PPS and CFs was investigated in a hot-pressed composite made from optimal commingled yarns. Commingling process optimization study define as optimal conditions the usage of the commercial air-jet with 1.5 bar of air pressure and an overfeed percentages for PPS and carbon fibres of 5 % and 3 %, respectively. Optimal commingled yarn was compared to PPS/CF yarn produced by parallel hybridization. Both have shown a similar linear density around 663 tex, however, while commingled yarn has shown a carbon fibre volume fraction of 52 %, parallel hybridized yarn this property was shown to be lower, 42 %. Visual inspections revealed an apparent better mingling between fibres in commingled yarn than in parallel hybridized yarn, this was confirmed by optical microscopy and SEM analysis. A higher number of broken and misalignment of CF on commingled yarn was also observed under SEM. Finally, mechanical bonding has shown to be the most dominant adhesion mechanism between PPS and CF after commingled yarns consolidation. Further optimizations of parallel hybridization process will be carried out as well as mechanical characterization of PPS/CF composites manufactured from commingled and parallel hybridized yarns.

Acknowledgements

This work was developed in the scope of “Carbo4Power” project, supported by the European Union under the HORIZON2020 Framework Programme Grant Agreement no. 953192.

5. References

[1] V. Nayana et al., *Polymer Testing*, vol. 91, no. July, p. 106774, 2020, doi: 10.1016/j.polymertesting.2020.106774.

[2] E. Selver et al., *Composites Part B: Engineering*, vol. 91, pp. 522–538, Apr. 2016, doi: 10.1016/j.compositesb.2015.12.035.

[3] P. J. Hogg, *Materials Science and Engineering A*, vol. 412, no. 1–2, pp. 97–103, Dec. 2005, doi: 10.1016/j.msea.2005.08.028.

[4] P. Kravaev et al., *Journal of Thermoplastic Composite Materials*, vol. 27, no. 3, pp. 350–363, 2014, doi: 10.1177/0892705712446167.

[5] M. M. B. Hasan et al., *Journal of Thermoplastic Composite Materials*, vol. 28, no. 12, pp. 1708–1724, 2015, doi: 10.1177/0892705715604677.

[6] J. P. Nunes et al., *Advances in Polymer Technology*, vol. 32, no. SUPPL.1, Mar. 2013, doi: 10.1002/adv.21279.

[7] H. Diao et al., *16th European Conference on Composite Materials, ECCM 2014*, no. June, pp. 22–26, 2014.

[8] M. S. Irfan et al., *Journal of Composite Materials*, vol. 48, no. 15, pp. 1813–1831, 2014, doi: 10.1177/0021998313490770.

MECHANICAL CHARACTERIZATION OF A THREE-DIMENSIONAL HYBRID WOVEN COMPOSITES

Benjamin, Ade[a,b], Bastien, Tranquart[b], Zoheir, Aboura[a]

a: Laboratoire Roberval de Mécanique, Sorbonne Universités, Université de technologie de Compiègne – benjamin.ade@utc.fr / benjamin.ade@safrangroup.com
b: Safran Composites, Itteville, France

Abstract: *A comprehensive analysis on the impact of the introduction of elastomer fibers in a epoxy-resin matrix reinforced by 3D-interlocks woven composites is given. At this aim, several configurations with different types of introduction of elastomer fibers and different thicknesses were tested. Analysis has been focused on the Young Modulus and on the apparition of the onset damage in the material through a multi-instrumentation. Stereo-digital image correlation (Stereo-DIC), acoustic emission (AE) and in-situ microscopy were used to identify the mechanical properties and onset damage mechanism of materials. The impact of hybridization was proven on the mechanical properties of each material, especially on the onset damage apparition.*

Keywords: mechanical properties; hybrid materials; woven composites

1. Introduction

Three-dimensional (3D) woven composites have progressively found their place in many industrial applications such as wind turbine blades, engine fans and construction applications (1). Through-the-thickness reinforcement allows an enhancement of out-of-plane properties and a higher impact damage tolerance (2). Like their mechanical behavior is different from the behavior of 2D composite laminates, many kinds of research were performed for accumulating knowledge about their mechanical properties and damage mechanisms. That is why studies on static (3), impact (4), multi-axial (5) and fatigue (6) loadings have been processed. Nowadays, the accumulation of knowledge on 3D woven composites is always an active field.

Over the past years, improvement of properties or capabilities of composites was also performed through functionalization and hybridization. Indeed, hybridization can provide an enhancement of a specific mechanical property (7,8) or can be used for structural health monitoring or process monitoring (9,10).

In this study, 3D woven composites have been hybridized to enhance damping properties through the introduction of elastomer fibers (11,12). Studies on the enhancement of damping properties through hybridization have been led previously for showing the increase or not of damping properties (7,13,14). Nevertheless, our objective was to study the impact of hybridization on the standard mechanical properties that are Young Modulus, onset damage, and damage mechanisms until failure.

At this aim, multi-instrumented tests were performed to establish a consequent knowledge of these hybrid materials. Multi-instrumentation as Digital Image Correlation (DIC), Acoustic Emission (AE), and in-situ microscopic observations have been used to analyze the mechanical behavior of these materials.

  doi:10.5075/epfl-298799_978-2-9701614-0-0

2. Materials

Epoxy-resin matrix reinforced by 3D-interlocks woven composites made of intermediate modulus (IM) carbon fibers were studied. Through the Jacquard Loom process, elastomer fibers have been introduced in the weft direction of the woven architecture (11,12). Then, materials are processed by Resin Transfer Molding (RTM) and are provided by SAFRAN Group. Figure 1 presents how elastomer fibers were introduced in the woven architecture. Elastomer fibers have been introduced into the weft direction thanks to the Jacquard Loom process and are not straight but undulated in the thickness of the material.

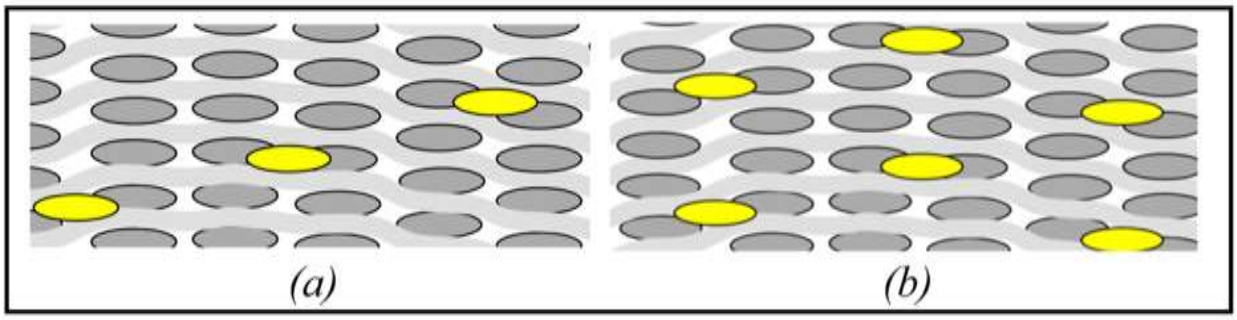

Figure 1 Insertion of the elastomer fibers in the weft direction: (a) config HYB1 (b) config HYB2 & HYBTW

Also, materials are unbalanced due which means the ratio between warp and weft fiber content is no even. The proportion of elastomer yarns and resin content changes accordingly. Indeed, elastomer fibers replaced resin matrix to keep as much as possible the stiffness of the material unchanged.

Several configurations with different ratios of hybridization have been studied and the following table lists (Fig.2) these different configurations.

Thickness 6mm	**0%**	**11,5%**	**11,5% + carbon**	**% elastomer in volume**
Configuration	6-REF	6-HYB2	6-HYBTW	
Thickness 13mm	**0%**	**3%**	**6%**	**% elastomer in volume**
Configuration	13-REF	13-HYB1	13-HYB2	

Figure 2 Ratios of elastomer for each configuration tested

  doi:10.5075/epfl-298799_978-2-9701614-0-0

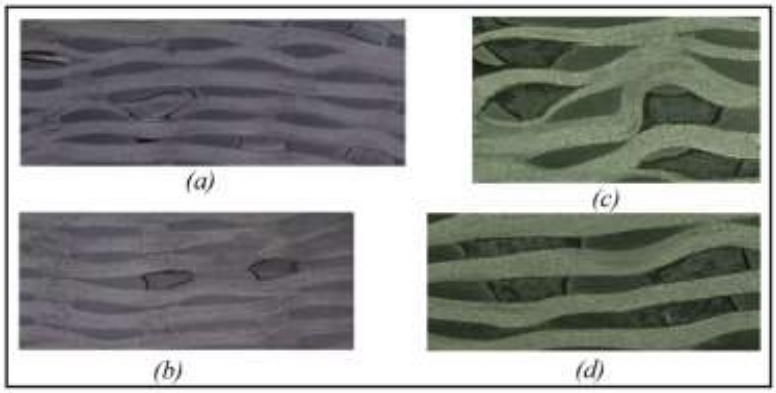

Figure 3 Microscopic (mesoscopic) view of: (a) 13-HYB2 (b) 13-HYB1 (c) 6-HYBTW (d) 6-HYB2

The physical properties of the elastomer disturbed the woven architecture during the process. Indeed, as we see in figure 3, the continuous elastomer fibers have been deformed and local shrinkages in the woven architecture were detected.

3. Methods

To analyze the impact of the hybridization on mechanical behavior, tensile tests on dog-bone specimens have been multi-instrumented. Figure 4 represents the sample preparation.

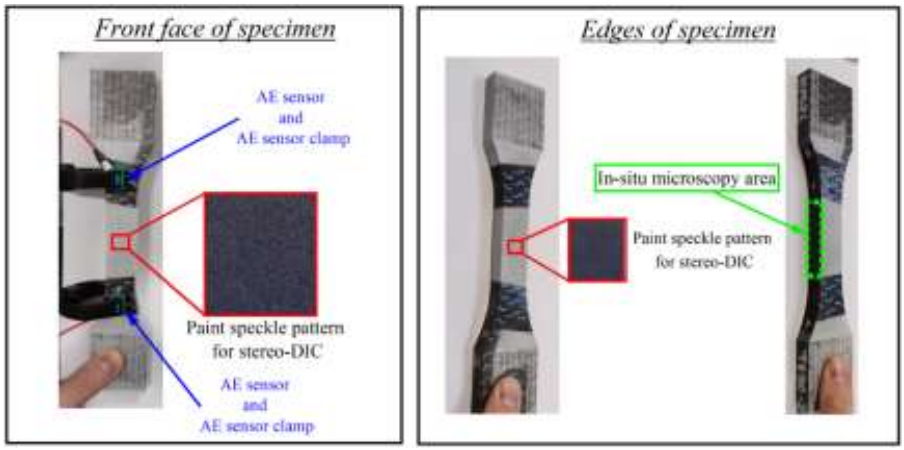

Figure 4 Sample preparation

Stereo-DIC, Acoustic Emission and in-situ microscopy were used. Stereo-DIC was preferred to ensure a better acquisition by taking into account any out-of-plane displacement. Acoustic emission records the material activity that is linked to damage in the material. In-situ microscopy identifies the apparition of damage in the edge of the dog-bone specimen.

This multi-instrumentation allows the identification of the two properties: Young Modulus and Stress at onset damage.

First, we measured the Young Modulus from DIC-extracted Stress-Strain curves between 0,1% and 0,3% strain (ε_{yy} : strain in the loading direction). Next, onset damage stress are obtained by analyzing the evolution of cumulative acoustic energy of localized event. These values are confirmed using two additional techniques: stereo-DIC and in-situ microscopy with an incremental tensile test. This method is illustrated in the figure 4.

  doi:10.5075/epfl-298799_978-2-9701614-0-0

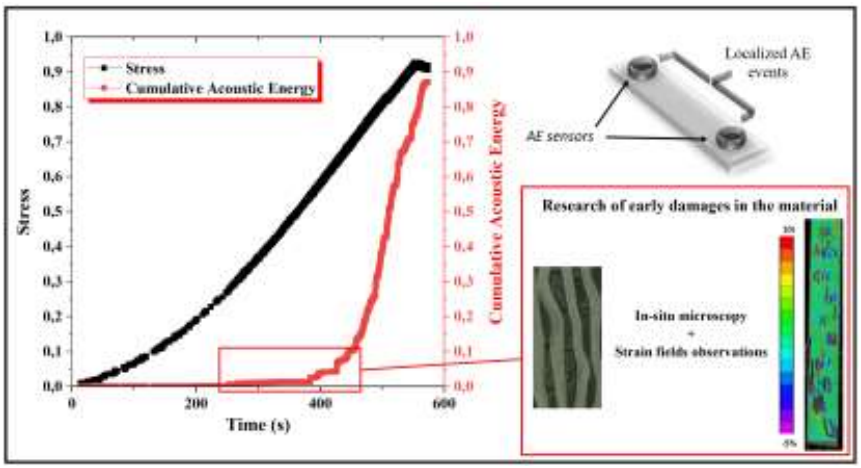

Figure 5 Multi-instrumentation procedure for identifying the onset damage

4. Results

Figure 6 represents the Young Modulus (normalized by the maximum Young Modulus) of the warp and weft dog-bone specimens with their standard deviation.

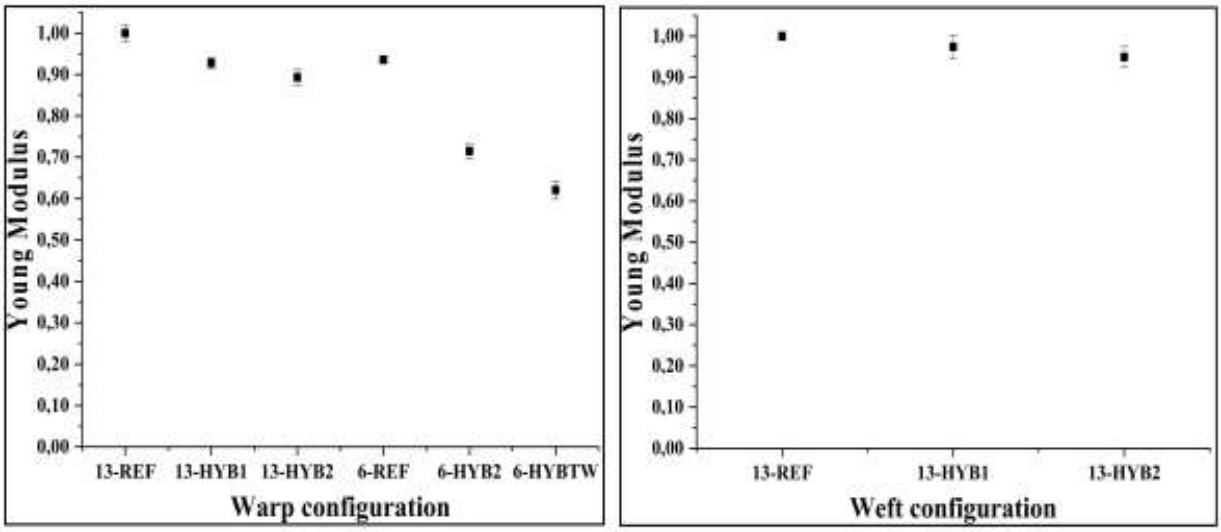

Figure 6 Comparison of Young Modulus

In the warp direction, reference materials have approximatively the same Young Modulus. First, as expected, there is a correlation between the percentage of elastomer and the degradation of stiffness. Configurations with the bigger ratio of elastomer (6-HYB2 and 6-HYBTW) have the lowest Young Modulus (loss of 23% and 33% compared to the reference).

As we saw in the material's description, these degradations can be explained by the perturbation in the weaving induced by the hybridization. First, the straightness of the warp tows is affected in the woven architecture by elastomer fibers. Moreover, it has been proved that the more the fibers are straight in a 3D woven composite, the more is the stiffness. Next, we replaced resin with elastomer fibers and the resin is more rigid so it is also normal for the stiffness of the material to drop.

  doi:10.5075/epfl-298799_978-2-9701614-0-0

That is why the degradation of the Young Modulus is correlated to the ratio of the elastomer in volume.

In the weft direction, the introduction of elastomer fibers induced a slight decrease of stiffness. A loss of 2.6% and 5.1% is observed for configurations 13-HYB1 and 13-HYB2 compared to the reference. The weft direction is less affected by the presence of elastomer fibers. This is due to an insignificant perturbation of the weaving in the weft direction.

After concluding on the impact of the hybridization on the Young Modulus, we put our interest on the onset damage. Figure 8 shows the Stress at onset damage (normalized by the maximum onset damage stress) of the warp and the weft dog-bone specimens with their standard deviation. For information, values presented were obtained through the tensile test until failure and then, they were validated through incremental tensile tests and correlation between instrumentations.

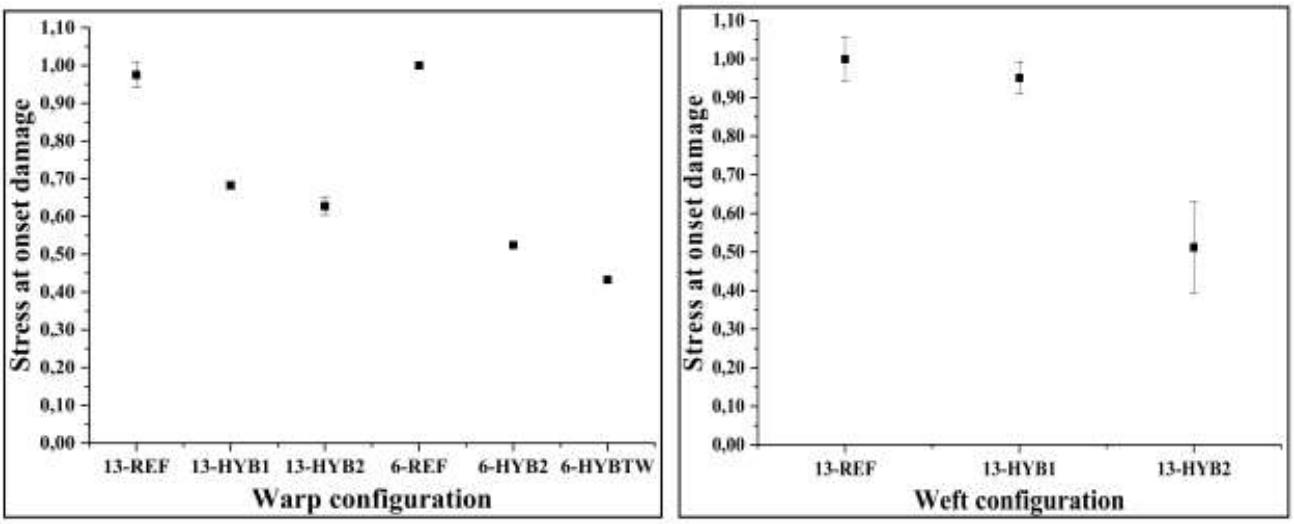

Figure 7 Comparison of Stress at onset damage

Reference materials have onset damage that appeared at approximately the same stress. First, we observe that hybridization of the material implies a significant degradation on the apparition of damage. Indeed, a decrease between 30% and 56% was noticed for the hybrid configurations compared to references. The degradation is correlated also with the percentage of the elastomer in the material. More the woven architecture is disturbed by hybridization lower the onset damage stress is. Indeed, the degradation induced in the carbon woven architecture by elastomer fibers provoked a first damage change compared to the reference materials. The change of onset damage on the 6mm-materials is shown in the figure 8. The apparition as onset damage of decohesion between carbon tows was observed and further, this onset damage induced a sooner failure of the hybrid materials.

  doi:10.5075/epfl-298799_978-2-9701614-0-0

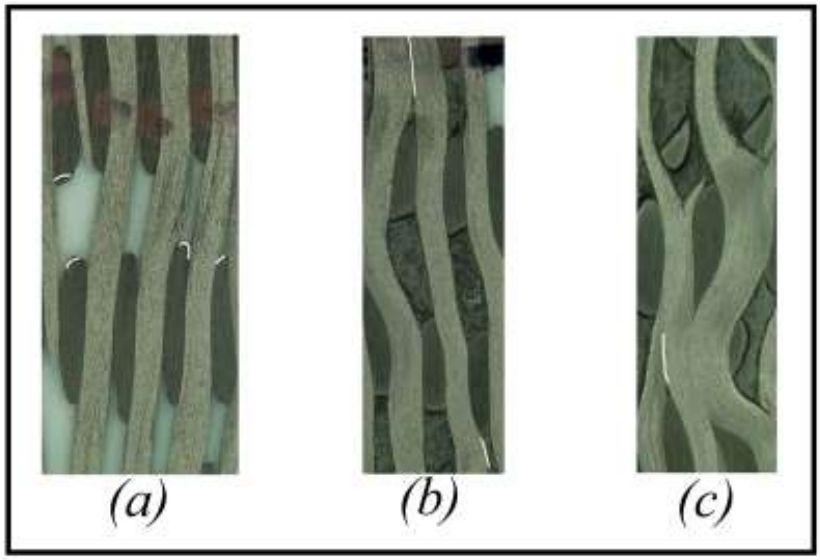

Figure 8 First damage of 6mm-materials: (a) 6-REF (b) 6-HYB2 (c) 6-HYBTW

In the case of the weft direction, the ratio of the elastomer in volume influences the onset damage. 3% of the elastomer in volume induced degradation of 4.9% (config. 13-HYB1) whereas 6% of the elastomer in volume induced a significant degradation of 49% (config. 13-HYB2).

5. Conclusion

Influence of elastomer fibers has been shown. Mechanical properties were degraded due to the woven perturbation occurring in the architecture. Indeed, the perturbation in the carbon reinforcement induced a loss of stiffness due to several local shrinkages in the warp direction of the material. Also, contact between carbon tows were established and the onset damage apparition is affected. That's why a sooner apparition of the onset damage is noticed.

Also, numerical analysis were performed to give us a predictive tool on the identification of the 3D elastic moduli and damage apparition. The computation of homogenized properties and damage initiation were performed with a meso-scale voxel-FE model. This tool helped us for continuing the improvement of the hybrid materials.

6. References

1. Mouritz AP, Bannister MK, Falzon PJ, Leong KH. Review of applications for advanced three-dimensional fibre textile composites. Compos Part A Appl Sci Manuf. 1999 Dec 1;30(12):1445–61.

2. Brandt J, Drechsler K, Arendts FJ. Mechanical performance of composites based on various three-dimensional woven-fibre preforms. Compos Sci Technol. 1996;56(3):381–6.

3. Saleh MN, Soutis C. Recent advancements in mechanical characterisation of 3D woven composites. Mech Adv Mater Mod Process [Internet]. 2017;3(1):12. Available from: https://doi.org/10.1186/s40759-017-0027-z

4. Umer R, Alhussein H, Zhou J, Cantwell WJ. The mechanical properties of 3D woven

  doi:10.5075/epfl-298799_978-2-9701614-0-0

composites. J Compos Mater [Internet]. 2016 Nov 30;51(12):1703–16. Available from: https://doi.org/10.1177/0021998316681187

5. Tableau N, Aboura Z, Khellil K, Laurin F, Schneider J. Multiaxial loading on a 3D woven carbon fiber reinforced plastic composite using tensile-torsion tests : Identification of the first damage envelope and associated damage mechanisms. Compos Struct. 2019 Nov 1;227:111305.

6. Yu B, Bradley RS, Soutis C, Hogg PJ, Withers PJ. 2D and 3D imaging of fatigue failure mechanisms of 3D woven composites. Compos Part A Appl Sci Manuf. 2015 Oct 1;77:37–49.

7. Martone A, Giordano M, Antonucci V, Zarrelli M. Enhancing damping features of advanced polymer composites by micromechanical hybridization. Compos Part A Appl Sci Manuf. 2011 Nov 1;42(11):1663–72.

8. Treviso A, Van Genechten B, Mundo D, Tournour M. Damping in composite materials: Properties and models. Compos Part B Eng. 2015 Sep 1;78:144–52.

9. Tuloup C, Harizi W, Aboura Z, Meyer Y, Ade B, Khellil K. Detection of the key steps during Liquid Resin Infusion manufacturing of a polymer-matrix composite using an in-situ piezoelectric sensor. Mater Today Commun. 2020 Sep 1;24:101077.

10. Martins AT, Aboura Z, Harizi W, Laksimi A, Hamdi K. Structural health monitoring by the piezoresistive response of tufted reinforcements in sandwich composite panels. Compos Struct. 2019 Feb 15;210:109–17.

11. Dambrine B, Tranquart B, Coupe D, Colot M-A. WO 2020/128367 A1 - Fibre reinforced composite part with increased vibration resistance. FRANCE; 2020. p. 23.

12. Dambrine B, Coupe D, Tranquart B. WO 2020/128191 A1 - Woven fibrous texture. FRANCE; 2020. p. 22.

13. Bandaru AK, Patel S, Sachan Y, Ahmad S, Alagirusamy R, Bhatnagar N. Mechanical characterization of 3D angle-interlock Kevlar/basalt reinforced polypropylene composites. Polym Test. 2016 Oct 1;55:238–46.

14. Baitab DM, Majid DL, Abdullah EJ, Hamid MFA. Tensile behavior of multilayer 3D smart woven composites embedded with shape memory alloy (SMA) wires. J Mater Res Technol. 2020 Sep 1;9(5):10876–85.

  doi:10.5075/epfl-298799_978-2-9701614-0-0

DESIGN AND CHARACTERIZATION OF TOUGH ARCHITECTURED CERAMIC-BASED COMPOSITES

Hamidreza, Yazdani Sarvestani [a], David, Backman [b], Marc, Genest [b], Behnam, Ashrafi [a]

a: Aerospace Manufacturing Technology Center, National Research Council Canada, 5145 Decelles Avenue, Montreal, QC H3T 2B2 Canada (hamidreza.yazdani@nrc-cnrc.gc.ca)
b: Structures and Materials Performance Laboratory, National Research Council Canada, Ottawa, ON K1A 0R6 Canada

Abstract:

Ceramic materials are excellent candidates for ambient and harsh environment applications. However, ceramics often suffer from brittle failure, which limit their applications when the potential for mechanical or thermal shocks may exist. Many natural materials demonstrate a ductile behaviour while mainly composed of brittle, mineral-based building blocks. In this study, inspired by natural materials, a simple, yet scalable procedure, based on laser-engraving and assembly is employed to fabricate architectured ceramic composites with enhanced toughness behaviour. Three types of multilayered architectured ceramics as well as a plain ceramic were manufactured. The mechanical response of the multilayered architectured and plain ceramics under three consecutive low-velocity impact loads was studied. It is found that the architectured composites demonstrate more energy absorption compared to plain ceramic panels. This comes at an expense of a decrease in stiffness and strength. The results reveal that the improved performance is rooted in relative sliding of neighbouring tiles which in turn results in frictional energy dissipation, a mechanism which is absent in plain ceramics.

Keywords: Ceramic composites; Lamination; Toughening mechanisms; Bio-inspiration.

1. Introduction

Ceramics have been widely used for many decades as structural materials, however due to their inherent brittleness their applications have been primarily limited to compressive loading conditions. General interest in the mechanical behaviour of ceramics is motivated by the in-service demand for structural components which often require the application of brittle materials, because of behaviors such as high stiffness and strength, low density, high temperature stability, oxidation, corrosion, hardness, and wear resistance. Further, most of the current advanced designs in aerospace, marine, automotive and armour industries require high toughness which implies potential limitations for ceramics due to their low fracture toughness [1].

Improving the toughness of ceramics is an advancing challenge. Through the process of evolution, biological materials have optimized their structure-property relationship and produced natural disordered microstructures. Borrowing the design of these biological structures from nature may inspire a promising strategy to overcome inherent brittleness of ceramics. Examples such as bone, bamboo, grassy stem, American white pelican feather, dragonfly wing, or crow skull present different organisms and constituent materials of which their structural properties prevent catastrophic and unexpected failure from fatigue or multi-

  doi:10.5075/epfl-298799_978-2-9701614-0-0

impacts as shown in Fig. 1. In these biological materials, control of the distribution of material as well as the complex and disordered structural phases generate very stiff, strong, and tough materials. These characteristics are necessary for function, and are traditionally mutually exclusive in traditional engineering materials [2].

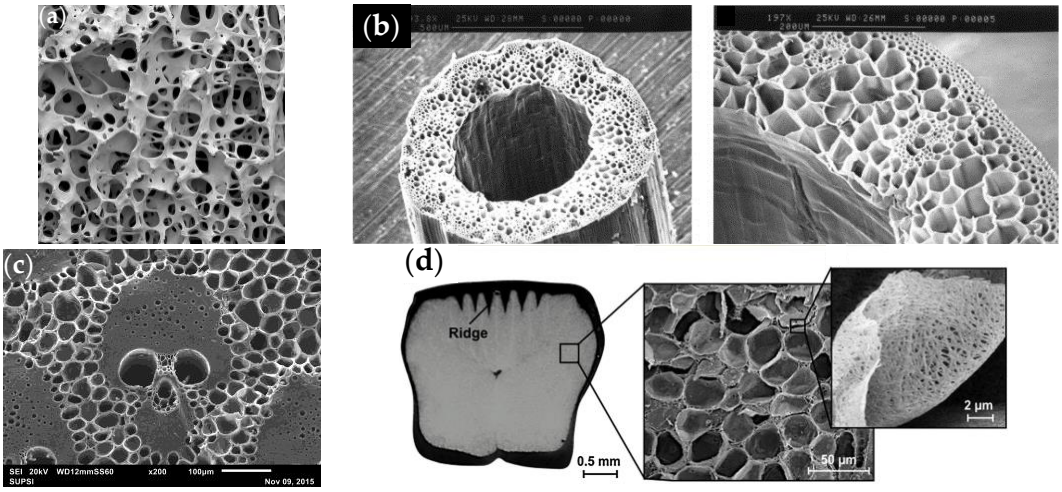

*Figure 1. Examples of natural disordered microstructures as a reverse engineering process: (**a**) Bone tissue [3], (**b**) Cross-sectional image of a grass stalk [4], (**c**) Bamboo cell structure [3], and (d) Architecture of American white pelican feather [5].*

Since the early 2000s, due to rapid advances in manufacturing technologies, using the aforementioned design methodologies has become increasingly feasible to accurately produce engineered materials by additive or subtractive manufacturing techniques. Stochastic or disordered designs are another common bioinspired development which through reverse-engineering strategy can improve toughness and multi-impacts behaviors of ceramic materials using advanced manufacturing. Disordered design methodology and its influence on the effective mechanical properties of two- and three-dimensional cellular solids has been the subject of various research efforts [6, 7]. However, in these works, special attention was given to lightweight and energy-absorbing applications such as three-dimensional sandwich cores [8, 9]. The arrangement of cell cores is well approximated by a so-called “Voronoi diagram”, a crucial tool to measure irregularity. Despite the efforts to duplicate tough materials based on the biological disordered design, only a few successful implementations of these strategies have been reported [10, 11], and less attention has been paid to the design, industrially scalable manufacturing, testing and exploration of toughening and strengthening mechanisms of stochastic ceramic-based bioinspired materials.

We recently demonstrated that laser machining can facilitate manufacturing architectured ceramics with an enhanced resistance to out-of-plane quasi-static and impact loads [12, 13]. By employing these promising bioinspired material architecture principles and disorder-induced mechanisms (quite similar to natural patterns such as bamboo cell structure, and/or dragonfly wing), and by exploiting an industrially scalable, efficient laser material removal system [14], a new class of high material-performance multilayered stochastic ceramic-based bioinspired materials is proposed. A group of multilayered plain, ordered (perfect hexagons) and disordered ceramics was fabricated and tested to show the potential of this strategy in the design of bioinspired stochastic ceramic-based systems. We established toughness, strength, and stiffness maps as functions of laser cut depth and stochasticity to improve the ceramics’ mechanical performance in low-velocity, multi-impact loading.

  doi:10.5075/epfl-298799_978-2-9701614-0-0

2. Materials and Methods

2.1 Stochastic Design

The models of the stochastic design investigated were constructed by parametric CAD integration. The first step in generating a stochastic design is to define the bounding area, A, in which nucleation points are contained, and the number of desired nuclei, n. The area was chosen as A = 100×100 mm^2, the same area of the ceramic tiles which used for the manufacturing purpose. A regular hexagonal design, with identical cells having six sides and vertex angles of 120°, can also be considered a stochastic design; for the special case in which all seed points are spaced identically apart as shown in Fig. 2a. This provides an upper bound to the spacing distance of seed points dispersed on a plane. The second step is to calculate the maximum spacing $r_{max} = \sqrt{\frac{2A}{n\sqrt{3}}}$ which accounts for the triangular nature of the distribution (see Fig. 2) [15]. Then, a stochastic design is constructed at any time when a minimum distance between seed points, s, is smaller than the maximum distance rmax. This distance is less than the maximum spacing (i.e., s ≤ rmax). If s is larger, it would be impossible to obtain n number of cells. A new simple parameter is defined so-called "regularity parameter", δ, used in designing the architectured designs and obtained as $\delta = \frac{s}{r_{max}}$. Therefore, it is clear than when δ = 1.0, the hexagonal ceramics condition is met. As the regularity parameter is lowered 0 < δ < 1.0, the seed localizations become distorted and the design transforms stochastically. The degree of stochasticity is inversely proportional to the magnitude of δ. Random points were generated one by one on A. Following each point deposition, its distance relative to all other previously deposited points were measured in a loop. Considering the desired value of regularity parameter δ, if a measured distance during the deposition falls below s, the point is discarded, and a new trial point was loaded. If all distances were greater than s, the new point was kept. This process was repeated up until *n* number of acceptable points were generated.

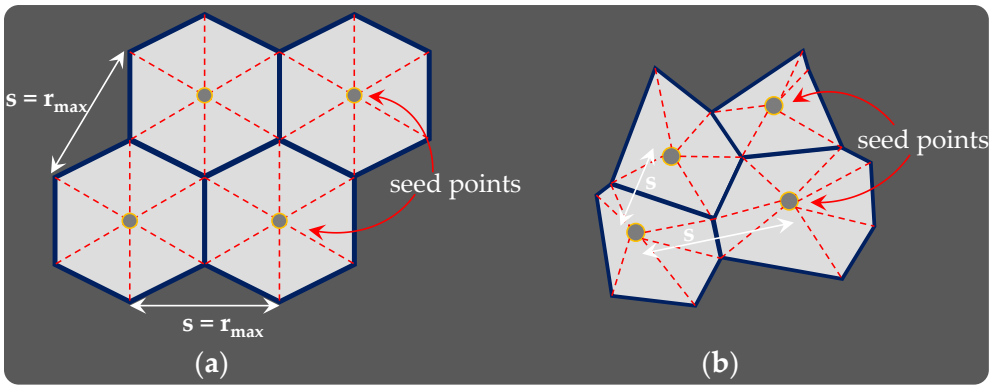

*Figure 2. Schematic showing (**a**) Identical spacing between highly ordered seed points, and (**b**) Spacing between disordered seed points.*

2.2 Hybrid Manufacturing

A mathematical "regularity parameter" controls the cell stochasticity of the designs for laser ablation. Four degrees of cell regularity, with almost the same number of cells, was chosen for this study which includes an ordered panel of perfect hexagons (δ = 1.0), two pseudo-random panels (δ = 0.8 and 0.5), and a disordered panel (δ = 0.1). In addition, non-architectured samples referred to as "multilayered plain ceramic" or "baseline" were manufactured for comparison. Alumina ceramic tiles of dimension 100×100×0.635 mm^3 were purchased off McMaster-Carr and

  doi:10.5075/epfl-298799_978-2-9701614-0-0 published under CC BY-NC 4.0 license

were used to manufacture a three-layer hybrid panel (high-tolerance fired non-porous alumina ceramic with 96% material composition, see Table 1). For each design, three alumina tiles were cut using an Ytterbium picosecond fiber laser (YLPP-25-3-50-R, IPG Photonics, USA). The laser produces a Gaussian spatial profile beam of a maximum power output of 50 W, with a 3 ps pulse duration and a 25 µJ average pulse energy of 1030 nm wavelength. In previous studies [13, 16], a procedure was developed using a circular wobble pattern with the laser scanner to ensure that thermal damage and micro-cracks were minimized. A comprehensive study of the effects of various laser processing parameters was conducted and the optimum process parameter settings that minimized material removal, roughness and manufacturing time were applied [14, 17]. However, due the laser material removal limitations, a stochasticity less than 0.1 was challenging for manufacturing.

Table 1. Material properties of non-porous alumina ceramic tiles.

Property	Value	Property	Value
Tensile strength	220 (MPa)	Modulus of Elasticity	303 (GPa)
Compressive strength	2070 (MPa)	Density	3875 (kg/m^3)

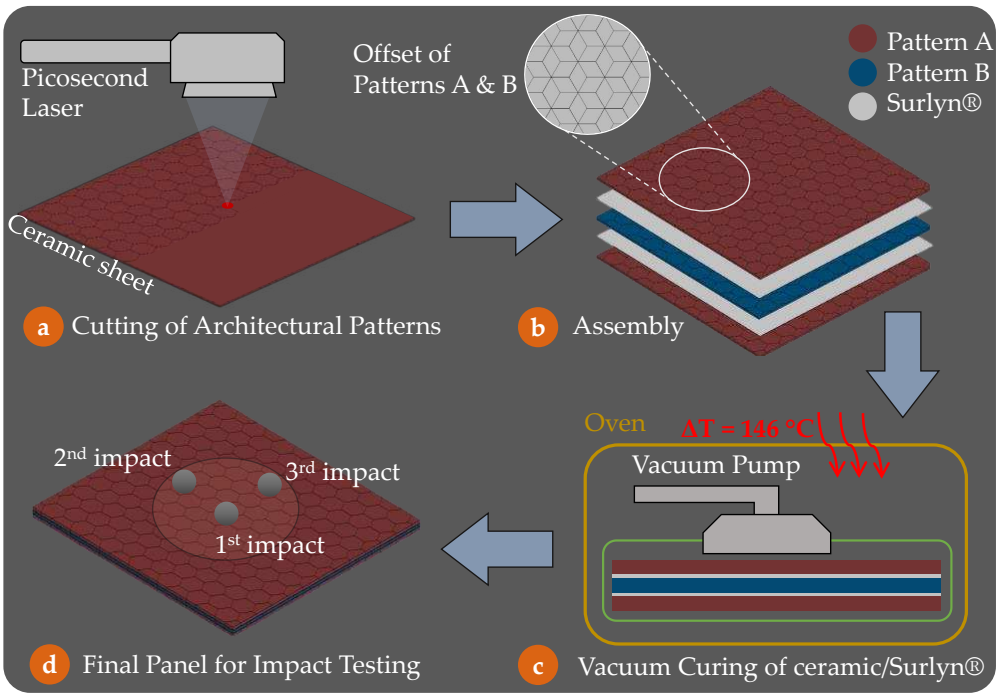

*Figure 3. Manufacturing of 3-layer stochastic ceramics highlighting (**a**) Cut patterns with the picosecond laser, (**b**) Assembly schematic with the pattern offset, (**c**) Vacuum bagging and curing of ceramics and commercial monomer Surlyn®, and (**d**) 3 consecutive low-velocity impact test configuration.*

Panels were manufactured to produce two cut depths: (i) 70% and (ii) 100%. The cut depths of 70% was found to have the highest energy absorption performance and multi-hit resistance of different cut depths previously tested [12, 18]. The ordered hexagonal pattern followed an *ABA* order, where cut designs were offset as shown in Fig. 3. Pattern B was offset such that the vertices of the hexagons were aligned with the centre of the hexagons on pattern *A*. The disordered panels used three different designs in an *ABC* order to compose the final manufactured panel. The cut panels were bonded by 101 µm thick Surlyn® interlayers and the deeper cuts are chosen to ensure that the polymer fills in the cavities of the cut ceramic panels

during the compression and vacuum curing process. To ensure that the three ceramic tiles were properly aligned, the layered assembly was placed into an aluminum frame and compressed between two tiles. This method allows for uniformity of the final panel thickness across all samples. The ceramic/Surlyn® assembly was then vacuum bagged and set to cure for 5 hours at 146 °C to bond the three ceramic layers into a single panel. The final panel was then demolded from the aluminum frame and sent for impact testing. Consequently, all final manufactured ceramics were 2.10 mm thick which include two 97.5 µm thick interlayers of Surlyn®. It is observed that all full and partial cuts of the panels were filled with Surlyn®.

3.1 Low-velocity Impact Test Configuration

Three consecutive low-velocity impact tests were performed on the multilayered architectured ceramics using a drop weight machine based on the guidelines given in the ASTM standard D3763 [19]. The impactor had a mass of 12.5 kg, a diameter of 5 mm with a semi-spherical tip and the impact velocity of 1.36 m/s with the total impact energy of 4.5 J.

3. Experimental Results

The effect of stochasticity on the multi-hit capabilities such as energy absorption performance, stiffness and maximum response load is investigated. Herein, the energy absorption performance is defined as: $\frac{\text{absorbed energy}}{\text{total impact energy}}$. Figure 4 presents the reaction force-displacement response and displacement and velocity histories of the impactor. The area under the experimental force-displacement curve was measured as the energy absorption of the ceramic systems as shown in Fig. 4a. The area after the maximum load up to the failure point is defined as the crack propagation energy and corresponding mechanisms (see Fig. 4a). The maximum displacement/force, and coefficient of restitution (COR) are also defined in Fig. 4b.

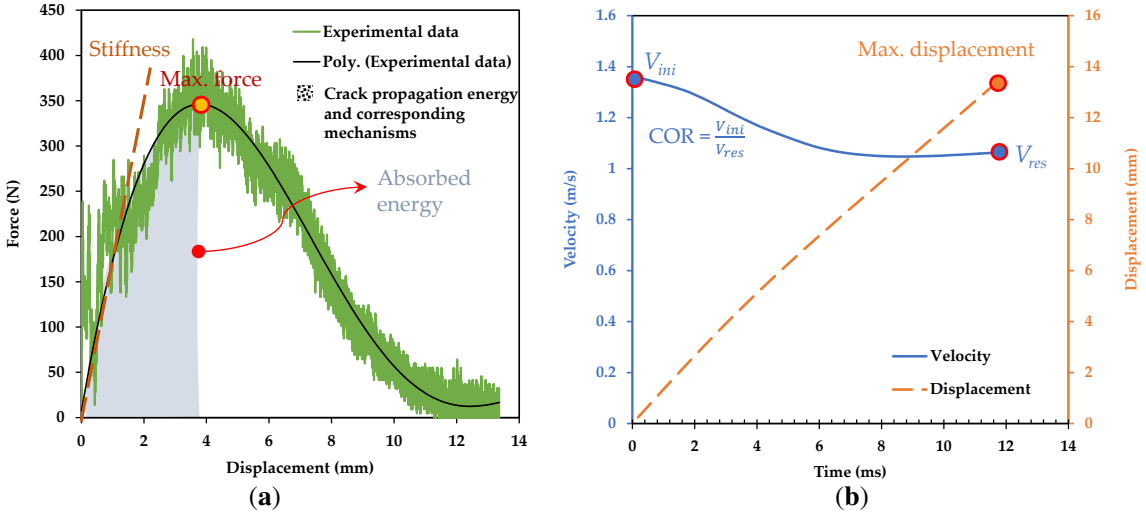

*Figure 4. (**a**) Reaction force-displacement response and (**b**) Displacement and velocity histories of the impactor (The maximum displacement/force, energy absorption, crack propagation energy and corresponding mechanisms as well as the coefficient of restitution (COR) are defined).*

Figure 5 presents the experimental results for the energy absorption performance, stiffness, and maximum response force of the multilayered architectured ceramics with the stochasticity of δ = 0.1, 0.5, and 0.8, and a perfect hexagonal design (δ = 1.0) as well as the baseline for the 70% and 100% cut-depths. The energy absorption performance of the architectured ceramics impressively increased during the 2nd and 3rd impacts up to 18% and 33%, respectively, unlike

the plain ceramic (i.e., baseline). Generally, the 70% cut-depth architectured ceramics have higher energy absorption performance compared to the 100% cut-depth ones for all three impacts up to 55%. Specifically, the 70% cut-depth stochastic ceramic with $\delta = 0.1$ absorbed 10% more energy during the 1st impact and up to 15% and 45% more energy during the 2nd and 3rd impacts compared to the fully-cut stochastic ceramic (100% cut depth with $\delta = 0.1$), respectively. As shown in Fig. 5a, increasing the stochasticity, δ, from 0.8 to 0.1 resulted in an increase in the energy absorption performance of ceramic systems for both partial- and fully-cuts. The crack propagation energy of the ceramic systems is also presented in Fig. 5a. It is seen that the crack propagation energy of the 3-layer architectured ceramics (for $\delta = 0.1$, 0.5, 0.8, and 1.0 with the 70% and 100% cut depths) increased during the 2nd and 3rd impacts in contrast to the baseline. After the 1st impact, frictional tile sliding becomes more important among all the toughening mechanisms. This mechanism is absent in the baseline. Considering the shear strength of the adhesive interlayer was overcome after the 1st impact, even more energy was dissipated by the plastic deformation of the adhesive interlayers in the architectured ceramic system. Furthermore, the partial-cuts cause the architectured ceramics to dissipate more energy through crack propagation occurred after the maximum response force. The maximum and minimum crack propagation energies occurred the 3rd impact of the 70% cut-depth stochastic ceramic with $\delta = 0.1$ and baseline, respectively. Observing from Fig. 5b, the ceramic's stiffness generally decreases after each impact independent of architecture. The stiffness of the baseline is higher than those of the architectured ceramics (ordered and stochastic designs) for the 1st impact. The reason is that some of the ceramic materials were removed during the laser removal processing and consequently, the architectured ceramic's stiffness was lower when compared to the baseline. However, for the 2nd and 3rd impacts, the perfect hexagonal ($\delta = 1.0$) and stochastic ceramic systems ($\delta = 0.1$, 0.5, and 0.8) have higher stiffness (up to 170%) compared to the baseline. Many cracks were propagated in the plain ceramic following the 1st impact and consequently, the plain ceramic loses its stiffness up to 25% (see Fig. 5b). In addition, the partial-cut ceramics (70% cut depth) have higher stiffness comparted to the fully-cut ceramic (100% cut depth) for all three impacts. As observed from Fig. 5c, the multilayered architectured ceramics have lower response forces compared to the baseline for all three impacts. Among the architectured ceramics, the 70% cut-depth disordered design ($\delta = 0.1$) and 100% cut-depth perfect hexagonal system have the highest and lowest strength, respectively. The strength of the ceramics decreases toward the 3rd impact since some cracks were propagated during the 1st and 2nd impacts. The number of propagated cracks depends on the ceramic system whether it is a partial/fully-cut or a stochastic/ordered design. In summary, the balanced material performance makes the 70% cut-depth stochastic ceramic with $\delta = 0.1$ a competitive candidate with a remarkable multi-hit resistant and stiffness. However, in terms of the strength, the appropriate selection between the 70% and 100% cut depths is dependent on the target application. For example, the 100% cut-depth ceramic has a lower response force compared to the 70% cut-depth one which is a better choice where less response force is required to transfer to the system such as personnel protective equipment.

  doi:10.5075/epfl-298799_978-2-9701614-0-0

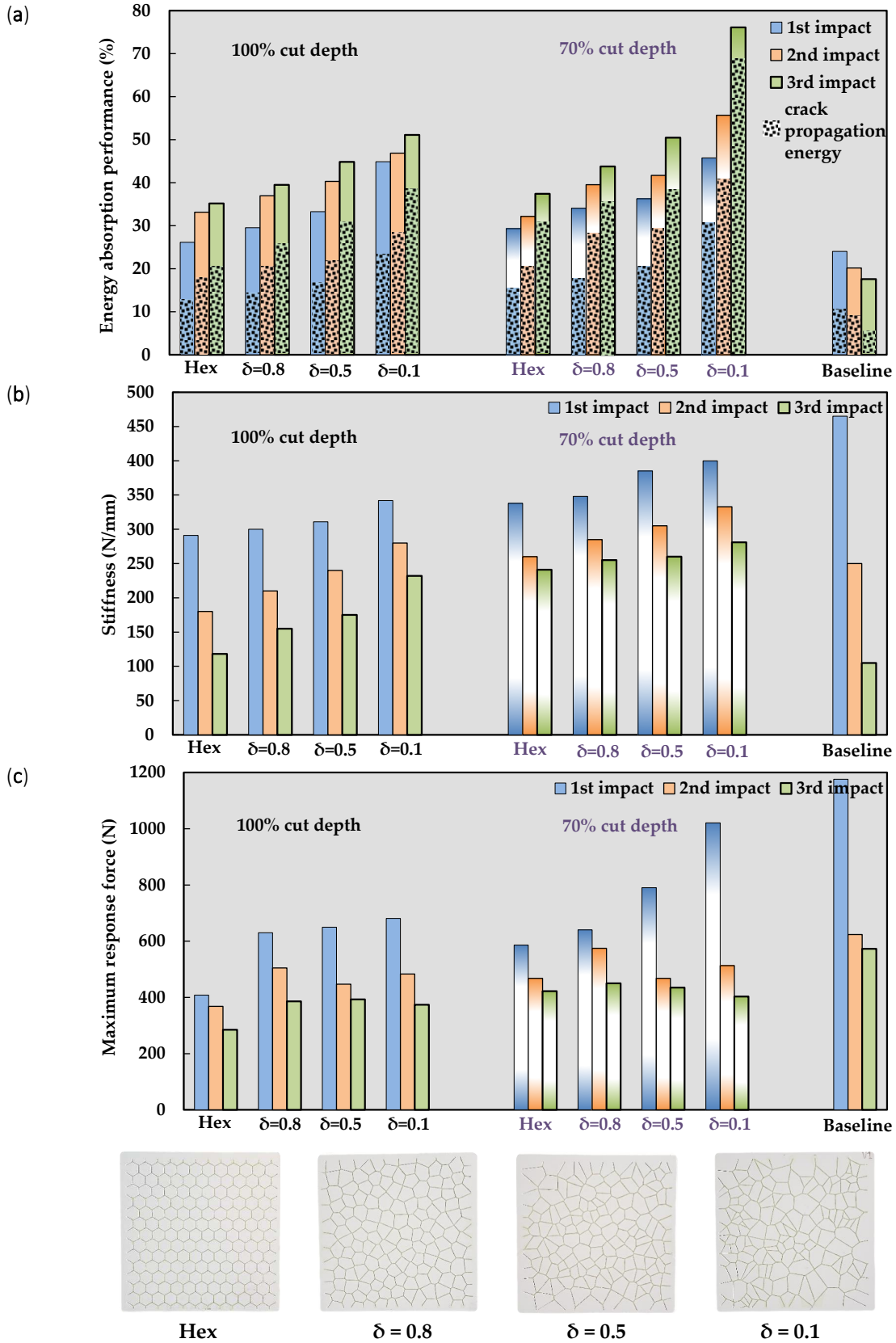

*Figure 5. Multi-hit properties of the 3-layer architectured ceramics with the stochasticity of δ = 0.1, 0.5, and 0.8, and a perfect hexagonal design (δ = 1.0) for the 70% and 100% cut-depths as well as the baseline: (**a**) Energy absorption performance, (**b**) Stiffness, and (**c**) Maximum response force.*

  doi:10.5075/epfl-298799_978-2-9701614-0-0 published under CC BY-NC 4.0 license

4. REFERENCES

1. Kingery, W.D., H.K. Bowen, and D.R. Uhlmann, *Introduction to ceramics*. Vol. 17. 1976: John wiley & sons.
2. Danzer, R., *A general strength distribution function for brittle materials.* Journal of the European Ceramic Society, 1992. **10**(6): p. 461-472.
3. Gibson, L.J., M.F. Ashby, and B.A. Harley, *Cellular materials in nature and medicine*. 2010: Cambridge University Press.
4. Gibson, L.J., *Biomechanics of cellular solids.* Journal of biomechanics, 2005. **38**(3): p. 377-399.
5. Sullivan, T.N., et al., *Extreme lightweight structures: avian feathers and bones.* Materials Today, 2017. **20**(7): p. 377-391.
6. Wang, S., et al., *Crushing behavior and deformation mechanism of additively manufactured Voronoi-based random open-cell polymer foams.* Materials Today Communications, 2020: p. 101406.
7. Chang, B., et al., *Crashworthiness design of graded cellular materials: An asymptotic solution considering loading rate sensitivity.* International Journal of Impact Engineering, 2020: p. 103611.
8. Li, K., X.-L. Gao, and G. Subhash, *Effects of cell shape and strut cross-sectional area variations on the elastic properties of three-dimensional open-cell foams.* Journal of the Mechanics and Physics of Solids, 2006. **54**(4): p. 783-806.
9. Zhu, H. and A. Windle, *Effects of cell irregularity on the high strain compression of open-cell foams.* Acta Materialia, 2002. **50**(5): p. 1041-1052.
10. Wu, K., et al., *Interfacial strength-controlled energy dissipation mechanism and optimization in impact-resistant nacreous structure.* Materials & Design, 2019. **163**: p. 107532.
11. Gutiérrez, A., et al., *The role of hierarchical design and morphology in the mechanical response of diatom-inspired structures via simulation.* Biomaterials science, 2018. **6**(1): p. 146-153.
12. Sarvestani, H.Y., et al., *Multilayered architectured ceramic panels with weak interfaces: energy absorption and multi-hit capabilities.* Materials & Design, 2019. **167**: p. 107627.
13. Sarvestani, H.Y., et al., *Architectured ceramics with tunable toughness and stiffness.* Extreme Mechanics Letters, 2020: p. 100844.
14. Beausoleil, C., et al., *Deep and high precision cutting of alumina ceramics by picosecond laser.* Ceramics International, 2020.
15. Zhu, H., J. Hobdell, and A. Windle, *Effects of cell irregularity on the elastic properties of 2D Voronoi honeycombs.* Journal of the Mechanics and Physics of Solids, 2001. **49**(4): p. 857-870.
16. Rahimizadeh, A., et al., *Engineering toughening mechanisms in architectured ceramic-based bioinspired materials.* Materials & Design. **198**: p. 109375.
17. Esmail, I., et al., *Engineered net shaping of alumina ceramics using picosecond laser.* Optics & Laser Technology, 2021. **135**: p. 106669.
18. Sarvestani, H.Y., et al., *Architectured ceramics with tunable toughness and stiffness.* Extreme Mechanics Letters, 2020. **39**: p. 100844.
19. Fragassa, C. and G. Minak. *Standard characterization for mechanical properties of photopolymer resins for rapid prototyping*. in *1st Symposium on Multidisciplinary Studies of Design in Mechanical Engineering, Bertinoro, Italy (Jun. 25-28, 2008)*. 2008.

  doi:10.5075/epfl-298799_978-2-9701614-0-0

BEARING STRENGTH HIGH PERFORMANCE FIBRE METAL THIN-PLY LAMINATES

B. Kötter[a], K.Yamada[b], J. Körbelin[a], K. Kawabe[b], M. Nishikawa[c], M. Hojo[c], H. Wittich[a], and B. Fiedler[a]*

a: Institute of Polymer and Composites, Hamburg University of Technology, Hamburg, Germany,
b: Industrial Center of Fukui Prefecture, Fukui, Japan,
c: Department of Mechanical Engineering and Science, Kyoto University, Kyoto, Japan
* Corresponding author (Wittich@tuhh.de)

Keywords: Stainless Steel Foil; Hybrid Composite; Thin-Ply; CFRP

Open access full paper: *Kötter, Benedikt and Yamada, Kohei and Körbelin, Johann and Kawabe, Kazumasa and Nishikawa, Masaaki and Hojo, Masaki and Fiedler, Bodo (2021). Steel foil reinforcement for high performance bearing strength in Thin Ply composites. Composites Part C: Open Access. 4. 100085*

1. Introduction

Conventional carbon fibre reinforced polymer (CFRP) laminates or structures do not exploit the full potential of the used carbon fibres. One approach to improve their performance is to reduce the layer thickness. The degree of freedom in design increases with decreasing layer thickness due to the larger number of used layers or more precise load-dependent design. As well, the failure behaviour is significantly dependent on the layer thickness. With decreasing layer thickness, the initiation of transverse microcracking shifts to higher strains and delaminations are suppressed. The failure mode changes from complex delamination dominated failure to a brittle failure mode, and tensile and compressive strength increases up to 42 % respectively 24 % [1]. With increasing strength, the requirements on the material increase in areas of load introduction and stress concentrations. Especially in areas of stress concentrations, adverse effects of the brittle failure behaviour can be observed. Studies demonstrate that in open hole tensile (OHT) tests the strength decreases with decreasing layer thickness [1, 2]. As pre-damages in the material are suppressed, stresses in areas of high concentration are not diverted or reduced by pre-damages, resulting in a high local stress concentration and results in premature failure. In the case of load introduction by bolts, although the bearing strength increases with decreasing layer thickness, the difference between un-notched and notched strength increases, so that the structure, material or number of bolts must be adapted to exploit the full potential of Thin-Ply laminates. This study investigates the influence of local stainless steel hybridisation of Thin- and Thick-Ply CFRP laminates on the open hole and bearing properties.

2. Materials and methods

The open hole tensile and bearing strength tests were performed according to ASTM D5766 and ASTM D5961, respectively, using a quasi-isotropic layup. Two layer thicknesses of CFRP unidirectional prepregs with the area weights of 40 g/m² and 160 g/m² were used. Stainless steel foil (1.4310) patches with the same thicknesses as the layers replaced locally 90° CFRP layers in

  doi:10.5075/epfl-298799_978-2-9701614-0-0

areas with high-stress concentrations or load introduction. The local stainless steel volume content varies from 6.25 %, 12.5 % to 25.0 %. If the steel content is lower than 25.0 %, the outer 90° layers are replaced symmetrical to the mid-plane (see figure 1). A high-performance sol-gel surface pre-treatment process using 3M's AC-130-2 surface pre-treatment system, an aircraft certified water-based system, was applied to increase the adhesion between steel and matrix.

3. Results and Discussion

The OHT strength of the neat Thin-Ply samples recorded a 9 % lower strength than the Thick-Ply specimens. The results correspond to other studies in this field [1, 2]. With increasing steel content, the OHT strength increases. With a local steel content of 25.0 %, the strength rises by 64 % ,and even the specific strength rises by up to 36 %. The specific open hole tensile strength represents the ratio of the strength and the global density of the specimen, and the notch sensitivity decreases.

In contrast to the thin layer fibre metal laminates, the laminates with thicker layers show delaminations between the stainless steel and the CFRP layers. These delaminations are initiated at the transition zone between the steel foils and the 90° CFRP layers. Digital Image Correlation System images show stress concentrations in the transition zone even at low strains. Due to the low layer thickness, it is possible to arrange the steel patches in a stepwise pattern in the area of the transition zone (see figure 1), thus reducing possible stress concentrations, and due to the higher number of interfaces between the layers, the interlaminar stresses decreased with decreasing layer thickness. Both effects results in no delaminations.

Due to the hybridisation with stainless steel foils, significantly higher bearing strengths can be observed. In contrast to the neat Thin-Ply samples with a bearing strength of 979.6 MPa, the strength of the samples with stainless steel foil increases to 1165.4 MPa in the case of 6.25 % stainless steel, via 1239.5 MPa in the case of 12.5 %, to 1513.9 MPa if all 90° layers are replaced by steel patches. In addition to the increased bearing strength, failure behaviour has changed. In contrast to the brittle failure of the Thin-Ply specimens, pre-damage occurs with increasing steel content, but the pre-damages do not result in final failure. The outer steel layers support the laminate through their relatively high bending stiffness so that local buckling does not lead to final failure. The results of the bearing strength are shown in figure 2. The diagram presents the maximum bearing strength, the offset strength at 2 % elongation and the stress of the first failure. As written above, although the maximum strength increases with increased steel content, the first damage of all hybrid configurations occurs at the same stress level and the offset limit defined for the design of a structure does not change. For the industrial application, a hybridisation of more than 6.25 % of steel content does not provide further advantages. The only significant increase is in the safety factor for ultimate failure. It is noticeable that the thick fibre metal laminates show the highest stresses concerning the first failure or offset stress. They exhibit the best bearing performance, because of the high bending stiffness of the thicker stainless steel foil patches.

This study shows that the hybridisation of Thin-Ply CFRP laminates with stainless steel patches in areas of stress concentration and load introduction significantly increases open hole tensile and bearing strength. The previous limitation of the gap between unnotched strength and open

hole or bearing strength can be reduced, allowing the potential of thin layers to be applied in structural light weight applications.

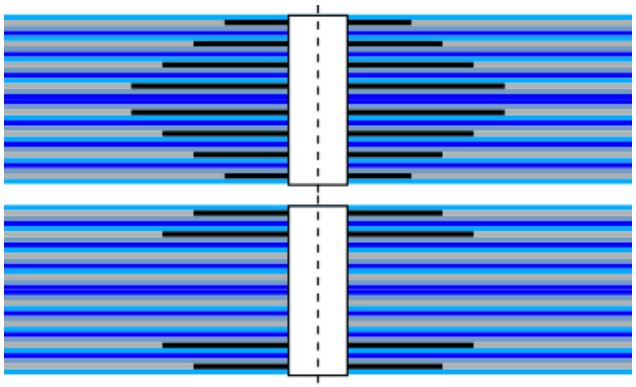

Fig. 1. Laminate layup for 25 % and 12.5 % stainless steel (black areas) content

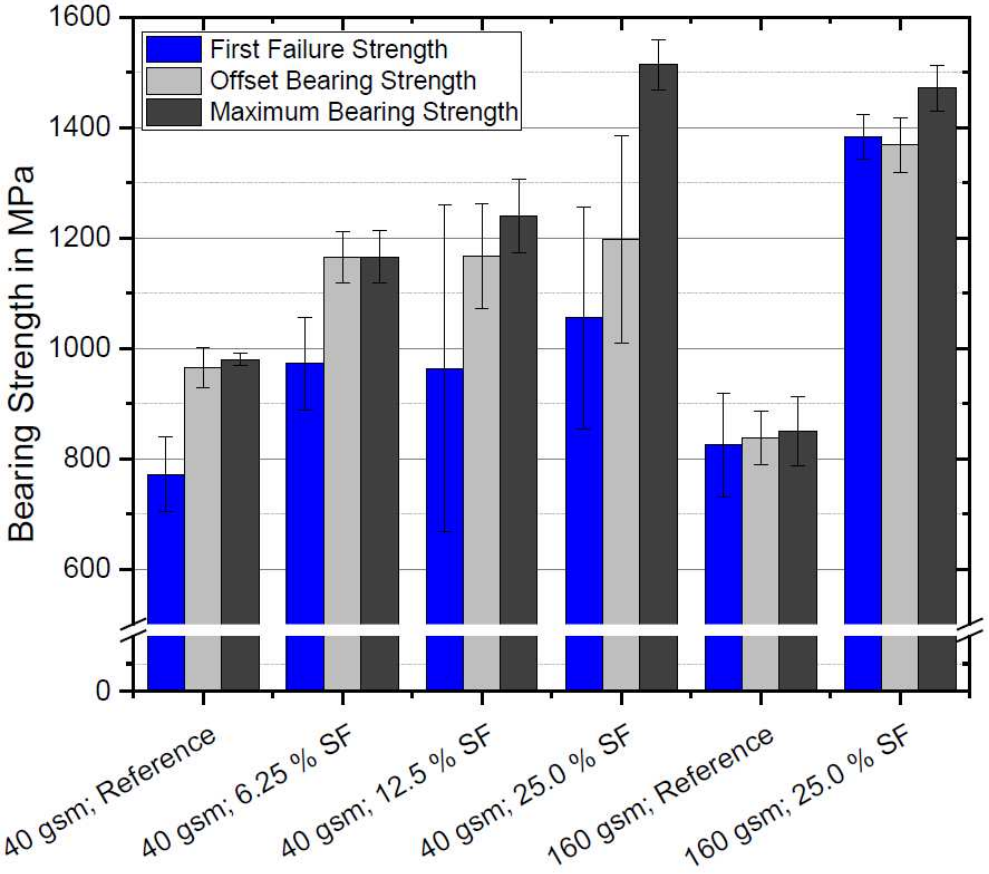

Fig. 2. First failure (blue), offset (grey) and maximum (black) bearing strength for neat and fibre metal laminates

4. References

1. R. Amacher, J. Cugnoni, J. Botsis, L. Sorensen, W. Smith and C. Dransfeld Thin ply composites: Experimental characterisation and modelling of size-effects Composite Science and Technology, Vol. 101, pp 121-132, 2014
2. S. Sihn, R. Kim, K. Kawabe, S. Tsai Experimental studies of thin-ply laminated composites Composite Science and Technology, 67, pp 996-1008, 2007

  doi:10.5075/epfl-298799_978-2-9701614-0-0

VISCOELASTIC AND VISCOPLASTIC CREEP MODELLING OF SHORT-GLASS FIBRE REINFORCED POLYPROPYLENE COMPOSITES

Michael Jerabek[a], Robert Wesenjak[b], Maxime Melchior[c], Simon Gastl[a]

a: Borealis Polyolefine GmbH, St.-Peter Strasse 25, 4021 Linz, Austria
Email: Michael.Jerabek@borealisgroup.com
b: MSC Software GmbH, a Hexagon company, Parkring 3, 85748 Garching b. München, Germany
c: MSC Software Belgium SA, a Hexagon company, Rue Emile Francqui 9, B-1435 Mont-Saint-Guibert, Belgium

Abstract: *For many under the hood applications, the creep behaviour of the component under a given thermo-mechanical load is key to validating the design and ensuring part integrity for the whole service lifetime. As comprehensive creep testing is costly and time-consuming, a new methodology based on tensile tests is introduced accompanied by a novel material model calibration routine connected to recent developments in Digimat. With the new viscoelastic-viscoplastic material model, the creep behaviour of short fibre reinforced materials in both elastic and plastic regimes can be predicted. Material model validation is carried out at the dumbbell level but also on a structural beam, both showing excellent agreement with the experimental result.*

Keywords: Short fibre composite; creep testing; material modelling; creep prediction

1. Introduction

The long-term behaviour of short glass-fibre reinforced Polypropylene (SGF-PP) composites is of crucial importance in many structural applications. This requires experimental characterization of the long-term creep and fatigue behaviour combined with adequate material models to support the virtual application development process. Since comprehensive creep characterization involves testing at several temperatures, creep loads and fibre orientations, significant effort is needed. Additionally, material model calibration procedures applied to creep data may be difficult. To predict the orientation-dependent behaviour of short fibre-reinforced Polypropylene composites, homogenized material models containing information about the composite microstructure are typically applied. While the glass fibre behaves fully elastic, the polymeric matrix shows time- and temperature-dependent behaviour. In the classical calibration procedure, a lot of model parameters need to be optimized to describe the creep curve of the composite.

To improve the calibration routine and to reduce the experimental costs for the extensive creep characterization, a new methodology is introduced in this paper based on conventional, strain rate dependent tensile tests. The idea is to extrapolate the measured tensile curves towards creep relevant strain rates and calibrate material model parameters in the reversible but also irreversible deformation regime. The resulting material model was capable to predict the creep deformation of an SGF-PP as a function of fibre orientation, time and creep load.

  doi:10.5075/epfl-298799_978-2-9701614-0-0

2. Materials and Methods

For the proposed methodology, specimens with different microstructures are required. For this reason, specimens were cut from the so-called glass fibre (GF) multitool; details about the geometry can be found in [1]. This injection-moulded part has a thickness of 2 mm and provides specimens with very distinct fibre orientations of 0°, 45° & 90° with respect to the main fibre alignment. Subsequently, tensile tests were conducted as a function of strain rate and temperature to collect the input data for the material modelling calibration routine.

To validate the methodology and to match the model predictions with experimental results, creep tests on specimens with distinct fibre orientations were carried out. In the applied test setup, a video extensometer measured the strain to avoid any direct influence on the measurement. To obtain long-term data, creep tests were run additionally at elevated temperatures and the time-temperature superposition principle was applied to generate creep master curves. In addition, 4-point bending creep tests were run on a structural beam, the testing setup and beam are shown in Figure 1.

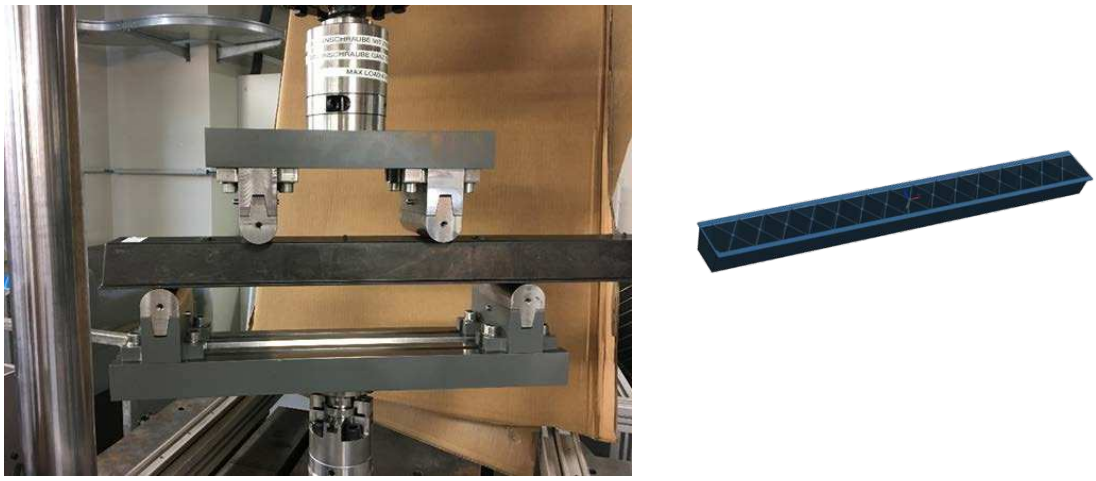

Figure 1. 4-point bending setup (left) and rib structure of the beam (right).

The material investigated in this study is a short glass fibre reinforced Polypropylene composite. The glass fibre content is 40w%.

3. Material modelling

For material modelling, the software Digimat [2] is used. The SGF- PP is modelled as a two-phase material with two major constituents: resin and fibres. The behaviour of the glass fibres is assumed to be elastic isotropic. For the resin, the material model has to capture the viscous behaviour of the material responsible for the time-dependent creep. Depending on the load level, specific material models can be selected:

- Viscoelastic material model if the load level stays low and only reversible deformation is considered.
- Elasto-viscoplastic material model, if the applied load is high and creep is mainly observed in areas showing plastic (irreversible) deformation.
- Viscoelastic-viscoplastic material model if the load history leads to both elastic and plastic deformation.

  doi:10.5075/epfl-298799_978-2-9701614-0-0

In addition to the selection of the material model for the fibres and the resin, the composite microstructure is described by specifying the volume or mass fraction of fibres, their orientation through an orientation tensor and their size.

3.1 Mean-Field Homogenization

Mean-Field homogenization combines the properties of the underlying constituents of a multi-phase material so that the original heterogeneous material is represented by an equivalent homogeneous one. Implemented in the software Digimat, this technology has proven to be effective for a broad range of materials. This semi-analytical solution has the advantage of very fast computation of the composite material behaviour. It is based on some assumptions that are sometimes not met in the real material:

- Fibres are ellipsoidal.
- Fibres are uniformly distributed in the resin with no clusters.
- Perfect resign / fibre interface.

Mean-Field homogenization is performed in three main steps as illustrated in figure 2:

1. The localization. The per-phase strain is computed from the strain applied on the composite.
2. The stress computation at the micro-level. The stress in each phase is computed from the strain obtained in step 1.
3. The averaging of stress. The stress at the composite level is computed through an averaging approach based on the stress at the level of the phases.

The results provided by the Mean-Field homogenization are limited to the average stress and strain in the composite and each phase (resin & fibres). This approach does not capture stress localizations that are observed in specific regions of the composite, for instance at the tip of fibres.

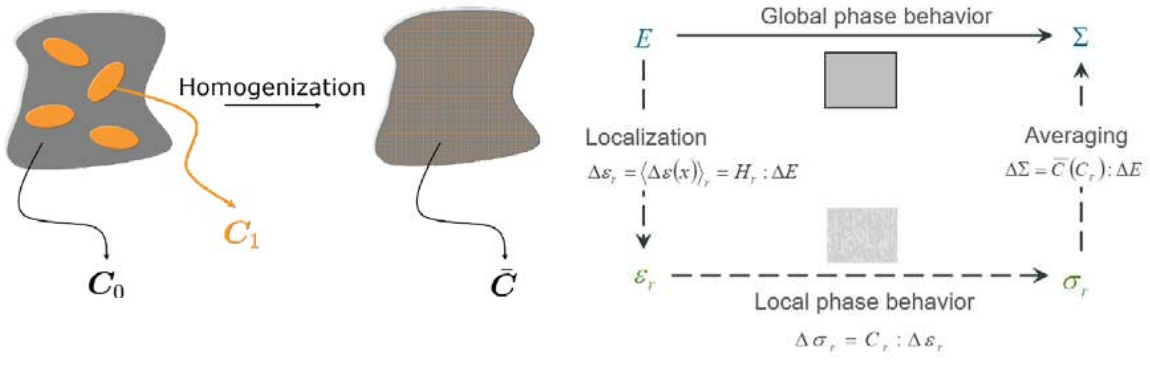

Figure 2: (a) Heterogeneous material (left) from which its equivalent stiffness $\bar{C}$ is computed from homogenization. (b) Three steps in the Mean-Field homogenization procedure: localization, per-phase stress computation and averaging.

  doi:10.5075/epfl-298799_978-2-9701614-0-0

3.2 Creep material model

In this study, the creep response of the material is modelled using a viscoelastic-viscoplastic constitutive law. The approach chosen to create this material model is specific to the software Digimat and works as follows:

- Identify the relevant strain-rate range of your application.
- Measure and/or generate tensile stress-strain curves for each strain-rate decade.
- Create (non-rate dependent) elasto-plastic material cards, one for each strain-rate decade within the identified range.
- Combine those elasto-plastic material cards into a so-called "strain-rate dependent elasto-plastic" (SREP) material in Digimat. This will create a single Digimat material card where all strain-rate dependent material properties (identified in the previous step) are combined into functions of strain-rate.
- Finally, this SREP card can be merged by Digimat into a viscoelastic-viscoplastic creep material card. During this merge process, viscous functions are employed to fit the overall material response given by the SREP card.

The advantage of this approach is that the amount of time needed to create a viscoelastic-viscoplastic creep material model is drastically reduced without any loss in quality. Furthermore, it is not required to conduct time-consuming creep tests to calibrate this material model since the elasto-plastic material cards are built on tensile stress-strain curves only. The challenge, however, is that experimental data for very low strain rates, i.e. 10-8 s^{-1} and lower is usually not available from testing and needs to be derived.

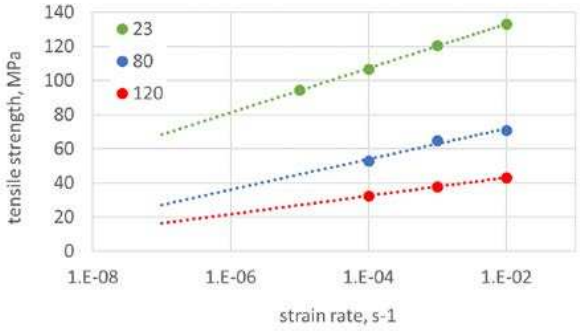

Figure 3. Tensile strength as a function of strain rate for three different temperatures measured in-fibre direction.

To extrapolate the quasi-static tensile curves towards creep relevant strain rates, knowledge about the deformation kinetics is required. In figure 3, tensile strength is plotted as a function of strain rate for different temperatures. The obtained log-linear correlation can be used for the extrapolation of the tensile curves within a certain strain rate range. However, as was shown in the literature [3-5], two independent micro-mechanisms of deformation can be found for Polypropylene. In figure 4, a typical example is depicted, showing clearly the bilinear correlation between the material yield stress and strain rate. Furthermore, the transition point where the linear slope changes, is characteristic of the material and strongly temperature-dependent. This information is required not only for the prediction of the virtual tensile curves for the low strain rate range but also when calibrating the elasto-plastic material model to each strain rate for the

  doi:10.5075/epfl-298799_978-2-9701614-0-0

three fibre orientations considered in this work. In this context, proper choice of the model parameters for the elasto-plastic matrix for each strain rate is key.

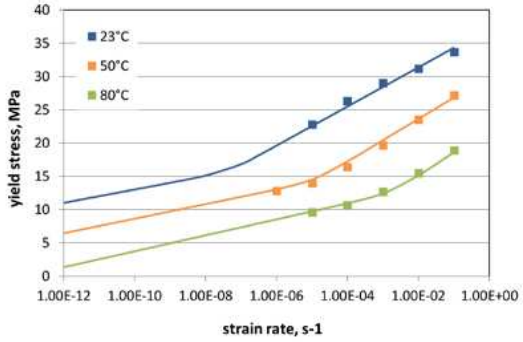

Figure 4. Example of the yield-stress evolution as a function of strain rate for Polypropylene. The characteristic bilinear correlation based on the testing temperature can be seen.

4. Results and discussion

The calibrated, anisotropic and strain rate dependent material model was applied to predict the behaviour of the material in a long-term creep test. Figure 5 depicts the experimental result obtained in-fibre direction at 16 MPa creep load. The information on the specimen microstructure (fibre orientation) and the creep load of 16 MPa is sufficient to describe the specimen behaviour – the blue line in figure 5. A very good agreement between measurement and prediction could be achieved. To demonstrate the capabilities of viscoelastic (VE) and elasto-viscoplastic (EVP) material models, these results are also plotted. Within some limits, still accurate predictions can be obtained, but either not providing information on the amount of irreversible deformation (VE) or do not cover the time-dependency correctly (EVP).

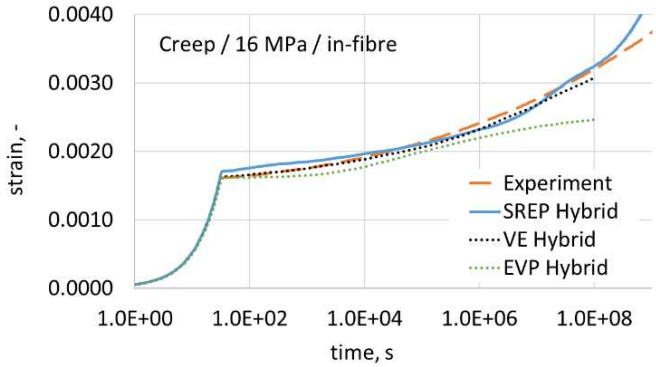

Figure 5. Creep strain vs. creep time in-fibre direction, comparing experiment with material model predictions.

These deficiencies of the “simpler” material models can be better observed when moving to a more matrix-dominant microstructure. In figure 6 the experimental result and model predictions are depicted perpendicular to the fibre direction. As can be seen, the absolute strain values are considerably larger than the in-fibre direction, finally resulting in ultimate specimen failure. The significant plastic strain accumulation as a function of time requires appropriate material model calibration strategies. While the viscoelastic-viscoplastic material model (SREP) captures the experimental result nicely, VE based models cannot describe plastic strain evolution and thus

  doi:10.5075/epfl-298799_978-2-9701614-0-0

underestimates creep strain significantly. On the other hand, EVP models tend to overestimate creep strain, as time-dependent reversible deformation (VE) is not included.

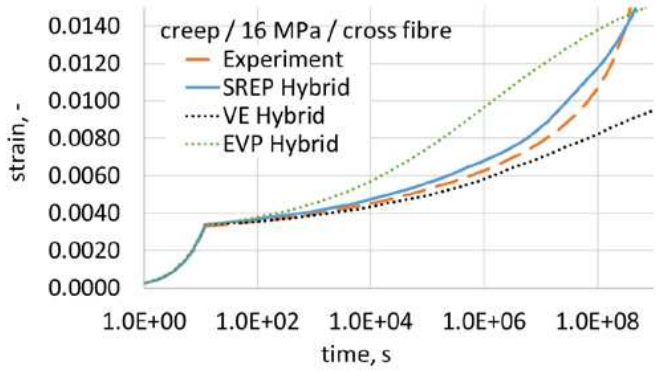

Figure 6. Creep strain vs. creep time perpendicular to the fibre direction. Experimental creep result and model predictions are depicted.

To investigate the capabilities along the whole simulation chain, a structural beam was injection-moulded and tested in 4-point bending. In order to obtain the fibre orientation distribution in the beam, Autodesk Moldflow® was used to simulate the conversion process and to predict the local microstructure. This microstructure was then mapped to the structural mesh. This investigation used Abaqus FEA as the CAE solver. The Digimat based material model was included in the simulation as a user material. The result for a creep load of 6500 N is plotted in figure 7. As can be seen, an excellent agreement between the experiment and model prediction was found.

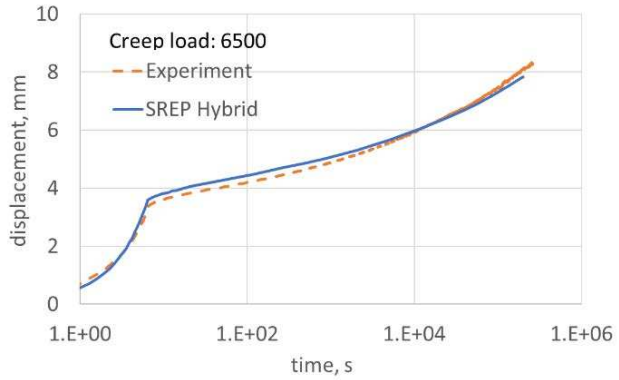

Figure 7. 4-point bending creep test result conducted on the structural beam together with the simulation results.

5. Summary

In this research study, a new material model calibration procedure for the long-term behaviour of SGF-PP composites was introduced. Instead of using costly long-term creep tests as input data, simple strain rate dependent tensile tests can be utilized. Knowledge about the appropriate deformation kinetics of PP allows to remarkably extend the experimentally observable strain rate range towards creep relevant ranges. The calibrated viscoelastic–viscoplastic material model nicely captured the long-term creep behaviour in- but also perpendicular to the fibre direction. Additionally, the methodology was successfully applied on a structural beam loaded in 4-point bending creep.

  doi:10.5075/epfl-298799_978-2-9701614-0-0

6. References

1. Hartl, A., Jerabek, M. and Lang, R.W. ”Anisotropy and compression/tension asymmetry of PP containing soft and hard particles and short glass fibres”. eXPRESS Polymer Letters, 2015, 9, 658 – 670.
2. Hexagon, "Digimat documentation Release 2021.4", 2021.
3. Kanters, M. “Prediction of Long-Term Performance of Load-Bearing Thermoplastics”, Dissertation, Eindhoven University of Technology. 2015.
4. Eyring, H. “Viscosity, Plasticity, and Diffusion as Examples of Absolute Reaction Rates". The Journal of Chemical Physics, 1936. 4, 283-291.
5. Ree, T. and Eyring, H. “Theory of Non-Newtonian Flow. I. Solid Plastic System". Journal of Applied Physics, 1955. 26, 793-800.

  doi:10.5075/epfl-298799_978-2-9701614-0-0

3D PRINTED SHORT CARBON FIBRES REINFORCED POLYAMIDE: TENSILE AND COMPRESSIVE CHARACTERISATION AND MULTISCALE FAILURE ANALYSIS

Andrea Canegrati [a], Luca M. Martulli [a], Gabriele Bolzoni [a], Milutin Kostovic [b], Gennaro Rollo [b], Andrea Sorrentino [b], Michele Carboni [a], Andrea Bernasconi [a]

a: Politecnico di Milano, Via La Masa 1, I-20156 Milano, Italy
andrea.canegrati@polimi.it
b: Polymer, Composites and Biomaterials Institute, National Research Council (CNR), Via Previati 1/E, 23900 Lecco (LC), Italy

Abstract: *The use of fused filament fabrication technology as a competitor of the conventional manufacturing processes for end-use parts production is of a great interest. However, a deep knowledge of the mechanical properties and failure behavior of printed parts is required to safely design final usable components. The present work aims to characterize the mechanical properties of a 3D printed short carbon fiber reinforced polyamide and to investigate the relationship between its unique morphology and its failure behavior. Tensile tests were conducted on rectangular specimens printed with an alternating sequence of layers with 0°/90° and ±45° raster orientation. Fracture surfaces of failed specimens were analyzed by Scanning Electron Microscopy (SEM). Possible failure mechanisms were then inferred by surface morphology analysis. Moreover, several specimens' geometries were designed and printed to characterize the in-plane and out-of-plane material compressive properties. Considerations about the longitudinal strength of the material were eventually drawn.*

Keywords: Fused Filament Fabrication; 3D printing; short fiber reinforced polymer; material characterization; failure analysis

1. Introduction

Fused Filament Fabrication (FFF), an extrusion-based 3D printing process, is nowadays one of the most common additive manufacturing technologies for Short Fiber Reinforced Polymers (SFRP).

There are major challenges related to the mechanical characterization of FFF printed composites. First, the manufacturing process induces anisotropy of the final part regardless the presence of the reinforcing phase. Testing FFF printed neat polymers parallel to the printing direction allows the highest mechanical properties to be evaluated [1]. In addition to this, short fibers preferentially align with the filament's deposition direction, thus strengthen the neat polymer in longitudinal direction. Transverse mechanical properties appear to be governed by the intra-layer bond quality between adjacent filaments and inter-layer bonding between different layers. [1-2]

Then, there is a complex and conflicting dependence of the overall mechanical performance of the FFF printed component on both printing and material parameters. [1,3-4] Finally, it is challenging to determine the actual cross section of specimens manufactured by FFF due to the

  doi:10.5075/epfl-298799_978-2-9701614-0-0

large extent of voids and to the elliptical cross section retained from the printed filaments. Thus, assuming a nominal cross section, the load carrying areas could be overestimated. [1]

Efforts of researchers were mainly focused on the optimization of printing parameters to achieve the highest performances of the final printed specimens. Material characterization plays a fundamental role as a baseline for developing models able to predict the mechanical properties of printed parts. However, an extensive investigation of the failure mechanism of FFF printed SFRP is still missing. This work aims to characterize the anisotropic properties of Onyx specimens obtained via FFF and investigate their failure mechanism under tensile and compressive quasi-static loads.

2. Materials and methods

2.1 Specimens fabrication

Test specimens were all produced via FFF technology by making use of a Markforged Onyx series printer. The material used to realize the specimens is a micro carbon fibre reinforced polyamide, whose tradename is Onyx, a micro-carbon fibres reinforced polyamide provided by Markforged [5] The filament width and layer height were 0.4 and 0.1 mm, for all the printed specimens, respectively.

Tensile specimens were designed with a rectangular shape, which was 175 mm long and 30 mm wide. By stacking 32 layers, the specimens' thickness resulted to be 3.2 mm. This specimens' geometry was selected to avoid premature failure due to stress concentration at the fillet radii of dog-bone specimens, that might be caused by the printing pattern of the layer. [6] The Markforged's slicing software, namely Eiger, offers limited freedom in setting the printing parameters. It is prevented to print a unidirectional specimen using the software's default options. Because of this technological limitation, two sets of tensile specimens were printed with ±45° and 0°/90° stacking sequence of the layers.

Moreover, Eiger software requires the printing of a contour shell to envelope the part. Two concentric onyx rings were selected to this purpose. This results in lateral walls of the specimen's cross section that run parallel to the longitudinal axis of the specimens. A schematic layout of the tensile specimens is reported in Fig.1.

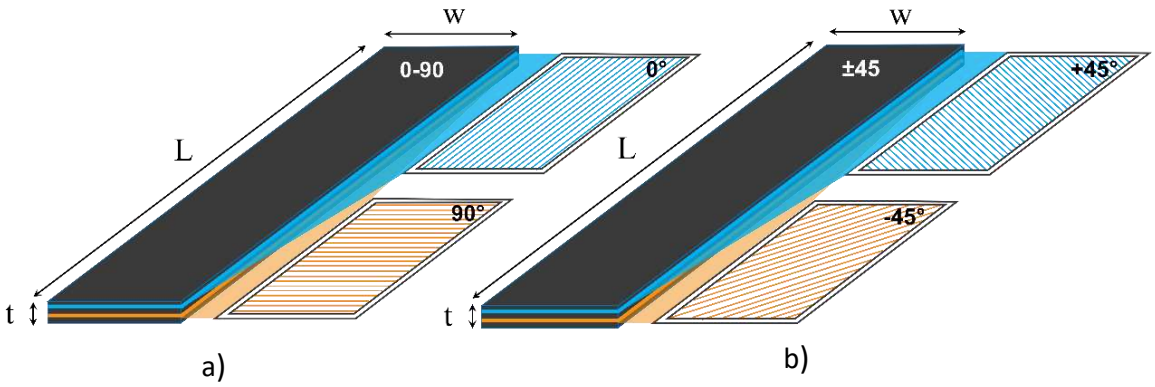

Figure 1. Schematic layout of the tensile specimens, a) 0°-90°, b) ±45° layers stacking sequence

Onyx end tabs, with dimensions of 50 mm x 30 mm x 2 mm, were separately printed by the same FFF printer used for the specimens. Tabs displayed an alternated sequence of layers with raster angles of ±45°. A low-cost, commercially available bicomponent epoxy resin glue was used to paste the tabs at the ends of the tensile specimens. The resulting gauge length of the specimens after the application of the tabs, was 75 mm.

For the characterization of the in-plane compressive properties of the material, prismatic specimens were printed. Each specimen's layer is made up by fifteen concentric contours only, no infill was used. The printing pattern of a single layer is reported in Fig. 2 This led to stack layers displaying unidirectional filaments at 0°. The overall dimensions of the specimens were 12 mm wide, 30 mm high and 35 mm long as shown in Fig 2.a. Load aligns parallel to the 0° filaments.

Two types of specimens were printed to evaluate the out-of-plane material properties. One geometry was a hollow cylinder with outer diameter of 30 mm, and internal diameter of 15.6 mm. The other geometry was a hollow prism with square section, whose external and internal sides were 25 mm and 9 mm long, respectively. The height of both specimens' geometries was 10 mm. Each specimens' layer was made up by concentric contours only, as shown in Fig 2.b-c.

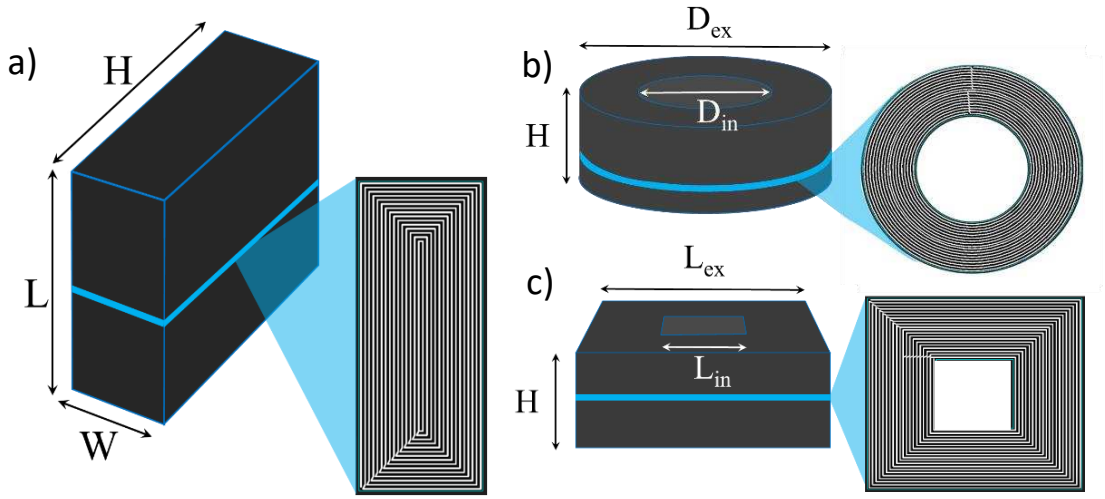

Figure 2. Schematic layout of the compression specimens: a) prism, b) hollow cylinder, c) hollow prism

2.2 Testing

Quasi-static tensile tests were performed according to ISO 527-4 [6]. Seven 0°/90° specimens and six ±45° specimens were tensile tested on an MTS Alliance RF testing machine. An extensometer of 50 mm of initial length was used to record the axial strains. A load ramp with a displacement rate of 0.75 mm/min (corresponding to 0.1 % of the specimens' gauge length) was first applied to the specimens up to 0.2 mm of axial displacement. This allowed an accurate evaluation of the Young's modulus of the specimens according to what prescribed in [6]. After the unloading of the specimens at the same speed, they were loaded up to failure at 5 mm/min of crosshead displacement rate.

Quasi-static compressive tests were carried out on two prismatic specimens, one hollow-prism and one hollow-cylinder. The specimens were tested on an MTS Alliance RF/150 to determine

  doi:10.5075/epfl-298799_978-2-9701614-0-0

the material's compressive properties. The compressive load was applied with a crosshead displacement rate of 0.2 mm/min.

2.3 Microscopy

The fracture surface of one tensile specimen per type was observed on a Zeiss EVO 50XVP Scanning Electron Microscope (SEM). The specimens' surfaces underwent a gold coating prior to scan, to enhance the quality of the images. Observation of the compressive tested specimens were carried out by an optical microscope.

3. Results

3.1 Tensile

Results of the tensile tests are shown in Fig.3 in terms of stress-strain curves. The values of the main mechanical properties obtained from testing are reported in Table 1.

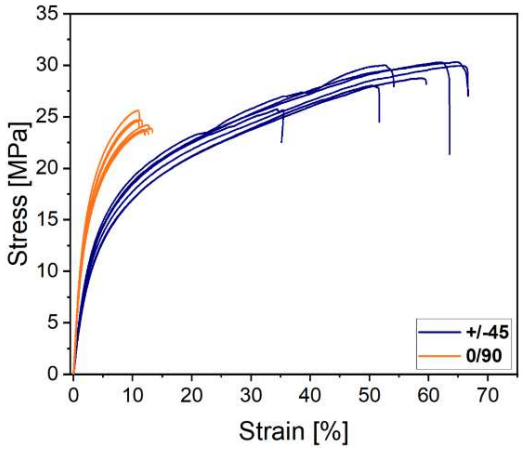

Figure 3. Stress-strain curves of tensile tested specimens

Table 1: Mean values and standard deviations of Young's modulus, tensile strength and strain at failure of tensile tested specimens.

	Young's modulus [MPa]	UTS [MPa]	Strain at failure [%]
±45	522 ± 37	29 ± 0.9	64.2 ± 9.2
0/90	967 ± 38	23.7 ± 0.6	11.8 ± 0.8

Specimens printed with 0°/90° raster angle displayed almost 85 % greater Young's modulus than the ±45° ones. Conversely, the strength of the ±45° specimens is about 22 % higher than that of the 0°/90° ones. According to what reported in [8], the ±45° specimens failed for strains about 450% larger than that of the 0°/90° specimens, thus displaying a more ductile behaviour.

Moreover, the failure of the 0°/90° specimens occurred over a surface oriented at 90° with respect to the specimens' axis. Instead, the fracture surface of the ±45° specimens is oriented either at +45° or -45° in the infill region, whereas it tended to preserve the orientation of 90° (perpendicular to the filaments of the contour) in the wall regions.

  doi:10.5075/epfl-298799_978-2-9701614-0-0

3.2 Compression

Results of the compressive tests carried are shown in Fig.4 in terms of stress-strain curves. The values of the main mechanical properties obtained from testing are reported in Table 2.

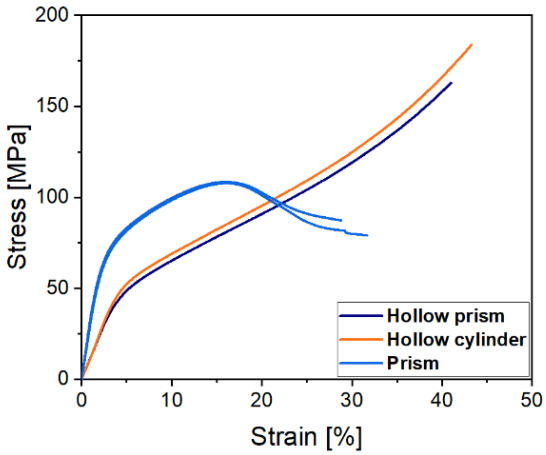

Figure 4. Stress-strain curves of tensile tested specimens

Table 2: Values of the compressive moduli and maximum compressive stress of the tested specimens.

	In-plane		Out-of-plane	
	Prism 1	Prism 2	Hollow prism	Hollow cylinder
Compressive modulus [GPa]	3.37	3.13	1.16	1.20
Max compressive stress [MPa]	108	108	-	-

Prismatic specimens allowed the evaluation of the compressive modulus of the material in the filament direction. It was found to be slightly greater than 3 GPa. The peak value of the stress in the filament direction was 108 MPa. Whereas two specimens' geometries were tested to evaluate the transversal moduli of the material. Good agreement existed between the resulting moduli, being 1.16 GPa and 1.20 GPa those obtained for the hollow-prism and the hollow-cylinder, respectively.

3.3 Fractography

Figure 5.a shows a SEM image of the fracture surface of a 0°/90° specimen. Two very different micromechanical behaviour of the material were inferred from the analysis of this fracture surface. A limited infill region experienced a micro-ductile failure mode. The matrix material of the filaments underwent large plastic deformation before failure, as clearly visible from the higher magnification images shown in Figure 5.b.

  doi:10.5075/epfl-298799_978-2-9701614-0-0

Conversely, micro-brittle failure occurred over an extended area of the specimen's cross section, including both walls and infill regions. The little to almost no plastic deformation of the filament's' matrix in those areas is highlighted in the close-up images of the filaments displayed in Figure 5.c and Figure 5.d.

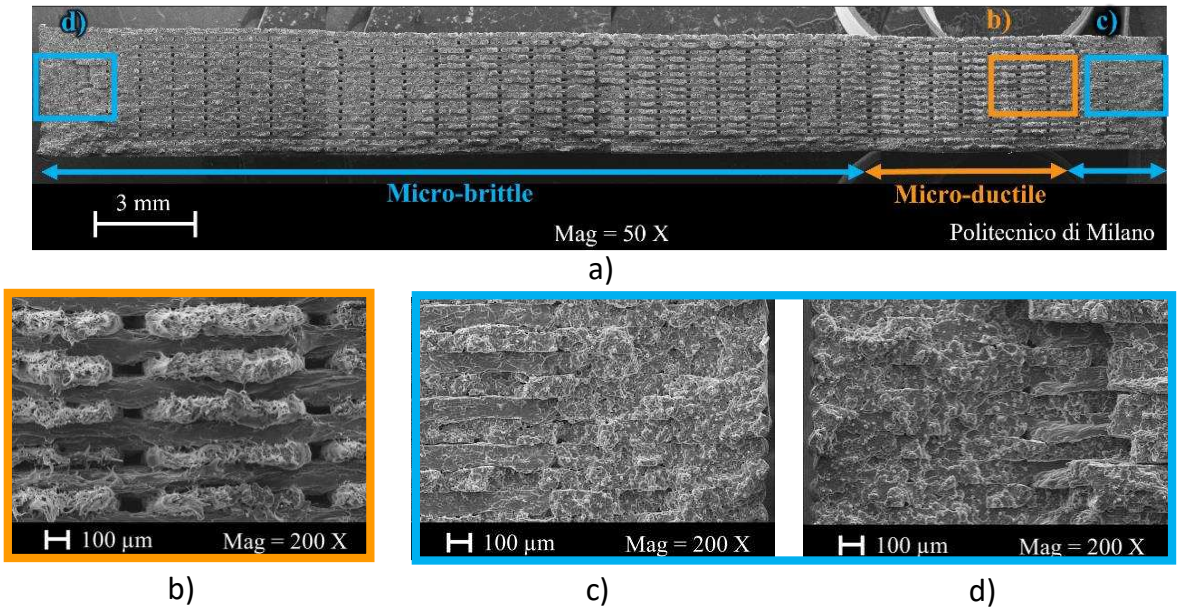

Figure 5. SEM images of: a) fracture surface of 0°/90° specimen, close up images 0 : b) micro-ductility of infill filaments, c-d) micro brittleness of the right and left walls respectively.

Figure 6.a displays a SEM image of the fracture surface of a ±45° specimen. The same micro-ductile and micro-brittle behaviour is observed. In the present case, the micro-ductile failure involved one of the two lateral walls and the filaments immediately adjacent to it. The large plastic deformation of this area is highlighted in Figure 6.b. The rest of the specimen's cross section displayed no evident plastic deformation, as shown in Figure 6.c.

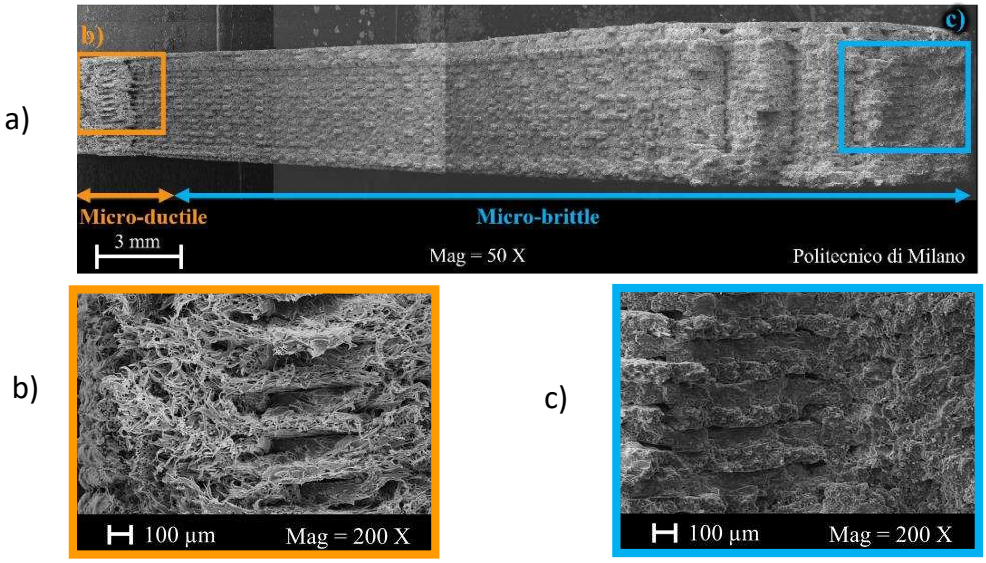

Figure 6. *SEM images of: a) fracture surface of ±45° specimen, close up images of: b) micro-ductility of left wall, c) micro brittleness of the right wall.*

A picture of the prismatic specimen tested under longitudinal compression is reported in Fig. 7.a. Shear bands formation and no evident inter-filaments debonding characterized the failure morphology of the prismatic specimens, as shown in the close-up images in Figure 7.a. Hollow prism and hollow cylinder specimens underwent small amount of barreling, however no debonding between adjacent filaments was detected.

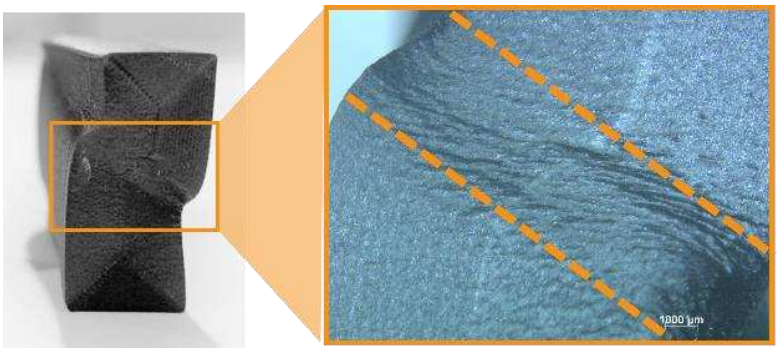

Figure 7. Failure morphology of the prismatic specimens under longitudinal load, close-up image of the shear bands.

4. Discussion

4.1 Tensile

The results of the tensile tests highlighted the influence of the raster orientation on both the stiffness and strength of the Onyx specimens printed via FFF technology. The higher stiffness of the 0°/90° specimens seemed to be mostly provided by the 0° filaments aligned with the load. By varying the angle between filaments and the load, as in the case of the ±45° specimens, the stiffness dramatically decreases.

In contrast, the 0°/90° specimens appeared to fail at lower stress values than the ±45° ones. However, it is worth to mention that the strength values reported in Table 1 were obtained by diving the applied load by the nominal resistant section (width times thickness). Moreover, the SEM images of the fracture surface of the 0°/90° specimens evidenced an intra-filaments at 0° and inter-filaments at 90° failure. This suggests that the effective resistant section is that provided by the 0° filaments only, thus lower than the nominal one. Therefore, the actual strength of 0°/90° specimens is most likely higher. Similar considerations can be applied to the strength of the ±45° specimens.

The onset of the specimens' failure might be associated to the micro-ductile areas of the specimens' fracture surface. There, large plastic deformation of the matrix most probably occurred at low strain rate. Once those regions have failed, a sudden failure of the remaining cross section yielded to the brittle failure of the rest of fracture surface.

4.2 Compression

Results of the compression tests highlight the anisotropic compressive behaviour of the FFF printed Onyx material. Longitudinal compression test of the prismatic specimens yielded to the highest mechanical properties. Seemingly the prismatic specimens did not fail for buckling.

Therefore, the maximum compressive stress obtained from testing could be assumed as a reliable estimation of the longitudinal compressive strength of the material. The transversal modulus seemed not to be influenced by the specimens' geometry used for the characterization. No sign of debonding between adjacent filaments were detected up to the maximum loads applied in the tests for all the tested specimens.

5. Conclusions

Mechanical characterization and failure analysis of an FFF printed short fibre reinforced polyamide were carried out. Results of tensile tests highlighted an effect of the raster angle on the mechanical properties of the printed specimens. Specimens printed with ±45° raster orientation were more compliant than those with 0°/90° raster orientation. The actual longitudinal tensile strength of the material could be underestimated by using the nominal cross-section. Failure of those specimens involved the filaments at 0° only, thus the effective resistant section is lower than the nominal one. The analysis of the fracture surface revealed that two different micro-mechanical behaviour were involved in the specimens' failure. The onset of the damage was confined in a limited portion of the cross-section, where large deformation occurred. Once this critical area fails, the remaining cross section fail at high strain rate, resulting in a micro-brittle failure behaviour.

Different in-plane and out-of-plane compressive properties resulted from the characterization of the Onyx material printed via FFF. The longitudinal compressive modulus was almost three times higher than the transversal one. The transverse modulus was not affected by specimens' geometry. The failure of unidirectional filaments longitudinally compressed occurred without buckling and debonding of adjacent filaments. Shear bands formation characterized the failed specimens' morphology. The maximum stress obtained by the test could be thus an accurate estimation of the compressive longitudinal strength of the material.

6. References

1. Brenken B, Barocio E, Favaloro A, Kunc V, Byron Pipes R, Fused filament fabrication of fiber-reinforced polymers: a review. Add Man 2018, 21:1-16.
2. Casavola C, Cazzato C, Moramarco V, Pappalettere C, Orthotropic mechanical properties of fused deposition modelling parts described by classical laminate theory. Materials & Design 2016,90:453-458.
3. Sanei SHR, Popescu D, 3D-Printed Carbon Fiber Reinforced Polymer Composites: A Systematic Review. J. Compos. Sci. 4, 98 (2020).
4. Krajangsawasdi N, Blok LG; Hamerton I; Longana ML., Woods BKS, Ivanov DS, Fused Deposition Modelling of Fibre Reinforced Polymer Composites: A Parametric Review. J. Compos. Sci. 5, 29 (2021).
5. Markforged, Onyx datasheet 2020: https://markforged.com/materials/plastics/onyx
6. Ahn S, Montero M, Odell D, Roundy S, Wright PK, Anisotropic material properties of fused deposition modelling ABS. Rapid Prototyping Journal 2002, 8(4):248-257.
7. EN ISO 527-4. Determination of tensile properties. 1997.
8. Jiang D, Smith DE. Anisotropic mechanical properties of oriented carbon fiber filled polymer composites produced with fused filament fabrication. Addit Manuf 2017;18:84–94.

  doi:10.5075/epfl-298799_978-2-9701614-0-0

ESTIMATION OF INTERFACIAL SHEAR STRENGTH OF LONG GLASS FIBRE COMPOSITES BY X-RAY COMPUTED TOMOGRAPHY

Dietmar Salaberger[a], Michael Jerabek[a], Wolfgang Stockreiter[a]

a: Borealis Polyolefine GmbH, St.-Peter Strasse 25, 4021 Linz, Austria, e-mail: dietmar.salaberger@borealisgroup.com

Abstract: X-ray computed tomography (CT) has been applied to fractured specimens after Charpy impact testing. A segmentation of all protruding fibres was done semi-automatically. Individual fibre characterisation lead to the knowledge of orientation and length of every protruding fibre. By taking the orientation into account and choosing only fibres that are aligned in direction of force, an estimation of the critical fibre length was performed on materials with long glass fibres and varying amount of coupling agent. Critical fibre length and shear strength, which was estimated using the Kelly-Tyson model, followed the expected trend.

Keywords: Long glass fibre composite; Computed tomography; Interfacial shear strength; Critical fibre length

1. Introduction

X-ray computed tomography (CT) has been established for the characterisation of discontinuous fibre reinforced polymers [1, 2]. The determination of features of every individual fibre has the advantage of getting many different values for each fibre. A feature that is usually determined by other methods is the interfacial shear strength τ [3]. This value is part of several other features like orientation and length distribution or local fibre fraction that describe the micro-mechanical behaviour of a material. The Kelly–Tyson model allows for the calculation of τ from the knowledge of the critical fibre length [4, 5]. Knowledge of real fibre length and orientation distribution are necessary to apply the Kelly-Tyson model in a proper way.

This contribution shows how CT and individual fibre characterisation can be used to estimate the interfacial shear strength for long glass fibre filled polymers.

2. Experimental

2.1 Materials

Polypropylene filled with 30 wt.% long glass fibres produced by injection moulding was analysed. Differences in fibre-matrix coupling was realised by adding different amount of coupling agent (CA). The amount for each specimen is shown in Table 1.
Charpy impact tests were performed on notched ISO standard test specimens. One part of the two broken parts was analysed by CT.

Table 1: Materials tested

ID number	1	2	3	4	5	6
CA content (wt. %)	0	0.5	1	1.5	2	2.5

  doi:10.5075/epfl-298799_978-2-9701614-0-0

2.2 Methods

CT scans were performed at a laboratory CT device (Heliscan, Thermo Fisher Scientific) applying 5 µm Voxel size. A comprehensive characterisation of the microstructure was performed using a tool developed at FH Wels [4] and allowing for the determination of fibre orientation and length. The chosen resolution allowed for the scan of the complete specimens cross section.

Data analysis started with the separation of protruding fibres and composite material. Therefore, all material other than air was segmented using a global threshold. This resulting region was the dilated and eroded in a way that missing holes were closed and the protruding fibres were excluded. At some points, manual optimization was necessary because of the presence of streaks and shadows. These were induced by the presence of fibre bundles and the complex, convex fracture surface (Figure 1). The inverted region contained only protruding fibres. This data set was analysed in order to determine fibre length and orientation of every individual fibre.

The contrast between fibres and background is much better compared to the composite and the fibres are better separated because only some of the fibres are pulled out of the other part. This is the basis for very good segmentation quality and accurate length determination.

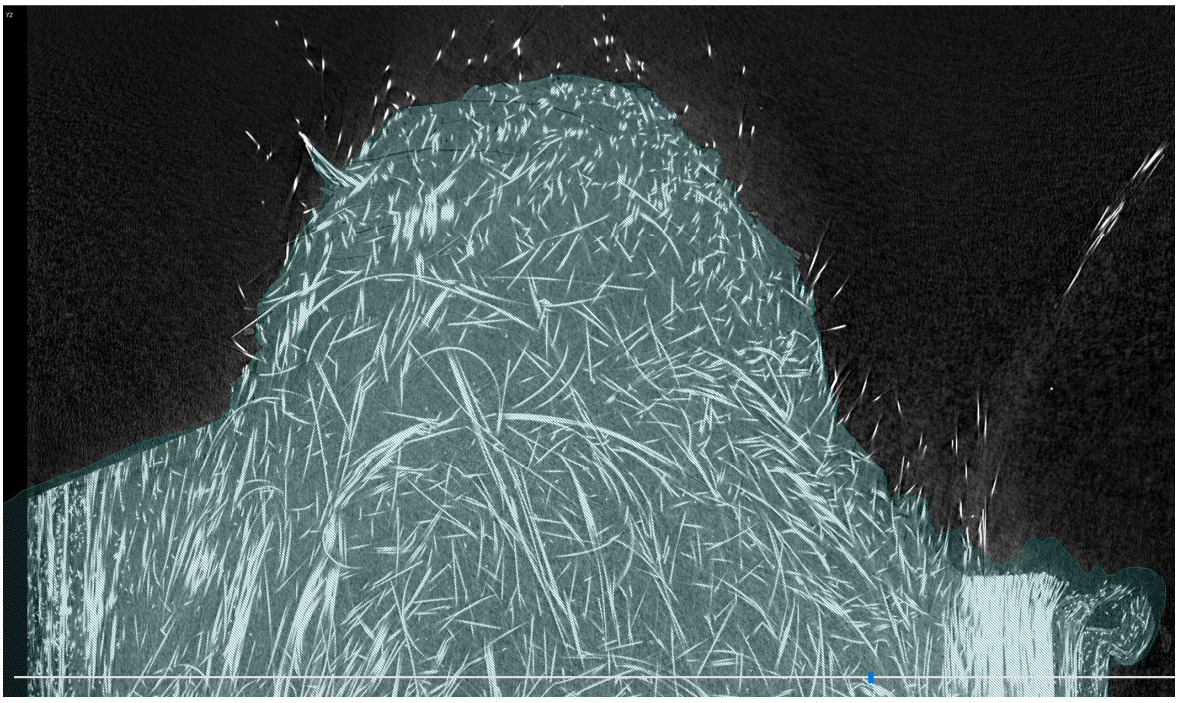

Figure 1: Cross sectional image of sample 3 (1 wt. % CA) showing the area that marked the border between protruding fibres and composite material

2.3 Calculation of interfacial shear strength

For the calculation of the interfacial shear strength according to Eq. (1), the critical fibre length has to be determined.

$$\tau = \frac{r_{f*}\sigma_f^u}{l_{crit}} \quad (1)$$

Since the stress distribution across the test specimens is non-uniform and the initial fibre orientation has an influence on the stress transfer from fibres into matrix, only fibres that are aligned in specimen longitudinal axis (Z) are considered. An arbitrary threshold of aZZ > 0.9 was defined. For these fibres, average length and orientation were determined.

For the critical length, the underlying model implies that the longest pulled out fibre ($l_{p,max}$) is the relevant and that it is pulled out of the other part by the same length as it is still in the composite material (Eq. (2)).

$$2 * l_{p,max} \leq l_{crit} \tag{2}$$

To reduce the influence of segmentation errors and deviations from the model of critical fibre length, the average of the longest 10 fibres with aZZ > 0.9 were used for the calculation of the critical fibre length.
For the radius of the fibres r_f a value of 8.5 µm was used and for the tensile strength of glass fibres σ_f^u a value of 1500 MPa was used.

3. Results and discussion

Visual analysis of the 3D data set reveal the distribution and orientation of fibres in the composite but also at the fracture surface and above. Figure 2 shows images of sample 5 (highest amount of coupling agent). Beside the fact that the fracture surface is highly convex which is visible by eye, CT reveals the orientation of the fibres closely underneath the fracture surface. Because of the high fibre length, the fibres especially in the centre are bent and the fracture surface is following the curvature of the fibres partly. The XY and XZ plane show the skin-core orientation profile induced be the differences in shear rate.

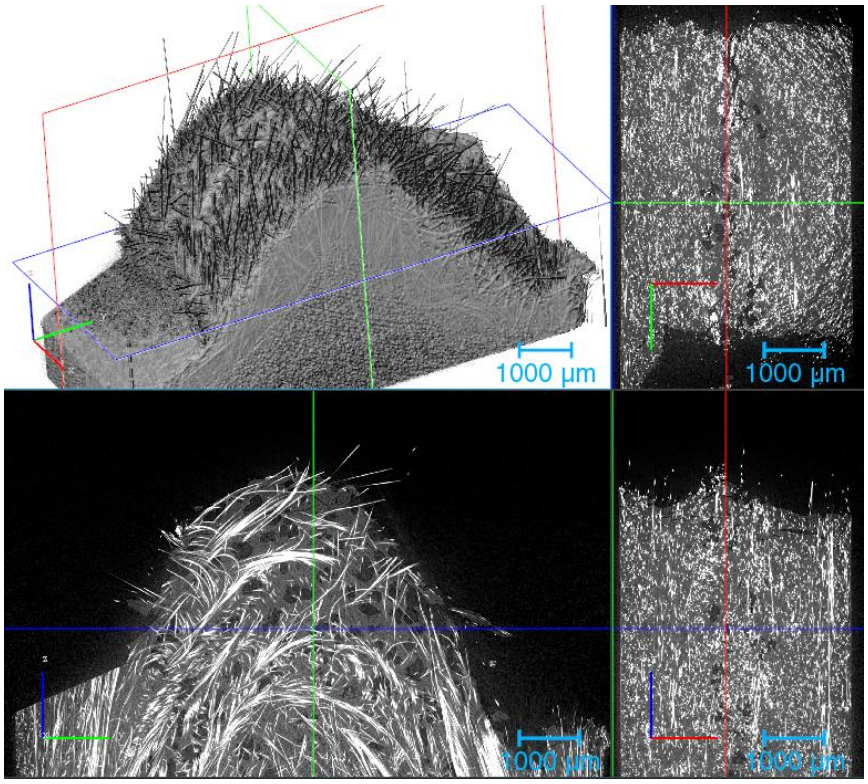

Figure 2: 3D and cross sectional images from different planes of specimens centre

Making an overlay of segmented, protruding fibres and the specimen underneath the fracture surface, on can see the influence of different amount of coupling agent (Figure 3). The fibres pulled out of the matrix are much longer without coupling agent (shown on the left) compared to the specimen with 2.5 wt.% of coupling agent (shown on the right). One can see the fibres are pointing in different directions. This can be explained by the non-uniform stress distribution that builds during Charpy impact testing and the complex fibre arrangement in the composite as such. The results for average orientation tensor show significant differences between the samples. These differences are not present when taking only well aligned fibres into account (Figure 4).

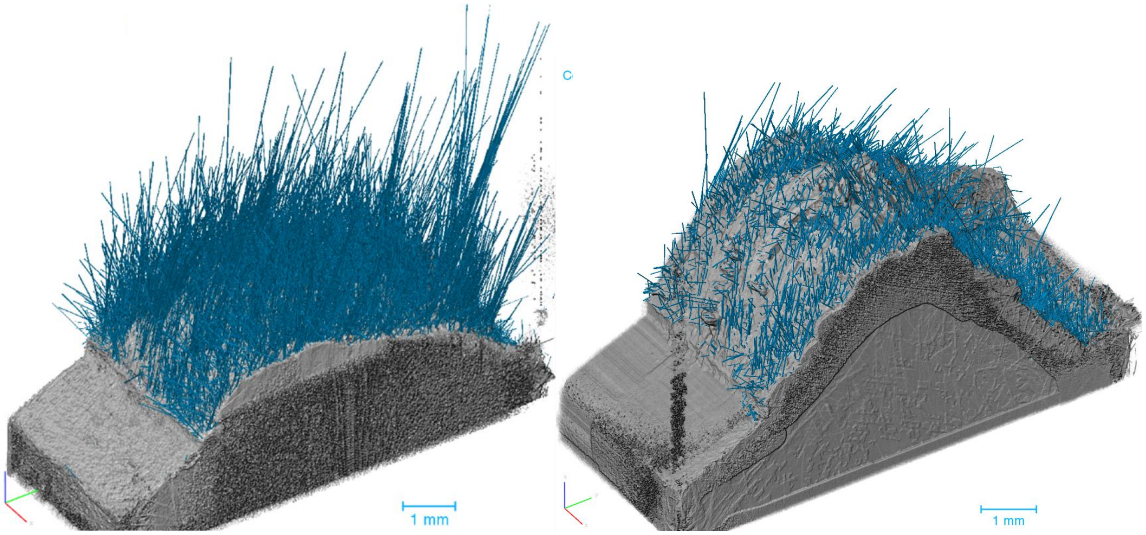

Figure 3: 3D rendered views of protruded fibres in blue and the bulk in grey: Sample 1 without coupling agent (left) and sample 5 with highest amount of coupling agent (right)

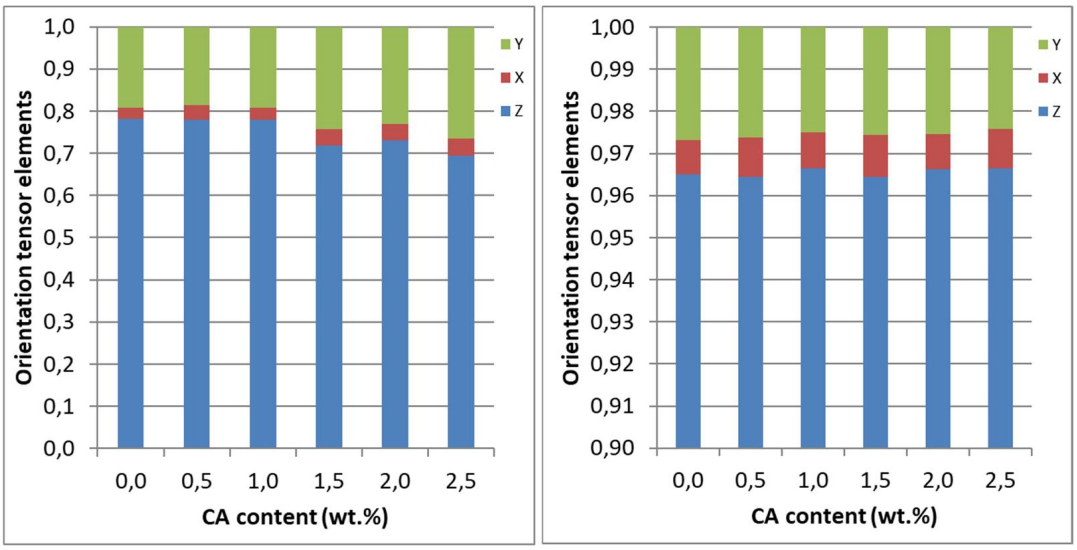

Figure 4: Main orientation tensor elements of all protruding fibres (left) and of fibres with aZZ > 0.9 only (right)

Both, average and weighted average length are monotonously falling with increased amount of coupling agent as shown in Figure 5. Especially for higher CA content above 1 wt.% the number of fibres protruding the surface decreases significantly. The plots of relative length

distribution show two regimes of fibre length where the CA content has the same influence on the trend: fibres with length below 300 µm and fibres with length above 2000 µm (Figure 6).

The calculated results for critical fibre length and interfacial shear strength follow the same trends as average fibre length. The specimen with 2.5 wt. % CA shows more than twice the shear strength of the specimen without CA. These values should be seen as estimates since the constraints for the underlying model are not fulfilled.

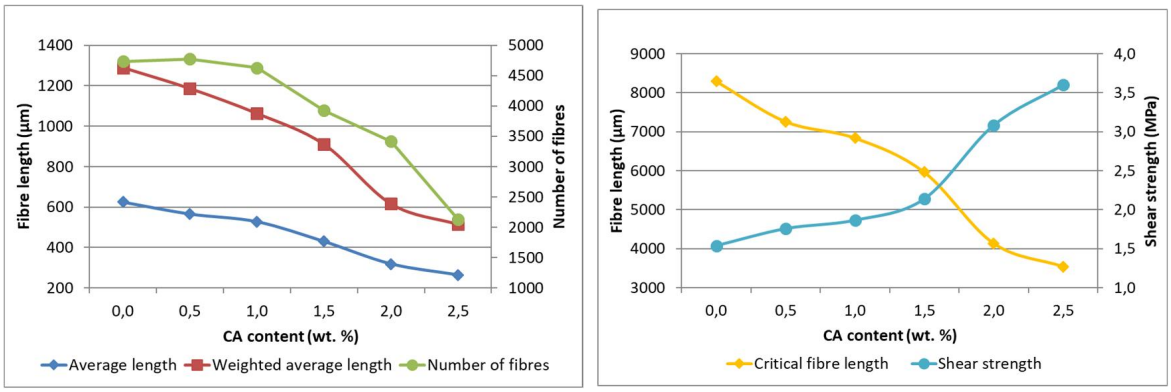

Figure 5: Average, weighted average fibre length and number of fibres (left); Critical fibre length and estimated shear strength (right). Only fibres with aZZ > 0.9 were taken into account

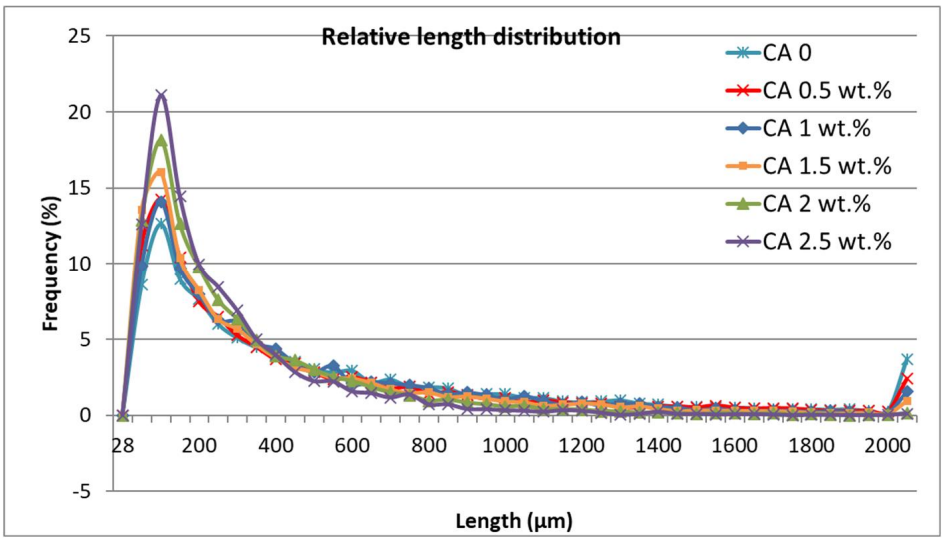

Figure 6: Fibre length distribution including all protruding fibres

4. Conclusions

The determination of features of individual fibres by X-ray computed tomography allows for the determination of critical fibre length and furthermore the interfacial shear strength. The resolution that can be achieved to scan the complete cross section of an ISO impact or tensile test specimen is sufficient for the accurate characterisation of protruding fibres.

CT artefacts that induces streaks or halo have to be reduces as much as possible in order to avoid manual optimization of fracture surface segmentation.

Although the trends for average fibre length, critical length and shear strength depending on amount of coupling agent meet the expectations, the absolute values are not yet confirmed by other methods. The definition of well aligned fibre and taking the average of the longest 10 fibres is arbitrary and should be verified.
For the accurate determination of shear strength, a tensile test would be better suited because of the more homogeneous stress distribution across specimen's cross section. The definition of direction of force would be more accurate and the fracture surface would be more flat. The assumptions for the Kelly-Tyson model (e.g. all fibres are aligned in direction of force) would be better fulfilled.

5. References

1. Bechara A S, Osswald T. Measuring Fibre Length in the Core and Shell Regions of Injection Molded Long Fiber-Reinforced Thermoplastic Plaques. Composites Science 2020; 4 (104)
2. Salaberger D. Micro-structure of discontinuous fibre polymer matrix composites determined by X-ray Computed Tomography. TU Vienna; 2019.
3. Thomason J L Interfacial strength in thermoplastic composites – at last an industry friendly measurement method?. Composites Part A: Applied Science and Manufacturing 2002; 33(10):1283-1288.
4. Wongpajan R, Mathurosemontri S, Takematsu R, Xu H Y, Uawongsuwan P, Thumsorn S, Hamada H. Interfacial Shear Strength of Glass Fiber Reinforced Polymer Composites by the Modified Rule of Mixture and Kelly-Tyson Model. Energy Procedia 2016; 89:328-334.
5. Vas L M, Ronkay F, Czigány T. Active fiber length distribution and its application to determine the critical fiber length. Polymer Testing 2009; 28(7):752-759.
6. D. Salaberger, K. A. Kannappan, J. Kastner, J. Reussner, and T. Auinger, Evaluation of Computed Tomography Data from Fibre Reinforced Polymers to Determine Fibre Length Distribution. International Polymer Processing 2011; 26(3):283-291.

  doi:10.5075/epfl-298799_978-2-9701614-0-0

MATERIAL CHARACTERISATION AND FATIGUE DATA CORRELATION OF SHORT FIBRE COMPOSITES: EFFECTS OF THICKNESS, LOAD RATIOS AND FIBRE ORIENTATION AT ELEVATED TEMPERATURES

Francesco Emanuele Fiorini[a], Luca Michele Martulli[b], Philippe Steck[a], Andrea Bernasconi[b]

a: thyssenkrupp Presta AG, Competence Center Mechanics, Principality of Liechtenstein – francesco.fiorini@thyssenkrupp-automotive.com
b: Politecnico di Milano, Department of Mechanical Engineering, Italy

Abstract: *In design engineering of short fiber reinforced components a given material can be used for two or more parts of the same system having different wall thicknesses. The thickness, together with numerous parameters, has an impact on the cyclic behavior of short fiber reinforced thermoplastics under fatigue loading. This research analyses and compares the fiber orientation by µCT as well as the quasi-static and cyclic behavior of two sets of specimens with 1.6 and 3 mm wall thicknesses made of PA6T/6I GF50. Fatigue criteria based on cyclic mean strain rate or on cyclic creep energy density are evaluated to assess the most accurate and independent of the thickness.*

Keywords: short fiber-reinforced thermoplastic; fatigue criterion; anisotropy; load ratio; thickness.

1. Introduction

In the last years, the automotive industry has been strongly impacted by the increase of restrictive CO_2 regulations on top of the already well-established aim for best cost solutions. Lightweight design and wide application of plastic materials is thus becoming of primary importance. This design can be achieved by using lightweight materials, such as Short Fibers Reinforced Polymers (SFRPs). These composite materials are usually injection molded into complex forms. Moreover, these materials can achieve a fair strength to weight ratio. To fully adopt SFRPs into automotive parts, it is necessary to be able to predict their fatigue strength. However, many challenges occur when predicting the fatigue behavior of SFRP composites. This is due to a various number of influencing parameters, which have a direct impact on the quasi-static and cyclic response. Some of these influencing parameters are the fiber orientation [1,2,3], fatigue loading [4,5], loading frequency [6] and mean stress [7]. The cyclic creep strain rate can be a unifying criterion for fatigue test results with positive stress ratios [8-10]. A unifying criterion is relevant due to its potential to accelerate the product's development time by reducing the testing effort, leading to higher efficiency and less costs. However, none of the above-mentioned authors take the wall thickness of the specimen into consideration as one potential influencing parameter. Complex systems developed for the automotive industry often comply with a modular product architecture to be able to meet the required increasing variation diversity. This results into building up components and sub-components by different means of design, one parameter being the wall thickness. In the present research, the dependency of the fatigue response of SFRPs on the thickness is investigated.

  doi:10.5075/epfl-298799_978-2-9701614-0-0

2. Material, specimen geometry and experimental method

2.1 Material

A Polyphtalamide PA6T/6I, filled with 50% weight short glass fibers (Ultramid® Advanced T1000HG10) was investigated. To investigate the influence of the thickness in combination with the fiber orientation on the mechanical properties, dog bone samples were extracted from injection molded plaques with a dimension of 150 x 150 mm and two different thicknesses t (1.6 mm and 3 mm). The plates were manufactured with the same material and appropriate process conditions by injection molding. Injection molding induces a heterogeneous orientation of the fibers through the thickness of the plates. The resulting microstructure can be described by three layers: the skin, the shell and the core [1, 11]. In the shell, the thickest part, fibers are aligned with the injection flow. A dog bone specimen was chosen for the quasi-static and cyclic characterization. Figure 1a showcases specimen's shape and dimensions (radiuses S and L are not reported due to confidentiality restrictions).

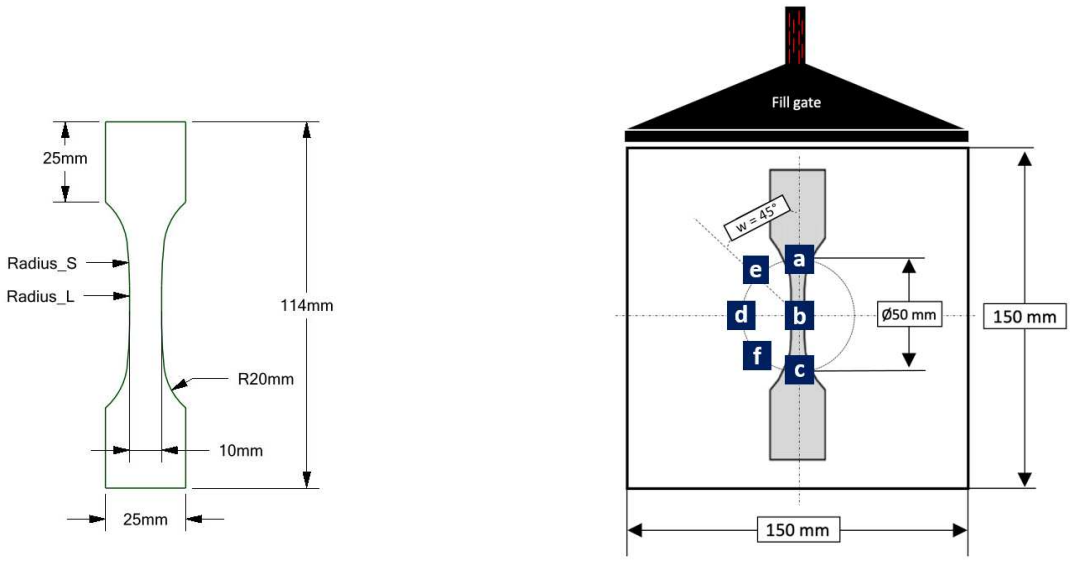

(a) *(b)*

Figure 1. Specimen dimension(a). Mold plaque dimensions and cutting sample orientation (b).

One coupon per plate was machined out by milling at 0° or 90° with respect to the main flow direction as shown in Figure 1b. The test temperature was 80°C. The relative humidity (RH) was kept under 0.1% wt., sealing the specimens in individual special bags to prevent any change in RH prior to the experiment after drying.

2.2 Methods

2.2.1 µCT Measurements

Micro Computed Tomography (µCT) samples were cut out from some of the dog bone specimens to measure the local fiber orientation. The µCT sample extraction points are shown in Figure 1b. In total, 6 positions for each plate thickness were measured. The µCT samples were 3 × 3 × t mm in size (t = 3 mm and 1.6 mm). A RX Solutions Destem 130 was used. Scanning resolution was 7 µm/voxel. Voltage acceleration and target current were 110 kV and 72 µA, respectively. Output data was processed with the software VGStudio Max by Volume Graphics.

  doi:10.5075/epfl-298799_978-2-9701614-0-0

2.2.2 Quasi-static testing

The quasi-static tests were conducted with an Inspect 300-1 Hegewald and Peschke test rig. The 3D camera optical measurement system GOM ARAMIS was used to measure the deformation of the specimens during the quasi-static experiments. A random speckle pattern was applied onto the specimens by white spray paints. To be able to carry out tests at 80°C, a temperature chamber equipped with a digital temperature controller was used. The displacement rate was 1 mm/min. Five specimens per thickness (3 mm and 1.6 mm) were tested for both orientations (0° and 90°).

2.2.3 Cyclic testing

Cyclic fatigue tests were performed at thyssenkrupp Presta AG using an Instron 8802 uniaxial servo hydraulic fatigue testing machine. A sinusoidal load function with constant amplitude at a frequency of 4 Hz was used. A mechanical extensometer was used to measure strain and a FLUKE thermal imaging camera to monitor the surface temperature. For a temperature effect study, an environmental chamber with an electronic heating element was employed. Complete specimen separation was the failure criterion. If the dog bone did not break after 10E+6 cycles, the coupon was considered a runout. Runouts were excluded for the derivation of the SN curve equation. Load ratios were R = 0.1 and R = 0.5.

3. Experimental results

3.1 Micro-structure – Fiber orientation analysis

In Figure 2a and 2b the measured eigenvalues a_{11} of the fiber orientation tensor are plotted against the position through the specimen's thickness. Two different thicknesses for the core layer of the t = 3 mm (Fig. 2a) and t = 1.6 mm (Fig. 2b) samples were detectable. Approximately 0.8 mm for the 3 mm and 0.2 mm for the 1.6 mm specimens.

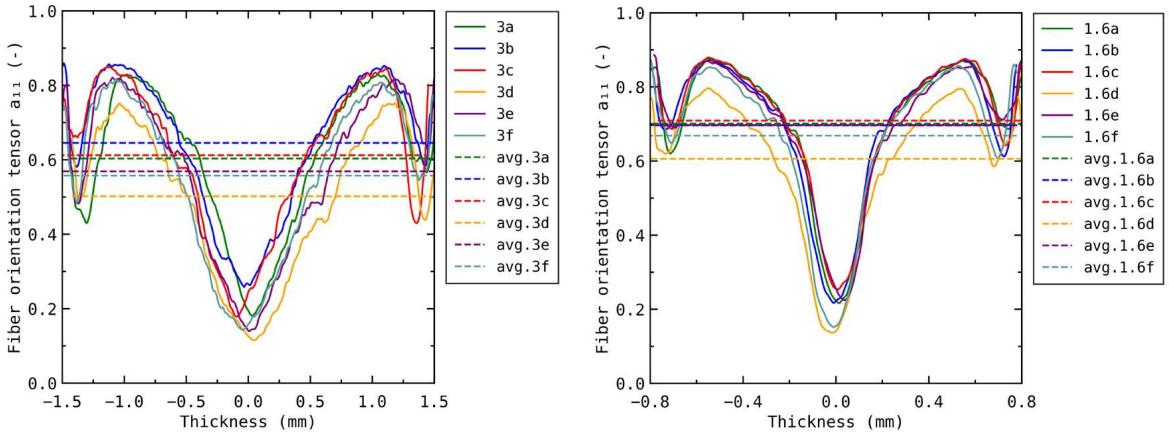

(a) *(b)*

Figure 2. Eigenvalue a_{11} in selected positions for plate thickness 3 (a) and 1.6 mm (b)

The µCT samples 3d, e and f have been extracted according to Figure 1b. A comparison of the average value 3a, 3b and 3c versus the µCT-measurements 3d, 3e and 3f showed a reduction of up to 23%. For the 1.6 mm specimens the delta lays around 13%. The average eigenvalues a_{11}

  doi:10.5075/epfl-298799_978-2-9701614-0-0

for the 1.6 mm specimen (a, b, c) milled out along the symmetry axis in flow direction were found to be constant. In all other cases a dependency of the extracted position was visible.

3.2 Quasi-Static material characterization

The stress-strain results from the quasi-static tests for two Fibre Orientation (FO) angles and two specimen thicknesses are shown in Figure 3. Strains at failure vary between 1.5 and 2.4%, depending on the FO angle. The test results are normalized by an arbitrary value for confidentiality reasons.

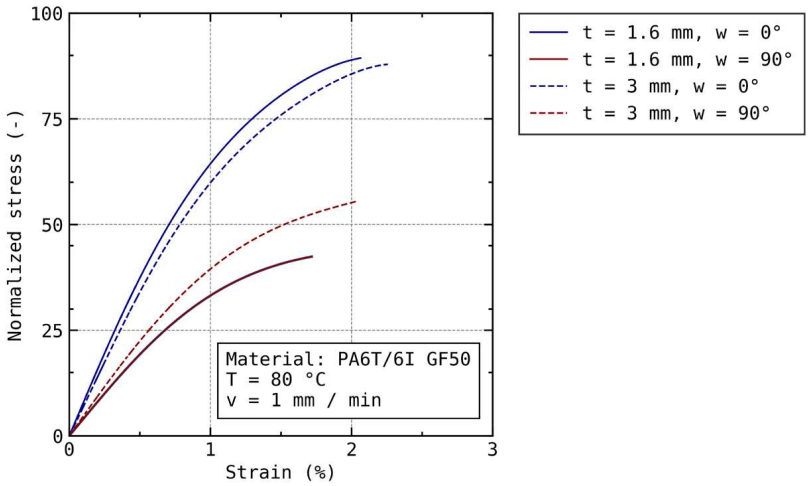

Figure 3. Comparison q. S. stress strain curves for 3 and 1.6 mm thick specimen at T = 80°C

3.3 Cyclic material characterization

Figure 4a and 4b present the fatigue test results as stress amplitude σ_a against the number of cycles to failure N_f in semi-logarithmic scale. All stress values have been normalized by an arbitrary value for confidential reasons.

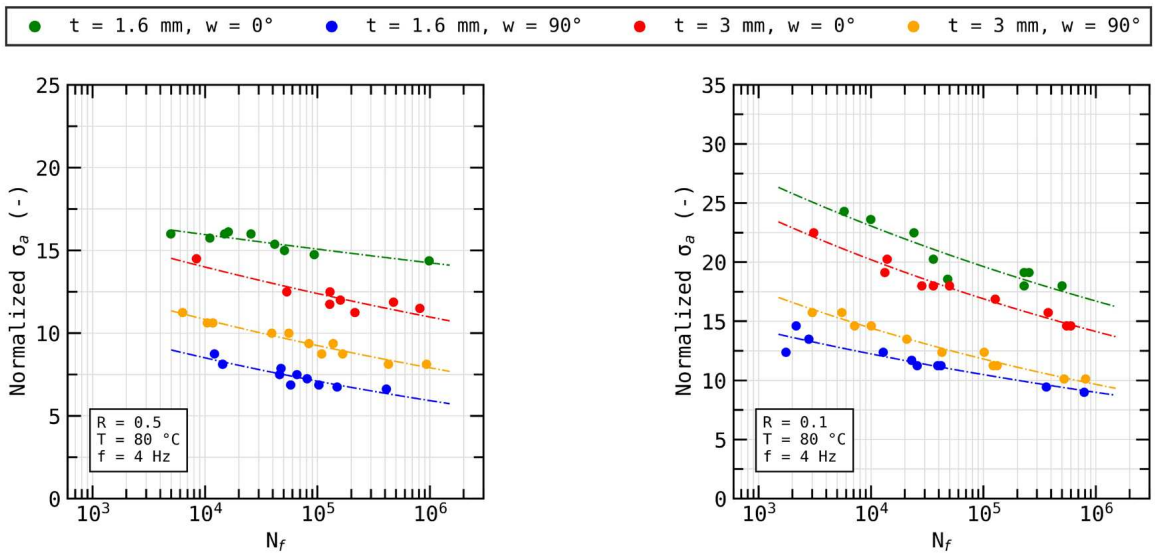

(a) *(b)*

Figure 4. Normalized S-N curves for 1.6 and 3 mm at R = 0.5 (a) 0.1 (b) for two orientations

  doi:10.5075/epfl-298799_978-2-9701614-0-0

Figures 5a and b display the quasi static and fatigue strength (residual strength at $N_f = 10^6$), normalized to the values at t = 1.6 mm thickness, as a function of specimen thickness. The quasi-static behavior is plotted for comparison purposes. The influence of the thickness on cyclic strength differs significantly from the correspondent influence on quasi-static strength, resulting in the conclusion that failure depends on the loading condition (static vs. cyclic). In regard to the R = 0.5 load ratio the normalized failure strength (extracted transversally, Figure 5b) drastically increases in comparison to the normalized failure strength of the coupon at R = 0.1 load ratio (extracted transversally, Figure 5a). The increase of around 24% leads to an approximation of the normalized failure strength in direction of the normalized quasi-static strength. For the longitudinal extracted specimens this trend cannot be confirmed. While quasi-static loading shows no significant difference in dependence of the thickness, the cyclic loading leads to a decrease of the fatigue strength. A higher decrease is detectable for R = 0.5.

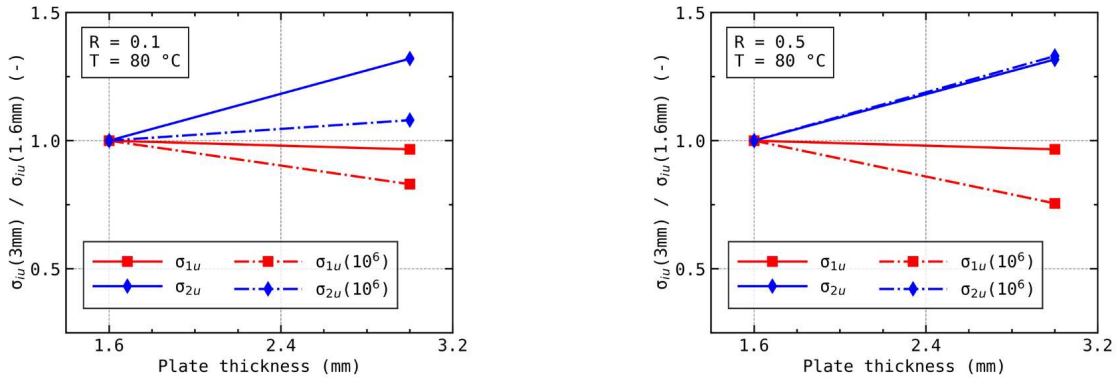

(a) *(b)*

Figure 5. Influence of thickness on normalized fatigue strength parameters for R = 0 (a) and R = 0.5 (b) compared to corresponding trends under quasi static loading

4. Fatigue criteria based one single set of parameters

In the present work the objective is to compare the ability of a strain and an energy-based criterion to predict fatigue failure. This criterion should be able to unify the fatigue data independently of the load ratio, fiber orientation, microstructure and specimen thickness using only one single set of parameters. Different criteria have been already proposed in [8-10]. Cyclic strain rate-based criteria showed good performance in regards to failure prediction. In this work, a comparison of the cyclic creep energy density and the cyclic creep strain rate is performed.

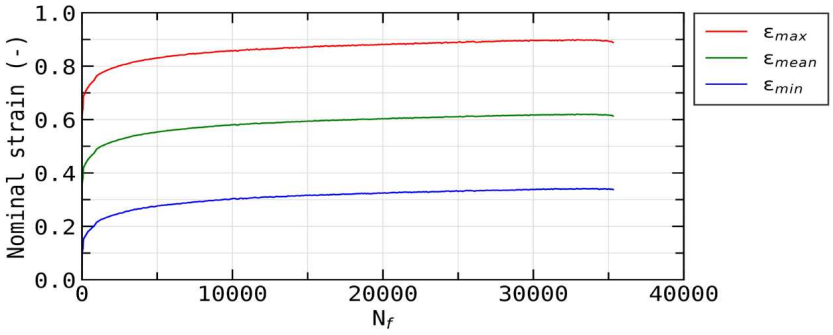

Figure 6. Trend of the maximal, minimal and mean strain until failure

  doi:10.5075/epfl-298799_978-2-9701614-0-0

Figure 6 depicts the trend of the minimum and maximum strain during fatigue testing of one of the tests performed on a longitudinally extracted 3 mm specimen, tested at R = 0.1. Based on these two values, the mean strain was also calculated. In this paper, the cyclic creep strain rate is calculated as the slope of the mean strain between 45% and 55% of the lifetime:

$$\dot{\varepsilon}_m = \frac{d\varepsilon_{mean}}{dN} \tag{1}$$

The calculated cyclic creep strain rate for the two analyzed thicknesses as well as the R-ratios was plotted as a function of cyclic to failure in Figure 7a.

The fatigue criterion allows to cluster the data independently of the thickness, fiber orientation and load ratio. The latter was possible since positive load ratios were considered within this investigation. The following power law criterion based on $\dot{\varepsilon}_m$ was identified:

$$\dot{\varepsilon}_m = aN_f^b \tag{2}$$

The Eq. (2) can be reformulated for the evaluation of the calculated lifetime as follows:

$$N_{f,calculate} = B(\dot{\varepsilon}_m)^p \tag{3}$$

The coefficients B and p are material dependent parameters.

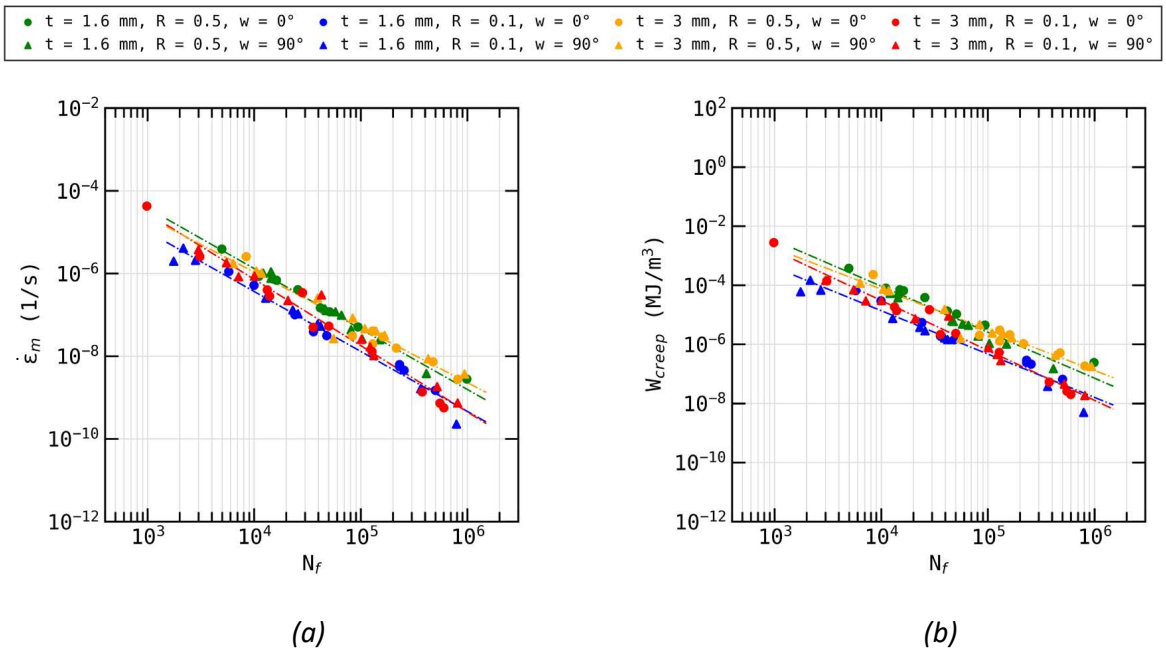

(a) *(b)*

Figure 7. Cyclic mean strain rate (a) and cyclic creep energy density (b) vs. number of cycles to failure for two load ratios, two specimen thicknesses and two orientations (dashed lines correspond to power-law fits, using one set of parameters for each R-Ratio, fiber orientation and specimen thickness).

The cyclic creep energy density (Fig. 7b) was determined by multiplying the cyclic mean strain rate $\dot{\varepsilon}_m$, between 45% and 55% of the lifetime, with the mean stress σ_{mean}. In this case, the cyclic creep energy density manages to group the two analyzed orientations and specimen thicknesses but fails to unify the results for different load ratios.

The following power-law criterion can be identified:

  doi:10.5075/epfl-298799_978-2-9701614-0-0

$$W_{creep} = aN_f^b \quad (5)$$

Eq. (5) can be rearranged for the evaluation of the lifetime such as:

$$N_{f,calculate} = B(W_{creep})^p \quad (6)$$

The coefficients B and p are material dependent parameters for the energy-based criterion.

The parameter set identification was carried out on the 0° fiber orientation specimen with a R-Value of 0.1 and a specimen thickness of t = 3 mm. To determine the criterion accuracy, the $N_{f,calculation}$ and $N_{f,experimental}$ are plotted on Fig. 8. The estimated lifetime $N_{f,calculation}$ is calculated by using Eq. (3) for the cyclic mean strain rate based criterion and Eq. (6) for the cyclic creep energy density. $N_{f,experimental}$ equals the experimental lifetime. For the cyclic mean strain rate based criterion, 76% of the calculated lifetime lays within scatter band two, whereas 98% was within scatter band three (Figure 8a). The calculated lifetime, compared with the one obtained experimentally, showed that the estimation of the cycles to failure by the cyclic mean strain rate based criterion can be used not only for the two R-Ratios and fiber orientations, but also for the wall thickness. For the cyclic creep energy based criterion, the usage of only one single set of parameters enables 71% of the fatigue lifetime data to be predicted by the criterion within a scatter band of a factor two. 90% of the predicted fatigue lifetimes are within a scatter band of factor three. The predictions were good for the analyzed load ratios.

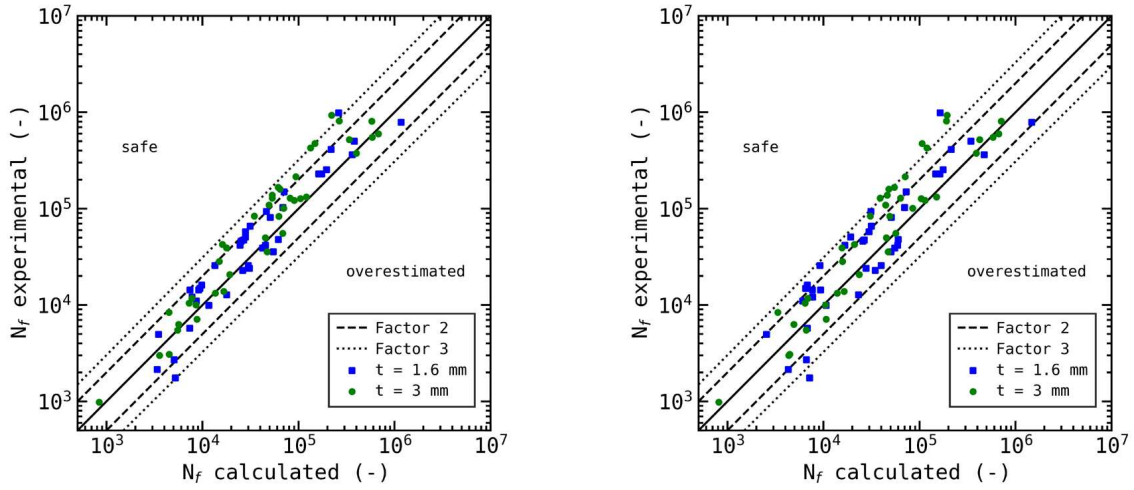

Figure 8. Fatigue criterion accuracy analysis based on one single set of parameters. (a) cyclic mean strain rate based and cyclic creep energy based criterion (b).

5. Conclusions

The present work analyzed the impact of the wall thickness onto the quasi-static and cyclic behavior. µCT scans were performed to evaluate the micro-structure as function of the thickness. The core layer thickness for the 3 mm specimens was approximately 0.8 mm and 0.2 mm for the 1.6 mm. In case of the 0° specimens, no significant static strength decrease could be detected in dependence of the wall thickness. The same did not apply for the 90° specimens, which showed an increase of the static strength with an increasing thickness of the probe. The 1.6 mm specimen always showed a higher fatigue strength compared to the 3 mm probe in case

  doi:10.5075/epfl-298799_978-2-9701614-0-0

of a longitudinal extraction to the main flow. An inverse behavior of the fatigue strength was witnessed, when analyzing the specimens which have been extracted transversally to the main flow direction. A strain-based and an energy-based criterion were chosen for the fatigue failure prediction using one single set of parameters. An independency of the thickness, fiber orientation and load ratio could be detected for the cyclic mean strain rate. The accuracy of the prediction lays between 76% (scatter band two) and 98% (scatter band three) in comparison to the experimentally determined lifetime. This research has been conducted by using only positive load ratios. To be able to evaluate a holistic material behavior with respect to the dependency of the wall thickness, an analysis including negative load ratios should be performed as well. Additionally, the conclusions drawn within this research should be tested and verified on a component or a system to understand if the procedure is still applicable for complex topologies. A final perspective could be to implement a cyclic mean strain rate numerical methodology in existing Finite Element tools.

6. References

1. Horst, J. J. (1997). Influence of fibre orientation on fatigue of short glassfibre reinforced Polyamide.
2. Bernasconi, A., Davoli, P., Basile, A., & Filippi, A. (2007). Effect of fibre orientation on the fatigue behaviour of a short glass fibre reinforced polyamide-6. International Journal of Fatigue, 29(2), 199-208.
3. De Monte, M., Moosbrugger, E., & Quaresimin, M. (2010). Influence of temperature and thickness on the off-axis behaviour of short glass fibre reinforced polyamide 6.6–cyclic loading. Composites Part A: Applied Science and Manufacturing, 41(10), 1368-1379.
4. Sauer, J. A., McMaster, A. D., & Morrow, D. R. (1976). Fatigue behavior of polystyrene and effect of mean stress. Journal of Macromolecular Science, Part B: Physics, 12(4), 535-562.
5. Sonsino, C. M., & Moosbrugger, E. (2008). Fatigue design of highly loaded short-glass-fibre reinforced polyamide parts in engine compartments. International Journal of Fatigue, 30(7), 1279-1288.
6. Bernasconi, A., & Kulin, R. M. (2009). Effect of frequency upon fatigue strength of a short glass fiber reinforced polyamide 6: a superposition method based on cyclic creep parameters. Polymer Composites, 30(2), 154-161.
7. Mallick, P. K., & Zhou, Y. (2004). Effect of mean stress on the stress-controlled fatigue of a short E-glass fiber reinforced polyamide-6, 6. International journal of fatigue, 26(9), 941-946.
8. Santharam, P., Marco, Y., Le Saux, V., Le Saux, M., Robert, G., Raoult, I., ... & Charrier, P. (2020). Fatigue criteria for short fiber-reinforced thermoplastic validated over various fiber orientations, load ratios and environmental conditions. International Journal of Fatigue, 135, 105574.
9. Raphael, I., Saintier, N., Rolland, H., Robert, G., & Laiarinandrasana, L. (2019). A mixed strain rate and energy based fatigue criterion for short fiber reinforced thermoplastics. International Journal of Fatigue, 127, 131-143.
10. Gillet, S., Jacopin, T., Joannès, S., Bedrici, N., & Laiarinandrasana, L. (2022). Short-term creep and low cycle fatigue unified criterion for a hybridised composite material. International Journal of Fatigue, 155, 106571.
11. Bernasconi, A., Cosmi, F., & Dreossi, D. (2008). Local anisotropy analysis of injection moulded fibre reinforced polymer composites. Composites Science and Technology, 68(12), 2574-2581.

  doi:10.5075/epfl-298799_978-2-9701614-0-0

LOCAL STRESS-STRAIN BEHAVIOUR IN SHORT GLASS FIBRE REINFORCED POLYMERS - A COMPARISON OF DIFFERENT SIMULATION APPROACHES WITH EXPERIMENTAL RESULTS BASED ON X-RAY COMPUTED TOMOGRAPHY DATA

Julia Maurer[a,b], Denise Krölling[b], Michael Jerabek[c], Dietmar Salaberger[c], Johann Kastner[a], Zoltán Major[b]

a: University of Applied Sciences Upper Austria, Stelzhamerstraße 23, 4600 Wels, Austria – julia.maurer@fh-wels.at
b: Institute of Polymer Product Engineering, JKU Linz, Altenberger Straße 69, 4040 Linz, Austria
c: Borealis Polyolefine GmbH, St. Peter-Straße 25, 4021 Linz, Austria

Abstract: *The objective of this work is the comparison of simulated and experimentally derived local stress-strain behaviour of short glass fibre reinforced polypropylene. For the local analysis, subvolumes of interest were extracted from computed tomography (CT) data and representative volume elements (RVEs) were simulated with Digimat. The selection was based on local strains measured by Digital Volume Correlation (DVC). Two different approaches were used for the simulations: namely the Digimat-FE Abaqus solver and the Digimat-FE FFT solver. The main focus was on the elastic behaviour, nevertheless new approaches for the comparison of the strain distribution in the plastic region were presented. Overall, the results from the Abaqus solver showed a stiffer behaviour compared to the FFT solver. Furthermore, good accordance between experiments and both simulation approaches were revealed for RVEs undergoing low strains.*

Keywords: Short Fibre Reinforced Polymers; X-ray Computed Tomography; Digital Volume Correlation; FE Simulation

1. Introduction

Discontinuous fibre reinforced polymers, especially glass fibre reinforced polypropylene, are used in many demanding engineering applications. Beside experimental characterization, numerical simulations gained importance over the last years. Thus, supporting the product design and material development. Microstructural characterization by X-ray computed tomography (CT) and interrupted in situ testing further contribute to a better understanding of the micro-mechanisms of failure and structure-property relationship.

Local strain evaluations can be performed based on a series of CT scans taken during in-situ tensile testing and evaluated using Digital Volume Corelation (DVC). This rather new approach developed 1999 [1] enables the determination of the local displacements and further the calculation of local strains in three dimensions. Therefore, the fibres are used as speckle pattern to correlate the reference volume (unloaded state) and the deformed volume (loaded state).

The modelling and simulation approaches of composites range from manufacturing process simulations to macro and micro scale simulations. Most of the microstructure details required for micromechanical models are based on process simulations or are provided by CT data. For microstructural computation of material properties, there are basically three options, namely homogenization, finite element (FE) modelling and the generalized method of cells.[2]

  doi:10.5075/epfl-298799_978-2-9701614-0-0

This study focused on finite element modelling and an alternate method based on Fast Fourier Transforms (FFT). The latter has the great advantage, that it uses a grid of regular spacing. Consequently, it avoids meshing and enables the use of real microstructure images, e.g. from CT [3]. Furthermore, the FFT approach may be considerably faster and has a smaller memory footprint [4].

The aim of these investigations is to get a deeper insight into the origin of local differences in the stress-strain behaviour inside a material. Simulations of various representative volume elements (RVEs) and the evaluation of the according experimental data was conducted.

2. Material and Methods

2.1 Short glass fibre reinforced polymers

The investigated material is short glass fibre reinforced polypropylene (homopolymer) with a fibre content of 24 wt% (PPsGF24). The glass fibre diameter is approximately 13 µm and the mean fibre length is around 470 µm.

Figure 1 shows the so-called GF-multitool, which has already been used for earlier investigations [5,6] and provides different test specimen geometries for material testing. The 0°, 45° and 90° test specimens were used to investigate the material behaviour and thus for the creation of a material model. All specimens have a thickness of 2 mm. The width and length are different, namely 10 mm and 100 mm for the 0° test specimen, 5 mm and 60 mm for the 45° specimen, and 10 mm and 50 mm for the 90° test specimen.

Constant radius (CR) test specimen geometries were milled out of the injection moulded plates in three different orientations (CR 0°, CR 45° and CR 90°). The CR specimens do have a length of 30 mm and a cross section of 3 x 2 mm² at the narrowest position. These specimens were tensile tested ex situ accompanied by Digital Image Correlation (DIC), as well as in situ by X-ray computed tomography (CT).

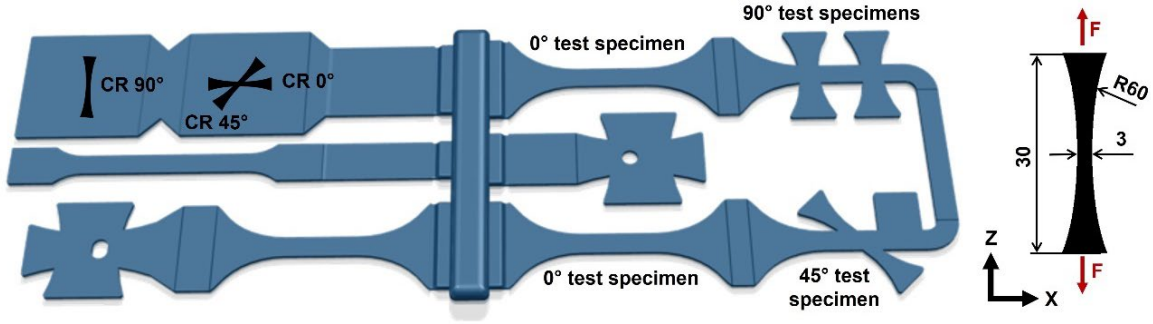

Figure 1. GF-multitool (left) with various test specimen geometries used for material testing and model generation, and CR test specimen geometry (right) used for ex and in situ testing.

2.2 Material testing

Ex situ experiments were performed with all test specimen geometries and accompanied by Digital Image Correlation (DIC). Additionally, CR test specimens were investigated in detail by X-ray computed tomography and interrupted in situ tensile tests were performed. Whereas ex situ tensile tests last only a few minutes, interrupted in situ tensile tests performed at X-ray laboratory CT devices last up to several hours, depending on the number of load steps. These

  doi:10.5075/epfl-298799_978-2-9701614-0-0

experiments were performed displacement controlled. After each load step the sample relaxes and when a steady state is reached a CT scan is performed. To minimize the necessary lead time before starting a CT scan, the relaxation behaviour was modelled with the Kohlrausch-Williams-Watts function according to [7] and the remaining lead time was estimated. Figure 2 schematically shows the difference of these two testing procedures.

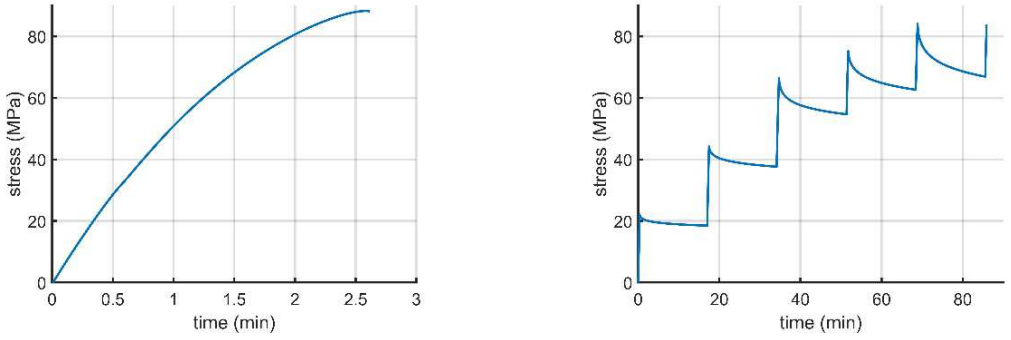

Figure 2. Stress-time curves of an monotonic ex situ tensile test (a) and an interrupted in situ tensile test (b)

The uniaxial ex situ tensile tests were performed with a Zwick/Roell Z010 testing machine and the Zwick TestXpert 146 II V3.7 software. For DIC a 1'' CCD Sensor with 6 147 megapixel and the Dantec Dynamics Istra 4D software was used. Interrupted in situ experiments were performed with the Deben CT500 tension/compression stage, designed for the use in X-ray computed tomography devices. Up to seven load steps were applied, defined as 30%, 52%, 60%, 68%, 76%, 84% and 92% of the tensile strength (estimated by an ex situ tensile test). All CR test specimen were tested with a strain rate of 1.9 x 10^{-4} s^{-1}, all others with 1 x 10^{-3} s^{-1}.

2.3 X-ray computed tomography

X-ray computed tomography (CT) allows for detailed microstructural investigation of composite materials. The CT scans were performed with a voxel edge length of 2 µm at the Nanotom 180 NF CT device (phoenix|X-ray, GE Sensing & Inspection Technologies GmbH, Wunstorf, Germany) equipped with a tungsten-on-diamond target. The acceleration voltage was 80 kV, the integration time 500 ms and the number of projection images 1800. Thus, resulting in a scanning time of approximately 1 hour. The available analysis volume is approximately 3 x 2 x 3.6 mm^3.

Based on CT data, the fibre orientation distribution was determined for all test specimen geometries with an in house developed software [8]. In addition, the fibre volume fraction was determined based on a gray value segmentation approach with Volume Graphics Studio Max (Version 3.5.1). An inclusion analysis was performed over the whole analysis volume. The gray value threshold was set in a way that a nominal fibre volume fraction of 10% was achieved. This results in a threshold value of ISO 39.5, which means that the threshold was set at 39.5% between background and material peak of the gray value histogram. According to this result, a binarization of the data set (fibre phase and matrix phase) was performed and used for the FFT simulations.

The interrupted in situ tensile tests provide additional information about the material behaviour, especially the local defect and strain formation. By using the Digital Volume Correlation (DVC) tool of Thermo Scientific™ Avizo™ Software (Version 2020.1), displacement

fields can be determined and strain tensors calculated. The necessary speckle pattern is provided by the short glass fibres and as the displacements are rather small, the global DVC approach can be used [9]. A tetrahedral mesh is generated based on the surface of the specimen, with approximately 15 000 elements using a mean edge length of approximately 200 µm. Subsequently, the correlation is performed between the reference volume data (unloaded specimen) and the deformed volume (loaded specimen).

For the selection of RVEs the analysis volume was divided into 144 subvolumes with a size of 500 x 500 x 500 µm³ and based on the local strain, some subvolumes were selected (see Figure 3). The microstructural information of these selected subvolumes was further used for FE simulations.

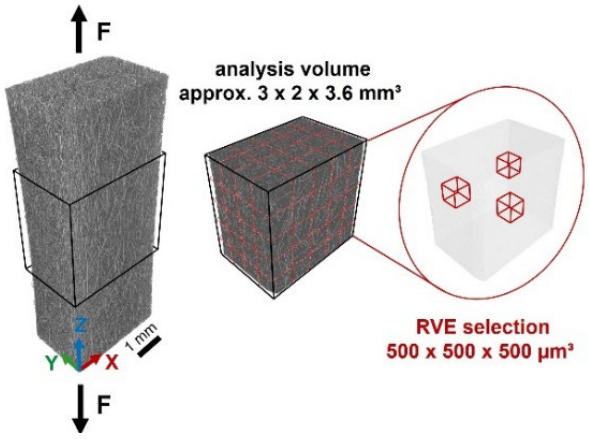

Figure 3. Schematical drawing of analysis volume and selected RVEs.

2.4 FE simulations

A suitable material model is required for the simulations, which was created by Digimat-MX (Version 2021.1). The results of the ex situ tensile tests of the 0°, 45° and 90° test specimens, as well as the fibre orientation distribution over thickness (gained by CT data evaluation) were used to calibrate a new material model by reverse engineering. Furthermore, perfectly bonded fibres were assumed, and an existing material model was used as initial condition. This iterative approach resulted in an elastic-plastic material model.

Simulations of representative volume elements (RVEs) were performed with Digitmat-FE (Version 2021.1). Two different approaches were used, namely the Digimat-FE Abaqus solver and the Digimat-FE FFT solver. Additionally, to the above mentioned elastic-plastic material model, periodic boundary conditions were applied to these simulations. No failure model was considered. The total analysis volume was divided into subvolumes with a size of 500 x 500 x 500 µm³ and based on the result of the strain analysis, several subvolumes were selected for the generation of the RVEs with the same size. Table 3 gives an overview of all simulated RVEs. For the Abaqus solver fibre properties estimated by CT data analysis - like fibre orientation, fibre length and fibre volume fraction - were used. Further, representative volume elements (RVE) were created based on the fibre characterization of the total analysis volume. The FFT solver used the binarized CT volume data (fibre phase and matrix phase). For the selected subvolumes, 8-bit raw data sets with a voxel edge length of 2 µm were analysed. The total analysis volume could not be simulated, as the data set would have been too big.

  doi:10.5075/epfl-298799_978-2-9701614-0-0

Table 3: Overview of generated RVEs (500 x 500 x 500 µm³) and information based on CT data.

RVE	aXX	aYY	aZZ	aXY	aXZ	aYZ	Fibre fraction [vol%]	Mean fibre length [µm]	Average strain [%] ($E_{zz\ last\ load\ step}$)	FE (Abaqus)	FE (FFT)
CR 0°	0.262	0.018	0.720	0.001	0.012	-0.001	10.0	494*	2.9	X	
CR 45°	0.488	0.018	0.493	-0.001	-0.235	0.003	10.0	494*	2.8	X	
CR 90°	0.674	0.025	0.301	-0.001	0.031	-0.002	10.4	494*	3.3	X	
CR 0°_#27	0.177	0.009	0.814	-0.002	-0.012	0.008	11.2	523	2.1	X	X
CR 0°_#49	0.164	0.010	0.826	-0.008	0.007	0.004	9.9	419	4.8	X	X
CR 0°_#61	0.309	0.032	0.659	0.008	-0.016	-0.010	9.1	476	4.2	X	X
CR 0°_#66	0.367	0.031	0.602	0.015	0.068	-0.027	10.4	455	2.2	X	X
CR 45°_#60	0.516	0.038	0.445	-0.001	-0.200	0.006	11.0	396	4.9	X	X
CR 45°_#116	0.445	0.009	0.545	-0.008	-0.274	0.005	10.3	510	1.8	X	X
CR 90°_#104	0.770	0.041	0.189	-0.018	0.038	-0.017	11.5	642	7.9	X	X
CR 90°_#115	0.686	0.015	0.299	-0.015	0.009	0.000	9.9	362	1.9	X	X

*nominal value (result of fixed aspect ratio and diameter)

3. Results and Discussion

3.1 Mechanical properties from experiments and simulations

For clarification of the mechanical properties and for the definition of the load steps of the in situ experiment, uniaxial tensile tests were performed. Based on these results, quantitative numbers for the mechanical properties were determined (Table 4). Further, Digimat-FE Abaqus simulations for these specimens (CR 0°, CR 45° and CR 90° RVE) were performed. The determined Young's modulus was comparable to the results gained by experiments, namely 5610 MPa (deviation of 5.5%), 3710MPa (deviation of -3.1%) and 3680MPa (deviation of 11.9%), respectively.

Table 4: Mechanical properties of the PPsGF24 CR 0°, CR 45° and CR 90° test specimen.

	CR 0°	CR 45°	CR 90°
Young's modulus [MPa]	5320	3830	3290
Tensile strength [MPa]	79.0	56.9	46.4
Nominal tensile strain at tensile strength [%]	3.0	3.7	3.9

For the selected subvolumes, the stiffness matrix was obtained with the FFT and the Abaqus solver. Figure 4 shows the results of the Young's modulus E33 and the Poisson's ratio v31 for both approaches. Overall, the results of the Abaqus approach revealed a stiffer material behaviour, which may be explained by the used meshing approach. In case of these simulations, linear mesh elements were used, which usually show a stiffer behaviour than quadratic mesh elements. Especially for high orientations in direction of the applied force (#27 and #49), the deviation in the Young's modulus was higher than 10%. This may be explained by a stronger influence of touching and connected fibres (in the binarized CT data set used for the FFT

  doi:10.5075/epfl-298799_978-2-9701614-0-0

approach) for samples with high fibre orientation. For the Poisson's ratio the differences in the results for both approaches are high, almost all exceeded 10% deviation.

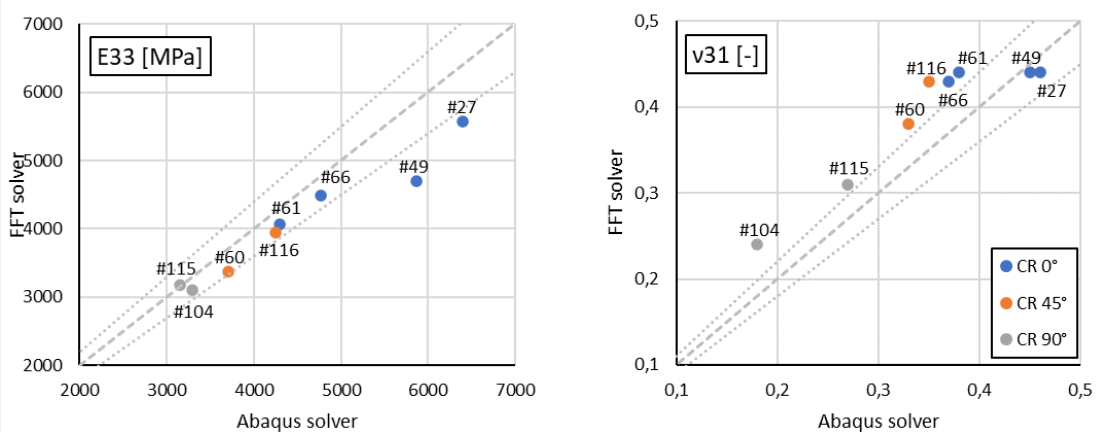

(a) (b)

Figure 4. Young's modulus E33 (a) and Poisson's ratio v31 (b) for the selected subvolumes, determined with two different simulation approaches (dotted lines mark the range of +/- 10%).

3.2 Global stress-strain behaviour

Since an elastic-plastic material model was used and perfectly bonded fibres were assumed, deviations from experimental results can be expected, especially in the plastic region. The global behaviour of in situ tested specimens show slightly lower stresses compared to monotonic tested specimens, due to the interrupted testing procedure (see Figure 5). Nevertheless, average curves were obtained based on the in situ results for all RVEs and compared with simulations.

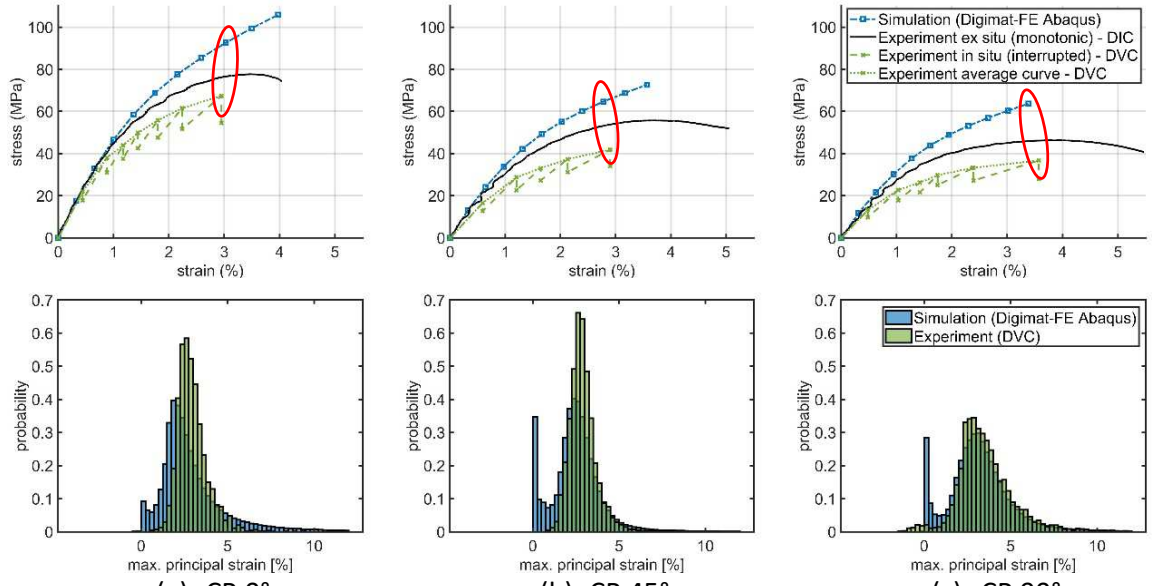

(a) CR 0° (b) CR 45° (c) CR 90°

Figure 5. Stress-strain curves (first row) and probability distributions of the maximum principal strain (second row) of experiments and simulations for 0° (a), 45° (b) and 90° (c) main fibre orientation (red ellipsoid marks increment used for probability distribution).

Concerning the strains, a distribution function was created for the Abaqus simulation result and the experimental result (Figure 5 second row). For the experimental data, the strain information

  doi:10.5075/epfl-298799_978-2-9701614-0-0 published under CC BY-NC 4.0 license

of approximately 3 600 nodes was available. In comparison, for the simulated data, the information of about 740 000 nodes was available. However, by normalizing the bins, the distributions can be compared. They showed good accordance and a clear tendency depending on the main fibre orientation. The CR 0° and the CR 45° test specimen showed the narrowest strain distribution, indicating a more homogeneous strain state, compared to the CR 90° specimen.

3.3 Local stress-strain behaviour

Good accordance between experiment and simulation was revealed for all RVEs in the elastic region, up to a strain of approximately 1.2% (selected ones are shown in Figure 6). Overall, simulations with the FFT solver showed increased accordance with the experimental data compared to the results gained with the Abaqus solver. This is also true for the plastic region. However, it must be pointed out that the stresses of the experimental curve are averaged values and not actual local values. Nevertheless, these curves can be considered as kind of limiting curves.

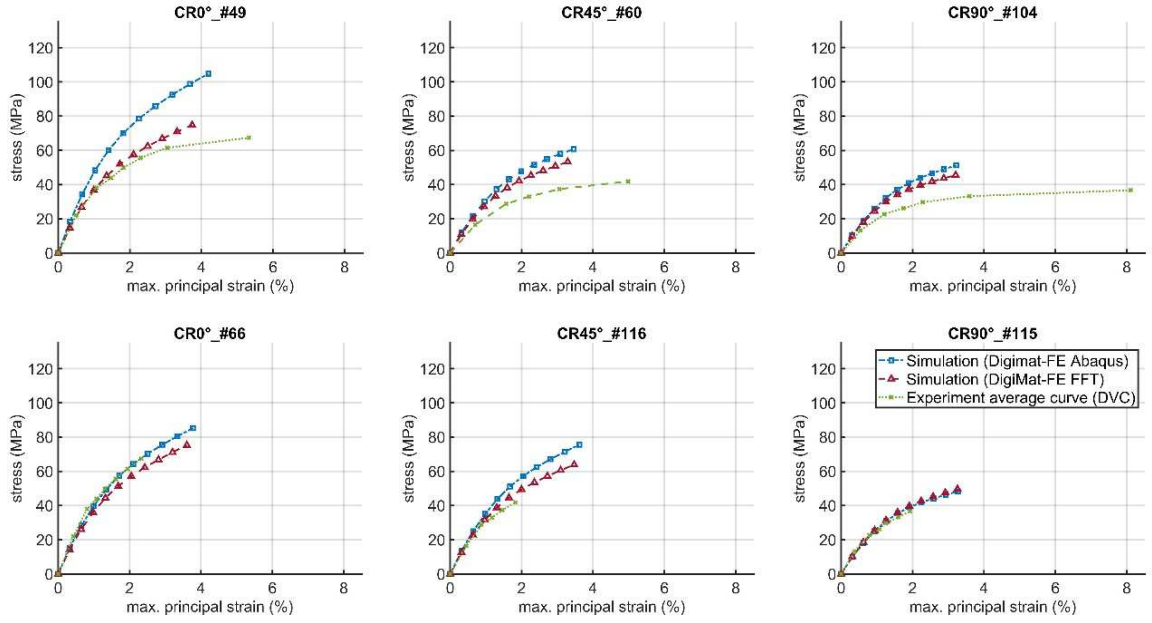

(a) CR 0° (b) CR 45° (c) CR 90°

Figure 6. Stress-strain curves from simulations and experiment for some selected subvolumes (first row - high strains, second - low strains) for CR 0° (a), CR 45° (b) and CR 90° test specimens.

4. Conclusion and Outlook

This study is one of the first publications that attempted to compare the results of the Digimat-FE FFT solver with another FE simulation approach and experimental results. The results demonstrated the influence of local fibre properties on the stress-strain behaviour. The main focus was on the elastic material behaviour, where experiments and simulations show good accordance. Further, the strain distributions of simulated and measured data were comparable. Nevertheless, more detailed DVC evaluations should be performed with smaller mesh sizes to compare results at the fibre level. The simulations at the plastic region could be further optimized by introducing a failure criterion. In addition, there are some smaller optimization parameters to focus on e.g. the settings of the mesh generation (in case of the Abaqus solver) or the voxel size and grey value threshold (in case of the FFT solver).

  doi:10.5075/epfl-298799_978-2-9701614-0-0

Acknowledgements

This project was funded by Borealis Polyolefine GmbH, Linz. Financial support was also provided by the Austrian research funding association (FFG) under the scope of the COMET programme within the research project 'Photonic Sensing for Smarter Processes (PSSP)' (contract # 871974). This programme is promoted by BMK, BMDW, the federal state of Upper Austria and the federal state of Styria, represented by SFG.

5. References

1. Bay BK, Smith TS, Fyhrie DP, Saad M. Digital volume correlation: Three-dimensional strain mapping using x-ray tomography. Exp Mech. 1999;39(3):217–26.
2. Gandhi UN, Goris S, Osswald TA, Song Y-Y. Discontinuous Fiber-Reinforced Composites - Fundamentals and Applications. Munich: Carl Hanser Verlag; 2020.
3. Moulinec H, Suquet P. A numerical method for computing the overall response of nonlinear composites with complex microstructure. Comput Methods Appl Mech Eng. 1998;157(1–2):69–94.
4. MSC Software Belgium SA. Digimat User's Manual. 2021.
5. Hartl AM. Mechanical Behavior of Short Glass Fiber Reinforced and Particle Modified Polypropylene Influence of Material Anisotropy and Loading Mode. JKU Linz ; 2014.
6. Kalteis A, Reiter M, Jerabek M, Major Z. Validation and Implementation of Failure Parameters in Integrated Simulations for Short Fibre Reinforced Polypropylene. Acta Polytech CTU Proc. 2016;7:22.
7. Maurer J, Jerabek M, Salaberger D, Thor M, Kastner J, Major Z. Stress relaxation behaviour of glass fibre reinforced thermoplastic composites and its application to the design of interrupted in situ tensile tests for investigations by X-ray computed tomography. Polym Test. 2022;109(March):107551.
8. Salaberger D. Micro-structure of discontinuous fibre polymer matrix composites determined by X-ray Computed Tomography. TU Vienna; 2019.
9. Buljac A, Jailin C, Mendoza A, Neggers J, Taillandier-Thomas T, Bouterf A, et al. Digital Volume Correlation: Review of Progress and Challenges. Exp Mech. 2018;58(5):661–708.

  doi:10.5075/epfl-298799_978-2-9701614-0-0

EFFECT OF FIBRE ORIENTATION, TEMPERATURE, MOISTURE CONTENT AND STRAIN RATE ON THE TENSILE BEHAVIOUR OF SHORT GLASS FIBRE-REINFORCED POLYAMIDE 6

D. Finazzi[a,b], R.D.B. Sevenois[a,b], L. Daelemans[a], K. De Clerck[a], W. Van Paepegem[a]

a: Department of Materials, Textiles and Chemical Engineering, Ghent University,
Technologiepark 46, 9052 Zwijnaarde, Belgium
E-mail: Daniele.Finazzi@ugent.be
b: SIM M3 Program, Technologiepark 48, 9052 Zwijnaarde, Belgium

Abstract: *The aim of this experimental study is to characterise the non-linear behaviour of short fibre-reinforced thermoplastics for the automotive industry. Tensile tests are performed on short glass fibre-reinforced polyamide 6 (PA6) and unfilled PA6 produced by injection moulding. The specimens are cut at different angles (0°, 45°, 90°) to the injection direction. Prior to testing, the material is either dried or saturated at 23°C/50% RH. The tests are then performed at different temperatures below and above the glass transition temperature (T_g), and at different strain rates (10^{-4}, 10^{-2} and 10^{-1} s^{-1}). The fibre orientation is found to affect the mechanical properties significantly. The test temperature relative to the T_g rules the transition from brittle to ductile response. Higher strain rates induce self-heating in PA6 due to plastic deformation and low thermal conductivity, although the effect on the composite is yet unknown.*

Keywords: thermoplastic composites; SFRP; glass/PA6; tensile tests; DIC

1. Introduction

Short fibre-reinforced thermoplastic composites are increasingly popular in the automotive industry thanks to low cost, short cycle times and recyclability. They can be easily injection-moulded into complex shapes. However, compared with thermoset composites or metals, they are more sensitive to environmental and loading conditions. A thorough understanding of their behaviour is thus required for safe use in components subjected to thermo-mechanical stresses, such as inlet manifolds and other parts near the engine.

Injection-moulded polyamide 6 (PA6) with short glass fibres offers attractive properties for this market and is currently being used for functional and structural parts. Some of its key features have already been investigated by various authors. Injection moulding produces a peculiar *shell-core* microstructure, whereby the fibres are mainly oriented along the injection flow direction, except for a thin layer (*core*, halfway between the mould walls) where the fibres arrange themselves at 90° to the flow direction[1,2]. This means that the material is anisotropic, and the resulting fibre orientation distribution can be quite complex according to the shape of the part. The effect of fibre orientation on the tensile performance and damage mechanism of Glass/PA6 is reported for example in [3,4,5].

PA6 is known to take up moisture from the surroundings. Water molecules break the hydrogen bonds between the chains in the amorphous phase, increasing their mobility and thus lowering the glass transition temperature (T_g). Since the material behaviour ranges from brittle below the T_g to ductile above the T_g, Parodi et al. [6] have suggested that a moisture-induced drop in

  doi:10.5075/epfl-298799_978-2-9701614-0-0

T_g is equivalent to an increase in temperature. Therefore, the effect of temperature and humidity can be combined into an *apparent temperature* $\bar{T}$ defined as follows:

$$\bar{T} = T + \left(T_{g,dry} - T_{g,wet}\right) \quad (1)$$

where T is the temperature, $T_{g,dry}$ and $T_{g,wet}$ are the T_g in the dry and moisturised conditions, respectively. This approach is successfully extended in other works to glass fibre-reinforced PA6 [4] and PA66 [7].

PA6 is also a strain rate-dependent material [8]. Wang et al. [9] have shown that the rate sensitivity of Glass/PA6 varies from below to above the T_g and is lower in the preferred fibre direction than normal to it. Moreover, polymers and polymer matrix composites are prone to self-heating: as the strain rate increases, the heat generated by plastic dissipation cannot be evacuated in time due to low thermal conductivity [10]. Although this effect is hardly touched upon for monotonic loading, and is generally relegated to dynamic tests, its relevance in quasi-static tests cannot be ruled out a priori.

Many works so far have focussed on combinations of the above-mentioned aspects: fibre volume fraction [11]; temperature and strain rate [9]; orientation and humidity [3]; orientation, temperature and humidity [4]; thickness, orientation, temperature and strain rate [5]. However, these factors are closely interconnected in determining the global behaviour of the composite. To date, a comprehensive investigation is still missing. The aim of this research work is to fully characterise the tensile behaviour of injection-moulded Glass/PA6 by assessing the impact of fibre orientation, temperature, humidity, and strain rate, including self-heating. Tests on unreinforced PA6 offer insights on the role of fibres in mitigating the matrix-dominated response.

2. Materials and methods

2.1 Materials and specimens

The material object of this study is a polyamide 6 reinforced with 50 wt% short glass fibres (DOMAMID 6LVG50H2 BK), provided by DOMO Chemicals as injection-moulded plaques (360 x 100 x 3 mm). The company has also provided plaques of unreinforced PA6. Dogbone specimens for tensile tests and rectangular beams for dynamic mechanical analysis (DMA) are machined from the plaques, at specific locations so as to minimise edge effects and at different angles (0°, 45°, 90°) to the injection direction. The shape and dimensions of the tensile specimens are shown in Fig. 1.

2.2 Conditioning

Before testing, the specimens are conditioned to equilibrium at two relative humidities: dry (0%RH) and 23°C/50%RH. Accelerated conditioning is used to speed up the sorption/desorption kinetics as follows:

- dry: the specimens are kept at 80°C for 7 days (enough for the weight to stabilise) and then stored in a desiccator with silica gel at room temperature;
- 50%RH: adhering to the ISO 1110 standard [12], the specimens are kept at 70°C inside a container with a saturated KI solution for 11 days, and then stored in a room with controlled atmosphere 23°C/50%RH.

  doi:10.5075/epfl-298799_978-2-9701614-0-0

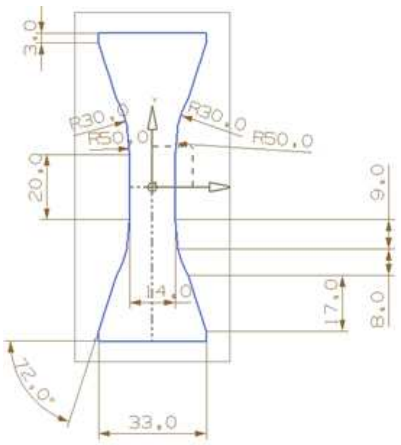

Figure 1. Dogbone specimen for tensile tests.

2.3 Dynamic mechanical analysis (DMA)

DMA tests are carried out in three-point bending on a TA Instruments Q800 Dynamic Mechanical Analyser. The T_g in the dry and 50%RH conditions is determined from a 2 °C/min temperature ramp at single frequency (1 Hz).

2.4 Tensile testing

The variables considered for the tensile test campaign are summarised in Table 1. Tests at room temperature are performed on both dry and 50%RH material. The choice of the other test temperatures is made by keeping the same distance from the T_g in the two cases.

Table 1. Summary of the test conditions. (RT = room temperature)

Fibre orientation	0°, 45°, 90°, PA6 (unfilled)
Humidity	dry, 50%RH
Temperature	*dry:* RT, 100°C, 120°C *50%RH:* RT, 50°C, 70°C
Strain rate	10^{-4} s^{-1}, 10^{-2} s^{-1}, 10^{-1} s^{-1}
Test mode	monotonic, loading/unloading/reloading

The tensile tests are performed on a servo-hydraulic Instron 8801 with a 50 kN load cell and an all-electric Instron ElectroPuls E10000 with a 10 kN load cell. The latter is equipped with an Instron 3119-600 Series environmental chamber, which is used for the tests above room temperature. Variation of the moisture content during a test at a given temperature is checked by weighing a reference sample before and after the test and is found to be acceptable in all cases. Strains are mapped full-field on the specimen surface by means of stereo digital image correlation (DIC), using two GS3-U3-51S5M-C 2/3" FLIR Grasshopper®3 cameras fitted with 35 mm-focal-length KOWA LM35JC lenses. A FLIR A6750sc infrared (IR) camera is calibrated together with the DIC cameras via the Vic-3D 9 software (Correlated solutions), so that the temperature field can also be tracked on the deformed surface, see Fig. 2. Synchronisation of all

  doi:10.5075/epfl-298799_978-2-9701614-0-0

the data streams (load cell analog signal, DIC images, IR images) is achieved by hardware triggering.

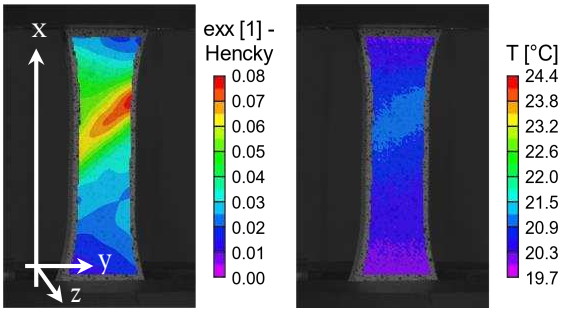

*Figure 2. Strain field (*left*) and temperature field (*right*) are mapped simultaneously during a tensile test, with* x *being the load direction. (The specimen represented here was cut at 45° to the injection direction.)*

The DIC images are processed with Vic-3D 9. True (logarithmic) strains are computed and the average value over the gauge region of the specimen is extracted.

True stress is calculated from the following formulation, under the assumption of transverse isotropy ($\varepsilon_{yy} = \varepsilon_{zz}$):

$$\sigma = \frac{F}{A_0} e^{-2\varepsilon_{yy}} \tag{2}$$

where: F is the force signal coming from the load cell; A_0 is the initial cross-sectional area, measured with a calliper on the specimen before the test; ε_{yy} is the transverse (true) strain, extracted from DIC as detailed above.

3. Results and Discussion

3.1 Glass transition temperature

The T_g (peak of $\tan\delta$) of PA6 is found to be around 68 °C in the dry state and 17 °C in the 50%RH state. Therefore, in Eq. (1) $T_{g,dry} - T_{g,wet} \approx 50$ °C. This justifies the choice of temperatures for the tensile tests.

3.2 Effect of fibre orientation

Representative stress-strain curves at room temperature, in the dry condition, at 10^{-4} s^{-1} are reported in Fig. 3 for the 0°, 45° and 90° orientations and the neat PA6. The results are in line with what reported in the literature [3,5]. The 0° orientation has the highest elastic modulus and tensile strength, but also the lowest strain at break: most of the fibres are favourably oriented to carry the load. The response at 45° seems closer to 90° than it is to 0°. In dry conditions and at room temperature, PA6 is below its T_g, producing a brittle behaviour. Overall, the reinforcing effect of glass fibres over neat PA6 is evident, both in terms of stiffness and strength.

  doi:10.5075/epfl-298799_978-2-9701614-0-0

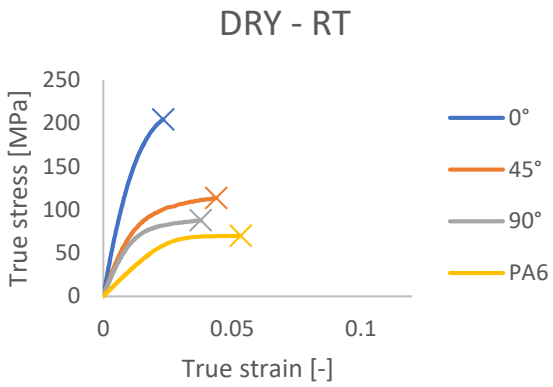

Figure 3. Stress-strain curves at room temperature in the dry condition (10^{-4} s^{-1}).

3.3 Effect of temperature and humidity

Figure 4 shows representative stress-strain curves at 10^{-4} s^{-1} for all the combinations of fibre orientation, temperature and humidity. At room temperature, a lower T_g in the 50%RH condition accounts for reduced strength and modulus and enhanced ductility compared to the dry material. The other temperatures have been chosen to produce the same apparent temperature (above T_g) between dry and 50%RH, thus expecting the similar response that is presented here. However, when looking at the quantitative properties, 50%RH gives a higher elastic modulus than dry for all orientations and apparent temperatures. Although more repetitions are needed for statistical significance, the increase ranges from +10% for 0° specimens to as high as +50% for unfilled PA6. This seems to contradict the temperature-humidity equivalence claimed by other authors. Further investigations are underway to get a clearer picture. Another remark, as noted by Jia and Kagan [13], is that, while temperature and moisture individually do improve ductility, the combination of moisture with high temperature seems to yield the opposite result. In fact, all the 50%RH specimens failed sooner than the dry counterparts tested at the same apparent temperature, although the reason for this is yet to be clarified.

3.4 Effect of strain rate: self-heating

Tests conducted on 50%RH PA6 at room temperature reveal that a strain rate of 10^{-2} s^{-1} is enough to produce self-heating in the specimens, see Fig. 5. This is not observed at 10^{-4} s^{-1}, nor on dry PA6 where failure occurs at relatively low strains. Thus, 10^{-2} s^{-1} could be taken as the critical strain rate in the transition from isothermal to adiabatic conditions. It should be noted that the critical strain is a function not only of the thermal diffusivity of the material, but also of the geometry of the test specimen [8]. Even steeper temperature rises are expected at 10^{-1} s^{-1}. The next step will be to assess the relevance on the composite and at higher temperatures, and how this interferes with the embrittling effect normally associated to higher strain rates.

  doi:10.5075/epfl-298799_978-2-9701614-0-0

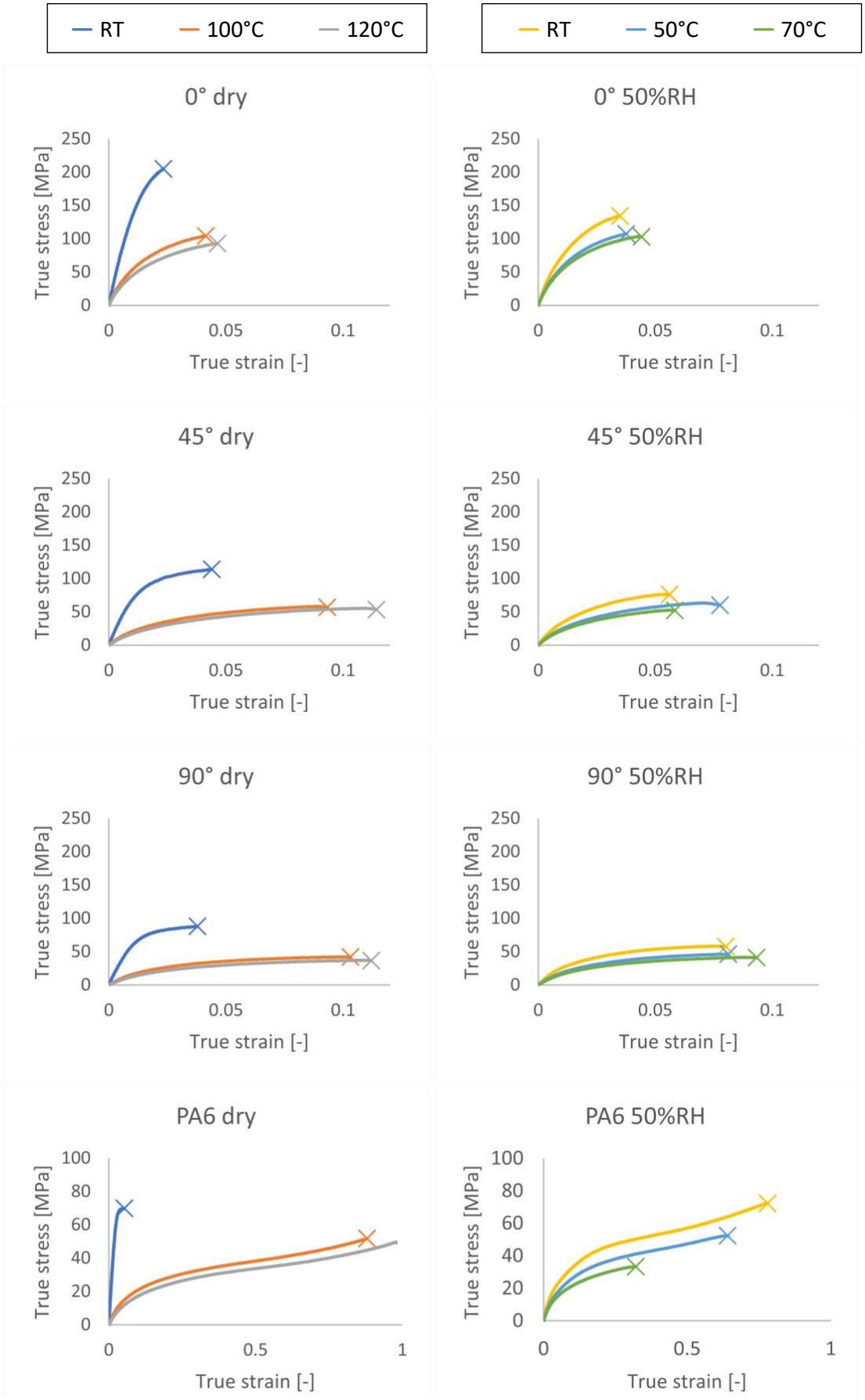

*Figure 4. Stress-strain curves at different temperatures for the dry (*left column*) and 50%RH (*right column*) conditions.*

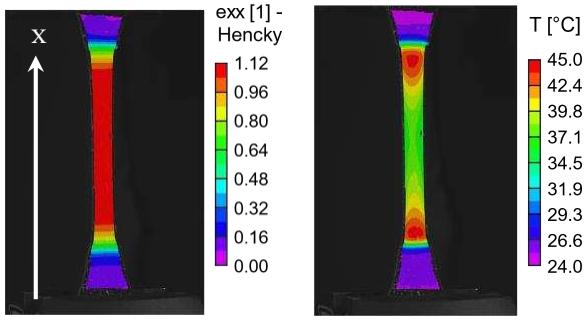

*Figure 5. Strain field (*left*) and temperature field (*right*) during a test at 10^{-2} s^{-1}, room temperature, on 50%RH PA6. The temperature reached by the material during deformation can grow significantly higher than the test temperature.*

4. Conclusion

The tensile response of injection-moulded Glass/PA6 has been studied under the influence of fibre orientation, temperature, humidity, and strain rate. The effect of the individual variables is in good agreement with previous studies. However, the equivalence between temperature and humidity is not fully confirmed in its simple, linear form. Also, quasi-static strain rates can induce self-heating in PA6, with possible influence on the rate-dependent response of the composite. Correct interpretation of these phenomena will be enabled as the test campaign proceeds.

The work will be completed by including:

- scanning electron microscopy (SEM) on fracture surfaces for interpretation of failure mechanisms;
- loading/unloading/reloading tests to capture the development of plastic deformation;
- analysis of fibre orientation distribution and fibre statistics by micro-computed tomography (CT);
- characterisation of viscoelastic behaviour (time-temperature superposition) by DMA;
- thermal analysis by differential scanning calorimetry (DSC).

Acknowledgements

The work leading to this publication has been funded by the ICON project “ProPeL”, which fits in the MacroModelMat (M3) research program, coordinated by Siemens (Siemens Digital Industries Software, Belgium) and funded by SIM (Strategic Initiative Materials in Flanders) and VLAIO (Flemish government agency Flanders Innovation & Entrepeneurship).

Research Foundation Flanders FWO, grant number 12R3221N.

The authors gratefully acknowledge DOMO Chemicals for providing the materials.

5. References

1. Bernasconi A, Cosmi F, Dreossi D. Local anisotropy analysis of injection moulded fibre reinforced polymer composites. Composites Science and Technology 2008; 68:2574-2581.

2. Rolland H, Saintier N, Robert G. Damage mechanisms in short glass fibre reinforced thermoplastics during in situ microtomography tensile tests. Composites Part B: Engineering 2016; 90:365-377.
3. Rolland H, Saintier N, Wilson P, Merzeau J, Robert G. In situ X-ray tomography investigation on damage mechanisms in short glass fibre reinforced thermoplastics: Effects of fibre orientation and relative humidity. Composites Part B: Engineering 2017; 109:170-186.
4. Pastukhov L, Leonid V, Kanters MJW, Engels TAP, Govaert LE. Influence of fiber orientation, temperature and relative humidity on the long-term performance of short glass fiber reinforced polyamide 6. Journal of Applied Polymer Science 2021; 138:1-19.
5. Mortazavian S, Fatemi A. Effects of fiber orientation and anisotropy on tensile strength and elastic modulus of short fiber reinforced polymer composites. Composites Part B: Engineering 2015; 72:116-129.
6. Parodi E, Peters GWM, Govaert LE. Prediction of plasticity-controlled failure in polyamide 6: Influence of temperature and relative humidity. Journal of Applied Polymer Science 2018; 135:45942.
7. Launay A, Marco Y, Maitournam MH, Raoult I. Modelling the influence of temperature and relative humidity on the time-dependent mechanical behaviour of a short glass fibre reinforced polyamide. Mechanics of Materials 2013; 56:1-10.
8. Shan G, Yang W, Yang M, Xie B, Feng J, Fu Q. Effect of temperature and strain rate on the tensile deformation of polyamide 6. Polymer 2007; 48:2958-2968.
9. Wang Z, Zhou Y, Mallick PK. Effects of temperature and strain rate on the tensile behavior of short fiber reinforced polyamide-6. Polymer Composites 2002; 23:858-871.
10. Sorini C, Chattopadhyay A, Goldberg R. Micromechanical modeling of the effects of adiabatic heating on the high strain rate deformation of polymer matrix composites. Composites Structures 2019; 215:377-384.
11. Bernasconi A, Cosmi F. Analysis of the dependence of the tensile behaviour of a short fibre reinforced polyamide upon fibre volume fraction, length and orientation. Procedia Engineering 2011; 10:2129-2134.
12. International Organization for Standardization. ISO 1110:1995. Plastics – Polyamides – Accelerated conditioning of test specimens. 1995
13. Jia N, Kagan V. Mechanical Performance of Polyamides with Influence of Moisture and Temperature – Accurate Evaluation and Better Understanding. Plastics Failure Analysis and Prevention 2001; 95-104.

  doi:10.5075/epfl-298799_978-2-9701614-0-0

A MODE II TESTING METHOD FOR HYBRID COMPOSITES

Tommaso, Scalici[a], Brian G., Falzon[b], Giuseppe, Catalanotti[c]

a: School of Mechanical and Aerospace Engineering, Queen's University Belfast, Ashby Building, Stranmillis Road, Belfast, BT9 5AH, United Kingdom – t.scalici@qub.ac.uk
b: School of Engineering, RMIT University, Melbourne, Victoria, 3000, Australia
c: Escola de Ciências e Tecnologia, Universidade de Évora, Colégio Luis António Verney, Rua Romão Ramalho, 59, Évora, 7000-671, Portugal

Abstract: *A modified Transverse Crack Tension (mTCT) test method previously proposed for the characterization of Mode II interlaminar fracture toughness in monolithic laminates is extended to the case of hybrid laminates. Variations in specimen geometry and materials are investigated numerically to derive an optimum geometry and explore the range of applicability.*

Keywords: Mode II delamination fracture toughness; transverse crack tension specimen; Hybrid composites.

1. Introduction

Carbon fibre composites have seen an increasing level of utilisation in transportation vehicles due to their high specific stiffness and strength. Moreover, the application of composite materials allows to better optimize the structure and increase its robustness [1].

Nonetheless, certain challenges still persist in the utilisation of composite materials, particularly in ensuring the integrity of structural joints, without extensive physical testing to meet certification requirements.

In general, mechanical fastening is the most reliable and preferred joining technique for metallic parts. Reversibility and relative ease of inspection are two of the characteristics that make this class of joint particularly appealing especially from the point of view of maintenance operations, reducing operational costs. In composite joints, stress concentrations and local delaminations, sometimes induced during manufacturing, (i.e, hole drilling) may dramatically reduce their efficiency [2]. It has been estimated that, in the case of composite laminates, the strength is reduced by up the 30% [3]. They are also prone to static failure (e.g., bearing, net tension [4], shear-out or pull-through [5]). To mitigate these inherent problems, a local increase in thickness around a mechanical fastener is often used, thus increasing the weight, the complexity of the manufacturing process and, as a consequence, the final cost of the structure. For the reasons presented above, the relatively low efficiency and reliability of conventional bolted joints in composites drastically limit their use. This has motivated researchers and engineers to explore this class of joints to gain a deeper understanding of the failure mechanisms aimed at informing new design approaches and strategies [6-9].

To enhance the compatibility of mechanically fastened joints with composite structures, usually, the part thickness is locally increased. This approach leads to complex geometries, an increase of total weight and higher costs due to a more complex manufacturing process. Moreover, from a mechanical point of view, eccentricities and variations in the thickness may lead to spurious loads that may affect the final performance of the structure. To prevent the effects due to

  doi:10.5075/epfl-298799_978-2-9701614-0-0

thickness variation, local hybridization with metallic interleaves has been proposed in recent years [10,11].

In Figure 1 three different regions can be identified: i) the hybrid region where metal plies are uniformly distributed through the material thickness and where the hole is usually located; ii) the transition region where the metal plies are terminated and where delaminations may initiate; iii) the CFRP/composite region consisting of a monolithic composite. Usually, the delaminations are mode II dominant due to the constraining action of the bolt head.

Figure 1 - Schematic representation of a locally hybridized mechanically fastened joint

It is clear that, with the aim to develop reliable numerical models and design approaches, the knowledge of the interface properties such as the strength and the interlaminar fracture toughness of the metal/composite interface is crucial. This work focuses on the development of an experimental method for the determination of the mode II interlaminar fracture toughness for cracks propagating between dissimilar materials; i.e. in the metal/composite interface in the case of hybrid laminates. In the case of monolithic composites, the End Notched Flexure (ENF) test was adopted as a standard method [12]. However, this standard requires a large number of test repetitions at different crack lengths for calibration purposes and secondary effects such as friction may affect the calculation of the energy release rate.

In a previous work [13], the Authors proposed to modify a Transverse crack tension test composite specimen to overcome the well-known drawbacks observed and reported in the available literature [11,15-17]. Through experimental observation, it was demonstrated that an mTCT (modified Transverse Crack Tension sample) allows measuring the steady-state value of the energy release rate in the case of a pure Mode II. In the present paper, the authors propose to extend the mTCT test to the case of a hybrid interface. In essence, each specimen geometry has two metallic plies over a unidirectional composite core split into two symmetric portions by a central transverse cut orthogonal to the fibre direction. Two release films are placed across the central cut (through-thickness crack) at the interface between the metal layers and the composite core, thus creating four symmetric crack tips. The tensile loading then activates four parallel cracks at the metal-composite interface (Figure 2).

A parametric numerical model was used to study how the mode-mixity vary with the elastic properties of the material and the sample geometry. Results show that the mTCT may be taken under consideration as a candidate for the assessment of the mode II fracture toughness properties of metal/composite interfaces.

  doi:10.5075/epfl-298799_978-2-9701614-0-0

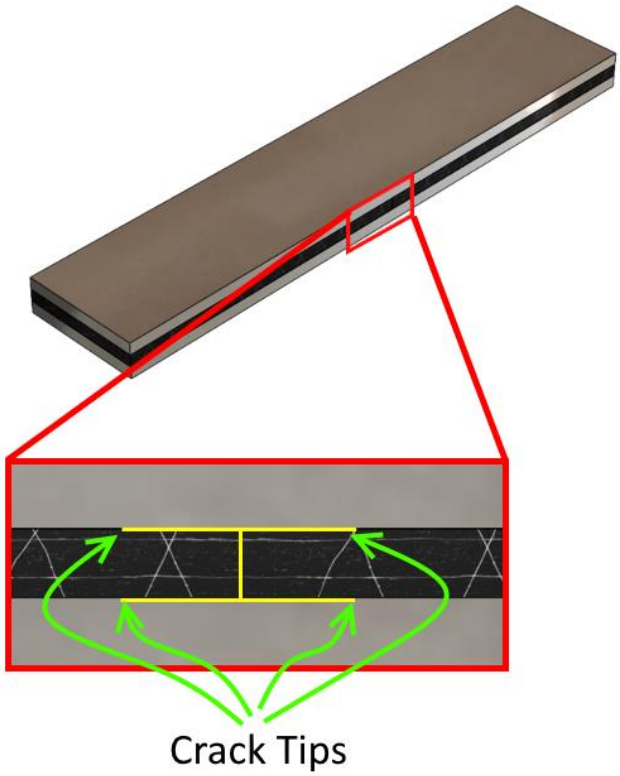

Figure 2 - Schematic view of a hybrid mTCT test specimen

2. Numerical model

2.1 Analytical framework

In the case of a monolithic composite, the Energy Release Rate (ERR) $\mathcal{G}_{II}$ can be computed as [11,13, 18-21]:

$$\mathcal{G}_{II} = \sigma^2 \frac{H}{2E_1}\left(\frac{1}{\eta} - 1\right) \quad , \tag{1}$$

where σ is the remote stress, E_1 is the Young's modulus of the composite, $\eta = \frac{\hat{H}}{H}$ with $2\hat{H}$ equal to the total thickness of the continuous layers and the other variables defined as in Figure 3.

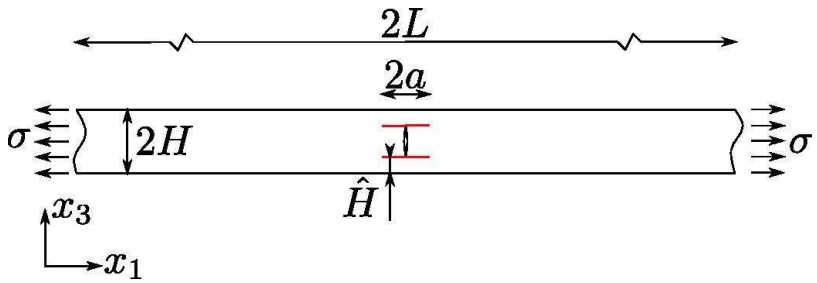

Figure 3 – Schematic representation of an mTCT sample

Alternatively, for an orthotropic material the ERR can be expressed in terms of the Stress Intensity Factor (SIF),

$$\mathcal{G}_{II} = \left(b_{11}b_{33}\frac{1+\rho}{2}\right)^{\frac{1}{2}}\lambda^{1/4}\mathcal{K}_{II}^2 \quad , \tag{2}$$

where

- $b_{ij} = s_{ij} - s_{i2}s_{j2}/s_{22}$;
- s_{ij} are the elements of the compliance matrix;
- $\lambda = b_{11}/b_{33}$;
- $\rho = \frac{2b_{13}+b_{22}}{2\sqrt{b_{11}b_{33}}}$;
- $\mathcal{K}_{II} = \sigma\sqrt{H}\chi$ is the stress intensity factor;
- χ is the geometry correction factor defined as $\chi = \chi(\alpha, \eta, \lambda, \rho)$ where $\alpha = \frac{a}{H}$;
- a is the crack length.

Moreover, for hybrid composites (Figure 2), Eq. 1 can be written as [11]

$$\mathcal{G}_{IIc} = \frac{1}{\Psi}(\sigma - \Delta T\Delta\alpha\eta E_m)^2 \quad , \tag{3}$$

with

$$\Psi = \frac{2E_1[(1-\eta)-(1-k)\varphi\eta][1-(1-k)\varphi\eta]}{H\eta} \quad , \tag{4}$$

where

- ΔT is the thermal step between test and laminate curing temperatures;
- $\Delta\alpha$ is the difference between the coefficients of thermal expansion;
- E_m is the Young's modulus of the metal;
- $\kappa = \frac{E_m}{E_1}$;
- $\varphi = \frac{Thickness\ of\ the\ metal\ layer}{Thickness\ of\ the\ cut\ plies}$;

If a thin layer of a room temperature cure adhesive (e.g., cyanoacrylate) is used to create the bonding interface, the contribution due to the coefficients of thermal expansion is negligible. To account for the influence of two different materials, the geometry correction factor can be modified to

$$\chi = \chi(\alpha, \eta, \varphi, \lambda, \rho, \kappa, \tau) \quad , \tag{5}$$

where $\kappa = \frac{E_m}{E_1}$ and $\tau = \frac{E_{metal}}{G_{metal}}$ were added to fully define the material.

Eq. 5 gives dimensionless material parameters that can be investigated by using numerical simulations. The consequential parametrical analysis allows the study of mode-mixity for this kind of geometry and calculate the geometry correction factor. To this aim, the parameter ψ is defined as:

$$\psi = \frac{\mathcal{G}_{II}}{\mathcal{G}_{II}+\mathcal{G}_{I}} \quad (6)$$

where $\mathcal{G}_I$ and $\mathcal{G}_{II}$ are the mode I and mode II energy release rate, respectively. It is worth noting that $\psi = 0.0$ corresponds to a pure mode I. Otherwise, $\psi = 1.0$ corresponds to a pure mode II.

Table 1 – Summary of the model parameters

Param.	Definition	Values
η	$\eta = \frac{\widehat{H}}{H}$	$[0.1,\ 0.25,\ 0.5]$
α	$\alpha = \frac{a}{H}$	$[0.05,\ 0.25,\ 0.5,\ 0.75,\ 1.0,\ 1.5,\ 2.0,\ 2.5, \infty]$
ρ	$\rho = \frac{2b_{13} + b_{22}}{2\sqrt{b_{11}b_{33}}}$	$[1.0,\ 5.0,\ 10.0,\ 15.0,\ 20.0]$
λ	$\lambda = b_{11}/b_{33}$	$[0.01, 0.02, 0.03, 0.05, 0.1, 0.2, 0.3]$
φ	$\varphi = \frac{Thickness\ of\ the\ metal\ layer}{Thickness\ of\ the\ cut\ plies}$	$[0.0,\ 0.1,\ 0.25,\ 0.5,\ 1.0]$
τ	$\tau = \frac{E_{metal}}{G_{metal}}$	$[1.0,\ 1.5,\ 2.0,\ 2.5,\ 3.0]$
κ	$\kappa = \frac{E_{metal}}{E_1}$	$[0.5,\ 0.75,\ 1.0,\ 1.25]$

A parametric analysis was used to compute the mode mixity for different geometry and material conditions by using Abaqus [22]. The test coupon was modelled as a 2D structure using rectangular shell elements CPE4R (four-node plane strain elements). Due to the high degree of symmetry, just a quarter of the sample was modelled. A linear-elastic analysis was performed. The Virtual Crack Closure Technique (VCCT) was used to compute $\mathcal{G}_I$ and $\mathcal{G}_{II}$. Table 1 summarizes the parameters used for the analysis.

3. Results

Figure 4 (a) reports the mode mixity ψ as a function of the normalized crack length, $\alpha = a/H$, with a being the crack length and H the sample thickness. From Eq. 6, $\psi = 0$ and $\psi = 1$ correspond to pure mode I and pure mode II, respectively.

  doi:10.5075/epfl-298799_978-2-9701614-0-0

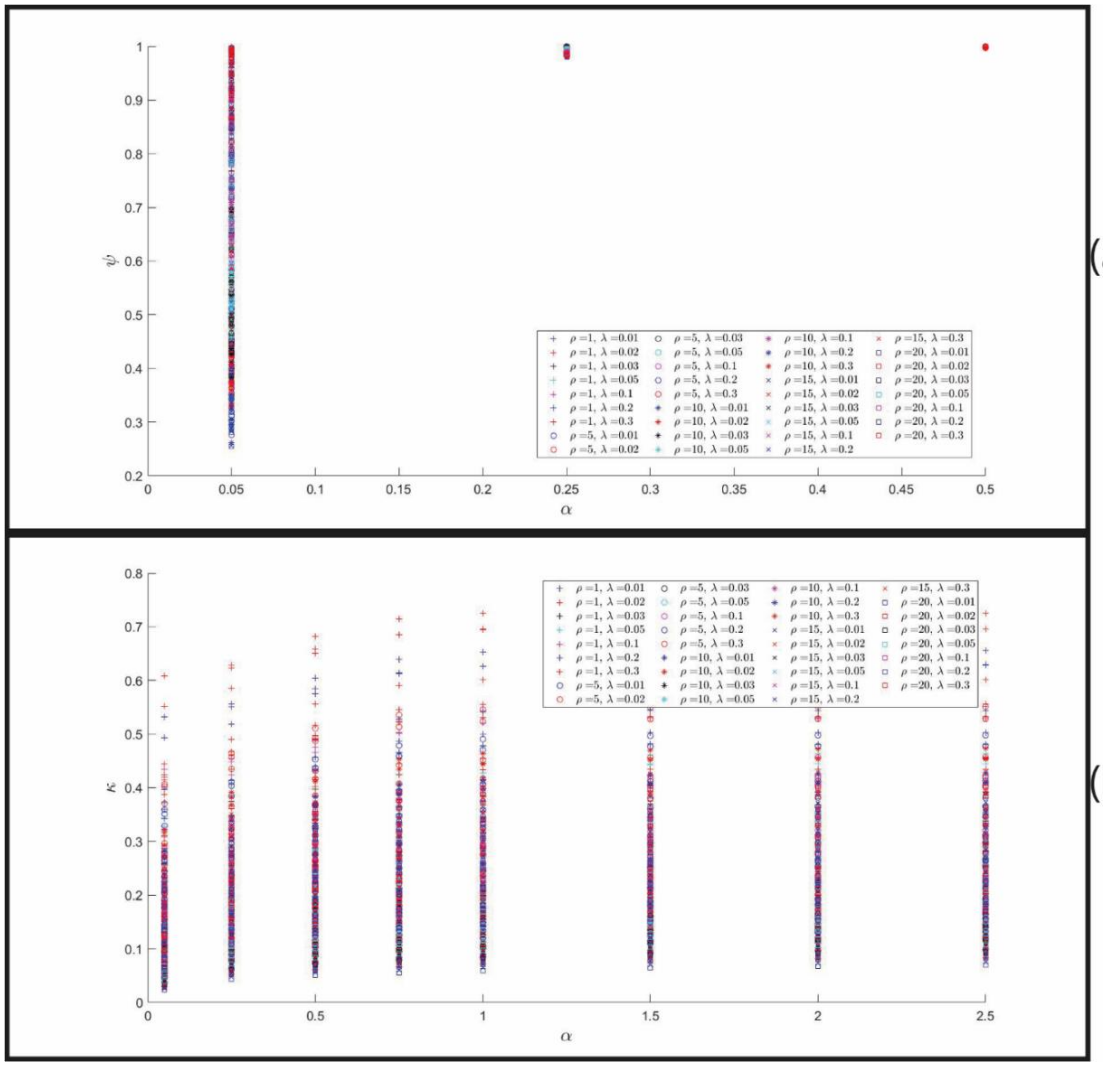

Figure 4 – Results of the parametrical analysis – (a) ψ $vs.\alpha$ curve; (b) χ $vs.\alpha$ curve

According to Figure 4 (a), the crack does not propagate in pure mode II as $\alpha \to 0$. The pure mode II conditions are reached for $\alpha > 0.25$. In other words, an artificial crack with a length greater than $0.25 * H$ must be used to obtain a pure mode II. Figure 4 (b) report the trends of the correction factors as a function of α. The values stabilize for $\alpha > 2.5$.

4. Conclusions

This work focused on the development of a robust method for the measurement of mode II fracture toughness in hybrid composites. The main conclusions may be summarized as follows:

- A parametrical numerical model was developed to simulate different specimen parameters to generalize the method;
- Results show that a robust and reliable test, based on a modified transverse crack tension (m-TCT) specimen can be utilised to assess the Mode II fracture toughness.

Acknowledgements

This study was conducted as part of the Belfast Maritime Consortium UKRI Strength in Places project, 'Decarbonisation of Maritime Transportation: A return to Commercial Sailing' led by Artemis Technologies, Project no. 107138.

5. References

1. Matthews FL. Load-carrying joints. In: Middleton DH, editor. Composite materials in aircraft structures. Longman aviation technology series; 1990.
2. Srinivasa DT, Finegan J, Gibson RF. Mechanics of mechanically fastened joints in polymer–matrix composite structures – a review. Composite Science and Technology 2009 ;69:301–29
3. Catalanotti, G. Hybrid joints for multi-material train structures, PhD dissertation, University of Porto, 2011.
4. Catalanotti, G., Camanho, PP., Ghys, P., Marques, AT. An efficient design method for multi-material bolted joints used in the railway industry. Composite Structures 2011; 94(1), 246-252.
5. Catalanotti, G., & Camanho, P. P. A semi-analytical method to predict net-tension failure of mechanically fastened joints in composite laminates. Composites Science and Technology 2013; 76, 69-76.
6. Camanho, PP, Matthews, FL. Stress analysis and strength prediction of mechanically fastened joints in FRP: a review. Composites: Part A 1997; 28A:529–47.
7. Fiore, V, Calabrese, L, Scalici, T, Bruzzaniti, P, Valenza, A. Experimental design of the bearing performances of flax fiber reinforced epoxy composites by a failure map. Composite Part B: Engineering 2018; 148:40-48.
8. Calabrese, L , Fiore, V, Scalici, T, Bruzzaniti, P, Valenza, A. Failure maps to assess bearing performances of glass composite laminates. Polymer Composites 2019; 40(3):1087-96.
9. Xiao Y, Ishikawa T. Bearing strength and failure behavior of bolted composite joints. Composite Science and Technology 2005; 65:1022–31
10. Kolesnikov, B, Herrmann, AS, Pabsch A. European patent EP 1 082 217 B1. In: Composite material with a reinforced connecting area. Applicant: German Aerospace Center DLR. Application date: March 1999.
11. Fink, A, Camanho, PP, Andrés, JM, Pfeiffer, E, Obst, A. Hybrid CFRP/titanium bolted joints: Performance assessment and application to a spacecraft payload adaptor. Composites Science and Technology 2010; 70:305-317.
12. ASTM D7905/D7905M-14, Standard test method for determination of the mode II interlaminar fracture toughness of unidirectional fiber-reinforced polymer matrix composites; 2014.
13. T Scalici T, Pitarresi, G, Catalanotti, G, van der Meer, FP, Valenza, A. The transverse crack tension test revisited: An experimental and numerical study. Composite Structures 2016;158:144-159
14. Prinz, R. Ermittlung der Energiefreisetzungsraten GIc und GIIc für das CFK-Laminat M40/Code69 1989. Internal document IB-131-89/34 German Aerospace Center
15. Prinz R, Gädke, M. Characterization of interlaminar mode I and mode II fracture in CFRP laminates 1991. In: Proceedings of international conference on spacecraft structures and mechanical testing; p. 97–102.
16. Wisnom, MR. On the increase in fracture energy with thickness in delamination of unidirectional glass fibre-epoxy with cut central plies. Journal of reinforced plastics 1992. 11(8):897-909

  doi:10.5075/epfl-298799_978-2-9701614-0-0

17. Cui, W, Wisnom, MR, Jones, M. An experimental and analytical study of delamination of unidirectional specimens with cut central plies. Journal of reinforced plastics 1994; 13(8):722-739
18. Pitarresi, G, Scalici, T, Dellaira, M, Catalanotti, G. A methodology for the rapid characterization of Mode II delamination fatigue threshold in FRP composites. Enginering fracture mechanics 2019; 220:106629
19. Catalanotti, G, Scalici, T, Pitarresi, G, Van Der Meer, FP. The effect of the through-the-thickness compressive stress on mode II interlaminar fracture toughness. In: ICCM International Conferences on Composite Materials, 2017.
20. Catalanotti, G, Furtado, C, Scalici, T, Pitarresi, G, van der Meer, FP, Camanho, PP. The effect of through-thickness compressive stress on mode II interlaminar fracture toughness. Composite Structures 2017. 182:153-163.
21. Pitarresi, G, Scalici, T, Catalanotti, G. Infrared Thermography assisted evaluation of static and fatigue Mode II fracture toughness in FRP composites. Composite structures 2019; 226:111220
22. Simulia, Abaqus (2018) User's Manual. Provid RI, USA DS SIMULIA Corp, 2018.

DEPLOYABLE COMPOSITE MESHES – MODELLING, MANUFACTURE AND CHARACTERISATION

Gokul Ganesh, Murali[a]; Paul, Robinson[a]; Alexander, Bismarck[b]; and Christoph, Burgstaller[c]

a: The Composites Centre, Department of Aeronautics, Imperial College London, South Kensington Campus, SW7 2AZ, London, United Kingdom. E-mail: g.murali@imperial.ac.uk

b: Polymer and Composite Engineering (PaCE) group, Department of Material Chemistry, University of Vienna, Waehringer Strasse 42, A-1090 Wien, Austria.

c: Transfercenter für Kunststofftechnik (TCKT), Franz-Fritsch-Straße 11, A-4600 Wels, Austria

Abstract: This paper describes the design and manufacture of a laminate which, when heated, will deploy into an expanded mesh. The design exploits the bending and/or twisting curvature that results when a non-symmetric laminate is subjected to a temperature change. To ensure the mesh laminate is almost flat after curing (i.e. prior to deployment), layups consisting of non-symmetric sublaminates separated by thermoplastic interleaves have been developed . When such a laminate is subsequently heated above the T_g of the thermoplastic layers, the mesh deploys. Two different layups are investigated; one deploys into a planar mesh and the other deploys into a mesh which forms a curved surface.

Keywords: Interleaved, Deployment, Non-symmetric, Thermoplastic, FEA

1. Introduction

Interleaved composites have been studied for their shape memory properties (1–7). In these studies, interleaved composite laminates have commonly been made of carbon fibre reinforced epoxy polymer (CFRP) plies interleaved with thermoplastic polystyrene (PS) films. When these composites are heated from room temperature, T^R, to T^H (where $\mathbf{T^R}<T_{g\text{-}PS}<\mathbf{T^H}<T_{g\text{-}CFRP}$ in which $T_{g\text{-}PS}$ is the glass transition temperature of PS, and $T_{g\text{-}CFRP}$ is the glass transition temperature of CFRP), the CFRP plies can slip relative to each other and, consequently, the flexural stiffness of the composite laminate is greatly reduced.

The shape memory behaviour of these interleaved composites is illustrated in Figure 1. In the low stiffness state (at T^H) the CFRP-PS composite is capable of large deformations at low deformation forces and bending stresses are developed in each CFRP ply as shown in the figure. If the deformed CFRP-PS composite is brought back to T^R and the deformation load is subsequently removed, the deformed shape will be retained with only a slight springback. The deformed shape of the composite is retained as the composite (now at T^R) once again possesses its full flexural stiffness. In this retained deformed shape, there are still stresses stored in the CFRP plies (see “Composite shape fixed” column of Figure 1). When the composite is reheated to temperature T^H, the CFRP plies are free to slide relative to each other, and so, return to their original flat shape.

  doi:10.5075/epfl-298799_978-2-9701614-0-0

Figure 1. Shape memory behaviour of interleaved composites

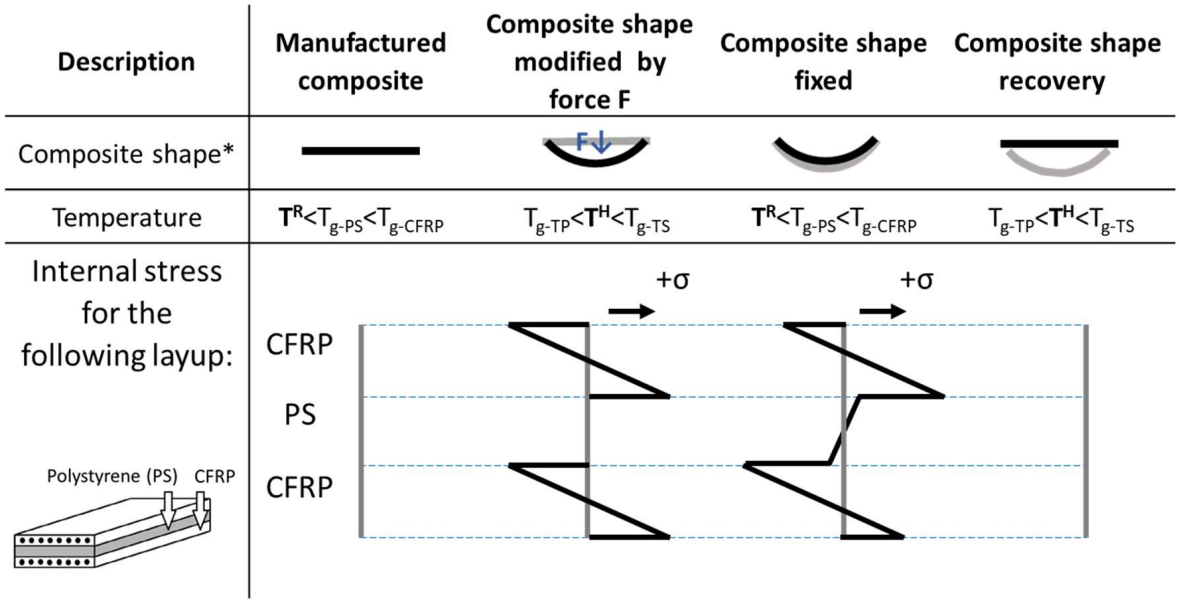

* Grey line – Initial shape, Black line – Final shape

2. Layup design for a deploying mesh

In the process shown Figure 1, the composite can be re-shaped from its cured shape and will return to its original as-cured shape on reheating. So, to achieve morphing of an interleaved composite from a Shape A to a Shape B, the interleaved composite has to be initially cured in Shape B and then deformed into Shape A at T^H and then cooled to T^R. After this, the interleaved composite can be deployed to Shape B by reheating to T^H.

To avoid having to cure the composite laminate in the form of an expanded mesh (i.e, in the deployed shape), it is possible to make use of the deformation that can develop in a non-symmetric laminate when cured at elevated temperature and cooled to room temperature (7). For example, the 90°/0° laminate of Figure 2 (a) will have the cured shape as shown due to the larger contraction of the 90° ply as the laminate is cooled. Figure 2 (b) also shows a laminate with a layup of $[[90°/0°/PS]_3/\ 90°/0°]$. This laminate is also non-symmetric and when removed from the autoclave after curing will have a curved shape, but this will have a much smaller curvature than that of the 90°/0° laminate.

If the $[[90°/0°/PS]_3/\ 90°/0°]$ laminate is now heated to T^H the PS will soften and the 90°/0° sublaminates will be free to slide relative to each other and will adopt a shape similar to the 90°/0° laminate in Figure 2 (a) but with a smaller curvature (since the PS regains it full stiffness when cooled to below its T_g). The $[[90°/0°/PS]_3/\ 90°/0°]$ laminate is therefore capable of deploying to a shape other than its cured shape. If the number repeats of the [90°/0°/PS] sublaminate is increased, then the cured shape would be flatter but the laminate would still deploy to a cured shape very similar to that of the $[[90°/0°/PS]_3/\ 90°/0°]$ laminate on reheating.

  doi:10.5075/epfl-298799_978-2-9701614-0-0

Figure 2. Morphing of composite using residual stress approach

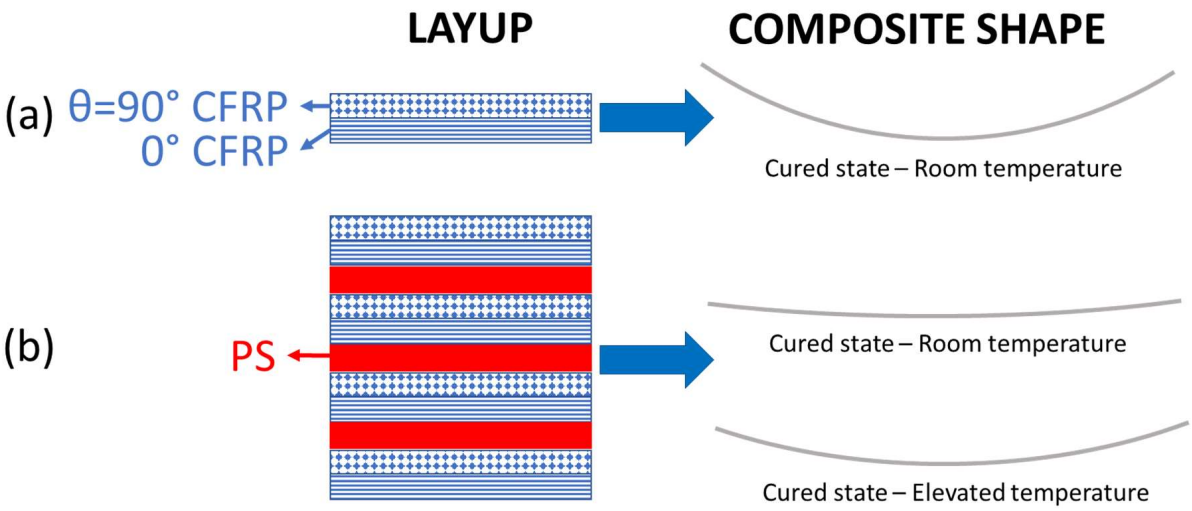

To create a single cell of a planar mesh, the layup shown in Figure 3 is used to form a quarter of the cell (the other quarters are formed of suitable mirror images of this layup). To create a single cell of a curved expanded mesh, a layup similar to the one shown in Figure 3 can be used, but by replacing the 90° plies with +/- 45° plies (See Figure 4).

Figure 3. Layup of the repeating segment of planar mesh. (Typical shape of a single cell of the mesh is shown, with the repeating segment highlighted)

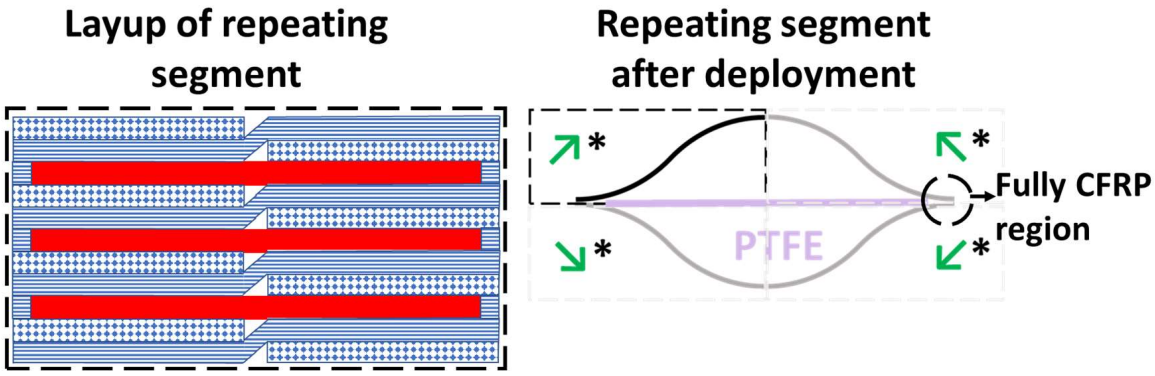

* The symbols ↗, ↖, ↘ and ↙ indicate the orientation of the mirrored repeating segments that form the mesh cell

Figure 4. Layup of the repeating segment of curved mesh

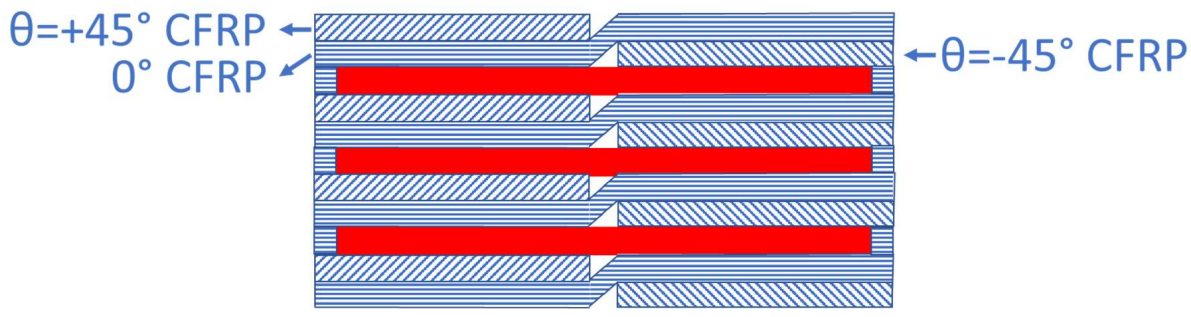

  doi:10.5075/epfl-298799_978-2-9701614-0-0

3. Materials and experimental details

Unidirectional Fibredux 914C-TS-5-34% carbon epoxy prepreg (Hexcel UK), which has a curing temperature of 175°C and a cured thickness of 125 μm, was selected as the carbon fibre reinforced polymer (CFRP) part of the layup. Empera/Styrolution 124N polystyrene film, produced at Transfercenter für Kunststofftechnik (TCKT) by film extrusion method, with a thickness of 70 μm and a glass transition temperature of 88 °C was selected as the interleaf. Aerovac MR-FILM polytetrafluoroethylene (PTFE) release film of 50 μm thickness was used to prevent bonding of the surfaces which are required to separate during mesh deployment. (See Table 1 for relevant thermal and mechanical properties of these materials.)

Table 1. Thermal and mechanical properties of the constituents of the proposed layup

Material	Property	Value
Fibredux 914C-TS-5-34% (also known as Hexcel T300/914)	E11	135 GPa[a]
	E22, E33	8.5 GPa[b]
	ν12	0.32[c]
	G12	5.27 GPa[c]
	α11	-4.5×10^{-7}/°C[a]
	α22	2.8×10^{-7}/°C[a]
PS	E	3.2 GPa[d] at $T<T_{g\text{-}PS}$ 0.1 MPa at $T>T_{g\text{-}PS}$
	ν	0.35[b]

[a] obtained from (8), [b] obtained from (6), [c] obtained from (9), [d] obtained from (10)

The layup sequences shown in *Figures 3 & 4* were used to manufacture composite laminates (400 mm x 170 mm) with the dimensions of the repeating segment of layup shown in Figure 5. The planned expanded mesh geometries to be achieved by repeating the layup segment are shown in Figure 6. Each PS and PTFE regions shown in Figure 4 were formed of two films to achieve thicknesses of 140 μm and 100 μm respectively so as to closely match the thickness of the CFRP ply. These layups would be almost flat upon curing and, on heating, would deploy into planar or curved expanded meshes.

Figure 5. Dimensions of the repeating segment of the layup

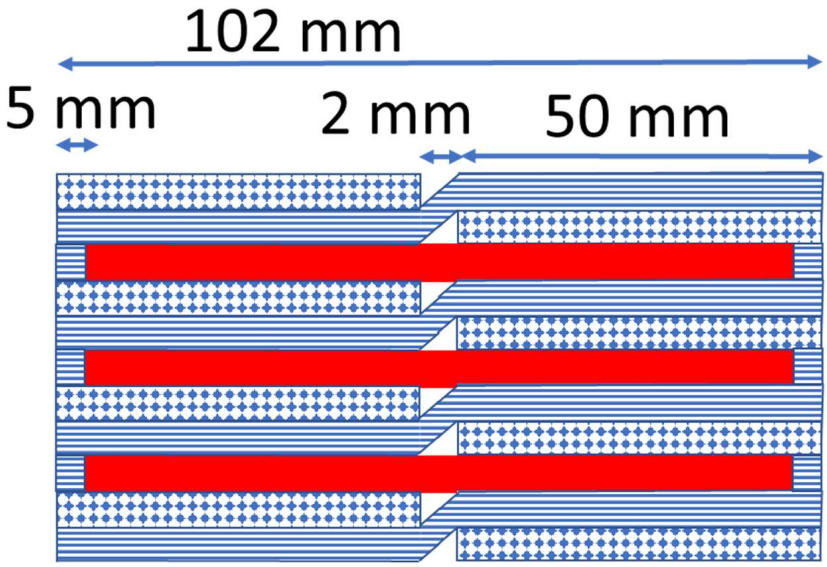

Figure 6. Typical deployment of a composite from a cured flat shape to a deployed mesh shape

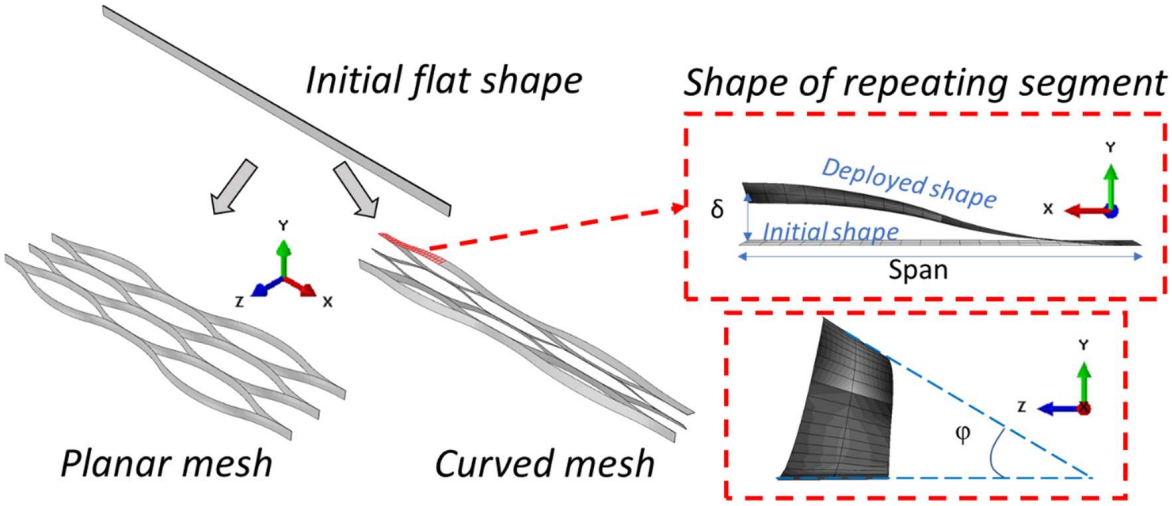

The composite panels were cured at 175°C at 7 bar pressure for 1 hour in an autoclave. The cured composite panels were then cut into 10 mm wide specimen strips (400 mm x 10 mm) using a waterjet cutter.

To deploy the composite meshes, the specimens were heated to 120°C in an oven and held at that temperature for 30 minutes before being cooled to room temperature. The resulting deployed shapes were measured to determine the mesh *Expansion Ratio* (100*δ/span – see Figure 6) and the mesh *Deployment Angle* (ϕ – see Figure 6).

4. Numerical modelling

The repeated segments shown in *Figure 3* and *Figure 4* were modelled using ABAQUS finite element analysis software (version 2020) using the geometry described in the experimental section.

The CFRP region was modelled as a 2D 4-node thermally coupled doubly curved general-purpose shell with finite membrane strains (S4T) and the PS region was modelled as a 3D 20-node thermally coupled brick with quadratic displacement distribution and linear temperature distribution (C3D20T). The plies were coupled together using a 'Tie' constraint with constrained rotational degree of freedom. Based on convergence studies, the global mesh size was fixed as 1 mm, resulting in the cell size of 1 mm x 1 mm for the 2D membranes and 1 mm x 1 mm x 0.125 mm for the 3D bricks. The ABAQUS standard solver was used for these analyses.

The model was designed to be initially flat with zero strain and displacement at a temperature of 175°C. Then, the model was made to cool down to $T_{g\text{-}PS}$ (88°C) with PS having a Young's modulus of 0.1 MPa. As a next step, the deformed mesh was imported to a new model. In this new model, the strains in CFRP plies were imported from the previous step, but the strains in PS plies were set to zero and the PS modulus was set to 3.2 GPa. The new model was then made to cool down to T^R (25°C).

In addition to the 90° and ±45° plies shown in Figure 3 and 4 respectively, the FE analyses were also performed for layups with different laminae orientations of θ = ±60°, ±75°, ±85°. The expansion ratio and the deployment angle of the deployed FE meshes were determined for each of the laminates investigated.

5. Results and discussions

The manufactured composite laminates in their initial almost-flat state after curing, and in their final deployed state are shown in *Figure 7*. The difference between planar and curved deployment is more evident when multiple samples are stacked on top of one another (as shown in the lowermost images in *Figure 7*). The comparison between the numerical predictions and experimental observations of the deployment parameters of the different meshes are shown in *Figure 8*. Although the numerical analysis used in this study overpredicts the deployment parameters of the meshes, the trends in expansion ratio and deployment angle with fibre orientation are reasonably well predicted. This discrepancy is most likely because the true temperature dependence of the properties of the CFRP and the PS are not accurately represented in the simple FE approach used here.

Figure 7. Deployable composites in their initial flat shape and final deployed mesh shape

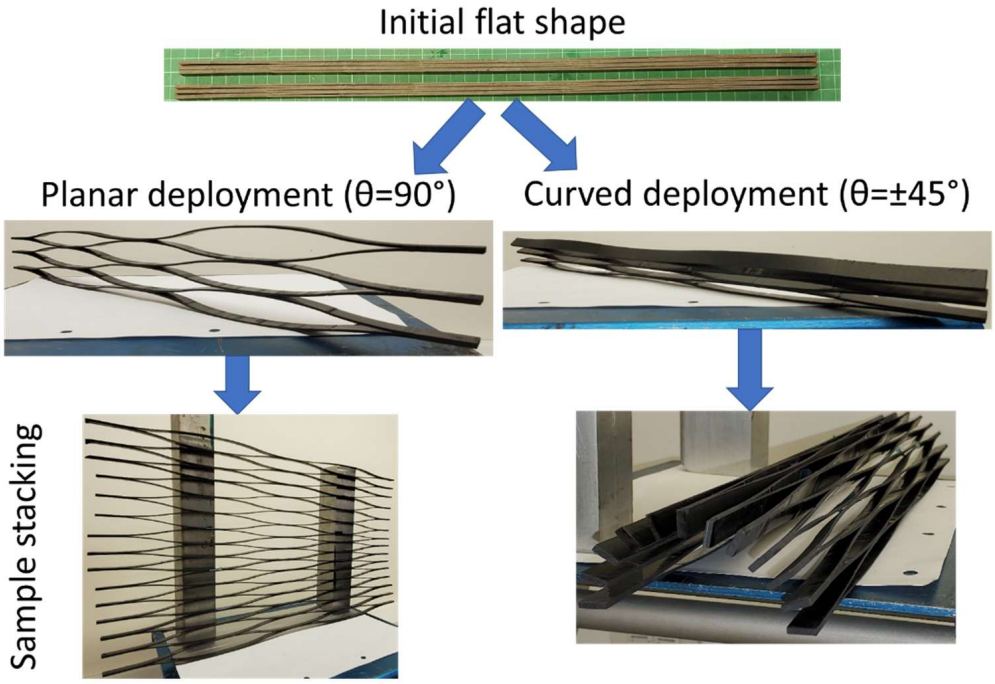

Figure 8. Deployment parameters of the deployable composites in numerical and experimental studies

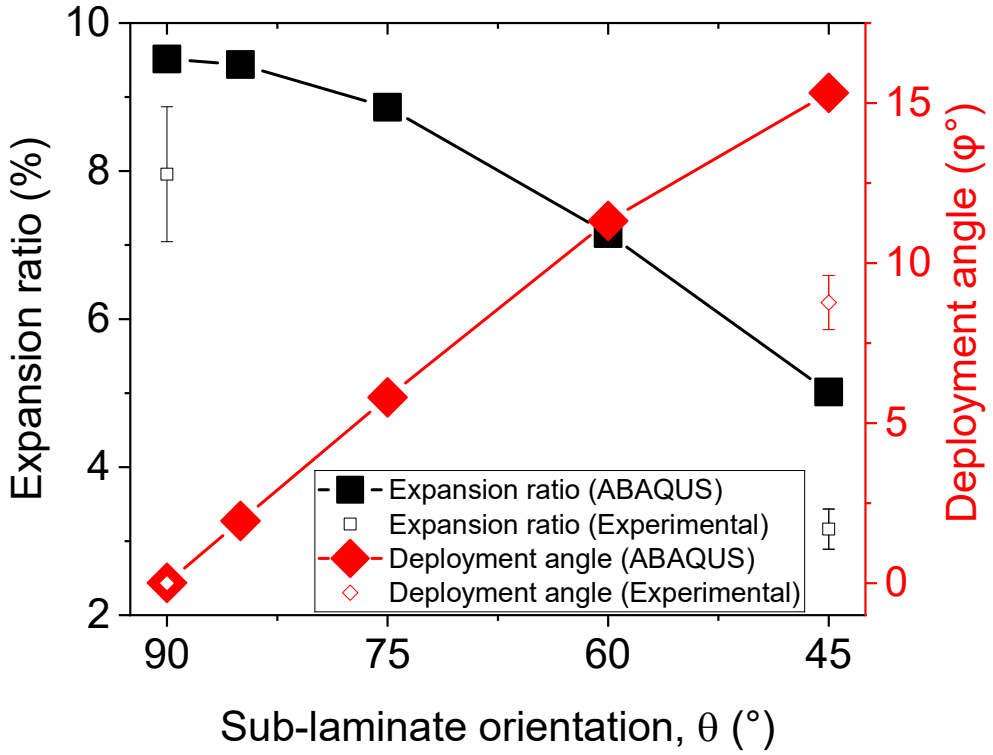

6. Conclusion

Composite laminates were designed which are almost flat after curing and can deploy upon heating to form planar and curved expanded meshes. Sample meshes were manufactured and the deployed shapes were measured. FE predictions showed reasonable agreement with the experimental results.

Acknowledgements

The research leading to these results has been performed within the framework of the HyFiSyn project and has received funding from the European Union's Horizon 2020 research and innovation programme under the Marie Skłodowska-Curie grant agreement No 765881.

7. References

1. Robinson P, Bismarck A, Zhang B, Maples HA. Deployable, shape memory carbon fibre composites without shape memory constituents. Compos Sci Technol [Internet]. 2017 [cited 2018 Nov 17];145:96–104. Available from: https://www.sciencedirect.com/science/article/pii/S0266353816316487?via%3Dihub

2. Zhang B. Interleaved composites for controllable stiffness, shape memory and easy repair capabilities (PhD thesis) [Internet]. Imperial College London; 2020. Available from: https://spiral.imperial.ac.uk/handle/10044/1/82298

3. Murali GG, Robinson P, Bismarck A, Burgstaller C. Improving flexural modulus of

interleaved composites using reinforced thermoplastic interleaves. In: SAMPE Europe Conference 2021. 2021.

4. Murali GG, Robinson P, Bismarck A, Burgstaller C. Design of a deployable composite mesh to form a segment of a circular cylindrical surface. In: HyFiSyn school and conference. 2021.

5. Murali GG, Robinson P, Bismarck A, Burgstaller C. Development of intrinsically heated, interleaved composites with controllable flexural stiffness and shape memory capability. In: MECHCOMP7 conference. 2021.

6. Waili MB. FE investigation of interleaved composites for controllable stiffness and morphing capabilities (Masters thesis). Imperial College London; 2019.

7. Zhang B, Tridech C, Maples H, Burgstaller C, Bismarck A, Robinson P. MADE TO ORDER: COMPOSITES WITH CONTROLLABLE STIFFNESS. In: ECCM18 Keynote lecture, Athens, Greece. 2018.

8. Ciba-Geigy Plastics. Fiberdux 914 High temperature resistant unidirectional prepregs (Information Sheet No. FTA 49f). Cambridge; 1989.

9. Bezazi A, Boukharouba W, Scarpa F. Mechanical properties of auxetic carbon/epoxy composites: Static and cyclic fatigue behaviour. Phys Status Solidi Basic Res [Internet]. 2009 Sep 1 [cited 2022 Mar 28];246(9):2102–10. Available from: https://onlinelibrary.wiley.com/doi/full/10.1002/pssb.200982042

10. Styrolution PS 124N/L | UL Prospector [Internet]. 2012 [cited 2022 Mar 11]. Available from: https://materials.ulprospector.com/en/profile/default?e=160634

ARE PSEUDO-DUCTILE ALL-CARBON HYBRID LAMINATES NOTCH INSENSITIVE IN OPEN HOLE TENSION?

Sergei B. Sapozhnikov [a], Valter Carvelli [b], Stepan V. Lomov [c], Yentl Swolfs [c]

a: South Ural State University, Chelyabinsk, Russia – sapozhnikovsb@susu.ru
b: Department A.B.C., Politecnico di Milano, Milan, Italy
c: Department of Materials Engineering, KU Leuven, Leuven, Belgium

Abstract: *The open hole tension response of multidirectional hybrid CFRP laminates with pseudo-ductile (PD) behaviour was investigated by using low- and high-elongation unidirectional (LE/HE UD) CFRP prepregs with conventional thickness. Two stacking sequences $[0/45/90/-45]_s$ (QI45) and $[0/60/-60]_s$ (QI60) were produced by the sub-laminate [HE/LE/HE] to achieve quasi-isotropy. PD sub-laminates were designed by combining Mitsubishi DIALEAD/ER450 (LE) and Toray T800/ER450 (HE) prepregs. The evolution of damage in the open hole laminates was monitored by digital image correlation (DIC) and acoustic emission (AE) recordings. For the considered laminates, with and without open hole, the pseudo-ductile plateau was clearly detected at almost the same stress level. Moreover, open hole QI60 laminates are notch-insensitive, and QI45 showed a limited notch sensitivity. These results can be helpful for the design of all-carbon hybrid composite components adopting small safety factors.*

Keywords: Carbon-carbon hybrid laminates; Pseudo-ductility; Quasi-isotropy; Notch insensitivity

1. Introduction

Hybrid effect and pseudo-ductile tensile behaviour in all-carbon hybrid composites is thoroughly investigated for laminates with thin prepreg plies [1,2] and (in previous publications of the present authors) for laminates with prepregs of conventional thickness [3,4]. Pseudo-ductile behaviour, with a well-developed plateau on the stress-strain diagram, creates post first failure safety, which is a desirable feature for applications where high loads can be present in design scenarios. In this context, the notch sensitivity is of considerable importance. The unnotched safety margin cannot be exploited if it is not preserved in the presence of a notch. The study presented in [2] has demonstrated that thin-ply all-carbon quasi-isotropic laminates preserve the pseudo-ductile behavior in an open hole tension test, and have very limited notch sensitivity. The behaviour has been motivated with the notch (un)sensitivity of ductile metals.

This paper investigates the strength sensitivity to open hole of all-carbon pseudo-ductile hybrid CFRPs made by standard thickness prepregs with a modified (toughened) matrix. The studied hybrids combine low elongation (LE) plies reinforced with high-modulus carbon fibres and high-elongation (HE) plies with intermediate-modulus carbon fibres.

2. Materials, specimens and test methods

Interlayer hybridisation of CFRPs has been realized using unidirectional prepregs with high-modulus DIALEAD fibres (MITSUBISHI) of thickness of about 220 µm and prepregs with high-strength fibres T800 (TORAY) of thickness of about 110 µm. Both prepregs had toughened ER450

  doi:10.5075/epfl-298799_978-2-9701614-0-0

epoxy resin [5, 6]. Everywhere below, prepregs with DIALEAD fibres are designated 'D', and T800 fibres are 'T'. During the production process, hybrid sublaminates were assembled, composed of three layers with parallel fibres [T/D/T]. Such sublaminates were laid according to the scheme $[0/45/90/-45]_s$ or $[0/60/-60]_s$ to obtain quasi-isotropic (QI) composites.

The laminates have been produced by hot pressing at a pressure of 5-6 bar and a temperature of 135°C for 2 hours. Heating and cooling rates were about 5°C/min. The same materials and processing techniques were used in a previous study on UD all-carbon hybrids [3, 4].

Specimens for mechanical tensile tests were cut from laminated plates with dimensions of 300x300 mm by a high-speed circular saw (water-cooled diamond disc). They had dimensions of 250x15 mm (prismatic specimens) and 200x25 mm with hole diameter of 6 mm (OH). Glass fibre composite tabs with dimensions of 50x15x2 mm were bonded to the specimen ends.

Loading was carried out on a universal electromechanical machine INSTRON 5978 with a 2 mm/min cross-head speed. A standard clip-on INSTRON 2620-829 extensometer with 50 mm gauge length was used to measure strain, alongside the registration of the grips displacement. Details of the damage process were monitored using the digital image correlation (DIC) [7], and acoustic emission (AE) signals by Vallen AMSY-5 system [8]. The main feature considered for AE analysis is the frequency at the maximum amplitude F_{max}, which has certain correlations with the damage mode at the signal origin.

3. Mechanical tests

Table 1 summarises the results of all tests (two UD, hybrid UD, two QI and two QI OH). The stress – cross-head displacement/strain diagrams were used to extract the characteristic values in Table 1, as illustrated in Figure 1: modulus of elasticity E_x, peak stress σ_p, pseudo-yield stress σ_{py}, ultimate stress X_T and OH strength sensitivity K_{py} and K_{max}.

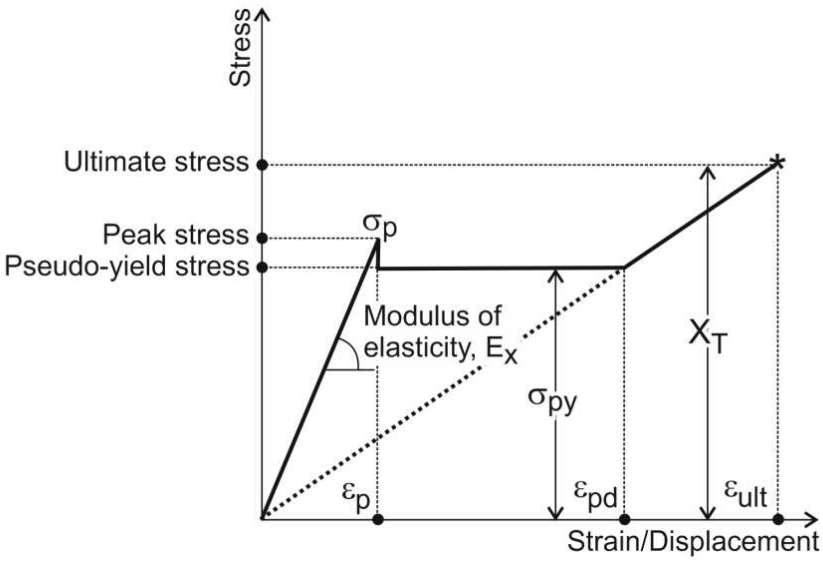

Figure 1. Schematics of the stress-strain/displacement diagram

Table 1: Mechanical properties of all-carbon hybrids, 4 – 6 specimens tested for each test type, ± means standard deviation.

Layup	Modulus of elasticity, E_X [GPa]	Peak stress, σ_p [MPa]	Pseudo-yield stress σ_{py} [MPa]	Ultimate stress, X_T [MPa]	OH peak stress sensitivity, K_{py} [-]	OH strength sensitivity, K_{max} [-]
UD [D_4]	382±36	1410±42	-	1410±32	-	-
UD [T_8]	148±10	2505±58	-	2505±58	-	-
UD [T/D/T]$_3$	255±16	960±12	810±15	1203±51	-	-
QI45	82.1±4.3	300±16	260±8.5	339±5	-	-
QI60	84.3±3.8	330±11	315±8.2	462±12	-	-
OH QI45	75.0±3.62[(1,2)]	285±13[(1)]	240±17[(1)]	295±13[(1)]	1.08±0.09	1.15±0.07
OH QI60	76.5±3.8[(1,2)]	340±18[(1)]	340±18[(1)]	444±29[(1)]	0.96±0.08	1.04±0.10

[(1)] net section of the specimens.
[(2)] with a hole at the base of the extensometer

The clip-on extensometer readings ("extensometer strain") increased monotonically up to the first peak at a strain of 0.38 ± 0.01%, corresponding to the breakage of the D-layer. Beyond the first peak, failure of the D-layers, the clip-on extensometer had sliding of the legs along the specimen surface . In this case, the extensometer readings became questionable, and, therefore, the tensile behaviour of unnotched and notched QI specimens are compared in Figure 2 in terms of "stress – displacement" curves.

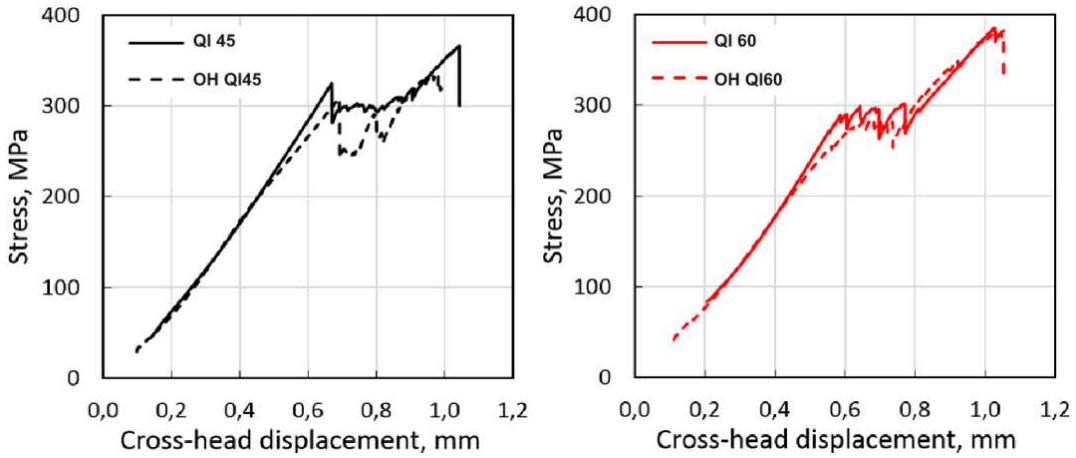

Figure 2. Typical 'stress – cross-head displacement' diagrams of unnotched specimens (solid lines) and 'net stress – cross-head displacement' diagrams of open hole QI45 and QI60 specimens (dot lines).

The diagrams in Figure 2 show that the notched specimens have similar pseudo-ductile behaviour to the unnotched specimens, with comparable levels of pseudo-yield stress (see Table 1). QI45 specimens fail at the end of the pseudo-ductile plateau without developing resistance of the HE plies. Correspondingly, the net ultimate stress of the notched specimens (295±13 MPa) is 13% lower than the unnotched one (339±5 MPa). This can be attributed to more intensive damage around the notch in the QI45 laminate, which led to the failure of the load-carrying 0° HE plies. The post-plateau behaviour of the notched QI60 specimens is similar to the unnotched

  doi:10.5075/epfl-298799_978-2-9701614-0-0

ones, with well-developed linear resistance of the HE plies and with the net ultimate stress (444±29 MPa) close to the one of the unnotched counterpart (462±12 MPa).

The OH strength sensitivity can be characterised as the ratio of the strength of unnotched and notched specimens, which is higher than 1 for a notch-sensitive material and close to 1 for a notch-insensitive one [9]. For pseudo-ductile QI laminates, two notch sensitivity ratios can be introduced:

$$K_{py} = \frac{\sigma_{py}}{\sigma_{py}^{OH}}, \quad K_{max} = \frac{X_T}{X_T^{OH}}.$$

The first, K_{py}, assesses the change of the pseudo-yield limit in the presence of the notch. It can be considered a helpful design limit when the (pseudo)-ductile deformation is unknown. The second, K_{max}, assesses the change in the ultimate load-carrying capability and is useful if post-yield safety is of concern. In both cases, the net stresses in the OH specimen are used.

Table 1 shows the notch sensitivity ratios for QI45 and QI60. Both types of QI laminates exhibit low notch sensitivity, especially compared to experimental data of QI carbon/epoxy laminates with comparable hole size [9], where values K_{max}~2 were measured. The low K_{py} can be explained by the failure of 0° LE plies, which is controlled by the failure strain of the LE fibres. A similar low K_{max} notch sensitivity was measured in thin QI all-carbon hybrids [2]. It was explained by analogy to the reduced notch sensitivity in ductile metals, which is related to the release of the stress concentration due to localised progressive damage.

4. Localised damage around the notch

Figure 3 shows the localisation of the AE events in a typical OH test. It reveals the location of the events X_{loc} in relation to the frequency at the maximum amplitude F_{max} of the signal. The centre of the notch corresponds to X_{loc} = 6 cm. The distribution shows the localisation of the damage near the notch. As discussed in [3], the frequency of the events can be interpreted as follows: the high-frequency events, with F_{max} ~ 1400...1500 kHz for LE and F_{max} ~ 700 kHz for HE fibres, can be associated to fibre breakage; the bands with F_{max} ~ 500 kHz and F_{max} ~ 200 kHz can be associated to off-axis cracking, including matrix cracks and interface damage.

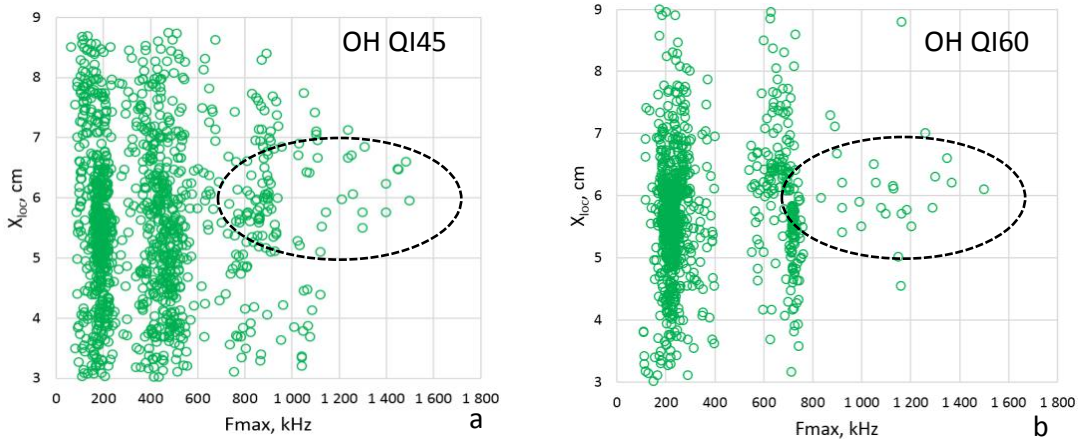

Figure 3. The relationships between the X_{loc} coordinate of the AE source and the frequency F_{max} for notched specimens OH QI45 (a) and OH QI60 (b). The ellipses show the position of high frequency (fibre breakage) events near the notch.

2D DIC was used to measure full-field strain on the surface of the samples near the hole during tension. The ε_{yy} strain maps are shown in Figure 4 just before and after the first load peak.

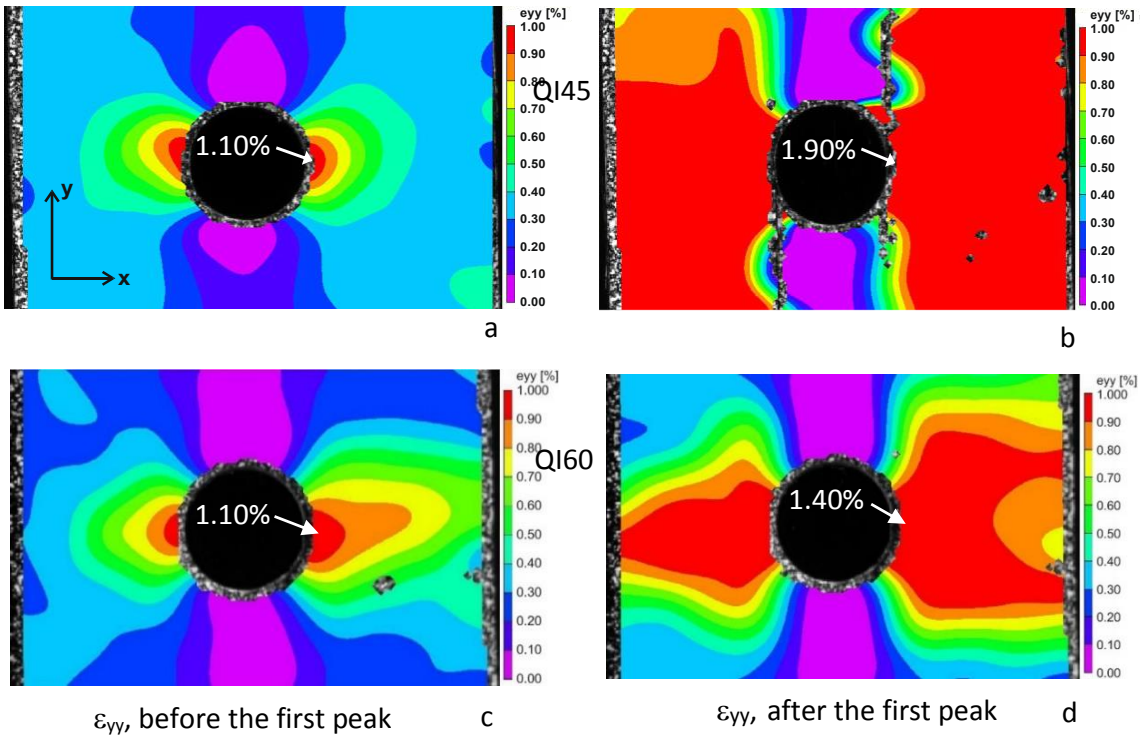

Figure 4. Strain maps ε_{yy} on the OH specimens surface, transition to unstable deformation after first peak failure, QI45 (a,b) and QI60 (c,d; (a,c) just before and (b,d) just after the first load peak.

The strain maps of QI45 just before the load peak (**Ошибка! Источник ссылки не найден.**a,c) are similar to the maps detailed in [9] for non-hybrid carbon/epoxy OH laminates with the layup $[0/45/90/-45]_s$. Failure of the LE ply drastically changes the strain field pattern, especially for QI45. Splitting of the 0° plies, seen in Figure 4b,d as non-correlated zones originating from the hole edge, separates the strain pattern into two parts. In the central part, the strain ε_{yy} is almost constant, as before the 0° LE failure. These maps are the witnesses of [0°] LE-ply failure near the hole, limited internal delamination (smearing of ε_{yy} in the net section) and shear splitting of outer HE-ply.

Conclusions

The paper reports an investigation of notch sensitivity of open-hole pseudo-ductile quasi-isotropic all-carbon hybrid laminates, combining low-elongation and high-elongation carbon fibre/epoxy plies of conventional thickness. Two types of QI laminates have been studied: QI45 - $[0/45/90/-45]_s$ and QI60 - $[0/60/-60]_s$. The results can be summarised as follows:

1. The OH QI hybrid laminates are almost notch-insensitive, with the notch sensitivity factors for pseudo-yield and ultimate stress below 1.15 (Table 1);
2. The notched specimens have similar pseudo-ductile behaviour to the unnotched specimens, with the same stress level (Figure 2);

  doi:10.5075/epfl-298799_978-2-9701614-0-0

3. The post-plateau linear resistance and the ultimate stress of HE plies are preserved in the notched specimens only for the QI60 case. Notched QI45 lose the post-plateau resistance of HE plies, and their ultimate stress decreases (Figure 2).

Acknowledgements

The work of Sergei B. Sapozhnikov was financially supported by the Russian Science Foundation (project No. 18-19-00377) and partially by KU Leuven. The authors are grateful to the Toray Group for providing prepreg materials and supporting the Toray Chair at KU Leuven, held by Stepan V. Lomov.

References

1. Czél G, Jalalvand M, Wisnom MR, Czigány T. Design and characterisation of high performance, pseudo-ductile all-carbon/epoxy unidirectional hybrid composites. Composites Part B: Engineering 2017; 111: 348-356.
2. Czél G, Rev T, Jalalvand M, Fotouhi M, Longana ML, Nixon-Pearson OJ, Wisnom MR. Pseudo-ductility and reduced notch sensitivity in multidirectional all-carbon/epoxy thin-ply hybrid composites. Composites Part A: Applied Science and Manufacturing 2018; 104: 151-164.
3. Sapozhnikov SB, Swolfs Y, Lomov SV. Pseudo-ductile unidirectional high modulus/high strength carbon fibre hybrids using conventional ply thickness prepregs. Composites Part B: Engineering 2020; 198: 108213.
4. Sapozhnikov SB, Swolfs Y, Lomov SV. Mode I and II interlaminar critical energy release rates in all-carbon interlayer unidirectional fibre-hybrids based on ultrahigh-modulus and high-strength fibres. Composite Structures, 2020; 236: 111886.
5. Composite Materials Italy (CIT), CFRP prepregs. http://www.composite-materials.it/pagina.php?cod=124.
6. ER450 epoxy resin. https://www.composite-materials.it/pagina.php?cod=124
7. VIC-2D, Correlated Solutions Inc., Irmo, SC, USA. https://correlatedsolutions.eu/vic-2d/
8. AMSY-5. Vallen Systeme Gmbh. https://www.vallen.de/
9. Oz F, Mehdikhani M, Ersoy N, Lomov SV. In-situ imaging of inter- and intralaminar damage in open-hole tension tests of carbon fibre-reinforced composites. Composite Structures 2020; 244: 112302.

  doi:10.5075/epfl-298799_978-2-9701614-0-0

REPARABILITY AS A NEW FUNCTION FOR HIGH-PERFORMANCE PSEUDO-DUCTILE HYBRID COMPOSITES

Gergely, Czél[a], Salvatore Giacomo, Marino[a]

a: Budapest University of Technology and Economics, Faculty of Mechanical Engineering, Department of Polymer Technology – czel@pt.bme.hu

Abstract: *Our study aimed to provide two desired features to high-performance composite materials for structural applications: pseudo-ductility and reparability. UD prepreg plies were selected for manufacturing the test laminates made of glass fibre/epoxy (GF/EP) and carbon fibre/epoxy (CF/EP) layers in symmetric sandwich architecture. Autoclave curing was utilised for the best reproducibility and quality. A novel approach to enable reparability based on interleaving thermoplastic films in interlayer hybrid laminates was used with discontinuous CF/EP layer. Stable, pseudo-ductile tensile stress-strain response was demonstrated in the first step. Then, partially damaged samples were generated and repaired under heat and pressure. The achievable stiffness recovery of the samples was up to 100%. Significant effect of the repairing pressure on the knee-point strain and stress was detected, with efficient recovery at pressures higher than 6 bar.*

Keywords: Hybrid composites; Glass fibre; Carbon fibre; Interleaving

1. Introduction

High-performance fibre reinforced polymer composites are an excellent choice for lightweight structural components. They have outstanding strength to weight ratio, and their corrosion and fatigue resistance are also appreciated in several demanding applications. Still, their usually catastrophic failure mode limits their spread towards safety-critical, high volume applications such as automotive and transportation. Unlike metals which can be repaired using the wide selection of welding technologies, composites suffer from the lack of intrinsic reparability. According to the state of the art, the lifetime of partially damaged structures can only be extended by removing material from the deteriorated zones and apply bonded repair patches to restore the original load-bearing capacity. This is a rather complicated, laborious and therefore expensive technique with limited scope. Alternatively, the loading condition of the damaged component has to be carefully limited, which is usually not feasible for multiple reasons including safety concerns.

Czél et al [1,2] recently proved the concept of making the failure mode of composites progressive, similar to that of ductile metals, by introducing pseudo-ductility through hybridisation of unidirectional (UD) glass and thin-ply carbon fibre reinforced epoxy plies in a sandwich architecture. The mechanisms enabling the progressive damage accumulation and failure mode of the materials are fragmentation of the low elongation (LE) fibre reinforced layer of the sandwich hybrids and stable delamination starting from the LE layer fractures. The resulting stress-strain response of the pseudo-ductile hybrid material consists of an initial linear part, a flat or slightly rising plateau and a second linear part (see Fig. 1), which provides clear warning before final failure The concept was developed further by hybridising different

  doi:10.5075/epfl-298799_978-2-9701614-0-0

types of carbon fibres [3] and using specific reinforcement orientations, such as bi-directional [4] and quasi-isotropic [5].

Czél et al [2] later demonstrated that the use of a unidirectional (UD) discontinuous carbon fibre/epoxy (CF/EP) layer in sandwich hybrid laminates together with UD continuous glass fibre/epoxy (GF/EP) layers, could also provide a pseudo-ductile, linear-plateau-linear type tensile stress-strain response with smooth transitions between the subsequent phases (see Fig. 1). The CF/EP layer has to release enough energy to initiate delamination before the fracture of the layer, therefore significantly thicker LE ply blocks are applied in this architecture than in the continuous one. This way, the CF/EP plies are prevented from fracturing during the benign damage process. The material's stiffness is degraded gradually by delamination between the discontinuous CF/EP and the continuous GF/EP layers before the final failure triggered by the fracture of the GF/EP layers. This controllable damage mechanism also enables the tailoring of the mechanical response to the requirements through careful design of the architecture of the material.

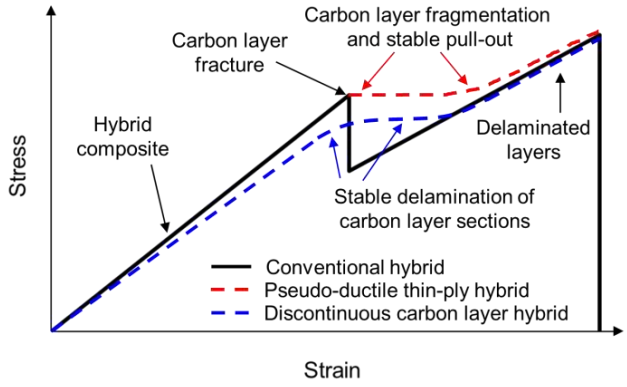

Figure 1. Schematic stress-strain responses of different sandwich hybrid composite configurations

The architecture made by the combination of discontinuous LE and continuous high elongation (HE) layers has a unique feature that the low elongation fibres (i.e. carbon fibres) do not break during the damage accumulation and final failure process. This enables the intrinsic reparability of delaminations in the material focusing only on the interfaces between the LE and HE layers. Thermoplastic polymers were applied successfully for improving the fracture toughness of composite layer interfaces [6], but full film interleaving is not a widespread approach to the best of the author's knowledge. Since a full layer of thermoplastic film can enable the re-bonding of deteriorated or fractured layer interfaces by heating the material under pressure after damage, we decided to study this approach. Full film interleaving is also a suitable technique as we apply prepreg sheets to manufacture our special hybrid laminate architectures for pseudo-ductile composite materials.

2. Materials, design, manufacturing

The materials considered for designing the pseudo-ductile and reparable hybrid laminates are GF/EP and CF/EP prepreg sheets and polyamide 12 (PA12) film. Their basic properties are summarised in Tables 1 and 2. The layered laminate architecture of the reparable material is shown in Fig. 2a. The CF/EP and GF/EP composite layers are separated by PA12 films, which are damaged when the composite is overloaded in tension, but can be repaired under heat

  doi:10.5075/epfl-298799_978-2-9701614-0-0

and pressure. Fig. 2b shows the designed discontinuities in the interleaved hybrid laminates which form CF/EP platelets between the continuous GF/EP layers.

Table 1. Basic properties of the fibres in the applied prepregs

Type	Manufacturer	Tensile elastic modulus [GPa]	Tensile strain to failure [%]	Tensile strength [MPa]	Density [kg/m^3]
Y-110 S-2 Glass	AGY	89	5.7	4890	2470
HexTow® IM7 Carbon	Hexcel	276	1.9	5516	1780

Table 2. Basic properties of the applied materials

Material designation	Fibre type	Nominal fibre areal density/ thickness	Fibre volume fraction	Cured ply thickness	(UD) elastic modulus
		[g/m^2]/[µm]	[%]	[µm]	[GPa]
GF/EP prepreg	S-glass	190 g/m^2	50	155	45.7
CF/EP prepreg	IM7	100 g/m^2	59	96	163.1
PA12 thermoplastic film	-	~20 µm	Melt temp.:	178 °C	1.1

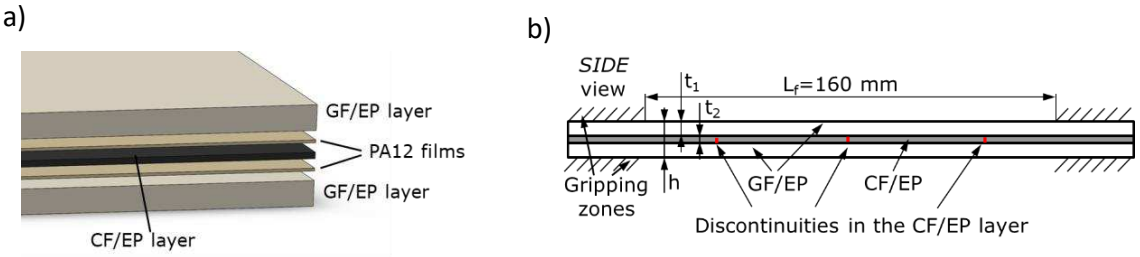

Figure 2. a) schematic of the interleaved laminate architecture, b) schematic of the hybrid laminate tensile specimen with discontinuous CF/EP layer

The key design considerations of the reparable hybrid laminates are summarised below based on [7]:

1. The GF/EP layers have to be thick enough to take the full load of the laminate at the discontinuous cross-sections even if the strain in the laminate reaches the breaking strain of the CF/EP layer. This criterion prevents the fracture of the continuous GF/EP layer during the damage process of the hybrid laminate. The formula for the minimum glass layer thickness is given in Eq (1).

$$t_1 = \frac{\varepsilon_{2b} E_2 t_2}{2E_1(\varepsilon_{1b} - \varepsilon_{2b})} \quad (1)$$

Where ε_{1b} and ε_{2b} are the breaking strains of the GF/EP and the CF/EP layers respectively, E_1 and E_2 are the elastic moduli of the GF/EP and the CF/EP layers respectively, t_1 is the thickness of the GF/EP layer.

2. We also have to make sure that delamination initiates before the fracture of the CF/EP platelets. For this, the mode II energy release rate (G_{II}) of the interface at CF/EP fracture has to be higher than the mode II fracture toughness (G_{IIC}) as shown in Eq. (2). The G_{IIC} of the interface was measured to be up to 4 kJ/m^2, which was used for design purpose here.

$$G_{II\ at\ CFEP\ fracture} = \frac{\varepsilon_{2b}^2 E_2 t_2 (2E_1 t_1 + E_2 t_2)}{8 E_1 t_1} > G_{IIC} \quad (2)$$

Where t_2 is the thickness of the CF/EP layer.

3. An important design factor is to have long enough platelets for effective load transfer from the GF/EP layer to the CF/EP platelets. We analysed the critical (or ineffective) length of the CF/EP platelets embedded in continuous GF/EP layers and came up with Eq. (3) for the critical platelet length L_{pc}. Minimum two times this L_{pc} was used for our repairable laminate architectures.

$$L_{pc} = \frac{E_2 \varepsilon_{2b} t_2}{\tau_{max}} \quad (3)$$

Where τ_{max} is the shear strength of the layer interface dominated by the shear strength of the interleaf film. It was measured separately that the shear strength of the interface does not exceed 36.2 MPa, therefore this value was used here for design purpose.

Table 3 presents the designed laminate configurations. The difference in platelet length (50 vs.60 mm) results only in a small change of the elastic modulus. On the other hand shorter platelets can adapt better to the geometric features of a real product, so they are considered more suitable from a practical point of view. It is also clear that the energy release rate is high enough to initiate delamination before breaking the platelets.

Table 3. Designed laminate configurations and key properties

Hybrid configuration (Abbreviation) [Lay-up sequence]	**Fibre areal densities of the constituent plies**	**Platelet length**	**Nominal thickness**	**CF/EP layer/full thickness ratio**	**Calculated G_{II} at CF/EP failure strain**	**Predicted elastic modulus**
	[g/m^2]	**[mm]**	**[mm]**	**[%]**	**[N/mm]**	**[GPa]**
(3G/PA12/3C-60 mm) [G_3/PA12/C_3/PA12/G_3]	[190_3/-/100_3/-/190_3]	60	1.22	23.6	8.907 at 1.9%	59.5
(3G/PA12/3C-50 mm) [G_3/PA12/C_3/PA12/G_3]	[190_3/-/100_3/-/190_3]	50	1.22	23.6	8.907 at 1.9%	57.3

The designed reparable pseudo-ductile hybrid composite laminates were manufactured from prepreg plies by manual lay-up with UD fibre orientations. The discontinuities in the CF/EP layer were introduced by rotary blade cutter manually. The interleaf films were also inserted in the laminates manually after degreasing with acetone. The laminates were vacuum bagged and cured in an autoclave at 130 °C for 60 min. Even though the thermoplastic interleaf films did not melt, excellent bonding to the composite layers was confirmed during the test procedures. 20 mm wide tensile test specimens were cut from the cured panels by a diamond cutting wheel.

  doi:10.5075/epfl-298799_978-2-9701614-0-0

3. Results and discussion

Testing of the parallel edge hybrid composite coupons was executed under uniaxial quasi-static tensile loading and displacement control at a crosshead speed of 5 mm/min on a computer-controlled Zwick Z250 type 250 kN rated universal electro-mechanic test machine fitted with a regularly calibrated 250 kN load cell and 100 kN rated Instron 2716-003 type manual wedge action grips. The strains were measured optically on one side of the specimens, with a Mercury Monet type video-extensometer using 60 and 100 mm gauge length fit to the platelet length of the given configuration. White markers (made with sharp tip paint marker) on a black background (made with blunt tip permanent marker) were used for high contrast and accurate tracking. The test sequence of the specimens was the following:

0. Quasi-static characterisation of the reparable pseudo-ductile hybrid laminates was completed to obtain a solid baseline for the reparability study (see Fig. 3). The specimens were strained until the first signs of damage in the GF/EP layers to preserve their integrity for further visual investigation.

1. Damage (delamination) is introduced to the specimen by tensioning until a specified strain value which is still safe against damaging the fibres. Fig. 3a also shows the developing delamination damage pattern (starting from the CF/EP layer discontinuities), because the translucent GF/EP plies enable visual damage detection in the specimens [8].

2. Damage was determined by re-loading the same specimen to the same strain approached in the damage introduction step. The stiffness reduction was used as the damage parameter, which was in the range of 37-47% (see Fig. 4).

3. Then, the damaged specimens were repaired under elevated pressure and temperature and tensioned once again to the strain specified for the damage introduction (see fig. 5) to assess the recovery of mechanical parameters.

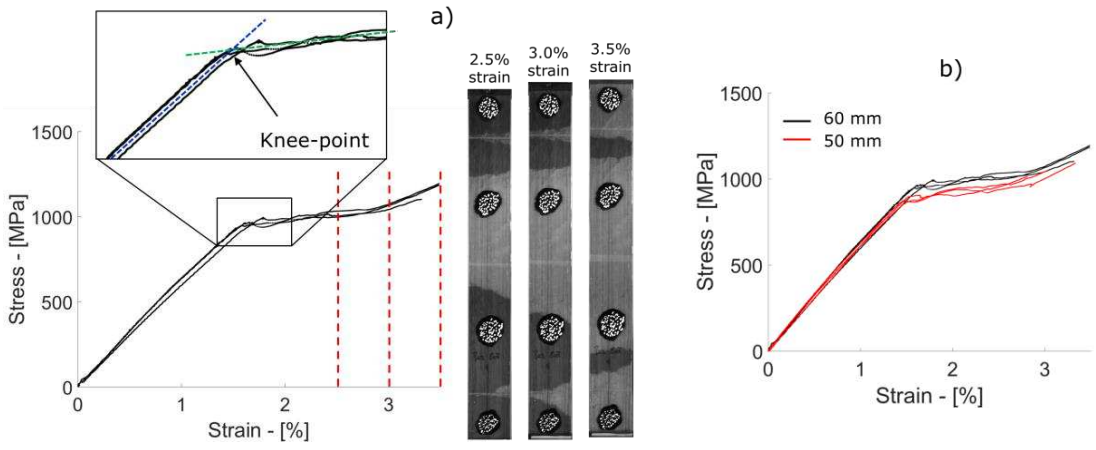

Figure 3. Baseline quasi-static test results of the a) 3G/PA12/3C-60 mm and b) 3G/PA12/3C-50 mm type specimens

It is interesting to note that the platelet length only changed the stress-strain response of the pristine hybrid specimens slightly. In case of the 50 mm platelet specimens, there were three discontinuities within the gauge length, while there were only two in the 60 mm platelet specimens. This means that there was a significantly larger volume subjected to stress

  doi:10.5075/epfl-298799_978-2-9701614-0-0

concentration and Mode II crack initiation in the 50 mm platelet length specimens, which led to earlier damage initiation (see knee points on Fig. 3).

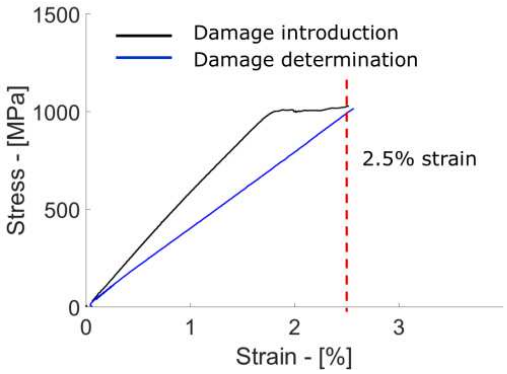

Figure 4. Typical stress-strain curves of damage introduction and detection steps of tensile testing

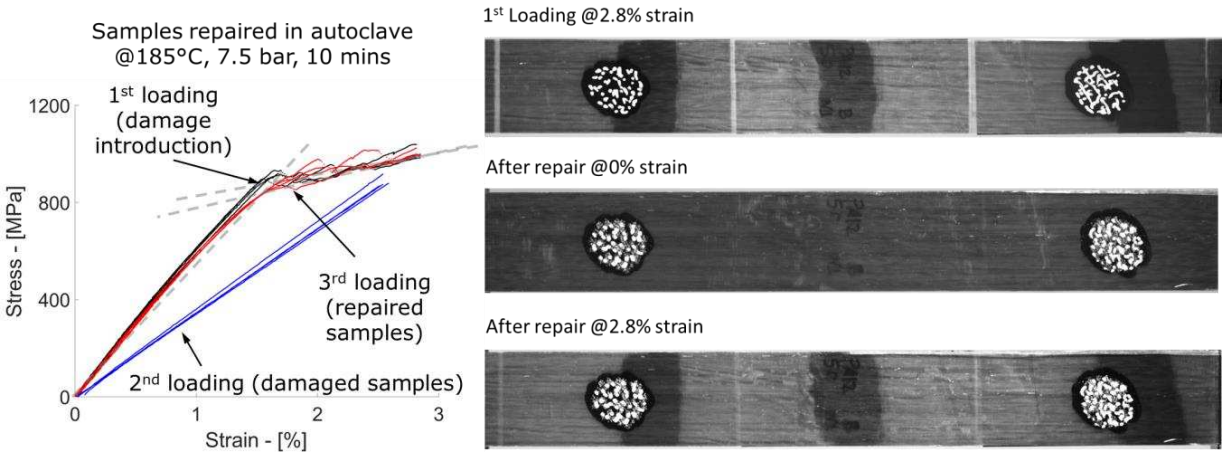

Figure 5. Typical test results of 3G/PA12/3C-50 mm specimens repaired at high pressure and high temperature in an autoclave.

Fig. 5 demonstrates that we managed to restore the initial modulus of our discontinuous CF/EP hybrid laminates by submitting the damaged specimens to a repairing cycle in the autoclave above the melt temperature of the thermoplastic interleaves at 185°C and 7.5 bar for 10 minutes. Fig. 5 also clearly shows that the visible delaminations disappeared from the specimen after the repairing cycle, confirming the successful re-bonding of the discontinuous CF/EP and the continuous GF/EP layers. Table 4 presents the summary of the test results. The moduli of the laminates were overestimated which suggest that the simple elastic-plastic material model applied in [7] and adopted here for modelling the mode II damage behaviour of the layer interface should be refined to capture the response of the modified interfaces more accurately. Repair efficiencies in Table 4 are calculated by dividing the given parameter value after the repair cycle with the corresponding parameter recorded during the damage introduction load step. The moduli of the damaged specimens were reduced by notable 37-47%, which was almost fully recovered by all repair cycles for both specimen configurations. On the other hand, the repairing pressure has a significant effect on the repair efficiency in case of the knee-point strain and stress.

Table 4. Results summary

Laminate configuration/repair pressure at 185 °C	Predicted elastic modulus	Measured elastic modulus (CoV)	Knee-point strain (CoV)	Knee-point stress (CoV)	Modulus reduction due to damage	Repair efficiency for elastic modulus	Repair efficiency for knee-point strain	Repair efficiency for knee-point stress
	[GPa]	[GPa]	[%]	[MPa]	[%]	[%]	[%]	[%]
3G/PA12/3C-60 mm /1 bar	59.5	63.4 (3.13)	1.667 (5.21)	990.6 (3.55)	36.9 (1.47)	~100 (1.64)	70 (3.65)	70 (3.21)
3G/PA12/3C-50 mm /6.5 bar	57.3	63.1 (2.61)	1.521 (3.53)	884.6 (3.18)	46.5 (0.77)	94 (1.49)	92 (4.52)	87 (5.85)
3G/PA12/3C-50 mm /7.5 bar					44.9 (2.60)	96 (3.11)	~100 (7.77)	99 (5.34)

4. Conclusion

- An industrially feasible material architecture and manufacturing process was proposed for reparable pseudo-ductile hybrid composite laminates.
- All tested configurations showed favourable pseudo-ductile stress-strain responses with a detectable damage initiation point (knee-point) and a wide margin before final failure.
- Small effect of the platelet length on the knee-point strain and stress was detected.
- It was possible to restore the elastic modulus of all damaged specimen types even with low pressure (1 bar) during the repair cycle.
- Almost full recovery of all the measured mechanical properties was achieved with high pressure (6.5-7.5 bar) repair cycles.
- Significant effect of the repairing pressure on the knee-point strain and stress was detected.

Acknowledgements

The research leading to these results has been performed within the framework of the HyFiSyn project and has received funding from the European Union's Horizon 2020 research and innovation programme under the Marie Skłodowska-Curie grant agreement no. 765881. The research was also supported by the National Research, Development and Innovation Office (NRDI, Hungary) through grant ref. OTKA FK 131882. The research reported in this paper is part of project no. BME-NVA-02, implemented with the support provided by the Ministry of Innovation and Technology of Hungary from the National Research, Development and Innovation Fund, financed under the TKP2021 funding scheme. Gergely Czél is grateful for funding through the Premium Postdoctoral Fellowship Programme of the Hungarian Academy of Sciences.

5. References

1. Czél G, Wisnom MR. Demonstration of pseudo-ductility in high performance glass/epoxy composites by hybridisation with thin-ply carbon prepreg. Composites Part A: Applied Science and Manufacturing 2013; 52:23-30

2. Czél G, Jalalvand M, Wisnom MR. Design and characterisation of advanced pseudo-ductile unidirectional thin-ply carbon/epoxy-glass/epoxy hybrid composites. Composite Structures 2016; 143:362-70.
3. Czél G, Jalalvand M, Wisnom MR, Czigány T. Design and characterisation of high performance, pseudo-ductile all-carbon/epoxy unidirectional hybrid composites. Composites Part B: Engineering 2017; 111:348-56.
4. Czél G. Development of bi-directional pseudo-ductile glass/carbon-epoxy hybrid composites for improved safety in structural applications. Composites Part B: Engineering 2022; 231:109546.
5. Czél G, Rev T, Jalalvand M, Fotouhi M, Longana ML, Nixon-Pearson OJ, Wisnom MR. Pseudo-ductility and reduced notch sensitivity in multi-directional all-carbon/epoxy thin-ply hybrid composites. Composites Part A: Applied Science and Manufacturing 2018; 104:151-64.
6. Boon YD, Joshi S. A review of methods for improving interlaminar interfaces and fracture toughness of laminated composites. Materials Today Communications 2020; 22: 100830.
7. Czél G, Jalalvand M, Wisnom MR. Demonstration of pseudo-ductility in unidirectional hybrid composites made of discontinuous carbon/epoxy and continuous glass/epoxy plies. Composites Part A: Applied Science and Manufacturing 2015; 72:75-84.
8. Rev T., Jalalvand M, Fuller J, Wisnom MR. Czél G. A simple and robust approach for visual overload indication - UD thin-ply hybrid composite sensors Composites Part A: Applied Science and Manufacturing 2019; 121, 376-385 (2019)

  doi:10.5075/epfl-298799_978-2-9701614-0-0

ON THE OPTIMAL DESIGN OF SMART COMPOSITE SENSORS FOR IMPACT DAMAGE DETECTION

Ali, Tabatabaeian[a], Sakineh, Fotouhi[a], Philip, Harrison[a], Mohammad, Fotouhi[a]

a: School of Engineering, University of Glasgow, Glasgow, UK – 2611578T@student.gla.ac.uk

Abstract: *This paper aims to study the feasibility of smart thin-ply hybrid glass/carbon sensors in quasi-static impact damage detection and analyse different design strategies to achieve an optimal sensor performance. A set of carbon fibre reinforced polymer (CFRP) specimens was manufactured, and the hybrid sensing layers were attached and evaluated. New architectures of hybrid sensing layers are proposed using woven prepregs and introducing pre-cuts to increase stress concentration. The sensors are used under indentation to detect the damage. Outcomes established key design insights, which will be used further in developing the self-sensing technology and may result in more sustainable composite structures that are light-weight, easy to inspect and last longer.*

Keywords: Self-sensing; Composite materials; Structural health monitoring

1. Introduction

Fibre reinforced polymer (FRP) composites are vastly applied in different sectors such as aerospace, automotive, wind turbine and civil engineering industries. Despite having several advantages over conventional engineering materials, there is still room for improving FRP composites, for example, developing new structural health monitoring (SHM) techniques to study their damage evolution and potentially enhance their failure mechanisms to avoid unexpected fracture or failure.

The damage detection using smart thin-ply hybrid glass/carbon composite sensors is a new chapter in SHM of composite structures, inspired by some early studies on the pseudo-ductile hybrid (PDH) composites [1-3]. PDH composites have recently been introduced as a new generation of FRP composites to address sudden and unexpected failure. When demonstrating pseudo-ductile behaviour in thin interlayer glass/carbon-epoxy hybrid composites, a pattern was observed by Czél and Wisnom [3] during the gradual failure of the specimens. The translucent nature of the constituent glass-epoxy layers made delamination detection possible to the naked eye. It was realised that this could be used for sensing damage on the surface of a structure, offering the potential for safer operation in service. This SHM technology is lightweight, bio-inspired, and wireless and has mainly been investigated in tensile loading [4].

This paper explores the feasibility of hybrid glass/carbon sensors in damage detection, specifically for FRP composite structures under indentation (quasi-static impact) loading conditions. To this end, after demonstrating the applicability of the sensing system to detect indentation damage, we made some developments in the design of the sensor: a) the unidirectional (UD) glass layer was replaced by a woven glass layer, and b) the influence of discontinuity in the sensor, in the form of pre-existed cuts, was studied. The results highlighted that woven glass can be a good alternative to UD glass, and the sensor activation threshold can be well set at a desired load level by applying cuts in carbon layer.

  doi:10.5075/epfl-298799_978-2-9701614-0-0

2. Experimental procedure

2.1 Design concept

The design concept is based on the change in the appearance of a hybrid glass/carbon sensor when loaded beyond a predefined strain. The sensor is on the component's surface and experiences similar strains as the material beneath. It consists of a 'sensing' layer (carbon layer) and an outermost layer (glass layer). The intact carbon layer absorbs the light through the translucent glass layer showing a dark appearance. After the strain exceeds the failure strain of the carbon layer, the carbon layer develops multiple fractures, and the light is reflected from the interfacial damaged glass/carbon are around the carbon layer fractures, demonstrating light stripes. The visible interfacial damage is caused by the fragmentation of the carbon fibre sensing layer followed by stable, dispersed delamination [5]. The schematic of the sensor-set up and its attachment to a substrate material is shown in Figure 1.

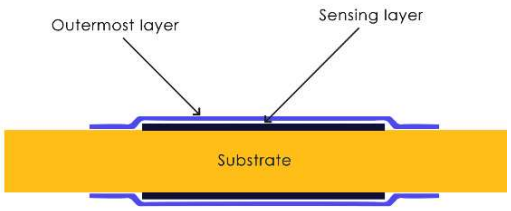

Figure 1. Schematic of hybrid thin-ply composite sensors attached to a substrate material

Various parameters can influence the design of the proposed hybrid composite sensors. Their geometry (length and width) can be varied as well as the stiffness ratio of the sensor to the substrate by either changing the thickness of the layers or by utilising different composite prepreg materials. This technology is an ongoing field in SHM of composites, and there is still much room for improvement, particularly in developing new designs for the thin-ply hybrid composite sensors to monitor low velocity impact and indentation damages.

2.2 Materials and manufacturing

Unidirectional IM7 carbon/913 epoxy prepreg supplied by Hexcel was used to fabricate the reference laminate with standard dimensions based on the ASTM D7136-07 (100 mm*150 mm). Two types of hybrid sensors, made from UD glass/YS 90A carbon and woven glass/YS 90A carbon with the same size as the reference laminates, were integrated into the front and back face of the laminates and cured at the same time as the core laminate. The core laminate was laid up in a quasi-isotropic $[+45/0/90/-45]_{4s}$ stacking sequence where 0 is the direction of unidirectional fibre orientation parallel to the long side of the plate. The sensors were composed of a single layer of the YS 90A carbon prepreg, with 90 orientation, sandwiched between the core laminate and a single layer of a glass prepreg with 90 orientation (Figure 2). It should also be noted that the total thickness of the sensor integrated specimens was 4.65 mm and 4.50 mm for specimens with UD and woven glass layers, respectively.

  doi:10.5075/epfl-298799_978-2-9701614-0-0

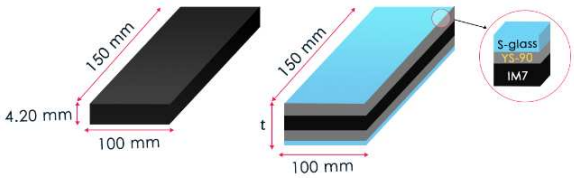

Figure 2. Schematic of the reference and sensor integrated specimens

In order to investigate the feasibility of the proposed sensing system, two sets of samples, with and without the sensor, were manufactured. Also, two other sets of sensor integrated samples was manufactured in which: an array of cuts was made in the sensing layer (carbon layer) using a V-shape blade (Figure 3) [6] in one group, and UD glass was replaced by woven glass layer in another group. Each coupon test was repeated three times, and the average amounts are reported in this paper. A schematic of different specimen groups manufactured in this study is represented in Figure 4.

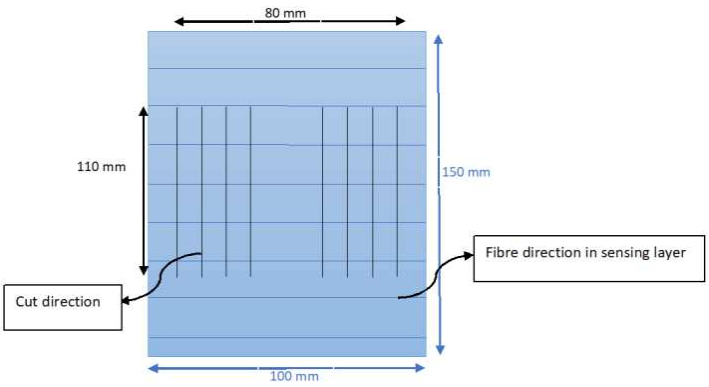

Figure 3. The cut pattern for the carbon layers of the discontinuous hybrid composite plates

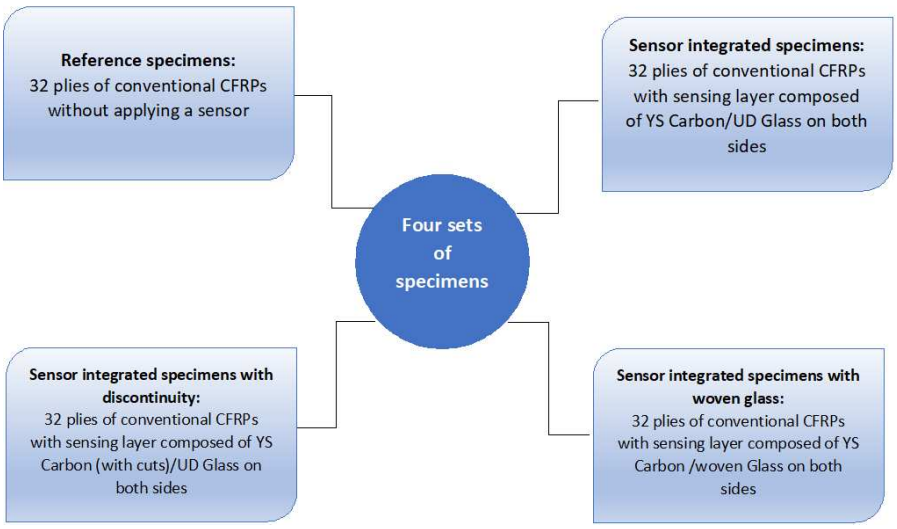

Figure 4. Different sets of manufactured specimens in this study

  doi:10.5075/epfl-298799_978-2-9701614-0-0

2.3 Indentation tests

In some cases, static indentation tests can be a suitable substitute for low velocity impact tests of laminated composite materials [7]. A Zwick 250 machine was used to perform indentation tests. The tests were carried out by mounting a 16 mm diameter steel indenter with the 150 mm*100 mm specimens simply supported on a 125 mm* 75 mm window and clamped lightly to it using four rubber-tipped clamps (Figure 5). The tests were conducted in controlled conditions imposing a displacement rate of 2 mm/min. Videos were also taken from both the front and back faces of the specimens during the test and related to different stages of the sensor activation.

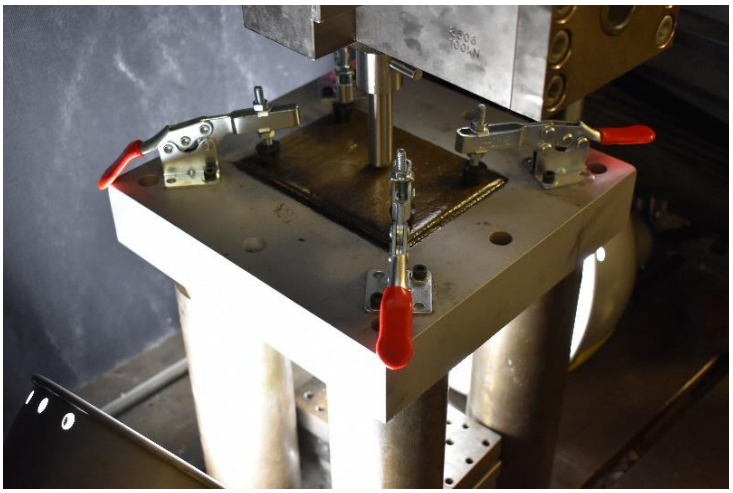

Figure 5. Experimental configuration for the static indentation tests

3. Results and discussion

3.1. Quasi-static impact behavior

The results of the indentation (quasi-static impact) tests of all four sets of specimens are shown in Figure 6. In all graphs, there are two major drops associated with the initiation and development of the damage in the form of delamination, where before the first drop, elastic behavior is observed. All the tests were continued until the force level of 12 KN, in which two main drops happened, but no fibre fracture was seen. A comparison of the four graphs indicates that integrating the sensors does not cause a significant difference in the force-displacement behavior of the CFRP composites under indentation loading. However, the reference specimen experienced a slightly higher deformation after the load drop compared to the sensor integrated specimens.

The results also clarify that the specimens equipped with woven glass in their sensing layer would undergo a higher deformation level under the same force value than samples with the UD glass layer, particularly after the first load drop. Moreover, a different force-deformation response is seen in specimens with woven glass layer after the second load drop, where multiple subsequent drops are observed. The force-deformation response provided by these graphs would help in the optimal designing of hybrid glass/carbon sensors by calculating the desired strain levels for sensor activation. This can also help determine the required critical energy level to induce delamination damage in drop-weight impact tests, as suggested in [7].

  doi:10.5075/epfl-298799_978-2-9701614-0-0

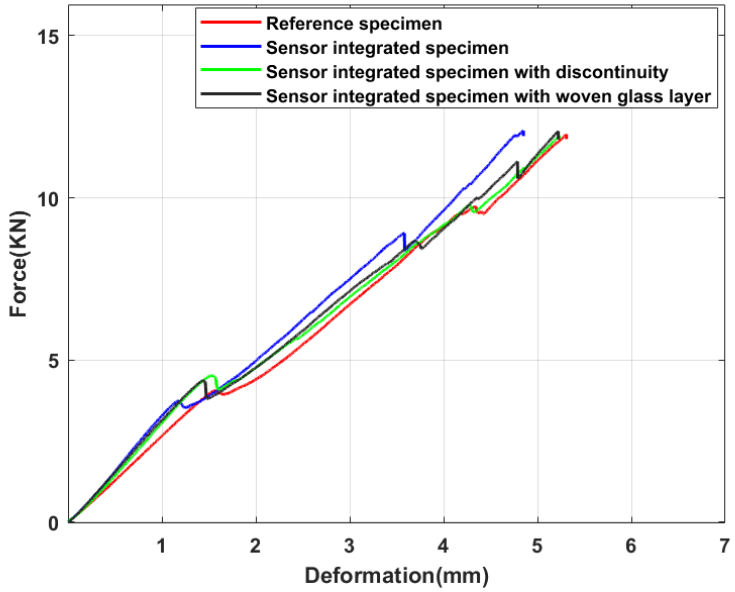

Figure 6. Quasi-static impact behavior of different sets of specimens

3.2. Sensor activation and visual observations

The specimens' back and front faces were monitored during the tests, and videos were taken from both sides to evaluate the sensor activation process. The time of each video was then related to the force-time graphs obtained by the indentation machine software. The load level at which sensor was activated is illustrated in Figure 7. In all three groups, the back face sensor was activated sooner than the front face one. Also, in all samples, the back and front face sensors were activated before the first and second load drops, respectively, which are way before the final fibre fracture.

As shown by Figure 7(b), sensor activation on two sides of the specimens happened at a lower force level compared to Figure 7 (a), especially in the front face, where the required force to activate the sensor has decreased from nearly 6.5 KN in intact specimens to 5 KN in specimens with discontinuities in their sensing layer, suggesting that initiation of the impact-induced delamination can be controlled by causing some discontinuities in the form of cuts.

Figure 7(c) demonstrates the required force level for sensor activation in the back and front faces of the specimens with the woven glass in their sensing layer. The load value for sensor activation in the back face is slightly higher than that of samples with the UD glass, while in the front face, sensors with the woven glass were activated at a lower force level. This suggests that the damage in the back face is due to tension and is dominated by the fibre properties, whereas for the front face, delamination damage is active. The earlier delamination damage in the woven is due to lower toughness of the woven glass prepreg compared with the UD glass that is an aerospace grade prepreg. A similar behavior was observed comparing the UD glass samples with and without discontinuities, where there is almost no difference between the damage in the back face initiation time, whereas the front face damage was initiated earlier for the sample with discontinuities due to the lower critical energy required for delamination initiation.

Figure 8 shows the back and front faces of the specimens after the quasi-static impact tests. It is seen that while there is no visible sign of damage in reference samples (Figure 8(a)), it can be

  doi:10.5075/epfl-298799_978-2-9701614-0-0 published under CC BY-NC 4.0 license

clearly observed in all sensor integrated specimens, and this is more visible in the back face. No significant difference can be seen in sensors with and without discontinuities (Figures 8(b) and 8(c)), but the specimens with woven glass have a different appearance after the test. Given the thinner thickness of the sensors with a woven glass layer and their required activation load, they could potentially be a good alternative to UD glass layers in particular applications where the use of woven glass is advantageous.

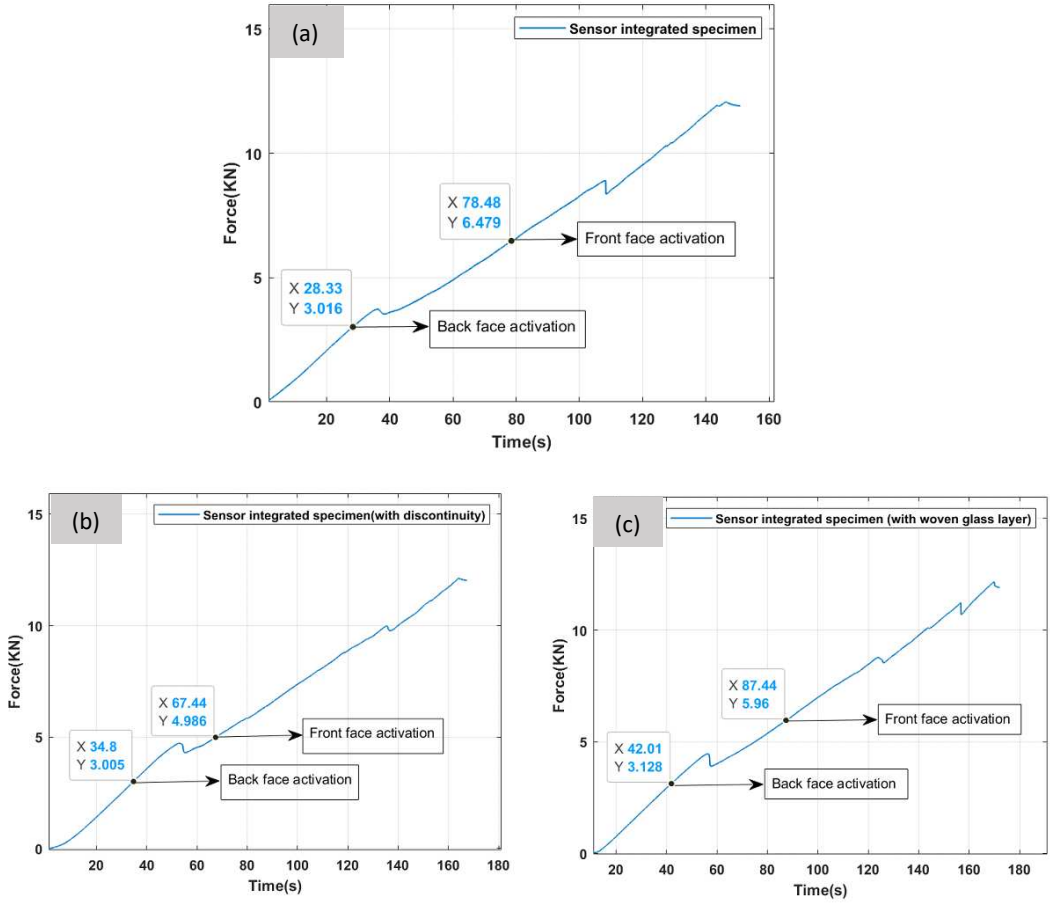

Figure 7. Sensor activation during quasi-static impact tests on the front face and back face of the samples

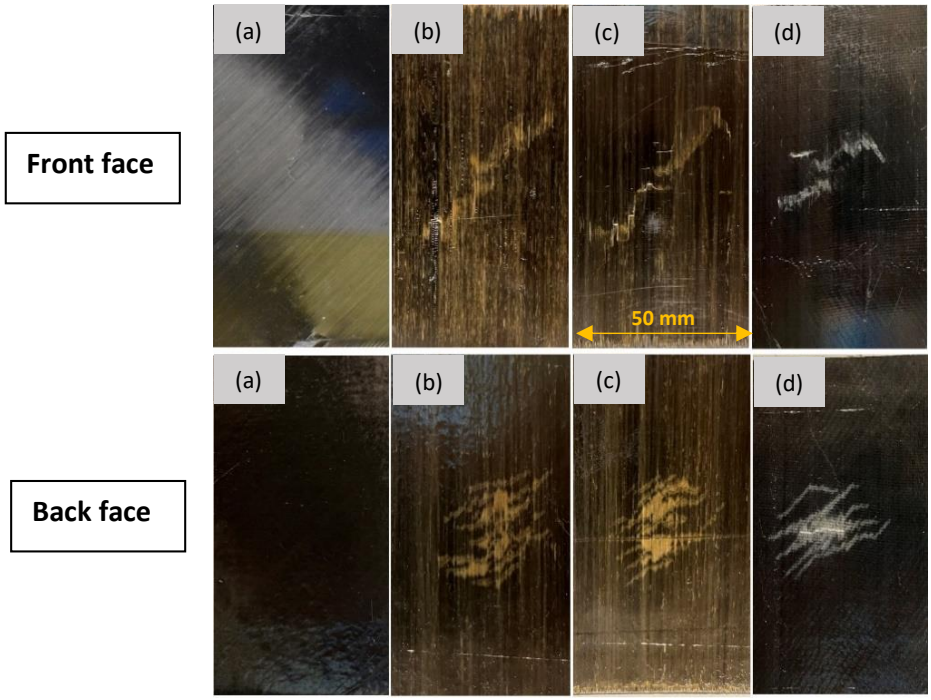

Figure 8. Visual observation of damage after quasi-static impact on the front face and back face of the samples: a) reference, b) with sensor (UD glass), c) with sensor (UD glass and discontinuity in carbon layer), d) with sensor (woven glass)

4. Conclusions

This paper explored the possibility of applying hybrid glass/carbon sensors on composite structures to monitor the quasi-static impact damage. Four different sets of specimens were manufactured, including reference samples (without sensor), sensor integrated samples with UD glass layer and without discontinuity, sensor integrated samples with UD glass layer and with discontinuity (in carbon layer), and sensor integrated samples with woven glass layer and without discontinuity. The feasibility of the proposed sensing technology and the influence of materials and pre-damages in the sensing layer were investigated experimentally. The results indicated that quasi-static impact damage could be well detected using hybrid thin-ply glass/carbon sensors, while they do not cause a significant difference in structural properties of the composites. It was seen that back and front face sensors are activated before the first and second load drop, respectively, which are way before the final fibre fracture. It was observed that the dominant front face damage in the sensor is delamination, whereas fibre properties are governing the back face damage.

The outcomes also suggested that initiation of the quasi-static impact-induced delamination can be well controlled by causing some discontinuities in the form of cuts. Another conclusion was that woven glass could potentially be a good alternative to UD glass in the sensing layer. The results of this work can be used in future research activities for optimal designing of self-sensing composites structures to trigger specific damage mechanisms under low-velocity impact loading conditions.

Acknowledgements

  doi:10.5075/epfl-298799_978-2-9701614-0-0

This work was funded under the UK Engineering and Physical Sciences Research Council (EPSRC) Grant EP/V009451/1 on Next generation of high-performance impact resistant composites with visibility of damage. The data necessary to support the conclusions are included in the paper.

5. References

1. Yu H, Longana ML, Jalalvand M, Wisnom MR, Potter KD. Pseudo-ductility in intermingled carbon/glass hybrid composites with highly aligned discontinuous fibres. Composites Part A: Applied Science and Manufacturing 2015; 73:35–44.
2. Jalalvand M, Czél G, Wisnom MR. Damage analysis of pseudo-ductile thin-ply UD hybrid composites - A new analytical method. Composites Part A: Applied Science and Manufacturing 2015; 69:83–93.
3. Czél G, Wisnom MR. Demonstration of pseudo-ductility in high performance glass/epoxy composites by hybridisation with thin-ply carbon prepreg. Composites Part A: Applied Science and Manufacturing 2013; 52:23–30.
4. Rev T, Jalalvand M, Fuller J, Wisnom MR, Czél G. A simple and robust approach for visual overload indication - UD thin-ply hybrid composite sensors. Composites Part A: Applied Science and Manufacturing 2019; 121:376–85.
5. Czél G, Jalalvand M, Wisnom MR. Design and characterisation of advanced pseudo-ductile unidirectional thin-ply carbon/epoxy–glass/epoxy hybrid composites. Composite Structures 2016; 143:362–70.
6. Czél G, Jalalvand M, Wisnom MR. Demonstration of pseudo-ductility in unidirectional hybrid composites made of discontinuous carbon/epoxy and continuous glass/epoxy plies. Composites Part A: Applied Science and Manufacturing 2015; 72:75–84.
7. Sun XC, Hallett SR. Barely visible impact damage in scaled composite laminates: Experiments and numerical simulations. International Journal of Impact Engineering 2017; 109:178–95.

  doi:10.5075/epfl-298799_978-2-9701614-0-0

IMPACT PROPERTIES OF FLAX-CARBON HYBRID COMPOSITES UNDER LOW-VELOCITY IMPACT

Mohsen, Bahrami [a], Mahoor, Mehdikhani [b], Yentl, Swolfs [b], Juana, Abenojar [a,c], Miguel Angel, Martínez [a]

a: In-Service Materials Performance Group, Universidad Carlos III de Madrid, Spain – mbahrami@ing.uc3m.es
b: Department of Materials Engineering, KU Leuven, Belgium
c: Mechanical Engineering Department, Universidad Pontificia Comillas, Madrid, Spain

Abstract: *In this study, the impact properties of interlayer hybrid thermoplastic composite were compared to the non-hybrid one. Hybrid laminates were produced using woven carbon and woven flax fibers and polyamide 12 matrix by hot-press with flax fiber plies as inner layers and carbon plies as outer layers. The non-hybrid carbon composite was also fabricated with similar thickness as a reference composite. The hybrid and non-hybrid composites were subjected to drop weight low-velocity impact with two different energies, namely 13.4 and 25.8 J. After hybridization, the absorbed impact energy decreased 12% and 16% for the 13.4 and 25.8-J impact energies, respectively. Moreover, characterization of the damage zone by X-ray micro-computed tomography confirmed the different damage mechanisms of hybrid composites compared to the non-hybrid ones for both impact energies.*

Keywords: Impact behavior; Hybrid laminate composites; Flax fibers; *X-ray computed tomography*

1. Introduction

Composite laminates with brittle fibers/matrices have a low resistance to dynamic loading, specifically to impact [1]. One of the current strategies to improve the mechanical performance of these composites is the hybridization of natural fibers with synthetic fibers to compensate for the disadvantages of one type with the advantages of the other type. Dealing with carbon fiber composites that suffer from limited toughness, introducing natural fibers as interlayer laminates apart from reduced cost and weight, can improve flexibility and compensate inherent brittleness of carbon fiber [2]. Another rationale for incorporating natural fibers in carbon composites would be obtaining various modes of damage propagation which can affect mechanical properties such as impact resistance [3].

Interlayer hybrid composites containing flax fibers have been studied by many researchers to improve the mechanical properties of carbon fiber-reinforced composites. Kumar et al. [4] showed that the tensile strength and fatigue life of laminated hybrid composites of flax, carbon and polyvinyl butyral with sandwich structure improved compared to the pure flax or pure carbon composites due to the high failure strain value of flax and its semi-brittle behavior. Kureemun et al. [5] reported higher tensile stiffness of woven carbon-flax hybrid composite with respect to the non-hybrid carbon-epoxy composite due to the architectural crimp mismatch between carbon and flax fabrics. In the study of Dhakal et al. [6], unidirectional flax/carbon

  doi:10.5075/epfl-298799_978-2-9701614-0-0

composites exhibited higher tensile modulus with less brittle damage mechanisms compared to plain carbon laminates.

Composite laminates can be subjected to two impact loading categories during maintenance or in service, depending on the impact mass and velocity: low- and high-velocity impact loading. The low-velocity (large mass) impacts occur in the range of 1–10 m/s; however, the high-velocity (small mass) impacts have a velocity range of 50-1000 m/s [7]. High-velocity impact loadings provide more visible and severe damages, which could cause immediate failure and are usually easily detectable. On the other hand, the low-velocity impact loadings could lead to barely visible impact damages within the plies or at the interfaces; thus, they are more complex to assess [8]. Matrix cracking is usually the first type of failure caused by relatively low-velocity applied loads [9]. It might be followed by delamination between plies which is the most critical damage mechanism in impact of composites. Delamination causes a significant loss of flexural strength and stiffness and consequently, the load-bearing capability of the laminate can be significantly reduced [10].

A wide range of characterization techniques could be applied to identify the damage modes during the impact. The main limitation of destructive methods such as conventional sectioning followed by microscopy is that they usually produce new damage and residual stress during the cutting process [1]. In contrast, the most commonly used non-destructive methods, i.e. thermography [10, 11], X-ray radiography [12] and ultrasound [13, 14], detect subsurface damages and keep structural integrity simultaneously. Recently, X-ray micro-computed tomography (micro-CT), as an advanced non-destructive inspection technique, has gained a lot of attention due to its capability to provide three-dimensional (3D) images of the damage zone [15]. In this method, X-ray radiographs are taken at many different angles, which are then reconstructed mathematically to obtain a 3D image. In the last decade, the CT imaging technique was often used to evaluate composite materials in terms of porosity and defects [16-19].

This work compares the impact behavior of carbon-flax-polyamide12 hybrid laminates with non-hybrid carbon-polyamide12. Both hybrid and non-hybrid laminates were subjected to the drop weight low-velocity impact at two different energy levels, generating non-perforated damage to determine the energy absorption and impact failure behavior of the composites. In addition, micro-CT observation was employed to characterize the impact damages and failure modes.

2. Experimentation

2.1 Materials

Two kinds of woven fabric have been used in this study; flax fabric (2x2 twill, 400 g/m^2) supplied by Composites Evolution Ltd. (Chesterfield, UK), and carbon fabric (2x2 twill, HR-12K, 600 g/m^2) supplied by Materiales Estructurales Ligeros S.L (Barcelona, Spain). Both fibers were stored at room ambient temperature and relative humidity (RT≈23 °C, RH≈33%) before composite fabrication. A commercial polyamide 12 (PA12) pellets were provided by Arkema (Madrid, Spain) as the thermoplastic matrix.

2.2 Surface treatment

Since flax fibers usually have poor bonding with polymer matrices [4], the atmospheric pressure plasma torch (Plasma treat GmbH, Steinhagen, Germany) was employed on the flax fabrics surface to improve their adhesion with the PA12 matrix. The device setup and technical details

  doi:10.5075/epfl-298799_978-2-9701614-0-0

were explained in a previous study [20]. The carbon fibers exhibited an excellent adhesion with the PA12 matrix without surface treatment.

2.3 Composite fabrication

The laminated composites were manufactured by a hot press machine (Fontijne Presses TPB374, Barendrecht, Netherlands). The maximum temperature and pressure were set to 200 °C and 3 MPa. Hot press parameters were selected based on the thermal and rheological properties of the matrix and fibers and other considerations. The non-hybrid composite consisted of four plies of woven carbon (CCCC) and the hybrid one included two inner plies of woven flax which were sandwiched between two outer plies of carbon (CFFC). A single PA12 layer was positioned between every ply as well as on the outside of the lay-up (see Fig. 1).

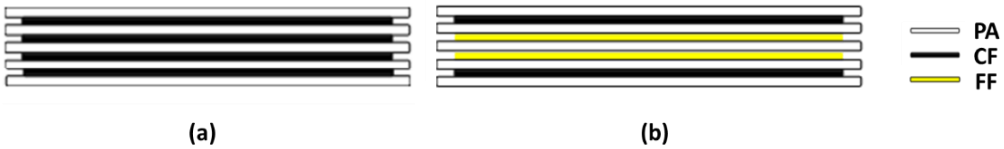

Figure 1: Manufacturing layup configurations: (a) non-hybrid carbon fiber composite (CCCC), (b) hybrid carbon-flax composite (CFFC).

2.4 Impact test

Drop-weight impact test in accordance with ASTM-D7136 standard was performed by an impact testing machine (CEAST/Instron 9340) with a hemispherical tup (diameter and mass of 16 mm and 5.41 kg, respectively) to study the low-velocity impact behavior of the composite laminates. Four specimens per composite type were tested at two energy levels of 13.4 and 25.8 J. The initial height of the impactor for both impact energies was set to 0.248 m, and for the higher impact energy, a 5-kg external weight was added to the tup weight. The composites specimens with a dimension of 60 x 60 x ~2.5 mm were clamped in a pneumatically actuated clamping fixture with an inner diameter of 40 mm. Moreover, the rebound brake was applied to prevent multiple impact events. Fig. 2 presents an overview of the drop-weight impact testing setup.

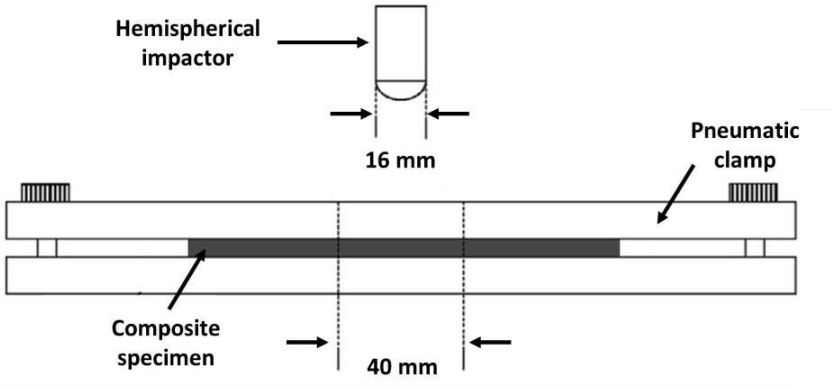

Figure 2: Schematic of the drop-weight impact test setup

2.5 Micro-CT image acquisition and processing

The post-impact inspection of the composites was performed using a micro-computed tomography system TeScan UniTom XL. The impacted specimens were mounted on the

scanner's rotation stage. The X-ray tube voltage and current for the scan were fixed to 80 kV and 200 mA, respectively. During each scan, which took about 100 min, 2400 radiographic projections were taken over a 360° rotation with an exposure time of 750 ms and voxel size of 15 µm. The reconstruction of the projection data to cross-sectional images was performed with the Octopus reconstruction software.

3. Results and discussion

A number of parameters could be defined by analyzing the impactor force-displacement curve obtained during the drop-weight impact test. The closed-loop area corresponds to the laminate's absorbed energy (E_a). The total area under the hysteresis cycle describes the incident energy (E_i). Rebound energy (E_r) is the difference between E_a and E_i. According to Fig. 3 and the resulting key impact parameters in Table 1, the absorbed energy ratio (E_a/E_i) decreased after hybridization by 12% and 16% for impact energies of 13.4 J and 25.8 J, respectively. It suggests that non-hybrid composites can dissipate a higher amount of impact energy. It is reasonable since the density of flax fibers (1.5 g/cm^3) is lower than carbon fibers (1.78 g/cm^3), non-hybrid composites have a higher overall fiber volume fraction (36 % vs. 25 %), which leads to the better impact behavior and higher absorbed energy. On the other side, compared to the non-hybrid composites, the peak force and the rebound energy increased in hybrid composites. Accordingly, by inserting flax plies in the middle of laminate, the force bearing capacity of the composite increased by about 20% and 35% for 13.4 J and 25.8 J impact energies.

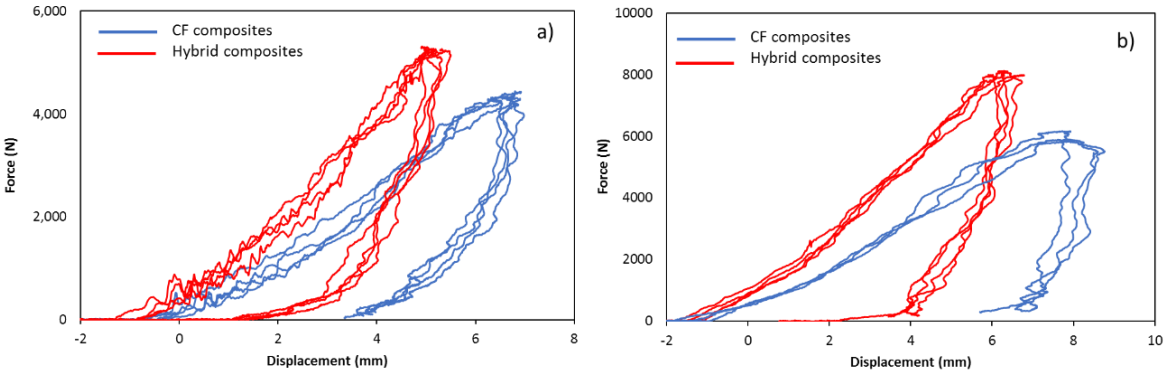

Figure 3: Impact hysteresis curves for the two types of composite laminates at different energies a) 13.4 J, b) 25.8 J

Table 1: Impact properties of composites tested at different impact energies

Composites	E_i [J]	E_a [J]	E_r [J]	Absorbed E ratio [%]	Peak force [kN]
CCCC	**13.4 J**				
	14.88 ± 0.44	10.77 ± 0.26	4.11 ± 0.32	72.39 ± 1.54	4.39 ± 0.05
	25.8 J				
	26.21 ± 1.67	23.42 ± 1.26	2.69 ± 0.87	89.43 ± 2.42	5.93 ± 0.12
CFFC	**13.4 J**				
	14.10 ± 0.55	9.10 ± 0.24	5.00 ± 0.35	63.58 ± 1.98	5.27 ± 0.02

			25.8 J		
	28.58 ± 2.17	21.48 ± 1.40	6.81 ± 1.19	75.30 ± 3.50	8.00 ± 0.17

Micro-CT images revealed more extensive internal damage of the hybrid composite compared to the non-hybrid one. During the impact, for both types of composites, the plies on the impacted face were compressed while those on the opposite face (back side) were stretched. In the non-hybrid CF composites, since the strength of carbon fiber composites under compression is weaker than in tension, the damaged area was more intense around the impact point. The damage in the woven carbon fiber composite (Fig. 4a and Fig. 5a) was predominantly inter-and intra-yarn debonding, delamination and longitudinal cracks. Another reason for less damage on the back side would be the locking tendency of composite layers together as an effect of impact [21].

On the other hand, in hybrid composites (Fig. 4b and Fig. 5b) compared to the non-hybrid ones, the damage appeared to be much more extensive on the back side, where the shear stress between adjacent layers of carbon and flax is more significant due to the considerable difference in modulus of these two layers. The carbon failure modes in the hybrid were similar to those in the non-hybrid composite. The damage of the flax fiber layer, which is less rigid and has a poorer bonding characteristic, was mainly intra-yarn debonding, inter-yarn transverse cracking, fiber/matrix debonding and fibers delamination. Moreover, the high transverse shear stress at the back side caused matrix cracking which propagated through the thickness. Passing from 13.4 J (Fig. 4) to the higher impact energy of 25.8 J (Fig. 5), delamination and transverse microcracks are more evident, especially in the hybrid laminates.

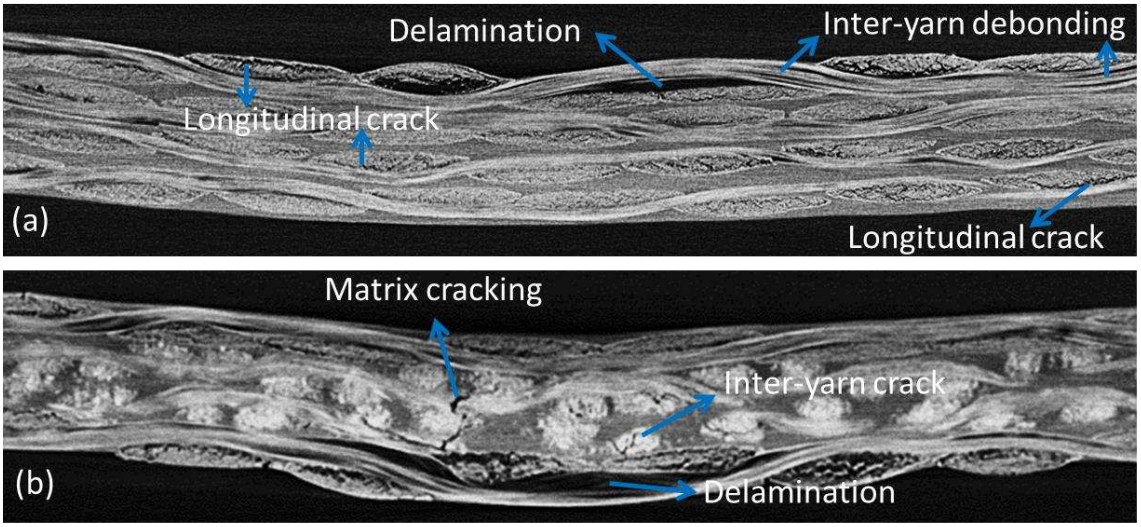

Figure 4: Micro-CT images of composites after impact (13.4 J): (a) non-hybrid; (b) hybrid

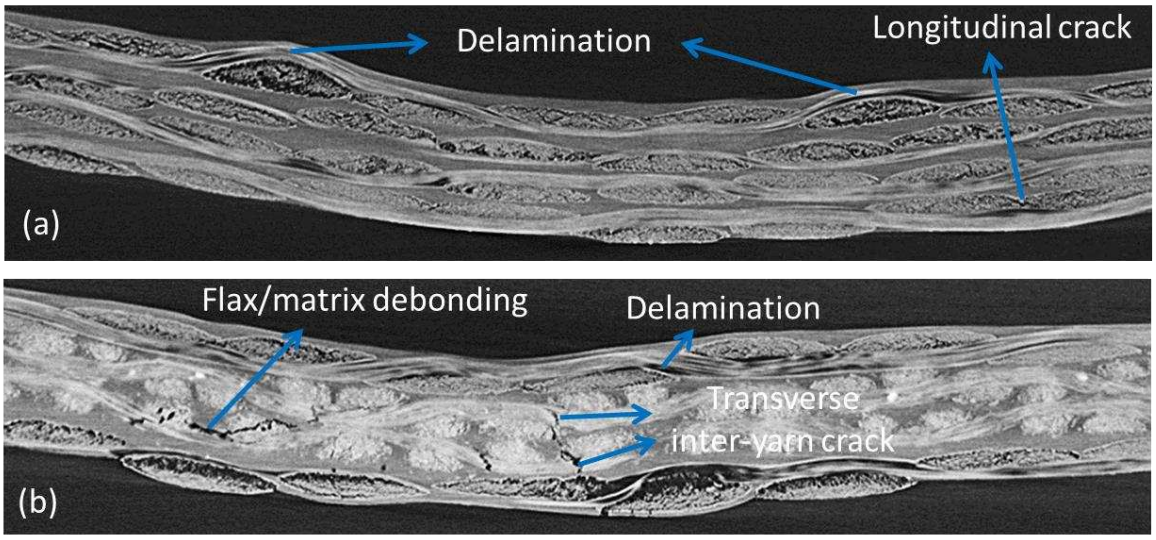

Figure 5: Micro-CT images of composites after impact (25.8 J): (a) non-hybrid; (b) hybrid

4. Conclusion

In this research work, the low-velocity impact behavior of the carbon-flax-PA12 hybrid composite was compared to the non-hybrid carbon-PA12 composite. The non-hybrid carbon composite (CCCC) had higher absorbed energy, while the hybrid (CFFC) tolerated higher peak force and rebound energy. In addition, micro-CT scans revealed higher damage development in the hybrid composite, likely caused by shear stress between flax and carbon layers. This resulted in more failure modes, which were mainly located on the back side. The investigated hybrid composite in this study had lower absorbed energy with different damage mechanisms, which can be assessed in future work by increasing the fiber volume fraction or modifying the lay-up sequence and plies number, which can affect the impact behavior of composite laminates.

Acknowledgments

The authors would like to acknowledge the KU Leuven XCT Core facility, and M. Mehdikhani would like to acknowledge his FWO Postdoc Fellowship, project ToughImage (1263421N).

5. References

1. Shyr T-W, Pan Y-H. Impact resistance and damage characteristics of composite laminates. Composite structures. 2003;62(2):193-203.
2. Wang A, Wang X, Xian G. Mechanical, low-velocity impact, and hydrothermal aging properties of flax/carbon hybrid composite plates. Polymer Testing. 2020;90:106759.
3. Santulli C. Mechanical and impact damage analysis on carbon/natural fibers hybrid composites: a review. Materials. 2019;12(3):517.
4. Kumar D, Faisal N, Layek A, Priyadarshi G, editors. Enhancement of mechanical properties of carbon and flax fibre hybrid composites for engineering applications. AIP Conference Proceedings; 2021: AIP Publishing LLC.
5. Kureemun U, Ravandi M, Tran L, Teo W, Tay T, Lee H. Effects of hybridization and hybrid fibre dispersion on the mechanical properties of woven flax-carbon epoxy at low carbon fibre volume fractions. Composites Part B: Engineering. 2018;134:28-38.

  doi:10.5075/epfl-298799_978-2-9701614-0-0

6. Dhakal HN, Sain M. Enhancement of mechanical properties of flax-epoxy composite with carbon fibre hybridisation for lightweight applications. Materials. 2020;13(1):109.
7. Safri S, Sultan M, Yidris N, Mustapha F. Low velocity and high velocity impact test on composite materials–a review. Int J Eng Sci. 2014;3(9):50-60.
8. Giurgiutiu V. Smart materials and health monitoring of composites. University of South Carolina, Columbia, SC, United States. 2017.
9. Richardson M, Wisheart M. Review of low-velocity impact properties of composite materials. Composites Part A: Applied Science and Manufacturing. 1996;27(12):1123-31.
10. Meola C, Carlomagno GM. Impact damage in GFRP: new insights with infrared thermography. Composites Part A: Applied Science and Manufacturing. 2010;41(12):1839-47.
11. Xie H, Fang H, Li X, Wan L, Wu P, Yu Y. Low-velocity impact damage detection and characterization in composite sandwich panels using infrared thermography. Composite Structures. 2021;269:114008.
12. Tan KT, Watanabe N, Iwahori Y. X-ray radiography and micro-computed tomography examination of damage characteristics in stitched composites subjected to impact loading. Composites Part B: Engineering. 2011;42(4):874-84.
13. Morokov E, Levin V, Chernov A, Shanygin A. High resolution ply-by-ply ultrasound imaging of impact damage in thick CFRP laminates by high-frequency acoustic microscopy. Composite Structures. 2021;256:113102.
14. Vandendriessche J, Orta AH, Verboven E, Van Paepegem W, Van Den Abeele K, Kersemans M. Probabilistic ultrasound C-scan imaging of barely visible impact damage in CFRP laminates. Composite Structures. 2022:115209.
15. Withers PJ, Preuss M. Fatigue and damage in structural materials studied by X-ray tomography. annual review of materials research. 2012;42:81-103.
16. Garcea S, Wang Y, Withers P. X-ray computed tomography of polymer composites. Composites Science and Technology. 2018;156:305-19.
17. Little JE, Yuan X, Jones MI. Characterisation of voids in fibre reinforced composite materials. NDT & E International. 2012;46:122-7.
18. Gigliotti M, Pannier Y, Gonzalez RA, Lafarie-Frenot MC, Lomov SV. X-ray micro-computed-tomography characterization of cracks induced by thermal cycling in non-crimp 3D orthogonal woven composite materials with porosity. Composites Part A: Applied Science and Manufacturing. 2018;112:100-10.
19. Quiney Z, Weston E, Nicholson PI, Pattison S, Bache MR. Volumetric assessment of fatigue damage in a SiCf/SiC ceramic matrix composite via in situ X-ray computed tomography. Journal of the European Ceramic Society. 2020;40(11):3788-94.
20. Bahrami M, Enciso B, Gaifami CM, Abenojar J, Martinez MA. Characterization of hybrid biocomposite Poly-Butyl-Succinate/Carbon fibers/Flax fibers. Composites Part B: Engineering. 2021:109033.
21. Nisini E, Santulli C, Liverani A. Mechanical and impact characterization of hybrid composite laminates with carbon, basalt and flax fibres. Composites Part B: Engineering. 2017;127:92-9.

  doi:10.5075/epfl-298799_978-2-9701614-0-0

ENHANCEMENT OF THIN-PLY COMPOSITES TRANSLAMINAR TOUGHNESS THROUGH FIBER-HYBRIDIZATION: TOWARDS A DISCRIMINATION WITH THE PLY THICKNESS EFFECT?

Guillaume Broggi[a], Joël Cugnoni[b], Véronique Michaud[a]

a: Laboratory for Processing of Advanced Composites (LPAC), Institute of Materials (IMX), Ecole Polytechnique Fédérale de Lausanne (EPFL), Station 12, 1015 Lausanne, Switzerland – guillaume.broggi@epfl.ch
b: School of Management and Engineering Vaud, University of Applied Sciences and Arts Western (HES-SO), Switzerland

Abstract: *Thin-ply composites are high-performance materials known for their superior mechanical properties and brittle failure at nearly the ultimate strain of the fiber, while ordinary thick-plies fail by transverse cracking and delamination at a fraction of that strain. Such a brittle failure results in poor translaminar toughness and is a significant shortcoming in the design of damage tolerant structural applications. Recent studies investigated the possibility to restore thin-ply translaminar toughness through fiber hybridization. However, the sole translaminar toughness results did not permit to differentiate the ply-thickness effect from the hybridization effect. In this work, a pull-out bundle characterization framework based on the systematic analysis of the fracture surfaces is introduced. Coupled to the mechanistic investigation of the energy dissipated by these bundles, it highlights phenomenological key differences enabled by the fiber hybridization.*

Keywords: thin-ply; fiber-hybrid; translaminar toughness; fracture mechanics

1. Introduction

By accounting for the presence of cracks in composite materials, damage tolerant design is one of the engineering methods allowing for lighter structures and a more sustainable mobility. Despite outstanding mechanical performance thoroughly studied over the past decade [1–3], thin-plies composites are unfortunately not optimal for this approach. Quasi-isotropic laminates were reported to fail in tension at a strain as close as 90% of the fiber ultimate strain whereas regular thick-ply equivalents would fail at 40% [4]. This remarkable result is attributed to a failure mechanism dominated by the fibers as the development of micro-cracking, transverse cracking and delamination is almost suppressed by the thin-ply effect [5]. Conversely, the absence of these distributed damage locations reduces the amount of energy dissipated during the crack propagation and translaminar toughness has been shown to significantly decrease with ply thickness [6,7]. Thus, thin-ply composites are not tolerant to translaminar cracking.

Recent studies investigated the reintroduction of distributed damage in thin-ply laminates before their failure through fiber hybridization [8,9]. Although distinctive failure modes were qualitatively observed, the contribution of the fiber hybridization to the toughness was barely distinguishable from the ply-thickness effect. This work aims to provide a quantitative characterization of the pull-out bundles, whose length has been shown to corelate with the translaminar toughness [6], in order to pave the way to a better understanding of the failure

  doi:10.5075/epfl-298799_978-2-9701614-0-0

mechanisms. The proposed method (i) maps in 3D the post mortem fracture surfaces, (ii) extracts 2D fracture profiles perpendicularly to the crack direction, (iii) postprocesses the profiles to (iv) output the bundle length, width and likelihood of occurrence and (v) link each bundle to an energy dissipated by debonding and rough friction through a finite element model. The results highlight phenomenological differences between fiber-hybrids and non-hybrids of equivalent ply-block thickness.

2. Materials and methods

2.1 Thin-ply fiber hybrids

Cross-ply thin-ply fiber-hybrid laminates were obtained by hand stacking low strain (subscript L) and high strain (subscript H) carbon prepregs, resulting in ply-by-ply hybrids. This study was restricted to commercially available materials, respectively a 30 gsm HR40 carbon fiber prepreg and a 60 gsm 34-700 carbon fiber prepreg, both produced by North Thin Ply Technology (NTPT) with the TP415 toughened epoxy system [10]. The layups, as reported in Table 1, were designed following the failure map proposed by Jalavand et al. [11], with the goal of delaying as much as possible the pseudo-ductility behavior while promoting the pull-out length. Indeed, a key aspect of thin-ply composites is arguably their outstanding mechanical performance and a too premature pseudo-ductility plateau leads to a low onset of damage and lowers their potential for structural applications. As illustrated in Figure 1, the influence of hybridization architecture was assessed by testing an unbalanced and a balanced ply-block – H2 and H3 hybrids, respectively – with the same ply thicknesses and fiber ratio.

Table 1: Laminates used in this study. t_H, t_L and $t_{Ply-block}$ are high strain, low strain and ply-block prepreg areal weight, respectively. Nb. is the number of crack surfaces observed.

Name	Lay-up	t_H $[gsm]$	t_L $[gsm]$	$t_{Ply-block}$ $[gsm]$	Sample thick. [mm]
Baseline B1	$[90^L\backslash 0^L]_{ns}$	0	30	30	4.39
Baseline B2	$[90^H\backslash 0^H]_{ns}$	60	0	60	3.99
Baseline B3	$[90_2^H\backslash 0_2^H]_{ns}$	120	0	120	4.07
Baseline B4	$[90_3^H\backslash 0_3^H]_{ns}$	180	0	180	4.15
Hybrid H1	$[90^H\backslash 90^L\backslash 0^H\backslash 0^L]_{ns}$	60	30	90	4.04
Hybrid H2	$[90_2^H\backslash 90_2^L\backslash 0_2^H\backslash 0_2^L]_{ns}$	120	60	180	4.26
Hybrid H3	$[90_1^H\backslash 90_2^L\backslash 90_1^H\backslash 0_1^H\backslash 0_2^L\backslash 0_1^H]_{ns}$	120	60	180	4.20

The plates were cured in an autoclave following NTPT instructions [10] and water-jet cut to run compact tension tests whose results were reported in a previous communication [9].

2.2 Fracture surface observations

Post-mortem upper and lower fracture surfaces – see Figure 2.a – were observed under 200x magnification with a VHX-5000 Keyence optical microscope for each compact tension specimen. The stitching feature along with the depth-of-field algorithm were used to map in 3D the fracture

  doi:10.5075/epfl-298799_978-2-9701614-0-0

surfaces, resulting in approximately $20000 \times 4000\ \mu m$ surfaces as depicted in Figure 2.b, with a resolution of $1.055\ \mu m \cdot px^{-1}$ in the focus plane. This approach was preferred over confocal or scanning electron microscopy based on a trade-off between scanning speed, size of the scanned area, and ease to derive quantitative data.

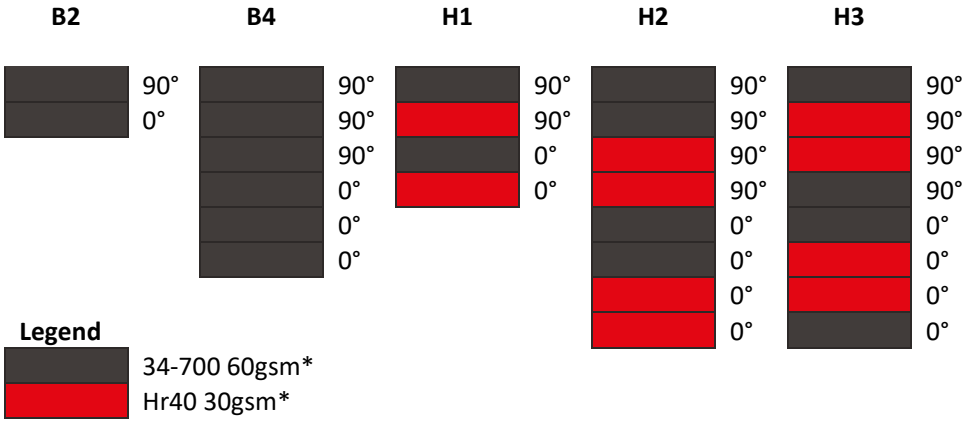

*Figure 1: Schematic illustrating the ply-block configuration and the cross-ply stacking of the samples used in this study. Not all baseline configurations are represented, refer to Table 1 for the exhaustive list. *Thicknesses are not to scale*

One-pixel-thick 2D fracture surface profiles in the transverse direction – i.e. along the direction perpendicular to the crack propagation – were then extracted every 10 pixels as shown in Figure 2.c, meaning that the features are analyzed with a resolution of $10\ \mu m$ in the crack propagation direction. Pre-crack and bridging areas were discarded to not bias the data. Similarly, the data after the last valid crack tip position as determined through the compact tension test were discarded.

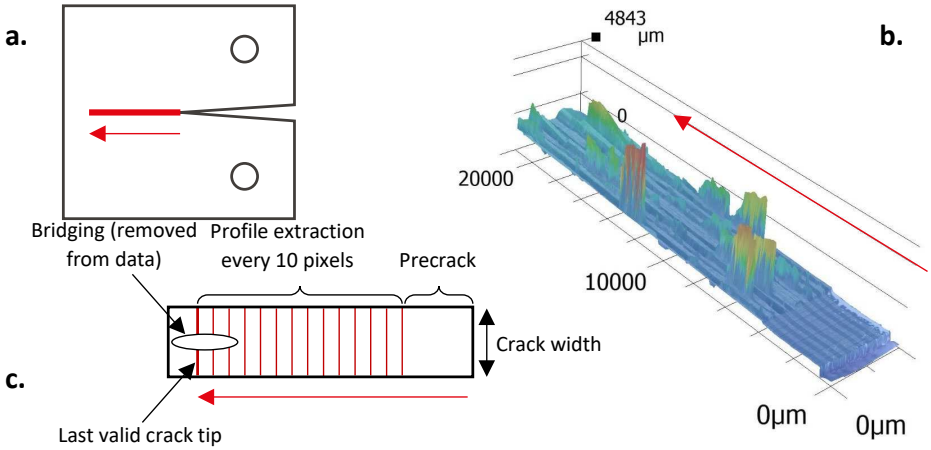

*Figure 2: **(a)** Schematic of a compact tension samples, lower fracture surface is highlighted in red; **(b)** Typical fracture surface observed by optical microscopy colored according to height; **(c)** Top view schematic of the fracture surface. The arrow stands for the crack propagation direction.*

2.3 Profile analysis

A typical crack profile is depicted in Figure 3 and illustrates the pull-out bundles observed at the crack surface. The profile appears asymmetric with respect to the crack plane. This is due to the

failure of the optical microscope to resolve deep and narrow openings – due for instance to a lack of light. To mitigate this issue, both lower and upper crack surfaces were observed. The positive bundles observed at one surface are supplemented by the positive bundles observed at the other surface to form the complete crack profile.

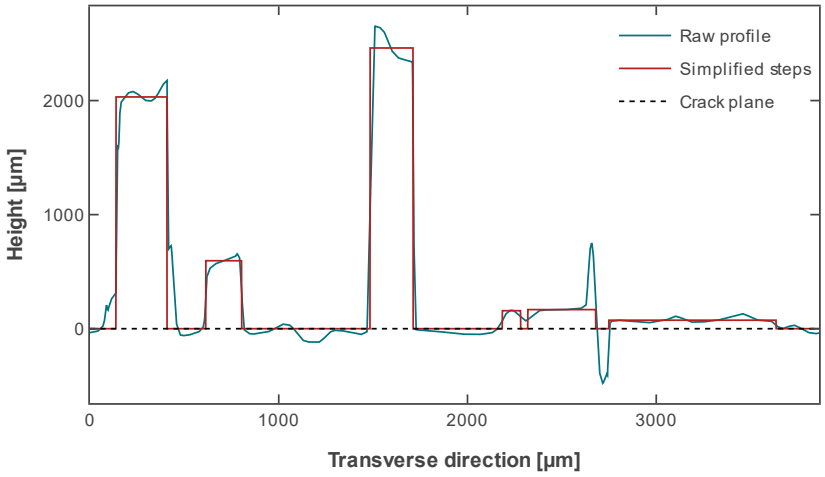

Figure 3: Typical fracture profile and simplified profile used to characterize pull-out bundles.

In practice, a crack plane was manually defined using the same 90° plies for both surfaces. Positive pull-out bundles were then measured with respect to this crack plane. Due to misalignments and optical artefacts, the profile matching from one surface to another is challenging. Each profile was thus treated as an independent observation. The resulting statistical descriptor is in fact only accounting for 50% of the information. With this approach, matching the profiles is not required and the whole procedure can be automatized but information is lost about the small pull-out bundles close to the crack plane, due to the incertitude regarding the crack position, and about the distance between two consecutive positive and negative bundles.

A Python algorithm was implemented to match simple steps with the profile as depicted in Figure 3. Small features whose dimensions were below $50\ \mu m$ were considered as noise and discarded. The height, width, and probability of step occurrence were used as statistical descriptors to characterize the pullout distribution for each material configuration. The developed lengths of the profiles were similarly aggregated to characterize the overall crack dimension.

2.4 Energy dissipation simulations

The fracture process in ply-by-ply fiber-hybrids laminates under longitudinal tensile loading is considered to start with ply fragmentation as shown in *Figure 4*.a. This process is described for instance by Mesquita et al. [12]. The low strain fibers fail as the strain increases. When a cluster of broken fibers reaches a critical size, a transverse crack propagates inside the low strain ply leading to its fragmentation. Thanks to the thin-ply effect the transverse crack does not propagate further and high strain plies keep carrying the load, preventing a catastrophic failure of the laminate. The ply block will finally also fail, most probably close to a transverse crack. This process is assumed to explain the presence of pull-out bundles at the crack surface. In the case of non-hybrids, weak points in the material may act as low strain fibers and explain the presence of pullout bundles.

  doi:10.5075/epfl-298799_978-2-9701614-0-0

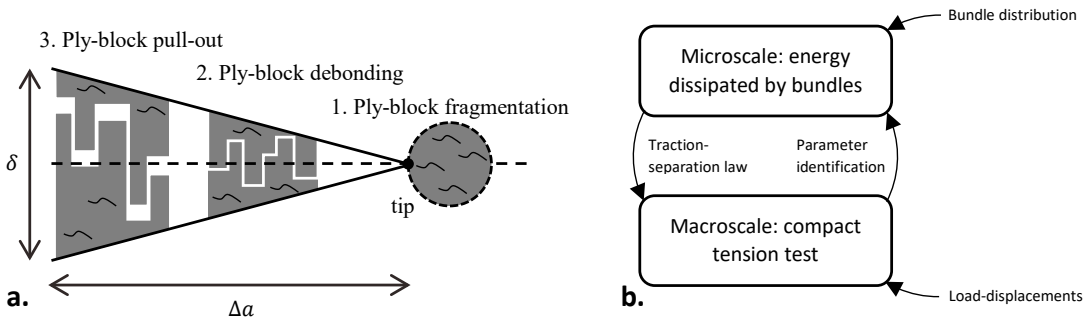

Figure 4: ***(a)*** *Damage sequence in thin-ply hybrids;* ***(b)*** *Overview of the modelling approach.*

Fragmentation and ply block failure happen at nearly zero crack opening displacement (COD) – few micrometers – but at high stresses. It corresponds to the initiation fracture toughness as measured in the compact tension test. As the crack progresses, consecutive mode II delamination followed by rough friction are expected to develop during pull-out of ply blocks. These processes involve much lower stresses but are acting on a large COD – over several millimeters. They are thus potentially very dissipative. These three steps may be efficiently accounted for by a macroscopic cohesive law [13].

Based on these assumptions, an Abaqus first-order dual scale finite element model was developed following the approach detailed in Figure 4.b. At the microscale, a shear cohesive law coupled to a Coulomb frictional behavior was implemented at pull-out interfaces to capture the energy dissipated by the pull-out of the bundles. A macroscale traction-separation law was derived from this model and implemented in a compact tension model. The debonding and frictional parameters were then obtained through inverse identification of the load-displacements curves from the compact tension tests. They were finally used to predict the energetic contribution of each pull-out bundle as a function of its length.

3. Results and Discussion

More than 64000 profiles were analyzed, and the corresponding pull-out bundle distributions are shown in Figure 5. Knowing that the profiles are 1 pixel-thick, the results were normalized by the crack area projected on to the crack plane for a direct comparison between the configurations. Material distributions were obtained by multiplying the results by a factor of 2 to account for the fact that only positive characteristics were analyzed.

Overall, the majority of bundles are below $400\ \mu m$ height. The contrast between thin-ply materials – baselines B1 and B2 whose ply thickness is 30 gsm and 60 gsm respectively – and thick-ply materials – baseline B4 with 180 gsm – is clearly highlighted in the first subplot, where the maximal pull-out length scales linearly with the ply-block thickness for the same material.

The distributions reveal two concomitant damage behaviors. The first one corresponds to crack deviations that stay close to the crack plane – bundles below $200\ \mu m$ – but which are distributed over a wide range of widths. This accounts for the large-scale crack variations over several plies that can be noticed as a "stair-case" on the crack surface. This behavior prevails in thin-plies as they exhibit almost no pull-out bundles confirming results already reported in the literature [6,7]. The second corresponds to the pull-out of actual medium-sized and large-scale fiber bundles – over $500\ \mu m$ – who are mostly confined to one ply-block and is more likely to occur in thick-plies.

  doi:10.5075/epfl-298799_978-2-9701614-0-0

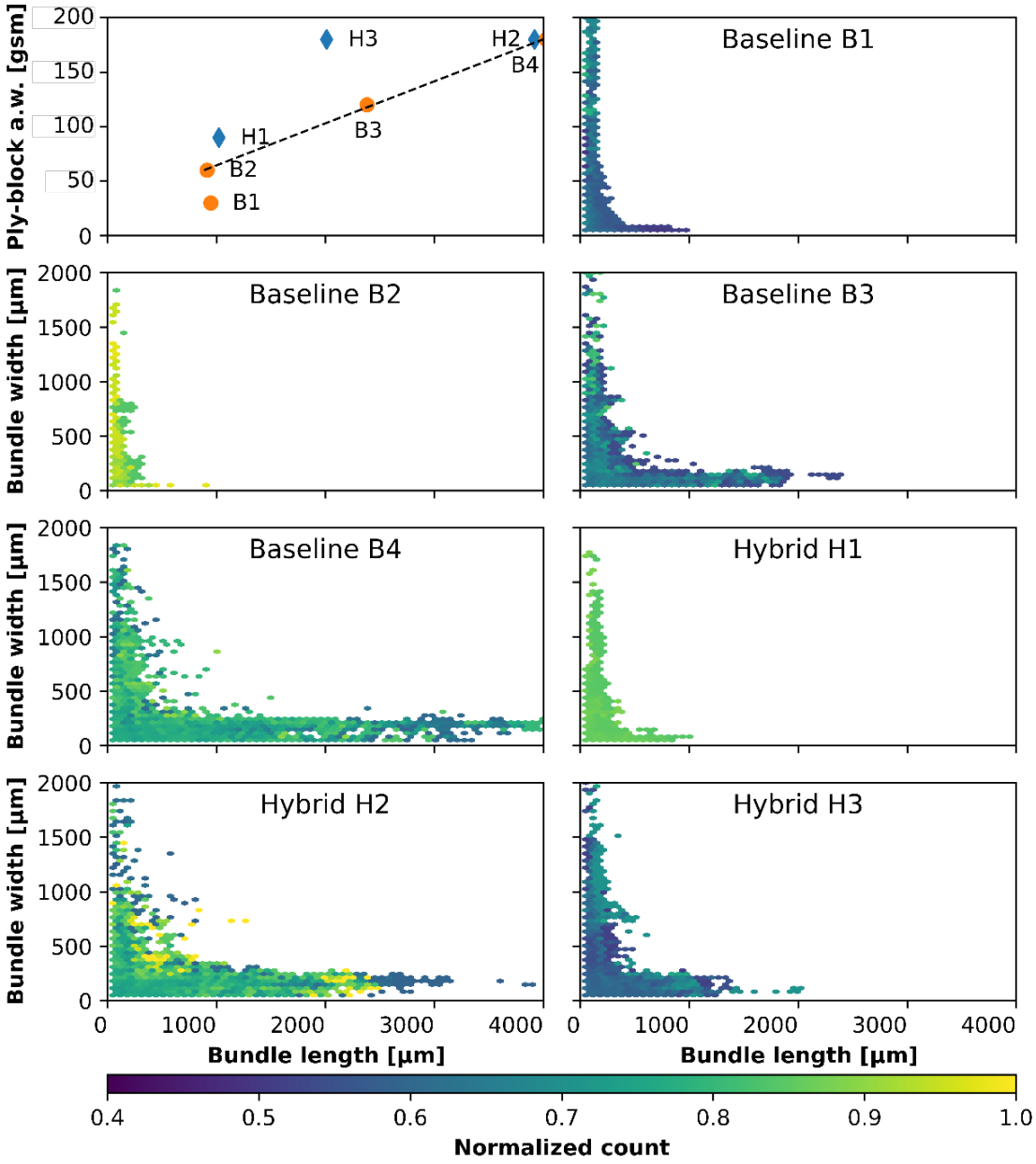

Figure 5: Heatmaps of the positive pull-out bundle distribution for each material configuration. Counts were normalized by the crack area projected on to the crack plane. The first subplot x-axis is the ply-block areal weight, the others are the bundle width.

Hybrid materials confirm these trends, with two noticeable differences. Hybrid H3 exhibits significantly shorter pull-out bundles compared to hybrid H2 even if they have the same ply-block thickness and the same fiber ratio. This difference is attributed to the hybridization architecture, an unbalanced ply-block H2 providing more extensive pull-out. Additionally, hybrid H2 shows less large-scale pull-out bundles close to $4000\ \mu m$ when compared to baseline B4, but much more medium-sized bundles around $600\ \mu m$, as highlighted in Figure 6.a.

The ratios of crack surfaces reported in Table 2 correlate these observations. Hybrid H2 offers more perpendicular surfaces – perpendicular with respect to the crack plane – per unit of projected crack area when compared to its equivalent baseline B4 – 2.72 vs. 2.36, +15 % – while hybrid H3 does significantly worse – 1.48 vs. 2.72, -37 %. These vertical surfaces are the interface

  doi:10.5075/epfl-298799_978-2-9701614-0-0

that dissipate energy during the pull-out. However hybrid H2 and baseline B4 offer a similar translaminar toughness [9]. It means that translaminar toughness does not scale linearly with the available vertical surface and another mechanism is at play.

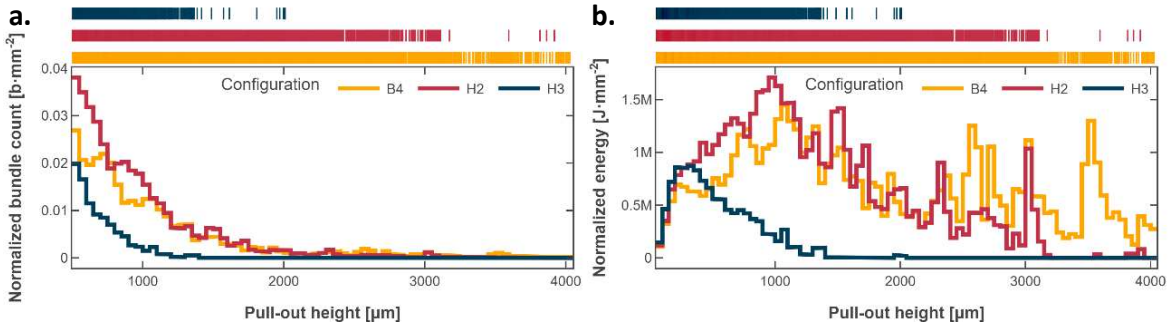

Figure 6: ***(a)*** *Close-up on the bundle length distribution over the range* $500 - 4000\ \mu m$ *for baseline B4, hybrid H2 and hybrid H3, all have a ply-block thickness of 180 gsm;* ***(b)*** *Corresponding energy dissipated by the bundles in debonding and friction predicted by the dual scale model. Counts and energies were normalized by the crack area projected on to the crack plane. Distributions are overlayed.*

As highlighted in Figure 6.b, the dual scale model proposed in this work predicts that longer pull-out bundles over $2000\ \mu m$ contribute far more to the dissipated energy than the smaller ones. The baseline B4 leads to a lower number of bundles and its developed crack area is smaller when compared to hybrid H2 but the few long B4 bundles dissipate as much energy as the numerous medium size H2 bundles.

Table 2: Crack surfaces as measured by the proposed method normalized by the crack area projected on to the crack plane.

Configuration	**B1**	**B2**	**B3**	**B4**	**H1**	**H2**	**H3**
Crack surface ratio	2.48	2.36	2.92	3.96	2.66	4.22	3.06
Crack perpendicular surface ratio	0.76	0.58	1.28	2.36	0.98	2.72	1.48

4. Conclusion

This work proposes a method to characterize the fracture surface of fiber hybrids tested in compact tension. The surfaces were systematically mapped in 3D with an optical microscope. The resulting data were then treated as series of 2D profiles that were simplified in order to extract statistical descriptors. Results show that the pull-out bundle height and width distributions are strongly impacted by the ply thickness in agreement with previous studies. More importantly, this work provides quantitative data about the influence of fiber hybridization and its architecture on the pull-out bundle distribution. It highlights two distinct dissipative mechanisms. In the hybrid case numerous medium-sized bundles provide similar energy dissipation as few large-scale bundles in the non-hybrid equivalent. It indicates that despite the absence of noticeable translaminar toughness improvement reported in recent studies on ply-by-ply hybrids, there is still room for new hybridization strategies that may tailor the pull-out distribution and the dissipative mechanisms to achieve toughness improvements.

  doi:10.5075/epfl-298799_978-2-9701614-0-0

5. Acknowledgements

The research leading to these results has been performed in the framework of the HyFiSyn project and has received funding from the European Union's Horizon 2020 research and innovation program under the Marie Skłodowska-Curie grant agreement No 765881.

6. References

[1] Sihn S, Kim R, Kawabe K, Tsai S. Experimental studies of thin-ply laminated composites. Composites Science and Technology 2007;67:996–1008. https://doi.org/10.1016/j.compscitech.2006.06.008.

[2] Amacher R, Cugnoni J, Botsis J, Sorensen L, Smith W, Dransfeld C. Thin ply composites: Experimental characterization and modeling of size-effects. Composites Science and Technology 2014;101:121–32. https://doi.org/10.1016/j.compscitech.2014.06.027.

[3] Arteiro A, Furtado C, Catalanotti G, Linde P, Camanho PP. Thin-ply polymer composite materials: A review. Composites Part A: Applied Science and Manufacturing 2020;132:105777. https://doi.org/10.1016/j.compositesa.2020.105777.

[4] Cugnoni J, Amacher R, Kohler S, Brunner J, Kramer E, Dransfeld C, et al. Towards aerospace grade thin-ply composites: Effect of ply thickness, fibre, matrix and interlayer toughening on strength and damage tolerance. Composites Science and Technology 2018. https://doi.org/10.1016/j.compscitech.2018.08.037.

[5] Kohler S, Cugnoni J, Amacher R, Botsis J. Transverse cracking in the bulk and at the free edge of thin-ply composites: Experiments and multiscale modelling. Composites Part A: Applied Science and Manufacturing 2019;124:105468. https://doi.org/10.1016/j.compositesa.2019.05.036.

[6] Frossard G. Fracture of thin-ply composites: effects of ply thickness 2017:189. https://doi.org/10.5075/epfl-thesis-8032.

[7] Teixeira RF, Pinho ST, Robinson P. Thickness-dependence of the translaminar fracture toughness: Experimental study using thin-ply composites. Composites Part A: Applied Science and Manufacturing 2016;90:33–44. https://doi.org/10.1016/j.compositesa.2016.05.031.

[8] Danzi F, Tavares R, Xavier J, Fanteria D, Camanho P. Effects of hybridization and ply thickness on the strength and toughness of composite laminates. Journal of Composite Materials 2021;55:4601–16. https://doi.org/10.1177/00219983211041762.

[9] Broggi G, Cugnoni J, Michaud V. Optimization of thin-ply fiber-hybrid composite translaminar toughness through ply-by-ply hybridization, 2021.

[10] NTPT-TDS_TP415_V1-0.pdf n.d. https://www.thinplytechnology.com/assets/mesimages/NTPT-TDS_TP415_V1-0.pdf (accessed April 27, 2022).

[11] Jalalvand M, Czél G, Wisnom MR. Damage analysis of pseudo-ductile thin-ply UD hybrid composites – A new analytical method. Composites Part A: Applied Science and Manufacturing 2015;69:83–93. https://doi.org/10.1016/j.compositesa.2014.11.006.

[12] Mesquita F, Swolfs Y, Lomov SV, Gorbatikh L. Ply fragmentation in unidirectional hybrid composites linked to stochastic fibre behaviour: A dual-scale model. Composites Science and Technology 2019;181:107702. https://doi.org/10.1016/j.compscitech.2019.107702.

[13] Frossard G, Cugnoni J, Gmür T, Botsis J. An efficient method for fiber bridging traction identification based on the R-curve: Formulation and experimental validation. Composite Structures 2017;175:135–44. https://doi.org/10.1016/j.compstruct.2017.04.032.

ASSESSING THE IMPACT BEHAVIOR OF HIGHLY ALIGNED FIBER HYBRID COMPOSITES

Arya, Aslani[a*], Stephen, J. Pickering[a], and Thomas, A. Turner[a]

a: Composites Research Group, Faculty of Engineering, the University of Nottingham, Nottingham, NG7 2GX, United Kingdom – arya.aslani1@nottingham.ac.uk

Abstract: *A novel fibre alignment method has been developed at the University of Nottingham whereby discontinuous fibres can be aligned to produce preforms that can be used to produce high fibre volume fraction composites at low moulding pressure. For example, a composite with 46% fibre volume fraction can be made in an autoclave.*

Several studies have been done on the tensile response of aligned discontinuous fibre hybrid composites, however, the impact properties of such new materials, one of the major requirements of structural materials, have yet to be determined. In addition, as fibre hybridization has been known as an effective way to improve the energy absorption and ductility of composites, this approach will be assessed to determine its influence on the impact behaviour of aligned fibre composites. In this study, carbon and glass fibers are hybridized in five different ratios with an intermingled architecture from 0% to 100% carbon. The impact samples are manufactured with ISO 6603 standard and the impact properties of them were assessed with the drop weight test.

Keywords: *Alignment; Hybridization; Impact.*

1. Introduction

The desire to design lighter vehicles to reduce fuel consumption, create an ever-increasing demand for Fibre Reinforced Composites (FRCs). However, two disadvantages have been always a concern. First, manufacturing virgin carbon fibres is energy intensive, which makes carbon fibres costly. Second, the increasing amount of wastes, either from manufacturing step or end-of-life scraps, must be limited to protect the environment. Implementation of circular economy on the composite industry to recover and reuse of valuable fibres can address these issues [1, 2]. There are three main methods to recycle FRCs: mechanical, thermal, and chemical. Each of these methods can be useful for specific applications, but thermal processes in general are the main recycling method in industry [3].

Fluidised bed (FB) was adapted to be used for composite materials at the University of Nottingham by Pickering et al. [4] to recover fibres with the same properties as the virgin ones. A variety of FRCs including Carbon Fiber Reinforced Composites (CFRCs) and Glass Fiber Reinforced Composites (GFRCs) have been recycled by different research groups. Based on the efforts to recycle carbon fibre (CF) and glass fibre (GF) by Pickering et al. [4] and Yip et al. [5] it was concluded that recovering CF is more efficient as CFs can fully retain their young's modulus

  doi:10.5075/epfl-298799_978-2-9701614-0-0

and 75% of their tensile strength. Pyrolysis can keep the properties of fibers as well, but this process is susceptible to create char on the fibers surface which can reduce the mechanical properties of subsequent composites [6].

Although the mechanical properties of carbon and glass fibres can be remained intact after recycling, their shape and size extremely change. FRCs with high stiffness and strength, typically contain continuous fibres; after recycling, these fibres turn to discontinuous fibres in a fluffy form. An example of the form of recycled carbon fibres is given in Figure 1. The subsequent usage of recovered fibres depends on the application. They can be used with random configuration and low volume fraction for applications in which high stiffness and strength is not desired. Nonetheless, to have structural composites, with the same mechanical properties as composites with continuous fibres, they must be aligned in a direction to increase the volume fraction of fibers and in-plane strength [7].

Figure 1 - Fluffy recycled carbon fibers.

A fibre alignment method has been developed at the University of Nottingham whereby discontinuous fibres can be aligned to produce preforms that can be used to manufacture high fibre volume fraction composites at low molding pressure. For example, a composite with 46% fibre volume fraction can be made in an autoclave [8].

One of the intrinsic characteristics of FRCs is their relative brittleness [9]. Fiber-hybridisation is an effective way to improve the ductility and energy absorption of composites without sacrificing their tensile stiffness and strength. Fiber-hybridisation is broadly defined as using two or more kinds of fibre within a composite, and can be divided into three configurations: intermingled, intralayer, and interlayer [9-12]. Figure 2 schematically illustrates the mentioned types of fibre-hybrid composites. 2a: mixture of fibres with random distribution, 2b: intralayer, with a controlled distribution of fibres within a layer; and 2c: interlayer, having different types of fibre in each layer.

  doi:10.5075/epfl-298799_978-2-9701614-0-0

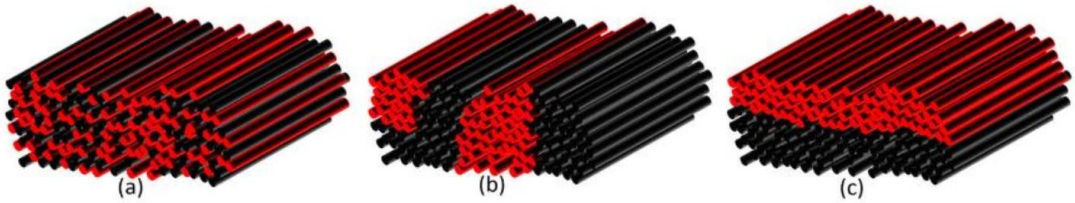

Figure 2 - An example of fibre hybrid architectures. Red and black represent different fibre types. a) intermingled b) intralayer [9].

In fibre hybridisation, it is possible to deviate from the rule of mixtures and have different properties than the one predicted by this simple and accurate model. This deviation can strengthen or weaken some properties in composites more than the predictions [9, 13]. An example of changing in a tensile behaviour of composites by fibre hybridisation can be seen in Figure 3. Combining two different fibres, one with low elongation (LE) and the other with high elongation (HE) fibres, results in a tensile behaviour between these two composites.

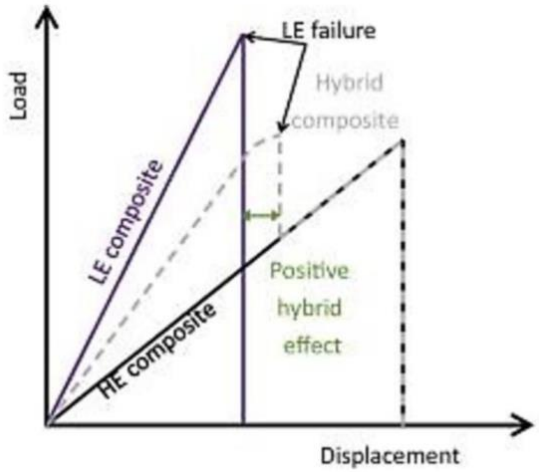

Figure 3 - Change in the tensile behaviour of low and high elongation fibre composites by fiber hybridisation [10].

However, most of the studies have focused on hybridisation of continuous fibres and the effect of it on the short fibre as well as aligned fibre composites remained unknown. A few research have been done on the effect of fibre hybridisation on aligned recycled fibres: H. Yu et al. worked on the hybridising of different grades of short carbon fibres and short E-glass fibres which were aligned by the HiPerDif method to achieve pseudo ductility [12]. In another study, they attempted to find the relation between plies distribution on the strain to failure of the interlaminated carbon and glass hybrid composites [14].

Until now, there is no study on the impact behavior of the aligned fibre composites. This lack of data is mainly due to the inability of other methods to produce mats with an adequate width for

  doi:10.5075/epfl-298799_978-2-9701614-0-0

impact samples. The aim of this study is to evaluate the effect of hybridization on the impact failure and energy absorption of aligned intermingled carbon/glass hybrid composites by performing impact tests on samples with different ratio of aligned carbon and glass fibres.

2. Materials and method

2.1 Materials

The samples were fabricated with 3mm carbon and glass fibres. Tenax®-A HT C124 carbon fibre staples with water soluble sizing supplied from Toho Tenax Europe GmbH, and the glass fibres were E-glass type and supplied by Jushi group co. The epoxy resin to form the final composite was Araldite LY 1556 by HUNTSMAN.

2.2. Aligned fiber tape manufacturing

The centrifugal alignment rig was used to produce aligned hybrid fiber mats. In this method, discontinuous fibres are dispersed in a viscous liquid, and the suspension then passes through a convergent nozzle to align the fibres and deposit them on the inner surface of a rotating drum. The inner surface of the drum is covered by a fine mesh and a vacuum is applied to the outside of it. The vacuum separates the liquid from the fibres leaving an aligned preform on the inside of the drum. A schematic diagram of the process can be found in Figure 4.

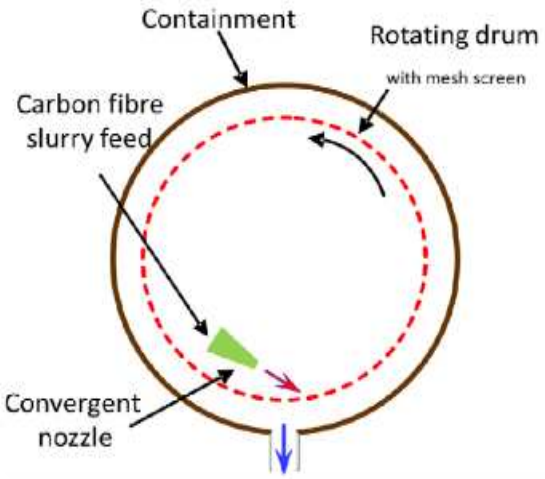

Figure 4 - Schematic view of fibre alignment by the rotating drum method.

2.3 Manufacture of aligned fiber composites

After the production of aligned fibre mats, the final laminates were made, firstly, by resin infusion of them under the vacuum to make a prepreg. Then, for each laminate, four prepregs were stacked together with cross-ply structure and cured at 120 C° for 2 hours.

2.4 Impact testing

The low velocity impact tests were done by INSTRON 9450 at Imperial College London. The samples were prepared to be compatible with ISO 6603-2 standard. This standard was chosen because it has the smallest sample dimension among all the standards for the low-velocity impact test and requires less materials which can speed-up the sample preparation stage. The schematic and real figure of test fixture can be found in figure 5. Specimens were tightly fixed between the test fixtures to not slip at the moment of impact. Impact energy was set to 25 J and was applied by a hemisphere shape impactor.

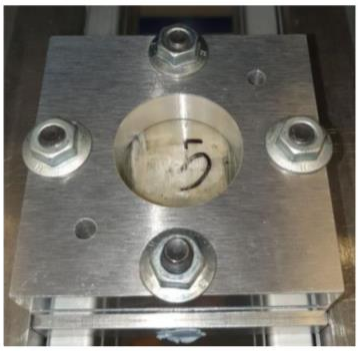

	Dimension (mm)
D2	40
D3	60
D4	>90
H	12
R	1

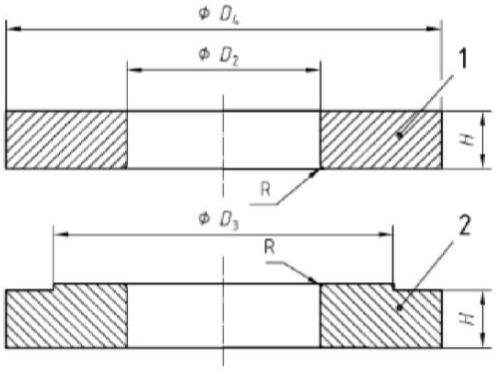

Figure 5 - Schematic and real figure of ISO 6603-2 test fixture.

Figure 6 shows two possible force-displacement curves for any sample which is tested in the drop weight impact test. By studying these curves, behaviour of different samples can be identified. A general trend can be seen in all the curves; each curve starts with an ascending force and reach to its own peak, then it is followed by a section of unloading. The ascending part of this curve can be interpreted same as the stress-strain curve in tensile test and can represent the bending stiffness of a sample during its resistance to the impact load. Then, the peak force is the point beyond which damage is initiated and propagated. The damage propagation continues till the impactor stops moving at some point or perforates the sample completely. If the impactor cannot fully penetrate the sample, normally the stored elastic energy of the material can push the impactor toward its opposite direction (Figure 6 b).

Another useful information which can be obtained from this curve is the energy absorption of the samples. The enclosed area beneath the curve is representative of energy absorption during the impact.

  doi:10.5075/epfl-298799_978-2-9701614-0-0

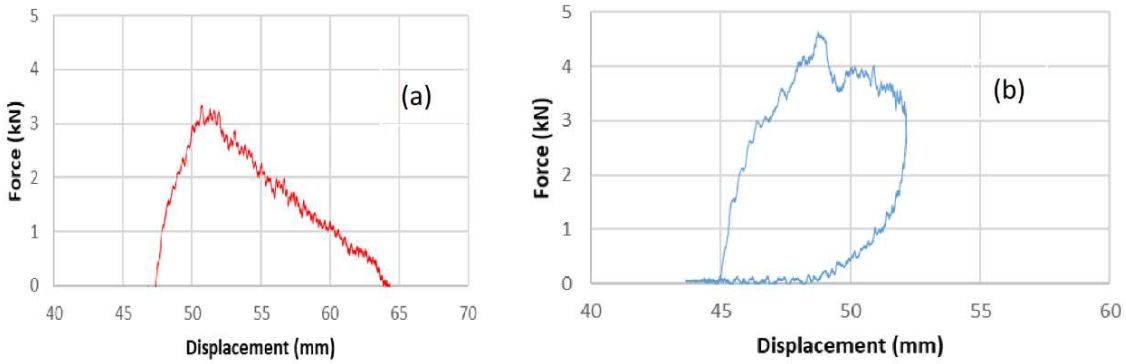

Figure 6 - Typical force-displacement behaviour of a) brittle and b) tough sample during the impact test.

3. Results and analysis

3.1. Peak force comparison

All the force-displacement curves of the samples from 100 % C to 100 % G were analysed and the comparison of their average peak forces is given in figure 7. Specimens with 100% G displays higher peak forces than the ones with 100 % C. This is due to the higher elongation of G fibres and the fact that C fibres break earlier than G fibres. However, the trend in hybrid samples is not linear. Although it is expected that with increasing C content lower peak forces would be observed, hybrid sample with 50 % C and 50 % G could sustain forces as much as glass fibres. This means hybridising G and C with a ratio of 1:1 can provide a positive hybrid effect, and G fibres can protect C fibres from early breakage. In other word, if any breakage occurred in C fibres, G fibres at the vicinity of it do not let the crack to propagate and damp the released stress waves [9].

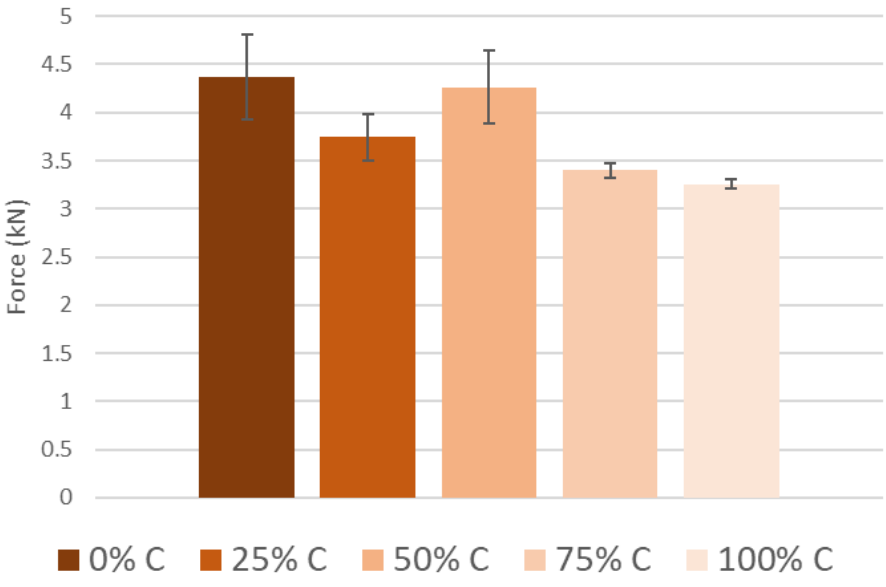

Figure 7 - Comparison of peak forces.

  doi:10.5075/epfl-298799_978-2-9701614-0-0

3.1. Energy absorption

The absorbed energies before initiation of the damage are compared in figure 8. Again, fully G fibre specimens absorbed more energy than fully C fibres, as expected, which is due to the brittle nature of carbon fibres. However, the trend in energy absorption do not obey the rule of mixture; and there is no change in energy absorption when the content of C fibres shifts from 25 % to 50 %. This can be a result of increase in crack length during propagation of impact cracks. When there are some intact glass fibres in between broken carbon fibres, the crack needs to travel around the intact fibres which helps with absorbing more energy.

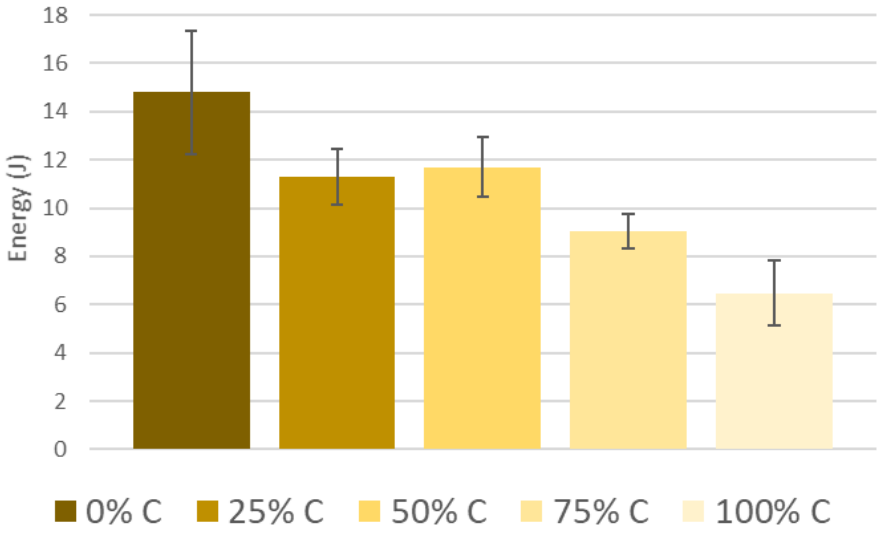

Figure 8 - Comparison of absorbed energy before initiation of the damage.

4. Conclusion

The impact behaviour of aligned discontinuous fibre composites have been assessed for the first time. It was shown that fibre hybridizing can be beneficial in shock absorption of samples and bearing more loads before damage initiation. The best hybrid effect was seen in samples with 50 % C and 50 % G due to the better dispersion of fibres. Using an equal volume fraction of different fibres eliminates the chance of having fibre clusters from one type of fibres and provide the maximum shock absorption, maintain the resistance to force without sacrificing the energy absorption capability.

Acknowledgements

The research leading to these results has been performed within the framework of the HyFiSyn project and has received funding from the European Union's Horizon 2020 research and innovation programme under the Marie Skłodowska-Curie grant agreement No 765881.

5. References

1. Rademacker, Tim. "Challenges in CFRP recycling." Breaking & Sifting-Expert exchange on the and-of-life of wind turbines. Onshore Wind Energy Agency, Berlin (2018): 24-25.

2. Utekar, Shubham, et al. "Comprehensive study of recycling of thermosetting polymer composites–Driving force, challenges and methods." Composites Part B: Engineering 207 (2021): 108596.

3. Yang, Y., et al., Recycling of composite materials. Chemical Engineering and Processing: Process Intensification, 2012. 51: p. 53-68.

4. McConnell VP (2010) Launching the carbon fibre recycling industry. Reinf Plast 54:33–37

5. Yip HLH, Pickering SJ, Rudd CD (2002) Characterisation of carbon fibres recycled from scrap composites using fl6idised bed process. Plast Rubber Compos 31:278–282

6. Rodrigues GGM, Faulstich De Paiva JM, Braga Do Carmo J et al (2014) Recycling of carbon fibers inserted in composite of DGEBA epoxy matrix by thermal degradation. Polym Degrad Stab 109:50–58

7. Longana, M.L., et al., Multiple closed loop recycling of carbon fibre composites with the HiPerDiF (High Performance Discontinuous Fibre) method. Composite Structures, 2016. 153: p. 271-277.

8. Liu, Zhe, et al. "Development of high-performance recycled carbon fibre composites with an advanced hydrodynamic fibre alignment process." Journal of Cleaner Production 278 (2021): 123785.

9. Swolfs, Y., I. Verpoest, and L. Gorbatikh, Recent advances in fibre-hybrid composites: materials selection, opportunities and applications. International Materials Reviews, 2019. 64(4): p. 181215.

10. Swolfs, Y., L. Gorbatikh, and I. Verpoest, Fibre hybridisation in polymer composites: a review. Composites Part A: Applied Science and Manufacturing, 2014. 67: p. 181-200

11. Kretsis, G., A review of the tensile, compressive, flexural and shear properties of hybrid fibre reinforced plastics. Composites, 1987. 18(1): p. 13-23.

12. Yu, H., et al., Pseudo-ductility in intermingled carbon/glass hybrid composites with highly aligned discontinuous fibres. Composites Part A: Applied Science and Manufacturing, 2015. 73: p. 35-44.

13. Such, M., C. Ward, and K. Potter, Aligned discontinuous fibre composites: a short history. Journal of Multifunctional Composites, 2014. 2(3): p. 155-68.

14. Yu, H., et al., Hybrid effect of carbon/glass composites as a function of the strength distribution of aligned short carbon fibres. 2016.

  doi:10.5075/epfl-298799_978-2-9701614-0-0

DEVELOPMENT AND CHARACTERIZATION OF HYBRID THIN-PLY COMPOSITE MATERIALS

Alexios Argyropoulos[a,c], Baris Caglar[b], Silvia Gomarasca[b], Thomas Ricard[c], Veronique Michaud[a]

a: Laboratory for Processing of Advanced Composites (LPAC), Institute of Materials (IMX), Ecole Polytechnique Fédérale de Lausanne (EPFL), Station 12, Lausanne, CH-1015, Switzerland – alexios.argyropoulos@epfl.ch
b: Aerospace Manufacturing Technologies, Faculty of Aerospace Engineering, Delft University of Technology, Kluyverweg 1, Delft 2629HS, The Netherlands
c: North Thin Ply Technology SARL, Chemin du Closel 3, 1020 Renens, Switzerland

Abstract: *The mechanical shaping process of calendering was employed for the manufacturing of hybrid pre-impregnated tapes of reduced thickness (thin-ply prepregs) by comingling various ratios of dissimilar carbon fibres with different processing parameters. A versatile image processing and microstructural analysis tool was developed to capture the arrangement of the different fibres in cross-sections of multi-layer laminates produced with the calendered materials. The performance of the calendering process as a method of manufacturing hybrid thin-ply prepregs was evaluated through the degree of hybridization that could be achieved and the effect of processing parameters on the overall microstructure of the hybrids.*

Keywords: hybrid composites; thin-ply; microstructural characterization

1. Introduction

Thin-ply composites are recognized as a key solution for the manufacturing of high-performance composite structures due to the unique mechanical properties and the increased design versatility that they offer. However, the high production cost due to the complexity of the manufacturing methods and their inherent brittleness limit their wider adoption by the composites industry [1]. In recent years, fibre hybridization (i.e., combining at least two types of fibres in a common matrix) is emerging as a promising approach for alleviating these drawbacks towards laminates with balanced characteristics in terms of mechanical properties and cost-efficiency [2]. Currently, most studies on hybrids employ simple interlayer (ply-level) configurations mainly due to difficulties in manufacturing more complex tow or fiber-level architectures[3]. However, simulation tools predict that notable improvements can be obtained from hybrids with an increased level of fiber dispersion [4]. The main aim of this work is to experimentally evaluate the efficiency of the calendering process as a new methodology for manufacturing prepregs that combine thin-ply and hybrid characteristics.

2. Materials and Methods

2.1 Materials

Two different grades of continuous tows of carbon fibres were selected for the present study. The high strain GRAFIL™ 34-700WD (HS: E_f=234 GPa, ε_f=2.06%) and the low strain PYROFIL™ HR 40 12M (LS: E_f=375 GPa ε_f=1.18%) both produced by Mitsubishi. The matrix was ThinPreg™ 415 (TP415), a rubber toughened epoxy formulation of North Thin Ply Technology (NTPT). The materials were processed by NTPT to produce single-fiber unidirectional (UD) thin-ply prepregs

  doi:10.5075/epfl-298799_978-2-9701614-0-0

with different ply fiber areal weight (FAW), that were used as an intermediate stage of hybrid prepreg manufacturing. Rolls with FAW of 30g/m^2 (gsm) and 60 gsm were manufactured with the 34-700 fibres and an ultra-thin ply format with FAW of 15 gsm was chosen for the HR40 fibres. The nominal resin content (RC) for all prepregs was set at 37% by weight.

2.2 Manufacturing of hybrid prepregs with the calendering process

A custom-made calender consisting of two heated counter-rotating steel rolls, schematically presented in Figure 1, was assembled for manufacturing the hybrid prepregs. Key production settings of the calender apparatus such as the rotational speed, the temperature, and more importantly the distance between the rolls that controlled the applied pressure on the unidirectional prepregs, could be accurately adjusted during production, securing a smooth and uninterrupted operation. To produce prepregs with an increased level of fibre co-dispersion and ideally fibre level hybrids, pairs of different single-fiber UD thin-ply prepregs manufactured at previous stages were aligned on top of each other and then guided in the tight nip created between the calender rolls at elevated temperatures. The pressure of the rolls forced the dissimilar fibres of the prepregs to interpenetrate and create fibre-level hybrid configurations. In total, four different calendered and two baseline non-calendered equivalent hybrid thin-ply prepregs were manufactured for this work, as described in *Table 1*. Hybrid composite laminates were manufactured with each material type by manually stacking hybrid plies on top of each other and the number of them was adjusted to reach a thickness of 2mm. The laminates were then cured in an autoclave following the curing profile recommended by NTPT (125^{0}C, 2h, 5atm peak pressure) to fully cross-link the TP415 epoxy matrix and reach optimal performance for the hybrid thin-ply composite.

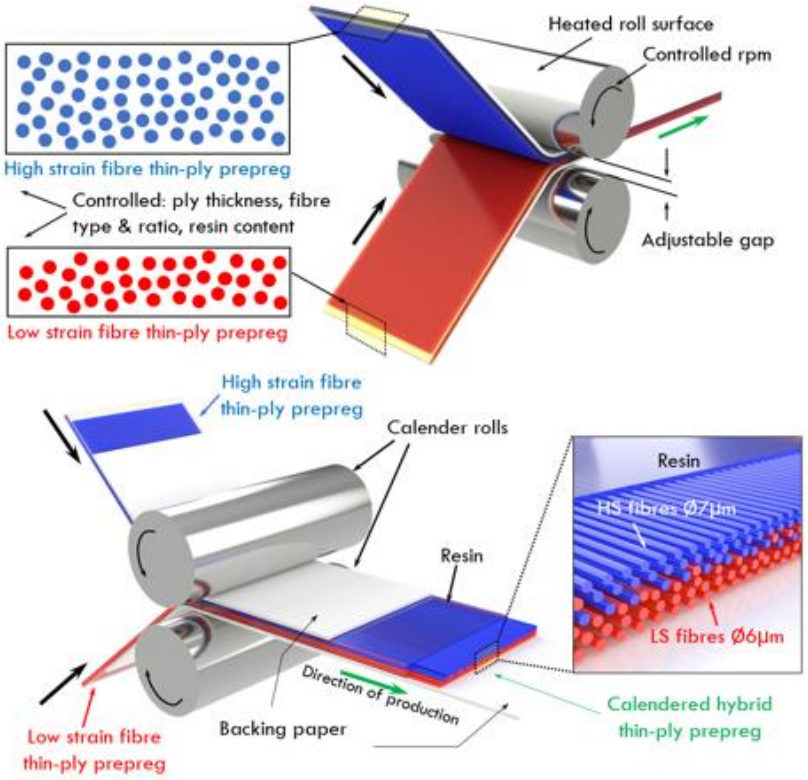

Figure 1 Schematic of the calendering process and calender apparatus employed for the manufacturing of hybrid thin-ply prepregs.

  doi:10.5075/epfl-298799_978-2-9701614-0-0

Table 1 Production characteristics and fibre composition of hybrid thin-ply prepregs

Calender Pressure	Low Strain Fibre (LS) HR40 (g/m^2)	High Strain Fibre (HS) 34-700 (g/m^2)	Hybrid FAW (g/m^2)	Sample Reference
Low	15	60	75	C LP 75
Low	15	30	45	C LP 45
High	15	60	75	C HP 75
High	15	30	45	C HP 45
Non-Calendered	15	60	75	NC 75
Non-Calendered	15	30	45	NC 45

2.3 Microstructural characterization of hybrid thin-ply composite laminates

Microstructural analysis techniques were used to quantify the effect of processing parameters on the overall microstructural profile of hybrid composites produced with calendered thin-ply prepregs. Cross-sections of the multilayer hybrid laminates were embedded into resin blocks that were ground with SIC abrasive papers (grain size P:400 - P:1200) and then polished for long cycles on a cloth pad with diamond abrasive suspension (particle size 1-3 µm) to obtain mirror-finished surfaces. These micrography samples were observed with a KEYENCE VHX-600 optical digital microscope under lighting conditions that could best produce high contrast between the matrix and the different reinforcements since the quality of the raw images can strongly affect the results of fibre identification and image analysis methods. The workflow for the identification of fibre position and type is shown in *Figure 2*. Matrix and fibres were segmented from the raw image in Fiji [5] via Minimum threshold. The following steps were conducted in Matlab. A morphological operation of opening was used to reduce thresholding artefacts prior to fibre identification via Circular Hough Transform. Analysis of the gradient magnitude on the location of each fibre was conducted on the raw image, leading to a bimodal distribution in which peaks correspond to each fibre type.

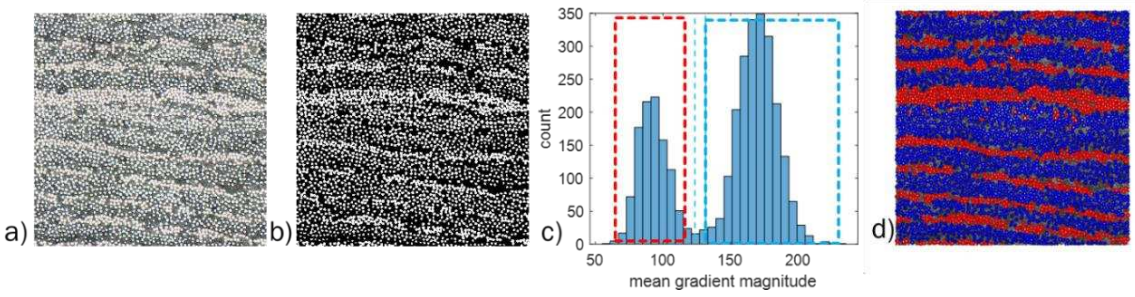

Figure 2 Workflow for fibre type identification: a) raw image b) image after thresholding and morphological operations c) histogram of the mean local gradient magnitude, showing a bimodal distribution where the two peaks can be associated to each fibre type (left: HR40 (low strain, LS); right: 34-700 (high strain, HS)) d) resulting fibre type assignment based on the bimodal distribution.

  doi:10.5075/epfl-298799_978-2-9701614-0-0

2.3.1 Hybrid parameters calculation

The metrics were based on the parameters of areal disorder [6], dispersion [2], and degree of hybridization [7]. To investigate the variability of the metrics for each material, the parameters were evaluated in three different regions of area 1600 µm by 1300 µm. Nominal fibre diameters were used for the calculations (7 µm for high strain (HS) fibres [8] and 6 µm for low strain (LS) fibres).

2.2.1 Areal disorder

The areal disorder (AD) was determined using a Delaunay tessellation as defined by Bray et al.[6]:

$$AD = \left(\frac{A}{\sigma} + 1\right)^{-1}, \quad (1)$$

where A is the mean area of the elements in the tessellation and σ is the corresponding standard deviation. In this work, AD was calculated for each sample on three different tessellations, one which considers globally all fibre centres and one considering LS fibres only and a third one considering HS fibres only.

2.2.2 Dispersion

In literature, the dispersion parameter was used to quantify the degree of fibre mixing by considering the proximity of two different fibre types F_A and F_B:

$$\text{Dispersion} = \text{mean}\left(\frac{R_{F_A}}{\sum_{i=1\ldots6} d(F_{Aj} \rightarrow F_{Bi})/6}\right) \text{ all j} \quad (2)$$

where R_{FA} is the nominal radius of fibre type F_A, $d(F_{A\,j} \rightarrow F_{B\,i})$ is the distance between the j-th fibre of type F_A and the six closest neighbouring fibres of type F_B. To understand the ability of the parameter to capture effects in an anisotropic fibre arrangement such as those encountered in this study, the parameter was calculated with reference to both low strain (LS) and high strain (HS) fibres, compared to only on low strain (LS) fibres as reported in the literature[2].

2.2.3 Degree of hybridization

The degree of hybridization compares the local fibre composition of a given microstructure to that of a microstructure with random fibre distribution [7]. A square moving window was used to determine the local areal ratio (AR) of the two fibre types over the region analysed, as:

$$AR = \frac{N_{F_A} D_{F_A}^2}{(N_{F_A} D_{F_A}^2 + N_{F_B} D_{F_B}^2)} \quad (3)$$

where N_{FA} and N_{FB} are the number of fibres of the two types, and D_{FA} and D_{FB} the corresponding nominal diameters. The window size was chosen equal to six times the nominal diameter as suggested in the literature [7] and was determined as the weighted ratio of the nominal values of the fibres diameters in the mean fibre composition for the dataset. The degree of hybridization (H) was then defined as the ratio between the coefficient of variation of the areal ratio distribution of each sample and that of a random hybrid microstructure, expressed as a percentage. For this analysis, the random microstructure was chosen to have same fibre type ratio, fibre number and positions as in each sample, but with a random fibre assignment.

  doi:10.5075/epfl-298799_978-2-9701614-0-0 published under CC BY-NC 4.0 license

3. Results and discussion

The samples show a range of volume fractions as shown in *Figure 3*. The resulting general trend shows an increase in global fibre volume fraction with increasing calendaring pressure. Additional effects arising from debulking cycles are not investigated.

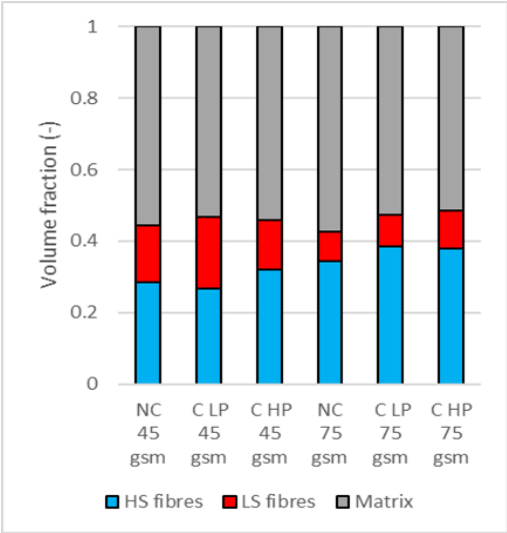

Figure 3 Laminate compositions expressed as volume fraction of the individual components.

3.1 Areal disorder

The results of the analysis of the areal disorder (AD) are reported in *Figure 4*a. The values of AD for the global fibre distributions are similar for all samples and lower than the values determined for either LS and HS fibre types taken individually. A higher value of global AD is observed for the non-calendered (NC) samples compared to calendered (C) samples. An increase in the value of AD for the LS fibres (in red) is observed for both increasing calendering pressure and for increasing nominal areal weight of HS fibres. For the HS fibres (in blue), the value of AD has a lower range of variation between samples compared to that for the LS fibres. A lower value of areal disorder corresponds to a more regular fibre distribution. For this reason, the AD for the global fibre architecture is always lower than for the individual phases, which have a greater variation in tessellation area due to the presence of alternated regions of higher packing density (within each individual layer), and empty regions occupied by the other fibre type. A slightly higher value of global AD is observed for non-calendered (NC) samples compared to calendered (C) samples, which might indicate a higher level of overall disorder in the material. Since the increase in HS fibres nominal areal weight from 30 gsm to 60 gsm translates into a greater spacing between layers of LS fibres, the latter phase appears overall less ordered, resulting in an increase in AD. For the HS fibres, the variability between samples can be appreciated less over this range of compositions.

3.2 Dispersion

As shown in *Figure 4*b, little variation in dispersion is observed between different samples for LS fibres (in red). Conversely, a general decrease of dispersion for HS fibres (in blue) is observed with the increase of the nominal HS fibre areal weight from 30 g/m^2 (gsm) to 60 g/m^2.

  doi:10.5075/epfl-298799_978-2-9701614-0-0

Since the areal weight of the LS fibre layer is similar for all samples, the resulting layer thickness is similar in all samples. For this reason, the distance to the six closest neighbours of the opposite fibre type varies only slightly between samples, leading to small changes in the values of dispersion. Conversely, for an increase in nominal HS fibres areal weight, the average distance to the six closest LS fibres will increase. This might have a different effect depending on the effective HS fibre fraction shown in *Figure 3*, which might determine a variation in the average layer thickness.

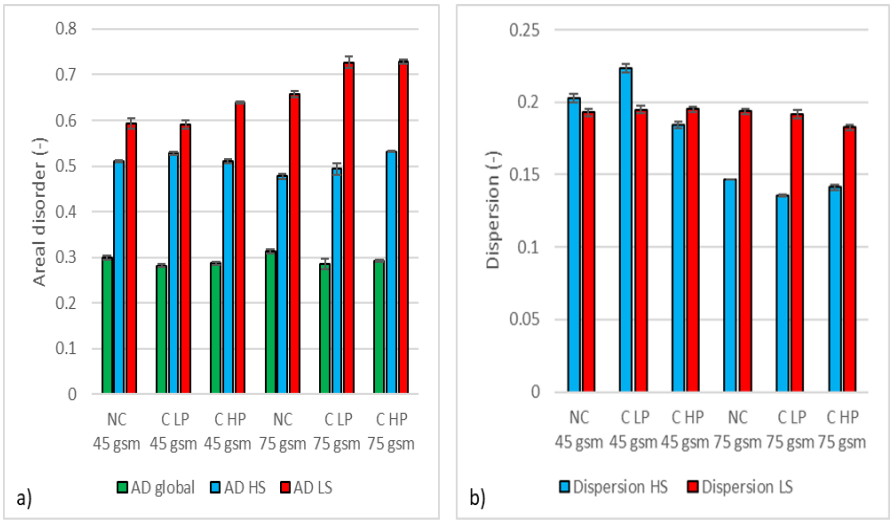

Figure 4 a) Areal disorder for the two fibre types (HS in blue and LS in red) and for the global fibre arrangement (in green) b) Dispersion for the two fibre types (HS in blue and LS in red).

3.3 Degree of hybridization

The distribution of areal ratios for each sample and for their corresponding random microstructures are shown in *Figure 4*a. A higher number of regions containing only HS fibres is present for increasing HS fibre nominal areal weight, which is shown by a higher bin count at AR=1. The resulting degree of hybridization shown in *Figure 4*b decreases with increasing HS fibre nominal areal weight and is highest for the non-calendered samples within each nominal composition. The degree of hybridization was calculated with reference to HS fibres. Choosing to refer to LS fibres instead would have led to a flipped distribution of areal disorder values, and therefore would not have affected the current analysis. A window size equal to six times the nominal fibre diameter was chosen as recommended in the literature [7], however, a different choice of size is expected to impact the result, as the greater the window size, the greater the microstructural homogenization in the resulting AR distribution. The choice of random microstructures tailored to each sample to match their fibre type composition was considered necessary to generate comparable datasets, due to the variations in fibre type composition shown in *Figure 3*. The greater degree of hybridization for the LS 15 gsm – HS 30 gsm sample series relates to a more homogenous microstructure within the window of observation chosen compared to the LS 15 gsm – HS 60 gsm series due to lower spacing between different layer types. Within each sample series, a greater degree of hybridization is observed for non-calendered samples compared to the calendered counterparts.

  doi:10.5075/epfl-298799_978-2-9701614-0-0

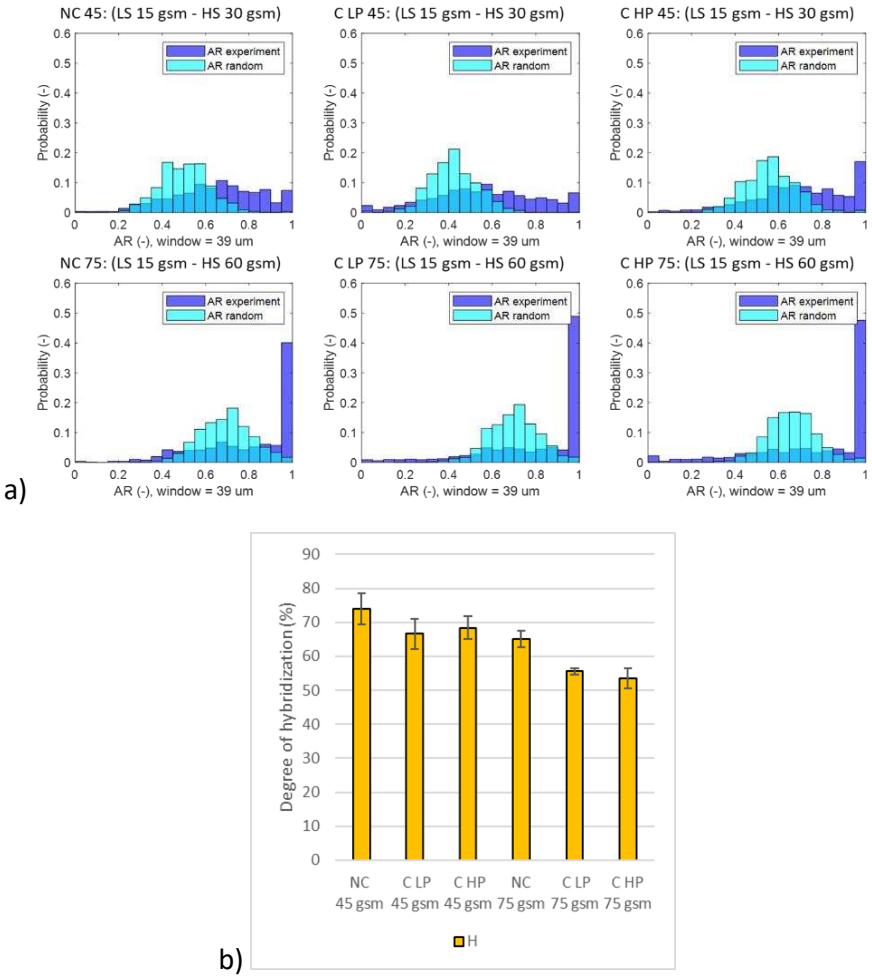

Figure 5 a) Distributions of areal ratio (AR) for the four samples b) resulting degree of hybridization (H)

4. Conclusions

Unidirectional hybrid pre-impregnated tapes were successfully manufactured via the newly developed calendering process by comingling various ratios of low strain (LS) and high strain (HS) carbon fibres under different processing conditions. Optical microscopy was used to reveal the microstructural features of cured multi-layer composite laminates manufactured with the calendered hybrid prepregs and a fiber identification and microstructural analysis tool was developed for the characterization of the new materials. Three parameters were used to describe the hybrid microstructure: areal disorder [6], dispersion [2] and degree of hybridization [7]. All parameters were able to capture differences between samples which are linked to size effects related to varying layer thickness. Calendering effects were mostly captured by areal disorder and degree of hybridization. Lower areal disorder in LS fibres and greater degree of hybridization were encountered for non-calendered samples compared to the high-pressure calendered counterpart, suggesting greater local fibre intermingling for the former.

  doi:10.5075/epfl-298799_978-2-9701614-0-0

Acknowledgments

The research leading to these results has been performed within the framework of the HyFiSyn project and has received funding from the European Union's Horizon 2020 research and innovation programme under the Marie Skłodowska-Curie grant agreement No 765881.

5. References

[1] J. Cugnoni *et al.*, "Towards aerospace grade thin-ply composites: Effect of ply thickness, fibre, matrix and interlayer toughening on strength and damage tolerance," *Compos. Sci. Technol.*, vol. 168, pp. 467–477, Nov. 2018, doi: 10.1016/j.compscitech.2018.08.037.

[2] Y. Swolfs, I. Verpoest, and L. Gorbatikh, "Recent advances in fibre-hybrid composites: materials selection, opportunities and applications," *Int. Mater. Rev.*, vol. 64, no. 4, pp. 181–215, May 2019, doi: 10.1080/09506608.2018.1467365.

[3] G. Czél, M. Jalalvand, and M. R. Wisnom, "Design and characterisation of advanced pseudo-ductile unidirectional thin-ply carbon/epoxy–glass/epoxy hybrid composites," *Compos. Struct.*, vol. 143, pp. 362–370, May 2016, doi: 10.1016/j.compstruct.2016.02.010.

[4] Y. Swolfs, R. M. McMeeking, I. Verpoest, and L. Gorbatikh, "The effect of fibre dispersion on initial failure strain and cluster development in unidirectional carbon/glass hybrid composites," *Compos. Part Appl. Sci. Manuf.*, vol. 69, pp. 279–287, Feb. 2015, doi: 10.1016/j.compositesa.2014.12.001.

[5] J. Schindelin *et al.*, "Fiji: an open-source platform for biological-image analysis," *Nat. Methods*, vol. 9, no. 7, pp. 676–682, Jun. 2012, doi: 10.1038/nmeth.2019.

[6] D. J. Bray, S. G. Gilmour, F. J. Guild, and A. C. Taylor, "The effects of particle morphology on the analysis of discrete particle dispersion using Delaunay tessellation," *Compos. Part Appl. Sci. Manuf.*, vol. 54, pp. 37–45, Nov. 2013, doi: 10.1016/j.compositesa.2013.07.003.

[7] H. Diao, A. Bismarck, P. Robinson, and M. R. Wisnom, "Production of continuous intermingled CF/GF hybrid composite via fibre tow spreading technology," *16th Eur. Conf. Compos. Mater. ECCM 2014*, Jan. 2014.

[8] F. Mesquita, Y. Swolfs, S. Bucknell, Y. Leray, S. V. Lomov, and L. Gorbatikh, "TENSILE PROPERTIES OF SINGLE CARBON FIBRES TESTED WITH AUTOMATED EQUIPMENT," p. 7.

  doi:10.5075/epfl-298799_978-2-9701614-0-0

TENSILE FATIGUE PERFORMANCE OF CARBON-CARBON HYBRID QUASI-ISOTROPIC LAMINATE

Valter, Carvelli [a], Sergei B., Sapozhnikov [b], Stepan V., Lomov [c], Christian, Breite [c], Yentl, Swolfs [c]

a: Department A.B.C., Politecnico di Milano, Milan, Italy – valter.carvelli@polimi.it
b: Aerospace Department, South Ural State University, Chelyabinsk, Russia
c: Department of Materials Engineering, KU Leuven, Leuven, Belgium

Abstract: *This experimental study has been focused on the tensile-tensile fatigue performance of a carbon-carbon fiber hybrid quasi-isotropic laminate. The laminate contained two unidirectional carbon fiber prepregs with the same epoxy matrix. One prepreg had carbon fibers T800 for the high-elongation layer (HE), the other prepreg had carbon fibers DIALEAD for the low-elongation layer (LE). The sub-laminate stacking sequence was [HE/LE/HE]. Sub-laminates have been piled to get a quasi-isotropic layup $[0/45/90/-45]_s$. The displacement (strain) controlled tension-tension tests were along the 0° fiber direction. Preliminary quasi-static tests provided the pseudo-ductile behavior considered for the fatigue loading levels. The evolution of the fatigue damage was macroscopically analyzed by the stiffness degradation, and microscopically by X-ray micro-CT observations. As main conclusions, the composite retains its load-carrying ability in the pseudo-ductile regime. The evolution of the fatigue damage involved fracture of 0° LE plies, transverse cracks in ±45° plies and delamination of 0°/+45°and ±45°/90° interfaces.*

Keywords: Carbon-carbon hybrid laminates; Pseudo-ductility; Fatigue; Damage.

1. Introduction

One of the main advantages of fiber reinforced composites is the design freedom, which can be better exploited using fiber-hybridization (coupling two or more fiber types). Fiber-hybrids reinforced plastics received particular attention due to the synergetic (or 'hybrid') effects [1,2], which can provide, among other features, the pseudo-ductility, namely a pseudo-ductile response by the combination of brittle composites [3]. Pseudo-ductility is often studied in quasi-static tension and the damage mechanisms underneath are reasonably well-understood [4,5].

Although cyclic loading is often the main condition on composite components in several industrial applications [6], the current knowledge on the fatigue behavior of fiber-hybrid composites is limited. Focusing the attention on tension-tension fatigue loading, being frequently adopted in experimental investigations as well as in the present study, the few available researches have been mainly dedicated to unidirectional hybrid laminates, coupling: carbon and glass fibers (e.g. [7]), carbon and basalt fibers (e.g. [8]) and all carbon fibers (e.g. [9]). The fatigue performance of hybrid laminates with other stacking sequences was barely investigated (see e.g. [10]). This is the aim of the present study, dedicated to an all-carbon interlayer hybrid quasi-isotropic laminate.

The hybrid laminate contained standard thickness prepregs, same matrix, reinforced with low elongation (LE) and high-elongation (HE) carbon fibers. The sub-laminates [HE/LE/HE] were stacked to have a quasi-isotropic layup $[0/45/90/-45]_s$.

  doi:10.5075/epfl-298799_978-2-9701614-0-0

The tension-tension strain-controlled cyclic loadings allowed to gain several insights, mainly related to: the fatigue life of the hybrid laminate for a wide range of maximum strain levels in the quasi-static tensile pseudo-ductile range and beyond it; the evolution of the fatigue damage by the stiffness retention as macroscopic metric; the damage observation by X-ray micro-CT imparted after selected number of cycles. The final goal of the study was the correlation of the macroscopic stiffness degradation and the evolution of the fatigue damage modes.

2. Carbon-carbon hybrid quasi-isotropic laminate

The laminate has been manufactured with two unidirectional carbon fiber prepregs supplied by Composite Materials Italy (CIT) – Toray Group, which had both the epoxy matrix ER450. The prepregs nominal fiber volume fraction was 55–56% (datasheet). The high contrast between the low-elongation (LE) and high-elongation (HE) composite stiffness and strain-to-failure (see fiber properties in Table 1) provides a pseudo-ductile plateau in quasi-static tension of UD hybrid laminates [11], which was related to the critical energy release rates [12].

One prepreg contained TORAY TORAYCA® T800 carbon fibers (in the following T) for the HE layer (thickness of 0.11 mm), the other prepreg was made of Mitsubishi Chemical DIALEAD™ K63720 carbon fibers (in the following D) for the LE layer (thickness of 0.22 mm). The considered laminate consisted of a set of sub-laminates. The sub-laminate had one ply of the D prepreg sandwiched between two plies of T [T/D/T]. Sub-laminates were stacked to create a quasi-isotropic layup $[0/45/90/-45]_s$. The laminates were then autoclave-cured for 2 hours at a temperature of 135 °C and a pressure of 4.5 bar. No post curing or conditioning was applied.

Table 1: Carbon fiber properties (manufacturer's data sheets).

ID	Fiber	Diameter [µm]	Elastic modulus [GPa]	Strength [MPa]	Failure strain [%]
T	TORAYCA® T800	5	294	5880	2
D	DIALEAD™ K63720	11	630	2620	0.4

3. Quasi-static and fatigue loading features

Preliminary quasi-static tensile tests were dedicated to the evaluation of the main mechanical features including the pseudo-ductile behavior. The results have been considered for the selection of the fatigue loading levels. The loading rate, along the 0° fiber direction, was set to 1 mm/min by an electromechanical machine INSTRON 5978. The tests were assisted by a digital camera to evaluate the full field strain on the specimen surface by the digital image correlation (DIC) technique (as in [11] for the hybrid UD counterpart). One surface of the prismatic specimens (dimensions 240 × 15 × ~3.7 mm^3) was painted white and then speckled by black spray paint. The stress was evaluated, as for cyclic tests, using the cross-sectional area of the pristine specimens.

Prismatic specimens have been dedicated to tension-tension fatigue loading. The displacement (strain) controlled cyclic loading was along the 0° fiber direction, by a hydraulic machine MTS 319. The constant displacement amplitude was imposed using a sinusoidal wave-form with a

  doi:10.5075/epfl-298799_978-2-9701614-0-0

ratio R = 0.1 (ratio of the minimum to the maximum displacement in the cycle) and a frequency of 5 Hz. The strain was estimated by the displacement of the actuator, assuming as the base length the distance between end tabs (140 mm). Several maximum strain levels have been applied close and beyond the pseudo-yield strain ε_P level (Figure 1). One specimen for each strain level has been cyclically loaded up to complete failure or runout after 1 million cycles. Despite the limited number of tests, statistically meaningless, the strain-controlled loadings provided a clear insight into the hybrid laminate fatigue response.

4. Quasi-static tensile behaviour

The preliminary quasi-static tensile tests provided the pseudo-ductile tensile response of the hybrid quasi-isotropic laminate as shown by a typical tress-strain diagram in Figure 1. The three main region of the diagram represents: the linear behavior (first region) whose slope E_0 (72.8 ± 2.9 GPa) is a combination of the stiffness of the LE and HE layers; the pseudo-ductile plateau (second region) with an almost constant stress level, starting at the pseudo-yield strain ε_P (0.41% ± 0.063), close to the ultimate strain of the LE component, and ending at the strain level ε_{PY} (1.15% ± 0.088); the almost linear trend of the third region, whose slope E_1 (15.3 ± 3.1 GPa) depends on the stiffness of the intact 0° HE plies and the residual stiffness of the damaged LE ones.

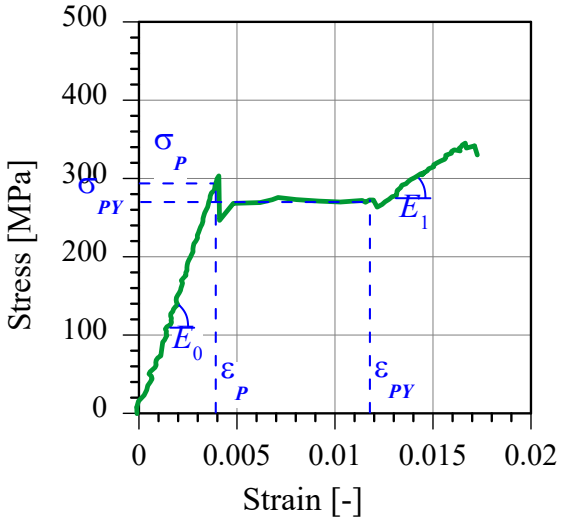

Figure 1. Typical quasi-static tensile pseudo-ductile stress-strain behavior.

5. Tensile-tensile fatigue behaviour

A broad range of maximum strain in the cycles has been considered to cover the quasi-static pseudo-ductility (second region) and post plateau linear behaviour (third region) of the hybrid laminate. Eight different maximum strain levels have been set in the range 0.46% - 1.7% (see Figure 2). The corresponding initial stress levels were close to σ_{PY} for strain levels in the second region and over it for the maximum strains in the third one (Figure 2).

All fatigue specimens did not fail after 1 million cycles, except the one subjected to the highest considered cyclic strain level (1.7%), which had a fatigue life of about 909 thousand cycles.

  doi:10.5075/epfl-298799_978-2-9701614-0-0

The peculiar fatigue response of the considered carbon-carbon hybrid quasi-isotropic laminate is observed overlapping the quasi-static stress-strain diagram, the fatigue strain levels and the initial and residual maximum fatigue stress.

The damage pattern created by the first loading cycle is hypothesized to contain different damage modes according to the strain level. The lower strain levels close to ε_P imparted fracture of the 0° LE plies, and transverse cracks in the ±45° and 90° plies. Those damage modes have been coupled to different stages of delamination for the strain levels up to ε_{PY}. The fatigue strain levels closer to ε_{PY} developed almost complete delamination leading to weak interactions between the damaged LE plies and the HE ones. This initial damage scenario evolved by further cyclic loading mainly with initiation and propagation of delamination. The damage pattern evolution for strain levels in the pseudo-ductile plateau is reflected on the residual fatigue maximum stress, depicted by green circles in Figure 2. Those residual stress levels fall on a line whose slope is almost that of the quasi-static tensile post plateau region (E_1). It demonstrates that the load at this stage of the fatigue life is mainly carried by the 0° HE plies.

The initial damage patterns of the fatigue strain levels higher than the quasi-static ε_{PY} (>1.2% in Figure 2) resulted in weak coupling of the damaged LE plies and the HE plies. Therefore, the cyclic load carrying capacity was mainly transferred to the 0° HE plies. Then, the further gradual damage imparted to the 0° HE plies during cyclic loading led to the reduction of the residual stress with increased strain level (Figure 2).

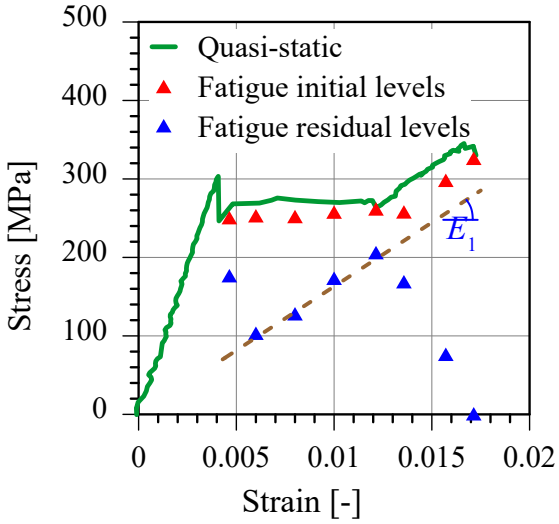

Figure 2. Initial and residual fatigue stress/strain levels compared to typical quasi-static stress-strain behavior.

The damage evolution can be macroscopically estimated considering the stiffness retention as a metric [7,8]. Figure 3 details the stiffness retention with the number of cycles for one strain level very close to the quasi-static ε_P, one strain level almost at mid of the pseudo-ductile plateau and one in the quasi-static post plateau liner region. They highlighted a considerable initial drop, limited to about 10% of the runout threshold. For the remaining cyclic loading, the stiffness kept almost a constant retention whose magnitude depends on the strain level. The initial drop is related to the mentioned fatigue damage development. The initial reduction of stiffness, for the lower strain level close to ε_P, could be connected to the onset of delamination and increase of transverse cracks in the ±45° and 90° plies, while the further continuous slight reduction could

  doi:10.5075/epfl-298799_978-2-9701614-0-0

be due to the slow propagation of the delamination at different interfaces. The initial stiffness drop of the strain level within the pseudo-ductile plateau could be the effect of the development of the intra- and inter-sub-laminates delamination, which led to a residual stress belonging to the quasi-static linear behavior of slope E_1 (Figure 2).

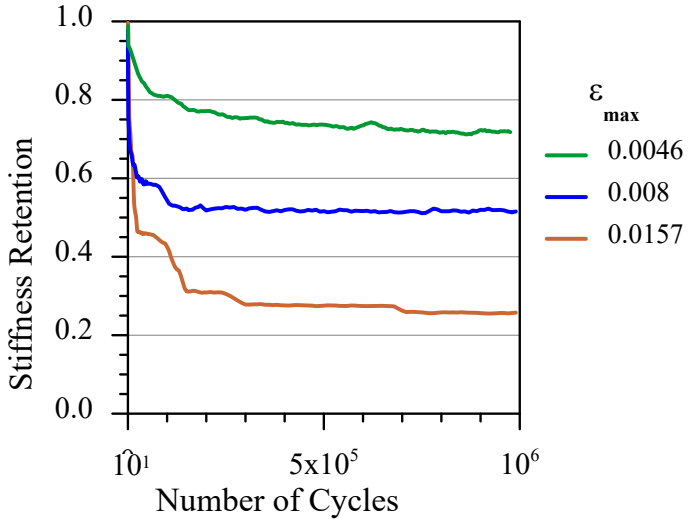

Figure 3. Fatigue tests: stiffness retention evolution during cyclic loading, for three levels of max strain (ε_{max}) in the cycle.

6. X-ray micro-CT fatigue damage observations

The evolution of the fatigue damage scenario was observed, to some extent, by X-ray micro-computed tomography (micro-CT). The cyclic loading with the lowest strain level of two specimens has been interrupted after 100 thousand and 1 million cycles (runout). The latter is here described for the sake of brevity. The central volume of the specimens was scanned by a TESCAN UniTOM XL, setting the acquisition parameters: tube potential 40 kV, power 15 W, source-object distance 30 mm, source-detector distance 800 mm, exposure 330 ms, 3000 projections. The resulting voxel size was 5.6 µm.

The damage scenario after 1 million cycles of maximum strain 0.46% is shown in Figure 4. At the initial fatigue stage, several cracks in the -45° central sub-laminates (see white ellipses in Figure 4) and onset of delamination at the +45°/90° interface were pinpointed, which mainly affected the initial loss of stiffness. The former damage mode evolved as delamination at the -45°/90° interfaces, while the latter enlarged covering almost half-width (see orange ellipses in Figure 4). A more extended delamination was generated at the two external 0° sub-laminates, namely: intra-sub-laminate at the LE/HE interface (yellow ellipses) and inter-sub-laminate delamination at the 0°/+45° interfaces (brown ellipses). The partial extension of the delamination through the width shows that the load was carried by the still connected plies and sub-laminates, as demonstrated by the residual stress of this strain level in Figure 2. This residual stress level is far from the linear segment representing the quasi-static tensile post plateau behavior. It shows that the LE and HE plies in the 0° sub-laminates still have a partial collaboration and the load is transferred to the 0° sub-laminates by the ±45° ones.

  doi:10.5075/epfl-298799_978-2-9701614-0-0 published under CC BY-NC 4.0 license

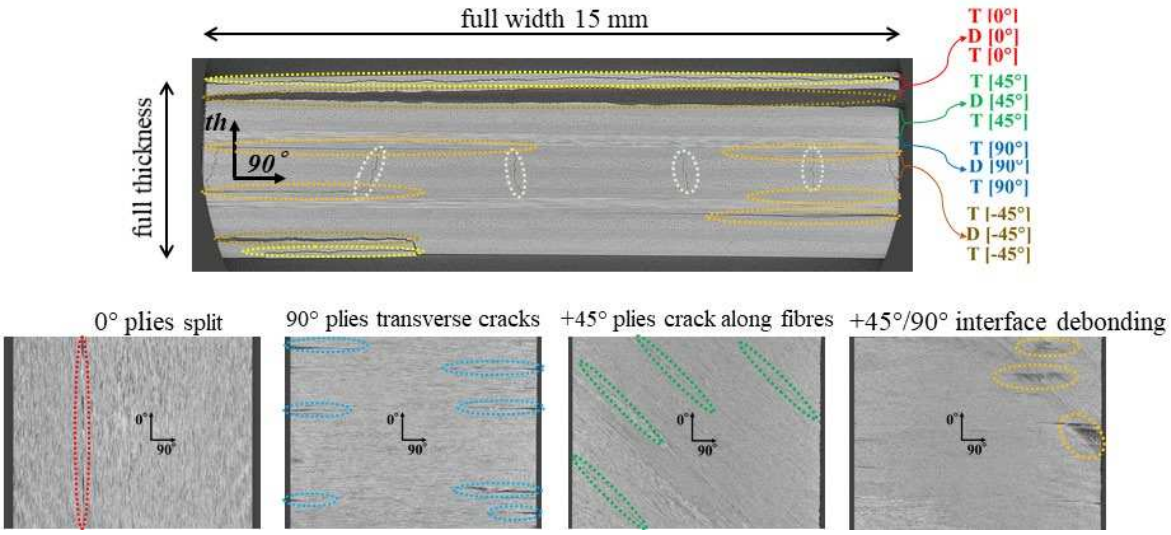

Figure 4. Fatigue tests, maximum strain ε_{max}=0.46%: X-ray micro-CT observations of the damage, after 1 million cycles, at center of the specimen.

7. Conclusions

This study was devoted to a specific aspect of the mechanical behavior of hybrid laminates, namely fatigue performance. The experimental study focused on the fatigue behavior of a carbon-carbon hybrid quasi-isotropic laminate, which has not been covered in the literature, to the authors' knowledge.

The tension-tension strain-controlled cyclic loading was designed considering the preliminary measurements of the tensile quasi-static pseudo-ductile behavior of the hybrid laminate.

The main achievement of this study was the connection between the macroscopic stiffness evolution, as a metric for the overall damage, and the damage modes observation by X-ray micro-CT. The damage scenario imparted during the early stage of the cyclic lower strain level, involved fracture of 0° LE plies, transverse cracks in ±45° plies and onset of delamination at +45°/90° interface, which were responsible of the initial drop of the stiffness retention. Further cyclic loading pointed out the very slow stiffness reduction which was motivated by the evolution of those damage modes as enlargement of the delamination at: the ±45°/90° interfaces, the 0° intra-sub-laminate LE/HE interfaces and the inter-sub-laminate 0°/+45° interfaces.

The measurements and observations of the fatigue damage modes evolution in the studied carbon-carbon hybrid quasi-isotropic laminate are not exhaustive and need further analyses. Nevertheless, the detailed understandings highlighted the effect of pseudo-ductility on the tensile cyclic loading response and are a valuable contribution to the knowledge on the fatigue behavior of hybrid fiber-reinforced plastics, which is needed in a wide range of advanced industrial applications.

  doi:10.5075/epfl-298799_978-2-9701614-0-0

Acknowledgements

The work of S. B. Sapozhnikov was supported by the Russian Science Foundation (project No. 18-19-00377) and partially by KU Leuven. The authors are grateful to the Toray Group for providing prepreg materials and for supporting the Toray Chair at KU Leuven, held by S.V. Lomov. The FWO large infrastructure I013518N project is acknowledged for their financial support of the X-ray infrastructure and the KU Leuven XCT Core facility is acknowledged for the 3D image acquisition and quantitative post-processing tools.

8. References

[1] Swolfs Y, Gorbatikh L, Verpoest I. Fibre hybridisation in polymer composites: A review. Compos Part Appl Sci Manuf 2014;67:181–200. https://doi.org/10.1016/j.compositesa.2014.08.027.
[2] Swolfs Y, Verpoest I, Gorbatikh L. Recent advances in fibre-hybrid composites: materials selection, opportunities and applications. Int Mater Rev 2019;64:181–215. https://doi.org/10.1080/09506608.2018.1467365.
[3] Czél G, Wisnom MR. Demonstration of pseudo-ductility in high performance glass/epoxy composites by hybridisation with thin-ply carbon prepreg. Compos Part Appl Sci Manuf 2013;52:23–30. https://doi.org/10.1016/j.compositesa.2013.04.006.
[4] Jalalvand M, Czél G, Wisnom MR. Damage analysis of pseudo-ductile thin-ply UD hybrid composites – A new analytical method. Compos Part Appl Sci Manuf 2015;69:83–93. https://doi.org/10.1016/j.compositesa.2014.11.006.
[5] Mesquita F, Swolfs Y, Lomov SV, Gorbatikh L. Ply fragmentation in unidirectional hybrid composites linked to stochastic fibre behaviour: A dual-scale model. Compos Sci Technol 2019;181:107702. https://doi.org/10.1016/j.compscitech.2019.107702.
[6] Swolfs Y. Perspective for Fibre-Hybrid Composites in Wind Energy Applications. Materials 2017;10:1281. https://doi.org/10.3390/ma10111281.
[7] Suwarta P, Fotouhi M, Czél G, Longana M, Wisnom MR. Fatigue behaviour of pseudo-ductile unidirectional thin-ply carbon/epoxy-glass/epoxy hybrid composites. Compos Struct 2019;224:110996. https://doi.org/10.1016/j.compstruct.2019.110996.
[8] Wu Z, Wang X, Iwashita K, Sasaki T, Hamaguchi Y. Tensile fatigue behaviour of FRP and hybrid FRP sheets. Compos Part B Eng 2010;41:396–402. https://doi.org/10.1016/j.compositesb.2010.02.001.
[9] Ribeiro F, Sena-Cruz J, Vassilopoulos AP. Tension-tension fatigue behavior of hybrid glass/carbon and carbon/carbon composites. Int J Fatigue 2021;146:106143. https://doi.org/10.1016/j.ijfatigue.2021.106143.
[10] Wu X, Fuller JD, Wisnom MR. An investigation into fatigue behaviour and damage progression in pseudo-ductile thin-ply angle-ply laminates. Compos Part Appl Sci Manuf 2021;149:106518. https://doi.org/10.1016/j.compositesa.2021.106518.
[11] Sapozhnikov SB, Swolfs Y, Lomov SV. Pseudo-ductile unidirectional high modulus/high strength carbon fibre hybrids using conventional ply thickness prepregs. Compos Part B Eng 2020;198:108213. https://doi.org/10.1016/j.compositesb.2020.108213.
[12] Sapozhnikov SB, Swolfs Y, Lomov SV. Mode I and II interlaminar critical energy release rates in all-carbon interlayer unidirectional fibre-hybrids based on ultrahigh-modulus and high-strength fibres. Compos Struct 2020;236:111886. https://doi.org/10.1016/j.compstruct.2020.111886.

VARIABLE STIFFNESS LATTICE STRUCTURES

Parham Mostofizadeh [a,b], Robert A. Dorey [b], Iman Mohagheghian [b]

a: EPSRC Centre for Doctoral Training in Micro- and Nanomaterials and Technologies, School of Mechanical Engineering Sciences, University of Surrey, Guildford, Surrey GU2 7XH, UK
p.mostofizadeh@surrey.ac.uk
b: Centre for Engineering Materials, School of Mechanical Engineering Sciences, University of Surrey, Guildford, Surrey GU2 7XH, UK

Abstract: *Lattice structures offer excellent stiffness to weight ratios and show promising potentials in decreasing the weight of structures. This has significant implications in reducing carbon footprint, especially in the automotive and aerospace sectors. In this paper, the aim is to enhance the efficiency of lattice structures further by embedding multiple functionalities into one structure. To reach this goal, a multi-material lattice structure was designed and manufactured using a Polyjet 3D printer capable of printing different polymers in a single print. By fabricating a lattice whose different struts were built from distinctive materials, it was possible to induce a continuous varying stiffness in the structure through temperature elevations. A compressive stiffness drop of more than 95% could be observed in the lattice with a 27-degree increase in temperature. The observations demonstrate the potential of using the proposed method in designing programmable lightweight structures which can be a leap forward in achieving more efficient and multi-purpose structures.*

Keywords: Lattice Structures; Variable Stiffness; Multi-material 3D Printing

1. Introduction

When compared to bulk materials, architected lattice materials are noted for their better structural efficiency. This makes them ideal candidates for use in a variety of industries, including aerospace and automotive. Even though various complex lattice topologies have been developed over years and at least analytically demonstrated to be weight-efficient, the realization of these lattices in smaller length scales became feasible only in recent years. This is thanks to the rapid development and proliferation of various additive manufacturing processes. It is now possible to manufacture complex lattice topologies in various length scales and more recently from multiple materials.

When it comes to efficiency, man-made structures often perform inferior to natural and biological materials. One of the main reasons behind this underperformance is the fact that man-made structures are often designed and manufactured to perform a single task. In the majority of applications, this task is to carry a specific load under a prescribed condition. In contrast, natural and biological materials have evolved to perform multiple tasks with minimum energy and available resources. Therefore, the next step to improve the efficiency of lattice structures is to embed several functionalities into a single structure. This means that rather than having a distinct structure for each function, a single structure is created to suit all the functional needs. In this regard, designing a *variable stiffness structure* is a promising method that helps achieve such multifunctionality within the structure.

  doi:10.5075/epfl-298799_978-2-9701614-0-0

Variable stiffness structures are defined as structures whose stiffness is changed considerably in response to external stimuli. The stiffness alteration can be achieved through either changing the material or the geometry [1]. The former involves alterations in material properties upon a change in an external condition. Shape memory alloys (SMAs), for example, can transform from the martensite phase to the austenite phase when heated above a certain temperature threshold and then revert to the martensite phase when cooled [2]. In each of these phases, the SMA exhibits a different behavior including having a different elastic modulus. Also, in polymers with an amorphous phase, a shift from the rubbery to glassy state takes place when cooled down below the glass transition temperature (T_g) [3]. These two states may have substantially different mechanical properties, which can be used to modify the stiffness of a structure. Yang et al. [4] based their work on this phenomenon and could observe stiffness change of roughly two orders of magnitude in additively built polymeric lattice structures by varying the temperature. Stiffness variability through geometrical changes, on the other hand, can be induced using a mechanism inside the structure, e.g., by dislocating certain elements resulting in an overall different mechanical behavior [1]. As an example, Overvelde et al. [5] reported an extruded-based 3D origami structure capable of morphing between multiple shapes upon imposing proper actuation, which then resulted in stiffness changes.

The two stiffness variation methods presented here can also be used in combination to build hybrid structures. Zappetti et al. [6], for example, designed a tensegrity structure modular unit with variable stiffness cables, using a hybrid strategy in which they changed both material properties and shape. A metal alloy with a low melting point was utilized as the variable stiffness material for the cables. To demonstrate its potential, they built a beam employing the unit structure. While softening the built-in cables through imposing electrical current, they noticed a considerable decrease in the beam's stiffness. Another example of using a hybrid strategy to create variable stiffness structures is the multi-layered beam designed by Henke et al. [7]. By adjusting the amount of friction between layers, using an electroactive polymer as the actuator, they tuned the second moment of inertia and consequently altered the bending stiffness of the beam.

The current study aims to utilize a hybrid approach that incorporates both geometric and material effects to create a variable stiffness lattice structure. This type of multifunctional structure can be used in a variety of industrial applications, including in soft robotics, where a transition between high load carrying capacity and deformability is required [8], and in aerospace, for applications such as deployable structures [9]. The methods of design and manufacturing of such a structure are described in the following section.

2. Methods

In order to build the variable stiffness lattice, a 2D multi-material unit cell was designed to be manufactured out of two different polymers. The unit cell, which is comprised of a square frame and a horizontal strut, is depicted in Figure 1. By heating up the structure, the horizontal strut, which is designed to have a lower T_g than the square frame, gradually becomes softer. This is especially more pronounced when the initial temperature is well below the glass transition temperature of the horizontal strut and the temperature rise continues until the glass transition region of the material is passed. It is reasonable to anticipate that when the horizontal strut gets significantly softer than the surrounding frame, the structure's nodal connectivity decreases,

  doi:10.5075/epfl-298799_978-2-9701614-0-0

relative to its initial state. As a result, the proposed method can result in a hybrid variable stiffness structure capable of stiffness changes due to both material and geometrical alterations.

To experimentally evaluate the mechanical behavior of the designed multi-material lattice, the designed unit cell was used to create a 3 by 3 lattice structure using Autodesk Inventor software (Autodesk, Inc., CA, USA). The total width and height of the lattice were designed to be 70.7 mm with a thickness of 10 mm. The value of 0.1 was considered for the t/l ratio (i.e. the ratio of struts' thickness to the square frame's strut length in Figure 1).

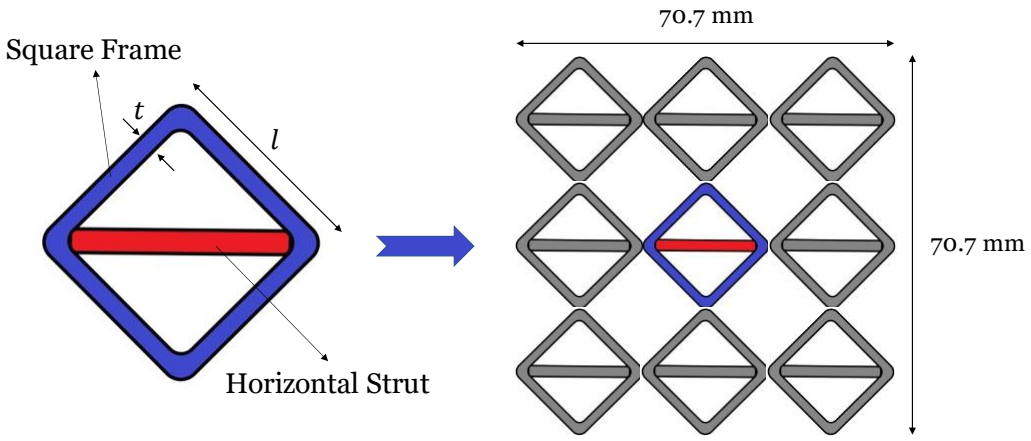

Figure 1. The 2D multi-material unit cell with a horizontal strut shown in red tessellated in two directions

An Objet260 Connex3 3D printer (Stratasys, MN, USA) was employed to fabricate the designed multi-material lattices. This 3D printer, which uses Polyjet technology, can manufacture samples from a variety of materials at the same time. To do this, the device combines two independent base materials to create a so-called "*Digital Material*" with properties falling between those of the base materials, depending on the mixture ratio. VeroWhite and TangoBlackPlus were chosen as the base materials in this study. The former base results in a rigid polymer, whilst the latter produces a rubbery product. VeroWhite was assigned to the diamond frame (shown in blue in Figure 1) while FLX9895-DM, a digital material with a mixture ratio of 62% TangoBlackPlus and 38% VeroWhite [10], was selected as the fabricating material for the horizontal strut (shown in red in Figure 1). The two materials were chosen due to their distinct mechanical properties and glass transition temperatures. The mechanical properties of these materials are summarized in Table 1.

Table 1: Mechanical properties of the Polyjet materials used in the current study.

Material	T_g [°C]	Tensile strength [MPa]	Elongation at break [%]
VeroWhite	52 – 60 [11,12]	50 – 65 [12]	10 – 25 [12]
TangoBlackPlus	~-5 [13]	0.8 – 1.5 [14]	170 – 220 [14]
FLX9895-DM	~30 [11]	8.5 – 10 [15]	35 – 45 [15]

  doi:10.5075/epfl-298799_978-2-9701614-0-0

During the manufacturing of the lattices, cylindrical samples with a diameter of 12.7 mm and a height of 25.4 mm were also printed and later tested under compression according to the ASTM D695 standard [16]. To account for 3D printing uncertainties, the exact dimensions of all manufactured samples were measured using a caliper and utilized for any additional calculations.

Compression tests were conducted on both cylindrical compression samples and the fabricated lattice structures at the strain rate of 10^{-4} s^{-1} and at four different temperatures: 23, 32, 40, and 50°C. Tests were conducted using an Instron 5500 universal machine fitted with an Instron 3119-005 environmental chamber. Each sample was maintained within the chamber for at least 5 minutes to ensure samples reached thermal equilibrium before operating the test. Three samples were tested at each temperature, and the average elastic modulus of the samples was recorded using the slope of the stress-strain curves at the early stages of deformation. A compliance test was also performed on a stiff sample to exclude the effect of the rig deformation and was utilized to correct the crosshead displacement results.

3. Results and Discussion

Quasi-static stress-strain curves of VeroWhite and FLX9895-DM in compression are shown in Figure 2 at different temperatures. As can be seen, both materials experience a reduction in their stiffness when the temperature increases from 23 to 50 °C. The reduction in stiffness is however not uniform for both polymers. VeroWhite shows the most notable decrease in stiffness when the temperature is raised from 40°C to 50°C, as it approaches its glass transition temperature (Table 1). In contrast to VeroWhite, FLX9895-DM demonstrates a more significant decrease when the temperature increases from 23°C to 32°C, since it has a lower glass transition temperature (Table 1).

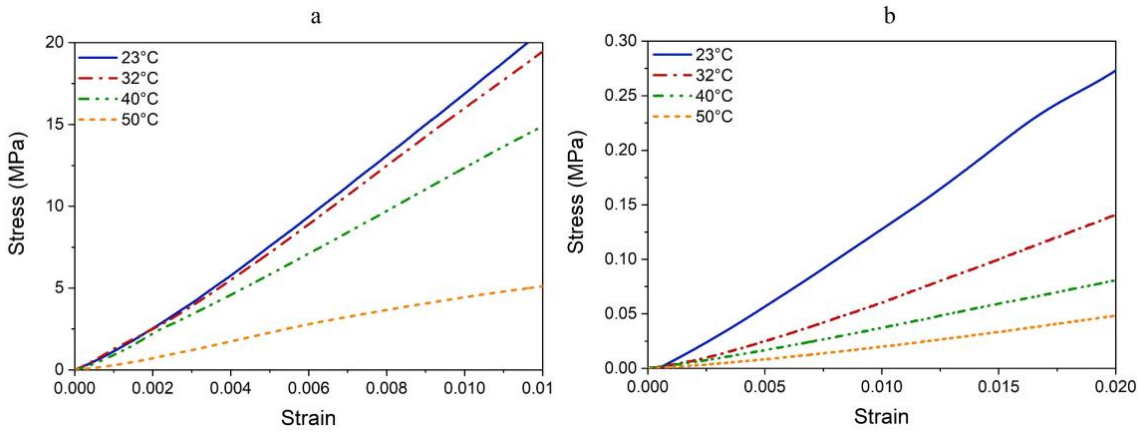

Figure 2. Quasi-static stress-strain curves at different temperatures for a) VeroWhite b) FLX9895-DM

Stiffness values for both VeroWhite and FLX9895-DM materials at different temperatures are depicted in Figure 3. The stiffness is extracted from the initial stages of deformation between the strain values of 0.8% and 1%. Figure 4 presents the results of compression tests on the multi-material lattice structures at four different temperatures. As can be seen in this figure, increasing the temperature from 23°C to 50°C causes the stiffness of the lattice structure to drop by more than 95%, from 8.4 MPa to 0.4 MPa. This was made possible by combining two materials with vastly different mechanical characteristics. When the temperature rises, the horizontal

  doi:10.5075/epfl-298799_978-2-9701614-0-0 published under CC BY-NC 4.0 license

strut softens more rapidly than the frame, potentially affecting the lattice's node connectivity. In other words, the rapid decline in the stiffness of the horizontal strut causes the strut to provide less resistance to deformation of the frame, promoting a more bending-dominated behavior in the frame. This can also be deduced from Figure 3, which indicates that FLX9895-DM has a sharper reduction in stiffness before 40°C than VeroWhite.

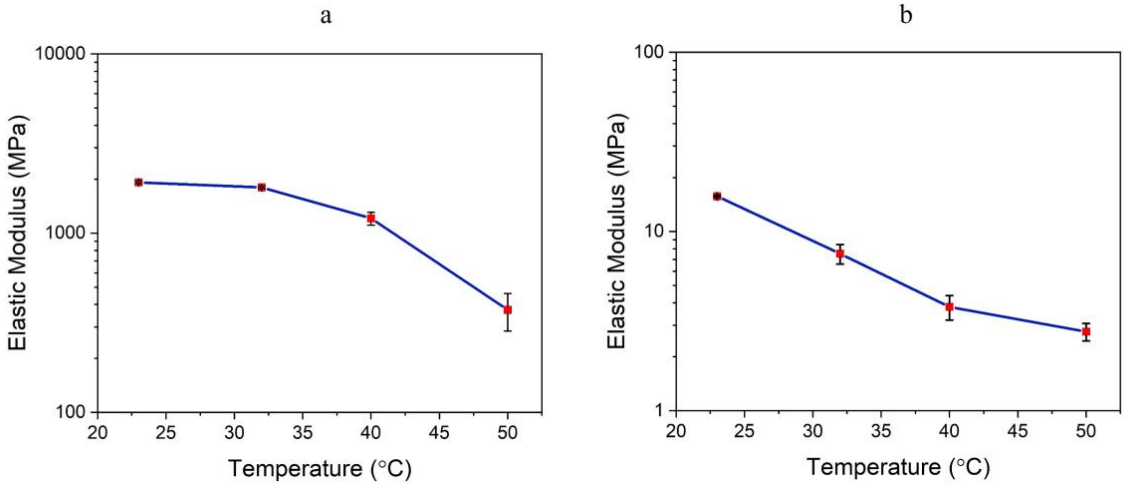

Figure 3. Elastic modulus variation with temperature for a) VeroWhite b) FLX9895-DM

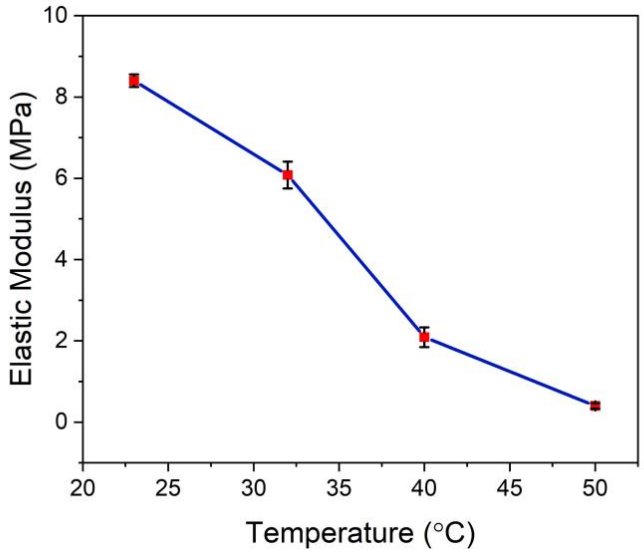

Figure 4. Effect of temperature on the vertical elastic modulus of the lattice structure

By employing multiple materials in the manufacture of a lattice structure, it is now possible to achieve greater stiffness variability by changing both the material and the geometry of the structure. This method allows designers to develop structures with more controllability over stiffness and the ability to carry loads at lower mass densities than conventional counterparts.

4. Conclusions

Owing to the emergence of new additive manufacturing techniques in recent years, a new door has opened to achieve more efficient structures unprecedented before due to production constraints. In the current study, the 3D printed structure was tested under quasi-static

  doi:10.5075/epfl-298799_978-2-9701614-0-0

compression at four different temperatures. By increasing the temperature from 23℃ to 50℃, a continuous reduction of more than 95% could be observed in the stiffness of the structure. The use of two materials with distinct mechanical properties in the lattice structure allowed for greater control over the structure's stiffness when exposed to a variable temperature. The acquired results illustrate the multi-material lattices' promise for applications requiring lightweight and stiffness changeable structures.

Acknowledgements

This work has been funded by the UK's Engineering and Physical Sciences Research Council (EPSRC, grant reference: EP/L016788/1) and the University of Surrey.

5. References

1. Kuder IK, Arrieta AF, Raither WE, Ermanni P. Variable stiffness material and structural concepts for morphing applications. Progress in Aerospace Sciences [Internet]. 2013;63:33–55. Available from: http://dx.doi.org/10.1016/j.paerosci.2013.07.001

2. Mohd Jani J, Leary M, Subic A, Gibson MA. A review of shape memory alloy research, applications and opportunities. Materials and Design [Internet]. 2014;56:1078–113. Available from: http://dx.doi.org/10.1016/j.matdes.2013.11.084

3. Rudin A, Choi P. Mechanical Properties of Polymer Solids and Liquids. In: The Elements of Polymer Science & Engineering [Internet]. Elsevier; 2013. p. 149–229. Available from: https://linkinghub.elsevier.com/retrieve/pii/B9780123821782000043

4. Yang C, Boorugu M, Dopp A, Ren J, Martin R, Han D, et al. 4D printing reconfigurable, deployable and mechanically tunable metamaterials. Materials Horizons. 2019;6(6):1244–50.

5. Overvelde JTB, de Jong TA, Shevchenko Y, Becerra SA, Whitesides GM, Weaver JC, et al. A three-dimensional actuated origami-inspired transformable metamaterial with multiple degrees of freedom. Nature Communications. 2016;7:1–8.

6. Zappetti D, Jeong SH, Shintake J, Floreano D. Phase Changing Materials-Based Variable-Stiffness Tensegrity Structures. Soft Robotics. 2020;7(3):362–9.

7. Henke M, Sorber J, Gerlach G. Multi-layer beam with variable stiffness based on electroactive polymers. Electroactive Polymer Actuators and Devices (EAPAD) 2012. 2012;8340(April 2012):83401P.

8. Zappetti D, Arandes R, Ajanic E, Floreano D. Variable-stiffness tensegrity spine. Smart Materials and Structures [Internet]. 2020 Apr 8;(December 2016):11–4. Available from: https://iopscience.iop.org/article/10.1088/1361-665X/ab87e0

9. McKnight G, Henry C. Variable stiffness materials for reconfigurable surface applications. Smart Structures and Materials 2005: Active Materials: Behavior and Mechanics. 2005;5761(May 2005):119.

  doi:10.5075/epfl-298799_978-2-9701614-0-0

10. Joshi VS, Qualters C, Chen E, Santiago JR, O'Neill K. Dynamic characterization of anisotropy effects in 3-D printed materials for high-G survivability. AIP Conference Proceedings. 2018;1979(July 2018).

11. Chen T, Shea K. An autonomous programmable actuator and shape reconfigurable structures using bistability and shape memory polymers. 3D Printing and Additive Manufacturing. 2018;5(2):91–101.

12. Stratasys Vero product data sheet [Internet]. Available from: stratasys.com

13. Saintsing CD, Yu K, Qi HJ, Tentzeris M. Planar monopole antennas on substrates fabricated through an additive manufacturing process. IEEE Radio and Wireless Symposium, RWS. 2015;2015-June(June):159–61.

14. Stratasys. Stratasys Tango Datasheet [Internet]. Stratasys Tango Datasheet. 2019. Available from: www.stratasys.com

15. Stratasys. Digital Materials Data Sheet [Internet]. Available from: www.stratasys.com

16. ASTM Standard D695 [Internet]. ASTM International. 2015. Available from: https://www.astm.org/

  doi:10.5075/epfl-298799_978-2-9701614-0-0

VIRTUAL-PHYSICAL ENGINEERING OF A GRADED CFRP/TITANIUM AIRCRAFT SUSPENSION STRUT

Robert Gottwald[a], Michael Birke[a], Sebastian Spitzer[a], Jan Luft[a], Jörg Meyer[b], Maik Gude[a]*

a: Technische Universität Dresden – michael.birke@tu-dresden.de
b: Liebherr-Aerospace Lindenberg GmbH

Abstract: *The paper presents an approach for the development of a novel design for high performance struts as used for landing gears in aviation. In order to significantly reduce the weight and increase the load bearing capability of such mechanical highly stressed structures, the use of carbon fiber reinforced polymers in combination with metal provides a promising perspective. The objective here is to achieve a better utilization of the respective material advantages. However, multi-axial loads in connection with anisotropic material behavior lead to a correspondingly demanding task for the stress-appropriate design. In this context for the development of a suitable strut concept, engineering-relevant approaches for material selection, load-oriented functional separation in the structure and partial hybridization for improved load transfer are introduced. In a systematic and linked procedure based on virtual and physical methods, the composition of the tension loops based on shape optimization and mechanical tests for proof of partial hybridization are demonstrated. For verification, complex specimens were manufactured on a laboratory scale and successfully tested.*

Keywords: development process; combined virtual and physical methods; fiber reinforced composites; hybrid structures

1. Introduction

Highly stressed components for landing gears in aerospace applications usually consist of materials with high specific strength and stiffness values. Steel, titanium or aluminum alloys are generally used for this purpose. These are suitable for use under the environmental conditions prevailing in the application environment.

In comparison, carbon fiber reinforced polymers (CFRP) can exhibit excellent specific anisotropic mechanical properties. Structures with defined uniaxial load conditions in broad areas predestine the use of CFRP to realize a high degree of lightweight [1]. In this context, specific development work is required for local load introduction areas in which mechanically complex, multi-axial stresses are present. In such areas, the advantageous properties of the materials used are to be exploited by targeted partial hybridization with metals, thus increasing the performance of the overall composite structure [2, 3].

In order to efficiently solve this task at a given level of complexity, a targeted combination of virtual and physical development process steps is necessary. The essential development methods presented below are examined using the reference example of a highly stressed aerospace landing gear strut previously manufactured from titanium material (cf. Figure 1).

  doi:10.5075/epfl-298799_978-2-9701614-0-0

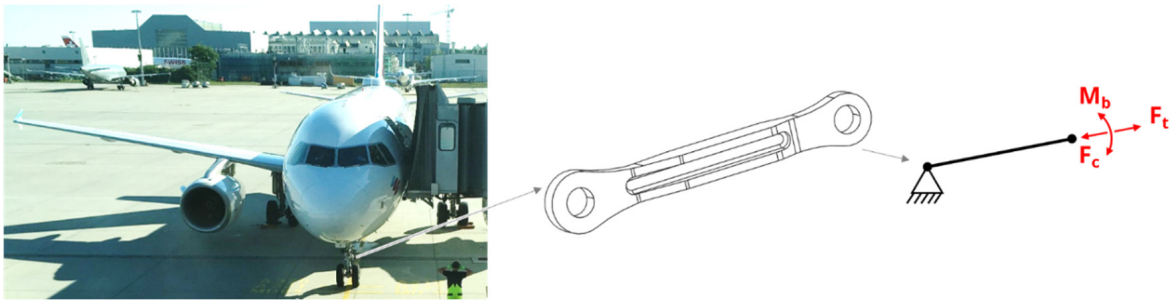

Figure 1. Aircraft (left) and principle shape of reference example strut from landing gear (middle) with simplified mechanical model (right) for development of high performance lightweight struts

2. Design approach for CFRP/titanium suspension struts

General guidance on the basic methodical procedure for the development of products is laid out, among others, in VDI 2221 [4]. In the context of finding solutions for strut structures where complex material behavior has to be taken into account, concepts for finding designs on a virtual basis are to be developed first, taking into account the given requirements. For efficient development, this requires selective physical experiments with regard to material properties, hybridization and structural behavior. This allows the determination of necessary characteristic values for the numerical calculations, as well as further important information on the structure-property relationships and technological influences.

To elaborate and validate the development approach, the focus is on modeling, manufacturing and testing using representative, complex test specimens. The work on the virtual level is not necessarily followed consistently by the work on the physical level, but both complement each other and can also take into account a feedback of the physical solutions into the virtual level, for example through non-destructive computed tomographic (CT) analyses, which sharpen the understanding of the structural behavior after the tests.

2.1 Concept based on material and structural mechanical aspects

In the procedure of developing lightweight strut structures, a scale-based view of the areas to be developed facilitates the formulation of solution approaches. In this case, it is advisable to first develop conceptual designs for finding a global component design in such a way that the main global functions are fulfilled. Based on this, local considerations can be made in order to counteract critical areas or undesirable local effects separately and thus finally to guarantee the function at the highest load conditions on the overall component.

For the mechanical design, the given installation spaces, boundary conditions, loads as well as media and temperature ranges in the associated use cases must be taken into account as external restrictions. As a result of the simplified considerations, a rough dimensioning and a possible material preselection can be derived.

Besides, a key function for the realization of lightweight fiber composite structures is taken on by the load introduction areas of the structure. Known concepts for load introduction into strut-like structures are adapted in such a way that the anisotropic material behavior is taken into account [5]. For the absorption of high tensile loads, a form-fit-based loop connection or a shear-based load introduction at the surface, e.g. via bonding or clamping, are established as ideal

  doi:10.5075/epfl-298799_978-2-9701614-0-0

load- and material-compatible solutions. The latter and also an axially oriented load application via the end face allow the application of high compressive forces. Depending on the application, other or superimposed load types may also have to be taken into account, such as stability effects or resulting bearing moments, which can induce an additional bending load due to their function.

Due to functional and assembly restrictions, the metal reference strut utilizes bolts for the introduction of loads. Therefore, the bolt eye and the surrounding structural design are of particular importance. Following the bolt geometry, a loop-based adaptation of the fiber course is basically appropriate for absorbing the tensile loads. The use of a compression strut arranged between the bearing eyes with a high fiber content in the load direction ensures both the introduction of high forces and a high compressive stiffness. This results in a differential design consisting of tension loop and compression strut for the design approach to the lightweight strut made of fiber composite material. (Figure 2). In this concept, however, only one of the two individual components would assume a load-bearing function, depending on the load case. Following the idea of a further increase in efficiency, the compression strut can also enclose the bolt eye over a large area with a correspondingly adapted design and thus also bear tensile forces proportionally in addition to the tension loop.

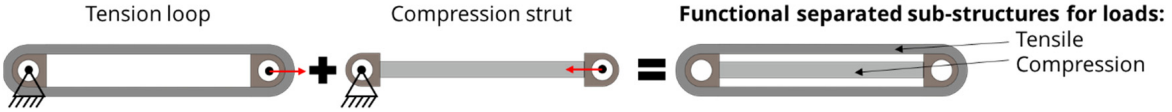

Figure 2. Separation of functions (left) within the tension-compression strut structure concept (right)

The work of Kolesnikov et al. [6] shows that fiber composite laminates can support a significantly higher bolt load if the load application area is designed as a layered fiber composite-metal hybrid structure. Supporting effects in the fiber composite were observed under face loading. Here, it is apparent that increasing homogenization of the materials and suitable grading of the material transitions improve the structural mechanical properties. This approach thus represents an increasing resolution of the hybrid-designed structure, with the increasing material homogenization in the actual sense producing a hybrid material (Figure 3).

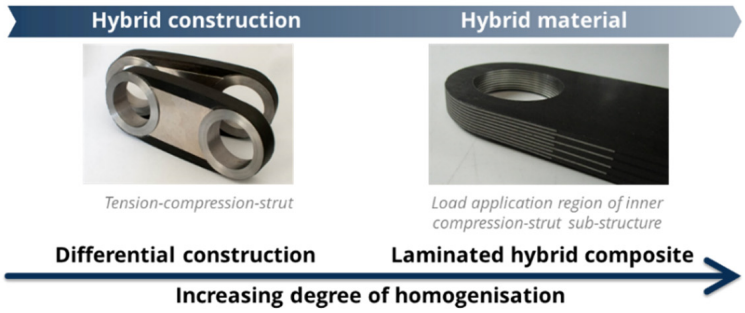

Figure 3. Hybrid design with increased degree of homogenization for the realization of graded material transitions for lightweight structures with high performance under complex loads

When designing tension loops, it should be noted that the tangential and radial stresses (σ_t, σ_r) are not constant across the cross-section, but decrease towards the outer edge. For high loop

  doi:10.5075/epfl-298799_978-2-9701614-0-0

thicknesses, it is therefore advisable to implement a graded multilayer or cascaded structure in which reinforcing fibers with higher stiffness are arranged on the outside [5].

In addition to the structural and material-mechanical aspects, further special load scenarios and specific issues relating to the hybrid design must be taken into account in the present case. The choice of subcomponents and the different materials result in failure-relevant stresses in the area of the interfaces with regard to mechanical and, above all, thermal (delta-alpha- and delta-T-problems) [7] and electrochemical influences, which are not discussed in detail here.

The design guidelines presented here for a lightweight strut in fiber composite construction provide a wide parameter range for possible variants in the design. This results in high requirements for efficient design, i.e. a design in which all the components involved are withstand the maximum load scenarios while at the same time using as little material as possible. Because design details can partially influence and affect each other, virtual parameter studies or suitable optimization methods are required (Figure 4).

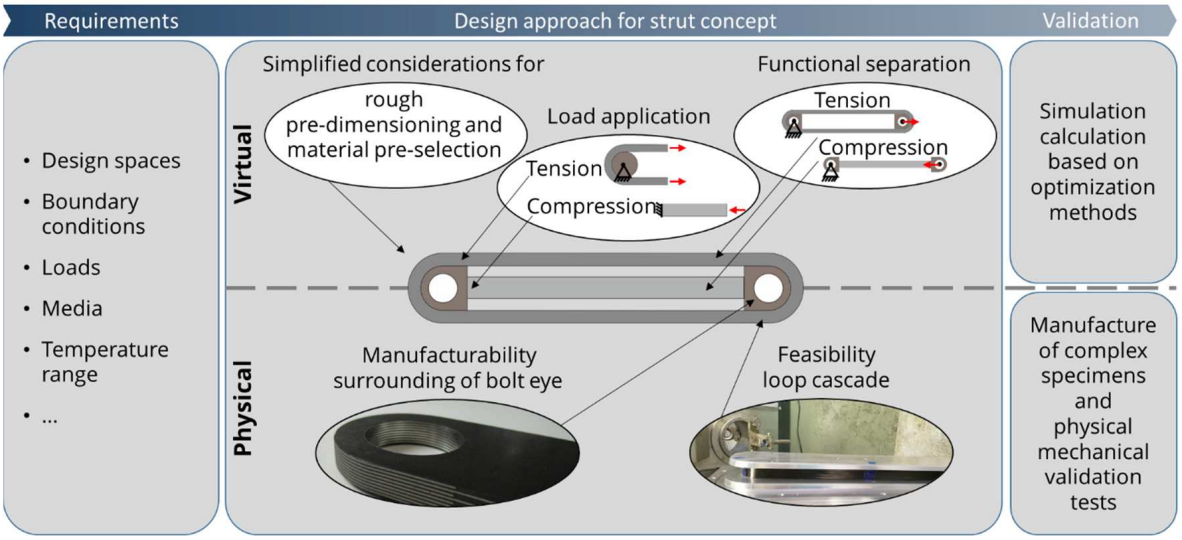

Figure 4 : Virtual-physical combined approach for design finding of the CFRP tension-compression strut with partial metallic hybridization in the load application region

2.2 Partial solutions for virtual – physical verification and validation

Virtual modeling and computational work must be performed for design identification of a fiber composite-based high-performance strut. These are carried out on abstracted and, if necessary, scaled designs in order to efficiently enable well-founded evaluations of the mechanical properties of the concept approaches. Based on this, promising partial solutions are further detailed.

Shape optimizations are carried out for the geometric design of the loop area and a consideration of the variations in the sequence of fibers of different stiffness in the circumferential loop. For this purpose, suitable specifications are to be defined with regard to permissible material parameters and geometries. As a result, the resulting variants are calculated. For an evaluation of influencing parameters, the evaluation of specific stresses $S_{xx,\,max,\,specif}$ and installation space, for example, is useful under lightweight design aspects. In this example, it becomes clear that if the fiber distribution is not optimal, load redistributions occur even with increasing loop thickness or more material, which promote at least a local induction

  doi:10.5075/epfl-298799_978-2-9701614-0-0

of failure. In particular, the distribution of the total thickness of the loop among the layer thicknesses of different carbon fiber types has a significant influence on the amount of maximum stress that occurs (Figure 5).

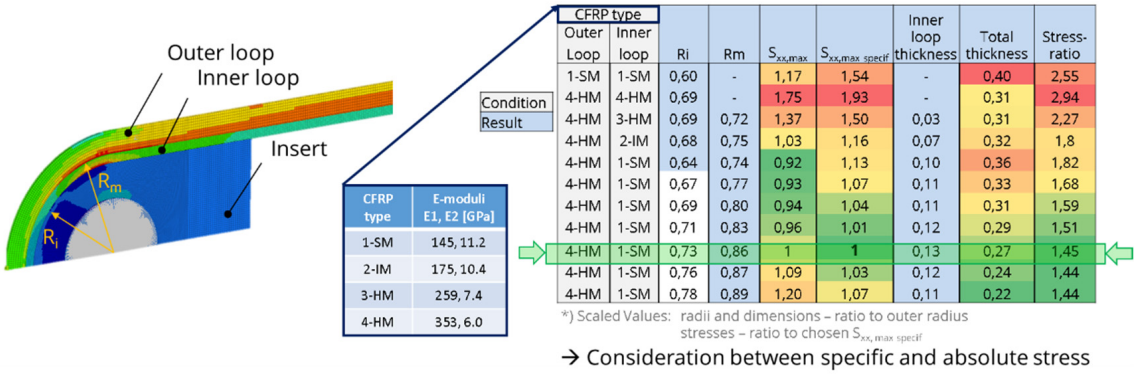

Figure 5 : Example of the scaled plane quarter model (approx. 1:2 to reference) with circumferential two-layer fiber composite loop (left) and result selection of the optimization study for the dimensioning of the loop sub-structures under tensile load (right)

In addition to literature data, physical tests on test specimens at coupon level are necessary to characterize the individual process-specific mechanical properties of the material composites. Specific problems for hybrid structures and detailed implementations are examined in physical mechanical tests. This requires test specimens with increased complexity between coupon and test structure level. For the bolt load introduction area, for example, there are studies on the use of layered metal/plastic composites for hybridization based on titanium or steel sheets with defined dimensions [6, 7]. A purely virtual transfer to the present strut structure and such considerations in this regard would be costly and are subject to many assumptions, e.g., due to the large number of interfaces. Therefore, corresponding CFRP specimens with and without partial metal hybridization are manufactured and experimentally verified. For reasons of sheet availability, the structural area around the bolt eye was initially tested on steel-CFRP laminates (Figure 6).

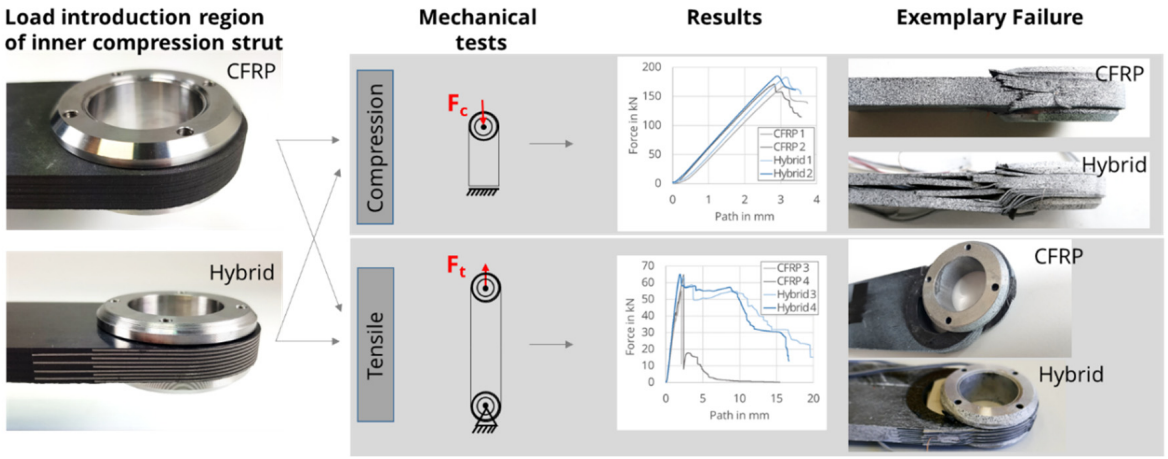

Figure 6. Compression strut specimen made of CFRP and hybrid laminate with approximate cross-section of 10 mm x 53 mm, results of mechanical load tests and failure of specimen

  doi:10.5075/epfl-298799_978-2-9701614-0-0

The tests confirmed the observation made by Both [7] that metal-CFRP laminates have higher strengths for bolt load introduction than pure CFRP designs, especially in limited installation space. In the case of high structural stiffness, as in the present example, it may be necessary to scale the size accordingly so that the failure behavior can be investigated on available testing machines in each case. Furthermore, the tests confirm a general increase in the load-bearing capacity of the test specimen structure compared to a conventional fiber composite construction. Especially in the tensile tests, a positive failure behavior with a high residual load-bearing capacity over the course of the test and thus a high energy absorption capacity can be observed.

For the experimental validation of the elaborated development methods, a process sequence for the manufacturing of complex test specimens, for the physical experimental testing as well as for the measurement of the mechanical behavior and associated damage detection are required.

The development of the production process chain will not be discussed in detail below. In accordance with the fiber composite material distribution and orientation developed for the strut concept, adapted manufacturing processes are used. These are based primarily on stacking in the thickness direction for the compression strut and on winding processes for the tangentially circulating tension loop (compare Figure 4 below) and thus allow effective, efficient and reproducible production. Support structures applied to the sides of the compression strut ensure sufficient stability against lateral buckling of the strut under compressive loading (Figure 7).

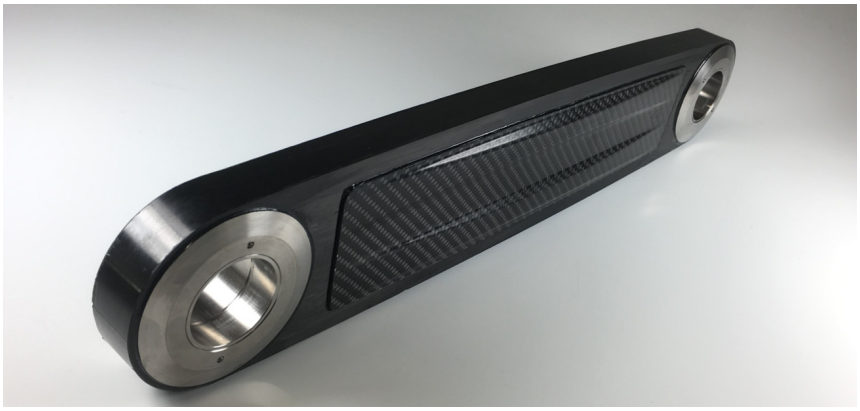

Figure 7 : Complex test specimen of the strut structure with novel CFRP-titanium hybrid design in overall dimensions of 515 mm x 36 mm x 95 mm, representing a scale of approximately 1:2 compared to the reference

2.3 Experimental physical validation of the strut structure under tensile and compressive load

For mechanical testing of the strut, suitable test setups with adapted load application adapters are to be developed. In a first step, the complex strut specimens are tested according to known load specifications with regard to defined limit load cases in quasi-static tests. Using optical 3D measurement technology, the resulting displacements and strains on the structural surface can be measured and the mechanical behavior with regard to deformations and failure can be analyzed. The scaled strut structure considered here was loaded and successfully tested up to a load of F = 600 kN under tension or compression, representing approx. 120 % of the ultimate load value (UL). The complex test specimens have not failed at end load (Figure 8). Only between

  doi:10.5075/epfl-298799_978-2-9701614-0-0

the substructures of the tension loop and the compression strut a delamination is identified, which does not lead to the total failure of the specimen. Compared to a conventional strut construction in titanium, the concept presented allows an estimated mass reduction of approx. 25 %.

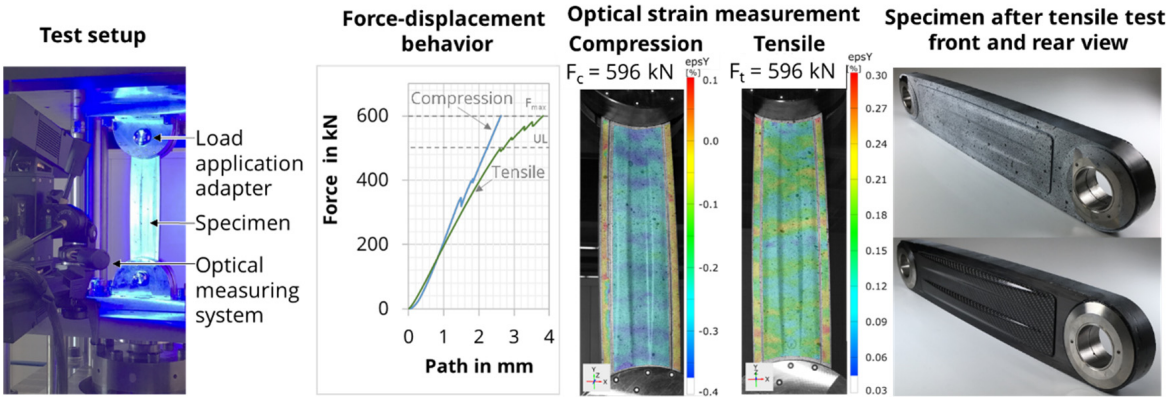

Figure 8 : Test set-up for experimental validation of the novel strut design, force-displacement behavior and strain results at maximum load (modified according to [3]) and tensile test specimen after successful testing

3. Discussions and conclusions

The presented considerations on the engineering of a CFRP aerospace landing gear strut with local metallic hybridization show an advanced method for the development of high performance tension-compression struts.

In addition to tensile and compressive loads, the selected reference strut structure also experiences a bending load due to its function, which are not discussed in detail in this paper. This is relatively small in relation to the axial forces and is taken into account by numeric analyses in the context of the optimization study presented here. For the experimental validation of the tensile or compressive load case with superimposed bending load, suitable test concepts and test techniques still need to be developed.

The physical experimental validation tests introduced only represent the static loading condition, which is used as an equivalent load for testing on metallic structures, considering safety factors. Nevertheless, further cyclic tests under a load that takes into account the operational stress are recommended to ensure the service life of the novel strut structure concept. Furthermore, testing under selected temperature and media boundary conditions or even dynamic loading can reproduce an increased closeness to reality. In this context, anisotropy- or hybrid-specific aspects, such as stiffness differences or delta-alpha problems, can also be considered in depth.

The delamination observed between the tension loop and compression strut substructures at high loading conditions is probably due to the different stiffness behavior. Here, further developments in the region of the interface are recommended in order to avoid delaminations while at the same time achieving the highest load capacity. Possible solutions here could be the development of a relatively elastic intermediate layer or a 3D reinforcement [8].

  doi:10.5075/epfl-298799_978-2-9701614-0-0

The presented aspects for the engineering of a CFRP strut with local titanium material hybridization show the high lightweight construction potential for complex-stressed high-performance structures, which in the field of landing gears in aviation usually consist of high-performance metals. With the help of a procedure in which tools of the virtual development environment are supported by physical experimental methods, it has been possible to develop effective and efficient approaches. The results obtained refer to a Technology Readiness Level (TRL) in which the structures were successfully mechanically tested as complex test specimens on a laboratory scale. The methods and the basic procedure are transferable to other strut structures in hybrid design, depending on the system similarity. It should be noted here that these always represent solutions tailored to the specific boundary conditions and loads, and that corresponding adaptations are usually required for other applications.

In particular, when transferring and applying the presented modular-based design methodology to other strut structures, it should be examined whether scaling effects affect the stressability of substructures like the composite metal hybrid laminate areas.

The reference example chosen here is a component that requires a great deal of effort, particularly due to the large dimensions, the availability of the semi-finished product made of a titanium alloy, the large machining volume and thus also the costs. The developed findings can therefore provide an important basis for improved lightweight construction solutions, which are also becoming increasingly important in consideration of ecological, economic and, where applicable, logistical aspects.

Acknowledgements

The project on which this work is based was funded by the German Federal Ministry for Economic Affairs and Climate Action under the funding code 20Y1505B (see also [3]). The authors are responsible for the content of this publication.

4. References

1. Klein B: Leichtbau-Konstruktion – Berechnungsgrundlagen und Gestaltung. Friedr. Vieweg & Sohn Verlag, GWV Fachverlage GmbH, 7. Aufl. Wiesbaden 2007.
2. Wiedemann J. Leichtbau – Elemente und Konstruktion. Springer-Verl. Berlin Heidelberg 2007.
3. Gude M et al.. Joint project FAWIBO: landing gear system for wide-body aircraft of the next generation: subproject: development of a modular design methodology for hybrid structures in highly loaded landing gear components. Final report. 2020.
4. NN. VDI 2221 Blatt 1:2019-11 Design of technical products and systems - Model of product design.
5. Schürmann H. Konstruieren mit Faser-Kunststoff-Verbunden. Deutschland: Springer. 2007.
6. Kolesnikov B, Herbeck L, Fink A. Fortschrittliche Verbindungstechniken von Faserverbundstrukturen. In: Deutscher Luft- und Raumfahrtkongress 2004, II, Seiten 1419-1428. Deutsche Gesellschaft für Luft- und Raumfahrt DGLR. Deutscher Luft- und Raumfahrtkongress 2004, 2004-09-20-23, Dresden. ISSN 0700-4083.
7. Both J C. Tragfähigkeit von CFK-Metall-Laminaten unter mechanischer und thermischer Belastung. Diss. TU München. 2014.
8. Havar T. Beitrag zur Gestaltung und Auslegung von 3D-verstärkten Faserverbundschlaufen. Diss. Uni Stuttgart. 2007.

  doi:10.5075/epfl-298799_978-2-9701614-0-0

MANUFACTURING AND PROPERTIES OF HYBRID COMPOSITES OF CONTINUOUS STEEL AND GLASS FIBERS MADE BY TAILORED FIBER PLACEMENT

Alexander Marx[a], Patrick Schiebel[b], Axel S. Herrmann[c]

a: Faserinstitut Bremen e. V. – amarx@faserinstitut.de
b: Faserinstitut Bremen e. V.
c: University of Bremen

Abstract. *In this study, the tailored fiber placement (TFP) technology was implemented to lay up high strength continuous steel fibers for manufacturing unidirectional hybrid composite laminates of glass and steel fibers. As result, the processing and impregnation of the steel fibers show good quality. Mechanical tests indicate a higher strength and lower strain of the steel fibers compared to glass fibers. A combination of the different fibers in hybrid laminates results in lower strength of the laminates, due to the steel fibers. Initial conclusions can be made on the mechanical tensile and bending behavior regarding the use to function integration through the steel fibers.*

Keywords: *Tailored fiber placement; Steel fiber; Hybrid composite*

1. Introduction

Fiber reinforced plastics (FRP) combine low density with excellent mechanical behavior, which make them a perfect match for lightweight constructions. Conventional structural reinforcing fibers such as carbon fibers (CF) or glass fibers (GF) are characterized by high strength and low strain behavior. The combination of different fiber materials into a hybrid composite generates a better balance in mechanical properties, but leads to a more difficult prediction of its properties [1]. Due to these characteristics, the combination of continuous ductile steel fibers (SF) with conventional reinforcing fibers increases the ductility and fracture toughness of FRP. The strain to failure of this combination is 3-4 times higher than the one of conventional composites parts from glass or carbon fibers [2]. On the other side, the strength of steel fiber composites can be increased by using silane treatments to modify the adhesion between the fibers and the matrix [3]. Most of the steel fibers used for hybridization of FRP have compared with conventional reinforcing fibers high strain to failure properties (>15%) but, low strength (< 1 GPa) and high diameters (30 µm) [4,5]. Besides the mechanical properties, steel fibers have additional benefits as is the possibility of integrating multiple new functions into composite parts, such as electric conductivity used for lighting strike protection [6].

However, the high density of steel requires a targeted use at essential points. Therefore, the approach of this study is to use tailored fiber placement (TFP) technology to specifically place SF and integrate them into a GF stack to a hybrid composite. The TFP technology is an established manufacturing process for textile preforms with conventional reinforcing fibers [7]. The TFP process allows a load predicted placement of reinforcing fibers aligned to the load direction with a high positioning precision and a variable arrangement of the reinforcing fibers [8].

  doi:10.5075/epfl-298799_978-2-9701614-0-0

Hence, for the purpose of this study a hybrid composite consisting of continuous high strength SF and GF is manufactured, allowing the analysis and investigation of the influence of SF on the quasi-static mechanical properties of hybrid composite.

2. Material and methods

2.1 Fiber and matrix material

The continuous SF selected for this study were BU 8/12.000 from Bekaert made of stainless steel AISI 302 A. The textile configuration was a non-crimp roving with 12 k filaments. The TFP technology was used to produce a textile of SF, which enables to place the SF with different distances in an unidirectional orientation on a base material. The placing was executed on a ZSK JGW 0200 550 TFP machine. The polyester sewing yarn Serafil 200/2 from Amann was used. A GF fabric with an area weight of 106 g/m² was used as base material. Two different types of textile SF-TFP-preforms were produced. The first TFP-preform type had a distance between SF rovings of 4.5 mm to ensure an areal layup by simultaneous low area weight. The second TFP-preform type had a roving distance of 10 mm to ensure just a partial amount of SF with reduced area weight. The TFP process parameters and the area weight of the manufactured TFP-preforms are shown in Table 1.

Table 1: TFP parameters of the manufactured SF preforms

TFP Preform	Roving distance [mm]	Stitch width [mm]	Stitch distance [mm]	Area weight [g/m²]
Areal	4.5	5	7	1046
Partial	10	5	7	576

To create hybrid laminates, the SF-TFP-preforms were integrated in the middle of 4 plies unidirectional (UD) GF non crimp fabric (NCF) with an area weight of 663 g/m². The configuration Hybrid 1 consists of the TFP-preforms Areal and the configuration Hybrid 2 consist of the TFP-preforms Partial. As reference, a laminate of 4 plies GF UD NCF (GFRP) and a laminate with 2 plies Areal TFP-preforms (SFRP) were manufactured. All laminates have UD orientation of 0° in tensile direction. The different laminate configurations are shown in Table 2.

Table 2: Lay up of the manufactured laminates

	Layers		
Laminate	GF NCF	SF	SF preform type
GFRP	4	-	-
SFRP	-	2	Areal
Hybrid 1	4	1	Areal
Hybrid 2	4	1	Partial

  doi:10.5075/epfl-298799_978-2-9701614-0-0

The composite was produced by vacuum infusion using the epoxy resin Hexion EPIKOTE RIMR 135 and the hardener Hexion EPIKURE RIMH 137 with a mixing ratio of 100:30 by weight. The impregnation was done at room temperature followed by a curing of 48 h at room temperature and a post-curing at 60 °C for 12 h. The manufactured laminates for the tensile tests are shown in Figure 1.

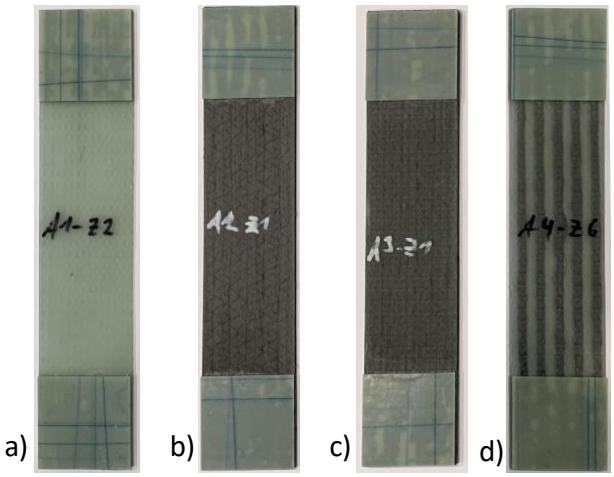

Figure 1. Manufactured laminates for tensile tests : a) GFRP; b) SFRP; c) Hybrid 1; d) Hybrid 2

2.2 Experimental methods

At first the selected BU 8/12000 SF were characterized using single filament tensile strength test according DIN EN ISO 5079 on a FAVIMAT+ system. A clamping length of 20 mm and a testing speed of 10 mm/min was applied. Scanning electron microscope (SEM) images were created to analyze the SF's surface. Micrographs of the laminates were used to investigate the impregnation quality. The fiber volume ratio was determined by pyrolysis. Due to the different fiber materials in the hybrid laminates, the amount of each fiber type was determined. The influence of SF content on the mechanical properties of the hybrid laminates was investigated by quasi-static tests, carried out on a Zwick Z250. Tensile tests were performed according to DIN-EN-ISO-527-4 with a testing speed of 2 mm/min. The length of the specimens was 250 mm by a width of 50 mm. To determine the elongation, strain gauges were attached to the specimens. In addition, three-point bending tests were performed according to DIN-EN-ISO-14125, for the investigation of the bending behavior of the laminates. The testing speed was 5 mm/min by a specimen size of 100 mm length and 15 mm width. In addition to the mechanical parameters, the failure of the laminates was investigated.

3. Results and discussion

3.1 Fiber characterization

At the single fiber tensile tests, the E-glass fibers from the UD NCF, with a diameter of 23.8 µm achieved a strength of 1.08 GPa at a strain of 1.5%. The SF, with a diameter of 7.9 µm, showed a stiffer behavior. The strength of 1.61 GPa is 49% higher, but the strain to failure of 1.0% is 33% lower than the E-glass fibers. The stress to strain curves of the different fibers are shown in Figure 2.

  doi:10.5075/epfl-298799_978-2-9701614-0-0

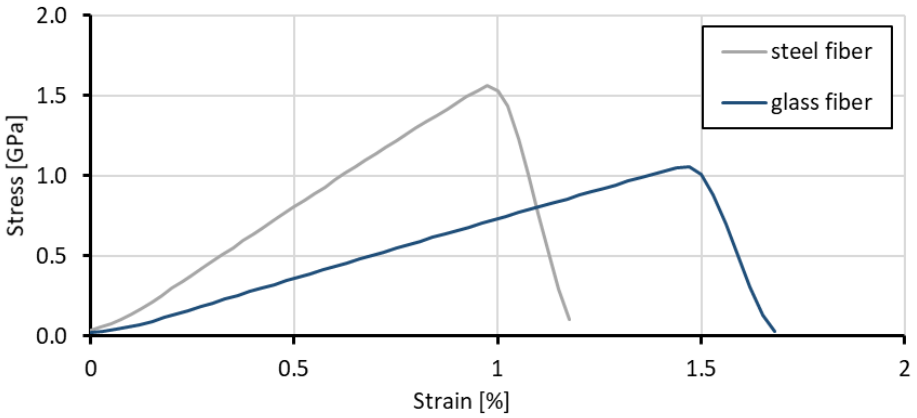

Figure 2. Representative stress stain curves of the single fiber tensile tests

Figure 3 shows the SEM images of the steel fibers. Compared to common reinforcing fibers like carbon or glass fibers, the surface is rough and the cross-section is not circular but polygonal.

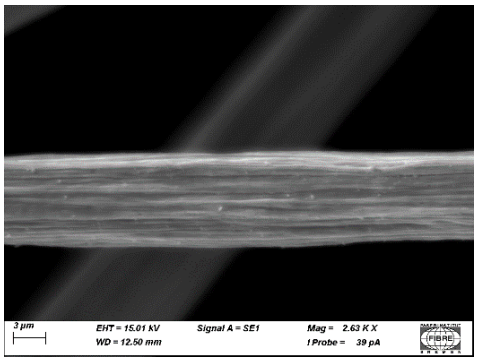

Figure 3. SEM image of the steel fibers

3.2 Micrographs

Figure 4 shows micrographs at the cross-section of the different laminates. No voids or defects were detected, which indicates a good impregnation quality of the laminates. Compared the GF, the SF are not packed as closely together, which leads to higher matrix portions inside the SF roving.

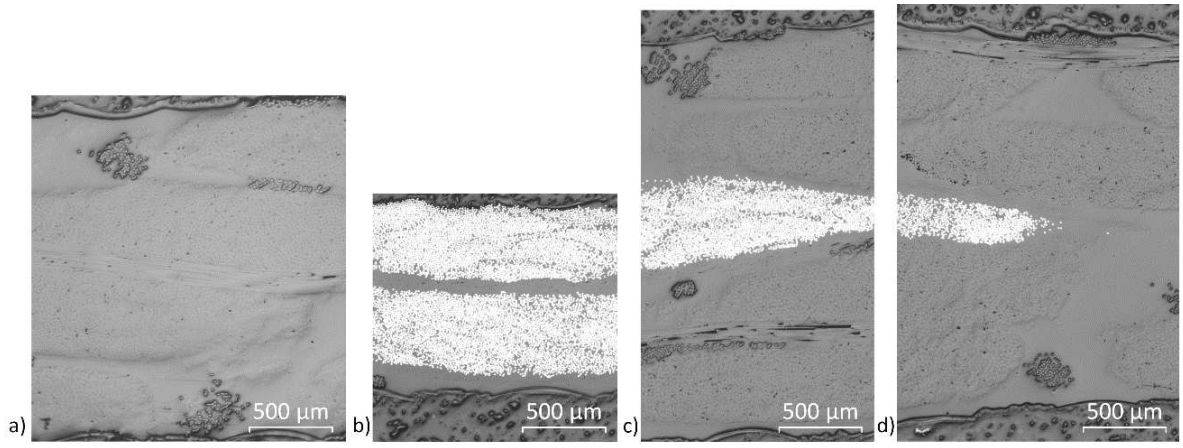

Figure 4. Cross-section micrographs of the laminates: a) GFRP; b) SFRP; c) Hybrid 1; d) Hybrid 2

  doi:10.5075/epfl-298799_978-2-9701614-0-0

3.3 Fiber volume ratio

The GFRP laminate shows the highest fiber volume ratio with 48.2%. As the other laminates consist of different fiber types, the amount of the consisting fibers was determined. The SFRP laminate shows the lowest fiber volume ratio with only 30.2%. This can be explained due to the not compact arrangement of the SF, see Figure 4. The hybrid laminates show with 39.6% for Hybrid 1 and 43.9% for Hybrid 2, a slightly higher fiber volume ratio. Responsible for the higher fiber volume ratio is the high amount of GF NCF in these laminates. The determined fiber volume ratio and thicknesses are listed in Table 3.

Table 3: Results of the fiber volume ratio and thickness

Laminate	Thickness [mm]	Fiber volume ratio [%]	Volume content [%]		
			GF NCF	SF	TFP base material
GFRP	2.33 ± 0.01	48.2	100	-	-
SFRP	1.28 ± 0.04	30.2	-	76.9	23.1
Hybrid 1	2.77 ± 0.04	39.6	85.0	11.7	3.3
Hybrid 2	2.72 ± 0.05	43.9	90.7	5.8	3.5

3.4 Tensile test

The results of the tensile tests are listed in Table 4. The highest tensile strength and strain to failure is reached by the GFRP laminate. The SFRP reaches 47% of that strength and just 32% of the strain. The samples of Hybrid 1 and 2 reach 86% and 87% of strength and almost the same strain to failure as the GFRP. Figure 5 shows the stress-strain curves of the tested laminates. The Hybrid 1 and 2 indicate a kink in the curve at the failure of the SFRP. The low strain of SF leads a brittle fracture appearance and complete failure of the SFRP. The breaking edge is flat with a 90° angle to the tensile direction. At the Hybrid 1 and 2 laminates the GF fibers burst of the body similar to the GFRP. The GF do not show a uniform fracture line, the broken fibers are all of different lengths and distributed on different levels of the body.

Table 4: Results of the tensile tests

Laminate	Breaking stress [MPa]	Strain to failure [%]	No. of samples
GFRP	842 ± 12.9	2.69 ± 0.36	4
SFRP	374 ± 29.5	0.85 ± 0.08	6
Hybrid 1	721 ± 15.7	2.67 ± 0.20	5
Hybrid 2	736 ± 33.7	2.62 ± 0.34	6

  doi:10.5075/epfl-298799_978-2-9701614-0-0

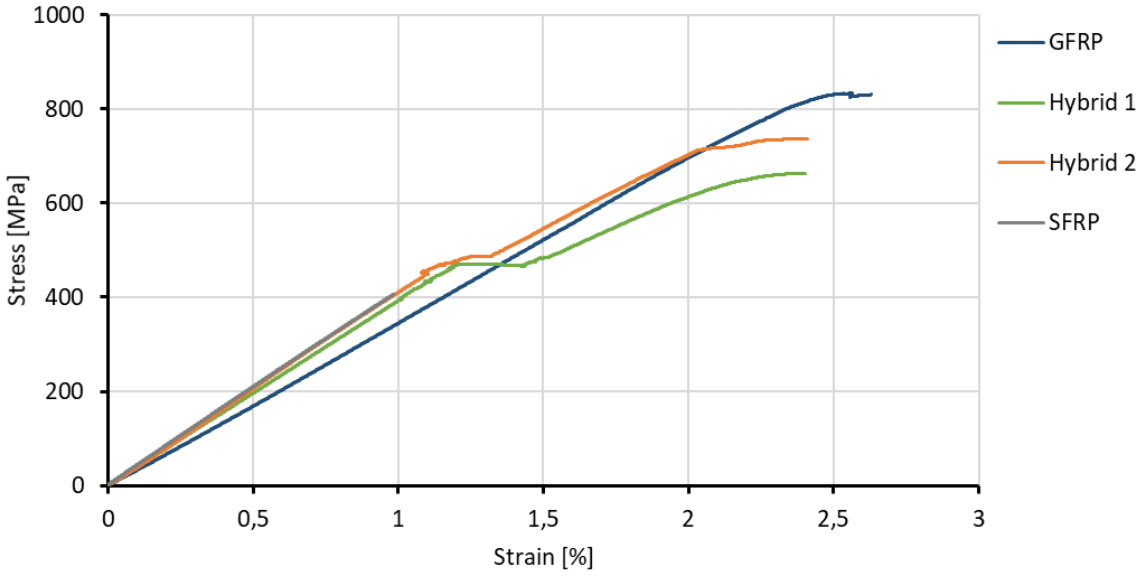

Figure 5. Representative stress-strain curves of the tensile tests

3.5 Bending test

The results of the three-point bending tests are listed in Table 5. The GFRP laminate reaches the highest bending strength of 682 MPa while the SFRP only reaches 54% of the strength. The Hybrid 1 and 2 laminates reach almost the bending strength of the GFRP. Figure 6 shows the bending stress-deformation curves. The curves of Hybrid 1 and 2 samples have a steeper ascent due to the stiffer steel fibers. The GFRP samples shows fractures of fibers at the top side induced by compressive stresses including delaminations of the first layer due to interlaminar shear stress. The SFRP samples show a fracture starting on the bottom due to tensile stress. Hybrid 1 and 2 show a similar behavior as the GFRP with fractures of the GF at the top through the compressive strength and delaminations.

Table 5: Results of the three-point bending tests

Laminate	Bending strength [MPa]	Deformation [%]	No. of samples
GFRP	682 ± 82.0	3.38 ± 0.38	6
SFRP	365 ± 22.9	1.79 ± 0.08	6
Hybrid 1	676 ± 48.5	3.44 ± 0.61	6
Hybrid 2	662 ± 80.4	2.79 ± 0.34	6

  doi:10.5075/epfl-298799_978-2-9701614-0-0

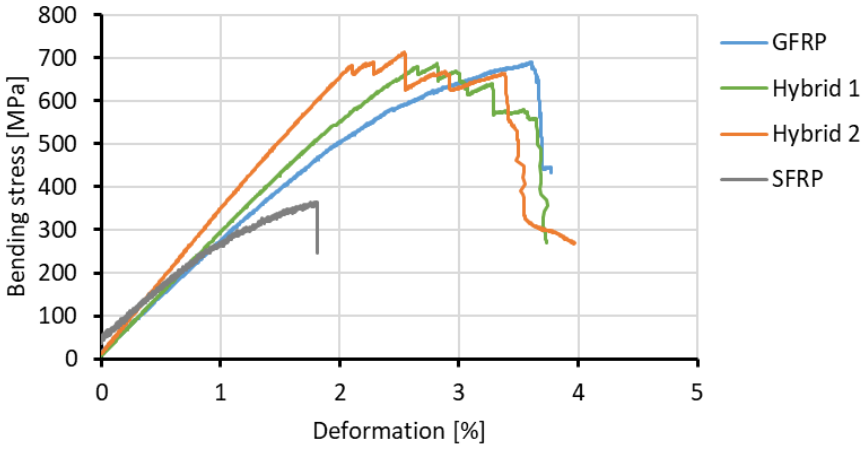

Figure 6. Representative bending stress-strain curves of the three-point bending tests

4. Conclusion

The results of this study show that the SF BU 8/12000 have a higher strength but lower strain to failure compared to the E-glass fibers. This certain properties are reflected in the mechanical tensile and three-point bending tests. At both tests, higher strengths are achieved by laminates with a high amount of GF. Due to the low strain, the content of SF lowers the strength of the hybrid laminates. Consequently, it can be stated that no positive effect due to hybridization occurs. Nevertheless, the results evidence a good processing of the SF via the TFP process and good impregnation quality of the hybrid laminates. Initial statements on the mechanical properties are shown, which will be useful for further SF application e.g. functional integration.

Acknowledgements

The presented results are from the project HyFiVE (03SX511C), which is supported via PTJ within the maritime research program of the Federal Ministry of Economic Affairs and Climate Action (BMWK), based on a resolution of the German Parliament.

Projektträger Jülich
Forschungszentrum Jülich

Federal Ministry
for Economic Affairs
and Climate Action

5. References

1. Swolfs Y, Gorbatikh L, Verpoest I. Fibre hybridisation in polymer composites: A review. Compos Part A Appl Sci Manuf [Internet]. 2014;67:181–200. Available from: http://dx.doi.org/10.1016/j.compositesa.2014.08.027

2. Callens MG, Gorbatikh L, Verpoest I. Ductile steel fibre composites with brittle and ductile matrices. Compos Part A Appl Sci Manuf [Internet]. 2014;61:235–44. Available from: http://dx.doi.org/10.1016/j.compositesa.2014.02.006

  doi:10.5075/epfl-298799_978-2-9701614-0-0

3. Callens MG, Gorbatikh L, Bertels E, Goderis B, Smet M, Verpoest I. Tensile behaviour of stainless steel fibre/epoxy composites with modified adhesion. Compos Part A Appl Sci Manuf. 2015;69:208–18.

4. Swolfs Y, Verpoest I, Gorbatikh L. Recent advances in fibre-hybrid composites: materials selection, opportunities and applications. Int Mater Rev [Internet]. 2019;64(4):181–215. Available from: https://doi.org/10.1080/09506608.2018.1467365

5. Allaer K, De Baere I, Lava P, Van Paepegem W, Degrieck J. On the in-plane mechanical properties of stainless steel fibre reinforced ductile composites. Compos Sci Technol [Internet]. 2014;100:34–43. Available from: http://dx.doi.org/10.1016/j.compscitech.2014.05.009

6. Hannemann B, Backe S, Schmeer S, Balle F, Breuer UP. Hybridisation of CFRP by the use of continuous metal fibres (MCFRP) for damage tolerant and electrically conductive lightweight structures. Compos Struct [Internet]. 2017;172:374–82. Available from: http://dx.doi.org/10.1016/j.compstruct.2017.03.064

7. Cherif C. Textile materials for lightweight constructions: Technologies - methods - materials – properties. Textile Materials for Lightweight Constructions: Technologies - Methods - Materials - Properties. 2016. 1–677 p.

8. Mattheij P, Gliesche K, Feltin D. Tailored Fiber Placement-Mechanical Properties and Applications. J Reinf Plast Compos [Internet]. 1998 Jun 18;17(9):774–86. Available from: http://journals.sagepub.com/doi/10.1177/073168449801700901

  doi:10.5075/epfl-298799_978-2-9701614-0-0

A NOVEL HYBRID THERMOSET-THERMOPLASTIC ROBOT-BASED PRODUCTION CONCEPT FOR LIGHTWEIGHT STRUCTURAL PARTS: A SPECIAL VIEW ON THE HYBRID INTERFACE

Philipp Bauer[a], Nicole Motsch-Eichmann[b], Sebastian Schmeer[b], Konstantin Mehl[b], Ingolf Müller[a], Joachim Hausmann[b]

a: Pforzheim University of Applied Science – philipp.bauer@hs-pforzheim.de
b: Leibniz-Institut für Verbundwerkstoffe GmbH (IVW), Kaiserslautern (Germany)

Abstract: *With the help of a robot-based 3d filament-winding process and a downstream injection molding process, highly loadable and functionalized hybrid thermoset-thermoplastic structures can be manufactured in a highly efficient, waste-free process. In this process, the continuous carbon fiber-reinforced filament-wound thermoset structures (CFRP) handle the main loads, and the short glass fiber-reinforced thermoplastic takes on additional functions, such as load transfer, functionalization by clips, planar surfaces and support of the truss-like CFRP reinforcement structures. To generate such a split of functions, there must be a highly loadable interface between the two dissimilar polymers. This can be created by a plasma pretreatment of the CFRP reinforcement structures. Here, the upper continuous fiber layer gets exposed, with which the thermoplastic injection molding material can then bond directly. In combination with the robot-based 3d filament-winding process, this creates an automated and cost-efficient process for manufacturing locally continuous fiber reinforced plastics.*

Keywords: Hybrid; Filament-Winding; TowPreg, Injection Molding; Interface;

1. Introduction

Continuous carbon fiber-reinforced plastics (CFRP) can be processed into highly loadable components with low mass, but this is usually very cost intensive due to the expensive materials and the complex process technology [1]. With a robot-based 3d filament-winding process, the thermoset CFRP material can be deposited along the load paths in a highly automated and waste-free process [2]. To make this possible, pre-impregnated rovings (TowPreg) are used for this process, which guarantee a higher winding speed (compared to classic winding with in-situ impregnation) and a very consistent impregnation quality of the fibers. In addition, the TowPreg allows leaving the geodesic paths due to the existing tackiness and thus more flexibility in the 3d filament-winding process [3, 4].

In order to increase the application range of such 3-dimensionally wound structures, the winding process is to be extended by a downstream injection molding process. With the aid of the injection molding process, complex components with a high degree of design freedom can be manufactured cost-effectively in an automated process [5]. For example, additional clips or load introduction elements can be created. Planar subareas of the highly loaded component that are not highly loaded can be manufactured more cost efficiently, too. As a result, such planar subareas do not have to be created with the expensive continuous fibers in this hybrid process. Furthermore, the injection molding material can support the truss-like wound CFRP reinforcement structures as an additional support structure. The tensile and compressive loads

  doi:10.5075/epfl-298799_978-2-9701614-0-0

can be carried by the thermoset CFRP and the shear loads by the thermoplastic material. To realize such functions, a highly loadable interface must be created between the wound structures and the injection molding material to transfer loads.

For an efficient process, the complete production chain of the hybrid thermoset-thermoplastic production concept must be considered (Figure 1). In the first step, adequate structural optimization must be carried out to identify the main load paths. Both, the anisotropic stiffness properties of the winding structure and the stiffness properties of the injection molding material, must be considered. The results of such an anisotropic topology optimizer based on the BESO algorithm were shown by Mehl et al. [10].

Figure 1. Hybrid thermoset-thermoplastic production concept

In the next step, the winding paths must be generated based on the topology-optimized structure. To do this, the structure can be broken down into individual winding paths (patterns), which are then reassembled to form an overall structure. Care must be taken to ensure that the winding paths are not traversed more often than it is actually required. The winding core can then be designed and manufactured using these results. The core can remain in the winding component as a lost core, be removed after curing or be demolded as a reusable mold.

Due to the low availability of TowPreg and its high costs on the market (compared to the cost of the base products by a factor of approx. 3), it is recommended to manufacture the TowPreg in-house. Above all, the choice of fibers and matrix can be made more flexible. The structural optimization determines the number of fibers in the roving (mainly by the geometric dimensions) and the core material, the core geometry as well as the later intended use of the component determine the properties of the matrix (tack, mechanical properties, curing temperature).

In the robot-based 3d filament-winding process, the fibers are deposited on the core (mounted on the external axis) with the help of a winding head mounted onto a 6-axis industrial robot (as shown in chapter 2.1). The winding head can deposit up to two TowPreg strands at the same time (1-50k filament possible). The continuous fibers follow the main load paths from the structural optimization on the core. This creates the load-bearing structure. If individual sections in the component are passed over too often due to the existing winding patterns, an automated separating and feeding unit at the winding head can switch between one and two TowPreg strands automatically so that no accumulation of TowPreg is generated which would lead to an oversized section.

The thermoset CFRP reinforcement structure is then cured under temperature and pressure. After curing, the structure must be pretreated to realize a high loadable interface. This pretreatment and the interface will be discussed in the following chapters. The final step, the overmolding of the CFRP reinforcement structure, is then carried out as usual within a standard injection molding process. The main point to consider is that the CFRP structure does not get dislocated in the injection mold. For this purpose, load introduction elements of the structure can be used to fix the CFRP reinforcement structure in the mold.

  doi:10.5075/epfl-298799_978-2-9701614-0-0

2. Hybrid Interface

The transmission of forces between two bonded plastics is possible via form-fit, a coherent connection or a frictional connection. In this process, the form-fit is generated by overmolding and thus encapsulating the CFRP reinforcement structure. The effect contributed by this is strongly varying depending on the geometry of the components. By roughening the CRFP component, a microform-fit can also be generated, which additionally contributes to the load transmission. In this hybrid process, the frictional connection is created by shrinkage of the cooling thermoplastic injection molding material but can be assumed to be very small. A coherent connection can be created in this hybrid process by connecting the molten thermoplastic material to the CFRP reinforcement structure.

Various preliminary studies have investigated different influences on the interface between the two materials. For example, the surface of the cured CFRP reinforcement structure can be roughened, which leads to an increase in the contact area of both materials and to an increase in the microform-fit. This has already been investigated in some publications, for example with peel plies or subsequent roughening using abrasive paper [6, 7]. Also, a coherent connection can be created by an additional component, such as hot melt adhesives shown by Karakaya et al. [8]. In contrast, Kazan et al. [9] overmolded and cured initially uncured prepreg directly in the injection molding process, but this leads to long occupancy times of the injection molding machine and is therefore unlikely to be practical for serial applications.

In this study, the focus on improving the load transmission for this hybrid process is the coherent connection between the two materials. For this purpose, the hybrid interface between the two dissimilar polymeric materials (thermoset & thermoplastic) will be investigated. First investigations have shown that an etching process seems to be very promising. The aim here is to create an interface that introduces the forces directly between the two matrix materials into the continuous fibers without detours (direct interface). For this purpose, the continuous fibers in the uppermost layer are exposed so that the injection molding material can bond directly to the fibers (Figure 2). This is done, for example, by etching away the epoxy matrix in a plasma process [7] or with the aid of a CO_2 laser [8]. In contrast to an indirect matrix interface, in which the loads from the thermoplastic matrix are first introduced via the thermoset matrix into the highly loadable continuous fibers, the direct fiber interface allows the thermoplastic matrix to be connected directly to the continuous fibers.

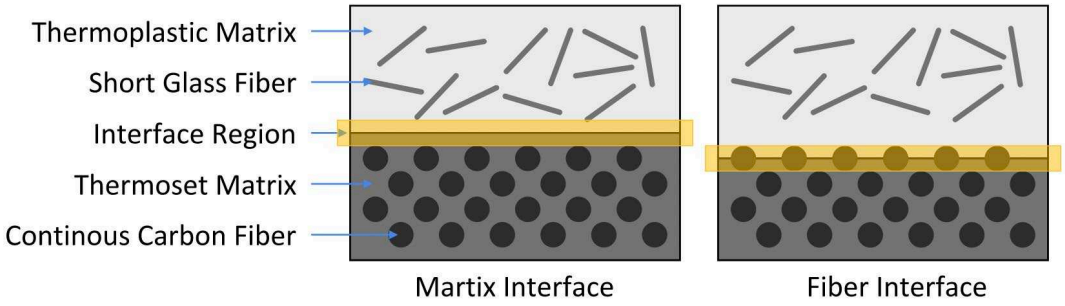

Figure 2. Scheme of a matrix interface (left) and fiber interface (right) with continuous carbon fiber-reinforced thermoset and short glass fiber-reinforced thermoplastic material

The aim of this publication is a special view on the fiber interface in this hybrid production process which was generated using a low-pressure plasma treatment.

3. Experimental

The averaged shear stress, as key parameter for the maximum load transmission in the interface, is to be investigated with the aid of a pull-out test [7]. A TowPreg from TCR (UF3325 - T700 12k) is used as the continuous fiber-reinforced thermoset material. This consists of a T700 roving (12,000 filaments from Toray) pre-impregnated with epoxy resin. Due to its high prevalence in low-load structural components, a polyamide 6 with 30% by weight short glass fiber reinforcement is used as the injection molding material. Here, “Celanese Nyflor B2GF30” material is used in tests v1-v3 and “Khimvolokno Grodnamid PA6-GF30-1” material in test v4.

2.1 Hybrid Sample Production

The first step is to manufacture the CFRP reinforcement structures. In the first test series v1, these were still manufactured by hand and had 10 layers of CFRP. For the test series v2-v4, a specially developed winding tool is used, which enables to manufacture the reinforcement structures with dimensions of 75 x 5 mm (length L x width W) directly in a robot-based winding process. Figure 3 shows the fabrication of the reinforcement structures and a final CRFP reinforcement structure. For demonstrations, 12 layers of CFRP were deposited in each of the first five channels and one layer in the sixth channel. In tests v2 and v3, 10 layers are processed to a thickness of 1.33 mm. In test v4, 12 layers are processed to a total thickness of 1.6 mm to increase the bending stiffness of the reinforcement structures (which is important in the injection molding process). The TowPreg strand is attached to the tool at the beginning and by rotating the external axis and moving the robot, 20 reinforcement structures can be produced at once. The TowPreg is not cut during the winding process and the robot-based production enables an exact and reproducible production of the CFRP reinforcement structures with a constant fiber tension. By varying the number of layers, reinforcement structures of different heights can be manufactured with this tool. After the CFRP reinforcement structures have been wound, an outer tool is attached to the upper and lower sides to compress the CFRP uniformly. The ends get cut before curing. The CFRP reinforcement structures are then cured in the mold by means of a vacuum bag around the three parted tool at 155°C for 1.5 hours. After cooling, the CFRP reinforcement structures get demolded and only the resin residues must be removed.

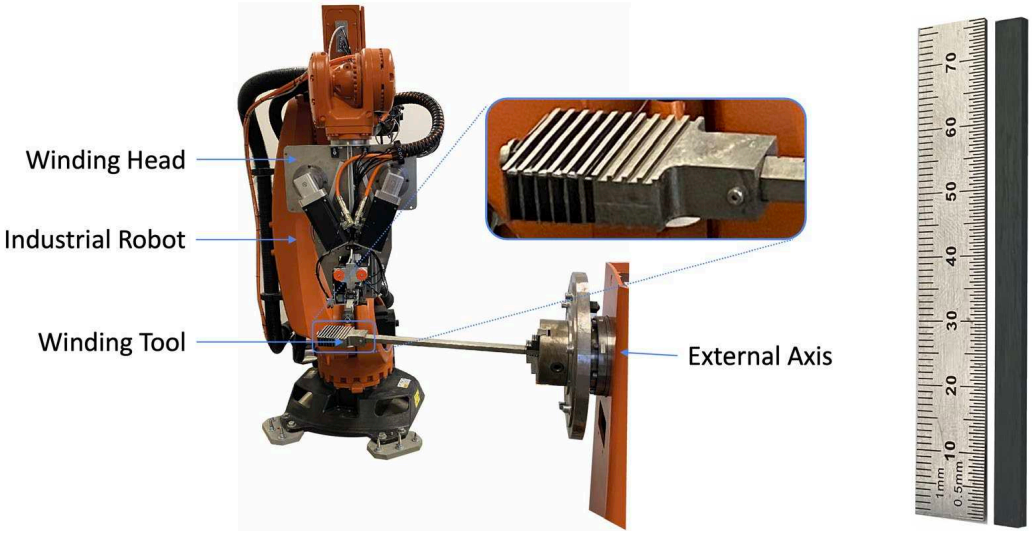

Figure 3. Robot-based filament-winding cell with a detailed view at the tool for manufacturing the CFRP specimen(left) and the final CFRP reinforcement structure *(right)*

After the reinforcement structures have been cleaned with acetone or isopropanol (to remove any release agent residues), they can be pretreated in different ways. As a comparison, a simple mechanical roughening with abrasive paper was done. All other pretreatments are based on a low-pressure plasma process. The etching rate in the plasma process can be changed by the parameters pressure, process duration, generator power and selecting different process gases. Furthermore, the selection of the process gas can influence the functional groups that are generated by the plasma. These also contribute to the coherent connection of the two composites.

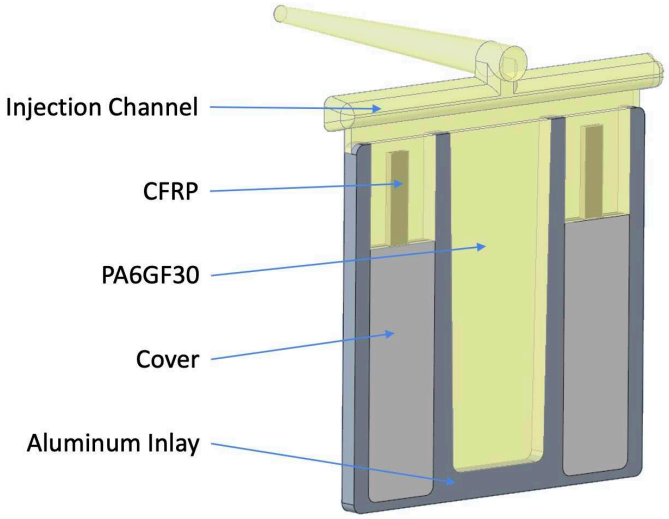

Figure 4. Aluminum inlay with covers, CFRP reinforcement structures, thermoplastic PA6GF30 and the injection channel

The final hybrid samples were produced using an aluminum inlay in a universal plate mold (80x80x4 mm) of the injection molding machine (Figure 4). The inlay is shaped in such a way that two samples (four samples in v1) can be produced with one injection molding cycle. The samples only need to be removed from the injection channel and otherwise do not need to be reworked. In test v1, the four hybrid samples have to be cut out of the molded plate. Table 1 shows an overview of the different production and test parameters in the different test series.

Table 1: Overview of different parameters for the four test series.

Parameter	Test v1	Test v2	Test v3	Test v4
Manufacturing	Hand lay-up	Robot-based	Robot-based	Robot-based
Nr. of CFRP plies	10	10	10	12
Diener plasma system	Pico (200W) Tetra 30 (500W)	Femto (100W)	Femto (100W)	Femto (100W)
Injection molding inlay	PTFE	Aluminum	Aluminum	Aluminum
Samples per shot	4	2	2	2
Thermoplastic material	Nyflor B2GF30	Nyflor B2GF30	Nyflor B2GF30	Grodnamid
Bracket type	Open	Open	Open	Closed

  doi:10.5075/epfl-298799_978-2-9701614-0-0

2.2 Pull-Out Test

For the average shear stress, the maximum pull-out force is related to the overmolded area (without the front area, since this can be neglected as the simulated flow of forces suggests). The pull-out test was described in detail in Bauer et al. [7] and Figure 5 shows the test setup schematically with the different hybrid specimen geometries.

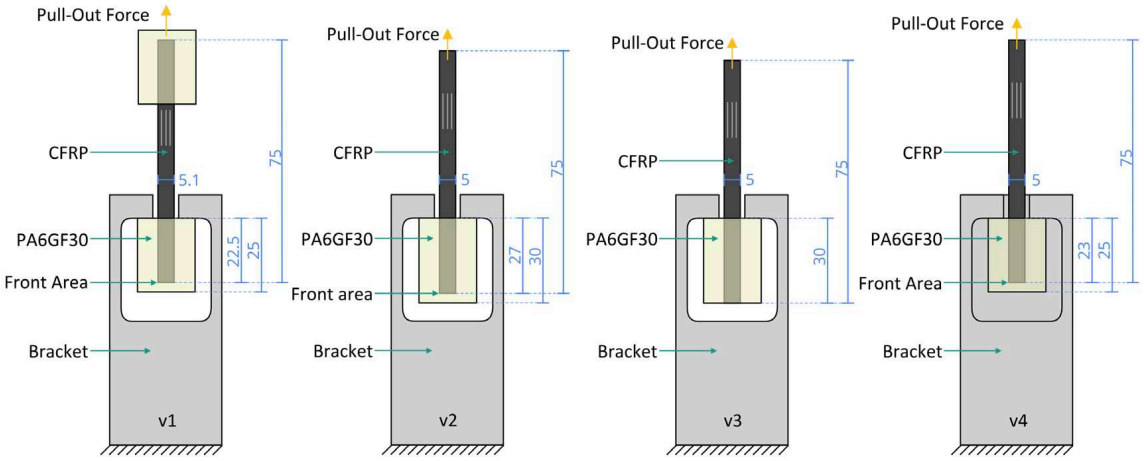

Figure 5. Different setups for the pull-out test in the four test series

While in test v1 both ends of the CFRP specimen were overmolded and one side was clamped and used for the force application in the pull-out test, only one side is overmolded in the tests v2-v4. This allows the force to be applied directly to the CFRP reinforcement structures. In test v4, the bracket is closed on both sides (the front side gets closed after placing the hybrid sample in the bracket) to prevent the specimen from tilting and to allow the CRFP specimen to be pulled out straight. During the start of the test, the hybrid sample is not in contact with the two closed sides of the bracket, so that no additional clamping forces are generated. If the sample starts to tilt, it supports itself with the lower edge of the thermoplastic material on one of the two closed sides so that the CFRP specimen is not pulled out slanted.

4. Results & Discussion

Figure 6 shows the main results of the four test series (v1-v4) and the number of samples tested for each single test set up. For the calculation of the average shear stress, the maximum pull-out force was divided by the overmolded CFRP area (the entire overmolded area, except the front area → Figure 5). In each of the four test series, a reference measurement was carried out with reinforcement structures that were only cleaned (v1 acetone, v2-v4 isopropanol). These references can be considered as an untreated matrix interface (Figure 2).

In the first series of tests, it was shown that roughening the surface with a 1200 grit sandpaper increased the strength of the interface by a factor of 3 (1-b). This is due to the increase in the surface area and the generation of microform-fit. An additional 5-minute oxygen low-pressure plasma treatment further doubled the interface strength (1-c). Since no etching process takes place during this short treatment period, the strength increase is due to the additional cleaning of the surface as well as the generation of functional groups. In a 30-minute etching process in a 300 W plasma system using oxygen low-pressure plasma, the averaged shear stress was increased by 7.6 times (1-d) compared to the reference sample.

  doi:10.5075/epfl-298799_978-2-9701614-0-0

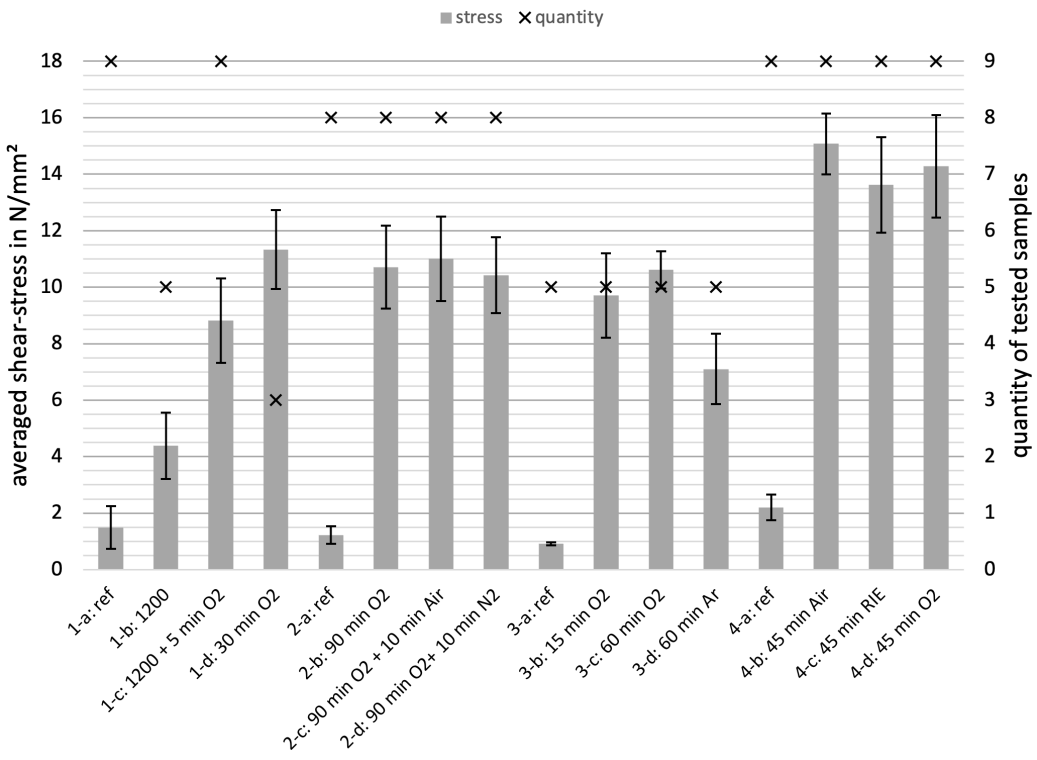

Figure 6. Averaged shear-stress for the different test series (1-4) and number of tested samples

In the second series of tests, the averaged shear stress was increased, due to a 90 minute treatment with low-pressure oxygen plasma, by a factor of 8.7 (2-b) compared to the corresponding reference. This is mainly due to the creation of a matrix interface by etching away the epoxy matrix in the area of the first continuous fiber layer. An additional 10 minute treatment with low-pressure air plasma (2-c) could apparently increase the interface strength a little more (but in the range of the standard deviation of both test series). An additional functionalization by means of a 10 minute low-pressure nitrogen plasma (2-d) slightly decreased the interface strength (again within the range of the standard deviation of both tests).

In the third series of tests, a change in plasma pretreating duration was investigated. By pretreating the CFRP reinforcement structures 60 (3-c) instead of 15 (3-b) minutes with oxygen plasma, the interface strength could be increased by another 9%. Furthermore, the effect of argon (3-d) as a process gas was investigated. Due to its inert behavior as a noble gas, the etching process here is purely physical based and not physical and chemical based as is the case with oxygen or nitrogen. For the same duration, oxygen plasma produces a much higher interface strength, which is due to the chemical etching effect and the addition of functional groups.

In the last series of tests, some minor optimizations were performed compared to the previous series of tests (more layers, closed bracket during pull-out) in order to generate a more reproducible failure of the samples, which was successfully achieved. Here it was shown that a 45 minute treatment with air low-pressure plasma could generate the highest interface strength with τ = 15.1 ± 1.1 N/mm^2 (4-b), 5% higher than with oxygen (4-d) as process gas. In contrast, pretreatment in oxygen plasma using the reactive ion etching (4-c) process deteriorated the interface strength compared to oxygen low-pressure plasma. This is due to the excessive etch rate and the resulting damage to the fibers at the interface as well as the very high temperatures acting on the CFRP reinforcement structures while placed on the electrode.

  doi:10.5075/epfl-298799_978-2-9701614-0-0

5. Conclusion

It has been demonstrated that the use of low-pressure air plasma can produce a high loadable interface between a continuous fiber-reinforced thermoset and a short glass fiber-reinforced thermoplastic. By exposing the upper continuous fiber layer, it is possible for the injection molding material to directly bond onto the continuous fibers, thus providing an optimum force flow in this direct interface. The interface strength created in this way is comparable to a structural bonding and therefore the basis for a hybrid manufacturing process based on anisotropic topology optimization, the robot-based 3d filament-winding process and a downstream injection molding process. Further investigations must show which is the most optimal pretreatment time (depending on plasma system, plasma power and generator frequency) for epoxy based CFRP reinforcement structures. An additional increase of the interface strength can possibly be generated by preheating the plasma treated CFRP reinforcement structures before overmolding.

6. References

1. AVK – Industrievereinigung Verstärkte Kunststoffe e.V. (Ed.). Handbuch Faserverbundwerkstoffe. Springer Fachmedien Wiesbaden. 2013.
2. Müller I, Bürgmann M, Heimann J, Stieglitz A, Sohl C, Hörtdörfer V. Method for producing a component and component. German Patent DE102017222579 (A1). 2017.
3. Holzinger M, Loy C, Gruber M, Kugler K, Bühler V. 3D Winding of Tailor-made Thermoplastic Rods for Locally Reinforced Injection Molded Components. ITHEC 2020 5th International Conference and Exhibition on Thermoplastic Composites, p. 92–95.
4. Nagakalyan S, Raghukumar B. Preparation and characterization of carbon/epoxy towpreg composite material. Materialstoday: Proceedings 2020; 23:499-506
5. Bonnet, M. Kunststofftechnik. Springer Fachmedien Wiesbaden. 2014.
6. Karakaya N, Papila M, Özkoc G. Overmolded hybrid composites of Pa6 on continuous carbon and glass fiber/epoxy composites: an assessment of the interface. Composites Part A 2020; 131:105771.
7. Bauer P, Becker YN, Motsch-Eichmann N, Mehl K, Müller I, Hausmann J. Hybrid Thermoset-Thermoplastic Structures: An Experimental Investigation on the Interface Strength of Continuous Fiber-Reinforced Epoxy and Short-Fiber Reinforced Polyamide 6. Composites Part C 2020; 3:100060.
8. Ding Y, Tang H, Shi W, He Q, Zhai Z. Enhancement of interfacial strength of overmolded hybrid structures of short fiber reinforced polyamide 6 on continuous fiber reinforced epoxy composites under various surface pretreatments. Polymer Composites 2022; 43:1038-1047.
9. Kazan H, Farahani S, Pilla S. Feasibility Study for Manufacturing CF/Epoxy – Thermoplastic Hybrid Structures in a Single Operation. Procedia Manufacturing 2019; 33:232-239.
10. Mehl K, Schmeer S, Motsch-Eichmann N, Bauer P, Müller I, Hausmann J. Structural Optimization of Locally Continuous Fiber-Reinforcements for Short Fiber-Reinforced Plastics. J. Compos. Sci. 2021; 5:118.

  doi:10.5075/epfl-298799_978-2-9701614-0-0

TENSILE PROPERTIES OF DEEP DRAWN IN-SITU POLYMERIZED FIBER-METAL-LAMINATES

Henrik Oliver Werner[a,b], Wilfried Liebig [a], Kay André Weidenmann [c]

a: Karlsruhe Institute of Technology (KIT), Institute for Applied Materials, Karlsruhe, Germany – henrik.werner@kit.edu
b: Karlsruhe Institute of Technology (KIT), Institute of Vehicle System Technology, Karlsruhe, Germany
c: University of Augsburg, Institute of Materials Resource Management – Hybrid Composite Materials (MRM), Augsburg, Germany

Abstract: *In previous work, we have introduced a new manufacturing process, which combines deep drawing with thermoplastic resin transfer molding. The fabric is infiltrated with a reactive resin during forming, which polymerizes to a tough poly (methyl methacrylate) matrix after completion of the forming process. In this contribution, miniaturized tensile specimen are tested. The tensile properties are location dependent due to the forming process. It is found, that FMLs Young's modulus and yield strength depends on the Young's modulus and yield strength of the metal. The ultimate tensile strength of the FML depends on the GFRP layer and its fiber orientation, as well as fiber volume content. Specimens with a ± 45° fiber orientation show higher failure strains compared to specimens with 0° and 90° fiber orientation.*

Keywords: FML; multi-material design; deep-drawing; sandwich; in-situ polymerization

1. Introduction

The climate change is the greatest challenge of our time. Sustainability has thus become a central issue in society, as well as in the design process of new products. Lightweight design is no longer considered exclusively under technical, but also under ecological boundary conditions. One example is the automotive industry, which has to reduce the CO_2 emissions of its vehicle fleet through legal framework conditions [1]. The automobile's energy consumption occurs 87 % of live time cycle during use and is thus proportional to the vehicle mass [2]. The result is the electrification of the powertrain and the use of new lightweight materials and strategies. In addition to steel and aluminum sheets [3], fiber-reinforced composites (FRP) are increasingly being used in car body design [4]. Joining or combining materials of different material classes has therefore become an essential part of the development process. Fiber-metal-laminates (FML) are a special form of multi-material design and combine the advantageous properties of metals and FRPs in a single layered material. FMLs exhibit excellent resistance to crack propagation, impact, and flammability [5].

In the 1980s, FMLs were developed and commercialized for the civil aviation industry [6,7]. The classical autoclave manufacturing process is time consuming, expensive, and the achievable geometric complexity of the components is low [8,9]. For mass production of FML components, the material and process costs have to be reduced and the producible complexity of the components has to be increased. A possible process could be the combination of deep drawing and thermoplastic resin transfer molding (T-RTM), as shown in Figure 1. In this one-step process,

  doi:10.5075/epfl-298799_978-2-9701614-0-0

an in-situ polymerizing matrix is injected during deep drawing. The metal sheets and the fabric layers are formed simultaneously, while the matrix infiltrates the fabrics. The matrix polymerizes after the deep drawing process, embedding the fibers and bonding the FRP to the metal sheets [10–16], shown in Figure 1. The mechanical properties of the FML are strongly influenced by the manufacturing process of the generic part geometry. Therefore, the mechanical properties have to be determined dependent on the generic part geometry, otherwise the structure-property relationships cannot be measured. For this purpose, tensile specimens from four regions of the generic part are extracted, shown in Figure 1. The regions differ in terms of their forming history, more precisely the degree of metal forming, fiber draping and infiltration.

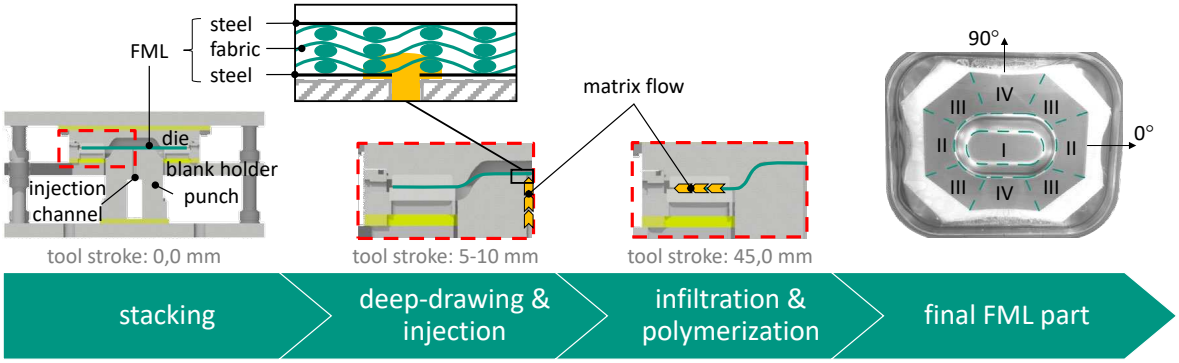

Figure 1. Process flow of combined deep drawing and resin transfer molding

2. Material

The FML layup is a sandwich construction with metal sheets as face sheets and thermoplastic reinforced twill weave fabrics as intermediate layer. The DC04 metal sheet thickness is 1 mm and six plies of 280 g/m² E-glass twill weave fabric 2/2 (Interglas 92125 FK800) are used. As resin system, a 1:1 mixture of acrylates Elium 130 and Elium 190 from Arkema S.A. with 2.5 % dibenzoyl peroxide (United Initiators, BP-50-FT) is used. The rolling direction of the metal sheet defines the 0° orientation, which is equal to the weft direction of the dry fabrics. In weft direction (0°), the fabric weight is 143 g/m² and 133 g/m² in warp direction (90°). The metal sheets were pretreated to increase the adhesion to the thermoplastic matrix according to [17] with manual grinding and a silane adhesion promoter (Evonik, Glymo). In addition, generic parts are produced with aluminum sheets of 1 mm AA5182-H111 and six plies of 280 g/m² E-glass twill weave fabric. The aluminum sheets are pretreated with release agent to be able to remove them after the manufacturing process to obtain GFRP parts without metal sheets. The draping influence of the fibers on the tensile properties of the FML is investigated using the GFRP parts.

The generic part geometry is divided into four general regions with different forming histories according to Figure 1. The samples are extracted by waterjet cutting from four different FML parts and two GFRP parts with equivalent process settings. The average fiber volume content of all parts is 70 % ± 3 % and is measured by thermal gravimetric analysis by the Fraunhofer Institute for Chemical Technology.

3. Experimental set-up

The tensile tests are performed on a Zwick/Roell ZMART.PRO 200 kN universal testing machine. The specimens are chosen according to DIN EN ISO 527-4:2022-03 [18] and ASTM D3039/D3039M−17 [19] with dimensions of 60 mm x 10 mm x 3 mm (LxBxt). For clamping 20

  doi:10.5075/epfl-298799_978-2-9701614-0-0

mm are required on each side, resulting in a free measuring length of 20 mm. Wooden spacers with a are placed between the clamping jaws due to the short clamping length. This prevents the clamping jaws from tilting. Strain is measured by using two-dimensional digital image correlation (GOM GmbH, Aramis 4M) with a recording frequency of 2 Hz for the FML specimens and 5 Hz for the GFRP specimens. An airbrush pistol with body paint is used for the speckled stochastic pattern to obtain a fine pattern for high resolution for high strains. The FML specimens are clamped rotated by 90° to measure the strain in stacking direction ε_z, shown in Figure 2. The GFRP specimens are not rotated and the transverse strain ε_y is recorded. The transverse velocity is v = 2 mm/min and corresponds to a strain rate of $\dot{\varepsilon}$ = 0.0016 1/s. A prestress of 2 MPa is applied via hydraulic jaws with a hydraulic pressure of 20 bar. Stresses and strains are calculated homogenized over the entire cross-section of the specimens. The Young's modulus is determined for strains between ε_x = 0.01 % and 0.07 % according to ASTM E1111 [20] by using linear regression with the method of least squares. The 0.05 % yield strength is determined as $R_{p0.05}$ for a plastic strain of ε_x = 0.05 %. The tensile strength R_m is calculated from the maximum measured force F.

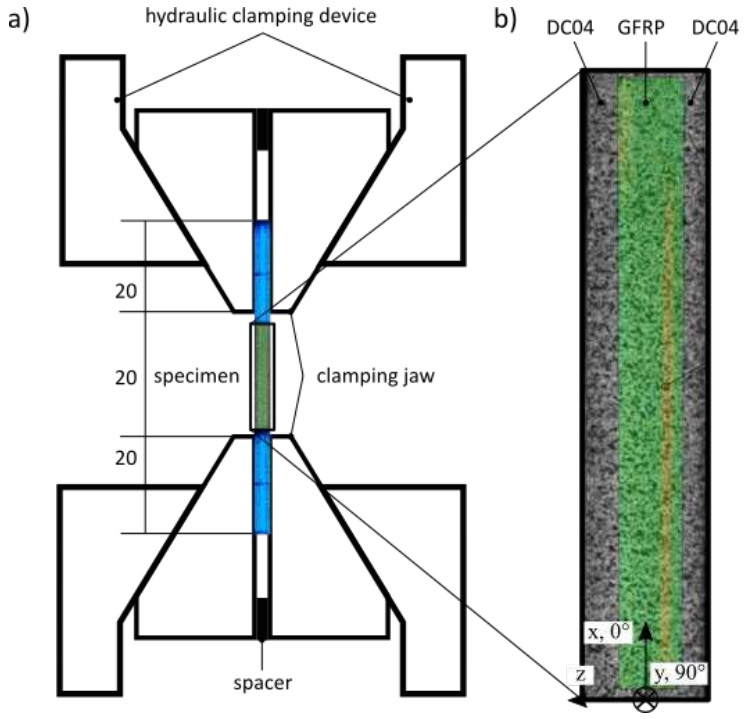

Figure 2. a) Experimental set up for tensile test with b) measured strain field of 2D-DIC system on a FML specimen

4. Results

Figure 3 summarizes the results in the form of box-plots. The tensile properties $(E, R_{p0.05}, R_m, e_b)$ show a strong dependence on region and orientation for the FML, as well as for the GFRP specimens. In general, the 0° orientation exhibits higher tensile properties than the 90° orientation within the respective region, with the exception of the FML specimens from region IV. The qualitative difference between 0° and 90° orientation is noticeable for all mentioned properties and is especially pronounced for ultimate tensile strength, except for FML specimen from region IV. The 45° orientation shows higher Young's modulus, yield strength and ultimate tensile strength compared to the 135° orientation for FML and GFRP specimens. The

  doi:10.5075/epfl-298799_978-2-9701614-0-0

highest failure strain is reached by the 135° orientation with $e_b \approx 6$ % for GFRP and $e_b \approx 10$ % for FML specimens compared to $e_b \approx 2$ % for FML and GFRP specimens in 0° and 90° orientation.

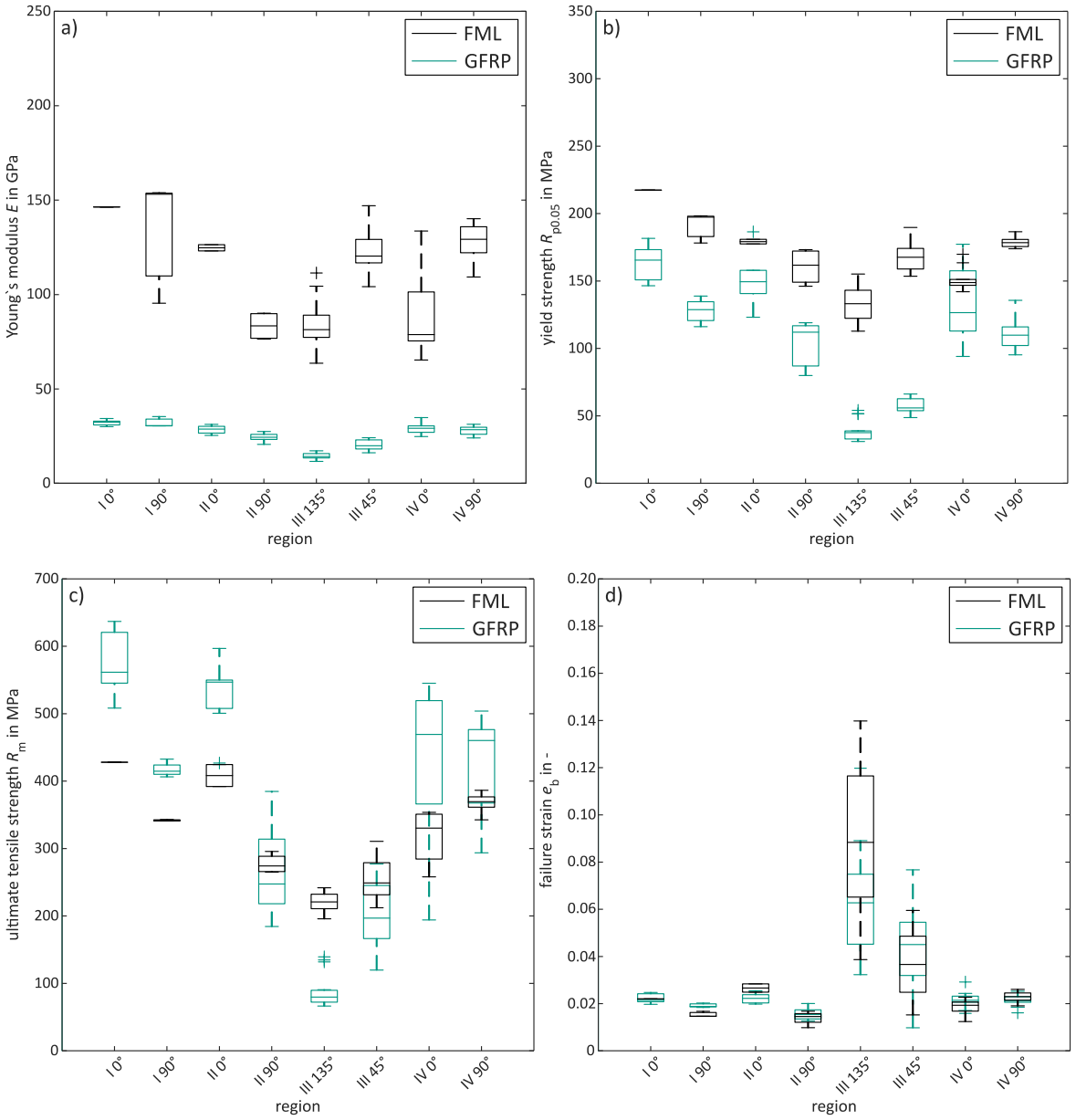

Figure 3. Box-plots of region dependent mechanical properties of GFRP and FML specimens a) Young's modulus, b) yield strength, c) ultimate tensile strength and d) failure strain

The stress-strain curves of the GFRP specimens in Figure 4 are linear elastic in 0° and 90° orientation, while in 45° and 135° orientation they are strongly nonlinear. The GFRP specimens in Figure 4 c) oriented in 135° show nearly ideal plastic flow behavior and differs from the stress-strain curve of 45° oriented specimens. All stress-strain curves of the FML specimens in 0° and 90° orientation show a bi-linear behavior, with a pronounced yield point. In 45° and 135° orientation, the stress-strain curves are strongly nonlinear and qualitatively similar to those from the GFRP specimens. In Figure 4 b) for region II, the stress-strain curves of GFRP and FML specimens oriented in 90° show significantly lower ultimate tensile strength. The ultimate tensile strength of GFRP and FML correlates directly. The same observation applies to the stress-strain behavior for GFRP and FML specimens in Figure 4 c) with 45° and 135° orientation and

  doi:10.5075/epfl-298799_978-2-9701614-0-0

less pronounced in Figure 4 a) with 0° and 90° orientation. As already mentioned for the box-plots, region IV in Figure 4 d) is an exception and shows no correlation between stress-strain behavior of GFRP and FML.

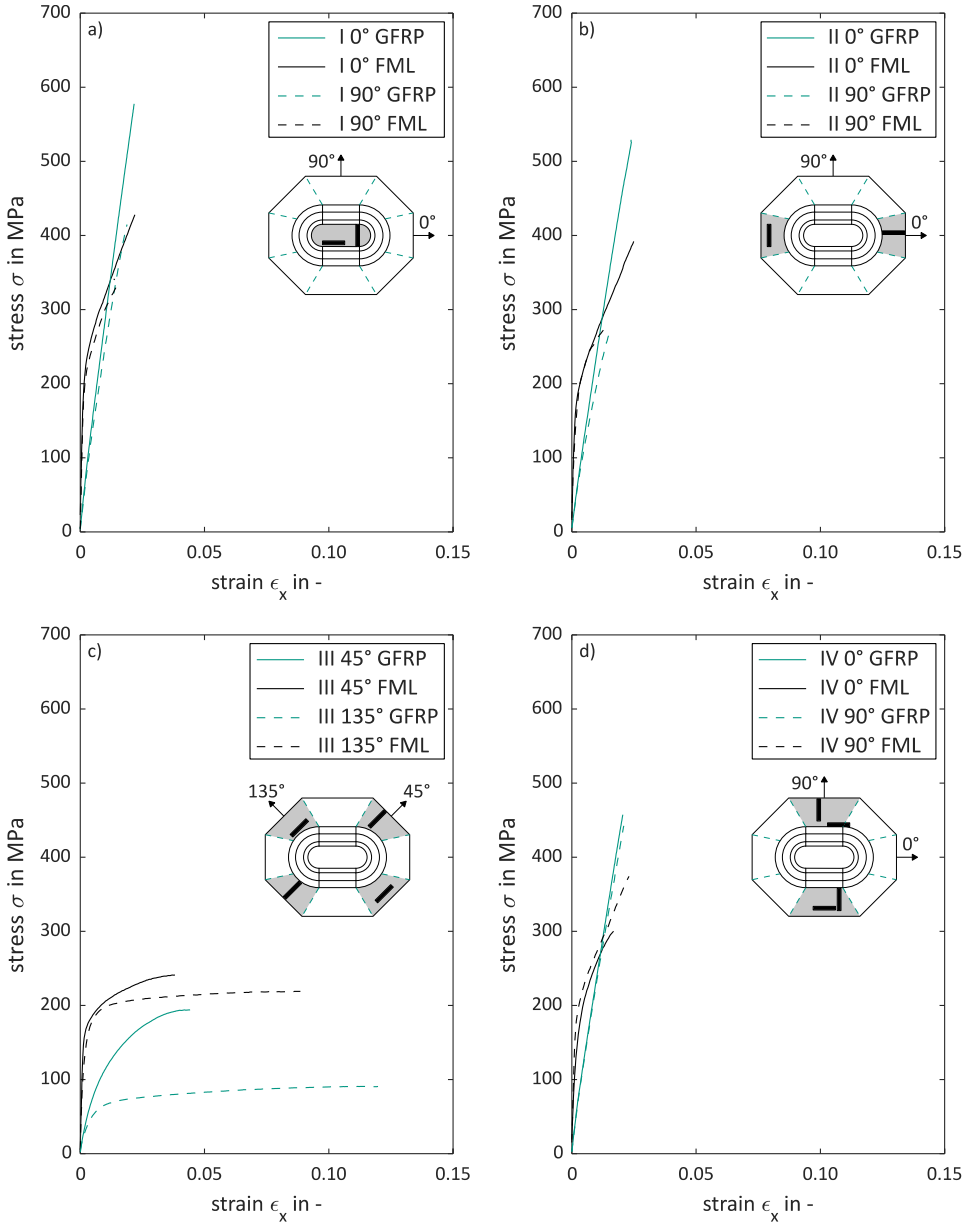

Figure 4. Representative stress-strain curves of GFRP and FML specimens from a) region I in 0° and 90° orientation, b) region II in 0° and 90° orientation, c) region III in 45° and 135° orientation and d) region IV in 0° and 90° orientation

5. Discussion

In region II and in region IV the fibers are drawn-in towards the center of the generic part. The fibers in 90° orientation in region II are draped transverse to loading direction. This results in a high fiber curvature and thus in low tensile properties. The same applies for the specimens in region IV in 0° orientation. Due to the shorter length of the geometry in region II compared to region IV, the fibers curvature is higher in region II, as shown in Figure 5.

  doi:10.5075/epfl-298799_978-2-9701614-0-0

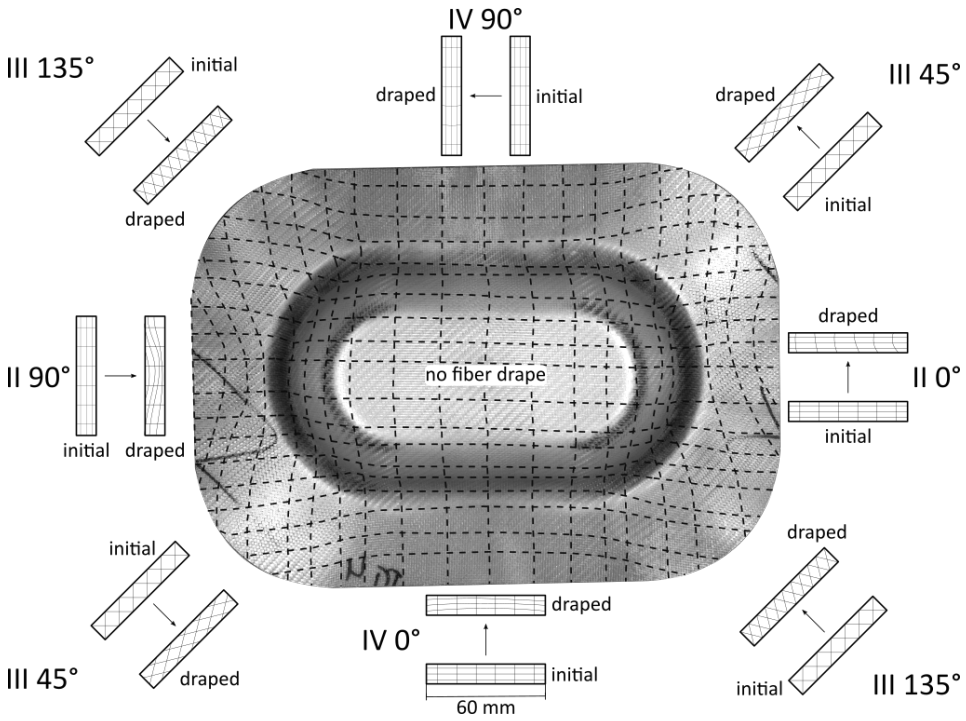

Figure 5. Fiber draping of representative generic GFRP part with removed metal sheets

The observed results can be explained by an analogous model consisting of two parallel springs representing the two metal layers and the GFRP layer [13]. The load distribution between the two layers, respectively the two springs, depends on the spring stiffness

$$c = \frac{EA}{L} \rightarrow \frac{c_1}{c_2} = \frac{E_1 t_1}{E_2 t_2} \tag{1}$$

with the Young's modulus E, the cross-section $A = bt$ and the length L, width b of the specimen and thickness t of the respective layer. The pronounced yield point of the FML stress-strain curves in Figure 4 is the load transition point between metal layers and GFRP layer. The stiffer DC04 metal sheets carry the main load up to the yield strength and then transfer the load to the GFRP layer. The GFRP layers ultimate tensile strength determines the ultimate tensile strength of the FML specimen, which depends on the fiber orientation of the GFRP layer due to fiber draping during forming. The more fibers are oriented in tensile direction, the higher is the ultimate tensile strength. The yield strength of the FML specimens depends on the degree of metal forming. For example, the influence of the GFRP yield strength on the FML yield strength is not be seen in Figure 3 b) for region I with 90° orientation and region III with 45° orientation, while the influence of the GFRP ultimate tensile strength correlates directly with the FMLs ultimate tensile strength in Figure 3 c) and failure strain in Figure 3 d). In region III with 45° orientation, the fibers are draped in loading direction, while in 135° orientation, the fibers are draped in transverse direction and the specimens have the largest proportion of fibers in transverse direction, which is why they have the lowest mechanical properties. The orientation and curvature of the fibers to the direction of loading significantly affects the ultimate tensile strength, as can be seen in Figure 4 b) and c). The specimens with higher fiber curvature in Figure 5, region II 90° and region III 135°, have lower tensile properties. This can also be seen in Figure 4 d) for the region IV with 0° and 90° orientation, with the 0° specimens exhibiting higher fiber curvatures due to draping and thus show lower tensile properties compared to the 90° orientation.

  doi:10.5075/epfl-298799_978-2-9701614-0-0

6. Conclusion

Results of tensile tests on GFRP and FML specimens of generic parts manufactured by combined deep-drawing with in-situ polymerization are presented. The study demonstrated that the mechanical properties in terms of Young's modulus, yield strength, ultimate tensile strength and failure strain are location dependent due to the forming process. The tested GFRP specimens show the influence of fiber draping due to forming on the tensile properties. The FMLs ultimate tensile strength and failure strain are dominated by the GFRP, while the results show no influence of the GFRPs Young's modulus and yield strength on the respective properties of the FML.

Acknowledgements

The German Research Foundation (DFG) kindly supports this research project (WE 4273/13-1 & -2, HE 6154/4-1 & -2). The Fraunhofer Institute for Chemical Technology kindly supports the manufacturing of the laminates. ARKEMA SA Colombes (France) kindly provided the polymer. United Initiators provided the peroxide and Evonik the coupling agent. The authors also thank their colleges for support, especially Thomas Mennecart from the IUL of the TU Dortmund and Moritz Kruse from the PPI of the Leuphana University Lüneburg for the great collaboration.

7. References

[1] European Parliament. Regulation (EU) 2019/631 of the European Parliament and of the Council of 17 April 2019 setting CO2 emission performance standards for new passenger cars and for new light commercial vehicles, and repealing Regulations (EC) No 443/2009 and (EU) No 510/2011; 2021.

[2] Mayyas A, Qattawi A, Omar M, Shan D. Design for sustainability in automotive industry: A comprehensive review. Renewable and Sustainable Energy Reviews 2012;16(4):1845–62. https://doi.org/10.1016/j.rser.2012.01.012.

[3] Tisza M, Czinege I. Comparative study of the application of steels and aluminium in lightweight production of automotive parts. International Journal of Lightweight Materials and Manufacture 2018;1(4):229–38. https://doi.org/10.1016/j.ijlmm.2018.09.001.

[4] Dröder K, Vietor T (eds.). Technologies for economical and functional lightweight design. Berlin, Heidelberg: Springer Berlin Heidelberg; 2019.

[5] Vlot A, Vogelesang LB, Vries TJ de. Towards application of fibre metal laminates in large aircraft. Aircraft Eng & Aerospace Tech 1999;71(6):558–70. https://doi.org/10.1108/00022669910303711.

[6] Vogelesang L, Vlot A. Development of fibre metal laminates for advanced aerospace structures. Journal of Materials Processing Technology 2000;103(1):1–5. https://doi.org/10.1016/S0924-0136(00)00411-8.

[7] Vlot A. Glare: History of the development of a new aircraft material. Dordrecht: Kluwer Acad. Publ; 2001.

[8] Gunnink JW, Vlot A, Vries TJ de, van der Hoeven W. Glare Technology Development 1997–2000. Appl Compos Mater 2002;9(4):201–19. https://doi.org/10.1023/A:1016006314630.

[9] Sinke J. Manufacturing of GLARE Parts and Structures. Appl Compos Mater 2003;10(4/5):293–305. https://doi.org/10.1023/A:1025589230710.
[10] Mennecart T, Werner H, Ben Khalifa N, Weidenmann KA. Developments and Analyses of Alternative Processes for the Manufacturing of Fiber Metal Laminates. In: Volume 2: Materials; Joint MSEC-NAMRC-Manufacturing USA. American Society of Mechanical Engineers; 2018.
[11] Werner HO, Dörr D, Henning F, Kärger L. Numerical modeling of a hybrid forming process for three-dimensionally curved fiber-metal laminates. In: Proceedings of the 22nd International ESAFORM Conference on Material Forming: ESAFORM 2019. AIP Publishing; 2019, p. 20019.
[12] Werner HO, Stern C, Weidenmann KA. Location-Dependent Mechanical Properties of In-Situ Polymerized Three-Dimensional Fiber-Metal Laminates. In: Hausmann JM, editor. 22nd Symposium on Composites. Zurich: Trans Tech Publications Limited; 2019.
[13] Werner HO, Liebig W, Weidenmann KA. Mechanical Properties of In-Situ Polymerized Fiber-Metal-Laminates. In: Hausmann JM, Siebert M, Hehl A von, Weidenmann KA, editors. Proceedings 4th International Conference Hybrid 2020 Materials and Structures; 2020.
[14] Werner HO, Poppe C, Henning F, Kärger L. Material Modeling in Forming Simulation of Three-Dimensional Fiber-Metal-Laminates – A Parametric Study. In: 23rd International Conference on Material Forming (ESAFORM 2020); 2020, p. 154–161.
[15] Werner HO, Schäfer F, Henning F, Kärger L. Material Modelling of Fabric Deformation in Forming Simulation of Fiber-Metal Laminates – A Review on Modelling Fabric Coupling Mechanisms. In: 24th International Conference on Material Forming; 2021.
[16] Mennecart T, Gies S, Ben Khalifa N, Tekkaya AE. Analysis of the Influence of Fibers on the Formability of Metal Blanks in Manufacturing Processes for Fiber Metal Laminates. JMMP 2019;3(1):2. https://doi.org/10.3390/jmmp3010002.
[17] Werner H, Sönmez I, Wendel R, Henning F, Weidenmann KA. Characterization of the interlaminar shear strength of fiber metal laminates with reactive processed thermoplastic matrix. In: SAMPE Europe Conference & Exhibition 2017 Stuttgart: Stuttgart, Germany, 14-16 November 2017. Red Hook, NY: Curran Associates Inc; 2017.
[18] Deutsches Institut für Normung e. V. DIN EN ISO 527-4:2022-03, Kunststoffe - Bestimmung der Zugeigenschaften - Teil 4: Prüfbedingungen für isotrop und anisotrop faserverstärkte Kunststoffverbundwerkstoffe (ISO 527-4:2021); Deutsche Fassung EN ISO 527-4:2021. Berlin: Beuth Verlag GmbH; 2022. https://doi.org/10.31030/3328116.
[19] D30 Committee. Test Method for Tensile Properties of Polymer Matrix Composite Materials. West Conshohocken, PA: ASTM International. https://doi.org/10.1520/D3039_D3039M-17.
[20] E28 Committee. Test Method for Youngs Modulus, Tangent Modulus, and Chord Modulus. West Conshohocken, PA: ASTM International. https://doi.org/10.1520/E0111-04R10.

MICRO-SCALE MODELLING OF COMPOSITES MADE OF RCF/ PA6 STAPLE FIBER YARNS WITH SPECIAL EMPHASIS ON FIBER LENGTH DISTRIBUTION

Thomas Gereke[a], Tobias Lang[a], Thi Anh My Huynh[a], M. M. Badrul Hasan[a], Anwar Abdkader[a], Chokri Cherif [a]

a: Technische Universität Dresden, Institute of Textile Machinery and High Performance Material Technology (ITM), Dresden (Germany), Email: thomas.gereke@tu-dresden.de

Abstract: *With the increasing demand and use of carbon fiber reinforced polymers (CFRP), the disposal or recycling of carbon fibers (CF) and end-of-life composite parts is becoming enormously important. Hybrid yarns from recycled CF (rCF) and a thermoplastic fiber (polyamide 6, PA6) were developed. The use of fibers with an initially higher fiber length should result in higher stiffness and strength of the composite. However, due to significant fiber damage during manufacturing the mechanical properties deteriorate. An algorithm is implemented to generate a finite element model of the yarn with probabilistic distribution of fiber length and fiber orientation. Fibers are coupled to elements of the thermoplastic matrix and the compaction step during composite manufacturing is simulated. The results of virtual tensile tests show the trend towards better composite properties at higher fiber lengths and at a fiber length distribution with lower variance. The model is very well suited for predicting composite properties as a function of various parameters in the production of staple fiber-based rCF/ PA6 hybrid yarns.*

Keywords: micro-scale; recycled carbon fiber; finite element model; thermoplastic; yarn

1. Introduction

Due to their excellent mechanical properties and their lightweight character, the application of carbon fiber reinforced polymers (CFRP) across different industries is steadily increasing. With the increasing demand and use of CFRP, the disposal of carbon fibers (CF) and end-of-life composite parts is becoming enormously important, especially from a sustainability perspective. As CF waste is not allowed to be thermally degraded or landfilled in the EU, the recovery of high quality recycled carbon fibers (rCF) and the introduction into a second life cycle is of great importance.

Powders of rCF are used as filler materials for plastics [1,2]. Short rCF are incorporated into thermoset compression moulding compounds [3,4]. Currently, the main use of rCF is for nonwovens [5,6] or injection moulded parts [7,8]. For injection moulding processes, rCF are used as short fiber reinforcement in thermoplastic compounds, for example in combination with polypropylene (PP), polyamide 6 (PA6) or polyphenylene sulfide (PPS) matrix [7,9,10]. Such materials lack of fiber orientation, have a low fiber volume content and, thus, low mechanical properties [11]. In the recycling of CF it is challenging to preserve high fiber length and to enable highly oriented fibers [12].

Probably the best alignment of rCF can be achieved by yarn spinning. In this process, the rCF web resulting from the opening is first processed into a tape. To homogenise it and to align the fibers, this sliver is then doubled and drawn [13,14]. Ring spinning, flyer spinning, friction spinning and wrap spinning are suitable methods to further process rCF [15]. At ITM of TU Dresden, hybrid yarns from rCF and a thermoplastic fiber (PA6) were developed. The spinning

  doi:10.5075/epfl-298799_978-2-9701614-0-0

of hybrid yarns from rCF for load bearing composite structures was realised and resulted in high performance composite parts [13,16,17]. The use of fibers with an initially higher fiber length should result in higher stiffness and strength of the composite. However, due to significant fiber damage during manufacturing, i. e. mainly during carding and drawing, the mechanical properties deteriorate.

Finite element models are widely employed to predict the mechanical properties of CFRP. Composites can be described at a microscale by modelling each fiber or a representative number of fibers. Approaches for composites made of continuous fibers [18,19] and short fibers were developed [20,21]. With the Digital Element Approach (DEA), textiles and composites were modelled with chains of beam elements that reduce the numerical effort [22–24]. Numerical models almost exclusively refer to textiles and composites made of continuous fibers with very low stretchability. However, yarns made of rCF are discontinuous in nature and the structure and mechanical behaviour of filament and staple fiber yarns differ significantly. Only a few empirical and analytical investigations on the mechanical behaviour of staple fiber yarns made of natural fibers are available [25–27].

2. Finite Element Model

The material used for the study is recycled carbon fibers (rCF) and polyamide 6 from which hybrid yarns are fabricated that are then processed to thermoplastic composites. Micro-scale models of spun yarns are generated based on information on the fibers, i. e. fiber length distribution and fiber orientation. The properties are implemented in the form of probability distributions. An algorithm is implemented that randomly adds fibers to a predefined volume until the respective fiber volume fraction is reached. By using a nearest neighbour search algorithm similar to the Random Sequential Adsorption Algorithm [28], overlapping of the fibers is avoided. Fibers that cross the boundaries of the unit cell during the yarn compilation are divided at the boundary and moved to the opposite side. This ensures the periodicity of the unit cell. The algorithm that generates the yarn structure is developed as a Python code. A length of 100 mm assures inclusion of the full trajectory of each fiber within the RVE.

Having generated the yarn structure based on the probabilistic algorithm, a finite element model of the composite is created in LS-Dyna. In the first step, the fiber network is compacted in a simulation step in order to account for the fiber volume content. The composite model then uses separate meshes for fibers and matrix. Fibers are modelled with beam elements; matrix is modelled with solid elements. Both meshes are coupled with kinematic constraints using the *CONSTRAINED_BEAM_IN_SOLID keyword in LS-Dyna. The procedure can be seen in Figure 1. Periodic boundary conditions are applied and homogenised tensile properties are calculated.

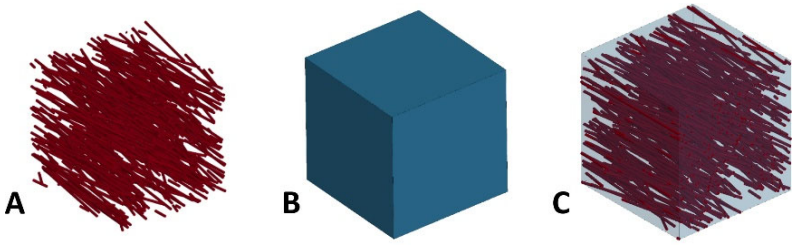

*Figure 1: Generated and compacted fiber network with beam elements (**A**), solid element mesh of the matrix (**B**), and composite model (**C**)*

  doi:10.5075/epfl-298799_978-2-9701614-0-0

3. Results and Discussion

A generated spun yarn model with a twist of 75 m^{-1} and fiber length distribution is shown in Figure 2. The results of the following compaction simulation and virtual tensile test are presented in Figure 3. Stresses are greatest near the fiber ends. Fiber failure dominates the tensile failure of the composite. Thus, overall composite failure occurs at the locations near the fiber ends.

Figure 2: Generated spun yarn model with twist of 75 m^{-1} and fiber length distribution

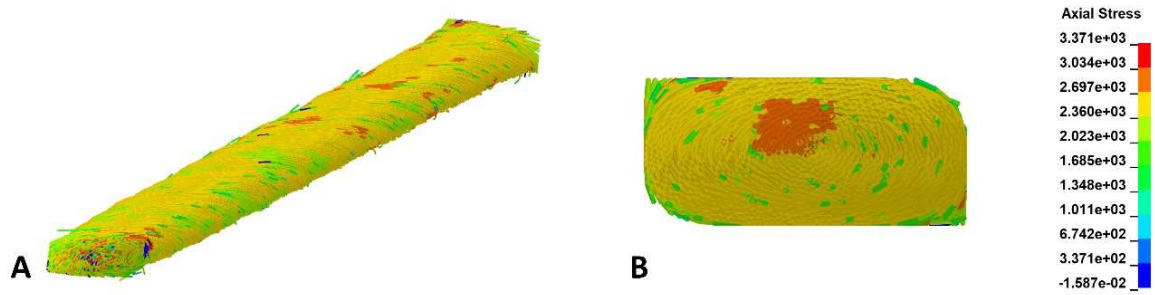

*Figure 3: Example of a compacted and tensioned composite model: **A** – Entire RVE, **B** – Cross-section*

The results of a study on yarn twist are shown in Figure 4 and Figure 5. The tensile modulus and strength of the composite reveal a dependence on yarn twist. A higher twist leads to higher fiber orientation and, thus, reduced mechanical properties. The comparison of simulation results and experiments shows a good correlation. Differences between virtual and simulated data are attributed to the idealised yarn model, which does not account for all the randomness in the real fiber network.

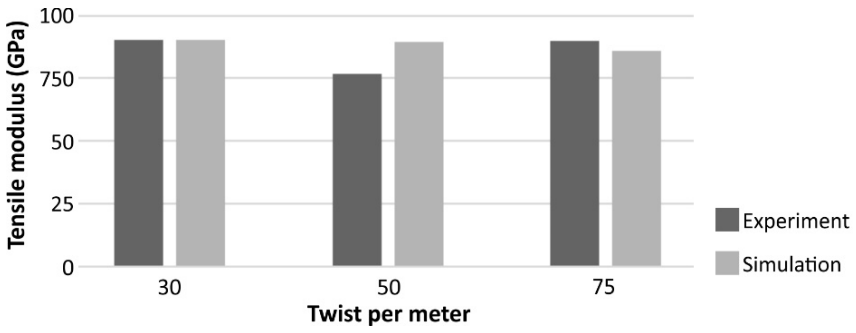

Figure 4: Tensile modulus in dependence on yarn twist

  doi:10.5075/epfl-298799_978-2-9701614-0-0

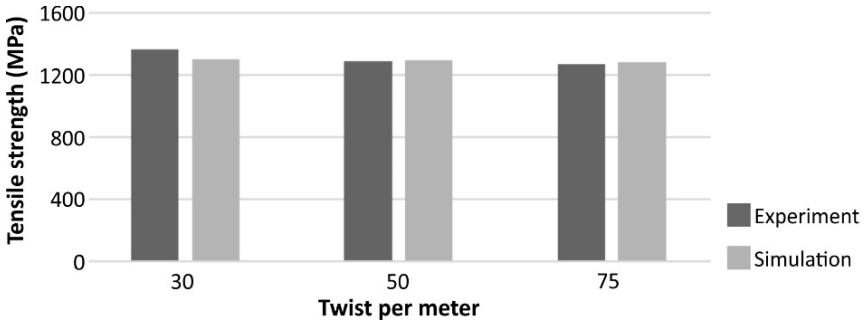

Figure 5: Tensile strength in dependence on yarn twist

A simulation study on the influene of the fiber length distribution within the composite is shown in Figure 6. The fiber length distribution is implemented in the model as follows:

$$P(l) = 1 - \exp\left[-\left(\frac{l}{l_0}\right)^m\right] \quad (1)$$

The influence of the parameter *m* shows a trend towards better composite properties with a distribution with lower variance. Thus, the damage of the fibers during processing should be minimised in order to reduce short fiber content.

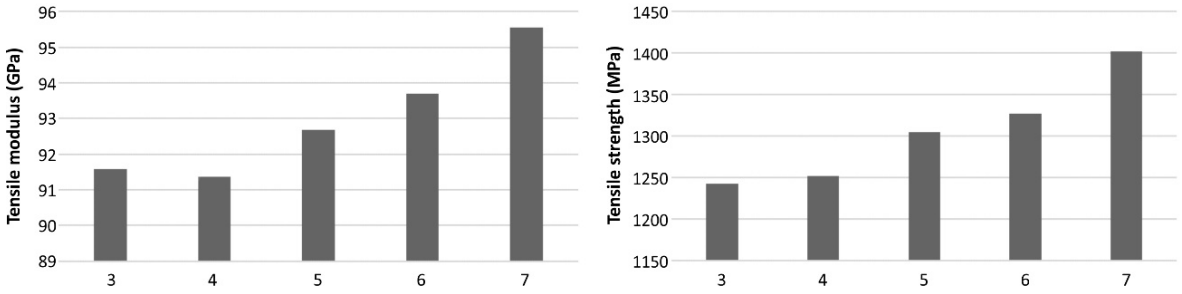

Figure 6: Influence of fiber length distribution (parameter m in Eq. 1) on composite behaviour

4. Conclusions

A numerical model has been established that simulates composite behaviour of rCF/ PA 6 based on input parameters such as fiber length, fiber orientation and yarn twist. The model is based on an algorithm that randomly generates the fiber network based on process parameters. A finite element model of the composite was used to perform parameter studies. Results show the influence of twist and fiber length on the composite properties. Future work should focus on reducing the yarn twist and the fiber damage during processing in order to increase composite properties. Nevertheless, the mechanical properties achieved are suitable for structural applications in automotive engineering or the like.

Acknowledgements

Funded by the Deutsche Forschungsgemeinschaft (DFG, German Research Foundation) – 407164652, 442070201.

  doi:10.5075/epfl-298799_978-2-9701614-0-0

5. References

1. Ahsan Q, Lin LM, Munawar RFB, Mohamad N. Effect of recycled carbon fiber reinforcement on the wear behavior of epoxy composite. Journal of Materials Research. 2016;31(13):1900–7.
2. Uhlmann E, Meier P. Carbon fibre recycling from milling dust for the application in short fibre reinforced thermoplastics. Procedia CIRP. 2017;66:277–82.
3. Allen BE. Characterization of reclaimed carbon fibers and their integration into new thermoset polymer matrices via existing composite fabrication techniques. Master thesis, North Carolina State University; 2008.
4. Palmer J, Savage L, Ghita OR, Evans KE. Sheet moulding compound (SMC) from carbon fibre recyclate. Composites Part A: Applied Science and Manufacturing. 2010;41(9):1232–7.
5. Wölling J, Schmieg M, Manis F, Drechsler K. Nonwovens from recycled carbon fibres - Comparison of processing technologies. Procedia CIRP. 2017;66:271–6.
6. Stegschuster G, Schlichter S. Perspectives of web based composites from RCF material. IOP Conference Series: Materials Science and Engineering. 2018;406(1):012022.
7. Connor ML. Characterization of recycled carbon fibers and their formation of composites using injection molding. Master thesis, North Carolina State University; 2008.
8. Meng F, Mckechnie J, Turner T, Wong KH, Pickering SJ. Environmental aspects of use of recycled carbon fiber composites in automotive applications. Environmental Science and Technology. 2017;51:12727–36.
9. Wong KH, Pickering SJ, Brooks R. Recycled carbon fibre reinforced polypropylene composites: effect of coupling agents on mechanical properties. In: Composites Innovation 2007 — Improved Sustainability and Environmental Performance. Barcelona, Spain; 2007.
10. Stoeffler K, Andjelic S, Legros N, Roberge J, Schougaard SB. Polyphenylene sulfide (PPS) composites reinforced with recycled carbon fiber. Composites Science and Technology. 2013;84:65–71.
11. May D, Goergen C, Friedrich K. Multifunctionality of polymer composites based on recycled carbon fibers: A review. Advanced Industrial and Engineering Polymer Research. 2021;4(2):70–81.
12. Khurshid MF, Abdkader A, Cherif C. Processing of waste carbon and polyamide fibres for high-performance thermoplastic composites: influence of carding parameters on fibre orientation, fibre length and sliver cohesion force. Journal of the Textile Institute. 2020;111(9):1277–87.
13. Hengstermann M, Raithel N, Abdkader A, Hasan MMB, Cherif C. Development of new hybrid yarn construction from recycled carbon fibers for high performance composites. Part-I : basic processing of hybrid carbon fiber/polyamide 6 yarn spinning from virgin carbon fiber staple fibers. Textile Research Journal. 2016;86(12):1307–17.
14. Goergen C, Schommer D, Duhovic M, Mitschang P. Deep drawing of organic sheets made of hybrid recycled carbon and thermoplastic polyamide 6 staple fiber yarns. Journal of Thermoplastic Composite Materials. 2020;33(6):754–78.
15. Abdkader A, Hengstermann M, Hasan MMB, Hossain M, Cherif C. Spinnverfahren zur Herstellung von Hybridgarnen aus recycelten Carbonfasern für CFK-Bauteile. melliand Textilberichte. 2017;(4):184–7.
16. Hengstermann M, Hasan MMB, Abdkader A, Cherif C. Development of a new hybrid yarn construction from recycled carbon fibers (rCF) for high-performance composites. Part-II: Influence of yarn parameters on tensile properties of composites. Textile

  doi:10.5075/epfl-298799_978-2-9701614-0-0

Research Journal. 2017;87(13):1655–64.
17. Hasan MMB, Nitsche S, Abdkader A, Cherif C. Carbon fibre reinforced thermoplastic composites developed from innovative hybrid yarn structures consisting of staple carbon fibres and polyamide 6 fibres. Composites Science and Technology. 2018;167:379–87.
18. Al Kassem G, Weichert D. Micromechanical material models for polymer composites through advanced numerical simulation techniques. PAMM. 2009;9(1):413–4.
19. Breuer K, Stommel M. RVE modelling of short fiber reinforced thermoplastics with discrete fiber orientation and fiber length distribution. SN Applied Sciences. 2020;2:1–13.
20. Bailakanavar M, Liu Y, Fish J, Zheng Y. Automated modeling of random inclusion composites. Engineering with Computers. 2014;30(4):609–25.
21. Islam M, Tudryn GJ, Picu CR. Microstructure modeling of random composites with cylindrical inclusions having high volume fraction and broad aspect ratio distribution. Computational Materials Science. 2016;125:309–18.
22. Zhou G, Sun X, Wang Y. Multi-chain digital element analysis in textile mechanics. Composites Science and Technology. 2004;64(2):239–44.
23. Wang Y, Miao Y, Swenson D, Cheeseman BA, Yen CF, LaMattina B. Digital element approach for simulating impact and penetration of textiles. International Journal of Impact Engineering. 2010;37(5):552–60.
24. Döbrich O, Gereke T, Cherif C. Modeling the mechanical properties of textile-reinforced composites with a near micro-scale approach. Composite Structures. 2016;135:1–7.
25. Zhang H, Guo X, Li Y. Mechanical properties of ring-spun yarn and its strength prediction model. FIBRES & TEXTILES in Eastern Europe. 2011;19(3):17–20.
26. Andersons J, Modniks J. A probabilistic model of the tensile strength of a UD flax-fabric-reinforced polymer composite. Polymer Composites. 2018;39(6):2101–9.
27. Antony S, Cherouat A, Montay G. Experimental, analytical and numerical analysis to investigate the tensile behaviour of hemp fibre yarns. Composite Structures. 2018;202:482–90.
28. Feder J. Random sequential adsorption. Journal of Theoretical Biology. 1980;87(2):237–54.

  doi:10.5075/epfl-298799_978-2-9701614-0-0

Composites Meet Sustainability – Proceedings of the 20th European Conference on Composite Materials,
ECCM20. 26-30 June, 2022, Lausanne, Switzerland

MICRO-CT BASED ASSESSMENT OF 3D BRAIDED AL_2O_3 REINFORCEMENT UNIFORMITY AND PERMEABILITY OF ALL-OXIDE CERAMIC MATRIX COMPOSITES PRODUCTION PROCESSES

Biltu Mahato[a], Stepan V. Lomov[a], Iskander S. Akhatov[a], Sergey G. Abaimov[a], Fabian Jung[2], Niels Grigat[2], Ben Vollbrecht[2], Martin Kolloch[2], Thomas Gries[2]

[a]Skolkovo Institute of Science and Technology, Centre for Design, Manufacturing, and Materials (CDMM), 121205 Moscow, Russian Federation, s.abaimov@skoltech.ru

[b]Institut für Textiltechnik (ITA), RWTH Aachen University, 52074 Aachen, Germany

Abstract: *The paper presents a methodology for processing micro-CT images of 3D braided preforms to assess the fiber orientation distribution uniformity and permeability. The micro-CT image is transformed into a voxel representation with identification of either fibre density and orientation, or absence of fibres in voxels, using VoxTex software. The voxel model allows calculation of the statistical parameters of the fibre spatial and orientation distribution, and characterization of the preform porosity. The voxel model is transferred to a Stokes solver in a commercial CFD software to calculate the preform permeability, using methods approbated during the International Virtual Benchmark Exercise.*

Keywords: 3D braiding, all-oxide CMC, digital twin, composite design, permeability

1. Introduction

Oxide ceramics are a suitable material class for high-temperature applications due to their high oxidation and corrosion stability. Although the operating time of oxide ceramics exceeds metallic high-temperature materials, e.g. nickel- or titanium-based alloys, the high brittleness of ceramics presents a challenge when used in applications of combined high temperature and high mechanical stress. To overcome the brittleness of ceramics, their damage tolerance can be improved through fibre reinforcements. For this purpose, oxide ceramic reinforcement textiles and matrix are combined to an all-oxide ceramic matrix composite (CMC).

Multidirectional 3D distribution of reinforcing fibre orientations is crucial to enable high damage tolerance of CMC [1, 2]. Currently, textile reinforcements in all-oxide CMC are realized by woven or scrim fabrics. The fibre orientation distribution in the laminate is 2D due to the absence of interlayer reinforcement. In woven layers the orientation of the fibres is bi-directional in-plane, with certain out-of-plane deviation (few degrees) due to crimp.

The high potential of three-dimensionally braided structures for high-temperature applications has been known since NASA's investigations in the 1970s. Like no other textile manufacturing technology, 3D braiding combines enormous process integration and automation potential with a geometric range of variation that has so far only been achieved in 3D printing. Compared to 2D braiding or weaving, it is thus possible to indirectly integrate entire process chains (e.g. surface production, cutting, draping, drilling, sewing) in one work step without waste and joining-related weak points in a resource-saving manner.

  doi:10.5075/epfl-298799_978-2-9701614-0-0

The 3D braiding process enables the production of complex and near net-shaped textiles by interlocking braided fibre layers, featuring a 3D multidirectional fibre orientation distribution. It increases the damage tolerance of all-oxide CMC by up to 95% [3]. Apart from the favourable fibre distribution, the preform permeability is a crucial parameter for defect-free infiltration with dispersed ceramic particles for further slip casting and sintering.
The paper presents a methodology for processing micro-CT images of 3D braided preforms to assess the fibre orientation distribution multidirectionality and permeability. The micro-CT image is transformed into a voxel representation with identification of either fibre density and orientation, or absence of fibres in voxels, using VoxTex software (KU Leuven, Belgium) [4]. The voxel model allows calculation of the statistical parameters of the fibre spatial and orientation distribution, and characterization of the preform porosity. The voxel model is transferred to a Stokes solver in a commercial CFD software to calculate the preform permeability, using methods approbated during the International Virtual Benchmark Exercise [5]. The methodology is demonstrated on three types of 3D braids, 3M Nextel 610 alumina fibres.

2. Materials

The alumina fibre 3D braids are produced on a 3D laboratory braiding machine in ITA (RWTH Aachen University, Germany). For the braiding operation, the 3M Nextel 610 alumina fibres are first rewound from the supplied mother spools onto braiding spools of 25 m each and inserted onto the braiding bobbins. The braiding machine is then loaded with the prepared bobbins. In the braiding operation, the 3D braid produced is continuously wound onto a take-off drum. The produced 3D braid is separated manually by cutting the textile to a defined length.

The fibres have diameter 10 – 12 µm, density 3.9 g/cm^3. Table 1 characterises the braids, which are modelled in the present work.

Table 1. Parameters of the fibres and braids

	Braid 1	Braid 2	Braid 3
Yarn linear density, den	4,500	10,000	10,000
Filament count	1,200	2,550	2,550
Braiding pattern	square	litz (wire)	litz (wire)
Braiding angle (with Z axis)	30°	6°	8°
Braiding yarns count	16	28	26
Inlays count	9	7	0
Braid width, mm	1.5	12	16
Braid fibre volume fraction	76%	64%	40%

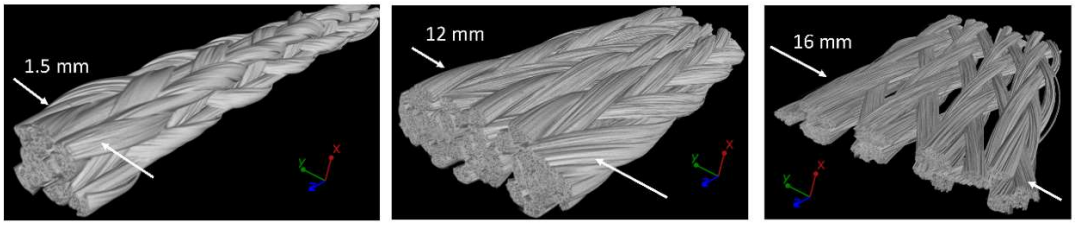

Braid 1 Braid 2 Braid 3

Figure 1. Braids images and dimensions

  doi:10.5075/epfl-298799_978-2-9701614-0-0

3. Micro-CT imaging

The computed-tomographic examinations are carried out on strip-shaped specimens with dimensions of 70.0 x 30.0 x 3.0 mm³ (L x W x H). For this purpose, preparation of the specimens is necessary. The 3D-braided textiles are cut by hand according to the required dimension. Before bringing the braids into the test chamber of the micro-CT, the bending stiffness of the textiles has to be evaluated. To prevent deposition of the limp braids during the scanning process, corresponding test specimens of length L = 70.0 mm are selected.

All images are taken with the help of a computer tomograph type CT-ALPHA (customized), ProCon C-Ray GmbH, Sarstedt, Germany. The scanned area is selected according to a repetitive braiding interval and is mapped to a resolution of 22.821 µm per pixel. The collected micro-CT data are processed using the reconstruction software VOLEX 10 (software package for X-ray and CT applications for digital information acquisition and evaluation) of the Fraunhofer Development Centre X-ray Technology EZRT, Fürth, Germany. The examined solid is built up as an image stack of scanned individual layers.

Figure 1 depicts the 3D images, which have been studied. Figure 2 shows succession of cross sections of the braids, revealing the braiding patterns.

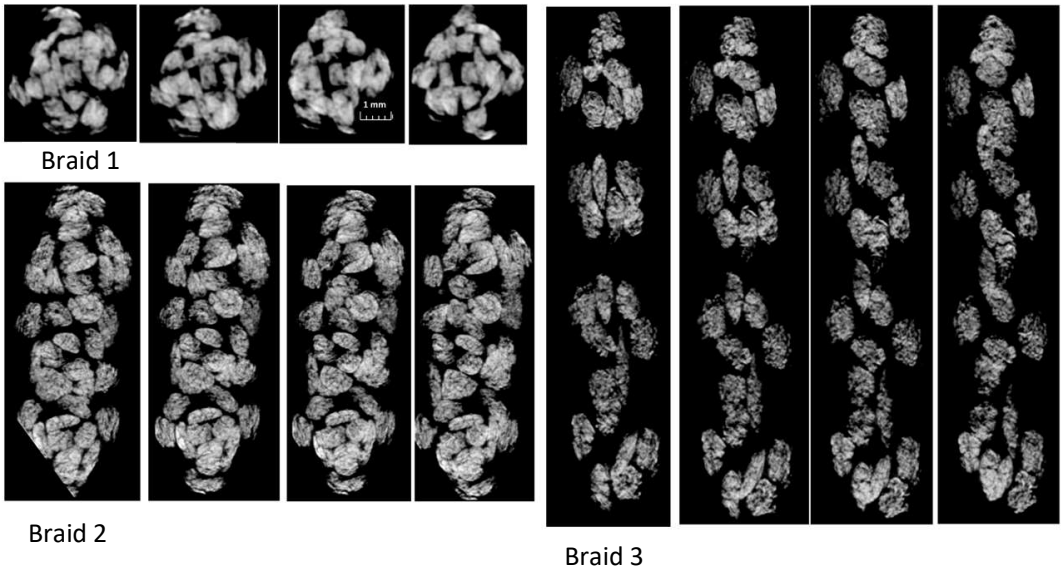

Figure 2. Successive cross sections of the braids. Distance between the cross sections 1 mm. The scale of all images is the same (shown for Braid 1)

4. Transformation into voxel mesh and segmentation

VoxTex software transforms the micro-CT image, as a 3D pixels array with the size of ~10^9 pix, into a voxels array. Each voxel is created by averaging properties of several pixels, with the step size 6 pix, and integration window size 4 pix. The resulting voxels array has a size of ~10^7 elements. The voxels, apart from the grey scale density, contain also information of anisotropy

  doi:10.5075/epfl-298799_978-2-9701614-0-0

index and the principle direction of the anisotropy, obtained using structure tensor analysis [4]. The voxel model can be segmented, labelling the voxels as belonging to the yarn volumes or to a void, based on two-parameters segmentation (density and anisotropy). Before the segmentation, a noise-reduction processing of the image is done (Gauss filtering). The segmentation limits are set for grey scale image density (8 bit, 0 – 255) and for degree of anisotropy, as shown in Fig 3c. The anisotropy limit includes only voxels with high degree of anisotropy, which represent fibrous material. The grey density limit cuts off empty spaces between the yarns. The thresholds are adjusted for the best visual fit between the original image and the result of the segmentation. The adjustment is done based on ten slices and remains subjective, especially given blurred edges of the yarns.
Only the central part of the braid is used for calculation of permeability, to exclude the influence of open edges of the braid. Figure 3 shows the transformation of the image into a segmented volume for permeability calculation.

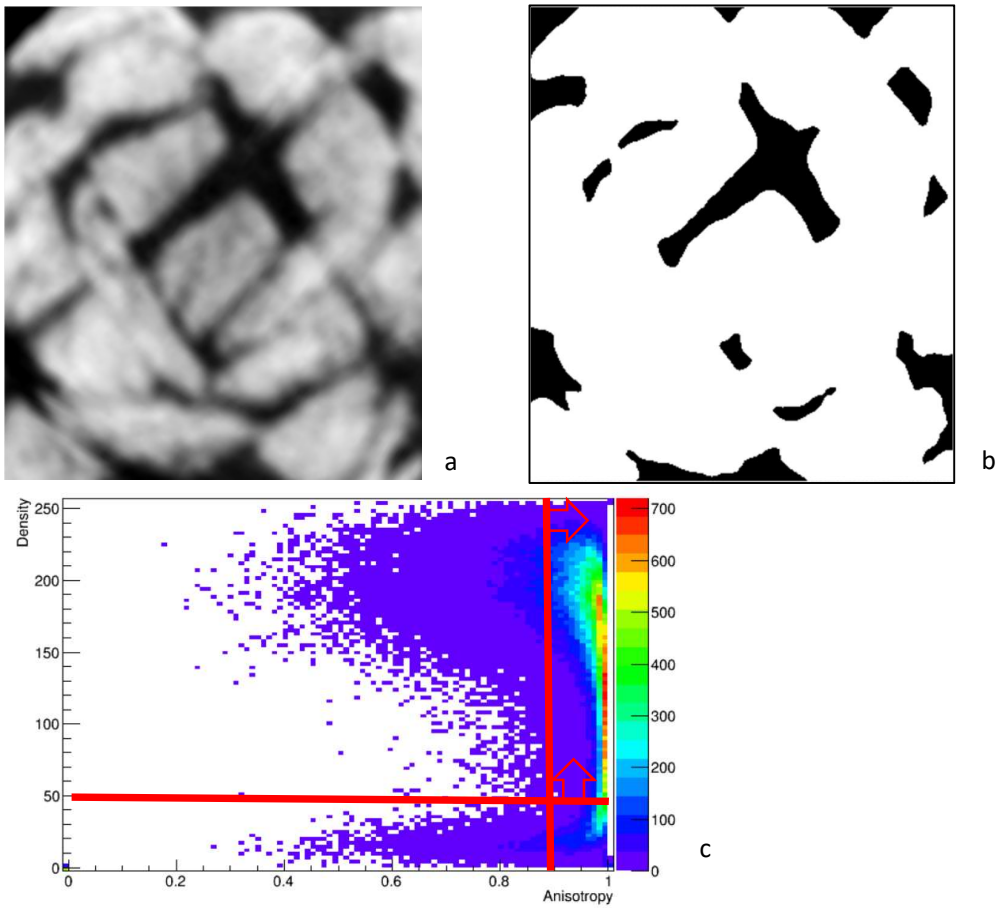

Figure 3. Segmentation of the image for permeability calculation, Braid 1: (a) central part of the braid, 3D image; (b) segmented image; (c) density-anisotropy histogram, lines show the thresholding limits. The colour scale gives number of voxels

  doi:10.5075/epfl-298799_978-2-9701614-0-0

5. Orientation distribution

Fibre orientation distribution in the core of the braids was evaluated using *VoxTex* software. This evaluation is based on calculation of structure tensor of the image in the voxels. The main direction of anisotropy (which is identified with the local fibre orientation) is given by the eigenvector of the structure tensor, corresponding to the smallest eigenvalue. The reader is referred for details to [4].

Figure 4 shows fibre orientation distributions. The distributions are represented as histograms of the orientation vector projection angles on plane YZ (in-plane orientation) and XZ (out-of-plane orientation).

Braid 1 has a wide fibre orientation distribution. Axial yarns (inlays) are responsible for fibres oriented close to axial (Z) direction. Braiding yarns "travel" from one side of the braid to another, creating strong deviations from the axial direction. This braid has the largest braiding angle of 30°, in comparison for Braid 2 and Braid 3.

Braids 2 and 3, of a "litz" ("wire") pattern, have, as the name implies, more narrow orientation distribution, concentrated near the axial direction. This is suggested by their low braiding angles.

Hence a square braiding pattern in combination with considerable braiding angle creates an orientation distribution, favourable from the point of view of damage tolerance of the braided composite.

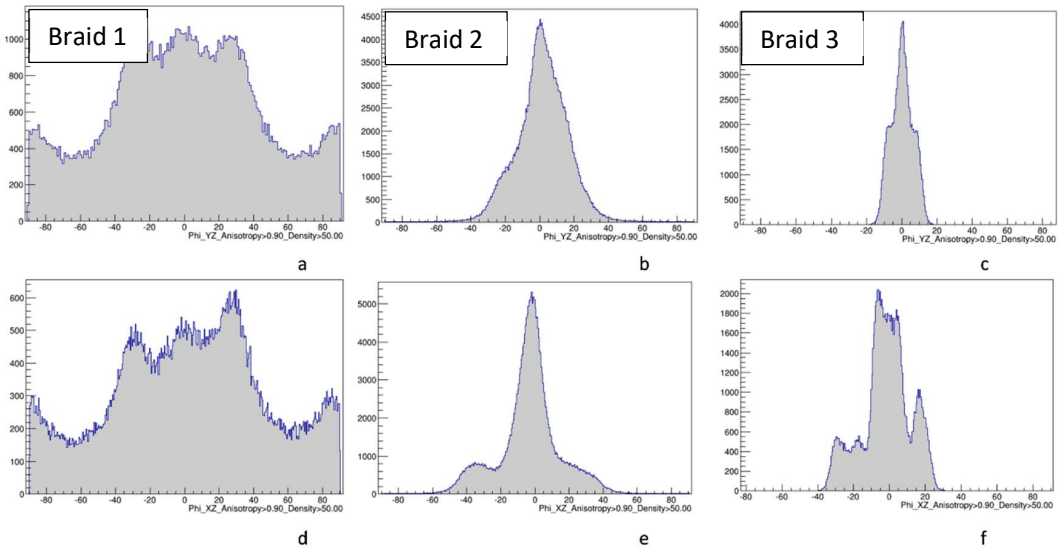

Figure 4. Orientation distributions for Braid 1 (a,d), Braid 2 (b,e), Braid 3 (c,f): (a-c) in-plane orientation angle (YZ plane), (d-f) out-of-plane orientation angle (XZ). 0° in the both cases corresponds to Z (axial) direction of the braids.

6. Permeability calculations

Permeability calculations are done using computational fluid dynamics (CFD) FlowTex software [6], integrated within VoxTex [7]. A flow of Newtonian incompressible fluid through the model is calculated. This calculation route (using another CFD package, namely CFX) has been

  doi:10.5075/epfl-298799_978-2-9701614-0-0

investigated by Skoltech in the framework of the International Virtual Permeability Benchmark [5]. The CFD software implements the numerical solution of the Stokes equations on a 3D regular grid, which is created directly from the segmented voxel model. The periodic boundary conditions were set along all the directions, simulating the resin flow in a thick braided preform. Because of the local variations of the fibrous structure, the periodic boundary conditions are weak, with coefficient of periodicity (the fraction of the corresponding boundary voxels on opposite faces, see [7]) about 0.6.

Table 2 shows results of the calculations. The fibre volume fractions are repeated here for easy reference. Figure 5 depicts dependencies of the permeability on the fibre volume fraction on the braids. These dependencies are close to linear in semi-logarithmic coordinates. The highest permeability component is the one along the braids, for all variants. For Braid 1 and Braid 2 permeability values in two directions across the braid are close one to another as is suggested by visual inspection of the fibre packing (Figure 2). For Braid 3 permeability in thickness (X) direction is five times higher than in width direction, because of presence of large empty spaces, seen in Figure 2.

Table 2. Computed permeability of the braided preforms

	Braid 1	Braid 2	Braid 3
Fibre volume fraction	76%	64%	40%
K_x, m^2 (thickness)	$7.2 \cdot 10^{-10}$	$2.2 \cdot 10^{-9}$	$2.1 \cdot 10^{-8}$
K_y, m^2 (width)	$8.1 \cdot 10^{-10}$	$1.8 \cdot 10^{-9}$	$4.4 \cdot 10^{-9}$
K_z, m^2 (length)	$13.1 \cdot 10^{-10}$	$6.2 \cdot 10^{-9}$	$3.8 \cdot 10^{-8}$

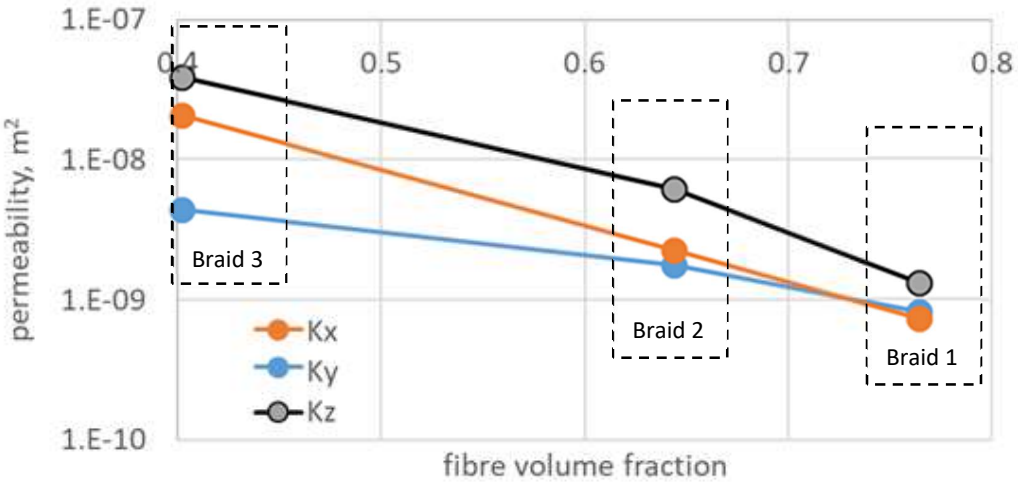

Figure 5. Calculated permeability of the braids in relation with fibre density

7. Conclusion

A methodology for processing of micro-CT images of 3D braided preforms, using VoxTex software and CFD Stokes solver is assessed and successfully used for evaluation of the fibre orientation distribution and permeability of 3D braided Al_2O_3 reinforcement.

  doi:10.5075/epfl-298799_978-2-9701614-0-0

References

1. Gonzalez-Julian, J., I. Kraleva, M. Belmonte, F.B. Jung, T. Gries, and R. Bermejo, Multifunctional performance of Ti2AlC MAX phase/2D braided alumina fiber laminates. Journal of the American Ceramic Society, 2022. 105(1): p. 120-130.
2. Kolloch, M., N. Grigat, B. Vollbrecht, and F. Jung, Simulation and modeling of the braiding process - Chapter 13, in Advances in Modeling and Simulation in Textile Engineering, N.T. Akankwasa and D. Veit, Editors. 2021, Woodhead Publishing. p. 351-394.
3. Kolloch, M., G. Puchas, N. Grigat, B. Vollbrecht, W. Krenkel, and T. Gries, Process chain development for the fabrication of three-dimensional braided oxide ceramic matrix composites. Materials, 2021. 14(21).
4. Straumit, I., S.V. Lomov, and M. Wevers, Quantification of the internal structure and automatic generation of voxel models of textile composites from X-ray computed tomography data. Composites Part A, 2015. 69: p. 150-158.
5. May, D., E. Syerko, T. Schmidt, C. Binetruy, L. Rocha da Silva, S.V. Lomov, and S. Advani, Benchmarking virtual permeability predictions of real fibrous microstructure, in 36th ASC Technical VIRTUAL Conference (ASC 2021). 2021. p. 2123 - 2132.
6. Verleye, B., S.V. Lomov, A.C. Long, I. Verpoest, and D. Roose, Permeability prediction for the meso-macro coupling in the simulation of the impregnation stage of Resin Transfer Moulding. Composites Part A, 2010. 41: p. 29-35.
7. Straumit, I., C. Hahn, E. Winterstein, B. Plank, S.V. Lomov, and M. Wevers, Computation of permeability of a non-crimp carbon textile reinforcement based on X-ray computed tomography images. Composites Part A, 2016. 81: p. 289-295.

  doi:10.5075/epfl-298799_978-2-9701614-0-0

MULTI-SCALE MODELING OF THE THERMO-VISCOELASTIC BEHAVIOR OF 3D WOVEN COMPOSITES

Martin Hirsekorn[a], Lionel Marcin[b], Thierry Godon[b]

a: DMAS, ONERA – Université Paris-Saclay, 29 avenue de la Division Leclerc, 92322 Châtillon, France – martin.hirsekorn@onera.fr
b: Safran Aircraft Engines, Rond point René Ravaud, 77550 Moissy Cramayel, France

Abstract: *A multi-scale modeling strategy is proposed that takes into account the temperature and cure dependence of the viscoelastic behavior of the constituent materials of a composite material and the effects of stress relaxation on thermal expansion and chemical shrinkage. A homogenization strategy is presented, which, starting from the constituent behaviors, yields the homogenized viscoelastic behavior of the composite with time-dependent expansion coefficients. This time-dependence is a direct consequence of the viscoelastic behavior of the constituents, as their expansion coefficients are supposed to be time-independent. In the simulation of a heating process, the model predicts sign changes in the thermal strain rate due to residual stress relaxation close to the glass transition temperature, which cannot be obtained with classical thermo-elastic homogenization methods.*

Keywords: Viscoelasticity; Thermal expansion; Chemical shrinkage; Homogenization

1. Introduction

Fiber reinforced composites with thermosetting polymer matrices are manufactured at much higher temperatures than typical in-service temperatures. During the curing process, the initially liquid resin polymerizes and forms a solid matrix material that holds the fibrous reinforcement together. At the end of the curing process, the composite part is cooled down to room temperature. As the coefficients of thermal expansion (CTE) of the fibers and the matrix material are not the same, residual stresses emerge within the composite, which may lead to part distortion and influence damage onset and evolution [1]. Furthermore, the resin shrinks during polymerization, which also contributes to the formation of residual stresses [2].

While the most common fiber materials (glass or carbon) are in a good approximation linear elastic and independent of temperature over the range of the cure cycle, the behavior of the polymer matrix is viscoelastic, leading to strain and stress evolutions in time even when temperature and degree of cure are constant [3,4]. This time-dependent component of the matrix behavior depends strongly on both temperature and degree of cure [4,5]. Therefore, in most recent published works on modeling residual stresses in composite materials, viscoelastic constitutive laws are used that take into account stress relaxation, which plays an important role in particular at the beginning of the cooling phase, when the matrix is still close to its glass transition temperature T_g [6-8]. The models are either identified directly from experimental observations of the time-dependent behavior of the composite [3] or obtained by viscoelastic homogenization starting from the constituent behaviors [8-11].

To predict residual stresses and shape distortions, time-independent average CTE and coefficients of chemical shrinkage (CCS) are used for the composite [8,11]. This means that

  doi:10.5075/epfl-298799_978-2-9701614-0-0

locally, changes of temperature or degree of cure only cause an instantaneous deformation of the material, which does not further evolve in time when temperature and degree of cure are kept constant. However, when looking at the lower scales, it becomes clear that due to the viscoelastic behavior of the matrix, residual stresses caused by, e.g., a temperature change evolve in time due to relaxation and creep phenomena, even if the temperature is kept constant. This effect leads to an evolution of the average strain of the composite after a change of temperature that has to be taken into account by time-dependent CTE (and likewise by time-dependent CCS for the relaxation of the stresses caused by chemical shrinkage).

In this contribution, we show how these phenomena can be taken into account in a multi-scale model of the thermo-viscoelastic behavior of polymer matrix composites with 3D woven reinforcements. The viscoelastic behavior is described in section 2. In section 3, it is shown how time-dependence can be taken into account in CTE and CCS using similar approaches as for the relaxation modulus of the viscoelastic behavior. A recently developed homogenization technique [12] is briefly outlined in section 4. It yields the homogenized viscoelastic behavior and the time-dependent CTE and CCS of the composite from the constituent behaviors. In section 5, the resulting model is used to predict the temperature dependence of the apparent elastic properties and the CTE of the composite.

2. Viscoelastic behavior

2.1 General formulation

We start from the general integral form of linear viscoelasticity, in which the stress tensor is expressed as the Stieltjes convolution of a 4th order tensor of (in general) anisotropic relaxation moduli $\underline{\underline{E}}$ with the mechanical strain $\underline{\varepsilon}^{ve}$ over a reduced time ξ

$$\underline{\sigma}(\xi) = \int_{-\infty}^{\xi} \underline{\underline{E}}(\xi - \xi') : \frac{\partial \underline{\varepsilon}^{ve}(\xi')}{\partial \xi'} d\xi' \tag{1}$$

The mechanical strain is obtained by subtracting the strain due to thermal expansion $\underline{\varepsilon}^{th}$ and due to chemical shrinkage $\underline{\varepsilon}^{ch}$ from the total strain tensor $\underline{\varepsilon}$.

$$\underline{\varepsilon}^{ve}(\xi) = \underline{\varepsilon}(\xi) - \underline{\varepsilon}^{th}(\xi) - \underline{\varepsilon}^{ch}(\xi) \tag{2}$$

The reduced time ξ accounts for horizontal shifts of the relaxation curves along the logarithmic time scale upon change of temperature and degree of cure if the time-cure-temperature superposition principle applies [13]

$$\xi(t) = \int_{-\infty}^{t} \frac{1}{a_T(t')} dt', \; \xi' = \xi(t') \tag{3}$$

where a_T is the shift factor, which, in general, depends on temperature and degree of cure.

If the relaxation moduli can be approximated by a Prony series

$$\underline{\underline{E}}(\xi - \xi') = \underline{\underline{E}}_{\infty} + \sum_{k=1}^{N} \underline{\underline{E}}_k e^{-\frac{\xi - \xi'}{\tau_k}} \tag{4}$$

with relaxation times τ_k, the integral form resolves to a generalized Maxwell model given by

$$\underline{\sigma}(\xi) = \left(\underline{\underline{E}}_{\infty} + \sum_{k=1}^{N} \underline{\underline{E}}_k\right) : \underline{\varepsilon}^{ve}(\xi) - \sum_{k=1}^{N} \underline{\underline{E}}_k : \underline{\varepsilon}_k^{ve}(\xi) \tag{5}$$

  doi:10.5075/epfl-298799_978-2-9701614-0-0

with tensorial internal variables $\underline{\varepsilon}_k^{ve}$ accounting for the strain history [14]. They evolve following the differential equations

$$\frac{d\underline{\varepsilon}_k^{ve}(\xi)}{d\xi} = \frac{1}{\tau_k}\left(\underline{\varepsilon}^{ve}(\xi) - \underline{\varepsilon}_k^{ve}(\xi)\right) \tag{6}$$

2.2 Viscoelastic model of the matrix

The epoxy matrix used in the modeled composite was characterized experimentally by multi-temperature relaxation tests on fully and partially cured specimens [4]. Relaxation master curves were built for different degrees of cure by shifting the relaxation curves observed at different temperatures along the logarithmic time scale. Below the glass transition temperature, the necessary shift factors can well be approximated by an Arrhenius model:

$$a_T(T, c) = \frac{H(c)}{R \cdot \ln 10}\left(\frac{1}{T} - \frac{1}{T_g(c)}\right) \tag{7}$$

Fitting Prony series to the obtained master curves, it was shown that the coefficients plotted against the relaxation times follow closely a continuous function of the form

$$G(\tau) = A \exp\left(-\left(\frac{\log_{10}\tau - \log_{10}\tau_{peak}}{l_{peak}}\right)^2\right) + \frac{B}{2}\left(1 - \operatorname{erf}\left(\frac{\log_{10}\tau - \log_{10}\tau_{peak}}{l_{peak}}\right)\right) \tag{8}$$

This function reproduces a Gaussian peak of height A, width l_{peak}, and center position τ_{peak}. For short relaxation times, the curve approximates a constant value of B. erf is the Gaussian error function, which makes the function tend towards zero for long relaxation times. Since this function is continuous, we may freely choose the relaxation times, as long as there is at least one relaxation time per decade. The corresponding weights of the Prony series are then given for the k^{th} relaxation time by

$$G_k = \frac{\log_{10}\tau_{k+1} - \log_{10}\tau_{k-1}}{2} G(\tau_k) \tag{9}$$

The parameters A, B, and l_{peak} are similar for the relaxation master curves obtained from partially cured specimens. The positions of the peaks for different degrees of cure superpose well, if the shift factors are defined with respect to the cure dependent glass transition temperature $T_g(c)$, as written in Eq. (7). T_g as a function of cure is given by the DiBenedetto equation [15]

$$T_g(c) = T_{g0} + (T_{g1} - T_{g0})\frac{\lambda c}{1 - c(1-\lambda)} \tag{10}$$

where T_{g0} is the glass transition temperature of the uncured and T_{g1} the glass transition temperature of the fully cured resin. The activation energy H in Eq. (7) decreases with increasing degree of cure. A linear function was used in [9] to take into account this effect.

A 3D version of this model developed in [4] was proposed in [9], based on the assumption of isovolumetric viscous effects. Thus, the tensors $\underline{\underline{E}}_k$ in the time-dependent terms of Eq. (4) take a purely deviatoric form

$$\underline{\underline{E}}_k = G_k\left(\underline{\underline{\mathbb{1}}} - \frac{1}{3}\underline{\mathbb{1}} \otimes \underline{\mathbb{1}}\right) \tag{11}$$

with the coefficients G_k given by Eqs. (8) and (9). The (purely elastic) bulk modulus is included into the time-independent term using for $\underline{\underline{E}}_\infty$ the general form for an isotropic elastic stiffness

$$\underline{\underline{E}}_\infty = K\frac{1}{3}\underline{\mathbb{1}}\otimes\underline{\mathbb{1}} + G_\infty\left(\underline{\underline{\mathbb{1}}} - \frac{1}{3}\underline{\mathbb{1}}\otimes\underline{\mathbb{1}}\right) \tag{12}$$

Here, $\underline{\mathbb{1}}$ is the 2nd order identity tensor and $\underline{\underline{\mathbb{1}}}$ the 4th order identity tensor with minor symmetry. The assumption of isovolumetric viscous effects implies that for long relaxation times at high temperatures the apparent Poisson ratio tends towards 0.5 [16]. The full list of parameters of the 3D model identified using the experimental data in [4] is given in [9].

3. Time-dependent expansion coefficients

Different formulations were proposed to integrate time-dependent effects of thermal expansion into viscoelastic constitutive models [14,17,18]. They use integral forms similar to the viscoelastic formulation given in Eq. (1) to express the time-dependent effects of thermal expansion on stress or strain. We use the formulation of [18] to write the thermal strain as

$$\underline{\varepsilon}^{th}(\xi) = \int_{-\infty}^{\xi} \underline{\alpha}^{th}\big(\xi-\xi', T(\xi'), c(\xi')\big) : \frac{\partial T(\xi')}{\partial \xi'} d\xi' \tag{13}$$

with time-dependent CTE $\underline{\alpha}^{th}$. The chemical shrinkage strain is written in an equivalent form

$$\underline{\varepsilon}^{ch}(\xi) = \int_{-\infty}^{\xi} \underline{\alpha}^{ch}\big(\xi-\xi', T(\xi'), c(\xi')\big) : \frac{\partial c(\xi')}{\partial \xi'} d\xi' \tag{14}$$

In the following, we will only show the expressions for the thermal strain, but the same formalism can be applied for the chemical shrinkage strain.

In addition to the reduced time-dependence of $\underline{\alpha}^{th}$ that describes the influence of a temperature change at ξ' on a later time $\xi > \xi'$, we also allow for an explicit dependence of the CTE on temperature and cure at the moment of the temperature change. This is represented by the arguments $T(\xi')$ and $c(\xi')$. As in the case of the relaxation moduli, we suppose that the time-dependence of the CTE can be approximated by a Prony series

$$\underline{\alpha}^{th}\big(\xi-\xi', T(\xi'), c(\xi')\big) = \underline{\alpha}_\infty^{th}\big(T(\xi'), c(\xi')\big) - \sum_{k=1}^{N} \underline{\alpha}_k^{th}\big(T(\xi'), c(\xi')\big) e^{-\frac{\xi-\xi'}{\tau_k}} \tag{15}$$

The evolution of thermal strain in reduced time is then given by [12]

$$\frac{d\underline{\varepsilon}^{th}(\xi)}{d\xi} = \Big(\underline{\alpha}_\infty^{th}\big(T(\xi), c(\xi)\big) - \sum_{k=1}^{N} \underline{\alpha}_k^{th}\big(T(\xi), c(\xi)\big)\Big)\frac{dT(\xi)}{d\xi} - \sum_{k=1}^{N}\frac{1}{\tau_k}\underline{\varepsilon}_k^{th}(\xi) \tag{16}$$

with tensorial internal variables $\underline{\varepsilon}_k^{th}$ accounting for the history of temperature and the CTE. They evolve following the differential equations

$$\frac{d\underline{\varepsilon}_k^{th}(\xi)}{d\xi} = \underline{\alpha}_k^{th}\big(T(\xi), c(\xi)\big)\frac{dT(\xi)}{d\xi} - \frac{1}{\tau_k}\underline{\varepsilon}_k^{th}(\xi) \tag{17}$$

For time-independent CTE, the classical definition

$$\frac{d\underline{\varepsilon}^{th}(\xi)}{d\xi} = \underline{\alpha}_\infty^{th}\big(T(\xi), c(\xi)\big)\frac{dT(\xi)}{d\xi} \tag{18}$$

of the CTE is recovered from Eq. (16).

  doi:10.5075/epfl-298799_978-2-9701614-0-0

4. Thermo-viscoelastic homogenization

According to the viscoelastic correspondence principle, the Laplace-Carson (LC) transform

$$\hat{f}(p) = p\int_0^\infty f(\xi)e^{-p\xi}d\xi \tag{19}$$

applied to a viscoelastic problem transforms it into an elastic problem in the LC-space [19] as a function of the transform parameter p. Applying Eq. (19) to Eqs. (1), (13), and (14) yields

$$\underline{\hat{\sigma}}(p) = \underline{\underline{\hat{E}}}(p)\colon\left(\underline{\hat{\varepsilon}}(p) - \underline{\hat{\alpha}}^{th}(p)\hat{T}(p) - \underline{\hat{\alpha}}^{ch}(p)\hat{c}(p)\right) \tag{20}$$

if the explicit dependence of $\underline{\alpha}^{th}$ and $\underline{\alpha}^{ch}$ on T and c is momentarily ignored. This corresponds to a thermo-elastic problem as a function of the transform parameter p. Classical thermo-elastic homogenization methods can therefore be applied in the LC-space to obtain the LC-transforms of the relaxation modulus, CTE, and CCS of the homogenized material [12]. Applying the LC-transform to the Prony series expression of the relaxation modulus (Eq. 4) yields for a given value p_i of the LC-transform parameter p

$$\underline{\underline{\hat{E}}}(p_i) = \underline{\underline{E}}_\infty + \sum_{k=1}^{N}\mathcal{L}_{ik}\underline{\underline{E}}_k \tag{21}$$

with

$$\mathcal{L}_{ik} = \frac{p_i}{p_i+\frac{1}{\tau_k}} \tag{22}$$

Likewise, for a given temperature T and a given degree of cure c, we obtain

$$\underline{\hat{\alpha}}^{th}(p_i,T,c) = \underline{\alpha}^{th}_\infty(T,c) - \sum_{k=1}^{N}\mathcal{L}_{ik}\underline{\alpha}^{th}_k(T,c) \tag{23}$$

We now assume that the relaxation modulus, CTE, and CCS of the homogenized thermo-viscoelastic behavior can also be well fitted by Prony series, whose weights follow continuous functions if plotted against the relaxation times on a logarithmic time scale. In this case, we can choose to represent the homogenized behavior by the same relaxation times as the matrix behavior, distributing the τ_k uniformly on the logarithmic time scale at one relaxation time per decade [9]. Then, the LC-transforms of the homogenized properties can also be written in terms of Eqs. (21) and (23), with the same transform matrix given by Eq. (22).

If this procedure is carried out for $M \geq N$ different p_i, the coefficients $\underline{\underline{E}}_\infty$, $\underline{\underline{E}}_k$, $\underline{\alpha}^{th}_\infty$, and $\underline{\alpha}^{th}_k$ of the homogenized behavior can be obtained by solving the least-squares problems given by the equation systems in Eqs. (21) and (23) [9,12]. This problem is often ill-conditioned, causing oscillations in the coefficients of the $\underline{\underline{E}}_k$ if plotted against the relaxation times [9], which may lead to non-positive definite tensors $\underline{\underline{E}}_k$. The proper choice of the p_i [9,19] improves the condition of the least squares problem, which reduces the oscillations [9]. If this is not sufficient, Tikhonov regularization can be used [12] to ensure positive definite $\underline{\underline{E}}_k$ and thus a thermodynamically admissible homogenized behavior.

5. Results

Two scale changes are needed to obtain the homogenized behavior of a 3D woven composite. In a first step, the homogenized behavior of the warp and weft yarns is determined using a hexagonal representative volume element (RVE) [9] and the thermo-viscoelastic behavior of

the matrix and the fibers (taking zero $\underline{\underline{E}}_k$, as the fibers are considered as linear elastic). Time-independent CTE and CCS are taken for the matrix and the fibres [12]. In the second step, the homogenized behaviors of the warp and weft yarns and the matrix behavior are used for thermo-elastic homogenizations on a mesoscopic RVE obtained from micro-tomography images of the composite material [9]. The thermo-elastic homogenizations in the LC-space are carried out by Finite Element (FE) calculations. The resulting homogenized behaviors reproduce accurately the average stresses and strains obtained from full-scale thermo-viscoelastic FE simulations on the respective RVEs using the same FE meshes [9,12].

The homogenized behavior of the composite was used to calculate the evolution of the secant moduli under tensile and shear loading as a function of temperature. The results are compared to experimental data in Figure 1. Up to about 120°C, the model only slightly underestimates the experimental observations. This difference may be due to the influence of the fibers on the polymerization of the resin during composite cure, which is not taken into account, as the predictions were made using exclusively the constituent properties identified on pure matrix specimens. Differences become more significant around T_g, at which the matrix characterization was less accurate due to the very soft and fragile specimens. Above T_g, the resin becomes very soft, and direct interactions between the fibers like friction, which are not take into account in the model, may influence the apparent properties of the composite.

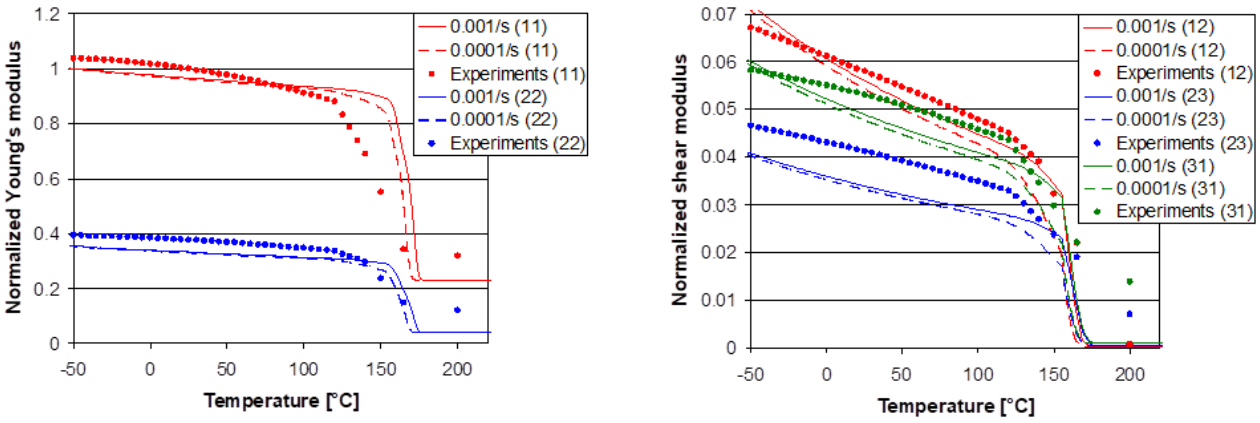

Figure 1. Secant moduli obtained with the homogenized viscoelastic behavior at strain rates of $0.001s^{-1}$ and $0.0001s^{-1}$ compared with experimentally measured moduli of the composite at $0.001s^{-1}$. The moduli are normalized by the measured tensile modulus in warp direction at 25°C.

The evolution of the average composite strain upon heating at 3°C/min from room temperature to 200°C predicted by the homogenized thermo-viscoelastic behavior is shown in Figure 2. The thermal expansion in the out-of-plane direction is significantly larger as in the plane, where it is limited by the fibers. The out-of-plane expansion increases considerably around T_g, as the CTE of the matrix increases. In the plane of the reinforcement, the thermal expansion is initially positive, but gradually slows down at growing temperatures. Close to T_g, the model yields a strong contraction, which is due to the relaxation of the matrix stresses. As a consequence, the composite strain becomes dominated by the fibers, which have a slightly negative CTE. The initially positive strain of the composite disappears when the internal stresses relax, leading to a strongly negative apparent CTE. The model also yields small average shear strains, as the RVE identified from tomography images of the composite, is not perfectly orthotropic with the axes of the coordinate system. These complex evolutions of the average

  doi:10.5075/epfl-298799_978-2-9701614-0-0

thermal strain with sign changes of the apparent CTE cannot be predicted by purely thermo-elastic homogenization or by viscoelastic homogenization without taking into account time-dependent effects of the average CTE.

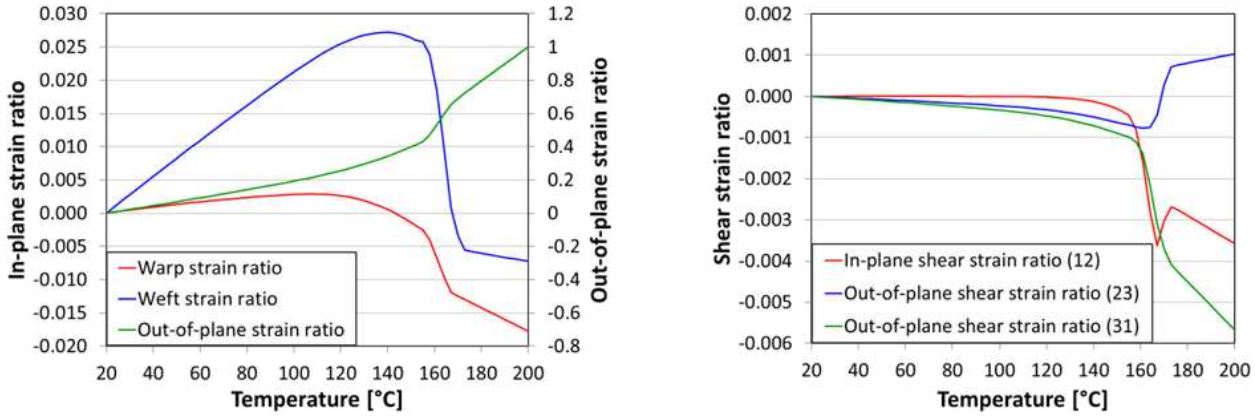

Figure 2. Average strain evolution of the fully cured composite upon heating at 3°C/min predicted by the homogenized thermo-viscoelastic behavior. The strains are normalized by the final out-of-plane strain at 200°C.

6. Conclusions

The viscoelastic behavior of the composite obtained with the presented homogenization method captures well the evolution of the apparent elastic properties with temperature. The time-dependent CTE that take into account stress relaxation at the lower scales predict a sign change of the in-plane average differential CTE of the composite that are not obtained with thermo-elastic or purely viscoelastic homogenization techniques. Experimental validation of the predicted effects is in progress. The presented methodology will be used in multi-scale simulations of the formation of residual stresses and shape distortions of composite parts. In particular, it can give indications on whether the shape of a composite part will evolve in time after the end of the curing process [8] and on relaxation of internal stresses when the parts are reheated.

Acknowledgements

The research presented in this article was funded by the Safran Group, France.

7. References

1. Wisnom MR, Gigliotti M, Ersoy N, Campbell M, Potter KD. Mechanisms generating residual stresses and distorting during manufacture of polymer-matrix composite structures. Composites: Part A 2006; 37:522-529.
2. Billotte C, Bernard F, Ruiz E. Chemical shrinkage and thermomechanical characterization of an epoxy resin during cure by a novel in situ measurement method. European Polymer Journal 2013; 49:3548-3560.
3. White SR, Kim YK. Process-induced residual stress analysis of AS4/3501-6 composite material. Mechanics of Composite Materials and Structures 1998; 5:153-186.

  doi:10.5075/epfl-298799_978-2-9701614-0-0 published under CC BY-NC 4.0 license

4. Courtois A, Hirsekorn M, Benavente M, Jaillon A, Marcin L, Ruiz E, Lévesque M. Viscoelastic behavior of an epoxy resin during cure below the glass transition temperature: Characterization and modeling. Journal of Composite Materials 2018; 53:155-171.
5. O'Brien D, Mather P, White S. Viscoelastic properties of an epoxy resin during cure. Journal of Composite Materials 2001; 35:883-904.
6. Zhang J, Zhang M, Li S, Pavier M, Smith D. Residual stresses created during curing of a polymer matrix composite using a viscoelastic model. Composites Science and Technology 2016; 130:20-27.
7. Ding A, Li S, Sun J, Wang J, Zu L. A thermo-viscoelastic model of process-induced residual stresses in composite structures with considering thermal dependence. Composite Structures 2016; 136:34-43.
8. Benavente M, Marcin L, Courtois A, Lévesque M, Ruiz E. Numerical analysis of viscoelastic process-induced residual distortions during manufacturing and post-curing. Composites Part A 2018; 107:205-216.
9. Hirsekorn M, Marcin L, Godon T. Multi-scale modeling of the viscoelastic behavior of 3D woven composites. Composites Part A 2018; 112:539-548.
10. Courtois A, Marcin L, Benavente M, Ruiz E, Lévesque M. Numerical multiscale homogenization approach for linearly viscoelastic 3D interlock woven composites. International Journal of Solids and Structures 2019; 163:61-74.
11. Trofimov A, Le-Pavic J, Ravey C, Albouy W, Therriault D, Lévesque M. Multi-scale modeling of distortion in the non-flat 3D woven composite part manufactured using resin transfer molding. Composites Part A 2021; 140:106145.
12. Hirsekorn M, Marcin L, Godon T. Thermo-viscoelastic homogenization of 3D woven composites with time-dependent expansion coefficients. Submitted to the International Journal of Solids and Structures 2022.
13. Eom Y, Boogh L, Michaud V, Sunderland P, Månson J-A. Time-cure-temperature superposition for the prediction of instantaneous viscoelastic properties during cure. Polymer Engineering and Science 2000; 40:1281-1292.
14. Sawant S, Muliana A. A thermo-mechanical viscoelastic analysis of orthotropic materials. Composite Structures 2008; 83:61-72.
15. Pascault J, Williams J. Relationships between glass transition temperature and conversion. Polymer Bulletin 1990; 24:115-121.
16. Tschögl N, Knauss WG, Emri I. Poisson's ratio in linear viscoelasticity – a critical review. Mechanics of Time-Dependent Materials 2002; 6(1):3-51.
17. Zocher MA, Groves SE, Allen DH. A three-dimensional finite element formulation for thermoviscoelastic orthotropic media. Internationa Journal for Numerical Methods in Engineering 1997; 40:2267-2288.
18. Pettermann H, DeSimone A. An anisotropic linear thermo-viscoelastic constitutive law: Elastic relaxation and thermal expansion creep in the time domain. Mechanics of Time-Dependent Materials 2018; 22:421-433.
19. Lévesque M, Gilchrist MD, Bouleau N, Derrien K, Baptiste D. Numerical inversion of the Laplace-Carson transform applied to homogenization of randomly reinforced linear viscoelastic media. Computational Mechanics 2007; 40:771-789.

  doi:10.5075/epfl-298799_978-2-9701614-0-0

ADVANCED NATURAL FIBRE TEXTILES FOR COMPOSITE REINFORCEMENT

C. Greb[a], C. Uthemann[a], J. Broening[a]

a: Institut für Textiltechnik (ITA) of RWTH Aachen University,
Otto-Blumenthal-Str. 1, D-52074 Aachen, Germany
Email: christoph.greb@ita.rwth-aachen.de, Web Page: www.ita.rwth-aachen.de

Abstract: *The use of natural fibres (NF) as reinforcement in composite materials has a long history. Yet, due to the growing awareness of global warming and the related societal demand for sustainability, its potential has never been more important. Compared to glass fibre-reinforced plastics (GFRP), natural fibre-reinforced plastics (NFRP) can be produced consuming up to 50 % less energy and emitting significantly less CO_2. While NFRP are already established for certain non-structural applications, they do not represent an adequate alternative to GFRP for structural components. One of the main reasons for this is the variation in fibre properties due to different fibre types, growing areas and climatic conditions. Another reason is the induced twist during the spinning of natural fibre yarns, which lowers the realisable fibre volume contents and reduces the mechanical properties of the composites. At the Institut für Textiltechnik (ITA) of RWTH Aachen University, ongoing research addresses these two deficits.*

Keywords: natural fibre-reinforced plastics; predictive model; mechanical properties; fibre orientation; non-crimp fabrics

1. Introduction

Fibre-reinforced plastics (FRP) offer the potential to be used in an energy- and resource-efficient way, which is why production volumes have risen significantly in recent years. In volume, the composite market was approx. 12.1 Mt in 2021 [1]. The annual growth rate of the market is estimated at 5 % for 2021-2026 [1]. Glass fibres are used for more than 90 % of FRP, which is due to the low fibre price (2-3 €/kg) in combination with good mechanical properties [1,2]. Despite their excellent specific mechanical properties (see Table 1), natural fibres are only used for about 5 % of FRP, mostly for non-structural applications [1].

Table 1: Mechanical properties of E-glass and typical natural fibres used for NFRP [3]

Fibre	Density [g/cm³]	Fibre length [mm]	Elongation at break [%]	Specific modulus [GPa/g*cm^{-3}]	Specific tensile strength [MPa/g*cm^{-3}]
Sisal	1.3-1.5	900	2.0-2.5	6.7-20	362-610
Jute	1.3-1.5	1.5-120	1.5-1.8	7.1-39	300-610
Ramie	1.5	900-1200	2.0-3.8	29-85	270-620
Hemp	1.5	5-55	1.6	39-47	370-740
Flax	1.5	5-900	1.2-3.2	18-53	230-1220
E-glass	2.5	∞	2.5	29	800-1400

  doi:10.5075/epfl-298799_978-2-9701614-0-0

When it comes to structural components, NFRP currently do not represent an adequate alternative to GFRP. This is due in particular to the fact that the potential of the fibres is not being fully exploited. One major reason for this are the fluctuations in the mechanical properties of the fibres, due to different fibre types, growing areas and changing climatic conditions over the years. This makes it very difficult to predict the achievable properties of the composite material. Another reason is the induced twist during the spinning when using natural fibre yarns, which negatively influences the fibre orientation, the impregnation behaviour of the reinforcement fabrics, the realisable fibre volume contents and thus reduces the mechanical properties of the composites [4,5]. Given the growing awareness of global warming and the related societal demand for sustainability, the need to address these issues has never been more important. After all, NFRP can be produced consuming up to 50 % less energy and emitting significantly less CO_2 compared to GFRP [6]. At the Institut für Textiltechnik (ITA) of RWTH Aachen University, ongoing research addresses the two deficits stated above.

2. Predicting the mechanical properties of NFRP

Currently, the mechanical properties of components made of NFRP are usually determined by means of complex destructive testing. Based on the results, the component design is iteratively adapted to the requirements. This procedure is a major hurdle for the usage of NFRP in series applications. One approach to solve this problem is to develop a model which allows for the prediction of the composite properties. This approach is being investigated within the IGF-project 21240 N “NaturePerformance” using the example of a thermoplastic NFRP, which is produced by means of thermoforming from a carded hybrid nonwoven.

2.1 Modelling approach

There are already different approaches, that allow for the calculation of the mechanical properties of NFRP (see Table 2). However, none of these methods is suitable for predicting the properties of nonwoven-based NFRP.

Table 2: Models for the calculation of the mechanical properties of NFRP

Model	Output
Mixing rule of Cox et al. [7,8]	Theoretical tensile strength and E-modulus of a unidirectional fibre-reinforced composite material
Equation of Moser [9]	E-modulus of a composite material made of NF with random fibre orientation and thermoplastic matrix
Model of Venkateshwaren [10]	Mechanical properties of natural fibre-reinforced thermosets
Halpin-Tsai-Equation [11]	Variation of the mixing rule of Cox et al. on the basis of empirical data
Shear-Lag-Theory [12]	Consideration of the fibre length and thus the shear forces, extension possible by using orientation factor

  doi:10.5075/epfl-298799_978-2-9701614-0-0

From these approaches, the Shear-Lag-Theory is currently the most promising one. However, under certain conditions, a highly modified Cox-Krenchel model can be used to calculate the tensile strength and E-modulus of NFRP. The equation used within the Cox-Krenchel method is:

$$E_C = \eta_0 \cdot \eta_{LE} \cdot V_f \cdot E_f + (1 - V_f) \cdot E_m \quad (1)$$

E_C = Modulus of elasticity of the composite material in fibre direction [GPa]
η_0 = Orientation factor according to Krenchel [-]
η_{LE} = Fibre length efficiency factor
V_f = Fibre volume fraction [%]
E_f = Modulus of elasticity of the fibres in longitudinal direction [GPa]
E_m = Modulus of elasticity of the matrix [GPa]

Eq. (1) takes into account the length of the individual fibres in addition to the modulus of elasticity. This also includes the effective transmission of shear forces in the component (Shear-Lag-Theory). In addition, Krenchel gives an extension of the Shear-Lag-Theory with which the fibre orientation can be included in the calculation. The equation can also be used to calculate the (tensile) strength of a component by replacing the elastic moduli with the (tensile) strengths. To use the model for nonwoven materials, it is necessary to further modify the equation, which is part of the ongoing research. In addition to the adaptation of the model, the determination of the necessary material properties is of particular interest.

2.2 Measurement of the fibre properties

Due to the inconsistent properties of the natural fibres, each fibre batch differs from another. To get accurate results from the predictive models, it is necessary to characterise the fibre properties from each batch that will be used in the production of NFRP. Some fibre properties strongly influence the properties of the produced textile and later composite, like e.g. the fibre length. While this property can be measured quite easily, determining other factors, such as the tensile strength, is costly and time-consuming. For industrial applications, faster measuring systems to determine the needed fibre properties are required. Within the current project, alternative testing methods and property correlations are therefore investigated. For instance, it is being investigated to what extent the colour and thickness of fibres can be used to derive information about the fibre strength.

3. Improving the mechanical properties of NFRP

Recent research has shown that NFRP can be produced with comparable specific stiffness to GFRP when achieving a very high fibre orientation and a good fibre-matrix adhesion. For most of the investigations, low twist or twist-free yarns were used. However, the processing of such yarns is limited in terms of the textile processes in which they can be used. [5,13] This is particularly critical when producing multiaxial non-crimp fabrics (NCF) on conventional warp knitting machines, as high yarn tension occurs during the weft insertion, which twist-free yarns can hardly withstand. As a result, the yarns necessarily need to be twisted, which has the following disadvantages:

  doi:10.5075/epfl-298799_978-2-9701614-0-0

- The twisting of the yarns leads to fibre undulation, resulting in lower mechanical properties within the composite [5].
- With increasing yarn twist, the fibre bundles are further compressed, leading to a reduction in impregnability and thus to a reduced fibre-matrix adhesion [5].
- The yarn production accounts for about 30 % of the process costs in NFRP production. [13,14]

These disadvantages were addressed in the IGF project 19400 N "HyPer-NFK". The solution approach was based on a machine modification enabling the processing of twist-free flax slivers during the production of NCF.

3.1 Production of non-crimp fabrics from twist-free flax slivers

In order to process flax slivers, a novel feeding and weft insertion device was developed and integrated into a warp knitting machine Copcentra Max 3 CNC from KARL MAYER Technische Textilien GmbH, Chemnitz (Germany) at ITA (see Figure 1). Measurements with a TS44/A1000E tensile force sensor from BTSR International, Olgiate Olona (Italy), showed that a tensile force of approx. 1.7 N has to be withstood in the feeding area of the machine up to the weft carrier system in order to prevent the slivers from slipping and tearing. Within the carrier system, the tensile force to be withstood is approx. 6.3 N. No significant dependence between yarn tension and production speed were found.

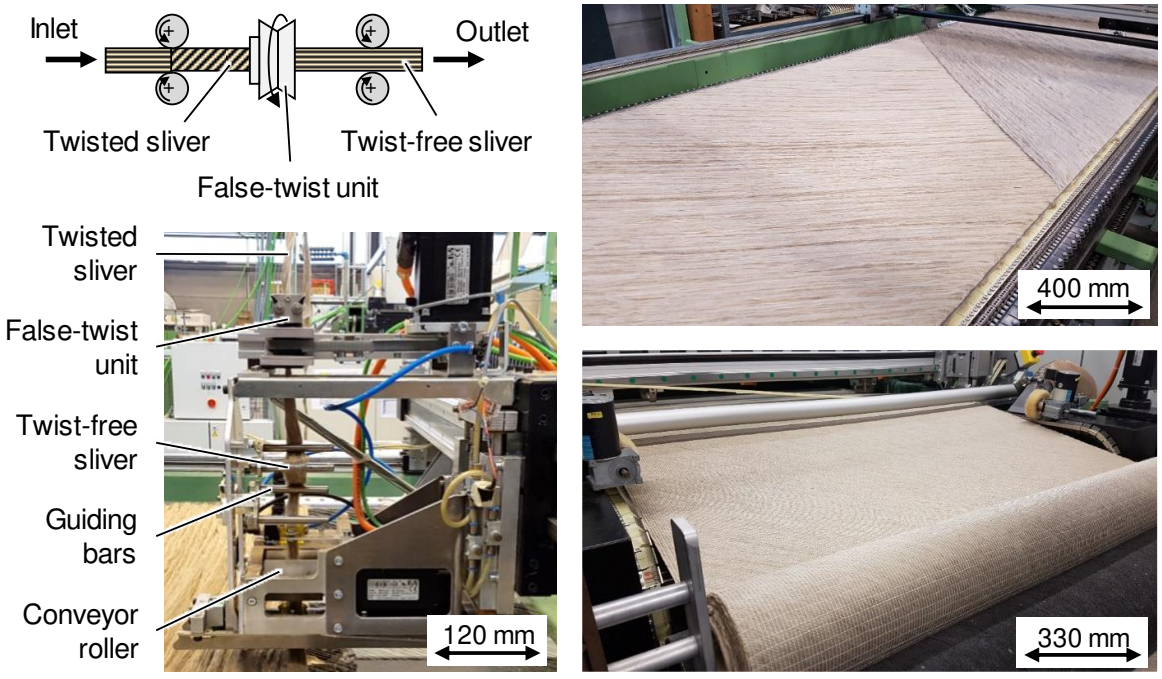

Figure 1. Modified weft carrier system of a warp knitting machine with false-twist device

The necessary cohesion of the slivers up to the weft carrier system is ensured using the false twist principle, commonly used for the texturing of yarns. The slivers are thus temporarily twisted in particularly critical sections of the feeding line. Flax slivers from SAFILIN, Sailly-sur-la-Lys (France) with a fineness of 5 ktex were used as raw material for the investigations. Applying a temporary twist of 10 turns per meter has been found suitable to transport the slivers. The inserted twist is released after passing through the false twist device within the carrier system.

Subsequently, the slivers are transported by a driven conveyor roller, which enables the tension-free deposition of the material. The new system allows for the production of flax NCF with a very higher fibre orientation and homogeneity of fibre distribution compared to yarn-based fabrics (see Figure 2).

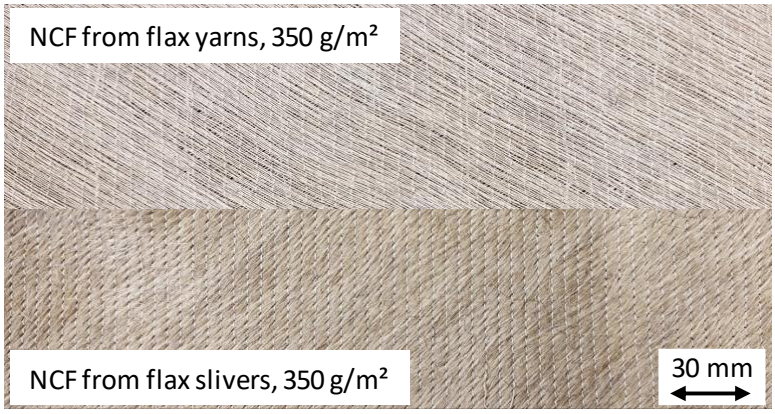

Figure 2. Comparison of NCF produced from flax yarns (top) and flax slivers (bottom)

Using the modified technology, a 1.27 m wide flax NCF with a fibre orientation of ±45° and an areal weight of approx. 350 g/m² was produced at a productivity of 25 m/h. The calculated production costs are approx. 20 % lower at 12.9 €/kg compared to the use of flax yarns. The produced NCF was subsequently vacuum infused with RIM-R134 epoxy resin and RIM-H-1366 hardener from Hexion Inc, Columbus, Ohio (USA) to form composite panels, from which coupon test specimens were taken to determine the resulting mechanical properties.

3.2 Resulting mechanical properties

Due to the higher fibre orientation and homogeneity of the novel flax NCF, the tensile properties of the resulting composite were increased by approx. 10 % compared to yarn-based products. Thus, a comparable specific tensile modulus to GFRP with a conventional glass fibre NCF reinforcement was achieved (see Figure 3).

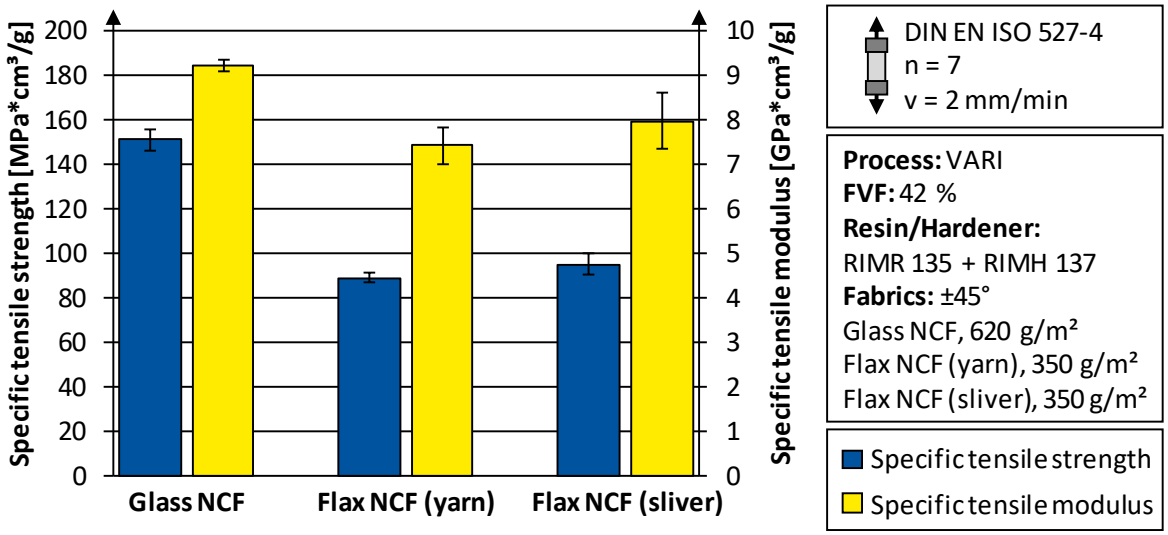

Figure 3. Specific tensile properties of composites made of glass and flax ±45° NCF

  doi:10.5075/epfl-298799_978-2-9701614-0-0

Conclusions

Within the ongoing IGF-project 21240 N “NaturePerformance”, models for calculating and predicting the properties of NFRP and methods for determining the necessary material properties are being investigated at ITA. It has already been shown that the properties of NFRP can be calculated to a certain extent, while the measurement effort remains manageable. With further research and the use of larger material databases, accurate predictions should be possible. Currently, the generated data is only suitable for nonwoven-based composites and components. Further research is needed to adapt the prediction models for other textile structures.

Within the IGF-projects 19400 N “HyPer-NFK”, the technical feasibility of the false-twist principle for conveying flax slivers in the production of NCF has been successfully demonstrated. Based on the new technology, new types of flax NCF were produced and qualified. The manufacturing costs for the fabrics could be reduced by approx. 20 % compared to yarn-based products. The mechanical properties of the composites produced using the novel fabrics could be increased by approx. 10 %. The combination of both effects could open up the potential for the use of natural fibres in load-bearing structures for series applications.

Acknowledgements

The IGF-projects 19400 N “HyPer-NFK” and 21240 N “NaturePerformance” of the Forschungskuratorium Textil e.V., Reinhardtstraße 14-16, 10117 Berlin were/are supported through the German Federation of Industrial Research Associations (AiF) as part of the programme for promoting the Industrial Collective Research (IGF) of the German Federal Ministry of Economic Affairs and Climate Action (BMWK) on the basis of a decision by the German Bundestag.

4. References

1. JEC Group. JEC Observer - Current trends in the global composites industry 2021-2026. Paris. JEC Group. 2022.
2. Bonten C. Kunststofftechnik: Einführung und Grundlagen. 2nd edition. Munich. Hanser. 2020.
3. Pickering K, Aruan Efendy M; Le T. A review of recent developments in natural fibre composites and their mechanical performance. Composites Part A: Applied Science and Manufacturing 2016. 83:98-112.
4. Verpoest I. The potential of natural fibres for composites: the case of flax fibres. 19th European Conference on Composite Materials (ECCM19). Nantes. 22.-26.06.2020. Online short-course for PhDs.
5. Goutianos S, Peijs T, Nystrom B, Skrifvars M. Development of Flax Fibre based Textile Reinforcements for Composite Applications. Applied Composite Materials 2006. 13(4):199-215.
6. nova-Institut Gmbh. Natural fibres show outstandingly low CO2 footprint compared to glass and mineral fibres - nova-Institute updates its reference study for the automotive and insulation industry. Hürth. nova-Institut GmbH. 2019.
7. Cox HL. The elasticity and strength of paper and other fibrous materials. British journal of applied physics 1952. 3(3):72-79.

  doi:10.5075/epfl-298799_978-2-9701614-0-0

8. Long AC. Design and manufacturing composites. Cambridge. Woodhead Publishing Limited. 2005.
9. Moser K. Faser-Kunststoff-Verbund: Entwurfs- und Berechnungsgrundlagen. Springer-Verlag. 1992.
10. Venkateshwaran N, Elayaperumal A, Sathiya GK. Prediction of tensile properties of hybrid-natural fiber composites. Composites Part B: Engineering 2012. 43(2):793-796.
11. Halpin JC, Kardos JL. The Halpin-Tsai Equations: A Review. Polymer Engineering and Science 1976. 16(5):344-352.
12. Krenchel H. Fibre Reinforcement. Copenhagen. Akademisk Forlag. 1964.
13. Shah DU, Schubel PJ, Clofford MJ. Can flax replace E-glass in structural composites? A small wind turbine blade case study. Composites Part B: Engineering 2013. 52:172-181.
14. International Textile Manufacturers Federation (ITMF). International Production Cost Comparison 2012. Zurich. ITMF. 2012.

  doi:10.5075/epfl-298799_978-2-9701614-0-0

CHARACTERIZATION OF INTERLOCK 3D PERMEABILITY TENSOR FOR C-RTM PROCESS

Gabriela, GAMBARINI[a,c], Boris, DUCHAMP[a],´Jérôme

OLHAGARAY[b], Marc, WARIS[b], Christophe, BINETRUY[c],

Sebastien,COMAS-CARDONA[c]

gabriela.gambarini@irt-m2p.fr
a: IRT M2P - 4 rue Augustin Fresnel, 57070 Metz
b: Safran Composites - 33, avenue de la Gare 91760 Itteville – France
c: Nantes Univesité, Ecole Centrale Nantes, CNRS, GeM, UMR 6183, F_44000 Nantes, France

Abstract: *The permeability characterization of the interlocks is crucial for the impregnation quality and its simulation. In this work, a continuous 3D permeability measurement technique [3] is used to measure the permeability evolution during compression of a saturated layer-to-layer interlock fabric. The in-plane and transverse permeability can be extracted for a range of fiber volume fraction which serves as support for simulation of applications such as C-RTM. The occurrence of flow-induced in-plane deformation and its effects on the fabric's apparent permeability is also investigated.*

Keywords: 3D weave; Permeability measurement; In-plane deformation; Interlock

1. Introduction

The interest of using 3D fibrous reinforcements for industrial applications have increased over the years. For example, they are considered for the manufacture of aircraft engine fan-blades. In comparison to 2D woven materials, 3D weaving provides more out of plane stiffness and prevents delamination. There is no need of ply stacking because the 3D weave already contains multiple ply, decreasing manufacture time. Therefore, the permeability characterization of those fabrics becomes of great interest to support the manufacture process.

Due to its elevated thickness and internal structure, several tens of bar are needed to compress the 3D weave to the desired fiber volume fraction (50% of its initial thickness) making necessary the use of specific equipment suitable for such pressure. This makes the permeability measurement challenging since the structure changes considerably from uncompressed to final state.

It is important to develop a reliable technique to measure the permeability evolution of the 3D fabric when it is under a large amount of pressure. In this work we will present a methodology to measure both in-plane and transverse permeability continuously and what happens to the structure when the viscous drag becomes higher than the friction forces between tows.

  doi:10.5075/epfl-298799_978-2-9701614-0-0

2. Materials and samples

2.1 Fabrics

The fabric used for both the saturated compression and injection methods is a carbon layer-to-layer interlock provided by Safran Composites. Details of the used tows can be seen on Table 1

Table 1: Interlock fabric information.

Warp density (thread/cm)	2.36
Weft density (thread/cm)	2.61
RCT(no. of warpwise tows in the repeating unit cell)	64.4/35.6
Warp tow	48K IM7
Weft tow	24K IM7
Number of layers	16

A 2D glass woven fabric (twill-weave, 600 g/m2 from CHOMARAT) is also studied [5] and used as comparative.

2.1 Fluids

Silicone oil

The model fluid for the continuous saturated compression is silicone oil sold by Carl Roth. The chosen silicone viscosities can be seen in Table 2:

Table 2: Silicone oil characteristics

	Density (g/cm³)	Viscosity range (Pa.s)	Melting point (°C)
M 100	0.97	0.095-0.105	-55
M 500	0.97	0.475-0.525	-47
M 1000	0.98	0.95-1.05	-50
M 5000	0.98	4.75-5.25	-50
M 10000	0.98	9.5-11	-50

Glycerol

The radial injection was made using a mixture of Glycerol and fluorescent pigment (Fluo Yellow 502 by Sennelier). The pigment concentration was 1.5% and later water was added to decrease the fluid viscosity in the proportions seen in Table 3:

  doi:10.5075/epfl-298799_978-2-9701614-0-0

Table 3: Glycerol + pigment (1.5%) water concentration.

Water %	Viscosity (Pa.s) @20 ° C
0.82	1.3
2.6	0.63
3.2	0.57

Sample conditioning for saturated components

It was observed that the saturated compression method is sensitive to the degree of saturation in a sample therefore, it is important to ensure a good fluid impregnation. Considering the specifics of the fabric (dense tows and an open geometry) some care needs to be taken to guarantee this proper saturation of the fabric. The samples are immersed in a container filled with fluid then they are degassed overnight in a vacuum chamber to expel air bubbles. The container is used to transport the sample and the fluid until it is time to be compressed, making sure the sample is always submerged. The sample and the fluid are then transferred to the receptacle where it is compressed using the universal testing machine.

2.2 Permeability measurement

Various methods to measure a 2D fabrics permeability have been published over the years as described by Sharma et al. [1]. When considering 3D woven fabrics and their complex internal structure work has been made investigating its mechanical properties as seen on Tan et al. [4]. However, regarding the permeability of 3D woven fabrics few papers have been published. The work of Umer et al. [2] measures the unsaturated in-plane radial and saturated through-thickness permeability data were obtained at several fiber volume fractions of an orthogonal, angle and layer-to-layer interlock.

2.2.1 Unidirectional compression

The principle of this method consists in compressing saturated fabric and extracting the in-plane and transverse fluid pressure to then calculate the permeability evolution during compression. For detailed description of the method, reference the work of Comas-Cadorna et al. [3].

The compression response of a saturated fabric is higher than of a dry or just lubricated fabric (Fig.1). For tests carried out on impregnated fabrics, the total compaction stress, σ_{zz} under Terzaghi hypothesis is written as:

$$\sigma_{zz} = \sigma_{zz}^{O} + p \quad (1)$$

Where σ_{zz}^{O} is the effective stress of the lubricated preform (fibers) and p the hydrostatic pressure generated by the fluid.

  doi:10.5075/epfl-298799_978-2-9701614-0-0

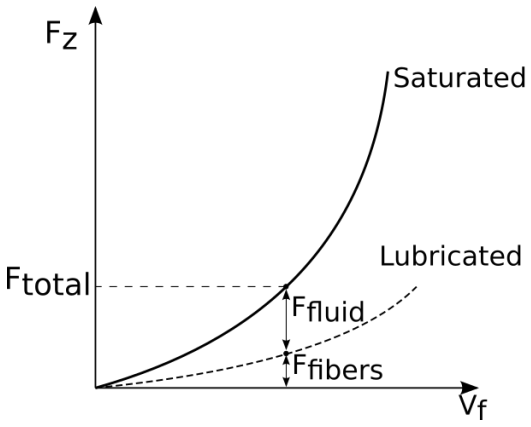

Figure 1 - Compression of a saturated and lubricated fabric

To determine σ_{zz}^{O} the compression force of a lubricated fabric is measured then divided by the compression platen area *S*. To generate the lubricated force ($F_z^{lubricated}$) the fabric is impregnated with a very low viscosity fluid (μ = 0.01 Pa.s) then compressed using a lower perforated platen (Fig. 2a) to minimize any fluid flow.

To measure the total force ($F_z^{Saturated}$) ,the fabric is impregnated with a high viscosity fluid and is compressed fully immersed in liquid as seen in Figure 2b, creating an in plane flow. The total stress σ_{zz} is then calculated as previously mentioned in Eq.1.

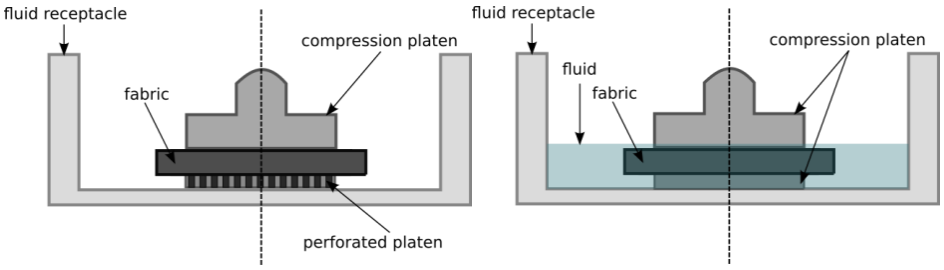

Figure 2 - Experimental setup for impregnated fiber reinforcement compression tests that generate through-thickness (a) and in-plane (b) fluid flow

The equivalent in plane permeability K_e is then calculated using Eq.2:

$$K_e(h) = \frac{\mu \dot{h} \pi R^4}{8h\left(F_z^{Saturated} - F_z^{lubricated}\right)} \quad (2)$$

Where R is the platen's radius h is the fabric's thickness, μ the fluid viscosity and $\dot{h}$ the compression speed.

  doi:10.5075/epfl-298799_978-2-9701614-0-0

3.2 Results

3.2.1 Permeability Measurements

We can see in Fig.3 the equivalent permeability K_e measured on the interval 45% < V_f < 60 %. During the transverse compression, the space between the fibers decrease and so does the permeability. The results from both methods (saturated compression and radial injection) are in good agreement, with the radial injection showing a slight higher permeability.

Differently from the saturation compression method, the radial injection was done once the fabric was already compressed to its desired V_f (50%, 55% and 60%) so the fabric is static and relaxed when the injection starts. The material's more relaxed configuration manifests in a higher K_e.

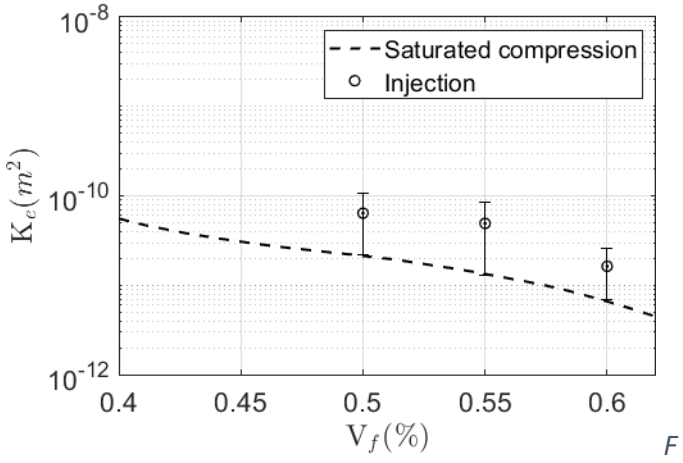

Figure 3 - Equivalent permeability K_e comparison between saturated compression (μ = 0.5 Pa.s $\dot{h}$ = 6 mm/min) and central injection.

3.2.2 In-plane deformation

The permeability is calculated considering that the structure only deforms transversely while compressed and that no deformation occurs in plane. As shown by the work of Hautefeuille et al. [5] if the viscosity of the resin and the mold closing speed are too high, the viscous-drag forces become higher than the friction between tows and it causes an in-plane washout (tow motion).

When comparing the theoretical fluid force calculated from Eq.3 and the experimental fluid force $\left(F_z^{Saturated} - F_z^{lubricated}\right)$ we can see that for higher fluid viscosity (μ=5 Pa.s and μ= 10 Pa.s) the responses do not match the theoretical baseline given by Darcy's law:

$$F_{fluid} = \int_0^R 2\pi P(r)\, dr = \frac{\mu \dot{h} \pi R^4}{8K_e(V_f)h} \quad (3)$$

  doi:10.5075/epfl-298799_978-2-9701614-0-0

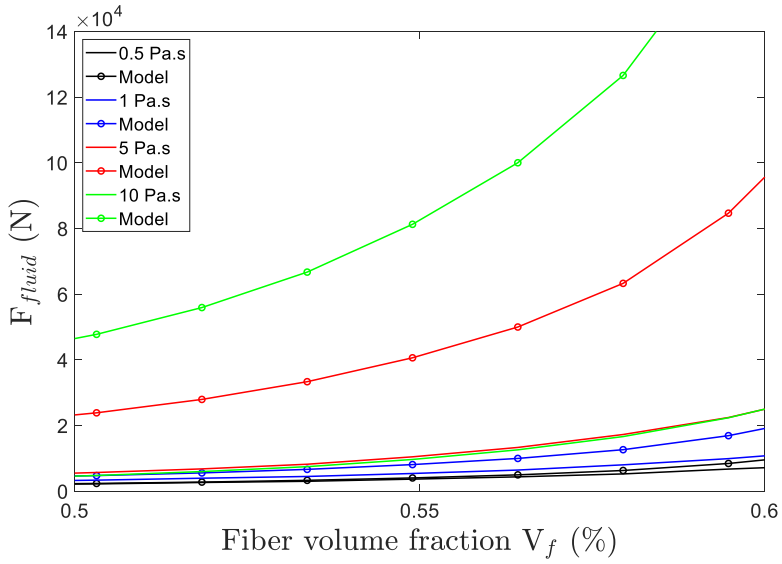

Figure 4 - Comparison between theoretical and experimental fluid force at $\dot{h}$= 6 mm/min

When the in-plane deformation occurs, the flow channels within the fiber reinforcement start to open to decrease the fabric's resistance to the flow. The apparent permeability becomes higher in comparison to its undeformed state. As seen in Figure 5, the viscosities μ= 5 Pa.s and μ = 10 Pa.s generate a permeability much higher than the reference (μ = 0.5 Pa.s) given by the Darcy's law for static fibrous bed.

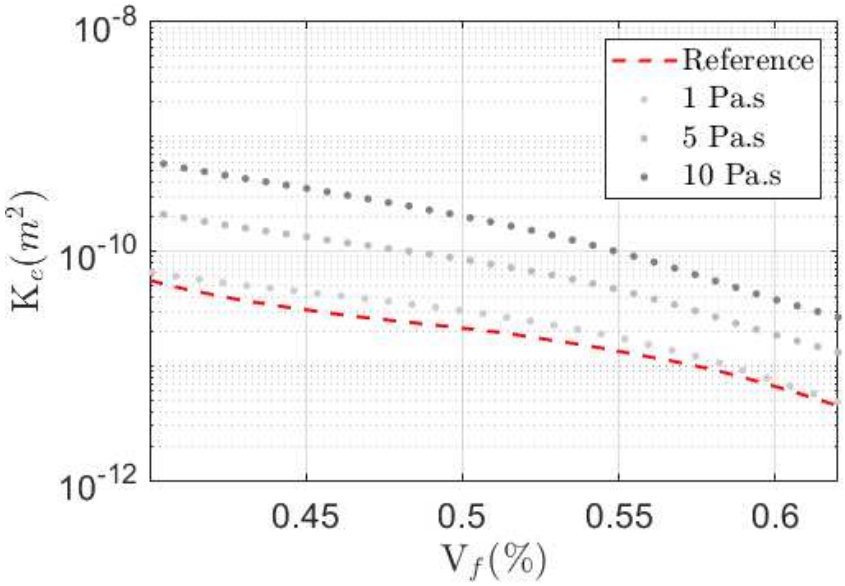

Figure 5 - In-plane permeability K_e calculated using Eq.2 with iso-speed of $\dot{h}$= 6 mm/min and chosen viscosities μ = 1 Pa.s, 5 Pa.s and 10 Pa.s

Hautefeuille et al. [5] worked on the experimental detection of flow-induced in-plane impregnation during compression of a woven fabric (twill weave, glass fiber, 600 g/m^2 from CHOMARAT).

  doi:10.5075/epfl-298799_978-2-9701614-0-0 published under CC BY-NC 4.0 license

He calculated the in-plane permeability $\boldsymbol{K_e}$ using Eq.2 for various fluid viscosities as seen in Figures 6 a and b.

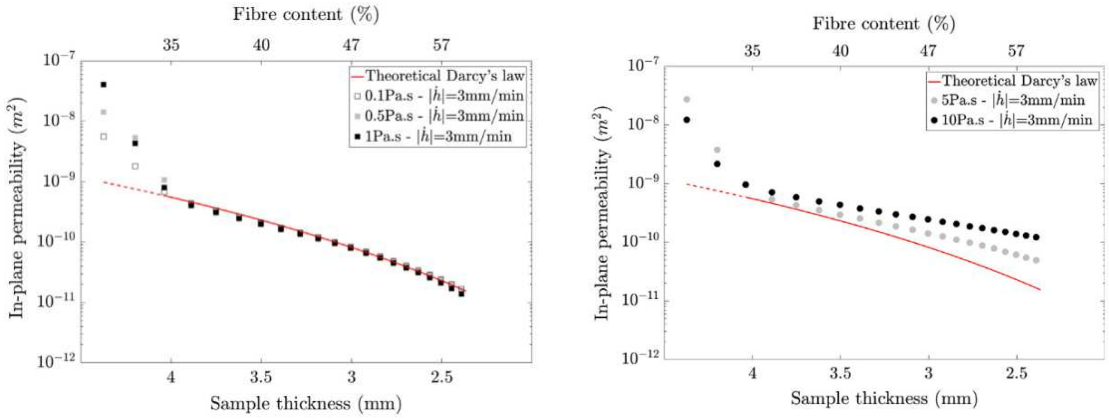

Figure 6 - In-plane permeability of the fibrous reinforcement with a μ= 0.1 Pa.s μ= 0.5 Pa.s, μ= 1 Pa.s and b) μ= 5 Pa.s and μ= 10 Pa.s [5]

Similar to what was observed with the interlock, higher fluid viscosities (Figure 6b) generate a higher apparent permeability. When comparing the compression behaviour between the twill weave (Figure 7a) and interlock (Figure 7b) as the fiber volume increases, the permeability of the twill weave distances more from the reference permeability (B-C). The lack of binding yarns lets the tows free to move and the permeability increases as the compression continues. On the other hand, the interlock has binding yarns that hold the tows to a determined position. We can see that at around V_f = 50% the curves tend to converge to a locked deformed configuration (E).

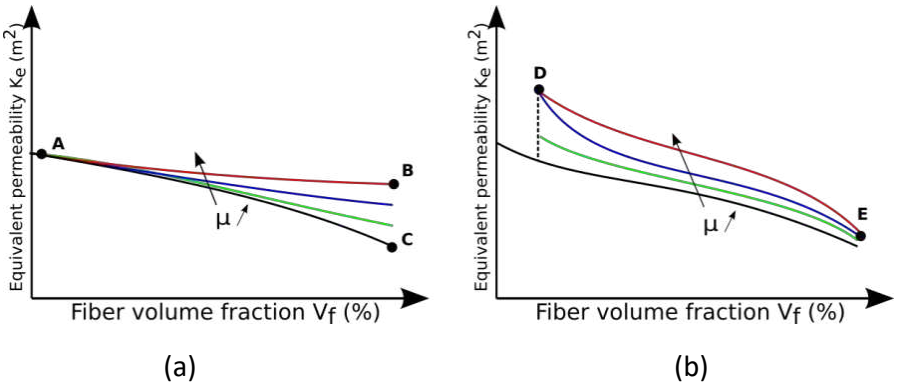

Figure 7 – In-plane deformation behavior of a 2D weave (a) and a 3D weave (b)

  doi:10.5075/epfl-298799_978-2-9701614-0-0

3. Conclusions

A methodology to measure the permeability of 3D fabric has been presented. The results show good agreement between the saturated compression and radial injection techniques. It is also possible to identify the flow-induced deformation when comparing the theoretical fluid force to the experimental one. The interlock structure and its binding yarns prevent the weft and warp tows to be moved after a certain point and it sustains the structure.

4. Acknowledgements

This work is being carried out within the framework of the national INCREASE project bringing together the partners IRT M2P, Safran Composites, ASMA, AXIOME, ESI, PEI and Civil and Mechanical Engineering Research Institute (GeM) of Nantes Université, Ecole Centrale Nantes. This project aims to develop innovative means and processes for the automated production of aeronautical components via C-RTM.

5. References

1. Sharma S, Siginer DA. Permeability measurement methods in porous media of fiber reinforced composites. Applied Mechanics Reviews. 2010 ;63(2).
2. Alhussein H, Umer R, Rao S, Swery E, Bickerton S, Cantwell WJ. Characterization of 3D woven reinforcements for liquid composite molding processes. Journal of materials science. 2016 ;51(6):3277-88
3. Comas-Cardona S, Le Grognec P, Binetruy C, Krawczak P. Unidirectional compression of fibre reinforcements. Part 1: A non-linear elastic-plastic behaviour. Composites science and technology. 2007 ;67(3-4):507-14.
4. Tan P, Tong L, Steven GP. Behavior of 3D orthogonal woven CFRP composites. Part II. FEA and analytical modeling approaches. Composites Part A: applied science and manufacturing. 2000;31(3):273-81.
5. Hautefeuille A, Comas-Cardona S, Binetruy C. Mechanical signature and full-field measurement of flow-induced large in-plane deformation of fibrous reinforcements in composite processing. Composites Part A: Applied Science and Manufacturing. 2019;118:213-22.

  doi:10.5075/epfl-298799_978-2-9701614-0-0

Automated G-Code to FE Mesh conversion – Modelling polymer penetration into a textile to generate a polymer-textile composite made by additive manufacturing

Ann-Malin Schmidt, Yordan Kyosev

TU Dresden, ITM, Chair of Development and Assembly of Textile Products –
ann-malin.schmidt@tu-dresden.de

Abstract: *Fused Deposition modelling creates 3D geometries in various shapes. Using FDM, it is possible not only to print on even surfaces; it is possible to print onto uneven substrates like textiles. The work at hand investigates the penetration of polymer into textiles. Whereby, the resulting geometry of the polymer within and on top of the textile is studied. The textile (woven textiles) is modelled at meso-scale (yarn-level). The G-code for the FDM machine is parsed, analysed and converted by means of a self-implemented Python algorithm. The trajectory of the nozzle is used to calculate and, subsequently, simulate the areas where the polymer gets in contact with the textile. The shape of the resulting polymer structure is meshed and can be utilized for analysis of the penetration behaviour of the polymer into the textile.*

Keywords: FEM mesh; textile-polymer composite; automatic generator; G-code analyser; 3D printing

1. Introduction

The use of Fused Deposition Modelling (FDM) to produce 3D structures is becoming more popular year on year. Also printing polymer on textiles to create polymer-textile composite prototypes are gaining in popularity. Currently developed prototypes purposes are mainly to investigate use cases such as replacement of anatomical structures in humans, structurally reinforced textiles for orthopaedic treatments and similar applications [1].

During the FDM process, melted polymer is stacked in thin layers one on top of the other in a generative manner. Depending on the kind of the 3D printer, moving part(s) are nozzle and/or printing bed. Often, the printing bed has integrated heating to prevent a fast cooling, in turn, preventing unwanted deformations of the polymer structure [1]. A convenient side-effect of a heated printing bed is improved adhesion between polymer and textile [2]. Before starting a 3D print, a 3D geometry is created digitally and sliced. Slicing converts the 3D object into machine commands for the printer. These machine commands include the moving directions of the nozzle and/or printing bed, heating temperatures, fan speed, display commands and many other parameter and is called G-code [3].

Creating a polymer-textile composite, the substrate is a textile, and the polymer is placed on the textile in a layered manner. Printing on the uneven textile surface makes the 3D printing process much more challenging compared to printing on a smooth metal surface. The uneven and porous surface can lead to a penetration of the polymer into the textile. Whereby, the polymer enclosures the textile fibres partly or fully. The degree of penetration and enclosure differs because they are strongly depended on the printing parameters and textile structure and, furthermore, influence the adhesion between textile and polymer (Figure 1) [4, 5]. Other factors

  doi:10.5075/epfl-298799_978-2-9701614-0-0

influencing the adhesion are polymer viscosity and thus its temperature during the print process, extrusion rate, the nozzle speed, nozzle diameter, z-distance between textile and nozzle [4] and other parameter.

Modelling textiles can be done on the micro- (fibre based), meso- (yarn based) and macro- (textile based) level. The micro-level is the most detailed simulation scale, but comes with high computational costs. The marco-scale has the smallest degree of details resulting in lower computation costs. Therefore, choosing the scale level is always compromise between havening a detailed enough simulation model and reasonable calculation time. Different approaches are available for the modelling, for instance finite element methods (e.g. LS-Dyna, Ansys), multi physics approaches (e.g. python modules) and other techniques [6].

Currently, the simulation of 3D printed geometry's are rare, especially when it comes to printing on textiles. Research to investigate the mechanical properties of printed objects in FEM or the adhesion between printed layers has been done [7–9]. All these simulations do not involve the penetration of polymer into the textile. Therefore, models involving the adaption of the polymer on the textile surface of the polymer-textile composite are more realistic and help to better understand the influences on the adhesion between of a polymer-textile composite.

This paper aims to create a computational method to generate a polymer-textile composite model fast, whereby polymer penetration can be calculated based on a given G-code.

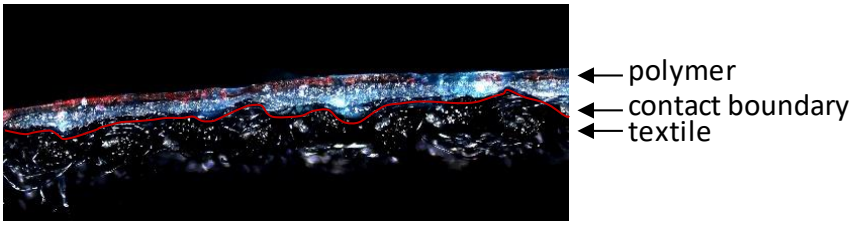

Figure 1 : Cross section of a polymer-textile composite

2. Methodology

The aim is to generate a mesh which represents the polymeric structure which results from the penetration of the polymer into the textile during the 3D print precisely. The method of creating a Finite Element mesh are the following steps. Firstly, the G-code of the printed geometry is analyzed. Because the G-code is a text file containing printing parameter and machine parameter, it can be read with almost any programming language which has libraries for it, in the current case python is chosen. A script is written to process the G-code and to extract the following printing parameter: nozzle path, nozzle velocity and extrusion rate. As a next step, the simulation environment ("world"), including boundary conditions, acting forces, damping etc. is set up. Part of this *world* are the textile and nozzle geometry. The WiseTex software is used to design the textile [10]. The nozzle geometry is created in Solidworks. Thirdly, the script to analyse G-code and components of the simulations environment are combined. Thus, the analysed nozzle path, -velocity and extrusion rate is transferred to the virtual environment. The nozzle path, nozzle velocity and extrusion rate can be adjusted within the script. Lastly, the resulting polymer shape is analysed and transferred as a finite element mesh.

  doi:10.5075/epfl-298799_978-2-9701614-0-0

3. Results

3.1. Automated analysis of G-code to extract printing parameters

The generated G-Code is parsed using python script and is filtered by relevant machine commands (Table 2, right). Lines starting with “G1” indicate information about the nozzle position, nozzle velocity and extrusion rate [11]. Other commands like M204 (Table 2, left) indicate a change in the nozzle acceleration or M73 is responsible for the display of the printing progress. The sections which are framed by “;WIPE_START” and “;WIPE_END” are irrelevant for the analysis, because those sections handle the cleaning of the nozzle. Subsequently, nothing is printed. Comments start with “;” are ignored. Only lines starting with “G1 Z”, “G1 X” and “G1 F” are kept for further processing (Table 2, right).

The relevant printing parameters for the simulation are the nozzle positions, nozzle velocities and extrusion rates. The nozzle path is stored in an array. An object of the array holds the x, y and z coordinates of one nozzle trajectory node, the nozzle velocity and the polymer extrusion rate at that trajectory node. “G1 Z” marks a positioning in z-direction. The command to change the z-coordinate occurs once per layer (Table 1, first row), because it stays the same for the following commands until the next layer begins. Therefore, that z-value is set for all trajectory nodes of that layer in the array. “G1 F” (Table 1, second row) describes the nozzle velocity for the movement to the following trajectory node. The velocity value remains constant for the following nodes until the next “G1 F” appears; hence, it is treated like the z-value. The G-code defines the nozzle velocity in $\frac{mm}{min}$. “G1 X” (Table 1, third row and following) sets the x- and y-coordinates and describes the nozzle trajectory. The extrusion rate is marked with an “E” and is placed after the fields for the x- and y- coordinates. It describes the amount of polymer, which is printed between two coordinate points (extrusion rate). The unit is mm. This information can be used to simulate the nozzle movement and extrusion rate.

Table 1 : Description of a G-code text file

G-code	**explaination**
G1 Z.65 F720	G1 Z: position z-axis
G1 F2700	F: velocity 2700 $\frac{mm}{min}$ = 45 $\frac{mm}{s}$
G1 X120.643 Y80.643 E1.25887 G1 X129.357 Y80.643 E.022706 G1 X129.357 Y129.357 E1.26929 G1 X120.643 Y129.357 E1.22706 G1 X120.643 Y129.357 E.00886 G1 X120.225 Y129.357 E10800	G1 X: position x-axis G1 Y: position y-axis E: extrusion volume between start and end point
G1 F1500	F: velocity 2700 $\frac{mm}{min}$ = 45 $\frac{mm}{s}$

  doi:10.5075/epfl-298799_978-2-9701614-0-0

Table 2 : Original and reduced G-code with machine commands

original G-code	**reduced G-code**
G1 X120.768 Y128.383 E.02448	G1 X120.768 Y128.383 E.02448
; stop printing object Streifen.STL id:0 copy 0 M106 S255 ;LAYER_CHANGE ;Z:0.65 ;HEIGHT:0.15 ;BEFORE_LAYER_CHANGE G92 E0.0 ;0.65 ;WIPE_START	
G1 F8640 G1 X121.429 Y129.044 E-.21584 G1 X122.023 Y129.044 E-.13712 G1 X120.956 Y127.977 E-.34837 G1 X120.956 Y127.723 E-.05866	G1 F8640 G1 X121.429 Y129.044 E-.21584 G1 X122.023 Y129.044 E-.13712 G1 X120.956 Y127.977 E-.34837 G1 X120.956 Y127.723 E-.05866
;WIPE_END G1 E-.04 F2100 G1 Z.9 F720 ;AFTER_LAYER_CHANGE ;0.65 ; printing object Streifen.STL id:0 copy 0	
G1 X120.643 Y128.957 F10800 G1 Z.65 F720 G1 E.8 F2100	G1 X120.643 Y128.957 F10800 G1 Z.65 F720 G1 E.8 F2100
M204 S800 ;TYPE:Perimeter ;WIDTH:0.45	
G1 F2700 G1 X120.643 Y80.643 E1.25887 G1 X129.357 Y80.643 E.22706 G1 X129.357 Y129.357 E1.26929 G1 X120.643 Y129.357 E.22706 G1 X120.643 Y129.017 E.00886	G1 F2700 G1 X120.643 Y80.643 E1.25887 G1 X129.357 Y80.643 E.22706 G1 X129.357 Y129.357 E1.26929 G1 X120.643 Y129.357 E.22706 G1 X120.643 Y129.017 E.00886
M204 S1000	
G1 X120.225 Y129.775 F10800	G1 X120.225 Y129.775 F10800
M204 S800 ;TYPE:External perimeter	
G1 F1500	G1 F1500

  doi:10.5075/epfl-298799_978-2-9701614-0-0

3.2. Setting up the simulation environment and simulating the printing process

The simulation environment is set-up with Python and the system is loosely based on a particle method. The meshes of the polymer, the nozzle and the textiles are loaded into the environment. An AABB algorithm is used to detect the contact between the meshes. Time iterations are performed using the Symplectic (semi-implicit) Euler Method. The environment offers the ability to import different kinds and shapes of textiles. The penetration of the polymer into the textile is strongly influenced by the type of textile. Using WiseTex, different textile shapes are created (Figure 2: (a) plain weave, (b) three-dimensional woven textile). The yarn parameter implemented in WiseTex represent a glass roving with 610 tex. The unit cell has a size of 6 x 6 x 0.5 mm^3 for a plain woven textile and 6 x 6 x 2 mm^3 for the three-dimensional textile. The nozzle of the 3D Printer has an opening with a diameter of 0.4 mm. The nozzle trajectory, nozzle velocity and extrusion rate can be regulated.

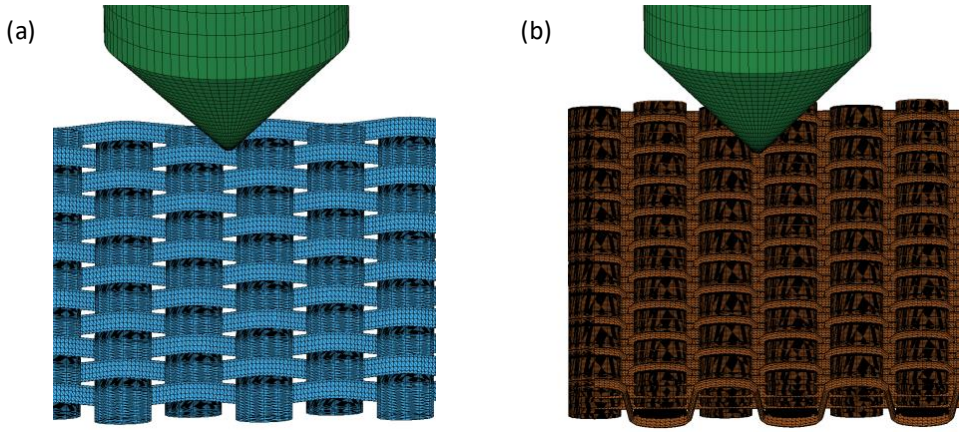

Figure 2 : Different textiles generated with WiseTex and imported in the simulation world,

3.3 Creating a finite element mesh of a penetrated polymer into a textile

After simulating the nozzle movement, the particles positions are used to reconstruct the resulting polymer 3D structure, which can be meshed and transferred into FEM software. In Figure 3 (a) the result of the simulated manufacturing of a polymer-textile-composite is shown from the nozzle view. Figure 3 (b) shows the polymer adapted shape to the textiles surface and structure in a sideview. Figure 3 (c) shows the polymers penetration through the textiles pore to the bottom of the textile from underneath.

  doi:10.5075/epfl-298799_978-2-9701614-0-0

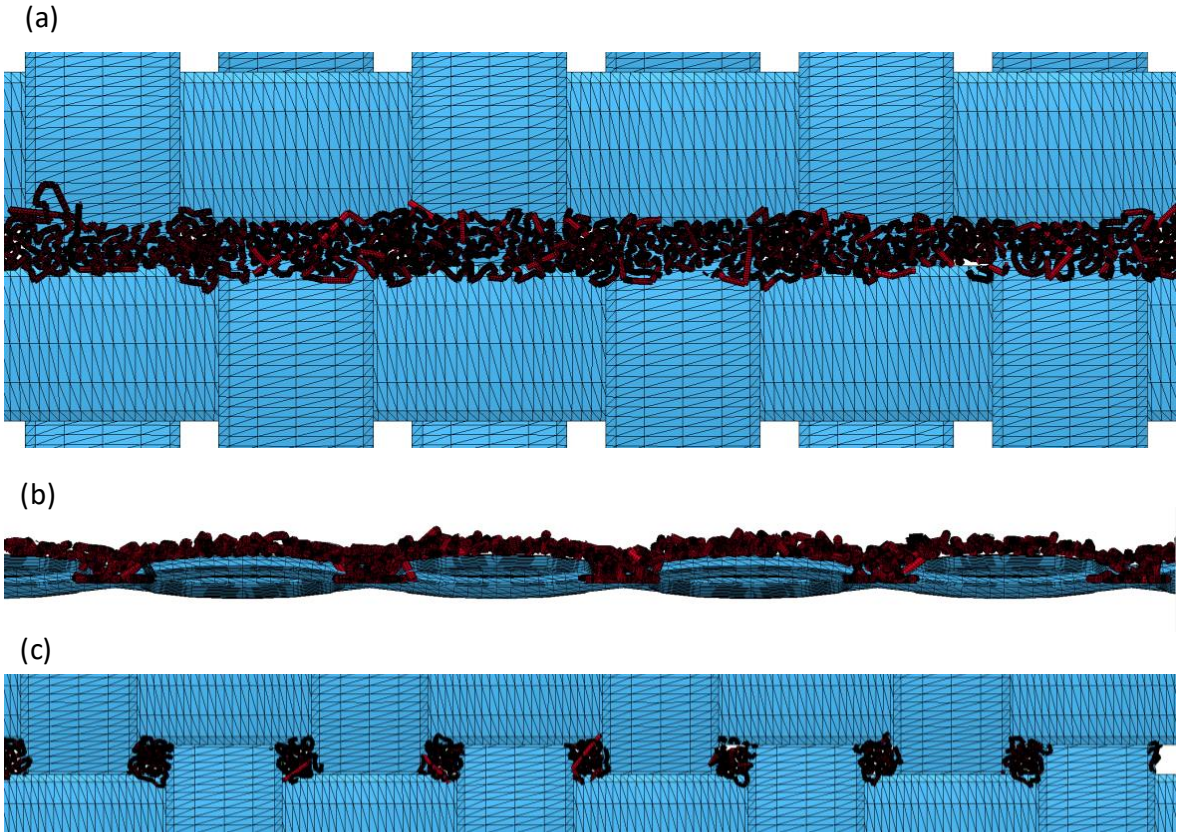

Figure 3: Meshed penetrated polymer and meshed textile (a) top view, (b) side view and (c) bottom view

4. Discussion

This work presents first step in the creation of a framework to remodel the penetration process of polymer into textile. The interactions of melted polymer with the yarn surface, their surface tensions, changing the state from melt to solid, temperature of the textile, of the air etc. are not considered at this point, but are part of upcoming steps in our research.

5. Conclusion

This work demonstrates first results of a virtual twin of the complete FDM process with textile as a printing substrate. The G-code is used to automatically generate the trajectory of the nozzle. Different types of textiles are generated using WiseTex and used as to be able to simulate the uneven textile substrate to print on, Polymer penetration and contact is modelled using particle methods. The adapted polymer is meshed as beams and a FEM model of a polymer-textile composite is generated. Although this work is based on simplifications, the first results provide already useful information to evaluate the FMD printing process on textiles.

  doi:10.5075/epfl-298799_978-2-9701614-0-0

5. References

1. Ahrendt D, Romero Karam A. Development of a computer-aided engineering–supported process for the manufacturing of customized orthopaedic devices by three-dimensional printing onto textile surfaces. Journal of Engineered Fibers and Fabrics. 2020;15:155892502091762. doi:10.1177/1558925020917627.
2. Eutionnat-Diffo PA, Chen Y, Guan J, Cayla A, Campagne C, Zeng X, Nierstrasz V. Stress, strain and deformation of poly-lactic acid filament deposited onto polyethylene terephthalate woven fabric through 3D printing process. Sci Rep. 2019;9:14333. doi:10.1038/s41598-019-50832-7.
3. Kishore R, Sivaraj S, Dhinakaran V, Padma Pravin Prabhagar V, Jawhar Srinivas S. Strength of 3D prints with variable print orientation. J. Phys.: Conf. Ser. 2021;2027:12021. doi:10.1088/1742-6596/2027/1/012021.
4. C Döpke, N Grimmelsmann, A Ehrmann. 3D printing on knitted fabrics.
5. Influence of Simple and Double-Weave Structures on the Adhesive Properties of 3D Printed Fabrics Enhanced Reader.
6. Weeger O, Sakhaei AH, Tan YY, Quek YH, Lee TL, Yeung S-K, et al. Nonlinear Multi-Scale Modelling, Simulation and Validation of 3D Knitted Textiles. Appl Compos Mater. 2018;25:797–810. doi:10.1007/s10443-018-9702-4.
7. Lalegani Dezaki M, Mohd Ariffin MKA. The Effects of Combined Infill Patterns on Mechanical Properties in FDM Process. Polymers (Basel) 2020. doi:10.3390/polym12122792.
8. Wolfs R, Bos FP, Salet T. Early age mechanical behaviour of 3D printed concrete: Numerical modelling and experimental testing. Cement and Concrete Research. 2018;106:103–16. doi:10.1016/j.cemconres.2018.02.001.
9. Stapleton SE, Kaufmann D, Krieger H, Schenk J, Gries T, Schmelzeisen D. Finite element modeling to predict the steady-state structural behavior of 4D textiles. Textile Research Journal. 2019;89:3484–98. doi:10.1177/0040517518811948.
10. Verpoest I, LOMOV S. Virtual textile composites software : Integration with micro-mechanical, permeability and structural analysis. Composites Science and Technology. 2005;65:2563–74. doi:10.1016/j.compscitech.2005.05.031.
11. Systems Management Council. INTERCHANGEABLE VARIABLE BLOCK DATA FORMAT FOR POSITIONING, CONTOURING, AND CONTOURING/POSITIONING, NUMERICALLY CONTROLLED MACHINES 2016. doi:10.4271/RS274D.

MICRO-CT-BASED NUMERICAL VALIDATION OF THE LOCAL PERMEABILITY MAP FOR THE B-PILLAR INFUSION SIMULATION

Oxana, Shishkina[a], Martine, Wevers[b], Stepan V., Lomov[b], Laszlo, Farkas[a]

a: Siemens Industry Software NV, Interleuvenlaan 68, 3001, Leuven, Belgium – oxana.shishkina@siemens.com
b: Department of Materials Engineering, KU Leuven, Kasteelpark Arenberg 44, 3001 Leuven, Belgium

Abstract: *Permeability of a fibrous reinforcement is an important input parameter for the simulation of the impregnation stage of the liquid composite molding process and its further optimization. In this work, an automatized workflow for the assessment of saturated permeability was developed as a part of Siemens Digital Industries Software solutions and its application was demonstrated on the case study of a composite B-pillar. X-Ray micro-computed tomography (micro-CT) was used to capture a realistic microstructure of the composite laminate in several locations of the B-pillar. The acquired images were segmented using VoxTex software developed by KU Leuven. Then, using the segmentation output, image-based models were generated in Simcenter 3D to predict homogenized local permeability. The obtained results showed a good agreement with the permeability map computed based on the draping simulations in Fibersim and verified against the experimental data of the flow front progression in the component infusion simulation in Simcenter STAR-CCM+.*

Keywords: Textile composites; X-ray computed tomography; Permeability; Finite element modeling

1. Introduction

Liquid composite molding (LCM) process is an often-used technique for manufacturing of polymer composite components, in which a dry fibrous reinforcement is impregnated with a liquid resin [1]. When the dry woven reinforcement is draped over a mold, local changes in its microstructure are introduced [2], e.g., fabric shear modifying the warp-weft angle, variations in the composite thickness etc. Such changes directly affect the fabric local permeability required for designing the impregnation process and its optimization, which nowadays can be performed virtually. For such simulations, *permeability* is an important input parameter which shows the ability of a resin to flow through a fibrous reinforcement when subjected to an external force (pressure) [3].

In this paper, the application of an automatized workflow is demonstrated for the assessment of saturated permeability developed in Simcenter 3D (Siemens Digital Industries Software) to numerically validate local permeability map required for the composite B-pillar infusion simulation.

2. Permeability calculation in Simcenter 3D

Simcenter 3D Materials Engineering is a module in the comprehensive, fully integrated Simcenter 3D simulation software [4], which aims aiding the engineers to virtually design and

  doi:10.5075/epfl-298799_978-2-9701614-0-0

test the performance of new materials as part of complex products, which drastically speeds up the design while lowering costs compared to a fully test-based approach [5]. In this work, an automatized workflow was developed for the assessment of the in-plane and out-of-plane components of the saturated permeability tensor. It was implemented as a part of the Materials Engineering module, thus, extending the capabilities towards the support of multiphysics simulations. The approach consists of two steps and can be orchestrated with the user interface (Fig. 1). The authors highlight that this workflow including, e.g., the boundary conditions (BCs) selection, modeling assumptions, was established based on numerous comparative studies and a careful choice between the model complexity and computational efficiency.

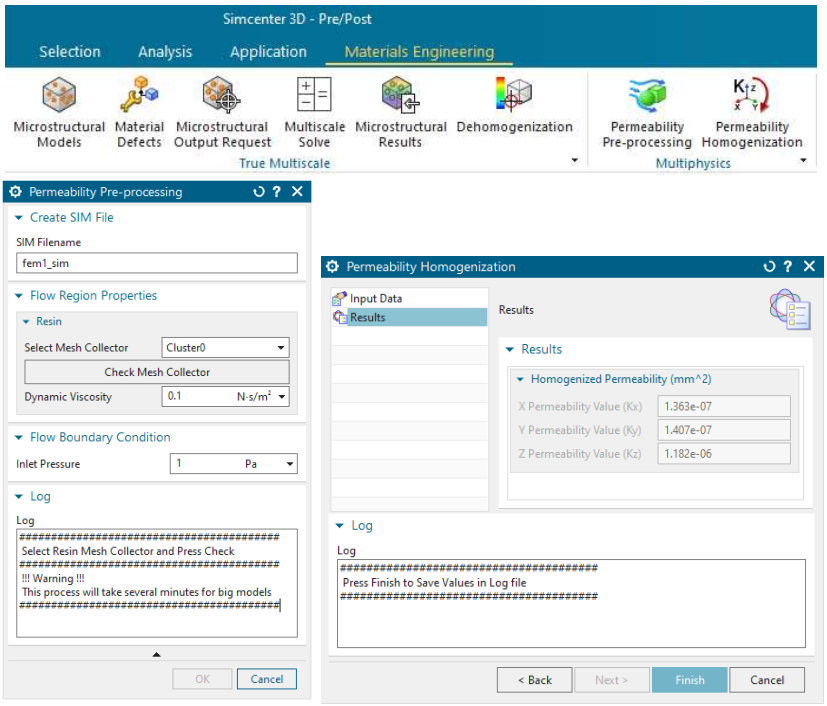

Figure 1. Simcenter 3D Materials Engineering: user interface of Permeability Pre-processing step and Homogenization step for the automatized computation of saturated permeability

2.1 Permeability Pre-processing

Permeability Pre-processing tool automatically sets up *three scenarios* for flow simulation through a unit cell (UC) of a composite reinforcement by defining a set of boundary and flow conditions in three orthogonal directions (Cartesian coordinates). The user input is restricted to the selection of the finite element (FE) mesh in which the flow will be simulated and to specifying the fluid (resin) dynamic viscosity and its pressure at the inlet (Fig. 1). Although permeability is the reinforcement property and should be independent of the dynamic viscosity and inlet pressure values [6], in virtual simulations they may affect the computed homogenized permeability [7] which is a numerical artefact. A high inlet pressure and/or a low viscosity increase Reynolds' number preventing the flow being laminar. To satisfy the laminar flow condition, 1 Pa and 0.1 Pa·s are the suggested default values (Fig. 1).

To gain computational efficiency, only the fluid (resin) mesh is considered in simulations (Fig. 2), thus, the model size is significantly reduced (by the number of elements in the reinforcement mesh). This assumption is valid for the microscale where fibers act as a solid blockage and are therefore neglected. The same assumption is also acceptable for the saturated permeability

  doi:10.5075/epfl-298799_978-2-9701614-0-0

computation on the mesoscale because the flow is dominated by channels between the yarns (the path of least resistance). Optionally, intra-yarn permeabilities can be activated in simulations, however, this will significantly increase computational time.

In three generated simulation scenarios, BCs are defined as follows (Fig. 2). The flow is driven by the pressure difference. For the outer side surfaces of the UC (not in the flow direction), slip wall condition is set which eliminates any surface drag calculations for the surface. For the fiber or yarn surfaces, no-slip wall condition (drag on a smooth wall) is defined. The flow solver computes the drag force by integrating the shear stress over the wall surface.

In the proposed workflow, Simcenter 3D Thermal/Flow solver solves Navier-Stokes equations with the FE-control-volume method to predict the fluid flow through a system of channels inside the reinforcement. As a result, the solver computes pressure and velocity fields which are used in the next step to compute the saturated permeability.

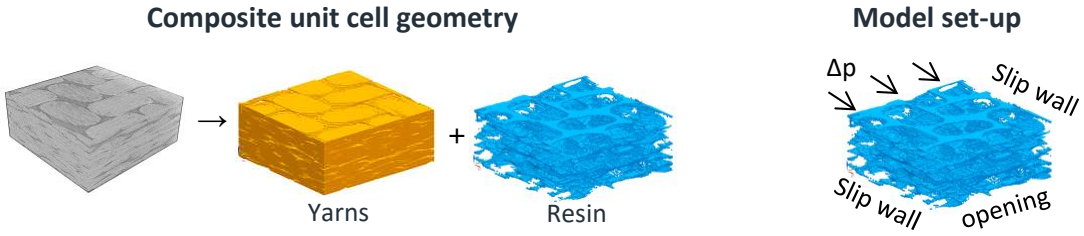

Figure 2. Example of a micro-CT image-based FE model of a woven composite and a model set-up for the saturated permeability computation in Simcenter 3D

2.2 Permeability Homogenization

Permeability Homogenization tool computes the homogenized saturated permeability of the reinforcement UC based on the results of three simulations. The permeability, K, is then calculated using Darcy's law (eq. 1) [8]:

$$K = -Q\eta L/(A\Delta p) \quad (1)$$

where Q – volume flow rate [mm^3/s] automatically extracted from the simulation results; η – fluid viscosity [Pa·s]; L – UC length [mm] in the flow direction; A – UC cross-sectional area [mm^2] which is perpendicular to the flow direction; Δp – pressure gradient [Pa] driving the flow. Δp is negative (the fluid flows from high pressure to low pressure), then the flow is positive.

3. Virtual permeability computation for the composite B-pillar

A composite B-pillar (an automotive application) was chosen as a case study for the developed workflow for saturated permeability. A schematic overview of the current study (blue boxes) and its position in the global case study (green/brown boxes) is presented in Fig. 3.

3.1 Brief description of the global case study

The composite B-pillar part was designed and manufactured in the past collaborative project by the partners Sirris, Com&Sens and Siemens Industry Software NV (see Acknowledgements). The objective was to perform, simulate and experimentally validate manufacturing of an automotive B-pillar with resin transfer molding process (RTM). Only the project key points relevant to the current study are here summarized. For more details, the reader is referred to [9].

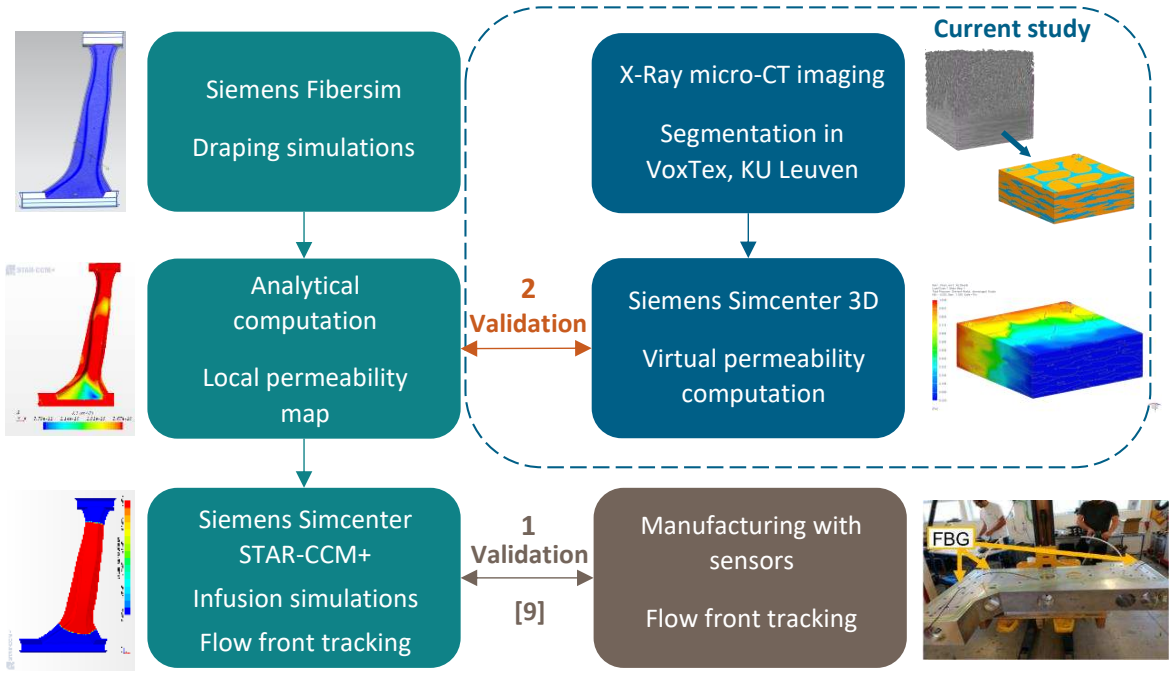

Figure 3. Schematic positioning of the presented study in the global case study context

Experimental part (brown box in Fig. 3)

The B-pillar was produced as a sandwich structure made of a foam core (Airex T92.100) glued to composite skins. Each composite skin was composed of five plies of the balanced woven carbon fiber fabric Chomarat C-WEAVE™ 285T 3K HS impregnated with the epoxy resin (Sicomin SR1710 with hardener SD8731) and had the layup of $(0°, 60°, -60°)_{S'}$ [2]. During the laying up of the dry woven fabric in the mold, optical fiber Bragg gratings (FBGs) were introduced into the layup for flow front tracking during the RTM process [2]. Thus, the experimental data for the validation of the infusion simulation was generated (Fig. 3, Validation 1 [9]).

Simulation part (green boxes in Fig. 3)

Draping of a dry woven fabric over a mold leads to local shearing (the warp-weft angle change) which directly affects the fabric permeability values and orientation of the flow front. The local fiber orientations needed in the infusion simulation were predicted in Fibersim (Siemens Digital Industries Software) [10] by the simulation of the reinforcement forming over the 3D CAD shape of the B-pillar (Fig. 4).

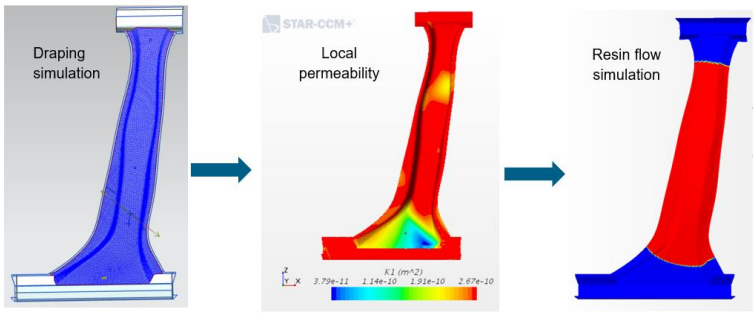

Figure 4. Simulation sequence: draping simulation; mapping of fiber orientations and computation of local permeability tensor, and resin flow simulation. Reproduced from [9]

During the next step, the Fibersim output (elements, warp and weft angles) was transformed into a local permeability map based on the analytical formulae of Demaria et al. [11] for the in-plane permeabilities of sheared fabrics. This local permeability map (Fig. 4) is our primary validation interest in the current study (Fig. 3, Validation 2).

During the final step, the permeability map was assigned to the B-pillar model in Simcenter STAR-CCM+ (Siemens Digital Industries Software) [12] as a porous viscous resistance tensor. The infusion simulation was solved by the finite volume solver and allowed to track the flow front progression (resin/air interface) with the volume of fluid approach (Fig. 4, the resin is shown in red). Fig. 5 illustrates a good agreement between the simulation and the experimental results (obtained via optical FBGs) of the flow front progression and supports the validity of the local permeability map.

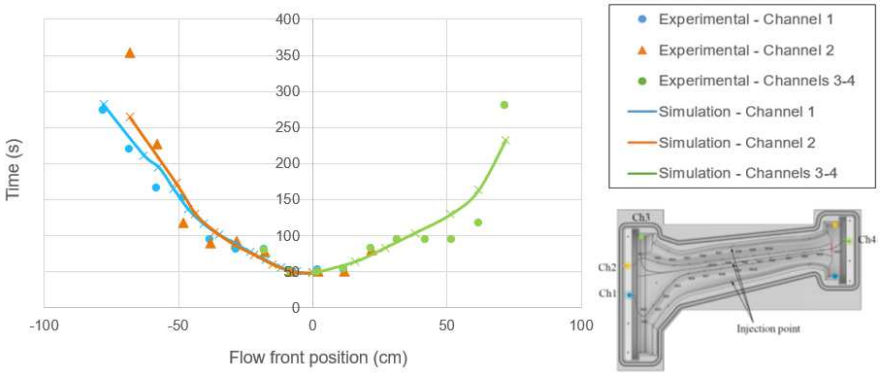

Figure 5. Time at which the flow front passes through each sensor location (symbols are experimental data; continuous lines are simulation results); on the right bottom corner, a scheme shows the sensor locations. Reproduced from [9]

3.2 Description of the current study

The objective of the current study (blue boxes in Fig. 3) was to perform numerical validation of the local permeability map (Fig. 4) by means of micro-CT image-based modeling.

From the draping simulation in Fibersim [10], zones of minimal (no shear) and maximal fabric shear were identified on the B-pillar. Their locations are illustrated in Fig. 6 (step 1) in green and red color respectively (the 60°-ply is depicted). Several specimens were cut from zones 1 (min shear) and 2 (max shear) such that they contained at least one UC of the fabric in every ply. The specimens were scanned with the resolution of 3.75 µm using GE Nanotom X-Ray CT-system at the X-ray CT center of KU Leuven. A 3D image of a specimen is shown in Fig. 6 (step 2).

The image acquisition was followed by their segmentation into material components, i.e., the yarn and resin regions (Fig. 6 step 3). For that purpose, a micro-CT data analysis software VoxTex developed by KU Leuven [13, 14] was used. From the scan, only the composite skin was considered, the foam core was neglected (Fig. 6 step 2). The image stacks were split into cubic sub-volumes ("voxels") with the edge of ~ 18-19 µm, inside which averaging was performed to decrease the noise coming from individual pixels. This also helped to reduce the resulting FE model size from a billion to several million of elements (one voxel = one finite element). The voxel classification in the yarns and resin clusters was completed by two feature variables approach based on the average grey value (density) and structural anisotropy. At the last step, voxel FE models of the specimens were generated in Simcenter 3D Materials Engineering using

a dedicated tool supporting direct import of VoxTex segmentation results [15]. The voxel models were seamlessly connected to the virtual permeability assessment workflow described in Section 2.

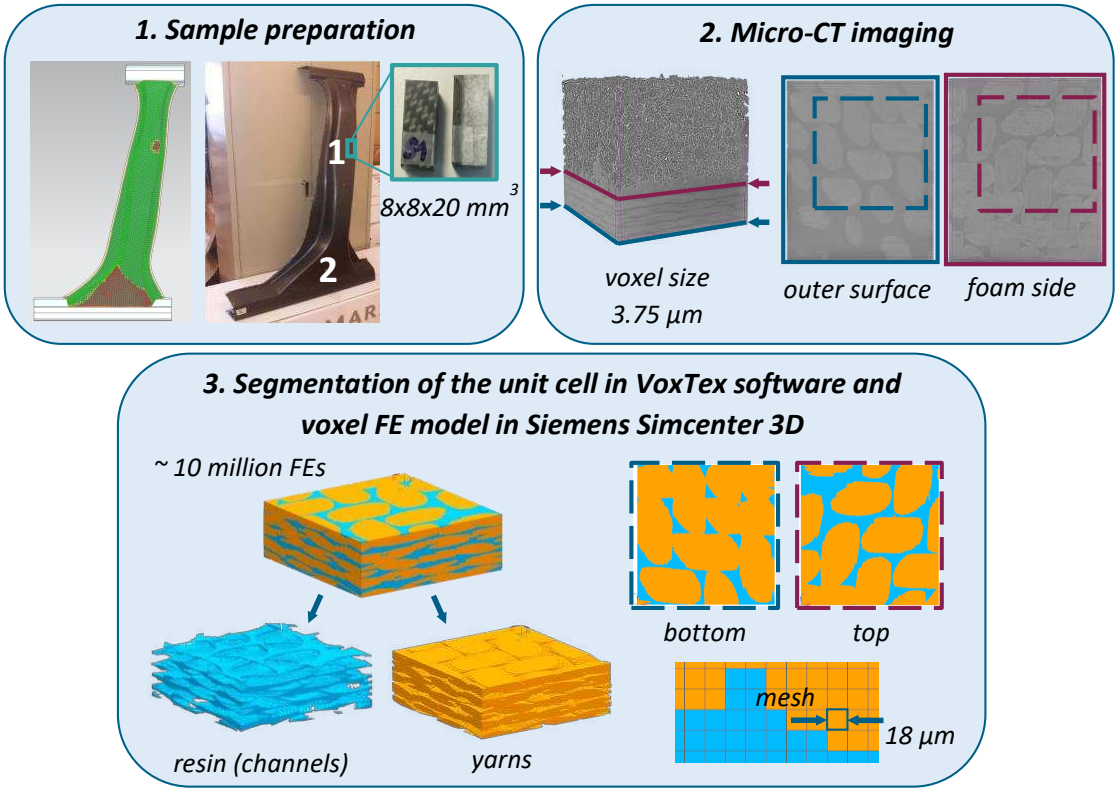

Figure 6. Steps of the image-based FE modeling using VoxTex and Simcenter 3D

4. Results and discussion

Table 1 reviews simulation results of the B-pillar in-plane permeability assessment using the micro-CT image-based modeling approach (Section 3.2).

Table 1: Micro-CT-based assessment of permeability in Simcenter 3D

Specimen label	Kx [m^2]	Ky [m^2]	Max abs shear angle [°]	K1 reference [m^2]
1	2.15E-10	2.34E-10	8.1	2.67E-10
2	1.36E-10	1.55E-10	5.5	2.07E-10
3	3.99E-11	4.62E-11	17.6	3.79E-11
4	1.09E-10	1.36E-10	13.6	1.77E-10
5	1.38E-10	1.43E-10	15.6	1.53E-10

Specimen labels and locations are indicated in Fig. 7 against the local permeability map calculated from the Fibersim draping simulation (Section 3.1). The permeability map reports the in-plane first principal permeability value, K1. For each micro-CT specimen two orthogonal in-plane (axial) permeability values (Kx and Ky) were computed. According to [11], the principal

permeability does not vary significantly for fabric shearing angles below 20°. Thus, K1 reference values (Table 1) can be compared with the simulated in-plane (axial) values, Kx and Ky. The fabric shear angles were measured on the micro-CT images and reported in Table 1. The simulation results showed a good agreement with the experimentally validated local permeability map.

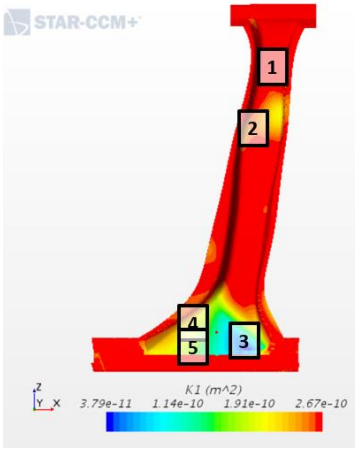

Figure 7. Specimen location on the B-pillar local permeability map

5. Conclusions

In this work, an automatized workflow for the assessment of saturated permeability in Simcenter 3D was demonstrated. The workflow was successfully applied to compute the local in-plane permeabilities of the composite B-pillar by means of the micro-CT image-based modeling.

Based on Fibersim predictions of the fabric draping, several small specimens were cut from various locations of the B-pillar component with the focus on the zones of minimal and maximal shear. Then, micro-CT images of the specimens were acquired using GE Nanotom CT-scanner and segmented into the yarn and resin regions using VoxTex software developed by KU Leuven. Afterwards, micro-CT-based FE models were set up in Simcenter 3D and the homogenized permeability of each specimen was computed using the developed workflow.

The simulation results showed a good agreement with the local permeability map which was analytically calculated from the Fibersim predictions. Additionally, this map was verified against the experimental data of the flow front progression in the component infusion simulation [9].

Acknowledgements

Siemens Industry Software NV (SISW) acknowledges VLAIO (Flemish government agency Flanders Innovation & Entrepreneurship) for their support of the collaborations with Flanders Make, Sirris Leuven-Gent Composites Application Lab and Com&Sense in creating the B-pillar component in the context of the SBO “Self-sensing composites” (n°120024) and ICON “VIDESPRO” (n°150533) projects. SISW also thanks P. Martinez Lera and K. Vanclooster for their contribution to the infusion simulation track. O. Shishkina thanks VLAIO for financing her work in the framework of the Innovation Mandate Project “MicroCT-based Model Generation Engine for Virtual Material Characterization” (n°HBC.2017.0189).

6. References

1. Mallick PK. Advanced materials for automotive applications: an overview. Book chapter in: Advanced Materials in Automotive Engineering. Woodhead Publishing. 2012.
2. Vanclooster K, Martinez Lera P, Luyckx G, Grefhorst R, Waeyenbergh B. Infusion simulation of the RTM process with experimental validation by using integrated optical sensors during the manufacturing. Presented at: EuroMech (Colloquium 602: Composite manufacturing processes. Analyses, modelling and simulations). Lyon, France. 2019.
3. Verleye B. Computation of the permeability of multi-scale porous media with application to technical textiles. PhD thesis, Katholieke Universiteit Leuven, Belgium. 2008.
4. Siemens Digital Industries Software Simcenter 3D product webpage. https://www.plm.automation.siemens.com/global/en/products/simcenter/simcenter-3d.html
5. Donders S, Farkas L, Erdelyi H, Souza F, Cornwell H. Virtual material and product design. Simcenter 3D helps manufacturers comply with regulations and meet customer expectations. Siemens Digital Industries Software. White paper 2021: 1-20.
6. Park CH, Krawczak P. Unsaturated and saturated permeabilities of fiber reinforcement: critics and suggestions. Frontiers in Materials 2015; 2:1-6 (article 38).
7. Swery EE, Meier R, Lomov SV, Drechsler K, Kelly P. Predicting permeability based on flow simulations and textile modelling techniques: comparison with experimental values and verification of FlowTex solver using Ansys CFX. Journal of Composite Materials 2016; 50:601-615.
8. Arbter R, Beraud JM, Binetruy C, Bizet L, Breard J, Comas-Cardona S, et al. Experimental determination of the permeability of textiles: A benchmark exercise. Composites Part A: Applied Science and Manufacturing 2011; 42:1157-1168.
9. Holt C. (ed.) Achieving lighter vehicles with the use of composites. Blogpost. Siemens Digital Industries Software. 2019. https://blogs.sw.siemens.com/simcenter/Achieving-lighter-vehicles-with-the-use-of-composites/
10. Siemens Digital Industries Software Fibersim product webpage. https://www.plm.automation.siemens.com/global/en/products/mechanical-design/composite-design-integration.html
11. Demaria C, Ruiz E, Trochu F. In-plane anisotropic permeability characterization of deformed woven fabrics by unidirectional injection. Part II: Prediction model and numerical simulations. Polymer Composites 2007; 28:812-827.
12. Siemens Digital Industries Software Simcenter STAR-CCM+ product webpage. https://www.plm.automation.siemens.com/global/en/products/simcenter/STAR-CCM.html
13. VoxTex software webpage. https://www.mtm.kuleuven.be/onderzoek/scalint/Composites/software/VoxTex
14. Straumit I. Prediction of the effective properties of textile composites based on X-ray computed tomography data. PhD thesis, KU Leuven, Belgium. 2017.
15. Shishkina O, Matveeva A, Wiedemann S, Hoehne K, Wevers M, Lomov SV, Farkas L. X-Ray computed tomography-based FE-homogenization of sheared organo sheets. In: Proceedings of the 18th European Conference on Composite Materials (ECCM-18). Athens, Greece. 2018; 1-8.

EFFECT OF TEMPERATURE ON DAMAGE ONSET IN THREE-DIMENSIONAL (3D) WOVEN ORGANIC MATRIX COMPOSITES FOR AERO-ENGINES APPLICATIONS

Salvador Orenes Balaciart[a], Yannik Pannier[a], Marco Gigliotti[a], David Mellier[a], Bastien Tranquart[b], Camille Guigon[b]

a: Institut Pprime, CNRS, ISAE-ENSMA (Department of Physics and Mechanics of Materials), Université de Poitiers, 1, Avénue Clément Ader F-86962 Futuroscope Chasseneuil, France
b: SAFRAN Composites, Conception \& Development Department 33, Avenue de la Gare F-91760 Itteville, France

Abstract: *The present work focuses on the characterization of the effect of temperature on damage onset in three-dimensional woven organic matrix composites for aero-engine applications. Damage initiation is characterised by X-ray µ-Computed Tomography (µCT) in-situ tensile tests at different temperatures supported by Acoustic Emission (AE). The synergy between these techniques allows an accurate damage characterization at the onset.*

Keywords: 3D woven composite; Onset damage mechanisms; high and low temperature *in-situ* test; tomography; acoustic emission

1. Introduction

Three-Dimensional Woven Organic Matrix Composites (3DOMC) have been used as structural elements in various parts of the aircrafts since last two decades due to excellent damage tolerance, improved fracture toughness and better through-the-thickness properties [1]. In the last decade, they are increasingly being used as elements of structural parts in the vicinity of aircraft engines and in the fan blades (for instance, LEAP engine). Thus, 3DOMC may operate in high-performance ranges for which their mechanical integrity is required at different temperatures.

Damage mechanisms in 3DOMC have been studied at room temperature in a wide range of mechanical test: static axial tensile load [2], tension-compression fatigue [3], low velocity impact [4] or off-axis tensile loading [5]. In mentioned works, damage mechanisms according to the type of test are studied up to failure of the specimens. Due to the complex damage mechanisms of such materials, the specific use of different experimental techniques is required to achieve a correct damage characterisation. For this reason, some authors have focused on developing complex tests by coupling different techniques. For instance, in [6] a multi-instrumentation analysis using digital image correlation (DIC), acoustic emission (AE) and *in-situ* microscopy was conducted in carbon fiber reinforced polymers (CFRP) in a compression-damaging scenario from first micro-damage to final failure. In [7] authors characterised damage evolution through real-time 3D observations in CFRP specimens under torsion coupled with X-ray computed tomography, which is a very rich technique as it allows a volume characterisation of the complex meso-structure and the damage mechanisms taking place in it. Because of the various experimental limitations, this type of testing becomes difficult to implement when attention is paid to damage occurring at high and low temperatures.

  doi:10.5075/epfl-298799_978-2-9701614-0-0

On the other hand, several studies emphasise the whole range of damage mechanisms, from initiation mechanisms up to catastrophic failure or rupture of the specimens. If this is done in this way, the mechanisms at the onset are neglected, or even studied post-mortem, which implies a lack of information of the structure behaviour at this stage. This context has prompted new *in-situ* testing methodologies whose target is to track the onset of damage. For instance, in [8] the authors proposed the coupling of two techniques (AE & DIC) to catch the onset through a progressively stepped loading. The onset is reached and analysed at the sample surface, however there is still a lack of information about the damage mechanisms at the core. Authors in [9] coupled AE and µCT to determine the initiation of damage. The criterion used to catch the onset was the accumulation of acoustic events to set a test interruption and perform a tomographic scan. To date, no studies of the onset of damage taking into account the effect of temperature have been found in the case of 3DOMC.

In the present work, the effect of temperature on damage onset in 3DOMC for aero-engines applications is investigated. For this purpose, an interruption protocol based on the cumulative energy released during the test is proposed, showing that damage initiation mechanisms are different for each temperature

2. Material & Experimental Setup

3D woven OMC materials samples made by Resin Transfer Molding (RTM) manufacturing techniques are provided by Safran Composites. At the level of constituents, commercial HexTow® IM7 carbon fiber and CYCOM® PR 520 epoxy resin are used. The material used in this study is a 4 plies interlock woven composite whose pitch size and fibre volume fraction has been designed for laboratory purpose. However, the RTM process is similar to that used in industrial parts. After curing the samples are cut from a 4 mm plate with high pressure water jet. The sample geometry (see Fig.1-d) is a trade-off between the *in-situ* experimental setup limitations and the fact of being able to visualize a RVE (RVE = 25.9 mm, see Fig.1-d). Furthermore, the specimens have been cut at 22.5° to the warp direction to induce multi-axial state of stress in the useful part.

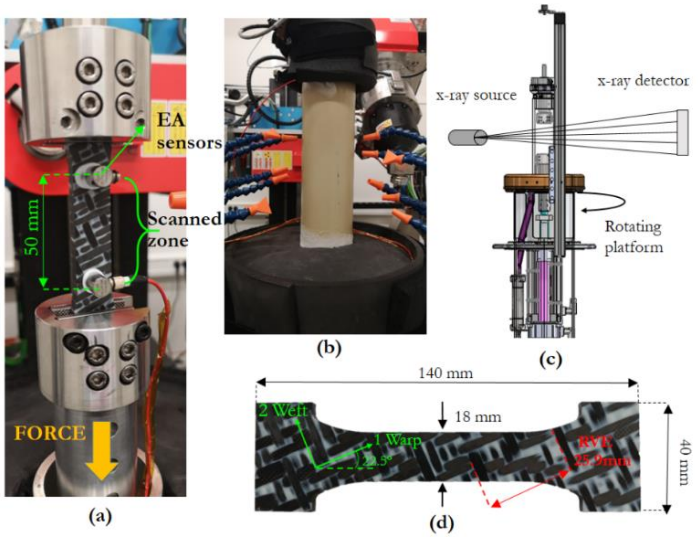

Figure 1. (a) Scanned area, AE sensors and grips; (b) isolation peek chamber used in warm and cold tests;(c) tensile machine and tomography coupling; (d) off-axis sample used in experiments.

Table 1: AE and µCT acquisition parameters.

Acoustic emission		**µCT**	
Gain [dB]	40	Voltage [kV]	50
Frequency [kHz]	100 – 1000	Current [mA]	280
Sensor	Mistras µ-80	Resolution [µm/vox]	14
Threshold [dB]	40	NB images	1120
		Frame rate [im/s]	6

The homemade temperature controlled tensile stage is shown in Fig.1 (a-b-c); it is integrated in the hollow rotation stage of an Ultratom RX-solutions µCT scanner. The maximum traction load hold by the machine is 20kN and the temperature operating range is +200°C to -40°C. The testing protocol consists of applying a monotonic displacement of 1mm/min to the lower grip and monitoring the load and released acoustic energy in the scanned zone of the specimen (Fig.1-a). The protocol followed to interrupt the test at the damage onset is based on the synergy between µCT and AE.

Tomography acquisition parameters are a compromise between image quality and scanning time to mitigate the effects of matrix relaxation. In the same way, the acquisition parameters of the acoustic chain have been selected to localise events in the scanned zone (see Fig.1-a) considering the material properties. These parameters are listed in Table.1.

3. Experimental Protocol

Tensile test is conducted within the µCT with 2 AE sensors monitoring damage onset, and those sensors are unplugged before launching the scan. The acoustic parameters involved in the protocol are:

- Amplitude: maximum level of the AE signal during a hit in Volts. It is converted into dB according to a reference voltage value and the preamplifier gain depending on the acquisition parameters.
- Duration: time from the first threshold crossing to the end of last threshold crossing of the AE signal.
- Energy: the magnitude taken into account is the MARSE (Measured Area under the Rectified Signal Envelope) energy, sometimes referred as energy counts (EC), which is the integral of the rectified voltage signal over the duration of the AE hit (or waveform). Commercially it is found as PAC-energy in the MISTRAS® packages used to record acoustic activity [10]. It depends on the amplitude and duration of a hit.

The criterion to stop the tensile test is based on two conditions: the AE events should be localized in the scanned zone and the Cumulated MARSE Energy (hereinafter, CME) should overcome a certain level. Since two hits are needed to register or localize an event, and depending on the relative distance of the hits to the sensors, they may measure different levels of energy due to material damping; it has been decided therefore to measure the average energy of both hits in each event localization.

  doi:10.5075/epfl-298799_978-2-9701614-0-0

Fig.2-a shows the load and the averaged and localized CME (between both piezoelectric sensors, according to Fig.1) as a function of test time. The CME at stop is called CME-Stop on Fig.2-a .Then a relaxation phase occurs, in which some events are still recorded, the CME after this relaxation phase is called CME-relaxation on Fig.2-a. In Fig.2-b are collected all the captured events in the scanned zone, as a function of time and its amplitude. Each event shown in Fig.2-b has its own weight in the cumulated energy in Fig.2-a. It can be observed how at the very beginning the first relatively small amplitude events whose impact in the cumulative energy is not very significant start to emerge, giving immediately way to a wider range of cascade events, between 40 and 70 dB. When the cumulative energy reaches a value equal to CME-Stop beyond a conventional threshold of around 40 EC (CME-Stop = 75EC in this case, Fig. 2a), the test is stopped by keeping constant the displacement at grips. Finally, when acoustic emission ceases and a steady value of CME is reached (CME-Relaxation = 100EC, in Fig. 2a), the tomographic scan is launched. Tomographic scans are very rich since they do provide information about the 3D internal morphology of the damage mechanisms and through image processing techniques it can be quantified in terms of the total cracked surface (Fig.2-c) and it can be related to the scalar value of CME released during the test, up to the relaxation phase (CME-Relaxation Fig.2-a).

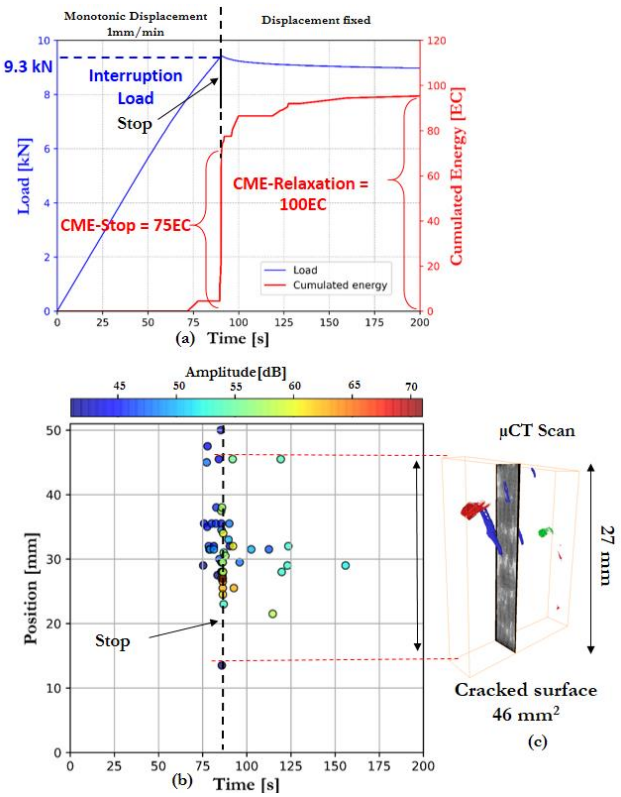

Figure 2. (a) CME and load in function of time; (b) localized AE events in the scanned zone; (c) segmented cracked surface. *Results at room (20°C) temperature.*

The lower the cumulated energy at which the test is stopped, the lower the cracked surface is observed; consequently this protocol can be sharpened towards the very early damage. Finally, it is important to point out the major limitation of this technique, which lies in the final quality of the image that can be achieved for the given setup, mostly in terms of contrast and resolution to discriminate a crack. Therefore, there is a possibility that for very low levels of cumulated energy, the resolution may not be sufficient to discriminate a crack.

  doi:10.5075/epfl-298799_978-2-9701614-0-0 published under CC BY-NC 4.0 license

4. Results

In-situ tensile tests have been conducted at 20°C, 120°C and -30°C on 3 specimens (A, B and C) respectively. Interrupted CME and loads levels following the above protocol as well as damage mechanisms are discussed below for each specimen. Furthermore, a crack classification with respect to the 3D-woven meso-structure is proposed.

4.1 Onset Damage mechanisms at room (20°C) temperature

The test at room temperature (RT) has been interrupted at CME-Stop level of 75 EC which has resulted in a load of 9.3 kN. This cumulated energy after relaxation has reached a value of 100 EC (CME-Relaxation) corresponding to a total cracked surface of 46 mm^2. Three different kind of cracks can be observed in Fig.3:

- Type I (red cracks in Fig.3): intra weft open crack, matrix crack inside weft yarns connected to a specimen cut edge,
- Type II (blue cracks in Fig.3): inter warp inner crack, matrix crack between two adjacent warp yarns not connected to specimen surfaces.
- Type III (green cracks in Fig3.): inter warp and weft crack, it consists in a matrix crack at the crossing point between warp and weft yarns. This type of crack is relatively limited at RT.

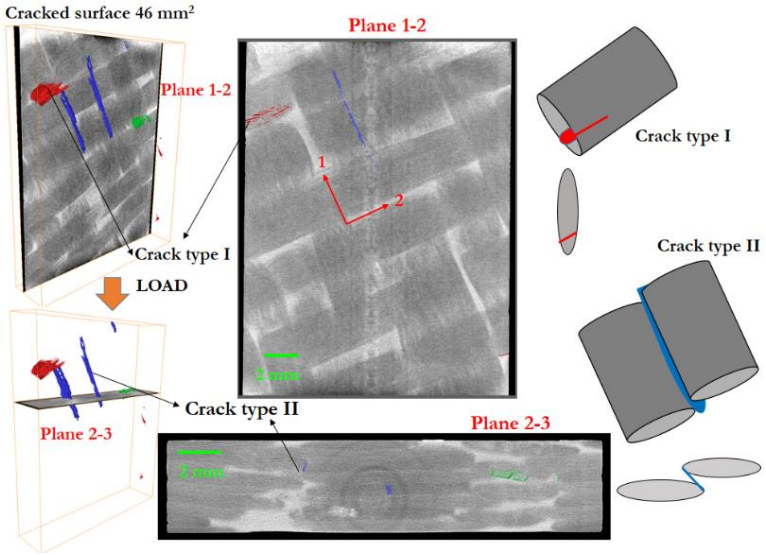

Figure 3. Segmentation and CT scan at damage onset at room (20°C) temperature [Specimen A]

4.3 Onset Damage mechanisms at high (120°C) temperature

The test at high temperature (HT) has been interrupted at CME-Stop level of 126 EC which has resulted in a load of 7.5 kN. This cumulated energy after relaxation has reached a value of 198 EC (CME-Relaxation) corresponding to a total cracked surface of 193 mm^2. One kind of crack can be observed in Fig.4:

- Type III: inter warp and weft crack, it consists in a matrix crack at the crossing point between warp and weft yarns (green cracks Fig.4), similar to the one found at RT, but much more developed. Having a look at Fig.4 it can be observed how the damage follows the weaving pattern. It can be supposed that shearing caused on the yarns by the multi-axial loading has a major impact; the increased viscosity of the matrix may also play an important role in this behaviour.

  doi:10.5075/epfl-298799_978-2-9701614-0-0

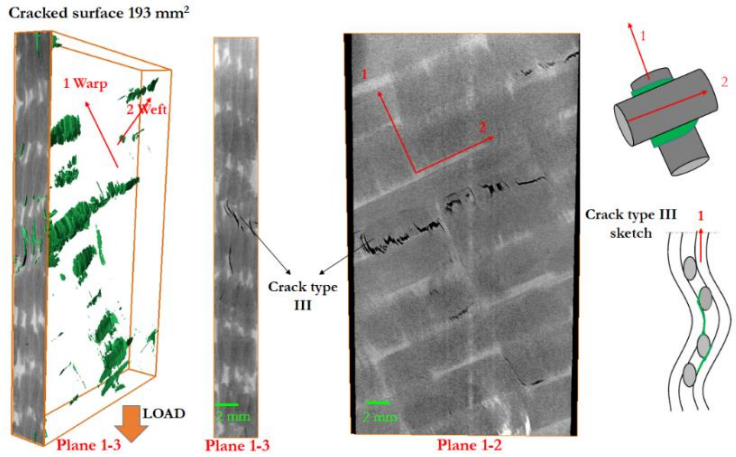

Figure 4. Segmentation and CT scan at damage onset at high (120°C) temperature [Specimen B]

4.3 Onset Damage mechanisms at low (-30°C) temperature

The test at low temperature (LT) has been interrupted at CME-Stop level of 180 EC which has resulted in a load of 9.2 kN. This cumulated energy after relaxation has reached a value of 192 EC (CME-Relaxation) corresponding to a total cracked surface of 5.9 mm^2. Two different kind of cracks can be observed in Fig.5:

- Type I (red cracks): same crack observed at 20°C, intra weft open crack, matrix crack inside weft yarns connected to a specimen cut edge,
- Type IV: it is an intra-crack given in the yarns middle section, both warp and weft (violet cracks Fig.5). The main difference with type I cracks (which are also intra-crack type) is that in the latter, cracks occurs in the yarn edge and normal to plane 1-3 (that is, edge of the sample), while at type IV cracks do appear in the middle of the yarn without connection to the cut edges, normal to plane 1-2.

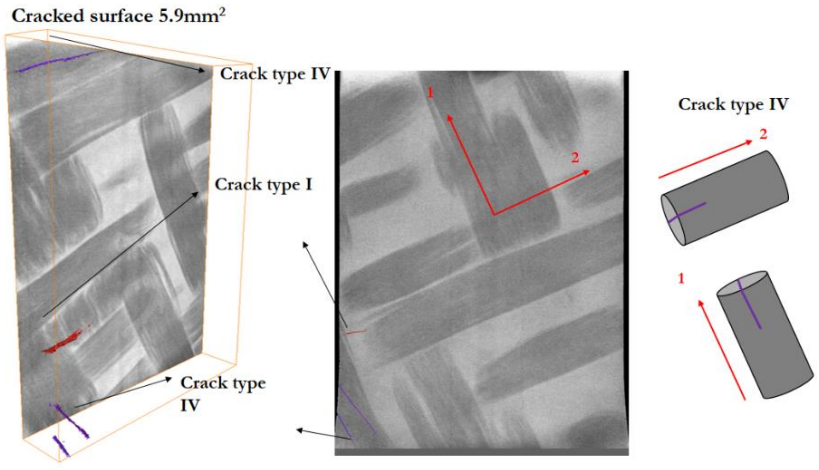

Figure 5. Segmentation and CT scan at damage onset at low (-30°C) temperature [Specimen C]

4.4 Discussion of results

For each test, the following parameters have been reported in Table.2: the cumulated energy at interruption time (CME-Stop) and the corresponding load at interruption; the cumulated energy

  doi:10.5075/epfl-298799_978-2-9701614-0-0 published under CC BY-NC 4.0 license

after the relaxation phase (CME-relaxation) as well as the corresponding number of events at interruption, and finally the total cracked surface which has been computed from segmentation of the µCT scans after interruption. Differences depending on temperature can be clearly appreciated:

- Energy values at interruption (CME-Stop inTable.2) exceed the established threshold of 40EC in all cases, but differ from each other depending on temperature; it has not been possible to interrupt the test for the same CME-Stop at the different temperatures as it is an instantaneous and different energy release for each case, probably linked to the difference in damage mechanisms already discussed.
- Paying attention to the cracked surface and load at interruption, the damage onset at HT is given at lower load levels, with respect to RT and LT. More cracked surface is given (193 mm^2) at a load level of 7.5 kN for HT, while at RT a lower surface of 46 mm^2 is given for a higher load of 9.3 kN. This results is even more marked for LT, in which a load of 9.2 kN only generated 5.9 mm^2 of cracked surface.
- Regarding the total energy released (CME-relaxation in Table.2), it can be observed that it is not proportional to the cracked surface: at RT 64 recorded events are responsible of 100 EC while at LT only 19 events are responsible of almost the double of energy (192 EC); while at HT a similar level of energy (198EC) is distributed in 250 events. In consequence, the lower the temperature, the higher the energy of the recorded events. This may be related to the fact that the damage mechanisms, as has been shown, are different for each temperature, and so it is the associated energy. There is also the possibility that the change in the mechanical properties of the material with temperature plays a role in the way elastic waves propagate, giving rise to more energetic events at lower temperatures due the increase in rigidity of the matrix. However, this last point needs to be studied in more detail.

Table 2: Parameters at the interruption at different temperatures.

Specimen & Temperature	CME-Stop [EC]	CME-Relaxation [EC]	Number of events	Total Cracked surface [mm^2]	Interruption Load [kN]
A (20°C)	75	100	64	46	9.3
B (120°C)	126	198	250	193	7.5
C (-30°C)	180	192	19	5.9	9.2

5. Conclusions

In this study a novel experimental *in situ* coupled technique for tracking the damage onset has been presented. This has allowed to interrupt a tensile test at different load levels depending on temperature. The CME interruption levels shown in the protocol differ according to temperature mainly because different mechanism of damage are involved. On the other hand, initiation damage mechanisms have turned out to be different depending on the temperature. At least one characteristic mode can be distinguished for each:

• Room (20°C) temperature: intra-crack between warp yarns at the core of the sample.

• High (120°C) temperature: intra-crack between warp and weft yarn at high waviness pattern zones

  doi:10.5075/epfl-298799_978-2-9701614-0-0

• Low (-30°C) temperature: inter-crack at yarn and weft yarn at 1-2 sample surfaces.

AE has allowed the test to be interrupted at a load level, while the tomography has provided information on the local location of this damage (and its relation with the meso-structure). The next step would be to use these inputs to create a finite element model based on µCT images that can answer at what level of local mechanical stress damage onsets.

Acknowledgements

Pprime Institute gratefully acknowledges “Contrat de Plan Etat - Région Nouvelle-Aquitaine" (CPER) as well as the "Fonds Européen de Développement Régional (FEDER)" for their financial support to the reported work. This work was partially funded by the French Government program “Investissements d'Avenir” (EQUIPEX GAP, reference ANR-11-EQPX-0018). ISAE-ENSMA is also acknowledge for the funding of the doctoral grant.

References

[1] T. Huang, Y. Wang, and G. Wang, “Review of the mechanical properties of a 3d woven composite and its applications,” Polymer-Plastics Technology and Engineering, vol. 57, no. 8, pp. 740–756, 2018.

[2] A. E. Bogdanovich, M. Karahan, S. V. Lomov, and I. Verpoest, “Quasi-static tensile behavior and damage of carbon/epoxy composite reinforced with 3d non-crimp orthogonal woven fabric,” Mechanics of Materials, vol. 62, pp. 14–31, 2013.

[3] J. Huang, L. Guo, L. Chen, Z.-X. Wang, and J. Li, “Damage evolution of 3d woven carbon/epoxy composites under the tension–compression fatigue loading based on multi damage information,” International Journal of Fatigue, vol. 154, p. 106566, 2022.

[4] B. Kazemianfar and M. R. Nami, “Influence of oblique low velocity impact on damage behavior of 2d and 3d woven composites: Experimental and numerical methods,” ThinWalled Structures, vol. 167, p. 108253, 2021.

[5] D. Zhang, X. Liu, Y. Gu, M. Sun, S. Yu, Y. Zhang, and K. Qian, “Effects of off-axis angle on shear progressive damage of 3d woven composites with x-ray micro-computed tomography,” Composites Part A: Applied Science and Manufacturing, vol. 115, pp. 311– 320, 2018.

[6] K. Hamdi, G. Moreau, and Z. Aboura, “Digital image correlation, acoustic emission and in situ microscopy in order to understand composite compression damage behavior,” Composite Structures, vol. 258, p. 113424, 2021.

[7] Y. Chai, Y. Wang, Z. Yousaf, N. T. Vo, T. Lowe, P. Potluri, and P. J. Withers, “Damage evolution in braided composite tubes under torsion studied by in situ x-ray computed tomography,” Composites Science and Technology, vol. 188, p. 107976, 2020.

[8] N. Tableau, Z. Aboura, K. Khellil, F. Laurin, and J. Schneider, “Multiaxial loading on a 3d woven carbon fiber reinforced plastic composite using tensile-torsion tests : Identification of the first damage envelope and associated damage mechanisms,” Composite Structures, vol. 227, p. 111305, 2019.

[9] F. Foti, Y. Pannier, S. O. Balaciart, J.-C. Grandidier, M. Gigliotti, and C. Guigon, “In situ multi-axial testing of three-dimensional (3d) woven organic matrix composites for aeroengine applications,” Composite Structures, vol. 273, p. 114259, 2021.

[10] Physical Acoustics Corporation, “Pci-2 based acoustic emission system user’s manual’’ Rev 3, April 2017.

  doi:10.5075/epfl-298799_978-2-9701614-0-0 published under CC BY-NC 4.0 license

SIMULATION OF FRICTIONAL CONTACT INTERACTIONS WITHIN JACQUARD HARNESS OF WEAVING LOOMS FOR 3D INTERLOCK FABRICS

Salah-Eddine, Mermouli [a,b], Pietro, del Sorbo[b], Damien, Durville[a], Bastien, Tranquart[b], Dominique, Coupé[b]

a: Université Paris-Saclay, CentraleSupelec, ENS Paris-Saclay, CNRS, Laboratoire de Mécanique Paris-Saclay
salah-eddine.mermouli@centralesupelec.fr
b: Safran Tech, Safran Composites

Abstract:

In Jacquard harness looms used for 3D interlocking fabrics, the relative motions between warp threads and heddles under confining effects induce frictional interactions that can damage the threads or block their motion and cause weaving errors. Based on an implicit solution scheme, a finite element approach is proposed to simulate these interactions. Simulation parameters are implemented according to the actual operating machine conditions. Simulation results for an interlock fabric with 20 warp threads will be presented. The resulting forces required to move the heddles are obtained as simulation results. In addition, the lateral force exerted by the rest of the harness on the portion considered is prescribed using rigid moving planes. The influence of the reed on the lateral confinement is highlighted along with various force evolution analyses of the heddles and warp threads over a few tens of shed openings.

Keywords: Jacquard harness; Frictional interactions; Finite element simulation; Shedding

1. Introduction:

The use of 3D interlock fabrics for manufacturing composite parts allows the making of stronger and lighter pieces. These fabrics are produced using Jacquard-weaving looms, in which a large number of heddles are gathered within the so-called Jacquard harness, and are operated to move the warp threads up and down to allow the insertion of weft threads.

Today, controls are done once the part has been produced and mostly manual operations are required to check them which generates time-consuming iterations. This study is concerned especially with the congestion mechanisms within the Jacquard harness. The harness is the part of the loom where the warp threads are the most subject to frictional effects. Our purpose is to provide a numerical tool that allows performing virtual testing representative of the real weaving process and provide technical locks to optimize the system.

Due to the high density of heddles and threads in a limited space, the relative motions between harness components induce frictional forces. These forces are of two types: thread friction against machine parts (that includes with heddles and especially at eyelets level and with the reed) and thread against thread friction. The interactions are particularly important when a large number of warps are moved along the harness depth and if friction forces within the harness can prevent some of them to reach their expected positions that causes a wrong weft thread insertion and thus an unexpected weaving pattern. These interactions are problematic for

  doi:10.5075/epfl-298799_978-2-9701614-0-0

weaving, resulting in a degradation of the state of the threads and subsequently leading both to a reduction in production rates and in the mechanical properties of the final reinforcement.

Based on an implicit solution scheme, a finite element approach [1] is used to simulate the interaction phenomena that occur in such harnesses. In this model, all elements involved in the studied part of the harness are represented using finite strain beam elements with different material properties. That includes the heddles, the warp threads, and the reed. Frictional contact elements are automatically created to account for frictional contact interactions.

To our knowledge, none of the works dedicated to the simulation of the weaving process [3-6] has addressed the congestion phenomena taking place in the Jacquard harness. The purpose of the present work is to deal specifically with this issue, in particular, to represent the frictional contact interactions between harness components in an accurate way and to provide a numerical tool that allows performing simulation representative of the real weaving process, in order to determine the variations of forces within the harness due to frictional forces and to prevent possible blocking events due to congestion through virtual testing.

After introducing the simulation model, the shedding device for 3D interlock fabrics and its operations are introduced. The representation of the rest of the harness on the portion of the harness selected in the model by the lateral pressure applied by moving planes is discussed. Results illustrating the ability of the proposed approach to determine the efforts in the heddles for the simulation of an actual case study are finally presented.

2. Simulation Model :

2.1 MULTIFIL: search for the mechanical equilibrium of a set of beams in frictional contact interactions

The finite element simulation approach used in this study was developed to model the mechanical behavior of wire or filament assemblies, subjected to frictional contact interactions and large displacements. This approach, based on an implicit solution scheme, presents an original procedure for the determination of contacts, the detailed description of which is provided in [1].

The beam model used to represent each wire or filament is based on kinematics that describes the displacement and deformation of each cross-section and bypasses the use of rotations. Complete Green-Lagrange deformation tensors are derived, allowing the implementation of three-dimensional constitutive equations.

A model of frictional contact between two spatial beams with circular cross-sections is proposed. After a global search, proximity zones are determined, and frictional contact interactions between two beams are taken into account by means of point-wise contact elements created for intermediate geometries generated for each proximity zone.

A regularized penalty model is used to determine the normal contact reactions. Quadratic regularization is considered for very small penetrations to smooth the transition between the contact and non-contact status. The penalty coefficient is adjusted at each proximity zone to control the maximum penetration for each proximity zone. A regularized friction model, taking into account a small reversible relative tangential displacement before the actual sliding, is considered for the friction interactions.

  doi:10.5075/epfl-298799_978-2-9701614-0-0

2.2 Components of the harness model

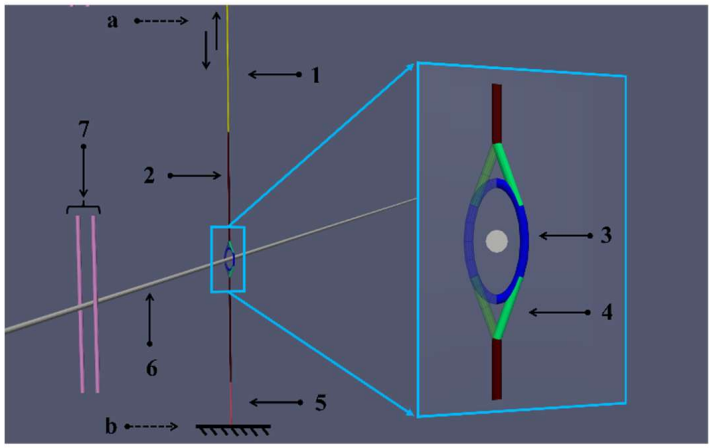

1. Nylon cord
2. metal rod (2)
3. Eyelet (2 half elliptical rings)
4. Eyelet (4 braces)
5. Spring
6. Warp thread
7. Reed vertical slits (2)

a. Bottom extremity blocked
b. Upper-end where the motion is applied

Figure 1. model of the harness components

2.2.1 Heddles

Each heddle is modeled by a set of beam elements, with different material properties, representing its different parts. These consist of, as shown in Fig. 1, the nylon cord at the top, two metal rods on either side of the eyelet, which itself consists of two half-elliptical rings and four braces, and lastly a spring element at the bottom end. Special connecting elements are used to ensure the bonding at the connection points between the different elements of the beam.

2.2.2 Warp threads

Each warp thread is modeled as a beam element. However, bending and twisting stiffness coefficients are adjusted to account for the very low bending and twisting stiffness of the considered carbon threads due to their multi-filamentary construction. In the case of a 48K carbon thread, the coefficient can be estimated as follows:

$$Coef = \frac{Number\ of\ macrofilaments}{Number\ of\ micro\ filaments} = \frac{1}{48000} \quad (2.1)$$

2.2.3 The reed

The reed is a frame with many vertical slits used for spacing the warp threads and for pushing the weft threads into place. Each vertical slit of the reed is modeled as a beam element with steel material properties.

3. Shedding Operation

3.1 Harness configuration building

The heddles respect the comber board positioning. The warp threads layers are arranged plane by plane with the specific thickness of the fabric while the thread board maintains their position at the opposite end. The reed is placed following and respecting the actual machine spacing and dimensions. We begin the simulation with a starting configuration in which the geometry of each element of the harness can be defined by simple geometries. Once the threads have been repelled on the right side, the starting configuration is then gradually changed until reaching the initial configuration in which each warp thread is inserted in its assigned eyelet resulting from a mechanical equilibrium, further details are provided in [2].

  doi:10.5075/epfl-298799_978-2-9701614-0-0

3.2 Estimation of the lateral pressure

The idea is to estimate the pressure exerted by the rest of the harness on the few heddles and warp threads being considered. This allows to represent the confining effects inside the harness on the few components being considered. Since the reed sets the width of the fabric, and the threads board sets warp threads positioning (bobbin bank side), the path of the warp threads between the board and the reed makes thus an angle at the eyelet level. Then the lateral force can be expressed using the angles and the thread tensions by the following formula:

$$F \approx T_1 \sin(\varphi) + T_2 \sin(\psi) \quad (3.1)$$

Given that the heddles do not remain straight also during shedding, they also generate a contribution to that lateral pressure expressed as:

$$F' \approx T'_1 \sin(\delta) + T'_2 \sin(\gamma) \quad (3.2)$$

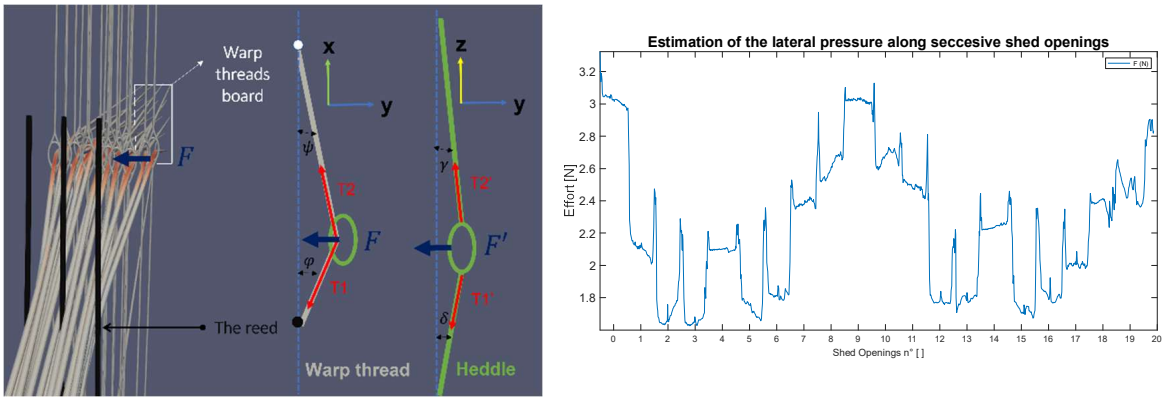

*Figure 2. T*he lateral pressure estimation

Once we know tensions and angles from the simulation results we can estimate the total pressure of an assembly of heddles and warps. See Fig. 2, during a dozen successive shedding motions of 20 heddles and warp threads, the total pressure obtained using formulas (3.1) and (3.2) for all heddles is about 3.25N.

3.3 Representation of the rest of the harness

Using moving rigid planes placed on both sides of the harness portion, which are assumed to be driven by the force estimated before, as demonstrated in Fig. 3, we can prescribe the lateral force exerted by the rest of the harness on the few heddles and warp threads being selected.

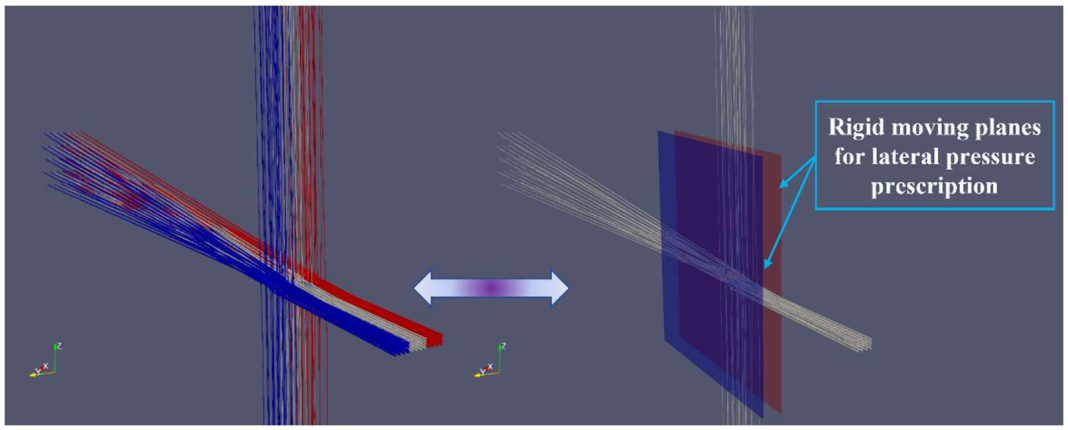

Figure 3. Representation of the rest of the harness using rigid planes

3.4 Successive shedding configurations during the weaving process

The shedding step allows the separation of the warp threads into two layers, thus creating the shed, necessary for the insertion of the weft. The raising and lowering of the threads are determined by the chosen weave constituting the elementary pattern of the desired fabric. It is represented by a binary matrix -the loom card- as shown in Fig. 4. Weaving errors are mainly related to events that prevent respecting the movements dictated by this card. The motions defined by the loom card for shedding are prescribed as displacements to the upper ends of the heddles.

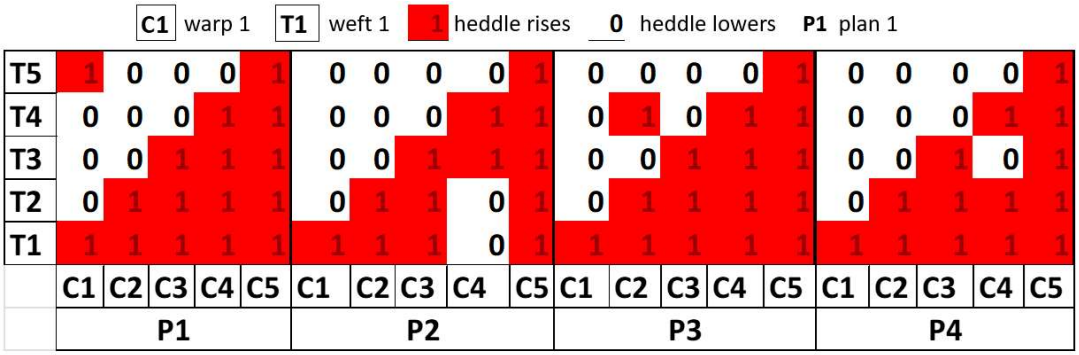

Figure 4. 3D interlock fabric weaving matrix portion

Warps tensile load, spring characteristics, heddles, and warps positioning are all implemented according to the actual operating conditions. Hereafter in Fig. 5 an overview of the simulation model at the shedding phase shows frictional contact interactions within the harness.

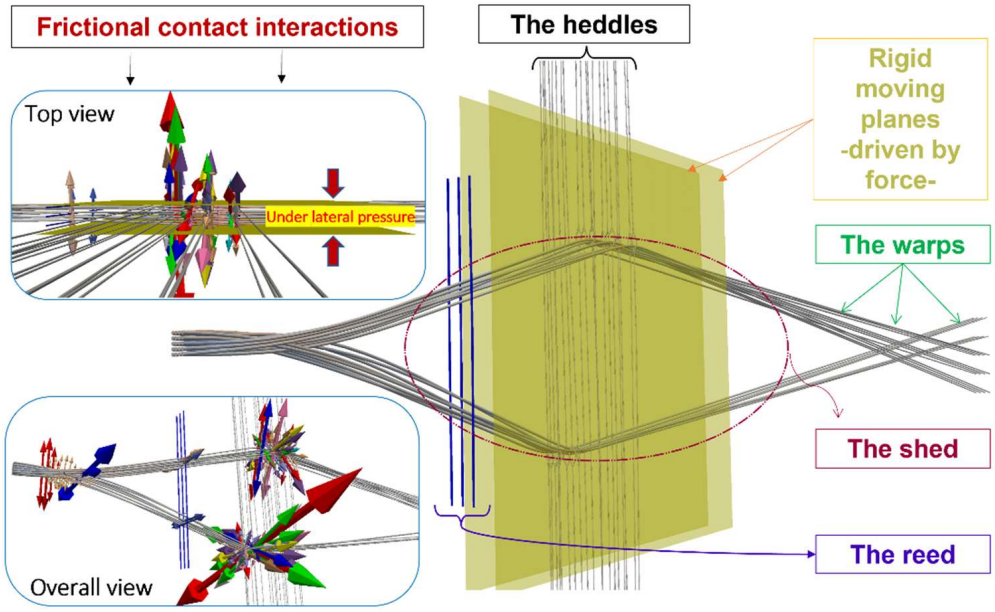

Figure 5. Simulation model at shedding phase showing frictional contact interactions

4. Multifil Simulation Results and Analysis

The case study presented is a portion of a harness that is composed of 20 heddles corresponding to 4 columns of warp threads arranged in 5 layers of carbon fiber of 48K (3200 Tex). Constrained by rigid planes on both sides driven by pressure force equivalent to the pressure of 20 heddles and warp threads, estimated at 325cN. The warp positions are locked on the fabric side when a nominal constant tension of 345cN is applied to the opposite end. Two planes of warp threads are placed per reed slits.

  doi:10.5075/epfl-298799_978-2-9701614-0-0

Firstly, the rigid planes are placed at a distance, then at the end of the initial phase the two planes are driven by displacement until they constrain the portion and the contact elements are created. At the beginning of the successive openings and closings of the shed, these planes are only driven by force. The transitions from the starting to the initial configurations, and between the successive shedding configurations and the taking-up phase are simulated incrementally, by prescribing the increments of displacements corresponding to each stage at the ends of the heddles and the warp threads. The taking up phase occurs in each 5 shed openings following the matrix card.

Friction between all elements is considered in the simulation represented with a friction coefficient of $\mu = 0.1$. The finite element total number is around 1400 for all the structures. With a shed opening amplitude close to 110 mm, the simulation phases occur. For 20 shed openings, the total loading steps calculation time is about 18 hours.

4.1 Effort evolution on heddles and warp threads

Fig. 6 represents simulation results. The vertical axis shows the force required to move the heddles and the horizontal axis presents the shed openings number.

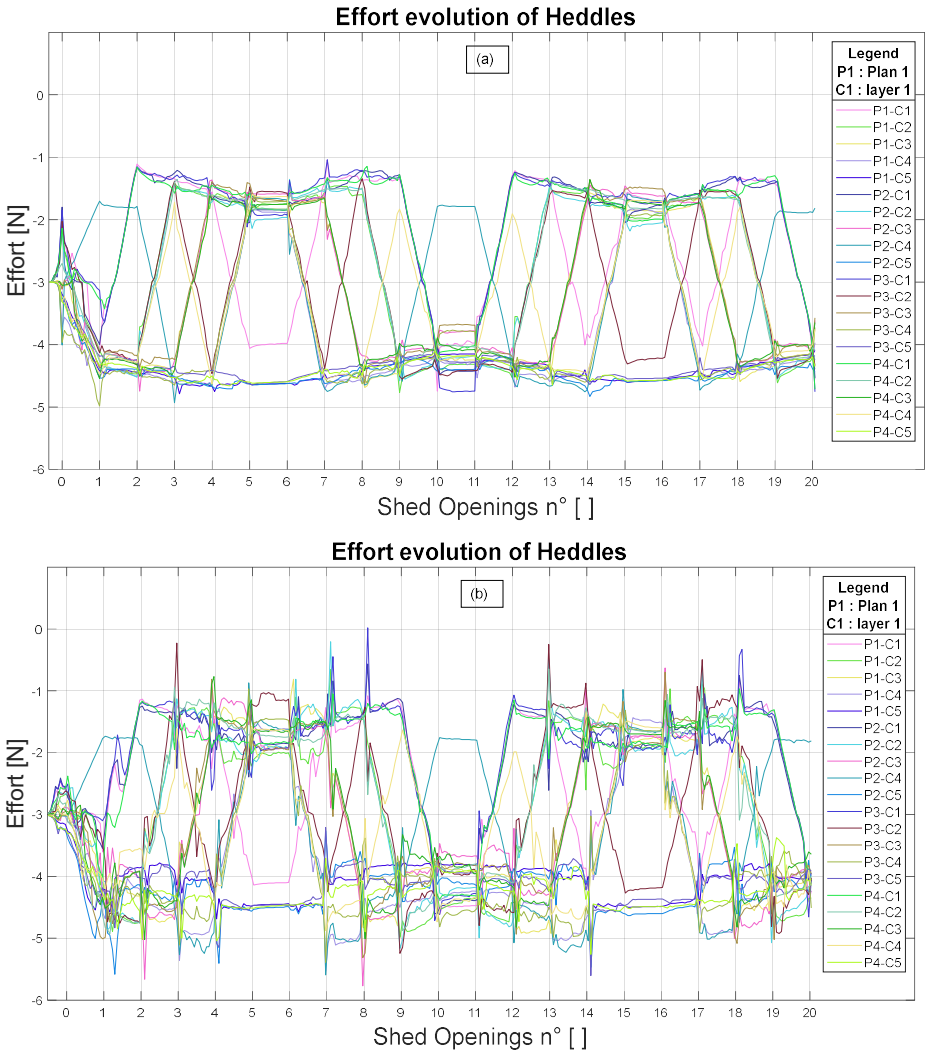

Figure 6. Heddles effort variation during successive shedding openings (a) without adding lateral pressure (b) with lateral pressure prescription

  doi:10.5075/epfl-298799_978-2-9701614-0-0

Mainly, two levels of effort corresponding to the upper and lower position of the heddles are highlighted. Besides irregularities, at one level, we notice that the heddles do not have the same value of equilibrium effort, this can be explained by the fact that each thread of these heddles has a significantly different position in the threads board. A difference in positioning generates different shed angles and since the effort in the heddle depends on the tension of the warps by the sinus of these angles, a difference in effort is exerted.
We can notice that simulation with lateral pressure (Fig.6 b) represents a different appearance compared with simulation without planes (Fig.6 a). More important irregularities in the two levels are observed for case b. Besides that area is the final expected position of heddles, when they arrive (or start to move) to their expected position, the contact interactions are more important with the others which are already in that position.

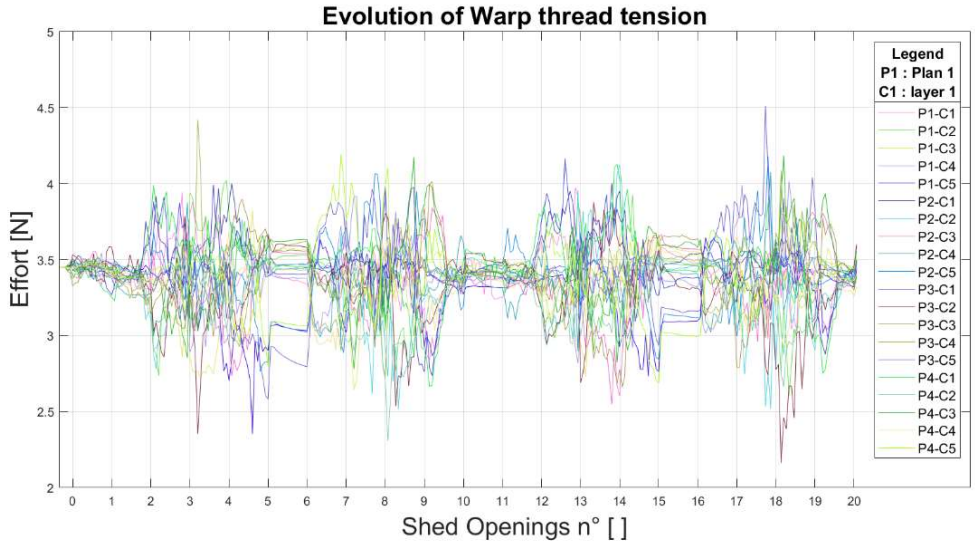

Figure 7. Warp threads tension evolution on the fabric side during shedding

The warp positions are locked on the fabric side when a nominal constant tension of 3.45N is applied to the opposite end. Figure 7 shows the evolution of thread tensions during successive shedding openings on the fabric side. It can be seen that the tension varies and an amount of ± 30 % of the nominal tension is reached during shedding. The tension changes are surely due to frictional interactions between threads and with heddles but also can be caused by the reed movements.

4.2 Example of blocking event

When we observe a singular peak that appears in heddles effort curves, that allows us to highlight that there is almost certainly a locking situation. Due to congestions, and especially hereafter when three warp threads are moved along the fabric depth at the same time. Friction forces within the harness prevent them to reach the expected position. We can notice clearly how threads remain blocked at a higher position compared with their eyelets due to the important frictional interactions involved. Figure 7, illustrate this blocking situation.

  doi:10.5075/epfl-298799_978-2-9701614-0-0

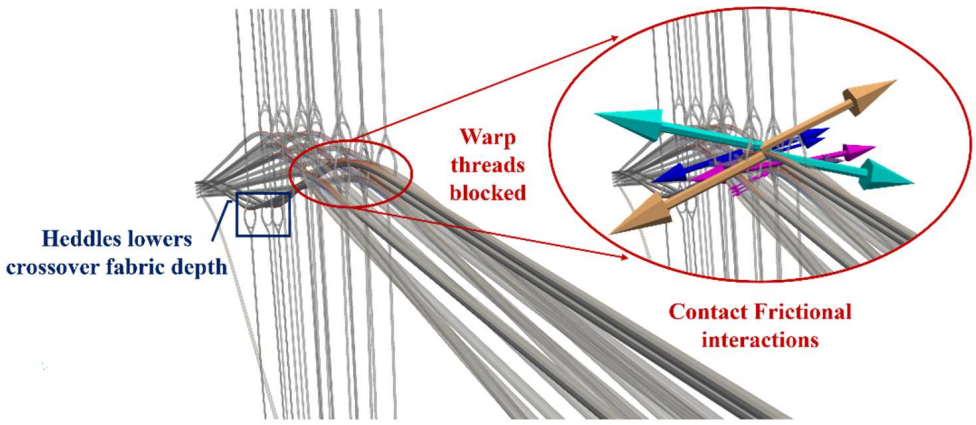

Figure 7. Blocking situation

5. Conclusion

The purpose of this research is to simulate the operation of a Jacquard harness to produce 3D interlock woven fabrics from carbon threads where a congestion phenomenon occurs within the harness components (heddles and warp threads). By simulating the motion of these elements, and by modeling the frictional contact interactions between them, the objective is to assess the tensile loads in the heddles in order to better understand and prevent the congestion effects responsible for various defects in the weave.

To limit the cost of simulation while remaining representative of the congestion phenomenon a formulation and implementation of the representation of the rest of the harness on the heddles and warp threads considered are carried out. The different effort curves allow the user to highlight blocking events. If a heddle remains blocked during its crossing, due to frictional forces, the user can notice it directly through the curves. The complete shedding process simulation of real 5-layer interlock fabric with 20 warp threads can be reached for a calculation time of 18 hours.

To validate the effort in the heddles predicted by the simulation, sensors will be used to obtain the loads measured directly on a real weaving case.

6. References

1. D. Durville, “Contact-friction modeling within elastic beam assemblies: an application to knot tightening,” Computational Mechanics, vol. 49, no. 6, pp. 687–707, 2012.
2. Mermouli, S. E., Del Sorbo, P., Durville, D., Tranquart, B., & Coupé, D. (2021, March). Simulation of Frictional Contact Interactions Between Warp Yarns and Heddles Within Jacquard Harness for 3d Weaving. In 14th WCCM-ECCOMAS Congress 2020 (Vol. 1000) .
3. H. Finckh, “Numerische simulation der mechanischen eigenschaften textiler fl¨achengebilde - gewebeherstellung,” LS-DYNA Anwenderforum, pp. 1–15, 2004.
4. J. Vilfayeau, Mod´elisation num´erique du proc´ed´e de tissage des renforts fibreux pour matériaux composites. PhD dissertation, L’institut national des sciences appliqu´ees de Lyon, 2014.
5. L. Russcher, E. Lamers, C. Dufour, F. Boussu, P. Wang, and D. Soulat, “Modelling the microstructure of multilayer woven fabrics,” In Proceedings of the 13th AUTEX World Textile Conference,Dresden, Germany, 22–24 May 2013.
6. X. Yang, Dynamic simulation of 3D weaving process. PhD dissertation, Kansas state university, Manhattan, Kansas, 2015.

  doi:10.5075/epfl-298799_978-2-9701614-0-0

LACCASE-ENZYME TREATMENT OF FLAX FIBRES FOR IMPROVED INTERFACIAL STRENGTH IN NATURAL FIBRE COMPOSITES

Hanna Brodowsky

hanna.brodowsky@htwk-leipzig.de ,
Leipzig University of Applied Sciences, Leipzig, Germany

Abstract: *Natural fibres are attractive reinforcement of polymer matrices, as they combine a high specific strength and modulus with sustainable production and reasonable prices. Modifying the fibre surface can increase the adhesion and thereby enhance the mechanical properties of composites. In this study, a novel sustainable surface treatment is presented: the fungal enzyme laccase was utilised with the aim of covalently binding the coupling agent dopamine to flax fibre surfaces. The goal is to improve the interfacial strength towards an epoxy matrix.*

SEM and AFM micrographs showed that the modification changes the surface morphology, indicating a deposition of dopamine on the surface. Fibre tensile tests, which were performed to check whether the fibre structure was damaged during the treatment, showed that no decrease in tensile strength or modulus occurred. Single fibre pullout tests showed a 30% increase in interfacial shear strength (IFSS) due to the laccase-mediated bonding of the coupling agent dopamine. These results demonstrate that a laccase + dopamine treatment modifies flax fibres sustainably and increases the interfacial strength towards epoxy.

Keywords: Natural fibres; fibre matrix adhesion; encymatic treatment

1. Introduction

The interphase between fibre and matrix is essential for the composites' mechanical properties. Reinforcing fibers such as glass, aramid or carbon fibres are usually treated with a sizing in order to improve the fibre matrix adhesion. Sizings are aquaeous solutions which aid in processing,. For better adhesion they contain coupling agents such as silanes, which can ideally covalently bind to both fibre and matrix. For a sustainable composite, sustainable interface modifications need to be found.

The study focuses on enzymatic fibre treatment: Flax fibres are treated with Laccase from a Cerrena unicolor polypore fungus. Laccase is e fungal enzyme abundant in nature and used e.g. in the food industry. Laccase catalyzes a ring opening reaction of lignin, inducing bonds to either amino or hydroxyl moieties. This may be used to covalently bind reactive species to the fibre which can then improve the fiber matrix interaction.

  doi:10.5075/epfl-298799_978-2-9701614-0-0

2. Materials and Methods

Flax fibre yarn (250 tex) was obtained from Composites Evolution (Chesterfield, UK). Once the outer winding yarn was removed, it contained mostly single fibres of 2–6 cm length and 20 µm diameter that could be used without further separation. Dopamine hydrochloride of TraceCERT® grade was obtained from Sigma (St. Louis, MO, USA). Epoxy resin/hardener systems RIM 135/RIM 137 and L + L were obtained from Hexion (Columbus, OH, USA) and R&G Faserverbundwerkstoffe GmbH (Waldenbuch, Germany) respectively.

Laccase enzyme from Cerrena unicolor fungus was kindly provided by the group of Bioprocess Engineering, Institute of Natural Materials Technology, Technical University Dresden, Germany. The fibre treatment was also performed by this group. Laccase and treatment are discussed in detail in Brodowsky et al. [1] and [2].

Four different fibre treatments were compared:

- fibre treated with laccase enzyme in presence of its substrate dopamine in malonate buffer

and three reference samples

- fibre treated with the malonate buffer only
- fibre treated with laccase in buffer but without dopamine
- fibre treated with dopamine in buffer but without laccase

3. Results and Discussion

In order to determine whether the laccase will not only modify the fibres' lignin but also harm the cellulose, the tensile strength of the treated fibres was measured in a 50 fold measurement. The single fibre tensile strength and Young's modulus as well as the Weibull distribution are shown in fig. 1

  doi:10.5075/epfl-298799_978-2-9701614-0-0

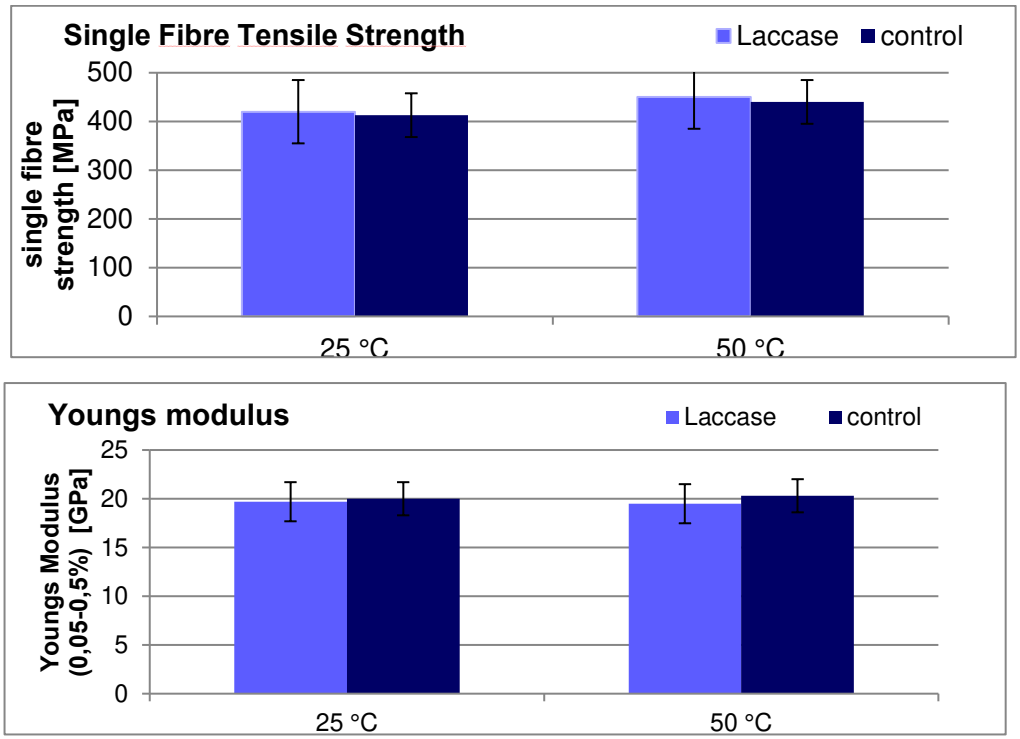

Figure 1. Results of single fibre single fibre tensile tests of Laccase treated fibres and control fibres for 25 °C and 50 °C.

Laccases mainly catalyze the ring opening reaction in Lignin, but could potentially damage the cellulose as a side effect. In current study, we can see this is not the case, not even at a higher reaction temperature. The treatment seems to have a tendency to improve fibre strength, perhaps rather due to other effects (such as recrystallization or removal of cement) than Laccase induced lignin catalysis. The treatment at higher temperature also improves the strength, while no difference between laccase treated fibre and control fibre are seen. The fibre modulus is not affected by the Laccase treatment. In the Weibull representation ot the data, the higher temperature strength probability data are shifted to higher strengths but there is no shift due to laccase activity [1].

The fibres were then exposed to laccase at 3,3 U/ml in malonate buffer with two substrates containing an amino and a hydroxyl moiety, namely dopamine and amino-hexanol. Both have been described to be substrates for Laccase [1]. Dopamine is a typical representative of Laccase substrates, which almost always have a ring structure. Amino-Hexanol is one of the few linear molecules that have been seen to act as Laccase substrates. The fibres are imaged by scanning electron microscopy (SEM) after treatment with buffer only, buffer and laccase, buffer + laccase + substrate, buffer+ substrate only. The dopamine binding effect of laccase is evident in REM [2] which is more pronounced than the polydopamin layer formed without Laccase. With amino-hexanol as a substrate, no fibre surface modifications are seen in REM or AFM [1]. In Figure 2, atomic force microscopy (AFM) images of buffer-only treated and laccase dopamine treated fibres are shown. The surface of the untreated fibre is smooth, whereas the modified fibre is covered by a flakey layer.

  doi:10.5075/epfl-298799_978-2-9701614-0-0

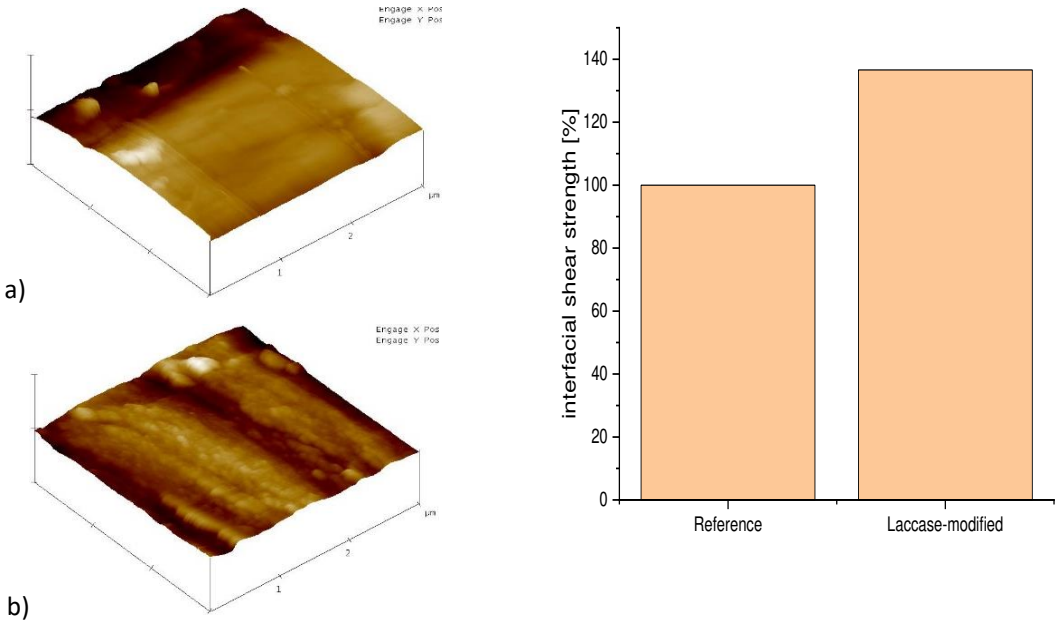

Figure 2. left: AFM images of fibre surface without (a) and with (b) laccase-modification. right: (c) interfacial shear strength of fibre epoxy composites

The interfacial shear strength (IFSS) of laccase modified interfaces was determined by micromechanical tests on single fibre model composites, namely single fibre pull out test and single fibre fragmentation test. The interfacial shear strength towards an epoxy matrix is improved by 30% in laccase-dopamine modified fibres as compared to buffer only treated fibres. IFSS from pullout measurements are shown in fig.2 The micromechaninca test results are thoroughly discussed in [2].

4. Conclusion

Natural fibres have a high potential as reinforcement of polymer matrices, as they combine a high specific strength and modulus with sustainable production and reasonable prices. Modifying the fibre surface is a common method to increase the adhesion and thereby enhance the mechanical properties of composites. In this study, a novel sustainable surface treatment is presented: the fungal enzyme laccase was utilised with the aim of covalently binding the coupling agent dopamine to flax fibre surfaces. The goal is to improve the interfacial strength towards an epoxy matrix. SEM and AFM micrographs showed that the modification changes the surface morphology, indicating a deposition of dopamine on the surface. Fibre tensile tests, which were performed to check whether the fibre structure was damaged during the treatment, showed that no decrease in tensile strength or modulus occurred. Single fibre pullout tests showed a 30% increase in interfacial shear strength (IFSS) due to the laccase-mediated bonding of the coupling agent dopamine. These results demonstrate that a laccase + dopamine treatment modifies flax fibres sustainably and increases the interfacial strength towards epoxy.

  doi:10.5075/epfl-298799_978-2-9701614-0-0

Acknowledgements

The author wants to thank Anne Hennig, of RWTH Aachen Germany for fruitful discussions, Steffi Preßler, Alma Rothe, Christina Scheffler of IPF Dresden Germany for the single fibre pullout test, also Annett Werner, TU Dresden, Germany, who performed the laccase treatments, and Serge Zhandarov, Academy of Sciences, Gomel, Belarus for the evaluation of the IFSS raw data.

References

1. Brodowsky, H.M.; Hennig, A.; Müller, M.T.; Werner, A.; Zhandarov, S.; Gohs, U. Laccase-Enzyme Treated Flax Fibre for Use in Natural Fibre Epoxy Composites. *Materials* **2020**, *13*, 4529. https://doi.org/10.3390/ma13204529
2. Brodowsky, H.M., Hennig, A. Micromechanical Tests on Natural Fibre Composites with Enzymatically Enhanced Fibre–Matrix Adhesion. *Mater Circ Econ* **4,** 5 (**2022**). https://doi.org/10.1007/s42824-021-00040-4

DIC-BASED MONITORING ON DEBONDING CRACK PROPAGATION IN WRAPPED COMPOSITE JOINTS

Weikang, Feng[a], Pei He[a], Mathieu Koetsier[a], Marko Pavlovic[a]

a: Department of Engineering Structures, College of Civil Engineering and Geoscience,
Technology University of Delft – w.feng@tudelft.nl

Abstract: *Wrapped composite joint is an innovative technique which connects steel hollow sections through bonding such that the fatigue performance is improved compared to welded joint. In this paper, a DIC-based method of monitoring surface strains is proposed to quantify the debonding crack propagation within the composite wrap layers during high cycle fatigue loading. A constant strain threshold was used to obtain crack length based on strain distribution curves extracted from DIC. Sensitivity analysis of such threshold showed that within the 'steady strain slope' region, the influence of threshold choice on calculated crack length is insignificant, but a good choice of threshold can help obtain more stable results. During cyclic loading, it was found that stiffness degradation and crack development of the joint is arrested due to friction effect at the cracked interface. Static tests after cyclic loading showed that the joint can still sustain its original static resistance.*

Keywords: Wrapped composite joints; Debonding crack propagation; Fatigue test; Digital Image Correlation

1. Introduction

Fatigue failure has been proved to be a common hazard for welded tubular joints, which are now widely used for circular hollow sections (CHS) of steel truss/jacket supporting structures of off-shore wind turbines, oil and gas platforms, steel bridges [1]. In recent years, fiber-reinforced polymers (FRP) have been widely used for enhancing static/fatigue performance of steel structures, due to their light weight, tailorability, high fatigue endurance and other excellent mechanical properties. In the previous study, an innovative joining technique, the wrapped composite joint was proposed by the authors [2], where composite wrap is used to connect steel members of hollow sections through bonding and welding can be completely avoided in the load transferring mechanism, and the low fatigue endurance due to welding is eliminated. Static [3] and fatigue [4] experiments on this kind of joints have shown their superior mechanical performance over their welded counterparts. However, monitoring the most important failure mode of the joint wrapped with thick laminates, debonding at the steel-to-composite interface still remains as a critical issue, which is of great importance for characterizing and predicting fatigue behaviour of wrapped composite joints.

During recent years, the non-destructive technique (NDT) has been widely used for mechanical damage assessment in composite structures [5], especially for monitoring debonding at composite-to-steel/concrete interface. Among these techniques, the Digital Image Correlation (DIC) technique has been widely used due to its advantages of non-contact, full field and real-time measurements. For example, Bahman Ghiassi [6], Pei Zhang [7] and Mohamad Ali-Ahmad [8] investigated debonding between FRP and substrates under quasi-static monotonic loads by DIC. Strain contours were captured under different load levels, where increased strains

  doi:10.5075/epfl-298799_978-2-9701614-0-0

indicated crack initiation or debonding at the interface. The DIC method was also applied for investigating debond behaviour under fatigue loading [9]. The strain plateau along the CFRP plate represented the debond length which increased gradually with the increasing number of loading cycles. However, monitoring technique for debonding crack propagation at curved interface under thick laminates still needs to be developed.

In this paper, fatigue tests on axial wrapped composite joints were carried out. A 3D DIC system was utilized for capturing surface strain of the specimen such that debonding crack propagation at the composite-to-steel interface was monitored. A constant strain threshold was utilized to calculate crack length, meanwhile sensitivity of such threshold was conducted. After fatigue tests, static tests were carried out to determine the remaining static resistance of the joints.

2. Specimens, test set-up and loading protocol

Geometry and dimensions of specimens are shown in Figure 1. Two steel tubes of Φ60.3×4 with steel grade S355 are bonded together by composite wrap. The laminate of the composite wrap is formed with multi-directional composition of E-glass reinforcement and vinyl-ester based thermoset resin system. The composite wrapping thickness is 12mm, while the total wrapping length is 480mm. A 25mm PTFE insert is applied at butt end of each tube forming 2 separate initial crack tips, such that the uncertainties related to crack initiation are reduced. A matt white paint was applied on the wrap, followed by a black speckle pattern to facilitate displacement and strain measurements using 3D DIC system. A total of 2 specimens were tested.

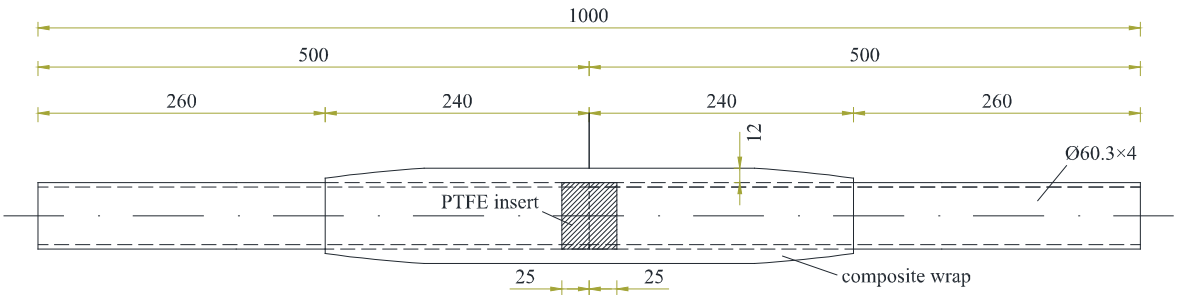

Figure 1. Geometry of specimen

Test set-up is shown in Figure 2. During the fatigue tests, all the specimens were loaded with the force range of 15-150kN (R=0.1), while the maximum force is approximately half of the static resistance obtained in separate tests. The loading frequency is 4Hz. Fatigue tests were stopped when stiffness degradation of the joint fully stabilized, then static tests were carried out on the same specimen to determine the remaining static resistance. The static tests were conducted through displacement control with the loading rate as 1mm/min. All the tests were carried out at room temperature.

GOM Aramis 3D DIC system with 12MPx cameras was positioned to acquire the local displacements and strains as shown in Figure 2. DIC measurement intervals during cyclic loading were controlled by the testing machine. At an interval of 1000 cycles, the cyclic loading is stopped, then photos are taken at the minimum and maximum forces, respectively.

  doi:10.5075/epfl-298799_978-2-9701614-0-0

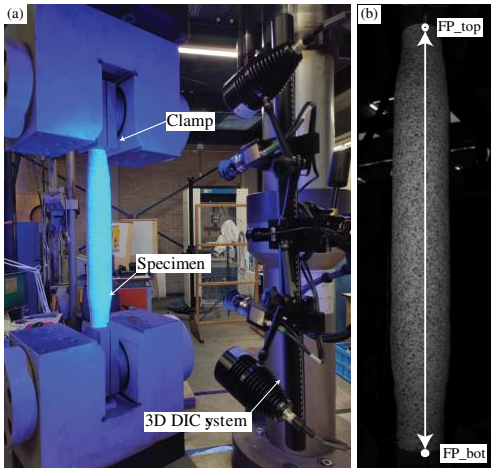

Figure 2. Test set-up and 3D DIC system

3. Test results and discussion

3.1 Stiffness degradation

To exclude any possible slip between the steel tube and grips of the testing machine at the load introduction point, the relative displacement, exclusively within the length of the specimen, measured by DIC technique was used to derive the stiffness degradation curves by Eq. (1).

$$k(N) = \frac{F_{max}(N) - F_{min}(N)}{\Delta L_{max}(N) - \Delta L_{min}(N)} \quad (1)$$

where $F_{max}(N)$ and $F_{min}(N)$ are the maximum and minimum applied forces at the Nth cycle, $\Delta L_{max}(N)$ and $\Delta L_{min}(N)$ are the elongations of the specimen between top and bottom facet points (see Figure 2 (b)) at the maximum and minimum loads respectively. Relative stiffness (k(N)/k(1)) against the number of cycles for both specimens are summarized in Figure 3. It can be seen from the figure that stiffness of the specimens degraded continuously during the cyclic loading due to crack propagation. It should be noted that the crack propagation can occur either as a debonding at the composite-to-steel interface or as an delamination within the composite wrap layers, which will be further discussed in section 3.2. Stiffness degradation shown in Figure 3 exhibits a stabilization trend for both tested specimens, namely a major (about 45%) stiffness degradation is found within the first 100,000 cycles, after which only 10% stiffness was lost until stop of the test at around 400,000 cycles. The stabilization phenomenon mainly results from stabilization of crack propagation, which will be discussed in section 3.3.

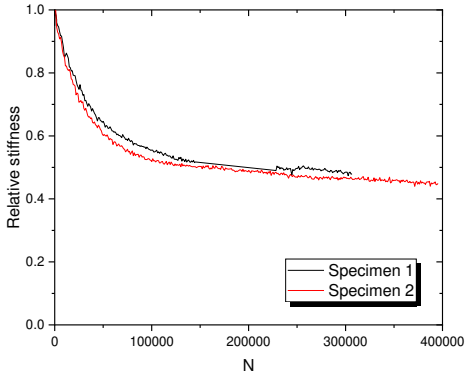

Figure 3. Stiffness degradation of specimens under fatigue load

3.2 Failure modes

During and after fatigue tests, no significant surface cracks were observed for both specimens. Further inspection was conducted through DIC system. Figure 4 (a) shows DIC contour plots of major principal strains on the surface of composite wrap corresponding to maximum loads at different cycles. It can be seen that the strain increased at the insert part at the first cycle. With increasing number of cycles, the strain-increased zone (in red colour) propagated steadily towards the wrapping ends. The increase of surface strains may be caused by multiple damage mechanisms, such as crack at the interface (debonding or delamination) and damage of the composite material. Considering the fact that the strain at the insert (middle) part, where force was only transferred by composite wrap, didn't increase so much during the cyclic loading shown in Figure 5, damage of the composite material can be neglected. Accordingly, the strain increase mainly reflected bonded interface crack propagation, which will be analysed quantitatively in the next section.

During the static test after cyclic loading, steel tubes were pulled out of the composite wrap for further inspection. It can be seen from Figure 4 (b) that there is still laminates remaining on the surface of steel tubes, indicating delamination occurring within the composite wrap layers.

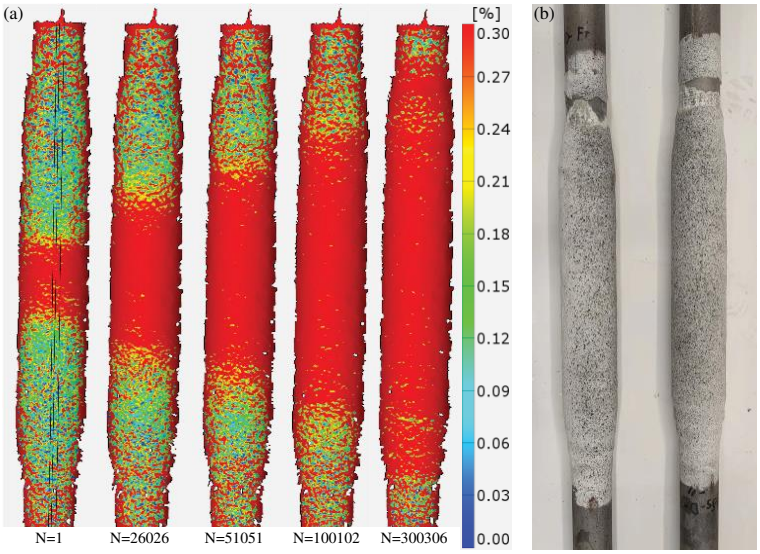

Figure 4. Failure modes of specimens (a) debonding crack propagation under cyclic loading; (b) steel tubes pulled out after static load

3.3 Debonding crack propagation

Strain distribution was extracted along the surface curves defined on the surface of composite wrap as shown in Figure 4 (a) for further analysis. The difference of strains at the maximum load and the minimum load was adopted here. The extracted strains at different number of cycles are plotted against distance to the middle of the joint in Figure 5. To average out some noise in the DIC strain measurements, the major strain was obtained along 3 surface curves and averaged. It shows that the strain is maximum in the middle, where there is the insert, and decreases gradually towards the wrapping ends. At the strain decreasing part, strain curves from different cycles are generally parallel to each other. Different from literature [9] which shows that there should be a strain plateau at the cracked part, the plateau is not obvious even at the insert part in the analysed case. This may be attributed to the shear deformation gradient of

  doi:10.5075/epfl-298799_978-2-9701614-0-0

such thick composite laminates, which is caused by restraining from the bonded part and friction effect at the cracked interface. To avoid scatter of strain distribution at this area with complex stress state, a relatively low strain threshold was taken around the 'steady strain slope' region (between 0.1%-0.2%) to calculate the crack increments. The crack length is calculated separately for each brace and equals to the summation of crack increments each cycle plus the initial crack length of 25mm. A sensitivity analysis of the strain threshold was carried out as shown in Figure 5 (b). The results show that within the 'steady strain slope' region, the influence of adopting different thresholds is insignificant, while a higher or lower threshold may result in scattering of calculated results due to scattering of strain distribution curves outside the 'steady strain slope' region. In the following analysis, strain threshold of 0.15% is adopted for the analysed case.

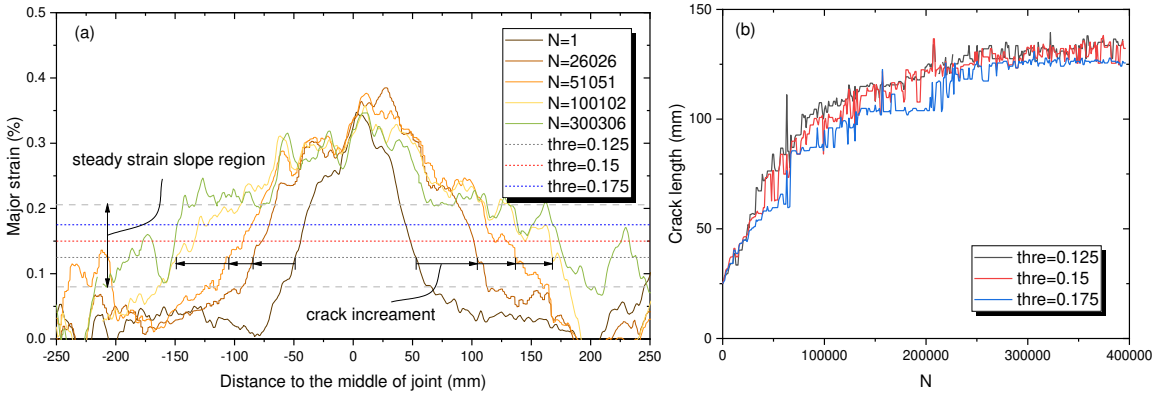

Figure 5. Crack length determination method (a) strain distribution along specimen (Specimen 2); (b) sensitivity analysis of thresholds for determining crack length (on bottom brace of Specimen 2)

The monitoring results for all the braces are summarized in Figure 6. It can be seen that for each specimen, crack propagations of top and bottom braces are identical, indicating symmetric fatigue performance of the specimens. Similarly to stiffness degradation, crack propagation rate also shows a stabilization trend. During the first 10,000 cycles, crack length increased steadily from 25mm to 115mm, while after that additional 15mm was achieved during the following 30,000 cycles leading to total crack length of 130mm. Considering that fatigue crack propagation is driven by strain energy release rate (SERR) at the crack tip according to Paris' law [10], this stabilization phenomenon is contradictory to the theory since the SERRs are constant at different crack lengths according to finite element analysis.

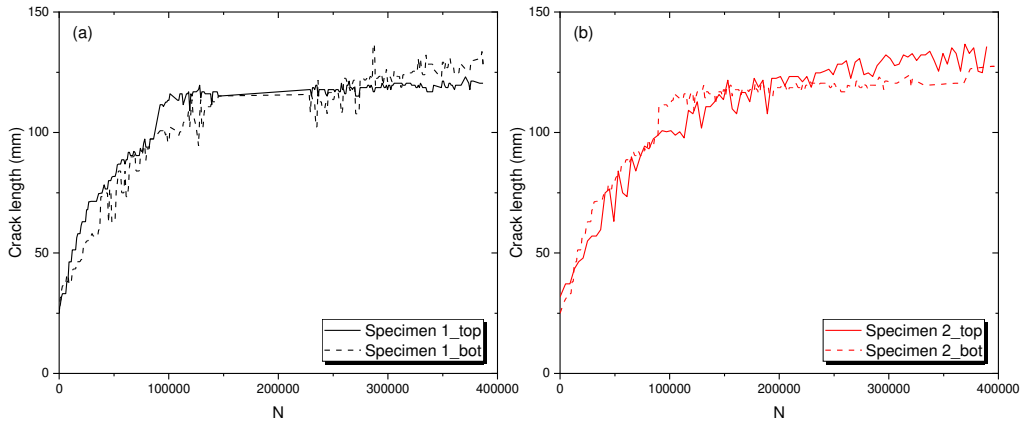

Figure 6. Crack growth on separate braces of (a) Specimen 1; (b) Specimen 2

An explanation can be made by looking at the failure mode given in Figure 4 (b), which is delamination within the first layer of composite wrap. The friction or fiber bridging effect at the cracked interface may dissipate part of the input energy, causing the SERR at the crack tip to reduce and leading to a smaller crack growth rate. Considering that fiber bridging effect is not predominate under mode II fatigue loading [11], the friction effect may dominate. This stabilization phenomenon is further studied out of the scope of this paper.

3.4 Static test after fatigue loading

After fatigue tests, the specimens were tested in monotonically increasing regime to check the influence of cyclic load on residual static resistance. The load-displacement curves are summarized in Figure 7. Results of specimens without being tested cyclically from previous study are also included for comparison. It can be seen that the initial stiffness of Specimen 1 and Specimen 2 is around 95kN/mm, which is 55% lower than that of previous specimens, namely 214kN/mm. This stiffness difference just equals to stiffness loss during cyclic load. After the elastic stage, a plateau due to steel yielding followed by hardening of steel materials was observed for Specimen 2 (The nominal yield strength of the steel tube is 252kN). The ultimate resistance of the specimen as well as the previous statically tested joint is around 300kN, after which a sudden failure occurred due to delamination as shown in Figure 4 (b). Considering that the remaining bond length for each braces is 240-130=110mm, the test results indicate that specimens with remaining bonding length of 1.5-2 diameters of the steel tube after cyclic loading can still sustain its original resistance. There is no sudden failure for Specimen 1, with the ultimate resistance being 260kN. After failure or ultimate resistance of the specimens, steel tubes were pulled out for further inspection which revealed that the failure plane is within the first layer of the composite laminate of the wrapped and not directly on the interface. This can be one explanation for steadily decreasing segment of the load-displacement curves.

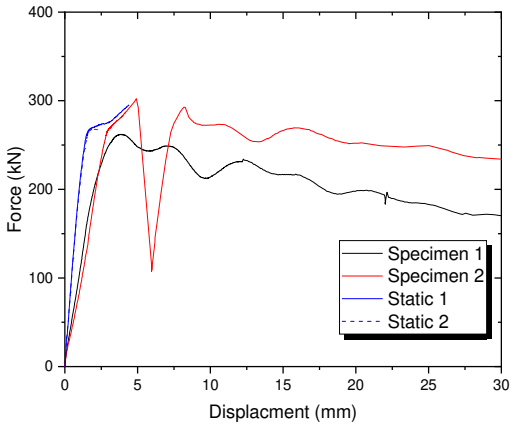

Figure 7. Load-displacement curve of specimens under static load after fatigue tests

4. Conclusions

Tensile fatigue tests were conducted on axial wrapped composite joints for 60mm diameter CHS steel tubes in this paper. 3D DIC system was employed to quantify the crack propagation within the specimen during cyclic load by monitoring surface strains on the composite wrap. A strain threshold was chosen after sensitivity analysis to determine the crack length. After fatigue tests, static tests were carried out to check the influence of cyclic load on residual static resistance of the joints. From studies mentioned above, main conclusions can be drawn as follows:

  doi:10.5075/epfl-298799_978-2-9701614-0-0

- Stiffness degradation of wrapped composite joints under cyclic loading is mainly due to delamination at the first composite wrap layer. The stiffness degradation exhibited a stabilization trend. A major stiffness degradation of 45% was found within the first 10,000 cycles, after which only 10% stiffness was lost in the remaining 390,000 cycles.
- Sensitivity analysis of strain threshold for determining crack length showed that the choice of threshold within the 'steady strain slope' region has insignificant influence on calculated crack length. A strain threshold of 0.15% was adopted in this study.
- After fatigue tests, the static resistance is the same with that of specimens without being tested cyclically.

Acknowledgements

The authors would like to express their gratitude to RVO for the financial support with Topsector Energiesubsidie van het Ministerie van Economische Zaken through WrapNode-I project. Acknowledgements are made towards GROW for their help in valorisation regarding renewable energy and energy transition and to Tree Composites B.V. for the production of specimens.

References

1. Wardenier J, Packer JA, Zhao XL, Van der Vegte GJ. Hollow sections in structural applications. Rotterdam, The Netherlands: Bouwen met staal. 2002.
2. Pavlovic M, Bogers P, Veljkovic M. Method for Making a Virgin Joint Between Two Separate Structural Hollow Sections. United States patent application US 17/052,303. 2021 Mar 18.
3. He P, Pavlovic M. Failure modes of bonded wrapped composite joints for steel circular hollow sections in ultimate load experiments. Engineering Structures 2022; 254:113799.
4. Feng W, Pavlovic M. Fatigue behaviour of non-welded wrapped composite joints for steel hollow sections in axial load experiments. Engineering Structures 2021; 249:113369.
5. Duchene P, Chaki S, Ayadi A, Krawczak P. A review of non-destructive techniques used for mechanical damage assessment in polymer composites. Journal of Materials Science 2018; 53:7915-38.
6. Ghiassi B, Xavier J, Oliveira D V., Lourenço PB. Application of digital image correlation in investigating the bond between FRP and masonry. Composite Structures 2013; 106:340-9.
7. Zhang P, Lei D, Ren Q, He J, Shen H, Yang Z. Experimental and numerical investigation of debonding process of the FRP plate-concrete interface. Construction and Building Materials 2020; 235: 117457.
8. Ali-Ahmad M, Subramaniam K, Ghosn M. Experimental Investigation and Fracture Analysis of Debonding between Concrete and FRP Sheets. Journal of Engineering Mechanics 2006; 132:914-23.
9. Wang HT, Wu G, Pang YY, Shi JW, Zakari HM. Experimental study on the bond behavior between CFRP plates and steel substrates under fatigue loading. Composites Part B 2019; 176:107266.
10. Anderson WE, McEvily AJ. A Critical Analysis of Crack Propagation Laws. Journal of Basic Engineering 1963; 85(4): 528-533.
11. Khan R. Fiber bridging in composite laminates: A literature review. Composite Structures 2019; 229:111418.

  doi:10.5075/epfl-298799_978-2-9701614-0-0

ULTRASOFT AND HYPERELASTIC ELECTRICALLY CONDUCTIVE NANOCOMPOSITES FOR STRAIN SENSING APPLICATIONS

Oliver Tomes, Han Zhang, Emiliano Bilotti, Dimitrios G. Papageorgiou

School of Engineering and Materials Science, Queen Mary University of London, London, UK – o.tomes@qmul.ac.uk

Abstract: *In this work we employed a highly scalable and solvent-free method to create electrically conductive composites capable of being stretched over several times their own length. The resulting flexible conductor has low elastic modulus in the order of 300 kPa and stretchability suitable for applications in wearable electronics. The electromechanical characterization of the nanocomposite system demonstrates strain sensing capabilities with sensitivities many times higher than traditional metal strain gauges.*

A three-roll mill was used to disperse reduced graphene oxide throughout a silicone rubber (SR) thermoset resin using mechanical forces only. The procedure offers a green alternative to many synthesis methods presented in current polymer nanocomposites research, whilst still achieving a highly effective dispersion of the nanofiller throughout the polymer matrix. Only small quantities of nanofiller are required to achieve the desired electrical properties (as percolation was achieved at ultra-low graphene contents), making synthesis of the high-performing multifunctional nanocomposite materials both sustainable and cost effective.

Keywords: nanocomposites; graphene; silicone rubber; strain sensing; wearable devices

1. Introduction

Conductive elastomer nanocomposites offer new opportunities for wearable electronics in applications such as health monitoring, detection of mechanical functions, temperature sensing, heating, power generation, energy storage, etc. [1]. Devices made using this relatively new class of materials offer improved compliance, robustness and sensitivities when compared with conventional silicon/metal-based devices [2]. Moreover, the effect of the elastic polymer matrix supporting a conductive filler network allows for repeatable strain sensing applications at unprecedented working ranges (10-1000% strain) [3, 4].

In this work we employed a highly scalable and solvent-free method to create electrically conductive composites capable of being stretched over several times their own length. Three-roll milling was used to disperse reduced graphene oxide throughout a silicone rubber (SR) thermoset resin using mechanical forces only. Within the three-roll mill (TRM), a combination of different roller speeds and microscale gap sizes generates large shearing forces which can facilitate high levels of dispersion and deagglomeration of the filler [5]. The process offers an eco-friendly alternative to many synthesis methods presented in current polymer nanocomposites research that commonly involve large quantities of solvents, whilst still achieving a highly effective dispersion of the nanofiller throughout the polymer matrix [6].

The resulting flexible conductor displays a low elastic modulus in the order of 300 kPa and stretchability suitable for applications in wearable electronics. Electromechanical properties

  doi:10.5075/epfl-298799_978-2-9701614-0-0

have been investigated revealing strain sensing capabilities with favorable sensitivities over large working ranges. Only small quantities of nanofiller are required to achieve the desired functionalities (as electrical percolation was achieved at ultra-low graphene contents), making synthesis of the high-performing multifunctional nanocomposite materials both sustainable and cost effective.

2. Materials and methods

2.1 Materials

Ecoflex 00-20 (platinum-catalyzed silicone rubber from Smooth-On) was used as the polymer matrix for all nanocomposites in this study. The filler used was reduced graphene oxide (rGO) supplied by Avanzare in powder form with an average thickness <3 nm and lateral size ∼40 μm according to the supplier.

2.2 Sample preparation and characterization

To prepare the silicone rubber/rGO (SR/rGO) nanocomposites, rGO powder was first dried at 60^{o}C for 2 hours to remove humidity. Powder was subsequently mixed manually with silicone resin precursor and crosslinker separately. Three-roll mill (80E EXAKT GmbH) was then used to disperse the filler throughout both parts of the silicone resin separately (precursor and crosslinker) for a total of 4 cycles before combining to cure. Parameters used for the three-roll mill were based upon the medium shear force method in Kernin *et al.* [7]. Samples were then compression molded into films using 25kN force (Rondol 10T Press) for 12 hours at room temperature to ensure proper cure.

Scanning electron microscopy (SEM) (ThermoFisher FEI Inspect F) was utilized in secondary electron imaging mode to observe thin films of rGO prepared via tip sonication followed by drop casting. Raman spectra were acquired using a Renishaw InVia Raman spectrometer with a laser wavelength of 442 nm and an objective of 50×, which produces a spot size of 1–2 μm. The level of reduction of the rGO nanofiller powder was measured via X-ray photoelectron spectroscopy (XPS) using a ThermoFisher Nexsa Surface Analysis System.

Electrical conductivity measurements were performed using the 4-probe method. Mechanical characterization was carried out using an Instron 5566. Tensile testing was completed according to ASTM D412 at a tensile rate of 500 mm/min. The electromechanical behavior was characterized by measuring the instantaneous two-point resistance of samples with a digital multimeter (Agilent, 34410A) while dynamic strain was applied via the Instron 5566. The measured trend of resistance against strain was then fit to an exponential function to an R^2 value of 99% in order to determine the sensitivity, G_{exp}, of samples over a range of filler loadings.

3. Results and discussion

3.1 Filler characterization

The rGO platelets seen in the SEM micrograph in Fig. 1a display a number of folds and wrinkles which are known to greatly reduce the mechanical reinforcing efficiency of 2D materials in polymers [8]. Raman spectroscopy (Fig. 1b) gave peak ratios of I_D/I_G = 1.56 which indicates a high defect density within graphene layers resulting in part from oxygen functional groups (primarily carboxyl, hydroxyl and epoxy) which remain after reduction of the graphene oxide [9]. These are

expected to facilitate good dispersion of the rGO, enable stronger bonding between the filler and the matrix through formation of chemical bonds and promote interfacial stress transfer in the nanocomposites [10]. Using XPS, the ratio of carbon to oxygen (see Fig. 1c) was measured to be 10.5 indicating high level of reduction for the rGO filler (C:O ratio typically ~2 for graphene oxide [11]). The wrinkled structure seen in the SEM and the high defect density indicated from the D and G Raman peaks can thus also be largely attributed to sp^3 hybridized carbon atoms left behind in sites of the basal plane where functional groups have been removed during reduction.

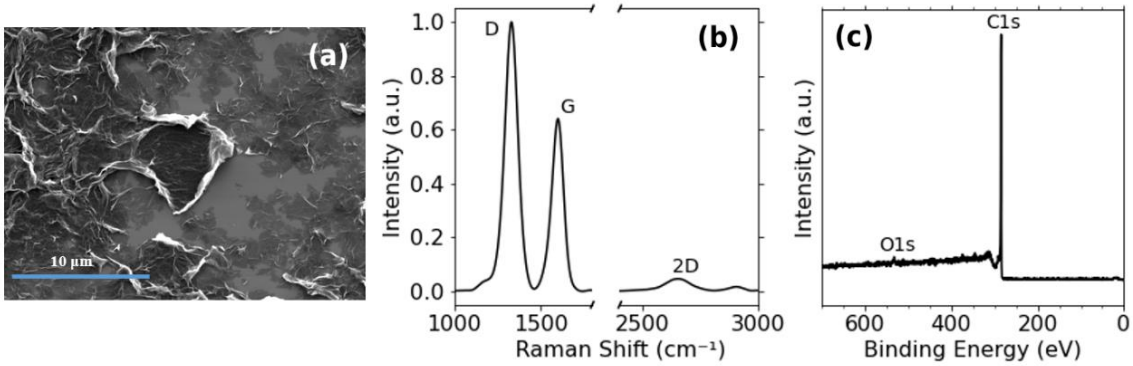

Figure 1. Characterization of rGO filler. (a) SEM image of rGO filler. (b) Raman showing D, G, and 2D peaks, respectively. (c) XPS showing C/O ratio = 10.5.

3.2 Composite properties

Mechanical testing of the silicone rubber matrix revealed that the pure polymer displays a very low Young's modulus of 0.04 MPa (Fig. 2a) and high failure strain of 740% (Fig. 2b). Incorporation of the rGO nanoplatelets led to a linear increase of the 100% modulus of the nanocomposite with filler loading, indicating good dispersion of rGO throughout the polymer matrix. A fit to the classic rule of mixtures gives a filler modulus of 44 MPa which is 3-4 orders of magnitude below values measured (~25 GPa) for few-layer reduced graphene oxide [12]. While the rule of mixtures model assumes perfect stress transfer between phases in a composite, the low filler modulus of the reinforcement ($E_f \approx 44$ MPa) suggests a particularly ineffective stress transfer at the polymer/platelet interface. This is not surprising, given the ultra-low shear modulus of the matrix and the fact that reinforcement takes place through shear at the filler-matrix interface. This is in accordance with a number of literature works on similar elastomer/graphene nanocomposites [13-15].

Notably the range of 100% modulus values for SR/rGO composites of the given loadings (0.09 – 0.38MPa) corresponds roughly to the range of stiffness associated with human skin (0.08 – 0.60MPa) [16]. This feature allows for wearable devices made of the nanocomposite material as it is expected to adhere favorably to the body and easily comply with body movements without causing any discomfort. As expected, higher loadings of graphene lead to fracture at lower strains, due to aggregates at higher filler loadings acting as internal defects. However, all conductive composites remained highly flexible, stretching 2-5 times their own length before breaking.

Although the reinforcing mechanism affecting the strength of the composite system is relatively unclear due to the statistical nature of tensile strength, the strength of the nanocomposites (Fig. 2c) does not degrade significantly with the addition of rGO to the polymer. The combination of

decreased failure strain and tensile strength at the highest loadings does mean that composites with >0.3wt.% content have considerably lower toughness (Fig. 2d) than the pure silicone rubber; however, the toughness of all specimens is still well suited for the intended applications.

Additionally, due to the highly elastic nature of the silicone rubber matrix, the composite material exhibits relatively low mechanical hysteresis when undergoing cyclic loading at high strains (Fig. 2e). This feature is particularly desirable for dynamic strain sensing applications in fields such as wearable electronics and soft robotics.

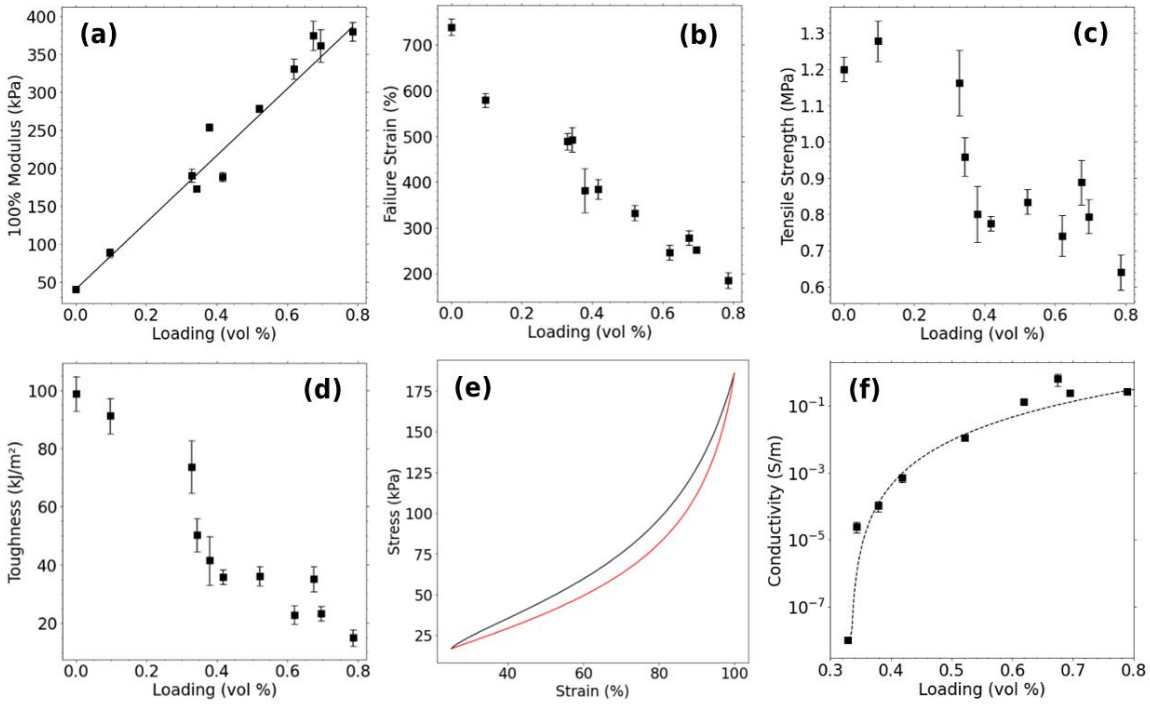

Figure 2. Electromechanical characterization of SR/rGO composites. (a) 100% modulus fit to rule of mixtures giving 44.0 MPa for filler modulus. (b) Strain at break versus rGO filler content. (c) Tensile strength versus rGO filler content. (d) Toughness versus rGO filler content. (e) Mechanical hysteresis of composite film (1.23wt.%). (f) Electrical conductivity versus rGO filler content exhibiting percolation at 0.33vol.% (0.59wt.%).

Electrical conductivity of the SR/rGO composite (seen in Fig. 2f) sets in at very low filler loadings and reaches values of 0.1-1 S/m near 1 wt.%. Electrical percolation occurs at 0.33 vol % (0.59wt.%) meaning conductive composites can be manufactured using ultra-low quantities of rGO filler. Combined with the relatively simple, solvent-free processing method, this renders high-performing devices made using the described nanocomposite system exceptionally cheap and sustainable to produce.

3.2 Strain sensing and sensitivity

The conductivity of stretchable elastomers reinforced with conductive fillers is altered when strain is applied across the material [17]. In most cases the conductivity will decrease due to the breakdown of the 3D network of conductive fillers up to the point where the network becomes too sparse to facilitate electrical conduction. Electromechanical measurements in this study show the resistance measured across the SR/rGO composites to increase exponentially with respect to the strain applied, up to a point which we will refer to as the critical strain, ε_{max}. This

  doi:10.5075/epfl-298799_978-2-9701614-0-0

can be seen in Fig. 3a which shows the relative change in resistance across a composite film with 1.10wt.% rGO content under a tensile strain rate of 2 mm/min. The critical strain was found to be 74% since the exponential trend in resistance with respect to strain is followed up to there. Past the critical strain, the rate of increase in resistance rises even more sharply as the strained material becomes electrically insulating.

For traditional strain gauges, sensitivity is measured using the gauge factor G, which corresponds to the rate at which resistance changes with respect to the strain applied. Typically these strain sensors are metallic foil based and have gauge factor values of G = 2 – 5 and stretchability limited to ~5% strain. Semiconductor based strain gauges possess a higher gauge factor G = 100-1000 however, much like with metals, their brittle and rigid nature and low fracture strains also limit their use for applications in wearable electronics [18, 19].

$$G = \frac{\Delta R}{R_0 \Delta \varepsilon} \tag{1}$$

Although not always followed in the literature when reporting on new polymer nanocomposite based strain sensors, this measure of sensitivity would conventionally be applicable only to a relatively small range of low strain values over which resistance increases linearly with respect to strain [4]. In the case of soft elastomer nanocomposites with conductive fillers such as the ones in this study, however, it is possible to calibrate the relationship between resistance and strain over much larger ranges using the following relationship [20].

$$R = R_0 e^{G_{exp}\varepsilon} \qquad (\varepsilon < \varepsilon_{max}) \tag{2}$$

Fitting experimental data to this relationship for SR nanocomposite samples with various rGO loadings gives values for the sensitivity G_{exp} shown in Fig. 3b. Also shown in this graph is the critical strain ε_{max}, corresponding to the working range that the resistance response to strain can be calibrated over using Eq. (2). As the conductive filler network is randomly distributed throughout the silicone matrix, the sensitivity of strain sensing measurements depends heavily on the filler content. We see that for the lowest filler contents, sensitivity is highest however the critical strain is lowest and vice versa. This is somewhat expected since while electrical conductivity does not vary significantly for loadings past electrical percolation, smaller quantities of randomly distributed conductive filler will require less strain to reach separations above that of the tunnelling distance of electrons to adjacent filler sites.

This trade off means that this nanocomposite material can be tailored to strain sensing applications. For applications where ultra-high sensitivity is required, lower loadings (0.6 - 1.1wt.%) can be used to measure strain over smaller strains, and where large strains are required, higher loadings (1.2 - 1.4wt.%) can be used with sensitivities still far superior to those of conventional metallic strain sensors. Furthermore, for applications of human body motion sensing and health monitoring, thanks to the ultra-soft silicone matrix, the highest filler loading samples are still compliant enough so as not be restrictive or cause discomfort when mounted to the skin.

  doi:10.5075/epfl-298799_978-2-9701614-0-0

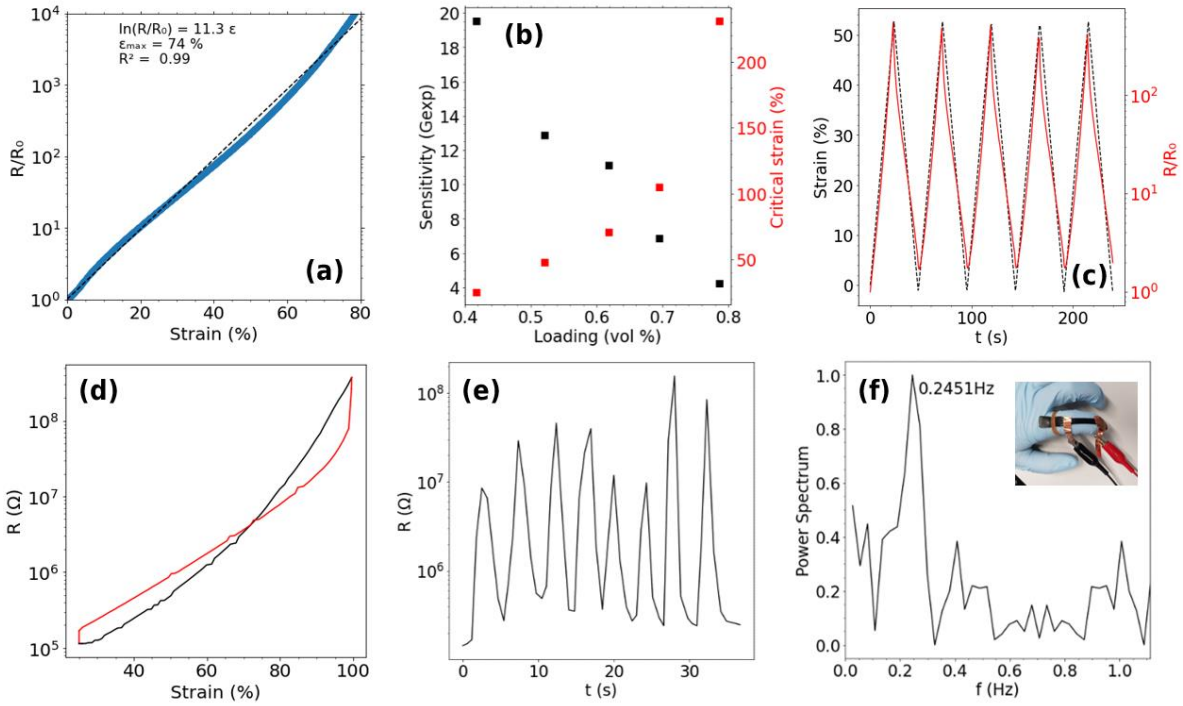

Figure 3. Strain sensing properties of SR/rGO composites.(a) Resistance variation of composite film (1.10wt.%) under tensile strain. (b) Resistance response (red line) of composite film (1.10wt.%) to cyclic strain (black dashed line) at 50mm/min. (c) Electromechanical hysteresis of composite film (1.23wt.%). (d) Sensitivity G_{exp} (black) and critical strain (red) versus rGO filler content. (e) & (f) Wearable strain sensing demonstration measuring repeated finger bending and associated frequency of motion from Fourier transform of signal (0.93wt.%).

Most importantly, unlike traditional metal strain gauges, the SR/rGO composite strain sensors are able to measure strain over of many strain cycles, allowing for monitoring of dynamic or cyclic motion. This makes them ideal for applications such as the detection of human motion, health monitoring and soft robotics. Fig. 3c shows the resistance measured when the samples were subjected to cyclic loading. The composite system exhibits some minor electromechanical hysteresis when undergoing repeated strain (see Fig. 3d) and there is some small variation in peak resistance values between cycles of the same strain amplitude which correspond to a standard deviation on strain measured at the peak of 1.2%.

It should be noted that despite the benefits of elastomeric nanocomposite strain sensors such as the ones in this study, uncertainty and drift in strain interpretation is somewhat inevitable due to viscoelastic behaviors of the polymeric matrix such as stress relaxation and creep [4]. This can affect the consistency of strain measurements in dynamic applications depending on the elastic properties of the polymer matrix. Notably, we would expect time data to be less affected by this limitation meaning that frequency measurements can also be obtained from the strain sensing output with considerable accuracy.

In Fig. 3e a demonstration of a wearable strain sensing device made with SR/rGO nanocomposite is presented where measurements have been taken on the bending of joints in the finger (roughly 30% strain). The finger is bent repeatedly roughly every 4 seconds with peaks in resistance corresponding to the position where the finger is most bent, and resistance minima where the finger is straight. Fig. 3f shows the frequency spectrum resulting from a Fourier

  doi:10.5075/epfl-298799_978-2-9701614-0-0

transform of the resistance data. A peak is seen representing the average frequency of motion measured during the joint bending motion.

4. Conclusions

Synthesis of highly flexible and stretchy conductive nanocomposites has been demonstrated via a scalable and solvent-free method. The low Young's modulus (0.1 – 0.4 MPa) and high stretchability (200-500%) of the conductive nanocomposites make them ideal for applications in wearable electronics as they are able to stretch and conform comfortably with the full range of bodily motions. Ultra-low electrical percolation threshold (0.33 vol %) renders synthesis of the high-performing conductive nanocomposite materials both sustainable and cost effective.

The highly flexible and stretchy conductive nanocomposites exhibit strain sensing capabilities with sensitivities many times higher than traditional metal strain gauges. The robust exponential resistance response to strain allows for dynamic strain monitoring with sensitivities of G_{exp} = 4-20 over ranges of 25-230% strain. This in combination with skin-compatibility means the nanocomposite system is a good candidate for use as wearable strain sensors in fields such as health monitoring, biomedical devices, human–machine interfaces, sports performance monitoring and soft robotics.

5. References

1. Wang B, Facchetti A. Mechanically Flexible Conductors for Stretchable and Wearable E-Skin and E-Textile Devices. Advanced Materials. 2019;31(28):1901408.
2. Chen J, Yu Q, Cui X, Dong M, Zhang J, Wang C, et al. An overview of stretchable strain sensors from conductive polymer nanocomposites. Journal of Materials Chemistry C. 2019;7(38):11710-30.
3. Choi S, Han SI, Kim D, Hyeon T, Kim D-H. High-performance stretchable conductive nanocomposites: materials, processes, and device applications. Chemical Society Reviews. 2019;48(6):1566-95.
4. Boland CS. Stumbling through the Research Wilderness, Standard Methods To Shine Light on Electrically Conductive Nanocomposites for Future Healthcare Monitoring. ACS Nano. 2019;13(12):13627-36.
5. Raza MA, Westwood AVK, Brown AP, Stirling C. Texture, transport and mechanical properties of graphite nanoplatelet/silicone composites produced by three roll mill. Composites Science and Technology. 2012;72(3):467-75.
6. Li Y, Zhang H, Crespo M, Porwal H, Picot O, Santagiuliana G, et al. In Situ Exfoliation of Graphene in Epoxy Resins: A Facile Strategy to Efficient and Large Scale Graphene Nanocomposites. ACS Applied Materials & Interfaces. 2016;8(36):24112-22.
7. Kernin A, Wan K, Liu Y, Shi X, Kong J, Bilotti E, et al. The effect of graphene network formation on the electrical, mechanical, and multifunctional properties of graphene/epoxy nanocomposites. Composites Science and Technology. 2019;169:224-31.
8. Liu M, Kinloch IA, Young RJ, Papageorgiou DG. Modelling mechanical percolation in graphene-reinforced elastomer nanocomposites. Composites Part B: Engineering. 2019;178:107506.
9. Stylianakis MM, Viskadouros G, Polyzoidis C, Veisakis G, Kenanakis G, Kornilios N, et al. Updating the Role of Reduced Graphene Oxide Ink on Field Emission Devices in Synergy with Charge Transfer Materials. Nanomaterials. 2019;9(2).
10. Li Z, Young RJ, Wang R, Yang F, Hao L, Jiao W, et al. The role of functional groups on graphene oxide in epoxy nanocomposites. Polymer. 2013;54(21):5821-9.

  doi:10.5075/epfl-298799_978-2-9701614-0-0

11. Compton OC, Nguyen ST. Graphene Oxide, Highly Reduced Graphene Oxide, and Graphene: Versatile Building Blocks for Carbon-Based Materials. Small. 2010;6(6):711-23.
12. Gómez-Navarro C, Burghard M, Kern K. Elastic Properties of Chemically Derived Single Graphene Sheets. Nano Letters. 2008;8(7):2045-9.
13. Liu M, Cataldi P, Young RJ, Papageorgiou DG, Kinloch IA. High-performance fluoroelastomer-graphene nanocomposites for advanced sealing applications. Composites Science and Technology. 2021;202:108592.
14. Liu M, Kinloch IA, Young RJ, Papageorgiou DG. Realising biaxial reinforcement via orientation-induced anisotropic swelling in graphene-based elastomers. Nanoscale. 2020;12(5):3377-86.
15. Liu M, Papageorgiou DG, Li S, Lin K, Kinloch IA, Young RJ. Micromechanics of reinforcement of a graphene-based thermoplastic elastomer nanocomposite. Composites Part A: Applied Science and Manufacturing. 2018;110:84-92.
16. Kim D-H, Lu N, Ma R, Kim Y-S, Kim R-H, Wang S, et al. Epidermal Electronics. Science. 2011;333(6044):838-43.
17. Boland CS, Khan U, Backes C, O'Neill A, McCauley J, Duane S, et al. Sensitive, High-Strain, High-Rate Bodily Motion Sensors Based on Graphene–Rubber Composites. ACS Nano. 2014;8(9):8819-30.
18. Qiu A, Li P, Yang Z, Yao Y, Lee I, Ma J. A Path Beyond Metal and Silicon:Polymer/Nanomaterial Composites for Stretchable Strain Sensors. Advanced Functional Materials. 2019;29(17):1806306.
19. Lu Y, Biswas MC, Guo Z, Jeon J-W, Wujcik EK. Recent developments in bio-monitoring via advanced polymer nanocomposite-based wearable strain sensors. Biosensors and Bioelectronics. 2019;123:167-77.
20. O'Mara MA, Ogilvie SP, Large MJ, Amorim Graf A, Sehnal AC, Lynch PJ, et al. Ultrasensitive Strain Gauges Enabled by Graphene-Stabilized Silicone Emulsions. Advanced Functional Materials. 2020;30(32):2002433.

MECHANICAL, RHEOLOGICAL AND THERMAL EVALUATION OF POLY(LACTIC ACID) (PLA) / MICRO FIBRILLATED CELLULOSE (MFC) PLASTICIZED BIOCOMPOSITES PRODUCED WITH FLAT DIE EXTRUSION AND CALENDERING

Vito Gigante[a,b], Laura Aliotta[a,b], Giovanna Molinari[a], Roberto D'Ambrosio[c], Maria Beatrice Coltelli[a,b], Luigi Botta[d], Francesco Paolo La Mantia[d], Andrea Lazzeri[a,b]

[a] *University of Pisa, Department of Civil and Industrial Engineering, Via Diotisalvi, 2, 56122, Pisa, Italy – vito.gigante@unipi.it*
[b] *Interuniversity National Consortium of Materials Science and Technology (INSTM), Via Giusti 9, 50121, Florence, Italy*
[c] *Istituto per i Processi Chimico-Fisici, IPCF-CNR, Via G. Moruzzi 1, 56124, Pisa, Italy*
[d] *Department of Engineering, RU INSTM of Palermo, University of Palermo, Viale delle Scienze Palermo, Italy*

Abstract: *The use of Micro Fibrillated Cellulose (MFC) as filler for polymeric matrices attempts an increasing interest both in academia and industry. In this framework, encouraging results have been obtained using plasticizers, as dispersing aids, during twin-screw extrusion that optimizes the process parameters and avoid MFC agglomeration. In this work, two commercial typologies of waterborne solution of MFC (Exilva and Celish) were melt-compounded in a PLA matrix through semi-industrial twin-screw extruder and calendered, producing films of 150 µm thickness. These films were mechanically and thermally characterized, moreover the migration of the plasticizer along the time was evaluated through analytical model and the diffusion coefficient was calculated.*

Keywords: Cellulose; PLA; biocomposites; Extrusion; Migration

1. Introduction

The need of finding new substitute materials, to minimize environmental footprint, is ever more pressing due to many ecological issues [1]. Polylactic acid (PLA) has gained interest because it can be synthesized from natural resources [2]. A common sustainable technique to improve the PLA performances is related to different strategies, such as the development of natural-filler-reinforced biocomposites [3]. Cellulose is known to improve barrier and mechanical properties of thermoplastic biopolymer films and currently special interest has been paid to PLA/microfibrillated cellulose (MFC) biocomposites [4] also for films applications.
As regards the production of PLA based films which can be carried out by flat die or blowing extrusion, the major drawback is represented from their excessive brittleness making them not commercially useful. To overcome this issue the mechanical flexibility of the PLA films can be improved through the addition of low-to-medium molecular weight plasticizers [5]. The choice of the most suitable plasticizer, especially in biobased applications, depends from the achievement of a good miscibility degree in order to avoid remixing, films opacity and, in

  doi:10.5075/epfl-298799_978-2-9701614-0-0

addition, its migration out of the film [6]. Moreover, the plasticizer migration also affects the final mechanical properties leading to a loss of flexibility and toughness [7].
Different approaches can be adopted to limit this phenomenon, filler addition is particularly interesting and, between the various nano- and micro-scale fillers available in commerce, cellulose is very attractive due to its well-known contribution in improving both the barrier and the mechanical properties of bio-plastics matrices [8,9]. This material is usually called micro-fibrillated cellulose (MFC), nano-fibrillated cellulose (NFC) or cellulose nanofibrils (CNF) and it is obtained as an aqueous suspension [10]. Nevertheless, by considering an exploitable industrial production of MFC based bio-composites, the critical drawback of cellulose agglomeration must be overcome to minimize its vulnerability to environmental attacks such as bio-damage, thermal deterioration and mechanical failure at the interface [11].
The aim of this study was to investigate mechanical and thermal properties, besides the plasticizer migration, of flat die extruded PLA based films reinforced with MFC as a filler using two different biobased plasticizers as dispersing agents (polyethylene glycol (PEG) and lactic acid oligomer (OLA)). Finally, the results have been compared after 50 days from the biocomposites manufacturing, evaluating the crystallinity and mechanical properties variations.

2. Materials and Methods

2.1 Materials

- Poly(Lactic Acid) (PLA), trade name PLA 2003D, purchased from Natureworks. ìdensity:1.24 g/cm^3; molecular weight (MW): 200,000 g/mol; melt flow index (MFI): 6 g/10 min at 190 ◦C: 2.16 kg).
- Poly(ethylene glycol) (PEG 400) purchased from Sigma-Aldrich (CAS number: 25322-68-3; MW: 400 g/mol, density: 1.12 g/cm^3; water solubility: 100 mg/mL).
- Lactic acid oligomer (OLA), trade name Glyplast OLA 2, provided by Condensia Quimica, (Barcelona,Spain) (ester content: >99%; density: 1.10 g/cm^3, water content (ASTM E 203): maximum 0.1%; molecular weight: 500 g/mol.
- MFC Exilva F 01-L 10% kindly provided by Borregaard (Sarpsborg, Norway) with a solid content of 1.5–2.4% (viscosity - in H_2O 2% - ≥ 14,000 mPa·s).
- MFC Celish KY100S 25% purchased from Daicel Miraizu Ltd. (Osaka, Japan) (CAS number: 9004-34-6).

Both MFC, morphologically analyzed in a previous work [10] are characterized by long and thin fibers arranged in a three-dimensional net- work interconnected to each other.

2.2 Methods

2.2.1 PLA/MFC compounding and flat die extrusion

The accurate MFC feeding into the extruder through the addition of bio-based plasticizers, has proved to be very effective in avoiding agglomeration issues. Furthermore, the procedure, successfully adopted and illustrated in [10] was used. The extrusion compounding was carried out on a semi-industrial COMAC EBC 25HT (L/D = 44) twin-screw extruder (COMAC, Cerro

Maggiore, Italy). The formulations obtained and their relative compositions are reported in *Table 1.*

Table 1: Formulation names and compositions

Name	PLA (wt.%)	PEG (wt.%)	OLA (wt.%)	Exilva (wt.%)	Celish (wt.%)
P_O	85	-	15	-	-
P_P	85	15	-	-	-
P_O_E	83.3	-	14.7	2	-
P_O_C	83.3	-	14.7	-	2
P_P_E	83.3	14.7	-	2	-
P_P_C	83.3	14.7	-	-	2

For the extrusion, PLA was added in the main extruder feeder while the plasticizer/MFC emulsions were fed through a peristaltic pump at 2/3 of the screws length. A vacuum pump (degassing system) positioned in proximity of the end of the screw ensured an efficient water stripping . The strands coming out of the extruder were cooled in a water bath and then pelletized by an automatic cutter. The granules were then dried in a DP604–615 PIOVAN dryer (Venezia, Italy) at 50 ◦C for 12 h before their flat die extrusion. The flat die extrusion has been carried out in a second extrusion step adding a flat die head, while the water bath was substituted by a AMUT calendering system. The temperature profile adopted in the extruder was the same used during the extrusion compounding with the flat die temperature set at 180°C °C. The correct homogeneity was obtained through a calendar apparatus regulated by setting the rollers cooling at 20 °C and the wind-up roll speed at 4 m/min. The obtained films were 20 mm width with a thickness of 150 µm.

2.2.2 Biocomposites characterization

Melt flow rate (MFR) measurements were carried out according to UNI EN ISO 1133 by a CEAST Melt Flow Tester MF20 (INSTRON, Canton, MA, USA). Five grams of pellets obtained by upscale extrusion were heated at 190 ◦C in a barrel and pushed through a normalized die (2.095 mm) under a constant load of 2.16 kg.

Tensile tests were carried out on an INSTRON universal testing machine model 5500R (Canton, MA, USA). The machine was equipped with a 100 N load cell interfaced with Merlin software. The specimens for tensile testing were shaped into ISO 527-2/5A dumbbell specimens with a manual Elastocon EP 08 cutting press (Elastocon, Brahmult, Sweden). The initial grip separation was equal to 25 mm and the deformation rate was set at 50 mm/min. Samples were cut in the machine direction (MD) and cross direction (CD) to evaluate the differences in the mechanical properties along the flow direction collected respectively by the wind-up roll (MD) and transverse (CD) direction. At least five specimens were tested for each formulation reporting the average values. The crystallinity degree was determined by calorimetric analysis using a Q200 TA-Instruments DSC equipped with an RSC cooling system. About 10-15 mg of material was cut

from the calendered film and it was sealed inside aluminum hermetic pan. In order to take into account the crystallinity of the system after the calendering process while monitoring its variation during the storage time, only the first heating run was considered. In particular, the following thermal program was adopted: heating from room temperature at 10 °C/min up to 190 °C. The melting temperature (T_m) and the cold crystallization temperature (T_{cc}) were registered at the maximum of the melting peak and at the minimum of the cold crystallization peak respectively. The enthalpies of melting (ΔH_m) and cold crystallization (ΔH_{cc}) were calculated integrating the areas under the corresponding peaks. The crystallinity percentages (X_{cc}) reached by the PLA were calculated as follows [12]:

$$X_{cc} = \frac{\Delta H_{m,PLA} - \Delta H_{cc,PLA}}{\Delta H°_{m,PLA} \cdot wt.\%_{PLA}} \quad (1)$$

Where $\Delta H°_{m,PLA}$ is the melting enthalpy of 100 % crystalline PLA and is equal to 93 J/g [13] while $wt._{\%PLA}$ is the total mass fraction of PLA in the formulation.

To evaluate the weight loss of films due to the plasticizers migration, three pieces of film for each formulation (40 x 40 x 0.2 mm) were put between two paper sheets. To accelerate the migration process making it more severe, the manufactured samples were kept in a ventilated oven at 60 °C (above the material T_g). Day by day the films were weighed to estimate the plasticizer weight loss over time. The film weight loss as a function of time was determined according to the following relationship [5]:

$$\%\, wt_{\,loss} = \frac{w_{t,film} - w_{t0,film}}{w_{t0,film}} \cdot 100 \quad (2)$$

where $w_{t,film}$ is the film weight at the time t and wt_0, film is the film weight at the beginning of the test (t = 0).

The MFC addition effect on the plasticizer migration was quantified according to the equations and procedure explained by Aliotta et al. in [5].

3. Results

3.1 Melt flow rate

A useful test to evaluate the processability of the studied formulations is the mass flow rate analysis. Form *Figure 1* it is possible to observe that, as expected, the fluidity of the plasticized matrices was much higher than those of all biocomposite formulations. More specifically, the PLA matrix plasticized with OLA showed a tremendous fluidity at 190 °C with a rather low melt strength and was hardly used for filming applications at such temperatures.

The melt strength was considerably improved with the inclusion of MFCs. The melt flow rate of the Celish–MFC composite was even 5 times lower than that of the Exilva–MFC. This result demonstrates that MFC can impart strengthening to the melt, but is necessary to verify if this viscosity increment can be associated with a better distribution of the cellulosic particles in the matrix and a better shielding action against plasticizer migration, going also to observe how this behaviour affects the mechanical properties

  doi:10.5075/epfl-298799_978-2-9701614-0-0

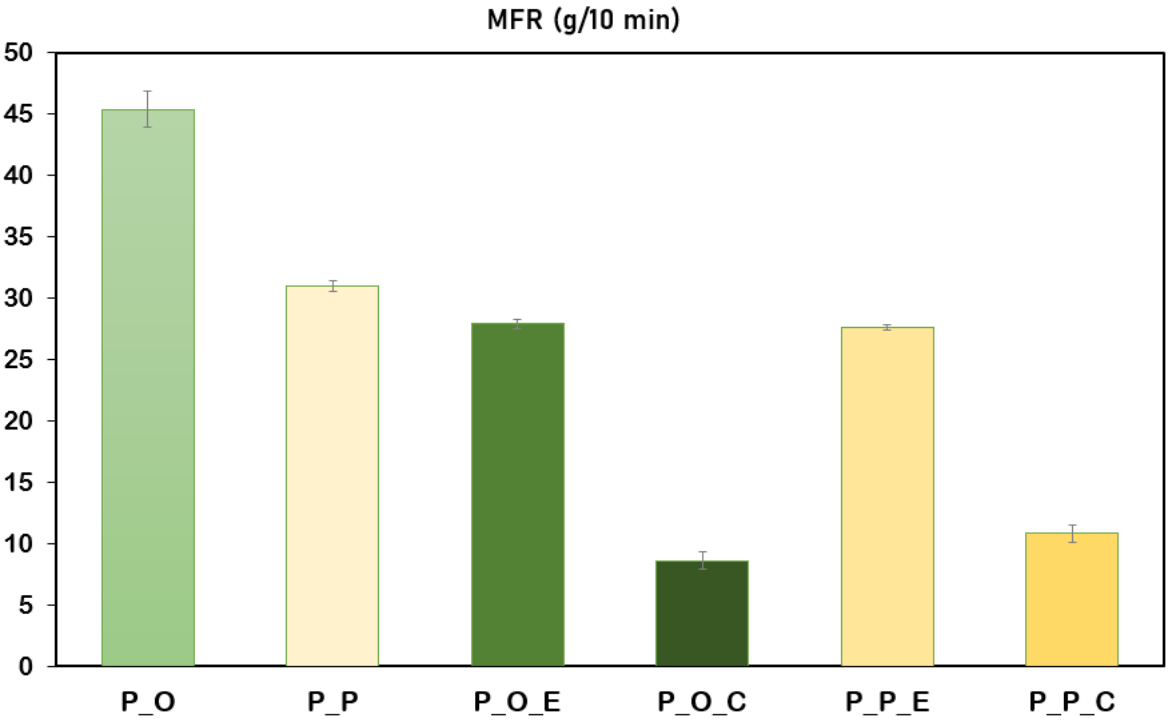

Figure 1. Mass flow rates (in g/10 min) of the PLA/MFC formulations achieved at 190 °C and with a weight of 2.16 kg

3.2 Control of the migration and associated with thermal and mechanical properties

The trends of the mass loss percentage as function of the square root time are reported for all formulations in *Figure 2*. It is interesting to observe how the formulations containing only the plasticizers showed a greater plasticizer loss over time than their counterparties containing MFC, confirming their ability in limiting the plasticizer migration. Specifically, OLA showed a greater tendency to migrate than PEG confirming the trends encountered during melt flow tests. The presence of the MFCs makes more impervious the plasticizer migration as also confirmed by the values of the calculated diffusion coefficients (using the second Fick's law [7]) that are reported in *Table 2.* The *D* values reported considered any eventual crystallization process which could have influenced the plasticizer migration, for this reason at day 1 and at day 50 crystallinity degree has been evaluated (also reported in Figure 2). Thermal results showed a general increment of crystallinity, but when the MFCs were added to the plasticized matrices, their effect resulted more marked thus significantly contributing to the plasticizer mass loss reduction. Also in this case, Exilva-MFCs showed a higher reduction of mass loss connected with a higher increase in crystallinity.

This concept is also evident from the variation of mechanical properties (tensile strength and elongation at break in MD to CD). The stress at break of the biocomposites grows over time in correlation to the loss of mass of the plasticizer; in parallel the elongation at break undergoes with an abrupt reduction for the plasticized matrices. The reduction in elongation at break over 50 days is less evident in biocomposites due to the ability of MFCs to retain the plasticiser in the mixture, thus preventing it from migrating to the surface and the film from losing its flexibility.

  doi:10.5075/epfl-298799_978-2-9701614-0-0

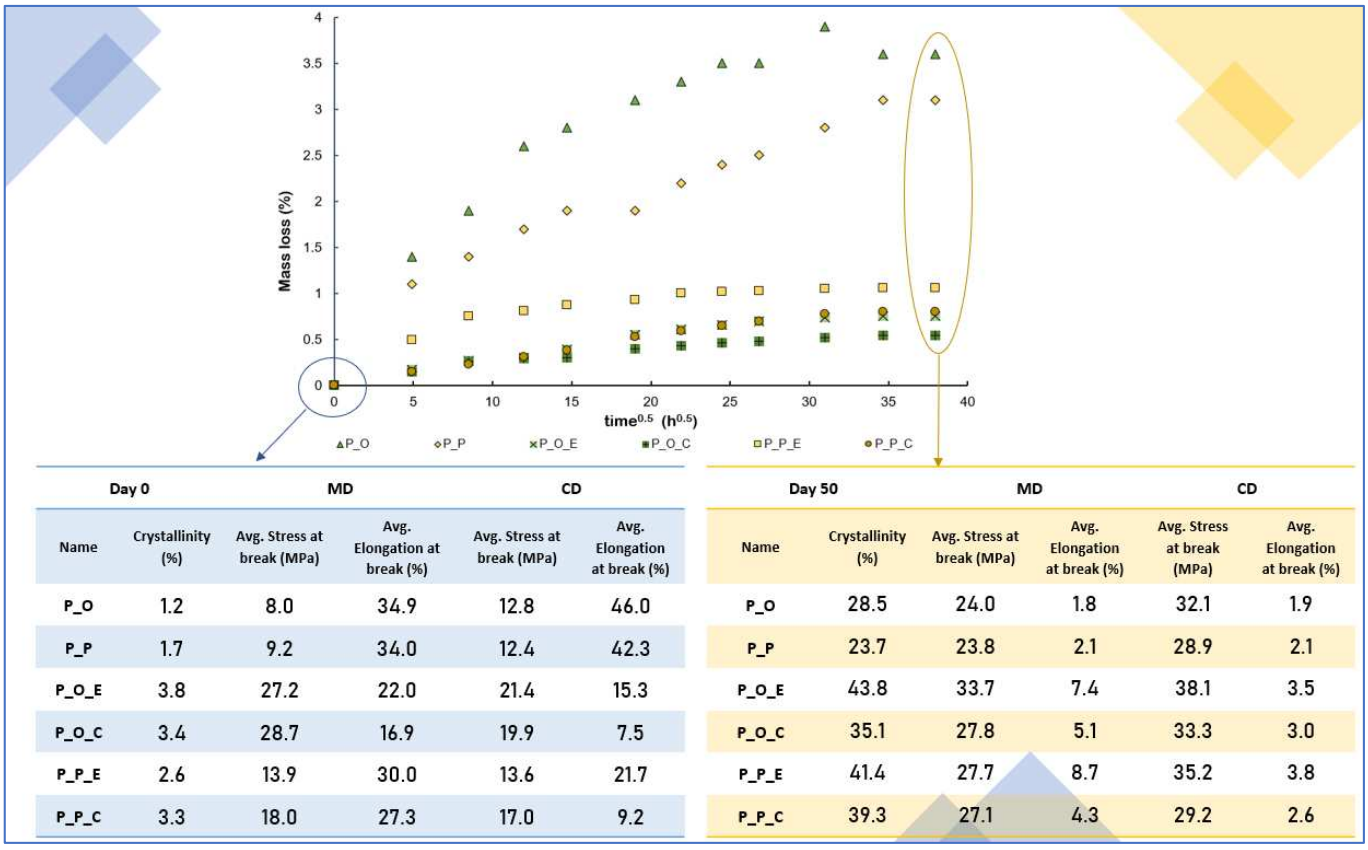

Day 0		MD		CD		Day 50		MD		CD	
Name	Crystallinity (%)	Avg. Stress at break (MPa)	Avg. Elongation at break (%)	Avg. Stress at break (MPa)	Avg. Elongation at break (%)	Name	Crystallinity (%)	Avg. Stress at break (MPa)	Avg. Elongation at break (%)	Avg. Stress at break (MPa)	Avg. Elongation at break (%)
P_O	1.2	8.0	34.9	12.8	46.0	P_O	28.5	24.0	1.8	32.1	1.9
P_P	1.7	9.2	34.0	12.4	42.3	P_P	23.7	23.8	2.1	28.9	2.1
P_O_E	3.8	27.2	22.0	21.4	15.3	P_O_E	43.8	33.7	7.4	38.1	3.5
P_O_C	3.4	28.7	16.9	19.9	7.5	P_O_C	35.1	27.8	5.1	33.3	3.0
P_P_E	2.6	13.9	30.0	13.6	21.7	P_P_E	41.4	27.7	8.7	35.2	3.8
P_P_C	3.3	18.0	27.3	17.0	9.2	P_P_C	39.3	27.1	4.3	29.2	2.6

Figure 2. Trend of mass loss over time, showing how crystallinity and mechanical properties vary from day 0 to day 50 on calendered films

Table 2: Diffusion coefficients of biocomposites studied

Name	Diffusion coefficient (D) (cm^2/s)
P_O	$2.4 \cdot 10^{-10}$
P_P	$2.3 \cdot 10^{-10}$
P_O_E	$1.4 \cdot 10^{-10}$
P_O_C	$1.4 \cdot 10^{-10}$
P_P_E	$1.9 \cdot 10^{-10}$
P_P_C	$1.35 \cdot 10^{-10}$

4. References

[1] Korhonen J, Honkasalo A, Seppälä J. Circular Economy: The Concept and its Limitations. Ecol Econ 2018; 143:37–46.

[2] Gálvez J, Correa Aguirre JP, Hidalgo Salazar MA, Vera Mondragón B, Wagner E, Caicedo

C. Effect of Extrusion Screw Speed and Plasticizer Proportions on the Rheological, Thermal, Mechanical, Morphological and Superficial Properties of PLA. Polymers (Basel) 2020; 12:2111.

[3] John MJ, Thomas S. Biofibres and biocomposites. Carbohydr Polym 2008; 71:343–364.

[4] Rigotti D, Checchetto R, Tarter S, Caretti D, Rizzuto M, Fambri L, Pegoretti A. Polylactic acid-lauryl functionalized nanocellulose nanocomposites: Microstructural, thermo-mechanical and gas transport properties. Express Polym Lett 2019; 13:858–876.

[5] Aliotta L, Vannozzi A, Panariello L, Gigante V, Coltelli MB, Lazzeri A. Sustainable Micro and Nano Additives for Controlling the Migration of a Biobased Plasticizer from PLA - Based Flexible Films. Polymers (Basel) 2020; 12:1–25.

[6] Mekonnen T, Mussone P, Khalil H, Bressler D. Progress in bio-based plastics and plasticizing modifications. J Mater Chem A 2013; 1:13379–13398.

[7] Aliotta L, Vannozzi A, Panariello L, Gigante V, Coltelli M-B, Lazzeri A. Sustainable Micro and Nano Additives for Controlling the Migration of a Biobased Plasticizer from PLA-Based Flexible Films. Polymers (Basel) 2020; 12:1366.

[8] Boldizar A, Klason C, Kubát J, Näslund P, Sáha P. Prehydrolyzed Cellulose As Reinforcing Filler for Thermoplastics. Int J Polym Mater Polym Biomater 1987; 11:229–262.

[9] Dufresne A. Cellulose nanomaterial reinforced polymer nanocomposites. Curr Opin Colloid Interface Sci 2017; 29:1–8.

[10] Molinari G, Gigante V, Fiori S, Aliotta L, Lazzeri A. Dispersion of Micro Fibrillated Cellulose (MFC) in Poly(lactic acid) (PLA) from Lab-Scale to Semi-Industrial Processing Using Biobased Plasticizers as Dispersing Aids. Chemistry (Easton) 2021; 3:896–915.

[11] Li Z, Reimer C, Wang T, Mohanty AK, Misra M. Thermal and mechanical properties of the biocomposites of Miscanthus biocarbon and poly(3-hydroxybutyrate-co-3-hydroxyvalerate) (PHBV). Polymers (Basel) 2020; 12.

[12] Aliotta L, Cinelli P, Coltelli MB, Righetti MC, Gazzano M, Lazzeri A. Effect of nucleating agents on crystallinity and properties of poly (lactic acid) (PLA). Eur Polym J 2017; 93:822–832.

[13] Fischer EW, Sterzel J. FL, and Wegner G. Investig Struct Solut Grown Cryst Lact Copolym by Means Chem React Coll Polym Sei 1973; 251:980–990.

  doi:10.5075/epfl-298799_978-2-9701614-0-0

OPTIMIZATION OF AN EXOSKELETON

Valentin SPIROUX [a], Laurent GUILLAUMAT [b]

a: PhD student – valentin.spiroux@ensam.eu
b: Professor – laurent.guillaumat@ensam.eu

Abstract: This work deals with the structure optimisation of a walking rehabilitation exoskeleton that acts on the lower limbs of the human body. We are focusing on the femur of the exoskeleton, which is an important part and whose mechanical performance influences the efficiency of the whole structure. To achieve this, we are developing a manufacturing process that allows the production of complex parts. This process combines filament winding and thermo-compression. The process was developed in our laboratory and then by controlling the angle of the fibres deposited after shaping by thermo-compression. For this, we work via microscopic image analysis and numerical simulation.

Keywords: Exoskeleton; Optimization; Filament winding; Carbon fiber; Thermoplastic

1. Introduction

Several exoskeletons exist for the medical field [1]. We are working on the creation of an exoskeleton specifically adapted to walking rehabilitation, intended for hemiplegic patients. In order to optimise its structure in terms of mechanical performance, we have chosen to focus initially on the connecting rod (so called: the femur of the exoskeleton) which allows the transfer of the torque developed by the motor to the patient's leg to create movement.

This large part plays an important role in the functioning of the exoskeleton. On the one hand its geometry will contribute to the comfort of the patient, the shape must therefore be adapted to the morphology of the patient while trying to limit the mass of the complete system. On the other hand, the stiffness of the femur will impact the movement of the exoskeleton and therefore the efficiency of the exercises proposed by the specialist in charge of the patient. In order to optimise these parameters, we have chosen to make this part in carbon fibre reinforced plastic composite (CFRP).

For the creation of this femur and because the shape is quite complex in 3D (not straight), we chose to develop a manufacturing process in two steps: first one is based on filament winding which will allow us to obtain a straight tube with a controlled angle of deposition [2]. The second step consist in doing a thermo-compression to manufacture the complex shape putting the tube in a mould. Filament winding lends itself well to mould shaping because the fibres can slide into a stable position without forming folds in the bent portions of the part.

The main difficulty is to control the fibres angle after shaping the wound tube in the mould. This angle will influence the mechanical performances of our part and in particular its stiffness. This study therefore consists of monitoring the final fibres angle in the femur by knowing the angle of the fibres deposited during the filament winding process which evolves during compression forming.

  doi:10.5075/epfl-298799_978-2-9701614-0-0

Working under a confidentiality agreement, we cannot reveal our data.

2. Presentation of Exoskeleton

The exoskeleton is specially designed for the medical field and is used exclusively in rehabilitation centers, so it cannot be used at home. Its field of application is focused on the rehabilitation of hemiplegic patients. The exoskeleton (Figure 1) replaces the physiotherapist in applying movement to the patient's leg(s). However, the specialist remains present during the session to look after the patient and adapts exercises from a control center. The exoskeleton offers progressive assistance during the therapy and is different for both legs. The aim of this exoskeleton is to get patients walking again as quickly as possible and to make them walk as naturally as possible. We therefore carried out a large study on the exoskeleton's joints, the positioning of their center of rotation and their level of functioning, i.e. free, passive with stiffness or controlled.

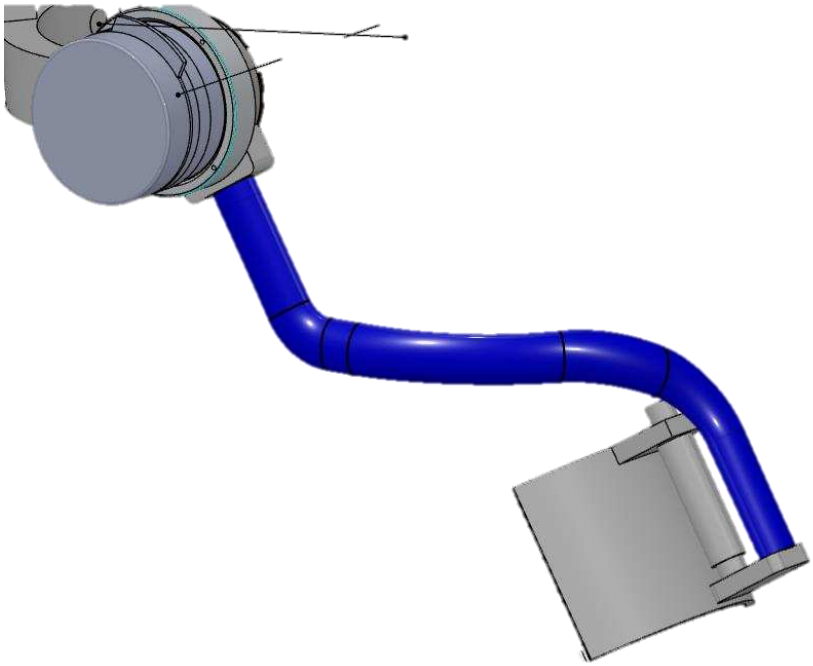

Figure 1: First exoskeleton prototype

3. Presentation of manufacturing process

To carry out the filament winding, as we did not have a machine designed for that, we adapted a numerically controlled lathe (Figure 2), by winding onto a rotating mandrel and depositing the wire via the movement of the machine's tool holder. By adjusting the correct ratio of chuck speed to tool transverse speed, the wire is deposited at a precise angle. In order to be able to modify the shape of the tube after winding to obtain the complex shape, we cannot consolidate our tube by heating our thermoplastic fibers mixed with carbon fibers, during winding. Nor can we cure the thermoset resin if we use one. With the tension of the wire, it may

  doi:10.5075/epfl-298799_978-2-9701614-0-0

be very difficult to remove the formed tube from the mandrel without changing the orientation of the fibers. We do this in two steps, the first being the use of a deformable mandrel. We designed a mandrel with an adjustable diameter. We wind on a desired mandrel diameter and then reduce the mandrel diameter to remove the tube without changing the winding sequence. The second step is to apply a thin layer of glue to the surface to stabilise fibers during handling before shaping.

Figure 2: CNC modified for filament winding

For the shaping, we first chose to make a simple mould (Figure 3) which compresses the tube completely via the use of a heating press, so as to obtain a solid part.

Figure 3: Mold for thermo-compression

4. Fibre angle microscopic analysis

The main objective concerning the measure of these angles is to relate the angle fibres in the part to those after winding and compression forming. Finally, we want to kwon which angle we have to consider for the winding to have a given value in the part. We have as samples 3mm thick specimens with bends of ±45°. The fibre angle will be obtained by geometric measurements on the ellipses formed by the section of the fibres.

  doi:10.5075/epfl-298799_978-2-9701614-0-0

4.1 Yurgartis method

The cutting of the specimens must be thought out in such a way as to highlight what we want to observe. In our case, it is the ellipses formed by the angular cutting of the fibres that interest us. The Yurgartis method [3] allows us to measure the angles of the fibres via a ratio between the largest diameter of the ellipse and the real diameter of the fibre. We will then try to maximise this large diameter in order to increase the accuracy of the subsequent measurement. The method therefore consists of cutting the fibre at an angle as close as possible to the initial angle of deposition. This must be done in two different planes (Figure 4) in order to obtain the overall deflection of the fibre.

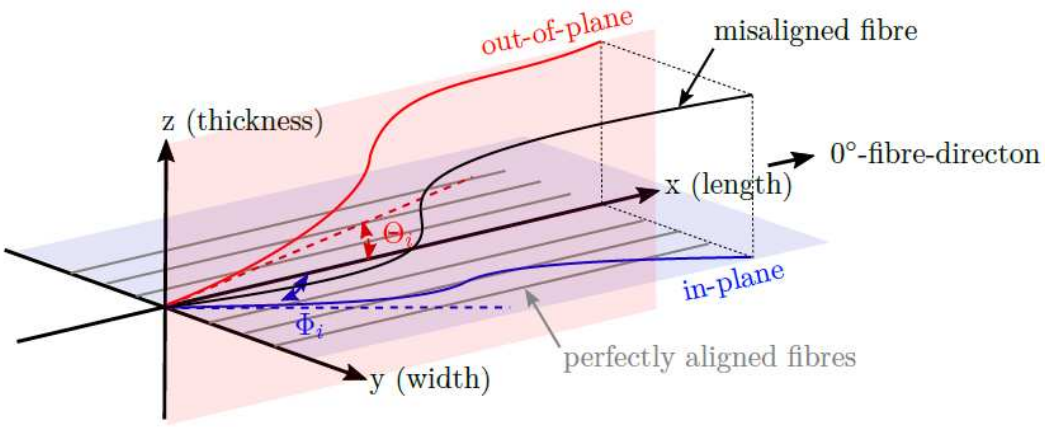

Figure 4: In plane and out plane cutting [4]

4.2 Microscopic pictures

The photographing using an optical microscope follows the cutting and mounting of the samples. The objective is to obtain the clearest possible photos, to locate them geographically on the sample in order to map the different areas of the sample at an given angle. To enable simplified location of future measurements, in first time, we take images of the entire section of the specimen (Figure 5). This can only be done if the detail of the photo can be zoomed in on a specific area to see precisely the contours of the different fibres, which is the case here (Figure 6). As the sample is large, we cannot study all areas. We therefore focus on the areas of interest (1; 2; 3; 4) that show significant variations or are typical of what will be found elsewhere.

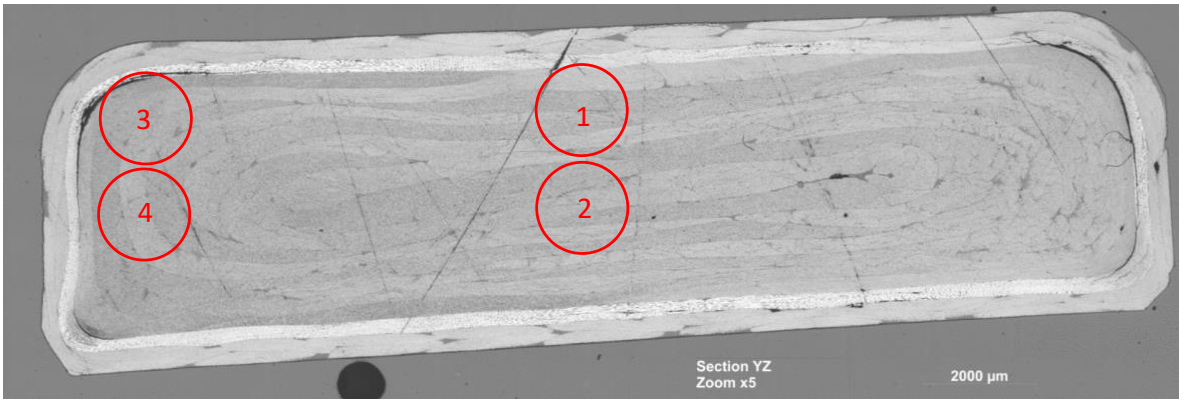

Figure 5: Sample section Zoom X5

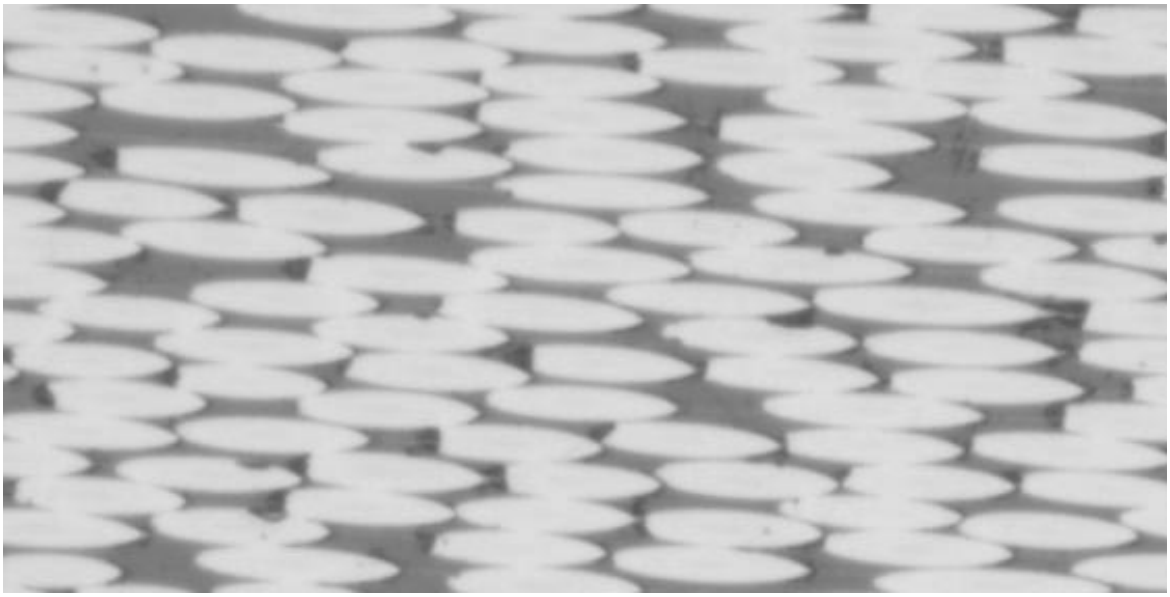

Figure 6: Sample section Zoom X50

2.3 Image analysis

Image analysis will enable us to obtain precise measurements of the diameters of the ellipses observed. To do this, we use the ImageJ software, which allows us to rework photos in order to bring out the colours and contours (Figure 7). This is done in several stages, the first being the segmentation of the image in order to separate the fibres in contact. Without this, we would be able to process fewer fibres and we could have erroneous data. The second step is to detect the contours of each fibre. Finally, an ellipse-type fit is applied to these contours, which will make an ellipse pass through the contours as best as possible. With this method, we process a maximum number of fibres as close as possible to the real section of the fibre.

  doi:10.5075/epfl-298799_978-2-9701614-0-0

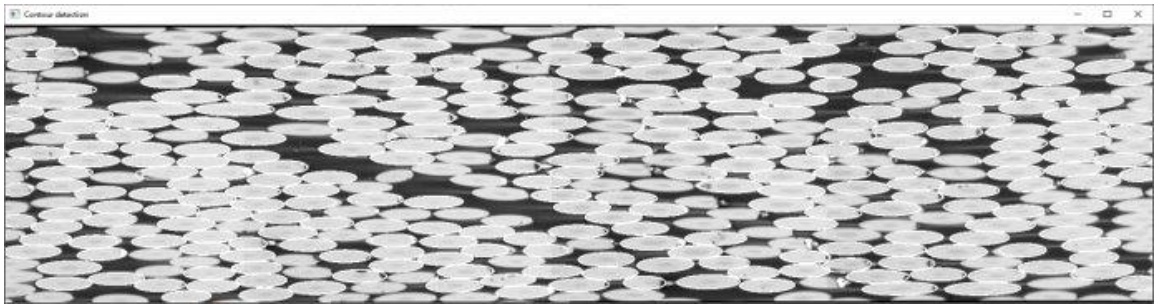

Figure 7: Detection of ellipse edges with ImageJ

Following the detection of the contours, the software gives us the values of the largest diameters of each ellipse located. The size of the ellipse will give its angle in relation to the cutting plane. The ratio between the large diameter L of the ellipse and the actual diameter l of the fibre (Eq.1) gives the angle α of the fibre to the cutting plane. Adding α to the cutting angle α_c (Eq.2) gives the misalignment angle α_f of the fibre with respect to the specimen axis.

$$\alpha = \cos^{-1}\left(\frac{l}{L}\right) \times \frac{180}{\pi} \quad (1)$$

$$\alpha_f = \alpha + \alpha_c \quad (2)$$

By doing this analysis in two planes, one with a cut in the height of the section, the other in the width, we obtain the global misalignment of the fibres per studied zone.

2.4 Results

For reasons of confidentiality, we cannot reveal the results of misalignment of the fibres by zone.

In order to understand the misalignment obtained, it is necessary to see whether the average of the angles found per zone is representative of the fibres panel studied, i.e. whether the measured angles are very scattered or whether they are relatively close to this average value. For this purpose, we carried out a short statistical study per zone (Figure 8). From these distributions, it can be seen that the mean values are representative of the populations observed in the vast majority of the areas observed. This means that the image analysis is working correctly, that globally the detected contours are close to the real contours. The discrepancy between some of the values may be due to misalignment of fibres due to winding of fibres within a yarn, removal or different slippage during compression. It may also be due to a poorer reading of the contour during the analysis.

  doi:10.5075/epfl-298799_978-2-9701614-0-0

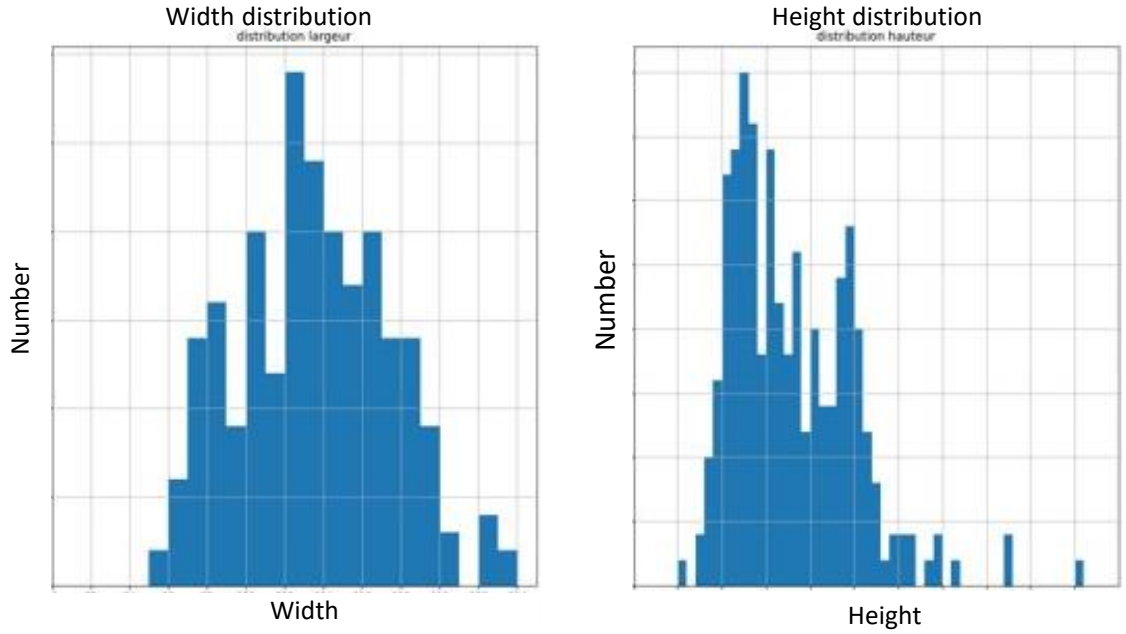

Figure 8: Example of distribution obtained for the width L of the ellipse on the left and the height l on the right

5. Conclusion

We are developing an innovative process combining filament winding of a composite tube made of carbon fibres and thermoplastic fibres with compression in a mould. This last step gives the tube a non-linear shape. We are working on the development of this process for the manufacture of a femur with a complex geometry. This involves controlling the angle of the fibres at the end of the shaping process. The mechanical performance of a composite part is extremely dependent on the angle of the fibres in relation to the stress. We therefore seek to know what angle is obtained following the compression of the tube in order to know what angle to apply during the winding of the tube to obtain the desired angle at the end. To do this we measure the angle of the fibres after compression using the Yurgartis method to obtain the overall misalignment of the fibres with respect to the initial angle. By modifying the initial lay-up angle to the extent of the observed misalignment we hope to obtain the desired final angle. The current method of measuring angles gives consistent and representative results on simple specimens. We now need to perform these measurements on complex geometries close to the final femur of the exoskeleton.

6. References

1. Jarrassé, 'Contributions à l'exploitation d'exosquelettes actifs pour la rééducation neuromotrice'.
2. Perez et al., 'Simulation Du Comportement Thermique Du Procede d'enroulement Filamentaire de Composites Thermoplastiques Assiste Par Chauffage Laser'.
3. Yurgartis, 'Measurement of Small Angle Fiber Misalignments in Continuous Fiber Composites'.
4. Gabow, 'Contribution to the investigation of the compressive strength and delamination of continuous fibre laminated composites in the context of competitive sailing'.

  doi:10.5075/epfl-298799_978-2-9701614-0-0

BANANA FIBRE AS SUSTAINABLE AND RENEWABLE RESOURCE FOR REINFORCEMENT OF POLYLACTIC ACID

Maryam Sodagar[a], Anne Hennig[a], Frederik Cloppenburg[a], Thomas Gries[a]

a: Institut für Textiltechnik of RWTH Aachen University, Otto-Blumenthal Straße 1, D-52074 Aachen, Germany; maryam.sodagar@ita.rwth-aachen.de

Abstract: *Banana fibres which are extracted from banana cultivation waste, contain high amount of cellulose which makes them a high strength renewable raw material to be used as composite reinforcement. The aim of the current work is to investigate the effect of using banana fibres as reinforcement for polylactic acid. Moreover, hybrid composites are also produced to investigate the effect of mixing banana fibers with flax and hemp fibres on the mechanical properties of the final product. First, nonwovens are made of PLA fibres, banana fibres, flax and hemp fibres in different compositions using airlay, carding and needle punching machines. Then they are hot-pressed to form the composite plates. Finally, tensile and three-point bending tests are carried out on the specimens according to DIN EN ISO 527-4 and DIN EN ISO 14125, respectively. The test results revealed that employing 60 wt.-% of pure banana fibres can increase the tensile strength and strain, as well as the flexural strength of the composites significantly, compared to hybrid composites made of banana, flax, and hemp fibres.*

Keywords: polylactic acid reinforced composite, natural fibre reinforced composite, banana fibres, nonwoven composite, hybrid fibre reinforced composite

1. Introduction

Recently due to ecological and environmental awareness, and price elevation of limited fossil resources, the demand for using alternative renewable biomaterials has increased in the composite industry. Due to their low cost, environmentally friendly characteristics, relatively good mechanical and properties, biodegradability, low density and recyclability, cellulose fibres have replaced various synthetic fibres for reinforced composites in many applications such as marine, automotive, aerospace, construction industries, etc [1–5].

The banana plant which is among the most cultivated plant in the world, can yield fruits only once in its lifetime. Once bananas are harvested the plant is cut and stems and leaves are considered as lignocellulose waste. The waste will either be landfilled or incinerated which produces greenhouse and noxious gases such as ammonia, hydrogen sulphide and methane [6, 7]. According to statistics, around 280 million tons of banana stem are wasted worldwide annually [8–10]. However, in a simple eco-friendly, low-cost mechanical process, banana fibres can be extracted from banana stem waste [11]. Banana fibre has a low density of 1.35 $\frac{g}{cm^3}$ [12] and is a high strength fibre as it contains 62.5 % cellulose [13]. These properties make it a suitable material to produce high strength lightweight composites.

As well as natural fibres, biodegradable polymers have also been developed from natural green resources, such as polylactic acid (PLA), which can be used as a matrix in the composites industry. According to market data compiled by European Bioplastics in cooperation with nova-Institute,

  doi:10.5075/epfl-298799_978-2-9701614-0-0

global biodegradable plastics production capacity may increase from around 1.05 million tonnes in 2019 to approximately 1.8 million tonnes in 2025 [14]. Due to its eco-friendliness, biocompatibility, processability and energy savings production process, recyclability and biodegradability, PLA has advantages compared to other biopolymers [15]. PLAs are very durable, UV-resistant, transparent and solid. [16]. Its tensile strength and Young's modulus are comparable to poly(ethylene terephthalate). However, higher cost, poor toughness and brittleness of PLA limits its use in certain applications [17, 18].

Incorporating natural fibres into polylactic acid can not only enhance the mechanical properties of PLA, but also reduce the final cost of the composite.

2. Materials and methods

2.1 Materials and samples compositions

In the current work banana fibre is sourced from Eco Green Unit, Tamil Nādu, India. The fibres are cut to 60 mm length to facilitate blending with the PLA fibres. Flax and hemp fibres are provided by Polyvlies Franz Beyer GmbH, Hörstel-Bevergern, Germany. The PLA fibre with a length of 60 mm and a fineness of 6.7 dtex has been received as a sample from Trevira GmbH, Bobingen, Germany.

In order to find the optimum fibre mass which leads to the highest tensile and flexural strength, 3 different banana fibre/PLA fibre compositions of 40/50, 50/50, and 60/40 wt.-% have been produced and tested.

The composition with the best mechanical properties has been selected for the investigation of the effect of using flax and hemp on the mechanical properties of the composites. To do so, the composites with the compositions of 40 wt.-% banana fibres/20 wt.-% hemp fibres/40 wt.-% PLA fibre, 40 wt.-% banana fibres/20 wt.-% flax fibres/40 wt.-% PLA fibre, and 40 wt.-% banana fibres/10 wt.-% hemp fibres/10 wt.-% flax fibre/40 wt.-% PLA fibre have been manufactured (see Table 1).

Table 1 : Compositions and labelling of the samples.

Sample	PLA fibre/Banana fibre/Hemp fibre/Flax fibre [wt.-%]
P4B6	40/60/0/0
P5B5	50/50/0/0
P6B4	60/40/0/0
P4B4H2	40/40/20/0
P4B4F2	40/40/0/20
P4B4H1F1	40/40/10/10

2.2 Manufacturing process

The fibres are first opened and blended using a Truetzschler CVT 3 fine opener, which is uses as an airlay machine. The blended fibres are then fed to Anton Guillot lab scale carding machine to

  doi:10.5075/epfl-298799_978-2-9701614-0-0

produce parallelised, oriented, and even distributed webs. The carded webs are afterwards needle punched, overlapped and again needle punched upside down to form the final nonwoven.

The needle punched hybrid nonwovens are cut to 200 × 300 mm dimensions and dried for 24 h at 60 ˚C before entering the hot press to reduce the moisture content, increase the fibre matrix adhesion and decrease the void contents in the final composite. Then the nonwoven mats are hot pressed at a temperature of 160 ˚C and a pressure of 10 bar for 13 minutes (see Figure 1).

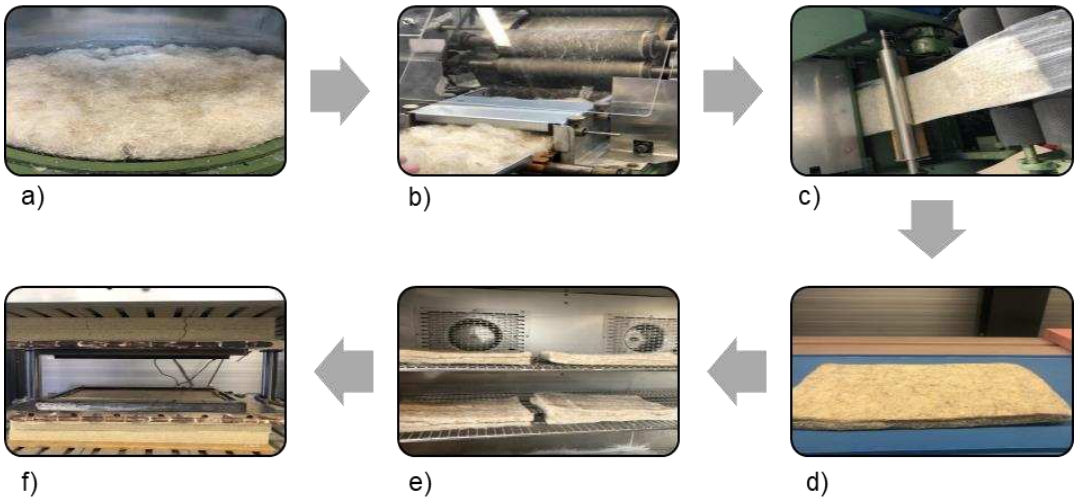

Figure 1 : Composite manufacturing process, a) Opening and blending; b) Carding; c) Needle punching; d) Cutting the nonwovens; e) Drying process of nonwovens, f) Hot press

To determine the tensile properties of anisotropic fibre reinforced polymers, tensile tests are carried out on the specimens in a standard climate of EN ISO 139 according to DIN EN ISO 572-4. Therefore 5 specimens with the dimensions of 250 mm×25 mm are cut from each sample. The tensile test in this experiment is conducted using a Z100 machine with the force transducer of 20 kN and testing speed of 2 mm/min.

In order to determine the flexural properties of thermoplastic fibre reinforced polymers, three-point bending tests are carried out on NFRCs in a standard climate of EN ISO 139 and according to DIN EN ISO 14125 procedure A class II. In this work the thicknesses of specimens are inconsistent and differ from the required thickness in the standard. Therefore, the lengths of each test specimens and the testing speed of each series are calculated using the ratio and equation given in DIN EN ISO 14125. According to the standard, the ratio L/h and l/h should be 16 and 20, respectively; and the testing speed of each series should also be calculated using equation 1.

$$v = \frac{\varepsilon' L^2}{6h} \tag{1}$$

3. Results and discussion

Figure 2 and Figure 3 show the summary of the tensile and bending tests results. As it can be seen, the composite sample with 60 wt.-% banana fibre content has the highest tensile strength, Young's modulus, flexural strength and bending E-modulus of 23.62, 5.306, 46.8 and 5.33,

  doi:10.5075/epfl-298799_978-2-9701614-0-0

respectively. However, its Young's modulus is almost the same as the sample with 50 wt.-% of banana fibre.

The tensile test results of the samples P4B6, P4B4H2, P4B4F2 and P4B4F1H1, in which the matrix contents are consistent, show that substituting only 20% of banana fibre with hemp or flax fibres leads to a decrease of 20% and 30% in tensile strength, 5% and 17% in Young's modulus, respectively. In addition, replacing 20% of banana fibres with flax and hemp fibres decreases the tensile strength and strain of the composite by 44% and 33%, respectively.

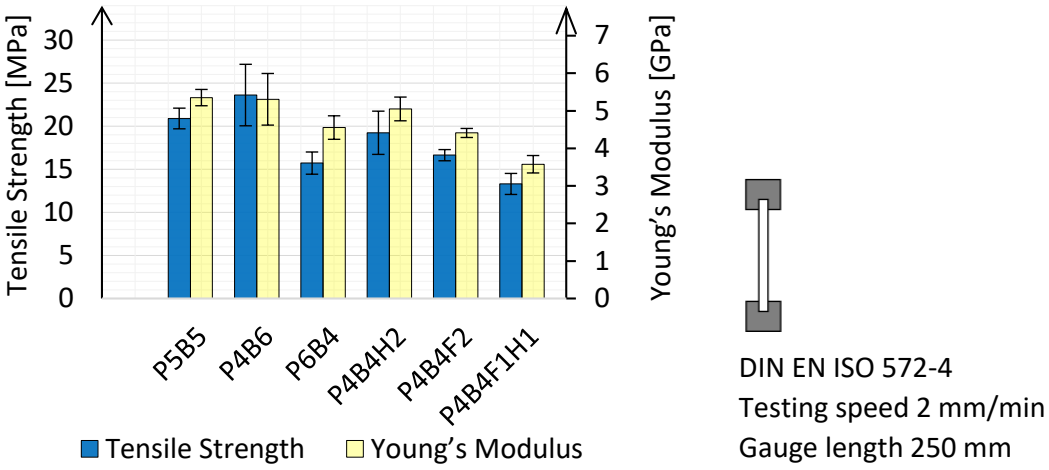

Figure 2 : Comparison of the tensile strength and Young's modulus of the composites

As it can be seen in the Figure 3, replacing 20% of banana fibre with flax and the combination of hemp and flax, decrease the flexural strength of the composite by around 5% and 10% respectively. Replacing 20% of banana fibre with hemp fibre does not change the flexural strength of the composite.

Moreover, mixing flax and hemp fibres with banana fibres decreases the bending E-modulus of the composites by 64% and 52%, respectively. The combination of flax and hemp fibres when they substitute 20% of banana fibres can lead to a decrease of 42% in bending E-modulus However, its Bending E-modulus is higher than that of banana/flax and banana/hemp reinforced composites.

The reasons to this phenomenon could be the type of the opening rollers in the airlay machine which may not be suitable for processing both coarse banana fibres and fine flax and hemp fibres. Therefore, it may cause damage and breakage of finer fibres during the opening process. This problem can be solved by using another opening cylinder which is specifically suitable for processing both fine and coarse natural fibres. Another reason could be the length of flax and hemp fibres. Despite banana fibres, that are cut to 60 mm fibres before the process of blending them with PLA fibres, flax and hemp fibres have variable staple length from 40 to 100 mm. This variation in length may lead to uneven inadequate blending during the airlay process and less mechanical properties accordingly. In addition, adding flax and hemp fibres, which are covered by small amount of wax in nature, may cause insufficient interfacial bonding between the reinforcing fibres and the PLA matrix. Poor adhesion between the polymer matrix and the fibres lead to poor force transfer from the matrix to the fibres and poor mechanical properties

accordingly. Surface treatment of flax and hemp fibres with NaOH can eliminate waxes from the surface of the fibres and therefore increase the fibre matrix bonding.

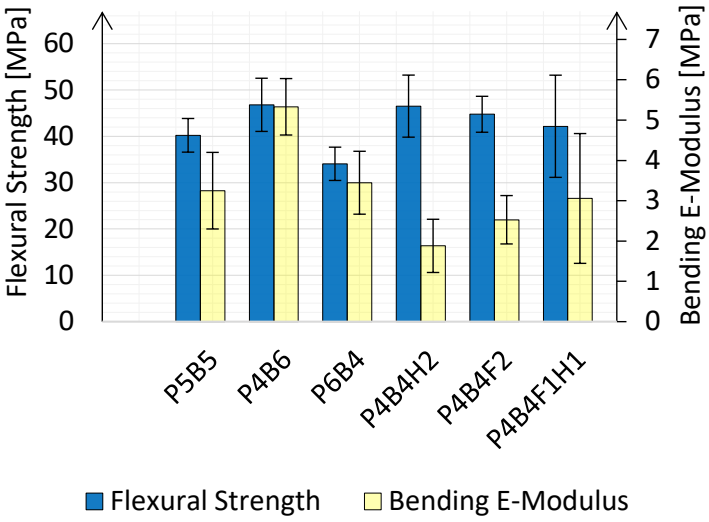

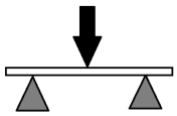

DIN EN ISO 14125
Testing speed 0.5 mm/min
Gauge length: Based on the thickness of each plate according to the standard

Figure 3 : Comparison of the flexural strength and bending E-modulus the composites

Although the manufacturing process of all the composites are identical, the PLA fibres in the sample P4B4F1H1 are not melted properly. The improper blending of PLA fibres may lead to uneven heat transfer from the outer PLA fibres to the inner PLA fibres. When the inner PLA fibres are not melted evenly, the loads cannot be transferred between the inner fibres. Therefore, the sample P4B4F1H1 shows the least mechanical properties with significantly high standard deviation. Using a different opening roller during blending process may solve this problem.

4. Summary and conclusion

The aim of current work is to investigate the effect of using banana fibre and its combination with flax and hemp fibres on the mechanical properties of PLA reinforced with said fibres. First, hybrid nonwovens are manufactured and then pressed under high pressure and temperature to form the consolidated composite plates. Three different composite samples with different banana fibre contents have been produced to find the optimum fibre content which leads to the highest tensile and flexural strength. It has been concluded that incorporating 60 wt.-% of banana fibre shows the highest tensile and flexural properties compared to the composites with 40 wt.-% and 50 wt.-% of banana fibre content. In order to investigate the effect of substituting 20 wt.-% of banana fibre with flax, hemp and its blends, 3 different hybrid composites of P4B4H2, P4B4F2 and P4B4F1H1 are manufactured. It has been concluded that replacing banana fibres with flax or hemp fibre leads to a decrease in the mechanical properties of the composites.

In the overall consideration, it can be concluded that banana fibre has a great potential to be used as reinforcement of polylactic acid. Replacing small amounts of banana fibre with flax or hemp fibre weaken the mechanical properties of the composite. However, using another method to produce the hybrid nonwovens may lead to better mechanical properties of those made of flax, hemp, and banana hybrid composites.

  doi:10.5075/epfl-298799_978-2-9701614-0-0

Acknowledgements

This research work was funded, in part, as a Speed Fund by the Hans Hermann-Voss-Stiftung, Germany. We thank our colleagues from Institut für Textiltechnik of RWTH Aachen who provided insight and expertise that greatly assisted the research.

4. References

1. Felix JM, Gatenholm P. The nature of adhesion in composites of modified cellulose fibers and polypropylene. J. Appl. Polym. Sci. 1991; 42:609–20. doi:10.1002/app.1991.070420307.
2. Porter ME, editor. The Competitive Advantage: Creating and Sustaining Superior Performance.; 1985.
3. C.J. Riensema, R.A.C. Koster, T.J.H.M. Hutten. Vlas 2000 : structuur en afzetperspectieven van de vlassector in Nederland: L.E.I; 1990.
4. Beckmann A., Kleinholz R., editors. Proceedings 2. Internationales Symposium “Werkstoffe aus Nachwachsenden Rohstoffen”; 1999.
5. M. Karus, M. Kaup, D. Lohmeyer. Study on Markets and Prices for Natural Fibres (Germany and EU), FNR-FKZ:99NR163, nova Institute; 2000.
6. Guerrero AB, Aguado PL, Sánchez J, Curt MD. GIS-Based Assessment of Banana Residual Biomass Potential for Ethanol Production and Power Generation: A Case Study. Waste Biomass Valor. 2016; 7:405–15. doi:10.1007/s12649-015-9455-3.
7. Muhammad Tahir Khan, Claudia Maurer, Dimitrios Argyropoulos, Mathieu, Brûlé, Joachim Mueller. Anaerobic Digestion of Banana Waste, a Potential Source of Energy in Uganda. In:
8. Pérez R. Feeding pigs in the tropics. Rome: Food and Agriculture Organization of the United Nations; 1997.
9. Foulkes D, Espejo S, Marie D, Delpeche M, Preston T. El plátano en la alimentación de bovinos. Composición y producción de biomasa. 1978;1983-1987.
10. AtlasBig. World Banana Production by Country. 1970. https://www.atlasbig.com/en-gb/countries-by-banana-production. Accessed 14 Dec 2021.
11. EcoIdeaz. Extracting Banana Fiber and Paper from Waste Banana Stems. 2015. https://www.ecoideaz.com/innovative-green-ideas/producing-banana-fiber-and-paper-from-waste. Accessed 22 Dec 2021.
12. Thyavihalli Girijappa YG, Mavinkere Rangappa S, Parameswaranpillai J, Siengchin S. Natural Fibers as Sustainable and Renewable Resource for Development of Eco-Friendly Composites: A Comprehensive Review. Front. Mater. 2019. doi:10.3389/fmats.2019.00226.
13. Mwaikambo LY, Ansell MP. Mechanical properties of alkali treated plant fibres and their potential as reinforcement materials. I. hemp fibres. J Mater Sci. 2006; 41:2483–96. doi:10.1007/s10853-006-5098-x.
14. Statista. Global bioplastic production capacity by type 2025 | Statista. 1/3/2022. https://www.statista.com/statistics/678684/global-production-capacity-of-bioplastics-by-type/. Accessed 3 Jan 2022.
15. Jamshidian M, Tehrany EA, Imran M, Jacquot M, Desobry S. Poly-Lactic Acid: Production, Applications, Nanocomposites, and Release Studies. Compr Rev Food Sci Food Saf. 2010;9:552–71. doi:10.1111/j.1541-4337.2010.00126.x.

16. Niedersachsen • Netzwerk Nachwachsende Rohstoffe und Bioökonomie e.V. Biopolymere | 3N Kompetenzzentrum. 7/12/2021. https://www.3-n.info/themenfelder/stoffliche-nutzung/biopolymere.html. Accessed 12 Jul 2021.
17. Auras R, Harte B, Selke S. An overview of polylactides as packaging materials. Macromol Biosci. 2004; 4:835–64. doi:10.1002/mabi.200400043.
18. S. Farah, K.R. Kunduru, A. Basu, A.J. Domb. Edition: 1st edition, Chapter: 8, Editors: P. M. Visakh, M. Liang. 2015:143–65.

HYBRID RATIO EFFECT ON FLEXURAL PROPERTIES FOR CFRP-NATURAL FIBER COMPOSITE HYBRID MATERIALS

Misaki Nakamura[a], Junji Noda[a] …

a: Kindai University – 2133730016d@waka.kindai.ac.jp

Abstract: *As the generalization of electric vehicles is strongly desired, we have to achieve the weight saving to make it be able to run more distance. The center pillar is important to protect people in the vehicle so it requires high bending stiffness. It was proposed that both of these requirements are achieved by using and combining CFRP and natural fiber composites(NFC). Then, the purpose of this study is to develop a beam which has CFRP skin and NFC core to apply car frames. First, the various conditions of molding were researched because a kind of matrix epoxy resin was different between CFRP and NFC prepregs. Next, a tensile and bending tests were conducted. In addition, it was conducted the test to reveal the relationship of water absorption. It was revealed that the material and mechanical properties of the hybrid material and the relationship between hybrid ratio and the bending fracture.*

Keywords: NFC; CFRP; Hybrid materials; Water absorption

1. Introduction

Unidirectional CFRP shows a strong anisotropy in modulus and strength. These days, the interest in Carbon neutral is increasing all over the world. As the generalization of electric vehicles is strongly desired, we have to achieve the weight saving to make it be able to run more distance. The center pillar is so important to protect people in the vehicle that it requires high bending stiffness. Center pillar also needs tensile modulus not to break when a car turns over, so it must have high modulus due to long fibers for core material. It was proposed that both of these requirements are achieved by using and combining CFRP and natural fiber composites(NFC). Then, the purpose of this study is to develop a beam which has CFRP skin and NFC core to apply car frames.

First, the various conditions of molding were researched because a kind of matrix epoxy resin was different between CFRP and NFC prepregs. Next, a tensile and bending tests were conducted. It was investigated that the material and mechanical properties of the hybrid material. It was investigated that the relationship between the components of laminates and the bending fracture strength, and the relationship between hybrid ratio and the bending fracture.

Furthermore, the 4-point bending test was conducted to prove the relationship between water absorption rate and bending properties.

  doi:10.5075/epfl-298799_978-2-9701614-0-0

2. Materials and test method

2.1 Material and method

In this study, CFRP prepreg (TR350G250S, Mitsubishi Chemical Co., Ltd.), and NFC prepreg (FLAXPLEG T-UD-110, Ecotechnilin Ltd.), were used. The thickness of each layer is 0.24 mm and 0.16 mm, respectively. The specimen was molded by the hotpress method. Before molding, NFC prepregs had dried at 40°C by drying oven for an hour to make it absolutely dried. Then, those were laminated and cured at 150 °C for 60 min while applying a pressure of 1 MPa. The stacking sequences for CFRP-NFC hybrid laminates was $[0^{CFRP}_2/0^{NFC}_2]$s, $[0^{CFRP}_2/0^{NFC}_4]$s which has the same CFRP layer thickness as $[0^{CFRP}_2/0^{NFC}_2]$s, $[0^{CFRP}/0^{NFC}_4]$s which has the same NFC layer thickness as $[0^{CFRP}/0^{NFC}_2]$s. Specimen were prepared to 100 mm × 15 mm. The thickness ware determined by the stacking sequences.

After molding, specimens were absolutely dried in dried oven again. Next, it was conducted the 4-point bending test. The conditions of the test were as follows:

- The length of the support span is 81 mm.
- The length of the indenter is 27 mm
- The velocity of testing is 1.0 mm/min

3. 4-point bending test of CFRP-NFC hybrid materials

3.1 Result and discussion

The results of 4-point bending tests were presented in Figure 1 and Figure 2. Because the deflection greatly exceeded the measurement range of the cantilever displacement measurement, the strain value was calculated by using the stroke mm. The resulting bending strength of $[0^{CFRP}/0^{NFC}_2]$s was 1123 MPa. The in-situ observation showed that the initial failure was buckling of the CFRP skin layer on the compression side, and that the thickness ratio of CFRP to NFC was about 2:5:2 in this stacking sequence, where the ratio of NFC was 57% by thickness. To compare with the bending strength of UD-CFRP with Poly-acrylonitrile-based carbon fiber is about 1600 MPa described in [1], in hybrid materials using CFRP as a skin layer, a method to increase the geometrical moment of inertia by using foam in the core layer, is considered to be a large value. These reduce the in-plane stiffness of the hybrid material. The center pillar, the subject of this study, requires high in-plane stiffness in compression to protect the occupants in the event of vehicle rollover, and the results show the superiority of a hybrid material with a NFC layer core that is less expensive than CFRP, exhibits specific stiffness equivalent to GFRP, and has high environmental friendliness.

  doi:10.5075/epfl-298799_978-2-9701614-0-0

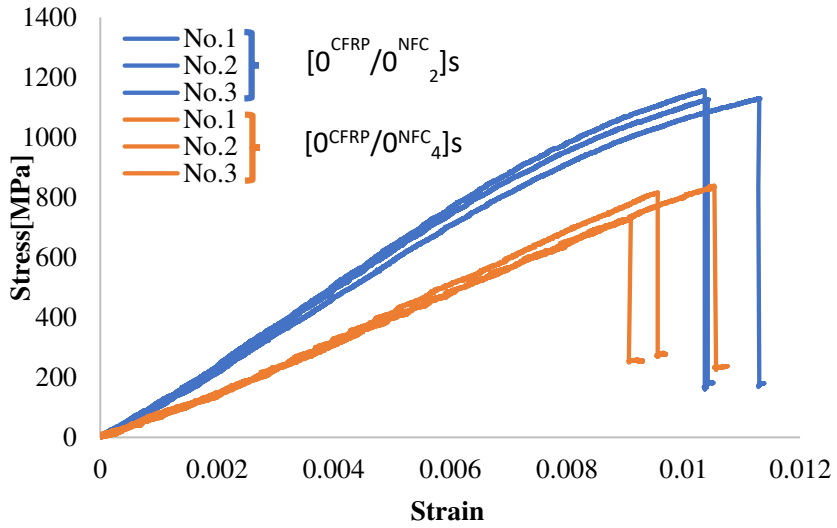

Figure 1 Stress-strain diagram (comparison between $[0^{CFRP}/0^{NFC}{}_2]s$ and $[0^{CFRP}/0^{NFC}{}_4]s$)

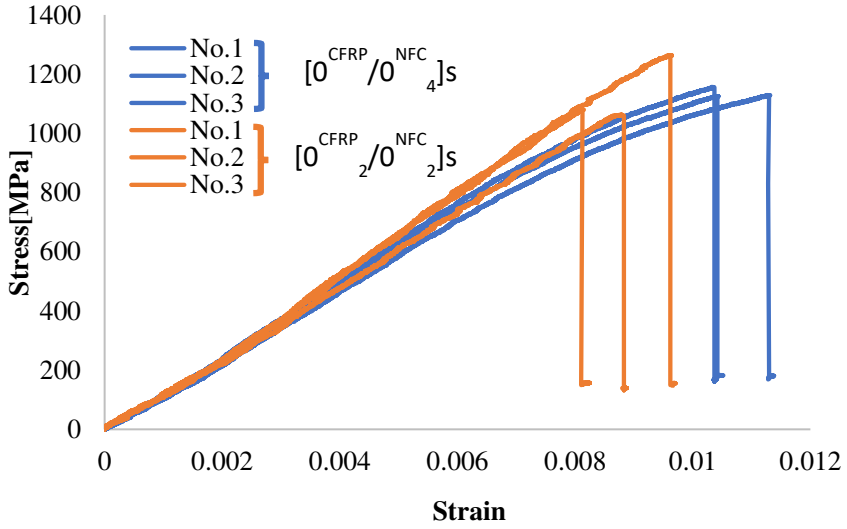

Figure 2 Stress-strain diagram (comparison between $[0^{CFRP}/0^{NFC}{}_2]s$ and $[0^{CFRP}{}_2/0^{NFC}{}_2]s$)

  doi:10.5075/epfl-298799_978-2-9701614-0-0

4. Water absorption behavior of CFRP-NFC hybrid materials

4.1 Deformational behavior during water absorption

In order to consider the difference in linear expansion coefficients between CFRP prepreg and NFC prepreg, specimens with asymmetric stacking sequence $[0^{CFRP}{}_4/0^{NFC}{}_4]$ were fabricated.

The molded CFRP-NFC hybrid material is shown in Figure 3(a). The curved shape was appeared. The maximum displacement of it was 12.0 mm. When the specimens were then held in an indoor environment, the curvature gradually decreased, and after 3 days the shape changed completely to a flat plate. To confirm the effect of humidity, the specimens had kept in a thermostatic chamber at 40 °C for 3 days and then removed. Figure 3 shows the appearance immediately after removal.

The laminate slightly regained its curvature, with a maximum displacement of 4.0 mm for the curved-formed plate.

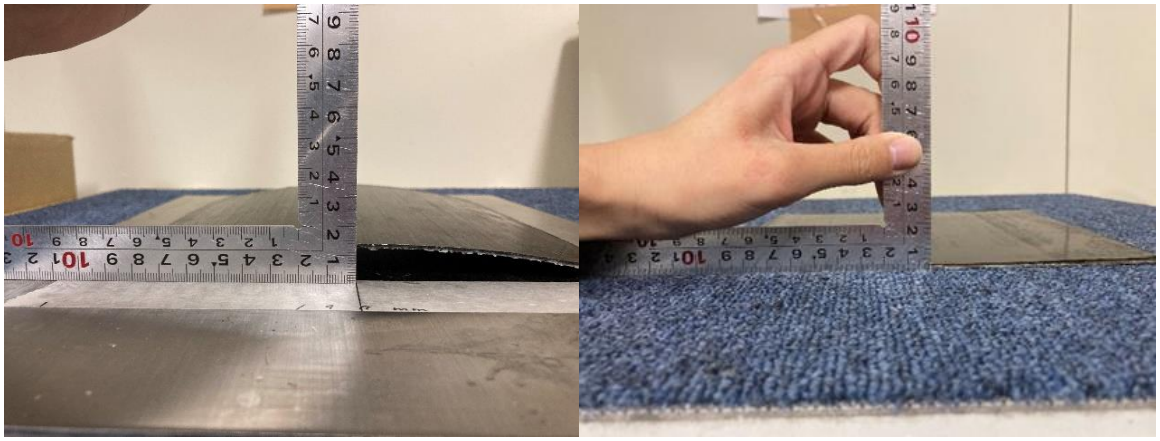

(a)After molding *(b) 3 days later*

Figure 3 Thermal deformation for $[0^{CFRP}{}_4/0^{NFC}{}_4]$

Figure 4 $[0^{CFRP}{}_4/0^{NFC}{}_4]$ After drying for 3 days

4.2 4-point bending test in wet condition

Based on these results, we conducted 4-point bending test on CFRP-NFC hybrid material with the stacking sequence $[0^{CFRP}/0^{NFC}{}_2]$s to reveal the relationship between water absorption and bending strength of NFC. The test was conducted by using the same specimen dimensions, the

  doi:10.5075/epfl-298799_978-2-9701614-0-0

length of support span, the length of indenter as in the test conducted in Chapter 2. Both specimen Dry-condition and Wet-condition were made by the same lot.

The specimen were absolutely dried in drying oven before mass measurement, and then we made it absorb water in the pool at 40 °C for 12 hours and conducted 4-point bending test after measuring mass after absorption. Table 1 shows the water absorption rate of the specimen and Figure 5 shows the comparison between dry and wet condition. It was abbreviated that dry-condition specimen has the initial D and wet-condition specimen has the initial W in Table 1 and Figure 5.

In the result, it is proved that water absorption greatly affects the bending strength of CFRP-NFC hybrid materials so it says we must be attention to environmental humidity or protect water absorption to apply this material to structures.

Table 1: Water absorption rate of Wet specimen

ID number	Weight [g]		Water absorption rate [wt%]
	Dry condition	Wet condition	
W-1	2.45	2.53	3.27
W-2	2.34	2.46	5.13
W-3	2.40	2.49	3.75

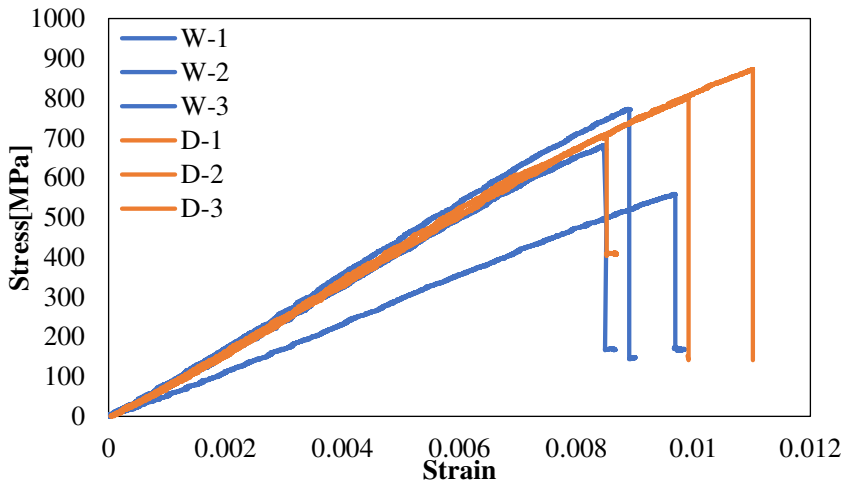

Figure 5 Stress-strain diagram (comparison between Wet and Dry condition of $[0^{CFRP}/0^{NFC}{}_2]s$)

5. Conclusions

In this study, it was revealed that the relationship between NFC ratio and bending properties, and between water absorption rate and bending properties.

- It was conducted the bending test of CFRP-NFC hybrid materials. As a result, it was revealed that The NFC layer can increase the bending strength by increasing the thickness at a low cost. The superiority of this materials was demonstrated.
- The strength of the NFC layer is significantly affected by humidity, and the shape of the laminate changes due to the effect of humidity. Therefore, the humidity at the time of use should be taken into account.

We will consider the deformation and strength of CFRP-NFC hybrid materials when molded into three-dimensional structures, taking into account its water absorption characteristics.

6. References

1. Fujimoto S, et al. Studies on the Machining Technology for CFRP (Part1) -Thermosetting resin- Ehime Institute of Industrial Technology. 2016.

  doi:10.5075/epfl-298799_978-2-9701614-0-0

INVESTIGATION OF THE ENERGY ABSORPTION CAPACITY OF NOVEL 3D-PRINTED GLASS FIBER REINFORCED THERMOPLASTIC BIO-INSPIRED STRUCTURES

Fatemeh, Ghorbania, Hussain, Gharehbaghia, Amin, Farrokhabadia, Amir, Bolourib

a: Department of Mechanical Engineering, Tarbiat Modares University, Tehran, Iran
b: School of Engineering, University of the West of England, Bristol, BS16 1QY, UK - Amir.Bolouri@UWE.AC.UK

Abstract: *This study has developed a novel glass-fiber-reinforced bio-inspired cellular structure with improved energy absorption capability. Extensive experimental analyses have been conducted to investigate their properties. The bio-inspired cellular structures of continuous glass fiber-reinforced PLA were manufactured using a Fused Deposition Modeling (FDM) printer. Quasi-static compression tests were conducted to analyze the energy absorption properties of the cellular structures. Results show that for the glass-fiber-reinforced PLA cellular structures, the energy absorption is ~250% higher than the unfiled PLA cellular structures. A topology optimization strategy was employed to tailor the energy absorption properties of the cellular structures by varying the stiffness of the unite cells. The key geometric parameters of the unite cells were identified and the cellular structures with different stiffnesses were designed and 3D printed. The energy absorption properties were measured and linked to the stiffnesses of the cells.*

Keywords: Fiber reinforced cellular structures; Optimization; Bio-inspired cellular structure; Energy absorption.

1.Introduction

Cellular structures are commonly used in lightweight applications due to their remarkable mechanical properties. They are used in various fields such as aerospace, biomedical engineering, transportation, and civil engineering[1]. Today the use of 3D printing technology to make complex cellular structures is associated with relatively low costs[2]. in recent years, different cellular structures have been studied for energy absorption applications. Xu et al. [3] studied the compressive response and energy absorption capacity of AuxHex structure, which consisted of auxetic and hexagonal honeycomb unit cells through theoretical, finite element simulation and experimental method. AuxHex structures exhibited superior young's modulus, collapse strength, and energy absorption than traditional honeycomb structures. Alomarah et al. [4] presented a re-entrant chiral auxetic structure (RCA) that combined topology features of re-entrant, tetrachiral, and anti-tetrachiral. Then the structure subjected to uni-axial compression test experimentally and numerically. RCA structure showed better performance than the other types of honeycombs in terms of strength and specific energy absorption under loading in the y-direction. Rahman et al.[5] investigated different graded structures by changing the unit cell size and relative densities made of soft and hard materials numerically. Their results revealed that graded changes in unit cell size and combination of soft and hard materials make cellular structures with maximum energy absorption and stiffness in comparison to those structure with a single material, interesting for multi-functional applications. Yin et al.[6]

  doi:10.5075/epfl-298799_978-2-9701614-0-0

evaluated hierarchial honeycomb based on three different structures: hexagonal, Kagome, and triangular. The presented structure was subjected to in-plane impact finite element simulation. Results showed that the triangular hierarchial honeycomb provides twice energy absorption than a regular honeycomb under the same loading condition. Ghazlan et al. [7] introduced a novel cellular structure inspired by cancellous bone and compared its performance with re-entrant and conventional honeycomb. Their results represented that bone-inspired cellular structure has more energy absorption than conventional honeycomb and re-entrant structures. In recent years the use of 3D printing technology to fabricate cellular structures with continuous fiber has expanded. The orthotropic cellular structures with complex geometry, low weight, and excellent mechanical properties can be achieved using this method. For example, Veisi and farrokhabadi [8] presented an analytical model using classical laminated theory (CTL) to obtain equivalent mechanical properties in a re-entrant unit cell with continuous fiber. They compared their results with previous experimental tests. Their results showed that the proposed model has good agreement with experimental tests. Farrokhabadi et al.[9] presented a novel analytical model based on the energy method to evaluate equivalent mechanical properties in cruciform honeycomb with continuous fiber for the first time. Experimental results demonstrated a 60% increase in the in-plane elastic stiffness of the cruciform honeycomb with glass fiber reinforcement. Farrokhabadi et al. [10] Proposed mechanical properties of a new orthotropic accordion honeycomb structure reinforced with glass fibers as a one-dimensional morphing structure. Quan et al. [11] investigated the stiffness and energy absorption in the re-entrant cellular structure using pure PLA and glass fiber reinforced PLA. They found that the compressive strength increased to 86% by adding fiber, and energy absorption increased to 100 %.In this study, the use of glass fiber-reinforced PLA and topology optimization have been evaluated for a bone-inspired cellular structure to improve the energy absorption properties. At first, fiber-reinforced PLA cellular structure and pure PLA structure are 3D printed and their properties are investigated. Then for improving energy absorption capabilities in bone-inspired cellular structure, an optimization algorithm is used to design unit cell with different stiffness to tailor energy absorption properties.

2. Experimental procedure

2.1 material and 3D printing method

Polylactic acid (PLA) filament was used to fabricate bio-inspired cellular structures. The cellular structures were reinforced with continuous glass fiber and fabricated using an FDM 3D printer machine shown in Figure 1(a). The mechanism for 3D printing of the composite cellular structures is shown in Figure 1(b). A nozzle was designed for the simultaneous impregnation system. The glass fiber enters the melting chamber through its inlet, and the impregnated fibers are guided out of the nozzle and placed on the building plate. The printing speed of the reinforced samples was 10 mm/s, and the nozzle temperature and the printing bed are set to 200° C and 60° C, respectively.

  doi:10.5075/epfl-298799_978-2-9701614-0-0

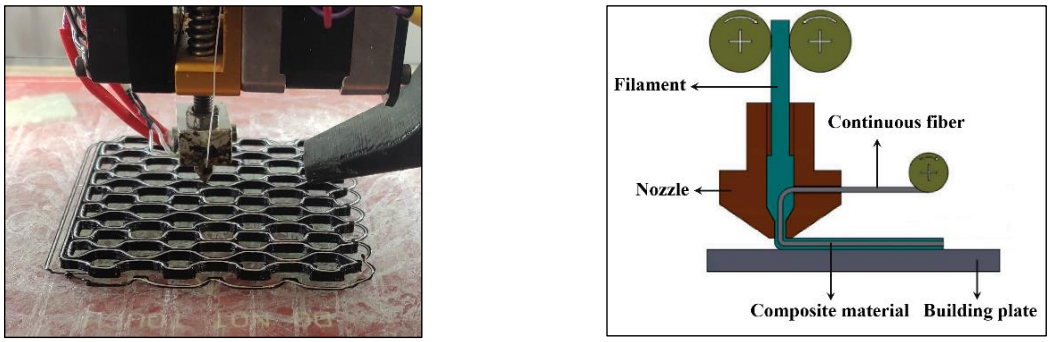

(a) (b)

Figure 1. Printing process of cellular structure (a), Mechanism of FDM 3D printing with continuous fibers [12] (b)

2.2. Tensile test for raw material

ASTM-D638 was utilized to obtain the mechanical properties of raw PLA as the base material [13]. A minimum of three dog bone specimens were printed and subjected to a tensile test at a 5 mm/min cross-head speed using instroon5500R machine. Table1 shows the mechanical properties of PLA material under the tensile test.

Table 1: Mechanical properties of Polylactic acid (PLA) material.

Type	Young modulus (GPa)	Poisson ratio	Yield stress (MPa)	Ultimate Tensile Strength (MPa)	Fracture Strain
PLA	3.3	0.35	22.76	58.29	0.01025

2.3. Compression test for cellular structures

To study the energy absorption capability for the cellular structures, uniaxial compression tests were conducted. A minimum of three specimens were fabricated using a FDM 3D printing machine and were subjected to a compression test. The crosshead speed was 5 mm/min for compression testing. A high-resolution and high-speed camera was used to investigate the deformation and failure in the specimens (Figure 2).

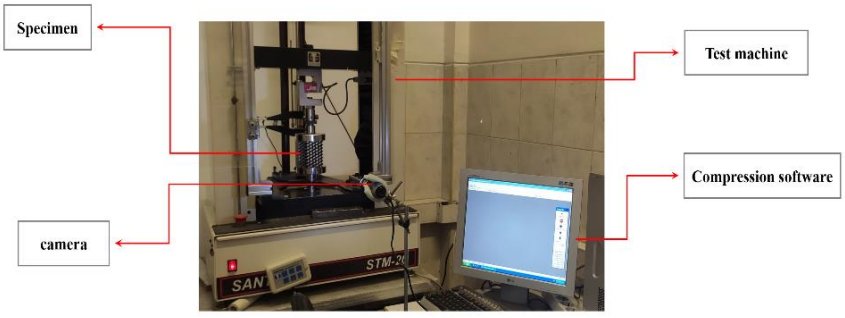

Figure 2. Experimental test of cellular structures under compression test.

  doi:10.5075/epfl-298799_978-2-9701614-0-0

2.3. Baseline cellular structure

For this study, a cellular structure is adopted and reproduced based on Ref [7]. Important geometric parameters are shown in Figure 3 and summarized in Table 2. The design is inspired by the cancellous bone to improve energy absorption properties of the structures.

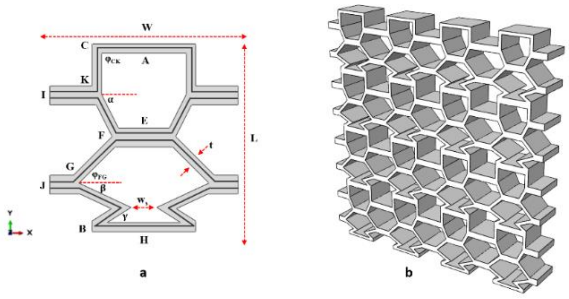

Figure 3. Representative unite cell with main parameters (a), Compression test sample (b)

Table 2: Geometric parameters of bone-inspired unit cell.

Variable	Value	Variable	Value	Variable	Value	Variable	Value
CA	5mm	FE	2.76mm	BH	3.8mm	φ_{FG}	90◦
CK	5mm	FG	7.07mm	HN	5.61mm	α	63.43◦
KI	5mm	GJ	2.24mm	t	1mm	β	25◦
KF	5mm	GB	5.92mm	φ_{CK}	45◦	γ	41.14◦

3. Results and discussion

3.1 Effect of glass fiber reinforcement on energy absorption

The cellular structures with glass fiber reinforcement were 3D printed. The structures were subjected to compression testing to measure the energy absorption. Total energy absorption is obtained by integrating the force-displacement curve, and it is equal to the area under the force-displacement diagram. Figure 4 compares the properties of pure and glass fiber-reinforced PLA cellular structures. It is demonstrated that the energy absorption considerably increases by ~250% for fiber-reinforced cellular structures.

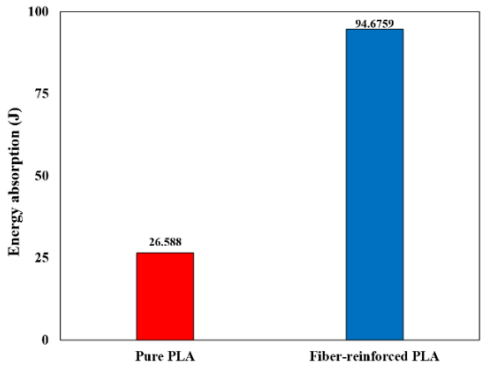

Figure 4. Comparison of energy absorption in fiber-reinforced-PLA and pure PLA structures.

  doi:10.5075/epfl-298799_978-2-9701614-0-0 published under CC BY-NC 4.0 license

3.2. Effect of unit cell designs on energy absorption

A particle swarm optimization (PSO) algorithm was developed to obtain optimized designs of the cellular structures to increase energy absorption capabilities. Raw materials properties were used for the calculations. The objective function was to design unit cells that maximize and double the stiffness in the cellular structures compared to the baseline cellular structure in Figure 3. This was to achieve only based on the design of unit cells. The analytical equations to get young's modulus in the y-direction were used as an objective function. The decision variables for optimization are α, β and γ. The unit cells proposed by the optimization algorithm are shown in Figures 5a and b, and geometric parameters are presented in Table 3.

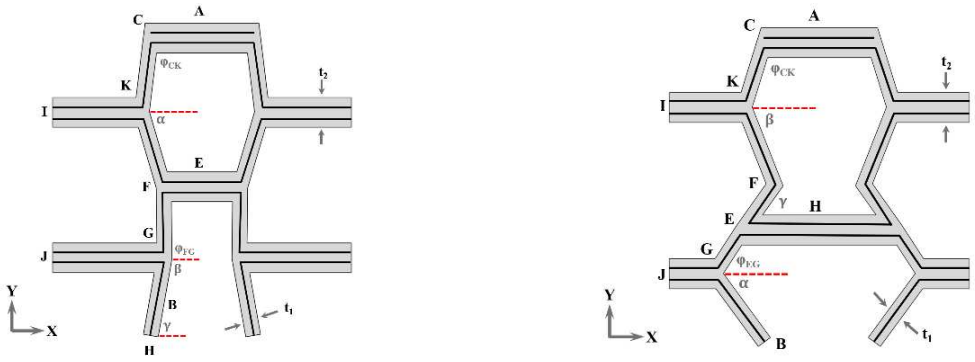

Figure 5. Unite cells with (a) maximum and (b) doubled stiffnesses compared to baseline unit cell.

Table 3: Geometric parameters of optimized unit cells.

(a) Unite cell with maximum stiffness							
Variable	Value	Variable	Value	Variable	Value	Variable	Value
CA	3.42mm	FE	2.55mm	BH	1.01mm	φ_{FG}	90.63◦
CK	5.03mm	FG	4.78mm	t_1	1mm	α	73.59◦
KI	5.97mm	GJ	7.49mm	t_2	2mm	β	80◦
KF	5.12mm	GB	4.28mm	φ_{CK}	96.9◦	γ	80◦
(b) Unite cell with doubled stiffness							
Variable	Value	Variable	Value	Variable	Value	Variable	Value
CA	3.66mm	FE	3.69mm	GB	5.64mm	φ_{EG}	122.91◦
CK	4.53mm	EH	5.1mm	t_1	1mm	α	53.79◦
KI	5mm	FG	3.48mm	t_2	2mm	β	68.62◦
KF	5.55mm	GJ	3mm	φ_{CK}	107.4◦	γ	54.76◦

  doi:10.5075/epfl-298799_978-2-9701614-0-0

The optimized structures were 3D printed using glass fiber-reinforced PLA and subjected to compression testing. Figure 6 shows energy absorption and specific energy absorption properties for designs with maximum and doubled stiffnesses compared to the baseline cellular structure. Specific energy absorption is one of the main parameters in comparing structures obtained from Eq. (1).

$$SEA = \frac{Total\ Absorbed\ Energy}{Total\ Specimen\ Mass} = \frac{\int Fdx}{m} \quad (1)$$

As illustrated, the amount of energy absorption and specific energy absorption in the optimized structures are increased. In the optimized cellular structures, the amount of stiffness has increased compared to the bone-inspired structure, which has increased the amount of energy absorption. The increase in the energy absorption properties for the structure with doubled stiffness is 30% while it is 90% for the structure with the maximum stiffness.

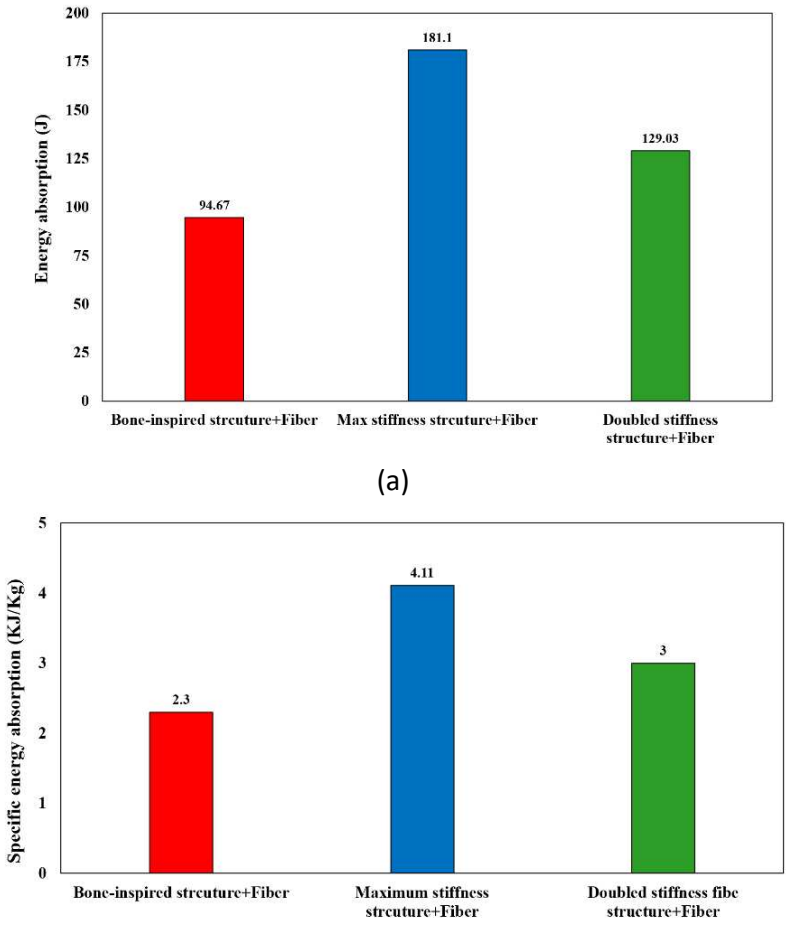

Figure 6. (a) Energy absorption and (b) specific energy absorption in bio-inspired and optimized cellular structures

4. Conclusion

This study investigated energy absorption in the bone-inspired cellular structure experimentally through material development and unit cell design optimization. The structures were 3D printed

using unfilled and glass fiber-reinforced PLA. Compared to unfilled cellular structures, the energy absorption for glass fiber-reinforced cellular structures increased by 250%. An optimization algorithm was employed with objective functions to obtain maximum and doubled stiffness (elastic modulus) in unit cells to increase energy absorption further. The energy absorption properties increase by 90% when the maximum stiffness in the structure was obtained.

References

1. Sadeghzade M, Gharehbaghi H, Farrokhabadi A. Experimental and analytical studies of mechanical properties of additively manufactured lattice structure based on octagonal bipyramid cubic unit cell. Addit Manuf [Internet]. 2021;48(PB):102403. Available from: https://doi.org/10.1016/j.addma.2021.102403

2. Evangelos G. Experimental and FE Analysis of 3Dprinted fiber reinforced honeycomb structured composite materials. 2018;(March):1–67.

3. Xu M, Xu Z, Zhang Z, Lei H, Bai Y, Fang D. Mechanical properties and energy absorption capability of AuxHex structure under in-plane compression: Theoretical and experimental studies. Int J Mech Sci [Internet]. 2019;159(May):43–57. Available from: https://doi.org/10.1016/j.ijmecsci.2019.05.044

4. Alomarah A, Masood SH, Sbarski I, Faisal B, Gao Z, Ruan D. Compressive properties of 3D printed auxetic structures: experimental and numerical studies. Virtual Phys Prototyp [Internet]. 2020;15(1):1–21. Available from: https://doi.org/10.1080/17452759.2019.1644184

5. Rahman H, Yarali E, Zolfagharian A, Serjouei A, Bodaghi M. Energy absorption and mechanical performance of functionally graded soft–hard lattice structures. Materials (Basel). 2021;14(6).

6. Yin H, Huang X, Scarpa F, Wen G, Chen Y, Zhang C. In-plane crashworthiness of bio-inspired hierarchical honeycombs. Compos Struct [Internet]. 2018;192:516–27. Available from: https://doi.org/10.1016/j.compstruct.2018.03.050

7. Ghazlan A, Nguyen T, Ngo T, Linforth S, Le VT. Performance of a 3D printed cellular structure inspired by bone. Thin-Walled Struct [Internet]. 2020;151(August 2019):106713. Available from: https://doi.org/10.1016/j.tws.2020.106713

8. Veisi H, Farrokhabadi A. Investigation of the equivalent material properties and failure stress of the re-entrant composite lattice structures using an analytical model. Compos Struct [Internet]. 2021;257(September):113161. Available from: https://doi.org/10.1016/j.compstruct.2020.113161

9. Farrokhabadi A, Ashrafian MM, Gharehbaghi H, Nazari R. Evaluation of the equivalent mechanical properties in a novel composite cruciform honeycomb using analytical and numerical methods. Compos Struct. 2021;275(July).

10. Farrokhabadi A, Ashrafian MM, Fotouhi M. Design and characterization of an orthotropic accordion cellular honeycomb as one-dimensional morphing structures with enhanced properties. J Sandw Struct Mater [Internet]. 2022 Jan 27;10996362211070248. Available from: https://doi.org/10.1177/10996362211070249

11. Quan C, Han B, Hou Z, Zhang Q, Tian X, Lu TJ. 3D Printed Continuous Fiber Reinforced Composite Auxetic Honeycomb Structures. Compos Part B Eng [Internet].

2020;187(February):107858. Available from: https://doi.org/10.1016/j.compositesb.2020.107858

12. Akhoundi B, Behravesh AH, Bagheri Saed A. Improving mechanical properties of continuous fiber-reinforced thermoplastic composites produced by FDM 3D printer. J Reinf Plast Compos. 2019;38(3):99–116.

13. ASTM D638-14. ASTM D638-14, Standard Practice for Preparation of Metallographic Specimens. ASTM Int. 2016;82(C):1–15.

14. Ghazlan A, Ngo T, Nguyen T, Linforth S, Van Le T. Uncovering a high-performance bio-mimetic cellular structure from trabecular bone. Sci Rep [Internet]. 2020;10(1):1–13. Available from: https://doi.org/10.1038/s41598-020-70536-7

RAPID FATIGUE LIFE PREDICTION OF CFRP LAMINATES BY COMBINING THE DATA OF SELF-HEATING WITH STIFFNESS DEGRADATION

Zijiao, Jia[a,b], Marie-Laetitia, Pastor[a], Christian, Garnier[b], Xiaojing, Gong[a]

a: Institut Clément Ader (ICA), CNRS UMR 5312, University of Toulouse, UPS, 1 rue Lautréamont, 65016 Tarbes, France – zijiao.jia@iut-tarbes.fr
b: LGP-ENIT-INP, University of Toulouse, 47 Avenue d'Azereix, BP 1629, 65016 Tarbes cedex, France

Abstract: *The thermographic approach is used to rapidly determine the fatigue properties of composite materials. In this work, a modified fatigue life prediction model based on self-heating data and stiffness degradation applied to unidirectional and ±45° CFRP (Carbon Fiber Reinforced Polymer) composites under traction loading (R=0.1) has been developed in order to avoid the conservativeness on the fatigue life of a quasi-isotropic CFRP laminate. A new parameter **r** is introduced to take more complex damage mechanisms in MultiDirectional (MD) laminates into account. It is demonstrated that predicted S-N curves using modified model has a better agreement with the experimental results.*

Keywords: fatigue life prediction; stiffness degradation; infrared thermography; damage accumulation; composite laminates

1. Introduction

Fatigue of Carbon Fiber Reinforced Polymer (CFRP) composite is one of the topics that receive more and more attention since these materials are frequently used for the manufacturing of loading-bearing components in the aeronautical, automotive and marine industries [1]. Investigating the fatigue properties of CFRP composite by the traditional fatigue tests is an expensive and time-consuming process [2]. Besides, the fatigue behavior of a composite laminate depends not only on loading parameters, but also on various material factors including constituent materials: fiber and matrix, architecture of reinforcement, stacking sequence, porosity, etc. Therefore, great efforts have been made to develop techniques and methods which allows for the rapid evaluation of fatigue behavior of composite laminates.

With the development of high resolution infrared camera and the improvement in relevant theories, InfraRed Thermography (IRT), as a non-contact, real-time, full-field technology, was extensively used for the rapid prediction of fatigue properties [3-14]. By monitoring the temperature increase of the specimen during an incremental stepwise loading procedure, Risitano et al. [3-4] firstly developed an empirical method to determine the fatigue limit of metallic materials and construct the S-N curves. Luong et al. [6-7] proposed a Two-Curve Methodology (TCM) to rapidly evaluate the fatigue limit of a mild steel Fe 510. Later, Colombo et al. [13] and Gornet et al. [14] extended the utilization of the method to Glass Fiber Reinforced Polymer (GFRP) and CFRP. Gornet et al. [5] adopted Risitano's method to rapidly determine the fatigue limit of CFRP and good agreement was achieved between predicted values and traditional experimental results.

  doi:10.5075/epfl-298799_978-2-9701614-0-0

Throughout the fatigue loading, three distinctive stages of damage evolution can be generally identified for the composite materials [15-16]. In the stage I, the damage developed rapidly, this is caused mainly by micro-cracks in the matrix. The development of damage results in a more gradual stiffness degradation of the material in the stage II, where the damage mode is considered to be delamination propagation [17]. The last stage of fatigue life (III) is involved with the fracture of fibers, which leads to a catastrophe decrease of mechanical properties and the failure of specimen [18-19]. With the accumulation of damages, the global stiffness degrades accordingly. Therefore, this correlation between stiffness and accumulated damages makes it possible to predict the fatigue life based on the stiffness degradation [20-21].

In a previous work, a fatigue life prediction model was proposed by Huang et al. [22] by combining the stiffness degradation with IRT data. The model succeeds to predict the S-N curves of braided, UD [22] and ±45° [23] CFRP in a short time (10-12 hours). In this study, firstly Huang's model is applied to a MD Quasi-Isotropic (QI) CFRP laminate; then it is modified by introducing a new parameter *r* so as to take the influence of more complex damage mechanisms into account. Finally, the results obtained by two models are compared with experimental data.

2. Materials and experimental setup

2.1 Materials and specimens

The material used is the unidirectional carbon prepreg composed of HexPly®M79 matrix reinforced with unidirectional high strength carbon fiber (38%/UD150/CHS). The stacking sequence of the laminates is $[0/45/90/-45]_s$, with thickness of 1.01 (± 0.025) mm. Curing was carried out in an autoclave at 2.0 bar and 80°C for 6 h with a heating rate of 1°C/min. According to the standard ISO 527-4: 2021 [24], the dimensions of the specimens were 250*25 mm². Glass fiber reinforced epoxy tabs were used at either end of the specimens to prevent gripping induced failure (Figure 1).

2.2 Experimental setup

The specimens were first statically tested to access the Ultimate Tensile Strength (UTS). Static tensile tests were carried out using INSTRON universal testing machine (INSTRON 5500R) with a 100 KN load cell. According to ISO 527-4: 2021 [24], the displacement rate is set as 2.0 mm/min. Two 8-bits Complementary Metal Oxide Semiconductor (CMOS) cameras with an Aramis 2M Digital Image Correlation (DIC) system (GOM Company, Germany) were used to measure the tensile strain fields on the specimens throughout the tests. Random black and white speckles were sprayed onto the surface of the specimen prior to the testing. The data was acquired with a rate of one image per second.

The tension-tension fatigue tests were performed in the servo-hydraulic Instron loading machine under load control mode, in accordance with the test standard ASTM D3479 [25]. All the tests were conducted at room temperature with a frequency of 5 Hz and a *R* value ($R = \frac{\sigma_{min}}{\sigma_{max}}$) of 0.1 was adopted. Traditional fatigue tests with constant load amplitude were conducted to produce a reliable S-N curve. Each test was conducted to failure or up to 10^6 cycles. The experimental stiffness *K(N)* was recorded at fixed time intervals of the fatigue life.

  doi:10.5075/epfl-298799_978-2-9701614-0-0

Besides traditional fatigue tests, step-loading fatigue tests at increasing loads were also performed. The maximum stress amplitude started from 30% UTS with steps of 5% UTS until the occurrence of final failure. For each stress level, the specimen is tested for a duration of 6000 cycles, which is sufficient to achieve temperature stabilization. During the fatigue tests, a FLIR X6800sc Series IR camera with a spatial resolution of 640×512 pixels and thermal sensitivity of 18 mK at 30°C was employed to measure the temperature field evolution of the specimen. The camera was placed in front of the specimen at a distance of 68 cm to achieve the optical field-of-view conditions. The acquisition frequency was set as 150 Hz. Before fatigue testing, the surface of the specimen was painted in black matt spray to increase surface emissivity properties. The detailed experimental set-up is depicted in Figure 1. A reference specimen is placed next to the test specimen. The surface temperature will be used to calculate the temperature increase ΔT.

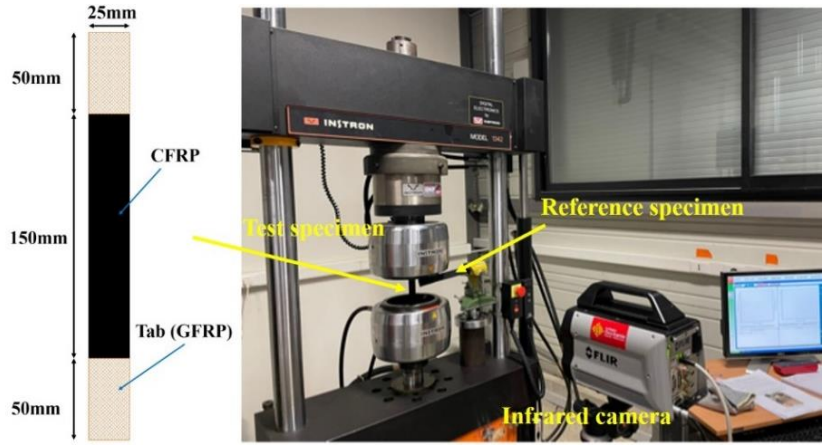

Figure 1. Experimental setup of fatigue tests with infrared thermography

3. Fatigue life prediction models

3.1 Huang's model

In the study of Huang et al. [22], the residual stiffness is adopted to describe the levels of accumulated damage in the laminates during fatigue loading. The damage index is defined as follows:

$$D(N) = \frac{1-k(N)}{1-k_f} \quad (1)$$

Where *N* is the number of loading cycles, $k(N)$ and k_f, defined as $\frac{K(N)}{K_0}$ and $\frac{K_f}{K_0}$, are normalized residual stiffness at N^{th} cycle and the end of second stage (N_f), respectively, K_0 is the initial stiffness.

The normalized stiffness *k(N)* can be calculated as a function of stabilized temperature rise according to the model proposed by Huang et al. [22]:

$$k(N) = 1 - p\Delta T_{stab} N^{\frac{1}{q}} \ (q \geq 1) \quad (2)$$

Where *p* and *q* are two constants, independent of temperature and loading cycles.

  doi:10.5075/epfl-298799_978-2-9701614-0-0

Taking Eq. (2) into Eq. (1) and considering the boundary condition that *D=1* when $N = N_f$, the expression for the fatigue life N_f can be obtained:

$$N_f = \left(\frac{1-k_f}{p\Delta T_{stab}(\sigma)}\right)^q \ (q \geq 1) \tag{3}$$

From Eq. (3), it can be seen that the application of Huang's model only requires the value of parameter *p*, *q* and the relationship between stabilized temperature rise ΔT_{stab} and applied stress.

3.2 Modified model

In the Eq. (2) of Huang's model, the role of parameter *p* and *q* is to regulate the influence of ΔT_{stab} and to control the shape of the function, respectively. However, throughout the fatigue loading, the damage modes inside the MD laminates are much more complex than UD and ±45° laminates since each ply of different orientation was subjected to different stresses. To account for this, Eq. (2) is modified by introducing a new parameter *r* into the original expression:

$$k(N) = 1 - p\Delta T_{stab}^r N^{\frac{1}{q}} \ (q \geq 1) \tag{4}$$

And the expression of fatigue life is modified accordingly:

$$N_f = \left(\frac{1-k_f}{p\Delta T_{stab}^r(\sigma)}\right)^q \ (q \geq 1) \tag{5}$$

In Eq. (5), the values of *p*, *q* and *r* can be determined empirically by fitting experimental data with MATLAB software. It should be noted that if the value of parameter *r* becomes close to *1*, the model will return to Huang's model.

4. Results and discussions

In this section, the two fatigue life prediction models are compared using the experimental data of QI CFRP laminates. The procedure and calibration details are listed below:

Step 1: determine fatigue limit and corresponding stabilized temperature rise based on thermographic data

The evolution of surface temperature rising with the number of cycles for one test specimen is depicted in Figure 2. It is observed that for all the stress levels indicated in the plot, the temperature profile reached a stabilized plateau after certain loading cycles. Figure 3 represents the stabilized temperature rising plotted as a function of the maximum applied stress. The improved graphic method in article [26] was employed. The point with maximum stress amplitude of 65% is chosen to divide the data points into two group. Since there is only one data point left above fatigue limit, which cannot form a line, the dividing point (65% UTS) is adopted for fitting. The fatigue limit is determined as 66.25% UTS and the corresponding stabilized temperature rise ($\Delta T_{stab_{fl}}$) is 4.31°C.

  doi:10.5075/epfl-298799_978-2-9701614-0-0

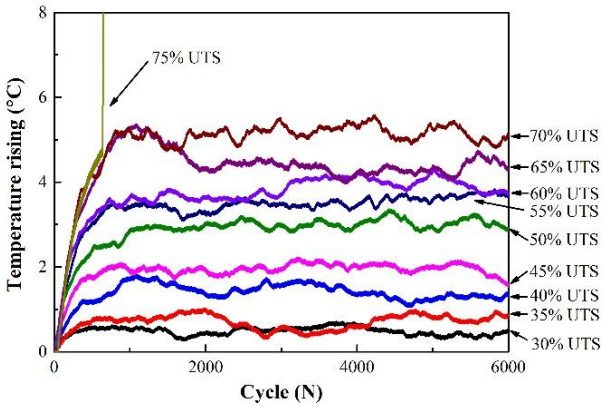

Figure 2. Evolution of temperature rising with the number of cycles

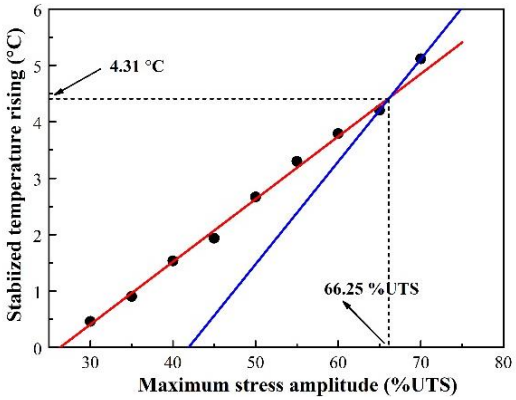

Figure 3. Fatigue limit determination by improved graphic method in [26]

Step 2: calibration of *p*, *q* and *r*

Figure 4 is a plot of the normalized stiffness degradation against the number of loading cycles and stabilized temperature rise for the specimens cycled at five stress levels: 45%, 50%,55%, 60% and 65% UTS. For each curve, 20 points were sampled, therefore, a total of 100 points were used for fitting. Herein, both Eq. (2) and Eq. (4) are employed to fit the experimental data (3D surface fitting in MATLAB). For Huang's model, the best fit values of *p* and *q* are 2.269e^{-2} $(°C^r \times cycle^{1/q})^{-1}$ and 12.155, respectively. As for the proposed model, the values of *p*, *q* and *r* are determined as 3.391e^{-2}$(°C^r \times cycle^{1/q})^{-1}$, 12.217 and 0.716, respectively.

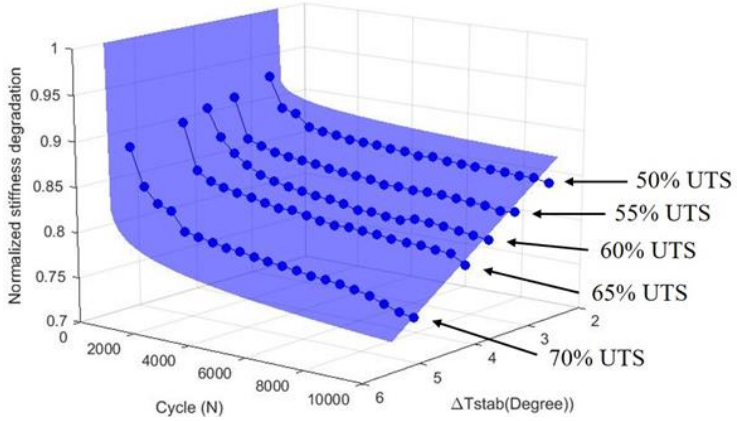

Figure 4. Surface fitting of Eq. (2) and Eq.(4) by MATLAB

Step 3: calculate failure threshold stiffness k_f

The number of loading cycles corresponding to the fatigue limit is usually taken between 10^6 and 10^7 cycles [27]. Hereby, both $k(N_{fl}=10^6)$ and $k(N_{fl}=10^7)$ were considered in the calculation. The values of failure threshold stiffness calculated by Eq. (2) and Eq. (4) were listed in Table 1.

Table 1: Failure threshold stiffnesses

Model	p [(°C ^{r} ×Cycle$^{1/q}$)$^{-1}$]	q	r	$k(N_{fl}=10^6)$	$k(N_{fl}=10^7)$
Huang	2.269e-2	12.155	1	0.6977	0.6347
Modified	3.391e-2	12.217	0.716	0.7010	0.6389

Step 4: prediction of S-N curve

Having the values of *p, q, r* and k_f, the whole S-N curve can be predicted. *Figure 5* displays the S-N curves predicted by two models. Traditional fatigue test results with 95% confidence interval are also included in the same figure for comparison.

As can be seen from the figure, the two predicted S-N curves using Huang's model are far below the 95% confidence interval. The predicted fatigue life is much lower than the traditional fatigue test results overall. When the loading amplitude is 85% UTS, the predicted fatigue life corresponding to $N_{fl}=10^6$ and $N_{fl}=10^7$ cycles using Huang's model is 815 and 8155 cycles, which is around 50 times and 4 times less than the value determined by the lower boundary line of 95% confidence interval. While both the predicted S-N curves corresponding to $N_{fl}=10^6$ cycles and $N_{fl}=10^7$ cycles using proposed model in this study are closer to the 95% confidence interval. In particular, the predicted S-N curve corresponding to $N_{fl}=10^7$ cycles lays totally in the confidence interval. This indicates that compared to Huang's model, owing to the introduction of parameter *r*, the modified model is more accurate in fatigue life prediction for QI CFRP laminates.

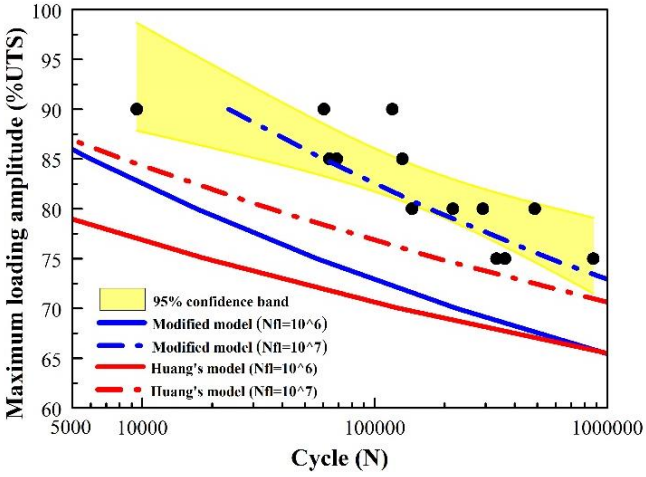

Figure 5. Comparison of predicted results by two models with traditional fatigue test results

5. Conclusions

The fatigue life prediction model proposed by Huang et al. [22] has been modified to take more complex damage modes in MD CFRP composites into account. A new parameter *r* is introduced into the original expression of normalized stiffness. When the value of parameter *r* becomes close to 1, the model will return back to Huang's model, therefore the modified model proposed in this study is more general in the fatigue life predictions of composite laminates. It is demonstrated that predicted S-N curves using Huang's model is too conservative and those obtained by modified model proposed in this study has a better agreement with the experimental results.

Acknowledgements

The author Zijiao Jia was supported by China Scholarship Council (CSC) for three years at the University of Toulouse.

6. References

1. Das M, Sahu S, Parhi D R. Composite materials and their damage detection using AI techniques for aerospace application: A brief review. Materials Today: Proceedings, 2021, 44: 955-960.
2. Pascual F G, Meeker W Q. Estimating fatigue curves with the random fatigue-limit model. Technometrics, 1999, 41(4): 277-289.
3. G Curti, G La Rosa, M Orlando, A Risitano. Analisi tramite infrarosso termico della temperatura limite in prove di fatica. XIV Convegno AIAS, 1986: 23-27.
4. Fargione G, Risitano A. Rapid determination of the fatigue curve by the thermographic method. International journal of fatigue, 2002, 24: 11−19.
5. Gornet L, Westphal O, Rozycki P, Stainier L, Kemlin G. Rapid determination of the fatigue properties of carbon fiber epoxy matrix composite laminates by self heating tests. ECCM16-16th European Conference on Composite Materials. 2014.
6. Luong M P. Fatigue limit evaluation of metals using an infrared thermographic technique. Mechanics of materials, 1998, 28(1-4): 155-163.
7. Luong M P. Infrared thermographic scanning of fatigue in metals. Nuclear engineering and design, 1995, 158(2-3): 363-376.
8. Colombo C, Libonati F, Pezzani F, Salerno A, Vergani L. Fatigue behaviour of a GFRP laminate by thermographic measurements. Procedia Engineering, 2011, 10: 3518-3527.
9. Peyrac C, Jollivet T, Leray N, Lefebvre F, Westphal O, Gornet L. Self-heating method for fatigue limit determination on thermoplastic composites. Procedia Engineering, 2015, 133: 129-135.
10. Montesano J, Fawaz Z, Bougherara H. Use of infrared thermography to investigate the fatigue behavior of a carbon fiber reinforced polymer composite. Composite structures, 2013, 97: 76-83.
11. Liakat M, Khonsari M M. Analysis and life prediction of a composite laminate under cyclic loading. Composites Part B: Engineering, 2016, 84: 98-108.
12. Amiri M, Khonsari M M. Rapid determination of fatigue failure based on temperature evolution: Fully reversed bending load. International Journal of Fatigue, 2010, 32(2): 382-389.
13. Colombo C, Libonati F, Pezzani F, Salerno A, Vergani L. Fatigue behaviour of a GFRP laminate by thermographic measurements. Procedia Engineering, 2011, 10: 3518-3527.

  doi:10.5075/epfl-298799_978-2-9701614-0-0

14. Gornet L, Wesphal O, Burtin C, Bailleul J L, Rozycki P, Stainier L. Rapid determination of the high cycle fatigue limit curve of carbon fiber epoxy matrix composite laminates by thermography methodology: Tests and finite element simulations. Procedia Engineering, 2013, 66: 697-704.
15. Vasiukov D, Panier S, Hachemi A. Direct method for life prediction of fibre reinforced polymer composites based on kinematic of damage potential. International Journal of Fatigue, 2015, 70: 289-296.
16. Shiri S, Yazdani M, Pourgol-Mohammad M. A fatigue damage accumulation model based on stiffness degradation of composite materials. Materials & Design, 2015, 88: 1290-1295.
17. Stinchcomb W W, Bakis C E. Fatigue behavior of composite laminates. Composite materials series, 1991, 4: 105-180.
18. Godines C, DorMohammadi S, Abdi F, Villa Montero M, Huang D, Minnetyan L. Damage tolerant composite design principles for aircraft components under static service loading using multi-scale progressive failure analysis. Journal of Composite Materials, 2017, 51(10): 1393-1419.
19. Razvan A, Reifsnider K L. Fiber fracture and strength degradation in unidirectional graphite/epoxy composite materials. Theoretical and applied fracture mechanics, 1991, 16(1): 81-89.
20. Shiri S, Yazdani M, Pourgol-Mohammad M. A fatigue damage accumulation model based on stiffness degradation of composite materials. Materials & Design, 2015, 88: 1290-1295.
21. Peng T, Liu Y, Saxena A, Goebel K. In-situ fatigue life prognosis for composite laminates based on stiffness degradation. Composite Structures, 2015, 132: 155-165.
22. Huang J, Pastor M L, Garnier C, Gong X. A new model for fatigue life prediction based on infrared thermography and degradation process for CFRP composite laminates. International Journal of Fatigue, 2019, 120: 87-95.
23. Huang J, Garnier C, Pastor M L, Gong X. Investigation of self-heating and life prediction in CFRP laminates under cyclic shear loading condition based on the infrared thermographic data. Engineering Fracture Mechanics, 2020, 229: 106971.
24. ISO 527-4:2021, Plastics - Determination of tensile properties - Part 4: Test conditions for isotropic and orthotropic fibre-reinforced plastic composites, 2021.
25. ASTM, D 3479/D 3479M–96. Standard test method for tension–tension fatigue of polymer matrix composite materials. ASTM, International, 2007.
26. Huang J, Pastor M L, Garnier C, Gong X. Rapid evaluation of fatigue limit on thermographic data analysis. International Journal of Fatigue, 2017, 104: 293-301.
27. De Los Rios E R, Rodopoulos C A, Yates J R. A model to predict the fatigue life of fibre-reinforced titanium matrix composites under constant amplitude loading. Fatigue & Fracture of Engineering Materials & Structures, 1996, 19(5): 539-550.

  doi:10.5075/epfl-298799_978-2-9701614-0-0

PERFORMANCE EVALUATION OF E-SKIN FOR STRUCTURAL DEFORMATION DETECTION

Yu-Jin, Jung[a], Seung-Jun, Lee[b], Sung-Hwan, Jang[c]

a: Department of Smart City Engineering, Hanyang University ERICA – yujin0421@hanyang.ac.kr
b: Department of Civil and Environmental Engineering, Hanyang University
c: Department of Civil and Environmental Engineering, Hanyang University ERICA – sj2527@hanyang.ac.kr

Abstract: *Damage detection systems of structures are considered one of the most important technologies for ensuring the safety of structures in various types of research. Among them, carbon nanotube polymer composite, which is easy to apply to structures and has no size limitations, has been reported as one of the most suitable methods for SHM systems. We developed E-Skin (Electronic Skin), a carbon nanotube polymer composite. Then, we confirmed the electrical change of E-Skin due to mechanical deformation. Mechanical deformation led to electrical changes in the E-Skin. Based on this phenomenon, we applied E-skin to the structure and checked the electrical changes of E-skin due to cracks and loads. We aim to develop a system that can monitor cracks and various loads of structures in real-time using E-Skin.*

Keywords: SHM; Structural deformation detection; Carbon nanotube polymer composite; E-Skin; Self-sensing system

1. Introduction

Concrete structures are aging over time, and they can be exposed to various loads and cause unexpected damage. In addition, hazardous environmental conditions and poor maintenance can accelerate structural performance, significantly reducing structural service life and leading to catastrophic losses.[1] The solution to this problem is to apply a Structural Health Monitoring (SHM) system that allows continuous monitoring of structures. We discussed the deformation sensor of the SHM system, which has no size limit and directly detects deformation to the structure.[2]

Deformation sensors that rely on direct contact exhibit electrical changes in response to structural damage.[3] The most widely used metal foil deformation sensors are often used for reliable performance and low cost but have low gauge coefficients, very low flexibility, and can only be fitted to surfaces of composite structures.[4, 5] As an alternative to this, we considered a stretchable deformation sensor using carbon nanotube polymer composites, a nanomaterial with no limitations in application.[6] Carbon nanotube polymer composites have excellent mechanical and electrical properties that can be used as deformation sensors and investigated through various studies.[7, 8]

This study developed a carbon nanotube polyurethane composite that detects various structural loads. We named it E-Skin and calculated the electrical conductivity of E-Skin according to the carbon nanotube content. Then, we considered the content of carbon nanotubes suitable for the sensor. We selected an applicable carbon nanotube content for the sensor. We confirmed

  doi:10.5075/epfl-298799_978-2-9701614-0-0

the electrical change of E-Skin according to the static and impact load by thickness. We applied E-Skin to the wall using this result. Finally, we have obtained useful conclusions regarding load detection performance through experiments.

2. Experimental

2.1 Materials

CNT was purchased from Nanolab, Inc. (MA, USA). CNT has a diameter of 15 nm, a length of 5-20 µm, and a purity of higher than 85 wt%. PU was obtained from Easy Composites Ltd. (Staffordshire, UK) with a density of 1.01-1.06 g/cm3 and hardness of 60. Acetone was used as a dispersant, and acetone with 99.7 % purity was purchased from Samchun chemicals Co., Ltd. (Gyeonggi, KOR).

2.2 Preparation of E-Skin

Figure 1 (a) shows the manufacturing process of E-Skin, a carbon nanotube polyurethane composite.[9] About 50 ml of acetone was used as a solvent for dispersion of CNT present as large agglomerates due to van der Waals intermolecular force between CNT. Acetone dissolved highly viscous polyurethane part A(resin) and enabled high-quality dispersion of CNT. An Q700CA ultrasonicator of Qsonica LLC. (CT, USA) was applied to break the van der Waals intermolecular force between CNT aggregates in the solution. The ultrasonicator was operated with a 90 % amplitude pulse model, and a total of 100,000 J energy was applied. The solution was placed on a hot plate at 60 °C for 24 hours to evaporate acetone in the solution. Then, PU part B(hardener) was added to the solution and mixed evenly by a TR50M three-roll mill of Trilos (CA, USA).

The electrode installation of the E-Skin is shown in Figures 1(b) and (c). Figure 1(b) shows the electrode design of the E-Skin for crack detection. After attaching the copper tape to both ends of the E-Skin for crack detection, the copper tape and the E-Skin were connected using silver paint to eliminate contact errors. Moreover, Figure (c) shows the electrode design of E-Skin for load detection. The electrodes are installed in the order of copper tape-E-Skin-Copper tape, with alternating bottom and top copper tapes.[10] The top and bottom lines meet to form a cell.

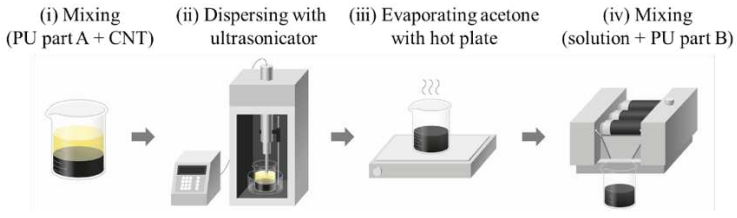

(a)

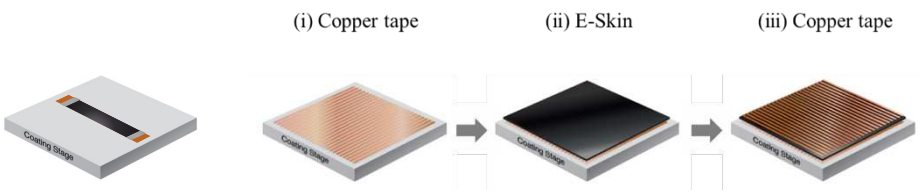

(b)

Figure 1. (a)Fabrication process of E-Skin, (b)Electrode installation process of E-Skin

2.3 Characterization of E-Skin

To select the carbon nanotube content of E-Skin suitable for the sensor, we investigated the electrical conductivity of E-Skin manufactured by carbon nanotube content before the experiment. The electrical conductivity was calculated using Eq. (1).

$$\sigma = \frac{\mathrm{L}}{\mathrm{AR}} \tag{1}$$

Where σ (S/m) is the electrical conductivity of the sample, L (m) is the distance between the electrodes, A (m^2) is the area of the electrode, and R (Ω) is the electrical resistance of the sample. The electrical resistance of E-Skin was measured using Keithley's 2450 SourceMeter (OH, USA), and we used a two-point probe measurement method.

Before applying E-Skin to the structure, the electrical behavior of E-Skin due to mechanical deformation was verified using UTM and an impact test machine. Also, as shown in Fig. 2(a), cracks occurred in the concrete coated with E-Skin using a 3-point bending tester. To find the exact location of the crack, the E-Skin was divided into 5 sections, and electrodes were installed. Furthermore, the real-time electrical change of E-Skin was measured using a multimeter. Figure 2(b) shows an E-Skin applied wall sensor. The E-Skin applied to the wall is installed across 48 horizontal and 48 vertical copper tapes. In addition, electrodes were installed at the ends and systems of the copper tape using copper wire. We applied static and impact loads to the E-Skin applied to the wall.

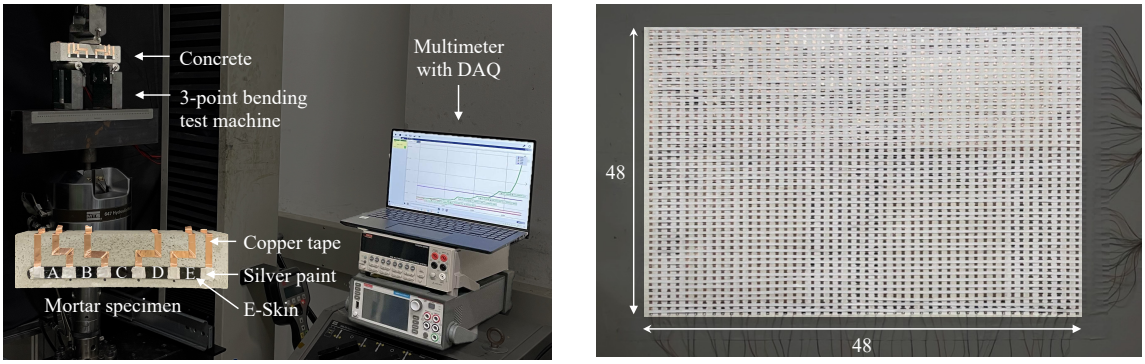

(a) (b)

Figure 2. (a)3-point bending test machine and multimeter with DAQ for crack detection test, (b)E-Skin coated wall load detection sensor

3. Results and Discussion

The electrical conductivity of the E-Skin we measured is shown in Figure 3. E-Skin showed an electrical percolation threshold at a carbon nanotube content of 1 wt%. The electrical percolation threshold allows the E-Skin to be used as a sensor. The electrical conductivity of the carbon nanotubes is governed by the contact resistance between the individual carbon nanotubes in the electrical percolation threshold. Therefore, as the carbon nanotube content increases, the tunneling effect gradually disappears, and the convergence of electrical conductivity appears. We confirmed that the electrical conductivity converges at the carbon nanotube content of 5 wt%.

  doi:10.5075/epfl-298799_978-2-9701614-0-0

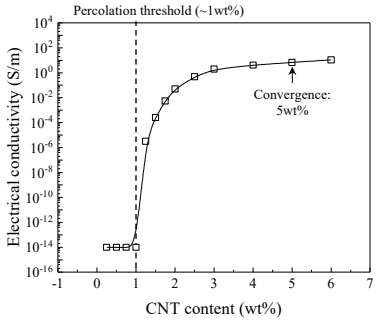

Figure 3. Electrical conductivity of E-Skin

Figure 4 shows the electrical changes in the E-Skin due to mechanical deformation. Figure 4(a) shows the electrical changes of the E-Skin according to strain. When strain is applied to the E-Skin, the electric tunneling gap between the carbon nanotubes in the carbon nanotube network increases. this change in the tunneling gap increases the contact resistance between the carbon nanotubes, increasing electrical resistance.[11]

Figure 4(b) shows the electrical changes of the E-Skin under static loads. E-Skin always has constant electrical conductivity. Therefore, the distance between E-Skin electrodes is greatly reduced by the static load, leading to a decrease in the electrical resistance of E-Skin.[12]

Figure 4(c) shows the electrical changes in the E-Skin due to the impact load. Impact load has the same principle as the result of static load. If the impact load of the E-Skin is applied, the area where the electrode is installed will be small. The same principle was applied to the impact load test as the result of the static load test. The electrode area of the E-Skin becomes very small during impact loading. The reduction in the distance between electrodes by the impact is negligible compared to a decrease in the area of the electrodes. Therefore, the change in electrical resistance is affected by the electrode area. Thus, the electrical resistance of the E-Skin tends to increase when the impact load is applied.

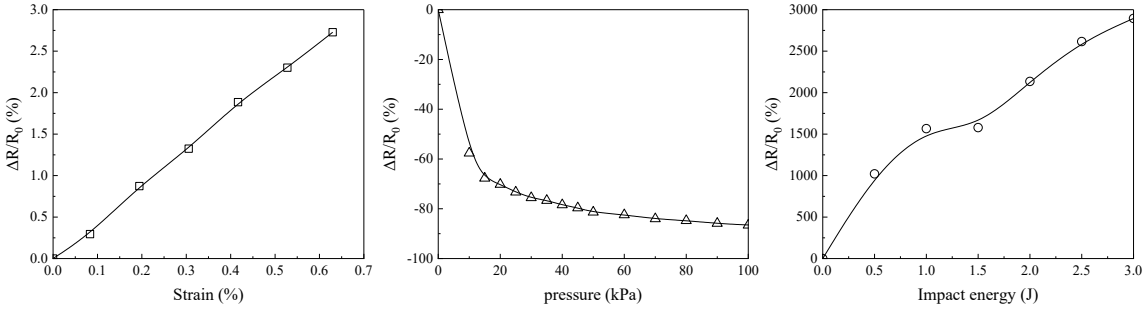

(a) (b) (c)

Figure 4. E-Skin Electrical Change (a)by strain, (b)by static load, (c)by impact load

The crack detection performance of the E-Skin applied to the structure is shown in Figure 5(a). Cracks in the structure appeared in the middle section C. The larger the crack, the greater the electrical resistance of the E-Skin. This is the same phenomenon as the tensile test, resulting in an increase in electrical resistance only in section C due to the rise in the electrical tunneling gap between the carbon nanotubes. Cracks occurred up to 5% on the concrete-coated E-Skin.

  doi:10.5075/epfl-298799_978-2-9701614-0-0

Considering that the strain at the breaking point of concrete is 0.3%, E-Skin is deemed suitable as a crack detection sensor.

The electrical changes in the E-Skin according to the load are shown in Figures 5(b) and (c). We manufactured a system that measures changes in electrical voltage in the same way as pressure sensors that are currently being commercialized.[13] We showed the output value of the system so that the voltage of 5V has a resolution of 2^{16}. Moreover, as evidenced by Ohm's law, it has an inverse property of electrical resistance and electrical voltage. This demonstrates the reverse sign of the electrical resistance change behavior of the E-Skin due to previous static and impact loads and the output value behavior of the multi-sensing system. As a result, it has been found that the tendency of electrical resistance changes under static and impact loads, and the direction of output values in the system are reversed. Furthermore, the voltage changes exactly where the load was applied. Therefore, we determined that E-Skin can detect static and impact.

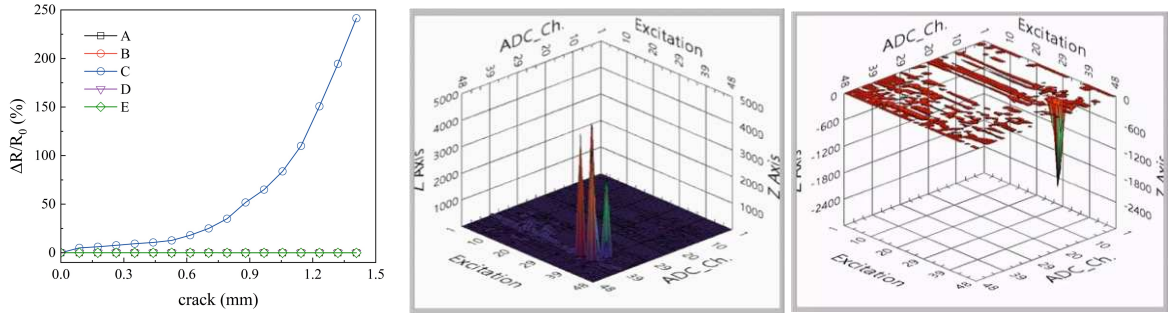

(a) (b) (c)

Figure 5. (a)Electrical Change of E-Skin by Crack in Concrete, Multi-sensing system screen according to (b)static load, (c)impact load

4. Conclusion

In this study, E-Skin, a carbon nanotube polymer complex for detecting the deformation of structures, was developed. We believe that the proposed approach is likely to revolutionize the current field of SHM because it enables high flexibility and accurate deformation detection of E-Skin. The results of conductive network formation and deformation detection of carbon nanotubes have the potential to be utilized in various engineering fields. We found E-Skin that can detect tensile and different loads. The E-Skin's crack detection and static and compressive load detection performance have been verified by application to concrete structures. Overall, the experimental results confirmed E-Skin's structural crack detection and load detection capabilities. Our future research will focus on electrical changes in the various loads of E-Skin applied to the floor of large structures.

Acknowledgement

This work presented in the paper was supported by the National Research Foundation of Korea(NRF) grant funded by the Korea government(MSIT) (No. 2020R1C1C1005273) and Korea Evaluation Institute of Industrial Technology(KEIT) grant funded by the Korea government(MOTIE) (No.20014127, Development of a smart monitoring system integrating 3D printed battery-free antenna sensor technology with AI optimization)

5. References

1. Yamaguchi T, Nakamura S, Saegusa R, Hashimoto S. Image-based crack detection for real concrete surfaces. IEEJ Transactions on Electrical and Electronic Engineering. 2008;3(1):128-135.
2. Tran Hoang P, Salazar N, Porkka TN, Joshi K, Liu T, Dickens TJ, et al. Engineering Crack Formation in Carbon Nanotube-Silver Nanoparticle Composite Films for Sensitive and Durable Piezoresistive Sensors. Nanoscale Res Lett. 2016;11(1):422.
3. Li S, Shu Y, Lin Y-A, Zhao Y, Yeh Y-J, Chiang W-H, et al. Distributed Strain Monitoring Using Nanocomposite Paint Sensing Meshes. Sensors. 2022;22(3):812.
4. Schumacher T, Thostenson ET. Development of structural carbon nanotube–based sensing composites for concrete structures. Journal of Intelligent Material Systems and Structures. 2013;25(11):1331-9.
5. Amjadi M, Yoon YJ, Park I. Ultra-stretchable and skin-mountable strain sensors using carbon nanotubes–Ecoflex nanocomposites. Nanotechnology. 2015;26(37):375501.
6. Boland CS, Khan U, Binions M, Barwich S, Boland JB, Weaire D, Coleman J. Graphene-coated polymer foams as tuneable impact sensors. Nanoscale. 2018;10(11):5366-75.
7. Zymelka D, Togashi K, Kobayashi T. Carbon-based printed strain sensor array for remote and automated structural health monitoring. Smart Materials and Structures. 2020;29(10):105022.
8. Cob J, Oliva-Avilés AI, Avilés F, Oliva AI. Influence of concentration, length and orientation of multiwall carbon nanotubes on the electromechanical response of polymer nanocomposites. Materials Research Express. 2019;6(11):115024.
9. Jang S-H, Yin H. Effective electrical conductivity of carbon nanotube-polymer composites: a simplified model and its validation. Materials Research Express. 2015;2(4):045602.
10. Njuguna MK, Yan C, Hu N, Bell JM, Yarlagadda PKDV. Sandwiched carbon nanotube film as strain sensor. Composites Part B: Engineering. 2012;43(6):2711-7.
11. Aly K, Li A, Bradford PD. Strain sensing in composites using aligned carbon nanotube sheets embedded in the interlaminar region. Composites Part A: Applied Science and Manufacturing. 2016;90:536-48.
12. Kim JH, Shin PS, Kim SY, Park JM. Evaluation of Adhesion and Electrical Properties of CNT/PU Topcoat with Different CNT Weight Fraction for A`ircraft. Compos Res. 2020;33(1):1-6.
13. Abot JL, Góngora-Rubio MR, Anike JC, Kiyono CY, Mello LAM, Cardoso VF, et al. Foil Strain Gauges Using Piezoresistive Carbon Nanotube Yarn: Fabrication and Calibration. Sensors. 2018;18(2):464.

  doi:10.5075/epfl-298799_978-2-9701614-0-0

TEMPERATURE DETECTABLE SURFACE COATING AND SELF-SENSING SYSTEM WITH CARBON NANO-TUBE/EPOXY COMPOSITES

Seung-Jun Lee[a], Yu-Jin Jung[b], Sung-Hwan Jang[c]

a: Department of Civil and Environmental Engineering, Hanyang University, Seoul, South Korea– sj5523@hanyang.ac.kr
b: Department of Smart City Engineering, Hanyang University ERICA, Ansan, South Korea
c: Department of Civil and Environmental Engineering, Hanyang University ERICA, Ansan, South Korea

Abstract: *In the machinery and construction industry, heat is a major factor causing damage and destruction. The safety and efficiency of most machines and structures are greatly affected by temperature, and temperature management and control are essential. In this study, a carbon nanotube (CNT) based temperature sensing coating that can be applied to machines and structures having various structural types were fabricated, and characteristics analysis and temperature sensing performance were evaluated. The temperature sensing coatings is composed of carbon nanotubes (CNT) and epoxy. Structural and electrical properties of CNT/epoxy coatings were analyzed through electron microscopy, and temperature sensing performance was evaluated according to the temperature change. As a result of the experiment, the CNT/epoxy coatings showed higher electrical conductivity as the CNT concentration increased. In addition, CNT/epoxy coatings exhibit high sensitivity in high and freezing temperature ranges. Therefore, the proposed CNT/epoxy coatings are promising for use as a material for high and freezing temperature sensing.*

Keywords: carbon nanotube; surface coating; temperature sensing; epoxy

1. Introduction

Temperature is the main parameter of most machines and structures, and temperature sensors account for a large part of the overall sensor market[1]. There are two main types of temperature sensors: contact and non-contact type. The contact type includes a thermocouple thermistor, silicon diode, platinum, etc., to measure the temperature in direct contact with the sensing point. Compared to the non-contact type, the contact type is simpler and more accurate temperature measurement. However, for accurate temperature measurement, sufficient contact surface must be secured. Also, when thermal energy is not enough, heat loss occurs and slow response. Silicon diode-based sensors are insensitive and require reliable interface electronics. Also, platinum sensors are expensive. To compensate for the shortcomings of these existing temperature sensors, research on various temperature sensors is being actively conducted.

Carbon nanotube (CNT) is one of the widely used functional fillers, and the composite with CNT is applied and utilized in various industrial fields. The structural morphology of CNTs can be used as a composite mixed with other materials to impart electrical and thermal conductivity and/or mechanical properties [2-4]. In particular, dispersing these kinds of nanoparticles in a polymer

  doi:10.5075/epfl-298799_978-2-9701614-0-0

system provides a means to improve thermal stability, light oxidation resistance and mechanical properties while expressing the functional properties of nanocomposites [5, 6].

The effect of temperature on CNT reinforced composites has been studied for different filler-resin composites. Gojny and Schulte [7] investigated the effect of multi-walled CNTs on the thermo-mechanical properties of multi-wall carbon nanotubes (MWCNTs)/epoxy composites and found that increasing concentrations of MWCNTs as well as functionalizing MWCNTs leads to an increase of the glass transition temperature with higher interfacial interaction between the CNT and the polymer matrix. For example, Jang and Yin [8, 9] fabricated highly sensitive strain and fracture sensors by dispersing carbon nanotubes as well as ferromagnetic particles in polydimethylsiloxane (PDMS). In addition to sensing applications, other capabilities have been reported for a decade. Jang and Park [10] proposed carbon nanotube-reinforced composite materials for dual functions such as temperature sensing and de-icing. Yum and Jang [11] proposed multi-functional road coating materials with self-sensing consisting of CNTs and a polyurethane (PU) matrix, widely used materials for road marking, for future transportation systems. Epoxy resins are one of the structurally suitable polymer systems among various polymer systems [12-14]. Due to their high stiffness, strength, dimensional stability, chemical resistance and durability, these resins are useful for a variety of industrial applications, particularly in the electronics, automotive and aerospace industries [15, 16].

In this study, a novel temperature-sensing coating composed of carbon nanotube and epoxy matrices applicable to various industrial fields was proposed. The CNT/epoxy coating is manufactured by solution casting for high electrical conductivity. The electrical conductivity of CNT/epoxy coatings was analyzed as a function of CNT concentration. The temperature sensing performance was analyzed through the resistance of CNT/epoxy composites to temperature change.

2. Materials and Methods

2.1 Materials

Industrial grade multi-walled carbon nanotubes were purchased from Nanolab, Inc. (MA, USA). The CNTs have a diameter of 15 nm, a length of 5-20 μm, and purity of higher than 85 wt %. Epoxy was obtained from Easy Composites Ltd. (Staffordshire, UK) with a density of 1.12-1.18 g/cm^3 and viscosity of 200-450 mPa.s. The dispersant used acetone from Samchun pure chemical Co., Ltd. (Gyeonggi-do, South Korea) with a purity of 99.7 %.

2.2 Fabrication Procedure

The fabrication procedure of CNT/epoxy coating was shown in Figure 1. Epoxy resin (20 g) and acetone (50 g) were added to a 200 ml beaker and hand-mixed using a spatula. Then, various concentrations of CNTs(from 0 to 5 wt %) were put into a beaker and mixed in the same way. An ultrasonicator (Q700CA, Qsonica LLC., USA) was applied to disperse CNTs in the solution. In this study, the ultrasonicator was operated in a pulse model with 90 % amplitude, and ice was placed around the beaker to prevent the evaporation of acetone due to the heat from the ultrasonicator. After dispersion, the sample was placed on a hot plate (60 °C) for 24 hours to fully evaporate acetone. Then, a curing agent (6 g) added into the sample and mixed it evenly in a 3-roll mill (TR 50M, Trilos, USA). After molding to the test, the CNT/epoxy coating was placed into the vacuum chamber and operated for 30 minutes to remove air bubbles inside the sample.

  doi:10.5075/epfl-298799_978-2-9701614-0-0

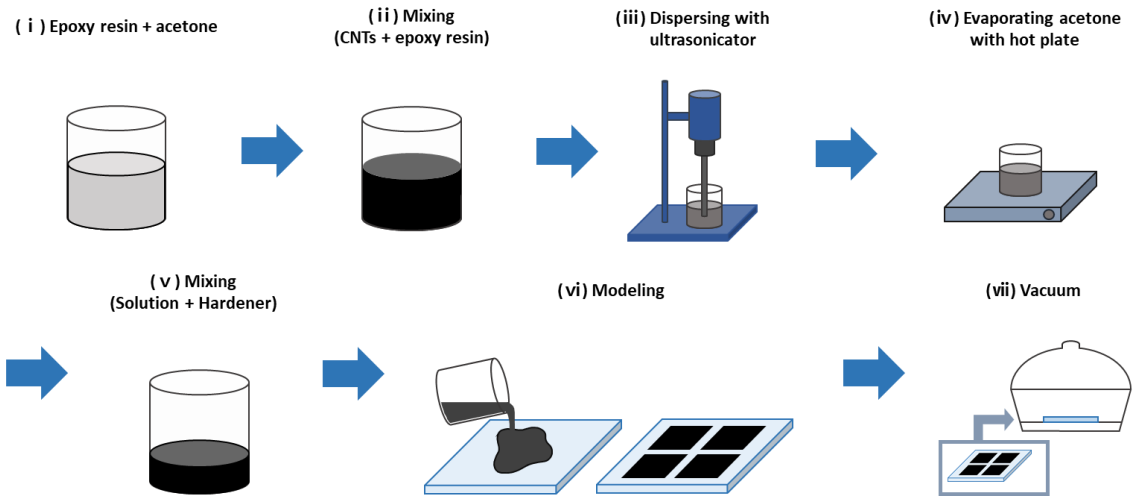

Figure 1. Fabrication of CNT/epoxy coating

2.3 Characterization

The resistance of the CNT/epoxy coatings were measured using a Keithley 2450 (Tektronix, Beaverton, USA) for a high resistance above $10^9\Omega$ and Keithley 2700 (Tektronix, Beaverton, USA) for normal resistance. The specimens prepared with a size of 50 mm x 30 mm x 1 mm. High-purity silver paint was applied to both ends of the specimens to minimize the contact resistance between the coating and the tip probe. The electrical conductivity (σ) of the specimens were calculated by

$$\sigma = \frac{L}{RA} \tag{1}$$

where R is the resistance of the coating (Ω), A is the area of the coating (m^2) and L is the length of the coating (m).

For the microstructure of the CNT/epoxy coatings, the cross-section of the specimen was observed through a scanning electron microscope (MIRA3 FE-SEMs, TESCAN, Brno, Czech) at 15 kV. For a high magnification measurement of more 10,000 times, the CNT/epoxy coating cross-section was coated with platinum using sputter coating (QUORUM-Q150T S, Laughton, UK) for 10 minutes.

For resistance-temperature dependence in CNT/epoxy coatings, the change in resistance of CNT/EP coatings as a function of temperature was measured in an environmental chamber using a digital multimeter (Keithley 2700, Tektronix, Beaverton, USA) with an externally connected data acquisition system, as shown in Figure 2(a). The resistance of CNT/epoxy coatings was measured from -20 °C to 60 °C in 10-degree increments. Note that the samples remain constant at each temperature for 1 h for the steady-state temperature of the CNT/epoxy coatings. For cyclic piezoresistive response of CNT/epoxy coatings, the test exposed the samples to high and low temperature of -20 °C and +20 °C. The temperature change will cycle 50 times as shown in Figure 2(b).

  doi:10.5075/epfl-298799_978-2-9701614-0-0

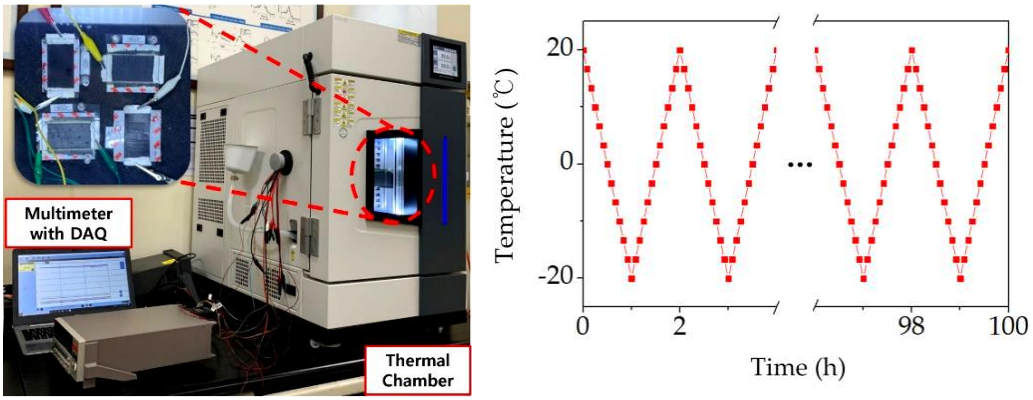

Figure 2. Temperature sensing performance equipment and details: (a) static and cycle sensing test; (b) temperature cycle in thermal chamber

3. Results

Figure 3 showed the electrical characteristics of the CNT/epoxy coatings. Figure 3(a) shows the electrical conductivity for the CNT/epoxy coating as a function of CNT concentrations. Pure epoxy is non-conductive material with 1×10^{-16} S/m. A dramatic increase in electrical conductivity was observed when the concentration of CNTs increased from 0.5 wt % to 1.25 wt %. This behavior has been attributed to the occurrence of a percolation threshold [17, 18]. The percolation threshold, i.e., the minimum CNT concentration in the matrix after which no significant change in the electrical conductivity is observed, occurred at around 0.63 wt % CNTs. The observed increased in electrical conductivity of the CNT/epoxy coating is due to a well-developed CNT network structure (conducting pathways) created within the matrix material as shown in Figure 3(b). The electrical conductivity showed a slight increase even with an increase in the CNT concentrations.

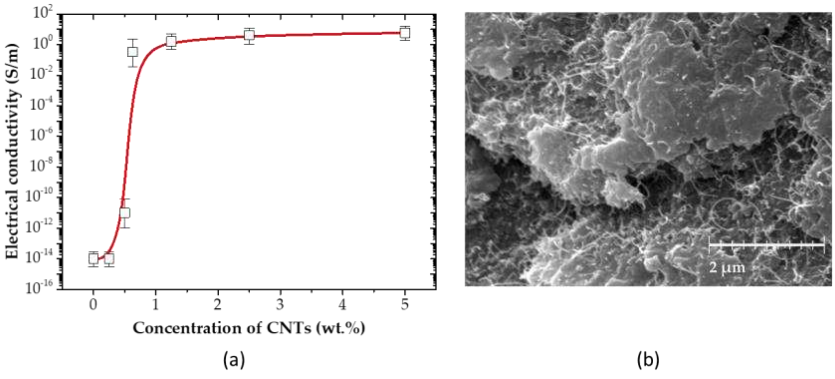

Figure 3. Electrical characteristics of CNT/epoxy coatings; (a) electrical conductivity; (b) scanning electron microscope (SEM) images of magnifications showing the morphology of the fracture surface

Figure 4 shows the effect of temperature on the resistance of the CNT/epoxy coatings. As shown in Figure 4(a), the resistance of all CNT/epoxy coatings significantly decreased with the increasing temperature, demonstrating that CNT/epoxy coatings have a negative temperature coefficient of resistance (TCR). This behavior can be attributed to the thermal activation of charge carriers that overcome the potential barrier between MWCNTs and result in a decrease of resistance of the nano-composite [19-21]. In this study, the resistance of all CNT/epoxy

  doi:10.5075/epfl-298799_978-2-9701614-0-0

coatings varied linearly with temperature except for 0.63 wt % CNT/epoxy coating due to high sensitivity. By fitting the normalized resistance relative to room temperature (20 °C) in Figure 4(b). TCR was lower as the CNT concentration increased, and the difference was smaller at high concentrations [22].

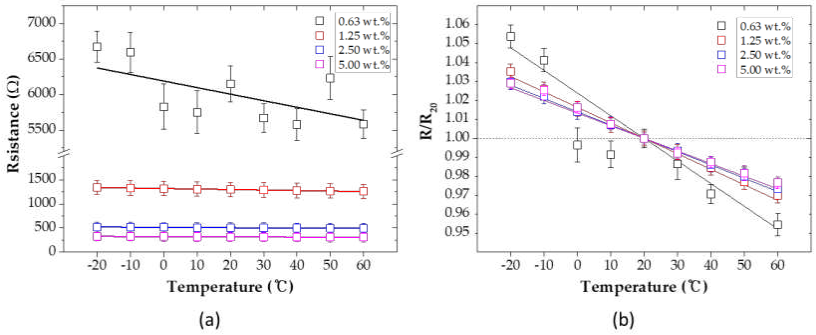

Figure 4. The effect of temperature on the change at rest resistance results of the CNT/epoxy coatings; (a) resistance by temperature; (b) normalized resistance by temperature

Figure 5 shows the cyclic piezoresistive response of CNT/epoxy coating (5.0 wt.%) for 50 temperature cycles. The repetition of the response was constant. This consistent resistance change demonstrates the long-term and repeatable use of CNT/epoxy coatings. The proposed sample can monitor the temperature with high stability.

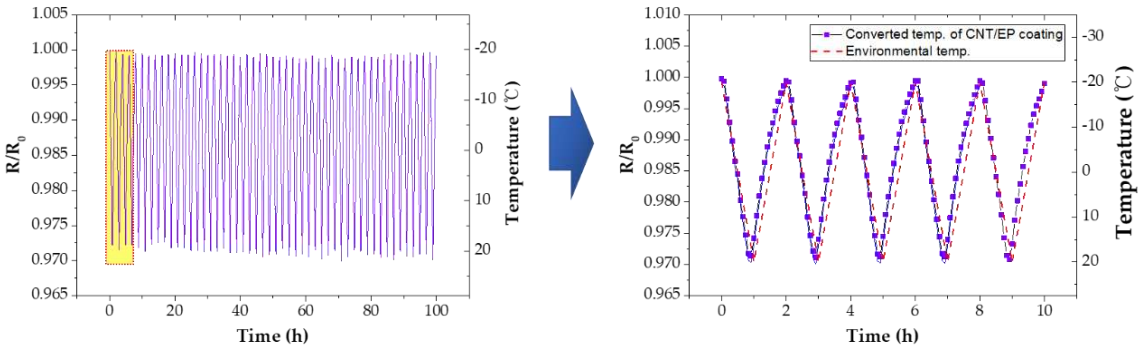

Figure 5. Temperature sensing performance of the CNT/epoxy coating according to cyclic temperature change

4. Conclusion

This study demonstrates the potential of CNT/epoxy temperature sensor coating applicable to the machinery and construction industries. Highly electrically conductive coatings have been successfully prepared by dispersing CNTs in an epoxy matrix. The addition of CNTs showed improved electrical conductivity. The proposed CNT/epoxy coatings also provided temperature sensing due to its negative temperature coefficient. As a result, CNT/epoxy coatings with higher CNT concentrations are more suitable for temperature monitoring. CNT/epoxy coatings are capable of general temperature sensing as well as freezing temperature sensing. It has also applicability as a temperature-sensing coating for winter maintenance and mechanical and industrial equipment in extreme environments.

Acknowledgements

This work was supported by the Technology Innovation Program (20014127, Development of a smart monitoring system integrating 3D printed battery-free antenna sensor technology with AI optimization) funded By the Ministry of Trade, Industry & Energy (MOTIE, Korea) and the National Research Foundation of Korea (NRF) grant funded by the Korea government (MSIT) (NRF-2020R1C1C1005273).

5. References

1. Webb, C. Infrared: faster; smaller; cheaper. Control and Instrumentation 1997; 29(4), 44-5.
2. Lirong Kong and Wei Chen. Carbon nanotube and graphene-based bioinspired electrochemical actuators. Advanced materials 2014; 26(7); 1025-1043.
3. L. Guadagno, B. De Vivo, A. Di Bartolomeo, P. Lamberti, A. Sorrentino, V. Tucci, L. Vertuccio and V. Vittoria. Effect of functionalization on the thermo-mechanical and electrical behavior of multi-wall carbon nanotube/epoxy composites. Carbon 2011; 49(6); 1919-1930.
4. Wolfgang Bauhofer and Josef Z. Kovacs. A review and analysis of electrical percolation in carbon nanotube polymer composites. Composites science and technology 2009; 69(10) ; 1486-1498.
5. Liberata Guadagno, Luigi Vertuccio, Carlo Naddeo, Elisa Calabrese, Giuseppina Barra, Marialuigia Raimondo, Andrea Sorrentino, Wolfgang H. Binder, Philipp Michael and Sravendra Rana. Reversible self-healing carbon-based nanocomposites for structural applications. Polymers 2019; 11(5); 903.
6. Y. El Assami, M. Drissi Habti and V. Raman. Stiffening offshore composite wind-blades bonding joints by carbon nanotubes reinforced resin–a new concept. Journal of Structural Integrity and Maintenance 2020; 5(2); 87-103.
7. Florian H. Gojny and Karl Schulte. Functionalisation effect on the thermo-mechanical behaviour of multi-wall carbon nanotube/epoxy-composites. Composites science and technology 2004; 64(15); 2303-2308.
8. Sung-Hwan Jang and Huiming Yin. Characterization and modeling of the effective electrical conductivity of a carbon nanotube/polymer composite containing chain-structured ferromagnetic particles. Journal of Composite Materials 2017; 51.2; 171-178.
9. Sung-Hwan Jang and Huiming Yin. Effect of aligned ferromagnetic particles on strain sensitivity of multi-walled carbon nanotube/polydimethylsiloxane sensors. Applied Physics Letters 2015; 106(14); 141903.
10. Sung-Hwan Jang, Yong-Lae Park. Carbon nanotube-reinforced smart composites for sensing freezing temperature and deicing by self-heating. Nanomaterials and Nanotechnology 2018; 8; 1847980418776473.
11. Sang-Guk Yum, Huiming Yin and Sung-Hwan Jang. Toward multi-functional road surface design with the nanocomposite coating of carbon nanotube modified polyurethane: Lab-scale experiments. Nanomaterials 2020; 10(10); 1905.
12. Sung-Hwan Jang, Donghak Kim and Yong-Lae Park. Accelerated curing and enhanced material properties of conductive polymer nanocomposites by joule heating. Materials 2018; 11(9); 1775.
13. Jang-Kyo Kim and Yiu-Wing Ma. Engineered interfaces in fiber reinforced composites. Elsevier 1998.
14. L. Vertuccioa, L. Guadagnoa, G. Spinellib, P. Lambertib, M. Zarrellic, S. Russod, G. Iannuzzod. Smart coatings of epoxy based CNTs designed to meet practical expectations in aeronautics. Composites Part B: Engineering 2018; 147; 42-46.

  doi:10.5075/epfl-298799_978-2-9701614-0-0

15. Kausar, Ayesha, Irum Rafique, and Bakhtiar Muhammad. Aerospace application of polymer nanocomposite with carbon nanotube, graphite, graphene oxide, and nanoclay. Polymer-Plastics Technology and Engineering 2017; 56(13); 1438-1456.
16. Fan-Long Jin, Xiang Li, Soo-Jin Park. Synthesis and application of epoxy resins: A review. Journal of Industrial and Engineering Chemistry 2015; 29; 1-11.
17. Beate Krause, Petra Potschke, Evgeniy Ilin and Mikhail Predtechenskiy. Melt mixed SWCNT-polypropylene composites with very low electrical percolation. Polymer 2016; 98; 45-50.
18. Hu, Lea, D. S. Hecht, and G. Grüner. Percolation in transparent and conducting carbon nanotube networks. Nano letters 2004; 4(12); 2513-2517.
19. Abdulkadir Sanli, Abderrahmane Benchirouf, Christian Müller, Olfa Kanoun. Piezoresistive performance characterization of strain sensitive multi-walled carbon nanotube-epoxy nanocomposites. Sensors and Actuators A: Physical 2017; 254; 61-68.
20. Zhi-Dong Xiang, Tao Chen, Zhong-Ming Li and Xiang-Cheng Bian. Negative temperature coefficient of resistivity in lightweight conductive carbon nanotube/polymer composites. Macromolecular Materials and Engineering 2009; 294(2); 91-95
21. Mohammad Mohiuddin and Suong Van Hoa, Electrical resistance of CNT-PEEK composites under compression at different temperatures. Nanoscale research letters 2011; 6(1); 1-5.
22. Q. Li, Q. Z. Xue, X. L. Gao and Q. B. Zheng. Temperature dependence of the electrical properties of the carbon nanotube/polymer composites. Express Polym Lett 2009; 3(12); 769-777.

  doi:10.5075/epfl-298799_978-2-9701614-0-0

SOLUBILITY BEHAVIOR OF GRAPHENE-OXIDE WITH VARIOUS SOLVENTS

Sung-Woong Choi[a]

a: Department of Mechanical System Engineering, Gyeongsang National University – younhulje@gmail.com

Abstract: *Dispersion is one of the most important factors in the manufacture of composite materials. In the manufacture of composite materials, solvents are used to better disperse the reinforcement, nano-filler in the matrix. Since dispersion is affected with solvents, it is necessary to study which solvent is adopted to get good dispersion. In this study, the dispersion behavior and solubility of graphene oxide (GO) were examined under various solvents (DMF, NMP, ethylene glycol, Acetone, DI water) to identify dispersion. As a result of UV-Vis spectroscopy absorbance measurement, it was found that DMF and ethylene glycol had the best dispersibility, whereas DI water showed the lowest dispersibility. In addition, as a result of visually observing the dispersion according to the surface tension and time, it was found that the dispersibility was excellent in the order of DI water, ethylene glycol, NMP, DMF, and acetone, which was consistent with the Hansen solubility parameter value.*

Keywords: Composite materials; Graphene oxide; Solvent; Solubility parameter;

1. Introduction

Composite materials are materials in which two or more different forms and compositions exist [1]. Due to its lightweight characteristics and excellent mechanical performance, it is used in various fields such as automobiles, sports, leisure, aerospace, and biotechnology [2]. Composite materials consist of a base material and a reinforcing material, and the total surface area of the reinforcing material for the same amount of reinforcing material increases significantly with how well the reinforcing material is dispersed in the base material. In addition, it has a great influence on the mechanical and thermal properties of the final composite material, such as physical, electrical, and thermal properties [3, 4]. In addition, it greatly affects the quality of manufactured products and can cause problems directly related to safety. Therefore, it can be seen that dispersion plays a very important role in composite materials.

For the thermosetting epoxy and graphene oxide (GO), their mixture of matrix and GO are soluble in a solvent with a similar chemical structure. Therefore, solubility and dispersion can be one of the crucial criteria as a solvent because it becomes soluble under similar conditions [5].

In the present study, the dispersion behavior and solubility of GO/solvents was examined to identify suitable solvents for dispersion. Various solvents, DMF, NMP, Ethylene glycol, Acetone, and DI were selected to determine the degree of dispersion of GO. The degree of solubility was obtained through UV-Vis spectroscopy absorbance measurement. The degree of dispersion for each solvent was investigated with comparison of solubility measurements.

2. Experimental

2.1 Materials

  doi:10.5075/epfl-298799_978-2-9701614-0-0

Graphene GO (Grapheneall, Korea) were prepared to dispersion material. Various solvents of DMF, NMP, Ethylene glycol, Acetone, DI water were prepared, and its material properties are listed in Table. 1.

Table 1: Properties of Solvents

Solvent	Chemical formula	Viscosity (Pa·s)	Density (kg/m^3)
DMF	C_3H_7NO	151.6	0.95
NMP	C_5H_9NO	114.7	1.03
Ethylene glycol	$C_2H_6O_2$	52.7	1.12
Acetone	CH_3COCH_3	106.1	0.79
DI water	H_2O	50.8	1.00

2.2 Experimental method

Go was mixed with 0.125 mg/mL of solvents listed in table 1. Go mixed with solvents were treated with ultrasonicate homonizer (SONIC&MATERIALS, Inc., VC505) during 1 hours and magnetic stirrer during 30 mins. Dispersion of GO with different kinds of solvents was observed: visual inspection and UV-vis spectroscopy. Visual inspection was conducted to observe the degree of dispersion with time. Also, dispersion was observed quantitatively using UV-Vis spectroscopy (human corporation, X-ma1200 V).

3. Results

3.1 UV-Vis spectroscopy

Dispersion of GO with different solvents was carried out to obtain solubility coefficients through UV-Vis spectroscopy absorbance measurement. From the data measured by UV-Vis spectroscopy, the absorbance gradient can be obtained by extracting the concentration values of each solvent at the specific wavelength.

Fig. 1 shows a representative UV-Vis spectroscopy for the GO with DI water at the stabilized wavelength of 660 nm. The change rate of the absorbance value can be observed according to the difference of the GO concentration. The absorbance value and Extinction coefficient were obtained using in Eq. (1).

$$A = \varepsilon bc \tag{1}$$

where A, ε, b, and c represents absorbance, extinction coefficient, the distance through which light passes, and the molar concentration of the sample, respectively. Becasue the dispersion of GO/solvents with different concentrations have different absorbances, GO/solvents have different molar extinction coefficients. From the Eq. (1), extinction coefficient and absorbance have a proportional relationship and the degree of dispersion can be identified with extinction coefficient.

  doi:10.5075/epfl-298799_978-2-9701614-0-0

The UV-Vis spectroscopy concentration of GO/ solvents was measured with absorbance and the results are shown in Table. 2. It can be seen that DMF and ethylene glycol showed high degree of dispersion and DI water has low degree of dispersion.

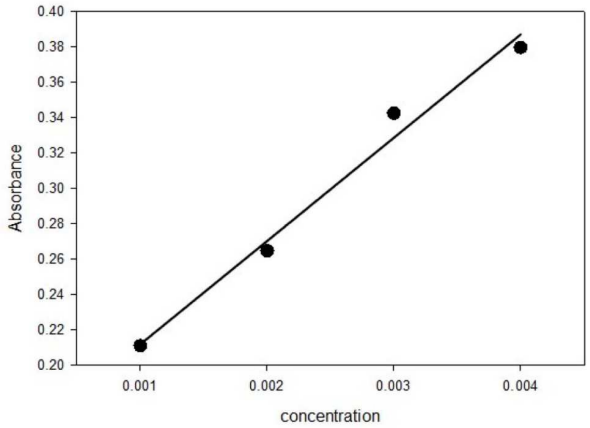

Figure 1. Absorbance slope graph by concentration of 660 nm wavelength of DI water using UV-Vis spectroscopy

Table 2: UV-Vis spectroscopy concentration

Solvent	Absorbance
DMF	118.6
NMP	114.7
Ethylene glycol	120.3
Acetone	106.1
DI water	59.39

3.2 Visual inspection

After dispersing the same amount of GO for each solvent, the degree of dispersion was examined after dispersion of GO/solvents with 1, 7, and 14 days, and the results are shown in Fig. 2. With visual observation, the degree of dispersion of GO/solvents was observed in the order of DI water, ethylene glycol, DMF, NMP, and acetone, which was consistent with the Hansen solubility parameter values [11,12].

  doi:10.5075/epfl-298799_978-2-9701614-0-0

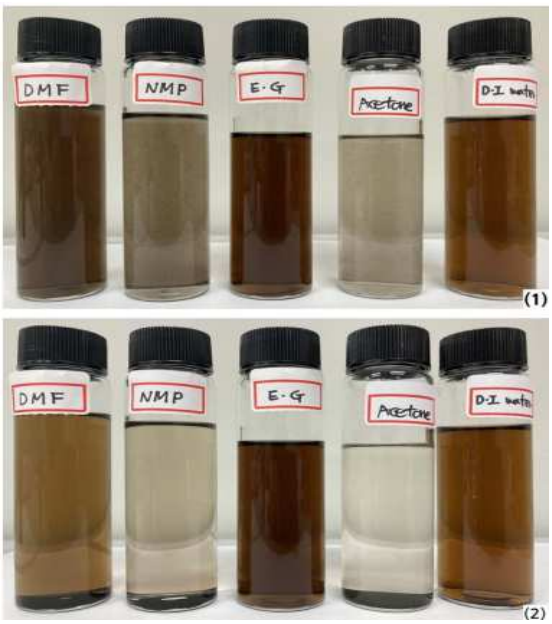

Figure 2. Results of GO dispersion experiments for each solvent conducted to observe long-term dispersion stability; (1) 0 s, (2) after 2 weeks later

4. References

1. Bae, J.M., “Fiber-reinforced Composites,” The Journal of the Korean Dental Association, Vol. 47, No. 1, 2009, pp. 17-24.

2. Park, C.R., “High-performance fiber Materials for Reinforcing Composite Materials,” Polymer Science and Technology, Vol. 10, No. 1, 1999, pp. 55-64.

3. Lee, B.N., Kim, C.H., Kweon, J.H., and Choi, J.H., “Evaluation of Dispersivity and Resistance of the Adhesive Joint According to Dispersion Methods of CNT,” Composites Research, Vol. 28, No. 6, 2015, pp. 348-355.

4. Jang, J.H., Yi, J.W., Lee, W.O., Lee, H.G., Um, M.K., Kim, J.B., and Byun, J.H., “Dispersion and Property Evaluation of Nano┐composites by Aspect Ratio of MWCNT,” Composites Research, Vol. 23, No. 3, 2010, pp. 58-63.

5. Chae, H.Y., “Development Status of Graphene Materials,” Vacuum Magazine, Vol. 2, No. 2, 2015, pp. 46-48.

  doi:10.5075/epfl-298799_978-2-9701614-0-0

BIODEGRADABLE POLYMER-BASED COMPOSITES FILLED WITH BIOCHAR FOR TUNABLE RELEASE OF CARVACROL

Luigi, Botta[a], Francesco, Lopresti[a], Giulia, Pernice[a], Giuliana, Garofalo[b], Raimondo, Gaglio[b]

a: Dipartimento di Ingegneria, Università degli Studi di Palermo, RU INSTM, Viale delle Scienze, 90128 Palermo, Italy. Mail: luigi.botta@unipa.it
b: Dipartimento Scienze Agrarie, Alimentari e Forestali, Università degli Studi di Palermo, Viale delle Scienze 4, 90128 Palermo, Italy

Abstract: Bio-composites are commonly obtained by combining biodegradable polymers with fillers collected from natural resources. In this context, biochar (BC) is attracting high interest as filler for polymer-based composites due to its challenging properties, including eco-sustainability. This study aimed to prepare and characterize bio-composites with antimicrobial properties evaluating the role of the filler in the release kinetics. In particular, BC as filler and carvacrol (CRV) as antimicrobial agent, were incorporated via melt-compounding in poly(butylene adipate-co-terephthalate) (PBAT) samples. The rheological, tensile, and antimicrobial properties of the obtained bio-composites were evaluated paying particular attention to the influence of BC concentration, i.e., 5, 10, and 20 wt%, on the investigated properties. Moreover, the influence of BC content on the release kinetics of carvacrol was studied and mathematically modeled to evaluate the release mechanism. The results showed that the presence of biochar modified the carvacrol release in comparison with the unfilled system thus allowing to tune the release kinetics.

Keywords: PBAT; carvacrol; bio-composites; biochar

1. Introduction

In recent years, polymers and polymer-based systems have been widely investigated as materials for thin-film preparation. Usually, thermoplastic polymers offer low raw material costs and a well-established manufacturing process that can be easily scaled to large-scale production. However, major concerns for traditional thermoplastics used for film preparation, commonly derived from fossil fuels, refer to the non-renewability and non-biodegradability of the raw materials chosen for their production, thus causing environmental issues [1–3]. Due to the rising attention towards eco-sustainable products, it is unsurprising that more and more research groups and industries are exploring the possibility of using new biodegradable and compostable polymers suitable for different applications [4–6] .

A wide plethora of biodegradable polymers, such as polysaccharides, proteins, and lipids, were proposed as suitable materials for thin-film preparation [4,7,8]. In this context, poly(butylene adipate-co-terephthalate) (PBAT) is an aliphatic/aromatic copolyester that is biodegradable and compostable and, due to its interesting properties, is considered among the most promising biopolymers for packaging film, agricultural film, and compost bag fabrication [9–11].

Over recent years, several additives, including natural compounds, peptides, enzymes, metals, chelating agents, and antibiotics, were incorporated into bio-polymeric matrices to provide antimicrobial activity [12–14]. Among them, plant essential oils (EOs) are interesting natural antimicrobial agents to be incorporated into the biopolymeric films or membranes due

  doi:10.5075/epfl-298799_978-2-9701614-0-0

to their high inhibitory potential against a wide spectrum of microorganisms [15,16]. Among the great variety of EOs, carvacrol (CRV), commonly present as the main compound in thyme and oregano EOs, has gained greater acceptance among food technologists due to its ability to inhibit undesired pathogenic and spoilage microorganisms [17,18]. Furthermore, CRV is a "generally recognized as safe" food additive and is approved by the U.S. Food and Drug Administration (FDA) for use in foods and drinks.

However, CRV release from thin biopolymeric films can lead to rapid (burst) release of the bioactive compound thus hindering a long-term release.

In order to mitigate the burst effect, it is usually preferable adding a third component, such as a filler. In fact, from a physical point of view, the presence of a filler may force the molecules to follow a tortuous path throughout the matrix before reaching the surface [12]. Moreover, from a chemical point of view the eventual strong interaction between filler and drug may decrease the amount released and the kinetics delivery.

In this context, biochar (BC) is attracting high interest as filler for polymer-based composites due to its challenging properties, such as high thermal and chemical stability combined with its cost-effectiveness and eco-sustainability [19,20]. BC is usually produced by the pyrolysis of wastes from the forestry and agricultural industries, and its structure can be modified by tuning the pyrolysis conditions [21].

Recently, several remarkable articles about the efficacy of BC as filler for the fabrication of green composites were published but its effect on the release kinetic of a natural antimicrobial compound was never reported so far [22,23].

Therefore, in this work, biocomposite films based on PBAT, biochar, and CRV were produced via melt mixing and filmed in hot press. The PBAT-based films were loaded with 20 wt% of CRV and filled with 5, 10, or 20 wt% of BC. The rheology of the melts was evaluated via frequency sweep analysis. The mechanical properties of the PBAT-based films were evaluated through tensile tests. The release profile of CRV from was evaluated via UV–Vis measurements and it was fitted with a power-law model.

2. Experimental part

2.1 Materials

PBAT (ecoflex® F Blend C1200, Basf, SE, Ludwigshafen, Germany) is a film grade with a melt flow rate (MFR) of 2.7–4.9 g/10 min (190 °C, 2.16 kg), a density in the range of 1.25–1.27 g/cm^3, and a melting temperature in the range of 110–120 °C.

Commercial biochar powder (hereafter coded as BC) used in the food industry (Special Ingredients) was chosen as filler. In particular, as reported in the technical data sheet of the supplier, this biochar was obtained from the pyrolysis of coconut shells.

Carvacrol (purity ≥98%) was purchased by Sigma Aldrich.

2.2 Film preparation

PBAT-based films were prepared by combining melt mixing and compression molding. More in detail, PBAT was fed to a batch mixer (Brabender PLE-330 T = 170 °C, n = 60 rpm) and processed

  doi:10.5075/epfl-298799_978-2-9701614-0-0

for 4 min, then the additives (BC and CRV) were added and mixed with PBAT for 1 min in order to minimize the evaporation of CRV. The PBAT-based mixtures were then fed out and rapidly quenched in liquid nitrogen in order to stop the CRV evaporation due to the high temperature. BC concentration was 5, 10, and 20 PHR while a single CRV concentration (equal to 20 PHR) was added to each composite. Therefore, five materials were produced and coded as PBAT (pure PBAT), PBAT/CRV (without BC) or PBAT/CRV/BC_N where N is equal to the PHR of BC in the sample. PBAT-based systems were then filmed in a Carver laboratory press at 170 °C and 140 bar in 15 cm × 15 cm × 0.2 mm height square molds for 3 min. In order to avoid the loss of CRV due to evaporation during the storage stages, all the PBAT/CRV and PBAT/CRV/BC films were stored at 2 °C and characterized within 24 h of preparation.

2.3 Rheological characterization

Rheological investigations of the melts were carried out through a plate–plate rotational rheometer ARES-G2 (TA Instruments, New Castle, DE, USA) equipped with a parallel-plate geometry (25-mm diameter). Frequency sweep tests, from 0.1 to 100 rad/s, were performed at 170 °C. The PBAT-based samples for rheological tests were prepared via compression molding of the melt mixed systems in a 25-mm diameter and 1.5-mm thick stainless-steel mold at the same conditions above described. Before testing, all the samples were let to dry under vacuum overnight at 70 °C.

2.4 Tensile tests

All PBAT-based films were mechanically tested in uniaxial tensile mode by using an Instron 3365 (Instron, Norwood, MA, USA) universal testing machine equipped with a 1 kN load cell. The tests were performed on rectangular film specimens (10 × 90 mm) until fracture with a uniform crosshead speed of 1 mm/min. At least 7 specimens were tested for each sample.

2.4 Carvacrol release kinetics

It is well known that the maximum absorbance peak of CRV in water detectable by UV–Vis measurements can be detected at 272 nm [1]. A series of CRV/water solutions containing from 1 to 50 mg/L of CRV were prepared and analyzed via UV–Vis (model UVPC 2401, Shimadzu Italia s.r.L., Milan, Italy) in order to obtain a calibration curve correlating the absorbance peak intensity and the CRV concentration (mg/L). In this range of concentration, the calibration curve was found to be linear (ABS_{272nm} = 0.0142 [CRV]; R^2 = 0.99998). The release of the essential oils from the films was investigated by immersing a pre-weighed sample (a section of 3 × 20 × 3 mm, approximately 120 mg) in 10 mL of distilled water at 37 °C. The absorbance of the medium at 272 nm was measured at specific time intervals and converted CRV concentration by using the calibration line. After each measurement, the samples were immersed in 10 mL of fresh distilled water at 37 °C, and the cumulative release of CRV here reported was calculated by sequentially adding the CRV released after each step.

2.4 Antibacterial activity determination

PBAT-based films containing CRV and BC at different concentrations were tested for antibacterial activity applying the paper disc diffusion method [24] with a few modifications. Briefly, a water agar (2% w/v) base support [25] was overlaid with 7 mL of the optimal soft agar (0.7% w/v) medium for each indicator strain inoculated at approximately 10^7 CFU/mL. MB foams discs (6-mm diameter) containing CRV were placed onto the surface of the double agar layer.

  doi:10.5075/epfl-298799_978-2-9701614-0-0

Sterile filter paper discs (Whatman no. 1) of the same diameter were soaked with streptomycin (10% w/v) and used as positive controls, while discs of MB foams without CRV represented the negative controls.

The inhibitory activity was evaluated after incubation at the optimal temperature (reported above) for each strain. The inhibitory activity was scored positive when a definite clear area was detected around the discs. The diameters of the inhibitory halos around the paper discs were measured. The experiments were performed in triplicate.

3. Results and discussion

3.1 Rheological properties

The effect of the filler and the essential oil on the rheological properties of the biocomposites was analyzed by measuring the storage modulus (G '), the loss modulus (G' ') and the complex viscosity (η *) as a function of frequency. In pure PBAT, a decrease of the complex viscosity with frequency was observed. More in detail, a pseudo-Newtonian behavior of the matrix at low frequencies was followed by a shear thinning behavior at high frequencies, as also reported by the studies of Adrar et al. [26]. Both the moduli and the viscosity decrease with the introduction of CRV, thus indicating the plasticizer action of this essential oil to PBAT, as already observed for other biopolymeric matrices. The addition of BC to the PBAT/CRV systems caused an increase of the complex viscosity at the lower frequencies. On the other hand, the complex viscosity of the melts containing or not BC were overlapped at the higher frequencies. Upon increasing the BC concentration, the shear thinning behavior of the melt became more evident reflecting a solid-like behavior. Similarly and coherently, the values of G 'and G'' increased at the lower frequencies upon increasing the content of BC while remained almost independent from the BC concentration at the higher frequencies. These results let us reasonably conclude that CRV has an evident plasticizer action on PBAT and that the further addition of BC slightly modified this behavior, in particular at the higher frequencies.

3.2 Mechanical properties

Tensile tests were performed to investigate the influence of BC and CRV addition on the mechanical behavior of PBAT-based films.

Table 1 displays the tensile properties investigated, and specifically the elastic modulus (E), the tensile strength (TS) and the elongation at break (EB).

Table 1. Tensile properties of the PBAT-based films

Sample	E [Mpa]	TS [Mpa]	EB [%]
PBAT	63 ± 4.0	26.0 ± 3.3	1245 ± 79
PBAT/CRV	18.6 ± 2.2	10.3 ± 1.3	759 ± 72
PBAT/CRV/BC_5	18.9 ± 2.2	7.1 ± 0.5	493 ± 52
PBAT/CRV/BC_10	22.3 ± 1.4	6.2 ± 0.4	288 ± 41
PBAT/CRV/BC_20	23.4 ± 2.2	5.4 ± 0.3	212 ± 33

  doi:10.5075/epfl-298799_978-2-9701614-0-0

Pure PBAT is a polymer with a relatively low elastic modulus (~63 MPa), with a relatively high tensile strength (~26 MPa) and high deformation at break (~1245%), values consistent with those found in the literature [27,28]. The high tensile strength values are due to the fact that, when they are subjected to high elongations, the polymer chains of the PBAT reorganize to undergo a stress-induced crystallization, thus increasing the force required to break.

The addition of CRV leads to a worsening of the mechanical properties with respect to the neat matrix. Upon increasing the BC concentration a slight increase of the elastic modulus was observed. The addition of biochar gives greater rigidity and a reduction in the mobility of the polymer chains which results in an increase in the elastic modulus. At the same time, the tensile strength, and the elongation at break of the PBAT-based films decreased upon increasing the BC content. This phenomenon can be ascribed to the formation of clusters that acted as stress-concentrators thus reducing the elongation at break and the tensile strength of the samples containing BC.

3.3 Carvacrol release kinetics

In order to investigate the release mechanism of CRV in water from the PBAT-based films, the experimental data of the release kinetic were fitted using the power law model:

$$\frac{M_t}{M_\infty} = kt^n \quad (1)$$

where *t* is the release time, *k* is a kinetics constant and *n* is the diffusion exponent related with the release mechanism. In particular, the release is diffusion-controlled when *n* is lower than 0.5 (Fickian) and it is swelling-controlled when *n* is equal to 1.0. If *n* is in the range 0.5–1.0 it can be assumed a release due to the superposition of both phenomena that is defined as anomalous transport by Peppas et al. [29].

In Table 2 there are summarized n, k and the R^2 values for each system here investigated.

Table 2. Power law parameters obtained from the release kinetics of CRV.

Sample	I Stage			II Stage			III Stage		
	k [h^{-1}]	n	R^2	k [h^{-1}]	n	R^2	k [h^{-1}]	n	R^2
PBAT/CRV	0.172	0.922	0.993	0.254	0.491	0.989	0.588	0.139	0.970
PBAT/CRV/BC_5	0.168	0.915	0.997	0.245	0.496	0.993	0.579	0.137	0.966
PBAT/CRV/BC_10	0.200	0.883	0.997	0.299	0.448	0.990	0.691	0.096	0.953
PBAT/CRV/BC_20	0.207	0.896	0.996	0.316	0.440	0.984	0.687	0.106	0.995

For all the systems, the release of CRV was characterized by three phases: (i) a burst phase, (ii) a second phase characterized by slower release rate, and (iii) a release plateau.

The release can be defined as diffusion-controlled when n is lower than 0.5 (Fickian) and it is swelling-controlled when n is equal to 1.0. The superposition of both phenomena occurs if n is

  doi:10.5075/epfl-298799_978-2-9701614-0-0

in the range 0.5–1.0. In this case, Peppas et al. defined this behavior as anomalous transport [29].

According to Peppas, the CRV release showed an anomalous mechanism of release during the first stage, and a Fickian release during the second and third release stages.

As highlighted by k values in table 2, the kinetic release of CRV was slowened by lowest concentration of BC while it increased upon furtherly increasing the BC concentration to 10 wt% and 20 wt%.

3.4 Antibacterial properties

Results of the screening of the antibacterial activity in vitro revealed that among the active materials tested the only ones to be effective on high concentrations of indicator strains were those produced at 10% and 20% of BC which also showed the faster kinetics of carvacrol release. In particular, the inhibitory effect was detected against spoilage bacteria, i.e. *Brochotrix thermosphacta* (SP10) and pathogenic bacteria, i.e *Stenotrophomonas maltophilia* (ICE272), while no effect was detected against pro-technological bacteria. While requiring further studies, this result highlights the potential use of this active material in applications in the food packaging sector. In fact, in a possible in vivo application, the presence of microorganisms with potential pro-technological and probiotic aptitudes in the food matrix in contact with the active material would not be compromised while the presence of alterative microorganisms responsible for reducing the shelf-life of the product would be inhibited.

4. References

1. Lopresti F, Botta L, La Carrubba V, Di Pasquale L, Settanni L, Gaglio R. Combining carvacrol and nisin in biodegradable films for antibacterial packaging applications. International Journal of Biological Macromolecules 2021; 193: 117-126.
2. Mistretta MC, Botta L, Arrigo R, Leto F, Malucelli G, La Mantia FP. Bionanocomposite Blown Films: Insights on the Rheological and Mechanical Behavior. Polymers 2021;13(7):1167.
3. Mistretta MC, Botta L, La Mantia FP, Di Fiore A, Cascone M. Film Blowing of Biodegradable Polymer Nanocomposites for Agricultural Applications. Macromolecular Materials and Engineering 2021; 306(9):2100177.
4. Mohamed SAA, El-Sakhawy M, El-Sakhawy MA-M. Polysaccharides, protein and lipid-based natural edible films in food packaging: A review. Carbohydrate Polymers 2020; 238: 116178.
5. Swaroop C, Shukla M. Development of blown polylactic acid-MgO nanocomposite films for food packaging. Composites Part A: Applied Science and Manufacturing 2019; 124.
6. Wu F, Misra M, Mohanty AK. Sustainable green composites from biodegradable plastics blend and natural fibre with balanced performance: Synergy of nano-structured blend and reactive extrusion. Composites Science and Technology 2020; 200.
7. Zubair M, Ullah A. Recent advances in protein derived bionanocomposites for food packaging applications. Critical Reviews in Food Science and Nutrition 2020; 60: 406-434.
8. Li X, Wei Y, Jiang S, et al. Full Bio-Based Soy Protein Isolate Film Enhanced by Chicken Feather Keratin. Macromolecular Materials and Engineering 2021; 306: 2100004.
9. Qiu S, Zhou Y, Waterhouse GIN, et al. Optimizing interfacial adhesion in PBAT/PLA nanocomposite for biodegradable packaging films. Food Chemistry 2021; 334:127487.

  doi:10.5075/epfl-298799_978-2-9701614-0-0

10. Balaji S, Venkatesan R, Mugeeth L, Dhamodharan R. Hydrophobic nanocomposites of PBAT with Cl-fn-POSS nanofiller as compostable food packaging films. Polymer Engeeniring & Science 2021; 61:314-326.
11. Botta L, Titone V, Mistretta MC, et al. PBAT based composites reinforced with microcrystalline cellulose obtained from softwood almond shells. Polymers 2021; 13: 2643.
12. Basavegowda N, Mandal TK, Baek K-H. Bimetallic and trimetallic nanoparticles for active food packaging applications: A review. Food and Bioprocess Technology 2020; 13:30-44.
13. Scaffaro R, Lopresti F, Marino A, Nostro A. Antimicrobial additives for poly(lactic acid) materials and their applications: current state and perspectives. Applied Microbiology and Biotechnology 2018; 102: 7739-7756.
14. Tkaczewska J. Peptides and protein hydrolysates as food preservatives and bioactive components of edible films and coatings-A review. Trends in Food Science & Technology 2020; 106: 298-311.
15. Scaffaro R, Maio A, D'Arrigo M, et al. Flexible mats as promising antimicrobial systems via integration of Thymus capitatus (L.) essential oil into PLA. Future Microbiology 2020; 15: 1379-1392.
16. Biddeci G, Cavallaro G, Di Blasi F, et al. Halloysite nanotubes loaded with peppermint essential oil as filler for functional biopolymer film. Carbohydrate Polymers 2016; 152:548-557.
17. Scaffaro R, Maio A, Lopresti F. Effect of graphene and fabrication technique on the release kinetics of carvacrol from polylactic acid. Composites Science and Technology 2019; 169: 60-69.
18. Campos-Requena VH, Rivas BL, Pérez MA, Garrido-Miranda KA, Pereira ED. Release of essential oil constituent from thermoplastic starch/layered silicate bionanocomposite film as a potential active packaging material. European Polymer Journal 2018; 109:64-71.
19. Giorcelli M, Khan A, Pugno NM, Rosso C, Tagliaferro A. Biochar as a cheap and environmental friendly filler able to improve polymer mechanical properties. Biomass and bioenergy. 2019; 120:219-223.
20. Botta L, Teresi R, Titone V, Salvaggio G, La Mantia FP, Lopresti F. Use of Biochar as Filler for Biocomposite Blown Films: Structure-Processing-Properties Relationships. Polymers 2021; 13:3953.
21. Tomczyk A, Sokołowska Z, Boguta P. Biochar physicochemical properties: pyrolysis temperature and feedstock kind effects. Reviews in Environmental Science and Bio/Technology 2020; 19:191-215.
22. Aup-Ngoen K, Noipitak M. Effect of carbon-rich biochar on mechanical properties of PLA-biochar composites. Sustainable Chemistry and Pharmacy 2020; 15:100204.
23. George J, Azad LB, Poulose AM, An Y, Sarmah AK. Nano-mechanical behaviour of biochar-starch polymer composite: Investigation through advanced dynamic atomic force microscopy. Composites Part A: Applied Science and Manufacturing 2019; 124:105486.
24. Kelmanson JE, Jäger AK, van Staden J. Zulu medicinal plants with antibacterial activity. Journal of Ethnopharmacology 2000; 69: 241-246.
25. Cruciata M, Gaglio R, Scatassa ML, et al. Formation and characterization of early bacterial biofilms on different wood typologies applied in dairy production. Applied Environmental Microbiology 2018; 84: e02107--17.
26. Adrar S, Habi A, Ajji A, Grohens Y. Combined effect of epoxy functionalized graphene and organomontmorillonites on the morphology, rheological and thermal properties of poly

  doi:10.5075/epfl-298799_978-2-9701614-0-0

(butylenes adipate-co-terephtalate) with or without a compatibilizer. Applied Clay Science 2017; 146:306-315.

27. Moustafa H, Guizani C, Dupont C, Martin V, Jeguirim M, Dufresne A. Utilization of torrefied coffee grounds as reinforcing agent to produce high-quality biodegradable PBAT composites for food packaging applications. Acs Sustainable Chemistry & Engineering 2017; 5:1906-1916.
28. de Andrade MF, de Lima Silva ID, da Silva GA, et al. A study of poly (butylene adipate-co-terephthalate)/orange essential oil films for application in active antimicrobial packaging. LWT 2020; 125:109148.
29. Peppas NA, Sinclair JL. Anomalous transport of penetrants in glassy polymers. Colloid and Polymer Science 1983; 261:404-408.

  doi:10.5075/epfl-298799_978-2-9701614-0-0

DESIGNING BICONTINUOUS SILICA-EPOXY NANOCOMPOSITES

Charles M.D. Shaw[a], David B. Anthony[b], Joseph Garguili[c], Ian Hamerton[c], Milo S.P. Shaffer[b]

a: Department of Materials, Imperial College London, UK – c.shaw20@imperial.ac.uk
b: Department of Chemistry, Imperial College London, UK
c: Bristol Composites Institute, Department of Aerospace Engineering, University of Bristol, UK

Abstract: *A nanocomposite reinforced with a 3D, connected, stiff framework should offer better performance than a simple dispersion of nanoparticles. Monolithic porous silica can be used as this framework by providing a fully connected but open porous supporting skeleton for reinforcing organic polymers. Infusion of epoxy resin into silica aerogel pores may produce a bicontinuous material that more efficiently exploits the intrinsic properties of each solid phase: bicontinuous aerogel and polymer matrix component. Matrix infusion into an aerogel monolith in principle allows greater silica content than shear mixing (of particles) which is limited by aggregation and high shear viscosities. Silica content is maximised by producing aerogels of unusually high envelope density (0.2 g.cm^{-3} – 0.8 g.cm^{-3}).*

Keywords: Silica; Aerogel; Bicontinuous; Hybrid; Nanoreinforcement

1. Introduction

Epoxies are widely used in structural composites due to their high toughness, ease of processing, and good interfacial compatibility with reinforcing materials. However, they lack stiffness when compared to inorganic materials and some high-end thermoplastics. Silica particles dispersed within epoxy resin can improve elastic modulus without loss of toughness [1]. However, this approach increases resin viscosity which hinders processing [2], and lacks any long-range connectivity between the particles. By pre-forming a porous silica monolith, and backfilling with epoxy, a structure consisting of a fully bicontinuous, silica-epoxy network may be achieved. In this architecture, the reinforcement is evenly distributed. forming an interlocked inorganic-organic hybrid with characteristic lengthscales of less than 10 nm. The bicontinuous structure facilitates improved load transfer for greater stiffness and introduces additional failure modes for greater energy absorption [3].

Silica aerogel was chosen as the porous silica phase for this material for its simple, low-temperature synthesis and controllable mesoporosity. Pure silica aerogel is intrinsically brittle due to the weakness of interparticle neck regions in its “pearl necklace” morphology. Improved mechanical performance has been reported when the fragile network is crosslinked with organic polymers to give an X-aerogel [4]. Aerogel-based hybrids are typically made with low loadings of secondary materials to preserve the characteristic low density and thermally insulating properties of the aerogel. In this work, we aim to use the aerogel as a 3D reinforcing element in which the pores are completely backfilled with a commercially available epoxy resin, encasing the silica network as a stiff skeletal reinforcement to the epoxy. A comparison of the microstructures of the various silica-epoxy nanocomposites so far described is shown in Figure 1.

  doi:10.5075/epfl-298799_978-2-9701614-0-0

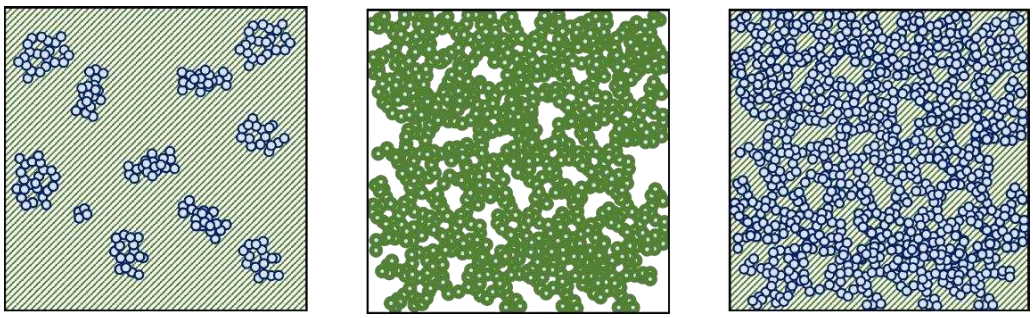

Figure 1. Cartoons depicting the microstructures of epoxy-silica nanocomposites. Left: Epoxy resin (green) reinforced with powdered silica aerogel (blue). Centre: Epoxy-crosslinked silica X-aerogel (light blue aerogel with dark green epoxy crosslinking. Right: Bicontinuous silica-epoxy hybrid monolith (blue aerogel and green epoxy).

Silica aerogel has previously been used produce a composite polymer electrolyte by backfilling with poly(ethylene oxide) (PEO) under reduced pressures [5]. In this material, the stiff silica backbone reinforces the mechanically weak PEO enabling suppression of lithium dendrite formation. We propose that a similar vacuum technique can be applied to fill mesoporous silica monoliths with epoxy resin, combining tough epoxy with stiff silica to produce a bicontinuous composite with greater stiffness than unreinforced epoxy without loss of toughness. Silica content is maximised by producing aerogels of unusually high envelope density (0.2 $g.cm^{-3}$ - 0.8 $g.cm^{-3}$). Aerogel density is restricted by the limited miscibility of siloxane precursors with water; high densities are achieved by maximising miscibility to give high siloxane concentrations. In this work, gels are dried from supercritical CO_2 to limit the influence of pore shrinkage on the final monolith density and, hence, envelope density is controlled directly from the precursor siloxane concentration. We describe the process to make such materials on a scale suitable for mechanical testing, and these tests will be conducted at a later stage.

2. Experimental

2.1 Materials

For the synthesis of silica aerogel monoliths tetramethylorthosilicate (98%, TMOS) and chlorotrimethylsilane (≥ 98%, TMCS) were purchased from Sigma Aldrich, and acetone (technical grade), ethanol (absolute), water (HPLC grade), and *n*-hexane (dehydrated) were purchased from VWR. An epoxy resin with its associated hardener (Gurit Prime 27 epoxy resin and Prime Extra Slow hardener, Marineware Ltd.) were infused into the silica aerogel monoliths to produce silica-epoxy bicontinuous composites. The epoxy and hardener were mixed according to manufacturer's instructions and degassed before use. All chemicals were used as received.

2.2 Silica Aerogel Synthesis and Characterisation

Silica aerogel monoliths were produced by combining water and TMOS in a molar ratio of 24:1. This mixture was stirred for 1 h at 25 °C to give a single transparent sol phase which was then poured into a mould. Cylindrical aerogel samples were cast in moulds made by machining 20 mm thick high-density polyethylene (HDPE) sheet (PE 300, Direct Plastics) on an AXYZ CNC router. Gelled samples were aged for 4 days at 25 °C to ensure complete reaction before exchanging from residual solvent to ethanol. Hydrophobisation of the silica surface was performed by immersion in a TMCS:*n*-hexane:ethanol mixture (1:1:8 ratio by volume). Samples were then

  doi:10.5075/epfl-298799_978-2-9701614-0-0

exchanged back to ethanol before a final exchange to acetone over 3 days. Finally, samples were dried from supercritical CO_2 using a Leica EM CPD300 critical point dryer. Envelope densities were determined by Archimedes' balance method in de-ionised water. Skeletal density was determined by helium pycnometry (Micrometrics AccuPyc II 1340). Specific surface area, pore volume, and pore radius distributions were determined from gas sorption isotherms (N_2) using a Quantachrome NOVAtouch gas sorption analyser.

2.4 Epoxy Infusion in Silica Aerogel Monoliths to Produce Composites

Silica aerogel cylinders (diameter ≈ 5.5 mm, length ≈ 15 mm) were backfilled with epoxy by immersion in epoxy resin/hardener mixture under reduced pressure. The chosen commercially available resin system has low viscosity (170 cP to 180 cP at 25 °C) and long vacuum flow time (7 h 40 min at 25 °C). Owing to their fragility, aerogel monoliths were supported in heat-shrink tubing during infusion. Once immersed, the entire system was evacuated to 1 mbar in a vacuum oven for 6 h at 25 °C.

2.5 Composite Characterisation

The degree of infusion of epoxy into the porous silica structure was quantified as a backfill volume percentage (β) using Equation (1),

$$\beta = \frac{\Delta\rho_b}{\varphi.\rho_e} \quad (1)$$

where $\Delta\rho_b$ is the difference in envelope density between the unmodified silica aerogel monolith and the epoxy-infused silica aerogel monolith, φ is the porosity of the silica aerogel monolith, and ρ_e is the cured epoxy density determined by Archimedes' balance method. The change in morphology following epoxy backfilling is observed by scanning electron microscopy using a LEO Gemini 1525 FEG SEM set at 5 kV with In lens detector.

3. Results and Discussion

The silica aerogel synthesis employed here was designed for scalability and processability. TMOS was chosen for its ability to react with water and self-mix from an initially biphasic liquid by evolving methanol without the need for additional solvents or catalysts. This miscibility is higher than that for alternative orthosilicates facilitating the formation of aerogels with higher bulk density giving a higher loading of silica reinforcement in the silica-epoxy composite. Samples were dried from supercritical CO_2 to eliminate capillary pressures resulting from solvent evaporation. This process minimises pore collapse which would otherwise result in increased envelope density and smaller pore radii which may inhibit infusion of epoxy. Samples were hydrophobised by reacting TMCS with surface silanol (OH) groups. This treatment was performed for the following reasons:

- Hydrophilic (non TMCS-treated) samples formed in this work were found to fracture in the presence of ambient moisture.
- Hydrogen bonded water molecules would be difficult to remove ahead of epoxy infusion. This residual water could affect the epoxy cure and produce voids in the composite structure.
- Furthermore, functionalisation with trimethylsilyl groups prevents silanol groups from reacting chemically with epoxy resin or hardener. This reaction may alter the

  doi:10.5075/epfl-298799_978-2-9701614-0-0

stoichiometry of the epoxy resin/hardener mixture. Silica-epoxy bi-continuous materials with a designed covalent interface will nevertheless be explored in future work.

Density and pore structure characteristics for the silica aerogel are summarised in Table 1. The BJH pore size distribution indicates that most of the porosity comprises mesopores with radii between 2 nm and 3.2 nm (Figure 2). The large specific surface area of silica aerogel (951 $m^2.g^{-1}$) results in an equally large silica-epoxy interface. This may increase the toughness of the material through crack pinning and deflection. Dry silica aerogel monoliths were translucent and bluish in colour due to Rayleigh scattering in the porous structure (Figure 3). Following epoxy infusion, the composite was uniform in appearance with greater transparency than uninfused aerogel (Figure 3) due to reduced scattering and closer matching of refractive indices [5]. Once cured, excess epoxy was removed, and the dimensions of the cylinder were measured to ensure that only the epoxy-silica composite remained. The mean backfill vol.%, β = 99.3% was calculated for six samples using Eq. (1) as summarised in Table 2. This value indicates that infusion of liquid epoxy into the porous epoxy structure was almost complete. Scanning electron microscopy images show the filling of pores by epoxy (Figure 4).

Table 1: Silica aerogel monolith properties where ρ_b *is envelope density,* ρ_s *is skeletal density,* SSA *is specific surface area,* r_{pore} *is mean pore radius and* V_{pore} *is pore volume.*

ρ_b ($g.cm^{-3}$)	ρ_s ($g.cm^{-3}$)	SSA ($m^2.g^{-1}$)	r_{pore} (nm)	V_{pore} ($cm^3.g^{-1}$)
0.226 ± 0.009	1.50 ± 0.02	951 ± 25	2.60 ± 0.17	3.81 ± 0.25

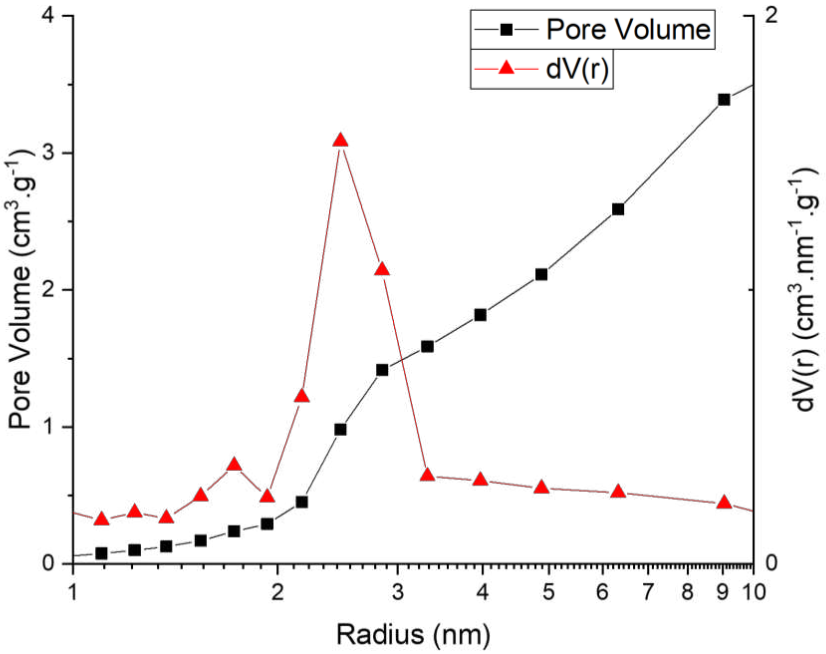

Figure 2: BJH plot calculated from silica aerogel gas sorption isotherm with the differential with respect to the pore radius included.

  doi:10.5075/epfl-298799_978-2-9701614-0-0 published under CC BY-NC 4.0 license

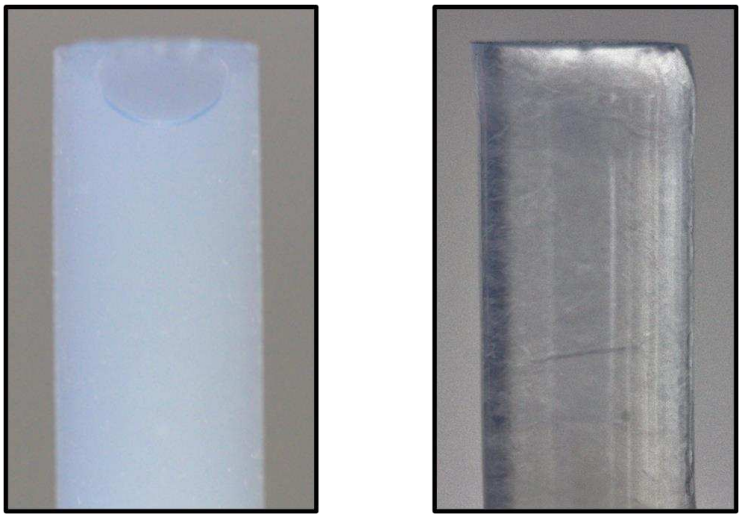

Figure 3: Photograph of silica aerogel monolith (left) and epoxy-infused silica aerogel monolith (right).

Table 2: Summary of composition of bicontinuous silica-epoxy material. Uncertainty is given as one standard deviation.

ρ_f ($g.cm^{-3}$)	Backfill vol.%	Void vol.%	Silica wt.%	Epoxy wt.%
1.189 ± 0.016	99.3 ± 1.9	0.6 ± 1.6	18.5 ± 0.7	81.5 ± 0.7

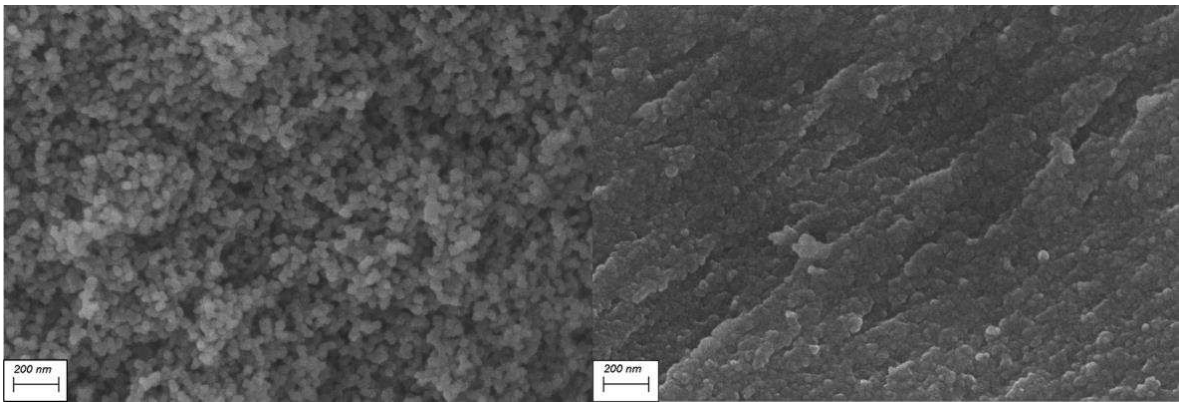

Figure 4: Scanning electron micrographs for silica aerogel before (left) and after (right) infusion with epoxy resin.

4. Conclusions

A silica-epoxy inorganic-organic bicontinuous hybrid composite material has been produced by backfilling mesoporous monolithic silica aerogel with liquid epoxy resin. Backfill vol.% was calculated from pre- and post-infusion envelope densities and indicated that 99.3 pore vol.% was filled resulting in a void content of 0.6 vol.%. This low void content shows that silica pores with radii of 2.0 nm - 3.2 nm uptake liquid epoxy resin. The resulting composite has a continuous 3D silica reinforcement which will provide the epoxy resin with improved stiffness by facilitating long range load transfer. Pre-forming the silica network as a monolithic structure also enables

  doi:10.5075/epfl-298799_978-2-9701614-0-0

high weight loadings of reinforcement without incurring the high viscosities seen in dispersed particulate systems. A simple two component silica aerogel synthesis has been employed which could enable modification of precursor composition to produce higher silica aerogel envelope densities leading to a higher silica content in the bicontinuous composite. Future work will test monolithic samples in compression to determine the optimum silica content for improved mechanical performance. Higher silica volume fractions could also be achieved through application of a lower porosity aerogel with a larger mean pore radius. Such a material may be achieved through selection of appropriate alternative monomers and catalysts or application of templating techniques. This material is currently limited to small scale test samples due to the geometric limitations imposed by critical point drying. Large scale structural elements will require the use of mesoporous silica materials which are stable to ambient pressure drying.

Acknowledgements

The authors kindly acknowledge the funding for this research provided by UK Engineering and Physical Sciences Research Council (EPSRC) programme Grant EP/T011653/1, Next Generation Fibre-Reinforced Composites: a Full Scale Redesign for Compression in collaboration with University of Bristol.

5. References

1. Salimian S, Zadhoush A. Water-glass based silica aerogel: unique nanostructured filler for epoxy nanocomposites. Journal of Porous Materials. 2019; 26(6):1755-65.
2. Rahatekar SS, Koziol KKK, Butler SA, Elliott JA, Shaffer MSP, Mackley MR, *et al.* Optical microstructure and viscosity enhancement for an epoxy resin matrix containing multiwall carbon nanotubes. Journal of Rheology. 2006; 50(5):599-610.
3. Quaresimin M, Schulte K, Zappalorto M, Chandrasekaran S. Toughening mechanisms in polymer nanocomposites: From experiments to modelling. Composite Science and Technology. 2016; 123:187-204.
4. Meador MAB, Fabrizio EF, Ilhan F, Dass A, Zhang G, Vassilaras P, *et al.* Cross-linking Amine-Modified Silica Aerogels with Epoxies: Mechanically Strong Lightweight Porous Materials. Chemistry of Materials. 2005; 17(5):1085-98.
5. Lin D, Yuen PY, Liu Y, Liu W, Liu N, Dauskardt RH, *et al.* A Silica-Aerogel-Reinforced Composite Polymer Electrolyte with High Ionic Conductivity and High Modulus. Advanced Materials. 2018; 30(32):1802661.

  doi:10.5075/epfl-298799_978-2-9701614-0-0

ROBUST CONTINUOUS PRODUCTION OF CARBON NANOTUBE-GRAFTED STRUCTURAL FIBRES: A ROUTE TO HIERARCHICAL FIBRE REINFORCED COMPOSITES

Hassan Almousa[a], Hugo G De Luca[a], David B Anthony[b], Emile S Greenhalgh[c], Alexander Bismarck[d], Milo SP Shaffer[a,b]

a: Department of Materials, Imperial College London, UK – h.almousa19@imperial.ac.uk
b: Department of Chemistry, Imperial College London, UK
c: Department of Aeronautics, Imperial College London, UK
d: Department of Materials Chemistry, University of Vienna, Austria

Abstract: *Growth of carbon nanotubes (CNTs) onto the fibre surface by direct chemical vapour deposition (CVD) offers a convenient means to integrate synthesis with assembly. This method delivers the nanostructures where they have the greatest influence on fibre-matrix interface or interphase. However, CVD is usually limited to small batches of short fibre lengths, and can damage the primary properties. Here, we describe a robust process to produce carbon nanotube-grafted-fibres continuously at tow level with a uniform coverage of short (sub-500 nm length), 10-20 nm diameter CNTs. Different CNT growth conditions, such as temperature [650-950 °C], duration [0.72-50 min], line speed [0.6-10 m/h], potential difference [0-1000 V], and reactive gas flow/compositions were investigated. Following optimisation, the fabrication of an entirely "fuzzy" fibre reinforced hierarchical composite was achieved.*

Keywords: Chemical vapor deposition; Carbon nanotubes; Carbon fibres; Hierarchical composites

1. Introduction

The structural response of fibre-reinforced composites is strongly influenced by the fibre-matrix interface or interphase. The inclusion of carbon nanotubes in conventional fibre composites promises to address many matrix- or interface-dominated failures. Research on these 'hierarchical composites' has focused predominantly on the addition of nano-reinforcement either in the bulk matrix, or locally on the fibre surface [1]. Grafting carbon nanotubes (CNTs) onto the fibre surface offers a convenient means to integrate synthesis with assembly and to deliver the nanostructures where they have the greatest influence. However, the outcome of direct chemical vapour deposition (CVD) growth depends on the underlying substrate material. On inorganic fibres, such as silica and alumina, long CNTs grow, often producing an undesirable "Mohawk" motif, which decreases the local fibre volume fraction and generates local high stress states that ultimately lead to premature failures. On carbon fibres (CFs), CVD can damage the primary fibre surface, as a result of the high temperature treatment in the presence of catalyst. In addition, CVD is usually limited to small scale batches of short fibre lengths. To make the process more applicable for industrial adoption, the production of continuous carbon nanotubes-grafted-fibres (CNT-g-Fs) must also be robust, uniform, and maintain the primary fibre characteristics.

  doi:10.5075/epfl-298799_978-2-9701614-0-0

In this paper, we describe a process to produce upwards of 50 m of CNT-g-CFs continuously on 12K tow level [2]. A continuous in-line deposition of an efficient bi-catalyst precursor system, both in terms of composition and concentration was followed by CNT synthesis in an open CVD reactor. This patented technology [3] produces a uniform coverage of short (sub-500 nm length), 10-20 nm diameter CNTs, ideal for maintaining primary fibre loading fraction. The continuous process allows for various growth parameters to be studied systematically. Different CNT growth conditions, such as temperature, duration, line speed, potential difference, and reactive gas flow / composition were investigated. Following optimisation and scale-up, the production of 50 m per day, allowed the fabrication of an entirely "fuzzy" fibre reinforced hierarchical composites. The promising potential for CNT-g-CFs suitability as reinforcement in thermoplastic matrices (e.g., polypropylene) is due to the mechanical interlocking [4], and work is ongoing to evaluate our material in such systems. In due course, this approach has the potential to produce higher performance yet recyclable and sustainable composites.

2. Experimental

2.1 Materials

Commercially-availabe unsized polyacrylonitrile-based carbon fibres (AS4-12K) supplied by Hexcel Composites (Hexcel, GB) were used as a continous tow with a diameter of ~7 µm. Iron (III) nitrate nonahydrate (≥98% ACS reagent, Merch, DE), nickel (II) acetylacetonate (≥98%, VWR, GB) and ethanol (>99.7% BDH Prolabo, VWR, GB) were used to prepare the catalyst precursor. Acetylene in nitrogen (N2 98.7 vol% and C2H2 1.3 vol%, C certificate, BOC gases, GB), hydrogen in nitrogen (N2 97.6 vol% and H2 2.4 vol%, C certificate, BOC gases, GB), nitrogen (99.998 vol% minimum, BOC gases, GB) were used for continuous CVD CNT synthesis. EPON 828 liquid epoxy (Netmro, US) and Jeffamine T-403 curing agent were used as matrix for the short beam shear test. Carbon fibers and all chemicals were used as-received.

2.2 Continuous CVD set-up

Production of CNT-g-CFs is conducted over two consecutive processes. First, the deposition of catalyst precursor particles on unsized and plasma treated AS4 CFs. Second, the growth of CNTs from the deposited catalyst precursor. The catalyst deposition is performed in-line by passing the CFs through a bath consisting of 1 wt.% iron (III) nitrate nonahydrate and nickel (II) acetylacetonate (1:0.64 mol.%) in ethanol for 1 minute. After, the coated CFs are dried in two infared furnaces. The bi-catalyst deposited CFs are then pulled continuously through a three-zone CVD reactive chamber (Figure 1) and exposed to different gas conditions through adjustable arrangement of internal quartz tubes at a speed of 2.4 m/h. As the CF tow enters the furnace, it is first exposed to nitrogen (10000 sccm) then in the hot-zone (770 °C) to hydrogen in nitrogen (2.4 vol.% hydrogen, 3400 sccm) for catalyst reduction. Following reduction, the tow then is subjected to acetylene in nitrogen (1.3 vol.% acetylene, 325 sccm) which acts as the carbon source for CNT synthesis for a duration of ~ 12 minutes. Finally, the CFs then are passed through another nitrogen region to exit the reactor.

  doi:10.5075/epfl-298799_978-2-9701614-0-0

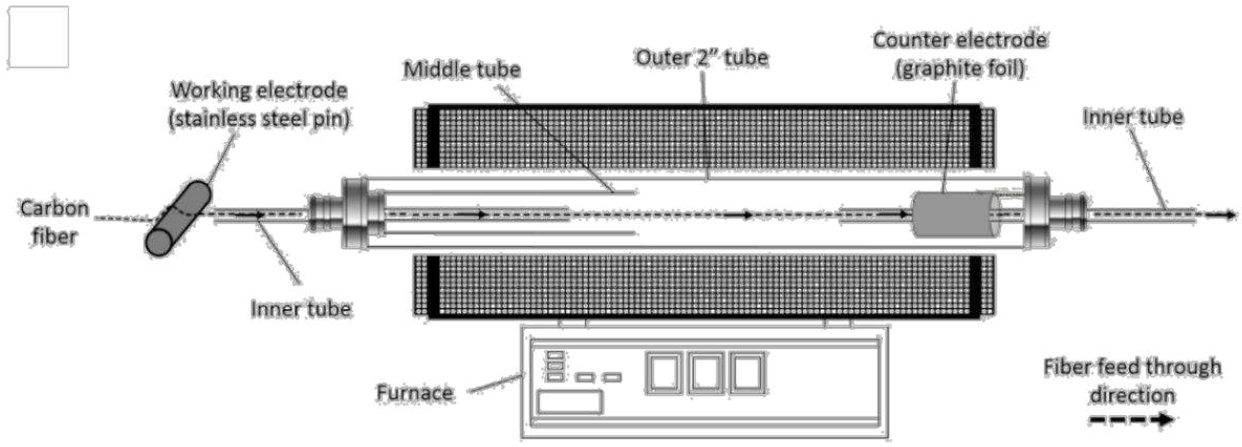

Figure 1. Continuous open spool-to-spool CVD reactor schematic [6].

3. Parameter space of CNT-synthesis via in-line CVD

CNT growth characteristics are strongly influenced by the temperature, active gas composition, reduction, and growth durations [5]. Varying these CNT growth parameters in a continuous process, allows the study of a wide range of conditions in-line and their effect on the produced CNT-g-CFs. A list of variables used to conduct a parametric study and the refinment of CVD conditions for CNT synthesis are listed in table 1. In this section, critical parameters for industrial adoption are discussed.

Table 1: CVD line associated process variables and refined synthesis conditions.

Variable	Unit	Range	Refined
Temperature	°C	[650 – 950]	770
Line-speed	m/h	[0.6 – 10]	2.4
Potential difference	V	[0 – 1000]	300
Reduction time	min	[0.72 – 10]	2
Growth time	min	[3.1 – 50]	12.5
C_2H_2:H_2	-	1:[10-80]	1:19.3
Gas-flow	sccm	[7500 – 12000] N_2	10000 N_2
		[3400 – 6800] H_2 in N_2	3400 H_2 in N_2
		[162 – 650] C_2H_2 in N_2	325 C_2H_2 in N_2

3.1 Effect of temperature

It is often observed when CNTs are synthesised at higher temperatures (above 800 °C) that less defective CNTs are grown. However, reduced temperatures are preferred as it reduces energy consumption and limits the damage to the primary CFs. Growth of CNTs on CF surface at temperatures below 720 °C in the continuous CVD reactor was not possible (Figure 2.a). At 770 °C, a dense and even coverage of CNTs were grown on CFs surface (Figure 2.b).

  doi:10.5075/epfl-298799_978-2-9701614-0-0

Temperatures above 870 °C altered the appearance of the catalyst and particle size (observed *ex-situ*) resulting in poor growth (Figure 2.c).

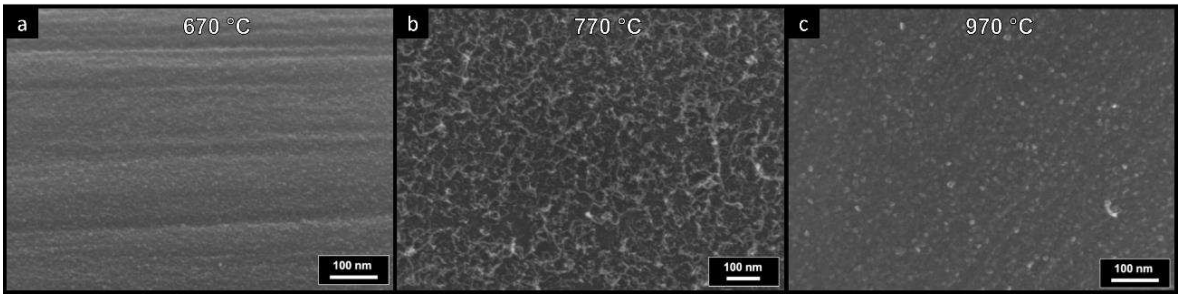

Figure 2. SEM micrographs of CNT-g-CF growth temperatures (a) 670 °C, (b) 770 °C, (c) 970 °C.

3.2 Effect of applied potential difference

Applying a potential difference of 300 V to the CFs was previously shown to enhance CNT growth and prevent catalyst pitting effect to CFs [6]. In the absence of a potential difference, the growth of CNTs was irregular and the CF surface was damaged. Therefore, a small step changes in potential difference applied to the CFs were conducted between 0 and 200 V. Potential differences over 200 V resulted in homogeneous and dense coverage of CNTs (Figure 3.c) that was comparable to applying potential different of 300 V. Any further increase in the potential difference up to 1000 V did not provide any significant improvement in CNT synthesis.

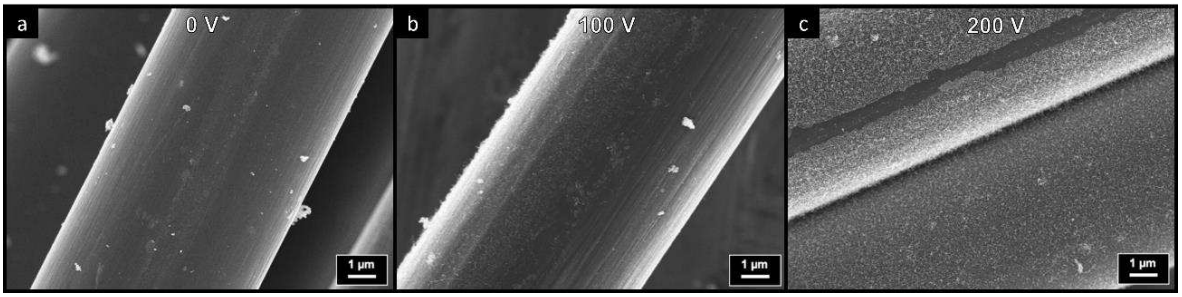

Figure 3. SEM micrographs of CNT-g-CF grown with an applied potential difference of (a) 0 V, (b) 100 V, (c) 200 V.

3.3 Effect of line speed

A conventional speed of carbon fibre production line is about 10 m/h. Therefore, matching this speed is important for future industrial adoption. A range of line speeds were investigated from 0.6 to 6.7 m/h (current design limitations). While longer growth dwell times can yield longer CNTs, premature termination of the growth can result from catalyst poisoning. Consequently, an increase of speed to 2.4 m/h resulted in uniform CNT coating with a thickness of ~ 200 nm (Figure 4.b). Further increases in the line speed up to 4.8 m/h led to thicker and homegenized CNTs coating as shown in (Figure 4.c). However, beyond this speed the growth declined due to incomplete catalyst reduction step.

  doi:10.5075/epfl-298799_978-2-9701614-0-0

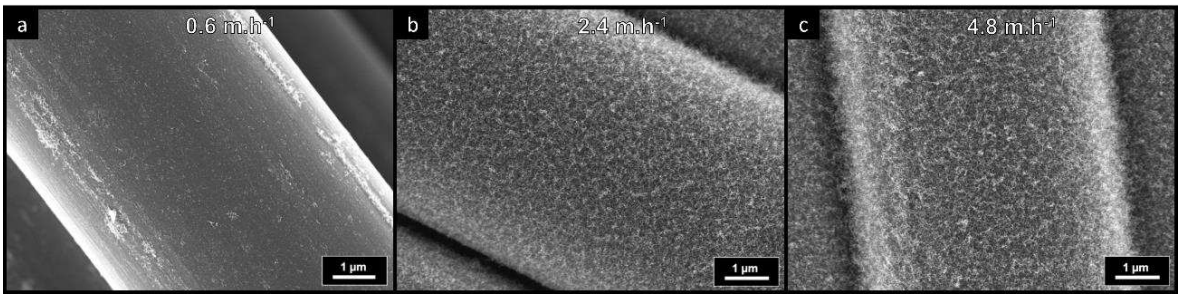

Figure 4. SEM micrographs of CNT-g-CF synthesized with line speeds (a) 0.6 m/h, (b) 2.4 m/h, (c) 4.8 m/h.

4. Processing CNT-g-CF composite specimen

Single-fibre measurement of apparent interfacial shear strength provide indications of the potential benefit of CNTs-g-CFs at the macroscale. However, a more complete mechanical evaluation accounting for macroscale deformation mechanism in a structural composite requires the fabrication of coupons. This step was unattainable until a scaled-up production of the CNT-g-CFs made it feasible to produce larger composite specimens. A process was developed for short beam shear (SBS) coupons fabrication within the specification of ASTM D2344 standard [7]. CFs were wrapped around stainless-steel pins (Ø 1.5 mm) to assemble four layers with an angle of 3.0° (±1.5°) between them. This method allowed for a fibre volume fraction of 50-69 vol.% in the final SBS hierarchical composite coupon.

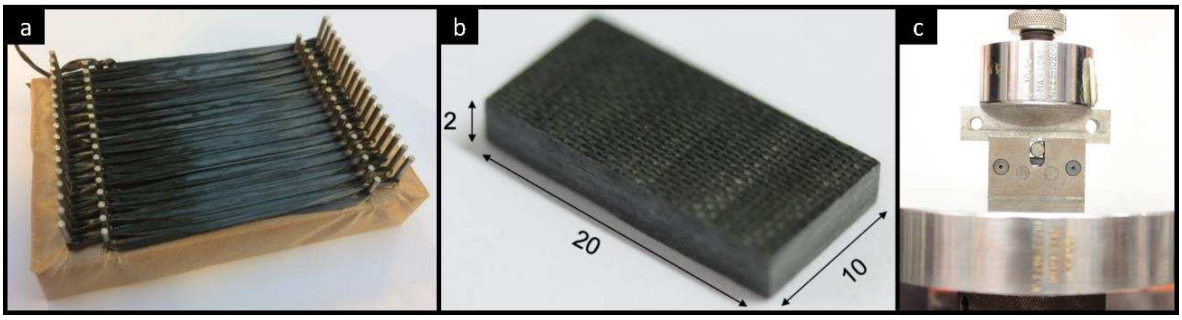

Figure 5. Images of (a) CNT-g-CFs 12K tow loomed around pins, (b) ASTM D2344 hierarchical composite sample (dimensions in mm), (c) SBS hierarchical composite coupon under load.

5. Conclusion

A continuous in-line deposition of bi-catalyst on fibres and continuous CVD system were successfully developed. In combination, these processes enabled comprehensive investigation of the effect of different parameters of CNT growth on CFs, such as temperature, duration, line speed, potential difference, and reactive gas flow/compositions. The refined conditions allowed for a robust route to producing CNT-g-CFs with dense and homogeneous growth of CNTs. After achieving a production of over 50 meters per day of CNT-g-CFs, a process for fabricating SBS CNT-g-CF specimen was developed to study the system's mechanical properties at macroscale. In due course, the CNT-g-CFs will be embedded in thermoplastic-based composite system to produce higher performance yet recyclable and sustainable composites.

  doi:10.5075/epfl-298799_978-2-9701614-0-0

Acknowledgements

The authors DBA, MSPS, and ESG kindly acknowledge the funding for this research provided by UK Engineering and Physical Sciences Research Council (EPSRC) programme Grant EP/T011653/1, Next Generation Fibre-Reinforced Composites: a Full Scale Redesign for Compression in collaboration with University of Bristol. HGDL kindly acknoledge the Lloyd's Register Foundation and the Ministry of Defence, Singapore (MINDEF) for the financial support of this work, and Hexcel for supplying the AS4 carbon fibres.

References

1. A Clancy, et al. Applied Materials & Interfaces, 12, 15955-15975, 2020
2. M Shaffer and D Anthony, Patent WO2016009207 A1, 2016
3. D Anthony, et al. Nanotechnology, Vol. 28, No. 30, 305602, pp 12, 2017
4. S Yumitori, et al. Computational Methods and Experimental Measurements XVI, 2013
5. V. Jourdain and C. Bichara, Carbon 58, 2-39, 2013
6. D Anthony, et al. Composites Part A: Applied Science and Manufacturing, 112, 525–538 2018
7. A. international, Astm D2344 / D2344m-16, 2016

  doi:10.5075/epfl-298799_978-2-9701614-0-0

PRINTED CIRCUIT BOARDS MADE FROM CELLULOSE FIBRILS

Thomas Geiger[a], Christine K. Geiger[b], Katrin G. Hoffmann[a], Gustav Nyström[a]

a: Laboratory for Cellulose & Wood Materials, Empa – Swiss Federal Laboratories for Materials Science and Technology, Überlandstrasse 129, 8600 Dübendorf, Switzerland – thomas.geiger@empa.ch
b: Cantonal School Zurich North, Birchstrasse 107, 8090 Zürich, Switzerland

Abstract: *Using cellulose nanofibrils (CNF) and bacterial cellulose (BC), rigid substrates were prepared with a special dewatering tool and drying step. These substrates exhibit exceptional mechanical properties with very high Young's moduli and strengths. Printed circuit boards (PCBs) are important components of many industrial and consumer electronic devices. The materials of today's PCBs are derived from petroleum-based sources and are based on epoxy resins, polyesters or polyimides, often in combination with paper, glass fibers, ceramic powders and additives. Our concept for a replacement of PCB substrates consists in the use of the rigid substrates made of sustainable, bio-based and bio-degradable CNF and BC. An electronic circuit was realized by conventional wet chemical etching and soldering with tin solder on the cellulose substrates. To demonstrate the PCB material biodegradability, the assembled circuit boards were composted for five months. Afterwards, the PCBs were fully decomposed and copper tracks and electronic components were recovered from the soil.*

Keywords: cellulose nanofibrils; bacterial cellulose; printed circuit board; home composting

1. Introduction

Printed Circuit Boards (PCB) are important components of many devices in industrial or consumer electronics. The materials of today's PCBs are derived from petroleum-based sources and based on epoxy resins, polyesters, or polyimides often in combination with paper, glass fibers, ceramic powders and additives (flame retardants). Many of these materials cause serious health and environmental issues when being manufactured, incinerated or recycled. Increasing environmental awareness among consumers, rising raw material prices worldwide, problems with the disposal and recycling of e-waste, and stricter environmental legislation are all driving forces for the research for alternatives to conventional PCB materials.

The excellent material properties of glass fiber-reinforced epoxy resins for conventional PCBs motivated many research groups to develop more environmentally friendly and sustainable composites by combining epoxy resins derived from bio-based monomers with natural fibers. Bio-polyester based on polylactic acid (PLA) [1] and polyhydroxybutyrate (PHB) [2] are other potential biopolymer classes which have been investigated for use as PCB materials. However, these polymers need to be produced chemically or biotechnologically from bio-based or petrol-based monomers. In contrast, plant (wheat gluten) and animal (chicken feathers) proteins can be isolated directly from renewable feedstock sources and have been tested as matrix [3] or fiber reinforcing [4] materials in PCBs.

  doi:10.5075/epfl-298799_978-2-9701614-0-0

Our concept for a PCB substrate replacement is the use of sustainable cellulose fibrils produced from cellulose pulp or directly by bacteria [5]. Cellulose nanofibrils (CNF) and bacterial cellulose (BC) were processed into rigid boards via thermal compression. The boards were mechanically characterized by tensile and flexural tests. An electronic circuit was realized on these rigid substrates using conventional wet chemical etching of an applied copper foil. The electronic components required for the circuit were connected to the conductor paths by simple soldering with tin solder. The assembled PCBs were then stored in an outdoor home compost for five months.

2. Experimental section

2.1 Materials

CNF suspensions at a solid content of 2 wt. % were obtained from elemental chlorine-free pulp (ECF from Mercer Stendal, Zellstoff Stendal GmbH, Arneburg, Germany). The pulp was disintegrated by using an ultra-fine friction grinder (supermass-colloider MKZA10-20 J CE, Masuko Sangyo Co., Ltd., Kawaguchi/Saitama, Japan) with an energy input of 9 kWh/kg pulp. Subsequently, the aqueous suspensions were dewatered under pressure to around 10 wt. %. Bacterial cellulose was obtained as a solid aqueous gel (around 1 wt. %) in the form of 5 mm thick sheets from fzmb GmbH (Bad Langensalza, Germany). All electrical components needed for the PCB (self-adhesive copper foil, capacitors, resistors, LEDs, transistors, solder (Sn99.3/Cu0.3)) were purchased from a local electronics store. Anhydrous iron(III)chloride (98 %) from Alfa Aesar (Thermo Scientific Chemicals) was used for the etching process.

2.3 PCB substrate

For the production of the PCB substrate, (100 x 100 x 0.8–2) mm^3, corresponding amounts of aqueous CNF suspension and BC sheets were dewatered. For this, the CNF and BC was pressed in a specially designed compression mold (Figure 1) in a laboratory hot press (Carver Inc., Wabash, IN, USA). The mold allows drainage of the escaping water due to the use of several layers of metal mesh inside the mold and holes in the base plate as well as the plunger body of the mold. Dewatering was carried out manually controlled under continuous pressure increase (0 – 11 t) for 1 h and at constant 11 t to for another hour. Subsequently, the dewatered CNF and BC plates were dried in a convection oven under a weight of 10 kg and at 100 °C for 12 h.

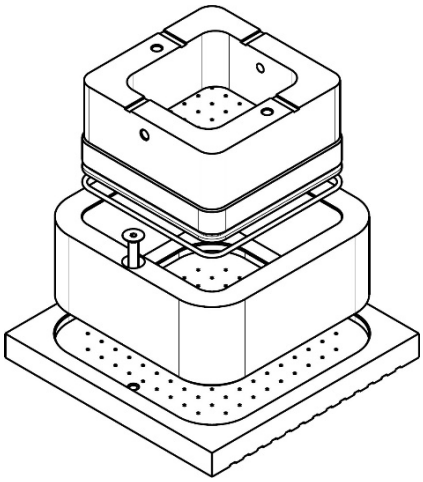

  doi:10.5075/epfl-298799_978-2-9701614-0-0

Figure 1. Specially designed compression mold with drainage channels.

2.4. Three-point flexural and tensile testing

Three-point flexural and tensile tests were carried out with a universal testing machine 1120 (ZwickRoell GmbH & Co. KG, Ulm, Germany) at 23 °C and 50 % RH following the standards DIN ISO 178 and DIN EN ISO 527-2, respectively. Five specimens each for the flexural and tensile tests were fabricated by laser cutting from the previously dewatered and dried CNF and BC substrates and stored under controlled climate conditions (23 °C and 50 % RH) for 72 h.

2.4 Etching

Rectangular pieces with a size of (60 x 33) mm^2 were sawn out of the previously dewatered CNF and BC boards to be used as PCB substrates. The substrates were covered with a self-adhesive copper foil. The track layout of a regenerative circuit (astable multivibrator) was used as example, which was printed mirror-inverted on a thin glossy catalog page with a laser printer. It is important that the melted toner is not absorbed from the glossy paper during the xerographic printing process. In the next step, an ethanol-acetone mixture (1:1) is spread dropwise onto the copper surface of the substrate and the glossy paper with the toner tracks was carefully placed with the toner side down on the solvent film. After a swelling time of 40 s and a light contact pressure of 30 s, the solvent was allowed to evaporate completely after another two minutes. Removal of the glossy paper and thus toner transfer to copper surface is achieved by rinsing in cold water. The toner remains on the copper surface as a mask. For the etching, the substrate was immersed in an aqueous ferric-(III)-chloride solution (40 wt. %) at 50 °C for 15 min until the unmasked copper was completely dissolved. Finally, the toner and all other residues were dissolved with acetone and removed from the remaining copper tracks.

2.5 Assembling

All electronic through-hole components required for the astable multivibrator are mounted with their wire leads passing through the board and being soldered to the copper tracks on the other side. The holes required for the leads were previously drilled into the substrate. Soldering was carried out with a soldering iron using lead-free Sn99.3/Cu0.3 solder at 270 °C. The contact time of soldering iron, solder, electronic component and PCB substrate was kept as short as possible in order to obtain a homogenous connection between leads and tracks and avoiding heat damage of the components. An astable multivibrator assembled on a copper laminated and etched glass fiber-reinforced epoxy resin substrate was used as reference.

2.4. Composting

A 200 liter plastic compost bin was completely filled with organic material (grass, leaves, forest soil, potting soil and compost activator) and kept moist for two weeks. Afterwards, half of the material was removed again and complete PCBs with CNF, BC and epoxy substrates (five each) were placed within the compost. The bin was then refilled and sealed again. The location of the compost was chosen so that it was exposed to alternating weather conditions. After 154 days (5 months), the bin was opened again. During this period, no organic material was added or removed and complete drying was prevented by moderate addition of water. The resulting soil was removed in layers down to the original location of the PBCs and then any material that had not decayed was collected, cleaned, and identified.

  doi:10.5075/epfl-298799_978-2-9701614-0-0

3. Results and Discussion

Fibrillary cellulose structures, formed by the supramolecular arrangement of cellulose macromolecules, originate either from the cell wall of wood generated during the growth of a tree, or from pellicles built up during the fermentation of glucose by bacteria. While the isolation of these cellulose fibrils requires delignified wood pulp to be broken down chemically and mechanically, the cellulose fibrils in the gel-like pellicles are already present in an isolated state. Both suspensions, CNF and BC, have in common that water stabilizes the cellulose fibrils and prevents renewed build-up of the hydrogen bonds among the fibrils and thus aggregation (hornification). For the production of mechanically stable and rigid PCB substrates, it is necessary to compress and dewater the cellulose fibrils (CNF or BC) back to their maximum material density of 1.5 g/cm^3. A number of publications described combinations of (thermo)-compression and drying steps with intensively homogenized CNF to form sheets of millimeter thickness [6-8]. BC gel sheets were usually only dried and pressed to thin paper-like layers [9-11]. Using a specially developed dewatering mold (Figure 1), we were able to show that CNF and BC can also be compressed easily by compression using a slow pressure build-up to 11 t and post-drying at 100 °C under a weight pressure of 10 kg. Figure 2 shows the CNF and BC substrates cut to size for PCB fabrication and the reference, a substrate of glass fiber-reinforced epoxy.

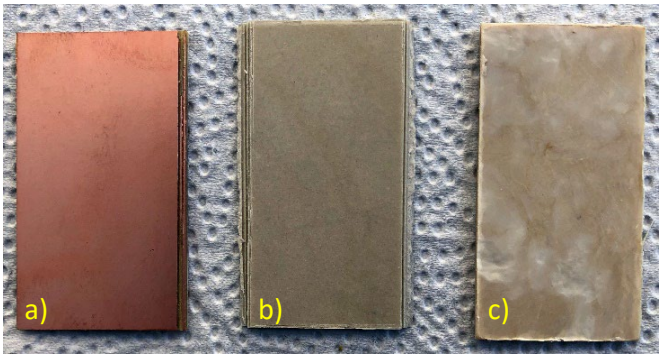

Figure 2. PCB substrates – a) glass-fiber reinforced epoxy with copper layer, b) CNF, c) BC

Substrates acting as a starting product for the manufacture of PCBs must have specific properties, such as high temperature resistance, good mechanical and chemical properties, as well as a low coefficient of thermal expansion, in order to withstand various loads during operation. These requirements are very well met by filled resins. In addition to the epoxy resins already mentioned, phenolic resins, cyanate esters, polyimides or Teflon are reinforced with various fillers, such as glass fiber or Kevlar fibers. In addition, the substrates must be flame retardant and pass the UL94 test. To achieve this, flame retardants are added to the resins. Minimum requirements and test methods are divided into classes FR-1 to FR-6 in the NEMA standards that govern PCB substrates [12].

The chemical and physical properties of cellulose are well known [13], and the authors are aware that not all properties of commercial PCB substrates based on, for example, glass fiber-reinforced epoxy resin can be achieved. This work aims to show a sustainable and environmentally friendly alternative. One property of cellulose fibrils is their mechanical stability, which can be transferred to the millimeter-thick substrates. In the framework of mechanical analyses, bending properties, with a flexural modulus of about 11 GPa and a flexural

  doi:10.5075/epfl-298799_978-2-9701614-0-0

strength of about 200 MPa, and tensile properties, with a tensile modulus of about 11 GPa and a tensile strength of about 120 MPa, were determined for samples made of CNF. In the case of the BC substrates, a flexural modulus of about 19 GPa and a flexural strength of about 197 MPa, and tensile properties, with a tensile modulus of about 21 GPa and a tensile strength of about 115 MPa have been determined (Table 1). It is important to note that all measurements were performed under the climate conditions of 23 °C and 50 % RH. Much higher moduli and strength values are obtained when the specimens are fully dried and stored and measured under exclusion of humidity (details are described elsewhere). At a density of 1.5 g/cm^3, the flexural and tensile moduli of compacted cellulose samples are almost in the range of fiber-reinforced composites.

Table 1: Results of the mechanical analyses of CNF and BC substrates at 23 °C and 50 % RH.

	flexural modulus [GPa]	flexural strength [MPa]	tensile modulus [GPa]	tensile strength [MPa]
CNF	11	200	11	120
BC	19	197	21	115

For the fabrication of the complete PCBs with all electronic components (Figure 3), a wet chemical process was deliberately applied for etching the copper traces and low temperature solder wire was used for not stressing the substrates in consequence of harsh process conditions. Neither the solvent-induced toner transfer from the carrier paper to the copper foil nor the etching in aqueous ferric chloride solution had any apparent substantial effect on the dimensional stability of the CNF and BC substrates. Likewise, no delamination of the entire copper foil or copper traces was observed after the solvent exposure, complete cleaning and soldering of the electrical components. It is also noteworthy that a short-term high temperature exposure to 270 °C through the soldering iron and solder tin, apparently did not lead to degradation of the CNF or BC.

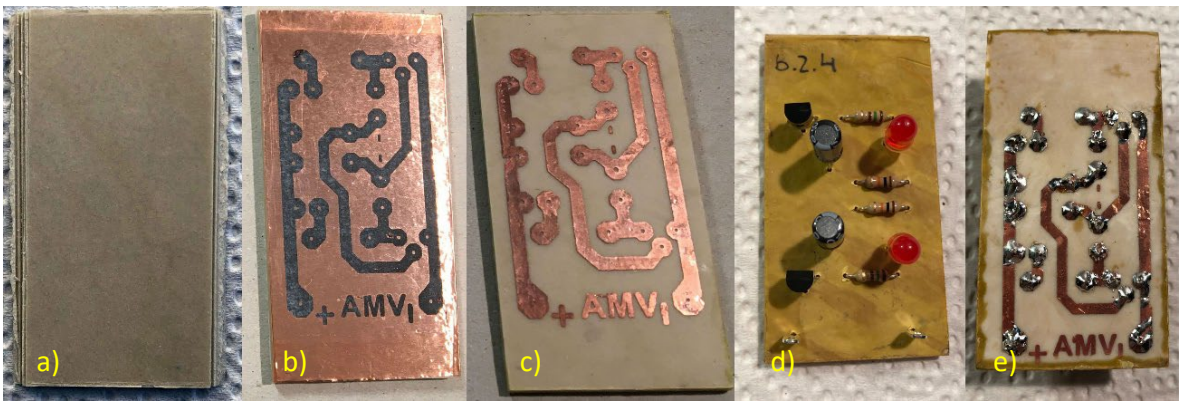

Figure 3. Process steps in PCB fabrication - a) CNF substrate, b) masked copper foil on CNF substrate, c) etched copper tracks on CNF substrate, d) soldered electronic compounds on CNF substrate, e) back of CNF substrate with tracks and soldered wire leads.

The astable multivibrator was operated by connecting a 9 V block battery, with the LEDs flashing alternately. After several months of in-house storage under non-controlled climate-conditions

  doi:10.5075/epfl-298799_978-2-9701614-0-0

of around 20–24 °C and 40–60 % RH, the CNF and BC substrates showed no change in their dimensions, no delamination of the tracks was detected and the electrical circuit with its components was still fully functional.

After the end of life of the PCBs, separation and recycling of all components is essential for environmental protection. In the case of the CNF and BC substrates, incineration of the cellulose can be considered, but this may be disadvantageous in terms of air pollution due to the electronic components. Alternatively, the authors suggest biodegradation of the cellulose in a compost. It is assumed that all other components of the PCBs are almost inert to the compost environment and can be easily separated from the newly formed soil after degradation of the cellulose. Figure 4 shows the compost bin with organic filling and the PCBs placed inside the compost. Figure 5 shows close-ups of a degraded CNF-PCB and an epoxy-PCB after five months of composting in the soil. A selection (Figure 6) of almost separated electronic components and copper traces as well as preserved epoxy-PCBs are presented.

Figure 4. a) Compost bin with organic filling,
b) CNF, BC and epoxy PCBs placed inside the compost.

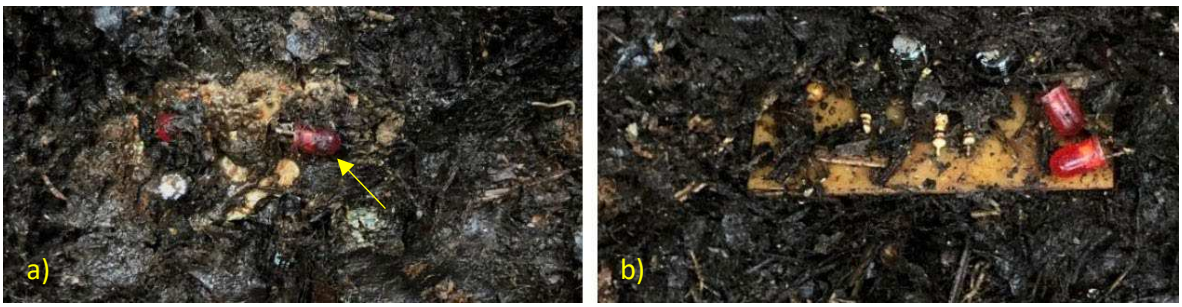

Figure 5. a) Fully degraded CNF substrate (an LED can be seen in the center of the image),
b) well preserved PCB made of glass fiber reinforced epoxy.

In summary, it can be stated that the cellulose was completely biodegraded under the conditions prevailing in the compost. Remarkably, the copper, tin, wire, and plastic of the components did not appear to have a direct effect on the degradation of the cellulose. The references (fiber-reinforced epoxy PCBs) were removed from the soil almost undamaged, and only partial corrosion of the wire leads of the electronic components was observed. The metals and

  doi:10.5075/epfl-298799_978-2-9701614-0-0

electronic components separated from the degraded CNF and BC could now be transferred to further recycling processes.

Figure 6. Selection of PCB copper tracks and electrical components where the cellulose has been completely degraded and intact boards made of glass fiber reinforced epoxy substrate.

4. Conclusion

We were able to present a novel concept for replacing printed circuit board substrates using sustainable cellulose fibrils produced from wood pulp or directly by bacteria. The cellulose nanofibrils and bacterial cellulose can be processed into mechanically stable, rigid boards by dewatering under compression using a special mold and subsequent drying step. The substrates possess exceptional tensile and flexural stiffness and strength, approaching these of fiber reinforced plastic materials. An electronic circuit (astable multivibrator) was realized on these substrates by conventional wet chemical etching of an applied copper foil. The electronic components required for the circuit were connected to the traces by simple soldering with tin solder. The assembled circuit boards were then stored in an outdoor compost for five months. The complete degradation of the cellulose allowed the circuit traces and electronic components to be easily separated from the resulting soil. The authors are aware that essential properties for industrial use, such as hydrophobicity, flammability, arc resistance, permittivity and resistance, still need to be specifically evaluated and studied in detail.

Acknowledgements

Urs Hintermüller and Erwin Pieper are acknowledged for the design and construction of the compression mold as well as the many valuable discussions.

  doi:10.5075/epfl-298799_978-2-9701614-0-0

5. References

1. Géczy A, Nagy D, Hajdu I, Kmetty Á, Szolnoki B, editors. Investigating mechanical performance of PLA and CA biodegradable printed circuit boards. 2015 IEEE 21st International Symposium for Design and Technology in Electronic Packaging (SIITME); 2015 October 2015.
2. Schramm R, Reinhardt A, Franke J, editors. Capability of biopolymers in electronics manufacturing. 2012 35th International Spring Seminar on Electronics Technology; 2012 May 2012.
3. Guna VK, Murugesan G, Basavarajaiah BH, Ilangovan M, Olivera S, Krishna V, et al. Plant-Based Completely Biodegradable Printed Circuit Boards. IEEE T Electron Dev. 2016;63(12):4893-8.
4. Zhan MJ, Wool RP. Design and evaluation of bio-based composites for printed circuit board application. Composites Part a-Applied Science and Manufacturing. 2013;47:22-30.
5. Geiger CK. Cellutronic - The circuit board of the future. Graduation work, Cantonal School Zürich Nord; 2020.
6. Yano H, Nakahara S. Bio-composites produced from plant microfiber bundles with a nanometer unit web-like network. Journal of Materials Science. 2004;39(5):1635-8.
7. Yousefi H, Azad S, Mashkour M, Khazaeian A. Cellulose nanofiber board. Carbohydr Polym. 2018;187:133-9.
8. Rol F, Rouilly A, Bras J. Thermo-compression of cellulose nanofibrils. Cellulose. 2019;27(1):25-40.
9. Yamanaka S, Watanabe K, Kitamura N, Iguchi M, Mitsuhashi S, Nishi Y, et al. The Structure and Mechanical-Properties of Sheets Prepared from Bacterial Cellulose. J Mater Sci. 1989;24(9):3141-5.
10. Skvortsova ZN, Gromovykh TI, Grachev VS, Traskin VY. Physicochemical Mechanics of Bacterial Cellulose. Colloid Journal. 2019;81(4):366-76.
11. Li Z, Li X, Ren J, Wu B, Luo Q, Liu X, et al. Robust All-Cellulose Nanofiber Composite from Stack-Up Bacterial Cellulose Hydrogels via Self-Aggregation Forces. J Agric Food Chem. 2020;68(9):2696-701.
12. https://www.nema.org/
13. Dufresne A. Nanocellulose: From Nature to High Performance Tailored Materials, Berlin, Boston: De Gruyter, 2017.

  doi:10.5075/epfl-298799_978-2-9701614-0-0

SANDWICH TYPE SHAPE MEMORY POLYMER COMPOSITE ACTUATORS TO INCREASE THE RECOVERY MOMENT AND DEFORMABILITY

Dajeong Kang [a], Jae-moon Jeong[a], Kwang Ill Jeong[a], Seong Su Kim[a]

a: Department of Mechanical Engineering, Korea Advanced Institute of Science and Technology, 291 Daehak-ro, Yuseong-gu, Daejeong 305-701, Republic of Korea – dajeong0115@kaist.ac.kr

Abstract: *As the space technologies continue to accelerate, large space structures such as satellite panels and reflectors are needed. Therefore, to enable the efficient storage of such large space structures into limited spacecraft space, deployable structures have become key technologies. Shape memory polymer composites (SMPCs) are promising next-generation materials that have the ability to return from a deformed shape to their original shape when induced by an appropriate stimulus with several advantages like lightweight and high mechanical properties. However, the trade-off relationship between deformability and recovery moment should be resolved to fulfill the requirements of simultaneous improvement on deformability and recovery moment. In this study, novel structural design is proposed to solve this problem. New concept of a sandwich type SMPC bending actuator is suggested with two features: multiple neutral axes skins and a deployable core.*

Keywords: Shape memory polymer composite, Multiple neutral axes, Deployable core, Recovery moment, Deformability

1. Introduction

Space deployable structures allow the further space development by transporting large structures into space with efficient packaging [1, 2]. In order to change the large volume of the space structures extremely, actuators that change the space structure configurations should have large recovery force and deformability. Up until now, electric motor-based actuators have been used for most space deployable structures due to their high driving force. Although, the problems still remain such as the heavy weight and complexity [3]. Therefore, shape memory polymer composites (SMPCs) have emerged as one of the promising materials that can alternate the conventional actuators with shape memory ability [3, 4]. SMPCs are the materials that have enhanced mechanical properties than shape memory polymers (SMPs) themselves with fillers inside. Among many fillers such as carbon nanotube (CNT) [5], carbon fiber [6], and carbon black [7], continuous carbon fiber reinforced SMPCs are the most widely studied materials as structural materials due to their high specific stiffness and strength. However, continuous carbon fiber reinforced SMPC actuators have a critical trade-off relationship between the recovery moment and deformability since keeping their thickness thin for large deformability causes the limitation on the recovery moment increase [8]. Therefore, in this study, a novel structural design of SMPC actuator which includes the mechanisms for the simultaneous increase of the recovery moment and deformability was introduced. A new concept of sandwich type bending actuator was designed and fabricated with two features: multiple neutral axes

  doi:10.5075/epfl-298799_978-2-9701614-0-0

(MNA) skins and a deployable core. Each feature has its own mechanical purpose to the sandwich type bending actuator. In order to improve deformability, MNA skin was designed with two SMPC layers and a polydimethylsiloxane/ethodxylated polyethylenimine (PDMS/PEIE) soft layer [9]. Furthermore, in order to increase the recovery moment, a deployable core was applied, which changes its height through compression and deployment during the shape memory process.

2. Experimental

2.1 Fabrication

In order to fabricate the SMPC skin, epoxy-based SMP resin (YD-114, Kukdo chemical, Republic of Korea) was mixed with curing agent (D230, Kukdo chemical, Republic of Korea) with mixing ratio of 3:1 in weight, and carbon fabric (T700-12K twill, Saenal Tech Tex, Korea) was impregnated with this solution. Compression molding was performed to cure the SMPC skin at 120°C for 2h. After demolding, cured SMPC was cut into 30 mm in width and 200 mm in length.

MNA skin was fabricated with the following procedures. First, PDMS (Sylgard184, Dowcorning, USA) base, curing agent, and PEIE solution (80% solution of ethoxylated Polyethylenimine, 37 wt% in H2O, average Mw = 100,000, Sigma-Aldrich, USA) was mixed with mixing ratio 10:1:0.08 in weight. Second, to enhance the interlayer adhesion force, the surface of the prepared SMPC skin surface was treated by oxygen plasma (Covance, Femto Science, Korea) with plasma etch mode of 100 W for 30 s. Third, the space between the two plasma-treated SMPC skins was filled with the PDMS/PEIE solution, and then the specimen was cured in a vacuum oven at 90°C for 8h. Table 1 shows the information of the SMPC skins and MNA skins that are examined in this paper.

Table 1: Different types of SMPC skins.

ID	Hard layer [mm] * number of layers	Soft layer [mm]	Total thickness [mm]	Layer feature
SMPC 1	0.5 *1	-	0.5	-
SMPC 2	1.0*1	-	1.0	-
SMPC 3	1.5*1	-	1.5	-
SMPC 4	2.0*1	-	2.0	-
MNA 1	0.5*2	0.5	1.5	Hard layer / Soft layer / Hard layer
MNA 2	1.0*2	0.5	2.5	Hard layer / Soft layer / Hard layer

  doi:10.5075/epfl-298799_978-2-9701614-0-0

2.2 Shape memory process

The shape programming process and the recovery process of the sandwich type SMPC bending actuator is shown in Figure 1. In the shape programming process, deformation was performed with the two steps, compression and bending. Universal testing machine (Instron 4469, Instron Corp, USA) and heating chamber was used for the deformation. Specifically, inside the heating chamber, specimens were heated up above the T_g (48.4°C) which is 70°C and the compression was performed with the head speed of 2mm/min. After deformation, specimens were cooled down to the room temperature and maintained the compressed shape. Thereafter, bending was applied with a bending jig that has 15 mm bending radius at the tip.

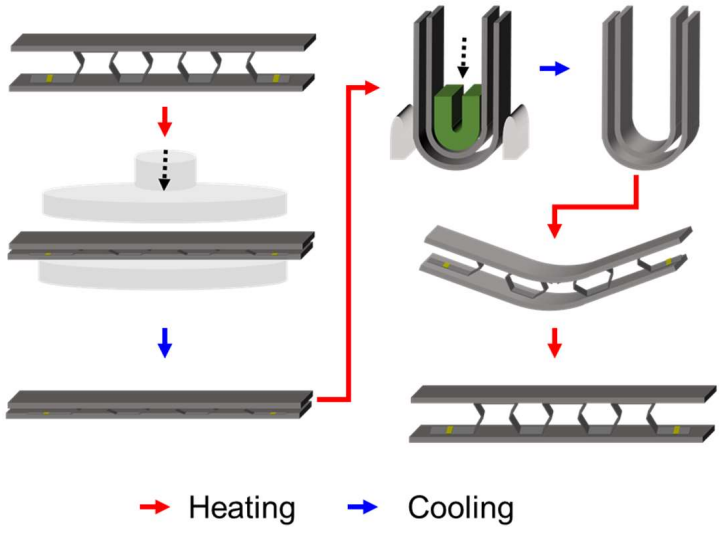

Figure 1. Shape memory process

2.3 Shape memory process

Failures can affect the degradation of the recovery moment so the surface morphology was conducted to check the failures and its negative influence on the performance. Continuous carbon fiber is more fragile to compression than tension. For this reason, failures are likely to happen on the inner surface under the bending deformation, which is caused by the micro-buckling generation when the temperature is above T_g. Therefore, the surface image of the deformed specimen inner surface was investigated after the shape programming process.

2.4 Recovery moment measurement

The recovery moment measurement system is composed of a 100 N load cell, fixed bar, and Arduino board. In order to measure the recovery force, one end of the SMPC actuator contacts the fixed bar and the other side of the actuator is attached to the load cell. Reaction force was measured when the attached specimen end pushes the load cell as the temperature rises. Until the load cell reaches the maximum force, the specimen was fixed at the initial bending angle. The load cell signal was converted to the force and displayed. The recovery moment was calculated from the force using following conversion equation (1) [10]:

  doi:10.5075/epfl-298799_978-2-9701614-0-0

$$M = r \times F_{measured} = (l_1 + l_2)F_{measured} = \left(l_1 + \rho cos\left(\frac{\theta}{2}\right)\right)F_{measured} \quad (1)$$

where r is the moment arm; $F_{measured}$ is the force measured from the load cell as shown in Figure 2.

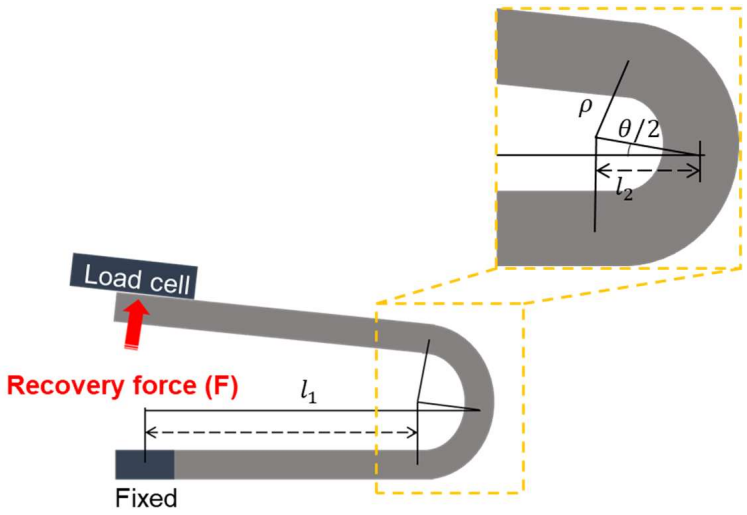

Figure 2. Schematic of the recovery moment measurement system

3. Discussion

3.1 MNA skin

Figure 3(a) shows the inner surfaces of the bent SMPC 1-4. In the SMPC 1 and 2, only small wrinkles or micro-buckling were observed without any significant failures. Whereas, with the SMPC 3 and 4, the unrecoverable large size micro-buckling was observed resulting in significant failures including fiber breakage and delamination. This is because as the SMPC skin thickness increases, the maximum compressive strain at the innermost surface increases substantially. However, as shown in figure 3(b) in case of the MNA 1, it showed a smooth surface with only as small degree of the micro-buckling as SMPC 1 even though its thickness of the total SMPC layer is twice of SMPC 1. The reason why the degree of the micro-buckling was kept small without failures is that a large amount of shear strain occurred in the soft PDMS/PEIE layer in the case of the MNA 1 and 2. Due to the large difference of the SMPC stiffness (31.3 GPa) and PDMS/PEIE (79.5 kPa) stiffness, as the PDMS/PEIE layer is inserted between the SMPC layer, multiple neutral axes are generated at each SMPC layer as shown in figure 3(c). Subsequently, the tensile and compressive axial strain significantly decreases, and the multiple neutral axes increased the deformability of MNA 1 [11, 12]. The same tendency was captured as well in MNA 2 in comparison with SMPC 2 and 4. Moreover, multiple neutral axes effect on deformability was dramatically increased. The surface of the MNA 2 had only wrinkles or micro-buckling without any severe failures that were observed at the surface of the SMPC 4 in spite of having the same total SMPC layer thickness. The degree of the micro-buckling and wrinkles of MNA 2 were similar to SMPC 2 that has half of the SMPC layer thickness.

  doi:10.5075/epfl-298799_978-2-9701614-0-0

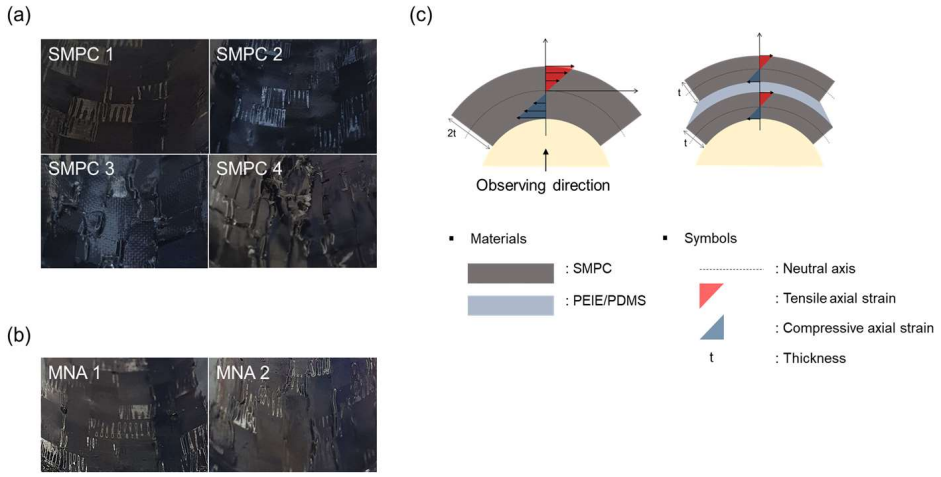

Figure 3. Inner surface image of SMPC 1-4 (a) and MNA 1 and 2(b). Schematic of the multiple neutral axes effect(c).

Figure 4(a) shows the recovery moment of the SMPC 1-4, and MNA 1 and 2. As the thickness of SMPC increased, the recovery moment increased. As shown in figure 4(b) MNA 1 showed the recovery moment of 14.58 N·cm and it is 212% larger and 11% smaller than that of the SMPC 1 and SMPC 2 respectively. This is because MNA 1 is composed of two SMPC 1 layers and the total amount of stored strain energy which transforms to the recovery moment was increased. In the meantime, owing to the existence of the PDMS/PEIE layer, the magnitude of the axial strain inside the SMPC layers in MNA 1 is smaller than that of the SMPC 2 and it led to the smaller amount of stored strain energy in MNA 1. On the other hand, in case of the MNA 2, recovery moment showed 50.40 N·cm and it is not only 211% larger than that of SMPC 2 but also 40% larger than that of SMPC 4. This result demonstrates that unlike MNA 1, MNA 2 is located under that condition where MNA effect can effectively prevent the failures like matrix crack and fiber breakages. Consequently, MNA 2 has a larger recovery moment with enhanced deformability than SMPC 4 by preventing energy loss resulted from failures.

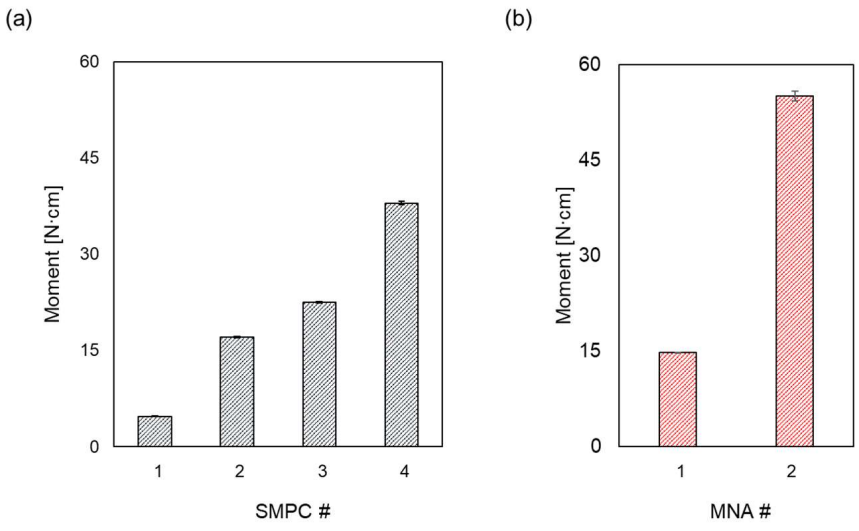

Figure 4. Recovery moment of SMPC 1-4(a) and MNA 1 and 2(b)

  doi:10.5075/epfl-298799_978-2-9701614-0-0

3.2 Deployable core

Figure 5 shows the recovery moment of the sandwich type SMPC bending actuators. First two sandwich type actuators with SMPC 2 as skins were measured under the two different conditions: core fixed and core free. Wherein core fixed condition means that the deployable core was tied and not able to recover its original height during the shape recovery process. On the other hand, core free condition means that the deployable core is free to recover. The recovery moment under core free condition was 92.10 N·cm which is 46% larger than that under the core fixed condition. This recovery moment gap comes from the existence of the deploying force of the deployable core during the shape recovery process.

In order to maximize the recovery moment of the sandwich type SMPC bending actuator, MNA 2 that has as large deformability as SMPC 2 replaced SMPC 2 as skins. The recovery moment showed 143.30 N·cm which is 56% larger than that of the sandwich type bending actuator with SMPC 2 as skins.

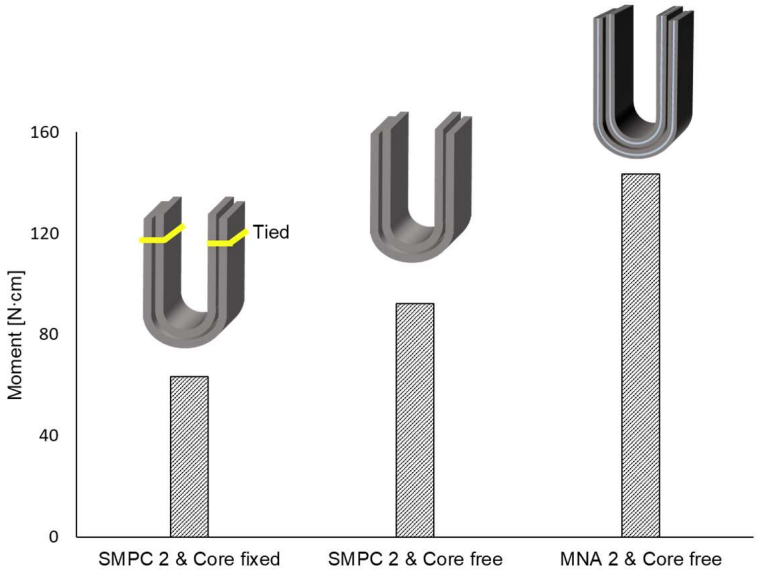

Figure 5. Recovery moment of the sandwich type SMPC bending actuators

4. Conclusion

This study suggested a new sandwich type SMPC bending actuator to obtain improved performance in terms of the deformability and the recovery moment with its two unique features: multiple neutral axes (MNA) skins and deployable core. The effect of MNA skins and deployable core on simultaneous enhancement of the deformability and recovery moment were analyzed through surface morphology and recovery moment measurement. Results obtained from the tests were summarized as follows

(1) Applying multiple neutral axes effect on SMPS skins led to significant strain reduction in SMPC layers in both MNA 1 and 2 when they are under bending deformation. In

  doi:10.5075/epfl-298799_978-2-9701614-0-0

particular, failures of MNA 2 were prevented owing to the large shear strain inside the PEIE/PDMS soft layer.

(2) From the recovery moment comparison, MNA skin 2 rather showed higher recovery moment of 50.40 N·cm than that of SMPC 4 (36.27 N·cm). This is because the soft layer was inserted and the failures which cause the loss of the stored deformation energy were effectively prevented.

(3) By exploiting the shape memory effect of the deployable core, recovery moment was increased with the contribution of the core deploying force during the shape recovery process.

Acknowledgements

This work was supported by the National Research Foundation of Korea(NRF) grant funded by the Korea government(MSIT) (No. 2020R1A2C201096512).

References

[1] Gantes CJ, Connor JJ, Logcher RD, Rosenfeld Y. Structural analysis and design of deployable structures. Computers & Structures. 1989;32(3-4):661-9.
[2] Hanaor A, Levy R. Evaluation of deployable structures for space enclosures. International Journal of Space Structures. 2001;16(4):211-29.
[3] Leng J, Lan X, Liu Y, Du S. Shape-memory polymers and their composites: stimulus methods and applications. Progress in Materials Science. 2011;56(7):1077-135.
[4] Li F, Liu Y, Leng J. Progress of shape memory polymers and their composites in aerospace applications. Smart Materials and Structures. 2019;28(10):103003.
[5] Bai Y, Zhang Y, Wang Q, Wang T. Shape memory properties of multi-walled carbon nanotube/polyurethane composites prepared by in situ polymerization. Journal of Materials Science. 2013;48(5):2207-14.
[6] An Y, Yu W-R, editors. Three-dimensional printing of continuous carbon fiber-reinforced shape memory polymer composites. AIP Conference Proceedings; 2019: AIP Publishing LLC.
[7] Leng J, Lv H, Liu Y, Du S. Synergic effect of carbon black and short carbon fiber on shape memory polymer actuation by electricity. Journal of Applied Physics. 2008;104(10):104917.
[8] Lan X, Liu L, Liu Y, Leng J, Du S. Post microbuckling mechanics of fibre-reinforced shape-memory polymers undergoing flexure deformation. Mechanics of Materials. 2014;72:46-60.
[9] Jeong SH, Zhang S, Hjort K, Hilborn J, Wu Z. PDMS-based elastomer tuned soft, stretchable, and sticky for epidermal electronics. Advanced Materials. 2016;28(28):5830-6.
[10] Dao TD, Goo NS, Yu WR. Blocking force measurement of shape memory polymer composite hinges for space deployable structures. Journal of Intelligent Material Systems and Structures. 2018;29(18):3667-78.
[11] Shi Y, Rogers JA, Gao C, Huang Y. Multiple neutral axes in bending of a multiple-layer beam with extremely different elastic properties. Journal of Applied Mechanics. 2014;81(11):114501.
[12] Su Y, Li S, Li R, Dagdeviren C. Splitting of neutral mechanical plane of conformal, multilayer piezoelectric mechanical energy harvester. Applied Physics Letters. 2015;1(4):041905.

  doi:10.5075/epfl-298799_978-2-9701614-0-0

SUPERCRITICAL CO_2 ASSISTED FOAM EXTRUSION FOR AERONAUTICAL SANDWICH STRUCTURE MANUFACTURING

Evangelos DIMOS[a], Raffaele D'ELIA[a], Martial SAUCEAU[b], Romain SESCOUSSE[b], Luis QUIROGA CORTES[a], Leonardo SANCHES[c] and Guilhem MICHON[c]*

a: IRT Saint-Exupéry, 3 rue Tarfaya – CS34436 – 31405 Toulouse Cedex 4, France
b: Centre RAPSODEE, IMT Mines Albi, CNRS, Université de Toulouse – 81013 Albi, France
c: Université de Toulouse, ISAE, ICA, CNRS, 3 rue Caroline Aigle – 31400 Toulouse, France

* corresponding author (raffaele.delia@irt-saintexupery.com)

Abstract: *Sandwich structures represent a very interesting approach for the development of new multifunctional and lightweight materials for aerospace and space applications. Nomex® or aluminum honeycomb is at this date the most widely used core materials for sandwich structures, given their extraordinary strength-to-weight-ratio. However, these materials exhibit some important drawbacks as a poor vibrational and acoustic damping [1], along with a limited impact energy absorption capability. Several studies are in progress in order to develop new composite materials with enhanced acoustic and vibrational damping properties [2-8]. A very promising solution to overcome these issues is represented by thermoplastic foams, having several advantages as ease of processing, good impact energy absorption, recyclability and enhanced properties in terms of thermal and acoustic isolation [9-12], along with the possibility to modify their intrinsic properties through micro and nano-particles addition.*

A relatively new and promising technique to develop thermoplastic foams is represented by supercritical CO_2 (sc-CO_2) assisted foam extrusion [13,14], with sc-CO_2 acting as Physical Blowing Agent (PBA). Sc-CO_2 has limited environmental impact, given its low toxicity and energetic requirements to attain its supercritical conditions (31 C, 74 bars), making this process economic, sustainable and totally green. In the frame of this work, a continuous process has been used to produce PLA foams with different microstructures depending on the operating conditions. Typical densities range from 20 to 60 kg/m^3, crystallinity from 10 to 30 % and cell size from 90 to 500 µm.

Keywords: Supercritical CO_2, PLA polymer, extrusion foaming, sandwich structures, aeronautical materials

1. Introduction

Classic sandwich structures are widely used in several industrial sectors but have significant shortcomings such as low damping and sound insulation rates [1], as well as low impact resistance. In aeronautical structures, noise can have significant effects on the health of passengers and aircrew [15] and several studies are in progress with the aim of developing new solutions with enhanced sound insulation [2-6, 16]. Through its potentially nonlinear viscoelastic properties, the intrinsic damping of the core material influences the amplitude of the vibration and acoustic response of the structure. Thus, the study of the vibro-acoustic behavior of the core material is fundamental.

  doi:10.5075/epfl-298799_978-2-9701614-0-0

A promising solution is to use cellular core materials such as thermoplastic polymer foams. Poly lactic acid (PLA) is a biopolymer that has been extensively studied in recent years, due to its promising potential in reducing waste by replacing petroleum-based polymers. Indeed, PLA monomers can be derived from renewable sources such as corn starch [17,18]. Furthermore, PLA has been considered as a non-toxic/eco-friendly polymer, with a good combination of mechanical properties and ease of processing. This family of materials has in fact several advantages, such as ease of implementation, the ability to absorb energy during an impact (resilience), recyclability and increased properties in terms of thermal and acoustic insulation [19,22]. Moreover, their intrinsic properties can be easily optimized by the dispersion of nano or micro particles.

In this context, the development of alveolar composites shows significant scientific and industrial interest. A certain number of technologies allow the realization of alveolar structures, most conventional using physical blowing agents (PBA) and chemical blowing agents (CBA) which are incorporated into the molten polymer. The gas formed in situ by chemical reaction (CBA) or injected into the polymer (PBA) will create pores or cells and will thus generate porosity in the polymer. However, the use of these compounds poses several problems: (i) CBAs, which are generally carbonated salts that decompose into gases under the action of heat, leave residues in the polymer after formation of the porous network and their decomposition often requires high temperatures; (ii) PBAs, such as freons (CFCs, HCFCs, etc.), are harmful to the environment by attacking the ozone layer or, like hydrocarbons such as pentane or butane, pose safety issues due to their flammability.

Supercritical fluid technology, and more particularly supercritical CO_2 (sc-CO_2), could respond to these problems by offering an alternative free of the aforementioned defects [14]. It is widely described in the literature and, in recent years, has been extensively studied with biopolymers in order to manufacture "green" foams with a clean process. The process has also been applied to technical thermoplastics such as polyphenylene sulphide and polyamide [23-26], but only with batch foaming processes which involve long implementation times, in particular for the saturation of the polymer by the fluid under pressure. It is possible to overcome these very long saturation times and thus increase the production rate by carrying out the polymer-supercritical fluid mixture continuously in an extruder [27-30]. In this continuous process, the polymer is melted, then sc-CO_2 is injected and the mixing actions of the extrusion screw allow to obtain a single-phase mixture. Nucleation then takes place at the injection point. However, the injection process remains a semi-discontinuous process and it seems relevant to think about a totally continuous implementation to reach the highest production rates.

The purpose of the study concentrated in the manufacturing of polymer foams and tested their properties in order to come to a stage that could be integrated in aeronautical structures. At a first stage, an extrusion foaming process of PLA polymer was examined at different operating conditions. Samples with a range of porosity were managed to be fabricated.

2. Materials and methods

2.1. Materials

The basic raw materials used in this study are PLE 005-A from NaturePlast supplied in the form of granules and a sc-CO_2 fluid used as physical blowing agent.

  doi:10.5075/epfl-298799_978-2-9701614-0-0

2.2. Extrusion foaming process

Experiments of extrusion foaming are performed on a single-screw extruder, described in details in previous publications [14]. A schematic representation of the equipment is shown in Figure 1. The single-screw extruder has a 30 mm screw diameter and a length-to-diameter ratio (L/D) of 37 (Rheoscam, Scamex). PLA is inserted into the hopper, while the screw drives the transportation of the solid granulated polymer to the end of the extruder where a die is placed. Along the way towards the exit, the polymer is melted and subsequently mixed with sc-CO_2. The foaming process of the polymer takes place when it flows out from a homemade die.

The extruder is thermo-regulated at six locations: T_1 and T_2 before the CO_2 injection port, T_3 and T_4 after the injection port, T_5 in the static mixer and T_6 at the die. There are three temperature and four pressure sensors: P_1 after the CO_2 injector, P_2 and T_{mat1} before the second gastight ring, P_3 and T_{mat2} before the static mixer and P_4 and T_{mat3} close to the die.

The sc-CO_2 is injected into the extruder using a syringe pump (260D, ISCO) between the second and the third temperature control device at the same pressure as that of the polymer (P_1). The screw rotation speed is kept constant at 30 rpm during the whole experiment and a constant volume flow rate of sc-CO_2 (Q_{CO2}) is used. Temperatures T_1 to T_4 are kept constant, while T_5 and T_6 are progressively decreased while keeping them equal. Samples are collected once a steady state is established [27-30].

The mass fraction of CO_2 ω_{CO2} in the CO_2-polymer mixture is calculated as follows:

$$\omega_{CO2} = \frac{Q_{CO2}\rho_{CO2}^{pump}}{Q_{CO2}\rho_{CO2}+\dot{m}_p} \quad (1)$$

$\dot{m}_p$ is the mass flow rate of the polymer measured by weighing outside of the die and ρ_{CO2}^{pump} is the density of CO_2, in the pump. This density is obtained from NIST website [31].

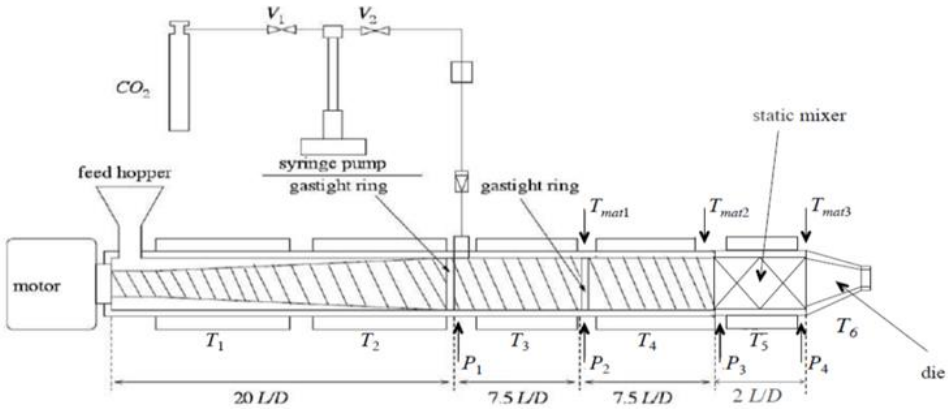

Figure 1. The experimental system used [25].

2.3. Influence of operating conditions on porosity

The supercritical CO_2 assisted extrusion process has shown that the expansion rate or the type of porosity were dependent on temperature. Indeed, with a die temperature too high, a loss of CO_2 is present which limits the expansion of the foam. Decreasing the temperature of the die, the surface of the foam is more quickly solidified and retains CO_2. Moreover, with the decrease in temperature, the diffusion of gas at the surface of the polymer decreases and therefore more gas remains in the foam to contribute to its expansion. However, an excessive die temperature

  doi:10.5075/epfl-298799_978-2-9701614-0-0 published under CC BY-NC 4.0 license

decrease penalizes the expansion, the surface of the extruded sample becoming too rigid and therefore limiting expansion. In the case of a semi-crystalline polymer, this surface stiffening is often related to crystallization. Furthermore, it was observed that the temperature upstream of the die also had an influence while it reduces the coalescence of cells thanks to an increase in the melt strength. The CO_2 content also plays a key role. With decreasing temperature, the viscosity polymer increases which can lead to pressure increases within the extruder. Adding more CO_2 in the extruder plasticizes the polymer and therefore reduces viscosity and pressure, which allows working at lower temperatures [14].

2.4. Foam characterization

Porosity (ε_{sample}) is defined as the ratio of void volume to total volume and is calculated as follows:

$$\varepsilon_{sample} = \frac{v_{porosity}}{v_{Total}} = 1 - \frac{\rho_m^{H_2O}}{\rho_P^{H_2O}} \quad (2)$$

$\rho_m^{H_2O}$, is the apparent density of the foamed sample determined by water pycnometry, while $\rho_P^{H_2O}$ is the density of the solid polymer determined on a sample after extrusion by water pycnometry.

The samples obtained by extrusion foaming process are characterized by Scanning Electron Microscopy (SEM) in order to define the cells microstructure and diameter. Cells diameters (*di*) and surfaces (S_i) are measured using ImajeJ open source software for image analysis. The average cell size of the foamed samples is calculated according to the following equation:

$$d_{sample} = \sum_{i=1}^{n} \frac{S_i d_i}{S_i} \quad (3)$$

Sample crystallinity of the extruded foams is measured using Differential Scanning Calorimetry (DSC), applying a constant heating rate of 10 °C/min from 20 to 200°C to samples obtained directly after the extrusion. For each grade of material five samples of 10-15 mg were tested using sealed aluminum pans. The defined thermal cycle allows evaluating the cold crystallization enthalpy (ΔH_c) and the enthalpy of fusion (ΔH_m). These parameters are necessary to compute the degree of crystallinity (X_c) of the PLA foam, determined according to Equation (4) [13, 14]:

$$X_c = \frac{\Delta H_m - \Delta H_c}{\Delta H_\infty} \quad (4)$$

Where ΔH_∞ is the theoretical enthalpy of fusion of the material equal to 93 J/g [14].

3. Results and discussion

3.1. Porosity of PLA foamed samples

Five samples were taken at the extruder outlet and are listed in table 1. This table indicates the temperature $T_{5\text{-}6}$ of the static mixer and die, the pressure P_4 before the die, the mass fraction of CO_2 ω_{CO2}, porosity ε_{sample}, density $\rho_m^{H_2O}$, diameter d_{sample} and crystallinity X_c.

Figure 2 represents the pressure before the die P_4, and the final material porosity $\rho_m^{H_2O}$, both measured as a function of the final temperature $T_{5\text{-}6}$. The two variables follow a similar tendency,

  doi:10.5075/epfl-298799_978-2-9701614-0-0 published under CC BY-NC 4.0 license

inversely proportional to temperature. Indeed, when the temperature decreases, an increase of the porosity can be observed. This increase is small as the porosity level is already high. The pressure also increases due to the increase of the polymer viscosity, despite the plasticizing effect of the increasing mass fraction of the CO_2.

Table 1: Overview of PLA foamed samples.

N°	$T_{5\text{-}6}$ (°C)	P_4 (bar)	ω_{CO2} (%)	ε_{sample} (%)	ρ_{sample} (g/cm³)	d_{sample} (µm)	X_c (%)
1	110	122	2.5	97.5	0,037	500	7
2	105	135	3	97.6	0,032	380	14
3	100	137	3.5	97.6	0,029	290	12
4	95	145	4	97.9	0,025	220	23
5	90	160	4.5	98.1	0,023	140	24

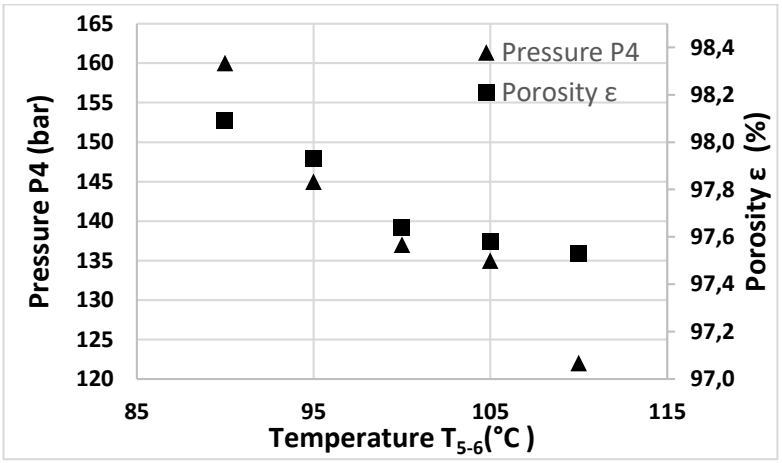

Figure 2. Behavior of porosity in temperature and pressure

3.2. Scanning electron microscope SEM

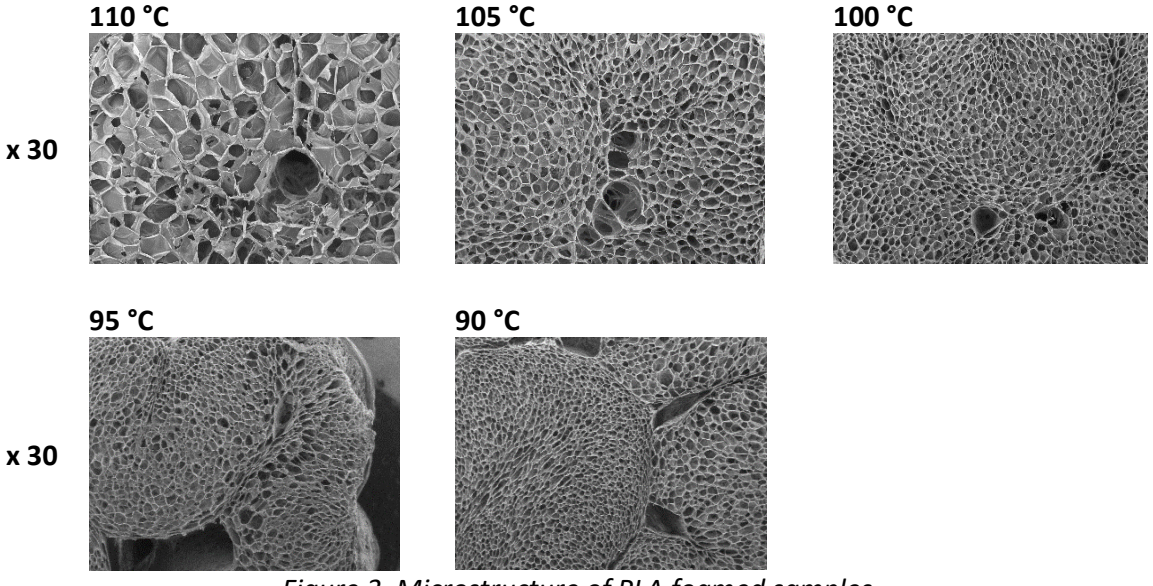

Figure 3. Microstructure of PLA foamed samples

The SEM photomicrographs of the different foams are shown in Figure 3. The images indicate the influence of temperature on the size and number of cells. The first image shows that, at high die temperature, few pores are present, they are very large and the structure is very coarse. All the other images represent that the pores are smaller at lower temperatures. In addition, the pore walls are slightly torn, confirming that the porosity is closed at the same time. The big cell in the middle is due to the annular shape of the die. The average cell diameters are presented in Table 1 (equation 3). It confirms that the mean diameter decreases with the temperature from 500 µm at 110°C to 140 µm at 90°C. This variation with temperature is obtained at a high level of total porosity which is more or less constant and it shows that it is possible to tune the porous structure by means of the temperature.

3.3. Crystallization properties of PLA foamed samples

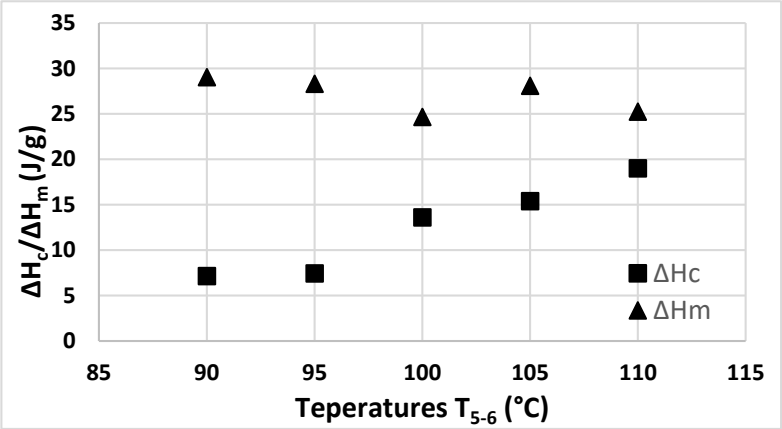

Figure 3. Behavior of crystallinity with temperature

After completing a first heating cycle for all five samples, the crystallinity of the samples was calculated using equation 4. The results are summarized in Table 1 and plotted in Figure 3, where the evolution with temperature of the two enthalpies is presented: the melting enthalpy (ΔH_m) and the cold crystallization enthalpy (ΔH_c). It has to be noticed that the crystallinity X_c is proportional to the difference between these two enthalpies. As the die temperature decreases, the melting enthalpy seems to slightly increase, while a more important evolution is observed for the cold crystallization, which decreases. It results in an increase of the sample crystallinity with decreasing temperature, the sample at the lower temperature (90 °C) having a crystallization degree of 24 %, while the sample at the higher temperature (110 °C) presenting a level of only 7 %.

A possible explanation arises from the viscosity of the polymer, which increases with the temperature decrease. Indeed, this viscosity increase provokes a decrease of the Reynold number (the flowrate being more or less constant) and thus the obtention of a more laminar flow inside the die. This flow evolution is favorable to the organization of the polymer chains and thus to the increase of the degree of crystallinity of the final material.

4. Conclusions

PLA polymer was the principal material used in this study for the foam's fabrication by continuous extrusion foaming. A series of characterization techniques were implemented including water pycnometry in order to determine the apparent density, scanning electron microscopy to reveal the inner structure of cells and differential scanning calorimetric to

  doi:10.5075/epfl-298799_978-2-9701614-0-0

measure the crystallization properties of the foam. All these parameters are strongly influenced by the processing temperature and thus to CO2 mass fraction which has to be increased to reach the lower temperatures. Finally, it is possible to tune the cellular structure of the foam at a high level of porosity (97-98 %) by means of the operating temperatures: a more crystalline porous structure (24 %) with a smaller cell mean diameter (140 µm) can be obtained while a more amorphous one (7 %) with higher cell mean diameter (400 µm) is obtained at higher temperatures. These materials will be further investigated in the following, in order to integrate them in composite sandwich structures and a full study of the acoustic and damping mechanical properties is planned.

5. Acknowledgement

The authors would like to thank the STAE Foundation (Science & Technologies pour l'Aeronautique & l'Espace) for their financial contribution in the ONOMATOPE project (élabOration de NOuvelles Mousses AéronauTiques avec Optimisation des Performances Elasto-plastiques).

6. References

1. Petrone G, D'Alessandro V, Franco F, De Rosa S, Numerical and experimental investigations on the acoustic power radiated by aluminium foam sandwich panels, Compos. Struct. 118 (2014) 170–177.
2. Li Z. Vibrational and acoustical properties of sandwich composite materials. Ph.D. Thesis, Auburn University; 2006.
3. Sargianis, Suhr. Effect of core thickness on noise and vibration mitigation in sandwich composites. Compos Sci Technol 2012; 72:724–30.
4. Liang JZ. Prediction of sound transmission losses for polymer/inorganic particle composites. Polym. Compos. 2015: 36: 2059–2065.
5. Liang JZ, Jiang XH. Sound proofing effect of polypropylene / inorganic particle composites. Compos. B. Eng. 2012; 43: 1995–1998.
6. Zhao HG, Liu YZ, Wen JH, et al. Dynamics and sound attenuation in viscoelastic polymer containing hollow glass microspheres. J. Appl. Phys. 2007; 101: 123.
7. Piolleta, E., Poquillon, D., Michon, G., Dynamic hysteresis modelling of entangled cross-linked fibres in shear, Journal of Sound and Vibration, 383, 248-264, 2016.
8. Quiroga Cortes, L., Sanches, L., Bessaguet, C., Chevalier, M., Lacabanne, C., Dantras, E., G. Michon. Improving damping capabilities of composites structures by electroactive films containing piezoelectric and conductive fillers, Smart Materials and Structures 2021, vol. 30 (8), 085008.
9. Hanssen AG, Girard Y, Olovsson L, Berstad T, Langseth M. A numerical model for bird strike of aluminium foam-based sandwich panels. Int J Impact Eng 2006; 32:1127–44.
10. Hou S, Li Q, Long S, Yang X, Li W. Crashworthiness design for foam filled thinwalled structures. Mater Des 2009; 30:2024–32.
11. Mills NJ, Fitzgerald C, Gilchrist A, Verdejo R. Polymer foams for personal protection: cushions, shoes and helmets. Compos Sci Technol 2003; 63:2389–400.
12. Reglero JA, Rodríguez-Pérez MA, Solórzano E, de Saja JA. Aluminium foams as a filler for leading edges: Improvements in the mechanical behaviour under bird strike impact tests. Mater Des 2011; 32:907–10.
13. Chauvet M, Sauceau M, Fages J. Extrusion assisted by supercritical CO2: a review on its application to biopolymers. J. Supercrit. Fluids, 2017, 120, 408-420.

  doi:10.5075/epfl-298799_978-2-9701614-0-0 published under CC BY-NC 4.0 license

14. Chauvet M. Extrusion assistée par CO2 supercritique appliquée au moussage d'un biopolymère, le poly (acide lactique), seul ou en mélange à de l'amidon : étude expérimentale et modélisation. 2017. Doctorat de l'Université de Toulouse.
15. Mellert V, Baumann I, Freese N, Weber R, Impact of sound and vibration on health, travel comfort and performance of flight attendants and pilots, Aerosp. Sci. Technol. 12 (1) (2008) 18–25.
16. Sargianis J, Suhr J. Core material effect on wave number and vibrational damp- 99 ing characteristics in carbon fiber sandwich composites, Compos. Sci. Technol. 100 72 (13) (2012) 1493–1499.
17. Murariu M, Dubois P. PLA composites: from production to properties. Adv Drug Deliv Rev 2016; 107:17–46.
18. Lasprilla AJ, Martinez GA, Lunelli BH, Jardini AL, Maciel Filho R. Poly-lactic acid synthesis for application in biomedical devices—a review. Biotechnol Adv 2012;30 (1):321–8.
19. Hanssen AG, Girard Y, Olovsson L, Berstad T, Langseth M. A numerical model for bird strike of aluminium foam-based sandwich panels. Int J Impact Eng 2006; 32:1127–44.
20. Hou S, Li Q, Long S, Yang X, Li W. Crashworthiness design for foam filled thinwalled structures. Mater Des 2009; 30:2024–32.
21. Mills NJ, Fitzgerald C, Gilchrist A, Verdejo R. Polymer foams for personal protection: cushions, shoes and helmets. Compos Sci Technol 2003; 63:2389–400.
22. Reglero JA, Rodríguez-Pérez MA, Solórzano E, de Saja JA. Aluminium foams as a filler for leading edges: Improvements in the mechanical behaviour under bird strike impact tests. Mater Des 2011; 32:907–10.
23. Ma Z, Zhang G, Shi X, Yang Q, Li J, Liu Y, Fan X, Microcellular foaming of poly (phenylene sulfide)/poly (ether sulfones) blends using supercritical carbon dioxide. Journal of Applied Polymer Science 132(40), 2015.
24. Liu WH, Huang YM. Carbon Dioxide-Blown Expanded Polyamide Bead Foams with Bimodal Cell Structure. Ind. Eng. Chem. Res., 2019, 58, 2958-2969.
25. Xu M, Yan H, He Q, Wan C, Liu T, Zhao L, Park CB. Chain extension of polyamide 6 using multifunctional chain extenders and reactive extrusion for melt foaming. Eur. Polym. J., 2017, 96, 210-220.
26. Royer JR, Siripurapu S, Henon FE, Genzer J. Processing of polyamide 11 with supercritical carbon dioxide. Ind. Eng. Chem. Res., 2001, 40, 5570-5577.
27. Villamil Jiménez J A, Le Moigne N, Bénézet J C, Sauceau M, Sescousse R, Fages J. Foaming of PLA Composites by Supercritical Fluid-Assisted Processes: A Review. *Molecules* 2020, *25*, 3408.
28. Le Moigne N, Sauceau M, Benyakhlef M, Jemai R, Benezet J C, Rodier E, Lopez-Cuesta J M, Fages F. Foaming of poly(3-hydroxybutyrate-co-3-hydroxyvalerate)/ organo-clays nano-biocomposites by a continuous supercritical CO2 assisted extrusion process. European Polymer Journal, Elsevier, 2014, 61, pp.157-171.
29. Le Moigne N, Sauceau M, Chauvet M, Benezet JC, Fages J. Microcellular foaming of (nano)biocomposites by continuous extrusion assisted by supercritical CO2. In: Biomass Extrusion and Reaction Technologies: Principles to Practices and Future Potential., 2018, Ed.
30. Common C, Rodier E, Sauceau M, Fages J. Flow and mixing efficiency characterisation in a CO2-assisted single-screw extrusion process by residence time distribution using Raman spectroscopy. Chem. Eng. Res. Design, 2014, 92, 1210-1218.
31. NIST. Carbon dioxide, NIST Chemistry WebBook. 2016. url: http://webbook.nist.gov/cgi/cbook.cgi?ID=124-38-9 (cf. p. 61, 62).

  doi:10.5075/epfl-298799_978-2-9701614-0-0

Composites Meet Sustainability – Proceedings of the 20th European Conference on Composite Materials,
ECCM20. 26-30 June, 2022, Lausanne, Switzerland

KINETIC STUDIES AND ITS INFLUENCE ON PHASE TRANSITION BEHAVIOUR OF MULTICOMPONENT AMINE-CURED EPOXY BLEND

Suihua He, Carwyn Ward, Ian Hamerton*

Bristol Composites Institute, Department of Aerospace Engineering, School of Civil, Aerospace, and Mechanical, Engineering, Queen's Building, University Walk, University of Bristol, Bristol BS8 1TR, UK
* Corresponding author (silva.he@bristol.ac.uk)

Abstract: *Isothermal and non-isothermal kinetic studies of liquid processable multicomponent commercial amine-cured epoxy resin were evaluated. The corresponding viscosity development and phase transition behaviour of this amine-cured epoxy blend were investigated. The rate constants of each combination were calculated highlighting the reaction speed between different components in various reaction processes, indicating the reaction probability between each component. As expected, the epoxy resin cured with highly reactive hardeners shows a higher Tg, presumably due to the formation of a more densely cross-linked network in this blend. However, it is worth noting that incorporating a high reactive hardener did not significantly influence the Tg of the multi-component blend. This was attributed to the participation of IDPA and POP in the following bridge-forming process after the ring-opening process instigated by AEPIP.*

Keywords: Kinetic studies; Amine-epoxy resin; Glass transition temperature

1. Introduction

Unlike traditional power, wind energy is one of the most promising renewable energy sources that can significantly reduce water consumption, greenhouse gas emission, and air pollution [1]. Advantages like inherently plentiful, renewable and widely distributed, making wind energy to be an increasingly attractive source of energy in the past decade. However, several problems would be faced when pushing forward the construction of a wind farm, especially for constructing offshore wind farms. While offshore wind farms would suffer strong tides and most seriously, punishing storms and repair costs could be very high, up to $30,000, and can take a couple of weeks before the seas are calm enough for a work vessel to fix it [2]. Thus, it is necessary to develop and design novel materials that have the better physical performance to the extent of the working lifetime of blades. Curing behaviour and correlated phase transition behaviour are essential factors that should be considered in the very beginning for designing a suitable formulation to manufacture wind turbine blades with desirable properties. Thus, the curing behaviour and phase transition behaviour of a commercial liquid processable epoxy resin, which is widely used for fabricating wind turbines were estimated in the present study. Further, we report the relationship between the curing kinetics and the phase transition behaviour in this paper.

  doi:10.5075/epfl-298799_978-2-9701614-0-0

2. Methodology

2.1 Materials

RS-M135 (PRF Composites, UK) is an epoxy resin produced from bisphenol A and epichlorohydrin (DGEBA) (CAS No. 25068-38-6) with a number average molecular weight, Mn <700 g/mol. (70–90 % w/w) and containing an added proportion of 1,6-hexanediol diglycidyl ether (DGEH) (CAS No. 16096-31-4) as a reactive diluent. RS-MH137 (PRF Composites, UK), which is a hardener contains (a) isophorodiamine abbreviated as IDPA (3-aminomethyl-3,5,5-trimethylcyclohexylamine) (CAS No. 2855-13-2) 35–50 % w/w, and (b) poly(oxypropylenediamine) abbreviated as POP, (CAS No. 9046-10-0) 50–70 % w/w. 1-(2-aminoethyl)piperazine (AEPIP) was purchased from Sigma Aldrich (CAS No. 140-31-8). The epoxy resin and hardener were mixed in a 10:3 weight ratio for all samples. The multicomponent blend was cured by the hardener with RS-MH137 and AEPIP in a 7:2 weight ratio.

2.2 Characterization

2.2.1 Differential Scanning Calorimetry (DSC)

In this study, DSC experiments were performed using a Netzsch DSC 204F1. Aluminum pans were used, with sample masses of ~5 mg (uncured samples) and 5.1 ± 0.5 mg (cured samples). Sealing is required to prevent evaporation or sublimation from the pan. Samples were equilibrated at 20 °C and cooled down to -50 °C immediately and isothermal for 5min, then heated to 250 °C at a heating rate of 10 °C min^{-1}, unless otherwise stated, with the sample cell kept under a constant nitrogen flow of 50 cm3 min^{-1}. Heat/cool/heat scans, using a cooling rate of 10 °C min^{-1}, were employed to determine whether residual curing exotherms were present. DSC kinetics were studied, using heating rates of 5, 7, 10, and 15 °C min^{-1}. In addition, to determine the cure degree over time, isothermal tests were performed at 25 and 60 °C, respectively.

2.2.2 Rheological Analysis

Rheology measurements were performed using a TA Discovery HR-1 hybrid rheometer instrument equipped with a parallel plate fixture. Disposable aluminum plates of 25 mm in diameter with a gap of 0.3 mm were used. To determine how the viscosity change over time, an isothermal test was performed at 25 and 60 °C with a shear rate of 5 s^{-1}. This was followed by a temperature ramp program. Samples were heated from room temperature to 60 °C (well below their gel point), at a heating rate of 2.5 °C min^{-1}. The strain frequency used was 1 Hz, and an oscillation amplitude of 50% was selected as this fell well within the linear viscoelastic regime.

2.2.3 Thermogravimetric Analysis

STA measurements were performed using a Netzsch STA 449 F3 Jupiter instrument equipped with alumina sample pans. Experiments were undertaken on cured samples with masses of ~5 mg in an N_2 environment. Samples were equilibrated at 20 and then heated to 550 °C at a heating rate of 20 K min^{-1}.

  doi:10.5075/epfl-298799_978-2-9701614-0-0

3. Results and discussions

In order to identify the formation order of each type of building block, kinetic studies were determined using the following equation, which is better suited to an autocatalytic system than an nth-order model. Therefore, first-order reaction kinetics are assumed, and the Kissinger methods were used as a preliminary assessment of the resin kinetics for the three main reaction peaks of each blend. Using the Kissinger method[3], the activation energy, E_a and the pre-exponential factor, A was determined by Eq.(1),

$$ln\left(\frac{\beta}{T_{max}^2}\right) = ln\left(\frac{AR}{E_a}\right) - \frac{E_a}{RT} \quad (1)$$

where β is the heating rate, T_{max} is the exothermic peak maximum (K), E_a is the activation energy, which is the energy barrier that the reaction must overcome for the reaction to proceed, A is the pre-exponential factor, which is interpreted as the frequency of collisions between reactant molecules at a standard concentration (leading to a reaction or not) per second, R is the gas constant (8.314 J K-1 mol^{-1}). By plotting a graph of lnβ = $(T_{max})^2$ versus 1/T_{max}, the activation energy and pre-exponential factor can be determined from the gradient and y-intercept respectively. The Kissinger method also enables the rate constant for the reaction, which is interpreted as the frequency of collisions between molecules that results in a reaction, to be calculated, using the Arrhenius equation as given in Eq.(2),

$$k = Ae^{\left(\frac{-E_a}{RT}\right)} \quad (2)$$

where, k is the rate constant (s^{-1}) and T is the temperature of the reaction (298 K or 25 °C, selected as this was the cure temperature used throughout the study). The values calculated are given in Table 1. The rate constants of each combination highlight the reaction speed between different components in various reaction processes, indicating the reaction probability between each component. Thus, the reaction subsequence probability should be: DGEBA-AEPIP > DGEBA-IDPA > DGEH-AEPIP ≈ DGEBA-POP ≈ DGEH-IDPA > DGEH-POP. As the epoxy-amine reaction is a multi-step reaction, peaks were fitted to the DSC exothermic plots and details of the multi-step reaction could be seen from the results of peak deconvolution (Fig.1). The initial stages of each reaction are being drawn out so that several consecutive reactions occur, the first peak is associated with ring-opening; the second peak is associated with bridge forming[4].

Table 1: Kissinger kinetic analysis for the amine-cured resin blends.

Blend	Kissinger method E_a (kJ mol^{-1})	Pre-exponential factor A (s^{-1})	Rate constant at 298 K k (10^{-2}) (s^{-1})
DGEBA-IDPA	43.1	1.8 x 10^6	4.8
DGEBA-POP	55.9	6.0 x 10^7	0.9
DGEBA-AEPIP	56.4	4.7 x 10^8	6.1
DGEH-IDPA	48.2	3.4 x 10^6	0.8
DGEH-POP	57.8	4.2 x 10^7	0.3
DGEH-AEPIP	67.6	7.3 x 10^9	1.0

  doi:10.5075/epfl-298799_978-2-9701614-0-0 published under CC BY-NC 4.0 license

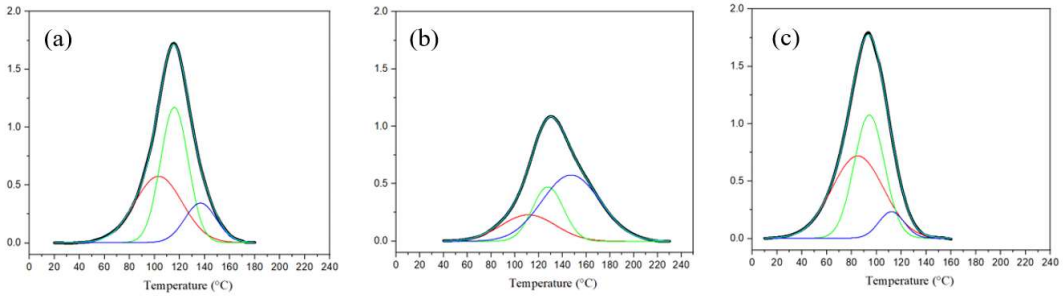

Figure 1. Peak fitting for DSC data at 2 K/min for different pairs (a) DGEBA-IDPA, (b) DGEBA-POP, and (c) DGEBA-AEPIP.

The kinetic parameters obtained from dynamic DSC experiments have enabled comparison to be made of the resin blends in terms of their activation energies, pre-exponential factors, and reaction rates at cure temperature. However, the Kissinger method only enables certain cure kinetic parameters to be estimated by assuming first-order cure kinetics, but these models do not enable the degree of cure to be estimated as the reaction progresses [5]. Thus, the isothermal cure kinetics must be assessed to validate a cure kinetics model which most accurately captures the resin cure behaviours [6]. The isothermal DSC measurements were used to determine the reaction rate and degree of cure. Assuming that the cure rate of the resin system, $d\alpha \ / \ dt$, is proportional to the rate of heat flow, $dH \ / \ dt$, thus, the cure rate can be expressed as Eq.(3),

$$\frac{d\alpha}{dt} = \frac{1}{H}\frac{dH}{dt} \tag{3}$$

The plot of reaction rate versus time for the isothermal cure at the ambient temperature of various combinations is shown in Fig. 2a. It could be seen that the reaction rate of the blends with AEPIP is much higher than the other blends (all the blends are amine excesses). On this basis, regarding the blend only incorporated with AEPIP, the reaction rate first increases, reaches a maximum and then decreases, which is attributed to the fast ring-opening process caused by AEPIP and then the rapidly increasing viscosity. This observation is in agreement with the non-isothermal measurement. While the following reduction is owing to the dramatically increasing viscosity (Fig.2b) caused by the reaction, which then hinders the mobility of molecules for the reaction [7]. For the blends with IDPA and the one with POP, it is clear that the reaction rate is very much low (three times lower than AEPIP) and remains stable during the polymerization process. This is because the reaction of the ring-opening process is hard to be instigated by the low reactive hardeners, and thus the bridge-forming process was delayed. Considering the blends containing AEPIP/IDPA/POP, the reaction rate decreases with the process of polymerization, which might be due to the consumption of AEPIP (which contributes only 15wt% of the curing agent) and the participation of IDPA in the following bridge-forming process.

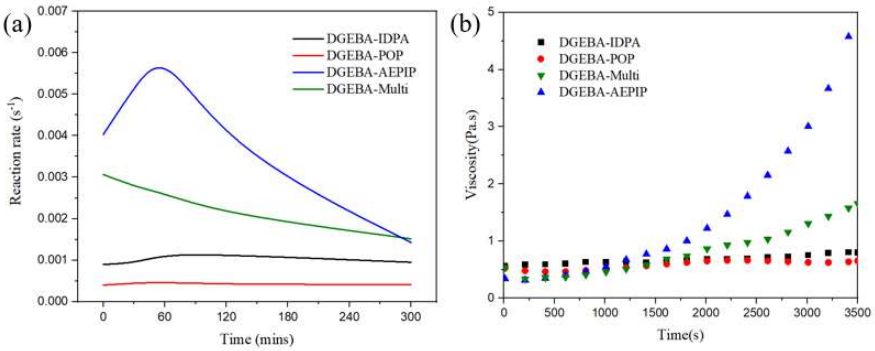

Fig.2. The plot of (a) reaction rate and (b) viscosity of amine-cured resin blends.

As shown in Fig.3, the variation of glass transition temperature (Tg) could be seen for different blends. As expected, the epoxy resin cured with highly reactive hardeners shows a higher Tg, presumably due to the formation of a more densely cross-linked network in this blend. However, it is worth noting that incorporating a high reactive hardener did not significantly influence the Tg of the multi-component blend. This was attributed to the participation of IDPA and POP in the following bridge-forming process after the ring-opening process instigated by AEPIP.

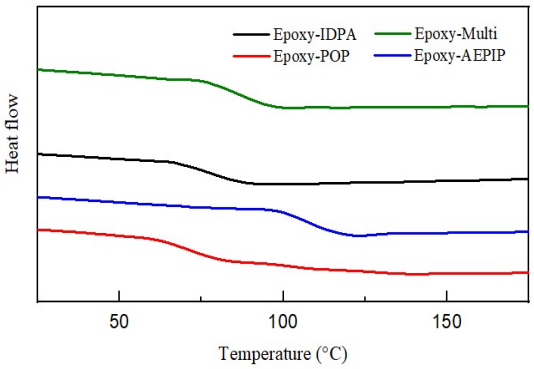

Fig.3. DSC curve of amine-cured resin blends.

4. Conclusion

By evaluating the kinetic studies of liquid processable multicomponent commercial amine-cured epoxy resin, the reaction subsequence and reaction rate during the curing process of each component pair is determined. At a specific temperature, the hardener present highly reactive would have a significant larger ring-opening peak when compared to other hardeners. While the reaction rate first increases and then decreases, which is attributed to the fast ring-opening process caused by the highly reactive hardener and then the rapidly increasing viscosity. Comparatively, the difficulty of instigating the ring-opening process of low reactive hardeners delayed the bridge-forming process, and thus the reaction rate of low reactive hardeners remained stable during the polymerization process. However, even though the highly reactive

hardener would increase the reactivity and T_g of the multi-component blend, the co-polymerization of each pair led to the subtle difference in phase transition behaviour. This study provides an essential clue for optimizing the curing parameter of a commercial blend to fabricate composite with desired performance for wind turbine blade applications.

Acknowledgements

S.H. is supported through the China Scholarship Council/University of Bristol (CSC-UOB) Joint Research Scholarship and wishes to thank the Faculty of Engineering Research Pump Priming Fund (UOB).

5. References

1. Lindenberg S. 20% Wind Energy By 2030: Increasing Wind Energy¿ s Contribution to US Electricity Supply: diane publishing; 2009.
2. BEGLEY D, DODD C, MCCALLA J, T, editors. Lightning protection for wind turbine electronics. 2nd Terrestrial Energy Systems Conference; 1981.
3. Kissinger HE. Variation of peak temperature with a heating rate in differential thermal analysis. J Res Natl Bur Stand. 1956;57(4):217-21.
4. Hamerton I, McNamara LT, Howlin BJ, Smith PA, Cross P, Ward S. Examining the initiation of the polymerization mechanism and network development in aromatic polybenzoxazines. Macromolecules. 2013;46(13):5117-32.
5. Hardis R. Cure kinetics characterization and monitoring of an epoxy resin for thick composite structures: Iowa State University; 2012.
6. O'Brien DJ, White SR. Cure kinetics, gelation, and glass transition of a bisphenol F epoxide. Polymer Engineering & Science. 2003;43(4):863-74.
7. Garschke C, Parlevliet PP, Weimer C, Fox BL. Cure kinetics and viscosity modelling of a high-performance epoxy resin film. Polymer Testing. 2013;32(1):150-7.

  doi:10.5075/epfl-298799_978-2-9701614-0-0

Non-Isocyanate Polyurethanes based composites: a new route to sustainable fully biobased structural composites

Guillem Seychal[a,b], Connie Ocando[a], Nora Aranburu[b], Bruno Grignard[c], Christophe Detrembleur[c], Haritz Sardon[b], Leila Bonnaud[d], Jean-Marie Raquez[a]

a: Laboratory of Polymeric and Composite Materials, Center of Innovation and Research in Materials and Polymers (CIRMAP), University of Mons, Place du Parc 23, 7000 Mons, Belgium – guillem.seychal@umons.ac.be

b: POLYMAT and Advanced Polymers and Materials: Physics, Chemistry and Technology, Faculty of Chemistry, University of the Basque Country UPV/EHU, Paseo Manuel de Lardizabal 3, 20018 Donostia-San Sebastián, Spain

c: Department of Chemistry, Center for Education and Research on Macromolecules (CERM), CESAM Research Unit, University of Liège, Sart-Tilman, B6A, 4000 Liège, Belgium

d: Materia Nova asbl, Parc Initialis, Avenue Copernic 1, 7000 Mons, Belgium

Abstract: *Polyurethanes (PU) are a versatile class of polymer widely used for their interesting and tuneable properties. However, PU synthesis requires the use of highly hazardous isocyanates and phosgene. New routes for synthesizing Non-Isocyanate Polyurethanes (NIPU) have been proposed, particularly the design of Poly(hydroxy)urethanes (PHU) as obtained by polyaddition of cyclic carbonates and polyamines. Interestingly, in addition to the implementation of biobased diamines, these cyclic carbonates can be directly obtained by coupling CO_2 to biobased epoxidized derivatives (e.g., epoxidized vegetable oils), leading to PHUs of reduced environmental footprint. The resulting PHUs present hydroxyurethane moieties along their backbone that can be considered as an interesting feature for improving adhesion of such polymer with highly hydrophilic cellulosic fibres (flax, hemp, jute…) in composite applications. In this work, we propose to investigate the feasibility of flax/PHU composites through rheological and thermomechanical properties. For a sake of comparison, a flax/epoxy composite was also evaluated. Finally, we propose examples of the resulting composites.*

Keywords: Biobased composites, non-isocyanate polyurethanes, natural fibres, poly(hydroxyurethane)s

1. Introduction

The need to design more sustainable materials with enhanced physical properties have pushed forward the conception of biobased composites during the last twenty years. Although natural fibres such as flax, hemp or sisal have shown promising properties that can challenge glass fibres [1], biobased polymer matrices for such structural composites suffer from a lack of satisfying properties to compete with conventional petroleum-based polymers and research is still ongoing [2].

Among the most used polymers, polyurethanes have shown high versatility and satisfying properties for numerous applications. However, conventional polyurethanes require the use of diisocyanate precursors that are classified carcinogenic, mutagenic and reprotoxic by REACH regulation in addition to their petroleum origin [3,4]. Obtaining non-isocyanate polyurethane (NIPU) has become a major breakthrough. The synthesis of poly(hydroxyurethane)s (PHU) through aminolysis of polyfunctional cyclic carbonates (CC) by polyamines offers a great opportunity to obtain fully biobased NIPU matrices with tuneable properties. Numerous

  doi:10.5075/epfl-298799_978-2-9701614-0-0

biobased cyclic carbonates can be obtained by carbonatation of epoxidized vegetable oils or glycerol-based precursors with CO_2 [5]. Biobased diamines can also be obtained from fatty acids, vegetable oils, sugar and lignin derivatives…[6]. Interestingly, the presence of hydroxyl groups within the PHU backbone could also offer further good adhesion with natural fibres (NF) for the manufacture of biobased composites. To the best of the authors' knowledge, no study has been conducted on NIPU-NF composites for structural applications.

In this work, we investigate the opportunities offered by PHU – NF composites and their possible applications. More precisely, we propose to evaluate a potentially biobased cyclic carbonate with different commercially available polyamine precursors (Hexamethylene Diamine -HMDA, m-Xylylene Diamine-MXDA) to design suitable NIPU matrices for high performance composites. Interestingly, recent studies highlighted the possibility to obtain the aromatic MXDA from biomass derived furfural [7] and aliphatic HMDA from sugar [8], leading to potentially fully biobased NIPU. The PHU formulations are compared to their epoxy equivalent (i.e., non-carbonated glycidyl ether monomer). Rheological properties were evaluated during curing as a first approach. Final properties of fully cured neat matrices were then evaluated. Unidirectional laminates made of the selected PHU and epoxy resins and aligned flax fibres are then manufactured by thermocompression. The obtained laminates were tested to assess the physical and mechanical properties of the composites.

2. Experimental

2.1 Materials

Trimethylol Propane Triglycidyl Ether (TMPTGE) and TetraButyl Ammonium Iodide (TBAI) were purchased from SigmaAldrich. Carbon Dioxide was provided by Air Liquide. m-Xylylene Diamine (MXDA) and Hexamethylene Diamine (HMDA) were purchased from ThermoScientific. Flax unidirectional fibres tape (FlaxTape UD110, 110 g/m²) were purchased from EcoTechnilin. Molecular structures are shown in Figure 1a.

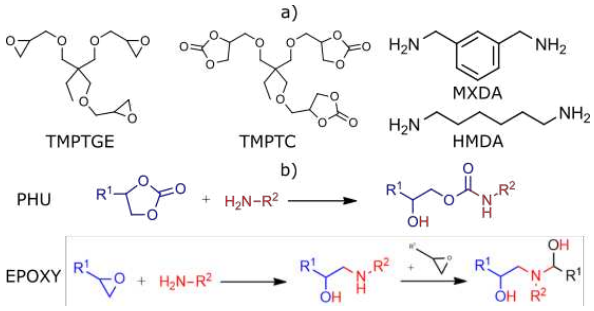

Figure 1: a) (Macro)molecular structures of the resins precursors, and b) PHU and epoxy model reaction.

2.2 Synthesis of cyclic carbonates

TrimethylolPropane TriCarbonated (TMPTC) was synthesized using CO_2 under supercritical conditions. About 60 g of TMPTGE was mixed with TBAI (2.5 mol%) and poured into a high-pressure stainless steel reactor. The reactor was then filled with CO_2 and maintained under supercritical conditions at 80°C and 100 bars for 24 h at 350 rpm. The resulting mixture was then degassed several times at 70°C under vacuum until no bubbling occurred to remove unreacted remaining CO_2. Reaction completion was evaluated by means of ^{1}H-NMR spectroscopy in

  doi:10.5075/epfl-298799_978-2-9701614-0-0

deuterated chloroform. Properties of the resin reactant are presented in **Erreur ! Source du renvoi introuvable.**.

2.3 Synthesis of epoxy and PHUs matrices

Cyclic Carbonates or epoxy functions were cured with a stoichiometric amount of amine groups. TMPTGE or TMPTC was thoroughly mixed manually for 5 minutes with the curing diamine (HMDA or MXDA) at room temperature. The tested formulations are listed in Table 2. The mixture was then degassed at room temperature under vacuum for 5 minutes three times before being used. For the assessment of physical properties, the mixture was poured into a silicon mould. Epoxy matrices were cured for one hour at 80°C with an additional post-curing at 150°C for 30 min. PHU matrices were cured for 20 h at 80°C followed by 4 h at 100°C with an additional post-curing at 150°C for 30 minutes. The model reaction of PHUs and epoxy are shown in Figure 1b.

Table 1: Characteristics of the resins precursors.

Name	Ref	EEW[1] (g/eq)	CEW[2] (g/eq)	AHEW[3] Epoxy (g/eq)	AHEW PHU (g/eq)	$\eta_{25°C}$ (Pa.s)
TriMethylolPropane Triglycidyl Ether	TMPTGE	145	-	-	-	0.12
TriMethylolPropane TriCarbonate	TMPTC	-	175	-	-	148
HexaMethylene DiAmine	HMDA	-	-	29	58	-
M-Xylylene DiAmine	MXDA	-	-	34	68	-

[1]Epoxy Equivalent Weight EEW= Mw/#oxirane functions; [2]Carbonate Equivalent Weight CEW = Mw/#CC functions; [3]Amine Hydrogen Equivalent Weight AHEW=Mw/#functional hydrogens (2 for each primary amine for oxirane, 1 for CC)

2.4 Composite Manufacturing

Composite plates were manufactured by hand lay-up and cured by thermocompression. Six aligned plies were alternatively put in the mould with a line of resin in the middle of the ply into a Teflon coated steel mould with resins. The two edges in the length of the mould were let opened to allow air and matrix excess to flow out from the mould. 3.5 bar pressure was slowly applied to fully impregnate the fibres. This particular process inspired from [9] was set to improve impregnation and process. The plates were then cured under this pressure following the same temperature process described in 2.3. The post-curing was realised in an oven after unmoulding. According to ASTM D3039 [10], 15x150x1.3 mm³ rectangular tensile test samples were cut by laser cutting and conditioned for at least two weeks at 23°C and 50% RH prior to test.

3. Results and discussion

3.1 Rheological curing properties

Rheological properties of the formulations during curing were measured using an Anton Paar Modular Compact Rheometer MCR302. Two disposable parallel aluminium plates of 25 mm diameter, with a 1 mm air gap were used. A 2% strain was applied at 1 Hz. Isothermal rheological

analyses were performed at 80°C for all formulations to assess the difference in evolution of the reaction between epoxy and PHUs. Additional 70°C, 90°C and 100°C analyses were performed for TMPTC/MXDA formulation to evaluate the effect of the temperature. For each sample, about 1 g of cyclic carbonate or epoxy product was mixed with the stoichiometric amount of cyclic carbonates and amine groups.

The viscosity curves for the four formulations at 80°C are presented in Figure 2a and numerical values are summarized in Table 2. As it can be seen in Table 2, the initial viscosity of the PHU formulations is significantly higher (between 70 and 500 times higher than the epoxy), which could result in a complicated infusion process for the manufacture of composites. The viscosity behaviour of PHU and epoxy formulations is slightly different: a continuous increase of the viscosity is observed in the case of PHUs. Subsequently, this behaviour begins to be less pronounced until a plateau is reached. Conversely, the viscosity of the epoxy resin does not evolve significantly at the beginning of the test and gelation starts very quickly after a few minutes. This high reactivity with a pot life and gel point of less than 10 minutes is often a problem in composite manufacturing as sufficient time is required to fully impregnate the laminates. As it can be seen in Table 2, the pot life is slightly higher for PHU, while gelation requires a significantly longer period of time to occur.

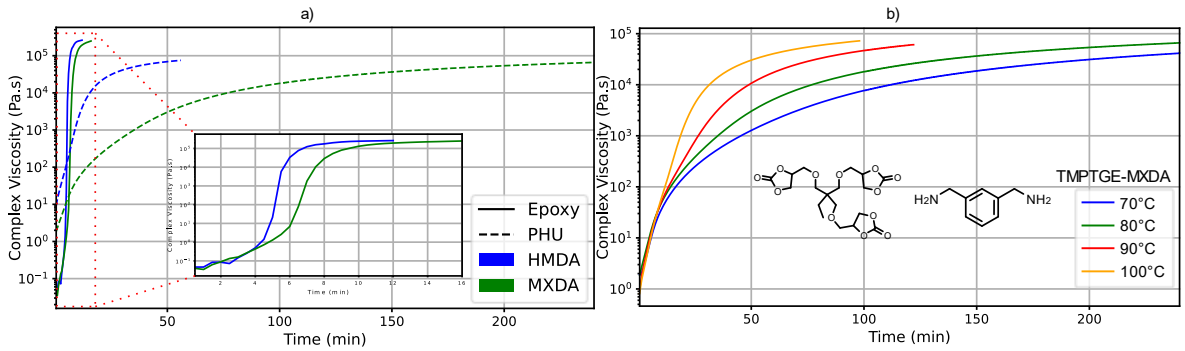

Figure 2 : Viscosity evolution over time for a) PHU and Epoxy formulations at 80°C, b) PHU TMPTC/MXDA formulation at 70°C, 80°C, 90°C and 100°C.

In general, the relative reactivity of the amines to crosslink the epoxy or the carbonate remains unchanged, the aliphatic diamine being much more reactive than the aromatic one. This can be also a problem, as the processing window in this case does not seem to be enhanced enough, while the curing time is significantly increased. This change in the viscosity behaviour can be explained by the increase of hydroxyl group during the curing of PHU, which can create secondary H-bonding in the mixtures, resulting in higher viscosity while lowering the reactivity of unreacted functions to crosslink due to the steric bulk hindrance effect. These observations are in accordance with the work proposed by Blain et al. whereby they highlighted that hydrogen bonds affect the polymerization progress in linear PHUs [11]. The effect of the temperature was also investigated for the TMPTC/MXDA formulations at 70°C, 80°C, 90°C and 100°C. The viscosity evolution is presented in Figure 2b. The temperature tends to play a minor role in the beginning of the reaction, as the viscosity tends to increase at the same speed between 0 and 15 minutes regardless the temperature. These observations are also confirmed by the pot life that only decreases from 28 to 14 minutes, while the gelation time is significantly reduced when higher temperatures are used, going from 209 minutes at 70°C to 20 minutes at 100°C. Therefore, the manufacture of matrices and composites could be optimised by controlling the curing and

  doi:10.5075/epfl-298799_978-2-9701614-0-0

processing in order to counterbalance the viscosity of the mixtures. However, it is worth noting that at higher temperature than 100°C side reactions can occurs as already reported in literature [3,12], for these reasons this study was carried at temperature up to 100°C .

Table 2 : Rheological curing properties of the Epoxies and PHUs formulations

Epoxy/PHU	Formulation	Temperature (°C)	Pot Life[1] (min)	Gel Point[2] (min)	$\eta_{initial}$ (Pa.s)	η_{10min} (Pa.s)
Epoxy	TMPTGE/HMDA	80	5	5	0.048	243000
PHU	TMPTC/HMDA	80	6	10	13.38	1800
Epoxy	TMPTGE/MXDA	80	6	6	0.033	131000
PHU	TMPTC/MXDA	70	28	209	2.00	35
PHU	TMPTC/MXDA	80	22	82	2.31	47
PHU	TMPTC/MXDA	90	19	40	1.38	50
PHU	TMPTC/MXDA	100	14	20	1.18	57

[1]Pot Life : Time before the resin reached 300Pa.s were it becomes unprocessable; [2]Approximative Gelation Time were Storage Modulus (G') becomes greater than Loss Modulus (G")

3.2 Mechanical and physical properties

The TMPTGE and TMPTC formulations were set in ASTM D638 type V dog bone shape silicon moulds for monotonic tensile testing. At least 3 samples were tested for each formulation on Zwick-Roell Z2.5 tensile machine equipped with a 2.5 kN load cell at a crosshead speed of 1 mm/min. Strain-Stress curves are presented in Figure 3. Glass transition temperature (T_g) and complete curing of the resins were assessed by Differential Scanning Calorimetry using a temperature ramp from -80°C to 200°C at 10°C/min. Density was measured through Archimedes' principle in ethanol. All numerical values are reported in Table 3.

For both PHUs and Epoxy, the T_g, Young's modulus and the tensile strength are higher when cured with MXDA than with HMDA. This is due to the presence of rigid aromatic rings in MXDA compared to the flexible aliphatic chains from HMDA. The aliphatic chains also allow higher ductility of the matrices than aromatic rings. This is due to a higher mobility within the networks cured with HMDA than MXDA, which leads to a higher strain at break for the matrices cured with HMDA. It can be observed that PHUs present higher T_gs than their epoxy equivalent. This increase in the glass transition of PHUs formulation with respect to the epoxy ones is more pronounced when the aromatic MXDA curing agent is used. It can be explained first, by the higher amount of aromatic rings in the PHU resins than the epoxy as a higher proportion of curing amine is required in PHUs formulations. However, the T_g of the aliphatic HMDA cured PHU is also slightly higher than the TMPTGE/HMDA formulation. This moderate increase can also be attributed to the higher density of hydroxyl functions in the PHU matrix leading to intra and inter molecular bonding, decreasing the chain mobility and, thus, increasing the T_g.

  doi:10.5075/epfl-298799_978-2-9701614-0-0

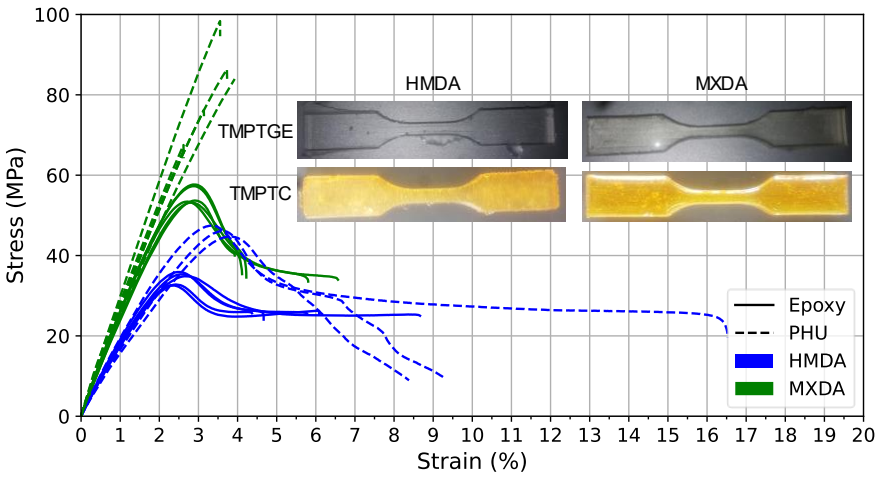

Figure 3 : Monotonic tensile curves of the Epoxy (TMPTGE) and PHUs (TMPTC) formulations for the two different amines (HMDA and MXDA) and their respective dog bone shape samples.

The thermal properties of the matrices are in accordance with the observed mechanical behaviour. Indeed, as shown in Figure 3, the behaviour of the PHUs is rather different from the epoxy. TMPTC/MXDA formulation present a slightly higher Young's Modulus of 2600 ± 160 MPa as compared to the 2300 ± 70 MPa from the TMPTGE one, while HMDA cured formulations have a comparable modulus. Moreover, the two epoxy matrices present a yield point at 2.5 ± 0.1% and 2.9 ± 0.1%, respectively, with a ductile zone, while in the case of the TMPTC/MXDA, the behaviour is typical of a brittle-elastic material, with no yield. TMPTC/HMDA still presents a ductile behaviour due to the aliphatic chains but with quite important scattering in this zone prior to failure that can be related to the effect of remaining trapped air bubbles acting as failure ignition sites. Interestingly, maximum stress and strain at yield are improved for PHUs compared to epoxy with significantly higher admissible stress (35 and 45% higher for HMDA and MXDA, respectively) and improved strain (44 and 15% higher for HMDA and MXDA, respectively).

Table 3: Properties of the neat matrices formulations (mean value ± standard deviation)

Monomer	Amine	T_g[1] (°C)	ρ[2] (g.cm^{-3})	E[3] (MPa)	σ_y (MPa)	ε_y (%)	ε_{break} (%)
TMPTGE	HMDA	35	1,19 ± 0,01	1600 ± 50	34 ± 1	2.5 ± 0.1	6.0 ± 1.5
TMPTC		40	1.22 ± 0,01	1570 ± 144	46 ± 1	3.6 ± 0.2	11.4 ± 3.6
TMPTGE	MXDA	43	1,20 ± 0,04	2300 ± 70	55 ± 2	2.9 ± 0.1	4.9 ± 1.0
TMPTC		60	1.31± 0,02	2600 ± 160	80 ± 11	3.3 ± 0.5	3.3 ± 0.5

[1]T_g determined by DSC;[2]ρ determined by Archimedes' principle;[3]Modulus calculated by linear regression between 0.05% and 2.0% in strain

3.3 Flax composite results

Monotonic tensile test was performed on a Lloyd LR10K equipped with a 10 kN cell force at a crosshead speed of 1 mm/min with an initial gauge length of 70 mm. Tensile curves are presented in Figure 4 and the values are summarized in Table 4. The behaviour of flax composite is assumed to be bilinear: the first apparent modulus (E_1) was calculated by linear regression between 0.05 % and 0.15 % longitudinal strain, the second apparent modulus (E_2) was calculated between 1.0

% and 3.0 % longitudinal strain. Fibres volume fraction (V_f) and porosities volume fraction (V_p) were calculated following equation (1) and (2). As fibres volume fraction are significantly different between epoxy and PHU based laminates, Rule-Of-Mixtures (ROM) was used to normalize modulus (equation 3) and stress (equation 3) at break values and allow comparison. The values of ROM are presented in [1]ρ determined by Archimedes' principle;[2] determined using equation (1);[3] determined using equation (2);[4] determined between 0.05 % and 0.15 % longitudinal strain; [5] determined between 1.0% and 3.0 % longitudinal strain

Table 5.

$$V_f = \frac{\frac{n \times A_r \times S}{\rho_f}}{\frac{n \times A_r \times S}{\rho_f} + \frac{m_c - \frac{n \times A_r \times S}{\rho_f}}{\rho_m}} \quad (1)$$

$$V_p = 1 - \rho_c \times \left(\frac{W_m}{\rho_m} + \frac{W_f}{\rho_f}\right) \quad (2)$$

$$E_{ROM} = V_f \times E_f + V_m \times E_m \quad (3)$$

$$\sigma_{ROM} = V_f \times \sigma_f + V_m \times \sigma_m \quad (4)$$

With V_i being the volume fraction, m_i the mass, n the number of plies, A_r the areal surface weight of the reinforcement, S the surface, ρ_i the density (1.53 g/cm³ for flax), E_i the modulus (53 GPa for flax) and σ_i the stress at break (700 MPa for flax). Indexes f, c, p and m refers to fibres, composite, porosities and matrix, respectively.

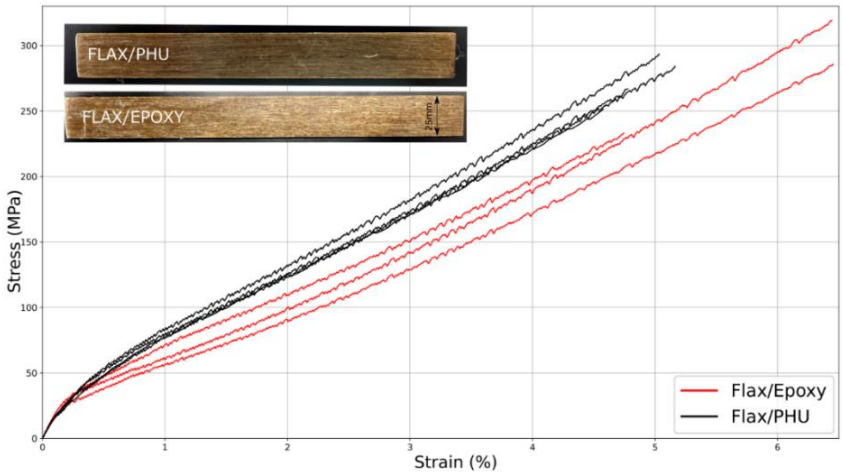

Figure 4 : Monotonic tensile behaviour of flax/epoxy (TMPTGE/MXDA) and flax/PHU(TMPTC/MXDA) composites laminates

From both tensile curves, the behaviour is similar and typical from monotonic tensile curves of Flax/thermosets composites with a bilinear behaviour, a first step with a high apparent modulus (15.1 ± 1.1 GPa for TMTPGE and 14.5 ± 1.9 GPa for TMPTC matrices) followed by a decrease around 0.2% strain down to 4.8 ± 0.1 GPa for PHU and 3.8 ± 0.2 GPa for epoxy. This behaviour is found to be similar to the results obtained by Jeannin et al. [13,14], where the same reinforcement was used with a DGEBA-based epoxy resin. Interestingly, it can be noted that even with 10% less flax fibres within the laminate, the Flax/PHU composite present comparable properties to the epoxy one. When normalized to ROM, to compare results while not taking into account the fibre volume fraction and to assess the quality of the adhesion between the fibre

and the matrix, it can be noted that E/E_{ROM} and σ/σ_{ROM} ratios are 22% and 16% higher for the PHUs matrix, respectively. This higher ratio tends to show a better affinity between the fibres and the PHUs matrix due to the high number of hydroxyl functions in the network. One must keep in mind that these results remains preliminary and further composite process optimisation, characterisation and investigations are needed to confirm the feasibility of PHUs as matrices for structural composites.

Table 4 : Mechanical properties of the flax-epoxy and flax-PHU composites (mean value ± standard deviation).

Formulation	ρ^1 ($g.cm^{-3}$)	V_f^2 (%)	V_v^3 (%)	E_1^4 (GPa)	E_2^5 (GPa)	σ_{max} (MPa)	ε_{max} (%)
Flax/TMPTGE/MXDA	1.24 ± 0.01	44.1 ± 3.2	8.0 ± 0.7	15.1 ± 1.1	3.8 ± 0.2	279 ± 35	5.9 ± 0.8
Flax/TMPTC/MXDA	1.35 ± 0.01	33.7 ± 0.3	2.5 ± 0.1	14.5 ± 1.9	4.8 ± 0.1	274 ± 16	4.9 ± 0.2

[1]ρ determined by Archimedes' principle;[2] determined using equation (1);[3] determined using equation (2);[4] determined between 0.05 % and 0.15 % longitudinal strain; [5] determined between 1.0% and 3.0 % longitudinal strain

Table 5 : Comparison of results by use of the Rule-Of-Mixtures.

Formulation	V_f^1 (%)	E_{ROM}^2 (GPa)	σ_{ROM}^3 (MPa)	E_1^4 (GPa)	σ_{max} (MPa)	E/E_{ROM}	σ/σ_{ROM}
Flax/TMPTGE/MXDA	44.1 ± 3.2	27.3	340	15.1 ± 1.1	279 ± 35	0.55	0.82
Flax/TMPTC/MXDA	33.7 ± 0.3	21.6	290	14.5 ± 1.9	274 ± 16	0.67	0.95

[1] determined using equation (1);[2] determined using equation (3);[3] determined using equation (4);[4] determined between 0.05 % and 0.15 % longitudinal strain

4. Conclusion

Poly(hydroxyurethane)s are a new class of polymers that offer several opportunities for green chemistry and biobased materials through insertion of CO_2 in epoxidized molecules. Until now, most of the PHUs formulations were dedicated to adhesives, coatings[15] and foams[16]. In this work, we proposed a preliminary study to assess opportunities and challenges in using PHUs as matrices for structural biobased composites. We showed that the rheological behaviour as the viscosity of the PHUs mixture tends to make the processing harder than epoxy but remains feasible. For neat matrices, PHUs showed better thermal and mechanical properties than epoxies. Moreover, the resulting flax/PHU composites, even with a significantly lower fibre volume fractions, presented comparable mechanical properties and a better adhesion to the fibres than epoxy/flax composites. Thus, this preliminary study shows that even if the process and formulation are not optimised so far for PHUs, this new route could be an asset in future green materials by increasing properties of biobased epoxies by the carbonatation of the oxirane groups to produce cyclic carbonates, while capturing CO_2 and decreasing the environmental footprint.

Acknowledgements

The authors would like to thank the financial support provided by the NIPU-EJD project; this project has received funding from the European Union's Horizon 2020 research and innovation

programme under the Marie Skłodowska-Curie grant agreement No 955700. The authors are also grateful to Materia Nova technological platform (Mons, Belgium) for the support in rheology and characterisation. C.D. is FNRS Research Director and thanks FNRS for funding.

5. References

[1] Bourmaud A, Beaugrand J, Shah DU, Placet V, Baley C. Towards the design of high-performance plant fibre composites. Prog Mater Sci 2018;97:347–408. https://doi.org/10.1016/j.pmatsci.2018.05.005.
[2] Bobade SK, Paluvai NR, Mohanty S, Nayak SK. Bio-Based Thermosetting Resins for Future Generation: A Review. Polym-Plast Technol Eng 2016;55:1863–96. https://doi.org/10.1080/03602559.2016.1185624.
[3] Cornille A, Auvergne R, Figovsky O, Boutevin B, Caillol S. A perspective approach to sustainable routes for non-isocyanate polyurethanes. Eur Polym J 2017;87:535–52. https://doi.org/10.1016/j.eurpolymj.2016.11.027.
[4] Khatoon H, Iqbal S, Irfan M, Darda A, Rawat NK. A review on the production, properties and applications of non-isocyanate polyurethane: A greener perspective. Prog Org Coat 2021;154:106124. https://doi.org/10.1016/j.porgcoat.2020.106124.
[5] Blattmann H, Fleischer M, Bähr M, Mülhaupt R. Isocyanate- and Phosgene-Free Routes to Polyfunctional Cyclic Carbonates and Green Polyurethanes by Fixation of Carbon Dioxide. Macromol Rapid Commun 2014;35:1238–54. https://doi.org/10.1002/marc.201400209.
[6] Błażek K, Datta J. Renewable natural resources as green alternative substrates to obtain bio-based non-isocyanate polyurethanes-review. Crit Rev Environ Sci Technol 2019;49:173–211. https://doi.org/10.1080/10643389.2018.1537741.
[7] Scodeller I, Mansouri S, Morvan D, Muller E, de Oliveira Vigier K, Wischert R, et al. Synthesis of Renewable *meta* -Xylylenediamine from Biomass-Derived Furfural. Angew Chem 2018;130:10670–4. https://doi.org/10.1002/ange.201803828.
[8] Wang X, Gao S, Wang J, Xu S, Li H, Chen K, et al. The production of biobased diamines from renewable carbon sources: Current advances and perspectives. Chin J Chem Eng 2021;30:4–13. https://doi.org/10.1016/j.cjche.2020.12.009.
[9] Cadu T, Berges M, Sicot O, Person V, Piezel B, Van Schoors L, et al. What are the key parameters to produce a high-grade bio-based composite? Application to flax/epoxy UD laminates produced by thermocompression. Compos Part B Eng 2018;150:36–46. https://doi.org/10.1016/j.compositesb.2018.04.059.
[10] D30 Committee. Test Method for Tensile Properties of Polymer Matrix Composite Materials. ASTM International; 2021. https://doi.org/10.1520/D3039_D3039M-17.
[11] Blain M, Cornille A, Boutevin B, Auvergne R, Benazet D, Andrioletti B, et al. Hydrogen bonds prevent obtaining high molar mass PHUs. J Appl Polym Sci 2017;134:44958. https://doi.org/10.1002/app.44958.
[12] Maisonneuve L, Lamarzelle O, Rix E, Grau E, Cramail H. Isocyanate-Free Routes to Polyurethanes and Poly(hydroxy Urethane)s. Chem Rev 2015;115:12407–39. https://doi.org/10.1021/acs.chemrev.5b00355.
[13] Jeannin T, Gabrion X, Ramasso E, Placet V. About the fatigue endurance of unidirectional flax-epoxy composite laminates. Compos Part B Eng 2019;165:690–701. https://doi.org/10.1016/j.compositesb.2019.02.009.
[14] Jeannin T, Berges M, Gabrion X, Léger R, Person V, Corn S, et al. Influence of hydrothermal ageing on the fatigue behaviour of a unidirectional flax-epoxy laminate. Compos Part B Eng 2019;174:107056. https://doi.org/10.1016/j.compositesb.2019.107056.
[15] Gomez-Lopez A, Panchireddy S, Grignard B, Calvo I, Jerome C, Detrembleur C, et al. Poly(hydroxyurethane) Adhesives and Coatings: State-of-the-Art and Future Directions. ACS Sustain Chem Eng 2021;9:9541–62. https://doi.org/10.1021/acssuschemeng.1c02558.
[16] Monie F, Grignard B, Detrembleur C. Divergent Aminolysis Approach for Constructing Recyclable Self-Blown Nonisocyanate Polyurethane Foams. ACS Macro Lett 2022;11:236–42. https://doi.org/10.1021/acsmacrolett.1c00793.

MXENE NANOPARTICLES TO IMPART MULTIFUNCTIONAL PROPERTIES TO FIBRE REINFORCED PLASTIC COMPOSITES

Daiva Zeleniakiene[a], Gediminas Monastyreckis[a], Maria Omastova [b], and Andrey Aniskevich [c]

a: Department of Mechanical Engineering, Kaunas University of Technology, Lithuania,
daiva.zelenikiene@ktu.lt
b: Polymer Institute, Slovak Academy of Sciences, Slovakia
c: Institute for Mechanics of Materials, University of Latvia, Latvia

Abstract: *In this work, the possibilities of MXene usage for imparting multifunctional properties such as damage sensing and de-icing to glass fibre reinforced plastic composites (FRPC) were studied. After the FRPC surface plasma treatment, water-based delaminated MXenes suspension was sprayed on the FRPC surface. Characterisation of structure and morphology of MXene nanocoating through SEM and AFM analysis was performed. As the focus of this study was to investigate the electrical resistance response of MXene-coated FRPC samples under tensile-tensile fatigue loading, the samples were tested under varying amplitudes with high tensile loads. The results demonstrated that MXenes are a suitable material for strain-sensing coatings in FRPC structures. It was also found that MXene coatings can work great for the de-icing as it heats up well and can melt ice quickly and efficiently.*

Keywords: Fibre reinforced plastic composites; MXene nanoparticles; multifunctional properties

1. Introduction

In the development of advanced composite materials, not only strength and low weight are important, but also the possession of additional multifunctional properties. Damage sensing, electromagnetic interference shielding, and other functions can be achieved using electrically conductive nanoparticles [1, 2]. Polymer composites doped with carbon-based nanoparticles such as graphene and carbon nanotubes provide even greater mechanical properties. Much less studied class of new 2D nanomaterials called MXenes, have recently been of great interest to scientists [3]. MXenes are transition metal carbides and/or nitrides discovered in the last decade. MXene $Ti_3C_2T_z$ is particularly noteworthy as it has a unique combination of electrical conductivity, hydrophilicity and excellent mechanical properties [4, 5]. In the case of mass production, this MXene is very likely to be much cheaper than previously mentioned electrically conductive nanoparticles. Motivation for the usage of MXene in structural composites is further enhanced by the fact that MXene has good adhesion to epoxy resin [6], which is commonly used in structural composites as a matrix. With application of delaminated MXenes solution it is possible to produce especially thin MXene layers and coatings [7, 8], and thusly obtaining additional functionalities without a weight penalty.

Therefore, the aim of this study was to investigate the possibilities of using MXene nanoparticles coating of fibre reinforced plastic composites (FRPC) to tailor the additional functionalities to FRPC, such as damage sensing and de-icing of the composite structure. The main idea of this work is presented in Figure 1.

  doi:10.5075/epfl-298799_978-2-9701614-0-0

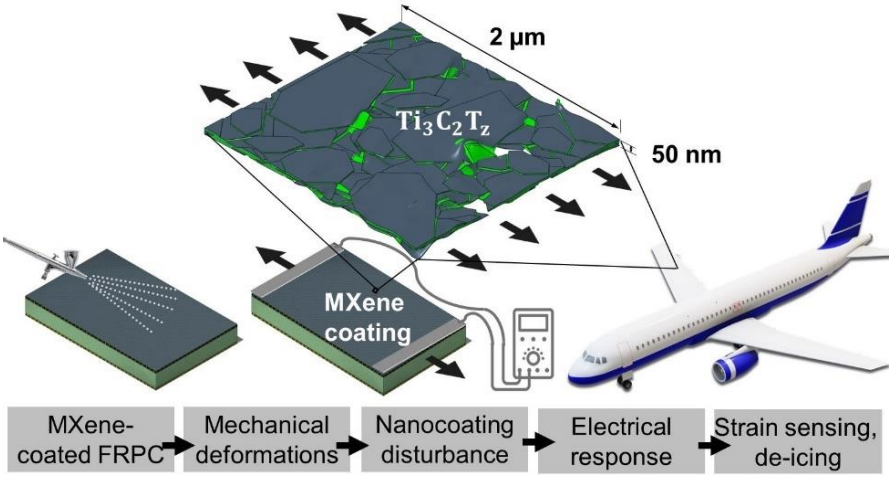

Figure 1. MXene nanocoatings for damage sensing and de-icing of FRPC structure

2. Materials and methods

$Ti_3C_2T_z$ MXenes were obtained from Ti_3AlC_2 MAX phase by etching Al with hydrochloric acid and lithium fluoride. MXenes were delaminated and reconcentrated to 3 mg/mL aqueous solution.

Glass FRPC tensile specimens for damage sensing and sandwich-type FRPC specimens for de-icing investigations were prepared by hand-layup and vacuum bagging methods. The epoxy resin Bisphenol F and an amine curing agent were mixed at a ratio of 10:3. Tensile specimens (15 × 1.5 cm) were made of 5 plies of twill-weave 2/2 (163 g/m²) glass fibres, and sandwich specimens (10 × 10 cm) were made of a total of 8 plies and 4 mm thick AIREX C70.75 foam. All specimens were cured at room temperature for 24 h and post-cured in a convection oven for 5 h at 100 °C. Plasma treatment of FRPC surface was used for all specimens. Two layers of MXene solution for sensing specimens and five – for de-icing were spread. Copper wires were directly soldered onto the MXene coating and silver ink was applied for coating edges. Specimens are shown in Figure 2.

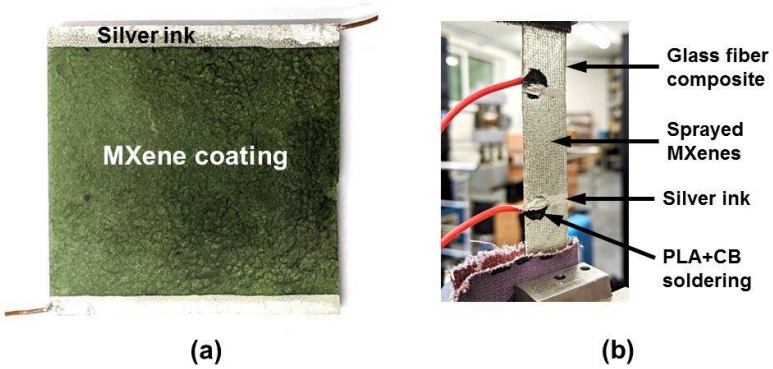

Figure 2. FRPC specimens for de-icing (a) and damage sensing (b) investigation

The initial electrical resistance values were monitored using a Fluke 287 True-RMS logging multimeter. The coatings were applied with DC voltage using an external power supply. The temperatures were evaluated using an infrared camera FLIR-SC7500. Fatigue tests were performed using the universal testing machine Instron ElectroPuls E10000T. Deformations were measured using Manta G-146B visual extensometer. For the tensile-tensile fatigue tests,

electrical resistance values were measured using Arduino Mega 2560 microcontroller and ATmega2560 microchip.

3. Results

3.1 MXene coating characterisation

Scanning electron microscopy (SEM) images of MXene coating (see Fig. 3 a) showed that MXene nanosheets are well delaminated and form a neat coating of oriented and overlapping 2D nanoparticles. Bumps of incompletely delaminated MXenes occur in some places. These coating's irregularities are also reflected in the atomic force microscopy (AFM) analysis study shown in Figure 3 b. The averaged thickness of the coating according to AFM investigation varied from 30 to 60 μm.

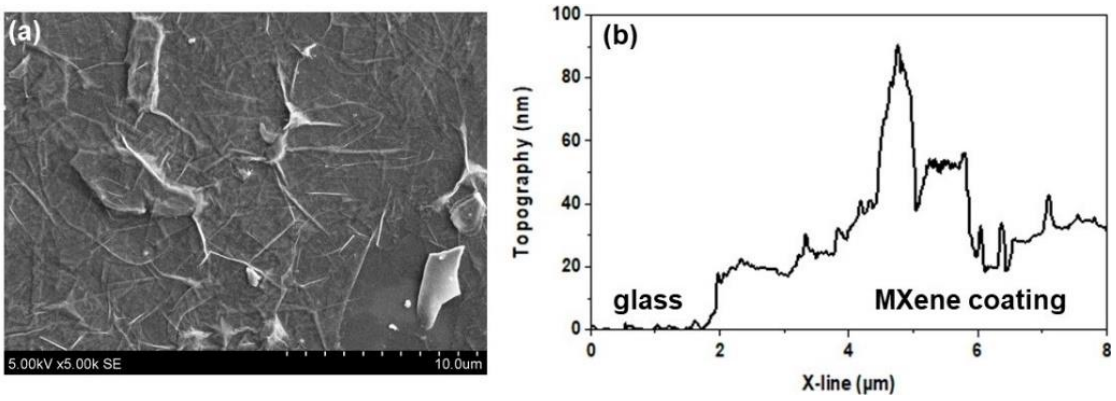

Figure 3. Characterisation of MXene coating: SEM image (a), and AFM analysis (b)

3.2 FRPC de-icing investigation

Thermal behaviour of MXene coating under 7.44 W was investigated. The temperature distribution of the coatings and the average temperature upon time is shown in Figure 4. It can be seen that the temperature distribution in the MXene coating is quite uniform. It can be seen that the thermal irregularities are due to the uneven thickness of the coating, the uniformity of which is difficult to ensure using the manual spraying method. The coating is able to heat up to 50°C in 120 s.

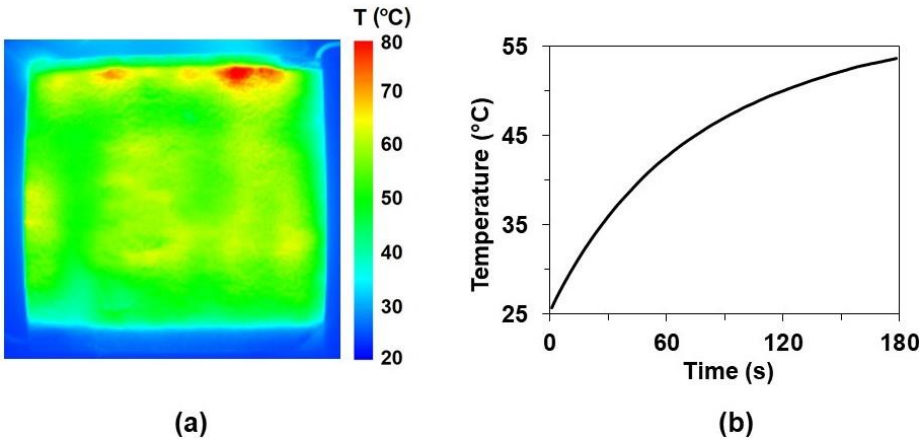

Figure 4. Thermal behaviour of MXene coating: temperature distribution of the coatings under 7.44 W power and 180 s (a); average temperature upon time at 7.44 W

3.3 FRPC damage sensing investigation

The tensile-tensile fatigue tests were performed under two different loading amplitudes (see Fig. 5). The first amplitude of 0.25–1.25 kN was repeated for 10 000 cycles and unloaded, after which the electrical resistance of MXene coating increased permanently by 18%. The second amplitude was 1–2 kN, where 2 kN corresponded to 264 MPa stress and 1.86% strain. The electrical resistance of MXene coating between these loads changed by 2.76%. Finally, the sample broke after 16245 cycles, and the resistance of the coating increased to infinite. A magnified region shown in Figure 5 represents the last several cycles before sample fracture. Here we can notice a slight increase in the coating's resistance, which suggests the first cracking of the glass FRPC specimen.

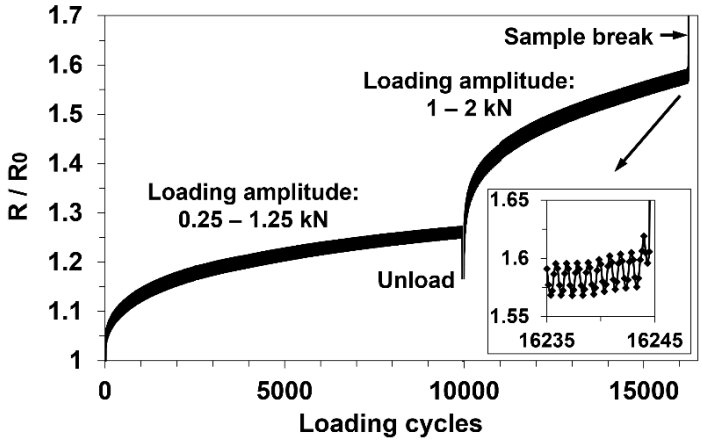

Figure 5. Electrical resistance response of MXene-coated FRPC under tensile-tensile fatigue test at two different loading amplitudes

4. Conclusions

The investigation showed that MXene coatings are able to impart multifunctional properties such as damage sensing and de-icing to glass fibre reinforced plastic composites. MXene coatings can heat up and melt the ice quickly and efficiently. The fatigue tests demonstrate that MXene coating is responsive to different amplitude loads and capable of tracking composite damage such as laminate cracks.

Acknowledgements

This project has received funding from the European Union's Horizon 2020 research and innovation programme under the Marie Skłodowska-Curie grant agreement No 777810.

5. References

1. Stankevich S, Bulderberga O, Tarasovs S, Zeleniakiene D, Omastova M and Aniskevich A. Electrical Conductivity of Glass Fiber-Reinforced Plastic with Nanomodified Matrix for Damage Diagnostic. Materials 2021; 14:4485.
2. Shimpi P, Aniskevich A and Zeleniakiene D. Improved method of manufacturing carbon nanotube infused multifunctional 3D woven composites. Journal of Composite Materials 2021; 56:479-489.

3. Zeleniakiene D, Monastyreckis G, Aniskevich A and Griskevicius P. Deformation and Failure of MXene Nanosheets. Materials 2020; 13:1253.
4. Kilikevičius S, Kvietkaitė S, Mishnaevsky J, Leon, Omastová M, Aniskevich A and Zeleniakienė D. Novel Hybrid Polymer Composites with Graphene and MXene Nano-Reinforcements: Computational Analysis. Polymers 2021; 13:1013.
5. Monastyreckis G, Mishnaevsky L, Hatter CB, Aniskevich A, Gogotsi Y and Zeleniakiene D. Micromechanical modeling of MXene-polymer composites. Carbon 2020; 162: 402-409.
6. Zukiene K, Monastyreckis G, Kilikevicius S, Procházka M, Micusik M, Omastová M, Aniskevich A and Zeleniakiene D. Wettability of MXene and its interfacial adhesion with epoxy resin. Materials chemistry and physics 2021; 257:123820.
7. Shimpi P, Omastova M, Aniskevich A and Zeleniakiene D. In Situ Deformation Monitoring of 3D Woven Composite T-Profile Using MXene Nanoparticles. Materials 2022; 15 :2730.
8. Monastyreckis G, Stepura A, Soyka Y, Maltanava H, Poznyak SK, Omastová M, Aniskevich A and Zeleniakiene D. Strain Sensing Coatings for Large Composite Structures Based on 2D MXene Nanoparticles. Sensors 2021; 21: 2378.

  doi:10.5075/epfl-298799_978-2-9701614-0-0

COMBOO – PROPERTIES OF A NOVEL BAMBOO BASED HONEYCOMB CORE MATERIAL FOR COMPOSITE SANDWICH STRUCTURES

Andreas Loth[a], Ralf Förster [a]

a: BHT Berlin, Germany, aloth@bht-berlin.de

Abstract: *This paper presents investigation results around a bamboo based honeycomb like core structure for sandwich applications. Due to excellent compressive strength values at a significantly reduced weight in comparison to plywood, the material could be a substitute in suitable applications. Light transmission through GFRP sheets was investigated as well, offering interesting fields of application for the combined sandwich structure.*

Keywords: Sandwich structure; Bamboo; lightweight; CO_2 footprint; compression test

1. Introduction

Fiber reinforced polymers usually consist of petrochemical products in combination with technical fibers like glass, aramid or carbon materials. The combination with suitable core materials leads to sandwich structures, providing superior mechanical properties like stiffness and weight compared to the base products and to many other unmodified materials too. The core materials are mainly polymer or metal foams, polymer, cardboard or metal honeycomb structures and sometimes lightweight wood as balsa.

The dependency on high amounts of energy or oil for producing the materials is somehow problematic. The prices for polymer products, epoxy or polyester resin and for fibers already increased rapidly since 2020 as the logistic chains and production were disturbed by Corona pandemic and increasing requirement in Asia. [1-4]

Another problem in the production of conventional sandwich components can be seen in the CO_2 emissions caused by the usage of energy and oil. The balsa wood production in mono cultures is also problematic.

Scientists worldwide are searching for products with a better ecological footprint. Interesting results are for example commercially available epoxy resins with a portion of up to 56 % of linseed oil. [5] Natural fibers like flax can be purchased as woven products to substitute glass or carbon fibers.

Nevertheless a wider focus on yet unknown or not yet useful materials like coconut or bamboo fibers, banana leaves, rice straw an many other natural products could decrease the dependency on the negative correlated resins and fibers.

A new approach for green core materials for sandwich applications can be COMBOO. COMBOO is a honey**COMB** structure made of bam**BOO**. [6] It consists of in a honeycomb pattern arranged bamboo rings. Top and bottom of the core were covered with GFRP, natural fibers, plywood and timer in several combinations. Previous investigations with this approach revealed a high bending strength and a nice appearance.

  doi:10.5075/epfl-298799_978-2-9701614-0-0

Bamboo is an extremely fast growing grass. Growth rates of up to 1m/day were reported. It is native to all continents except of Europe and Antarctica. Over 1000 different species can be found on earth. Bamboo has a density of approximately 0.6 – 0.7 g/cm^3 considering the solid material only. Tensile strength, hardness and bending capabilities are very high too. It ca be harvested after 5-7 years. Bamboo rods consist of longer hollow cylindrical parts divided by nodes and is conical which limits the direct usage for industrial processes in western countries. Therefore the bamboo is sliced and or cut, grinded, pressed, soaked with resin, glued and processed in several other ways to form standardized beams, chopping boards or floor coverings. Other extensive processing steps lead to fibers for clothes. Asian countries use bamboo and its products for ages in a more traditional way as building materials, for weapons, furniture, household stuff, cooking material and even for scaffolds for skyscrapers.

The concept of COMBOO is using the bamboo in a very little modified way, to preserve the superior properties and to reduce necessary machining steps. The density of COMBOO is with around 0.22 g/cm^3 significantly lower than bamboo wood considering that for the honeycomb structure over 70 % consist of air.

Another interesting (but environmental problematic) core material could be palm wood made of oil palms. Palms were like bamboo no trees either, even if the look like and reach heights of several tens of meters. One of the most popular palms for industry are oil palms as they deliver an organic oil that can be used in food, cosmetics, biofuel, detergents and many more. [7] Main producers of palm oil are Indonesia and Malaysia.

After approximately 25 years the economic life span of an oil palm ends. [8] reports of 100-120 million m^3 of palm wood trunks every year in near future that have to be replaced. While in the beginning push-fell and burn method was used to reduce biomass other methods are use nowadays as the previous one led to a gigantic CO_2 production and air pollution. Nevertheless the recent strategies (push-felled and windrow; push-felled, chip and windrow and under-planting) to decrease the large amount of decaying palms lead to diseases or pests. [7]

A much better strategy is using the palm wood for furniture, wood pellets and lightweight materials as density is relatively low. In contradiction to common timber density is high in outer regions with 0.4 g/cm^3 and low in the inner part. Density values vary with referred source from 0.15 g/cm^3 - 0.3 g/cm^3 for inner regions and 0.4 g/cm^3 - 0.7 g/cm^3 for outer regions, also varying with height. [7 - 10]

The investigation of these interesting materials as core materials for sandwich applications is one part of this paper. The other part refers to optical phenomena when using different resins, different fibers and different numbers of fiber layers. The COMBOO structure as a honeycomb provides several hollow parts, as can be seen in Figure 1 (l). When using glass fibers as top and bottom material for sandwich structures, light is passing through it. One possible application for these kind of sandwich could be in civil engineering, architecture or trade fair construction. Therefore the modification of light, its brightness or wavelength were under investigation.

  doi:10.5075/epfl-298799_978-2-9701614-0-0

2. Materials and methods

2.1 Materials and manufacturing of COMBOO structure

Manufacturing of COMBOO structure is relatively simple and requires a low level of machining equipment. It also uses a large part of the bamboo without chemical modifications and difficult processing steps. Hence it is suitable for easy production also in not fully industrialized countries.

First recommended step is a grinding procedure of the whole bamboo rod. The bamboo rod is much easier to handle than the smaller rings of a later processing level. Different grinding procedures like grinding, sandblasting and also milling to a hexagonal shape have been investigated and compared with unmodified bamboo in a shear test. [11] It was found that preparation is strongly recommended to enhance shear strength. Shear strength means in this case ability of movement ring against ring as shown in Figure 1. Previous bending tests often led to a failure due to the movement of a whole line of bamboo rings according to low shear strength.

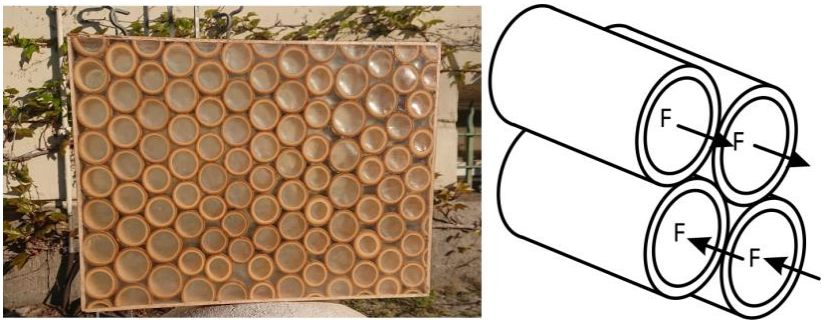

Figure 1. COMBOO structure – 600 x 400 x 80 mm (l), shear test of bamboo rings (r)

The improvement by grinding led to an increase of up to 40 % in shear tests. Grinding and milling were the most appropriate procedures, while grinding is very easy to perform. [11]

Second step is sawing the bamboo rod to rings with similar length. Several test have been made using different kinds of saws. Bamboo rings here were cut manually by using a band saw. Cutting is the most difficult step, as the bamboo rod is conical, sometimes not cylindrical and nodes are disturbing a good handling.

Only a few experiments have been performed yet to reduce the nodes as the most important problem. Grinding steps for example with an ankle grinder led to satisfying results. The size of the nodes depends also on bamboo species. The most common one from China, Moso bamboo has often larger nodes, especially when using bamboo rods with a diameter of less than 30 mm. Species like bamboo hitam, an Indonesian species shows no or only very low differences in diameter of cylindrical part and node.

Third step is arranging the cut bamboo rings in the honeycomb pattern. The pattern depends on allowed ring diameters. Arranging could hence influence the bending strength of the structure, which have to be investigated in further projects.

After arranging of the rings, lamination or better covering steps of top and bottom sheet occur as the last processing step. Different sheet materials have been tested. In this work plywood

  doi:10.5075/epfl-298799_978-2-9701614-0-0

sheets and glass fiber reinforced polymers (GFRP) have been used for experiments. Plywood was reduced to 2 layers (in two horizontal directions) for compression test.

The palm wood specimen have been received from palmwoodnet initiative and only cut into the required size. The fiber arrangement of the palm wood core (1 & 3 layer) was horizontal (to top and bottom material), covered with a plywood sheet of unknown origin. For comparison a birch plywood of 15 layers has been chosen. All test specimen were cut to side length of 50 x 50 mm. Differences in height were accepted, as the palm wood board was higher than the plywood and COMBOO board.

2.2 Materials and manufacturing of specimen for optical investigations

Nine different glass weavings (unidirectional, plain, twill weave) have been selected at different weights (25-220 g/m^2), in different numbers of layers (1-4) and two types of epoxy resin (Epoxy Resin L / Hardener CL, R&G Faserverbundwerkstoffe GmbH, Waldenbuch, Germany and SR Surf Clear EVO / SD EVO, Sicomin, France) for the optical experiments. Selected materials and materials combinations are shown in Table 1. Fabrics were processed in hand lamination technique, cured between two glass plates for surface quality and cut on a CO_2 laser cutter to the desired shape and size. It was tried to reach similar weight values of about 100 g / m^2 for the materials or a fraction of it for better comparison.

Table 1. Materials for optical investigations (UD – unidirectional weave)

ID nr	Weave	weight [g/m^2]	Number of layers	Total weight [g/m^2]	Resin
1	plain	25	1	25	Epoxy Resin L
2	plain	25	4	100	Epoxy Resin L
3	plain	49	1	49	Epoxy Resin L
4	plain	49	2	98	Epoxy Resin L
5	plain	108	1	108	Epoxy Resin L
6	plain	108	2	216	Epoxy Resin L
7	twill	105	2	210	Epoxy Resin L
8	UD	220	1	220	Epoxy Resin L
9	plain	49	2	98	Surf Clear Evo

For better comparison of optical measurements, two different hole patterns (diameter 20 and 40 mm) and two different thicknesses for one hole diameter (19 and 38 mm at hole diameter of 40) were machined to simulate a quasi-standard COMBOO structure. Therefore medium-density fiberboards (MDF) were milled or laser structured. GFRP sheets were glued onto to structures for transmission measurements, as will be described in chapter 3.

2.3 Testing methods

Compression test according to DIN EN 408 have been chosen to compare the different sandwich materials. Therefore a compression testing machine (TESTING Bluhm & Feuerherdt GmbH,

  doi:10.5075/epfl-298799_978-2-9701614-0-0

Berlin, Germany) was selected as its technical parameters met the requirements, received from initial tests. Results like compression strength, compressive stress at specific deformation and the stress strain behavior can be obtained.

Light measurement system was the portable spectrometer MK350 (UPRtek, Taiwan). The spectrometer acquires and calculates 5 different light values in the interesting spectrum of 380 - 780 nm. A closed MDF chamber was built and covered with mat black color to prevent reflections. The spectrometer was placed inside the chamber, controlled via cable by a computer and test specimen were placed at the open side. Test setup and a few test specimen are presented in Figure 2. The aperture of the box was 250 x 250 mm. Four different light sources with different power have been used according to Table 2.

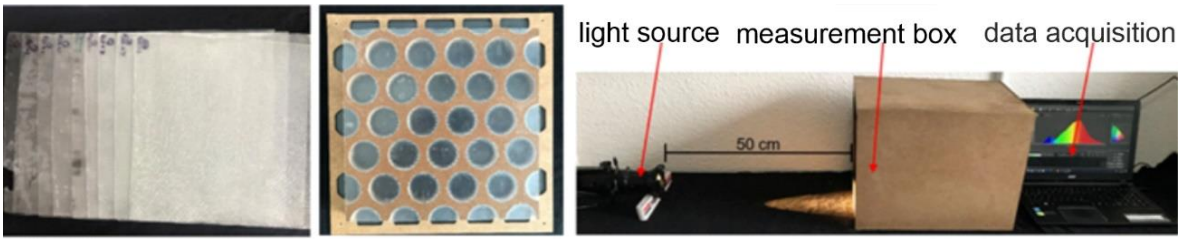

Figure 2. GFRP sheets, specimen holder and test setup (l. to r.) for optical measurements [13]

Table 2. Light sources for optical measurements

Nr	Source	Manufacturer	Power [W]	Color
1	Halogen	Strand lightung	650	Warm white
2	LED	ETC	14	Warm white
3	Fluorescent tube	Osram	36	Neutral white
4	Sun	-	-	Daylight

3. Experiments and results

3.1 Compression tests

Four different material classes of 7 samples each have been tested during compression tests. The specimen were placed under the plunger and the load was increased until failure criteria has been reached. Criteria were either exceeding the maximum load of 300 kN (not reached) or a maximum way of 20 percent of original thickness.

The results of the investigation are presented in Figure 3 (r). It can be seen, that the palm wood can only reach very low values of 1.7 N/mm^2 (one layer) and 2.3 N/mm^2 (three layers). It is known, that compression tests with timber in grain direction show much higher compression strength than perpendicular to the orientation.

The compressive strength values of plywood and the COMBOO board are much higher. The COMBOO board reached approximately 15 N/mm^2 und the plywood 13.4 N/mm^2. The weight of the COMBOO board is around 20 % lower than the plywood board, offering a wide field of applications.

  doi:10.5075/epfl-298799_978-2-9701614-0-0

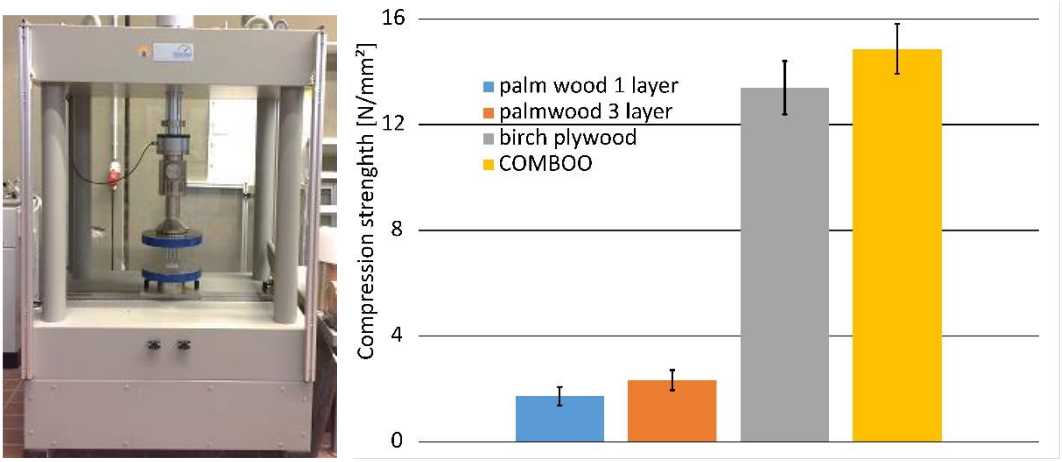

Figure 3. Testing machine (l), results of compression tests (r)

3.2 Light tests

Several test have been made to qualify the materials and the COMBOO structure as well. After preparing the light source at a distance of 500 mm, mounting the specimen in front of the box and calibration of spectrometer, test were performed while acquiring the interesting data on a computer.

For the first test the different GFRP samples without COMBOO structure were compared for all light sources. Figure 4 shows the transmission values for the most significant light source, the halogen lamp. LED lamp and sunlight show similar results, while the effects of the neon tube are less obvious

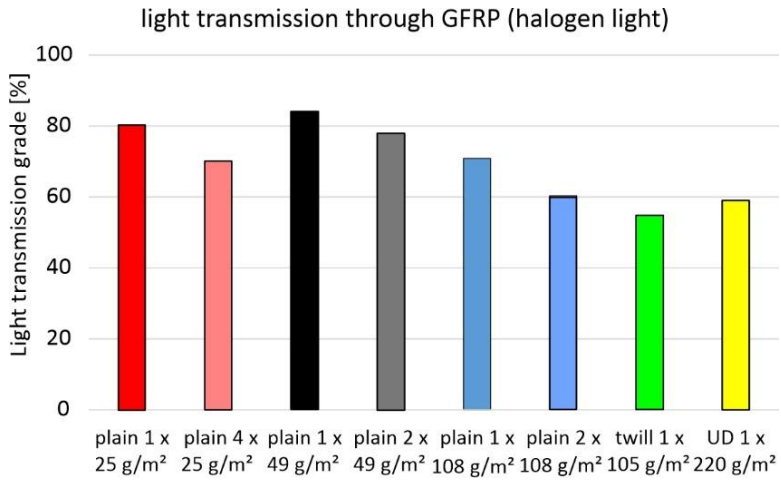

Figure 4. Light transmission measurements (different weave, number of layers and weight [13]

It can be seen, that the number of layers always reduces the transmission grade of approximately 10 percent. The single layer of plain weave fabric of 49 g /m^2 reaches higher transmission values than a single layer at 25 g /m^2. This effect is attributed to thinner fibers and more dense arrangement, as was observed under the microscope. The transmission trough plain weave fabric of 108 g /m^2 is a little different. While 2 layers of 49 g /m^2 show 78 % a single layer of 108 g /m^2 has a transmission grade of just 71 %. Twill weave (single layer) has the lowest transmission of just 55 %, as the binding is obviously very dense. Even the 220 g /m^2 UD fabric has a 4 % higher transmission. A difference in this effect was observed at sunlight only. [13]

It is interesting that the weight / m^2 has lower influence on transmission than the number of layers or the type of weave.

Second test was a comparison of epoxy resin. Using similar fabric (2 layers at 49 g /m^2) and the two different resins, light transmission depends on light source. While halogen light and sunlight led to significantly higher transmission values at the epoxy system L + CL, values at LED light were inverted. The neon tube light resulted in nearly equal values. This effect is attributed to the wave length, power and light spectrum. The Surf Clear Evo material is designed for longer exposure in sunlight without degradation. Hence it can be assumed that light could not penetrate or pass the resin, protecting deeper layers.

Third test refers on hole diameter of a simulated COMBOO structure. As expected a higher diameter leads to more light passing and higher transmission grades. Especially the sunlight provides the highest transmission of 34 % (20 mm) and 75 mm (40 mm). For other light sources transmission is sometimes up to 6 times higher (halogen lamp) for the larger diameter. This effect might be explained by the parallel sunbeams while the other light sources diverge from a source with defined distance and hence an angular side effect, especially while the usual focus of the theater lamps is somewhere behind 500 mm.

Fourth test has shown the effect of varying the light axis and using a deeper (38 mm thickness, hole diameter 40 mm) COMBOO structure. The effect was measured with the LED light only. It was found, that the grade of light transmission is reduced by 30 % if the angle is adjusted 15° of the perpendicular path. At 30 ° already more than 66 % of light are lost. Under 45°, more than 90 % of light cannot pass through the structure. With higher ring diameter and / or decreasing depth of the COMBOO board a higher amount of light transmission will be received.

It was finally found, that the colour rendering index or CRI – value were not affected by GFRP sheets. The value is nearly similar using no sheet or sheets with one / two layers. [13]

4. Summary and Discussion

In this paper two different topics of lightweight structures were under investigation connected by a novel interesting bamboo based core material for sandwich applications called COMBOO. After a brief introduction about bamboo and the manufacturing strategy of the COMBOO core material another natural material – oil palm wood has been presented too. Furthermore the materials and preparations for transmission tests depending on GFRP at different layers, weights and resins have been introduced.

In a compression test 4 different materials, 2 palm wood series and a plywood series were tested against the COMBOO structure. A much lower compressive strength has been identified for the 1 and 3 layer palm wood in contradiction to plywood and the COMBOO board. The COMBOO board reached 10 % higher average compressive strength value than the plywood board at up to 20 % lower weight. Hence COMBOO boards might be a good alternative to thick plywood boards. It is assumed, that the main remaining problem might be the closure of the outer rim of such a plate to prevent moisture coming into the structure, preventing a swelling.

The so called optical measurements were mainly transmission measurements of light from different sources through different weave and weights of GFRP. After initial tests with plain GFRP sheets other combinations were placed in front of and behind of a substitute COMBOO

  doi:10.5075/epfl-298799_978-2-9701614-0-0

structure. The substitute was chosen to reduce the influence of different sizes (inner / outer diameter) of natural bamboo.

It was identified that single layer GFRP provide higher transmission values then multi-layer arrangements. A higher weight of the fabric provides higher transmission values than the same weight reached by combining several layers. Twill weave has a significantly lower transmission than plain weave or UD fabric. The choice of an epoxy resin affects the transmission, depending probably manly on wave length. The CRI value was not affected by GFRP layers in comparison to undisturbed light.

Depending on the type of application, a protection against sunlight in separating walls or window replacements might be an interesting approach. It was found that already a moderate angle of 15° leads to a significant decrease of light transmission. An angle of 45° reduces the light to about 10 % of the original transmission value. Choosing a small wall thickness of the single bamboo rods and higher wall thickness of the whole COMBOO board might work well as a nice shading structure. Another advantage of the enclosed air between the two GFRP sides is an insulation effect.

Acknowledgements

The authors would like to thank Prof. Dr.-Ing. M. Beck, Dipl.-Ing. Olaf Linde for the support of compression measurements, Dipl.-Ing. M. Eng. Karsten Jäkel and Dipl.-Ing. Sarah Kamender for light measurements and woodworking.

5. References

1. https://www.farbeundlack.de/artikel/preisexplosion-bei-epoxidharzen, acquired 1.4.2022
2. https://bi-medien.de/fachzeitschriften/baumagazin/wirtschaft-politik/preisentwicklung-rohstoffverknappung-mc-bauchemie-erhoeht-die-preise-b13673, acquired 20.3.2022
3. https://www.plastverarbeiter.de/markt/alles-zur-rohstoffknappheit-in-der-kunststoffindustrie-258.html, acquired 1.4.2022
4. https://www.kiweb.de/default.aspx?pageid=2065, acquired 17.4.2022
5. https://www.timeout.de/news/bio-epoxidharz-sicomin/, acquired 1.3.2022
6. Loth, A. et al. Evaluation and comparison of a lightweight bamboo composite, AIP Conference Proceedings 1769, 170010, 2016
7. Erwinsyah, Improvement of Oil Palm Wood Properties Using Bioresin, Doctoral Thesis, TU Dresden, 2008
8. https://www.wbpionline.com/features/oil-palm-wood-an-untapped/, acquired 17.4.2022
9. Srivaro, S., et. al Property gradients in oil palm trunk. J Wood Sci 64, 709–719, 2018
10. Fathi, L., Structural and mechanical properties of the wood from coconut palms, oil palms and date palms, Doctoral Thesis, Universität Hamburg, 2014
11. Loth, A., Förster, R. COMBOO - a novel core material for composite sandwich structures from renewable sources, ECCM18, Athens, 2018
12. DIN EN 408, Timber structures - Structural timber and glued laminated timber - Determination of some physical and mechanical properties, Beuth, 2012
13. Jomeah, Y. Akustische und photometrische Untersuchung von bambusbasierten Leichtbaustrukturen, Masterthesis, Beuth University of Applied Science, 2020

  doi:10.5075/epfl-298799_978-2-9701614-0-0

EFFECT OF ASPECT RATIO AND BULK DENSITY OF CARBON NANOTUBE ON THE ELECTRICAL CONDUCTIVITY OF POLYCARBONATE/MULTI-WALLED CARBON NANOTUBE NANOCOMPOSITES

Shichoon, Lee[a], Youngon, Son[b]…

a: Department Aero-Materials Engineering, Jungwon University, 85 Munmu-ro Goesan-eup, 28024, Republic of Korea – tonygren@jwu.ac.kr
b: Division of Advanced Materials Science and Engineering, Kongju National University, Cheonan, Chungnam 31080, S. Korea – sonyg@kongju.ac.kr

Abstract: *We investigated electrical conductivity of PC/MWCNT nanocomposites prepared by both compression and injection molding. Three different MWCNTs with same diameter but different length were used in this study. Three different MWCNTs show different electrical conductivity of the nanocomposites especially in the injection molded samples. Among three MWCNTs used, two of them have same aspect ratio (L/D = 2000) but different bulk density (BD, 40 and 26 Kg/m3). We could investigate the effect of bulk density more clearly with these two MWCNTs. The other MWCNT has highest aspect ratio (16,000) and lowest BD (10 Kg/m3). Among three MWCNTs, the MWCNT with L/D = 2000, BD = 26 provided highest electrical conductivity of the nanocomposites. By various investigations, we found that the individualization and dispersion from the primary agglomerates is more decisive factor affecting the dispersion state and final electrical properties of the composite rather than the aspect ratio.*

Keywords: MWCNT; bulk density; aspect ratio; polycarbonate

Introduction

Polymer/carbon nanotube (CNT) composites have attracted extensive attention in terms of the electrical conductivity. Many factors such as properties of CNT, viscosity of matrix, aspect ratio (AR) and the fabrication methods of nanocomposites on the electrical conductivity have been explored. In order to study the effect of AR exclusively, one must prepare the CNTs of which ARs are different but the other properties are same. Many studies manipulated the AR with same length and different diameter of CNTs. In this study, we used three different multiwall carbon nanotubes (MWCNT) from same manufacturer. They have same thickness but different length. By various investigations, we found that individualization and dispersion from the primary agglomerates are more critical than the AR.

Experimental

Three different MWCNTs (Hanhwa Chemical, South Korea) with varying AR and BD were investigated. Characteristics of the MWCNTs are summarized in Table 1

Polycarbonate (PC)/MWCNT nanocomposites were prepared in a twin screw extruder at a speed of 150 rpm at 280 oC. For some samples, re-extrusion was performed. Pelletized nanocomposites was dried, fed into the hopper and extruded again. This procedure was

  doi:10.5075/epfl-298799_978-2-9701614-0-0

repeated with designated times. The extruder was a co-rotating twin screw extruder (BA-11, BAUTEK Co., Republic of Korea) with a screw length of 440 mm and a screw diameter of 11 mm.

The volume resistivity was measured by using the two-probe method with a manual probe station (SUMMIT-11862B, Cascade Microtech Inc.) and a semiconductor characterization system (4200-SCS/F, Keithley Instruments Inc.)

Table 1: Characteristics of As-Received CNTs.

Commercial Name	CM130	CM130 (upgraded)	CM280
Notation	AR2k-BD40	AR2k-BD26	AR16k-BD10
Length (μm)	25	25	200
Diameter (nm)	12.5	12.5	12.5
Aspect Ratio (L/D)	2 000	2 000	16 000
Bulk Density (g/cm^3)	~ 0.040	~ 0.026	~ 0.010

Results and discussions

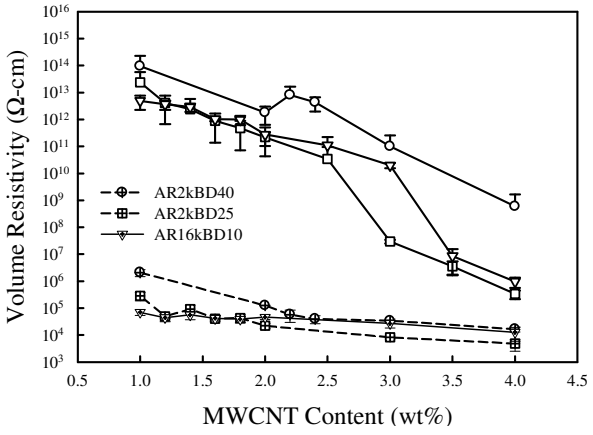

(b)

Figure 1. Volume resistivity of compression (crossed symbols, ⊕⊞⩛) and injection (open symbols, ○□▽) molded PC/MWCNT nanocomposites as a function of MWCNT concentration. circlar symbols: AR2kBD40, rectangular symbols: AR2kBD26, triangular symbols: AR16kBD10.

Figure 1 shows the volume resistivity of PC/MWCNT nanocomposites as a function of MWCNT content. In this study, three different MWCNTs were employed. Two of them are of same AR but different BD. When looking at the data of the samples having same AR (AR2k-BD40 and AR2k-BD26), it is certain that low BD sample leads to lower electrical resistivity. Carbon nanotubes must form an electrically conductive network within the polymer matrix in order to exhibit high electrical conductivity. The first step is to ensure disentanglement of CNTs from its primary agglomerates. Once dispersed, the individualized CNTs form an electrically conductive

  doi:10.5075/epfl-298799_978-2-9701614-0-0

network which enhances the final electrical properties of the composites. If the nanotubes are restricted in remaining primary agglomerates and are not nicely dispersed, the composites do not have enough amount of CNTs which build the conductive networks and consequently lead to the poor electrical conductivity. MWCNTs of the lower BD have higher probability for better dispersion due to its less entangled structure and provide the higher electrical conductivity. The AR2k-BD26 used in this study is an improved batch of CNT under the same commercial name with the AR2k-BD40. To our knowledge, slight modifications on the synthesis process were applied to improve the overall characteristics of the AR2k, which can significantly change the overall characteristics of the nanotubes. Such details on the process improvements remain undisclosed by the manufacturer.

When looking at the data for AR2k-BD26 and AR16k-BD10, unexpected result are seen. AR2k-BD26 provides the higher electrical conductivity in spite of lower AR and higher BD. This is more profound in injection molded samples. Up to date most studies has reported that CNT with higher AR provides higher electrical conductivity of the nanocomposites because the conductive network can be built at lower concentration for the CNT having the higher AR. Most studies on the effect of the AR do not provide information of the BD or CNTs with higher AR showed lower BD in the studies that provide the BD. Since CNTs with higher AR have lower BD in general, it is difficult to conclude which of AR (increase in possibility of tube-tube contacts) and BD (enhanced dispersion and individualization from the primary agglomerates) is more decisive factor in the electrical conductivity of polymer/MWCNT nanocomposites. Our experimental finding shows that the lowest BD and the highest AR do not always guarantee the higher electrical conductivity. MWCNTs with the high AR can bend, be coiled for higher AR and even tangle like a long polymer molecules for the highest AR. Their shapes are regarded as somewhere between a rigid slender body and polymer molecule. Thus, the AR may not affect the conductivity beyond the critical value.

In order to get fundamental insight into the reason of this unexpected result, we carried out the additional repeated extrusion. Fig. 2 shows the volume resistivity of PC/MWCNT nanocomposites as a function of extrusion times for AR2k-BD26 and AR16K-BD10. It is observed that the resistivity of the nanocomposite decreases with number of extrusions. Both AR2k-BD26 and AR16K-BD10 show decrease of the resistivity with number of extrusions but the decreasing rates are different. PC/AR16k-BD10(97/3) shows more rapid decrease. After third extrusion, PC/AR16K-BD10 (97/3) shows lower resistivity than that of PC/AR2k-BD26. It is certain that the dispersion of the MWCNTs in the PC matrix is enhanced with the number of repeated extrusions. Thus, the decrease of the electrical resistivity with the number of extrusions is explainable. The unexpected result that PC/AR2k-BD26(97/3) shows lower electrical resistivity than PC/AR16K-BD10 in spite of lower AR and higher BD is most probably due to different dispersion ability of two MWCNTs. Inherently, CNTs with higher AR has better ability to form a conductive network once they are dispersed and individualized from the primary agglomerates. However, it is more difficult to disperse CNTs with higher AR because longer CNTs has more entanglement between CNTs.

  doi:10.5075/epfl-298799_978-2-9701614-0-0

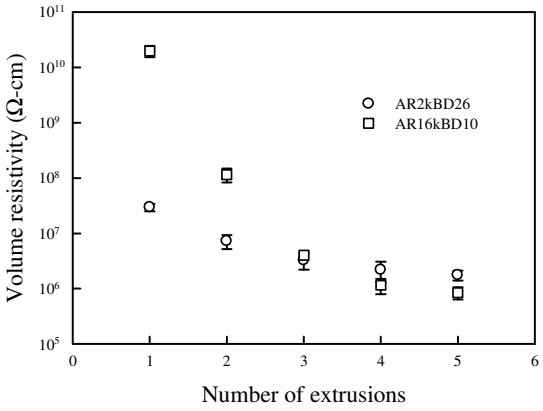

Figure 2. Electrical resistivity of PC/MWCNT nanocomposites extruded several times.

From the repeated extrusion experiments with AR2k-BD26 and AR16kBD10, we concluded that dispersion and individualization of CNTs from the primary agglomerates are more crucial. The repeated extrusion improves the dispersion of CNTs and AR16kBD10 provides the highest electrical properties after 4 repeated extrusion among three MWCNTs investigated. However, repeated extrusion is not economical in the industrial view. Therefore, practical way to achieve the highest electrical conductivity is using optimal AR and lower BD. Higher AR does not always guaranties the higher conductivity. This misleading is from the fact that higher AR normally accompanies lower BD. Theory on the maximum packing fraction of the randomly oriented glass fiber suggests that the maximum packing fraction is inversely proportional to the AR of glass fiber. It is most likely that the packing of the pristine MWCNT shows similar behavior.

So far most studies emphasized the importance of the AR. Only a few studies were conducted on the effect of BD. In this study, we found that BD is more important in some aspect and more studies on the BD should be conducted from now on.

Conclusion

Our study demonstrated that MWCNT aspect ratio does not solely determine the final electrical properties of the nanocomposites. In this study, it was observed that the MWCNTs with the highest AR and the lowest BD did not provide the highest electrical conductivity of PC/MWCNT nanocomposites. By various investigations, it was concluded that the higher AR is beneficial to build the conductive path but unfavorable for better dispersion since the longer MWCNTs tend to be more entangle and thus have higher resistance for disintegration of agglomerate. The bulk density of MWCNTs, inherent dispersive abilities caused by MWCNT entanglements, and intrinsic MWCNT alignment also play a very crucial role in the dispersion of MWCNTs in the polymer matrix, thereby also assisting in the final electrical property of the nanocomposites.

  doi:10.5075/epfl-298799_978-2-9701614-0-0

HIERARCHICAL SOLUTIONS TO COMPRESSIVE PROBLEMS IN FIBRE-REINFORCED COMPOSITES

David B Anthony[a,b], Cameron G Woodgate[c], Charles MD Shaw[e], Mayank Patni[d], Dimitrios Bikos[d], Rupam Gogoi[a], Torquato Garulli[b], Laura R Pickard[c], Gustavo Q Quino[c], Joseph F Gargiuli[c], Soraia Pimenta[d], Giuliano Allegri[c], Silvestre T Pinho[b], Ian Hamerton[c], Emile S Greenhalgh[b], Stephen J Eichhorn[c], Paul Robinson[b], Michael R Wisnom[c], Richard S Trask[c], Milo SP Shaffer[a,e]

a: Department of Chemistry, Imperial College London, UK
b: Department of Aeronautics, Imperial College London, UK
c: Bristol Composites Institute, Department of Aerospace Engineering, University of Bristol, UK
d: Department of Mechanical Engineering, Imperial College London
e: Department of Materials, Imperial College London, UK

d.anthony08@imperial.ac.uk

Abstract: *Currently, the useable compressive properties of a composite are restricted by set design limits well below the expected intrinsic performance of the materials contained within. The next generation of high-performance fibre-reinforced polymer composites will need to address the challenge of improving the absolute performance of composites in compression. This task requires a rethink of the whole system; not only to address practical limitations of current materials, but their combination, interface, and their architecture. The mechanisms involved do not simply act over the nano-, macro-, or meso-level independently, but are mutually related at the system level, complicating the approach.*

Keywords: Hierarchical; Compression; Fibre-reinforced composites

1. Introduction

In natural materials, such as wood and bone, a hierarchical framework is employed with precise structural features at all lengthscales [1]. Whilst this level of intricacy is still beyond current composite production, similar motifs can be made from intrinsically superior constituents, in order to improve (artificial non-natural) composite compression response. This hierarchical approach, with new constituent materials, and advanced assembly processes, when coupled with digital sandboxes, permits a fresh look at the failure mechanisms, providing opportunities to redirect, or suppress, failure modes to improve overall composite performance. The problem can be broken down into a number of interconnected components with attention given to the fibres, matrix and their interface/interphase, the design and lay-up of these constituents, and investigations using new analytical frameworks. This paper will outline the fibre-reinforced compressive weaknesses and approaches to resolve them, providing an insight into current state-of-the-art hierarchical composites.

  doi:10.5075/epfl-298799_978-2-9701614-0-0

2. Fibre-reinforced composites and bio-inspiration for hierarchical motifs

Fibre-reinforced composite materials are prominent in a range of applications with tensional loading conditions demonstrating their greatest performance (in the fibre axis). Whilst fibre-reinforced composites are used in other loading conditions, their compressive strength is approximately 60% of their tensile strength. Composite failure does not depend on a single element but rather a complex interconnectivity between the fibres, matrix, their interface, and the architecture of the specimen. In some instances, improving one area, for instance a high interface matrix-fibre adhesion, alters the failure mode of the composite e.g. inducing cohesive matrix failure, which can be an undesirable mechanism leading to a lower ultimate composite performance. For these reasons a holistic approach to address the compressive weakness in composites is sought with hierarchical architectures an intriguing approach to solve the weakness observed in compression. Looking to nature for inspiration [2, 3], a number of quite different approaches are observed; for example, multiscale reinforcing elements with particular orientation and support (Figure 1) [4], systems that have a strut and skeletal formation with minimal matrix content (fibrous), or conversely brick-and-mortar (layered) like formations using short reinforcing structures that dissipate stresses within the system, amongst other motifs. Alternative methods to dissipate energy or impacts through shear stiffening responses in the bulk of the material are observed but not commonly associated with a fibre-like scaffolds.

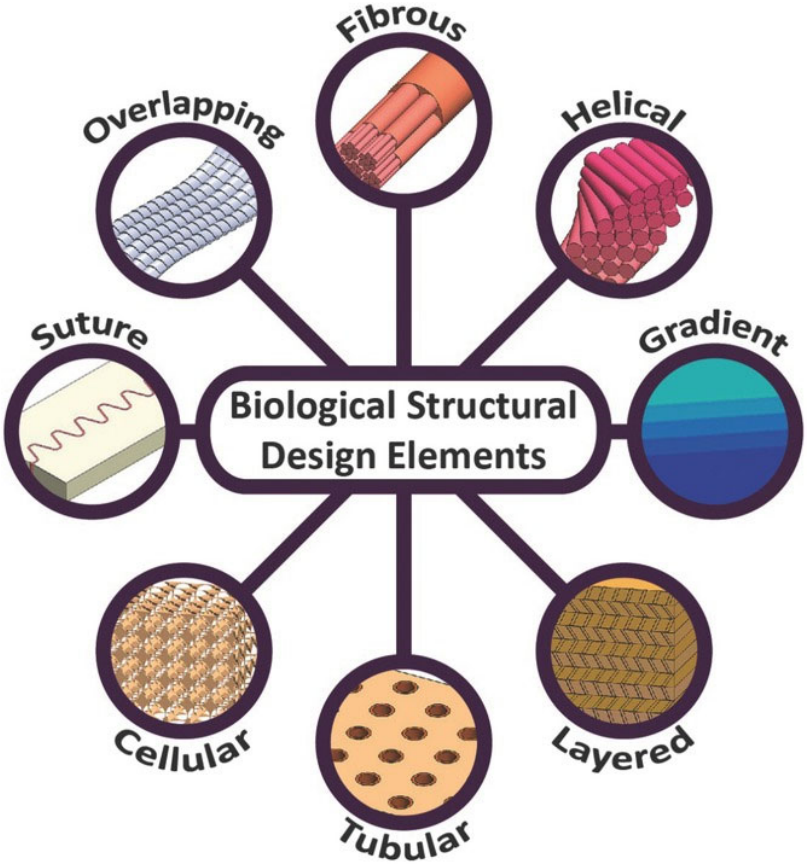

Figure 1. Diagram of the eight most common biological structural design elements [3]. [Used with permission from John Wiley and Sons]

  doi:10.5075/epfl-298799_978-2-9701614-0-0

In most instances, modifications to continuous fibre-reinforced composite materials fall broadly into categories that include, improving the interface of fibre-matrix components, introducing mechanisms to deflect, distribute, or dissipate stress to limit areas of high stress-concentrations, initiate tougher failure in a controlled manner to either defect or arrest the generated crack (introducing toughen response), or targeting the generally poor delamination strength (resin rich regions) between plies.

3. Current hierarchical composites designs and approaches

It is desirable to have fibres orientated in specified loading axis and to contain continuous fibres as these are more efficient with respect to mechanical loading [5]. Even with these design constraints, hierarchical approaches can be implemented to improve composite compression properties. A schematic of the composite designs discussed in the later sections are shown in Figure 2.

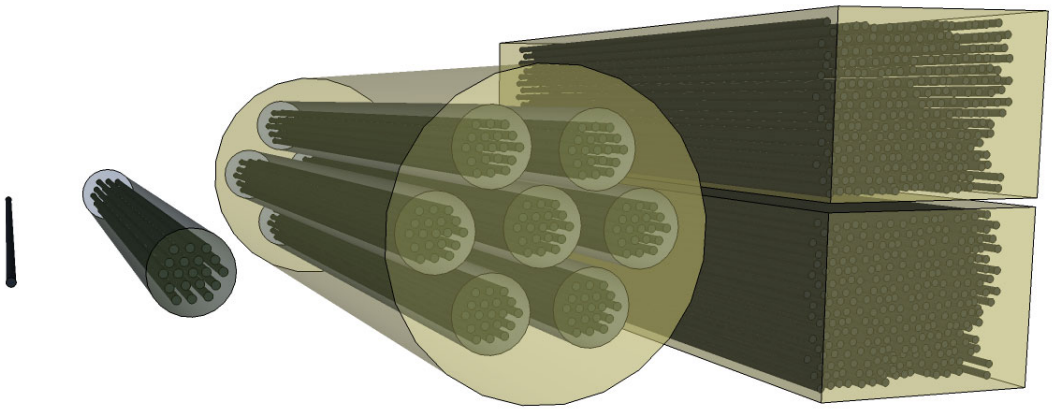

Figure 2. A schematic of the various length scales of the composite designs, from left to right, a single fibre (matrix omitted), a bundle of fibres in a matrix, a bundle-of-bundle composite, and a representation of a traditional unidirectional composite for comparison (shown with a gap to more clearly illustrate the plies).

3.1 Fibres

The shape and form of high performance (non-natural) fibres have usually been chosen for improved tensile properties and are uniform, continuous, circular, and small in diameter (~5-20 µm), but these characteristics may not be the optimal form for compressive loads. In Nature, the form of fibril scaffolds are normally non-circular, have defined periodicals of morphological changes, for instance bird feathers [6], and vary in diameter depending on their primary function. Another major difference between naturally occurring fibril/fibres and those artificially produced fibres are their hollow construction which allows for the transport of fluids throughout the organism, or to reduce weight for specific applications (e.g. flight); these features are not necessary for achieving ultimate mechanical performance using high performance constituents. Natural fibrils are often supported through a helical arrangement, or through a change in density of a porous or foam-like local structures (cellular and gradient). The complexity and refinement of the reinforcing elements of the structure changes from large features to smaller structures, which themselves can have specific alignment to aid support, when arranged about the parent fibril-structure. This alignment and change in length-scale is a key feature in improved lateral

  doi:10.5075/epfl-298799_978-2-9701614-0-0

support exhibited by these materials. These laterally supporting architectures provide adequate dissipation and non-stress localising properties and are desirable for high performance systems in a bid to reduce the failure mode(s) associated with the onset of kink-band formations. The failure of composite materials in compression is often driven by poor lateral support and early formation of kink-bands as a result of the instabilities of the loads experienced by the primary reinforcing fibres. To mimic this lateral supporting motif, there have been multiple attempts to add nanoreinforcement to the fibre surface/interphase which has the added benefit of reducing stiffness mismatch between the fibre and the matrix [7]. Methods include directly synthesising/growing nanomaterials on the surface, or depositing pre-made nanomaterials by electrophoretic deposition or some other chemical grafting process; the simplest approach is to coat the fibres in a size containing dispersions of nanomaterials. All these approaches suffer from some limitations for instance difficulties in scaling production, or poor alignment of the nanomaterial. Alignment of the nanomaterials, on the parent structure, is of particular significance, and is one of the most challenging aspect of adding nanomaterials to mimic the arrangements observed in biological systems. It is expected that if the nanoreinforcement is aligned in the axis of the parent fibre there may be limited lateral support in the surrounding interphase. However, increases in surface areas from these processes improve the mechanical interlocking of the fibre with the surrounding matrix which can improve the interfacial/interphase properties. Altering the morphology of the fibres' cross-section (unduloid or cross section shape) is a less studied approach to create supporting motifs, with either commercial fibres acquired and further processed [8] or produced/synthesised in-house to create the desired forms [9]. Depending on the materials chosen (carbon, glass, etc.) synthesising non-circular cross-section fibres can have significant cost, equipment, and processing constraints. There is also interest in well aligned nanomaterial based fibres/veils, which satisfy the requirements for local alignment whilst containing strong, stiff, and tough reinforcement.

3.2 Matrix

The most commonly used and modified composite matrix is epoxy (thermoset) due to the ease of handling and manipulation at the laboratory scale. Whilst thermoplastics are generally tougher, they require high temperatures and pressures to form around fibres, and as such they have been studied less often. Additionally, thermoplastic moduli are low resulting in less support for the fibres in compressive loading conditions; this along with poor compatibility between the thermoplastic matrix and fibres leads to a reduced fibre-matrix interface and overall composite performance. Methods to improve epoxy toughness includes the introduction of rubber particles, and for improved stiffness the introduction of nanomaterials (typically carbon) [10]. Chemical functionalisation is frequently used to improve the dispersibility of nanomaterials in an epoxy matrix resin system. However, the addition of nanomaterials to the matrix, even if unagglomerated, can alter the processability, increasing viscosities, and leading to self-filtering of the nanomaterials by the parent fibres. In natural materials there is often localised reinforcement leading to a heterogeneous structure, yet in the majority of composite systems a homogenous reinforcement is preferred. Further investigations into the impact of localising adequately dispersed nanoreinforcement and their effect on failure modes [11] is an exciting area of investigation.

  doi:10.5075/epfl-298799_978-2-9701614-0-0

3.3 Bundle systems

Bundle systems are similar, but one order of magnitude greater in size than the fibres systems previously described. Analogous adaptations for bundle composites are consequently desired, with off-axis reinforcement sought. Bundle-like pultruded composite rods are commercially available, with high alignment, allowing research into the surrounding matrices to form bundle-of-bundles composites and hybridisations. Bundle composites bridge the reinforcement length scales between fundamental systems and the ply level.

3.4 Ply level systems

In natural layer structures, deformation and localised failures are promoted to limit damage progression into the whole system. To achieve the same effect in high performance materials, the alignment of fibres within a ply may be exploited to alter and manipulate the failure modes observed. At the ply level, the introduction of misalignment (to the loading direction) or confined reinforcement to an area can alter the composite properties drastically. Choosing specific arrangements that benefit the compressive properties of the system are a challenge, and it is likely that suppression of the kink-band formation through careful consideration of materials and layup will be a route to success.

4. Outlook

The approach of introducing hierarchical constructs to fibre-reinforced composites is not new, however, in the most challenging loading condition of compression, there are very limited studies. Taking a step back, the use of existing materials, processes, and architectures needs to be revised for their suitability for use in hierarchical composite for compressive loading conditions. Whilst the focus will remain on the constituents of the composite for improvements, the combinations and arrangement need to be investigated to truly establish their performance in compression. A collaboration between Imperial College London and the University of Bristol, along with industrial partners are taking on this challenge in a five-year UK Engineering and Physical Sciences Research Council (EPSRC) funded project. We hope to share our investigations and results shortly.

Acknowledgements

The authors kindly acknowledge the funding for this research provided by UK Engineering and Physical Sciences Research Council (EPSRC) programme Grant EP/T011653/1, Next Generation Fibre-Reinforced Composites: a Full Scale Redesign for Compression a collaboration between Imperial College London and the University of Bristol.

5. References

1. Lakes R. Materials with Structural Hierarchy, Nature, 1993; 361:511-515, DOI: 10.1038/361511a0.
2. Bruck HA, Evans JJ, Peterson ML. The Role of Mechanics in Biological and Biologically Inspired Materials. Experimental Mechanic 2002; 42:361–371, DOI: 10.1007/BF02412140.
3. Naleway SE, Porter MM, McKittrick J, Meyers MA. Structural Design Elements in Biological Materials: Application to Bioinspiration. Advanced Materials 2015; 27:5455-5476, DOI: 10.1002/adma.201502403.

  doi:10.5075/epfl-298799_978-2-9701614-0-0

4. Masselter T, Hesse L, Böhm H, Gruhl A, Schwager H, Leupold J, Gude M, Milwich M, Neinhuis C, Speck T. Biomimetic optimisation of branched fibre-reinforced composites in engineering by detailed analyses of biological concept generators. Bioinspiration & Biomimetics 2016; 11:5:055005, DOI: 10.1088/1748-3190/11/5/055005.
5. Halpin JC, Kardos JL. Strength of Discontinuous Reinforced Composites: I. Fiber reinforced composites. Polymer Engineering and Science 1978; 18:6:496-504, DOI: 10.1002/pen.760180612.
6. Lingham-Soliar T, Bonser RHC, Wesley-Smith J. Selective biodegradation of keratin matrix in feather rachis reveals classic bioengineering. Proceedings of the Royal Society B 2010; 277:1161-1168, DOI: 10.1098/rspb.2009.1980.
7. Khan SU, Kim JK. Impact and Delamination Failure of Multiscale Carbon Nanotube-Fiber Reinforced Polymer Composites: A Review. International Journal of Aeronautical and Space Science 2011; 12:2:115-133, DOI: 10.5139/IJASS.2011.12.2.115.
8. Rodricks CW, Greenfeld I, Wagner HD. Polymer beads as interfacial obstacles in fibre composites. Composite Science and Technology 2021; 210:108793, DOI: 10.1016/j.compscitech.2021.108793.
9. Lee YS, Basova YV, Edie DD, Reid LK, Newcombe SR, Ryu S.K. Preparation and characterization of trilobal activated carbon fibers. Carbon 2003; 41:13:2573-2584, DOI: 10.1016/S0008-6223(03)00376-2.
10. Kinloch IA, Suhr J, Lou J, Young RJ, Ajyan PM. Composites with carbon nanotubes and graphene: An outlook. Science 2018; 362:6414:547-553, DOI: 10.1126/science.aat7439.
11. Abidin MSZ, Herceg TM, Greenhalgh ES, Shaffer MSP, Bismarck A. Enhanced fracture toughness of hierarchical carbon nanotube reinforced carbon fibre epoxy composites with engineered matrix microstructure. Composites Science and Technology 2019; 170:85-92, DOI: 10.1016/j.compscitech.2018.11.017.

  doi:10.5075/epfl-298799_978-2-9701614-0-0

TOUGH POLY(ETHYLENE GLYCOL)-SIZED BACTERIAL CELLULOSE SHEET FOR HIGH IMPACT STRENGTH LAMINATED ACRYLIC COMPOSITES

Natalia Herrera[a], Joanne Li[a], Koon-Yang Lee[a,b]

a: Department of Aeronautics, Imperial College London, SW7 2AZ, London United Kingdom
b: Institute for Molecular Science and Engineering, Imperial College London, SW7 2AZ, London, United Kingdom

Abstract: *Dried and well-consolidated sheet of bacterial cellulose (BC) nanofibrils is a material structure that possesses high modulus and strength but is also brittle, which limits its potential in various advanced composite applications. Here, we report a simple method of enhancing the toughness of BC sheet by sizing the BC nanofibrils with poly(ethylene glycol) (PEG). This hinders interfibril hornification and facilitates large-scale BC nanofibril debonding, slippage and reorientation upon deformation. The PEG-sized BC sheets show high tensile strain-at-failure and work of fracture compared to neat BC sheet. PEG-sized BC reinforced laminated acrylic composites achieve a flatwise Charpy impact strength of up to 26 kJ m 2. This is a remarkable increase over the impact strength of neat impact-modified acrylic of only 12 kJ m-2, especially when the BC loading required to achieve this radical improvement is only 0.2 wt-%. Our study opens new paradigm in using low BC loading to achieve performance improvements suitable for high value composite applications.*

Keywords: Nanocomposite; Biocomposite; Fracture toughness; Nanocellulose; Bacterial cellulose

1. Introduction

Bacterial cellulose (BC) is an ultrapure form of cellulose nanofibrils synthesised by cellulose-producing *Komagataeibacter* ssp. through the fermentation of low molecular weight sugars (1). It is bio-synthesised naturally as a nanomaterial (2) with a fibril width of 20-100 nm and an indeterminate length (3) to form a jellylike translucent mass, *i.e.,* a pellicle, floating at the air-liquid interface of the culture medium. BC is highly crystalline, with a measured degree of crystallinity of 90% (4). This results in the high tensile properties of BC nanofibrils. The Young's modulus of a single BC nanofibril was measured to be 78 GPa in bending using atomic force microscopy (5). Molecular deformation measurements based on Raman spectroscopy further estimated the tensile modulus of a single BC nanofibril to be 114 GPa (6). Whilst the tensile strength of a single BC nanofibril has not been reported, recent work based on sonication-induced fragmentation of (2,2,6,6-tetramethylpiperidin-1-yl)oxyl (TEMPO)-oxidised cellulose nanofibrils estimated the tensile strength to be between 1.6 and 6 GPa, depending on the source of cellulose (7). Therefore, BC could potentially serve as glass fibre alternative for the production of high-performance composite materials given their low toxicity and density (~1.6 g cm^{-3}) (8).

The ability of BC to act as nano-reinforcement in various advanced composite settings for load-bearing applications has been demonstrated by various authors (9-12). Despite this, BC has not yet been commercialised as reinforcement for polymers. A recent cost analysis estimated the break-even price of the large scale production of BC to be US$25/kg (wet basis, 99% moisture

  doi:10.5075/epfl-298799_978-2-9701614-0-0

content) (13). Such high-cost stems from capital expenditure as BC is grown most efficiently in static culture, as well as the low production rate of ~0.5 g (wet basis) L^{-1} h^{-1}. Thus, BC is an expensive nano-reinforcement, especially when high loading fraction of BC in a polymer matrix is required (>30 vol.-%) to demonstrate significant mechanical improvements over conventional engineering polymers (9). It can be anticipated however that the high cost of BC can be offset by designing BC composites containing only low loading fraction of BC but still offering dramatically improved mechanical performance that conventional materials cannot achieve. A defining characteristic of BC is that it is biosynthesised as a continuous network of cellulose nanofibrils into a tough pellicle, especially in the plane of growth (14). If the toughness of the pellicle can be translated into a composite setting, it will introduce additional energy-dissipating mechanisms, including BC nanofibril-nanofibril debonding, BC nanofibril re-orientation and fracture, improving the fracture resistance and impact strength of the resulting BC-reinforced composite materials. This is a sought-after property as advanced BC fibre composites are often brittle (15-20).

In the manufacturing of BC composites however, BC is first dehydrated prior to subsequent composite processing, such as resin impregnation followed by crosslinking or thermoplastic lamination (15, 18, 19, 21). The dehydration step leads to interfibril hornification (22), i.e., the formation of irreversible hydrogen bonds between the adjacent cellulose nanofibrils upon drying, producing a brittle BC sheet with poor fracture resistance. The introduction of such brittle BC sheet into a polymer matrix also reduces the fracture resistance of the resulting BC composites. Here, we report a simple concept based on the sizing BC nanofibrils with low molecular weight poly(ethylene glycol) (PEG) to prevent interfibril hornification, thereby preserving the original toughness of the pellicle. Low molecular weight PEG is ideal as it exists as a liquid at room temperature (up to 600 g mol^{-1}). This allows the BC nanofibrils in the resulting BC sheet to reorientate and/or slip during mechanical deformation. Such effect cannot be achieved with solid PEG as the BC sheet would fracture brittlely in the solid PEG matrix. We further show in this article that these low molecular weight PEG-sized BC can be used as two-dimensional reinforcement in a laminated composite construct to enhance the impact properties of polymeric materials even at low loading fraction (0.2 wt.-%) without sacrificing tensile performance.

2. Experimental

2.1 Materials

Methyl methacrylate (MMA) (Aldrich, purity ≥ 99%, inhibited with ≤ 30 ppm monomethyl ether hydroquinone) and 2,2'-azobis(2-methylpropionitrile) (AIBN) (Aldrich, purity ≥ 98%) were purchased from Sigma-Aldrich. Triethyl citrate (TEC) (Alfa Aesar, purity ≥ 99%), sodium hydroxide pellets (AnalaR NORMAPUR®, purity > 98.5%,) and PEG, namely PEG-200 (Merck Chemicals Ltd., M_w = 200 g mol^{-1}, ρ = 1.124 g cm^{-3} @ 20°C, T_m = -50°C), PEG-400 (Merck Chemicals Ltd., M_w = 400 g mol^{-1}, ρ = 1.13 g cm^{-3} @ 20°C, T_m = 5°C), as well as PEG-600 (Merck Chemicals Ltd, M_w = 600 g mol^{-1}, ρ = 1.13 g cm^{-3}, T_m = 17-22°C) were purchased from VWR International Ltd. (Lutterworth, UK). These chemicals were used as received without further purification. Commercially available impact-modified acrylic sheets (Plexiglas 0RA65 GT, 3 mm thick) were purchased from Röhm (Darmstadt, Germany). BC in the form of 30 cm × 30 cm × 1 cm pellicle with a water content of 98.7 wt.% was purchased from a commercial retailer (Vietcoco International Co. Ltd., Ho Chi Minh City, Vietnam). It was purified with 0.1 N sodium

  doi:10.5075/epfl-298799_978-2-9701614-0-0

hydroxide in house following a previously described protocol (20) and stored in a 4°C fridge prior to subsequent use.

2.2 Preparation of tough PEG-sized BC sheets

Purified BC pellicle with dimensions of 65 mm × 65 mm × 10 mm (wet weight = 31 ± 7 g, Fig. 1a) was immersed in PEG (200 g) and magnetically stirred at room temperature for 30 min to promote the mixing of water molecules in the BC pellicle with the surrounding liquid PEG. This suspension was then subjected to a reduced pressure at 200 mbar for 2 h (Fig. 1b) to further draw out the water in the BC pellicle. The PEG-impregnated BC pellicle was carefully removed, allowing excess PEG to drip away, before placing it on a petri-dish and heated to 50°C for 24 h to slowly evaporate the excess water. After this pre-drying step, the PEG-impregnated BC pellicle was sandwiched between two filter papers (Qualitative filter paper 413, VWR International Ltd., Lutterworth, UK) and two blotting papers (Grade 3MMCHR, GE Healthcare, Buckinghamshire, UK), followed by hot pressing (4122CE, Carver Inc., Wabach, IN, USA) at 120°C for 30 min under a weight of 1 t to remove any residual moisture and excess PEG, consolidating the 10 mm thick PEG-impregnated BC pellicle into PEG-sized BC sheet of 66-150 µm in thickness, depending on the PEG used (Fig. 1c). Simple gravimetric measurement showed that the mass fraction of PEG-200, PEG-400 and PEG-600 in the BC sheets were 57 ±9 wt.-%, 55 ± 8 wt.-% and 49 ± 10 wt.-%, respectively. Even though liquid PEG was used in the sizing of BC, the resulting PEG-sized BC sheets did not have a “wet feel” to it as the liquid PEG was held strongly within the consolidated BC nanofibril network structure through capillary forces. As a control, neat BC sheet (70 g m^{-2}) without PEG sizing was also produced following the previously described pre-drying and hot-pressing steps. The porosity of neat BC sheet was found to be 30% and all the PEG-sized BC sheet possessed a porosity of ~12% based on density measurements (see Table S1 in the supplementary information). All (PEG-sized) BC sheets were kept dry in a desiccator containing silica gels before subsequent use.

2.3 Fabrication of laminated acrylic composites reinforced with (PEG-sized) BC sheets

In this work, 3 mm thick acrylic composites with a laminated construct consisting of (PEG-sized) BC sheet sandwiched between two 1.5 mm thick impact-modified acrylic sheets were produced. Triethyl citrate-plasticised poly(methyl methacrylate) (TEC-plasticised PMMA) was used as the interlayer adhesive. Firstly, the TEC-plasticised PMMA interlayer adhesive was produced by adding TEC (5 g, 25 wt.-%) and AIBN (60 mg, 0.3 wt.-%) into 20 g of MMA. This solution was magnetically stirred for 10 min, followed by pre-polymerisation in a water bath at 75°C for 35 min until a viscous syrup was obtained. The syrup was then immediately cooled in an ice bath to quench the polymerisation reaction. The viscous TEC-plasticised PMMA syrup was then flow coated onto a prefabricated 1.5 mm thick impact modified acrylic sheet (compression moulded from the 3 mm thick sheets using a weight of 1 t at 190 °C), followed by the placement of a (PEG-sized) BC sheet (Fig. 1d). The composite construct was then assembled with another coating of viscous TEC-plasticised PMMA syrup on the topside of the (PEG-sized) BC sheet and the placement of another prefabricated 1.5 mm thick impact modified acrylic sheet. Care was taken at each stage to ensure that no bubbles were trapped in between the layers. Finally, the assembled composite construct was heated in an oven at 70°C for 4 h under a weight of 5 kg to fully polymerise the TEC-plasticised PMMA interlayer adhesive, producing (PEG-sized) BC-reinforced laminated acrylic composite (Fig. 1e). The loading fraction of BC in the laminated composites was 0.2 wt.-% based on simple weight gain measurement. Dynamic mechanical

  doi:10.5075/epfl-298799_978-2-9701614-0-0

thermal analysis revealed that the different PEGs did not affect the degree of polymerisation of the TEC-plasticised PMMA interlayer as they possessed similar glass transition temperatures at ~60 °C (see Fig. S1 in the supplementary information). As a control, laminated composite consisting of TEC-plasticised PMMA interlayer adhesive without BC reinforcement was also produced.

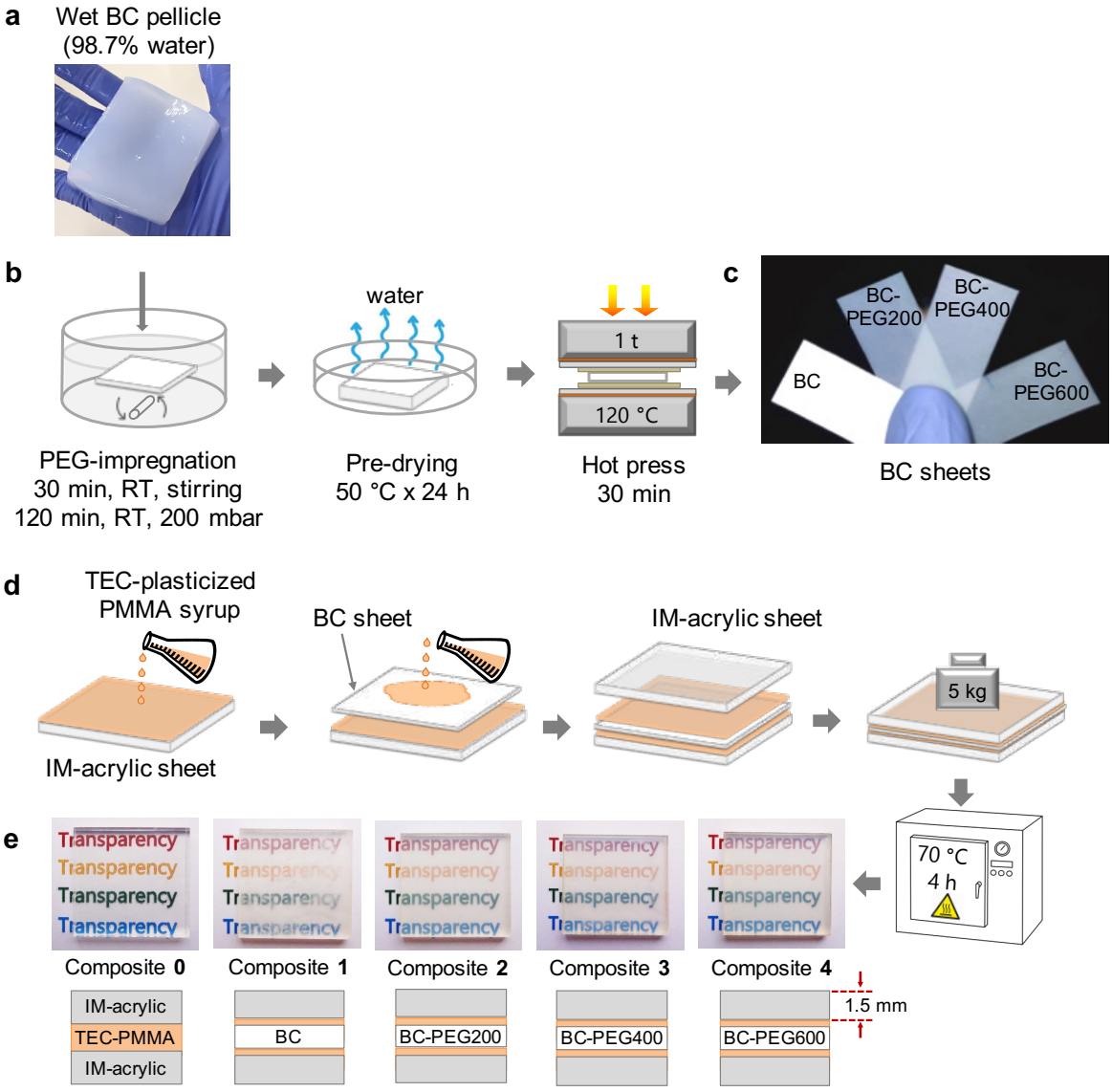

Fig 1. (a) A wet BC pellicle (65 mm × 65 mm x 1 cm), (b) schematic representation of PEG-impregnated BC sheets preparation, (c) visual appearance of (PEG-impregnated) BC sheets, (d) schematic representation of composite preparation and (e) visual appearance of the translucent (PEG-sized) BC sheet-reinforced impact-modified (IM)-acrylic composites.

2.4 Materials characterisation

Prior to tensile testing, the samples were cut into miniaturised rectangular test specimens of 5 mm in width and 40 mm in length using a Zwick/Roell ZCP 020 manual cutting press (Zwick Testing Machines Ltd., UK). Two dots were marked on the surface of the test specimen in the direction of the applied load. The test specimen was then mounted onto a micro tensile tester (MT-200, Deben UK Ltd., Woolpit, UK) equipped with a 200 N load cell. The distance between

  doi:10.5075/epfl-298799_978-2-9701614-0-0

the grips was set to be 25 mm. A crosshead displacement speed of 0.5 mm min^{-1}, which corresponded to a strain rate of 3 × 10^{-4} s^{-1}, was used. The strain of the test specimen during tensile loading was measured using a non-contact video extensometer (iMetrum Ltd., Bristol, UK) based on the movement of the two previously marked dots. Tensile test was performed at room temperature (20°C) and a relative humidity of 40%. Average results of five test specimens were reported for each sample.

3. Results and discussion

The representative tensile stress-strain curves of (PEG-sized) BC sheets are presented in Fig. 2. After the initial linear elastic response, followed by yielding and a small degree of plastic deformation, neat BC sheet fractures catastrophically (Fig. 2, red curve). This is characterised by a single sharp decrease in stress to zero after peak load is reached (3.4% strain for neat BC sheet). Neat BC sheet possesses a tensile modulus and strength of 16.5 GPa and 177 MPa, respectively (Table 1). These values are consistent with the tensile properties of dried and well-consolidated BC sheet at similar grammage produced from pristine pellicle reported by Yamanaka et al. (23) and Nakagaito et al. (18) A recent study also confirmed that the theoretical maximum tensile strength of a sheet of randomly oriented cellulose nanofibrils was ~200 MPa (24), consistent with our findings. It is worth mentioning that BC sheet produced from disintegrated pellicle possesses lower mechanical properties than those made from pristine pellicle (8).

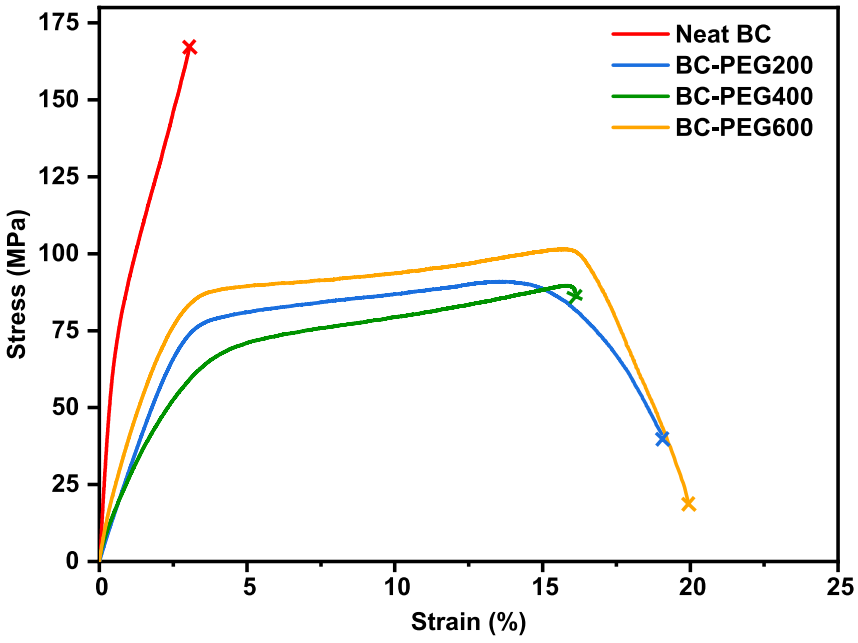

Fig 2. Representative tensile stress-strain curves of (PEG-sized) BC sheets

All PEG-sized BC sheets, on the other hand, exhibit a ductile response, with prolonged plastic deformation prior to fracture at a strain of ~17% (Fig. 2, blue, orange and green curves). The sizing of BC with PEG also leads to a decrease in both the tensile modulus and strength (Table 1). BC-PEG200 possesses the lowest tensile modulus of 3.0 GPa, followed by BC-PEG400 of 3.4 GPa and BC-PEG600 of 4.5 GPa. This increase in tensile modulus can be attributed to the increase in the viscosity of PEG with increasing molecular weight (see Fig. S2 in the supplementary information). All PEG-sized BC sheets possess similar tensile strength of ~90

  doi:10.5075/epfl-298799_978-2-9701614-0-0

MPa, independent of the type of PEG used. The brittleness of neat BC sheet also led to lower tensile work of fracture (U_T, calculated from the area under the stress strain curves, Table 1) of 4 MJ m^{-3} compared to the more ductile PEG-sized BC sheets of ~14 MJ m^{-3}.

As the tensile properties of a sheet of cellulose fibrils are a function of the tensile properties of the fibril, fibril length and the degree of fibril-fibril bonding (25, 26), the observed decrease in both tensile modulus and strength must be due to a reduction in the degree of fibril-fibril bonding as both the BC nanofibril length and BC nanofibril tensile properties are the same for all samples. The large number of physical crosslinking points between adjacent BC nanofibril due to interfibril hornification prevents large-scale nanofibril debonding and slippage, as well as reorientation. This leads to the observed high tensile modulus and strength of the neat BC sheet but also limits its plastic deformation, resulting in low strain-at-failure and a catastrophic fracture. A previous study (27) confirmed that the hydroxyl groups of cellulose and the hydroxyl end groups of PEG would form strong hydrogen bonds. Therefore, the sizing of BC with PEG leads to a decrease in the number of hydrogen bonds formed between adjacent BC nanofibrils, hindering the interfibril hornification process. This facilitates BC nanofibril reorientation and/or slip during tensile deformation, resulting in the observed large strain-at-failure, overcoming the inherent brittleness of BC sheets. The lack of interfibril hornification also corroborates with the results that the tensile strength of the PEG-sized BC sheets is independent of the molecular weight of PEG used as the failure mechanism is now governed by the degree of entanglement of the BC nanofibrils in the original pellicle, which is similar for all PEG-sized BC sheets.

Table 1. Mechanical properties of (PEG-sized) BC sheets. *E, σ* and ε_B denote the tensile modulus, tensile strength and tensile strain-at-failure, respectively.

Sheet	E (GPa)	σ (MPa)	ε_B (%)
Neat BC	16.5 ± 0.2	177 ± 13	3.4 ± 0.4
BC-PEG200	3.0 ± 0.2	92 ± 6	15.9 ± 3.7
BC-PEG400	3.4 ± 0.5	91 ± 5	17.7 ± 1.4
BC-PEG600	4.5 ± 0.8	94 ± 10	18.2 ± 3.7

4. Conclusions

The toughness of dried and well-consolidated sheet of BC nanofibrils was enhanced by sizing the BC with liquid PEG of different molecular weights, namely PEG-200, PEG-400 and PEG-600. Whilst the PEG sizing reduced both the tensile modulus and strength of the BC sheet, the tensile strain-at-failure and toughness improved by ~400% and ~900%, respectively, over neat BC sheet. The sizing of BC with liquid PEG, independent of molecular weight, minimises the number of contact or physical crosslinking points via hydrogen bonding between adjacent BC nanofibrils, reducing the efficacy of interfibril hornification. This study also shows the potential of PEG-sized BC sheet in a laminated composite construct (to be presented in the presentation), whereby radical improvement in the impact resistance of the laminated composites can be achieved with only just 0.2 wt-% of BC. This also keeps the overall cost of the BC composites low as the cost of BC is often cited as the bottleneck for using BC in various advanced composite applications.

5. References

  doi:10.5075/epfl-298799_978-2-9701614-0-0

1. Florea M, Hagemann H, Santosa G, Abbott J, Micklem CN, Spencer-Milnes X, et al. Engineering control of bacterial cellulose production using a genetic toolkit and a new cellulose-producing strain. Proceedings of the National Academy of Sciences of the United States of America. 2016;113(24):E3431-E40.
2. Klemm D, Kramer F, Moritz S, Lindström T, Ankerfors M, Gray D, et al. Nanocelluloses: A new family of nature-based materials. Angewandte Chemie - International Edition. 2011;50(24):5438-66.
3. Brown Jr RM, Willison JHM, Richardson CL. Cellulose biosynthesis in Acetobacter xylinum: visualization of the site of synthesis and direct measurement of the in vivo process. Proceedings of the National Academy of Sciences of the United States of America. 1976;73(12):4565-9.
4. Lee KY, Bismarck A. Susceptibility of never-dried and freeze-dried bacterial cellulose towards esterification with organic acid. Cellulose. 2012;19(3):891-900.
5. Guhados G, Wan W, Hutter JL. Measurement of the elastic modulus of single bacterial cellulose fibers using atomic force microscopy. Langmuir. 2005;21(14):6642-6.
6. Hsieh YC, Yano H, Nogi M, Eichhorn SJ. An estimation of the Young's modulus of bacterial cellulose filaments. Cellulose. 2008;15(4):507-13.
7. Saito T, Kuramae R, Wohlert J, Berglund LA, Isogai A. An ultrastrong nanofibrillar biomaterial: The strength of single cellulose nanofibrils revealed via sonication-induced fragmentation. Biomacromolecules. 2013;14(1):248-53.
8. Santmarti A, Zhang H, Lappalainen T, Lee KY. Cellulose nanocomposites reinforced with bacterial cellulose sheets prepared from pristine and disintegrated pellicle. Composites Part A: Applied Science and Manufacturing. 2020;130.
9. Lee KY, Aitomäki Y, Berglund LA, Oksman K, Bismarck A. On the use of nanocellulose as reinforcement in polymer matrix composites. Composites Science and Technology. 2014;105:15-27.
10. Neves RM, Ornaghi HL, Zattera AJ, Amico SC. Recent studies on modified cellulose/nanocellulose epoxy composites: A systematic review. Carbohydrate Polymers. 2021;255.
11. Oksman K, Aitomäki Y, Mathew AP, Siqueira G, Zhou Q, Butylina S, et al. Review of the recent developments in cellulose nanocomposite processing. Composites Part A: Applied Science and Manufacturing. 2016;83:2-18.
12. Qiu K, Netravali AN. A review of fabrication and applications of bacterial cellulose based nanocomposites. Polymer Reviews. 2014;54(4):598-626.
13. Fourado F, Fontão AI, Leal M, Rodrigues AC, Gama M. Process Modelling and Techno-Economic Evaluation of an Industrial Airlift Bacterial Cellulose Fermentation Process. In: Lee KY, editor. Nanocellulose and Sustainability: Production, Properties, Applications and Case Studies. Boca Raton: CRC Press; 2018. p. 1-16.
14. Brown AJ. XLIII. - On an acetic ferment which forms cellulose. Journal of the Chemical Society, Transactions. 1886;49:432-9.
15. Hervy M, Blaker JJ, Braz AL, Lee KY. Mechanical response of multi-layer bacterial cellulose nanopaper reinforced polylactide laminated composites. Composites Part A: Applied Science and Manufacturing. 2018;107:155-63.
16. Hervy M, Bock F, Lee KY. Thinner and better: (Ultra-)low grammage bacterial cellulose nanopaper-reinforced polylactide composite laminates. Composites Science and Technology. 2018;167:126-33.
17. Lee KY, Tammelin T, Schulfter K, Kiiskinen H, Samela J, Bismarck A. High performance cellulose nanocomposites: Comparing the reinforcing ability of bacterial cellulose and nanofibrillated cellulose. ACS Applied Materials and Interfaces. 2012;4(8):4078-86.

  doi:10.5075/epfl-298799_978-2-9701614-0-0

18. Nakagaito AN, Iwamoto S, Yano H. Bacterial cellulose: The ultimate nano-scalar cellulose morphology for the production of high-strength composites. Applied Physics A: Materials Science and Processing. 2005;80(1):93-7.
19. Quero F, Nogi M, Yano H, Abdulsalami K, Holmes SM, Sakakini BH, et al. Optimization of the mechanical performance of bacterial cellulose/poly(L-lactic) acid composites. ACS Applied Materials and Interfaces. 2010;2(1):321-30.
20. Santmarti A, Teh JW, Lee KY. Transparent Poly(methyl methacrylate) Composites Based on Bacterial Cellulose Nanofiber Networks with Improved Fracture Resistance and Impact Strength. ACS Omega. 2019;4(6):9896-903.
21. Yano H, Sugiyama J, Nakagaito AN, Nogi M, Matsuura T, Hikita M, et al. Optically transparent composites reinforced with networks of bacterial nanofibers. Advanced Materials. 2005;17(2):153-5.
22. Iguchi M, Yamanaka S, Budhiono A. Bacterial cellulose - a masterpiece of nature's arts. Journal of Materials Science. 2000;35(2):261-70.
23. Yamanaka S, Watanabe K, Kitamura N, Iguchi M, Mitsuhashi S, Nishi Y, et al. The structure and mechanical properties of sheets prepared from bacterial cellulose. Journal of Materials Science. 1989;24(9):3141-5.
24. Kontturi KS, Lee KY, Jones MP, Sampson WW, Bismarck A, Kontturi E. Influence of biological origin on the tensile properties of cellulose nanopapers. Cellulose. 2021;28(10):6619-28.
25. Page DH. A theory for the elastic modulus of paper. British Journal of Applied Physics. 1965;16(2):253-8.
26. Page DH. A theory for the tensile strength of paper. Tappi Journal. 1969;52:674-81.
27. Liang XH, Guo YQ, Gu LZ, Ding EY. Crystalline–Amorphous Phase Transition of a Poly(ethylene glycol)/Cellulose Blend. Macromolecules. 1995;28(19):6551-5.

  doi:10.5075/epfl-298799_978-2-9701614-0-0

EXPERIMENTAL INVESTIGATION AND MODELLING OF THE MORPHOLOGY AND INDUCED THERMAL PROPERTIES EVOLUTION BY CONSOLIDATION OF FLAX FIBRES REINFORCED THERMOPLASTIC COMPOSITE

Henri Perrin, Margot Lucas, Noha-lys Senoussaoui, Yao Koutsawa

Luxembourg Institute of Science and Technology – henri.perrin@list.lu

Abstract: *This study is focused on the understanding of the morphology evolution and associated thermal properties during consolidation of unidirectional and hybrid lay-up enabling the prediction of consolidation behavior under non-isothermal conditions. The literature presents a significant number of studies, describing the thermal conductivity measurement and prediction for a defined material configuration. Authors propose in this paper an original approach, based on the experimental characterization of the thermal and compression behaviors as function of the compression rate, their numerical modelling enabling the consolidation process simulation in non-isothermal environment. First, an experimental morphology analysis during consolidation was performed, based on an interrupted consolidation method. Thermal conductivity measurements were performed, using a Hot disk method, to quantify this evolution as function of the consolidation rate. A theoretical model, based on a two-level homogenization method, and a Mori-Tanaka model is proposed, considering the three-phases material, and correlate with experiments with a good agreement, but limited predictivity for porosity level above 15%.*

Keywords: thermoplastic composite; structure-properties; consolidation behavior; thermal properties

1. Introduction

Lightweight was the most important drivers in material development during the last decade. However, sustainability is becoming the main driver of new mobility solutions. Due to the depletion of inorganic material, natural based material finds increasingly non-structural applications in transport industry. Structural applications are still dominated by non-renewable material solutions due to lack of affordable alternative. Indeed, continuous natural fibers reinforcement composite (NFRC) have been developed and recently commercialized, as dry fabric or pre impregnated layers. Fast production rate of thermoplastic composite requires an accurate control of the thermal behavior, enabling to form by stamping or weld above the fusion temperature when pressure is applied. The heating up phase prior to this step, and the transfers time induced thermal gradient, which must be anticipated and predicted. By NFRC, both the thermoplastic resin and the fibers itself are sensitive to overheating, presenting a thermal degradation closed to the processing window.

In this study, authors are focused on the understanding of the morphology evolution and associated thermal properties during consolidation of unidirectional and hybrid lay-up enabling the prediction of consolidation behavior under non-isothermal conditions.

Transverse thermal conductivity of NFRC, i.e., through the thickness, is widely studied in the literature. An overview is presented on Figure 1, as function of the fiber volume fraction. 0% of fiber correspond to the neat polymer, and 100% correspond to the pure natural fiber. In-between, measured values at the composite level are presented. On neat polymer, mainly PP

  doi:10.5075/epfl-298799_978-2-9701614-0-0

properties are reported, the values are strongly varying depending on methods and polymer grade. Few experimental values on pure natural fibers are reported, presenting transversal conductivities in-between 0.02 to 0.12 $W.m^{-1}.K^{-1}$. Several thermal conductivities on NFRC are reported, as function of their fibers volume fraction. No clear trend is obviously visible, probably due to the too wide range of materials range, fibers architecture and methodology investigated in the respective papers [1-10].

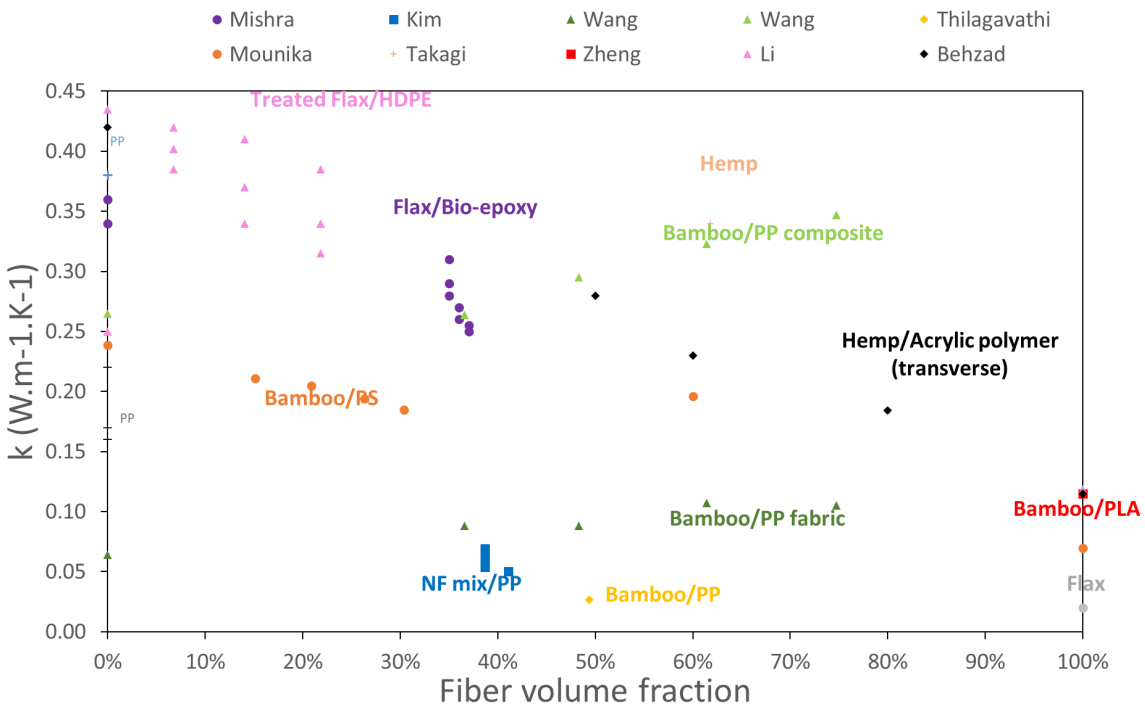

Figure 1: Transverse thermal conductivity of NFRC

Regarding in-plane thermal conductivity, i.e. the conductivity in fiber direction of a unidirectional NFRC, only one author [9] was found. The related study estimated an in-plane thermal conductivities of the hemp fibers of 1.48 $W.m^{-1}.K^{-1}$ and for the polymer of about 0.115 $W.m^{-1}.K^{-1}$. The in-plane thermal conductivity of a unidirectional Hemp/acrylics composite were experimentally investigated as function of the fiber volume ration. A good agreement is noticed

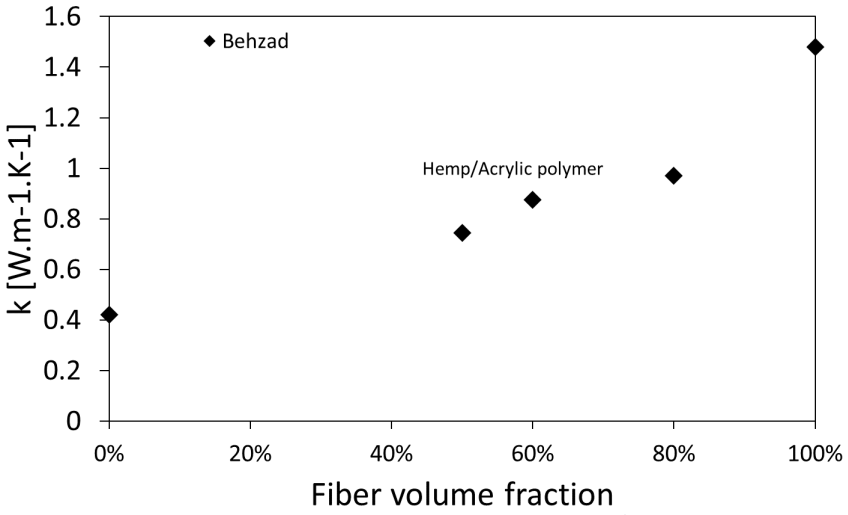

Figure 2: in-plane thermal conductivity of NFRC

  doi:10.5075/epfl-298799_978-2-9701614-0-0 published under CC BY-NC 4.0 license

by comparing the experimental data with the theoretical one, obtained from the rule of mixture model.

In this paper, authors proposed to investigate the evolution of the transversal and in-plane thermal conductivities, during the consolidation of the prepreg raw materials. During the consolidation step, where the pressure is applied on the raw materials above the melting temperature of the resin, a gradual voids disappearance took place, up to the final state where the no void is expected inside the materials. To this aim, the evolution of the morphology is experimentally investigated. Then, thermal conductivities are measured at different consolidation stage. Finally, a correlation with theoretical values, based on measured and estimated inputs parameters is proposed.

2. Materials and sample manufacturing

2.1 Raw materials

In this study, the prepreg manufactured by the company BPREG, called EcoRein® UD 50 is used. EcoRein® UD is thermoplastic-based prepreg reinforced with unidirectionally aligned flax fibers. The tape presents a theoretical mass fraction of 50% of flax fibers inside a polypropylene matrix. The process of BPREG allows to assure a very good alignment of the fiber tows (see Figure 2-A). The tape is pre-consolidated, it means that fibers tows are well impregnated with the PP matrix. In-between tows, air gaps are visible in white on the micro-Computed Tomography (µ-CT) view Figure 2-B made on a prepreg sample of 10*10 mm. the transversal view (see Figure 2-C) shows that tows create independent cluster, presenting a random cross section, with a regular patterning. The Figure 2-D shows in-plane µ-CT view of prepreg sample. The individual flax fibers orientation inside a tow aren't fully unidirectional. The twisting of the tow during manufacturing induced unique fiber misalignment at the microscale.

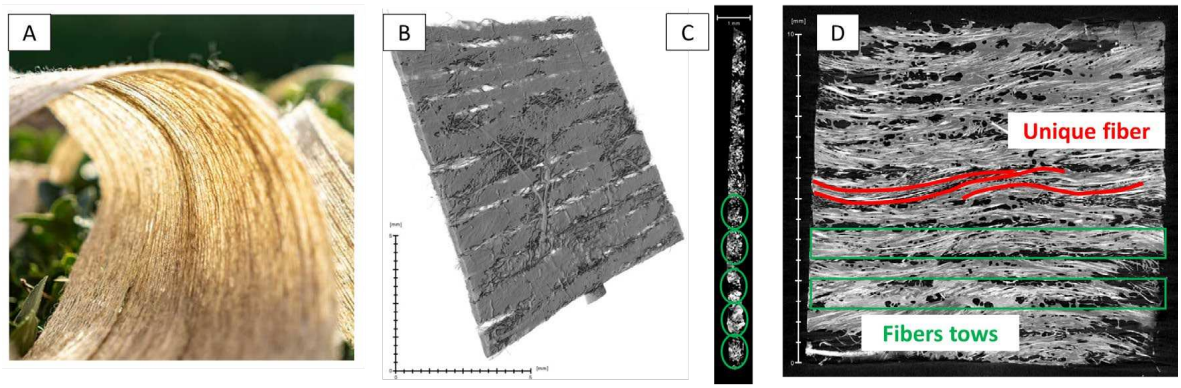

Figure 3: EcoRein® UD 50 prepreg morphology

The polymer matrix, constituting part of the prepreg, is a polypropylene matrix. The fusion peak is at about 165°C, confirm by DSC analysis. The processing temperature was defined accordingly at 190°C. At this temperature, the degradation kinetics is rather low, as confirm by isothermal TGA made at 190°C after a pre-drying phase one hour at 80°C (See Figure 3).

  doi:10.5075/epfl-298799_978-2-9701614-0-0

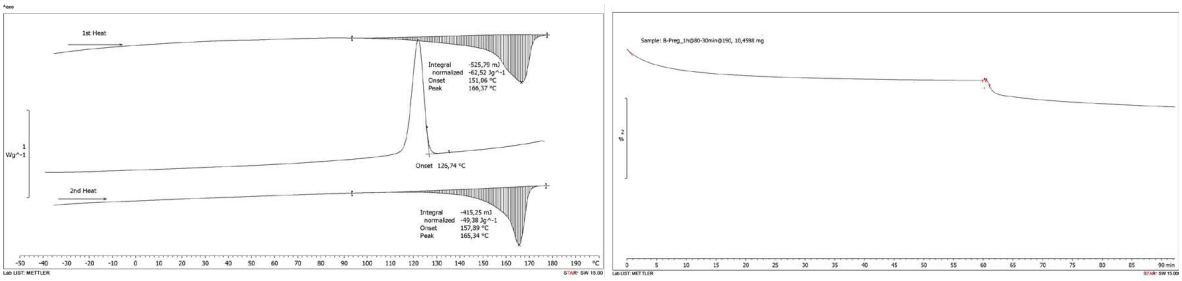

Figure 4: left; EcoRein® UD 50 analysis by DSC (left) and isothermal TGA (right)

As the value in the literature are strongly varying as function of the grade of matrix, neat PP polymer plate was made based on the polymer fibres used for the prepreg manufacturing. PP polymer fibres were placed in the same mould under the same consolidation conditions than the NFRC. A slight difference between in plane and transverse conductivity is observed, certainly induced by the initial intrinsic polymer fibres properties (See Table 1).

Table 1: Thermal conductivity measurement of neat PP

Heating power [mW]	Measurement time [s]	Transverse thermal conductivity [$W.m^{-1}.K^{-1}$]	In-plane thermal conductivity [$W.m^{-1}.K^{-1}$]
15	10	0.156	0.182
20		0.157	0.177
30		0.157	0.174
35		0.158	0.171
40		0.158	0.170
45		0.159	0.167
Average		**0.158**	**0.172**

2.2 Samples manufacturing

The NFRC of this study are manufactured by a thermal compression process. A male and female molds were used to applied a constant pressure after reaching the consolidation temperature of 190°C. The process cycle consists :

i) Place the prepreg layer inside the female mould and closing it with the male mold. Gaps inbetwe both mold is about 10 µm, eabling the release of air, and avoidung any resin of fibre flow outite the cavities. This is very mportant for our study, as I's assure to cisider a material conservation during the process.

ii) The closed molds is placed inbetwen the press platte, preh-heated at 200 °C. The temperarute of the mold is monitoried during the whole process. As soon as a mold temperature reach 190°C, starts 10 min waiting time for temperature homogenization purposes.

iii) Then, a pressure of about 10 bars is applied constantly and the water cooling down of the press platte is started. Pressure is maintain during the whole cooling down phase.

iv) Demolding occurs at a temperature below 30°C.

This procedure enables to produce the reference material, as the high consolidation pressure applied on the NFRC during the consolidation and cooling down phase enable to produce the highest compression rate possible, i.e. release all the residual porosities. A pressure-controlled FEI Quanta FEG 200 scanning electron microscope (SEM) from FEI Company was used to obtain

  doi:10.5075/epfl-298799_978-2-9701614-0-0 published under CC BY-NC 4.0 license

information about the morphology in cross sections of the reference material. Figure 4-A shows the reference material morphology. Very few porosities are visible on this cross section. Flax fibers are well homogeneously distributed. Individual flax fibers and fibers bundles are observed. Image analyses enable to measure the fibers volume content of 34% inside the produced material was measured. µ-CT analysis of a 10x10x2.3 mm sample, a small focal spot has been selected, with following parameters filament, 70 kV – 160 µA – 18 W FR=1.60 – Avg=10. It provides a voxel size of 6 µm. The 3D view of the fibers and the porosities are showed on Figure 4-B and C respectively. An average porosities amount of less than 0.7 % have been quantified.

Figure 5: Reference material analysis by SEM and µ-CT

Thermal conductivities measurement required thick composite sample, in-between 12 to 16 mm. To prevent through the thickness gradient of morphology, 3 individual plates made of 17 prepreg layers were manufactured first, then are consolidated, together, in a second step according to the same procedure.

3. Experiments

3.1 Morphology evolution during consolidation

The study of consolidation is made by producing samples at different consolidation rate. To this aim, adjustable blocks are placed outside the cavity, in between the male and female mold, enabling to control the final cavities thickness. The consolidation rate is defined as :

$$Consolidation\ rate_{\ \text{intermediate}} = \frac{t_{\text{intermediate}}}{t_{\text{reference}}} x\ 100\%$$

Where $t_{\text{reference}}$ correspond to the reference thickness, $t_{\text{intermediate}}$ the sample thickness at the intermediate consolidation state. For our material of interest, a single prepreg layer, fully consolidated and considered as reference presents a thickness of 243 µm.

For this study, complementary to the reference material, which is considered as 100% of consolidation, 4 intermediates consolidation state were manufactured, up to 135%. As start, without any consolidation, the lay-up of prepreg correspond to 170%. This range of consolidation will be explored in a follow-up study, as experimental methods need to be adjusted consequently.

Several techniques are reported in the literature for porosities measurements of NFRC [XX]. Due to the high porosities amount, especially for sample presenting a law consolidation rate, the combination of cross section image analysis and µ-CT observation were selected.

  doi:10.5075/epfl-298799_978-2-9701614-0-0 published under CC BY-NC 4.0 license

For imaging, 12x15x15 mm samples were embedded in epoxy casting resin and subsequently ground and polished until a scratch-free surface was obtained. Immediately after polishing, samples were cleaned and dried at 80°C for 1 hour, avoiding an unexpected porosities growth induced by moisture ageing.

Figure 5 shows the morphology evolution from 100 % up to 134 % of consolidation rate. The fiber bundles are well impregnation as start. The consolidation process consists mainly here in the fibers bundles re-arrangement, enabling the reduction of macro-scale porosities.

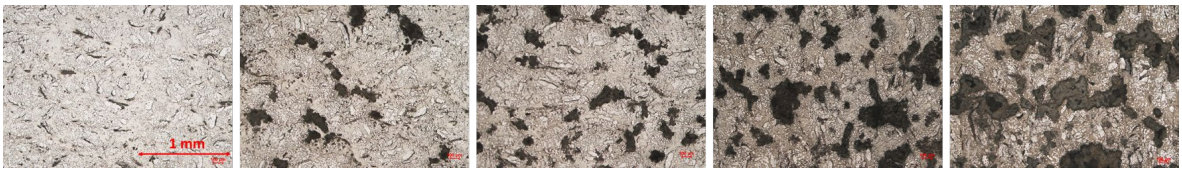

Figure 6: Consolidation evolution as function of the compression rate: 100, 106, 117 ,127 and 134 %

The µ-CT view enables to catch the porosities shape in 3D. At a consolidation rate of 134%, the dominant porosities population presents mainly channel shape with a typical diameter of 200 to 300 µm. Micro round-shape porosities are visible also inside fibres bundles as well as decohesion in-between fibres bundles interface. At a consolidation rate of 106%, majority macro scale channels are completely disappeared and still few of them are still visible but are strongly shrank.

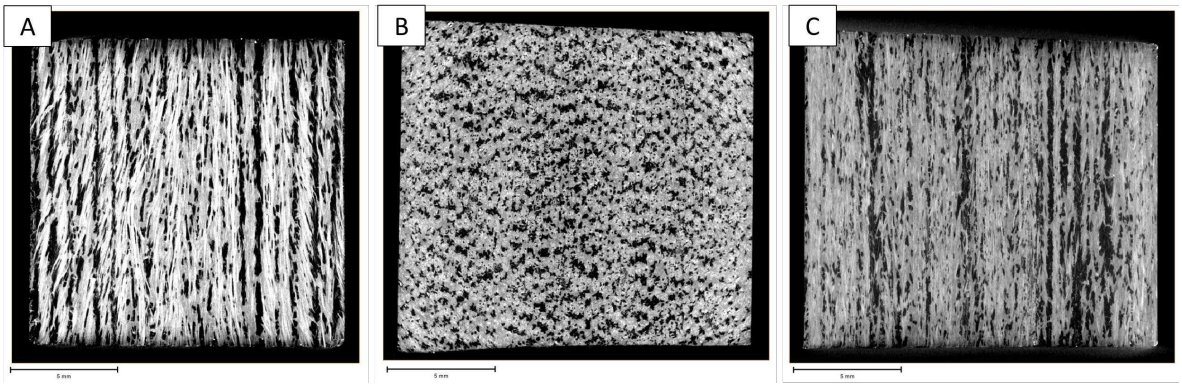

Figure 7: µ-CT view of a 16x15x15mm sample at 134% of consolidation

3.2 Thermal conductivity measurement

A Hot disk method, also call transient plan source (TPS), is used to measure anisotropic thermal conductivity, in both directions: transverse, means in the direction of fibers for a unidirectional composite, and in-plane, means in the perpendicular plane to the direction of fibers (see Figure 7). Measurement was performed according EN ISO 22007-2:2015. The Hot Disk is a TPS 2500 S from Hot Disk instruments with a Kapton-insulated sensor, named 7577 (a = 2.001mm radius).

  doi:10.5075/epfl-298799_978-2-9701614-0-0

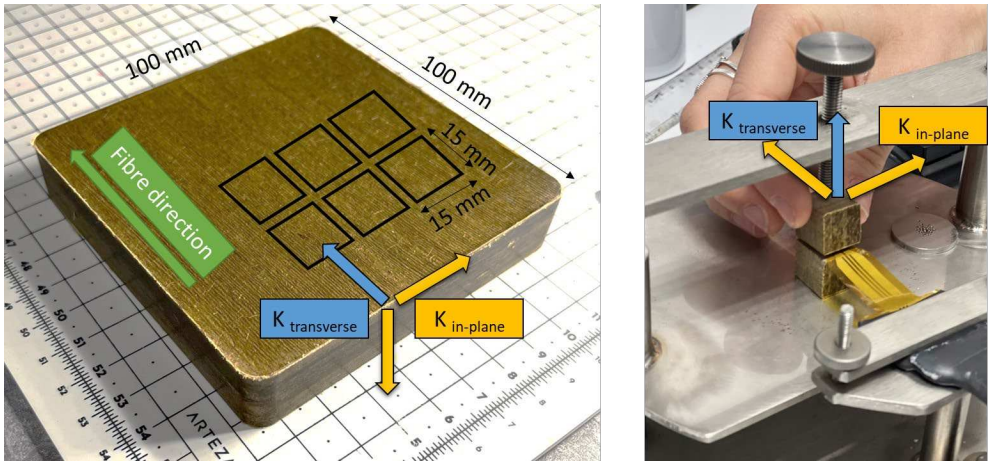

Figure 8: Thermal conductivity measurement method

6 samples of each configurations were water jet cut, enabling to perform 3 measurements per configurations. 2 samples are need for a single measurement. One measurement is obtained by the average value of the thermal conductivities at a constant measurement time of 10 s, and a varying input power, set at 15, 20, 30, 40 and 50 mW.

The thermal conductivity measurements are reported in Table 2. The standard deviation for both transverse and in-plane conductivities is very low, less than 0.8 % and 6.5 % respectively for transverse and in-plane thermal conductivity, by considering the highly heterogenous aspect ratio, their size, and the spatial distribution of observed pores.

Table 2: Morphology and thermal conductivities evolution as function of the consolidation rate

Consolidation rate	Porosity volume	Fibre volume rate	Sample thickness [mm]	Transverse thermal conductivity [W.m-1.K-1]	Standard deviation [W.m-1.K-1]	In-plane thermal conductivity [W.m-1.K-1]	Standard deviation [W.m-1.K-1]
100%	0%	34%	12.400	0.531	0.002	0.170	0.004
106%	6%	32%	13.150	0.470	0.004	0.176	0.011
117%	15%	29%	14.540	0.437	0.001	0.170	0.003
127%	21%	27%	15.700	0.337	0.001	0.152	0.006
134%	25%	25%	16.590	0.281	0.002	0.171	0.011

4. Homogenization model

The two-level homogenization method proposed in [11] for elastic composites and extended to thermal and electrical conductivity in [12] is used here to predict the effective thermal conductivity of the three-phase (flax fibers, pores, and polypropylene matrix) NFRC. The two-level method is based on nested homogenization levels. At the deepest level, the real matrix material is homogenized with a first family of reinforcements. The effective material thus obtained plays the role of a fictitious matrix which is reinforced with another set of reinforcements to constitute an upper-level composite. This procedure is repeated until all reinforcements families have been taken in account. In this study, the Mori–Tanaka model is used at a given level to homogenize the basic two-phase composite. The two-level method can deliver excellent predictions when the right choice of the nested homogenization levels is made. It is shown that for reinforcements with different material properties, when going from the

deepest level to the upper level, the inclusions should be added from the most compliant to the most rigid. More details on the model's equations can be found in [12].

Reverse calculation based on the reference material is used to determine the model input parameters. A flax fibre transversal thermal conductivity of 1.232 $W.m^{-1}.K^{-1}$ and in-plane thermal conductivity of 0.170 $W.m^{-1}.K^{-1}$ were calculated and implemented in the theoretical model. The theoretical values present a good agreement with experiments. The hypothesis of spherical pores is certainly responsible for the poor prediction of the theoretical model. Extended experimental data will be required to be able to consider the pore aspect ratio in predictive model.

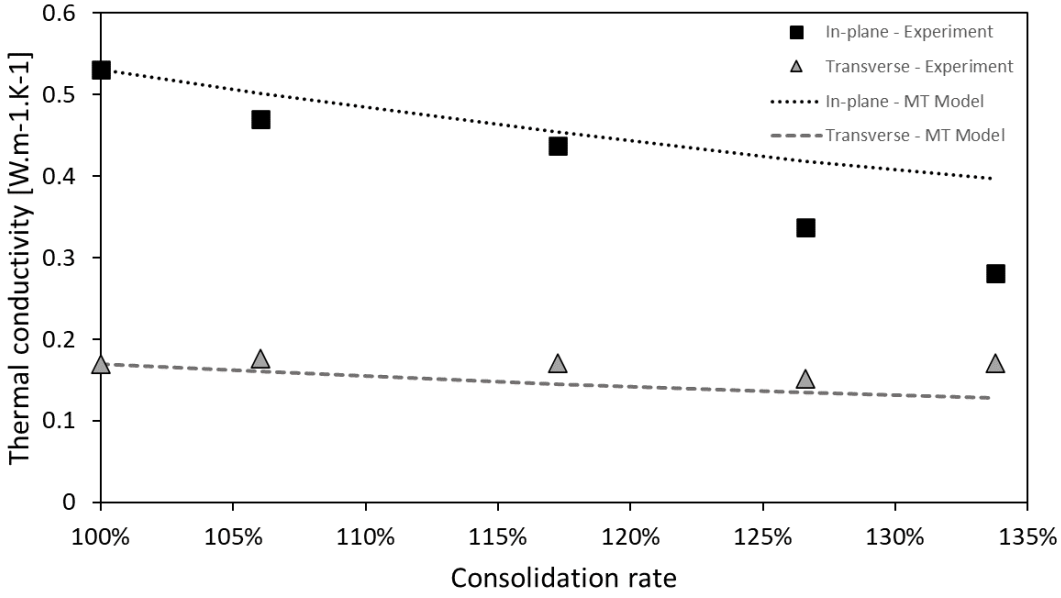

Figure 9: Comparison between experiments and theoretical model

5. Conclusions and perspectives

i. Morphology evolution during consolidation were characterized for a prepreg material of NFRC, though the coupling of image analyses and µ-CT. The dominant pore reduction is driven at macro-scale, through large channel progressive compaction, located in-between fibres bundles. Micro-scale porosities are considered negligible with the studied material. Constituting phase distribution was experimental determined enabling to set up reliable theoretical model.

ii. Anisotropic thermal conductivity measurements were performed as function of the compression rate, with a very satisfying standard deviation. The transverse thermal conductivity isn't affected significantly during the consolidation. However, the in-plane thermal conductivity is divided by a factor 2 between the 100 % and 134 % consolidation rate.

iii. A theoretical model, based on a two-level homogenisation method, and a Mori-Tanaka model is proposed, considering the three-phases material, and correlate with experiments with a good agreement, but limited predictivity for porosity level above

  doi:10.5075/epfl-298799_978-2-9701614-0-0

15%. The aspect ratio for this range of consolidation cannot be considered as spherical and the typical channel shape of porosity must be integrated in the theoretical model.

Acknowledgments

The authors gratefully thank Loïc Borghini and Sébastien Klein for their support in sample manufacturing and preparation, Dr. Doriane Del Frari for the µ-CT measurement, Régis Vaudemont and Benoit Marcolini for thermal analysis.

Funding

The project, called NATALINA, leading to this application has received funding from Luxembourg National Research Fund under the reference INTER/MERA/19/13991124 in frame of M-ERA.Net . All authors gratefully thank the Luxembourg National Research Fund as well as the NATALINA's project partners BPREG and KAREL KALIP and their funding agency TUBITAK.

6. References

1. Mishra, R., Wiener, J., Militky, J., Petru, M., Tomkova, B., & Novotna, J. (2020). Bio-Composites Reinforced with Natural Fibers: Comparative Analysis of Thermal, Static and Dynamic-Mechanical Properties. Fibers and Polymers, 21(3), 619–627. https://doi.org/10.1007/s12221-020-9804-0
2. Kim, S. W., Lee, S. H., Kang, J. S., & Kang, K. H. (2006). Thermal Conductivity of Thermoplastics Reinforced with Natural Fibers. International Journal of Thermophysics, 27(6), 1873–1881. https://doi.org/10.1007/s10765-006-0128-0
3. Wang, C., Zuo, Q., Lin, T., Anuar, N. I. S., Mohd Salleh, K., Gan, S., Yousfani, S. H. S., Zuo, H., & Zakaria, S. (2020). Predicting thermal conductivity and mechanical property of bamboo fibers/polypropylene nonwovens reinforced composites based on regression analysis. International Communications in Heat and Mass Transfer, 118, 104895. https://doi.org/10.1016/j.icheatmasstransfer.2020.104895
4. G. Thilagavathi, E. Pradeep, T. Kannaian, L. Sasikala, Development of natural fiber nonwovens for application as car interiors for noise control, J. Ind. Text. 39 (2010) 267–278.
5. M. Mounika, K. Ramaniah, K. Ramaniah, A.V. Ratna Prasad, K. Mohana Rao, K. Hema Chandra Reddy, Thermal conductivity characterization of bamboo fiber reinforced polyester composite, J. Mater. Environ. 3 (2012) 1109–1116.
6. H. Takagi, S. Kako, K. Kusano, A. Ousaka, Thermal conductivity of PLA-bamboo fiber composites, Adv. Compos. Mater. 16 (2007) 377–384.
7. Zheng, G. Y. (2014). Numerical Investigation of Characteristic of Anisotropic Thermal Conductivity of Natural Fiber Bundle with Numbered Lumens. Mathematical Problems in Engineering, 2014, 1–8. https://doi.org/10.1155/2014/506818
8. Li, X., Tabil, L. G., Oguocha, I. N., & Panigrahi, S. (2008). Thermal diffusivity, thermal conductivity, and specific heat of flax fiber–HDPE biocomposites at processing temperatures. Composites Science and Technology, 68(7–8), 1753–1758. https://doi.org/10.1016/j.compscitech.2008.02.016
9. Behzad, T., & Sain, M. (2007). Measurement and prediction of thermal conductivity for hemp fiber reinforced composites. Polymer Engineering & Science, 47(7), 977–983. https://doi.org/10.1002/pen.20632

10. Ineos. (2014, April). Typical Engineering Properties of Polypropylene. https://www.ineos.com/globalassets/ineos-group/businesses/ineos-olefins-and-polymers-usa/products/technical-information--patents/ineos-engineering-properties-of-pp.pdf
11. Naili C., Doghri I., Demey J., Porous materials reinforced with short fibers: Unbiased full-field assessment of several homogenization strategies in elasticity, Mech. Adv. Mater. Struct. (2021), pp. 1-16, https://doi.org/10.1080/15376494.2021.1880674.
12. Koutsawa Y., Rauchs G., Fiorelli D., Makradi A., Belouettar S., A multi-scale model for the effective electro-mechanical properties of short fiber reinforced additively manufactured ceramic matrix composites containing carbon nanotubes, Composites Part C: Open Access, Volume 7, 2022, https://doi.org/10.1016/j.jcomc.2022.100234.

AVOIDING COMPLETE FAILURE OF COMPOSITE T-JOINTS BY EMBEDDING SACRIFICIAL CRACKS INSIDE THE BONDLINE

A. Wagih, M. Hashem, G. Lubineau

Mechanics of Composites For Energy and Mobility Lab, Mechanical Engineering Program, Physical Science and Engineering Division, King Abdullah University of Science and Technology (KAUST), Thuwal 23955-6900, Kingdom of Saudi Arabia

Abstract: A novel CFRP bioinspired adhesive T-joint that mimics the structure of the bondline of a biological systems that has excellent adhesion, *mytilus californianus*, was designed. We embedded sacrificial tailored defects inside the adhesive bondline to allow progressive failure mode in the bioinspired T-joint by delocalizing the damage from the skin/adhesive interface. The presence of the sacrificial cracks inside the bondline improves the interlaminar fracture toughness of the stiffener/skin interface and hence improve the joint toughness. The improvement of the interface toughness delays the catastrophic failure of the joint and lead to initiation of damage inside the stiffener and the skin that further increase the toughness and provide progressive damage mode. The strength and toughness of the bioinspired T-joints are 2 and 17 times larger than the conventional T-joint, respectively. The growth of progressive damage inside the skin and the stiffener inhibited the catastrophic and complete failure of the joint.

Keywords: Composites; T-joints; Adhesive joints; Bioinspired; Pull-off strength.

1. Introduction

Joining is one of the most common difficulties in composites applications. T-joints are applied widely in aircraft structures to transfer loads from the horizontal panels such as aircraft body to vertical panels, which are stiffeners. Stiffeners are usually joined with the body panels using adhesives. However, the toughness of this joints is relatively low. These T-joints might fail at the interface between the stiffener and the skin as delamination. Once the delamination initiates, it rapidly propagates causing catastrophic failure [1].

Various toughening techniques were developed in CFRP T-joints to provide an improved interface bonding. Such techniques include modifying the geometry of the delta-fillet region or using bio-inspired designs to minimize the stress concentrations, increasing the resistance by using toughened resins, and employing through-the-thickness pinning or stitching [2-4]. Despite their efficiency to improve the global response of the T-joints, the improvement rate is relatively low compared to the complexity of implementing these techniques. Moreover, in some of these techniques, the in-plane stiffness and strength of the skin might be highly influenced, i.e, pinning and stitching. Additionally, the safety of the toughened T-joint using most of this technique is similar to the conventional joint, where catastrophic failure is not inhibited.

Here, a novel bioinspired CFRP adhesive T-joint that mimics the structure of the bondline in the *mytilus californianus* adhesion system, was designed. We embedded sacrificial cracks inside the adhesive bondline to activate nonlocal damage mechanisms such as crack migration and ligament formation. Pull-off tests were deployed to characterize the toughness and strength of

  doi:10.5075/epfl-298799_978-2-9701614-0-0

the developed bioinspired T-joints. Microcomputed tomography was deployed to characterize the different damage modes inside the joints.

2. Material and experiments

The developed bioinspired adhesive joint was inspired by the bondline in the *mytilus californianus* adhesion system, where voids were observed inside the bondline [5]. Fig. 1 shows schematic of the bioinspired T-joint. In the joint, sacrificial cracks were embedded at the bondline between the stiffeners and the skin to simulate the presence of voids in the biological adhesion system.

Unidirectional carbon fiber prepregs composed of epoxy resin and carbon fibers (HexPly T700/M21, Hexcel) were used to manufacture the T-joints. The nominal ply thickness was 250 µm and the fiber volume fraction was 57 %. The skin was manufactured using hand lay-up of 16 plies with stacking sequence $[0/45/-45/90]_{2s}$ over a commercial polyamide sheet, resulting in a laminate of 4 mm nominal thickness. The stacked plies were cured by compression molding process using hydraulic hot pressing machine at 180 °C temperature and 7 bar pressure and held for 2 h dwell time. The heating and cooling rates were kept constant at 3 °C/min. The L-shape stiffener was manufactured using the hand lay-up technique as well with $[0/45/-45/90]_s$ stacking sequence.

The bonding process of the T-joint was composed of bonding the two L-shape stiffeners to form a T-shape stiffener using Araldite 420 A/B two-component epoxy adhesive. Then, the same adhesive was applied to the T-shape and skin surfaces equally. To generate tailored defects inside the bond line that mimics the bondline of *mylitus californianus* adhesion system (see Fig. 1), PTFE film was placed over the adhesive layer on the stiffener. To control the adhesive thickness at 0.8 mm, nylon wires of 0.8 mm diameter were placed at the edges of the stiffener. The skin was placed over the stiffeners and pressed using the T-joint mold. Curing of the bonded T-joint was done at 60 °C for 2 h under vacuum using universal oven. The width of sacrificial crack in this case was considered as 2 mm and the gap between two successive cracks was equal 5 mm. These values were applied based on previous investigation on the effect of crack width and the gap between two cracks on the mode I and II toughness of adhesive joints [5,6].

The strength and toughness of the T-joints were characterized using Pull-off tests that was performed using universal testing machine with 10 kN load cell and loading rate of 2 mm/min. The samples were simply supported using the fixture as shown in Figure 1(b). The stiffener was loaded vertically allowing the upper surface of the skin to be pulled against the rollers through the load application set. Three samples were tested for each configuration.

The different damage modes after testing were recognized using X-ray micro-computed tomography. The system parameters were set as follows: 120kV voltage, 140 µA intensity, 250 ms exposure time, 11.27 µm voxel size and 26 mm field view. The machine carried out 2500 projections during the 360° rotation for each specimen examined.

  doi:10.5075/epfl-298799_978-2-9701614-0-0

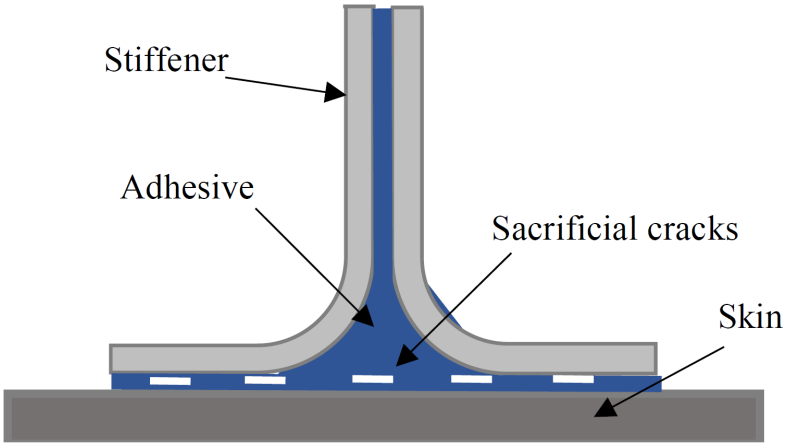

(a) Bioinspired adhesive T-joint

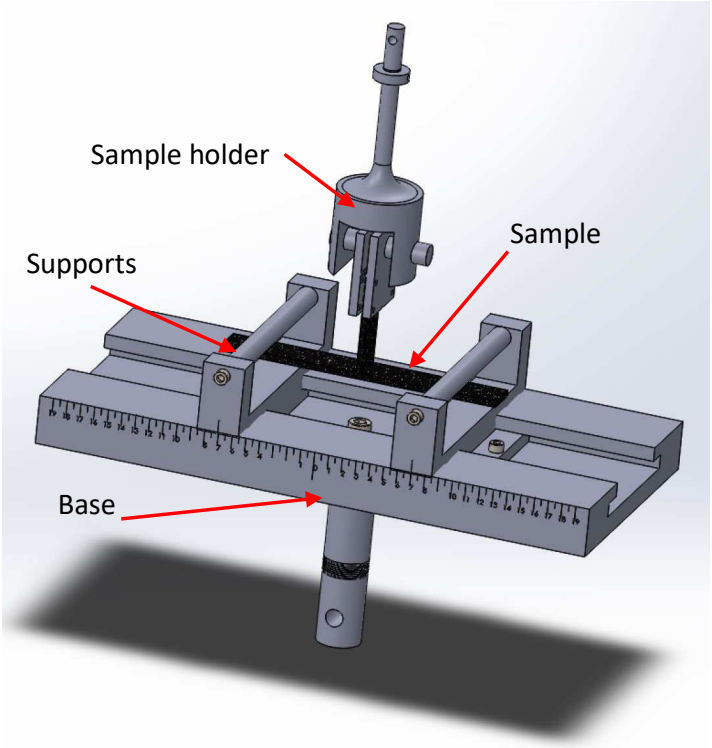

(b) Pull-off test for T-joints

Figure 1. Schematic of the bioinspired adhesive joint and the pull-off test fixture.

3. Results and discussion

Figure 2 shows the load-displacement response of all the samples of conventional and bioinspired T-joints. The figure reflects good repeatability of the test for both joints. The response of the bioinspired T-joint differs from the conventional joint. For the conventional joint, the response was characterized by increase of the load with increasing displacement until complete and brittle failure occurs. However, for the bioinspired T-joint, the load increases monotonically with increasing the applied displacement until the maximum load. Then, small load drop occurs due to the initiation of the damage. After that, the load increases again until a second load drop occurs, which indicates a progressive failure mode of bioinspired adhesive joints. It is valuable highlighting that the conventional T-joint fail in catastrophic mode, where once the crack initiates at the skin-adhesive interface, it propagates suddenly causing loss of the

  doi:10.5075/epfl-298799_978-2-9701614-0-0

structural integrity of the joint and at this stage the joint can sustain zero load. However, for the bioinspired T-joint, even after several load drops, and at a pull-off displacement three times larger than the conventional T-joint, it can sustain a load around 700 N, which is almost 70 % of the maximum load of the conventional joint even after failure.

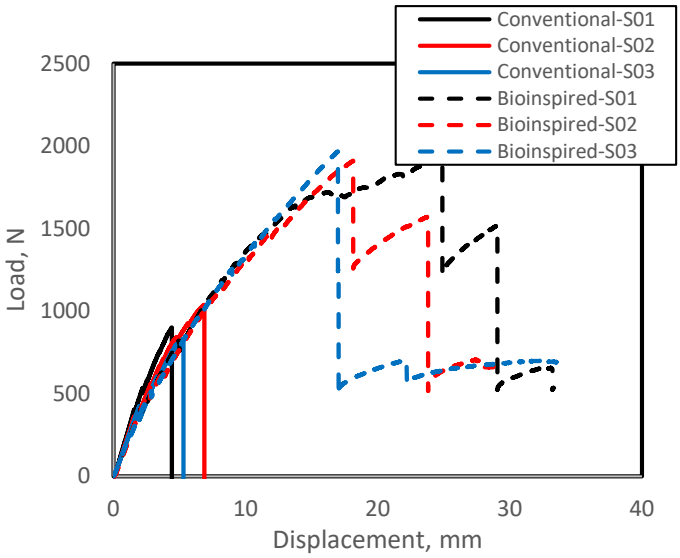

Figure 2. Load-displacement response of conventional and bioinspired T-joints.

Figure 3 shows the different damage modes that allows the changes of the failure modes from catastrophic mode for the conventional T-joints to progressive mode for the bioinspired T-joint. For conventional T-joint, a single delamination grows at the interface between the adhesive layer and the skin as shown in Figure 3(a). During pull-off test, shear stresses are localized at the interface between the skin and the adhesive layer, which exceed the energy applied to this interface. Once this energy exceeds the interlaminar fracture toughness of the interface a crack initiate. The initiation of this crack increases the stress intensity factor at this crack tip, which lead to fast propagation of the crack causing the catastrophic failure. However, for the bioinspired T-joint, different damage modes propagate during the loading. For instance, Figure 3(b) shows the propagation of delaminations between stiffener and skin plies and fiber breakage of the skin lower plies. The presence of the sacrificial cracks inside the adhesive layer promotes relative deformation inside the adhesive layer during pull-off test and improves the interface toughness. Previous studies done by the authors showed more than 2 times improvement of the mode I and II fracture toughness of adhesive joints with sacrificial cracks compared to conventional joints [5,6]. The improvement of the interface fracture toughness results in propagation of delaminations between stiffener plies especially at the fillet region where high shear stresses occurs during loading. The propagation of these delaminations reduces the energy exerted to the interface, which inhibit the initiation of a crack at the interface and thus allow larger deformation of the joint. Increasing the applied displacement results in higher compressive strains at the fibers in the lower plies of the skin, which exceed the fiber failure strain and hence fiber breakage occur. After fiber breakage occurs at the skin, delamination grows between skin plies. Thus, for the bioinspired T-joints, the damage was dispersed inside the stiffener and skin rather than localized at the skin-adhesive interface, which inhibit the complete failure of the joint.

  doi:10.5075/epfl-298799_978-2-9701614-0-0

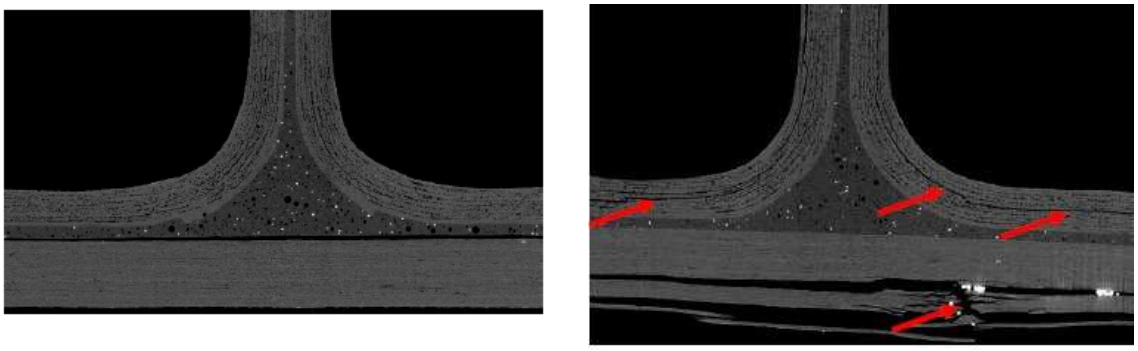

(a) Conventional T-joint (b) Bioinspired T-joint

Figure 3. Damage modes in conventional and bioinspired T-joint.

Based on the obtained results, the strength of the bioinspired T-joint is 2 times larger than the conventional T-joint (see Figure 2). The higher strength is attributed to the dispersion of the damage inside the stiffener and skin that suppress the interfacial damage at the interface and hence increase the joint strength. Moreover, the energy dissipated for the failure of the joint (the area under the load-displacement curve) is 17 times larger for the bioinspired T-joint compared to the conventional T-joint. This larger toughness is due to the dissipation of higher energy to grow delaminations and fiber breakage inside the stiffener and the skin. Additionally, the bioinspired T-joints fails in progressive manner and it does not lose all its integrity after failure. The bioinspired T-joint after failure can sustain 70% of the load capacity of the conventional T-joint, which clearly shows more safety and integrity of the joint.

4. Conclusions

A novel bioinspired T-joint design with improved strength and toughness is proposed in this work by embedding sacrificial defects inside the adhesive bondline to mimic the bondline of an excellent adhesion biosystem, *mytilus californianus*. We used pull-off test to characterize the manufactured T-joints. The results showed great enhancement in the strength and toughness of the bioinspired T-joints compared to the conventional one. The improvement were due to the improvement of the skin/adhesive interlaminar toughness that prohibits the propagation of delamination at that interface and initiate delaminations between stiffener plies instead. However, the damage in the conventional T-joints was pure interfacial delamination at the skin/adhesive interface. Additionally, at large displacement, the compressive stresses at the lower plies of the skin increases resulting in fiber breakage of the lower plies of the skin. These progressive damage mechanisms increase the energy dissipation, which enhances the toughness of the joint reaching 17 times larger than the conventional T-joint and provides safer joint.

Acknowledgements

This research was funded by King Abdullah University of Science and Technology (KAUST) Office of Sponsored Research (OSR) under award number OSR-2017-CRG-3388.01.

References

1. Trask R, Hallett S, Helenon F, Wisnom M. Influence of process induced defects on the failure of composite T-joint specimens. Composites Part A 2012; 43(4):748-757.

2. Boerio F, Roby B, Dillingham R, Bossi R, Crane R. Effect of grit-blasting on the surface energy of graphite/epoxy composites, The Journal of Adhesion 2006; 82:19–37.
3. Prolongo S, Gude M, Del Rosario G, Urena A. Surface pretreatments for composite joints: study of surface profile by SEM image analysis, Journal of adhesion science and technology 2010; 24:1855–1867.
4. Holtmannspotter J, Czarnecki J, Wetzel M, Dolderer D, Eisenschink C. The use of peel ply as a method to create reproduceable but contaminated surfaces for structural adhesive bonding of carbon fiber reinforced plastics, The Journal of Adhesion 2013; 89:96–110.
5. Wagih A, Tao R, Lubineau G. Bio-inspired adhesive joint with improved interlaminar fracture toughness. Composites Part A 2021; 149:106530.
6. Wagih A, Lubineau G. Enhanced mode II fracture toughness of secondary bonded joints using tailored sacrificial cracks inside the adhesive. Composites Science and Technology 2021; 204:108605

  doi:10.5075/epfl-298799_978-2-9701614-0-0

Mechanical analysis of the indentation behavior of short fiber-reinforced composites using finite element method

Hyonwoo,Pang [a], Doyoung ,Kim [a], Jeong-Min Cho [b], Woong-Ryeol Yu [a]*

a: Department of Materials Science and Engineering and Research Institute of Advanced Materials (RIAM), Seoul National University, Gwanak-ro 1, Gwanak-gu, Seoul 08826, Korea – *E-mail: woongryu@snu.ac.kr

b: R&D Division, Hyundai Motor Company, 150 Hyundai Yeonguso-ro, Hwaseong-si 18280, Korea

Abstract:

Due to the significance of identifying macroscopic mechancial properties in specimen level, the indentation test has been developed as one of the effective methods for evaluating the mechanical properties of industrial parts in nondestructive manner. However, such method has been shown to be inapplicable for directly obtaining the tensile properties of short fiber reinforced composites (SFRCs) due to their time-depndent matrix and anisotropic fiber orientation effect. In this study, commercial finite element software (ABAQUS) was used to analyze the indentation behavior of SFRCs and identify the source of the discrepancy. By accomodating the optimized material properties based on mechancial characterizations and fiber orientation analysis, DIGIMAT enabled the coupled simulation of the ball-tip indentation of SFRCs. Finally, by analyzing the various stress field and its interactions during the indentation process, a correlation between indentation modulus and macroscopic mechanical property of SFRCs was explored through this finite element analysis.

Keywords: short fiber reinforced composites; ball-tip indentation; finite element analysis; mechanical property prediction

1. Introduction

Effective determination of the mechanical properties of composite materials, in particular their industrial parts, is an inevitable issue taken for consideration in industrial fields. Among various characterization methods, the indentation test has emerged as an instrumented and efficient method for evaluating the mechanical properties of industrial parts composed of such isotropic materials as metal and ceramic [1,2]. However, for the case of short fiber reinforced composites (SFRCs), the indentation method shows inconsistent agreement between reduced elastic modulus and experimental one, leading to difficulty in using indentation test as direct method for correlating with longitudinal tensile properties [1]. This is due to the fact that the mechanical performance of injection molded SFRCs heavily depends on anisotropic fiber orientation formed throughout the manufacturing process. In addition to this anisotropic nature of SFRCs, several researches pointed out the viscoelastic

  doi:10.5075/epfl-298799_978-2-9701614-0-0

effect of constituent polymer matrix makes it difficult to apply indentation test for characterizing their mechanical properties [3].

Various researches have been developed so far to identify the unique indentation behavior of polymer matrix by showing accurate modeling compared with experimental result [4] and suggesting viscoelastic parameter extraction method from nanoindentation method [5]. However, current researches have been limited in the case of isotropic polymer matrix which required the necessity of further study regarding the indentation behavior of anisotropic SFRCs.

In this study, commercial finite element software (ABAQUS) was used to investigate the indentation behavior of SFRCs for analyzing the influence of unique stress distribution. First, the homogenization of anisotropic composite was completed in unit cell level by DIGIMAT-MF software with material property optimization based on micro-CT scan, static tensile test and dynamic mechanical analysis for identifying viscoelastic-viscoplastic polymer matrix. Then, by obtaining the homogenized material properties in specimen level, an analysis model was built to simulate the ball-tip indentation of SFRCs. Finally, by scrutinzing the interaction of stress field distributions during the indentation process, a relationship between indentation modulus and macroscopic mechanical property of SFRCs was inspected through this numerical simulation.

2. Theological background

2.1 Olive-Pharr method

The Olive-Pharr method was originally developed to measure the hardness and reduced elastic modulus (indentation modulus) of isotropic elasto-plastic material from the indentation load-depth curve (Fig.1). By substituting the values obtained from the graph to following equations (1)~(3), the indentation modulus (E^*) of tested material was able to be calculated [6]. This method was proven to be applicable in industrial fields where required the nondestructive testing of macroscopic properties. The effectiveness of this following evaluation method was also applied in the indentation case of SFRCs in this study.

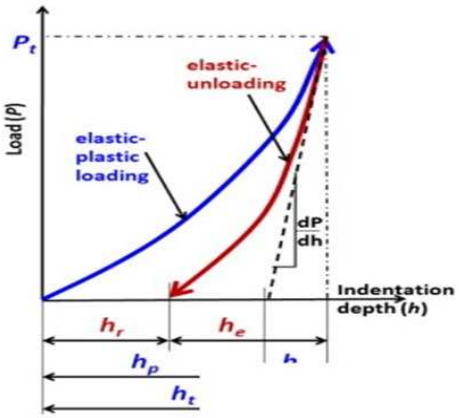

$$\mathbf{S} = \frac{\mathbf{dF}}{\mathbf{dD}} \qquad \textbf{(1)}$$

$$\mathbf{E}^* = \frac{\mathbf{S}\sqrt{\boldsymbol{\pi}}}{\mathbf{2\beta}\sqrt{\mathbf{A_c}}} \qquad \textbf{(2)}$$

$$\frac{\mathbf{1}}{\mathbf{E}^*} = \frac{\mathbf{1-v_i^2}}{\mathbf{E_i}} + \frac{\mathbf{1-v^2}}{\mathbf{E}} \qquad \textbf{(3)}$$

Fig.1 Oliver Pharr method for indentation modulus calculation

  doi:10.5075/epfl-298799_978-2-9701614-0-0

3. Experimental section

3.1 Materials and specimen

SFRCs used in this research were prepared by injection molding of polyamide-6 (PA6) base and 30wt% short glass fibers (denoted as PA6-GF30). The specimens were prepared in two ways: First, the tensile specimens were injection-molded through a gate on the shorter edge into a dog bone shape (thickness: 4mm). Second, a large rectangular plate (thickness:3mm) was injection-molded for ball-tip micro indentation test.

3.2 Micro-indentation test

Micro-indentation test was performed in the air under isothermal conditions at room temperature (25°C) using a tungsten carbide ball (spherical) indenter (FRONTICS AIS 3000, USA). Following experiments were conducted in displacement-controlled mode and the testing speed was set as 1mm/min along with 0.5 seconds of holding time at maximum depth (150μm). Fig.2 shows the picture of indentation process with test specimen.

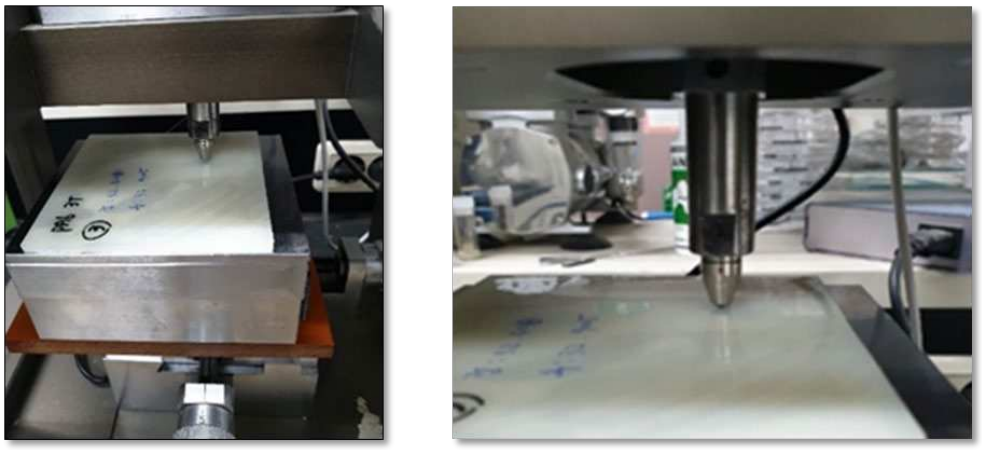

Fig.2 Micro-indentation process image

3.3 Mechanical characterization: Tensile test and Dynamic mechanical analysis

Static tensile tests were performed at room temperature (25°C) using a tensile testing machine (Instron 8801; Instron, Norwood, MA, USA) according to ISO 527 standard to measure the basic mechanical properties. Two cameras and a digital image correlation system (VIC-3D7 software; Correlated Solutions, USA) were also used along the obtain the strain of testing specimen.

Dynamic mechanical properties were obtained by using dynamic mechanical analyzer (DMA Q800, TA instrument, USA). A temperature-frequency sweep mode was employed for measuring storage and loss modulus from 0°C to 140°C and a frequency range from 0.1 to 100 Hz.

  doi:10.5075/epfl-298799_978-2-9701614-0-0

3.4 Micro-CT examination

Nondestructive examination of internal structure of PA6-GF30 was conducted using X-ray CT (SKYSCAN 1272Bruker, Belgium) for fiber orientation analysis. The specimen was cut into 80 mm^3 and mounted vertically on a holder using a wax (Fig.3). The scanning of CT specimen was performed under scanning voltage of 40kV and voxel resolution size at 2.5μm.

Fig.3. Micro-CT scan of PA6-GF30 specimen

4. Result and Discussion

4-1. Micro-indentation test result

Fig.4 shows the ball-tip indentation result of SFRCs and the corresponding indentation modulus calculated from previously mentioned Oliver Pharr method. Considerable modulus difference was observed both for the PA6 base and PA6-GF30 specimen due to the time-dependent depth recovery of polymer and anisotropic stress distribution. Numerical simulation was conducted to identify the source of discrepancy.

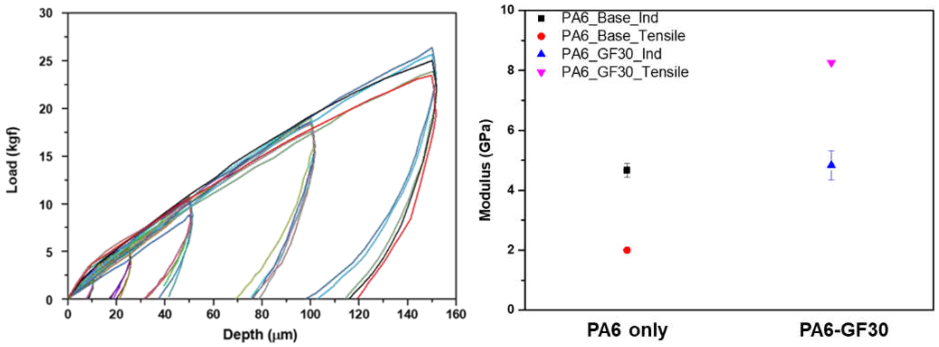

Fig.4 (a) Micro-indentation result (b) Modulus comparison of PA6 base and PA6-GF30

4-2. Material parameter optimization of composite material

For accurate material modeling, the process of obtaining optimized material parameters was conducted by using the homogenization scheme of DIGIMAT software by using the data based on tensile and viscoelastic test results. In addition, in order to consider the anisotropic fiber orientation effect in specimen level, fiber orientation result was extracted from injection molding simulation by MOLDEX 3D software (Fig. 5).

  doi:10.5075/epfl-298799_978-2-9701614-0-0

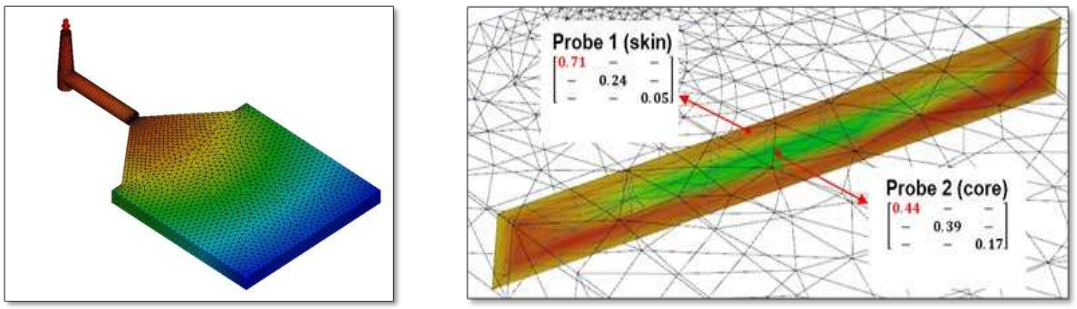

Fig.5. (a) Injection molding simulation by MOLDEX 3D Simulation and (b) fiber orientation result in skin-core layers

4-2. ABAQUS-DIGIMAT interactive simulation

By accommodating the optimized polymer material parameters and anisotropic fiber orientation effect, DIGIMAT software enabled the coupled finite element analysis with ABAQUS to predict tensile behavior of given SFRC specimen (Fig.6) and applied similar methodology to indentation simulation (Fig.7). Fig.8 shows the Von Mises stress distribution difference of isotropic PA6 base and anisotropic PA6-GF30 during the indentation process. Detailed discussion regarding the stress/force distribution during the indentation simulation and correlation with macroscopic mechanical properties will be shown at the conference.

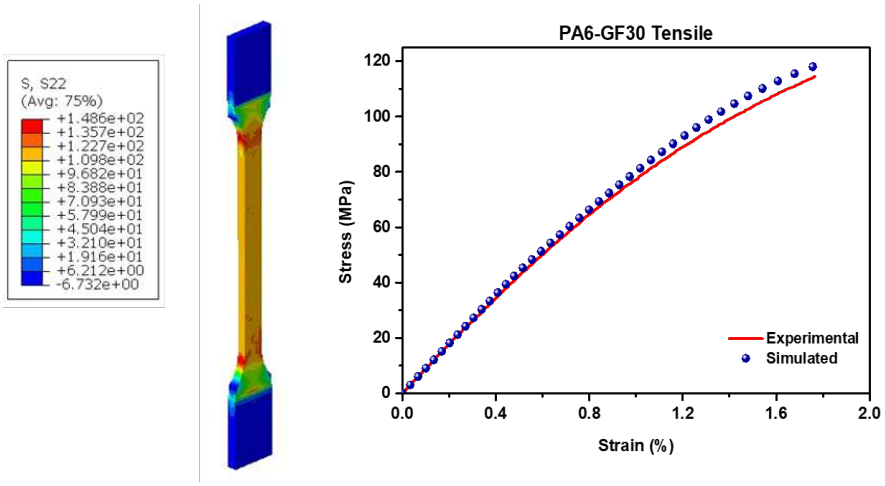

Fig.6. Uniaxial tensile test simulation result of PA6-GF30 specimen

  doi:10.5075/epfl-298799_978-2-9701614-0-0

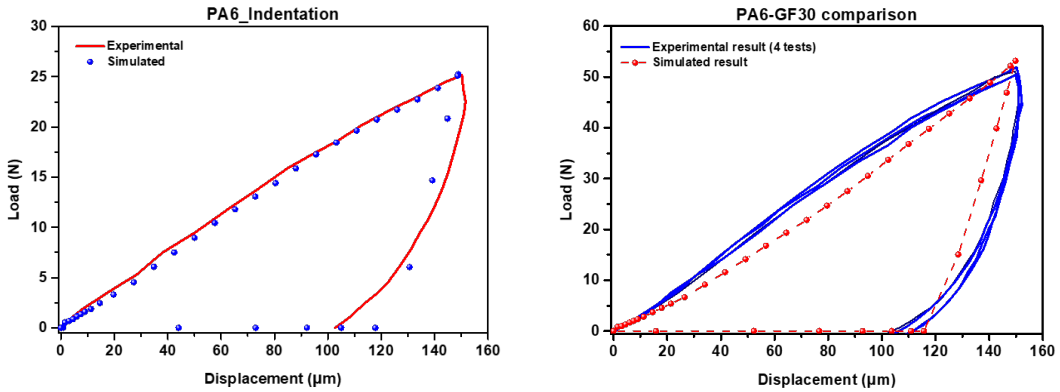

Fig.87. Indentation behavior simulation result of (a) PA6 base and (b) PA6-GF30

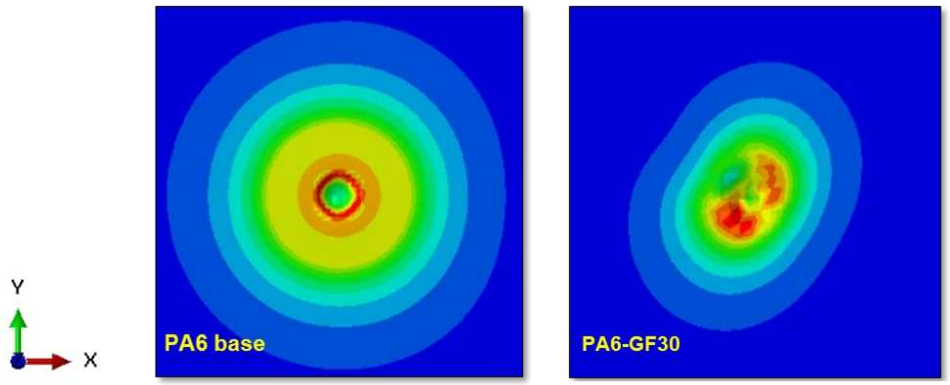

Fig.8. Von Mises stress distribution of (a) PA6 base and (b) PA6-GF30

5. Conclusion

Numerical simulation of micro-indentation test of SFRC specimen was conducted to analyze the correlation between indentation modulus and macroscopic mechanical properties. For accurate modeling of corresponding material, homogenization of composite properties was based on experimental characterization and consideration of fiber orientation effect. By using the capability of coupled simulation between DIGIMAT and ABAQUS, tensile and indentation behavior of SFRC was predicted. Detailed discussion of indentation simulation results will be provided at the conference.

6. Acknowledgements

This work was supported by Hyundai Motor Group (0676-20190009) in Republic of Korea.

7.Reference

1. Hardiman, Mark, Ted Joseph Vaughan, and Conor T. McCarthy. "A review of key developments and pertinent issues in nanoindentation testing of fibre reinforced plastic microstructures." *Composite structures* 180 (2017): 782-798.

2. Karimzadeh, A., M. R. Ayatollahi, and M. Alizadeh. "Finite element simulation of nano-indentation experiment on aluminum 1100." *Computational Materials Science* 81 (2014): 595-600.Mays GC, Hutchinson AR. Adhesives in civil engineering. Cambridge University Press. 1992.

3. Hardiman, Mark, Ted Joseph Vaughan, and Conor T. McCarthy. "The effects of pile-up, viscoelasticity and hydrostatic stress on polymer matrix nanoindentation." *Polymer Testing* 52 (2016): 157-166.

4. Li, Hongzhou, et al. "Determining the constitutive behavior of nonlinear visco-elastic-plastic PMMA thin films using nanoindentation and finite element simulation." *Materials & Design* 197 (2021): 109239.

5. Wang, Yuemin, et al. "Measurement of viscoelastic properties for polymers by nanoindentation." *Polymer Testing* 83 (2020): 106353.

6. Kan, Qianhua, et al. "Oliver–Pharr indentation method in determining elastic moduli of shape memory alloys—a phase transformable material." *Journal of the Mechanics and Physics of Solids* 61.10 (2013): 2015-2033.

  doi:10.5075/epfl-298799_978-2-9701614-0-0

MICRO-SCALE MEASUREMENTS ON EPOXY USING IN-SITU MICROSCOPIC TECHNIQUES

Olivier, Verschatse[a], Lode, Daelemans[a], Wim, Van Paepegem[a] and Karen, De Clerck[a]

a: *Department of Materials, Textiles and Chemical Engineering (MaTCh), Ghent University, Technologiepark 70A, B-9052 Zwijnaarde, Belgium* – Olivier.verschatse@ugent.be

Abstract: *Fiber reinforced composite materials are typically comprised of two phases, e.g. the reinforcing fibers and a surrounding matrix. As a result, the matrix phase in unidirectional composites is composed of many interconnected, microscale (1 – 200 µm), tube-like volumes confined by the reinforcing aligned fiber bundles. Only very little is known on the micromechanical behavior of these small epoxy. Here, we show that the microscale behavior is clearly different and has extreme ductility not observed in the bulk scale brittle behavior. The confined microsize epoxy volumes have a plastic deformation behavior resulting in a substantially higher ultimate tensile strength (up to 380 MPa) and strain at break (up to 130 %) compared to their bulk counterpart (68 MPa and 8%). Polarized light microscopy confirmed the internal epoxy network structure rearrangement during loading. This work thus provides novel insights on the epoxy material behavior at the confined microscale as present in fiber reinforced composite materials.*

Keywords: Scanning Electron Microscopy (SEM); micromechanical testing; yielding; plasticity

1. Introduction

The specific build-up of fibre reinforced polymer composites where individual fibres are surrounded by matrix material, results in the presence of very small zones of matrix material (order of µm) in between the individual fibres. These micro volumes of matrix material tend to have different properties than is expected from standard testing of bulk scale specimens. This has important consequences towards the deformation behaviour and especially the microscale modelling of composite materials, where the current material models are still lacking.

Several researchers pointed out that these microscaled resin regions may have different mechanical properties than their macroscopic/bulk counterpart [1–4]. This has important consequences towards understanding the deformation behavior of fiber reinforced polymer composites. For example, microscale modelling of composites [5] is done very frequently to predict and optimize a composite material without the requirement of expensive time-consuming experimental trial-and-error. Yet, this requires accurate input of the material behavior at the microscale [6]. Nevertheless, most characterization of composites is performed at the bulk scale, typically using the prescribed standardized test methods such as ASTM D638 or ISO 527, while the research into microscale matrix properties is still very limited [1,2,4].

In this respect, a better understanding of epoxy at the microscale is of utmost importance as it is the most used matrix material in composites. Yet, for thermoset materials such as epoxies only a handful of studies are available [1–4]. Hobbiebrunken et al. introduced a production method which enabled the production of microfibers from epoxy resin that have a similar volume as the volumes present in composite materials (fiber diameters between 22 and 52 µm) [1]. Such microfibers indeed offer a good model for the pillar like matrix zones in between the

  doi:10.5075/epfl-298799_978-2-9701614-0-0

reinforcing fibers. An increase in ultimate tensile strength and strain showed that microscale fibers have a higher strength than larger bulk scale specimens. Misumi et al. expanded the research by also studying the yield strength and stiffness in addition to the ultimate tensile strength for five different epoxy systems [3]. They observed an increase in both yield and ultimate tensile strength for all systems. Recently, Sui et al. conducted a study over a broader range of microfiber diameters to compare the mechanical properties at the microscale with those at the bulk scale [4]. Again a decrease in diameter resulted in an increase in ultimate strength and strain.

Overall, it is clear that the mechanical behavior of epoxies may change depending on its size. However, there is currently no agreement whether these changes are induced by a size-effect (related to the amount of defects inside the material), by a difference in microstructure (e.g. orientation of polymer chains) and/or by the production method of the specimens (e.g. a difference in conversion degree). While several researchers describe necking and ductility of the epoxy microfibers, only post-mortem observations are currently available. Furthermore, the amount of tested samples is limited and there is a large variability reported in the results.

Therefore, we studied the deformation behavior of microscale epoxy fibers through tensile testing, thermal analysis (study of glass transition temperature and conversion) and in-situ (electron) microscopy (observation of necking behaviour). The combination of these techniques allows a deeper analysis of the epoxy behavior. In addition, polarized light optical microscopy enabled to study possible rearrangements in the internal network structure of the microscale epoxy samples due to deformation since this was only briefly discussed up till now.

2. Materials and methods

Fine epoxy fibers were made via an optimized method based on the work of Hobbiebrunken et al. [1] by drawing fibers from a vitrifying degassed epoxy mixture. For the specific system used in this paper, the resin was first cured 24h at room temperature in an acclimatized room. This was followed by heating up the resin to 80°C. After 7 minutes this led to the possibility of drawing fibers out of the resin. Fibers were drawn from the resin using an in-house developed automated dip-coater at a constant speed of 10 mm/s (Figure 1-a). The produced fibers are placed on a rack and put in an electrically heated oven at 80°C for 15 hours to complete the curing cycle (Figure 1-b). The complete cured fibers are glued onto paper supports with a two-component 5-minute epoxy glue (Figure 1-c). In total, 42 microfibers were produced with a diameter ranging from 30 to 400 µm and a standard deviation of less than 10%.

Both bulk and microscaled epoxy specimens were produced using the same curing conditions to minimize any change in properties induced by a difference in conversion. This was confirmed by Modulated Differential Scanning Calorimetry (TA instrument Q2000 DSC, heating rate of 3°C/min, modulation of 0.5°C/min, scan from 0°C to 150°C). The glass transition temperature (Tg) of bulk scale and microscale specimens was 86.8 ± 1 °C and 87.3 ± 3 °C respectively. As the Tg is directly linked to the conversion degree [7], this shows that both bulk and microscale specimens have a similar conversion degree. In addition, no additional exothermic peak was measured above the Tg for both types of specimens.

  doi:10.5075/epfl-298799_978-2-9701614-0-0

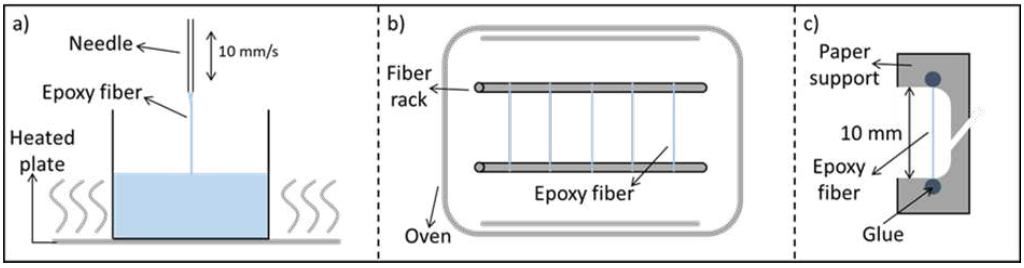

Figure 1 Production method. (a) Epoxy fibers are drawn from the vitrifying resin. (b) The produced fibers are cured at 80°C in an oven for 15h. (c) The final fibers are glued on paper supports, ready to be tested.

The tensile properties of the fibers were determined through tensile tests that agreed both with the ISO 527-1 (strain rate) and ISO 11566 standard (specimen geometry, strain rate), for bulk and fiber materials respectively, utilizing a dedicated fiber testing machine (Textechno Favimat™, force resolution 0.01 mN). The fiber is placed between the clamps at the glued points, the gauge length is 10 mm for all tests. A constant strain rate of 10%/min was selected. Mechanical data for the bulk scale was reused from previous research obtained in our group as published by Allaer et al. [8].

An Olympus BX-51 optical microscope with polarized light was used to inspect all fibers before and after testing. At least 5 pictures were used to measure the diameter of the fibers over the complete gauge length. In addition to the tensile experiments, several specimens were mechanically tested while observed with a Scanning Electron Microscope (SEM, Phenom XL, FEI). Here, a dedicated tensile stage was used (Tensile Sample Holder for Phenom XL, 150N load cell) that could be controlled during SEM imaging.

3. Results and discussion

Mechanical analysis of the microfiber epoxy samples revealed a high overall ductility with nominal strains reaching over 100%, this in contrast to bulk epoxy samples with the same conversion rate. A representative force-displacement curve for a microfiber epoxy sample, Figure 2, illustrates linear elasticity (zone I) followed by plastic deformation (zone II). For bulk scale samples this almost immediately leads to fracture, as only minor plastic deformation before failure is encountered for the majority of epoxy systems used in composites. On the other hand, the microfibers sustain this local decrease in diameter leading to a stable necking process and fracture is only encountered in a much later stage. Generally the microfibers show a lower stiffness and yield stress compared to the bulk samples (figure 3). The necking proceeds throughout the whole microfiber resulting in a large plateau in the force - displacement curve, resulting in an extreme ductility of the microfiber specimens (zone III, drawing of the microfibers). Finally, an increase in stress is observed (zone IV) and brittle fracture occurs. The increase in stress is likely related to strain hardening occurring during the necking of the microfiber.

An increase in E-modulus can be observed with decreasing microfiber diameter, the smaller the fibers become the stiffer they are (Figure 3a). This is probably due to a more perfect network structure with very few or no defects. Yet, the presence of small defects will have a large influence on the fibers resulting in more variability of the reported values compared to their bulk counterparts [3,4]. It has to be noted that for the microscale tests, the crosshead displacement of the tensile stage was used to determine the strain. This likely leads to an

underestimation of the E-modulus since any fixture compliance (e.g. slippage, backlash, …) results in an artificially increased strain. It can thus explain why the bulk scale modulus, which was accurately measured through DIC and clip-on extensometers, is higher than those of the microfibers. Indeed, one would expect that the more perfected network structure of the microfibers would result in a higher stiffness.

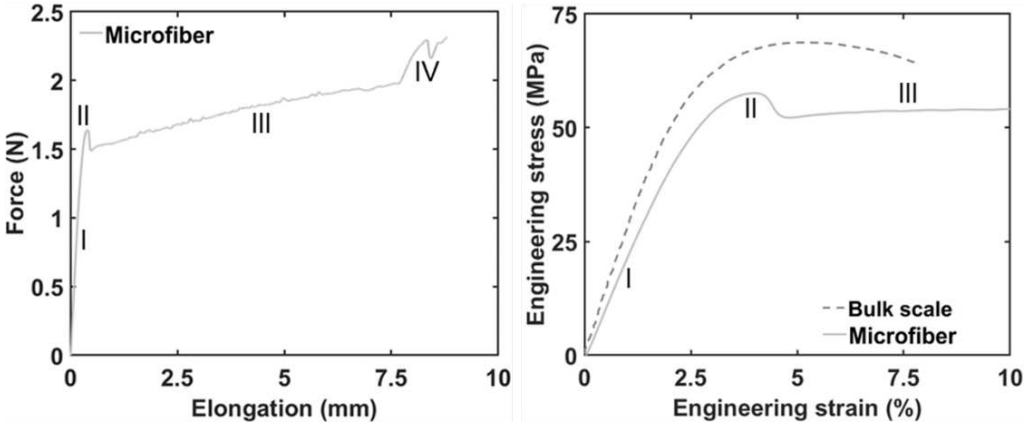

Figure 2 Stress-strain curve of a microfiber and bulk scale (the latter adapted from previous work. [23]). Representative force - displacement curve of a microfiber. Four zones can be observed: I - linear elastic zone, II - necking formation III - constant necking IV - strain hardening.

The microfibers show a similar yielding behavior over the full tested diameter range. In general the observed yield stress is somewhat lower than the values obtained for the bulk sample, while the yield strain is similar to the bulk values (Figure 3c and 3d). The latter can likely again be attributed due to the strain being based on crosshead displacements.

After yielding, the microfibers start to deform plastically resulting in necking. Similar to the yield stress, the necking stress and strain remain relatively unaffected by the diameter range tested here. The necking stress of the microfibers averages around 55 – 60 MPa (Figure 3e) while the necking strain averages around 4.5% of strain (Figure 3f). This indicates that for the microscale specimens there is somewhat less restriction for the epoxy network to deform and network chains possibly slip over one another resulting in reorientation of the chains in the internal network [4,9], somewhat similar to the deformation behavior of thermoplastics.

A drastic increase in ultimate tensile strength is observed as well. Whereas the bulk material has a ultimate tensile strength of around 68 MPa the fibers show a ultimate tensile strength up to 380 MPa. Moreover, an increasing trend in the ultimate tensile stress is observed for decreasing fiber diameters (Figure 3h). Similarly to the ultimate tensile strength, the strain at break increases drastically for all of the microfibers, with values going up to 130% (the bulk material has a strain at break of 8%).

Not all fibers reach these very high ultimate tensile strains as some fracture earlier during the necking process (zone III) which may be attributed to the presence of voids or defects. Due to the small volume, the chance of a void or defect being present is low which results in higher possible strengths [1]. Yet, if a void is present this will largely influence the mechanical behavior of the microfiber, resulting for example in early failure.

  doi:10.5075/epfl-298799_978-2-9701614-0-0

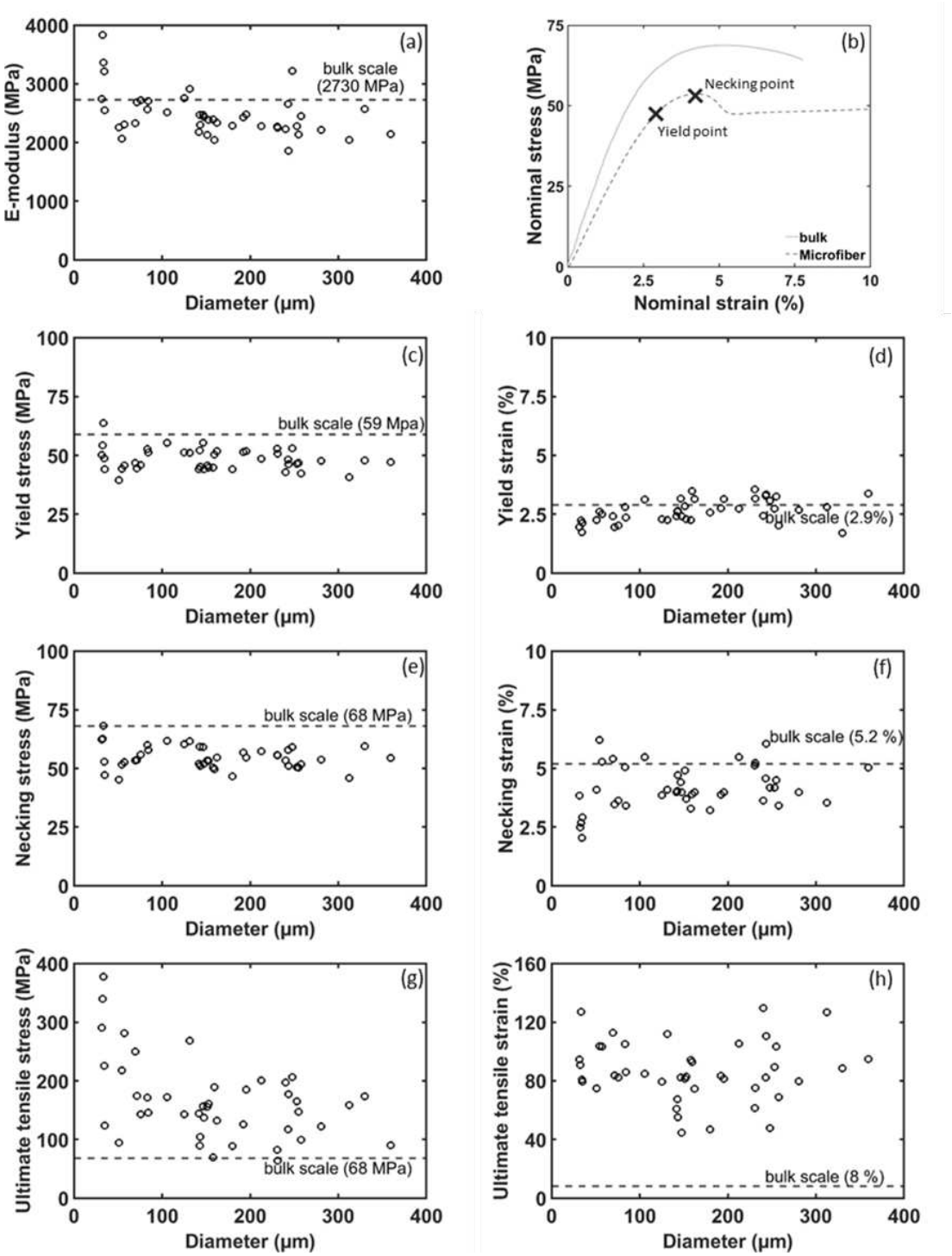

Figure 3 Representation of all mechanical data (a) E-modulus (b) engineering stress – engineering strain curve of representative microfiber tensile test with indication of necking and yield point (c) yield stress (d) yield strain (e) necking stress (f) necking strain (g) ultimate tensile stress and (h) ultimate tensile strain.

Figure 4 schematically illustrates the change in network structure during the deformation of the microfiber specimens, resulting in an oriented network structure after necking. Initially, the epoxy network is similar to that of a bulk material and can be considered random. During necking, the network has the possibility to align itself in the tensile direction by sliding and reorientation of the network chain segments, explaining the sudden and relatively large decrease in cross-sectional area. This reorientation is indeed confirmed by the sharp increase in

stress once the necking has proceeded completely through the gauge area of the fiber. (Figure 2, zone IV). This (local) strain hardening effect can be explained by a more oriented state of the molecular network. After this reorientation, the stress increases and the epoxy network finally fractures via the rupture of chains (chain scission) as it cannot accommodate the increasing tensile strain anymore.

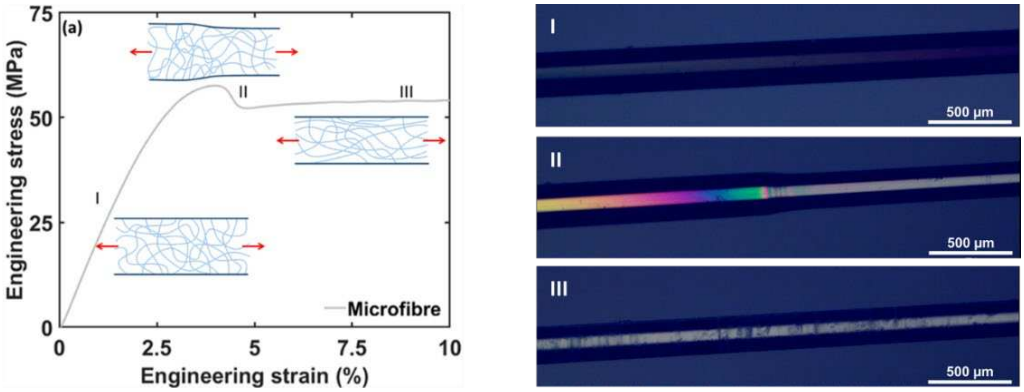

Figure 4 Schematic representation of the rearrangement of the epoxy network under tensile stress. Polarized optical microscopy confirms an oriented molecular microstructure in the necked zone of the specimens.

Polarized optical microscopy of tested fibers further confirm the change in orientation of the molecular network in the necked zone (Figure 4). Before stress is applied, the sample barely interacts with the light, resulting in a low amount of light passing through the second polarizer and thus a dark zone. Once stress is applied on the sample it starts to interact with the polarized light due to straining of the network structure. Around the necking zone, the network starts to orient. The oriented network interacts with the polarized light resulting in a bright zone showing a difference in internal structure with the unnecked zone. This confirms that a random network is present with no preference for any direction before necking, while a reorientation at molecular level occurs during necking.

To have a better view of the necking behavior several microfibers were mechanically tested with in-situ scanning electron microscopy. Via the obtained SEM pictures the diameter of the fiber is accurately measured which gives the possibility to calculate the change in diameter due to necking and the corresponding change in length (Eq. 1). Assuming a constant volume (v = 0.5, plasticity), the strain in the fiber direction can be calculated from the diameter variation via Equation 1:

$$Tensile\ strain = \frac{(D_1^2 - D_2^2)}{D_2^2} \quad (1)$$

Where D_1 and D_2 are the diameter just in front of the neck and just behind the neck (Figure 5).

The necking process that takes place during the plastic deformation of the microfibers can be clearly seen in Figure 5. All tested microfibers showed a decrease in diameter between 16 and 20%, with an average value of 18.3%, corresponding to a strain in the fiber direction ranging from 40 to almost 60% (average of 49.9%). Note the measured contraction is only due to the necking process, the tensile strain developed in the linear elastic zone or after necking of the fiber is not considered here.

  doi:10.5075/epfl-298799_978-2-9701614-0-0

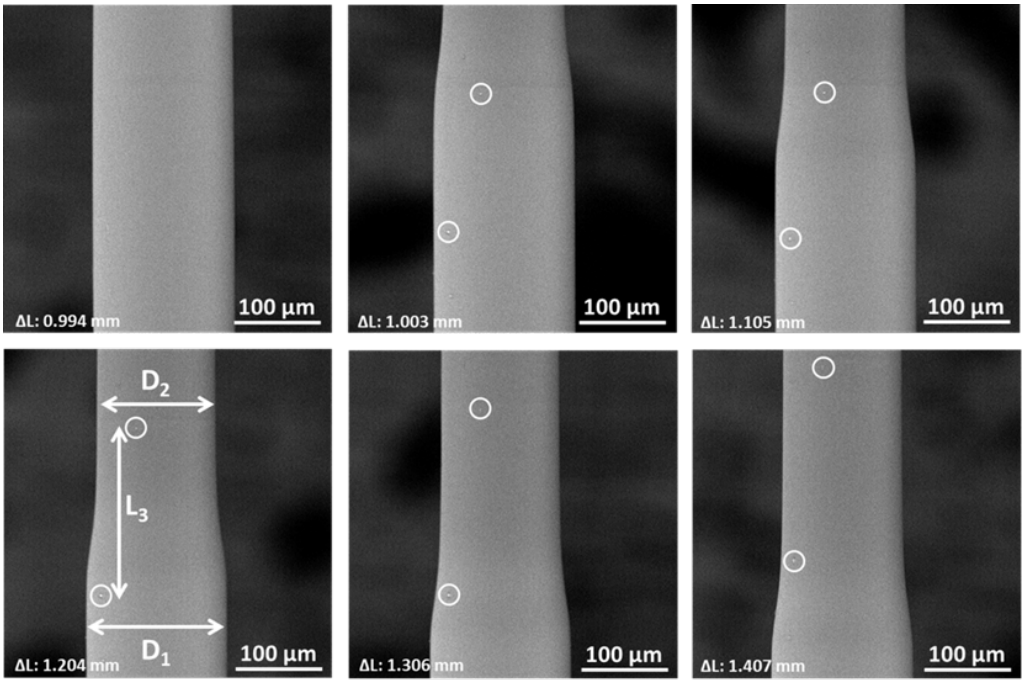

Figure 5 Sequential SEM images of necking in a microfiber. ΔL indicates the displacement of the clamps.

In addition to calculating the strain according to Eq. (1), the idea of video-extensometry is proposed as well to directly measure the increase in tensile strain after necking. We therefore deliberately handled a couple of specimens without gloves, resulting in small contamination onto the surface of the specimens that are ideal as surface markers, see Figure 5. These surface markers allowed to directly calculate the tensile strain. The results are listed Table 1 and confirm that the values obtained through Eq. (1) are correct.

Table 1 Comparison of the strain calculated based on the diameter reduction and the surface markers.

	Calculated strain via diameter (%)	Strain (%)
Microfiber 1	50.1	52.5
Microfiber 2	52.1	53.7
Microfiber 3	41.8	41.0

4. Conclusion

A set of microfibers was produced and studied via standard tensile testing. The deformation behavior of the confined microfiber epoxy samples was substantially different compared to bulk epoxy behavior, while thermal analysis confirmed a similar conversion rate of the epoxy in both the microfiber and the bulk state. During both linear elastic deformation and yielding, the microfibers behaved very similar to bulk samples. Yet, after necking, the behavior of the microscale and the bulk scale samples is very different. Indeed, the bulk scale samples show fracture shortly after yielding, whereas the microfiber specimens showed a large plastic deformation via the formation of a necked zone that extended throughout the fiber. As a result, much higher strains at break (up to 130% vs. 8% for bulk) and ultimate tensile strengths (up to 380 MPa vs. 68 MPa for bulk) were observed for these confined microfibers.

  doi:10.5075/epfl-298799_978-2-9701614-0-0

This high plastic deformation is attributed to a rearrangement of the epoxy network structure in the microfibers, as confirmed by polarized optical microscopy and the occurrence of strain hardening. In-situ electron microscopy moreover allowed to accurately observe the deformation behavior of these microfibers and measure tensile strains and diameter contractions during loading. An increase in length of around 50% was observed due to necking only.

The remarkable difference between the deformation behavior of epoxy resin at the micro- and macroscale clearly illustrates the need of microscale testing. Indeed, the resin pockets in fiber reinforced polymer composites are confined microsized regions as well that cannot be accurately characterized via bulk testing. Especially for predictive modelling tools, such as micromechanical modelling, this necessitates the use of microscale measured properties to obtain correct data and insights.

5. References

1. Hobbiebrunken T, Fiedler B, Hojo M, Tanaka M. Experimental determination of the true epoxy resin strength using micro-scaled specimens. Compos Part A Appl Sci Manuf. 2007;38(3):814–8.

2. Odom EM, Adams DF. Specimen size effect during tensile testing of an unreinforced polymer. Vol. 27, Journal of Materials Science. 1992. p. 1767–71.

3. Misumi J, Ganesh R, Sockalingam S, Gillespie JW. Experimental characterization of tensile properties of epoxy resin by using micro-fiber specimens. J Reinf Plast Compos. 2016;35(24):1792–801.

4. Sui XM, Tiwari M, Greenfeld I, Khalfin RL, Meeuw H, Fiedler B, et al. Extreme scale-dependent tensile properties of epoxy fibers. 2019;13(11):993–1003.

5. Vaughan TJ, McCarthy CT. Micromechanical modelling of the transverse damage behaviour in fibre reinforced composites. Compos Sci Technol [Internet]. 2011;71(3):388–96. Available from: http://dx.doi.org/10.1016/j.compscitech.2010.12.006

6. Totry E, Molina-Aldareguía JM, González C, LLorca J. Effect of fiber, matrix and interface properties on the in-plane shear deformation of carbon-fiber reinforced composites. Compos Sci Technol. 2010;70(6):970–80.

7. Hardis R, Jessop JLP, Peters FE, Kessler MR. Cure kinetics characterization and monitoring of an epoxy resin using DSC, Raman spectroscopy, and DEA. Compos Part A Appl Sci Manuf [Internet]. 2013;49:100–8. Available from: http://dx.doi.org/10.1016/j.compositesa.2013.01.021

8. Allaer K, De Baere I, Van Paepegem W, Degrieck J. Direct fracture toughness determination of a ductile epoxy polymer from digital image correlation measurements on a single edge notched bending sample. Polym Test [Internet]. 2015;42:199–207. Available from: http://dx.doi.org/10.1016/j.polymertesting.2015.01.014

9. Andrew T. Detwiler AJL. Aspects of Network Formation in Glassy Thermosets. J Appl Polym Sci. 2010;117(2):1021–34.

STUDY ON CURE SHRINKAGE OF EMC USING DIELECTRIC SENSOR AND FBG SENSOR

Jeong-Hyeon Baek[a], Dong-Woon Park[a], Simon Park[b] and Hak-Sung Kim[a,c]*

a: Department of Mechanical Engineering, Hanyang University, 222 Wasngsimni-ro, Seongdong-gu, Seoul 133-791, Republic of Korea
b: Department of Mechanical and Manufacturing Engineering, Schulich School of Engineering, University of Calgary, 2500 University Drive NW, Calgary, AB T2N 1N4, Canada
c: Institute of Nano Science and Technology, Hanyang University, 222 Wasngsimni-ro, Seongdong-gu, Seoul 133-791, Republic of Korea

Abstract: *The curing status and internal strain of epoxy molding compound (EMC) were monitored using a dielectric sensor and a fiber Bragg grating (FBG) sensor under curing conditions similar to the actual semiconductor packaging process. The dissipation factor was measured with a dielectric sensor during the molding process, and a gelation point, which is the starting point of effective cure shrinkage, was defined. Also, differential scanning calorimetry (DSC) test and rheometer test were performed and analyzed with dielectrometry measurement. In addition, Bragg wavelength (BW) was measured with the FBG sensor during the whole curing process and the cure shrinkage of the EMC was obtained. From these results, the effective cure shrinkage of the EMC that actually affects the residual stress of the EMC after curing processing was obtained.*

Keywords: Cure shrinkage; Gelation point; Dielectric sensor; FBG sensor; EMC;

1. Introduction

Semiconductor technologies such as nano-scale line widths and more than 10 million cells continue to develop in various forms. Packaging technologies, on the other hand, do not keep up with that level, so they do not fully support semiconductor technologies to achieve optimum efficiency. Among the various issues related to packaging technology, warpage is one of the major concerns. This is because the warpage causes a variety of problems in the surface mount technology (SMT) process, such as inducing mounting errors when mounting a chip or poor contact of solder joints between the package and printed circuit board (PCB) [1]. Since this problem significantly lowers manufacturability, it is required to control the warpage generated during the curing process. The cure shrinkage is well known as a main factor that makes warpage prediction difficult [2]. Furthermore, as the package is getting thinner, the importance of cure shrinkage is being emphasized more and more. Therefore, the effective cure shrinkage of the epoxy molding compound (EMC), which occurs after the gelation point and induces the residual stress of the EMC, must be accurately measured [3]. However, the method to measure the effective cure shrinkage has not yet been completely established. One of the reasons that make this difficult is the detection of the gelation point. Since the gelation point does not affect the curing reaction significantly, it is difficult to detect the gelation point with a method such as differential scanning calorimetry (DSC) [4]. Therefore, molecular analysis is required to detect the gelation point which is a microscopic phenomenon.

  doi:10.5075/epfl-298799_978-2-9701614-0-0

In this study, the effective cure shrinkage of the EMC was obtained under the curing condition similar to the actual packaging process using the dielectric sensor and FBG sensor. The curing status of the EMC was monitored by measuring the dielectric properties using a dielectric sensor during the heating process for the molding. From this result, the gelation point was defined and the curing status was analyzed by comparing the dynamic scanning results of the DSC test and the rheometer test with the same heating rate. In addition, the cure shrinkage of the EMC was measured using the FBG sensor during the entire curing process. Finally, the effective cure shrinkage of the EMC was derived from the measured cure shrinkage generated from the detected gelation point.

2. Experiments for the properties of the EMC

2.1 Measurement method of effective cure shrinkage

Dielectric analysis (DEA) is a powerful method to monitor the cure state of thermosetting plastic for an in-molding system [5]. In this study, the cure status of the EMC was analyzed with the dissipation factor measured using a dielectric sensor during the heating process for molding [6]. As shown in Figure 1 (a), the dielectric sensor was embedded in the EMC and connected to an alternating electric field. Then, the EMC can be electrically modeled as shown in Figure 1 (b). As the EMC undergoes the curing process, mobility of ions and dipoles change correspondingly and the degree of this movement can be represented as a dissipation factor. That is, the dissipation factor increases as the EMC becomes a viscous liquid, and then decreases again as it is cured into a solid. Furthermore, a curing initiation point and a gelation point are defined by the rate of dissipation factor being maximum and minimum [7].

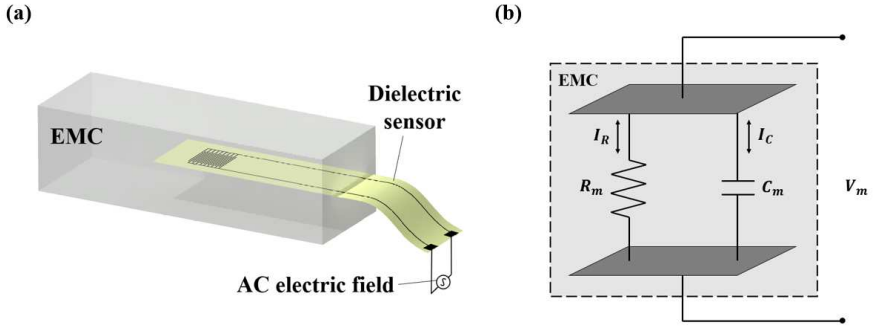

Figure 1. Schematics of (a) a dielectric senor embedded in the EMC and (b) an equivalent electrical circuit for a dielectric material.

The FBG sensor has the characteristic of reflecting and transmitting a specific frequency spectrum that satisfies the Bragg condition due to Bragg grating engraved in the middle of the optical fiber. This specific frequency spectrum can be expressed in Bragg wavelength (BW), λ_B, which is shifted with temperature and stress-induced deformation (see Eq. 1).

$$\Delta\lambda_B = \Delta\lambda_B^i + \Delta\lambda_B^d \quad (1)$$

$\Delta\lambda_B^i$ is "intrinsic" BW shift that is related to the temperature, and $\Delta\lambda_B^d$ is "deformation" induced BW shift that is related to stress-induced deformation [8]. Since intrinsic BW shift has a linear relationship with temperature change, it is measured in advance through a calibration

  doi:10.5075/epfl-298799_978-2-9701614-0-0

experiment using a bare FBG sensor [9]. Then, the $\Delta\lambda_B^d$ can be obtained by subtracting the $\Delta\lambda_B^i$, which is calculated from the measured temperature, from the BW shift.

If the length "b" of EMC which is distance from center to edge is greater than 200 times the fiber radius "a" (see Figure 2), it can be assumed that only a uni-axial loading along the fiber longitudinal direction is applied on the FBG sensor. Then, the internal strain (ε) of the EMC can be calculated as [10]

$$\varepsilon = \frac{\Delta\lambda_B^d}{\lambda_B(1-P_k)} \tag{2}$$

where P_k is the equivalent strain-optic constant.

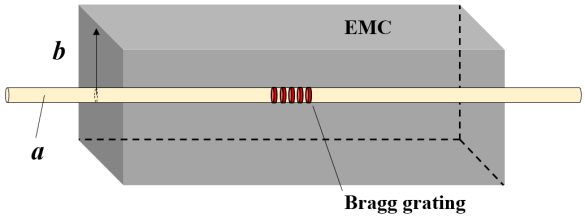

Figure 2. Schematic of an FBG sensor embedded in the EMC.

2.2 Monitoring of curing process

The EMC was cured under the temperature profile including molding and post-curing process in Figure 3. The EMC was filled in the mold which is designed considering the above length ratio to use equation (2) as shown in Figure 4. Then, the dielectric sensor, the FBG sensor, and thermocouple were embedded together. The mold was vacuum bagged and heated with a pressure of about 20 kPa for the molding process. After molding, the mold was removed from the EMC and the post-curing process was performed using a thermal chamber. Dissipation factor was measured with dielectric sensor until the molding process, and BW and temperature were measured with FBG sensor and thermocouple during the entire curing process.

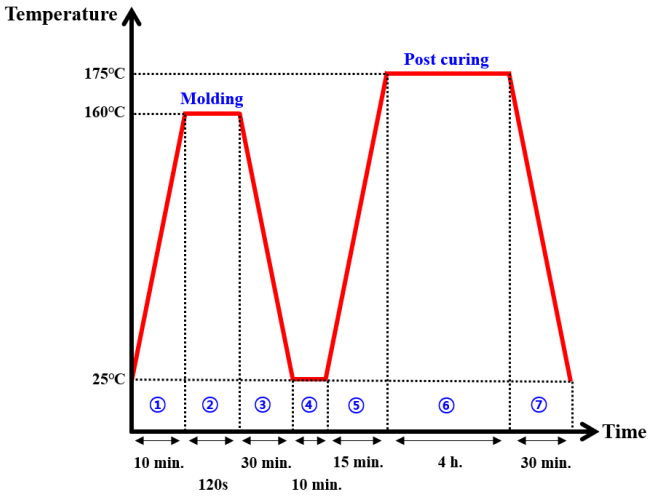

Figure 3. Temperature profile for curing the EMC.

  doi:10.5075/epfl-298799_978-2-9701614-0-0

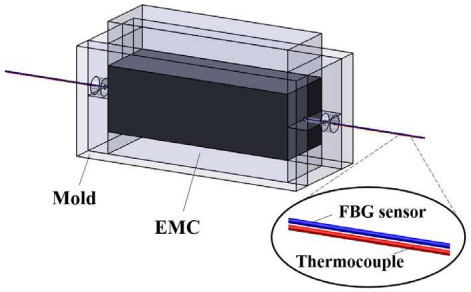

Figure 4. Schematic of the mold set-up

2.3 Characterization

The DSC is a universal thermoanalytical technique to obtain the degree of cure of polymer. DSC Q20 (TA Instruments, USA) was employed to determine the degree of cure of the EMC during the heating process for molding temperature of 160℃. Dynamic scanning was performed at a heating rate of 13°C/min used for effective cure shrinkage measurement.

The viscoelastic properties of the EMC were measured during the dynamic scanning at a heating rate of 13°C/min using the parallel plate fixture of a strain-controlled rheometer ARES-G2 (TA Instruments, USA). When the bottom plate was oscillating at a constant shear rate (1/sec) and constant frequency (1Hz), the torque generated by the shear stress of the EMC between the parallel plate was measured with the torque sensor at a constant shear rate. As a result, storage and loss modulus of the EMC were calculated using the measured shear stress and the shear rate.

3. Results and discussion

Figure 5 shows the dissipation factor (*D*) and the rate of dissipation factor (*dD/dt*) during the heating process for the molding. The curing initiation point was detected at 114°C with a maximum *dD/dt*, and the gelation point was detected at 151°C with a minimum *dD/dt*.

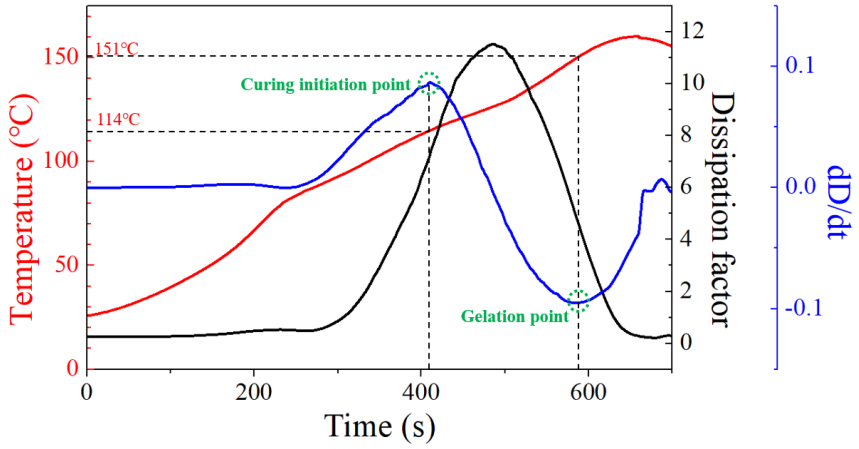

Figure 5. Dissipation factor (D) and the rate of dissipation factor (dD/dt) during the heating process for molding.

Figure 6 shows the results of the rheometer test, DSC test, and the rate of dissipation factor (*dD/dt*). The degree of cure at the gelation point detected by dielectrometry was about 0.28 which is in the general range of the degree of cure at the gelation point of the EMC [11]. In addition, it was confirmed that the temperature of the maximum point of *dD/dt* and the curing initiation point obtained from the DSC result coincided as 114°C. From these results, the reliability of the dielectrometry results was verified.

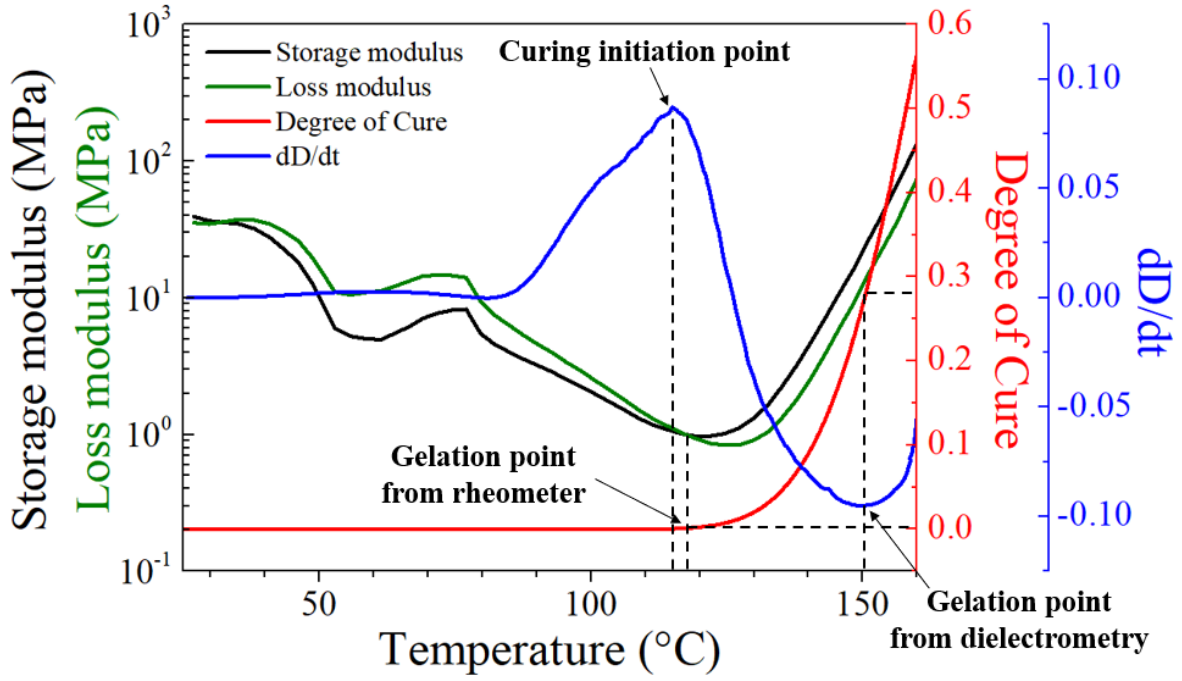

Figure 6. Results of rheometer test, DSC test and the dD/dt

DMA or rheometer test is the common method to determine the gelation point by analyzing changes in mechanical properties. However, a general definition of the gelation point using mechanical properties has not yet been determined. Nonetheless, the most representative method to define the gelation point is to detect the crossover point where the storage modulus and the loss modulus cross [12]. As shown in Figure 6, the storage modulus and the loss modulus cross at 118°C where the degree of cure is about 0.01. However, it is difficult to regard this point as the gelation point, considering the general degree of cure at the gelation point of the EMC. Although this method could show a high accuracy for homogeneous polymer, the gelation point of the EMC is not properly detected due to the influence of the silica filler as the EMC is a composite material composed of high content of silica filler and epoxy. Therefore, it was verified that the dielectrometry is an effective method to detect the gelation point of the EMC.

Figure 7 shows the calibration result of the bare FBG sensor. Through linear fitting, the intrinsic BW shift was obtained as a linear function of temperature as:

$$\Delta\lambda_B^i = 0.0119 \cdot T \tag{3}$$

where *T* is the temperature in °C unit.

  doi:10.5075/epfl-298799_978-2-9701614-0-0

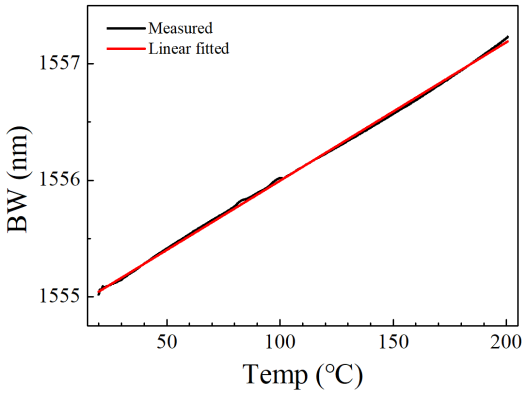

Figure 7. Calibration result of bare FBG sensor

Using eq. (3), intrinsic BW was calculated from the temperature measured during the whole process. Then, the deformation BW, $\Delta\lambda_B^d$, was calculated by subtracting the intrinsic BW from the measured BW from the FBG sensor during the entire curing process. Finally, the internal strain of the EMC was obtained using Eq. (2) where $P_k = 0.18$ [13]. Figure 8 (a) shows the internal strain of the EMC and dD/dt with the temperature at the beginning of molding. It was confirmed that the strain abruptly decreased at the temperature of 151℃ which is the gelation point detected by the dielectric sensor. As a result, the cure shrinkage of 0.04% in the molding process and 0.032% in the post-curing process occurred, resulting in a total cure shrinkage of 0.072% (see Figure 8 (b)).

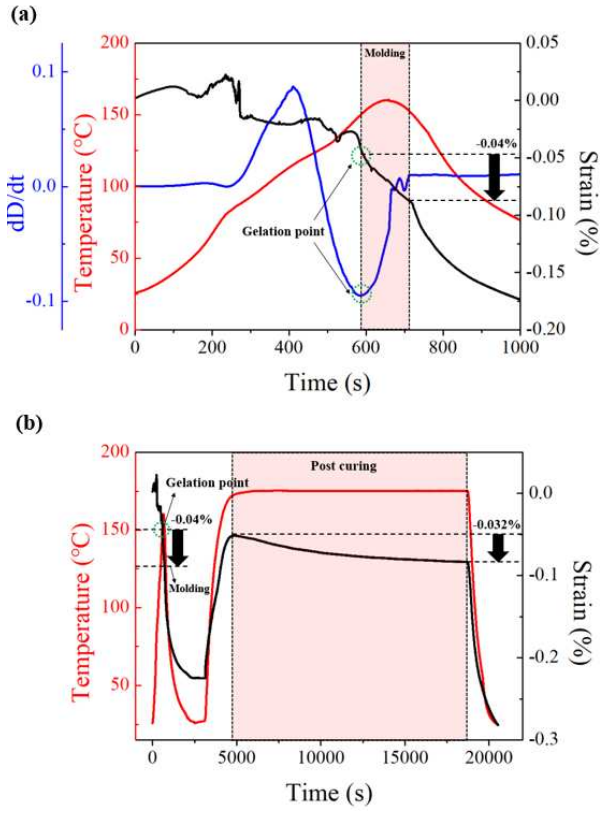

Figure 8. Experimental results of (a) strain, dD/dt during the beginning part of molding, and (b) strain evolution with temperature.

  doi:10.5075/epfl-298799_978-2-9701614-0-0

4. Conclusions

In this study, a new method to measure the effective cure shrinkage of the EMC using the dielectric sensor and the FBG sensor is proposed. It would contribute to predicting the accurate warpage behavior of semiconductor packages. Furthermore, the effective cure shrinkage measurement method proposed in this study could be applied to thermosetting polymer-based composites manufacture.

Acknowledgements

This research was supported by the MOTIE (Ministry of Trade, Industry, and Energy) in Korea, under the Fostering Global Talents for Innovative Growth Program (P0008748, Global Human Resource Development for Innovative Design in Robot and Engineering) supervised by the Korea Institute for Advancement of Technology (KIAT). This work was also supported by Korea Institute of Energy Technology Evaluation and Planning(KETEP) grant funded by the Korea government(MOTIE)(20202020800360, Innovative Energy Remodeling Total Technologies(M&V, Design, Package Solutions, and Testing & Verifications Technologies) for the Aging Public Buildings and 20212020800090, Development and Demonstration of Energy-Efficiency Enhanced Technology for Temperature-Controlled Transportation and Logistics Center).

References

1. B. Bilyeu, W. Brostow, K.P. Menard, Epoxy thermosets and their applications II. Thermal analysis, Journal of Materials Education 22(4/6) (2000) 107-130.
2. J. Botsis, L. Humbert, F. Colpo, P. Giaccari, Embedded fiber Bragg grating sensor for internal strain measurements in polymeric materials, Optics and lasers in Engineering 43(3-5) (2005) 491-510.
3. W. Brostow, S.H. Goodman, J. Wahrmund, Handbook of Thermoset Plastics: 8. Epoxies, Elsevier Inc. Chapters2013.
4. S. Han, K. Wang, Integrated flow analysis during filling and post-filling stage of semiconductor encapsulation, J. Electron. Packag. 122(1) (2000) 20-27.
5. R. Hardis, J.L. Jessop, F.E. Peters, M.R. Kessler, Cure kinetics characterization and monitoring of an epoxy resin using DSC, Raman spectroscopy, and DEA, Composites Part A: Applied Science and Manufacturing 49 (2013) 100-108.
6. G. Hu, J.-E. Luan, S. Chew, Characterization of chemical cure shrinkage of epoxy molding compound with application to warpage analysis, (2009).
7. D.-H. Kim, H.-S. Kim, Smart cure cycle to improve tensile load capability of the adhesively bonded joint, Journal of adhesion science and technology 27(16) (2013) 1739-1754.
8. H.S. Kim, Reduction of fabricational thermal residual stress of the hybrid co-cured structure using a dielectrometry, Composites science and technology 67(1) (2007) 29-44.
9. S.P. Phansalkar, C. Kim, B. Han, P.J. Gromala, Volumetric effective cure shrinkage measurement of dual curable adhesives by fiber Bragg grating sensor, Journal of materials science 55(22) (2020) 9655-9664.

  doi:10.5075/epfl-298799_978-2-9701614-0-0

10. F. Ren, W. Zhang, Y. Li, Y. Lan, Y. Xie, W. Dai, The temperature compensation of FBG sensor for monitoring the stress on hole-edge, IEEE Photonics Journal 10(4) (2018) 1-9.
11. N. Tanaka, Y. Okabe, N. Takeda, Temperature-compensated strain measurement using fiber Bragg grating sensors embedded in composite laminates, Smart materials and structures 12(6) (2003) 940.
12. Y. Wang, B. Han, D. Kim, A. Bar-Cohen, P. Joseph, Integrated measurement technique for curing process-dependent mechanical properties of polymeric materials using fiber bragg grating, Experimental mechanics 48(1) (2008) 107-117.
13. W. Xia, M. Xiao, Y. Chen, F. Wu, Z. Liu, H. Fu, Thermal warpage analysis of PBGA mounted on PCB during reflow process by FEM and experimental measurement, Soldering & Surface Mount Technology (2014).

  doi:10.5075/epfl-298799_978-2-9701614-0-0

THERMOPLASTIC COATING ON CARBON FIBER FOR THE DESIGN OF SUSTAINABLE COMPOSITE MATERIALS

Mónica Peñas Caballero[a], Enrico Chemello[b], Antonio Mattia Grande[b], Marianella Hernández Santana[a], Raquel Verdejo[a], Miguel Ángel López-Manchado[a]

[a]: Institute of Polymer Science and Technology (ICTP-CSIC) (Madrid, Spain) – mpcaballero@ictp.csic.es
[b]: Department of Aerospace Science and Technology, Politecnico di Milano, (Milan, Italy)

Abstract:

Self-healing carbon fiber reinforced plastics have been developed through the deposition of poly(ethylene-co-methacrylic acid) (EMAA) nanoparticles on the fiber surface, by aerography. EMAA nanoparticles are homogeneously distributed, showing a strong adhesion to the fiber. EMAA coating improves the fracture toughness, G_{IC} and provides self-healing capacity to the material. The healing efficiency decreases gradually with the number cycles, but retains more than 40% after a third cycle.

Keywords: Self-healing; Thermoset; Thermoplastic; Coating.

1. Introduction

Fiber reinforced plastics (FRP) have excellent properties, such as high fatigue and corrosion resistance, good dimensional stability and light weight, as well as an excellent strength-to-weight ratio. As a result, they have found widespread use in different sectors. In 2020, the FRP market was valued at €60 billion and is expected to grow to €96 billion in 2026 [1]. However, this growth implies an increase in the waste generated at the end-of-life of the products derived from these materials. In order to overcome this situation, research lines are emerging focusing on the design of sustainable FRPs. Different strategies are being considered, such as the use of thermoplastic matrices that can be easily recycled; the substitution of synthetic fibers by natural fibers (as flax, hemp or jute); or conferring self-healing capability to the FRP, among others.

Currently, there are different possibilities to address the self-healing strategy, such as the incorporation of capsules, vascular systems, or thermoplastics into epoxy matrices; being the latter the most industrially scalable. Poly (ethylene-co-methacrylic acid) (EMAA) is one of the prefer thermoplastic that has shown high healing efficiency due to its high coefficient of thermal expansion and its covalent cross-linking with the epoxy resin. Its healing mechanism has been ascribed to a pressure-delivery mechanism [2]. As the temperature increases, the EMAA melts and flows, driven by high-pressure gas-filled bubbles, produced by the reaction of the acid group of the thermoplastic with the hydroxyl group of the resin [3]. EMAA has been introduced into FRPs as discrete particles in the epoxy resin, and as sheets between the carbon fiber plies or as filaments that stitch carbon fiber yarns together. In this work, we will incorporate EMAA into the fiber by using a spray coating method, a versatile and easily scalable technique. The self-healing capability will be studied through the recovery of the interlaminar fracture toughness.

  doi:10.5075/epfl-298799_978-2-9701614-0-0

2. Materials and Methods

2.1 Materials

The used carbon fiber was unidirectional UD 12k, 340 g/m^2 and 45 µm supplied by *INP96*. The matrix was an epoxy resin Resoltech 1050/1053s, from Resoltech consisting of diglycidyl ether of bisphenol F (DGEBF 50-80 %), diglycidyl ether of bisphenol A (DGEBA, 10-40 %) and 1,6 hexanediol diglycidyl ether, with a hardener of polioxialcalinoamine/n-aminoetilpiperacine/dietiletriamine, at specific resin:hardener ratio of 100:35 in parts by weight. According to the supplier specifications, the curing reaction is carried out at 60 ° for 16 h. As healing agent, we used pellets of poly (ethylene-co-methacrylic acid) (EMAA) from Sigma-Aldrich.

2.2 Sample preparation

The coatings were prepared following three steps: 1) dissolution of the thermoplastic, 2) cooling, and 3) spraying and drying. In step 1, EMAA was dissolved in THF at a concentration of 0.012 g/ml; the solution was heated at 60 ^{o}C (below the boiling point of the THF) with stirring and assisted by an ultrasonic bath. Once the EMAA is completely dissolved, it is cooled in an ice bath and the solution turns milky white as a result of the formation of nano-sized particles [4]. Finally, the solution was sprayed onto the fiber surface to the required concentration (10 wt.%) and dried at 65 ^{o}C in the oven to remove the solvent, until the weight remained unchanged.

The coated fibers were placed unidirectionally and 14-layer laminates were prepared by vacuum-assisted resin infusion (VARI). The laminates were heated up to 60 ^{o}C and kept for 16 h for curing. The laminates were post-cured (150 °C/2 h) in the press to promote the compaction of the layers. The samples were cut on a Neurtek Brillant 220 precision cutting machine.

2.3 Characterization

The uncoated and EMAA-coated carbon fibers were observed with a Scanning Electron Microscope (SEM), Phillips, model XL30 with a tungsten filament and an accelerating voltage of 25 kV, after sputter-coating with gold. The healing fracture surface of the laminates was observed with an Optical Microscope Olympus, model DSCX1000.

The interlaminar fracture toughness properties under mode I static and fatigue loading were measured using the double cantilever beam (DCB), ASTM D55S8. The specimen's dimensions were 100 x 20 mm with a pre-crack of 40 mm. Two metallic tabs were bonded to the outer surface of the DCB specimen using a two-component epoxy adhesive (3M Scotch-Weld DP110). The composite was measured by applying a monotonically increasing crack opening displacement speed of 1 mm/min to the pre-cracked end of the DCB specimen using MTS 858 mini Bionix. Mode I interlaminar fracture toughness (G_{IC}) was calculated by the modified beam theory (MBT) method, using Load (N), displacement (mm), crack length (mm), specimen width (mm) and specimen thickness (mm). After testing, the DCB specimens were healed by heating them at 150 °C for 120 min. The healing efficiency was improved by applying pressure to the delaminated composite to minimize the volume of open crack that will be infiltrated by the thermoplastic. The cured samples were then cooled to room temperature and retested under the same conditions. The self-healing efficiency was calculated by:

η (%) = ($f^{repaired}/f^{virgin}$) x 100, where f is the studied property, peak load or G_{IC}.

3. Results and discussion

3.1 Coating

The SEM micrographs in Figure 1 show the uncoated and EMAA-coated carbon fibers. The EMAA nanoparticles uniformly and homogeneously coat the fiber, due to their large surface area. In addition, it was possible to manipulate the coated fibers without damaging the coating evidencing the good adhesion to the fiber surface. Thus, spray coating increases the roughness of the fiber and provides a scalable procedure to introduce the EMAA nanoparticles.

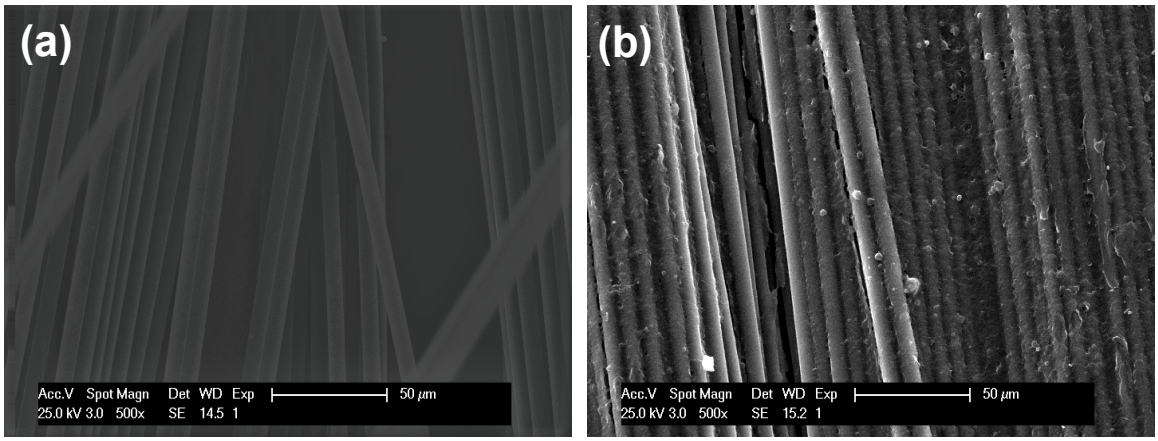

Figure 1. (a) Uncoated carbon fibers; (b) EMAA-coated carbon fibers.

3.2 Mode I Double Cantilever Beam testing

The effect of EMAA coating on the mode I interlaminar fracture toughness of the composite material is shown in Table 1. The peak load and G_{IC} values follow an opposite trend to that observed in the flexural tests, as the incorporation of EMAA leads to an increase in the properties. This effect may be due to the enhanced interfacial adhesion between the fiber and the matrix, thanks to the presence of the thermoplastic on the surface of the fiber. This behavior has been previously reported in the literature for mode I and mode II interlaminar fracture toughness [5,6].

Table 1. Peak load and interlaminar strength toughness of laminates with uncoated and EMAA-coated fibers.

Sample	Peak Load (kN)	G_{IC} (J/m^2)
Uncoated	104 ± 6	1070 ± 80
EMAA-coated	150 ± 30	2300 ± 300

The samples were re-measured after healing at 150 °C for 2 h under pressure. Figure 2 shows the repair efficiency based on the recovery of peak load and mode I interlaminar fracture toughness, after several healing cycles. Specimens achieved a mean peak load healing efficiency of 63 % in the first cycle, 54 % in the second and 43 % in the third one. The decrease in self-healing efficiency with the number of cycles is caused by the fact that the EMAA reactive compound is depleted in the reaction cycles and the crack surfaces become more irregular. However, this is quite significant as some studies in the literature only report values for a first

healing cycle [7]. The fracture toughness efficiency (44 %, 24 % and 18 %) was lower if compared to that reported in the literature [8]. This reduction and discrepancy with the peak load efficiency could be explained by the fact that the G_{IC} calculations assume a linear elastic behaviour in rigid materials, but the EMAA is ductile [9]. Nevertheless, these values are significant and decrease by only 20 % between the first and second cycle.

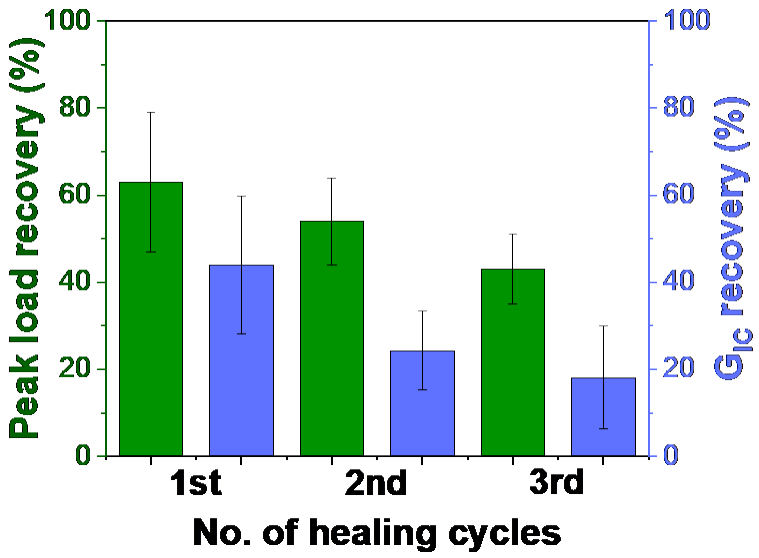

Figure 2. Peak load recovery (left) and GIC recovery (right) of EMAA-coated FRP after several healing cycles.

3.3 Fracture surface morphology

Optical microscopy was used for visual characterization of the healing process. Figure 3(a) shows a FRP with a crack width of approximately 50 µm, resulting after flexural testing. After heating his sample in the press at 150 °C for 2 h, the thermoplastic flows to the outside and appears to protrude from the crack (Figure 3(b)). Thus, the EMAA is capable of filling and sealing the crack. Previous studies have shown that EMAA remains strongly adhered to the matrix, and after cooling, it forms bridging stitches between the two crack surfaces [6,10].

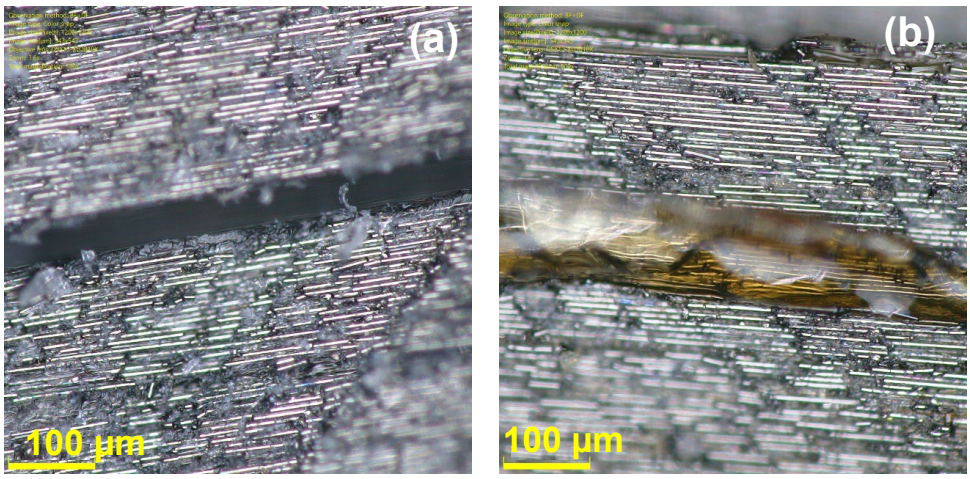

Figure 3. Micrographs of the (a) initial and (b) healed crack in an EMAA-coated FRP.

4. Conclusions

In this work, self-healing FRP composites were developed by coating carbon fibers with EMAA at 10 wt.%. The materials showed an improved interlaminar fracture toughness, and a good healing capability. After three healing cycles, the material kept a repair efficiency of more than 40%. These results are promising to consider that the deposition of EMAA on carbon fiber surface by aerography is a simple and easily scalable method, that enables the incorporation of high quantities of thermoplastic healing agent.

Acknowledgements

This research was funded by the Agencia Estatal de Investigación (AEI) through grants PID2019-107501RB-I00, RYC-2017-22837 and MAT2016-81138-R. Mónica Peñas-Caballero thanks for a Predoctoral contract (BES-2017-079899).

5. References

1. Fiber-Reinforced Plastic Market Research Report by Material, by Application, by Industry, by Region - Global Forecast to 2027 - Cumulative Impact of COVID-19 [cited 2022 Feb 21]. Available from: https://www.reportlinker.com/p06160105/Fiber-Reinforced-Plastic-Market-Research-Report-by-Material-by-Application-by-Industry-by-Region-Global-Forecast-to-Cumulative-Impact-of-COVID-19.html?

2. Meure S, Varley RJ, Wu DY, Mayo S, Nairn K, Furman S. Confirmation of the healing mechanism in a mendable EMAA-epoxy resin. European Polymer Journal 2012; 48(3):524–31.

3. Pingkarawat K, Wang CH, Varley RJ, Mouritz AP. Self-healing of delamination cracks in mendable epoxy matrix laminates using poly [ethylene-co-(methacrylic acid)] thermoplastic. Composites Part A: Applied Science and Manufacturing 2012; 43(8):1301–7.

4. Huang HC, Zacharia NS. Layer-by-layer rose petal mimic surface with oleophilicity and underwater oleophobicity. Langmuir 2015; 31(2):714–20.

5. Ladani RB, Nguyen ATTT, Wang CH, Mouritz AP. Mode II interlaminar delamination resistance and healing performance of 3D composites with hybrid z-fibre reinforcement. Composites Part A: Applied Science and Manufacturing 2019; 120:21–32.

6. Pingkarawat K, Wang CH, Varley RJ, Mouritz AP. Healing of fatigue delamination cracks in carbon-epoxy composite using mendable polymer stitching. Journal of Intelligent Material Systems and Structures 2014; 25(1):75–86.

7. Azevedo A, Fernandez F, Fábio S, Ferreira EPC, Daniel J, Melo D, et al. Addition of poly (ethylene-co-methacrylic acid) (EMAA) as self-healing agent to carbon-epoxy composites. Composite Part A 2020; 137:106016.

8. Shanmugam L, Naebe M, Kim J, Varley RJ, Yang J. Recovery of Mode I self-healing interlaminar fracture toughness of fiber metal laminate by modified double cantilever beam test. Composites Communications 2019; 16:25–9.

  doi:10.5075/epfl-298799_978-2-9701614-0-0

9. Meure S, Furman S, Khor S. Poly [ethylene-co-(methacrylic acid)] healing agents for mendable carbon fiber laminates. Macromolecular Materials and Engineering 2010; 295(5):420–4.

10. Pingkarawat K, Bhat T, Craze DA, Wang CH, Varley RJ, Mouritz AP. Healing of carbon fibre-epoxy composites using thermoplastic additives. Polymer Chemistry 2013; 4(18):5007–15.

  doi:10.5075/epfl-298799_978-2-9701614-0-0

FABRICATION OF CNT AEROGEL COMPOSITE THROUGH REACTIVE INFILTRATION OF POLYAMIDE 6

Suyeon, Lee[a], Ahram, Jeong[a], Minju, Jeong[b], Youngseok, Oh[b], Dong Gi Seong[a,c]*

a: School of Chemical Engineering, Pusan National University, Busandaehak-ro 63beon-gil 2, Geumjeong-gu, Busan, Republic of Korea
b : Composites Research Division, Korea Institute of Materials and Science, 797, Changwon-daero, Seongsan-gu, Changwon-si, Gyeongsangnam-do, 51508, Republic of Korea
c: Department of Polymer Science and Engineering, Pusan National University, Busandaehak-ro 63beon-gil 2, Geumjeong-gu, Busan, Republic of Korea

First/presenting author : sylee0631@pusan.ac.kr
Corresponding author : dgseong@pusan.ac.kr

Abstract: *Nano-fillers like Carbon nanotube, graphene have been hardly used ever for fabricating composites because of agglomeration and weak interfaces between nano-materials in matrices which may cause declined properties. Aerogels can solve these problems owing to its three-dimensional network structure. However, even though aerogel has a structural stability, fragility limits their application, so polymer infiltration method has been studied to make aerogels more durable. Among various kinds of resins, thermoplastics restrict to their application resulted from high viscosity despite of good impact strength and recyclability. Therefore, in-situ polymerization of thermoplastics can be suggested for fabricating structural composites. Moreover, thermoplastics Resin Transfer Molding (T-RTM) has been used to fabricate more dense structure of composite than dipping method.*

Keywords: CNT aerogel ; Nanocomposite ; Polyamide 6 ; Reactive infiltration

1. Introduction

Aerogels are unique and promising materials with high porosity and low density so that they have many potential application fields like electronics and catalysts. In particular, carbon based aerogels have achieved many attentions with an electrically conductive and other attractive properties. [1]-[3] Therefore, carbon aerogel composed of graphene and Carbon Nanotube (CNT) network are anticipated for the latest purpose as a highly conductive porous material. [4]

CNT has outstanding thermal, mechanical and electrical properties because of their high aspect ratio, an extensive research in the field of nano-composites has studied. The introduction of CNT in nano-composites can enhance the properties and therefore variety fields of application as electronics, field emitters can be expected for this reinforced composites. [5], [6] However, owing to worse dispersion, agglomeration and weak interfaces between nanomaterials may cause debased properties. [7], [8] To solve this drawback of nanocomposite, aerogel can play a key role because of its three-dimensional network structure. With controlled structure of aerogels, dispersion problems do not matter for fabricating filler-added composite since micro- or nano-sized fillers already have homogeneous arrangement. Recently, CNT

  doi:10.5075/epfl-298799_978-2-9701614-0-0

aerogels (CAs), a three dimensional structure of CNTs, have been used for high performance of polymer-based composites. [6],[9]-[11] Although CA has a structural stability because of its stereoscopic characteristic, fragility and mechanically weakness limits their application. Accordingly, many researches have studied with polymer infiltration to make aerogels more durable. [7], [12]-[14]

Most of the thermosetting polymers cause longer fabrication time and lower processability for producing filler-added composites. These disadvantages of matrix system are critical to application fields because of higher cost for production. Also, thermosetting polymers cause many environmental problems because of their non-recyclability. Meanwhile, thermoplastics restrict to their application resulted from high viscosity despite of good impact strength and recyclability. [15], [16] Thus, in situ polymerization of thermoplastics can suggest a solution owing to following diverse advantages. This method for synthesizing thermoplastics has been used to fabricate various composites due to fast processing speed and remarkable chemical affinity. Furthermore, low viscosity of monomer solution contribute to favorable impregnation of resin system. [17]-[20]

Among thermoplastic polymers, Polyamide 6 (PA6) is one of the most widely used engineering plastic because it has high toughness, thermal stability and wear resistant property. [21], [22] For polymerization of PA6, there are two ways which are hydrolysis and anion polymerization. Hydrolytic method is one of the common method for polymerizing PA6 but polymers using hydrolysis have lower mechanical property and longer reaction time while synthesis with anion polymerization has higher property with shorter reaction time. Thermoplastic resin transfer molding (T-RTM) has been suggested to fabricate composites through ring opening polymerization of Ɛ-caprolactam. [15], [21] With vacuum pressure of T-RTM, composites have more dense structure than simple dipping method which is contribute to much higher properties. As our best knowledge, there were few reports about CA reinforced nanocomposites using in situ polymerization of thermoplastics via T-RTM, contrary to the more conventional process.

In this study, CNT aerogel infiltrated with PA6 by in situ polymerization was manufactured through various methods. Dipping and T-RTM processes were compared to find the proper way to fabricate aerogel/polymer composites with high quality. These composites have structural stability for adding nano-fillers owing to 3D interconnected network of aerogel resulted in improved properties. Compression test and nano indentation are carried out to investigate the enhanced ductility of composites resulted from complementation effect of polymer. Also, due to improved electrical conductivity and thermal analyses of aerogel/polymer composites, they were expected to utilize for various applications in industrial fields.

2. Experiments

2.1 Materials

For synthesizing PA6, Ɛ-caprolactam (C2204, Sigma Aldrich, USA), which has a low melting point (68˚C) and 113.16 g/mol of molecular weight, was used as a monomer. Ethyl magnesium bromide solution (3.0M in diethyl ether, Sigma Aldrich, USA) and Hexamethylene diisocyanate (

  doi:10.5075/epfl-298799_978-2-9701614-0-0

≥98.0%, Sigma Aldrich, USA) were used as catalyst and initiator, respectively. All chemicals were used as received. CNT aerogel was kindly supported by Korea Institute of Materials Science.

2.2 Fabrication of CNT aerogel/PA6 composite (CAPA)

First of all, CNT aerogel and glass beakers were dried at 80˚C during overnight for eliminating moisture. Ɛ-caprolactam of 450 g was melted at 85 ˚C over 30 min with magnetic stirring and then the 11.93 ml of catalyst was added slowly. After that, degassing process of mixture was implemented more than 30 min. Meanwhile, CNT aerogel was located in the mold with vacuum for eliminating remained moisture. Finally, anionic in-situ polymerization of PA6 was started by injection into aerogel after adding a 3.93 ml of initiator to the mixture with mixing another 1 min. The amount of materials for dipping method was 100 g, 2.65 ml and 0.173 ml, respectively. As shown in Figure 1, CAPAs were fabricated by dipping and T-RTM method. Dipping process is simple and easy method to fabricate nanocomposites but it has difficulty of composite shape control and low quality of final product. On the other hand, T-RTM process has many advantages like easy impregnation of shape controllable composites and fabricating of composites with dense structure due to vacuum pressure.

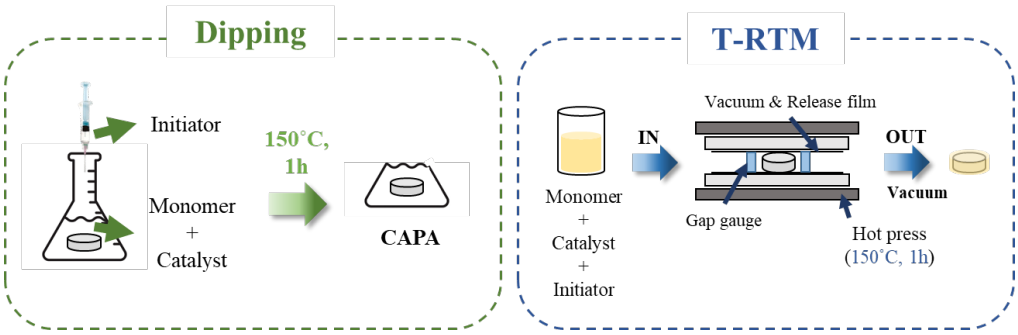

Figure 1. Schematic figure of dipping and TRTM process for fabricating CAPA.

3. Results and discussion

3.1 Structural properties of CAPA by dipping and TRTM method

Structure properties of CNT aerogel/PA6 composites (CAPA) was characterized by IR and XRD, shown in figure 2. The results of FT-IR were peaks at 1500-1600 cm^{-1}, 2700-2900 cm^{-1} and 3300 cm^{-1} correspond to the amide bond, -CH2 and N-H bond, respectively. As a results of XRD, Table 1 shows that the crystallite size of CAPA was same as neat PA6, indicating that 3D network structure of CA did not interrupt polymerization of PA6. These results can show the PA6 was successfully polymerized by anionic in-situ polymerization.

  doi:10.5075/epfl-298799_978-2-9701614-0-0

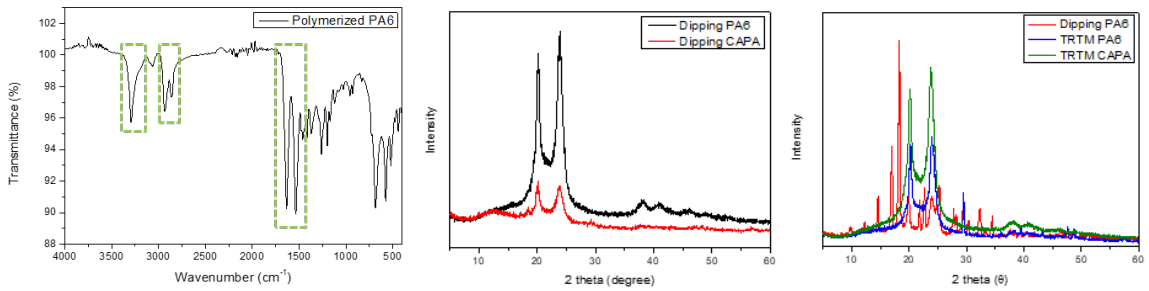

(a) (b)

Figure 2. FT-IR spectra of polymerized PA6 (a)and XRD patterns of PA6 and CAPA fabricated by dipping and T-RTM method (b).

Table 1. Full width at half maximum (FWHM) and crystallite size of polymerized PA6 and CAPA by different methods.

	FWHM	Crystallite size (nm)		FWHM	Crystallite size (nm)
PA6	2.66	2.94	PA6	3.21	2.44
(Dipping)	1.66	4.68	(T-RTM)	1.61	4.83
CAPA	1.24	6.31	CAPA	2.71	2.88
(Dipping)	1.68	4.63	(T-RTM)	1.86	4.18

3.2 Thermal stability

For investigating thermal stability of PA6 and CAPA, TGA and DSC were characterized, shown in figure 3. The specimens for TGA were achieved by cryogenic fracture because poor polymerization can occur in the middle of CAPA due to nano-sized pore of aerogel. The degradation temperature of CAPA by dipping was 161˚C, while T-RTM was 274˚C which means that polymerization of PA6 was successful. From the DSC results, slow annealing in oil bath and unpolymerized PA6 with dipping process led to two T_m peaks. Two T_c peaks of CAPA by both method occurred because CNT acts as a nucleation agent for forming crystalline structure of PA6.

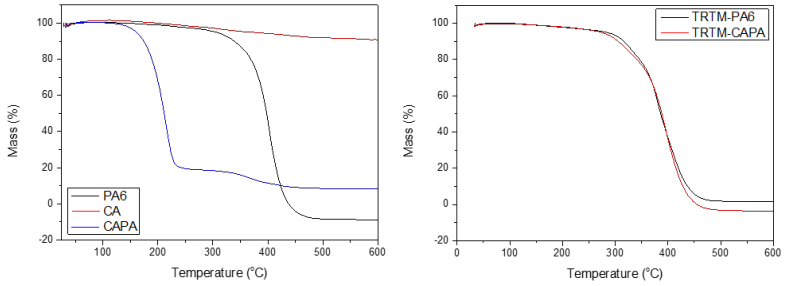

(a)

  doi:10.5075/epfl-298799_978-2-9701614-0-0 published under CC BY-NC 4.0 license

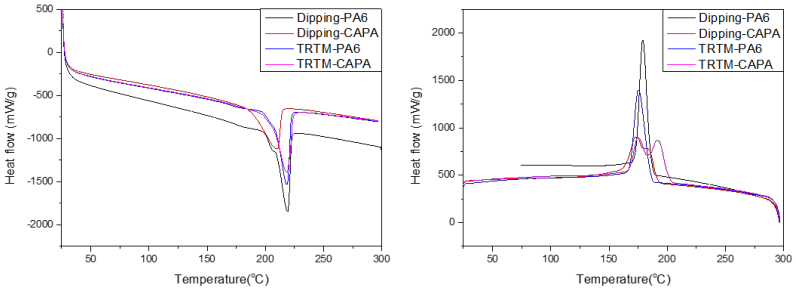

(b)

Figure 3. TGA results (a) and DSC results (b) of PA6 and CAPA by dipping and T-RTM method.

3.3 Mechanical properties and morphology of composites

Table 2 shows that tensile strength of various composites with 1wt% of CNT. Because PA6 is one of the strongest engineering plastic, CNT/PA6 nanocomposites have higher mechanical property than composites with other polymers. Also, comparing to nanocomposites with CNT powder and PA6, structural stability of CAPA was strengthened by 3D network of CNT aerogel. [23]-[30]

The FE-SEM images of composite was characterized for comparing morphology by different process as shown in figure 4. Nanocomposite using dipping process has many void while homogeneous and uniform surface was observed with T-RTM process. This is because T-RTM method uses vacuum pressure which is stronger than dipping.

Table 2. Tensile strength comparison of various composites with 1wt% of CNT

No.	Tensile strength (MPa)	Material	Reference
1	44.9	$CNT_{aerogel}$/PA6	**This work**
2	16	CNT/LLDPE	[23]
3	8	CNT/Epoxy	[24]
4	12	CNT/PE	[25]
5	20	CNT/PA6	[26]
6	25	CNT/PA6	[27]
7	40.3	CNT/PA6	[28]
8	13.6	$CNT\&GO_{aerogel}$/PS	[29]
9	2.3	$CNT_{aerogel}$/PDMS	[30]

  doi:10.5075/epfl-298799_978-2-9701614-0-0

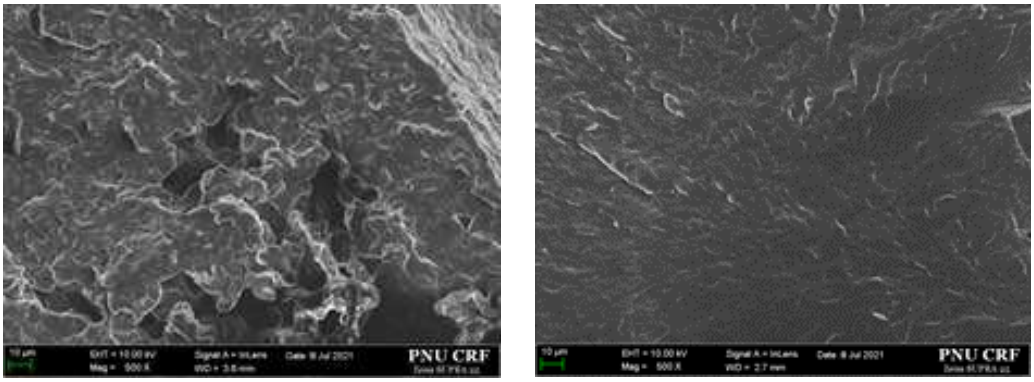

Figure 4. The SEM images of nanocomposites using dipping (left) and T-RTM (right) method.

4. Conclusion

We successfully fabricated nanocomposites with CNT aerogel impregnated PA6 by in-situ polymerization. 3D network of aerogel can improve structural stability of nanocomposites which have higher performance and uniformity. Through FT-IR, XRD and TGA characterization, it is confirmed that PA6 was successfully polymerized even in the middle of CAPA. Also, comparing the processes for fabricating CAPAs, we can suggest that T-RTM method is much more proper way to fabricate CAPA with dense structure. Furthermore, it is identified that CAPA by T-RTM process has higher tensile strength than nanocomposites with CNT powders or other polymers. In conclusion, our CAPA with controllable structure has higher performance than nanocomposites with same content of CNT so it can be applied for many industries as electronics and IT.

Acknowledgements

This work was supported by the Industrial Strategic Technology Development Program (20017530) funded by the Ministry of Trade, Industry and Energy (MOTIE) of Korea.

5. References

1. Ageyeva T, Sibikin I, Kovács JG. A review of thermoplastic resin transfer molding: Process modeling and simulation. Polymers 2019;11(10):1555.
2. An H, Wang Y, Wang X, Zheng L, Wang X, Yi L, et al. Polypyrrole/carbon aerogel composite materials for supercapacitor. J Power Sources 2010;195(19):6964-6969.
3. Baumann TF, Worsley MA, Han TY, Satcher Jr JH. High surface area carbon aerogel monoliths with hierarchical porosity. J Non Cryst Solids 2008;354(29):3513-3515.
4. Boros R, Sibikin I, Ageyeva T, Kovács JG. Development and validation of a test mold for thermoplastic resin transfer molding of reactive PA-6. Polymers 2020;12(4):976.
5. Chen X, Liu H, Zheng Y, Zhai Y, Liu X, Liu C, et al. Highly compressible and robust polyimide/carbon nanotube composite aerogel for high-performance wearable pressure sensor. ACS applied materials & interfaces 2019;11(45):42594-42606.

  doi:10.5075/epfl-298799_978-2-9701614-0-0

6. Cho B, Lee J, Hwang S, Han JH, Chae HG, Park Y. Enhancement in mechanical properties of polyamide 66-carbon fiber composites containing graphene oxide-carbon nanotube hybrid nanofillers synthesized through in situ interfacial polymerization. Composites Part A: Applied Science and Manufacturing 2020;135:105938.
7. Das S, Wajid AS, Shelburne JL, Liao Y, Green MJ. Localized in situ polymerization on graphene surfaces for stabilized graphene dispersions. ACS applied materials & interfaces 2011;3(6):1844-1851.
8. Dourani A, Haghgoo M, Hamadanian M. Multi-walled carbon nanotube and carbon nanofiber/polyacrylonitrile aerogel scaffolds for enhanced epoxy resins. Composites Part B: Engineering 2019;176:107299.
9. Duan X, Yu B, Yang T, Wu Y, Yu H, Huang T. In situ polymerization of nylon 66/reduced graphene oxide nanocomposites. Journal of Nanomaterials 2018;2018.
10. Fan W, Zuo L, Zhang Y, Chen Y, Liu T. Mechanically strong polyimide/carbon nanotube composite aerogels with controllable porous structure. Composites Sci Technol 2018;156:186-191.
11. Fan Z, Gong F, Nguyen ST, Duong HM. Advanced multifunctional graphene aerogel–poly (methyl methacrylate) composites: experiments and modeling. Carbon 2015;81:396-404.
12. Gojny FH, Nastalczyk J, Roslaniec Z, Schulte K. Surface modified multi-walled carbon nanotubes in CNT/epoxy-composites. Chemical physics letters 2003;370(5-6):820-824.
13. Irin F, Das S, Atore FO, Green MJ. Ultralow percolation threshold in aerogel and cryogel templated composites. Langmuir 2013;29(36):11449-11456.
14. Kim B, Cha S, Park Y. Ultra-high-speed processing of nanomaterial-reinforced woven carbon fiber/polyamide 6 composites using reactive thermoplastic resin transfer molding. Composites Part B: Engineering 2018;143:36-46.
15. Korkees F, Aldrees A, Barsoum I, Alshammari D. Functionalised graphene effect on the mechanical and thermal properties of recycled PA6/PA6, 6 blends. J Composite Mater 2021;55(16):2211-2224.
16. Lee H, Lee D, Cho J, Kim Y, Lim S, Youn S, et al. Super-insulating, flame-retardant, and flexible poly (dimethylsiloxane) composites based on silica aerogel. Composites Part A: Applied Science and Manufacturing 2019;123:108-113.
17. Li X, Shao L, Song N, Shi L, Ding P. Enhanced thermal-conductive and anti-dripping properties of polyamide composites by 3D graphene structures at low filler content. Composites Part A: Applied Science and Manufacturing 2016;88:305-314.
18. Lin Y, Wei T, Chien H, Lu S. Manganese oxide/carbon aerogel composite: an outstanding supercapacitor electrode material. Advanced Energy Materials 2011;1(5):901-907.
19. Liu N, Zhang S, Fu R, Dresselhaus MS, Dresselhaus G. Carbon aerogel spheres prepared via alcohol supercritical drying. Carbon 2006;44(12):2430-2436.
20. Worsley MA, Kucheyev SO, Kuntz JD, Olson TY, Han TY, Hamza AV, et al. Carbon scaffolds for stiff and highly conductive monolithic oxide–carbon nanotube composites. Chemistry of materials 2011;23(12):3054-3061.
21. Xu Z, Gao C. In situ polymerization approach to graphene-reinforced nylon-6 composites. Macromolecules 2010;43(16):6716-6723.
22. Zhang Q, Xu X, Li H, Xiong G, Hu H, Fisher TS. Mechanically robust honeycomb graphene aerogel multifunctional polymer composites. Carbon 2015;93:659-670.
23. Allaoui A, Bai S, Cheng H, Bai J. Mechanical and electrical properties of a MWNT/epoxy composite. Composites Sci Technol 2002;62(15):1993-1998.

  doi:10.5075/epfl-298799_978-2-9701614-0-0

24. Cho E, Chang-Jian C, Hsiao Y, Lee K, Huang J. Three-dimensional carbon nanotube based polymer composites for thermal management. Composites Part A: Applied Science and Manufacturing 2016;90:678-686.
25. Gorrasi G, Sarno M, Di Bartolomeo A, Sannino D, Ciambelli P, Vittoria V. Incorporation of carbon nanotubes into polyethylene by high energy ball milling: morphology and physical properties. Journal of Polymer Science Part B: Polymer Physics 2007;45(5):597-606.
26. Liu T, Phang IY, Shen L, Chow SY, Zhang W. Morphology and mechanical properties of multiwalled carbon nanotubes reinforced nylon-6 composites. Macromolecules 2004;37(19):7214-7222.
27. McNally T, Pötschke P, Halley P, Murphy M, Martin D, Bell SE, et al. Polyethylene multiwalled carbon nanotube composites. Polymer 2005;46(19):8222-8232.
28. Sahoo NG, Cheng HKF, Cai J, Li L, Chan SH, Zhao J, et al. Improvement of mechanical and thermal properties of carbon nanotube composites through nanotube functionalization and processing methods. Mater Chem Phys 2009;117(1):313-320.
29. Scaffaro R, Maio A, Tito A. High performance PA6/CNTs nanohybrid fibers prepared in the melt. Composites Sci Technol 2012;72(15):1918-1923.
30. Xu H, Li X, Li P, Ma L, Li H, Shi L, et al. Enhancing mechanical performances of polystyrene composites via constructing carbon nanotube/graphene oxide aerogel and hot pressing. Composites Sci Technol 2020;195:108191.

  doi:10.5075/epfl-298799_978-2-9701614-0-0

VOID REDUCTION IN GRAPHENE INTERLAYER ENHANCED CARBON FIBRE THERMOPLASTIC COMPOSITES

Christopher Leow[a], Peter Kreider[a], Silvano Sommacal[a], Paul Compston[a]

a: ARC Training Centre for Automated Manufacture of Advanced Composites, Australian National University, Canberra, Australia – christopher.leow@anu.edu.au

Abstract: *Graphene enhanced CF/PEEK composites are excellent candidates for aerospace applications where enhanced conductivity is integral, however including nanomaterials within the composite can also cause mechanical degradation, notably void formation. Surfactant stabilised graphene suspensions were used to generate graphene thin films for enhancing the interlaminar spaces in CF/PEEK. The presence of voids and mechanical strength was investigated with F108 and F68 surfactants and heat treatment of the thin film before hot pressing or hot embossing consolidation. Pluronic F68 yielded 3-4 layer graphene compared to F108, and when hot pressed had a 22% increase in shear strength compared to the control. The heat treated then hot pressed F108 graphene sample had the lowest void percentage of 1.7vol%. Heat treatment of thin films to remove excess surfactant combined with F68 surfactant will likely yield low void defect graphene enhanced CF/PEEK composites.*

Keywords: Nanocomposites; Nanomaterials; Carbon fiber thermoplastics; Graphene; Voids

1. Introduction

Carbon fibre reinforced polymers (CFRP) uniquely high strength to weight and stiffness ratio properties make them perfect for aerospace applications but are limited due to their insulative matrix phase. Polyether ether ketone (PEEK) is a high performance aerospace grade polymer due to the high temperature, chemical resistance and high strength properties, but it remains unsuitable for thermal regulation and electrical charge dissipation applications [1]. Graphene's high tensile strength, specific surface area, thermal and electrical properties make it an excellent candidate as an enhancing material for CFRP [2,3].

Liquid phase exfoliation (LPE) offers a scalable manufacturing method to synthesise high quality and purity graphene at a low cost [4], compared to chemical vapour deposition, and mechanical exfoliation which are limited by cost and purity, respectively [4]. High concentration suspensions require surfactants to aid exfoliation and reduce agglomeration effects, while aqueous graphene suspensions are economically and environmentally beneficial over their solvent counterparts [5,6]. Various surfactants have been studied in aqueous systems, but triblock copolymers have demonstrated high suspension stability and graphene quality [7].

Spray deposition of nanomaterial suspensions offers a scalable processing method for transferring nanomaterials into composite materials. Li *et al.* [8] spray deposited CNT/GNP nanomaterials onto aerospace grade CF epoxy prepreg tapes for increased fracture toughness, thermal and electrical conductivity properties. Multiwalled CNT interleaves (150 µm thick) reduced interlaminar properties due to localized resin evaporation, but increased electrical conductivity properties and demonstrated successful lightning strike protection [9].

Before composites with nanomaterial additions can be utilized in aerospace applications, void content is required to be below 1% [10]. Thermoset and thermoplastic composites have different mechanisms in which defects may appear during manufacturing, but voids and porosity

  doi:10.5075/epfl-298799_978-2-9701614-0-0

have been identified and most detrimental to mechanical properties [11]. The introduction of nanomaterials to composite phases only adds additional complexity to the understanding of void formation during manufacturing.

The focus of this study will be to investigate the mechanical properties of CF/PEEK composites manufactured using different consolidation methods and graphene suspension formulations. Aqueous graphene suspensions stabilized with either pluronic F108 or F68 surfactant were spray deposited onto CF/PEEK plies and were either hot pressed or hot embossed with and without heat treatment. The interlayer regions were studied using Raman spectroscopy, and interlaminar shear strength (ILSS) properties characterized using compression shear testing (CST). The microstructure and void distribution were characterised in 3D using micro-computed tomography.

2. Experiment

2.1 Materials

Highly concentrated aqueous graphene suspension (~1.5 wt%), acquired from FlexeGRAPH, was synthesised through LPE methods [12]. Graphite (~1 µm flake size) starting material was exfoliated in a high-volume ultrasonic flow cell with continuous addition of non-ionic pluronic F108 and F68 surfactant (Sigma Aldrich). The AS-4 CF/PEEK (40 mm x 90 mm) unidirectional tapes (Toray Cetex, fibre volume fraction 59%) were used as the substrates to study the graphene thin film.

2.2 Spray deposition

The methodology applied to fabricate graphene interlayer enhanced CF/PEEK composites using spray deposition methodologies follows the same approach reported in an earlier work Leow et al. [13] (Figure 1a). Average graphene flake size in the spray deposited thin films was measured to be 413 ± 61 nm [13]. The aqueous graphene suspension was aerosolised at 1 bar air pressure fed through a NE-300 syringe pump (New Era Pump Systems Inc.) at a feed rate of 5 $mLmin^{-1}$. Deposition was done using a flat fan air atomising nozzle (SUE15, Xinhou Industrial Co. Ltd) onto CF/PEEK ply substrates from a distance of 300mm for 30s followed by drying on a hot plate at 50°C for five minutes; this deposition process was defined as a pass and repeated to generate graphene thin films of varying thickness. The CF/PEEK plies were sprayed with four (34 ± 1.5 mg), five passes (40 ± 1.5 mg and 30 ± 1.5 mg) of F108 stabilised graphene suspension and ten passes of F68 (30 ± 1.5 mg) stabilised graphene suspension to create thin films that were further dried at room temperature for a minimum of 24 hrs. The nineteen graphene enhanced CF/PEEK plies coated with five pass (40 ± 1.5 mg) F108 graphene suspension were heat treated in an oven (O75, Steridium) at 110°C for 30 mins to remove any water absorbed (Figure 1b). The temperature was then raised to 250°C for 60 mins to vapourise non-ionic pluronic surfactant, following the methodology outlined in Mansukhani *et al.* [14], and were then cooled at a rate of ~20°C/min.

2.3 Consolidation

Consolidated composites were manufactured using a hot press (PW220C-X4A, Phi Hydraulics) and in a vacuum environment using a hot embosser (EVG520 HE, EV Group) in a picture frame mould following the methodology outlined in Cogswell [15] (Figure 1c). A single set of nineteen

  doi:10.5075/epfl-298799_978-2-9701614-0-0

graphene enhanced CF/PEEK plies were laid up unidirectionally with an unmodified ply on top to create a $[(90)_{20}]$ composite layup with ~1 wt% graphene thin film interlayer additions.

The CF/PEEK composite without graphene additions (control), heat treated (HT) control, 10 pass F68, 5 pass F108, and heat treated 5 pass F108 graphene thin film samples were also consolidated using the hot press. The consolidated composite parts with 0, ~1wt% F68 and ~1wt% F108 loadings manufactured using hot press (HP), heat treatment of plies and consolidation using the hot press (HT+HP) and hot embossing (HE) are henceforth referred to as the Control (HP), Control (HE), Control (HT+HP), F68 (HP), F108 (HE), F108 (HT+HP), and F108 (HP) respectively.

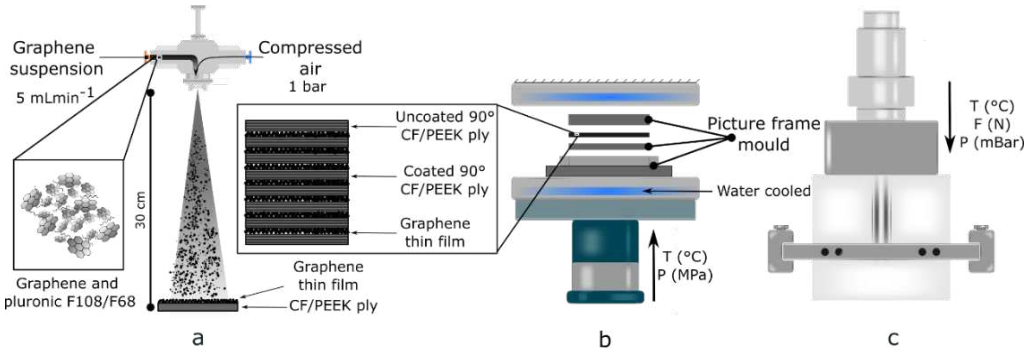

Figure 1. (a) Aerosolised spray-deposition of the graphene suspension onto CF/PEEK ply substrate. (b) Schematic of water-cooled hot press and picture frame mould with partial unidirectional layup with graphene interlayers illustrated in the inset used to manufacture consolidated composites. (c) Schematic of hot-embosser used to consolidate composites under vacuum.

2.4 Sample preparation

The consolidated CF/PEEK samples were milled into 10 mm x 10 mm coupons for compression shear testing (CST) using a desktop CNC machine (Nomad 3, Carbide 3D) with a 2-fillet square carbide tip (Nomad Tools, Carbide 3D). Coupons were subsequently casted in epoxy resin to allow for direct chemical characterisation of interlaminar regions by viewing the composites in cross-section. One coupon was secured end-on flush against the base of the resin-casting mould using double sided tape. The samples were then cast in epoxy resin (EpoFix), de-gassed under vacuum to remove bubbles prior to a 24 hour cure, and polished according to the procedure outlined in Leow *et al.* [13].

2.5 Characterisation

2.5.1 Raman Spectroscopy

The graphene thin film quality post consolidation in the interlaminar regions were chemically characterised on a confocal Raman microscope (Renishaw inVia Reflex) at a magnification of x100. Samples were exposed to a 532 nm wavelength laser at 0.5 mW power with use of a 2400 mm-1 grating to isolate the signal and measurements were integrated over a period of 10 s with 3 accumulations to reduce signal to noise ratios. Data were baseline corrected and normalised against the G peak.

  doi:10.5075/epfl-298799_978-2-9701614-0-0

2.5.2 Compression shear testing

The compression shear testing device used here followed the methodology outlined for flat specimens in Zinnecker et al. [16]. The loading noses translate vertically to induce pure shear stress on the samples. All specimens were loaded with a 0.2 mm gap between the loading noses to ensure shearing of the midplane as ply thicknesses were 0.1 mm pre-consolidation. Manually adjustable support blocks were used to ensure symmetrical and flush alignment to the loading noses without gaps. The CST device was placed in a universal testing machine (8074, Instron USA) with a 25kN load cell. Five specimens from each graphene loading condition were tested at a 1 mm/min displacement rate. Samples that failed due to a 40% load drop but did not shear were excluded from the data set in accordance with ASTM D2344.

2.5.3 Micro-computed tomography (µCT)

X-ray micro-computed tomography (µCT) was utilised to characterise the microstructure and further investigate in 3D the quality of consolidated CF/PEEK Control and graphene specimens of ~2.5 x 3 mm (cross-section) by 7mm (length). This technique is increasingly used for composite characterisation and has recently proven successful to characterise in detail the microstructure and map and quantify void distribution and content in CF/PEEK samples of comparable volumes [17]. The samples were imaged using an HeliScan™ micro-CT instrument hosted at the ANU CTLab, equipped with a 60 kV X-ray micro-focus source and a 3040 x 3040 pixels flat panel detector. Image acquisition time was about 9 hours per sample, scanning resolution (i.e. voxel size) ~2.0 µm. Image reconstruction, processing and analysis were carried out using proprietary ANU software [18].

Results and Discussion

3.1 Chemical quality and interlayer validation

The graphene thin film interlayers were analysed for chemical quality after consolidation using Raman spectroscopy (Figure 2). The G and D peaks were fit with a single Lorentzian curve centered at 1582 cm^{-1} and 1345 cm^{-1} corresponding to carbon ring stretching and defects evident within the samples, respectively. The peak intensity ratio, $I_D/I_{D'}$ = ~2.5, ~2.0, ~2.8 for F108 (HE), F108 (HT+HP) and F68 (HP), which reveals the most common defect within the sample is likely edge defects [19]. The least defects present occur within the heat treated sample likely due to the heat reducing the number of grain boundaries present within the graphene flakes. The effects of corrugations, topological defects and atomic vacancies in graphene manifest themselves as disorder peaks: D (1345 cm^{-1}), D' (1615 cm^{-1}) and D+G (2935 cm^{-1}). The disorder of graphene is measured using intensity ratio I_D/I_G = ~0.8 across all F108 (HE), F108 (HT+HP) and F68 (HP) samples. This corresponds to a high number of graphite like structures present which is likely due to the compact nature of the thin film interlayer after consolidation [20].

Fitting the 2D peak can help gain further insights into the number of graphene layers and in few layer graphene (<5 layers) is fitted with four Lorentzian peaks to correspond to the two phonons with opposite momentums interacting with the electronic band structures [21]. The four peaks occurred at 2652, 2682, 2710, and 2732 cm^{-1}; 2682, 2704, 2720, 2738 cm^{-1}; 2667, 2686, 2708, 2732 cm^{-1}; for F108 (HE), F108 (HT+HP), and F68 (HP), respectively as depicted in Figure 2. The I_G/I_{2D} intensity ratio equals ~2.2 for all F108 (HE), F108 (HT+HP), and F68 (HP) samples, corresponding to ~5 layered graphene. The full width half maximum (FWHM) of the 2D peak is

  doi:10.5075/epfl-298799_978-2-9701614-0-0

~67, 61, ~67 and centered at 2704, 1706, 2705 cm^{-1} for F108 (HT+HP), F68 (HP) and F108 (HE), respectively. This indicates 4-5 layered graphene in the F108 (HT+HP) and F108 (HE) samples, while the F68 sample has 3-4 layered graphene [22].

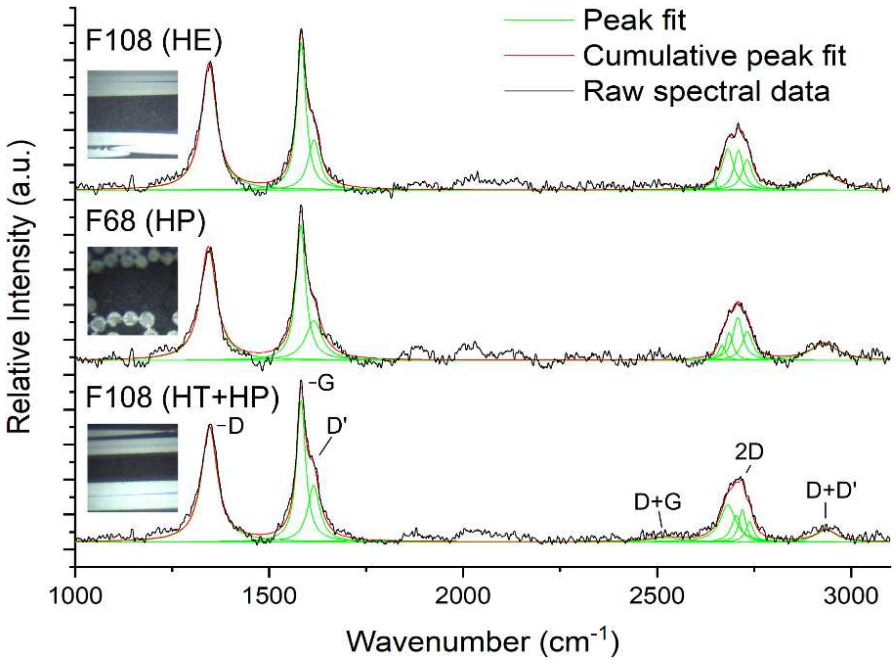

Figure 2. Cross sectional Raman spectra and peak fits of hot embossed F108, hot pressed F68, and heat treated-hot pressed F108 graphene additions into the interlaminar region of CF/PEEK composites. Acquired spectra were obtained from the interlaminar region of the inset images.

3.2 Interlaminar shear strength

The compressive shear strength of the consolidated composite as a function of graphene weight percent loading is shown in Figure 3a. The mean shear strength of the CF/PEEK Control samples were 65.54 ± 5.51 MPa, 60.30 ± 5.66 MPa, and 25.41 ± 1.38 MPa for hot embossed, heat treated and hot pressed, respectively. The Control (HE) and Control (HT+HP) samples are significantly higher than CF/PEEK shear strength data (~34 MPa) previously reported in literature [23]. The measured shear strength decreases with the addition of F108 stabilised graphene thin films. Heat treated samples had a 61% decrease (23.36 ± 1.72 MPa), while hot embossed samples had a 56% decrease (29.01 ± 2.99 MPa) in shear strength. Hot pressed F108 stabilised graphene thin films had a 34% reduction (16.83 ± 0.09 MPa) in strength compared to the control, but F68 stabilised graphene thin film additions saw an increase of 22% in shear strength to 32.72 ± 1.69MPa.

The strongest graphene enhanced sample was the F68 hot pressed sample despite no heat treatment suggesting there was good interlocking between fiber, matrix and thin film phases within the interlaminar region [24]. Graphene enhanced hot embossed and heat treated samples' lower ILSS properties may have been a result of poor bonding between plies and the interlaminar region due to a limited mixing between the thin film and the matrix phase. Further investigation into sample microstructures, void content and defect distribution using µCT imaging was conducted to understand the mechanisms controlling ILSS properties.

  doi:10.5075/epfl-298799_978-2-9701614-0-0

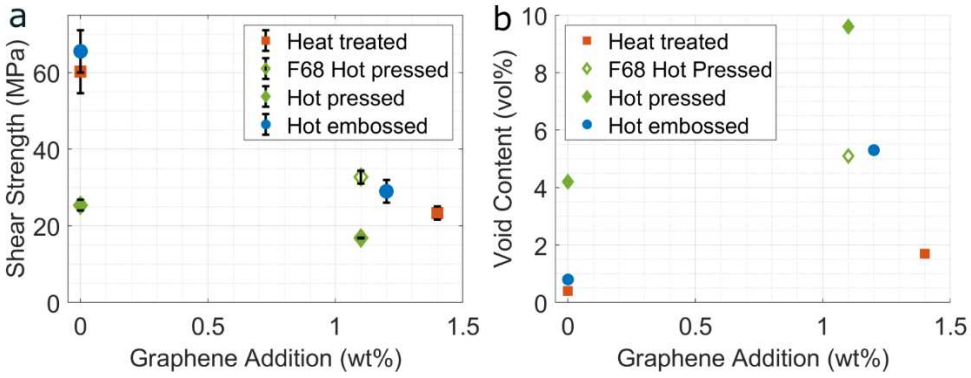

Figure 3. (a) Compressive shear strength of CF/PEEK samples with relation to graphene weight percent loadings added to the interlaminar regions. Error bars denote one standard deviation of the mean. (b) Void percentage of CF/PEEK samples with relation to graphene weight percentage loadings added to the interlaminar regions.

3.3 Micro-Computed Tomography (µCT)

Each image was segmented, void content quantified (vol%), void shape, size and distribution mapped and visualised in 3D. Lowest void content for the control samples was 0.4%, 0.8% and 4.2%, for heat treated, hot embossed and hot pressed, respectively. The F108 (HT+HP) sample had a lower void content (1.7%) compared to F108 (HE, 5.3%) and F108 (HP, 9.6%). The F68 (HP) sample had a void content of 5.1%, similar to F108 (HT+HP). Although, F68 (HP) had a higher mean ILSS than F108 (HT+HP), the void content is drastically higher suggesting the importance of heat treatment of the thin film to remove surfactant cannot be discounted in the manufacturing process of integrating interlaminar graphene additions.

The images in figure 4 illustrate voids running parallel to the plies and distributed throughout the volume. Increased void content correlates strongly to the reduction in mean compressive shear strength (r=-0.75). The concentration of voids within the interlaminar region likely resulted in crack propagation along the interlaminar plane causing reduced mechanical stress. Void formation was likely the result of pluronic triblock copolymers (T_b = ~150°C) vapourising during high composite processing temperatures. The F108 (HE) sample demonstrated that even under vacuum vapourised surfactant remains trapped within the interlayers compared to heat treatment which allowed for vapourisation of most surfactant.

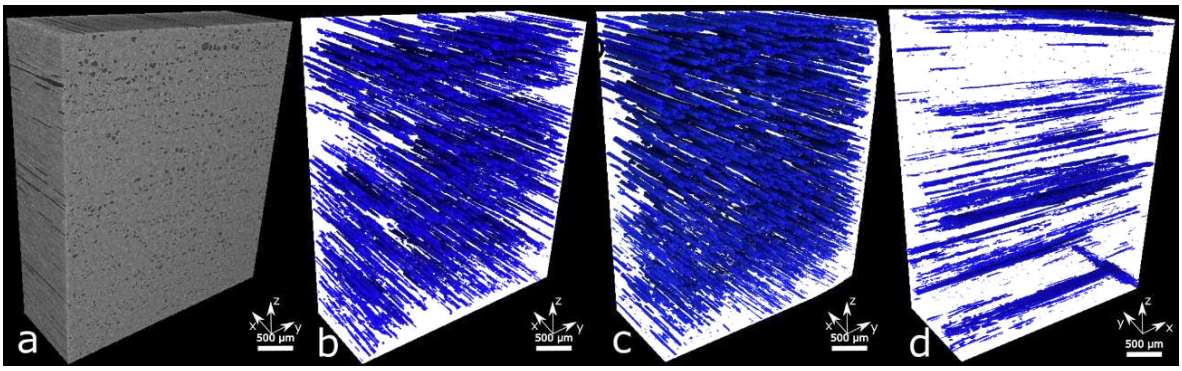

Figure 4. 3D visualisations of (a) F108 (HE) sample tomogram image and (b) corresponding segmented image showing voids in blue with matrix and fibres 100% transparent; (c) segmented F68 (HP) image (d) and segmented F108 (HT+HP) image processes at 90°

  doi:10.5075/epfl-298799_978-2-9701614-0-0

Conclusion

This study investigated the effects of manufacturing method (hot press vs hot embossing) and graphene film heat treatment on interlaminar graphene additions to CF/PEEK composite tapes. The graphene quality was characterized using Raman spectroscopy and revealed 3-4 layer and 4-5 layer graphene for F68 and F108 stabilised suspensions respectively, post consolidation. Heat treated samples had the lowest void percentage with F108 (HT+HP) having only a 1.7 vol% compared to ~5vol% that was measured in F108 (HE) and F68 (HP) samples. The highest shear strength among graphene-enhanced samples was the F68 (HP) which increased 22% compared to Control (HP). The addition of surfactant remains important to the LPE graphene synthesis process to prevent agglomeration and therefore cannot be entirely removed from the process. Heat treated spray deposited thin films combined with use of F68 surfactant allows for the synthesis of few layer graphene while removing surfactant from the thin film prior to consolidation.

Acknowledgements

This project was conducted within the ARC Training Centre for Automated Manufacture of Advanced Composites (IC160100040), supported by the Commonwealth of Australia under the Australian Research Council's Industrial Transformation Research Program. The authors acknowledge the scientific and technical assistance, of the Australian Microscopy & Microanalysis Research Facility at the Centre of Advanced Microscopy, ANU; the support of ANFF ACT Node (ANFF @ ANU); FlexeGRAPH for supplying the graphene suspension; and J. Bradby and C. Nothoff for providing the facilities and expertise for Raman spectroscopy measurements.

3. References

1. Díez-Pascual AM, Naffakh M, Gómez MA, Marco C, Ellis G, Martínez MT, et al. Development and characterization of PEEK/carbon nanotube composites. Carbon N Y [Internet]. 2009;47:3079–90.

2. Lee C, Wei X, Kysar JW, Hone J. Measurement of the Elastic Properties and Intrinsic Strength of Monolayer Graphene. Science (80-) [Internet]. 2008;321:385–8.

3. Zhu Y, Murali S, Cai W, Li X, Suk JW, Potts JR, et al. Graphene and graphene oxide: Synthesis, properties, and applications. Adv Mater. 2010;22:3906–24.

4. Raccichini R, Varzi A, Passerini S, Scrosati B. The role of graphene for electrochemical energy storage. Nat Mater. 2015;14:271–9.

5. Samoilov VM, Danilov EA, Nikolaeva A V., Yerpuleva GA, Trofimova NN, Abramchuk SS, et al. Formation of graphene aqueous suspensions using fluorinated surfactant-assisted ultrasonication of pristine graphite. Carbon N Y [Internet]. Elsevier Ltd; 2015;84:38–46.

6. Tao H, Zhang Y, Gao Y, Sun Z, Yan C, Texter J. Scalable exfoliation and dispersion of two-dimensional materials-an update. Phys Chem Chem Phys. Royal Society of Chemistry; 2017;19:921–60.

7. Ager D, Arjunan Vasantha V, Crombez R, Texter J. Aqueous Graphene Dispersions–Optical Properties and Stimuli-Responsive Phase Transfer. ACS Nano [Internet]. 2014;8:11191–205.

8. Li Y, Zhang H, Liu Y, Wang H, Huang Z, Peijs T, et al. Synergistic effects of spray-coated hybrid carbon nanoparticles for enhanced electrical and thermal surface conductivity of CFRP laminates. Compos Part A Appl Sci Manuf [Internet]. Elsevier Ltd; 2018;105:9–18.

9. Kumar V, Sharma S, Pathak A, Singh BP, Dhakate SR, Yokozeki T, et al. Interleaved MWCNT

  doi:10.5075/epfl-298799_978-2-9701614-0-0 published under CC BY-NC 4.0 license

buckypaper between CFRP laminates to improve through-thickness electrical conductivity and reducing lightning strike damage. Compos Struct [Internet]. Elsevier; 2019;210:581–9.

10. Liu L, Zhang BM, Wang DF, Wu ZJ. Effects of cure cycles on void content and mechanical properties of composite laminates. Compos Struct. 2006;73:303–9.

11. Saenz-Castillo D, Martín MI, Calvo S, Rodriguez-Lence F, Güemes A. Effect of processing parameters and void content on mechanical properties and NDI of thermoplastic composites. Compos Part A Appl Sci Manuf [Internet]. Elsevier; 2019;121:308–20.

12. Notley SM. Highly concentrated aqueous suspensions of graphene through ultrasonic exfoliation with continuous surfactant addition. Langmuir. 2012;28:14110–3.

13. Leow C, Kreider PB, Notthoff C, Kluth P, Tricoli A, Compston P. A graphene film interlayer for enhanced electrical conductivity in a carbon-fibre/PEEK composite. Funct Compos Mater. 2021;2.

14. Mansukhani ND, Guiney LM, Kim PJ, Zhao Y, Alducin D, Ponce A, et al. High-Concentration Aqueous Dispersions of Nanoscale 2D Materials Using Nonionic, Biocompatible Block Copolymers. Small [Internet]. 2016;12:294–300.

15. Cogswell FN, Neil F. Platen pressing of carbon fibre/PEEK laminates. Thermoplast Aromat Polym Compos Mater. Oxford: Butterworth Heinemann; 1992. p. 249.

16. Zinnecker V, Stokes-Griffin CM, Khudiakova A, Wolfahrt M, Compston P. A comparative study for shear testing of thermoplastic-based composites and metal-composite hybrids. Compos Part A Appl Sci Manuf [Internet]. 2020;137:105953.

17. Sommacal S, Matschinski A, Drechsler K, Compston P. Characterisation of void and fiber distribution in 3D printed carbon-fiber/PEEK using X-ray computed tomography. Compos Part A Appl Sci Manuf [Internet]. Elsevier Ltd; 2021;149:106487.

18. Sheppard A, Latham S, Middleton J, Kingston A, Myers G, Varslot T, et al. Techniques in helical scanning, dynamic imaging and image segmentation for improved quantitative analysis with X-ray micro-CT. Nucl Instruments Methods Phys Res Sect B Beam Interact with Mater Atoms [Internet]. Elsevier B.V.; 2014;324:49–56.

19. Narayan R, Lim J, Jeon T, Li DJ, Kim SO. Perylene tetracarboxylate surfactant assisted liquid phase exfoliation of graphite into graphene nanosheets with facile re-dispersibility in aqueous/organic polar solvents. Carbon N Y [Internet]. Elsevier Ltd; 2017;119:555–68.

20. Lu H, Yao Y, Huang WM, Hui D. Noncovalently functionalized carbon fiber by grafted self-assembled graphene oxide and the synergistic effect on polymeric shape memory nanocomposites. Compos Part B Eng. Elsevier Ltd; 2014;67:290–5.

21. Ferrari AC, Meyer JC, Scardaci V, Casiraghi C, Lazzeri M, Mauri F, et al. Raman spectrum of graphene and graphene layers. Phys Rev Lett. 2006;97:1–4.

22. Hao Y, Wang Y, Wang L, Ni Z, Wang Z, Wang R, et al. Probing layer number and stacking order of few-layer graphene by Raman Spectroscopy. Small. 2010;6:195–200.

23. Rosselli F, Santare MH. Comparison of the short beam shear (SBS) and interlaminar shear device (ISD) tests. Compos Part A Appl Sci Manuf [Internet]. 1997;28:587–94.

24. Gao X, Huang Z, Zhou H, Li D, Li Y, Wang Y. Higher mechanical performances of CF/PEEK composite laminates via reducing interlayer porosity based on the affinity of functional s-PEEK. Polym Compos. 2019;40:3749–57.

  doi:10.5075/epfl-298799_978-2-9701614-0-0

HIGHLY DEFORMABLE AND PROCESSABLE POLY(3-HYDROXYBUTYRATE) IN PRESENCE OF FERULIC ACID-BASED ADDITIVES

Lionel LONGÉ[a,b], Laurent MICHELY[b], Antoine GALLOS[a], Agustin RIOS DE ANDA[b], Henri VAHABI[c], Estelle RENARD[b], Michel LATROCHE[b], Florent ALLAIS[a], Valérie LANGLOIS[b].

a: URD Agro-Biotechnologies Industrielles (ABI) (Thiais, FR)
b : Institut de Chimie et des Matériaux Paris-Est (CNRS) – agustin.rios-de-anda@u-pec.fr
c: Université de Lorraine, Centrale Sup´elec.

Abstract: *Poly(3-hydroxybutyrate), PHB, has gathered a lot of attention for its promising properties, in particular its biobased nature and high biodegradability. Although PHB is prime candidate for the packaging industry, the applications are still limited by a narrow processing window and thermal degradation during melt processing. In this work, three novel additives based on ferulic acid esterified with butanediol, pentanediol and glycerol, namely BDF, PDF and GTF, respectively are used as plasticizers and antioxidative additives to improve mechanical properties of PHB. Elongation at break up to 270 % was obtained in presence of BDF and the processing window was improved nearly tenfold. The Pawley method was used to identify the monoclinic space group P2 of the BDF. The estimated crystallite size (71 nm) agrees with a crystalline additive. With $PHB_{70}BDF_{30}$ blends, even higher elongations at break were obtained though dwindled with time. However, these properties could be recovered after thermal treatment. The high thermal stability of this additive leads to an increase in the fire retardancy property of the mate-rial, and the phenolic structure induced antioxidant properties to the samples as demonstrated by radical scavenging tests, further highlighting the possibilities of the PHB/additives blends for packaging applications.*

Keywords: PHB; polyhydroxybutyrate; biopolymer; plasticizer; ferulic acid

1. Introduction

Since their production method was streamlined a few decades ago, poly(3-hydroxyalkanoate)s (PHAs) which are produced by a fermentation process have shown a growing amount of interest [1-3]. Indeed, PHAs, are one of the most promising renewable biocompatible and biodegradable polyesters [4]. Produced by microorganisms in presence of natural substrates, they offer an excellent alternative to petroleum-based plastics. Poly(3-hydroxybutyrate), PHB, is one of the simplest members of the PHAs family. PHB is a linear semi-crystalline isotactic polyester with high crystallinity, high melting temperature and excellent resistance to solvents. Similarly, to other PHAs, PHB exhibits complete biodegradability [5-8]. However, industrial applications are still limited today by its high brittleness, low value for elongation at break and thermal degradation during melt processing. The short permanence above melting point induces degradation that involves a cis-elimination reaction and the formation of crotonic acid [9]. To improve PHB thermal and mechanical properties a lot of efforts have been put to find different solutions or formulations with additives [10]. A common workaround is to synthesize copolyesters of PHB with other 3-hydroxyalkanoates moieties, such as 3-hydroxyvalerate and 3-hydroxyhexanoate [11]. Poly(3-hydroxyvalerate) is the most common co-monomer for this application and the resulting copolymer, PHBHV, exhibits significant improvement in the

  doi:10.5075/epfl-298799_978-2-9701614-0-0

elongation at break depending on monomers ratio. Internal plasticization of PHB have been developed using the bacterial fermentation of copolymers.

On the other hand, the external plasticization is an efficient and rapid method to improve some mechanical properties of polymers. Additives as plasticizers, blend partners, fillers and crosslinkers may also affect the processing and mechanical properties [12]. Blending PHB with plasticizers may offer the advantage to improve the processability. Plasticizing additives for PHB are diverse, and include aromatic compounds, fatty acids, alcohols, ester, and polymers themselves [13-16]. Vegetable oils and their derivatives have also been extensively studied as promising additives into PHA formulations [17]. Semi-interpenetrated networks in which PHB is embedded in network based on sunflower oil and trithiol exhibited a toughening improvement of this polyester [18]. Plasticized PHB formulations were recently prepared with monoterpenes such as linalool, geraniol, and geranyl acetate [19]. Blending with terpenes leads to a decrease of the Tg values and a remarkable increase in the elongation at break combined with a decrease in Young's mod-ulus with regard to pure PHB. The effect is more pronounced with geranyl acetate due to the presence of the segment bearing ester group that increases free volume and molecular mobility. However, there are still challenges to be overcome to open the applications of PHB. Ferulic acid is a biobased compound that can be extracted though different processes from lignocellulosic biomass. Due to the various functional groups, it can be easily functionalized and its phenol group usually carry-on antioxidant properties even after functionalization. Ferulic acid derivatives were recently found to have plasticizing effects on polylactic acid and polycaprolactone [20].

The objective of this study is to develop the appropriate plasticizer for improving mechanical properties. We aim at preparing plasticized PHB with ferulic derivatives. The bis-O-dihydroferuloyl 1,4-butanediol (BDF) was blended in PHB to have a direct comparison with the observed plasticizing effect of BDF in PLA. Two others ferulic acid derivatives (bis-O-dihydroferuloyl 1,5-pentanediol and tris-O-dihydroferuloyl glycerol) hereafter named PDF and GTF were also blended with PHB to study the effect of various molecular designs. PHB was blended with BDF, PDF and GTF in the melt state by using extrusion process. The influence of the chemical structure of these compounds on the thermal properties, mechanical properties, dynamic mechanical properties, thermal stability and flammability behavior of PHB was studied. A special attention was paid to the evolution of the mechanical properties and recrystallization of the blends over time.

2. Results and discussion

All materials and additives synthesis, processing, and characterization techniques have been thoroughly detailed in [21]. The major drawback of PHB during hot melt extrusion is that the melting point and the extrusion temperature are very close to the degradation temperature. Therefore, if PHB residence time in the extruder is prolonged, temperature and shear stress will start to de-grade the polymer, causing oxidation (i.e. seen as samples browning) and a distinctive odor re-lease attributed to crotonic acid and loss of mechanical properties. To overcome this in-convenient, PHB and the ferulic acid-based additives were combined by hot melt extrusion in a twin-screw mini-extruder and injected directly into a mold. By using a mini-extruder, PHB residence time is diminished, which limits the polymer degradations. Different formulations of PHB_xBDF_y blends were prepared to study the influence of BDF concentrations ranging from 0 to 100 wt%. Theoretical glass transition temperature of BDF (-17.7°C) matches quite closely with

  doi:10.5075/epfl-298799_978-2-9701614-0-0

the experimental T_g measured by DSC (-19 °C). Furthermore, the measured T_g for the PHB_xBDF_y blends also line up closely to the theoretical values determined by the Fox equation when the blends contain less than 30 wt% of BDF. The crystallinity of the PHB is nearly unchanged whatever the content of BDF, as shown by the values of the melting enthalpies in the different blends. Even if the BDF concentrations above 20 wt% start to hinder PHB crystallization, the BDF interference with PHB is only limited to a shift in melting point T_m from 177°C to 167°C. This decrease of T_m is certainly due to the decrease of crystallite sizes as the total amount of crystalline PHB part remains constant. The diffraction pattern of PHB is shown in Figure 1. The phase is crystalline though a broadening of the diffraction peaks is observed in the range 20-25° in 2θ. The diffraction pattern was indexed with the orthorhombic cell proposed by Kawaguchi and Doi [22]. The structure was refined with the atomic positions given by Brückner et al. [23] in space group P212121. The cell parameters were obtained from the Rietveld and Loopstra method [24]. The estimated crystallite size (286 nm) agrees with a semi-crystalline material. For the X-ray pattern of BDF, the phase is crystalline though the diffraction peaks are relatively broad. The Pawley method [25] was used to determine the space group and cell parameters of BDF. The diffraction lines can be fully indexed with a monoclinic space group P2.

The estimated crystallite size (71 nm) agrees with a crystalline material. The calculated density (1.282) of BDF deduced from the chemical formula $C_{24}H_{30}O_8$ (M=446.5 g) and the cell volume obtained by the Pawley method (V=1156.7 Å3) is in good agreement with the measured one (1.277), assuming Z=2. The diffraction pattern of the $PHB_{70}BDF_{30}$ is also shown as prepared (1 day) in Figure 2. The pattern can be described by a combination of the two single phases BDF and PHB, though BDF looks much less crystalline than the pristine material. All diffraction peaks can be accounted, and the sample can be seen as a physical mixture of the two phases without significant chemical reactions between them. It can be stated that introducing 30 wt% BDF lowers the melting temperature of PHB by 10°C, which allows to decrease the processing temperature of the samples by extrusion. It is possible that BDF not only acts as a chain spacer in the amorphous phase of PHB but plays the same role during the melting and extrusion process. By spacing the chains, BDF can reduce the polymers viscosity and melting point, leading to lower overall processing temperatures. This is beneficial as the heat extrusion effect on the polymer degradation is reduced. For the remaining of the investigation, a concentration of 30 wt% of additive in the blends was considered.

Mechanical properties showed that the incorporation of the ferulic acid-based additives induces a substantial increase in the elongation at break of the material which was measured three hours after extrusion in the case of $PHB_{70}GTF_{30}$ and $PHB_{70}BDF_{30}$. For $PHB_{70}GTF_{30}$, it jumps from 11 % for pure PHB to 178 % (Figure 3, Table 1). This increase is paralleled by a decline of the Young's modulus E and of the stress at break σ_r. Indeed, σ_r decreases from 29.7 for pure PHB to 5.8 MPa for $PHB_{70}GTF_{30}$. This means that both GTF and BDF act also as mechanical plasticizers, yielding toughened PHB formulations. For $PHB_{70}PDF_{30}$, no increase of the elongation at break could be detected compared to pure PHB. Additionally, it was found that during storage at room temperature, some oily sub-stance exuded from the samples. Unlike BDF and GTF, PDF is a liquid at room temperature which explains that this behavior is not observed for these compounds. For those reasons, PDF could not be considered as a good candidate for improving the toughening mechanical properties of PHB or for medium-long term packaging applications contrary to BDF and GTF.

  doi:10.5075/epfl-298799_978-2-9701614-0-0

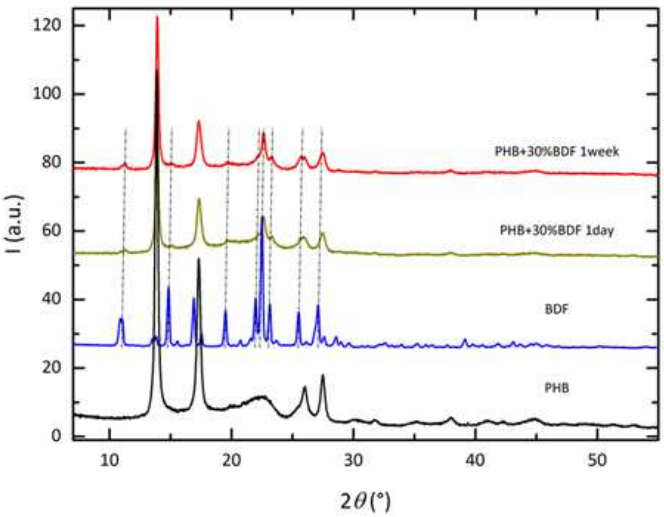

Figure 1. X-ray diffraction patterns of (from bottom to top) PHB (black), BDF (blue), $PHB_{70}BDF_{30}$ as-prepared (one day), and $PHB_{70}BDF_{30}$ after one week. Dotted lines are a guide for the eyes.

Table 1: Mechanical Properties of PHB and blends three hours after extrusion.

	Young's modulus [MPa]	Stress at break [MPa]	Elongation at break [%]
PHB_{100}	1169 ± 38	29.7 ± 1.6	11 ± 2
$PHB_{70}BDF_{30}$	417 ± 38	11.4 ± 1.1	42 ± 14
$PHB_{70}PDF_{30}$	510 ± 82	12.3 ± 1.7	12 ± 6
$PHB_{70}GTF_{30}$	211 ± 93	5.8 ± 0.8	178 ± 49

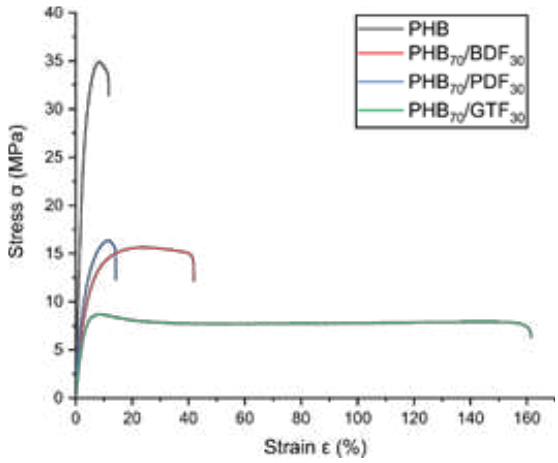

Figure 2. Strain-stress curve of PHB/additive samples, three hours after extrusion: $PHB_{70}BDF_{30}$, $PHB_{70}PDF_{30}$, $PHB_{70}GTF_{30}$ and pure PHB.

PHB mechanical properties are known to quickly evolve with time after solidifying. After three hours, PHB properties are usually mostly settled but can still slightly evolve. The evolution of the mechanical properties was therefore followed over time and to see if this phenomenon is reversible, the samples were subjected to thermal treatments at 120°C, *i.e.* above the T_m of BDF but well below the T_m of PHB. It turns out that three anneals at 120 °C for 5 minutes were

  doi:10.5075/epfl-298799_978-2-9701614-0-0

necessary for the sample to recover its initial properties, i.e. an elongation at break of 260%, as shown in Figure 6. Five minutes after extrusion, PHB samples already have low elongation at break around 11%, while for $PHB_{70}BDF_{30}$ it is twenty-five times higher, at 253%. This value decreases rapidly, and after one hour it is already down to 27%. Simultaneously the BDF was observed to crystallize in the sample as the normalized fusion enthalpy increases steadily to a plateau around 65 J/g. Even though the two phenomena seem connected, they do not happen concomitantly. Indeed, the decline in elongation at break occurs marginally before the increase of ΔH_m. After one week, the samples were annealed 5 min at 120 °C. Elongation at break increased by 3 %, five times higher than annealed PHB. Following three anneals, properties like the fresh samples could be recovered. 262 % of elongation at break was measured five minutes after annealing, and 190 % after one hour. Compared to the non-annealed samples, the drop in ε_r was about ten time slower, while, at the same time, the crystallization kinetic was slightly faster. These results are shown in Figure 3.

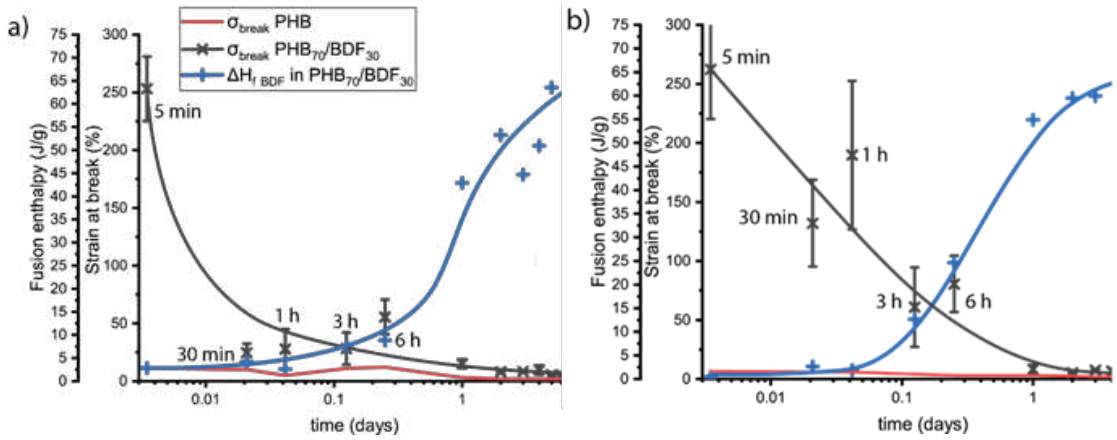

Figure 3. Follow up of polymer deformation at break for PHB (gray) and PHB70BDF30 (red) a) after extrusion and b) after annealing at 120°C. Blue dashed line represents the fusion enthalpy of BDF in the $PHB_{70}BDF_{30}$.

BDF is a phenolic compound that exhibits two phenol groups per molecule. As such, some radical-scavenging property is expected. Accordingly, by blending BDF and PHB the resulting material is anticipated to exhibit antioxidant behavior. Radical scavenging activity (RSA) can be measured by reduction of DPPH in solution. The DPPH radical scavenging assay is widely used to assess the antioxidant activity of phenolic compounds [26-27]. At 517 nm, this relaxation and swelling control radical has an absorbance maxi-mum. When this molecule reacts with a hydrogen donor such as an antioxidant, the absorbance decreases and a change in color of the solution from purple to yellow is observed. Concentrations as low as 5 wt% was found to reduce 81 % of DPPH in solution. With 20 wt% and above, 94 % radical scavenging activity can be obtained. This behavior makes BDF a promising additive for applications where antioxidant properties are sought after.

Figure 4 shows the loss of mass as a function of temperature as measured by TGA. This loss of mass is due to the loss of volatile fragments following the important degradations of polymer chains leading to small molecules. The temperature at which 20% mass loss is observed is 280°C for PHB and 360°C for BDF. The introduction between 5 and 40 wt% of BDF increases the thermal stability by 10°C and the 20% mass loss is now observed at 290°C. Pyrolysis combustion flow calorimetry (PCFC) tests were performed according to ASTM D7309 to evaluate the flammability

  doi:10.5075/epfl-298799_978-2-9701614-0-0 published under CC BY-NC 4.0 license

of PHB_{100}, $PHB_{80}BDF_{20}$ and $PHB_{70}BDF_{30}$ samples [28]. Pure PHB shows a highly flammable character demonstrated by an intense pHRR 1074 W/g at 305 °C. The presence of BDF in PHB significantly changed the flammability behavior of PHB. The slope of HRR curves were decreased by increasing the percentage of BDF. Moreover, the pHRR was meaningfully decreased and reached 723 W/g and 659 W/g for $PHB_{80}BDF_{20}$ and $PHB_{70}BDF_{30}$, respectively. Furthermore, the temperature at pHRR was increased from 305 °C for pure PHB to 310 °C for $PHB_{70}BDF_{30}$, while for $PHB_{80}BDF_{20}$ it remained similar that of pure PHB, at 305.5 °C. It was also noticed that there is quite no change in THR for samples containing BDF compared to pure PHB.

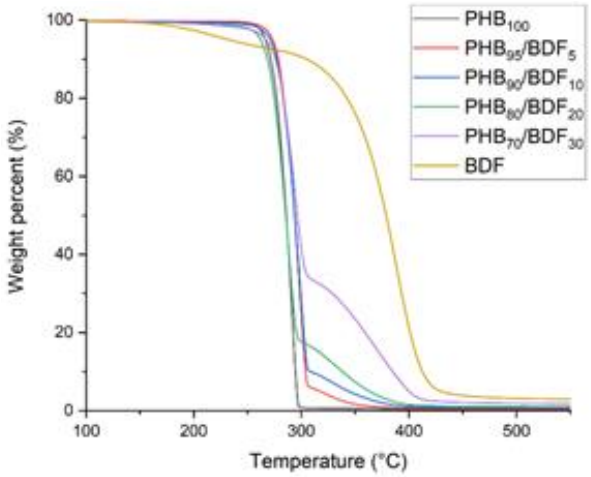

Figure 4. Thermal stabilities of different PHB-BDF blends measured by TGA.

3. Conclusion

Among the three ferulic acid derivatives, only BDF and GTF showed a plasticizing effect of PHB with a clear increase in elongation at break unlike PDF. However, the mechanical properties of the mixtures vary with time due to the crystallization of the additives. This effect is very important in the case of GTF because the specimens become so brittle after one week that it is no longer possible to handle them. The BDF is very promising because it increases the elongation at break from 11% for PHB to 260% for the $PHB_{70}BDF_{30}$ blend. Although this value is not stable over time, it is possible to recover this property after a short five-minute heat treatment of PHB at a temperature much lower than the melting temperature of PHB but just above the melting temperature of BDF. For this purpose, an X-ray diffraction study has allowed for the first time to specify the crystal structure and the lattice parameters of BDF. This derivative which had already shown its properties as plasticizer for PCL and PLA confirms here all its interest during the formulation of PHB. The reversibility of the mechanical properties according to the temperature combine with the antioxidant properties and the resistance to the flammability will undoubtedly allow to consider new applications for the PHB. The incorporation of BDF decrease the hydrophobicity of PHB surface as it was shown by the values of contact angle with water from 70° to 63.5° in presence of BDF. The effect of ferulic acid-based derivatives on the kinetics of enzymatic and hydrolytic degradations required a further study to precise the long-term behavior of these biodegradable polyesters.

  doi:10.5075/epfl-298799_978-2-9701614-0-0

Acknowledgements

Financial support from ANR PRCI (SeaBioP Project, France) is sincerely acknowledged. The Région Grand Est, the Conseil Départemental de la Marne and the Grand Reims are gratefully acknowledged for supporting these works.

4. References

1. Steinbüchel A, Valentin HE. Diversity of Bacterial Polyhydroxyalkanoic Acids. FEMS Microbiol. Lett. 1995; 128:219-228.
2. Sudesh K, Abe H, Doi Y. Synthesis, Structure and Properties of Polyhydroxyalkanoates: Biological Polyesters. Prog. Polym. Sci. 2000; 10:1503-1555.
3. Lenz RW, Marchessault RH. Bacterial Polyesters: Biosynthesis, Biodegradable Plastics and Biotechnology. Biomacromolecules 2005; 6:1-8.
4. Akaraonye E, Keshavarz T, Roy I. Production of Polyhydroxyalkanoates: The Future Green Materials of Choice. J. Chem. Technol. Biotechnol. 2010; 85: 732-743.
5. Guerin P, Renard E, Langlois V. Degradation of Natural and Artificial Poly[(R)-3-Hydroxyalkanoate]s: From Biodegradation to Hydrolysis. In Plastics from Bacteria; Microbiology Monographs. Springer. 2010.
6. Jendrossek D, Handrick R. Microbial Degradation of Polyhydroxyalkanoates. Annu. Rev. Microbiol. 2002; 56: 403-432.
7. Renard E, Walls M, Guérin P, Langlois V. Hydrolytic Degradation of Blends of Polyhydroxyalkanoates and Functionalized Polyhydroxyalkanoates. Polym. Degrad. Stab. 2004; 85: 779-787.
8. Tokiwa Y, Calabia BP. Review Degradation of Microbial Polyesters. Biotechnol. Lett. 2004; 26: 1181-1189.
9. Grassie N, Murray EJ, Holmes PA. The Thermal Degradation of Poly(-(d)-β-Hydroxybutyric Acid): Part 2-Changes in Molecular Weight. Polym. Degrad. Stab. 1984; 6: 95-103.
10. Gigante V, Cinneli P, Segginai M, Alavarez VA, Lazzer A. Processing and thermomechanical properties of PHA; The Handbook of polyhydroxyalkanoates. CRC press. 2020.
11. Qiu YZ, Han J, Quo JJ, Chen GQ. Production of Poly(3-hydroxybutyrate-co-3-hydroxyhexanoate) from Gluconate and Glucose by Recombinant Aeromonas hydrophila and Pseudomonas putida, Biotechnol Lett. 27; 2005: 1381-1386.
12. Jost V. Mechanical and permeation properties of PHA-based blends and composites; The Handbook of polyhydroxyalkanoates. CRC press. 2020.
13. Vieira MGA, da Silva MA, dos Santos LO, Beppu MM. Natural-Based Plasticizers and Biopolymer Films: A Review. Eur. Polym. J. 2011; 47: 254-263.
14. Hong S, Hsu HW, Ye MT. Thermal Properties and Applications of Low Molecular Weight Polyhydroxybutyrate. J. Therm. Anal. Calorim. 2012; 111: 1243-1250.
15. Brunel DG, Pachekoski WM, Dalmolin C, Agnelli JAM. Natural additives for poly (hydroxybutyrate-CO-hydroxyvalerate)-PHBV: effect on mechanical properties and biodegradation. Materials Research 2014; 17: 1145-1156.
16. Choi JS, Park WH. Effect of Biodegradable Plasticizers on Thermal and Mechanical Properties of poly(3-Hydroxybutyrate). Polym. Test. 2004; 23: 455-460.
17. Audic JL, Lemiègre L, Corre YM, Thermal and Mechanical Properties of a Polyhydroxyalkanoate Plasticized with Biobased Epoxidized Broccoli Oil. J. Appl. Polym. Sci. 2014; 131: 1-7.

  doi:10.5075/epfl-298799_978-2-9701614-0-0

18. Mangeon C, Modjinou T, Rios de Anda A, Thevenieau F, Renard E, Langlois V. Renewable Semi-Interpenetrating Polymer Networks Based on Vegetable Oils Used as Plasticized Systems of Poly(3-hydroxyalkanoate)s. ACS Sustain Chem Eng 2018; 6: 5034-5042.
19. Mangeon C, Michely L, Rios de Anda A, Thevenieau F, Renard E, Langlois V. Natural Terpenes Used as Plasticizers for Poly(3-hydroxybutyrate). ACS Sustain Chem Eng 2018; 6: 16160-16168.
20. Gallos A, Paës G, Legland D, Beaugrand J, Allais F. Microstructural and Chemical Approach To Highlight How a Simple Methyl Group Affects the Mechanical Properties of a Natural Fibers Composite. ACS Sustain Chem Eng. 2017; 5: 10352-10360
21. Longé LF, Michely L, Gallos A, Rios De Anda A, Vahabi H, Renard E, Latroche M, Allais F, Langlois V. Improved Processability and Antioxidant Behavior of Poly (3-hydroxybutyrate) in Presence of Ferulic Acid-Based Additives. Bioengineering 2022; 3: 100.
22. Kawaguchi Y, Doi Y. Structure of native poly(3-hydroxybutyrate) granules characterized by X-ray diffraction. FEMS Microbiology Letters. 1990; 70: 151-156.
23. Brückner S, Meille SV, Malpezzi L, Cesàro A, Navarini L, Tomblini R. The structure of Poly(D-(-)-β-hydroxybutyrate). A Refinement based on the Rietveld method. Macromolecules 1988; 21: 967-971.
24. Rietveld HM. A profile refinement method for nuclear and magnetic structures. J. Appl. Crystallogr. 1969; 2: 65-71.
25. Le Bail A. Whole powder pattern decomposition methods and applications: A retrospection. Powder Diffraction 2005; 20: 316-326.
26. Sureshkumar M, Lee PN, Lee CK. Facile preparation of a robust and flexible antioxidant film based on self-polymerized dopamine in a microporous battery separator. RSC Adv. 2012; 2: 5127-5129.
27. Engman L, Persson J, Vessman K, Ekström M, Berglund M, Andersson CM. Organotellurium compounds as efficient retarders of lipid peroxidation in methanol. Free Radic. Biol. Med. 1995; 19: 441-452.
28. Sonnier R, Vahabi H, Ferry L, Lopez-Cuesta JM. Pyrolysis-combustion flow calorimetry: A powerful tool to evaluate the flame retardancy of polymers, Fire and polymers VI: new advances in flame retardant chemistry and science 2012; 361-390.

  doi:10.5075/epfl-298799_978-2-9701614-0-0

CHITOSAN NANOPARTICLES WITH GINKGO BILOBA EXTRACT IN AN ALGINATE CARRIER AS A SYSTEM FOR THE SLOW RELEASE OF THE ACTIVE SUBSTANCE

Monika, Owczarek[ab], Lucyna, Herczynska[b], Izabella, Krucinska[b]

a: Łukasiewicz Research Network – Lodz Institute of Technology, Sklodowskiej-Curie 19/27, 90-570 Lodz, Poland – monika.owczarek@lit.lukasiewicz.gov.pl
b: Institute of Materials Science of Textiles and Polymer Composites, Faculty of Material Technologies and Textile Design, Lodz University of Technology, Zeromskiego 116, 90-924 Lodz, Poland

Abstract: *The Chitosan is a natural, cationic polysaccharide with many properties, incl. biocompatibility, bactericide and fungicide, it is non-toxic, biodegradable and hemostatic. This polymer is used in various sectors, especially in medical, pharmaceutical, dental and veterinary applications. Chitosan is also used as a carrier component of organic drug delivery systems (mainly nanoparticles - NPs) for loading and releasing compounds of plant extracts eg Ginkgo biloba extract. Ion gelation is one of the most frequently used NPs production procedures in which the matrix is chitosan, which has the ability to act as a polyelectrolyte. The sizes of nanoparticles range from 1 to 1000 nm in diameter, which ensures a high surface to volume ratio and correlation with the structural size of biological components: they are small enough to pass through biological barriers. Moreover, the encapsulation of NPs in the structures of another polymer, e.g. alginate, provides a good basis for the development of a slow release system of the active substance (microparticles with nanoparticles encapsulated in them).*

Keywords: nanoparticles; microparticles; *Ginkgo biloba* extract; drug release

1. Introduction

Since ancient times, *Ginkgo biloba* leaf extract (GB) has been used in the prevention and treatment of many diseases due to its low side effects. It is used as one of the most commonly consumed dietary supplements that improve memory and concentration [1]. It has also been shown that GB effectively improves blood microcirculation in the brain and in the limbs by increasing the supply of oxygen and nutrients, prevents the formation of clots, strengthens capillary walls and protects nerve cells against damage with limited oxygen in the environment [1,2]. GB is a source of various compounds: flavonoids, terpene lactones, terpenoids, polyphenols, organic acids, carbohydrates, EFAs, inorganic salts, amino acids and others [3-5]. As a result of biological studies, it has been shown that the therapeutic activity is caused by the fraction of flavone glycosides and terpene derivatives [5, 6].

In recent decades, a trend has been observed to enclose plant extracts and medicinal substances in microcapsules (MCs). Microencapsulation is an effective method that enables long-term storage, protection of the properties of sealed substances and the extension of their release time at the application places. MCs are obtained in various ways: emulsion methods, extrusion methods, spray drying, fluidized layer coating, drum coating, hot melt dispersion, interfacial polymerization and coacervation in an aqueous or anhydrous environment [7]. Recently, researchers have also focused on the development of therapeutically active

  doi:10.5075/epfl-298799_978-2-9701614-0-0

nanoparticles (NPs) with a size in the range of 1-1000 nm, in order to improve the penetration of drugs by various ways, including by alimentary (active endocytosis), respiratory, injection or transdermal [8]. Therefore, NPs are more promising as carriers of medicinal substances than microcapsules. NPs based on various polymers are usually prepared using ionic or covalent cross-linking methods, precipitation methods, polymerization or self-assembly [9]. The matrix of polymer NPs and MCs usually consists of natural polymers (chitosan, gelatin, alginate, etc.), synthetic polymers (PLA, PCL, PLGA, cyclodextrin, etc.) and their blends [10, 11].

The most frequently studied nanoparticles from natural polymers for dermal applications are NPs based on chitosan [11-13]. This cationic polymer is biocompatible and has anti-inflammatory, antibacterial and homeostatic properties and can bind with negatively charged active substances due to electrostatic interactions, thus increasing cell bioavailability and internalization [9, 14]. Several mechanisms of drug release from NPs and MCs are known, such as: polymer swelling, bound drug diffusion, drug diffusion through the polymer coating, polymer erosion or degradation, and a combination of erosion and degradation. The initial process of the release of the active ingredient from NPs clearance from MCs is due to either polymer swelling, pore formation, or drug diffusion from the polymer surface. Fick's first law is a mathematical reflection of the diffusion process taking place [15].

Karavelioglu et al. in their research developed chitosan nanoparticles with *Ginkgo biloba* extract, which due to their small sizes (<200 nm) are suitable for crossing the blood-brain barrier and may have a potential neuroprotective effect [1]. Nanocarriers as transdermal systems are used in the transdermal administration of vaccines, antihypertensive drugs, anti-parkinsonian drugs and chemotherapeutic agents [8].

The aim of the presented work was to obtain and characterize nanoparticles with *Ginkgo biloba* extract – Ch(GB)NPs, microcapsules containing the above-mentioned nanoparticles - Al(Ch(GB)NPs), and microcapsules with *Ginkgo biloba* extract – Al(GB). Chitosan was used as the shell material in Ch(GB)NPs and alginate was used for Al(Ch(GB)NPs) and Al(GB). The rate of release of the core material from Ch(GB)NPs, Al(Ch(GB)NPs) and Al(GB) was tested in 2 research media to check which test system allows for constant and slow release of the active substance over time.

2. Materials and methods

2.1 Materials

The following materials were used: chitosan (Primex, Chitoclear fg 95, average M_W ~ 234.55 kDa, DD=86.8%, 99.17 cP viscosity measured for 1% water solution in 20°C, Iceland), acetic acid (Avantor, 80%, pure, Poland), Sodium tripolyphosphate pentabasic-TPP (Sigma-Aldrich-Merck, purum p.a., ≥98.0%, Cat. No.: 72061), commercial medicinal product *Tinctura Ginkgo bilobae* - water-ethanol extract from green leaves of *Ginkgo biloba* (Phytopharm, 10%, Poland), Poly(vinyl alcohol) – PVA, (POCh, average M_W 20000, Poland), sodium alginate *Manucol DH* (FMC Biopolymer UK, 56 cP viscosity measured for 1% water solution in 20 °C, Ireland), calcium chloride (Chempur, pure, Poland), sodium chloride (Chempur, pure, Poland), methyl alkohol (Stanlab, 99.5%, pure, Poland), distilled water.

2.2 Methods

2.2.1 Preparation of Ch(GB)NPs

Ch(GB)NPs were prepared based on the ionotropic gelation method developed by Calvo et al. [16] and Porras-Gómez et al. [17] with a small modification. Briefly, chitosan was dissolved at

0.5% w/w in 0.5 % v/w acid acetic solution. TPP was dissolved in distilled water to obtain a 0.5% w/w concentration. PVA was dissolved in distilled water to obtain a 1% w/w concentration. 1 ml of GB was added into 10 ml of chitosan solution and then 4 ml of 1% PVA solution (as a surfactant) was added and later 2,5 ml of the TPP solution was added drop-wise to the chitosan and GB solution and homogenized for 1 h. The final suspension was centrifuged at 12,000 rpm for 20 min.

2.2.2 Preparation of Al(Ch(GB)NPs) and Al(GB)

Al(Ch(GB)NPs) were prepared by coacervation method Sodium alginate 5 % (w/w) was dissolved in distilled water and then mixture of 1 g of Ch(GB)NPs and 2 ml methanol (to prevent complexing) was added into this solution and stirred. Sodium alginate solutions with Ch(GB)NPs were dropped through a syringe and blown with compressed air into a calcium chloride solution (5% w/w) for obtaining Al(Ch(GB)NPs) respectively. Composed microcapsules were incubated in calcium chloride solution for hardening about 45 min. Then, the Al(Ch(GB)NPs) were filtered. The microcapsules were dried in a vacuum oven at 50 °C for 5 h.
The method of obtaining Al(GB) is similar with the only difference that 5 ml of extract are added into alginate solution.

2.2.3 Characterization of Ch(GB)NPs and Al(Ch(GB)NPs)

The size analysis of Ch(GB)NPs

Mean diameter and polydispersity index (PDI) of the nanoparticles were analyzed by the Zetasizer Nano ZS (Malvern, UK) instrument. Measurements were made at 25 ^{o}C in water.
In order to determine the particle size and PDI values, 1 ml of sample was placed in the ZEN0040 cuvette (Malvern, UK), and the results were measured using the dynamic light scattering (DLS) technique. In order to analyze the influence of nanoparticle aggregation on the size and polydispersion, measurements were carried out for nanoparticle solutions without preliminary sonication and after 5 and 10 minutes preliminary sonication. Each sample has been measured 3x11 times and the results were analyzed by Malvern Instruments Ltd. software.

The morphology of Ch(GB)NPs and Al(Ch(GB)NPs)

The surface structure and shape of the obtained microcapsules and nanoparticles was analyzed using microphotography obtained by means of a scanning electron microscope-SEM (FEI, USA, Quanta 200 model, with the Q150R S vacuum sputtering machine) in 1500, 12000, 20000 and 100000 x magnification.

2.2.4. The rate of release of GB from Ch(GB)NPs, Al(Ch(GB)NPs) and Al(GB)

3xThe Perkin Elmer UV-Vis spectrophotometer with Lambda 2 software was used to study the kinetics of the core material release (GB). Ch(GB)NPs, Al(Ch(GB)NPs) and Al(GB) samples were prepared in the form of tablets for the study of release kinetics. 0.05 g of each sample was pressed into a tablet with a diameter of 12 mm and poured over 5 ml of the test medium (the tests were carried out in water and saline). The flasks with the tested samples were closed tightly and placed in an incubator at 33 °C. Absorption studies were performed at the rutin wavelength in the range of 257-270 nm. Measurements were made at specified intervals by collecting 2 ml of the medium containing the above-mentioned samples, and the same volume of fresh medium was supplemented with the tested systems to the baseline volume.

  doi:10.5075/epfl-298799_978-2-9701614-0-0

3. Results and discussion

Characteristic of nanoparticles and microcapsules

Chitosan-coated nanoparticles were obtained by ion gelation as a result of the reaction between positively charged amino groups of chitosan and negatively charged TPP groups. *Ginkgo biloba* extract was dissolved in a 0.5% chitosan solution, and then TPP crosslinker was added to allow the active ingredient to be encapsulated. Brown-colored Ch(GB)NPs were obtained, proving that the *Ginkgo biloba* extract was effectively sealed. The shape and morphology of Ch(GB)NPs were observed by scanning electron microscopy (SEM; Figure 1). As can be seen, all nanoparticles were quite spherical and uniform in shape.

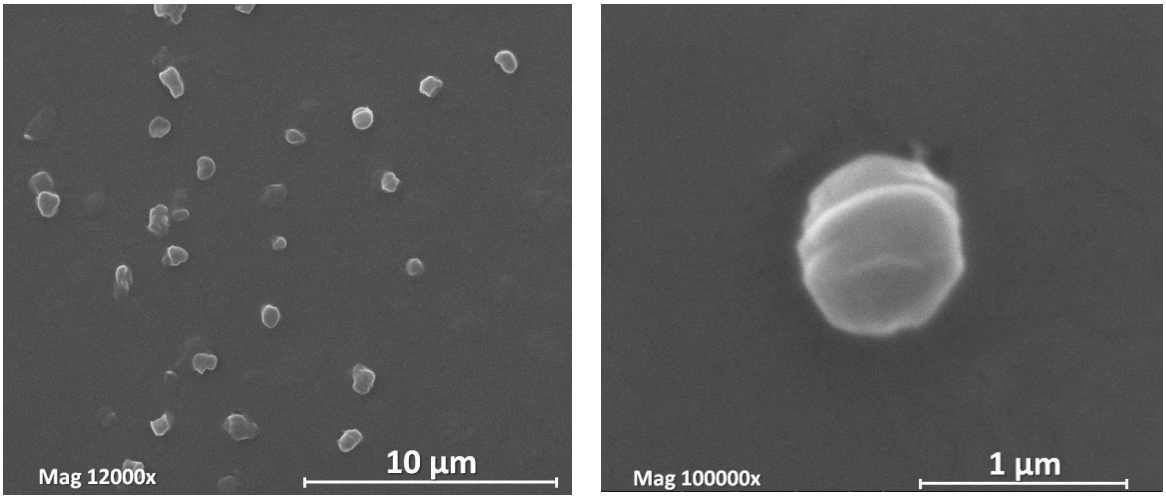

Figure 1 SEM pictures of Ch(GB)NPs at 12000x and 100000x magnification

The hydrodynamic diameter in water and the corresponding polydispersity index (PDI) of the nanoparticles were observed by the DLS method, and the results are presented in Table 1.

Table 1: Particle size and polydispersity index of Ch(GB)NPs (with and without initial sonication for 5 and 10 minutes).

Sample	Sonification (min)	Size (nm)	PDI
Ch(GB)NPs	-	436.7	0.512
Ch(GB)NPs	5	374.9	0.512
Ch(GB)NPs	10	358.9	0.474

The average diameter of the nanoparticles tested in the sample was 436.7 nm. A high PDI polydispersity index indicates the presence of nanoparticles of various sizes. The Ch(GB)NPs fraction was observed with an average diameter of 19.6; 102.5; 568.8 and 835.3 nm. Initial sonication of nanoparticle solutions changed the diameter of the tested particles and their polydispersion, which would suggest the formation of small agglomerates of nanoparticles in the aqueous environment. Therefore, we can note that the material obtained contains Ginkgo biloba extract, which, after application, will be able to penetrate the body, e.g. through skin appendages, as demonstrated by Patzelt et al. These researchers observed that for nanoparticles with a size ranging from 122 nm to 1000 nm in *in vitro* tests on the skin of the pig's ear, NPs with a diameter of 643 nm was transported the furthest through the hair follicles [18].

  doi:10.5075/epfl-298799_978-2-9701614-0-0

Alginate microcapsules containing Ch(GB)NPs: Al(Ch(GB)NPs) or *Ginkgo biloba extract* - Al(GB) were obtained by the coacervation method. A 5% solution containing Ch(GB)NPs nanoparticles was added dropwise to the solution of calcium chloride crosslinker. The obtained microcapsules with nanoparticles had a light brown color. Based on the SEM images (Figure 2), it can be observed that Al(Ch(GB)NPs) microcapsules have a spherical shape with a smooth, homogeneous surface.

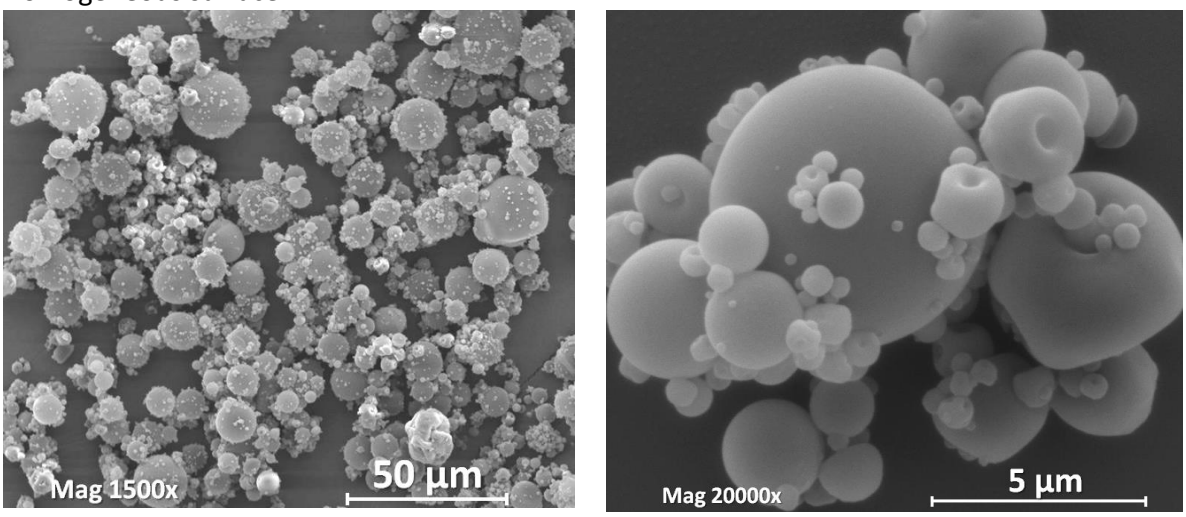

Figure 2 SEM pictures of Al(Ch(GB)NPs) at 1500x and 20000x magnification

Al(Ch(GB)NPs) microcapsules with an average transverse dimension of 11.7 µm were obtained.

Kinetics of core material release

The release of *Ginkgo biloba* extract in water and in saline from the obtained Ch(GB)NPs, Al(Ch(GB)NPs) and Al(GB) at the temperature of 33 °C was carried out. The concentration of the released core material was determined by UV-Vis spectroscopy, examining the absorption at a wavelength in the range of 257-270 nm characteristic for rutin.

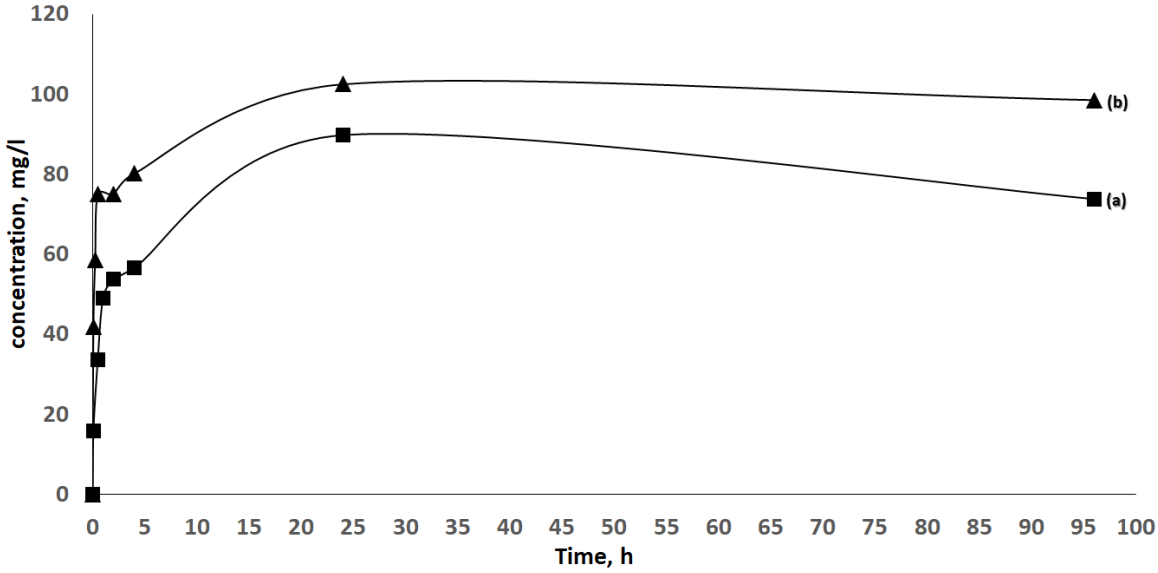

Figure 3 The rate of release of Ginkgo biloba extract from Ch(GB)NPs in water (a) and in saline (b)

  doi:10.5075/epfl-298799_978-2-9701614-0-0

Figure 3 shows the release curves of *Ginkgo biloba* extract from Ch(GB)NPs obtained in the ion gelation process. Based on the results presented in Figure 3, it can be concluded that nanoparticles containing *Ginkgo biloba* are characterized by a different release rate of the core material depending on the medium used. We can see that after 24 hours the amount of released core material does not change significantly in both water and saline.

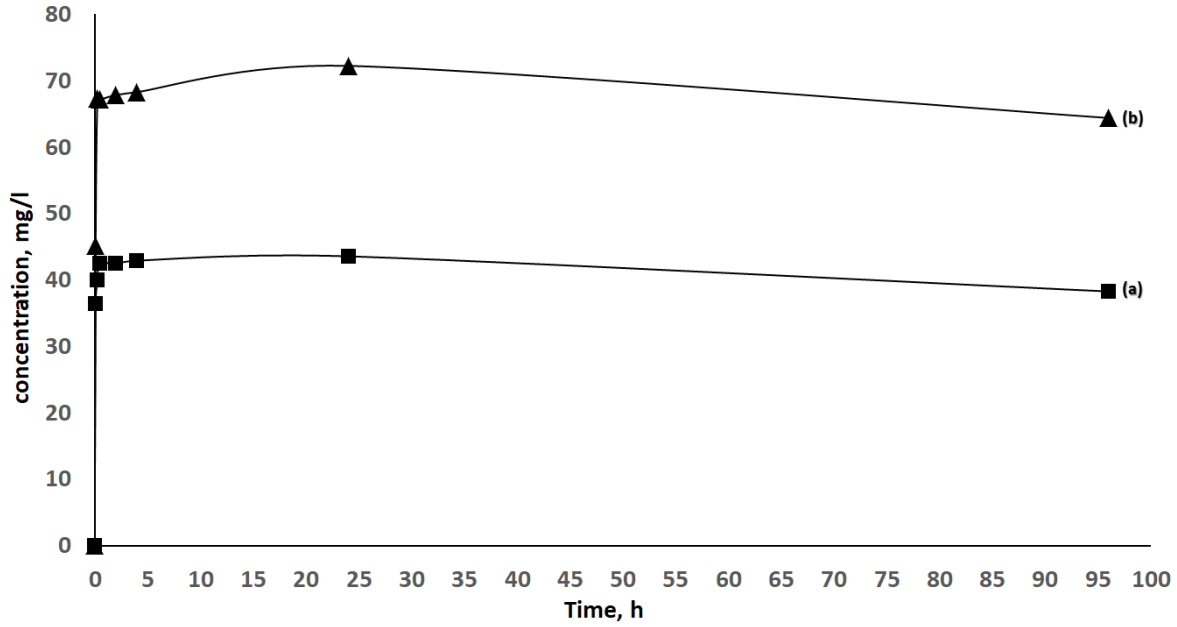

Figure 4 The rate of release of Ginkgo biloba extract from Al(GB) in water (a) and in saline (b)

In the case of Al(GB) capsules, which contain *Ginkgo biloba* extract, there is also a rapid release of the core material, which decreases slightly in the following hours of the test (Figure 4). Also in this case, more intense releasing of the extract in the saline solution can be observed. It is probably related to the better solubility of *Ginkgo biloba* extract in saline than in water.

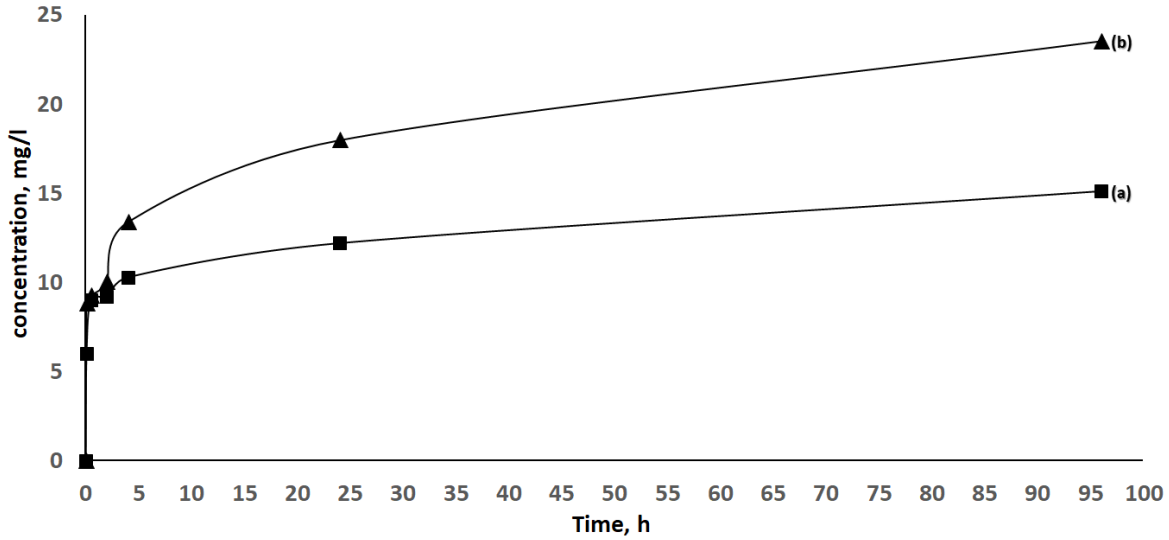

Figure 5 The rate of release of Ginkgo biloba extract from Al(Ch(GB)NPs in water (a) and in saline (b)

Based on the results presented in Figure 5, it can be observed that the process of releasing the Al(Ch(GB)NPs) extract has an upward trend throughout the study. It is presumed that this is related to the passage of the extract first through the chitosan shell and then through the

Al(Ch(GB)NPs) alginate shell, so that the extract is released in a steady and slow manner. The intensity of core material releasing, similar to that of Ch(GB)NPs and Al(GB), is higher for saline. Based on the research on the kinetics of the release of the core material from Ch(GB)NPs, Al(Ch(GB)NPs) and Al(GB), it can be concluded that in all cases the release of the active substance takes place by passive diffusion. The active substance penetrates from the inside of the polymer matrix into the surrounding environment, and the polymer coating constitutes a diffusion barrier, hindering and slowing down the rate of penetration of the extract into the test medium. In the case of release from Ch(GB)NPs and Al(GB), the extract has only one barrier to overcome, therefore the release of the extract at the beginning is greater and stabilizes over time. On the other hand, in the case of Al(Ch(GB)NPs) there are two diffusion barriers (chitosan and alginate), which allow for a constant, slow release of the extract from polymer coatings. The use of a material with two diffusion barriers will allow you to control the release of the active substance, and small amounts of the released substance will prevent the irritating effect of the released core material.

Conclusion

Ginkgo biloba extract was encapsulated in chitosan nanoparticles, alginate microcapsules and chitosan nanoparticles which were then encapsulated in alginate microcapsules. The release of *Ginkgo biloba* extract in water and in saline from the obtained nanoparticles – Ch(GB)NPs, and microcapsules - Al(Ch(GB)NPs) and Al(GB), at the temperature of 33 °C was carried out. Based on the research on the kinetics of the release of the core material from Ch(GB)NPs, Al(Ch(GB)NPs) and Al(GB), it can be concluded that in all cases the release of the active substance takes place by passive diffusion. The active substance penetrates from the inside of the polymer matrix into the surrounding environment, and the polymer coating constitutes a diffusion barrier, hindering and slowing down the rate of penetration of the extract into the test medium. It was possible to obtain a material (Al(Ch(GB)NPs)) which allows for a slow and steady release of the active substance. Controlled release of the active substance applied to the skin, for example, prevents irritation.

4. References

1. Karavelioglu Z, Cakir-Koc R. Preparation of chitosan nanoparticles as *Ginkgo Biloba* extract carrier: *In vitro* neuroprotective effect on oxidative stress-induced human neuroblastoma cells (SH-SY5Y). International Journal of Biological Macromolecules 2021;192:675-683.
2. Singh B, Kaur P, Gopichand, Singh RD, Ahuja PS. Biology and chemistry of *Ginkgo biloba*. Fitoterapia 2008; 79(6):401-418.
3. Sabaner MC, Dogan M, Altin SS, Balaman C, Yilmaz C, Omur A, Zeybek I, Palaz M. *Ginkgo Biloba* affects microvascular morphology: a prospective optical coherence tomography angiography pilot study. Int Ophthalmol 2021; 41:1053-1061.
4. DeFeudis F, Drieu K. *Ginkgo biloba* extract (EGb 761) and CNS functions basic studies and clinical applications. Curr Drug Targets 2005; 1(1):25-58.
5. Pereira E, Barros L, Ferreira I. Chemical characterization of Ginkgo biloba L. and antioxidant properties of its extracts and dietary supplements. Ind. Crops Prod. 2013; 51:244–248.
6. Kobus-Cisowska J, Flaczyk E, Siger A, Kmiecik D. Effect of the extraction process on yield and composition of selected extracts from maidenhair tree green and yellow leaves. Nauka Przyr. Technol. 2015; 9.1.#9:1-15.

  doi:10.5075/epfl-298799_978-2-9701614-0-0

7. Bartkowiak A, Brylak W. Hydrogel microcapsules containing natural or chemically modified oligochitosan - mechanical properties and porosity. Polimery 2006; 51, 7-8:547-554.
8. Palmer B, DeLouise L. Nanoparticle-Enabled Transdermal Drug Delivery Systems for Enhanced Dose Control and Tissue Targeting. Molecules 2016; 21(12).1719:1-17.
9. Goyal R, Macri LK, Kaplan HM, Kohn J. Nanoparticles and nanofibers for topical drug delivery. Journal of Controlled Release 2016; 240:77-92.
10. Yuan L, Pan M, Shi K, Hu D, Li Y, Chen Y, Qian Z. Nanocarriers for promoting skin delivery of therapeutic agents. Applied Materials Today 2022; 27.101438:1-19.
11. Carter P, Narasimhan B, Wang Q. Biocompatible Nanoparticles and Vesicular Systems in Transdermal Drug Delivery for Various Skin Diseases. International Journal of Pharmaceutics 2019; 30.555:49-62.
12. Zhang X, Zhang H, Yin L, Hu R, Qiu T. Yin Y. Xiong X. Zheng H. Wang Q. A pH-sensitive nanosystem based on carboxymethyl chitosan for tumor-targeted delivery of daunorubicin. Journal of biomedical nanotechnology 2016; 12(8):1688-1698.
13. Hu R, Zheng H, Cao J, Davoudi Z, Wang Q. Synthesis and in vitro characterization of carboxymethyl chitosan-CBA-doxorubicin conjugate nanoparticles as pH-sensitive drug delivery systems. Journal of Biomedical Nanotechnology 2017; 13(9):1097-1105.
14. Zheng Z, Tsai PC, Ramezanli T, Michniak-Kohn BB. Polymeric nanoparticles-based topical delivery systems for the treatment of dermatological diseases. Wiley Interdisciplinary Reviews: Nanomedicine and Nanobiotechnology 2013; 05.5(3):205-218.
15. Mohammed MA, Syeda JTM, Wasan KM, Wasan EK. An Overview of Chitosan Nanoparticles and Its Application in Non-Parenteral Drug Delivery.Pharmaceutics 2017; 9(4): 53.
16. Calvo P, Remunan-Lopez C, Vila-Jato JL, Alonso MJ. Novel hydrophilic chitosan-polyethylene oxide nanoparticles as protein carriers. Journal of applied polymer science 1997; 63(1):125-132.
17. Porras-Gómez M, Vega-Baudrit J, Núñez-Corrales S. Ampicillin-loaded chitosan nanoparticles for in vitro antimicrobial screening on *Escherichia coli*. In Chitin-Chitosan-Myriad Functionalities in Science and Technology. IntechOpen. 2018.
18. Patzelt A, Richter H, Knorr F, Schafer U, Lehr CM, Daehne L, Sterry W, Lademann J. Selective follicular targeting by modification of the particle sizes. Journal of controlled release 2011; 150(1):45-48.

  doi:10.5075/epfl-298799_978-2-9701614-0-0

ECCM
26-30 JUNE
2022
LAUSANNE
SWITZERLAND

ECCM20 - Proceedings

ISBN: 978-2-9701614-0-0
DOI: 10.5075/epfl-298799_978-2-9701614-0-0